

**Second Edition**

# An Introduction to Applied and Environmental Geophysics

**John M. Reynolds**





# **An Introduction to Applied and Environmental Geophysics**



# **An Introduction to Applied and Environmental Geophysics**

**2nd Edition**

**John M. Reynolds**

*Reynolds International Ltd*

 **WILEY-BLACKWELL**

A John Wiley & Sons, Ltd., Publication

This edition first published 2011 © 2011 by John Wiley & Sons, Ltd.

Wiley-Blackwell is an imprint of John Wiley & Sons, formed by the merger of Wiley's global Scientific, Technical and Medical business with Blackwell Publishing.

*Registered office:* John Wiley & Sons, Ltd, The Atrium, Southern Gate, Chichester, West Sussex, PO19 8SQ, UK

*Editorial offices:* 9600 Garsington Road, Oxford, OX4 2DQ, UK  
The Atrium, Southern Gate, Chichester, West Sussex, PO19 8SQ, UK  
111 River Street, Hoboken, NJ 07030-5774, USA

For details of our global editorial offices, for customer services and for information about how to apply for permission to reuse the copyright material in this book please see our website at [www.wiley.com/wiley-blackwell](http://www.wiley.com/wiley-blackwell).

The right of the author to be identified as the author of this work has been asserted in accordance with the UK Copyright, Designs and Patents Act 1988.

All rights reserved. No part of this publication may be reproduced, stored in a retrieval system, or transmitted, in any form or by any means, electronic, mechanical, photocopying, recording or otherwise, except as permitted by the UK Copyright, Designs and Patents Act 1988, without the prior permission of the publisher.

Designations used by companies to distinguish their products are often claimed as trademarks. All brand names and product names used in this book are trade names, service marks, trademarks or registered trademarks of their respective owners. The publisher is not associated with any product or vendor mentioned in this book. This publication is designed to provide accurate and authoritative information in regard to the subject matter covered. It is sold on the understanding that the publisher is not engaged in rendering professional services. If professional advice or other expert assistance is required, the services of a competent professional should be sought.

Library of Congress Cataloging-in-Publication Data

Reynolds, John M.

An introduction to applied and environmental geophysics / John M. Reynolds. – 2nd ed.

p. cm.

Includes index.

Summary: "The book covers a range of applications including mineral and hydrocarbon exploration but the greatest emphasis is on the use of geophysics in civil engineering, and in environmental and groundwater investigations" – Provided by publisher.

ISBN 978-0-471-48535-3 (hardback) 978-0-471-48536-0 (paperback)

1. Geophysics—Technique. 2. Seismology—Technique. I. Title.

QC808.5.R49 2011

624.1'51—dc22

2010047246

A catalogue record for this book is available from the British Library.

This book is published in the following electronic format: ePDF 9780470975015, ePub 9780470975442

Set in 9.5/12pt Minion by Aptara Inc., New Delhi, India.

First Impression 2011

# Contents

<b>Preface to the 2<sup>nd</sup> Edition</b>	<b>xi</b>			
<b>Acknowledgements</b>	<b>xiii</b>			
<b>1 Introduction</b>	<b>1</b>			
1.1 What are 'applied' and 'environmental' geophysics?	1	2.5.3 Latitude	35	
1.2 Geophysical methods	3	2.5.4 Free-air correction	35	
1.3 Matching geophysical methods to applications	5	2.5.5 Bouguer correction	36	
1.4 Planning a geophysical survey	5	2.5.6 Terrain correction	38	
1.4.1 General philosophy	5	2.5.7 Building corrections	41	
1.4.2 Planning strategy	5	2.5.8 Eütvüs correction	41	
1.4.3 Survey constraints	7	2.5.9 Isostatic correction	44	
1.5 Geophysical survey design	9	2.5.10 Miscellaneous factors	45	
1.5.1 Target identification	9	2.5.11 Bouguer anomaly	45	
1.5.2 Optimum line configuration and survey dimensions	9	2.6 Interpretation methods	45	
1.5.3 Selection of station intervals	11	2.6.1 Regionals and residuals	46	
1.5.4 Noise	13	2.6.2 Anomalies due to different geometric forms	47	
1.5.5 Position fixing	15	2.6.3 Depth determinations	51	
1.5.6 Data analysis	16	2.6.4 Mass determination	52	
<b>2 Gravity Methods</b>	<b>19</b>	2.6.5 Second derivatives	53	
2.1 Introduction	19	2.6.6 Sedimentary basin or granite pluton?	55	
2.2 Physical basis	19	2.7 Applications and case histories	59	
2.2.1 Theory	19	2.7.1 Mineral exploration	59	
2.2.2 Gravity units	20	2.7.2 Engineering applications	59	
2.2.3 Variation of gravity with latitude	20	2.7.3 Archaeological investigations	66	
2.2.4 Geological factors affecting density	22	2.7.4 Hydrogeological applications	67	
2.3 Measurement of gravity	24	2.7.5 Volcanic hazards	71	
2.3.1 Absolute gravity	24	2.7.6 Glaciological applications	78	
2.3.2 Relative gravity	25			
2.4 Gravity meters	26	<b>3 Geomagnetic Methods</b>	<b>83</b>	
2.4.1 Stable (static) gravimeters	27	3.1 Introduction	83	
2.4.2 Unstable (astatic) gravimeters	27	3.2 Basic concepts and units of geomagnetism	83	
2.4.3 Marine and airborne gravity systems	31	3.2.1 Flux density, field strength and permeability	83	
2.5 Corrections to gravity observations	34	3.2.2 Susceptibility	84	
2.5.1 Instrumental drift	34	3.2.3 Intensity of magnetisation	84	
2.5.2 Tides	34	3.2.4 Induced and remanent magnetisation	85	
		3.2.5 Diamagnetism, paramagnetism, and ferri- and ferro-magnetism	85	
		3.3 Magnetic properties of rocks	87	
		3.3.1 Susceptibility of rocks and minerals	87	
		3.3.2 Remanent magnetisation and Künigsberger ratios	88	

3.4	The Earth's magnetic field	89	4.3.1	Reflection and transmission of normally incident rays	149
3.4.1	Components of the Earth's magnetic field	89	4.3.2	Reflection and refraction of obliquely incident rays	150
3.4.2	Time variable field	94	4.3.3	Critical refraction	151
3.5	Magnetic instruments	95	4.3.4	Diffractions	151
3.5.1	Torsion and balance magnetometers	95	4.4	Loss of seismic energy	152
3.5.2	Fluxgate magnetometers	95	4.4.1	Spherical divergence or geometrical spreading	152
3.5.3	Resonance magnetometers	97	4.4.2	Intrinsic attenuation	153
3.5.4	Cryogenic (SQUID) magnetometers	99	4.4.3	Scattering	154
3.5.5	Gradiometers	99	4.5	Seismic energy sources	154
3.5.6	Airborne magnetometer systems	100	4.5.1	Impact devices	155
3.6	Magnetic surveying	100	4.5.2	Impulsive sources	157
3.6.1	Field survey procedures	100	4.5.3	Explosive sources	159
3.6.2	Noise and corrections	101	4.5.4	Non-explosive sources	159
3.6.3	Data reduction	103	4.5.5	High-resolution waterborne sources	162
3.7	Qualitative interpretation	103	4.5.6	Vibrators	163
3.7.1	Profiles	105	4.5.7	Animals	166
3.7.2	Pattern analysis on aeromagnetic maps	105	4.6	Detection and recording of seismic waves	169
3.8	Quantitative interpretation	107	4.6.1	Geophones and accelerometers	170
3.8.1	Anomalies due to different geometric forms	110	4.6.2	Hydrophones and streamers	171
3.8.2	Simple depth determinations	112	4.6.3	Seismographs	177
3.8.3	Reduction to the Pole (RTP)	115	<b>5</b>	<b>Seismic Refraction Surveying</b>	<b>179</b>
3.8.4	Modelling in two and three dimensions	115	5.1	Introduction	179
3.8.5	Depth determinations and Euler deconvolution	118	5.2	General principles of refraction surveying	179
3.9	Applications and case histories	123	5.2.1	Critical refraction	179
3.9.1	Regional aeromagnetic investigations	123	5.2.2	Field survey arrangements	181
3.9.2	Mineral exploration	125	5.3	Geometry of refracted raypaths	182
3.9.3	Detection of underground pipes	126	5.3.1	Planar interfaces	182
3.9.4	Detection of buried containers	127	5.3.2	Irregular (non-planar) interfaces	185
3.9.5	Landfill investigations	128	5.4	Interpretational methods	186
3.9.6	Acid tar lagoon survey	133	5.4.1	Phantoming	187
3.9.7	UneXploded Ordnance (UXO)	136	5.4.2	Hagedoorn plus-minus method	188
<b>4</b>	<b>Applied Seismology: Introduction and Principles</b>	<b>143</b>	5.4.3	Generalised reciprocal method (GRM)	190
4.1	Introduction	143	5.4.4	Hidden-layer problem	191
4.2	Seismic waves	144	5.4.5	Effects of continuous velocity change	192
4.2.1	Stress and strain	144	5.4.6	Seismic refraction software	193
4.2.2	Types of seismic waves	145	5.5	Applications and case histories	193
4.2.3	Seismic wave velocities	147	5.5.1	Rockhead determination for a proposed waste disposal site	193
4.3	Raypath geometry in layered ground	149	5.5.2	Location of a buried doline	197

5.5.3	Assessment of rock quality	199	6.6.4	Geophysical diffraction tomography in palaeontology	283
5.5.4	Landfill investigations	201	6.6.5	Forensic seismology	286
5.5.5	Acid-tar lagoons	203			
5.5.6	Static corrections	205			
5.5.7	Locating buried miners	207			
5.6	Shear wave methods	208	<b>7</b>	<b>Electrical Resistivity Methods</b>	<b>289</b>
5.6.1	Ground stiffness profiling	208	7.1	Introduction	289
5.6.2	Multichannel Analysis of Shear Waves (MASW)	211	7.2	Basic principles	289
5.6.3	Earthquake hazard studies	215	7.2.1	True resistivity	289
			7.2.2	Current flow in a homogeneous earth	292
<b>6</b>	<b>Seismic Reflection Surveying</b>	<b>217</b>	7.3	Electrode configurations and geometric factors	293
6.1	Introduction	217	7.3.1	General case	293
6.2	Reflection surveys	217	7.3.2	Electrode configurations	294
6.2.1	General considerations	217	7.3.3	Media with contrasting resistivities	298
6.2.2	General reflection principles	218	7.4	Modes of deployment	301
6.2.3	Two-dimensional survey methods	219	7.4.1	Vertical electrical sounding (VES)	301
6.2.4	Three-dimensional surveys	221	7.4.2	Automated array scanning	303
6.2.5	Vertical seismic profiling (VSP)	224	7.4.3	Electrical resistivity tomography (ERT)	306
6.2.6	Cross-hole seismology: tomographic imaging	225	7.4.4	Constant separation traversing (CST)	307
6.3	Reflection data processing	228	7.4.5	Field problems	308
6.3.1	Preprocessing	229	7.5	Interpretation methods	311
6.3.2	Static corrections (field statics)	230	7.5.1	Qualitative approach	311
6.3.3	Convolution and deconvolution	233	7.5.2	Master curves	313
6.3.4	Dynamic corrections, velocity analyses and stacking	236	7.5.3	Curve matching by computer	314
6.3.5	Filtering	241	7.5.4	Equivalence and suppression	317
6.3.6	Migration	243	7.5.5	Inversion and deconvolution	318
6.4	Correlating seismic data with borehole logs and cones	246	7.5.6	Modelling in 2D and 3D	321
6.4.1	Sonic and density logs, and synthetic seismograms	246	7.6	ERT applications and case histories	326
6.4.2	Correlation with cone penetration testing	247	7.6.1	Engineering site investigations	326
6.5	Interpretation	250	7.6.2	Groundwater and landfill surveys	330
6.5.1	Vertical and horizontal resolution	250	7.6.3	Mineral exploration	333
6.5.2	Identification of primary and secondary events	252	7.6.4	Glaciological applications	333
6.5.3	Potential interpretational pitfalls	256	7.7	Mise-à-la-masse (MALM) method	336
6.6	Applications	257	7.7.1	Mineral exploration	338
6.6.1	High-resolution seismic profiling on land	257	7.7.2	Civil engineering pile testing	341
6.6.2	Seismic reflection surveys for earthquake prediction studies	265	7.7.3	Study of tree roots	344
6.6.3	High-resolution seismic profiling over water	266	7.7.4	Groundwater flow	344
			7.8	Leak detection through artificial membranes	346
			<b>8</b>	<b>Spontaneous (Self) Potential Methods</b>	<b>349</b>
			8.1	Introduction	349
			8.2	Occurrence of self-potentials	349
			8.3	Origin of self-potentials	349
			8.3.1	Electrokinetic potentials	350

	8.3.2 Electrochemical potentials	351	10.1.3 Types of EM systems	404
	8.3.3 Mineral potentials	352	10.2 Principles of EM surveying	407
8.4	Measurement of self-potentials	353	10.2.1 Electromagnetic waves	407
8.5	Corrections to SP data	354	10.2.2 Polarisation	410
8.6	Interpretation of self-potential anomalies	354	10.2.3 Depth of penetration of EM radiation	411
	8.6.1 Qualitative interpretation	354	10.3 Airborne EM surveying	411
	8.6.2 Quantitative interpretation	355	10.3.1 Background	411
8.7	Applications and case histories	357	10.3.2 Frequency-domain EM (FEM)	412
	8.7.1 Geothermal exploration	357	10.3.3 Time-domain EM (TEM)	414
	8.7.2 Mineral exploration	359	10.3.4 Airborne VLF-EM	418
	8.7.3 Hydrogeology	361	10.4 Seaborne EM surveying	418
	8.7.4 Landfills and contaminant plumes	363	10.4.1 Background	418
	8.7.5 Leak detection	364	10.4.2 Details of marine EM systems	421
	8.7.6 Mapping mine shafts	370	10.5 Borehole EM surveying	426
8.8	Electrokinetic (EK) surveying	371		
<b>9</b>	<b>Induced Polarisation</b>	<b>373</b>	<b>11 Electromagnetic Methods: Systems and Applications</b>	<b>431</b>
9.1	Introduction	373	11.1 Introduction	431
9.2	Origin of induced polarisation effects	374	11.2 Continuous-wave (CW) systems	431
	9.2.1 Grain (electrode) polarisation	374	11.2.1 Tilt-angle methods	431
	9.2.2 Membrane (electrolytic) polarisation	375	11.2.2 Fixed-source systems (Sundberg, Turam)	432
	9.2.3 Macroscopic processes	375	11.2.3 Moving-source systems	433
	9.2.4 Ionic processes	376	11.2.4 Interpretation methods	437
9.3	Measurement of induced polarisation	376	11.2.5 Applications and case histories	441
	9.3.1 Time-domain measurements	376	11.3 Pulse-transient (TEM) or time-domain (TDEM) EM systems	467
	9.3.2 Frequency-domain measurements	377	11.3.1 TDEM/TEM surveys	467
	9.3.3 Spectral IP and complex resistivity	379	11.3.2 Data processing and interpretation of TEM surveys	468
	9.3.4 Noise reduction and electromagnetic coupling	381	11.3.3 Applications and case histories	470
	9.3.5 Forms of display of IP data	382		
	9.3.6 Inversion and fitting dispersion spectra	383		
9.4	Applications and case histories	384	<b>12 Electromagnetic Methods: Systems and Applications II</b>	<b>495</b>
	9.4.1 Base metal exploration	384	12.1 Very-low-frequency (VLF) methods	495
	9.4.2 Hydrocarbon exploration	389	12.1.1 Introduction	495
	9.4.3 Geothermal surveys	390	12.1.2 Principles of operation	495
	9.4.4 Groundwater investigations	391	12.1.3 Effect of topography on VLF observations	498
	9.4.5 Environmental applications	392	12.1.4 Filtering and interpretation of VLF data	498
	9.4.6 Geological investigations	398	12.1.5 Applications and case histories	499
<b>10</b>	<b>Electromagnetic Methods: Introduction and Principles</b>	<b>403</b>	12.2 The telluric method	502
10.1	Introduction	403	12.2.1 Principles of operation	502
	10.1.1 Background	403	12.2.2 Field measurements	503
	10.1.2 Applications	404	12.3 The magnetotelluric (MT) method	505
			12.3.1 Principles of operation	505
			12.3.2 Field measurements	505
			12.3.3 Interpretation methods	507

	CONTENTS	ix
12.3.4 Applications and case histories	509	
12.4 Magnetic Resonance Sounding (MRS)	519	
12.4.1 Principles of operation	519	
12.4.2 Field measurements	522	
12.4.3 Interpretation methods	525	
12.4.4 Case histories	525	
<b>13 Introduction to Ground-Penetrating Radar</b>	<b>535</b>	
13.1 Introduction	535	
13.2 Principles of operation	537	
13.3 Propagation of radiowaves	539	
13.3.1 Theory	539	
13.3.2 Energy loss and attenuation	540	
13.3.3 Horizontal and vertical resolution	544	
13.4 Dielectric properties of earth materials	546	
13.5 Modes of data acquisition	552	
13.5.1 Radar reflection profiling	552	
13.5.2 Wide-angle reflection and refraction (WARR) sounding	553	
13.5.3 Trans-illumination or radar tomography	553	
13.6 Data processing	554	
13.6.1 During data acquisition	556	
13.6.2 Wide-angle reflection and refraction (WARR) sounding	556	
13.6.3 Post-recording data processing	557	
13.7 Interpretation techniques	560	
13.7.1 Basic interpretation	560	
13.7.2 Quantitative analysis	562	
13.7.3 Interpretational pitfalls	562	
<b>14 Ground-Penetrating Radar: Applications and Case Histories</b>	<b>565</b>	
14.1 Geological mapping	565	
14.1.1 Sedimentary sequences	565	
14.1.2 Lacustrine environments	567	
14.1.3 Geological faults	570	
14.2 Hydrogeology and groundwater contamination	571	
14.2.1 Groundwater contamination	571	
14.2.2 Mapping the water table	576	
14.3 Glaciological applications	578	
14.3.1 Polar ice sheets	578	
14.3.2 Snow stratigraphy and crevasse detection	581	
14.3.3 Temperate glaciers	583	
14.3.4 Glacial hazards	586	
14.4 Engineering applications on manmade structures	587	
14.4.1 Underground storage tanks (USTs), pipes and cables	588	
14.4.2 Transportation infrastructure	592	
14.4.3 Dams and embankments	594	
14.4.4 Golf courses	597	
14.5 Voids within manmade structures	599	
14.5.1 Voids behind sewer linings	600	
14.5.2 Buried crypts and cellars	600	
14.5.3 Coastal defences	602	
14.6 Archaeological investigations	603	
14.6.1 Roman roads	603	
14.6.2 Historical graves	603	
14.6.3 Buried Roman structures	604	
14.6.4 Burial mounds	605	
14.7 Forensic uses of GPR	607	
14.8 Wide-aperture radar mapping and migration processing	607	
14.9 Borehole radar	609	
14.9.1 Hydrogeological investigations	612	
14.9.2 Mining	613	
14.10 UXO and landmine detection	617	
14.11 Animals	618	
<b>15 Radiometrics</b>	<b>625</b>	
15.1 Introduction	625	
15.2 Natural radiation	625	
15.2.1 Isotopes	625	
15.2.2 $\alpha$ and $\beta$ particles, and $\gamma$ radiation	626	
15.2.3 Radioactive decay series and radioactive equilibria	626	
15.2.4 Natural gamma-ray spectra	627	
15.3 Radioactivity of rocks	628	
15.4 Radiation detectors	628	
15.4.1 Geiger-Müller counter	628	
15.4.2 Scintillometers	629	
15.4.3 Gamma-ray spectrometers	630	
15.4.4 Radon detectors	630	
15.4.5 Seaborne systems	631	
15.4.6 Borehole logging tools	632	
15.5 Data correction methods	633	
15.5.1 Detector calibration	633	
15.5.2 Thorium source test	633	
15.5.3 Dead time and live time	633	
15.5.4 Geometric corrections	633	
15.5.5 Environmental factors	634	
15.5.6 Compton scattering	634	
15.5.7 Terrain clearance corrections	634	
15.5.8 Radio-element ground concentrations	635	
15.6 Radiometric data presentation	635	

15.7 Case histories	636	<b>Appendix</b>	<b>645</b>
15.7.1 Mineral exploration	636		
15.7.2 Engineering applications	638	<b>References</b>	<b>649</b>
15.7.3 Soil mapping	639		
15.7.4 Nuclear waste disposal investigations	642	<b>Index</b>	<b>681</b>

# Preface to the 2<sup>nd</sup> Edition

The idea for this book originated in 1987 while I was preparing for lectures on courses in applied geology and environmental geophysics at Plymouth Polytechnic (now the University of Plymouth), Devon, England. Students who had only very basic mathematical skills and little if any physics background found most of the so-called ‘introductory’ texts difficult to follow owing to the perceived opacity of text and daunting display of apparently complex mathematics. To junior undergraduates, this is immediately offputting and geophysics becomes known as a ‘hard’ subject and one to be avoided at all costs.

I hope that the information on the pages that follow will demonstrate the range of applications of modern geophysics – most now very well established, others very much in the early stages of implementation. It is also hoped that the book will provide a foundation on which to build if the reader wishes to take the subject further. The references cited, by no means exhaustive, have been included to provide pointers to more detailed discussions.

The aim of this book is to provide a basic introduction to geophysics, keeping the mathematics and theoretical physics to a minimum and emphasising the applications. Considerable effort has been expended in compiling a representative set of case histories that demonstrate clearly the issues being discussed.

The first edition of this book was different from other introductory texts in that it paid attention to a great deal of new material, or topics not previously discussed in detail: for example, geophysical survey design and line optimisation techniques, image-processing of potential field data, recent developments in high-resolution seismic reflection profiling, electrical resistivity Sub-Surface Imaging (tomography), Spectral Induced Polarisation, and Ground Penetrating Radar, amongst many other subjects, which until 1997, when the first edition was published, had never featured in detail in such a book. While retaining much of the basic theory and principles from the first edition, the scope of material has been expanded considerably in the second edition to reflect the changes and developments in the subject. Consequently, there is much new material. Many new and unpublished case histories from commercial projects have been included along with recently published examples of applications.

The subject material has been developed over a number of years, firstly while I was at Plymouth, and secondly and more recently while I have been working as a geophysical consultant. Early drafts of the first edition book were tried out on several hundred second- and third-year students who were unwitting ‘guinea pigs’ – their comments have been very helpful. While working in industry, I have found the need for an introductory book all the more evident.

Many potential clients either appear unaware of how geophysics could possibly be of help to them, or have a very dated view as to the techniques available. There has been no suitable book to recommend to them that explained what they needed and wanted to know or that provided real examples.

Since publication of the first edition, the development of new instruments, improved data processing and interpretation software and increased understanding of physical processes have continued at a seemingly ever-faster rate. Much of this has also been fuelled by the availability of ever more powerful computers and associated technology. It has been difficult keeping abreast of all the new ideas, especially with an ever-growing number of scientific publications and the huge resource now available through the Internet. What is exciting is that the changes are still occurring and we can expect to see yet more novel developments over the next few years. We have seen new branches of the science develop, such as in forensic, agro- and bio-geophysics, as well as techniques mature, particularly in environmental geophysics and applications to contaminated land, for example. There has been a move away from just mapping to more monitoring and time-lapse surveys. There has also been a greater blurring of the boundaries between industrial sectors. Hydrocarbon exploration analytical techniques are now being used in ultra-high resolution engineering investigations, and electromagnetic methods have ventured offshore to become established in hydrocarbon exploration, just two examples amongst many.

It is my hope that this book will be seen as providing a broad overview of applied and environmental geophysics methods, illustrating the power and sophistication of the various techniques, as well as the limitations. If this book helps in improving the acceptance of geophysical methods and in increasing the awareness of the methods available, then it will have met its objective. There is no doubt that applied and environmental geophysics have an important role to play, and that the potential for the future is enormous.

It is inevitable with a book of this kind that brand names, instrument types, and specific manufacturers are named. References to such information does not constitute an endorsement of any product and no preference is implied, nor should any inference be drawn over any omissions. In books of this type the material covered tends to be flavoured by the interests and experience of the author, and I am sure that this one is no exception. I hope that what is included is a fair reflection of the current state of applied and environmental geophysics. Should any readers have any case histories that they feel are of particular significance, I should be most interested to receive

them for possible inclusion at a later date. Also, any comments or corrections that readers might have would be gratefully received.

Another major difference with this edition is that while all the figures included herein are published in black and white greyscale, colour versions of many are included on an accompanying website at: [www.wiley.com/go/reynolds/introduction2e](http://www.wiley.com/go/reynolds/introduction2e), along with the list

of web URLs given in the Appendix. Furthermore, the book is also available in electronic form in its entirety and also as e-chapters, all of which are available for purchase through the Wiley website at [www.wiley.com](http://www.wiley.com).

The figures with a [C] in the captions indicates that the full colour version is available on the website.

# Acknowledgements

Thanks are due to the many companies that have very kindly supplied material, and colleagues around the world for permitting extracts of their work to be reproduced as well as their kind comments about the first edition. A key feature of any technical book is the graphical material. Most of the figures that featured in the first edition and have been used in the second have been redrawn or updated; there have been many brand new figures and extensive graphical work done to enhance the material presented. I must show due recognition to a number of people who have assisted with this mammoth task and worked on the figures for me, especially Holly Rowlands, who has undertaken the majority of this work. Thanks are also due to my colleague Dr Lucy Catt for technical discussions and for her contribution in generating a number of the figures. I

must also thank the editorial and production staff at John Wiley & Sons Ltd for their understanding and patience in waiting so long for the final manuscript, especially Fiona Woods and Rachael Ballard.

My final acknowledgement must be to my wife, Moira, for her support, encouragement and long-suffering patience while I have been closeted with ‘The Book’. Without her help, encouragement and forbearance, this second edition would never have been completed.

John M. Reynolds  
Mold, Flintshire, North Wales, UK  
*May 2010*



# 1

## Introduction

### 1.1 What are 'applied' and 'environmental' geophysics?

In the broadest sense, the science of *geophysics* is the application of physics to investigations of the Earth, Moon and planets. The subject is thus related to astronomy. Normally, however, the definition of 'geophysics' is used in a more restricted way, being applied solely to the Earth. Even then, the term includes such subjects as meteorology and ionospheric physics, and other aspects of atmospheric sciences.

To avoid confusion, the use of physics to study the interior of the Earth, from land surface to the inner core, is known as *solid earth geophysics*. This can be subdivided further into *global geophysics*, or alternatively *pure geophysics*, which is the study of the whole or substantial parts of the planet, and *applied geophysics*, which is concerned with investigating the Earth's crust and near-surface to achieve a practical and, more often than not, an economic aim.

'Applied geophysics' covers everything from experiments to determine the thickness of the crust (which is important in hydrocarbon exploration) to studies of shallow structures for engineering site investigations, exploring for groundwater and for minerals and other economic resources, to trying to locate narrow mine shafts or other forms of buried cavities, or the mapping of archaeological remains, or locating buried pipes and cables – but where in general the total depth of investigation is usually less than 100 m. The same scientific principles and technical challenges apply as much to shallow geophysical investigations as to pure geophysics. Sheriff (2002: p. 161) has defined '*applied geophysics*' thus:

*Making and interpreting measurements of physical properties of the Earth to determine sub-surface conditions, usually with an economic objective, e.g. discovery of fuel or mineral depositions.*

'Engineering geophysics' can be described as being:

*The application of geophysical methods to the investigation of sub-surface materials and structures that are likely to have (significant) engineering implications.*

As the range of applications of geophysical methods has increased, particularly with respect to derelict and contaminated land investigations, the subdiscipline of '*environmental geophysics*' has developed (Greenhouse, 1991; Steeples, 1991). This can be defined as being:

*The application of geophysical methods to the investigation of near-surface bio-physico-chemical phenomena that are likely to have (significant) implications for the management of the local environment.*

The principal distinction between engineering and environmental geophysics is more commonly that the former is concerned with structures and types of materials, whereas the latter can also include, for example, mapping variations in pore-fluid conductivities to indicate pollution plumes within groundwater. Chemical effects can be equally as important as physical phenomena. Since the mid-1980s in the UK, geophysical methods have been used increasingly to investigate derelict and contaminated land, with a specific objective of locating polluted areas prior to direct observations using trial pits and boreholes (e.g. Reynolds and Taylor, 1992). Geophysics is also being used much more extensively over landfills and other waste repositories (e.g. Reynolds and McCann, 1992). One of the advantages of using geophysical methods is that they are largely environmentally benign – there is no disturbance of subsurface materials. An obvious example is the location of a corroded steel drum containing toxic chemicals. To probe for it poses the real risk of puncturing it and creating a much more significant pollution incident. By using modern geomagnetic surveying methods, the drum's position can be isolated and a careful excavation instigated to remove the offending object without damage. Such an approach is cost-effective and environmentally safer.

There are obviously situations where a specific site investigation contains aspects of engineering as well as environmental geophysics, and there may well be considerable overlap. Indeed, if each subdiscipline of applied geophysics is considered, they may be represented as shown in Figure 1.1, as overlapping. Also included are six other sub-disciplines whose names are largely self-explanatory: namely, *agro-geophysics* (the use of geophysics for agriculture and soil science),

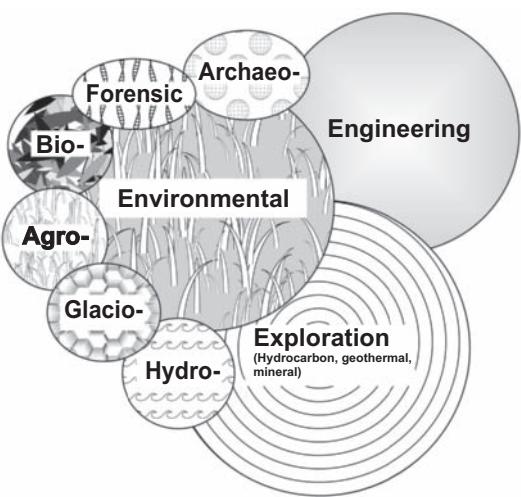


**Figure 1.1** Inter-relationships between the various subdisciplines of applied geophysics. [C]

*archaeo-geophysics* (geophysics in archaeology), *bio-geophysics* (geophysical manifestation of microbial activity within geological materials), *forensic geophysics* (the application of geophysical methods to investigations that might come before a court of law), *glacio-geophysics* (geophysics in glaciology) and *hydro-geophysics* (geophysics in groundwater investigations; see Pellerin *et al.* (2009) and accompanying papers). Glacio-geophysics is particularly well established within the polar scientific communities and has been since the 1950s. The application of ground-based geophysical techniques for glaciological studies (and particularly on temperate glaciers) has come of age especially since the early 1990s (see for example the thematic set of papers on the geophysics of glacial and frozen materials, Kulessa and Woodward (2007)). Forensic geophysics is now recognised as a subdiscipline of forensic geoscience ('geoforensics'; cf. Ruffell and McKinley, 2008) and is used regularly in police investigations in searches for mortal remains, buried bullion, and so on: see Pye and Croft (2003) and Ruffell (2006) for a basic introduction and signposting to other literature. The subdiscipline of bio-geophysics has emerged over the last decade or so (e.g. Williams *et al.* 2005; Slater and Atekwana, 2009) and examines the geophysical signatures of microbial cells in the Earth, the interaction of micro-organisms and subsurface geological materials, and alteration of the physical and chemical properties of geological materials as a result of microbial activity. The microbial activity may be natural, as in microbial bio-mineralisation, or artificial as in the insertion of bacteria into the ground to remediate diesel spills, for example. Perhaps the newest branch is agro-geophysics (Allred *et al.*, 2008; Lück and Müller, 2009), which has emerged over the last decade. Recent examples of these applications of geophysics include water retention capacity of agricultural soils (Lück *et al.*, 2009, effects of long-term fertilisation on soil properties (Werban *et al.*, 2009), and influences of tillage on soil moisture content (Müller *et al.*, 2009).

The general orthodox education of geophysicists to give them a strong bias towards the hydrocarbon industry has largely ignored these other areas of our science. It may be said that this restricted view has delayed the application of geophysics more widely to other

disciplines. Geophysics has been taught principally in Earth Science departments of universities. There is an obvious need for it to be introduced to engineers and archaeologists much more widely than at present. Similarly, the discipline of environmental geophysics needs to be brought to the attention of policy-makers and planners, to the insurance and finance industries (Doll, 1994).

The term 'environmental geophysics' has been interpreted by some to mean geophysical surveys undertaken with environmental sensitivity – that is, ensuring that, for example, marine seismic surveys are undertaken sympathetically with respect to the marine environment (Bowles, 1990). With growing public awareness of the environment and the pressures upon it, the geophysical community has had to be able to demonstrate clearly its intentions to minimise environmental impact (Marsh, 1991). By virtue of scale, the greatest likely impact on the environment is from hydrocarbon and some mineral exploration, and the main institutions involved in these activities are well aware of their responsibilities. In small-scale surveys the risk of damage is much lower, but all the same, it is still important that those undertaking geophysical surveys should be mindful of their responsibilities to the environment and to others whose livelihoods depend upon it.

While the term 'applied geophysics' covers a wide range of applications, the importance of 'environmental' geophysics is particularly highlighted within this book. Although the growth of this discipline has increased dramatically since the 1990s, it has not been as universally accepted as some anticipated. The reasons for this include the reluctance of some engineers to adopt modern geophysical methods, site investigation companies make more money out of drilling and trial pitting, and the perceived high cost of using geophysics rather than appreciating the subsequent 'whole project life' cost-benefit. What is clear, however, is that engineering and environmental geophysics are becoming increasingly important in the management of our environment.

A further major advantage of the use of environmental geophysics in investigating sites is that large areas of the ground can be surveyed quickly at relatively low cost. This provides information to aid the location of trial pits and boreholes. The alternative and more usual approach is to use a statistical sampling technique (e.g. Ferguson, 1992). Commonly, trial pits are located on a 50 m by 50 m grid, and sometimes 25 m by 25 m. The disadvantage of this is that key areas of contamination can easily be missed, substantially reducing the value of such direct investigation. By targeting direct investigations by using a preliminary geophysical survey to locate anomalous areas, there is a much higher certainty that the trial pits and boreholes constructed will yield useful results. Instead of seeing the geophysical survey as a cost, it should be viewed as adding value by making the entire site investigation more cost-effective. For instance, consider the example shown in Table 1.1. On this particular site in northwest London, three successive site investigations had been undertaken over a former industrial site, involving trial pits, boreholes, and stripping 0.3 m off the ground level. For a 2 ha area, only 32 trial pits would have been used to characterise the site, representing sampling of less than 1% by area. Typically, as long as a field crew can gain access to the site on foot and the majority of obstacles have been removed, a geophysical survey can access more than 90% by area of a site. A typical geophysical survey

**Table 1.1** Statistics of the use of geophysical surveys or trial pitting on a 2 ha site.

	Trial pits	Geophysics
Total site area	20,000 m <sup>2</sup>	20,000 m <sup>2</sup>
Area sampled	192 m <sup>2</sup> [<1%]	19,000 m <sup>2</sup> [95%]
Number of samples	32 pits [3 m by 2 m]	9,500 to >38,000 stations
Depth of sampling	1–5 m (notional) <sup>a</sup>	5–6 m (notional)
Contracting costs	~£3,500	~£6,300
Cost/m <sup>2</sup>	£18.23	£0.33
Typical success rate <sup>b</sup>	<10%	>90%
Sampling grid	25 m by 25 m	2 m x 1 m [EM31]; 2 m x <0.2 [mag]
Time on site	4 days	5 days

<sup>a</sup>Depends upon the reach of the mechanical excavator;  
<sup>b</sup>Assuming the target has an area of 5 m by 5 m and has physical properties contrasting with those of the host material.

over a brownfield (former industrial) site would consist of a ground conductivity and magnetic gradiometry survey, using dGPS for position fixing. Consequently, the line interval would commonly be 2 m and with a station interval along the line as small as 0.1 m, using a sampling rate of ten measurements a second and a reasonable walking pace for hand-carried instruments. The relative depths of penetration are as deep as a mechanical excavator can reach, typically down to 5 m below ground level; for the geophysical survey, this is a function of the method and the effective contribution of the target to form an anomaly. For a ground conductivity meter (e.g. Geonics EM31), the nominal depth of penetration is 6 m.

Had intrusive methods alone been used, then the probability of finding a target with dimensions of 5 m by 5 m would be <10%, whereas with geophysical methods (in this case ground conductivity and magnetic gradiometry) the success rate would be greater than 90%. Unfortunately, some clients see only the relative costs of the two methods, and geophysics loses out each time on this basis. However, if the cost-benefit is taken on the basis of the degree of success in finding objects, then the geophysical survey wins by a large margin. This is the difference between *cost* and *cost-benefit*!

Instead of trying to have a competition between intrusive methods OR geophysics, the best practice is to use BOTH, where it is appropriate. By so doing, the geophysical survey can be used to target trial pits onto features that have been identified as anomalies by the geophysical survey. The benefit of this can be seen by reference to the two sets of ground models shown in Figure 1.2 (Reynolds, 2004b). The first model (Figure 1.2A) was produced purely as a consequence of four trial pits and one borehole. The second (Figure 1.2C) was derived following a geophysical survey (Figure 1.2B) and excavating on the locations of geophysical anomalies. It is clear that the combined approach has provided a much better knowledge of the subsurface materials.

Geophysical methods are being seen increasingly not just as a set of tools for site investigation but as a means of risk management. With the growing requirements for audit trails for liability, the risks associated with missing an important feature on a site may

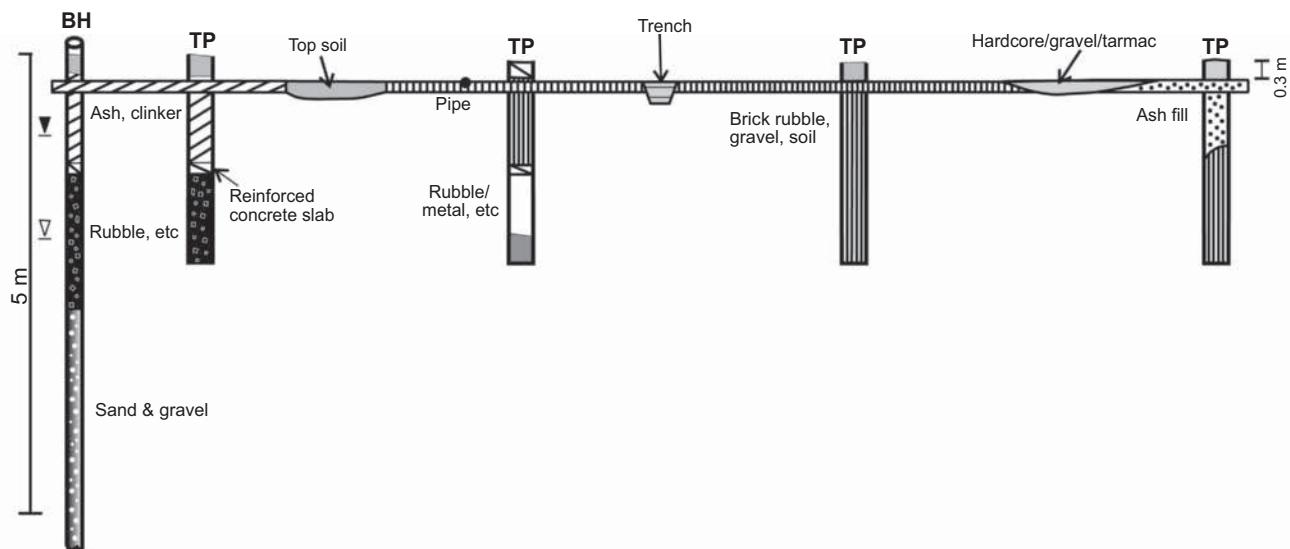
result in large financial penalties or legal action. For example, an environmental consultant may operate with a warranty to their client so that if the consultant misses a feature during a ground investigation that is material to the development of the site, they become liable for its remediation. A drilling contractor may want to have assurance that there are no obstructions or Unexploded Ordnance (UXO) at the location of the proposed borehole. Sites may be known to have natural voids or man-made cavities (cellars, basements) that, if not located, could represent a significant hazard to vehicles or pedestrians passing over them, with the risk that someone could be killed or seriously injured. Geophysical methods can locate live underground electricity cables effectively. Failure to identify the location of such a target could result in electrocution and death of a worker involved in excavation, and damage to such a cable.

## 1.2 Geophysical methods

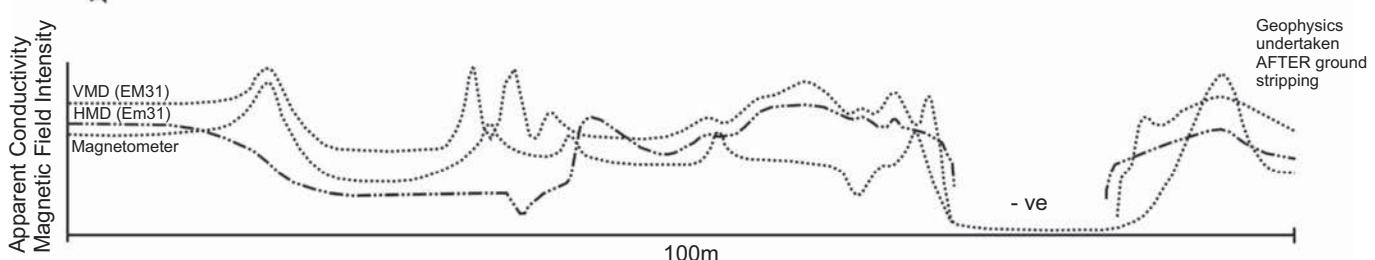
Geophysical methods respond to the physical properties of the subsurface media (rocks, sediments, water, voids, etc.) and can be classified into two distinct types. *Passive* methods are those that detect variations within the natural fields associated with the Earth, such as the gravitational and magnetic fields. In contrast are the *active* methods, such as those used in exploration seismology, in which artificially generated signals are transmitted into the ground, which then modifies those signals in ways that are characteristic of the materials through which they travel. The altered signals are measured by appropriate detectors whose output can be displayed and ultimately interpreted.

Applied geophysics provides a wide range of very useful and powerful tools which, when used correctly and in the right situations, will produce useful information. All tools, if misused or abused, will not work effectively. One of the aims of this book is to try to explain how applied geophysical methods can be employed appropriately,

(A)



(B)



(C)

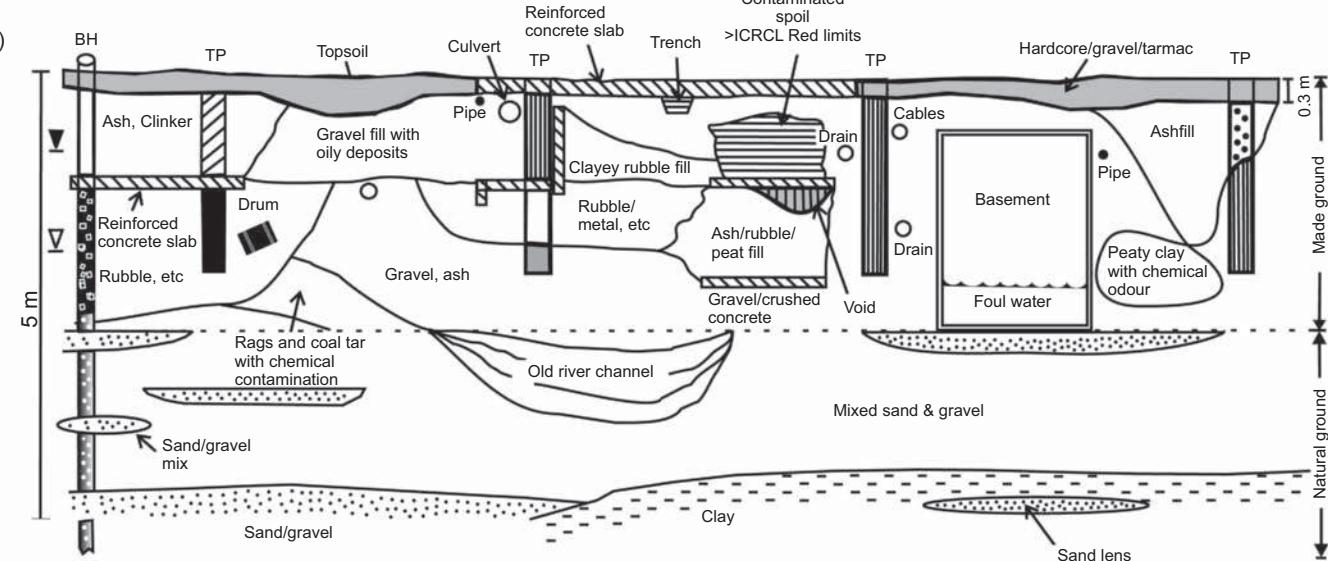


**Figure 1.2** Ground models derived from (A) an intrusive investigation only, (B) a combined profile from a comprehensive geophysical survey, and (C) final interpretation of a subsequent intrusive investigation targeted on the geophysical anomalies. [C]

and to highlight the advantages and disadvantages of the various techniques.

Geophysical methods may form part of a larger survey, and thus geophysicists should always try to interpret their data and communicate their results clearly to the benefit of the whole survey team and particularly to the client. An engineering site investigation, for

instance, may require the use of seismic refraction to determine how easy it would be to excavate the ground (i.e. the 'rippability' of the ground). If the geophysicist produces results that are solely in terms of seismic velocity variations, the engineer is still none the wiser. The geophysicist needs to translate the velocity data into a rippability index with which the engineer would be familiar.

Few, if any, geophysical methods provide a *unique* solution to a particular geological situation. It is possible to obtain a very large number of geophysical solutions to some problems, some of which may be geologically nonsensical. It is necessary, therefore, always to ask the question: 'Is the geophysical model geologically plausible?' If it is not, then the geophysical model has to be rejected and a new one developed which does provide a reasonable geological solution. Conversely, if the geological model proves to be inconsistent with the geophysical interpretation, then it may require the geological information to be re-evaluated.

It is of paramount importance that geophysical data are interpreted within a physically constrained or geological framework.

## 1.3 Matching geophysical methods to applications

The various geophysical methods rely on different physical properties, and it is important that the appropriate technique be used for a given type of application.

For example, gravity methods are sensitive to density contrasts within the subsurface geology and so are ideal for exploring major sedimentary basins where there is a large density contrast between the lighter sediments and the denser underlying rocks. It would be quite inappropriate to try to use gravity methods to search for localised near-surface sources of groundwater where there is a negligible density contrast between the saturated and unsaturated rocks. It is even better to use methods that are sensitive to different physical properties and are able to complement each other and thereby provide an integrated approach to a geological problem. Gravity and magnetic methods are frequently used in this way.

Case histories for each geophysical method are given in each chapter, along with some examples of integrated applications where appropriate. The basic geophysical methods are listed in Table 1.2 with the physical properties to which they relate and their main uses. Table 1.2 should only be used as a guide. More specific information about the applications of the various techniques is given in the appropriate chapters.

Some methods are obviously unsuitable for some applications but novel uses may yet be found for them. One example is that of ground radar being employed by police in forensic work (see Chapter 12 for more details). If the physical principles upon which a method is based are understood, then it is less likely that the technique will be misapplied or the resultant data misinterpreted. This makes for much better science.

Furthermore, it must also be appreciated that the application of geophysical methods will not necessarily produce a unique geological solution. For a given geophysical anomaly there may be many possible solutions each of which is equally valid geophysically, but which may make geological nonsense. This has been demonstrated very clearly in respect of a geomagnetic anomaly over Lausanne in Switzerland (Figure 1.3). While the model with the form of a question-mark satisfies a statistical fit to the observed data, the model is clearly and quite deliberately geological nonsense in order

to demonstrate the point. However, geophysical observations can also place stringent restrictions on the interpretation of geological models. While the importance of understanding the basic principles cannot be over-emphasised, it is also necessary to consider other factors that affect the quality and usefulness of any geophysical survey, or for that matter of any type of survey whether it is geophysical, geochemical or geotechnical. This is done in the following few sections.

## 1.4 Planning a geophysical survey

### 1.4.1 General philosophy

Any geophysical survey tries to determine the nature of the subsurface, but it is of paramount importance that the prime objective of the survey be clear right at the beginning. The constraints on a commercial survey will have emphases different from those on an academic research investigation and, in many cases, there may be no ideal method. The techniques employed and the subsequent interpretation of the resultant data tend to be compromises, practically and scientifically.

There is no short-cut to developing a good survey style; only by careful survey planning, backed by a sound knowledge of the geophysical methods and their operating principles, can cost-effective and efficient surveys be undertaken within the prevalent constraints. However, there have been only a few published guidelines: British Standards Institute BS 5930 (1981), Hawkins (1986), Geological Society Engineering Group Working Party Report on Engineering Geophysics (1988), and most recently, their revised report published in 2002 (McDowell *et al.*, 2002), although see a review of this publication by Reynolds (2004b). Scant attention has been paid to survey design, yet a badly thought-out survey rarely produces worthwhile results. Indeed, Darracott and McCann (1986: p. 85) said that:

*dissatisfied clients have frequently voiced their disappointment with geophysics as a site investigation method. However, close scrutiny of almost all such cases will show that the geophysical survey produced poor results for one or a combination of the following reasons: inadequate and/or bad planning of the survey, incorrect choice or specification of technique, and insufficiently experienced personnel conducting the investigation.*

It is important that geophysicists maintain a sense of realism when marketing geophysical methods, if expectations are to be matched by actual outcomes. Geophysical contractors tend to spend the vast majority of their time on data acquisition and a minimal amount of time on interpretation and reporting. It is hoped that this chapter will provide at least a few pointers to help construct cost-effective and technically sound geophysical field programmes.

### 1.4.2 Planning strategy

Every survey must be planned according to some strategy, or else it will become an uncoordinated muddle. *The mere acquisition of data does not guarantee the success of the survey.* Knowledge (by way of

**Table 1.2** Geophysical methods and their main applications

Geophysical method	Chapter number	Dependent physical property	Applications (see key below)											
			1	2	3	4	5	6	7	8	9	10	11	12
Gravity	2	Density	P	P	s	s	s	s	x	x	s	x	x	x
Magnetic	3	Susceptibility	P	P	P	P	x	m	x	P	P	x	x	P
Seismic refraction	4, 5	Elastic moduli; density	P	P	m	s	s	s	x	x	x	x	x	x
Seismic reflection	4, 6	Elastic moduli; density	P	P	m	s	s	m	x	x	x	x	x	x
Resistivity	7	Resistivity	m	m	P	P	P	P	P	s	P	P	m	x
Spontaneous potential	8	Potential differences	x	x	P	m	P	m	m	m	x	P	x	x
Induced polarisation	9	Resistivity; capacitance	m	m	P	m	s	m	m	m	m	P	m	x
Electro-Magnetic (EM)	10, 11	Conductance; inductance	s	P	P	P	P	P	P	P	P	m	m	P
EM - VLF	12	Conductance; inductance	m	m	P	m	s	s	s	m	m	x	x	x
EM - GPR	13, 14	Permittivity; conductivity	x	x	m	P	P	P	s	P	P	m	P	s
Magneto-telluric	12	Resistivity	s	P	P	m	m	x	x	x	x	x	x	x
Magnetic Resonance	12	Magnetic moment; porosity	x	x	x	x	P	x	m	x	x	x	x	x
Sounding (MRS)														
Radiometrics	15	$\gamma$ -radioactivity	s	s	P	s	x	x	x	x	x	x	x	x

**P** = primary method; **s** = secondary method; **m** = may be used but not necessarily the best approach, or has not been developed for this application;  
**x** = unsuitable

**Applications**

- 1 Hydrocarbon exploration (coal, gas, oil)
- 2 Regional geological studies (over areas of 100s of km<sup>2</sup>)
- 3 Exploration/development of mineral deposits
- 4 Engineering/environmental site investigation
- 5 Hydrogeological investigations
- 6 Detection of subsurface cavities
- 7 Mapping of leachate and contaminant plumes
- 8 Location and definition of buried metallic objects
- 9 Archaeogeophysics
- 10 Biogeophysics
- 11 Forensic geophysics
- 12 Unexploded Ordnance (UXO) detection

masses of data) does not automatically increase our *understanding* of a site; it is the latter we are seeking, and knowledge is the means to this.

One less-than-ideal approach is the ‘blunderbuss’ approach – take along a sufficient number of different methods and try them all out (usually inadequately, owing to insufficient testing time per technique) to see which ones produce something interesting. Whichever method yields an anomaly, then use that technique. This is a crude statistical approach, such that if enough techniques are tried then at least one must work! This is hardly scientific or cost-effective.

The success of geophysical methods can be very site-specific and *scientifically-designed* trials of adequate duration may be very worthwhile to provide confidence that the techniques chosen will work at a given location, or that the survey design needs modifying in order to optimise the main survey. It is in the interests of the client

that suitably experienced geophysicists are employed for the vital survey design, site supervision and final reporting. Indeed, the latest guidelines (McDowell *et al.*, 2002) extol the virtues of employing what is being called in the UK an *Engineering Geophysics Advisor* (EGA). Some of the benefits of employing an Engineering Geophysics Advisor are:

- The survey design is undertaken objectively;
- The appropriate geophysical contractor(s) is/are selected on the basis of their capability and expertise, not on just what kit they have available at the time;
- The contractor is supervised in the field (to monitor data quality, survey layout, deal with issues on site, gather additional information to aid the interpretation);

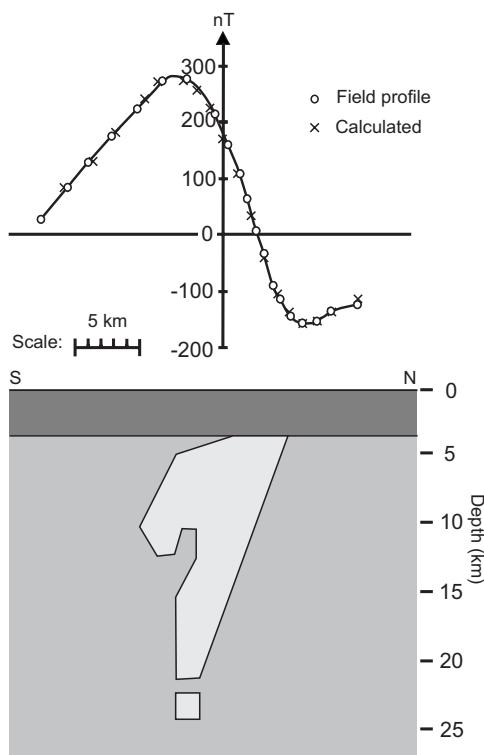


**Figure 1.3** A magnetic anomaly over Lausanne, Switzerland, with a hypothetical and unreal model for which the computed anomaly still fits the observed data. After Meyer de Stadelhofen and Juillard (1987).

- The contractor's factual report is reviewed objectively;
- The field data and any processed data from the contractor are scrutinised prior to further analysis and modelling;
- The analysis, modelling, and interpretation can be undertaken by specialists who have the time and budget to do so, to extract the necessary information to meet the survey objectives for the Client;
- The analysis can incorporate additional information (geological, historical, environmental, engineering, etc.) and integrate it to produce a more holistic interpretation and more robust recommendations for the Client.

So what are the constraints that need to be considered by both clients and geophysical survey designers? An outline plan of the various stages in designing a survey is given in Figure 1.4. The remainder of this chapter discusses the relationships between the various components.

### 1.4.3 Survey constraints

The first and most important factor is that of *finance*. How much is the survey going to cost and how much money is available? The cost will depend on where the survey is to take place, how accessible

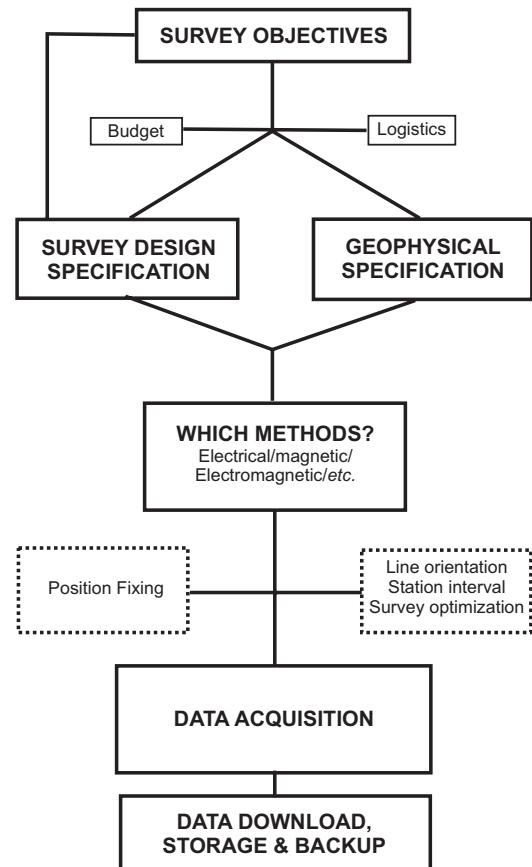


**Figure 1.4** Schematic flow diagram to illustrate the decision-making leading to the selection of geophysical and utility software. After Reynolds (1991a).

the proposed field site is, and on what scale the survey is to operate. An airborne regional survey is a very different proposition to, say, a local, small-scale ground-based investigation. The more complex the survey in terms of equipment and logistics, the greater the cost is likely to be.

It is important to remember that the geophysics component of a survey is usually only a small part of an exploration programme and thus the costs of the geophysics should be viewed in relation to those of the whole project. Indeed, the judicious use of geophysics can save large amounts of money by enabling the effective use of resources (Reynolds, 1987a). For example, a reconnaissance survey can identify smaller areas where much more detailed investigations ought to be undertaken, thus removing the need to do saturation surveying. The factors that influence the various components of a budget also vary from country to country, and from job to job, and there is no magic formula to guarantee success.

Some of the basic elements of a survey budget are given in Table 1.3. This list is not exhaustive but serves to highlight the most common elements of a typical budget. Liability insurance is especially important if survey work is being carried out as a service to others. If there is any cause for complaint, then this may manifest itself in legal action (Sherrell, 1987).

**Table 1.3** Basic elements of a survey budget.

<b>Staffing</b>	Management, technical, support, administration, etc.
<b>Operating costs</b>	<i>Including logistics</i>
<b>Cashflow</b>	<b>Assets versus useable cash</b>
<b>Equipment</b>	<b>For data acquisition and/or data reduction/analysis - computers and software; whether or not to hire, lease or buy</b>
<b>Insurances</b>	<b>To include public, employer's and professional indemnity insurances, as appropriate</b>
<b>Overheads</b>	<b>Administration; consumables; etc.</b>
<b>Development costs</b>	<b>Skills, software, etc.</b>
<b>Contingencies</b>	<b>Something is bound to go wrong at some time, usually when it is most inconvenient</b>

It may seem obvious to identify *logistics* as a constraint, but there have been far too many surveys ruined by a lack of even the most basic needs of a survey. It is easy to think of the main people to be involved in a survey – i.e. geologists, geophysicists, surveyors – but there are many more tasks to be done to allow the technical staff the opportunity to concentrate on the tasks in hand. Vehicles and equipment will need maintaining, so skilled technicians and mechanics may be required. Everybody has to eat, and it is surprising how much better people work when they are provided with well-prepared food: a good cook at base camp can be a real asset. Due consideration should be paid to health and safety, and any survey team should have staff trained in first aid. Admittedly it is possible for one person to be responsible for more than one task, but on large surveys this can prove to be a false economy. Apart from the skilled and technical staff, local labour may be needed as porters, labourers, guides, translators, additional field assistants, or even as armed guards!

It is all too easy to forget what field conditions can be like in remote and inaccessible places. It is thus important to remember that in the case of many countries, access in the dry season may be possible, whereas during the rains of the wet season, the so-called roads (which often are dry river beds) may be totally impassable. Similarly, access to land for survey work can be severely hampered during the growing season with some crops reaching 2–3 metres high and consequently making position fixing and physical access extremely difficult. There is then the added complication that some surveys, such as seismic refraction and reflection, may cause a limited amount of damage for which financial compensation may be sought. In some cases, claims may be made even when no damage has been caused! If year-round access is necessary, the provision of all-terrain vehicles and/or helicopters may prove to be the only option, and these are never cheap to operate.

Where equipment has to be transported, consideration has to be given not only to its overall weight but to the size of each container.

It can prove an expensive mistake to find that the main piece of equipment will not pass through the doorway of a helicopter so that alternative overland transport has to be provided at very short notice; or to find that many extra hours of flying time are necessary to airlift all the equipment. It may even be necessary to make provision for a bulldozer to excavate a rough road to provide access for vehicles. If this is accounted for inadequately in the initial budgeting, the whole success of the survey can be jeopardised. Indeed, the biggest constraint in some developing countries, for example, is whether the equipment can be carried by a porter or will fit on the back of a pack-horse or yak.

Other constraints that are rarely considered are those associated with *politics, society* and *religion*. Let us take these in turn.

**Political constraints** This can mean gaining permission from land-owners and tenants for access to land, and liaison with clients (which often requires great diplomacy). The compatibility of staff to work well together also needs to be considered, especially when working in areas where there may be conflicts between different factions of the local population, such as tribal disputes or party political disagreements. It is important to remember to seek permission from the appropriate authority to undertake geophysical fieldwork. For example, in the UK it is necessary to liaise with the police and local government departments if survey work along a major road is being considered, so as to avoid problems with traffic jams. In other cases it may be necessary to have permission from a local council, or in the case of marine surveys, from the local harbour master so that appropriate marine notices can be issued to safeguard other shipping. All these must be found out well before the start of any fieldwork. Delays cost money!

**Social constraints** For a survey to be successful it is always best to keep on good terms with the local people. Treating other people with respect will always bring dividends (eventually). Each survey should be socially and environmentally acceptable and not cause a nuisance. An example is in not choosing to use explosives as a seismic source for reflection profiling through urban areas or at night. Instead, the seismic vibrator technique should be used (see Chapter 4). Similarly, an explosive source for marine reflection profiling would be inappropriate in an area associated with a lucrative fishing industry because of possibly unacceptably high fish-kill. In designing the geophysical survey, the question must be asked: ‘Is the survey technique socially and environmentally acceptable?’

**Religious constraints** The survey should take into account local social customs which are often linked with religion. In some Muslim countries, for example, it is common in rural areas for women to be the principal water-collectors. It is considered inappropriate for the women to have to walk too far away from the seclusion of their homes. Thus there is no point in surveying for groundwater for a tubewell several kilometres from the village (Reynolds, 1987a). In addition, when budgeting for the provision of local workers, it is best to allow for their ‘Sabbath’. Muslims like to go to their mosques on Friday afternoons and are thus unavailable for work then. Similarly, Christian workers tend not to like being asked to work on Sundays, or Jews on Saturdays, and so on. Religious traditions must be respected to avoid difficulties.

## 1.5 Geophysical survey design

### 1.5.1 Target identification

Geophysical methods locate boundaries across which there is a marked contrast in physical properties. Such a contrast can be detected remotely because it gives rise to a *geophysical anomaly* (Figure 1.5) which indicates variations in physical properties relative to some background value (Figure 1.6). The physical source of each anomaly is termed the *geophysical target*. Some examples of targets are trap structures for oil and gas, mineshafts, pipelines, ore lodes, cavities, groundwater, buried rock valleys, and so on.

In designing a geophysical survey, the type of target is of great importance. Each type of target will dictate to a large extent the appropriate geophysical method(s) to be used, and this is where an

understanding of the basic geophysical principles is important. The physical properties associated with the geophysical target are best detected by the method(s) most sensitive to those same properties.

Consider the situation where saline water intrudes into a near-surface aquifer; saline water has a high conductivity (low resistivity) in comparison with fresh water and so is best detected using electrical resistivity or electromagnetic conductivity methods; gravity methods would be inappropriate because there would be virtually no density contrast between the saline and fresh water. Similarly, seismic methods would not work as there is no significant difference in seismic wave velocities between the two saturated zones. Table 1.1 provides a ready means of selecting an appropriate technique for the major applications.

Although the physical characteristics of the target are important, so are its shape and size. In the case of a metallic ore lode, a mining company might need to know its lateral and vertical extent. An examination of the amplitude of the anomaly (i.e. its maximum peak-to-peak value) and its shape may provide further information about where the target is below ground and how big it is.

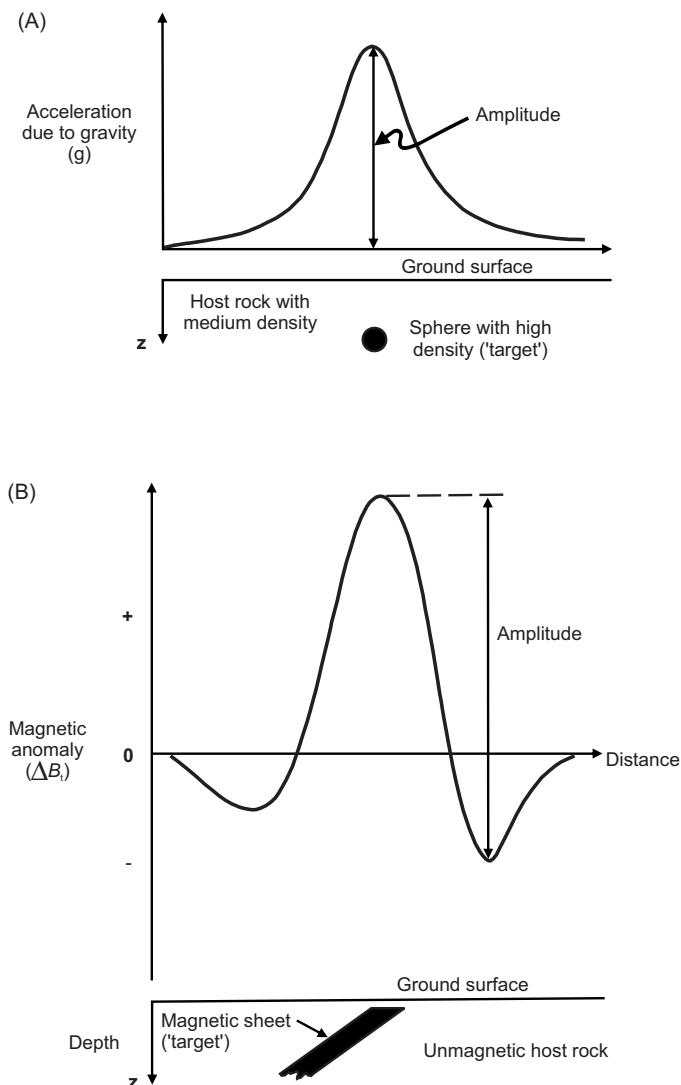


**Figure 1.5** Examples of (A) a gravity anomaly over a buried sphere, and (B) a magnetic anomaly over an inclined magnetic sheet. For further details of gravity and magnetic methods, see Chapters 2 and 3 respectively.

### 1.5.2 Optimum line configuration and survey dimensions

So far only the types of geological target and the selection of the most appropriate geophysical methods have been discussed. In order to complete a technically competent survey several other factors need to be given very careful thought. How are the data to be collected in order to define the geophysical anomaly? Two concepts need to be introduced, namely *profiling* and *mapping*.

Profiling is a means of measuring the variation in a physical parameter along the surface of a two-dimensional cross-section (Figure 1.7A). Consideration needs to be given to the correct orientation and length of the profile (see below). Data values from a series of parallel lines or from a grid can be contoured to produce a *map* (Figure 1.7B) on which all points of equal value are joined by *isolines* (equivalent to contours on a topographic map). However, great care has to be taken over the methods of contouring or else the resultant map can be misleading (see Section 1.5.3). There are many other ways of displaying geophysical data (Figure 1.7C), especially if computer graphics are used (e.g. shaded relief maps as in Figure 1.7D), and examples are given throughout the book.

The best orientation of a profile is normally at right-angles to the strike of the target. A provisional indication of geological strike may be obtained from existing geological maps and mining records. However, in many cases, strike direction may not be known at all and test lines may be necessary to determine strike direction prior to the main survey. The length of the profile should be greater than the width of the expected geophysical anomaly. If it is not, then it may be impossible to define a background value to determine the true anomaly amplitude and the value of the survey would be reduced greatly. The choice of line orientation also has to take into account sources of noise (see Section 1.5.4). If a map is required then it is advisable to carry out 'tie-lines' (cross-cutting profiles), the intersections (*nodes*) of which should have identical values. If the data are not the same at the nodes then the values need to be

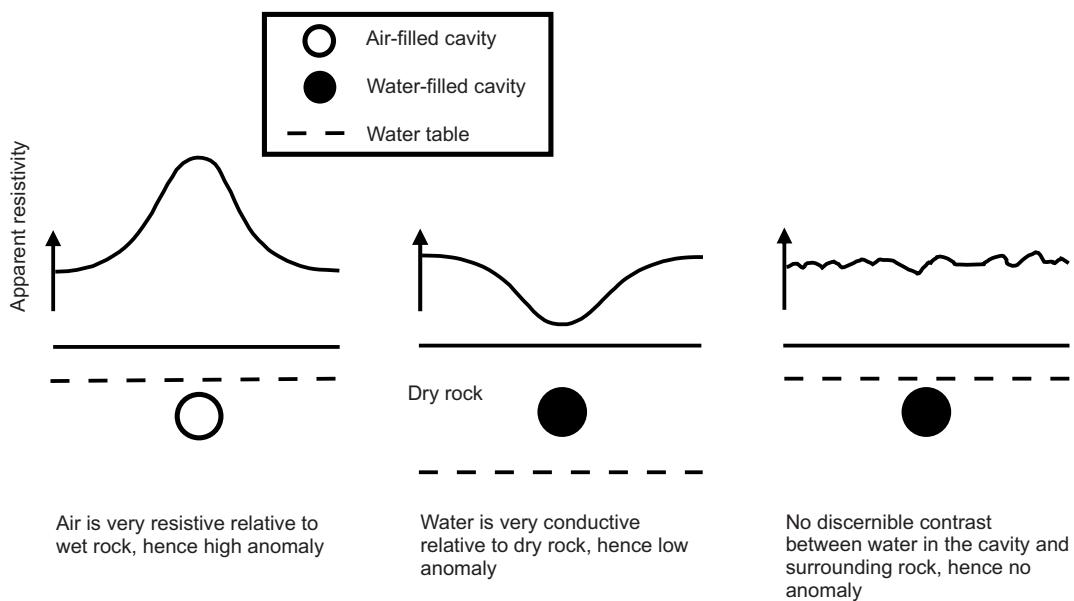


**Figure 1.6** Contrasts in physical properties from different geological targets give rise to a target. When there is no contrast, the target is undetectable geophysically. [C]

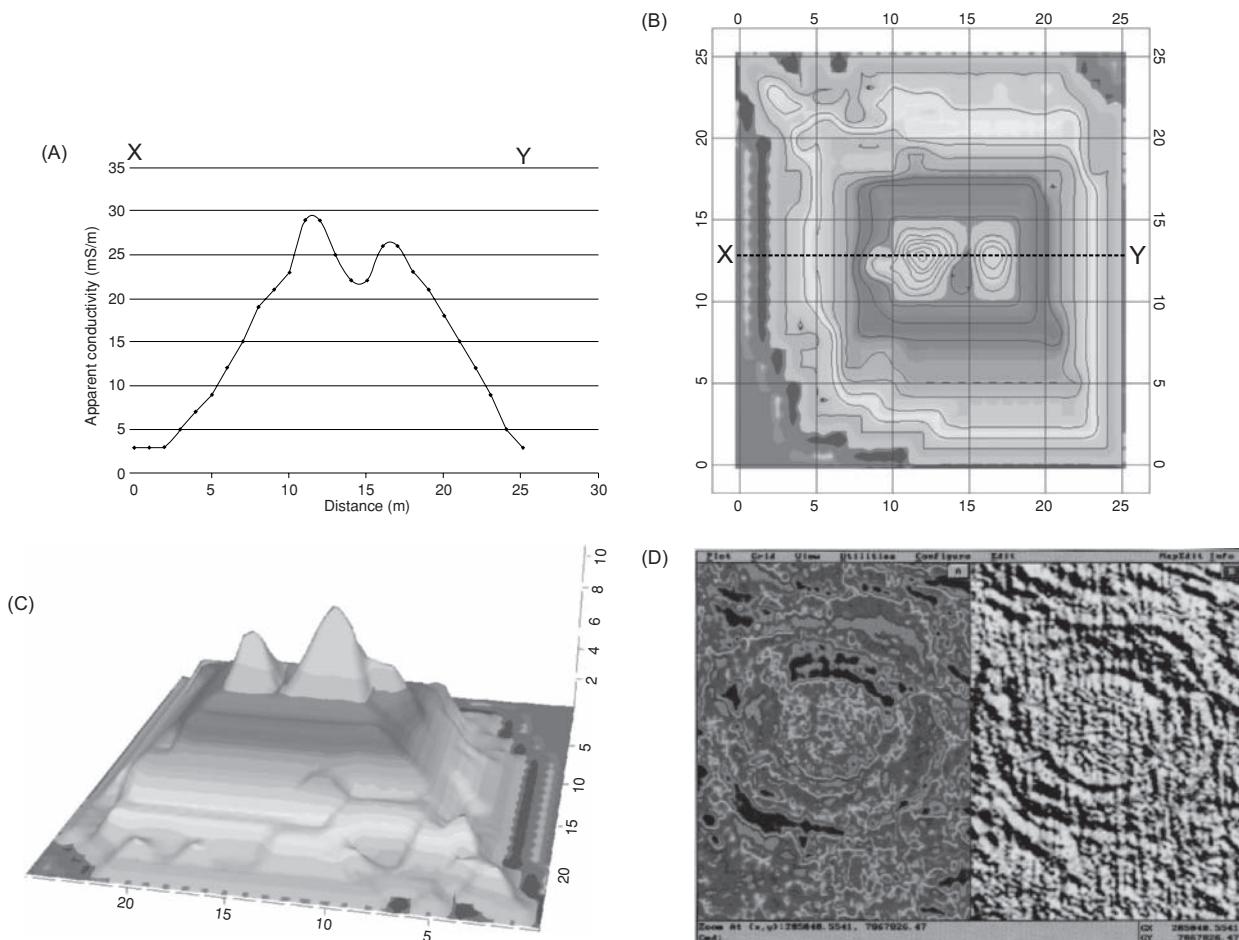


**Figure 1.7** Geophysical anomaly plots: (A) profile, (B) map, and (C) isometric projection. All three plots are from the same set of electromagnetic ground-conductivity data (see Chapter 11). (D) A shaded relief/grey-scale shadow display can enhance features that otherwise would be hard to visualise – in this case the display is of magnetic data over an area in which faulting appears as a series of features that possibly may be part of a meteorite impact crater. Photo courtesy of Geosoft Europe Ltd. [C]

checked in case there has been a simple misprint in data entry, or there might have been an error in fixing position or in instrumental calibration. When such data are compared, make sure all necessary data corrections have been made (see the individual chapters for details and examples) so that like is compared with like. Nodal values are vital for data quality control.

Geophysical investigations can take the form of four types of dimensional survey to investigate the spatial ( $x,y,z$ ) and temporal ( $t$ ) variations in the geophysical properties of the subsurface. A one-dimensional (1D) *sounding* at a specific location yields information as a function of depth ( $z$ ), such as with the Vertical Electrical Sounding method (see Chapter 7, section 7.4.1). Profiling (2D) along a given ( $x$  or  $y$ ) transect as illustrated in Figure 1.7A indicates variations in geophysical properties with depth ( $z$ ). When a series of parallel 2D ( $x,z$ ) profiles is surveyed, the results may be gridded and interpolated in the  $y$ -direction to present the data in map and/or isometric projection form (as shown in Figures 1.7B and 1.7C) or as a data volume. While the results may look three-dimensional, they should be referred to as *2.5 dimensional*, or *pseudo-3D*. True 3D spatial surveys take the form of a geophysical source that transmits a signal that is detected after passing through the subsurface to a *grid* rather than a *line* of sensors laid out on the ground surface, for example. When time-lapse surveys are undertaken, this can be referred to as providing an additional (time,  $T$ ) dimension to the survey, so that a 4D survey would comprise a true 3D ( $x,y,z$ ) spatial survey repeated over the same sensor layout after a period of time ( $t$ ). Similarly, 2D surveys repeated as time lapse investigations, such as in monitoring remediation of ground contamination, could also be referred to as being 3D ( $x,z,t$ ), but this would cause confusion with a 3D ( $x,y,z$ ) spatial survey. To differentiate between them a 2D time lapse survey can be referred to as a 2D-T survey, rather than 3D. A repeated time-lapse sounding ( $z,t$ ) can be referred to as a 1D-T survey to differentiate it from a 2D ( $x,z$ ) spatial survey.

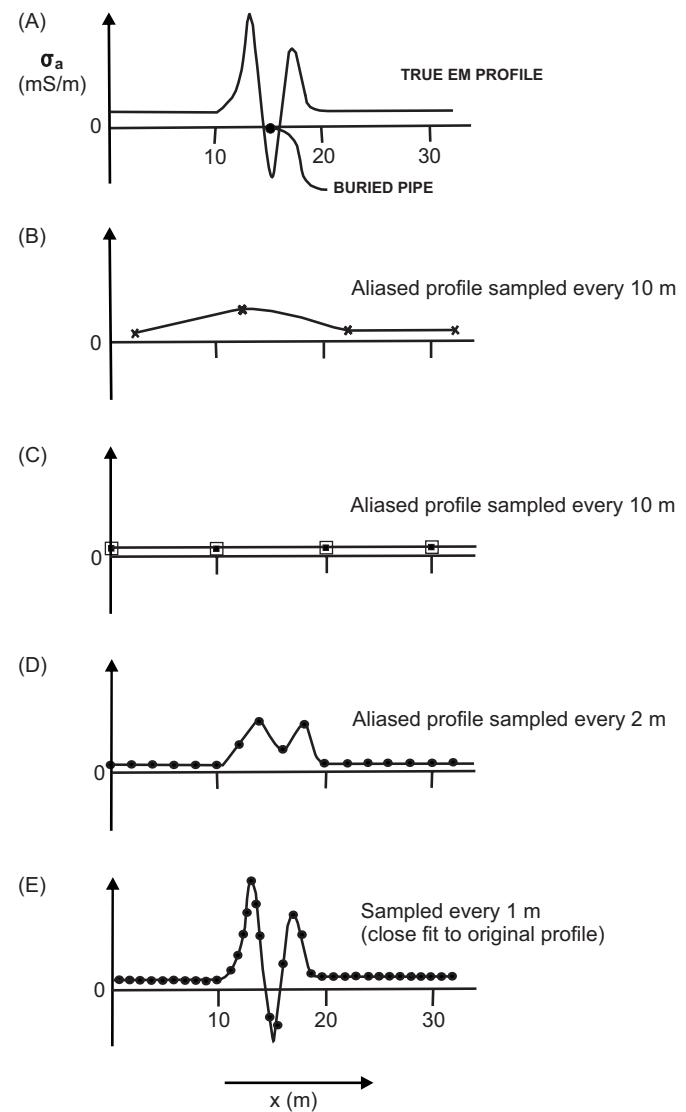


**Figure 1.8** Examples of various degrees of spatial aliasing using different sampling intervals. (A) shows a continuously sampled profile. (B) and (C) show sampling every 10 m, but at different points along the profile. (D) shows sampling every 2 m: the profile is still aliased. (E) shows sampling every 1 m: this profile is the closest fit to that in (A).

### 1.5.3 Selection of station intervals

The point at which a discrete geophysical measurement is made is called a *station* and the distances between successive measurements are *station intervals*.

It is fundamental to the success of a survey that the correct choice of station intervals be made. It is a waste of time and money to record too many data and equally wasteful if too few are collected. So how is a reasonable choice to be made? This requires some idea of the nature and size of the geological target. Any geophysical anomaly found will always be larger than the feature causing it. Thus, to find a mineshaft, for example, with a diameter of, say, 2 m, an anomaly with a width of at least twice this might be expected. Therefore, it is necessary to choose a station interval that is sufficiently small to be able to resolve the anomaly, yet not too small as to take far too long to be practicable.

Reconnaissance surveys tend to have coarser station intervals in order to cover a large area quickly, and to indicate zones over which a more detailed survey should be conducted with a reduced station interval and a more closely spaced set of profiles.

Consider Figure 1.8A in which a typical electromagnetic anomaly for a buried gas pipe is shown. The whole anomaly is 8 m wide. If a 10 m sampling interval is chosen, then it is possible either to clip the anomaly, as in Figure 1.8B, or to miss it entirely (Figure 1.8C). The resultant profiles with 2 m and 1 m sampling intervals are shown in Figures 1.8D and 1.8E respectively. The smaller the sampling interval, the better the approximation is to the actual anomaly (compare with Figure 1.8B or C). The loss of high-frequency information, as in Figures 1.8B and C, is a phenomenon known as *spatial aliasing* and should be avoided.

Another form of spatial aliasing may occur when gridded data are contoured, particularly by computer software. If the grid network is too coarse, higher-frequency information may be smeared

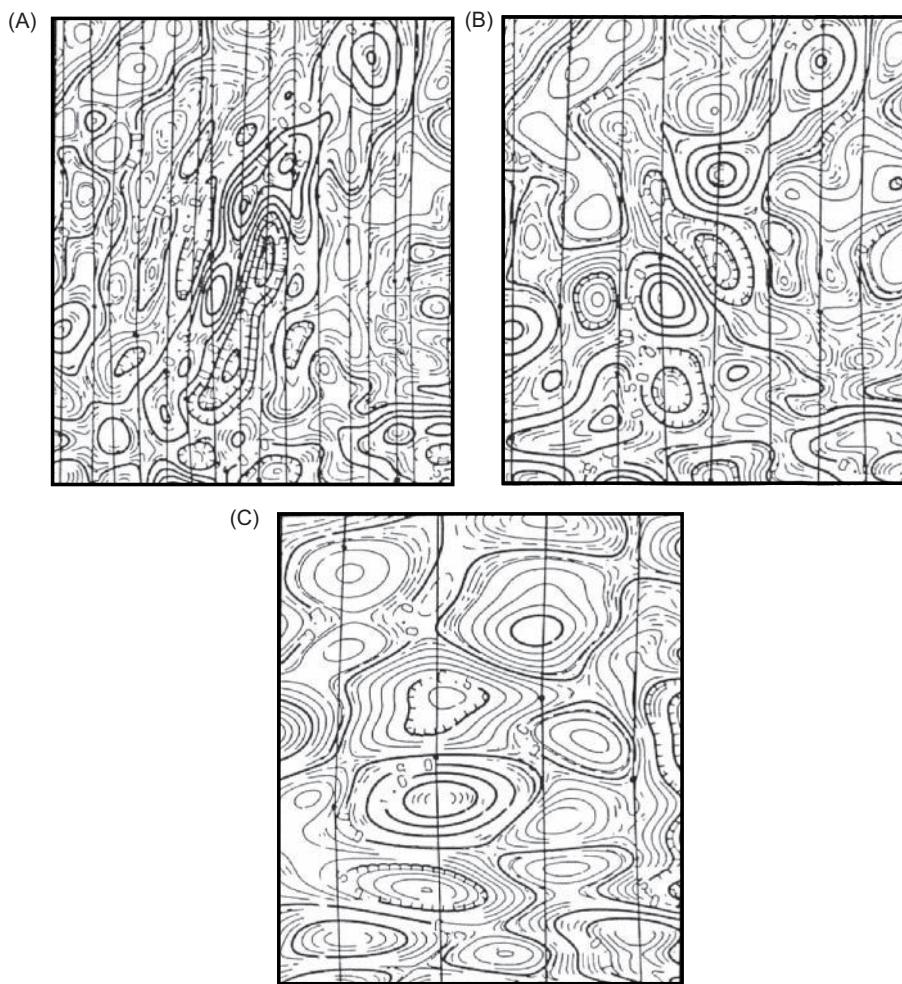


**Figure 1.9** Example of spatial aliasing on aeromagnetic data, showing the loss of higher-frequency anomalies, increasing separation between flight lines and the increased 'bullseye' effect caused by stretching the data too far. From Hood *et al.* (1979), by permission.

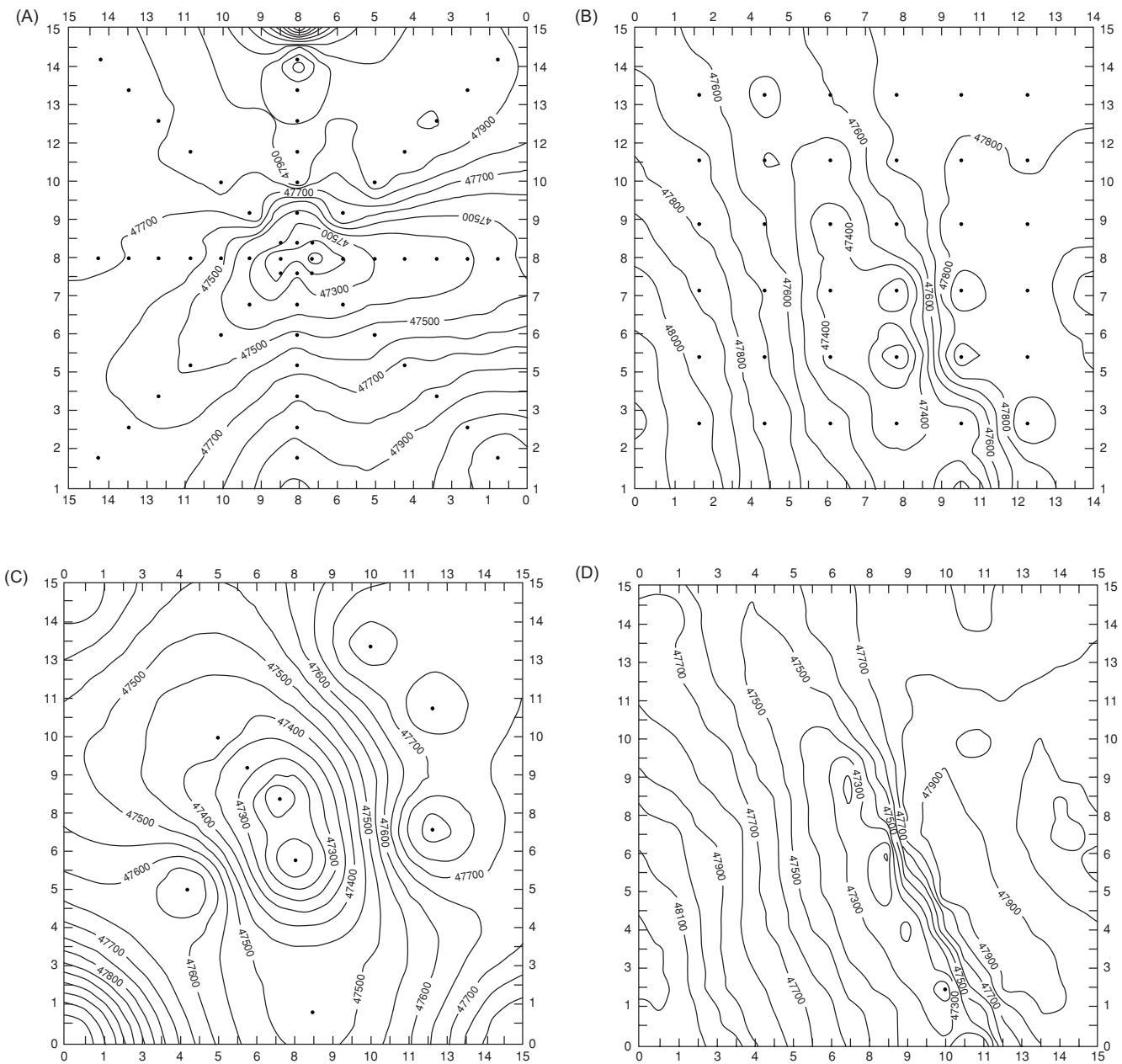
artificially and appear as lower-frequency anomalies. A common characteristic of spatially aliased gridded data is the 'bullseye' effect (see Figure 1.9) where the contouring program has had too little information to work on and so has contoured around individual data points or has linked data together unjustifiably (Cameron *et al.*, 1976; Hood *et al.*, 1979; Reid, 1980; Wu, 1990). This kind of problem can be created by an inadequately detailed or inappropriately designed field programme.

Figure 1.9 shows a hypothetical aeromagnetic survey. The map in Figure 1.9A was compiled from contouring the original data at a line spacing of 150 m. Figures 1.9B and C were recontoured with line spacings of 300 m and 600 m respectively. The difference between the three maps is very marked, with a significant loss of information between Figures 1.9A and C. Noticeably the higher-frequency anomalies have been aliased out, leaving only the longer-wavelength (lower-frequency) features. In addition, the orientation of the major anomalies has been distorted by the crude contouring in Figure 1.9C.

Spatial stretching occurs on datasets acquired along survey lines separated too widely with respect to along-line sampling. This spa-

tial aliasing can be removed or reduced using mathematical functions, such as the Radon Transform (Yuanxuan, 1993). This method provides a means of developing a better gridding scheme for profile line-based surveys. The specific details of the method are beyond the scope of this chapter, and readers are referred to Yuanxuan's paper for more information. Further advice about the effects of different gridding routines is available from the relevant software providers either through their manuals, software 'help' keys or online via the Internet. Do not just use the default settings and hope for the best!

Similar aliasing problems associated with contouring can arise from radial survey lines and/or too few data points, as exemplified by Figure 1.10. Figure 1.10A and B both have 64 data points over the same area, and two effects can be seen very clearly: in Figure 1.10A the orientation of the contours (one marked 47,500 nT) artificially follows that of the line of data points to the top left-hand corner, whereas the orientation is more north-south in Figure 1.10B. The even grid in Figure 1.10B highlights the second effect (even more pronounced in Figure 1.10C), which is the formation of bullseyes around individual data points. The inadequacy of the number of data points is further demonstrated in Figure 1.10C, which is based



**Figure 1.10** Examples of contouring different patterns of data. (A) shows set of radial lines, and (B) an even grid of data, both with 114 points per square kilometre. (C) has too few data points unevenly spread over the same area (23 data points per square kilometre). (D) shows an even grid of 453 points per square kilometre. The contours are isolines of total magnetic field strength (units: nanoteslas); the data are from a ground magnetometer investigation of northwest Dartmoor, England.

on only 13 data values, by the formation of concentric contours that are artificially rounded in the top left and both bottom corners. For comparison, Figure 1.10D has been compiled on the basis of 255 data points, and exposes the observed anomalies much more realistically.

#### 1.5.4 Noise

When a field survey is being designed it is important to consider what extraneous data (*noise*) may be recorded. There are various

sources of noise, ranging from man-made sources ('cultural noise') as diverse as electric cables, vehicles, pipes and drains, to natural sources of noise such as wind and rain, waves, and electrical and magnetic storms (Figure 1.11).

Some aeromagnetic and electrical methods can suffer badly from cathodic currents that are used to reduce corrosion in metal pipes (Gay, 1986). Electrical resistivity surveys should not be conducted close to or parallel to such pipes, nor parallel to cables, since power lines will induce unwanted voltages in the survey wires. Before a survey starts, it is always advisable to consult with public utility

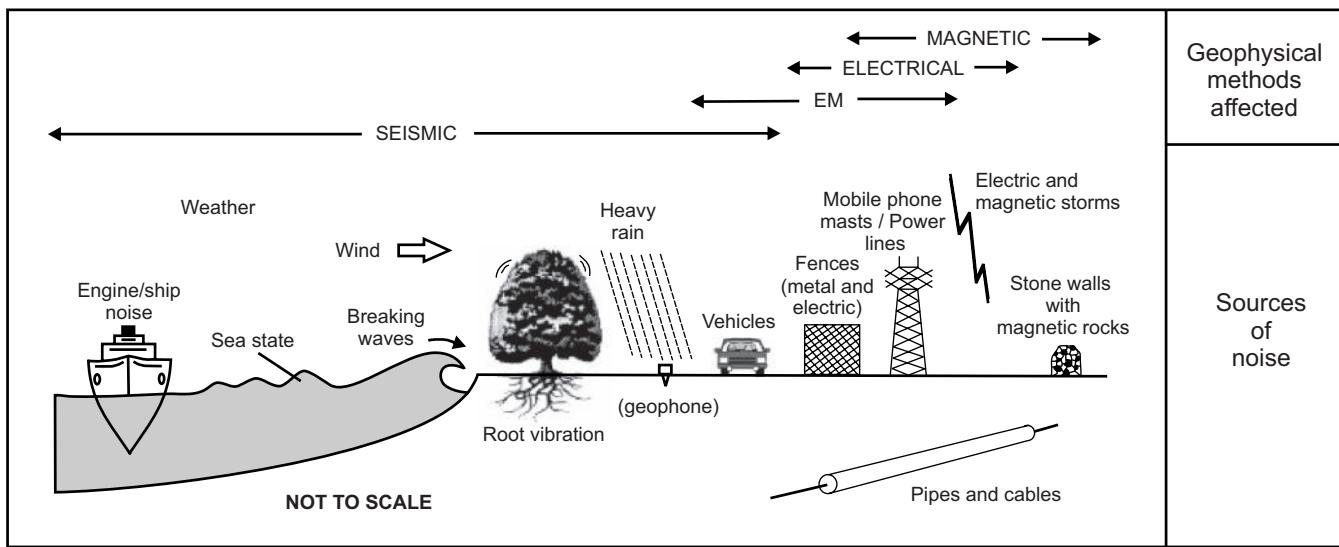


**Figure 1.11** Schematic illustrating some common sources of geophysical noise.

companies which should, given enough time, provide maps of their underground and overhead facilities. It is important to check on the location of water mains, sewers, gas pipes, electricity cables, telephone cables and cable-television wires. In many cases such utilities may mask any anomalies caused by deeper-seated natural bodies. Furthermore, should direct excavation be required, the utilities underground may be damaged if their locations are not known.

It is also worth checking on the type of fencing around the survey area. Wire mesh and barbed wire fences, and metal sheds, can play havoc with electromagnetic and magnetic surveys and will restrict the area over which sensible results can be obtained. It also pays to watch out for types of walling around fields, as in many areas wire fences may be concealed by years of growth of the local vegetation. In addition, when undertaking a magnetic survey, be on the lookout for stone walls built of basic igneous rocks, as these can give a noticeable magnetic anomaly.

There are two forms of noise (Figure 1.12). *Coherent noise*, such as that produced by power lines, occurs systematically (Figure 1.12A) and may degrade or even swamp the wanted signals. As coherent noise usually occurs with a definable frequency (e.g. mains electricity at 50–60 Hz), appropriate filters can be used to remove or reduce it.

In contrast, *incoherent noise*, such as that due to waves breaking on a seashore or to traffic, is random. When summed together it tends to cancel to some extent, so reducing its overall effect (Figure 1.12B).

High but incoherent noise levels are often associated with surveys along road verges. Metal-bodied vehicles passing by during an electromagnetic survey can cause massive but brief disturbances. Vehicles, particularly heavy lorries, and trains can set up short-lived but excessive acoustic noise which can ruin a seismic survey. So, too, can the effects of waves washing onto beaches or the noise of turbulent river water close to geophone spreads on a seismic survey. In exposed areas, geophones that have not been planted properly may pick up wind vibration acting on the geophones themselves and on the connecting cable, but also from trees blowing in the

breeze, as the motion transmits vibrations into the ground via their root systems. Similar effects can be observed close to man-made structures. Unprotected geophones are very sensitive to the impact of raindrops, which can lead to the curtailment of a seismic survey during heavy rain.

Cultural and unnecessary natural noise can often be avoided or reduced significantly by careful survey design. Increasingly, modern technology can help to increase the *signal-to-noise ratio* so that, even when there is a degree of noise present, the important geophysical signals can be enhanced above the background noise levels (Figure 1.13). Details of this are given in the relevant sections of later chapters. However, it is usually better to use a properly designed field technique to optimise data quality in the first instance, rather than relying on post-recording filtering. Further details of field methods are given, for example, by Milsom (2003).

Where a survey with a single instrument lasts longer than a day, it is recommended that a base line is established that can be re-surveyed quickly each day to check on the repeatability of the method. If the sets of data taken on two consecutive days are not similar it suggests there is a problem with the instrument set-up. Also any day-on-day drift of the equipment will become apparent, and this drift will need to be corrected in any subsequent data processing of the combined dataset. Furthermore, the repeatability check also indicates the variations that occur in the data due to the way the instrument is being deployed (different operator, slightly different carrying position, etc.). These differences will help in determining the minimum contour interval that should be selected when displaying the data. For example, if the repeatability check indicates that there is a  $\pm 1$  milliSiemens/m difference on readings, then there is no justification for displaying the data with a 0.5 mS/m contour interval, as this is significantly smaller than the uncertainty in the readings and is not physically significant. It is possible to apply a more statistically rigorous approach and calculate the standard deviation of the data. The minimum contour interval should not be smaller than the standard deviation.

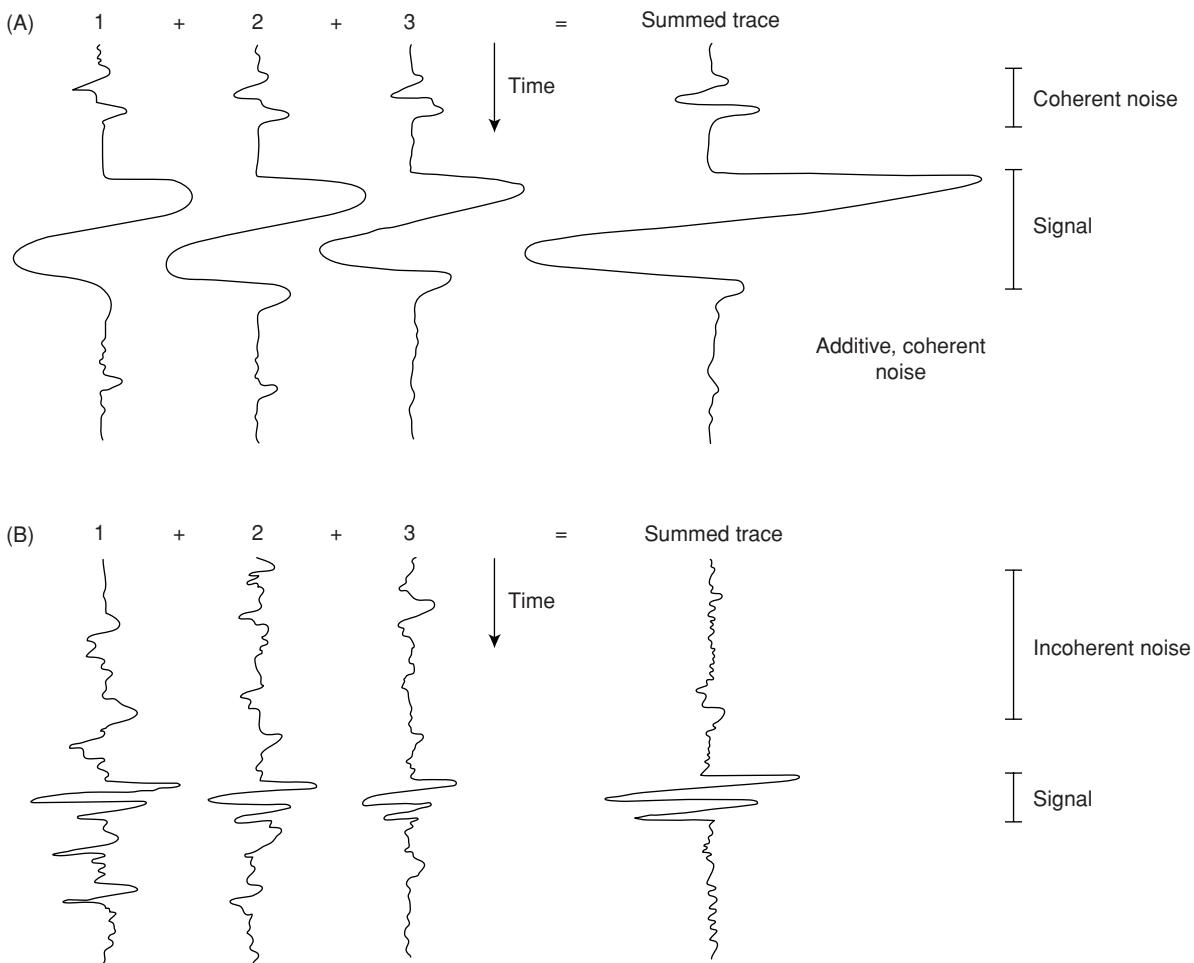


**Figure 1.12** The effect of summing three traces with (A) coherent and (B) incoherent noise.

## 1.5.5 Position fixing

Knowing the position of any data point accurately within a survey and relative to prominent ground features is essential. This can vary from being able to deploy a tape measure through to making integrated measurements using differential Global Positioning Systems (dGPS). The key is that whichever method is used, it is possible to

re-occupy a given location to within the specified accuracy of the survey. There have been too many examples of where an intrusive test (such as a trial pit) is excavated over what is supposed to be the position of a geophysical anomaly, but the errors in surveying mean that the two are not coincident. The trial pit effectively samples the wrong ground and no association is made between what was causing the geophysical anomaly and the ground truth result.

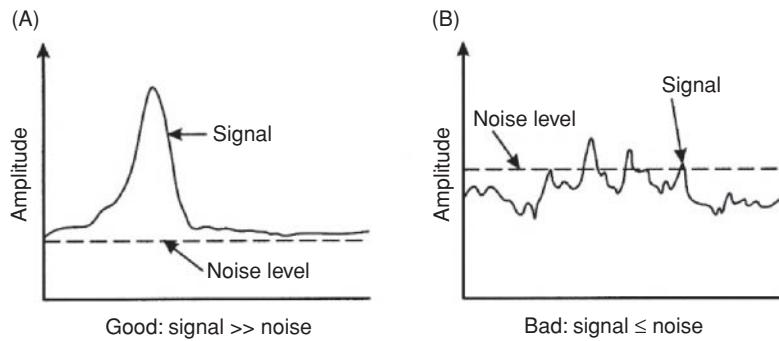


**Figure 1.13** Signal-to-noise ratio. In (A) the signal has a much larger amplitude than that of the background noise, so the signal can be resolved. In (B) the signal amplitude is less than, or about the same as, that of the noise and thus the signal is lost in the noise.

A key benefit of using geophysical methods is to be able to target intrusive tests on the basis of the geophysical data. Obtaining accurate ground truth information is very important to correlate with the geophysical results so that the physical interpretations can be extrapolated spatially on the basis of the geophysical data. It is essential, therefore, that being able to set out a survey, whether for a geophysical investigation or locating the correct position for a borehole or trial pit, is carried out accurately (e.g. Crawford, 1995).

When using dGPS, there is often an issue about being able to plot dGPS positions of features onto their corresponding position on a local map, for example. In some cases, there may be several metres difference between the dGPS position and the position on a site plan using local coordinates. It then becomes important to be able to reconcile different map systems.

The World Geodetic System 1984 (WGS84) is a global coordinate system designed for use anywhere in the world, with coordinates usually expressed as latitude, longitude and ellipsoid height. A high-accuracy version of WGS84, known as the International Terrestrial Reference System (ITRS), has been created in a number of versions since 1989, and is suitable for international high-accuracy applications, such as in geophysical surveys. As the continents are moving in relation to each other, up to 0.12 m per year, there is a problem in maintaining the accuracy of a coordinate system. The European Terrestrial Reference System 1989 (ETRS89) was established as the standard precise GPS coordinate system throughout Europe which accounts for continental motion. The relationship between ITRS and ETRS89 is precisely defined at any point in time by a simple transformation published by the International Earth Rotation Service (ITRS). Most national mapping agencies in Europe have adopted the ETRS89 as a standard coordinate system for precise GPS surveying.

Survey data can be exported from data-logging instruments in World Geodetic System 1984 (WGS84) format and imported into Geosoft's Oasis Montaj software, for example, where they can be transformed to OSGB 1936, the British National Grid coordinates, using an automatic transform. Furthermore, to cope with slight distortions in the OSGB36 *Terrestrial Reference Frame* (TRF) it is necessary to use a 'rubber-sheet' stretch-style transformation that works with a grid expressed in terms of easting and northing coordinates. The grids of easting and northing shifts between ETRS89 and OSGB36 cover Britain at a resolution of one kilometre. From these grids a northing and easting shift for each point to be transformed is obtained by a bilinear interpolation, which is called the National Grid Transformation OSRTN02 (Ordnance Survey, 2008). To account for the slight difference in the WGS84 to British National Grid transform a Geosoft '.wrf' file can be created to rectify the data to a DXF version of a site plan supplied by the client. This way, the dGPS positions for the acquired data plot in the correct position on a digital site plan provided in OSGB coordinates. In the UK the Ordnance Survey provides automatic transforms via its website ([www.ordnancesurvey.co.uk/gps](http://www.ordnancesurvey.co.uk/gps)). Geographical Information System software also provides coordinate transformation algorithms. For surveys undertaken outside of the UK, reference should be made to the relevant national survey institution or agency to obtain the relevant coordinate transformation algorithms, where necessary.

Care should also be taken when alternative coordinate systems are used, such as by metro companies and mining companies where their underground coordinate systems may be slightly skewed relative to those at the surface. When integrating data, the coordinate systems need to be transformed so that they are consistent with each other. In addition, long sinuous survey tracks, such as those for railways, pipelines and roads, may take advantage of the 'Snake' projection (Iliffe *et al.*, 2007; Iliffe, 2008a,b). The original route of the infrastructure (pipe, railway or road) is passed to the 'Snake-maker' design software in the form of seed points at discrete intervals along the route. The program then fits a three-dimensional trend line through these, along which the scale factor is unity. The program generates a curvilinear rectangle along the trend line, indicating the region in which scale factor distortion is less than the permitted maximum, usually 20 ppm for rail projects (see also Iliffe and Lott, 2008).

With some equipment used with a dGPS antenna, the location of any data point and that of the antenna will be coincident. However, in other cases, there may be a physical separation between the location of the measurement point and that of the antenna, creating a *layback* or *offset*, which has to be corrected for in any subsequent data display. Furthermore, if direction of travel and layback are not taken into account when correcting positions of data, artefacts can be introduced into the contoured data such as the herringbone effect. Methods such as EM31 ground conductivity profiling (Chapter 11) are particularly prone to this, depending upon the orientation of the dipole boom. If alternate lines are surveyed in opposite directions, the data are acquired with the transmitter and receiver in opposite directions and this can also generate a 'herring bone' effect; the transmitter-receiver orientation must be kept constant throughout the survey. In other methods, such as in high-resolution over-water sub-bottom seismic reflection profiling or marine magnetometry, the offset between instrument platforms and the dGPS antenna can be significant (tens of metres). Fix positions marked on the recorded seismic sections must have layback applied so that the position of the seismic trace is correct with respect to its location on the ground. An example of a layback diagram from a marine survey is shown in Figure 1.14. See Chapter 4, Section 4.6.2, for further details of marine survey positional issues.

In marine surveys in tidal regions, it is also essential that records are kept of tidal levels with respect to specified chart datums. In the UK, the chart datum is defined as that at Newlyn in Cornwall. Bathymetric data must be corrected to that specific datum so that seabed levels can be expressed in terms of elevations relative to chart datum. This makes correlation with borehole data far easier, as geological interfaces on borehole logs are defined in terms of both depth below a specific level (typically the moon pool of a drilling rig – the platform through which the drill string passes) and elevation relative to datum. Vertical profiles through the water column to measure the speed of sound in water should be acquired regularly in order to correct echo sounding results accurately to water depths.

## 1.5.6 Data analysis

All too often, data are acquired without regard for how they are to be processed and analysed. This oversight can lead to inadequate

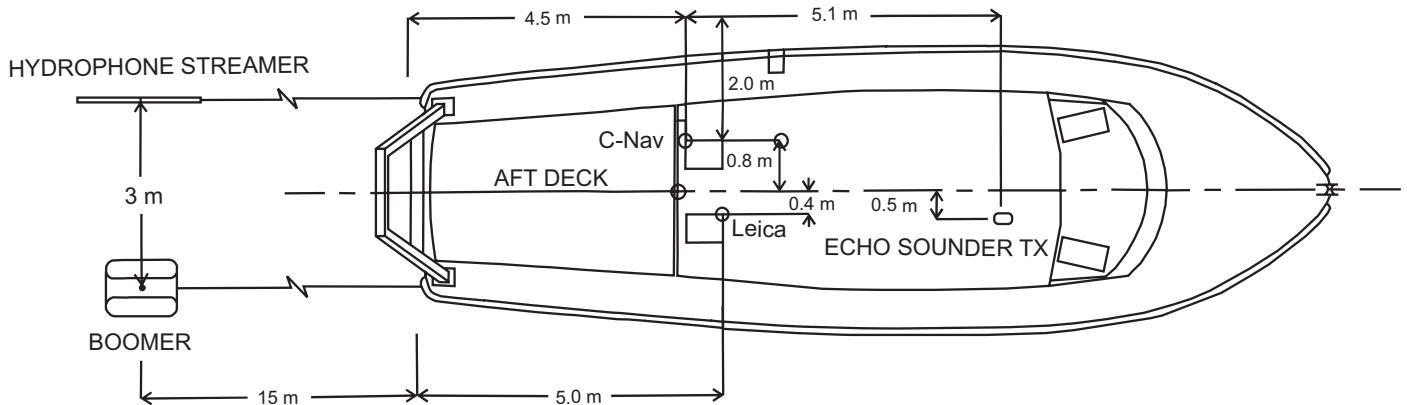


**Figure 1.14** Example of field geometry diagram for an over-water Sub-Bottom Profiling and water bathymetry survey.

data collection or the recording of data in such a way that vast amounts of tedious transcribing or typing-in of measurements has to be undertaken. Not only is this unproductive in terms of the person who has to do all the 'number crunching', but it often allows the introduction of errors into the datasets. The consequent back-checking to find the bad data takes up valuable time and money. It therefore pays dividends to think through how the data are to be collected in relation to the subsequent methods of data reduction and analysis.

As automatic data-logging with simultaneous position fixing with dGPS and computer analysis have become commonplace, it is increasingly important to standardise the format in which the data are recorded to ease the portability of information transfer between computer systems. This also makes it easier to download the survey results into data-processing software packages. It is also important to be able to manage large volumes of data. For example, a major survey using ground penetrating radar can easily generate many gigabytes of data per day. Making standard back-ups becomes no trivial matter. To make computer analysis much simpler, it helps to plan the survey well before going into the field to ensure that the collection of data and the survey design are appropriate for the type of analyses anticipated. Even here, there are many pitfalls awaiting the unwary. How reliable is the software? Has it been calibrated against proven manual methods, if appropriate? What are the assumptions on which the software is based, and under what conditions are these no longer valid, and when will the software fail to cope and then start to produce erroneous results? (For an example of this, see Section 7.5.3.)

The danger with computers is that their output (especially if in colour) can have an apparent credibility that may not be justified by the quality of the data input or of the analysis. Unfortunately there are no guidelines or accepted standards for much geophysical software (Reynolds, 1991a) apart from those for the major seismic data-processing systems. However, the judicious use of computers and of automatic data-logging methods can produce excellent and very worthwhile results. Comments on some of the computer methods available with different geophysical techniques are made in the relevant chapters of this book, and some have been discussed more fully elsewhere (Reynolds, 1991a).

For users of personal computers, there has been a proliferation of software. One major software house generating commercially available geophysical computer packages is Geosoft Ltd in Canada, who also produce gridding and contouring packages, as does Golden Software (USA), producers of SURFER. Commercial products vary widely in their ranges of applications, flexibility and portability between different computers. Intending users of any software package should evaluate the software prior to purchase if possible. A search on the Internet produces a plethora of lists of software, freeware and commercially-available packages. Intending users should take considerable care about the selection of software to find those packages that are well-established (i.e. the majority of bugs have been resolved) and have demonstrated their reliability. In the UK over the last few years the Association of Geotechnical Specialists (AGS) have established a file format for the production of intrusive investigation results, including borehole geophysics. Many clients now require contractually that datafiles are produced in AGS format or are compatible with this format. Increasingly, such datafile formats provide communication with major engineering Computer Aided Design (CAD) and Geographical Information System (GIS) software. In addition, geophysical software (Geosoft Oasis Montaj) can be linked to a GIS (such as ArcGIS) using their bridging software (Target), which greatly enhances the scope of geo-rectified and integrated outputs. Other software systems may also provide comparable capabilities. However, some proprietary interpretation software packages may be distinctly limited in their capability. Anyone intending to use the results should ensure that they are aware of how the data are analysed and what implications this might have for the use of any interpretations arising. It is strongly advised that clients engage an independent geophysical consultant to advise them so that they commission surveys that meet their needs, not just satisfy the desires of bidding contractors.

There is also a growing recent trend amongst contractors to try to develop ways in which data can be downloaded, gridded and interpreted on the same day that the data are acquired, and the faster the better. This is not necessarily a beneficial step. While it might provide a selling point for the contractor, experience suggests that this is not necessarily in the client's interests. Firstly, the acquisition of far greater quantities of data in shorter time periods often

results in the data not being viewed as regularly during acquisition as was done previously. Bad data, spikes, and the like, are now often only identified back in the office when it is too late to re-acquire data. Furthermore, the ubiquitous ‘default’ setting on software allows people not to think about what they are producing – as long as the output looks alright, it must be alright! This is not always the case. In shallow seismic reflection profiling, as undertaken for marine dredge surveys, for instance, semi-automatic horizon picking software may miss or mis-pick events. It is not uncommon for marine geophysics contractors to dump datasets on clients without undertaking appropriate data quality control checks. Unless there is a conscious effort to apply some reasonable quality control, the final deliverables for the Client may be incorrect, incomplete or both.

The increased use of gridding packages means that subtle details in the individual profiles may be missed; maxima are reduced and minima increased through the gridding routines. In some cases this ‘filtering’ can result in important anomalies being missed completely. While rapid data gridding and data visualisation are important parts of quality control, when it is applied correctly, they should not be substitutes for interpretation, an aspect that is worryingly on the increase.

## Further reading

See also monographs and special publications produced by the Society for Exploration Geophysicists (SEG), and by the Environmental and Engineering Geophysical Society (EEGS). The latter holds an annual Symposium on the Application of Geophysics to Engineering and Environmental Problems (SAGEEP) and publishes the proceedings. Other organisations of note are the Australian Society of Exploration Geophysics (ASEG), the Canadian Exploration Geophysics Society, the South African Geophysical Association, and the European Association of Geoscientists and Engineers (EAGE), among others.

ASEG publishes the quarterly journal *Exploration Geophysics*; SEG publishes the journals *Geophysics* and *Geophysics: The Leading Edge*, and books, monographs and audio-visual materials (slides, videos, etc.). Since 1995, the EEGS has published the *Journal of Environmental and Engineering Geophysics*. In January 1996 the European Section of the EEGS launched the first issue of the *European Journal of Environmental and Engineering Geophysics*, which since 2003 has been published under the title *Near Surface Geophysics* by the EAGE. The EAGE also publishes *Geophysical Prospecting* and *First Break*. The journal entitled *Archaeological Prospection* has been available since 1995.

The list above gives a general idea of what is available. For those interested particularly in archaeological geophysics, very useful guidelines have been produced by the English Heritage Society (David *et al.*, 2008), which are also available online at [www.english-heritage.org.uk/upload/pdf/GeophysicsGuidelines.pdf](http://www.english-heritage.org.uk/upload/pdf/GeophysicsGuidelines.pdf).

The rapid growth in the number of journals and other publications in environmental and engineering geophysics demonstrates the growing interest in the subject and the better awareness of the applicability of modern geophysical methods.

## Bibliography

### General geophysics texts

- Milsom, J. (2003) *Field Geophysics* (3<sup>rd</sup> edn). Chichester: John Wiley & Sons Ltd.
- Telford, W.M., Geldart, L.P., Sheriff, R.E. and Keys, D.A. (1990) *Applied Geophysics* (2<sup>nd</sup> edn). Cambridge.

# 2

## Gravity Methods

### 2.1 Introduction

Gravity surveying measures variations in the Earth's gravitational field caused by differences in the density of subsurface rocks. Although known colloquially as the 'gravity' method, it is in fact the variation of the acceleration due to gravity that is measured. Gravity methods have been used most extensively in the search for oil and gas, particularly in the early twentieth century. While such methods are still employed very widely in hydrocarbon exploration, many other applications have been found (Table 2.1), some examples of which are described in more detail in Section 2.7. It should be noted that the gravity field refers to the gravitational force or acceleration due to gravity exerted on a unit mass at a point in space (see Zeng and Wan, 2004) as opposed to the definition cited by Sheriff (2002) that refers to the space in which an effect is measurable.

Micro-gravity surveys are those conducted on a very small scale – of the order of hundreds of square metres – and which are capable of detecting cavities, for example, as small as 1 m in diameter within 5 m of the surface.

Perhaps the most dramatic change in gravity exploration in the 1980s was the development of instrumentation that permits airborne gravity surveys to be undertaken routinely and with a high degree of accuracy (see Section 2.5.8). This has allowed aircraft-borne gravimeters to be used over otherwise inaccessible terrain and has led to the discovery of several small but significant areas with economic hydrocarbon potentials. Further advances have included the development of increasingly compact, mobile absolute gravimeters. Nabighian *et al.* (2005) provided an overview of the gravity method in large-scale exploration.

### 2.2 Physical basis

#### 2.2.1 Theory

The basis upon which the gravity method depends is encapsulated in two laws derived by Sir Isaac Newton, which he described in

*Principia Mathematica* (1687) – namely his Universal Law of Gravitation, and his Second Law of Motion.

The first of these two laws states that the force of attraction between two bodies of known mass is directly proportional to the product of the two masses and inversely proportional to the square of the distance between their centres of mass (Box 2.1). Consequently, the greater the distance separating the centres of mass, the smaller is the force of attraction between them.

#### Box 2.1 Newton's Universal Law of Gravitation

$$\text{Force} = \text{gravitational constant} \times \frac{\text{mass of Earth}(M) \times \text{mass}(m)}{(\text{distance between masses})^2}$$
$$F = \frac{G \times M \times m}{R^2} \quad (1)$$

where the gravitational constant ( $G$ ) =  $6.67 \times 10^{-11} \text{ N m}^2 \text{ kg}^{-2}$ .

Newton's law of motion states that a force ( $F$ ) is equal to mass ( $m$ ) times acceleration (Box 2.2). If the acceleration is in a vertical direction, it is then due to gravity ( $g$ ).

#### Box 2.2 Newton's Second Law of Motion

$$\text{Force} = \text{mass } (m) \times \text{acceleration } (g)$$
$$F = m \times g \quad (2)$$

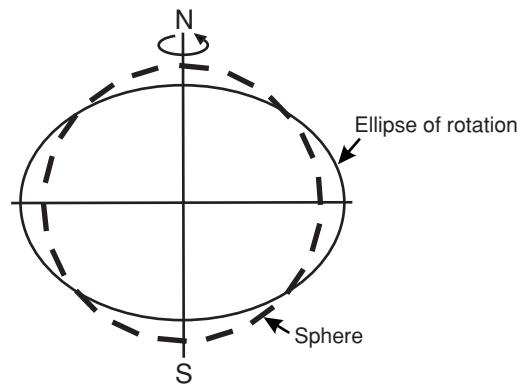
Equations (1) and (2) can be combined to obtain another simple relationship:

$$F = \frac{G \times M \times m}{R^2} = m \times g; \quad \text{thus } g = \frac{G \times M}{R^2} \quad (3)$$

This shows that the magnitude of the acceleration due to gravity on Earth ( $g$ ) is directly proportional to the mass ( $M$ ) of the Earth

**Table 2.1** Applications of gravity surveying.

- Hydrocarbon exploration
- Hydrocarbon reservoir monitoring
- Monitoring of CO<sub>2</sub> containment underground
- Regional geological studies
- Isostatic compensation determination
- Exploration for, and mass determination of, mineral deposits
- Detection of subsurface cavities (micro-gravity), e.g. mine workings, caves, solution features, tunnels
- Location of buried rock valleys
- Determination of glacier thickness
- Tidal oscillations
- Archaeogeophysics (micro-gravity), e.g. location of tombs, crypts
- Shape of the earth (geodesy)
- Military (especially for missile trajectories)
- Satellite positioning
- Monitoring volcanoes
- Hydrological changes in the geoid

**Figure 2.1** Exaggerated difference between a sphere and an ellipse of rotation (spheroid).

## 2.2.2 Gravity units

The first measurement of the acceleration due to gravity was made by Galileo in a famous experiment in which he dropped objects from the top of the Leaning Tower of Pisa. The normal value of  $g$  at the Earth's surface is 980 cm/s<sup>2</sup>. In honour of Galileo, the c.g.s. unit of acceleration due to gravity (1 cm/s<sup>2</sup>) is the *Gal*. Modern gravity meters (gravimeters) can measure extremely small variations in acceleration due to gravity, typically 1 part in 10<sup>9</sup> (equivalent to measuring the distance from the Earth to the Moon to within a metre). The sensitivity of modern instruments is about ten parts per million. Such small numbers have resulted in sub-units being used such as the milliGal (1 mGal = 10<sup>-3</sup> Gal) and the microGal (1 µGal = 10<sup>-6</sup> Gal). Since the introduction of SI units, acceleration due to gravity is measured in µm/s<sup>2</sup>, which is rather cumbersome and so is referred to as the gravity unit (g.u.); 1 g.u. is equal to 0.1 mGal [10 g.u. = 1 mGal]. However, the gravity unit has not been universally accepted and 'mGal' and 'µGal' are still widely used.

## 2.2.3 Variation of gravity with latitude

The value of acceleration due to gravity varies over the surface of the Earth for a number of reasons, one of which is the Earth's shape. As the polar radius (6357 km) is 21 km shorter than the equatorial radius (6378 km), the points at the poles are closer to the Earth's centre of mass (so smaller value of  $R$ ) and, therefore, the value of gravity at the poles is greater (by about 0.7%) than that at the equator (Figure 2.3) (see Equation (3) under Box 2.2). Furthermore, as the Earth rotates once per sidereal day around its north-south axis, there is a centrifugal acceleration acting which is greatest where the rotational velocity is largest, namely at the equator (1674 km/h; 1047 miles/h) and decreases to zero at the poles (Figure 2.3). The centrifugal acceleration, which is equal to the rotational velocity ( $a$ ) squared times the distance to the rotational axis ( $d$ ), serves to decrease the value of the gravitational acceleration. It is exactly the same mechanism as that which keeps water in a bucket when it is being whirled in a vertical plane.

The value of gravity measured is the resultant of that acting in a line with the Earth's centre of mass with the centrifugal acceleration

and inversely proportional to the square of the Earth's radius ( $R$ ). Theoretically, acceleration due to gravity should be constant over the Earth. In reality, gravity varies from place to place because the Earth has the shape of a flattened sphere (like an orange or an inverted pear), rotates, and has an irregular surface topography and variable mass distribution (especially near the surface).

The shape of the Earth is a consequence of the balance between gravitational and centrifugal accelerations causing a slight flattening to form an oblate spheroid. Mathematically it is convenient to refer to the Earth's shape as being an *ellipse of rotation* (Figure 2.1).

The sea-level surface, if undisturbed by winds or tides, is known as the *geoid* and is particularly important in gravity surveying as it is horizontal and at right angles to the direction of the acceleration due to gravity everywhere. The geoid represents a surface over which the gravitational field has equal value and is called an *equipotential surface*. The irregular distribution of mass, especially near the Earth's surface, warps the geoid so that it is not identical to the ellipse of rotation (Figure 2.2). Long-wavelength anomalies, which can be mapped using data from satellites (Wagner *et al.*, 1977), relate to very deep-seated masses in the mantle (Figure 2.2A), whereas density features at shallow depths cause shorter-wavelength warps in the geoid (Figure 2.2B). Consequently, anomalies within the gravitational field can be used to determine how mass is distributed. The particular study of the gravitational field and of the form of the Earth is called *geodesy* and is used to determine exact geographical locations and to measure precise distances over the Earth's surface (*geodetic surveying*).

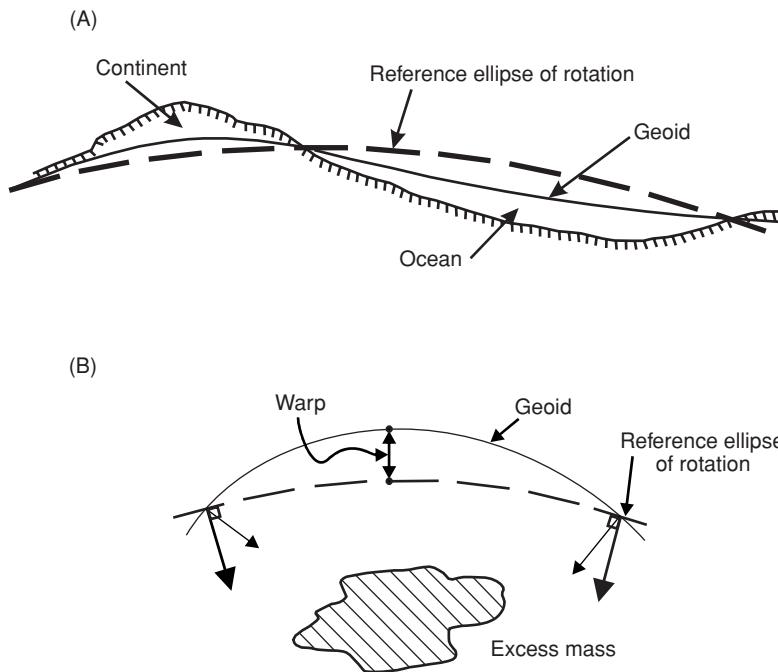


**Figure 2.2** Warping of the geoid: (A) continental-scale effects, and (B) localised effects due to a subsurface excess mass.

(Figure 2.4). The resultant acts at right-angles to the ellipsoid of rotation so that a plumb line, for example, hangs vertically at all locations at sea-level. The angle  $\varphi$  in Figure 2.4 defines the geodetic (ordinary or geographic) latitude. The resultant gravity at the poles is 5186 mGal (51,860 g.u.) greater than at the equator and varies systematically with latitude in between, as deduced by Clairaut in 1743.

Subsequent calculations in the early twentieth century, based on Clairaut's theory, led to the development of a formula from which it was possible to calculate the theoretical acceleration due to gravity ( $g_\varphi$ ) at a given geographic latitude ( $\varphi$ ) relative to that at sea-level ( $g_0$ ). Parameters  $\alpha$  and  $\beta$  are constants which depend

on the amount of flattening of the spheroid and on the speed of rotation of the Earth.

In 1930 the International Union of Geodesy and Geophysics adopted the form of the *International Gravity Formula* (Nettleton, 1971: p. 20) shown in Box 2.3. This became the standard for gravity work. However, refined calculations using more powerful computers and better values for Earth parameters resulted in a new formula, known as the *Geodetic Reference System 1967* (GRS67), becoming the standard (Woppard, 1975) (Box 2.4). If gravity surveys using the 1930 gravity formula are to be compared with those using the 1967 formula, then the third formula in Box 2.4 should be used to compensate for the differences between them. Otherwise, discrepancies due to the differences in the equations may be interpreted

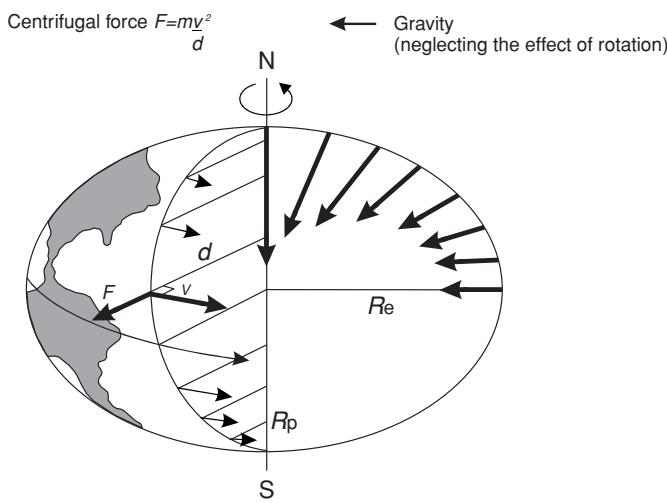


**Figure 2.3** Centrifugal acceleration and the variation of gravity with latitude  $\varphi$  (not to scale).

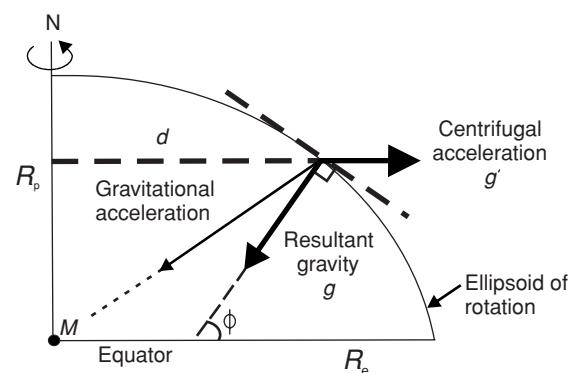


**Figure 2.4** Resultant of centrifugal acceleration ( $g'$ ) and the acceleration due to gravity ( $g$ ) (not to scale); the geographic (geodetic) latitude is given by  $\varphi$ . After Robinson and Coruh (1988), by permission.

**Box 2.3** General form of the International Gravity Formula

$$g_\varphi = g_0(1 + \alpha \sin^2 \varphi - \beta \sin^2 2\varphi)$$

wrongly as being due to geological causes. In 1980 a new Geodetic Reference System (GRS80) was developed (Moritz, 1980) that led to the World Geodetic System 1984 (WGS84) which is now used for satellite positioning. The latest equation for the calculation of  $g_\varphi$  adopted by the International Association of Geodesy (IAG) for Geodetic Reference System (Blakely, 1995; Sheriff, 2002) is shown in bold in Box 2.4.

## 2.2.4 Geological factors affecting density

Gravity surveying is sensitive to variations in rock density, so an appreciation of the factors that affect density will aid the interpretation of gravity data. Ranges of bulk densities for a selection of different material types are listed in Table 2.2 and shown graphically in Figure 2.5.

It should be emphasised that in gravity surveys, the determination of densities is based on rocks that are accessible either at the surface, where they may be weathered and/or dehydrated, or from boreholes, where they may have suffered from stress relaxation and be far more cracked than when *in situ*. Consequently, errors in the determination of densities are among the most significant in gravity surveying. This should be borne in mind when interpreting gravity anomalies so as not to over-interpret the data and go beyond what is geologically reasonable.

There are several crude ‘rules of thumb’ that can be used as general guides (Dampney, 1977; Telford *et al.*, 1990; Nettleton, 1971, 1976). Sedimentary rocks tend to be the least dense (average density about  $2.1 \pm 0.3 \text{ Mg/m}^3$ ). Within the three fundamental rock classifications there are crude trends and associations which are outlined in the next section. Commonly, units are quoted in terms of grams per cubic centimetre ( $\text{g/cm}^3$ ) but are herein referred to in the SI-derived units of  $\text{Mg/m}^3$ , which are numerically equivalent.

**Box 2.4** Standard formulae for the theoretical value of  $g$  at a given latitude  $\varphi$ 

$$g_\varphi(1930) = 9.78049(1 + 0.0052884 \sin^2 \varphi - 0.0000059 \sin^2 2\varphi) \text{ m/s}^2$$

$$g_\varphi(1967) = 9.78031846(1 + 0.005278895 \sin^2 \varphi + 0.0000023462 \sin^4 \varphi) \text{ m/s}^2$$

$$g_\varphi(1967) - g_\varphi(1930) = (136 \sin^2 \varphi - 172) \text{ m/s}^2 (\text{g.u.})$$

$$\begin{aligned} g_\varphi(1987) &= 9.7803267714 \\ &\times (1 + 0.00193185138639 \sin^2 \varphi) \\ &\times (1 - 0.00669437999013 \sin^2 \varphi) \text{ m/s}^2 \end{aligned}$$

**Table 2.2** Densities of common geological materials (modified from Telford *et al.*, 1990).

Material type	Density range ( $\text{Mg/m}^3$ )	Approximate average density ( $\text{Mg/m}^3$ )
<b>Sedimentary rocks</b>		
Alluvium	1.96–2.00	1.98
Clay	1.63–2.60	2.21
Gravel	1.70–2.40	2.00
Loess	1.40–1.93	1.64
Silt	1.80–2.20	1.93
Soil	1.20–2.40	1.92
Sand	1.70–2.30	2.00
Sandstone	1.61–2.76	2.35
Shale	1.77–3.20	2.40
Limestone	1.93–2.90	2.55
Dolomite	2.28–2.90	2.70
Chalk	1.53–2.60	2.01
Halite	2.10–2.60	2.22
Glacier ice	0.88–0.92	0.90
<b>Igneous rocks</b>		
Rhyolite	2.35–2.70	2.52
Granite	2.50–2.81	2.64
Andesite	2.40–2.80	2.61
Syenite	2.60–2.95	2.77
Basalt	2.70–3.30	2.99
Gabbro	2.70–3.50	3.03
<b>Metamorphic rocks</b>		
Schist	2.39–2.90	2.64
Gneiss	2.59–3.00	2.80
Phyllite	2.68–2.80	2.74
Slate	2.70–2.90	2.79
Granulite	2.52–2.73	2.65
Amphibolite	2.90–3.04	2.96
Eclogite	3.20–3.54	3.37

### 2.2.4.1 Sedimentary rocks

At least seven factors affect the density of sedimentary materials: composition, cementation, age and depth of burial, tectonic processes, porosity and pore-fluid type. Any or all of these may apply for a given rock mass. The degree to which each of these factors affects rock density is given in Table 2.3; but experience shows that, under normal circumstances, the density contrast between adjacent sedimentary strata is seldom greater than  $0.25 \text{ Mg/m}^3$ .

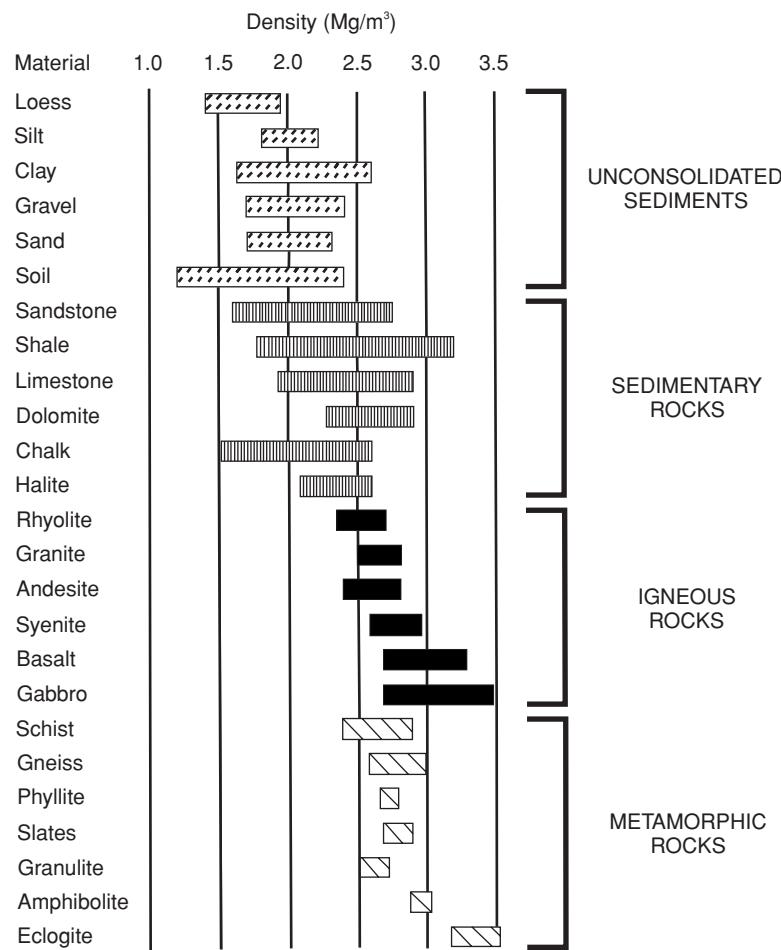


Figure 2.5 Variations in rock density for different rock types. Data from Telford et al. (1990).

Density varies depending on the material of which the rock is made, and the degree of consolidation. Four groups of materials are listed in order of increasing density in Table 2.4. Sediments that remain buried for a long time consolidate and lithify, resulting in reduced porosity and consequently an increased density.

In sandstones and limestones, densification is achieved not by volume change but by pore spaces becoming infilled by natural cement. In shales and clays, the dominant process is that of com-

paction and, ultimately, recrystallisation into minerals with greater densities.

#### 2.2.4.2 Igneous rocks

Igneous rocks tend to be denser than sedimentary rocks, although there is overlap. Density increases with decreasing silica content, so basic igneous rocks are denser than acidic ones. Similarly, plutonic rocks tend to be denser than their volcanic equivalents (see Table 2.5).

Table 2.3 The effects of different physical factors on density.

Factor	Approximate percentage change in density
Composition	35%
Cementation	10%
Age and depth of burial	25%
Tectonic processes	10%
Porosity and pore fluids	10%

Table 2.4 Approximate average densities of sedimentary rocks.

Material type	Approximate average density (Mg/m³)
Soils and alluvium	2.0
Shales and clays	2.3
Sandstones and conglomerates	2.4
Limestone and dolomite	2.6

**Table 2.5** Variation of density with silica content and crystal size for selected igneous rocks; density ranges and, in parentheses, average densities are given in Mg/m<sup>3</sup>. Data from Telford *et al.* (1990).

Crystal size	Silica content		
	Acid	Intermediate	Basic
Fine-grained (volcanic)	Rhyolite 2.35-2.70 (2.52)	Andesite 2.4-2.8 (2.61)	Basalt 2.7-3.3 (2.99)
Coarse-grained (plutonic)	Granite 2.5-2.81 (2.64)	Syenite 2.6-2.95 (2.77)	Gabbro 2.7-3.5 (3.03)

### 2.2.4.3 Metamorphic rocks

The density of metamorphic rocks tends to increase with decreasing acidity and with increasing grade of metamorphism. For example, schists may have lower densities than their gneissose equivalents. However, variations in density within metamorphic rocks tend to be far more erratic than in either sedimentary or igneous rocks and can vary considerably over very short distances.

### 2.2.4.4 Minerals and miscellaneous materials

As the gravity survey method is dependent upon contrast in densities, it is appropriate to highlight some materials with some commercial value for which the method can be used for exploration purposes. Gravity surveying becomes increasingly appropriate as an exploration tool for those ore materials with greatest densities. The densities of a selection of metallic and non-metallic minerals and of several other materials are listed in Table 2.6.

**Table 2.6** Densities of a selection of metallic and non-metallic minerals and some miscellaneous materials. Data from Telford *et al.* (1990).

Material type	Density range(Mg/m <sup>3</sup> )	Approximate average density (Mg/m <sup>3</sup> )
<i>Metallic minerals</i>		
<i>Oxides, carbonates</i>		
Manganite	4.2-4.4	4.32
Chromite	4.2-4.6	4.36
Magnetite	4.9-5.2	5.12
Haematite	4.9-5.3	5.18
Cuprite	5.7-6.15	5.92
Cassiterite	6.8-7.1	6.92
Wolframite	7.1-7.5	7.32
Uraninite	8.0-9.97	9.17
Copper	No data	8.7
Silver	No data	10.5
Gold	15.6-19.4	17.0
<i>Sulphides</i>		
Malachite	3.9-4.03	4.0
Stannite	4.3-4.52	4.4
Pyrrhotite	4.5-4.8	4.65
Molybdenite	4.4-4.8	4.7
Pyrite	4.9-5.2	5.0
Cobaltite	5.8-6.3	6.1
Galena	7.4-7.6	7.5
Cinnebar	8.0-8.2	8.1
<i>Non-metallic minerals</i>		
Gypsum	2.2-2.6	2.35
Bauxite	2.3-2.55	2.45
Kaolinite	2.2-2.63	2.53
Baryte	4.3-4.7	4.47
<i>Miscellaneous materials</i>		
Snow	0.05-0.88	No data
Petroleum	0.6-0.9	No data
Lignite	1.1-1.25	1.19
Anthracite	1.34-1.8	1.50
Concrete	1.6-3.2	No data
Asphalt	2.5-2.6	No data

## 2.3 Measurement of gravity

### 2.3.1 Absolute gravity

Determination of the acceleration due to gravity in absolute terms requires very careful experimental procedures and is normally only undertaken under laboratory conditions. Two methods of measurement are used, namely the falling body (Figure 2.6) and swinging pendulum methods. However, it is the more easily measured relative variations in gravity that are of interest and value to explorationists. More detailed descriptions of how absolute gravity is measured are given by Garland (1965) and Nettleton (1976). A popular account of gravity and its possible non-Newtonian behaviour has been given by Boslough (1989); see also Parker and Zumberge (1989).

In the late nineteenth century, F.R. Helmut established the Vienna Gravity System in Austria based on pendulum measurements with an estimated relative accuracy of  $\pm 10$  mGal. By 1909 this system was replaced by the Potsdam (East Germany) Gravity System, with a relative accuracy of  $\pm 3$  mGal, and corrected the Vienna System by  $-16$  mGal. By the 1960s, it was recognised that the Potsdam datum

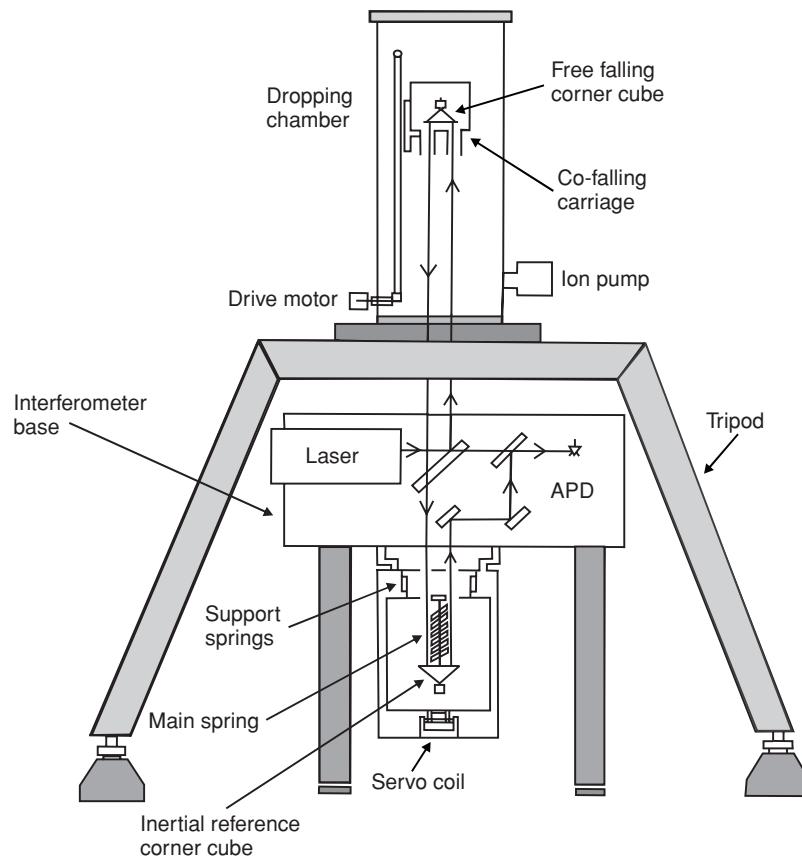


**Figure 2.6** Schematic through an absolute gravity meter (from National Oceanic and Atmospheric Administration, USA).

was off by about  $-14$  mGal, but this is still the datum used internationally. Absolute values of gravity have also been determined at other locations such as the Smithsonian Museum, Washington, DC, USA, the National Bureau of Standards at Gaithersburg, USA, the National Physical Laboratory at Teddington, England, and Universidad Nacionale de Colombia, Bogata, Colombia, among others. In the late 1950s and 1960s a series of measurements of absolute gravity worldwide was integrated and became known as the *International Gravity Standardisation Net 1971* (IGSN 71) (Morelli, 1971) and was established in 1963 by Woppard and Rose (1963). About 1900 worldwide sites were in this network, where each site had an estimated standard error of less than  $\pm 50$   $\mu$ Gal, with a correction of  $-14$  mGal at the Potsdam site. It is thus possible to tie in any regional gravity survey to absolute values by reference to the IGSN 71 and form a primary network of gravity stations.

One of the benefits of portable absolute gravity meters is that they have been used to measure the rate of land rebound in the continental interior of North America far from the ocean due to the delayed response to the removal of the Laurentide ice sheet. A project by the Geological Survey of Canada (assisted by the Geodetic Survey) and the USA National Oceanic and Atmospheric Administration (NOAA) has involved measuring absolute gravity at Churchill, Manitoba, Canada, and International Falls, Minnesota, USA. The data up to 1999 reveal a decrease in gravity at a rate of  $2.1 \mu\text{Gal}/\text{year}$  at Churchill and  $0.9 \mu\text{Gal}/\text{year}$  at International Falls, which equate to a land uplift of  $14 \text{ mm/year}$  and  $6 \text{ mm/year}$  at the

respective locations. For further details, see the Geological Survey of Canada website.

Continuing developments in instrumentation is enabling absolute gravity meters to become increasingly portable. Indeed, in remote areas where repeat occupation of base stations to calibrate surveys is both time-consuming and physically difficult, the use of a portable absolute gravity meter becomes an attractive option, especially in time-lapse gravity monitoring of active volcanoes (Battaglia *et al.*, 2008), for example. There may come a time when the use of portable absolute gravity meters replaces that of relative gravity meters for some applications.

### 2.3.2 Relative gravity

In gravity exploration it is not normally necessary to determine the absolute value of gravity, but rather it is the relative variation that is measured. A base station (which can be related to the IGSN 71) is selected and a secondary network of gravity stations is established. All gravity data acquired at stations occupied during the survey are reduced relative to the base station. If there is no need for absolute values of  $g$  to be determined, the value of gravity at a local base station is arbitrarily designated as zero. Details of the data reduction procedure are given in Section 2.5.

The spacing of gravity stations is critical to the subsequent interpretation of the data. In regional surveys, stations may be located with a density of  $2\text{--}3$  per  $\text{km}^2$ , whereas in exploration for

hydrocarbons, the station density may be increased to 8–10 per km<sup>2</sup>. In localised surveys where high resolution of shallow features is required, gravity stations may be spaced on a grid with sides of length 5–50 m. In micro-gravity work, the station spacing can be as small as 0.5 m.

For a gravity survey to achieve an accuracy of  $\pm 0.1$  mGal, the latitudinal position of the gravimeter must be known to within  $\pm 10$  m and the elevation to within  $\pm 10$  mm. Furthermore, in conjunction with multiple gravity readings and precision data reduction, gravity data can be obtained to within  $\pm 1 \mu\text{Gal}$ . The most significant causes of error in gravity surveys on land are uncertainties in station elevations. At sea, water depths are measured easily by using high-precision echo sounders. Positions are determined increasingly by satellite navigation; and in particular, the advent of the Global Positioning System (GPS) (Bullock, 1988), with its compact hardware and fast response time, is resulting in GPS position-fixing becoming more precise. This is particularly true with reference to airborne gravity measurements.

#### Box 2.6 Differences in gravitational acceleration

$$\text{Gravity difference} = -2 \times \text{gravity} \times \frac{\text{difference in periods}}{\text{period}_1}$$

$$\delta g = -2g \frac{(T_2 - T_1)}{T_1}$$

it was used in exploration from 1915 to the late 1940s (Bell and Hansen, 1998). The method, which measures variations in only the horizontal component of gravity due to terrain and not vertical gravity, is capable of very great sensitivity (to 0.001 mGal) but is awkward and very slow to use in the field. The method is described in more detail by Telford *et al.* (1990). It has been suggested that a double torsion balance using balance beam designs could be used on moving platforms (Speake *et al.*, 2001).

Since about the early 1930s, variations in relative gravity have been measured using gravity meters (gravimeters), firstly stable (static) and more recently unstable (astatic) types. Practical aspects of how to use such instruments have been detailed by Milsom (2003). Gravimeters are sophisticated spring balances from which a constant mass is suspended (Figure 2.8). The weight of the mass is the product of the mass and the acceleration due to gravity. The greater the weight acting on the spring, the more the spring is stretched. The amount of extension ( $\delta l$ ) of the spring is proportional to the extending force, i.e. the excess weight of the mass ( $\delta g$ ). (Remember that weight equals mass times acceleration due to gravity.) The constant of proportionality is the elastic spring constant  $\kappa$ . This relationship is known as Hooke's Law (Box 2.7).

As the mass is constant, variations in weight are caused by changes in gravity ( $\delta g$ ). By measuring the extension of the spring ( $\delta l$ ), differences in gravity can then be determined. As the variations in  $g$  are very small (1 part in  $10^8$ ) the extension of any spring will

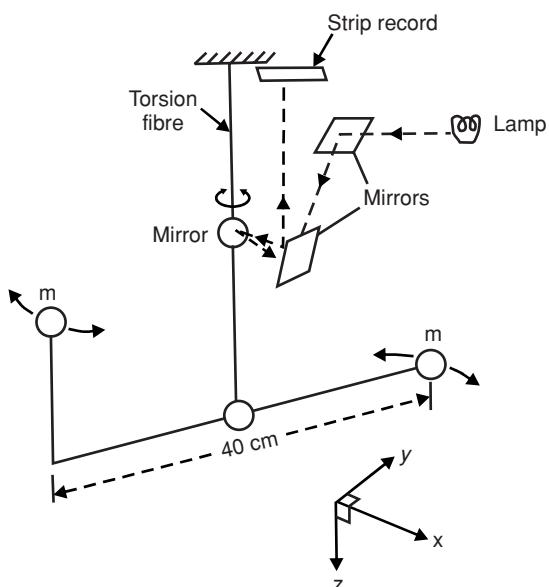


Figure 2.7 Schematic of a torsion balance.

## 2.4 Gravity meters

No single instrument is capable of meeting all the requirements of every survey, so there are a variety of devices that serve different purposes. In 1749, Pierre Bouguer found that gravity could be measured using a swinging pendulum. By the nineteenth century, the pendulum was in common use to measure relative variations in gravity. The principle of operation is simple. Gravity is inversely proportional to the square of the period of oscillation ( $T$ ) and directly proportional to the length of the pendulum ( $L$ ) (Box 2.5). If the same pendulum is swung under identical conditions at two locations where the values of accelerations due to gravity are  $g_1$  and  $g_2$ , then the ratio of the two values of  $g$  is the same as the ratio of the two corresponding periods of oscillation  $T_1$  and  $T_2$ .

Furthermore, the magnitude of the difference in acceleration due to gravity ( $\delta g$ ) between the two locations is (to the first order) equal to the product of gravity and twice the difference in periods ( $T_2 - T_1$ ) divided by the first period (Box 2.6). This method is accurate to about 1 mGal if the periods are measured over at least half an hour. Portable systems were used in exploration for hydrocarbons in the 1930s.

Another method of determining relative gravity is that of the torsion balance (Figure 2.7). English physicist Henry Cavendish devised this system to measure the gravitational constant in 1791. The method was developed for geodetic purposes in 1880 by a Hungarian physicist, Baron Roland von Eötvös. After further modification

#### Box 2.5 Acceleration due to gravity from pendulum measurements

$$\text{Gravity} = \text{constant} \times \text{pendulum length}/\text{period}^2 \quad g = 4\pi^2 L/T^2$$

$$\frac{(\text{Period}_1)^2}{(\text{Period}_2)^2} = \frac{\text{gravity}_2}{\text{gravity}_1} \quad \frac{T_2^2}{T_1^2} = \frac{g_2}{g_1}$$

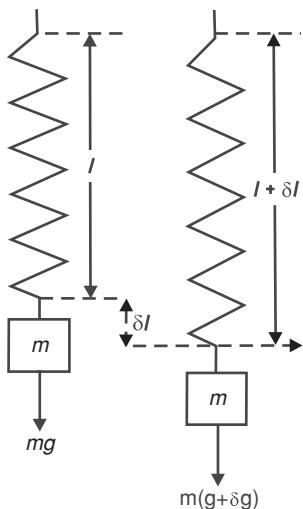


**Figure 2.8** Extension ( $\delta l$ ) of a spring due to additional gravitational pull ( $\delta g$ ).

also be extremely tiny. For a spring 30 cm long, changes in length of the order of  $3 \times 10^{-8}$  m (30 nanometres) have to be measured. Such small distances are even smaller than the wavelength of light (380–780 nm). Consequently, gravimeters use some form of system to amplify the movement so that it can be measured accurately.

### 2.4.1 Stable (static) gravimeters

Stable gravimeters (Figure 2.9), which were developed in the 1930s, are less sensitive than their more modern cousins, the unstable gravimeters, which have largely superseded them. The stable gravimeter consists of a mass at the end of a beam which is pivoted on a fulcrum and balanced by a tensioned spring at the other end. Changes in gravity affect the weight of the mass which is counter-balanced by the restoring action of the spring. Different configurations of stable gravimeters are shown in Figure 2.10 and are discussed in more detail by Garland (1965), Nettleton (1976), Telford *et al.* (1990) and Parasnis (1986). A brief description of three stable gravimeters is given below.

#### 2.4.1.1 Askania

A beam with a mass at one end is pivoted on a main spring S (Figure 2.10A). Changes in gravity cause the beam to tilt, so producing a deflection in a beam of light which is reflected off a mirror placed on the mass. A photoelectric cell, the output of which is displayed on a galvanometer, measures the displacement of the light beam.

#### Box 2.7 Hooke's Law

$$\text{Extension to spring} = \text{mass} \times \frac{\text{change in gravity}}{\text{spring constant}} \quad \delta l = \frac{m\delta g}{\kappa}$$

$$\text{Change in gravity} = \text{constant} \times \text{extension/mass} \quad \delta g = \frac{\kappa\delta l}{m}$$

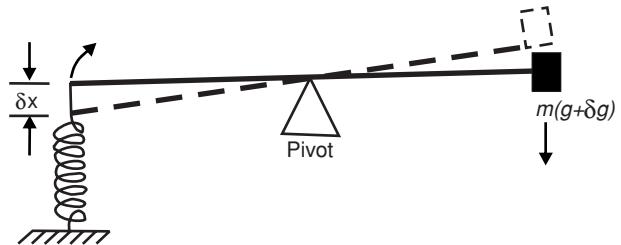


**Figure 2.9** Basic principle of operation of a stable gravimeter.

An auxiliary spring (AS) is re-tensioned using a micrometer to restore the mass to its rest position, which is indicated when the galvanometer reading is returned to zero (nulled).

#### 2.4.1.2 Boliden

The Boliden gravimeter uses the principle that the capacitance of a parallel-plate capacitor changes with the separation of the plates (Figure 2.10B). The mass has the form of a bobbin with a plate at each end and is suspended by two springs between two other capacitor plates. With a change in gravity, the mass moves relative to the fixed plates, changing the capacitance between the upper plates; this movement can be detected easily using a tuned circuit. The lower plates are connected to a d.c. supply which supports the bobbin mass by electrostatic repulsion. With a change in gravity and the consequent displacement of the bobbin relative to the fixed plates, the original or a reference position can be obtained by changing the direct voltage between the lower pair of plates. The overall sensitivity is about 1 g.u. (0.1 mGal). A modern version has been produced by Scintrex (Model CG-3), which operates on a similar principle (see Figure 2.10C), with a standard resolution of 1  $\mu$ Gal. Any displacement of the mass due to a change in gravity is detected by a capacitor transducer and activates a feedback circuit. The mass is returned to its null position by the application of a direct feedback voltage (which is proportional to the change in gravity) to the plates of the capacitor, which changes the electrostatic force between the plates and the mass (Robinson and Coruh, 1988).

#### 2.4.1.3 Gulf (Hoyt)

The Gulf gravimeter comprises a coiled helical ribbon spring which rotates as it changes length (Figure 2.10D). The rotation of the free end of the spring is much larger than the change in length and so is more easily measured. The range of measurement is quite small, being only 300 g.u. (30 mGal), although this can be overcome to some extent by re-tensioning the spring, and the accuracy of measurement is to within 0.2–0.5 g.u. (0.02–0.05 mGal).

### 2.4.2 Unstable (astatic) gravimeters

Since the 1930s, unstable gravimeters have been used far more extensively than their stable counterparts. In a stable device, once the system has been disturbed it will return to its original position, whereas an unstable device will move further away from its original position.

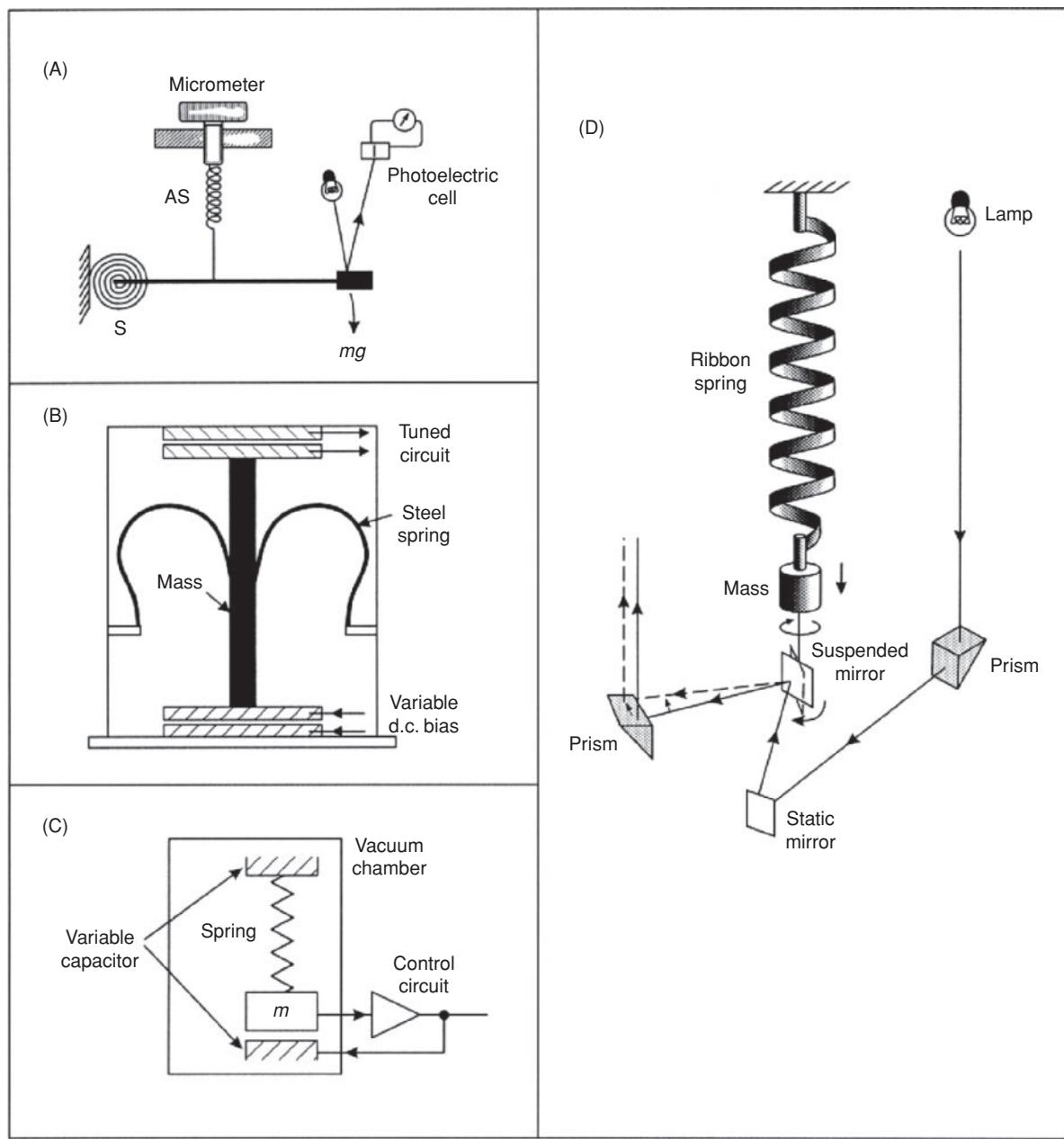


**Figure 2.10** Types of stable gravimeter: (A) Askani; (B) Boliden; (C) Scintrex CG-3; and (D) Gulf (Hoyt). After Garland (1965), Telford et al. (1990), and Robinson and Coruh (1988), by permission.

For example, if a pencil lying flat on a table is lifted at one end and then allowed to drop, the pencil will return to being flat on the table. However, if the pencil starts by being balanced on its end, once disturbed, it will fall over; that is, it becomes unstable, rather than returning to its rest position. The main point of the instability is to exaggerate any movement, so making it easier to measure, and it is this principle upon which the unstable gravimeter is based.

Various models of gravimeter use different devices to achieve the instability. The principle of an astatic gravimeter is shown in Figure 2.11. An almost horizontal beam hinged at one end supports a mass at the other. The beam is attached to a main spring which is connected at its upper end to a support above the hinge. The spring

attempts to pull the beam up anticlockwise by its turning moment, which is equal to the restoring force in the spring multiplied by the perpendicular distance from the hinge ( $d$ ). This turning moment is balanced by the gravitational turning moment which attempts to rotate the beam in a clockwise manner about the hinge and is equal to the weight of the mass ( $mg$ ) times the length of the beam ( $I$ ) multiplied by the cosine of the angle of the beam from the horizontal ( $\theta$ ) (i.e.  $mgl \cos \theta$ ). If gravity changes, the beam will move in response but will be maintained in its new position because the main spring is a ‘zero-length’ spring. One virtue of such a spring is that it is pre-tensioned during manufacture so that the tension in the spring is proportional to its length. This means that if all forces

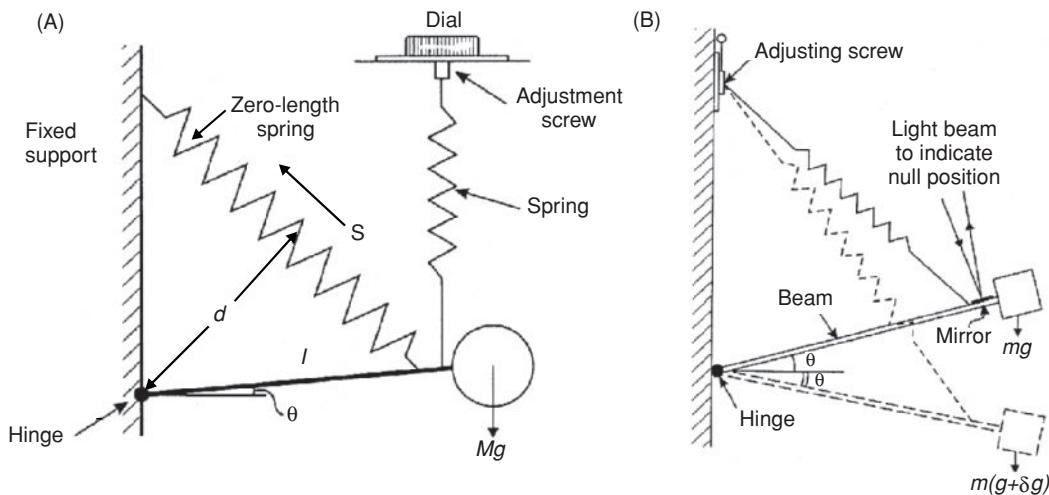


**Figure 2.11** (A) Principle of operation of an astatic gravimeter, and (B) schematic of a LaCoste & Romberg gravimeter (after Kearey and Brooks, 1991, by permission).

were removed from the spring it would collapse to zero length, something which is impossible in practice. Another virtue of the zero-length spring is that it results in an instrument which is linear and very responsive over a wide range of gravity values. Astatic gravimeters do not measure the movement of the mass in terms of changes in gravity, but require the displaced mass to be restored to a null position by the use of a micrometer. The micrometer reading is multiplied by an instrumental calibration factor to give values of gravity, normally to an accuracy within 0.1 g.u. (0.01 mGal) and in some specialist devices to within 0.01 g.u. (0.001 mGal = 1  $\mu$ Gal).

#### 2.4.2.1 Thyssen

Although obsolete, this gravimeter demonstrates the instability concept extremely well and is included for this reason. An extra mass is placed above a balanced beam (Figure 2.12) so producing the instability condition. If gravity increases, the beam tilts to the right and the movement of the extra mass enhances the clockwise rotation about the pivot, and conversely for a reduction in gravity. When used, this type of gravimeter had a sensitivity of about 2.5 g.u. (0.25 mGal).

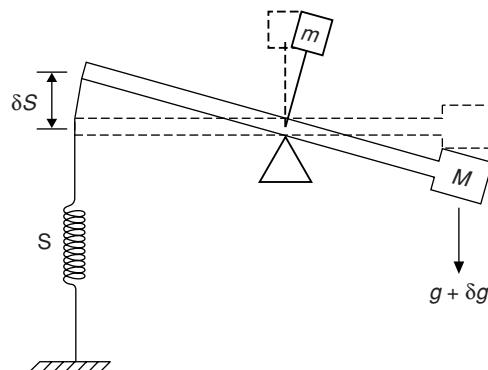


**Figure 2.12** Schematic of a Thyssen gravimeter.

#### 2.4.2.2 LaCoste-Romberg

This device is a development of LaCoste's long-period seismograph (LaCoste, 1934) and is illustrated in Figures 2.11B and 2.13A. The spring is made of metal with a high thermal conductivity but cannot be insulated totally to eradicate thermal effects, and so has to be housed permanently in an enclosed container in which a stable temperature is maintained to within 0.02°C by a thermostat element. The null point is obtained by the observer viewing a scale through an eyepiece onto which a beam of light is reflected from the beam when it is in its rest position. In order to restore the position of the beam, the operator rotates a micrometer gauge on the outer casing which turns a screw to adjust the beam position. The long length of the screw means that the gravimeter can be used worldwide without having to undergo any resets, which is a major advantage over other makes for surveys where this is important. When this type of gravimeter was manufactured in the 1930s it weighed a massive 30 kg, but modern technology has made it possible for the weight to be reduced to only about 9 kg, including the battery required to maintain the heating coils. The springs can be clamped and so the gravimeter is more easily transportable than other makes and also less sensitive to vibration. It is possible for some models of LaCoste-Romberg gravimeters (e.g. Graviton-EG with Aliod 100x) to measure to 0.1  $\mu$ Gal with a repeatability of 3  $\mu$ Gal; a similar performance can be achieved using a Scintrex CG-5. The LaCoste & Romberg Model G gravimeter has been further developed to achieve a system resolution of 0.1  $\mu$ Gal and a repeatability of 1  $\mu$ Gal (Super-G Gravity System). For most land-based micro-gravity surveys, a station repeatability of 3–5  $\mu$ Gal is readily achievable. It has been noted (Ander *et al.*, 1999) that proof mass within the instrument can change over the time-scale of a regional gravity survey. Temporal proof-mass variations can generate instrumental errors (*tares*) up to several tens of  $\mu$ Gal resulting from dust specks or tiny blobs (0.1  $\mu$ g) of oil transferred from the tips of the clamping pins around the proof mass during the clamping-unclamping process.

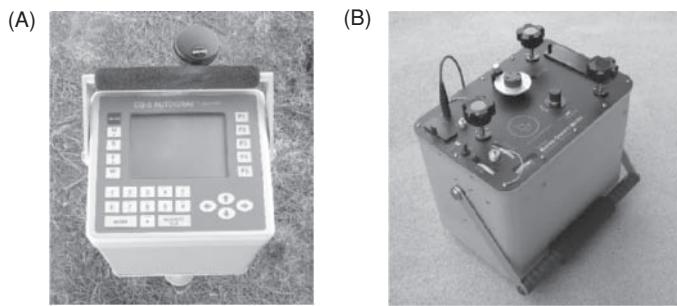


**Figure 2.13** (A) A LaCoste & Romberg CG-5 gravimeter and (B) a Burris gravimeter. [C]

### 2.4.2.3 Burris

A variant on the zero-length spring concept is a gravity meter designed by Larry J. Burris and developed by ZLS Corporation since the early 1990s (Figure 2.13B). It uses UltraGrav™ control electronics developed by Herbert Valliant who also developed the increasingly industry-wide UltraSys™ control system for land, marine and airborne gravity meters (cf. Valliant, *et al.* 1985). The Burris gravity meter has a reading resolution of 1  $\mu\text{Gal}$ , a range of 7000 mGal and has an on-board levelling system.

### 2.4.2.4 Worden

Unlike the LaCoste-Romberg gravimeter, the Worden is made entirely of quartz glass springs, rods and fibres (Figure 2.14). The

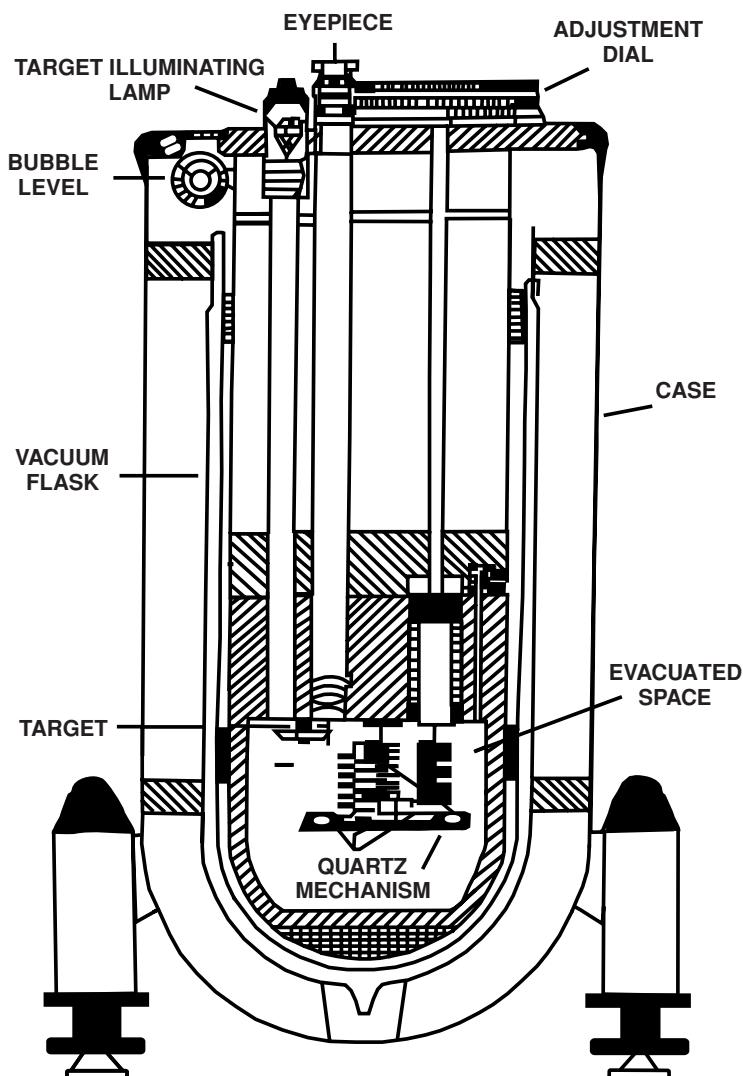
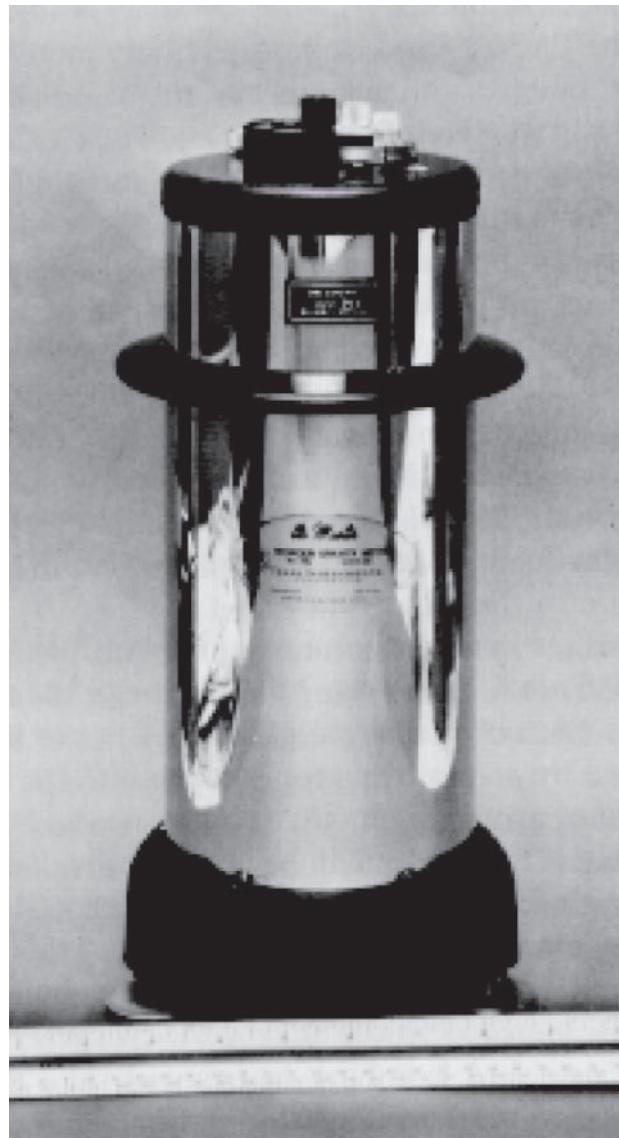


**Figure 2.14** (A) Picture of the exterior of and (B) a cross-section through a Worden gravimeter (Texas Instruments Ltd). From Dunning (1970), by permission.

**Box 2.8 Determination of  $g$  using a vibrating string**

$$\text{Gravity} = \frac{4 \times \text{string length}^2 \times \text{frequency}^2 \times \text{string mass}}{\text{suspended mass}}$$

$$g = \frac{4L^2 f^2 m_s}{M}$$

quartz construction makes it much easier to reduce thermal effects. Indeed, the whole assembly is housed in a glass vacuum flask and some models have an electrical thermostat. As the spring cannot be clamped, the Worden gravimeter is sensitive to vibration and has to be transported extremely carefully. The range of the instrument is about 20,000 g.u. (2000 mGal) with an accuracy to within 0.1–0.2 g.u. (0.01–0.02 mGal). However, quartz gravimeters such as the Worden can be quite difficult for inexperienced operators to read and a realistic accuracy may be more like 1 g.u. (0.1 mGal). The Worden gravimeter has two auxiliary springs, one for coarse and the other for fine adjustments.

#### 2.4.2.5 Vibrating string

The earliest vibrating string gravimeter was developed in the 1940s and consisted of a central element of flat beryllium-copper ribbon about 50 mm long, suspended in the field of a permanent magnet, with a 65 g mass at its lower end (Gilbert, 1949). More modern instruments have been based on one, two or three strings (Jones, 1999). If a mass is suspended on a fibre which is forced to oscillate by an a.c. circuit, then the frequency of vibration, which can be measured electronically, will vary with changes in gravity. For a fibre of length  $L$ , and mass per unit length  $m_s$ , from which a mass  $M$  is suspended, by measuring the frequency of vibration ( $f$ ), gravity can be determined (Box 2.8). However, the technology is not sufficiently developed to provide the same resolution and accuracy as other gravimeters, but it does give the impression that even more compact and lightweight gravimeters may be forthcoming in the future. Vibrating string gravimeters have tended to be used on shipborne platforms in marine gravity surveys where gravity can be measured to an accuracy of better than 1 mGal in moderate sea conditions. However, such instruments are subject to erratic drift. Such instruments are likely to be superseded by Full Tensor Gravity Gradiometers (TGFs) (see Section 2.4.3) in marine gravity surveys.

#### 2.4.3 Marine and airborne gravity systems

Prior to around 1960, marine gravity surveys were undertaken in submarines (Harrison *et al.*, 1966) largely due to excessive accelerations of surface vessels arising from rough sea states. When stabilised platforms and highly-damped sensors were introduced (LaCoste, 1967), submarine-based marine gravity surveys ceased as surface surveys proved to be cheaper and easier logically. In relatively shallow water, surveys have been undertaken using a land gravimeter deployed in a waterproof housing that is lowered overboard to the seabed and the instrument operated and read remotely. This

requires the instrument to be placed on the seabed for each station at which measurements are to be made, and thus the procedure is extremely slow. An adaptation of this method is to use a marine gravimeter, such as the LaCoste-Romberg Sea Gravity Meter, where the instrument is connected to the mother ship via a coaxial cable which carries the gravimeter signals to the ship (see e.g. Hildebrand *et al.*, 1990; Stevenson *et al.*, 1994). This still required the marine gravimeter to be lowered to the sea bed for each measurement. Further complications with seabed measurements included the difficulty in determining local terrain corrections associated with seabed topography. A further adaptation was developed by Zumberge *et al.* (1997) where an adapted LaCoste & Romberg Model S marine gravimeter was deployed within a spherical pressure housing and mounted on a submersible platform that could be towed just above the seabed at a speed of 0.5–1.0 m/s (1–2 knots), thereby increasing the speed with which measurements could be acquired (Figure 2.15) relative to seabed surveys. Other methods have also been developed to deploy high-resolution gravity meters to the seafloor, such as the ROVDOG (Remotely Operated Vehicle-deployed Deep Ocean Gravimeter), which was based on a Scintrex SG-3 land gravimeter that was installed on gimbals within a watertight housing capable of withstanding water pressures rated to 4500 m depth (Sasagawa *et al.*, 2003). Standard deviation of measurements achieved was 19 µGal and a positional accuracy (water-pressure derived) of 0.78 m. Since then an 11-day quiet series standard deviation of 1.1 µGal has been achieved with this system (Sasagawa *et al.*, 2008).

A key development of marine gravimeters has been the muting the accelerations due to ship heave and yaw by using forced-feedback systems, rather than by isolating the gravimeter from those accelerations by towing the instrument behind the ship using a decoupling interface or by placing the instrument on the seabed. One such instrument (the BGM-3) is manufactured by Bell Aerospace Company, which incorporated in its sensor a feedback system to counteract the displacement of a weight subject to an acceleration (Bell and Watts, 1986) and is not subject to cross-coupling of the platform's horizontal and vertical accelerations. The key element of the instrument (Figure 2.16) comprises an accelerometer proof-mass around which a coil is wrapped and which is constrained to move vertically between two permanent magnets. At equilibrium the downward gravitational force on the mass is balanced by an upward electromagnetic force induced by the coil around the mass. When the mass moves out of equilibrium, such as in response to a change in gravity or wave movement, its motion is detected by a servo loop that regulates the currents in the coil, changing its magnetic moment, to return the mass to its balanced position. The changes in the current in the coil are proportional to the change in the vertical acceleration, which is a combination of the vertical acceleration acting upon the ship (or aircraft) and gravity. The effects of motion of the vessel on the accelerometer are removed by applying a weighted average filter to the output, which is then a measure of the local acceleration due to gravity.

The ZLS Dynamic Meter™ has recently been introduced commercially by Austin Exploration Inc. as a new airborne and shipborne gravity instrument. According to its manufacturer, it is designed to eliminate cross-coupling errors, frequent damper adjustments, and vibration sensitivity problems associated with

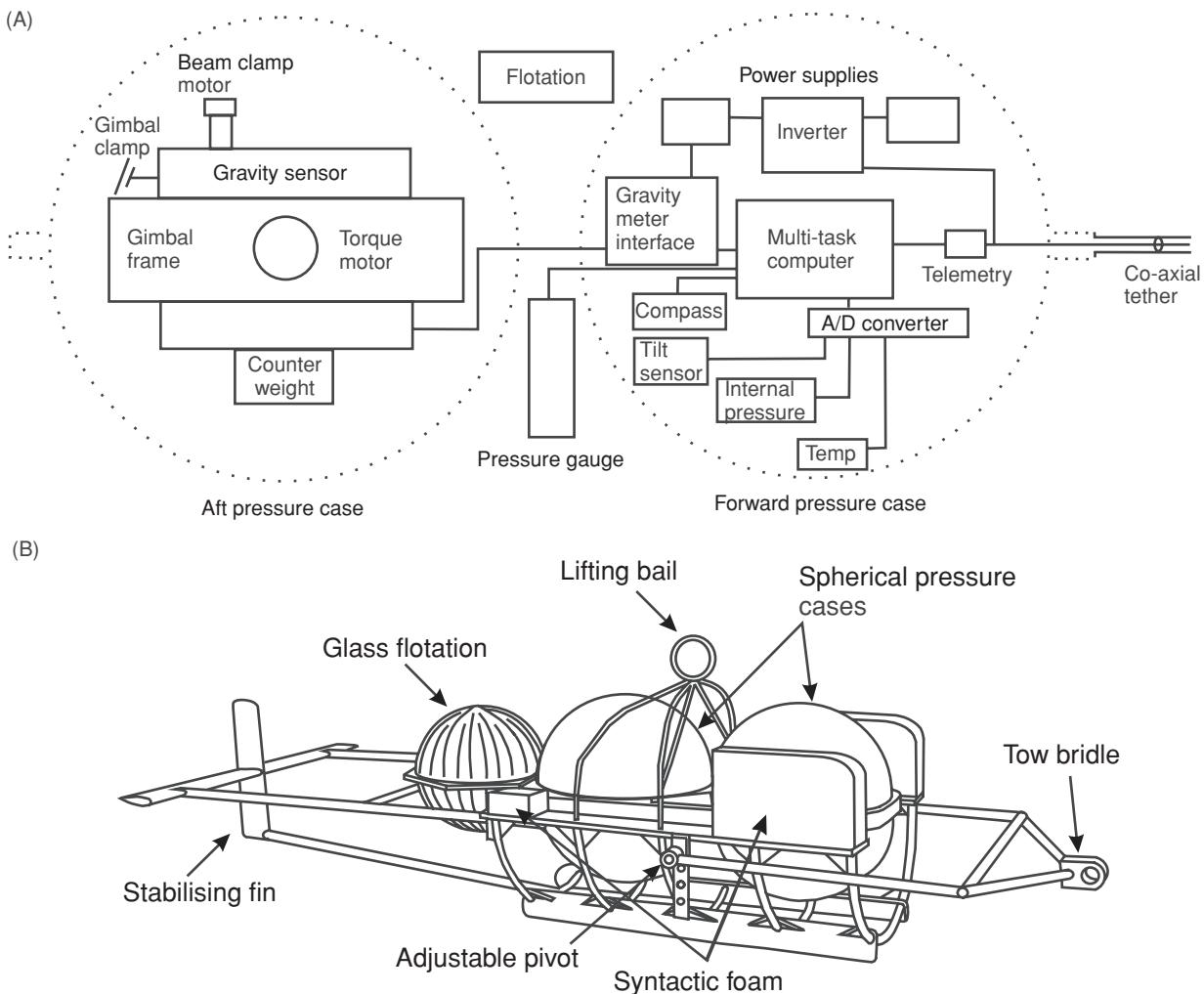


**Figure 2.15** (A) A block diagram of the towed gravity meter and (B) a schematic illustration showing the major exterior components. The gravity meter used is a modified LaCoste & Romberg Model S. After Zumberge *et al.* (1997), by permission.

beam-type gravity meters. Its accuracy at sea is typically less than 1 mGal and has a range of 7000 mGal, and for airborne systems the range is 10,000 mGal. Like many other systems it also utilises the UltraSys™ platform and sensor control functions.

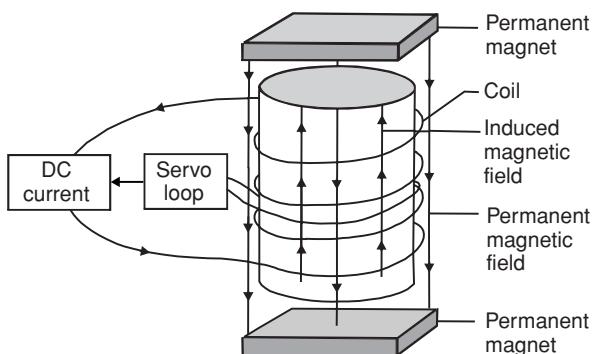


**Figure 2.16** The principle of operation of the accelerometer unit of the Bell marine gravimeter. After Bell and Watts (1986), by permission.

In the last ten years some military technology has been declassified for civilian purposes, enabling significant technological benefits to become available commercially. For example, a system developed by the USA government and Lockheed Martin Federal Systems as a stealth navigation system for Trident-class nuclear-powered submarines has been modified for use in exploration for hydrocarbons and minerals (Eaton, 2003). The instrument is a gravity gradiometer, typically weighing around 450 kg and costing several million dollars, and is usually mounted on the most stable part of an aircraft's interior.

The instrument comprises four pairs of opposing accelerometers mounted on a rotating disc (Figure 2.17). When airborne and in motion, the linear inertial acceleration is cancelled out. The gravity gradient is measured in the plane of the rotating disc and represents the difference between values measured by two opposing accelerometers. FALCON, the world's first airborne gradiometer, began commercial production in 1999 following a decade-long \$30 million investment programme by BHP Billiton and Lockheed Martin. The system is being flown under contract from BHP Billiton by Fugro.

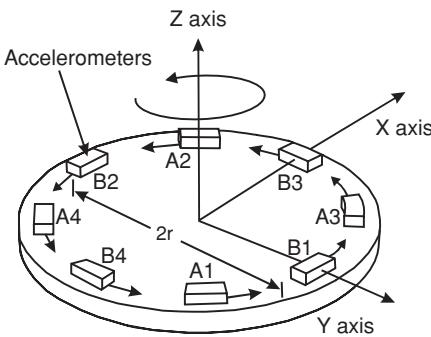


**Figure 2.17** Opposing pairs of accelerometers are mounted on a horizontal disc that rotates at a specified frequency. Another set of accelerometers (the B set) doubles the measured gradients. After Eaton (2003), by permission.

The Lockheed Martin gradiometer has also spawned another offspring to compete with the FALCON. In February 2003, Bell Geospace announced its commercialisation of its Air-FTG™ system which is based upon Bell Geospace's Full Tensor Gradient (3-D FTG) acquisition system. The 3-D FTG system measures three gravity vectors (in  $x$ ,  $y$  and  $z$  directions) and three tensors for each vector – each vector has three coordinate components ( $G_x$ ,  $G_y$  and  $G_z$ ; Figure 2.18). By measuring the rate of change of the three components of the gravity vector, the tensor gradient is obtained (Box 2.9). This produces nine measured components. However, of the nine, five gradients are independent and four are redundant. The  $x$ -direction measures east–west gradients, the  $y$ -direction north–south. The

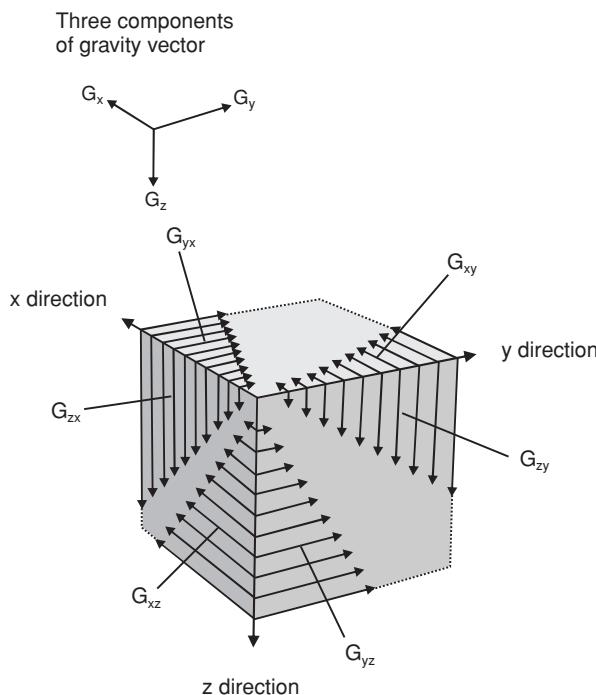


**Figure 2.18** Description of the relationship between gravity vectors and the tensor components. After Hammond and Murphy (2003), by permission.

#### Box 2.9 Tensor gravity gradients (see Figure 2.18)

A nine-component symmetric tensor that defines the rate of change of the three components of the gravity gradient is given by:

$$T_{i,j} = \begin{bmatrix} T_{xx} & T_{xy} & T_{xz} \\ T_{yx} & T_{yy} & T_{yz} \\ T_{zx} & T_{zy} & T_{zz} \end{bmatrix}$$

The independent gradients are shown in bold; the redundant tensor gradients are:

$$\begin{aligned} T_{xy} &= T_{yx} \\ T_{xz} &= T_{zx} \\ T_{yz} &= T_{zy} \\ T_{zz} &= -(T_{xx} + T_{yy}) \end{aligned}$$

(From Hammond and Murphy, 2003)

$z$ -direction is vertical and most closely represents geological structures. Bell's shipborne 3-D FTG system was first used in commercial surveys in 1999. Physically the acquisition system comprises three rotating disks (gravity gradiometer instruments, GGIs) each containing two pairs of orthogonally mounted accelerometers (Figure 2.19). Each GGI is rotated at a set frequency to avoid bias in the measurement in the direction of the primary components. The difference in the gravity field sensed by each pair of accelerometers is used to compensate for most of the turbulence experienced by the aircraft. This also helps to retain the high frequency signal that is essential to provide the high quality of data required for mineral exploration. The FTG system is normally positioned near to the centre of pitch, roll and yaw of the aircraft (currently a Cessna Grand Caravan 208B), thus minimising rotational accelerations. Survey flying heights as low as 80 m and line spacings in the range of 50 m to 2000 m are usual, depending upon the type of target and the style of survey being undertaken.

12 Accelerometers, 3 Disks

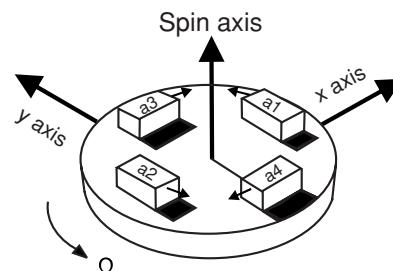


**Figure 2.19** Bell Geospace's 3-D FTG systems consists of three gravity gradiometer instruments (GGIs). Internal to each GGI is a rotating disk with four accelerometers. After Hammond and Murphy (2003), by permission.

The Lockheed Martin gradiometer system has also generated another new entry to the airborne gravity gradiometry arena in the form of a modified FTG system based upon a levitated superconducting proof mass. The principle of the system relies upon the fact that a superconducting proof mass can be levitated by passing currents through coils close to its surface in a module operated at  $-269^{\circ}\text{C}$ . The motion of the levitated mass can then be monitored and controlled without the complications of physical attachments required to constrain the motions of a physical spring. The advantage of this system is that it should have unprecedented sensitivity, resolution and stability, postulated by its developers to be almost an order of magnitude more sensitive than current systems. The Exploration Gravity Gradiometer (EGG), as it is known, entered into commercial service in the first quarter of 2006 operated by Fugro Airborne Surveys on behalf of its developers ARKex, Cambridge, UK. For more details of this system, see the paper by Lumley *et al.* (2008, accessible from [www.arkex.com](http://www.arkex.com)).

Airborne gravimetry has been used extensively since 1977, initiated by the Soviets (Aleshkova *et al.*, 2000), in investigating the subglacial environment in polar regions. During the 1990s more than 275,000 km of data were collected by USA researchers using a DHC-6 Twin Otter aircraft using either a Bell Aerospace BGM-3 marine gravimeter or a LaCoste & Romberg S-gravimeter modified by ZLS Corporation (Blankenship *et al.*, 2001). Similarly, European and Australian researchers (Jones *et al.*, 2002; McLean and Reitmayer, 2005) have used LaCoste & Romberg air/sea gravimeters and a ZLS Ultra-Sys LaCoste & Romberg air/sea gravimeter, respectively. In 2007 tests were undertaken to compare different airborne gravimeter systems with the potential of producing higher resolution data in polar regions whilst improving flight efficiency (Studinger *et al.*, 2008). Studinger and colleagues tested an AIRGrav system (Sander Geophysics Ltd) and a Canadian Micro Gravity (CMG) GT-1A system (based on Russian Federation technology) on a DHC-6 Twin Otter, flying both systems side by side.

The CMG GT-1A system comprises an airborne, single-sensor, vertical scalar gravimeter with a Schuler-tuned three-axis inertial platform (Gabell *et al.*, 2004). The Sanders AIRGrav system consisted of a three-axis stabilised inertial platform using three orthogonal accelerometers and two two-degrees-of-freedom gyroscopes (Sander *et al.*, 2004). It was found that both systems would allow broader potential applications for polar use compared with the previously used BGM-3 and LaCoste & Romberg gravimeters. Of the two instruments tested against each other, the AIRGrav system was found to have a lower noise level and greater accuracy and to be less sensitive to changing flight conditions than the GT-1A system.

## 2.5 Corrections to gravity observations

Gravimeters do not give direct measurements of gravity. Rather, a meter reading is taken which is then multiplied by an instrumental calibration factor to produce a value of observed gravity ( $g_{\text{obs}}$ ). Before the results of the survey can be interpreted in geological terms,

**Table 2.7** Corrections to gravity data.

Correction	Book sections
Instrument drift	2.5.1
Earth tides	2.5.2
Latitude	2.2.3 and 2.5.3
Elevation	
Free-air correction	2.5.4
Bouguer correction	2.5.5
Terrain	2.5.6
Buildings	2.5.7
Eötvös	2.5.8
Isostatic	2.5.9

these raw gravity data have to be corrected to a common datum, such as sea-level (geoid), in order to remove the effects of features that are only of indirect geological interest. The correction process is known as *gravity data reduction* or *reduction to the geoid*. The difference between the value of observed gravity ( $g_{\text{obs}}$ ) and that determined either from the International Gravity Formula/Geodetic Reference System for the same location, or relative to a local base station, is known as the *gravity anomaly* (cf. Chapin, 1996). For a discussion of the geodetic versus the geophysical perspectives of the gravity anomaly and further comments on the various corrections to gravity data, see Hackney and Featherstone (2003); the nature of the Bouguer anomaly has been discussed further by Vaníček *et al.* (2004). The various corrections that can be applied are listed in Table 2.7, with the sections of this book in which each one is discussed.

### 2.5.1 Instrumental drift

Gravimeter readings change (drift) with time as a result of elastic creep in the springs, producing an apparent change in gravity at a given station. The instrumental drift can be determined simply by repeating measurements at the same stations at different times of the day, typically every 1–2 hours. The differences between successive measurements at the same station are plotted to produce a *drift curve* (Figure 2.20). Observed gravity values from intervening stations can be corrected by subtracting the amount of drift from the observed gravity value. For example, in Figure 2.20 the value of gravity measured at an outlying station at 12.30 hours should be reduced by the amount of drift  $d$ . The range of drift of gravimeters is from a small fraction of one g.u. to about ten g.u. per hour. If the rate of drift is found to be irregular, return the instrument to the supplier – it is probably faulty!

### 2.5.2 Tides

Just as the water in the oceans responds to the gravitational pull of the Moon, and to a lesser extent of the Sun, so too does the solid

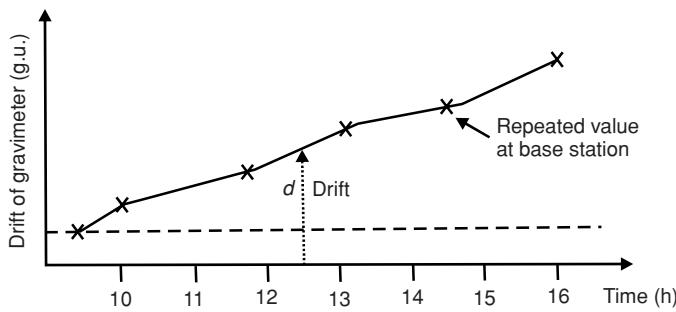


**Figure 2.20** An instrumental drift curve.

earth. Earth tides give rise to a change in gravity of up to three g.u. with a minimum period of about 12 hours. Repeated measurements at the same stations permit estimation of the necessary corrections for tidal effects over short intervals, in addition to determination of the instrumental drift for a gravimeter (Figure 2.21).

### 2.5.3 Latitude

The latitude correction is usually made by subtracting the theoretical gravity calculated using the International Gravity Formula ( $g_\varphi$ ) (Section 2.2.3) from the observed value ( $g_{\text{obs}}$ ). For small-scale surveys which extend over a total latitude range of less than one degree, and not tied into the absolute gravity network, a simpler correction for latitude can be made. A local base station is selected for which the horizontal gravity gradient ( $\delta g_L$ ) can be determined at a given degree of latitude ( $\varphi$ ) by the expression in Box 2.10.

Note that the correction is negative with distance northwards in the northern hemisphere or with distance southwards in the southern hemisphere. This is to compensate for the increase in the gravity field from the equator towards the poles. For a latitude of

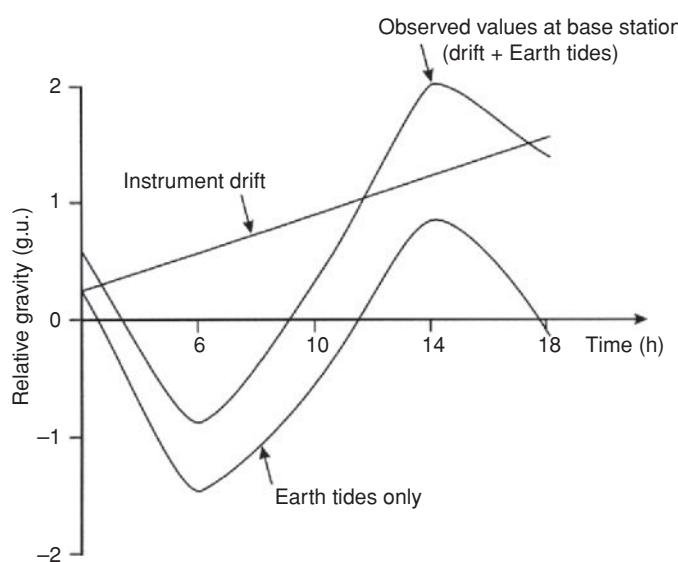


**Figure 2.21** Graph of the effects of Earth tides and instrumental drift on the acceleration due to gravity.

#### Box 2.10 Local latitude correction

$$\delta g_L = -8.108 \sin 2\varphi \text{ g.u. per km N}$$

51°N, the local latitude correction is about 8 g.u./km. For gravity surveys conducted with an accuracy of  $\pm 0.1$  g.u., the latitudinal position of the gravity station needs to be known to within  $\pm 10$  m, which is well within the capability of modern position-fixing. For micro-gravity surveys in engineering applications, position fixing must be considerably more accurate (i.e. to within  $\pm 0.1$  m).

### 2.5.4 Free-air correction

The basis of this correction is that it makes allowance for the reduction in magnitude of gravity with height above the geoid (see Figure 2.22A and Box 2.11), irrespective of the nature of the rock below. It is analogous to measuring gravity in the basket of a hot-air balloon in flight – hence the term free-air correction. The free-air correction is the difference between gravity measured at sea-level and at an elevation of  $h$  metres with no rock in between. A value of 3.086 g.u./m is accepted for most practical applications and is positive at elevations above sea-level, and negative below. The free-air

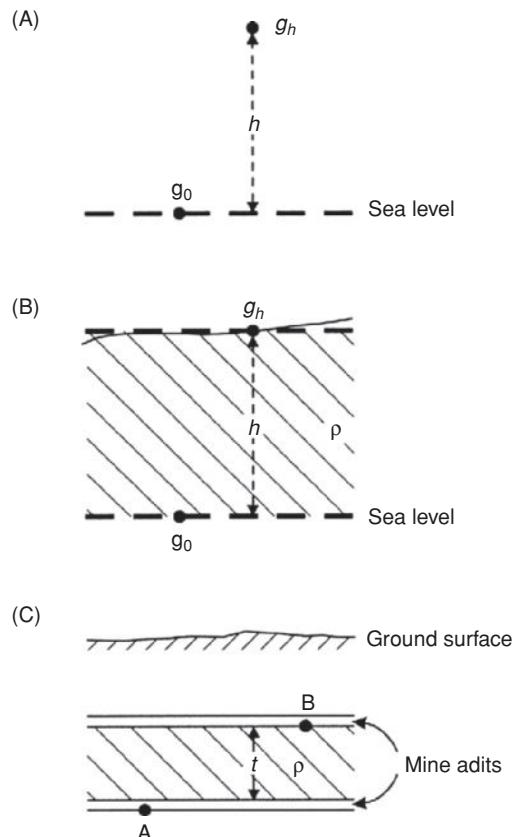


**Figure 2.22** Schematic showing (A) the free-air correction, (B) the Bouguer correction, and (C) the Bouguer correction for measurements made underground.

**Box 2.11 Free air correction (see also Figure 2.22)**

Taking the Earth to be a sphere (rather than an oblate spheroid) with its mass concentrated at its centre of mass, then the value of gravity at sea level is:

$$g_0 = GM/R^2.$$

The value of gravity at a station at an elevation of  $h$  metres above sea-level is:

$$g_h = GM/(R + h)^2 = \frac{GM}{R^2} \left( \frac{1 - 2h}{R} \dots \right).$$

The difference in gravity between sea-level and at  $h$  metres is the free-air correction:

$$\delta g_F = g_0 - g_h = \frac{2g_0h}{R}.$$

With  $g_0 = 9,817,855$  g.u.,  $R = 6,371,000$  m, and with  $h$  in metres,

$$\delta g_F = 3.082h \text{ g.u.}$$

Taking into account that the Earth is an oblate spheroid, rather than a sphere, the normally accepted value of the free-air correction is:

$$\delta g_F = 3.086h \text{ g.u.}$$

correction term varies slightly with latitude from 3.083 g.u./m at the equator to 3.088 g.u./m at the poles. With the normal measuring precision of modern gravimeters being around 0.1 g.u., elevations must be known to within 3–5 cm, and for high precision surveys, to within 1–2 cm.

The reduction in  $g$  with increasing height above the ground is important in airborne gravimetry. Anomalies detected by helicopter-mounted gravimeters will have decreased amplitudes and longer wavelengths compared with those obtained from land-based surveys. To compare land gravity survey data with airborne, it is necessary to correct for the free-air attenuation of the gravity anomaly by using *upward continuation*, which is discussed in Section 2.6.

The quantity calculated by applying both the latitude and the free-air corrections is called the *free-air anomaly* and is commonly used to display corrected gravity data for oceans and continental shelves (see, e.g., Talwani *et al.*, 1965).

## 2.5.5 Bouguer correction

Whereas the free-air correction compensates for the reduction in that part of gravity due only to increased distance from the centre of mass, the Bouguer correction ( $\delta g_B$ ) is used to account for the rock mass between the measuring station and sea-level (Figure 2.22B).

**Box 2.12 Bouguer correction**

Bouguer correction ( $\delta g_B$ ) =  $2\pi G\rho h = \beta\rho h$  (g.u.), where:

$$\beta = 2\pi G = 0.4192 \text{ g.u. m}^2 \text{ Mg}^{-1}$$

$$G = 6.67 \times 10^{-8} \text{ m}^3 \text{ Mg}^{-1} \text{ s}^{-2}.$$

Density ( $\rho$ ) is in  $\text{Mg m}^{-3}$  and height ( $h$ ) is in metres.

For marine surveys, the Bouguer correction is given by:

$$\delta g_B = \beta(\rho_r - \rho_w)h_w \text{ (g.u.)}$$

where  $\rho_r$  and  $\rho_w$  are the densities of rock and sea water respectively, and  $h_w$  is the water depth in metres.

The Bouguer correction calculates the extra gravitational pull exerted by a rock slab of thickness  $h$  metres and mean density  $\rho$  ( $\text{Mg/m}^3$ ) which results in measurements of gravity ( $g_{\text{obs}}$ ) being overestimated by an amount equal to  $0.4192\rho h$  g.u. (Box 2.12). The Bouguer correction should be subtracted from the observed gravity value for stations above sea-level. For an average rock density of  $2.65 \text{ Mg/m}^3$ , the Bouguer correction amounts to 1.12 g.u./m. For marine surveys, the Bouguer correction is slightly different in that the low density of seawater is effectively replaced by an equivalent thickness of rock of a specified density (Box 2.12).

A further development of this correction has to be made for gravity measurements made underground (Figure 2.22C). In this case, the Bouguer correction has to allow for the extra gravitational pull ( $= 0.4191\rho t$  g.u.) on Station A caused by the slab of thickness  $t$  metres between the two stations A and B, whereas the value of gravity at Station A is underestimated by the equal but upward attraction of the same slab. The difference in gravity between the two stations is twice the normal Bouguer correction ( $= 0.8384\rho t$  g.u.). Allowances also have to be made for underground machinery, mine layout and the variable density of local rocks, and this is sometimes referred to as the *Gallery correction* (Figure 2.23).

The Bouguer correction on land has to be modified by allowances for terrain roughness (see Section 2.5.6) in areas where there is a marked topographic change over a short distance, such as an escarpment or cliff. In such a situation the approximation of a semi-infinite horizontal slab of rock no longer holds true, and more detailed calculations are necessary (Parasnis, 1986: p. 72).

The free-air and Bouguer corrections are commonly combined into one *elevation correction* ( $\delta g_E$ ) to simplify data handling (Box 2.13). It should be noted that in some cases, the resulting gravity anomaly may be misleading and the combined calculation should be used judiciously. For a density of  $2.60 \text{ Mg/m}^3$ , the total elevation correction is 2 g.u./m, which requires elevations to be known to an accuracy within 5 cm if gravity readings are to be made to within 0.1 g.u.

One of the main problems with the Bouguer correction is knowing which density to use. For example, a difference of  $0.1 \text{ Mg/m}^3$  in density for a gravity measurement made at an elevation of 250 m will result in a discrepancy of more than 10 g.u. in the Bouguer

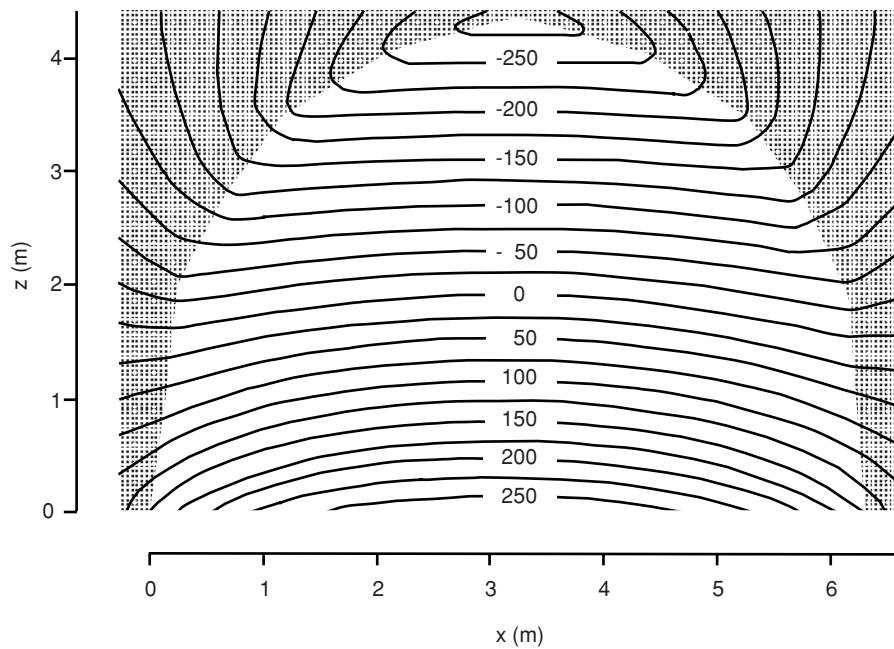


**Figure 2.23** Micro-isogals for a typical gallery in a deep coal mine; the contour interval is 25 µGal and the density of the host rock is 2.65 Mg/m<sup>3</sup>. From Casten and Gram (1989), by permission.

correction. In many cases, it may be possible to obtain an estimate of rock densities from appropriate surface samples, or from borehole samples, if available. Caution should be used in the latter case, as rock-core samples will relax mechanically, producing many cracks, and expanding slightly in response to the reduced pressure at the surface, giving rise to an underestimate of *in situ* density.

Nettleton (1939, 1940) found a very simple way of determining the appropriateness of the chosen density using a graphical method. Corrected gravity data should show no correlation with topography, as all such effects should have been removed through the data reduction process. If a range of densities is chosen and the resulting elevation corrections computed along one gravity profile, the density that shows least correlation with topography is taken as the ‘correct’ one (Figure 2.24). It is known, however, that this method becomes less accurate if there is any topographic expression due to dipping beds with a significant density contrast to those above and below. Examples of where this might occur are in association

with an inclined dense igneous intrusion, or in a marked structural feature with significant variations in density.

A generalised Nettleton method has been proposed by Rimbert *et al.* (1987) that allows for density to vary over a geographical area. The topographic data of an area are smoothed and reduced to produce a surface that lies just below the low topographic points on the survey, and which they refer to as the ‘regional topography’. The density between the ‘regional’ and the actual topography is considered as constant ( $\rho_0$ ) for a fixed radius around each station. The density below the ‘regional’ topography is taken as uniform throughout the area of the survey. The variations in density above the ‘regional’ topography are accounted for statistically but can be plotted in map form to demonstrate the areal variation in density which can be correlated independently with maps of the known geology. Rimbert *et al.* (1987) have achieved accuracies to within 3–4 g.u. with this method in an area in the south of France where the observed gravity anomalies ranged from 40 to 150 g.u.

Another method to calculate density is to plot a graph of the latitude-corrected gravity data from an area without marked gravity anomalies, against station elevation (Reeves and MacLeod, 1986). The resulting straight-line graph yields a gradient that is numerically equal to the elevation correction. Using the result in Box 2.16 and rearranging the equation to make density the subject of the equation, it is possible to solve and find a value for the density. Reeves and MacLeod used this method on data for a survey in Belgium, and produced a graphical elevation correction of 2.35 g.u./m which gave a density estimate of 1.74 Mg/m<sup>3</sup>, compared with 1.6 Mg/m<sup>3</sup> determined using the Nettleton method.

The danger with a graphical method – even if linear regression statistics are used to determine the gradient of the best straight-line fit through the data – is that a small difference in the graphical

#### Box 2.13 Elevation correction

Elevation correction ( $\delta g_E$ ) = (Free air – Bouguer) corrections:

$$\delta g_E = \delta g_F - \delta g_B.$$

Substituting in the terms  $\delta g_F = 3.086h$  and  $\delta g_B = 0.4192\rho h$ :

$$\delta g_E = (3.086 - 0.4192\rho)h(\text{g.u.})$$

where  $\rho$  is the average rock density in Mg/m<sup>3</sup>.

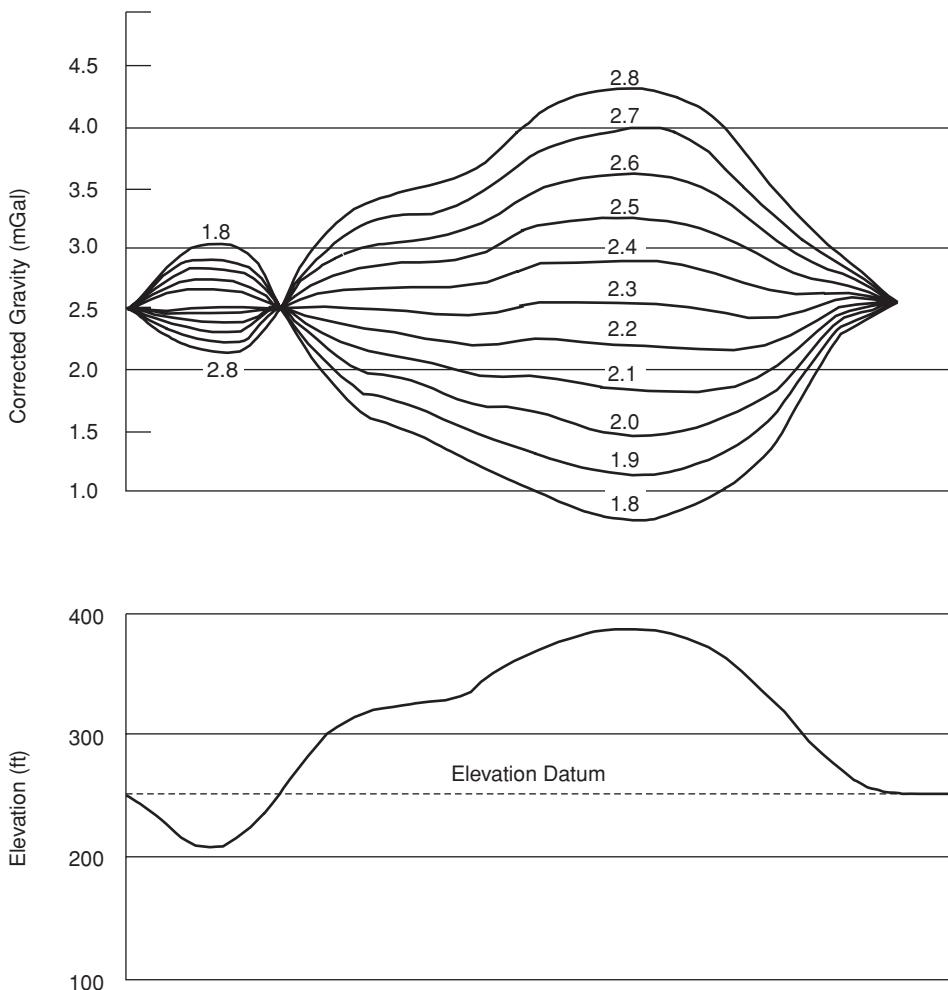


**Figure 2.24** The Nettleton method for determining the density of near-surface rock formations with the topography as shown. The most appropriate density is about  $2.3 \text{ Mg/m}^3$  (least correlation with the topography). Corrections are referred to a height of 76 m. From Dobrin (1976), by permission.

gradient can result in an unacceptably large density discrepancy, and this makes the method rather insensitive to small changes in density. For example, the data presented by Reeves and MacLeod, rather than showing a single trend with elevation, indicate two: data up to an elevation of 215 m yield a density of  $1.43 \text{ Mg/m}^3$  and the remaining data up to 280 m yield a density of  $1.79 \text{ Mg/m}^3$ , a difference of  $0.36 \text{ Mg/m}^3$ . Densities should be determined to better than  $0.1 \text{ Mg/m}^3$  if possible.

In underground gravity surveys, a similar method is employed (Hussein, 1983). The vertical gravity gradient (i.e.  $\delta g_E$ ) is obtained by measuring  $g$  at two or more elevations separated by only 1.5–3 m at the same location within an underground chamber. The density can then be calculated as described above. As the measurements of  $g$  are strictly controlled, the error in density can be minimised routinely to within  $0.08 \text{ Mg/m}^3$  (Casten and Gram, 1989).

Rock densities for depths below which it is not possible to sample can also be estimated using the relationship of density with P-wave velocities as described, for example, by Nafe and Drake (1963), Woppard (1950, 1959, 1975), Birch (1960, 1961), and Christensen and Fountain (1975).

## 2.5.6 Terrain correction

In flat countryside, the elevation correction (the combined free-air and Bouguer correction) is normally adequate to cope with slight topographic effects on the acceleration due to gravity. However, in areas where there are considerable variations in elevation, particularly close to any gravity station, a special *terrain correction* must be applied. The Bouguer correction assumes an approximation to a semi-infinite horizontal slab of rock between the measuring station and sea-level. It makes no allowance for hills and valleys and this is why the terrain correction is necessary.

The effect of topography on  $g$  is illustrated in Figure 2.25. Consider a gravity station beside a hill as in Figure 2.25A. The slab of rock which comprises the hill (mass  $M$ ) has its centre of mass above the plane on which the gravimeter is situated. There is a force of attraction between the two masses. If the force is resolved into horizontal and vertical components and the latter only is considered, then it can be seen that the measurement of  $g$  at the gravity station will be underestimated by an amount  $\delta g$ . Conversely, if the gravity station is adjacent to a valley, as indicated in Figure 2.25B, then the

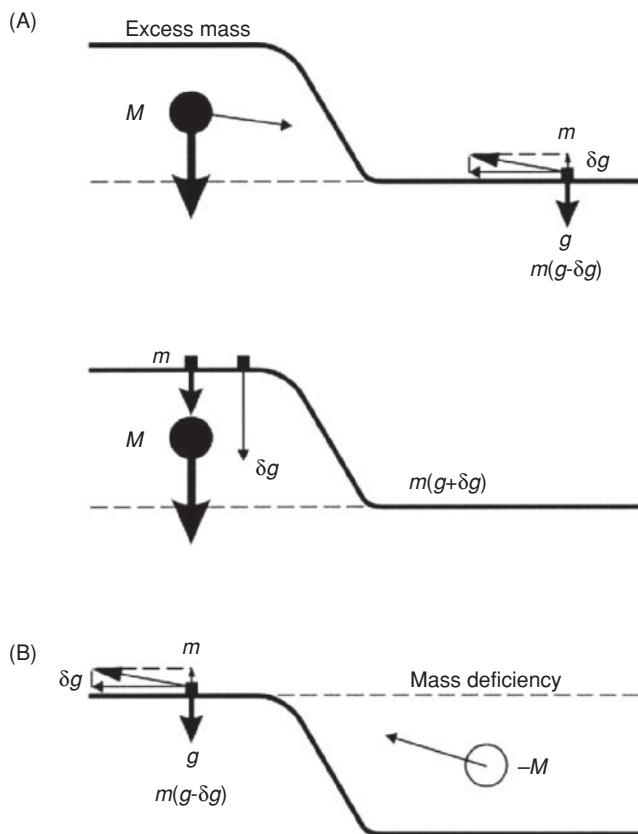


**Figure 2.25** The effects of (A) a hill and (B) a valley on the measurement of gravity, illustrating the need for terrain corrections.

valley represents a mass deficiency which can be represented by a negative mass ( $-M$ ). The lack of mass results in the measurement of  $g$  to be underestimated by an amount  $\delta g$ . Consequently, a gravity measurement made next to either a hill or a valley requires a correction to be added to it to make allowance for the variable distribution of mass. The correction effectively removes the effects of the topography to fulfil the Bouguer approximation of a semi-infinite rock slab.

Physical computation of the terrain correction is extremely laborious as it has to be carried out for each and every station in an entire survey. A special transparent template, known as a *Hammer chart* after its originator Sigmund Hammer (1939), consists of a series of segmented concentric rings (Figure 2.26). This is superimposed over a topographic map and the average elevation of each segment of the chart is estimated. The outer radius of the furthest zone is 21.9 km, beyond which the effect of topography on  $g$  is negligible. In some cases, the range of the chart is extended to 50 km. Special tables (Table 2.8) are used to derive the terrain correction in g.u. for each segment, and then all the values are summed to produce a statistically weighted terrain correction for a given gravity station, each ring of the Hammer chart having a different weighting. For example, for a mean height difference of 34.7 m between the gravity station and a segment in zone D, a terrain correction of 0.95 g.u. can be determined from Table 2.8.

The terrain correction method works on the principle of determining the value of  $g$  at the centre of an annulus of inner and outer radii  $r_1$  and  $r_2$  (Figure 2.27) using the equation given in Box 2.14. Although topographic maps can be digitised and the terrain corrections calculated by computer (Bott, 1959; Kane, 1962) for the outer rings of the Hammer chart, it is still necessary to compute the terrain corrections for the innermost rings manually.

There is no theoretical reason as to why the terrain correction needs to be calculated on the basis of a circular division of the

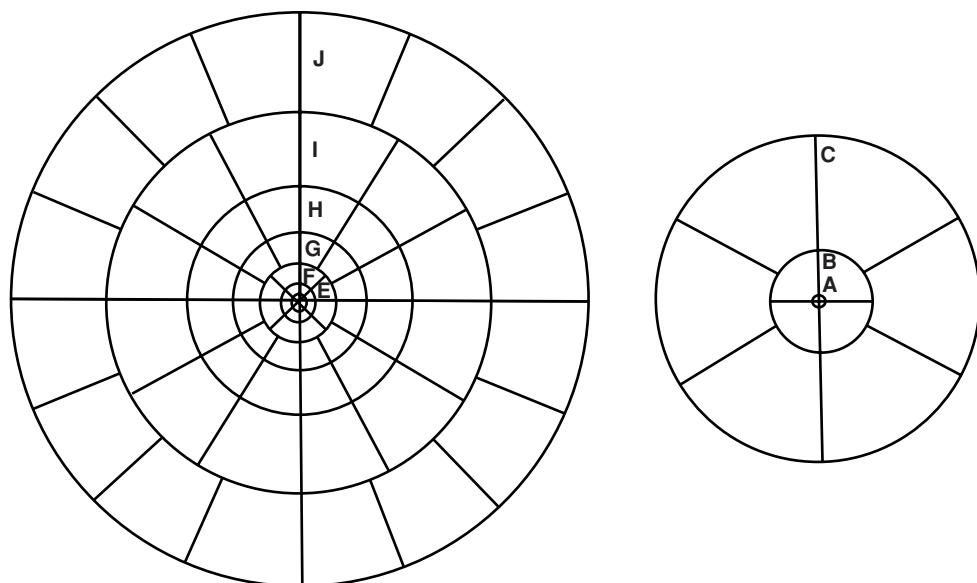


**Figure 2.26** Hammer terrain correction chart with inner rings A-C shown for clarity. After Dobrin (1976) and Milsom (2002), by permission.

**Table 2.8** Terrain corrections for Hammer zones B to M. From Milsom (2002) by permission.

Zone No. of compartments:	B 4	C 6	D 6	E 8	F 8	G 12	H 12	I 12	J 16	K 16	L 16	M 16
Correction (g.u.)	Heights (metres)											
0.01	0.5	1.9	3.3	7.6	11.5	24.9	32	42	72	88	101	125
0.02	0.7	2.6	4.7	10.7	16.3	35.1	46	60	101	124	148	182
0.03	0.8	3.2	5.8	13.1	19.9	43.1	56	74	125	153	186	225
0.04	1.0	3.8	6.7	15.2	23.0	49.8	65	85	144	176	213	262
0.05	1.1	4.2	7.5	17.0	25.7	55.6	73	95	161	197	239	291
0.06	1.2	4.6	8.2	18.6	28.2	60.9	80	104	176	216	261	319
0.07	1.3	5.0	8.9	20.1	30.4	65.8	86	112	191	233	282	346
0.08	1.4	5.4	9.5	21.5	32.6	70.4	92	120	204	249	303	370
0.09	1.5	5.7	10.1	22.9	34.5	74.7	96	127	216	264	322	391
0.10	1.6	6.0	10.6	24.1	36.4	78.7	103	134	228	278	338	413
0.20	2.4	8.7	15.1	34.2	51.6	111.6	146	190	322	394	279	586
0.30	3.2	10.9	18.6	42.1	63.3	136.9	179	233	396	483	587	717
0.40	3.9	12.9	21.7	48.8	73.2	158.3	206	269	457	557	679	828
0.50	4.6	14.7	24.4	54.8	82.0	177.4	231	301	511	624	759	926
0.60	5.3	16.5	26.9	60.2	90.0	194.7	253	330	561	683	832	1015
0.70	6.1	18.2	29.3	65.3	97.3	210.7	274	357	606	738	899	1097
0.80	6.9	19.9	31.5	70.1	104.2	225.6	293	382	648	790	962	1173
0.90	7.8	21.6	33.7	74.7	110.8	239.8	311	405	688	838	1020	1244
1.00	8.7	23.4	35.7	79.1	117.0	253.2	328	427	726	884	1076	1312

Note: These tables list the exact height differences which, assuming a density of 2000 kg/m<sup>3</sup>, will produce the tabulated terrain effects. Thus, a height difference of 32 m between gravity station and average topographic level in one compartment of zone E would be associated with a terrain effect of 0.20, or possibly 0.19, g.u. Almost all commercial gravity meters have sensitivities of 0.1 g.u. but an additional decimal place is necessary if large 'rounding off' errors are to be avoided in summing the contributions from all the compartments. The inner radius of zone B is 2 m. Zone outer radii are: B: 16.6 m. C: 53.3 m. D: 170 m, E: 390 m, F: 895 m, G: 1,530 m, H: 2.61 km, I: 4.47 km, J: 6.65 km, K: 9.9 km, L: 14.7 km, M: 21.9 km.

terrain. It is computationally better for a regular grid to be used, in which case digitised topographic data can be used quite readily. Ketelaar (1976) suggested a method in which the topography is represented by square prisms of side length  $D$  with an upper surface sloping at an angle  $\alpha$ . The terrain correction due to each prism can be calculated using the expression in Box 2.15. An example of

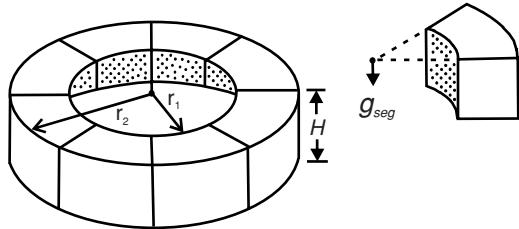


**Figure 2.27** Segmented cylindrical ring used to compute terrain corrections. From Robinson and Coruh (1988), by permission.

computer analysis of terrain corrections for micro-gravity surveys has been given by Blizkovsky (1979), in which he also considers the gravitational effects of walls, vertical shafts and horizontal corridors. In micro-gravity surveys, an area of radius 2 m centred on the

#### Box 2.14 Gravity of a Hammer chart segment (see Figure 2.27)

Gravity of a Hammer chart segment ( $\delta g_{\text{seg}}$ ):

$$\delta g_{\text{seg}} = \frac{2\pi\rho G}{N} [r_2 - r_1 + (r_1^2 + z^2)^{1/2} - (r_2^2 + z^2)^{1/2}] \text{ (g.u.)}$$

where  $N$  is the number of segments in the ring,  $z$  is the modulus of the difference in elevation between the gravity station and mean elevation of the segment, and  $\rho$  is the Bouguer correction density (Mg/m<sup>3</sup>).

**Box 2.15** Terrain correction for a square prism

Terrain correction due to a square prism of side length  $D$ :

$$\delta g_{\text{prism}(i,j)} = G\rho D(1 - \cos \alpha)K(i, j)$$

where  $K(i, j)$  is the matrix of prism coordinates within the grid.

measurement station should be flat. For terrain effects of less than 1 µGal, height variations of less than 0.3 m in Hammer zone B and up to 1.3 m in zone C can be tolerated.

The calculation of terrain corrections is labour-intensive, time-consuming, and adds considerably to the total cost of the survey if undertaken manually. It is only undertaken when dictated by the roughness of the local topography. However, it is possible to use software to calculate the terrain corrections where the necessary data are available from Digital Elevation Models (DEMs) (e.g. Parker, 1995, 1996; García-Abdeslem and Martín-Atienza, 2001). However, the use of DEMs, which normally describe only the mean elevation in a geographical cell, omit near-station effects that, depending upon the resolution of the DEM and the roughness of the topography, can reach several mGal (Leaman, 1998; Nowell, 1999). In the case of airborne gravity gradiometry surveys, compensation for surface topography is also essential. In areas where DEMs are not already available or are not accurate enough, airborne laser scanning data acquired during the airborne gravity survey can be used to generate suitably accurate DEMs that are properly registered to the aircraft position (Stone and Simsky, 2001).

## 2.5.7 Building corrections

One additional aspect of terrain corrections is the effect of buildings adjacent to the gravimeter during data acquisition in built-up areas. Modern, thin-walled buildings may contribute only a small effect (of the order of 1–5 µGal), but older thick-walled constructions may give rise to an effect of 10–30 µGal depending upon the distance between the building and the gravity meter. In these cases, it is preferable to position the gravimeter more than 2.5 m away from such a building in order to keep the effect to less than 5 µGal (Milsom, 2003). Otherwise, it is necessary to determine the localised effects of buildings. There are three approaches to dealing with the effects of buildings: (a) ignore them – not acceptable these days; (b) empirical approach to remove the effects; or (c) calculate and remove the effect.

The empirical approach is to measure the gravity effect around a comparable building, assuming one exists, away from the survey area, and to carry out an adjustment of the actual survey data. Bishop *et al.* (1997) described a field survey of the Al-Dahr residential area in Kuwait following the collapse of four sinkholes in 1988–89. The estate consisted of six sectors with each sector being subdivided into essentially symmetrical quadrants positioned around a central area containing a school. The main area of concern, Quadrant 1, associated with a number of collapsing sinkholes, was surveyed using micro-gravity (Figure 2.28A). A corresponding area (Quadrant 4) with the same layout and style of buildings and known not to be af-

fected by sinkholes was also surveyed. The Bouguer anomaly data of Quadrant 4 (unaffected by sinkholes but still containing the effects of the buildings) were subtracted from the Bouguer anomaly data of Quadrant 1, thereby removing the effects of the buildings and residualising the anomalies (Figure 2.28B) associated with formerly unknown sinkholes. Had the survey been commissioned now, the additional costs of the micro-gravity survey of Quadrant 4 would have to be evaluated against those of directly calculating and removing the gravity effect of the buildings without surveying the additional area.

A micro-gravity survey was undertaken in Field Road, Reading, UK, following the collapse of chalk mine workings beneath a row of terraced Victorian houses (Reynolds, 2004b). Experiments were undertaken to model the gravitational effect of the different architectural styles of buildings, from Victorian terrace houses, to more modern 1980s flats and houses. Different combinations of walls, wall thicknesses and heights were modelled to gauge their relative values on the data collected within the main part of Field Road. It was shown to be possible to produce a map of the gravitational effects of the buildings along Field Road, even taking into consideration basements where they were known to occur. The density of the typical house bricks was obtained from brick manufacturers and was found to be  $2.1 \text{ Mg m}^{-3}$ . It was shown that the anomalies arising purely from the buildings was of the order of up to 20 µGal but the field decayed to less than 5 µGal within less than 1 m of the front walls (Figure 2.29). For example, five gravity stations were occupied across a 4.25 m wide alley between two houses (Figure 2.29A). The gravity field over the same profile was modelled (Figure 2.29B) and used to correct the Bouguer anomaly profile. It can be seen in the corrected profile (Figure 2.29C) that the three data values along the right-hand end of the profile are generally the same whereas the first two show lower values by around 12 µGal. This zone was later shown by the probe drilling to be, as predicted from the geophysical interpretation, due to collapsed backfilled mine workings. This approach was taken across the entire survey area to produce a Bouguer anomaly fully corrected for the effects of buildings. Obtaining mini-profiles orthogonal to major walls and comparing them with calculated building corrections is a useful way of determining the effectiveness of the building correction and the rate of decay of the field from the building, especially in the case of more complex architectural detail and different building materials.

Budgetary constraints may preclude detailed data reduction, in which case the effectiveness of the micro-gravity survey may be jeopardised. Such considerations need to be made at the design stage of the survey. In some cases, the effects of adjacent buildings are assumed to be negligible and are ignored unjustifiably as they are thought to be too difficult to determine. Commercially-available software permits the rapid determination of the effects of buildings, but such corrections need to be applied with considerable care if small anomalies associated with targets being sought are not to be missed.

## 2.5.8 Eötvös correction

For a gravimeter mounted on a vehicle, such as a ship or a helicopter, the measured gravitational acceleration is affected by the vertical

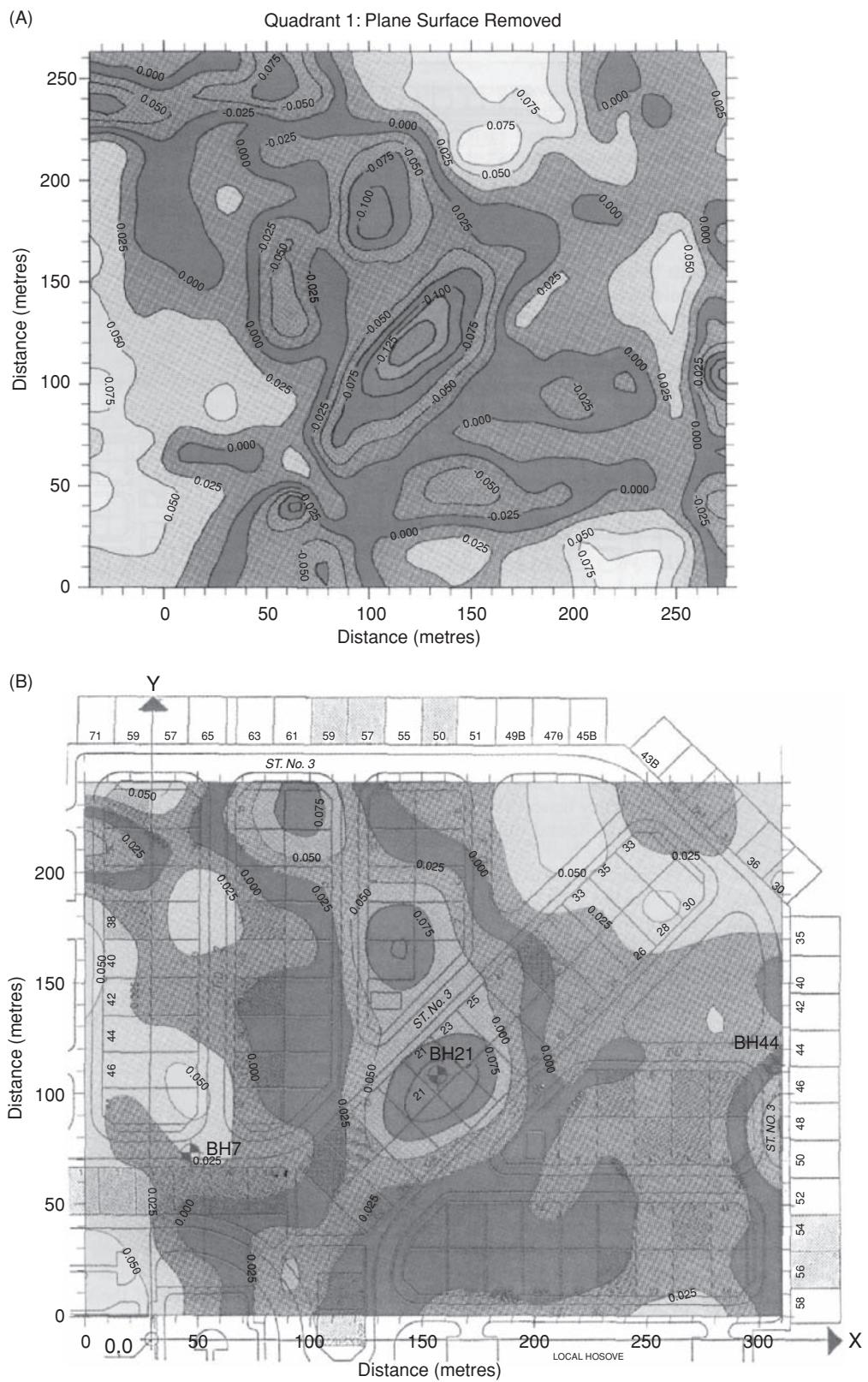


**Figure 2.28** Quadrant 1, Sector 1: Al Dhahar Estate, Kuwait: (A) residual Bouguer anomaly map, and (B) residual difference Bouguer anomaly map with street plan superimposed. After Bishop *et al.* (1997).

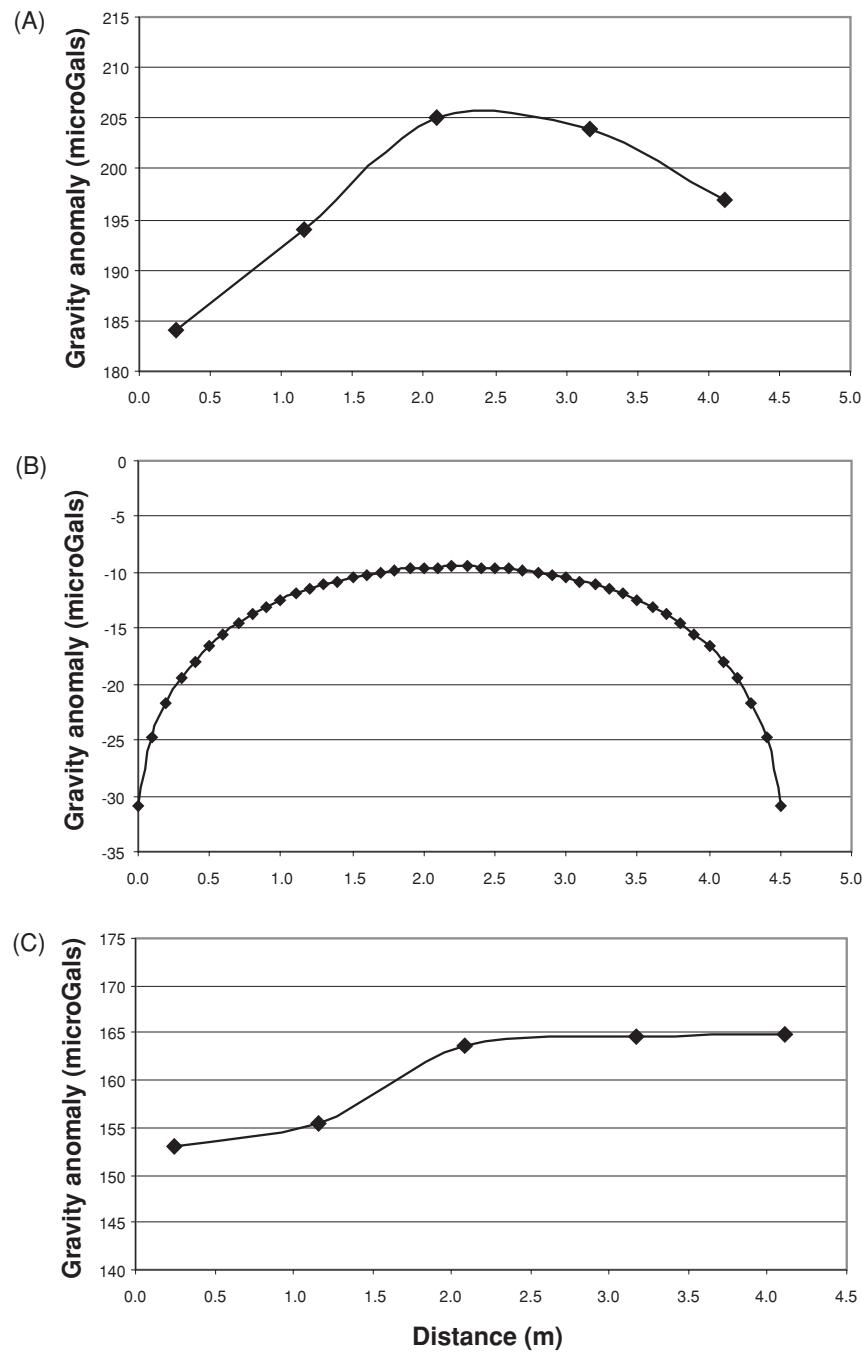


**Figure 2.29** Corrections to Bouguer anomaly data to account for the effects of buildings and front garden walls. (A) Uncorrected Bouguer anomaly data; (B) the modelled effects of two house walls at either end of the profile; and (C) the residual anomaly arising from the corrected data revealing the presence of backfilled collapsed ground (within the first 2 m of data). From Reynolds (2004b), by permission.

component of the Coriolis acceleration, which is a function of the speed and direction in which the vehicle is travelling. To compensate for this, gravity data are adjusted by applying the Eötvös correction, named after the Hungarian geophysicist Baron von Eötvös who described this effect in the late 1880s.

There are two components to this correction. The first is the outward-acting centrifugal acceleration associated with the movement of the vehicle travelling over the curved surface of the Earth,

and the second is the change in centrifugal acceleration resulting from the movement of the vehicle relative to the Earth's rotational axis. In the second case, an object that is stationary on the Earth's surface is travelling at the speed of the Earth's surface at that point as it rotates around the rotational axis in an east–west direction. If that same object is then moved at  $x$  km/h towards the east, its speed relative to the rotational velocity is increased by the same amount. Conversely, if it travels at a speed of  $y$  km/h in a westerly direction,

**Box 2.16 Eötvös correction**

The Eötvös correction is given by:

$$\delta g_{\text{EC}} = 75.08 V \cos \varphi \sin \alpha + 0.0416 V^2 \text{ (g.u.)}$$

or

$$\delta g_{\text{EC}} = 40.40 V' \cos \varphi \sin \alpha + 0.01211 V'^2 \text{ (g.u.)}$$

where  $\varphi$  is the degree of geographical latitude,  $\alpha$  is the azimuth in degrees, and  $V$  and  $V'$  are the speeds of the vehicle in knots and kilometres per hour respectively.

The error in the Eötvös correction [ $d(\delta g_{\text{EC}})$ ] in g.u. due to errors in speed ( $dV$ ) and azimuth ( $d\alpha$ ) is:

$$d(\delta g_{\text{EC}}) = (0.705 V' \cos \varphi \cos \alpha) d\alpha + (40.40 V' \cos \varphi \sin \alpha + 0.02422 V') dV.$$

its relative speed is slowed by the same amount. Any movement of a gravimeter which involves a component in an east–west direction will have a significant effect on the measurement of gravity. For shipborne gravimeters the Eötvös correction can be of the order of 350 g.u. For airborne gravity measurements, where speeds over 90 km/h (about 50 knots) are common, the Eötvös correction can be as high as 4000 g.u. The expression governing the Eötvös correction is given in Box 2.16, with a fuller mathematical explanation in Box 2.17.

At a latitude of  $25^\circ$ , a change of 0.1 knot (0.2 km/h) with a half a degree shift off course, will result in over 7 g.u. difference in Eötvös correction while on an easterly course ( $\alpha = 90^\circ$ ), or 3 g.u. on a northerly course ( $\alpha = 0^\circ$ ), assuming a speed of 10 km/h. Consequently, for an airborne survey to be accurate to within 10 g.u., extremely tight controls need to be kept on navigation and on the general movement (roll, pitch, yaw) of the helicopter or plane; such accuracies are now thought to be routinely achievable (Hammer, 1982, 1984). From the last equation in Box 2.15, it can be seen that there is the greatest sensitivity to errors in speed in an east–west direction, and to errors in azimuth on a north–south course.

### 2.5.9 Isostatic correction

If there were no lateral variations in density in the Earth's crust, the fully reduced gravity data, after application of all the corrections so far outlined, would be the same. However, where there are lateral variations, a gravity anomaly results which is known as the *Bouguer anomaly* (discussed in more detail in Section 2.5.11). The average Bouguer anomaly in oceanic areas is generally positive, while over mountainous regions it is usually negative. These effects indicate that the rock beneath the oceans is more dense than normal while that beneath the mountains is less dense.

**Box 2.17 Derivation of the Eotvos correction equation (see Figure 2.30)**

In general, the centrifugal acceleration  $a_1$  is  $(\text{velocity})^2/d$ . The total east–west speed of the vehicle is the linear speed of rotation of the Earth ( $v$ ) plus the *east–west* component of the speed of the vehicle ( $V_E$ ). Thus the centrifugal acceleration  $a_1 = (v + V_E)^2/d$ .

Centrifugal acceleration ( $a_2$ ) along the radius vector, due simply to the movement of the vehicle in a *north–south* direction, is  $a_2 = V_N^2/R$ .

However, it is the *change* in acceleration that is required, so the centrifugal acceleration acting on a static body ( $a_3$ ) needs to be removed:  $a_3 = v^2/d$ .

The total change in acceleration acting in a vertical sense is:

$$\delta g_E = a_1 \cos \varphi + a_2 - a_3 \cos \varphi \quad (4)$$

We note that:

$$d = R \cos \varphi$$

$$v = \omega R \cos \varphi$$

$$V = (V_N^2 + V_E^2)^{1/2} \text{ (from Pythagoras' theorem)}$$

$$V_E = V \sin \alpha, \text{ where } \alpha \text{ is the bearing to true north.}$$

Substituting into Equation (4) we obtain:

$$\delta g_E = \frac{(v + V_E)^2}{R \cos \varphi} \cos \varphi + \frac{V_N^2}{R} - \frac{v^2 \cos \varphi}{R \cos \varphi}$$

Simplifying, this becomes:

$$\delta g_E = [(v + V_E)^2 + V_N^2 - v^2]/R$$

which reduces to:

$$\delta g_E = [2vV_E + (V_E^2 + V_N^2)]/R$$

Rewriting this in terms of  $\omega$ ,  $R$ ,  $\varphi$  and  $\alpha$  using the above expressions, this becomes:

$$\delta g_E = 2\omega V \cos \varphi \sin \alpha + V^2/R \quad (5)$$

Given the following values:

$$\omega = 7.2921 \times 10^{-5} \text{ radians/s}$$

$$R = 6.371 \times 10^8 \text{ cm}$$

$$1 \text{ knot} = 51.479 \text{ cm/s}$$

$$1 \text{ Gal} = 10^4 \text{ g.u.}$$

then Equation (5) can be rewritten (in terms of g.u.) as:

$$\delta g_E = 2(7.2921 \times 10^{-5} \times 51.479 \times 10^4) V \cos \varphi \sin \alpha + (51.479 V)^2 \times 10^4 / 6.371 \times 10^8$$

Finally:

$$\delta g_E = 75.08 V \cos \varphi \sin \alpha + 0.0416 V^2 \text{ (g.u.)} \text{ [with } V \text{ in knots].}$$

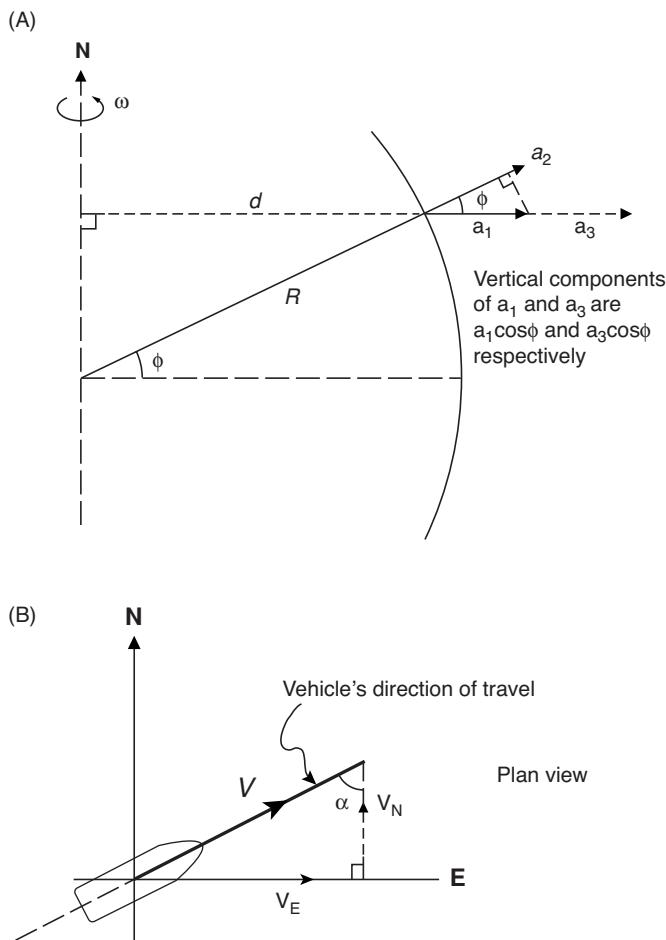


**Figure 2.30** Schematic illustrating the components that contribute to the Eötvös correction (see Box 2.17).

Two hypotheses were proved in the 1850s to account for this large-scale systematic variation in density (Figure 2.31). The geodesist G.B. Airy (1855) proposed that while mountain chains had deep roots, beneath the oceans the crust, which was assumed to have constant density everywhere, was thin. In contrast, an English Archdeacon J.H. Pratt (1859) thought that the crust extended to a uniform depth below sea-level, but that density varied inversely with the height of the topography.

Airy's isostatic model is preferred geologically and seismologically, whereas Pratt's model is easier to use to calculate the isostatic

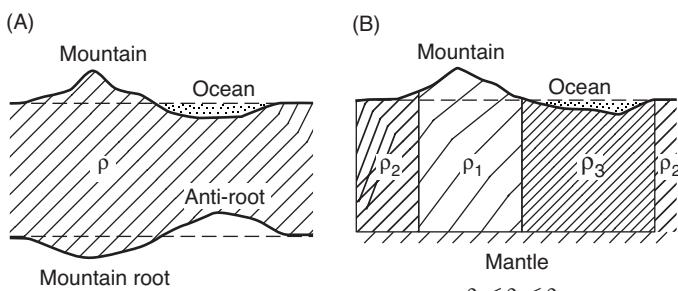


**Figure 2.31** (A) Airy and (B) Pratt's models for isostacy.

correction (e.g. Rimbert *et al.*, 1987), but the results are similar. Pratt's model was developed by Heiskanen (1938), who suggested that density changes laterally with variable thickness of crust and that density increases gradually with depth. The aim of the isostatic correction is that effects on  $g$  of the large-scale changes in density should be removed, thereby isolating the Bouguer anomaly due to lateral variations in density in the upper crust (Hayford and Bowie, 1912). The isostatic correction is discussed in more detail by Garland (1965), and the implications for isostatic rebound due to crustal loading and the viscosity of the mantle are discussed by Sharma (1986).

### 2.5.10 Miscellaneous factors

In Sections 2.5.1–2.5.8, calculable corrections to gravity data have been discussed. Gravimeters are sensitive not only to these factors, but also to several others which tend to be erratic, temporal and difficult to quantify so that they may constitute gravitational noise. Such factors are: meteorological loading produced by atmospheric pressure changes; inertial acceleration caused by seismic and microseismic waves, including the effect of wind pressure on the gravimeter, and vibration from traffic and industrial machinery; and electrical noise from the gravimeter itself. Changes in atmospheric pressure can be corrected for using an atmospheric pressure coefficient, for example  $<0.15 \mu\text{Gal}/\text{kPa}$ , although modern instruments (e.g. Scintrex CG-5) house the sensing element in a vacuum chamber to protect it from changes in atmospheric pressure, which are accounted for automatically. Modern gravimeters used in micro-gravity surveys can filter out most noise above 10 Hz, and reject the microseismic noise between 0.1 and 2 Hz, so that standard deviations on gravity readings can be less than 0.05 g.u. ( $5 \mu\text{Gal}$ ) with a standard resolution of  $1 \mu\text{Gal}$ .

### 2.5.11 Bouguer anomaly

The main end-product of gravity data reduction is the Bouguer anomaly, which should correlate only with lateral variations in density of the upper crust or near-surface environment and which are of most interest to applied geophysicists and geologists. The Bouguer anomaly is the difference between the observed gravity value ( $g_{\text{obs}}$ ), adjusted by the algebraic sum of all the necessary corrections ( $\Sigma(\text{corr})$ ; see Table 2.7 and Box 2.18), and that at some base station ( $g_{\text{base}}$ ). The variation of the Bouguer anomaly should reflect the lateral variation in density such that a high-density feature in a lower-density medium should give rise to a positive Bouguer anomaly. Conversely, a low-density feature in a higher-density medium should result in a negative Bouguer anomaly.

## 2.6 Interpretation methods

There are two approaches to the interpretation of Bouguer anomaly data. One is direct where the original data are analysed to produce an interpretation. The other is indirect, where models are constructed to compute synthetic gravity anomalies that are compared in turn

### Box 2.18 Bouguer anomaly

The Bouguer anomaly ( $\Delta g_B$ ) is the difference between the observed value ( $g_{\text{obs}}$ ) duly corrected, and a value at a given base station ( $g_{\text{base}}$ ) such that:

$$\Delta g_B = g_{\text{obs}} + \Sigma(\text{corr}) - g_{\text{base}}$$

with

$$\begin{aligned} \Sigma(\text{corr}) = & \Delta g_L + (\Delta g_F - \Delta g_B) + \Delta g_{\text{TC}} \pm \Delta g_{\text{EC}} \\ & \pm \Delta g_{\text{IC}} - \Delta g_{\text{D}}^* \end{aligned}$$

where the suffices refer to the following corrections:

$L$  = latitude;  $F$  = free-air;  $B$  = Bouguer;  $TC$  = terrain correction;  $EC$  = Eötvös correction;  $IC$  = isostatic correction; and  $D$  = drift (including Earth tides).

\*For micro-gravity surveys in built-up areas, then  $\Sigma(\text{corr})$  must also include a term to account for the effects of buildings and basements ( $\pm \Delta g_{\text{BLDG}}$ ).

with the observed Bouguer anomaly. The model producing the best fit, however, will not be unique as several alternative models may be found that also produce an equivalent fit (Figure 2.32). It is because of this type of ambiguity, which has already been discussed in Section 1.3 (see also Figure 1.3), that different geophysical methods are used together to constrain the geological model.

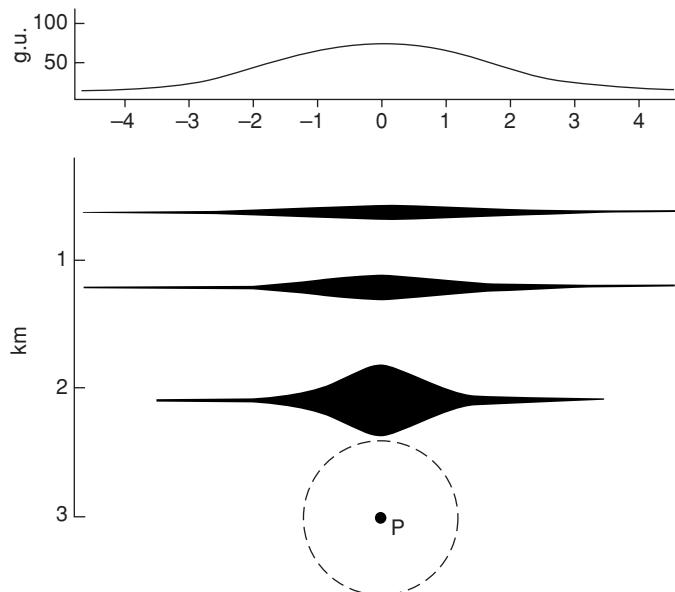


**Figure 2.32** Ambiguity in geological models, all of which produce the gravity anomaly shown at the top. The lens-shaped bodies have a gravity anomaly identical to that of a sphere at  $P$  of radius 600 m and density contrast  $1.0 \text{ Mg/m}^3$ . The thickness of the bodies is exaggerated by a factor of 3. From Griffiths and King (1981), by permission.

### 2.6.1 Regionals and residuals

Bouguer anomaly maps are rather like topographic maps with highs and lows, linear features and areas where the contours (isogals) are closely packed and others where they are further apart. There may be a gentle trend in the gravity data, reflecting a long-wavelength gravity anomaly attributable to deep-seated geological features; this is known as a regional anomaly. Shorter-wavelength anomalies arising from shallower geological features are superimposed on the regional anomaly, and it is these anomalies that are often to be isolated for further analysis. Separation of the regional from the Bouguer anomaly will leave a residual anomaly (Figure 2.33).

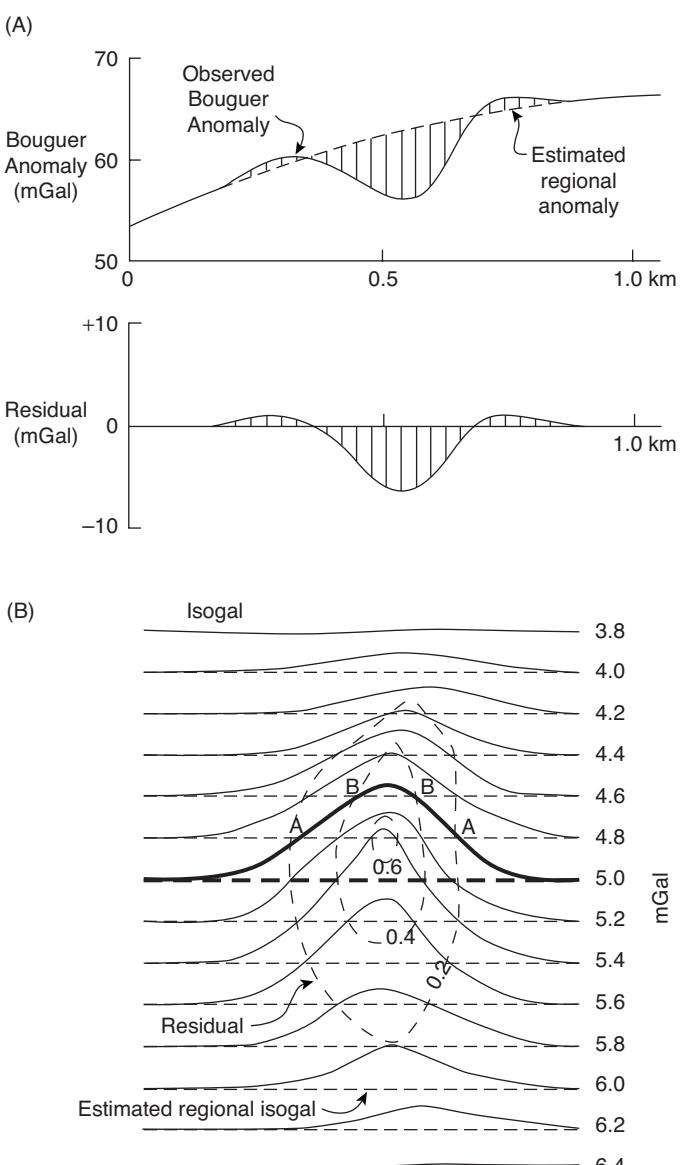


**Figure 2.33** (A) Removal of a residual gravity anomaly from a regional anomaly, and (B) how a residual gravity map is constructed (see text for an explanation). After Dobrin (1976), by permission.

There are a number of different methods with varying degrees of complexity and effectiveness by which residual anomalies can be isolated (Nettleton, 1954). These range from curve-sketching, which is purely subjective, through to computer-based analytical methods. Graphical methods include sketching in estimated regional trends by eye on a profile (Figure 2.33A) or calculating the residual from estimated isogals on a map. Figure 2.33B illustrates how the residual is calculated. The 5.0 mGal isogal, which has been highlighted, intersects several estimated regional isogals. At points A and B, the difference (i.e. the residual) between the 5.0 mGal line and those it crosses are respectively +0.2 and +0.4 mGal, and contours are drawn of the same residual value.

An example of the quantitative analytical method consists of fitting a low-order polynomial expression to the Bouguer anomaly data and then subtracting the calculated values from those observed to produce residual values, which are then plotted in map form. A more sophisticated method is the application of Fourier analysis by which a power spectrum is obtained for the Bouguer anomaly (Spector and Grant, 1970; Syberg, 1972). This highlights the different wavelengths of anomaly present and so allows a form of filtering to be undertaken to remove the unwanted anomalies (e.g. Granser *et al.*, 1989). Dobrin (1976), Grant and West (1965) and Telford *et al.* (1990) have discussed the various techniques in more detail.

Although the analytical methods appear more rigorous and thorough, there are occasions when the manual interpretation can take into account known variations in local geology more readily than an automated system.

the associated gravity anomalies. The use of the half-width ( $x_{1/2}$ ) is discussed in more detail in sections 2.6.3 and 2.6.4.

The range of geometric forms given above is by no means complete. Details of other forms and their interpretations, such as by the use of characteristic curves, are given by Grant and West (1965) and Telford *et al.* (1990).

Calculation of gravity anomalies using the above methods should be regarded as a first step in the interpretation process. There are other, more sophisticated, and commonly computerised methods of gravity anomaly analysis. However, it is worth noting that for more complicated geological features of irregular shape which do not approximate to any of the geometrical forms, two other broad approaches can be adopted. The first is the use of graphical methods, and the second is an analytical approach. In the graphical methods, a template, which is divided into segments, is superimposed on an irregular cross-section of the geological feature to be modelled. The gravity at a point on the surface can be calculated by summing the effects of all the individual segments covering the cross-section of the feature.

Graphical methods can also be used for three-dimensional bodies. In this case, the appropriate template is superimposed on contours of the geological feature in the horizontal plane, thereby dividing it into a pile of horizontal slabs each with a thickness equal to the contour interval.

Most computer-based analytical methods (e.g. Bott, 1960) are based on the premise proposed by Talwani *et al.* (1959) that a cross-section of a two-dimensional body can be approximated by representing it by a multi-sided polygon (Figure 2.35A). This was developed by Talwani and Ewing (1960) for three-dimensional bodies (Figure 2.35B), which are approximated by a stack of polygonal laminae. The gravity effect of each lamina is computed and summed to give a total gravity anomaly. Enhancements of these methods have largely been centred upon improving the ease of use of the software on computers that have dramatically increased in power and efficiency, and on the portability of software from mainframe machines to personal microcomputers (Busby, 1987). There are now a number of commercially available software packages that can be used on PCs and laptops (e.g. Potent for use with Geosoft).

A development of the three-dimensional approach is to consider a geological body as a stack of cubic blocks of uniform size, each having a specified density contrast. Each little cube is considered as a point mass and thus the total gravity anomaly for the entire body is obtained by summing the constituent gravity components for each mini-cube. The resultant gravity anomaly is compared with that observed and, if necessary, the model is adjusted by trial and error, or by automatic iterative methods (e.g. non-linear optimisation (Al-Chalabi, 1972)) until the differences between the computed and observed anomalies are reduced to an acceptable, statistically defined level. Better resolution is obtained by reducing the size and increasing the number of individual cubes within the model. By having a regular cube size, the computation is eased considerably. An example of the application of this technique is given in Figure 2.36, where gravity data from Guernsey, Channel Islands, have revealed that a gabbro body, which outcrops to the northeast of the island near St Peter Port, has the form of a laccolith 0.8 km thick and about 4 km in diameter (Briden *et al.*, 1982).

## 2.6.2 Anomalies due to different geometric forms

Certain geological structures can be approximated to models with known geometric forms (Nettleton, 1942). For example, a buried cavity may be represented by a sphere, a salt dome by a vertical cylinder, a basic igneous dyke by an inclined sheet or prism, and so on. Another factor to be considered is whether the target to be modelled should be considered in two or three dimensions. If  $g$  is computed across a profile over a buried sphere, then that profile should hold true for any direction across the sphere. However, if the profile is across a buried horizontal cylinder, then the profile along the long axis of the cylinder will be quite different from that across it. Also, if the strike length of the feature is greater than 20 times any other dimension, then it may be considered a two-dimensional body. Where this does not hold true, any profile will also sense the effects of the third dimension ('edge effects') and thus will not be modelled accurately if considered only in two dimensions.

Several common geometric forms are illustrated in Figure 2.34, with their associated gravity profiles and the types of geological features they approximate. The equations used to calculate the maximum anomaly for each geometric feature are given in Box 2.19. No attempt is made here to explain the derivations of these formulae, all of which are discussed much more fully by Dobrin (1976), Telford *et al.* (1990) and Parasnis (1986). The equations in Box 2.19 are intended only as guides to estimate the maximum values of

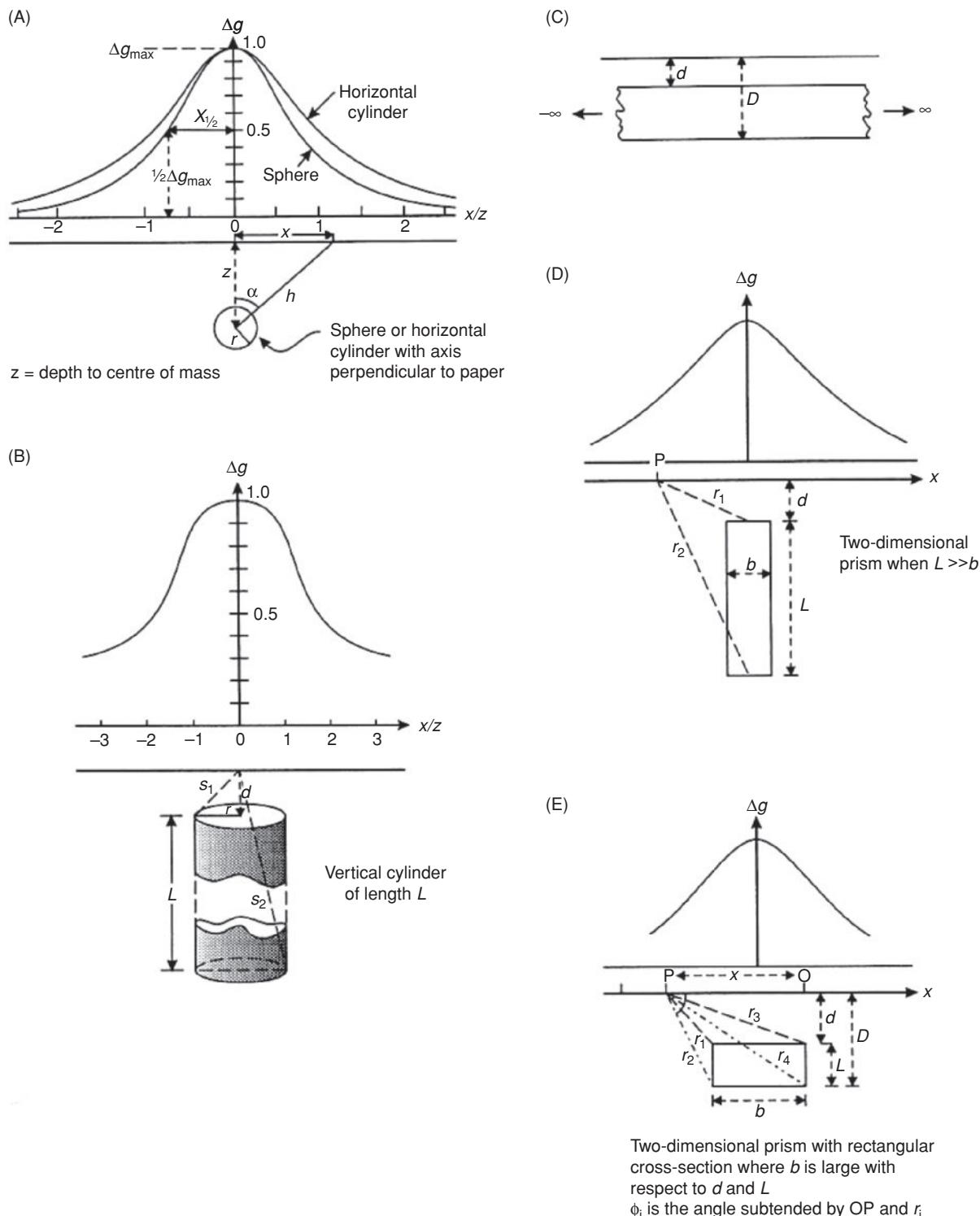


**Figure 2.34** Representative gravity anomalies over given geometric forms: (A) a sphere or horizontal cylinder with its long axis perpendicular to the paper; (B) a vertical cylinder; (C) a semi-infinite horizontal slab (a Bouguer plate when  $d = 0$ ); (D) a vertical rectangular prism; and (E) a horizontal rectangular prism.

**Box 2.19** Gravity anomalies associated with geometric forms (see Figure 2.34)

Models	Maximum gravity anomaly	Notes
<i>Sphere</i>	$\Delta g_{\max} = (4/3)\pi G \delta \rho r^3 / z^2$	$z = 1.305x_{1/2}$ (m)
<i>Horizontal cylinder</i>	$\Delta g_{\max} = 2\pi G \delta \rho r^2 / z$	$z = x_{1/2}$ (m)
<i>Vertical cylinder</i>	$\Delta g_{\max} = 2\pi G \delta \rho (s_1 - d)$ $\Delta g_{\max} = 2\pi G \delta \rho r$ $\Delta g_{\max} = 2\pi G \delta \rho (L + s_1 - s_2)$	If $L \rightarrow \text{infinity}$ If $d = 0$ If $L$ finite $z = x_{1/2} \sqrt{3}$
<i>Buried slab</i> (Bouguer plate)	$\Delta g_{\max} = 2\pi G \delta \rho L$	For $L = 1$ km and $\delta \rho = 0.1$ Mg/m
<i>Infinite slab</i>	$\Delta g_{\max} = 2\pi G \delta \rho (D - d)$ $\Delta g_p = 2G \delta \rho \left[ x \ln \left( \frac{r_1 r_4}{r_2 r_3} \right) + b \ln \left( \frac{r_2}{r_1} \right) + D(\phi_2 - \phi_4) - d(\phi_1 - \phi_3) \right]$	
<i>Horizontal rectangular prism</i>	$\Delta g_{\max} = 2G \delta \rho [b \ln(d/L)]$	$L \gg b$
<i>Vertical rectangular prism</i>	$\Delta g_{\max} = 2G \delta \rho [x \ln(r_4/r_3) + \pi(D - d) - D\varphi_4 + d\varphi_3]$	
<i>Step</i>		

All distances are in metres unless stated otherwise;  $\Delta g_{\max}$  in mGal and  $\delta \rho$  in Mg/m<sup>3</sup>, and factor  $2\pi G = 0.042$ .

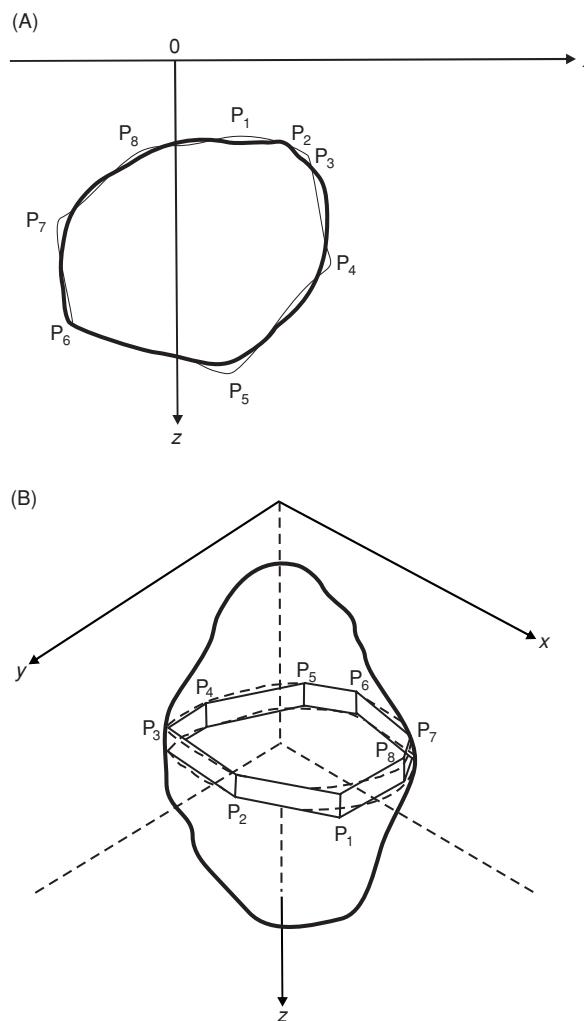


**Figure 2.35** (A) Polygonal representation of an irregular vertical section of a two-dimensional geological feature. (B) Representation of an irregular three-dimensional geological feature by polygonal laminae.

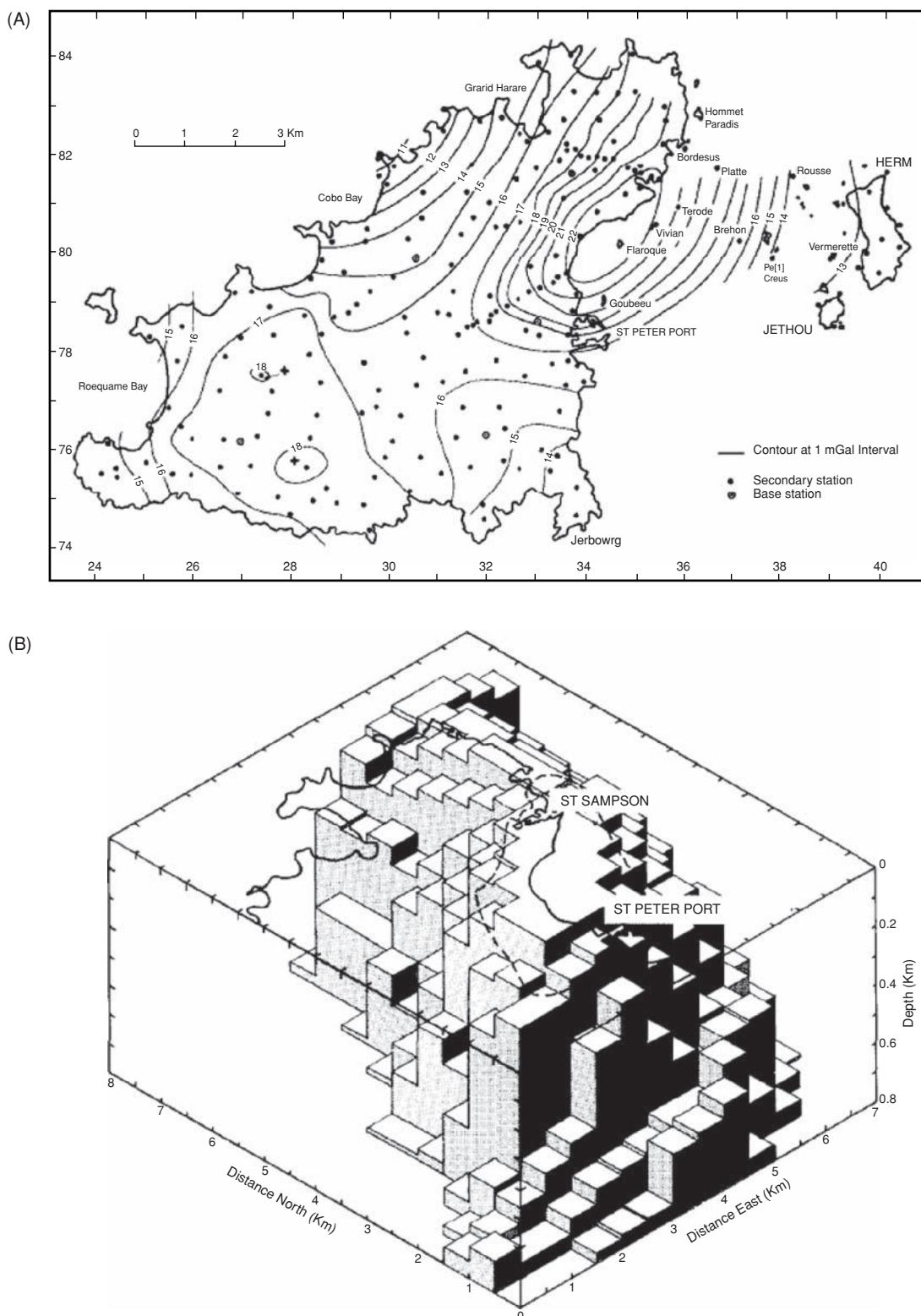


**Figure 2.36** (A) Bouguer anomaly map for Guernsey, Herm and Jethou, Channel Islands, and (B) a three-dimensional model of the underlying St Peter Port Gabbro (density contrast  $0.27 \text{ Mg/m}^3$ , vertical exaggeration 5:1). The coastline and the outline of the gabbro outcrop are indicated. The gabbro is thus interpreted as a laccolith approximately 4 km in diameter and 0.8 km thick. From Briden *et al.* (1982), by permission.

### 2.6.3 Depth determinations

Of major importance in the interpretation of any gravity data is the determination of depth to the centre of mass and/or to the top of the body causing the anomaly. The maximum depth at which the top of any particular geological body can be situated is known as the limiting depth. Methods of obtaining this information depend upon which interpretational technique and model are being used. Let us consider various direct or forward methods where the actual gravity anomaly data are used to derive depths and also estimates of anomalous masses of the features causing the anomalies.

The commonest rules of thumb concern the use of the half-width of the anomaly; that is, the half-width ( $x_{1/2}$ ) of the anomaly where the amplitude is half the maximum value. Some workers define the half-width as the entire width of the anomaly at half peak amplitude, and the form of the depth and mass determination equations will differ accordingly. Whichever formulae are used, care should be taken when calculating the limiting depth. The causative body has finite size and its mass is not concentrated at its centre of mass, and thus any estimate of depth will be overestimated. Also, the method will only give an approximation of depth in cases where all the constituent components have the same sense of density contrast (i.e. all negative or all positive). These formulae will also not be

#### Box 2.20B Example of calculation for a sphere

An air-filled cavity in rock of density  $2.5 \text{ Mg/m}^3$  can be modelled by a sphere of radius  $r$  and depth to centre of mass,  $z$  (m). The resultant gravity anomaly is shown in Figure 2.37.

Given  $\Delta g_{\max} = 0.048 \text{ mGal}$ ,  $x_{1/2} = 2.2 \text{ m}$ , and  $\delta\rho = 2.5 \text{ Mg/m}^3$ :

$$z = 1.305 \times 2.2 \text{ m} = 2.87 \text{ m.}$$

Radius of sphere =  $r$ :

$$r^3 = 0.048 \times (2.87)^2 / (0.0286 \times 2.5) = 5.53 \text{ m}^3.$$

So  $r = 1.77 \text{ m}$ . Depth to top of sphere  $d = 2.87 - 1.77 = 1.10 \text{ m}$ .

*An air-filled cavity of this size so close to the surface could constitute a hazard.*

effective for compact mineral bodies. Formulae for a selection of given geometric forms are given in Box 2.20A, and an example of one calculation is given in Box 2.20B (see Figure 2.37).

Several basic ‘rules’, known as the *Smith Rules* after their originator (Smith, 1959, 1960), have become established in the calculation of limiting depths. Two rules (1 and 2 in Box 2.21) use a *gradient-amplitude ratio* method. Consider any geological body that gives an isolated gravity anomaly (Figure 2.38) entirely of either sign with a maximum gravity ( $\Delta g_{\max}$ ) that varies along the line of the profile and thus has a horizontal gradient that reaches a maximum value

#### Box 2.20A Depth estimates for given geometric forms

Form	Formula	Notes
Sphere	$z = 1.305x_{1/2}$ $d = z - r$	$z$ is depth to centre of mass $d$ is depth to top of sphere of radius $r$ $r^3 =  \Delta g_{\max} z^2 / (0.0286\delta\rho)$ from Box 2.18
Horizontal cylinder	$z = x_{1/2}$ $d = z - r$	$z$ is depth to cylinder axis $d$ is depth to top of sphere of radius $r$ $r^2 =  \Delta g_{\max} z / (0.042\delta\rho)$ from Box 2.18
Vertical cylinder	$z = 1.732x_{1/2}$	$z$ is depth to top end of cylinder (overestimates $z$ )
Thin dipping sheet	$z \approx 0.7x_{1/2}$	$z$ is depth to top of sheet; $z \approx$ dip length of sheet <i>When length of sheet is very large or sheet dips at less than 60°, no reliable solution is possible.</i>
Thick prism	$z \approx 0.67x_{1/2}$ $z \approx 0.33x_{1/2}$	$z$ is depth to prism top = prism width, and depth to prism base is twice width. When depth to prism base is 10 times prism width. <i>In both cases, estimates of <math>z</math> are unreliable.</i>

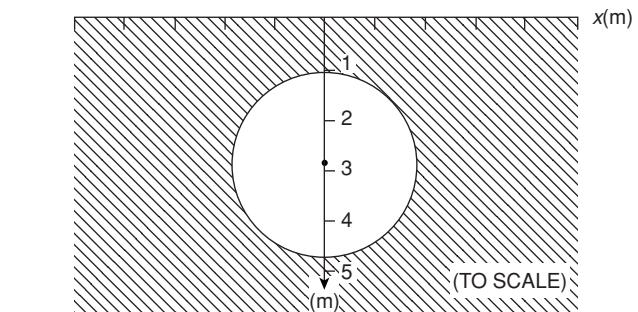
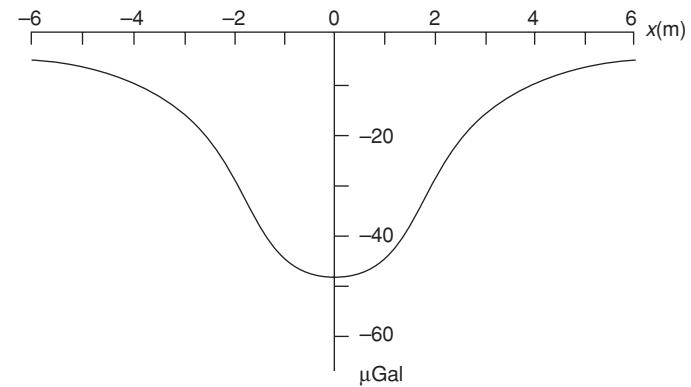


Figure 2.37 Gravity anomaly over an air-filled cavity of radius  $1.77 \text{ m}$  and  $2.87 \text{ m}$  depth to centre, in rock of density  $2.5 \text{ Mg/m}^3$ .

**Box 2.21 Smith Rules**

(1) Where the entire anomaly has been isolated:

$$d \leq C \cdot \Delta g_{\max} / \Delta g'_{\max}$$

where  $C = 0.65$  for a 2-D body and  $C = 0.86$  for a 3-D body.

(2) When only part of an anomaly is isolated, for any point  $x$ :

$$\leq K \Delta g_x / \Delta g'_x$$

where  $K = 1.00$  for a 2-D body and  $K = 1.50$  for a 3-D body.

(3) For a maximum density contrast  $\delta\rho_{\max}$  and a maximum value of the second horizontal gradient ( $\Delta g''_{\max}$ ) (that is, the rate of change of  $\Delta g'$  with  $x$ ):

$$d \leq 5.4 G \delta\rho_{\max} / \Delta g''_{\max}$$

at  $\Delta g'_{\max}$ . The Smith Rules describe the various relationships between the limiting depth  $d$  to the top of any geological body and the maximum gravity ( $\Delta g_{\max}$ ) and its horizontal gradient ( $\Delta g'_{\max}$ ) as listed in Box 2.21.

The third Smith Rule adopts a second-derivative method that uses the rate at which the gravity gradient changes along the profile. It is thought that second-derivative methods produce more accurate estimates of limiting depths. Second derivatives are discussed in more detail in Section 2.6.5.

## 2.6.4 Mass determination

*Anomalous mass* is the difference in mass between a geological feature and the host rock. There are two basic methods of calculating either an excess mass due to a high-density body or a mass deficiency caused by a body with a lower density.

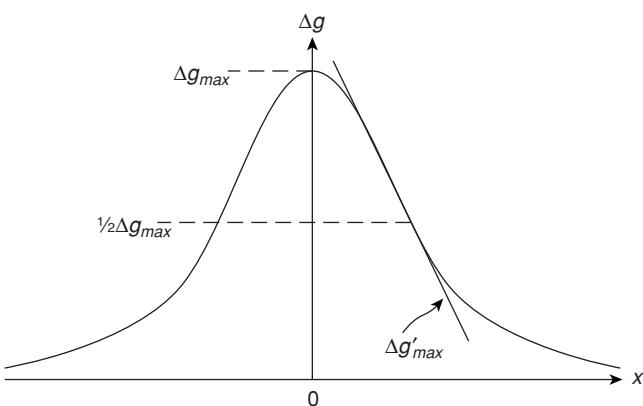


**Figure 2.38** Limiting depth calculations: half-width method and gradient-amplitude ratio method (see text for details).

**Box 2.22 Mass of a sphere**

$$\text{Total mass } M \approx 255 \Delta g_{\max} (x_{1/2})^2 \text{ tonnes}$$

where  $\Delta g_{\max}$  is in mGal and  $x_{1/2}$  in metres.

**Example:** For the air-filled cavity described in Box 2.20B, the total mass deficiency of the sphere is equal to the mass of the rock that would have been in the cavity, times its density (2.5 Mg/m<sup>3</sup>):

$$\text{Mass} = \text{density} \times \text{volume} = 2.5 \times (4/3)\pi 1.77^3 = 58 \text{ tonnes.}$$

Using the gravity data:

$$\text{Mass} \approx 255 \times 0.048 \times 2.2^2 = 59 \text{ tonnes.}$$

The first method uses a rule of thumb based on the gravity anomaly half-width ( $x_{1/2}$ ) and an assumption that the geological feature approximates to a given geometric form, such as a sphere (Box 2.22). The anomalous mass can be calculated by subtracting the mass due to a sphere (density times volume) from the mass estimated using gravity data. In the example below, the actual mass of an air-filled cavity is negligible, so the mass deficiency calculated is the mass of the missing rock.

The second method is based on Gauss's Theorem in potential theory (Grant and West, 1965) and is particularly important for two reasons. Firstly, the total anomalous mass of a geological feature can be calculated from the associated gravity anomaly without any assumptions being necessary about the body's shape or size. Secondly, the total anomalous mass can be very important in the determination of tonnage of ore minerals (Hammer, 1945). For this method to work effectively, it is important that the regional gravity field be removed and that the entire residual anomaly be isolated clearly. The survey area is divided into a series of rings, each of which is further divided into segments of area  $\delta A$ . The gravity effect of each segment is determined and the total for each ring is obtained and summed together (Box 2.23). Having determined the excess mass, it is then a simple matter to calculate the actual mass ( $M$ ) if the densities of the host rock ( $\rho_0$ ) and the anomalous body ( $\rho_1$ ) are known.

Parasnis (1966) gave an example where the total anomalous mass of the Udden sulphide ore body in northern Sweden was calculated to be 568,820 tonnes. Assuming the densities of the ore and host rock to be 3.38 and 2.70 Mg/m<sup>3</sup> respectively, the actual mass of the ore was found to be 2.83 million tonnes, a value consistent with drill hole estimates. A further example was provided by Bishop *et al.* (1997) where the total mass deficiency associated with gravity anomalies caused by sinkholes beneath a housing estate in Kuwait was calculated to be ~9030 tonnes. This estimate was also useful in that it can be used to estimate the total quantity of grout required for remedial work. Repeated surveys post-treatment can be used to assess the efficacy of the remediation work by confirming that the gravity anomaly has been eradicated.

**Box 2.23 Anomalous and actual masses**

(1) Total anomalous mass ( $M_E$ )

$$M_E = 23.9 \Sigma (\Delta g \delta A) \text{ tonnes}$$

where  $\Delta g$  is in mGal and  $\delta A$  in square metres.

(2) Actual mass of a geological body ( $M$ ):

$$M = M_E \frac{\rho_1}{(\rho_1 - \rho_2)} \text{ tonnes } (\rho_1 > \rho_2)$$

## 2.6.5 Second derivatives

### 2.6.5.1 Second vertical derivative (SVD) maps

One of the problems inherent within the interpretation of Bouguer anomaly maps is that it is difficult to resolve the effects of shallow structures from those due to deeper-seated ones. The removal of the effect of the regional field from the Bouguer anomaly data results in an indeterminate and non-unique set of residuals. It is possible to separate the probable effects of shallow and deeper structures by using second vertical derivatives.

The gravity field ( $g$ ) that is measured by gravimeters varies with height; that is, there is a vertical gradient ( $\partial g / \partial z = g'$ ). Over a non-uniform Earth in which density varies laterally, the vertical gradient changes and the rate of change ( $\partial g' / \partial z$ ) is thus the second vertical derivative of the gravity field ( $\partial^2 g / \partial^2 z$ ). This quantity is very sensitive to the effects of shallow features (and to the effects of noise and topography).

As an illustration of how the gravity effects of shallow and deep structures can be separated, consider two equal point masses ( $m$ ) at two different depths, say at depths of 1 unit and 4 units. The value of  $g$  for a point mass at a depth  $z$  is simply equal to the product of the gravitational constant ( $G$ ) and the mass divided by the depth  $z$  squared, so  $g = Gm/z^2$ . If this is differentiated twice with respect to  $z$ , it becomes  $g'' = 6Gm/z^4$ . This tells us that the second derivative of the two masses,  $g''$ , is inversely proportional to  $z^4$ . Hence the ratio of the two derivatives will be, for  $z_1 = 1$  and  $z^4 = 4$ ,  $g''_1/g_4 = 256$ .

It is possible to compute and plot maps of the second vertical derivative of Bouguer anomaly data. The zero contour should indicate the edges of local geological features. The contours have units where  $10^{-6} \text{ mGal/cm}^2 \equiv 10^{-9} \text{ cm}^{-1} \text{ s}^{-2} \equiv 1 \text{ E cm}^{-1}$  (E stands for an Eötvös unit =  $10^{-6} \text{ mGal/cm}$ , which is a measure of gravitational gradient).

It should be emphasised that it is not possible to undertake any quantitative analyses of SVD maps except to produce characteristic profiles over known geometric forms. The main advantage of SVD maps is to highlight and clarify features spatially, as can be seen from Figures 2.39 and 2.40. In the first of these, the Bouguer anomaly map appears to have a consistent trend in the direction of the gravity gradient (increasingly positive to the east) with isogals aligned in a

NW–SE direction. There is no obvious major feature evident on the Bouguer anomaly map. In contrast, the SVD map shows a major ENE–WSW linear feature with three closures, and it has picked out the outline of the Cement Field in Oklahoma extremely well. Figure 2.39 illustrates the case when a single Bouguer anomaly is really the envelope of several smaller anomalies. In this atypical and rather extreme case, several deep boreholes were drilled on the large minimum indicated on both the Bouguer and the residual anomaly maps; they were found to be dry, having missed the appropriate target, presumed to be a single salt dome. In contrast, the SVD map highlights three salt domes accurately.

Unfortunately, SVD also amplifies noise and so can produce many second-derivative anomalies that are not related to geology. Consequently, in some cases, SVD analyses provide no real advantage over the Bouguer anomaly map. An example of where extraneous anomalies shroud the geologically related features is given in Figure 2.41. Although it is possible to see on the SVD map the two main features present on the Bouguer anomaly map (Figure 2.41A) of the Jjaure titaniferous iron-ore region in Sweden, the SVD map (Figure 2.41B) also has a number of small maxima and minima that are of no structural interest. To resolve which anomalies are of geological importance, it is necessary to go back to the original gravity map and to any other source of geological information. It may even be prudent to refer back to the raw observations and corrections.

### 2.6.5.2 Downward and upward continuation

The effect on gravity of a geological mass at considerable depth is far less than if it were close to the surface (see Figure 2.31). The principle of continuation is the mathematical projection of potential field data (gravity or magnetic) from one datum vertically upwards or downwards to another datum. Effectively, the continuation process simulates the residual Bouguer anomaly at levels below or above sea-level as if the gravity data had been obtained at those levels.

Upward continuation is relatively straightforward as the projection is usually into free space. Upward continuation serves to filter out the shorter-wavelength anomalies and reduce their amplitudes and decrease noise.

Downward continuation is far more problematical as there is an inherent uncertainty in the position and size of the geological features as represented by the Bouguer gravity data. Furthermore, downward continuation aims to reduce each anomaly's wavelength and increase its amplitude. This mathematical amplification will also work on noise within the data, and the resultant information may prove unsuitable for further analysis.

Continuation also forms a method of gravitational stripping (Hammer, 1963) where the gravity effects of upper layers are necessarily removed to reveal the anomalies due to deeper-seated geological structures (e.g. Hermes 1986; Abdoh *et al.* 1990). The method uses the concept of an equivalent stratum (Grant and West, 1965). The Bouguer gravity field is continued downwards to a level that corresponds to a previously identified interface, such as from seismic reflection surveys, and an equivalent topographic surface is constructed at that level. This equivalent stratum should account for any residual anomalies at the surface arising from the interface.

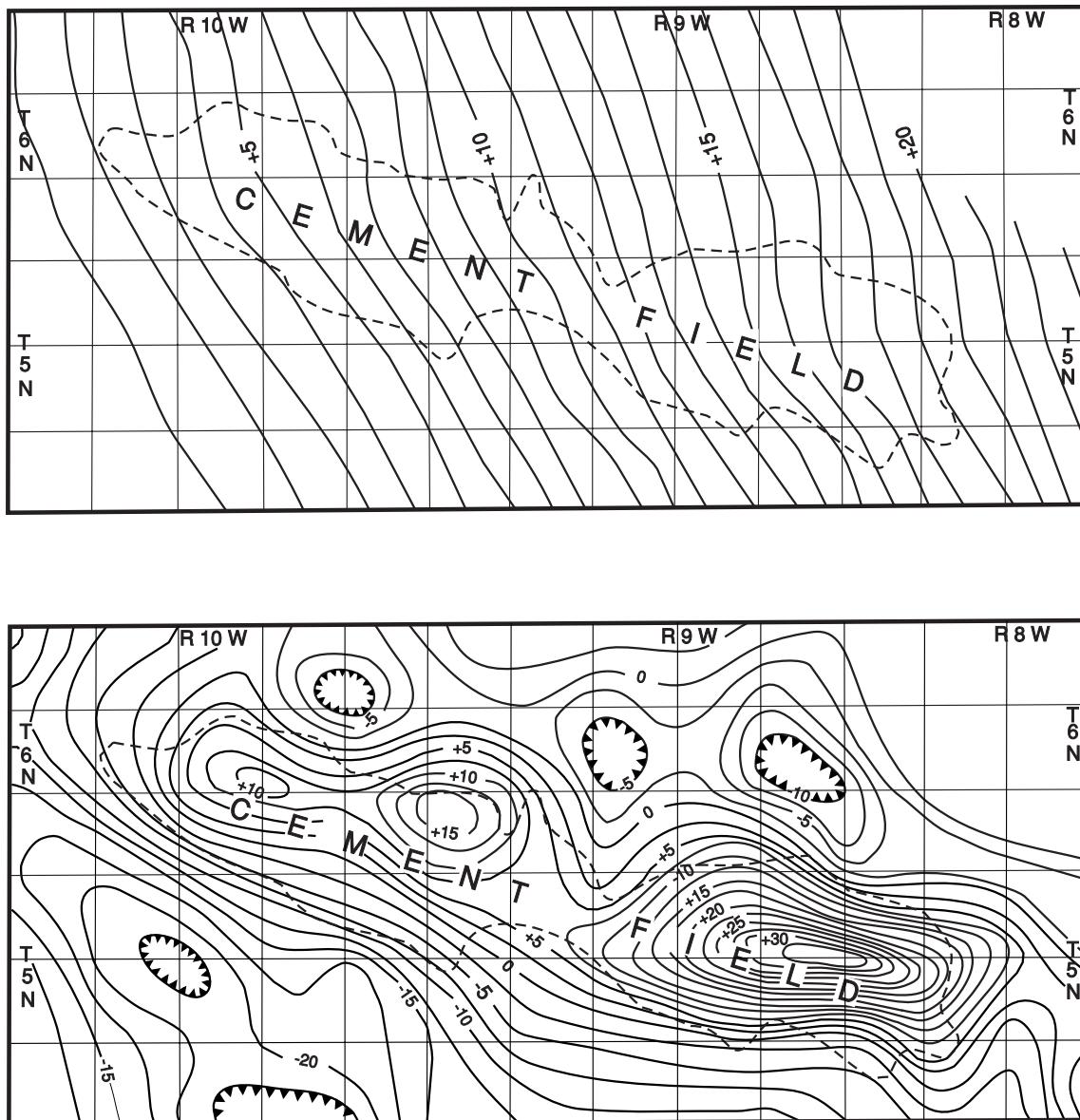


**Figure 2.39** Observed Bouguer anomaly (contour interval 1 mGal) and second vertical derivative ( $2.5 \times 10^{-15}$  c.g.s.u.) maps over the Cement Field in Oklahoma. From Elkins (1951), by permission.

Continuation is discussed in much more detail by Grant and West (1965) and by Telford *et al.* (1990).

Upward continuation is used in comparisons of ground-based gravity anomalies with airborne data. It is usual to continue ground data upwards rather than to work downwards so as not to amplify noise. An example of such a comparison is shown in Figure 2.42 (Hammer, 1982, 1984). Two gravity minima associated with low-density salt have shorter-wavelength maxima superimposed which are due to the high-density cap rocks. These maxima attenuate with increased elevation, and the agreement between the upwardly continued land Bouguer data and the airborne is better than 5 g.u. except in the immediate vicinity of the cap rocks.

One of the major considerations in the interpretation of particularly regional gravity data is the amount of computer process-

ing required. Considerable effort has been expended in developing computer-based methods of data enhancement. For example, image processing of data on computer-compatible tapes (CCTs) permits considerable manipulation of the data for display purposes to aid analysis and interpretation. Processes include edge enhancement to highlight lineaments (e.g. Thurston and Brown, 1994), amplitude displays and spectral modelling (Figure 2.43). It is usually only economically viable to undertake such sophisticated processing on very large datasets.

### 2.6.5.3 Euler deconvolution

Euler deconvolution has been developed primarily for geomagnetic surveys (see Chapter 3) and has been applied increasingly for

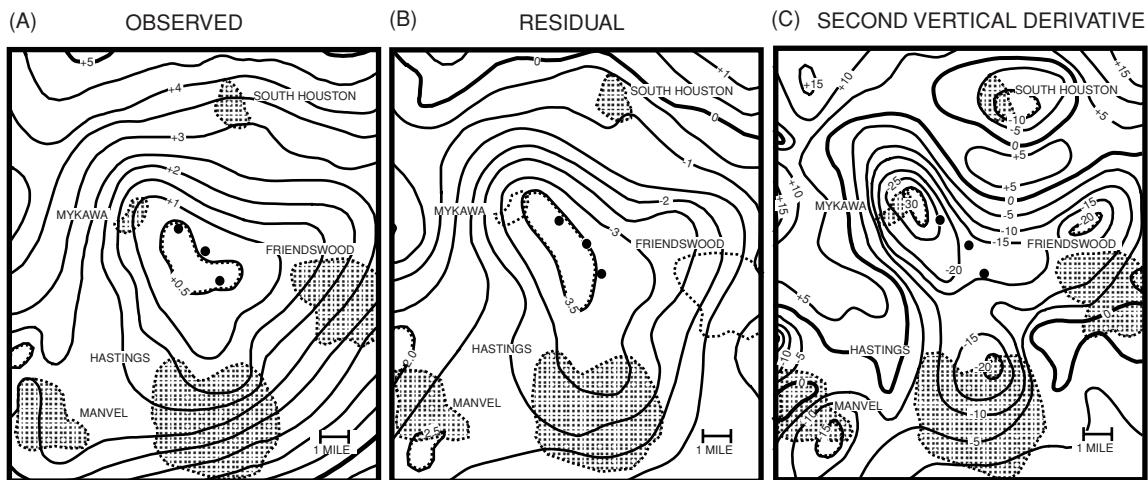


**Figure 2.40** (A) Observed gravity, (B) residual gravity (contour interval 0.5 mGal), and (C) second vertical derivative (contour interval  $5 \times 10^{-15}$  c.g.s.u.) maps for Mykawa, Texas Gulf Coast. • indicates dry boreholes. From Elkins (1951), by permission.

the interpretation of gravity data since the late 1980s. 3-D Euler deconvolution was developed for geomagnetic data by Reid *et al.* (1990) and has since been developed for gravity tensor gradient data (Zhang *et al.*, 2000).

The Euler deconvolution technique aids the interpretation of any potential field (gravity or magnetic) data in terms of depth and geological structure. The discussion here focuses on gravity data, but the principle also applies to magnetic data. Conventional Euler deconvolution utilises three orthogonal gradients of gravity data as well as the gravity values themselves to determine depths and the locations of source bodies. The basic Euler deconvolution equation is given in Box 2.24 and the equations for tensor Euler deconvolution are given in Box 2.25. Derivations of specific formulae for specific source types are beyond the scope of this book. The primary data used for the Euler deconvolution analyses comprise series of survey profiles of airborne gravity, the locations of each measurement point being known.

Zhang *et al.* (2000) have developed the Euler deconvolution method and compared their new tensor deconvolution process, which uses all tensor gradients, against the conventional method where three gradients of the vertical component of the gravity vector are used. They used three target model shapes for the comparison, namely point, prism and cylindrical mass. The results they presented are shown in Figure 2.44, in which it is clear to see that the grid tensor Euler process provides the clearest results.

## 2.6.6 Sedimentary basin or granite pluton?

It is very important in the interpretation of gravity data for hydrocarbon exploration to be able to distinguish between a sedimentary basin (a good possible hydrocarbon prospect) and a granitic pluton (no prospect for hydrocarbons), as both can produce negative gravity anomalies of comparable magnitude.

For example, Arkell (1933) interpreted a minimum in an initial Bouguer gravity survey in the Moray Firth, northeast Scotland, as being due to a granite pluton. It was only after further geological

work (Collette, 1958) and gravity work (Sunderland, 1972) that it was realised that the minimum was due to a sedimentary basin. Simultaneously, the Institute of Geological Sciences undertook seismic reflection surveys and initiated some shallow drilling. It was not until 1978 that the Beatrice Field was discovered (McQuillin *et al.*, 1984). Had the 1933 interpretation been different, the history of the development of the North Sea as a major hydrocarbon province might have been very different.

In 1962, Bott proposed a set of criteria to distinguish between a sedimentary basin and a granite boss as interpretations of gravity minima. His argument was based on the second vertical derivative of the gravity anomaly due to a semi-infinite two-dimensional horizontal slab with a sloping edge. He found that the ratio of the moduli of the maximum and minimum second vertical derivative ( $|\Delta g'_{\max}|/|\Delta g'_{\min}|$ ) provides a means of distinguishing between the two geological structures, as outlined in Box 2.26 and illustrated in Figure 2.45. McCann and Till (1974) have described how the method can be computerised and the application of Fourier analysis to Bott's method. Some authors calculate the second *horizontal* derivative ( $\delta^2 g/\delta x^2$ ) (e.g. Kearey *et al.*, 2002: Fig. 6.19), which responds in exactly the same way as the *vertical* derivative except that the maxima and minima are reversed, as are the criteria in Box 2.26. In order for the method to work, the gravity anomaly attributed to the appropriate geological feature (sedimentary basin or granitic pluton) needs to be clearly isolated from adjacent anomalies due to other features. The method is not applicable, however, in cases where extensive tectonic activity has deformed either a sedimentary basin by basin shortening or a granitic pluton by complex faulting, thereby changing the gradients of the flanks of both types of model.

The vertical variation of density of sediments with depth in a sedimentary basin can be represented in a number of ways. Moving away from Bott's uniform density model, consideration of the variation in density in terms of exponential and hyperbolic density contrast has been given by Rao *et al.* (1993, 1994), for example.

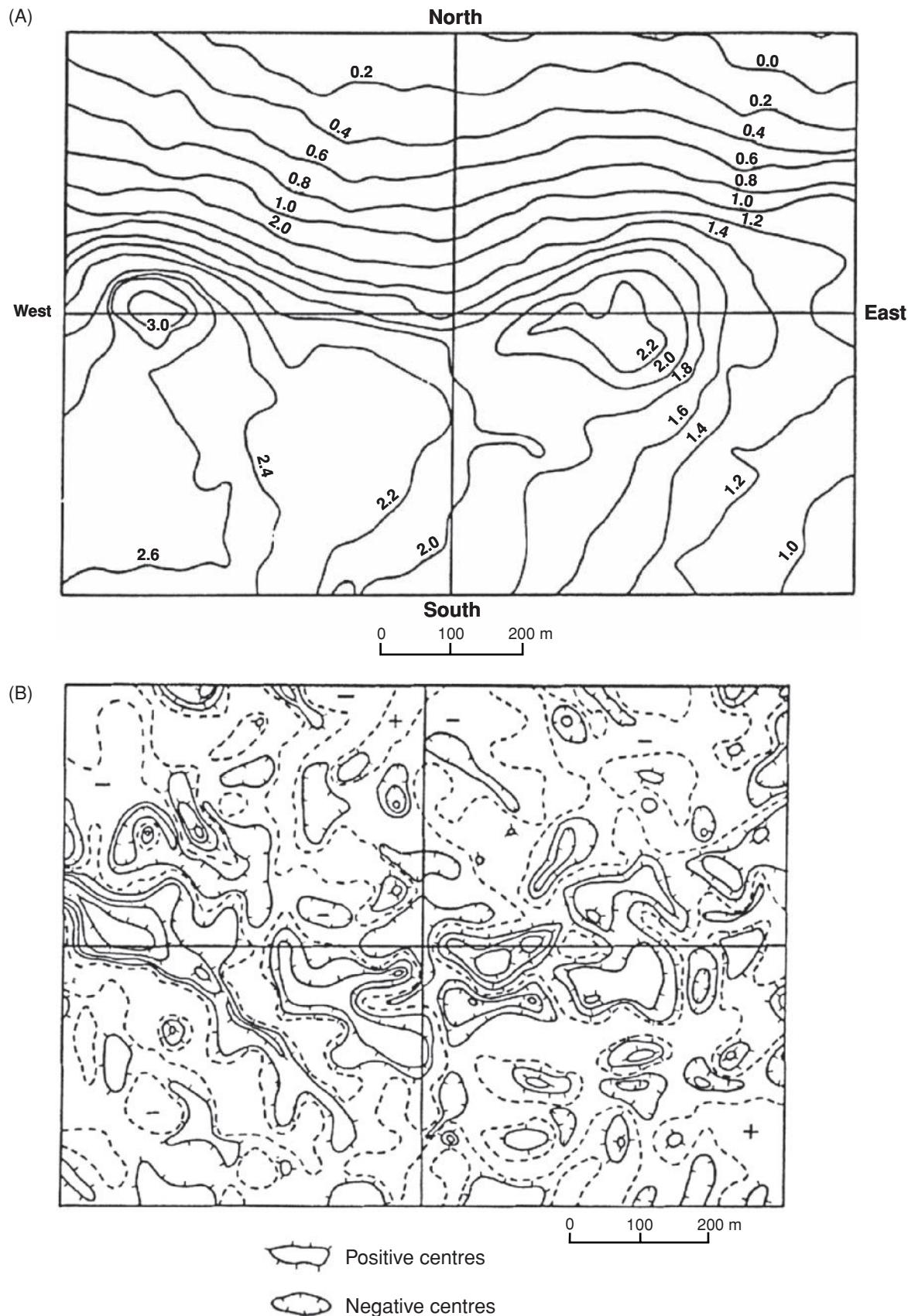


**Figure 2.41** An example where the Bouguer anomaly map (A) (contour interval 2 mGal) exhibits more than the corresponding second vertical derivative map (B) for the Jjaure titaniferous iron-ore region in Sweden. Contours: 0 (dashed),  $\pm 0.1$ ,  $\pm 0.2$ ,  $\pm 0.4$  in units of  $0.0025 \text{ mGal/m}^2$ . From Parasnis (1966), by permission.

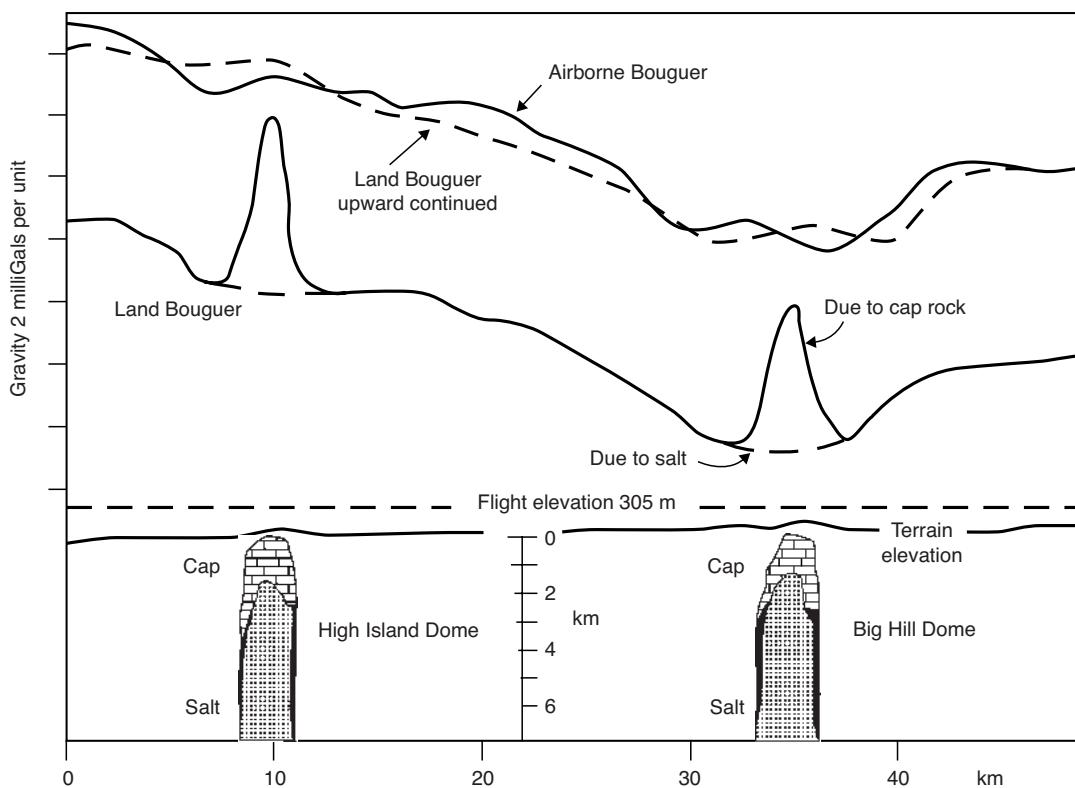


**Figure 2.42** Comparison of airborne and upward continued land Bouguer gravity data with those obtained by airborne gravity surveying. From Hammer (1984), by permission.

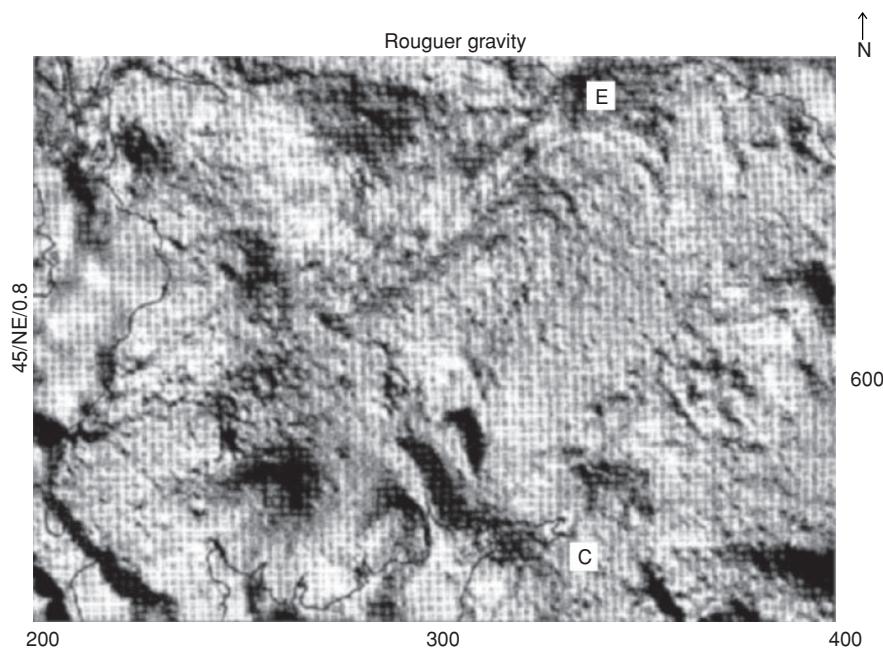


**Figure 2.43** Structural analysis, based on lineations from a series of colour and greyscale shaped-relief images of geophysical data, can provide a basis for reassessment of regional structure, mineralisation potential and fracture patterns. This image is of observed regional Bouguer gravity data, over an area of 200 km x 140 km of the Southern Uplands, Scotland (C: Carlisle; E: Edinburgh). The data have been reduced to Ordnance Datum using a density of  $2.7 \text{ Mg/m}^3$ , interpolated to a square grid of mesh size 0.5 km and displayed as a greyscale shaded-relief image. Sun illumination azimuth and inclination are NE and  $45^\circ$ , respectively. A series of NE trending features parallel to the regional strike and the Southern Uplands fault have been suppressed by the NE illumination, whereas subtle NW trending features linked to development of the Permian basins are enhanced and seen to be more extensive. For comparison, see Figure 3.50. Image courtesy of Regional Geophysics Group, British Geological Survey.

**Box 2.24** Conventional Euler deconvolution equation (Zhang et al., 2000)

The conventional Euler deconvolution equation is given by:

$$(x - x_0)T_{zx} + (y - y_0)T_{zy} + (z - z_0)T_{zz} = N(B_z - T_z)$$

for the gravity anomaly vertical component  $T_z$  of a body having a homogeneous gravity field. The parameters  $x_0$ ,  $y_0$  and  $z_0$  represent the unknown coordinates of the source body centre or edge to be estimated, and  $x$ ,  $y$  and  $z$  are the known coordinates of the observation point of the gravity and gradients. The values  $T_{zx}$ ,  $T_{zy}$  and  $T_{zz}$  are the measured gravity gradients along the  $x$ ,  $y$  and  $z$  directions;  $N$  is the structural index, and  $B_z$  is the regional value of the gravity to be estimated.

Rewriting the first equation, we have:

$$x_0 T_{zx} + y_0 T_{zy} + z_0 T_{zz} + NB_z = xT_{zx} + yT_{zy} + zT_{zz} + NT_z$$

in which there are four unknown parameters ( $x_0$ ,  $y_0$ ,  $z_0$  and  $B_z$ ).

**Box 2.25** Tensor Euler deconvolution equations (Zhang et al., 2000)

In addition to the first equation given in Box 2.24, tensor Euler deconvolution uses two additional equations:

$$(x - x_0)T_{xx} + (y - y_0)T_{xy} + (z - z_0)T_{xz} = N(B_x - T_x)$$

$$(x - x_0)T_{yx} + (y - y_0)T_{yy} + (z - z_0)T_{yz} = N(B_y - T_y)$$

where the values  $T_x$  and  $T_y$  are the horizontal components of the gravity vector along the  $x$  and  $y$  directions, respectively. The values  $T_{xx}$ ,  $T_{xy}$ ,  $T_{xz}$ ,  $T_{yx}$ ,  $T_{yy}$  and  $T_{yz}$  are gravity tensor gradients.  $B_x$  and  $B_y$  are the regional values of the horizontal components to be estimated if values of  $T_x$  and  $T_y$  are available. Otherwise  $(B_x - T_x)$  and  $(B_y - T_y)$  can be estimated in the process.

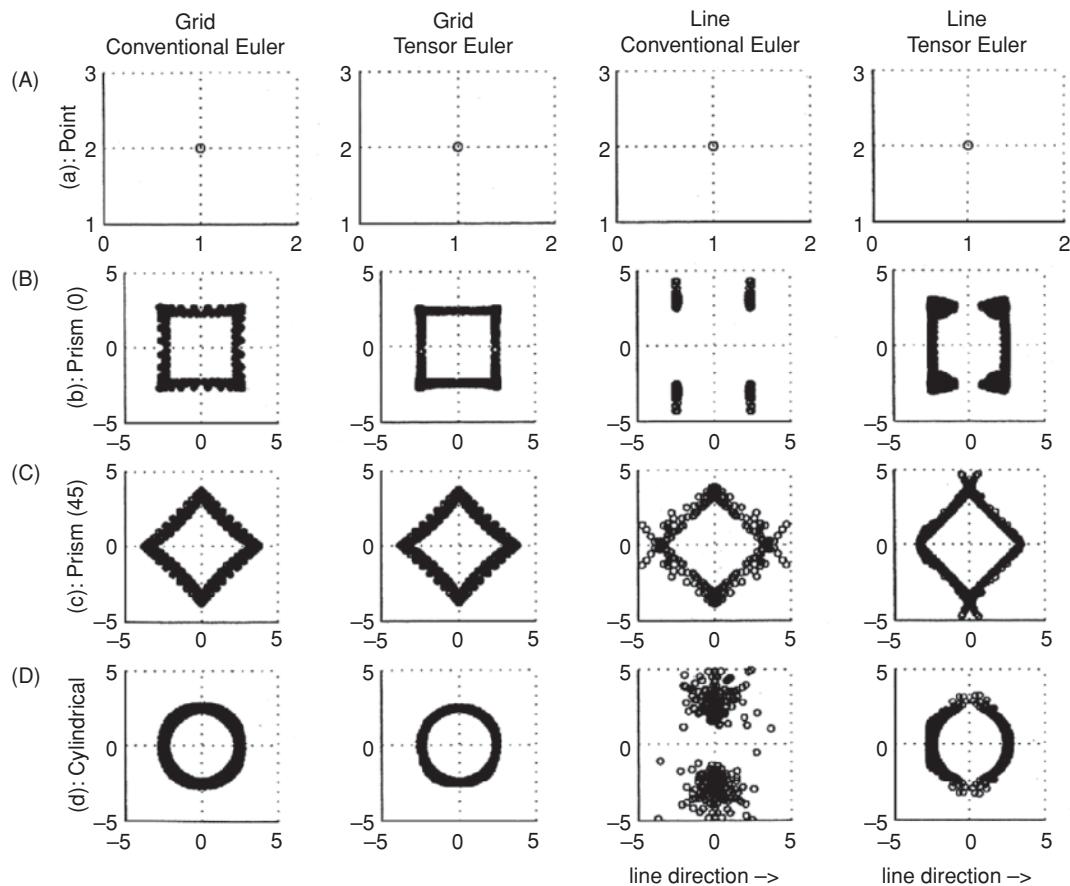


**Figure 2.44** Euler deconvolution results from four models (a small circle denotes the position of each solution). From Zhang et al. (2000), by permission.

**Box 2.26 Bott criteria (see also Figure 2.45)**

(1) For a sedimentary basin:

$$|g''_{\max}| / |g''_{\min}| > 1.0$$

Basin sides slope *inwards*.

(1) For a granite pluton:

$$|g''_{\max}| / |g''_{\min}| < 1.0$$

Granite pluton sides slope *outwards*.

the gravity anomalies (Figure 2.47) correlated extremely well with the distribution of the mineralisation within the ore body. Additionally, the gravity data were used successfully to estimate total ore tonnage. Electrical resistivity (see Chapter 7) produced low-amplitude anomalies with a broad correlation with the position of the ore body, and a TURAM electromagnetic survey (see Chapters 10 and 11) was singularly unsuccessful and produced virtually no anomaly at all. The induced polarisation chargeability produced a spectacular anomaly.

**2.7.1.3 Sourton Tors, Dartmoor, SW England**

This is an example of where gravity did not work at all in association with a known occurrence of mineralisation (Figure 2.48), whereas electrical, electromagnetic and magnetic methods all produced significant anomalies (Beer and Fenning, 1976; Reynolds, 1988). The reason for the failure of the gravity method in this case is two-fold:

- The scale of mineralisation, which is a stockwork of mineralised veins, was of the order of only a few metres wide.
- The sensitivity of the gravimeter was insufficient to resolve the small density contrast between the sulphide mineralisation and the surrounding rocks.

Had a gravimeter capable of measuring anomalies of the order of tens of  $\mu\text{Gal}$  been available, and the station interval been small enough, then the zone of mineralisation may have been detectable. At the time of the survey (1969) sensitive gravimeters were not as widely available as they are today.

**2.7 Applications and case histories**

In this section, a limited number of case histories are described to illustrate the diversity of applications to which the gravity method can be put. Other geophysical methods are discussed as appropriate, where they have been used in conjunction with, or to contrast with, the gravity results. These other methods are explained in their respective chapters as appropriate.

**2.7.1 Mineral exploration**

Gravity surveys fulfil two roles in exploration for minerals: (1) for search and discovery of the ore body; and (2) as a secondary tool to delimit the ore body and to determine the tonnage of ore.

**2.7.1.1 Discovery of the Faro lead-zinc deposit, Yukon**

An integrated airborne and land geophysical exploration programme, of which gravity surveying was an integral part, led to the discovery of the Faro lead-zinc deposit in the Yukon, northern Canada (Brock, 1973). Gravity was found to be the best geophysical method to delimit the ore body (Figure 2.46). It was also used to obtain an estimate of the tonnage (44.7 million tonnes), which compared very well with a tonnage proven by drilling of 46.7 million tonnes (Tanner and Gibb, 1979). In contrast, vertical magnetic mapping provided an anomaly with too shallow gradients to be used, as Figure 2.46 shows.

**2.7.1.2 Pyramid ore body, North West Territories**

The Pyramid lead-zinc ore body, at Pine Point in the North West Territories, Canada, was discovered using the ‘induced polarisation’ (IP) method (Seigel *et al.*, 1968). For further details of IP, see Chapter 9. Gravity was used to optimise development drilling since

**2.7.1.4 Central Mineral Belt Uranium Project, Labrador**

Uranium was first discovered in central Labrador, Newfoundland, in 1956 through the use of geological mapping and radiometric surveying. In the late 1970s, Shell drilled 72 exploration boreholes. However, in the 1980s there followed a period of very low uranium prices during which time exploration at the prospect ceased. In 2003 an airborne gravity survey was conducted that revealed the presence of a kilometre-long elliptical anomaly in an area with known occurrences of uranium.

Further airborne geophysical surveys were undertaken along with ground gravity surveys to help to define the extent of the uranium find. With an extensive programme of further drilling and sediment sampling, a 4.5-km long mineralised corridor was identified. This prospect is currently being managed by Crosshair Exploration and Mining Corporation through its Northstar Division.

**2.7.2 Engineering applications**

The size of engineering site investigations is normally such that very shallow (<50 m) or small-scale (hundreds of square metres) geological problems are being targeted. Consequently, the resolution

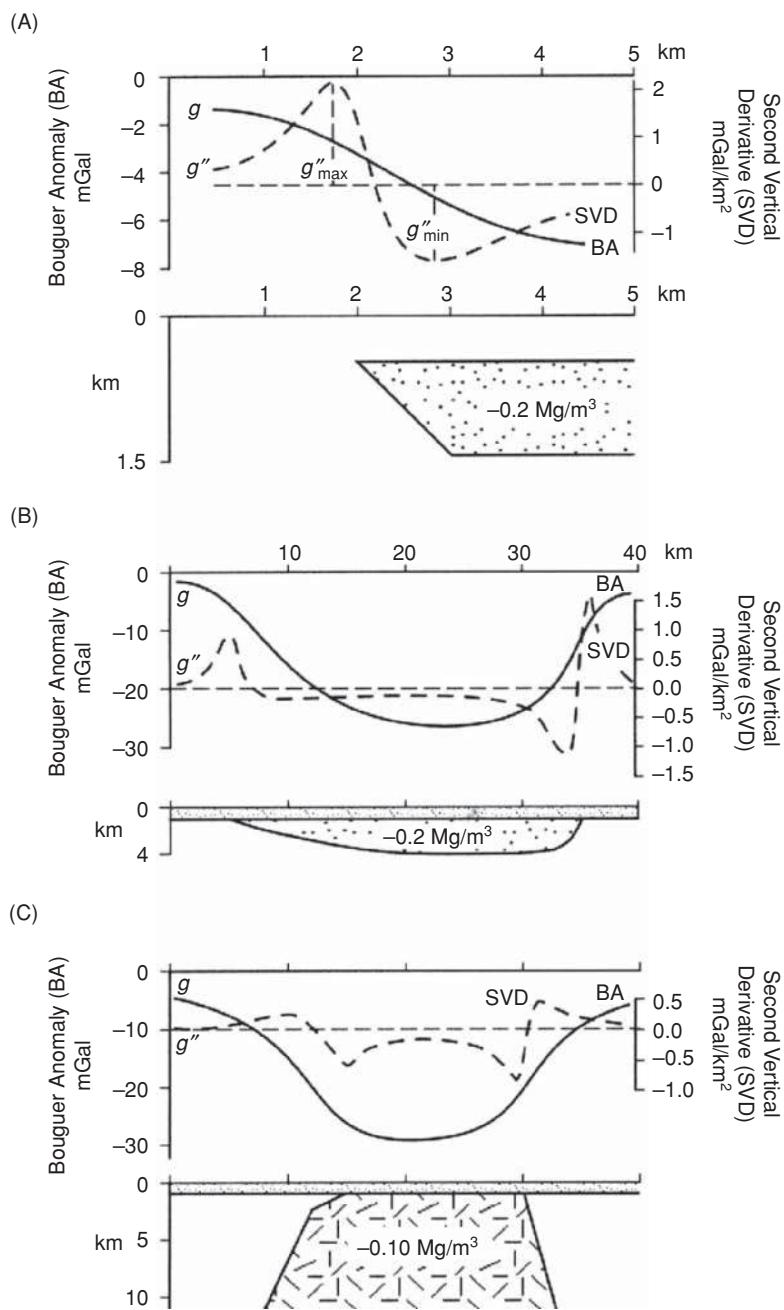


**Figure 2.45** Bott criteria to distinguish between the Bouguer gravity profile over (A) a horizontal prism, (B) a sedimentary basin, and (C) a granitic pluton. After Bott (1962), by permission.

required for gravity measurements is of the order of  $<5 \mu\text{Gals}$ . The use of gravity is commonly to determine the extent of disturbed ground where other geophysical methods would fail to work because of particularly high levels of electrical or acoustic noise, or because of the presence of a large number of underground public utilities (Kick, 1985). Additionally, gravity is used to assess the volume of anomalous ground, such as the size of underground cavities or of ice lenses in permafrost. There are often no records of where ancient quarrying or mining has been undertaken, and the

consequent voids may pose considerable hazards to people and to property (see next section). The increasing development of higher latitudes brings its own engineering problems, and the application of gravity surveying, amongst other applied geophysical methods, is playing a growing and important role in site investigations in these areas. Furthermore, it is also true to say that with the increased use of geophysical methods, the very geological phenomena under investigation are becoming better studied and better understood.

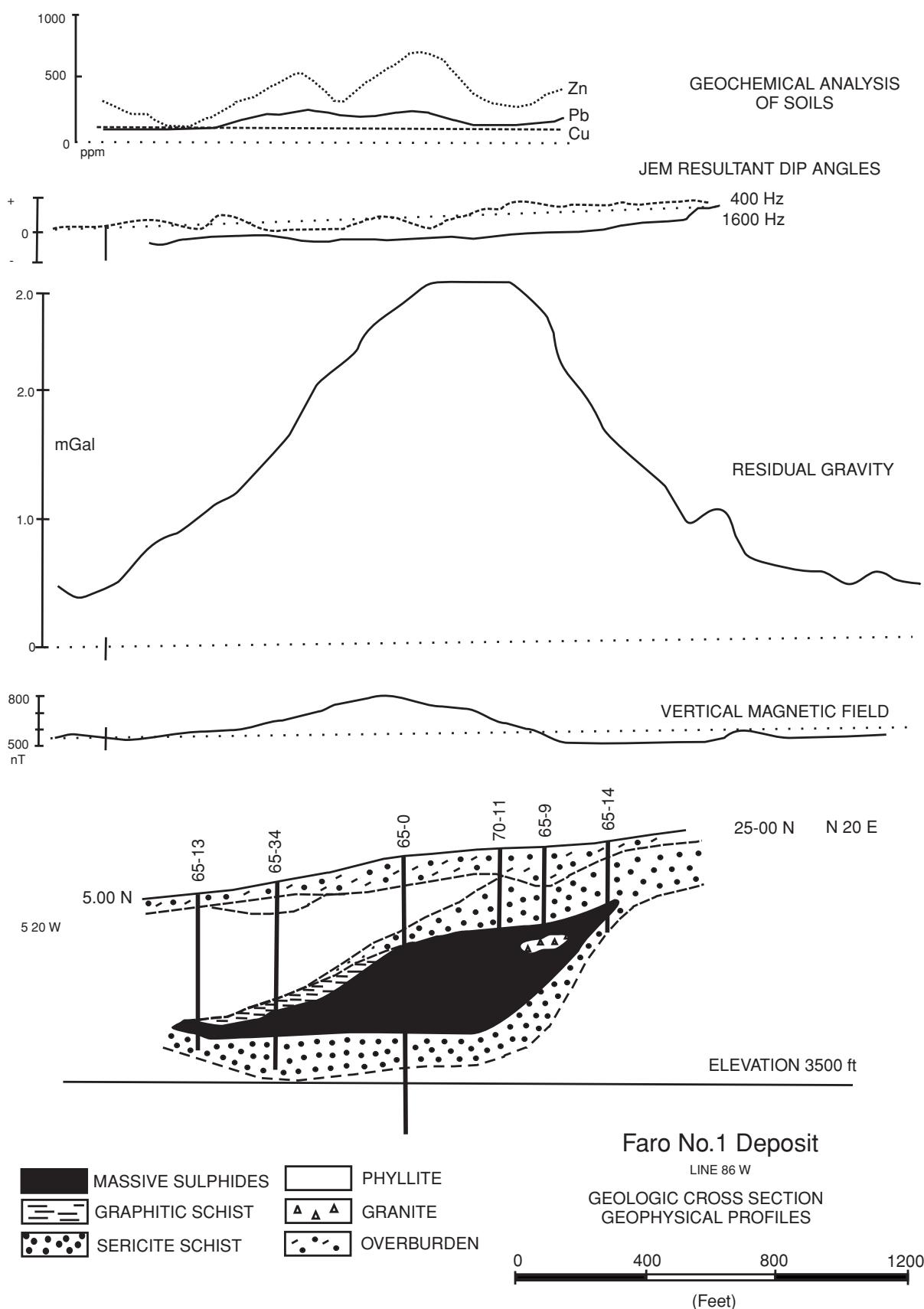


Figure 2.46 Various geophysical profiles, including residual gravity, across the Faro lead-zinc deposit in the Yukon. From Brock (1973) and Tanner and Gibb (1979), by permission.

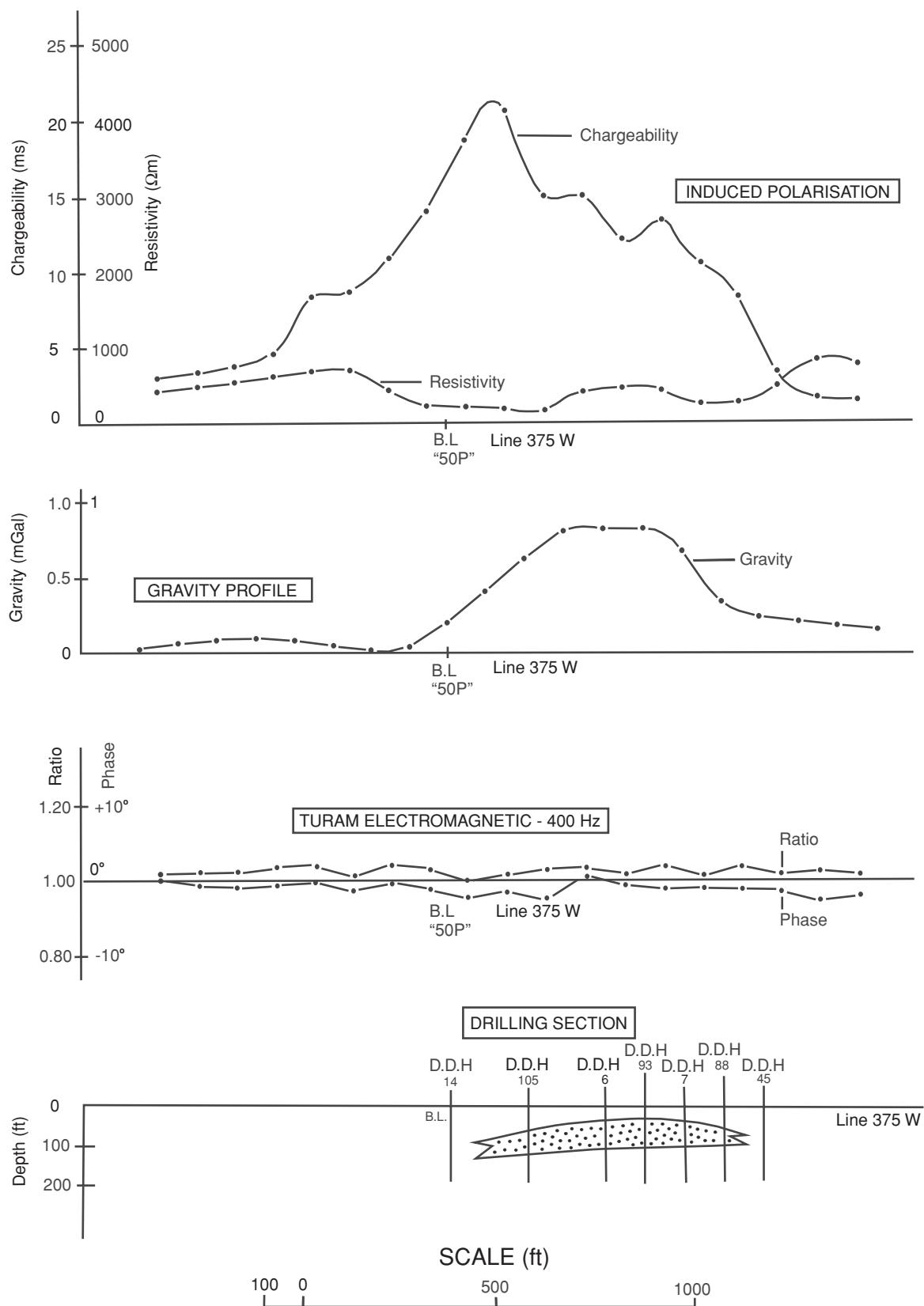
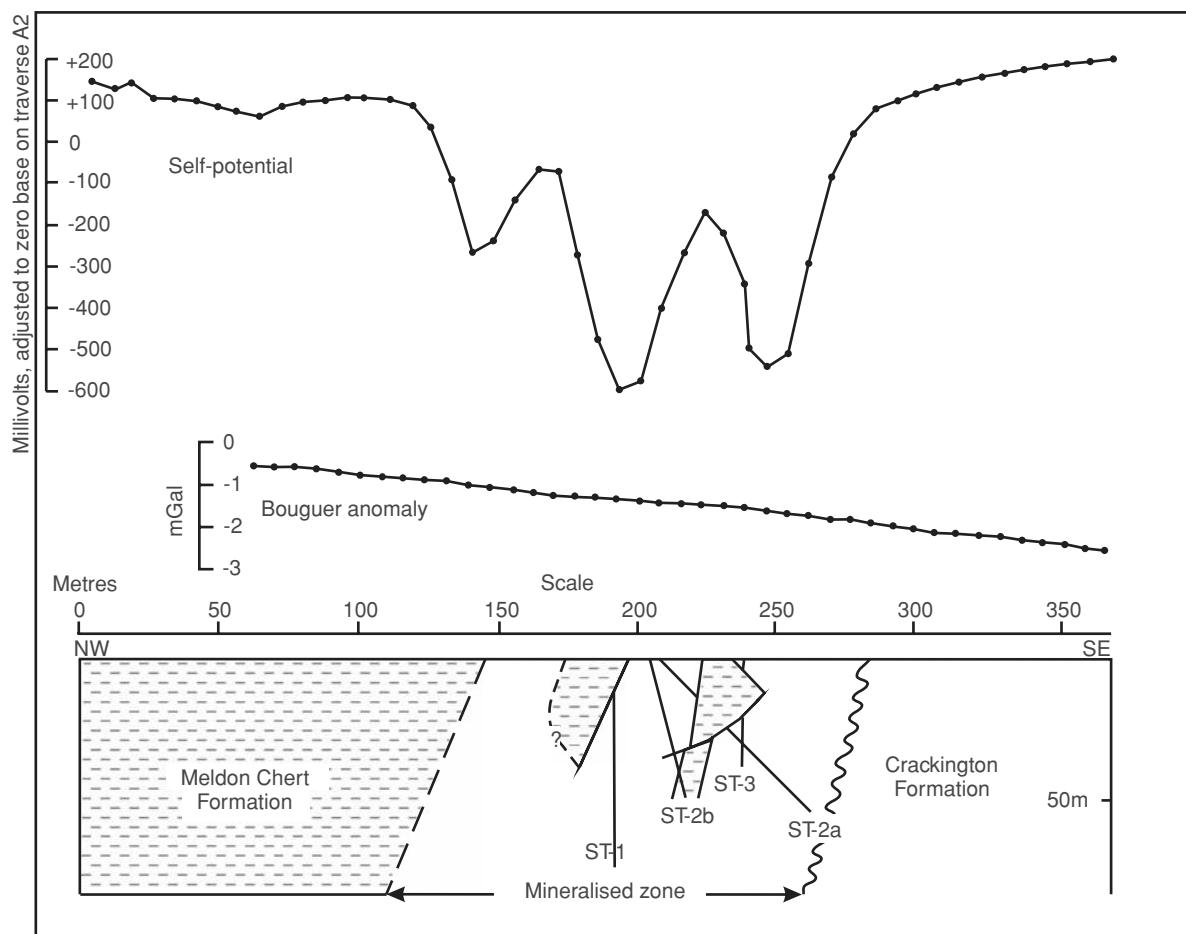


Figure 2.47 Various geophysical profiles including residual gravity, across Pyramid no. 1 ore body. From Seigel et al. (1968), by permission.



**Figure 2.48** A Bouguer gravity profile across mineralised zones in chert, Sourton Tors, northwest Dartmoor, showing no discernible anomalies. From Beer and Fenning (1976), by permission.

### 2.7.2.1 Detection of natural and man-made cavities

Hidden voids within the near-surface can become serious hazards if exposed unwittingly during excavation work, or if they become obvious by subsidence of the overlying ground (Figure 2.49). The detection of suspected cavities using gravity methods has been achieved in many engineering and hydrogeological surveys (e.g. Colley, 1963).

An example of the application of micro-gravimetry to the detection of underground cavities has been given by Fajkiewicz (1986). Over many years he has investigated the gravity effect of both natural and man-made cavities and has helped to develop a method of detection based on calculating the vertical gradient of the gravity field. He has found that the amplitude of the gravity anomaly is commonly greater than that predicted (Figure 2.50) for reasons that are still not clear.

A micro-gravity survey was carried out in the town of Inowroclaw, Poland, where karst caverns occur to depths of around 40 m in gypsum, anhydrite, limestone and dolomite. The cavities develop towards the ground surface and have resulted in the damage and destruction of at least 40 buildings within the town. The density

contrast between the cavity and the surrounding material in Figure 2.50A is  $-1.8 \text{ Mg/m}^3$  and for Figure 2.50B is  $-1.0 \text{ Mg/m}^3$ , slightly lower due to the presence of rock breccia within the cavity. Fajkiewicz has demonstrated that the cavity in Figure 2.50B should not have been detectable assuming that its gravity field is due entirely to a spherical cavity at the depth shown. Even the theoretical anomaly from the vertical gravity gradient is too broad to indicate the presence of a cavity, yet the observed anomaly is quite marked.

A similar approach can be taken using horizontal gravity gradients ( $\Delta g/\Delta x$  or  $\Delta g/\Delta y$ ), in which case the point at which the gravity anomaly reaches a minimum or maximum, the gradient goes through zero, and that point should lie over the centre of the body causing the anomaly (Butler, 1984). An example of this (Figure 2.51) is given by Casten and Gram (1989) for a test case where gravity data were measured in a deep coal mine along an inclined drift which was known to pass at right-angles over a pump room.

Furthermore, micro-gravimetry can be used to determine the rate and extent of the development of strength-relaxation around underground excavations, as shown in Figure 2.52 (Fajkiewicz, 1986; Glusko *et al.*, 1981). As the rock relaxes mechanically it cracks, thereby reducing its bulk density. As the cracking continues and develops, so the changes in density as a function of time can be



**Figure 2.49** Catastrophic failure of the roof of an ancient flint mine in Chalk in Norwich. Photo courtesy of Eastern Daily Press. [C]

detected using highly sensitive micro-gravimeters, and then modelled.

In 2003 and 2004, geophysical surveys were commissioned for a rural site in the Peak District in the UK that was proposed for development for residential properties. However, the site was known to overlie limestone bedrock in which natural solution features were present. Water was observed to drain through a series of interconnected underground caves, some of which had been explored and partially mapped by speleologists. In addition to obvious entrants to the caves, conspicuous surface depressions were also visible that possibly correlated with collapsed and/or partially backfilled solution voids. Several coincident profiles were acquired using both electrical resistivity tomography (ERT) and micro-gravity across these features and correlated with both the surface geomorphology and available borehole results. The ERT inversions were used to develop suitable inputs for the gravity modelling so that a consistent interpretation of the subsurface could be determined (Figure 2.53). The open air-filled voids are evident as high-resistivity anomalies, and these coincided with areas of greatest density contrast such that a good fit was achieved between the synthetic and observed gravity data. Limestone bedrock affected by joints and solution features form an area of lower density material relative to limestone apparently unaffected by such features. It was clear that the combined use of both micro-gravity and resistivity methods to form an integrated interpretation was a significant benefit to the overall risk assessment for the footprints of the proposed structures of the new develop-

ment. It also enabled the house builder to ensure that the designs for the house foundations were appropriate for the level of risk associated with possible solution features. Surface structures and associated ground loading were relocated to minimise the possible adverse effects associated with the possible collapse of underground solution features.

On 4 January 2000 a crater opened up in a residential area of Reading, Berkshire, creating a hole with an estimated volume of 200 m<sup>3</sup> (Figure 2.54), rupturing a gas main and requiring the emergency evacuation of over 200 local residents. The hole was thought to be due to the collapse of historical chalk mine workings. Once the gas main was repaired, 17 families had to be rehoused urgently. The catastrophic collapse and ensuing plight of the local residents received substantial media coverage both locally and nationally (Soames, 2000). It was considered essential that further investigations were undertaken urgently. An extensive programme of probe drilling was undertaken in order to define the extent of the suspected mine workings, and to complement this, two micro-gravity surveys were carried out in February–March and June 2000 (Emanuel, 2002; Reynolds and Edmonds, 2001). The geophysical interpretation was confirmed by the probe drilling and provided sufficient accuracy in order to help direct the location of the intrusive investigation.

A Scintrex CG-3M Autograv gravimeter was used to acquire the data (Figure 2.55) on a grid 2 m by 2 m along the roads, in alleyways and in back gardens where space permitted. Although the site was near a major road and probe drilling was being undertaken while the gravity survey was being carried out, the standard deviation of measured micro-gravity results was generally better than 5 µGal. The observed data were corrected for all the standard factors but also for the buildings, taking into account building typology (cf. Section 2.5.7), and presented as Bouguer anomaly maps (Figure 2.56). Individual profiles were modelled (e.g. Figure 2.57) and the results used to provide a summary interpretation of the distribution of air-filled and infilled mine workings. This also included locating a backfilled quarry from which it is thought that the mine adits were driven. The survey clearly demonstrated the benefit of using micro-gravity to detect shallow mine workings, even though the site was located in the middle of a busy city and was close to major roads and a railway line. The success of the survey was attributable to specific survey design, well-controlled data acquisition and appropriate data reduction (especially the building corrections) and careful modelling. Indeed, following the site investigation, two further collapses occurred in locations where mine workings had been identified from the gravity survey. One collapse (Figure 2.58) exposed the crown of the underlying mine workings. The site has subsequently been remediated.

Branston and Styles (2003) described a time-lapse micro-gravity survey undertaken at Northwich, Cheshire, NW England. Salt was discovered in the area in 1670 and was mined extensively during the nineteenth century. As a result there is ongoing subsidence of the surrounding area. A particular area of terraced houses in east Northwich had been affected by subsidence, with several having been demolished in 1985. Further subsidence was reported and an initial micro-gravity survey undertaken in 1998. A second survey was completed in 2001 along the same transects. Over the

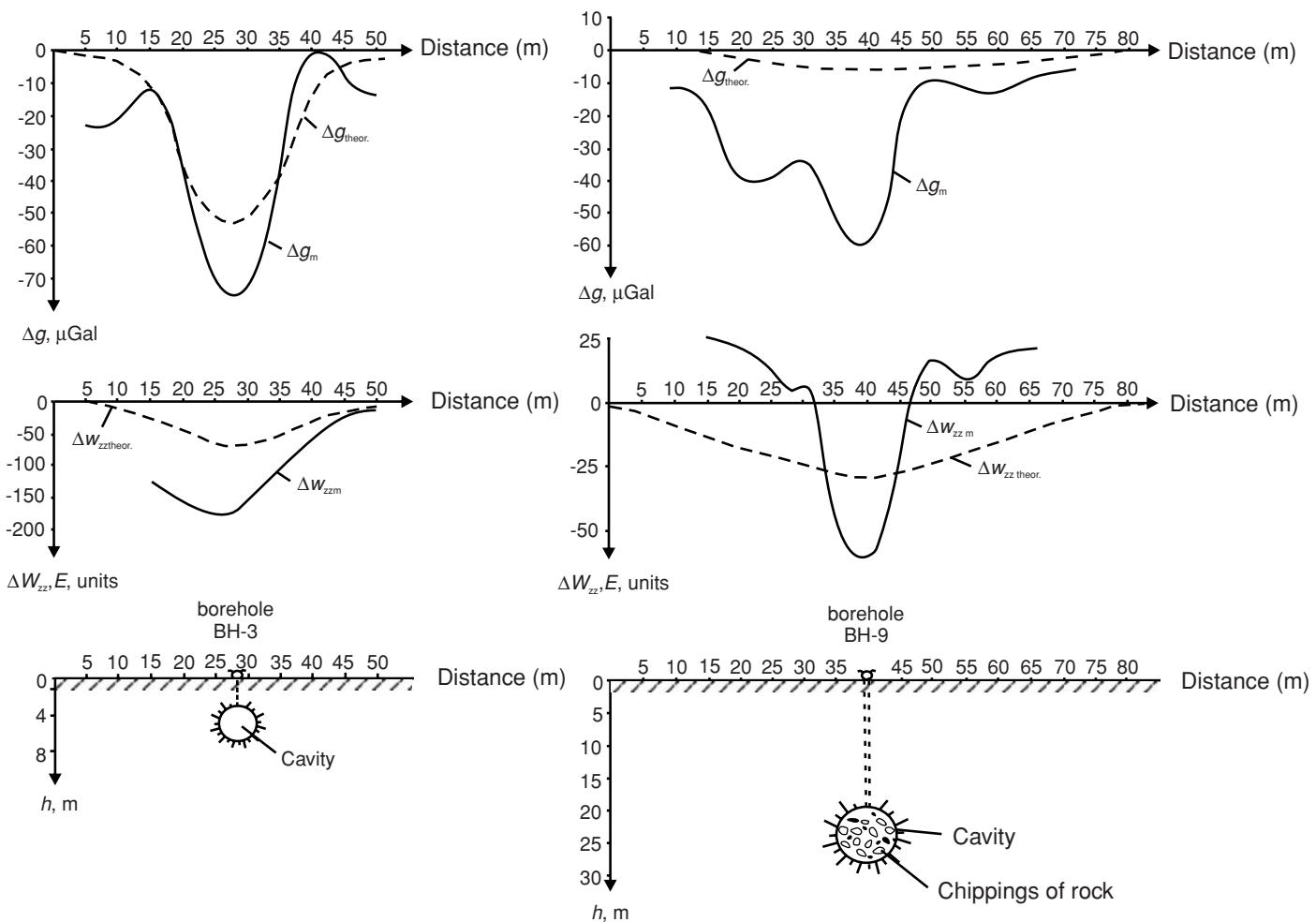


**Figure 2.50**  $\Delta g_m$  and  $\Delta W_{zz,m}$  – micro-gravity anomalies and gravity gradient anomalies respectively – over (A) an air-filled cavity (BH-3), and (B) one partially infilled by rock fragments (BH-9). Curves labelled with suffix 'theor' represent the theoretical anomalies based on the parameters of the cavity alone. From Fajklewicz (1986), by permission.

intervening time the ground had subsided by a further 23 cm. The data from coincident profiles obtained in 1998 and 2001 were modelled using GRAVMAG (Figure 2.59) and the calculated results from the models fit the observed data well. The density value attributed to each polygon labelled in Figure 2.59 is listed in Table 2.9. By comparing the models for each survey it was possible to determine any differences between them. The main feature interpreted was that the void and associated collapse breccia had changed over the intervening time, with the crown of the void migrating towards the ground surface by around 4 m, with a corresponding rise in the level of the collapse breccia from around 16 m below ground level to around 13.5 m below ground level. From the density information and modelling it was suggested that the void was largely filled with loose material (polygon no. 9) rather than being air-filled, with denser brecciated material lying beneath (polygon no. 12). Euler deconvolution solutions for the main feature identified indicated a depth of 8 m for the model in 1998 and 6 m for that in 2001.

Branston and Styles (2006) have also described a further case history showing the use of micro-gravity surveying at another site

in Northwich. Careful data acquisition followed by modelling using Euler deconvolution was used to target further intrusive investigations. The results of the drilling corresponded well with the predicted extent of the anomalous ground conditions derived from the geophysical survey.

Ripon, in NE England, is another area of the UK particularly prone to subsidence arising from dissolution of gypsumiferous Permo-Triassic strata, and has been the focus of a number of high-resolution micro-gravity surveys. One such survey has been described by Patterson *et al.* (1995). Following a desk study, a micro-gravity survey was undertaken on an 8 m grid with adjacent lines offset by 4 m to provide adequate ground coverage (Figure 2.60A). This included obtaining measurements inside an adjacent office block. The resulting residual gravity anomaly had a peak amplitude of -74  $\mu\text{Gal}$ . Subsequent static core probing, rotary drilling and trial trenching confirmed the existence of a potentially unstable breccia pipe centred on the gravity anomaly low (Figure 2.60B). A basic ground model, derived by modelling the gravity anomaly prior to the intrusive investigation, is shown superimposed on the section profile

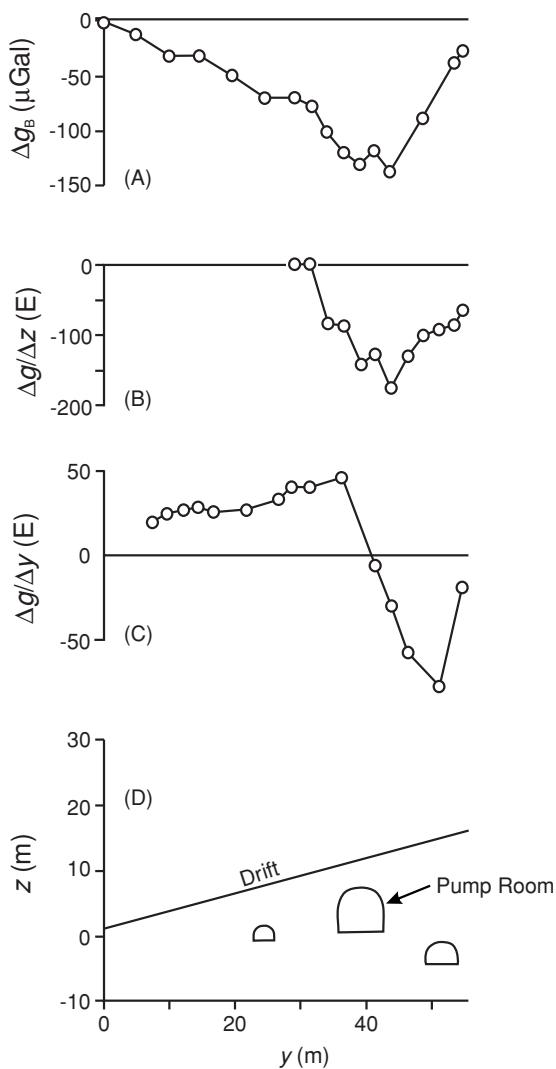


**Figure 2.51** A micro-gravity survey within a deep coal mine as measured along a drift cut over a pump room and other known cavities. (A) shows observed residual gravity data; (B) observed and computed vertical gravity gradients; (C) observed horizontal gravity gradient, and (D) underground positions of known cavities from mine plans. From Casten and Gram (1989), by permission.

in Figure 2.60B and demonstrated that the model was substantially correct.

A similar survey was undertaken in 2004 at another site in Ripon, but using a 2.5 m grid with adjacent lines offset by 2.5 m. A number of residual gravity anomaly lows were identified, with amplitudes of the order of  $-70 \mu\text{Gal}$  (Figure 2.61). Removing further localised regional fields, the resultant anomalies reduce to  $-16 \mu\text{Gal}$ . One such anomaly, which has been modelled in detail (Figure 2.61), indicates a breccia pipe with lower density material in its upper reaches and a discrete void at a depth below  $\sim 17$  m. Subsequent intrusive investigation on this location confirmed the gravity model.

In contrast with the applications described above, sinkholes in a palaeokarst basin may not provide a potential geotechnical hazard, but an important source of fossil flora and fauna. One such occur-

rence is the Gray Fossil Site, Washington County, Tennessee, USA, which has produced a remarkable Mio-Pliocene fauna and flora (Whitelaw *et al.*, 2008). Drilling indicated that the fossils occurred in fill material within a series of sinkholes. The distribution of these features could not be determined using drilling. To image the sink-hole basin more adequately, a high-resolution micro-gravity survey was undertaken comprising some 1104 measurement stations. These data were used to create complete Bouguer and residual gravity anomaly maps and a 3D density model via inversion methods. The residual gravity anomaly map reveals the presence of seven separate sinkholes. However, the 3D inverse modelling constrained by drill-hole depths and density indicate that there are 11 separate sinkholes, ranging between 20 m and 44 m in depth. The identified depocentres provide targets for the acquisition of additional complete cores to bedrock, and a focus for palaeontologists.

### 2.7.2.2 Detection of massive ice in permafrost terrain

The thawing of massive ice masses and associated ice-rich permafrost can cause severe engineering and environmental problems. The detection and identification of such ground phenomena is thus extremely important.

Kawasaki *et al.* (1983) provided an example of the use of gravity surveying to detect the presence and the volume of massive ice within an area of permafrost at Engineer Creek, near Fairbanks, Alaska, along the route of a proposed road cut. It is well known that large bodies of massive ice, such as occur within pingos, give rise to significant gravity anomalies (Mackay, 1962; Rampton and Walcott, 1974). Permafrost without discrete segregated ice has a density of about  $1.6 \text{ Mg/m}^3$ , compared with the density of solid ice ( $0.88\text{--}0.9 \text{ Mg/m}^3$ ) and with that of typical Alaskan soils ( $1.35\text{--}1.70 \text{ Mg/m}^3$ ) and should give rise to detectable residual gravity anomalies if measured with a sufficiently sensitive gravimeter.

Kawasaki and colleagues demonstrated that, although massive ice can be detected by correlation with the gravity minima along the profile shown in Figure 2.62, the measurements were also sensitive to variations of density within the schist bedrock.

The gravity method is considered an excellent tool for detailed investigation of construction sites where massive ice is suspected, but it is too slow a method for use as a reconnaissance tool over long profiles. Other geophysical methods such as electrical resistivity, electromagnetic ground conductivity and ground-penetrating radar are more efficient, particularly for reconnaissance (Osterkamp and Jurick, 1980).

### 2.7.3 Archaeological investigations

Gravimetry is increasingly of interest to archaeologists searching, for example, for ancient crypts or passages within Egyptian pyramids, such as has been achieved within the Kheops (see *First Break*, 1987, 5(1): 3) with what is called ‘endoscopic micro-gravity’ (see also Lakshmanan, 1991).

Blizkovsky (1979) provided an example of how a careful micro-gravity survey revealed the presence of a suspected crypt within

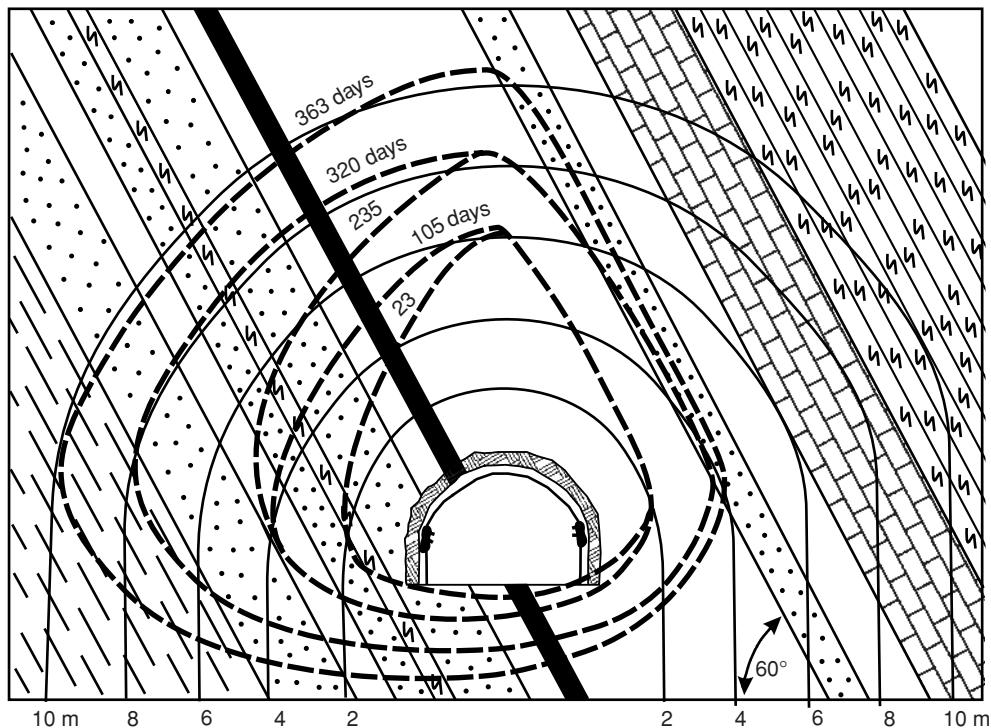


**Figure 2.52** The time-dependent strength-relaxation around an underground gallery at 540 m depth as deduced from micro-gravity surveying in the Tchesnokov Colliery in the Don Basin over a period of 363 days. From Glusko *et al.* (1981) and Fajkiewicz (1986), by permission.

the St ‘Venceslas church, Tovačov, Czech Republic, which was later proven by excavation work. The dataset consisted of 262 values measured on a 1 m<sup>2</sup> or 4 m<sup>2</sup> grid to an accuracy of  $\pm 11 \mu\text{Gal}$ , corrected for the gravity effect of the walls of the building (Figure 2.63). Two significant gravity minima with relative amplitudes of  $-60 \mu\text{Gal}$  were located, which indicated mass deficiencies associated with the previously unknown crypts.

## 2.7.4 Hydrogeological applications

Gravity methods are not used as much as electrical methods in hydrogeology, but can still play an important role (Carmichael and Henry, 1977). Their more normal use is to detect low-density rocks that are thought to be suitable aquifers, such as alluvium in buried rock valleys (Lennox and Carlson, 1967; van Overmeeren, 1980).

Rather than interpret Bouguer anomalies, it is possible to use a gravimeter to monitor the effect of changing groundwater levels. For example, in a rock with a porosity of 33% and a specific retention of 20%, a change in groundwater level of 30 m could produce a change in  $g$  of  $170 \mu\text{Gal}$ . It is possible, therefore, to use a gravimeter to monitor very small changes in  $g$  at a given location. The only changes in gravity after corrections for instrument drift and Earth tides should be the amount of water in the interstices of the rock. Consequently, for an aquifer of known shape, a measured change in gravity, in conjunction with a limited number of water-level observations at a small number of wells, can be translated into

an estimate of the aquifer’s specific yield. Similarly, repeated gravity measurements have been used to estimate the volume of drawdown, degree of saturation of the steam zone (Allis and Hunt, 1986) and the volume of recharge of the Wairakei geothermal field, North Island, New Zealand (Hunt, 1977).

### 2.7.4.1 Location of buried valleys

Buried Pleistocene subglacial valleys are important geological structures in northern Germany and are used extensively for groundwater production (Gabriel, 2006). However, the distribution and internal structure of these valleys are not known completely. In order to ensure future water supplies, more details are needed about the locations of buried Pleistocene subglacial valleys as well as the characterisation of the physical properties of their sedimentary infill. In order to obtain such information, intrusive methods with down-hole geophysical logging are used in combination with a variety of geophysical methods, including reflection seismic surveys, airborne EM, and gravity.

Of four subglacial valleys investigated by Gabriel, only that in the Ellerbek valley in Schleswig-Holstein produced a negative anomaly (Figure 2.64). The geometry of the valley and its sandy infill was derived from seismic surveys. The simplest model comprised two source bodies: the Pleistocene valley fill and the surrounding Neogene sediments with a density contrast of  $50 \text{ kg/m}^3$ . The Trave valley in the same area of Germany, however, produced a positive

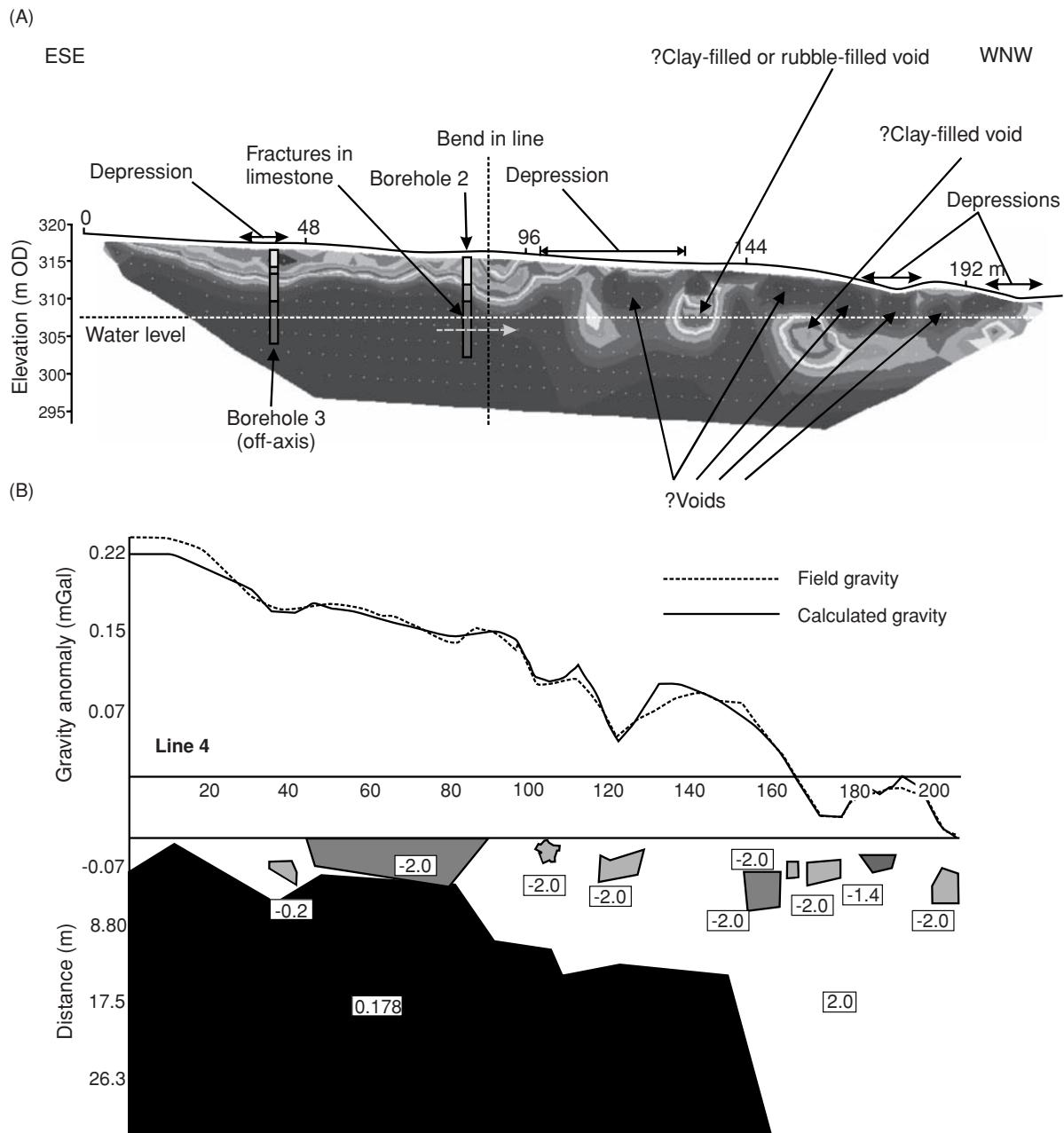


**Figure 2.53** (A) Electrical resistivity pseudo-section and (B) corresponding micro-gravity profile and model for a coincident traverse across an area of limestone affected by dissolution voids in the Peak District, UK.

gravity anomaly (Figure 2.65), its infill being boulder-clay with a density of  $2.075 \text{ Mg/m}^3$ . The valley is buried beneath Quaternary sediments (density  $1.93 \text{ Mg/m}^3$ ) and lies within Tertiary bedrock with a density of  $1.85 \text{ Mg/m}^3$ .

Most of the mines in the semi-arid Yilgarn region of Western Australia, east of Perth, rely upon groundwater for mining and ore processing. Granitoid greenstone terranes of the Archaean Yilgarn craton have been incised by palaeochannels and filled with Tertiary sediments. The best supply of large volumes of water are basal sand and gravel sections of the palaeochannels, which constitute aquifers

of highly saline water (Jenke, 1996). Holzschuh (2002) described an integrated geophysical exploration of these palaeochannels, predominantly using detailed P- and S-wave seismic reflection surveying with some refraction and micro-gravity profiles. Electrical and EM techniques are not appropriate here due to the high salinity of the groundwater. Holzschuh demonstrated that the micro-gravity technique could be used as a suitable reconnaissance method to map the bedrock tomography and to help determine the most likely aquifer locations in order to focus the subsequent seismic surveys and drilling.



**Figure 2.54** Collapse of mine-workings in chalk at Reading, UK. From Emanuel (2002), by permission. [C]



**Figure 2.55** A Scintrex CG-3M is use in Reading city centre, UK. [C]

#### 2.7.4.2 Microgravity monitoring in the oil industry

Since October 1996, Statoil and its partners in the Sleipner Field in the North Sea have injected CO<sub>2</sub> into a saline aquifer at a depth of 1012 m below sea-level, some 200 m below the top of the reservoir. The first seabed gravity survey was acquired in 2002 with 5.19 Mt of CO<sub>2</sub> in the injected plume. The survey comprised measurements of relative gravity at each of 30 benchmarked locations deployed in two perpendicular lines spanning an area some 7 km east–west and 3 km north–south and overlapping the subsurface footprint of the CO<sub>2</sub> plume, which had also been monitored over the corresponding time interval using time-lapse seismic imaging. The final detection threshold was estimated at  $\sim 5 \mu\text{Gal}$  for individual stations in 2002, and  $3.5 \mu\text{Gal}$  for a repeat survey undertaken in September 2005, with  $\sim 7.76 \text{ Mt}$  of CO<sub>2</sub> in the plume.

Based upon the calculated gravity response of gridded 3D plume models, with detailed CO<sub>2</sub> distributions and densities defined by reservoir flow simulations (the latter calibrated by the seismic surveys), four model scenarios were considered: a lower temperature reservoir with and without CO<sub>2</sub> dissolution, and a higher temperature reservoir with and without dissolution. The observed gravity anomalies associated with the CO<sub>2</sub> plumes in 2002 and 2005 were respectively from  $-11$  to  $-31 \mu\text{Gal}$  and from  $-16$  to  $-44 \mu\text{Gal}$ . The changes observed are shown in Figure 2.66 (Arts *et al.*, 2008). Alnes *et al.* (2008) provide further information about monitoring gas production and CO<sub>2</sub> injection at the Sleipner field using time-lapse gravimetry.

Knowledge of the magnitude and distribution of water influx can be essential for managing water-drive gas fields. Geophysical fieldwide monitoring can provide valuable information,

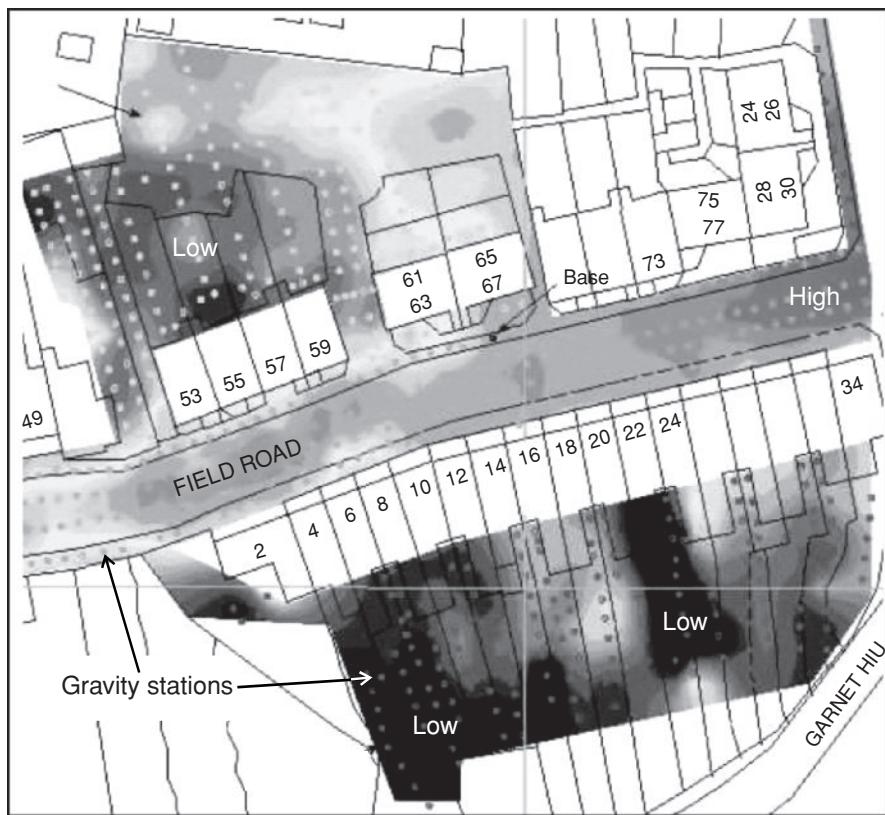


**Figure 2.56** Extract of a Bouguer anomaly map corrected for the gravitational effect of buildings for a survey of chalk mine workings in Reading, UK. [C]

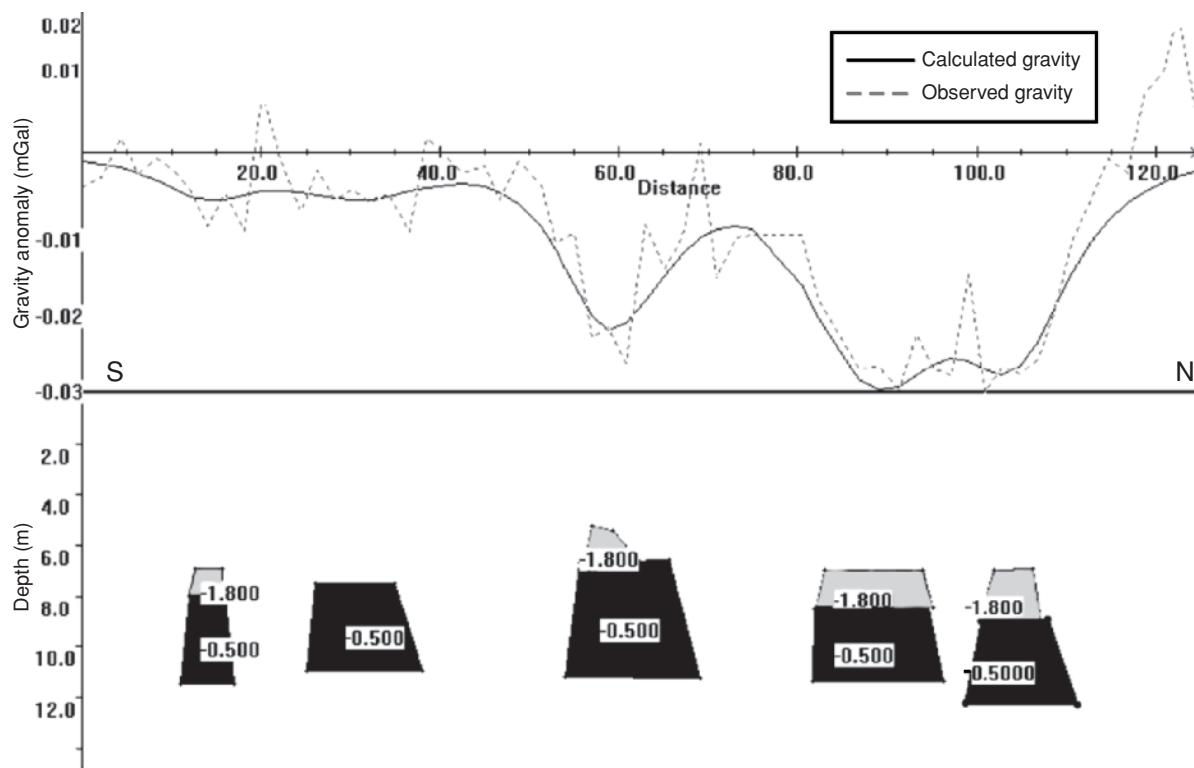


**Figure 2.57** An example Bouguer anomaly profile and derived model from a micro-gravity survey of chalk mine workings in Reading, UK. The majority of the interpreted mine galleries were later confirmed by probe drilling. [C]



**Figure 2.58** Collapse in Reading city centre reveals the crown of underlying chalk mine workings located using micro-gravity surveys and follow-up probe drilling. From Emanuel (2002), by permission. [C]

particularly offshore where well control is sparse and observation wells are expensive. Advances in the accuracy of sea-floor time-lapse gravimetry, a ten-fold improvement between 1998 and 2006, have made this method feasible, as described by Stenvold *et al.* (2008). Flooded areas can be quantified, providing complementary information to well-monitoring, production and 4D seismic data. It is now considered feasible to monitor displacement of gas by water in reservoirs that are only a few metres thick. Gravimetric monitoring is now applicable for gas reservoirs of modest volumes ( $\sim 2 \times 10^8 \text{ m}^3$  *in situ* gas volume) at medium depths ( $\sim 2 \text{ km}$ ).

It is clear that routine sub-centimetre elevation measurements correspond to gravity changes of a few microgals, which is now within the resolution of modern gravimeters (typically  $\leq 5 \mu\text{Gal}$ ) (Biegert *et al.*, 2008). It is now possible to combine large-scale GPS and gravity surveys (i.e. hundreds of stations over hundreds of square kilometres) (Ferguson *et al.*, 2008) with a similar precision being achievable with seafloor gravity measurements (Zumberge *et al.*, 2008). Consequently many more applications of time-lapse (4D) gravimetric surveys, not only in the hydrocarbon industry, may be forthcoming in the future.

## 2.7.5 Volcanic hazards

With the advent of highly accurate surveying equipment and methods, and the availability of very sensitive gravimeters, it is possible to monitor small changes in the elevations of the flanks of active volcanoes – ultimately with a view to predicting the next eruption. Such studies are often accompanied by seismic monitoring (e.g. Cosentino *et al.*, 1989). Sanderson *et al.* (1983) carried out such a gravity monitoring and levelling programme on Mount Etna, Sicily, during the period August 1980 to August 1981, during which time a flank eruption took place (17–23 March 1981) from which a lava flow resulted which narrowly missed the town of Randazzo. A series of schematic diagrams is shown in Figure 2.67 to illustrate the three clear stages of the fissure eruption.

Changes in gravity in association with elevation increases were interpreted as the injection of new magma at depth during the intrusion of a new dyke at about 1.5 km depth (Figure 2.67A). Gravity decreases were observed when eruptions took place because of the reduction in material (Figure 2.67B). Where increases in gravity were observed without an increase in elevation, this was interpreted as being due to the density of the magma increasing by the enforced emplacement of new material at depth (Figure 2.67C). The magnitude of the gravity changes ( $\approx 2\text{--}25 \mu\text{Gal}$ ) coupled with the known variations in elevation ( $\leq 20 \text{ cm}$ ) provide a means of determining where within the volcano's plumbing the intrusions of new material and/or density changes are taking place.

Rymer and Brown (1987, 1989) summarised the micro-gravity effects resulting from vertical movements of the magma/rock interface, vesiculation cycles with the magma column and radial changes in the dimensions of the magma body for Poas volcano in Costa Rica. The individual internal processes in this particular volcano can be clearly differentiated by using the ratio of the gravity effects measured at the volcano flank and summit. However, not all subterranean activity is associated with seismic signatures. Indeed, Rymer (1993) reported on an increase in gravity at Mt Etna between June 1990 and June 1991 with no corresponding seismic activity. Large increases in gravity were observed around the summit craters and along an elongated zone following the line of a fracture formed during a previous eruption in 1989. Surface elevation changes surveyed between 1990 and 1991 were only of the order of less than 3 cm. The gravity changes were an order of magnitude larger than would have been expected on the basis of elevation changes alone, which suggested that there must have been some subsurface increase in mass. This was calculated to be of the order of  $10^7 \text{ Mg}$  and was caused by the intrusion of magma into fractures left by the 1989 eruption. The magma migrated passively into the pre-existing fractures so there was no corresponding seismic activity. Consequently, the micro-gravity measurements, in conjunction with elevation surveys, produced the only evidence of an impending eruption. The eruption of Mt Etna lasted for 16 months from 1991 to 1993, during which time lava poured out of the vent at a rate of  $10 \text{ m}^3/\text{s}$ , making this the largest eruption there for 300 years (Rymer, 1993; Rymer *et al.*, 1993).

When monitoring volcanic behaviour it is important to recognise that the changes in the gravity field occur as a result of a number of interrelated factors. Changes in mass, such as by the influx of

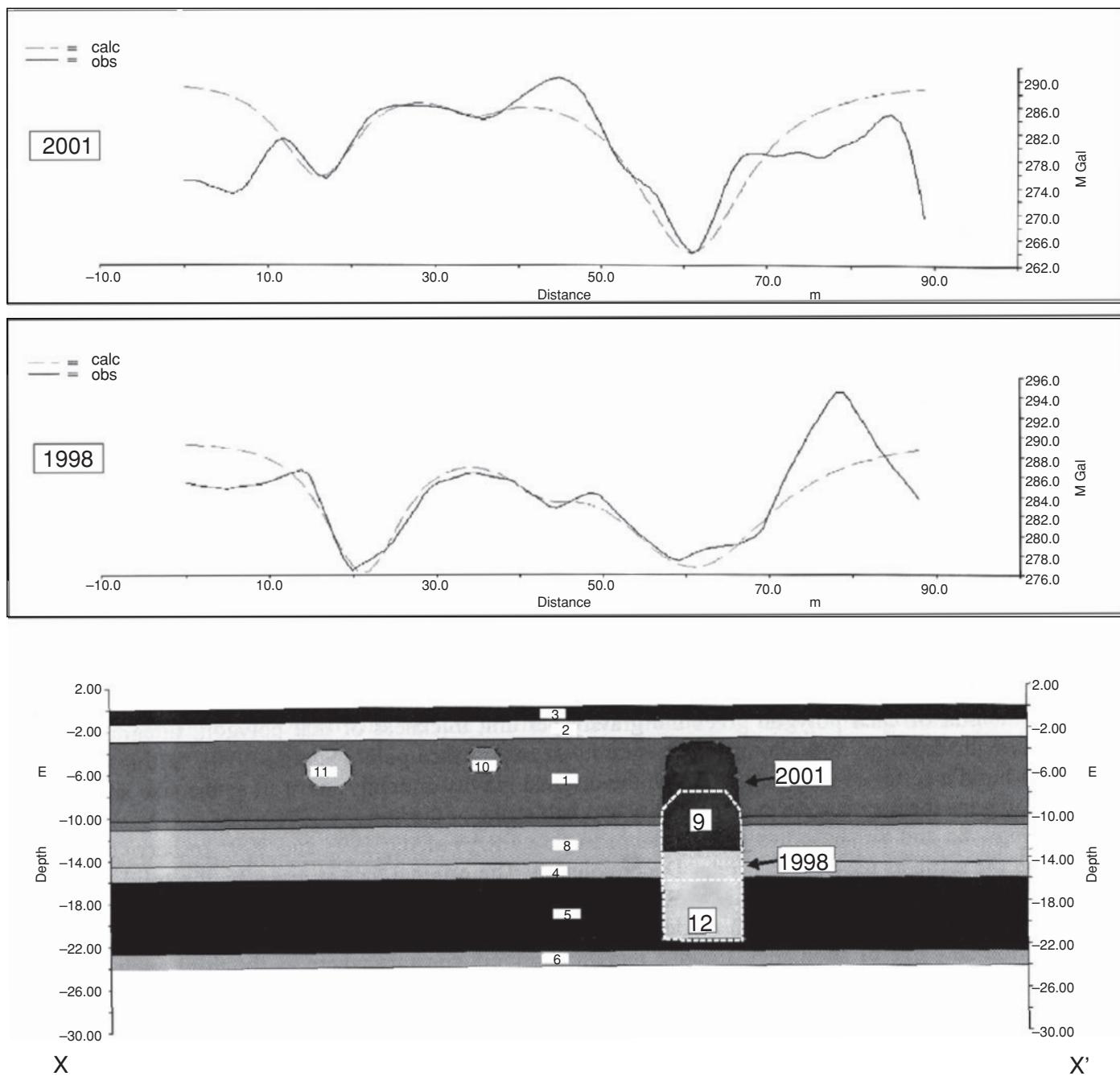


**Figure 2.59** Gravity models (2.5D) produced using GRAVMAG in 1998 and 2001 with the observed and calculated profiles attained in each year. The only interpreted difference between the two surveys is the upward migration of the low-density block (#9) towards the surface and the corresponding shallowing of the underlying material (#12). Adapted from Branston and Styles, (2003), by permission.

denser magma, can give rise to a rise in gravity, whereas mass loss through eruption or changes in composition of magma including foaming can cause the gravity to decrease. The elevation of the flanks of the volcano may change through inflation and deflation, causing a decrease or increase respectively in gravity. A study was undertaken by Currenti *et al.* (2007) of the 1993–1997 inflation phase on Mt Etna. They established a 3D finite element model

(FEM) in which they used the real topography (including geometry and seismic tomography) to infer crustal heterogeneities. Different geodetic surveying techniques clearly detected the inflation phase that showed a uniform expansion of the overall volcano edifice. In order to obtain a reliable estimate of depth and density of an intrusion, joint modelling of the geodetic and gravity data should be undertaken. They showed that the application of FEMs allows

**Table 2.9** Densities derived from an adjacent borehole and attributed to the polygons shown in Figure 2.59.

Polygon no.	Density ( $\text{Mg/m}^3$ )	Polygon no.	Density ( $\text{Mg/m}^3$ )	Polygon no.	Density ( $\text{Mg/m}^3$ )
1	2.65	5	2.69	9	2.44
2	2.70	6	2.20	10	2.45
3	2.30	7	2.65	11	2.2
4	2.65	8	2.72	12	2.55

for a more accurate modelling procedure and may help to reduce the misinterpretations of geophysical observations undertaken in volcanic areas.

There is a trend to install continuous gravity monitoring on volcanoes. This has the benefit of providing better environmen-

tal controls on the gravimeters used to restrict the thermal effects, and reduces the temporal aliasing arising from comparing gravity data acquired over different time sequences. For instance, if the acquisition of repeat data at a given station is too infrequent, discrete events within the volcano may be missed. Battaglia *et al.* (2008) provide an example of a significant, but short-lived, event that was observed in continuous gravity monitoring during the 2002–2003 eruptive phase of Mt Etna (Figure 2.68). During temporary switches from vigorous lava fountains to mild Strombolian explosions, marked gravity decreases were observed to occur simultaneously with tremor-amplitude increases (Carbone *et al.*, 2006). These changes in gravity were assumed to reflect collapses of the magma/gas mixture within the upper level of the system feeding the active vent. The collapsed column diminished gas flow to the shallowest levels of the discharge system to the atmosphere, creating conditions under which a foam layer forms. By substituting denser material (magma), a foam layer can induce a local mass (gravity) decrease. It can also radiate seismic energy by coupled oscillations

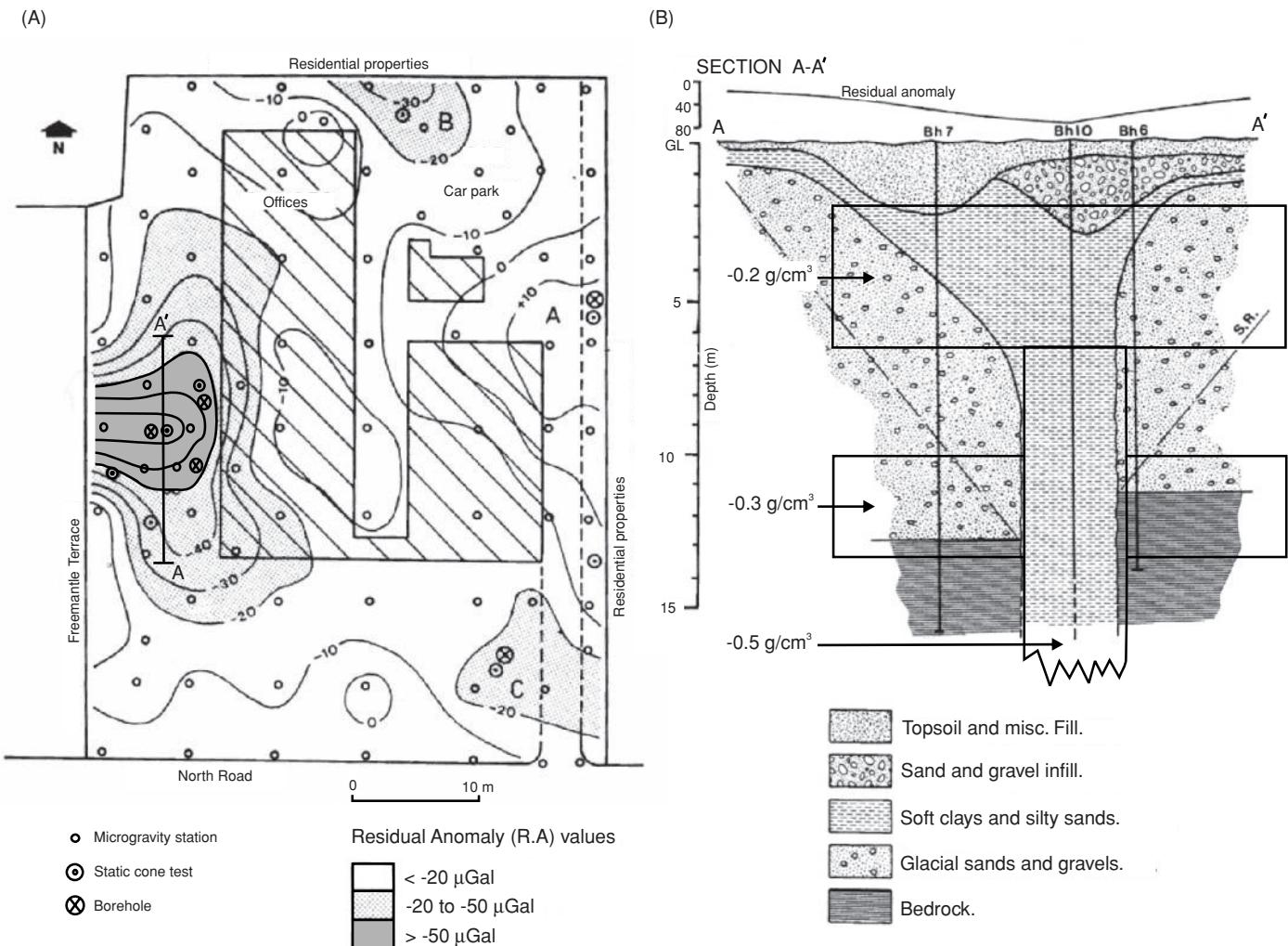


**Figure 2.60** Micro-gravity survey (A) at Ripon, NE England, with the composite results of drilling and trenching along profile A-A' on which the initial basic gravity model has been superimposed. S.R. = angle of shearing resistance assumed to be  $50^\circ$ . Adapted from Patterson *et al.* (1995), by permission.

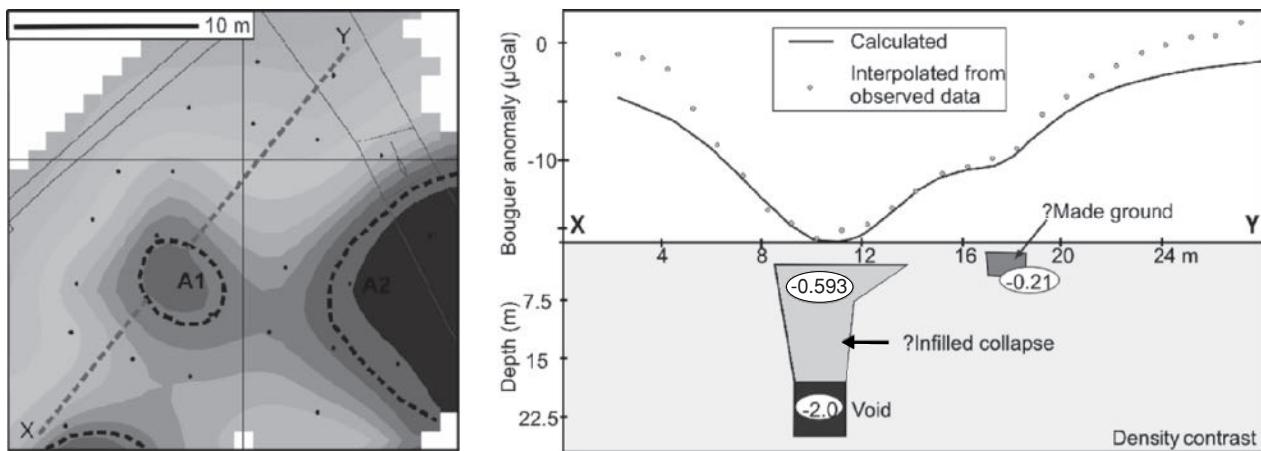


**Figure 2.61** (A) Residual gravity anomaly map over a prominent gravity 'low' in Ripon, NE England, with (B) the derived geological model indicating a dissolution breccia pipe and void at depth.

of the bubbles inside it. Growth of a foam layer could thus explain the observed joint gravity/tremor anomalies (Figure 2.68).

Montesinos *et al.* (2003) have described a detailed gravity investigation undertaken over a volcanic crater in Terceira Island, part of the Azores archipelago. The island has been badly affected by earthquakes not only historically (e.g. in 1614 and 1841) but also in 1980, when the strongest earthquake to strike the Azores occurred (magnitude 7.2); other strong earthquakes have also occurred subsequently (1997, 1998). The majority of these earthquakes have been felt across the island but with higher intensity in the São Sebastião volcanic crater, in the southeastern corner of the island. The village of São Sebastião is located within this crater, which has an average diameter of 1100 m and a depth of about 50 m. Parts of this village have suffered more damage from earthquake activity than others. To

try to understand why, Montesinos *et al.* (2003) undertook a gravimetric investigation, looking for a correlation among the geological, tectonic and volcanic characteristics of the area. The geology of the area is illustrated in Figure 2.69A, with the distribution of gravity stations shown in Figure 2.69B. The resulting Bouguer anomaly map of the area is shown in Figure 2.70, for which a terrain density of  $2.48 \text{ Mg/m}^3$  has been used. The gravity map indicates an anomaly trending SSE from São Sebastião, which has been interpreted as indicating a volcanic and tectonic lineament. 3D regional modelling of the gravity data indicate a shallow mass deficiency in the centre of the crater, which is shown in cross-section and plan view in Figure 2.71. The anomalous seismic response observed in the São Sebastião depression may be associated with a weak zone dominated by subsurface low-density structures, which are confined within

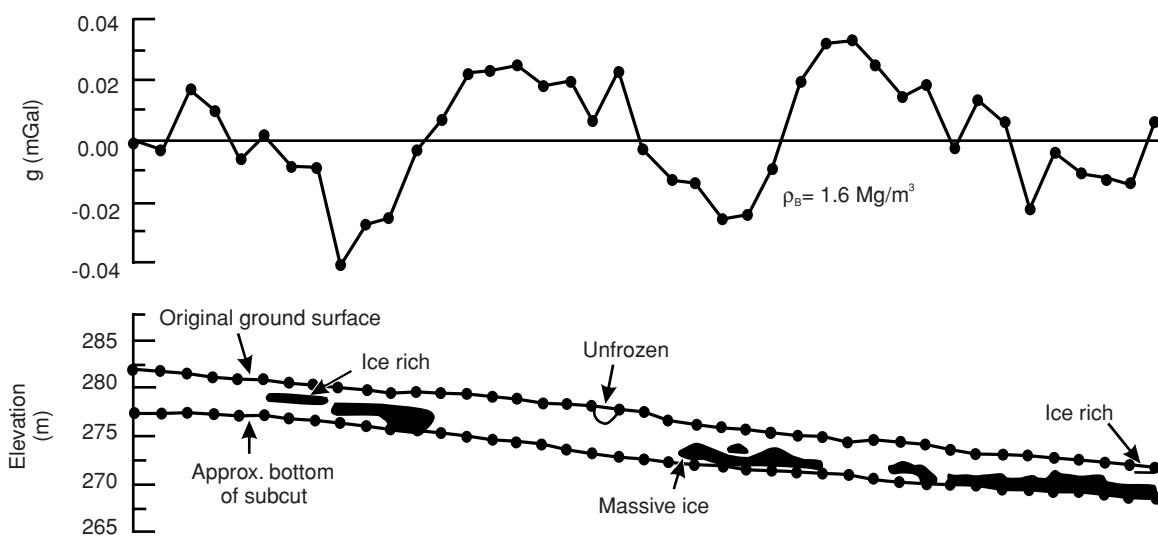


**Figure 2.62** Gravity profile across massive ground ice in a road cut, Engineer Creek, near Fairbanks, Alaska. After Kawasaki *et al.* (1983), by permission.

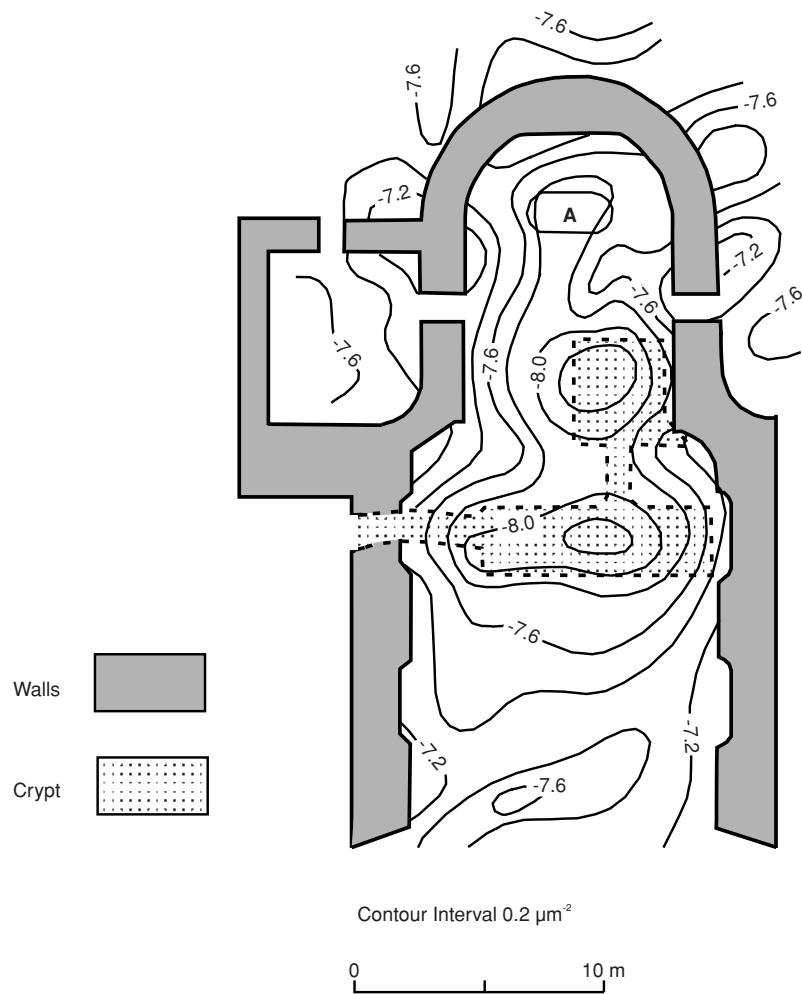


**Figure 2.63** Micro-gravity map St 'Venceslas Church, Tovačov, Czech Republic, showing marked anomalies over previously unknown crypts. From Blizkovsky (1979), by permission.

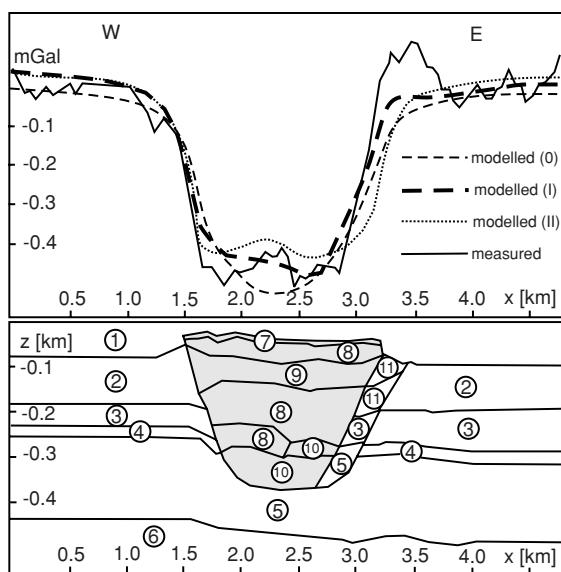


**Figure 2.64** Gravity profile across the Ellerbek valley, Germany, with the valley geometry taken from the interpretation of seismic reflection profiles. After Gabriel (2006), by permission.

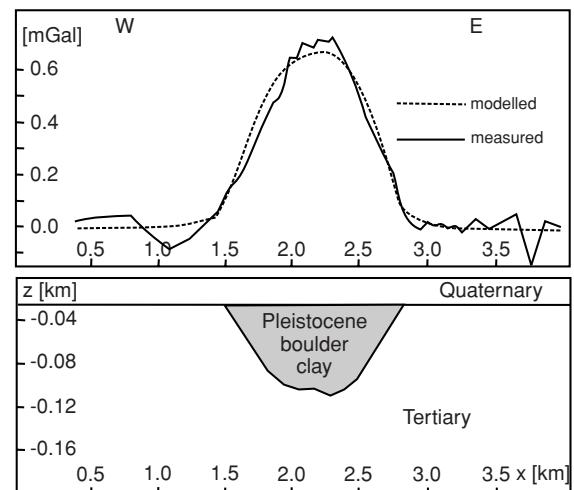


**Figure 2.65** Gravity profile across the Trave valley, Germany, with the location of the valley based on a seismic reflection survey. After Gabriel (2006), by permission.

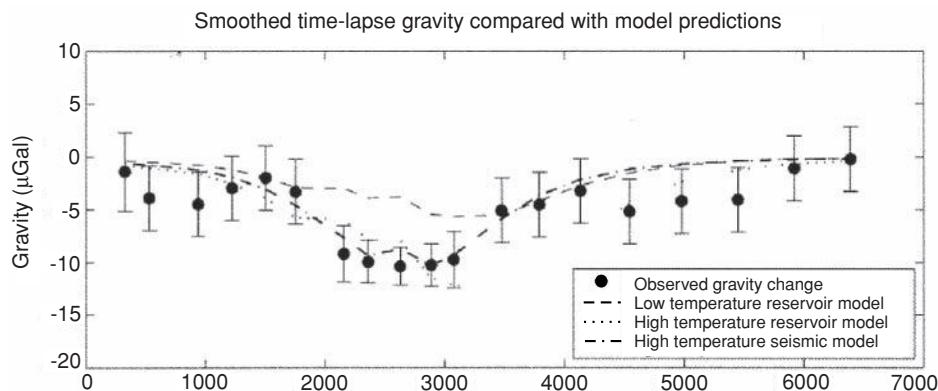


**Figure 2.66** Smoothed observed time-lapse gravity change plotted with modelled gravity change for high (average  $\text{CO}_2$  density  $550 \text{ kg/m}^3$ ) and low reservoir temperatures (average  $\text{CO}_2$  density  $700 \text{ kg/m}^3$ ) models. After Arts *et al.* (2008), by permission.

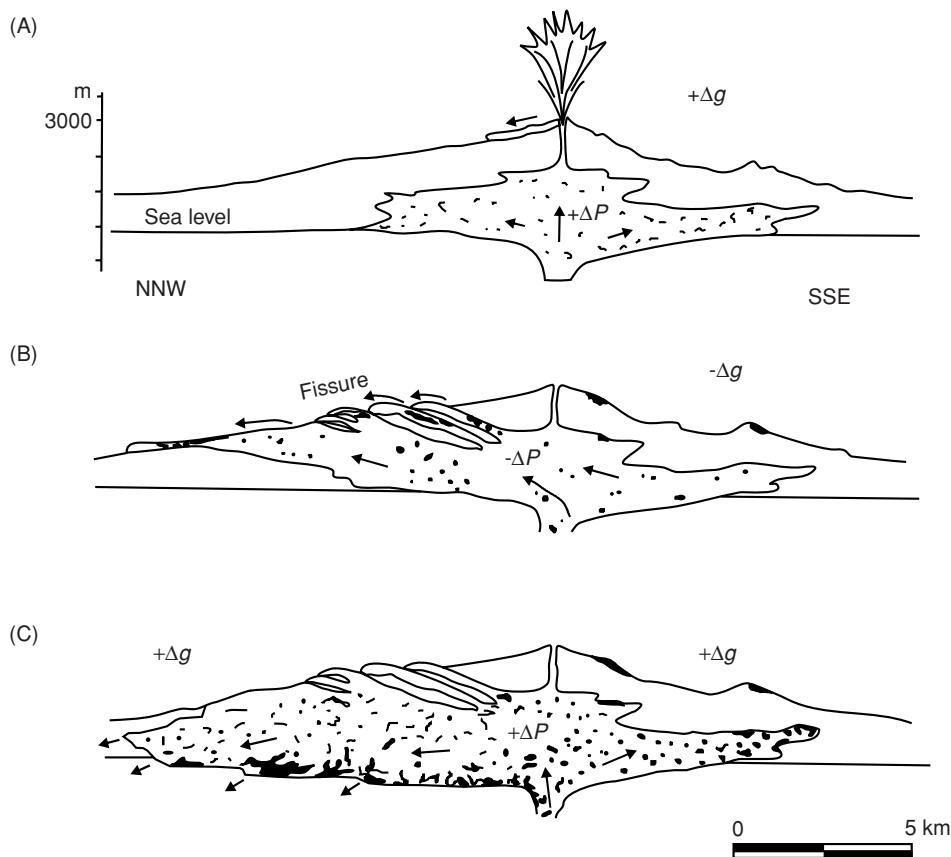


**Figure 2.67** Sketches of the stages of fissure eruptions on Mt Etna, Sicily, with gravity trends. After Sanderson *et al.* (1983) and Cosentino *et al.* (1989), by permission.

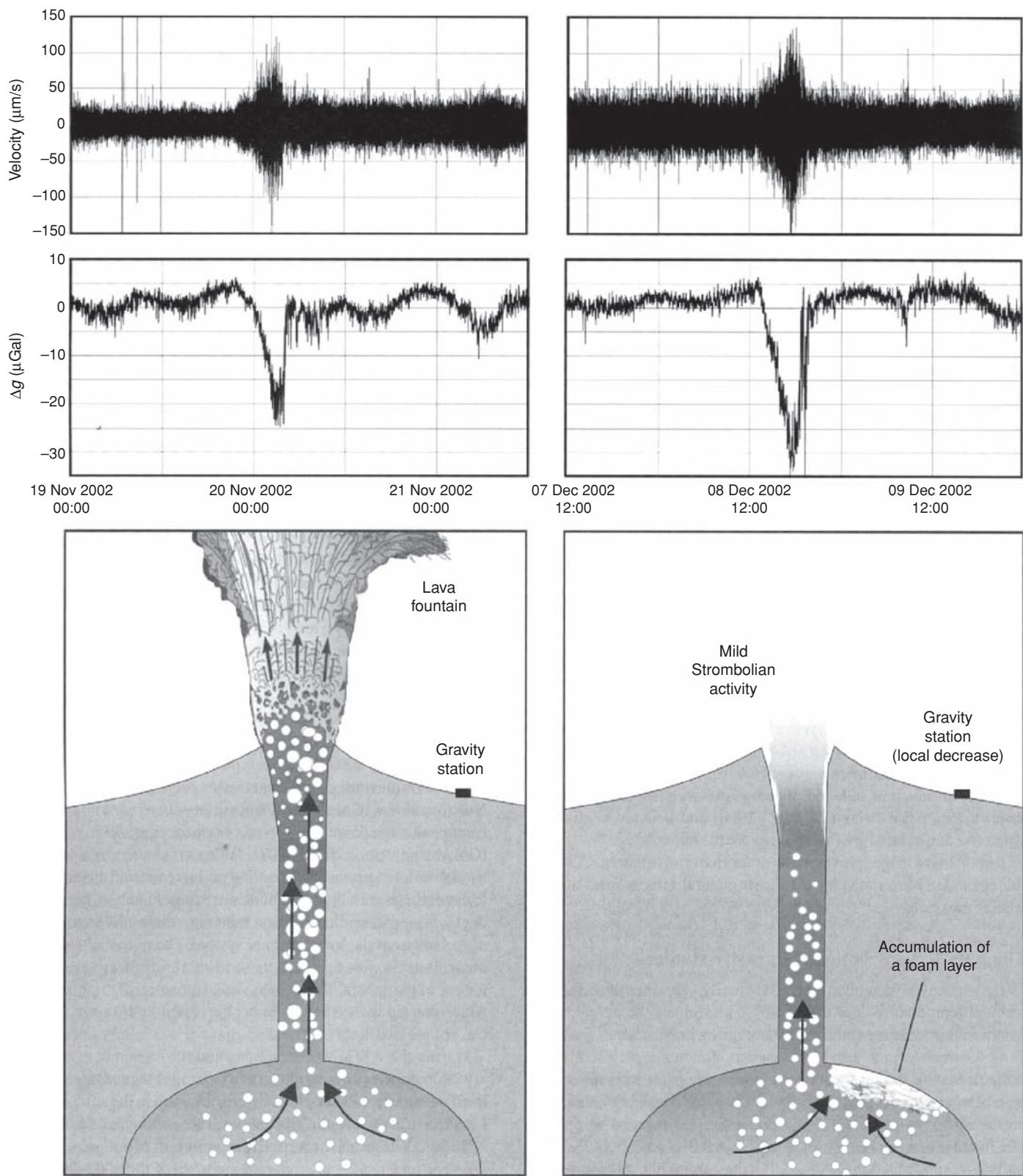


**Figure 2.68** During the 2002–2003 Mount Etna eruption, gravity decreases lasting a few hours were observed simultaneously with increases in amplitude of the volcanic tremor. From Battaglia *et al.* (2008), by permission.

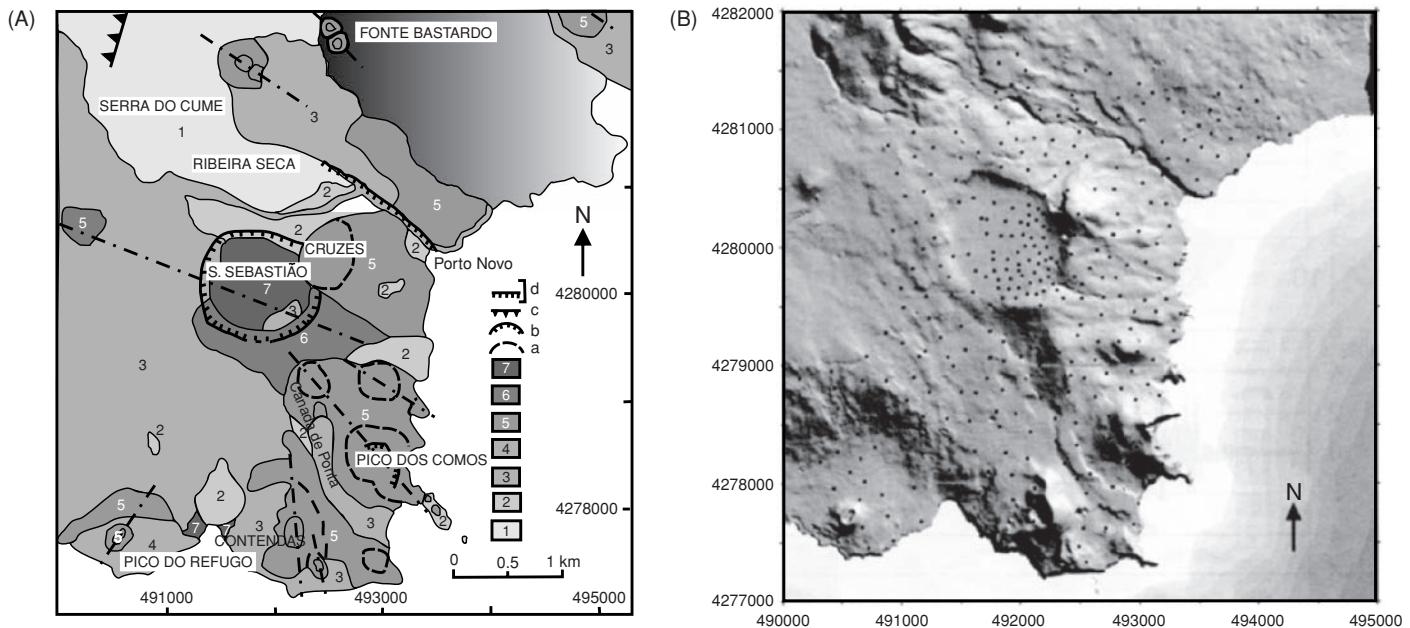


**Figure 2.69** (A) Volcanological map of the São Sebastião area of SE Terceira Island, part of the Azores Archipelago. (1) Old trachyte lava flows (Serra do Cume volcano); (2) old basaltic lava flows; (3) intermediate-age basaltic lavas; (4) recent basaltic lava flows; (5) basaltic scoria and lapilli deposits; (6) lahar; (7) fluvial and slope deposits; (a) scoria cone base; (b) crater rim; (d) volcanic and tectonic lineaments. (B) Location of 344 gravimetric observation sites (dots) on a digital terrain model of the corresponding area. The highest point is 335 m. From Montesinos *et al.* (2003), by permission. [C]

the crater and flanked by several denser bodies forming a resonant basin.

In a separate study, Camacho *et al.* (2007) have measured values of gravity at 253 stations across the volcanic island of Faial, part of the Azores archipelago, and lying on the Paial-Pico Fracture Zone which forms the current boundary between the Eurasian and African plates in the Azores area. The structural fabric can be seen in Figure 2.72A.

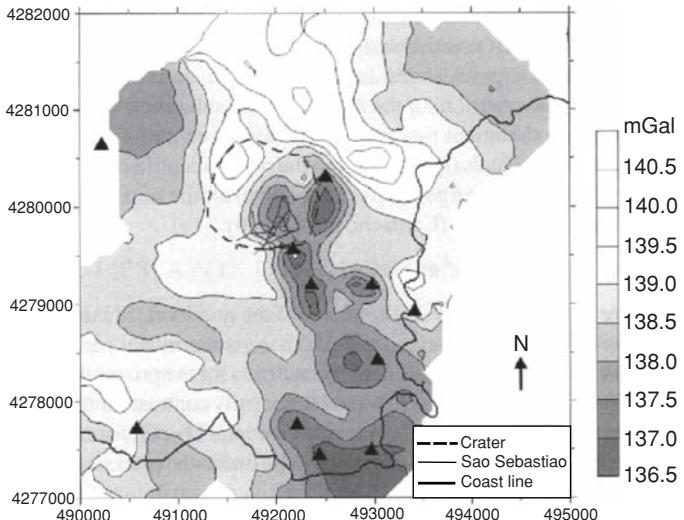


**Figure 2.70** Bouguer anomaly map corresponding to a terrain density value of  $2.48 \text{ Mg/m}^3$ . Triangles indicate scoria cone eruptive centres. From Montesinos *et al.* (2003), by permission.

Their 3D inversion shows a subsurface anomalous structure for the island, the main feature being an elongated high-density body (Figure 2.72B and C). This forms a wall-like structure extending from a depth of 0.5 to 6 km b.s.l., and is thought to correspond to an early fissural volcanic episode controlled by regional tectonics.

Micro-gravity monitoring coupled with the distinctive patterns of the frequency of seismic activity (volcanic tremor spectra) provide a very comprehensive model for volcanic eruptions, such as those at Mt Etna, and their associated processes. Many other volcanoes now have active monitoring programmes utilising gravity, seismic and thermal investigations. Monitoring gas emissions is also proving to be a valuable additional indicator of impending volcanic activity (e.g. Pendick, 1995, on the work of S. Williams). If these data can be obtained for individual volcanoes in conjunction with thermal radiation as measured by satellite, then the probability of identifying recognisable precursors to eruptions may be enhanced significantly, leading to a better prediction of volcanic activity and mitigation of potential hazards (Rymer and Brown, 1986; Eggers, 1987).

## 2.7.6 Glaciological applications

For a regional gravity survey to be complete in areas such as Antarctica and Greenland, measurements have to be made over ice sheets and valley glaciers. Very often, these areas have incomplete information about the depth or volume of ice. The large density difference between ice ( $0.92 \text{ Mg/m}^3$ ) and the assumed average rock density ( $2.67 \text{ Mg/m}^3$ ) means that easily measured gravity anomalies can be

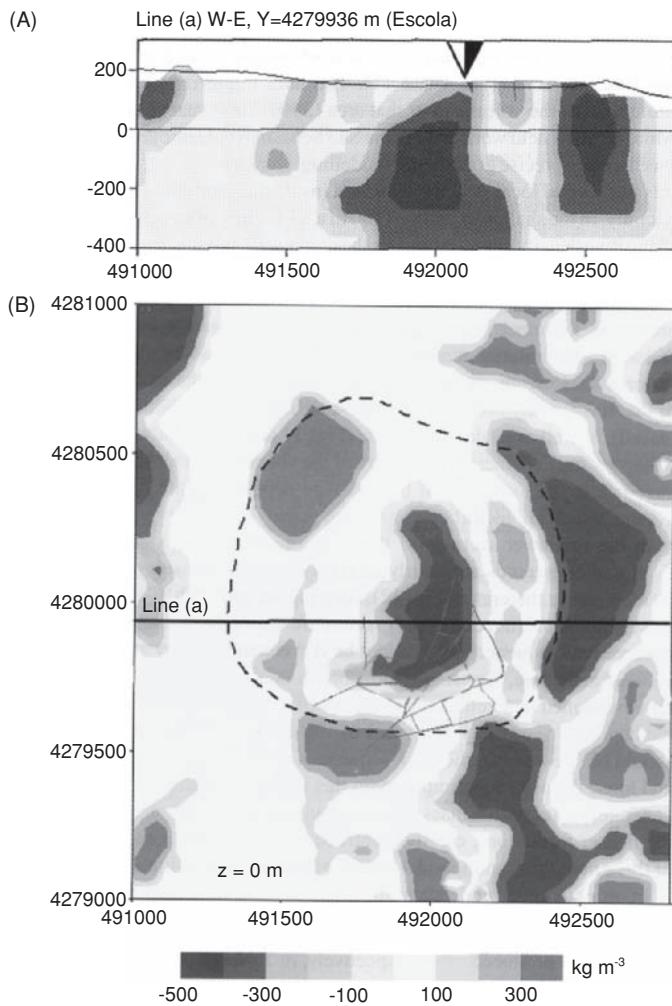


**Figure 2.71** (A) Map of density contrasts at 0 m a.s.l. and the E-W profile for the line shown in (B) as derived from the gravity model. The outline of the crater is shown by a dashed line; the web of lines indicate streets within São Sabastião. From Montesinos *et al.* (2003), by permission. [C]

observed and the bottom profile of the ice mass (i.e. the subglacial topography) can be computed.

Micro-gravity measurements have also formed part of a more comprehensive geophysical survey at Petrov Lake, Kyrgyzstan, as part of a glacial hazards investigation. While the quality of the gravity data was very good, the uncertainties in local density variations made it difficult to make specific interpretations about the presence of stagnant glacier ice within a moraine dam. However, in conjunction with electrical resistivity tomography and self potential measurements, the micro-gravity survey can provide additional contextual information that can help to constrain the overall geological model.

### 2.7.6.1 Glacier thickness determinations

An example of this has been given by Grant and West (1965) for the Salmon Glacier in British Columbia (Figure 2.73), in which a gravity

survey was undertaken in order to ascertain the glacier's basal profile prior to excavating a road tunnel beneath it. A residual gravity anomaly minimum of almost 40 mGal was observed across the glacier, within an accuracy of  $\pm 2$  mGal due to only rough estimates having been made for the terrain correction. An initial estimate of local rock densities was  $2.6 \text{ Mg/m}^3$ , and the resultant depth profile across the glacier proved to be about 10% too deep (Figure 2.73B) compared with depths obtained by drilling. Considering the approximations taken in the calculations, the agreement was considered to be fair. In addition, it was found that the average density of the adjacent rocks was slightly lower ( $2.55 \text{ Mg/m}^3$ ). This could have indicated that there was a significant thickness of low-density glacial sediments between the sole of the glacier and the bedrock. However, had more detailed modelling been undertaken on data corrected fully for terrain, the discrepancy could have been reduced.

Increasingly, ice thickness measurements are being made by seismic reflection surveying (see Chapter 5), electromagnetic VLF measurements (see Chapter 9, Section 9.6.6.3) and radio echo-sounding (see Chapter 9, Section 9.7.4.2). Comparisons between the various geophysical methods indicate that agreements of ice thickness to within 10% can be readily obtained. Gravity measurements over large ice sheets (e.g. Renner *et al.*, 1985; Herrod and Garrett, 1986) have been considerably less accurate than standard surveys for three reasons:

- The largest errors were due to the imprecise determination of surface elevations; heights were determined to within 5–10 m;
- Inaccurate corrections for sub-ice topography vary by hundreds of metres, in areas without radio echo-sounding control. An error in estimated ice thickness/bedrock depth of 100 m can introduce an error of  $\pm 74$  g.u.
- As in all gravity surveys, the estimate of the Bouguer correction density is also of critical importance. Major ice sheets obscure the local rock in all but a few locations, and the sub-ice geology, and its associated densities, may vary significantly.

In high mountain areas, the main disadvantage for the use of the gravity method, in addition to some of the issues raised for surveys over ice sheets, is the extreme topography and hence the need for detailed elevation information with which to apply appropriate terrain corrections. Seldom are such data available at the required resolution, so the inherent inaccuracies in the terrain correction are likely to be of the same order as some of the anomalies being sought. For example, in the Tien Shan mountains in Kyrgyzstan, a detailed micro-gravity survey was undertaken over a terminal moraine that dams a glacial lake in order to locate buried stagnant ice within the moraine. The uncertainty over the levels and accuracies of the necessary terrain corrections, as well as significant variations in local densities of the glacial sediments, makes the interpretation ambiguous. However, there is merit in developing this application if the control on the corrections can be improved.

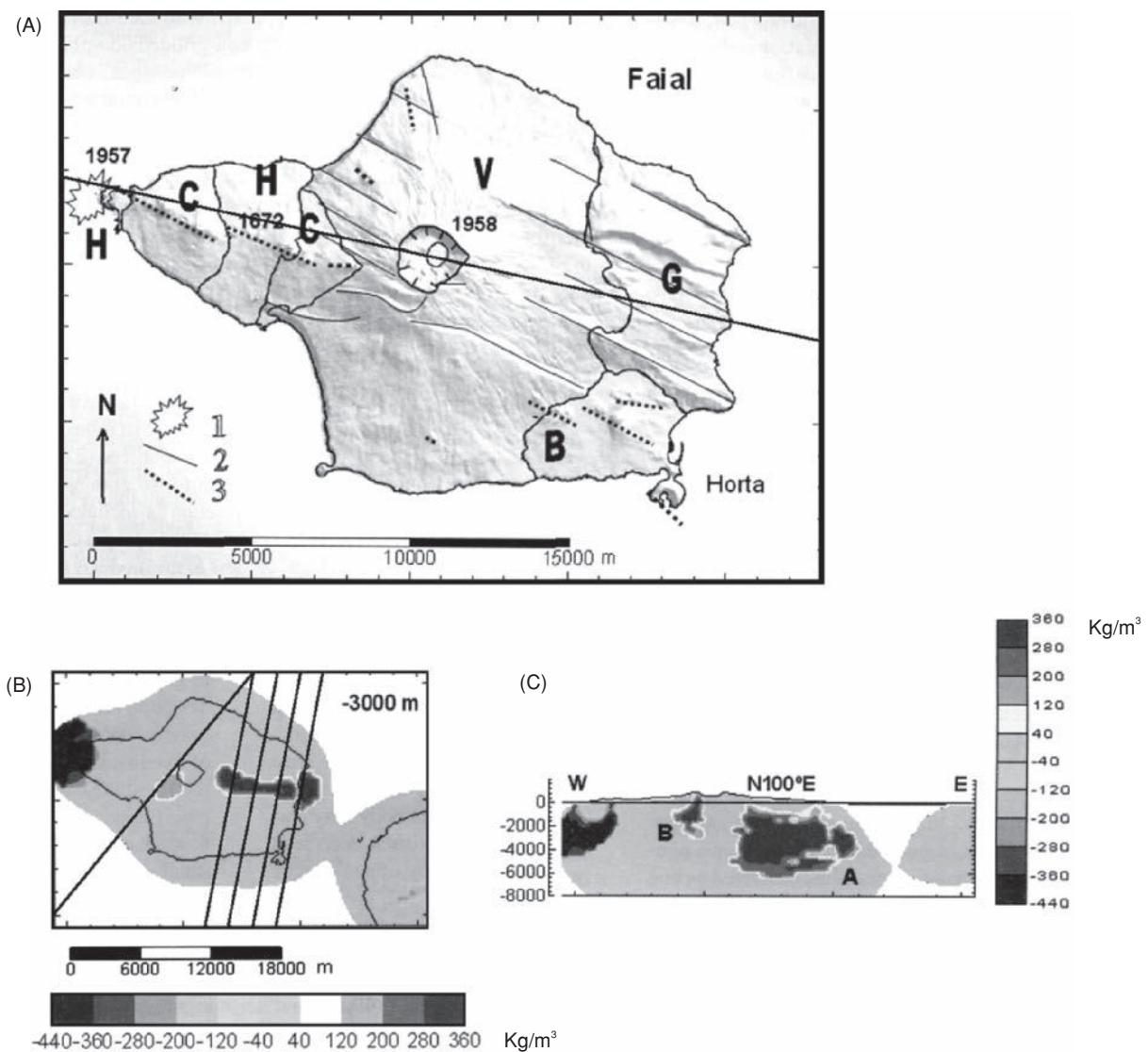


**Figure 2.72** (A) Digital elevation model for Faial Island with the main volcano-tectonic structures superimposed. (1) Capelinhos Volcano; (2) faults and (3) main volcano-tectonic lineaments. General volcano-stratigraphy: H: historical eruptions (with year of occurrence); C: Capelo Volcanic Complex; V: Caldeira Volcano; B: Horta Basaltic Zone; G: Ribeirinha Volcano and Pedro Miguel Graben. (B) Example density model depth slice for 3 km depth, showing the high-density structure trending  $110^\circ$ . (C) Density sections W-E and N-S along the profiles shown in (A). Adapted from Camacho *et al.* (2007), by permission.

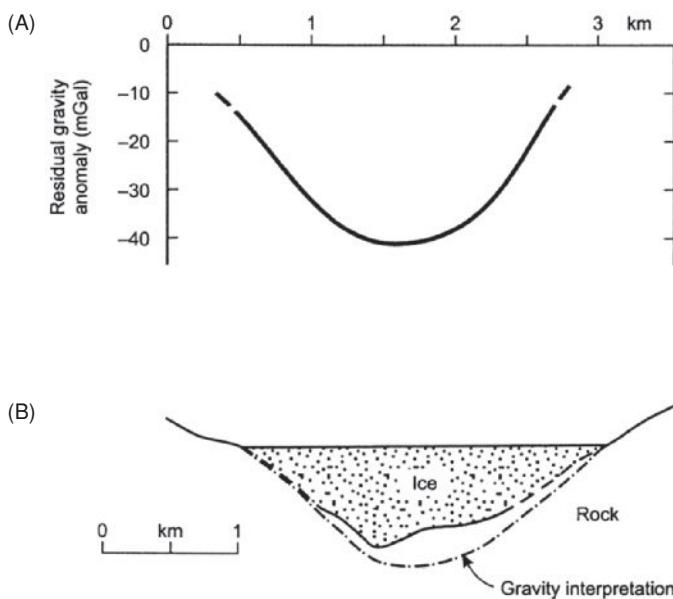


**Figure 2.73** A residual gravity profile across Salmon Glacier, British Columbia, with the resulting ice thickness profile compared with that known from drilling. After Grant and West (1965), by permission.

### 2.7.6.2 Tidal oscillations of Antarctic ice shelves

Another glaciological application of the gravity method is the use of a gravimeter to measure oceanic tidal oscillations by the vertical movements of floating ice shelves in the Antarctic (Thiel *et al.*, 1960; Stephenson, 1984). The resulting tidal oscillation pattern can be analysed into the various tidal components and hence relate the mechanical behaviour of the ice shelf to ocean/tidal processes. If tidal oscillations are not found at particular locations, this may indicate that the ice shelf is grounded. Independent measurements with tilt meters, strain gauges and radio echo-sounding should be used to confirm such a conclusion (Stephenson and Doake, 1982).



# 3

## Geomagnetic Methods

### 3.1 Introduction

It is thought that the Chinese first used lodestone (magnetite-rich rock) in primitive direction-finding as early as the second century BC. It was not until the twelfth century in Europe that reference was made to the use of a magnetic compass for navigation. The first scientific analysis of the Earth's magnetic field and associated phenomena was published by the English physicist William Gilbert in 1600 in his book *De Magnete*. Measurements of variations in the Earth's magnetic field were made in Sweden to locate iron ore deposits as early as 1640. In 1870, Thalen and Tiberg developed instruments to measure various components of the Earth's magnetic field accurately and quickly for routine prospecting.

In 1915, Adolf Schmidt made a balance magnetometer that enabled more widespread magnetic surveys to be undertaken. As with many geophysical methods, advances in technology were made during the Second World War which enabled more efficient, reliable and accurate measurements to be made thereafter. In the 1960s, optical absorption magnetometers were developed which provided the means for extremely rapid magnetic measurements with very high sensitivity, ideally suited to airborne magnetic surveys. Since the early 1970s, magnetic gradiometers have been used which measure not only the total Earth's magnetic field intensity, but also the magnetic gradient between sensors. This provides extra information of sufficient resolution to be invaluable in delimiting geological targets.

Geomagnetic methods can be used in a wide variety of applications (Table 3.1) and range from small-scale investigations to locate pipes and cables in the very near surface, and engineering site investigations, through to large-scale regional geological mapping to determine gross structure, such as in hydrocarbon exploration. Commonly in the larger exploration investigations, both magnetic and gravity methods are used to complement each other. Used together prior to seismic surveys, they can provide more information about the subsurface, particularly the basement rocks, than either technique on its own. Subsequent seismic reflection surveys are then used to provide more detailed imaging of the subsurface, which is

of more value to hydrocarbon exploration. The range of magnetic measurements that can now be made is extremely large, especially in the area of palaeomagnetism, which will not be dealt with here. Palaeomagnetism is discussed in detail by Tarling (1983) and by Gubbins and Herrero-Bervera (2007), for example.

### 3.2 Basic concepts and units of geomagnetism

#### 3.2.1 Flux density, field strength and permeability

Around a bar magnet, a magnetic flux exists, as indicated by the flux lines in Figure 3.1, and converges near the ends of the magnet, which are known as the magnetic poles. If such a bar magnet is suspended in free air, the magnet will align itself with the Earth's magnetic field with one pole (the positive north-seeking) pointing towards the Earth's north pole and the other (the negative south-seeking) towards the south magnetic pole. Magnetic poles always exist in pairs of opposite sense to form a dipole. When one pole is sufficiently far removed from the other so that it no longer affects it, the single pole is referred to as a monopole.

If two magnetic poles of strength  $m_1$  and  $m_2$  are separated by a distance  $r$ , a force exists between them (Box 3.1). If the poles are of the same sort, the force will push the poles apart, and if they are of opposite polarity, the force is attractive and will draw the poles towards each other. Note the similarity of the form of the expression in Box 3.1 with that for the force of gravitational attraction in Box 2.1; both gravity and magnetism are *potential fields* and can be described by comparable potential field theory.

The closeness of the flux lines shown in Figure 3.1, the flux per unit area, is the *flux density*  $\mathbf{B}$  (and is measured in weber/m<sup>2</sup> = teslas).  $\mathbf{B}$ , which is also called the 'magnetic induction', is a vector quantity (the former c.g.s. units of flux density were gauss, equivalent to 10<sup>-4</sup> T.) The units of teslas are too large to be practical in geophysical work, so a subunit called the nanotesla (nT = 10<sup>-9</sup> T)

**Table 3.1** Applications of geomagnetic surveys.**Locating**

- Pipes, cables and ferrous metallic objects
- Buried military ordnance (shells, bombs, etc.)
- Buried metal drums (of contaminated or toxic waste, etc.)
- Concealed mine shafts and adits

**Mapping**

- Archaeological remains
- Concealed basic igneous dykes
- Metalliferous mineral lodes
- Geological boundaries between magnetically contrasting lithologies, including faults
- Large-scale geological structures

**Box 3.2** Relationship between magnetic flux density  $B$ , magnetising force  $H$ , and susceptibility  $\kappa$ 

Given:

$$B = \mu H$$

[units :  $\mu$ (Wb/Am).  $H$ (A/m) = Wb/m<sup>2</sup> = teslas]

Since  $\mu = \mu_r \mu_0$ :

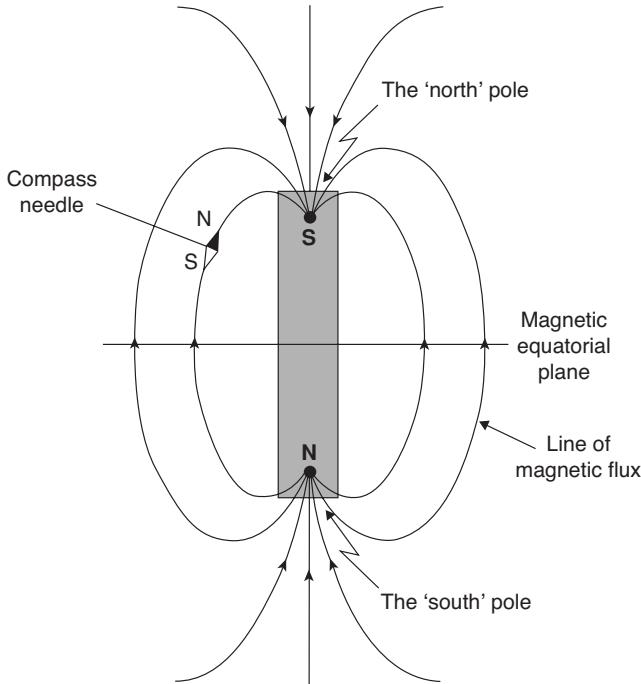
$$B = \mu_r \mu_0 H.$$

Rearranging to introduce  $k = \mu_r - 1$ :

$$\begin{aligned} B &= \mu_0 H + \mu_0 (\mu_r - 1) H \\ &= \mu_0 H + \mu_0 k H = \mu_0 H + \mu_0 J. \end{aligned}$$

Hence:

$$B = \mu_0 H(1 + k) \text{ and } J = kH.$$

**Figure 3.1** Lines of magnetic flux around a bar magnet.**Box 3.1** Force between two magnetic poles

$$F = \frac{m_1 m_2}{4\pi \mu r^2}$$

where  $\mu$  is the magnetic permeability of the medium separating the poles;  $m_1$  and  $m_2$  are pole strengths and  $r$  the distance between them.

is used instead, where 1 nT is numerically equivalent to 1 gamma in c.g.s. units (1 nT is equivalent to  $10^{-5}$  gauss).

The magnetic field can also be defined in terms of a force field which is produced by electric currents. This *magnetising field strength*  $H$  is defined, following Biot-Savart's Law, as being the field strength at the centre of a loop of wire of radius  $r$  through which a current is flowing such that  $H = 1/2r$ . Consequently the units of the magnetising field strength  $H$  are amperes per metre (A/m).

The ratio of the flux density  $B$  to the magnetising field strength  $H$  is a constant called the *absolute magnetic permeability* ( $\mu$ ). Practically, the magnetic permeability of water and air can be taken to be equal to the *magnetic permeability of free space* (a vacuum), denoted  $\mu_0$  which has the value  $4\pi \times 10^{-7}$  Wb A<sup>-1</sup> m<sup>-1</sup>. For any medium other than a vacuum, the ratio of the permeabilities of a medium to that of free space is equal to the *relative permeability*  $\mu_r$ , such that  $\mu_r = \mu/\mu_0$  and, as it is a ratio, it has no units.

### 3.2.2 Susceptibility

It is possible to express the relationship between  $B$  and  $H$  in terms of a geologically diagnostic parameter, the *magnetic susceptibility*  $\kappa$  (see Box 3.2 and Section 3.3.1). Susceptibility is in essence a measure of how susceptible a material is to becoming magnetised. For a vacuum,  $\mu_r = 1$  and  $\kappa = 0$ . Although susceptibility has no units, to rationalise its numerical value to be compatible with the SI or rationalised system of units, the value in c.g.s. equivalent units (e.g. unratinalised units such as e.m.u., electromagnetic units) should be multiplied by  $4\pi$ . Some materials have negative susceptibilities (see Section 3.3).

### 3.2.3 Intensity of magnetisation

From the last expressions given in Box 3.2, it is clear that for a vacuum,  $B = \mu_0 H$  (as  $\kappa = 0$ ). The penultimate expression in Box

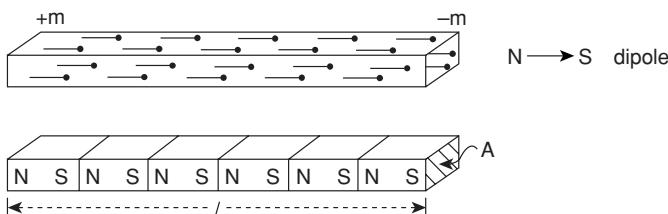


**Figure 3.2** Schematic of a uniformly magnetised bar magnet as a collection of aligned dipoles producing a pole strength of  $\pm m$  and as a series of minor bar magnets.

3.2 indicates that in a medium other than a vacuum, an extra magnetising field strength of  $\kappa H$ , called the *intensity of magnetisation*  $J$ , is induced by the magnetising force,  $H$ .

Another way of visualising the intensity of magnetisation is to examine a bar magnet of length  $I$  and cross-sectional area  $A$  which is uniformly magnetised in the direction of the long axis. The bar magnet can be thought of as consisting of a series of much smaller bar magnets or dipoles all aligned parallel to the long axis of the whole bar magnet (Figure 3.2). The magnetic intensities due to all the individual north and south poles will cancel out except at the end faces of the whole magnet, thus giving the whole magnet an overall magnetisation. The surface concentration of free poles, or pole strength  $m$  per unit area, is a measure of the intensity of magnetisation  $J$  (Box 3.3). The stronger the magnetisation, the greater will be the concentration of free poles. Furthermore, if a body of volume  $V$  is magnetised uniformly with intensity  $J$ , then that body is said to have a magnetic moment  $M$  which is defined as the product of the magnetic pole strength  $m$  and the length  $I$  separating the poles (Box 3.3). The intensity of magnetisation, which is thus the magnetic moment per unit volume, is of fundamental importance in describing the magnetic state of any rock mass.

#### Box 3.3 Intensity of magnetisation, $J$ (amps/metre)

$$J = m/A$$

where  $m$  is the pole strength (amp.metre) and  $A$  is the cross-sectional area of the bar magnet ( $\text{m}^2$ ). In terms of the *magnetic moment*,  $M$  (amp.metre $^2$ ):

$$J = M/V = m.l/V$$

where  $I$  is the length of the dipole,  $V$  is the volume of the magnetised body, and  $M = m.l$ .

The intensity of the induced magnetisation,  $J_i$  in rock with susceptibility  $\kappa$ , caused by the Earth's magnetic field  $F$  (tesla) in the sense of the flux density, i.e. the  $B$ -field, is given by:

$$J_i = \kappa.F/\mu_0$$

where  $\mu_0$  is the permeability of free space, and  $F = \mu_0 H$ , with  $H$  being the magnetising force.

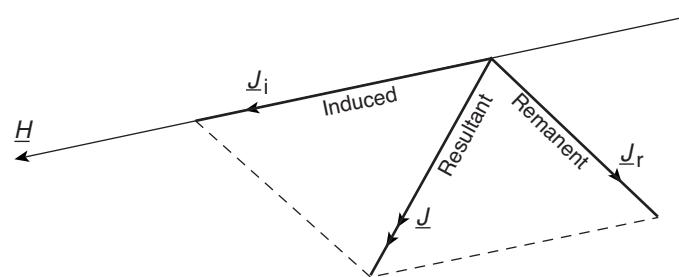


**Figure 3.3** Vectorial summation of induced and remanent intensities of magnetisation.

#### 3.2.4 Induced and remanent magnetisation

So far the discussion has centred upon a magnetisation that is induced by an applied field  $H$  where the induced intensity of magnetisation is denoted by  $J_i$ . In many cases, in the absence of an applied field ( $H$ ), there is still a measurable intensity of magnetisation which is sustained by the internal field strength due to permanently magnetic particles. The intensity of this *permanent* or *remanent magnetisation* is denoted by  $J_r$ .

A rock mass containing magnetic minerals will have an induced as well as a remanent magnetisation. These magnetisations may have different directions and magnitudes of intensity (Figure 3.3). The magnitude and orientation of the resultant  $J$  dictate both the amplitude and shape of a magnetic anomaly, respectively. Consequently, interpretation of magnetic data is complicated by having greater degrees of freedom of the magnetic parameters and physical properties compared with gravity, which is largely dependent upon only rock density.

#### 3.2.5 Diamagnetism, paramagnetism, and ferri- and ferro-magnetism

All atoms have a magnetic moment as a result of the orbital motion of electrons around the nucleus and the spin of the electrons. According to quantum theory, two electrons can exist in the same electron shell (or state) as long as they spin in opposite directions. The magnetic moments of two such electrons, called *paired electrons*, will cancel out. In the majority of substances, when there is no external applied magnetic field, the spin magnetic moments of adjacent atoms are distributed randomly, so there is no overall magnetisation. In a *diamagnetic* material, such as halite, all the electron shells are complete and so there are no unpaired electrons. When an external magnetic field is applied, a magnetisation is induced. The electrons orbit in such a way so as to produce a magnetic field that opposes the applied field, giving rise to a weak, negative susceptibility.

Unpaired electrons in incomplete electron shells produce unbalanced spin magnetic moments and weak magnetic interactions, between atoms in *paramagnetic* materials such as fayalite, amphiboles, pyroxenes, olivines, garnets and biotite. In an external applied field, the magnetic moments align themselves into the same direction, although this process is retarded by thermal agitation. The result is a weak positive susceptibility, but one which decreases

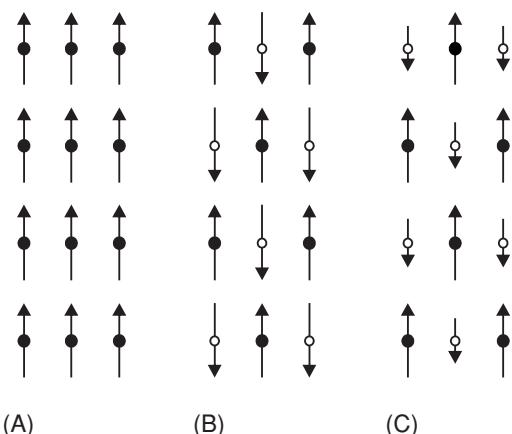


**Figure 3.4** Schematic of magnetic moments in (A) ferromagnetic, (B) anti-ferromagnetic, and (C) ferrimagnetic crystals. After Nagata (1961), by permission.

inversely with the absolute temperature according to the Curie-Weiss Law. Paramagnetism is generally at least an order of magnitude stronger than diamagnetism.

In *ferromagnetic* materials the susceptibility is large but is dependent upon temperature and the strength of the applied magnetic field. The spin moments of unpaired electrons are coupled magnetically due to the very strong interaction between adjacent atoms and overlap of electron orbits. A small grain in which magnetic coupling occurs forms what is called a single *magnetic domain* and has dimensions of the order of one micron. This gives rise to a strong spontaneous magnetisation, which can exist even when there is no external applied field. The magnetic coupling can be such that the magnetic moments are aligned either parallel (Figure 3.4A) or anti-parallel as in an anti-ferromagnetic substance (Figure 3.4B).

A *ferrimagnetic* material, such as magnetite ( $\text{Fe}_3\text{O}_4$ ), is one where one of the two anti-parallel magnetic moments is stronger than the other. This produces a net remanent magnetisation even in the absence of an external magnetic field (Figure 3.4C). Ferrimagnetic materials, such as magnetite and greigite ( $\text{Fe}_3\text{S}_4$ ), can occur as crystals 42 nm long within magnetosomes that link together to form chains. These are known to occur within bacterial magnetoreceptors, such as the bacterium *Magnetospirillum magnetotacticum* (Johnson and Lohmann, 2008). The torque on the chain of magnetosomes is so large that it can rotate the entire organism to align with the Earth's magnetic field. Such magnetoreceptors have been found in a wide range of species including honeybees, birds, salmon and sea turtles.

Truly ferromagnetic materials occur only rarely in nature, but include substances such as cobalt, nickel and iron, all of which have parallel alignment of moments. Ferromagnetism disappears when the temperature of the materials is raised above the *Curie temperature*  $T_C$ , as inter-atomic magnetic coupling is severely restricted and the material thereafter exhibits paramagnetic behaviour. In *anti-ferromagnetic* materials such as haematite, the moments are aligned in an antiparallel manner. Although the magnetic fields of the oppositely orientated dipoles cancel each other out, crystal lattice defects result in a net residual moment or *parasitic (anti)-ferromagnetism*. In ferrimagnetic materials, of which magnetite, titanomagnetite

and ilmenite are prime examples, the sublattices are unequal and antiparallel. This results in a net magnetisation. Spontaneous magnetisation and large susceptibilities are characteristics of ferrimagnetic materials, such as in the case of pyrrhotite. Although the temperature dependence of ferrimagnetic behaviour is complex, ferrimagnetism disappears at temperatures above the Curie temperature. The majority of naturally occurring magnetic minerals exhibit either ferrimagnetic or imperfectly anti-ferromagnetic characteristics.

The Curie temperature varies with different minerals and will be different for whole rocks depending upon the composition of magnetic minerals present. In a granitic rhyolite, for example, the Curie temperature for titanomagnetite is between 463 and 580°C, whereas for the ilmenite-haematite series it is in the range 130–220°C. Oxidation of the iron-titanium oxides generally causes a rise in the Curie temperature. When low-temperature oxidation occurs, i.e. at temperatures lower than 300°C, in addition to increases in the Curie temperature, the intensity of magnetisation decreases. In order of increasing oxidation and decreasing intensity of magnetisation, titanomagnetite ( $T_C = 100$ –200°C) alters to titanomaghemite (150–450°C) then to magnetite (550–580°C) and ultimately to haematite (650–680°C) (Petersen, 1990). Haematite has the lowest intensity of magnetisation. The alteration of magnetic minerals is important to remember when it comes to the interpretation of magnetic anomalies. Rocks that should display large susceptibilities and greatest intensities of magnetisation may exhibit much weaker magnetic properties owing to geochemical alteration of the magnetic minerals.

For a multi-domain material in a field-free space ( $H = 0$ ), the spontaneous magnetisation of the magnetic domains within a crystal is related to the crystal axes (Figure 3.5). The magnetisation directions of all domains cancel each other out, so there is no net magnetisation intensity ( $J = 0$ ). On increasing the applied magnetic field ( $H$ ), the domain walls can move easily and reversibly, should  $H$  be reduced at this point. As  $H$  increases, so the various domains

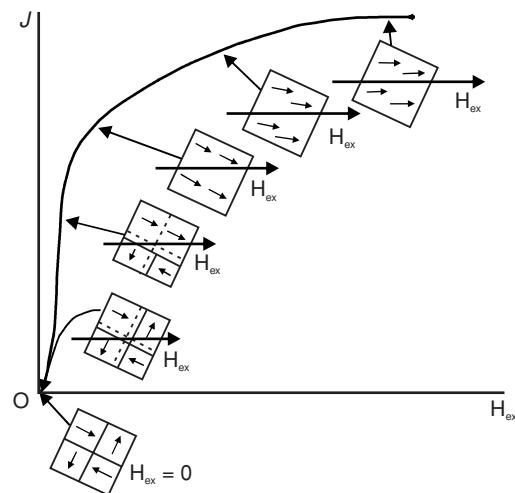


**Figure 3.5** Process of magnetisation of a ferromagnetic substance according to domain theory. From Sharma (1986), by permission.

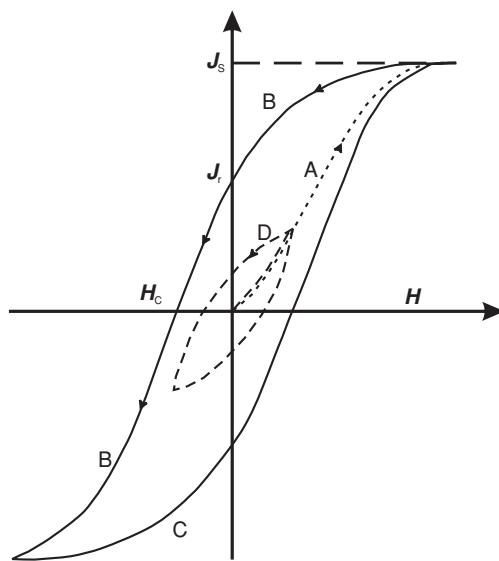


**Figure 3.6** Hysteresis loop illustrating a cycle of magnetisation (curves A, B, C) of a ferromagnetic material. Small loop (D) shows the magnetisation cycle without saturation. From Sharma (1986), by permission.

reorientate themselves parallel to the applied field, but in discrete steps called *Barkhausen jumps*, which are permanent. When there is no further increase in magnetisation intensity with increasing applied field strength, all the domains are orientated parallel to the applied field direction and the material is said to be magnetically *saturated*. On reducing  $H$  to zero following saturation, only some of the magnetic domains are able to return to their former orientation, which results in a remanent magnetisation  $J_r$ .

If the magnetic permeability ( $\mu$ ) of a medium is independent of the magnetising force ( $H$ ), the material is said to be linear in its behaviour. However, if a ferromagnetic or ferrimagnetic material, such as magnetite or pyrrhotite, with grains larger than 10 microns is placed in an increasing applied magnetic field, its magnetic intensity  $J$  increases to the point of saturation following a hysteresis loop (Figure 3.6). The physical processes by which this happens have already been described in terms of domain theory. After reaching saturation, the applied field  $H$  is reduced to zero, at which point the intensity of magnetisation is that attributed to the remanent magnetisation. To eliminate this magnetisation, a negative field,  $-H_c$ , the *coercive force*, has to be applied. The *coercivity*,  $H_c$ , is an indication as to the ‘hardness’ or permanence of the magnetisation. Consequently, larger magnetic grains, which thus contain more magnetic domains, are easier to magnetise (and therefore have a higher susceptibility), than fine grains which are magnetically hard, as indicated by a relatively high coercivity and low susceptibility. On increasing the applied magnetic field to full saturation, the hysteresis loop is completed. It follows that, for minerals that exhibit a non-linear behaviour, no unique value of susceptibility exists. Values cited for such materials are usually for weak values of  $H$  and prior to saturation ever having been reached. For much more detailed discussion of rock magnetism, see the monographs by Nagata (1961), Stacey and Banerjee (1974) and O'Reilly (1984).

### 3.3 Magnetic properties of rocks

#### 3.3.1 Susceptibility of rocks and minerals

Magnetic susceptibility is an extremely important property of rocks, and is to magnetic exploration methods what density is to gravity surveys. Rocks that have a significant concentration of ferro- and/or ferrimagnetic minerals tend to have the highest susceptibilities. Consequently, basic and ultrabasic rocks have the highest susceptibilities, acidic igneous and metamorphic rocks have intermediate to low values, and sedimentary rocks have very low susceptibilities in general (Table 3.2 and Figure 3.7). In this compilation of data,

**Table 3.2** Susceptibilities of rocks and minerals (rationalised SI units).

Mineral or rock type	Susceptibility*
<b>Sedimentary</b>	
Dolomite (pure)	-12.5 to +44
Dolomite (impure)	20,000
Limestone	10 to 25,000
Sandstone	0 to 21,000
Shales	60 to 18,600
Average for various	0 to 360
<b>Metamorphic</b>	
Schist	315 to 3000
Slate	0 to 38,000
Gneiss	125 to 25,000
Serpentinite	3100 to 75,000
Average for various	0 to 73,000
<b>Igneous</b>	
Granite	10 to 65
Granite (m)	20 to 50,000
Rhyolite	250 to 37,700
Pegmatite	3000 to 75,000
Gabbro	800 to 76,000
Basalts	500 to 182,000
Oceanic basalts	300 to 36,000
Peridotite	95,500 to 196,000
Average for acid igneous	40 to 82,000
Average for basic igneous	550 to 122,000
<b>Minerals</b>	
Ice (d)	-9
Rocksalt (d)	-10
Gypsum (d)	-13
Quartz (d)	-15
Graphite (d)	-80 to -200
Chalcopyrite	400
Pyrite (o)	50 to 5000
Hematite (o)	420 to 38,000
Pyrrhotite (o)	1250 to $6.3 \times 10^6$
Illmenite (o)	314000 to $3.8 \times 10^6$
Magnetite (o)	70,000 to $2 \times 10^7$

(d) = diamagnetic material; (o) = ore; (m) = with magnetic minerals.

\*  $\kappa \times 10^6$  rationalised SI units; to convert to the unratinalised c.g.s units, divide by 4π.

Data from Parasnis (1986), Sharma (1986) and Telford et al. (1990)

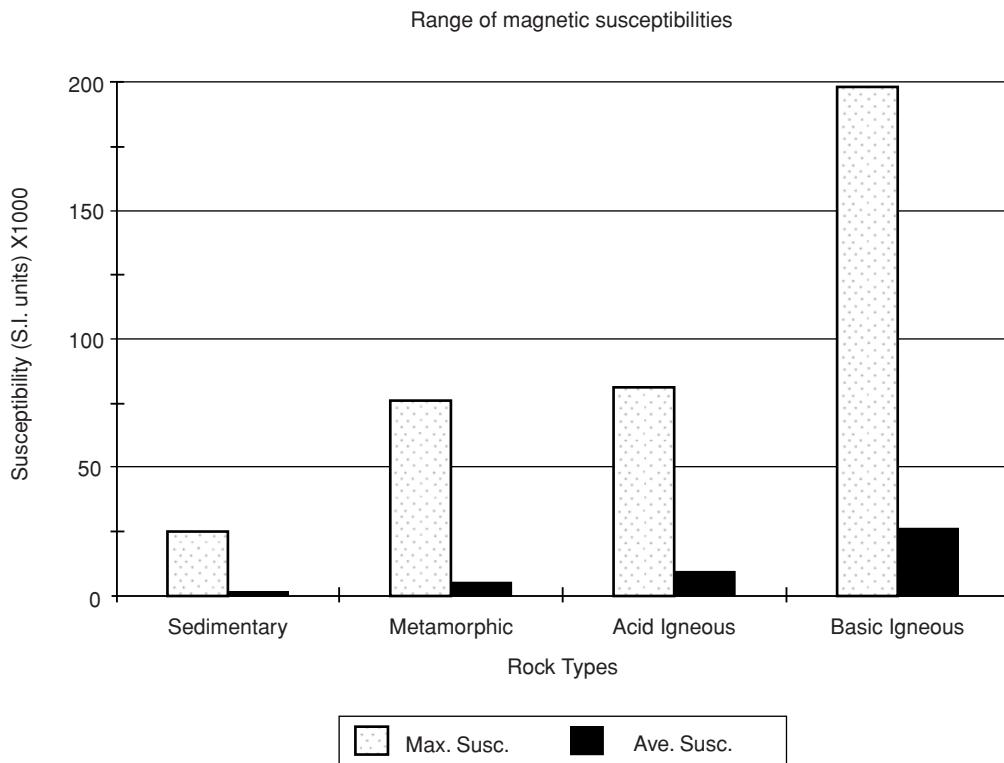


**Figure 3.7** Susceptibilities of major rock types.

specific details of rock types are not available and so the values cited should be taken only as a guide. Metamorphic rocks are dependent upon their parent material, and metapsammites are likely to have different susceptibilities compared with metapelites, for example.

Whole rock susceptibilities can vary considerably owing to a number of factors in addition to mineralogical composition. Susceptibilities depend upon the alignment and shape of the magnetic grains dispersed throughout the rock. If there is a marked orientation of particles, such as in some sedimentary and metamorphic rocks, a strong physical anisotropy may exist. The variation of magnetic properties as a function of orientation and shape of mineral grains is known as the *magnetic fabric*. Magnetic fabric analysis provides a very sensitive indication as to the physical composition of a rock or sediment, which in turn can be important in interpreting physical processes affecting that rock. For example, it is possible to correlate magnetic fabric variation in estuarine sediments with sonograph images of the estuary floor. In conjunction with Thematic Mapper images obtained from low-flying aircraft and simultaneous water sampling from boats, it is possible to establish a detailed model of estuarine sediment dynamic processes, as has been achieved for Plymouth Sound in southwest England (Fitzpatrick, 1991). For further details of the magnetic fabric method, see the discussions by Lowrie (1990) and Tarling (1983), for example.

For magnetic ore bodies with extremely high susceptibilities ( $\kappa \geq 10^6$  SI), the measured susceptibility – more correctly referred to rock types as the *apparent susceptibility*  $\kappa_a$  – can be reduced substantially by a shape demagnetisation effect (see Box 3.4). This involves a *demagnetisation factor*  $N_\alpha$  which depends on a direction  $\alpha$ . For a

**Box 3.4 Apparent susceptibility  $\kappa_a$  and the demagnetisation factor  $N_\alpha$**

$$\kappa_a = \kappa / (1 + N_\alpha \kappa)$$

sphere,  $N_\alpha = 1/3$  in all directions. In the case of a thin sheetlike body with a high true susceptibility ( $\kappa \sim 10^6$  SI):  $N_\alpha \sim 1$  in the transverse direction, giving a susceptibility  $\kappa_a \sim 0.5\kappa$ ; and  $N_\alpha \sim 0$  in the longitudinal direction, so that  $\kappa_a \approx \kappa$ . Demagnetisation factors are discussed further by Parasnis (1986) and Sharma (1986).

Susceptibilities can be measured either in the field using a hand-held susceptibility meter such as the kappameter, or on samples returned to a laboratory where they can be analysed more accurately.

### 3.3.2 Remanent magnetisation and Königsberger ratios

In addition to the induced magnetisation, many rocks and minerals exhibit a permanent or *natural remanent magnetisation* (NRM) of intensity  $J_r$  when the applied field  $H$  is zero. The various processes by which rocks can acquire a remanent magnetisation are listed in Table 3.3 and discussed in more detail by Merrill (1990), Sharma (1986), Tarling (1983), and especially by Gubbins and Herrero-Bervera (2007) and contributions therein.

**Table 3.3** Types of remanent magnetisation (RM). After Merrill (1990), by permission.

Types of RM	Process
Natural (NRM)	Acquired by a rock or mineral under natural conditions.
Thermal (TRM)	Acquired by a material during cooling from a temperature greater than the Curie temperature to room temperature (e.g. molten lava cooling after a volcanic eruption).
Isothermal (IRM)	Acquired over a short time (of the order of seconds) in a strong magnetic field at a constant temperature (e.g. such as by a lightning strike).
Chemical (CRM)	Also crystallisation RM; acquired at the time of nucleation and growth or crystallisation of fine magnetic grains far below the Curie point in an ambient field.
Thermal-chemical (TCRM)	Acquired during chemical alteration and cooling.
Detrital (DRM)	Also depositional RM; acquired by the settling out of previously magnetised particles to form ultimately consolidated sediments which then have a weak net magnetisation, but prior to any chemical alteration through diagenetic processes.
Post-depositional (PDRM)	Acquired by a sediment by physical processes acting upon it after deposition (e.g. bioturbation and compaction).
Viscous (VMR)	Acquired after a lengthy exposure to an ambient field with all other factors being constant (e.g. chemistry and temperature).
Anhysteretic (ARM)	Acquired when a peak amplitude of an alternating magnetic field is decreased from a large value to zero in the presence of a weak but constant magnetic field.

Primary remanent magnetisations are acquired by the cooling and solidification of an igneous rock from above the Curie temperature (of the constituent magnetic minerals) to normal surface temperature (TRM) or by detrital remanent magnetisation (DRM). Secondary remanent magnetisations, such as chemical, viscous or post-depositional remanent magnetisations, may be acquired later on in the rock's history. This is especially true of igneous rocks that have later undergone one or more periods of metamorphism, particularly thermal metamorphism.

The intensity of the remanent magnetisation  $J_r$  may swamp that of the induced magnetisation  $J_i$ , particularly in igneous and thermally metamorphosed rocks. The ratio of the two intensities ( $J_r/J_i$ ) is called the *Königsberger ratio*,  $Q$ , which can be expressed in terms of the Earth's magnetic field at a given locality and the susceptibility of the rocks (Box 3.5). Just as susceptibility can vary within a single rock type, so too can the Königsberger ratio. However, similar rock types have characteristic values of  $Q$ , some of which are listed in Table 3.4. Nagata (1961) made four broad generalisations on the basis of  $Q$ :

- $Q \sim 1$  for slowly crystallised igneous and thermally metamorphosed rocks in continental areas;
- $Q \sim 10$  for volcanic rocks;
- $Q \sim 30-50$  for many rapidly quenched basaltic rocks;
- $Q < 1$  in sedimentary and metamorphic rocks, except when iron ore is involved.

**Box 3.5 Königsberger ratio,  $Q$** 

$$Q = J_r/\kappa(F/\mu_0)$$

where  $J_r$  is the intensity of remanent (NRM) magnetisation,  $\kappa$  is the susceptibility,  $\mu_0$  is the permeability of free space and  $F$  is the magnitude of the Earth's magnetic field (in tesla) at a given location in the same sense as the  $B$ -field (flux density).

It is also very important to consider that not only may  $J_r$  exceed  $J_i$ , but the direction of remanent magnetisation may be quite different from that of the ambient induced field at a location. Consequently, the resultant magnetisation (i.e. the vectorial sum of the remanent and induced magnetisations) will give rise to characteristic magnetic anomalies (refer back to Figure 3.3) when reversely magnetised rocks are present.

## 3.4 The Earth's magnetic field

### 3.4.1 Components of the Earth's magnetic field

The geomagnetic field at or near the surface of the Earth originates largely from within and around the Earth's core. Currents external to the Earth in the ionosphere and magnetosphere associated with the Van Allen radiation belts (Figure 3.8), currents induced in the Earth

**Table 3.4** Examples of values of the Königsberger ratio.

Rock type	Location	<i>Q</i>
Basalt	Mihare volcano, Japan	99-118
Oceanic basalts	Northeast Pacific	15-105
Oceanic basalts	Mid-Atlantic Ridge	1-160
Seamount basalts	North Pacific	8-57
Cainozoic basalts	Victoria, Australia	5
Early Tertiary basalts	Disko, West Greenland	1-39
Tholeiite dykes	England	0.6-1.6
Dolerite sills	North England	2-3.5
Dolerite	Sutherland, Scotland	0.48-0.51
Quartz dolerite	Whin Sill, England	2-2.9
Gabbro	Småland, Sweden	9.5
Gabbro	Minnesota, USA	1-8
Gabbro	Cuillin Hills, Scotland	29
Andesite	Taga, Japan	4.9
Granite	Madagascar	0.3-10
Granite plutons	California, USA	0.2-0.9
Granodiorite	Nevada, USA	0.1-0.2
Diabase	Astano Ticino, Switzerland	1.5
Diabase dykes	Canadian Shield	0.2-4
Magnetite ore	Sweden	1-10
Magnetite ore	South India	1-5

by external field variations, and the permanent (remanent) and steady-state induced magnetisations of crustal rocks, also contribute to the overall geomagnetic field. The magnetosphere is vital for the survival of life on Earth as it forms the primary force field that protects the planet from harmful radiation from the Sun. The various components of the geomagnetic field affect exploration surveys in a variety of ways which will be discussed in turn. For a comprehensive review of geomagnetism and palaeomagnetism, readers are referred to Gubbins and Herrero-Bervera (2007).

### 3.4.1.1 The main dipole field

The main component of the geomagnetic field is called the *dipolar field* as it behaves, to a first-order approximation, like a dipolar electromagnet located at the centre of the Earth but inclined at  $11\frac{1}{2}^\circ$  to the Earth's rotational axis (Figure 3.9).

The *geomagnetic poles*, the positions on the Earth's surface through which the axis of the best-fitting dipole passes, are not the same as the *magnetic* or *dip poles*. These are located where the magnetic field is directed vertically. The positions of the geomagnetic and dip poles change with time (see also Section 3.4.2)

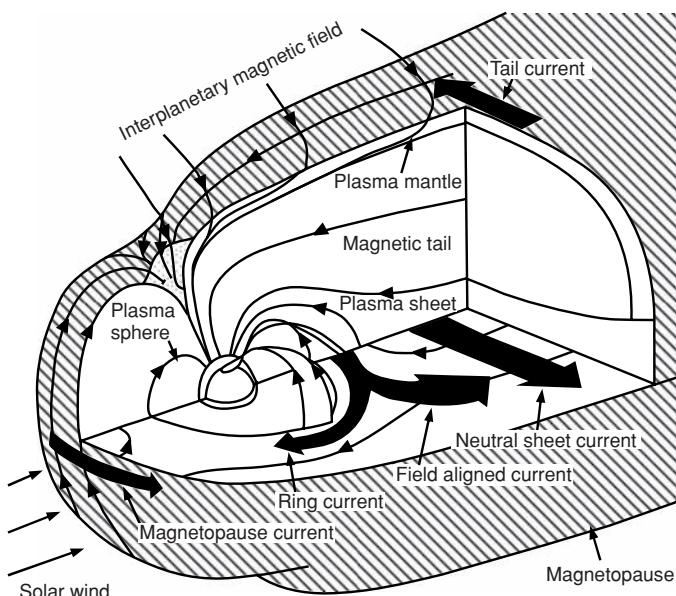


**Figure 3.8** The geomagnetic field showing the magnetosphere, magnetopause and Van Allen radiation belts. From James (1990), by permission.

with varying rates of movement. The north *geomagnetic pole* is at  $80.02^\circ\text{N}$ ,  $71.98^\circ\text{W}$  (2010), on the eastern side of Ellesmere Island in the Canadian Arctic Archipelago, and is moving northwestwards at around  $50\text{ km/yr}$  (Figure 3.10A, Olsen and Mandea, 2007b). If it continues at its present speed and direction, it will cross the Arctic Ocean and arrive at Severnaja Zeml'A, an island off northern

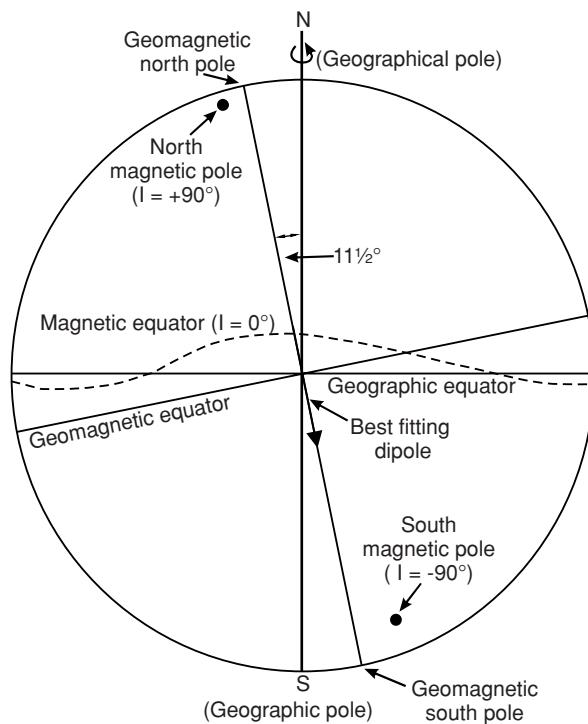


**Figure 3.9** The field due to an inclined geocentric dipole. After McElhinny (1973), by permission.

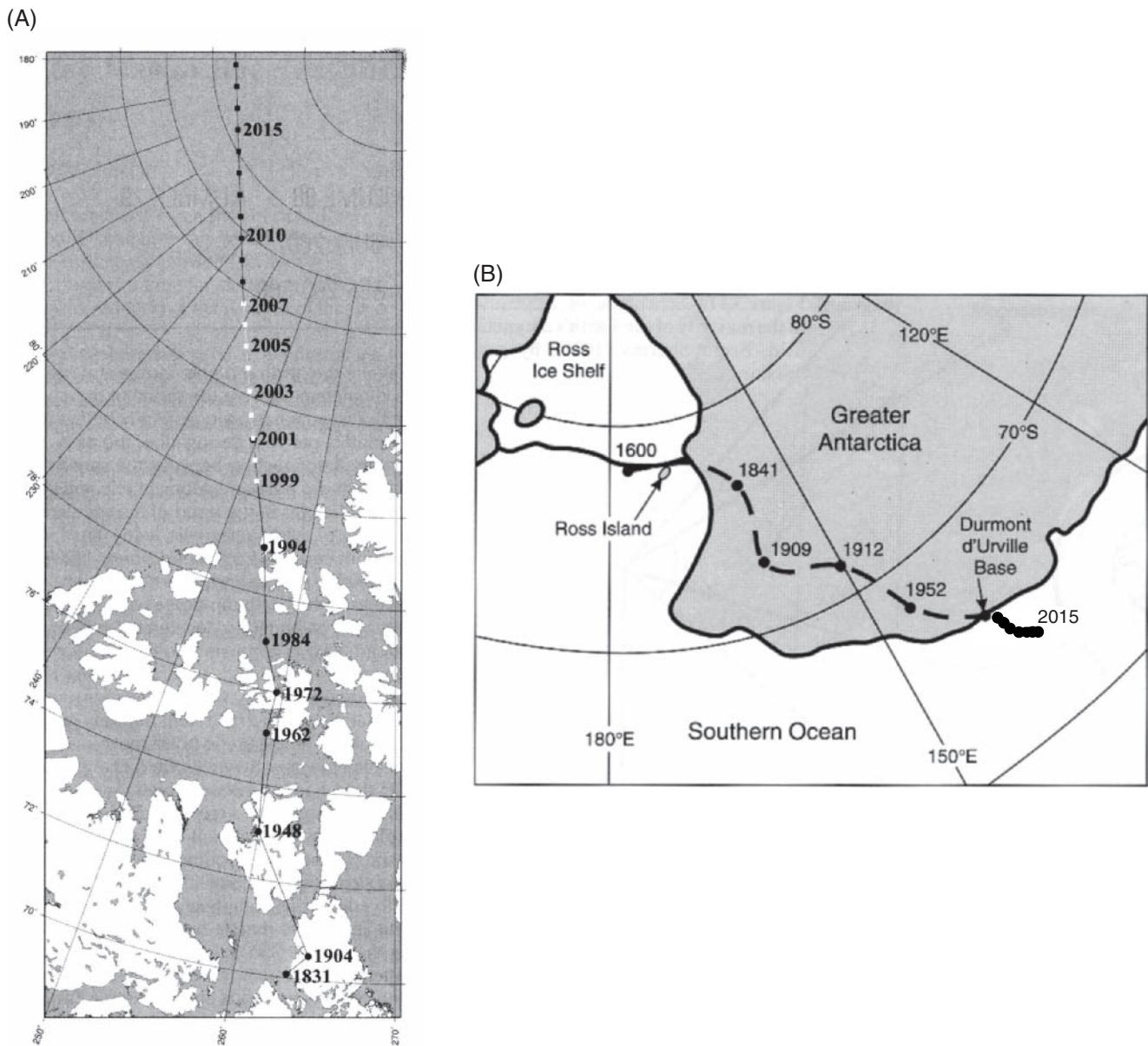


**Figure 3.10** (A) Location of the north magnetic dip pole and its drift from 1831 and its predicted trend from 2007 to beyond 2015 (from Olsen and Mandea, 2007b; IGRF-10 (2005)), and (B) the location of the south magnetic dip pole and its drift since the year 1600, with additional IGRF-11 data from Finlay et al. (2010).

Russia, in 2050. The northern *dip* pole is at  $85.19^{\circ}\text{N}$ ,  $133.16^{\circ}\text{W}$  (2010). The south dip pole is at  $64.44^{\circ}\text{S}$ ,  $137.44^{\circ}\text{E}$  (2010), offshore from the Adélie Coast of Greater Antarctica and moving northwards at a rate of 5–10 km/yr (Olsen and Mandea, 2007b). The southern geomagnetic pole is at  $80.02^{\circ}\text{S}$ ,  $108.02^{\circ}\text{E}$  (2010) and moving towards the geodetic south pole ( $90^{\circ}\text{S}$ ) (Figure 3.10B). Further updates on the movement and positions of both dip and geomagnetic poles can be found on the websites of the British Geological Survey and the Geological Survey of Canada (Appendix 1).

The geomagnetic field is produced by electric currents induced within the conductive liquid outer core as a result of slow convective movements within it (Figure 3.11). It is for this reason that the analogy of the Earth's field to that induced by an electromagnet

is preferred to that of a permanently magnetised bar magnet. The liquid core behaves as a geodynamo, but the precise nature of the processes involved has yet to be resolved. Models to explain the disposition of the magnetic field must also account for the slow but progressive change in field intensity and westward drift in direction known as the secular variation. Furthermore, the model must also explain how the Earth's magnetic field goes through reversals of magnetic polarity. The study of how the Earth's magnetic field has changed through geological time is known as *palaeomagnetism*. The use of magnetic reversals to provide global chronometric calibration of geological events is known as *magnetostratigraphy* (Tauxe, 1990).

The geomagnetic field can be described in terms of the declination,  $D$ , inclination,  $I$ , and the total force vector  $\mathbf{F}$  (Figure 3.12).

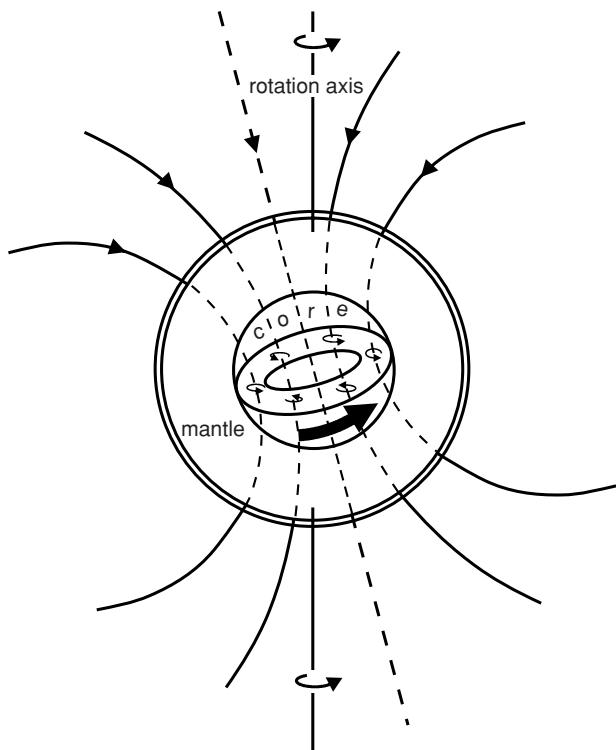


**Figure 3.11** Schematic of the cause of the majority of the Earth's magnetic field. From Sharma (1986), by permission.

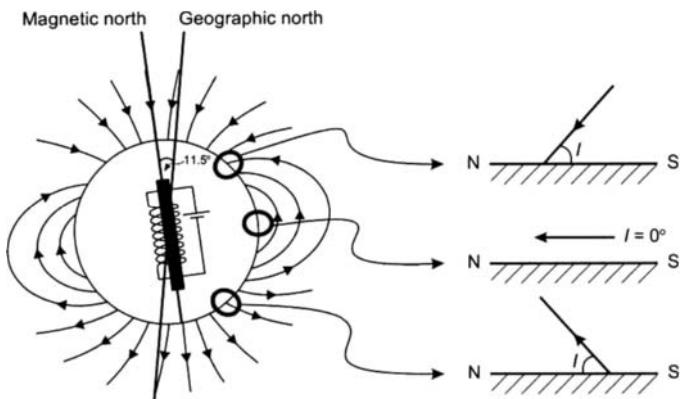


**Figure 3.13** Variation of inclination with latitude.

A freely suspended magnetised needle will align itself along the  $F$  vector so that at the magnetic (dip) north, the inclination is  $90^\circ$ ; i.e. the needle will point vertically downwards. At the south magnetic (dip) pole, the needle will point vertically upwards. At the magnetic equator, the needle will lie horizontally (Figure 3.13). Furthermore, the vertical component of the magnetic intensity of the Earth's magnetic field varies with latitude, from a minimum of around 30,000 nT at the magnetic equator to 60000 nT at the magnetic poles.

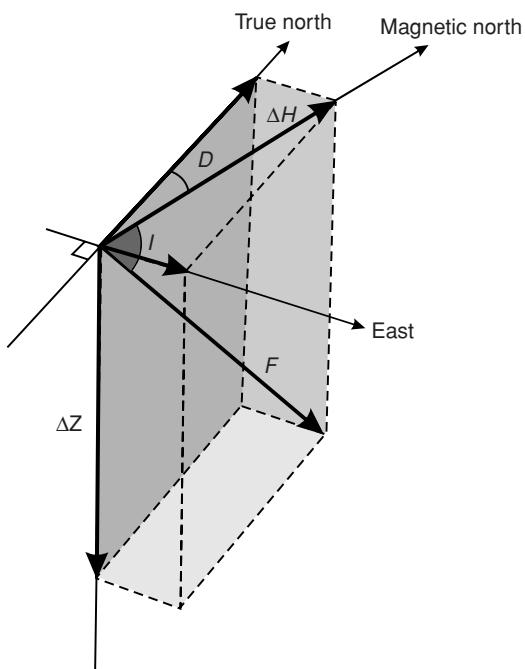


**Figure 3.12** Elements of the magnetic field: inclination  $I$ , declination  $D$ , and total magnetic force  $F$ .

### 3.4.1.2 The non-dipolar field

While the single dipole field approximates to the Earth's observed magnetic field, there is a significant difference between them, which is known as the *non-dipole field*. The total intensity for the non-dipole field is shown in Figure 3.14, from which several large-scale features can be seen with dimensions of the order of several thousand kilometres and with amplitudes up to 20,000 nT, about a third of the Earth's total field. Using the method of spherical harmonic analysis, it can be demonstrated that the non-dipole field and the associated large-scale features can be represented by a fictitious set of 8–12 small dipoles radially located close to the liquid core. These dipoles serve to simulate the eddy currents associated with the processes within the liquid core.

A further use of the spherical harmonic analysis is that it provides a means whereby the spatial distribution and intensity of the total magnetic field can be calculated for the whole globe. The total field, which is calculated every five years, is called the *International Geomagnetic Reference Field* (IGRF) and the year of calculation is known as the *epoch*. The main field, with sources inside the Earth, is the negative gradient of a scalar potential  $V$ , the mathematical form of which is given in Box 3.6. The coefficients are a function of time and, for the IGRF, are assumed to vary at constant rates for five-year periods. For more details on main-field modelling, see the discussions by Chapman and Bartels (1940) and Langel (1987). It has to be recalculated regularly because of the secular variation. The IGRF is now in its eleventh generation, having been revised in 2010 (Finlay *et al.*, 2010). Consequently, it is possible to obtain a theoretical value for the field strength of the Earth's magnetic field for any location on Earth (Figure 3.15). However,

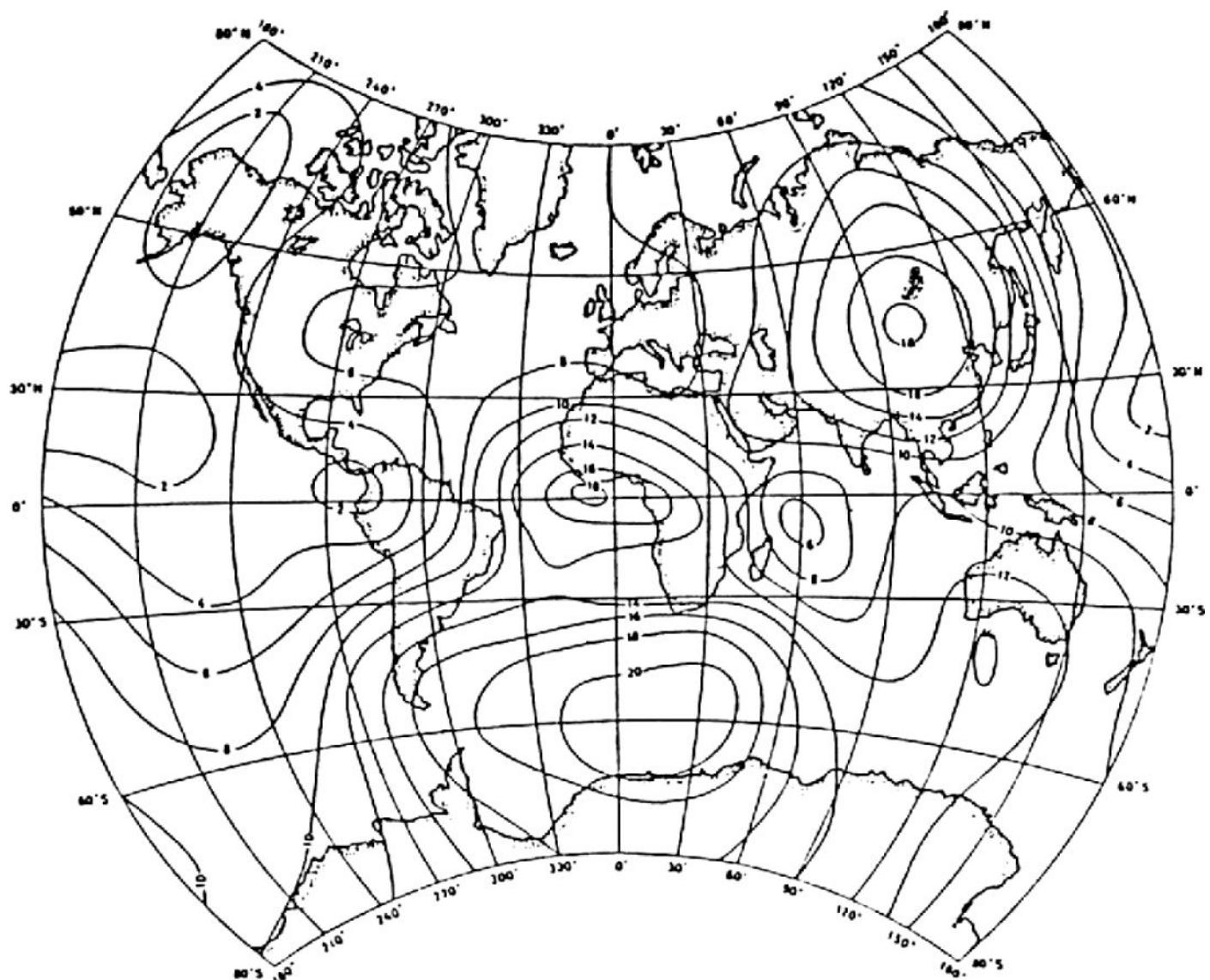


**Figure 3.14** Variation in the intensity of the non-dipole field for epoch 1980. From Sharma (1986), by permission.

#### Box 3.6 IGRF equation (Macmillan and Maus, 2005)

The main field is the negative gradient of the scalar potential  $V$ :

$$V(r, \theta, \lambda, t) = R \sum_{n=1}^{n_{\max}} (R/r)^{n+1} \sum_{m=0}^n (g_n^m(t) \cos m\lambda + h_n^m(t) \times \sin m\lambda) P_n^m(\theta)$$

where  $r, \theta, \lambda$ , are geocentric coordinates ( $r$  is the distance from the centre of the Earth,  $\theta$  is the co-latitude, i.e.  $90^\circ$ -latitude, and  $\lambda$  is the longitude),  $R$  is a reference radius (6371.2 km);  $g_n^m(t)$  and  $h_n^m(t)$  are the coefficients at a time  $t$ , and  $P_n^m(\theta)$  are the Schmidt semi-normalised associated Legendre functions of degree  $n$  and order  $m$ .

readers are strongly advised to read the IGRF 'health warning' to be found at [www.ngdc.noaa.gov/ILAGA/vmod/igrfhw.html](http://www.ngdc.noaa.gov/ILAGA/vmod/igrfhw.html) about the numerical accuracy with which the IGRF calculates values for the main magnetic field. It can be seen from this figure that instead of the anticipated two maxima consistent with a truly dipolar field, there are in fact four maxima. The significance of the IGRF in processing magnetic data is discussed in Section 3.6.3. Maps of the components of the IGRF are available from a number of sources such as the USGS and BGS (see web details in Appendix 1).

Some time after a given epoch for the IGRF, a definitive version is derived for a given time period and is known as the *Definitive Geomagnetic Reference Field* (DGRF). For example, IGRF-10 (2005) is valid for the period 1900–2010, and Definitive for the period 1945–2000.

Data used in the computation of revisions of the International Geomagnetic Reference Field have been obtained by satellite (e.g. during 1965–71, Polar Orbiting Geophysical Observatory series,

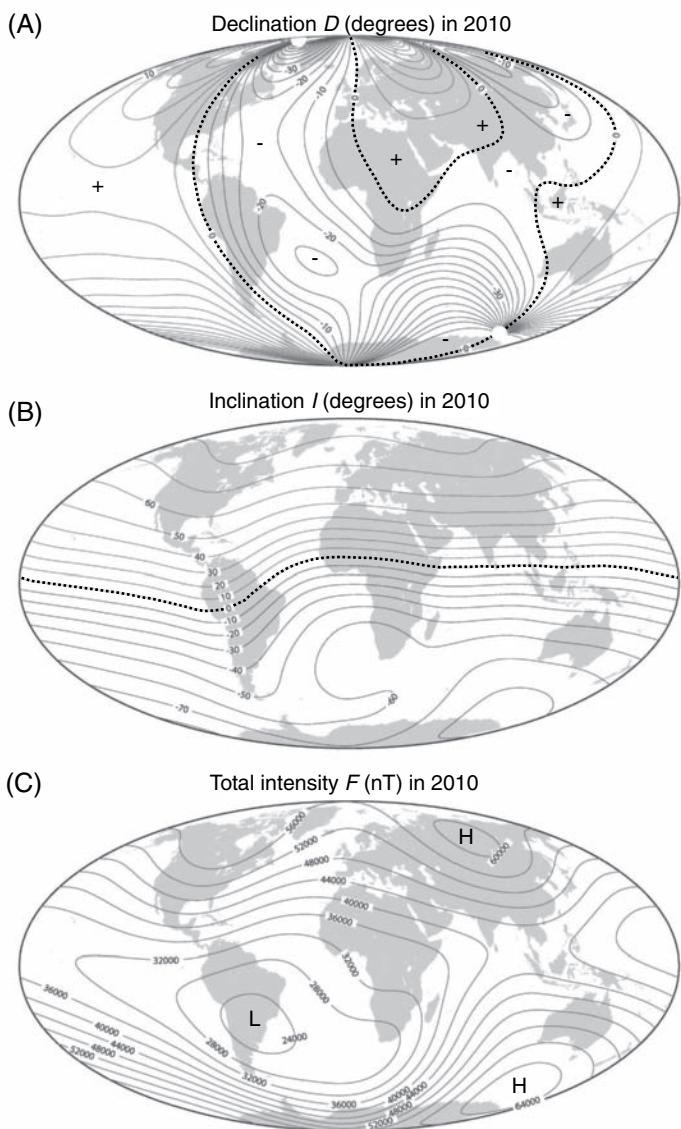


**Figure 3.15** Maps of the magnetic declination  $D$  (A) and (B) inclination  $I$  (middle, units are degrees) – zero line is shown dotted, positive areas shown with +, and negative areas with –; and (C) total intensity  $F$  at the Earth's surface in 2010.0 from the model IGRF-11. Mollweide projection is used. Modified from Finlay *et al.* (2010), by permission. [C]

POGO; October 1979 to June 1980, MAGSAT; and from 1999, Ørsted (Lowes *et al.*, 2000) and CHAMP data). However, at satellite orbit ranges, perturbations in the Earth's magnetic field caused by magnetic materials in the crust are not resolvable. Surface or airborne measurements can detect high-amplitude small-scale features within the crust down to a depth of 25–30 km where the Curie isotherm is reached. These features may be caused by induction due to the Earth's field, or remanent magnetisation, or a mixture of both.

### 3.4.2 Time variable field

Observations of the Earth's magnetic field have been made for over four centuries at London and Paris. From these data, it is clear

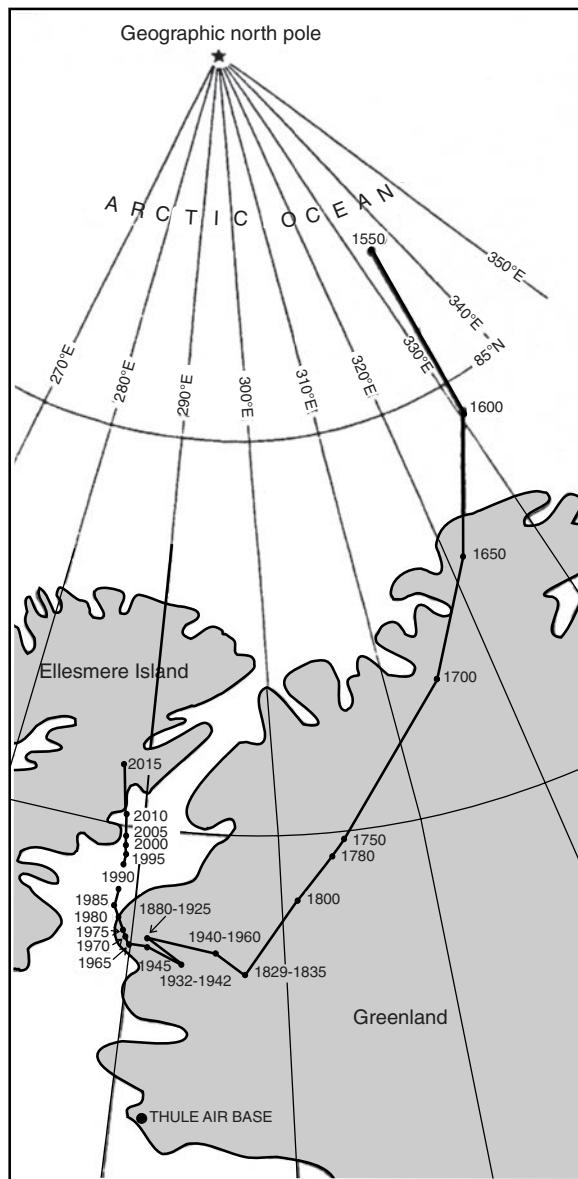


**Figure 3.16** Map of the drift of the north geomagnetic pole position from 1550 to 1990 (James, 1990), and projected to 2015 using IGRF-11 data (Finlay *et al.*, 2010), by permission.

that the geomagnetic and magnetic pole positions drift with time, known as the secular variation in the magnetic field (Figure 3.16). In addition, the intensity of the main magnetic field is decreasing at about 5% per century. These rates of change, although very significant on a geological timescale, do not affect data acquisition on a typical exploration survey unless it covers large geographical areas and takes many months to complete, or if such surveys are being used to compare with historical data.

Abrupt changes in the trend of the secular variation in the geomagnetic field over short periods of time (less than four years), known as geomagnetic jerks, have been modelled (e.g. Le Huy *et al.*, 1998) and observed (e.g. the 2003 geomagnetic jerk, Olsen and Mandea, 2007a). They are thought to be due to a change in the

fluid flow at the surface of the Earth's core (Bloxham *et al.*, 2002), although their physical origin is still not understood.

The Earth's magnetic field changes over a daily period, the *diurnal variations*. These are caused by changes in the strength and direction of currents in the ionosphere. On a magnetically 'quiet' (Q) day, the changes are smooth and are on average around 50 nT, but with maximum amplitudes up to 200 nT at the geomagnetic equator. The changes are least during the night when the background is almost constant, and decrease in amplitude from dawn to midday, whereupon they increase to the daily maximum about mid-late afternoon before settling down to the night-time value.

Magnetically disturbed (D) days are marked by a rapid onset of fluctuations of the order of hundreds of nanoteslas followed by slower but still erratic fluctuations with decreasing amplitude. These disturbances, which are called *magnetic storms*, may persist for several hours or even days. Such frenetic magnetic activity is caused by sunspot and solar activity resulting in solar-charged particles entering the ionosphere. This may happen on fine sunny days and not necessarily in stormy weather. Magnetic observatories around the world provide an advance warning service to advise of the probability of magnetic storm activity. In severe storms, all magnetic surveying has to stop as it is not practicable to correct for such extreme fluctuations. In minor disturbances, if a continuous-reading base station magnetometer is used, the diurnal variations can be corrected. In aeromagnetic surveys, it is necessary to specify contractually what constitutes a magnetic storm. Survey data adversely affected by magnetic disturbances may have to be reflown, and this obviously has cost implications. Practical details of how to correct for diurnal variations are given in Section 3.6.2.

## 3.5 Magnetic instruments

The earliest known device which responded to the Earth's magnetic field was a magnetised spoon used by Chinese geomancers (diviners) in the first century AD. Compass needles were introduced for navigation around the year 1000 in China, and in Europe about 200 years later. The first accurate measurement of the inclination of the Earth's field was made at Radcliffe in London in 1576 by Robert Norman. He described his instruments and collected data in his book *The Newe Attractive* (1581), which was the first book ever to be devoted to geomagnetism.

Magnetometers used specifically in geophysical exploration can be classified into three groups: the torsion (and balance), fluxgate and resonance types, of which the last two have now completely superseded the first. Torsion magnetometers are still in use at 75% of geomagnetic observatories, particularly for the measurement of declination. Magnetometers measure horizontal and/or vertical components of the magnetic field ( $F_h$  and  $F_z$  respectively) or the total field  $F_t$  (see Figure 3.12).

### 3.5.1 Torsion and balance magnetometers

Historically the first to be devised (1640), these comprise in essence a magnetic needle suspended on a wire (torsion type) or balanced on a pivot. In the Earth's magnetic field the magnet adopts an

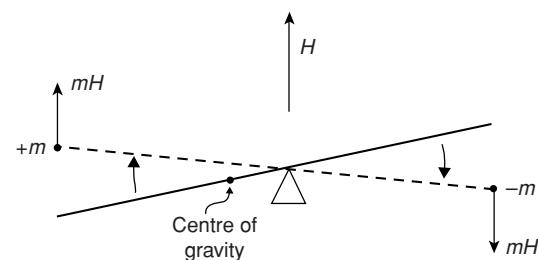


**Figure 3.17** Basic principle of operation of a torsion or balance-type magnetometer.

equilibrium position. If the device is taken to another location where the Earth's magnetic field is different from that at the base station, or if the magnetic field changes at the base station, the magnet will align itself to the new field and the deflection from the rest position is taken as a measure of the Earth's magnetic field. The Swedish mine compass, Hotchkiss superdip, and Thalén-Tiberg magnetometer are all early examples of this type of device. In 1915, Adolf Schmidt devised his variometer in which a magnetic beam was asymmetrically balanced on an agate knife edge (Figure 3.17) and zeroed at a base station.

Deflections from the rest position at other locations were then read using a collimating telescope. To be used it had to be orientated at right-angles to the magnetic meridian so as to remove the horizontal component of the Earth's field. The device was calibrated using Helmholtz coils so that the magnitude of the deflection was a measure of the vertical component of the field strength.

A development of the Schmidt variometer was the compensation variometer. This measured the force required to restore the beam to the rest position. In exploration work, the greatest precision with a balance magnetometer was only 10 nT at best. For further details of these devices, see the descriptions by Telford *et al.* (1990).

### 3.5.2 Fluxgate magnetometers

The fluxgate magnetometer was developed during the Second World War to detect submarines. It consists of two parallel cores made out of high-permeability ferromagnetic material. Primary coils are wound around these cores in series but in opposite directions (Figure 3.18). Secondary coils are also wound around the cores but in the

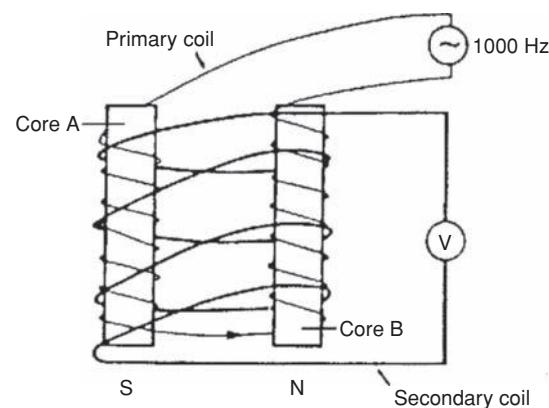


**Figure 3.18** Basic operating principle of the fluxgate magnetometer.

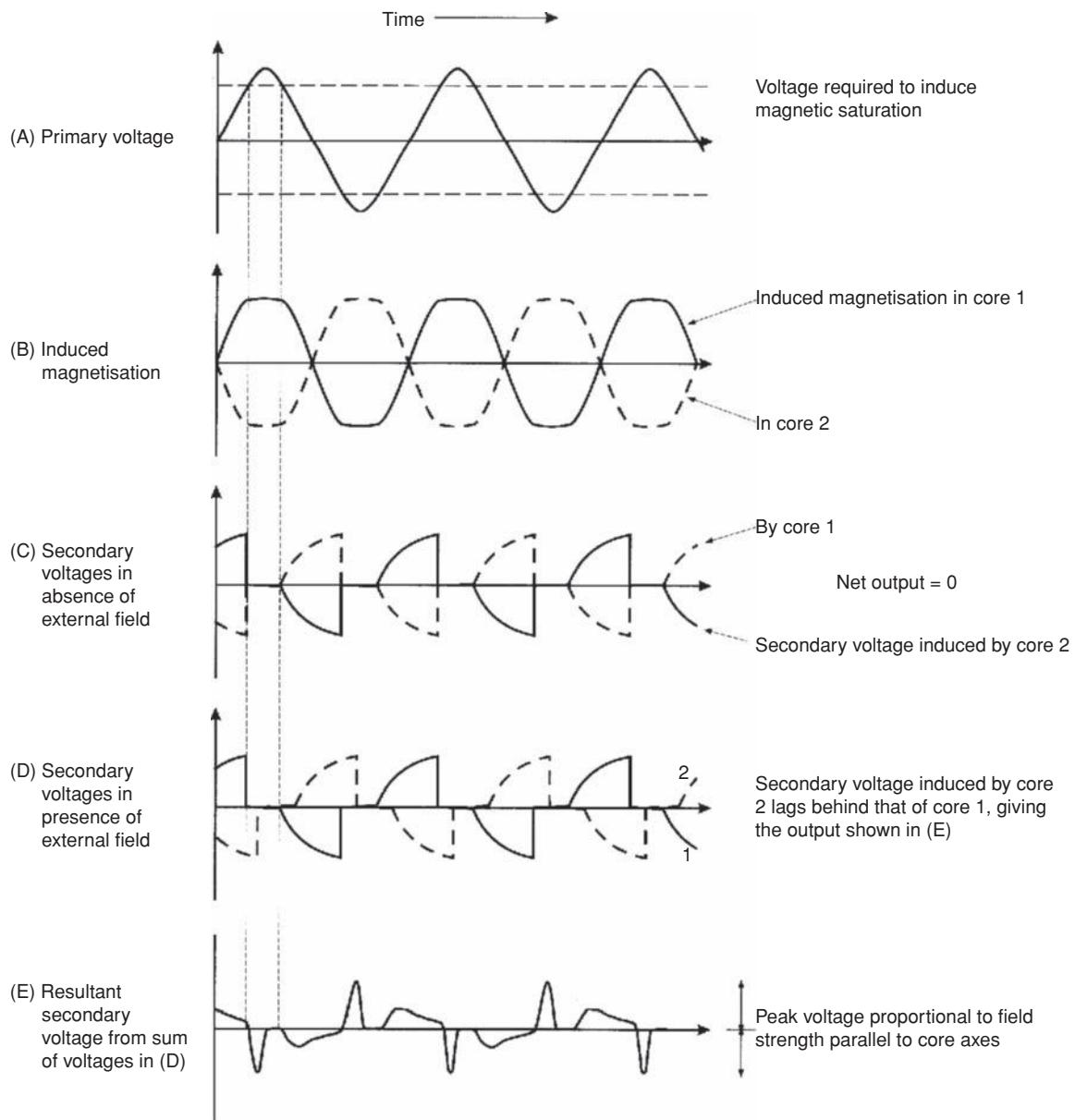


**Figure 3.19** Response characteristics of primary and secondary circuits in a fluxgate magnetometer.

opposite sense to the respective primary coil. A current alternating at 50–1000 Hz (Figure 3.19A) is passed through the primary coils which drives each core through a  $B$ - $H$  hysteresis loop (cf. Figure 3.6) to saturation at every half-cycle (Figure 3.19B) in the absence of an external field, so inducing a magnetic field in each core. The generated alternating magnetic field induces an in-phase voltage within the secondary coils. This voltage reaches its maximum when the rate of change of the magnetic field is fastest (Figure 3.19C). As the coils are wound in opposing directions around the two cores, the secondary voltages are in phase but have opposite polarity (Figure 3.19C) so that the sum of the two voltages is at all times zero. However, when the cores are placed in the Earth's magnetic field, a component of that field will be parallel to the orientation of the cores. Consequently, the core whose primary field is reinforced by

the ambient external field will reach saturation earlier than the other core whose magnetic field is opposed by the external field. This has the effect of shifting the phases of the secondary voltages (Figure 3.19D) so that the sum of the two secondary voltages is now non-zero (Figure 3.19E). The peak amplitude of the pulsed output of the combined secondary coils is proportional to the magnitude of the external field component (Primdahl, 1979).

The fluxgate magnetometer can be used to measure specific magnetic components with the same attitude as the sensor cores. As the fluxgate magnetometer is relatively insensitive to magnetic field gradients, it has the advantage that it can be used in areas where very steep gradients would militate against the use of resonance-type devices, which are affected. Some portable fluxgate magnetometers suffer from temperature effects owing to inadequate thermal



**Figure 3.20** A Bartington Grad601-2 dual fluxgate gradiometer in use for an archaeological survey. Courtesy of Wessex Archaeology Ltd, by permission. [C]

insulation, which can reduce the resolution to only  $\pm 10$  to  $20$  nT, this being inadequate for ground exploration surveys. They are used quite widely in airborne surveys where better thermal insulation can be ensured and additional devices can be used to aid the consistent orientation of the sensor cores. In such cases, an accuracy to within  $\pm 1$  nT can be achieved. In addition, fluxgate instruments can provide a continuous output which is another advantage for airborne applications. Fluxgate magnetometers can also be used in downhole logging applications in mineral exploration and as dual gradiometers in archaeological investigations, such as those manufactured by Bartington Instruments (Figure 3.20).

### 3.5.3 Resonance magnetometers

There are two main types of resonance magnetometer: the *proton free-precession magnetometer*, which is the best known, and the *alkali vapour magnetometer*. Both types monitor the precession of atomic particles in an ambient magnetic field to provide an absolute measure of the total magnetic field,  $F$ .

The proton magnetometer has a sensor which consists of a bottle containing a proton-rich liquid, usually water or kerosene, around which a coil is wrapped, connected to the measuring apparatus (Figure 3.21). Each proton has a magnetic moment  $M$  and, as it is always in motion, it also possesses an angular momentum  $G$ , rather like a spinning top. In an ambient magnetic field such as the Earth's ( $F$ ), the majority of the protons align themselves parallel with this field, with the remainder orientated antiparallel (Figure 3.22A). Consequently, the volume of proton-rich liquid acquires a net magnetic moment in the direction of the ambient field ( $F$ ).



**Figure 3.21** (A) A nuclear proton precession magnetometer in use (courtesy of Geometrics), and (B) a caesium vapour magnetometer. [C]

A current is applied to the coil surrounding the liquid, generating a magnetic field about 50 to 100 times stronger than, and at right-angles to, the Earth's field. The protons align themselves to the new magnetic direction (Figure 3.22B). When the applied field is switched off, the protons precess around the pre-existent ambient field  $F$  (Figure 3.22C) at the *Larmor precession frequency* ( $f_p$ ) which is proportional to the magnetic field strength  $F$  (Box 3.7). As protons are charged particles, as they precess they induce an alternating voltage at the same frequency as  $f_p$  into the coil surrounding the sensor bottle. Interaction between adjacent protons causes the precession to decay within 2–3 seconds, which is sufficient time to measure the precession frequency. To obtain a value of  $F$  to within  $\pm 0.1$  nT, frequency must be measured to within  $\pm 0.004$  Hz, which is quite easily achieved. This resolution is equivalent to 1 part in  $10^6$ , which is 100 times less sensitive than in gravity measurements.

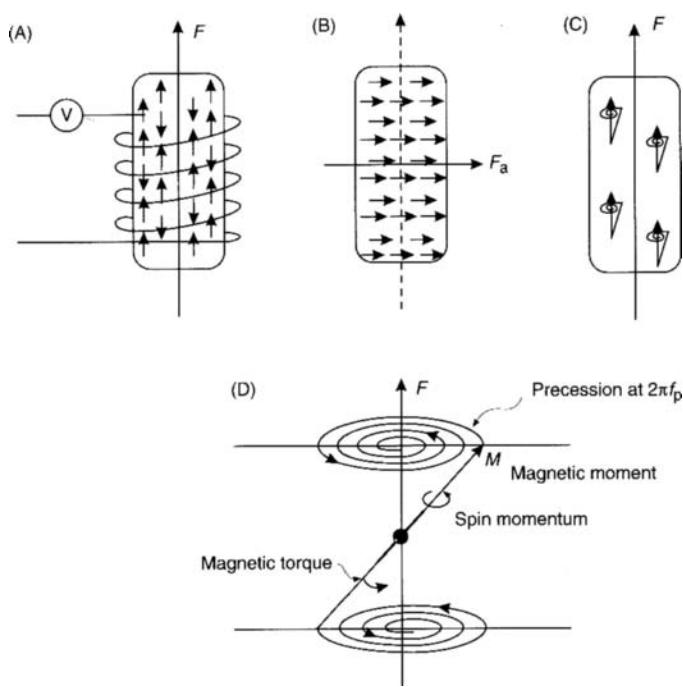


**Figure 3.22** Basic operating principles of a proton magnetometer. After Kearey et al. (2002), by permission.

One of the limiting factors of the proton magnetometer is that its accuracy is reduced in areas of high magnetic gradient. As the sensor bottle is of the order of 15 cm long, a strong field gradient of 500 nT/m, for example, means that there is a 75 nT difference in field strength between the top and bottom of the sensor and the rate of damping is increased. The accuracy of measurement of the precession frequency is thus reduced. As a guide, if the gradient is 400 nT/m, the precision is at best 1 nT; for 200 nT/m it is 0.5 nT.

As the precession frequency is only a function of field strength, there is no need to orientate the field sensor. Modern proton magnetometers give a direct readout of the field strength in nanoteslas and

#### Box 3.7 Magnetic field strength, $F$ , and precession frequency, $f_p$

$$F = 2\pi f_p / \Phi_p$$

where  $\Phi_p$  is the gyromagnetic ratio of the proton, which is the ratio of the magnetic moment and spin angular momentum (see Figure 3.22); and

$$\Phi_p = 0.26753 \text{ Hz/nT} \text{ and } 2\pi/\Phi_p = 23.4859 \text{ nT/Hz.}$$

Thus:

$$F = 23.4859 f_p$$

For example, for  $F = 50,000 \text{ nT}$ ,  $f_p = 2128.94 \text{ Hz}$ .

data can be automatically output into a datalogger for subsequent downloading onto a computer.

Proton magnetometers are used extensively not only in land surveys but also at sea and in airborne investigations. In marine surveys, the magnetometer sensor bottle, which is located in a sealed unit called a 'fish', is deployed two or three ship's lengths astern so as to be sufficiently removed from magnetic interference from the ship. In the case of aircraft, two techniques are used. One is to tow the sensor bottle at least 30 m below and behind the aircraft in what is called a 'bird', or place it in a non-magnetic boom called a 'stinger' on the nose, on the tail fin or on a wingtip of the aircraft. In the fixed mode, special magnetic compensation measures can be taken to annul the magnetisation of the aircraft; the excellence of the compensation is called the *figure of merit* (FOM) rating. The fitting of active compensation systems in modern aircraft has improved FOM values and reduced the time taken for compensation, and so helped to improve the cost-effectiveness of airborne surveys. In addition to ground, marine and airborne applications, proton magnetometers can be deployed down boreholes, and can be particularly useful in mineral exploration programmes.

A limitation on proton magnetometers, particularly in airborne surveys, is the rate at which measurements can be made. As the proton precession and measurement take a finite time (of the order of a second or longer), continuous readings are not possible and this can be restricting in some situations.

One manufacturer (GEM Systems Inc.) has produced a modified precession instrument that utilises the Overhauser Effect. An electron-rich fluid containing free radicals is added to a standard hydrogen-rich liquid. The combination increases the polarisation by a factor of 5000 in comparison with standard liquids. Overhauser proton precession uses a radio-frequency (RF) magnetic field and so needs only minimal power, in contrast with high-power direct current fields used in traditional proton precession magnetometers. Polarisation and magnetisation can occur simultaneously, and thus rapid sampling of the total field strength (two readings per second) can be achieved.

The second type of resonance magnetometer is the *alkali vapour magnetometer* or *optical absorption magnetometer*, which utilises the optical pumping technique (Bloom, 1962). The principle on which this method is based is illustrated in Figure 3.23. Under normal conditions of temperature and pressure, electrons exist at certain energy states (A and B) around the nucleus of the atom. According to quantum physics, it is only possible to transfer an electron from a lower energy state (A) to one with higher energy (B) in discrete jumps. If a vapour of an element such as rubidium or caesium is illuminated by a light whose filament is made of the same element, the light emitted is at the correct wavelength for incident photons to be absorbed by the vapour and the low-energy state electrons excited up to higher levels. If the incident light is circularly polarised, only electrons in the A1 orbit will be excited or 'optically pumped' up to the B orbit. At this point, the excess photons will be transmitted through the excited vapour and will be detected by the photocell as an increase in light intensity.

A small alternating current is passed through a coil at a frequency of between 90 and 300 kHz to induce a magnetic field around the alkali vapour cell. The frequency is tuned until it is locked into the

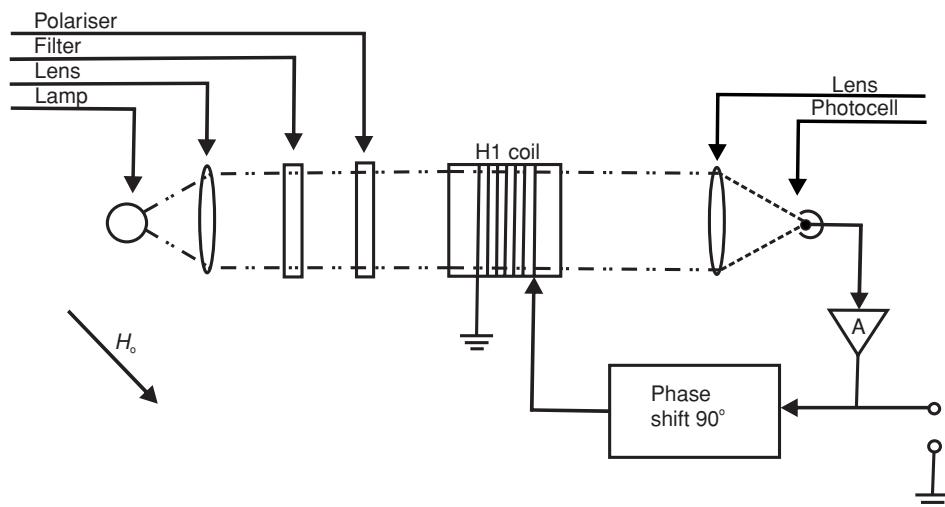


**Figure 3.23** Optical pumping principle of the alkali vapour magnetometer. From James (1990), by permission.

Larmor frequency for the alkali vapour concerned. This small magnetic field energises some electrons back into their vacant A ground states. The consequence of this is that the light intensity at the photocell diminishes as photons are absorbed by the alkali vapour in the cell, until saturation is reached again. Photons will continue to be absorbed until all the available electrons have been excited to the B state, when the light at the photocell will again be at its most intense. Consequently, the cycled optical pumping produces a light at the photocell that flickers at the Larmor precession frequency, which can easily be measured. As the precession frequency is dependent upon the ambient field strength of the Earth (see Box 3.6), the total field strength can be determined from a measurement of the precession frequency. The factor  $2\pi/\Phi_p$  is approximately equal to 0.2141 and 0.1429 nT/Hz for rubidium and sodium respectively, which give corresponding precession frequencies of 233.5 and 350 kHz in a field of 50000 nT. As long as the light beam axis is not parallel or antiparallel to the Earth's magnetic field (when no signals would be produced), the precession frequency can be measured with sufficient accuracy so that the magnetic field strength can be determined to within +0.01 nT. The measurement time is extremely small, and so alkali vapour magnetometers can be used as virtually continuous reading instruments, which makes them ideally suited to airborne surveys.

For land-based archaeological or environmental geophysical applications, self-oscillating split-beam caesium vapour magnetometers have been developed, largely from military ordnance detection instruments (e.g. the Geometrics G-822L magnetometer). Sampling rates of up to 10 readings per second are possible with a sensitivity of 0.1 nT.

### 3.5.4 Cryogenic (SQUID) magnetometers

The most sensitive magnetometer available is the cryogenic magnetometer which operates using processes associated with superconductivity, details of which have been given by Goree and Fuller (1976). These magnetometers are perhaps better known as *SQUID*

(Superconducting QUantum Interference Device) magnetometers. Used extensively in palaeomagnetic laboratories, the SQUID magnetometer has also been developed for use in aeromagnetic surveying since the early 1980s, particularly as a gradiometer. SQUIDs can have a measurement sensitivity of  $10^{-5}$  nT/m; this means that two sensors need only be placed 25 cm or less apart, thus making it possible to have the entire sensor system in a very small space. This has great advantages in mounting the equipment in aircraft, in borehole probes and in submarine devices where space is at a premium. Measurement accuracy of the total field strength is within  $\pm 0.01$  nT.

Technical difficulties over the use of liquid helium, which has to be maintained at a temperature of 4.2 K for superconductivity to occur, limit the widespread deployment of SQUID magnetometers. They are rarely used in surface magnetic measurements.

### 3.5.5 Gradiometers

A gradiometer measures the difference in the total magnetic field strength between two identical magnetometers separated by a small distance. In ground instruments, a separation of 0.5 m to 1.5 m is common. The magnetic field gradient is expressed in units of nT/m and taken to apply at the mid-point between the sensors. A major advantage of gradiometers is that because they take differential measurements, no correction for diurnal variation is necessary as both sensors will be equally affected. As gradiometers measure the vertical magnetic gradient, noise effects from long-wavelength features are suppressed and anomalies from shallow sources are emphasised. For detailed high-resolution surveys exploring for mineral targets, magnetic gradiometry is the preferred method (Hood, 1981).

Fluxgate and resonance-type magnetometers are commonly used in ground surveys. Where continuous-reading devices are required, such as when automatic data-logging is being used, fluxgate gradiometers are preferable (e.g. Sowerbutts and Mason, 1984). A detailed although dated comparison of the different types of gradiometers and magnetometers has been made by Hood *et al.* (1979).

A more recent review of magnetic gradiometry has been provided in *The Leading Edge* (January 2006; McConnell and Dragoset (2006), and papers therein).

Self-oscillating split-beam caesium vapour gradiometers have also been developed for small-scale land-based surveys, such as Geometrics Inc.'s G-858 instrument. These instruments can sample at up to 10 readings per second with a sensitivity of 0.05 nT. An additional feature of this particular instrument is that it can be connected to a differential Global Positioning System for the simultaneous logging of position and magnetic data. The system was first tested at Stanford University, USA, in March 1993. As with any geophysical instruments, it is always best to check with equipment manufacturers for the latest technical specifications.

### 3.5.6 Airborne magnetometer systems

Magnetic surveys are commonly acquired using aircraft, either fixed wing or helicopters. Magnetometers can be fitted to aircraft either as single or multiple sensors depending upon the type of measurements to be made. The sensors can be rigid mounted as booms (from the front of the aircraft nose) or stingers (from the aircraft's tail) (Figure 3.24A) or at the end of the aircraft's wing tips (especially useful in horizontal gradiometer mode to provide as large a horizontal separation of the sensors as possible). Where the aircraft to be used is not specifically adapted for magnetic surveying, temporary mounts can be added or the sensors can be deployed from helicopters using a towed 'bird' (Figure 3.24B). Sensors can be single, dual (either as horizontal or vertical gradiometers) or triaxial gradiometers (Figure 3.24C) or as multiple sensors in order to sample the vertical and horizontal gradients sufficiently (Doll *et al.*, 2006, 2008a,b; and Billings and Wright, 2009, respectively). Sensors can either be mounted as a discrete entity or bundled with other sensors, such as electromagnetic systems (see Chapter 10, Section 10.3), to permit simultaneous measurements during the same flight.

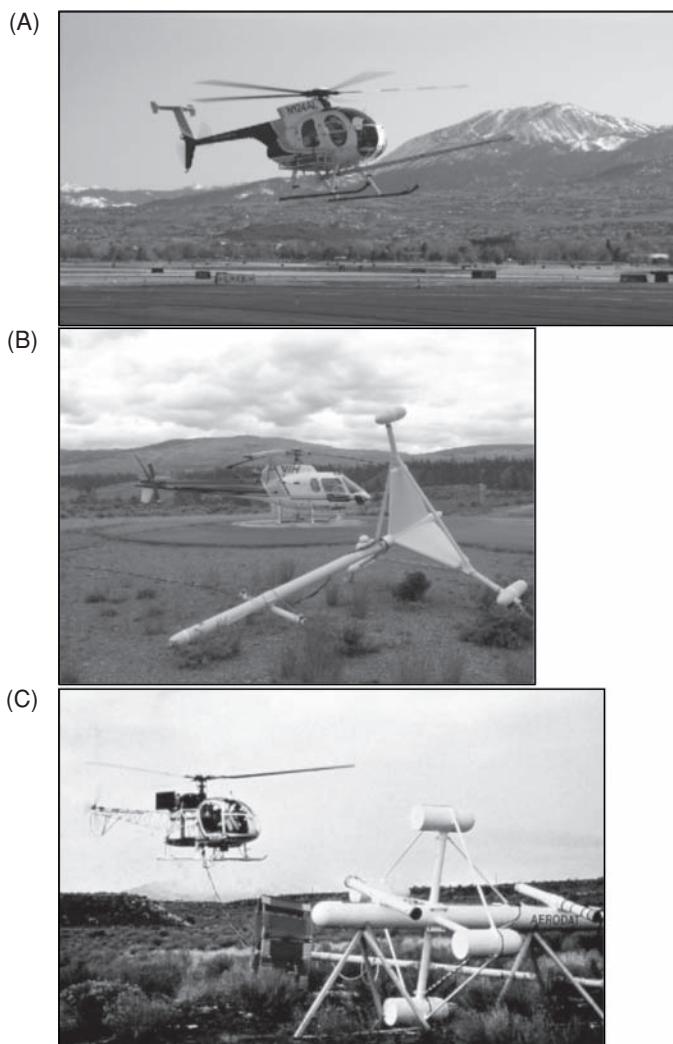


**Figure 3.24** (A) Single-sensor magnetic boom or stinger; (B) vertical gradiometer bird (courtesy of AeroQuest Ltd, Canada); and (C) Eurocopter AS315 about to lift a 3-axis magnetic gradiometer system. Originally courtesy of Aerodat Inc., Canada, now part of Fugro Airborne Surveys. [C]

## 3.6 Magnetic surveying

### 3.6.1 Field survey procedures

As with every geophysical survey, the keeping of detailed and accurate field notes cannot be emphasised too strongly, even if data-loggers or memory-magnetometers are used. Orderly record-keeping permits more efficient and accurate data processing. Practical details of how magnetic surveys should be undertaken have been given by Milsom (2003).

In the vast majority of cases where the magnetic targets have a substantial strike length, survey profiles should, where possible, be conducted across strike with tie-lines along strike. In cases such as some archaeological and engineering site investigations where the targets are more equidimensional, such as the ruins of a Roman villa or a brick-lined mineshaft, north–south and east–west orientations are commonly used.

In ground-based surveys, it is important to establish a local base station in an area away from suspected magnetic targets or magnetic noise and where the local field gradient is relatively flat. A base station should be quick and easy to relocate and re-occupy. The precise approach to the survey will depend on the type of equipment. If a manual push-button proton magnetometer is deployed, the exact time of occupation of each station is needed and at least three readings of the total field strength should be recorded. Each of the three values should be within  $\pm 1$  or 2 nanoteslas; an average of these three readings is then calculated. As the survey progresses, the base station must be re-occupied every half or three-quarters of an hour in order to compile a diurnal variation curve for later correction (see next section). Next to each data entry, where required, should be any comments about the terrain or other factors that may be considered to be important or relevant to subsequent data processing and interpretation.

**Table 3.5** Degree of aliasing (Reid, 1980).

$h/\delta x$	$F_T$	$F_G$
0.25	21	79
0.5	4.3	39
1	0.19	5
2	0.0003	0.03
4	0	0

$F_T$  and  $F_G$  are the aliased power fraction (%) expected from surveys of total field and vertical gradient respectively.

If a continuous-reading base-station magnetometer is used to measure the diurnal variation, it is still worth returning to base every 2–3 hours, just in case the base magnetometer fails.

When data-loggers or memory magnetometers are used, regular checks on the recording of data are vital. It is all very well occupying hundreds of stations and taking perhaps several thousand measurements, only to find that the logger is not functioning or the memory has been corrupted.

One golden rule is always to check your data as they are collected and at the end of each survey day. This serves two purposes. Firstly, it provides a data quality check and allows the operator to alter the survey in response to the magnetic values measured. For example, if a 50 m station interval was selected at the outset and the field values indicate a rapid change over a much shorter interval, the separation between stations must be reduced in order to collect enough data to image the magnetic anomaly. Secondly, it provides a check on the consistency of the data. Odd anomalous values may indicate something of geological interest which may need to be followed up, or may highlight human error. In either case, the next day's survey can take this into account and measurements can be made to check out the oddball values.

In the case of aeromagnetic or ship-borne surveys, the specifications are often agreed contractually before an investigation begins. Even so, there are guidelines as to what constitutes an adequate line separation or flying height, orientation of survey line, and so on. As an example, Reid (1980) compiled a set of criteria based on avoidance of spatial aliasing (Tables 3.5 and 3.6). For example, if a mean flying height over magnetic basement ( $h$ ) of 500 m is used with a flight line spacing ( $\delta x$ ) of 2 km, then  $h/\delta x = 0.5/2 = 0.25$ , which would indicate that 21% aliasing would occur in measurements of the total field, and as much as 79% if the vertical magnetic gradient were being measured (Table 3.5). Neither value is acceptable. The larger the value of  $h/\delta x$ , the less aliasing will occur; a survey is considered reasonably designed if  $h/\delta x \geq 0.5$ , depending on survey type. At this minimum value, about 5% maximum aliasing is acceptable if contouring is to be undertaken on total field data. Other maximum flight line spacings are given in Table 3.6. There have been examples of commercially flown surveys in Egypt, for instance, where the flying height was 400 m above ground, but with 1 km thickness of sedimentary cover over magnetic basement (hence  $h = 1.4$  km) and the line spacing was 21 km. This gives a value of  $h/\delta x \sim 0.07$ , result-

**Table 3.6** Maximum line spacings (Reid, 1980).

Survey type	Intended use	$\delta x_{\max}$
Total field	Contour map	$2h$
Total field	Computation of gradient, etc., maps	$h$
Vertical gradient	Gradient contour maps	$h$
Total field	Modelling of single anomalies	$h/2$

ing in more than 65% aliasing. The contour maps of these surveys, which covered thousands of square kilometres, are virtually useless. To have been contoured adequately, the flight line spacing for data acquired at a flying height of 1.4 km above basement should have been no more than 2.8 km; i.e. from Table 3.6,  $\delta x < 2h$ .

The choice of survey parameters will also affect the success (or otherwise) of subsequent computer contouring. These guidelines can also apply to surface surveys using a proton magnetometer where  $h = 3$  m (1 m of overburden over a magnetic target, plus 2 m for the magnetometer sensor pole), for example. In this case, an acceptable maximum line spacing would be 6 m if a contour map of the total field were required. Survey design parameters and automated contouring have been described briefly in Chapter 1 and in detail by Hood *et al.* (1979) and by Reid (1980).

### 3.6.2 Noise and corrections

All magnetic datasets contain elements of noise and will require some form of correction to the raw data to remove all contributions to the observed magnetic field other than those caused by subsurface magnetic sources. In ground magnetometer surveys, it is always advisable to keep any magnetic objects (keys, penknives, some wristwatches, etc.), which may cause *magnetic noise*, away from the sensor. Geological hammers put next to the sensor bottle of a proton magnetometer will have a significant effect, as demonstrated by students trying to simulate a magnetic storm so that they could abandon the survey and retire to the nearest hostelry! It is also essential to keep the sensor away from obviously magnetic objects such as cars, metal sheds, power lines, metal pipes, electrified railway lines, or walls made of mafic rocks.

The most significant correction is for the *diurnal variation* in the Earth's magnetic field. Base station readings taken over the period of a survey facilitate the compilation of the diurnal 'drift' as illustrated in Figure 3.25. Measurements of the total field made at other stations can easily be adjusted by the variation in the diurnal curve. For example, at point A in Figure 3.25, the ambient field has increased by 10 nT and thus the value measured at A should be reduced by 10 nT. Similarly, at B, the ambient field has fallen by 19 nT and so the value at B should be increased by 19 nT. Further details of diurnal corrections have been given by Milsom (2003). Gradiometer data do not need to be adjusted as both sensors are affected simultaneously and the gradient remains the same between them.

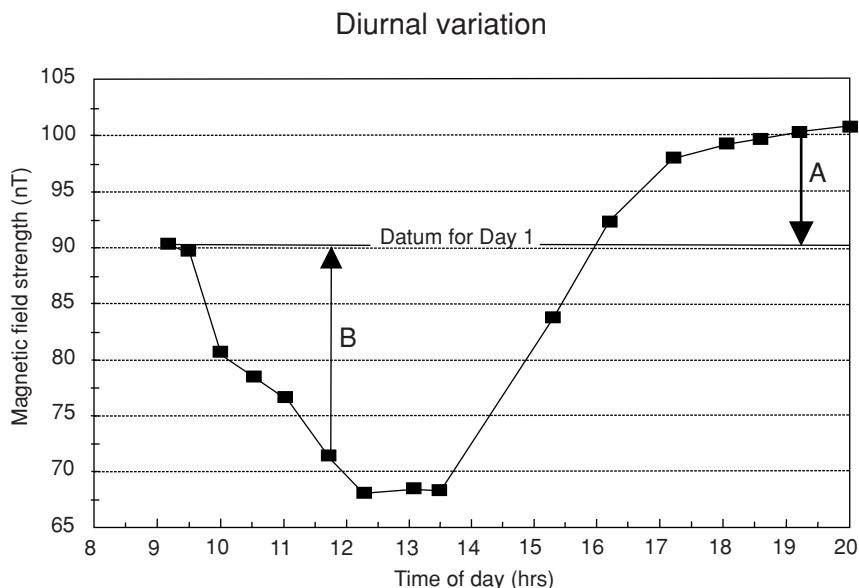


Figure 3.25 Diurnal drift curve measured using a proton magnetometer.

In airborne and shipborne surveys, it is obviously not possible to return to a base station frequently. By designing the survey so that the track lines intersect (Figure 3.26), the dataset can be appropriately corrected. Some surveys use profiles and tie-lines at the same spacing to give a regular grid. Other surveys have tie-lines at 10 times the inter-profile line spacing. In addition to checking on diurnal variations, tie-lines also serve as a useful control on navigational and measurement accuracy. In regional surveys, a further tie is to a local geomagnetic observatory, if there is one within 150 km, at which all the magnetic components are measured and which can

provide diurnal variations. It would then have to be demonstrated that the curve obtained from the observatory applied in the survey area.

The degree of data processing is dependent upon the resolution required in the final dataset. For a broad reconnaissance survey, a coarser survey with lower resolution, say several nanoteslas, may be all that is required. In detailed surveys, however, an accuracy to within 0.1 nT will need a finer survey grid, more accurate position-fixing and diurnal drift corrections.

Rarely, a *terrain correction* may need to be applied when the ground over which a survey is conducted is both magnetic and topographically rough. Unlike the gravity case where terrain corrections, although laborious, are relatively easy to calculate, corrections for terrain for magnetic data are extremely complex. If the rough terrain is made up largely of low-susceptibility sedimentary rocks, there will be little or no distortion of the Earth's magnetic field. However, if the rocks have a significant susceptibility, a terrain factor may have to be applied. Anomalous readings as large as 700 nT have been reported by Gupta and Fitzpatrick (1971) for a 10 m high ridge of material with susceptibility  $\kappa \approx 0.01$  (SI). Furthermore, magnetic readings taken in a gully whose walls are made of basic igneous rocks will be anomalous owing to the magnetic effects of the rocks above the magnetic sensor. Considerable computational effort (see Sharma, 1986: Appendix C) then has to be applied to correct the data so that they are interpretable. Similar geometric effects can also occur in radiometric surveys.

Another way of correcting for the effects of topography, or of reducing the data to a different reference plane, is by *upward continuation*. This permits data acquired at a lower level (e.g. on the ground) to be processed so that they can be compared with airborne surveys. The effect of this is to lessen the effects of short-wavelength high-amplitude features, as the magnetic force is indirectly proportional to the square of the distance between source and sensor (see Box 3.1). The rate of change of the field with elevation (akin to the

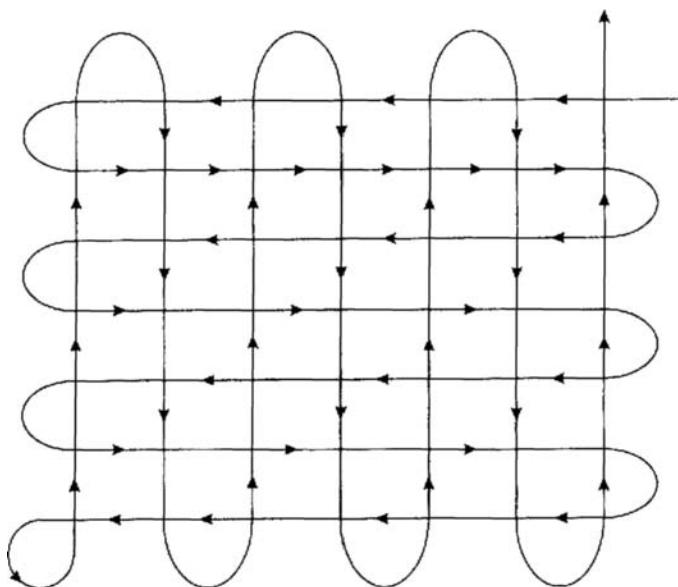


Figure 3.26 Tracks of a shipborne or airborne magnetic survey. Some surveys, rather than having spacings between all tracks, have tie-lines at 10 times the normal interline spacing.

gravitational free-air correction) is between 1.5 and 3.5 nT/100m, with the maximum gradient being at the poles. In areas where the range of elevations of the ground surface is large, such as in the Rockies, Andes and Himalayas, maintaining a constant terrain clearance is not practicable (or safe!). Indeed, in areas of extreme altitude, airborne surveys are not possible as the ground can be higher than the flying ceiling of available aircraft owing to the rarified atmosphere. Different flying heights can be specified for particular areas within a survey region, and the various datasets processed to the same flying height or alternative datum.

In some regions, metal pipes can become inductively magnetised by currents in the atmosphere (Campbell, 1986) or are cathodically protected by passing a large direct current (1–7 amps) through them to reduce internal corrosion. The presence of such pipes can contribute a significant anomaly on high-resolution aeromagnetic data (Gay, 1986). In hydrocarbon exploration over sedimentary basins up to 6 km depth, basement faulting, which affects basement-controlled traps and reservoirs, can be identified from their respective magnetic anomalies which can have amplitudes of only several nanoteslas. There is then a problem over differentiating between a geologically significant fault and a cathodically protected pipe, as their respective magnetic anomalies may appear to be similar.

Iron pipes have a permanent magnetisation acquired at the foundry at the time of manufacture. Being magnetisable, they also acquire a magnetisation induced by the Earth's magnetic field. Current injected into the pipes will also generate a magnetic field according to the right-hand rule. This states that a conductor carrying electrical current, indicated by the thumb on the right hand, will generate a magnetic field in the direction indicated by the coiled fingers of the right hand (Figure 3.27A). The injection of current at specific points along a pipe has one marked effect (Figure 3.27B and C). The polarity of the magnetic anomaly will be reversed either side of the injection point as the current is flowing in opposite directions away from it and into the ground. The point at which the polarity reverses (Figure 3.27B) indicates the position of current injection. The figure shows the magnitudes and senses of the western and eastern anomaly peaks for each survey line. Lines 9–13 have a positive western peak and corresponding negative eastern peak, while lines 14–17 south of the injection point have a negative western peak and positive eastern peak (Figure 3.27C). The magnitude of the anomaly will also decrease away from the injection point. The magnitudes determined for survey lines south of the injection point are slightly larger than those for northern lines as the flying height was 40 m lower to the south. Mean flying height was 257 m. These characteristics are diagnostic of cathodically protected pipes and can be used to tell them apart from linear fault structures whose polarity does not switch along its length, although its magnitude may vary along the strike of the fault. Having identified a linear anomaly as being due to a cathodically protected pipe, the anomaly can be filtered out of the dataset.

### 3.6.3 Data reduction

In order to produce a magnetic anomaly map of a region, the data have to be corrected to take into account the effects of latitude and, to a lesser extent, longitude. As the Earth's magnetic field strength

varies from 25000 nT at the magnetic equator to 69000 nT at the poles, the increase in magnitude with latitude needs to be taken into account. Survey data at any given location can be corrected by subtracting the theoretical field value  $F_{\text{th}}$ , obtained from the International Geomagnetic Reference Field, from the measured value,  $F_{\text{obs}}$ . This works well in areas where the IGRF is tied-in at or near to geomagnetic observatories, but in many places the IGRF is too crude. Instead, it is better to use a local correction, which can be considered to vary linearly over the magnetic survey area. Regional latitudinal ( $\phi$ ) and longitudinal ( $\theta$ ) gradients can be determined for areas concerned and tied to a base value ( $F_0$ ), for example, at the southeast corner of the survey area. Gradients northwards ( $\delta F/\delta\phi$ ) and westwards ( $\delta F/\delta\theta$ ) are expressed in nT/km and can easily be calculated for any location within the survey area. For example, in the UK, gradients of 2.13 nT/km north and 0.26 nT/km west are used. Consequently, the anomalous value of the total field ( $\delta F$ ) can be calculated arithmetically, as demonstrated by the example in Box 3.7.

Another method of calculating the anomalous field  $\delta F$  is to determine statistically the trend of a regional field to isolate the higher-frequency anomalies, which are then residualised in the same way that gravity residuals are calculated. The regional field is subtracted from the observed field to produce a residual field ( $\delta F$ ) (Figure 3.28A). If the survey is so laterally restricted, as in the case of small-scale archaeological, engineering or detailed mineral prospecting surveys (e.g.  $< 500 \text{ m} \times 500 \text{ m}$  in area), the use of regional gradients is not practicable. Instead, profile data can be referred to a local base station ( $F_b$ ) which is remote from any suspected magnetic sources. In this case, the anomalous field  $\delta F$  is obtained by subtracting the base value ( $F_b$ ) from every diurnally corrected observed value  $F_{\text{obs}}$  along the profile ( $\delta F = F_{\text{obs}} - F_b$ ), as illustrated in Figure 3.28B.

## 3.7 Qualitative interpretation

Once magnetic data have been fully corrected and reduced to their final form, they are usually displayed either as profiles (Section 3.7.1) or as maps (Section 3.7.2) and the interpretation procedures are different for the two cases. However, it must always be borne in mind that, although the techniques used are similar to those for gravity surveys, there are two important complications. Firstly, the Earth's magnetic field is dipolar, which means that a single anomaly can have the form of a positive peak only, a negative peak only, or a doublet consisting of both positive and negative peaks. Secondly, the single largest unknown is whether there is any remanent magnetisation and, if there is, its intensity and direction ( $J_r$ ) need to be ascertained. It must also be remembered that many geophysical interpretations may fit the observed data and that a given interpretation may not be unique (see Chapter 1, and Figure 1.1 in particular). For this reason, it is always useful to use other geophysical methods in the same area to help to constrain the interpretations. If some geological information already exists for the area, then this should be used to help with the geophysical interpretations. However, a word of warning: be careful that some

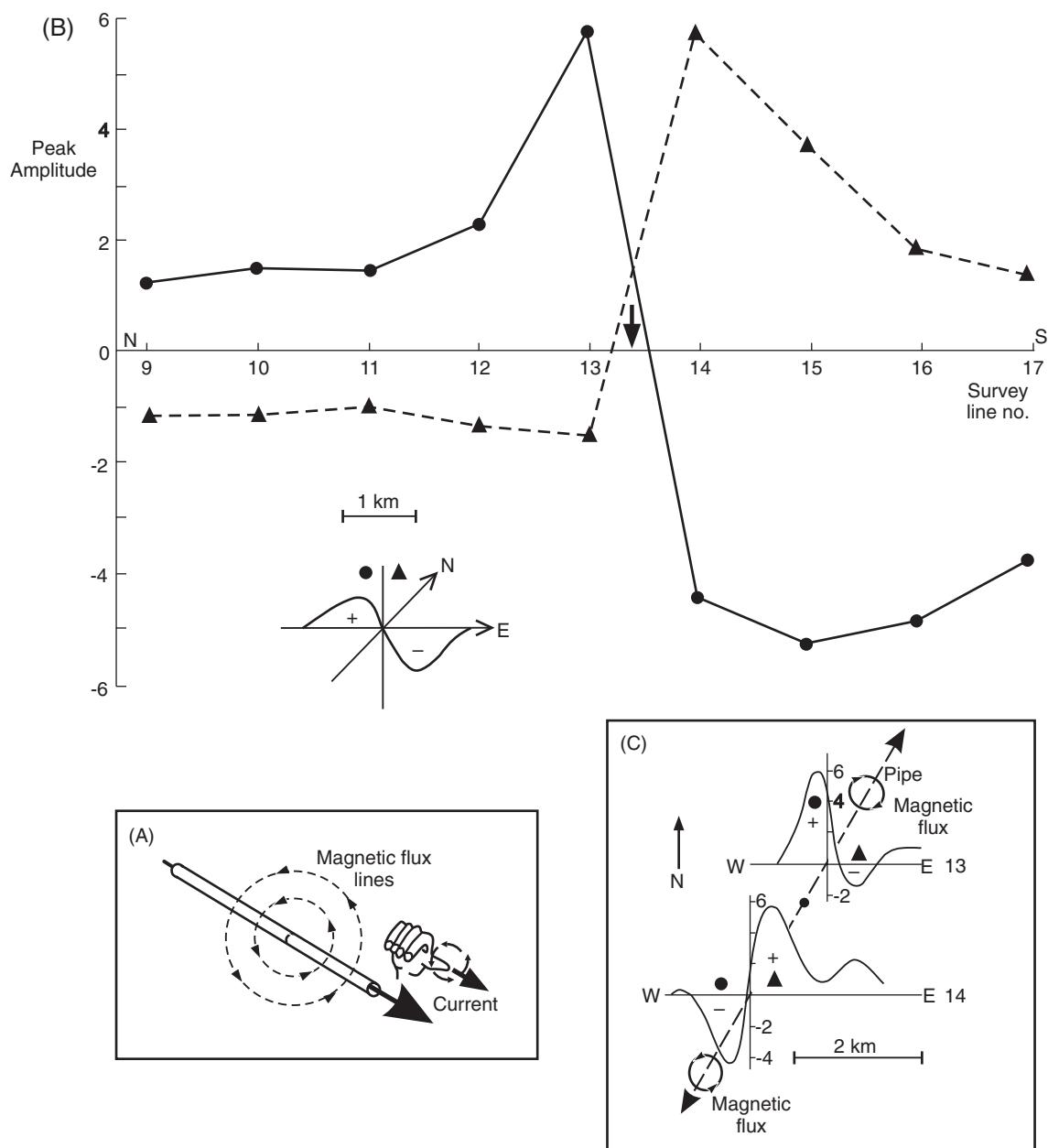


**Figure 3.27** Magnetic anomalies associated with a cathodically protected pipe in northeast Oklahoma, USA. (A) Right-hand rule applied to a pipe through which a current is passed to show direction of magnetic flux lines. (B) Peak amplitudes for western and eastern parts of profile anomalies, of which two for lines 13 and 14 are shown in (C). Note the relative amplitudes of the anomalies on lines 13 and 14 either side of the current injection point (arrowed). Data from Gay (1986), by permission.

geological information may itself be an interpretation and should not be considered to be the only solution. The geophysics may disprove the geological hypothesis!

A magnetisable body will have a magnetisation induced within it by the Earth's magnetic field (Figure 3.29A). As magnetisation is a vector quantity, the anomaly shape will depend upon the summation of the vectors of the Earth's field ( $F$  (with intensity  $J$ ) and the induced field ( $J_i$ ) from the subsurface body and from any remanent magnetisation ( $J_r$ ). It can be seen from Figure 3.29(A and B) how any magnetic anomaly is produced. The maximum occurs

when the induced field is parallel to the Earth's field; the anomaly goes negative when the induced field vector is orientated upwards as at D. As the magnetic data have been corrected to remove the effect of the Earth's magnetic field, the anomaly will be due to the vectors associated with the source body. The sign convention is positive downwards, negative upwards. Where there is no remanent magnetisation, a magnetised body in the northern hemisphere will always have a negative anomaly on its northern side and a positive anomaly on its southern side. The opposite is true for the southern hemisphere.

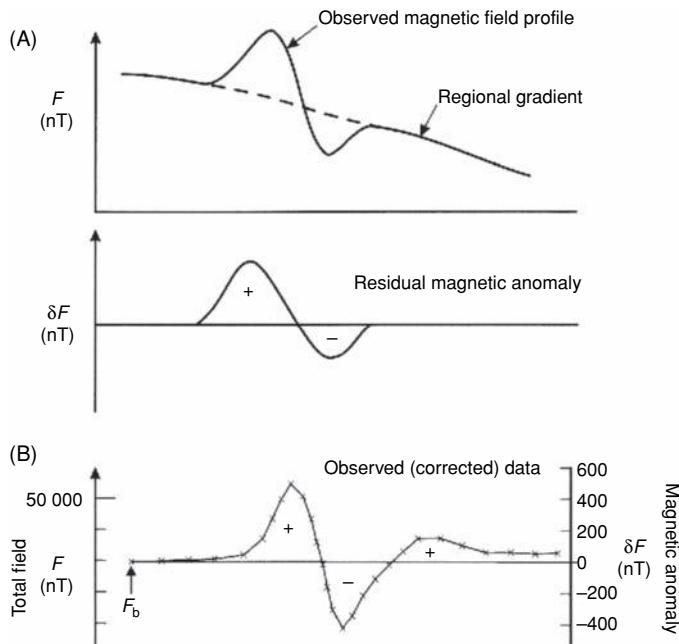


**Figure 3.28** Magnetic residuals: (A) Subtraction of a regional field gradient, and (B) reference to a local arbitrary base station.

For the two anomalies shown in Figure 3.30, anomaly A has a short wavelength compared with anomaly B, indicating that the magnetic body causing anomaly A is shallower than the body causing B. As the amplitude of anomaly B is identical to that of anomaly A, despite the causative body being deeper, this must suggest that the magnetisation of body B is much greater than for body A, as amplitude decreases with increasing separation of the sensor from the magnetised object.

Some general guidelines for the qualitative interpretation of magnetic profiles and maps are listed in Table 3.7, and an example in Figure 3.31. The list of guidelines should be used like a menu from which various combinations of parameters apply to specific

#### Box 3.7 Anomalous total field strength $\delta F$

$$\delta F = F_{\text{obs}} - (F_0 + \delta F/\delta\varphi + \delta F/\delta\theta) \text{ (nT)}$$

where  $F_{\text{obs}}$  is the measured value of  $F$  at a point within the survey area with coordinates  $(x, y)$ ;  $F_0$  is the value at a reference point  $(x = 0; y = 0)$ ;  $\delta F/\delta\varphi$  and  $\delta F/\delta\theta$  are the latitudinal and longitudinal gradients respectively (in units of nT/km).

**Example:** For a station 15 km north and 18 km west of a reference station at which  $F_0 = 49\,500$  nT, with gradients  $\delta F/\delta\varphi = 2.13$  nT/km north, and  $\delta F/\delta\theta = 0.26$  nT/km west, and the actual observed field  $F_{\text{obs}} = 50\,248$  nT, the magnetic anomaly  $\delta F$  is:

$$\begin{aligned} \delta F &= 50\,248 - (49\,500 + 2.13 \times 15 + 0.26 \times 18) \text{ nT} \\ &= 711 \text{ nT} \end{aligned}$$

anomalies. For instance, a short-wavelength, high-amplitude doublet anomaly with negative to the north, and positive to the south, with an elongation in the east–west direction in the mid-latitudes of the northern hemisphere, suggests a near-surface, moderate-to-high susceptibility magnetic feature with induced magnetisation in a sheet-like body with an east–west strike and northerly dip.

### 3.7.1 Profiles

The simplest interpretation technique is to identify zones with different magnetic characteristics. Segments of the profile with little variation are termed magnetically ‘quiet’ and are associated with rocks with low susceptibilities. Segments showing considerable variation are called magnetically ‘noisy’ and indicate magnetic sources in the subsurface. The relative amplitudes of any magnetic anomalies (both positive and negative) and the local magnetic gradients can all help to provide an indication of the subsurface.

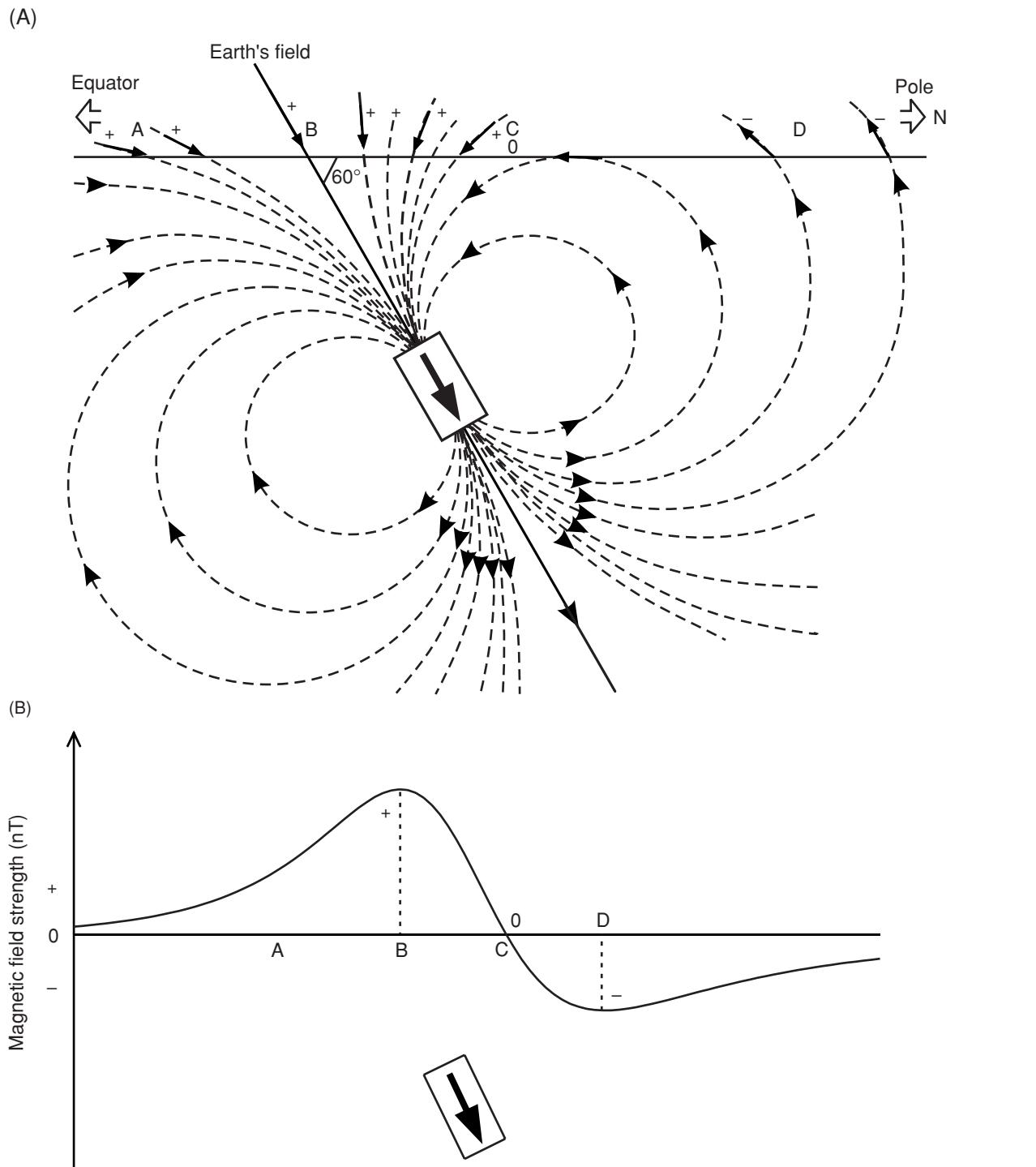
Figure 3.32 illustrates the differences between noisy and quiet zones in a profile over Sourton Tors, north Dartmoor, England, where the magnetically noisy segments indicate metalliferous mineralisation. The negative occurring as the northern part of the doublet indicates that there is little remanent magnetisation and that the anomaly is due largely to induction ( $J_i \gg J_r$ ).

Figure 3.33 shows a profile measured at Kildonnan, Isle of Arran, Scotland, across a beach section over a series of vertical dolerite dykes. Two of the three dykes (A and B) give rise to large positive anomalies, while a third dyke (C) produces a broader low. All the dykes have virtually identical geochemistry and petrology and hence similar susceptibilities. The difference in magnetic character associated with dyke C compared with dykes A and B is attributed to there having been a magnetic reversal between the intrusion of dyke C relative to the other two. It is well known that in the British Tertiary Igneous Province, which includes the Western Isles of Scotland, a phase of doleritic intrusion occurred which lasted 10 million years and straddled a magnetic reversal (Dagley *et al.*, 1978). Some dykes are normally magnetised and others have a reversed polarity. The different magnetic characters therefore provide a means of identifying which dykes were associated with which phase of the intrusion episode, whereas it is virtually impossible to make such an identification in the field on the basis of rock descriptions.

Having identified zones with magnetic sources, and possibly having gained an indication of direction of dip (if any) of magnetic targets and relative intensities, either more detailed fieldwork can be undertaken to obtain more information and/or the existing data can be interpreted using quantitative methods (see Section 3.8).

### 3.7.2 Pattern analysis on aeromagnetic maps

Magnetic data acquired over a grid with no spatial aliasing are displayed as contoured maps, as three-dimensional isometric projections, or as image-processed displays (see Section 3.8.3). The various displays can be interpreted in terms of the guidelines in Table 3.7. Commonly, even such a basic level of interpretation can yield important information about the subsurface geology very quickly.



**Figure 3.29** The magnetic field generated by a magnetised body inclined at 60° parallel to the Earth's field (A) would produce the magnetic anomaly profile from points A-D shown in (B). See text for details.

One major advantage of airborne surveys is that they can provide information about the geology in areas covered by water.

An aeromagnetic survey was acquired over the southeastern part of the Shetland Islands, northeast Scotland, and described in detail by Flinn (1977). The original aeromagnetic data were extracted from part of a British Geological Survey map and are shown in

Figure 3.34A. The corresponding pattern analysis for the same area is shown in Figure 3.34B and compares very well with Flinn's interpretation (Figure 3.35). Magnetic lows in band A are associated with psammites and migmatised psammites which have been heavily injected by pegmatite. The lows in band B correspond to gneissified semipelites and psammites intruded by granites and pegmatites.

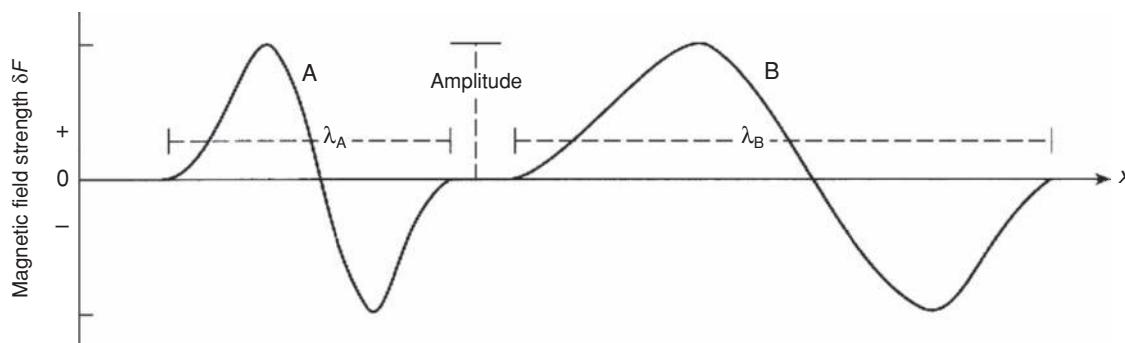


**Figure 3.30** Two magnetic anomalies arising from buried magnetised bodies (see text for details).

The short-wavelength but large-amplitude highs just east of band A are attributed to the magnetic pelitic schist and gneiss. In the central part of Figure 3.34A, truncation of NE–SW trending contours can be seen to be associated with the Whalsay Sound Fault. Other faults, such as the Lunning Sound Fault and the Nesting Fault, separate zones of differing magnetic character and lie parallel to the local aeromagnetic contours. A series of three localised positive highs in the southeast corner (*h*, *i* and *j* along the thrust beneath the Quarff Nappe; Figure 3.35) is thought to be due to phyllites with 4% hematite, which in itself cannot explain the anomaly amplitudes. However, suitably orientated remanent magnetisation could account for these magnetic features. The large-amplitude anomaly (*k*) in the southeast corner is attributed to a large buried intrusive which is also evident on gravity data. However, this and similar anomalies in the vicinity with similar character all occur under sea and have not been sampled, and so the exact nature of the rock remains unknown.

More detailed discussions on the interpretation of aeromagnetic maps have been given, for example, by Vacquier *et al.* (1951), Nettleton (1976) and Hinze (1985). An overview of the magnetic method in exploration has been provided by Nabighian *et al.* (2005).

## 3.8 Quantitative interpretation

The essence of quantitative interpretation is to obtain information about the depth to a particular magnetic body, its shape and size, and details about its magnetisation in two possible ways. One is direct, where the field data are interpreted to yield a physical model. The other is the inverse method, where models are generated from which synthetic magnetic anomalies are generated and fitted statistically against the observed data. The degree of detail is limited by the quality and amount of available data and by the sophistication of either the manual methods or the computer software that can be used.

**Table 3.7** Guidelines to qualitative interpretation of magnetic profiles and maps.

Applies to:	Magnetic character	Possible cause
Segments of a profile and areas of maps	Magnetically quiet	Low $\kappa$ rocks near surface.
Anomaly	Magnetically noisy Wavelength $\pm$ amplitude	Moderate – high $\kappa$ rocks near surface. Short $\Rightarrow$ near-surface feature Long $\Rightarrow$ deep-seated feature Indicative of intensity of magnetisation
Profile*	Anomaly structure <sup>†</sup> and shape	Indicates possible dip and dip direction. Induced magnetisation indicated by negative to north and positive to south in northern hemisphere and vice versa in southern hemisphere; if the guideline does not hold, implies significant remanent present.
Profile and maps	Magnetic gradient	Possible contrast in $\kappa$ and/or magnetisation direction
Maps	Linearity in anomaly	Indicates possible strike of magnetic feature
Maps	Dislocation of contours	Lateral offset by fault
Maps	Broadening of contour interval	Downthrow of magnetic rocks

\* Can be determined from maps also.

Structure = composition of anomaly, i.e. positive peak only, negative peak only or doublet of positive and negative peaks.  
 $\kappa$  = magnetic susceptibility.

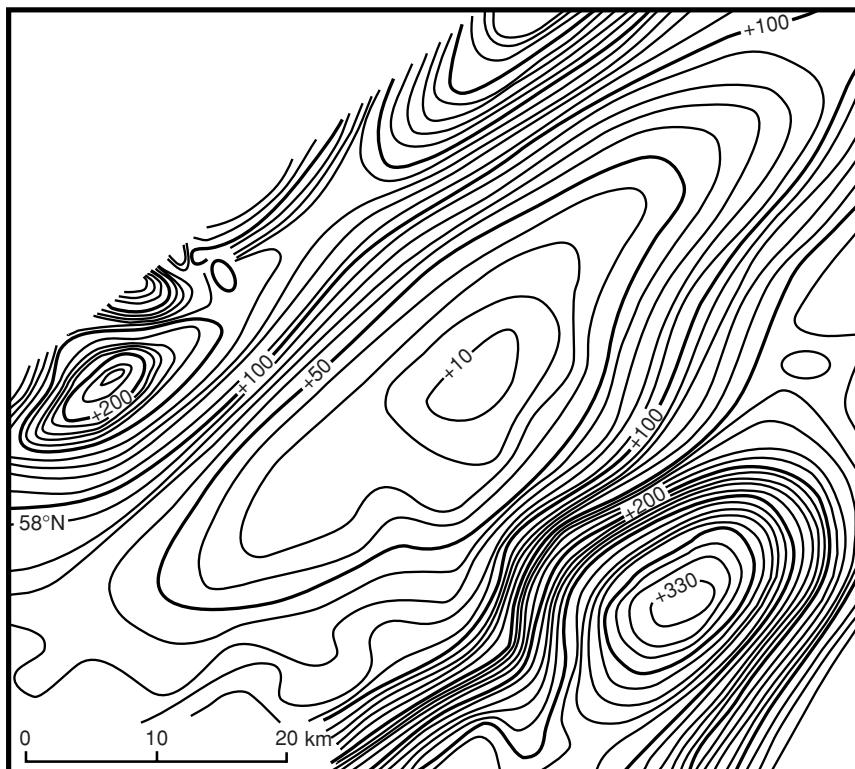


**Figure 3.31** Magnetic anomaly map associated with a fault-bounded sedimentary basin with upthrown horst block to the southeast – Inner Moray Firth, Scotland. After McQuillin *et al.* (1984), by permission.

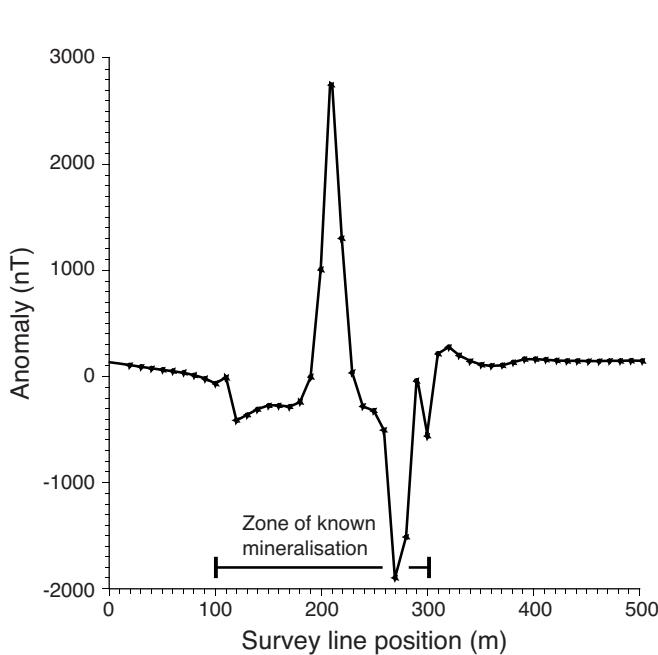


**Figure 3.32** Magnetic zonation of a proton magnetometer profile across Sourton Common, north Dartmoor, England.

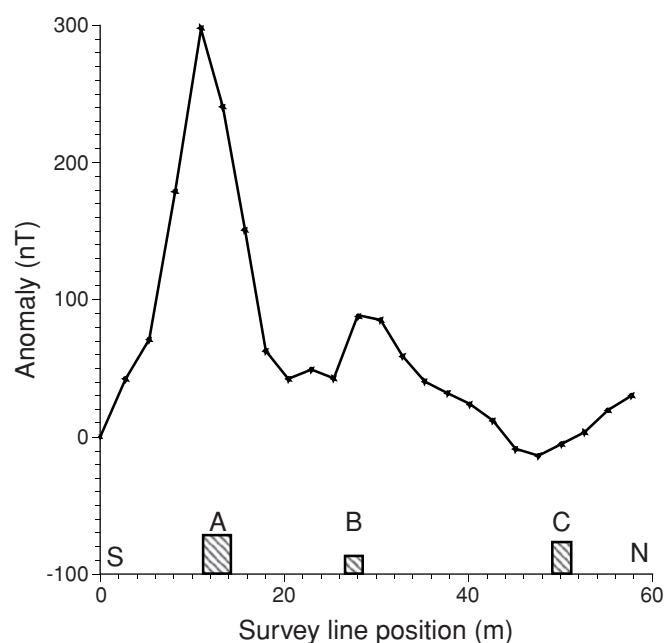


**Figure 3.33** Proton magnetometer profile across three vertical dolerite dykes at Kildonnan, Isle of Arran, Scotland, which were intruded during a period when the Earth's magnetic polarity changed.

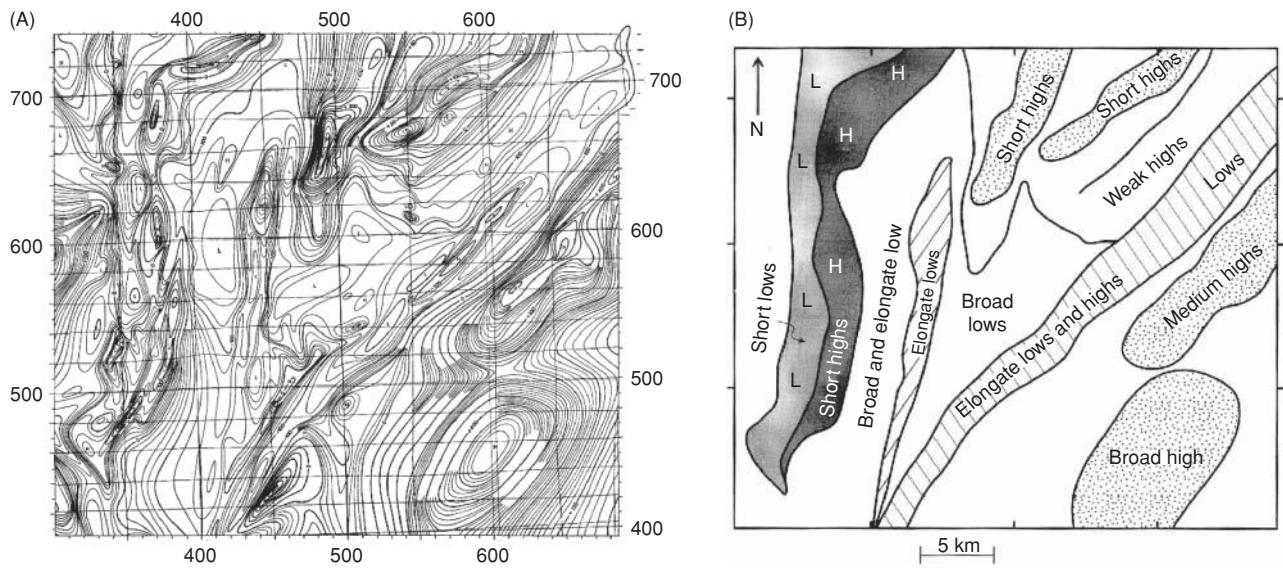


**Figure 3.34** (A) Aeromagnetic map of the southeast part of the Shetland Islands, Scotland (Flinn, 1977); (B) zonation of (A) in terms of magnetic characteristics.

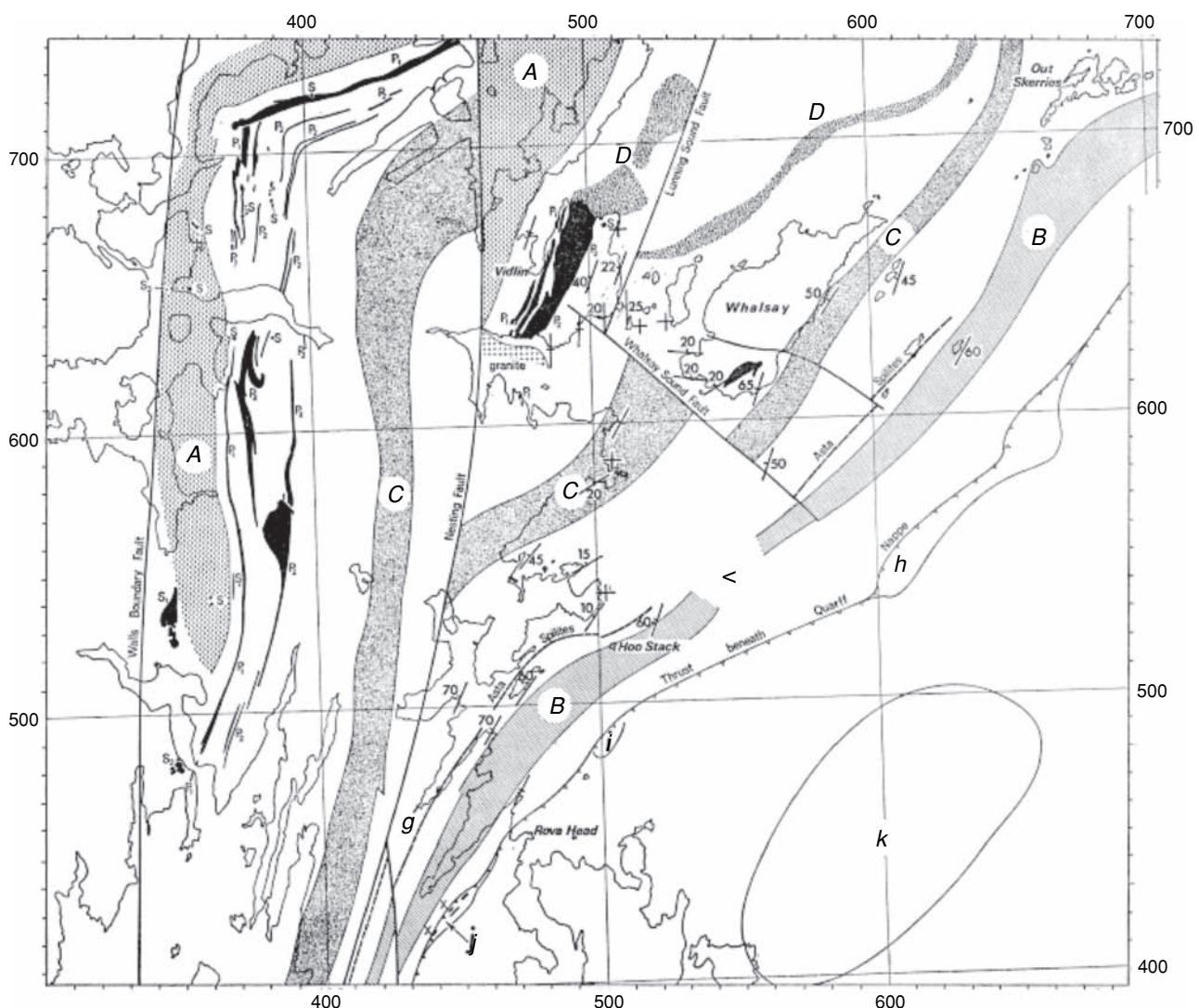


**Figure 3.35** Geological interpretation of the aeromagnetic map shown in Figure 3.34 of the southeast part of the Shetland Islands, Scotland. From Flinn (1977), by permission.

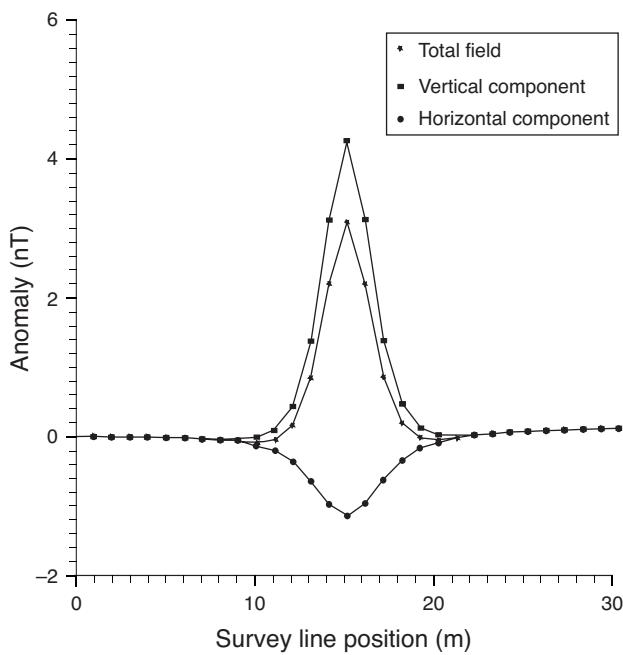


**Figure 3.36** Horizontal and vertical components and the total field over a uniformly magnetised sphere with a radius of 1 m and whose centre lies at 3 m depth at position  $x = 15$  m.

### 3.8.1 Anomalies due to different geometric forms

Just as with gravity data, magnetic data can be interpreted in terms of specific geometric forms which approximate to the shapes of subsurface magnetised bodies. This tends to be true where profiles are to be interpreted only in terms of two dimensions. Three-dimensional models are far more complex and can be used to approximate to irregularly shaped bodies (see Section 3.8.3). Detailed mathematical treatments of the interpretation of magnetic data have been given by Grant and West (1965), Parasnis (1986), Telford *et al.* (1990), Mushayandebvu *et al.* (2004), Cooper (2009), Guspí and Novara (2009), Keating (2009), and Li *et al.* (2010), for example.

The commonest shapes used are the sphere and the dipping sheet, both of which are assumed to be uniformly magnetised and, in the simplest cases, have no remanence. Total field anomalies ( $\delta F$ ) for various types of model are illustrated in Figures 3.36–3.39; except where otherwise stated, the field strength is 50000 nT, inclination  $I = 60^\circ$ , declination  $D = 0^\circ$ , and susceptibility  $\kappa = 0.05$  (SI).

In the example of a uniformly magnetised sphere (Figure 3.36), the horizontal and vertical components are shown in addition to the total field anomaly. The anomalies associated with vertical bodies of various thicknesses are shown in Figure 3.37. The anomaly produced by a 50-m-thick vertical dyke (Figure 3.37A) is both wider and has a significantly larger amplitude (830 nT) than that of the 5-m-thick dyke (peak amplitude 135 nT). Notice also that the anomaly shape changes considerably with strike direction, from being a positive–negative doublet when the dyke is striking east–west (with the negative on the northern side) to being a single symmetric positive peak when the dyke strikes north–south. In

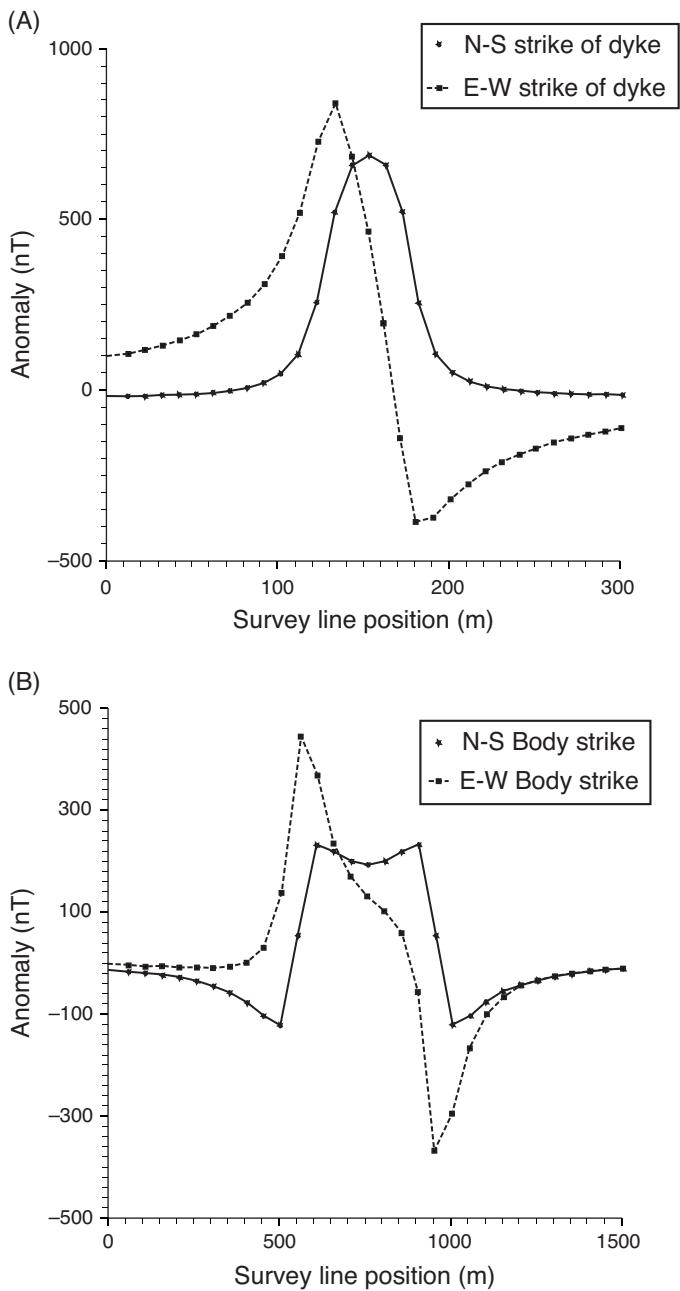


**Figure 3.37** Total field anomalies over a vertical sheet-like body. (A) 50 m and (B) 400 m wide.

all cases, when an inductively magnetised body of regular shape is orientated north–south, its anomaly is symmetric. For a 70-m-thick, 400-m long magnetised slab with its top 30 m below ground, a symmetric M-shaped anomaly is produced with the strike in a north–south direction (Figure 3.37B). When striking east–west, the positive–negative doublet is stretched to form an inflection in the middle; again, the negative is on the northern side.

The effects on anomaly shape caused by changing the depth to the top of a vertical magnetised dyke are illustrated in Figure 3.38. With increasing depth, the anomaly decreases in amplitude and widens. At any given latitude, the anomaly shape will also be affected by any

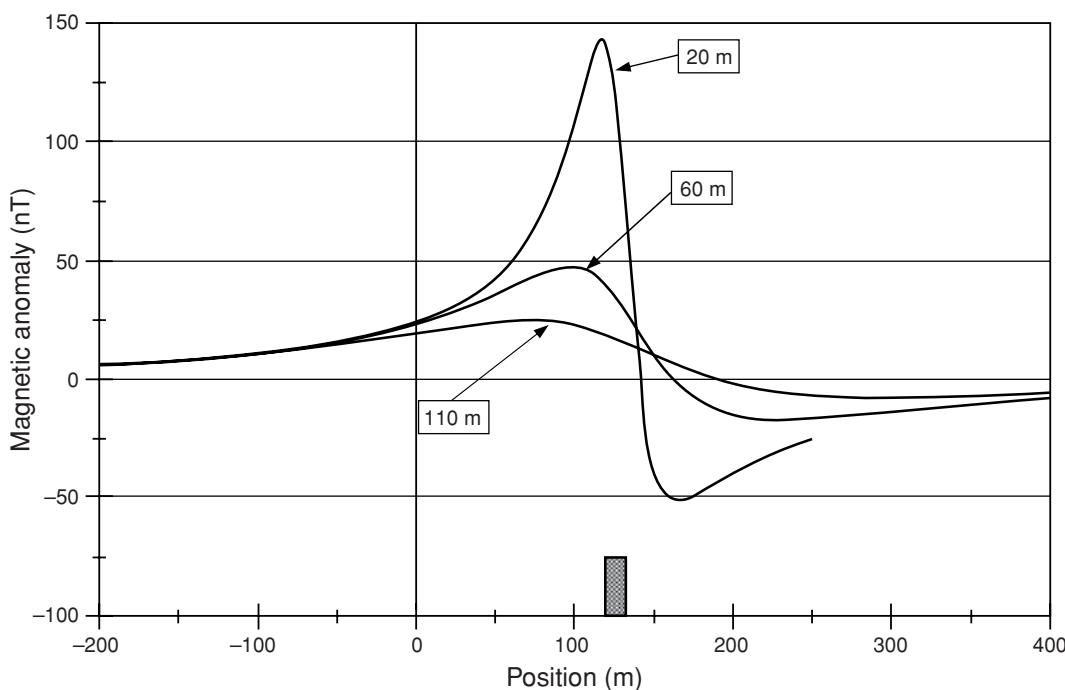


**Figure 3.38** Total field anomalies over a 10 m wide vertical sheet-like body orientated east–west and buried at depths of 20 m, 60 m and 110 m; the position of the magnetised body is indicated.

dip (*a*) of a sheet-like body, such as the inductively magnetised sheet (5 m thick) striking east–west (dip direction is towards the north) indicated in Figure 3.39. With zero dip, the body behaves like a thin horizontal slab with its northern edge off the scale of the figure.

If one end of a thick horizontal slab is sufficiently far enough away from the other, the model effectively becomes a vertical boundary separating two contrasting magnetic media (Figure 3.40A). The anomaly produced when the boundary strikes east–west has a significantly larger field strength (peaking around 1870 nT) than when in the other orientation.

The direction and degree of dip of a fault plane in a magnetised body also has a distinctive anomaly shape (Figure 3.40B). The negative anomaly is associated with the downthrown side. The anomaly shape is very similar to half of the M-shaped anomaly in Figure 3.37B.

Anomalies produced over a near-semicylindrical, low-susceptibility body within magnetised basement, to simulate a buried rock valley infilled by sediments in magnetic bedrock, are shown in Figure 3.41. The symmetric anomaly is obtained when the semicylinder is orientated north–south. When this body is orientated north–south, the negative anomaly is on the southern side and so can be distinguished from the anomaly over a thin vertical dyke. Furthermore, the minimum anomaly amplitude is far greater in the case of the low-susceptibility semicylinder than for a vertical dyke.

One of the largest effects on anomaly shape for a given geological structure is latitude. Anomalies in the northern hemisphere over a 5-m-thick dyke dipping at 45° to the north decrease in amplitude (partly a function of the reduced field strength towards the magnetic equator) and the negative minimum becomes more pronounced (Figure 3.42A). If the same geological structure exists at different latitudes in the southern hemisphere, this trend continues (Figure 3.42B) but with the slight growth of the now northern positive anomaly. These curves were calculated along the 0° Greenwich Meridian where the field strengths in the southern hemisphere

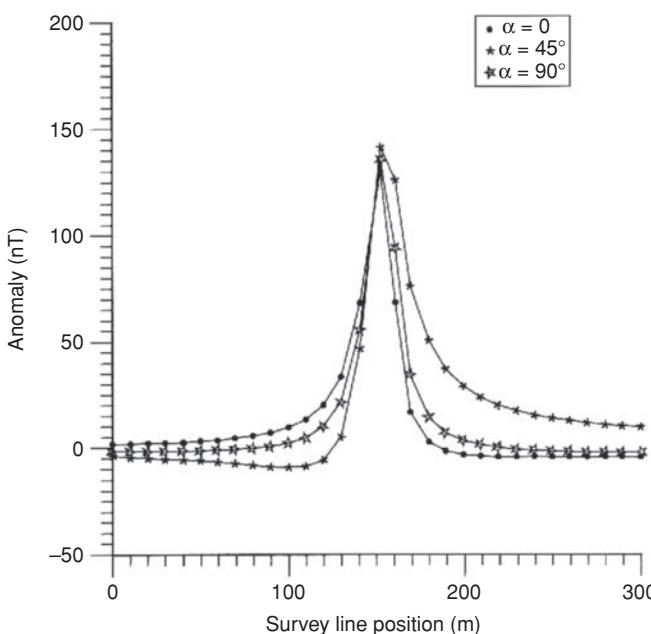
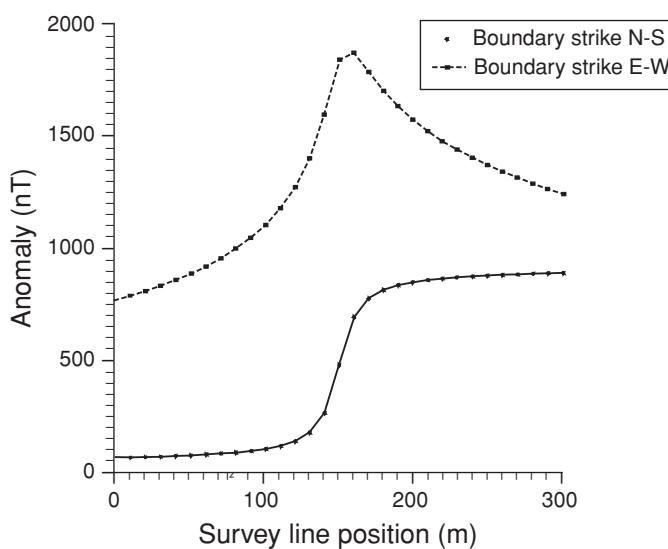


**Figure 3.39** Total field anomalies over a thin dyke (5 m wide) dipping to the north at angles from  $\alpha = 90^\circ$  to  $\alpha = 0^\circ$ ; body strike is east–west.

(A)



(B)

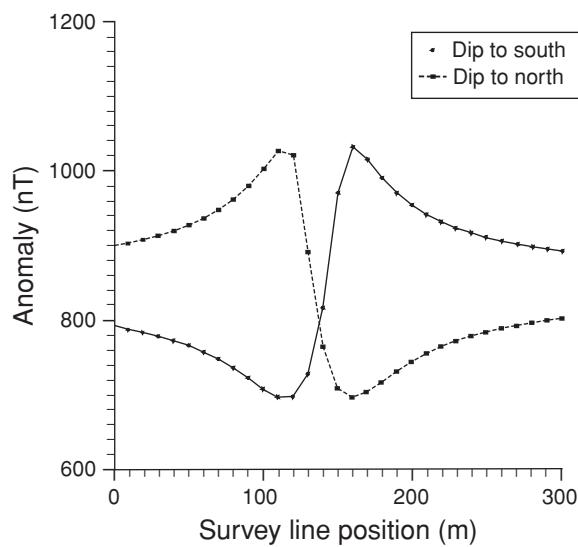


**Figure 3.40** Total field anomalies over (A) a vertical contact between contrasting magnetised bodies, and (B) over a fault plane dipping at  $45^\circ$  to the south and to the north for a north-south fault strike direction.

are significantly less than at equivalent latitudes in the northern hemisphere. Profiles along other lines of longitude would produce anomalies of similar shapes but with different amplitudes. It is also worth remembering that a given geological model, which produces a significant magnetic anomaly at one latitude and strike direction, may produce only a negligible anomaly at a different latitude and strike (Figure 3.42C) and so could be overlooked.

In all the above cases, it was assumed that there was no remanent magnetisation, yet if present, it can affect the shape of an anomaly significantly (Green, 1960). In Figure 3.43, four profiles are illustrated, one where there is no remanence, and three

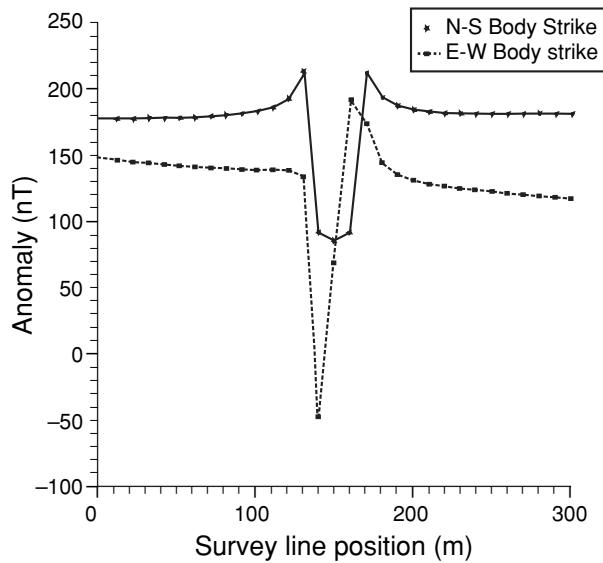


**Figure 3.41** Total field anomalies over a semicylindrical body of low susceptibility within a magnetised basement.

others where the intensity of remanent magnetisation is constant at  $0.12 \text{ A/m}$  (giving a strength of  $150 \text{ nT}$ ). A schematic vector diagram is shown to illustrate the effects of remanence and the significance of the vertical component in high magnetic latitudes ( $>45^\circ$ ). When the direction of permanent magnetisation is antiparallel to the Earth's field (A), the resultant amplitude is  $F'_a$  ( $\ll F$ ), so the anomaly amplitude is substantially reduced. In the case B, where the remanent magnetisation is at right-angles to the Earth's field, the resultant  $F'_b$  ( $< F$ ) has a smaller vertical component than  $F$ , and so the amplitude is slightly reduced. In case C, where the remanent magnetisation is also at right-angles to the Earth's field but has the same positive downwards sense,  $F'_c$ , although the same magnitude as  $F'_b$ , has a larger vertical component than even the Earth's field and so the anomaly amplitude is increased substantially. In low magnetic latitudes ( $<45^\circ$ ), the horizontal vector component becomes more important than the vertical component when considering remanent magnetisation.

A range of different anomaly shapes demonstrating the effects of strike, latitude, dip, depth and body size has been provided above for comparison. When a field profile is to be interpreted, there is usually some background information available about the local geology (how else was the survey designed?). Consequently, many of the variables can be constrained so that a reasonable interpretation can be produced. The biggest unknown in many cases is the presence or otherwise of any remanence. Commonly it is assumed to have no effect unless found otherwise from measurements of remanence of retrieved rock samples. However, to obtain a more exact interpretation it is necessary to model the observed data using computer methods (see Section 3.8.3).

### 3.8.2 Simple depth determinations

It is possible to obtain a very approximate estimate of depth to a magnetic body using the shape of the anomaly. By referring to either

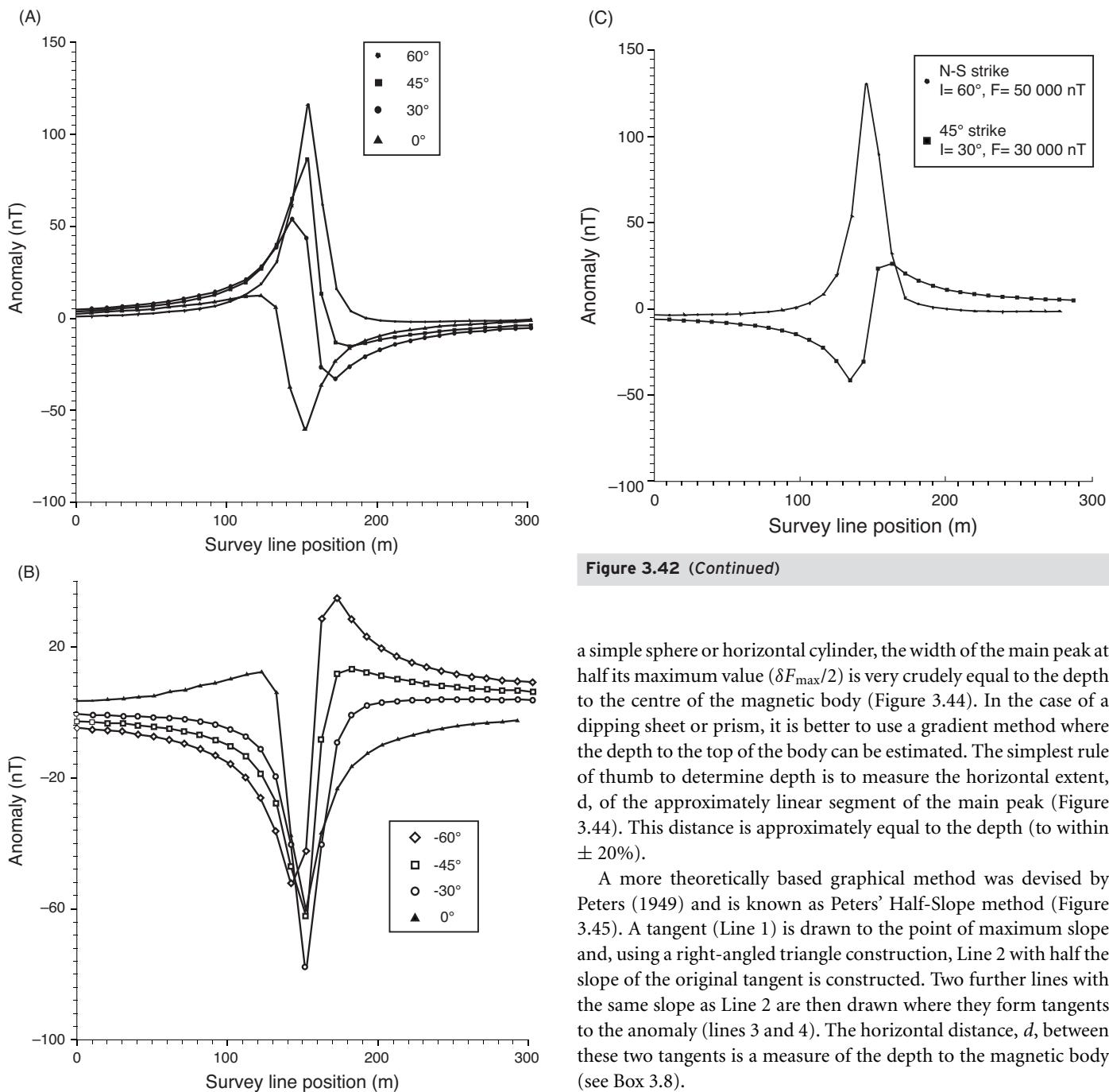


Figure 3.42 (Continued)

a simple sphere or horizontal cylinder, the width of the main peak at half its maximum value ( $\delta F_{\max}/2$ ) is very crudely equal to the depth to the centre of the magnetic body (Figure 3.44). In the case of a dipping sheet or prism, it is better to use a gradient method where the depth to the top of the body can be estimated. The simplest rule of thumb to determine depth is to measure the horizontal extent,  $d$ , of the approximately linear segment of the main peak (Figure 3.44). This distance is approximately equal to the depth (to within  $\pm 20\%$ ).

A more theoretically based graphical method was devised by Peters (1949) and is known as Peters' Half-Slope method (Figure 3.45). A tangent (Line 1) is drawn to the point of maximum slope and, using a right-angled triangle construction, Line 2 with half the slope of the original tangent is constructed. Two further lines with the same slope as Line 2 are then drawn where they form tangents to the anomaly (lines 3 and 4). The horizontal distance,  $d$ , between these two tangents is a measure of the depth to the magnetic body (see Box 3.8).

Parasnis (1986) derived alternative methods of depth determination for a magnetised sheet of various thicknesses and dips using the anomaly shape as well as amplitude. Given an asymmetric anomaly (Figure 3.46) over a dipping dyke of known latitude, dip and strike directions, the position of, and the depth to, the top of the dyke can be determined from the anomaly shape. If the maximum and minimum numerical values are denoted  $\delta F_{\max}$  and  $\delta F_{\min}$  respectively (i.e. irrespective of sign), the position of the centre of the top edge of the dyke is located at the position of the station where the anomaly amplitude equals the sum of the maximum and minimum values (taking note of their respective signs, positive or negative) and which lies between the maximum and minimum values. For example, if  $\delta F_{\max} = 771$  nT and  $\delta F_{\min} = -230$  nT, the position

**Figure 3.42** Total field anomalies over a 5-m-thick dyke dipping at 45° to the north with an east-west strike direction but with different magnetic inclinations along the 0° Greenwich Meridian, with (A) the northern hemisphere, and (B) the southern hemisphere, taking account changes in magnetic field strength with latitude. (C) The total field anomaly for a vertical dyke but at two different magnetic latitudes and directions, to illustrate how the magnetic anomaly over a magnetised body can become insignificant by only changing the magnetic latitude (inclination) and strike direction.

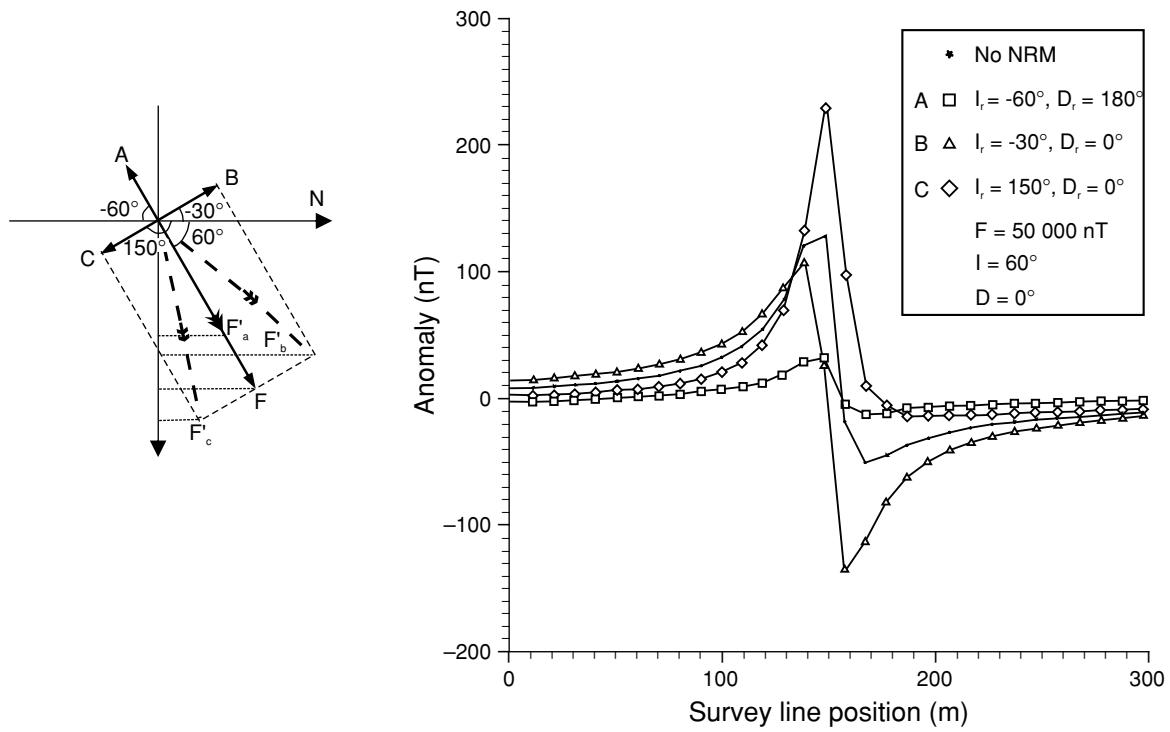


**Figure 3.43** Total field anomalies over a vertical dyke striking east-west with either no remanent magnetisation (\*), or remanent magnetisation of 150 nT in three directions as indicated by the schematic vector diagram.

of the centre of the dyke would be located where  $\delta F = 771-230$  nT = 541 nT. Expressions from which the depth to the top of the dipping sheet can be derived (see Box 3.9) relate the amplitudes of the minimum and maximum values and their respective separations. Expressions for thick dipping sheets and other models are much more complicated to calculate and are not discussed further here. Derivations of mathematical expressions and full descriptions of methods to determine shape parameters for a variety of dipping sheet-like bodies have been given by Gay (1963), Åm (1972),

Parasnis (1986) and Telford *et al.* (1990), for example. Manual calculation of parameters has been largely superseded by the ease with which computer methods can be employed.

For the analysis of aeromagnetic data and where source structures have vertical contacts, there is no remanent magnetisation and the magnetisation is either vertical or has been reduced to the pole (see the next section), the magnetic tilt-depth method can be used to derive estimates of the depth to the magnetised structure (Salem *et al.*, 2007). The magnetic tilt angle is a normalised derivative based upon the ratio of the vertical and horizontal derivatives of the Reduced to the Pole field (RTP), as described originally by Miller and Singh (1994); the expressions for these two derivatives have been described by Nabighian (1972). In short, the tilt angle ( $\theta$ ) is restrained between  $\pm 90^\circ$  and is equal to the arc tangent of the ratio of the horizontal distance ( $h$ ) and depth to the magnetised structure ( $z$ ), i.e.  $\tan \theta = h/z$ . The location at which the tilt angle becomes zero lies over the vertical contact (Figure 3.47). The depth to the magnetised structure is equivalent to half the horizontal distance between the  $\pm 45^\circ$  contours of the tilt angle profile. The method can be applied to aeromagnetic data to produce maps of the tilt angle from which the locations at which  $\theta = 0^\circ$  can be determined (the  $0^\circ$  contour on a tilt angle map), and the corresponding distances between the  $+45^\circ$  and  $-45^\circ$  contours computed, from which values of  $z$  can be derived (see also the paper by Salem *et al.*, 2008). This method is most suited to the analysis of aeromagnetic data for hydrocarbon exploration or large-scale regional geological studies, and is less useful for mineral exploration unless the qualifying criteria apply and the scale of the targets is large enough.

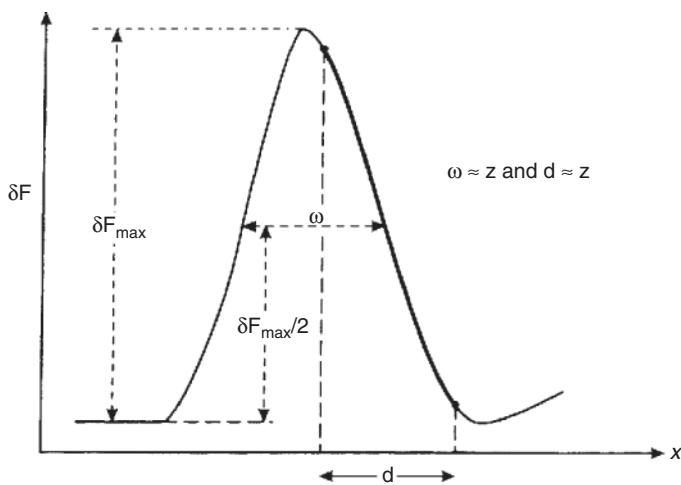


**Figure 3.44** Simple graphical methods to estimate the depth to the top of a magnetised body.

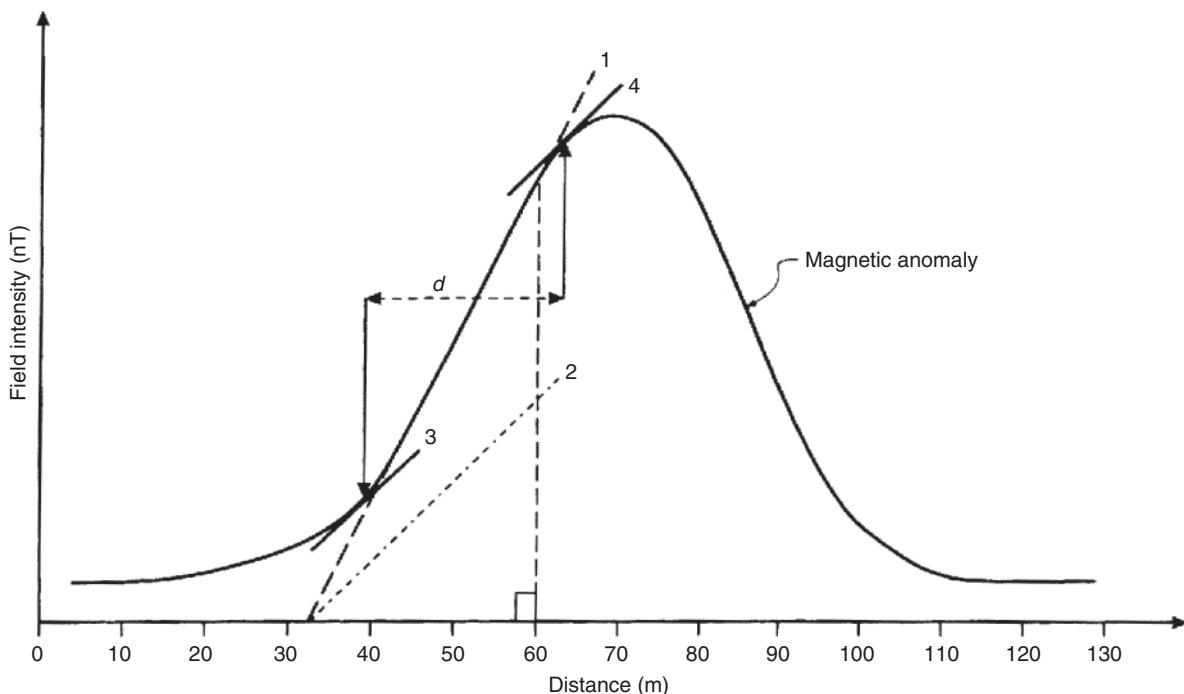


**Figure 3.45** Peters' Half-Slope method of determining the depth to the top of a magnetised dyke (see text for further details).

**Box 3.8** Peters' Half-Slope method of depth determination (see Figure 3.45)

The depth ( $z$ ) to the top of the magnetised body is:

$$z = (d \cos \alpha) / n$$

where  $d$  is the horizontal distance between half-slope tangents;  $1.2 \leq n \leq 2$ , but usually  $n = 1.6$ ;  $\alpha$  is the angle subtended by the normal to the strike of the magnetic anomaly and true north.

**Example:** If  $d = 24$  m,  $n = 1.6$  and  $\alpha = 10^\circ$ , then  $z \approx 15$  m.

approaches  $\pi/2$  (a north–south feature), the operator  $L(\theta)$  approaches infinity.

Variations in anomalies produced by an east–west and north–south striking, vertically-dipping magnetised dyke are shown in Figure 3.48 (MacLeod *et al.*, 1993). For the east–west striking dyke, the amplitude remains the same across all magnetic latitudes but the shape changes. For the north–south striking dyke, the anomaly shape remains the same but the amplitude is reduced as the inducing magnetic vector is rotated to lie parallel to the strike at the magnetic equator, by which point the anomaly disappears. The RTP method amplifies noise especially within TMI data over survey areas at low magnetic latitudes, and also is affected by the presence of remanent magnetisation within source bodies. The presence of high-frequency, high-amplitude anomalies within a TMI gridded dataset also generates noise. If the half-wavelength of these anomalies is comparable to the grid cell size in dimensions, high-frequency ringing will be propagated through the grid, which can obscure the geological signals and be amplified by further processing. Commercially-available software permits the rapid Reduction to Pole by applying an appropriate RTP filter, and offers ways to filter artefacts out of the process. In order to address the latitude-related effects on the TMI and assumptions about the directions of magnetisations, other processing techniques have been developed, such as the 3D Analytical Signal (see Section 3.8.5).

### 3.8.3 Reduction to the Pole (RTP)

It is clear that the shape and amplitude of magnetic profiles over a given magnetised feature vary depending upon the magnetic latitude at which the source lies. This can lead to difficulties in interpreting Total Magnetic Intensity (TMI) anomaly maps directly. One way to simplify the interpretation is to remove the effects of geomagnetic latitude by applying a mathematical filter to the gridded TMI data to produce an anomaly map that would have resulted had the area of interest been surveyed at the magnetic pole. This process is known as Reduction to the Pole (RTP) and was originally developed by Baranov (1957) and Baranov and Naudy (1964).

Assuming that all the measured magnetic field of a survey area is due to magnetic induction, pole reduction can be calculated in the frequency domain using a mathematical operator (Box 3.10) devised by Grant and Dodds (1972). It can be seen that as the inclination approaches zero (the magnetic equator) and  $(D-\theta)$  ap-

### 3.8.4 Modelling in two and three dimensions

Manual calculations of depths to the top of a particular magnetised body may provide an approximate figure, provided an individual

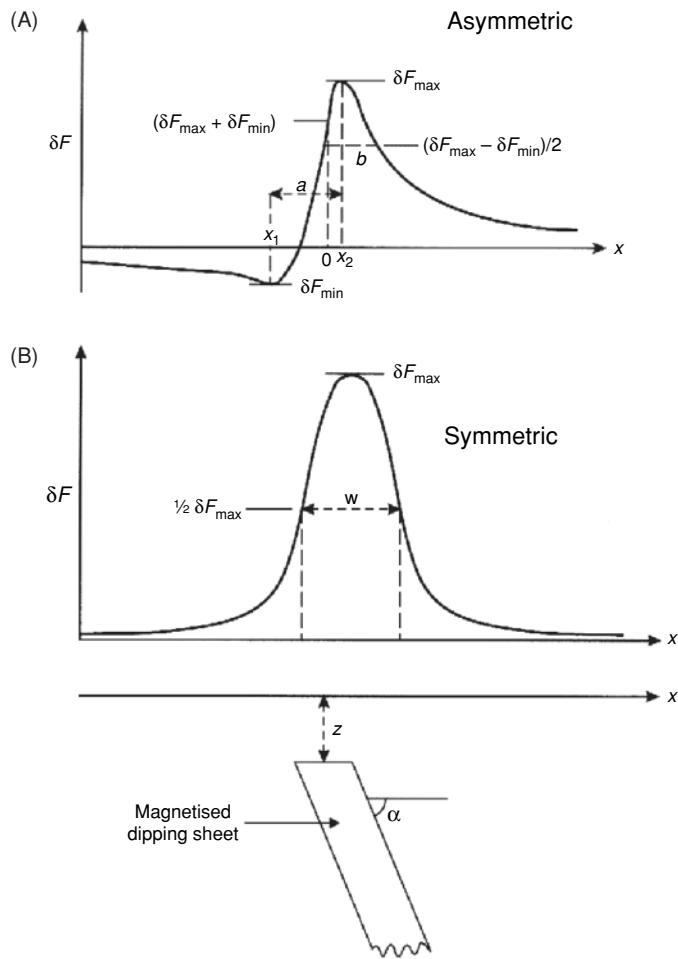


**Figure 3.46** ParASNIS' (1986) method of determining the position of the centre of and the depth to the top of, a magnetised thin sheet. (A) An asymmetric profile, and (B) a symmetric profile.

#### Box 3.9 Depth estimations (see Figure 3.46 for definitions of parameters)

##### Thin sheet (depth to top of body $z$ )

*Asymmetric anomaly:*

$$z = (-x_1 \cdot x_2)^{1/2} \quad (x_1 \text{ or } x_2 \text{ is negative})$$

$$\text{and } z = (a^2 - b^2)^{1/2} \cdot |C|/2 \cdot (1 + C^2)^{1/2}$$

where  $1/C = \tan(I + i - \alpha)$ ;  $|C|$  is the magnitude of  $C$ ;  $I$  = inclination of the Earth's magnetic field;  $i$  = inclination of any remanent magnetisation; and  $\alpha$  = angle of dip of the sheet.

*Symmetric anomaly:*

$$z = w/2$$

where  $w$  = anomaly width at  $\delta F_{\max}/2$ .

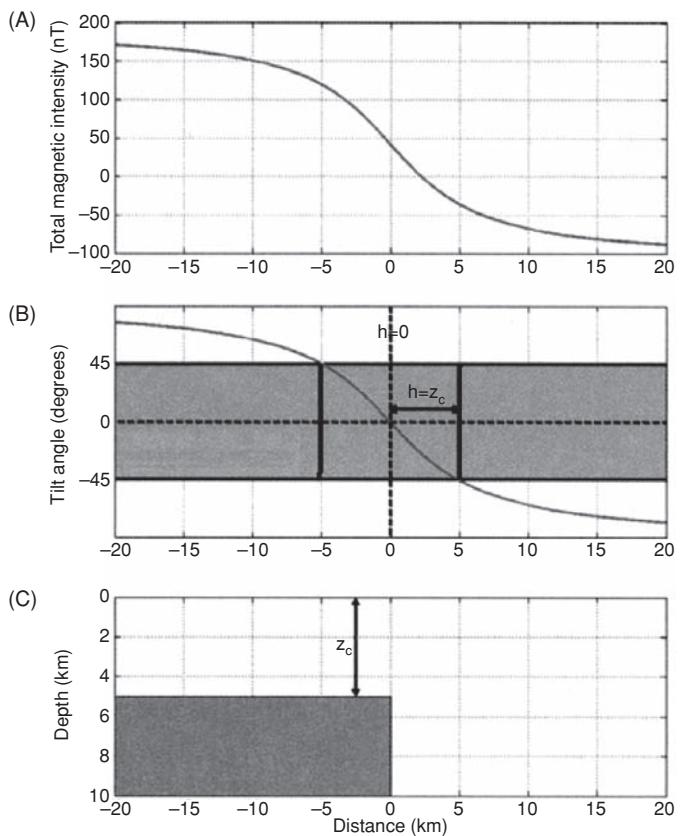


**Figure 3.47** (A) RTP profile of the magnetic anomaly, and (B) the tilt derivative over a vertical contact (C) for RTP (or vertical inducing field). The contact coincides with the tilt angle  $\theta = 0^\circ$  crossing point and the depth to the structure ( $z$ ) is given by half the horizontal distance between the  $+45^\circ$  and  $-45^\circ$  contours, as indicated in (B). From Salem et al. (2007).

anomaly can be isolated from the background adequately. One common problem is when two magnetised bodies are so close to each other spatially that their magnetic anomalies overlap to form a complex anomaly (Figure 3.49). Sometimes such an anomaly may be misinterpreted as being due to a much thicker body with lower susceptibility than the actual cause, and so gives rise to an erroneous interpretation. Geological control may help, but having the ability to generate models quickly by computer is a great boon. 'What if . . . ?' models can be constructed to test to see what anomaly results

#### Box 3.10 Reduction to the Pole operator (Grant and Dodds, 1972)

$$\text{RTP Operator } L(\theta) = 1/[\sin(I) + i \cos(I) \cos(D - \theta)]^2$$

where:

$\theta$  is the wave number direction;  $I$  is the magnetic inclination; and  $D$  is the magnetic declination.

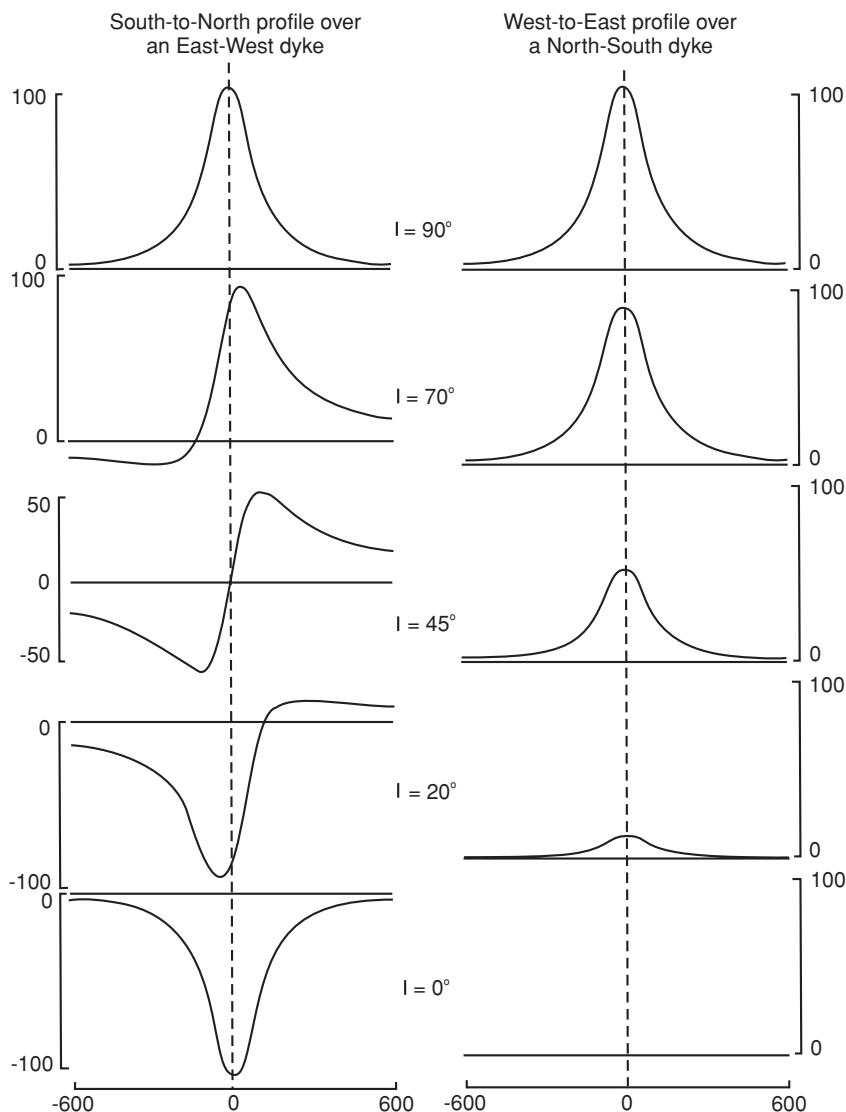


**Figure 3.48** Total magnetic field intensity profiles over a vertically-dipping dyke for striking (left) east-west and (right) north-south with magnetic inclinations ranging from  $90^\circ$  to  $0^\circ$ . From MacLeod *et al.* (1993).

if different configurations of magnetised bodies are considered. A basis for many computer programs was provided by Talwani *et al.* (1959) and Talwani (1965). In essence, two-dimensional modelling requires that the body being modelled has a lateral extent at least 20 times its width so that the end effects can be ignored. For many geological features this restriction is adequate, and anomalies from such bodies can be analysed successfully. In many other cases, it is necessary to use more sophisticated computer methods.

With any set of profile data and the analysis of anomalies, it is absolutely essential that there be sufficient data to image the correct shape of the anomaly. Too few data leads either to incorrect evaluation of amplitude maxima or minima (consider the effects on simple depth determinations if the peak positions are not adequately defined), or in more extreme cases to severe aliasing (see Chapter 1). Limitations can be caused by too few field data values and/or by computer models producing too few point values at too large a

station interval. It is therefore essential that, if computer methods are to be employed, the user is aware of what the software is actually trying to do and how it does it, and that adequate field data, both in number of values and data quality, are used.

A wide variety of computer methods exist, ranging from simple two-dimensional packages that can be run on low-cost personal computers and laptops, up to extremely sophisticated 2.5-dimensional and three-dimensional modelling packages on more powerful workstations. Two-and-a-half dimensional modelling is an extension of two-dimensional modelling but allows for end effects to be considered (e.g. Busby, 1987). Some packages provide a statistical analysis on the degree of fit between the computer-generated anomaly and the observed data. Others allow successive iterations so that each time the software completes one calculation it generates better input parameters automatically for the next time round, until certain quality parameters are met. For example,

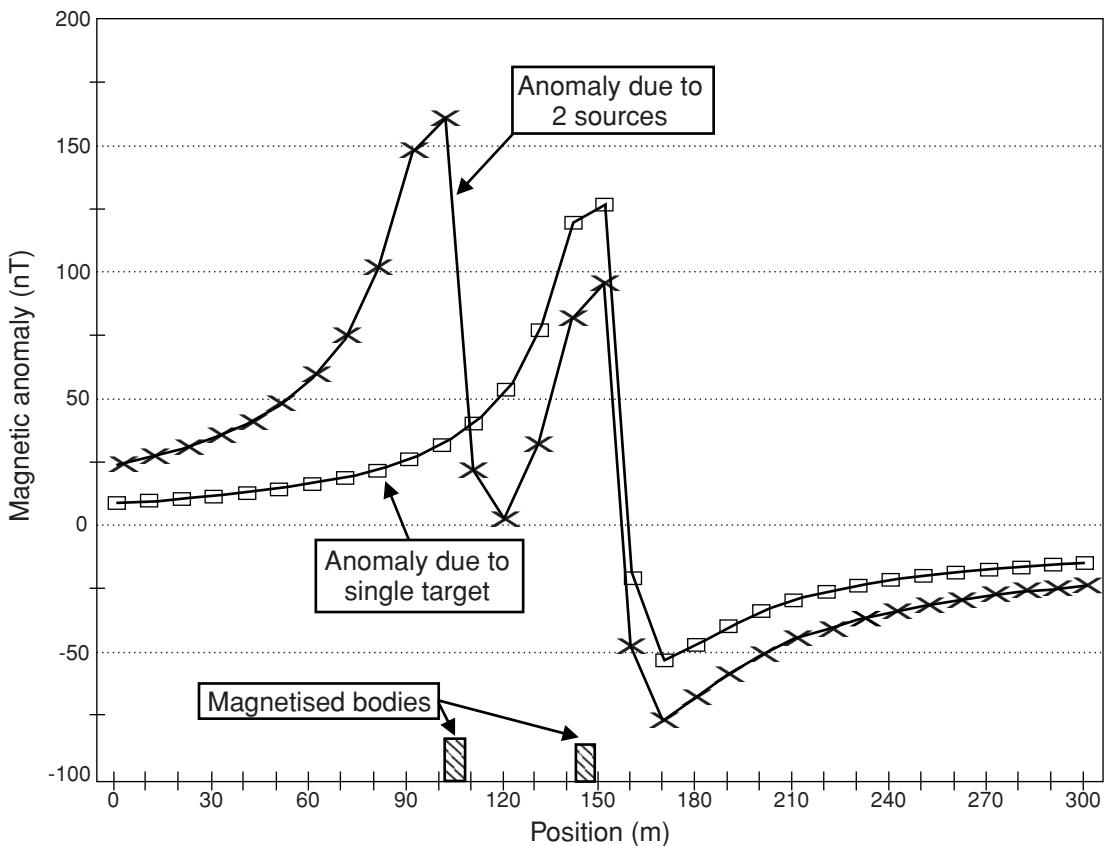


**Figure 3.49** Total magnetic anomalies over two identical 5-m-wide vertical dykes whose centres are separated by 45 m (their locations are indicated), and in contrast, the magnetic anomaly arising from just one of the dykes (position 145 m), ignoring the other.

a computer program may run until the sum of the least-squares errors lies within a defined limit.

One other factor that needs to be borne in mind with magnetic modelling is that some software packages compute the anomaly for each body and then sum them arithmetically at each station. This ignores the fact that adjacent magnetised bodies will influence the magnetic anomalies of the other bodies. Consequently, the computed anomalies may be oversimplifications; and even if statistical parameters of the degree of fit are met, the derived model may still be only a crude approximation. In the majority of cases involving small-scale surveys in archaeology or site investigations, these problems are not likely to be as significant.

Modelling in three dimensions permits the construction of irregularly shaped bodies made up of a stack of magnetised polygons and takes into account edge effects. An example of three-dimensional interpretation of magnetic (and gravity) data is given in Section 3.9.1.

In addition to the spatial modelling, another method of assisting interpretation is the use of spectral analysis. The magnetic field is expressed by Fourier analysis as an integral of sine and/or cosine waves, each with its own amplitude and phase. In this, the amplitude or power spectrum is plotted as a function of wavelengths (from short to long), expressed in terms of wavenumber (1/wavelength). A number of methods exist to determine the power spectrum (*e.g.* Spector and Parker, 1979; Garcia-Abdeslem and Ness, 1994). They

attempt to isolate the regional field so that the residual anomalies can be identified. Once the frequency of the residuals has been determined, the dataset can be filtered to remove the regional field, thus facilitating the production of anomaly maps on which potential target features may be highlighted. It is also possible to produce susceptibility maps from this type of analysis. From the form of the Fourier spectrum, estimates of depth to the magnetised bodies can be made (Hahn *et al.*, 1976). The power spectrum yields one or more straight-line segments, each of which corresponds to a different magnetised body. A recent example of such an analysis of aeromagnetic data associated with the Worcester Graben in England has been described by Ates and Kearey (1995). Further analysis of magnetic data in the wavenumber domain has been discussed by Xia and Sprowl (1992), for example.

### 3.8.5 Depth determinations and Euler deconvolution

There have been two important developments in the display and processing of magnetic data. Where a large dataset exists for a regional aeromagnetic survey, say, the data have been displayed conventionally as a contoured anomaly map. With the advent since the 1970s of image processing using computers, it is possible to digitise and process data recorded previously in analogue form. Instead

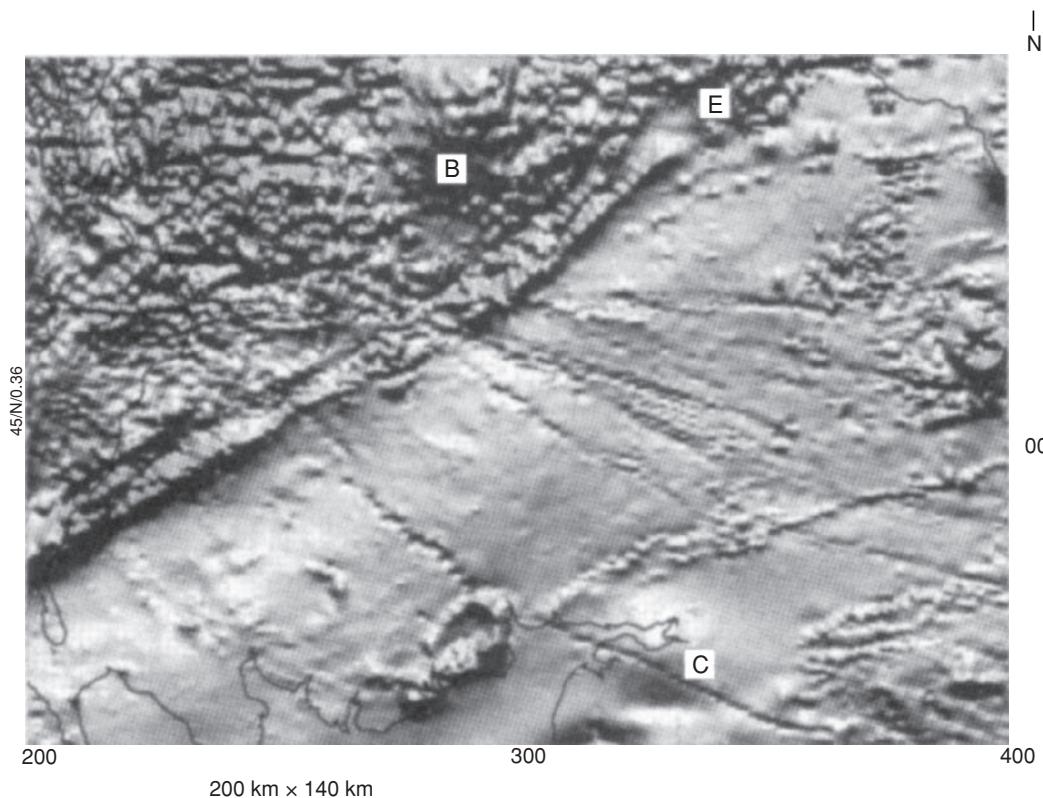


**Figure 3.50** This image shows total field aeromagnetic data collected over an area of 200 km x 140 km of the Southern Uplands, Scotland (B: Bathgate; C: Carlisle; E: Edinburgh). The data were acquired in analogue form along flight lines spaced approximately 2 km apart, with tie lines 10 km apart and with a mean clearance of 305 m. The data were digitised, interpolated to a square grid of mesh size 5.0 km and displayed as a greyscale shaded-relief image. Sun illumination azimuth and inclination are N and 45° respectively. East-west lineations through the high-amplitude Bathgate anomaly are related to quartz-dolerite Permo-Carboniferous dykes. Numerous Tertiary dykes can be mapped trending NW-SE across the Southern Uplands. For comparison, see Figure 2.43. Image courtesy of Regional Geophysics Group, British Geological Survey.

of contouring, the area covered is divided into rectangular cells, each of which is assigned a total field strength value. These cells are manipulated and displayed as individual pixels. The resultant display is a colour image with blue indicating negative anomalies and red the positive anomalies. Shades of colour indicate intensities, so dark red indicates a high-amplitude positive anomaly while deep blue a high-amplitude negative anomaly. Image-processing software analogous to that used to process satellite image data, such as Landsat, is used to analyse the aeromagnetic (or indeed gravity) data (Figure 3.50).

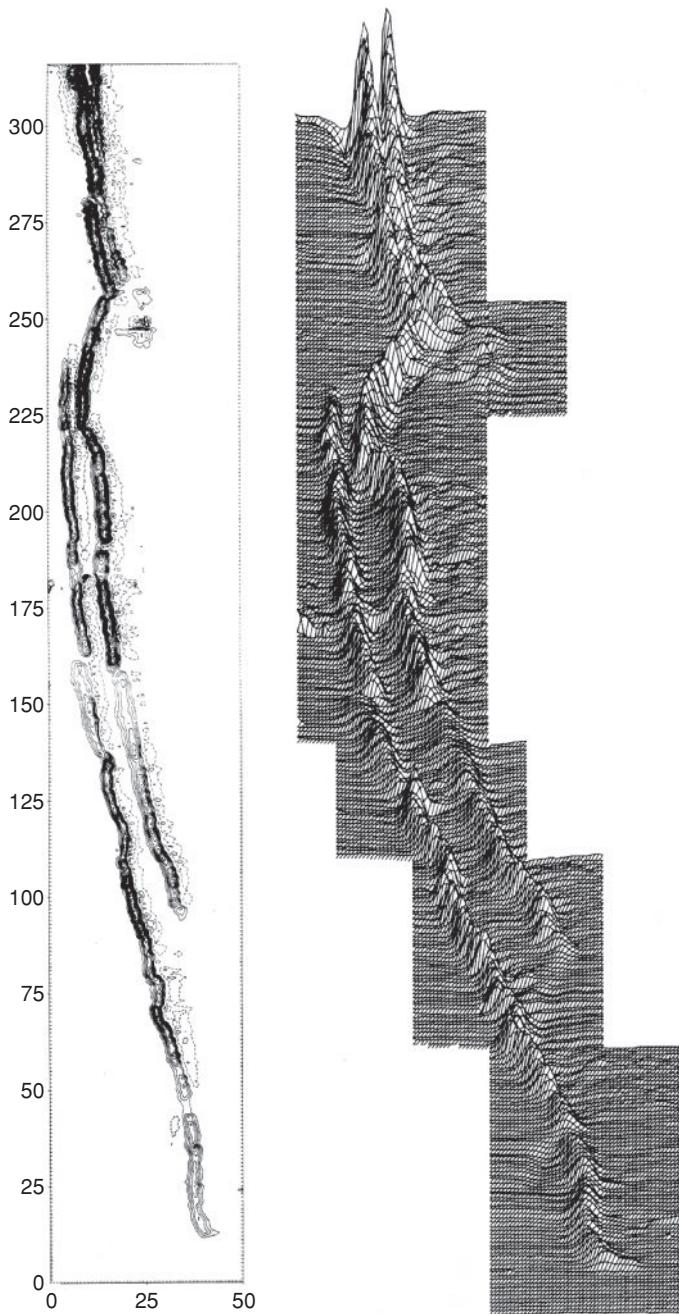
Lineaments suggestive of faults can be identified using edge filters. Spatial filters can be applied to resolve the data into regional and residual datasets, and zoom facilities allow the accurate expansion of subsets of data for high-resolution analysis of much smaller areas, thus permitting the identification of any low-amplitude anomalies. Green (1983), for example, has discussed digital image processing in detail.

Image-processing methods need not be restricted to datasets covering very large areas. The only prerequisite for image processing to be possible is that there must be a large enough dataset. Dataloggers attached to magnetometers and memory-backed magnetometers or gradiometers can also be used for ground surveys where very high

spatial discrimination is required (Sowerbutts and Mason, 1984). Scollar *et al.* (1986) reviewed the various data processing and display methods used in archaeology where very high resolution is also required.

Sowerbutts (1987) mapped the largely concealed Butterton Dyke in central England using a microcomputer-based fluxgate gradiometer. More than 16800 magnetic measurements were made in one day by one person. Data were recorded at 0.5 m intervals along 317 parallel traverses 1 m apart and the results plotted as a contour map and as an isometric display (Figure 3.51). The lines of the olivine dolerite dykes are obvious. The survey produced an extremely accurate map of the dyke, which was totally concealed in the area of the survey, and demonstrated that the dyke was not terminated by a fault, as previously thought, but died out naturally.

Calculating depths to magnetic features is still the most significant aspect of magnetic surveys. Since Peters' classic paper in 1949 there has been a steady stream of publications describing new or modified methods of depth determination. In the 1980s, one technique, known as the Euler deconvolution method, was developed to process magnetic data and convolve them to a point source at depth (Thompson, 1982). The method operates on the data directly and provides a mathematical solution without recourse to any



**Figure 3.51** Butterton Dyke anomalies displayed as a magnetic gradient contour map with a contour interval of 20 nT/m (positive values, solid; negative values, dashed). From Sowerbutts (1987), by permission.

geological constraints. This has the advantage that the Euler-derived interpretation is not constrained by any preconceived geological ideas and thus can be used critically to appraise geological, and particularly structural, interpretations.

The Euler method utilises the magnetic field strength at any point in terms of the gradient of the total magnetic field, expressed in Cartesian coordinates. Furthermore, these gradients are related to different magnetic sources by a function termed the *Structural*

### Box 3.11 Euler's equation

$$(x - x_0) \frac{\delta T}{\delta x} + (y - y_0) \frac{\delta T}{\delta y} - z_0 \frac{\delta T}{\delta z} = N(B - T)$$

where  $x_0, y_0, z_0$  are the coordinates of a magnetic source whose total field intensity  $T$  and regional value  $B$  are measured at a point  $(x, y, z)$ ;  $N$  is the degree of homogeneity and is referred to as the *Structural Index*.

For two dimensions  $(x, z)$ , Euler's equation reduces to:

$$x_0 \frac{\delta T}{\delta t} + z_0 \frac{\delta T}{\delta z} + NB = x \frac{\delta T}{\delta x} = NT(*)$$

The only unknowns are  $x_0, z_0$  and  $N$ ; gradients of  $T$  with respect to  $x$  and  $z$  can be derived from the measured magnetic data;  $\delta T/\delta y$  is assumed to be equal to zero.

#### Structural indices $N$ :

Vertical geological contact	Edge of large tank	0 - <0.5
Infinite sheet		0
Thick step		0.5
Irregular sill	Metal sheet	1
Vertical cylinder	Well/drum	2-2.25
Cylinder with unknown orientation	Drum	2.5
Horizontal cylinder	Pipeline/drum	2-2.75
Point dipole		3
Sphere	Tank	3

*Index,  $N$ .* Euler's equation is given in Box 3.11. Considering the equation asterisked, a series of seven equations can be determined from observed data by evaluating this equation in at least seven places within a window placed on the data. This provides seven equations to solve for three unknowns using a least-squares procedure. The output consists of determinations of the depth to the magnetic body ( $z_0$ ) producing the anomaly which can be plotted on a map as a circle, the increasing size of which indicates greater depth. Solutions that lie outside predetermined statistical bounds are rejected, thus constraining the possible number of solutions.

Reid *et al.* (1990) used the Euler method to aid the interpretation of an area in south-central England. A simplified geological map of the survey area is given in Figure 3.52 with the aeromagnetic survey data. The Euler solutions have been plotted in Figure 3.52C which has been interpreted to form a structural map shown in Figure 3.52D. The Euler display has picked out the two north-south striking boundary faults marking the central block. Depth solutions for the Eastern Boundary Fault were within 0.3 km of those derived by other means. The magnetic anomalies over the central block yield very few Euler solutions and this may be due to overlapping anomalies making Euler solutions statistically unacceptable and so these have been rejected. Alternatively, there are insufficient data to represent the area adequately. In the southwest corner there is a strong cluster of solutions with large depth values. This has been interpreted as being due to a magnetic body intruded at a depth of about 10 km. The main benefit of using the Euler method

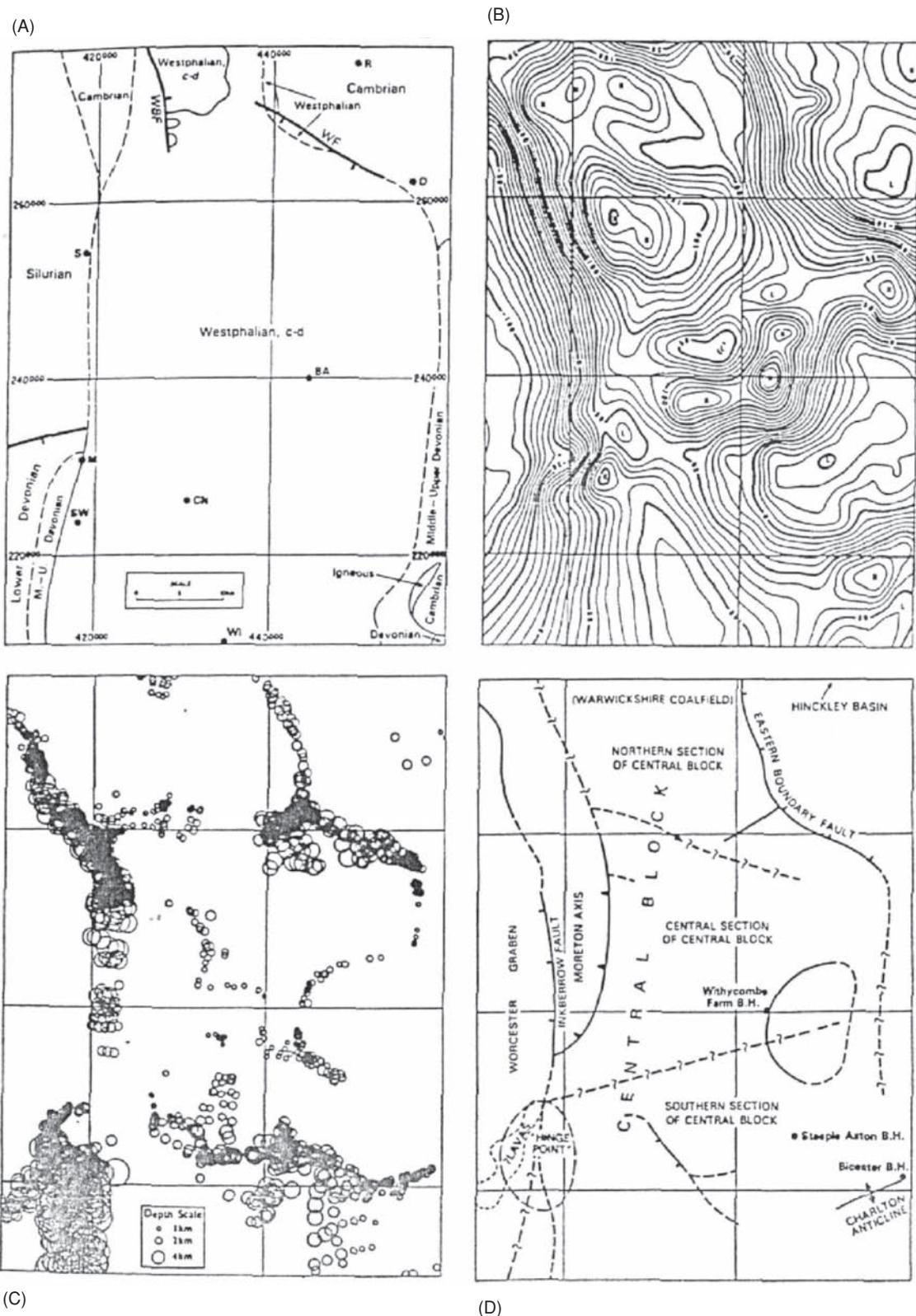


**Figure 3.52** (A) Simplified geological map of the south-central part of England. (B) Aeromagnetic map of the area shown in (A). (C) Euler solutions derived from the aeromagnetic data calculated for a structural index of 1. (D) Structural interpretation of the Euler solutions. From Reid *et al.* (1990), by permission.

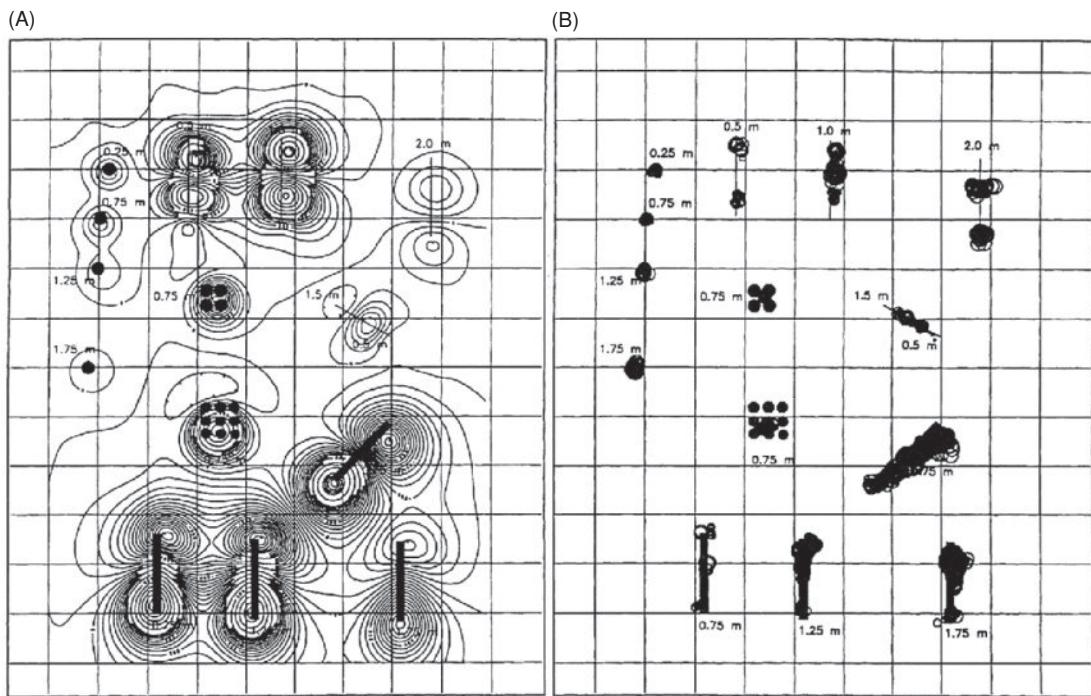


**Figure 3.53** (A) Total magnetic field anomaly map over the Columbia Test Site, University of Waterloo, Canada, with the known depths to the various targets listed. (B) The solutions calculated from (A). From Yaghoobian *et al.* (1992), by permission.

appears to be the delimitation of lineaments due to faults or major linear intrusions, and these features are best imaged by the Euler solutions if they are dipping, rather than vertical. The technique offers a method of independent interpretation which can be used to appraise existing geological models.

Euler's method has been incorporated into commercially available software and has been demonstrated to be applicable to the location of near-surface utilities (pipes, drums, etc.) in addition to regional structural features. Examples of the use of the method in locating buried manmade targets have been given by Yaghoobian *et al.* (1992). They have described a detailed magnetic survey carried out at the Columbia Test Site, University of Waterloo, Canada, and corresponding Euler analysis. The results are shown in Figure 3.53. This example is perhaps too contrived to demonstrate the effectiveness in a real situation with a typical amount of background noise, but it does serve to show that the method works. Where there is a significant background noise problem, accurate depths and/or locations may be hard to achieve, especially if the measured data yield only weak signals. With careful analysis and selection of processing parameters (especially the Structural Index and GRIDDEPTH window size), best-possible solutions may be obtained. It is also important that the field data be of as high quality as can be achieved and that appropriate filtering to remove obvious noise is undertaken before Euler analysis.

In addition to Euler analysis, increasing attention is being paid to the use of three-dimensional analytical signals (Nabighian, 1984; Roest *et al.*, 1992; MacLeod *et al.*, 1993). The general principle behind the method is illustrated schematically in Figure 3.54. Given a magnetic anomaly (in the case illustrated, this arises from a square prism magnetised in an arbitrary direction), the three derivatives

can be obtained from which the analytical signal is derived (Box 3.12). The amplitude of the 3-D analytical signal of the total magnetic field produces maxima over magnetic sources irrespective of their magnetisation direction (MacLeod *et al.*, 1993; Parlowski *et al.*, 1995). The 3-D analytical signal can be calculated readily from an accurately gridded dataset. A  $3 \times 3$  filter can be applied to obtain the horizontal gradients ( $\delta T/\delta x$  and  $\delta T/\delta y$ ). A fast Fourier transform (FFT) can be used to obtain the vertical gradient ( $\delta T/\delta z$ ). Alternatively, if a gradiometer has been used to acquire the data, the vertical gradient is a measured parameter.

From the form of the resultant analytical signal, solutions are obtained as to the location ( $x$ ,  $y$ ,  $z$ ) of the source. These are shown graphically as circles, much the same as from Euler solutions. The distance between the inflection points of the analytical signal anomaly is directly proportional to the depth to the top of the magnetic source. It has been demonstrated that both Euler and analytical solutions can be used to produce an integrated model of the causative magnetised structure: the analytical signal can be used to delineate the magnetic contrasts and give estimates of their approximate depths, while the Euler solution yields more detailed interpretation at depth (Roest *et al.*, 1992; Parlowski *et al.*, 1995). It should be noted that the use of analytical signals can also be applied to gravity data or a combination of potential-field data.

In shallow environmental applications, sources at very shallow depth (< 1 m) give rise to extremely high-frequency signals, which are difficult to resolve using these techniques. It is probably more cost-effective to dig with a shovel on the position of magnetic anomalies to locate the target source than to go through the analytical procedures outlined above. However, as soon as the depth is beyond easy excavability, the value in the use of analytical

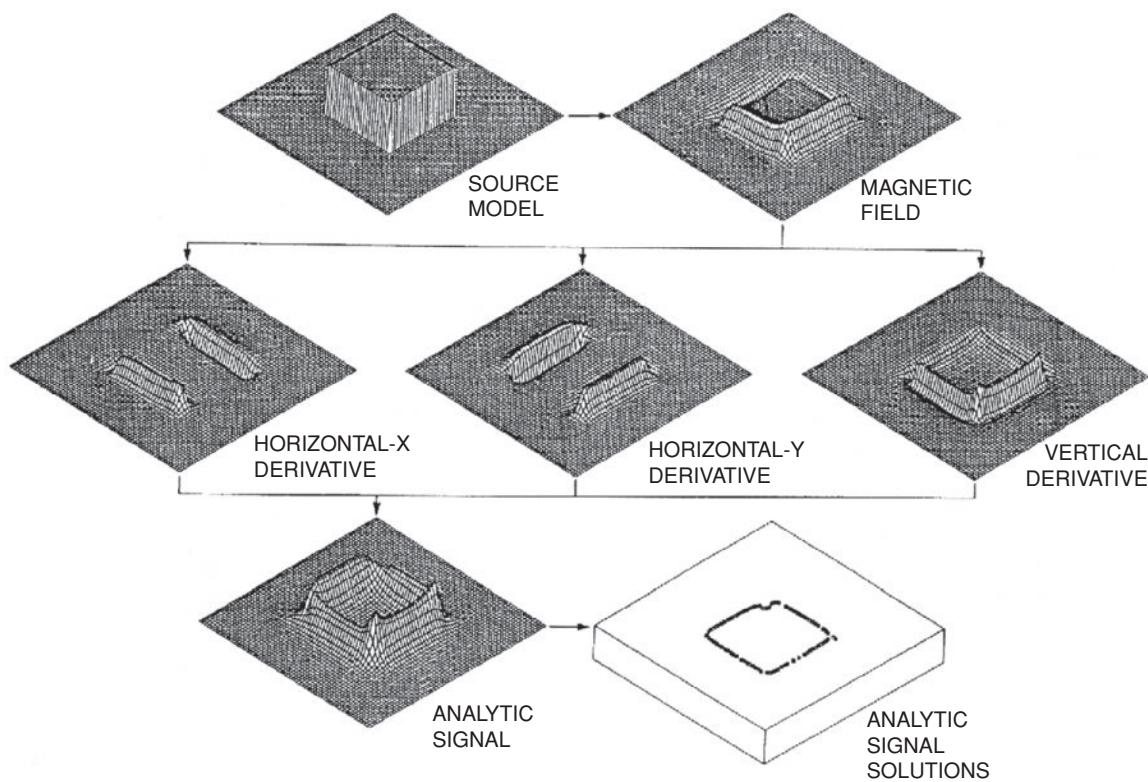


**Figure 3.54** Schematic outline of the analytical signal method. Horizontal and vertical derivatives are calculated from the total field anomaly over a square prism and combined to yield the absolute value of the analytical signal. The locations of the maxima and the shape of this signal can be used to find body edges and corresponding depth estimates. From Roest *et al.* (1992), by permission.

**Box 3.12** The amplitude of the three-dimensional analytical signal (MacLeod *et al.*, 1993)

The amplitude of the analytical signal ( $|A(x,y)|$ ) at any location  $(x,y)$  is given by:

$$|A(x, y)| = [(\delta T/\delta x)^2 + (\delta T/\delta y)^2 + (\delta T/\delta z)^2]^{1/2}$$

where  $T$  is the measured field at  $(x, y)$ .

solutions increases. Accuracies in depth determination are of the order of 30% of the target depth. This figure is one that may be improved upon in time with future developments and experience.

## 3.9 Applications and case histories

### 3.9.1 Regional aeromagnetic investigations

An aeromagnetic survey over the Lizard Peninsula in Cornwall, which was interpreted in conjunction with gravity data (Rollin, 1986), provides an example of three-dimensional interpretation. The Lizard Complex comprises what is thought to be an ophiolite

suite made up of a lower tectonic sheet of hornblende schists and metasediments and structurally overlain by peridotite and gabbro. This upper sheet shows lateral variation from harzburgite peridotite, gabbro and a dyke complex in the east, to lherzolite peridotite and cumulate complex to the west. Comparison of the simplified geological map with the corresponding aeromagnetic map (Figure 3.55) demonstrates the correlation of the most prominent magnetic feature, a magnetic high which extends offshore to the east, onshore across the harzburgite peridotite south of Coverack, northwestwards with diminishing amplitude over the Traboe Cumulate Complex. Western Lizard is characterised by small localised anomalies over the western peridotite. These features correlate with small outcrops of interlayered basic gneiss. A summary of the tectonic units and their respective schematic geophysical responses are shown in Figure 3.56. From this it can be seen that the Iherzolite peridotite has a much smaller magnetic effect than the harzburgite peridotite, while they both have comparable effects on the gravity field. It was found that the harzburgite peridotite was depleted particularly in  $TiO_2$  compared with the Iherzolite peridotite. Low concentrations of titanium in these rocks are indicative of complex geochemical processes which affected the formation of magnetite during serpentinisation.

When modelling these aeromagnetic anomalies, Rollin found that it was necessary to investigate the remanent magnetisation which is significant, as might be expected for such a suite of rocks. On the basis of field and laboratory measurements, the overall

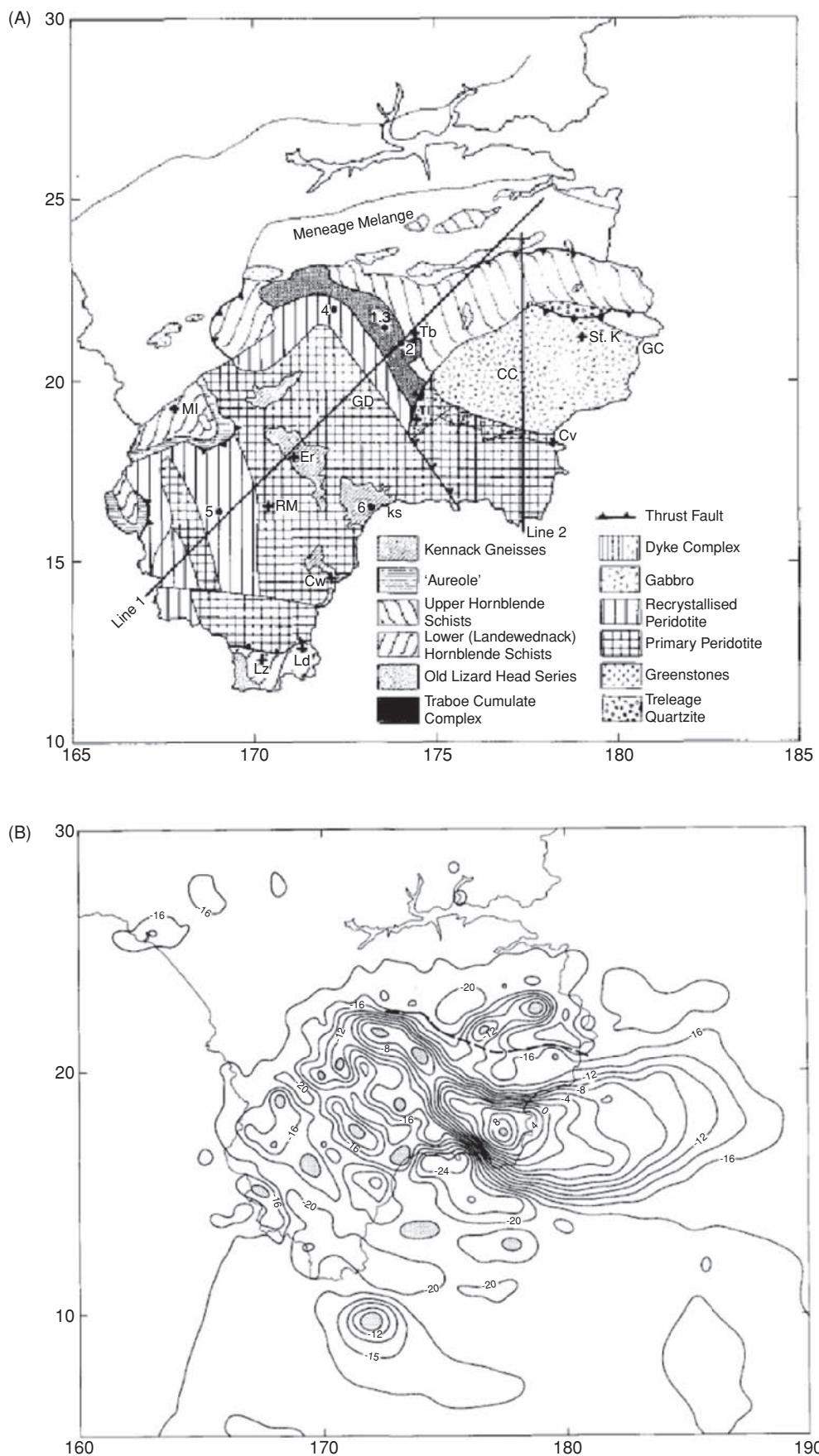


**Figure 3.55** (A) Simplified geological map of the Lizard Peninsula, south Cornwall, and (B) the corresponding aeromagnetic map. From Rollin (1986), by permission.

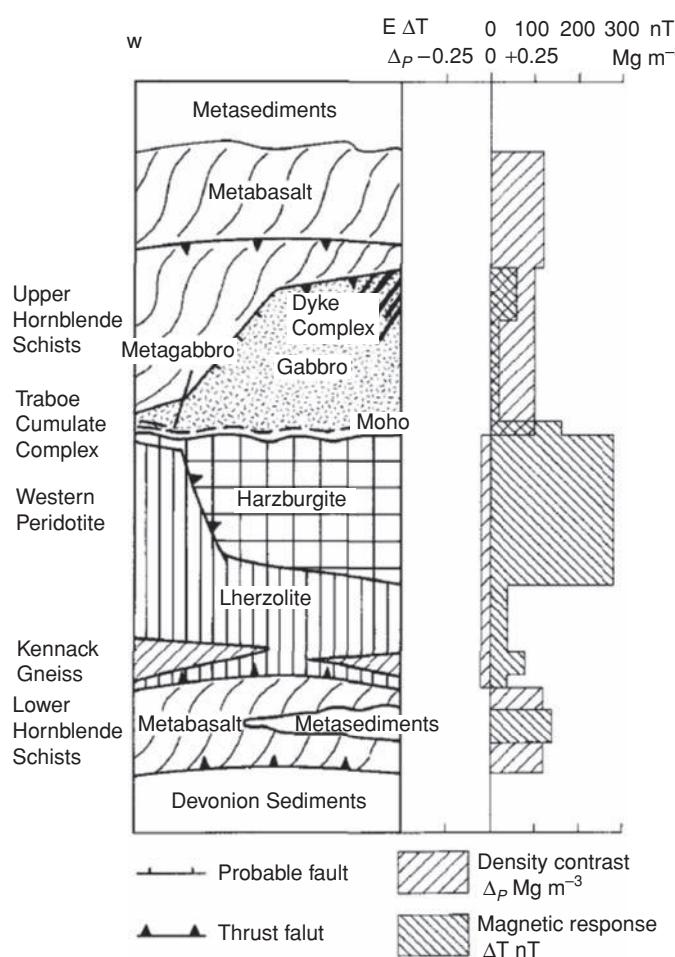


**Figure 3.56** Tectonic units of the Lizard and a schematic representation of their geophysical responses. From Rollin (1986), by permission.

Königsberger ratio (remanent:induced magnetisation) was taken to be 0.43, with a declination and inclination of the remanent magnetisation of 286° and 75° respectively, with a resultant magnetisation up to 220 nT and a mean susceptibility of 0.0774 (SI). A simple 3D model comprising stacked horizontal polygons was then constructed for the eastern area, which produced a calculated anomaly (Figure 3.57) comparable to the observed aeromagnetic anomaly. The magnetic interpretation indicated that the Traboe Complex has a thickness of only 150 m while the eastern harzburgite peridotite is about 500 m thick (Figure 3.58). Independent gravity modelling gave the thickness of the eastern peridotite as 560 m, which is in reasonable accord with the magnetic interpretation.

Mushayandebvu *et al.* (2004) provided an example of the use of an adapted Euler deconvolution method to resolve 2D from 3D targets from an aeromagnetic survey over a section of the Great Dyke of Zimbabwe. Outputs from their approach include not only depths to the source bodies but also strike and dip and susceptibility contrasts. The Great Dyke is 550 km long and up to 11 km wide and cuts across the Archaean Zimbabwe craton. It extends in a north-northeast trending direction from the Limpopo Belt in the south to

the Zambesi Belt in the north. The dyke comprises the remains of a number of synclinally layered mafic igneous complexes. These pass downwards into true dyke feeders to the complexes. Lying parallel to the Great Dyke for its entire length are true satellite dykes: the Umvimeela (to the west) and the East dykes (to the east). The satellite dykes are essentially vertical, with a mean dip of 84° towards the Great Dyke for the Umvimeela Dyke and 89° away from the Great Dyke for the East Dyke, and with average widths of 200 m and 100 m, respectively.

The aeromagnetic data were acquired during a nationwide survey of the entire country at a mean terrain clearance of 305 m with traverse lines spaced 1 km apart and tie lines every 14 km. An extract of the Total Magnetic Intensity dataset is shown in Figure 3.59A and the grid Euler deconvolution results in Figure 3.59B. The locations of the three dykes are indicated.

### 3.9.2 Mineral exploration

In Finland, in regions of Precambrian basement comprising black graphite-schists, the location of sulphide ores is becoming increasingly difficult. The easy-to-find ores have already been identified. The more difficult ones, such as pyrrhotite-rich black schists and associated mineralisation, have been more easily eroded by glacial ice than the surrounding rocks and have become buried beneath a veneer of overburden, commonly up to 30 m thick. The overburden is characterised by high resistivities, so the relatively conductive ore zones can be located using electrical methods. However, this is not always practicable, so magnetic methods have also been used in conjunction with geochemical surveys. Furthermore, it is difficult to discriminate between the geophysical anomalies produced by economic sulphide mineralisation and those caused by the black schists and other rocks. Consequently, the identification of copper ores is particularly difficult.

The Saramäki ore body, located about 370 km northeast of Helsinki, forms a compact copper mass with some cobalt, and occurs in geological complexes comprising serpentinites, dolomites, skarns, quartzites and black schists, in a country rock of mica schist. The exploration strategy has been discussed in detail by Ketola (1979). The whole mineralised complex can be traced using aero-geophysical methods for over 240 km. The specific ore body, which was located in 1910 by drilling, is 4 km long, 200–400 m wide and extends down to about 150 m. Average copper content is 3.8% with 0.2% cobalt.

Problems with identification of the ore body can be seen by reference to Figure 3.60. The electrical resistivity (SLINGRAM) anomalies are caused by the black schists. The whole skarn zone forms a denser block (0.23 Mg/m<sup>3</sup> higher) compared with the country rock and so the subunits within the mineralised zone cannot be differentiated using gravity. Susceptibility measurements made using the boreholes suggested that the mineralised zone was magnetised heterogeneously and that its upper part influenced the magnetic anomaly. In addition it was found by two-dimensional modelling that the main magnetised zones had significant remanent magnetisation. If remanence is ignored, the dip of the two main zones is inconsistent with the known dips derived from drilling, even

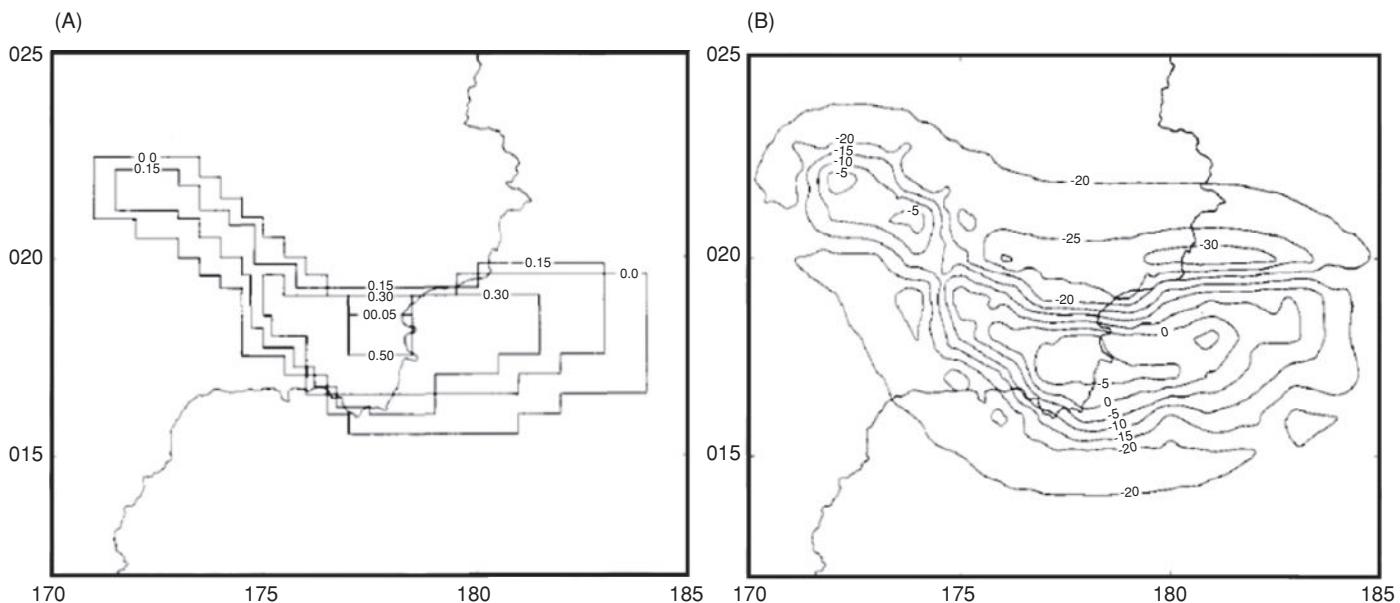


**Figure 3.57** Three-dimensional modelling of the southeast part of the Lizard. (A) Stacked horizontal polygons, and (B) the resulting calculated magnetic anomaly. From Rollin (1986), by permission.

though the computed anomaly fits the observed one very well (Figure 3.61A). By incorporating remanence, with inclination  $45^\circ$  and declination  $90^\circ$  (compared with  $75^\circ$  and  $7^\circ$ , respectively for the Earth's field), geologically compatible models were then produced which were also in accord with those used in the gravity modelling (Figure 3.61B).

Ketola concluded from this and other similar examples in Finland that geophysical or geochemical methods alone were insufficient to resolve these complex ore bodies. It was necessary to use a wide variety of geophysical and geochemical techniques together, in conjunction with drilling, to provide a successful differentiation of the subsurface geology.

Other illustrations of magnetic anomalies over mineralised bodies have been shown in Figure 1.10D, for a lode at Wheel Fanny, northwest Devon, where the course of the lode is picked out clearly by the linear magnetic anomalies. Figure 3.32 illustrates a ground magnetometer profile over sulphide mineralisation at Sourton Tors, northwest Dartmoor, Devon.

Ground-based magnetic profiling is often undertaken as part of reconnaissance exploration for iron ore in the Philippines, which lies at a low geomagnetic latitude. Anomalies across steeply dipping magnetised dykes have the form of a large amplitude negative to the north but a very subdued positive to the south (Figure 3.62). Such a profile also indicates that although modern magnetometers can sample at rates of up to ten measurements per second, such a sampling rate would be excessive in this case; a station interval of 10 m would be adequate for this scale of survey.

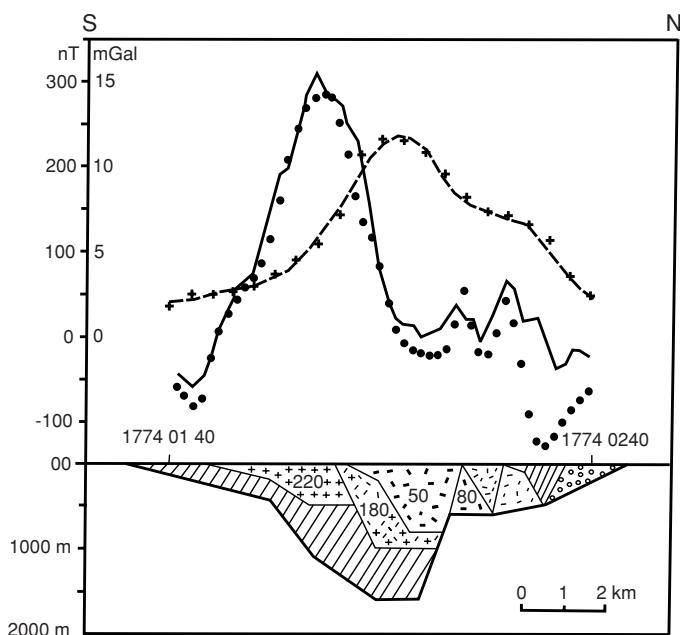


**Figure 3.58** Aeromagnetic and gravity anomaly profiles along line (Figure 3.55A) across the southeastern part of the Lizard. From Rollin (1986), by permission.

### 3.9.3 Detection of underground pipes

Sowerbutts (1988) has provided a clear example of how high-resolution magnetic gradient surveys can identify not only the location of underground metal pipes, but also the position of joints between individual sections of pipe. If joints can be located remotely, the amount of excavation required to examine and repair a pipe can be minimised, saving time, money and inconvenience.

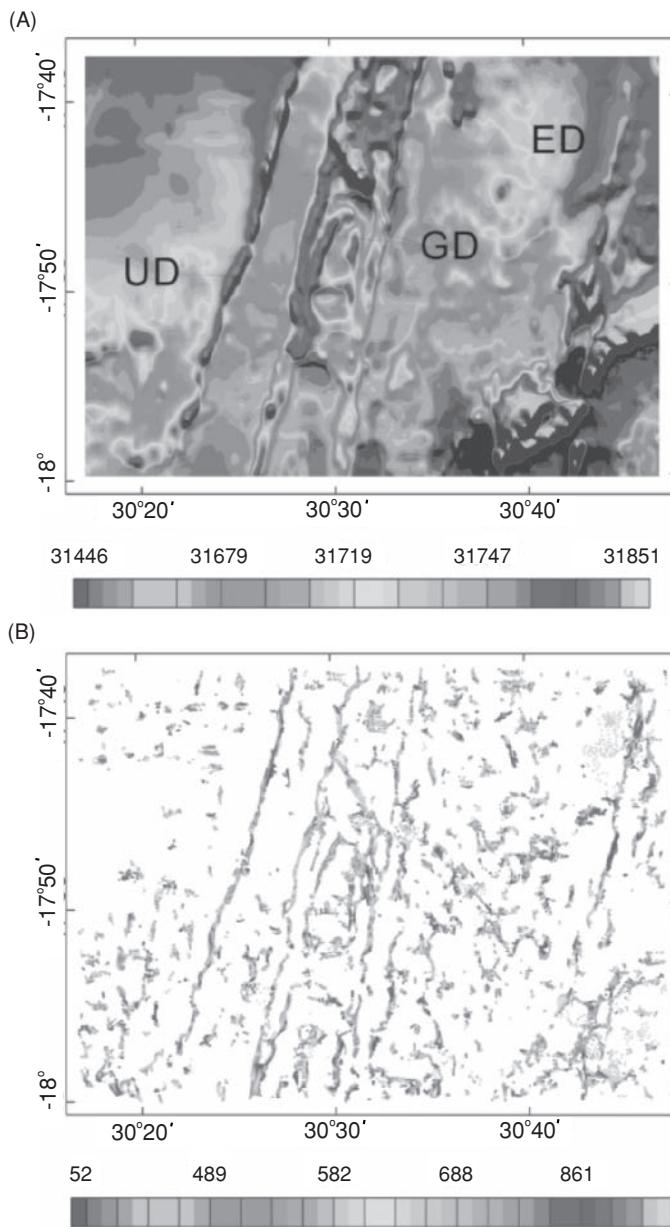


**Figure 3.59** (A) Total Magnetic Intensity map over the Great Dyke region of Zimbabwe, with (B) the corresponding grid Euler deconvolution map of depths to sources. From Mushayandebvu et al. (2004). [C]

The magnetic anomaly along a pipe consists of a series of smaller anomalies, each of which corresponds to an individually cast segment of pipe which behaves like a magnetic dipole. For a pipe buried close to the surface and away from extraneous magnetic sources, a clear repetition of anomalies can be identified (Figure 3.63A). In the case illustrated, the pipe had a diameter of 0.5 m and was made of ductile iron in 6.3 m long sections and buried at a depth of 0.5 m. Magnetic highs, with gradients up to 4000 nT/m, are centred between 0.5 m and 1.0 m along from the socket end. For a pipe orientated east–west, a typical negative (north) and positive (south) anomaly doublet is produced along a profile aligned north–south

in the northern hemisphere (cf. Figure 3.37A). A magnetised body orientated north–south produces a more symmetric positive-only or negative-only anomaly, and this is also seen in pipes orientated north–south (Figure 3.63B). For a smaller 76 mm diameter pipe (Figure 3.63C) this anomaly doublet effect is clearly repeated along the line of this north–south orientated pipe. In an urban environment, identifying the anomalies associated specifically with the buried pipe can be very difficult. Other magnetic materials are likely to be nearby and this can obscure or de-focus the pipeline anomaly (Figure 3.63D). In the last case, the pipe was of 0.15 m diameter and buried about 1.5 m down. Local metal grids produce large magnetic anomalies. The anomaly pattern associated with this pipe is now irregular and complex, and it is not possible to identify pipe joints. Even seamless steel pipes with welded joints can be identified in areas with a quiet magnetic background.

A further example of the use of magnetometry to locate near-surface pipes has been given by Geometrics Inc., who acquired data over a test site at Stanford University, USA, using a caesium magnetometer. The data were contoured and displayed as both a map and an isometric projection, which are shown with a map of the utilities in Figure 3.64. The correlation between buried objects and the corresponding magnetic anomalies is obvious.

Anomalies have been produced that have been characteristic of induced magnetisation in many cases, but what has not been considered is that pipes acquire a permanent magnetisation on cooling during manufacture. It may be necessary to examine the orientation of the pipes as they cool at their respective foundries (hence determine the inclination and declination of permanent magnetisation). Having ascertained the permanent magnetisation, and knowing where these pipes have been buried, it should then be possible to determine more accurately the magnetic anomaly due to each segment of pipe.

### 3.9.4 Detection of buried containers

There are many situations where it is imperative that potentially harmful objects, such as bombs, drums of toxic waste or steel underground storage tanks (USTs), be located passively. Drilling holes to locate drums of poisonous waste, or using electromagnetic signals to detect hidden bombs, could have devastating consequences. As these types of object will produce a magnetic anomaly, it is possible to use magnetic methods to locate them without risk of interacting with them directly. The amplitudes of magnetic anomalies detectable for various types of ordnance of different size and depth of burial are illustrated in Figure 3.65, assuming a maximum detectability of 0.1 nT. However, in practice, the smallest anomaly to be discernible above background noise is likely to be around 1 nT. This means that it would technically be possible to detect a 1000 lb bomb buried at a depth of 22 m.

Metal drums also give rise to strong magnetic anomalies and, if dumped together in a random way, will produce large-amplitude but highly variable anomalies that will stand out from background noise. To resolve the number of drums and their possible size, it may be preferable to use a gradiometer survey so that the anomalies can be imaged with greater resolution. The local anomaly amplitudes

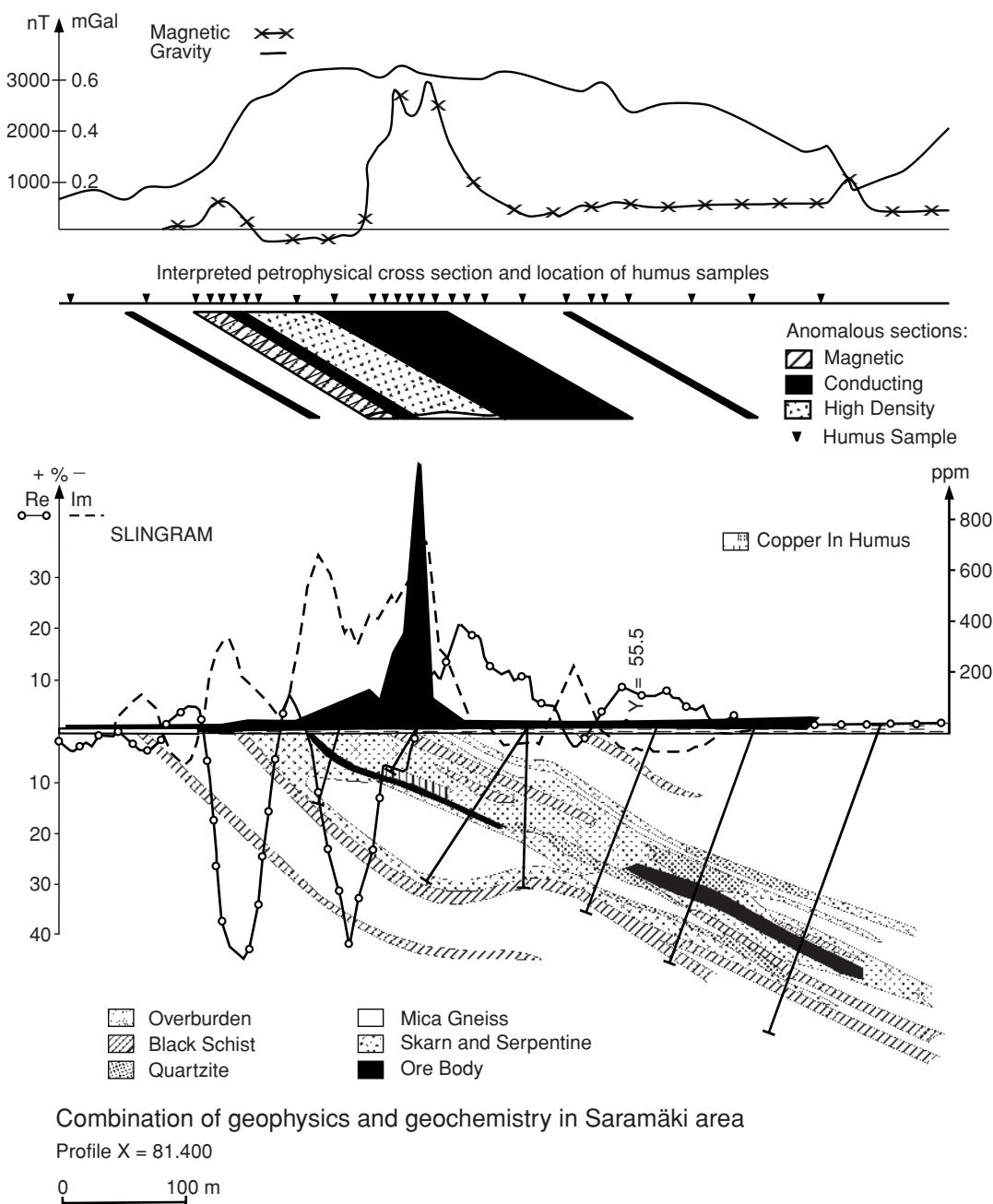


**Figure 3.60** Magnetic, gravity and SLINGRAM electrical data with a geological cross-section for the Saramäki orebody, Finland. From Ketola (1979), by permission.

over a steel drum may be as high as several thousand nanoteslas, and field gradients of several thousand nanoteslas per metre (Leech and Johnson, 1992). The main difficulty with locating illegally buried drums of toxic waste is that they are usually dumped in ground with other rubbish that might mask their anomalies. However, by careful analysis of the anomaly shapes, amplitudes, orientations and overall characteristics, it should be possible to differentiate between various buried objects, if not actually identify them individually. Further examples of this are given in the next section.

### 3.9.5 Landfill investigations

Landfills are likely to contain large amounts of ferro-metallic debris deposited at irregular angles. Consequently, a magnetic anomaly map produced over a former landfill will show a considerable amount of high-frequency noise from near-surface ferro-metallic objects. There is perhaps a tendency to think that such noise is likely to dominate the magnetic anomaly map to produce a highly chaotic and largely unhelpful anomaly map. To achieve useful results less affected by the near-surface metal detritus, the sensor should be

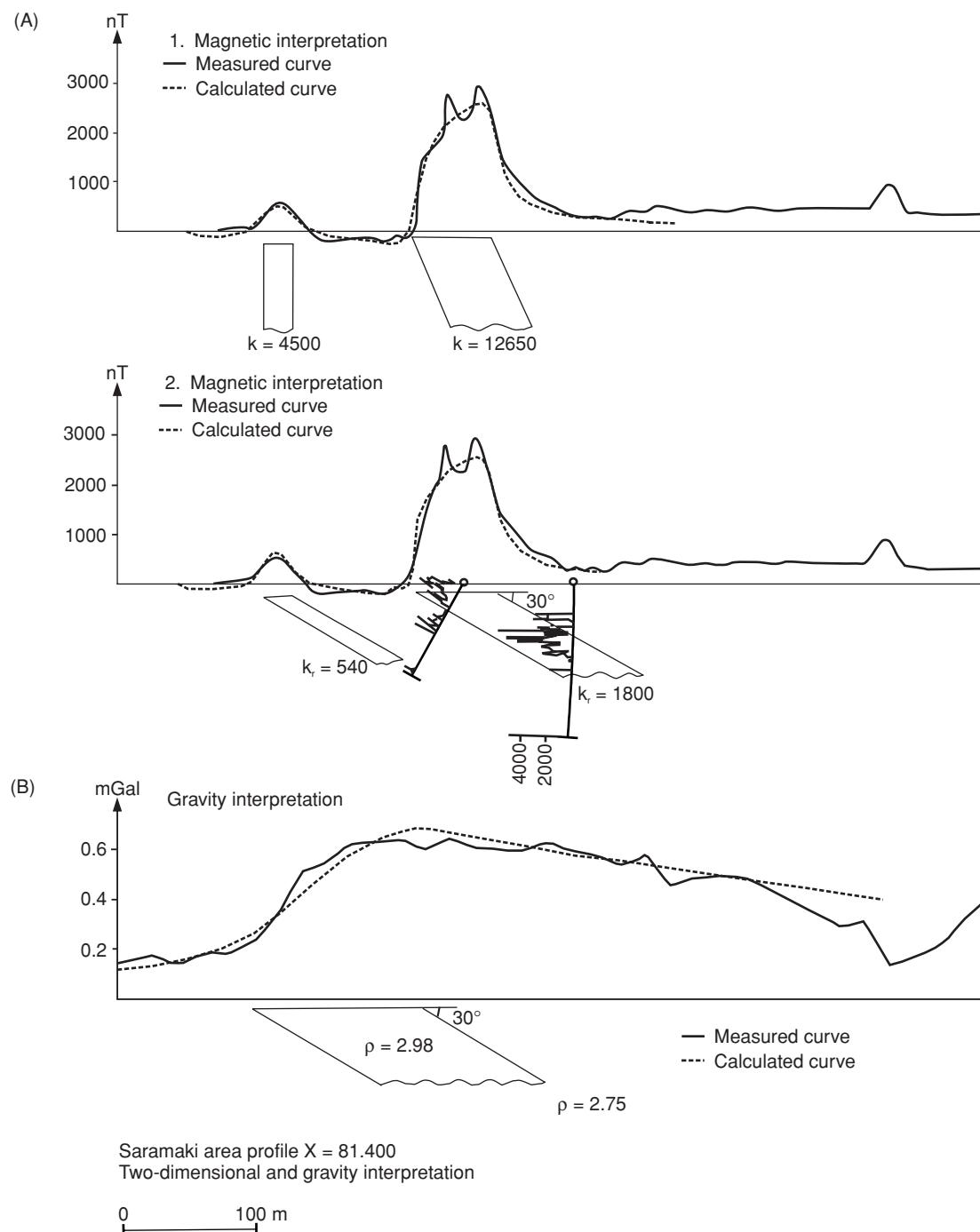


**Figure 3.61** Modelling of the Saramäki orebody. (A) Induced magnetisation only; (B) induced and remanent magnetisation modelled and compared with a gravity model. From Ketola (1979), by permission.

raised above the surface. Anomalies associated with deeper targets will become more apparent and less noisy, making the results more useful.

One aspect of old closed landfills is that their previous tipping history may have been lost, or was never recorded. It might be useful to be able to obtain some idea as to whether a site has had different tipping sequences, such as periods of waste of a similar character being tipped and then having another type of waste with

different magnetic properties. Consequently, the magnetic method lends itself to the rapid surveying of closed landfills in order to assess previous tipping histories and the zonation of waste types within a site.

Magnetic anomalies over landfills containing a range of wastes demonstrate that zones within a landfill will generate broader anomalies than just a mass of high-frequency noise. As landfills also tend to contain conductive leachate, the use of ground conductivity

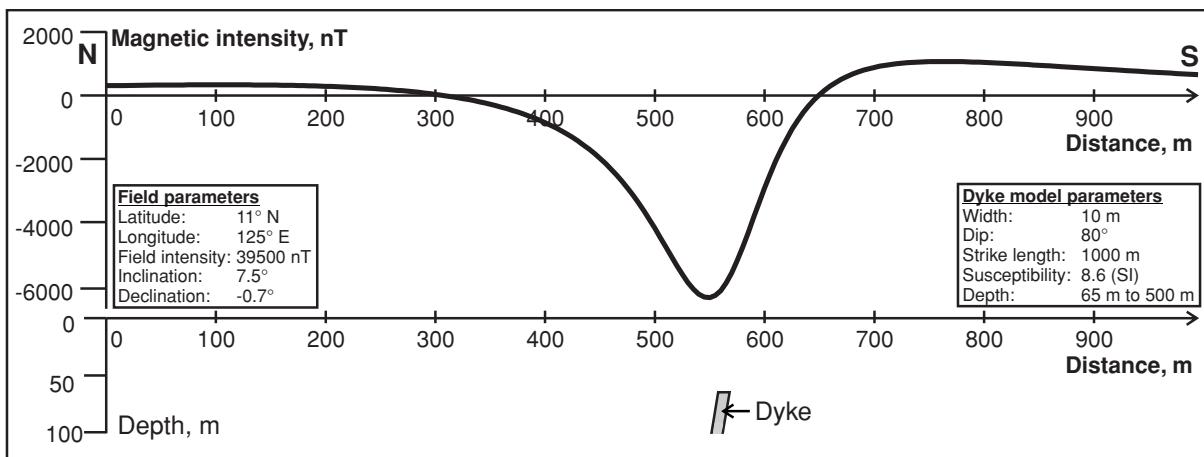


**Figure 3.62** Example of a magnetic profile across iron ore deposits in the Philippines to illustrate the profile shape at a low geomagnetic latitude.

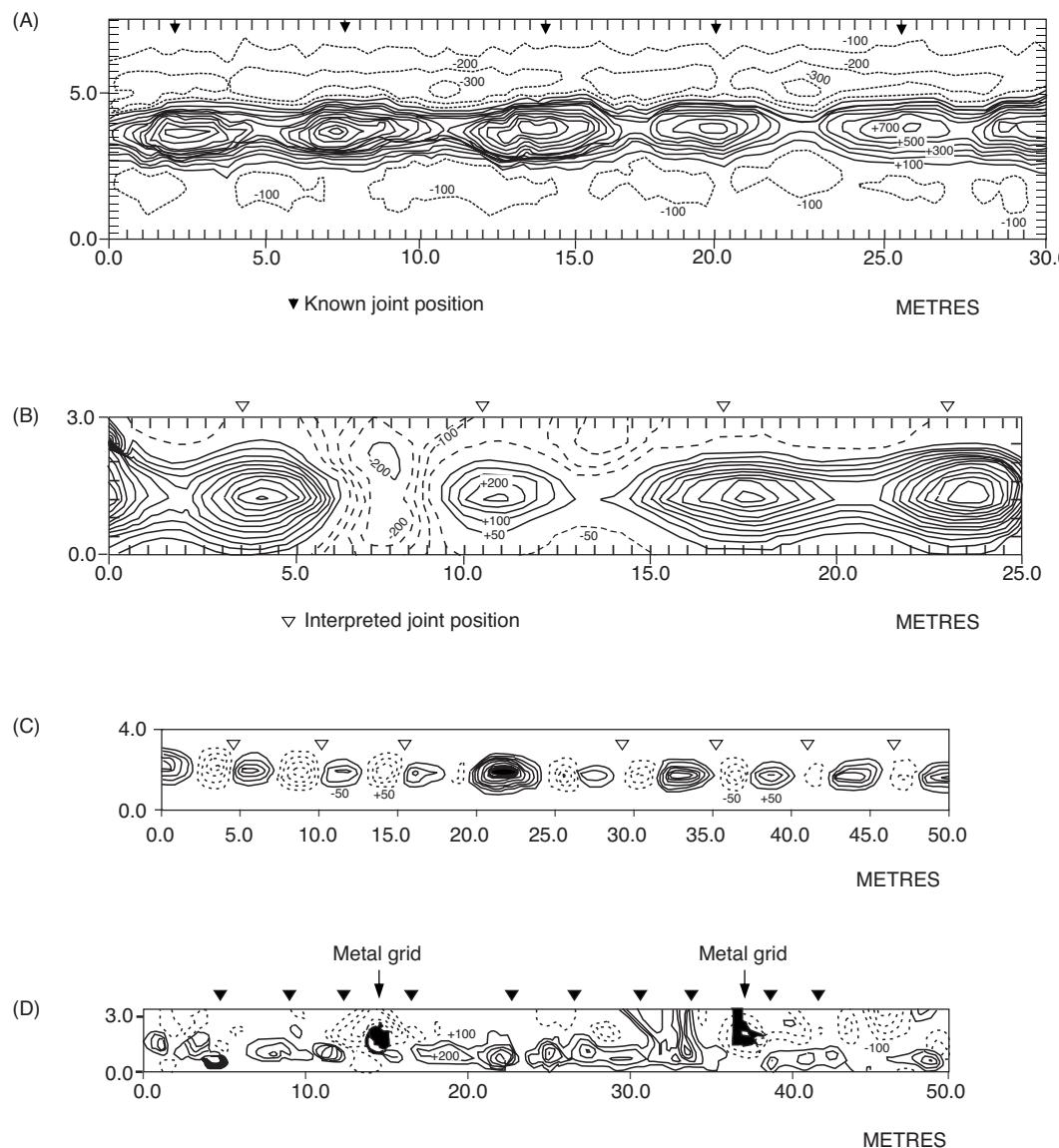


**Figure 3.63** Magnetic gradiometer anomalies over buried pipelines: (A) Ductile iron pipe, diameter 0.5 m buried at 0.5 m depth, E-W trend of pipe; contour interval 200 nT/m. (B) Cast iron pipe, N-S trend of pipe; contour interval 50 nT/m. (C) 76 mm diameter cast iron gas pipe trending N-S. (D) 0.15 m diameter pipe, buried about 1.5 m down, in an urban environment with extraneous magnetic anomalies caused by adjacent metal grids. From Sowerbutts (1988), by permission.

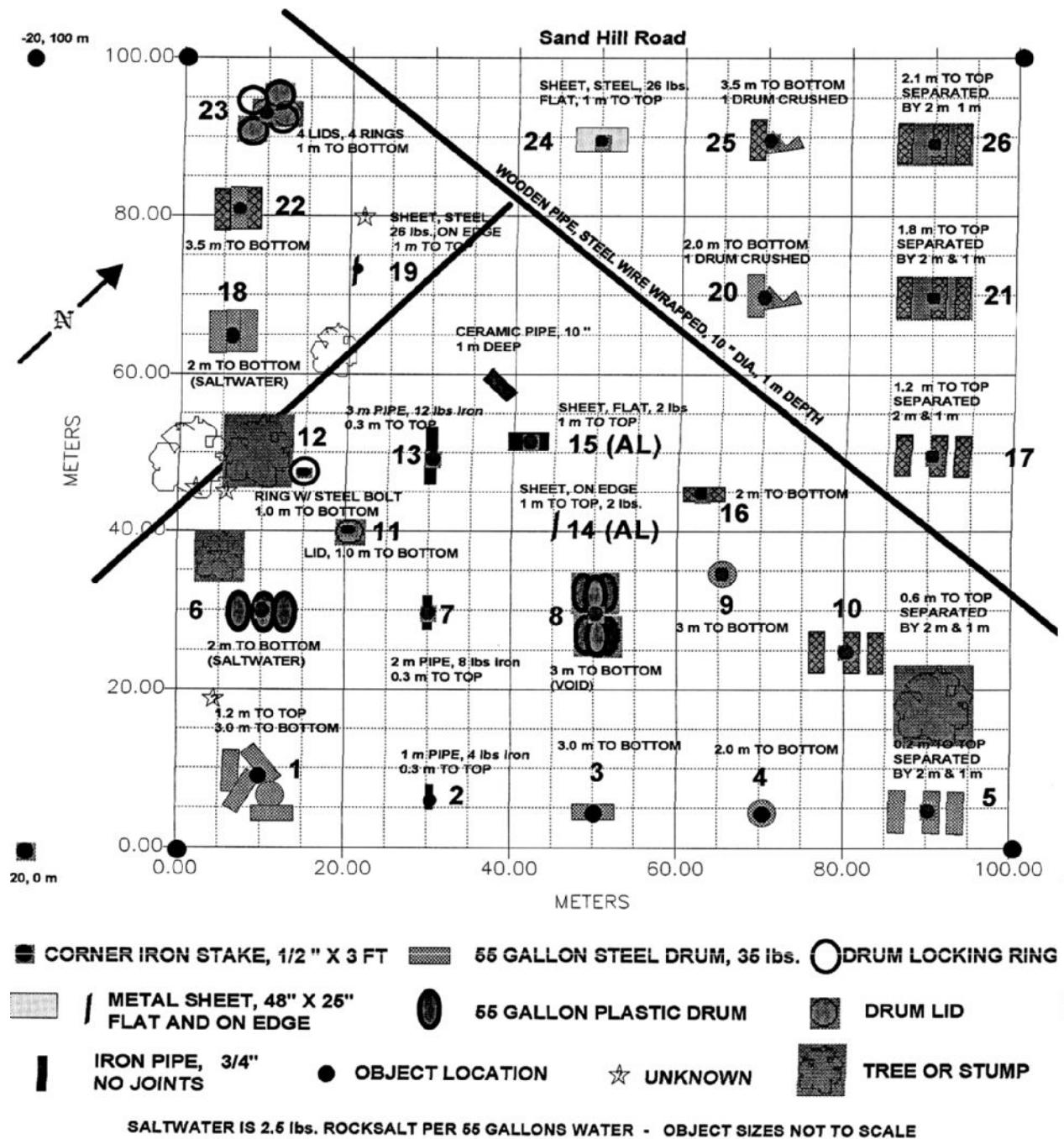


**Figure 3.64** (A) Map of the Stanford University, US, environmental test site showing the details of the various buried targets. (B) Magnetic anomaly map produced using a caesium magnetometer sampling at 10 readings per metre along survey lines at 2 m spacings. (C) Isometric projection of the data in (B). Courtesy of Geometrics Inc. [C]

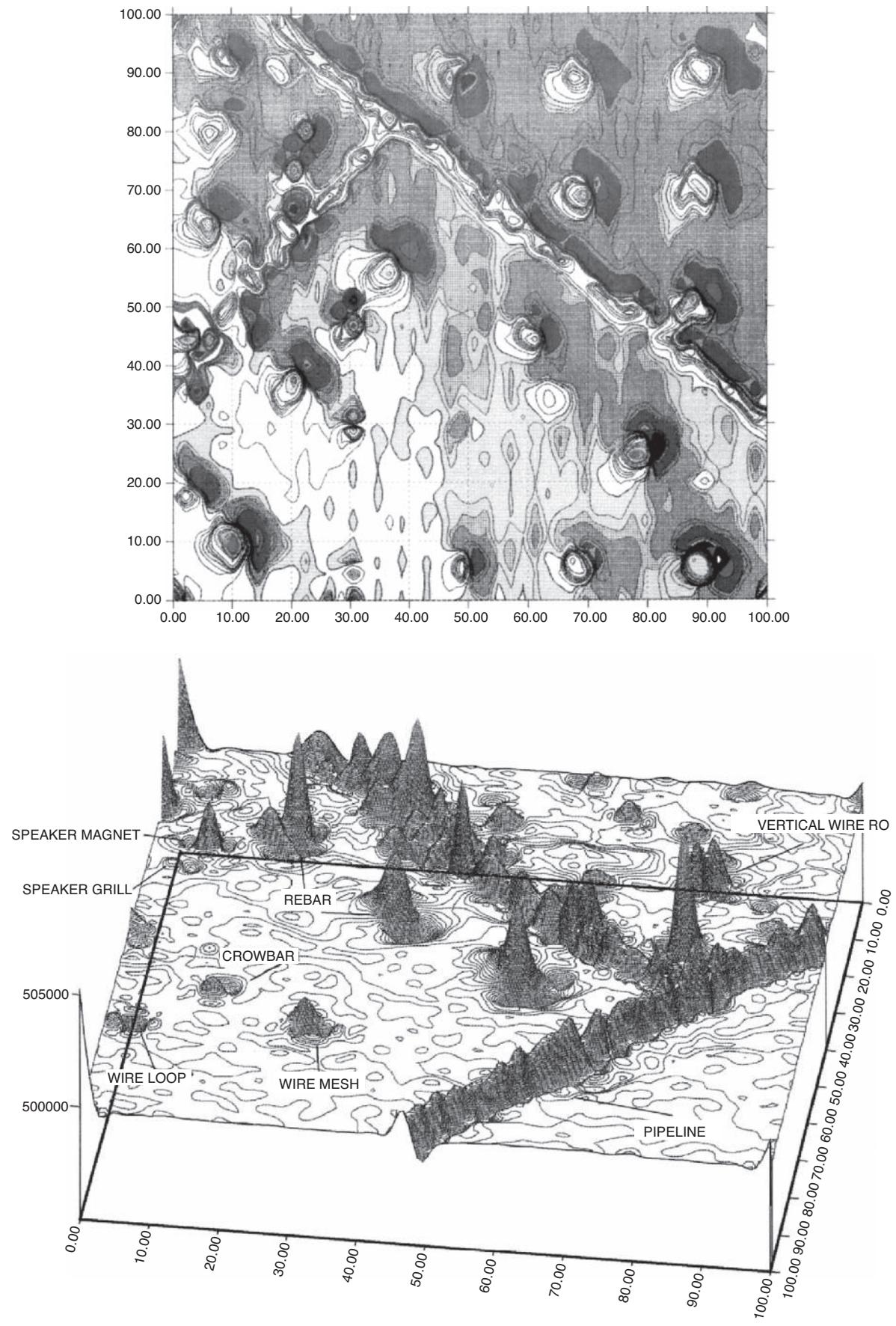
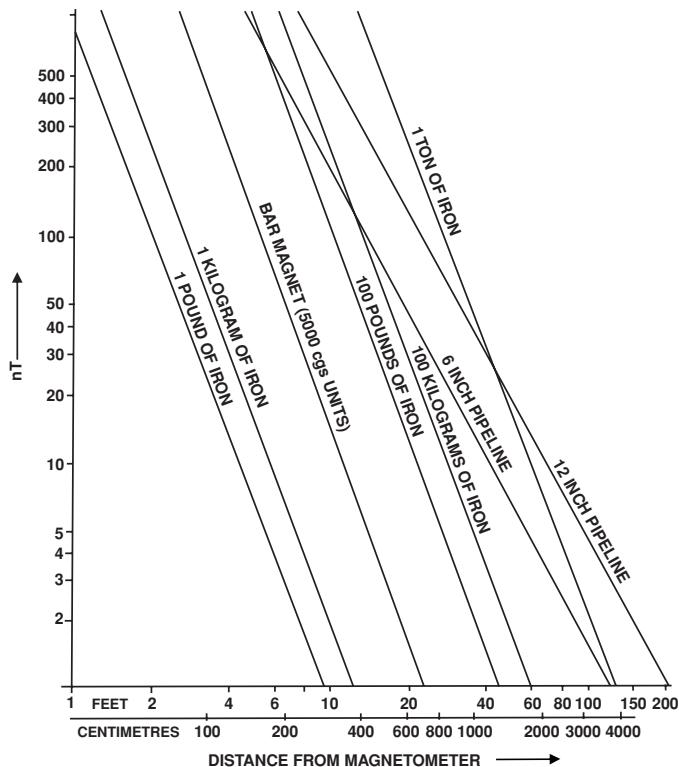


Figure 3.64 (Continued)



**Figure 3.65** Minimum detectable anomaly amplitudes for different types of ordnance at various depths of burial. Note that the distances cited are those between the sensor and the target, not the depth below ground of the target. From Breiner (1981), by permission.

mapping (Chapter 11) is also useful to help to define boundaries and internal zones. Cross-sections through landfills can be helpfully achieved using electrical resistivity tomography (Chapter 7).

An example is given of an integrated geophysical investigation undertaken over a closed landfill site in the UK. The three geophysical methods mentioned above were used and each demonstrated different aspects of the former landfill. Whereas the brief from the client was to identify the landfill boundary, it proved possible to not only do this but also to differentiate different zones within the landfill on the basis of the electrical and magnetic anomalies measured. The total magnetic field intensity anomaly map of part of the site is shown in Figure 3.66A. The interpreted outline of the landfill is shown along with the internal division boundaries identified from the geophysical survey. It was thought that different types of waste materials had been dumped through the active period of operation of the site, giving rise to distinct geophysical zonation. The magnetic anomalies indicated areas with large numbers of buried steel drums. The ground conductivity anomaly map for the same area is shown in Figure 3.66B, and one resistivity cross-section is illustrated in Figure 3.66C. Differences in the apparent conductivity anomaly maps using a Geonics EM31 ground conductivity meter indicated possible lateral migration of leachate southwards at shallow depths. The areas of buried drums also coincide with areas with elevated apparent conductivities. The corresponding zones are also clearly seen in the resistivity section.

### 3.9.6 Acid tar lagoon survey

A byproduct of the refining of petroleum products in the 1970s and 1980s from Venezuelan crude oil was an acid tar that was often disposed of in former quarries. One such case (Reynolds, 2002) is that of Llywneinion in northeast Wales, UK, a site that has an industrial legacy dating back over 250 years. Coal mining and iron smelting are believed to have taken place from c. 1750 to 1860, followed by quarrying associated with brick making from c. 1820 to 1964. The site has also been mined for coal, and three uncapped mineshafts were thought to exist beneath the quarry. During the late 1950s to 1960s the quarried clay resource became depleted and tipping of industrial waste products commenced, comprising acid sludges and drums of unknown chemicals. Up to 1972, c. 94000 tonnes of sulphuric acid mixed with tar-like hydrocarbons, and 7500 tonnes of spent bentonite containing absorbed heavy oil were deposited, together with perhaps 1000 55-gallon metal drums of uncertain contents. The acid tar waste originated predominantly from benzole refining at an oil refinery at Ellesmere Port, 32 km to the north. In 1980 the local government authority purchased the site for £1 from the estate of the family that had operated the quarry, due to concerns over the state of the site. Since then, simple clean-up work and security fencing have been undertaken and various remediation options considered, but as yet the site remains untreated. One estimated cost of the remediation of the site is £100 million.

In August 1980, the 1.3 ha site comprised a 75-mm layer of volatile hydrocarbon floating on about 0.5 m of water (with a pH of <2.5) over the tar waste, which was thought to be up to 10 m thick. One of the steel drums may have contained a sodium product so that, when the drum corroded, water contacted the sodium and ignited. The ensuing fire, the largest ever seen in north Wales, burnt off the volatile hydrocarbon (solving one problem!), the heat evaporated the acid water and ignited the acid tar beneath. The acrid smoke plume could be seen in Ellesmere Port. The entire neighbouring town had to be evacuated until the fire was extinguished. Since then, there has generally been about 0.5 m of acid water covering the tar waste. Given the uncertainty as to what is in the old steel drums, there is a reluctance to probe intrusively into the lagoon to determine the nature of the infill material. Consequently a comprehensive geophysical investigation was designed and implemented. In essence it comprised a magnetic gradiometry survey to locate and map the steel drums, and a seismic survey to determine the thickness and degree of solidification of the tar. Health and safety considerations meant that over-water access had to be achieved remotely.

A Geometrics MagCat (Figure 3.67) was set up with the magnetic gradiometer sensors (Geometrics G858) on the front of the platform, with the measuring instrument housed in a waterproof plastic container at the rear. The measured data were telemetered to the shore via a radio modem. Accurate positioning was achieved by placing an active prism at the rear of the MagCat, which was tracked continuously from the shore by a robotic geodimeter. To mobilise and control the MagCat over the lagoon, the platform was attached front and rear to polyethylene ropes (acid resistant) connected to shore-based winches. The MagCat could be hauled along each traverse by controlling the speed of the manual winches, providing a

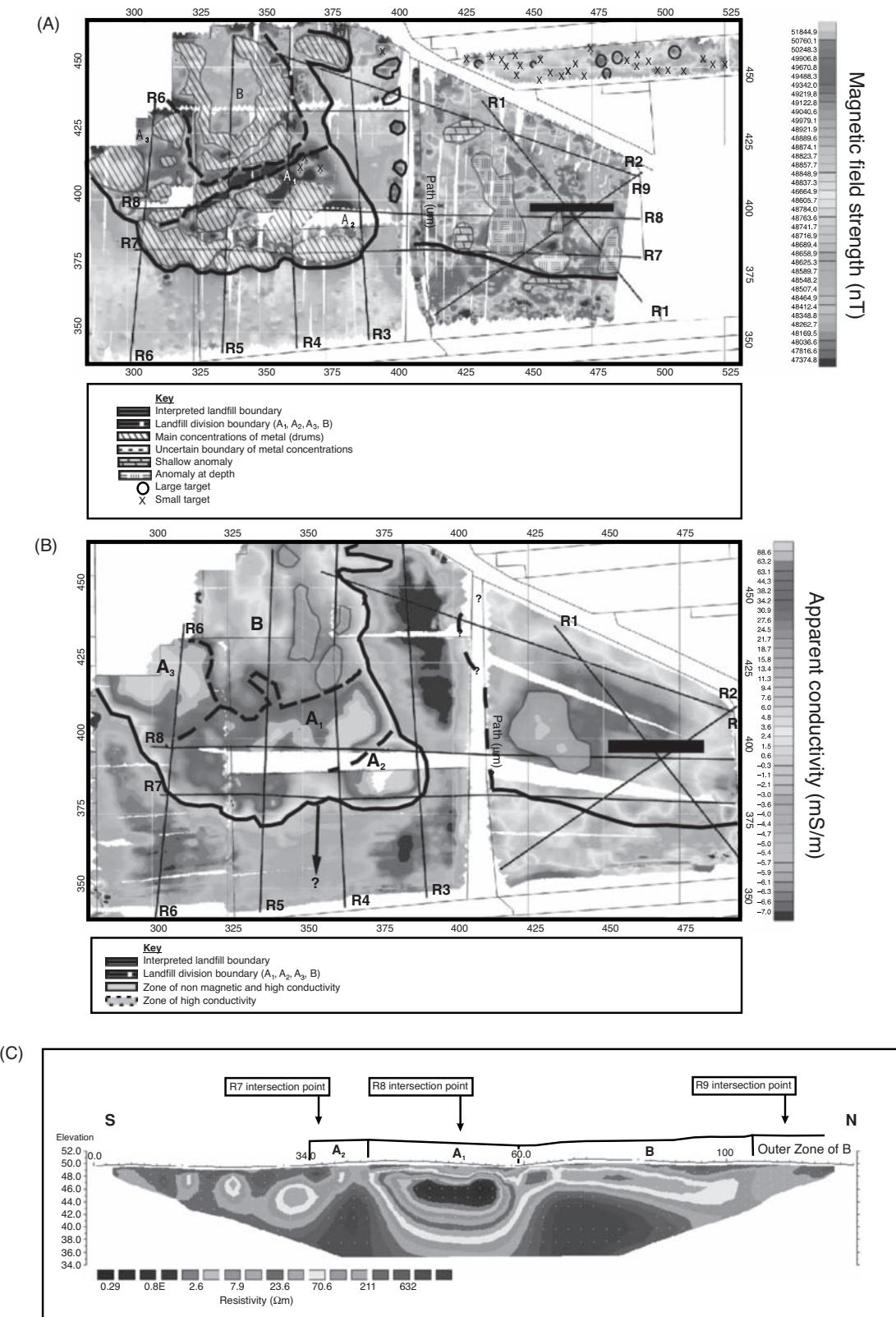


**Figure 3.66** (A) Magnetic anomaly map over a closed former landfill with (B) the corresponding apparent conductivity map from a Geonics EM31 (vertical dipole), and (C) an electrical resistivity section along the profile indicated in A and B. The interpreted outer boundary of the landfill is shown along with internal divisions within the landfill based on the geophysical anomaly patterns from the three different techniques. [C]

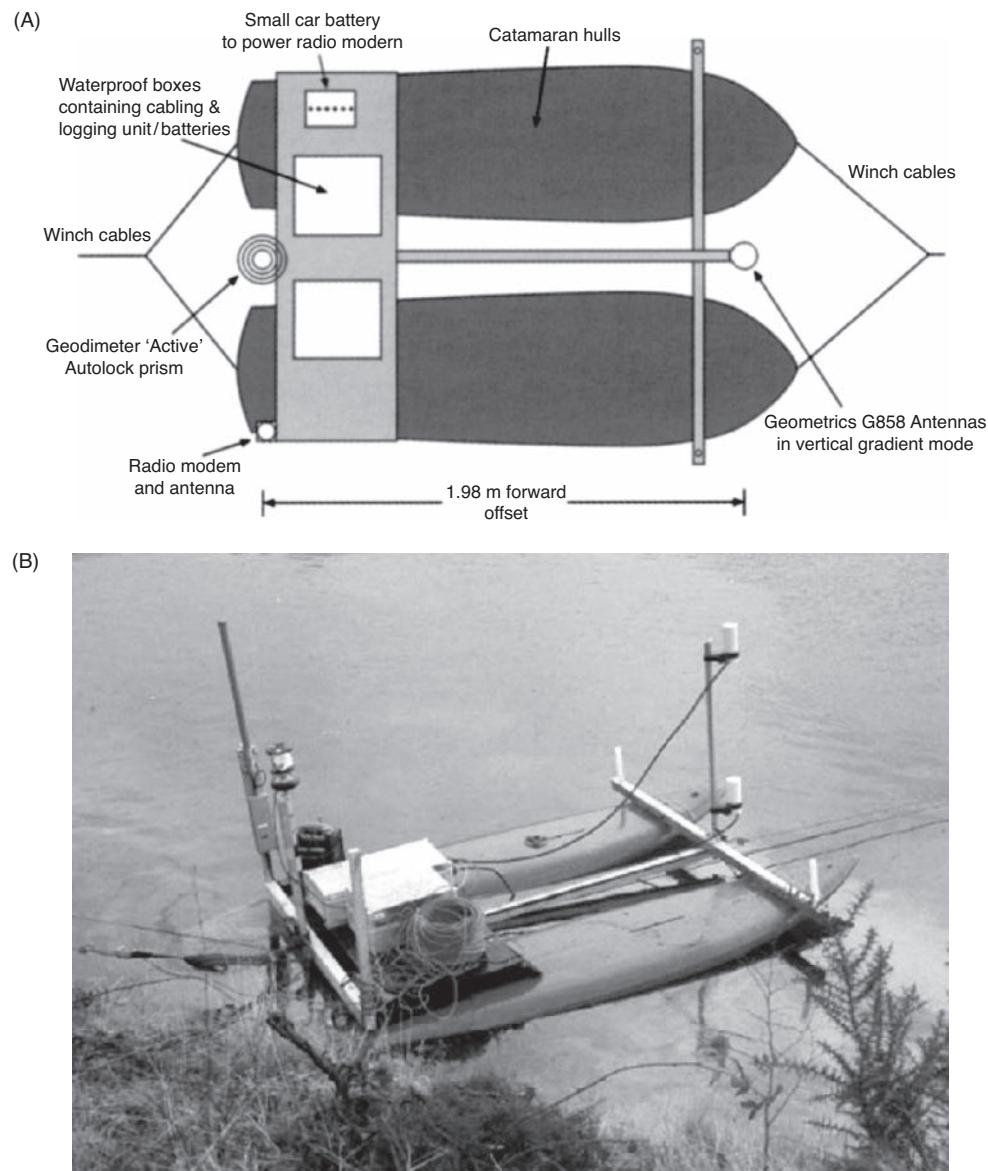


**Figure 3.67** Details of the Geometrics MagCat platform: (a) instrument deployment offset diagram, and (b) the equipment in use. A vertical gradiometer (two white sensors) is mounted on the dual surf boards with an active prism at the rear (for position fixing) and telemetry aerial (for remote communication with the shore station). From Reynolds (2002), by permission. [C]

spatial sampling interval of  $<0.2$  m along each profile. The whole winch assemblies were moved along each opposite shore to provide a line interval of 2.5 m.

Measurements of total magnetic field intensity at each sensor were captured (e.g. Figure 3.68A) and the resulting vertical gradient obtained. Maps of the magnetic parameters provided a spatial perspective across the lagoon from which it was possible to identify the locations of drum graves and, in many cases, individual drums, as well as, importantly, areas without any drums present. Each magnetic profile was modelled using commercially available software in order to locate the position of the magnetic targets along each transect and its depth below the lagoon surface. As well as a visual inspection of each magnetic anomaly identified, commercially available software for the identification of UnExploded Ordnance

(UXO) was also used to help to define the location of the magnetic targets (see next section). The resulting output was a map (Figure 3.68B) showing the interpreted locations of the drums and exclusion zones around them in which there was a risk of encountering a drum (or drums) in case any subsequent intrusive work was to be undertaken. It was also noted during this project that the magnetic signature associated with the drums was also strongly influenced by the amount of degradation of the metal through corrosion, with the weakest signatures being associated with the most corroded drums. This aspect and that of the orientation of each drum with respect to the Earth's magnetic field will result in a variety of different anomaly characteristics. The implications of these factors has been considered by Emerson *et al.* (1992) and Furness (2002, 2007).

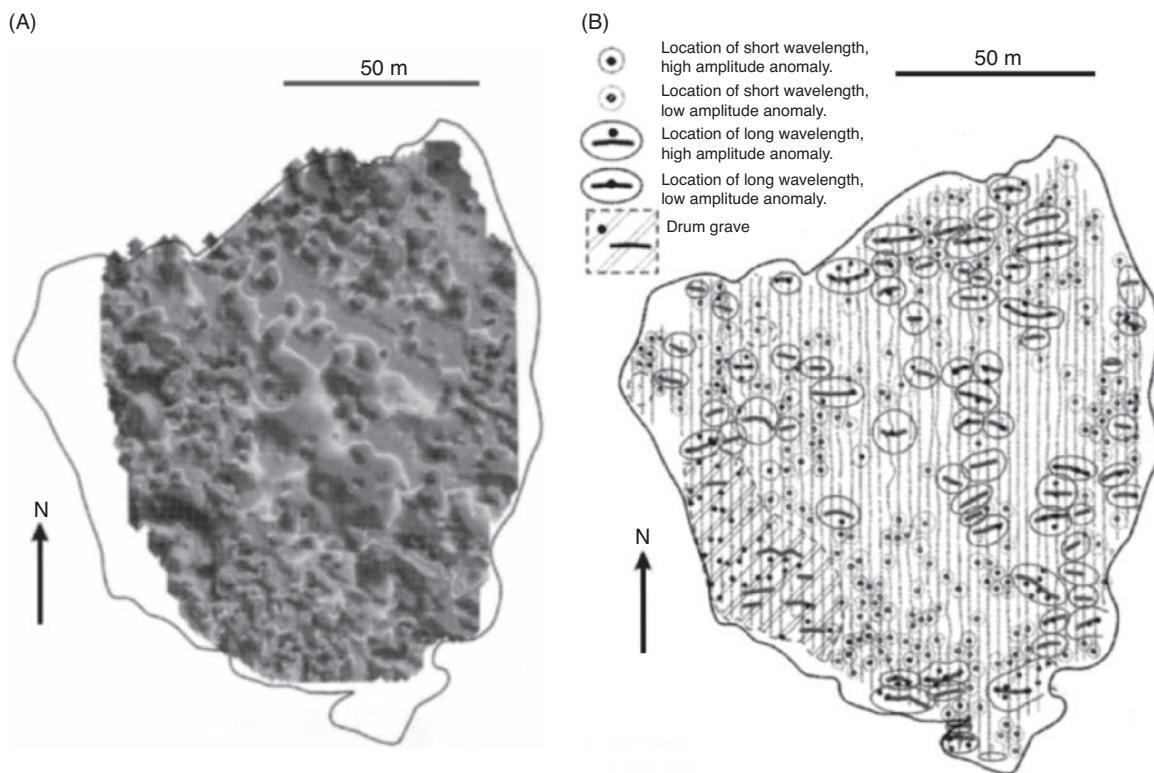


**Figure 3.68** (A) Magnetic anomaly map (bottom sensor) from the magnetic gradiometer and (B) the corresponding map of interpreted zones of influence of steel drums and drum graves. From Reynolds (2002), by permission. [C]

In addition to the magnetic survey, a seismic refraction investigation was also undertaken (see Chapter 5, Section 5.5.5). Where both magnetometry and seismic refraction data were obtained over the same transects, it was possible to integrate the analysis. From this it was possible to identify the locations of the drums and to see where within the tar they may be located. One such integrated profile is shown in Figure 3.69. It was clear that the drums tended to be located in the tar that had the lightest viscosity (as evidenced by the lowest seismic P-wave velocity values).

### 3.9.7 UneXploded Ordnance (UXO)

Magnetic methods are among the most commonly used to detect UneXploded Ordnance (UXO), both in over-ground and over-water surveys, down boreholes and in magnetometer Cone Penetration Tests. The technique is based upon the assumption that the ferrous metal components of the ordnance produce a magnetic anomaly of sufficient amplitude to be detected by a remote sensor. There is also an issue in being able to discriminate ordnance-related targets from other near-surface metallic clutter and geological noise, both of which are likely to yield false alarms and unnecessary clearance efforts. The selection of non-ordnance-related targets gives rise to excessive false alarm rates (FARs), and therefore a great deal of effort is being taken to develop techniques to reduce these. Stanley and Clark (2003) have provided an example of the detection depths likely to be achieved for a remote magnetic sensor for a range of UXO types (Figure 3.70). They have also indicated a nominal assurance probability, given a known survey sampling specification and known magnetic noise from geological, cultural or electromagnetic sources. The 100% confidence limit shown in Figure 3.70 indicates the level at which the risk of an item remaining undetected within the depth indicated is insurable, nominally less than 1 in 100000. It is also clear from this chart that to achieve a high level of confidence, detection of ordnance equivalent to a high-explosive (HE) 105 mm shell or smaller, the distance between the sensor and the ordnance must be less than 3.5 m, with the maximum distance decreasing for smaller-sized items. It has been observed that intact ordnance tend to become demagnetised after impact, whereas shrapnel tends to retain a significant component of remanent magnetisation. Consequently, if a magnetic anomaly indicates a direction of magnetisation with a large deviation from the direction of the Earth's magnetic field, then it might suggest the greater probability of the target being shrapnel than intact ordnance. In order to determine this, it is necessary to undertake detailed analysis of the magnetic anomaly, and this is a non-trivial task.

Traditionally, detection of a ferrous metal target in mid-geomagnetic latitudes is based upon identifying a magnetic anomaly couplet, with a low to the north and a high to the south (in the northern hemisphere), as typified in the profile shown in Figure 3.69, for example. Commercial software is available by which such anomalies can be identified and is commonly used for UXO detection. An example of the analytical signal and total magnetic field extracted from a larger magnetic survey is shown in Figure 3.71. One anomaly identified (circled) in Figure 3.71B has a crosshair at what the

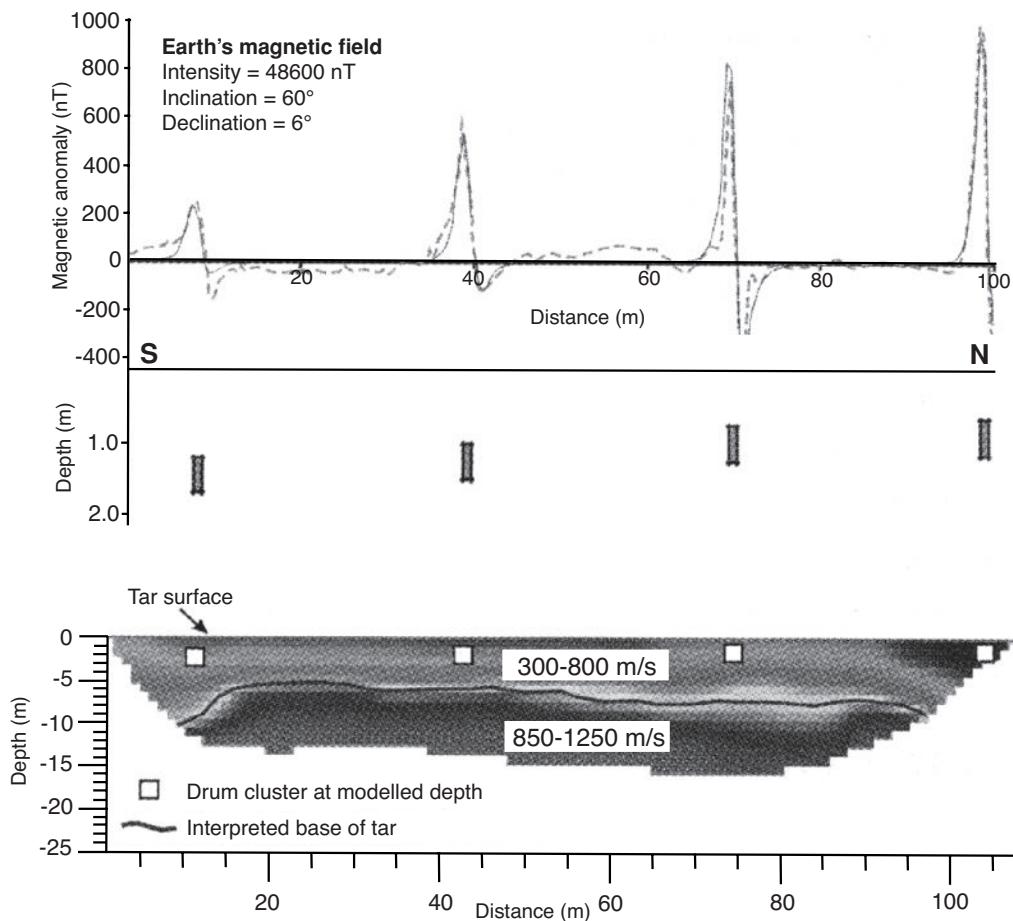


**Figure 3.69** (Top) Magnetic profile and model across the acid tar lagoon with modelled responses, and (bottom) a seismic velocity section with the locations of the four magnetic targets indicated. From Reynolds (2002), by permission. [C]

software has determined to be the  $x,y$  location above the target. Other anomalies are present on the magnetic field data but have not been selected by the software. UXO-automated picking software may not be as reliable as manual selection by an experienced operator. In one survey over a former Ministry of Defence munitions site, the military UXO system detected 85% of targets identified by a manual operator. It also failed to deselect targets associated with known non-ordnance features such as a large manhole cover! It is essential that the known locations of such features are identified so that corresponding magnetic anomalies can be deselected. It is also helpful to use the analytical signal to help clarify features that may represent anomalies associated with targets of interest. To the eye, there is less clutter on the analytical signal data shown in Figure 3.71A than on the total field magnetic data in Figure 3.71B. Specific correlations between the anomalies picked by the automated UXO-detection software can be seen in the screen capture shown in Figure 3.72. The target location is indicated by the position of the crosshair and the target identification number, target depth and target weight are displayed on the map and also indicated in tabular form and as separate graphical displays. The target weight is an effective weight based upon an assumption of the magnetic susceptibility of the metal in the targets. More sophisticated database

correlations can give a more direct indication as to the type of munitions that best fits the parameters determined from the magnetic anomaly. On sites used as artillery or bombing ranges, the types of munitions used should be well documented and thus the degree of uncertainty can be constrained. However, in areas of former military conflict, this information may not be so easily obtained. It should also be stressed that magnetic methods are not particularly useful in detecting anti-personnel mines that have been specifically designed to have minimal metal content to avoid detection.

Another aspect of importance is being able to identify whether a magnetic anomaly is being caused by a single piece of ordnance or a cluster. While on small-scale sites the identification of individual items of UXO is important, on much larger sites, *wide-area assessments* to map clusters rather than individual items may be sufficient (Gamey, 2008). The ratio of the target separation to sensor height (separation/height ratio – SHR) determines the amount of response overlap between targets. If the target separation is more than 1.5 times the sensor height (i.e.  $SHR > 1.5$ ), then the overlap is sufficiently small to indicate that the targets must be treated as discrete objects. If the SHR is between 0.5 and 1.5 there is some overlap, but it is insufficient to increase significantly the response amplitudes. Individual peaks may still be recognisable, but it is difficult to

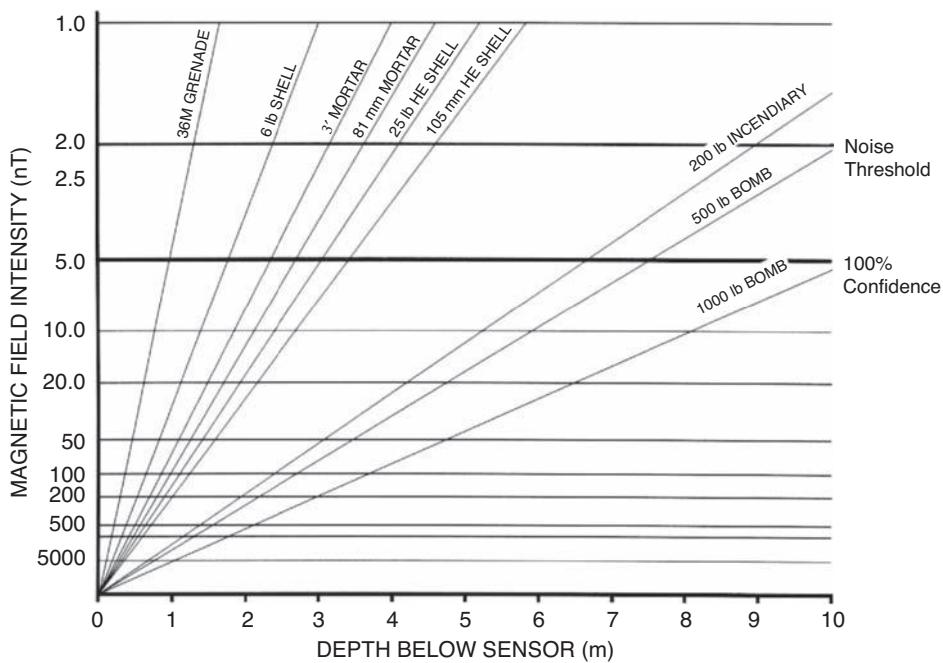


**Figure 3.70** Typical magnetic intensity amplitudes plotted as a function of depth below a magnetic sensor for a range of UXO types. From Stanley and Clark (2003), by permission.

determine the magnetic parameters of any constituent objects. When the magnetic anomalies of objects overlap significantly, then the usual UXO performance metrics start to fail. It is also important to try to resolve individual targets but when their respective magnetic anomalies overlap, this can mask diagnostic anomaly shapes. To differentiate between targets, high-pass, two-dimensional filtering can be undertaken (René *et al.*, 2008). This filtering process can

provide more accurate estimates of magnetic dipole parameters, and help to improve detection, discrimination and characterisation of identified magnetic anomalies and reduce false alarms.

Modelling of magnetic data to identify UXOs is complicated by the fact that the normal inversion assumes that the target is a spheroid of arbitrary size, shape, orientation and location. There are an infinite number of spheroids that can generate exactly the same

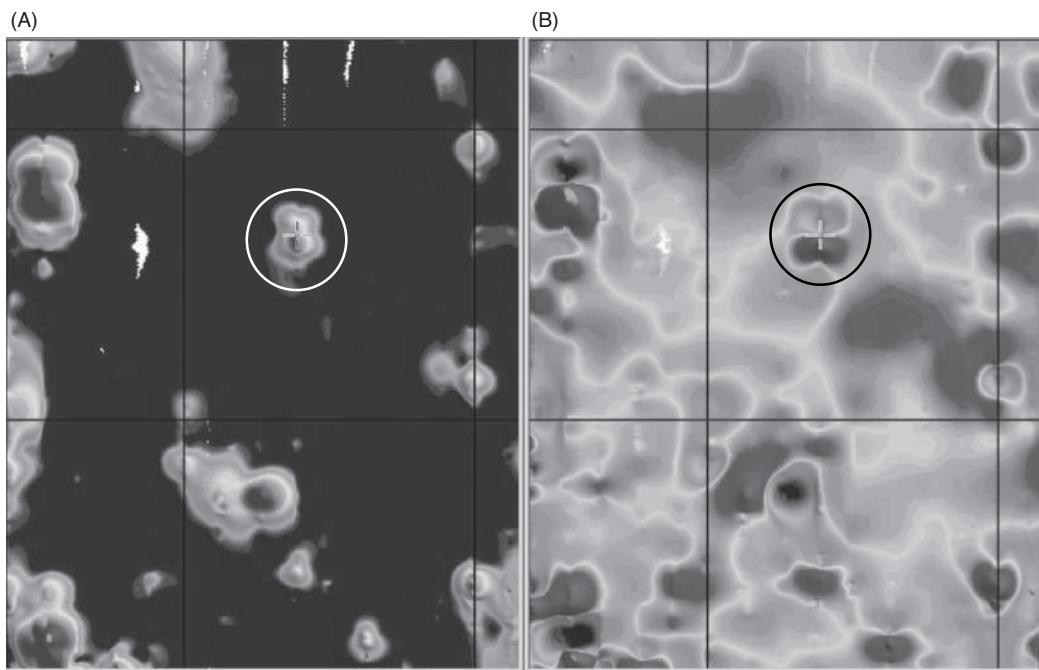


**Figure 3.71** (A) Analytical signal and (B) total magnetic field showing an anomaly (circled) picked by the automatic anomaly identification software (marked by the crosshair). [C]

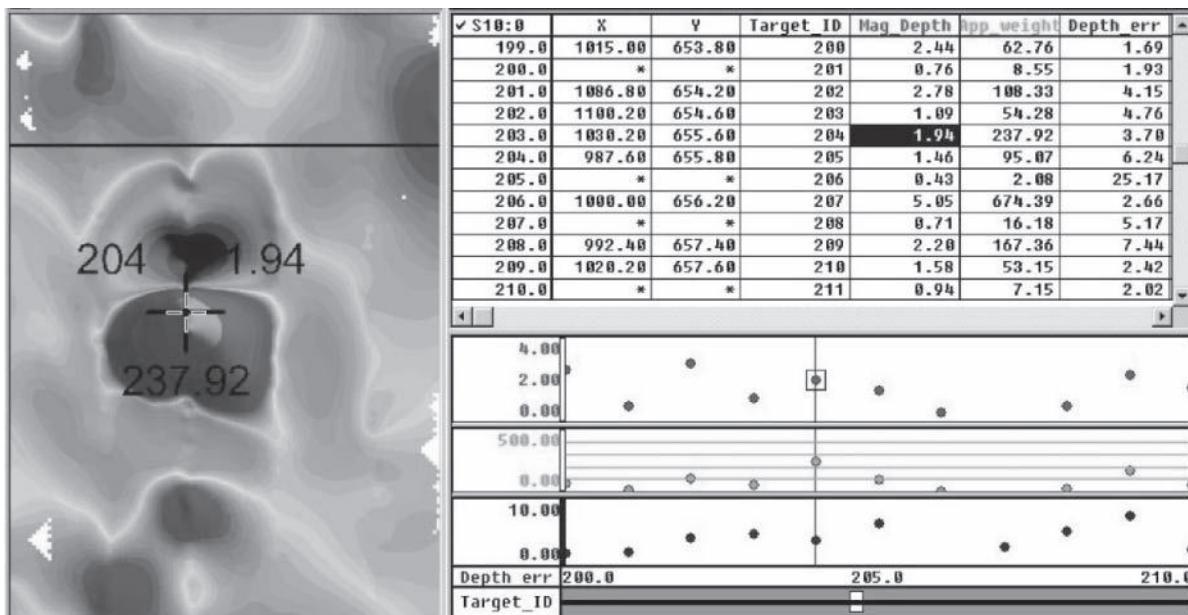


**Figure 3.72** Extract of screen view using automated anomaly-picking software showing (A) the selected anomaly with the target identification number (204), target depth (1.94 m), and effective target weight (237.92 kg), with (B) a view of the associated database. [C]

magnetic dipole moment to satisfy the inversion of the observed magnetic field. If electromagnetic induction (EMI) techniques are used, such as with a Geonics EM63 TEM instrument, the resulting data can be inverted to help constrain the orientation of the target, which can then be used to refine the analysis of the magnetic data (Pasion *et al.*, 2008). The cooperative analysis using both TEM and magnetic inversion can help to reduce the number of false alarms by being able to identify more clearly the targets of interest

from clutter. This process has been taken further by developing a joint EMI-magnetometer instrument using a Geonics EM73 and Geometrics G823A caesium vapour magnetometer in one handheld UXO-detection device (Wright *et al.*, 2008).

To cover large areas of ground most efficiently it is possible to deploy multisensor magnetic gradiometers from a small helicopter that is flown with a minimal ground clearance, typically 0.5–1.5 m (Figure 3.73). The system illustrated is the Batelle VG-16,



**Figure 3.73** Helicopter-mounted VG-16 high-resolution magnetic gradient system. Courtesy of Batelle-Oak Ridge Operations, USA, by permission. [C]

which has been designed to produce better production rates on a wider swath on wide-area assessment surveys, whereas the VG-22 (see Figure 10.22B) was designed for high-resolution detection of small ordnance under good field conditions (Doll *et al.*, 2008a,b). Depending upon the sensors deployed and their geometry relative to the aircraft being used, it may be necessary to compensate for the effects of the aircraft's rotor blades as they pass across the sensor array (Billings and Wright, 2009) to improve data quality. To demonstrate the effectiveness of a low-altitude helicopter multi-sensor magnetic system, comparison surveys using a Hammerhead array, where the forward sensors are mounted on a rigid boom shaped like a T, and a TEM system (see also Figure 10.22A), took place over a test site at the Badlands Bombing Range, South Dakota, USA, where different types of munitions were buried along eight southwest to northeast trending rows (Figure 3.74; Beard *et al.*, 2008). The measured results for the magnetic and TEM trial surveys are shown in Figure 3.75A and B, respectively. Both systems were able to detect the larger ordnance (bombs and most artillery rounds), but the Hammerhead system failed to detect many of the medium ordnance items, such as mortar rounds, that the TEM was able to detect. Some non-ordnance items, such as iron pipes, nails and rebar rods, produced large magnetic responses but small or no TEM responses. The average flying height for both surveys was about 1 m above ground level. The Hammerhead system was an early boom-mounted system and its sensitivity has been surpassed by later total field and vertical gradiometer systems. A comparison of the results using the VG-22 magnetic system and a TEM-8 helicopter-mounted EM system is also illustrated in Figure 11.79 and discussed in Chapter 11, Section 11.3.3.6.

Airborne magnetic data can in some circumstances compare favourably with data acquired using ground-based systems; the

same cannot be said of airborne EM. The decay of the EM signal with altitude is too great for low-altitude airborne EM data to compete successfully with ground-based EM systems, although significant development is ongoing in both airborne EM and magnetic UXO-detection technologies.

In ground-based surveys, it is strongly recommended that the background geophysical response of a site is determined as the first stage in a UXO-detection survey, in order to help refine the investigation technique to ensure that the targets being sought lie within the detection limits of the equipment. Depending upon the ambient noise levels, different survey specifications might be necessary, such as profile line spacing, sensor elevation and along-line sampling interval. It is also essential that the claims made by any Explosive Ordnance Clearance (EOC) contractor as to detectability with their equipment are verified by a third party, as there have been occasions when equipment to be used clearly and demonstrably had insufficient detection range to identify the targets being sought. Had this not been checked, the EOC company might have given a site clearance certificate, when in fact they had not investigated the full depth of interest and a significant risk of UXO remained. Surface-based UXO systems have a limited depth of investigation, and if there is a demonstrable probability of large unexploded bombs (UXB) existing on a site, where the depth of burial may be up to 15 m in unconsolidated sediments, the only way to detect such devices is through borehole- or CPT-delivered magnetic sensors. In these cases a slim-line magnetometer is deployed either at vertical increments as a borehole is constructed, or via a CPT tool pushed into the ground. In both cases, the principle is that the magnetic sensor is looking a short distance ahead of the tool and to a radius around the hole or axis of the CPT profile, typically to around 1–2 m from the hole/CPT probe. Even in these cases, the maximum radius

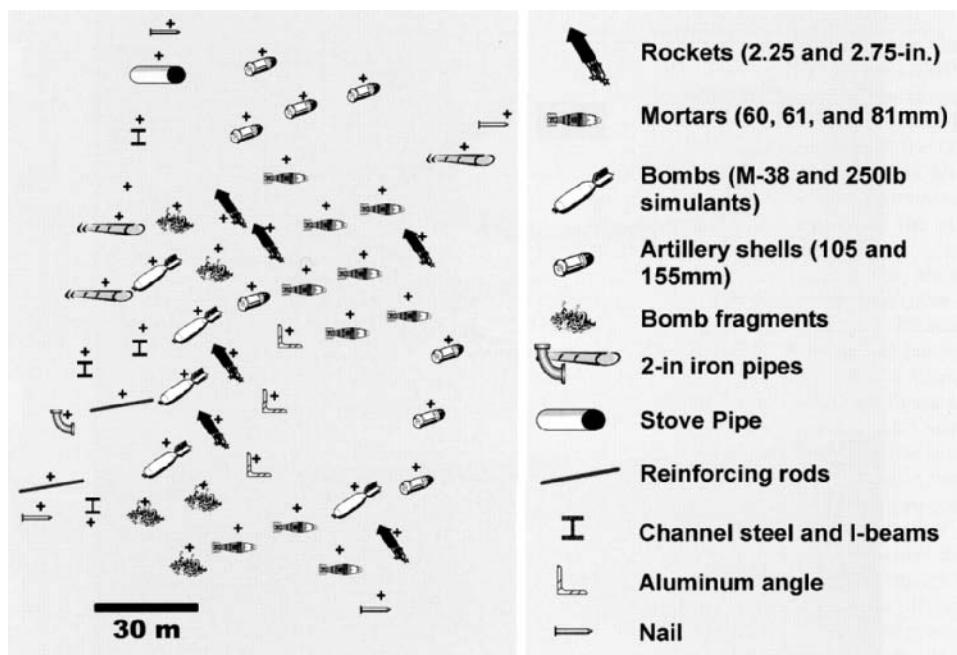
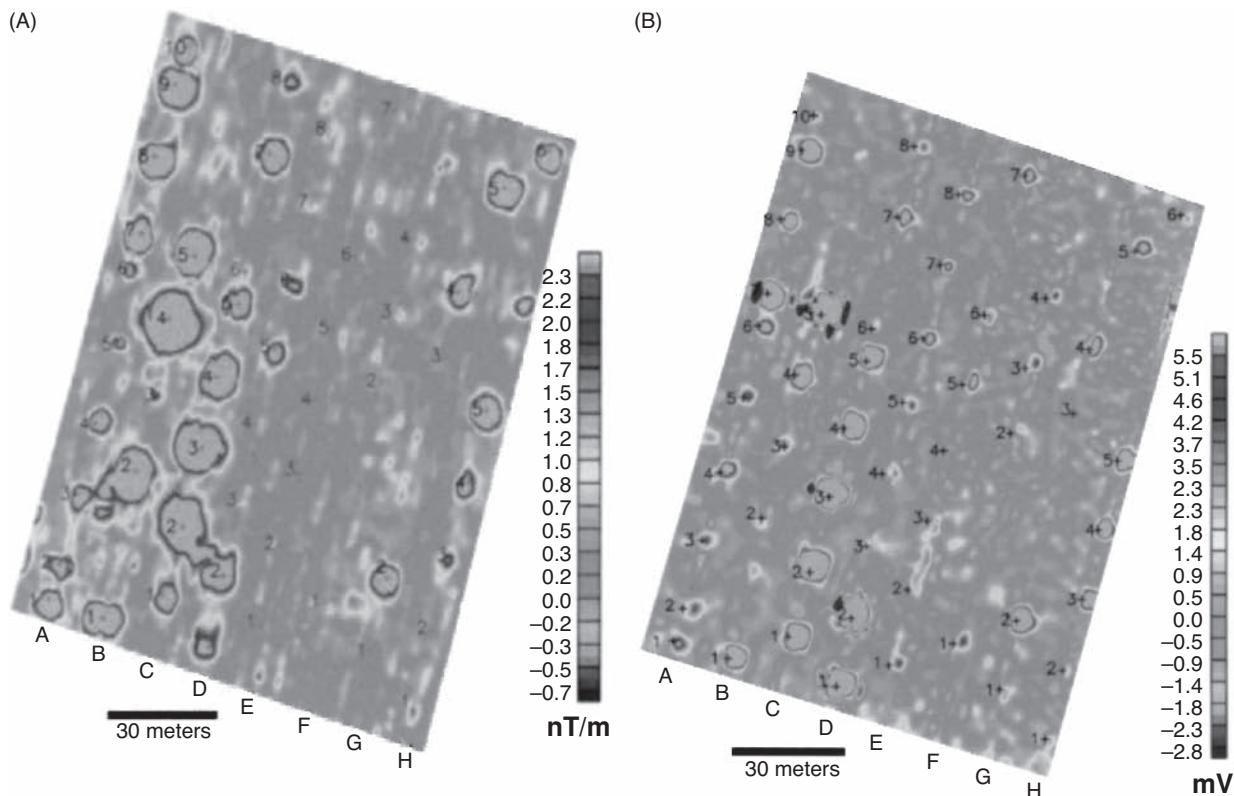


Figure 3.74 Indicative map of items buried along eight southwest to northeast trending rows at Badlands Bombing Range, USA. From Beard *et al.* (2008), by permission.



**Figure 3.75** Anomaly maps from the Badlands Bombing Range, USA. (A) Total magnetic field anomalies using a Hammerhead total-field magnetic system, and (B) ORAGS-TEM response 230 ms after end of transmitter turnoff ramp for a large loop configuration. From Beard et al. (2008), by permission. [C]

of detection may vary considerably depending upon site conditions. It is essential that the detection assurance level (i.e. 100% confidence that the target-size UXO can be detected) is indicated. It must not be assumed that because a detection range of 3 m was achieved on one site, that it will be the same on another; it may be significantly shorter. Detection ranges for even a 500 kg bomb may be as small as only 1 m. It is also important that EOC firms do not hide the technical limitations of their equipment using ‘military secrecy’ or

‘commercially proprietary technology’ as grounds to refuse to disclose limits of detectability. If they do not provide this information, do not use them. Any reputable company should be prepared to provide such information. To exaggerate claims of UXO detection depths for surface UXO surveys or detection radii for CPT probe or drilling UXO methods could result in tragic consequences. It is crucial that any intending client has an independent qualified third-party check over any such claims thoroughly.



# 4

## Applied Seismology: Introduction and Principles

### 4.1 Introduction

The basic principle of exploration seismology is for a signal to be generated at a time that is known exactly, and for the resulting seismic waves to travel through the subsurface media and be reflected and refracted back to the surface where the returning signals are detected. The elapsed time between the source being triggered and the arrival of the various waves is then used to determine the nature of the subsurface layers. Sophisticated recording and subsequent data processing enable detailed analyses of the seismic waveforms to be undertaken. The derived information is used to develop images of the subsurface structure and a knowledge of the physical properties of the materials present.

Exploration seismic methods were developed out of pioneering earthquake studies in the mid-to-late nineteenth century. The first use of an artificial energy source in a seismic experiment was in 1846 by Robert Mallet, an Irish physicist who was also the first to use the word ‘seismology’. John Milne introduced the drop weight as an energy source in 1885. His ideas were further developed by August Schmidt who, in 1888, devised travel time–distance graphs for the determination of seismic velocities. In 1899, G.K. Knott explained the propagation, refraction and reflection of seismic waves at discontinuity boundaries. In 1910, Andrija Mohorovicic identified distinct phases of P- and S-waves on travel-time plots derived from earthquake data. He attributed them to refractions along a boundary separating material with a lower velocity above and a higher velocity at greater depth. This boundary, which separates the Earth’s crust from the lower-lying mantle, is now called the ‘Moho’.

Significant developments in the refraction method were made during the First World War by both the Allies and Germany, particularly by Ludger Mintrop. Research was undertaken to develop methods by which the location of heavy artillery could be achieved by studying the waves generated by the recoil of the guns on firing.

This work was developed further by Mintrop who obtained the first patent for a portable seismograph in 1919 (Keppner, 1991). On 4 April 1921, Mintrop founded the company Seismos Gesellschaft in order to carry out seismic refraction surveys in the search for salt domes acting as trap structures for hydrocarbons. In 1924, the Orchard Salt Dome in Texas, USA, was discovered using seismic refraction experiments undertaken by Seismos on behalf of Gulf Production Co., thus demonstrating the effectiveness of the method as an exploration tool.

The first seismic reflection survey was carried out by K.C. Karcher between 1919 and 1921 in Oklahoma, USA, based on pioneering work by Reginald Fessenden around 1913. By 1927, the seismic reflection method was being used routinely in exploration for hydrocarbons, and within 10 years had become the dominant method worldwide in the exploration for oil and gas.

The use of fan shooting was also finding favour in the early 1920s due to the encouragement by L.P. Garrett who was head of seismic exploration at Gulf. Parallel to these developments, research work was also being undertaken at the USA Bureau of Standards. In 1928, O. von Schmidt, from Germany, derived a method of analysis of refraction data for dipping two-layer structures to obtain the angle of dip and true velocity within the lower layer. In 1931, he published a solution to solve the dipping three-layer case. The so-called Schmidt method is still commonly used to determine weathered layer corrections in seismic reflection surveying.

In 1938, T. Hagiwara produced a method whereby, in addition to determining the lower layer velocity, the depths to this horizon could be determined at all shot and receiver positions along a single profile. Details of contributions made by Japanese engineering seismologists have been given by Masuda (1981).

As with just about all geophysical methods, the Second World War provided advances in technology that increased the usefulness of the various seismic methods.

In 1959, J.G. Hagedoorn published his ‘Plus–Minus’ method (see Section 5.4.2). In 1960, Carl Savit demonstrated that it was possible to identify gaseous hydrocarbons directly using seismic methods

by identifying ‘bright spots’. In 1961, L.V. Hawkins introduced the ‘reciprocal method’ of seismic refraction processing that has been subsequently and substantially developed by D. Palmer (1980, 1991) as the ‘generalised reciprocal method’ (GRM; see Section 5.4.3). Both Hagedoorn’s and Palmer’s methods are similar to Hagiwara’s. A very good review of the seismic refraction method has also been given by Sjogren (1984).

Major developments in seismic methods have come about by revolutions within the computing industry. Processing once thought possible only by mainframe computers is now being handled on personal computers and stand-alone workstations. With the vast increase in computer power, currently at a rate of an order of magnitude every two years, has come the ability to process data far more quickly and reliably, and this has opened up opportunities for seismic modelling. Obviously, with the degree of sophistication and specialisation that now exists in the seismic industry, it is not possible to provide anything like a comprehensive account here. There are many books available that deal extensively with exploration seismology, such as those by Claerbout (1976, 1985), McQuillin *et al.* (1984), Hatton *et al.* (1986), Waters (1978), Yilmaz (2001), and Dobrin and Savit (1988), among others.

There are two main seismic methods – *refraction* and *reflection*. Since the 1980s there has been a major shift towards using high-resolution seismic reflection surveying in shallow investigations (i.e. to depths less than 200 m and especially less than 50 m). Previously, of the two seismic methods, refraction had been used principally within engineering site investigations. Neither seismic sources with suitably high frequencies, nor the data processing capability, were available or cost-effective for small-scale surveys. This is no longer so, and shallow seismic investigations are now much more common both on land and over water. Data obtained by signal-enhancement seismographs can be processed in similar ways to data acquired in large-scale hydrocarbon exploration surveys. Consequently, following a brief overview of the basic principles of applied seismology in this chapter, seismic refraction data processing and interpretation techniques are discussed in the next chapter, with seismic reflection surveying being discussed in detail in Chapter 6. These will provide a brief introduction to the shallow refraction and reflection methods (to which emphasis is given), and briefly to the processes used in the seismic industry for hydrocarbon exploration.

In addition to hydrocarbon exploration, seismic methods have a considerable number of other applications (Table 4.1), ranging from crude depth-to-bedrock determinations through to more subtle but fundamental information about the physical properties of subsurface media, and from the obvious applications such as site suitability through to the apparently obscure uses such as in forensic investigations in aircraft crashes on land, such as the Lockerbie air disaster in Scotland in 1989, and the location of miners trapped after roof collapses. Details of some of these applications are given in Section 6.6.

**Table 4.1** Derived information and applications of exploration seismology.

<b>Gross geological features:</b>
Depth to bedrock
Measurement of glacier thickness
Location of faults and fracture zones
Fault displacement
Location and character of buried valleys
Lithological determinations
Stratigraphy
Location of basic igneous dykes
<b>Petrophysical information:</b>
Elastic moduli
Density
Attenuation
Porosity
Elastic wave velocities
Anisotropy
Rippability
<b>Applications:</b>
Engineering site investigations
Rock competence
Sand and gravel resources
Detection of cavities
Seabed integrity (for siting drilling rigs)
Degassing or dewatering of submarine sediments
Preconstruction site suitability for:
new landfill sites
major buildings
marinas and piers
sewage outfall pipes
tunnel construction, etc.
Hydrogeology and groundwater exploration
Ground particle velocities
Forensic applications:
location of crashed aircraft on land
design of aircraft superstructures
monitoring Nuclear Test Ban Treaty
location of large bore military weapons
Location of trapped miners
Seismic hazard zonation

external force. The ratio of the force to area ( $F/A$ ) is known as stress. Stress can be resolved into two components, one at right-angles to the surface (normal or dilatational stress) and one in the plane of the surface (shear stress). The stressed body undergoes *strain*, which is the amount of deformation expressed as the ratio of the change in length (or volume) to the original length (or volume). According to *Hooke’s Law*, stress and strain are linearly dependent and the body behaves *elastically* until the *yield point* is reached. Below the yield point, on relaxation of stress, the body reverts to its pre-stressed shape and size. At stresses beyond the yield point, the body behaves in a *plastic* or *ductile* manner and permanent damage results. If further stress is applied, the body is strained until it fractures.

Earthquakes occur when rocks are strained until fracture, when stress is then released. However, in exploration seismology, the amounts of stress and strain away from the immediate vicinity of a seismic source are minuscule and lie well within the elastic behaviour of natural materials. The stress/strain relationship for any

## 4.2 Seismic waves

### 4.2.1 Stress and strain

When an external force  $F$  is applied across an area  $A$  of a surface of a body, forces inside the body are established in proportion to the

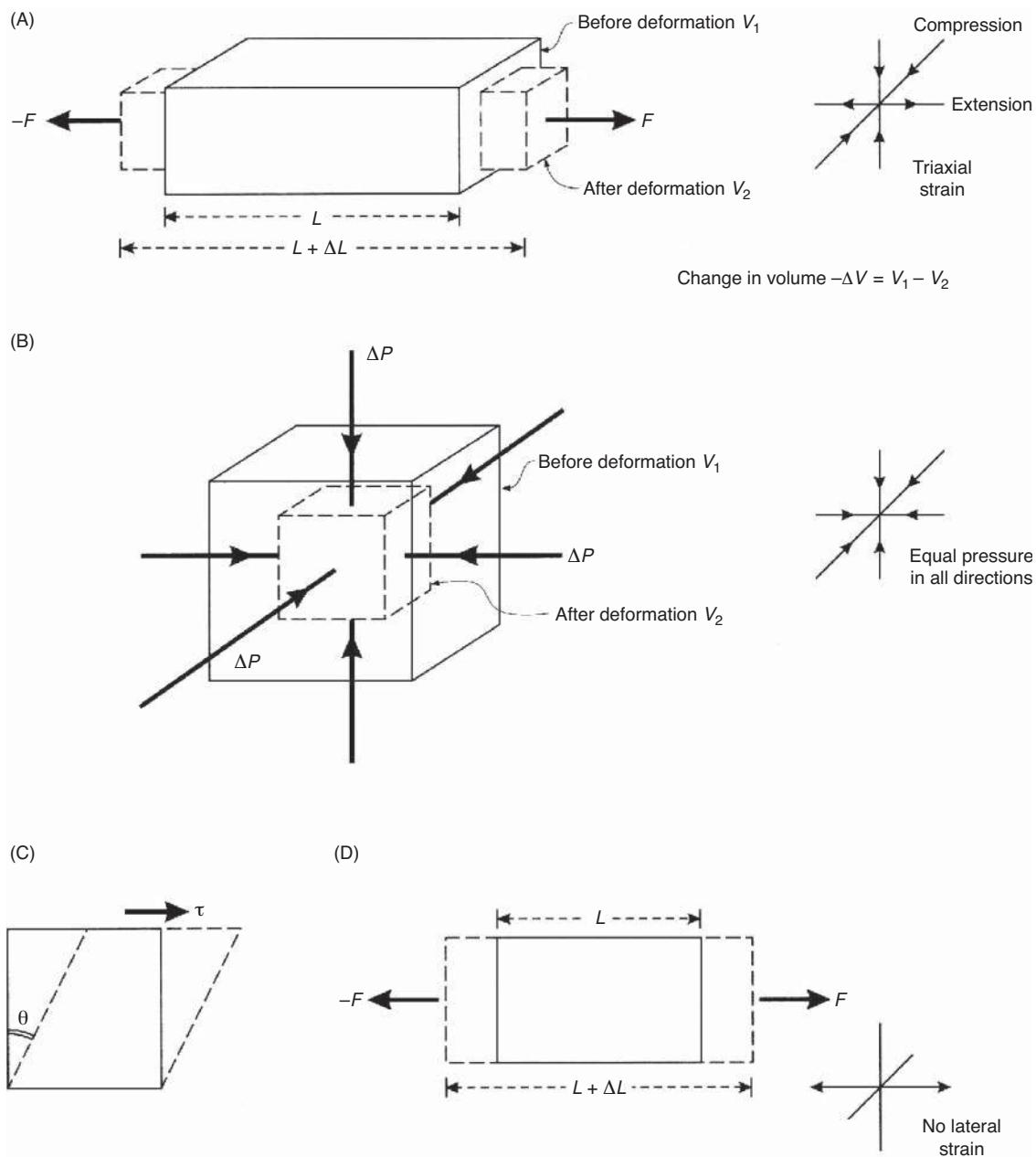


**Figure 4.1** Elastic moduli. (A) Young's modulus; (B) bulk (rigidity) modulus; (C) shear modulus; (D) axial modulus.

material is defined by various elastic moduli, as outlined in Figure 4.1 and Box 4.1.

## 4.2.2 Types of seismic waves

Seismic waves, which consist of tiny packets of elastic strain energy, travel away from any seismic source at speeds determined by the elastic moduli and the densities of the media through which they pass (Section 4.2.3). There are two main types of seismic waves: those that pass through the bulk of a medium are known as *body waves*; those confined to the interfaces between media with contrasting elastic properties, particularly the ground surface, are called

*surface waves*. Other types of waves encountered in some applications are *guided waves*, which are confined to particular thin bands sandwiched between layers with higher seismic velocities by total internal reflection. Examples of these are *channel* or *seam waves*, which propagate along coal seams (Regueiro, 1990a,b), and *tube waves*, which travel up and down fluid-filled boreholes.

### 4.2.2.1 Body waves

Two types of body wave can travel through an elastic medium. *P-waves*, which are the most important in exploration seismology, are also known as *longitudinal*, *primary*, *push*, or *compressional* waves.

**Box 4.1 Elastic moduli****Young's modulus**

$$E = \frac{\text{Longitudinal stress } \Delta F/A}{\text{Longitudinal strain } \Delta L/L} = \frac{\sigma}{\varepsilon}$$

(in the case of triaxial strain)

**Bulk modulus**

$$k = \frac{\text{Volume stress } \Delta P}{\text{Volume strain } \Delta v/v}$$

(in the case of excess hydrostatic pressure)

**Shear (rigidity) modulus** (a Lamé constant)

$$\mu = \frac{\text{shear stress } \tau}{\text{shear strain } \varepsilon}$$

 $(\mu \approx 7 \times 10^4 \text{ MPa}; \mu = 0 \text{ for fluids})$ **Axial modulus**

$$U = \frac{\text{Longitudinal stress } \Delta F/A}{\text{Longitudinal strain } \Delta L/L} = \frac{\sigma}{\varepsilon}$$

(in the case with no lateral strain)

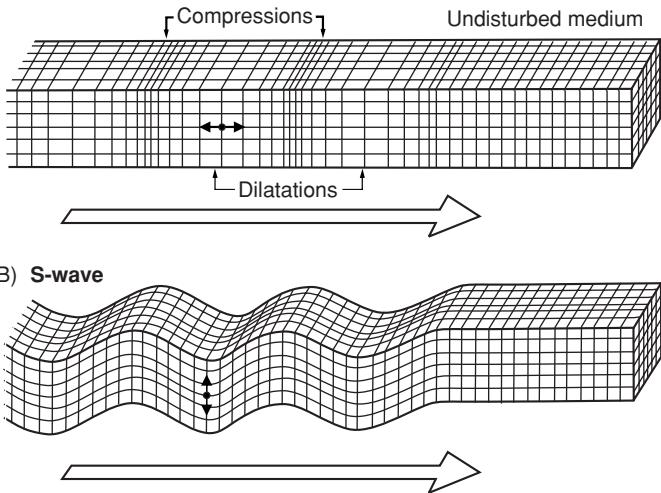
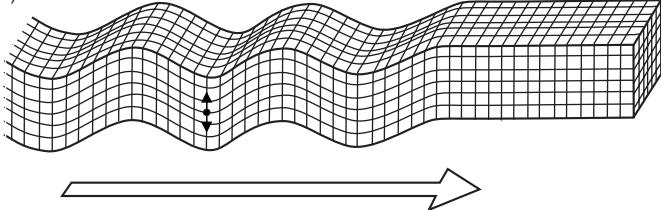
**Relationships between Young's modulus ( $E$ ), Poisson's ratio ( $\sigma$ ), and the two Lamé constants ( $\mu$  and  $\lambda$ )**

$$E = \frac{\mu(3\lambda + 2\mu)}{(\lambda + \mu)} \quad \sigma = \frac{\lambda}{2(\lambda + \mu)} \quad k = \frac{3\lambda + 2\mu}{3}$$

and

$$\lambda = \frac{E\sigma}{(1 + \sigma)(1 - 2\sigma)}$$

Poisson's ratio ranges from 0.05 (very hard rocks) to 0.45 (for loose sediments). Elastic constants for rocks can be found in handbooks of physical constants.

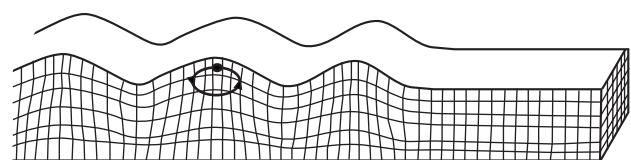
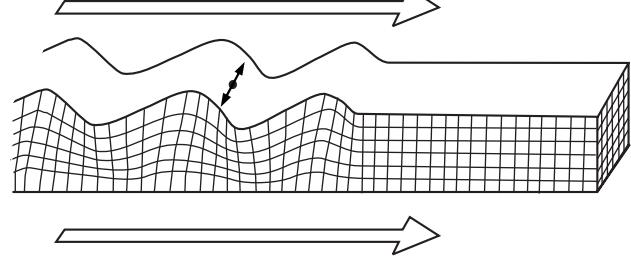
**(A) P-wave****(B) S-wave**

**Figure 4.2** Elastic deformations and ground particle motions associated with the passage of body waves. (A) A P-wave, and (B) an S-wave. From Bolt (1982), by permission.

**4.2.2.2 Surface waves**

Waves that do not penetrate deep into subsurface media are known as surface waves, of which there are two types, *Rayleigh* and *Love* waves. Rayleigh waves travel along the free surface of the Earth with amplitudes that decrease exponentially with depth. Particle motion is in a retrograde elliptical sense in a vertical plane with respect to the surface (Figure 4.3A) and, as shear is involved, Rayleigh waves can travel only through a solid medium. Love waves occur only where a medium with a low S-wave velocity overlies a layer with a higher S-wave velocity. Particle motion is at right-angles to the direction of wave propagation but parallel to the surface. These are thus polarised shear waves (Figure 4.3B).

Surface waves have the characteristic that their waveform changes as they travel because different frequency components propagate

**(A)****(B)**

**Figure 4.3** Elastic deformations and ground particle motions with the passage of surface waves. (A) A Rayleigh wave, and (B) a Love wave. From Bolt (1982), by permission.

Material particles oscillate about fixed points in the direction of wave propagation (Figure 4.2A) by compressional and dilatational strain, exactly like a sound wave. The second type of wave is the *S-wave*, also known as the *transverse*, *secondary* or *shear wave*. Particle motion is at right-angles to the direction of wave propagation and occurs by pure shear strain (Figure 4.2B). When particle motion is confined to one plane only, the S-wave is said to be *plane-polarised*. The identification and use of polarised shear waves in their vertical and horizontally polarised modes (SV and SH respectively) are becoming increasingly important in exploration seismology, as will be discussed later.

All the frequencies contained within body waves travel through a given material at the same velocity, subject to the consistency of the elastic moduli and density of the medium through which the waves are propagating.

at different rates, a phenomenon known as *wave dispersion*. The dispersion patterns are indicative of the velocity structure through which the waves travel, and thus surface waves generated by earthquakes can be used in the study of the lithosphere and asthenosphere. Surface wave dispersion has been described in detail by Grant and West (1965, pp. 95–107), by Gubbins (1990, pp. 69–80) and by Sheriff and Geldart (1982, p. 51). Body waves are non-dispersive. In exploration seismology, Rayleigh waves manifest themselves normally as large-amplitude, low-frequency waves called *ground roll* which can mask reflections on a seismic record and are thus considered to be noise. Seismic surveys can be conducted in such a way as to minimise ground roll, which can be further reduced by filtering during later data processing.

### 4.2.3 Seismic wave velocities

The rates at which seismic waves propagate through elastic media are dictated by the elastic moduli and densities of the rocks through which they pass (Box 4.2). As a broad generalisation, velocities increase with increasing density. Examples of P-wave velocities for a range of geological materials are listed in Table 4.2. The seismic wave velocities in sedimentary rocks in particular increase both with depth of burial and age (cf. Chapter 2, Section 2.2.4.1; see Box 4.3).

From the last equation (asterisked) in Box 4.2, it is clear that Poisson's ratio has a maximum value of 0.5 (at which value the denominator becomes zero). When Poisson's ratio equals 0.33,

#### Box 4.2 Seismic wave propagation velocity

Velocity of propagation  $V$  through an elastic material is:

$$V = (\text{Appropriate elastic modulus/density } \rho)^{1/2}$$

Velocity of P-waves is:

$$V_p = \left( \frac{k + 4\mu/3}{\rho} \right)^{1/2}$$

Velocity of S-waves is:

$$V_s = (\mu/\rho)^{1/2}.$$

The ratio  $V_p/V_s$  is defined in terms of Poisson's ratio ( $\sigma$ ) and is given by:

$$\frac{V_p}{V_s} = \frac{(1 - \sigma)^{1/2}}{(1/2 - \sigma)} (*)$$

Note that  $\mu = 0$  for a fluid, as fluids cannot support shear, and the maximum value of Poisson's ratio is 0.5;  $\sigma \approx 0.05$  for very hard rocks,  $\approx 0.45$  for loose, unconsolidated sediments, average  $\approx 0.25$ .

**Table 4.2** Examples of P-wave velocities.

Material	$V_p$ (m/s)
Air	330
Water	1450–1530
Petroleum	1300–1400
Loess	300–600
Soil	100–500
Snow	350–3000
Solid glacier ice*	3000–4000
Sand (loose)	200–2000
Sand (dry, loose)	200–1000
Sand (water saturated, loose)	1500–2000
Glacial moraine	1500–2700
Sand and gravel (near surface)	400–2300
Sand and gravel (at 2 km depth)	3000–3500
Clay	1000–2500
Estuarine muds/clay	300–1800
Floodplain alluvium	1800–2200
Permafrost (Quaternary sediments)	1500–4900
Sandstone	1400–4500
Limestone (soft)	1700–4200
Limestone (hard)	2800–7000
Dolomites	2500–6500
Anhydrite	3500–5500
Rock salt	4000–5500
Gypsum	2000–3500
Shales	2000–4100
Granites	4600–6200
Basalts	5500–6500
Gabbro	6400–7000
Peridotite	7800–8400
Serpentinite	5500–6500
Gneiss	3500–7600
Marbles	3780–7000
Sulphide ores	3950–6700
Pulverised fuel ash	600–1000
Made ground (rubble, etc)	160–600
Landfill refuse	400–750
Concrete	3000–3500
Disturbed soil	180–335
Clay landfill cap (compacted)	355–380

\* Strongly temperature-dependent for polar ice (Kohnen, 1974).

S-wave velocities are half P-wave velocities. Of the surface waves, Love waves travel at approximately the same speed as S-waves, as they are polarised S-waves, but Rayleigh waves travel slightly slower at about  $0.92 V_s$  (for Poisson's ratio = 0.25).

Care has to be taken in comparing seismic velocities. Velocities can be determined from seismic data (see Sections 6.3.4 and 6.4.1 as to how this is done) and from laboratory analysis. When velocities have been determined using seismic refraction, the range of velocities obtained for a given type of material should be cited, and preferably with the standard deviation. *In situ* measurements made using refraction studies may yield velocities that are significantly different from those obtained from laboratory measurements. This occurs when the *in situ* rock is heavily jointed or fractured. The

**Box 4.3** Elastic wave velocity as a function of geological age and depth (after Faust, 1951)

For shales and sands, the elastic wave velocity  $V$  is given by:

$$V = 1.47(ZT)^{1/6} \text{ km/s}$$

where  $Z$  is the depth (km) and  $T$  the geological age in millions of years.

refraction velocities sample the rock and the discontinuities, whereas a laboratory measurement on a solid sample cannot, by virtue of the scale of the sample. Detailed measurements which may yield more representative *in situ* velocities on a fine scale are those obtained using a Schmidt hammer system. Two geophones are attached to the exposed material at a small distance apart. A hammer is used to generate a P-wave directly on to the rock at a known distance from the receivers. The velocity is obtained from the difference in travel time between the two receivers relative to their separation. No one velocity is absolute. In the case of laboratory measurements, ultrasonic transducers are used to transmit a pulse through a sample of the material in question. From the measured travel time of this pulse through the material, whose length is known, a velocity can be calculated. Ultrasonic frequencies (0.5–1.5 MHz) are three to four orders of magnitude higher than typical seismic frequencies, and so the velocities may not be directly comparable.

In addition to knowing the frequency of the transducers, it is also important to determine whether the samples have been measured dry or fully saturated, and if the latter, the salinity of the fluid used and the temperature at which the sample was measured. Of greater significance is the problem over mechanical relaxation of retrieved core pieces. If a sample of rock is obtained from significant depth below ground where it is normally at substantial pressure, the rock specimen expands on its return to the surface, resulting in the formation of microcracks due to the relaxation of confining pressure. These microcracks thereby increase the porosity and decrease the density of the rock. In the case of saturated samples retrieved from below the seabed, gas bubbles form within the sample as the pressure is reduced and these can reduce the acoustic velocity significantly compared with the *in situ* velocity. This may be noticeable even if samples are retrieved from less than 10 m of water depth.

In porous rocks, the nature of the material within the pores strongly influences the elastic wave velocity; water-saturated rocks have different elastic wave velocities compared with gas-saturated rocks; sandstones with interstitial clay have different propagation characteristics compared with clean sandstones, for example. Seismic velocities can be used to estimate porosity using the time-average equation in Box 4.4. If the P-wave velocities of both the pore fluid and the rock matrix are known, the porosity can be deduced. The form of this equation applies both for water-saturated and frozen rocks. In the case of permafrost, the velocity depends upon (a) the type of geological material, (b) the proportion of interstitial

**Box 4.4** Time-average equation to estimate rock porosity

The P-wave velocity  $V$  for a rock with fractional porosity ( $\varphi$ ) is given by:

$$\frac{1}{V} = \frac{\varphi}{V_f} + \frac{1 - \varphi}{V_m}$$

where  $V_f$  and  $V_m$  are the acoustic velocities in the pore fluid and the rock matrix respectively (Wyllie *et al.*, 1958).

Typical values:  $V_f = 1500 \text{ m/s}$ ,  $V_m = 2800 \text{ m/s}$ .

ice, and (c) the temperature. The importance of seismic velocities in interpretation is discussed in Chapter 6. The P-wave velocity in water is dependent upon temperature and salinity (Box 4.5), but is normally considered to be around 1500 m/s for a salinity of 35 parts per thousand at 13°C. In high-resolution surveys conducted where water masses with different temperatures and salinities occur, such as at the mouth of a river where fresh river water flows into and over salt water, the stratigraphy of the water column can become important in determining the correct P-wave velocities for use in subsequent data processing.

In stratified media, seismic velocities exhibit anisotropy. Velocities may be up to 10–15% higher for waves propagating parallel to strata than at right-angles to them. Furthermore, some materials with strongly developed mineral fabrics can also demonstrate anisotropy, as for example in glacier ice and in highly foliated metamorphic rocks. In high-resolution surveys over sediments with marked anisotropy, significant differences in seismic character and data quality may be observed. In situations where such anisotropy is anticipated, it is essential to run test lines orientated at different azimuths in order to identify directions of shooting which either degrade the data quality or provide good resolution and depth penetration. For example, at the mouth of a fast-flowing river, lines parallel and at right-angles to water flow would be good directions to try. Once tests have been undertaken, an appropriate survey grid can then be established to ensure that the best-quality data are acquired. Towing the hydrophone streamer against the water flow produces better control and signal-to-noise ratios than across the water currents. Cross-track currents can also lead to excessive feathering of the source–receiver system (see sections 4.6.2 and 6.3.2.2).

**Box 4.5** P-wave velocity as a function of temperature and salinity in water

$$V = 1449.2 + 4.6T - 0.055T^2 + 0.0003T^3 \\ +(1.34 - 0.01T)(S - 35) + 0.016d$$

where  $S$  and  $T$  are the salinity (parts per thousand) and the temperature (°C);  $d$  is depth (m) (Ewing *et al.*, 1948; cf. Fofonoff and Millard, 1983).

## 4.3 Raypath geometry in layered ground

### 4.3.1 Reflection and transmission of normally incident rays

Huygens' Principle is of critical importance to the understanding of the propagation of seismic waves through layered ground. Huygens' Principle states that every point on a wavefront can be considered to be a secondary source of spherical waves. The new wavefront is the envelope of these waves after a given time interval (Figure 4.4). If this is borne in mind, it is easier to understand how reflection, refraction and diffraction occur. Instead of always considering the wavefront of each wave, it is often easier to consider a line at right-angles ('normal') to the wavefront as a ray along which energy travels. Consequently, the propagation of seismic waves is frequently discussed in terms of rays and raypaths.

Whenever a wave impinges upon an interface across which there is a contrast in elastic properties, some of the energy is reflected back off the interface, and the remainder passes through the boundary and is refracted upon entering the second medium. The relative amplitudes of the partitioned energy at such an interface into reflected and transmitted components are described by Zoeppritz-Knott equations in terms of the seismic velocities and densities of the two layers (Sheriff and Geldart, 1982; see Telford *et al.*, 1990, pp. 155ff, for a detailed discussion). The product of the density ( $\rho$ ) and the seismic velocity ( $V$ ) for each respective layer is known as the acoustic impedance ( $Z$ ). Generally speaking, the more consolidated a rock, the greater will be its acoustic impedance. In order to propagate seismic energy most efficiently across a boundary, the acoustic impedance contrast should be small.

In the case of normal incidence, if the amplitude of incident energy is  $A_0$  and those of the reflected and transmitted energy are respectively  $A_1$  and  $A_2$  (Figure 4.5), then, assuming no loss of energy along any raypath, the energy within the incident wave must equal

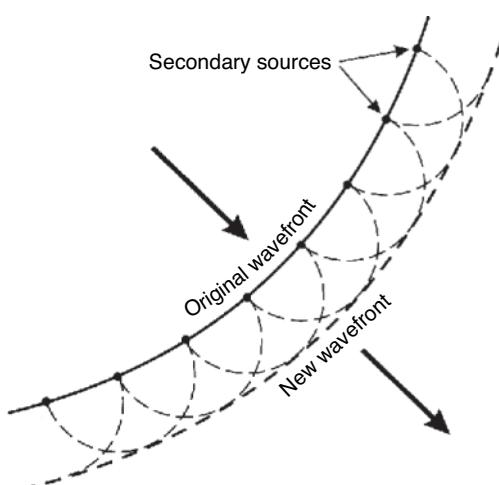


**Figure 4.4** Propagation of a wavefront according to Huygens' Principle.

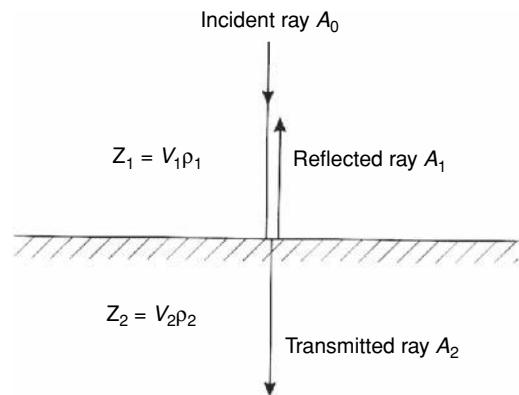


**Figure 4.5** Partitioning of energy from a normally incident ray with amplitude  $A_0$  into reflected and transmitted rays with respective amplitudes  $A_1$  and  $A_2$ .  $Z_1$  and  $Z_2$  are the acoustic impedances of the two layers.

the sum of the energy contained within the reflected and transmitted waves (i.e.  $A_0 = A_1 + A_2$ ).

The degree of reflectivity of an interface for normal and low angles ( $<20^\circ$ ) of incidence is described by the *reflection coefficient* ( $R$ ), which is the ratio of the amplitudes of the reflected wave ( $A_1$ ) and the incident wave ( $A_0$ ). Furthermore, the reflection coefficient is also a solution to Zoeppritz's equations, and is given by the ratio of the difference in acoustic impedances to the sum of the impedances (Box 4.6).

It can be seen that the magnitude of the reflection coefficient lies in the range of -1 to 1. When a ray passes from a high-velocity medium into one with low velocity, the reflection coefficient is negative and a phase reversal occurs ( $\pi$  or  $180^\circ$ ) within the reflected ray. Typical values of  $R$  are between  $<0.1$  (weak reflection), 0.1–0.2 (moderate reflection), or  $>0.2$  (strong reflection). In the case of an emergent ray in water impinging upon the water-air interface, such as from a submerged seismic source, the reflection coefficient is -1 and the reflected ray undergoes a phase reversal at the interface. (To calculate this as a check, the values used are:  $V_{\text{water}} = 1500 \text{ m/s}$ ;  $\rho_w = 1.0 \text{ Mg/m}^3$ ;  $V_{\text{air}} = 330 \text{ m/s}$ ,  $\rho_a = 1.293 \text{ kg/m}^3$  at sea-level. As we are dealing here with an emergent ray from water to air, layer one is the water, and layer two is the air.)

The degree of *transmittivity* of an interface for normal and low angles ( $<20^\circ$ ) of incidence is described by the *transmission coefficient* ( $T$ ), which is the ratio of the amplitudes of the transmitted wave ( $A_2$ ) and the incident wave ( $A_0$ ). Furthermore, the transmission coefficient is also a solution to Zoeppritz's equations, and is given by the ratio of twice the acoustic impedance of the first layer to the sum of the impedances (Box 4.6).

The proportions of *energy* that are reflected or transmitted are also referred to as the reflection and transmission coefficients. However, in this case, the forms of the equations are different (see Box 4.6). It should be noted that the sum of the reflected and transmitted energy must equal one.

If the reflection coefficient is  $\pm 1$ , or  $E_R = 1$ , then all the incident energy is reflected and none is transmitted (i.e.  $T = 0$  and  $E_T = 0$ ). Conversely, if  $R = 0$  and  $E_R = 0$ , then all the incident energy is

**Box 4.6** Reflection and transmission coefficients (see Figure 4.5)

For normal and low angles ( $<20^\circ$ ) of incidence:

**Reflection coefficient**

$$R = A_1/A_0 = (Z_2 - Z_1)/(Z_2 + Z_1)$$

$$R \leq \pm 1.$$

**Transmission coefficient**

$$T = A_2/A_0 = 2Z_1/(Z_2 + Z_1).$$

$Z_1$  and  $Z_2$  are the acoustic impedances of the first and second layers, respectively.  $Z = V\rho$ , where  $V$  and  $\rho$  are the seismic velocity and density of a given layer;  $A_0$ ,  $A_1$  and  $A_2$  are the relative amplitudes of the incident, reflected and transmitted rays, respectively.

Of the incident energy, the proportions of energy reflected ( $E_R$ ) and transmitted ( $E_T$ ) are given by:

**Reflected energy**

$$E_R = (Z_2 - Z_1)^2/(Z_2 + Z_1)^2$$

**Transmitted energy**

$$E_T = 4Z_1Z_2/(Z_2 + Z_1)^2$$

Note that  $E_R + E_T = 1$ .

For the derivation of these formulae, see Telford *et al.* (1990, p. 156).

transmitted ( $T = 1$  and  $E_T = 1$ ), suggesting that there is no contrast in acoustic impedance across the interface (i.e.  $Z_1 = Z_2$ ). In such a situation there still may be differences in both velocity and density between the two materials. For example, if the seismic velocities and densities for layers 1 and 2 are 1800 m/s, 1.6 Mg/m<sup>3</sup> and 1600 m/s, 1.8 Mg/m<sup>3</sup>, respectively, there would be no contrast in acoustic impedance as  $Z_1 = Z_2 = 2880$  Mg/m<sup>2</sup>s.

In the above discussion, it has been assumed that the reflection from an interface arises from a point. In reality, it is generated from a finite area of the reflector surface as defined by the first Fresnel zone (Figure 4.6). The second and subsequent Fresnel zones can be ignored in the case of normal incidence. Effectively, the incident wavefront has a discrete footprint on the reflector surface. The reflection coefficient for a given interface is thus the average response over the first Fresnel zone.

Furthermore, surface roughness of the interface also becomes important if the amplitude of the roughness is of the same order or greater than the quarter-wavelength of the incident wave. The rougher the surface, the more it behaves as a specular reflector, returning rays at a very wide variety of angles. The amount of energy reaching the surface is therefore much reduced and the observed

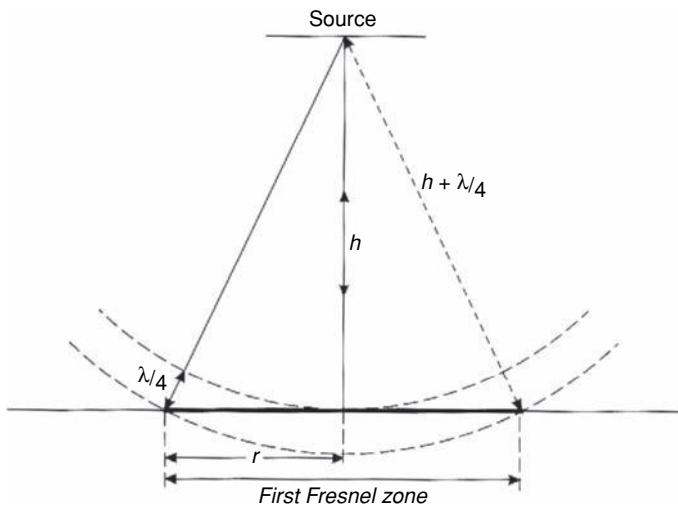


**Figure 4.6** The first Fresnel zone on a reflector at a depth  $h$  below the source of the incident spherical wave.

reflection coefficient is much less than that predicted for a given contrast in acoustic impedances. The radius ( $r$ ) of the first Fresnel zone is related to the depth of the reflector below the source ( $h$ ) and the wavelength of the incident wave ( $\lambda$ ), such that  $r^2 \approx \lambda h/2$  (Box 4.7). As two-way travel times are considered, the quarter-wavelength is used as opposed to classical optics where only a half-wavelength is used. For a more detailed discussion, see McQuillin *et al.* (1984), Yilmaz (2001), Knapp (1991) and Eaton *et al.* (1991). It is clear from this that the first Fresnel zone becomes larger as a result of increasing depth and decreasing frequency (i.e. greater wavelengths). The effect that this has on horizontal resolution is considered in Chapter 6 for seismic reflection surveying, and in Chapter 12 for ground penetrating radar. The determination of Fresnel zones for travel-time measurements has been discussed in detail by Hubral *et al.* (1993).

### 4.3.2 Reflection and refraction of obliquely incident rays

In the case of an incident wave impinging obliquely on an interface across which a contrast in acoustic impedance exists, reflected and

**Box 4.7** First Fresnel zone (see Figure 4.6)

The radius ( $r$ ) of the first Fresnel zone is given by:

$$r^2 = \lambda h/2 + \lambda^2/16 \approx \lambda h/2$$

$$r \approx (\lambda h/2)^{1/2} = (V/2)(t/f)^{1/2}$$

where  $h$  is the distance between the source and the reflector, and  $\lambda$  is the wavelength of the incident wave of frequency  $f$ , with propagation speed  $V$  in the material and a reflector at a two-way travel time  $t$  on a seismic section.

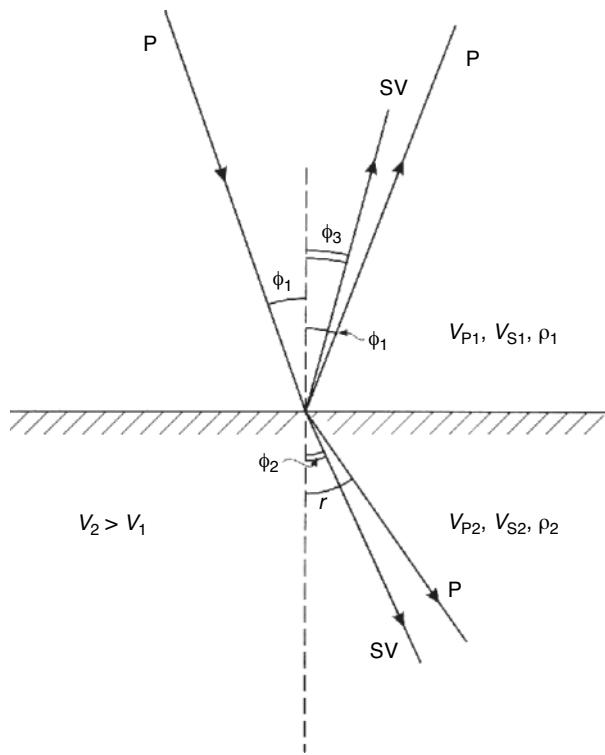


**Figure 4.7** Geometry of rays associated with a P-wave (shown as a ray incident obliquely on a plane interface), and converted vertically polarised S-waves (SV; shown as a ray).  $V_p$  and  $V_s$  are the respective P- and S-wave velocities and  $\rho$  is the density. Suffixes 1 and 2 depict the layer number.

transmitted waves are generated as described in the case of normal incidence. At intermediate angles of incidence, reflected S-waves generated by conversion from the incident P-waves (Figure 4.7) may have larger amplitudes than reflected P-waves. This effect is particularly useful in the study of deep reflection events in crustal studies where very large offsets (source-receiver distances) are used.

In general, the P-wave amplitude decreases slightly as the angle of incidence increases. This is equivalent to a decrease in P-wave amplitude with increasing offset. However, there are cases where this does not occur, such as when Poisson's ratio changes markedly, perhaps as a result of gas infilling the pore space within a rock. This phenomenon has been reported by Ostrander (1984) for seismic field records obtained over gas reservoirs and can be used as an indicator of the presence of hydrocarbon gas.

When a P-wave is incident at an oblique angle on a plane surface, four types of waves are generated: reflected and transmitted P-waves and reflected and transmitted S-waves. The relative amplitudes of these various waves are described by Zoeppritz's equations (Telford *et al.*, 1990). The direction of travel of the transmitted waves is changed on entry into the new medium, and this change is referred to as refraction. The geometry of the various reflected and refracted waves relative to the incident waves is directly analogous to light and can be described using Snell's Laws of refraction (Box 4.8). These state that the incident and refracted rays, and the normal at the point of incidence, all lie in the same plane; for any given pair of

#### Box 4.8 Laws of reflection and Snell's Laws of refraction (Figure 4.7)

##### Snell's Laws:

$$\frac{\sin i}{V_{P1}} = \frac{\sin r}{V_{P2}} = \frac{\sin \beta_1}{V_{S1}} = \frac{\sin \beta_2}{V_{S2}} = p$$

where  $i$  and  $r$  are the angles of incidence and refraction respectively, and  $V_1$  and  $V_2$  are the speeds of propagation in layers 1 and 2 respectively for P- and S-waves as indicated by the suffix, and where  $p$  is the raypath parameter. Conversely:

$$\frac{\sin i}{\sin r} = \frac{V_1}{V_2}$$

In the case of critical refraction:

$$\frac{\sin i_c}{\sin 90^\circ} = \frac{V_1}{V_2}$$

Since  $\sin 90^\circ = 1$ ,  $\sin i_c = V_1 / V_2$ , where  $i_c$  is the critical angle.

##### Laws of reflection:

- The angle of incidence equals the angle of reflection.
- The incident, reflected and refracted rays and the normal at the point of incidence all lie in the same plane.

media, the ratio of the sine of the angle of incidence to the sine of the angle of refraction is a constant. In its generalised form, Snell's Law also states that for any ray at the point of incidence upon an interface, the ratio of the sine of the angle of incidence to the velocity of propagation within that medium remains a constant, which is known as the *raypath parameter*.

### 4.3.3 Critical refraction

When the angle of incidence reaches a particular value, known as the critical angle, the angle of refraction becomes  $90^\circ$ . The refracted wave travels along the upper boundary of the lower medium, whose speed of propagation is greater than that of the overlying medium (i.e.  $V_2 > V_1$ ). The material at the interface is subject to an oscillating stress from the passage of the refracted wave, which in turn generates upward-moving waves, known as head waves, which may eventually reach the surface (Figure 4.8). The orientation of the ray associated with the head wave is also inclined at the critical angle (Figure 4.8). Critical refraction is discussed further in Chapter 5.

### 4.3.4 Diffractions

If a wave impinges upon a surface that has an edge to it, such as a faulted layer, then the wavefront bends around the end of the feature and gives rise to a diffracted wave (Figure 4.9). Similarly, boulders whose dimensions are of the same order as the wavelength of the

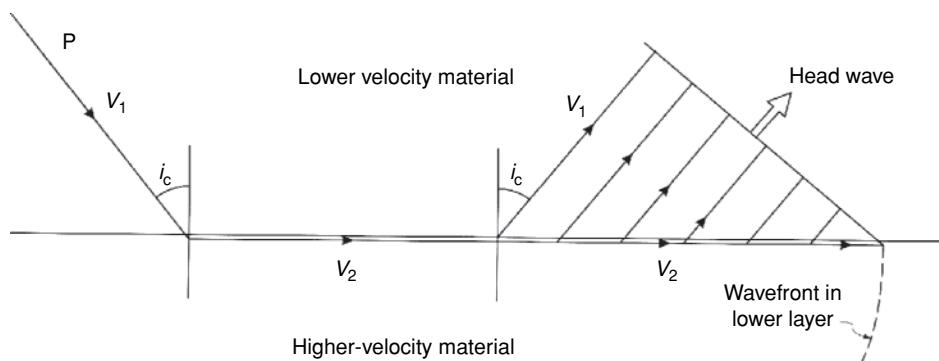


**Figure 4.8** Critical refraction at a plane boundary and the generation of a head wave.

incident signal can also give rise to diffractions. The curvature of the diffraction tails are a function of the velocity of the host medium (Figure 4.10). While diffractions are usually considered as noise and attempts are made at resolving them through data processing, they can be used as an interpretational aid (see Chapter 6).

The reason that diffraction occurs is best explained by Huygens' Principle of secondary wavefronts. The object causing the diffraction acts as a secondary source of waves which spread out spherically from that point and can travel into areas where, according to ray theory, there should be no signals observed, such as the shadow zone shown in Figure 4.9. In the case of an isolated cause, such as a boulder, where the shot is located over the source of the diffraction, a hyperbolic travel-time response is obtained (Figure 4.10; see also Box 4.9). For comparison, the two-way travel time for a shot-receiver pair with increasing offset (i.e. starting with both at station 6, then shot-receiver at 5 and 7, 4 and 8, 3 and 9, etc.) is given in Figure 4.10.

Whereas a diffraction from a point source in a uniform-velocity field is symmetrical, a diffraction caused by the termination of a reflector undergoes a 180° phase change on either side of a diffracting edge (Troyer, 1970; see Figure 4.11).

## 4.4 Loss of seismic energy

The loss of amplitude with distance travelled by a seismic wave occurs in three main ways: spherical divergence, intrinsic attenuation, and scattering. These are summarised in Figure 4.12. The amount of transmitted energy also decreases each time a boundary in acoustic impedance is crossed, since a proportion of energy is reflected (see Section 4.3.1).

### 4.4.1 Spherical divergence or geometrical spreading

Seismic wave energy propagates radially away from the source and decreases in amplitude with increasing distance. The loss of amplitude can be considered by reference to Figure 4.13. The total energy ( $E$ ) generated at the shot instant is spread out over a spherical shell with a radius ( $r$ ) that increases with time. The energy is spread out over the surface of the sphere such that the energy density (i.e. energy per unit area) is  $E/4\pi r^2$ . Some time later, when the shell has radius  $R$ , the energy density is  $E/4\pi R^2$ . As  $R > r$ , the energy density

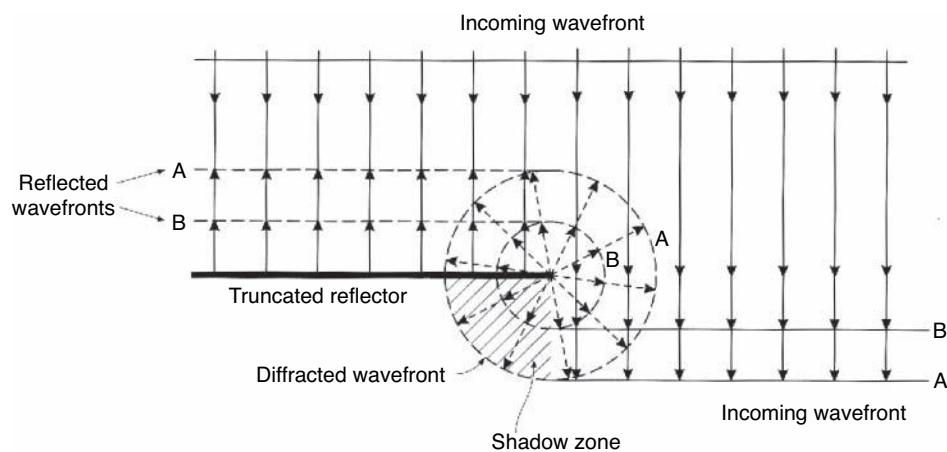


**Figure 4.9** Diffracted wavefronts arising from a truncated reflector. The shaded area is a shadow zone where, according to ray theory, no energy should be observed. Huygens' Principle of wavefront generation explains why signals are observed in this shadow zone.

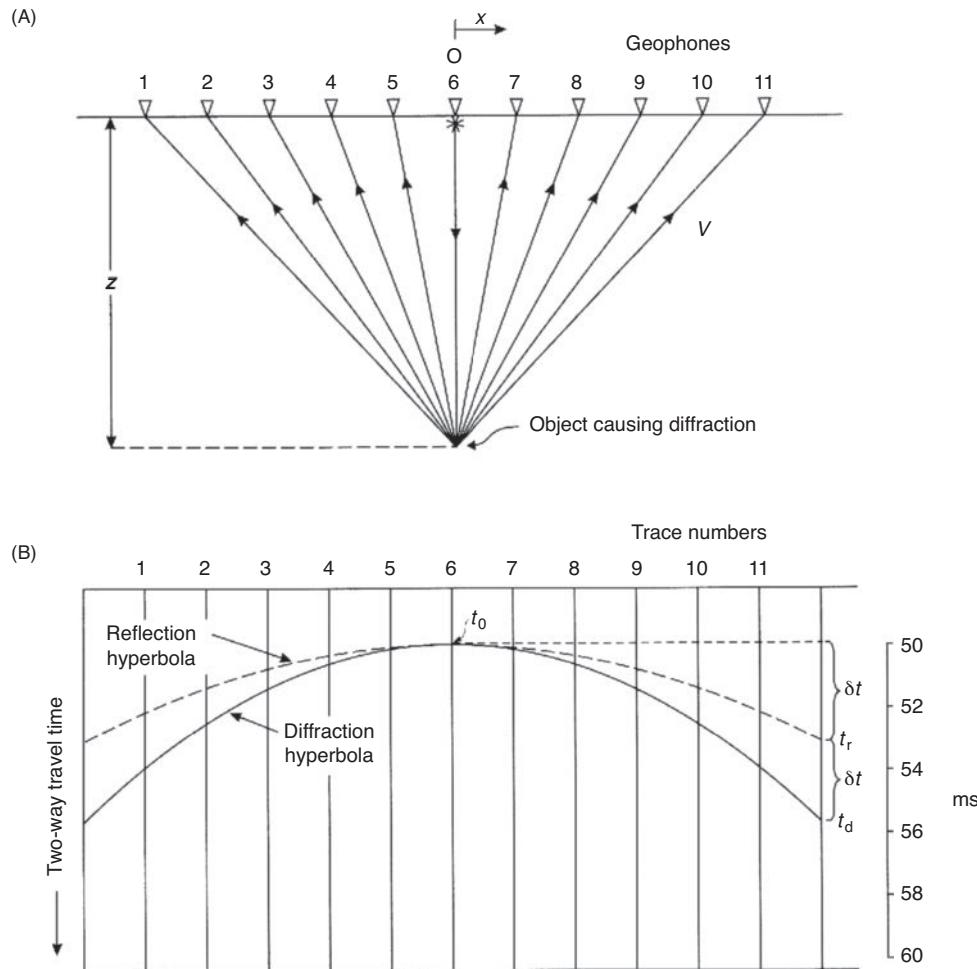


**Figure 4.10** (A) Raypath geometry for diffracted rays arising from a point target situated beneath a short position; reflections arise from increasing offset between shot-receiver pairs 6 and 6 (coincident), 5 and 7, 4 and 8, etc. Depth  $z = 45$  m, in a material with  $V_p = 1800$  m/s. The geophone interval is 5 m. (B) Corresponding time section to illustrate the shape and symmetry of the diffraction as compared with the reflection hyperbola.

is now smaller. The energy thus diminishes in proportion to  $1/r^2$ . Amplitude, which is proportional to the square-root of the energy density, thus varies in proportion to  $1/r$ .

#### 4.4.2 Intrinsic attenuation

In addition to spherical divergence, elastic energy is absorbed by the medium by being transferred into heat by the friction of individual particles moving against each other as the seismic wave passes through the medium, amongst other mechanisms.

The exact processes by which seismic waves are attenuated are still not clearly understood. However, it is known that this energy absorption or intrinsic attenuation decreases exponentially with distance travelled. Attenuation also varies with the type of material through which the wave passes, and is characterised by the attenuation coefficient  $\alpha$ . If both spherical divergence (the  $1/r$  term) and absorption ( $\exp(-\alpha r)$ ) are combined together, the reduction in amplitude with distance is given by the expression in Box 4.10, in which a further coefficient is introduced, namely

the *quality* (or *slowness*) factor ( $Q$ ) and the *specific dissipation function*  $Q^{-1}$ .  $Q$  has been used extensively in seismological studies in plate tectonics (Jacobs, 1992) and particularly around island arcs. The attenuation coefficient is physically diagnostic of different types of rock. Much attention is now being paid to methods of determining  $Q$  directly from seismic data, particularly in shallow seismic surveys. Attenuation data have been traditionally obtained from laboratory measurements using ultrasonic transducers and through VSP experiments. It is through this kind of work that the processes of attenuation are being investigated (e.g. Jones, 1986; Klimontos and McCann, 1990). One of the outstanding problems which is receiving much attention with respect to hydrocarbon exploration is the effect of clay on the petrophysical properties of sandstones and shales. With the increase in capability of imaging the subsurface with finer resolution, unconsolidated sediments near the surface should also be studied in more detail.

The attenuation coefficient is a measure of the fractional loss of energy per unit distance, and  $2\pi/Q$  is the fractional loss per wavelength. Therefore the more cycles that occur, the greater will

**Box 4.9** Diffraction travel time calculations (see Figure 4.10)

Two-way travel time for a reflected signal,  $t_r$ , is given by:

$$t_r = (x^2 + 4z^2)^{1/2}/V \approx 2z/V + x^2/4Vz$$

For normal incidence, the two-way travel time,  $t_0$  is given by:

$$t_0 = 2z/V \quad \text{and} \quad \delta t = x^2/4Vz.$$

Hence

$$t_r = t_0 + \delta t$$

Total travel time for a diffracted wave ( $t_d$ ) with a source at O is given by the sum of the travel time along OT ( $= z/V$ ) and the travel time along any oblique raypath, such as TA ( $= (x^2 + z^2)^{1/2}/V$ ), such that:

$$\begin{aligned} t_d &= z/V + (x^2 + z^2)^{1/2}/V \\ &= 2z/V + x^2/2Vz = t_0 + 2\delta t. \end{aligned}$$

Note that the difference between the two travel times is that  $t_d$  is delayed by an extra term  $\delta t$  relative to the reflected arrival.

be the attenuation. From the first equation shown in Box 4.10, it is clear that the attenuation coefficient increases with increasing frequency, and so low-frequency waves will be attenuated more slowly than a higher-frequency wave. The effect of this on the shape of a wave pulse is for the higher frequencies to be attenuated faster than the low frequencies, which produces a pulse lengthening with distance travelled (Figure 4.14).

### 4.4.3 Scattering

Scattering of incident energy is evident as an apparent attenuation that takes place by reflection, refraction and diffraction of seismic

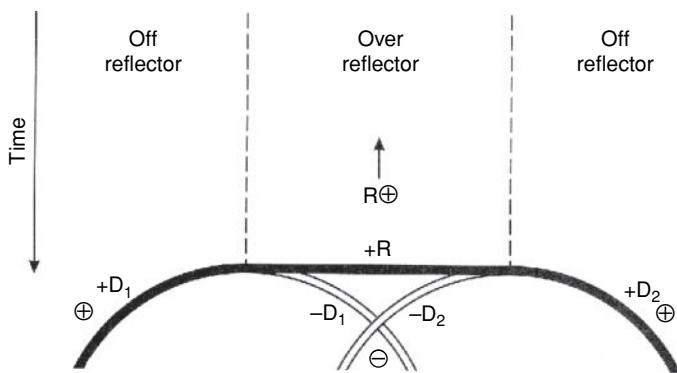


**Figure 4.11** Change of polarity by 180° (from + to -) on either side of a diffracting edge.  $D_1$  and  $D_2$  are diffractions with their polarities indicated; R is a reflection. After Trefry (1970) and Waters (1978).

waves. There are three levels of scattering that can be described in terms of the product of the wavenumber ( $k = 2\pi f / V$ ) and scale of the heterogeneity ( $a$ ).

- When  $ka \ll 0.01$ , the material through which the seismic waves are travelling is said to be *quasi-homogeneous*, and the scatterers are too small to be seen by the seismic waves except as an apparent anisotropy if enough cracks within the rock are aligned.
- Where the wavelength of the seismic waves is large compared with the heterogeneities ( $ka < 0.1$ ), *Rayleigh scattering* occurs and produces an apparent attenuation. This situation is the most common.
- In areas where there is very rapid variation in seismic wave velocity and density laterally and vertically, such as over old landfill sites, scattering can be very significant and will be evident on the seismic record as a chaotic jumble of signals that appears as noise. In this case,  $ka$  lies in the range 0.1 to 10, and the energy dissipation is known as *Mie scattering*.

In high-resolution shallow seismic surveys, sediments such as boulder-clay with boulders of the order of 0.5–1 m across are sufficiently large relative to the wavelength of the incident wave for scattering to be a significant cause of amplitude loss. For a survey with seismic waves of frequency 500 Hz, in a medium with P-wave velocity 2000 m/s, boulders of the size given above would yield a value of  $ka$  between 0.8 and 1.6, in which case Mie scattering would occur.

## 4.5 Seismic energy sources

The prime requirements of a seismic source are listed in Table 4.3. The aim of using any seismic source is to produce a large enough signal into the ground to ensure sufficient depth penetration and high enough resolution to image the subsurface. There are a large number of different sources that can be used in a wide variety of environments, and a great deal of development has been and is being done to make seismic sources more efficient and effective. Selection of the most appropriate source type for a particular survey is very important. Overviews of different source types have been given by Miller *et al.* (1986, 1992, 1994) with particular reference to engineering and environmental applications.

Generally speaking, there are three types of seismic source: impact, impulsive and vibrator. They can be used on land, in water and down boreholes, and are summarised in Table 4.4. In selecting a source, there is always a trade-off between depth penetration and minimum resolution, which is dependent upon one-quarter wavelength. To achieve good depth penetration requires a low-frequency source, but this has a lower resolution. High-resolution shallow seismic surveys require higher-frequency sources and thus have restricted depth penetration. The broad relationship between depth penetration and frequency for several high-resolution water-borne seismic sources is given in Figure 4.15. Detailed discussions

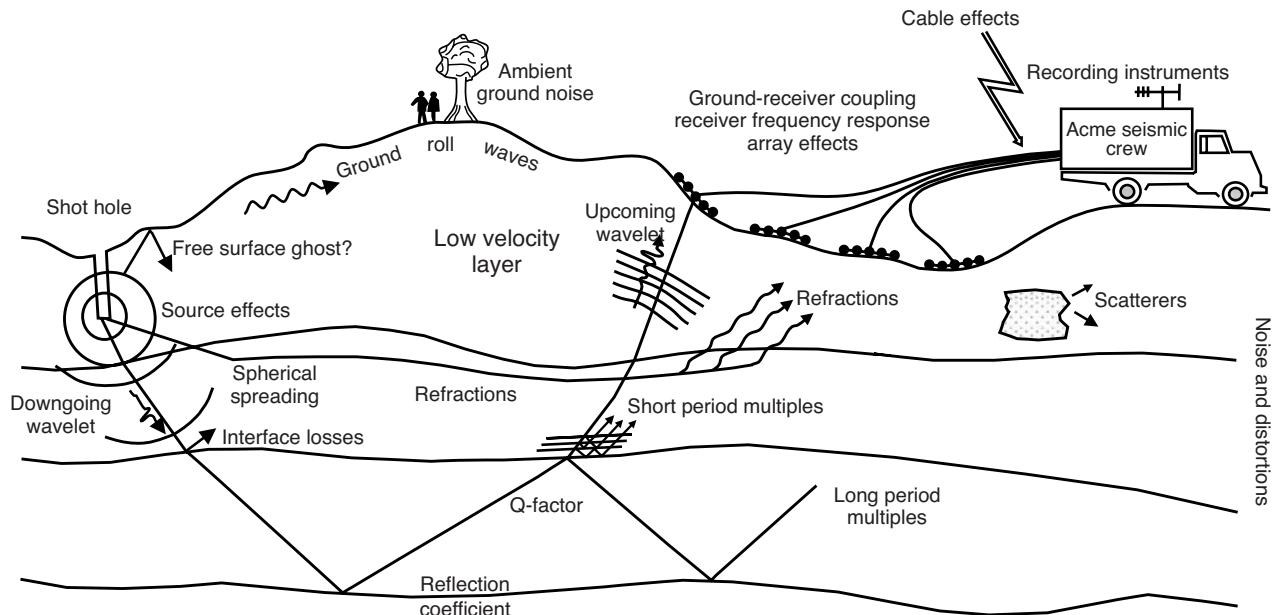


**Figure 4.12** Phenomena causing degradation of a seismic wave. Courtesy of BP.

of seismic sources and their characteristics have been given by Lugg (1979), Sieck and Self (1977) and Reynolds (1990a), among others.

### 4.5.1 Impact devices

These are devices where the seismic signal is generated by the impact of anything from a heavy sledge hammer through to a 3 tonne block being dropped from 4 m from the back of a drop-weight truck.

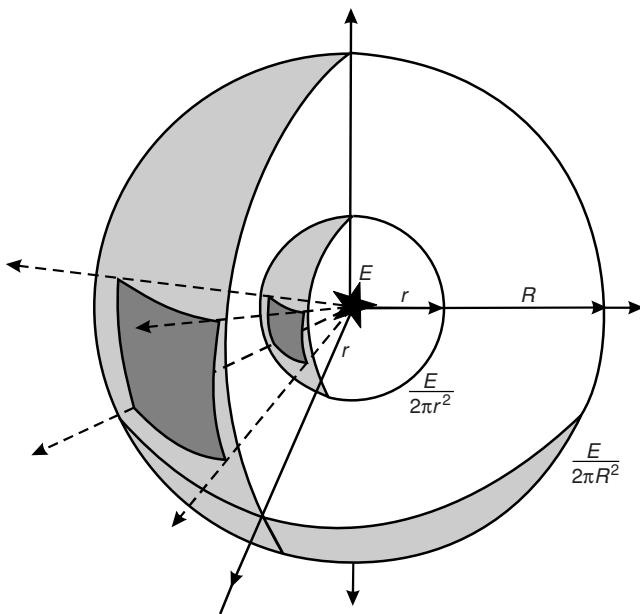


**Figure 4.13** The progressive diminution of energy per unit area caused by spherical propagation from an energy source at  $E$ .

#### 4.5.1.1 Sledge hammer

The easiest of all sources must be the humble sledge hammer. A standard sledge hammer is struck against a heavy-duty rubber baseplate. An inertia switch on the hammer handle or a geophone beneath the baseplate triggers the seismograph when the hammer head strikes the plate. The source is easily repeatable, although to obtain similar

#### Box 4.10 Attenuation of seismic waves

For a homogeneous material:

$$\frac{A}{A_0} = \frac{r_0}{r} \exp\{-\alpha(r - r_0)\}$$

where  $A$  and  $A_0$  are the amplitudes at distance  $r$  and  $r_0$  from the source, respectively;  $\alpha$  is the attenuation coefficient, which is related to the velocity of elastic waves ( $V$ ) and their frequency ( $f$ ) by:

$$\alpha = \pi f / QV \quad \text{and} \quad Q^{-1} = 2\alpha\lambda$$

where  $Q$  is the quality factor and  $\lambda$  the wavelength.

For sandstones with porosity  $\varphi$  (%) and a clay content  $C$  (%):

$$\alpha = 0.0315\varphi + 0.241C - 0.132 \text{ (dB/cm)}$$

and:

$$Q = 179 C^{-0.843}$$

at 1 MHz and 40 MPa (Klimentos and McCann, 1990).

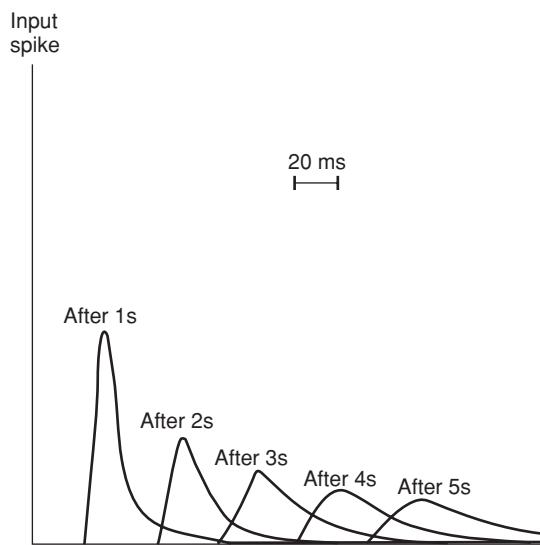


**Figure 4.14** The progressive change of shape of an original spike pulse during its propagation through the ground, due to the effects of absorption.

source pulses the same person should use the hammer for each set of shots. Even with the same weight of hammer head, operators who are not the same height (or even build) swing the hammer differently, so producing source signals that are not exactly reproducible. Furthermore, if care is not taken, the more a baseplate is hit at one location, the more it tends to angle away from the operator, giving some sense of directionality to the signal generated and an increase in ground roll. The hammerer must also try to stop the hammer head from bouncing on the baseplate after the main strike, as even slight bounces may produce a tail to the source pulse.

In engineering work, signal enhancement seismographs stack the signal to improve the signal-to-noise ratio. The bad news for the

**Table 4.3** Requirements of a seismic source.

**Technical:**

1. Sufficient energy to generate a measurable signal with a good signal-to-noise ratio
2. Short-duration source pulse with high enough frequency for the required resolution
3. A source wave of known shape (or minimum phase)
4. Minimal source-generated noise

**Operational:**

5. Efficient to use, especially if multiple shots or fast repetition rates are required
6. Repeatable pulse shape
7. Safe to operate and with minimal maintenance
8. To be operated by as few people as possible
9. Reasonably priced both to buy/hire and to use

**Table 4.4** Seismic sources.

		On land	On water
<i>Impact:</i>	Sledge hammer Drop-weight Accelerated weight		
<i>Impulsive:</i>	Dynamite	Airgun	Pinger Boomer Sparker
		Detonating cord Airgun Shotgun Borehole sparker	Gas gun Sleeve gun Water gun Steam gun
<i>Vibrator:</i>	Vibroseis Vibrator plate	Multipulse GeoChirp	Rayleigh wave generator

person wielding the hammer is that to improve the signal-to-noise ratio ten times requires the plate to be struck 100 times! The rate of improvement corresponds to the square-root of the number of shots or hits.

The advantage of this source is that it is cheap, causes minimal environmental damage and is extremely easy to use. For shallow seismic work, the hammer source may provide sufficient energy for spreads up to refraction line lengths of over 200 m, and interface depths of 30 m or more, depending on the local geological conditions.

#### 4.5.1.2 Drop-weight devices

The depth penetration obtainable from drop-weight sources is dependent upon the momentum of the mass as it strikes the ground. For lightweight portable systems, a small weight is suspended from an electromagnet at the top of a tube 3 m long. On triggering the seismic recording system, the electromagnet releases the weight, causing it to fall through the tube and strike a baseplate. The disadvantage with this system is that often the falling weight rattles against the side of the tube during its descent, triggering the recording system prematurely. Also the weight may bounce on the baseplate unless a catcher device is incorporated, giving rise to additional but unwanted signals. The converse of this system is for a small hollow metal cylinder (e.g. 5 kg) to fall from a height guided by a pole down which the weight slides until it strikes a base plate (Toteva and Long, 2007).

Portable gantry systems can be used where a tower is constructed out of pre-assembled sections to reach up to 5 m high. An electromagnet again is used to release the weight. In this case the weight used can be something like an old gas cylinder filled with concrete. The heavier the drop-weight and the taller the gantry, the less portable the system becomes.

In the seismic industry, special weight-drop trucks (Figure 4.16A) have gantries that can drop a 3 tonne weight from 4 m height routinely with reproducible source characteristics. Often more than one shot is used so that the total source signal is made up of a number of wallops and the received signals are summed. The disadvantages

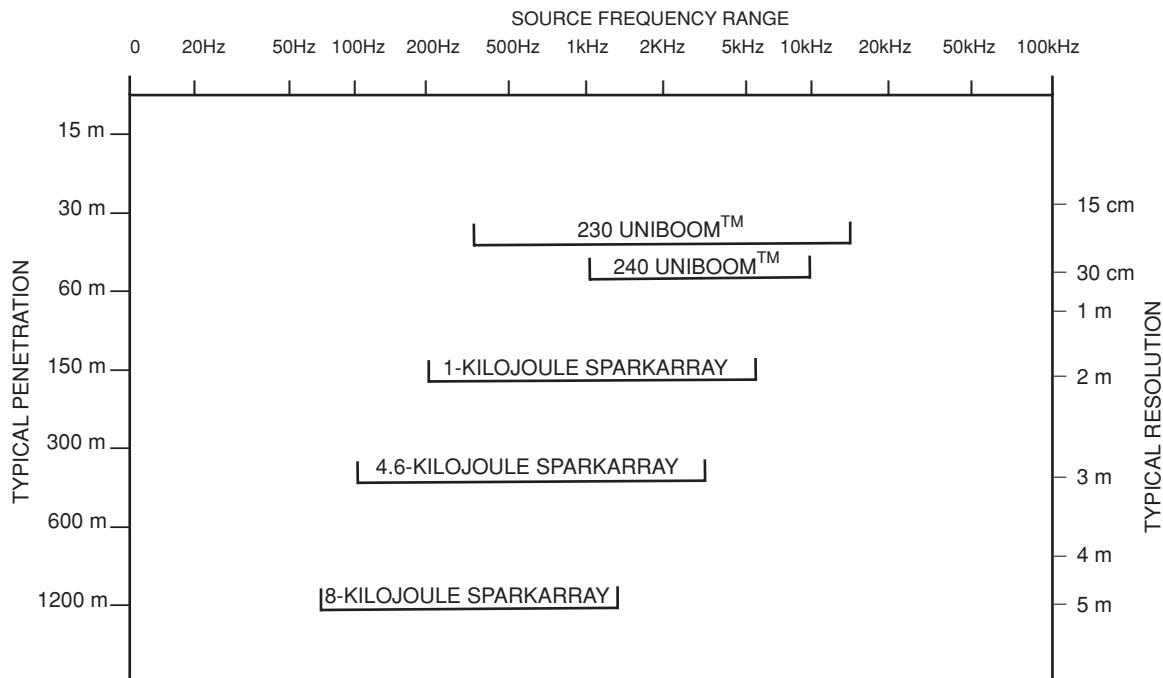


**Figure 4.15** Typical penetration and resolution for Uniboom and Sparker sources as a function of their respective frequency bandwidth.  
Courtesy of EG & G.

are the relative expense of such a system, and the fact that the source noise is often high, making it only useful in regions, such as deserts, with very low ambient noise levels. Furthermore, with some drop-weights, they fall unevenly so that one edge lands before the rest and so slaps the ground rather than providing a sharp impulse. Consequently, the source shape is often not evenly reproducible or well constrained. However, the field effort involved in undertaking an extensive programme with a weight-drop truck can be less than that required for shooting with explosives for which pre-drilled holes in which to fire the shots are required. Given the issues over the control of the source characteristics, the environmental footprint and safety issues, weight-drop sources have fallen out of favour recently in the hydrocarbon exploration industry.

#### 4.5.1.3 Accelerated weight drop (AWD)

In order to maintain a lightweight system yet not sacrifice depth penetration, accelerated weight drop devices have been developed. These use a shorter tower and smaller weight, but have a mechanical system to accelerate the weight towards the baseplate rather than allowing it to freefall. The Dinoiseis uses compressed air. An alternative propulsion system is the vertical slingshot method employed in the elastic wave generator (Bison Instruments Inc.). Thick elastic slings and gravity accelerate a 250 kg hammer into a steel anvil on the ground surface (Figure 4.16B). Other, more compact systems also exist such as the PEG source, which propels a steel bar vertically downwards against a steel baseplate (Figure 4.16C) and can repeat the process automatically for stacked shots. Whereas the use of traditional heavy weight-drop sources has declined in recent years, accelerated weight drops have begun to find increasing favour. This

is due in part to the more acceptable environmental footprint but also to the better control now achievable on the source characteristics. A new system has been developed by Polaris Explorer Ltd (Explorer 860 AWD; Figure 4.16D), which uses a hydraulic system to raise and lower a weight of approximately 1180 kg (Monk *et al.*, 2004). The system is mounted on the back of a vehicle in such a way that allows the gimballed baseplate to be deployed so that the weight of the vehicle holds the baseplate on the ground prior to the initiation of a shot, and so that the accelerated mass always hits the baseplate perpendicularly, ensuring repeatability of the source characteristics. The projectile weight is located at the centre of the system and its direction of travel is controlled by a central spindle. The weight can be raised about 61 cm (2 ft) and released under pressure onto the baseplate which has a similar mass. The peak output force achievable is 3825 kN (860,000 lbs), although the best results are achieved at typically 65% of peak output (due to reduced ground roll). The overall reflection characteristics achieved are better than those obtained using dynamite. In a tradition 3D seismic survey, the productivity rate is controlled by the drilling of shot holes. When using an AWD, the controlling factor is the rate at which the receiver strings can be moved. More than 1000 shot points can be acquired in a day.

#### 4.5.2 Impulsive sources

A further type of source is one that uses the detonation of a small charge to propel either lead shot, bullets or wadding into the ground. A common make is the so-called ‘Buffalo gun’ that comprises a metal pipe inserted vertically up to 1 m or so into the ground. A shotgun shell located at the lower end is detonated via a firing rod, which

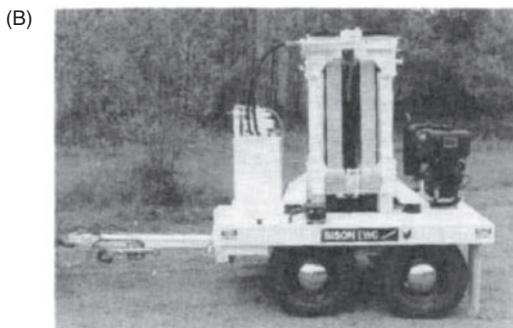


**Figure 4.16** (A) Weight-drop truck (courtesy of BP). The mass is dropped from the gantry at the rear of the vehicle. (B) Accelerated weight-drop system from Bison Instruments Inc. (C) PEG source. (D) Explorer 860 AWD (Courtesy of Polaris Explorer Ltd).

protrudes to the surface, being struck by a mallet. In some countries, such as the UK, and depending on the policy of local police forces, a firearms certificate may be needed before such a device can be used. Cartridges made up with different gunpowder mixes coupled with variable amounts of wadding present will affect the amount of energy discharged with each shot. Subsequent shots made into the

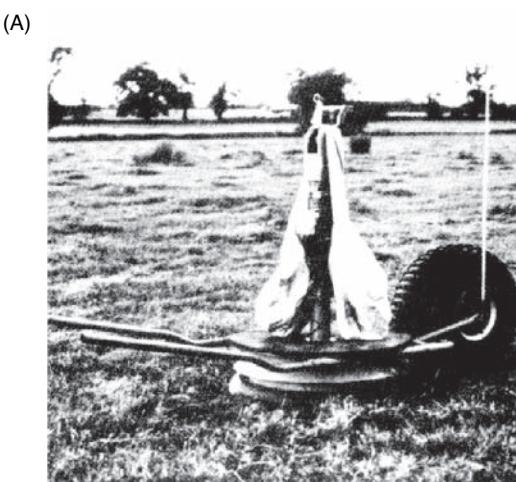


**Figure 4.17** (A) Betsy gun. The bags suspended from the barrel are used to hold live and spent cartridges. (B) Generation of S-waves using a sledge hammer against a wooden sleeper weighted down by a heavy vehicle.

same hole may produce different source characteristics due to the effect of the cavity made during the first blast.

A modification of this which does not require a hole to be predrilled is called the Betsy gun™ (Betsy Seisgun) where the entire assembly is housed in a wheelbarrow assembly that is wheeled to the required location and the shot fired on to the ground surface inside a protected chamber (Figure 4.17A). Another source consists of a 0.5 calibre machine-gun mounted on the back of a pickup truck with the barrel pointing vertically downwards into a muzzle. Belts of standard ammunition are fed through the gun and fired in bursts. There are restrictions in some parts of the USA on using such weaponry as seismic sources because of the resulting subsurface lead pollution. For sources of shear waves, mortars and anchored Howitzer artillery guns have been used when firing blanks so as to utilise the recoil to produce S-waves.

A less dramatic and perhaps safer way to generate shear waves is to place a heavy wooden beam on the ground and weight it down using the front wheels of a heavy vehicle. The end of the beam can be struck using a pivoted sledge hammer (Figure 4.17B).

### 4.5.3 Explosive sources

Explosives are now used in only 40% of land seismic surveys. Once the main source in marine shooting, the high fish kill occasionally caused by the shock wave from the explosion was considered to be environmentally unsatisfactory and has led to its decline in usage. Also, explosions were not identically repeatable, nor could the exact time of detonation be obtained with the accuracy required in modern seismic surveying. In land shooting, a single shot can provide enough energy into the ground and with sufficient frequency bandwidth for rapid coverage of survey lines. It is necessary for the shot to be acoustically coupled to the ground. This is best achieved by blasting in water-filled holes.

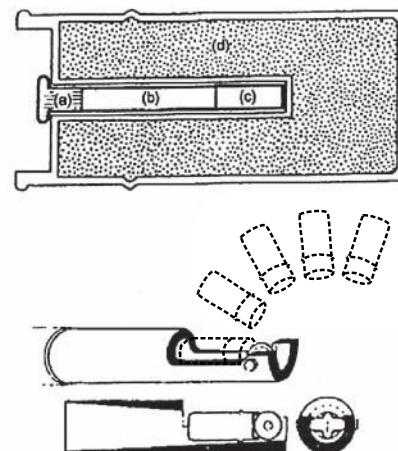
The common form of explosive is dynamite or gelignite (ammonium nitrate), which is quite safe when handled properly as it can only be detonated by very high temperatures as achieved by the shock from detonator caps. Handling gelignite causes headaches if the chemicals make contact with the skin. Anyone considering using explosives should attend appropriate safety courses and become fully conversant with the safe use of such material. Although explosives provide a very lightweight and portable high-energy source, the practical problems involved with transporting and storing explosives can be a major disadvantage. So, too, can be the problem of dealing with explosives that have failed to detonate. Liaison with local police is almost universally necessary, and in many countries only licensed explosives-handlers are permitted to work as shot firers.

For very shallow work, detonator caps on their own can be used as a source. It is best to use 'zero delay' seismic detonators because other types, as used for example in quarry blasting, have a finite delay of several milliseconds between being triggered and detonating. Detonator caps need to be handled with great care as, although small, they can still blow off fingers or hands. Another form of explosive is detonating cord, such as Primacord™ (Ensign Bickford Co.), Geoflex™ and its marine equivalent, Aquaseis™ (both Imperial Chemical Co.). Explosive cord is ploughed into the ground using special bulldozer rippers and detonated as a line rather than a point source. The explosion starts at a point but ripples along the cord and may be used to trigger other explosives attached along its length. Alternatively, cord can be deployed from hovercraft or other platforms in shallow waterborne surveys.

In marine multichannel seismic surveying, various configurations of detonation of small amounts of explosives are available, such as the Maxipulse™ (Western Geophysical Co.) and Flexotir™ (Compagnie Général de Géophysique) (Figure 4.18). In the Maxipulse system, a small explosive charge (Figure 4.18A) of nitrocarbonate is flushed down a hose to the trigger mechanism. The charge strikes its detonator on a firing wheel as the charge is ejected and triggers a delay fuse which detonates the main charge at between 7 and 15 m depth after a period sufficient for the gun to have been towed from the vicinity. The ensuing bubble pulse train has to be removed by specialised processing.

In the Flexotir system, a very small amount of charge (typically about 60 g) is pumped down a flexible hose by water under pressure into a steel cage rather like a spherical colander in which the charges are detonated (Figure 4.18B). Water expelled by the explosion flows in and out through the holes in the cage.

(A)



(B)

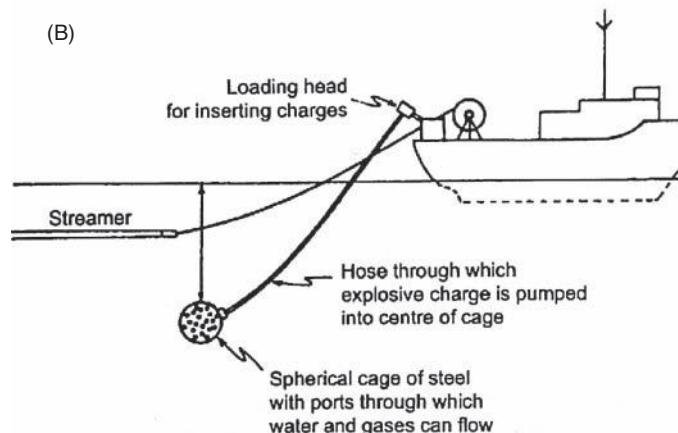


**Figure 4.18** (A) A schematic cross-section of the Superseis charge used in the Maxipulse system: (a) = rim fire percussion cap; (b) = delay column; (c) = booster; and (d) = nitrocarbonate main charge. Underneath is shown the Maxipulse gun. A perspective view of the gun shows the charge striking the firing wheel, then successive stages of ejection. The cross-section and end views show the charge in the gun at the instant of striking the firing wheel. Courtesy of Western Geophysical, McQuillin et al. (1984) with kind permission from Kluwer Academic Publishers. (B) Flexotir system. After Sheriff (2002), by permission.

### 4.5.4 Non-explosive sources

All the non-explosive marine sources (cf. Table 4.4) give rise to varying degrees of a bubble pulse. When the source is discharged, cavitation occurs when the surrounding water is displaced by the formation of a gas bubble, usually of air. Hydrostatic pressure causes the bubbles to collapse, so pressurising the gas which heats up and expands to reform smaller bubbles, which too, in turn, collapse and reform (Figure 4.19A), until such time that the hydrostatic pressure is too great and the remaining gas dissolves in the water or

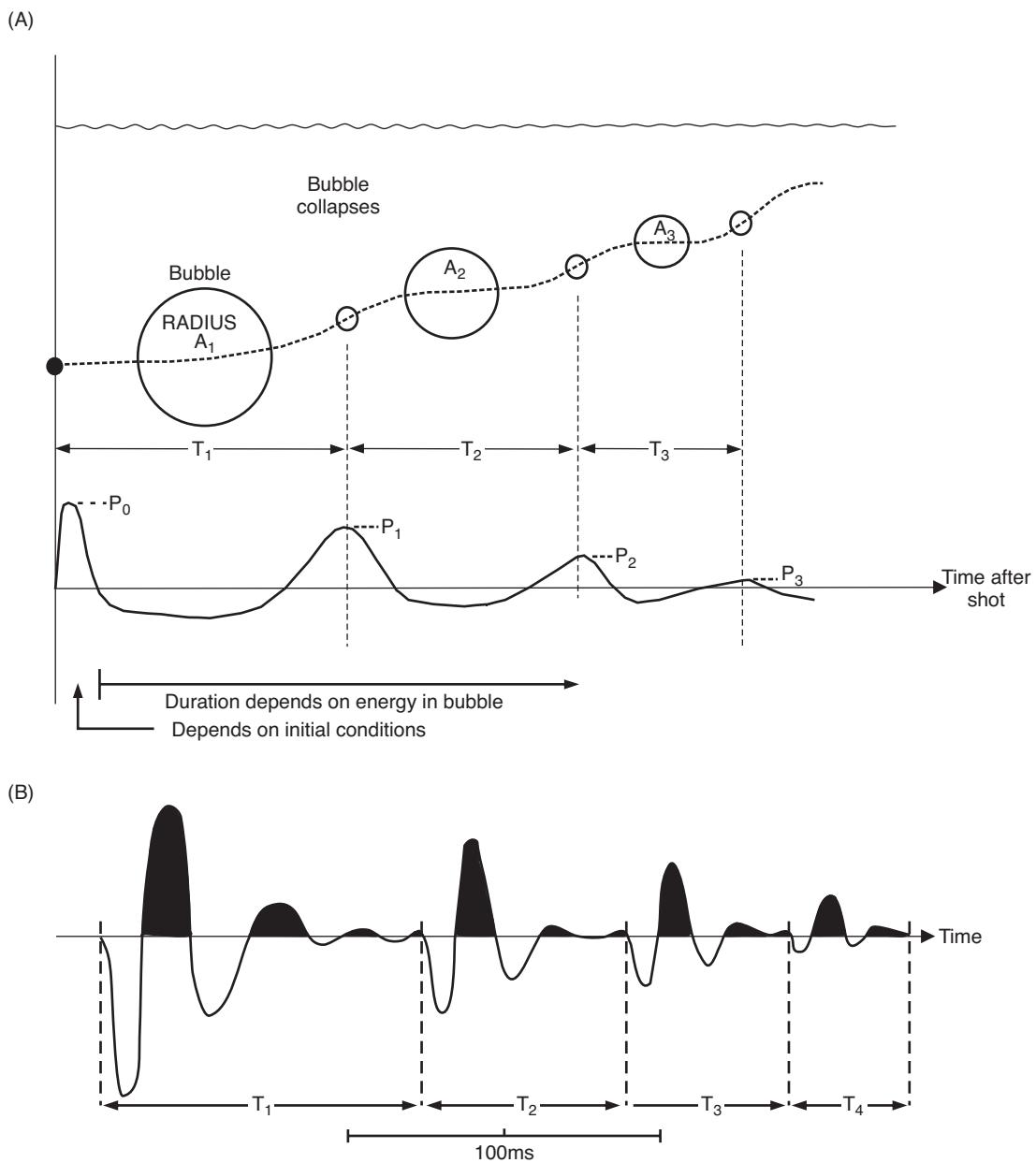


**Figure 4.19** (A) Archetypal marine source showing the response of the bubble from the point of forming at the firing of the source through to venting at the water surface. The respective bubble pulse periods ( $T$ ) and amplitudes ( $P$ ) are indicated as a function of time. Courtesy of BP. (B) The corresponding bubble pulse train.

finally vents to the surface. The acoustic noise from the successive collapses of the bubbles produces noise which is undesirable (Figure 4.19B) and which can either be removed by later processing or is minimised using a tuned array of sources. Airguns (see next section) with different volume capacities are fired simultaneously, but the respective bubble pulses occur at different times and with varying amplitudes. By summing all the individual signatures of an array, a much more acceptable overall source signature can be produced (Figure 4.20). Bubble pulses can also be reduced by using a waveshape kit within each airgun, for example. Air is bled under pressure into the expanding bubble, thereby reducing the rate at

which it collapses, with a consequent reduction in the overall length and severity of the bubble train. The effectiveness of a marine source can be measured in terms of the ratio of the amplitudes of the primary to first bubble signal. A summary of marine airgun arrays has been provided by Amundsen and Landrø (2010a,b).

#### 4.5.4.1 Airguns and sleeve guns

An airgun is used to inject a bubble of highly compressed air into the surrounding water and is the most commonly used of all seismic sources (Figure 4.21). Airguns, although usually deployed in marine

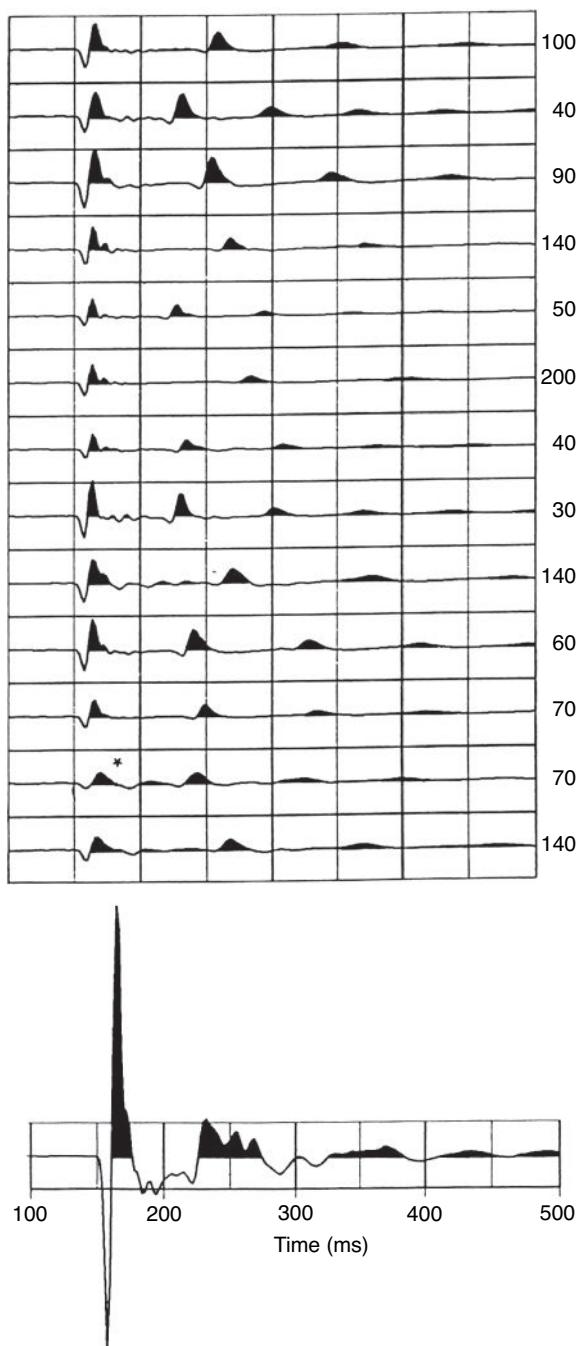


**Figure 4.20** Individual airgun signatures and the simulated array signature produced by summing them. The asterisk indicates a malfunction. Courtesy of BP.

surveys, can also be used in modified form in marshlands, in a land airgun, and as a borehole source. Compressed air is fed through a control chamber (Figure 4.22A) into a lower main chamber and in so doing a shuttle is depressed, closing off the external ports. Opening a solenoid valve (Figure 4.22B) releases the sealing pressure in the upper control chamber and the shuttle moves rapidly upwards, so releasing the high-pressure air in the lower chamber to vent explosively through the ports (Figure 4.22C and D). The shape of

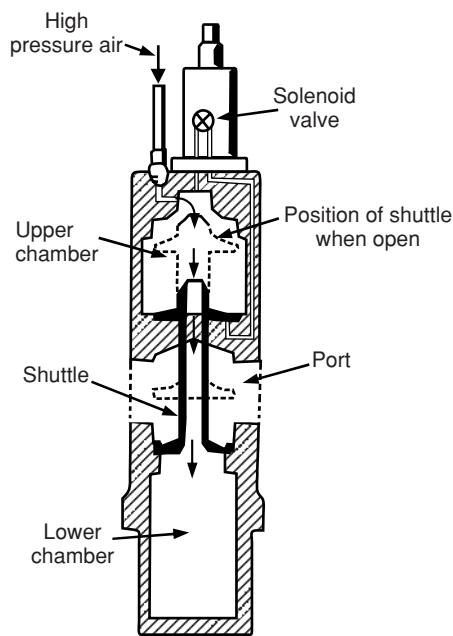


**Figure 4.21** Schematic cross-section through an airgun. High-pressure air flows continuously into the upper chamber and through the shuttle into the lower chamber. Opening the solenoid valve puts high-pressure air under the upper shuttle seat, causing the shuttle to move upward, opening the lower chamber and allowing its air to discharge through the ports to form a bubble of high-pressure air in the surrounding water. The size of an airgun is indicated by the volume in cubic inches of its lower chamber (1991). Courtesy of Bolt Associates.

the source pulse is dependent upon the volume of air discharged, its pressure, and the depth at which the gun is discharged. It has been found (Langhammer and Landrø, 1993) that airgun signatures are also affected by the temperature of the surrounding water. The primary-to-bubble ratio and the bubble time period both increase with increasing water temperature.

Airguns range in volume capacity (lower chamber) from a few cubic inches to around 2000 cubic inches ( $0.033 \text{ m}^3$ ), and pressures from 2000 to 4000 pounds per square inch ( $1400\text{--}2800 \text{ Mg/m}^2$ ). Older airguns had 4 or 6 cylindrical holes through which air was expelled. More recently, sleeve guns have been developed which allow the air to escape through an annulus as a doughnut-shaped bubble (Figure 4.23) and the effect is to reduce the bubble pulse. When the gun is fired, instead of an internal shuttle moving, an external sleeve moves.

#### 4.5.4.2 Water guns

Instead of expelling compressed air into the surrounding water, which often has had deleterious effects on local fish stocks, air is used to force a piston forward which discharges a slug of water. When the piston stops, cavitation occurs behind the expelled water, resulting in an implosion which creates the seismic pulse. The firing sequence is outlined in Figure 4.24. The major advantage of a water gun is that no real bubble pulse is produced.

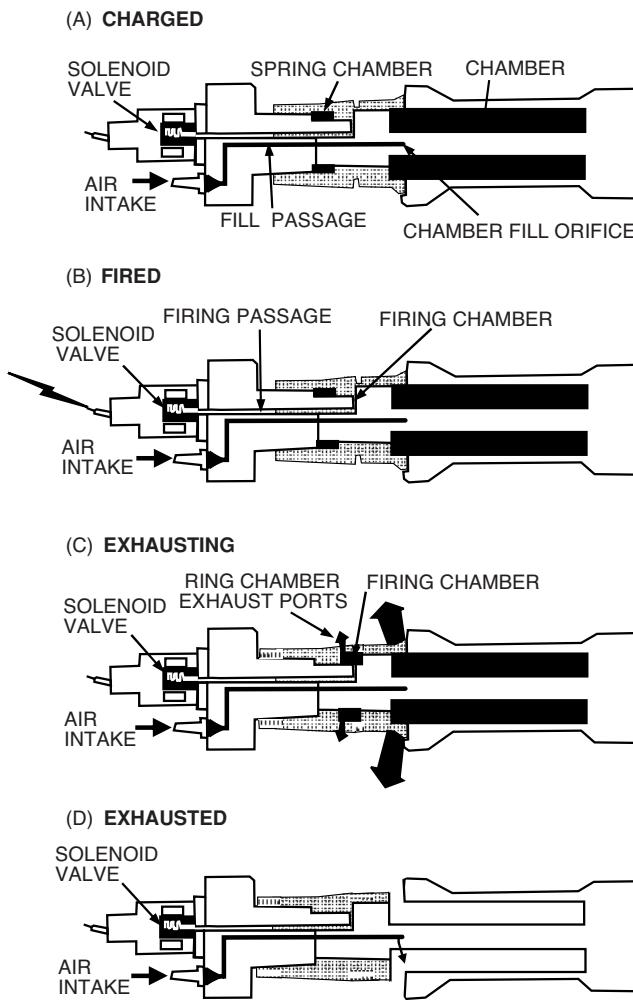


**Figure 4.22** The operation of a sleeve gun is very similar to that of an airgun. Instead of a shuttle moving to release the compressed air, an outer sleeve is used instead. (A) The sleeve gun charged ready to fire; (B) fired; (C) the lower chamber discharges its compressed air into the surrounding water, until (D) the lower chamber is exhausted of air.

#### 4.5.4.3 Gas guns/sleeve exploders

A mixture of butane or propane with oxygen or air is exploded under water using a gas gun. Alternatively, the mixture is detonated inside a tough rubber bag that expands to contain the explosion, and then collapses creating an implosion which is the main source pulse. The exhaust gases are vented from the sleeve, up hosing to the surface, so that there is no bubble pulse. A major trade name is Aquapulse™ (Esso Production Research) and the system is used under licence by several seismic contractors.

#### 4.5.4.4 Steam gun and Starjet

Compagnie Générale de Géophysique (CGG) has developed a steam gun under the name Vaporchoc™. Steam generated on board ship is fed into the water through a remotely controlled valve (Figure 4.25A). This releases a bubble of steam, causing a small amount

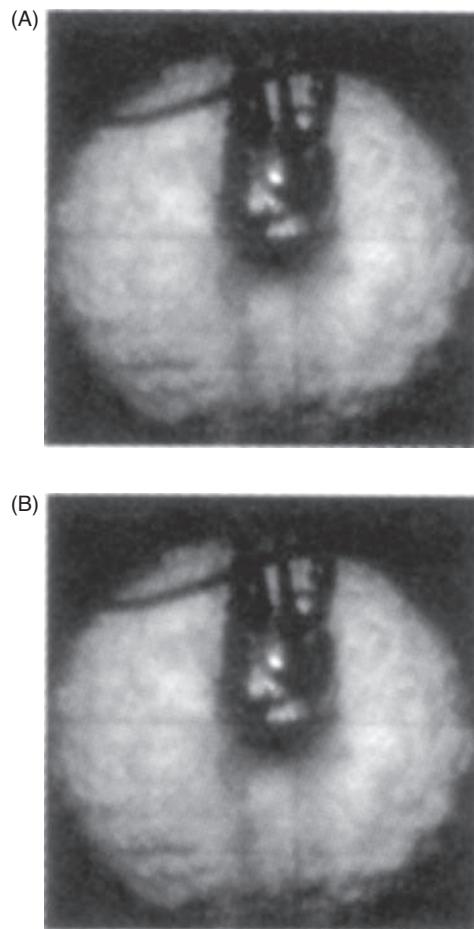


**Figure 4.23** The exhaust bubbles from (A) a conventional airgun, and (B) a sleeve gun. Courtesy of Texas Instruments.

of acoustic noise which precedes the main seismic pulse. This pre-emptive noise is known as the *source precursor*. On closing the valve, steam in the bubble condenses and the internal gas pressure drops to less than hydrostatic pressure, so causing the bubble to implode, radiating acoustic energy with negligible bubble pulse. However, to overcome the problems over the precursor signal, CGG has developed the Vaporchoc principle in a system known as Starjet, which uses four systems, each of which has four tunable guns. By varying the timing of the discharge of each of these systems, the precursors can be manipulated to become self-cancelling. The overall source pulse shape is far cleaner with minimum ringing, as can be seen in Figure 4.25B.

#### 4.5.5 High-resolution waterborne sources

In the last few years an increasing amount of attention has been paid to high-resolution waterborne surveys using high-frequency sources. The types of applications for such surveys are listed in Table 4.5. There are three main types of source in this category, namely pingers, boomers and sparkers (Figure 4.26), each with a different frequency bandwidth, resolution and depth penetration (see Table 4.6).

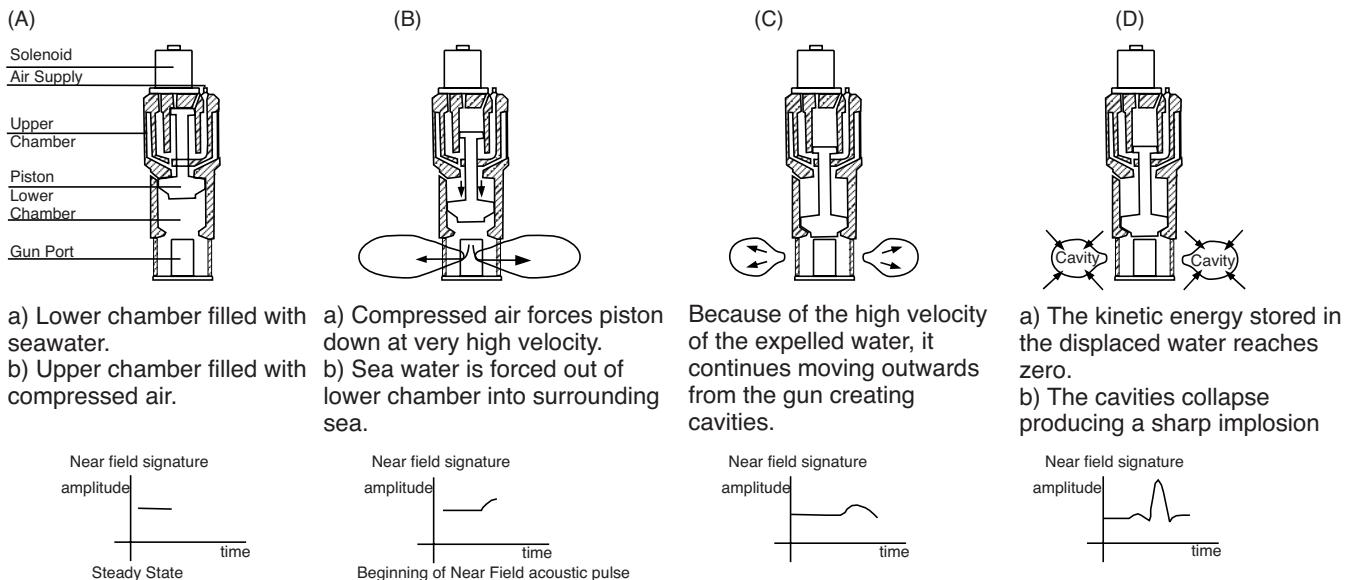


**Figure 4.24** The operation of a water gun: (A) charged ready to fire; (B) fired; (C) discharge of water from the gun creates cavities surrounding the gun; (D) the cavities collapse, producing a sharp implosion impulse. Courtesy of SSL.

A *pinger* has the highest frequency of the three types, and greatest resolution but least penetration. A *boomer* consists of a capacitor bank that discharges through a transducer which consists of two flat parallel plates. Eddy currents are established in the plates, forcing them suddenly apart (by magnetic repulsion) to produce a low-pressure region between the plates into which surrounding water rushes, creating an implosive pressure wave. The boomer is a surface tow device which is very portable (liftable by two people) and can easily be operated out of relatively small vessels, making it ideal for inshore work. A deep-tow version can be used for deep-water applications where the energy source is deployed close to the seabed to maximise the energy transmission into the substrate.

A *sparker* consists of a capacitor bank that discharges through a submerged cage, which houses a number of electrodes (3–300). An electric arc is created between the electrode tips and the frame, so ionising the seawater to produce hydrogen bubbles that then implode, creating the pressure pulse. In freshwater environments normal sparkers do not operate effectively (due to the low conductivity of fresh water). In these environments a close circulation system needs to be employed where saline water is circulated over the electrode tips so that they can spark. A downhole sparker had been developed that contained the electrode elements in a saline solution within a rubber enclosure. Such a device could also be used in open water conditions within lakes and rivers.

Of the three types of sources, sparkers undoubtedly have the most variable source characteristics. The source pulse shape depends critically on the output power of the system and the number and configuration of the electrodes in the sparker array (Reynolds, 1990a). Better pulse shapes are achieved by increasing the number of electrode tips, although higher-powered systems tend to have fewer electrodes. Typical pulse shapes for squid and delta sparkers are shown in Figure 4.27. During a survey some electrode tips may burn back to the insulation and cease to work, thereby reducing the

number of active tips and the effective output – both of which serve to degrade the pulse shape. It is important, therefore, to check on the state of the electrode tips during each day's survey and to monitor signal quality. In addition, the depth of the frame below the water surface also affects the pulse shape by virtue of the interference of the surface ghost and bubble pulse.

## 4.5.6 Vibrators

### 4.5.6.1 Vibroseis

On land, an alternative to explosive or impulsive sources is the use of a vibrating plate to generate a controlled wave train. A system developed by Conoco, known as Vibroseis and described in detail by Baeten and Ziolkowski (1990), consists of a vibrator plate mounted on the underside of a special truck. When on location the plate is set on the ground surface and the truck is jacked up so that its weight is transferred to the plate (Figure 4.28). A low-amplitude sinusoidal vibration of continuously varying frequency (between 60 and 235 Hz) is applied over a *sweep period* which lasts between 7 and 60 seconds.

Progressively increasing frequencies are used in *upsweeps* and progressively decreasing frequencies with time are used in *downsweeps*. Usually the change of frequency is linear, although non-linear sweeps may be used where higher frequencies are used for longer to compensate for loss of high-frequency information through the propagation of the signal. The resulting field record is the superposition of the reflected wavetrains (Figure 4.29) and is correlated with the known source sequence (pilot sweep). At each sample point along each trace the pilot is cross-multiplied with the superimposed signals to produce a *correlogram* trace. When the pilot sweep matches its reflected wavetrain (i.e. autocorrelates) it produces a significant zero-phase wavelet (known as a *Klauder*

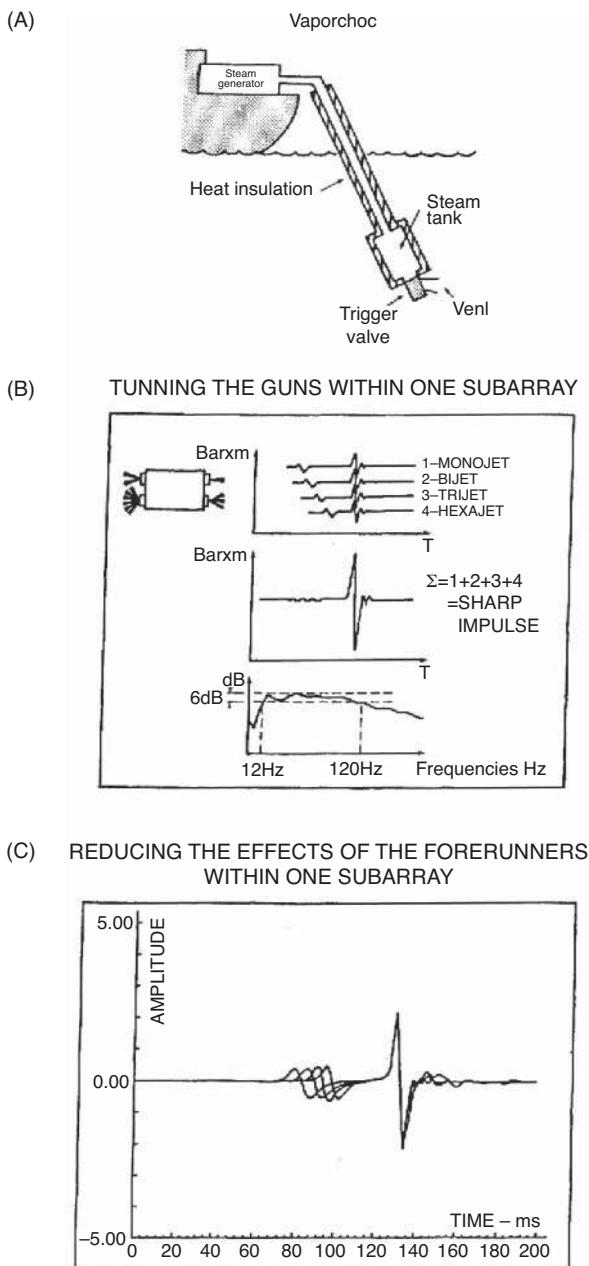


**Figure 4.25** (A) The Vaporchoc system. (B) and (C) The use of Starjet to modify the source characteristics.

wavelet) on the trace (Figure 4.29). The display of adjacent correlogram traces produces a seismic section or correlogram which resembles its conventional seismic counterpart obtained using a high-energy impulsive source.

A major advantage of the Vibroseis method is that it is a rapid and easily repeatable source that is convenient to use, especially in urban areas. The cross-correlation data-reduction method enables the extraction of sensible signals even in areas with high cultural noise. Furthermore, the Vibroseis method does not damage the ground surface and thus can be used with care on macadamised roads and over public utilities.

**Table 4.5** Principal applications of commercial waterborne site investigation using high-resolution seismic methods.

**Near/inshore marine/estuarine environments:**

- Bridges, tunnels, viaducts
- Harbours, jetties, quay walls, marinas, canals
- Pipelines and sewage outfalls
- Dredging for access channels to ports/harbours

**Marine:**

- Hydrocarbon pipelines
- Hydrocarbon production platforms/wellheads
- Siting of drilling rigs
- Shallow gas surveys
- Sand and gravel resources
- Dredge and contaminated spoil-dump surveys
- Wind-farm foundation surveys

In order to increase the energy input into the ground for greater depth penetration, a number of vibrators can be used simultaneously in a group provided they are phase-locked, i.e. they all use the same sweep at exactly the same time. Multiple sweeps can be used and summed (stacked) to improve the signal-to-noise ratio. It is possible to improve the results from vibroseis methods for shallow investigations using the groundforce signal of the vibrator as a correlation operator and applying sweep deconvolution (Buness, 2007).

Very large vibrators have also been developed for crustal and earthquake studies where the actuator mass is of the order of 100 tonnes (Kovalevsky *et al.*, 2009). Vibroseis interferometry was used with 10-minute periods of vibration at three separate frequencies (7, 8 and 9 Hz).

#### 4.5.6.2 Small-scale land vibrators

On a much reduced scale, the Vibroseis principle can be used in the form of a number of small vibrator sources. One of these is the Mini-Sosie source which consists of a pneumatic hammer impacting on a baseplate. The thumper delivers a random series of blows to the baseplate on which a detector is located which records the source sweep. The variable-frequency source wavetrain with low amplitude is transmitted into the ground. The detected signals are cross-correlated with the recorded pilot sweep to produce correlograms. The source can produce 10 pops/second and several hundred pops are summed at each shot point. The frequency range of this method is higher than for dynamite, thereby providing higher resolution. Another type of P- and S-wave vibrator is *Elvis* (Electrodynamic Vibrator System) (Figure 4.30A), which uses sweep frequency control software to control the operation of both the seismograph (e.g. Geode) and the vibrator from the same computer. It can generate a peak force of  $\sim 450$  N, has a frequency range of 5–360 Hz and can generate signals to about 100 m, and to 200 m for zero-offset vertical seismic profiles (VSPs).

For a shallow hydrocarbon exploration, mining or geotechnical surveys, a number of small land vibrators were developed during the early 1990s. One of these was described by Christensen (1992).

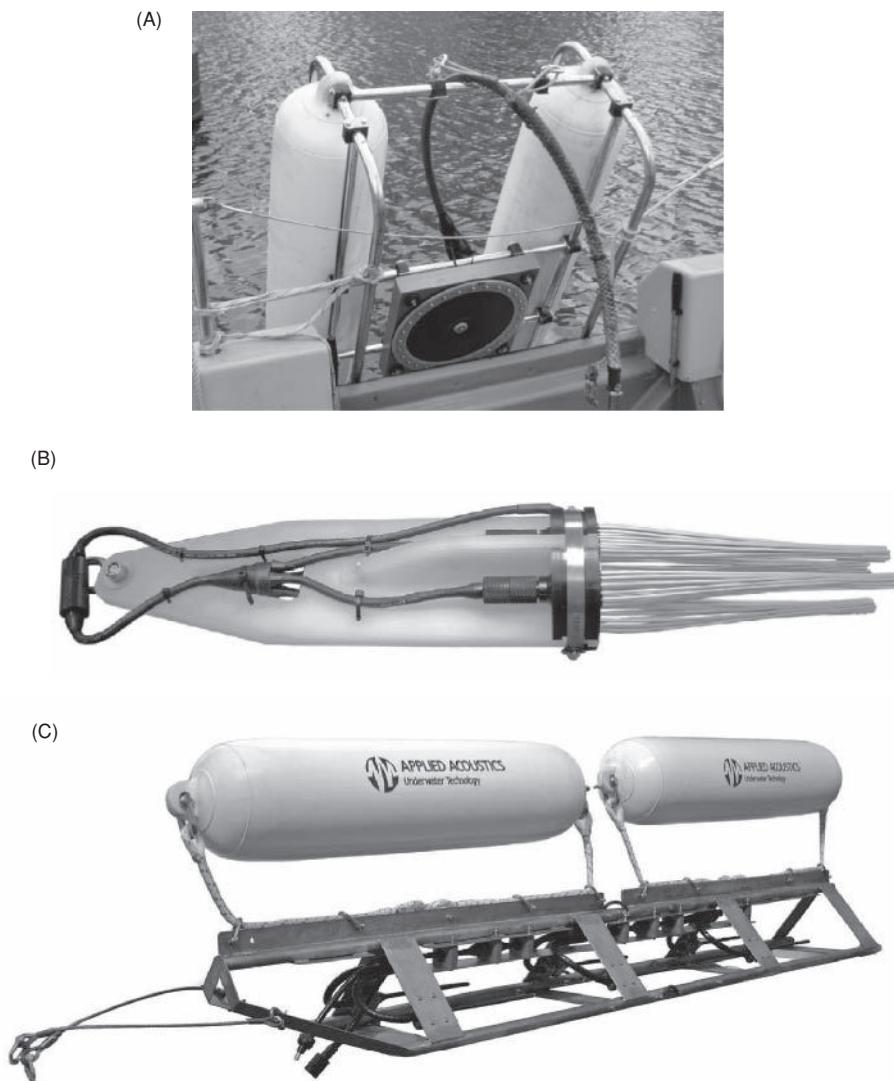


**Figure 4.26** (A) Boomer plate with a surface-tow catamaran; (B) a Squid sparker system, and (C) a Delta sparker system where the electrode tips are the spikes within the A-frame. (B) and (C) courtesy of Applied Acoustics.

His device consists of a 0.91 m diameter baseplate on which a 136 kg mass is located (Figure 4.30B). A small engine drives a hydraulic pump which energises the vibrator over a frequency bandwidth of 10–550 Hz at 4.4 kN output. The peak force is 30.5 kN. By slanting the mass-actuator through 45° (Figure 4.31), both P- and S-waves can be generated. A PC-based controller drives the vibrator using open-loop amplitude and phase control. It also measures the

output of the vibrator, utilising appropriate sensors, and records this information for signal correlation purposes.

It is becoming increasingly important to measure *in situ* stiffness of the ground rather than relying solely on measurements made on samples in a laboratory. One way to achieve this is to use a Rayleigh wave generator. A mass is suspended in a small gantry (Figure 4.32) that can be excited by a signal oscillator. The inertia of the mass is such that the vibrations that are in a horizontal plane are used to strain the ground by generating Rayleigh waves (Abbiss, 1981; Powell and Butcher, 1991). See Section 5.6.2.

**Table 4.6** Theoretical resolution and depth penetration of three common high-frequency source types.

Source	Frequency bandwidth (kHz)	Resolution (m)	Depth of penetration (m)
Pingers	3.5–7	0.1–1	≤tens
Boomers	0.4–5	≈1	tens to 100 +
Sparkers	0.2–1.5	2–3	≥1000

#### 4.5.6.3 Marine vibrators

In 1988, Western Geophysical introduced the Multipulse™ (Hydroacoustics Inc.) marine vibrator, which operates over the frequency range 5–100 Hz and has a sweep period of 6 seconds. The

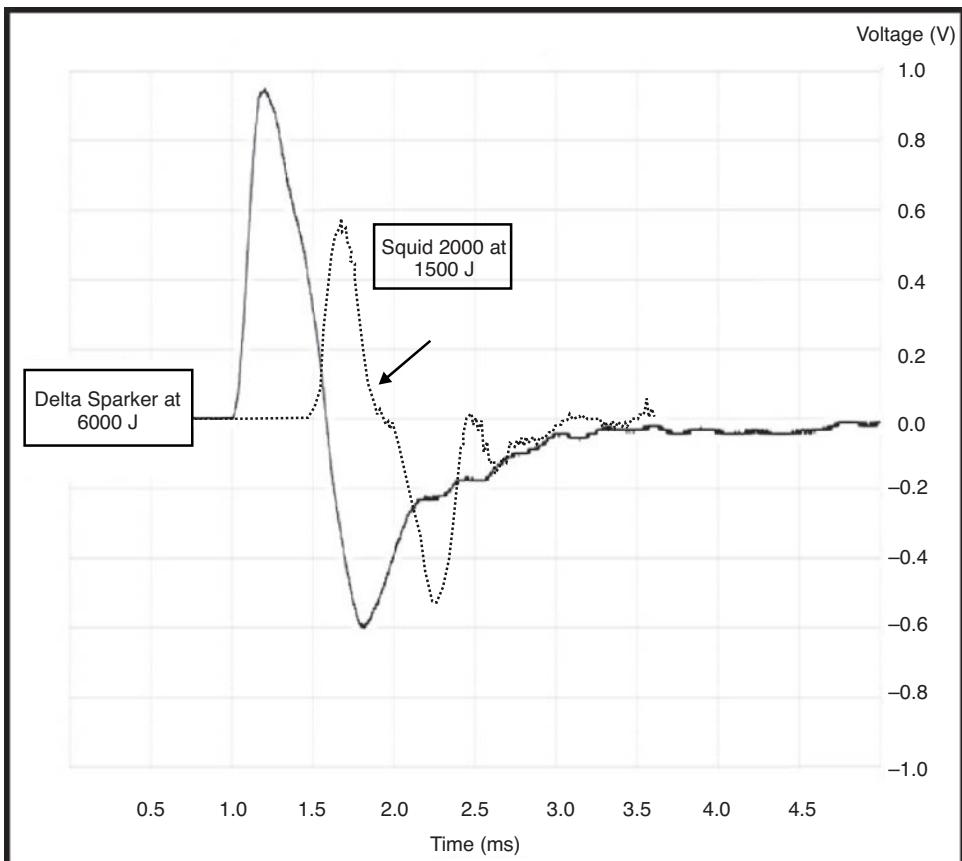


**Figure 4.27** Typical pulses from (A) a squid sparker at 1.5 kJ and (B) a delta sparker at 6 kJ. Courtesy of Applied Acoustics.

advantages of this system over traditional airgun arrays are the minimal disturbance to marine life due to reduced cavitation; a smaller radius of interference away from the source so that it can be operated near production platforms without affecting diving activities; and particularly, that the source characteristics are extremely well known and controlled. The vibrator plates are powered by a pneumatic-nitrogen supply and compressed air, and are deployed in a flotation gantry. Marine vibrators have been discussed in more detail by Baeten *et al.* (1988).

For smaller scale surveys, a system has been developed by GeoAcoustics Ltd, UK, (now part of Kongsberg Maritime, Norway), called the GeoChirp. The system can be deployed in either an over-the-side mounted assembly or as a towed fish (Figure 4.33). The instrument consists of up to four source transducers with frequency bandwidths of either 2–8 kHz or 1.5–11.5 kHz. An upsweep of frequencies (the ‘chirp’) is transmitted in a pulse lasting either 16 or 32 ms, and repeated 4 or 8 times a second.

Immediately behind the source mounting, which looks like the head of a tadpole, is located an 8-element streamer that is about 1 m long. As the source transducer characteristics have been measured by the manufacturer, the system is programmed with these characteristics in order to provide an autocorrelated ‘de-chirped’ analogue output. This can be printed directly on to a hard-copy device, such as a thermal linescan printer. Alternatively, the analogue signals can

be put through a sonar enhancement processing unit that provides facilities for real-time filtering, gain control, and so on, and then output as required.

Another Chirp-type system has been introduced by IXSEA (Echoes 1500), which uses a single transducer repeatable sound source. The single transducer is suspended from a buoy and towed as necessary. The manufacturer claims the system has a 27 cm resolution.

A shear-wave source that is being developed uses the principle of a vibrating mass embedded within the ground (VibroPile). The source vibrates horizontally, thereby generating shear waves. For reservoir monitoring, a configuration would have 25 installed piles into the seabed with one moveable S-wave source. Each pile is  $\sim 0.6$  m in diameter and has a length of about 2 m. The vibrator itself weighs around 1.5 tonnes. The total weight with the submerged power unit is 6 tonnes. A linear sweep through 10 Hz to 80 Hz is used with a duration of 10 s. It is thought that by using shear waves it is possible to study reservoirs beneath gas clouds, to monitor fracture development and to help optimise production in oil fields.

#### 4.5.7 Animals

It is now recognised that animals, especially the African and Asian elephants, are able to generate seismic signals for the purpose of

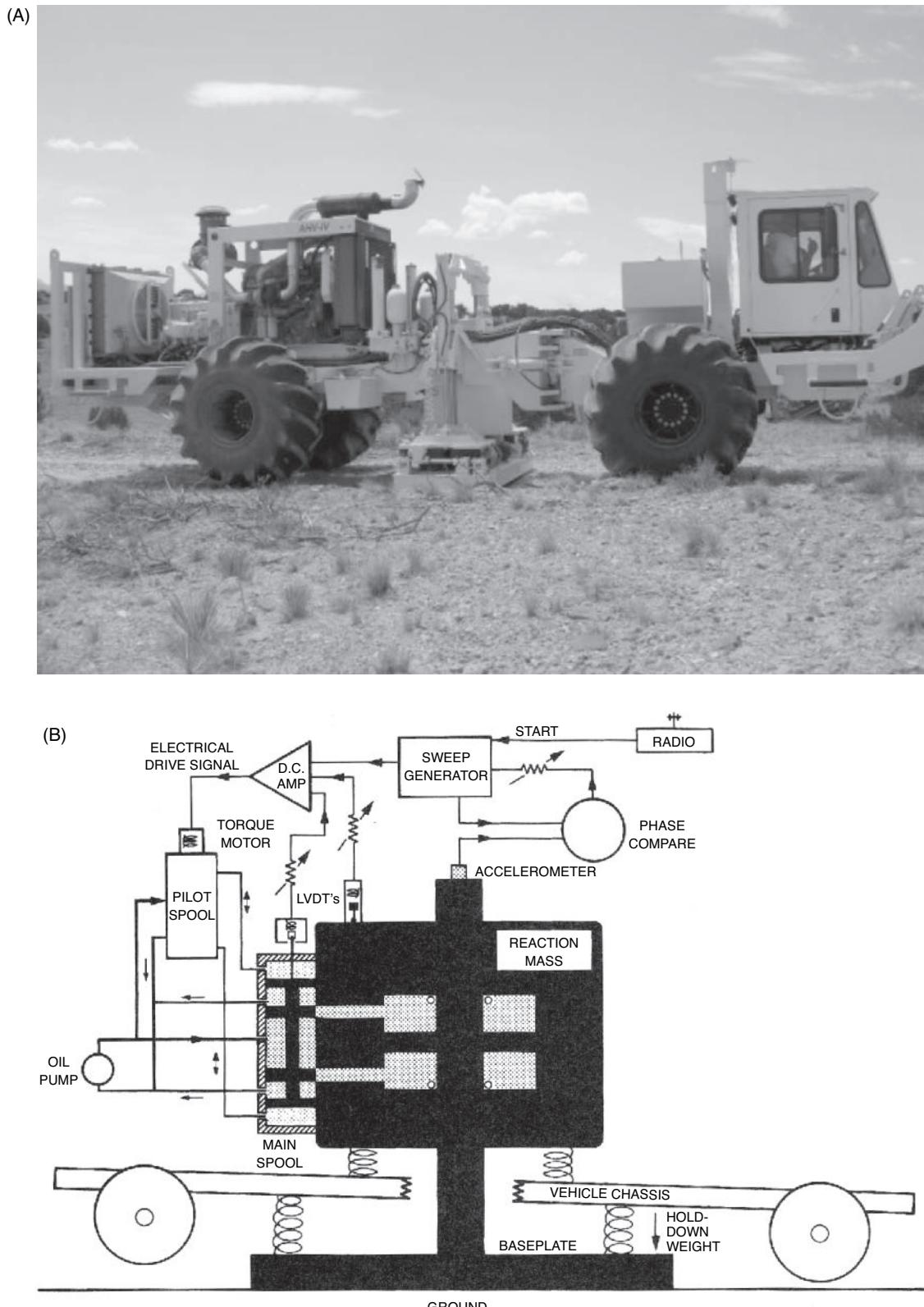


**Figure 4.28** (A) A Vibroseis truck. The weight of the vehicle is transferred to the jack in the middle of the vehicle when operating. Courtesy of ION Geophysics Inc. (B) Schematic of a Vibroseis truck. Courtesy of BP. [C]

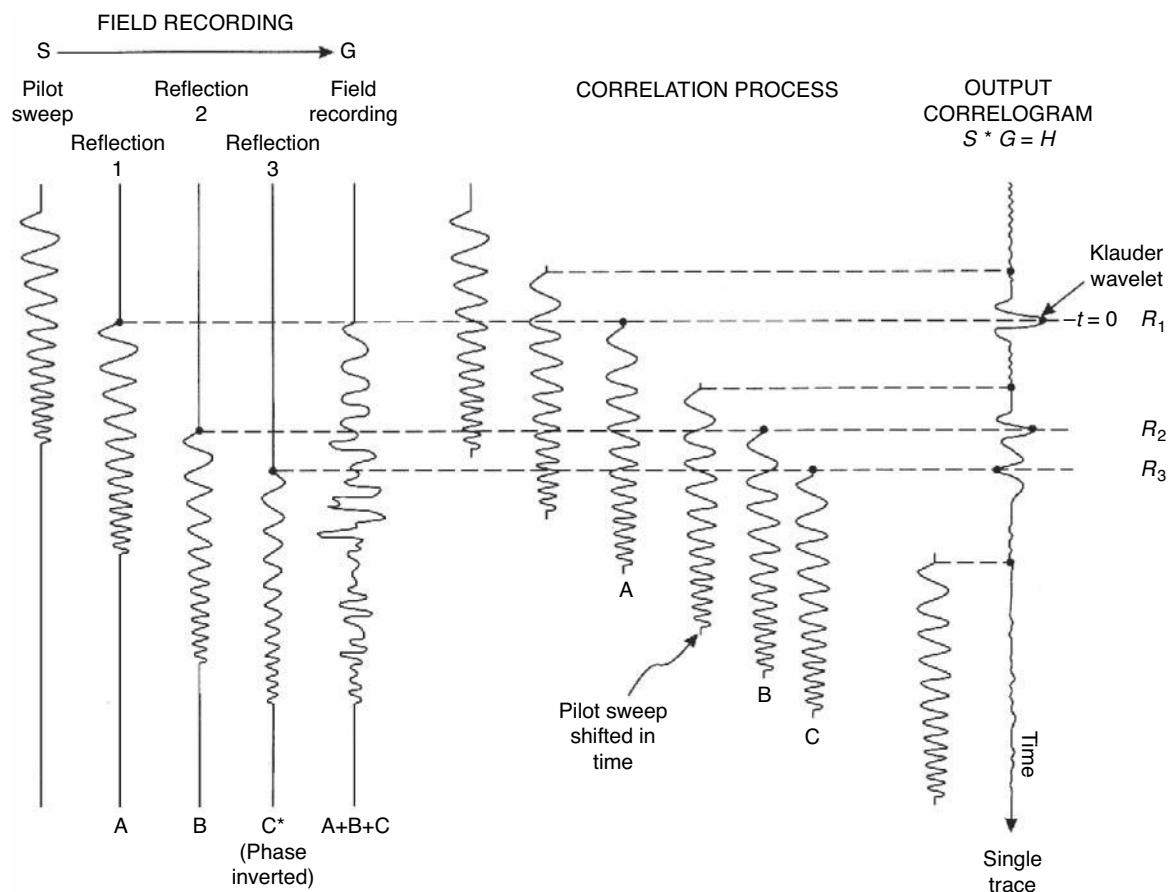


**Figure 4.29** Schematic to illustrate the process of generating a Vibroseis pilot sweep, acquiring field recordings and correlating the field record with the pilot sweep to obtain the output correlogram with Klauder wavelets.

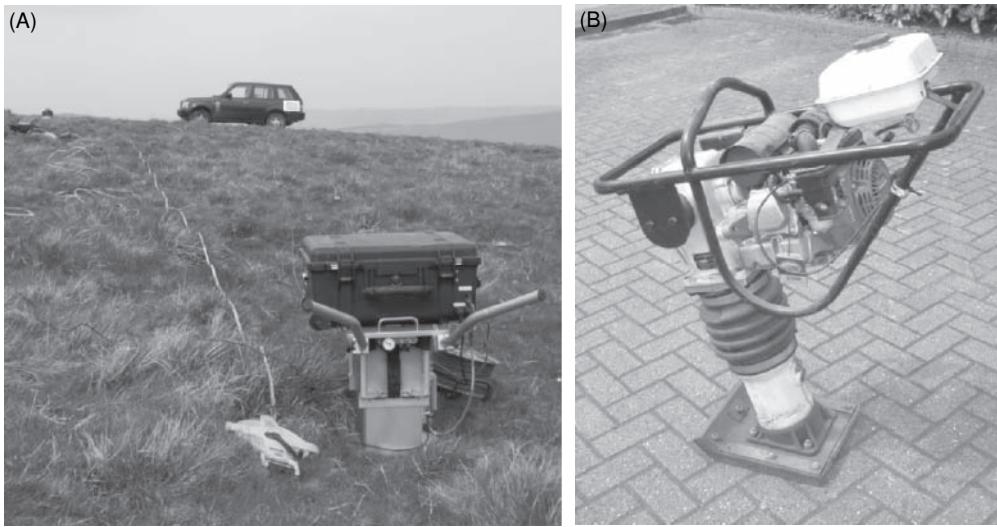


**Figure 4.30** (A) Elvis land vibrator (box in direct contact with the ground) in use as a SH source using a Geode (box with screen, top left) as the recording seismograph. (B) Mini-Sosie land vibrator source. Courtesy of Geomatrix Earth Science Ltd. [C]

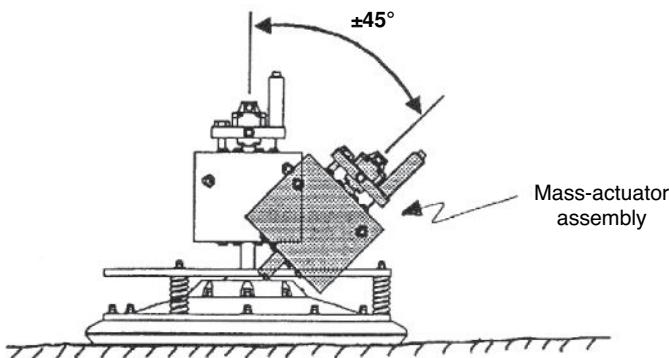


**Figure 4.31** Land vibrator that can be used to generate both P- and S-waves. From Christensen (1992), by permission.

communication over large distances (O'Connell-Rodwell, 2007). Elephants produce such signals in two ways: (a) by stomping on the ground, and (b) by vocalising at around 20 Hz at high amplitude. An elephant weighing 2720 kg, for example, can stomp on the ground hard enough to generate a signal that has been modelled to travel for 32 km. Vocalisations can be made with amplitudes of 103 dB Sound Pressure Level (SPL) and 90 dB SPL at 5 m, respectively. Such low-frequency vocalisations at high amplitude couple with the ground and form Rayleigh waves that propagate along the ground surface for large distances, and further than can be achieved by the sound waves in air.

Elephants have an additional seismic sophistication in that they can orientate themselves to the sources of low frequency seismic

signals by using their feet and trunk to detect the phase of the ground vibrations. Rayleigh waves travelling at a speed of 210–250 m/s, for example, in the case of some elephant habitats, have a wavelength of ~12.5 m. The distance between the front and rear feet of an adult elephant (2–2.5 m) makes the phase difference of an incident wave discernable. By lifting a front leg and using its trunk, an elephant can orientate itself to the direction of travel of the incoming ground wave. It is also thought that elephants use simultaneously the difference in the arrival times of the sound wave and the Rayleigh waves to determine the distance to the source of the signals. The animals sense these signals as part of their defence mechanisms. Elephants possess a cartilaginous fat pad in the heel of each foot that is thought to facilitate impedance matching of signals between the ground and the elephant's body.

Asian elephants have been reported to respond vigorously to earthquakes (Jackson, 1918) or to trumpet loudly at the approach of an earthquake (Nicholls, 1955). Their inconsistent behaviour after the 2004 tsunami in southeast Asia suggests that there is need for further research in this area of earthquake response (Wikramanayake *et al.*, 2006).

## 4.6 Detection and recording of seismic waves

Seismic surveys would not be possible without sensors to detect the returned signals. These detectors are called *geophones* and are used on a substrate of some kind, normally the ground surface, or down boreholes. They are used to convert seismic energy into



**Figure 4.32** Rayleigh wave generator (left), signal processing and recording equipment (right) and the first of a series of geophones is circled. [C]



**Figure 4.33** GeoChirp configuration with the transmitting transducers mounted in the tadpole head and a short streamer aft. Courtesy of GeoAcoustics Ltd. [C]

a measurable electrical voltage. A special form of geophone is the *accelerometer* which, as its name suggests, is used to measure acceleration. The waterborne equivalent of a geophone is a *hydrophone*, and these, too, can be used down water-filled boreholes. Traditionally all components of the seismic survey are interconnected by cables. However, since 2003, it has been possible to have a cableless system, where the interconnectivity is provided by a broadband cellular radio network, such as that provided by Wireless Seismic Inc. The layout and principles of the wifi seismic survey are exactly the same as for the traditional systems, the only difference being the mode of interconnectivity.

#### 4.6.1 Geophones and accelerometers

Most geophones, which are also known as jugs (and people who implant geophones are known as ‘jug-handlers’ or ‘juggies’), are of the ‘moving-coil’ type. A cylindrical coil is suspended by a leaf-spring in a magnetic field provided by a small permanent magnet which is fastened to the geophone casing (Figure 4.34). By suspending the coil from a spring, an oscillatory system is created with a resonant frequency dependent upon the mass of the spring and the stiffness of the suspension. The geophone is implanted into the ground with a spike attached to the base of the casing (Figure 4.34A) to ensure good ground coupling. Shear-wave geophones are slightly different in that they can have two spikes mounted side-by-side. Typical geophone construction is shown in Figure 4.34B. Some geophones are used as transducers to monitor vibrations in heavy engineering machinery, but these work on exactly the same principles as their geological counterparts.

The passage of a seismic wave at the surface causes a physical displacement of the ground which moves the geophone case and magnet in sympathy with the ground, but relative to the coil because of its inertia. This relative movement of the magnet with

respect to the coil results in a small voltage being generated across the terminals of the coil in proportion to the relative velocity of the two components (above the natural frequency of the geophone). Geophones thus respond to the *rate* of movement of the ground (i.e. particle velocity), not to the *amount* of movement or displacement. The maximum sensitivity of any geophone occurs when the coil axis is parallel to the direction of the maximum ground movement. As the incident reflected and refracted P-waves are usually steeply orientated with respect to the ground surface and produce a vertical displacement of the ground, geophones with vertical coil orientations are deployed to detect them. Similarly, as horizontally polarised shear waves tend to produce ground displacements in the plane of the surface, the coil assembly is mounted horizontally in shear-wave geophones. Deployment of geophones with a specifically orientated coil axis can filter out orthogonal responses. If either P- or S-wave geophones are planted crookedly, they are designed to stop working and give a ‘dead trace’. This condition is usually looked for at the beginning of any survey and the problem rectified by replanting the misaligned geophone.

Geophones need to respond quickly to the arrival of seismic waves, but should not ring as this would affect their ability to sense other seismic arrivals. Thus geophones need to be damped so that, after their initial response to ground movement, the relative movement of the coil and casing stop quickly ready for the arrival of the next event. *Critical damping* ( $\mu_c$ ) is the minimum amount required which will stop any oscillation of the system from occurring (Figure 4.35A). Geophones are inherently damped as the oscillatory movement of the coil is retarded by the relative movement of the coil and magnet. Current generated in the coil by the initial relative movement of the permanent magnet induces a magnetic field which interacts with that of the permanent magnet in such a way as to oppose the motion of the coil. This damping can be changed by the addition of a shunt resistance across the coil terminals. This resistance controls the amount of current in the coil; the lower the resistance, the greater is the degree of damping. Most geophones are slightly underdamped, typically around 0.6–0.66  $\mu_c$  (Figure 4.35B). Geophones are designed to respond to different frequencies, with the common natural frequencies being in the range 4–30 Hz for seismic refraction and deep reflection surveys. For shallow high-resolution reflection surveys, geophones with a natural frequency greater than or equal to 100 Hz should be used. Near and below the natural frequency, the geophone response is heavily attenuated and for most seismic work this helps to filter out unwanted very-low-frequency noise. Well above the natural frequency, the geophone response is usually flat (Figure 4.35B and C).

An accelerometer is a device whose output is proportional to the acceleration to which it is subjected. A geophone or seismometer whose response is below its natural frequency can be used as an accelerometer. They are used in inertial navigation systems and with shipboard and airborne gravimeter systems to record variations in acceleration which are necessary for the reduction of the gravity data (see Section 2.5.7).

Seismometers are devices used to measure the waveform of earthquake-type waves and are normally installed in specially engineered recording stations. Extremely good ground coupling is

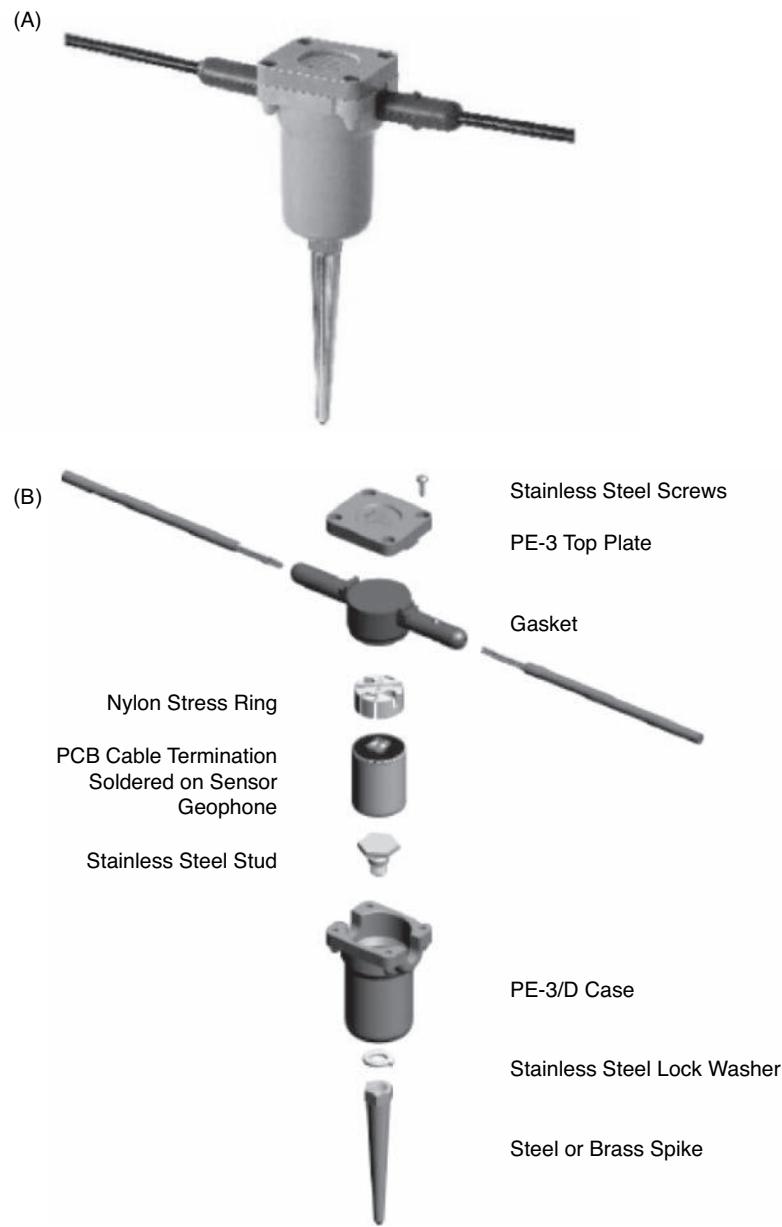


**Figure 4.34** (A) Field geophone with spike. (B) Typical geophone construction. Courtesy of Sensor Nederland b.v. [C]

achieved by bolting the device to bedrock or to a concrete plinth which is in contact with bedrock. Multicomponent seismometers record in two horizontal but orthogonal directions and vertically. The output goes to three channels recording simultaneously. Further details of the operating principles of seismometers have been given by Howell (1990).

The earliest known seismometer or seismoscope was built in China in the year 132 by Heng Zhang, Imperial Historian, and represents not only a remarkable piece of early engineering but also a beautiful work of art (Figure 4.36). The device consisted of a hollow dome in which was suspended a pillar. Eight cups in the shape of dragons' heads were arranged symmetrically around the upper periphery. In the mouth of each dragon was a delicately poised

ball. Immediately below each dragon's head was an ornamental frog with an open mouth pointing upwards. When the instrument was disturbed, ostensibly by an earthquake wave, the suspended pillar swayed in the direction of motion and triggered a mechanism which knocked the ball out of the nearest dragon's head and into the mouth of the frog beneath (Wartnaby, 1957). It is known that the device registered an earthquake in Gansu Province in China in 138.

## 4.6.2 Hydrophones and streamers

A hydrophone is in essence a waterborne equivalent of a geophone, although the principle of operation is quite different. A hydrophone responds to variations in pressure, whereas a geophone responds

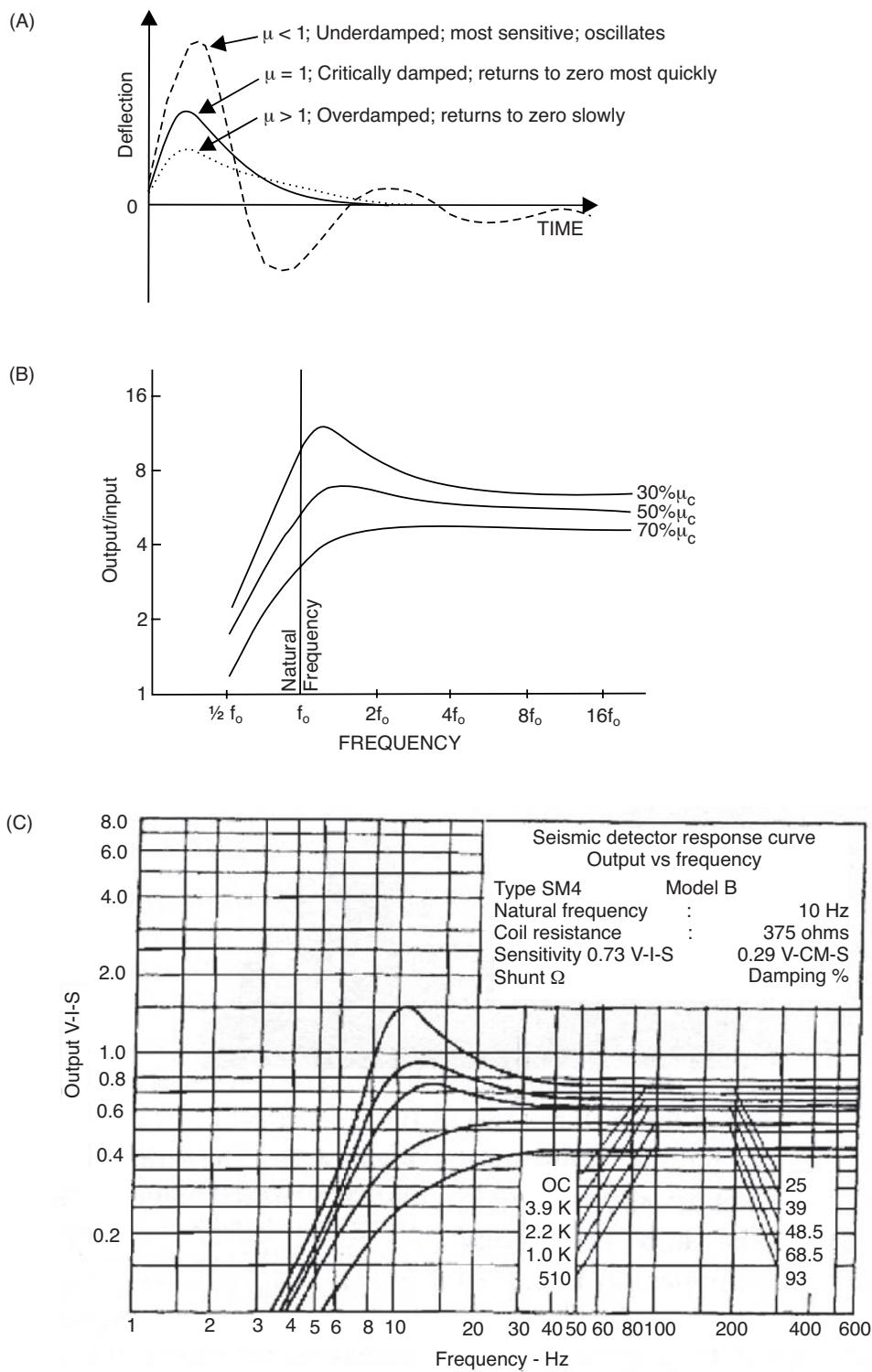


**Figure 4.35** (A) Deflection as a function of time for underdamped, critically damped and overdamped modes of a geophone. (B) The amplitude response as a function of frequency in three states of underdamping to critical damping ( $\mu_c$ ). (C) Variation of response with frequency for a typical moving-coil geophone. Courtesy of Sensor Nederland BV.



**Figure 4.36** The earliest known seismoscope was developed in 132 by Heng Zhang and was used successfully to indicate the occurrence of an earthquake in the year 138. Courtesy of Stop Disasters and the World Intellectual Property Organization.

to ground particle motion. Hydrophones can be used in open water, down a water-filled borehole, and in water-saturated marshy conditions.

A hydrophone consists of two piezoelectric ceramic discs (e.g. barium titanate or lead zirconate) cemented to a hollow sealed copper or brass canister (Figure 4.37A). A pressure wave effectively squeezes the canister and bends the piezoelectric disc, thus generating a voltage between the top and bottom of each disc. The two discs are polarised and connected in series so that the voltage generated by the passage of a pressure wave (i.e. seismic wave) are added, but those due to acceleration will cancel (Figure 4.37B). Piezoelectric hydrophones have a high electrical impedance and thus any signals must pass through impedance-matching transformers before being transmitted through to the recording instruments.

In marine work, hydrophones are deployed in a *streamer*, a marine cable up to 9 km long, which is designed to be towed continuously through the water. A streamer is made up of a number of elements (Figure 4.38). The main section comprises active or live sections (groups) in each of which 30 hydrophones are connected in parallel with impedance-matching transformers. In multiplexing cables, the signals from each hydrophone group are amplified, multiplexed, and converted into digital form within the cable, and then transmitted to the recording vessel along a single wire. The individual hydrophones are acoustically coupled to the surrounding water by being immersed in oil, which also assists in keeping the streamer neutrally buoyant. Such streamers are typically towed in the depth

range of 5–9 m. High-resolution streamers, as used in engineering type investigations, are normally towed at the water surface. In 2007, PGS introduced a new form of streamer (*GeoStreamer*<sup>®</sup>) that is filled with a Buoyancy Void Filler, which is introduced into the streamer as a fluid but transforms into a solid gel during a curing process. The *GeoStreamer*<sup>®</sup> also uses dual pressure and particle velocity sensors that allow the streamer to be towed at greater depths, typically 15–25 m, and is thus less affected by surface weather noise. The dual sensor also permits the receiver ‘ghost’ wave to be removed, thereby improving the signal-to-noise ratio across all frequencies and giving better vertical resolution. The reflection wavelet’s ghost reflection (from the reflection of the upgoing wave on the underside of the sea surface), as sensed by the particle velocity sensor, has the opposite polarity to that of the same ghost reflection wavelet as sensed by the pressure sensor. Combining the two cancels out the ghost reflection (Carlson *et al.*, 2007; Tenghamn and Dhelie, 2009).

The streamer skin, which is kept from collapsing by plastic bulkheads in the case of oil-filled streamers, is made either of PVC for use in warm water, or of polyurethane for use in cold water. If the wrong skin is used – for example, if a warm-water skin is used in cold water – the streamer stiffens, which generates acoustic noise as the cable is towed through the water.

From the front end of the streamer, the first section encountered is the towing bridle, which takes the strain of towing and connects the hydrophone communication cables to the ship’s recording systems. At the rear end of the lead-in section is a depressor hydrovane (paravane), which is used to keep the nose of the streamer at a given level below the surface. Immediately aft of this is a compliant or stretch section which is designed to absorb and attenuate the jerks caused by uneven tow rates and/or sea conditions, and to isolate the streamer from shocks to the ship (such as ploughing through a swell). Another stretch section is located right at the end of the streamer where it is connected to the tail buoy, which is a polystyrene raft housing a radar reflector and radio antenna, and is used to isolate the streamer from jerks from uneven movement of the tail buoy.

Along the line of the streamer, depth controllers are located at specific points. These devices have servo-controlled fins which change their aspect in order to keep the streamer at a predefined depth below the surface. Pressure sensors on each controller are used to measure float depth, and if the streamer deviates from the required level the fin angles are adjusted to compensate. Also, a series of compasses is located along the length of the streamer (Figure 4.39) and each transmits signals back to the ship so that the position of each active group of the streamer can be determined and plotted (see Section 6.2.2.3). Different commercial operators may deploy their own systems. One system (*Nautlius*<sup>®</sup>, developed by Sercel) comprises a series of tri-finned acoustic transceivers (Figure 4.39) spread along the streamer on airgun sub-arrays and the tailbuoy or navbuoy. These provide accurate and quality-controlled acoustic range measurements to the navigation system. If the ship is towing a long streamer across a side current, which causes the streamer to drift off track (called *feathering*), the feather angle and the streamer position can still be determined (Figure 4.40). Such information is

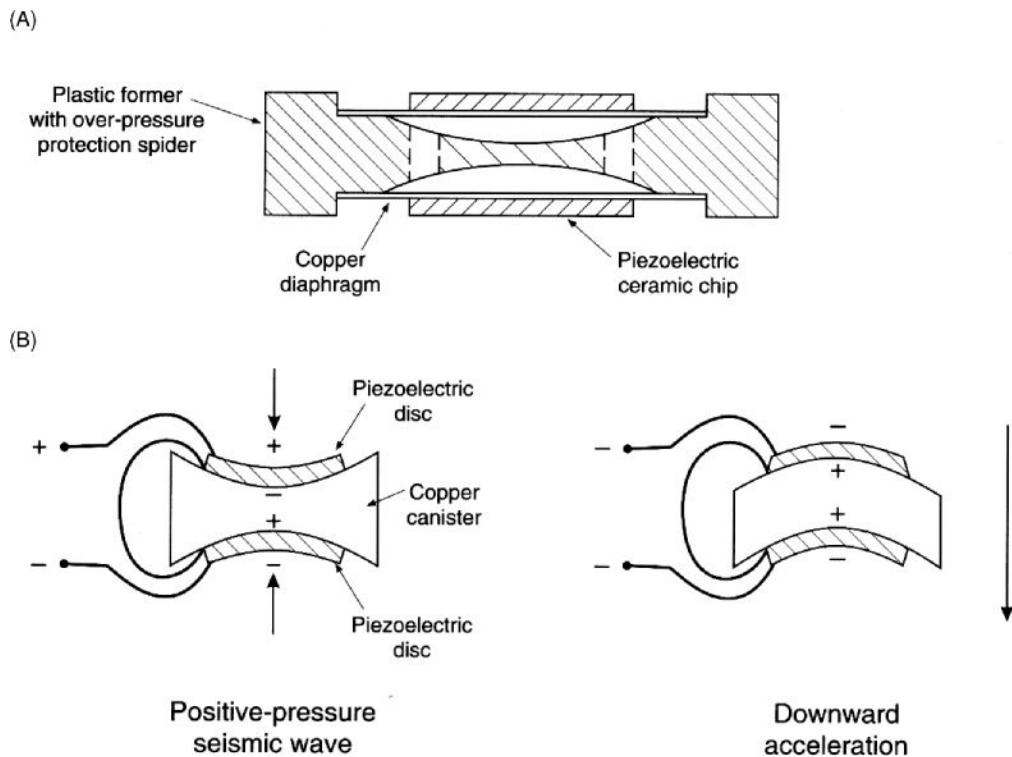


**Figure 4.37** (A) Hydrophone construction, and (B) acceleration-cancelling hydrophone. Courtesy of SSL.

vital for subsequent data processing. Knowing the position of each towed element is vital not only for the success of the seismic survey, but also for marine safety. Seismic surveys are sometimes undertaken in busy shipping lanes, and other ships need to know where the streamers are so as to be able to avoid snagging them. When a streamer is not being used it is coiled up on a drum on the ship's deck (Figure 4.41).

Knowing the precise location of the streamers deployed is all the more important when three-dimensional seismic data are being acquired. Usually, up to four streamers, each up to 6 km long, are deployed from two ships steaming parallel to each other. In addition, there may be four seismic gun arrays deployed from the same

two ships. The most modern seismic vessels are capable of deploying 12–16 streamer arrays each 6 km long, and longer in special cases, 9 km not being unusual. In order to be able to deploy so many streamers, a specially designed fleet of ships has been built (the *Ramform* series) based on the Norwegian intelligence-gathering 'stealth' ship, the *Marjatta*. The 83 m long *Ramform Explorer*, which is operated by the Norwegian Petroleum Geo-Services Group (PGS), was radically different from previous seismic vessels when she entered service in 1995 in that she is triangular in shape with a 40 m aft beam (Figure 4.42A) and automatic streamer spooler system. The latest Ramform S-class vessels are designed to tow up to 22 streamers. The wide beam and massive deck space of this ship are sufficient

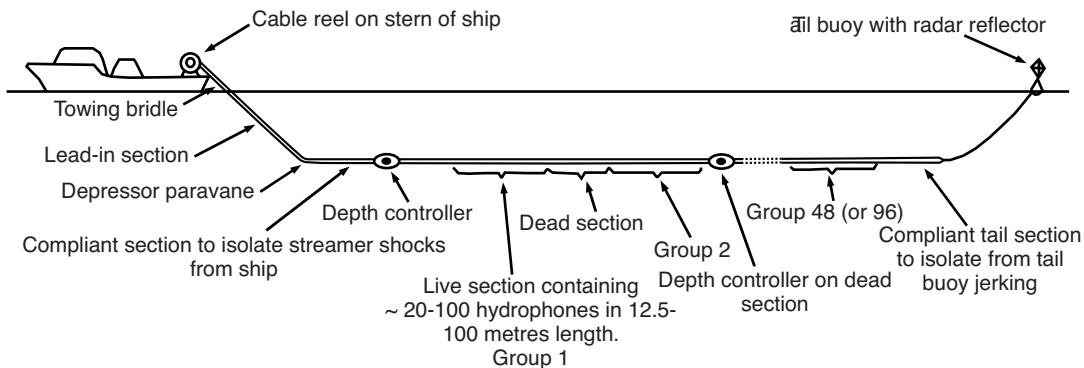


**Figure 4.38** Basic structure of a hydrophone streamer. From Sheriff (2002), by permission.

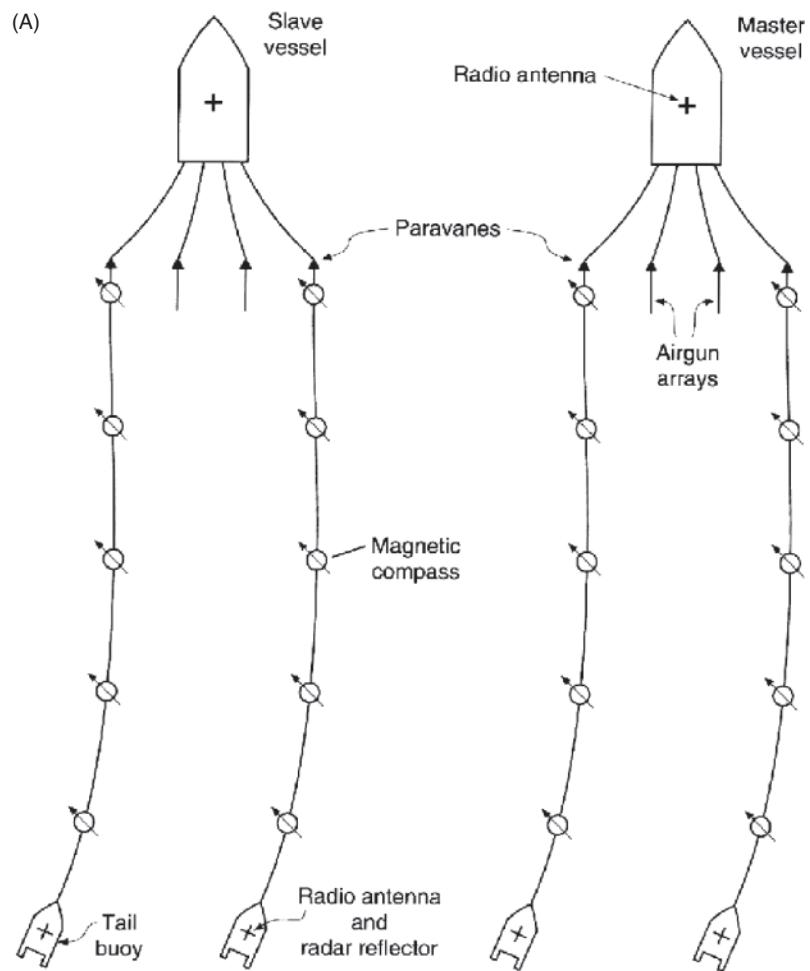


**Figure 4.39** (A) Three-dimensional multi-streamer deployment. Each streamer has a series of fins (B) by which to control its position – Nautilus system (courtesy of Sercel); (C) integrated tailbuoy in use (courtesy of Seemap). [C]

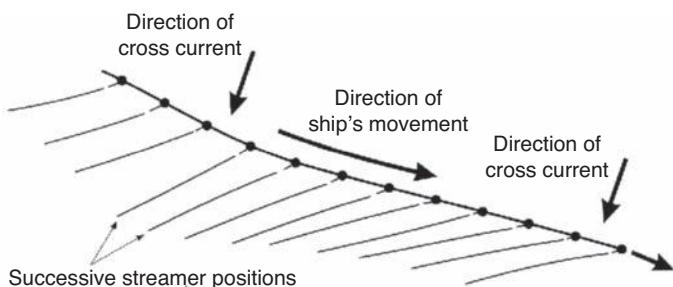


**Figure 4.40** Schematic plot of successive streamer locations – significant feathering occurs caused by strong cross-track currents.

to accommodate a Chinook-size helicopter operation. This allows for complete crew changes at sea, thereby increasing the ship's productive time. The simultaneous use of up to 17 streamers is for the acquisition of 3D seismic data. The *Ramform Sovereign*, which became operational in 2008, set the record (to date in February 2009) for towing 17 streamers, the widest tow ( $14 \times 100$  m), and the largest total streamer length deployed ( $14 \times 8100$  m). When fully deployed these ships are each towing in excess of \$60 million worth of sensitive seismic equipment (Greenway, 2009). The distinctive and novel Ulstein X-BOW (Figure 4.42B) is being used for a new generation of seismic survey vessels that came into operation in 2009, the first of which was *WG Columbus*, operated by WesternGeco. These ships are capable of deploying up to 12 streamers each and are designed for both 2D and 3D data acquisition, depending upon the individual vessel specification.

Towed streamers have also been developed for use on land ('*land streamers*') and have been in use since the mid-1970s (e.g. Kruppenbach and Bedenbender, 1975, 1976). However, a significant amount



**Figure 4.42** (A) *Ramform Explorer* in operation showing the distinctive broad stern. Photograph courtesy of PGS Exploration, Norway. (B) The distinctive Ulstein X-BOW® design of a new series of seismic survey vessels operated by WesternGeco. © Polarcus Ltd. Both types of vessels can deploy up to 12 streamers simultaneously. [C]



**Figure 4.41** Coiled streamers on the aft deck of the *Ramform Sovereign* survey vessel. From Greenway (2009), by permission. [C]

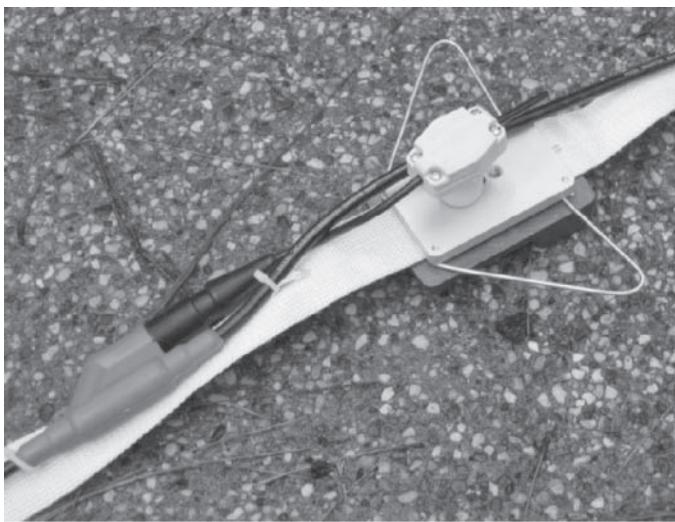


**Figure 4.43** Detail of a geophone mount and stabilising wing on a land streamer. Courtesy of Geostuff. [C]

of development has taken place in the last decade and commercial systems are now available. Geometrics has provided an overview of land streamer systems in their March 2003 issue of *Geoprofiles*. In essence, the traditional seismic spread layout is exactly the same as for a fixed land survey, except the geophones have their ground spikes removed and are instead fixed to some form of baseplate to aid ground coupling and in turn broad webbing or other non-stretch material that is used to tow the system (Figure 4.43) but which itself does not provide any inter-geophone coupling. The geophones are connected to the usual multi-core take-out cables that are secured to the top of the webbing. Wings are variably available to provide stability to the spread as it is being towed so that it does not flip over or become entangled as it is moved along. Van der Veen and Green (1998) and Van der Veen *et al.* (2001) provided more details of a system developed at ETH in Switzerland. Some workers have used wooden blocks to mount and protect each geophone (COWI, Denmark); Kansas Geological Survey mounts the geophones inside heavy duty fire hose. Each geophone is screwed into an external three-pointed cutter that carves a groove into the ground surface over which it is being dragged. Loose material is pushed aside and light vegetation is sliced, leaving firmer ground that improves coupling. Additional weights are added to improve the ground coupling as necessary. The fire hose protects the cable, reduces tow noise, isolates each receiver and is strong enough to be pulled by a vehicle. Where standard geophones are used in a towed array, they must be used correctly and be protected from damage through being dragged over the ground surface. It is important therefore that the geophone array is the correct way up when being dragged across the ground and when in use. In Montana Tech's system, the geophones are gimballed and mounted onto a broad weighted rubber mat with the cables secured on the upper side to avoid becoming entangled. This system has been developed further so that four separate land streamers in a 96-channel 3D array can be towed behind a vehicle simultaneously with a separate vehicle deploying the seismic source.

Unlike marine deployment of streamers where the data acquisition is continuous, the land streamer method is 'stop-start'. The streamer is dragged to the required position and left to stand. The seismic source is moved to the back of the array and fired to provide the initial shot record. The source is then moved up the array in sequence. Once the source has arrived at the front of the array the shot-front receiver offset is maintained. After each shot the source and land streamer are moved up one shot increment and, once the streamer has settled for a few seconds, another shot is fired. The process is then repeated as many times as required to cover the designated profile length.

For use in snow-covered areas, a gimballed geophone 'snow streamer' has been developed (Eiken *et al.*, 1989) after field trials for an exploration survey in 1988 in Svalbard. The system comprised a main cable with a central stress member surrounded by insulated conductors. Half-gimballed geophones were connected to the main cable by short geophone cables up to a few metres long. The survey was carried out using a tracked over-snow vehicle towing the snow streamer. Each geophone sensor was self-orientating along one horizontal axis and was enclosed in an oil-filled cylindrical metal case (20 cm long, diameter 4.5 cm with a mass of 1 kg). The weight of the sensor in its case coupled well with soft snow. For each shot, the streamer was stationary. No appreciable difference in data quality was noted between data acquired using the streamer and using standard spiked geophones implanted within the snow cover. However, the increased speed of surveying achieved using the streamer resulted in significant savings in survey time and hence costs. The snow streamer has also been used in the Antarctic. Given the increased amount of exploration work, particularly in the Arctic, both onshore and over sea-ice, the use of the snow streamer is likely to increase.

### 4.6.3 Seismographs

There is a wide variety of seismographs available designed for different applications and budgets. For small-scale engineering studies, a single-channel seismograph is available for operation by one person using constant offset profiling, although most systems are now multichannel (typically 24- or 48-channel). The advantage of signal enhancement instruments is that, instead of having to supply all the required energy in a single blast, many but smaller 'shots' can be used to build up the seismic record. By so doing, the process of summation also helps to reduce incoherent noise, thus improving the signal-to-noise ratio. To illustrate what the control panel of a modern seismograph looks like, the top panel of a Geometrics ES-2401 seismograph is shown in Figure 4.44. Comparable seismographs are also produced by other manufacturers. Increasingly, systems for use in shallow engineering and environmental surveys are being packaged to be controlled by a laptop, such as the ES-3000 seismodule developed by Geometrics.

For large-scale three-dimensional land surveys, multichannel systems capable of handling up to many hundreds of channels have been developed for use by specialist seismic contractors, predominantly for use in hydrocarbon exploration (Bertelli *et al.*, 1993). Modern digital seismographs are also used in vertical seismic



**Figure 4.44** The display panel of an ES-2401 seismograph.  
Courtesy of Geometrics Inc. [C]

profiling surveys, cross-hole investigations, as well as for surface applications. The amplifier gains are adjusted automatically each time the record is sampled. Consequently, both large-amplitude first breaks and small-amplitude late arrivals can be recorded precisely. There is growing attention to reduce the requirement for cables linking recording devices to the geophones and for wireless connections to be used (WiFi systems). The use of radio communications and the Internet to link geophysical systems is increasing in popularity and will become more commonplace as the technology improves.

It is currently feasible to acquire field data in a remote part of the world and for those data to be transmitted and monitored virtually in real time across the other side of the world.

Modern seismographs have pre-loaded software for refraction processing so that in-field solutions can be obtained very quickly. Not only does this provide rapid preliminary interpretation, but, more importantly, it highlights bad first-break picks and inconsistent modelling. With the increased field production rates, it is also possible to undertake preliminary surveys and, with the benefit of the in-field analysis, to obtain additional data to provide for detailed information where it is needed while the field crews are still deployed. By producing high-quality digital data, powerful seismic data processing techniques can be applied in order to retrieve the maximum amount of information (see Chapter 6).

Seismic acquisition technology and recording systems are developing at such a rate that reference should be made to the websites of appropriate manufacturers for the latest specifications. Websites of a number of manufacturers are listed in Appendix 1.

In the case of over-water surveys, acquisition and interpretation systems are often combined with an emphasis on obtaining as fast a turn-around of the interpretation as possible, often utilising automated interpretation systems. In cases where the subsurface geology is simple and the seismo-acoustic facies are well defined, such an approach may be justified. However, in other cases an experienced geophysicist, who has recourse to additional data processing tools coupled with good interpretational software plus, where available, other geological information, should undertake the interpretation. There have been too many cases where the automated software has produced a totally incorrect interpretation and this has not been identified prior to being issued to the client. This is discussed further in Chapter 6.

# 5

## Seismic Refraction Surveying

### 5.1 Introduction

Seismic refraction experiments can be undertaken at three distinct scales: global (using earthquake waves), crustal (using explosion seismology), and near-surface (engineering applications). For the purposes of this book, emphasis is placed on shallow investigations.

The major strength of the seismic refraction method is that it can be used to resolve lateral changes in the depth to the top of a refractor and the seismic velocity within it. The most commonly derived geophysical parameter is the seismic velocity of the layers present. From such values, a number of important geotechnical factors can be derived, such as assessing rock strength, determining rippability (the ease with which ground can be ripped up by an excavator), and potential fluid content. In addition to the more conventional engineering applications of foundation studies for dams and major buildings, seismic refraction is increasingly being used in hydrogeological investigations to determine saturated aquifer thickness, weathered fault zones, and so on. The location of faults, joints, and other such disturbed zones using seismic refraction is of major importance in the consideration of the suitability of potential sites for the safe disposal of particularly toxic hazardous wastes.

### 5.2 General principles of refraction surveying

#### 5.2.1 Critical refraction

The seismic refraction method is based on the principle that when a seismic wave (P- and/or S-wave) impinges upon a boundary across which there is a contrast in velocity, then the direction of travel of that wave changes upon entry into the new medium. The amount of change of direction is governed by the contrast in seismic velocity across the boundary according to Snell's Law as described in Chapter 4 (see Boxes 4.8 and 5.1, and Figures 4.7 and 5.1). The critical angle for a given boundary for P-waves may be different from that for

#### Box 5.1 Snell's Law (see Figure 5.1)

**Snell's Law:**

$$\sin i / \sin r = V_1 / V_2 \text{ for general refraction}$$
$$\sin i_c = V_1 / V_2 \text{ for critical refraction}$$

where  $i_c$  is the angle at which critical refraction occurs, and  $V_2$  is greater than  $V_1$ .  $V_1$  and  $V_2$  are the seismic velocities of the upper and lower layers respectively;  $i$  and  $r$  are the angles of incidence and refraction.

S-waves, as the respective ratio in velocities between the two layers for P- and S-waves may not be the same.

The refraction method is dependent upon there being an increase in velocity with depth. If, however, the lower medium has a velocity lower than that from which the wave is emerging (i.e.  $V_2$  is less than  $V_1$ , a *velocity inversion*), then the refracted wave will bend towards the normal. This gives rise to a situation known as a *hidden layer*, which is discussed in more detail in Section 5.4.4.

It is assumed in the refraction method that the thickness of each layer present is greater than the wavelength of the incident energy, and that each successive layer is as thick as, or is thicker than, the one lying above it. A further assumption is that the raypaths are constrained to lie in the vertical plane of the refraction profile line such that there is no seismic energy (refracted or reflected) arising from boundaries out of that plane – a phenomenon known as *sidewipe*. In some engineering applications, this factor is significant and has to be considered during data acquisition.

In a refraction survey, only the P-wave is usually considered. There are occasions when the additional use of S-waves is beneficial to the overall interpretation. For the purposes of the discussion that follows, we shall confine our considerations to P-waves only.

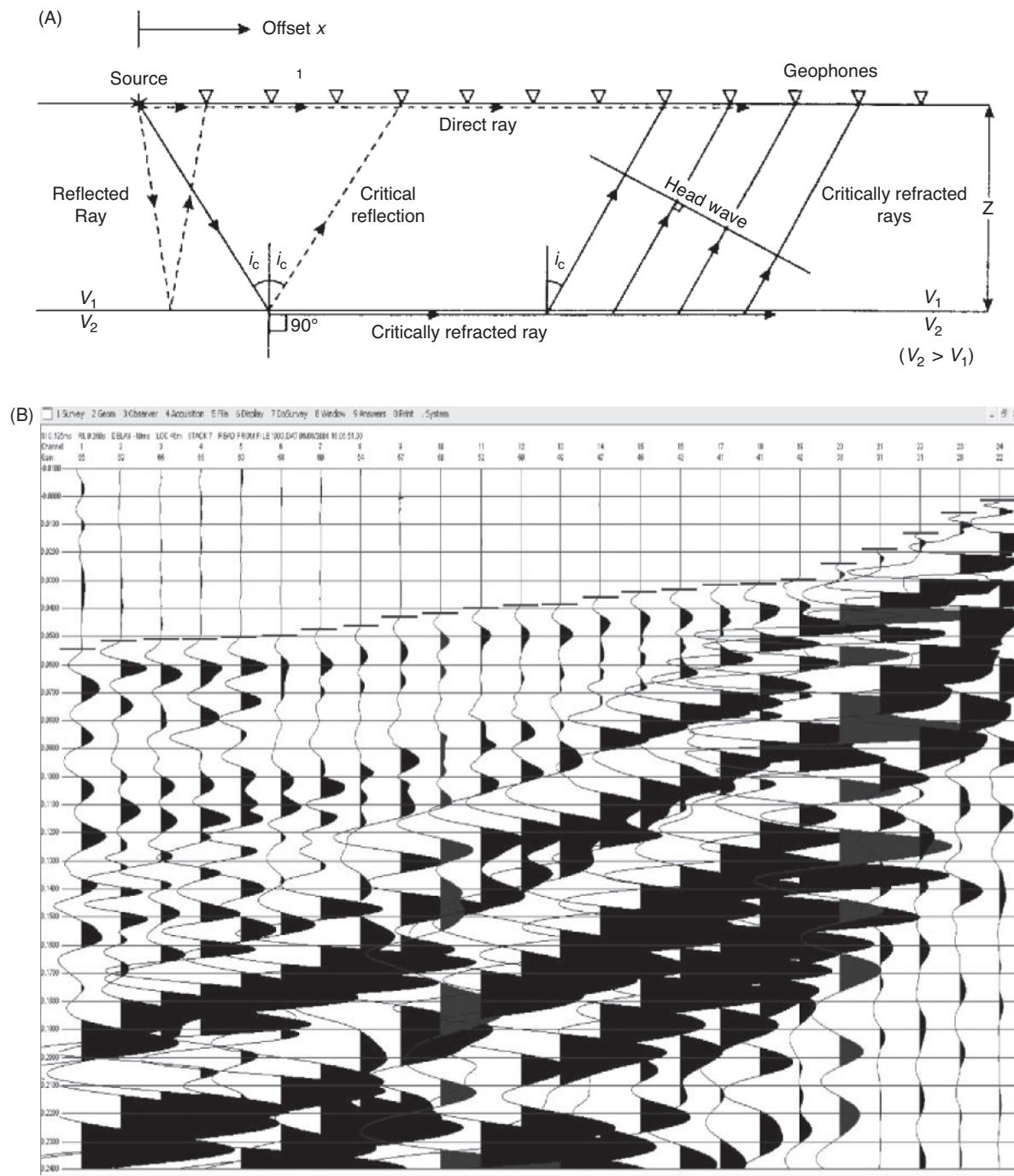


**Figure 5.1** (A) Raypath diagram showing the respective paths for direct, reflected and refracted rays. (B) Example of a seismic refraction record as seen on the display of an EG&G Smartseis seismograph, with first arrivals picked on each trace (indicated by the small cross lines); courtesy of Geomatrix Earth Science Ltd.

The basic components of a seismic refraction experiment are shown schematically in Figure 5.1A. A source, such as a sledge hammer on a baseplate or shotgun blanks in a buffalo gun, is used to generate the P-waves. The waves produced travel in three principal ways: directly along the top of the ground surface (direct wave); by reflection from the top of the refractor; and, of greatest importance, by critical refraction along the top of the refractor(s). The arrival

of each wave is detected along a set of geophones and recorded on a seismograph, with the output of each geophone being displayed as a single trace. The onset of each arrival for each geophone is identified (Figure 5.1B) and the associated travel time is measured and plotted on a time-distance graph (Figure 5.1C).

At a distance called the *critical distance*, the reflected arrival is coincident with the first critically refracted arrival and the travel

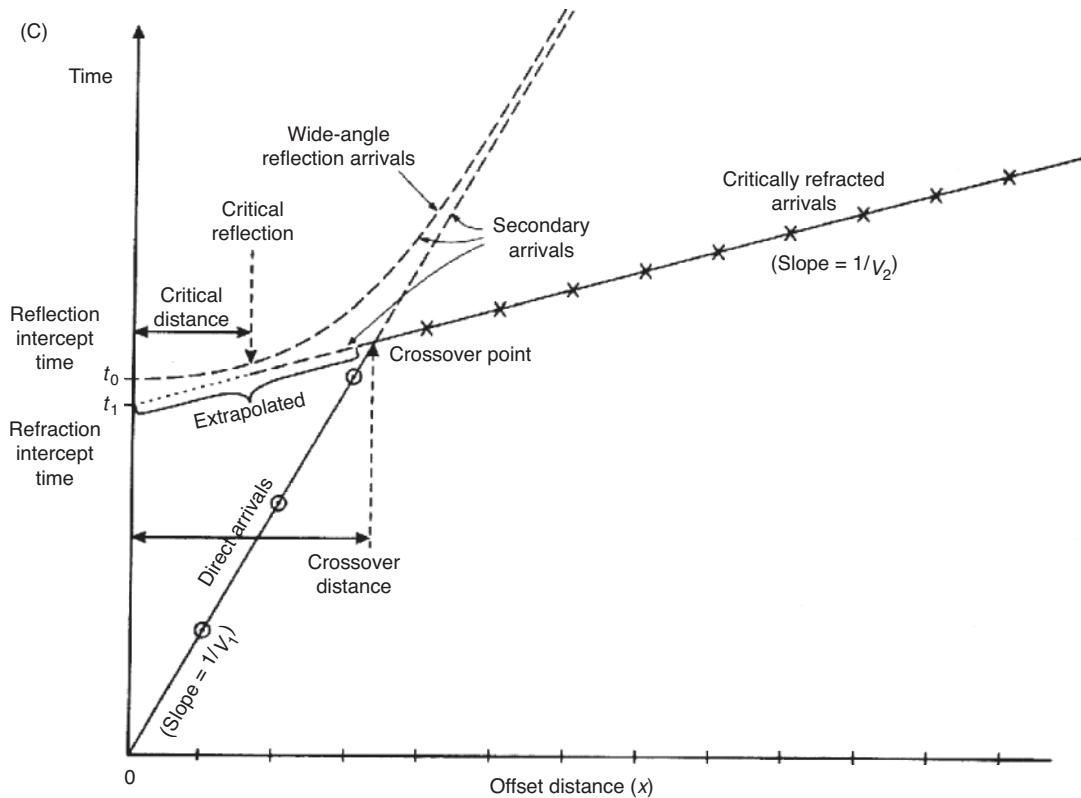


**Figure 5.1 (Continued) (C)** Arrival times plotted on a time-distance graph.

times of the two are identical. The critical distance is thus the offset at which the reflection angle equals the critical angle. This distance should not be confused with the *crossover distance*, which is the offset at which the critically refracted waves precede the direct waves. The crossover point marks the change in gradient of the time-distance graph from the slope of the direct arrivals segment to that for the refracted signals. While the travel-time hyperbola associated with reflected arrivals is shown in Figure 5.1C, only direct and refracted arrival times are usually considered in the refraction analysis.

## 5.2.2 Field survey arrangements

### 5.2.2.1 Land surveys

For a seismic refraction survey on land, the basic layout is shown in Figure 5.2. A number of geophones, usually 24 or 48, are laid

out along a cable with a corresponding number of takeouts along a straight line. This set of geophones constitutes a 'spread'; it should be noted that this is not a geophone 'array' (see Chapter 6). The seismic source (shot), whatever type it happens to be for a given survey, is located in one of five locations. The simplest case is for the shot to be positioned at the start and the end of the spread ('end-on' shots). A source located at a discrete distance off the end of the spread is known as an 'off-end' shot. A source positioned at a location along the spread is known as a 'split-spread' shot; usually this is either at mid-spread or at a quarter or three-quarters along a spread. Shots are usually fired into a spread from each end (end-on and off-end shots) in forward and reverse directions. The positioning of shots relative to a given spread is to achieve adequate coverage of the refractor surface and to provide adequate lateral resolution. As will be described in later sections, for each shot, appropriate travel times can be picked on each trace on the seismic

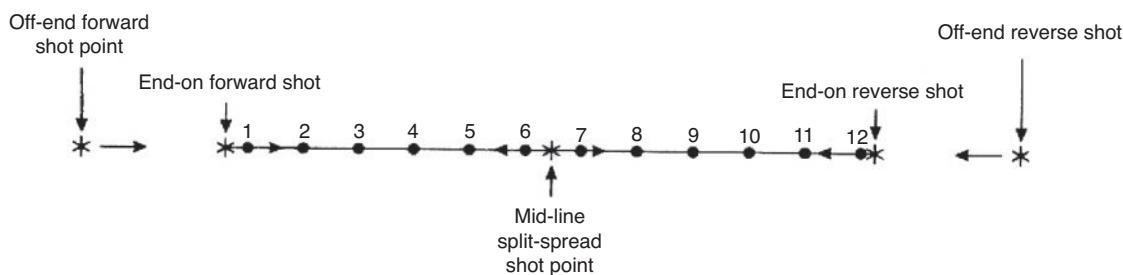


**Figure 5.2** Geophone spread for a refraction survey with shot locations indicated.

record obtained. With each shot location into the same spread, additional data are acquired to provide sufficient information for detailed data reduction and analysis.

### 5.2.2.2 Waterborne surveys

Seismic refraction can also be undertaken in an aquatic environment, but special systems are required. There are two main methods of detecting the critically refracted signals: one is to use a bottom-drag hydrophone cable, and the other is to use sonobuoys. Each will be described briefly in turn.

A bottom-drag cable is similar to a normal reflection hydrophone streamer but is usually only 55 m long. A boat housing all the shot-firing and seismograph recording systems tows the cable on to station, when the cable is allowed to sink to the river/seabed. In some cases, divers are used to anchor the cable to the substrate as required. Shots are fired as necessary and then the cable is towed to the next station and the process repeated. By careful operation of the boat and the positioning of the bottom-tow cable, long seismic refraction lines can be acquired.

The sonobuoy method does away with hydrophone streamer cables and is not limited by streamer cable lengths. The sonobuoy consists of a flotation device containing batteries which, when in contact with seawater, are activated, causing a radio telemetering antenna to be raised and one or more hydrophones to be suspended on cables from below. When a shot is fired from the survey ship, the signals received by the hydrophones are radioed back to the ship where they are recorded. The offset between the shot and the sonobuoy is determined from the travel time of the direct wave through the water. In the case of inshore surveys, land-based surveying methods can be used to track the sonobuoy. One advantage of the sonobuoy method, if used during a major marine seismic reflection survey, is that the sonobuoys are expendable and sink after a finite period. The refraction data can, however, be acquired while the reflection survey is in progress.

A third method of marine seismic refraction surveying requires at least two ships, one towing the hydrophone streamer and the other firing the shots. If reverse shooting is to be used, a third ship may be required – two ships steam in opposite directions firing shots in sequence, while a third ship steams along the profile track towing a hydrophone streamer.

In hydrocarbon exploration, the use of multiship surveys and the slow rate of data acquisition make this an extremely expensive operation. Similarly, waterborne refraction surveys in harbours and estuaries take considerably longer to acquire than a comparable line-meterage of reflection profiling. Marine refraction surveys are very valuable in investigations for proposed tunnel routes under harbours for sewerage schemes, for example.

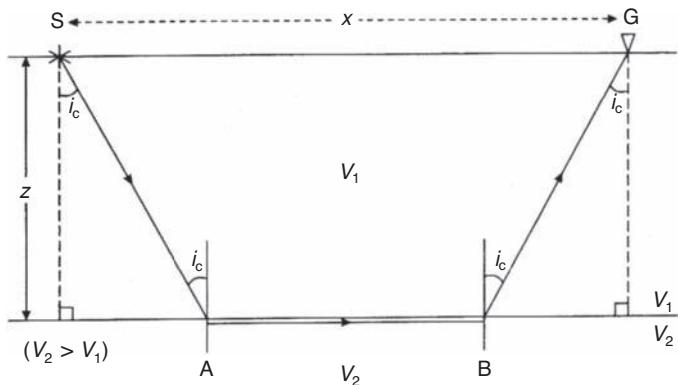


**Figure 5.3** Simple raypath for a two-layer structure.

### 5.3.1 Planar interfaces

#### 5.3.1.1 Two-layer case

In Figure 5.3, it can be seen that the raypath taken by a signal originating from the source S travels to A, where it undergoes critical refraction and travels towards and ultimately beyond position B. The headwave originating from the refractor at B travels through layer 1 where it is detected by a geophone at G. The geophone is offset from the shot by a distance  $x$ . The total travel time taken is the sum of the three component travel times, details of which are presented in Box 5.2. The time-distance graph for the two-layer case (Figure 5.1C) is used to calculate the velocities of the two layers,  $V_1$  and  $V_2$ , from the gradients of the two straight-line segments (gradient =  $1/V$ ). The extrapolation of the segment from the critically refracted arrivals on to the time axis gives an intercept time  $t_i$  from which the depth to the refractor ( $z$ ) can be calculated (Box 5.2, Equation (8)), given values of  $V_1$  and  $V_2$  derived from the time-distance graph.

On Figure 5.1, it can be seen that the travel times for the direct and critically refracted rays are the same at the crossover distance. Consequently, solving Equation (1) in Box 5.3 in terms of the crossover distance  $x_{\text{cross}}$  provides an additional means of calculating the depth to the refractor. Furthermore, Equation (2) in Box 5.3 shows that the depth to the refractor is always less than half the crossover distance.

#### 5.3.1.2 Three-layer case

The simple raypath geometry for critical refraction to occur in a three-layer model with horizontal interfaces is shown in Figure 5.4A, and its corresponding travel time-distance graph in Figure 5.4B. The expressions governing the travel time-velocity relationships are given in Box 5.4. The effect of reducing the thickness of layer 2 on the time-distance graph is to reduce or even remove completely the straight-line segment corresponding to refracted arrivals from the top of layer 2 (Lankston, 1990). The signal travels from the source down to the first refractor (at A), where it is refracted into the second medium through to the second interface (at B), at which point it is then critically refracted. From there the generated head wave from

### 5.3 Geometry of refracted raypaths

The basic assumption for seismic refraction interpretation is that the layers present are horizontal or only dipping at shallow angles, and are, in the first instance, planar surfaces.

**Box 5.2** Travel-time calculations for a two-layer case (see Figures 5.1 and 5.3)

$$\text{Total travel time is: } T_{SG} = T_{SA} + T_{AB} + T_{BG} \quad (1)$$

where:

$$T_{SA} = T_{BG} = z/(V_1 \cos i_c) \quad (2)$$

$$T_{AB} = (x - 2z \tan i_c)/V_2. \quad (3)$$

Substituting expressions (2) and (3) into (1), we obtain:

$$T_{SG} = z/(V_1 \cos i_c) + (x - 2z \tan i_c)/V_2 + z/(V_1 \cos i_c)$$

$$\text{which simplifies to: } T_{SG} = (1/V_2)x + 2z(\cos i_c)/V_1. \quad (4)$$

This has the form of the general equation of a straight line,  $y = mx + c$ , where  $m$  = gradient and  $c$  = intercept on the y-axis on a time-distance graph. So, from equation (4), the gradient is  $1/V_2$  and  $c$  is the refraction time intercept  $t_i$  (see Figure 5.1) such that  $t_i = 2z(\cos i_c)/V_1$ .

Remember that  $\sin i_c = V_1/V_2$  (Snell's Law), and hence:

$$\cos i_c = (1 - V_1^2/V_2^2)^{1/2} \text{ (from } \sin^2\theta + \cos^2\theta = 1\text{).}$$

An alternative form to Equation (4) is:

$$T_{SG} = x(\sin i_c)/V_1 + 2z(\cos i_c)/V_1 \quad (5)$$

or

$$T_{SG} = x/V_2 + t_i \quad (6)$$

where

$$t_i = 2z(V_2^2 - V_1^2)/V_1 V_2 \quad (7)$$

$$z = t_i V_1 V_2 / 2(V_2^2 - V_1^2)^{1/2} \quad (8)$$

the lowest refractor travels back from C through the overlying layers to arrive at the geophone at G.

The analysis works by determining  $V_1$ ,  $V_2$ ,  $t_1$  and  $t_2$  from the travel-time graph for the top two layers, and hence the thicknesses of the first two refractors can be calculated using the equations in Box 5.4. The thicknesses of refractors are usually underestimated by about 3%, with the percentage inaccuracy increasing with the larger the number of layers involved.

### 5.3.1.3 Multilayer case

The general expressions governing the travel time-velocity relationships for the situation where more than three horizontal planar layers are present are given in Box 5.5. The form of the equations and of the analysis of the travel-time graphs follow the procedures

**Box 5.3** The use of crossover distance to calculate refractor depth

Travel time of direct ray at the crossover distance is  $x_{\text{cross}}/V_1$ .

Travel time of critically refracted ray at the crossover distance is (from Equation (6) in Box 5.2) given by:

$$T = x_{\text{cross}}/V_2 + 2z(V_2^2 - V_1^2)^{1/2}/V_1 V_2$$

Hence, at the crossover point:

$$x_{\text{cross}}/V_1 = x_{\text{cross}}/V_2 + 2z(V_2^2 - V_1^2)^{1/2}/V_1 V_2 \quad (1)$$

Solving for  $x_{\text{cross}}$  and reorganising gives:

Depth to the refractor:

$$z = 1/2 x_{\text{cross}}[(V_2 - V_1)/(V_2 + V_1)]^{1/2} \quad (2)$$

Crossover distance:

$$x_{\text{cross}} = 2z[(V_2 + V_1)/(V_2 - V_1)]^{1/2}$$

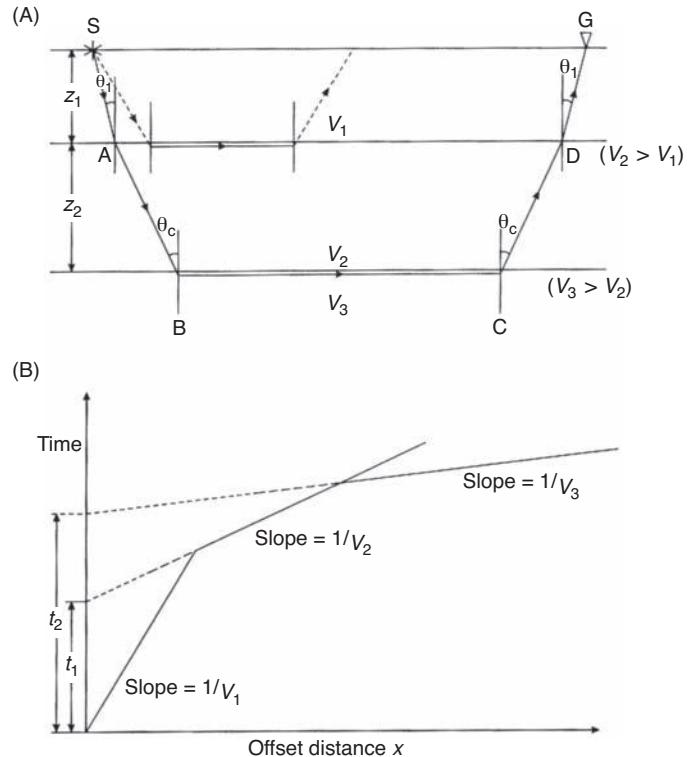


**Figure 5.4** (A) Simple raypath diagram for refracted rays, and (B) their respective travel time-distance graphs for a three-layer case with horizontal planar interfaces.

**Box 5.4** Travel-time calculations for a three-layer case (see Figure 5.4)

Total travel time is:

$$T_{SG} = T_{SA} + T_{AB} + T_{BC} + T_{CD} + T_{DG}$$

where:

$$T_{SA} = T_{DG} = z_1/V_1 \cos \theta_1$$

$$T_{AB} = T_{CD} = z_2/V_2 \cos \theta_c$$

$$T_{BC} = (x - 2z_1 \tan \theta_1 - 2z_2 \tan \theta_c)/V_3.$$

Combining these gives:

$$T_{SG} = x/V_3 + (2z_2 \cos \theta_c)/V_2 + (2z_1 \cos \theta_1)/V_1 \quad (1)$$

$$T_{SG} = x/V_3 + t_2 \quad (2)$$

where

$$\frac{\sin \theta_1}{V_1} = \frac{\sin \theta_c}{V_2} = \frac{1}{V} \quad \text{from Snell's Law.}$$

Thicknesses of refractors are given by:

$$z_1 = t_1 V_1 V_2 / 2(V_2^2 - V_1^2)^{1/2}$$

$$z_2 = t_2 V_2 V_3 / 2(V_3^2 - V_2^2)^{1/2} - z_1 V_2 (V_3^2 - V_1^2)^{1/2} / V_1 (V_3^2 - V_2^2)^{1/2}$$

explained for a three-layer case, but are extended to the relevant total number of layers.

In engineering applications, it is unusual to have more than three or at most four layers present; commonly only two-layer cases are used, with any variations in velocity within the first layer being taken into account by consideration of the value of the first layer velocity being an average. Commonly, in areas of alluvial fill or over glacial sediments, the local lateral and vertical variations in velocity

**Box 5.5** Travel-time calculations for a multilayer case

The total travel time  $T_{SG}$  in an  $n$ -layer case is given by:

$$T_{SG} = x/V_n + \sum_{i=1}^{n-1} [(2z_i \cos \theta_i)/V_i]$$

where  $\sin \theta_i = V_i/V_n$ .

Note that  $\theta_i$  are not critical angles except for  $\theta_{n-1}$ .

can be significant. It is often advisable to undertake micro-spreads, with geophone intervals as small as 1 m, in order to measure the near-surface velocities along a spread. If it is known from desk study work that the area has Quaternary and/or Recent sediment cover, the survey design should include micro-spreads in order to provide better control on the determination of local velocities. The variation in near-surface velocities makes it quite inappropriate to quote calculated values of velocity to the nearest metre per second. Careful thought should be given to determining the statistical significance of variations in P-wave velocities determined from refraction surveys. Calculated values of velocity should be quoted to perhaps the nearest 50 m/s, for example, with an estimation of the standard deviation as calculated from a relevant statistical analysis. If due consideration is not given to careful analysis of the variation of velocities, any depth estimates arising from the refraction survey are likely to be inaccurate, possibly being as much as 30–40% of the actual refractor depth. Depths determined to a refractor should be quoted with *realistic* error bars, not ‘hoped-for’ values!

Where refraction surveys are carried out as part of a hydrocarbon exploration programme or for crustal research, larger numbers of refractors can be encountered. However, there still needs to be a very careful appraisal of the errors and inaccuracies involved in whatever analysis is undertaken.

### 5.3.1.4 Dipping-layer case

When a refractor lies at an angle to the horizontal, the simple geometries so far described are complicated by the *angle of dip*. It is no longer adequate to undertake only one direction (forward) of shooting; it becomes necessary to carry out both forward and reverse shooting in order to determine all the parameters required to solve for the refractor geometry. Furthermore, the refractor velocities determined in the case of dip are referred to as *apparent* velocities, as the values of velocity determined from the inverse gradients of the straight-line segments on the travel time-distance graphs are higher in the upslope direction ( $V_u$ ) and lower in the downslope direction ( $V_d$ ).

The raypath geometry for a dipping two-layer case is shown in Figure 5.5A, with its travel time-distance graph in Figure 5.5B. Following the logic used in discussing the two-layer planar refractor in Section 5.3.1.1, a set of equations can be produced (Box 5.6) that relate velocity, layer thickness and angle of refractor dip, from which the geometry of the dipping refractor can be determined. The depths ( $d_a$  and  $d_b$ ) to the refractor vertically below the spread end-points can easily be calculated from the derived values of perpendicular depths ( $z_a$  and  $z_b$ ) using the expression  $d = z/\cos \alpha$ .

It should also be noted that the total travel times obtained from both forward and reverse shooting should be the same ( $T_{AD} = T_{DA}$ ) and these are hence also known as ‘reciprocal times’. When undertaking forward and reverse shooting, the reciprocity of the measured travel times should be checked. If the total travel times are not the same, the picking of first arrivals and the offsets of the geophones should be checked for errors.

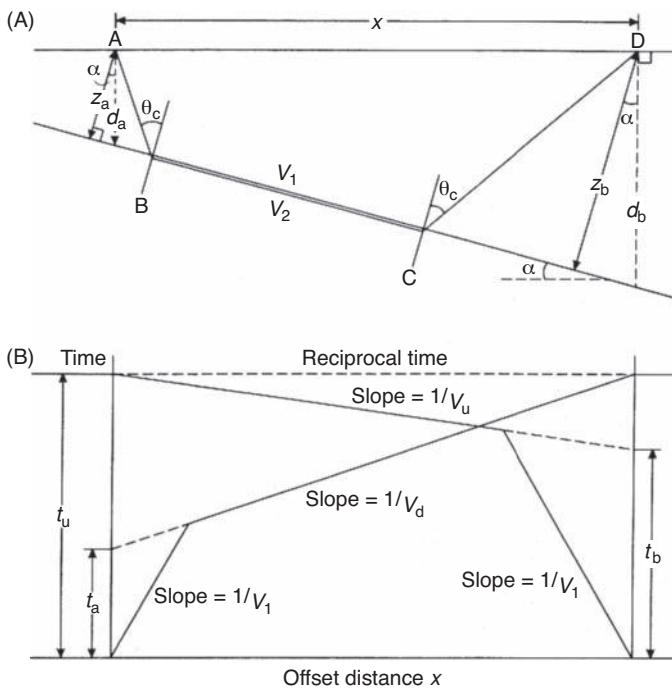


**Figure 5.5** (A) Raypath geometry over a refractor dipping at an angle  $\alpha$ , and (B) the respective travel time-distance graph for the forward (down-dip) and reverse (up-dip) shooting directions.

### 5.3.1.5 The case of a step discontinuity

So far the refractor has been assumed to be planar and continuous. There are situations where a step discontinuity may occur in the refractor, such as in an old backfilled quarry where a former quarry face has been covered over with backfill material (Figure 5.1B). In such a situation, the refractor velocity should remain the same along its length; the only perturbation arises from the distortion in raypath (Figure 5.6).

If the step discontinuity has been caused by a normal fault, for example, there may be an additional complication of the refractor velocity having different magnitudes across the fault plane; if the throw on the fault is significant, different geological materials may now be juxtaposed with consequent differences in seismic velocities. Indeed, the presence of a lateral change in refractor velocity in a two-layer case may give rise to a travel time-distance graph from a single end-on forward shot identical to that produced by three horizontal layers but with uniform layer velocities. The easiest way to discriminate between the two cases is to carry out an off-end forward shot. If the crossover point on the travel time-distance graph is shifted laterally (i.e. along the  $x$ -axis), this indicates that the three-layer case is correct. If, instead, the crossover point is shifted vertically on the time axis (i.e. there is a delay time) then this is indicative of a two-layer case, such as across a fault plane at which there is no topographic effect on the refractor, but where there is a significant velocity contrast. This situation has been discussed in more detail by Lankston (1990).

Where the size of the step discontinuity is small with respect to the depth of the refractor, then a simple equation (Box 5.7) can

### Box 5.6 Travel-time calculations for a dipping refractor (see Figure 5.5)

Total travel time over a refractor dipping at an angle  $\alpha$  is given by:

$$T_{ABCD} = (x \cos \alpha)/V_2 + [(z_a + z_b) \cos i_c]/V_1$$

where  $V_2$  is the refractor velocity, and  $z_a$  and  $z_b$  are the distances perpendicular to the refractor.

The down-dip travel time  $t_d$  is given by:

$$t_d = x[\sin(\theta_c + \alpha)]/V_1 + t_a \quad (1)$$

where  $t_a = 2z_a (\cos \theta_c)/V_1$ , and the up-dip travel time  $t_u$  is given by:

$$t_u = x[\sin(\theta_c - \alpha)]/V_1 + t_b \quad (2)$$

where  $t_b = 2z_b (\cos \theta_c)/V_1$ .

Equations (1) and (2) above can be written in terms of the apparent up-dip velocity ( $V_u$ ) and down-dip velocity ( $V_d$ ) such that:

$$\begin{aligned} t_d &= x/V_d + t_a, & \text{where } V_d = V_1/\sin(\theta_c + \alpha) \\ t_u &= x/V_u + t_b, & \text{where } V_u = V_1/\sin(\theta_c - \alpha). \end{aligned}$$

An approximate relationship between true and apparent velocities for shallow angles of dip ( $\alpha < 10^\circ$ ) is given by:

$$V_2 \approx (V_d + V_u)/2.$$

be used to estimate the difference in depth to the refractor. While the delay time ( $\delta t$ ) may be observed on a time-distance graph from a shot in a forward direction, commonly the amplitudes of the refracted signals from a reverse shot are very small and it may not be possible to obtain satisfactory data from a reverse shot.

### 5.3.2 Irregular (non-planar) interfaces

The preceding discussion has been for planar layers that are either horizontal or dipping uniformly and with no lateral variation in velocity in the refractor, or vertical variation in velocity within the surface layer. It is important whenever a refraction survey is

### Box 5.7 Determination of depth to a refractor with a step discontinuity (see Figure 5.6)

The step size ( $\delta z$ ) in a discontinuity in a refractor is given by:

$$\delta z = \delta t V_1 V_2 / (V_2^2 - V_1^2)^{1/2}.$$

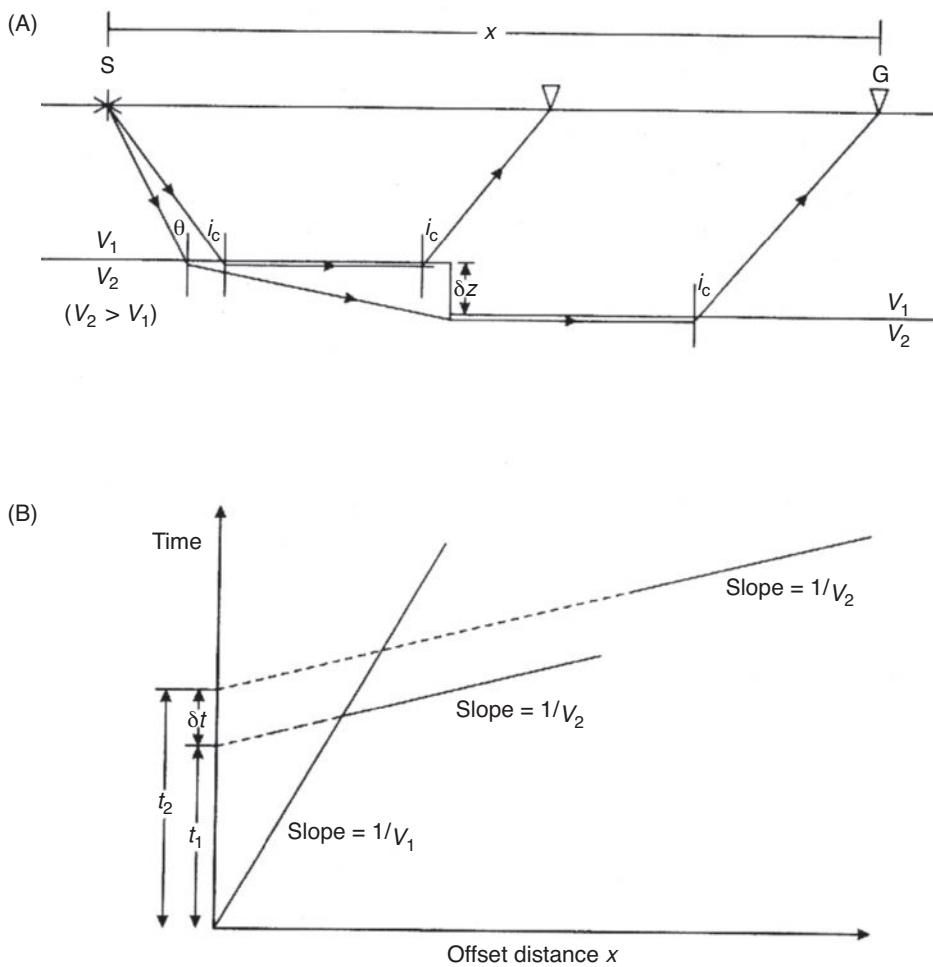


**Figure 5.6** (A) Raypath geometry over a refractor with a step discontinuity but no lateral change in layer velocity, and (B) the corresponding travel time-distance graph.

designed and then executed that consideration be given to the type of layer case present, as judged from the quality and nature of travel time-distance data obtained. In a significant number of cases the simple models are obviously not appropriate, as in the situation of a refraction survey over a buried rock valley, for instance. It becomes necessary to carry out interpretation on the basis that the refractor is no longer planar or necessarily horizontal, but irregular in form, and where the wavelength of variation in refractor elevation is greater than the depth to the refractor. When an irregular refractor is encountered, it is usually analysed on the basis of only a two-layer case, details of which are given in the next section.

## 5.4 Interpretational methods

Before any detailed interpretation can begin, it is important to inspect the travel time-distance graphs obtained, (a) as a check on quality of the data being acquired, and (b) in order to decide which interpretational method to use – simple solutions for planar layers and for a dipping refractor, or more sophisticated analysis for the

case of an irregular refractor. Checks to be considered are listed in Table 5.1, and some of the associated time anomalies ((iii)–(vi)) are illustrated in Figure 5.7. Indiscriminate smoothing of ‘cusps’ in travel time data can obscure what might be important features and result in serious errors of interpretation.

Several different interpretational methods have been published, falling into two approaches: delay-time and wavefront construction

**Table 5.1** Travel time anomalies (see Figure 5.7).

- (i) Isolated spurious travel time of a first arrival, due to a mispick of the first arrival or a misplot of the correct travel-time value
- (ii) Changes in velocity or thickness in the near-surface region
- (iii) Changes in surface topography
- (iv) Zones of different velocity within the intermediate depth range
- (v) Localised topographic features on an otherwise planar refractor
- (vi) Lateral changes in refractor velocity

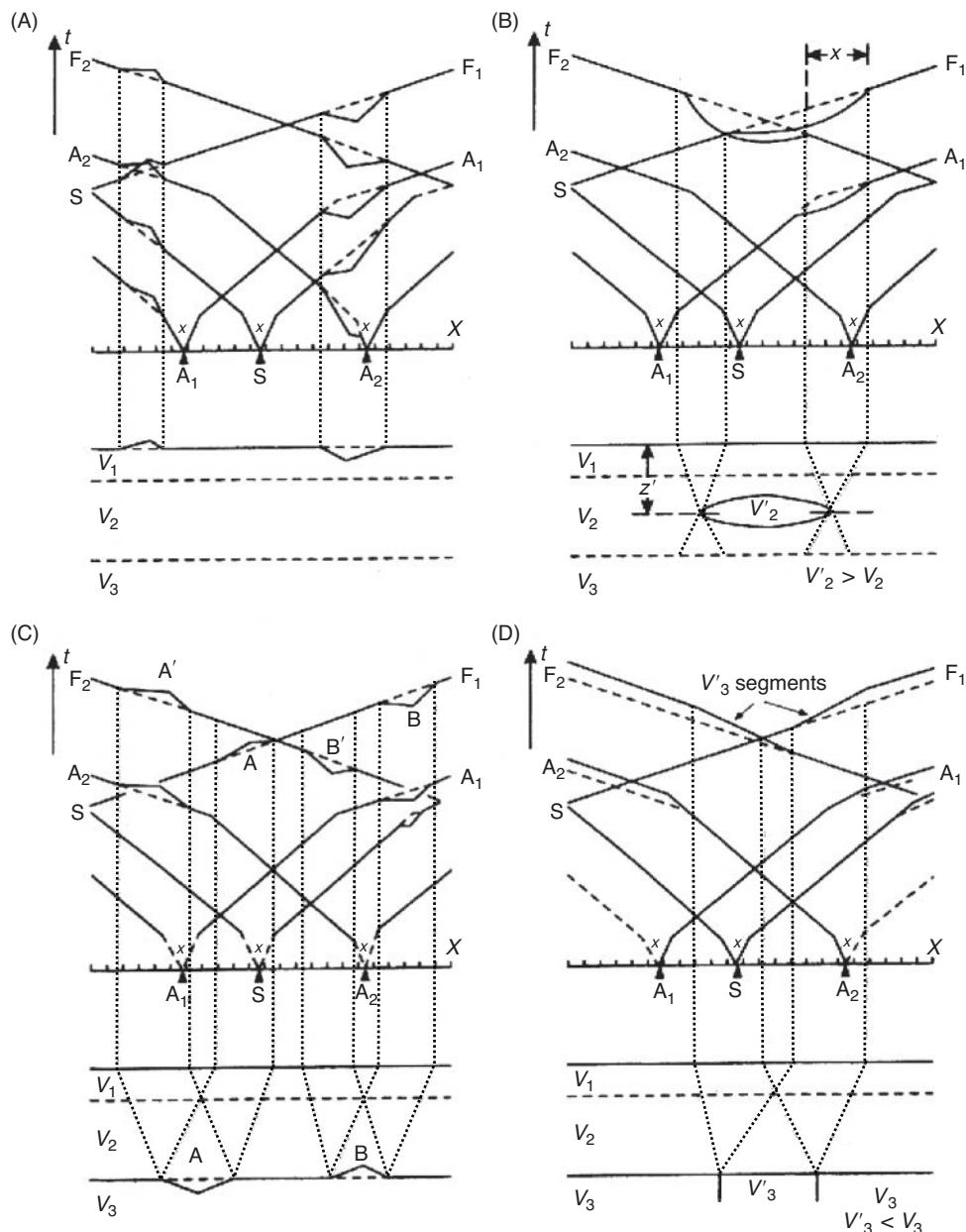


**Figure 5.7** Travel-time anomalies and their respective causes. (A) Bump and cusp in layer 1. (B) Lens with anomalous velocity ( $V'_2$ ) in layer 2. (C) Cusp and bump at the interface between layers 2 and 3. (D) Vertical but narrow zone with anomalous velocity ( $V'_3$ ) within layer 3. After Odins (1975), in Greenhalgh and Whiteley (1977), by permission.

methods. Examples of the former are Gardner (1939, 1967), Wyrobek (1956), Barry (1967) and Palmer (1980), and those of the latter are Thornburgh (1930), Hales (1958), Hagedoorn (1959), Schenck (1967), Hill (1987), Vidale (1990), and Aldridge and Oldenburg (1992). However, two methods emerge as the most commonly used, namely Hagedoorn's 'plus-minus' method (Hagedoorn, 1959) and the generalised reciprocal method (GRM) (Palmer, 1980), which are described in Sections 5.4.2 and 5.4.3 respectively. The more recent publications tend to be modifications of earlier methods or new computational procedures – see Section 5.4.6.

#### 5.4.1 Phantoming

The subsurface coverage of a dipping refractor obtained by both forward and reverse shooting overlaps along only part of the refractor, and is not totally coincident, as shown in Figure 5.8 (Lankston, 1990). The apparent velocities obtained up-dip and down-dip are in fact derived from different segments of the refractor. If the interface is planar, then the use of such apparent velocities to derive layer thicknesses and dip angles is justified.

In order to increase the subsurface coverage, and depending on the suitability of the local geology, both the shot locations and the

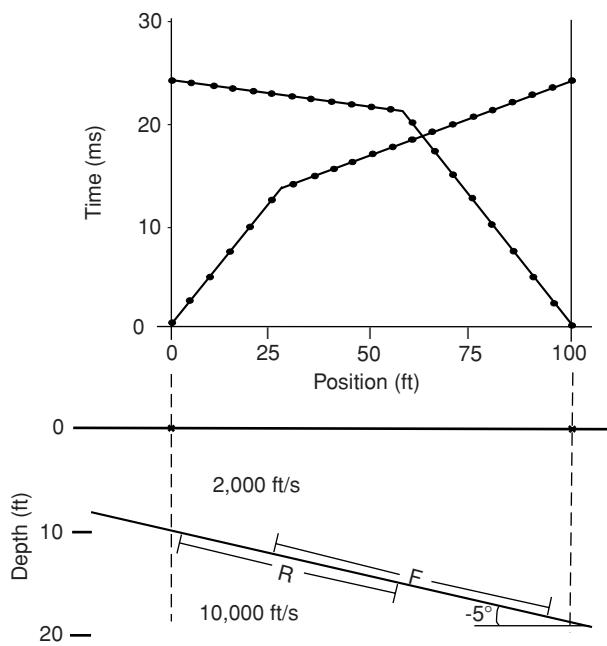


**Figure 5.8** Overlapping zones of subsurface coverage from forward and reverse shooting over a dipping refractor, and corresponding travel time-distance graphs. From Lankston (1990), by permission.

geophone spread have to be moved along the line of the profile. If there is no lateral variation in refractor velocity, then the resultant travel time-distance graph from a headwave generated from shot at increased offset is delayed in travel time but has the same gradient as that from the end-on shot (Figure 5.9). The observed parallelism of the two travel-time graphs indicates that the difference in travel time is a constant for each geophone location. By subtracting this time difference from the headwave arrivals from the refractor in the second, offset shot, then the reduced travel times are those that would have been recorded from the first shot over the distance between the end-on shot and the crossover distance.

The time-shifted arrivals are known as *phantom arrivals* (Redpath, 1973) and the process of time-shifting is referred to as *phantomming*. This process provides a means of obtaining real first-arrival information between the end-on shot and the original crossover distance which could not have been recorded from the first shot. The phantom arrivals, therefore, remove the necessity to extrapolate the travel-time graph from beyond the crossover point back to the zero-offset point to obtain the intercept time, as indicated previously in Figure 5.1.

#### 5.4.2 Hagedoorn plus-minus method

In Hagedoorn's method, it is assumed that the layers present are homogeneous, that there is a large velocity contrast between the layers, and that the angle of dip of the refractor is less than 10°. The method uses intercept times and delay times in the calculation of the depth to a refractor below any geophone location. Referring to Figure 5.10, the delay time ( $\delta t$ ) is the difference in time between

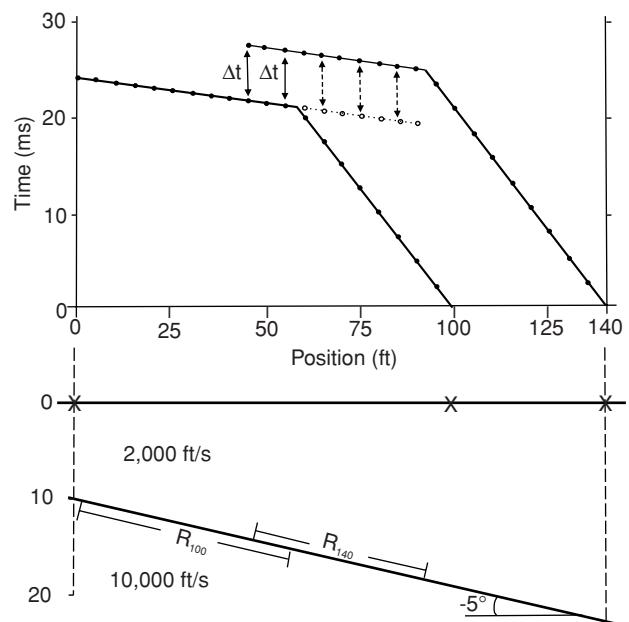


**Figure 5.9** Travel time-distance graphs and subsurface coverage from two overlapping reverse direction spreads; open circles denote phantom arrivals. From Lankston (1990), by permission.

(1) the time taken for a ray to travel along a critically refracted path from the source via the subsurface media and back to the surface ( $T_{SG}$  along SABG), and (2) the time taken for a ray to travel the equivalent distance of the source–geophone offset ( $x$ ) along the refractor surface (i.e.  $T_{PQ}$  along the projection PQ of the refracted raypath on to the refractor surface). The total delay time ( $\delta t$ ) is effectively the sum of the 'shot-point delay time' ( $\delta t_s$ ) and the 'geophone delay time' ( $\delta t_g$ ). In cases where the assumptions on which the method is based are realistic, it is sufficiently accurate to consider the distance PQ to be approximately the same as the source–geophone offset (SG). The mathematical equations relating the various delay times and velocities are given in Box 5.8.

Hagedoorn's plus-minus method of analysing refraction data from both forward and reverse shooting provides a means of determining the delay times and hence the layer velocities and the depth to the refractor beneath any given geophone.

In Figure 5.11A, A and B are the locations of the forward and reverse shot points, and G is an arbitrary location of a geophone

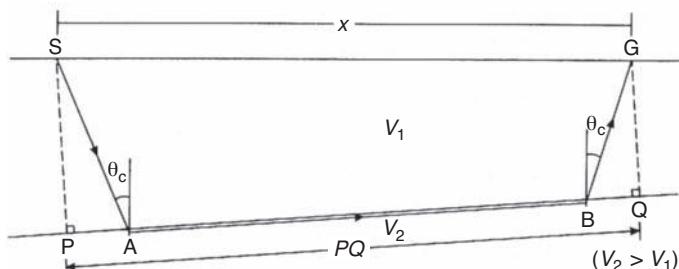


**Figure 5.10** The principle of delay time (see text for details).

**Box 5.8 Determination of delay times (see Figure 5.10)**

The total delay time is given by:  $\delta_t = T_{SG} - T_{PQ}$

and by:  $T_{SG} = (SA + BG)/V_1 + AB/V_2$  and  $T_{PQ} = PQ/V_2$ .

Thus:  $\delta_t = (SA + BG)/V_1 - (PA + BQ)/V_2$

$$\begin{aligned} &= (SA/V_1 - PA/V_2) + (BG/V_1 - BQ/V_2) \\ &= \delta t_s + \delta t_g \approx T_{SG} - x/V_2. \end{aligned}$$

Alternatively:  $T_{SG} = x/v_2 + \delta t_s + \delta t_g$  (1)

where  $\delta t_s$  and  $\delta t_g$  are the shot-point and geophone delay times.

In the case of a horizontal refractor,  $\delta t = t_i$ , the intercept time on the corresponding time-distance graph (see Figure 5.1 and Box 5.2, Equation (6)).

in between. Using Equation (1) from Box 5.8, the travel time for a refracted ray from a shot point to any geophone G can be defined in terms of the respective delay times (see Box 5.9). Hagedoorn's 'plus term' ( $T^+$ ) is the sum of the travel times from shot to the geophone from each end, minus the overall travel time between one shot point

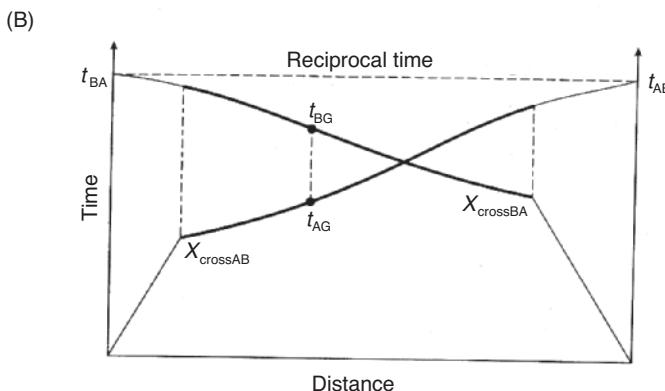
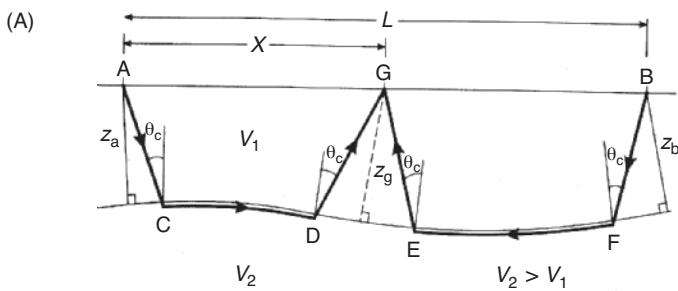


**Figure 5.11 (A)** Raypath geometry for forward and reverse shots over a refractor with irregular surface topography, and (B) the corresponding travel time-distance graphs. The segments between respective crossover distances are highlighted by thicker lines as it is these segments that are used in Hagedoorn's plus-minus analysis.

**Box 5.9 Hagedoorn plus-minus terms (see Figure 5.11)**

The travel time of a refracted ray at any geophone G is given by:

$$t_{AG} = x/V_2 + \delta t_g + \delta t_a \quad (1)$$

$$t_{BG} = (L - x)/V_2 + \delta t_g + \delta t_b \quad (2)$$

$$t_{AB} = L/V_2 + \delta t_a + \delta t_b \quad (3)$$

Hagedoorn's plus term  $T^+$  is given by:

$$T^+ = t_{AG} + t_{BG} - t_{AB} = 2\delta t_g = 2z_g(\cos \theta_c)/V_1 \quad (4)$$

Therefore, the depth to the refractor beneath any geophone ( $z_g$ ) is given by:

$$z_g = (T^+)/V_1/2 \cos \theta_c = (T^+)/V_1 V_2/2(V_2^2 - V_1^2)^{1/2}. \quad (5)$$

Hagedoorn's minus term  $T^-$  is given by:

$$T^- = t_{AG} - t_{BG} = (2x - L)/V_2 + \delta t_a - \delta t_b. \quad (6)$$

and the other (Box 5.9, Equation (4)). Hagedoorn's 'minus term' ( $T^-$ ) is the difference in travel times taken by rays from each shot point to a given geophone.

$T^-$  values can be plotted on a graph either against offset distance directly, in which case the velocity is determined from the slope which is  $2/V_2$ , or against  $(2x - L)$  in which case the velocity is simply the inverse slope ( $1/V_2$ ). Values of the first layer velocity can be obtained in the conventional way from the inverse slope of the time-distance graph ( $1/V_1$ ). In each case, the  $T^-$  term provides a means of examining the lateral variation in refractor velocity with a lateral resolution equal to the geophone separation. Better accuracy of the estimate of velocity can be achieved, whichever graphical method is used, by carrying out linear regression analysis over the appropriate segments of the graph to determine the slope(s) most accurately and to provide some means of determining standard deviations.

Once values of layer velocities have been calculated, the depth ( $z_g$ ) perpendicular to the refractor below each geophone can be computed using the T-term. Calculations are made easier if velocities are expressed in km/s and time in milliseconds, as depths are then given in metres. Given the assumptions made, the accuracy of the depth calculation should be to within 10%.

An example of the graphical output from the plus-minus method is shown in Figure 5.12.

The Hagedoorn plus-minus method is readily adapted for calculation using either a spreadsheet on a personal computer or stand-alone proprietary software. Seismograph manufacturers also provide their own interpretational software with their instruments.

The interpretation procedure is very straightforward. Having picked the first-arrival times, the values are put into their respective spreadsheet cells for their given offset distance. By inspection of the time-distance (T-X) graphs, the reciprocal times can be found

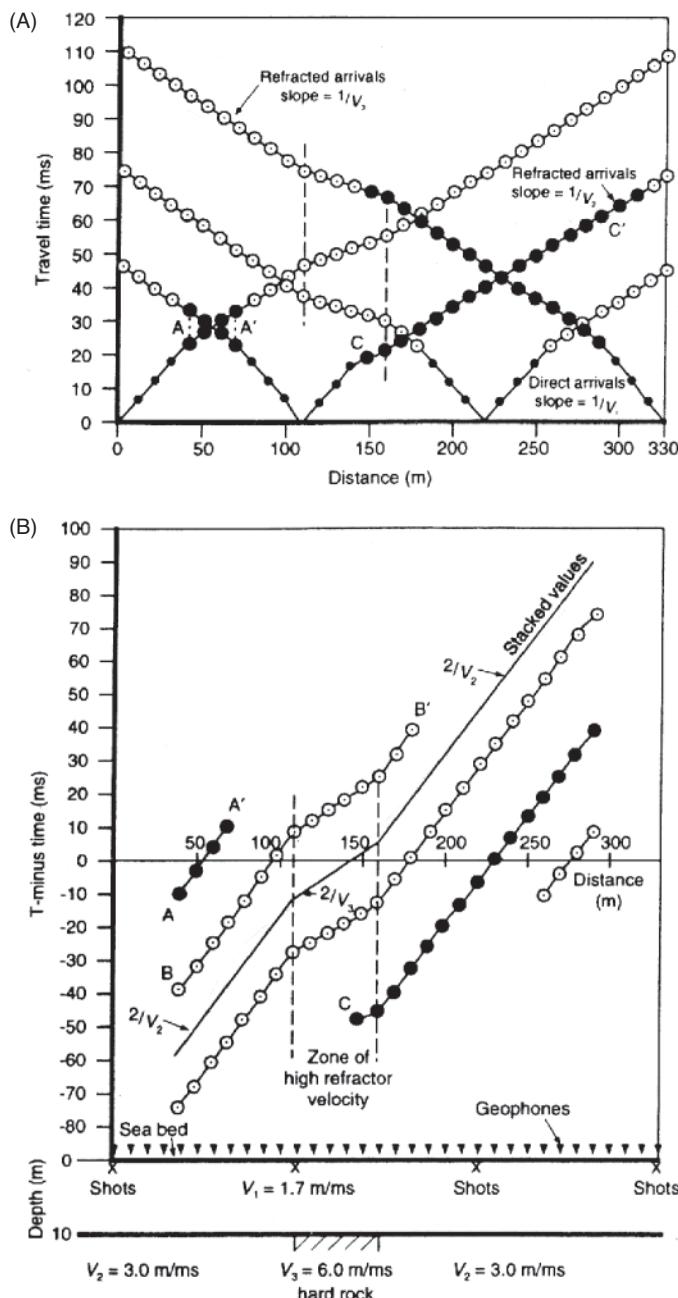


**Figure 5.12** (A) Composite travel time-distance graphs; (B) Hagedoorn  $T^-$  graph; and (C) calculated depths to a refractor. After Gardner (1992), by permission.

and checked; the distances between end-to-end shots and hence the values of the distance  $L$  are known from the survey layout. The  $T-X$  graphs are inspected to separate out which portions of which graph are to be used in the analysis (i.e. which data give information about  $V_1$  and which about  $V_2$ , etc.). Velocities are found using linear regression analysis on the relevant portions of the  $T-X$  graph (for  $V_1$ ) and of the  $T^-$  distance graphs (for  $V_2$ ). These values are then used with the  $T^+$  term to derive values of depth to the refractor at each geophone location. All the graphical output and

the calculations can be achieved using just one software package, thus making it very convenient to carry out the analysis.

The plus-minus method assumes also that the refractor is uniform between the points of emergence on the interface (i.e. between D and F in Figure 5.11 A). If this assumption does not hold but the method is used, then the non-planarity of the refractor is smoothed and an oversimplified interpretation would be obtained. This smoothing is overcome by the generalised reciprocal method, which is discussed in the next section.

### 5.4.3 Generalised reciprocal method (GRM)

The generalised reciprocal method (Palmer, 1980) is an inversion technique which uses travel-time data from both forward and reverse shots and which provides a graphical solution to resolve the geometry of subsurface refractors. The method uses refraction migration to obtain the detailed structure of a refractor and information about any localised lateral variations within it. Refraction migration uses the offset (migration) distance which is the horizontal separation between a point on the refractor where a ray is critically refracted, and that at the surface where the ray emerges.

It has been pointed out (Sjögren, 1984), however, that the migration distance does not satisfactorily define narrow zones with low seismic velocities. As such zones are often the targets for refraction surveys, it is important that the interpretational method is capable of resolving them. Palmer (1991) demonstrated that the migration distance selected to define the refractor surface is not necessarily the same as that which provides the optimum information about refractor velocities. Consequently, if the GRM is used to its full effect, it can be used successfully to define narrow low-velocity zones (see also Section 5.5.1). In order to increase the accuracy of the GRM, Zanzi (1990) proposed that consideration should be given to non-linear corrections in the case of an irregular refractor.

A principal difference of the GRM compared with the plus-minus method is that the critically refracted rays emerge at or very near the same point on the refractor, thereby removing the smoothing problem discussed in the previous section. They arrive at two different geophone locations separated by a distance  $XY$  (Figure 5.13).

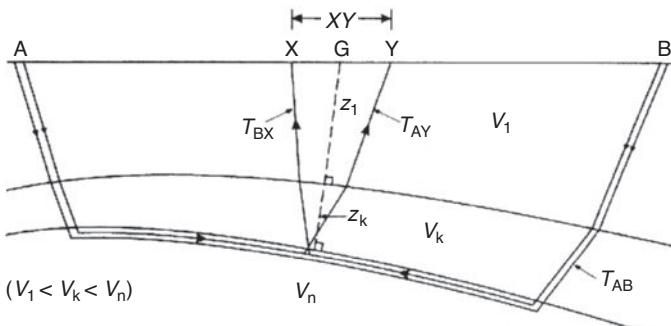


**Figure 5.13** Schematic summary of parameters used in the generalised reciprocal method (GRM).

**Box 5.10** GRM velocity analysis and time functions  
 (see Figure 5.13)

The refractor velocity analysis function ( $t_v$ ) is given by:

$$t_v = (T_{AY} - T_{BX} + T_{AB})/2 \quad (1)$$

where the distances  $AY$  and  $BX$  can be defined in terms of the distances  $XY$  and  $AG$ , such that:

$$AY = AG + XY/2 \quad \text{and} \quad BX = AB - AG + XY/2.$$

A graph of  $t_v$  plotted as a function of distance  $x$  has a slope =  $1/V_n$ , where  $V_n$  is the seismic velocity in the refractor (which is the  $n$ th layer).

The time-depth function ( $t_G$ ) is given by:

$$t_G = [T_{AY} + T_{BX} - (T_{AB} + XY/V_n)]/2 \quad (2)$$

The time-depth function, plotted with respect to position G, is related to the thicknesses ( $z_{jG}$ ) of the overlying layers, such that:

$$t_G = \sum_{j=1}^{n-1} z_{jG} (V_n^2 - V_j^2)^{1/2} / V_n V_j \quad (3)$$

where  $z_{jG}$  and  $V_j$  are the perpendicular thickness below G and velocity of the  $j$ th layer, respectively.

The optimum distance  $XY$  ( $XY_{\text{opt}}$ ) is related to layer thickness  $z_{jG}$  and seismic velocities  $V_j$  and  $V_n$  by:

$$XY_{\text{opt}} = 2 \sum_{j=1}^{n-1} z_{jG} \tan \theta_{jn} \quad (4)$$

where  $\sin \theta_{jn} = V_j/V_n$ .

Given a value of  $XY_{\text{opt}}$ , an average velocity ( $V'$ ) of all the layers above the refractor (layer  $n$ ) is given by:

$$V' = [V_n^2 X Y_{\text{opt}} / (X Y_{\text{opt}} + 2 t_G V_n)]^{1/2} \quad (5)$$

Two functions are computed within the generalised reciprocal method: the velocity analysis function ( $t_v$ ) and the time-depth function ( $t_G$ ). The latter is determined with respect to a position G (Figure 5.13) at the mid-point between the points of emergence at the surface of forward and reverse rays at Y and X, respectively. Both functions are expressed in units of time and are detailed in Box 5.10. Equations (1) and (2) in that box are similar to Hagedoorn's  $T^-$  and  $T^+$  terms, respectively, when the points X and Y are coincident (see Box 5.9). In cases where the maximum angle of dip is less than  $20^\circ$ ,

the GRM, as detailed here, provides estimates of refractor velocities to within 5%.

Both the velocity analysis and time-depth functions are evaluated and presented for a range of  $XY$  values from zero to one considerably larger than the optimum value. The increment in values of  $XY$  is usually taken as being equivalent to the geophone separation. Thus, if geophones are spaced at 5 m intervals,  $XY$  is incremented in steps of 5 m.

At the optimum value of  $XY$ , both the forward and reverse rays are assumed to have been critically refracted at or very near the same point on the refractor. The optimum value of  $XY$  in the analysis of velocity is determined as being that which gives a time-depth function that approximates most closely to a straight line. Where there are lateral variations in refractor velocity, the optimum value of  $XY$  may differ with distance (see, for example, the case history in Section 5.5.1). In the selection of the optimum value of  $XY$  for the time-depth function, the graph that exhibits most detail should be the one chosen. In general, the optimum value of  $XY$  should be the same for both the velocity analysis and time-depth functions.

Having determined the value(s) of refractor velocity from the velocity analysis function ( $t_v$ ), and hence determined the optimum value of  $XY$ , then Equation (3) in Box 5.10 can be used to calculate the perpendicular depth to the refractor below each geophone position. This depth value is, however, the locus of depths centred on any given geophone position. Hence, an arc is drawn centred on a given geophone location with a radius equivalent to the calculated depth. The refractor surface is constituted by drawing the tangent to the constructed arcs, so that the true geometry of the refractor is migrated to the correct location in space. A further example of the application of this method is given in Section 5.5.1 (Lankston, 1990).

#### 5.4.4 Hidden-layer problem

A *hidden layer* or *blind zone* occurs when a layer that is present is not detected by seismic refraction. There are four causes of this problem: velocity inversion; lack of velocity contrast; the presence of a thin bed; and inappropriate spacing of geophones (Figure 5.14). In the situation where a layer with a lower velocity underlies one with a higher velocity, then the lower-lying layer may not be detected using seismic refraction methods. No critical refraction can occur in such a situation and thus no headwaves from the interface are produced. If there is little velocity contrast, then it may be extremely difficult to identify the arrivals of headwaves from the top of this zone. In addition, in the case where velocities increase with depth, but the thickness of a layer is less than one wavelength of the incident wave, then the thin bed would not be evident on the corresponding time-distance graph and would therefore effectively be hidden. Furthermore, the portion of travel-time graph arising from this thin bed may not be sampled if the geophone interval is too large (Lankston, 1990).

The hidden-layer problem precludes seismic refraction surveys from being undertaken where there is known to be a velocity

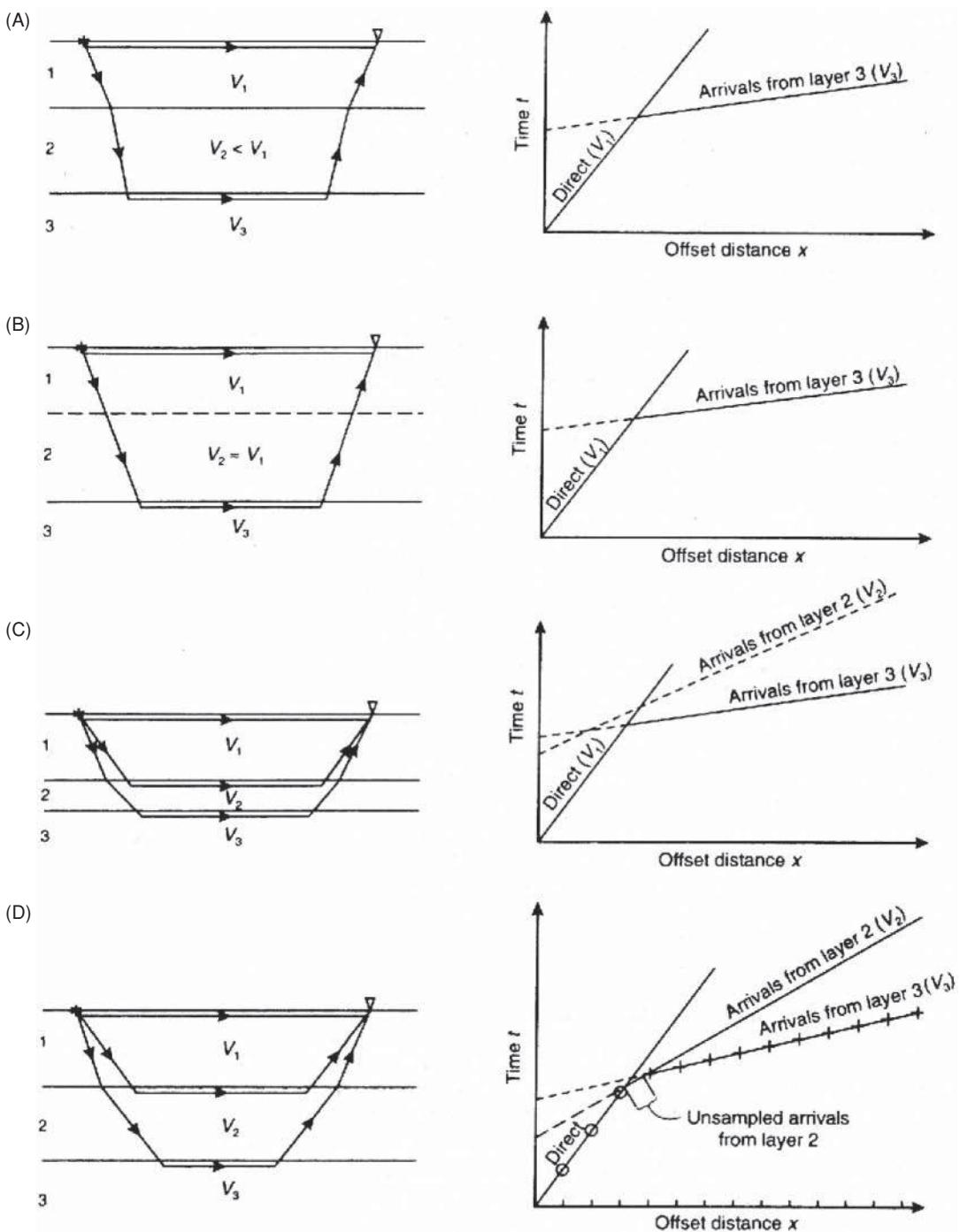


**Figure 5.14** Depiction of the 'hidden layer' problem due to: (A) velocity inversion ( $V_2 < V_1$ ); (B) lack of velocity contrast ( $V_2 \sim V_1$ ) and (C) a thin layer (layer 2) sandwiched between layers 1 and 3. In (D) the distance between geophones is too large to permit the identification of layer 2.

inversion, such as where there is a layer of strongly cemented material in less consolidated material at shallow depth, such as hard-pan or duricrust. The only way seismic refraction can be undertaken in such circumstances is for each shot and geophone to be located below this hard, higher-velocity layer. This solution can lead to considerable logistical problems and reduced production rates, with a corresponding increase in cost.

#### 5.4.5 Effects of continuous velocity change

So far it has been assumed that each layer has a uniform velocity both horizontally and vertically. In reality there are some materials where a uniform velocity is not observed. Examples of such materials are: sedimentary sequences in which grain size varies as a function of

depth (fining-up and fining-down sequences), or where the degree of cementation increases with depth; some igneous bodies where fractionation has occurred, giving rise to more dense material at depth; and in polar regions over snowfields, where the degree of compaction from snow to ice increases with depth (firnification). In these situations, there is a gradual change in velocity with depth (e.g. Kirchner and Bentley, 1979; Beaudoin *et al.*, 1992; King and Jarvis, 1992) and hence there is no obvious crossover point on the time-distance graph. Instead, the graph is curved, and the change from one so-called layer to another is gradational, making the usual methods of analysis inappropriate.

#### 5.4.6 Seismic refraction software

The Delay Time Method (DTM) and Reciprocal Method (RM) of refraction interpretation originated as graphical approaches, and as discussed above, make simplifying assumptions about the velocity structure and do not take into account adequately heterogeneity, lateral discontinuities, and gradients (Sheehan *et al.*, 2005). New software has been developed that uses seismic refraction tomography, which is not subject to these constraints. There are now a number of different packages available on the market (e.g. REFLEXW (Sandmeier, 2007); SeisOpt®@2D™ (Optim LLC, 2002); \*SeisImager™ (Geometrics and OYO, 2003); REFRACT (Leung *et al.*, 1997); \*RAYRACT™ (Rohdewald, 2006); \*GeoCT-II (GeoTomo, 2007) – see Appendix 1 for corresponding websites for further details). GeoTomo have also produced a 3D tomography package (TOMO3D). The three packages asterisked were evaluated by Sheehan *et al.* (2005). Most seismograph manufacturers package basic first-arrival picking and display/processing software. Other seismic refraction interpretation software packages and variations also exist. For example, Whiteley (2004) has adapted Leung's (1997) approach to interactive interpretation of shallow refraction data on a PC using Visual Interactive Ray Trace (VIRT) modelling. Rayfract uses the Wavepath Eikonal Traveltime (WET) method (Schuster and Quintus-Bosz, 1993; Woodward and Rocca, 1988), which uses a Fresnel volume approach (Watanabe *et al.*, 1999), whereas SeisImager and GeoCT, for example, use wavefront propagation methods for travel-time modelling (Geometrics and OYO, 2003; Zhang and Toksoz, 1998). Interpretation limitations of tomographic sections include artefacts arising from insufficient subsurface raypath coverage. VIRT, WET and RM methods have been compared by Whiteley and Eccleston (2006) for regolith mapping. This is especially important in places like Australia where the regolith is highly variable. If seismic refraction tomography is to be used, then the number of shot points per spread needs to be increased relative to the usual practice for the GRM method in order to ensure that subsurface raypath coverage is sufficiently high not to have blind spots or undersampled zones. This means at least seven, preferably nine or even eleven shots per spread: a minimum of two end-on, one mid-spread, at least two asymmetric split spread, and at least two off-end shots (this includes forward and reverse shooting). Additional off-end shots should be considered with different offsets from the spread to ensure subsurface raypath coverage.

## 5.5 Applications and case histories

### 5.5.1 Rockhead determination for a proposed waste disposal site

Lankston (1990) provided an example of the use of seismic refraction surveying with respect to a municipality granting a permit for a waste disposal site. The proposed location was an isolated site adjacent to a major river. Basalt, which was exposed along the side of the site farthest from the river, formed the underlying bedrock. Overlying bedrock was alluvium and windblown sand which in areas formed dunes 1–2 m high. Owing to the presence of loose sand at the surface, a sledgehammer source was ineffective, so explosives were used. The geophone interval was 50 ft (15.2 m). Each refraction spread was surveyed using one long and one short offset shot at each end, plus one mid-spread shot. Each successive spread overlapped with the previous one by two geophone positions.

The forward-direction travel time-distance graphs along one survey line are shown in Figure 5.15. The data are indicative of a two-layer case, with good parallelism evident in the high-velocity, deeper layer arrivals, except between 700 and 800 ft (213 m and 244 m) along the line. It is evident that the geophone interval is too large to provide the required resolution here. It is a good example of the occurrence of the problem illustrated in Figure 5.14D. The presence of an intermediate layer is indicated at 750 and 800 ft (indicated by the letter A in Figure 5.15).

The reverse-direction travel-time graphs for the same survey line are given in Figure 5.16. However, these data do not help to resolve the problem over the presence of an intermediate layer or to what extent the feature occurs laterally.

The data were phantomed (Figure 5.17) using the method described by Lankston and Lankston (1986). Forward data from the shot at 325 ft (99 m) and reverse data from the shot at 1125 ft (343 m) were used. Between each observed (or phantomed) point on the travel time-distance graph, travel times were interpolated in order to improve the resolution of the optimum XY value using the general reciprocal method. The resulting velocity analysis is shown in Figure 5.18. Applying Palmer's (1980) criterion of least detail, the curve for  $XY = 0$  was considered to be the best for defining the refractor's velocities. Applying Palmer's (1980) maximum detail criterion to the time-depth data in Figure 5.19, an optimum  $XY = 0$  was also chosen. In generating the time-depth graphs, the refractor velocity was required; three values were interpreted along the refractor as indicated in Figure 5.20.

With such a large inter-geophone spacing (50 ft), quantifying any change in the optimum XY value on the basis of the data acquired was not possible. However, had the layer thicknesses and velocities been known, the optimum XY value could have been predicted. By working backwards in this example from the interpreted velocities and depths, the optimum XY value was predicted to be equal to about 6 m (20 ft).

Having determined the refractor velocities and, from micro-spreads, the velocities of the near-surface layers, within the constraints of the actual survey, the depth of the refractor below each geophone position was determined. The uppermost layer was

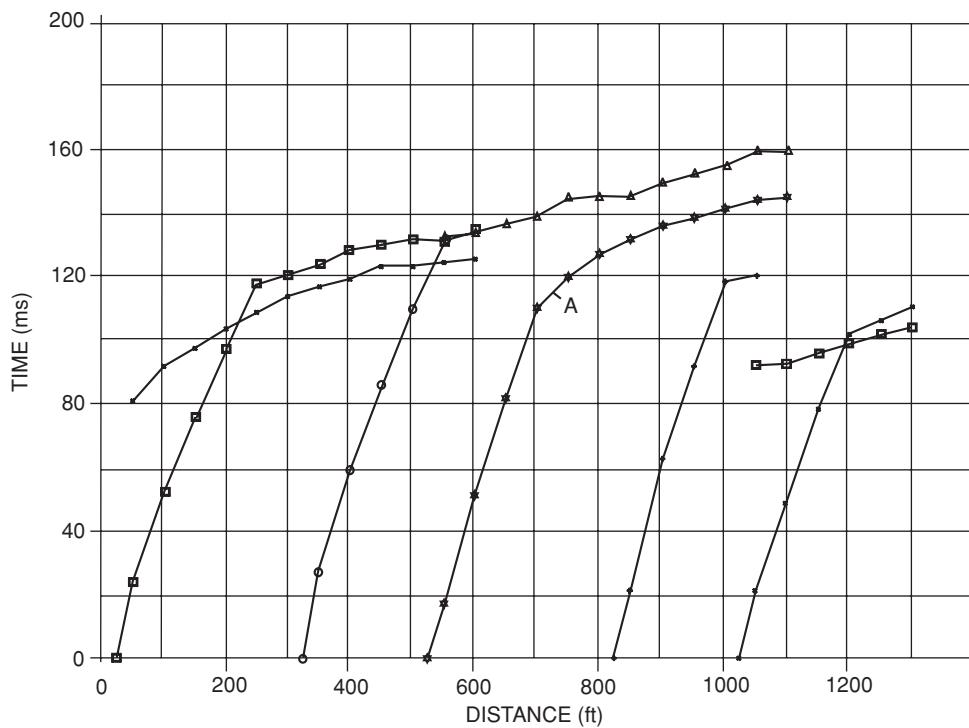


**Figure 5.15** Travel time-distance graphs for forward-direction shots. The first breaks for the far-offset shots (shown as crosses) for the leftmost spread arrive earlier than those from the near-offset shot (shown by squares) for this spread. This occurs when the distance between the shotpoint and the refractor decreases significantly between the near- and far-offset shots. From Lankston (1990), by permission. See text for details.

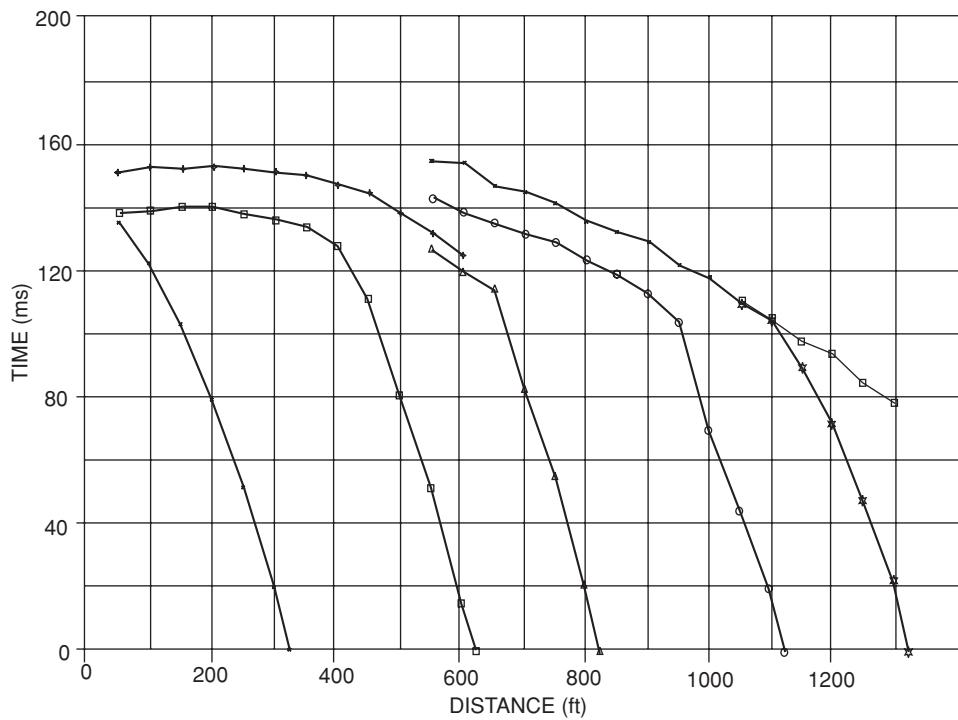


**Figure 5.16** Travel time-distance graphs for the reverse-direction shots. From Lankston (1990), by permission.

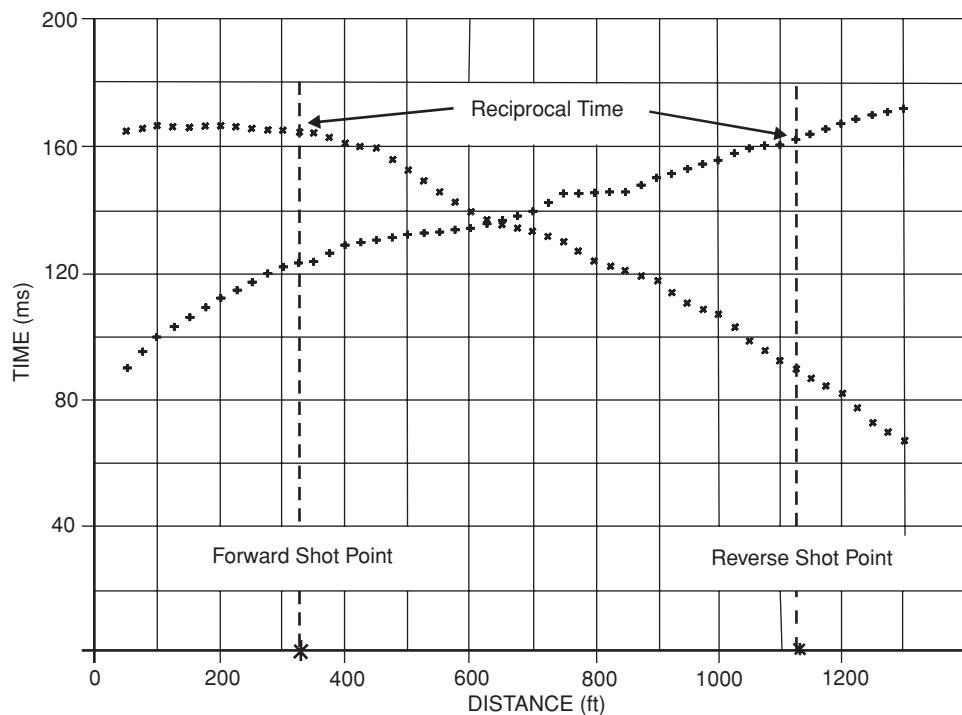


**Figure 5.17** Forward- and reverse-direction travel time-distance graphs after intra-line phantoming and interpolation of new arrivals at locations halfway between observed arrivals. The reciprocal time as interpreted from the forward and reverse direction experiments is indicated. From Lankston (1990), by permission.

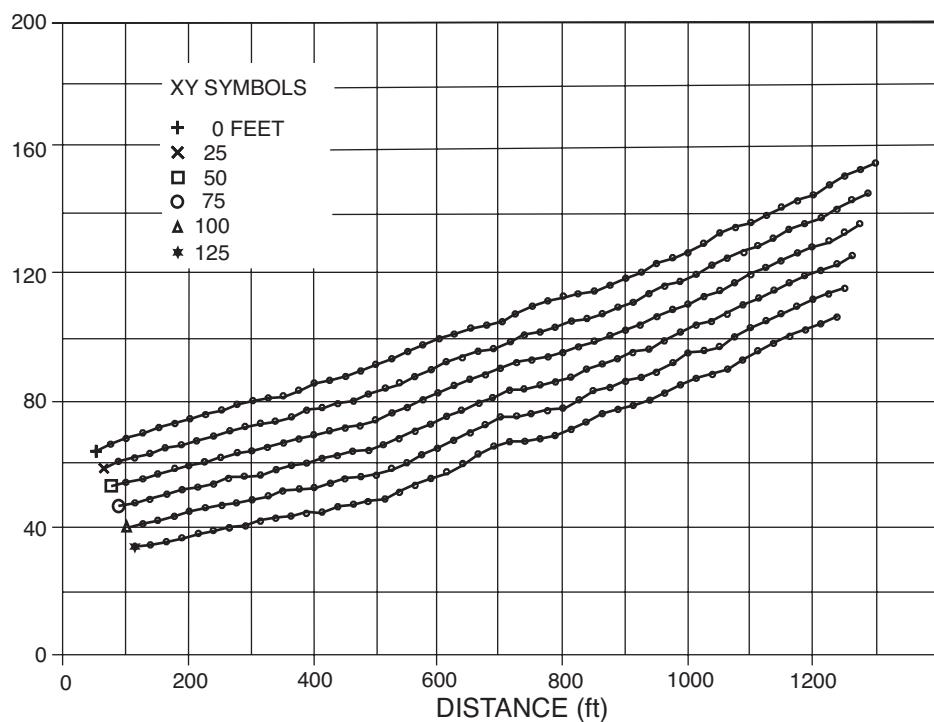


**Figure 5.18** Velocity analysis curves for XY spacings from zero to 48 m (125 ft). From Lankston (1990), by permission.

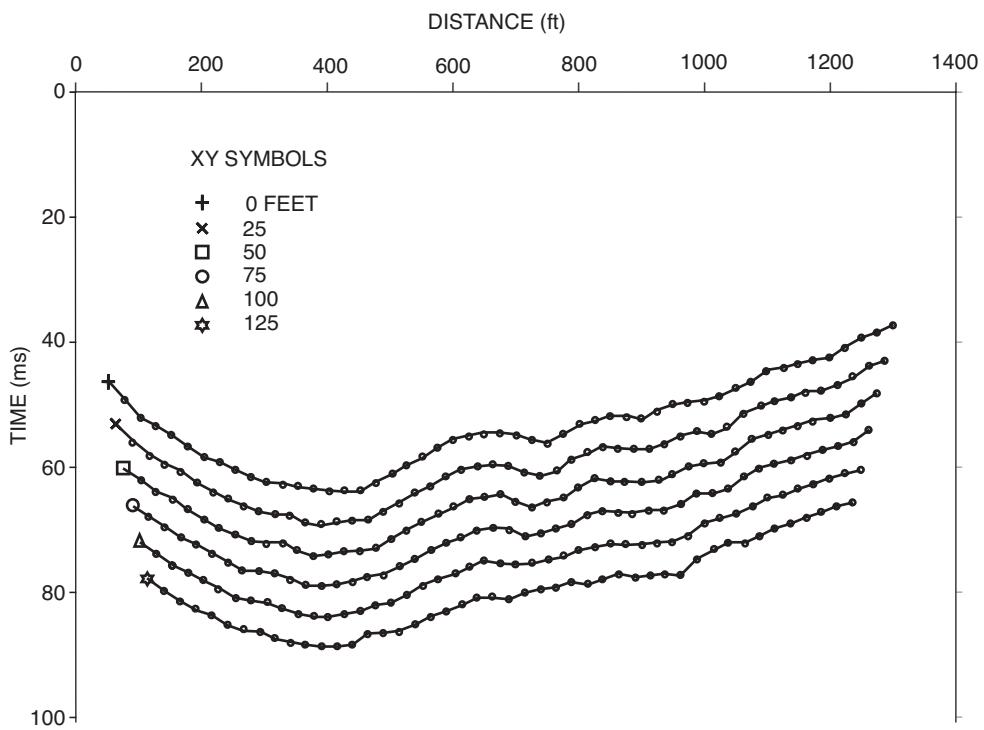


**Figure 5.19** Time-depth curves for XY spacings from zero to 48 m (125 ft). Refractor velocities used to generate these curves are indicated in Figure 5.20. From Lankston (1990), by permission.

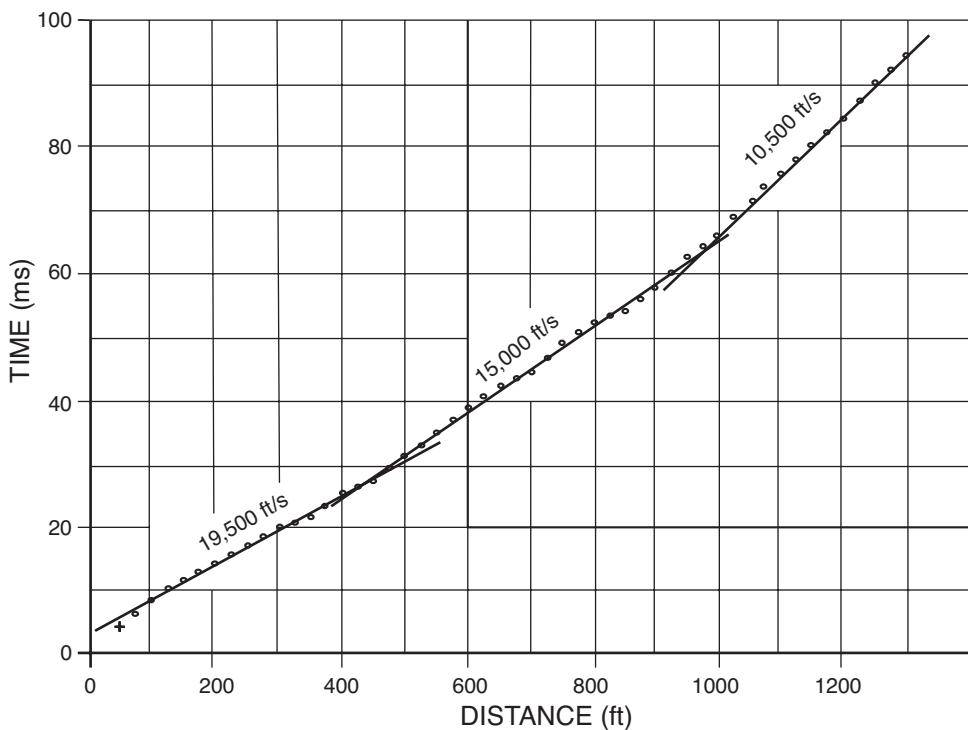


**Figure 5.20** Velocity analysis curve for the XY = 0 case; the refractor is interpreted to have two lateral velocity changes. From Lankston (1990), by permission.

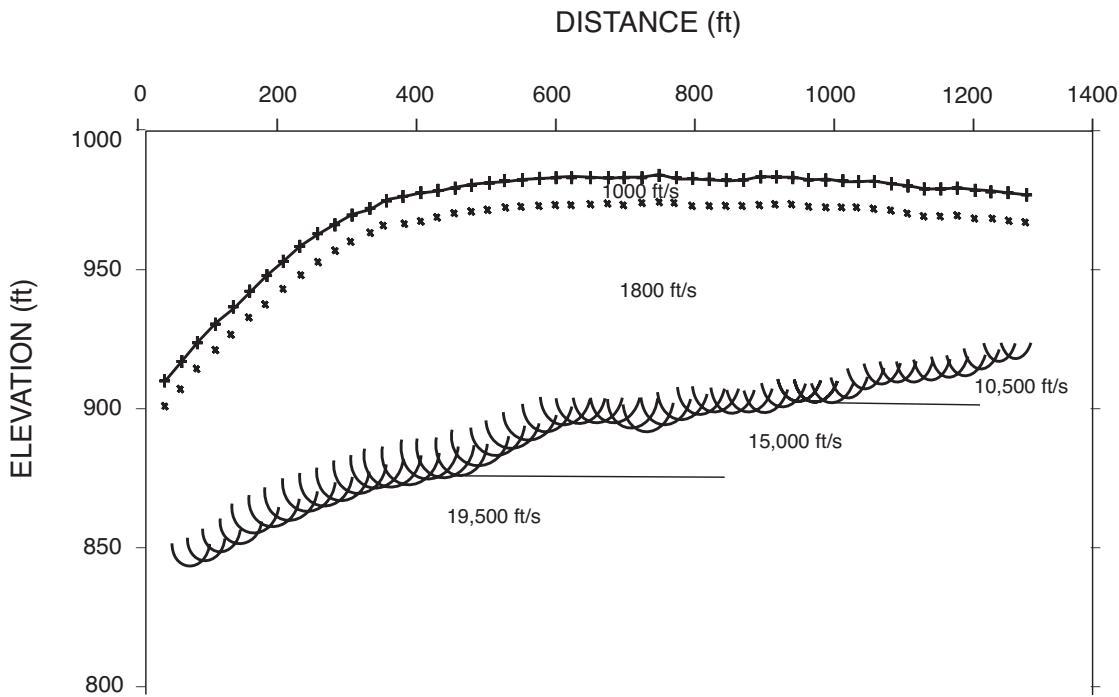


**Figure 5.21** Final migrated section. The refractor surface is the envelope of the tangents to the suite of arcs. The arcs are mathematically circular, but they appear elliptical because of vertical exaggeration of the elevation scale. The ground surface is denoted by the continuous curve. The small crosses represent the interface between the 305 m/s (1000 ft/s) unit and the underlying 550 m/s (1800 ft/s) unit. The positions of the lateral velocity changes from Figure 5.20 are shown and have been interpreted as being due to layering with the basalt. From Lankston (1990), by permission.

determined to have a velocity of 305 m/s (1000 ft/s) and a thickness of 3.1 m (10 ft) along the length of the survey line. The second layer was assigned a velocity of 550 m/s (1800 ft/s). The calculated depth to the refractor is shown graphically below the appropriate geophone as an arc whose radius is equal to the calculated depth at that point (Figure 5.21). The actual surface of the refractor is then indicated by the envelope of tangents to the circular arcs. Also indicated in Figure 5.21 are the three values of refractor velocity. As it was known that the bedrock was basalt and that its structure was generally flat-lying, then the interpreted structure depicted in Figure 5.21 appears to be reasonable, with the three intra-refractor velocities corresponding to layers within the basalt.

Having produced the interpretation shown in Figure 5.21, this does not necessarily reflect the true geological picture. Earlier, it was suggested that there was an intermediate layer whose presence was intimated in the data in Figure 5.15 (at A). This has not been taken into account in the final model. If it had been, the depression evident in the refractor surface at 750 ft along the profile (which corresponds to the location of A) would have had a greater calculated depth to its surface.

In this example, Lankston (1990) reported that at the intersection of cross-lines, the interpreted depths to the refractor agreed to within 5%. It was also stated that the final model produced was a fair reflection of the geological structure and that the survey had achieved the client's objectives.

## 5.5.2 Location of a buried doline

Palmer (1991) described a seismic refraction survey over a known collapsed doline (sinkhole) in Silurian metasediments in central eastern Australia. In contrast to the previous example, the geophone interval was 2.5 m with a shot point interval nominally of 30 m. The travel time-distance graphs obtained are shown in Figure 5.22.

The refractor velocity analysis for shots at stations 12 and 83 are shown in Figure 5.23 for values of XY from zero to 15 m, in increments of 2.5 m. Velocity analysis for the refractor revealed values of 2750 m/s between stations 24 and 46, and 2220 m/s between stations 46 and 71. Palmer determined that the optimum value of XY was 5 m. The travel time-depth graphs over the same spread and range of XY values are shown in Figure 5.24. From these graphs the optimum value of XY was confirmed as being 5 m. A deepening of the refractor is evident between stations 40 and 52.

Evaluating Equation (5) in Box 5.10 with an optimum value of XY of 5 m, a time-depth of 15 ms is obtained and a refractor velocity of 2500 m/s, with an average seismic velocity of 600 m/s for the material above the refractor. This latter value is comparable to that determined directly from travel time-distance graphs. The similarity of the near-surface velocities determined using the two approaches suggests strongly that there is no hidden-layer problem. Using these velocities, a depth section was produced (Figure 5.25).

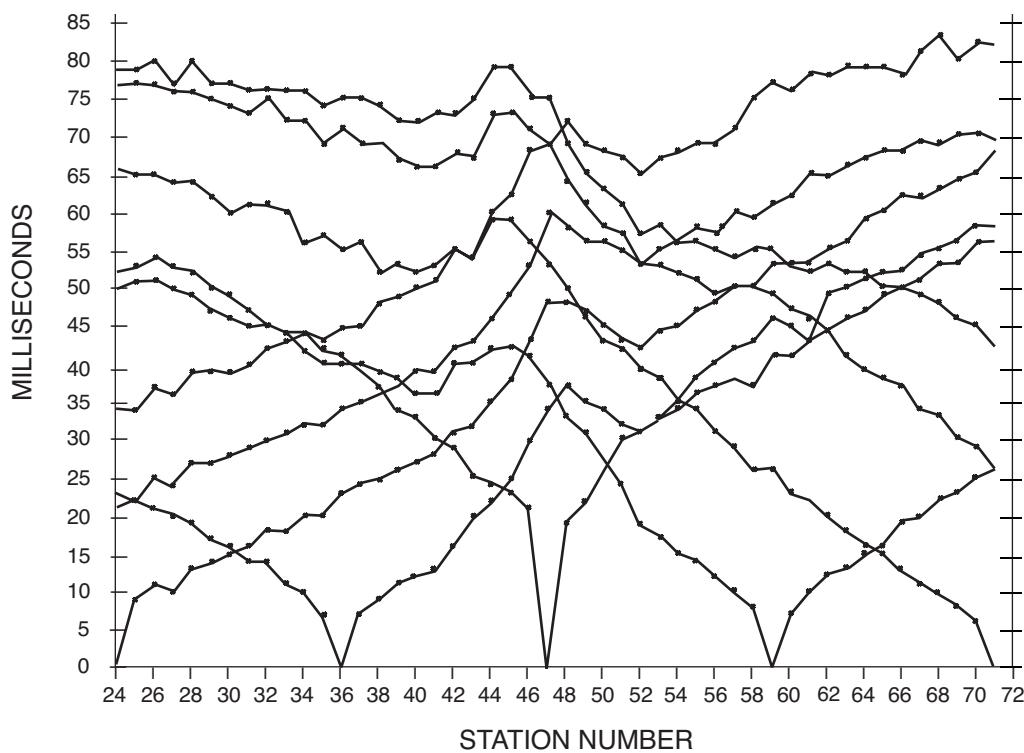


**Figure 5.22** Travel time-distance graphs recorded over a collapsed doline in eastern Australia; the inter-geophone spacing is 2.5 m. From Palmer (1991), by permission.

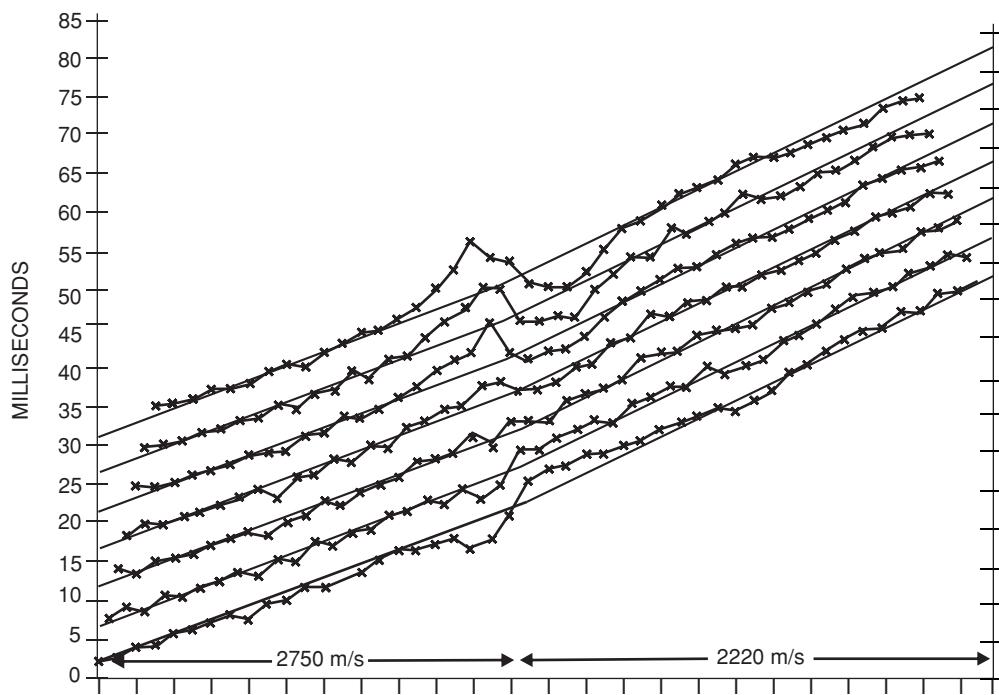


**Figure 5.23** The GRM velocity analysis function computed with XY values from zero, the lower set of points, to 15 m, the upper set of points, in increments of 2.5 m. The reciprocal time has been increased by 10 ms for each XY value for clarity of display. From Palmer (1991), by permission.

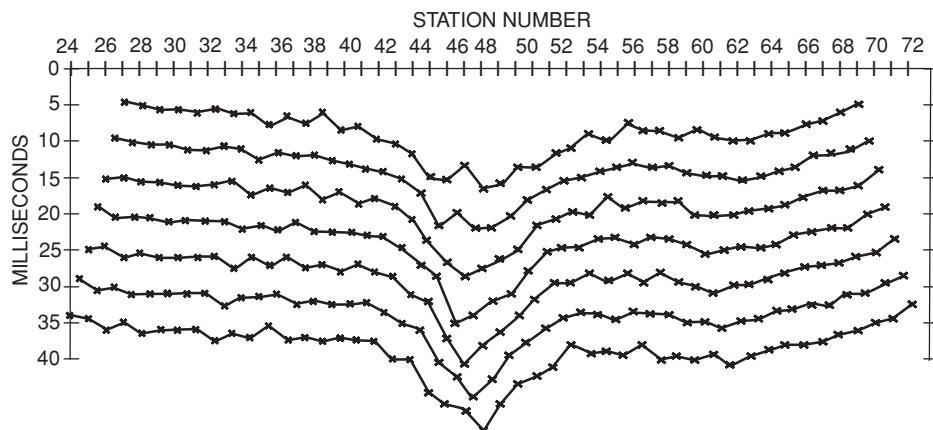


**Figure 5.24** The GRM travel time-depth function computed with XY values from zero, the lower set points, to 15 m, the upper set points, in increments of 2.5 m. The reciprocal time has been increased by 10 ms for each XY value for clarity of display. From Palmer (1991), by permission.

In Figure 5.25, the arcs, representing the loci of the refractor surface beneath stations 39 and 46, all intersect in a cluster beneath station 39. Similarly, the arcs from stations 47 and 54 cluster beneath station 53. Such clusters indicate that all arrivals associated with the collapsed doline at these locations are diffractions from the edges. The refractor surface shown in Figure 5.25 is the minimum equivalent refractor rather than a true image of the doline. A drill hole sited near station 47 intersected almost 50m of siliceous sandstone and voids. It was concluded that, with the large vertical extent of the doline relative to its 30m diameter, and a roughly circular plan section, most of the seismic energy probably travelled around the doline rather than underneath it. Consequently, the minimum equivalent refractor was thought to be a hemisphere with a diameter of about 30 m.

From this analysis using the GRM, it was also concluded that there was no low-velocity zone associated with the collapsed doline. If a value for XY of zero was used in the velocity analysis function, it was possible to infer a seismic velocity of about 750 m/s between stations 44 and 47. This in itself would warrant further investigation. However, as it was thought that the seismic energy travelled around the doline, the volume beneath the feature was thought not to have been adequately sampled. Nevertheless, it was concluded that any low-velocity zone, if there was one, would have been of only limited lateral extent.

Another feature of this example is that it demonstrates the ability of the GRM to take diffractions into account without having to recognise them beforehand. In this respect, the migrated depth section (Figure 5.25) is very useful in revealing the clusters of arcs that are indicative of the diffractions. Furthermore, inclusion of the drilling results also helped to elucidate the mechanism of wave propagation in the vicinity of the collapsed doline. The combined interpretation that resulted was more realistic than if either the refraction survey or the drilling had been used in isolation.

### 5.5.3 Assessment of rock quality

There is an increasing requirement for geophysical surveys carried out during geotechnical investigations to provide direct information about rock quality or other geotechnical parameters. With the paucity of information to correlate geophysical results with actual rock properties, this is still difficult to achieve. Much more research needs to be done to address this. However, New (1985) has described one detailed study designed specifically to investigate this matter.

As part of the UK's radioactive waste management research programme, the Transport and Road Research Laboratory undertook a short programme of seismic velocity measurements at Carwynnan, Cornwall. The site was an experimental excavation in massive

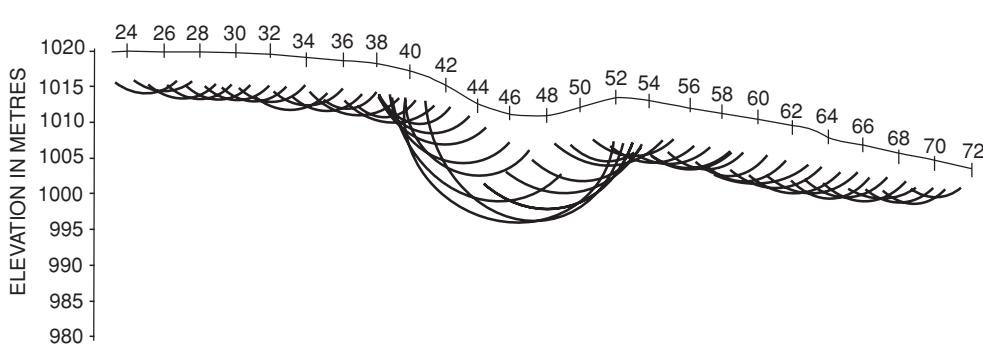


**Figure 5.25** The depth section computed with XY = 5 m and an average velocity in the overburden of 600 m/s; the position of the collapsed doline is evident. From Palmer (1991), by permission.

granite towards the northwestern margin of the Carnmenellis Granite boss. The Cornubian batholith, of which the Carnmenellis boss is part, is predominantly coarse-grained biotite–muscovite granite with phenocrysts of potassium feldspar. The rock is generally very strong and is weakly weathered. A predominant subvertical joint set, with a  $120^\circ$  strike direction and a joint spacing usually greater than 1 m, was found throughout the test site area.

The survey was undertaken within three horizontal headings at a depth of 30 m below ground level. Twenty reference points were fixed along three sides of a rectangular section of rock some  $900 \text{ m}^2$  in area. Transmitting and receiving locations were numbered from 0 to 19 (Figure 5.26A). Geophones were bolted rigidly to the rock and surveyed to an accuracy of  $\pm 0.5 \text{ cm}$ . The seismic source used was a sledgehammer.

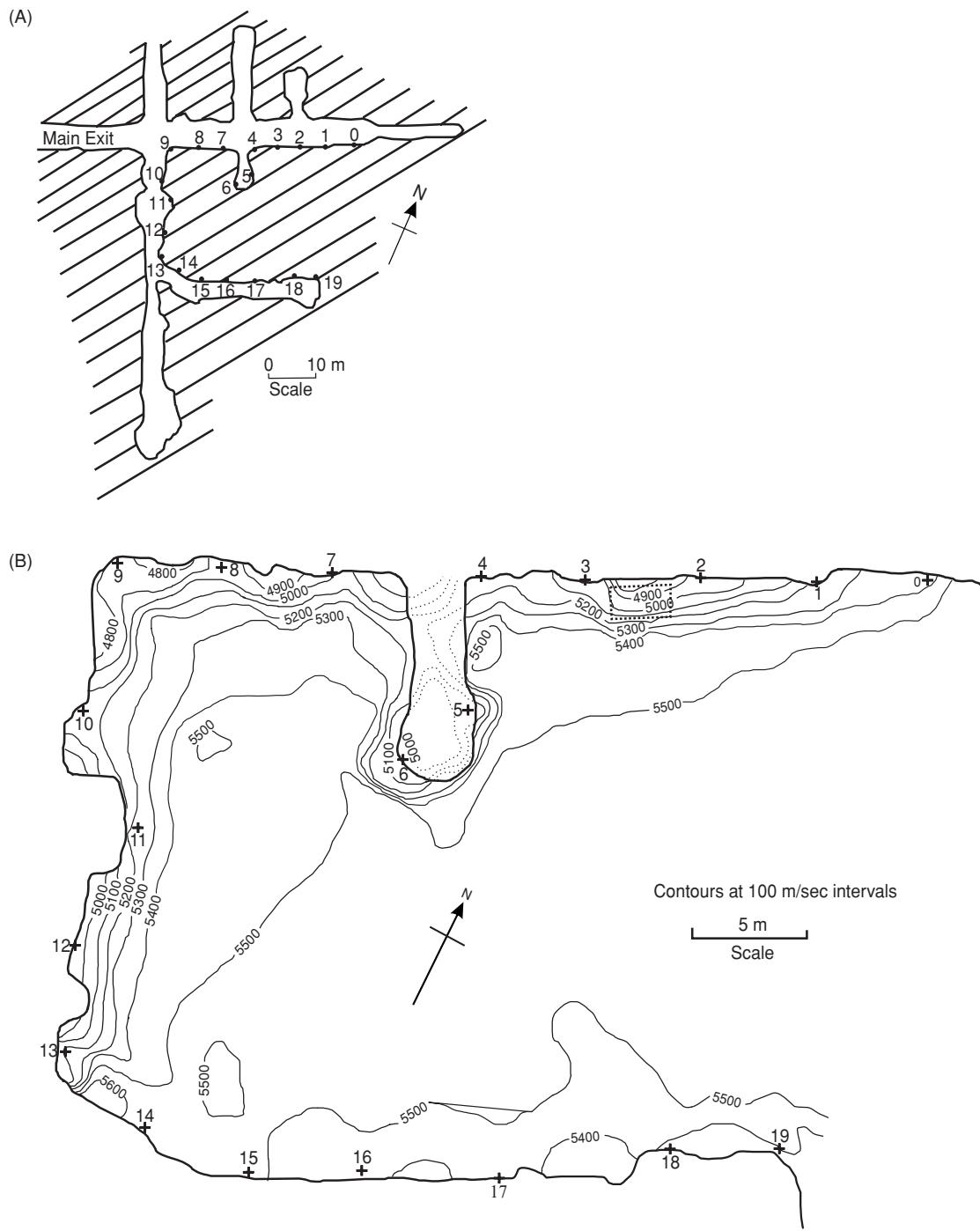


**Figure 5.26** (A) Map of the three underground headings with source-receiver locations numbered. (B) Contoured map of the representative velocity ( $V_R$  in m/s), based on measurements between reference locations. From New (1985), by permission.

The travel times and waveforms of the seismic signal were recorded and analysed using Fourier processing and a representative velocity ( $V_R$ ) determined for each cell of a grid calculated for the rock mass. Contoured values of  $V_R$  were displayed in map form (Figure 5.26B). It is obvious that rock affected by the excavation of the headings has a reduced seismic velocity (<5000 m/s) in comparison with that for undisturbed rock (~5500 m/s).

A site-specific rock classification system was used to derive a numerical classification value ( $C$ ) for each area of wall between reference points. This parameter depended upon:

- the spacing of the joints;
- the condition of the joints (aperture, filling, etc.);
- the general intact rock condition;
- the degree of excavation-induced blast damage;
- the density of shot holes in a given area – these depths of between 1 m and 3 m.

The representative seismic velocity ( $V_R$ ) was plotted as a function of the derived rock quality classification number ( $C$ ) (Figure 5.27) for each pair of reference points.

It is clear from Figure 5.27 that there is a correlation between the seismic velocity and the rock quality. Indeed, New (1985) calculated the correlation as  $V_R = 48.4C + 4447$  (with a correlation factor  $r^2 = 0.86$ ). The very lowest velocities were found to be associated with a damaged and weathered area of rock with several major joints at the western extremity of the survey area. The northwestern and southwestern walls of the test area had been affected by heavy blast damage and extensively drilled compared with the smaller heading along the southeastern wall.

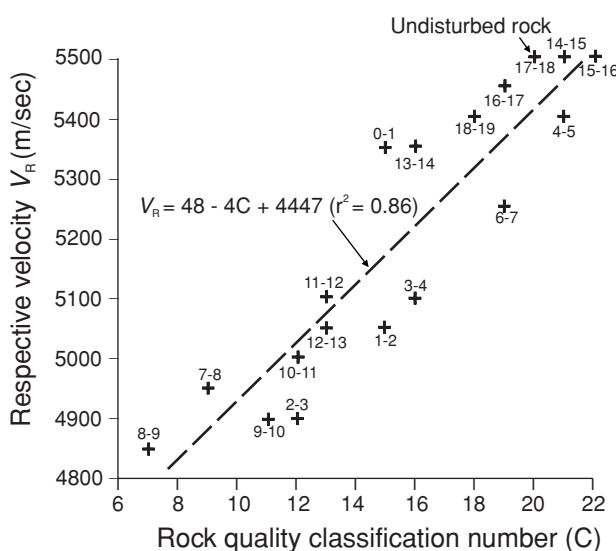


**Figure 5.27** Correlation of representative velocity with rock quality classification. From New (1985), by permission.

This experiment, although limited in extent, did demonstrate that the classification of rock using seismic methods can satisfactorily indicate the engineering properties of a rock mass: see also papers by Sjögren *et al.* (1979) and Gardener (1992).

A very well-known application of seismic velocities is the determination of rippability – the ease with which the ground may be excavated using machines. In 1958, the Caterpillar Tractor Company developed the use of seismic velocities determined from surface refraction experiments to produce a practical chart (Figure 5.28) of rippability. Using this, contractors can estimate the ease (or otherwise) of excavating a given tract of ground using a mechanical device. Obviously, the chart is not exhaustive, but it provides general guidelines for practical use. Similarly, rippability is also a function of vehicle size, power and machine type. More specific charts relate geological material and rippability to machine types (Caterpillar Tractor Co., 2000). Other charts have been produced by other bulldozer manufacturers (e.g. Komatsu). However, disputes have arisen because the determination of rippability is not precise and contractors have found that ground reported to be rippable was patently not so, or their production rates were considerably slower than expected because of greater difficulty in excavating the ground. The estimation of rock rippability, including the use of seismic velocities, has been reviewed extensively by MacGregor *et al.* (1994).

## 5.5.4 Landfill investigations

Refraction rather than reflection seismology has been used on landfills for three principal reasons:

- most landfills are too shallow for reflection seismology to be of much use;
- landfill material is highly attenuating and thus it is difficult to put much energy into the material and detect any significant signals;
- the cost of seismic reflection surveys tends to be greater than that of refraction surveys.

Even refraction surveys are seldom used over closed landfills (Reynolds and McCann, 1992). One of the reasons for this is the difficulty in energy input – a hammer source may not be powerful enough and shotgun shells cannot be used where there is an active generation of methane gas! The general use of seismic methods on landfills is thus quite uncommon.

For selected sites where conditions permit, refraction seismology can be used to determine: (1) the depth of fill; (2) P-wave velocities of the fill and substrates; (3) the location of old quarry walls that may delimit the edge of a landfill; and (4) the state of a clay cap, if it is of sufficient thickness. An example of a seismic refraction record, with displaced first arrivals due to a vertical step associated with a step within an old backfilled quarry, is shown in Figure 5.29.

Knight *et al.* (1978) have described the results of a seismic refraction survey carried out at a waste disposal site at Lucas Heights near

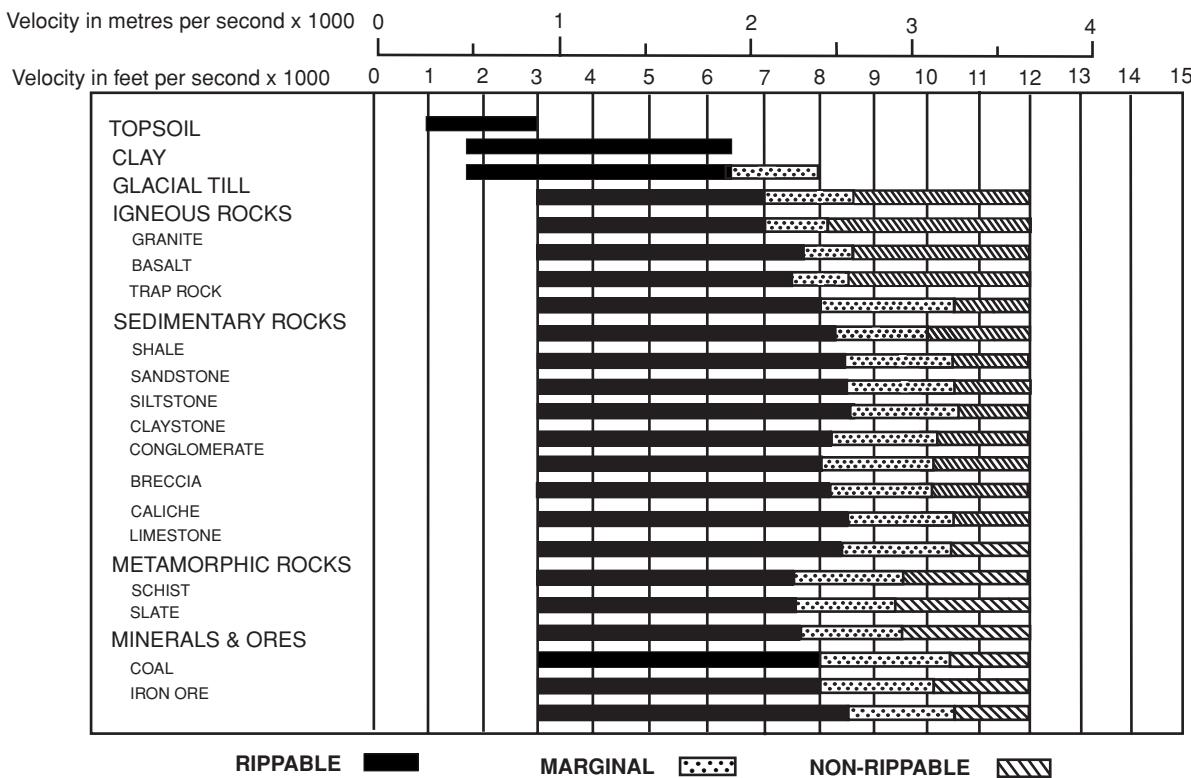


Figure 5.28 Typical chart of ripper performances related to seismic P-wave velocities. © Caterpillar Tractor Company, by permission.

Sydney, Australia, to determine the depth of the fill material and the properties of the underlying bedrock. The fill material was made up of glass, metal and plastic, with small quantities of paper, cardboard and wood. At the base of the fill was a 'brown viscous sludge' at a depth of about 4 m below ground surface. The depth of fill was 6.5 m and it was underlain by sand containing a second water table and shale at a depth of 19 m. Their results were generally of poor quality because of the high attenuation of the seismic energy in the fill material. With a geophone interval of 3 m, the close-spaced survey indicated a P-wave velocity of 450 m/s for the fill material and 1900 m/s for the underlying sand.

Nunn (1978) described a refraction survey to determine the depth of fill at a landfill site at Brownhills, Warwickshire, UK. The fill material was colliery spoil and domestic waste. The actual site was an old lake bed over a shallow depression in Etruria Marl. The fill material was underlain by an unknown thickness of glacial drift deposits, interbedded clays, sands and gravels, which were known to vary both laterally and vertically. Nunn found P-wave velocities of 500 m/s for unsaturated fill material, and 1300 m/s for saturated fill below the water table. There was no direct evidence of the saturated drift layer in the results, and thus it was thought that this layer was 'hidden'.

As far as the assessment of the geotechnical properties of a landfill is concerned, the work of Baoshan and Chopin (1983) on the measurement of shear waves in a tailings deposit at four tailings dam sites in China is of particular significance. Surface to borehole and cross-hole seismic measurements were made to determine the

shear wave velocity ( $V_s$ ). Their results showed excellent correlation between  $V_s$  and the geotechnical properties of the tailings material.

An integral part of the successful management of an enclosed landfill is the maintenance of the integrity of the compacted clay cap overlying the waste material. As long as this impermeable layer remains intact, gases are kept beneath (to vent in a controlled manner through appropriate outlets) and rainwater/snow melt is kept out to run off into surface drains. However, erosion can occur into this clay cap and it can also degrade through differential settlement of the waste beneath.

Carpenter *et al.* (1991) reported on their use of both seismic refraction and electrical resistivity surveys to examine the integrity of a clay cap over a municipal landfill at Mallard North, near Chicago, USA. They demonstrated that detailed mapping of P-wave velocities could be used to identify areas where the clay cap had been fractured (giving rise to low P-wave velocities) compared with the intact clay cap (with higher P-wave velocities). Similarly, variability in electrical resistivity with azimuth around a central point indicated the orientation of fractures within the clay cap. Maps of the site and of their survey locations are shown in Figure 5.30.

Carpenter and coworkers found that average P-wave velocities determined along survey lines parallel and perpendicular to fractures were around  $370 \pm 20$  m/s and  $365 \pm 10$  m/s, respectively, compared with a value of  $740 \pm 140$  m/s over unfractured clay cap. They also reported difficulty in obtaining refracted arrivals in some areas owing to the P-wave velocity in the underlying waste being lower than that for the clay cover. It is thought that where clay caps

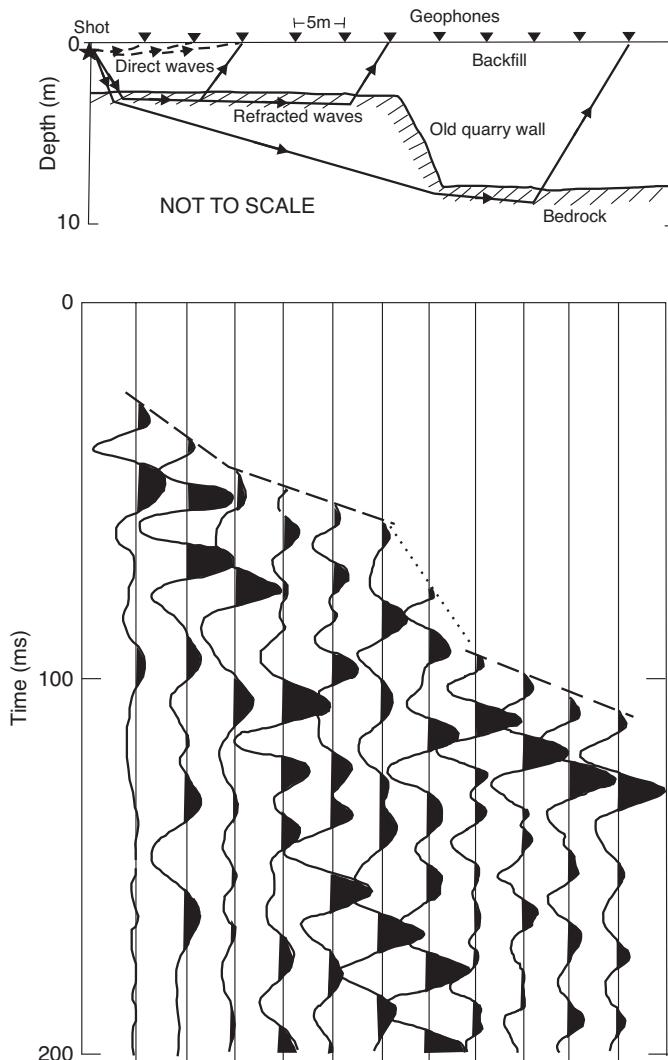


**Figure 5.29** Seismic section over a buried quarry face within a landfill site backfilled with marl, with the corresponding refraction record; the lines of the first breaks are indicated by the dashed and dotted lines. From Reynolds and McCann (1992), by permission.

are of the order of 1.5–2 m thick, as in this case, electrical resistivity subsurface imaging could provide a quick and reliable method of measuring the thickness non-intrusively.

As part of a major investigation for a road scheme in England, an extensive amount of geophysical surveys were designed and undertaken across areas known to contain closed landfills (with domestic and inert waste, and colliery spoil) that had been operated within former limestone quarries. Three techniques were used principally: seismic refraction, ground stiffness, and electrical resistivity tomography (ERT). Seismic refraction profiles were obtained using a Geometrics Geode 48-channel engineering seismograph with either a Propelled Energy Generator (PEG) source or ‘Buffalo gun’, with GeoSpace geophones implanted at 1 m to 2.5 m intervals, depending upon the spread length and desired depth of penetration. The seismic first-arrival data were input to SeisImager to produce

raypath coverage displays and seismic velocity sections. All sections were cross-correlated with the corresponding electrical resistivity profiles and available borehole logs. Example coincident ERT and refraction profiles are shown in Figure 5.31. The resistivity profile reveals conductive material associated with the landfill waste and consistent depths with those derived from the seismic velocity sections, where the P-wave velocities within the waste range from 300 m/s to 1000 m/s, with lower, more dense parts of the waste having velocities in the 1000–1800 m/s range; in this area solid bedrock has a seismic velocity in excess of 3000 m/s. Resistivity values of the waste were found to be in the range of 5–20  $\Omega$ m, while those for bedrock were measured to be >80  $\Omega$ m. Depths derived from the ERT data tended to be greater than those from the seismic refraction results. The resistivity data may be indicating a degree of leachate migration into the underlying sandstone bedrock, as the landfills were unlined.

### 5.5.5 Acid-tar lagoons

In Chapter 3, Section 3.9.6, the site of an acid tar lagoon in northeast Wales, UK, was described over which both magnetic gradiometry and seismic refraction surveys were undertaken (Reynolds, 2002). The magnetic survey was discussed in Chapter 3. The seismic survey component was undertaken using a Geometrics MagCat dual surfboard as a floating platform from which the seismic source (sleeve gun) was deployed (Figure 5.32A). A sleeve gun was chosen as the source rather than a water gun, so that the ports of the gun would not become clogged by tar and detritus from the lagoon floor when the source was fired. Although the gun was suspended just below the water surface between the boards, only a limited splash-back occurred when the gun was fired (Figure 5.32B). The location of the platform was determined using the same system as that for the magnetic survey. Deployed separately was a 24-channel ultra-high resolution marine hydrophone streamer with 2 m group intervals. The array was laid out across a 46-m long section of the lagoon at a time, and left to sit in the soft tar surface during acquisition of the data over that spread length. The MagCat with the seismic source was winched across the lagoon and the sleeve gun fired at 2 m intervals over the hydrophone spread and slightly beyond to obtain the necessary ground coverage. Once the first spread was completed, the MagCat was held stationary while the hydrophone cable was dragged on to cover the next 46 m of profile. The MagCat was reversed and several off-end shots acquired before moving to the next length of the hydrophone spread. The hydrophone streamer was moved as many times as necessary in order to cover the required length of the lagoon. Seismic refraction profiles were obtained at 10 m line intervals across the lagoon with two oblique transverse lines; orthogonal lines were not possible due to the restricted access along parts of the lagoon shoreline.

As a shot record was obtained at each shot location into 24 channels (Figure 5.33), data quality could be assessed at each geophone/shot location. Time-distance graphs were obtained for each profile and a combination of reciprocal ‘delay time’, Hagedoorn’s ‘plus-minus’, and basic intercept time methods of analysis were used to determine basic 2D models along each seismic profile. In

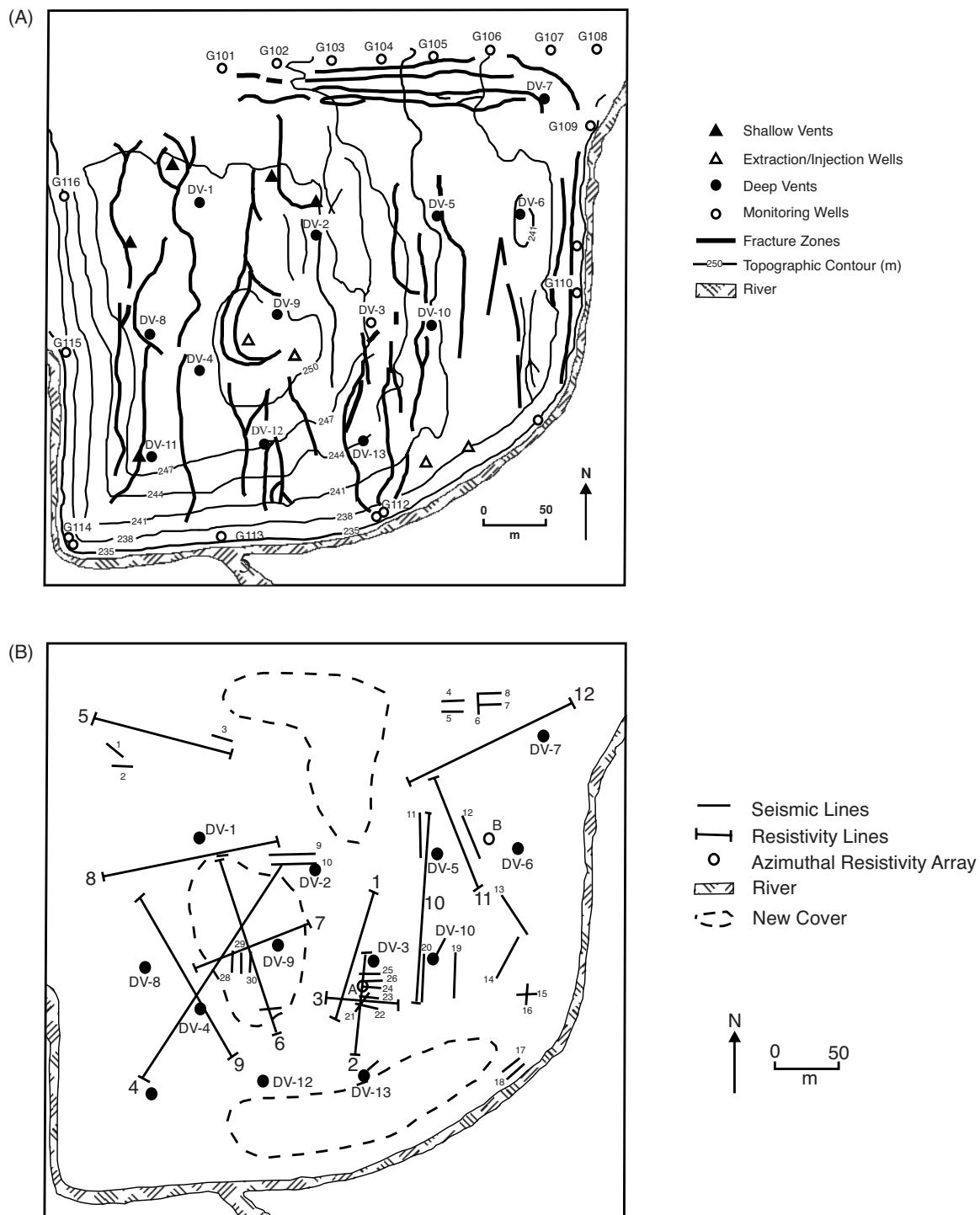


**Figure 5.30** Map of the Mallard North landfill, showing (A) topography, major fissures, shallow/deep gas vents, and monitoring wells, and (B) lines of resistivity soundings, refraction profiles, and azimuthal resistivity arrays marked ('A' and 'B'). Areas of cover replacement during the experiment are also shown in (B). From Carpenter *et al.* (1991), by permission.

addition, the refraction data were also processed using SeisOpt@2D to produce 2D P-wave velocity panels for each section. Note that on the shot record (Figure 5.33) reflections can also be identified.

The seismic refraction analysis revealed a four-layer structure, with three layers existing within the tar itself. A thin uppermost

layer was found to have a P-wave velocity of 200–800 m/s within the tar body itself, and the next two layers were found to have P-wave velocities of  $1560 \pm 20$  m/s and  $1715 \pm 65$  m/s, respectively, with the velocity increasing with depth. The surface low-velocity layer within the tar was found to vary across the site, with the

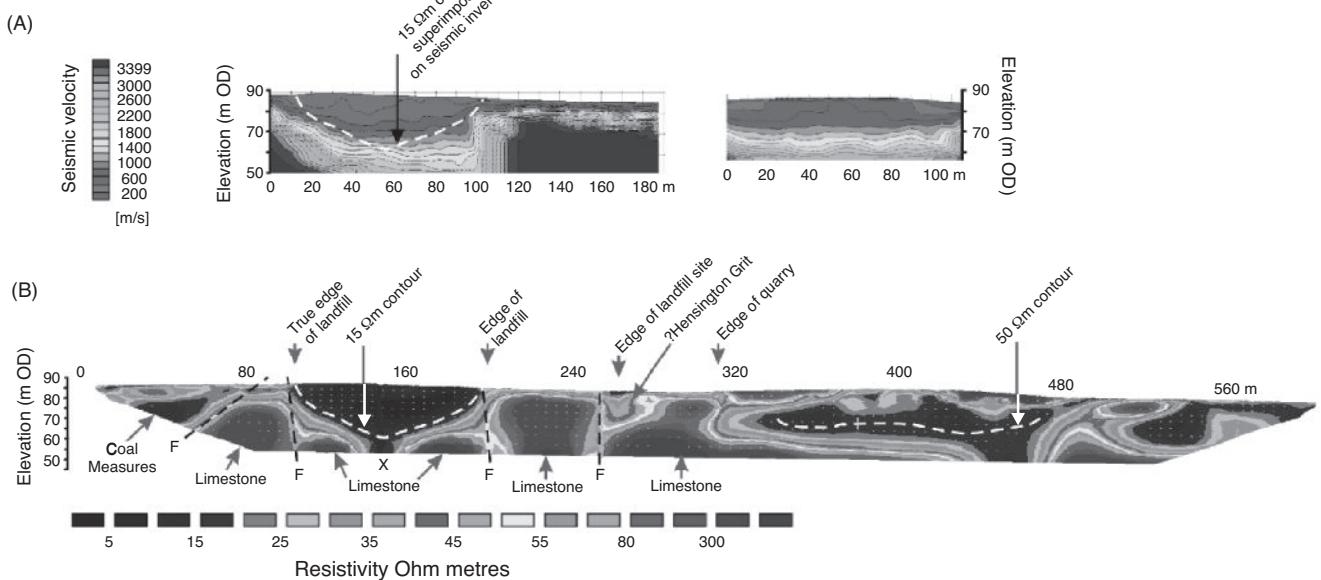


**Figure 5.31** (A) Seismic refraction velocity profile and (B) electrical resistivity tomography section across a closed landfill in a former limestone quarry. [C]

lowest velocities being recorded in association with the softest parts of the tar surface and where gas bubbles and free hydrocarbons were observed to emerge at the surface. These areas also coincided with zones identified on a dual-frequency transponder survey (for water depth, tar surface bathymetry) where penetration into the tar was greater using the lower frequency transponder than with the higher frequency source. The P-wave velocity range for the bedrock underlying the tar was found to be in the range 2150–3600 m/s. The seismic survey resulted in depths to the base of the tar being determined over 80% of the area of the quarry floor. This contrasts with an intrusive survey previously undertaken where only three piston sampling sites out of 17 actually reached the base of the tar. The combined geophysical survey provided more information than most of the previous intrusive investigations undertaken over the previous 22 years.

## 5.5.6 Static corrections

The topic of static corrections for large-scale seismic reflection exploration is very large, and it is not intended to give an overview here; an excellent one has been provided by Cox (1999). A special set of papers on statics was published in *The Leading Edge* (*TLE*) in February 2009 that provides a useful brief update. However, it is perhaps germane to highlight some key developments in this area as they pertain to refraction tomographic methods.

Deere (2009), in his introduction to the special topic in *TLE*, identified three trends in the application of statics corrections within the seismic processing workflow:

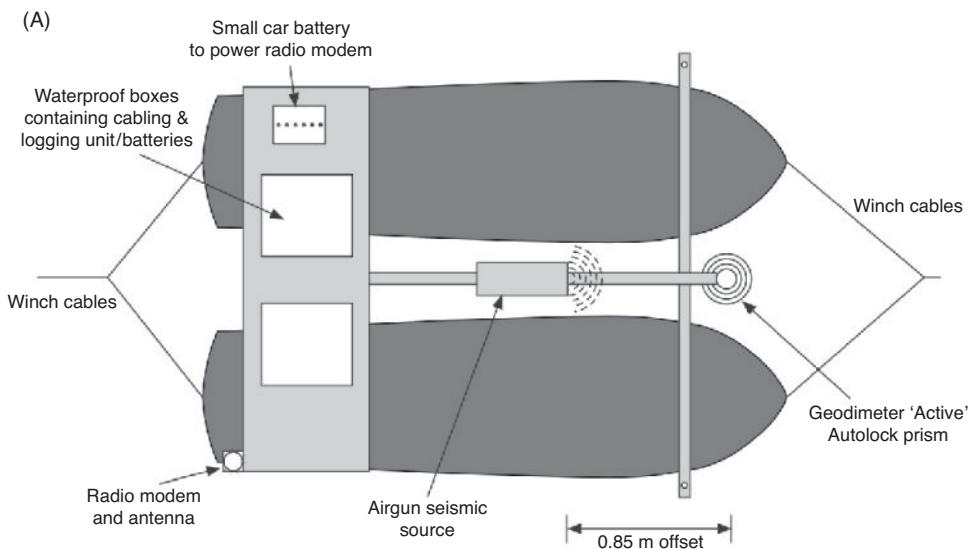
- Tomographic statics have become more common, especially in areas with rapid lateral velocity variations;

- The calculation of often large S-wave statics has become an issue with the increased use of multi-component data;
- Increased use of time-lapse analysis has necessitated careful attention to static corrections on baseline and monitoring surveys.

There is increasing attention being paid to the use of non-seismic remote sensing methods to characterise geomorphological near-surface features. Satellite imagery and LIDAR<sup>1</sup> scanning both feature in this approach, the latter to produce high-resolution Digital Elevation Models (DEMs). Lithological and topographic classification enables the generation of a 3D near-surface geological model. Using standardised elastic properties for the rock types identified within the initial classification, it is possible to convert a 3D geological model into a corresponding 3D elastic model. Statics are estimated assuming vertical propagation of the seismic waves through the layers within the elastic model. Laake and Zaghloul (2009) have demonstrated that this approach can generate statics corrections to within 10 ms of refraction statics. Refraction statics commonly use first-break picking over large offset ranges to produce a large-scale, low-pass filtering of the refraction velocities with a typical filter length of at least 1000 m. Statics based on remote sensing can provide a much finer texture due to the better spatial resolution (10–15 m). LIDAR and ortho-photography can produce DEMs with a ground resolution of 2.5 m.

For large-scale marine reflection surveys the seafloor may dip in a cross-line direction, such as over the UK continental shelf, where the water bottom two-way travel time varies from 200 ms to 800 ms. In such a case, it is possible to see some water-column variations within one survey as well as between surveys undertaken on different

<sup>1</sup>LIDAR: Light Detection And Ranging.



Note: During the echo sounder survey the prism was mounted directly above the echo sounder transducer.



**Figure 5.32** Details of the Geometrics MagCat platform set up for the seismic refraction survey at Llwyneinion acid-tar lagoon. (A) Seismic survey offset diagram; (B) the equipment in use during the firing of the sleeve gun seismic source suspended midway beneath the surf boards. From Reynolds (2002), by permission. [C]

occasions (time lapse surveys). Compensation for variations in the P-wave velocity in seawater and tide correction may both have to be applied in order to dejitter the 3D CMP gathers. For instance, the P-wave velocity in seawater may vary for each sail line from  $\sim 1485$  m/s to 1497 m/s. After correction, a reference velocity is selected (e.g. 1495 m/s). Lacombe *et al.* (2009) have provided an example of how differential GPS measurements can be used to calculate tidal corrections and use a derived reference P-wave velocity in seawater to compensate for dynamic time-dependent changes in the seawater velocity profile.

In exploration with 2D and 3D seismic data, optimising static corrections can have significant benefits to the final data quality, with substantial improvements in reflector continuity being achieved. In Saudi Arabia, for example, exploration blocks can cover a wide variety of terrains with a corresponding range of static correction issues. For instance, the terrain can include large sand dunes, cliffs of carbonate outcrops (known locally as *jebels*), *sabkhas* (salt flats), desert *wadis* and areas with near-surface variations due to the dissolution of a thick layer of anhydrite. Some outcrops can be dissected by gorges up to 100 m deep, the bases of which are filled with

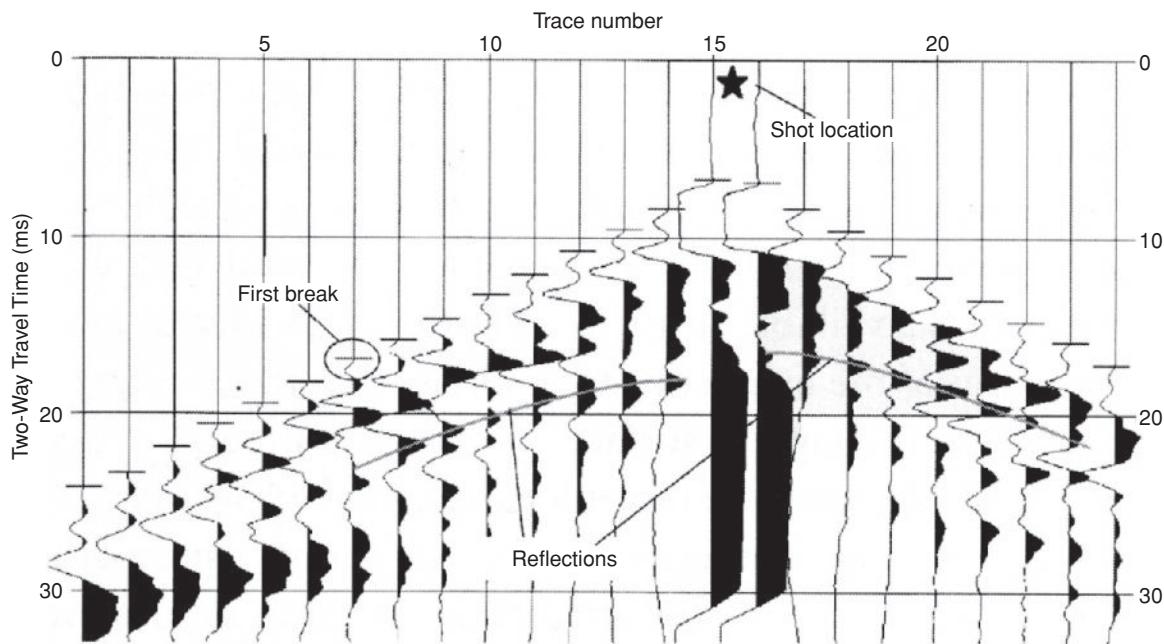


**Figure 5.33** Example shot record acquired over the acid-tar lagoon. From Reynolds (2002), by permission.

mixed unconsolidated sediments ranging in size from fine particles to boulders. Some of these gorges are covered with featureless sand and gravel, but the effects on surface seismic measurements can be pronounced. It is essential, therefore, that accurate static corrections are applied. Bridle (2007, 2009) has described the lengths to which Saudi Aramco, for example, has gone in order to improve their seismic acquisition for hydrocarbon exploration in the region. Bridle has described the use of the delay-time method using both the plus-minus and GRM techniques. He concluded that no single refraction interpretation method can model the entire range of near-surface geological features. The plus-minus method focuses on the time horizons where there are small changes in the refractor depth. The GRM method was found to be successful in defining the structure of a varying depth refractor. In areas with source acquisition gaps (due to lack of access over farms, gorges, severe topography, for example) the confidence in the delay-time method has been improved through updating by reduced travel-time analysis.

Taking the issue of severe topography one stage further, Becerra *et al.* (2009) described a statistical approach to evaluating static corrections derived for a seismic survey acquired in the Catatumbo Basin, Norte de Santander, Colombia, S. America. The exploration area has rough topography where the weathering layer has highly variable thicknesses and velocities due to the dense vegetation, high precipitation, humidity and temperature, and where the resulting seismic images have a low signal:noise ratio. Becerra *et al.* described their approach with respect to a survey profile with a topographic range of around 300 m to 875 m in a 10-km long profile. Seismic velocities within the weathering layer were found to vary in the range 800 m/s to 1500 m/s. They applied four different statistical methods to the seismic tomographic data: jackknifing, checkerboard test, Monte Carlo and bootstrapping methods (the details of which are beyond the scope of this section). The essence of the conclusion

was that by applying a statistical analysis to static corrections, zones with less reliable results may be defined and may provide additional information to estimate the errors associated with static correction calculations. Identifying areas of non-uniqueness within the statistical solutions suggests where additional information is required to obtain a better solution. For large-scale hydrocarbon exploration projects, the additional statistical analysis suggested is possibly justified; at the scale of most engineering refraction studies, it is probably not. However, it does flag up the need to be circumspect when calculating static corrections – the first solution may not be the best statistically and may not yield the optimum solution; different methods of calculating static corrections may need to be tried before arriving at an acceptable and more physically meaningful result, and an appropriate comparison should be made.

## 5.5.7 Locating buried miners

Sadly, deadly mine collapses are all too common. Locating trapped miners soon after a collapse occurs can save lives and avoid searches in the wrong locations, which can lead to fatalities and casualties among rescuers. Many methods have been proposed for finding trapped miners, such as echo location. Unfortunately such a method is not reliable partly because the signal:noise ratio of the signals from the miners is too weak for conventional imaging techniques. Gajewski and Tessmer (2005) introduced a seismic migration technique to image unknown source locations with hidden excitation times. The principle of the method is shown in Figure 5.34. A buried source at position *S* excites the scattered events seen in Figure 5.34A. Direct waves, primary reflections, and multiples are recorded along the surface array of geophones. Back-projecting these events is equivalent to having a series of sources at the same locations as the geophones and reversing the time history of the

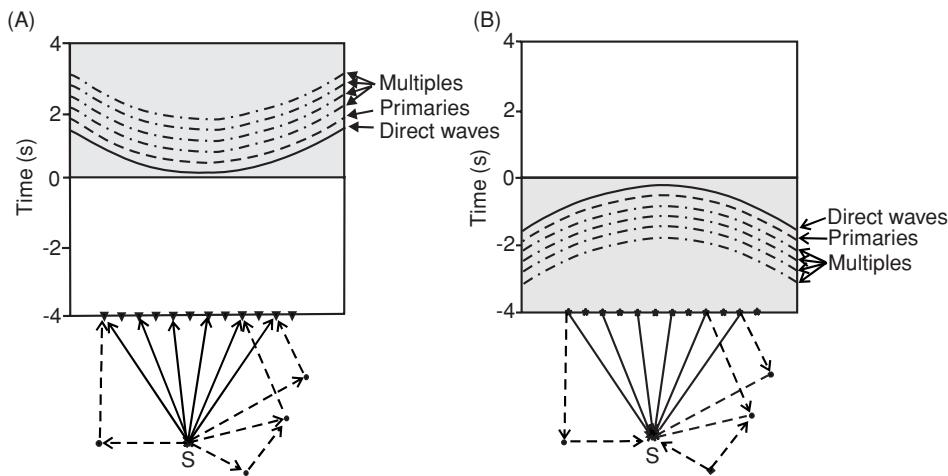


**Figure 5.34** (A) Forward modelled data and (B) backward modelled seismic events for a source located at S and recording at N geophones at the ground surface. Solid dots represent scatterers. From Hanafy *et al.* (2009), by permission.

event from source S. It is equivalent to making the surface act as a so-called *time-reverse mirror* (TRM). As shown in Figure 5.34B, backward modelling returns the recorded events coherently to their common source at the time of the source excitation. The estimated migration amplitude,  $m(x,0)$ , is a maximum at the source point location S because all back-projected direct waves, primaries and multiples are simultaneously in phase at the source excitation time.

The difficulty with this method is that the source occurs at an unknown time and location. To resolve these issues, Hanafy *et al.* (2009) adapted the method by migrating the passive data (i.e. the signals generated by trapped miners) with recorded calibration signals. These are acquired during normal mining operations. A series of geophones is established across the mine site. A hammer source is used to generate signals at a number of pre-determined locations within and along a given mine level. The records generated by this approach become the calibration records.

In a field test undertaken at an experimental site at San Xavier, Tucson, USA, sources were triggered in two mine tunnels at 30 m and 45 m below ground level with 120 geophones at 0.5 m separations at the surface. Within each mine tunnel level, 25 source locations were used at 0.5 m and 0.75 m intervals respectively. For each shot two records were acquired: one represented the miners' signal with a one-stack shot gather; the other represents the calibration record with 16 and 22 stacks for the two mine tunnel levels, respectively. Migrating the records and convolving with the calibration records produced a value of  $m(x,0)$  at each geophone location. The maximum value of  $m(x,0)$  occurs (Figure 5.35A) at the geophone location vertically above the source location where the trapped miners were located (in the simulation experiment). As the time of the source is not known (as would be the case for trapped miners), the migration and convolution process was repeated with a time shift and it can be seen (Figure 5.35B) that the correct location of the source SOS occurs at the maximum of  $m(x,t)$  and with the correct time shift. The TRM method was demonstrated to work even when the signal:noise ratio was very small (0.0005). The method shows promise for relatively shallow mine tunnels but has

yet to be demonstrated for deeper mines; one hopes that this will be achieved in due course.

## 5.6 Shear wave methods

Use of surface waves in geotechnical site investigations began in the early 1960s when small vibrators were used as wave generators to gather ground stiffness information about road beds (e.g. Jones, 1958, 1962). Shear wave methods developed along two paths:

- (i) ground stiffness measurements, especially since the late 1970s, using (a) *Spectral Analysis of Shear Waves* (SASW), which uses only two to six geophones and a hammer source (Nazarian *et al.*, 1983), and (b) *Continuous Surface Wave Systems* (CSWS), which use a tunable 70 kg vibrator and a linear array of typically five geophones (Sutton and Snelling, 1998; Menzies, 2001);
- (ii) since 1999, Multichannel Analysis of Shear Waves (MASW), which uses typically 24 or more channels (Park *et al.*, 1999) and can use either an active source (e.g. hammer) or passive sources (e.g. traffic noise) or both, as developed by Kansas Geological Survey.

### 5.6.1 Ground stiffness profiling

The shear modulus  $G$  is becoming a more valuable parameter for ground stiffness and is readily determined through seismic investigation. The advantage of using a seismic method is that it is not affected either by insertion effects or by sampling disturbance. The stress-strain relationship exhibited by weak rock and soils is non-linear, such that high stiffness values result from small strains. For a strain of less than 0.001% the stiffness becomes constant and is therefore the maximum stiffness possible ( $G_{\max}$ ). Seismic methods apply strains of approximately this magnitude. For intermediate strains (0.001–0.1%) the stiffness is proportional to the strain, and

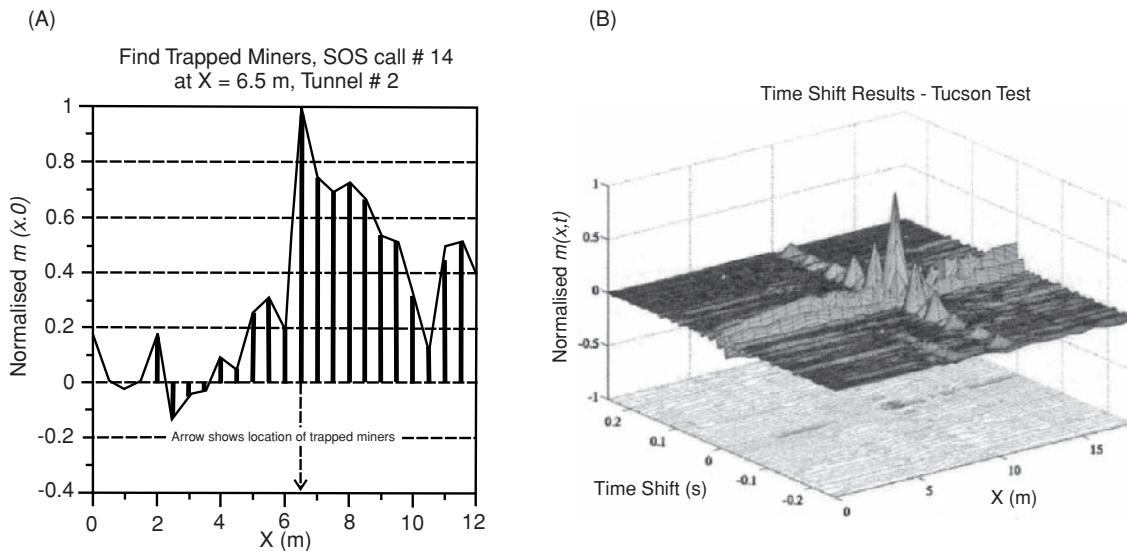


**Figure 5.35** (A) Tuscon field test data from the 30 m depth mine tunnel – the actual SOS call location is at  $x = 6.5$  m, which coincides with the maximum value of  $m(x,0)$ . (B) Migration image,  $m(x,t)$  for the results from the tunnel at 45 m depth, with the maximum peak at the correct SOS location and correct zero times. From Hanafy *et al.* (2009), by permission.

for larger strains ( $>0.1\%$ ) the soil exhibits plastic behaviour and the stiffness becomes less sensitive to strain and approaches a minimum value as the material is brought to failure.

Field observations of ground deformations around full-scale structures can be predicted using non-linear models where the initial strains are very small. These discoveries have closed the gap between static and (small strain) dynamic measurements of stiffness, such as seismic observations, and have made seismic investigation a viable method of determining ground stiffness. Field tests of the geophysical approach to ground stiffness determination have demonstrated that the resultant values are often more useful to engineers than those determined by traditional invasive means.

### 5.6.1.1 Spectral Analysis of Shear Waves (SASW)

The SASW method uses the spectral analysis of the ground roll generated by an impulsive source (e.g. hammer strike) and recorded by a pair or up to six geophones in a linear array. Data are recorded in the frequency domain to produce a dispersion curve by calculating the phase difference between each successive pair of geophones. If a single pair of geophones is used they have to be configured and reconfigured (depending upon the wavelength required) as many times as necessary to sample the desired frequency range (Park *et al.*, 1999).

Commercial SASW systems tend to use a tunable vibrator source, which can be as light as 5 kg, with two to six 4.5 Hz geophones (sometimes 12 geophones can be used). The vibrator is tuned to an individual frequency and the responses across the geophone array recorded. The vibrator is tuned to the next frequency in the range to be used, and another record obtained, and so on until the complete suite of frequencies has been sampled. The system first undertakes a coherence calculation, then an instantaneous Fast

Fourier Transform (FFT) after each data acquisition set (see, for example, data sheets provided by GDS Instruments). For practical reasons, the SASW method has been largely superseded by the Continuous Surface Wave method.

### 5.6.1.2 Continuous Surface Wave System (CSWS)

The equipment used is portable and requires a field crew of two people to operate it. The system consists of a Rayleigh wave vibration generator (typically 70 kg vibrator mass) and a linear array of two to six connected geophones (Figure 5.36A) set out with a geophone separation ( $d$ ) (Figure 5.36B). Ideally the spacing  $d$  is slightly less than the wavelength to be measured. This is impractical for every reading, but increasing  $d$  from 2.5 m to 5 m when reducing the vibrator frequency below 20 Hz is advantageous.

The vibrator generates Rayleigh waves at a sweep of frequencies between 5 Hz and 400 Hz. The frequency of the source is set per sweep and the waveforms received at each geophone are compared. The change in waveform phase angle ( $\varphi$ ) between the geophones is measured using a low-frequency spectrum analyser or a frequency response analyser. In most soils, Rayleigh waves travel at a depth of between one half and one third wavelength below the surface, so a reduction in vibrator source frequency forces the effective depth of surface waves to increase. By varying the source frequency, a range of values for frequency and phase angle change can be obtained. As a general guide, acquisition of each ground stiffness profile requires an hour after set-up to complete.

The path taken by a Rayleigh wave is more controlled than that of a shear or compressional wave, as it is bounded by the free space of an elastic medium (i.e. the ground surface). The particle motion of a Rayleigh wave is elliptical, with the long axis of the ellipse

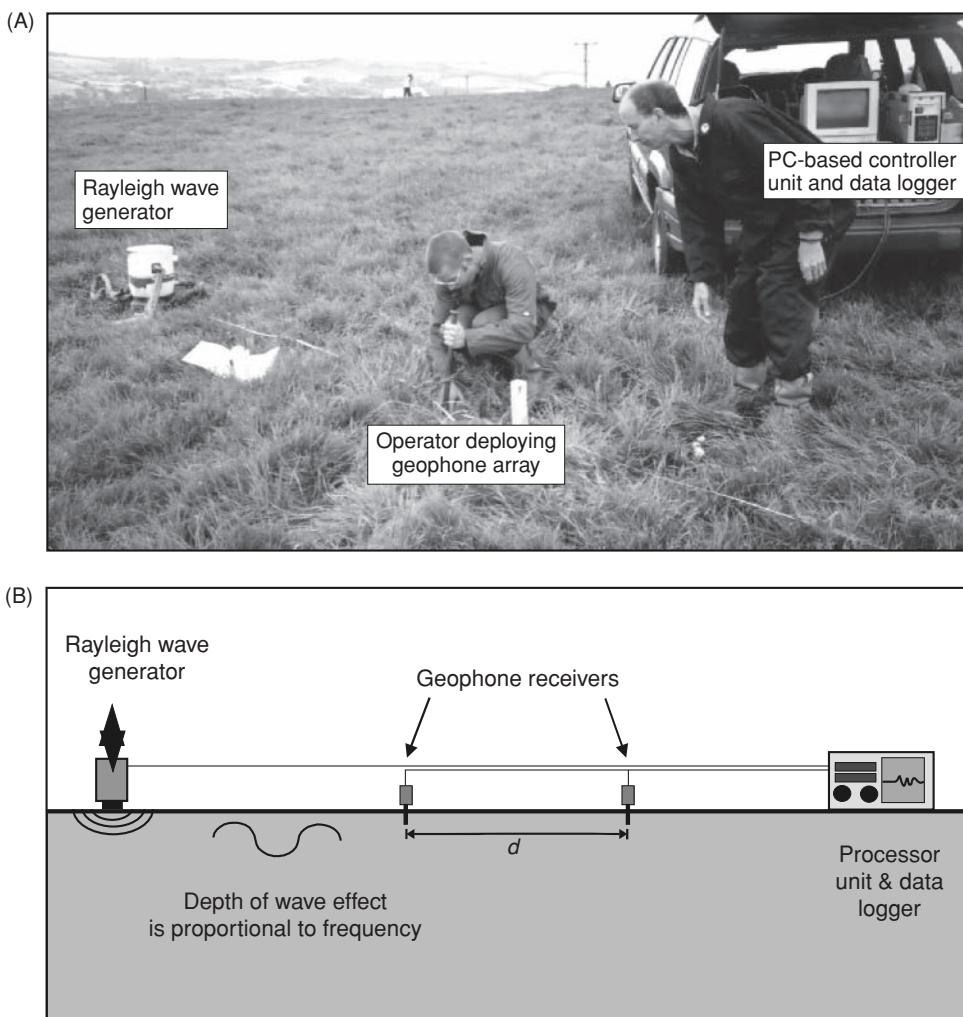


**Figure 5.36** (A) Ground stiffness equipment being deployed. (B) Example field layout. [C]

perpendicular to the boundary of the half space. The short axis is parallel to the half space boundary and the plane of propagation of the wave is in the plane of the particle motion.

Knowing the frequency of the source ( $f$ ), the distance between the geophones ( $d$ ) and the measured phase angle ( $\varphi$ ), the wavelength ( $\lambda$ ) and Rayleigh wave velocity ( $V_R$ ) may be calculated as shown in Box 5.11 (Butcher and Powell, 1996). This allows the variation in Rayleigh wave velocity with depth to be determined.  $V_R$  is typically 5% slower than the shear wave velocity ( $V_S$ ) in most soils, so a correction to the Rayleigh wave velocity provides values for  $V_S$  as a function of depth (Figure 5.37). In this example, three different sources were used. Two lightweight vibrators (14 kg) were used, with frequency ranges of 0–20 Hz and 15–7000 Hz. The third had a source weight of 1200 kg and frequency range 0–40 Hz. It can be seen from Figure 5.37 that each source, with different energy and frequency characteristics, yielded complementary information. The higher-frequency lightweight source clearly profiles the shallowest portion of the profile (to 3 m depth) but fails to detect the silty clay beneath the sand, which was detected by the low-frequency lightweight source. By using the heaviest low-frequency

source and extending the inter-geophone separation from 2.5 m to 5 m provided information to the greatest depths (to 20 m). This demonstrates the need to match the source weights and frequency ranges. However, intermediate weight vibrator masses (e.g. 70 kg) with a tunable frequency range (5–600 Hz) can provide a similar depth range especially when operated over unconsolidated sediments (Moxhay *et al.*, 2001). When stiffness increases gradually with depth, the depth of investigation is approximated to be one third of the wavelength.

The S-wave velocity is then converted to a shear modulus using Poisson's ratio and the bulk density of the subsurface material. If these values are not known, a value for Poisson's ratio is assumed, yielding a maximum error of 10% in the final result. The information obtained through this technique takes the form of a plot of shear modulus against depth, usually to a total depth of 15–20 m below ground level (Figure 5.38). Note that the measured stiffness values are the greatest ( $G_{\max}$ ) at minimum strain levels. Clays can be seen to have low values of  $G_{\max}$  (<100 MPa), whereas the range for chalk is considerably higher (up to 3000 MPa) (Matthews *et al.*, 1996).

**Box 5.11 Rayleigh wave velocity variation and ground stiffness ( $G_{\max}$ ) (Matthews et al., 1996)**

The Rayleigh wave velocity ( $V_R$ ) is given by:

$$V_R = C \cdot V_S$$

where  $C$  is dependent on Poisson's ratio and varies from 0.911 to 0.955 for the range of Poisson's ratio associated with most soils and rocks (ignoring anisotropy), and  $V_S$  is the S-wave velocity.

$$V_R = f \cdot \lambda$$

where:  $\lambda = (360/\varphi) \cdot d$

If  $\rho$  is the bulk density of the medium,  $G_{\max}$  is given by:

$$G_{\max} = \rho \cdot V_S^2$$

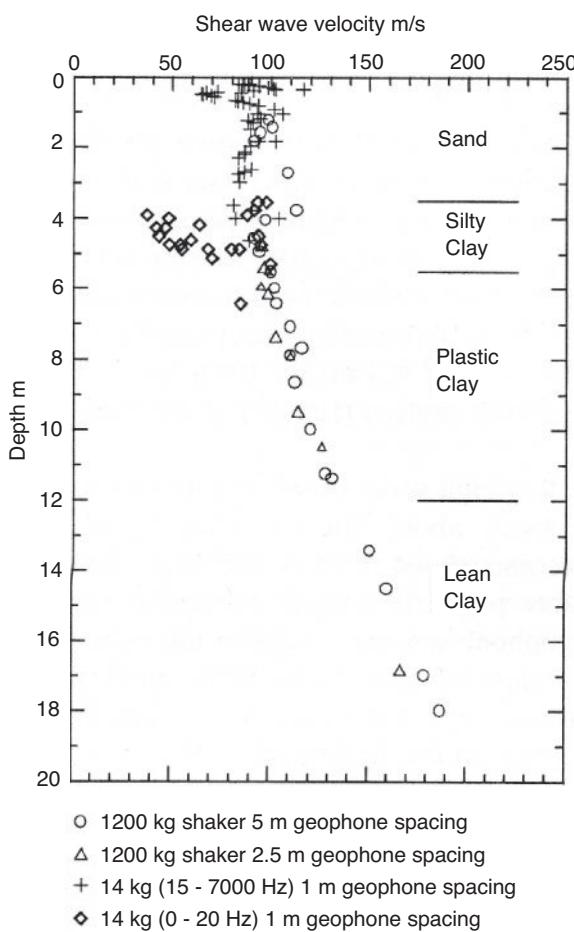


**Figure 5.37** Shear wave velocity profile as a function of depth. From Butcher and Powell (1996), by permission.

In a survey over a closed landfill, ground stiffness profiles over areas known not to contain waste produced  $G_{\max}$  values greater than 350 MPa (Figure 5.39A), whereas values for landfill waste were less than 70 MPa (Figure 5.39B). The shape of the profiles at locations over the landfill indicated an increased stiffness within the capping layer (50–90 MPa) overlying a low-stiffness layer down to ~7 m depth (within the waste). Below the waste, the ground stiffness is seen to increase sharply.

Commercially-available software permits ground stiffness and  $V_S$  profiles to be inverted to derive a layered earth model. Where ground stiffness increases gradually with depth, the derived values of  $G_{\max}$  are a reasonable approximation to the values of the material being investigated. However, where sharp contrasts exist (i.e. step-wise variations in a layered earth) the observed values of  $G_{\max}$  do not approximate to those of the materials being tested, and specialist software (e.g. WinSASW2) should be used to derive an accurate stiffness/depth model.

## 5.6.2 Multichannel Analysis of Shear Waves (MASW)

Over the last decade, the use of shear waves to investigate the near surface has increased markedly and has been used extensively to investigate voided ground, areas affected by near-surface structures, and to determine the shallow shear-wave velocity variability for seismic hazard micro-zonation. The method deals with surface waves in the lower frequencies (e.g. 1–30 Hz) and has a shallow range of depth of investigation (to a few tens of metres depending on site conditions). The passive MASW method may provide information to greater depths.

The field layout is as for a traditional seismic refraction survey, with geophones laid out at 1 or 2 m separation, a hammer and plate seismic source, and 24-channels with an engineering seismograph. The method can also be used with a land streamer. The primary difference is in how the shot records are processed. Unlike refraction surveys, where ground-roll has to be minimised as much as possible, with the MASW method, ground roll is to be encouraged. A typical MASW shot record is shown in Figure 5.40A with key features identified.

In order to understand the MASW process it is necessary first to explain the concept of wave dispersion. In the normal case of seismic velocity increasing with depth, the longer wavelengths propagate faster than the shorter wavelengths, so the frequency content of the wave disperses with transit time (Figure 5.41A). A dispersion curve is a plot of the frequency versus the propagation (phase) velocity (Figure 5.41B). The dispersion curve with the slowest phase velocity is known as the fundamental mode. In the case where more than one phase velocity exists for a given frequency (like a vibrating string), faster dispersions occur for higher modes (harmonics). It is common for a number of modes to be present. The clarity (or otherwise) with which an individual mode can be identified affects the quality of interpretation. If a higher mode is misidentified as being the fundamental mode, the resulting determination of shear-wave velocities will be anomalously high. In some cases, the second or even higher mode may be very evident,

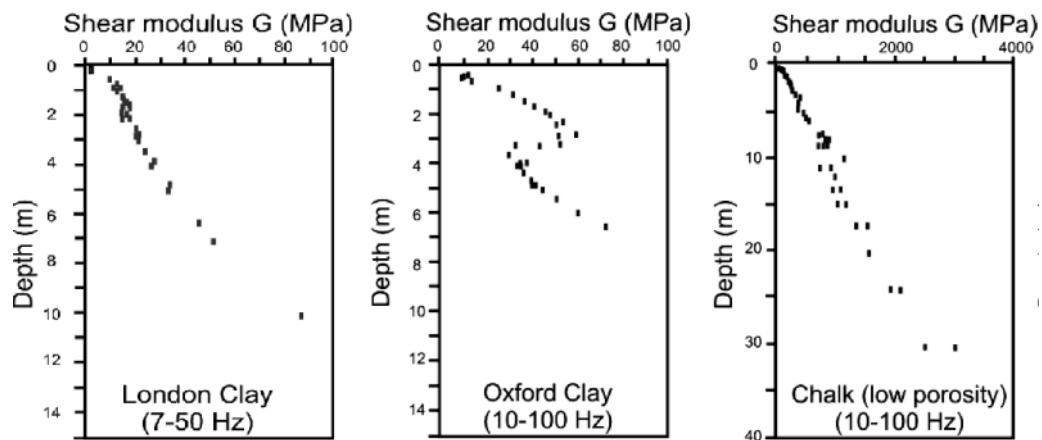


Figure 5.38 Examples of  $G_{\max}$  profiles across three different sets of geological materials. From Matthews *et al.* (1996), by permission. [C]

while the fundamental mode may appear to be absent. This is a key issue in the quality and robustness of the interpretation of MASW data. Identified features on a shot record (Figure 5.40A) give rise to the corresponding features on the associated dispersion curve (Figure 5.40B).

Having obtained a dispersion curve for each spread (Figure 5.42A), one 1D  $V_s$  profile with depth is derived that gives theoretical dispersion curves closest to the extracted curves (Figure 5.42B). As the seismic spread is moved to the next location across the ground, each adjacent spread will give rise to one 1D  $V_s$  profile

with depth, which when plotted together give rise to a 2D  $V_s$  image (Figure 5.43).

MASW can be deployed in three modes: *active* (using a source such as a hammer and plate), *passive* (using ambient noise, especially that generated by vehicle traffic, as the source), and *combined*. When the passive (or combined) mode is selected, the geophone array should be set out preferably as a cross (two orthogonal spreads) or as a circle. This has been discussed further by Park and Miller (2008). The passive method can achieve significantly greater depths of penetration than those achieved using the active method. It should also

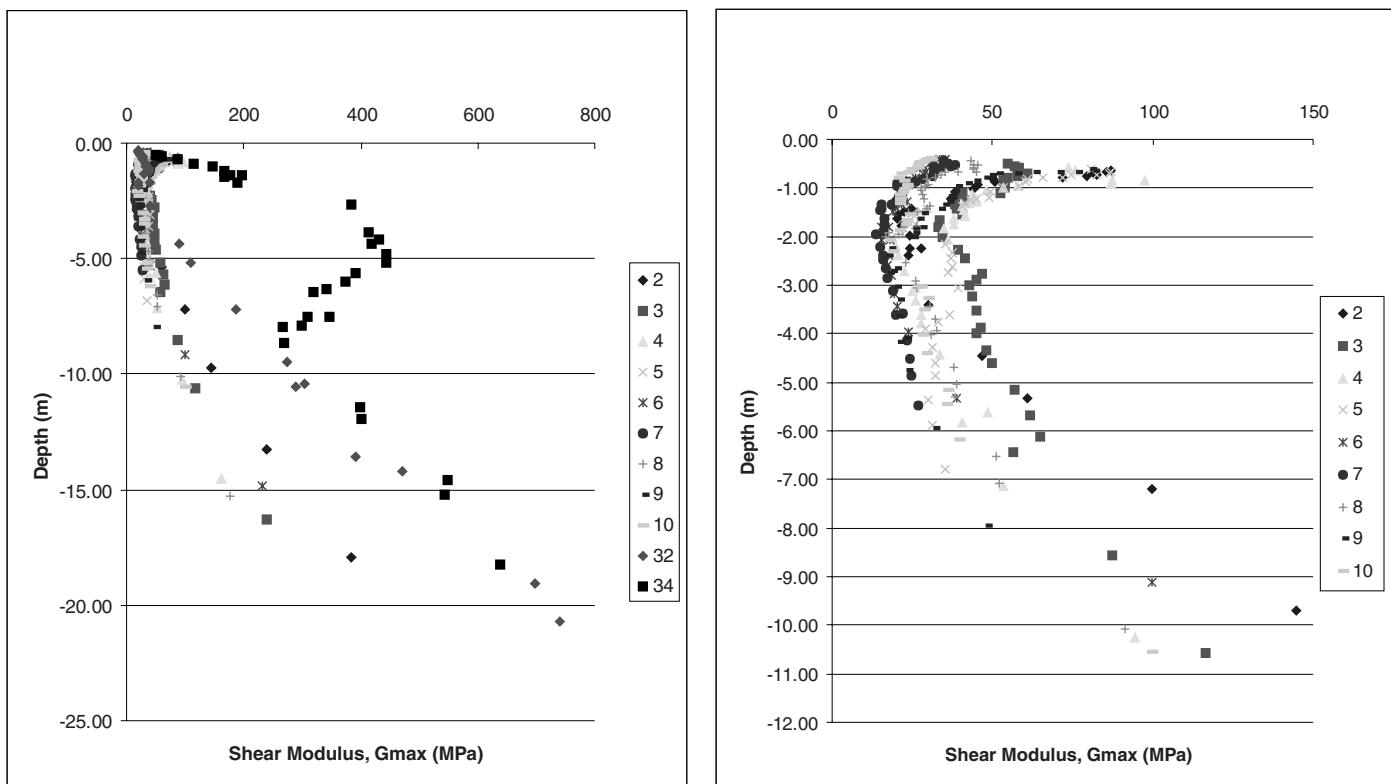
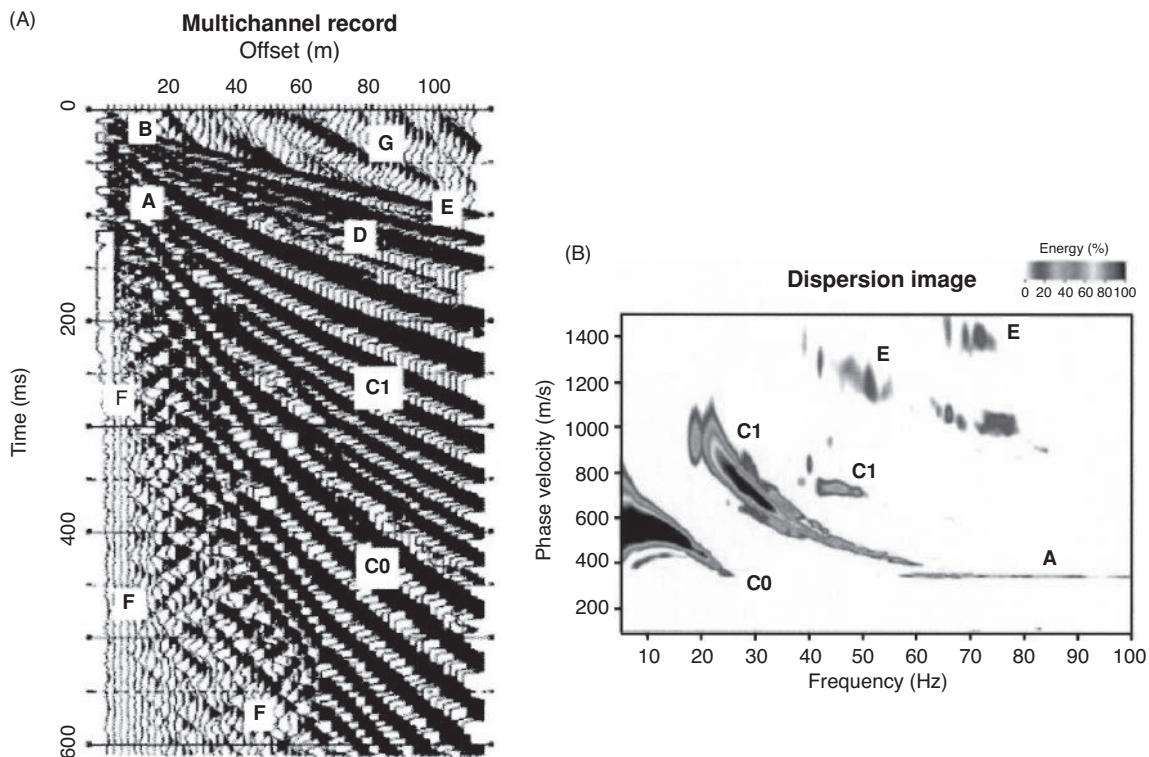
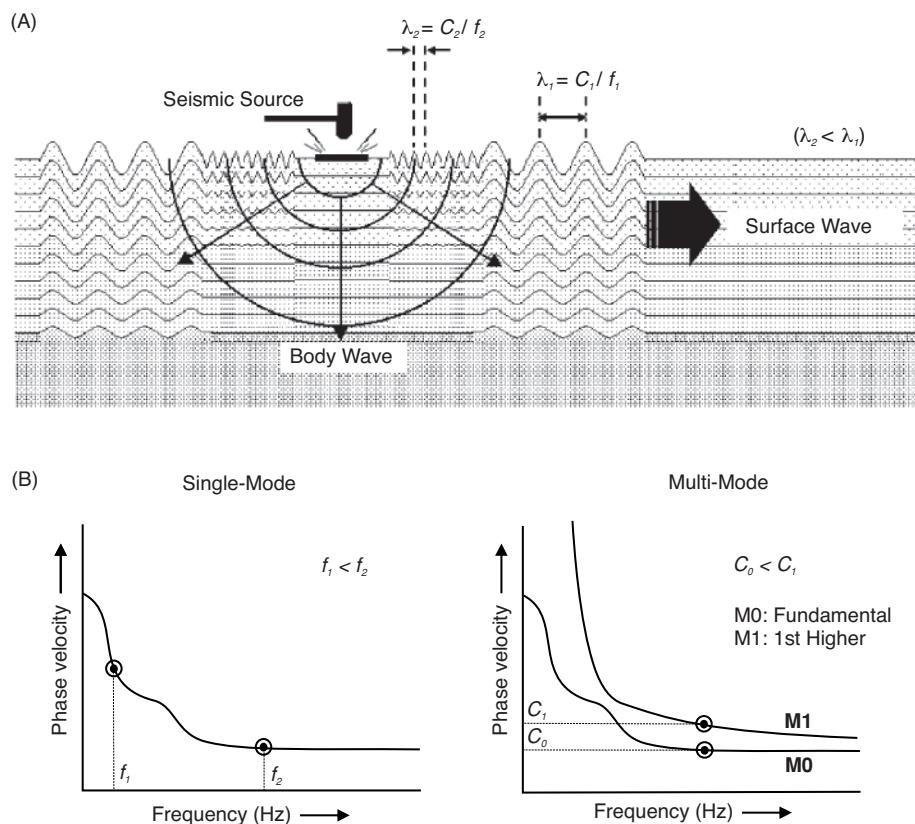


Figure 5.39 Ground stiffness profiles over (A) areas outside and (B) over a closed landfill. [C]

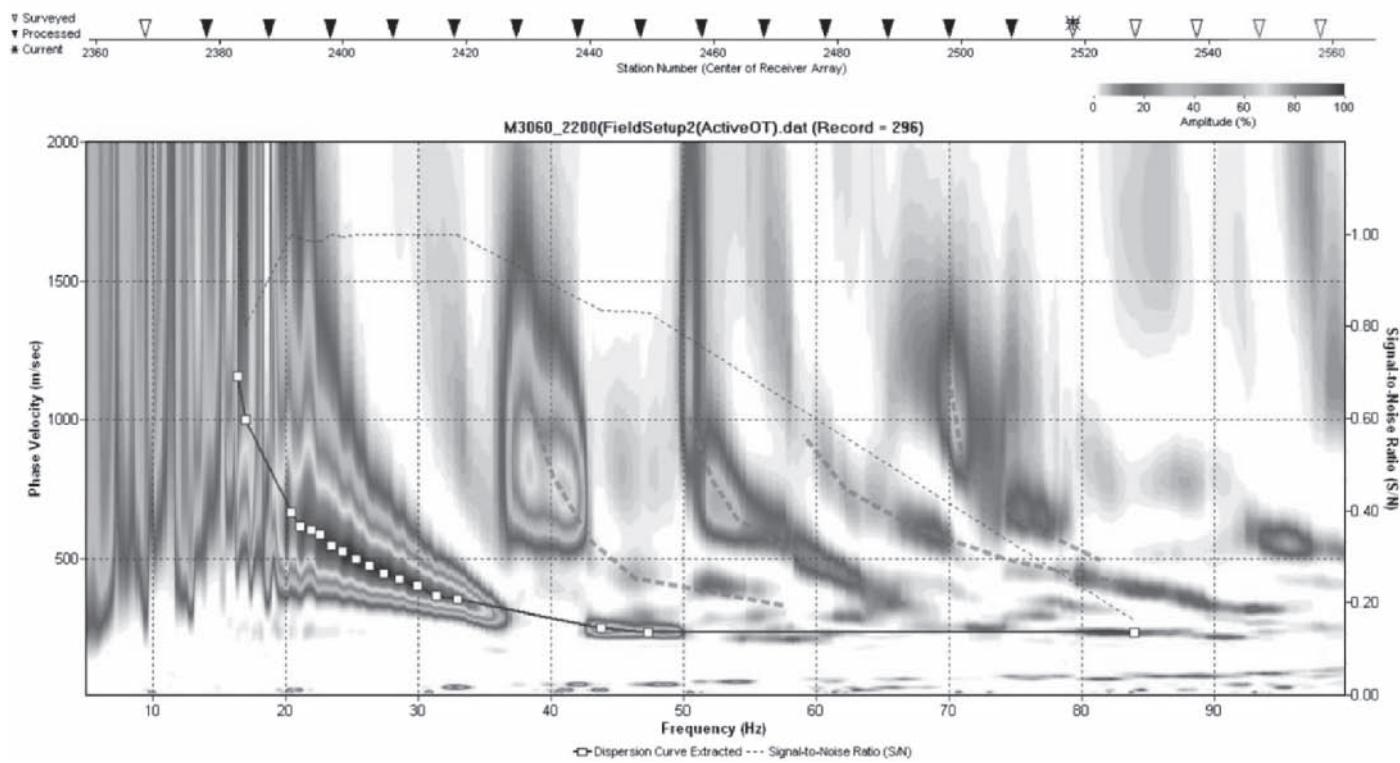


**Figure 5.40** (A) Multichannel MASW shot record; A: Air wave; B: Direct wave; Surface wave fundamental mode, C0, and higher mode(s), C1; D: Reflection; E: Refraction; F: Back-scattering of surface wave; G: ambient cultural noise. (B) Dispersion image with modes arising from features identified in (A). From Park et al. (2007), by permission. [C]



**Figure 5.41** Concept of wave dispersion: (A) longer wavelength surface waves travel faster and deeper than shorter wavelength waves in the case of increasing seismic velocity with depth. (B) Single and multi-mode dispersion curves.

(A)



(B)

### 1D S-velocity ( $V_s$ ) profile

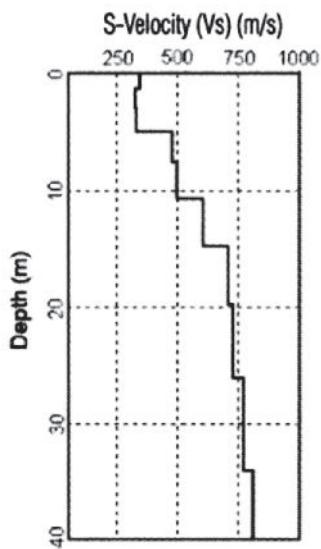


**Figure 5.42** (A) Dispersion curve showing the fundamental and higher modes. (B) 1D  $V_s$  profile versus depth for a single seismic spread. [C]

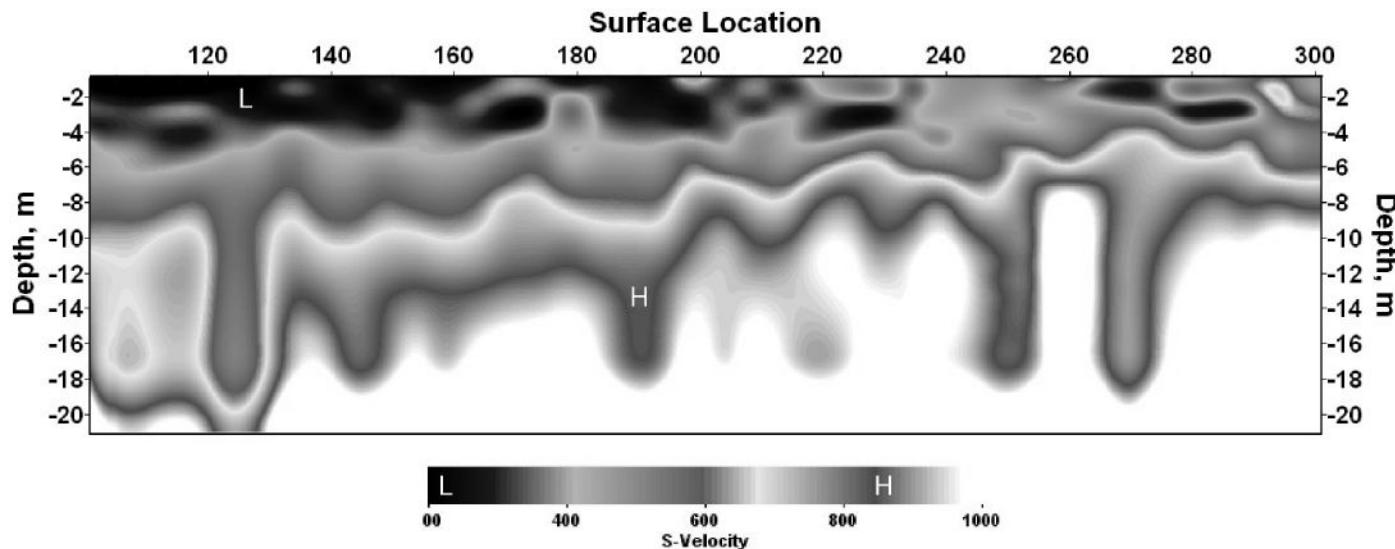


**Figure 5.43** An example 2D  $V_s$  section integrating adjacent 1D  $V_s$  depth profiles. [C]

be noted that the passive MASW method had been studied many years earlier in Japan under the name of the *Micro-tremor Survey Method* (MSM) (Aki, 1957; Tokimatsu *et al.*, 1992).

### 5.6.3 Earthquake hazard studies

Over the last decade, significant and increasing attention has been paid to micro-zonation studies of major cities, by which to define the seismic hazard in earthquake-prone areas. This has been a consequence of the *Global Seismic Hazard Project* (GSHAP), which concluded in 1999. Micro-zonation of urban areas is being undertaken partly to help with the design of preparedness strategies, but also to inform seismic engineers about the design parameters necessary for vital structures to withstand probable seismic events, the so-called *design earthquakes*. Active seismic profiling is undertaken for two principle reasons: (i) to identify and characterise local soil conditions, and (ii) to determine P- and S-wave velocities within the near surface, in conjunction with standard penetration tests (SPTs) in boreholes. Maps of the average value of S-wave velocities estimated for specific depth increments (e.g. 5 m to 30 m below ground level in 5 m increments) have been produced. In addition to the usual seismic refraction method, Multichannel Analysis of Shear Waves (MASW; see Section 5.6), down-hole seismic profiling, borehole seismic tomography, and seismic Cone Penetrometer Tests (CPTs) are also used increasingly frequently in seismic hazard site studies (Fardis *et al.*, 2005). It is stated in EN 1998-1 (Part 1 of Eurocode 8) that '*The site should be classified according to the value of the average shear wave velocity  $V_{s,30}$ , if this available. Otherwise the value of  $N_{SPT}$  should be used*'. Seismic refraction and MASW techniques have the advantage over borehole-dependent methods, especially when operating in congested urban areas, in that they do not require the construction of boreholes.

Statistical correlations have been developed, principally in Japan, between SPT  $N$ -values (the number of blows required to drive a penetrometer a given vertical distance, usually 10 cm, within a borehole) and the small deformation shear modulus ( $G_0$ ) or the S-wave velocity ( $V_s$ ) (Box 5.12). Examples of the use of this approach have been given by Fardis *et al.* (2005).

On 1 October 1995 an earthquake ( $M_S = 6.1$ ) occurred in the Dinar region of Turkey, killing 90 people and destroying more than 4000 buildings. The extremely high level of damage was surprising given the moderate size of the earthquake. At that time, no appropriate soil condition map existed based on extended high-density measurements. Kanli *et al.* (2006) described the subsequent acquisition of surface seismic wave soundings at 50 locations across Dinar city and its surrounding areas. Special low-frequency vertical geophones (2.5 Hz natural frequency) and a seismic source were used for the study. The seismic source was an 80 kg mass (called SR-II - Kangaroo) operated by a blank 12-bore shotgun cartridge fired

**Box 5.12** Correlation between  $V_s$  and  $N_{SPT}$  (Ohta and Goto, 1978)

$$V_s = 68.5 N_{60}^{0.17} z^{0.2} f_A f_G$$

where  $V_s$  is in metres per second,  $N_{60}$  is the SPT count at a depth  $z$  (metres) below ground level,  $f_A$  is the age factor of soil deposits, and  $f_G$  is the soil-type factor.

The values of  $f_A$  are: 1.0 for materials of Holocene age (last 100,000 years), and 1.3 for materials of Pleistocene age (up to 600,000 years).

The values of  $f_G$  are: 1.00 for clay; 1.10 for sand; and 1.45 for gravel.

by an electric starter device. Shear wave velocity profiles were obtained at the investigation sites.  $V_S$  distribution maps were drawn for different depths. The derived  $V_{S,30}$  map of the Dinar region was transformed to UBC (Universal Building Code) and Eurocode-8 standards. Shear wave velocities within the range 160–240 m/s (cat-

egories C and D, Eurocode-8) correlated with being in an alluvial basin that had the highest levels of building damage. Hilly and transition zones had better soil conditions (B category, Eurocode-8) and had comparatively high shear wave velocities ( $V_{S,30}$ ) and suffered less severe damage.

# 6

## Seismic Reflection Surveying

### 6.1 Introduction

Seismic reflection surveying is the most widely used geophysical technique, and has been since the 1930s. Its predominant applications are hydrocarbon exploration and research into crustal structure, with depths of penetration of many kilometres now being achieved routinely. Since around 1980, the method has been applied increasingly to engineering and environmental investigations where depths of penetration are typically less than 200 m. Applications of shallow high-resolution seismic reflection surveying include mapping Quaternary deposits, buried rock valleys and shallow faults; hydrogeological studies of aquifers; shallow coal exploration; and pre-construction ground investigations for pipe, cable and sewerage tunnel schemes, and offshore wind farms.

One of the principal reasons for the increased use of shallow seismic reflection surveying has been the improvement in equipment capabilities and the availability of microcomputers and portable digital engineering enhancement seismographs. Computing power is such that preliminary data processing can be accomplished while still in the field in some cases. This has facilitated real-time processing on board ships for quality assurance and control, the availability of portable data-processing centres which can be housed within a container and flown into remote areas by helicopter, through to self-contained, highly sophisticated seismographs which can be carried by one person. Perhaps more importantly, the growth of computer power has also provided the means whereby three-dimensional data acquisition can be undertaken much more cost-effectively. Data manipulation and management can be accomplished much faster than was possible 15 years ago. In the late 1970s, the costs of three-dimensional seismic surveying were at least double that of conventional two-dimensional acquisition, and it was only undertaken as a last resort. Now, 3D seismics have become much more cost-effective and currently constitute in excess of 60% of the market share in the seismic industry.

As seismic reflection surveying is such an established technique, and as a very large amount of research and development has been

undertaken within the hydrocarbon industry, there is a vast technical literature available. Members of the International Association of Geophysical Contractors, for example, are usually keen to respond to requests for the very latest details of proprietary techniques, new equipment for data acquisition and processing methods.

The literature in relation to shallow applications is, however, surprisingly sparse, with little attention having been paid to this growing area of work. This chapter deals particularly with shallow seismic reflection surveying, but also provides an overview of the wider issues of the methods where appropriate.

### 6.2 Reflection surveys

#### 6.2.1 General considerations

The essence of the seismic reflection technique is to measure the time taken for a seismic wave to travel from a source (at a known location at or near the surface) down into the ground where it is reflected back to the surface and then detected at a receiver, which is also at or near the surface at a known position. This time is known as the *two-way travel time* (TWTT). The seismic method is used to obtain important details, not only about the geometry of the structures underground, but also about the physical properties of the materials present. After all, the ultimate objective of hydrocarbon exploration is to find oil in sufficiently large quantities in places from where it can be extracted cost-effectively. In engineering applications, everything is scaled down and depths of penetration are typically of the order of 10–50 m, and the sizes of mappable targets are correspondingly reduced in size.

The most important problem in seismic reflection surveying is the translation of two-way travel times (in the time domain) to depths (in the space domain). While travel times are measured, the one parameter that most affects the conversion to depth is seismic velocity. Consequently, a great deal of effort in research is devoted to improving our understanding of this parameter. Although this chapter is devoted to seismic reflection methods, analytical

techniques used and interpretational problems are equally valid for ground-penetrating radar data (see Chapter 12).

A further difficulty with seismic reflection surveying is that the final results obtained from data processing undertaken by contractors are likely to be different. Although the basic processing routines may be exactly the same, the choice of parameters to be used in the various stages of processing is more subjective. Thus, the final output from a variety of processors may have different frequency content and signal-to-noise ratios, and even differences in structural detail. Interpreters beware! Furthermore, some data processing may be carried out that adds nothing to the technical content of the data but which focuses attention by the form of display on to specific zones within the data. This 'cosmetic' processing, which may have some benefit to the contractor in marketing terms, has no specific technical justification.

## 6.2.2 General reflection principles

The reflection method requires a source of seismic energy and an appropriate method of both detection (geophones or hydrophones) and recording (seismographs). Details of these three sets of components are discussed in Chapter 4. For a seismic wave to be reflected back to the surface, there has to be a subsurface interface across which there is a contrast in acoustic impedance ( $Z$ ), which is the product of the seismic velocity ( $V$ ) and the density ( $\rho$ ) of each layer (i.e.  $Z = V_i \rho_i$  for the  $i$ th layer). The amplitude of the reflected wave is described by the *reflection coefficient* (see Section 4.3.1).

If a seismic source is discharged at a given shot point S and the reflected waves are detected at geophone locations laid out in a line each side of the shot, then the resulting raypaths are as shown in Figure 6.1. At each point of incidence on a subsurface interface, over an area corresponding to the first Fresnel zone (see Section

4.3.1), the incident waves are reflected back. The point of reflection is halfway between the source and the detecting geophone. The spacing between reflection points on the interface is always half that of the geophone spacing. Consequently, the total subsurface coverage of an interface is half the total geophone spread length. The distance from the source to any geophone is known as the *offset*.

If more than one shot location is used, reflections arising from the same point on the interface will be detected at different geophones (Figure 6.2A). This common point of reflection is known as the *common midpoint* (CMP). Sometimes the terms *common depth point* (CDP) and *common reflection point* (CRP) are used as being equivalent to CMP. This is true, however, only in the case of flat horizons with no lateral velocity variation. If the reflector is dipping, the points of reflection are smeared along the interface (Figure 6.2B). According to Snell's Law, the angle of reflection equals the angle of incidence, and it is for this reason that the point of reflection moves upslope with greater shot–geophone offset. It is recommended that only the term '*common midpoint*' be used.

The number of times the same point on a reflector is sampled is known as the *fold of coverage*. If a subsurface point is sampled only once, as in common-offset shooting, then this is termed *single-fold* or 100% coverage. If 12 different shot–geophone locations are used to sample the same point on a reflector, for example, then this is said to have *12-fold* or 1200% coverage. Folds of coverage of 6, 12, 24, 48 and 96 are frequently used in the hydrocarbon industry, with up to 1000-fold being used exceptionally; in engineering surveys, 12-fold coverage is usually considered excessive. From the number of shots providing the fold of coverage, it is possible to gather together all the traces arising from the same CMP to produce a *common midpoint gather* (CMG) (Figure 6.3). The use of CMP gathers is described in more detail in Sections 6.3.3 and 6.3.4.

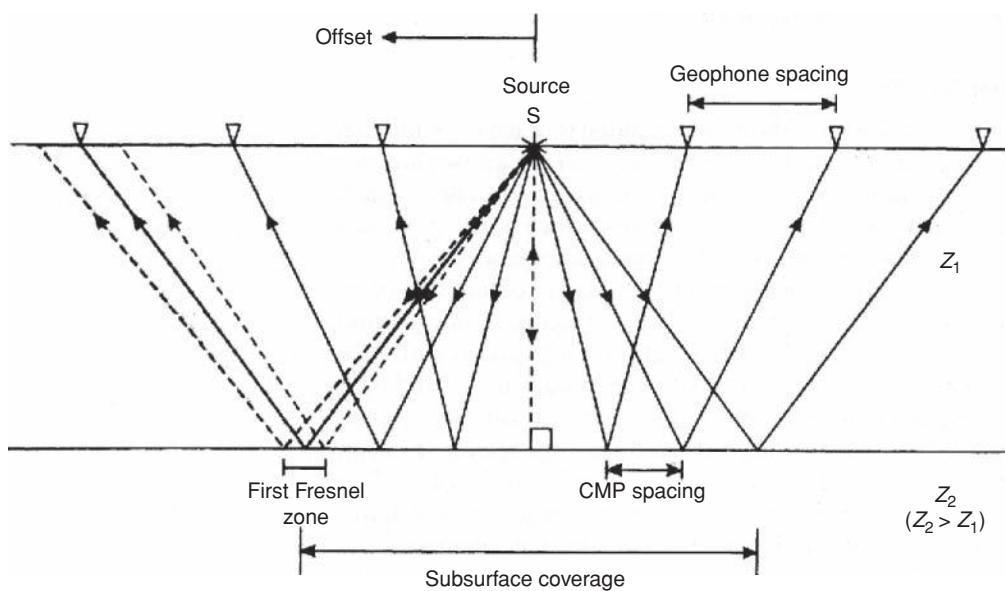


**Figure 6.1** Schematic of reflection raypaths over a horizontal interface across which there is a contrast in acoustic impedance  $Z$  ( $Z_2 > Z_1$ ); the first Fresnel zone at just one location is indicated.

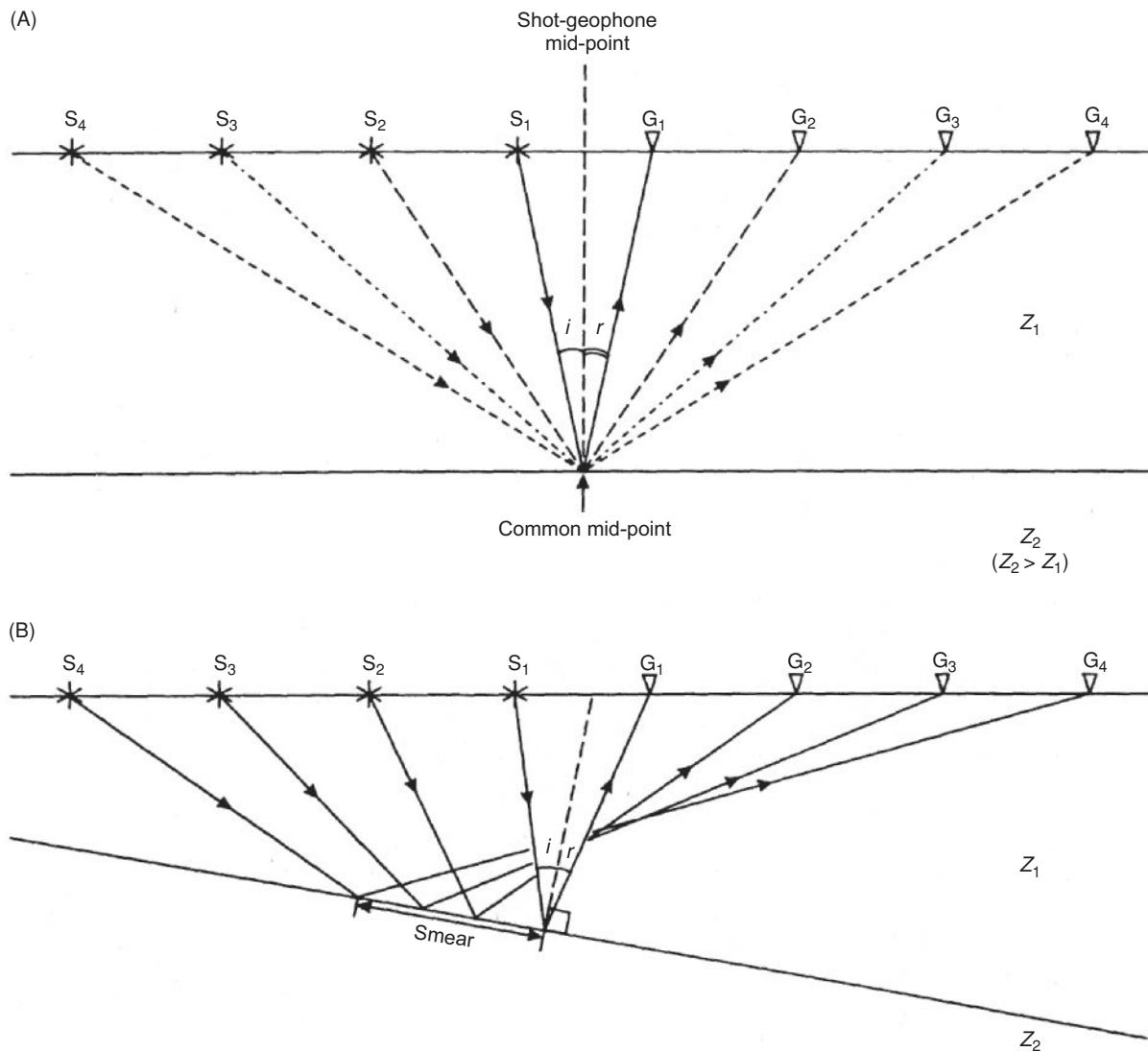


Figure 6.2 Principle of the common midpoint over (A) a horizontal and (B) a dipping interface.

### 6.2.3 Two-dimensional survey methods

Survey designs vary according to the requirements of the investigation. Survey layouts for engineering investigations are considerably simpler than for large-scale hydrocarbon exploration, with corresponding differences in costs.

For an engineering shallow investigation, the layout consists of a shot of some description, and a set of 12, 24 or occasionally 48 geophones with a fundamental frequency of at least 100 Hz connected by a multicore cable (with the appropriate number of takeouts) to an engineering seismograph. The output from each geophone is displayed as one trace on the field record (seismogram).

For larger-scale surveys, more than one geophone may be connected together to form a 'group' or 'array' of geophones, the output of which is summed together and recorded in one channel. There is a variety of different group layouts: the 'in-line array', where all the geophones within the group lie along the line of the survey; the 'perpendicular array', where the geophones are aligned at right-angles

to the survey line; and the 'cross array', which is a combination of the previous two. Other examples are given by Sheriff (2002). In some cases the number of geophones in a group may be as many as several hundred laid out in a rectangular grid, in which case the set of geophones is known as a *patch*. When multiple geophones are used per recording channel, the offset distance is taken as that between the shot and the centre of the group. The distance between centres of adjacent geophone groups is known as the *group interval*.

The use of multiple sets of geophones gives a directional response to the array, designed to enhance the near-vertical upward-travelling reflected waves and to minimise any horizontally travelling coherent noise, which can be correlated from trace to trace, in contrast to random noise which has no coherency between traces. Coherent noise may be in the form of a Rayleigh wave, for example. If the individual geophones in a given group have a spacing equivalent to a half-wavelength of the Rayleigh wave, then the signals at alternate geophones will be out of phase and will be cancelled by the

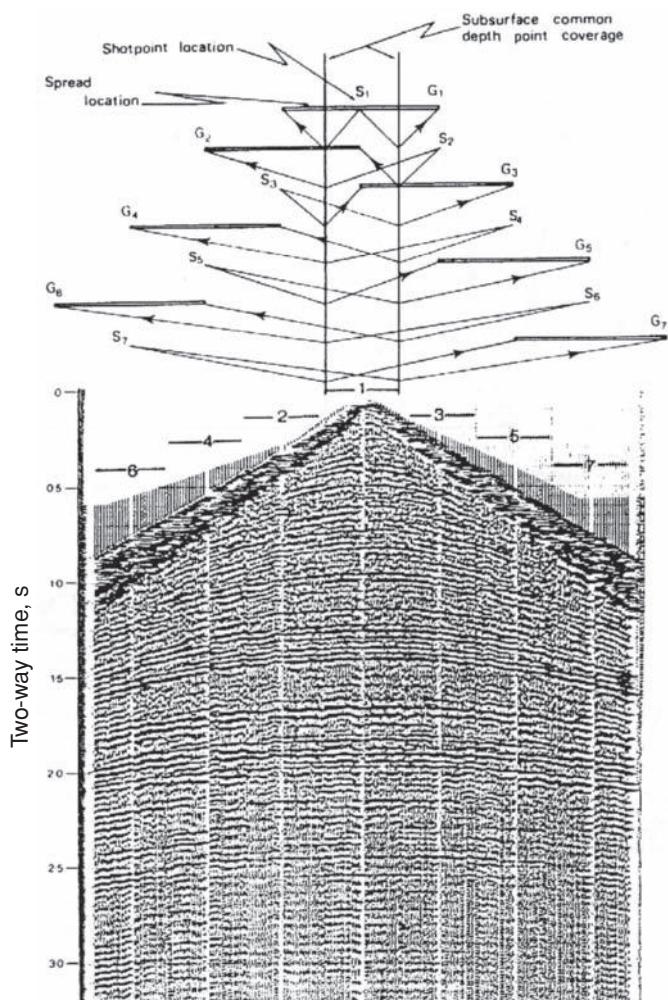


**Figure 6.3** Example of a common midpoint gather.

summation of the outputs from the geophones. An upward-travelling reflected body wave, however, should arrive at the geophones simultaneously, and the total output is then the sum of all the in-phase signals from all the geophones within the group. This has the advantage that it also helps to filter out some random noise and has the overall effect of increasing not only the signal strength, but also the signal-to-noise ratio.

Just as geophones can be laid out in groups, so too can the source shots, and for very much the same reasons. For engineering surveys, however, it is unusual to use either source or geophone arrays.

The shooting arrangements for reflection surveys on land are normally end-on shots, firing into a line of geophones, or split-spread shots, where the source is located within the line of geophones. It is usual for a reflection profile to be built up from end-on shots with split-spread shots as required. For example, if geophones have been laid out along the survey line at an interval of 2 m, the shot may be fired at the end of the line, and then every 2 m along the line, but slightly offset at right-angles from it. The fold of coverage of a reflection profile can be calculated from the expression  $N/2n$ , where  $N$  is the total number of geophone groups in a spread and

$n$  is the number of group intervals by which the entire spread is moved along the survey line between shots (i.e. the move-up rate). Thus for a 24-geophone spread ( $N = 24$ ), with a move-up rate of one interval per shot interval ( $n = 1$ ), the fold of coverage would be  $24/2 \times 1 = 12$ -fold. An example of the successive shot-spread layouts required to achieve a 6-fold coverage from a single 12-channel spread is given in Figure 6.4.

In waterborne surveys for hydrocarbon exploration, shots are fired using one or more tuned airgun arrays, into one or more hydrophone streamers in which a number of hydrophones are interconnected to form an active group, the summed output from which feeds one channel. See Section 4.6.2 for more details of hydrophone streamers. In small-scale engineering surveys, a single airgun or higher-frequency source may be used (see Section 4.5.4) with a short hydrophone streamer, perhaps less than 10 m long, with the output from each hydrophone being summed to give one channel only. Given adequate digital data-recording systems with fast enough sampling rates, very high quality records can be produced even though only single-fold coverage is achieved. The compactness of size of equipment, and the shortness of the streamer, permit seismic reflection surveys to be undertaken from small boats (<10 m long) in small rivers and narrow canals.

In land-based shallow engineering and hydrogeological investigations, the simplest form of reflection surveying uses a single geophone offset from the source by a constant amount. This survey configuration is known as the *constant-offset* method. The source and receiver are moved progressively along the survey line in equal increments, with one trace being produced from the single geophone from each shot (Figure 6.5). The seismic record is obtained by displaying successive traces side-by-side. The main advantage is that, as the incident raypath is virtually perpendicular to the ground surface, there is virtually no data processing required in order to obtain a seismic section. For short survey lines requiring only very basic information, simple and cheap seismographs are available for constant-offset surveys. For larger surveys, it is better to lay out a geophone cable with 12 or 24 takeouts and to shoot with optimum offset into one active geophone at a time, with all the rest switched off. The benefit of this approach depends upon the optimum offset chosen and the geophone interval selected for most efficient data acquisition and reflector imaging.

The method has been developed further by the Geological Survey of Canada into what is known as the *optimum-offset* method. If the source and single receiver are located at virtually the same point, ground roll and perhaps the airwave from the shot would swamp the geophone and no useful information would be obtained. In order to reduce the effect of the ground roll, it is necessary to offset the geophone from the source by an optimum amount (Figure 6.6). This offset distance is best determined from trial reflection shots to gauge the most appropriate offset in order to image the reflectors required.

The optimum-offset window is the range of offsets at which the bedrock reflection arrives before either the ground roll or air wave. The choice of incremental move-up distance between shots is dependent upon the type of target being imaged. If the reflector in question has significant dip or surface topography, then a short spacing is best (typically 1–3 m). If the reflector targeted is

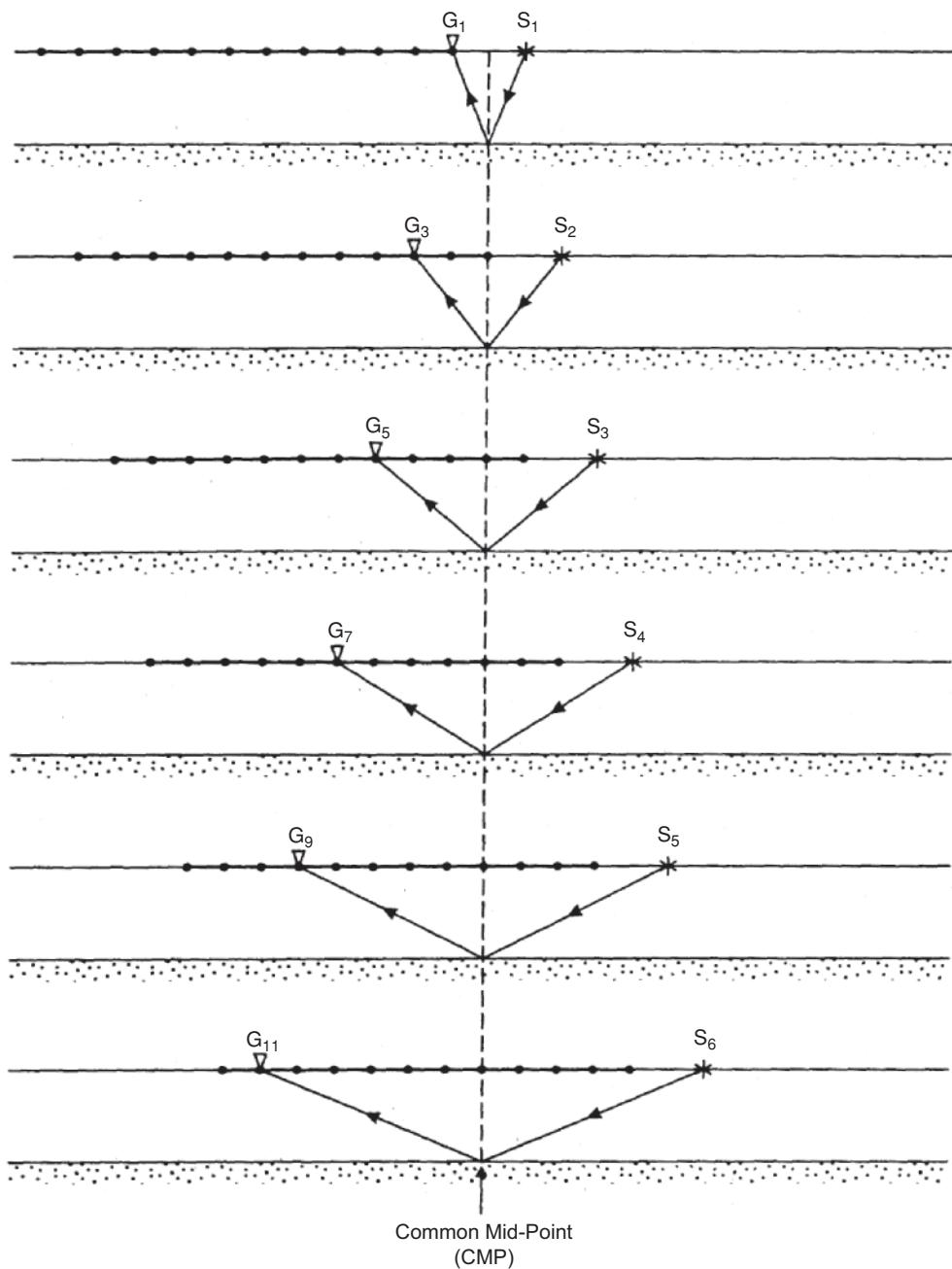


**Figure 6.4** Sequence of survey layouts to acquire 6-fold coverage; S indicates the source and G a geophone (or hydrophone).

reasonably planar, then the spacing can be increased, perhaps to 5 m or more. Further details of the method have been summarised by Pullan and Hunter (1990).

#### 6.2.4 Three-dimensional surveys

Three-dimensional surveys were first undertaken in 1975. Since then there has been a rapid growth in the use of this mode of survey, particularly after 1985. Previously, it was only used over mature producing fields with good prospects for hydrocarbon recovery. With substantial improvement in three-dimensional acquisition ef-

ficiency and processing, the costs have fallen such that the method is now used increasingly as part of primary exploration surveys to aid appraisal of new fields, as well as over producing fields. Three-dimensional surveys are also used to evaluate trends in reservoir quality. The proven advantages of 3D over 2D surveys have resulted in a massive increase in its usage; for example, of its annual expenditure on seismic methods, Shell invested 75% in 3D (Nestvold, 1992). Indeed, it is likely that 3D seismics will become the primary survey method in hydrocarbon exploration in many areas.

While the method is obviously highly successful in the hydrocarbon industry, in engineering investigations it is used only where the

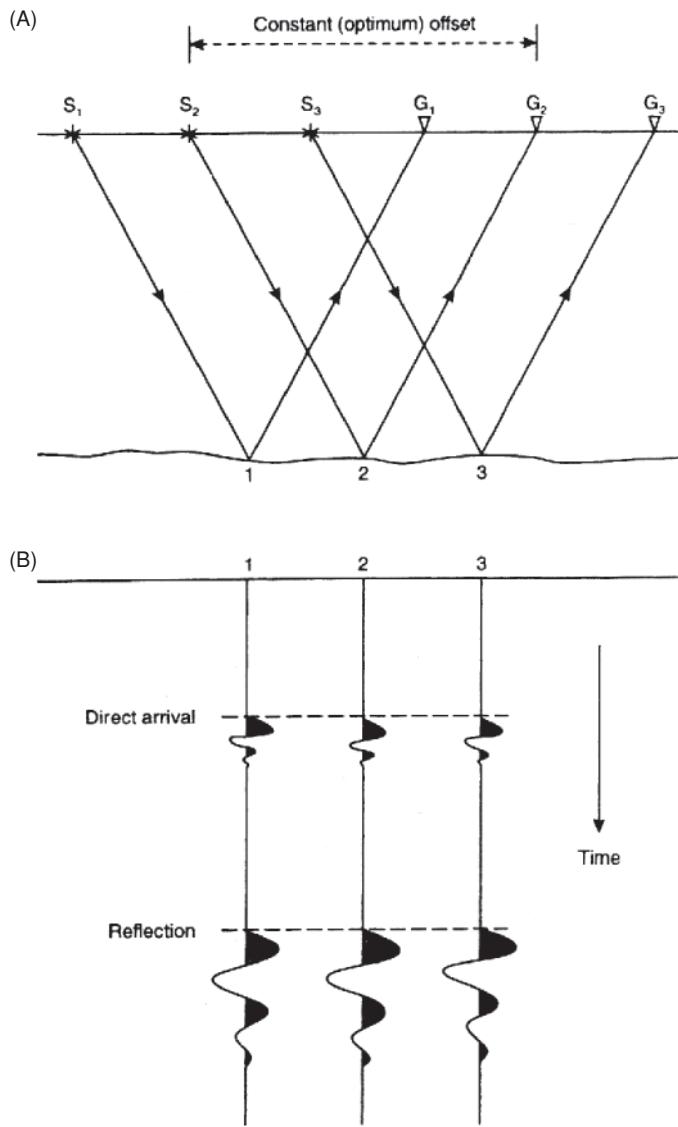


**Figure 6.5** Constant-offset seismic reflection surveying using the optimum-offset window. (A) Raypaths and (B) three adjacent traces obtained using the layout shown in (A).

high cost can be justified, such as in major investigations for nuclear power stations or for sites for the safe disposal of highly radioactive waste material deep underground. Henriet *et al.* (1992) published an account of very-high-resolution 3D seismic reflection surveying for geotechnical investigations with a bin size of only  $1\text{ m}^2$ . Two sources were used, namely an EG&G Boomer<sup>TM</sup> and a Sodera 15 in<sup>3</sup> modified airgun firing into an array of 12 dual-channel streamers at 1 m separation; the array was orientated at right-angles to the boat track, giving a 5.5 m wide swath. The survey imaged a clay diapir (with a reported accuracy of better than 0.25 m) over a depth range of 50 m to about 25 m below ambient ground level, with a 60 m diameter.

A three-dimensional survey requires extremely careful design so as to avoid spatial aliasing. In the field, the data are acquired in subsets known as *common shot gathers*. When all the subsets are

taken together, these common shot gathers form a complete 3D dataset.

A marine 3D survey is accomplished by shooting closely spaced parallel lines, known as *line shooting*. On land or over shallow water, the survey uses a number of receiver lines deployed parallel to each other with the shot points located along lines at right-angles in a configuration known as *swath shooting*. In marine surveys, the direction in which the shooting vessel sails (boat track) is known as the *in-line direction*, whereas in land 3D surveys the receiver cable is deployed along the in-line direction. The line at right-angles to the in-line direction is known as the *cross-line direction*. The line spacing in marine 3D surveys is typically less than 50 m, and may be as small as 12.5 m. Consequently, it is essential that the locations of all shots and receivers be accurately known at all times in order to locate the area on each reflector from where the reflection originates. In 2D surveys, traces are collated as CMP gathers; in 3D surveys, traces are collected together as common cell gathers ('bins'). Effectively, the common point of reflection from a large number of source-receiver pairs lies within an area ('bin') on the reflector (Figure 6.7), with a typical size of  $25 \times 25$  m. The fold of coverage is then the number of traces that pertain to a given bin.

Three independent coordinate sets need to be considered: travel time ( $t$ ), and two spatial coordinates, midpoint ( $x_m$ ) and offset ( $x_0$ ). The same data can be described in terms of travel time ( $t$ ), source coordinate ( $x_s$ ) and receiver coordinate ( $x_r$ ). The relationship between these sets of coordinates is given in Box 6.1 and illustrated in Figure 6.8 (Vermeer, 1991).

The two methods of displaying shot-receiver geometries in Figure 6.9 are known as a *surface diagram* (shot-receiver coordinate system) and a *subsurface or stacking diagram* (midpoint-offset coordinate system). The design of sampling using 3D seismics is dealt with in more detail by Vermeer (1991), for example. As the range of applications diversifies, so too does the option of source-receiver geometry in 3D acquisition. Additional survey layouts include:

- the *wide-line layout* (Compagnie Général Geophysique), in which a single line of groups of geophones is straddled obliquely by four source points, each with a different offset (Figure 6.10A);
- *zigzag* (Figure 6.10B), where the source boat zigzags a track relative to a straight streamer track (Bukovics and Nooteboom, 1990);
- *block layout*, where several parallel lines of geophones are recorded simultaneously from an orthogonal line of shots (Figure 6.10C);
- *Seisloop*, where both geophones and source points are located around the perimeter of a square (Figure 6.10D);
- and *Rich Azimuth* (RAZ) geometry (Figure 6.10E) (Ross, 2008).

Rich Azimuth (RAZ) surveys have been developed to exploit a complete  $360^\circ$  range of azimuths and combine the *Multi-Azimuth* (MAZ) and *Wide Azimuth* (WAZ) geometries. The WAZ geometries typically employ three or four vessels simultaneously with parallel towed streamer acquisition, with multiple vessels enabling a larger cross-line offset. The MAZ method uses a single vessel that acquires

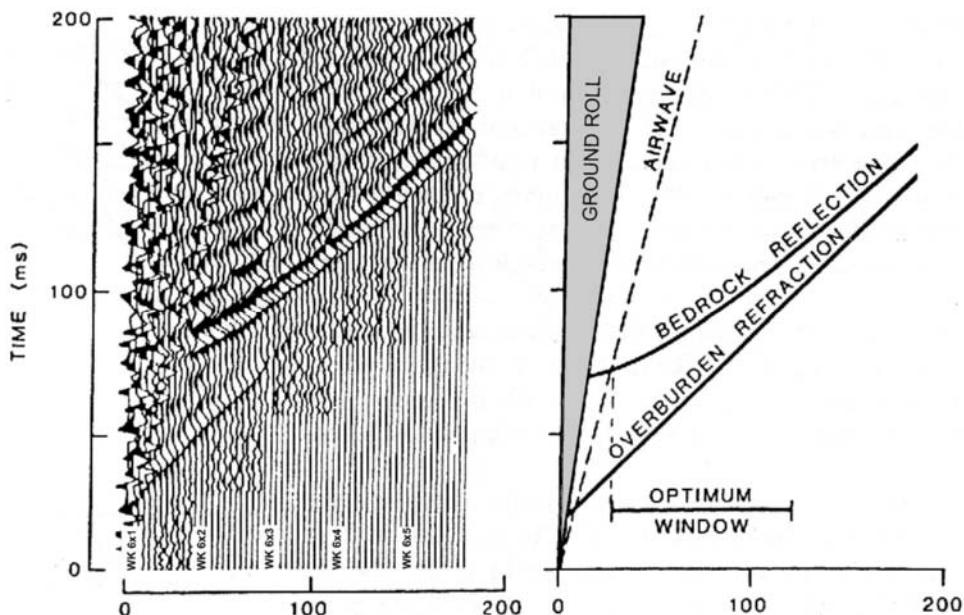


**Figure 6.6** (A) Composite shallow reflection record made up of separate 12-channel records, each of which was recorded with a different time delay between the shot instant and the start of recording. (B) Corresponding time-distance graph identifying the major seismic events on the record. The optimum window is that range of source-receiver separations that allows the target reflection to be observed without interference from other events. From Slaine *et al.* (1990), by permission.

a conventional 3D survey in several directions over the same survey area. Kapoor *et al.* (2007) found that wider cross-line offsets led to better images, and that the best were with a complete range of 360° range of azimuths. A subset of geometries producing such azimuthal

sampling became known as ‘rich azimuthal’ (RAZ) geometries. A new development of the RAZ geometry has been *coil shooting* (Amundsen and Landrø, 2009; Ross, 2008), where a single vessel sails in a series of concentric intersecting circles in the pattern, for example, of a dahlia (Figure 6.10E). The method is a proprietary development of WesternGeco. As an indication of productivity, 18 circles were shot centred on a 2.6 km by 2.6 km square in four days, with a coil radius of 5.6 km, with ten streamers each 4.5 km long, separated by 75 m. The concept of coil shooting was first patented by French (1984).

In a marine survey, a two-boat system was devised by GECO in 1988 to provide rapid and cost-effective acquisition of 3D seismic reflection data. It is known as Quad/Quad because it consists of four hydrophone streamers (each 3 km long with 120 hydrophones

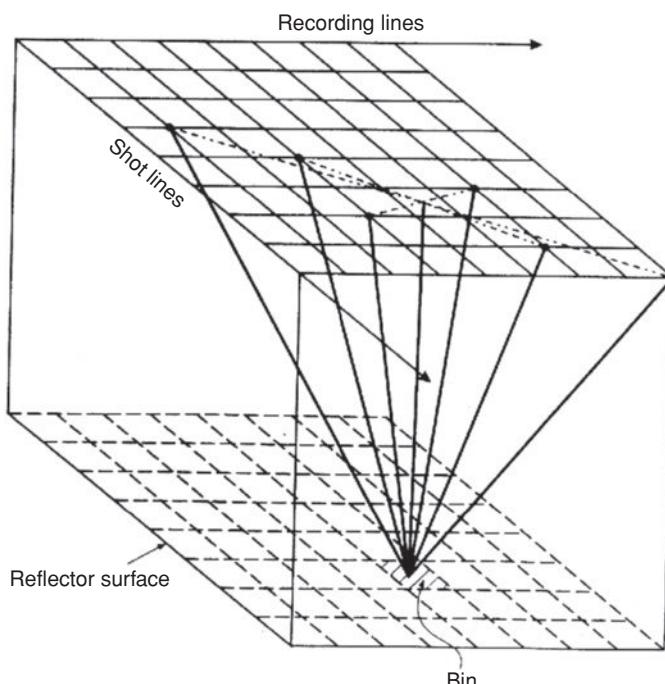


**Figure 6.7** Three-dimensional survey with a small number of raypaths shown for a given bin for a common cell gather. There is no requirement for the bin size to be the same as the shot-receiver grid – these are shown schematically.

#### Box 6.1 Spatial coordinate system for SD seismic surveys (see Figure 6.8)

The distances between a coordinate reference point (0, 0) and the seismic source ( $x_s$ ) and receiver ( $x_r$ ) produce a distance to the shot–receiver midpoint ( $x_m$ ) with offset being given by  $x_o$ . Thus:

$$x_m = (x_s + x_r)/2 \quad x_s = x_m + x_o/2$$

and

$$x_o = x_s - x_r \quad x_r = x_m - x_o/2$$

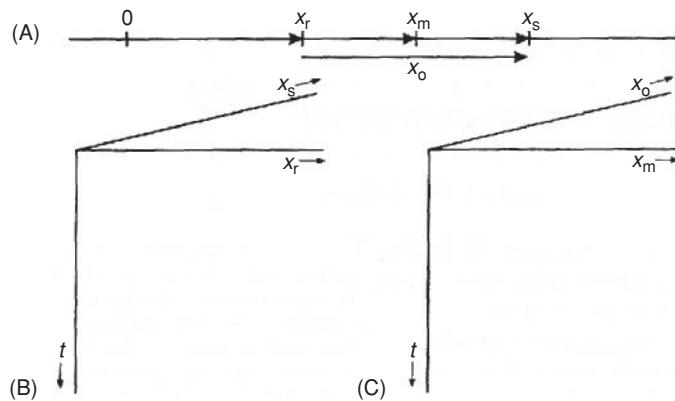


**Figure 6.8** Pre-stack data coordinate systems: (A) the four spatial coordinates in relation to the seismic line; (B) the shot-receiver coordinate system; and (C) the midpoint-offset coordinate system. From Vermeer (1991), by permission.

groups) and four source arrays towed behind two seismic vessels. One vessel is designated the master ship with the second acting as slave. All survey operations are controlled from the master ship. The field and shooting configurations are shown in Figure 6.11. Each source array is fired in turn at 10-second intervals; at a typical cruising speed of 5 knots (9.3 km/h), the ships sail a distance of 25 m during this time interval, giving rise to a shot ('pop') interval of 25 m and a CMP interval of 12.5 m. The reflected wavefield from the subsurface is recorded using all four streamers. By sequencing the firing, complete subsurface coverage can be achieved across a swath typically 300 m wide.

Three-dimensional surveys are also achieved using a single streamer with one source array where the streamer is allowed to drift off the boat track line. The feathering of the streamer caused by cross-currents provides a swath of coverage of the subsurface (Figure 6.12). By careful monitoring of the positions of the streamer at regular time intervals, the positions of the active hydrophone groups can be determined relative to the source, and hence the locations of the respective midpoints can be calculated.

A further development in 3D data acquisition has been Concentric Circle Shooting (CCS - trademark by Grant Tensor and patented by W. French) for improved imaging of salt domes. The first deployment of this method in Europe was in Block 29/2c in the North Sea in October 1991 by Mobil (Hird *et al.*, 1993). Concentric Circle Shooting uses a single ship from which a dual streamer/dual source is deployed where each source array is fired alternately (the *flip-flop* method). The ship sails in a circle of a predetermined radius in order to acquire the subsurface coverage needed. The radius of each circle is decreased until a minimum size is achieved, which is then infilled using straight survey lines.

In a salt diapir environment, the CCS method permits the acquisition of data in essentially the strike direction, which minimises non-hyperbolic move-out distortion of the shot records and maximises the energy returns along the entire length of the streamer (Reilly and Comeaux, 1993). Another advantage of the circular shooting geometry is that it provides optimal imaging of any radial or non-linear fault pattern within the survey area.

Of critical importance to 3D data acquisition is positional accuracy. While 3D data acquisition has resulted in a 10-fold increase in seismic data collected, the amount of survey data has mushroomed 30-fold. The collection of navigational data, and the mathematical processing of information, for instance, from up to 48 compasses (12 per streamer), 6 radio positions and 92 acoustic ranges for each and every shot fired, is a non-trivial exercise. Consequently, there has been a substantial growth in the supply of specialist navigational control software and associated technology (see also Chapter 4).

## 6.2.5 Vertical seismic profiling (VSP)

*Vertical seismic profiling* (VSP) is effectively seismic surveying using boreholes. Seismic detectors are located at known levels within a borehole and shots fired at the surface, and vice versa. The VSP method utilises both the downgoing wavefield as well as the reflected and/or diffracted wavefield to provide additional information about the zone imaged by the method. In areas of structural complexity, seismic data acquired from only the surface may not provide the clarity of imaging necessary to resolve the detail required. Furthermore, additional information may be needed in areas now occupied by drilling rigs and oil platforms. As drilled holes already exist in these cases, it makes economic as well as technical sense to use them.

The basic layout of a VSP survey is shown schematically in Figure 6.13. There are several different types of VSP configurations such as static VSP, with one string of detectors at a fixed position with a single shot at the surface (shown in Figure 6.13); single-level walkaway VSP, where shots are fired into one downhole detector from source points with increasing distance from the wellhead (i.e. walking away from the hole); and multilevel walkaway VSP – the same as for single-level walkaway VSP but with a string of downhole detectors over a wide range of depth levels.

In the case of a single-level walkaway VSP, a double wavefield situation is created in which it is difficult to differentiate between the downgoing and upgoing signals (Figure 6.14). If such a VSP is undertaken along radial transects around a wellhead, the zone of illumination has the form of an inverted paraboloid (shaded section in Figure 6.14A). In the case of a multilevel walkaway VSP survey, the corresponding schematic raypaths and associated common-shot point gathers are as shown in Figure 6.15. Use of the multilevel walkaway survey helps to resolve the problem of identifying the downgoing and upgoing wavefields. An added advantage of the VSP method is that it can utilise shear waves as well as P-waves.

Incident P-waves can be mode-converted under suitable conditions to vertically polarised S-waves (SV), or S-waves can be generated specifically (e.g. Edelmann, 1992). As the S-wave velocity is between 50 and 75% that of P-waves, the S-wave wavelength is significantly shorter, thereby increasing the resolution available. In addition, highly fractured zones tend to attenuate S-waves preferentially with respect to P-waves, as the S-waves are more directly affected by changes in the rigidity modulus or density of the medium. Also, Poisson's ratio, estimates of porosity and attenuation ( $Q$ ) can be computed, giving more engineering attributes for the host rock (Ahmed *et al.*, 1986). In addition, where a VSP survey is undertaken on land, and where S-waves can be generated specifically as well as P-waves, then the shear-wave splitting (polarisation into

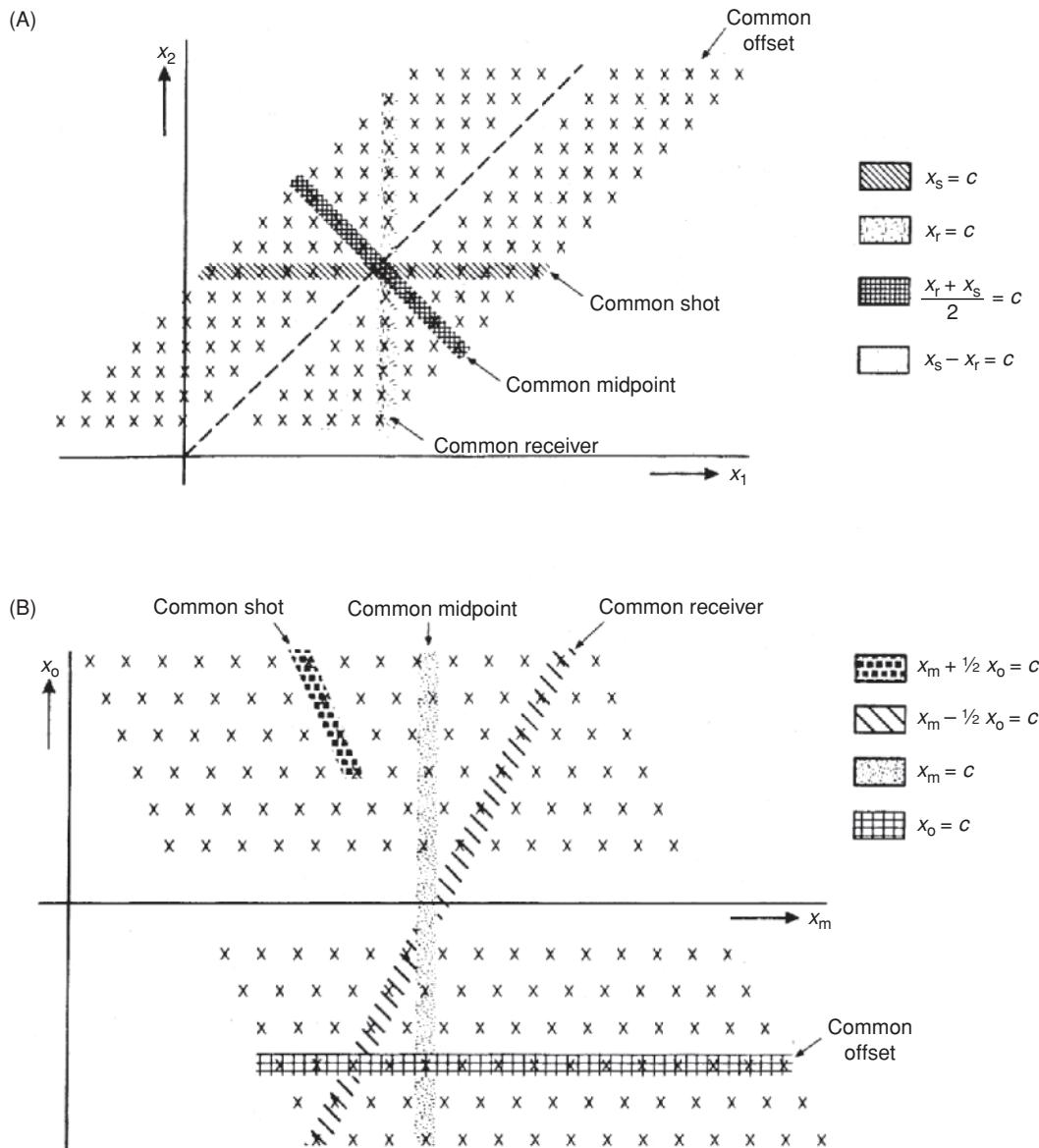


**Figure 6.9** Descriptions of a pre-stack seismic data set in: (A) shot-receiver coordinate systems (a surface diagram); and (B) midpoint-offset coordinate systems (a subsurface diagram or stacking diagram). From Vermeer (1991), by permission.

components) can be used to determine anisotropy of the host media at a resolution much less than the wavelength (e.g. Crampin, 1985; Douma *et al.*, 1990). Further details of VSP surveys have been given by Hardage (1985) and Maio *et al.* (1995), for example, and their use is discussed further in Section 6.4.2.

### 6.2.6 Cross-hole seismology: tomographic imaging

Of increasing importance in seismic investigations is the use of hole-to-hole (*cross-hole*) surveys, also known as *borehole tomography*. Two or more boreholes may be used simultaneously, with one hole being used to deploy a source at one or more levels, and the other borehole(s) to house geophone or hydrophone strings. The basic configuration is shown in Figure 6.16.

The essence of the method is that the raypath lengths between sources and receivers are known, and that by measuring the travel times along these paths, the average velocity along each can be determined. The plane in between the source and receiver holes is divided into a grid of cells. Each constituent cell is assigned a velocity, and the synthetic travel time through it along the portion of ray path intersecting the cell is calculated. By summing the incremental travel times of imaged cells along a given ray path and comparing the total against the measured travel time, the assigned velocities in the various cells can be changed iteratively so that the difference between the observed and modelled travel times is reduced to a minimum. As some cells are imaged by many ray paths, the iterative process can produce very good estimates of cell velocity. Consequently, any zones with anomalous velocity lying in the imaged plane between boreholes can be identified. The method of producing tomographic

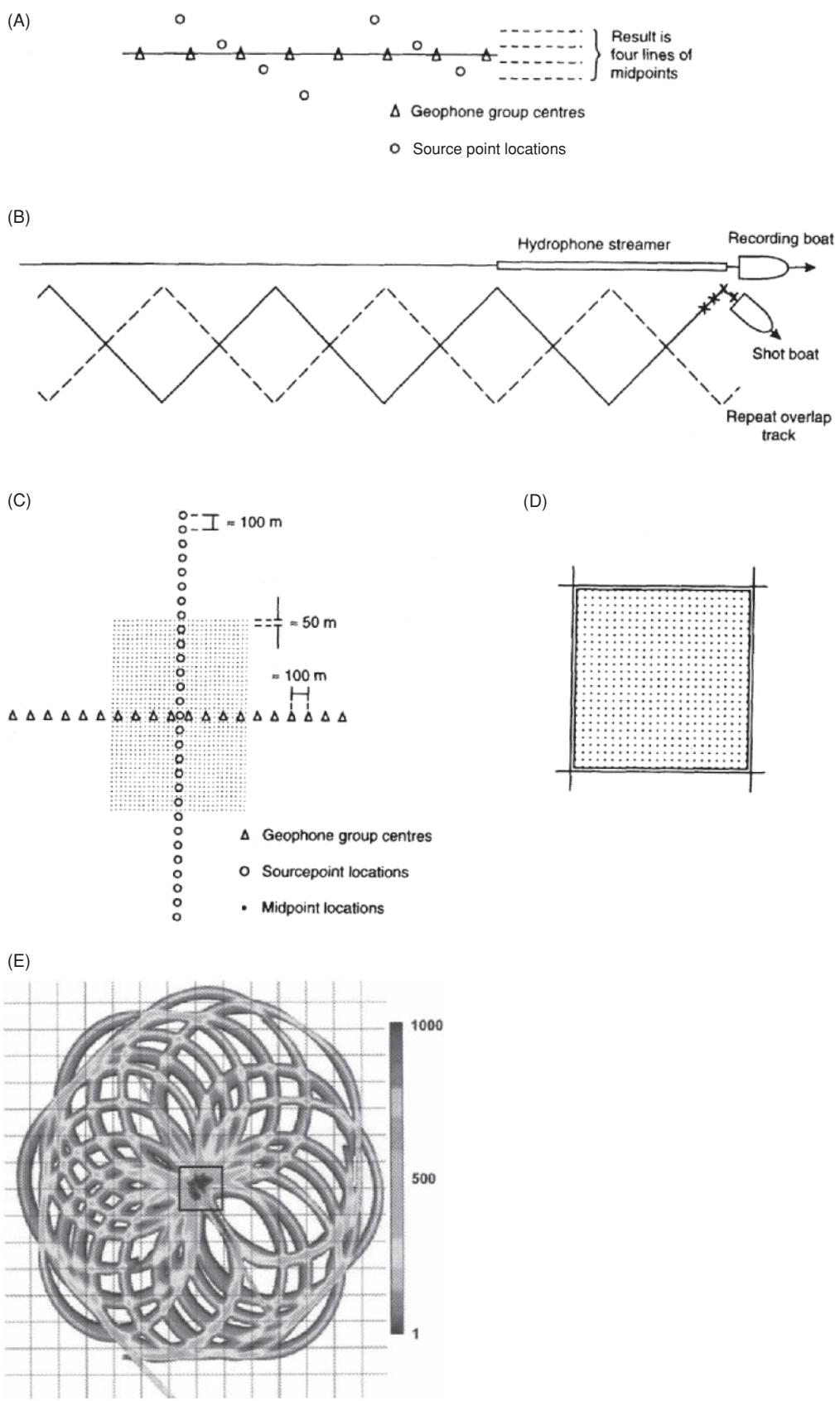


**Figure 6.10** Survey layout for investigations: (A) wide-line layout; (B) zigzag (Bukovics and Nooteboom, 1990); (C) block layout; (D) Seisloop where the geophones and sources are located around the perimeter; and (E) Rich Azimuth geometry. A-D after Sheriff (2002), and E after Amundsen and Landrø (2009), by permission. [C]

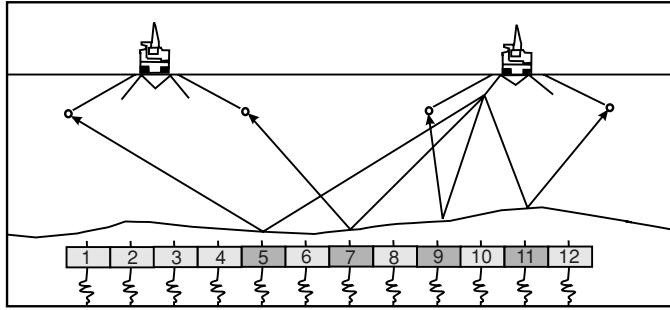
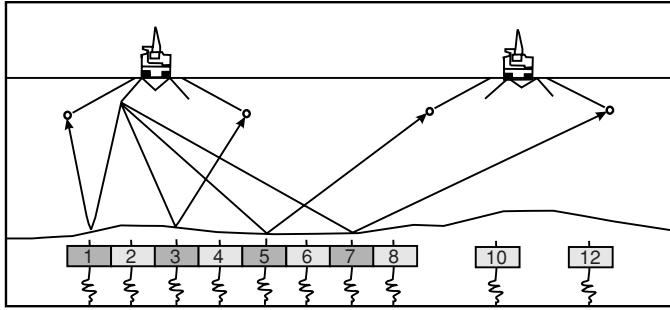
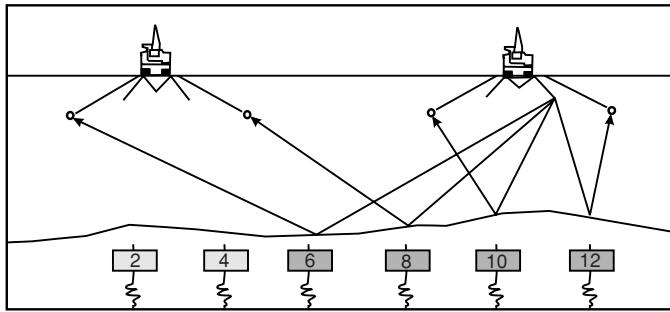
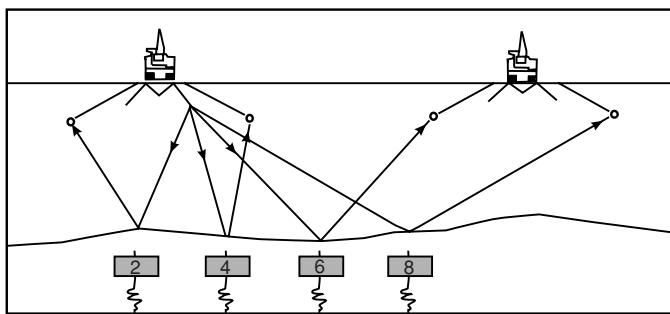


**Figure 6.11** The sequence of firing four source arrays to obtain subsurface coverage in the Quad/Quad system. This firing sequence is similar to that of a car's engine – in the sequence 1, 3, 4, 2. After four arrays have been fired, 12 common midpoints (CMPs) have been recorded across a swath of about 300 m. From Hansen *et al.* (1989), by permission.

images is based upon similar principles to those used for medical scanning in hospital radiological or orthopaedic departments.

Just as seismic velocities (P- and S-wave) can be determined, so too can Poisson's ratio and relative attenuation, thus providing important engineering information about the host materials. In applications for engineering site investigation, for example, the inter-borehole separation should be no more than 10–15 times the

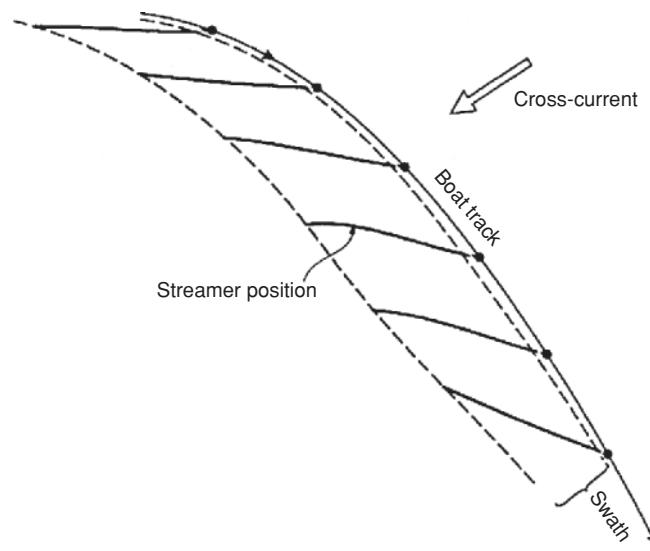


**Figure 6.12** Feathered hydrophone streamer locations at discrete intervals of time showing the swath covered by this geometry.

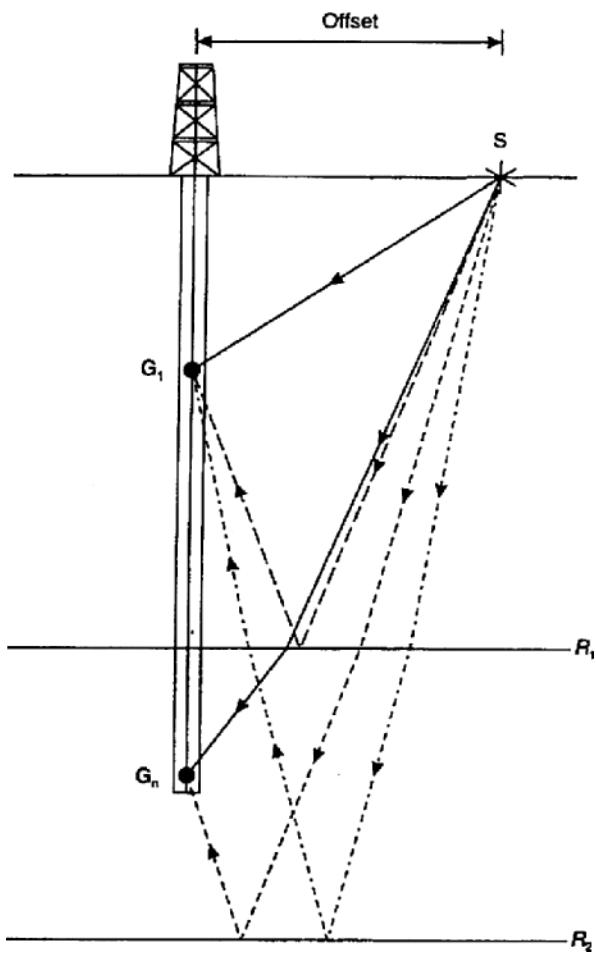


**Figure 6.13** Schematic showing the principle of vertical seismic profiling (VSP). A string of geophones or hydrophones is suspended down a borehole and a shot is fired at S. Direct, reflected and diffracted wavefields are detected along the string of geophones  $G_1$  and  $G_n$ .  $R_1$  and  $R_2$  are successive reflectors.

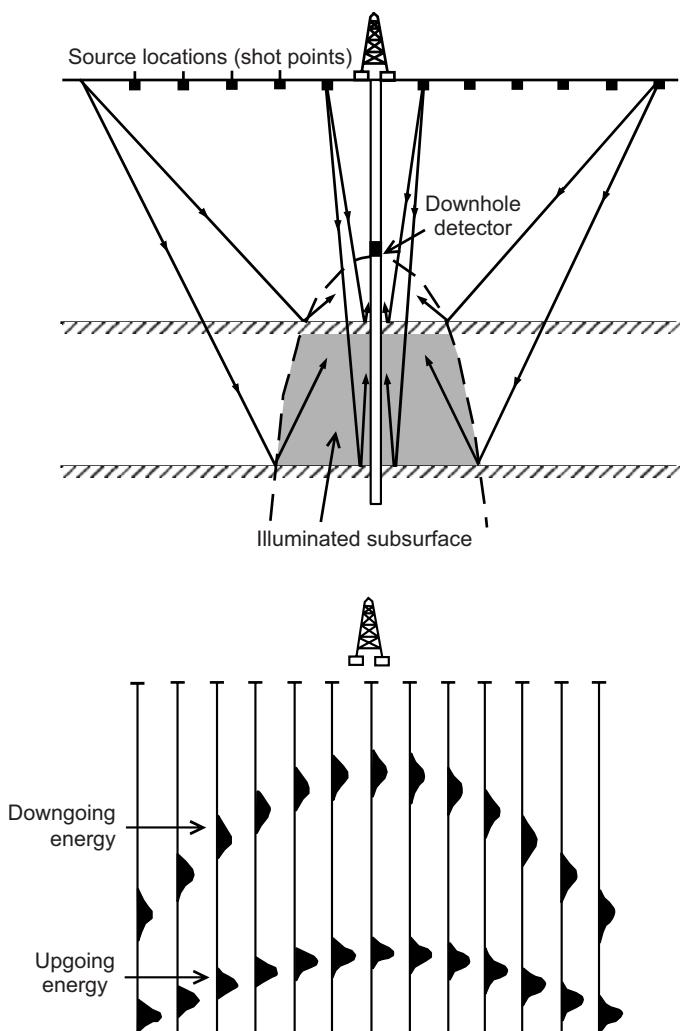


**Figure 6.14** Single-level walkaway VSP with sample raypaths showing (A) a section through the inverted paraboloid zone of illumination, and (B) downgoing and upgoing wavefield signals recorded at a single detector. After Ahmed *et al.* (1986), by permission.

maximum size of target being imaged. In hydrocarbon surveys, the distance between boreholes may be of the order of 1 km.

A major advantage of the cross-hole survey is that high-frequency sources can be used and introduced to geological horizons at depths inaccessible from surface surveys owing to the attenuation of the high frequencies near the surface. Consequently, the resolution possible using this method is much better than with either surface or VSP surveys. A major disadvantage in the oilfield situation is the requirement to have simultaneous access to two boreholes, especially if they are part of a producing field. In engineering surveys, cross-hole boreholes are usually drilled specifically for the survey, and the cost of drilling the holes has to be considered as part of the overall expense of the survey. Further details of cross-hole surveys are given, for example, by Stewart (1991), Tura *et al.* (1994) and Lines *et al.* (1993), and of the data processing methods by Hatton *et al.* (1986) and Sandmeier (2007).

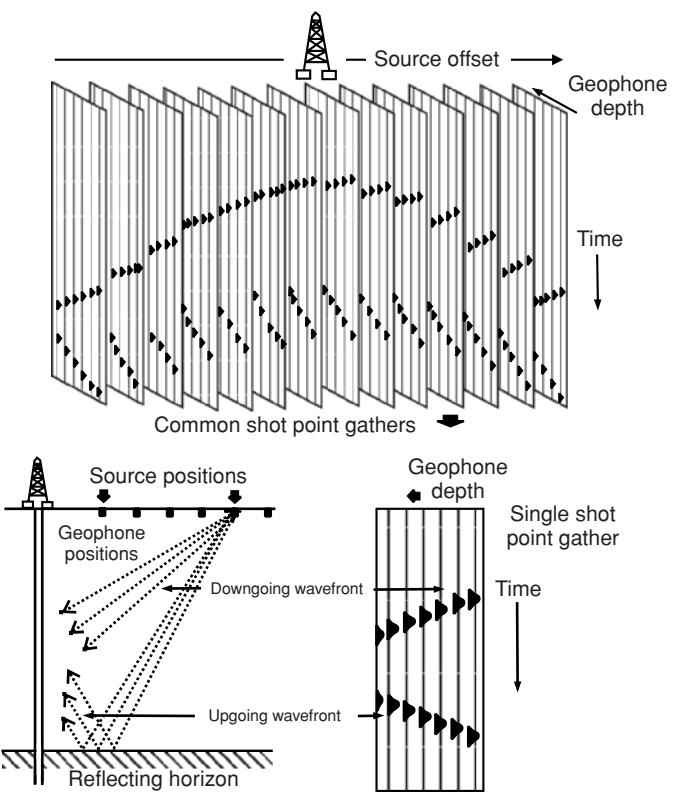


**Figure 6.15** Multilevel walkaway VSP survey schematic and shot-point gathers. After Ahmed *et al.* (1986), by permission.

### 6.3 Reflection data processing

There are three principal stages in seismic data processing: deconvolution, stacking and migration. In addition, there are many auxiliary processes that are necessary to improve the primary processes. While maintaining a particular sequence of processing is essential for the principal stages, other ‘commutative’ processes can be undertaken at any stage; ‘commutativity’ means that the final results can be achieved irrespective of the order in which the processes are undertaken. The success of an individual process is dependent not only on the choice of most appropriate parameters, but also on the effectiveness of the processing stages already completed (Yilmaz, 2001). Conventional data processing is based upon certain assumptions. Many of the secondary processes are designed to make data compatible with the assumptions of the three primary processes (Yilmaz, 2001):

- Deconvolution assumes a stationary, vertically incident, minimum-phase source wavelet and reflectivity series containing all frequencies, and which is noise-free.
- Hyperbolic move-out is assumed for stacking.
- Migration is based on a zero-offset (primaries only) wavefield assumption.

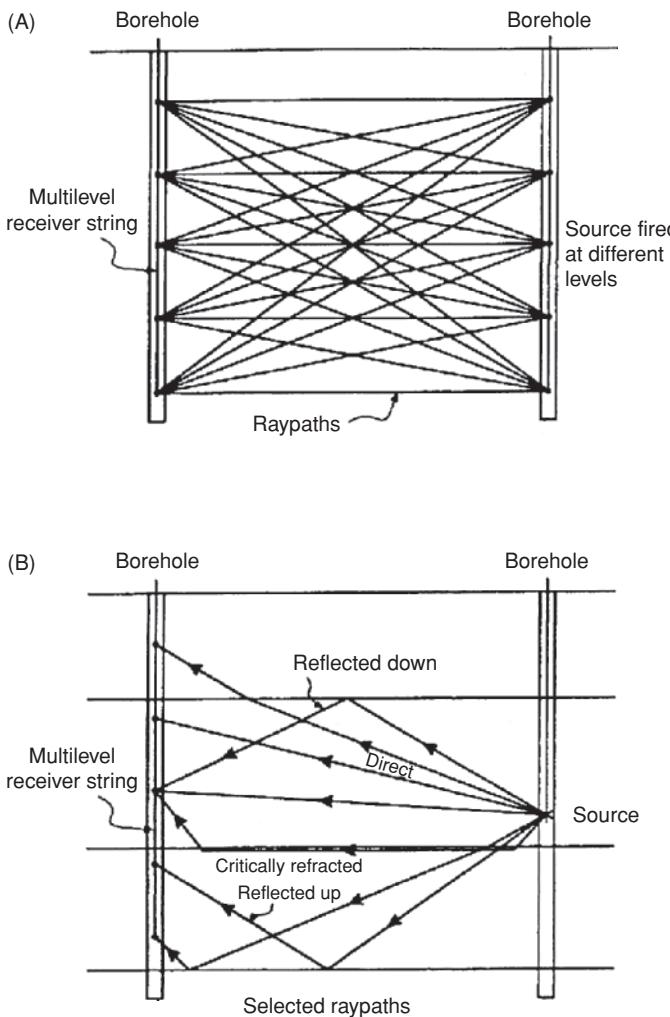


**Figure 6.16** Cross-hole surveying. (A) Raypaths from a source fired at different levels, and (B) from a single source position, into a multilevel string of receivers.

Although these assumptions are not exactly valid, drilling results have confirmed the accuracy of the processing, thus demonstrating the validity of these methods. This is also true because the various processes are in themselves robust and their performance is relatively insensitive to the underlying assumptions.

The following sections are designed to provide a brief overview of the main seismic data processing stages required to convert raw data into an interpretable seismic record. The main stages in data processing are shown in Figure 6.17 and are described briefly in turn. Seismic data processing has been discussed much more fully by Hatton *et al.* (1986) and by Yilmaz (2001), for example.

### 6.3.1 Preprocessing

#### 6.3.1.1 Demultiplexing

Signals received from detectors are digitised at small increments in time, known as the *sampling interval*. In large-scale seismic surveys, this may be 2 ms or 4 ms over a total two-way travel time range

#### Field tapes and Observer's log

1. Reprocessing
  - Demultiplexing
  - Reformatting
  - Editing
  - Geometric spreading correction
  - Set-up of field geometry
  - Application of field statics
2. Deconvolution and trace balancing
3. CMP sorting
4. Velocity analysis
5. Residual statics corrections
6. Velocity analysis
7. NMO correction
8. DMO correction
9. Inverse NMO correction
10. Velocity analysis
11. NMO correction, muting and stacking
12. Deconvolution
13. Time-variant spectral whitening
14. Time-variant filtering
15. Migration
16. Gain application

**Figure 6.17** Basic data processing flowchart. After Yilmaz (2001), by permission.

of 6–7 seconds. For higher-resolution surveys the sample interval may be reduced to 0.25 ms, and in very-high resolution, such as in single-channel marine engineering surveys using pingers, the sample interval may be as short as 15 µs.

The format in which the data are stored is usually the industry standard SEG (SEG stands for Society of Exploration Geophysicists). There are a number of recognised versions such as SEG-B, SEG-D and SEG-Y; the latter format was revised in 2002 (Rev.1) and SEG-D was revised (Rev. 2.1) in 2006. Details of SEG formats are available through the SEG website ([www.seg.org](http://www.seg.org)) under Technical Standards. The UK Offshore Operators Association (UKOOA) also produces standards for tape storage.

The recorder stores data in multiplexed time-sequential form, where the record contains the first sample from each trace (trace 1, sample 1; trace 2, sample 1; trace 3, sample 1; . . . last trace, sample 1; then trace 1, sample 2; trace 2, sample 2; etc.). While this is convenient for recording purposes, it is not so for processing. Consequently, the order of samples is changed by demultiplexing from time-sequential order to trace-sequential order (trace 1, all samples in order; trace 2, all samples in order, etc.). In this format

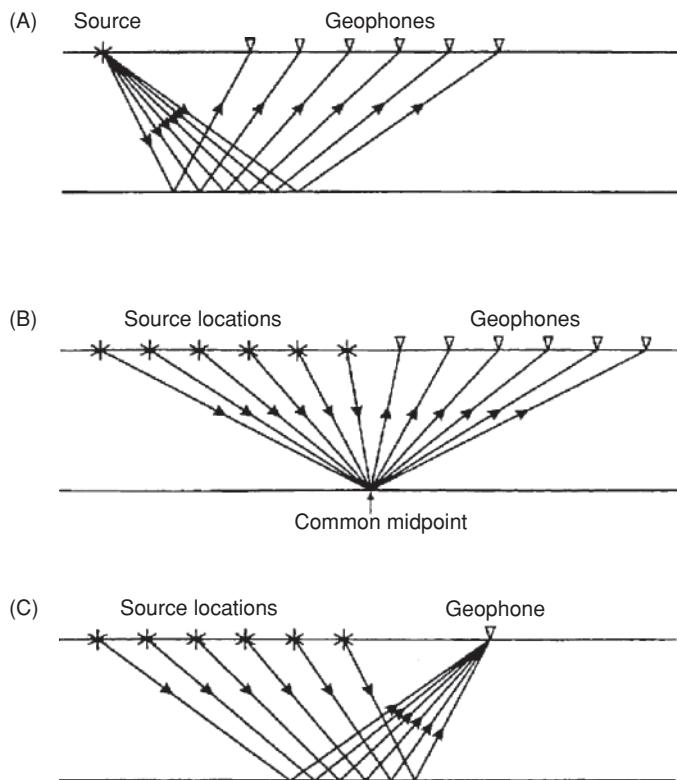


**Figure 6.18** Layouts for (A) a common-shot gather; (B) a common midpoint gather; and (C) a common receiver gather.

all the samples for one trace are contained in one block and can be managed as a discrete dataset very easily. The recognised format of demultiplexed data is SEG-Y, which is supposed to be universally compatible. However, in engineering seismology, manufacturers of seismographs have developed instruments that follow the SEG-Y format but in their own modified forms, which can cause problems when transferring data to processing software. Individual data processing houses demultiplex data to the form of SEG-Y that is most appropriate for their processing system. Further details of SEG formats have been given by Hatton *et al.* (1986). However, commercially-available software exists that purports to be able to transfer any format into any other format.

Once into trace-sequential format, the traces recorded from a single shot (Figure 6.18A) can be displayed as a *common shot gather*, for example. This is the standard display of a seismic record on an engineering seismograph. Traces pertaining to the same midpoint on a reflector can be collated as a *common midpoint gather* (Figure 6.18B; see also Figure 6.3). Traces recorded at the same receiver but from different shot locations can be collated as *common receiver gathers* (Figure 6.18C).

### 6.3.1.2 Editing

Once the data have been demultiplexed, they can be edited to remove dead traces (i.e. those containing no information) or those with monocyclic waveforms caused by electronic interference (e.g. a sinusoidal waveform with constant amplitude and wavelength),

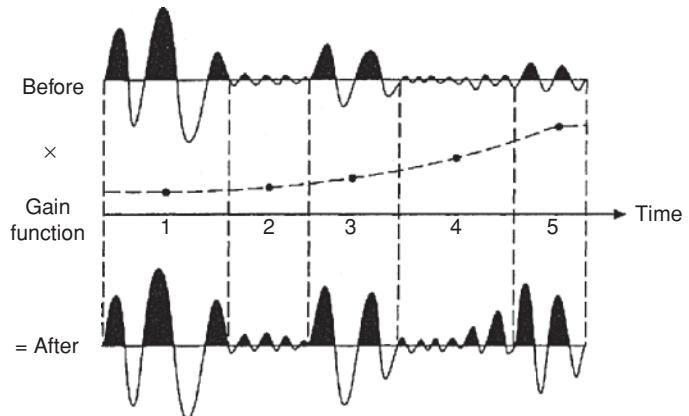


**Figure 6.19** The application of a time-varying gain function to a waveform exhibiting spherical divergence, in order to recover signal amplitudes at later travel times. Gain functions are applied in discrete windows (labelled 1 to 5 shown here).

to reverse the polarity of traces recorded the wrong way around, or those with excessive noise. Editing effectively is cleaning the dataset of bad traces that would otherwise pollute the quality of the remaining data if used in subsequent data processing.

### 6.3.1.3 Gain recovery

In Section 4.4.1, it was explained how energy is lost as a seismic wave travels away from its source by geometric spreading or spherical divergence. As the rate of energy loss can be calculated, it can be compensated by applying a gain function to the data in order to restore the signal amplitudes with increasing two-way travel times. Just as geologically significant reflection signals are amplified by the application of a gain function, so too is noise (Figure 6.19); this is a disadvantage of the process.

### 6.3.2 Static corrections (field statics)

Static corrections ('statics') are made to take into account the effect on travel times of irregular or changing topography and of near-surface velocity variations such as in the weathered layer (Cox, 1999). This has been discussed briefly in Section 5.5.6. Indeed, the application of statics represents the most significant challenge to improving the resolution of land seismic reflection data (Ait-Messaoud *et al.*, 2005). In the preceding descriptions of survey layouts, it has been assumed that the source and receivers are all located at the ground (or water) surface. While this may be true of seismic surveys using an impact or vibrator source into a spread of surface-laid geophones, in many cases the source and/or the detectors may be located at different levels within the ground. To compensate for the different lengths of ray paths associated with a buried source to a spread of geophones over an irregular topography, corrections may have to be applied so that the processed data refer to a specified datum that is taken to be horizontal and to contain no lateral variations in seismic velocity. This process of referring to an arbitrary datum is also known as *datuming*. If these adjustments are not made, reflections on adjacent traces may be shifted in time,

producing irregular and incoherent events. As these adjustments are applied to a fixed source–receiver geometry for a given survey, they are known as static corrections or *field statics*.

In addition to the source–receiver geometric corrections, adjustments to travel times also have to be made to account for the near-surface weathered zone in land reflection surveys. Seismically this weathered zone refers to the portion of the subsurface above the water table where pore spaces are filled by air rather than water. The seismic weathered layer does not necessarily conform to the depth of geological weathering. This layer may exhibit anomalously low velocities (from 150 to 800 m/s) and hence is often referred to as the *low-velocity layer* (LVL). Smaller-scale seismic refraction surveys are commonly undertaken in order to determine the thickness and velocity of the weathered zone. This information is used to determine the appropriate depths at which the shots should be placed below the base of the weathered layer, and to provide the travel-time corrections at each detector position in the main reflection survey.

It is important to consider the spatial consistency of any near-surface model derived throughout a survey area before computing statics corrections. Otherwise mis-ties between intersecting reflection lines may be introduced by inconsistent selection of appropriate statics. It is not currently feasible for the low-velocity layer to be defined precisely seismically. Consequently, errors or inaccuracies remaining in the data are known as *residuals*. These may lead to a reduction in the coherence of individual reflection events on seismic sections. A specific process of *residual static analysis* is undertaken during the pre-stack data processing to refine the statics corrections. Such processing can lead to substantial reduction in trace-by-trace jitter of individual reflection events.

The various static corrections, which are described in turn in the following three sections, have been reviewed succinctly by Marsden (1993a,b,c). For more detailed discussions, refer to Cox (1999) and the special set of papers on statics in *The Leading Edge* (February 2009).

### 6.3.2.1 Source-receiver geometry

In a survey undertaken over an irregular surface, the differences in elevation of the source and the individual receivers have to be taken into consideration in order to compensate for the differences in travel times caused by the irregular topography. Given the situation shown in Figure 6.20A, a time correction can be calculated such that the final travel times then refer to a plane datum. The travel time taken from a reflector to a given geophone will be delayed by the difference in elevation divided by the seismic velocity of the near-surface layer. The greater the elevation of the geophone relative to the datum, the larger will be the time delay. Similarly, the time delay associated with a shot location above a given datum is simply the distance of the shot above the datum divided by the layer velocity. The total time delay due to elevation is given simply by the sum of the time delays of the shot and those associated with each geophone. The actual expressions for the time correction are shown in Box 6.2. The assumption is usually made that the downgoing and upgoing raypaths are virtually vertical.

An estimate of the average near-surface velocity can be obtained by measuring the uphole travel time from the shot to a geophone at

the surface immediately above. As the shot depth ( $h$ ) is known, and the uphole time ( $t_{uh}$ ) is measured, the average near-surface velocity can be calculated very simply ( $V = h/t_{uh}$ ).

Velocities derived from uphole shots are never likely to be exactly appropriate for the elevation component of field statics, as they are still averaged values. Similarly, the average velocity defined over too large a vertical shot interval may not be locally representative. This is especially true in cases where the velocities change markedly over vertical distances significantly shorter than the vertical shot interval.

Only one uphole survey may be undertaken in an entire survey area, in which case the velocities obtained for the near-surface materials may be totally unrepresentative away from the uphole survey hole. This applies particularly where Quaternary deposits are present in the near-surface.

Velocity can also be determined using refraction statics (see Section 6.3.2.3) and *data smoothing statics* methods. The latter method is automated and relies on statistical means of minimising the jitter in reflection events between adjacent traces.

For small-scale seismic surveys for engineering or environmental applications, an individual seismic trace is obtained from each geophone. However, for large-scale hydrocarbon exploration, often the output from a whole array, comprising two parallel lines of 12 geophones deployed over a horizontal distance of  $\sim 46$  m, is used to give one output trace at a location marked by the centre of gravity of the array (Figure 6.21). If the ground surface is uneven across this spread and the weathered layer has lateral and vertical heterogeneity, then the upgoing waves will arrive at the individual geophones at slightly different times. When the signals from all the geophones are aggregated to form the resulting output trace, the frequency content is often lower than that of each of the individual input signals and with a lower amplitude. This is known as the *(intra-)array effect* and degrades the quality and resolution of the seismic data (Ait-Massaoud *et al.*, 2005). This has led WesternGeco to develop its innovative Q-land system that effectively digitises the outputs from each geophone individually, rather than from a group of geophones. This effectively increases the number of live channels for a hydrocarbon exploration land survey from perhaps 4000–5000 to more than 20,000. This ‘point-source, point-receiver’ approach increases data volume by an order of magnitude. Given the appropriate computing power to handle this massive increase in data, there is a significant improvement in the quality and resolution of the recorded data.

If the twin-parallel geophone array system is deployed, as described above, the assumption that the geophones are recording a wave travelling from the reflector vertically towards the ground surface is not valid with respect to the first arrivals. These will have travelled from refractors much closer to the ground surface and will propagate more horizontally. Consequently, there will be a dispersion within the refracted waves as they pass through the geophone array. This will result in the quality of the summed first break from the 24-geophones into one trace being reduced. This is especially true if there is a deep weathering layer with strongly contrasting near-surface velocity variations, such as in areas with deep sand. It is thought (Palmer, 2009) that in some cases the inhomogeneities within the surface soil layer are as important a source of intra-array statics as variations in topography and thickness of the weathered

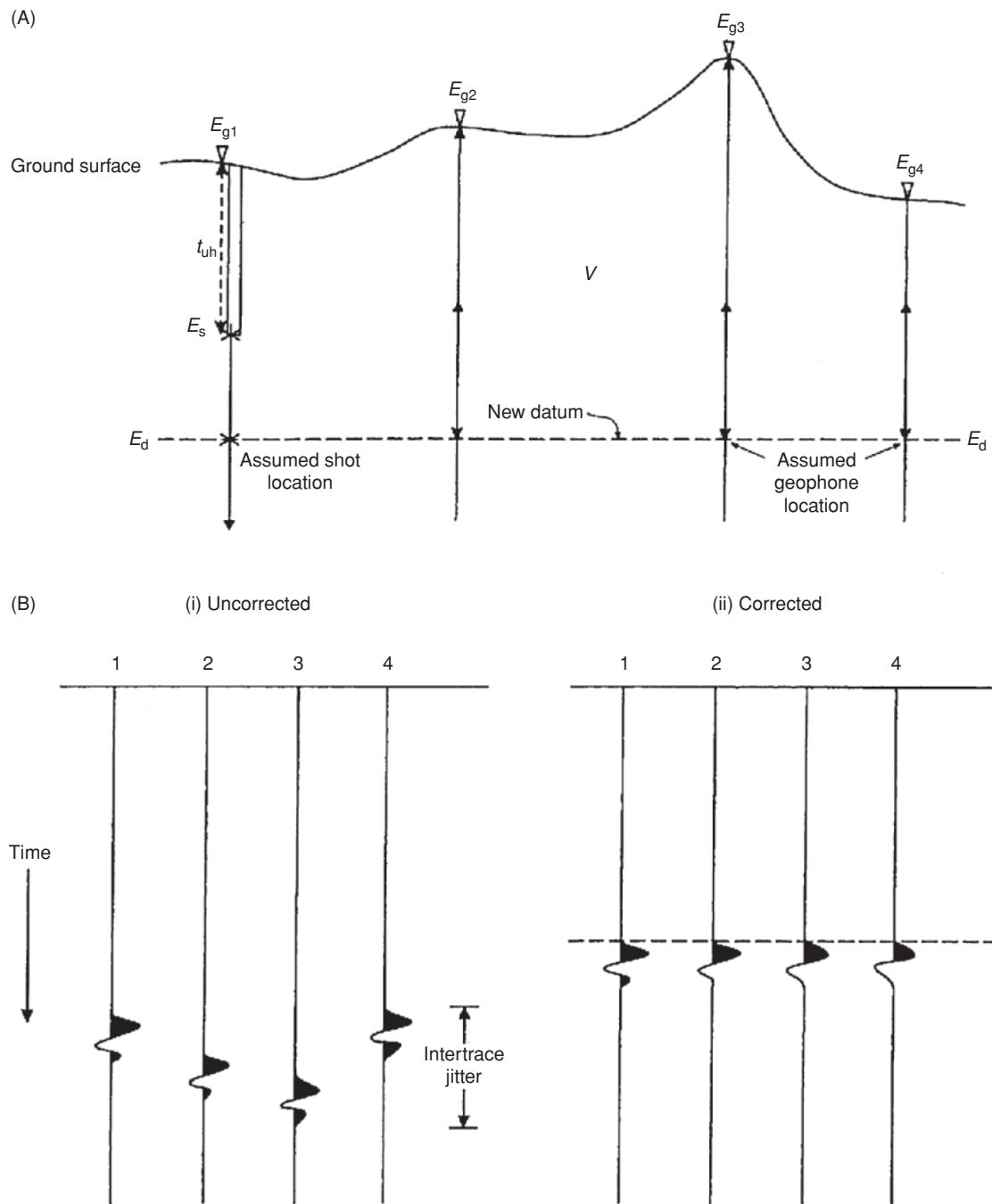


**Figure 6.20** (A) Field static corrections to account for topography.  $E$  and  $E_d$  are the elevations of geophones and the new datum, respectively. (B) (i) Uncorrected traces showing the amount of inter-trace jitter, and (ii) traces corrected for differences in elevation shown in (A).

layer. It is important, therefore, to ensure that the designs of the source-receiver and geophone array geometries are optimised to produce the best quality first arrivals.

Marine statics refer to the depth of the shot and the streamer below a given datum level – not the ambient sea-level, which fluctuates with the tide. For example, a typical level in the UK is Ordnance Datum (Newlyn). Particularly in high-resolution engineering surveys, tidal corrections need to be made accurately since the water depth will change over a tidal cycle.

An additional correction is sometimes made to allow for the seabed topography. If a depression exists in the seabed, the additional depth of water over this provides a time delay that is manifest as a downwarping in deeper planar reflection events. For instance, a depression 7.5 m deep will add a time delay of 1.67 ms (assuming a contrast in P-wave velocity between seawater and seabed sediments of 300 m/s).

In single-channel marine seismic surveys in shallow water, it is sometimes necessary to allow for the offset between the hydrophone

**Box 6.2 Static correction for elevation (see Figure 6.20)**

The time delay due to the difference in elevation between source and datum ( $t_s$ ) is given by:

$$t_s = (E_s - E_d)/V.$$

The time delay due to the difference in elevation between a given geophone and datum ( $t_g$ ) is given by:

$$t_g = (E_g - E_d)/V.$$

Total static correction due to elevation ( $t_e$ ) is given by:

$$t_e = t_s + t_g$$

Velocity in the near-surface can be calculated from the measurement of the uphole travel time ( $t_{uh}$ ) and the depth of the shot ( $h$ ), such that:

$$V = d/t_{uh}.$$

$E_s$ ,  $E_g$  and  $E_d$  are the elevations of the shot, any geophone and the reference datum respectively.

streamer and source. This is because, with the shallow depth, the offset results in significant differences in the total ray path length compared with normal incidence. As all reflection events are considered assuming normal incidence, a time reduction is necessary to produce accurate two-way travel times to reflection events. This correction can also apply to constant-offset seismic reflection profiling on land, especially when the optimum offset is comparable to the depth to the first reflector. An alternative method that avoids the problems of source-receiver geometry in marine surveys is to determine the elevation of the seabed using echo-sounding. Distances to reflectors are determined from the two-way travel times using an assumed reduction velocity relative to the seabed.

**6.3.2.2 Feathering**

A further consideration in marine seismic reflection profiling is the position of the streamer relative to the source at any given time. When significant cross-currents occur, the streamer can drift off track to a considerable degree. This deviation from the boat track is known as *feathering*, and the angle of the streamer to the boat track is the *feathering angle*. However, with streamers up to 6 km long, they do not keep straight. Consequently, the positions of the tail buoy and mid-streamer compasses need to be logged at regular time intervals. This information is needed to determine the appropriate common midpoints and subsurface coverage (see also Section 4.6.2).

**6.3.2.3 Weathered layer**

Of particular importance to seismic reflection surveying is accurate determination of field statics. In addition to elevation corrections, consideration has to be given to the presence of a near-surface weathering zone that may have anomalously low velocities and can exhibit considerable variation in seismic velocities.

The weathering zone, when present, can range in thickness from only a few metres to several hundreds of metres. When this zone is only thin, source shots can be located relatively easily beneath the weathered layer. When the zone is very thick, this is no longer feasible owing to the costs of having to drill such deep shot holes and to the reduction in production rates that this would cause. Consequently, it is necessary to calculate the delay-time effect of the weathered zone.

Incorrect evaluation of the weathering layer can result in corruption of stacking (see Section 6.3.4) and may even introduce spurious features into deep reflectors. The importance of correct determination of the weathering layer has led to the development of a host of different methods (e.g. Hatherley *et al.*, 1994) to account for the weathering layer with increasing sophistication, such as 2D refraction tomography (e.g. Docherty, 1992). Refraction statics are an important method of investigating the weathering layer, and special refraction surveys are used.

While many of the different methods produce virtually identical statics corrections, the differences in the speed of computation can be very marked. For industrial applications, rapidity of calculation is an important factor, and methods that produce the correct best estimates of statics corrections in the least time are obviously preferred. As an example, Marsden (1993b) described a test undertaken by Amoco in which a comparison was made between using the slope/intercept method and refraction tomography. The former method took three days to calculate, whereas the tomographic method took only three hours. One example of a rapid method of statics determination has been given by Zanzi and Carlini (1991). They demonstrated that if the calculations are undertaken after Fourier transformation of reflection data, then the calculation process can be substantially reduced without loss of accuracy.

**6.3.3 Convolution and deconvolution**

An initial waveform ( $W$ ) propagating into the ground is filtered by layers with different acoustic impedances (which form a reflectivity time series denoted by  $R$ ) through which the signal passes, resulting in a modified waveform ( $S$ ) observed on a seismogram. This ‘convolution’ process is denoted by  $S = W^* R$ , where  $*$  represents the process of convolution. The seismic method generates a waveform whose initial shape should be known and the resulting seismogram  $S$  is measured. The principle of this process is shown in Figure 6.22. The only unknown is  $R$ . In order to unravel the seismogram to obtain this time series of ground properties, the seismogram needs to be ‘deconvolved’. The main complication is that the time series  $R$  consists not only of primary reflection events, but also reverberation, ghosting, diffractions, multiples and noise. Consequently the deconvolution process requires methods of removing or suppressing unwanted signals and of compressing the initial waveform to as

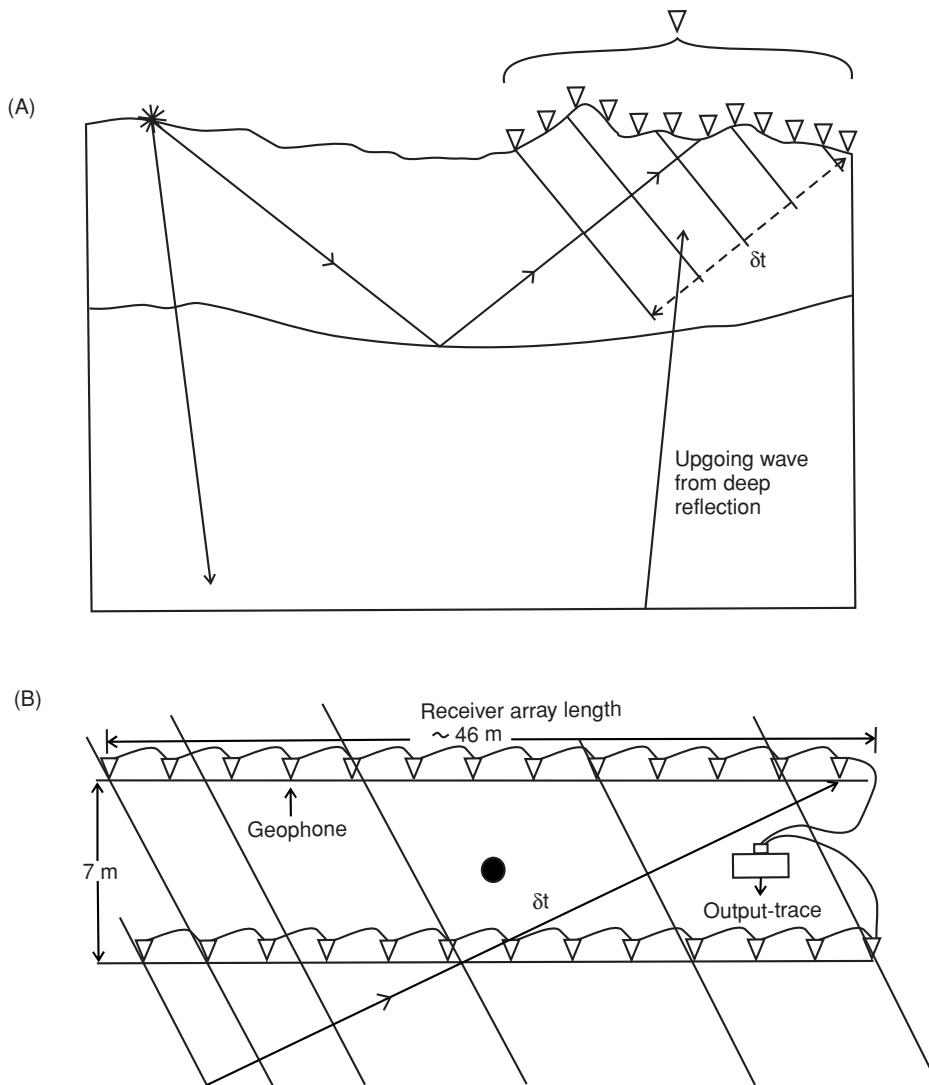


**Figure 6.21** (A) Location of a geophone spread over uneven ground with near vertical upgoing waves from deep reflectors, and more horizontally directed near-surface first arrivals showing a spread of arrival times ( $\delta t$ ) across the array. (B) Strings of geophones hard-wired together average the individual sensor measurements and deliver one aggregated output trace whose location is denoted by the centre of gravity of the array (solid dot). A spread of arrival times ( $\delta t$ ) is shown illustratively. Modified from Ait-Messaoud *et al.* (2005).

close to a spike (Dirac) pulse as possible. By so doing, the geologically significant components of the time series  $R$  may then become clearer.

Deconvolution is an analytical procedure to remove the effects of previous filtering such as that arising from convolution. There are a number of different deconvolution processes:

- *Dereverberation* or *deringing* refers to the process by which ringing associated with multiple reflections within a water layer or other near-surface layer is strongly attenuated. Specific filters can be designed to remove certain simple types of reverberation, such as the Backus filter.
- *Deghosting* is designed to remove the effects of energy that leaves a source and travels upwards and is reflected back down to the receiver. Ghosting is caused by signals bouncing off the under-

surface of the water/air interface or the weathered layer where its lowermost boundary is well defined.

- *Whitening* (trace equalisation) adjusts the amplitudes of all frequency components to be the same within a bandpass. The effect of this is to make the amplitudes of adjacent traces comparable over some predetermined time interval. This may have the effect of worsening the signal-to-noise ratio in situations where the signal amplitude is already weak and where the window length across which the trace equalisation is applied is inappropriate.

The effect of each of the three processes described above is to shorten the pulse length on the processed seismograms, thereby improving the vertical resolution. The ultimate objective, which cannot as yet be achieved, is the compression of each waveform into

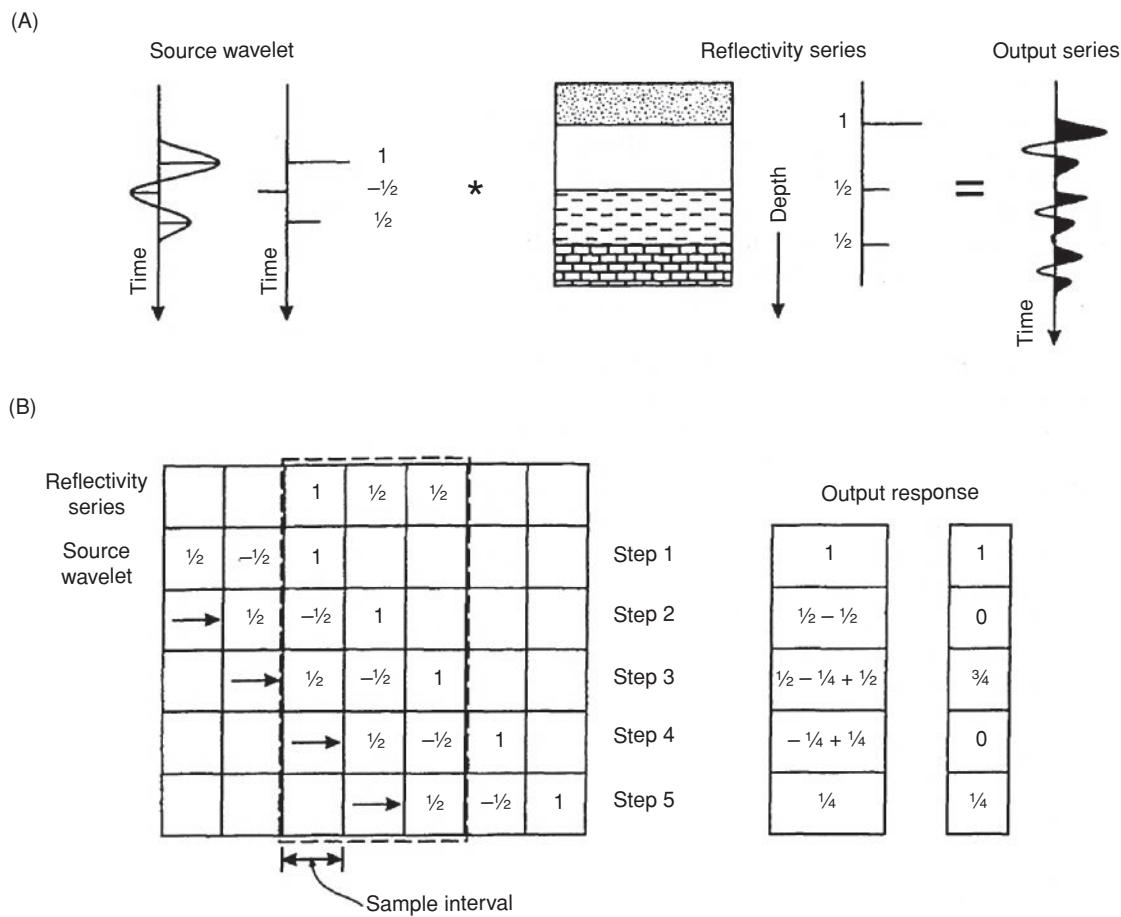


**Figure 6.22** The principle of convolution:

Step 1: Convolve source wavelet and reflectivity series by multiplying the first sample of the source wavelet (1) by the first component of the reflectivity series ( $\frac{1}{2}$ ) to give the first constituent of the output response.

Step 2: Move the source array on one sample and convolve; hence  $(1 \times \frac{1}{2}) + (1 \times -\frac{1}{2}) = \frac{1}{2} - \frac{1}{2} = 0$ .

Step 3: Move the source wavelet array on one sample and convolve; hence  $(\frac{1}{2} \times 1) + (\frac{1}{2} \times -\frac{1}{2}) + (1 \times \frac{1}{2}) = \frac{1}{2} + (-\frac{1}{4}) + \frac{1}{2} = \frac{3}{4}$ .

Step 4: Move the source wavelet array on one sample and convolve; hence  $(\frac{1}{2} \times -\frac{1}{2}) + (\frac{1}{2} \times \frac{1}{2}) = -\frac{1}{4} + \frac{1}{4} = 0$ .

Step 5: Move the source wavelet array on the sample and convolve; hence  $(\frac{1}{2} \times \frac{1}{2}) = \frac{1}{4}$ .

a single spike (Dirac pulse,  $\delta$ ) such that each reflection is also a simple spike. By so doing, it should be feasible to determine the reflectivity series that defines the subsurface geological stratigraphic sequences. The deconvolution operator (or inverse filter) ( $I$ ) is designed by convolving it with a composite wavelet  $W$  to produce a spike pulse (i.e.  $I^*W = \delta$ ); see also Box 6.3. The designed inverse filter ( $I$ ) can then be convolved with the seismogram trace  $S$  to produce the reflectivity series  $R$  (i.e.  $I^*S = R$ ). The type of filter that best achieves (as judged statistically) the reduction of the wavelet to a spike is known as a *Wiener filter*. This stage of deconvolution is referred to as *spiking* or *whitening deconvolution*. The latter name refers to the fact that in a spike, all the frequency components have the same amplitude.

When a deconvolution operator is changed as a function of travel time, instead of remaining the same for all travel times, the process is known as *time-variant deconvolution*. The need for such a time-variant function is that the frequency content of a wavelet changes along its raypath because of the preferential attenuation of higher-

frequency components by the ground. Consequently, the wavelet increases in wavelength with travel time, i.e. the bulk of the energy occurs at decreasing frequencies with increasing travel time.

A method of removing multiples is to predict when they might be expected and then remove them. This is the process of *predictive deconvolution*. By knowing the arrival times of particular primary events, the arrival times of multiples can be predicted. For this method it is assumed that there is no systematic distribution of subsurface reflectors, and that the composite waveform from an active seismic source has the bulk of its energy at the start of the pulse rather than somewhere down the tail of the waveform.

The use of predictive deconvolution leads on to a further process for identifying key primary or even secondary reflection events, namely *correlation techniques*. A multiple is a duplication of the primary reflection and hence should have the same or very similar characteristics as the primary event. For instance, the wavelet pulse shape associated with the seabed reflection is also evident in the first and successive multiples of the seabed reflection. If the wavelet

**Box 6.3 Deconvolution processes**

A source wavelet ( $W$ ) convolved (indicated by  $*$ ) with a reflectivity series ( $R$ ) produces the observed seismic trace ( $S$ ), which is denoted:

$$R^* W = S. \quad (1)$$

A deconvolution operator ( $D$ ) can be designed such that when it is convolved with the source wavelet ( $W$ ) it produces a spike output ( $\delta$ ):

$$D^* W = \delta. \quad (2)$$

As seismic data processing aims to image the subsurface geology, the objective of the deconvolution process is to unwrap the seismic trace to reveal the reflectivity series ( $R$ ):

From Equation (1) above,  $D^* S = D^* R^* W = D^* W^* R$ .

From Equation (2) above,  $D^* W^* R = \delta^* R = R$  (as  $\delta = 1$ ).

shape of the seabed reflection is isolated, it can be moved along each trace and compared against the remaining seismogram. Where its shape is present in the seismogram at later travel times, the degree of correlation is high (a value of 1 indicates a perfect match). Successive multiples should be evident by having a high correlation coefficient. Correlating one signal against a time-shifted copy of itself is known as *autocorrelation*. Comparing one time series with another to obtain a quantitative measure of similarity is referred to as *cross-correlation*, of which autocorrelation is a special case.

### 6.3.4 Dynamic corrections, velocity analyses and stacking

The most critical parameter in seismic surveying, irrespective of the type or scale of application, is the determination of seismic velocity. It is this factor which is used to convert from the time domain (the seismogram) to the depth domain (the geological cross-section). Consequently, correct analysis of velocities is of vital importance.

In a horizontally layered sequence (Figure 6.23), where each layer has a diagnostic seismic ‘interval’ velocity  $V_i$ , the single-way travel time of a seismic wave through each layer is equal to the layer thickness ( $z_i$ ) divided by the appropriate velocity ( $V_i$ ) (see Box 6.4). Clearly, the two-way travel time is double this time. The overall travel time at normal incidence is thus the sum ( $\Sigma$ ) of all the individual two-way travel times ( $\Sigma(z_i/V_i)$ ). The average velocity  $V'$  is assumed to apply only to specific straight-raypath travel. In the case of normal incidence, the average velocity is simply the total raypath distance divided by total travel time. The weighted-average velocity is termed the root-mean-square (RMS) velocity ( $V_{\text{RMS}}$ ) and applies to horizontal layers and normal incidence. Typically the RMS velocity is a few per cent higher than the average velocity.

**Box 6.4 Definition of velocity analysis terms (see Figure 6.23)**

Interval velocity  $V_i$  = layer thickness  $z_i$ /interval transit time  $t_i$ :

$$V_i = z_i/t_i.$$

Average velocity  $V'$  is total raypath length ( $Z$ ) divided by total travel time  $T_0$ :

$$V' = Z/T_0.$$

The root-mean-square velocity is:

$$V_{\text{RMS}} = \left[ \sum V_i^2 t_i / \sum t_i \right]^{1/2}$$

Two-way travel time of a ray reflected from the  $n$ th interface at a depth  $z$  is:

$$t_n = (x^2 + 4z^2)^{1/2} / V_{\text{RMS}}$$

where  $x$  is the offset distance.

**Dix Formula:** The interval velocity ( $V_{\text{int}}$ ) over the  $n$ th interval is

$$V_{\text{int}} = \left[ \frac{(V_{\text{RMS},n})^2 t_n - (V_{\text{RMS},n-1})^2 t_{n-1}}{(t_n - t_{n-1})} \right]^{1/2}$$

where  $V_{\text{RMS},n}$ ,  $t_n$  and  $V_{\text{RMS},n-1}$ ,  $t_{n-1}$  are the RMS velocity and reflected ray two-way travel times to the  $n$ th and  $(n - 1)$ th reflectors respectively.

Neither of these two statistical parameters should be used uniquely as being diagnostic of the seismic velocity in a given material.

The travel times associated with geophones at large offsets are greater than those at short offsets, by virtue of the increased ray path distances (Figure 6.24). In the case of a horizontal reflector at a depth  $z$  below ground level, the difference in travel time at the largest offset from normal incidence is known as the *normal moveout* (NMO). From traces collated together in a common midpoint (CMP) gather, the same problem arises. The intention is to stack all the traces relating to the same CMP in order to improve the signal-to-noise ratio and thus emphasise the coherent signals at the expense of the incoherent signals minimised by destructive interference. In order to ensure that the stacking process is undertaken accurately, it is important to estimate the correct ‘stacking’ velocity. In the case of horizontal isotropic media, the stacking velocity is the same as the normal move-out velocity. However, when the reflector dips, it is important to carry out *dip move-out* to compensate for dip as well as the finite offset between source and detectors.

The calculation of NMO correction is given in Box 6.5. The larger the offset, the greater will be the NMO correction. The greater the two-way travel time, with a corresponding increase in velocity (as velocity tends to increase with depth as a general rule), the smaller

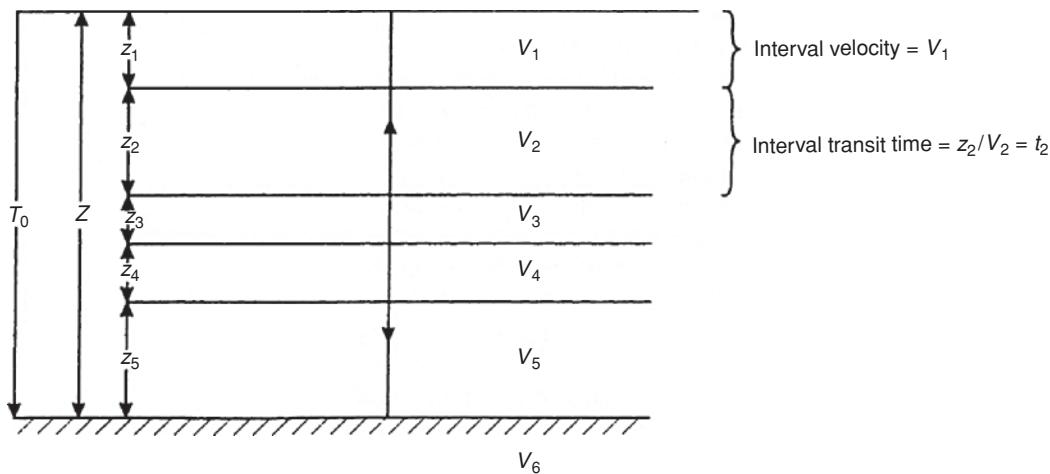


**Figure 6.23** Definition of seismic velocity analysis terms (see Box 6.4). In the example illustrated, the total number of layers ( $n$ ) = 6 and so  $n - 1$  refers to the fifth layer.

will be the NMO correction at a given offset. The rate of increase in NMO correction with greater offset is hyperbolic (see Box 6.5), giving a curved reflection on a CMP gather. As velocity increases with depth, the size of the NMO correction (degree of curvature) decreases, i.e. effectively flattens at greater two-way travel times.

Just as ray paths increase in length with increasing offset from a single shot into a spread of detectors and give rise to normal

move-out, the same situation occurs with the ray paths associated with a common midpoint gather (Figure 6.25). The whole point of acquiring multichannel seismic data, as opposed to single-channel data, is to be able to improve the signal-to-noise ratio and increase the resolution of geologically significant reflection events at the expense of incoherent noise. Consequently, the traces associated with a given CMP can be gathered and stacked. Obviously, in order

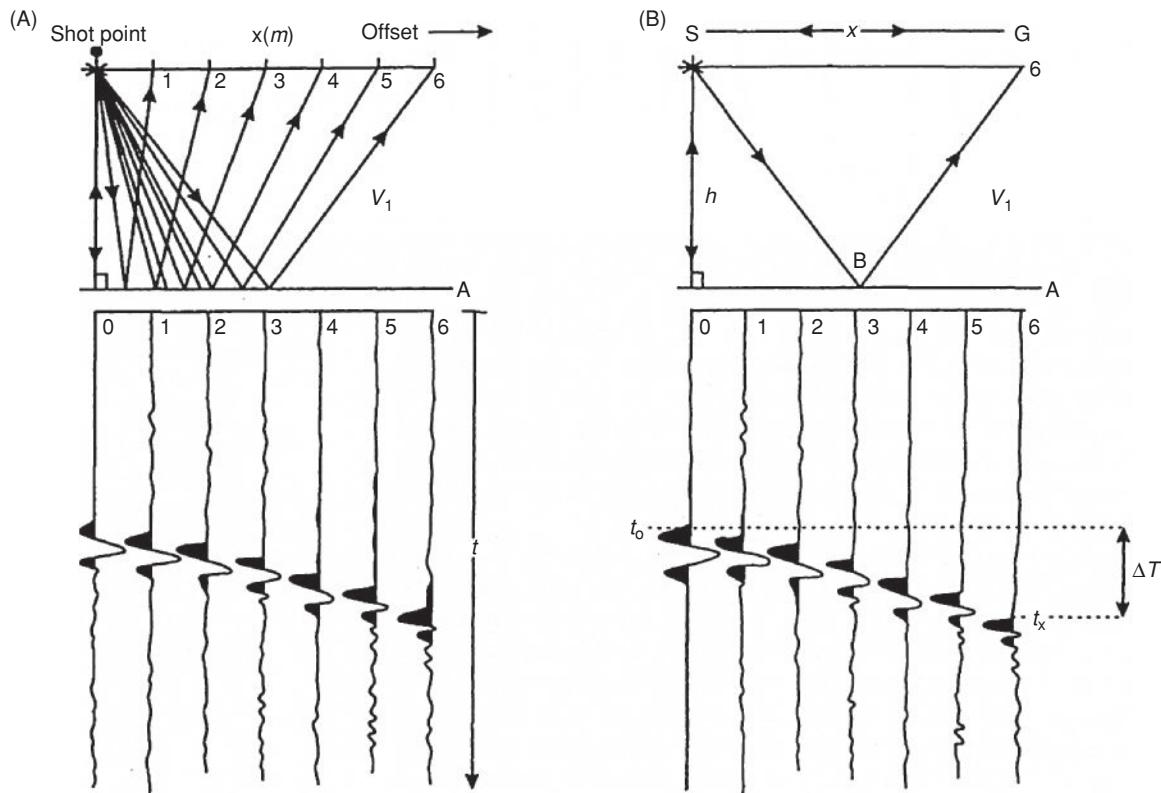


**Figure 6.24** Selected raypaths and corresponding seismic traces illustrating the effect of normal move-out (NMO). After Dohr (1981), by permission.

**Box 6.5** Normal move-out (NMO) correction (Figure 6.24)

For a medium with a seismic velocity  $V$  and a depth to a reflector  $z$ , the two-way travel time S-B-G is:

$$t_x = t_{SB} + t_{BG}$$

The raypath  $SB = BG$  can be determined using Pythagoras' theorem such that:

$$BG^2 = (x/2)^2 + z^2, \text{ so } BG = \{(x/2)^2 + z^2\}^{1/2}$$

The total travel time is thus  $t_x = (2/V) \cdot \{(x/2)^2 + z^2\}^{1/2}$  as time  $= x/V$ . Substituting for  $z$  (from the two-way travel time for S-A-S), we obtain:

$$t_x = (2/V) \cdot \{(x/2)^2 + Vt_0/2\}^{1/2} \quad (1)$$

and

$$t_x^2 = x^2/V^2 + t_0 \quad (\text{where } t_0 = 2z/V). \quad (2)$$

Equation (2) is the equation of a straight line of the form  $y = mx + c$ , where  $m$  is the gradient and  $c$  is the intercept. By plotting a graph of  $t_x$  against  $x^2$ , it can be seen that the gradient  $m = 1/V^2$  and the intercept  $c = t_0^2$ , so  $V$  and  $t_0$  can be obtained.

Equation (1) can be rewritten in hyperbolic form as:

$$(V^2 t^2)/4z^2 - x^2/4z^2 = 1. \quad (3)$$

At zero offset ( $x = 0$ ), Equation (3) reduces to  $t_0 = 2z/V$ .

Equation (3) can be rewritten making time the subject:  $t^2 = 4z^2/V^2 + x^2/V^2$ . In turn this can be expressed in binomial form, such that:

$$t = (2z/V) \cdot \{1 + (x/2z)^2\}^{1/2} = t_0 \{1 + (x/Vt_0)^2\}^{1/2}. \quad (4)$$

By binomial expansion, and limiting the case to small offsets with  $x/Vt_0 \ll 1$ , and with  $t_n$  at  $x = x_n$ , this equation reduces to:

$$t_n \approx t_0 \{1 + \frac{1}{2}(x/Vt_0)^2\}. \quad (5)$$

*Move-out* is the difference in travel time at the two different offsets, such that:

$$t_2 - t_1 \approx (x_2^2 - x_1^2)/2V^2 t_0.$$

In the case of the *normal moveout correction* ( $\Delta T$ ), the difference in times is relative to zero offset ( $x=0$ ), so the last equation becomes:

$$\Delta T = t_x - t_0 \approx x^2/2V^2 t_0.$$

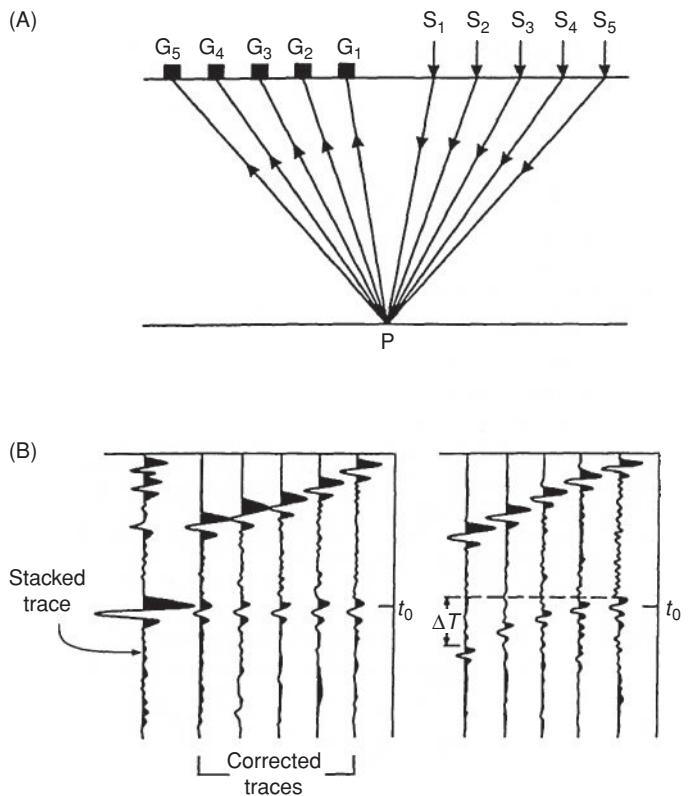


**Figure 6.25** Given the source-receiver layout and corresponding raypaths for a common depth spread, shown in (A), the resulting seismic traces are illustrated in (B), uncorrected (on the right), corrected (in the middle) – note how the reflection events now are aligned – and the final stacked trace on the left. After Dohr (1981), by permission.

to achieve the correct stacking, an appropriate NMO correction needs to be applied for each reflection event down the record. It is possible to determine the RMS velocity to a given reflector by plotting a  $T^2 - X^2$  graph; the gradient of the straight-line segment appropriate for each selected reflection is  $1/(V_{\text{RMS}})^2$ .

The volume of data acquired in modern seismic surveys necessitates an automated method of determining the correct stacking velocities. One such method uses *constant-velocity gathers* (CVGs). Given a CMP gather, it is assumed that the RMS velocity is constant throughout the entire raypath. This RMS velocity is applied to the CMP gather to correct for NMO. A panel of CVGs is produced in which the RMS velocity applied to the CMP gather is increased by a given increment from one CVG to the next (Figure 6.25). Where the correct RMS velocity has been applied, any particular reflection events should appear horizontal. Where the RMS velocity is too low, the reflection, instead of being straight, curves upwards (smiles); where the RMS velocity is too fast, the reflection curves downwards (frowns). By inspection of a panel of CVGs, the correct RMS velocities can be picked for particular reflection events.

Three picked events (labelled A, B and C) are encircled in Figure 6.26. As the amount of NMO decreases with increasing travel time, so too does the sensitivity of the velocity analysis. This can be seen

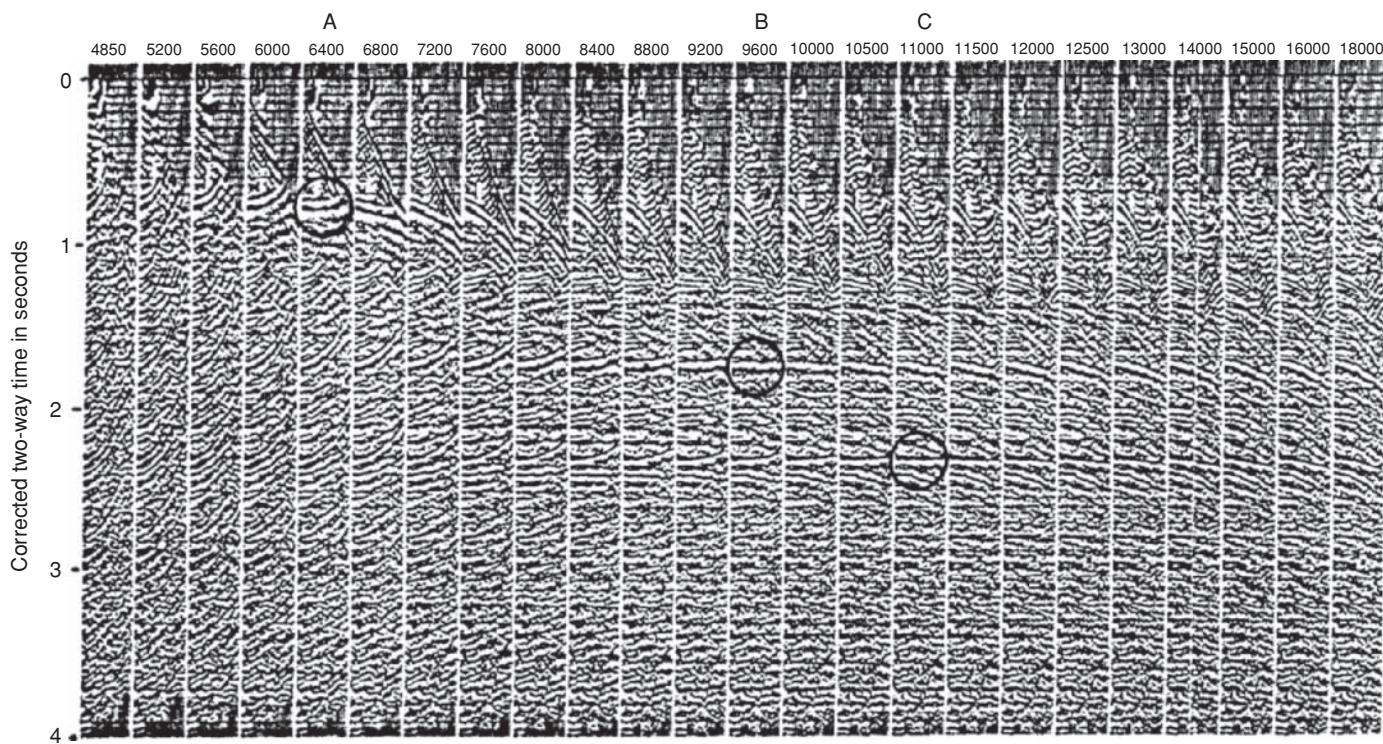


**Figure 6.26** A constant-velocity gather (CVG). The same seismic data are shown in each panel, the only difference being the RMS velocity applied to the data (labelled at the top of panel in ft/s). Three events have been encircled (A, B and C) – see text for details. The two-way travel time (in seconds) and RMS velocity (in ft/s) for the three events are respectively: Event A at 0.8 s, 6400 ft/s; Event B at 1.7 s, 9600 ft/s; and Event C at 2.3 s, 11,000 ft/s. After McQuillin *et al.* (1984), with kind permission from Kluwer Academic Publishers.

by comparing the curvature of the events on panels either side of the ones picked for each of the three events. For event A at 0.8 seconds, the event is flattest for a RMS velocity of 6400 ft/s. The slight upturned tail of the event suggests that even this velocity is slightly too slow. Panels for 6000 ft/s and 6800 ft/s clearly show a smile and a frown respectively. For event B at 1.7 seconds, the amount of curvature on the adjacent panels is much smaller, making the choice of velocity harder. However, for event C at 2.3 seconds, velocities of 10,500 ft/s and 11,500 ft/s appear to be virtually indistinguishable from that chosen (11,000 ft/s). Reflections occurring at shorter two-way travel times will have lower RMS velocities, and those further down the records will have larger RMS velocities. It is thus possible to pick the correct RMS velocities for all principal reflection events on a given CMP gather to produce a vertical velocity profile.

It is usual to display the velocity information as a scaled *velocity semblance spectrum* (Figure 6.27). *Semblance* is a measure of the coherence of the stacking process; when it equals 1 it implies perfect selection of the normal move-out correction. *Coherence* is a measure of the degree of fit of a theoretically derived hyperbolic curve at a given travel time for a chosen RMS velocity. Scaled semblance profiles are usually plotted alongside any velocity spectrum (Figure 6.27).

It is normal practice to provide velocity analyses at regular but widely separated intervals along a seismic reflection line, so as to ensure that the stacking is undertaken properly. For example, ve-

locity analyses may be undertaken every 3 km along a survey line while shot intervals are as small as 50 m or less. By compiling a display of velocity profiles along a section (Figure 6.28), it is possible to identify (1) anomalous velocity picks due to incorrect velocity analysis, and (2) zones where velocity changes are associated with significant geological structures. When particular marker horizons have been identified, it is possible to carry out *horizontal velocity analysis* (HVA), by which velocity information is obtained at every CMP position along a survey line. HVA is usually undertaken only where there are considered to be significant and important velocity changes due to geological structure. The improved knowledge of the lateral velocity changes can be input into the stacking process to improve the overall visualisation of the structure being imaged (Figure 6.29).

Two further methods of velocity analysis have been developed. One is the use of *travel-time tomography* and the other is *pre-stack depth migration* (PDM) (Lines *et al.*, 1995; Whitmore and Garing, 1993). The objective of travel-time tomography is to match modelled travel times obtained by ray tracing to interpreted travel times produced prior to stacking. The main difficulty with the method is obtaining reliable travel-time measurements. Plane-wave pre-stack depth migration is based on the principle that plane-wave depth migration should be independent of the angle of plane-wave illumination, if the velocities are correct. PDM uses an estimate of the velocity field to map plane-wave gathers into depth for each of the

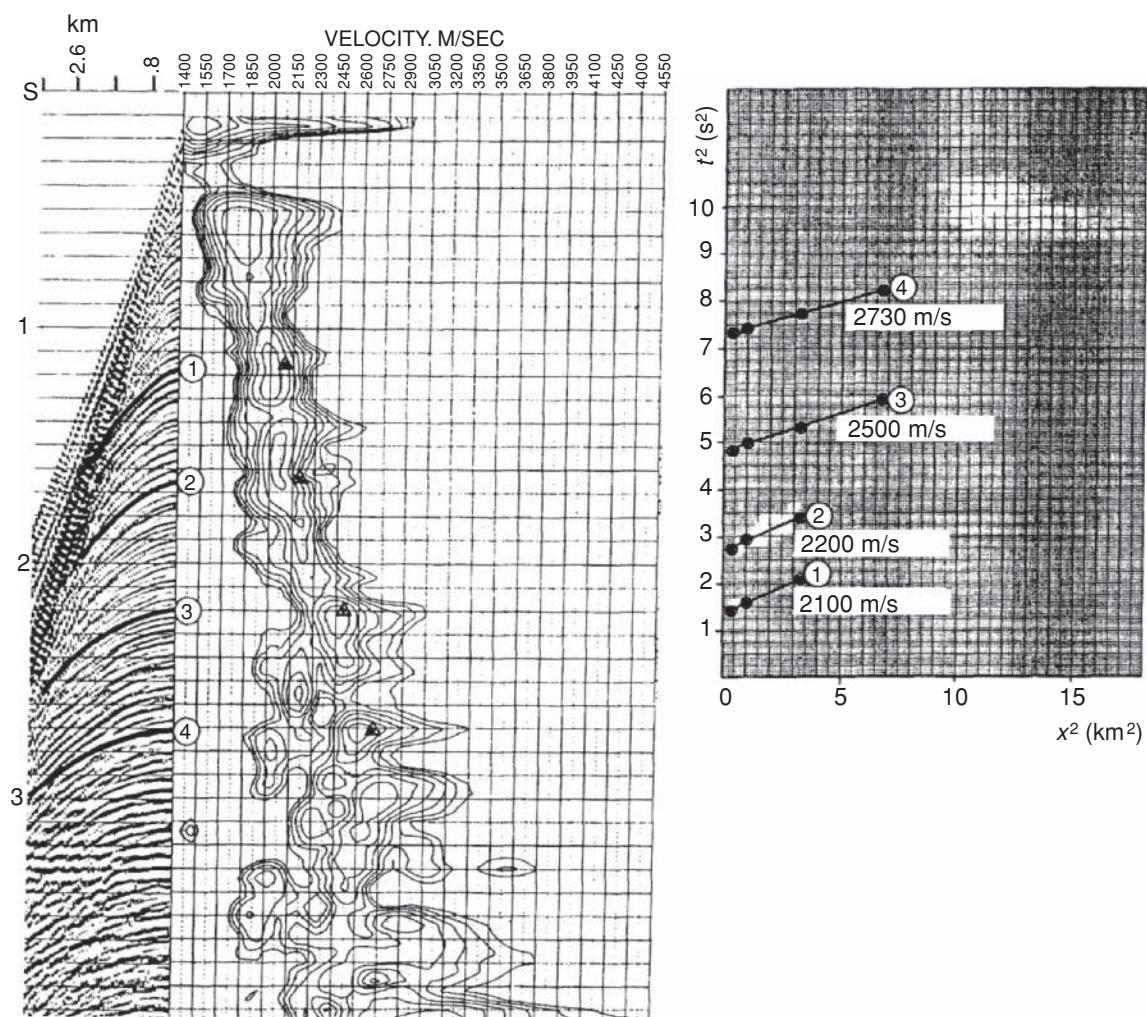


**Figure 6.27** The  $(t^2 - x^2)$  velocity analysis applied to a CMP gather. The triangles on the velocity spectrum (left panel) represent velocity values derived from the slopes of the lines shown on the graph at the right. From Yilmaz (2001), by permission.

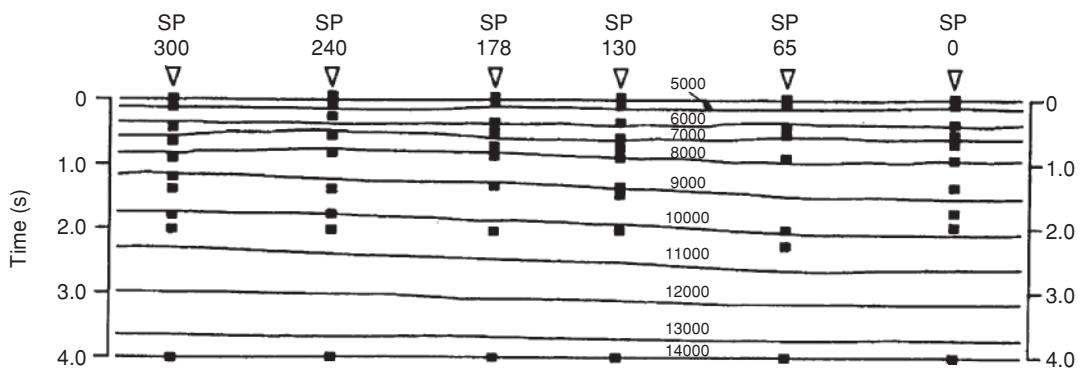


**Figure 6.28** Constant-velocity profile along a seismic line. Velocity analyses have been carried out at the shot points indicated and the velocities are labelled in units of ft/s. From McQuillin *et al.* (1984), with kind permission from Kluwer Academic Publishers.

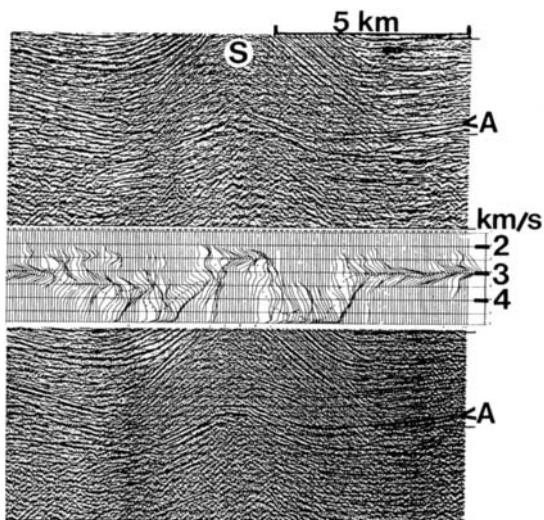


**Figure 6.29** A CMP stacked section obtained by sparsely spaced conventional velocity analysis (top) and horizontal velocity analysis (HVA) (bottom). The HVA for horizon A below the salt dome (S) is shown in the centre. From Yilmaz (2001), by permission.

plane-wave orientations. When the data are sorted on the basis of ‘common reflection points’, the migrated depth images should not be dependent upon angle. A migrated event should appear flat as a function of plane-wave angle, when the correct velocity has been applied (Figure 6.30). If velocities are too slow, the migrated event will have an upward curvature (smile); if the velocities are too fast, the curvature will be downwards (frown).

There are other forms of stacking which constitute migration processes, such as diffraction stacking, and some are discussed briefly in Section 6.3.6.

### 6.3.5 Filtering

The term ‘filtering’ covers a very wide range of data processing techniques whose purpose is to modify a waveform or change its frequency composition in some controlled manner. If an input =  $f(A) + f(B)$ , then the output is equal to output (A) plus output (B). Algebraically, given an ‘impulse response function’ [F] (i.e. a filter) and an input [G] (a waveform), then the output [H] is described by  $H = G^*F$ , where  $*$  represents the process of convolution.

A filter can be designed to remove reverberations within a dataset associated, for example, with a ringy seabed, such as may occur when overcompacted glacial clays form the seabed. The effect of such a filter designed to remove unwanted components of a signal is shown in Figure 6.31. A successfully designed filter, when applied to the data, should produce the required output. However, in the example provided, there is no noise present, which is very unrealistic. With noise, the filter is never perfect but may reduce unwanted signals substantially, if not remove them entirely.

Other types of filter are used to remove specific frequency elements, such as low-frequency groundroll or high-frequency jitter. To remove such band-limited signals, specific filters are designed

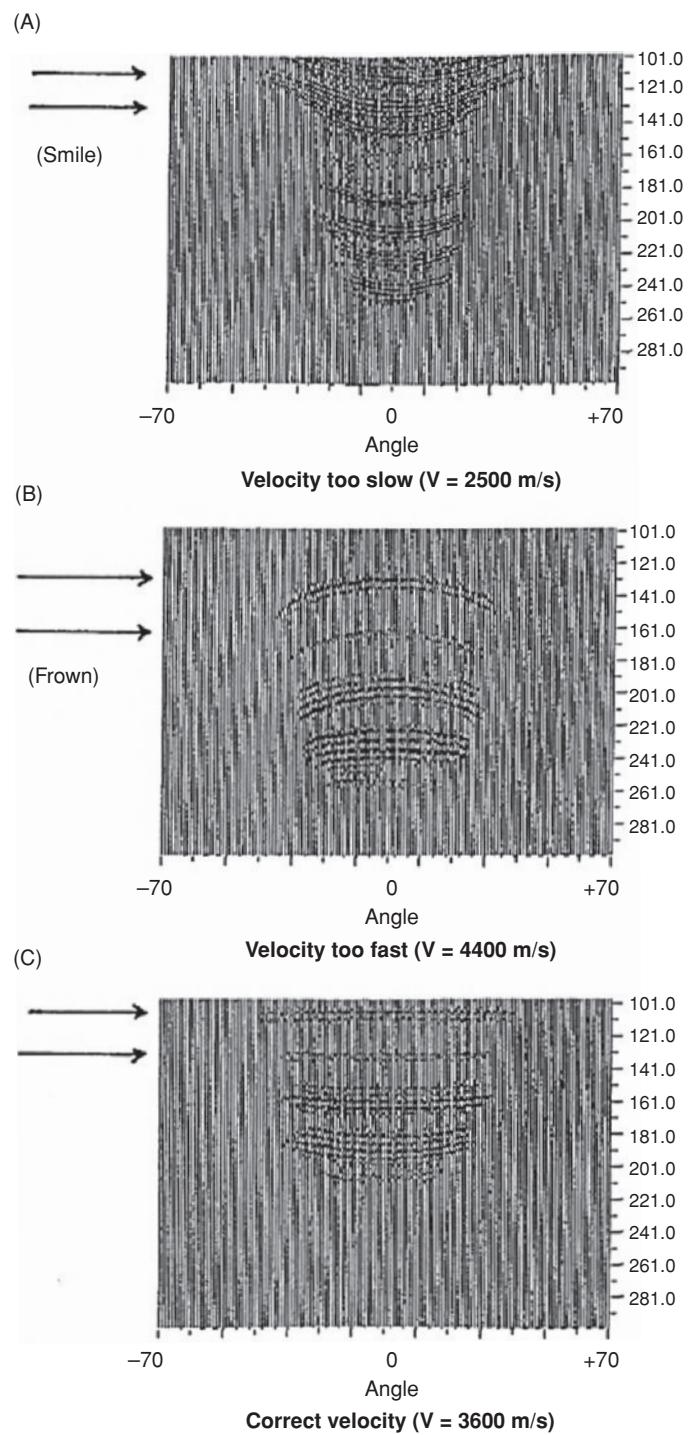


**Figure 6.30** (A) Migration panel for CRP showing a ‘smile’ caused by a low velocity estimate in layer 1 (arrowed). (B) Migration panel for CRP showing a ‘frown’ created by a high velocity estimate in layer 1. (C) Migration panel for CRP shows a flat event in the case of a correct velocity. The depth of the reflected event is dependent upon offset – a requirement for the correct velocity. From Lines et al. (1993), by permission.

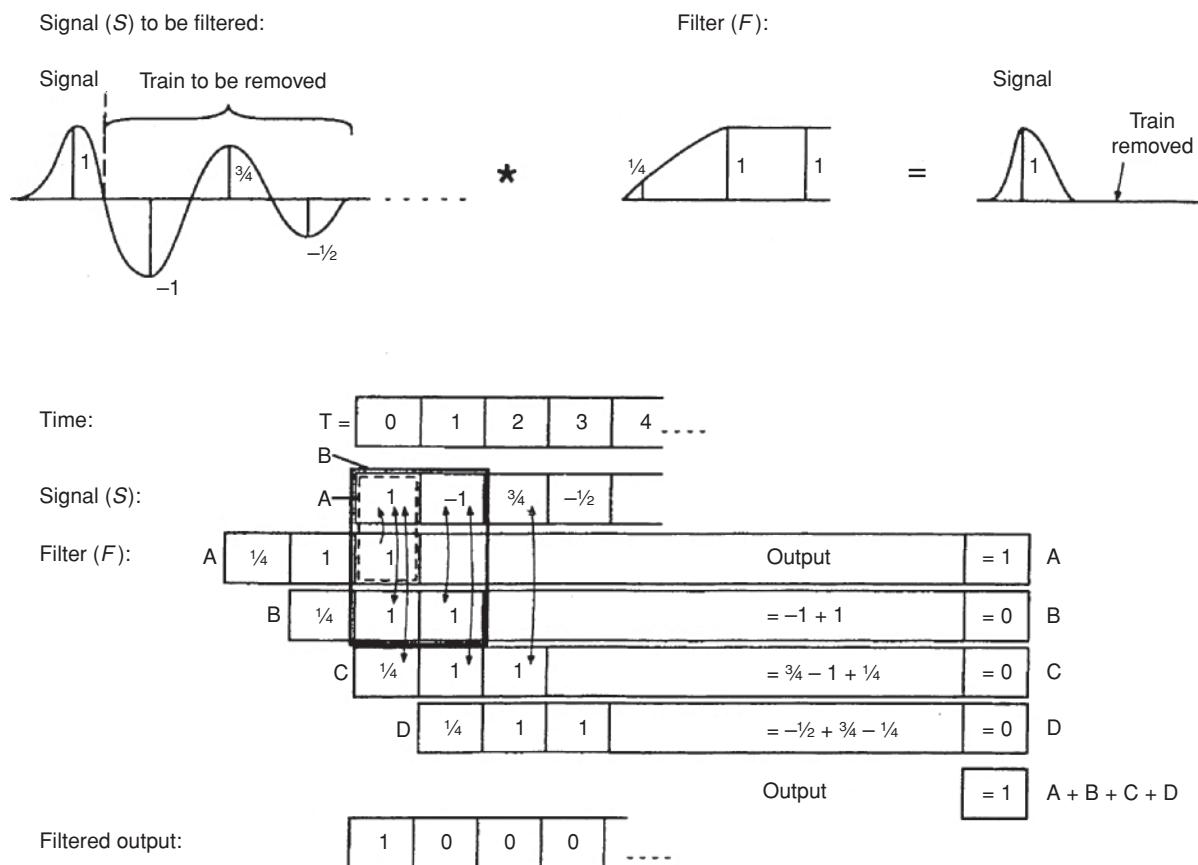


**Figure 6.31** Filtering out a reverberant signal:

At each relevant time sample (i.e.  $T = 1, 2, \dots$ ) the signal amplitude  $S$  is multiplied by the corresponding segment of the filter  $F$ . Hence for  $T = 1$ , the calculation is simply of the form signal  $\times$  filter ( $S^*F$ ) such that  $[1 \times (-1)] + (1 \times 1) = -1 + 1 = 0$ . Taking this a stage at a time, we have:

**Stage A:** At  $T = 0$ , the first element of the filter (1) is multiplied by corresponding sample of the signal (1), hence the output = 1.

**Stage B:** At  $T = 1$ , the first element the filter (1) is multiplied by the corresponding sample of the signal (-1) giving a value of -1. This is added to the product of the second element of the filter (1) and its corresponding sample of the signal (1) to give a value of 1 and an overall output of  $-1 + 1 = 0$ .

**Stage C:** As for Stage B but shifted by one time sample ( $t = 2$ ).

**Stage D:** As for Stage C but shifted by one time sample ( $t = 3$ ).

to operate over the required frequency ranges. For example, to remove groundroll, a low-cut filter can be used (i.e. cuts out the low-frequency signals associated with the groundroll). To reduce high-frequency jitter, where the jitter occurs at frequencies significantly greater than those associated with the primary signals, a high-cut filter can be used. Sometimes, electricity mains cause interference at 50 to 60 Hz. To eradicate this, a 'notch filter' is used which attenuates those frequencies most strongly.

Different shaped filters are shown in Figure 6.32. A bandpass filter allows frequencies within the specified range (the bandwidth) to pass without attenuation by the filter; all other frequencies are affected by the filter. Similarly a low- or high-cut filter selectively removes the low or high frequencies, respectively. A low-cut filter is thus the same as a high pass filter, and a high-cut filter is the same as a lowpass filter.

As has been mentioned previously, high frequencies are progressively attenuated by the filter response of the ground. Consequently,

it may be inappropriate to apply the same filter design to signals at later travel times as was applied to those at short travel times. This requires a filter whose design changes with increasing travel time (i.e. a time-variant filter). A seismic record may be divided into a discrete number of time sections (windows), such as from 0 to 2 seconds, 2–3 seconds, 3–4 seconds and 5–6 seconds. A different filter design may be selected for each of these four time windows. It is important, however, that the change in design of filters between adjacent windows is not so extreme as to cause significant variations in the character of dipping events across the window frame.

Instead of using an impulse response function in the frequency domain, a filter can be expressed in terms of a series of sine and cosine waves of different frequencies and amplitudes in the time domain. The final response is the sum of all the constituent sine and cosine waves. The analysis of time series data to provide this information is called *Fourier analysis*. Consider a function  $f(t)$  over the time interval  $t = 0$  to  $t = T$ . It can be expressed as a constant

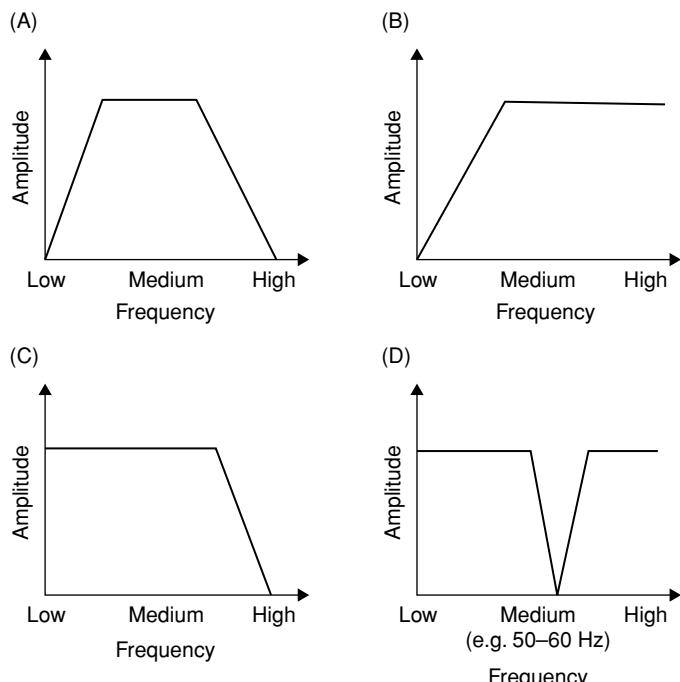


**Figure 6.32** Types of filter: (A) bandpass; (B) low-cut (highpass); (C) high-cut (lowpass); and (D) notch.

plus the sum of all cosine waves plus the sum of all sine waves. Each of the constituent waves is expressed as an amplitude multiplied by the sine or cosine as a function of time (see Box 6.6). More detailed discussion of Fourier analysis is beyond the scope of this book. Further details can be found in texts by McQuillin *et al.* (1984), Yilmaz (2001) and Hatton *et al.* (1986), among many others.

### 6.3.6 Migration

Migration is the process of restoring the geometric relationships between seismic events on a time section to take account of structural complexities and steeply dipping interfaces. A steeply dipping reflector gives rise to a seismic event on a stacked seismic section that is not in its correct geometric position (see Figure 6.33). The pur-

#### Box 6.6 Fourier description of a waveform in the time domain

A function  $f(t)$  over the time interval  $t = 0$  to  $t = T$  can be expressed by:

$$f(t) = a_0 + \sum_{j=1}^{\infty} a_j \cos(2\pi jt/T) + \sum_{j=1}^{\infty} b_j \sin(2\pi jt/T)$$

where  $a_0$  is a constant. The amplitude  $A$  and phase  $\varphi$  at each frequency is given by:

$$A_j = (a_j^2 + b_j^2)^{1/2} \text{ and } \phi_j = \arctan b_j/a_j.$$

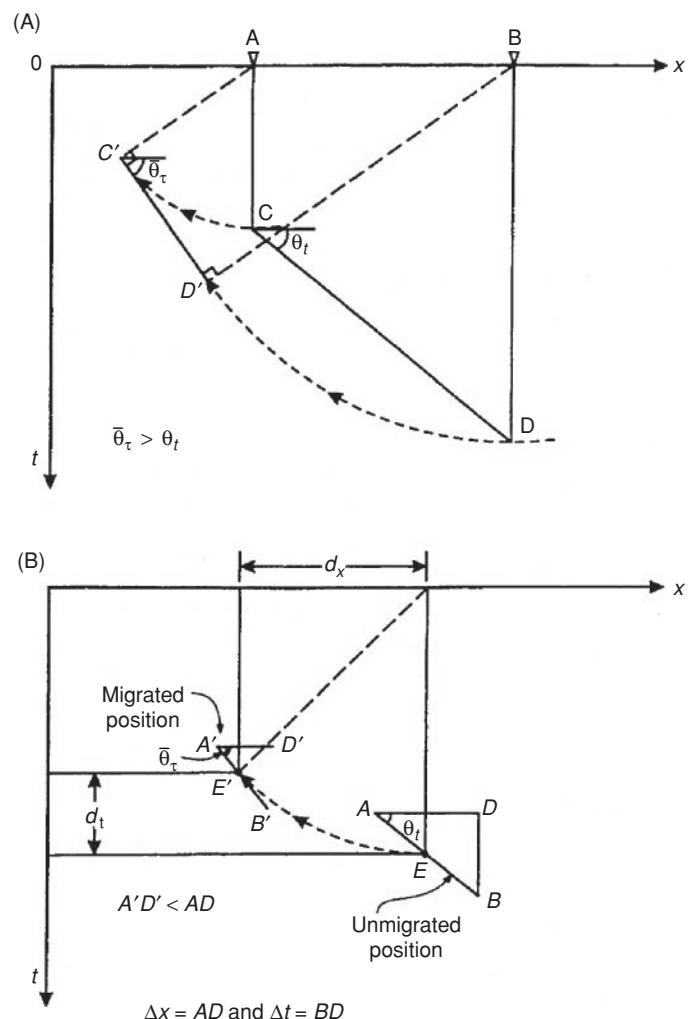


**Figure 6.33** The principle of migration. (A) For dipping reflector C-D, a stacked section is migrated to correct geometry C' – D'. (B) The migration process moves an event (E) a lateral distance  $d_x$  and vertically  $d_t$ . The gradient of the event increases from  $\theta_t$  to  $\theta$ . After Yilmaz (2001), by permission.

pose of the migration process is to place a given seismic event in its correct position on the time section. A further benefit of migration is the collapse of diffraction hyperbola to their points of origin, and the consequent clarification of seismic events (for example, seismic rollover) associated with discontinuities within interfaces such as at fault planes. As a common midpoint stack smears dipping events (see Section 6.2.2), dip move-out (DMO) processing is commonly undertaken before stacking; DMO is sometimes considered to be a migration process.

There are a number of different migration procedures, such as Kirchhoff (Claerbout, 1985), finite-difference, frequency-wavenumber ( $f - k$ ) domain (Stolt, 1978), and turning-wave migration; with the exception of the last method, they are described and discussed in considerable detail by Berkhout (1984) and Yilmaz (2001), among others. Turning-wave migration or imaging

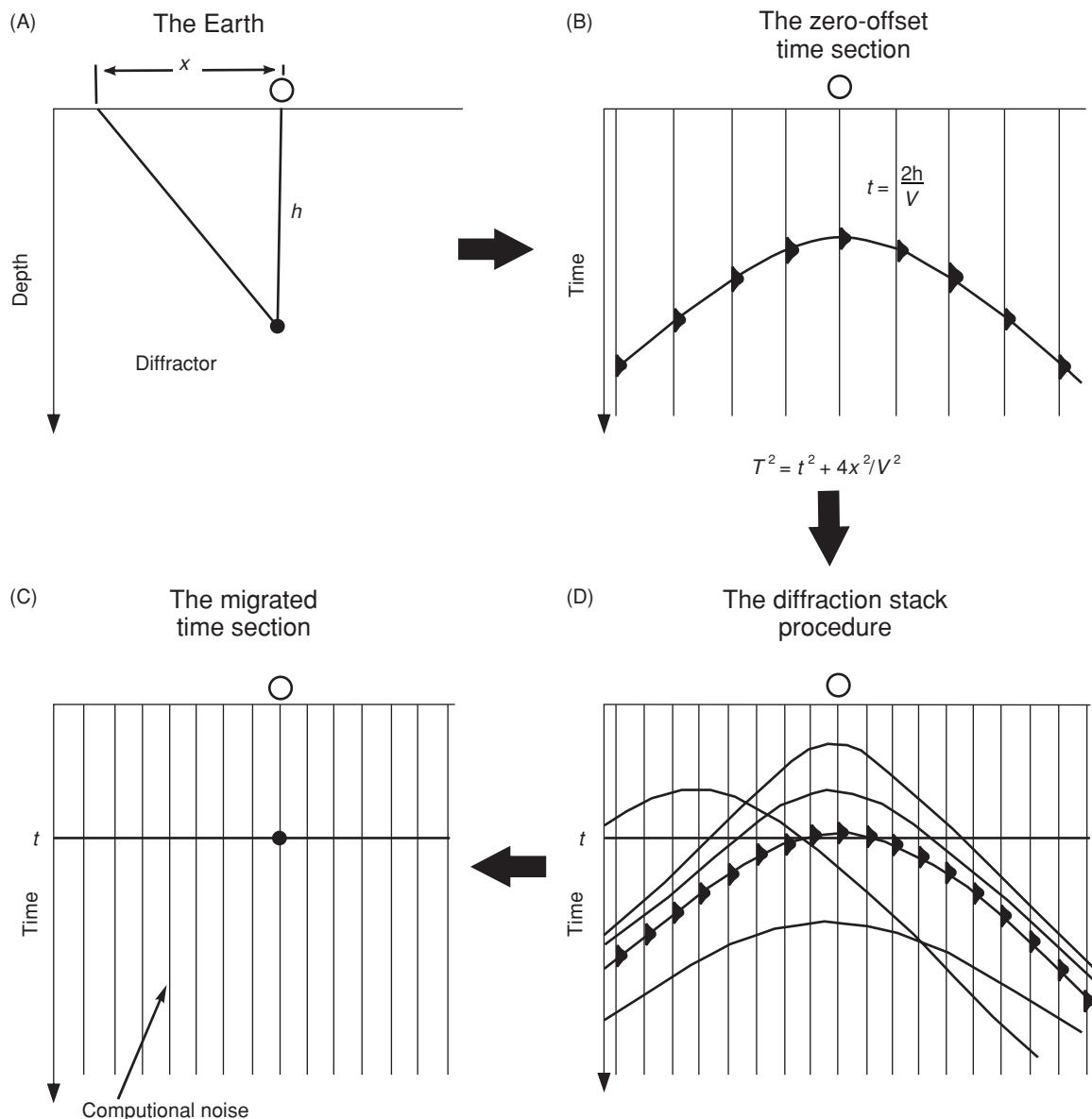


**Figure 6.34** The principle of the diffraction stack or Kirchhoff migration. (A) A diffractor lies at a depth  $h$  vertically below a receiver and gives rise to a diffraction event (B) on a seismic reflection record. (C) A diffraction stack hyperbola for a known velocity is matched against the observed diffraction. Given a correlation along the hyperbola, all the same-phase events are summed and the observed diffraction is shrunk back to a point (D). Courtesy of BP.

has been described by Claerbout (1985), Hale *et al.* (1991), Meinardus *et al.* (1993) and Ratcliff *et al.* (1991), among others.

Time migration from a stacked section (i.e. zero offset) produces a migrated time section and is appropriate in the absence of strong lateral velocity variations. When such velocity gradients are present, time migration does not produce an accurate image of the subsurface. Instead, depth migration should be used, the output of which is a migrated depth section. Ray-tracing is used particularly to generate depth sections.

The basis of the migration method is Huygens' secondary source principle: that any point on a wavefront can act as a secondary source producing circular wavefronts when viewed in two dimensions, or

spherical wavefronts in three dimensions. The process of migration is to collapse the apparent secondary wavefronts to their points of origin. For example, a point source generates a diffraction hyperbola (see Figure 6.34). By scanning an appropriate number of adjacent traces, the hyperbola can be collapsed back to the point source by the migration process. The number of adjacent traces scanned is known as the *migration aperture*. When the seismic velocity is slow, the curvature of the diffraction hyperbola is steep, and consequently the number of traces required is small. As the hyperbola curvature decreases (flattens) with increasing seismic velocity, the migration aperture also has to increase (Figure 6.35). Incomplete collapse of diffraction hyperbolae occurs if insufficient aperture widths are

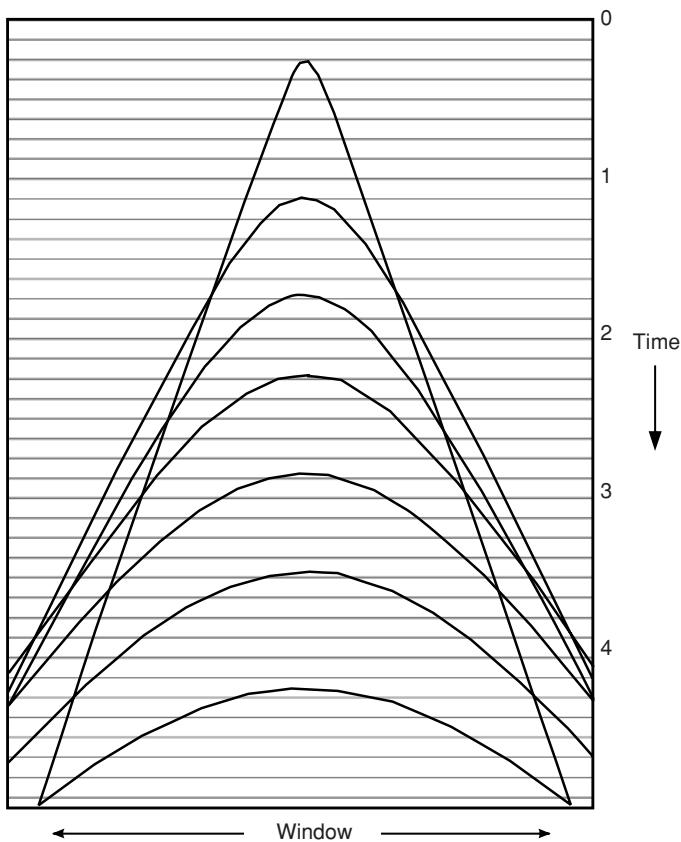


**Figure 6.35** Diffraction hyperbolae calculated using increasing velocities. A slow velocity results in a tight hyperbola (uppermost curve), while that associated with the fastest velocity has both the broadest window and the flattest of the curves. After Yilmaz (2001), by permission.

chosen. It is also important to ensure that the migration aperture is large enough to capture all the required data for a given geological target.

The horizontal and vertical displacements between the unmigrated and migrated sections can be calculated (see Box 6.7). At a two-way travel time of 4 s and with a seismic velocity of 4000 m/s, the horizontal (in km) and vertical displacements (seconds) are 6.4 km and 1.6 s respectively. Even at a two-way travel time of 1 s and with a seismic velocity of 2500 m/s, the displacements are 625 m and 0.134 s. It is thus obvious that the degree of displacement is very significant, and that even small errors in the migration process can have large practical implications when choosing potential well sites.

The migration process has three basic effects when compared with events on unmigrated sections. Migration (a) steepens reflections, (b) shortens reflections, and (c) moves reflections up-dip (see Figure 6.32).

Kirchhoff migration has a tendency to generate noise but handles all required dips and can cope with horizontal and vertical velocity variations. Finite-difference migration produces little noise and can also cope with velocity variations; but in the case of steep dips the computational time is lengthy and hence expensive. The  $f-k$  migration handles all dips very quickly but has difficulty in coping

**Box 6.7** Vertical and horizontal displacements through migration (see Figure 6.33)

Horizontal (distance) and vertical (time) displacements  $d_x$  and  $d_t$  and dip angle after migration ( $\theta_\tau$ ) can be expressed in terms of material velocity  $V$ , two-way travel time  $t$  and apparent dip ( $\theta_t$ ) of the reflection as measured on an unmigrated section using the following expressions:

$$\begin{aligned} d_x &= (V^2 t \tan \theta_t)/4 \\ d_t &= t\{1 - [1 - (V^2 \tan^2 \theta_t)/4]^{1/2}\} \\ \tan \theta_\tau &= \tan \theta_t [1 - (V^2 \tan^2 \theta_t)/4]^{1/2} \\ \tan \theta_t &= \Delta t/\Delta x. \end{aligned}$$

with velocity variation in the cross-dip situation. It also only works for constant-velocity models, so there is a requirement to undertake comprehensive velocity-depth conversions.

Kirchhoff migration uses a hyperbola in 2D or hyperboloid in 3D. For pseudo 3D migration, the migration process is run in two stages that are basically a 2D migration in the  $x$ -direction and then a 2D migration in the  $y$ -direction. This process is known as '2D2' and may require some 600 traces for one migration run; in contrast a full 3D migration for the same coverage might require 70,000 traces, a correspondingly longer calculation time and greater costs.

Turning wave migration is of particular importance in imaging the overhanging sides of salt diapirs (Hale *et al.*, 1991). Turning waves travel downwards initially, pass through a turning point and travel upwards before being reflected from the salt–rock interface (Figure 6.36). Figure 6.37A shows a stacked section from the Gulf of Mexico (Meinardus *et al.*, 1993) after application of dip move-out and has three events highlighted; event 3 arises from turning waves at an apparent distance of over 5 km from the salt dome. The salt–rock interface giving rise to these reflections lies at a two-way travel time of 1.3 s on the turning-wave migrated section (Figure 6.37B), compared with 4.5 s on the TV DMO section. The improvement

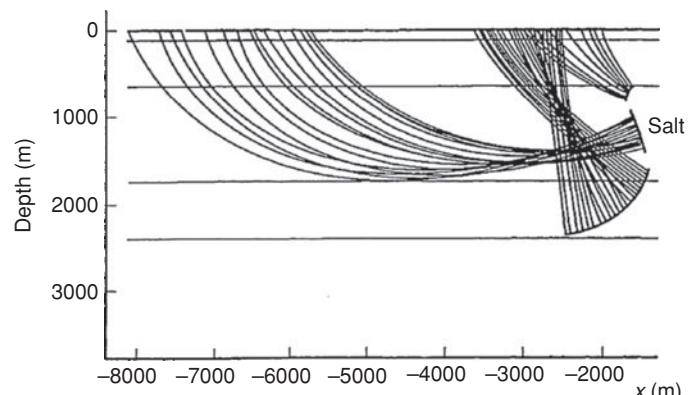


**Figure 6.36** The overhang face of the salt dome on the right edge is recorded with turning waves as indicated by their ray paths. From Meinardus *et al.* (1993), by permission.

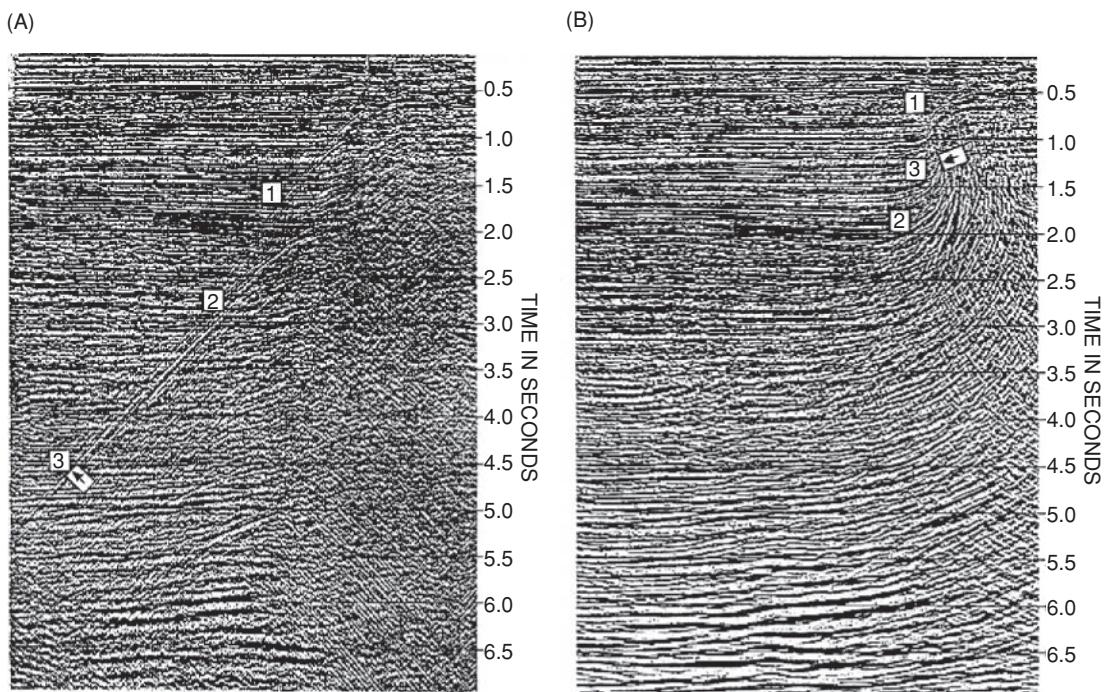


**Figure 6.37** (A) Stack of a seismic reflection record in the Gulf of Mexico after the application of time-variant dip move-out (DMO). Three events are indicated by numbers. (B) The same section after turning-wave migration. The difference in position of event (3) (arrowed) between the two sections is very marked, with the event being restored to the salt overhang on the migrated section. From Meinardus *et al.* (1993), by permission.

in clarity of imaging is quite spectacular. The scale of geometric repositioning achieved by migration (of the order of kilometres) in large-scale hydrocarbon exploration surveys demonstrates the importance of the method in providing much more reliable and realistic images of the subsurface in structurally complex areas. However, for small-scale engineering investigations, migration may not be either technically or financially justifiable (Black *et al.*, 1994).

Along with major developments in migration methods (whether pre- or post-stack), advances in computing hardware have facilitated the processing of the vastly increased amount of data. Of major significance has been the application of 'massively parallel processors' (e.g. the Cray T3D system). Undoubtedly, developments in computer technology will continue to have major effects on the capabilities of the seismic processing industry.

While all of the above discussion has been in relation to seismic data, migration processes can also be applied to ground-penetrating radar data (see Chapter 12). The issues concerning velocity determination in order to translate from the time domain to the depth domain apply equally to radar surveys.

tation that represents what is actually present within the ground. The proof of the model interpretation is in the drilling! However, geophysical interpretation is an iterative process. Working with a forward model, an initial interpretation is obtained. Given independent data, the model can be refined or constrained. Given yet more information, the interpretation can be revised yet further. With each iteration, the model should represent the actual ground structure more realistically each time. In the following section, several different methods of correlation are described briefly, ranging from the use of boreholes, the comparison with synthetic seismograms, through to correlation in engineering surveys with Dutch cone logs.

#### 6.4.1 Sonic and density logs, and synthetic seismograms

A well-established method of correlation is to use borehole geophysical logs to produce reflectivity series for comparison with the seismic sections. Significant primary reflections should occur where there is significant contrast in acoustic impedance. Borehole sonic and density logs provide the information from which acoustic impedances can be derived over vertical distances much shorter than the seismic wavelength.

A sonic logging tool consists of two transmitters, one at each end of the tool, and two pairs of detectors located in between the transmitters. A sound wave is generated from one source and is refracted along the borehole wall, and the critically refracted waves are

## 6.4 Correlating seismic data with borehole logs and cones

It is of great importance to constrain geophysical models with independent information where possible, so as to produce an interpre-

detected at each of one pair of receivers separated by a known distance. A second signal is then generated from the other source in the opposite direction, and the critically refracted arrivals are detected by the second pair of receivers. The instrumentation measures the travel time taken for the signal to travel through the distance of the borehole wall equivalent to the separation between the pairs of receivers. The travel time from shooting in one direction is averaged with that obtained for the reverse direction, to make allowance for the tilt of the tool with respect to the borehole wall. The average single-way transit time is then logged for that interval.

Typically the transit time is recorded in units of  $\mu\text{s}/\text{ft}$ . To convert these times to a seismic velocity, a simple conversion factor can be used: given the single-way transit time ( $T$ ) in  $\mu\text{s}/\text{ft}$ , then the seismic velocity  $V$  in  $\text{km}/\text{s}$  is given by  $V = 304.79/T$ . For example, if  $T = 9011 \mu\text{s}/\text{ft}$ , then  $V = 304.79/90 = 3387 \text{ km}/\text{s}$ . Consequently, the sonic data give a measure of the seismic velocity. The density log gives a corrected reading in  $\text{Mg}/\text{m}^3$ . If the numerical values of each of these two logs are cross-multiplied (i.e. velocity times density), then a log of the acoustic impedance  $Z$  is produced.

From an inspection of the acoustic impedance log, significant interfaces across which there is a marked contrast in impedance can be readily identified. Such interfaces can also be correlated with the other available borehole geophysical and geological logs to provide a lithological as well as a chronological stratigraphy. The acoustic impedance log can be used to derive a vertical reflectivity series; that is, across each interface the reflection coefficient can be determined. This can be used with an artificial wavelet to generate a synthetic seismogram which can be compared directly with the observed seismogram. The added advantage of direct correlation with borehole logs is that there is an actual measurement of depth against which the seismic section can be constrained.

An example of the use of a synthetic seismogram to correlate with measured seismic data is shown in Figure 6.38A (Varela *et al.*, 1993). The strong reflections seen in the segments of seismic section match those in the synthetic seismogram very well. It is unusual in engineering investigations to have the luxury of synthetic seismograms, but more normally, it may be possible to use one or preferably a pair of boreholes, logged geotechnically and stratigraphically, with which to correlate adjacent seismic sections (Figure 6.38B). However, it should be noted that boreholes logged geotechnically may not record all the possible interfaces or changes in material, as they may not be visible to the person logging the material. Consequently large sequences within a borehole log may describe the material as being just one unit, London Clay, for example, yet high-resolution seismic sections may show reflections arising from within the same unit. Of critical importance in making such correlations is the choice of interval velocity by which to convert the depths or thicknesses provided by the borehole logs to two-way travel times that can then be correlated directly with the seismic sections. In surveys over tidal waters it is also important to make the necessary tidal corrections to level the sections to the relevant datum. Otherwise it is impossible to make the correct correlations since the levels cannot be constrained. In the example shown in Figure 6.38B, the boreholes and seismic section have been levelled to ensure that where the line between the two boreholes crosses the seismic section, the river bed is at the correct level with respect to the local datum. In this case the

seismic section was acquired along the centre line of the river and the intersection between the seismic section and the line between the borehole pairs is indicated by the vertical dashed line. At this line of intersection the interfaces in the borehole pairs are interpolated across and correlated with reflections. The correlation is possible in this case as the vertical scale of the seismic section has been selected using a seismic velocity of 1800  $\text{m}/\text{s}$ , a value derived from velocity analysis which demonstrated that significantly higher or lower velocities (i.e.  $<1700 \text{ m}/\text{s}$  or  $>1900 \text{ m}/\text{s}$ ) resulted in significantly poorer correlation with the borehole data. It is important only to make the correlation where a seismic reflection event can be identified clearly. Multiples must be excluded from the correlation, as confusing these with geological interfaces will result in completely incorrect correlations.

In marine dredging operations or other offshore shallow investigations, correlations between reflection sections are often made with vibrocore results and/or shallow boreholes. The principle is the same, whereby the intrusive sampling yields information about the lithologies present and the thicknesses of the various units sampled. However, a common problem in such surveys is not having the intrusive testing reach deep enough to ensure that each seismo-acoustic facies and boundary are sampled and identified. It is not uncommon for a contract to stipulate that the intrusive sampling should be undertaken routinely to 6 m only, to find that seismically a key interface lies at a depth of say 6.2 m below seabed, and that the depth of, and material underlying, the interface remain unsampled. Ideally, locations at which intrusive sampling is undertaken should be determined by inspection of the seismic sections, which should also indicate the most appropriate depth to which sampling should be made. All too commonly, the order of the work is the reverse, and the possible correlations are all the poorer as a result, resulting in both a lower cost–benefit and a less technically robust interpretation.

## 6.4.2 Correlation with cone penetration testing

In shallow land and marine engineering applications, it is possible to correlate seismic reflection records with cone and standard penetration test (CPT and SPT, respectively) logs. There are now many types of CPT available, and for a review of the available technology, readers are referred to books by Brouwer (2007), Mayne (2007) and Schnaid (2009); see also the website listed in Appendix 1. By way of example, two types of cone testing correlation methods are described as follows.

A *cone penetrometer test* (CPT) consists of vertical insertion into the ground of an instrumented 3.6–4.4 cm diameter cone on the end of an extension rod (Figure 6.39). Typically, the platform from which the cone is deployed is a truck with a cabin, which houses all the instrumentation and the hydraulic rams that drive the cone and rods into the ground. By pushing the rods into the ground at a constant rate (e.g. 2  $\text{cm}/\text{s}$ ), the resistances on the cone tip and sleeve can be measured and displayed as a function of depth (Figure 6.40). Vertical resolution is of the order of 2 cm.

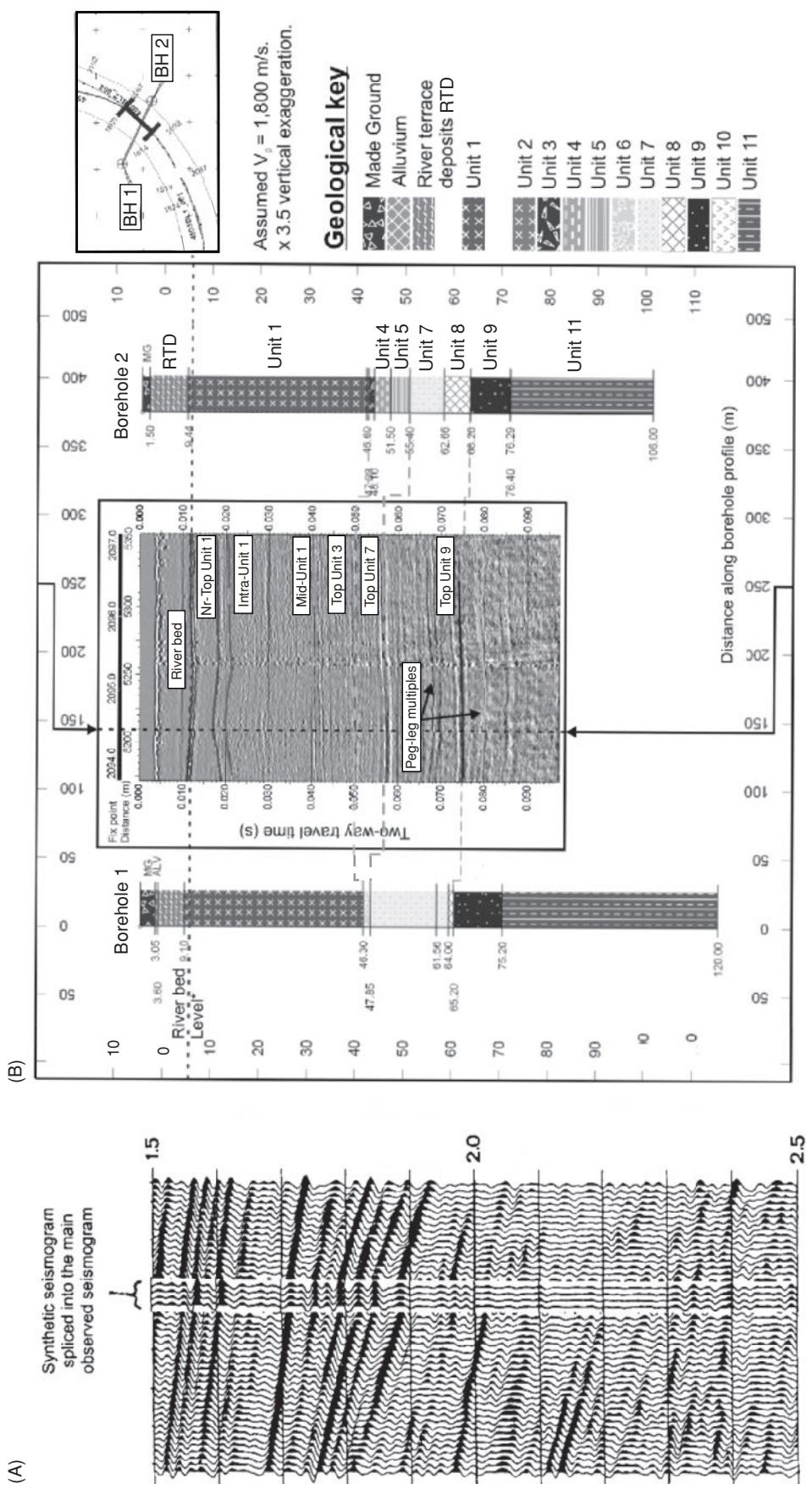


**Figure 6.38** (A) Part of a seismic record from the Campos Basin, offshore Brazil, into which a synthetic seismogram has been inserted in order to demonstrate the correlation between the observed and the synthetic data. From Varela *et al.* (1993), by permission. (B) Inter-borehole correlation with Boomer data, River Thames. [C]

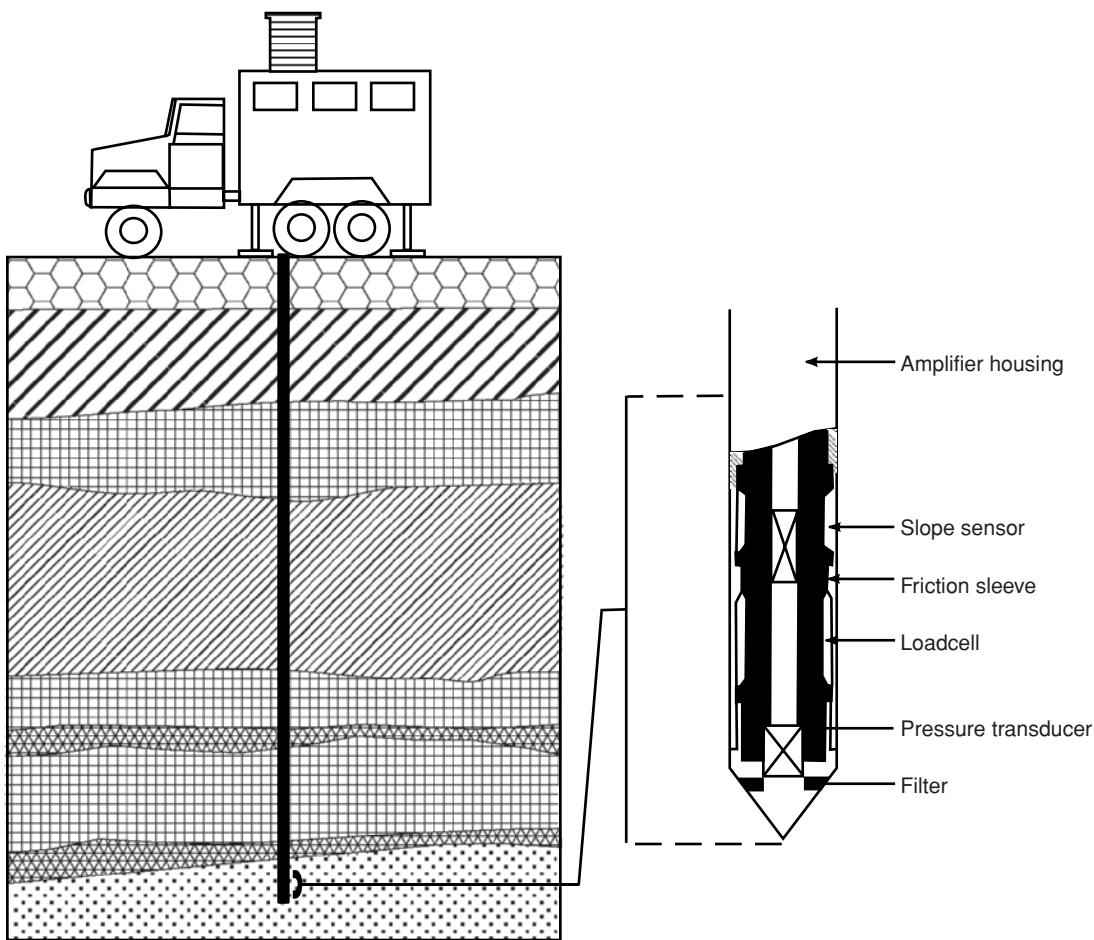


**Figure 6.39** Cone penetration testing (CPT) system with a piezocone tip in detail. From Hunt (1992), by permission.

Whereas all the usual cone tips measure physical or chemical parameters in the immediate vicinity of the instrumented cone, the seismic cone works on a different principle. Here, only the geophone is placed within the cone head. The seismic source remains at the ground surface (Figure 6.41A). For example, a large piece of heavy-duty timber (such as a railway sleeper) is anchored to the ground to ensure good ground coupling. A sledgehammer is struck against one end of the timber to generate a shear wave that propagates down into the ground, where it is detected by the stationary cone sensor. Another hammer blow is applied but to the opposite end of the timber to produce a shear wave of opposite polarity to the first. The use of two opposite-polarity shear waves helps the identification of the onset of the shear wave (Figure 6.41B). The two waveforms are logged against the position of the sensor depth. The cone and rods are pushed an incremental distance further into the ground (typically 0.25 m or 0.5 m) and the two surface seismic shots are fired again. The difference in total travel time measured between adjacent sensor positions can be inverted to give an S-wave velocity averaged over the incremental distance plotted as a function of depth. The process is repeated until the required depth has been reached or it is not possible to push the rods any further into the ground. Alternatively, and more conventionally, the sledgehammer is impacted on to a rubber baseplate to generate P-waves.

Averaged P-wave velocities can be obtained in the same way as for S-waves. Zones of higher-velocity material produce short travel times, while the converse is true for materials with slow elastic-wave velocities. Given the development of a uniform seismic source, other parameters may be determinable using this method (relative attenuation, Poisson's ratio, elastic moduli, etc.). The use of two seismic cones deployed side-by-side would permit the equivalent of cross-hole seismic tomography. One cone tip would have to be replaced by an appropriate source to permit transmission of the seismic energy from one cone laterally through the ground to the other.

A further method that can be used with the seismic cone is the equivalent of the walkaway VSP. If the surface source is moved to larger offsets, with the sensor located at the same vertical depth, then the slant-angle raypath geometry can be explored. Additionally, the source can be moved around the cone position at a common offset to give azimuthal information. This may be particularly beneficial in materials that possess a strongly developed anisotropic fabric. Three-dimensional seismic cone tomography has yet to be fully developed commercially. The basic method is only just starting to be accepted amongst the engineering community, but the potential for its usage is considerable. Similarly, the scope for development of other active cone tips (e.g. EM, electrical resistivity, etc.)

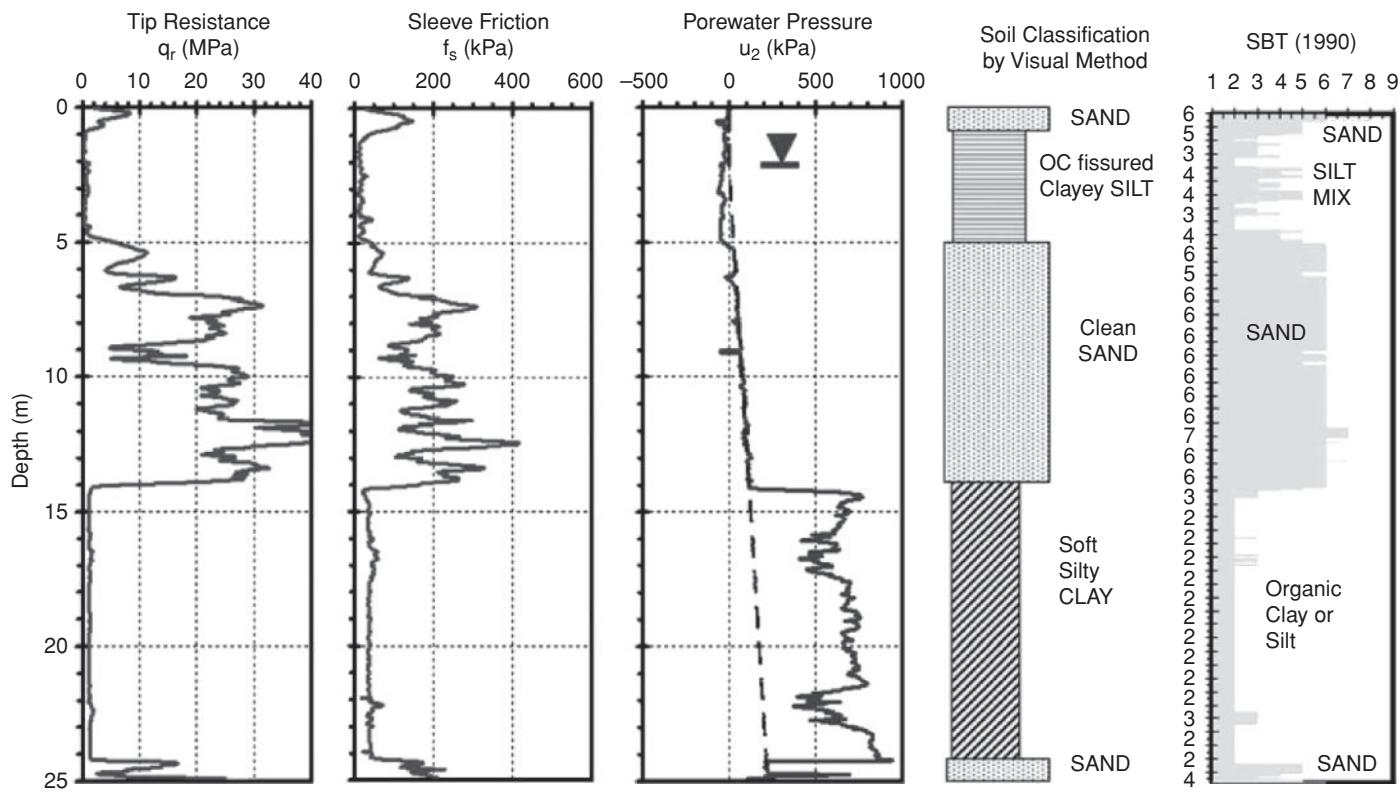


**Figure 6.40** Examples of the output from cone penetration testing with the corresponding soil classification. From Mayne (2007), by permission. [C]

and deployed in ‘walkaway’ profiling and cross-hole tomography is enormous. The combination of ‘clever’ cone sensors and surface geophysical methods is perhaps one of the most exciting areas of development in environmental geophysics and ground investigation. It is surprising, therefore, that greater use of these techniques has not been made, given the clear technical and cost benefits achievable.

In the drilling of boreholes, whether on land or afloat, *standard penetration testing* is a very basic method of testing the hardness of the material being drilled through. In essence it is a measure of the number of blows of a shell-and-auger rig tool to penetrate a given distance, usually 10 cm. The larger the number of blows, the harder is the material. Similarly, the use of *dynamic probing* works on a similar principle – a rod is driven continuously into the ground and the distance driven and the energy imparted are measured (e.g. Russell and Gee, 1990). For further details of techniques for site investigation see guidelines produced by the International Society for Soil Mechanics and Geotechnical Engineering (Danson, 2005). Consequently, if a borehole is constructed through materials in which there are distinct changes in hardness, the interfaces across which hardness changes should also be evident in seismic reflection records due to the differences in acoustic impedance. Thus, where hardness changes, so acoustic impedance should also. By correlating a good-quality, high-resolution marine seismic reflection record with SPT logs, significant reflections should be readily identifiable at interfaces identified with the SPTs. For example, in a commercial marine resource evaluation project in Hong Kong, SPT logs proved to be very valuable in aiding the interpretation of seismic reflection

records to derive a general seismic stratigraphy for the area. The degree of correlation between the seismic records and SPT logs was extremely good.

Once the reflections on the seismic sections have been correlated with borehole and cone data, the seismic time series record becomes interpretable in geological terms. Depths, interval seismic velocities, seismic characteristics associated with particular lithological units, and so on, can be determined with confidence. With the advent of more detailed quantitative analysis of high-resolution single-channel seismic data, further information about the geotechnical parameters of the soils and sediments present can be obtained.

## 6.5 Interpretation

### 6.5.1 Vertical and horizontal resolution

Determination of resolution within seismic surveying depends upon four factors: quality of raw data, frequency bandwidth, source response characteristics, and the nature of the vertical sequence of possible reflectors. Each of these is discussed briefly.

The acquisition of raw seismic data has to be undertaken in such a manner that the quality of the records obtained is suitable for the task in hand. This requires two stages: the first is to ensure that the correct equipment is specified to start with, and secondly, that the equipment used is operated properly. There are still too

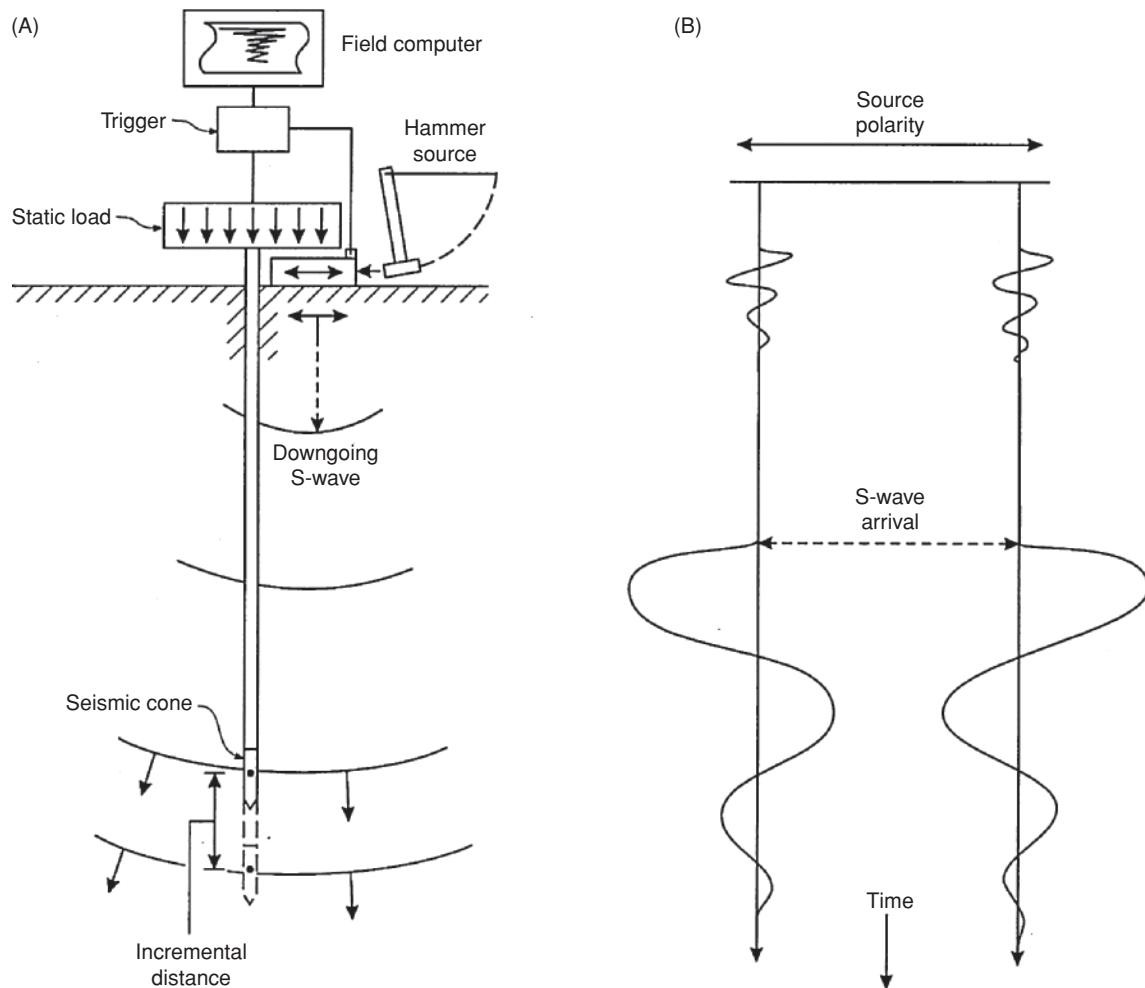


**Figure 6.41** Seismic cone test. (A) Schematic of the survey components. (B) The first breaks of S-waves with opposite polarities can be clearly identified. The polarity of the downgoing P-waves is not reversed.

many occasions when the wrong kit has been used or the right equipment has been used badly. No amount of processing will transform substandard data into high-quality records.

Another point is that it is essential that the appropriate frequency range system is used for the objective of the survey. There is no point using a lower-frequency sparker system if shallow penetration and high resolution are required. Conversely, the selection of a Pinger, with its high frequency and restricted bandwidth, is inappropriate to obtain even moderate penetration through gravels. In essence, however, resolution (see Section 4.5.5 and Table 4.6) is dependent upon frequency. High-frequency sources provide greater resolution than low-frequency sources. The Rayleigh resolution limit is equal to one-quarter of the dominant wavelength of the incident waveform. The Widness limit is an eighth of the wavelength. This has been discussed in more detail by, for example, Phadke and Kanasewich (1990).

The third consideration is *source response*. In hydrocarbon exploration, seismic contractors are obliged to record the seismic source pulse. It is seldom done in shallow engineering surveys. With the increased usage of digital acquisition systems in engineering type

surveys, and with the sophistication of analysis now available, it is becoming increasingly important that the source pulse should be recorded on each and every survey. By having a knowledge of the shape and duration of the source pulse, the subsequent interpretation of the seismic record is made more realistic, if not easier. Source pulse shape and duration are fundamental aspects of interpreting seismic (and ground-penetrating radar) records (Reynolds, 1990a). If a source pulse is ringy, so too will be the reflections; if the source comprises three bars, for example, so will the subsequent reflections, although the tails of later reflections may become more subdued and less obvious. If the source pulse is 'clean', then the reflections arising from this are also likely to be sharp. When many reflectors lie in close proximity to each other, the ability to resolve between them is determined in part by the cleanliness of the source signal. It is more difficult to resolve units with a ringy source than with a clean one, as the tail of the earlier reflection interferes with the onset of the next, and the two wavetrains may coalesce to cause a complex and unresolvable mess.

To some extent the cleanliness of the source can be improved by filtering the data during acquisition (Figure 6.42) and with

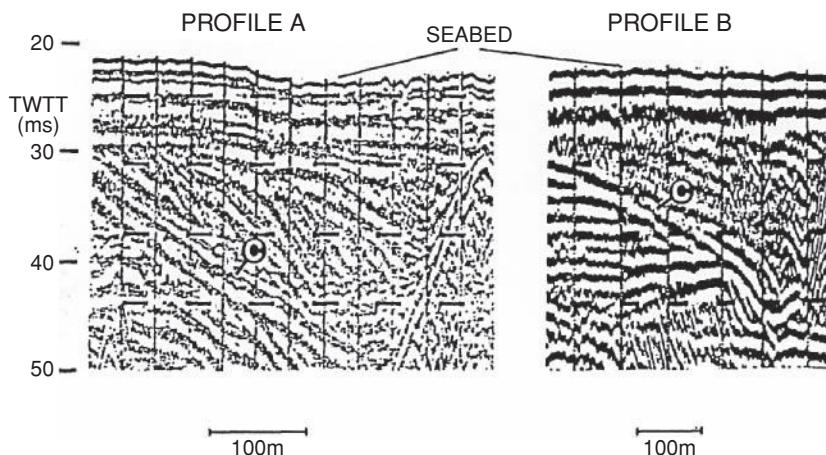


**Figure 6.42** Two sparker records acquired over the same ground but using different frequency filters. From Reynolds (1990a), by permission.

post-processing. It is important that, during the setting up of any acquisition system, the source be optimised to produce the sharpest signal possible. It should also be remembered that source quality drifts, and periodic checks of the source characteristics should be made during each day of a survey to ensure consistency.

Related to this third factor is the directionality of the source used in marine surveys. Spatial smearing occurs owing to the finite size of the source array: the source is not infinitesimal but has a finite footprint. Consequently, the in-line and cross-line responses may be different and these need to be considered, especially in 3D surveys. Roberts and Goult (1990) provided an example where directional deconvolution of the signature from a marine source array was achieved in conjunction with pre-stack migration or dip move-out (DMO) processing. A particular benefit of undertaking this processing sequence is that shallow, dipping reflections have better lateral continuity and frequency content. Consequently, the processing takes into account a source characteristic and improves the lateral resolution.

The fourth factor to be considered is the very nature of the sequence of reflectors present within the subsurface. Flat-lying, widely spaced reflectors are much easier to image than are those that are closely spaced and/or steeply dipping. The resolvability of thinly bedded strata is of great concern to the hydrocarbon industry, and much effort has been made to improve the techniques used for unravelling such sequences. The minimum thickness of a bed that gives rise to an identifiable reflection is known as the *detectable limit* or the *limit of visibility*. Numerically, this is taken as being equivalent to one 30th of the dominant wavelength of the incident waveform.

Horizontal resolution of unmigrated seismic sections is usually taken as being equivalent to the width of the first Fresnel zone (see Section 4.3.1). If horizontal stacking of traces has been carried out, then this may lead to smearing of features with a consequent loss of horizontal resolution. This effect is also present on some ground-penetrating radar sections. It is always advisable for those involved in the interpretation of seismic and radar sections to be familiar with the methods of data acquisition and processing used in the production of their sections.

In the case of steeply dipping reflectors, careful consideration needs to be given to the geometry of features in real space with respect to unmigrated versus migrated sections. Horizontal resolution in these situations is largely a function of the efficiency and accuracy of the migration process.

### 6.5.2 Identification of primary and secondary events

A fundamental aspect of interpreting time sections (seismic or ground-penetrating radar) is being able to distinguish between primary events (i.e. caused by the local subsurface features) and secondary events that are artefacts of the data-acquisition geometry and instrumentation (i.e. multiples, reverberations, instrument noise, interference, and so on). In the vast majority of surveys, great effort is made to remove or reduce secondary events. In the case of analogue shallow seismic reflection surveys undertaken over water, multiples and off-section reflections (from harbour walls, moored boats, etc.) can mask primary information that is of greatest interest. Under such circumstances, the benefits of the survey are very limited. However, modern digital acquisition systems have been developed for use in exactly these circumstances, and provide methods whereby particularly the seabed or lake-bed multiple can be suppressed (Haynes *et al.*, 1993). Primary events that would otherwise have been masked then become more visible and hence more interpretable. As a general rule, the gradient of a multiple of a dipping event is always steeper than its primary reflection, with second multiples steeper than the first multiple, and third multiples steeper than the second and so on (Figure 6.43). Where the major problem often lies is in differentiating multiples in the case of horizontally bedded units when the multiples are parallel to the primary events. Under these circumstances it can be difficult to distinguish between the two types of event.

Since the late 1980s, attention has been paid to the information content of multiples. It has been noted that, in some surveys, discrete areas exhibit anomalously high reflection strengths giving rise to strong multiples. The areas concerned tend to be found in rivers,

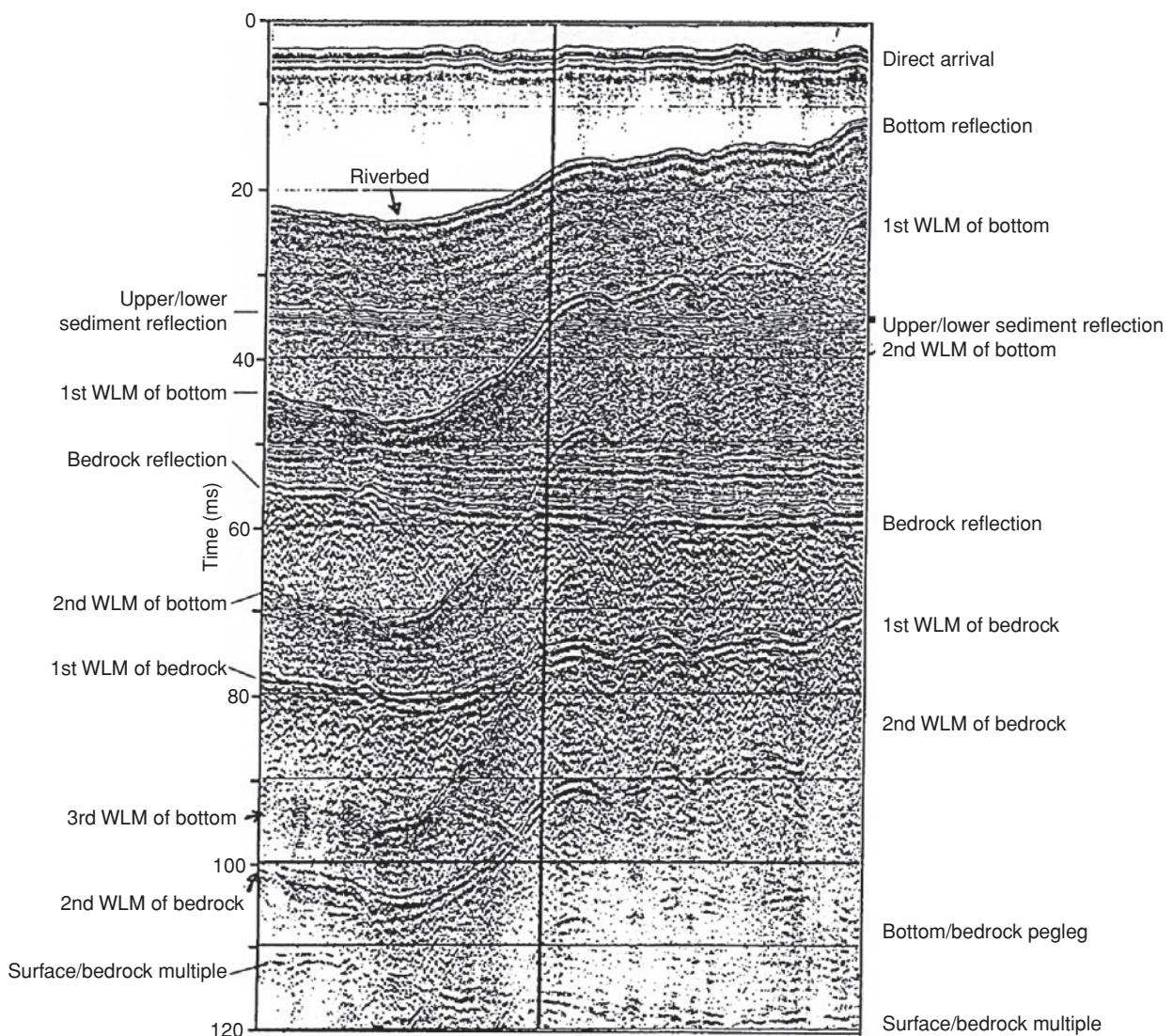


**Figure 6.43** Analogue seismic profile across the Saint Clair River, on the Canada–USA border, north of Detroit, showing all types of multiples for a two-layer situation. WLM = water-layer multiple. After McGee (1990), by permission.

bays and estuaries, and particularly those affected by industrial effluent. In other areas, the absence of multiples is indicative of highly attenuating material such as cellulose (from wood pulp mills) or decaying organic matter.

McGee (1990) analysed multiples from a number of high-resolution surveys in order to determine what information can be gleaned about the near-surface materials. Figure 6.44 shows an analogue seismic record across the Saint Clair River at the Canadian–USA border near Detroit, where waste material had been dumped at the base of a rock outcrop. A discontinuous reflection from the river bed is faintly visible below the waste material. The water-layer multiple decays more rapidly over the waste material than elsewhere. This indicates that the reflectivity of the waste is greater than that of both the natural river sediments and the bedrock outcrop.

Figure 6.45 shows another profile across the Saint Clair River from Sarnia, Ontario, Canada, to Port Huron, Michigan, USA. The

concave-downward event at 23 ms near the centre-line is a reflection from the top of a 6 m diameter railway tunnel that passes obliquely beneath the river. The dredged area on the Canadian side is associated with a commercial wharf. The soil there is soft clay over firm clay. On the USA side the soil is sand over firm clay. Except for these locations the tunnel was excavated in firm clay containing large boulders and lenses of sand and gravel. It is thought that the diffractions seen just below the river-bed reflection have been caused by these heterogeneities. The lower part of the tunnel lies in a sand layer, the top of which gives rise to the weak reflection a couple of milliseconds above the first water-layer multiple (WLM) of the river bottom. The strong reflection beneath has been produced by the top of bedrock, the Detroit Sandstone. The presence of water-layer multiples of second and higher order is obvious, but the tunnel produces only one multiple. Considering that it is lined with cast iron, this is somewhat surprising. However, the lack of higher-order multiples associated with the tunnel was thought by

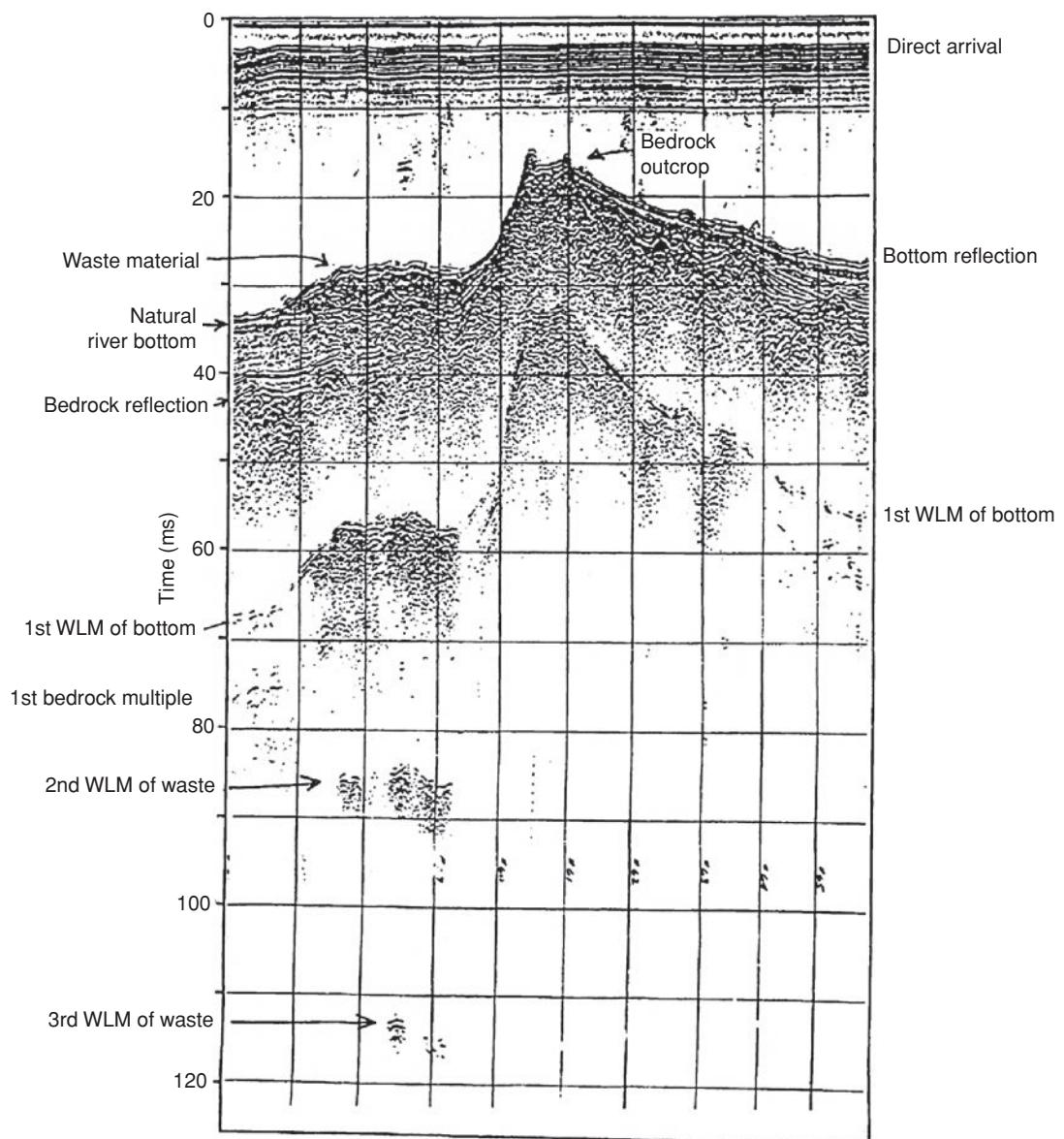


**Figure 6.44** Analogue seismic profile across the Saint Clair River near Detroit, USA, showing reflections and multiples arising from a waste dump adjacent to a bedrock outcrop. After McGee (1990), by permission.

McGee to be due to its curvature, causing reflected wavefronts to diverge.

Figure 6.46 shows another sequence across the Saint Clair River in which several areas of pegleg multiples are evident. A portion of this record has been enlarged to show the multiple sequences in more detail. Several orders and combinations of water-layer and pegleg multiples can be identified on the basis of their arrival time. Slight differences in apparent dip between the water-bottom reflection and the anomalous reflection become greatly exaggerated by the higher-order events. Soft grey clay over firm blue clay was found in a borehole drilled nearby. The interface between the two clays was encountered within 0.3 m of the depth calculated from the reflection time by assuming that the seis-

mic velocity in both the water and the upper soil was 1500 m/s. The postulated cause of the higher reflectivity in certain locations was an anomalously large density contrast between the two clays.

Higher reflectivity is often observed associated with channel lag deposits in rivers or palaeochannel infills. As the sediment coarseness increases from fine sands on the channel rim to gravels and even cobbles at the lowermost point, so the reflectivity increases. Consequently, higher-order multiples often arise from the gravel part of the lag deposits, with the reflectivity decaying laterally and in sympathy with the decrease in sediment grain size. Commonly, gravel bands give rise to pulse broadening too, so producing a characteristic reflection pattern.

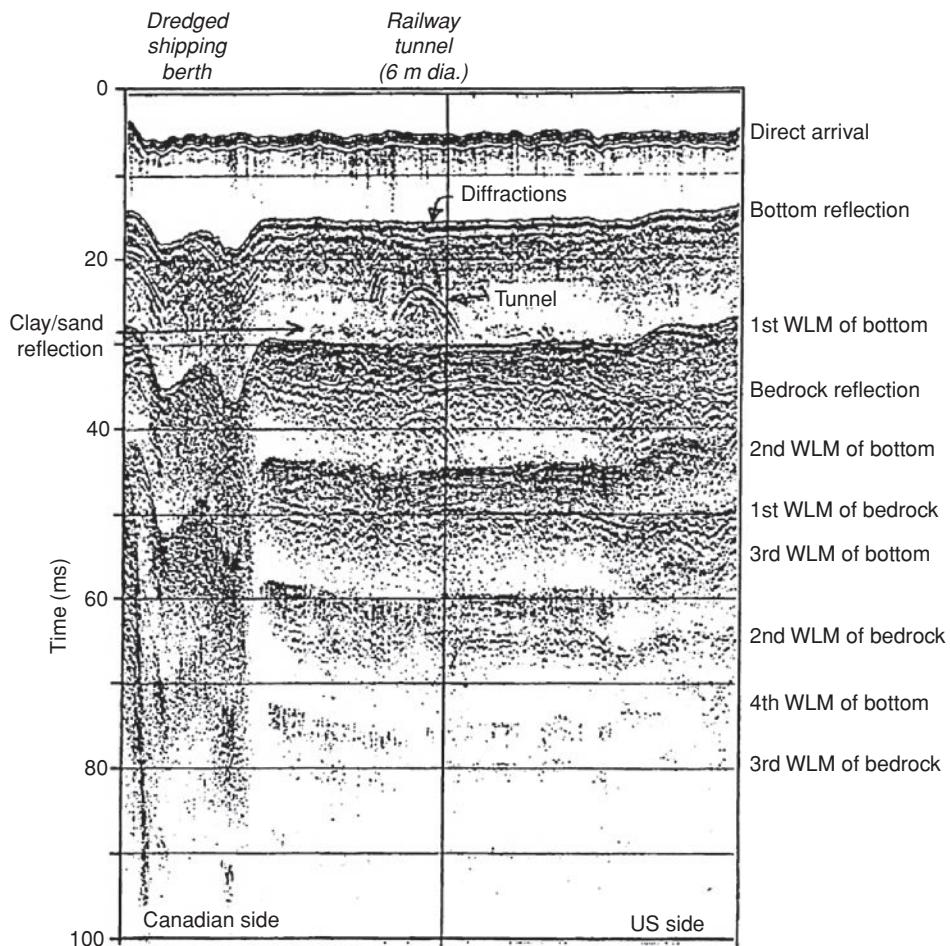


**Figure 6.45** Analogue seismic profile across the Saint Clair River in the vicinity of a railway tunnel. After McGee (1990), by permission.

McGee (1990) also argued that, when the data are recorded digitally and with sufficient dynamic range, the amplitudes of the multiples can yield valuable information. For example, in water-saturated and weakly consolidated sediments, the seismic velocity in most of the materials is approximately 1500 m/s. Any reflections that arise do so, therefore, from a contrast in density only. If the reflection coefficient can be computed from the digitally recorded data for the water-seabed interface, then the density of the soil can be estimated. Using this, and the measured decay in subsequent amplitudes, and still assuming a saturated soil velocity of 1500 m/s, the densities of deeper soil horizons can be estimated. In areas of anomalously high reflectivity, the increase in density of the material causing the effect can be calculated.

Although not routinely done, the format of reflection seismic data from shallow engineering over-water surveys can be output in SEG-Y format with (dGPS) positional data in the trace header. These data can be processed using commercially available workstations or oil industry software on powerful laptops or PCs to utilise the full processing power normally reserved for hydrocarbon exploration surveys. Knowing what data processing and analytical

methods are available, high-resolution over-water surveys are now being designed with a high degree of interline spacing (e.g. 10 m) across survey corridors hundreds of metres wide. By so doing it is possible to process and interpret the data as a 3D project. Reflection picks along long lines can be tied in to cross-lines to check the intersection mis-ties, and help to ensure consistency in picking reflection events around a loop of survey transects. The sampled reflection picks can be output to georeferenced databases and gridded to form rendered surfaces that can be viewed in 3D and cross-correlated with borehole data (where available in AGS or similar format). Furthermore, by having access to the SEG-Y data, more detailed analysis using attributes may yield more information about the geotechnical properties of the materials being imaged. Although parameters of direct interest to geotechnical engineers and engineering geologists, as outlined in Figure 6.47, would be desirable, seldom is the budget large enough to justify the time of expert interpreters to derive these parameters. It is also rare for surveys to be designed to such a high level of sophistication to have the data available to achieve such outcomes. There is still a disproportionately small amount of a project's budget being allocated to high-quality ground investigation.

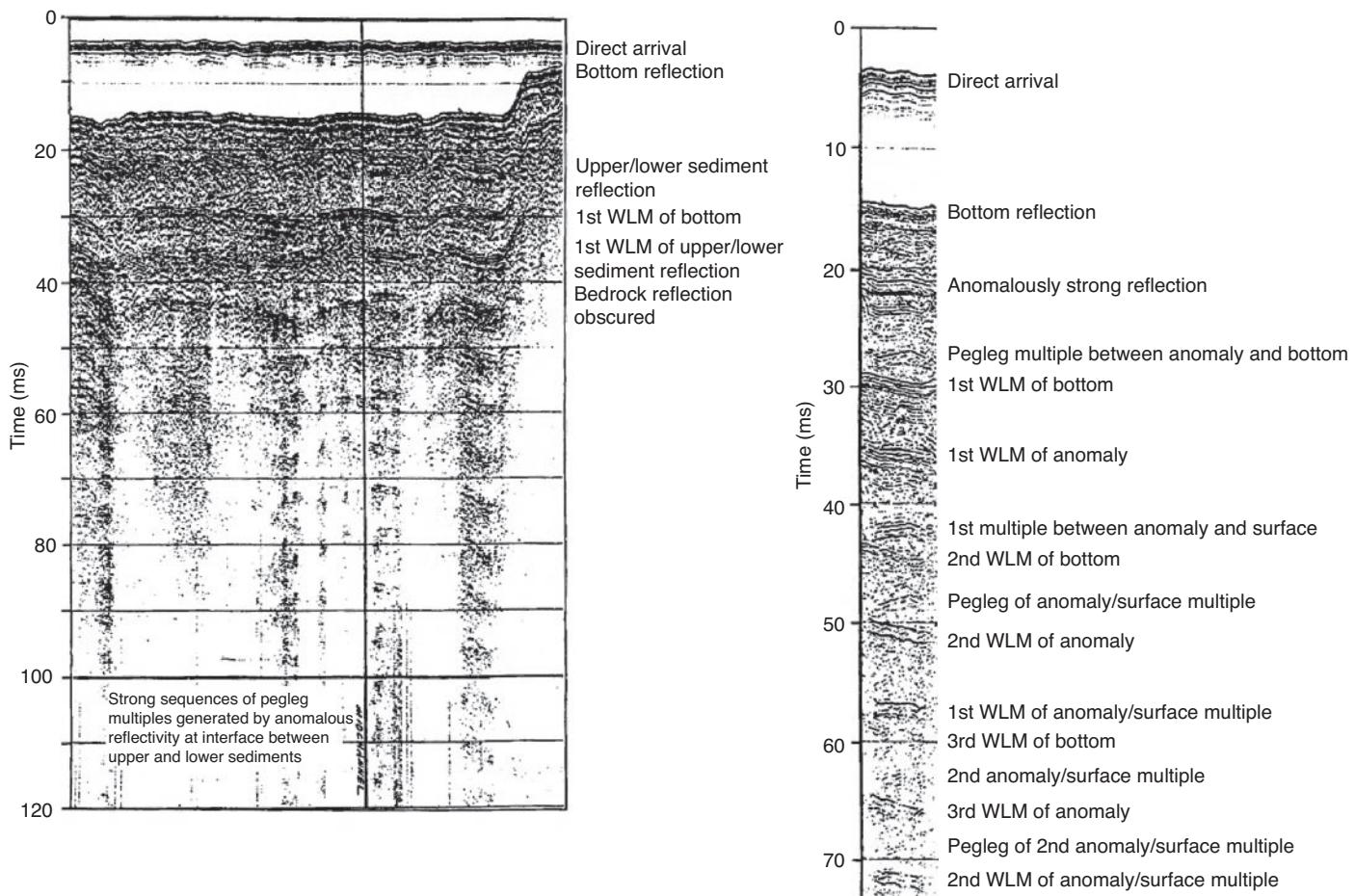


**Figure 6.46** On the left is a digital seismic profile across the Saint Clair River showing numerous patches of anomalous reflectivity indicated by pegleg multiples. On the right is enlargement of the portion located immediately to the right of the mid-channel line, showing the multiple sequences in detail. After McGee (1990), by permission.

### 6.5.3 Potential interpretational pitfalls

Pitfalls in seismic interpretation have been discussed in detail by Tucker and Yorston (1973), Tucker (1982) and Steeples and Miller (1994). The most basic difficulty is translating from the time-domain seismic ‘image’ to the geological cross-section, and the biggest uncertainty is in determining the seismic velocities and their lateral and vertical variations. Just two aspects are highlighted here, both of which are related to velocity.

The first aspect is apparent dip on a seismic reflector produced by velocity variation within a layer (Figure 6.48A). As the velocity increases or decreases along the horizon, so the travel time through that material decreases or increases respectively, even though the reflector is horizontal.

The second aspect is apparent bulges or cusps in an otherwise planar reflector. These are caused by velocity ‘pull-ups’ or ‘push-downs’ due to areas with an anomalous velocity above the reflector (Figure 6.48B). A ‘pull-up’ occurs when the overlying velocity is faster than that adjacent to it, so the travel time through the anomalous zone is

shorter than elsewhere. Conversely, a velocity ‘push-down’ occurs when the overlying velocity is lower than that adjacent, giving rise to a longer travel time.

One other common pitfall in interpretation, particularly of marine seismic profiles, is the ‘apparent thickness’ of the seabed sediment. Often the seabed reflection comprises a train of pulses which masks any inclined reflections that actually reach to the seabed surface. A common mistake is to calculate the period of the seabed reflection (in milliseconds) from the first break to the end of the wave train, and then compute an apparent thickness. This is completely wrong. No apparent thickness can be determined at all unless the thickness of the sediment cover exceeds that derived from the seabed wave train. For example, given a period of 5 ms two-way travel time for the seabed reflection wave train, and a sea-floor sediment P-wave velocity of 1500 m/s, the seabed sediment layer would have to be thicker than 1.88 m before the base of the seabed sedimentary layer could be imaged. Any thinner than this, and the base of the sediment layer would be masked by the tail of the seabed reflection wave train.

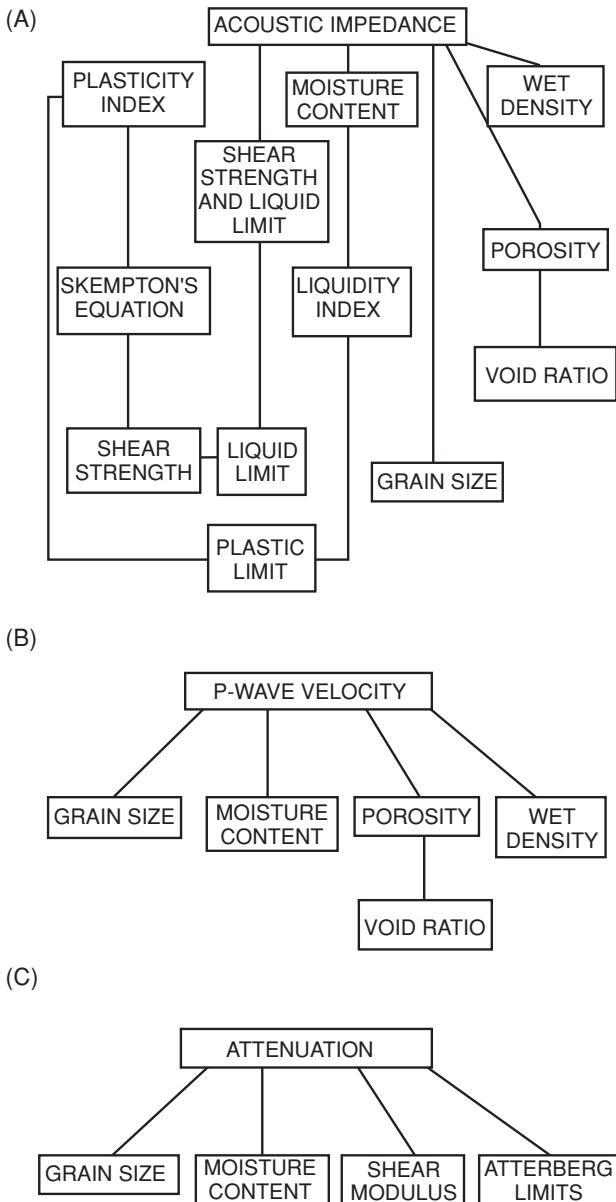


**Figure 6.47** Schematics showing the empirical relationships between geotechnical properties of a marine or estuarine sediment and its seismo-acoustic properties: (A) acoustic impedance; (B) P-wave velocity; and (C) attenuation. From Haynes *et al.* (1993), by permission.

well seismic reflection surveys can image the subsurface as well as indicating different applications.

The first example, provided by Pullan and Hunter (1990), describes the imaging of a buried rock valley beneath flat farmland at Dryden, Ontario, Canada. An in-hole shotgun source was used with the optimum offset of 15 m between source and receiver. High-frequency (100 Hz) geophones were used and data were recorded through a 300 Hz highpass filter on the seismograph. The recorded data were amplified using automatic gain control (AGC) and filtered with a digital bandpass filter (240–800 Hz) before final display. The minimum depth of visible reflections is around 7.5 m, about half the typical optimum offset distance.

The processed seismic section is shown in Figure 6.49, in which the buried rock valley is obvious. The geology of the site comprises flat-lying units of sand and clay (Quaternary) above Precambrian quartz-pegmatite bedrock. The natural groundwater level is at only 1 m depth. Consequently, the seismic source was fired into fully water-saturated fine-grained sediments – ideal conditions for high-resolution seismic reflection profiling. Despite the site being completely flat, the bedrock topography is marked – bedrock lies at a depth of only 15 m at each end of the 500 m long seismic line, but is about 65 m below ground level in the middle of the rock valley. The vertical geological sequence was determined from a borehole drilled as part of a Quaternary mapping project in the area, and a simplified log is spliced into the section for the sake of correlation. It can be seen that the major interfaces have been imaged successfully.

The depth scale shown in Figure 6.49 has been derived from a detailed velocity analysis, but the image does not show the exact geometry for the bedrock reflector because of the steep dip of the rock valley sides. Pullan and Hunter (1990) estimated that the error in the depth scale with respect to the valley sides is only 6–8%, so the unmigrated section provides a reasonable image of the buried rock valley. This accuracy is certainly adequate for the siting of boreholes for engineering or groundwater purposes.

The second example, also provided by Pullan and Hunter (1990), is an 850-m long optimum offset section from Shawville, Quebec, Canada, which crosses the proto-Ottawa River valley. The present-day Ottawa River lies 5 km to the west of the site. The seismic section (Figure 6.50) shows the buried valley to be about 500 m wide and over 100 m deep. The channel is incised into Precambrian marble and gneiss, and is infilled with glacio-lacustrine sediments.

In comparison with the previous example, the source used in this case was a 16 pound (7 kg) sledgehammer, with four strikes at the baseplate to generate sufficient energy to produce a sensible bedrock reflection. The optimum offset used here was 60 m, which is much larger than in the previous example because of the significant airwave generated by the hammer striking the baseplate. There was virtually no airwave generated in the first case as the shot was fired within the ground. The data were filtered using 100 Hz geophones and a 100 Hz highpass filter on the seismograph, followed by filtering with a digital bandpass filter (100–400 Hz) during subsequent processing.

The section in Figure 6.50 gives a general indication of the form of the buried channel. Several diffraction events (produced by knolls or depressions on the bedrock surface) can also be seen on the section, producing a more rounded impression of the bedrock topography.

## 6.6 Applications

### 6.6.1 High-resolution seismic profiling on land

In this section a number of examples are given to demonstrate the efficacy of the technique under suitable conditions. The surveys described range from the mapping of buried channels and of glacial stratigraphic sequences, and the evaluation of permitting (licensing) hazardous-waste injection. These case histories illustrate how

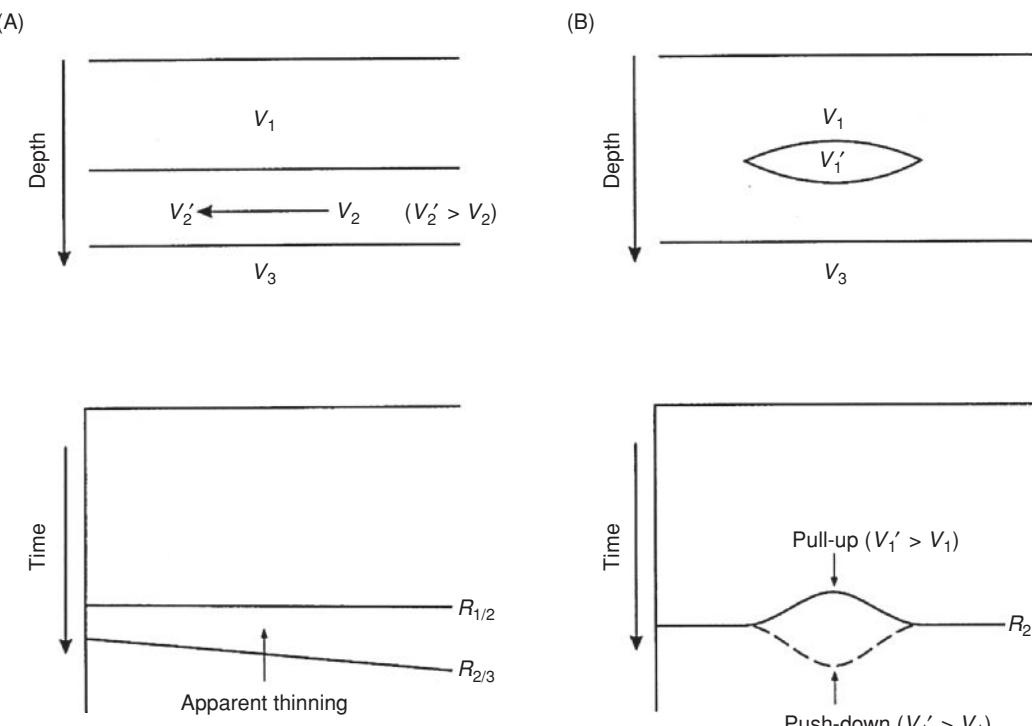


**Figure 6.48** Depth and corresponding time sections to illustrate (A) apparent thinning of a horizon due to lateral velocity changes; and (B) pull-up and push-down of a lower reflection due to the presence of a lens with a higher or lower velocity, respectively, relative to that of surrounding material. These interpretational features are relevant to both seismic reflection profiling and to ground-penetrating radar surveys.

The section is presented here to demonstrate that penetration of up to 100 m (achieved using just a hammer source), coupled with the benefit of the optimum offset technique, produced a good-quality image of the bedrock surface.

The third example, provided by Slaine *et al.* (1990), was acquired during a comprehensive investigation of the overburden and bedrock in the vicinity of the Ontario Waste Management Corporation's (OWMC) proposed site for a hazardous waste treatment

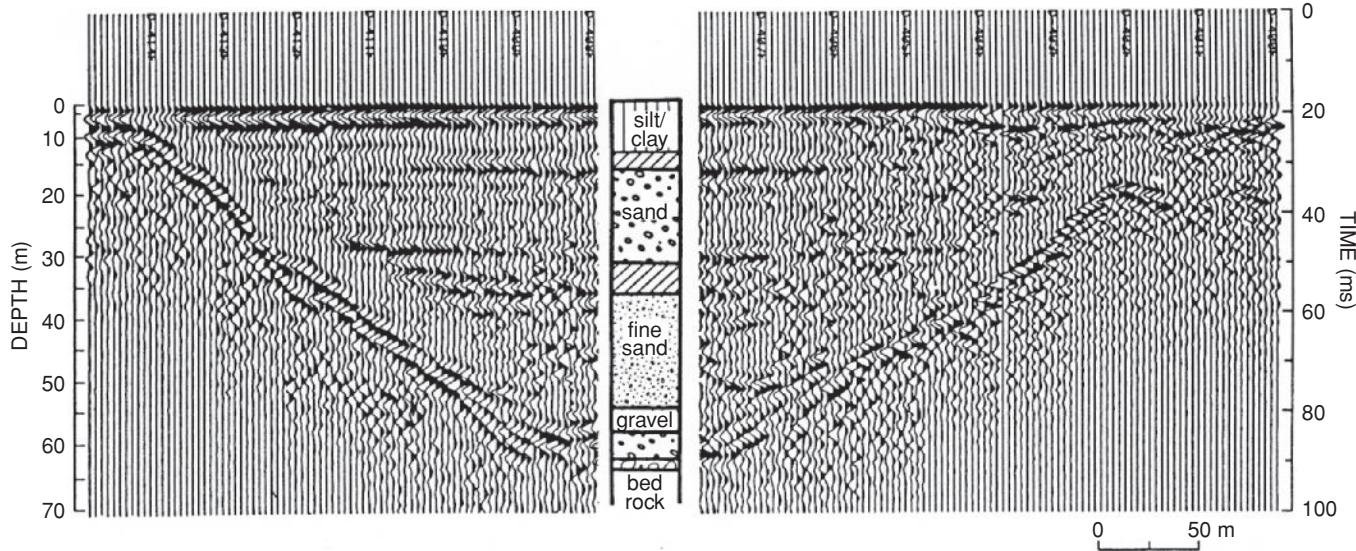


**Figure 6.49** Unmigrated optimum offset reflection section from Dryden, Ontario, showing a steep-sided bedrock valley filled with clay and sand deposits; the section is around 500 m long. From Pullan and Hunter (1990), by permission.

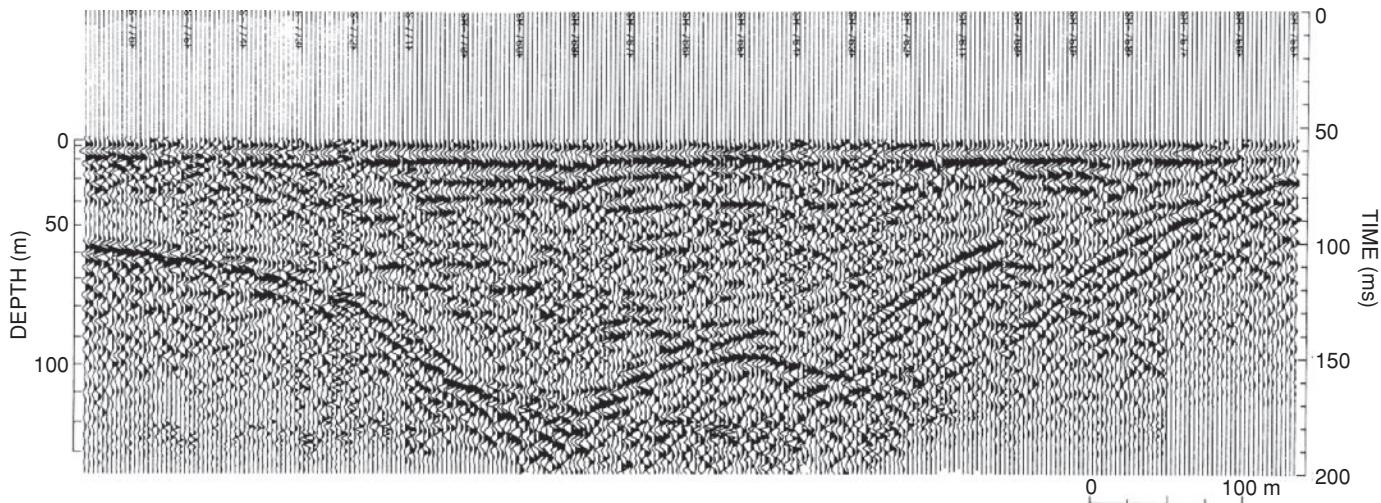


**Figure 6.50** Optimum offset reflection section from Shawville, Quebec, showing a broad (ca. 500 m wide) buried river channel, part of the proto-Ottawa River. From Pullan and Hunter (1990), by permission.

facility. It was also claimed to have been the first commercial seismic reflection survey for the evaluation of a proposed hazardous waste site in Canada. The objective of the seismic survey was to determine the continuity of subsurface overburden conditions between borehole locations on-site and beyond the site boundaries.

Stratigraphic control was provided by geological logs from 19 boreholes. The geology of the site was found to consist of four Quaternary glacio-lacustrine/glacial units. The Upper and Lower Glacio-lacustrine units (silt-clay) and the Halton Unit, an interbedded till, have a total thickness of 35 m. These units overlie a lower dense sandy-silt till (Wentworth (Lower) Till), commonly 1–2 m thick, which in turn overlies the Guelph Dolostone (dolomitised limestone) bedrock.

The seismic survey was undertaken using a 12-gauge in-hole shotgun source, with 100 Hz geophones buried at 0.5 m with a geophone interval of 5 m, and a 300 Hz highpass filter on the engineering seismograph. The data were processed by filtering with a bandpass filter (500–1000 Hz), corrected for surface statics, and displayed after applying AGC. Velocity analyses were also undertaken in order to determine the lateral and vertical variability in velocity. However, it was found that, as the sediments were predominantly water-saturated, there was no systematic variation in velocity with depth and that a value of 1600 m/s was representative of the overburden. Further details of the velocity analyses used are given by Slaine *et al.* (1990). The depth scale for the optimum offset section was calculated using the formula:

$$\text{Depth (m)} = \frac{1}{2} |(VT)^2 - X^2|^{1/2}$$

where  $V = 1600$  m/s,  $T$  is the two-way travel time in seconds, and  $X$  is the optimum offset (m). Depths to interfaces determined from the seismic sections were on average within 4% of the depths found by drilling.

Three laterally-continuous reflections were identified on the sections, one of which is shown in Figure 6.51. From the correlation

with the borehole logs, it was found that the three principal reflections were associated with interfaces between the units as shown in the figure. It was found, therefore, that the seismic survey met the original objectives and provided information about the subsurface materials that was not readily obvious from the borehole logs alone.

Miller *et al.* (1995) examined the vertical resolution achievable using high-quality seismic reflection profiling at a site in south-eastern Kansas, USA. A 12-fold common depth point profile was designed to image geometric changes greater than 2 m at depths from 25 m to 100 m in a depositional shelf-to-basin environment dominated by limestones, sandstones and shales. At the time of the survey the water table was more than 10 m deep.

The seismic data were acquired with a 15-bit EG&G Geometrics 2401 seismograph using a half-millisecond sampling rate, and 100 Hz low-cut and 500 Hz high-cut analogue filters. The source used was a downhole 0.50-calibre shotgun and receivers consisted of three 40 Hz geophones at 1 m spacing to form a group centred on each station with a station interval of 2.5 m. The optimum recording window had a source-to-nearest-receiver group offset of 12.5 m and a source-to-farthest-receiver group offset of 70 m, giving a total spread length of 58 m. Details of the data processing and modelling are discussed in detail by Miller *et al.* (1995).

The uninterpreted seismic record is shown in Figure 6.52. A borehole, Clarkson #2, is located at CDP 494, and the geological cross-section and corresponding geophysical logs (gamma ray and neutron density) are shown in Figure 6.53. A model derived for the seismic section was consistent with the borehole control from Clarkson #2, and the velocities and densities correlate with the lithologies encountered in the borehole core. The derived model is shown in Figure 6.54, with the interpreted version of Figure 6.52 shown in Figure 6.55. The buried channel has been imaged quite clearly, as have several of the principal rock units.

A comparison of Figure 6.52 with Figure 6.49 is quite striking. Both were acquired over the same travel-time range (ca. 100 ms) with comparable systems, although the survey shooting

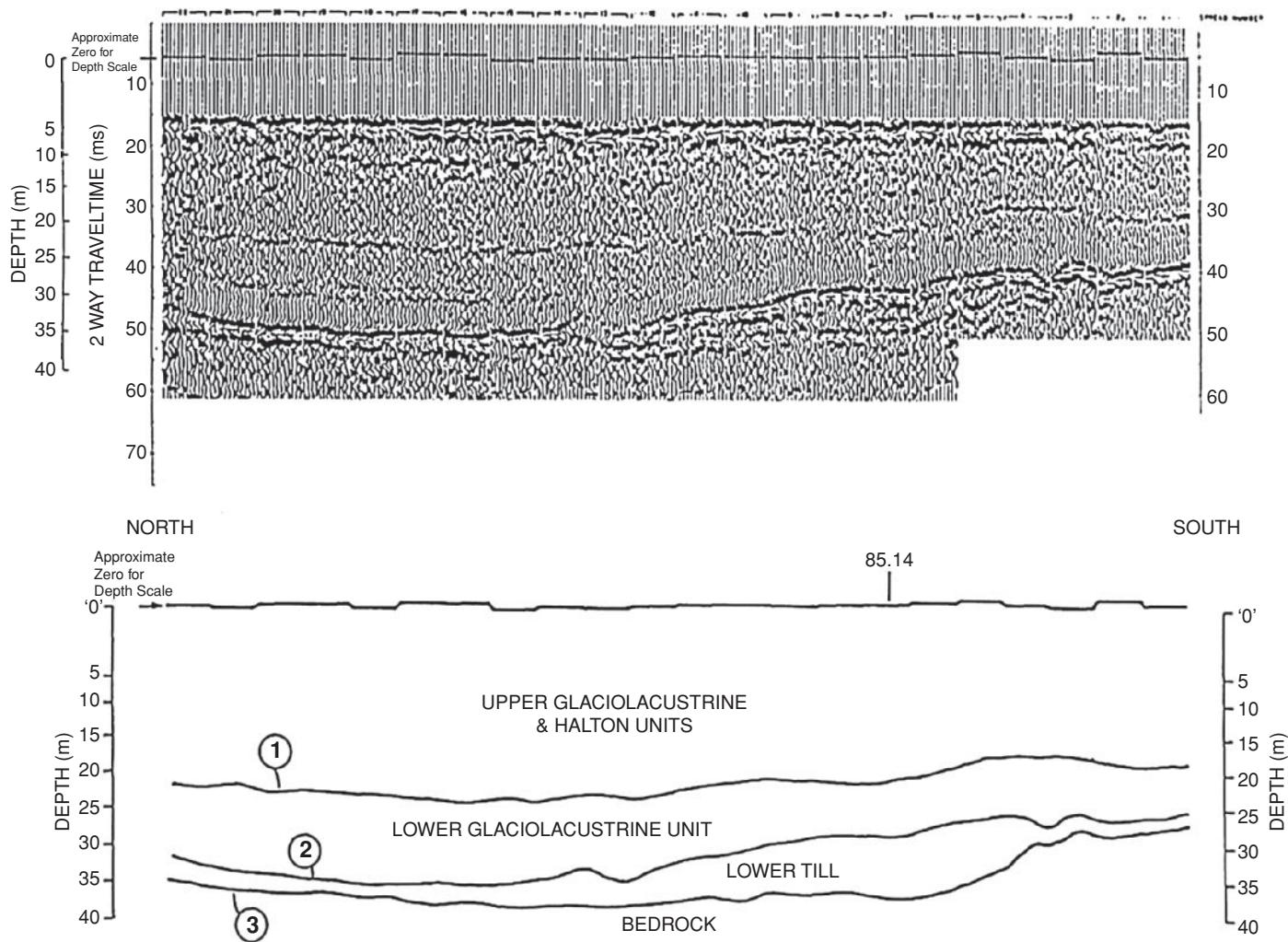


**Figure 6.51** (A) Seismic and (B) geological cross-sections along an 850 m long optimum offset reflection section acquired in Ontario. From Slaine et al. (1990), by permission.

configurations were different (12-fold CDP profiling versus the use of the optimum offset technique). Two other prime differences should be noted:

- In the present example the water table was deep and shots were fired in the unsaturated zone, in contrast with the fully water-saturated situation in the earlier example.
- In the present case the geology is mainly a cyclic, thinly-bedded sequence of the Late Carboniferous, compared with unlithified Quaternary sediments.

The vertical resolution apparent in Figure 6.49 is about 2–3 m, whereas that determined for the present case is about 7 m for a wavelength of approximately 21 m at a depth of 70 m. This latter value corresponds to one-third wavelength resolution rather than the more usual one-quarter wavelength. This comparison demonstrates that high-resolution seismic reflection profiling is better suited to sites with fine-grained, saturated near-surface conditions.

In north Wales, UK, the bridge Pont Melin Rûg (Figure 6.56A) was constructed in 1792 and is designated an Ancient Monument. It was originally designed to take horse-drawn stagecoaches that travelled the route between London and Holyhead en route to Dublin, then an increasingly busy route following the Act of Union between the two parliaments of Great Britain and Ireland. The bridge was incorporated into a new road scheme developed by the father of engineering, Thomas Telford, in 1820, a prime objective of which was to enable stagecoach horses to easily and rapidly trot along the entire road at an average speed of 13 km/hr. While the narrow humpbacked bridge remains visually appealing and architecturally significant, its location with tight radii bends with poor forward visibility, and awkward junction configurations on both sides of the bridge, had resulted in it becoming the focus of many road traffic accidents; while adequate for stagecoaches, the bridge was increasingly less so for modern juggernauts and tourist-towed caravans! It was decided to construct a new bridge upstream of the old one, and straighten the highway alignment. However, preliminary borehole investigations to 40 m depth failed to identify the base of soft to

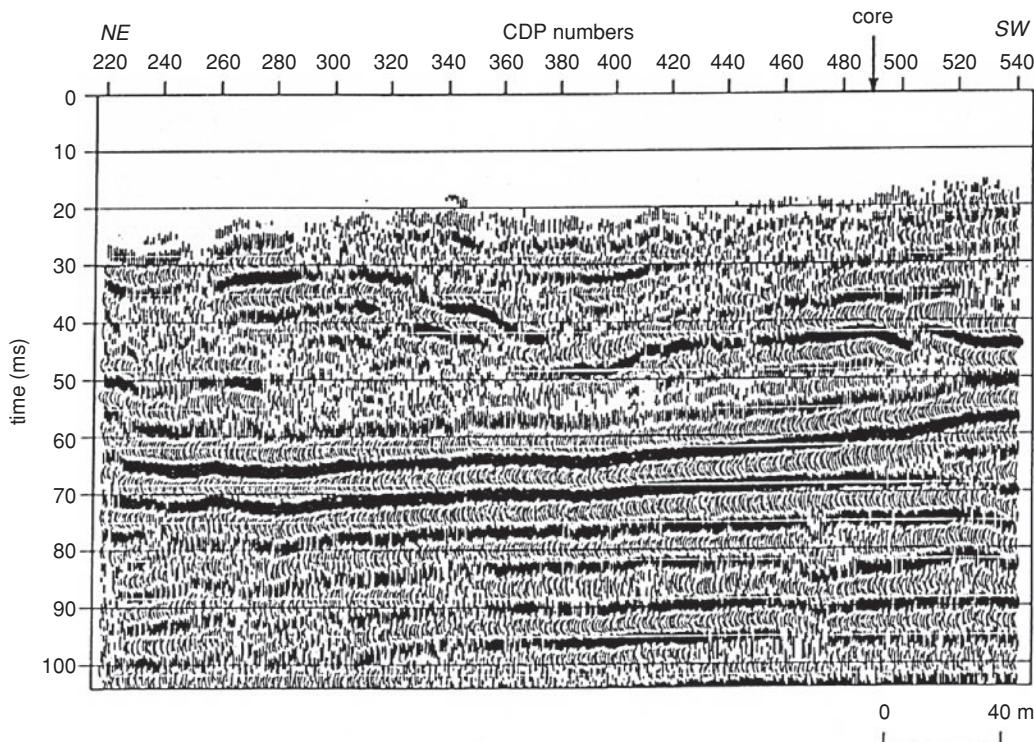


**Figure 6.52** Uninterpreted seismic reflection profile at a site in southeastern Kansas. From Miller et al. (1995), by permission.

very soft glaciolacustrine silts (Rûg Silts), although found a layer of contemporary alluvial gravels at the surface. The site lies within what was a substantial former glacial lake (Llyn Edeirnion) which silted up during the deglaciation from the Meirionnydd Ice Cap after the Pleistocene (Late Devensian) glaciation. It was decided that the only viable method of determining the depth of the base of the

Rûg Silts was to undertake a seismic reflection survey (Nichol and Reynolds, 2002).

Two 75-m long seismic profiles were established either side of the river Afon Alwen and as close as possible to the centre line of the proposed new route (Figure 6.56B). The river at this location is fast-flowing, and so seismic surveying was not continuous across

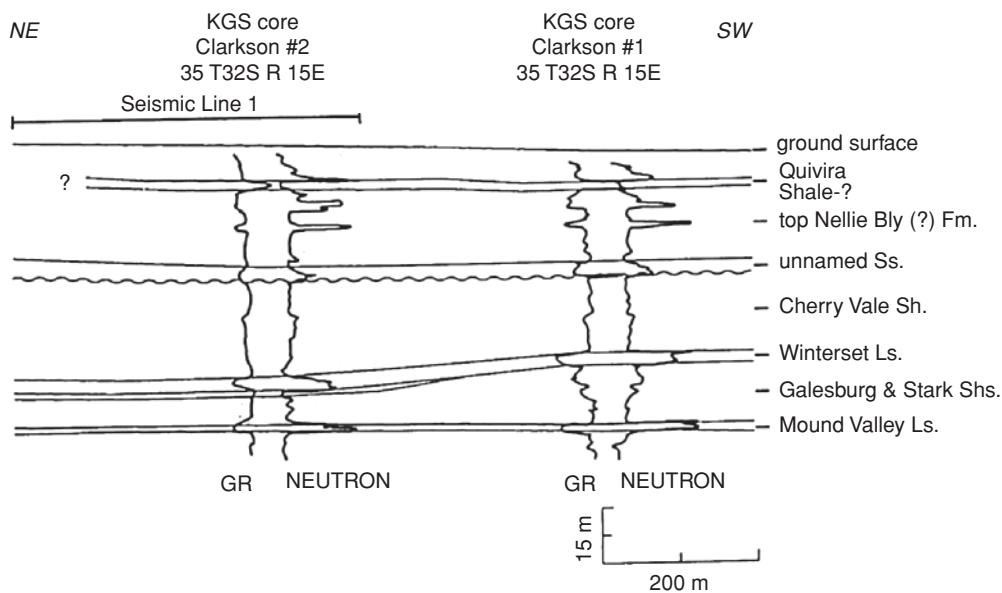


**Figure 6.53** Geological cross-section based on borehole lithological core and geophysical (gamma ray and neutron density) logs; the zone corresponding to the seismic line in Figure 6.52 is shown shaded. From Miller et al. (1995), by permission.

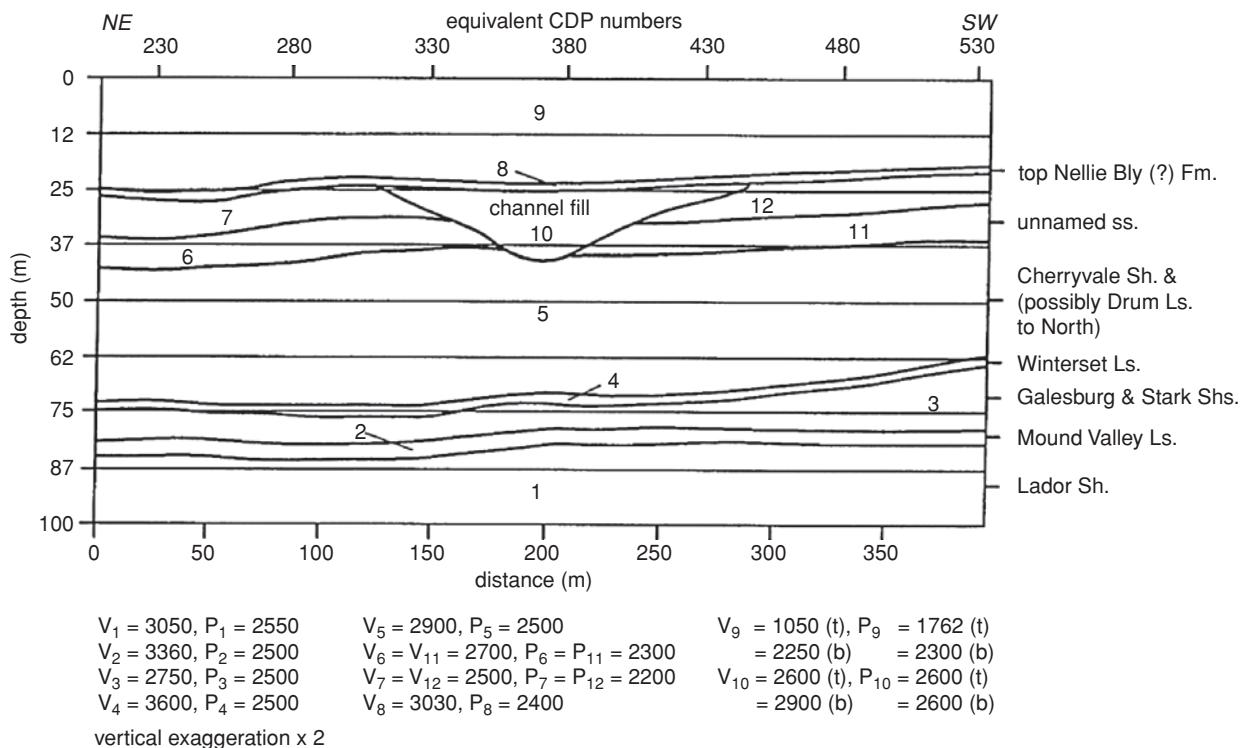


**Figure 6.54** Two-dimensional geological model derived from the seismic survey and correlated with borehole data. For this model, seismic velocity ( $V$  in m/s) and density ( $P$ ) in  $\text{kg}/\text{m}^3$  are defined at each interface and at the top (t) and bottom (b) of the channel fill. From Miller *et al.* (1995), by permission.

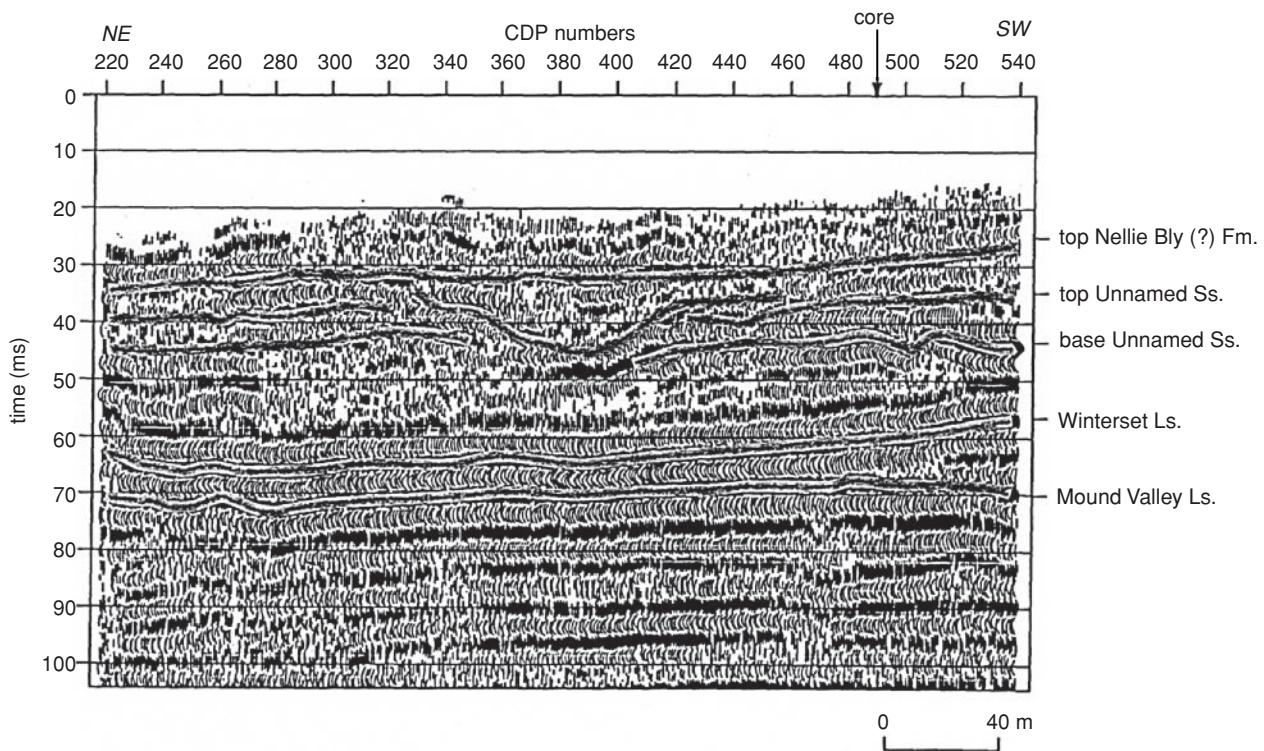


**Figure 6.55** Interpreted version of the 12-fold CDP stacked section shown in Figure 6.52. From Miller *et al.* (1995), by permission.

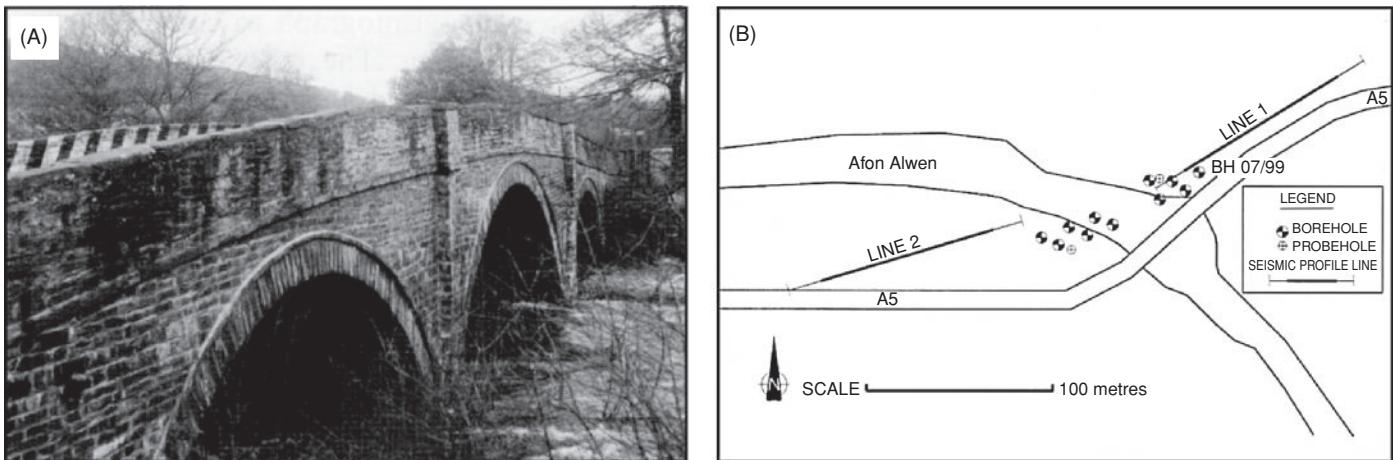


**Figure 6.56** (A) View of Pont Melin Rûg, Corwen, north Wales. (B) Location of seismic reflection profiles and boreholes. From Nichol and Reynolds (2002), by permission.

the river partly for logistical reasons but also because of the high noise levels generated by the turbulent water flow conditions. Time, budget and logistical constraints also prohibited the potential to undershoot the river using shots on one side and sources on the other. The central part of the survey line had been extensively drilled previously.

The results of the seismic survey (Figure 6.57) indicated that the base of the Rûg Silts lies at a depth of between 32 m and 49 m below ground level with the deepest section below the present Afon Alwen. Beneath the Rûg Silts, glaciofluvial gravel deposits between 36 m and 59 m thick consist of dense to very dense silts, sands, gravels and boulders. Within this unit, one prominent channel feature appears infilled by stratified material, and numerous other more subdued channel structures also exist. Rockhead is interpreted to range from 72 m to 114 m deep.

The findings of the high-resolution seismic reflection survey were confirmed by a single borehole (BH07/99; Figure 6.57) constructed to a depth of 49.1 m, which penetrated the full thickness of the Rûg Silts and permitted determination of an average seismic velocity of 1270 m/s for the unit. The investigations also proved a potential foundation stratum for the new bridge at 45.8 m in the basal fluvioglacial gravel unit (seismically determined depth of  $46.0 \pm 5$  m). The understanding of the geology at the bridge site provided by the geophysical investigation aided the deliberations on foundation selection and provided a major influence on the final design process. A new bridge has been constructed successfully using rafted foundations.

In the last example in this section, the scale of investigation is increased. In the USA, deep-well injection is used to dispose of hazardous liquid waste products. It is usual to use well-log data to assess the viability of such disposal, particularly in respect of the presence of faults that could act as fluid conduits, allowing hazardous waste to migrate beyond its intended destination. Underground sources of drinking water could easily become contaminated if such unforeseen leakage were to occur. In the present case, discussed in detail by

Zinni (1995), seismic surveys were used in conjunction with well-log data to help to delineate known subsurface faults and to locate previously unknown faults in St John the Baptist Parish, Louisiana, USA. Municipal water wells near Ruddock supply freshwater from the Covington aquifer, the principal local source of drinking water. A chemical manufacturer has been disposing of liquid hazardous waste into a zone encompassing the Covington aquifer (Figure 6.58) for 30 years via four injection wells. A recent deep geological investigation in the area had suggested that the Covington aquifer might be connected hydrologically with two of these waste-injection reservoirs. Under the local authority's regulations pertaining to contamination of any underground sources of drinking water (USDW), the confining zone(s) of a hazardous-waste injection reservoir should be free of bisecting transmissive faults and fractures. The seismic investigation was used to assess the structural, and hence hydrogeological, conditions in relation to licensing liquid hazardous-waste disposal. The geographical layout of the various wells and seismic line 1094 is shown in Figure 6.59.

The seismic survey was completed using between 24- and 30-fold coverage with asymmetrical split-spread geophone arrays with geophone group and shot intervals of 67 m and 134 m, respectively, and both hydrophone group and shot intervals of 67 m (for lake recording). The energy source was dynamite. Processing included dip move-out and migration.

The seismic record for line 1094 (shown in Figure 6.60) reveals four previously unknown faults, three of which (A, C and D in Figure 6.59) bisect the injection reservoirs and the Covington aquifer. The presence of these faults significantly increases the possibility of hydrological communication by providing pathways (fault planes) along which fluids may migrate. Alternatively or in addition, sand units could have been juxtaposed against other sand units, permitting leakage to occur across the contacts. Furthermore, the upper injection reservoir was found to be part of a fluvial system that in places had scoured down into the Covington aquifer. Sand had evidently been deposited directly from the injection reservoir interval

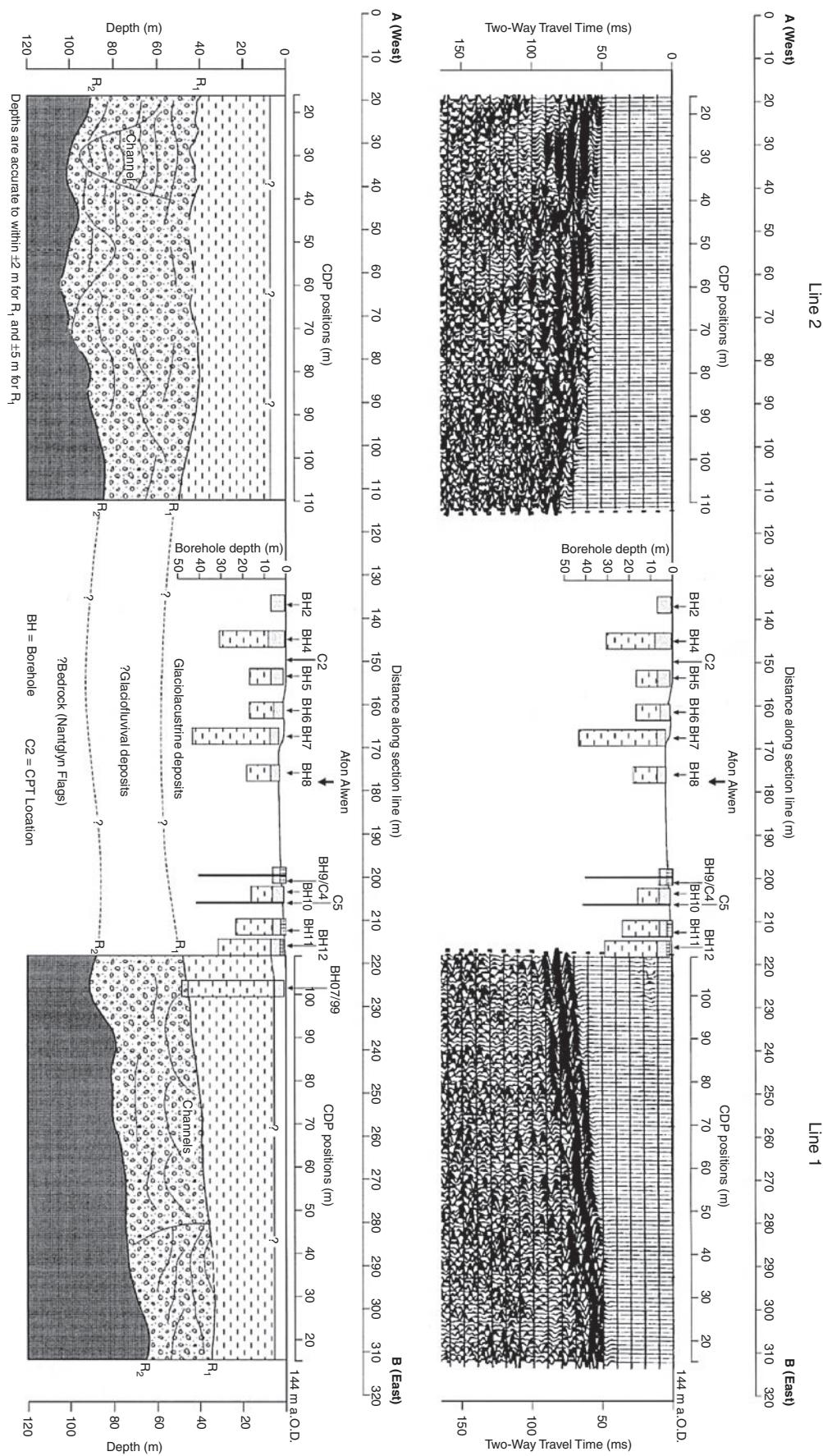


**Figure 6.57** Integrated interpretation of seismic reflection survey results and site investigation data. The new borehole is indicated at BH07/99. From Nichol and Reynolds (2002), by permission. [C]

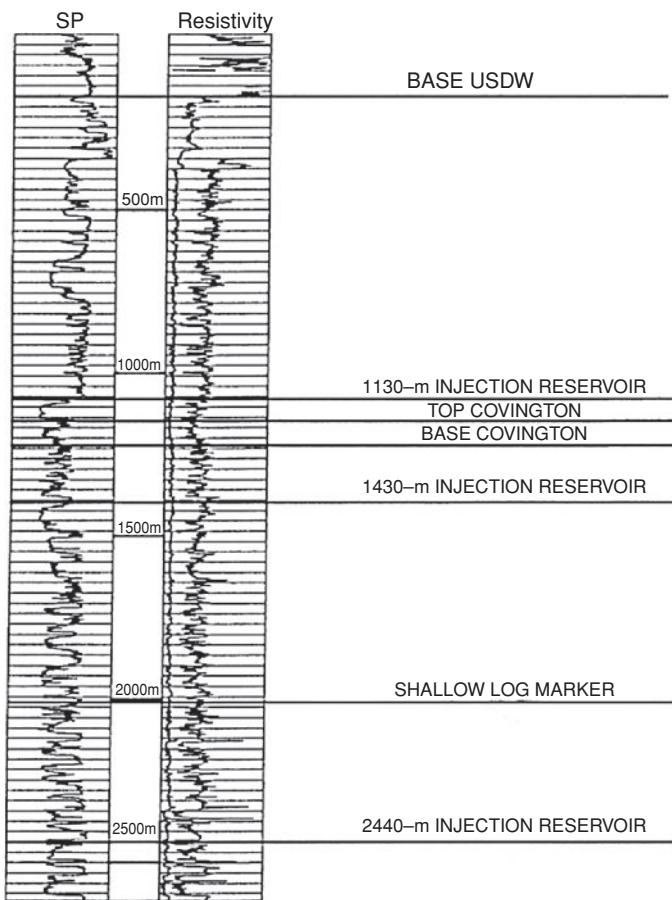


**Figure 6.58** Borehole logs at Dupont #8 Pontchartrain Works (for the location, see Figure 6.59). This well is the deepest of the four injection wells (total depth 2592 m), and has penetrated the 1130, 1430 and 2440 m injection reservoirs and the Covington aquifer. The base of the underground source of drinking water (USDW) is at 245 m depth. From Zinni (1995), by permission.

on the Covington aquifer sands. Consequently, the injection reservoir was thought by Zinni to be in hydrological communication with the Covington aquifer.

If vertical migration of liquid hazardous waste occurs along the fault planes following injection into the underground reservoirs, the water quality of the Covington aquifer could be adversely affected. Similarly, other shallow freshwater aquifers could also be jeopardised. Without the use of the seismic survey, the risk of contaminating underground sources of drinking water would not have been assessed properly.

In northeast England, subsidence occurs as a consequence of dissolution of gypsumiferous material, commonly chimney-collapse subsidence resulting in the formation of pipe breccia, and this is especially true around the market town of Darlington. At one site, known as Hell Kettles, ponds have formed in the subsidence depressions and are up to 100 m in diameter. A trial survey using the 3D seismic reflection method was undertaken following successful experiments acquired along 2D seismic profiles in an area nearby to one of the largest subsidence ponds, where another 0.5 m deep

subsidence depression is located. A strong seismic reflection had been recorded previously from the boundary of the Roxby Formation (mudstone) and the underlying Seaham Formation (limestone) (Sargent and Goult, 2009a). Foundering of the Seaham Formation is thought to have originated from the deeper-lying Hartlepool Anhydrite Formation. It was considered, therefore, that by mapping the top of the Seaham Formation using 3D seismic reflection might reveal additional and hitherto unknown possible collapse features (foundering). These might be evident on the seismic profiles by dislocations within the otherwise continuous reflection from the top of the Seaham Formation (Figure 6.61). The detailed field procedure built up a 3D seismic volume comprising 64 in-line and 84 cross-line sections of 6-fold CMP bins with dimensions 2 m × 2 m covering a total subsurface area of 128 m × 128 m. Improved detail of the reflection from the Seaham Formation was obtained from the 3D survey compared with the coincident results from the 2D survey (Sargent and Goult, 2009b; Figure 6.62).

The overall dip direction of the Seaham Formation across the 3D area is to the northeast, with a corresponding increase in the two-way travel time from 41 ms to 57 ms, equivalent to depths of 41–57 m below the datum. A contoured map of the two-way travel time to the top of the Seaham Formation (Figure 6.63A) was produced by manually picking the limestone reflection response throughout the 3D survey area. A quadratic polynomial regression surface, computed from the top Seaham Formation two-way travel time slice, represents the long-wavelength content of the horizon slice in Figure 6.63B. Subtraction of the regression surface from the original horizon slice reveals short-wavelength deviations in the limestone surface (Figure 6.63C). Several subcircular depressions within the limestone surface are evident, varying in size from 5 m to 20 m in diameter. The location of the shallow depression evident at the ground surface is indicated by the short arrow; the other three features as yet do not have any surface expression (Sargent and Goult, 2009b).

This case study demonstrates that using a very high-resolution 3D seismic survey produced images of subsurface foundering at the top of the Seaham Formation limestone at depths of around 50 m that could not have been produced by any other geophysical method.

## 6.6.2 Seismic reflection surveys for earthquake prediction studies

Of potentially enormous consequences are the possible effects of major earthquakes ( $M_L \sim 7$ ) on mega-cities such as Mexico City, Istanbul, and especially Tehran, where the potential numbers of casualties in such an event could exceed 500,000 with economic losses in excess of \$300 billion. As urbanisation has occurred, often unchecked and unplanned, ground becomes enveloped by buildings, making it extremely hard to map the location and extent of near-surface faults that could become activated. Yet a knowledge of where such faults exist and their orientation and characteristics may prove extremely useful in helping to reduce the consequences of major seismic events. In Tehran, for example, it is proposed to undertake a 26-km long north-south transect through the city

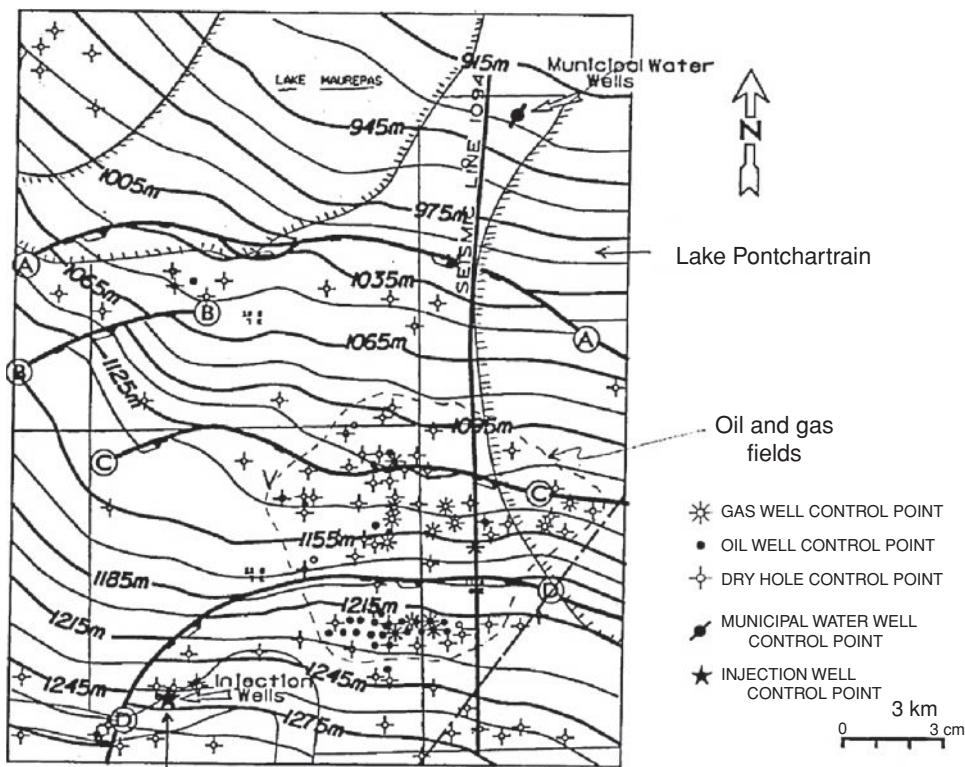


Fig 6.58

**Figure 6.59** Location map of the survey and well-field area, Louisiana, USA. The position of each of the municipal water wells, injection wells, velocity survey well (V), and the approximate outline of the Frenier, Laplace and Bonnette Carre oil and gas fields, are marked. After Zinni (1995), by permission.

along a major road using Vibroseis in order to map the location and vertical extent of faults beneath the city. This study is being coordinated by the International Institute for Earthquake Engineering and Seismology in conjunction with an international oil company.

### 6.6.3 High-resolution seismic profiling over water

There has been a substantial growth in the use of high-resolution seismic surveys for the determination of suitable foundations for offshore wind farms, as well as for dredging and marine resource evaluations, and mapping subsurface geological structures for the construction of tunnels and pipes.

When these surveys are undertaken, they are often accompanied by hydrographic surveys, where the depth to seabed and the nature and texture of the seabed are determined. For this reason, a brief explanation of hydrographic surveys is provided in the next section, followed by examples of the use of high-resolution seismic surveys in a variety of applications over water.

#### 6.6.3.1 Hydrographic surveys

Hydrographic surveys usually comprise one or more methods of determining the water depth or more particularly the surface ele-

vation of the seabed or riverbed. In tidal areas, it is necessary to measure the variation of the water depths with the tidal cycle, so that the elevations of the river/seabed can be determined relative to a particular datum (e.g. Newlyn within the UK). Note that for surveys along rivers, due to the river gradient, different datums may apply for different reaches of the river. In order to know what value of speed of sound in water to use to correct transit times to water depths, it is necessary to conduct vertical profiles to measure the variation in the speed of sound as a function of water depth. In oceanographic investigations, this is often done in tandem with vertical salinity profiling using a single instrument to measure both parameters. It is advisable to make measurements on the descent as well as the ascent of the instrument. An example profile of the speed of sound in water is given in Figure 6.64.

**Echo sounding:** Two types of echo sounding are available: (a) Normal incidence depth measurement, and (b) swath bathymetry. In the first case, a single or dual frequency transducer is deployed that emits pulses of sound, and the transit time of the echo is measured. Using a value for the speed of sound through water, the transit time can be converted to a distance, i.e. water depth. Most boats use a standard single frequency echo sounder to provide an indication of water depth, but for hydrographic surveys, dual-frequency transducers can be used. These operate at two different frequencies, for example, 33.8 kHz and 210 kHz, in the range 3.5 kHz to 250 kHz. Where the substrate is hard, the transit times from both frequencies are likely

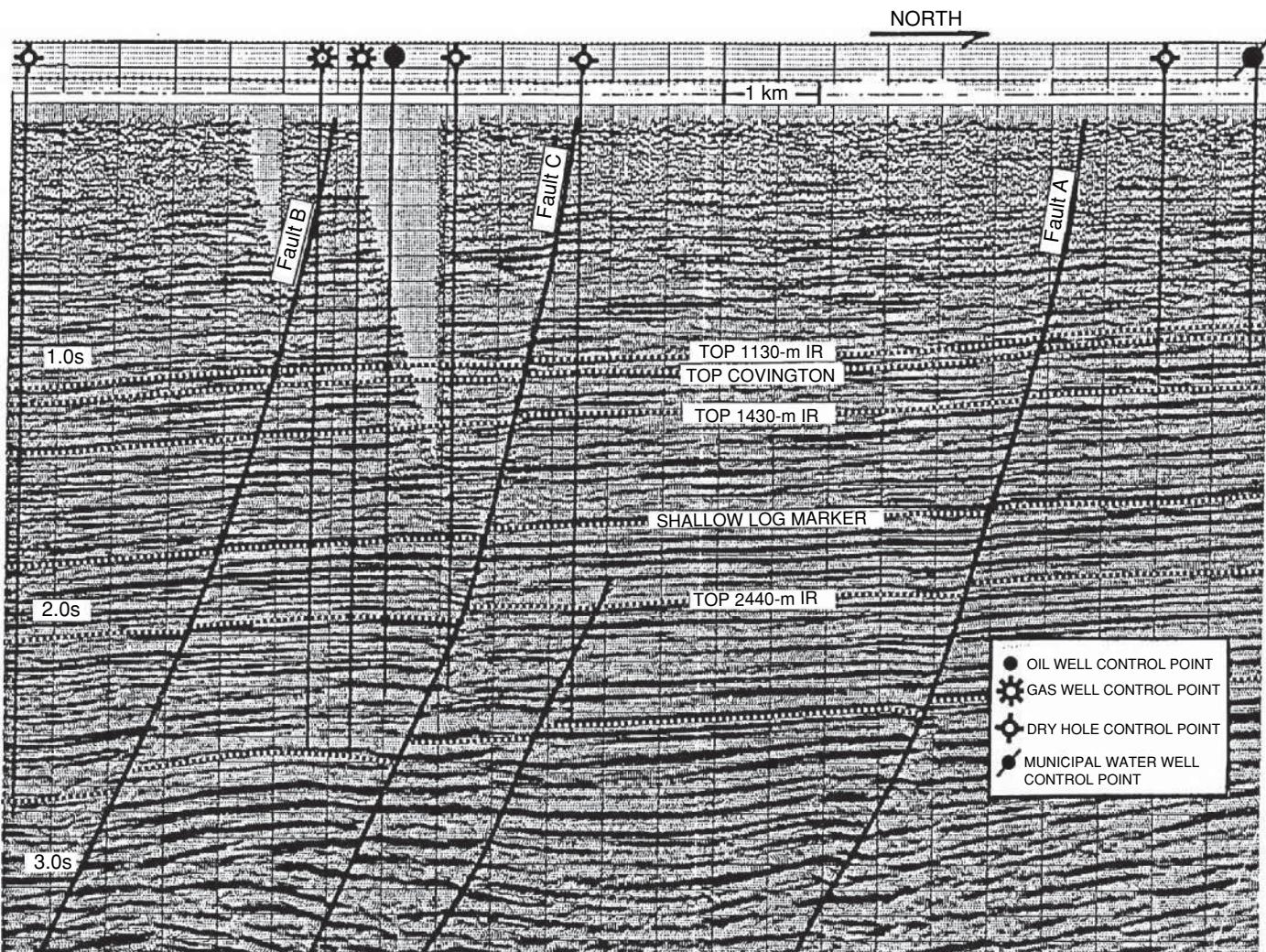


**Figure 6.60** Seismic line 1094 (location marked in Figure 6.59). Faults A, C and D intersect the 1130, 1430 and 2440 m injection reservoirs (IR) and the Covington aquifer. From Zinni (1995), by permission.

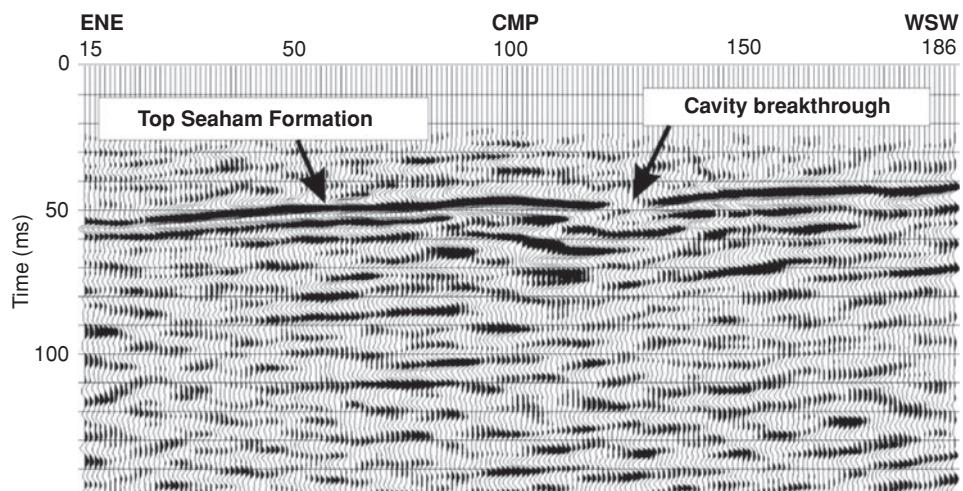


**Figure 6.61** Migrated 2D section showing a gap in the reflection from the top surface of the Seaham Formation limestone. Trace separation is 1 m. From Sargent and Goult (2009a), with permission.

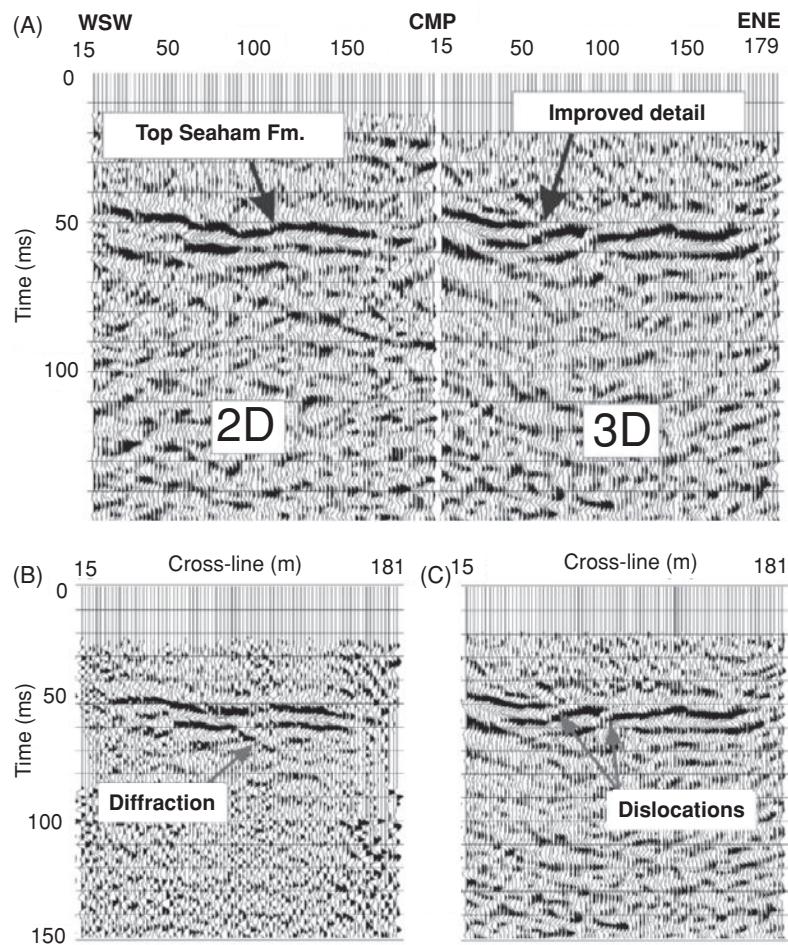


**Figure 6.62** (A) Comparison of a migrated 2D section with the section at the same location extracted from the migrated 3D volume. Trace spacing is 2 m. (B) 2D stacked section and (C) time-migrated section of one line from the 3D survey block. From Sargent and Goult (2009a and b), respectively, with permission.

to be the same; however, where there is a soft ooze a few centimetres thick above a harder substrate, the depths from the two different frequencies may differ. The low frequency signals will respond to the hard substrate, while the high frequency signals will respond to the top of the ooze.

Utilising the differences between the water depths derived using the two frequencies can yield information about the nature of the substrate. For example, at Llwyneinion in north Wales, a dual-frequency echo sounder was used across a shallow lagoon over a tar pit (Reynolds, 2002). Differences in depth obtained by the two frequencies indicated areas of soft tar, whereas when they were the same it indicated that a crust had formed. The soft areas also corresponded with areas of observed gas seeps from within the tar where it had not set hard.

**Swath bathymetry:** A single high-frequency signal from a fixed-mounted transducer is swept at right angles across the path of a vessel to a slant range that is typically four times the water depth (Figure 6.65). The transit time is determined and software used to correct for the increasing raypath distances with increasing offset from the vessel track, to produce a value of water depth for each

discrete pixel across the swath insonified. Typically pixel sizes are of the order of 25 cm or 50 cm, depending upon the system deployed. This system is capable of providing very high-resolution maps of water depth with a very high spatial sampling; typical pixel size is 0.25 m. The recorded data can be mosaiced using specialist software to produce a single map of water depth derived from a variety of traverses with different azimuths. This is sometimes necessary to avoid the shadow effect produced, for example, by bridge piers and piles or other obstructions.

**Side-scan sonar:** A single towed sensor that emits sound pulses from sideways-looking transducers can be used to map underwater objects from their echo returns (Figure 6.66). Moderns side-scan sonars have been developed from those invented during the Second World War for submarine detection (ASDIC = Anti-Submarine Detection Investigation Committee systems). As the sensor is moved forward at speeds typically of 3.5–9 km/hr, the echoes from each increment along the profile line are recorded according to the slant ray path and displayed as a *sonograph*. Typically the sensors contain transducers with two different frequencies (e.g. 130 kHz and 445 kHz) which have correspondingly different resolutions and

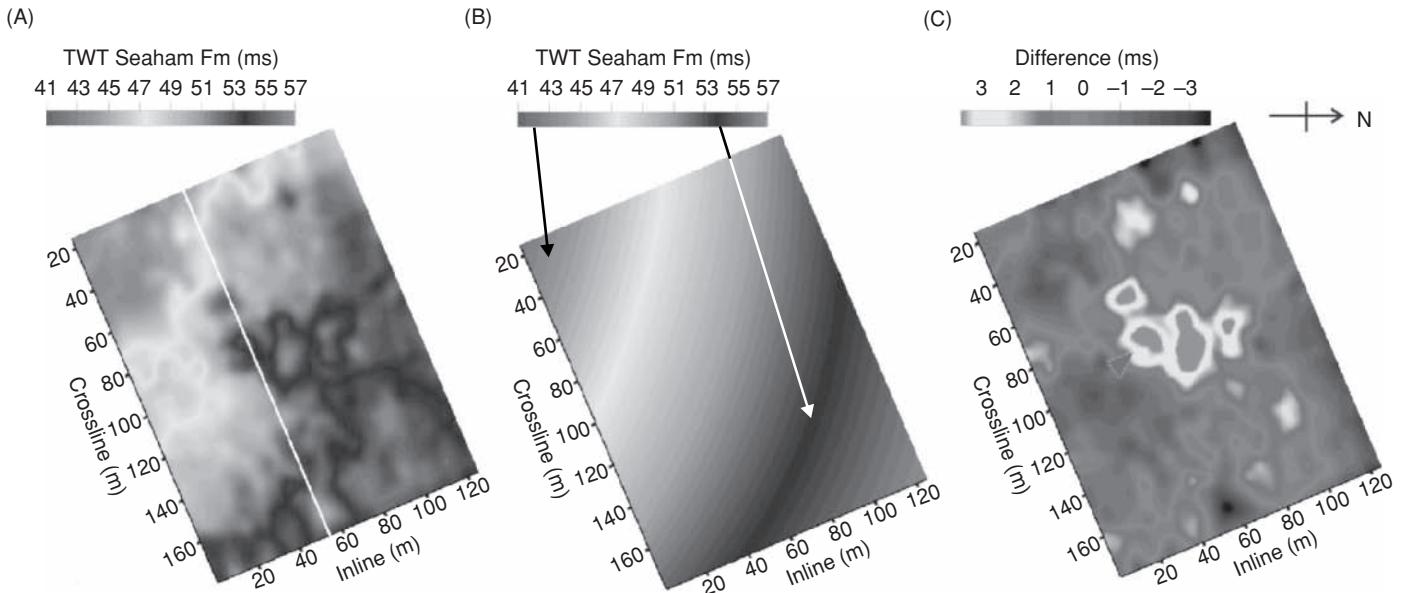


**Figure 6.63** (A) Top Seaham Formation horizon time slice, unfiltered. The line of the 2D section in Figure 6.62B and C is shown by the white line. (B) Polynomial regression surface. (C) Top Seaham Formation horizon slice after subtracting the regression surface. To the ENE of crossline 160 the horizon picks are noisy due to low fold and poor data quality. From Sargent and Goult (2009b), with permission. [C]

sonar ranges, the low frequency range (<450 m) being perhaps three times longer than that of the high frequency system. The sensor ('fish') can be towed at shallow depth or at significant depth depending upon the system being deployed. Modern systems are capable of depth ratings to 6 km. When used for shallow water

applications, the resolution is sufficient to be able to detect objects such as discarded car tyres, anchor chains, pipes, shipwrecks, and so on, as well as to map the seabed texture to differentiate between areas of mud, sand, gravel and exposed bedrock.

The principle of side-scan sonar is also illustrated in Figure 6.67. A number of targets both on the sea floor and within the water column (Figure 6.67A) are insonified by sonic pulses from the towfish at different slant ranges (Figure 6.67B). The minimum echo time is given by the distance between the towfish and the seabed ( $t_0$ ) in which time there is usually no echo evident on the sonograph, which gives rise to a central stripe on the image (Figure 6.67C). The different targets produce a variety of echo types and, if the target is upstanding from the seabed, it is possible to determine the height of the object above the seabed from the corresponding shadows.

An example of the results of a high-resolution swath bathymetry survey are shown in Figure 6.68A for comparison with the corresponding sonograph from side-scan sonar (B) over a feature on the riverbed, seen at low tide (C). It is thought that this is a crater formed from the impact of an unexploded WW2 bomb, with the entry on impact at the narrow portion displacing material into the rump in the foreground of the picture. A magnetic target was also located here!

Specialist systems used in deep ocean surveys since the 1960s, such as GLORIA (Geological Long Range Inclined Asdic) provide coverage of large areas of seafloor per day, typically of the order of 20,000 km<sup>2</sup> (Jones, 1999). GLORIA is usually towed at a depth of 50 m and up to 400 m astern of the towing vessel at speeds of 10–20 km/hr. Nominal cross-track sonar ranges of 45 km can be achieved. TOBI (Towed Ocean Bottom Instrument) uses a 30 kHz side-scan, along with other sensors, that is towed 400 m above the seabed at about 3 km/hr producing a sonograph about 3 km

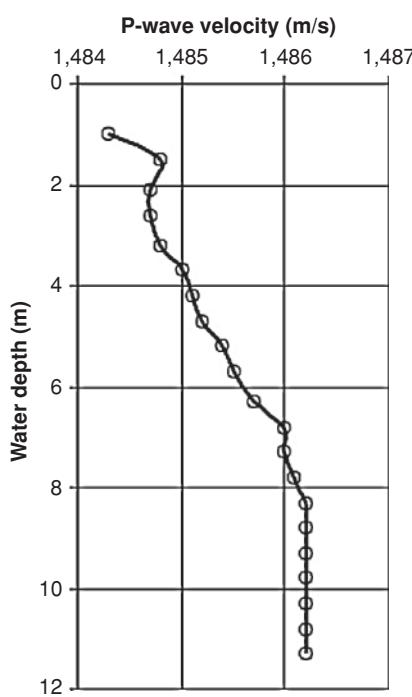


**Figure 6.64** Example of a vertical profile of the speed of sound in water.

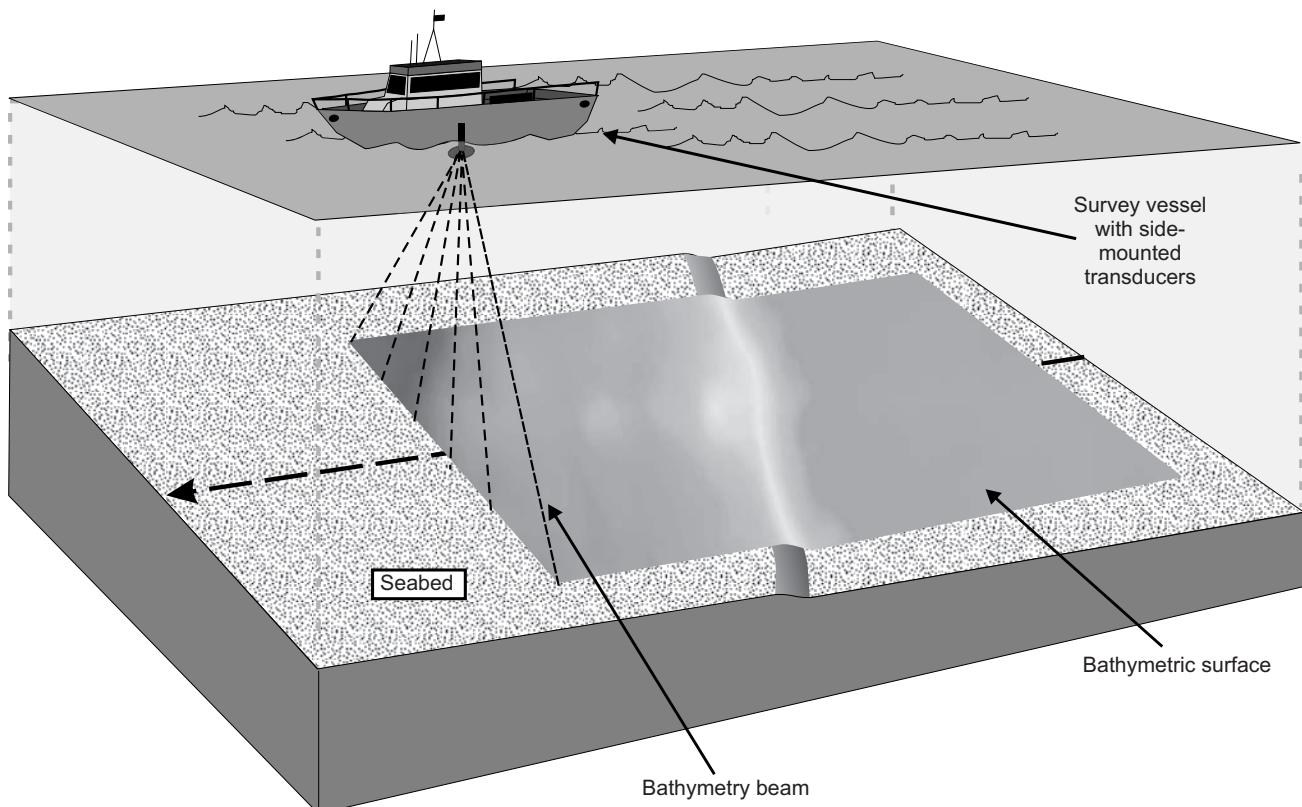


**Figure 6.65** Cartoon showing multi-beam swath bathymetric data acquisition. [C]

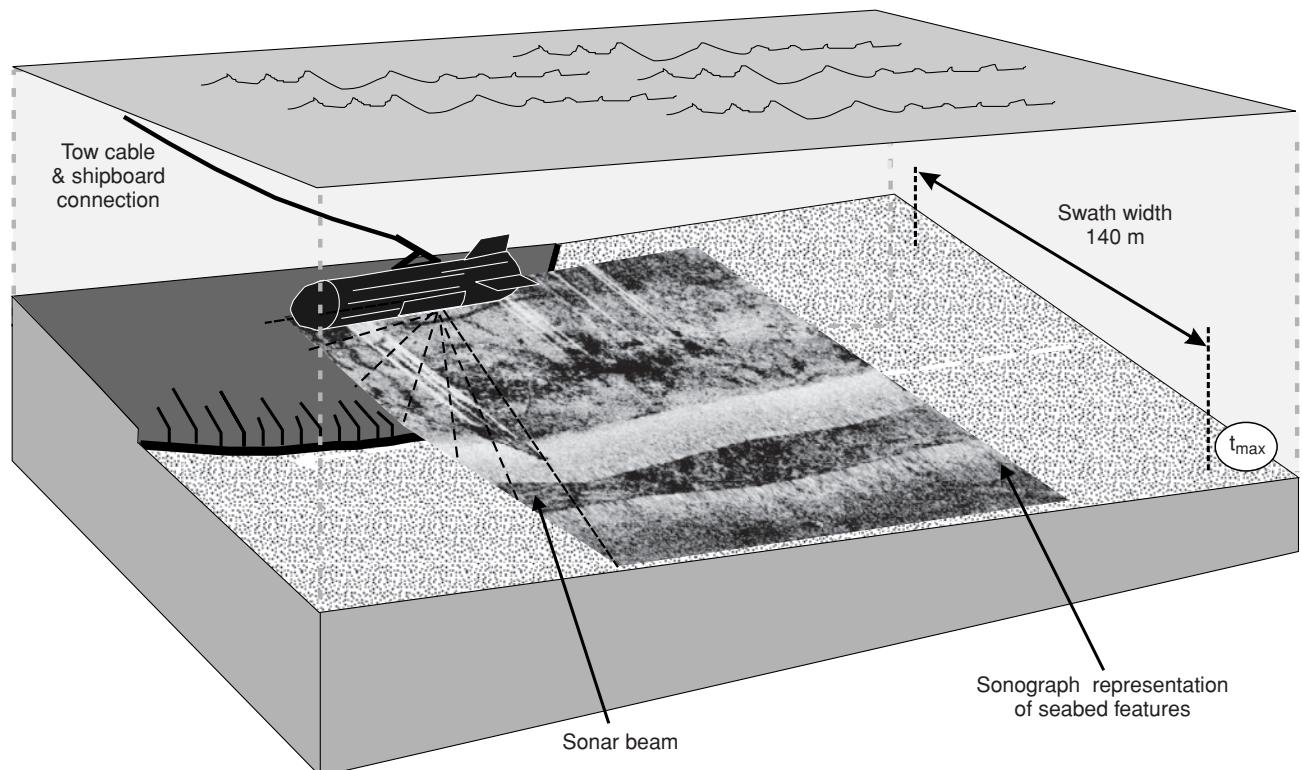


**Figure 6.66** Cartoon representation of typical side-scan sonar survey deployment, demonstrating the relationship between seabed features and sonograph data. [C]

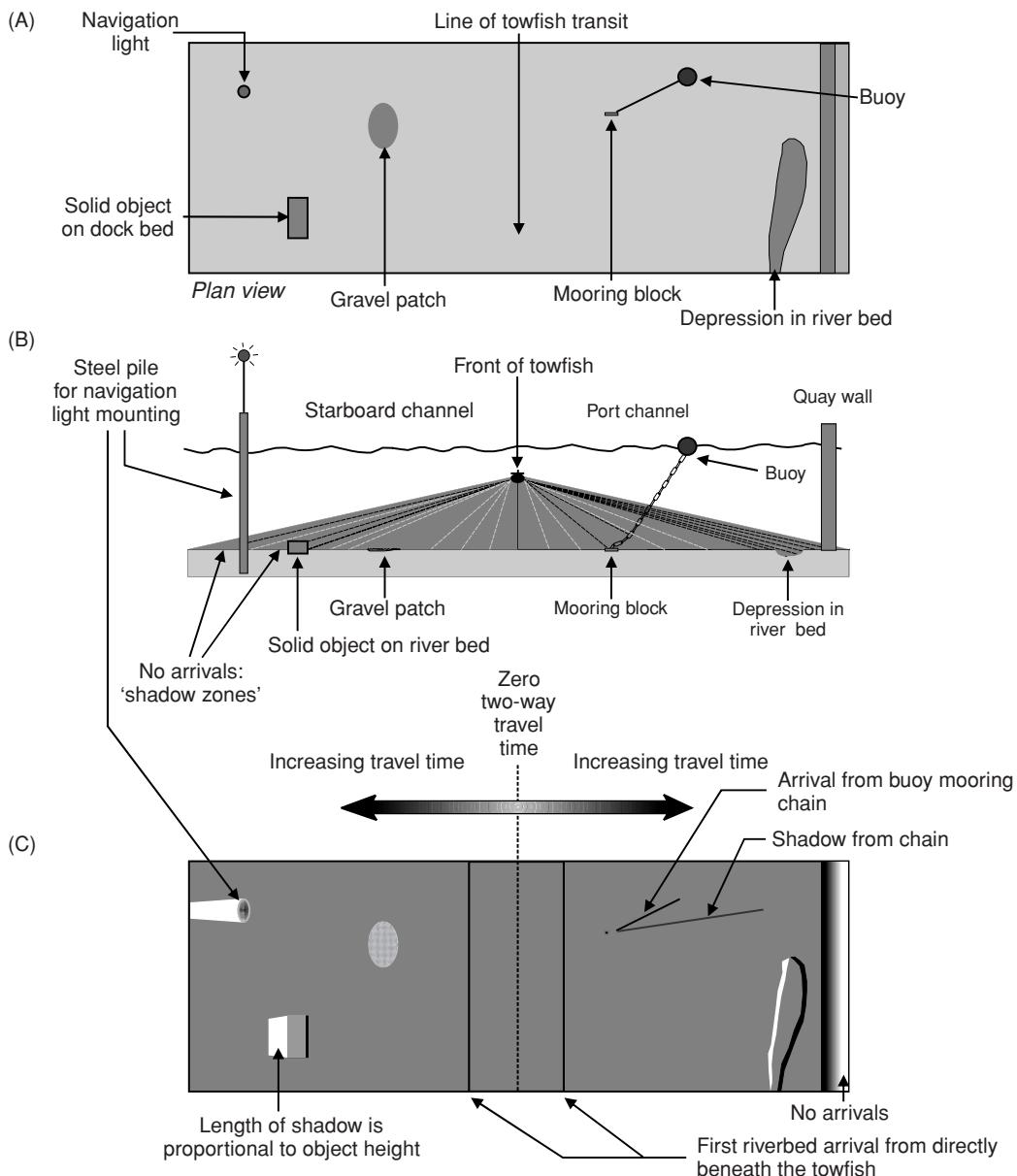


**Figure 6.67** Schematic depicting simulated acquisition of a side-scan sonar sonograph over a section of river bed whose features are shown in plan view (A), and represented as a single vertical plane (B). Reflections from these targets are represented by dashed lines; darker lines indicate stronger reflections and white lines represent areas of zero return ('shadow zones'). In the synthetic sonograph (C), solid objects and variations in riverbed texture are represented by characteristic reflection patterns. [C]

wide from port to starboard. TOBI can be towed at depths down to 6 km. These systems are used in large-scale geological research to map the bedrock geology, investigate seabed resources, survey deepwater routes for pipelines and telecommunications cables, and to detect marine geohazards.

### 6.6.3.2 Fresh-water surveys

An example of what can be achieved with equipment with a good specification is shown in Figure 6.69, from a survey at Lake Windermere in Cumbria, UK (Haynes *et al.*, 1993). The system used

was a Carrack SAQ-V that was capable of sampling up to 12 channels with a total throughput of 48 kHz (i.e. three channels at 16 kHz, 12 channels at 4 kHz, etc.). The system was PC-based, making it small enough to be deployable on small boats for use in very shallow water surveys. The section illustrated in Figure 6.69 was obtained using an ORF 'Geopulse' Model 5819B source, operated at 280 J with a trigger length of 0.5 s and a sweep length of 150 ms. The signals were received by an EG&G Model 265 hydrophone streamer and recorded using a Dowty Waverley Model 3700 thermal linescan recorder.

Lake Windermere is an ideal location to undertake a very-high-resolution seismic survey, as on a calm day the lake surface is

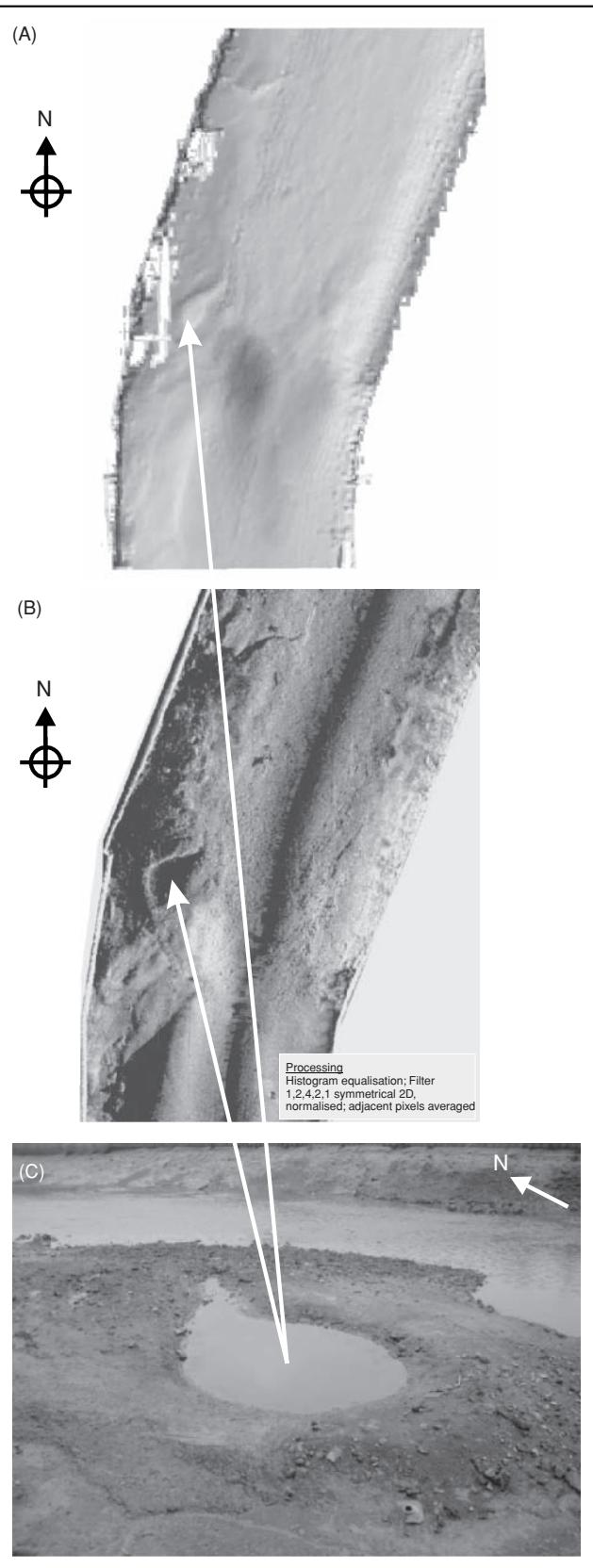


**Figure 6.68** Comparison of riverbed features imaged by (A) multi-beam swath bathymetry and (B) side-scan sonar, with (C) the corresponding part of the riverbed as seen at low tide. [C]

mirror-like and acoustically it is very quiet. The data obtained are of very high quality and, on the section shown, reflectors can be resolved to better than 20 cm down to a sediment depth in excess of 15 m. Four different sediment types can be distinguished: lake-bed mud, slumped and varved (seasonally laminated) clays, and glacial till.

### 6.6.3.3 Marine geohazard surveys

In estuarine and marine engineering investigations, a major difficulty encountered is the presence of shallow gas accumulations, thought to be associated with the decay of organic matter within near-surface sediments or to have migrated from depth. In some cases, the gas escapes to the surface of the water and vents naturally as 'flares'. In other, more dramatic cases, the gas release may be triggered by drilling activity leading to blowouts which can be highly dangerous. Drilling rigs and boats have been lost through degassing of sediments. Past gas escapes from the seafloor are commonly characterised by seabed pockmarks or scars. The issue of marine geohazards, especially shallow gas, has had to be addressed extremely seriously by both the hydrocarbon industry and increasingly the engineering community.

A detailed discussion of seabed pockmarks and associated seepages has been given by Hovland and Judd (1988), and the authoritative text on shallow gas, gas hydrates and gas seepages is by Judd and Hovland (2007). Shallow gas strongly influences the mechanical and acoustic properties of sediments and is manifest by increased attenuation of sound, scattering of acoustic energy, variability in sound velocity, and so on. Seismically, this leads to poor definition, acoustic opacity, rapid signal attenuation and masking of underlying reflection events. Only a small quantity of gas, 0.5% of sample volume as bubbles, is sufficient to decrease the P-wave velocity in affected sediments by up to a third that of a normally saturated and bubble-free equivalent sediment.

There are three recognised forms of shallow gas accumulations as seen on high-resolution seismic profiles (Taylor, 1992): (1) gas curtains (the most common); (2) gas blankets; and (3) gas plumes. The lateral extent and acoustic characteristics of each of these is listed in Table 6.1.

An example of the seismic expression of each of these three forms of shallow gas accumulation is shown in Figure 6.70. In each case, the surveys were acquired using a Uniboom sub-bottom profiler. Taylor (1992) reported that in one survey, in the Firth of Forth, Scotland, both a Uniboom and a 30 in<sup>3</sup> sleeve-gun failed to produce sufficient energy to propagate through a shallow gas accumulation. Instead, a marine refraction experiment was undertaken with a 10 in<sup>3</sup> airgun as a source and bottom-mounted hydrophones on the far side of the gassified sediments in order to undershoot the gas. Refracted head waves from bedrock were recorded despite the presence of the shallow gas.

Further examples of the effects of shallow gas on high-resolution seismic data have been given by Naudts *et al.* (2009) from surveys in the Dnepr palaeodelta in the northwestern Black Sea. They used and compared three sources (5-kHz pinger, a sparker and an airgun).

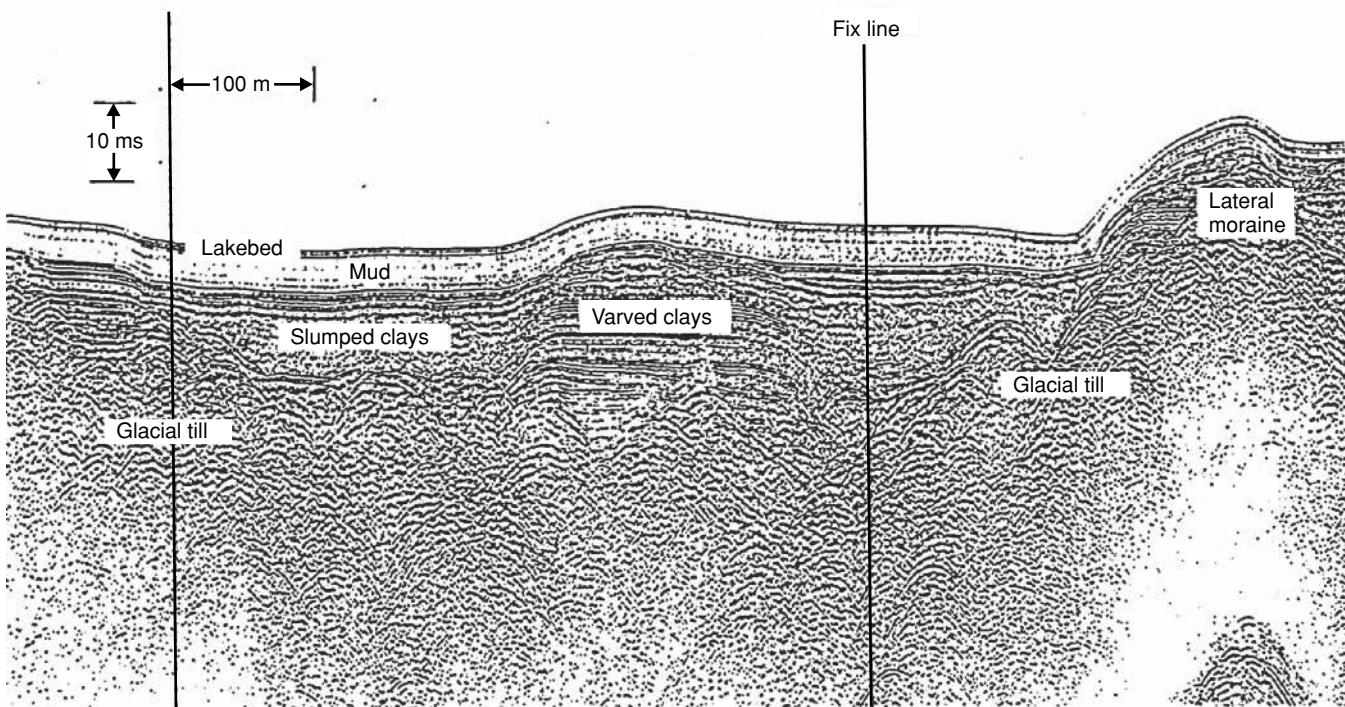


**Figure 6.69** Example of high-resolution seismic data obtained at Lake Windermere, Cumbria, UK, using a Boomer-type source. From Haynes *et al.* (1993), by permission.

The very shallow parts of the survey area were investigated using the pinger, which was deployed with a side-scan sonar transducer in a towfish flown at an elevation of 50–200 m above the sea floor. The theoretical resolution with this system is 0.3 m, with a maximum penetration of 35 ms. Similar features to those described by Taylor are evident in the Black Sea dataset (Figure 6.71). Enhanced reflections (Figure 6.71C) on high-resolution data are analogous to bright spots seen on lower-frequency seismic reflection data used in the hydrocarbon exploration. These occur as reflections with anomalously high amplitudes and are thought to be caused by the accumulation of small amounts of free gas below a particular horizon. The gas results in a negative acoustic impedance across that boundary and the subsequent large amplitude, phase-reversed reflection event seen on the seismic data. The enhanced reflection event is at the *gas front*

**Table 6.1** Classification of types of shallow gas accumulations (Taylor, 1992).

Name	Lateral extent	Acoustic characteristics
Plume	<50 m	Edges distinct, apparent vertical connection to source
Curtain	100–500 m	Edges distinct, no apparent vertical connection to source
Blanket	>500 m	Edges often difficult to resolve; no apparent vertical connection to source

(Figure 6.71), i.e. the topmost level of the gas accumulation, below which the gas blanket or curtain masks or blanks out later data (e.g. Figure 6.71C and E) through *acoustic turbidity*. This is caused by the attenuation (absorption and scattering) of the acoustic energy by the gas bubbles within the sediment. Acoustic attenuation is greatest when the acoustic frequency matches the resonant frequency of the bubbles, which is a function of the size of the bubbles. Consequently, seismic sources with different frequency bandwidths are likely to show variations in the characteristics of the gas front and of the later acoustic signals.

In places the gas front domes up towards the sea floor (Figure 6.71B and G), like the gas plumes in Figure 6.70C, and if the gas breaches the sea floor, can give rise to a 'flare' (Figure 6.71B), which is a hydro-acoustic water-column anomaly caused by the gas bubbles rising from the sea bed. The exit point of the gas seep from the sediments is often indicated by a *pockmark* on the sea floor, which may be large enough to be imaged by side-scan sonar or multi-beam bathymetry insonification.

By combining the gas-front surface from the pinger data with the sea floor surface, Naudts *et al.* (2009) were able to produce a 'depth-to-gas-front' map (Figure 6.72). From this and the observed surface locations of seeps, it was possible to observe that the majority occur where the gas front reaches within a couple of meters of the sea floor. It is also possible to note that the gas fronts dome up towards the sea floor at morphological highs. They also observed that, in this survey area, the gas fronts tended to stay below the sedimentary infill of incised channels and only come up to the sea floor at the margins of the palaeochannels.

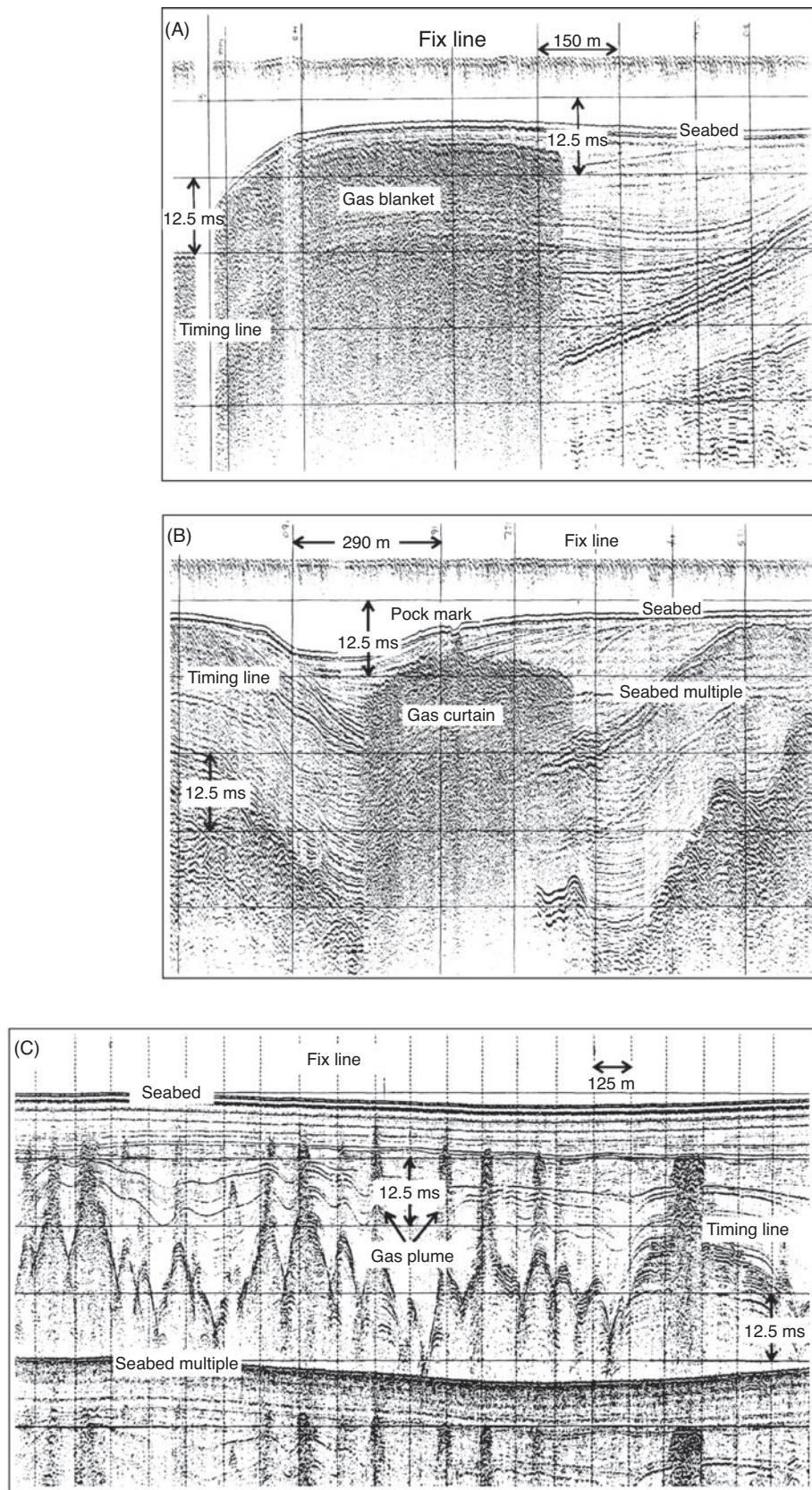


**Figure 6.70** Uniboom sub-bottom profiles showing (A) a gas blanket, and (B) a gas curtain in the Firth of Forth, Scotland; and (C) gas plumes in the northeast Irish Sea. From Taylor (1992), by permission.

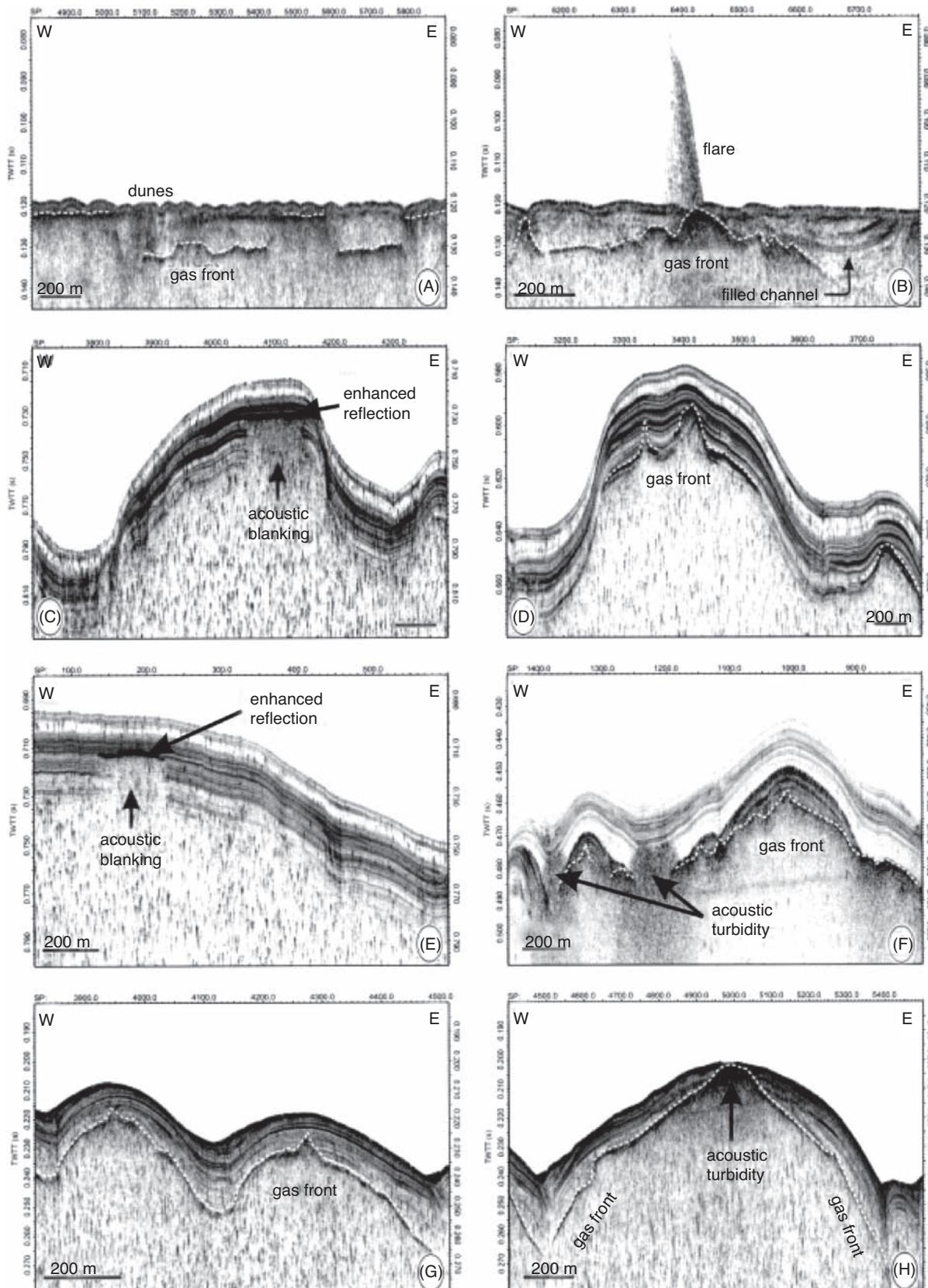


**Figure 6.71** Various shallow gas signatures showing different behaviours on 5-kHz pinger data. From Naudts *et al.* (2009), by permission.

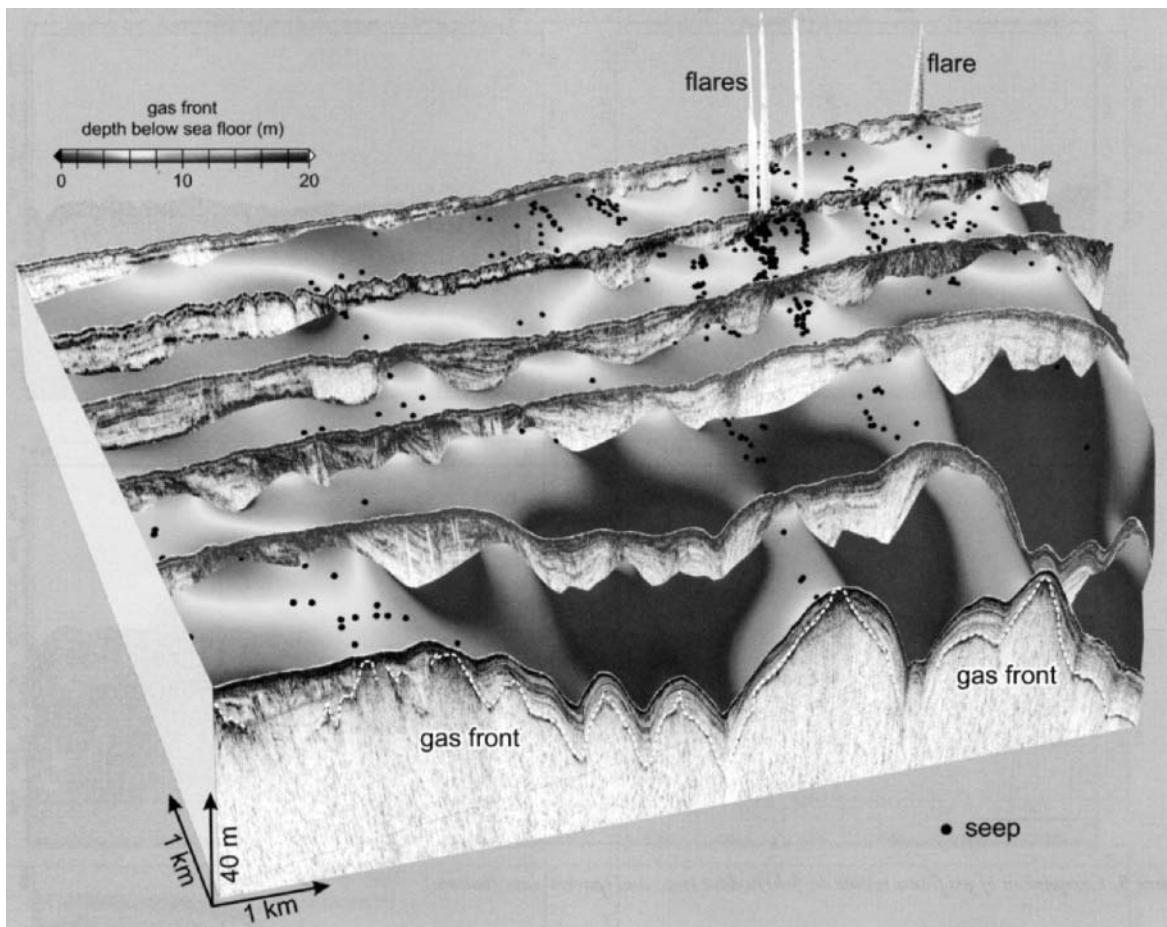


**Figure 6.72** Three-dimensional view showing the depth variation of the gas front as a depth map overlain by an isopach map with 5-kHz pinger profiles. From Naudts *et al.* (2009), by permission. [C]

#### 6.6.3.4 Marine resource evaluation and dredging

In marine resource evaluation surveys or for dredging, it is important to be able to recognise the required soil types by their respective seismo-acoustic facies characteristic. Data acquisition and recording systems have been developed that allow the rapid collection of digital data which can be filtered, enhanced and output as a line interpretation almost in real time. The ‘interpretation’ is undertaken by event tracking. A specific reflection event is identified and the software tracks the same phase of the chosen wavelet on adjacent traces and follows the event along the section. The two-way travel time picks to each selected event can be output for presentation as CAD sections or similar. However, these systems should never be used without the results being reviewed by an experienced geo-physical interpreter. There have been many examples of where the software follows one event, which dives away to greater two-way travel times along the section, but is replaced by another event at about the same two-way travel time. The software may identify these two events as being the same and attribute them to the same interpreted interface. In reality, the second event is unrelated to the first and the interpretation is then incorrect.

An example of a Boomer section for a dredge survey is shown in Figure 6.73. In this case the source signal has an extensive wave train associated with it, as seen by the parallel events recorded above the seabed. This characteristic is then mirrored in any subsequent reflection. These source signal tails can cloud the interpretation of the data at later two-way travel times. It should be a priority during acquisition to make the source signal as clean as possible and with as short a tail as possible. In Figure 6.73, the seabed multiple is evident around 40 ms. A strong reflection event lies at the surface at the left of the section and becomes buried beneath a sequence of different materials towards the north. At the northern end of this section events can be seen dipping in different directions separated by an unconformity (A). The seismo-acoustic characteristic of the material in zone B is different to that above the boundary A and in zone C. These indicate that the materials present are different from each other. It would require direct intrusive testing to sample each of these zones to be able to assign a material classification to each. Frequently in such surveys this is seldom achieved, either by the lack of intrusive sampling on a fine-enough spatial interval, or by not penetrating deep enough.

It is possible, however, to determine some basic information about materials from the seismic characteristics within each

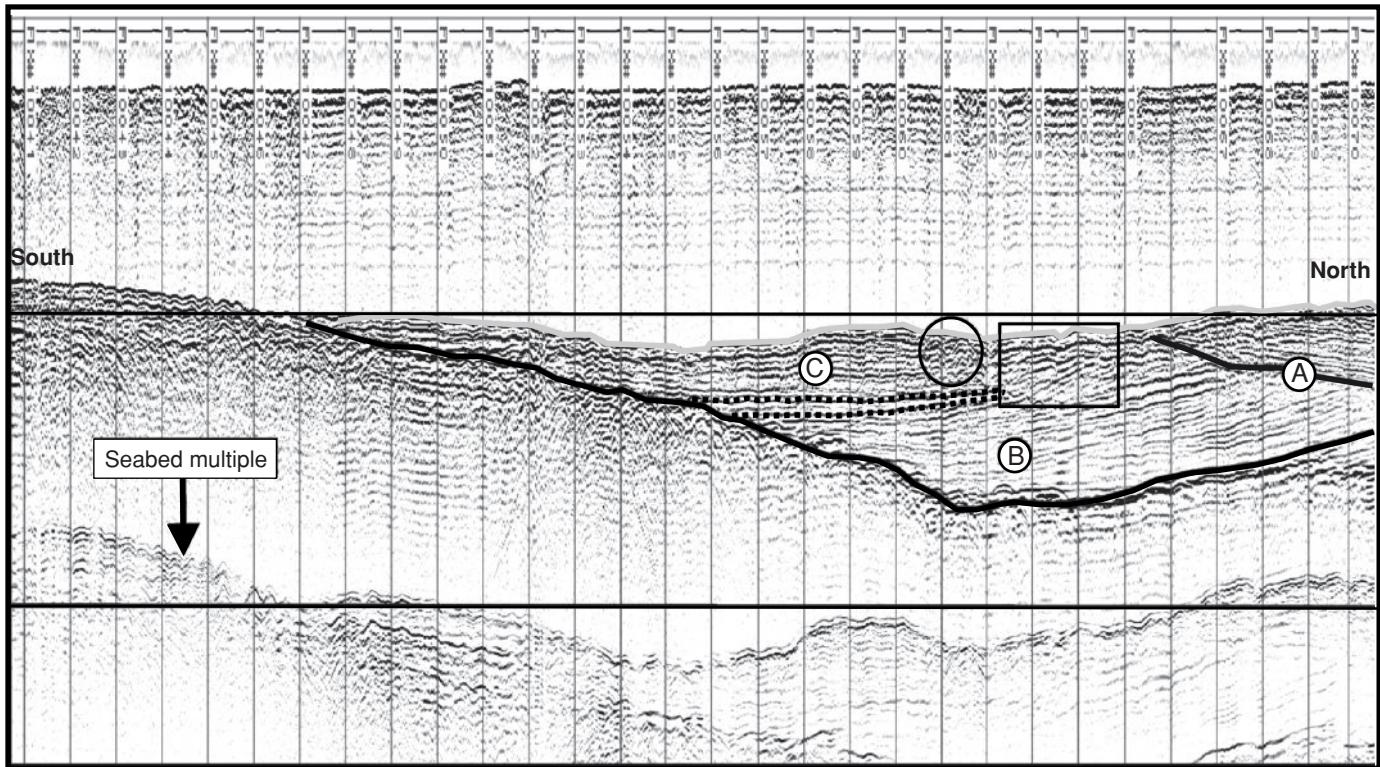


**Figure 6.73** Extract of Boomer record showing different reflection characteristics. See text for details. [C]

sedimentological facies. In the rectangle in Figure 6.73, the reflection characteristics indicate both a different orientation and reflection strength of events compared with adjacent parts of the section, indicating that perhaps this formed part of a channel infill and might contain a different grain-size profile to that in area A, for instance. Similarly, in the ellipse, diffraction events can be identified that might be caused by coarser material (gravel or cobbles, for example). If the source of the diffractions lies at the seabed, reference to the appropriate side-scan sonograph should help to identify the nature of the objects. If the diffractions originate only from the seabed, then the material is likely to be superficial drape that may or may not be of geological interest. Sometimes such material can be discarded objects from passing vessels. If the diffractions originate within the seismic facies, this might indicate that the material is coarse: i.e. the dimension of the object is comparable to one quarter of the wavelength of the incident seismic signals. In the region between zones B and C is a wedge of material picked out by dashed lines. There are no diffractions from this area so it might be interpreted that the material is finer grained.

An important aspect of high-resolution seismic surveys is the correlation with intrusive sampling (e.g. vibro-coring, boreholes, etc.). The correlation between the seismic record and the borehole log, for example, is possible depending upon the quality of both the seismic data and of the geological logging of the borehole. In Figure 6.74, for example, a borehole has been constructed through the sequence imaged. This provides two sources of key information. First is the sequence of geological materials with their respective

layer thicknesses. The second is that by correlating with the seismic record, both the average seismic velocity for the sequence and the interval velocity within discrete seismo-acoustic facies can be determined. Commonly, seismic velocities are assumed for a sequence on the basis of published results for similar materials and layer thicknesses, and resource volumes calculated accordingly. Yet one of the most significant uncertainties when converting from time sections produced from sub-bottom profiling to depth sections is seismic velocity, which is discussed in more detail below. The other feature illustrated in Figure 6.74 is the correlation between the borehole log and the seismic section, especially in the Upnor Formation. Principal reflections have been highlighted for the boundaries between the Terrace Gravels at the surface and the Upnor Formation, and the Upnor Formation and the underlying Thanet Sands. The latter interface has a weak, but discernable, seismic reflection strength, but no interface has been identified on the borehole log. Within the Upnor Formation a clay band is present on the borehole log, and this can be seen clearly to be associated with seismic reflection events at the top and bottom of this layer. The seismic characteristic of this band is that it is virtually transparent to the seismic waves and no features are evident within this layer. This example demonstrates that just because an interface has not been identified on a borehole log does not mean that it is not detectable seismically, and vice versa.

Correlation between intrusive tests and sub-bottom profiling data might reveal variations in seismic velocities associated with different soil types. For example, at one location of a marine CPT

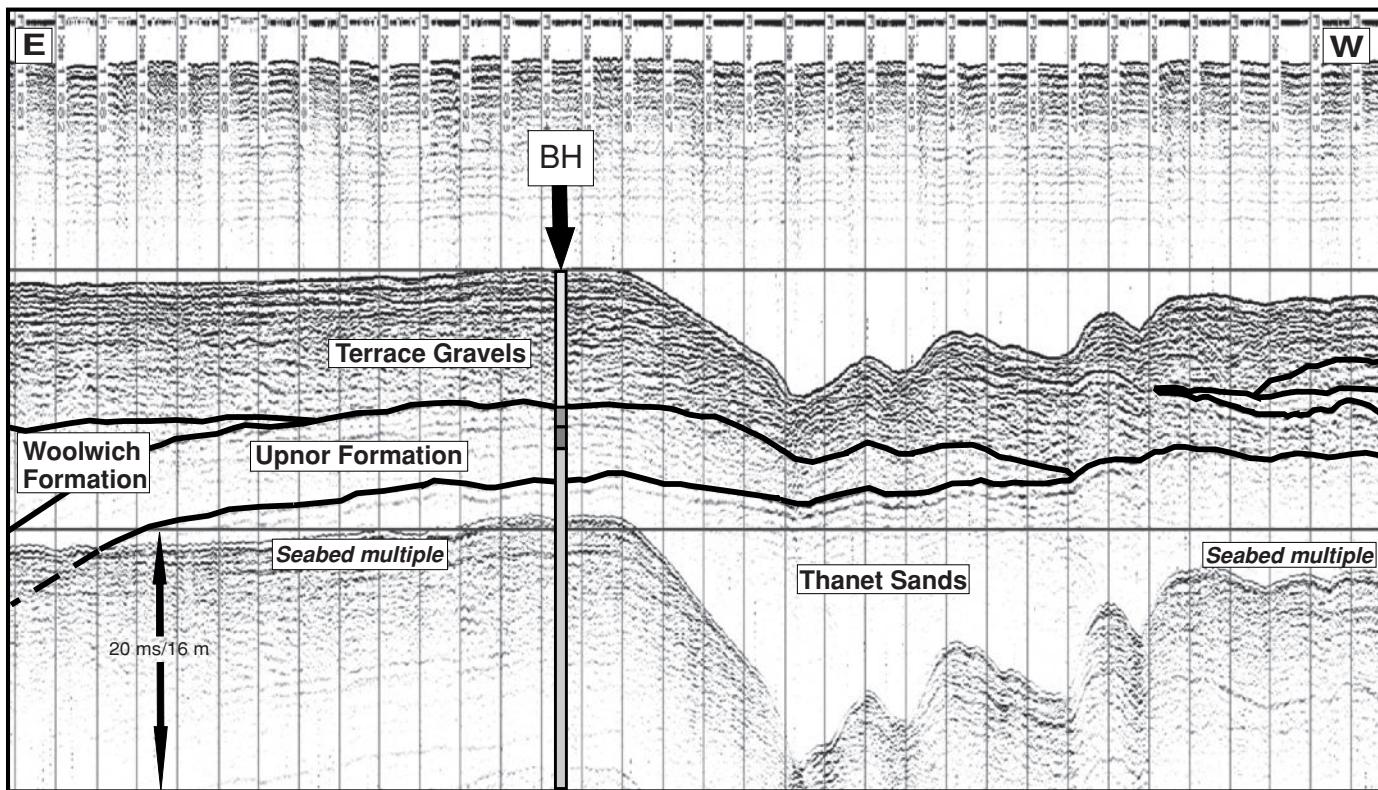


**Figure 6.74** Correlation of (offset) marine borehole with Boomer record. Assumed seismic velocity is 1600 m/s. [C]

the soil sequence was interpreted to comprise silty SAND (2.66 m thick) over CLAY (2.66 m thick) over dense sandy GRAVEL, based on net cone resistance values. However, a different sequence could be identified using friction values for the same CPT (thicknesses of 2.3 m and 3.35 m). Using the seismic velocity of 1600 m/s assumed by the contractor, corresponding two-way travel times (TWTTs) were calculated, but these did not correlate directly with principal reflections evident on the seismic section. By associating the principal reflectors' TWTTs with the measured depths, the interval velocity for each of the top layers was calculated. This produced values of 1810 m/s for the silty SAND layer, 1510 m/s for the CLAY layer, and 1570 m/s for the sandy GRAVEL. Weighting these velocities using the layer thicknesses gives a statistically weighted velocity for the entire sequence of 1660 m/s. While this might appear close enough to the assumed value of 1600 m/s, the significance of the deviation from this assumed value for specific soil layers becomes important when considering the volume of such material. To put this in context, estimates of the thickness of the silty SAND layer, using the assumed seismic velocity rather than the derived interval velocity, underestimates the thickness by ~12%, and overestimates the thickness of the underlying layers by between 2% and 6%. Elsewhere, local interval velocities were found to vary between 1200 m/s and 2090 m/s, with corresponding implications for estimates of layer thicknesses. Such variation in seismic velocity have been reported elsewhere for estuarine sediments (Eddies and Reynolds, 1988; Reynolds, 1990a). For a range in velocities of 1200–2000 m/s, relative to an assumed value of 1600 m/s, the resulting uncertainty

in layer thicknesses in the case above was of the order of 10–15%, which could be significant and make a difference to the viability of a commercial project.

Figure 6.75 shows a seismic section across a postulated fault zone, where the seismic data indicate a complex association of materials. However, the only intrusive sampling was achieved by a very shallow vibrocoring which did not penetrate through the base of the uppermost and spatially restricted surface unit. The identification of the other materials present was made on the basis of extrapolation from other parts of the survey area, where intrusive sampling was deep enough to provide sufficient information to characterise the seismo-acoustic facies of key soil types. The specific soil types had been defined on the basis of particle size analysis. In Figure 6.75, the material type associated with the top of the postulated fault zone (indicated by the question-mark) is unknown as it remains unsampled.

Figure 6.76 provides an example of the different effects associated with a range of surface sedimentological bedforms. At location A, there are small localised diffractions probably associated with a veneer of gravel at the top of the Terrace Gravels. At B, being in a slight depression in the seabed, the diffractions are stronger and start to show clear apices, indicating that the source of each diffraction is larger than those in area A. At location C, the surface bedforms are sand waves with sufficient vertical topographic expression to produce not just diffractions but reflections from each wave. Further information about the nature of the surface bedforms could be provided by reference to side-scan sonographs.

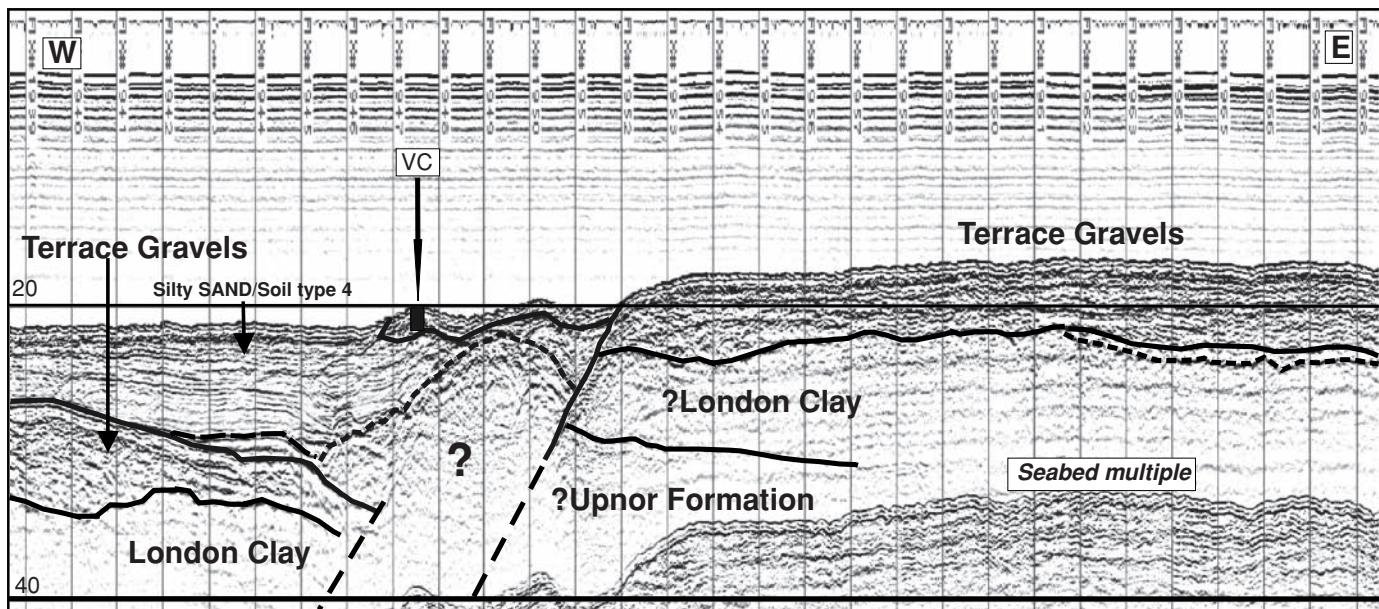


Figure 6.75 Complex sequence imaged in a Boomer section. [C]

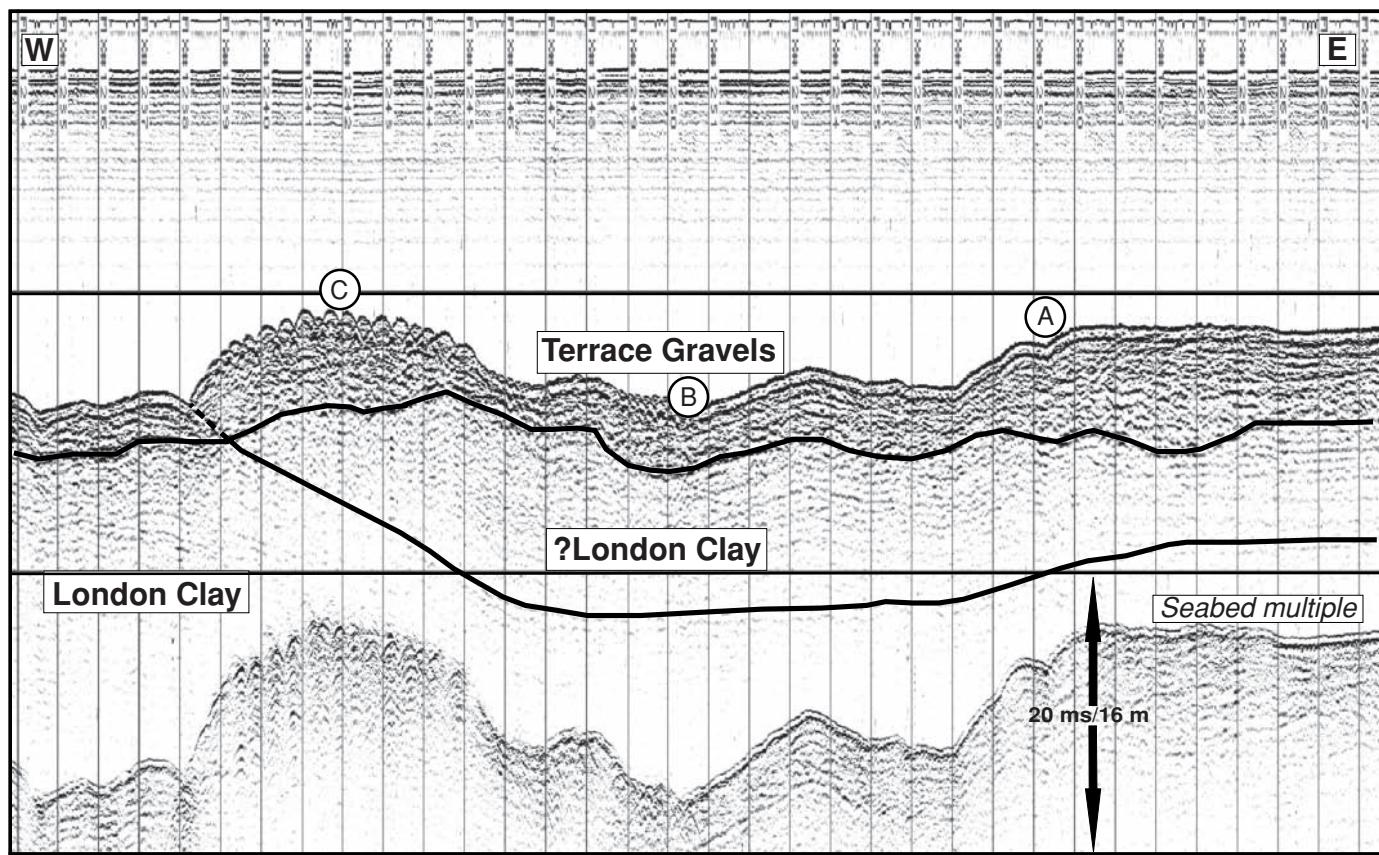


Figure 6.76 Structure within the solid geology being reflected in the seabed topography and influencing seabed sedimentation. [C]

### 6.6.3.5 Tunnels

In London there are significant infrastructure developments being constructed involving railway tunnels, such as for the Docklands Light Railway, and Crossrail Line 1 which is proposed to link east and west London. Another is the Thames Tideway project by which a 7.2-m diameter storm drain will ultimately be constructed for a distance of about 26 km underneath and predominantly along the route of the River Thames as part of a massive scheme to capture and treat storm-water effluent and improve the water quality of the river. In each case, high-resolution seismic surveys have been designed and undertaken.

In the case of the Woolwich Reach survey (Lenham *et al.*, 2006), boomer data were acquired on a 10-m line interval offset across the river Thames, and key information of high resolution was obtained to more than 40 ms. Five boreholes were constructed along the route of the proposed tunnel to a depth of 32–39 m below riverbed level and extending at least 15 m below the proposed tunnel invert. Example boomer sections are shown with borehole information in Figure 6.77. Correlation with borehole data indicated that extensive shallow-dipping reflection events visible in this section represent bedding surfaces within the chalk bedrock. The true dip of these beds was calculated as around 2° SE to ESE. Interpretation of the seismic data also identified the presence of a probable backfilled feature within the chalk-head surface on the northern side of the riverbed. This was confirmed by borehole logs for TRC1 and TRC2 (Figure 6.77) and identified the backfill material as being primarily alluvium and river terrace deposits. The significance of this is that

the running tunnels were anticipated to intersect the base of the basin feature, which was thought to be in hydraulic connectivity with the river above.

The combined desk study, geophysical and intrusive investigation at Woolwich Reach in the River Thames provided key information for tunnel design and construction. This included determination of the nature and thickness of the ground cover over the tunnels; detailed stratigraphic logging of chalk core to identify key marker beds and flint bands within the chalk; identification of a possible east–west trending fault of limited throw towards the centre of the river; and discovery of a filled-basin feature of limited lateral and vertical extent. The running tunnels have been built successfully.

As part of the Thames Tideway project, a reconnaissance high-resolution seismic survey was undertaken along 39 km of the River Thames from Hammersmith in the west to Beckton downstream in the east. The data acquired in January 2008 were later converted into SEGY, underwent further data processing, and were interpreted using a 2D/3D oil industry interpretation software package. The significant improvement in data quality as a result of the processing led to a higher resolution of interpretation. This resulted in being able to identify previously unrecorded faults within the local bedrock (Figure 6.78). The benefits achieved by this approach led to a new and more comprehensive survey being designed and undertaken along the same stretch of the river in 2009. The design of the new survey was able to take into account improvements in both the methods of data processing and interpretation to influence the choice of data acquisition parameters.

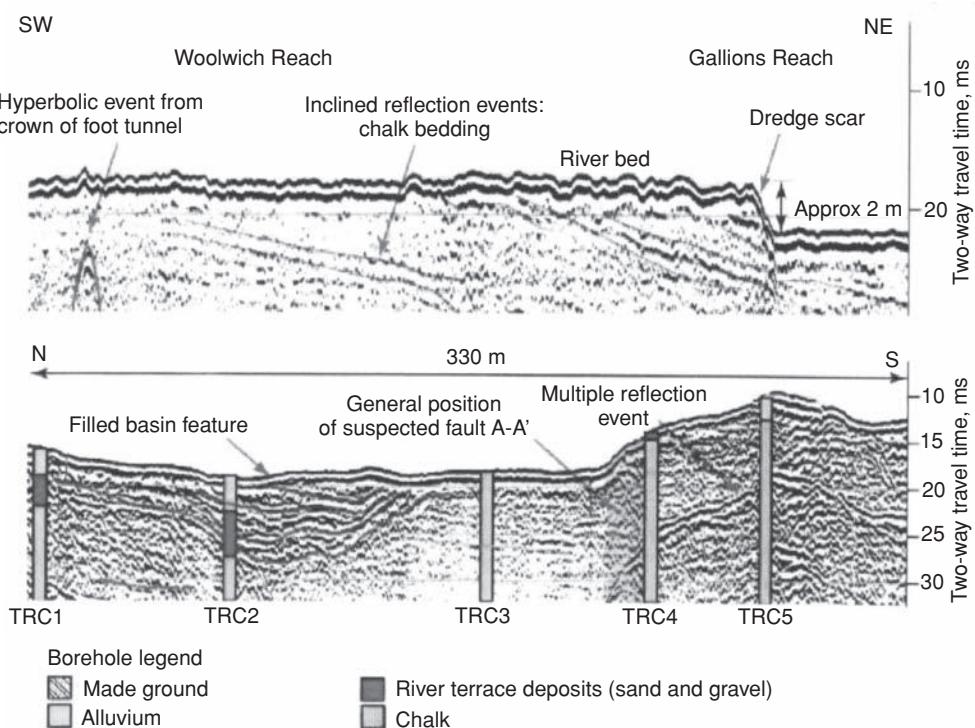


**Figure 6.77** Seismic Boomer data acquired parallel to (top) and across (bottom) the River Thames at Woolwich Reach, together with logs from nearby boreholes. From Lenham *et al.* (2006), by permission. [C]

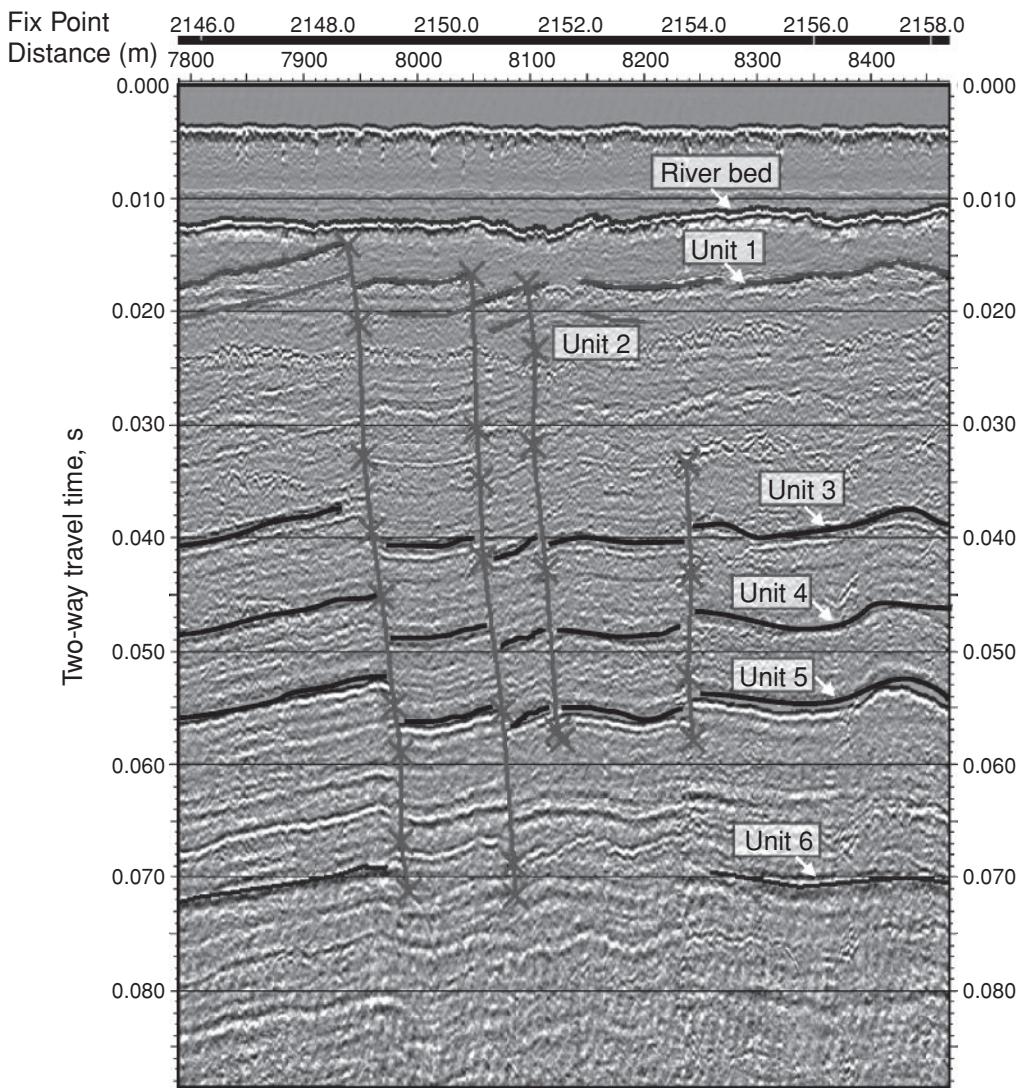


**Figure 6.78** Seismic Boomer data, converted to and processed in SEGY format, reveal faulting within the bedrock beneath the River Thames. [C]

### 6.6.3.6 Estuarine environments

While the acquisition of high-quality digital data using high-specification systems is extremely desirable, it is not always either practicable or financially justified as perceived by clients. It is possible, however, even with basic analogue systems, to produce reliable information about the vertical and lateral distribution of geological interfaces. One such example is a series of analogue surveys in Plymouth Sound, Devon, UK, using a Boomer surface-tow source and a sparker to map an infilled rock valley (Reynolds, 1990a). Two boreholes were drilled within Plymouth Sound to provide vertical geological correlation. An example of an analogue sparker section with details from one of the boreholes is shown in Figure 6.79. The sedimentary sequence consisted of contemporary estuarine muds overlying fine-coarse sands with gravel lenses. The lower interface of the sand unit was marked by a prominent, partially cemented shelly gravel overlying organic muds, finely laminated in parts with

silts. The base of the sediments was marked by coarse gravel overlying weathered Devonian slate at a depth of 26.6 m below the seabed. The upper sand unit was characterised by dipping reflections (Figures 6.79 and 6.42) thought to be associated with point bar foresets. The top of the organic muds, which was dated provisionally at 8300 BP on the basis of microfossils, could be traced laterally over a substantial part of the central portion of Plymouth Sound, and thus served as an isochron. The sediments infilling the rock valley formed during a period of rising sea-level following the end of the last ice age. The interfaces between the principal units mirror the temporal changes in the proto-River Tamar as it flowed through Plymouth Sound.

Using a grid of survey lines, posted two-way travel time maps of the principal, laterally extensive subsurface reflections were produced (Figure 6.80) from the analogue records. The travel-time data were contoured using a simple graphical package (SURFER from Golden Software Inc., USA). From these, isometric projections were

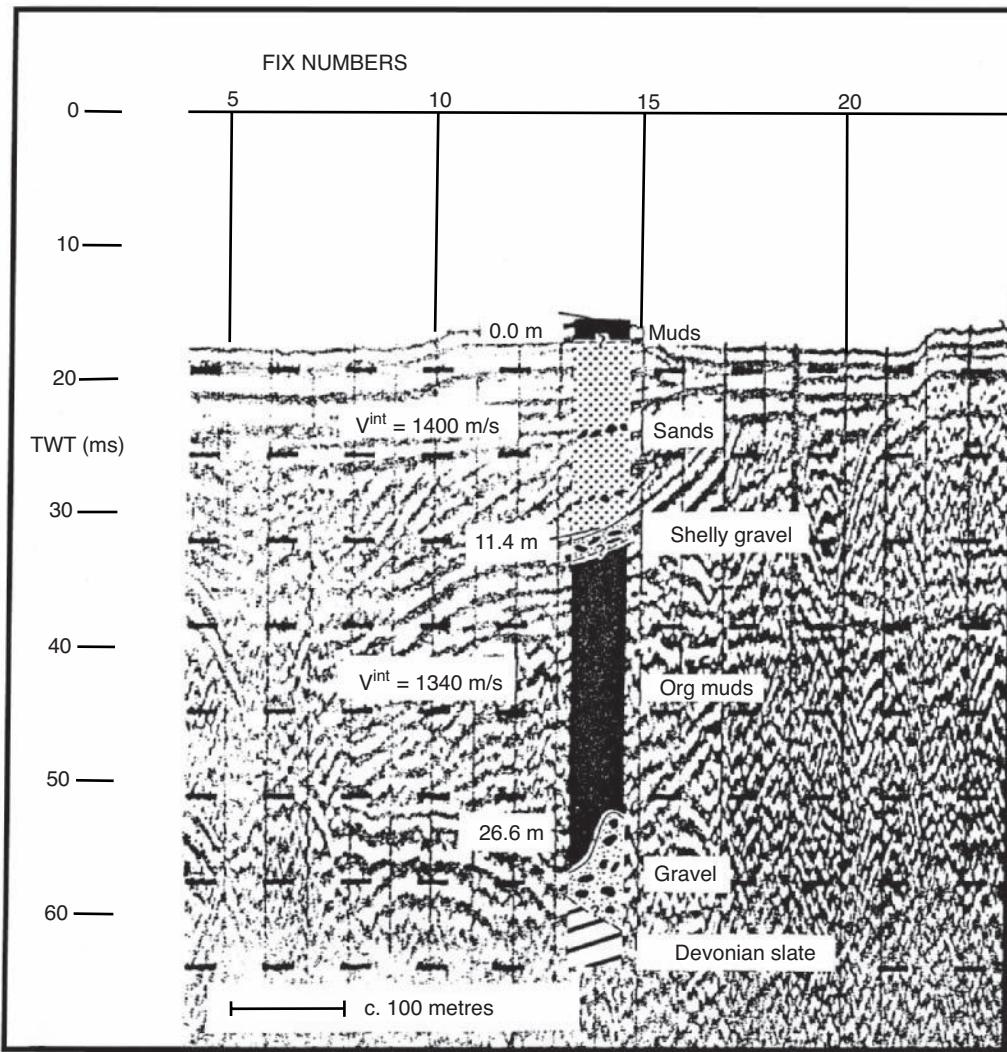


**Figure 6.79** Analogue sparker record over a buried rock valley within Plymouth Sound, Devon, with the main geological sequences as found by drilling. Two preliminary average interval velocities were determined for the main sequences corresponding to the depth ranges 0–11.4 m and 11.4–26.6 m using the observed two-way travel (TWT) times and the measured depths below seabed to the corresponding interfaces from the borehole lithological log. From Reynolds (1990a), by permission.

also produced for each reflection and are shown stacked in Figure 6.81. The travel times were normalised to a time datum 60 ms below Ordnance Datum (Newlyn) for the graphical display. In Figure 6.81, the knoll evident on the eastern side of the valley is bedrock, which is why there are few changes in this region between the lower three projections. However, the main sediment deposition was on the western side and the gradual shallowing of the channel can be seen clearly.

The last example in this section is of a three-dimensional seismic reflection survey undertaken in the River Scheldt in Antwerp, Belgium, to map a clay diapir as part of a geotechnical investigation (Henriet *et al.*, 1992). The clay diapir in Rupelian Clay had been discovered during a survey in 1982 close to a site proposed for a metro tunnel under the river. The 1982 survey was shot using an EG&G Uniboom source, and a sample seismic section is shown in Figure 6.82. The diapir has an apparent diameter of 60 m. The re-

flections bulge upwards with a vertical amplitude increasing from a few decimetres at 50 m depth to a few metres at about 25 m depth. Higher horizons are pierced by the diapir.

Many reflections from within the Rupelian Clay are prominent as clusters of diffraction hyperbolae (marked with solid triangles in Figure 6.82). The diffractions are associated with large concretions (septarian nodules) with diameters in the range between 0.5 m and 1 m and thicknesses of 0.2–0.3 m. The clay diapirs themselves were not thought to constitute a hazard, as their geotechnical properties had been found to be comparable to those of undisturbed clay. However, the formation of the diapiric structures was known to drag some septarian nodules vertically. The distribution of the nodules was important as it influenced the choice of drilling equipment for the tunnelling.

Following the successful 1982 survey, a more detailed investigation was undertaken in 1990 using a true 3D data-acquisition system

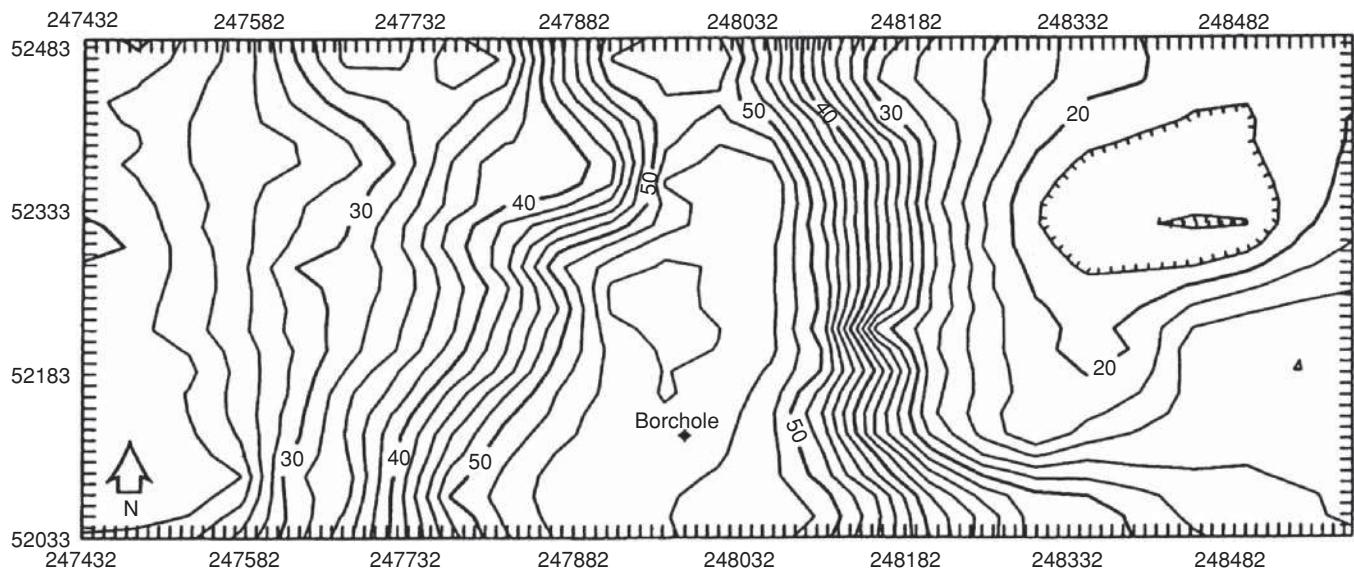


**Figure 6.80** Posted two-way travel time map to bedrock from a part of Plymouth Sound. Values along the x and y axes are Universal Transverse Mercator (UTM) coordinates. The location of the borehole is also shown. From Reynolds (1990a), by permission.

(Figure 6.83). The receiver configuration consisted of an array of 12 purpose-built micro-streamers, each with two hydrophone groups 1 m apart, that were towed from a modified Hobiecat catamaran from which the source was also deployed. The distance between each streamer was 1 m. Each shot generated 24 seismic traces in a swath 5.5 m wide centred along the boat track. The source–receiver catamaran was towed about 10 m behind the RV *Belgica*. The shot interval was 1 m. Positioning accuracy was to within decimetres and was necessarily accurate to permit  $1 \times 1 \text{ m}^2$  binning. Two seismic sources were used: an EG&G Uniboom and a modified Sodera 15 in<sup>3</sup> watergun lashed horizontally to a fender at 0.2 m depth.

In order to achieve the required shot interval and firing rate, a very slow ground speed was required (between 0.5 and 2 m/s). This could only be achieved realistically by sailing against the current, which in the River Scheldt is very strong. It was thus impractical to turn the 45 m long survey vessel for fear of disrupting the towed acquisition system. Consequently, the vessel sailed against the current, acquiring data *en route*. At the end of the survey line, the vessel moved across to the next track line and decreased her sailing speed to less than that of the river current, effectively sailing backwards while still maintaining headway into the current and keeping the towed array well stretched behind the vessel. The actual survey took three days to complete and about 20,000 shots were digitally recorded, translating into 250,000 common midpoints. The survey area was  $50 \times 180 \text{ m}^2$  in area, with at least 5-fold and in places in excess of 10-fold bin coverage. Details of the data processing have been discussed by Henriet *et al.* (1992).

It was demonstrated during this survey that the characteristics of the two sources were very similar and the data were stacked together – not something that is normally recommended. The record length for the watergun was 60 ms and about 80 ms for the Uniboom. The combined record is shown in Figure 6.84. The obvious change in signal character around 60 ms is due to the differences in record

length between the two sources. Slight updoming in the reflection at 58 ms is evident. The main clay diapir is in the centre of the record. Variation in signal character between the two sources was apparently due to differences in bin coverage. It is important, therefore, when interpreting seismic records by comparison, that such factors are taken into consideration if misinterpretation is not to happen. This case history has demonstrated that 3D seismic surveys can be translated down to the scale of geotechnical surveys and can provide valuable information with a high degree of spatial resolution.

#### 6.6.4 Geophysical diffraction tomography in palaeontology

In 1979, two hikers discovered partially exposed bones from the tail of a hitherto unknown species of dinosaur in the high desert of New Mexico (Witten *et al.*, 1992). Excavation began in 1985 in the Morrison Formation, a 145 million year old (Late Jurassic) sandstone well known for its dinosaur remains further north in the USA, but until then, unrecognised in New Mexico. By 1986, it was realised that the bones were from a relative of *Diplodocus* with a projected length of at least 33.5 m (110 ft). David Gillette, who first described the dinosaur, coined the informal name ‘seismosaurus’ for the new dinosaur, alluding to its considerable size making the earth shake when it moved. The geological setting of the bones indicated that the body had suffered from *rigor mortis* before burial and that the animal’s carcass had come to rest on a bend in a local river on a point bar, and had been buried subsequently by fine sand. The sandstone surrounding the skeleton is massive but predominantly homogeneous, thus providing an excellent medium for remote sensing.

The 1985–86 field excavations indicated that the skeleton extended into a cliff face, but the orientation and extent of the bones could only be conjectured. The projected orientation of the

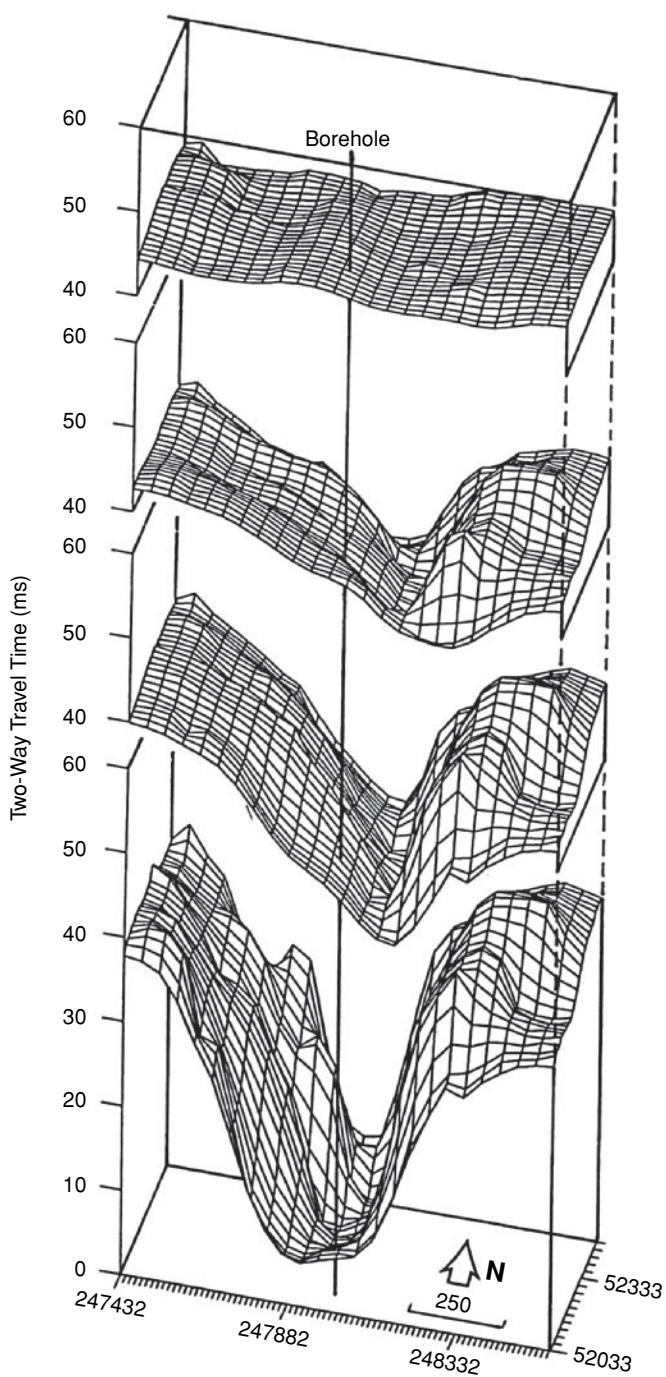


**Figure 6.81** Stacked isometric projections of normalised two-way travel time to, in order of increasing depth, the internal reflector in the upper sand unit, the shelly gravel layer between the upper sand and underlying organic clays, and bedrock. From Reynolds (1990a), by permission.

skeleton was at a level of at least 2.5 m (8 ft) beneath the surface. Traditional excavation using shovel, hammer and chisel would have been extremely slow and would have involved the removal of hundreds of tonnes of material. In April 1988, and again in July 1989,

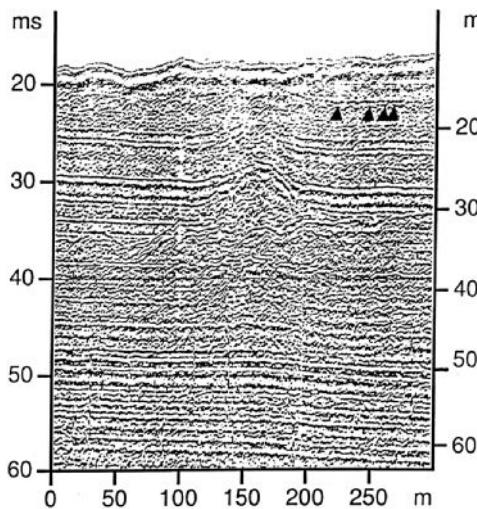


**Figure 6.82** Uniboom profile from the 1982 survey across a clay diapir in Rupelian Clay under the River Scheldt, Antwerp, Belgium. Diffraction hyperbolae (indicated by solid triangles) are associated with calcareous septarian nodules within the clay. The riverbed reflection occurs at about 18 ms. The effect of the diapir is evident at 150 m, especially around 30 ms. From Henriet et al. (1992), by permission.

the site was investigated using geophysical diffraction tomography (GDT).

Geophysical diffraction tomography can take two forms: back-projection or back-propagation, the concepts of which are illustrated schematically in Figure 6.85. For both methods, it is assumed that a series of receivers is located down a borehole and a series of sources is placed along the ground surface. In back-projection, it is assumed that the energy emanating from a source travels through the subsurface in straight lines or as rays from source to a given receiver, whose distance from the source is known exactly. The measured travel time of the first arriving signal and its amplitude are related to local variations in wave speed or wave attenuation. Reconstructing an image from variations in measured parameters is achieved mathematically by using data from many raypaths, which intersect the same unit cells, to iterate towards a solution, which is displayed as a pixelated image (i.e. each cell is assigned a value from the iteration which is displayed as one pixel in the final image). Back-projection has been used for imaging inhomogeneities such as karst features, imaging the Earth's mantle, and in producing electrical images from arrays of electrodes. Back-projection assumes straight raypaths and ignores any refraction effects.

A preferred alternative is back-propagation, which is reputed to provide sharper images and take into account refraction effects. The field system is exactly the same as in back-projection, but the effect being sought here is the distortion of the wavefront caused by inhomogeneities within the ground being imaged. The distortion of the waveform in both time and space are measured at the receivers. A benefit of the back-propagation method is that it utilises information contained in the received signals regarding the constructive and

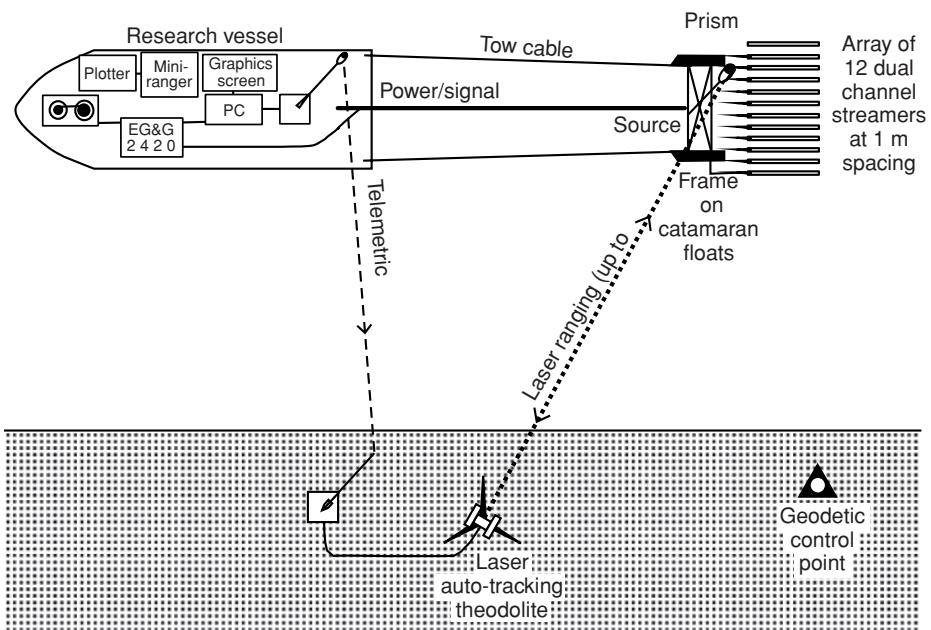


**Figure 6.83** Layout of the system used in the 1990 three-dimensional survey at Antwerp, Belgium. From Henriet *et al.* (1992), by permission.

destructive interference associated with multiple raypaths between source and receiver. The methods are described in more detail by Witten and King (1990a).

The GDT survey undertaken in April 1988 produced one image displaying a feature that was believed to be due to a dinosaur bone (Figure 6.86). In early July 1989, a dorsal vertebra and partial rib were exposed at the location indicated by the geophysical survey.

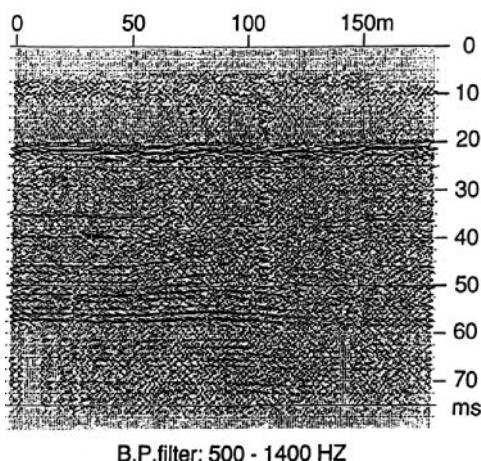


**Figure 6.84** Composite stacked section combining both watergun data from 0 to 60 ms and Uniboom data from 0 to the end of the record, across a clay diapir at Antwerp, Belgium. Slight updoming of the reflection at 58 ms is evident. The seismic responses from the main diapir are in the centre of the record. From Henriet *et al.* (1992), by permission.

The field acquisition layout is shown in Figure 6.87. Approximately 1 m of overburden was removed from a rectangular plot about 9 m × 12 m, of which a flat L-shaped area was used in the GDT survey. A series of four boreholes (A–D in Figure 6.87) were constructed. They were 6 m deep, lined with PVC casing capped at the bottom, and the annulus around the outside of the casing within the borehole was backfilled with sand. Each borehole was filled with water and a hydrophone receiver array with active elements at 0.15 m intervals deployed down the borehole. Source positions were defined along radial lines emanating from the boreholes, with the first source position 1.2 m from the borehole and successive positions at intervals of 0.6 m. The source consisted of a commercially available seismic Betsy gun. Further details of the data acquisition and processing have been described by Witten *et al.* (1992).

The results of the GDT survey are summarised in Figure 6.88. Dinosaur bones identified by image reconstruction are shaded black, those found by direct excavation are shaded grey and the postulated positions of undiscovered bones, based upon experience of the disposition of other dinosaur skeletons that have been found with a *rigor mortis* posture, are unshaded. One of the reasons why the method worked at this site is that the material surrounding the bones was found to have a P-wave velocity of only 450 m/s, in stark contrast to that of the bones with a velocity of 4500 m/s.

The use of GDT as part of this palaeontological investigation has been beneficial in the location of significant parts of the skeleton of this giant dinosaur. It has also demonstrated the usefulness of the technique in being able to image objects successfully.

The GDT method has also been applied to imaging artificial buried objects such as metal drums, pipes and tunnels (e.g. King

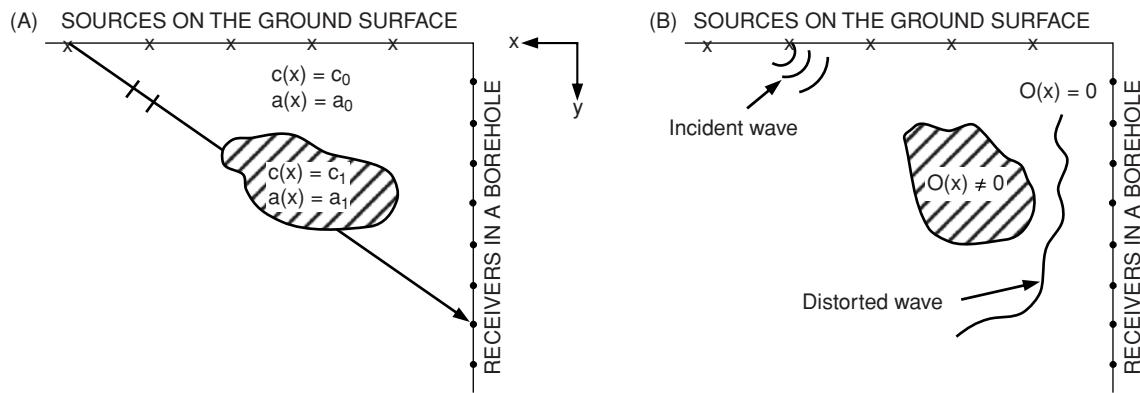


**Figure 6.85** Schematic of the concepts of (A) back-projection imaging, and (B) back-propagation imaging. From Witten and King (1990a), by permission.

et al., 1989; Witten and King, 1990a,b). One such example is illustrated in Figure 6.89. A field test was conducted under controlled conditions by burying waste-simulating targets at known locations and then imaged using back-propagation imaging. The targets were 55-gallon metal drums with a diameter of 0.61 m and 1 m tall, either empty or water-filled, and plastic bags containing styrofoam packing pellets. The positions of the targets relative to a borehole are shown in Figure 6.89A. An array of 29 uniformly spaced hydrophones spanning a depth interval of 0.61 m to 4.9 m was located in a cased monitoring well. Source positions were established along two lines, one of which is shown in Figure 6.89. The sources were located over a distance of 1.8–14.6 m from the well. The resulting image is shown in Figure 6.89B in which the water-filled drum is evident as a faster-velocity anomaly, and the

empty drum and the styrofoam are associated, weakly, with low-velocity zones. Note that in the image there is a velocity anomaly which smears obliquely across the image from the location of the drum towards the base of the well. This is an artefact of the GDT method, and such elongation of features occurs in the predominant direction of incident wave propagation. In this case, the sources were at the surface and the waves travelled down towards the well.

## 6.6.5 Forensic seismology

The impact of the main segments of a Boeing 747 aircraft that crashed at Lockerbie in Scotland on 21 December 1988, as a result of a bomb blast on board, was equivalent to a small earthquake measuring  $1.3 M_L$  on the Richter scale (Redmayne and Turbitt, 1990). The event was detected by a series of seismometers at Eskdalemuir, Scotland, a wider network established and monitored routinely by the Seismology Unit of the British Geological Survey. As the location of the impact was known, it was possible to calibrate and check their algorithms for locating epicentres. Their best fit for the Lockerbie impact was only some 300 m in error.

Records from these seismological stations are analysed to provide the approximate location of an aircrash event to within an area of about  $1 \text{ km}^2$ . In remote and largely unpopulated areas covering many hundreds of square kilometres, such information can help to target the search area and reduce the time taken to locate a crashed aircraft. The impact at Lockerbie was also used to calibrate the relationship between the energy of a falling mass and the resulting seismic magnitude of the impact. This kind of information is useful in the search for meteorite impacts.

Information arising from events recorded by the seismological network is passed to the British Ministry of Defence at Aldermaston. Analysis of the records from the event at Lockerbie indicated that the crash could have been felt up to 1 km away from the point of impact, and that structural damage from seismic waves alone could have been caused to buildings up to 100 m away.

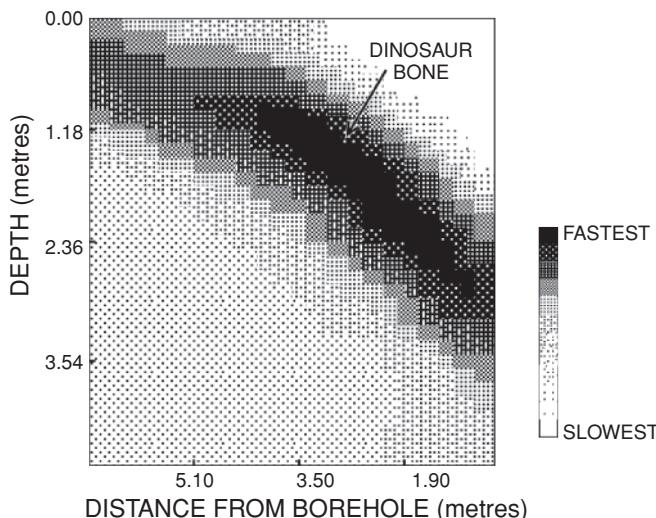


**Figure 6.86** Tomographic image displaying a velocity anomaly interpreted as being due to a dinosaur bone in a near-homogeneous sandstone formation, New Mexico. The interpretation was confirmed by subsequent excavation. From Witten and King (1990a), by permission.

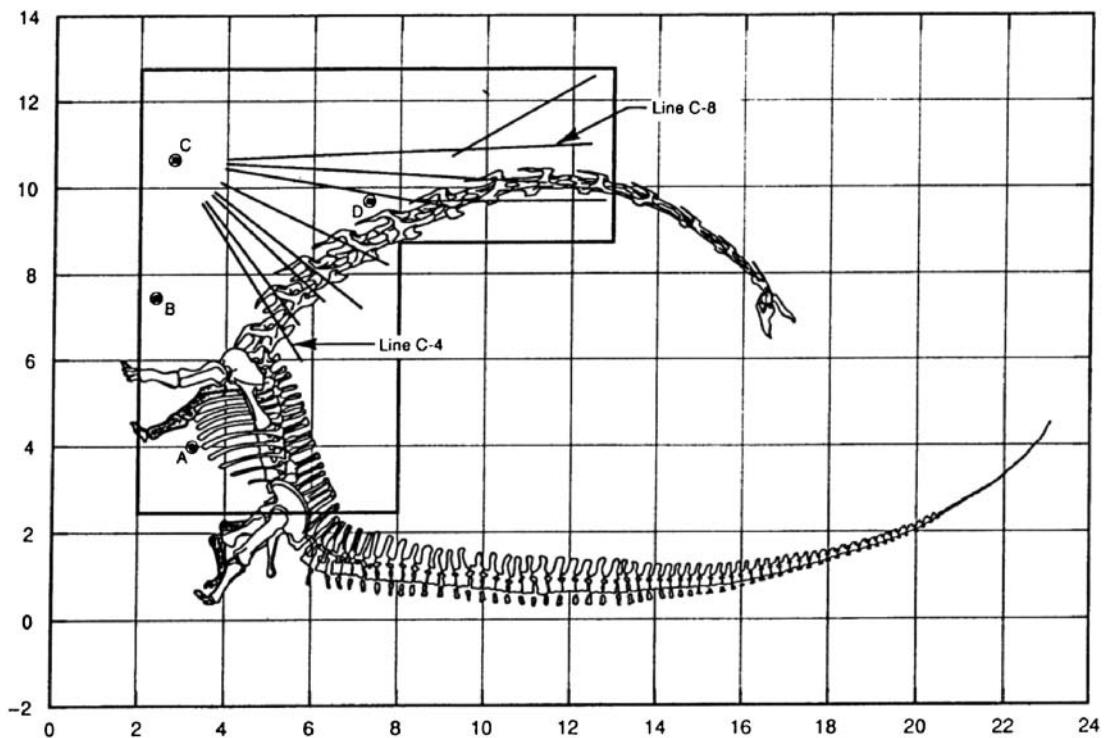


**Figure 6.87** Illustration of the L-shaped study area and the horizontal extent and positions of the 10 offset VSP survey lines around the remains of the 'seismosaurus' skeleton. Grid cells are  $2\text{ m} \times 2\text{ m}$ . The borehole positions are indicated by the letters A-D. From Witten et al. (1992), by permission.

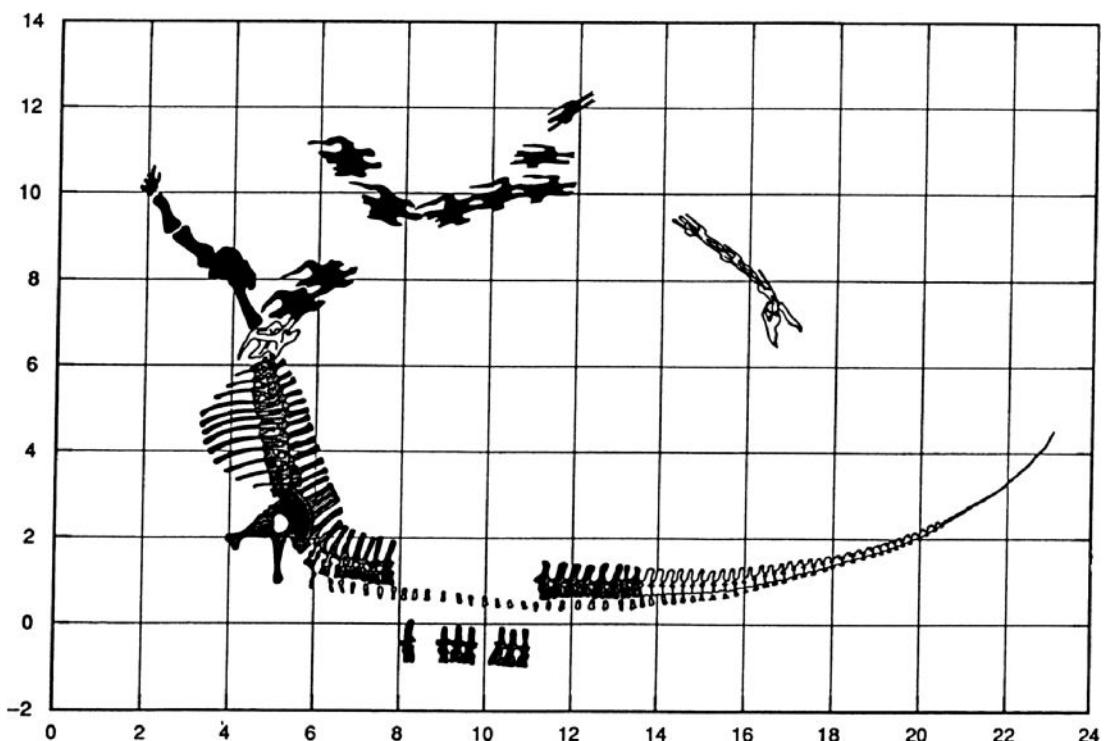


**Figure 6.88** Interpretation of skeletal position based on known bone locations and the results of the GDT surveys. Bones identified by image interpretation are shaded black; those found by excavation are shaded grey; bones conjectured as being present are unshaded. The skeletal drawing is schematic and is not intended to demonstrate anatomical details. From Witten et al. (1992), by permission.

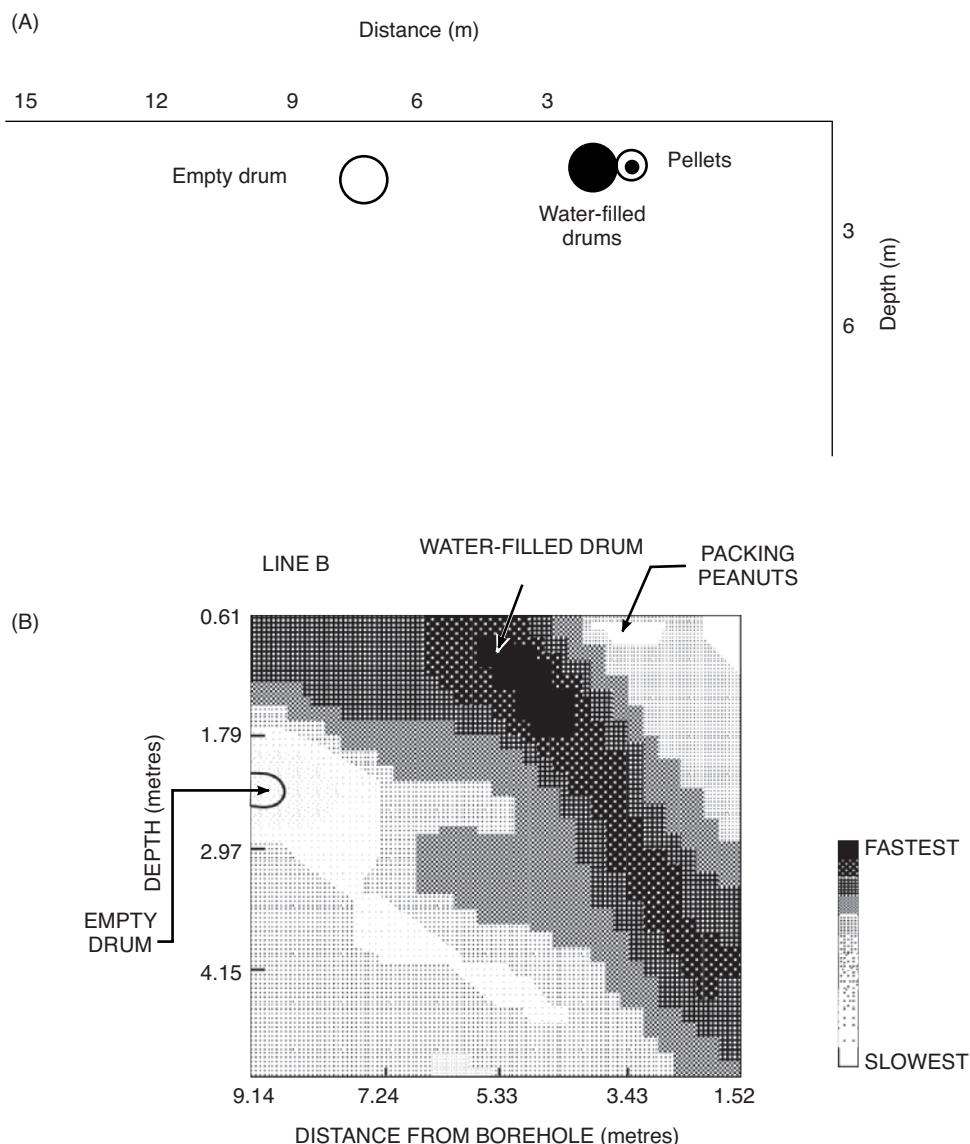


**Figure 6.89** A GDT survey undertaken at a test site over buried known targets: (A) the layout of the targets, and (B) a tomographic image obtained along the line in (A). From Witten and King (1990b), by permission.

Two other implications arise from the analysis of seismic waves generated from air crashes. The first is that the magnitude of the peak particle velocity can be estimated, and hence sensitive buildings and structures can be designed to withstand such ground dis-

turbance. The second is that the knowledge of the force of impact, determined using the seismic evidence in conjunction with other information, combined with a study of how a particular plane behaves on impact, can help to improve aircraft design.

# 7

## Electrical Resistivity Methods

### 7.1 Introduction

Electrical resistivity methods were developed in the early 1900s but have become very much more widely used since the 1970s, due primarily to the availability of computers to process and analyse the data. These techniques are used extensively in the search for suitable groundwater sources and also to monitor types of groundwater pollution; in engineering surveys to locate subsurface cavities, faults and fissures, permafrost, mine shafts, and so on; and in archaeology for mapping out the areal extent of remnants of buried foundations of ancient buildings, amongst many other applications. Electrical resistivity methods are also used extensively in downhole logging. For the purposes of this chapter, applications will be confined to the use of direct current (or very-low-frequency alternating current) methods.

Electrical resistivity is a fundamental and diagnostic physical property that can be determined by a wide variety of techniques, including electromagnetic induction. These methods will be discussed in their respective chapters. That there are alternative techniques for the determination of the same property is extremely useful, as some methods are more directly applicable or practicable in some circumstances than others. Furthermore, the approaches used to determine electrical resistivity may be quite distinct – for example, ground contact methods compared with airborne induction techniques. Mutually consistent but independent interpretations give the interpreter greater confidence that the derived model is a good approximation of the subsurface. If conflicting interpretations result, then it is necessary to go back and check each and every stage of the data acquisition, processing and interpretation in order to locate the problem. After all, the same ground with the same physical properties should give rise to the same model, irrespective of which method is used to obtain it.

### 7.2 Basic principles

#### 7.2.1 True resistivity

Consider an electrically uniform cube of side length  $L$  through which a current ( $I$ ) is passing (Figure 7.1). The material within the cube resists the conduction of electricity through it, resulting in a potential drop ( $V$ ) between opposite faces. The resistance ( $R$ ) is proportional to the length ( $L$ ) of the resistive material and inversely proportional to the cross-sectional area ( $A$ ) (Box 7.1); the constant of proportionality is the ‘true’ resistivity (symbol:  $\rho$ ). According to Ohm’s Law (Box 7.1), the ratio of the potential drop to the applied current ( $V/I$ ) also defines the resistance ( $R$ ) of the cube and these two expressions can be combined (Box 7.1) to form the product of a resistance ( $\Omega$ ) and a distance (area/length; metres), which is defined as the resistivity (units: ohm-metres,  $\Omega\text{m}$ ). The inverse of resistivity ( $1/\rho$ ) is conductivity ( $\sigma$ ), which has units of siemens/metre ( $\text{S}/\text{m}$ ) that are equivalent to mhos/metre ( $\Omega^{-1} \text{ m}^{-1}$ ). It should be noted that Ohm’s Law applies in the vast majority of geophysical cases unless high current densities ( $J$ ) occur, in which case the linearity of the law may break down.

If two media are present within the resistive cube, each with its own resistivity ( $\rho_1$  and  $\rho_2$ ), then both proportions of each medium and their geometric form within the cube (Figure 7.2) become important considerations. The formerly isotropic cube will now exhibit variations in electrical properties with the direction of measurement (known as *anisotropy*); a platy structure results in a marked anisotropy, for example. A lower resistivity is usually obtained when measured parallel to laminations in phyllitic shales and slates compared with that at right-angles to the laminations. The presence and orientation of elongate brine pockets (with high conductivity) strongly influence the resistivity of sea ice (Timco, 1979).

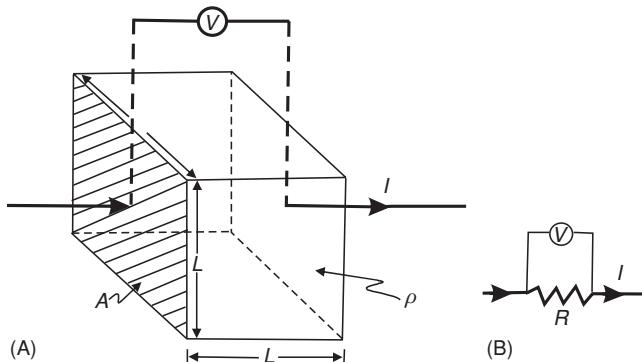


**Figure 7.1** (A) Basic definition of resistivity across a block of side length  $L$  with an applied current  $I$  and potential drop between opposite faces of  $V$ . (B) The electrical circuit equivalent, where  $R$  is a resistor.

The amount of anisotropy is described by the *anisotropy coefficient*, which is the ratio of maximum to minimum resistivity and which generally lies in the range 1–2. Thus it is important to have some idea of the form of electrical conductors with a rock unit. Detailed discussions of anisotropy have been given, for example, by Maillet (1947), Grant and West (1965) and Telford *et al.* (1990) (see also Section 7.3.3).

There are three ways in which electric current can be conducted through a rock: electrolytic, electronic (ohmic) and dielectric conduction. *Electrolytic conduction* occurs by the relatively slow movement of ions within an electrolyte and depends upon the type of ion, ionic concentration and mobility. *Electronic conduction* is the process by which metals, for example, allow electrons to move rapidly, so carrying the charge. *Dielectric conduction* occurs in very weakly conducting materials (or insulators) when an external alternating current is applied, so causing atomic electrons to be shifted slightly with respect to their nuclei. In most rocks, conduction is by way of pore fluids acting as electrolytes, with the actual mineral grains contributing very little to the overall conductivity of the rock (except where those grains are themselves good electronic conductors). At the frequencies used in electrical resistivity surveying, dielectric conduction can be disregarded. However, it does become important in ‘spectral induced polarisation’ and in ‘complex resistivity’ measurements (see Chapter 9).

### Box 7.1 True resistivity (see Figure 7.1)

Resistance ( $R$ ) is proportional to length ( $L$ ) divided by area ( $A$ ):  $R \propto L/A$ . This can be written as  $R = \rho L/A$ , where  $\rho$  is the true resistivity.

#### Ohm's Law

For an electrical circuit, Ohm's Law gives  $R = V/I$ , where  $V$  and  $I$  are the potential difference across a resistor and the current passing through it, respectively. This can be written alternatively in terms of the electric field strength ( $E$ ; volts/m) and current density ( $J$ ; amps/m<sup>2</sup>) as:

$$\rho = E/J (\Omega m)$$

Resistivity is defined by:

$$\rho = \frac{VA}{IL} (\Omega m)$$

The resistivity of geological materials exhibits one of the largest ranges of all physical properties, from  $1.6 \times 10^{-8} \Omega m$  for native silver to  $10^{16} \Omega m$  for pure sulphur. Igneous rocks tend to have the highest resistivities; sedimentary rocks tend to be most conductive, largely due to their high pore fluid content; and metamorphic rocks have intermediate but overlapping resistivities. The age of a rock is also an important consideration: a Quaternary volcanic rock may have a resistivity in the range 10–200  $\Omega m$ , while that of an equivalent rock but Precambrian in age may be an order of magnitude greater. This is a consequence of the older rock having far longer to be exposed to secondary infilling of interstices by mineralisation, and compaction decreasing the porosity and permeability.

In sedimentary rocks, the resistivity of the interstitial fluid is probably more important than that of the host rock. Indeed, Archie (1942) developed an empirical formula (Box 7.2) for the effective resistivity of a rock formation which takes into account the porosity ( $\varphi$ ), the fraction ( $s$ ) of the pores containing water, and the resistivity of the water ( $\rho_w$ ). Archie's Law is used predominantly in borehole logging. Korvin (1982) has proposed a theoretical basis to account for Archie's Law. Saline groundwater may have a resistivity as low as 0.05  $\Omega m$  and some groundwater and glacial meltwater can have resistivities in excess of 1000  $\Omega m$ .

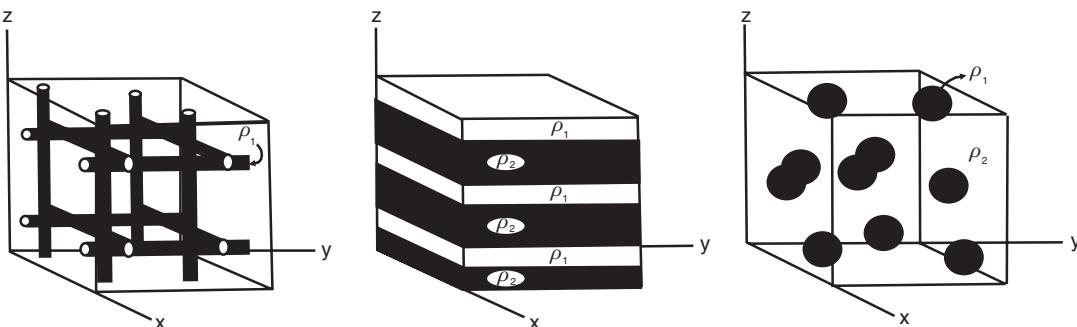


**Figure 7.2** Three extreme structures involving two materials with true resistivities  $\rho_1$  and  $\rho_2$ . After Grant and West (1965), by permission.

**Table 7.1 Resistivities of common geological materials.**

Material	Nominal resistivity ( $\Omega\text{m}$ )
<i>Sulphides:</i>	
Chalcopyrite	$1.2 \times 10^{-5} - 3 \times 10^{-1}$
Pyrite	$2.9 \times 10^{-5} - 1.5$
Pyrrhotite	$7.5 \times 10^{-6} \times 1^{-2}$
Galena	$3 \times 10^{-5} - 3 \times 10^2$
Sphalerite	$1.5 \times 10^7$
<i>Oxides:</i>	
Haematite	$3.5 \times 10^{-3} - 10^7$
Limonite	$10^3 - 10^7$
Magnetite	$5 \times 10^{-5} - 5.7 \times 10^3$
Ilmenite	$10^{-3} - 50$
Quartz	$300 - 10^6$
Rock salt	$30 - 10^{13}$
Anthracite	$10^{-3} - 2 \times 10^5$
Lignite	9-200
Granite	$300 - 1.3 \times 10^6$
Granite (weathered)	30-500
Syenite	$10^2 - 10^6$
Diorite	$10^4 - 10^5$
Gabbro	$10^3 - 10^6$
Basalt	$10 - 1.3 \times 10^7$
Schists (calcareous and mica)	$20 - 10^4$
Schist (graphite)	10-100
Slates	$600 - 4 \times 10^7$
Marble	$100 - 2.5 \times 10^8$
Consolidated shales	20-2000
Conglomerates	$2 \times 10^3 - 10^4$
Sandstones	$1 - 7.4 \times 10^8$
Limestones	$50 - 10^7$
Dolomite	$350 - 5 \times 10^3$
Marls	3-70
Clays	1-100
Alluvium and sand	10-800
Moraine	$10 - 5 \times 10^3$
Hydrocarbon reservoir	25 – 27.5
Sherwood sandstone	100-400
Soil (40% clay)	8
Soil (20% clay)	33
Topsoil	250-1700

**Table 7.1 (Continued)**

Material	Nominal resistivity ( $\Omega\text{m}$ )
London clay	4-20
Lias clay	10-15
Boulder clay	15-35
Clay (very dry)	50-150
Mercia mudstone	20-60
Coal measures clay	50
Middle coal measures	>100
Chalk	50-150
Coke	0.2-8
Gravel (dry)	1400
Gravel (saturated)	100
Quaternary/Recent sands	50-100
Ash	4
Colliery spoil	10-20
Pulverised fuel ash	50-100
Laterite	800-1500
Lateritic soil	120-750
Dry sandy soil	80-1050
Sand clay/clayey sand	30-215
Sand and gravel	30-225
Unsaturated landfill	30-100
Saturated landfill	15-30
Acid peat waters	100
Acid mine waters	20
Rainfall runoff	20-100
Landfill runoff	<10-50
Glacier ice (temperate)	$2 \times 10^6 - 1.2 \times 10^8$
Glacier ice (polar)*	$5 \times 10^4 - 3 \times 10^5*$
Permafrost	$10^3 - >10^4$

\* $-10^\circ\text{C}$  to  $-60^\circ\text{C}$ , respectively; strongly temperature-dependent (Reynolds, 1985).

Based on Telford *et al.* (1990) with additional data from McGinnis and Jensen (1971), Reynolds (1987a), Reynolds and Paren (1980, 1984) and many commercial projects.

Resistivities of some common minerals and rocks are listed in Table 7.1, while more extensive lists have been given by Telford *et al.* (1990).

Some minerals such as pyrite, galena and magnetite are commonly poor conductors in massive form, yet their individual crystals have high conductivities. Hematite and sphalerite, when pure, are virtual insulators, but when combined with impurities they can

**Box 7.2 Archie's Law**

$$\rho = a\varphi^{-m}s^{-n}\rho_w$$

where  $\rho$  and  $\rho_w$  are the effective rock resistivity, and the resistivity of the porewater, respectively;  $\varphi$  is the porosity;  $s$  is the volume fraction of pores with water;  $a$ ,  $m$  and  $n$  are constants where  $0.5 \leq a \leq 2.5$ ,  $1.3 \leq m \leq 2.5$ , and  $n \approx 2$ .

The ratio  $\rho/\rho_w$  is known as the Formation Factor ( $F$ ).

become very good conductors (with resistivities as low as  $0.1 \Omega\text{m}$ ). Graphite dispersed throughout a rock mass may reduce the overall resistivity of otherwise poorly conducting minerals. For rocks that have variable composition, such as sedimentary rocks with gradational facies, the resistivity will reflect the varying proportions of the constituent materials. For example, in northern Nigeria it is possible, on the basis of the interpreted resistivities, to gauge whether a near-surface material is a clayey sand or a sandy clay. Resistivities for sandy material are about  $100 \Omega\text{m}$  and decrease with increasing clay content to about  $40 \Omega\text{m}$ , around which point clay becomes the

dominant constituent and the values decrease further to those more typical of clay: well-formed and almost sand-free clay has a value in the range  $1-10 \Omega\text{m}$  (Reynolds, 1987a).

The objective of most modern electrical resistivity surveys is to obtain true resistivity models for the subsurface, because it is these that have geological meaning. The methods by which field data are obtained, processed and interpreted will be discussed later.

The *apparent resistivity* is the value obtained as the product of a measured resistance ( $R$ ) and a *geometric factor* ( $K$ ) for a given electrode array (see Section 7.3.2), according to the last expression in Box 7.1. The geometric factor takes into account the geometric spread of electrodes and contributes a term that has the unit of length (metres). Apparent resistivity ( $\rho_a$ ) thus has units of ohm-metres.

## 7.2.2 Current flow in a homogeneous earth

For a single current electrode implanted at the surface of a homogeneous medium of resistivity  $\rho$ , current flows away radially (Figure 7.3). The voltage drop between any two points on the surface can be described by the potential gradient ( $-\delta V/\delta x$ ), which is negative

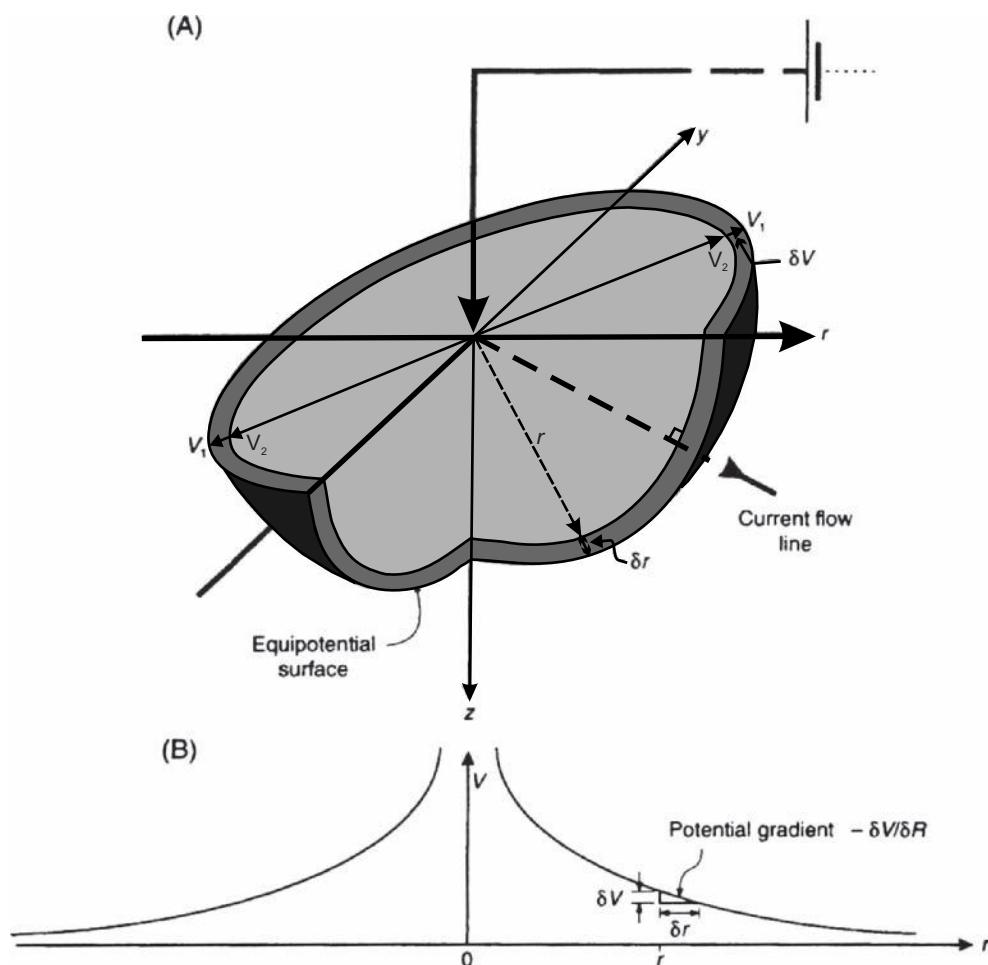


**Figure 7.3** (A) Three-dimensional representation of a hemispherical equipotential shell around a point electrode on a semi-infinite, homogeneous medium. (B) Potential decay away from the point electrode.

**Box 7.3** Voltage at a point from a current source (see Figure 7.3)

The potential difference ( $\delta V$ ) across a hemispherical shell of incremental thickness  $\delta r$  is given by:

$$\frac{\delta V}{\delta r} = -\rho \cdot J = -\rho \frac{I}{2\pi^2 r}.$$

Thus the voltage  $V_r$  at a point  $r$  from the current point source is:

$$V_r = \int \delta V = - \int \rho \cdot \frac{I \delta r}{2\pi r^2} = \frac{\rho I}{2\pi} \cdot \frac{1}{r}.$$

because the potential decreases in the direction of current flow. Lines of equal voltage ('equipotentials') intersect the lines of equal current at right-angles. The current density ( $J$ ) is the current ( $I$ ) divided by the area over which the current is distributed (a hemisphere;  $2\pi r^2$ ), and so the current density decreases with increasing distance from the current source. It is possible to calculate the voltage at a distance ( $r$ ) from a single current point source (Box 7.3). If, however, a current sink is added, a new potential distribution occurs (Figure 7.4) and a modified expression is obtained to describe the voltage at any point (Box 7.4).

## 7.3 Electrode configurations and geometric factors

### 7.3.1 General case

The final expression in Box 7.4 has two parts, namely a resistance term ( $R$ ; units  $\Omega$ ) and a term that describes the geometry of the

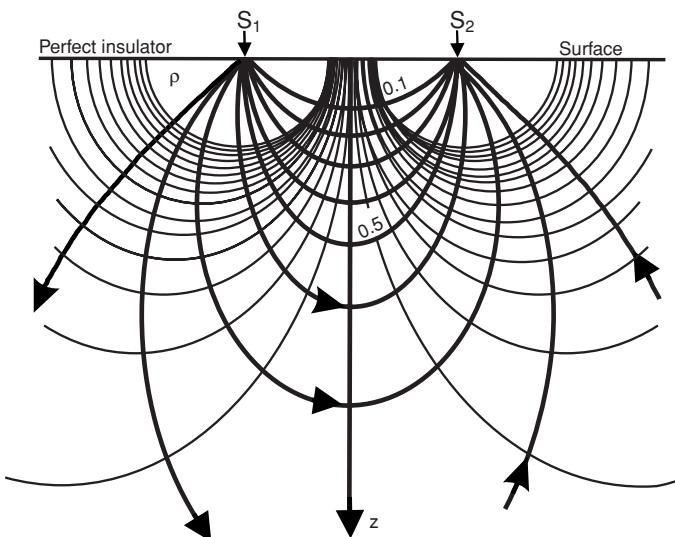


**Figure 7.4** Current and equipotential lines produced by a current source and sink. From van Nostrand and Cook (1966), by permission.

**Box 7.4** Resistivity as a function of electrode array geometry (see Figure 7.5)

For a current source and sink, the potential  $V_P$  at any point  $P$  in the ground is equal to the sum of the voltages from the two electrodes, such that:  $V_P = V_A + V_B$  where  $V_A$  and  $V_B$  are the potential contributions from the two electrodes, A(+I) and B(-I).

The potentials at electrode M and N are:

$$V_M = \frac{\rho I}{2\pi} \left[ \frac{1}{AM} - \frac{1}{MB} \right], \quad V_N = \frac{\rho I}{2\pi} \left[ \frac{1}{AN} - \frac{1}{NB} \right]$$

However, it is far easier to measure the potential difference,  $\delta V_{MN}$  which can be rewritten as:

$$\rho V_{MN} = V_M - V_N = \frac{\rho I}{2\pi} \left\{ \left[ \frac{1}{AM} - \frac{1}{MB} \right] - \left[ \frac{1}{AN} - \frac{1}{NB} \right] \right\}$$

Rearranging this so that resistivity  $\rho$  is the subject:

$$\rho = \frac{2\pi\rho V_{MN}}{I} \left\{ \left[ \frac{1}{AM} - \frac{1}{MB} \right] - \left[ \frac{1}{AN} - \frac{1}{NB} \right] \right\}^{-1}$$

electrode configuration being used (Box 7.5) and which is known as the *geometric factor* ( $K$ ; units m). In reality, the subsurface ground does not conform to a homogeneous medium and thus the resistivity obtained is no longer the 'true' resistivity but the *apparent resistivity* ( $\rho_a$ ), which can even be negative. It is very important to remember that the apparent resistivity is not a physical property of the subsurface media, unlike the true resistivity. Consequently, all field resistivity data are for apparent resistivity, while those obtained by interpretation techniques are 'true' resistivities.

Figure 7.6 shows that, in order for at least 50% of the current to flow through an interface at a depth of  $z$  metres into a second medium, the current electrode separation needs to be at least twice – and preferably more than three times – the depth. This has obvious practical implications, particularly when dealing with situations where the depths are of the order of several hundreds of metres, so requiring very long cable lengths that can produce undesirable inductive coupling effects. For very deep soundings where the

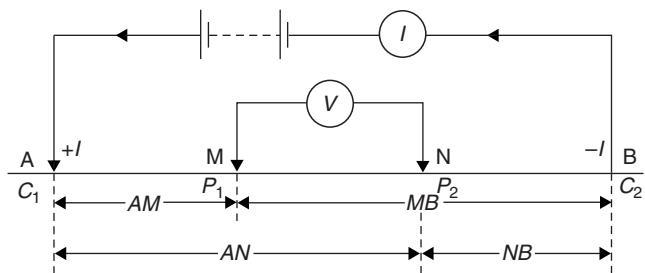


**Figure 7.5** Generalised form of electrode configuration in resistivity surveys.

**Box 7.5** The geometric factor (see Figure 7.5)

The geometric factor ( $K$ ) is defined by the expression:

$$K = 2\pi \left[ \frac{1}{AM} - \frac{1}{MB} - \frac{1}{AN} + \frac{1}{NB} \right]^{-1}$$

Where the ground is not uniform, the resistivity so calculated is called the *apparent resistivity* ( $\rho_a$ ):

$$\rho_a = R K, \text{ where } R = \delta V/I.$$

electrode separation is more than several kilometres, telemetering the data becomes the only practical solution (e.g. Shabtaie *et al.*, 1980, 1982). However, it should be emphasised that it is misleading to equate the depth of penetration with the current electrode separation as a general rule of thumb in the region of a resistivity survey. This aspect is discussed in Section 7.3.3.

### 7.3.2 Electrode configurations

The value of the apparent resistivity depends upon the geometry of the electrode array used, as defined by the geometric factor  $K$ . There are at least 102 different surface array types now recognised (Szalai and Szarka, 2008), most of which are rarely used; for a previous review of array types, see Whiteley (1973). Additional arrays exist involving either combined surface and downhole or just downhole arrays. Downhole arrays are often variants of surface array types. There are three main types of electrode configuration in common use, two of which are named after their originators – Frank Wenner (1912a,b) and Conrad Schlumberger – and a range of subtypes (Table 7.2 and Figure 7.7). The geometric factors for these arrays

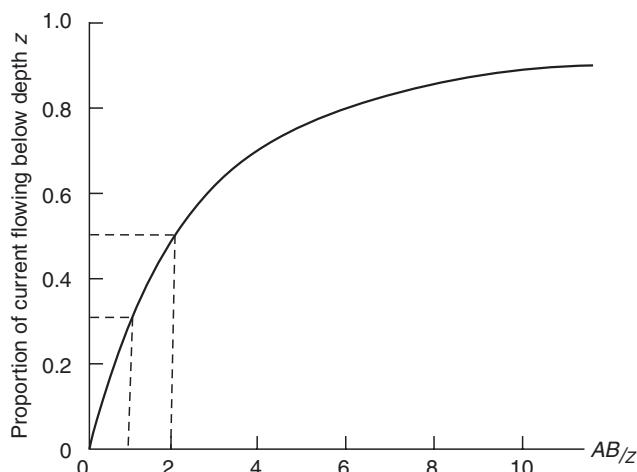


**Figure 7.6** Proportion of current flowing below a depth  $z$  (m);  $AB$  is the current electrode half-separation.

**Table 7.2** Selected electrode configurations (see also Figure 7.7).

<b>Wenner arrays</b>	<b>Standard Wenner</b>
	<b>Offset Wenner</b>
	Lee-partitioning array
	Tripotential ( $\alpha$ , $\beta$ and $\gamma$ arrays)
<b>Schlumberger array</b>	<b>Standard Schlumberger</b>
	Brant array
	Gradient array
<b>Dipole-dipole arrays</b>	<b>Normal</b> (axial or polar)
	Azimuthal
	Radial
	Parallel
	Perpendicular
	Pole-dipole
	<b>Equatorial</b>
	<b>Square</b> (special form of equatorial)

are given in Box 7.6 and a worked example for the Wenner array is given in Box 7.7. Arrays highlighted in bold in Table 7.2 are those most commonly used. That there are so many different array types is indicative of the flexibility of the resistivity technique, but it is important to recognise the advantages and disadvantages of each array; the choice of array is often a function of the user's previous familiarity with the array type, availability of cabling and data acquisition software, and of data processing and inversion software, as well as site-specific factors. For example, RES2DINV, a very popular and widely available software package (Geotomo Software, 2009a; Loke, 2009), supports ten surface array types and two cross-borehole arrays.

Dipole–dipole arrays have been used extensively by Russian geophysicists since 1950, and especially in Canada, particularly for 'induced polarisation' surveys (see Chapter 9) in mineral exploration, and in the USA in groundwater surveys (Zohdy, 1974). The term 'dipole' is misapplied in a strict sense because the inter-electrode separation for each of the current or potential electrode pairs should be insignificant with respect to the length of the array, which it is not. However, the term is well established in its usage.

These different types and styles of electrode configuration have particular advantages, disadvantages and sensitivities. Factors affecting the choice of array type include the amount of space available to lay out an array, and the labour intensity of each method. Other important considerations are the sensitivity to lateral inhomogeneities (Habberjam and Watkins, 1967a; Barker, 1981) and to dipping interfaces (Broadbent and Habberjam, 1971).

A graphic example of the different responses by the three main electrode configurations is given by so-called 'signal contribution sections' (Barker, 1979) shown in Figure 7.8. These sections are

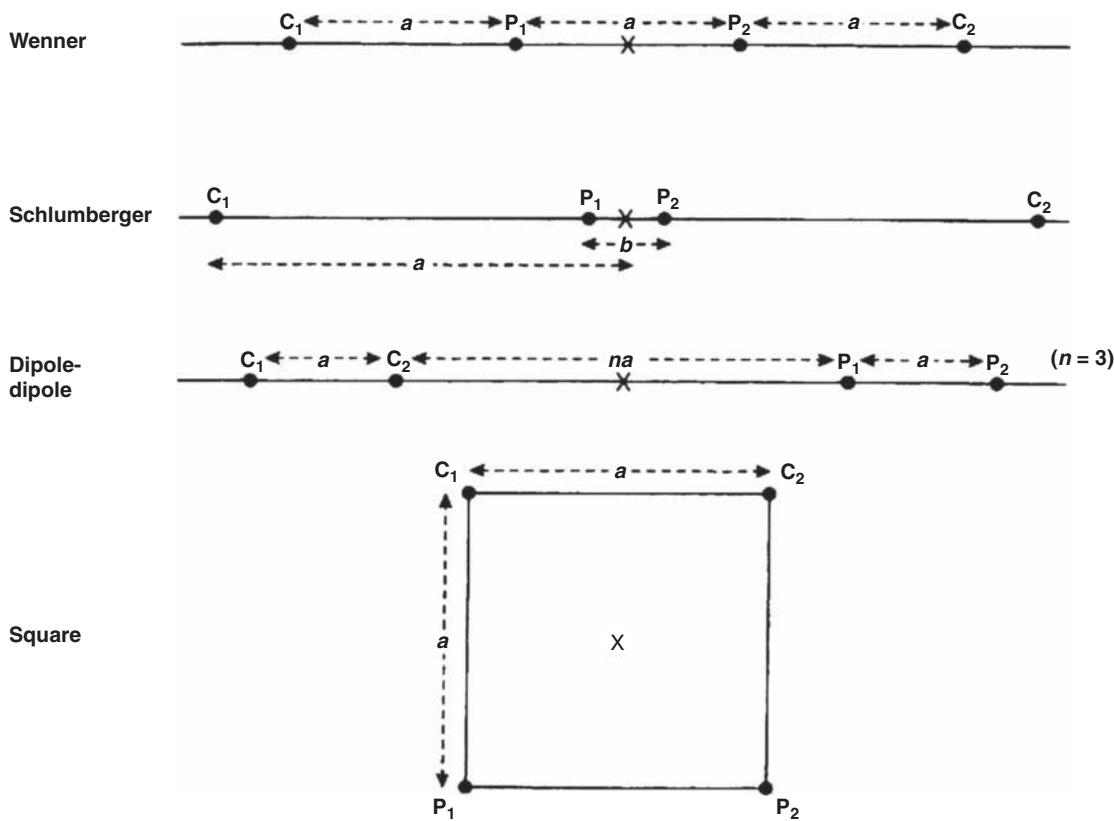


Figure 7.7 Electrode configurations used in electrical surveys.

contoured plots of the contribution made by each unit volume of the subsurface to the voltage measured at the surface.

Figure 7.8A shows the signal contribution for a Wenner array. In the near-surface region, the positive and negative areas cancel each

other out and the main response, which originates from depth, is largely flat (see the 1 unit contour). This indicates that for horizontally layered media, the Wenner array has a high vertical resolution. The Schlumberger array has almost as high a vertical resolution, but note that the form of the signal contribution at depth is now concave-upwards (Figure 7.8B). For the dipole-dipole array (Figure 7.8C), the lobate form of the signal contribution indicates that there is a poor vertical resolution and that the array is particularly sensitive to deep lateral resistivity variations, making it an unsuitable array for depth sounding (Bhattacharya and Patra, 1968). Nevertheless, this sensitivity can be utilised in resistivity profiling (see Section 7.4.4).

#### Box 7.6 Apparent resistivities for given geometric factors for electrode configurations in Figure 7.7

Wenner array:  $\rho_a = 2\pi aR$  (alpha/beta arrays)

$\rho_a = 3\pi aR$  (gamma rays)

Two-electrode:  $\rho_a = 2\pi aR$

Lee array:  $\rho_a = 4\pi aR$

Schlumberger array:  $\rho_a = \frac{\pi a^2}{b} \left[ 1 - \frac{b^2}{4a^2} \right] R; \quad a \geq 5b$

Gradient array:  $\rho_a = 2\pi \frac{L^2}{a} \cdot \frac{1}{G} \cdot R$   
where  $G = \frac{(1-X)}{(Y^2 + (1-X)^2)^{3/2}}$   
 $\quad \quad \quad + \frac{(1+X)}{(Y^2 + (1+X)^2)^{3/2}}$

Dipole-dipole array:  $\rho_a = \pi n(n+1)(n+2)aR$

Pole-dipole array:  $\rho_a = 2\pi n(n+1)aR$

Square array:  $\rho_a = \pi a(2 + \sqrt{2})R$

#### Box 7.7 Worked example of how to calculate a geometric factor

Using the expression previously defined in Box 7.5 (see also Figure 7.5), and substituting the correct values for the Wenner array:

$$K = 2\pi \left[ \frac{1}{a} - \frac{1}{2a} - \frac{1}{2a} + \frac{1}{a} \right]^{-1} = 2\pi \left[ \frac{2}{a} - \frac{2}{2a} \right]^{-1} = 2\pi a.$$

Hence, as  $\rho_a = KR$ ,  $\rho_a = 2\pi aR$ .

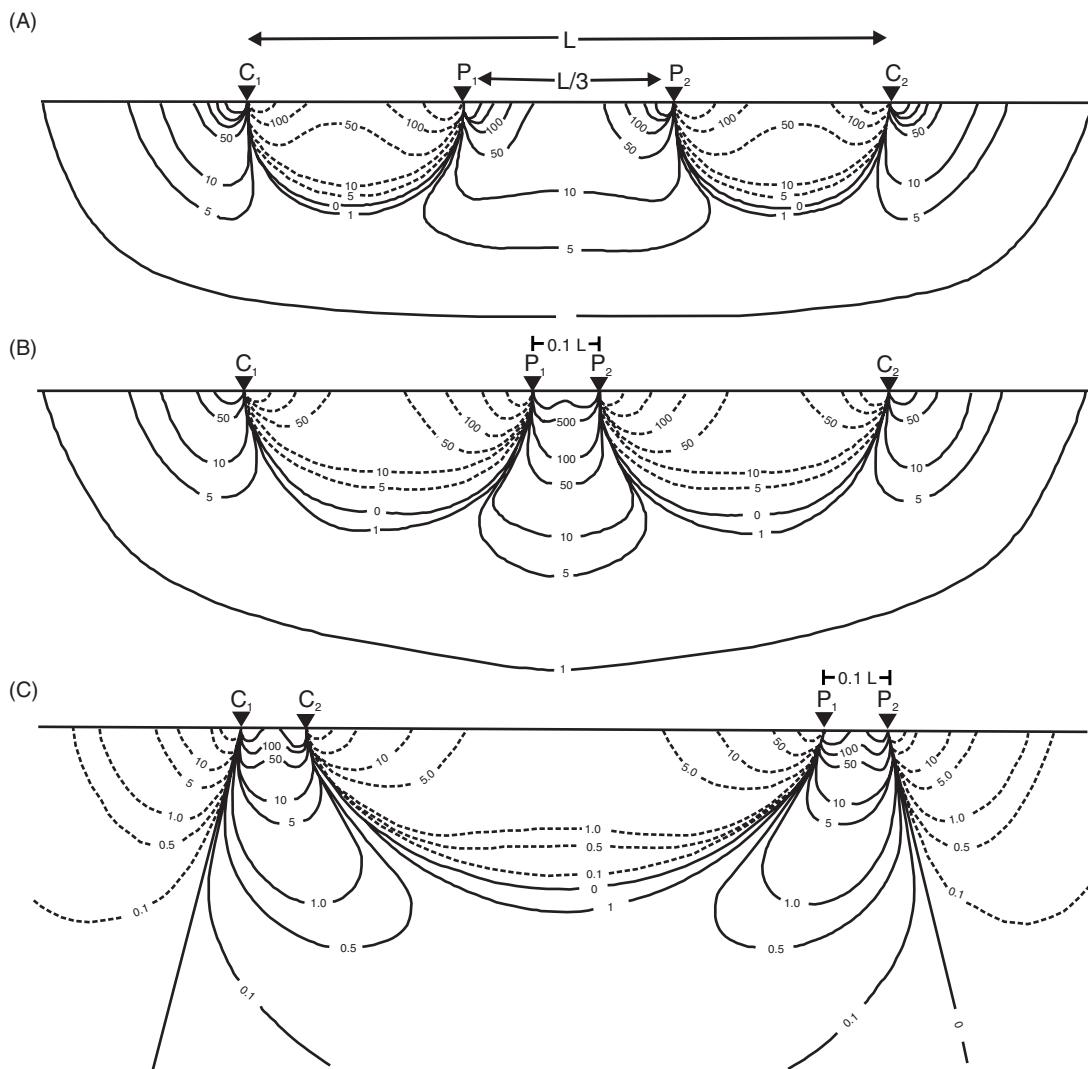


**Figure 7.8** Signal contribution sections for (A) Wenner, (B) Schlumberger and (C) dipole-dipole configurations. Contours indicate the relative contributions made by discrete volume elements of the subsurface to the total potential difference measured between the two potential electrodes  $P_1$  and  $P_2$ . From Barker (1979), by permission.

A modified electrode array (Lee partitioning array) was devised by Lee (Lee and Schwartz, 1930) in an attempt to reduce the undesirable effects of near-surface lateral inhomogeneities. An alternative tripotential method was proposed by Carpenter (1955) and Carpenter and Habberjam (1956) which combined the apparent resistivities obtained for the alpha, beta and gamma rays (Figure 7.9). The method has been discussed further by Ackworth and Griffiths (1985). A smoothing technique using the tripotential method was produced by Habberjam and Watkins (1967).

An alternative technique, called the *Offset Wenner* method (Barker, 1981), has been readily adopted for its ease of use. The method is extremely simple in concept. Figure 7.10 shows a single contribution section for a standard Wenner array. A conducting sphere buried in a semi-infinite homogeneous medium with true resistivity of  $100 \Omega\text{m}$  is located in a positive region of the signal contribution section (Figure 7.10A). The corresponding apparent resistivity, calculated using an exact analytical method (Singh, 1976),

is  $91.86 \Omega\text{m}$ . Offsetting the Wenner array one spacing to the right (Figure 7.10B), the previously positive areas are now negative and vice versa, and the buried sphere is located in a negative region resulting in an apparent resistivity of  $107.81 \Omega\text{m}$ . The average of these two apparent resistivities is  $99.88 \Omega\text{m}$ , thereby reducing the error due to a lateral inhomogeneity from around  $\pm 8\%$  to only  $0.1\%$ .

One array that is seldom used, but which has two major advantages, is the square array. This is a special form of the equatorial dipole-dipole array for  $n = 1$ . The square array is particularly good for determining lateral azimuthal variations in resistivity. By swapping  $P_1$  and  $C_2$ , the square is effectively rotated through  $90^\circ$  and thus the apparent resistivity can be determined for two orthogonal directions. For ground that is largely uniform, the two resistivities should be the same, but where there is a difference in resistivity due to a form of anisotropy (*transverse anisotropy* as it is measured only in the  $x-y$  plane), the two resistivities will differ. The ratio of the two resistivities is an indication of the transverse anisotropy.

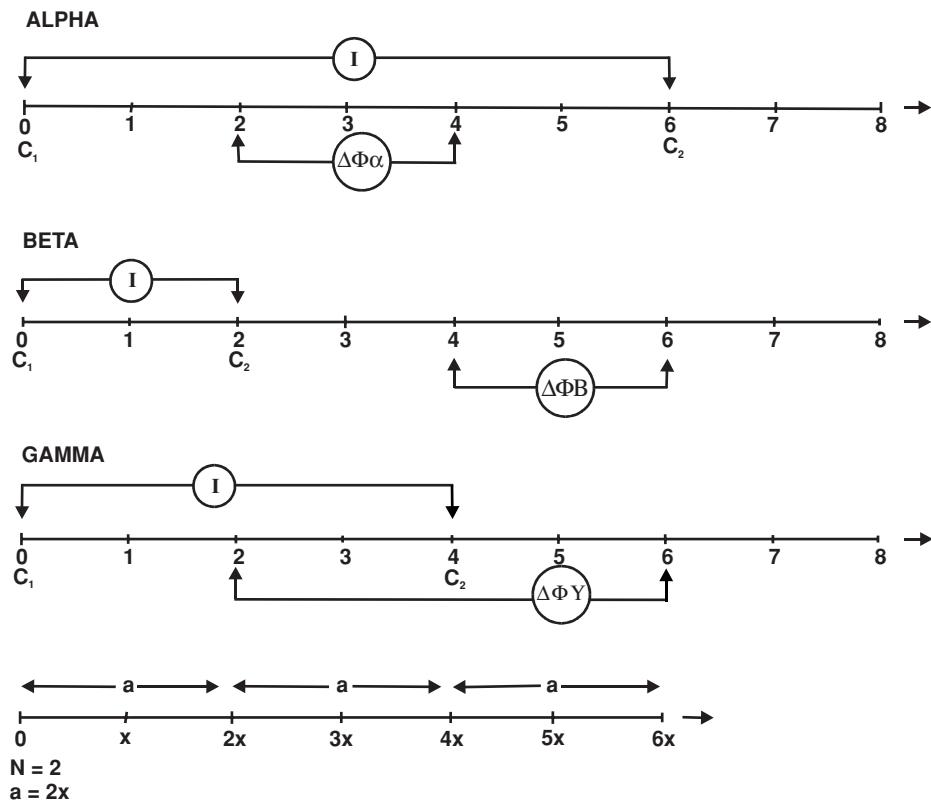


**Figure 7.9** Wenner tripotential electrode configurations for  $N = 2$ ;  $x$  is the fixed electrode separation, and the active electrode separation is  $2x$ . From Ackworth and Griffiths (1985), by permission.

Profiles and maps of transverse anisotropy can be interpreted qualitatively to indicate anomalous ground. The second advantage of the square array is that it lends itself to rapid grid mapping. By moving two electrodes at a time, the square can be moved along the transect. By increasing the dimensions of the square, and thus generally increasing the depth penetration and repeating the same survey area, three-dimensional models of the resistivity distribu-

tion can be obtained. Of all the electrode configurations, the square array is the least sensitive to steeply dipping interfaces (Broadbent and Habberjam, 1971) and thus it can cope in situations where the subsurface media are not horizontally layered. Being a particularly labour-intensive field method, it is best restricted to small-scale surveys where the electrode separation is only of the order of a few metres. This technique has particular value in 3D mapping of

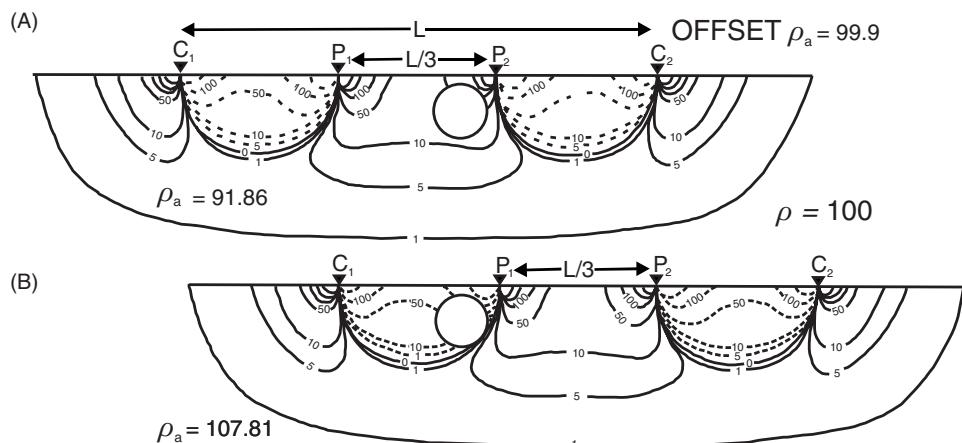


**Figure 7.10** (A) Signal contribution section for a Wenner array with a conducting sphere (negative  $K$ ) in a positive region in a medium with resistivity  $100 \Omega\text{m}$ . (B) Offset Wenner electrodes in which the sphere is now in a negative region. Distortion of contours due to the presence of the sphere is not shown. From Barker (1981), by permission.

**Table 7.3** Comparison of dipole-dipole, Schlumberger, square and Wenner electrode arrays.

Criteria	Wenner	Schlumberger	Dipole-dipole	Square
Vertical resolution	✓✓✓	✓✓	✓	✓✓
Depth penetration	✓	✓✓	✓✓✓	✓✓
Suitability to VES	✓✓	✓✓✓	✓	✗
Suitability to CST	✓✓✓	✗	✓✓✓	✓✓✓
Sensitivity to orientation	Yes	Yes	Moderate	No
Sensitivity to lateral inhomogeneities	High	Moderate	Moderate	Low
Labour intensive	Yes (no*)	Moderate (no*)	Moderate (no*)	Low
Availability of interpretational aids	✓✓✓	✓✓✓	✓✓	✓

✓ = poor; ✓✓ = moderate; ✓✓✓ = good; ✗ = unsuitable.  
 \* When using a multi-core cable and automated electrode array.

buried massive ice and in shallow archaeological investigations, for example.

A general guide to the suitability of the dipole-dipole, Schlumberger, square and Wenner electrode configurations is given in Table 7.3. An important consideration for the suitability of a given array is the scale at which it is to be deployed. For example, a square array is not really appropriate for depth sounding ('vertical electrical sounding'; VES) or for 'constant separation traversing' (CST) with a large square side; whereas it is perhaps better than either the Wenner or Schlumberger arrays for applications concerned with very shallow depths (<2 m), such as in archaeological investigations. While the main electrode configurations are now well established in their major applications, small-scale mini-resistivity surveys have yet to realise their full potential other than in archaeo-geophysical investigations. In such surveys, twin-electrode or four-point (Wenner) electrode arrays are used where the electrode separation is of the order of 0.5 m in order to sample the very near-surface materials.

### 7.3.3 Media with contrasting resistivities

A geological section may show a series of lithologically defined interfaces which do not necessarily coincide with boundaries identified electrically. For example, in an unconfined sandstone aquifer, there is a capillary zone above the water table making the boundary from 'dry' to 'saturated' a rather diffuse one. Furthermore, different lithologies can have the same resistivity and thus would form only one electric unit.

A geoelectric unit is characterised by two basic parameters: the *layer resistivity* ( $\rho_i$ ) and the *layer thickness* ( $t_i$ ) for the  $i$ th layer ( $i = 1$  for the surface layer). Four further electrical parameters can be derived for each layer from the respective resistivity and thickness; these are called the *longitudinal conductance* ( $S_L$ ; units mS); *transverse resistance* ( $T$ ; units  $\Omega\text{m}^2$ ); *longitudinal resistivity* ( $\rho_L$ ; units  $\Omega\text{m}$ ); and *transverse resistivity* ( $\rho_T$ ; units  $\Omega\text{m}$ ). They are defined in Box 7.8 for the model shown in Figure 7.11. The sums of all the longitudinal conductances and of the transverse resistances for a layered ground are called the Dar Zarrouk 'function' and 'variable',

respectively. (The curiously named Dar Zarrouk parameters were so called by Maillet (1947) after a place near Tunis where he was a prisoner of war.)

The importance of the longitudinal conductance for a particular layer is that it demonstrates that it is not possible to know both the true layer conductivity (or resistivity) *and* the layer thickness, so giving rise to layer *equivalence*. For example, a layer with a longitudinal conductance of 0.05 mS can have a resistivity of 100  $\Omega\text{m}$  and thickness 5 m. Layers with the combination of resistivity 80  $\Omega\text{m}$  and thickness 4 m, and 120  $\Omega\text{m}$  and 6 m, are all equivalent electrically. Equivalence needs to be considered during interpretation of sounding curves (see Section 7.5.4) and generally in the interpretation of electrical data, whether obtained by contact electrical or electromagnetic induction methods.

Where a point current source is located close to a plane boundary between two homogeneous media, the lines of current flow (and hence of equipotential) are refracted at the boundary in proportion to the contrast in resistivity between the two media (Figure 7.12

#### Box 7.8 Dar Zarrouk parameters

For a given layer:

$$S_L = h/\rho = h \cdot \sigma$$

$$T = h \cdot \rho$$

$$\rho_L = h/S$$

$$\rho_T = T/h$$

$$A = \rho_T / \rho_L$$

For  $n$  layers:

$$S_L = \sum_{i=1}^n (h_i / \rho_i) = \frac{h_1}{\rho_1} + \frac{h_2}{\rho_2} + \frac{h_3}{\rho_3} + \dots + \frac{h_n}{\rho_n}$$

$$T = \sum_{i=1}^n (h_i \cdot \rho_i) = h_1 \rho_1 + h_2 \rho_2 + h_3 \rho_3 + \dots + h_n \rho_n$$

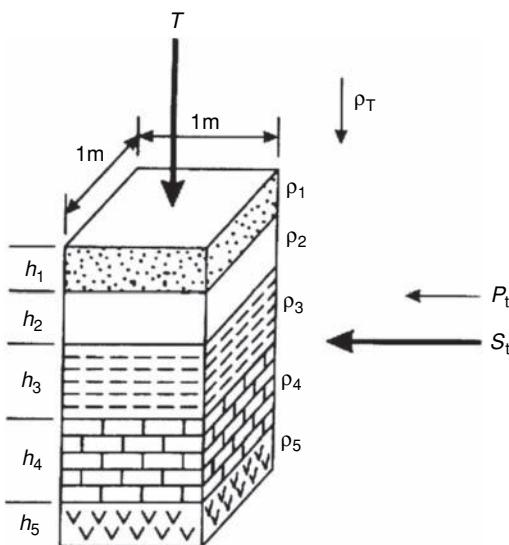


**Figure 7.11** Thickness ( $h$ ) and true resistivity ( $\rho$ ) of component layers with an indication of the total longitudinal conductance ( $S_L$ ) and total transverse resistance ( $T$ ); subscripts L and T refer to longitudinal and transverse, respectively.

and Box 7.9). In a homogeneous material with no boundaries in the vicinity, current flow lines are symmetrically radial. If a boundary is nearby, the current flow lines will become distorted (Figure 7.12B): current flowing towards a medium with a higher resistivity will diverge from the radial pattern and current densities adjacent to the boundary will decrease, whereas the current converges upon approaching a medium with a lower resistivity, with a consequent increase in current densities. The potential at a point adjacent to a plane boundary can be calculated using optical image theory (Figure 7.12C). If a current source of strength  $S$  is placed in one medium of resistivity  $\rho_1$ , the source's image point lies in the second medium of resistivity  $\rho_2$  (where  $\rho_2 > \rho_1$ ) but has a reduced strength  $kS$ , where  $k$  is dependent upon the resistivity contrast between the two media and lies in the range  $\pm 1$ . This  $k$  factor is akin to the reflection coefficient in optics and in reflection seismology, and has the form given in Box 7.10. If the current passes from a lower resistivity medium to one with a higher resistivity,  $k$  is positive; if it passes into a medium with a lower resistivity,  $k$  is negative.

In the case when the boundary is vertical, different types of anomaly will be produced dependent upon the electrode configuration used and whether it is developed at right-angles or parallel to the boundary. Examples of the types of anomalies produced are illustrated in Figure 7.13. The cusps and discontinuity in (A), (B)

**Box 7.10** Electrical reflection coefficient,  $k$  (see Figure 7.12C)

Potential at P:

$$V = \frac{I\rho_1}{4\pi} \left[ \frac{1}{r_1} + \frac{k}{r_2} \right]$$

Potential at Q:

$$V = \frac{I\rho_2}{4\pi} \left[ \frac{1+k}{r_3} \right]$$

At the interface,  $V = V'$  and  $r_1 = r_2 = r_3$ . Hence:

$$\rho_1/\rho_2 = (1-k)/(1+k)$$

$$\text{or } k = (\rho_2 - \rho_1)(\rho_2 + \rho_1)$$

and (C) are due to the positioning of the electrodes relative to the vertical boundary, with each cusp occurring as one electrode crosses the boundary. In the case of the Wenner array, it can be explained in detail (Figures 7.13D and E) as follows.

As the array is moved from the high-resistivity medium towards the low-resistivity medium (case (i) in Figure 7.13), the current flow lines converge towards the boundary, increasing the current density at the boundary but decreasing the potential gradient at the potential electrodes. The apparent resistivity gradually falls from its true value until a minimum is reached when the current electrode  $C_2$  is at the boundary (ii). Once  $C_2$  has crossed into the low-resistivity unit (iii), the current density increases adjacent to the boundary but within the low-resistivity medium, causing the potential gradient between the potential electrodes to rise. When the entire potential electrode dipole has crossed the boundary (iv), the current density is highest in the high-resistivity medium, causing the potential gradient across  $P_1-P_2$  to fall dramatically. With the current electrode  $C_1$  now into the low-resistivity unit (v), the current adjacent to the boundary is divergent. This results in an elevated potential gradient between  $P_1$  and  $P_2$  which falls to a normal value when the entire collinear array is sufficiently far away from the boundary. At this point the current flow is radial once more. The magnitude of the cusps and discontinuities is dependent upon the resistivity contrast between the two media. However, if the array is orientated parallel to the boundary such that all electrodes cross it simultaneously, the cusping is reduced (Figure 7.13B, dashed line).

The anomaly shape is similarly varied over a vertical dyke (Figure 7.14) in which the width of the anomaly varies not only with electrode configuration but also with the ratio of the dyke width to electrode separation. An example of an apparent resistivity profile across a buried hemi-cylindrical valley is shown in Figure 7.15. The field and modelled profiles are very similar. The mathematical treatment of apparent resistivity profiles across vertical boundaries is discussed in detail by Telford *et al.* (1990).

The important consideration arising from this discussion is that different array types and orientations across an identical boundary between two media with contrasting resistivities will produce

**Box 7.9** Refraction of current flow at a plane boundary (see Figure 7.12A)

Refraction of current flow at a plane boundary:

$$\tan \theta_2 / \tan \theta_1 = \rho_1 / \rho_2.$$

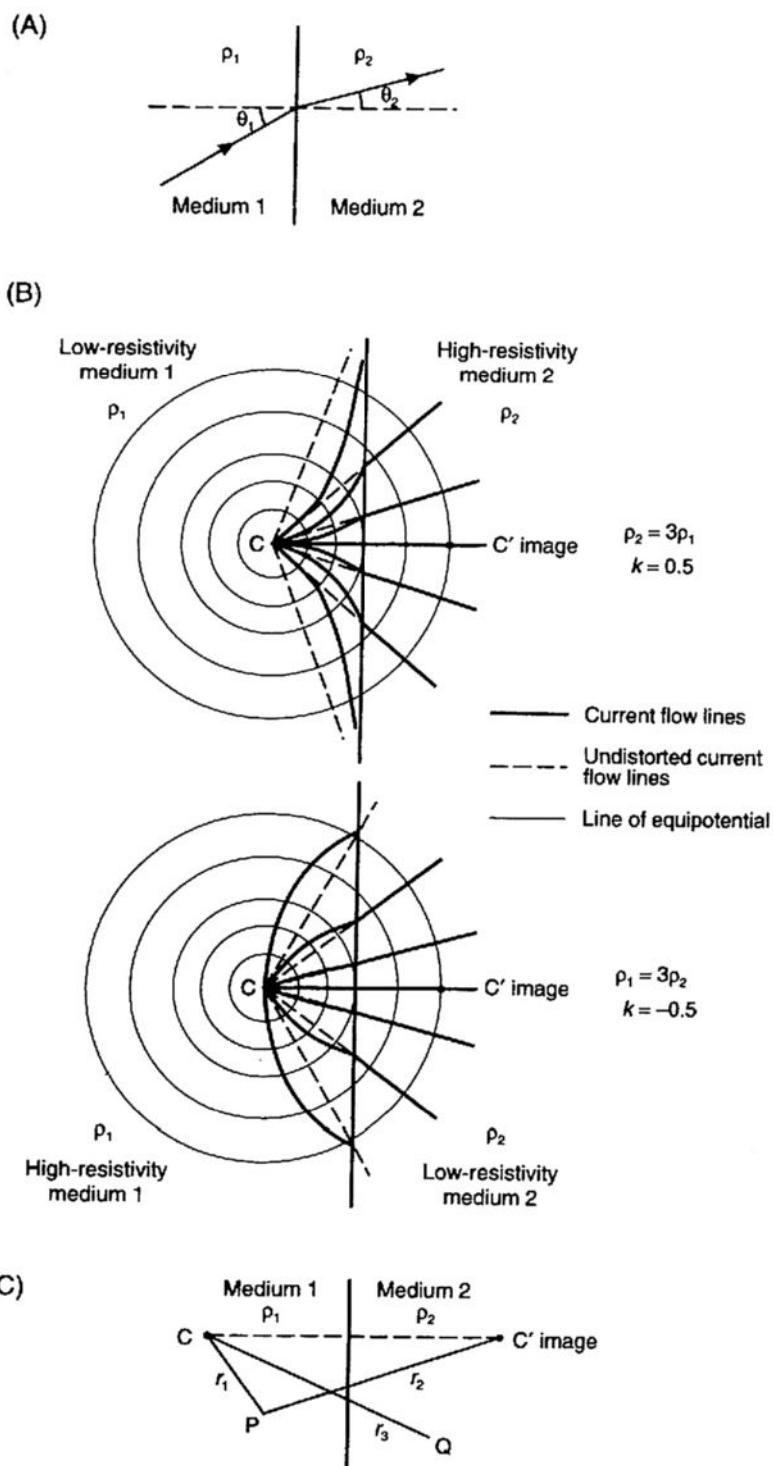
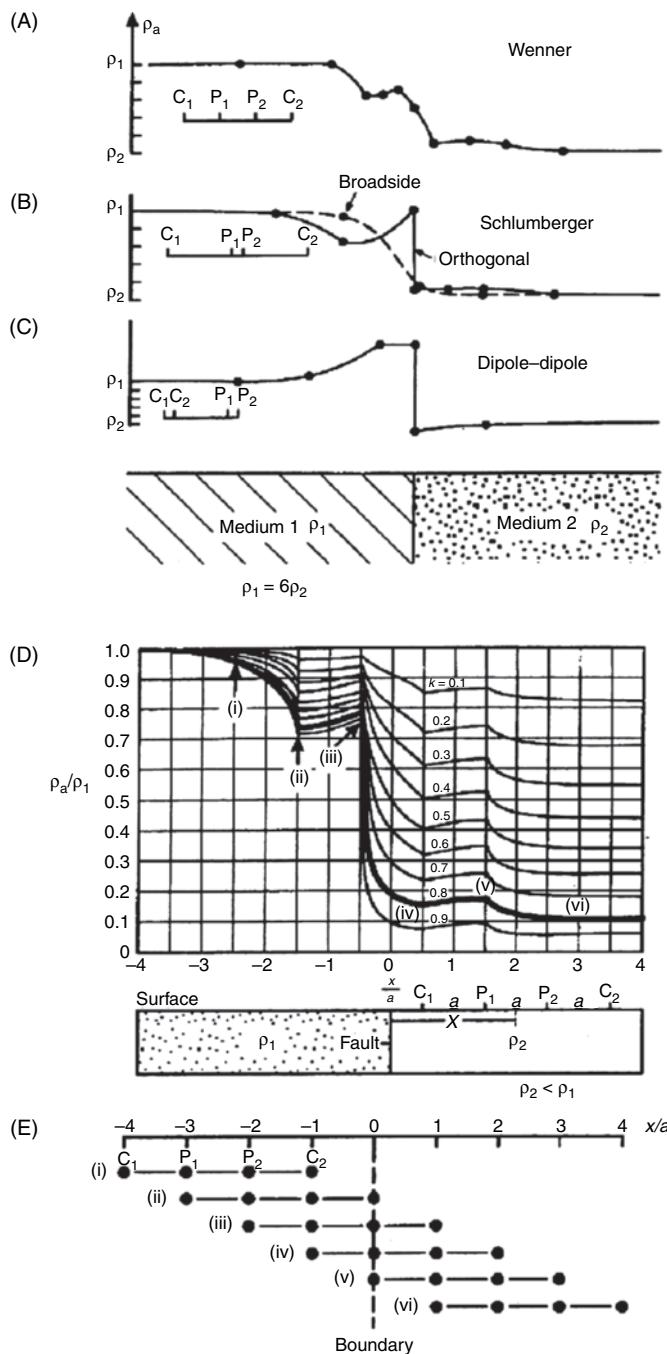


Figure 7.12 (A) Refraction of current flow lines, and (B) distortion of equipotential and current flow lines from a point electrode across a plane boundary between media with contrasting resistivities (Telford et al., 1990). (C) Method of optical images for the calculation of a potential at a point (see text for details).



**Figure 7.13** Apparent resistivity profiles measured over a vertical boundary using different electrode arrays: (A) Wenner (with its characteristic W-shaped anomaly), (B) Schlumberger and (C) dipole-dipole. After Telford et al. (1990), by permission of Cambridge University Press. (D) Profile shapes as a function of resistivity contrast. From van Nostrand and Cook (1966), by permission. (E) Plan view of successive moves of a Wenner array with electrode positions indicated for six marked points in (D).

markedly different anomaly shapes. Thus interpretation and comparison of such profiles based simply on apparent resistivity maxima or minima can be misleading; for example, if maxima are used to delimit targets, a false target could be identified in the case of maxima doublets such as in Figure 7.14. Similar complex anomalies occur in electromagnetic data (Section 9.4.3). Furthermore, the type of anomaly should be anticipated when considering the geological target so that the appropriate electrode configuration and orientation can be chosen prior to the commencement of the survey.

## 7.4 Modes of deployment

There are two main modes of deployment of electrode arrays. One is for depth sounding (to determine the vertical variation of resistivity) – this is known as *vertical electrical sounding* (VES; Section 7.4.1). The other is for producing either a horizontal profile (lateral variation of resistivity) using a fixed electrode separation (called *constant separation traversing*, CST; Section 7.4.4) or both a lateral and vertical variation in resistivity (called *subsurface imaging*, SSI, or *electrical resistivity tomography*, ERT; Section 7.4.3). SSI/ERT, for example, is used for very high resolution mapping of the near-surface in archaeological, engineering and environmental investigations, and can be deployed in 2D and 3D acquisition configurations.

### 7.4.1 Vertical electrical sounding (VES)

As the distance between the current electrodes is increased, so the depth to which the current penetrates is increased. In the case of the dipole-dipole array, increased depth penetration is obtained by increasing the inter-dipole separation, not by lengthening the current electrode dipole. The position of measurement is taken as the mid-point of the electrode array. For a depth sounding, measurements of the resistance ( $\delta V/I$ ) are made at the shortest electrode separation and then at progressively larger spacings. At each electrode separation a value of apparent resistivity ( $\rho_a$ ) is calculated using the measured resistance in conjunction with the appropriate geometric factor for the electrode configuration and separation being used (see Section 7.3). The values of apparent resistivity are plotted on a graph ('field curve'), the  $x$ - and  $y$ -axes of which represent the logarithmic values of the current electrode half-separation ( $AB/2$ ) and the apparent resistivity ( $\rho_a$ ), respectively (Figure 7.16). The methods by which these field curves are interpreted are discussed in detail in Section 7.5.

In the normal Wenner array, all four electrodes have to be moved to new positions as the inter-electrode spacings are increased (Figure 7.17A). The offset Wenner system (Figure 7.17B) has been devised to work with special multi-core cables (Barker, 1981). Special connectors at logarithmically spaced intervals permit a Wenner VES to be completed by using a switching box which removes the necessity to change the electrode connections physically. Note that the offset Wenner array requires one extra electrode separation to cover the same amount of the subsurface compared with the normal Wenner array. When space is a factor, this needs to be considered in the survey design stage.

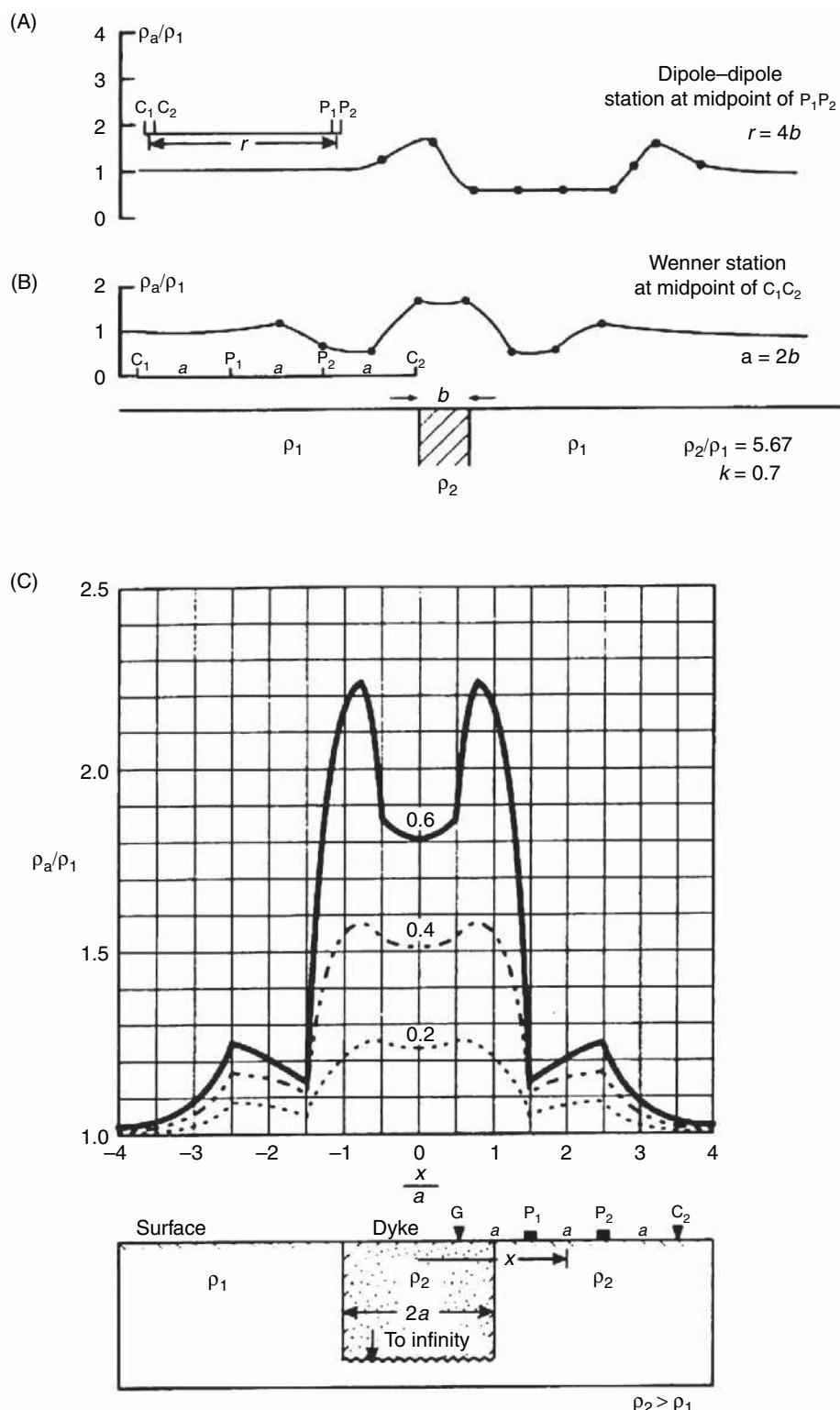


**Figure 7.14** Apparent resistivity profiles across a thin vertical dyke using (A) a dipole-dipole array and (B) a Wenner array. (C) Computed normalised resistivity profiles across a thin vertical dyke with different resistivity contrasts. After van Nostrand and Cook (1976), by permission.

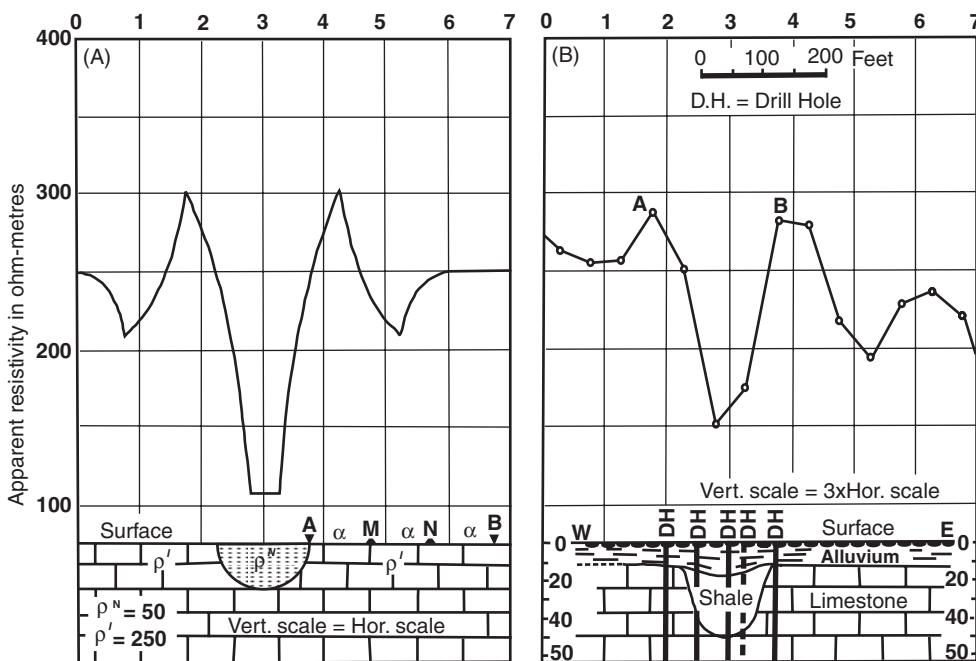


**Figure 7.15** Apparent resistivity profiles across a buried valley: (A) theoretical profile, and (B) measured profile. After Cook and van Nostrand (1954) (see ParASNIS, 1986).

In the case of the Schlumberger array (Figure 7.17C), the potential electrodes ( $P_1P_2$ ) are placed at a fixed spacing ( $b$ ) which is no more than a fifth of the current-electrode half-spacing ( $a$ ). The current electrodes are placed at progressively larger distances. When the measured voltage between  $P_1$  and  $P_2$  falls to very low values (owing to the progressively decreasing potential gradient with increasing current electrode separation), the potential electrodes are spaced more widely apart (spacing  $b_2$ ). The measurements are continued and the potential electrode separation increased again as necessary until the VES is completed. The tangible effects of so moving the potential electrodes is discussed at the end of Section 7.4.5. A VES

using the Schlumberger array takes up less space than either of the two Wenner methods and requires less physical movement of electrodes than the normal Wenner array, unless multi-core cables are used.

The dipole-dipole array is seldom used for vertical sounding as large and powerful electrical generators are normally required. Once the dipole length has been chosen (i.e. the distance between the two current electrodes and between the two potential electrodes), the distance between the two dipoles is then increased progressively (Figure 7.17D) to produce the sounding. The square array is rarely used for large-scale soundings as the setting-out is very cumbersome (Figure 7.17E). The main advantage of the electrode configuration is the simplicity of the method when setting out small grids. In small-scale surveys investigating the three-dimensional extent of subsurface targets, such as in archaeology, the square sides are of the order of only a few metres.

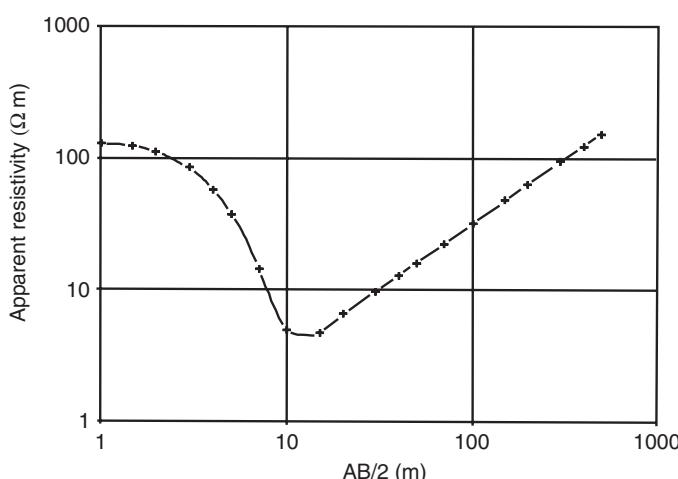


**Figure 7.16** A vertical electrical sounding (VES) showing apparent resistivity as a function of current electrode half-separation (AB/2).

## 7.4.2 Automated array scanning

In 1981 Barker published details of the offset Wenner array using multi-core cables and multiple electrodes for VES investigations. In 1985, Griffiths and Turnbull produced details of a multiple electrode array for use with CST. This theme was developed by van Overmeeren and Ritsema (1988) for hydrogeological applications, and by Noel and Walker (1990) for archaeological surveys. For deeper sounding, where multi-core cabling would become prohibitively heavy, the cable is wound into 50 m sections on its own drum, with an addressable electronic switching unit and power supply mounted in the hub of each cable reel. The switching units are controlled by a laptop computer which can switch any electrode to either of two current or two potential cables which connect the entire array of

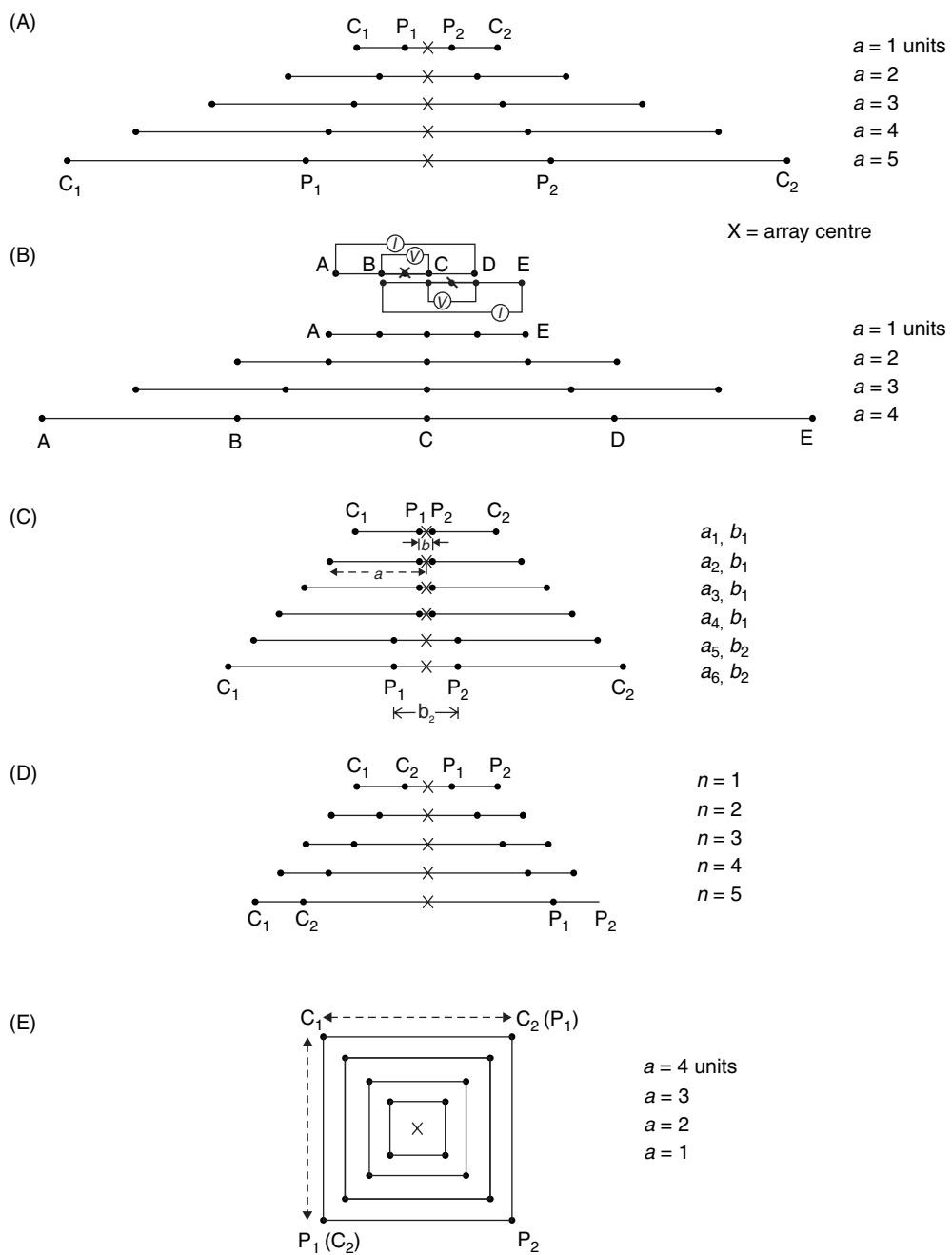


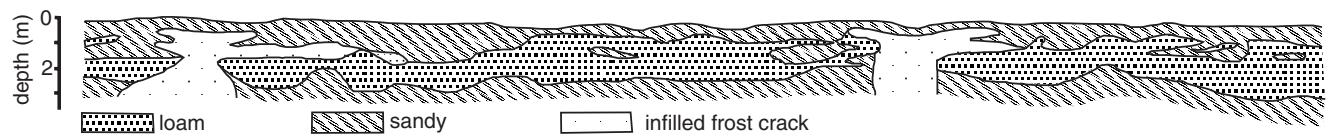
**Figure 7.17** Expanded arrays (with successive positions displaced for clarity) for: (A) Wenner, (B) offset Wenner, (C) Schlumberger, (D) dipole-dipole and (E) square arrays.

drum reels. This system is known as the *microprocessor-controlled resistivity traversing system* (Griffiths *et al.*, 1990).

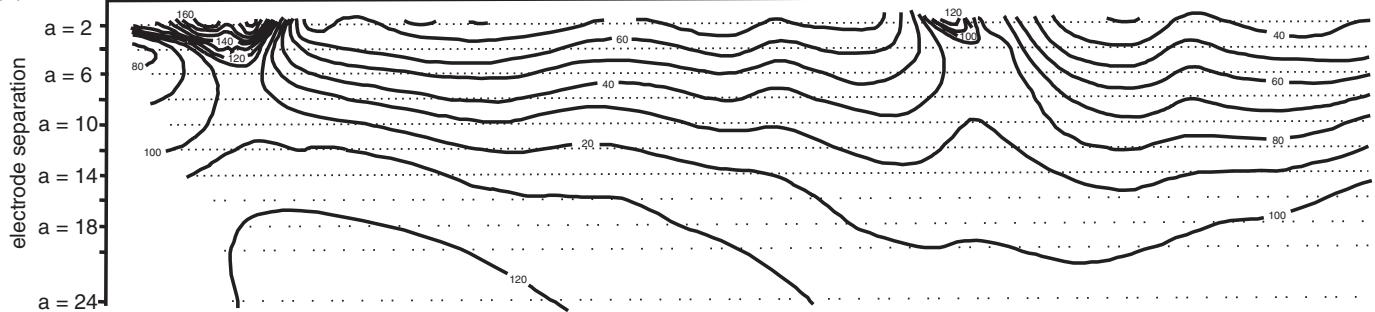
In van Overmeeren and Ritsema's (1988) *continuous vertical electrical sounding* (CVES) system, an array of multiples of 40 electrodes is connected to a microprocessor by a multi-core cable. Using software control, discrete sets of four electrodes can be selected in a variety of electrode configurations and separations, and a measurement of the resistance made for each. Instead of using one cable layout for just one VES, the extended electrode array can be used for a number of VESs, each one offset by one electrode spacing. If

the first VES is conducted with its centre between electrodes 15 and 16, for example, the next VES will be centred between electrodes 16 and 17, then 17 and 18, 18 and 19, and so on. A field curve is produced for each sounding along the array and interpreted by computer methods (see Section 7.5.3) to produce a geo-electric model of true layer resistivities and thicknesses for each VES curve. When each model is displayed adjacent to its neighbour, a panel of models is produced (Figure 7.18) in which the various resistivity horizons can be delimited. It is clear from Figure 7.18D that the CVES interpretation is closest to the known physical model

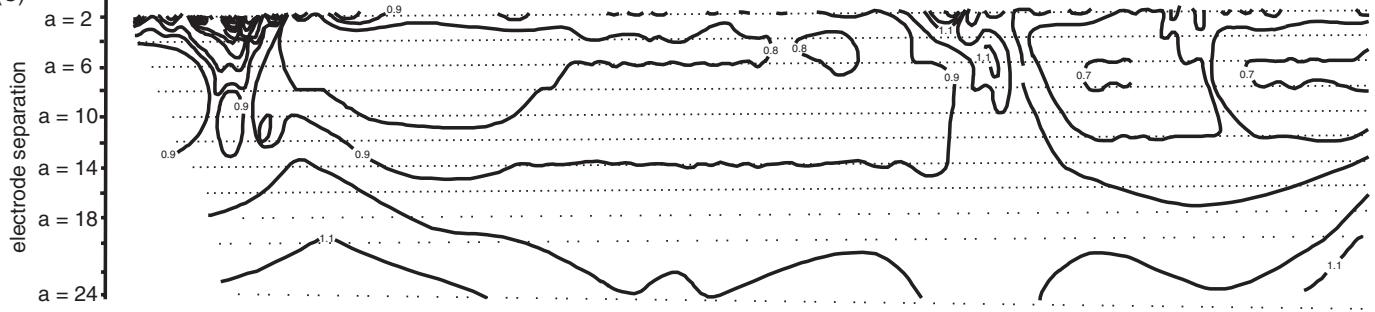
(A)



(B)



(C)



(D)

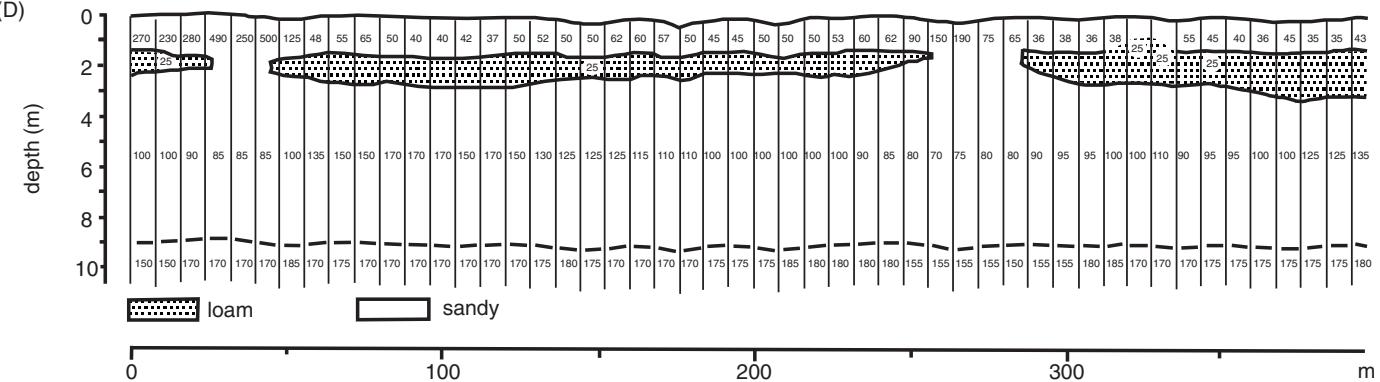


**Figure 7.18** High-resolution soil survey using a scanned array. (A) Soil section determined by shallow hand-drilling. Pseudo-sections obtained using (B) Wenner tripotential alpha and (C) beta/gamma arrays. (D) Continuous vertical electrical sounding (CVES) results with true resistivities indicated. From van Overmeeren and Ritsema (1988), by permission.

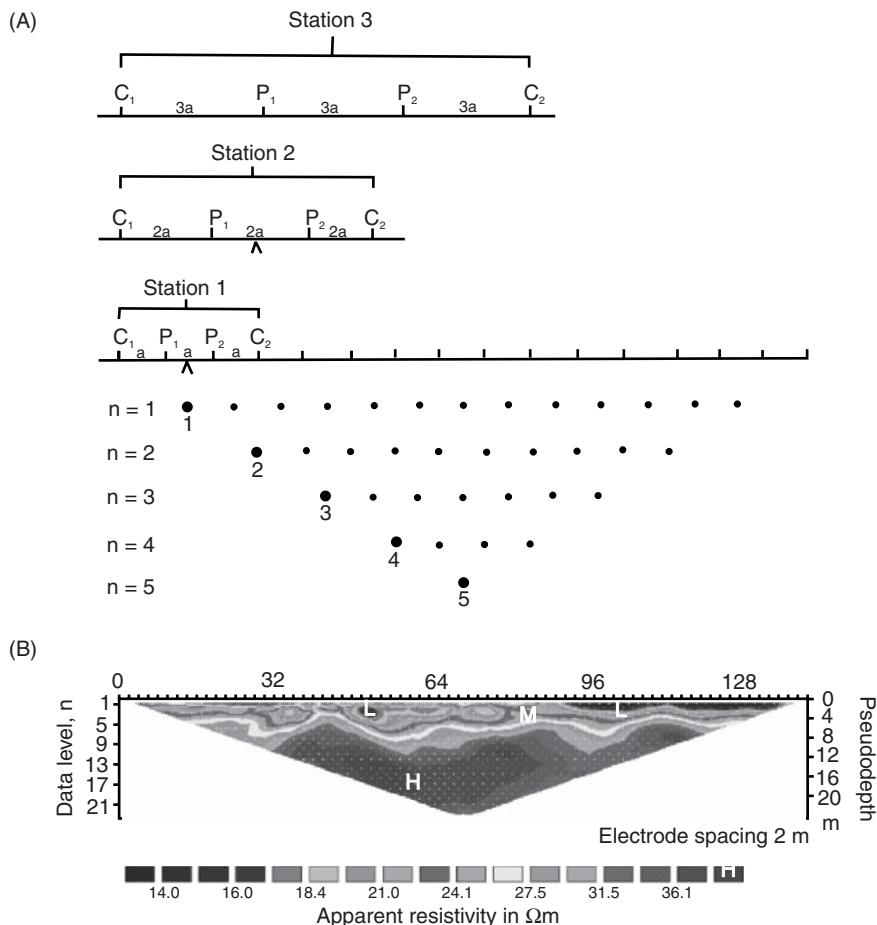


**Figure 7.19** (A) Example of the measurement sequence for building up a resistivity pseudo-section. Courtesy of Campus Geophysical Instruments Ltd. (B) Example of a measured apparent resistivity pseudo-section. [C]

compared with those for either the tripotential alpha or beta/gamma ratio sections (shown in Figure 7.18B and C respectively). This particular method requires special equipment and associated computer software, but it highlights a novel application of both field method and data analysis to improve the resolution of shallow resistivity surveys.

### 7.4.3 Electrical resistivity tomography (ERT)

In subsurface imaging (SSI), also known as electrical resistivity tomography (ERT), typically 50 electrodes are laid out in two strings of 25, with electrodes connected by a multi-core cable to a switching box and resistance meter, or a single cable connecting 72 or more electrodes. The whole data acquisition procedure is software-controlled from a laptop computer. Similar systems have been produced, such as the LUND Automatic Imaging System (ABEM), and MacOhm 21 (DAP-21) Imaging System (OYO), and the Sting/Swift (Advanced Geosciences Inc.), Campus Tigre, and IRIS system (Syscal), among others.

As with van Overmeeren and Ritsema's CVES method, a discrete set of four electrodes with the shortest electrode spacing ( $n = 1$ ;

see Figure 7.19A) is addressed and a value of apparent resistivity obtained. Successive sets of four electrodes are addressed, shifting each time by one electrode separation laterally. Once the entire array has been scanned, the electrode separation is increased by one electrode increment (e.g.  $n = 2$ , then 3, 4, 5, and so on), and the process repeated until the appropriate number of levels has been scanned. The values of apparent resistivity obtained from each measurement are plotted on a pseudo-section (Figure 7.19B) and contoured. Methods of interpretation are described in more detail in sections 7.5.5 and 7.5.6. There are considerable advantages in using SSI/ERT or equivalent methods. With multi-core cable and many electrodes, the entire array can be established by one person, although logically it is more efficient with more people. The acquisition of apparent resistivity data is controlled entirely by the software whose parameters are selected at the outset. By changing the inter-electrode spacing, the vertical and horizontal resolutions can be specified to meet the objectives of the survey. For example, the horizontal resolution is defined by the inter-electrode spacing, and the vertical resolution by half the spacing. For example, using a 2 m inter-electrode spacing, the horizontal and vertical resolutions are 2 m and 1 m, respectively, for the pseudo-section display. Whether subsurface features can be resolved at a comparable

scale is determined also by the lateral and vertical variations in true resistivity. Commercially-manufactured multi-core cables have electrode take-outs at 5 m and 10 m intervals, which also allows selection of shorter electrode intervals as needed.

#### 7.4.4 Constant separation traversing (CST)

Constant separation traversing uses a manual electrode array, usually the Wenner configuration for ease of operation, in which the electrode separation is kept fixed. The entire array is moved along a profile and values of apparent resistivity determined at discrete intervals along the profile. At its most basic level, one set of four electrodes can be used with single-core cables, and the array is migrated along the profile by leapfrogging the last electrode in advance of the first and the electrodes re-connected to maintain the correct geometry as the profile is advanced. This is very labour-intensive and slow. Another approach is to use a Wenner spacing of say 10 m, with perhaps 12 electrodes deployed at any one time at 5-m intervals. Alternate electrodes are used for any one measurement, and instead of uprooting the entire sets of electrodes, the connections are moved quickly and efficiently to the next electrode along the line, i.e. 5 m along the traverse. This provides a CST profile with an electrode separation of 10 m and station interval of 5 m. The values of apparent resistivity are plotted on a linear graph as a function of distance along the profile. Variations in the magnitude of apparent resistivity highlight anomalous areas along the traverse, such as the low apparent resistivity zone associated with clay infill in Figure 7.20. This technique is used to identify anomalous zones

with either high or low apparent resistivity values, and no further analysis or display of the data may be necessary. It can be a useful reconnaissance technique along single profiles. The technique has largely been superseded in commercial surveys by the ERT method and variants that, by virtue of the increasingly sophisticated equipment available, can acquire more data far more efficiently than can be inverted to 2D true resistivity models.

Sørensen (1994) has described a ‘pulled array continuous electrical profiling’ technique (PA-CEP). An array of heavy steel electrodes, each weighing 10–20 kg, is towed behind a vehicle containing all the measuring equipment. Measurements are made continuously. It is reported that 10–15 line kilometres of profiling can be achieved in a day. The quality of results is reported to be comparable to that of fixed arrays with the same electrode geometry.

In the case of VES, CRT and ERT on land, the electrodes need to be implanted into the ground at fixed points to achieve *galvanic* coupling. Modern towed arrays on land work on the principle of *capacitive* coupling with the ground, so that the electrodes merely need to be in contact with the ground; the electrode assembly can be dragged across the surface and measurements made as the array is moved along the profile (e.g. Geometrics Ohm Mapper; and Capacitive Resistivity Imaging (CRI) towed array (Kuras *et al.*, 2007); Figure 7.21). Different dipole separations can be configured so that the resulting display is a pseudo-section showing apparent resistivity to a nominal depth (depending on the dipole lengths used). Values achieved using a towed array have been found to be comparable to those acquired using galvanic electrodes in fixed arrays. The advantage with the towed array is the speed of data acquisition in terms of line-metres acquired per hour compared with that for fixed arrays. The disadvantage is that capacitive coupling can lead to increased electrode noise depending upon the coupling with the ground surface, so the signal:noise ratio may be worse than for a fixed array with much better electrode coupling and lower electrode contact resistances. Furthermore, the nature of the towed array means that the number of dipole lengths available are more limited (due to weight constraints) compared with a fixed array, so vertical discrimination may be poorer than for ERT profiling, depending upon the site. However, these limitations may be outweighed by the advantage of much faster ground coverage and use over hard surfaces than can be achieved with fixed galvanic arrays.

The concept of acquiring resistivity data over water has received an increasing amount of attention in recent years. It is possible to deploy waterproof multi-core cables with suitable graphite rather than metal electrodes at the take-out positions. Graphite electrodes are preferable to metal ones, which tend to corrode through electrolysis with seawater. Specially manufactured resistivity marine cables are available with graphite electrodes at intervals of 6 m, for example, with the leading pair of electrodes acting as a current dipole pair and the successive nine electrodes (eight electrode pairs) acting as potential dipoles along a floating ‘streamer’ (e.g. AGI SuperSting R8 marine system). Current is injected every three seconds and eight apparent resistivity values, equivalent to eight different depth levels, are acquired for each injection of current. The data are displayed as a conventional ERT apparent resistivity pseudo-section. Typically the total depth of penetration is approximately 20% of the electrode array length. The data can be acquired in formats suitable for input

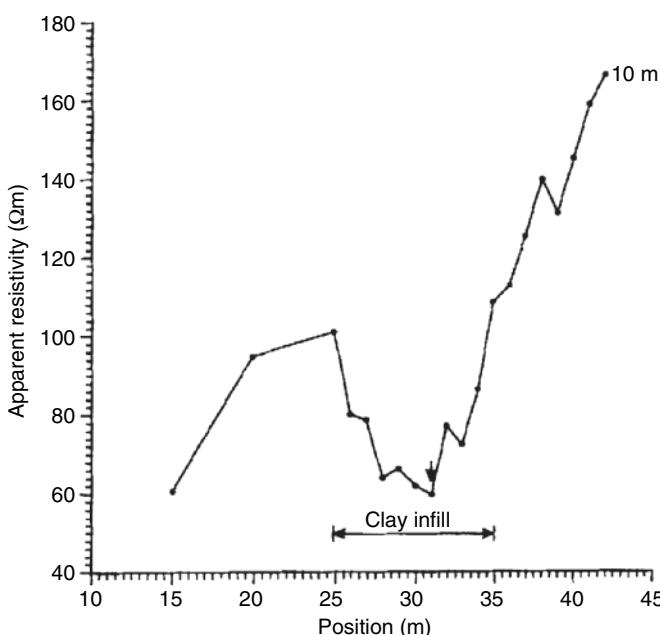


**Figure 7.20** A constant separation traverse using a Wenner array with 10 m electrode spacing over a clay-filled feature (position arrowed) in limestone.

(A)



(B)

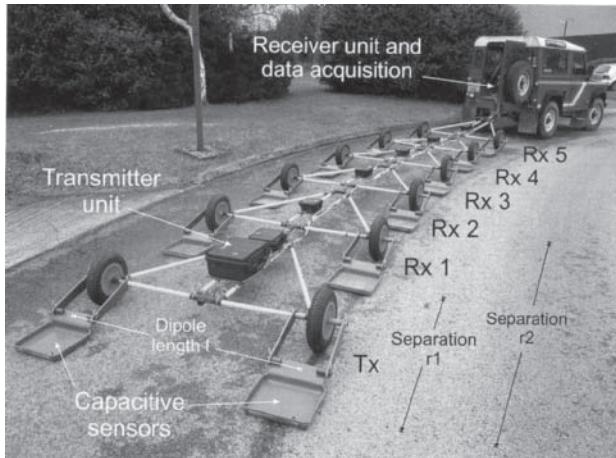


**Figure 7.21** (A) Geometrics' Ohm Mapper towed array in use. Courtesy of Geomatrix Earth Science Ltd. (B) Five-channel Capacitive Resistivity Imaging (CRI) towed array in use on a tarmac road. Courtesy of Kuras et al. (2007). [C]

to generally available commercial software (e.g. RES2DINV) which has the capacity to accommodate water layers and can invert the data to true resistivity models.

For relatively shallow water situations, such as in transition zone surveys or shallow lakes, it is possible to use a combination of marine multi-core cable and electrodes laid on the bed of the water body but with the recording equipment on land. In this case the cable is weighted so that it stays on the lake bed rather than refloating to the water surface. The advantage with this approach is that a far greater number of recording channels are available with a fixed electrode cable (e.g. >50) than for a floating marine system (less than ten channels), so that a much larger number of depth levels can be utilised than would be available for a floating towed system.

Some proprietary waterborne systems have been developed by survey contractors for which the data formats and inversion are commercially secret, and where external independent scrutiny of the inversion process is therefore not possible. This can lead to a contractor producing resistivity sections where the nature of output is not declared (true or apparent resistivity values?), and where there may be little or no correlation of the resistivity results with

coincident high-resolution seismic survey data and no means of determining why. It is strongly recommended, therefore, that data acquisition systems are used that provide apparent resistivity data in formats that can be input to programs like RES2DINV so that there is greater transparency in the way that the data are processed and inverted. Generally 'black box' data 'acquisition-to-interpretation' schemes where there is no opportunity to scrutinise the data independently, from acquisition through processing to inversion, should be avoided; this applies not just to waterborne resistivity surveys but to most geophysical investigations. Poor acquisition, processing and inversion procedures can be cloaked by proprietary secrecy.

#### 7.4.5 Field problems

In order for the electrical resistivity method to work using a collinear array, the internal resistance of the potential measuring circuit must be far higher than the ground resistance between the potential electrodes. If it is not, the potential circuit provides a low-resistance alternative route for current flow and the resistance measured is completely meaningless. Most commercial resistivity equipment has an input resistance of at least  $1 \text{ M}\Omega\text{m}$ , which is adequate in most cases.

In the case of low-temperature glacier ice, which itself has a resistivity of up to  $120 \text{ M}\Omega\text{m}$ , a substantially higher input resistance is required (preferably of the order of  $10^{14} \Omega$ ).

Electrical resistivity soundings on glaciers are complicated by the fact that ice does not conduct electricity electronically but by the movement of protons within the ice lattice, and this causes substantial polarisation problems at the electrode–ice contact. Consequently, special techniques are required in order to obtain relevant resistivity data on glacier ice (Reynolds, 1982).

Perhaps the largest source of field problems is the electrode contact resistance. Resistivity methods rely on being able to apply current into the ground. If the resistance of the current electrodes becomes anomalously high, the applied current may fall to zero and the measurement will fail. High contact resistances are particularly common when the surface material into which the electrodes are implanted consists of dry sand, boulders, gravel, frozen ground, ice or laterite. If the high resistance can be overcome (and it is not always possible), there are two methods that are commonly used. One is to wet the current electrodes with water or saline solution, sometimes mixed with bentonite. The second method is to use multiple electrodes. Two or three extra electrodes can be connected to one end of the current-carrying cable so that the electrodes act as resistances in parallel. The total resistance of the multiple electrode is thus less than the resistance of any one electrode (see Figure 7.22 and Box 7.11). However, if this method is used, the extra electrodes must be implanted at right-angles to the line of the array rather than along the direction of the profile. If the extra electrodes are in the line of the array, the geometric factor may be altered as the inter-electrode separation ( $C_1-P_1-P_2-C_2$ ) is effectively changed. By planting the electrodes at right-angles to the line of the array, the inter-electrode separation is barely affected. This problem is only acute when the current electrode separation is small. Once the current electrodes are sufficiently far apart, minor anomalies in

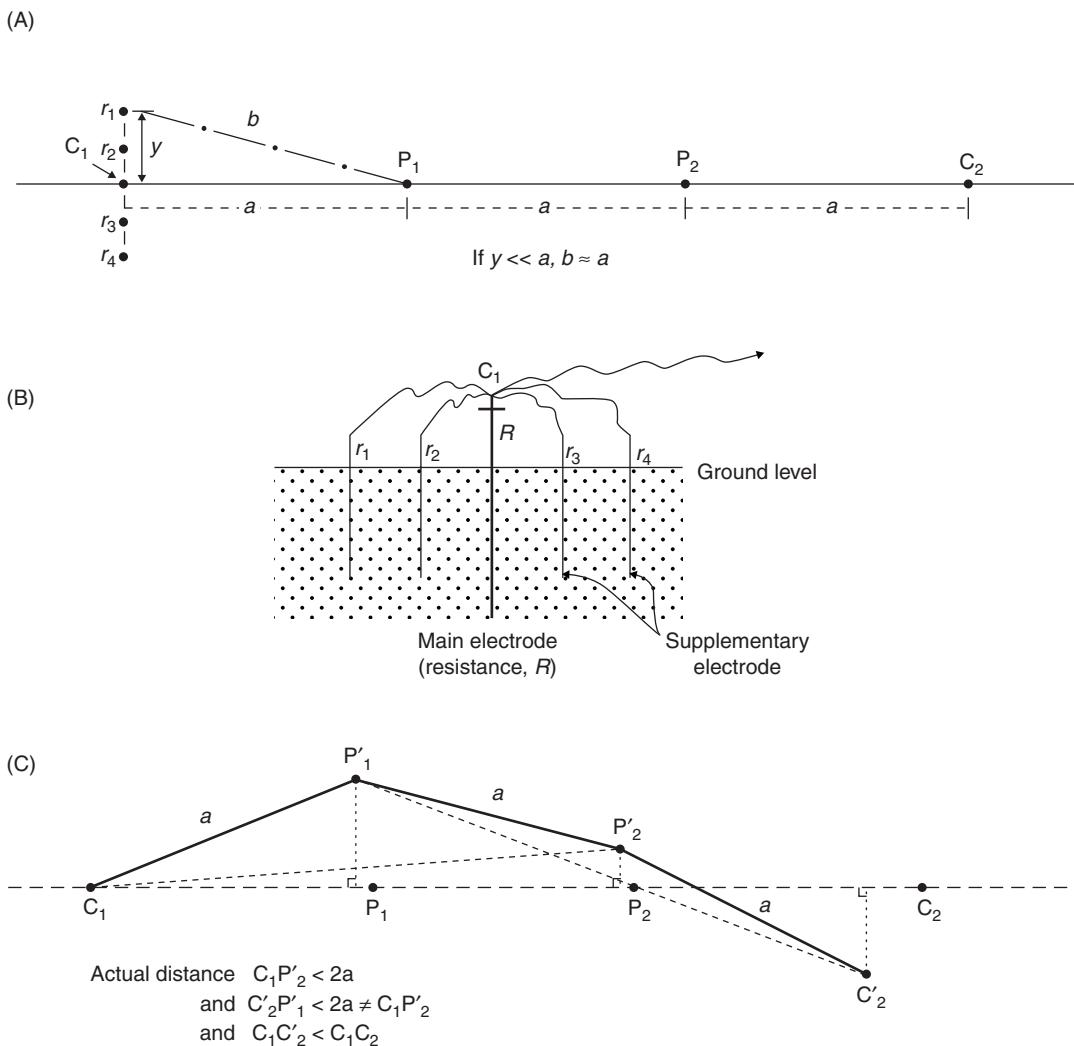


**Figure 7.22** (A) Supplementary electrodes planted in a straight line at right-angles to the main electrode have minimal effect on the geometric factor as long as the offset  $y \ll a$ . (B) Any number of additional electrodes act as parallel resistances and reduce electrode contact resistance. (C) An out-of-line electrode array will give rise to erroneous  $\rho_a$  values unless the appropriate geometric factor is used. A shortened  $C_1C_2$  produces elevated  $\Delta V$  between  $P_1$  and  $P_2$  and needs to be compensated for by a reduced value of the geometric factor.

positioning are insignificant. This also applies when laying out the survey line to start with.

Ideally, a VES array should be expanded along a straight line. If it curves significantly and/or erratically (Figure 7.22C), and no correction is made, cusps may occur in the data owing to inaccurate geometric factors being used to calculate apparent resistivity values. Cusps in VES field curves are particularly difficult to resolve if their cause is unknown. Even if the apparent resistivity values have been calculated correctly with appropriately modified geometric factors, ambiguities may arise in the field curve for which it may not be possible to model or interpret. In the case of CST/ERT data, if the correct geometric factors are used to derive the apparent resistivities, the CST/ERT profile may be interpreted normally. It always pays to keep adequate field notes in addition to recording the geophysical data so that appropriate corrections can be made with recourse to

#### Box 7.11 Resistances in parallel

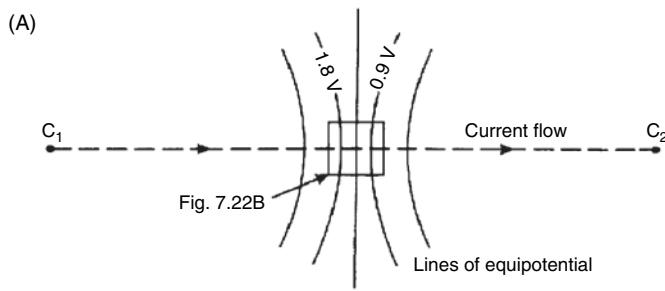
Total resistance of multiple electrodes is  $R_T$ :

$$1/R_T = 1/R_1 + 1/R_2 + 1/R_3 + \dots + 1/R_n = \sum_{i=1}^n (1/R_i)$$

For example, if  $r_1 = r_2 = 0.2R$  and  $r_3 = r_4 = 0.5R$ , then:

$$1/R_T = 1/0.2R + 1/0.2R + 1/0.5R + 1/0.5R + 1/R = 15/R.$$

Thus  $R_T = R/15$ , and  $R_T$  is much less than the lowest individual resistance ( $= R/5$ ).



(A)

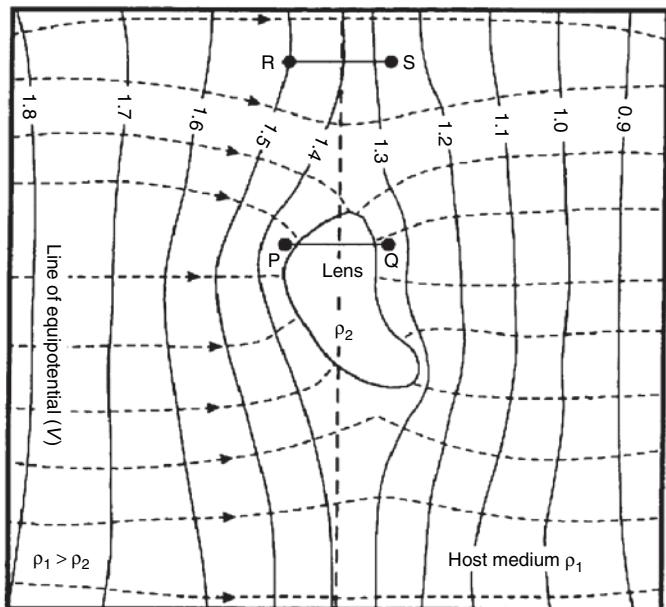


**Figure 7.23** Distortion of current flow lines and equipotentials around an anomalous feature. The boxed area in (A) is enlarged to show detail in (B). The magnitude of equipotentials is for illustrative purposes only.

the correct information, rather than to a rather hazy recollection of what may have been done in the field.

The presence of pipes, sand lenses or other localised features, which are insignificant in relation to the main geological target, can degrade the quality of the field data and thus reduce the effectiveness of any interpretation. If a conductive clay lens is present, for example, then when a current is applied from some distance away from it, the lines of equipotential are distorted around the lens and the current flow lines are focused towards the lens (Figure 7.23). The potential between P and Q ( $<0.1$  V) is obviously smaller than that measured between R and S ( $\approx 0.25$  V), which are outside the field of effect of the lens. The apparent resistivity derived using this value of potential is lower than that obtained had the lens not been there, hence the occurrence of a cusp minimum (Figure 7.24A). If the lens has a higher resistivity than the host medium, the current flow lines diverge and the potential between P and Q becomes anomalously high and results in a positive cusp (Figure 7.24B).

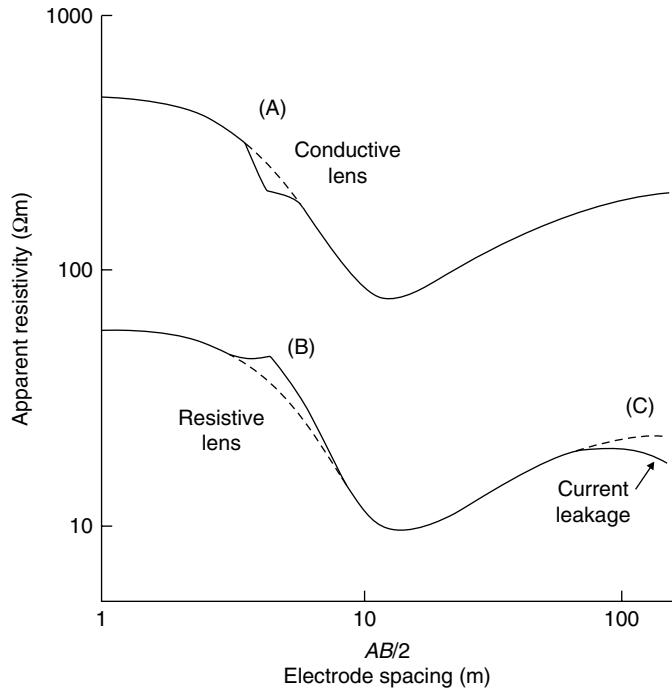


**Figure 7.24** Distortion of Schlumberger VES curves due to (A) conductive lens or pipeline, (B) a resistive lens, and (C) current leakage. After Zohdy (1974), by permission.

Another feature that may occur on VES profiles is current leakage, particularly at large current electrode separations, when the array is aligned parallel to a conductive feature such as a metal pipe or a surface stream. The values of apparent resistivity become increasingly erratic owing to the voltage between the potential electrodes falling to within noise levels and tending to decrease in value (Figure 7.24C). If the position and orientation of a pipe is known, there should be no ambiguity in interpretation. There is no point in extending the VES once it is obvious that current leakage is occurring.

A method of reducing the effects of these lateral inhomogeneities using the offset Wenner array has been described in Section 7.3.2. There is, however, no alternative method for the Schlumberger electrode configuration, and cusps can be removed by smoothing the curve (dashed lines in Figure 7.24).

An additional but easily resolvable problem can occur with Schlumberger depth soundings. When the separation of the potential electrode pair is increased ( $b_1$  to  $b_2$  in Figure 7.17C), the contact resistance may change, causing a discrete step up or down of the next segment of the curve (Figure 7.25). Although the value of the apparent resistivity may change from the use of one electrode pair to another, the gradient of the change of apparent resistivity as a function of current electrode half-separation should remain the same. Consequently, the displaced segments can be restored to their correct values and the curve smoothed ready for interpretation. Segments at larger potential electrode separations should be moved to fit the previous segment obtained with a shorter electrode separation. So in Figure 7.25, segment 3 is moved down to

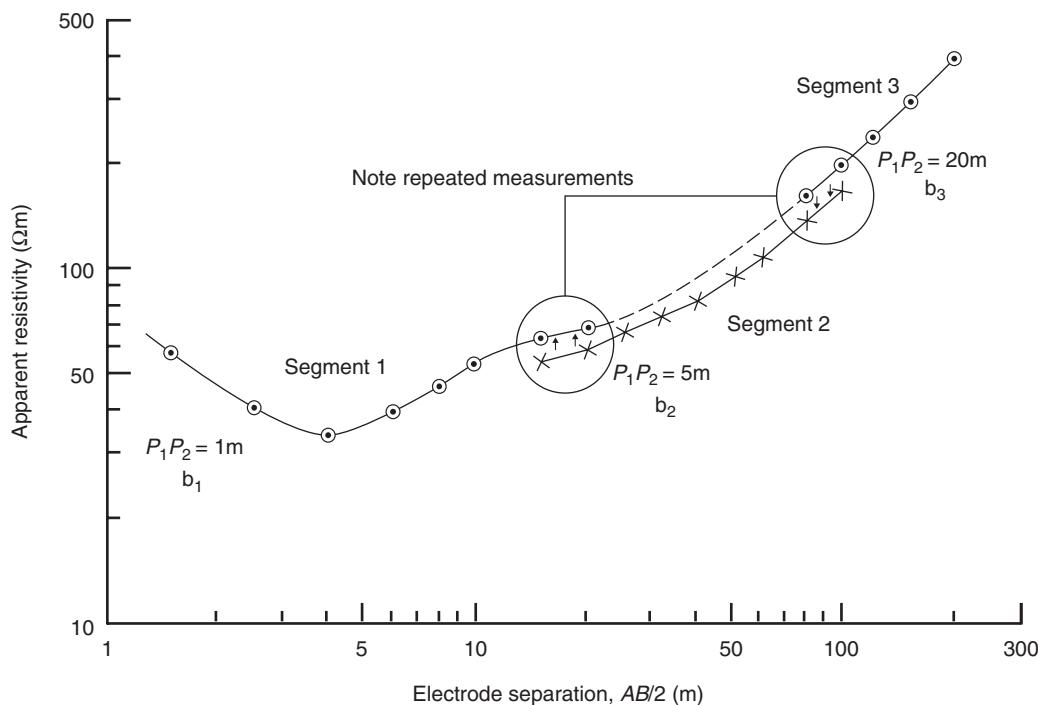


**Figure 7.25** Displaced segments on a Schlumberger vertical electrical sounding curve due to different electrode resistances at  $P_1$  and  $P_2$  on expanding potential electrode separations; segment 3 is displaced to fit segment 2, which is in turn displaced to fit segment 1 to produce a smoothed curve.

fit segment 2, which is moved up to join on the end of segment 1. Measurements of resistance should be repeated at both potential electrode separations when crossing from one segment to the next. As all the electrodes are moved when a manual Wenner array is expanded, there is no discernible displacement of segments of the curve. Instead, the field curve may appear to have lots of cusps and blips (data shown by dots) through which a smooth curve is then drawn, usually by eye (Figure 7.26). An alternative, preferable approach is to use the offset Wenner array (see section 7.3.2) which improves the quality of the acquired field data (crosses in Figure 7.26).

## 7.5 Interpretation methods

Vertical sounding field curves can be interpreted qualitatively using simple curve shapes, semi-quantitatively with graphical model curves, or quantitatively with computer modelling. The last method is the most rigorous but there is a danger with computer methods of overinterpreting the data. VES field curves may have subtle inflections and cusps that require the interpreter to make decisions as to how real or significant such features are. Often a noisy field curve is smoothed to produce a graph which can then be modelled more easily. In such a case, there is little point in spending large amounts of time trying to obtain a perfect fit between computer-generated and field curves. As a general rule, depending on how sophisticated the field acquisition method is, layer thicknesses and resistivities are accurate to between 1% and 10% RMS error, with poorer accuracies arising from the cruder field techniques. Furthermore, near-surface layers tend to be modelled more accurately than those at depth, primarily because field data from shorter electrode separations tend to be more reliable than those for very large separation, owing to higher signal-to-noise ratios.

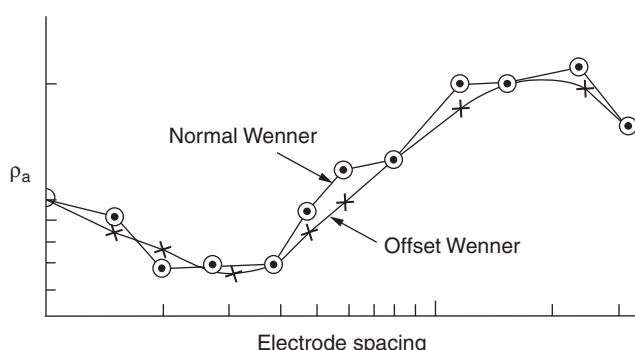


**Figure 7.26** The difference in data quality that can be obtained by using an offset Wenner array in place of a normal Wenner array; the normal curve is more noisy.

### 7.5.1 Qualitative approach

The first stage of any interpretation of apparent resistivity sounding curves is to note the curve shape. This can be classified simply for three electrical layers into one of four basic curve shapes (Figures 7.27A–D). These can also be combined to describe more complex

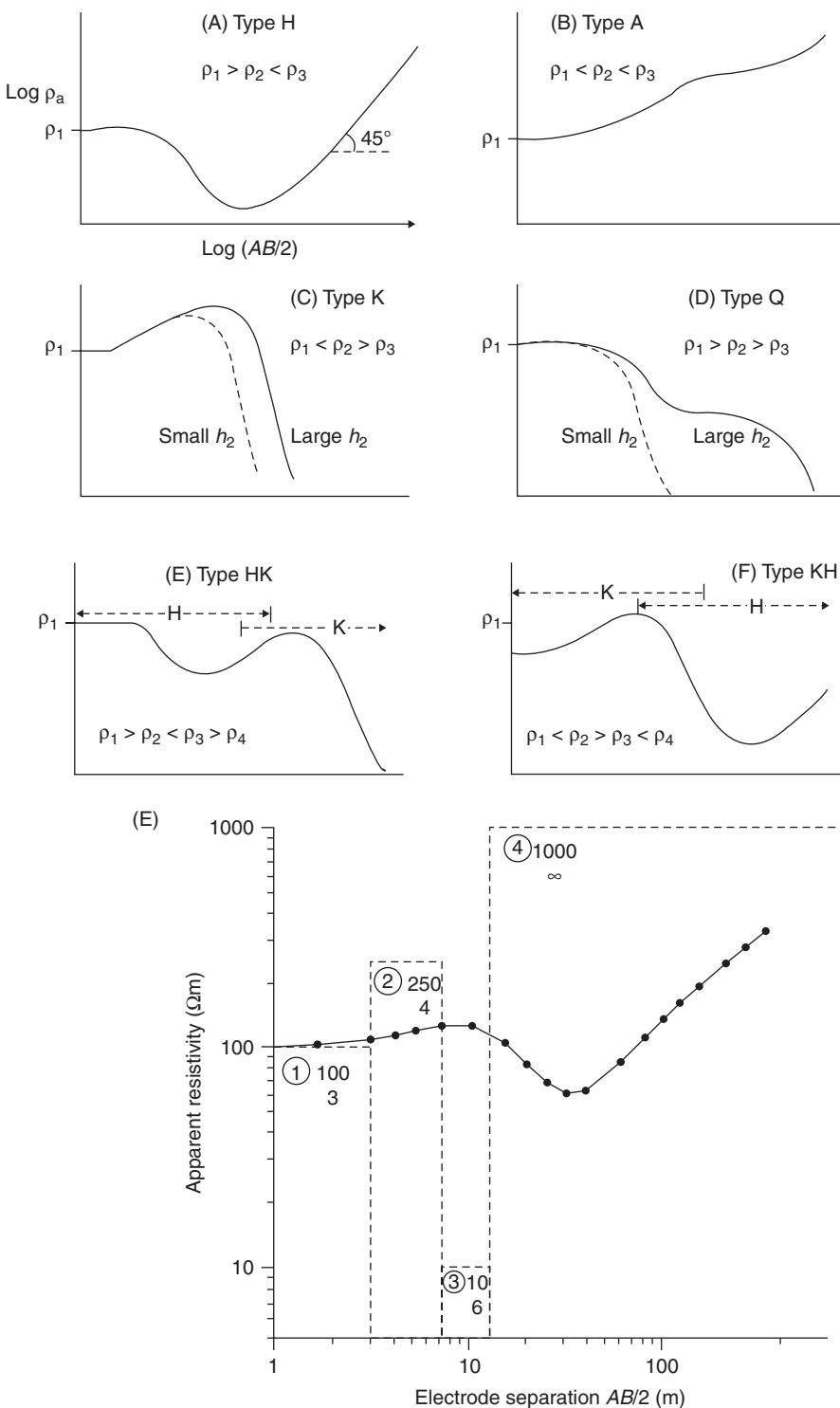


**Figure 7.27** Apparent resistivity curve shapes for different resistivity structures: (A) to (D) are three-layer models; (E) and (F) are four-layer models; (G) shows a block model for the layer resistivities and thicknesses and the resulting apparent resistivity curve. Neither the minimum nor the maximum apparent resistivities occur at electrode separations equivalent to the layer depths. To penetrate to bedrock, electrode separation should be about three times the bedrock depth for a Schlumberger array.

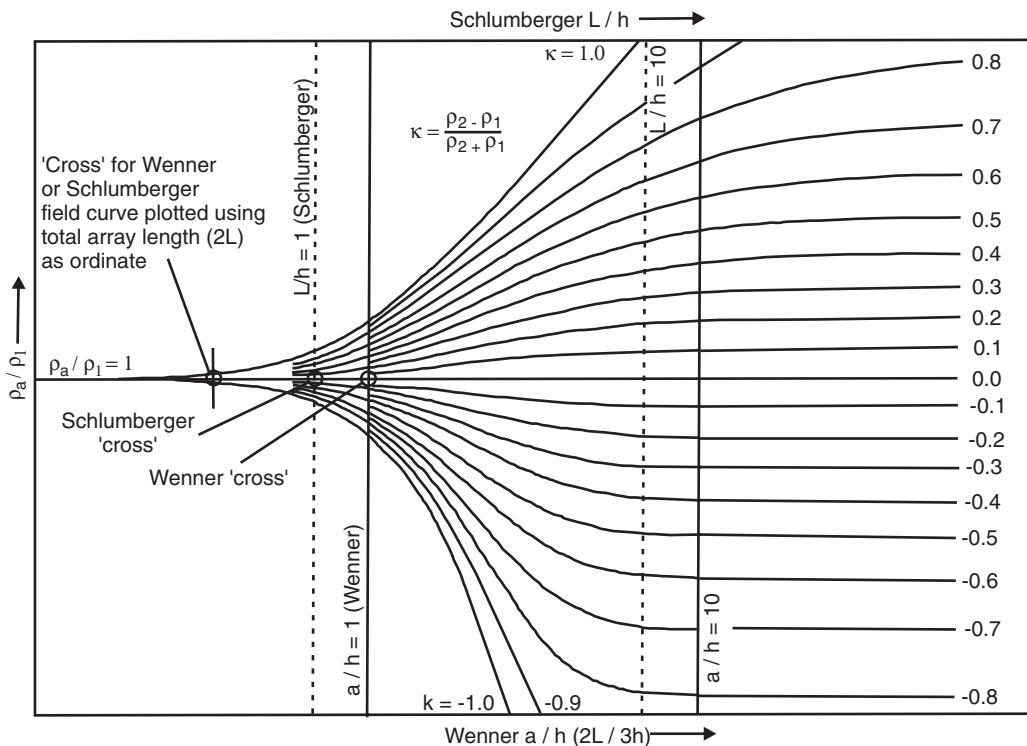


**Figure 7.28** Two-layer master curves for Schlumberger and Wenner arrays. From Milsom (2003), by permission.

field curves that may have several more layers. Note that the curve shape is dependent upon the relative thicknesses of the in-between layers (layer 2 in a 3-layer model; Figures 7.27C, D). The maximum angle of slope that the rising portion of a resistivity graph may have on a log–log graph is  $45^\circ$ , given the same scales on both axes (Figure 7.27A). If the field curve rises more steeply, then this suggests error in the data or that geometric effects due to steeply inclined horizons are distorting the data.

The *relative* magnitudes of the true resistivities obtained from the levels of the flat portions or shoulders of the graph are a useful starting point before more involved interpretation. For example, in Figures 7.27A and B, the only difference between the two models is the resistivity of layer 2. In Figure 7.27A, layer 2 resistivity is less than those for both layers 1 and 3. In Figure 7.27B, the second layer resistivity is between those for layers 1 and 3. In the case of Figure 7.27D, if the second layer is very thin (dashed line for small  $h_2$ ) it may not be evident on the curve that this layer exists, i.e. its effects are ‘suppressed’. Suppression is discussed in more detail in Section 7.5.4.

From Figure 7.27G, it can be seen that the number of layers identified is equal to the number of turning points (TP) in the curve, plus one. The presence of turning points indicates subsurface interfaces, so the number of actual layers must be one more than the number of boundaries between them. However, the coordinates of the turning points in no way indicate the depth to a boundary or provide specific information about the true resistivities (Figure 7.27G). From the curve shape alone, the minimum number of horizontal layers and the relative magnitudes of the respective layer resistivities can be estimated.

## 7.5.2 Master curves

Interpretation of field curves by matching against a set of theoretically calculated master curves is based on the assumptions that the model relates to a horizontally stratified Earth, and that successively deeper layers are thicker than those overlying. Although this second assumption is rarely valid, the use of *master curves* does seem to provide a crude estimate of the physical model.

Synthetic curves for two-layer models can be represented on a single diagram (Figure 7.28), but for three-layer models the range of graphs is very large, and books of master curves have been published (Mooney and Wetzel, 1956; European Association of Exploration Geophysicists, 1991). It is only practicable to use the master curves method for up to four layers. If more layers are present, the graphical approach is far too cumbersome and inaccurate. Three- and four-layer models can also be interpreted using master curves for two layers with the additional use of auxiliary curves (Figure 7.29) as outlined below.

The field data, smoothed and corrected as necessary, are plotted on a log–log graph on a transparent overlay at the same scale as the master curves. The overlay is placed on the master curves and, keeping the  $x$ - and  $y$ -axes of the two graphs parallel, the overlay is moved until the segment of the field curve at shortest electrode spacings fits one of the master curves and its  $k$  value is noted (Figure 7.30; in this case,  $k = -0.3$ ). The position of the origin of the master curve is marked (A) on the overlay, which is then placed over the auxiliary curve sheet and the line for the same  $k$  value is traced on to the overlay. The coordinates of A (which are read off the graph) are first estimates of the true resistivity and thickness of the top

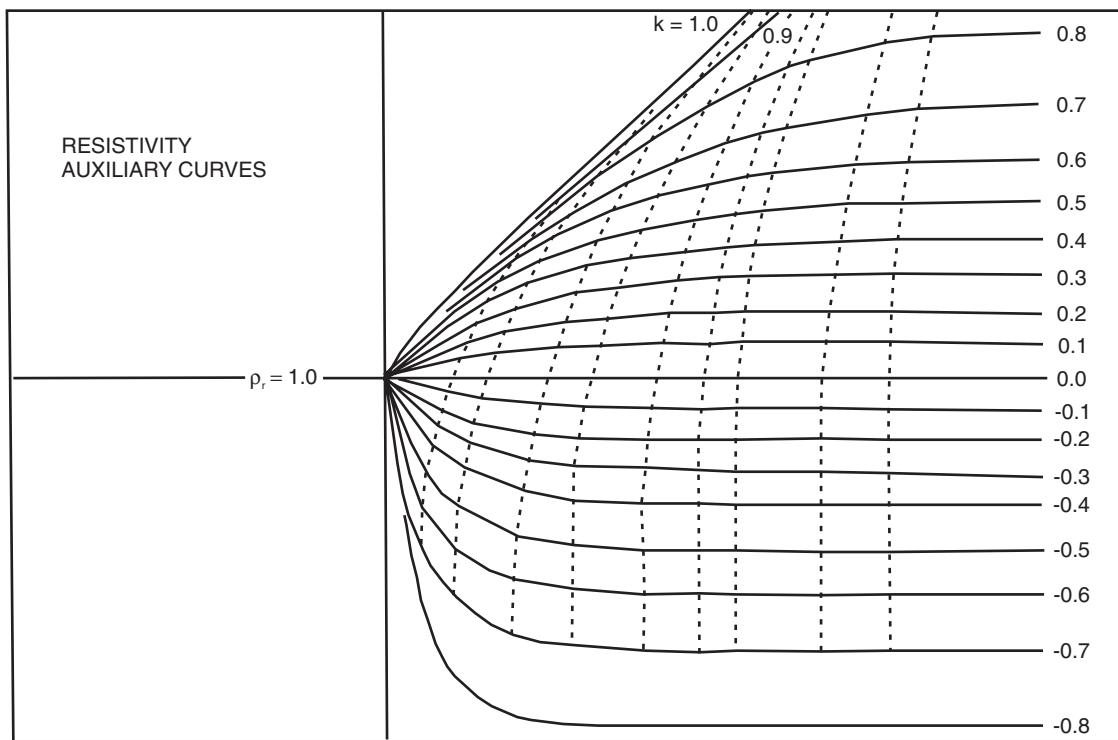


**Figure 7.29** Auxiliary curves for a two-layer structure.

layer. Next, the overlay is replaced over the master curve sheet and moved so that the traced auxiliary curve for  $k = -0.3$  always lies over the origin of the master curve, until the next portion of the field curve is coincident with one of the master curves beneath and the new  $k$  value noted; in the example in Figure 7.30, the second  $k$  value is +1.0. When a fit has been obtained, the new position of the origin of the master curves (B) is marked on to the traced auxiliary curve. The overlay is returned to cover the auxiliary curves and the point B is placed over the origin of the auxiliary curves and the line corresponding to the new  $k$  value is again traced on to the overlay. The coordinates of B (also measured off the graph) are first estimates of the resistivity of the second layer and of the total depth to the second interface. The above process is then repeated, going from master curve to auxiliary curves and back again, noting the new  $k$  values in each case until the entire field curve has been matched against master curves. The final result should be, for a three-layer case as the example, two points of origin A and B giving  $\rho_1$ ,  $t_1$  and  $\rho_r$  and  $(t_1 + t_2)$ , and hence  $t_2$ . From the first  $k$  value, the resistivity of the second layer can easily be calculated (see Box 7.10), and from the second  $k$  value,  $\rho_3$  can be estimated, thus completing the determination of the model parameters.

Curve-matching is constrained to fit the field curve with one calculated from a very limited range of master curves. If the resistivity contrasts do not give rise to a  $k$  value that corresponds to one of the master curves, then the accuracy of the fitting (and of the subsequent interpretation) will be reduced. Furthermore, the use of master curves does not allow the problems of equivalence and suppression to be resolved (see Section 7.5.4). Interpretations obtained using this graphical approach should be regarded as crude

estimates of the subsurface layer parameters which can then be put into a computer model to obtain much more accurate and reliable results.

### 7.5.3 Curve matching by computer

In 1971, Ghosh described a convolution method by which computers can be used to calculate master curves for vertical electrical soundings obtained using either a Wenner or Schlumberger array. The method uses what is called a 'linear digital filter', the details of which are given by Koefoed (1979).

The program synthesises an apparent resistivity profile for an  $n$ -layered model in which the variables are layer thickness and resistivity. Model profiles can then be compared with the field curves and adjustments to the layering and resistivity values can be made by trial and error to obtain as near correspondence as possible to the field curve.

However, in cases where a very good conductor underlies a comparatively resistive layer (where  $\rho_1 > 20\rho_2$  and  $-1 < k < -0.9$ ), Ghosh's method was found to produce inaccurate profiles owing to the structure of the filter, which had too few coefficients to track a rapidly falling resistivity curve.

A computer program can easily be checked to see whether it produces erroneous profiles by obtaining an apparent resistivity curve for a simple two-layer model where the resistivity contrast is at least 20:1 with the lower layer being the more conductive. If the program is unable to cope with such a contrast, the portion of the graph at larger electrode separations will appear to oscillate (Figure 7.31) rather than pass smoothly to the true resistivity of the second layer.

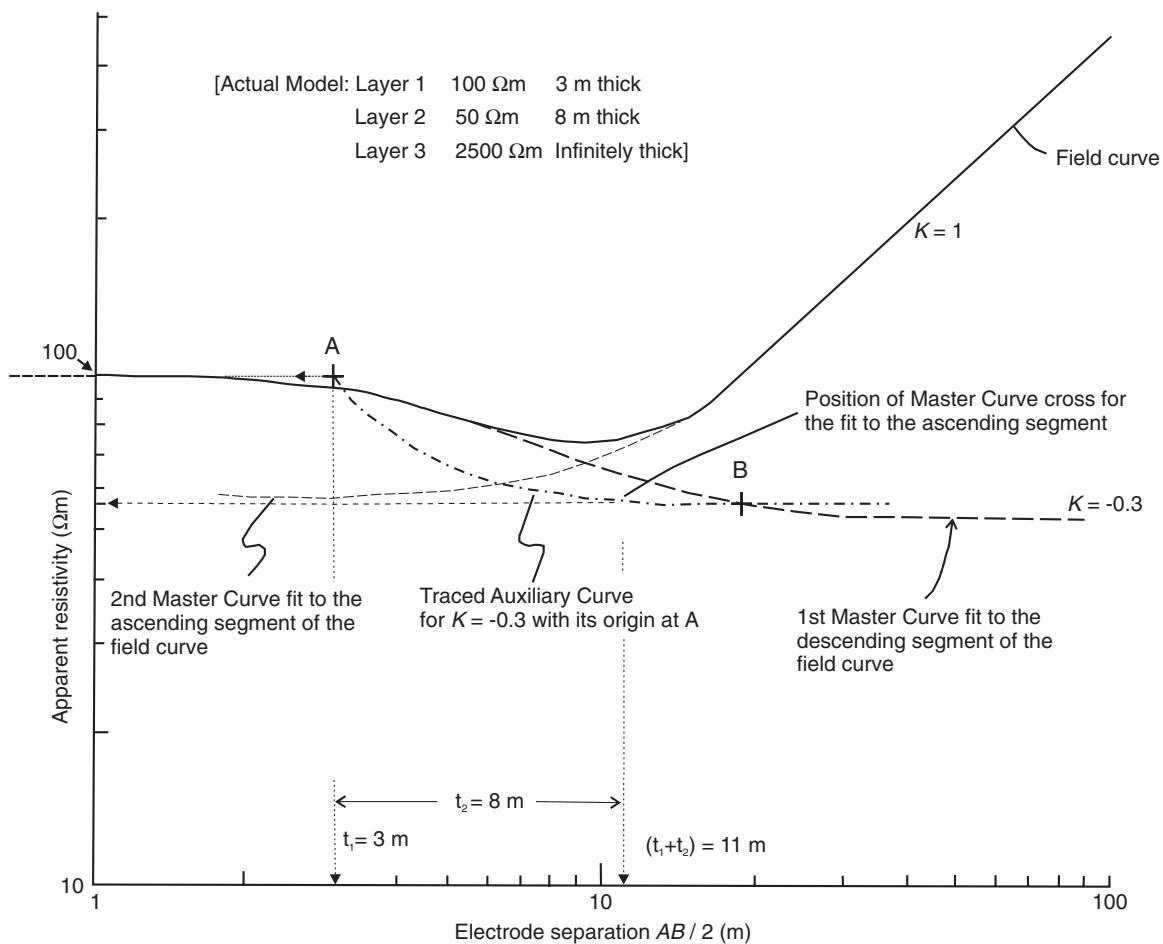


Figure 7.30 Fitting master and auxiliary curves to a Schlumberger VES curve; see text for details.

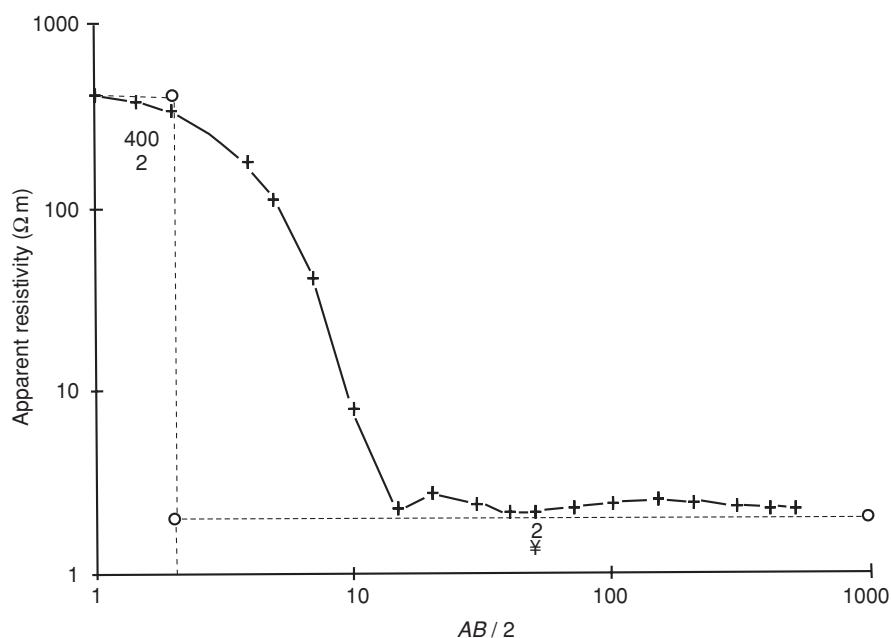
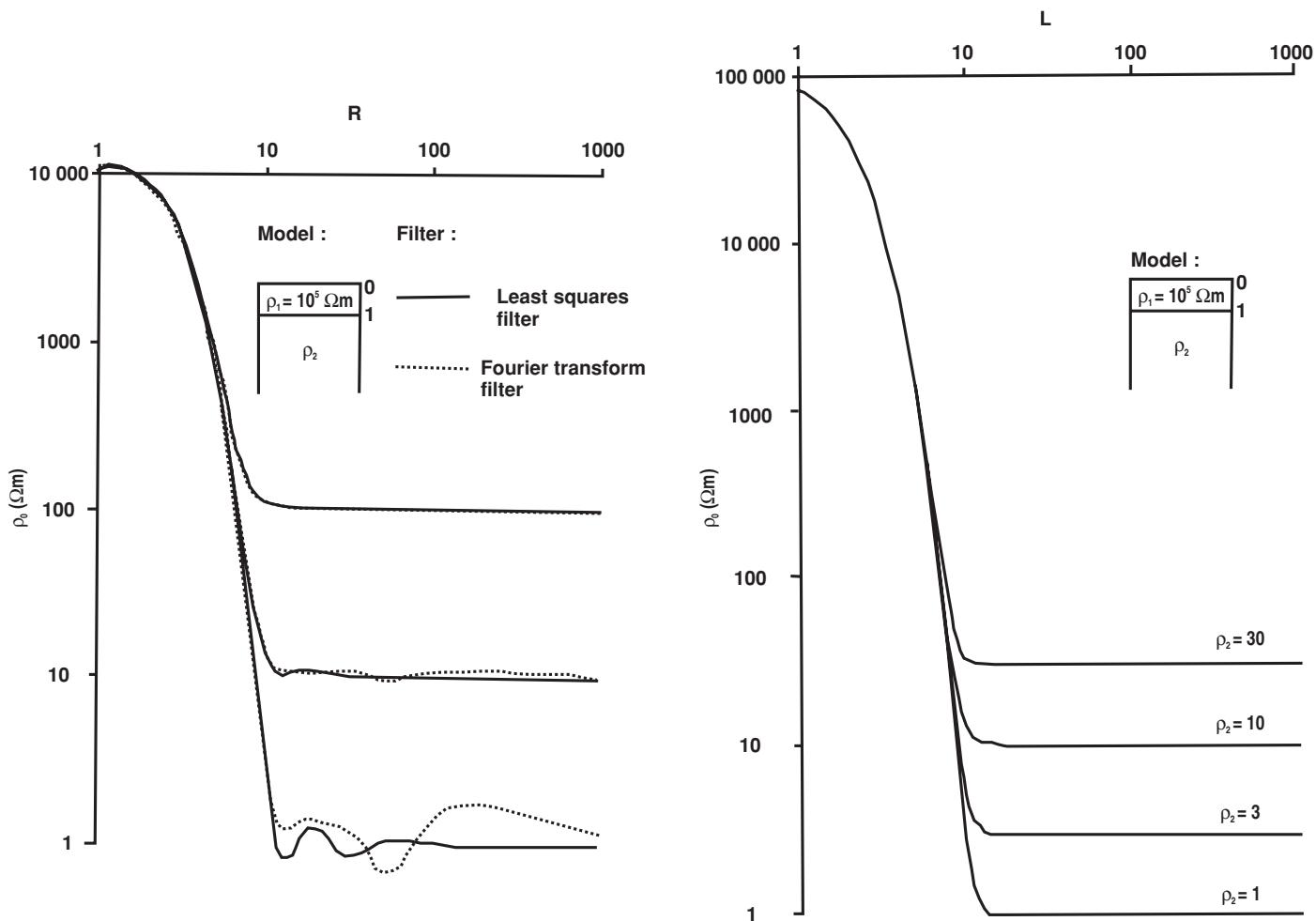


Figure 7.31 Oscillating tail produced by a computer program that has insufficient coefficients in its linear digital filter to cope with a resistivity contrast of more than 20:1.



**Figure 7.32** Effects of different computational methods on the scale of resistivity contrasts with which the various types of computer program can cope without producing erroneous data. From O'Neill and Merrick (1984), by permission.

Much work has gone into the design of linear digital filters to overcome this computational difficulty (e.g. O'Neill and Merrick, 1984), and now modern software packages can cope with even the most extreme resistivity contrasts. Although these packages can deal with as many as 25 layers, 2–6 layers are usually adequate to describe the subsurface. By increasing the number of layers beyond this, the length of time to produce an acceptable fit is increased dramatically (as there are so many more combinations of layer parameters to try) and, more often than not, the field data do not justify such a level of discrimination and may lead to overinterpretation.

As with master curves, it is always best to fit segments of the field curve at shortest electrode separations first and then to work progressively to greater separations. Once the top layers have been resolved, it is then easier to obtain good estimates of the parameters for the lower layers. The geoelectric basement (the lowest layer) is taken to be semi-infinite in depth and only the layer resistivity is required. Some computer packages display both the field and model curves simultaneously and may produce statistical parameters (RMS error) to describe the closeness of the fit. Optimisation of the interpretation can be achieved automatically by successive iterations to reduce the degree of misfit until it falls within a specified

and acceptable statistical limit. One such software package is IX1D v3 (Interpex, 2007).

A major advantage of the computer approach is that it provides an opportunity to investigate the problems of equivalence and suppression quickly and efficiently. See Section 7.5.4 for a more detailed discussion.

With the more sophisticated computer packages, some care has to be taken as to the method by which the convolution method is undertaken, as different results may be produced (Figure 7.32). Having said that, as long as the user of the computer program is aware of its advantages and disadvantages, then good and reliable interpretations will be obtained. The danger, as with all uses of computers, is that, for some inexplicable reason, computer-generated results may appear to have greater credibility than those produced by more traditional means, which is not necessarily justified. There is evidently an increasing and undesirable tendency for people to plug data into a computer package, and produce a result without thinking about the methodology or of experimental errors, or about the geological appropriateness of the model produced. As with all tools, computers must be used properly. With the availability of powerful, fast laptop computers, preliminary interpretation of results can be done while

**Table 7.4** Material types and their respective resistivity ranges for Kano State, northern Nigeria (Reynolds, 1987a).

Material	Resistivity range ( $\Omega\text{m}$ )
Sandy soil with clay	60–100
Clayey sandy soil	30–60
Clay	10–50
Weathered biotite granite	50–100
Weathered granite (low biotite content)	50–140
Fresh granite	750–8000

still in the field, with master and auxiliary curves being used as a backup in case of problems with the computer. However, modern generations of geophysicists are unlikely to have been exposed to master curve fitting, rather using computer-based methods. This has led to a reduction in the understanding of resistivity data processing, and overinterpretation of resistivity sections through a lack of appreciation of the pitfalls in interpretation. There has been too much emphasis on producing results quickly, often using default parameters during processing to produce the first output that looks reasonable. This does not make for good geophysics!

Once an acceptable layer model has been produced for each vertical electrical sounding, the models can be displayed side-by-side much like borehole logs. Between the various VES models, correlations are made between layers with comparable resistivities to build up a two-dimensional picture of both the vertical and lateral variations in resistivity. This can be extended into the third dimension so that maps of the individual layer thicknesses, akin to isopachyte maps, can be produced.

The final stage of a resistivity interpretation should be to relate each accepted VES model to the unknown local geology. Tables of resistivities, such as that in Table 7.1, or more geographically specific rock-type/resistivity ranges, can be used instead of referring to layer numbers. The interpretation can then be described in terms of rock units such as those listed in Table 7.4, which are from Kano State in northern Nigeria, for example. Thus a typical resistivity interpretation would consist of perhaps four layers with resistivities as given in Table 7.5.

**Table 7.5** Typical VES interpretation from Kano State, northern Nigeria (Reynolds, 1987a).

Layer	Resistivity ( $\Omega\text{m}$ )	Material type
1	95	Very sandy soil
2	32	Clay
3	75	Weathered granite*
4	3500	Fresh granite*

\*Granite type also determined from local geological mapping and from local hand-dug wells.

### 7.5.4 Equivalence and suppression

In the case of a three-layered model, if the middle layer is conductive relative to those around it, then current flow is focused through and virtually parallel to that layer. The longitudinal conductance  $S_L$  for this layer is  $h_2/\rho_2 = \text{constant}$ , and as long as the thickness and resistivity are changed (within limits) so as to maintain that ratio, there will be no appreciable change in the resulting apparent resistivity curve. All the pairs of  $h_2/\rho_2$  are electrically equivalent, and no single pair of values is preferable to any other.

However, if computer interpretation of VES curves is undertaken, the range of  $h$  and  $\rho$  values can be determined so that estimates of the ranges of both thickness and true resistivity can be made. This in itself can be extremely valuable. For example, in northern Nigeria, the subsurface consists of at least three layers – soil, weathered granite and fresh granite. It has been found that weathered granite with a resistivity in the range 50–140  $\Omega\text{m}$  provides a reasonable source of water (given a saturated thickness >10 m) to supply a hand-pump on a tubewell in a rural village. If the resistivity is less than 50  $\Omega\text{m}$ , this indicates that there is more clay present and the supply is likely to be inadequate. If the interpretation indicates a second-layer resistivity of 60  $\Omega\text{m}$  and thickness 12 m, which is characteristic of an acceptable water supply, this layer may be electrically equivalent to only 8 m of material (i.e. too thin) with a resistivity of 40  $\Omega\text{m}$  (<50  $\Omega\text{m}$ , thus probably clay-rich). This combination could prove to be problematical for a reliable water supply. If, however, the computer models demonstrate that the lowest limit of thickness is 10.5 m and of resistivity is 55  $\Omega\text{m}$ , then the site could still be used. On the other hand, if the equivalent layer parameters are well into those for the thin clay-rich range, then it is better to select another site.

Similarly, if the middle layer is resistive in contrast to those layers surrounding it, then current tends to flow across the layer and thus the product of the layer resistivity and thickness (which is the transverse resistance,  $T$ ; see Box 7.8) is constant. If, for example, a gravel layer with resistivity 260  $\Omega\text{m}$  and thickness 2 m is sandwiched between soil ( $\rho_1 < 200 \Omega\text{m}$ ) and bedrock ( $\rho_3 > 4500 \Omega\text{m}$ ), then  $T_2 = 520 \Omega\text{m}^2$ . If the model thickness is reduced to only 1 m, the gravel layer resistivity must be doubled. Similarly, if the resistivity is reduced, the thickness must be increased to compensate. Computer analysis can be used again to resolve the range of layer parameters which produce no discernible change in the apparent resistivity curve.

In the example illustrated in Figure 7.33A, a layer of resistivity 35  $\Omega\text{m}$  and thickness 2 m is sandwiched between an upper layer of resistivity 350  $\Omega\text{m}$  and thickness 6 m, and the bedrock of resistivity 4500  $\Omega\text{m}$  (upper bar below curve). The longitudinal conductance  $S_L$  for layer 2 is 0.057 siemens (2 m/35  $\Omega\text{m}$ ). The two other models depicted by horizontal bars are extreme values for the middle layer, but which have the same longitudinal conductance and which gave rise to model curves that are coincident with the one shown to better than 0.5%. The depths to bedrock thus range from 7.1 m to 10 m (in the models calculated), and there is no geophysical way of telling which model is ‘right’. It is by considering whether a 10 cm thick, highly conductive horizon is more geologically reasonable than a far thicker, more resistive band, that the most appropriate model

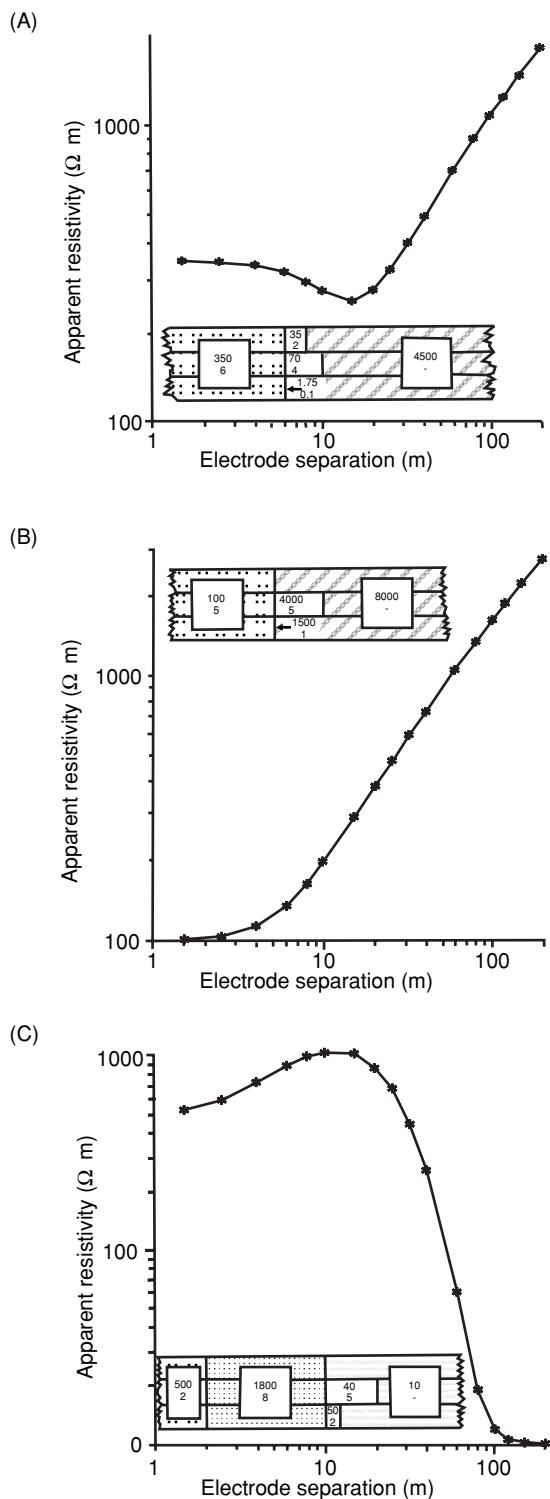


**Figure 7.33** (A) Equivalence test on a three-layer model. The models indicated in the lower two horizontal bars are electrically equivalent to the model in the top bar. Pairs of numbers are true resistivity ( $\Omega\text{m}$ ) above layer thickness (m). Suppression tests for (B) an ascending curve and (C) a four-layer descending curve.

can be chosen. If the layer thickness is determined independently, such as from a borehole, then the true resistivity for a layer can be determined.

An additional form of equivalence needs to be borne in mind at the interpretation stage, and that is the equivalence between an isotropic and an anisotropic layer. This Doll-Maillet equivalence (see Maillet, 1947) results in an overestimate of layer thickness in proportion to the amount of anisotropy which, if present, is of the order of 10–30%.

Apart from equivalence, the other interpretational problem is that of suppression. This is particularly a problem when three (or more) layers are present and their resistivities are ascending with depth (A-type curve; see Figure 7.27B) or descending with depth (Q-type curve; see Figure 7.27D). The middle intermediate layer may not be evident on the field curve and so its expression on the apparent resistivity graph is suppressed. The computer method is invaluable here to estimate (1) if there is a hidden layer present, and (2) if there is, its range of layer parameters. In Figure 7.33B, curves for three-layer models (middle and lower bars) with second layers of resistivity of 1500 to 4000  $\Omega\text{m}$  and thicknesses 1 to 5 m are graphically indistinguishable from that of a two-layer model (top bar). For a layer to be suppressed, its resistivity should approach that of the one below, so that the resistivity contrast between the top and the suppressed layer is comparable to that between the top and lowermost layers. The effects of missing such a suppressed layer can have major effects on the estimation of the depth to bedrock. In Figure 7.33C, a similar example is given but for descending resistivities. The curves for models with a suppressed layer (middle and lower bars) fit the three-layer case (top bar) to better than 1% and are indistinguishable graphically.

If the intermediate layers are thin with respect to those overlying, and if either equivalence or suppression is suspected, master curves will provide no solution. However, equivalent or suppressed layers can be modelled very effectively using computer methods in conjunction with a knowledge of what is geologically reasonable for the field area in question.

### 7.5.5 Inversion and deconvolution

Zohdy (1989) produced a technique for the automatic inversion of resistivity sounding curves. Least-squares optimisation is used in which a starting model is adjusted successively until the difference between the observed and model pseudo-sections is reduced to a minimum (Barker, 1992). It is assumed initially that there are as many subsurface layers as there are data points on the field sounding curve (Figure 7.34), and that the true resistivity of each of these assumed layers is that of the corresponding apparent resistivity value. The mean depth of each layer is taken as the electrode spacing at which the apparent resistivity was measured, multiplied by some constant. The value of this constant is one which reduces the difference between the observed and model resistivity curves to a minimum and is determined by trial and error.

A starting model is used to generate a theoretical synthetic sounding curve, which is compared with the field data. An iterative process is then carried out to adjust the resistivities of the model while

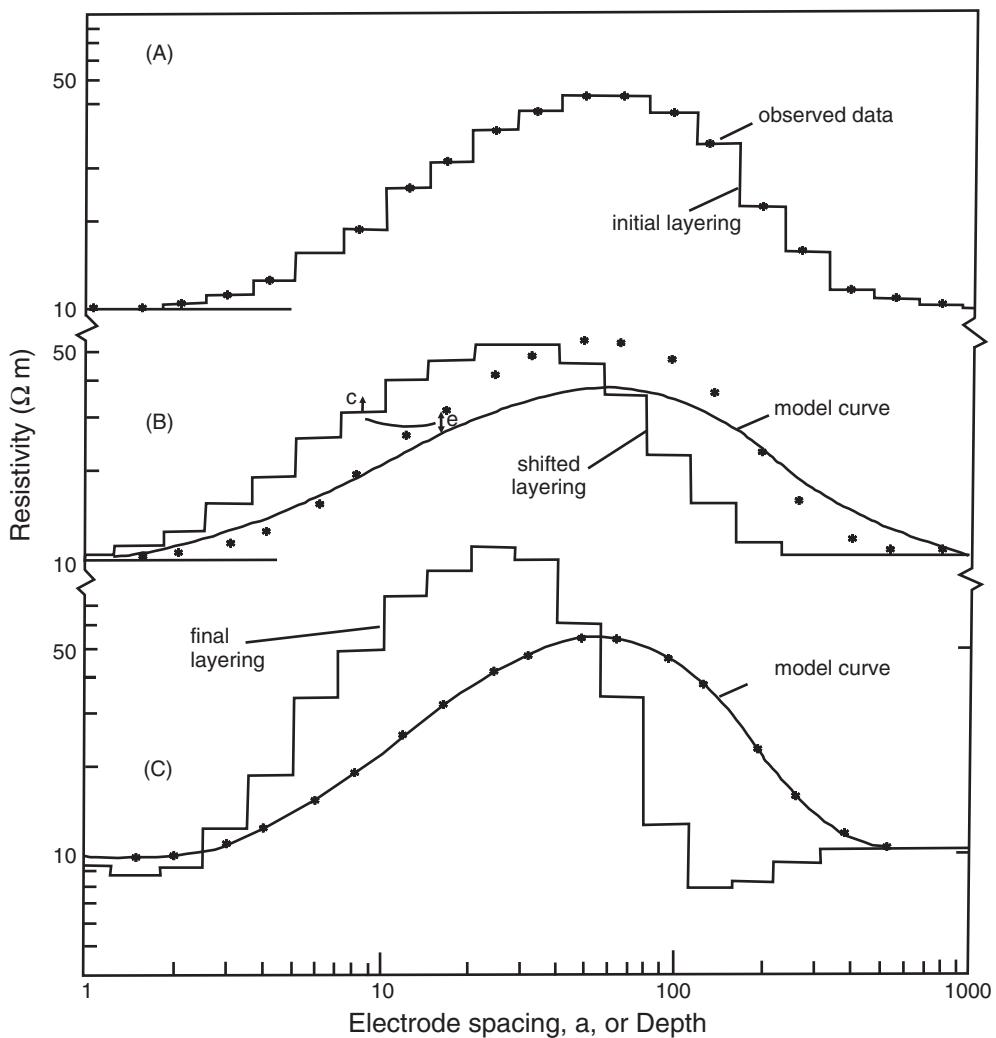


**Figure 7.34** Automatic sounding inversion technique. (A) Observed data and initial layering. (B) Shifted layering and resulting model sounding curve. The difference (e) between the model and observed curves is used to apply a correction (c) to the layering. (C) The final layering and resulting model curve that is closely similar to the observed data. From Barker (1992), by permission.

keeping the boundaries fixed. After each iteration the theoretical curve is recalculated and compared with the field data, and the degree of misfit is indicated by the percentage RMS error; the process is repeated until the RMS difference between the two curves reaches a minimum or an acceptable value (Figure 7.34).

Finite-element forward modelling can be undertaken using commercially available software. The resistivity response for a two-dimensional model is calculated and displayed as a pseudo-section for comparison with the original field data. This approach is used to help to generate realistic subsurface geometries in definable model structures (e.g. Figure 7.35).

In the case of an ERT dataset, before inverting the data, the raw apparent resistivity values should be reviewed for obvious data spikes, poor electrode contact resistances, missing data, and so on, otherwise such 'bad' data points will infect the inversion process and produce artefacts that might be confused later in the interpretation process as being physically significant. It is also possible to reduce the effect of known surface utilities. The (edited) mea-

sured apparent resistivity data are plotted as a pseudo-section as a function of *pseudodepth*, i.e. it is not yet a true depth scale (Figure 7.36A). The inversion routine calculates synthetic apparent resistivity data (Figure 7.36B), also as a function of pseudodepth, for a true resistivity-depth model for each iteration. Elevation data, if available, should also be used to correct for irregular topography at the start of the inversion process. The process is repeated automatically for either a set number of iterations or until the percentage RMS error falls below an acceptable value. The programme then displays the resulting true resistivity-depth model section (Figure 7.36C). The examples shown have been produced using RES2DINV (Loke and Barker, 1996a; Loke, 2010). Other inversion software is available such as that produced (e.g. DCIP2D) by the Geophysical Inversion Facility at the University of British Columbia. Other examples of inverted pseudo-sections for a range of applications are given in Section 7.7.

As with any computer analysis, it is important to understand how the data are to be processed and to review the results with an

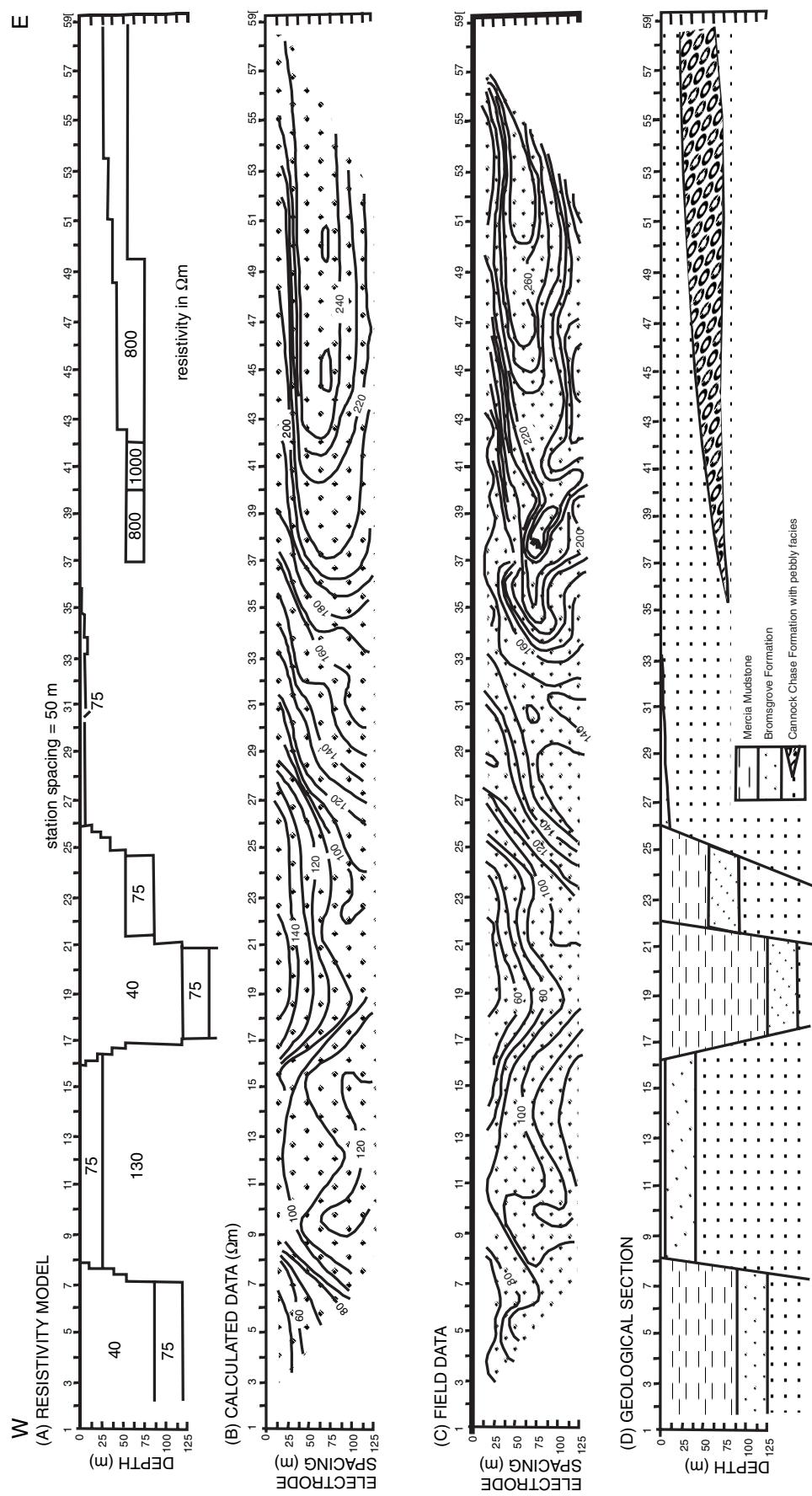
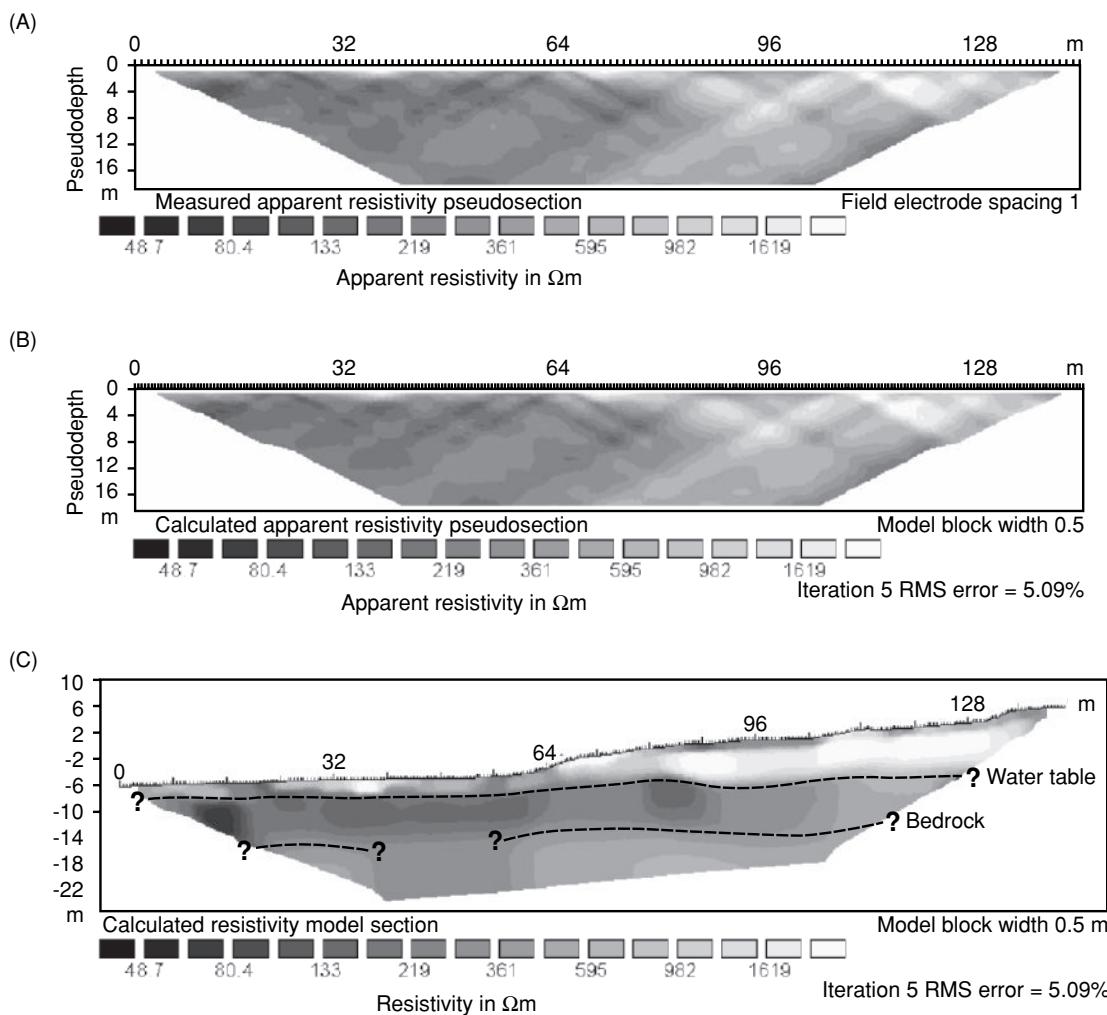


Figure 7.35 Final interpretation of a Triassic sequence in Staffordshire, UK. (A) Two-dimensional finite difference model. (B) Computed apparent resistivity pseudo-section. (C) Field data. (D) Geological interpretation based on (A) and additional information. From Griffiths *et al.* (1990), by permission.



**Figure 7.36** Example of pseudo-sections showing (A) raw apparent resistivity data, and (B) calculated apparent resistivity values, for (C) the derived true resistivity-depth model section. [C]

appreciation of the possible presence of artefacts within the data, such as from data acquisition, those that might occur as a function of the data processing itself, and the effects of ‘noise’. It is also important to recognise that different inversion methods are suited to specific types of targets, e.g. predominantly horizontally layered, or with sharp boundaries. These will affect the results obtained, and it is not adequate to use default settings to produce the first model with an acceptable RMS error (e.g. <10%). This does not constitute an interpretation. Indeed, it may be necessary to try a number of inversion methods to produce a suite of true resistivity–depth models that can be viewed in the light of independent geological information before a final interpretation is made. The same inversion process can be undertaken when processing 3D datasets (Loke and Barker, 1996b). It may also be necessary to try 2D and 3D modelling to test for additional extraneous influences on the data, as ERT data can be influenced by features that lie off the line or end of the profile. This is especially so in the presence of targets that have highly contrasting true resistivities. This is discussed more in the next section.

## 7.5.6 Modelling in 2D and 3D

Finite-element forward modelling can be undertaken using commercially available software. The resistivity response for a two-dimensional model is calculated and displayed as a pseudo-section for comparison with the original field data, and the degree of misfit is given in terms of percentage RMS error. This approach is used to help generate realistic subsurface geometries in definable model structures.

In order to help to understand how to interpret ERT true resistivity–depth sections, it is appropriate to consider a number of results derived from different simple but common models. The examples have all been produced using RES2DMOD (Geotomo Software), which is widely available.

It is important to recognise that the form of display of ERT sections is not a clear step function where the layer boundaries are picked out by sharp changes in true resistivity values. Rather, there is a gradient from one value to the next (Figure 7.37A). To interpret such a section it is necessary to look for maximum resistivity gradients and choose a true resistivity contour that best represents

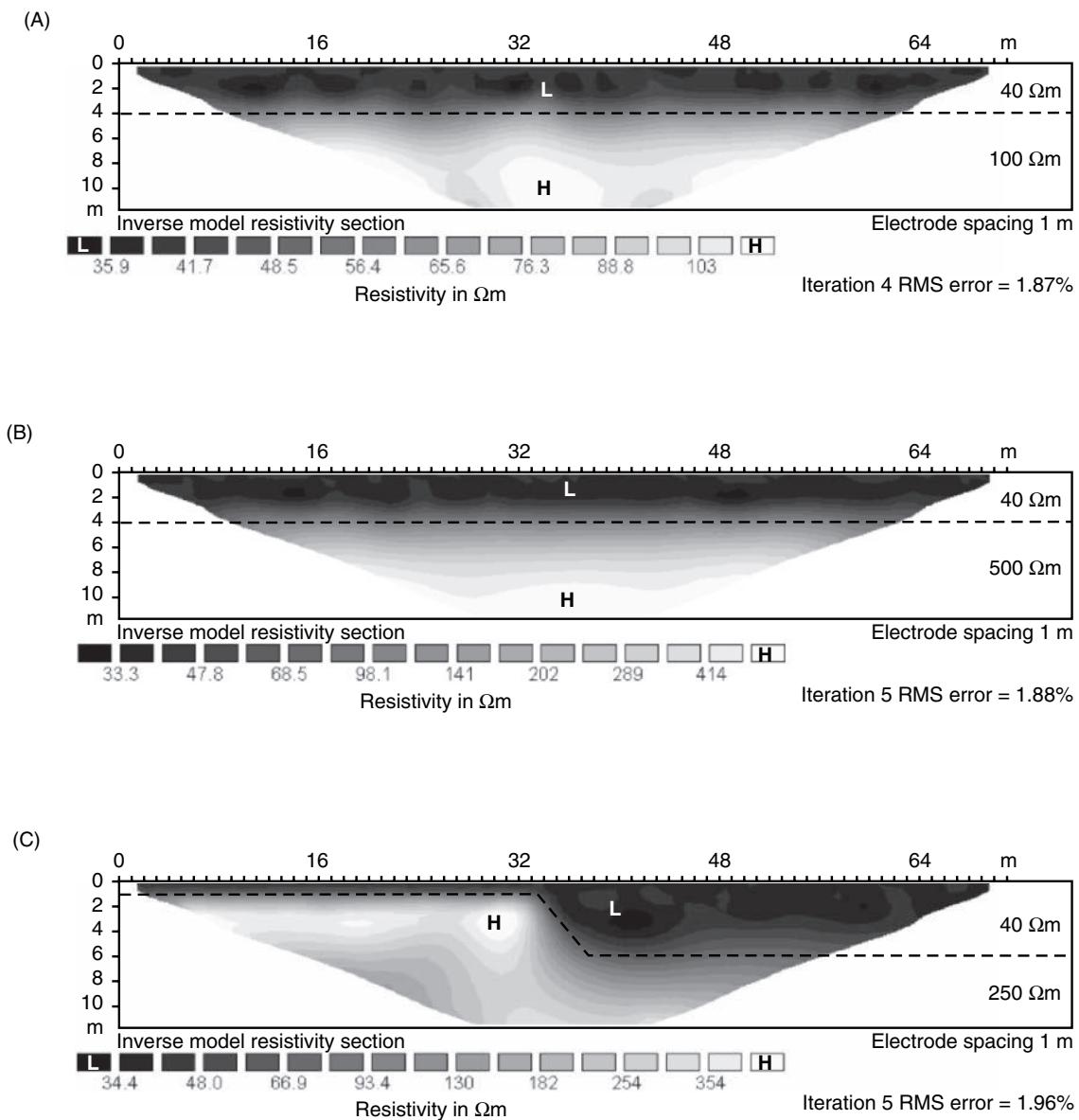


**Figure 7.37** Examples of model resistivity sections derived for a simple two-layer case with (A) a moderate contrast and (B) a high contrast in resistivity values between layers, and (C) a simple two-layer case with a normal fault. [C]

the postulated layer boundary. It might be possible to constrain the depth by using borehole correlation by which the layer thickness is known from the log. However, the choice of this contour can be difficult even in a simple two-layer case. Two examples are shown in Figure 7.37A and B where the physical model is exactly the same except for the contrast in layer resistivity between the first and second layer. The contrast in resistivity, as defined by the  $k$  value (see Box 7.10 and graphically represented by master curves in Figures 7.28 and 7.29), is moderate in Figure 7.37A ( $k \sim 0.4$ ;  $\rho_1 = 40 \Omega\text{m}$ ;  $\rho_2 = 100 \Omega\text{m}$ ), whereas it is equal to 0.85 in Figure 7.37B; *i.e.*  $\rho_2 \geq 10\rho_1$  ( $\rho_1 = 40 \Omega\text{m}$ ;  $\rho_2 = 500 \Omega\text{m}$ ). In each case, 2% noise has been added to the sections. Firstly, it should be noted that in Figure 7.37A, the true resistivity values range from less than 36  $\Omega\text{m}$  (whereas the model stipulated 40  $\Omega\text{m}$ ) to over 103  $\Omega\text{m}$

(whereas the model stipulated 100  $\Omega\text{m}$ ). The fluctuations below and above the model values are a function of the introduced noise. So is the apparent undulation in the layer boundary at 4 m depth. These fluctuations are less significant in Figure 7.37B due to the greater contrast in resistivity. Anomalous resistivities also appear in the model indicated in Figure 7.37C, which is a two-layer model but with a normal fault with a 4 m downthrow. The model generates resistivity values significantly above and below the specified maximum and minimum model values respectively. The apparent decrease in resistivity in the lower part of the left-hand side of Figure 7.37C is purely an artefact of the inversion process. In each of these three cases, the ERT sections show a resistivity gradient from the value close to that of the model first layer rising over a finite depth range to its maximum. The interface between the two layers is not

manifest as a step function but as a gradient. This makes interpreting the precise location of interfaces on field data difficult without other, independent information. Estimating depths to boundaries can be tricky. It is for this reason that it is useful to be able to invert field data to derive a true resistivity model, interpret it as a layer model with designated true resistivities, and then generate a synthetic true resistivity section for that model to compare with the field results. Through this process, physically implausible options may be eliminated.

In a three-layer case, the nature of the middle layer can be critical in whether or not it is identified on the ERT true resistivity–depth section. Examples of a thin (2 m) and thick (6 m) middle layer with exactly the same true resistivity sandwiched between layers with higher true resistivities are shown in Figure 7.38A and B. In the case of a thin middle layer it is hard to define exactly how thick this layer is and what its true resistivity value is from the resistivity section alone. It is only when the layer thickness becomes significant that the unit can begin to be resolved. There is an element of lack of definition arising from the inability to use suppression and equivalence tests on ERT inversion. This is demonstrated by comparison of Figure 7.38C with Figure 7.38D. The former has three layers with increasing resistivity values; the latter has a fourth layer between the second and third of the model in Figure 7.38C so that the resistivity gradient of the lowermost three layers is nearly identical in example D as for the lowermost two horizons in the three-layer case in C: this is an example of equivalence. The bulbous effect or cusp in the lowermost parts on each of the four sections in Figure 7.38 is an artefact of the inversion process.

The ideal geophysical model comprises an  $n$ -layered case where each layer is homogeneous, isotropic and semi-infinite, so that there are no edge effects in our models arising from the lateral boundaries of features. Clearly, nature is not like this, so our interpretations require that these boundary effects are taken into account. It is also important that the presence of a contrasting resistivity feature that lies off the end of an ERT profile, or offset from it, is also taken into account. This is demonstrated in Figure 7.39, which shows a final resistivity model by inversion of synthetic dipole–dipole array data. In Figure 7.39A, a very high resistivity body lies within 5 m of the end of the profile. The true resistivity values indicated in the ERT section show a low resistivity anomaly along the lower right edge of the pseudo-section, and both a horizontal low and underlying high resistivity anomaly (between 240 and 310 m), both of which are artefacts associated with the presence of the very high resistivity body off the end of the line. Without considering this off-end body the section might be interpreted as having a vertical true resistivity gradient within the materials, which is not the case. This is a real issue when interpreting ERT sections for glacial hazards where large bodies of buried temperate glacial ice may be present. These can have extremely high resistivity values ( $>2\text{ M}\Omega\text{m}$ ) compared with those of moraine ( $\sim 4000\text{ }\Omega\text{m}$ ) (i.e.  $k = 1$ ). This is discussed further in Section 7.6.4.

If there is a target lying offset from an ERT profile, it too can influence the section (Figure 7.39B). The question then is whether the target lies on the ERT line or is offset, and if offset, to which side and how far away? The only way that this might be determined is if there is a series of parallel ERT transects so that the effects of the

unidentified target can be seen preferentially on one or other of the adjacent lines, or modelled in 3D, if the dimensions and resistivity of the target are known. This uncertainty when mapping 3D targets using 2D profiling is a significant potential interpretational pitfall. It is also a case for deploying 3D acquisition methods where there is a cost and technical benefit in doing so.

Figures 7.39B to E show the final resistivity models produced by inversion of synthetic Wenner array data created using Res3DMod, where 2D sections were extracted from the 3D synthetic dataset and 2D inversion undertaken using Res2DInv for a number of different scenarios. Figure 7.39B shows the three-layer case with no additional off-line or off-end bodies present. It shows the same features and artefacts as highlighted in Figure 7.38B. The section in Figure 7.39C is as for B but with the inclusion of a 4-m-wide highly resistive ( $2\text{ M}\Omega\text{m}$ ) ‘dyke’-like air-filled feature extending to infinity at right angles to the line of the profile. The target is equivalent to an air-filled mine shaft but making no allowance for the lack of strike length at right angles to the profile, i.e. the inversion assumes that the mine shaft extends to infinity either side of the profile line (which clearly no mine shaft does!). This contrasts with a more realistic model where the strike distance is limited to 2 m either side of the profile line (Figure 7.39D). In this case the shaft is not properly imaged by a 2D survey even when passing directly over the top of the feature. The 2D inversion software assumes that the ground resistivity remains constant into and out of the section, and changes only along the profile and with depth. In reality, current flows in 3D, and if a high-resistivity feature below a survey line is surrounded by low resistivity material, the current will pass preferentially through the low resistivity material: an effect that cannot be accounted for with 2D acquisition and inversion. Effectively the current lines are refracted around the high-resistivity feature. The presence of the anomaly blob centred at 2 m depth might be sufficient to indicate the presence of the top of the mineshaft so that intrusive investigations could then be targeted appropriately. It does not provide any information about the nature of the mineshaft column to greater depth. Should the same mineshaft target be offset by one diameter (4 m in this case; Figure 7.39E), the effects of the mineshaft are almost impossible to distinguish. Very careful comparison of the section in E with that in B shows only a minute difference in the base of the  $50\text{ }\Omega\text{m}$  horizon. In reality, such a subtle feature would not be interpreted as being due to a mine shaft offset from the transect. This demonstrates that to detect a 4 m diameter mineshaft using 2D ERT, the maximum interline spacing used should be no more than half a diameter. To detect the mineshaft in the resistivity conditions indicated, the use of a shallow EM technique is likely to be much faster, more cost-effective, and yield more definite results to target intrusive follow-up investigations. However, if a number of parallel profiles are acquired, each offset from the other by a regular amount (say, 2–4 electrode spacings generally) then it might be possible to determine whereabouts the postulated mine shaft might be, even though it does not lie beneath any of the actual ERT profile lines. It should also be pointed out that the limitations described here refer to the use of 2D ERT lines to detect a spatially-limited discrete 3D target. The effectiveness of such a survey may also be improved by enhanced analysis of the 2D dataset into a 3D volume to produce horizontal resistivity slices.

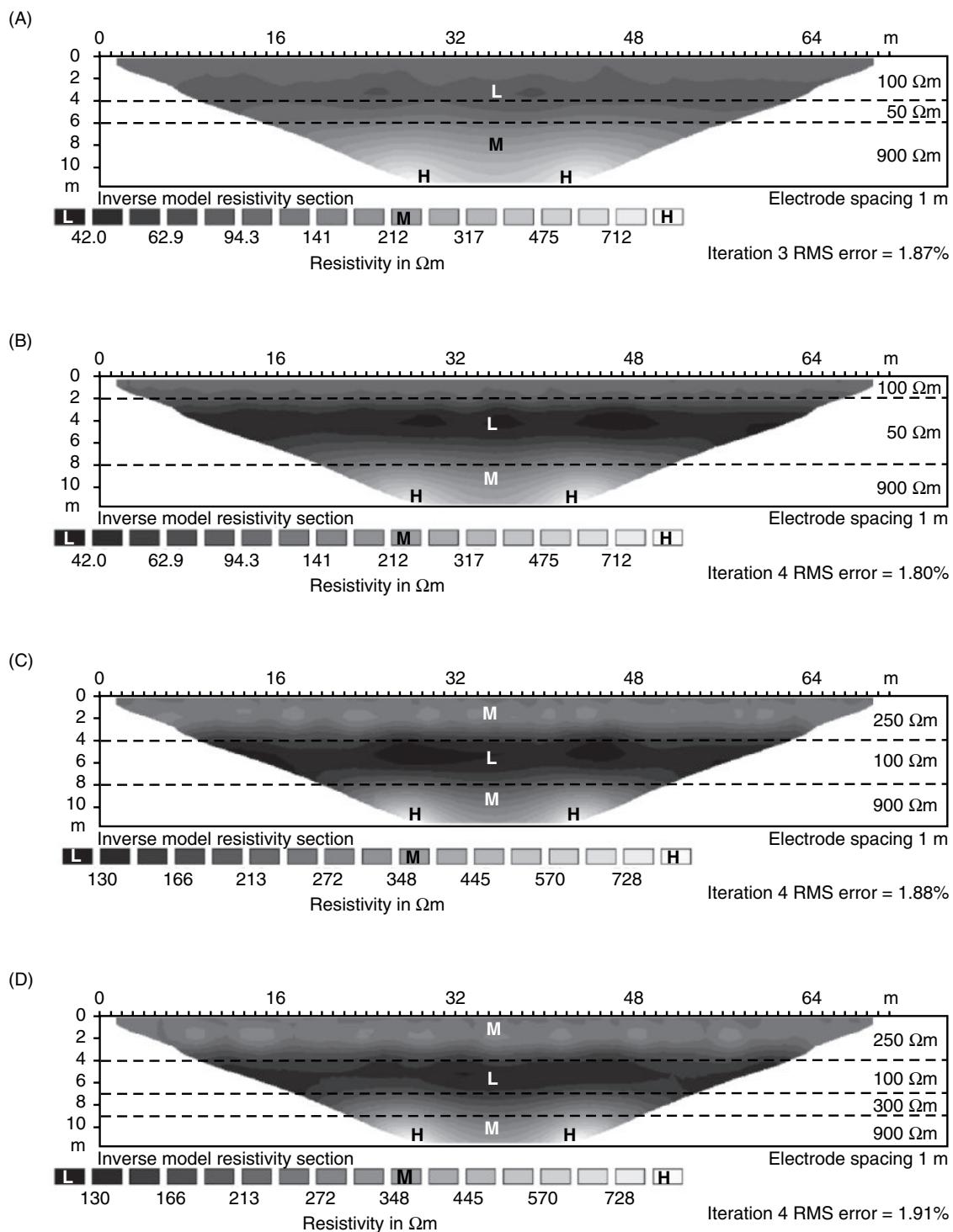


**Figure 7.38** Examples of model resistivity sections derived for three separate three-layer cases: (A) with a thin lower-resistivity middle layer; (B) the same resistivity model as in (A) but with a thicker middle layer; and (C) with increasing resistivity values with depth (3 layers) and (D) in four layers.

The interpretational aspects of the discussion above are also important considerations when taking a series of parallel 2D ERT model sections and interpreting them to create a '3D' (or more correctly a 2.5D or quasi-3D) resistivity model of the ground from which to produce true resistivity slices at a given depth to produce

'anomaly' maps. It is possible that artefacts within the 2D sections are interpolated into adjacent lines and give rise to ghost anomalies that have no physical significance. Similarly, consideration needs to be given to the methods of gridding true resistivity data with respect to the grid cell dimensions relative to the electrode separations used

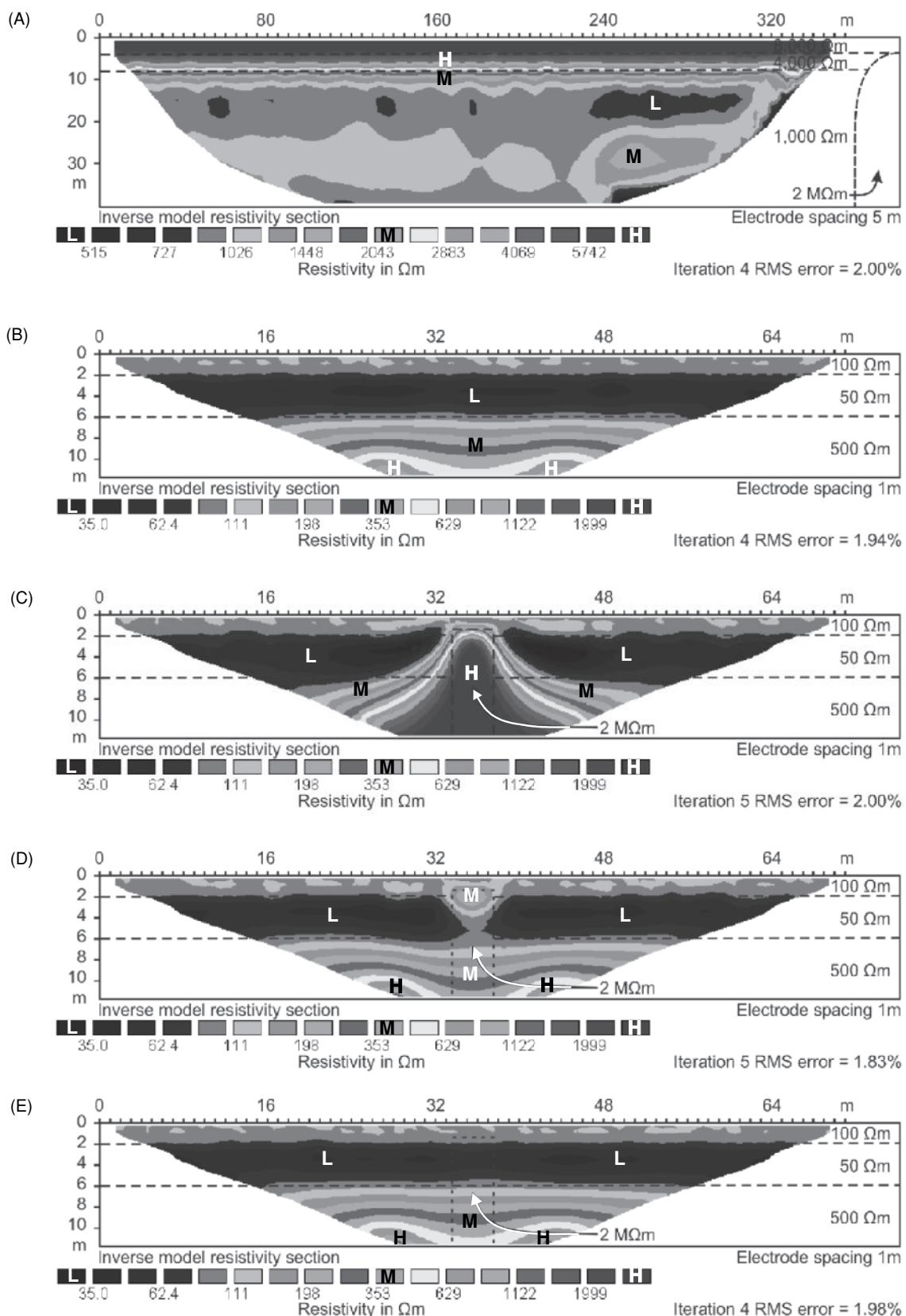


**Figure 7.39** (A) A resistivity section modelled to show the effects of a very high resistivity feature lying off the end of the line. (B) A 3-layer model section, and (C) the resulting modelled resistivity section with a 4-m wide vertical dyke with infinite strike located in the middle; and with (D) a 4-m wide mineshaft with a strike length of 2m either side of the ERT profile. (E) A modelled section with the mineshaft as in (D) but offset from the profile line by one diameter (4 m). [C]

to acquire the data, so that there is no geometric distortion of the resistivity anomalies due to the gridding process. From experience, it is best to screen such anomaly maps using dimensional analysis to filter out those ‘anomalies’ that are physically too small by area to be significant, or where the identification of anomalies is such that the apparent anomaly magnitude is less than the standard deviation of the variability of the resistivity values in the section. Are the anomalies present just noise? As with most geophysical interpretation, the true value lies in the depth and detail of the analysis, not just in producing colour maps or sections using default processing parameters.

Measure material was anticipated to be massive and strong and thus hard to excavate, while saturated superficial deposits and Coal Measure shales were thought to provide very unstable trench walls. The CST results using a Wenner array with 10 m electrode separation and 10 m station interval revealed locations where sandstone bedrock was interpreted to be close to the surface, which would have required blasting for the excavation for the new sewer (Figure 7.41). Seismic refraction was also used to obtain acoustic velocities, which in turn were used to determine whether blasting or ripping techniques should be used in the excavation.

## 7.6 ERT applications and case histories

### 7.6.1 Engineering site investigations

#### 7.6.1.1 Subsurface collapse features

In a small village in east Devon, a 5 m diameter hole appeared overnight in the middle of the road. The local water main had been ruptured and had discharged for over 12 hours and all the water had disappeared down a fissure into underlying limestone. Several of the local buildings started to crack badly, and on investigation it was found that the rafted foundations of several houses had broken and the houses were literally cracking open at the seams, resulting in the emergency evacuation of the residents.

A resistivity survey was initiated in order to determine the subsurface extent of the problem prior to drilling. Fortunately, the front gardens of the houses affected were all open-plan, so there was no difficulty in access, but space was still at a premium. A series of constant separation traverses was instigated using the Wenner array with electrode separations of 10, 15 and 20 m. The resulting apparent resistivity values were plotted as a contour map (Figure 7.40). It was clear that where the hole had appeared, there was a deep infill of clay. It was this that had slipped through a neck of a fissure into a cave beneath, resulting in subsidence beneath the foundations of the houses and the rupture of the water main. The discharging water disappeared into this newly discovered cavern. The clay depth decreased uphill and suddenly increased again, indicating further clay-filled fissures. On drilling these resistivity anomalies, the depth to limestone was confirmed. One drill hole penetrated the cave but failed to locate the bottom; the cave was at least 20 m deep.

#### 7.6.1.2 Burial of trunk sewer

A route for a proposed new trunk sewer in south Wales was investigated using electrical resistivity methods because access for drilling equipment was not possible. Both vertical electrical soundings and constant separation traverses were used along the route and compared with available borehole data from the National Coal Board (Prentice and McDowell, 1976). The material through which the sewer trench was to have been dug consisted of superficial deposits overlying Coal Measure sandstone and mudstone. The Coal

#### 7.6.1.3 Location of permafrost

The presence of massive ground ice and frozen ground provides considerable problems to engineers involved in construction projects. Firstly there are the difficulties in excavation, and secondly, substantial problems can emerge with the thawing of such affected ground. It is therefore vital that ice wedges and lenses, and the extent and degree of permafrost, can be determined well in advance.

Ice has a very high DC electrical resistivity in the range from 1 MΩm to 120 MΩm (Reynolds and Paren, 1984) and therefore forms a particularly resistive target. A variety of geophysical profiles over a proposed road cutting near Fairbanks in Alaska are illustrated in Figure 7.42. Data obtained in the spring show more variability and resolution than when an active layer of thawed ground is present, as in the autumn measurements (Osterkamp and Jurick, 1980). Other geophysical methods that are used successfully in this application are electromagnetic profiling, micro-gravity and ground radar surveying.

With changing climate, permafrost areas are thawing increasingly, leading to major engineering problems within previously frozen infrastructure corridors (roads, railways, pipelines, power grids, etc.), and to greater slope instability. There is a growing amount of attention to periglacial environments and the use of geophysical techniques (e.g. Hauck and Kneisel, 2008).

It has recently been demonstrated that the ERT method can be used to help to discriminate between types of rock glacier (Ikeda, 2008), such as between bouldery and pebbly rock glaciers, on the basis of their resistivity ranges (10–5000 kΩm, bouldery; and 0.5–20 kΩm, pebbly). These are illustrated in Figure 7.43 (bouldery type, A; pebbly type, B). Resistivities higher than 100 kΩm tend to indicate a highly ice-supersaturated layer in bouldery rock glaciers. In contrast, resistivities of pebbly rock glaciers indicate ice-cemented pebbles/cobbles with a relatively high unfrozen water content. The ERT method can play an important role in helping to detail the structure of frozen ground and structures, and especially to indicate if free water is present (Kneisel and Hauck, 2008).

#### 7.6.1.4 Location of buried foundations

As part of a trial survey in January 1993, electrical resistivity subsurface imaging was used at a disused railway yard in order to locate old foundations concealed beneath railway ballast. Details of the geophysical survey have been described in more detail by Reynolds (1994, 1995) and Reynolds and Taylor (1995).

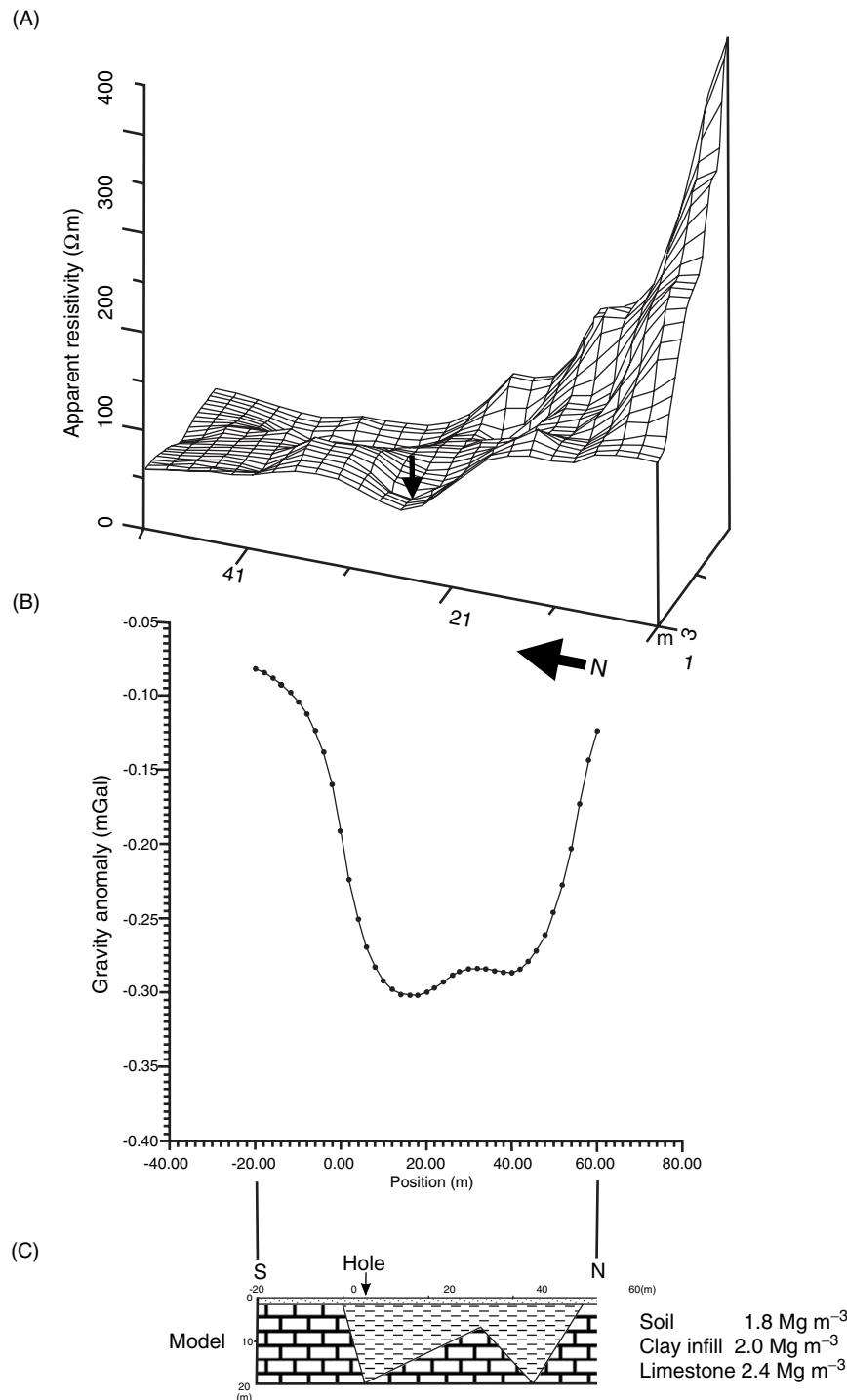


**Figure 7.40** (A) Apparent resistivity isometric projection obtained using constant separation traverses with an electrode separation of 10 m. (B) Modelled micro-gravity profile that would be expected for the geological model shown in (C): interpreted depth to limestone constrained by drilling. A north-south profile is shown in Figure 7.20. The position of a clay-filled solution feature is arrowed.

The ERT survey was carried out adjacent to a metal chain-link fence and an old diesel tank, and about 3 m from an existing building. It was thought that the remains of two former buildings might still be present beneath the railway ballast and the existing building. The site was totally unsuitable for electromagnetic

profiling, because of the above-ground structures. It was also unsuitable for ground-penetrating radar owing to the coarse ballast and potentially conductive ash also found on site. Despite extremely high electrode contact resistances, a 25 m long array was surveyed with an inter-electrode separation of 1 m. This provided a vertical

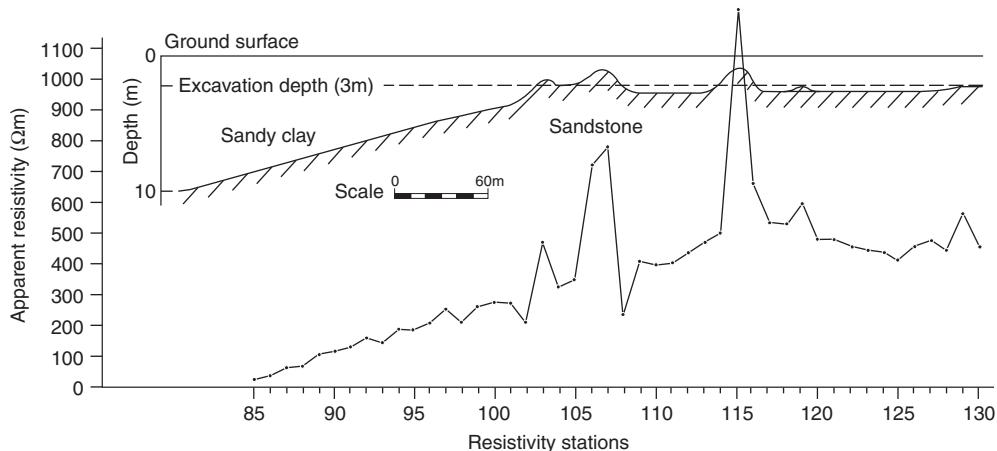


**Figure 7.41** Constant separation traverse data obtained along the proposed route of a new trunk sewer in south Wales, with the interpreted geological section. After Prentice and McDowell (1976), by permission.

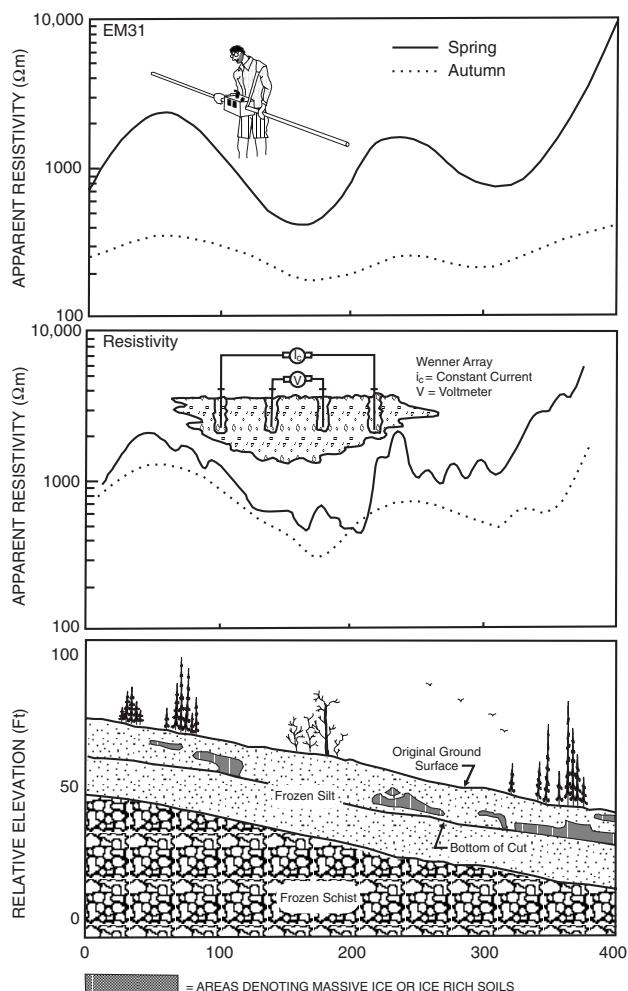


**Figure 7.42** Massive ice and frozen ground in a subsurface profile of a proposed road cut near Fairbanks, Alaska. Also shown are the spring and autumn survey data obtained using electrical resistivity constant separation traversing and electromagnetic induction (EM31). Massive ground ice produces significant apparent resistivity highs. From Osterkamp and Jurick (1980), by permission.

resolution of 0.5 m or better. The apparent resistivity data were filtered to remove noise spikes and displayed as a pseudo-section (Figure 7.44A), which was inverted using a deconvolution technique (Barker, personal communication). The final pseudo-section of true resistivities against depth shows a general increase in resistivity with depth (Figure 7.44B). In particular, it revealed two areas of extremely high resistivity ( $>125,000 \Omega\text{m}$ ) at a depth of about 1 m which had very flat tops to the anomalies. These were interpreted to be due to buried foundations. The main anomaly (between 6 and 11 m along the array) was found to correlate with the outline of one former building on an old plan. The second feature (starting at around 18 m) is thought to be due to the other old building. However, the location was found to be several metres further away from the first building than indicated on the plans. The depth to the foundation was thought to be reasonable, as adjacent brick slabs excavated a few metres away were found at a comparable depth.

### 7.6.1.5 Landslides

Electrical resistivity tomography lends itself to profiling across landslides in order to image the active sliding portion and the plane of décollement (sliding surface). An example is shown in Figure 7.45, which was acquired across a former landslide in northwest England as part of an investigation into a new road scheme. The photograph shows the landscape; the bowl-shaped depressions are part of the various components of the local landslide, which is made up of a series of rotational slope failures on the flanks of a drumlin. Where these failures meet the slope surface, spring lines emerge and are associated with patches of reeds. From the resistivity section, the landslide portion can be clearly seen as more resistive patches on a much more conductive substrate (glacial till). The boundaries indicated on the section correlate with geomorphological features mapped on the ground.

On steep slopes the electrodes should be implanted perpendicular to the ground surface, not vertically, to maintain the potential distribution at shallow depths. It is imperative that topographic corrections are applied so as to maintain the correct geometries, as

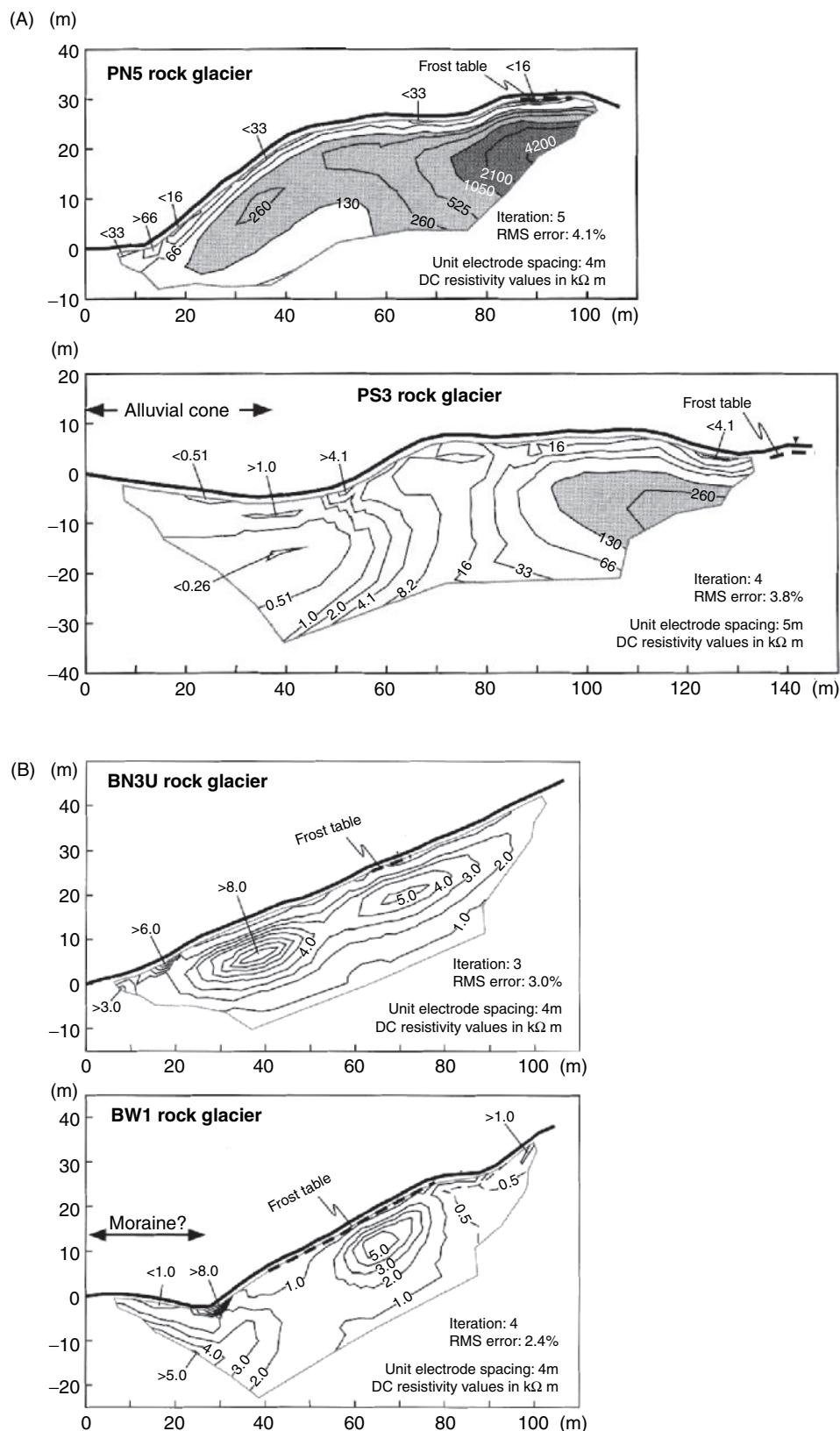


**Figure 7.43** ERT inversion results for (A) two bouldery rock glaciers and (B) two pebbly rock glaciers in the Swiss Alps. After Ikeda (2008), by permission.

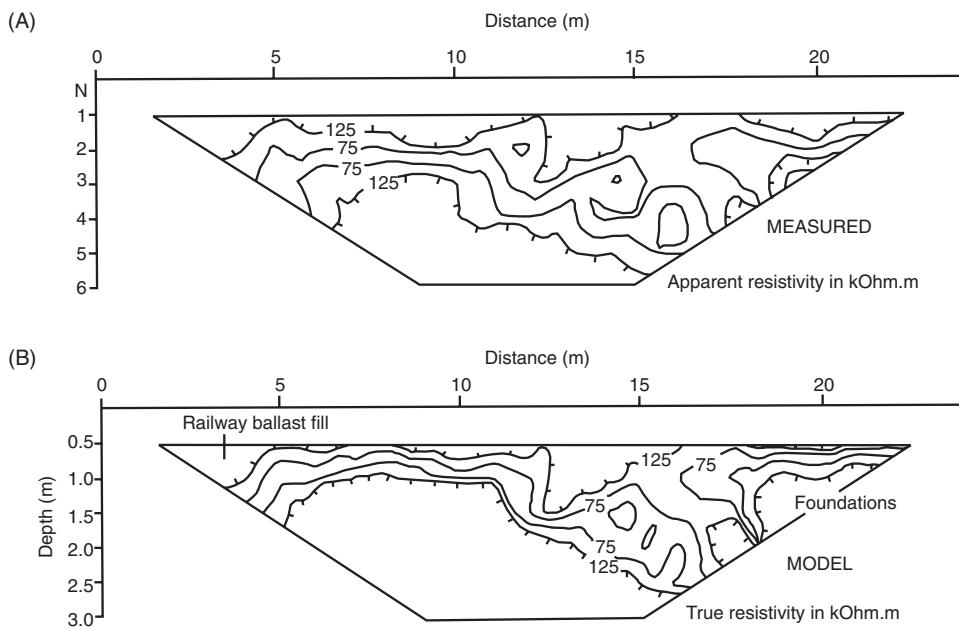


**Figure 7.44** Electrical resistivity subsurface imaging pseudo-sections: (A) apparent resistivity profile, and (B) true resistivity-depth profile, over buried concrete slabs at 1 m depth. From Reynolds and Taylor (1995), by permission.

demonstrated in this landslide example. In conjunction with intrusive methods, it is possible to provide a detailed 3D model of a landslide based on the interpolation of multiple ERT sections acquired downslope and across-slope. Such information can also be used to constrain geotechnical slope stability models. The limitations to this application tend to be logistical rather than geophysical, as often it can become difficult for field staff to access steep slopes without ropes. Nonetheless, resistivity profiles are routinely acquired down steep landslide slopes in the Himalayas, for example.

## 7.6.2 Groundwater and landfill surveys

### 7.6.2.1 Detection of saline groundwater

In the mid-1950s, a comprehensive electrical resistivity survey programme was initiated in order to map out saline groundwater in areas of the Netherlands below or at mean sea-level. Figure 7.46 shows schematically the nature of the hydrogeology in the western part of the Netherlands. The vertical electrical soundings provided a means of obtaining information about the vertical distribution of fresh, brackish and saline water bodies and their areal extent (Figure 7.47).

Pockets of saline water were found which were thought to be remnants from before the fifteenth century, after which time the present sea-dyke formed, cutting off the sea. To the west of Alkmaar, some 30 m of saline water was found above tens of metres of fresh water, separated by an impermeable clay layer. Major demands for construction sand for the building of new roads and urbanisation could have led to the extraction of sands with the demise of the clay barrier. This could have resulted in the mixing of the water bodies and the contamination of an otherwise potable water supply. Furthermore, correlation of resistivities from modelling of

VES data with borehole information about groundwater chemistry has led to a relationship between chloride content and resistivity. Consequently, it is possible to determine chloride content of the groundwater from the resistivity data.

### 7.6.2.2 Groundwater potential

In Kano state, northern Nigeria, an internationally funded aid programme was established in the 1980s to provide tubewells with hand-pumps for 1000 villages in rural areas. Village populations ranged from several hundred to no larger than 2000 people, but all were in very remote locations. Failure to obtain a reliable supply of water would have resulted in many of the villages being abandoned and the populations moving to the larger towns, thereby compounding the local problems of sanitation and health, education and employment, and the demise of rural culture and skills.

It was first recommended that geophysics was unnecessary to locate groundwater; boreholes drilled anywhere would succeed. In practice, borehole failures were in excess of 82% of holes drilled, particularly in the southern areas. Geophysical methods were then called upon to improve the success rate. Predominantly, vertical electrical soundings were used on sites selected following initial hydrogeological and photogeological inspection. Careful analysis of the VES data with the subsequent borehole information led to the compilation of a database of typical formation resistivities and their likely hydrogeological potential. It became apparent that certain geographical regions had better and more easily resolved groundwater resources, and six drilling rigs were kept working on these sites. This provided a window of several months in which the more problematic sites could be investigated further until they, too, were ready for drilling.

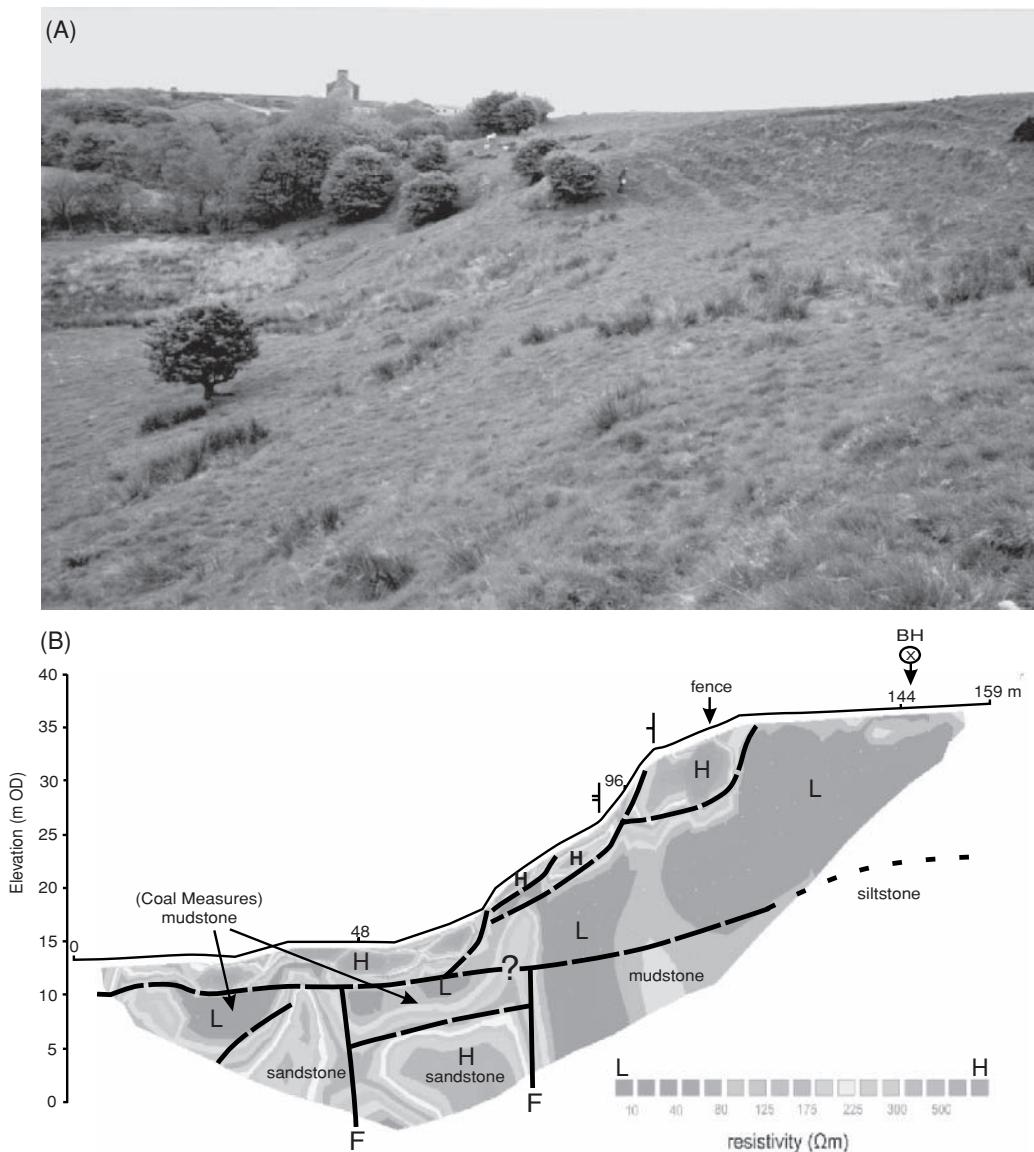


**Figure 7.45** A former landslide pictured in (A) across which (B) an electrical resistivity tomography pseudo-section was obtained, annotated with geological interpretation. [C]

Use of geophysics to help to identify the groundwater potential in particular areas, and to assist in the planning of drilling programmes, led to the borehole failure rate falling to 17% of holes drilled and a saving to the project of £5 million – at least 10 times the cost of the geophysical surveys (Reynolds, 1987a).

### 7.6.2.3 Landfills

There is an increasing amount of interest in the use of high-resolution resistivity surveys in the investigation of closed landfills, particularly with respect to potential leachate migration. Both resistivity sounding and subsurface imaging have been used very successfully.

There is no such thing as a typical landfill – some are extremely conductive, while others are resistive relative to the surrounding me-

dia, depending upon the material buried within. There are many variables geophysically (Reynolds and McCann, 1992), and care must be taken not to presume a particular geophysical response for any given site. For example, van Nostrand and Cook (1966) presented a very clear CST profile of apparent resistivity across a resistive landfill (Figure 7.48). Another example is provided in Figure 7.49. In this case, the boundary of the closed landfill was obtained using electromagnetic methods (see Chapter 10/11). Leachate was observed to be emerging from the lower parts of the capping layer on the downstream side of the landfill, and this was associated with dead vegetation (see Figure 11.48). An ERT profile across the landfill (along the hydraulic gradient) indicates that the leachate has filled the downstream part of the landfill and is emerging through a failed capping layer, which can be clearly identified on the ERT section.

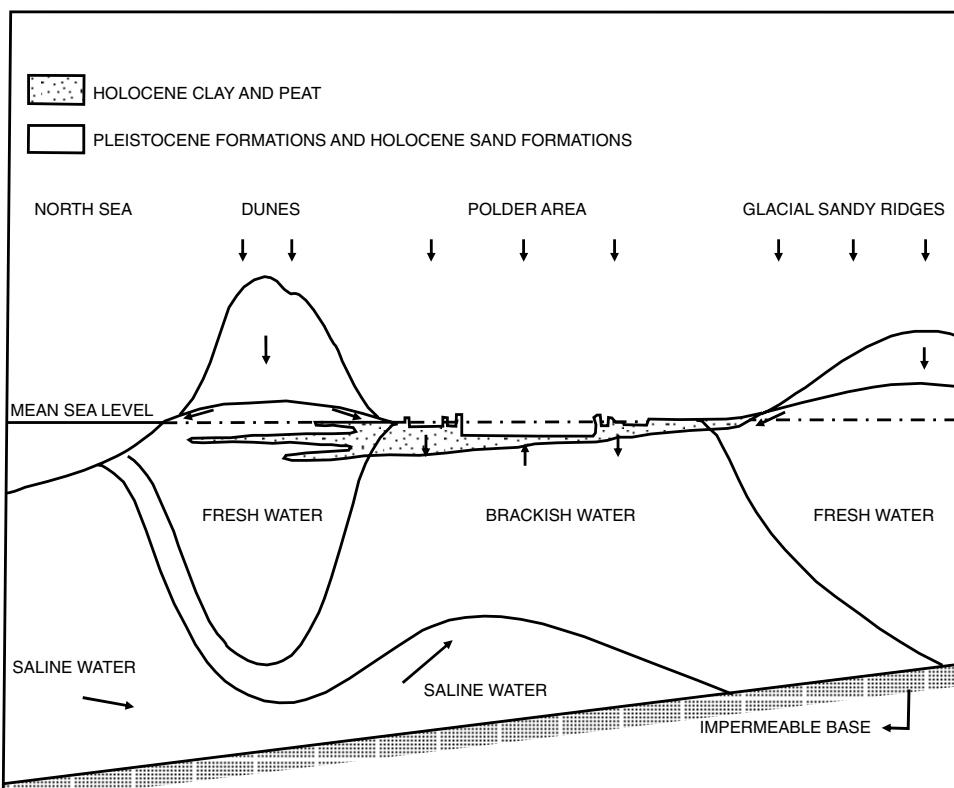


**Figure 7.46** Schematic hydrogeological cross-section for the western part of the Netherlands. From van Dam and Meulenkamp (1967), by permission.

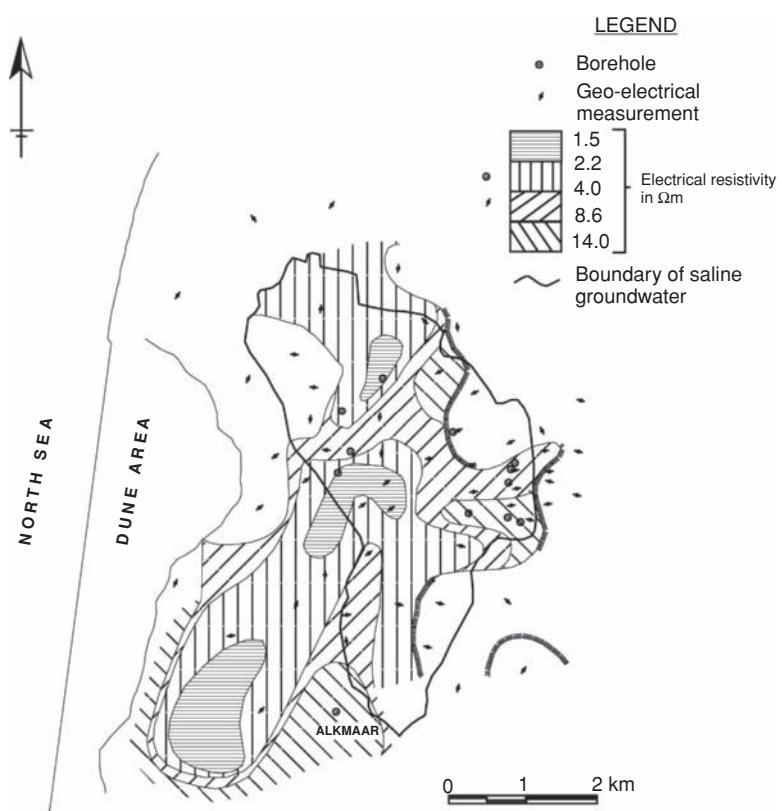


**Figure 7.47** Distribution of resistivities of a sand layer with a saline groundwater boundary in Noord Holland, as determined by many vertical electrical soundings. From van Dam and Meulenkamp (1967), by permission.

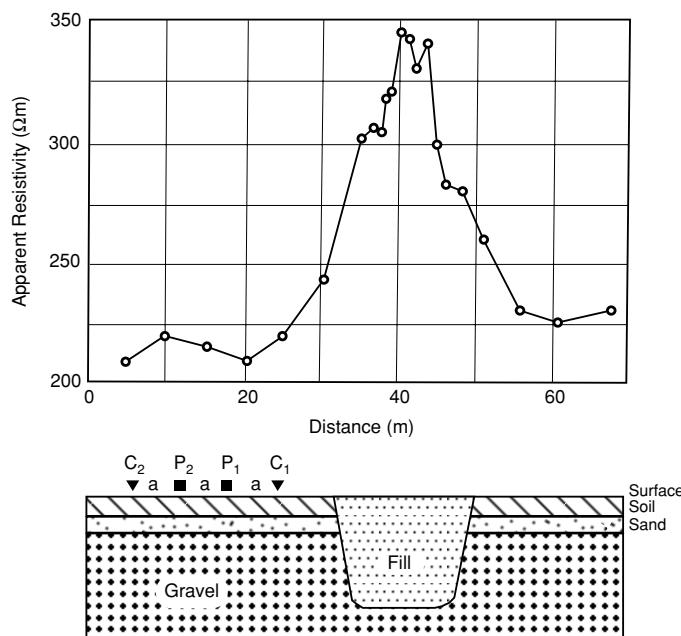


**Figure 7.48** Observed apparent resistivity profile across a resistive landfill using the Wenner array. From van Nostrand and Cook (1966), by permission.

Schlumberger soundings have been used by Monier-Williams *et al.* (1990) as part of a broader geophysical survey around the Novo Horizonte landfill in Brazil. Quantitative analysis of the soundings and displays as resistivity panels have revealed significant zones with anomalously low resistivities (Figure 7.50). These have been interpreted as being contaminant plumes arising from the landfill.

The displays shown in the figure are oriented parallel to the flank of the landfill, but at 10 m and 70 m distance away from it.

Subsurface imaging pseudo-sections across a landfill are shown in Figure 7.51. The three panels illustrate the observed apparent resistivity data, the inverted true resistivity-depth model and a schematic interpretation. In this case, the depth and geometry of the landfill were known at the outset. The zone of low resistivity associated with the saturated landfill extends more deeply than had been expected. This is interpreted as indicating the leakage of leachate through the base of the landfill (Barker, 1992).

A further example of an ERT pseudo-section inverted model is shown in Figure 7.52 (Reynolds, 1995). The data were acquired over a closed shallow landfill constructed as a 'dilute and disperse' site over river gravels. The electrical image shows the thin capping material, the waste material and the basal gravels quite clearly. The image is entirely consistent with depths known from boreholes on site.

### 7.6.3 Mineral exploration

Electrical resistivity tomography is used as part of mineral exploration, most often as an adjunct to induced polarisation surveys. Consequently, the commonest array type used is the dipole-dipole, with dipole lengths of 50 m or 100 m. However, the depths of penetration are often limited by using only 4–6  $n$  levels. Apparent resistivity pseudo-sections are inverted using the methods described in Section 7.5.5. Examples are provided in Chapter 9.

### 7.6.4 Glaciological applications

Electrical resistivity methods have been used since 1959 to determine glacier ice thickness. Measurements were first obtained on

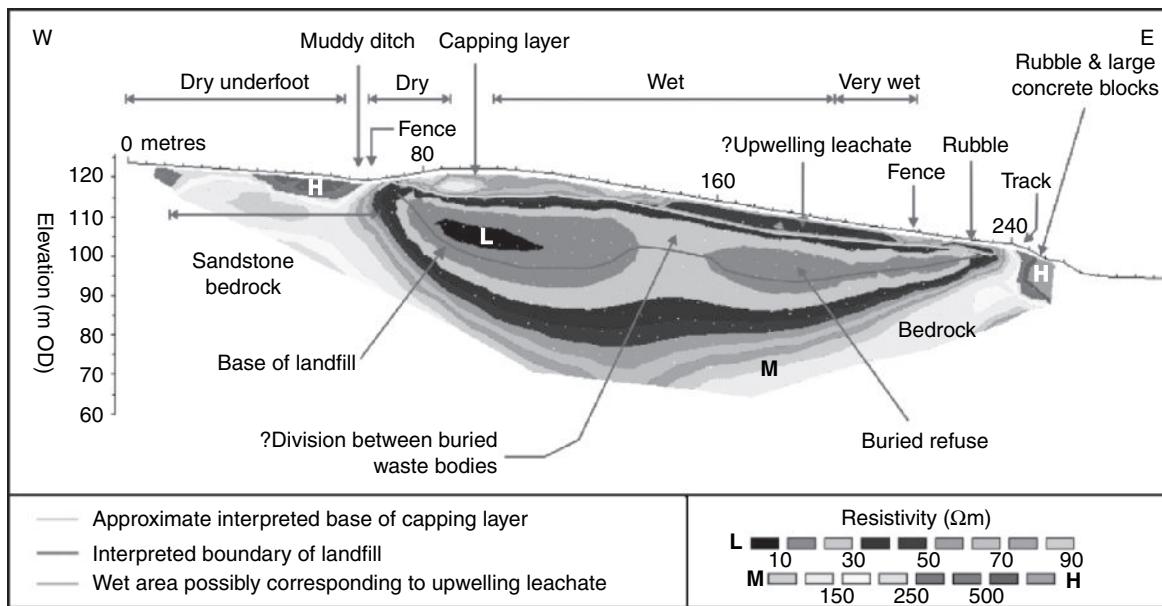


**Figure 7.49** Interpreted 2D resistivity section acquired across a closed landfill site. Low resistivity areas on the eastern flank of the site were associated with escaping leachate driven by groundwater gradients. [C]

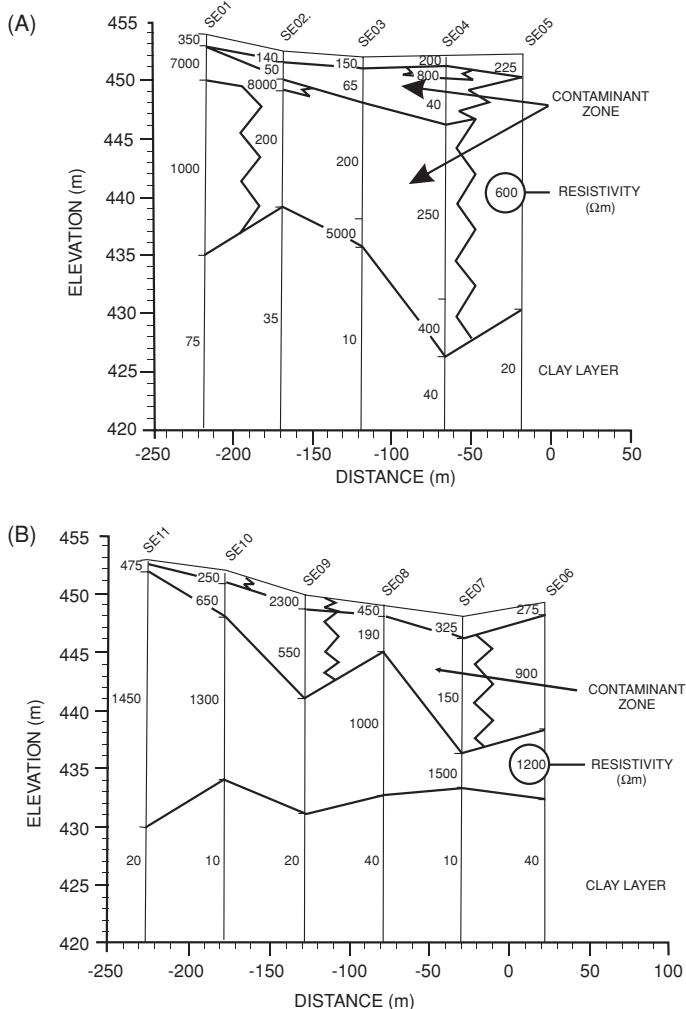


**Figure 7.50** Two parallel resistivity sections based on the interpretation of Schlumberger soundings at the Novo Horizonte landfill site, Brazil. The profile in (A) is closer to the landfill than that shown in (B). The background resistivities above the basal clay are high; the lower values in the centre of the sections are assumed to be due to contamination. Note that the conductive zone in (B) is apparently more shallow than in (A). From Monier-Williams *et al.* (1990), by permission.

European glaciers on temperate ice (i.e. ice at its pressure melting point). In 1962, resistivity measurements were made on polar ice (i.e. ice well below its pressure melting point) and were found to be anomalously low by up to three orders of magnitude compared with temperate ice values. Whereas the electrical resistivity behaviour of polar ice is now reasonably understood (Figure 7.53; Reynolds and Paren, 1984), the electrical behaviour of temperate ice is still poorly understood. In the 1970s a considerable amount of work was undertaken to develop field data acquisition in Antarctica. Interpretation methods were developed to yield information on vertical thermal profiles through the ice mass, and whether or not ice shelves afloat on seawater were melting or freezing at their base. All of these data contribute to an understanding of ice dynamics (rate of ice movement, etc.) and the structure of the ice masses under study.

A series of vertical electrical soundings has been made on George VI Ice Shelf along a flow line of the Goodenough Glacier, which flows westwards from the Palmer Land Plateau in the Antarctic Peninsula (Figure 7.54). The field curves were modelled to take into account thermal effects and the resulting interpretations are shown in Figure 7.55. The estimated ice thicknesses and rates of bottom melting were in good agreement with those determined independently (Reynolds, 1982).

Other uses of resistivity measurements have been made by Haeberli and Fisch (1984) who drilled holes with a hot-water jet drill through Grubengletscher, a local glacier in Switzerland. By using a grounded electrode beyond the snout of the glacier and the drill tip as a mobile electrode, they were able to detect the point at which the drill tip broke through the highly resistive ice into the more conductive substrate (Figure 7.56A). Consequently, they were able to determine the ice thickness much more accurately than by using either the drilling or surface radio echo-sounding. With debris-charged ice at the glacier base, it is difficult to tell when the glacier sole has been reached judging by thermal drilling rates alone. The radio echo-sounding depth measurements were found on average to be accurate to within 5%, but generally underestimated the depth. Electrodes were planted at the ice-bed interface at the ends of each of 14 boreholes, and standard resistivity depth soundings were undertaken as if the glacier were not there (Figure 7.56B).

Haeberli and Fisch (1984) discovered that the Grubengletscher was underlain by over 100 m of unconsolidated sediments. It had been thought previously that the glacier was in direct contact with bedrock. This work has demonstrated that by using subglacial electrodes, significant new information can be obtained about the nature of the materials underlying the glacier. This can have considerable benefits when trying to understand the subglacial hydrogeological regime, for example. This is of particular importance at Grubengletscher because of two proglacial lake outbursts in 1968 and 1970 which caused considerable damage to the nearby village of Saas Balen.

Electrical methods have been used to investigate high-altitude glacial environments since the 1970s, initially using vertical electrical soundings (e.g. Röthlisberger, 1967; Lliboutry, 1977). Electrical resistivity tomography was first used in the Himalayas in 1996 as part of the assessment of glacial hazards associated with a hydropower project in Nepal (Hanisch *et al.*, 1998; Pant and Reynolds, 2000). It has been used much more often subsequently and with extremely good results, not only in the Himalayas but also in other high mountain glacial environments. One of the advantages of this method for such applications is being able to locate buried ice masses by their very high resistivity values relative to those for glacial sediments. Such ice masses can lead to subsidence and mechanical failure of natural dams. Furthermore, it is also possible to use ERT to detect low resistivity features that might indicate piping through a moraine dam, which can ultimately lead to its failure and catastrophic flooding downstream.

Large glacial lakes exist in the Himalayas as the glaciers melt and retreat. Catastrophic failure of the natural dams can result in so-called glacial lake outburst floods (GLOFs) which can travel at speeds up to 80 kph and run-out over large distances, sometimes greater than 200 km. These floods can cause widespread

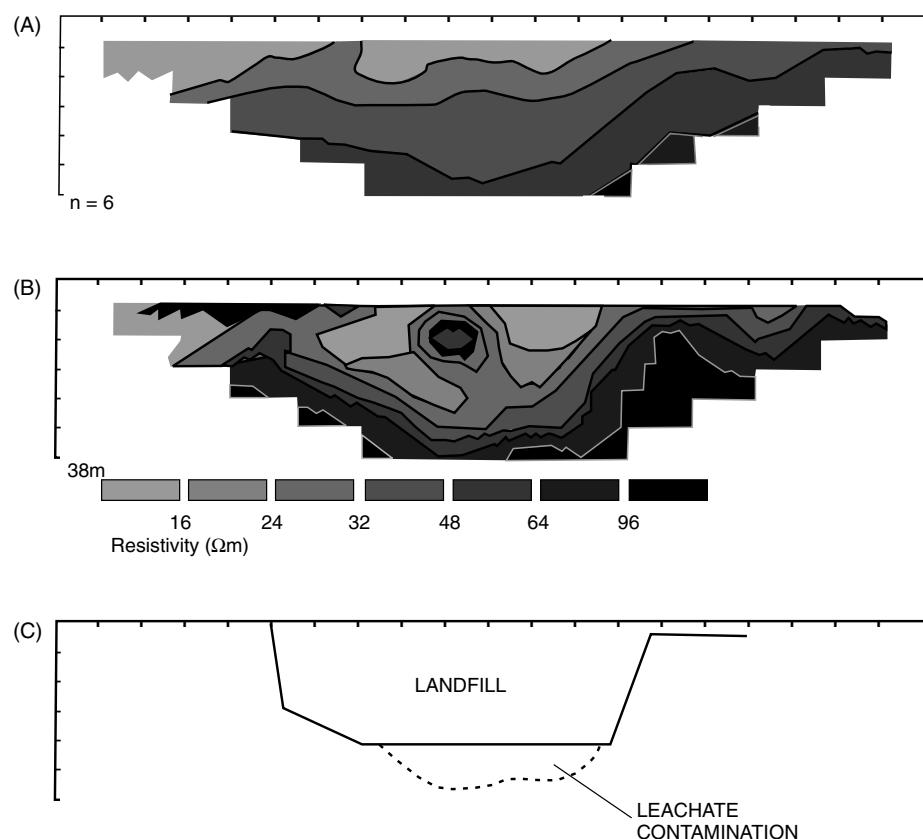


**Figure 7.51** (A) Wenner apparent resistivity pseudo-section measured across a landfill. Electrode spacing = 10 m. (B) Resistivity depth section obtained after eight iterations. (C) Approximate section across the landfill based on existing information. From Barker (1992), by permission.

damage measured in millions of dollars, as well as kill people and livestock.

The ERT method has been used successfully on a number of large debris-covered stagnant ice tongues associated with glacial lakes in Nepal (e.g. Thulagi: Pant and Reynolds, 2000; Tsho Rolpa: Rana

et al., 2000; and Imja Tsho: Figure 7.57A; Reynolds, 2006; Takenaka et al., 2010). In each case the ERT method was used to identify areas containing buried stagnant glacier ice as well as to confirm where ice was not present, in conjunction with ground-penetrating radar.

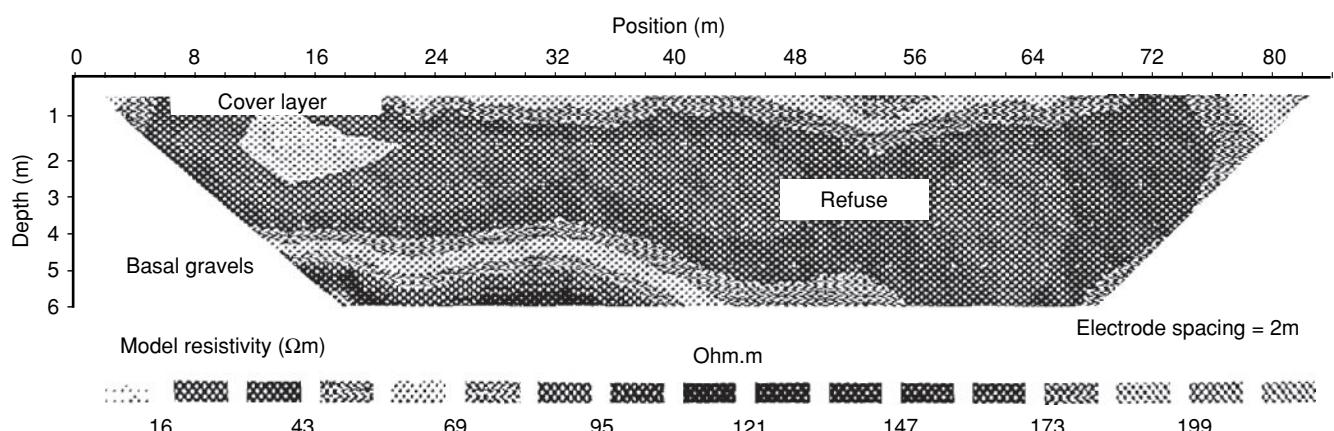


**Figure 7.52** Electrical resistivity pseudo-section acquired over a closed landfill in north Wales. From Reynolds (1995), by permission.

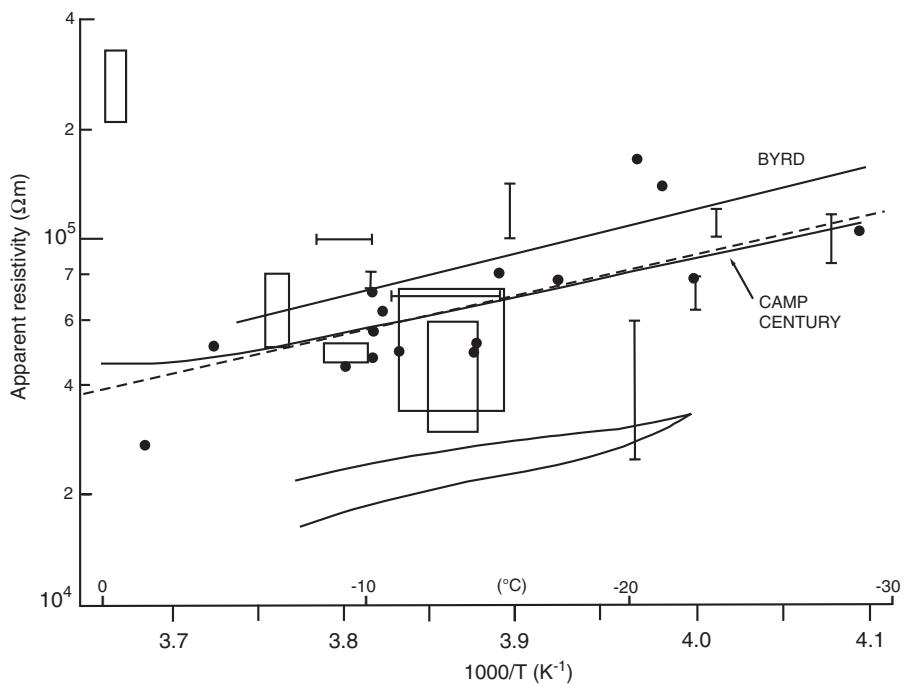


**Figure 7.53** Resistivity of ice as a function of temperature. Mean values from georesistivity sounding of ice at 100 m or deeper are plotted with estimated uncertainties against the estimated layer temperature from a wide variety of sources. Laboratory measurements on ice cores examined over a range of temperatures are shown by continuous lines. A regression line for the data is given by a dashed line. Given a particular temperature, the ice resistivity can be predicted within a factor of 2 or better. After Reynolds and Paren (1984), by permission.

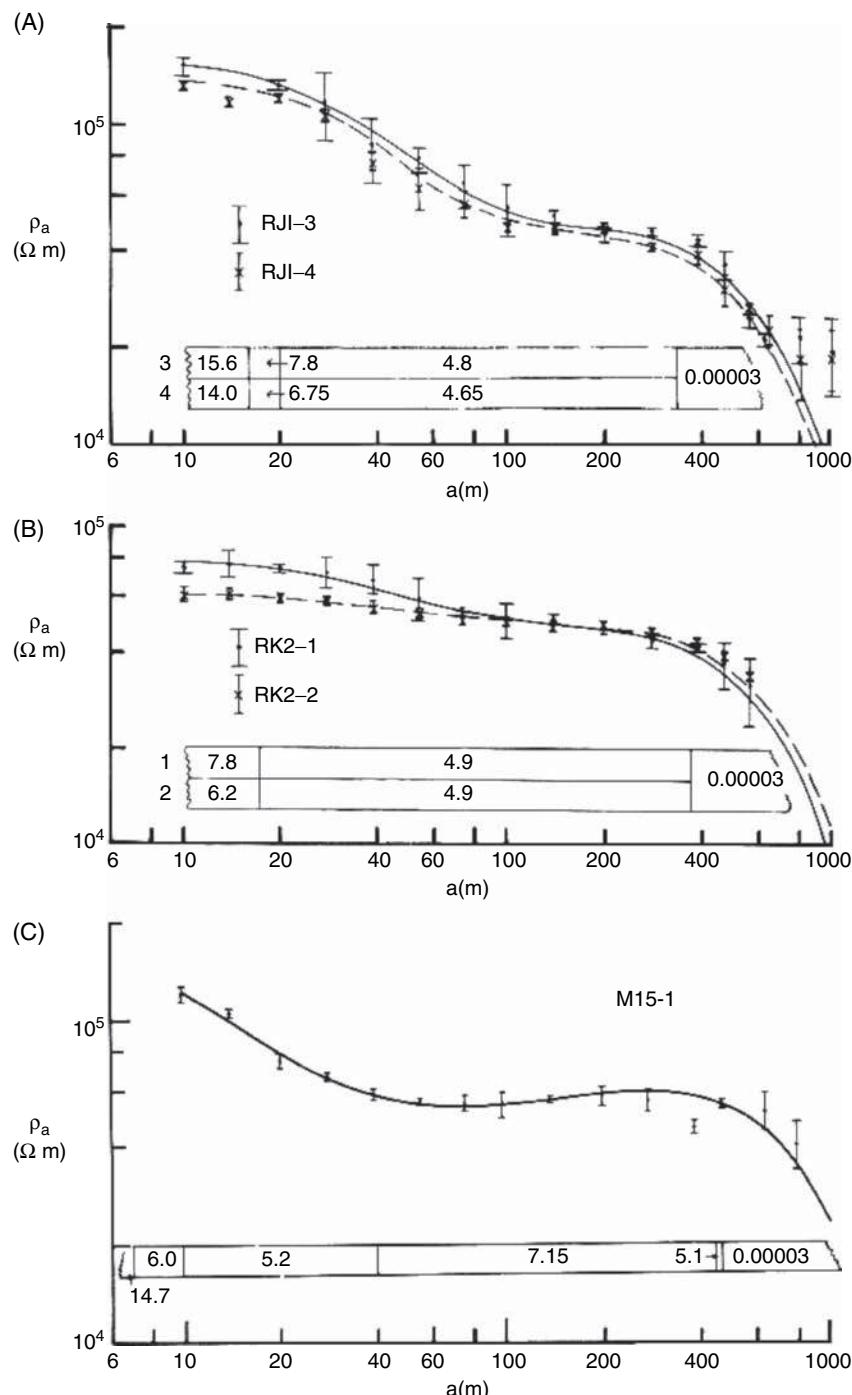
A series of coincident ERT and ground-penetrating radar sections were acquired at Imja Tsho, Solukhumbu, Nepal (Figure 7.57A), during a more comprehensive investigation for glacial hazard assessment. On the figure the lines of two profiles are indicated. One ERT profile, indicated by the short dashed lines, traversed stagnant glacier ice buried beneath a thin veneer of supraglacial moraine (Figure 7.57B; Reynolds, 2006; Hambrey *et al.*, 2008). The ice-free lateral moraine is clear at the right of the figure. That the buried ice is evident as two high-resistivity zones is consistent with it belonging to two discrete flow units from the original glacier upstream. By way of contrast, an ERT profile across moraine where no buried ice is present (the profile indicated by long dashes) is shown in Figure 7.58A with the corresponding ground-penetrating radar section (Figure 7.58B) (Hambrey *et al.*, 2008). The small high-resistivity blobs at and near the surface are associated with large boulders. The resistivity values for the general morainic material lie in the range 1000–10,000  $\Omega$ m. The interpretation derived from the ERT section is shown superimposed on the GPR section. The radar facies are broadly consistent with the resistivity interpretation shown in Figure 7.58B. Depth of penetration is around 40 m. These results have been replicated independently by a more recent ERT survey at the same location (Takanawa *et al.*, 2010).

current electrode within a conducting body and the other current electrode at a semi-infinite distance away on the surface (Figure 7.59). The voltage between a pair of potential electrodes is measured with appropriate corrections for any self-potentials. The method dates back to the 1960s (Ogilvy *et al.*, 1969) and has historically been used in mineral exploration and in groundwater investigations in countries of the former Soviet Union, eastern and central Europe and in China. It has been used in hydropower investigations in Nepal to examine groundwater flow in the proposed location of a new dam (Pant, personal communication). Other more diverse applications have been developed recently for this method. These include measuring the length of metal reinforcement in bored *in situ* concrete piles (Dong *et al.*, 2008), and mapping the extent and activity of tree root zones (Kepic *et al.*, 2008), as will be described below. The key issue in relation to the use of MALM is how to place an electrode into the conductor under scrutiny, and how then to measure and analyse the resulting equipotential distribution other than purely qualitatively, although for many applications, this may be adequate.

For an isolated conductor in a homogeneous medium, the lines of equipotential should be concentric around the conductor (Figure 7.60A). In reality, lines of equipotential are distorted around an irregularly shaped conductive ore body (Figure 7.60B) and can be used to delimit the spatial extent of such a feature more effectively than using the standard CST method. The mise-à-la-masse method is particularly useful in checking whether a particular conductive mineral-show forms an isolated mass or is part of a larger electrically connected ore body. In areas where there is rough topography,

## 7.7 Mise-à-la-masse (MALM) method

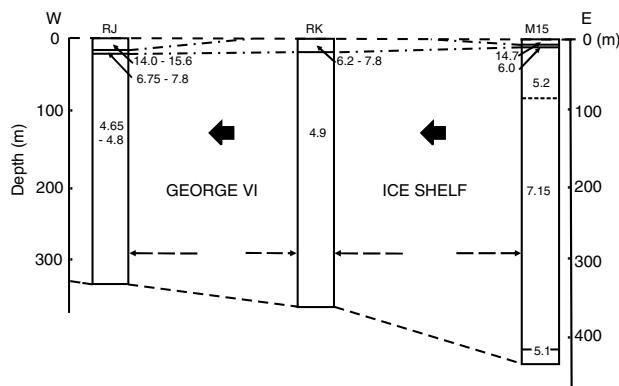
The mise-à-la-masse (MALM) or ‘charged-body potential’ method is a development of the CST technique, but involves placing one



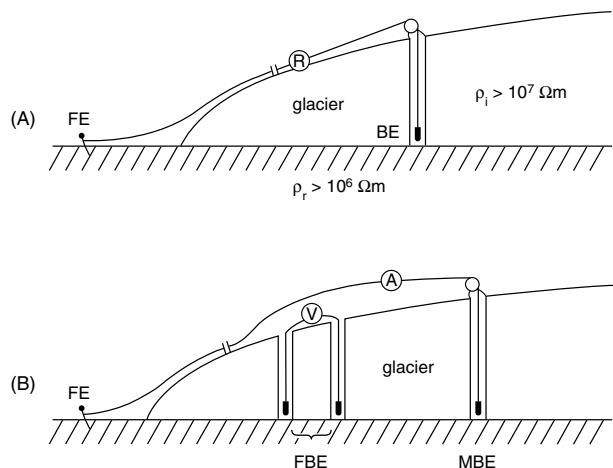
**Figure 7.54** Apparent resistivity sounding curves obtained using a Schlumberger array at three sites along a glacial flow line on the George VI Ice Shelf, Antarctica. In (A) and (B) two orthogonal soundings are shown at each site. Below each curve is the interpreted model in terms of true resistivities against depth within the ice sheet. The extremely low values of resistivity below the ice shelf indicate that it is afloat on seawater. Model resistivities are given in units of  $10 \text{ k}\Omega\text{m}$ . From Reynolds and Paren (1984), by permission.

terrain corrections may need to be applied (Oppliger, 1984). There are no general rules that can be applied to mise-à-la-masse data. Each survey is taken on its own merits and a plausible model constructed for each situation, although Eloranta (1984), for example, has attempted to produce a theoretical model to account for the

observed potential distributions. More recently, different workers have established their own empirical methods of interpretation, depending upon how they have collected their data, but 3D modelling has now been undertaken (Carey *et al.*, 2003) using a finite-element method (Zhou and Greenhalgh, 2001).



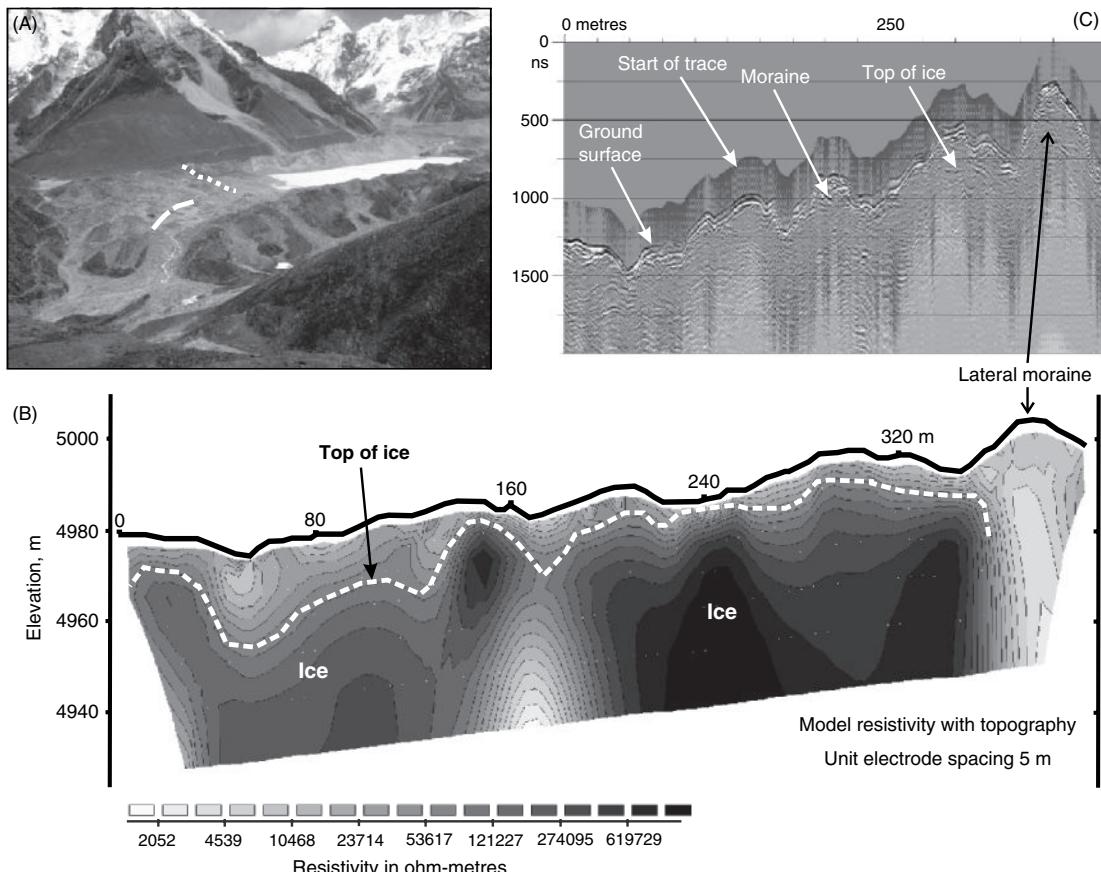
**Figure 7.55** Resistivity structure through the George VI Ice Shelf along a flow line. Resistivities are in units of  $10 \text{ k}\Omega\text{m}$ , and are plotted against depth within the ice sheet. From Reynolds and Paren (1984), by permission.



**Figure 7.56** Electrode arrays used for the determination of the exact position of the glacier bed (A) and for resistivity soundings of glacier beds (B). FE = fixed electrode outside the glacier margins; BE = borehole electrode for determination of glacier-bed position; FBE = 'fixed' borehole electrodes for resistivity soundings of glacier beds (corresponding to potential electrodes MN in traditional surface soundings); MBE = moving borehole electrode for resistivity soundings of glacier beds. R = resistivity meter; V = voltmeter; A = ammeter. From Haeberli and Fisch (1984), by permission.

### 7.7.1 Mineral exploration

There are two approaches in interpretation for mineral exploration. One uses the potential only and takes the maximum values as being indicative of the conductive body. The other converts the potential



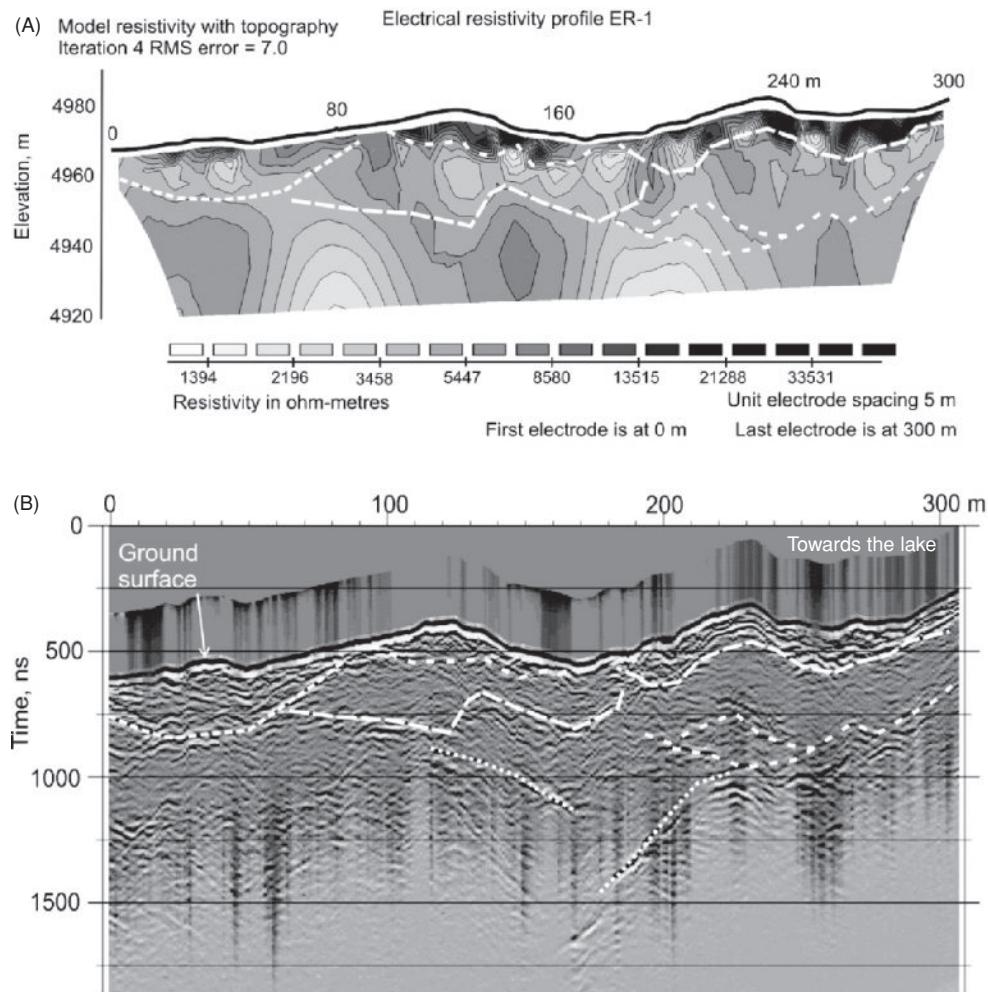


**Figure 7.58** Coincident (A) electrical resistivity and (B) ground-penetrating radar profiles at Imja Tsho, Nepal, along the line indicated by long dashes in Figure 7.57. The geophysical profiles indicate the absence of buried ice very clearly. Interpreted boundaries are indicated by white dashed lines, and highlight the consistency of the results from the two different methods. From Hambrey et al. (2008), by permission. [C]

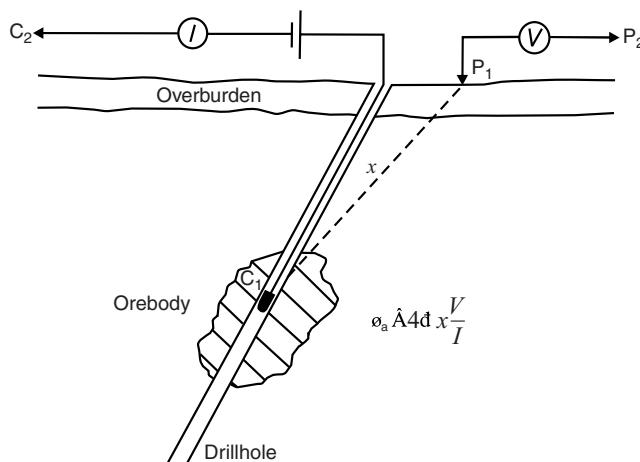


**Figure 7.59** Positions of electrodes used in a mise-à-la-masse survey. One form of geometric factor is given where  $x$  is the distance between the  $C_1$  electrode down the hole and the  $P_1$  mobile electrode on the ground surface.

data to apparent resistivities and thus a high surface voltage manifests itself in a high apparent resistivity ( $\rho_a = 4\pi x V / I$ , where  $x$  is the distance between  $C_1$  and  $P_1$ ).

Parasnis (1967) described an early mise-à-la-masse survey for prospecting for ore in Sweden. One current electrode was placed 65 m below ground, 89 m down an inclined borehole, and the surface potentials were mapped; they were found to be concentric around the main borehole. As there were so many boreholes available in this survey, it was possible to determine the vertical distribution of potentials as well as the surface equipotential distribution, and this too showed a concentric equipotential pattern. Combining all the available data, it was possible to obtain a three-dimensional image of the potential distribution associated with the target ore body and thus delimit its size, strike and structure. The analysis in this case was simply a matter of contouring the measured equipotential values to form a graphical display, with the greatest values being associated with the highest grade of mineralisation, and the long axis of the equipotential anomaly indicating its dip and direction.

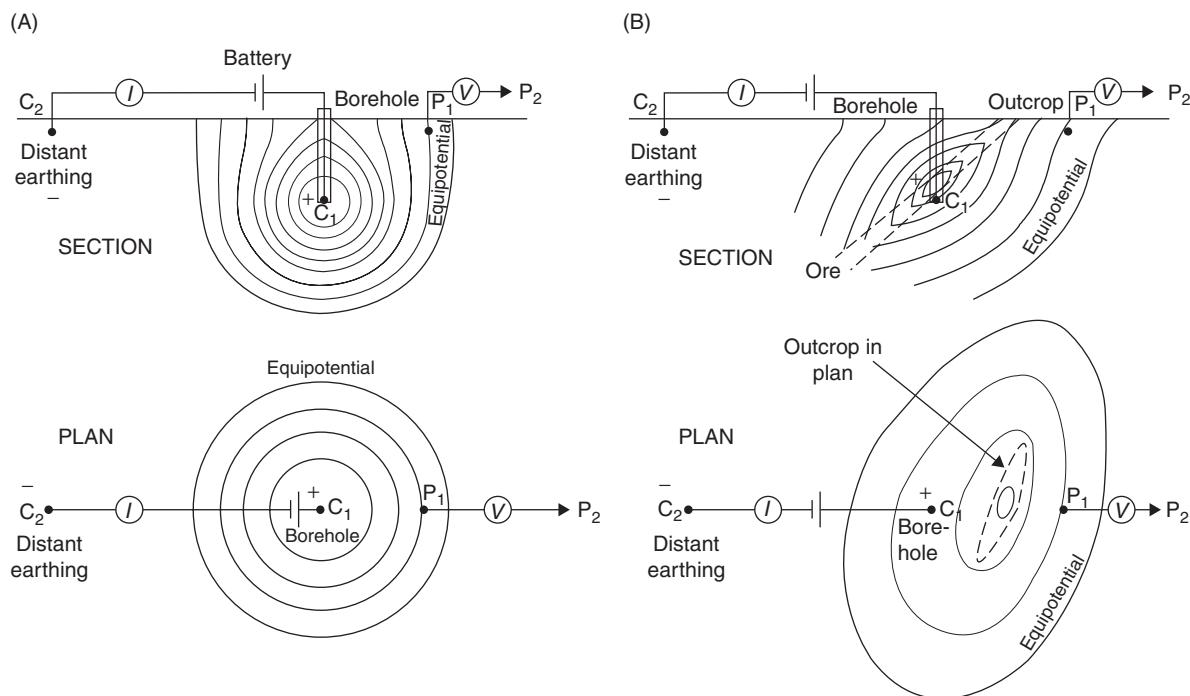


**Figure 7.60** (A) Concentric and symmetrical distribution of equipotential lines around a current electrode emplaced within a homogeneous medium. (B) Distortion of equipotentials due to the presence of an ore body. After Parasnis (1966), by permission.

A second example, shown in Figure 7.61, demonstrates the effects of terrain on the surface potentials. The positive electrode was placed at 220 m depth down a 1 km deep borehole (Figure 7.61A) and the surface potentials mapped (Figures 7.61B and C). Oppliger (1984) found that when terrain slopes exceed  $10^\circ$ , surface electric potentials can be adversely affected. The terrain-corrected surface potentials are shown in Figure 7.61C. The main differences are that the low of  $85 \Omega\text{m}$  and the high of  $168 \Omega\text{m}$  both change in value (to 100 and 150

$\Omega\text{m}$  respectively) and, in particular, the orientation of the elongate apparent resistivity high is rotated through  $30^\circ$ . The ridge form of this resistive anomaly suggests that a conductive body is bounded to the north and south (as indicated by the marked lows) and extends a limited way in an east–west direction. This interpretation has been confirmed by other investigations.

*Carey et al.* (2003) have provided an example of the MALM technique. Their experiment was undertaken at Scuddles Mine, Western

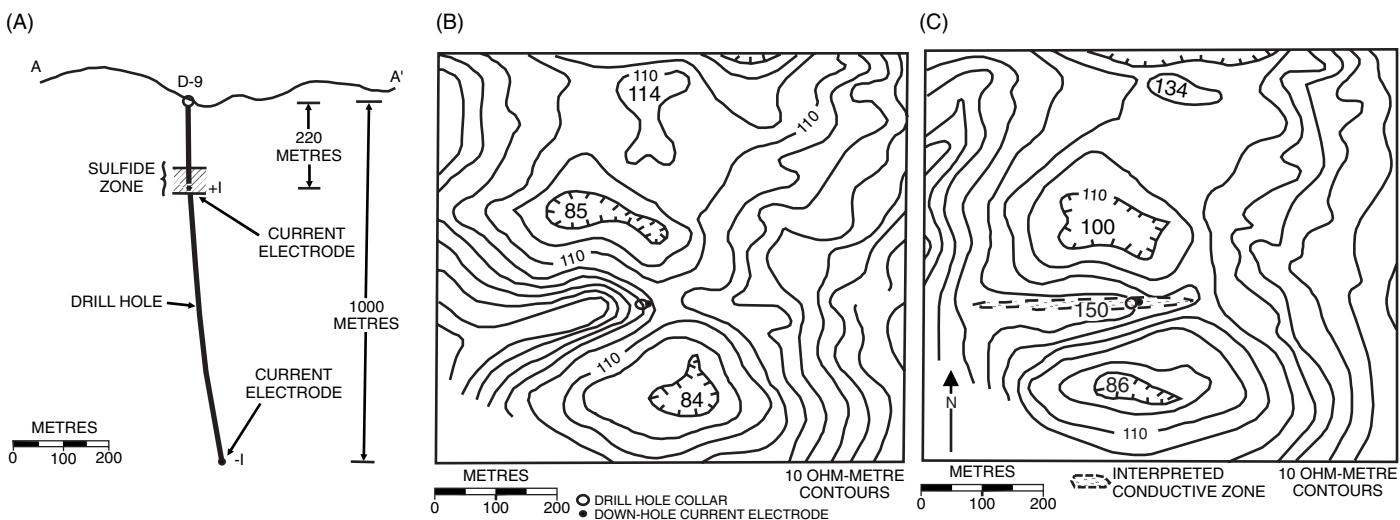


**Figure 7.61** (A) Current electrode configurations. (B) Actual mise-à-la-masse apparent resistivities measured on the surface around inclined borehole D-9. Contours are every 10  $\Omega\text{m}$ . (C) Terrain-corrected apparent resistivities for the same survey with an interpreted conductive zone indicated. From Oppliger (1984), by permission.

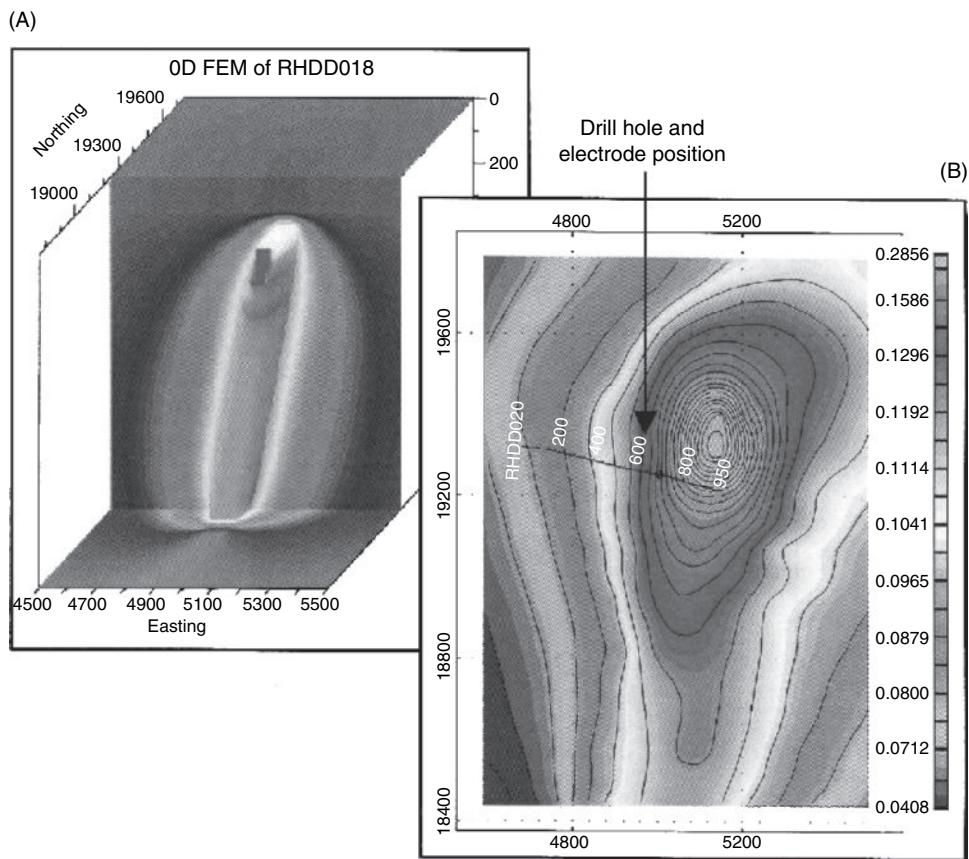


**Figure 7.62** (A) Three-dimensional model cross-section, and (B) surface potentials and electrode position within the ore body. The line of the drill hole is indicated with depths below ground level. The peak surface MALM anomaly is centred over the upper portion of the ore body. After Carey *et al.* (2003). [C]

Australia, which is a base metals operation involving a volcanic massive sulphide (VMS) with the primary target being a massive pyrite lode. A MALM survey was undertaken with the injection electrode located in contact with the massive pyrite body at 700 m depth (Figure 7.62). A 3D forward model was constructed (Figure 7.62A) with a uniform half-space with a resistivity of 1000  $\Omega\text{m}$  and a conductive body of 0.1  $\Omega\text{m}$ , striking north–south with an 80° dip towards the west. The upper surface of the body plunges to the north and is buried beneath 100 m thick overburden with a resistivity of 10  $\Omega\text{m}$ . The model cut-away (Figure 7.62A) shows an electrical potential halo surrounding the model ore body; this is equally distributed as the model ore body is homogeneous and isotropic. The mineralisation was energised by the injection electrode, and the peak surface anomaly (Figure 7.62B) was found to overlie the upper surface of the ore body.

Carey *et al.* (2003) also demonstrated the benefit of removing the effects of the injection electrode using the image-current technique (Telford *et al.*, 1990). This calculates the potential field from a buried electrode in a homogeneous half-space and subtracts it from the total electric potential as measured at the surface. The resultant residual potentials are then more indicative of the subsurface resistivity boundaries.

The technique was applied to two different sets of data acquired from different depths (450 m and 850 m) within the same drill hole. The response from the shallower MALM test (Figure 7.63A) was found to be significantly different to that from the deeper survey. The shallower anomaly was broad with the peak values to the southeast of the current electrode, whereas the deeper survey produced greatest values far to the south of the current electrode and with a different shape of the peak when compared with that of the shallower survey. The current electrode's position was modelled for each of the datasets and the modelled surface potentials subtracted from the acquired MALM data. Residual potentials from the shallow survey had their peak values on the southern border of the survey area, similar to the field data collected using the deeper injection electrode, whereas there was minimal change after removing the electrode effect for the deeper electrode (Figure 7.63B).

## 7.7.2 Civil engineering pile testing

The *in situ* determination of the length of steel reinforcement inside bored-in concrete piles can be important in the construction industry. One technique is to drill a borehole adjacent to the piles being investigated and to lower a magnetometer down the hole (where

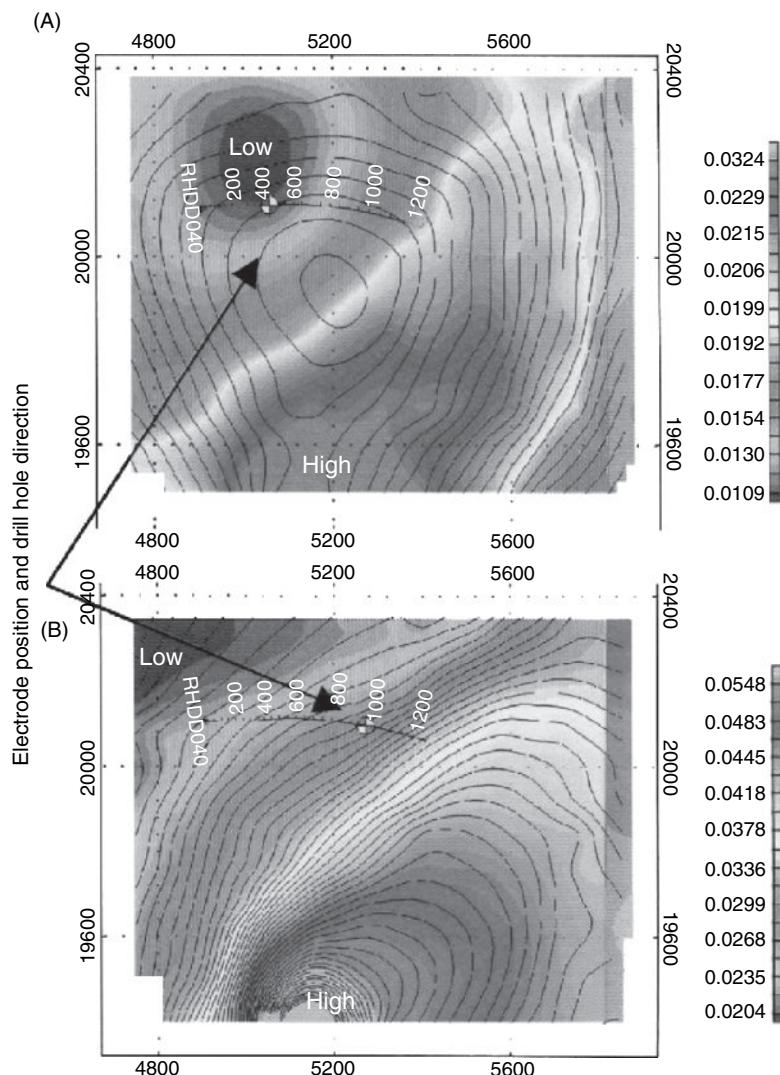


**Figure 7.63** Contour maps of (A) the original MALM data, and (B) after the removal of the electrode effect. The injecting electrode was moved from borehole 1a in (A) to borehole 1b in (B). After Carey *et al.* (2003). [C]

cased in plastic, not steel) and measure the magnetic field intensity. However, in magnetically noisy construction sites it can be difficult to achieve unambiguous results. Dong *et al.* (2008) have demonstrated that the mise-à-la-masse method can be effective, fast and convenient used in such testing. It has also been suggested that this technique can also be used in the survey of old steel piles, bridge footings and dam foundations.

The reinforcement of bored-in concrete piles typically comprises eight to a dozen main steel bars welded together by thin steel wire hoops forming a cage inside the pile (Figures 7.64A). The resistivity of the reinforcement is less than  $10^{-6}$   $\Omega\text{m}$ , whereas that of the concrete is greater than  $10^6$   $\Omega\text{m}$ , and surrounding soil and rock variably in the range  $10^{-1}$   $\Omega\text{m}$  to  $10^3$   $\Omega\text{m}$ , similar to that of the local groundwater. The potential field associated with the steel cage can be compared to that of an ellipsoid whose long axis lies along that of the pile. A vertical borehole is constructed at least 3 m

to 5 m deeper than the expected depth of the pile. The anode (electrode A, Figure 7.64A) of a battery power source ( $>90$  V) is attached to one of the main steel bars exposed at the pile cap. The cathode (electrode B, Figure 7.64A) is buried in soil at a distance not less than five times the expected length of the reinforcement cage. A potential electrode (N) is buried close to the pile top at the ground surface. The remaining roving potential electrode (M) is connected to the anode of a voltmeter and is lowered at increments (0.2–0.5 m) down the borehole, and at each point the potential is measured. If a vertical section is taken through A–A' (Figure 7.64A), the maximum value of the measured potential ( $V$ ) should remain constant within the depth range of the reinforced cage and the vertical gradient of the potential ( $dV/dz$ ) should be close to zero. At the base of the reinforcement cage beyond which the steel bars end, the potential  $V$  should drop very quickly and the associated gradient peak at the depth equivalent to the base of the cage (Figure 7.64B).

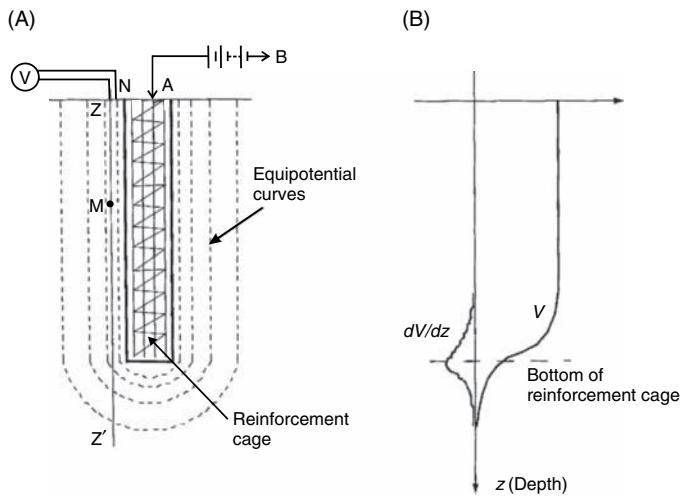


**Figure 7.64** Illustrations showing (A) the shape of hypothetical equipotential curves outside a reinforcement cage, and (B) the electrical potential curve and its gradient ( $dV/dz$ ) at the Z-Z' longitudinal cross-section. V is the electrical potential and z is the depth. Modified from Dong et al. (2008), by permission.

Dong et al. (2008) demonstrated that field results matched the expected theoretical profiles (Figure 7.65). The three sets of results show vertical profiles of the electrical potential and its vertical gradient from a borehole located at the centre of the pile (Figure 7.65A), and both the electrical potential (Figure 7.65B) and its vertical gradient (Figure 7.65C) for a series of boreholes at different distances (0.3 m to 1.7 m) from the pile. The structure of the 1-m diameter pile tested consisted of 8 mm diameter steel hoops placed at vertical increments of 200 mm down the pile to a depth of 16 m; the total concrete pile depth was 18.6 m. It is clear that the peak of the measured vertical gradient is greatest closest to the pile itself and decays with distance away. For boreholes at a distance of 1.07 m (> one pile diameter) or greater the vertical gradient profile results are virtually too small to distinguish the required peak to yield the required depth of the pile cage base. However, the results from closer boreholes provide anomalies above the background noise and the three recorded peaks all occur at the same depth (16 m). For standard determination of the depth to the base of reinforced pile cages, it would be expected that only one borehole would be constructed. It is therefore expected that this should be no further from the pile than one pile diameter.

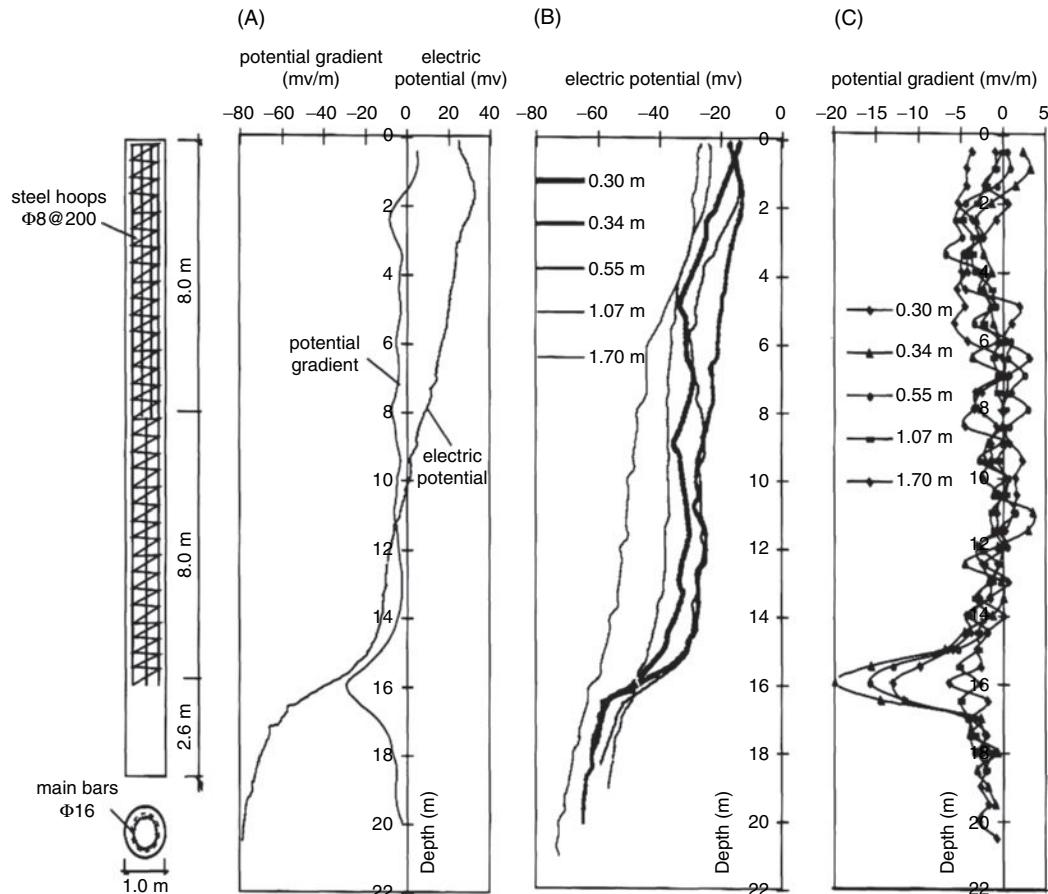


**Figure 7.65** Test results of the MALM method in a concrete pile. (A) Electrical potential curve and its gradient at a borehole located at the centre of the pile. (B) Electrical potential curves and (C) their gradients in boreholes at different distances away from the pile. After Dong et al. (2008), by permission.

### 7.7.3 Study of tree roots

The study of tree root zones (rhzosphere) requires that trees and their immediate environments are instrumented with some non-invasive sensors and let grow to some size, and then the entire tree with its root zone is dug up using a large mechanical excavator. This inevitably kills the trees being studied and disturbs the ground around the former root zone, rendering time-lapse studies impossible. Root zone environments can be investigated using ground-penetrating radar (to locate shallow roots) and electrical resistivity to monitor changes in soil moisture with time. However, it can be difficult to investigate both shallow root systems (that can be mapped to some extent geophysically) and the much deeper penetrating tap roots that hitherto could not.

Kepic *et al.* (2008) have described three experiments where they used the MALM method. In one, they effectively made the tree trunk itself the anode of a MALM system by boring a 10-mm diameter hole into the trunk and inserting a steel current electrode (which was removed after the tests). The second current electrode was placed several hundred metres from the survey grid, and a current between 80 and 90 mA applied (voltage of the order of 200 V). A 2-m by 2-m grid was used to measure electrical potential which was found to vary within the range  $\pm 0.5$  V. The results indicated that the injected current was passing through the deep tap root directly into the groundwater, and the shallow lateral roots that were located in dry soil were largely inactive. In the second experiment, it was clear from a map of the potential measured (Figure 7.66A) that the tree was transmitting the current from its trunk into the surrounding earth through its lateral root system, as indicated by the decreasing potential with distance away from the tree, which was located in the middle of the grid. A vertical derivative was calculated for the potential data (Figure 7.66B) with the expectation that current passing through the lateral roots would produce ridges leading out from the trunk. This was observed in the vertical gradient data, especially a group of three roots immediately to the east of the main trunk. These were confirmed subsequently by GPR profiling.

In their third experiment, Kepic and coworkers tested a single small gum tree, less than 2 m tall, located near the edge of an unused tailings dam that was undergoing rehabilitation. The depth of tailings in the area was about 4–5 m over bedrock. Two surveys were undertaken: one with the current electrode implanted onto the tree trunk and the other with the current electrode planted into the ground at the base of the tree (Figure 7.67A). Apparent resistivity values for a pole-dipole profile were calculated to normalise the data in each case (Figure 7.67B). The tree trunk was located about 1.5 m away from and 11 m along the profile. The difference between the two profiles in this case is due to the current being transmitted through the root sap relative to that being passed through the ground. The anomaly due to the difference in potential between the current passing through the root and through the ground demonstrates that the root system lies between 9 m and 13 m along the profile, equivalent to a root system radiating out to 3 m to 3.5 m, as was confirmed subsequently by trenching and counting root fibre density by soil scientists.

A serious concern to those who maintain railway networks is the effect that, in areas of expansive clays, soil heave and settlement

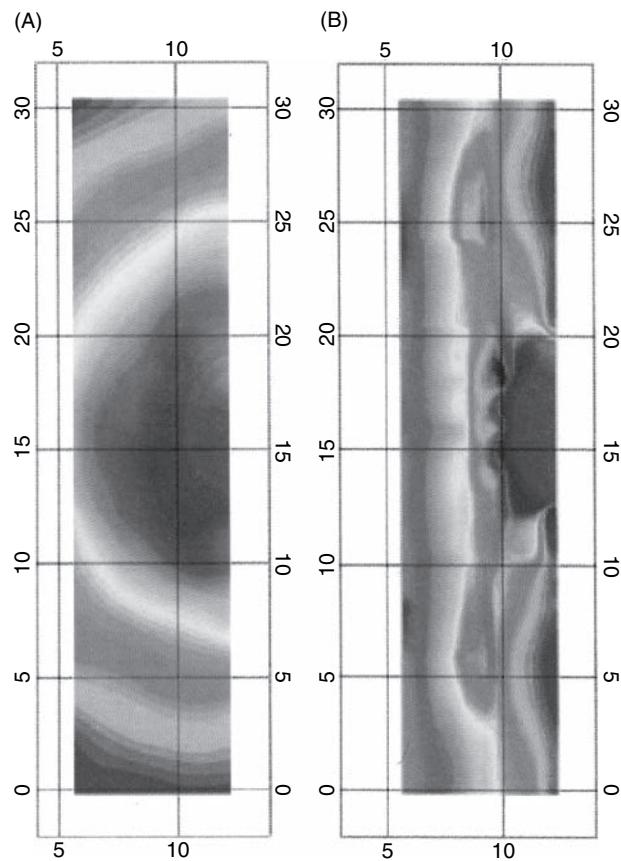


**Figure 7.66** MALM results (A) and the corresponding first vertical derivative (B) for a survey around a tree located in the middle of the grid. Note the presence of the effects of three large lateral roots (circled). From Kepic *et al.* (2008), by permission. [C]

can have on the running tracks. Seasonal variations in soil moisture content can result in vertical displacements with amplitudes of the order of 0.5 m, resulting in serious disruption to railway operations. Furthermore, changes in soil porewater pressures, especially from negative (suction) to positive (hydrostatic conditions), can lead to slope failures in cuttings and embankments. Chopping trees down (to avoid problems with overhanging foliage and leaf detritus on the tracks, for instance) may exacerbate the slope stability issue and lead unwittingly to increased slope failures. There is therefore a desire to study the soil moisture content and fluctuations non-invasively and non-destructively if possible. ERT lends itself to repeat time-lapse monitoring of soil moisture variability, and GPR can also be used to map primary lateral root systems (and animal burrows). It might also be possible to complement these studies with the use of MALM measurements in strategic heavily vegetated areas prior to any decisions being made about cutting trees down.

### 7.7.4 Groundwater flow

The Himalayas possess huge potential for the development of hydropower. Consequently, there is a large amount of development work being undertaken in India, Nepal and Bhutan, especially for

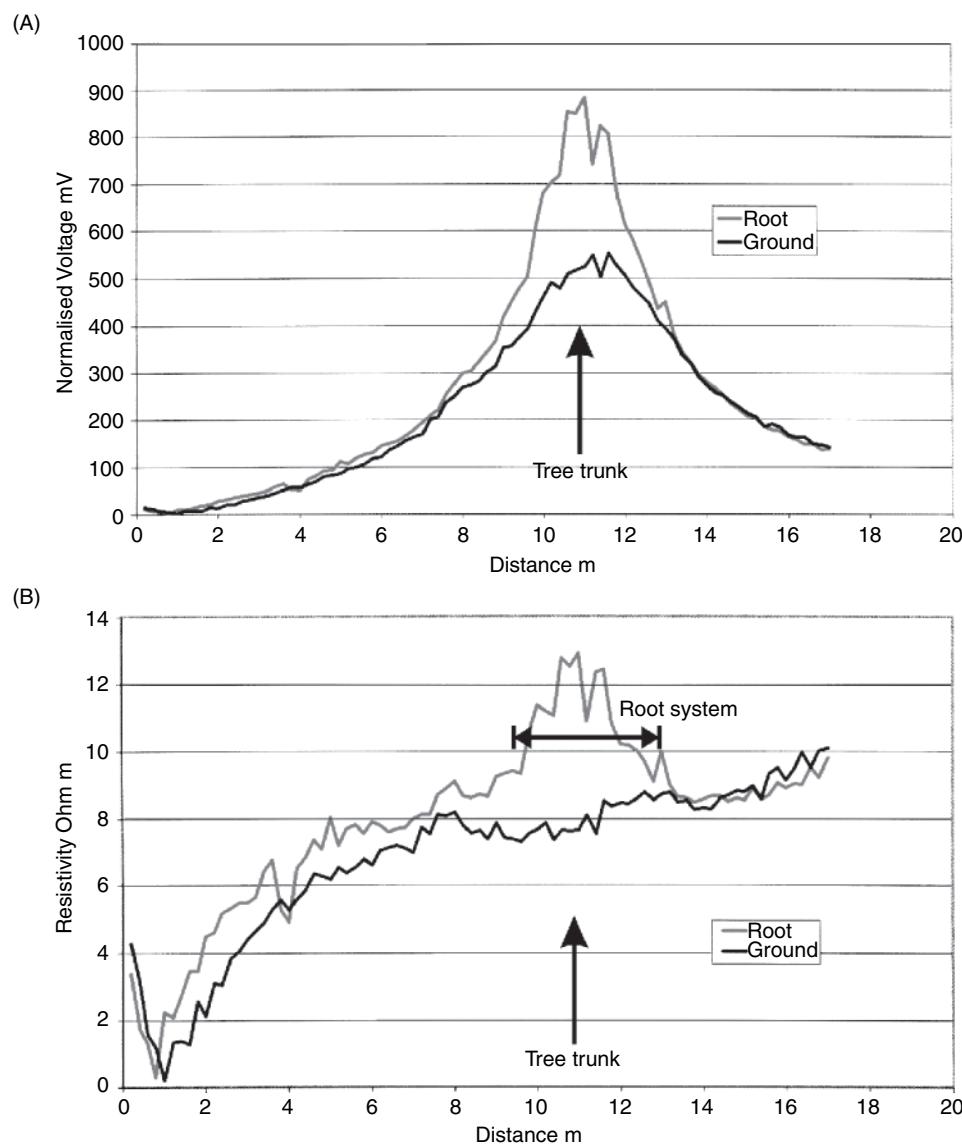


**Figure 7.67** Comparison between planting the current electrode directly into a tree trunk versus into the ground near the tree's base. (A) Normalised MALM potential, and (B) normalised resistivity profile. From Kepic *et al.* (2008), by permission. [C]

run-of-river projects. As part of these investigations, electrical techniques have become popular alternatives to seismic studies which hitherto had tended to use explosives as the seismic source of choice for refraction surveys. Due to political insurgency, restrictions were placed on the transport of explosives, making the seismic method logically and politically less feasible. The ERT, self-potential and MALM techniques have all become more popular as a consequence.

The MALM method has been used to assess groundwater flow direction and speed in a proposed dam area (Pant, personal communication). At the site under investigation, the predominant shallow material present was found to be coarse sand mixed with gravel, the resistivity of which was found to be  $\sim 500 \Omega\text{m}$  where saturated, and greater than  $1000 \Omega\text{m}$  where unsaturated. Pits into the ground were excavated reaching to the groundwater, the resistivity of which was measured to be  $83 \Omega\text{m}$  at a depth of 1 m. Archie's law was

used to determine the effective porosity of the local material (41% for the pit investigated). A portion of the groundwater that surrounded the pit was salted to create a highly electrically conductive body. One of the current electrodes and a slat bag were kept at the depth of the salted groundwater, while the other current electrode was placed a significant distance away. Eight observation profiles were established at radial intervals of  $45^\circ$  centred on the pit. One of the potential electrodes ( $N$ ) was kept fixed on the opposite side of the expected flow direction. The other potential electrode ( $M$ ) was moved along each of the profile lines to map the equipotentials.

The relationship between the hydraulic conductivity and the groundwater flow speed is given in Box 7.12 and is a product of the hydraulic conductivity ( $K$ ;  $\text{m/day}$ ) and the hydraulic gradient, which is locally derived. By measuring the potential along each arm of the radial array, it was possible to determine the direction and rate of flow of the salted groundwater (Figure 7.68). It was determined

**Box 7.12 Relationship between hydraulic conductivity and groundwater velocity**

The hydraulic conductivity ( $K$ , m/day) is related to the groundwater velocity ( $V$ ) by the expression:

$$K = V\alpha L/h$$

where  $\alpha$  is the effective porosity, and  $h/L$  is the hydraulic gradient.

that the local hydraulic conductivity was of the order of  $1-3 \times 10^{-3}$  m/s (Pant, personal communication).

## 7.8 Leak detection through artificial membranes

The detection of leaks through manmade linings to lagoons and landfills has become increasingly important in the last few years. The intention of lining waste disposal sites is to ensure containment of the waste. However, small tears or cuts in the lining can end up with major leaks of contaminants. Various methods have been developed to try to locate holes in the linings so that they can

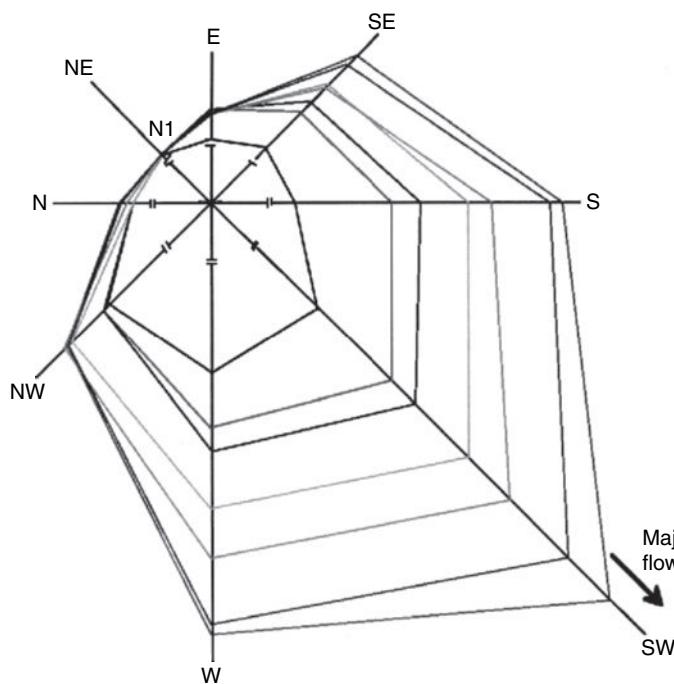
be repaired or mitigation measures can be taken to remedy the contamination.

The general principle behind all the methods is that the artificial lining (high-density polyethylene (HDPE) geomembrane) is effectively a resistive barrier as long as there are no holes through it. Typical resistivity of an HDPE geomembrane is  $> 10^7 \Omega\text{m}$ .

Electrical current is passed between two electrodes, one of which is outside the membrane but in contact with the local groundwater, and one is within the waste or in a wet sand layer immediately overlying the geomembrane (Figure 7.69A). The same system can be used in water-filled lagoons (Figure 7.69B). Either a pair of potential electrodes or a roving single potential electrode (with the second one located with the external current electrode) is used to detect anomalous electrical potentials. These occur where electrical current is able to penetrate through holes in the geomembrane. Tears as small as 1 mm at a depth of 0.5 m beneath a sand layer have been located successfully.

In addition to post-construction leak detection, modern containment landfills are being built with sub-liner detection systems installed permanently. Arrays of electrodes connected by sealed multi-core cables are buried at a depth of around 1 m below the geomembrane. A current circuit is provided by two electrodes as previously described. At the time of construction, measurements are made to check for holes in the liner so that they can be repaired before the disposal of any waste (Figures 7.69C and D). Instead of measuring potentials above the liner, as in the previous case, this technique permits the measurement of anomalous potentials *below* the liner. In addition, pseudo-sections of resistivity can be

(A)



(B)

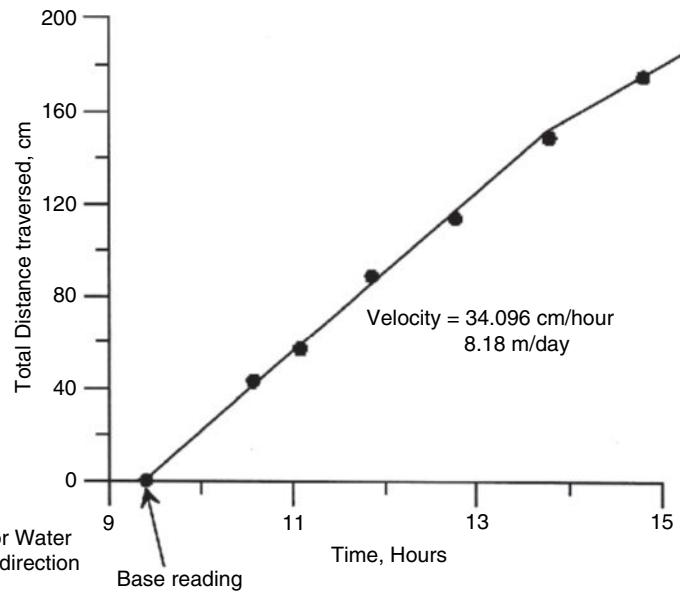


**Figure 7.68** Monitoring of MALM equipotential (A) within a shallow pit, and (B) the time-distance relationship in the southwest direction in (A). From Pant (2004), by permission. [C]

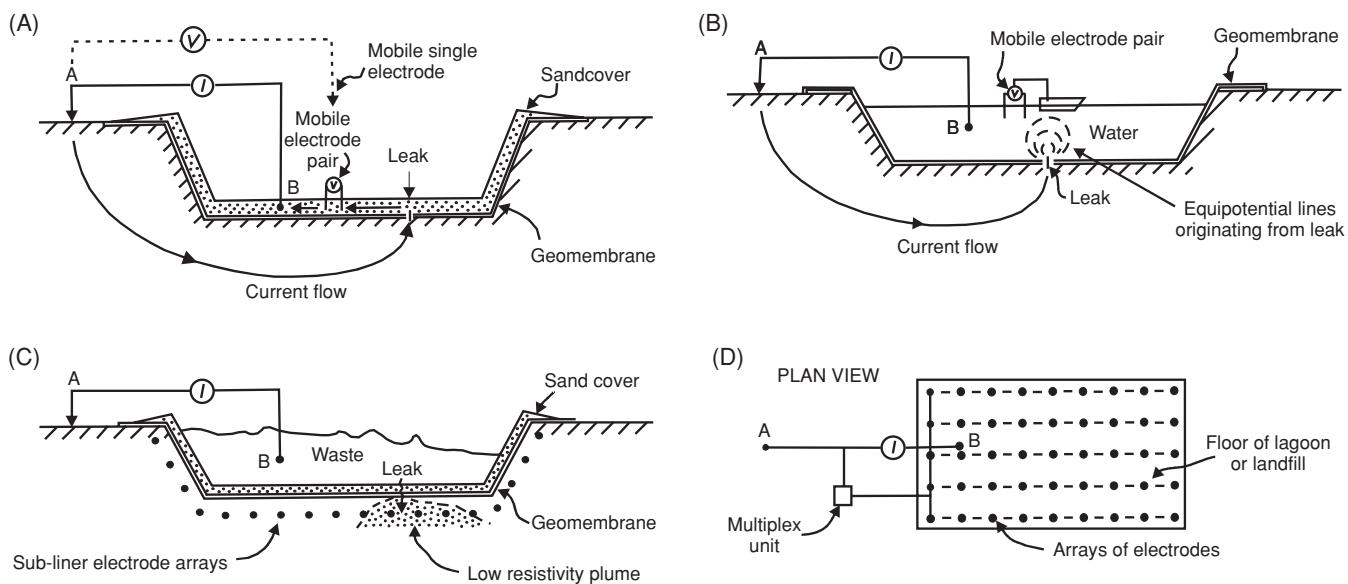


**Figure 7.69** Leak detection systems in waste repositories or lagoons with manmade geomembrane liners. The survey layout in the case where (A) the liner is covered with a thin (0.5 m) layer of sand and bentonite, and (B) the liner is filled with water. (C) A sub-liner leak detection system that uses permanently installed arrays of electrodes, with a typical plan layout shown in (D).

obtained by using the sub-liner arrays as subsurface imaging arrays (see Section 7.4.2), without using the surface current electrode pair. At the construction of the disposal site, baseline measurements can be made when it can be assured that there are no leaks. Once waste has begun to be put into the facility, the sub-liner array can be monitored routinely and repeat pseudo-sections acquired.

The data are normalised so that they display changes in values relative to the baseline dataset. If a leak develops at a later stage in the facility's life, it can be identified from the routine monitoring. By

using the array of subsurface electrodes, the spatial distribution of any sub-liner pollutant plume can be determined so that remedial action can be taken. This may include constructing abstraction wells downstream of a leaking landfill so that the contaminated water can be pumped out and treated. Examples of such leak detection systems have been given by Mazáč *et al.* (1990) and by Frangos (1994), among others. Many geophysical contractors are now offering remote leak detection surveys for containment waste repositories. The first landfill in the UK with a sub-liner leak detection system installed was constructed in 1995.



# 8

## Spontaneous (Self) Potential Methods

### 8.1 Introduction

The *self-potential* or *spontaneous polarisation* (SP) method was devised in 1830 by Robert Fox, who used copper-plate electrodes connected to a galvanometer to detect underground copper sulphide deposits in Cornwall, England. The method has been used since 1922, when Schlumberger introduced non-polarisable electrodes as a secondary tool in base metal exploration, characteristically to detect the presence of *massive* ore bodies, in contrast to the induced polarisation method (see Chapter 9) which is used predominantly to investigate *disseminated* ore bodies. The SP method has been extended to groundwater and geothermal investigations, and can also be used as an aid to geological mapping, for example, to delineate shear zones and near-surface faults. It has also been used in forecasting earthquakes (e.g. Corwin and Morrison, 1977; Varotsos and Alexopoulos, 1984) and volcanic eruptions (Zablocki, 1976), and investigating volcanic plumbing (Patella, 1997a; Lénat, 2007). The technique has also been used successfully in archaeological investigations (Wynn and Sherwood, 1984; Drahor, 2004). The method is increasingly being used in environmental studies such as in monitoring fluid contamination and bio-remediation. A useful general introduction to the method has been given by Corwin (1990).

The SP method ranks as the cheapest of the surface geophysical methods in terms of equipment necessary and amongst the simplest to operate in the field. Although the phenomenon of self-potentials is utilised more extensively in borehole well logging than in surface applications, downhole techniques will not be discussed further here.

### 8.2 Occurrence of self-potentials

The SP method is passive: differences in natural ground potentials are measured between any two points on the ground surface. The potentials measured can range from less than a millivolt (mV) to over one volt (exceptionally to over 10 V), and the sign (positive or

negative) of the potential is an important diagnostic factor in the interpretation of SP anomalies, as described later.

Self-potentials are generated by a number of natural sources (next section), although the exact physical processes by which some are caused are still unclear. A summary of the common types of SP anomaly are listed in Table 8.1 with their respective geological sources. In addition to compositional variations, the geometry of geological structures can also create SP anomalies, and so the sources listed should only be used as a guide. It is possible that observed SP potentials arise as a combination of different processes rather than as a result of a single process. Natural ground potentials consist of two components, one of which is constant and unidirectional and the other fluctuates with time. The constant component is due primarily to electrochemical processes, and the variable component is caused by a variety of different processes ranging from alternating currents induced by thunderstorms and by variations in the Earth's magnetic field, to the effects of heavy rainfall. In mineral exploration, components of the SP are called the *mineral potential* and the *background potential*, respectively. This terminology belies the usefulness of the so-called 'background' potentials as these can be used in geothermal and hydrogeological investigations as the main measured anomaly. The processes by which some of these potentials are generated are discussed briefly in the next section.

### 8.3 Origin of self-potentials

The common factor among the various processes thought to be responsible for many self-potentials is groundwater movement. The potentials are generated by the flow of water, by water acting as an electrolyte and as a solvent of different minerals, and so on. The types of potentials are listed in Table 8.2 (with their alternative names where appropriate) and their mathematical definitions are given in Box 8.1. There are three ways of conducting electricity through rocks: by dielectric, electrolytic and electronic (ohmic) conduction. The electrical conductivity ( $\sigma$ , the inverse of resistivity) of porous rocks therefore depends on their porosity (and the

**Table 8.1** Types of SP anomalies and their geological sources.

Source	Type of anomaly
<i>Mineral potentials</i>	
Sulphide ore bodies (pyrite, chalcopyrite, pyrrhotite, sphalerite, galena)	Negative ≈ hundreds of mV
Graphite ore bodies	
Magnetite + other electronically conducting minerals	
Coal	
Manganese	
Quartz veins	Positive ≈ tens of mV
Pegmatites	
<i>Background potentials</i>	
Fluid streaming, geochemical reactions, etc.	Positive +/- negative ≤ 100 mV
Bioelectric (plants, trees)	Negative, ≤ 300 mV or so
Groundwater movement	Positive or negative, up to hundreds of mV
Topography	Negative, up to 2 V

arrangement of the pores) and on the mobility of water (or other fluids) to pass through the pore spaces (hence dependent upon ionic mobilities and solution concentrations, viscosity ( $\eta$ ), temperature and pressure).

### 8.3.1 Electrokinetic potentials

An electrokinetic potential ( $E_k$ ) forms as a result of an electrolyte flowing through a capillary or a porous medium, the potential being measured across the ends of the capillary (Ahmad, 1961). The potentials arising from this process are alternatively referred to as *electrofiltration*, *electromechanical* or *streaming* potentials.

According to Helmholtz's law, the flow of electric current is related to the hydraulic gradient and a quantity known as the electrofiltration coupling (or streaming potential) coefficient ( $C_E$ ), which takes into account the physical and electrical properties of the electrolyte and of the network through the medium through which the electrolyte has passed. It is also important that the water flows parallel to either a geological boundary (Fitterman, 1978, 1979a) or to its free surface (i.e. the water table).

**Table 8.2** Types of electrical potentials.

Electrokinetic (Electrofiltration) (Electromechanical) (Streaming)	Variable with time
Diffusion potential	Electrochemical potential
Liquid-junction	
Nernst potential (shale)	Constant
Mineral potential	

### Box 8.1 Electrical potentials

#### Electrokinetic:

$$E_k = \frac{\varepsilon \mu C_E \delta P}{4\pi\eta}$$

where  $\varepsilon$ ,  $\mu$  and  $\eta$  are the dielectric constant, resistivity and dynamic viscosity of the electrolyte respectively;  $\delta P$  is the pressure difference; and  $C_E$  is the electrofiltration coupling coefficient.

#### Diffusion potential:

$$E_d = \frac{-RT(I_a - I_c)}{nF(I_a + I_c)} \ln(C_1/C_2)$$

where:  $I_a$  and  $I_c$  are the mobilities of the anions (+ve) and cations (-ve) respectively;  $R$  is the Universal Gas Constant (8.314 J K<sup>-1</sup> mol<sup>-1</sup>);  $T$  is absolute temperature (K);  $n$  is ionic valence;  $F$  is Faraday's Constant (96487 C mol<sup>-1</sup>);  $C_1$  and  $C_2$  are the solution concentrations.

#### Nernst potential:

$$E_N = \frac{-RT}{nF} \ln(C_1/C_2)$$

when  $I_a = I_c$  in the diffusion potential equation.

Graphs of electrokinetic potentials obtained for different geological situations with characteristic values of  $C_E$  for each geological unit are given in Figure 8.1A (Schiavone and Quarto, 1984). The potentials tend to increase in positiveness with the direction of water flow as the electric charge flows in the opposite direction. Consequently, negative charge flows uphill and can result in spectacular SP anomalies on topographic highs. Gay (1967) reported a potential of -1842 mV measured on a mountain top near Hualgayoc, Peru (mineralisation: alunite); Nayak (1981) measured a value of -1940 mV on a hill of unmineralised quartzites in Shillong, India; Corwin and Hoover (1979) reported a value of -2693 mV on the peak of Adagdak Volcano, Adak Island, Alaska. This topographic effect requires a correction to be applied (see Section 8.5) particularly where slope angles exceed 20°.

Superimposed on the topographic flow generation of self-potentials can be potentials of the order of 5 mV which are caused by the brief but rapid percolation of water such as from heavy rainfall (Fournier, 1989). Variation in soil moisture content may also produce locally variable SP signals (Corwin and Hoover, 1979), with the electrode in the wetter soil often becoming increasingly positive (Poldini, 1939). The small but measurable SP anomaly lasts only as long as the water flow. Potentials of the order of tens of millivolts can be induced artificially through pumping groundwater (Semenov, 1980). The hydraulic gradient is increased by water abstraction, thereby increasing the rate of water flow towards the borehole; hence a positive anomaly is observed (Figure 8.1B).

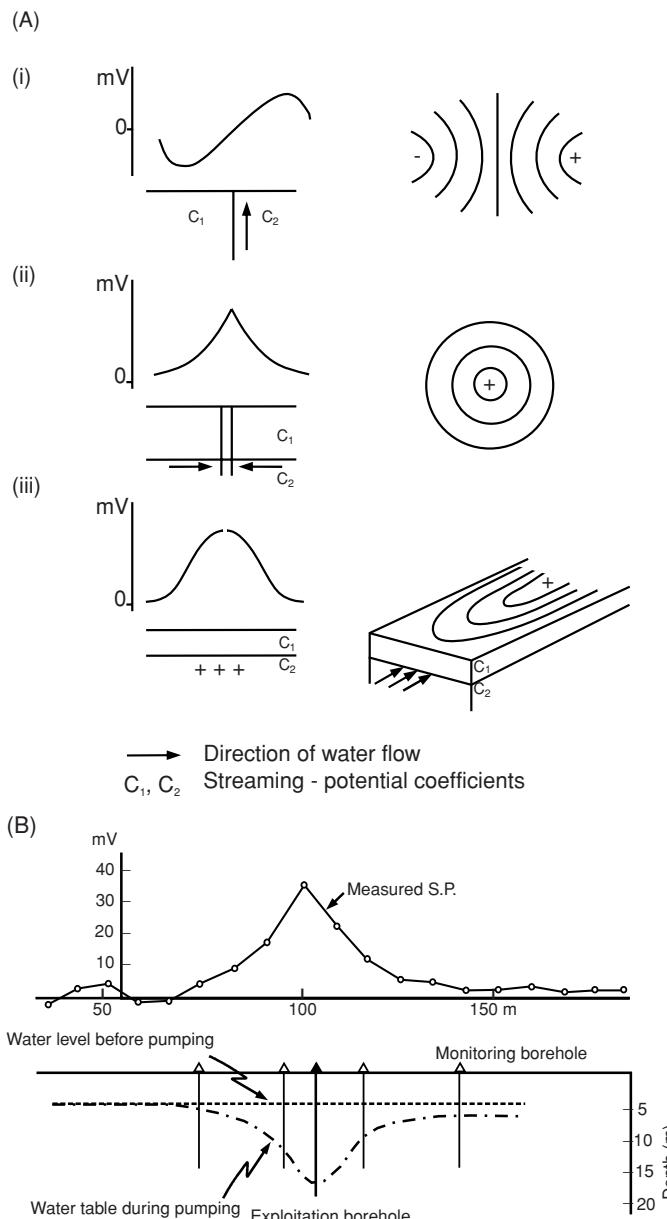


**Figure 8.1** (A) Idealised electro-filtration SP profiles and maps for the following models (from Schiavone and Quarto, 1984): (i) a vertical boundary with upwelling on the right; (ii) pumping from a well (injection into the well would produce the opposite sense of anomaly); (iii) horizontal boundary flow. Interfaces are marked by a contrast in streaming potential coefficients ( $C_1$  and  $C_2$ ). (B) Example of the SP anomaly produced by pumping from a well (after Semenov, 1980).

A further factor that needs to be taken into account is *thermo-electric coupling*, which is the production of a potential difference across a rock sample throughout which a temperature gradient is maintained. The effect may be caused by differential thermal diffusion of ions in the pore fluid and of electrons and donor ions in the rock matrix (Corwin and Hoover, 1979), a process called the *Soret Effect* (Heikes and Ure, 1961).

### 8.3.2 Electrochemical potentials

Transient background *diffusion* (or *liquid junction*) potentials ( $E_d$ ) of up to tens of millivolts may be due to the differences in the mobilities of electrolytes having different concentrations within groundwater. For this mechanism to explain the continued occurrence of background potentials, a source capable of maintaining imbalances in the electrolytic concentrations is needed, otherwise the concentration differences will disappear with time by diffusion.

The *Nernst (shale) potential* ( $E_N$ ) occurs when there is a potential difference between two electrodes immersed in a homogeneous solution and at which the concentrations of the solutions are locally different. It can be seen from Box 8.1 that the form of the equation for the Nernst potential is a special case of that for the diffusion potential and can easily be combined to form the *electrochemical potential*. For a solution of sodium chloride (NaCl) at 25°C with a ratio of concentrations of 5:1, the electrochemical potential is about  $\pm 50$  mV. The Nernst potential is of particular importance in well logging, in which case it is referred to as the *shale potential*. It can also be seen from Box 8.1 that the electrochemical potential is directly dependent upon the concentration differences ( $C_1/C_2$ ) and temperature. The higher the temperature and the greater the concentration differences, the larger the electrochemical potential will be. For this reason, the measurement of self-potentials is important in the exploration for geothermal resources (e.g. Corwin and Hoover, 1979) where the temperatures are obviously elevated and the concentrations of salts within the groundwater are also likely to be high.

Further electrochemical potentials are attributable to adsorption of anions on to the surface of veins of quartz and pegmatite, and are known as *adsorption* (or *zeta*) *potentials*. For example, an anomaly of up to +100 mV has been measured over vertical pegmatitic dykes within gneiss (Figure 8.2) (Semenov, 1980; cited by Parasnis, 1986). In addition, adsorption potentials may account for the observed anomalies over clays where the solid–liquid double layer may generate a potential.

The *redox potential* ( $E_H$ ), measured in volts, indicates the ability of a substance or solution to cause reduction or oxidation under non-standard conditions. The higher the value of the redox potential, the more oxidising the conditions. It is common practice to measure the redox potential in shallow pits in order to determine

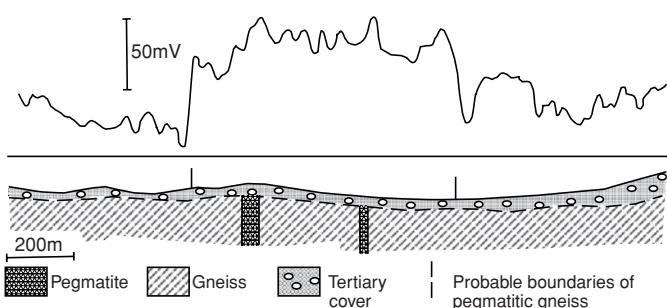


**Figure 8.2** An SP profile across pegmatite dykes in gneiss. From Semenov (1980), by permission.

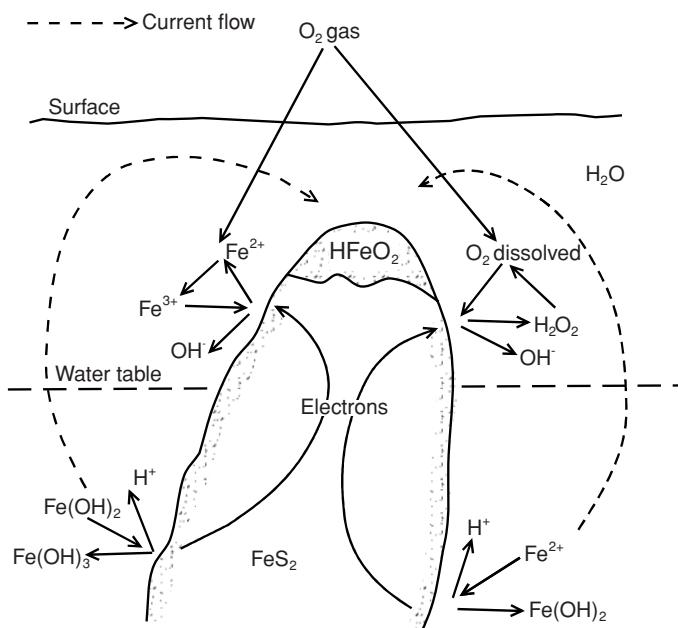


**Figure 8.3** Physico-chemical model proposed by Sato and Mooney (1960) to account for the self-potential process in a massive sulphide orebody. Reproduced by permission.

the aggressiveness of the soil to corrosion of metal reinforcement or grounding electrodes.

### 8.3.3 Mineral potentials

Of most importance in the use of SP in mineral exploration is the *mineral potential* such as that associated with massive sulphide orebodies. Large negative anomalies can be observed particularly over pyrite and chalcopyrite and other good electronic conductors. (Mineral potentials have also been observed over sphalerite and porphyry orebodies, somewhat surprisingly, as they are poor conductors.)

Sato and Mooney (1960) have provided the most often cited explanation of the electrochemical processes (Figure 8.3) that cause the observed self-potential anomalies, although no hypothesis is yet able to account for all the observed mineral potentials. Where a sulphide orebody straddles the water table, a cathodic electrochemical half-cell forms by the chemical reduction of the ions in the surrounding electrolyte, i.e. they gain electrons. In contrast, below the water table, an anodic electrochemical cell operates in which oxidation is dominant and ions lose electrons. The role of the massive orebody is to permit the flow of electrons from the lower half of the orebody to the upper half (i.e. a 'geo-battery'). The net result of this process is that the upper surface becomes negatively charged (hence the negative SP anomalies) and the lower half becomes positively charged. However, the fact that this hypothesis does not explain all the occurrences of self-potentials indicates that the actual physical processes are more complicated and not yet fully understood (Kilty, 1984). This is even truer when more than one orebody is involved resulting in complex SP anomaly shapes (e.g.

Becker and Telford, 1965). Nyquist and Corry (2002) have argued against the geo-battery hypothesis on the basis that there are too many examples of where this does not accord with what is observed geologically. For instance, Nyquist and Corry state that the Sato and Mooney model cannot account for voltages greater than about 800 mV based on the diffusion potential of sulphides. The maximum amplitude of an anomaly generated by either pole of the geo-battery relative to the reference electrode a large distance away is therefore only 400 mV. Yet in many instances, voltages in excess of 1000 mV have been reported over sulphides. Also, the Sato and Mooney model requires reasonably smooth voltage gradients, yet large and variable gradients have been measured at the surface, underground and by downhole logging. Nyquist and Corry also argue against the geo-battery model on the basis that SP measurements made on the surface, underground and in boreholes through ore bodies invariably produce negative anomalies relative to a remote base station, whereas a battery model should have both a negative and a positive pole. SP values associated with ore bodies appear to be stable over time and show no fluctuation, even though related water tables do. Ion transport would be expected to decrease with reducing temperatures, yet SP anomalies are evident within frozen Arctic terrains. Similarly, the geo-battery model does not account for SP potentials recorded where the orebody lies entirely below the water table. Clearly, an alternative model is necessary to account for these. Indeed, Nyquist and Corry postulate a redox SP model, where the SP electrodes measure the difference in redox potential between the base and a roving electrode, and not the voltage drop associated with a geo-battery discharging through resistive rock. As with any galvanic cell, no current will flow unless the electrodes are located in separate environments where the difference in redox potential would allow spontaneous reactions. In effect, it is the wire connecting the electrodes, not the orebody, that completes the circuit between oxidising and reducing zones (Figure 8.4). A redox SP potential will be produced when a wire is connected between two materials in electrolytic contact and where there is an oxidation-reduction potential between those materials such that they will react spontaneously. Further evidence in support of the redox model has been provided by Hamilton and Hattori (2008) who found SP anomalies to be spatially correlated with redox gradients in a survey over a forest ring that overlies a  $H_2S_{(aq)}$  accumulation in Ontario, Canada, where there is no metallic mineralisation.

Sato and Mooney's geo-battery model requires both a redox gradient and a buried conductor, whereas the redox SP model only requires a redox gradient to produce potentially large SP anomalies. This is important for environmental geophysics applications as it means that the SP technique may be applicable in many more situations in addition to mineral exploration and groundwater surveys. One potentially major application is in site bio-remediation where microbes are used to digest diesel. The process produces a reduced zone at the centre of the fuel plume which contrasts with the oxygen-rich uncontaminated groundwater beyond, thus providing an SP target. This will be discussed further later.

Where clay overlies a massive sulphide orebody, the mineral potential may be suppressed to the extent that no anomaly is observed (Telford *et al.*, 1990). This may be a result of the adsorption potential (which tends to be positive) having the same amplitude as the

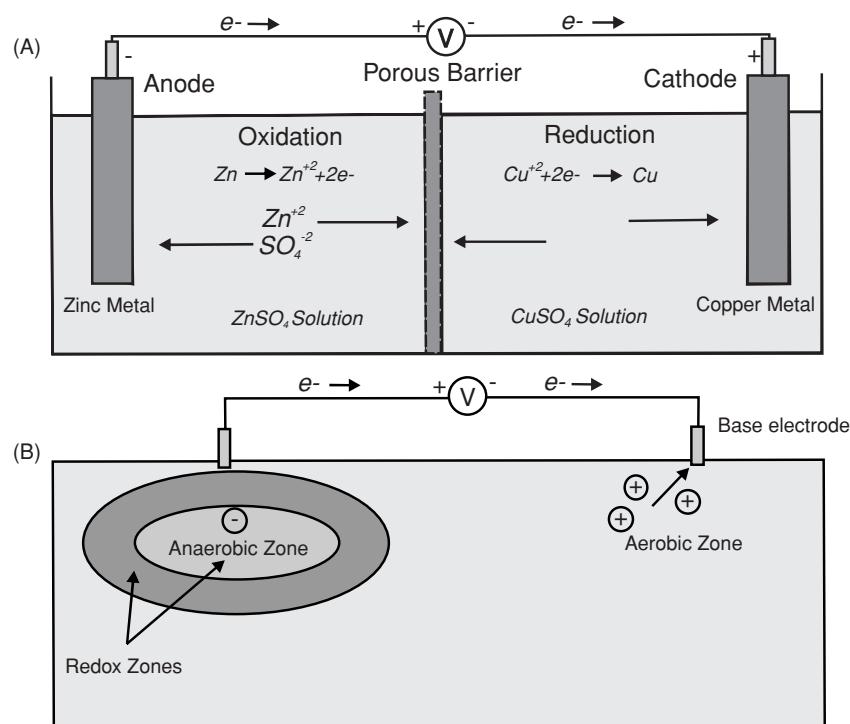


**Figure 8.4** (A) The redox potential difference between the two halves of a galvanic cell registers as an electrical voltage. (B) The analogous situation in the field, where a redox difference can be produced by, for example, the metabolism of hydrocarbons by bacteria. From Nyquist and Corry (2002), by permission.

mineral potential (negative polarity) and thus cancelling each other out.

## 8.4 Measurement of self-potentials

The measurement of self-potentials is very simple. Two non-polarisable porous-pot electrodes are connected to a precision multimeter with an input impedance greater than  $10^8$  ohms and capable of measuring to at least 1 mV. Each electrode is made up of a copper electrode dipped in a saturated solution of copper sulphate, which can percolate through the porous base to the pot (Figure 8.5A) in order to make electrical contact with the ground. Alternatively, a zinc electrode in saturated zinc sulphate solution or silver in silver chloride can be used. More rapid measurements can be made by using a so-called walking stick electrode (Figure 8.5B), which consists of either of a round-ended cylindrical porous pot or a conical Tufnol nose containing copper sulphate solution, with holes filled with a porous material to make contact with the ground. The electrode is connected to a walking stick probe that is used simply to push the electrode probe into the surface of the soil. By convention, the *negative* lead of the voltmeter should be connected to the base electrode.

There are two field techniques, both of which are carried out at right-angles to the suspected strike of the geological target. The *potential gradient method* uses two electrodes, at a fixed separation, typically 5 m or 10 m, between which the potential difference

measured is divided by the electrode separation to give a potential gradient (mV/m). The point to which this observation applies is the midpoint between the two electrodes. The two porous pots are leapfrogged along the traverse, but care has to be taken to ensure that the correct polarity of the potential is recorded. The procedure in the *potential amplitude method* is to keep one electrode fixed at a base station on unmineralised ground and to measure the potential difference (in mV) between it and the second one, which is moved along the traverse. This removes the problems of confusing polarity and accumulating errors. Care should be taken to ensure that the temperature of the electrolyte in the mobile pot does not differ significantly from that in the reference electrode, or else a potential difference will be produced. The temperature coefficient for copper–copper sulphate is about  $0.5\text{ mV}^\circ\text{C}$  (about  $0.25\text{ mV}^\circ\text{C}$  for silver–silver chloride electrodes).

As mentioned above, the self-potential consists of a static and a variable alternating component. The latter, which can have frequencies typically in the range of 5–10 Hz, is caused by atmospheric effects, and its long period component may have amplitudes that are of the same order as the static mineral potential. Where this signal is present, the mineral potential can be resolved by taking measurements along the same profile at different times of the day and averaging the results. Electrical noise can also result if measurements are made too soon after heavy rain or too close to running surface water, as streaming potentials may then swamp any mineral potentials. Other sources of manmade SP noise include the generation of an SP signal from an electric railway 1 km distant, interference from electric ore trains more than 20 km from a survey

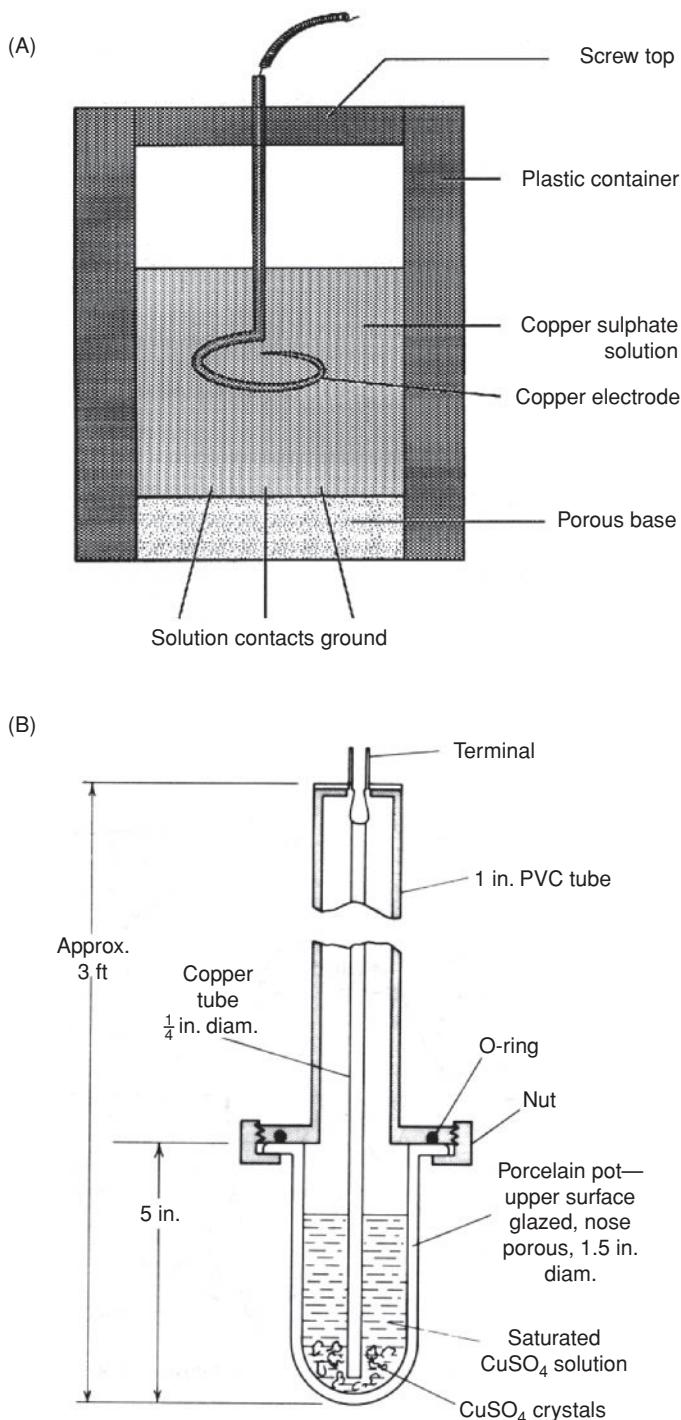


**Figure 8.5** (A) Cross-section through a non-polarisable porous-pot electrode. (B) Walking stick SP electrode. After Telford *et al.* (1990), by permission.

area (Nyquist and Corry, 2002), buried utilities (including those cathodically protected), grounded fences and equipment, and corroding scrap metal, to name but a few.

The maximum depth of sensitivity of the SP method is around 60–100 m, depending on the depth to the orebody and the nature of the overburden.

Self-potential measurements can also be made over water to measure streaming potentials (Corwin, 1973). The porous-pot electrodes are enclosed in special containers so that they can be towed through water without causing serious loss of electrolyte from the pots. This method will only work where there is little current flow (lateral or vertical) within the water column (Ogilvy *et al.*, 1969); the amplitude of any SP anomaly obtained within a saline water body (resistivity 0.3–1  $\Omega\text{m}$ ) tends to be very small.

## 8.5 Corrections to SP data

Self-potentials measured over a large area (of the order of many square kilometres) may have a regional trend due to ‘telluric’ currents (see Section 11.5) of  $\geq 100 \text{ mV/km}$ . The mineral potential may be superimposed upon this regional gradient. Thus, to interpret the anomaly due to mineralisation, its anomaly has to be isolated in much the same way as gravity residuals are obtained (see Section 2.6.1). Regional corrections must be applied before any adjustment for topography is made. However, for a local survey whose length is small in comparison with the regional wavelength, removing regional trends is usually unnecessary.

The association of negative anomalies with topographic highs has already been mentioned (Section 8.3.1). Telluric currents are also affected by changes in elevation. The combined effects are extremely hard to quantify explicitly, but can be corrected for in a general manner as prescribed by Yüngül (1950) and discussed further by Bhattacharya and Roy (1981) and Bhattacharya (1986). If the surface slope of a survey area is large ( $>20^\circ$ ), the SP minimum may be well displaced from its cause and subsequent drilling may miss the orebody completely. In any attempts to correct data for either regional or topographic effects, the SP anomaly for an individual polarised body should be isolated. If the observed anomaly is due to the superposition of a number of anomalies from different geological sources (and hence with different shapes and polarities), corrections cannot be carried out and the locations of the tops of the orebodies must be taken as very approximate; alternative geophysical methods should be used to try to delimit the geological structure more explicitly.

It may also be necessary to make allowance for the effects of bioelectric potentials caused by vegetation. Passing from bare ground into an area of vegetation can cause a negative potential of several hundred millivolts, comparable to a mineral potential due to a sulphide orebody. Basic field observations should clarify the situation.

## 8.6 Interpretation of self-potential anomalies

### 8.6.1 Qualitative interpretation

SP anomalies are often interpreted qualitatively by profile shape, amplitude, polarity (positive or negative) and contour pattern (see Figure 8.1). The top of an orebody is then assumed to lie directly

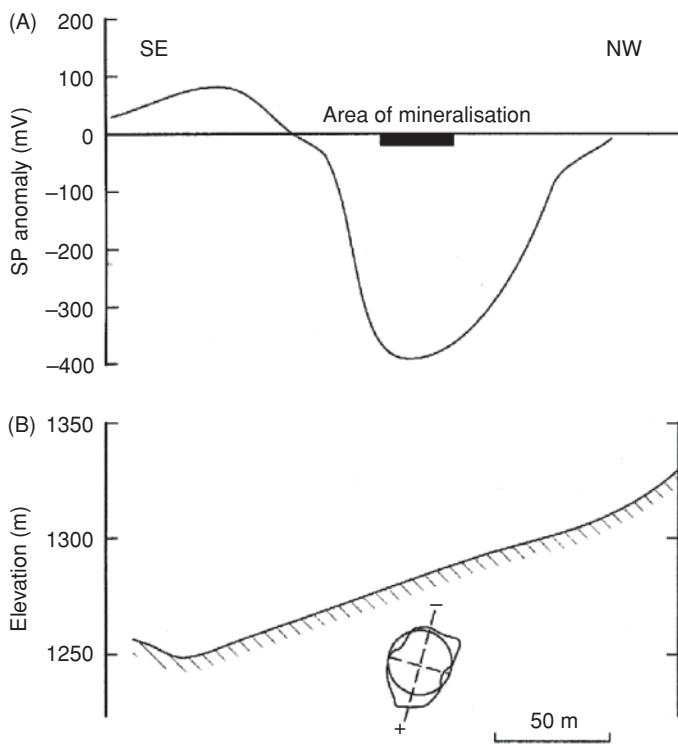


**Figure 8.6** (A) Weiss SP anomaly in Ergani, Turkey, with the causative ore body shown schematically in (B). Note that the axis of polarisation is inclined uphill. After Yüngül (1950), by permission.

beneath the position of the minimum potential. If the axis of polarisation (i.e. the axis between the cathode and anode on the orebody) is inclined from the vertical, the shape of the profile will become asymmetrical with the steepest slope and positive tail both lying on the downdip side (Figure 8.6).

Complications arise when two or more geological features give rise to superimposed SP anomalies. One such example (Nayak, 1981) is shown in Figure 8.7. An anomaly over graphitic phyllites is characteristically large ( $-740$  mV) owing to mineral electrochemical potentials. A second anomaly, with an amplitude of  $-650$  mV, has been produced by electrokinetic potentials associated with water flow through permeable disintegrated conglomerates. However, if similar-sized bodies are present but with different dips, the resultant anomaly can be used to resolve between them. Consider two graphite bodies in gneiss (Figure 8.8) in two different models (Meiser, 1962). The first is where the graphites dip towards each other in a synclinal structure, in which case the negative centres associated with each polarisable body are well separated, resulting in an anomaly with two negative minima. The second is where the graphite bodies dip away from each other in an anticlinal structure, in which case the two negative centres are very close together and may even combine to form one large negative minimum. The separation between the two minima is equal to the separation of the tops of the graphite bodies.

In the case of using SP to locate leaks through dams (artificial or natural), an SP profile across the probable leakage flow direction

may show negative anomalies; these can be simply interpreted as indicating the location directly above the flow of the electrolyte. See the example in Section 8.7.5.2.

## 8.6.2 Quantitative interpretation

The theoretical basis of quantitative interpretations of SP anomalies over a polarised sphere is attributed to Petrovski (1928) and developed by de Witte (1948), over a bar by Stern (1945) and over a dipping plate by Meiser (1962). Other forms of model and revised methods of calculation have been described more recently by Hongisto (1993). In mineral exploration, interpretation techniques use the comparison of field data with results from forward models based on charged geometric structures, such as planes, rods and ellipsoids, to represent the geometry of isolated mineral deposits (Cooper, 1997; Abdelrahman *et al.*, 2003). The model is then adjusted until the observed model and calculated profiles agree within prescribed statistical limits. While this method may work for very well constrained data, if the actual geological feature causing the SP anomaly does not conform to a given geometric shape, the problem becomes very much more complicated mathematically, and numerical methods of computation are required (e.g. Fitterman, 1979b; Patella, 1997a,b). One of the problems of some methods of interpretation is that the type of potential (electrokinetic, electrochemical, etc.) being generated is assumed, along with the associated physical process: an assumption that may prove to be incorrect.

The inverse approach is to manipulate the observed anomaly to produce a model. This method may be used to estimate the size of the geological feature prior to other, more detailed, geological and geophysical investigations (Sill, 1983). The approach is to make an *a priori* assumption about the geological feature and then to assume that it conforms to a given geometric form (Figure 8.9) for which depths to the centre of the body may be estimated using a half-width technique. Unfortunately this method is notoriously inaccurate, the most serious limitation of this approach being that the width of the anomaly may be more indicative of the physical breadth rather than the depth of the body, and so depth estimates may be in error by as much as  $\pm 100\%$ . Examples of actual graphite bodies and their respective SP anomalies are shown in Figure 8.10. The observed anomaly in Figure 8.10B is the envelope of the anomalies due to the individual geological components A–D.

Over the last decade, significant advances have been made in the quantitative modelling of SP data. For example, Bérubé (2007) described a graphical 3D finite element program for modelling self-potentials generated by flow through a porous medium. He based his approach on the theory of coupled flows. This is perhaps best suited to modelling flows through embankments and mine tailings dams. Sheffer and Oldenburg (2007) have developed a similar program that was also based on coupled flow.

In contrast, Patella (1997a,b; 1998) has developed a sophisticated mathematical approach that does not require any *a priori* assumptions about how the potentials are being generated. He termed his approach *self-potential tomography* (SPT). The general method is characterised by the presence of primary electric sources or sinks, located within any complicated resistivity structure where there is

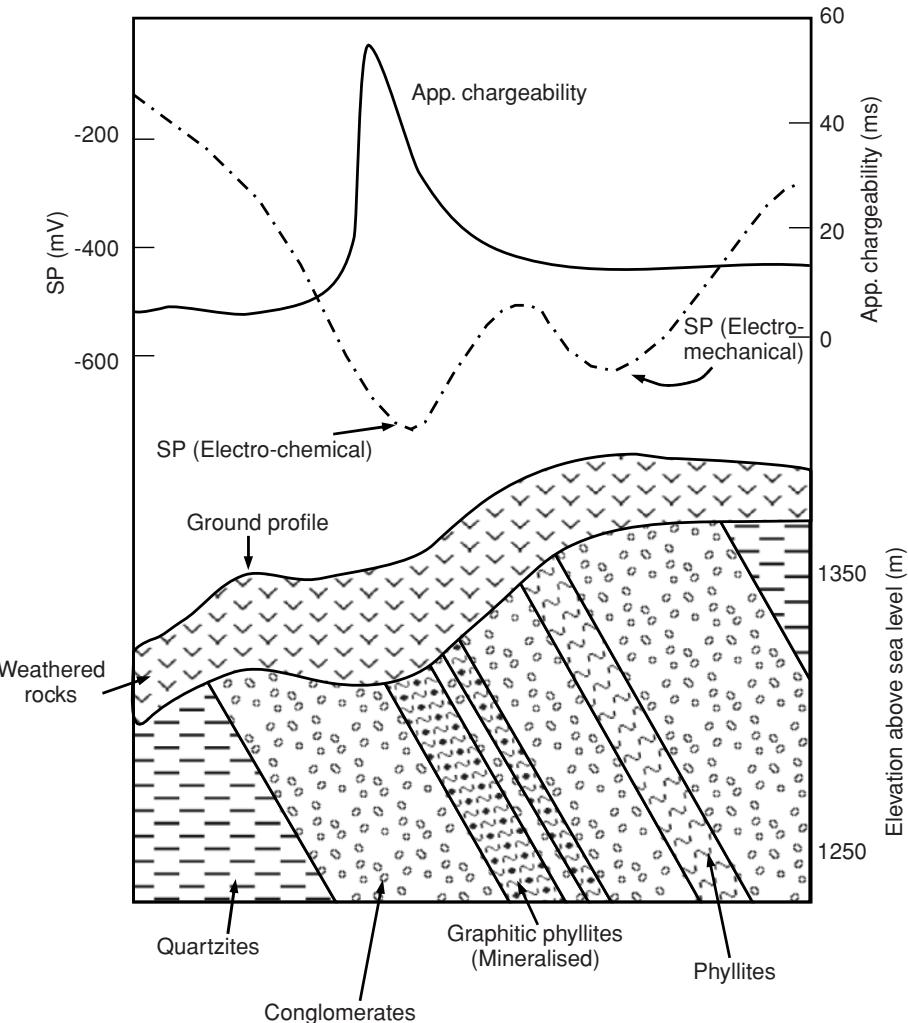


**Figure 8.7** Two SP minima with different causes: one produced by electrochemical processes associated with mineralised graphite phyllites, and one caused by electrokinetic processes due to the flow of water in permeable disintegrated conglomerates. From Nayak (1981), by permission.

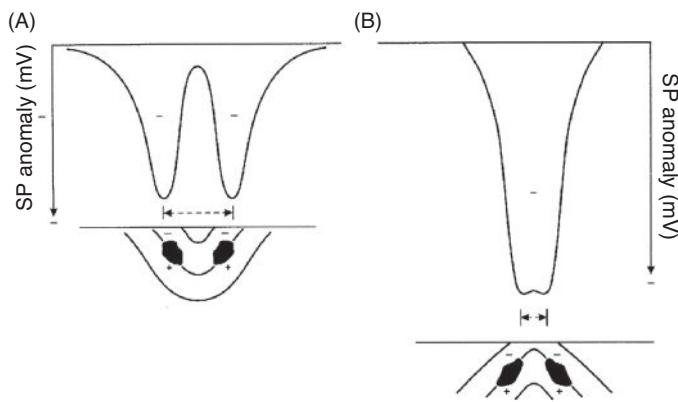


**Figure 8.8** SP anomalies due to (A) two graphite bodies with axes of polarisation inclined away from each other (in syncline), and (B) inclined towards each other (in anticline). After Meiser (1962), by permission.

either a flat air–earth surface boundary (Patella, 1997a) or where the topographic effects can be taken into account in a more robust 3D approach (Patella, 1997b, 1998).

Patella introduced the idea of a *scanning function*, which is the unit strength electric field component generated by an elementary positive charge. His method calculates the correlation between the observed surface potentials (measured from a traditional grid of SP data) and the potential from a scanning test charge. He developed this further with the *Charge Occurrence Probability* ( $\eta$ ) (COP) for the tomographic imaging of the charge distribution geometry as a function of depth. This function is defined as the cross-correlation product of the total observed electric field component and the scanning function, divided by the square root of the product of the respective variances. [Variance is a measure of the width of the probability distribution for a single random variable or the square of the standard deviation, cf. Sheriff (2002).] Values of COP lie in the range  $\pm 1$ ; a large value indicates an increased likelihood that charge has accumulated at that point, with the sense of the sign indicating

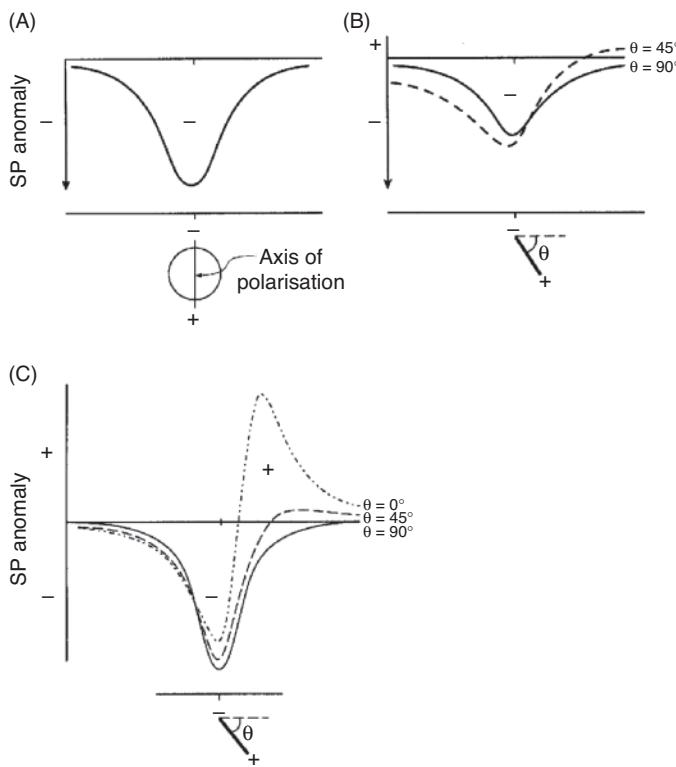


**Figure 8.9** Self-potential anomalies associated with (A) a sphere, (B) a dipping plate (Parasnis, 1986), and (C) a dipping rod (Telford *et al.*, 1990).

whether the accumulated charge is positive or negative. The 3D tomographic approach is the composition of the COP functions related to any two orthogonal surface components of the natural electric field, in order to account for the total surface component of the self-potential field.

Patella (1997b) described how the new approach was used successfully to delineate the nature of an entrance chamber tomb in the Sabine necropolis near Rome, Italy. From 360 surface SP measurements made with a sampling interval of 0.5 m across a grid 9 m by 9 m, a sequence of eight *tomopanes* (horizontal surfaces) at vertical depth increments of 0.5 m were constructed. These revealed a positive COP anomaly, shaped in horizontal outline like a double-rooted molar tooth, derived from the SP data that ranged in amplitude between -8 mV and +10 mV. COP values ranged between  $\pm 0.2$ . The 'molar root' part of the anomaly indicated a partially empty chamber tomb, while the main 'tooth' part of the anomaly indicated the entrance corridor (*dromos*) to the tomb. These results were subsequently confirmed using an integrated analysis of ground-penetrating radar and geoelectrical data. He gave a second example of the application of the same 3D tomographic method across the volcanological area of Mt Somma-Vesuvius (Naples, Italy). The SP data (1250 measurements) were collected over an area of about 170 km<sup>2</sup> using the gradient technique with a 100-m long passive dipole continuously displaced along a net of randomly distributed lines around the volcano, which has a very uneven topography. SP values were observed in the range -1600 mV to +800 mV. A series of

eight *tomopanes* (horizontal surfaces) at vertical depth increments of 400 m were constructed (from +800 m to -2000 m elevations). A widely extended positive anomaly in the central zone appeared to correspond to the summit portion of the Mt Vesuvius chimney, thought to be composed of cemented volcanic breccia. The same method has also been used to map the subsurface charge distribution of the Varco d'Izzo landslide (Perrone *et al.*, 2004).

## 8.7 Applications and case histories

### 8.7.1 Geothermal exploration

The hydrogeological regimes associated with geothermal fields are often complex. Water bodies can have highly differing temperatures and salinities, and be highly mobile (e.g. Cioni *et al.*, 1992). Consequently, streaming potentials may be well developed and hence may be measured using the SP method (see also Anderson and Johnson (1976) and Zohdy *et al.* (1973)).

#### 8.7.1.1 Roosevelt Hot Springs, Utah, USA

A self-potential profile carried out across the Dome Fault Zone, Roosevelt Hot Springs, Utah, is shown in Figure 8.11 (Corwin and Hoover, 1979). Alunite and pyrite occur in the zone, both of which normally produce negative polarity anomalies that may be evident on the profile within 1 km west of the reference electrode position. The area within 1 km to the east of the reference electrode has a positive anomaly of about +80 mV, which is thought to be due to the geothermal activity. Comparison of the thermal gradient profile with the SP transect indicates that the axis of the thermal gradient anomaly is coincident with the position of the reference electrode. The negative potentials associated with the mineralised areas within the zone may be degrading the anomaly due to the geothermal activity. The geothermal SP anomaly results from streaming potentials being driven by the convective cells within such a zone, and also from elevated diffusion potentials due to the higher temperatures.

#### 8.7.1.2 Cerro Prieto geothermal field, Mexico

Corwin and Hoover (1979) reported on a significant SP anomaly of some 150 mV peak-to-peak amplitude associated with the Cerro Prieto geothermal field in Mexico (Figure 8.12). The anomaly is centred over the Hidalgo Fault, which is thought to provide a major conduit for geothermal fluids. The actual geology of the field is still not fully understood, but it is clear that the production zone, which generates about 75 MW of electrical energy, is located between the maximum and minimum points of the SP anomaly which are 8 km apart (Fitterman and Corwin, 1982). The width of the SP anomaly is possibly owing to several faults acting as geothermal conduits rather than just the Hidalgo Fault.

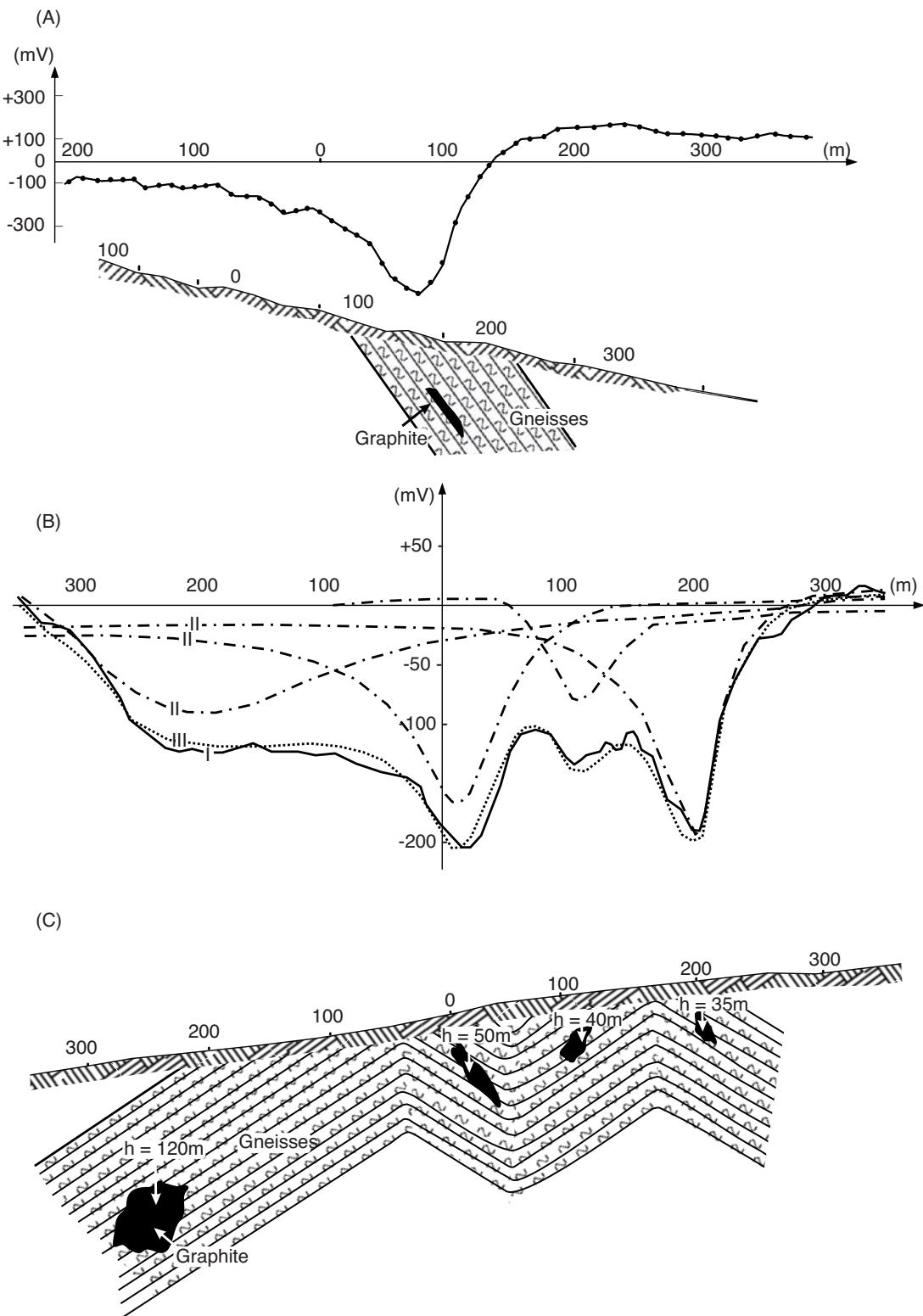


**Figure 8.10** (A) A self-potential anomaly across a single graphite body in gneiss. (B) Individual model SP anomalies for each of four graphite bodies in gneiss, and (C) the observed profile. From Meiser (1962), by permission.

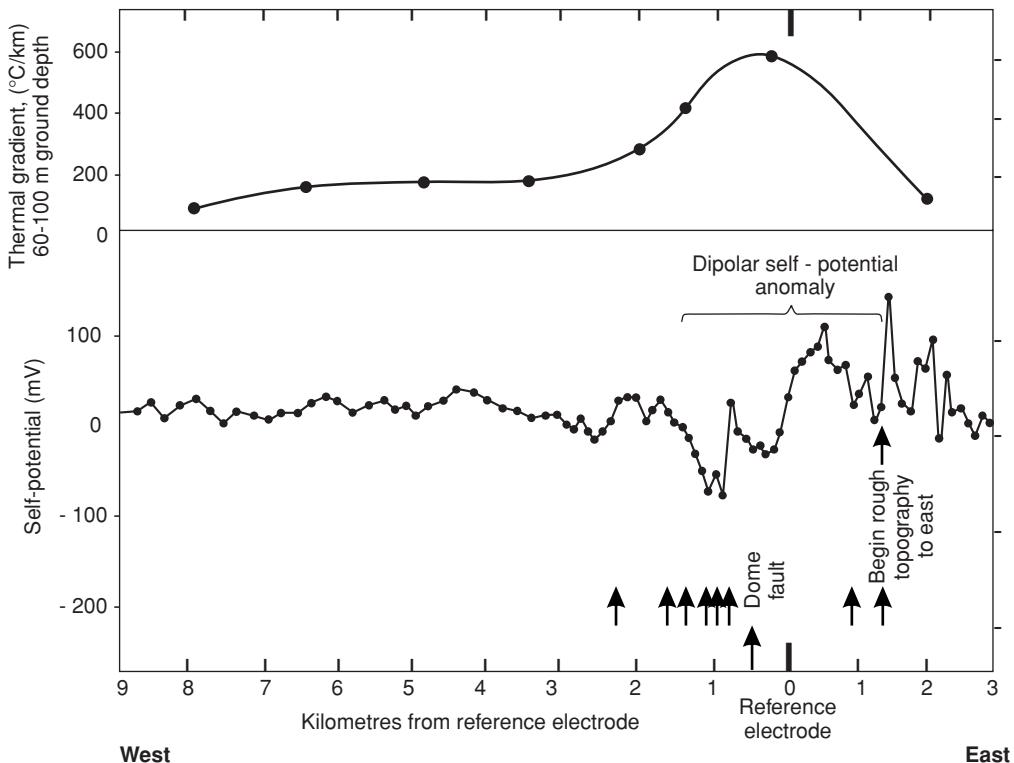


**Figure 8.11** Thermal gradient and self-potential profiles over the Dome Fault Zone, Roosevelt Hot Springs, Utah. Arrows denote points at which mapped faults cross the SP survey line. From Corwin and Hoover (1979), by permission.

## 8.7.2 Mineral exploration

### 8.7.2.1 Kimheden orebody, Skellefte, northern Sweden

The Kimheden orebody, which is mainly pyrite, occurs in steeply dipping sheets along a ridge in moraine-covered sericite-quartzite. The tops of the ore fragments are at no more than about 10 m depth. The SP contours (Figure 8.13) show several clear linear features that correlate extremely well with the known position of the orebodies (Parasnis, 1966), with one exception. The most western orebody (X) was found to have a particularly high resistivity, which may explain the absence of any anomaly (see Section 8.3.3).

### 8.7.2.2 Copper ore at Chalkidiki, northern Greece

The Chalkidiki area of northern Greece consists of gneisses and schists that are strongly sheared and intruded by mineralised granitic-granodioritic and ultrabasic structures (Figure 8.14). Pyrite, galena and sphalerite are associated with the acidic intrusions, and magnetite and chromite with the basic intrusions. Copper minerals and pyrite have resulted from Tertiary volcanic activity and are particularly associated with lava flows of trachytes, andesites and porphyritic granodiorite, and have been concentrated within a dense network of fractures and faults. There are three recognisable

zones of copper mineralisation, of which the shallowest consists of an oxidised leached zone (about 1% Cu). Below this is a zone of secondary enrichment 2–3 m thick in which copper concentrations are as high as 20% (malachite, azurite, eupyrite, etc.). The lowest zone, which represents the primary mineralisation of chalcopyrite, pyrite, bornite and syngenetic magnetite, begins at around 20–30 m depth and extends down to at least 300 m below surface. The magnetite within the volcanic rocks gives rise to distinctive magnetic anomalies, the maxima of which occur just within the margins of the trachyte dome. The minima of the self-potential anomalies occur specifically over the copper ore bodies. Where the oxidation of the copper sulphide is marked, which produces a low magnetic susceptibility, there is a corresponding cusp in the magnetic profile. This example also highlights the complementary use of two different geophysical methods (based on Zachos (1963) and Parasnis (1966)).

### 8.7.2.3 Sulphide orebody at Sariyer, Turkey

A classic, and oft cited, example of a self-potential anomaly over a sulphide orebody is the one given by Yüngül (1954) for a complex orebody at Sariyer in Turkey (Figure 8.15A). Chalcopyrite and pyrite occur in varying concentrations within a massive deposit within andesite and below Devonian schist. The area is characterised by a steep surface gradient which, if not corrected for, displaces the SP minimum downhill. The orebody comprises four regions, of

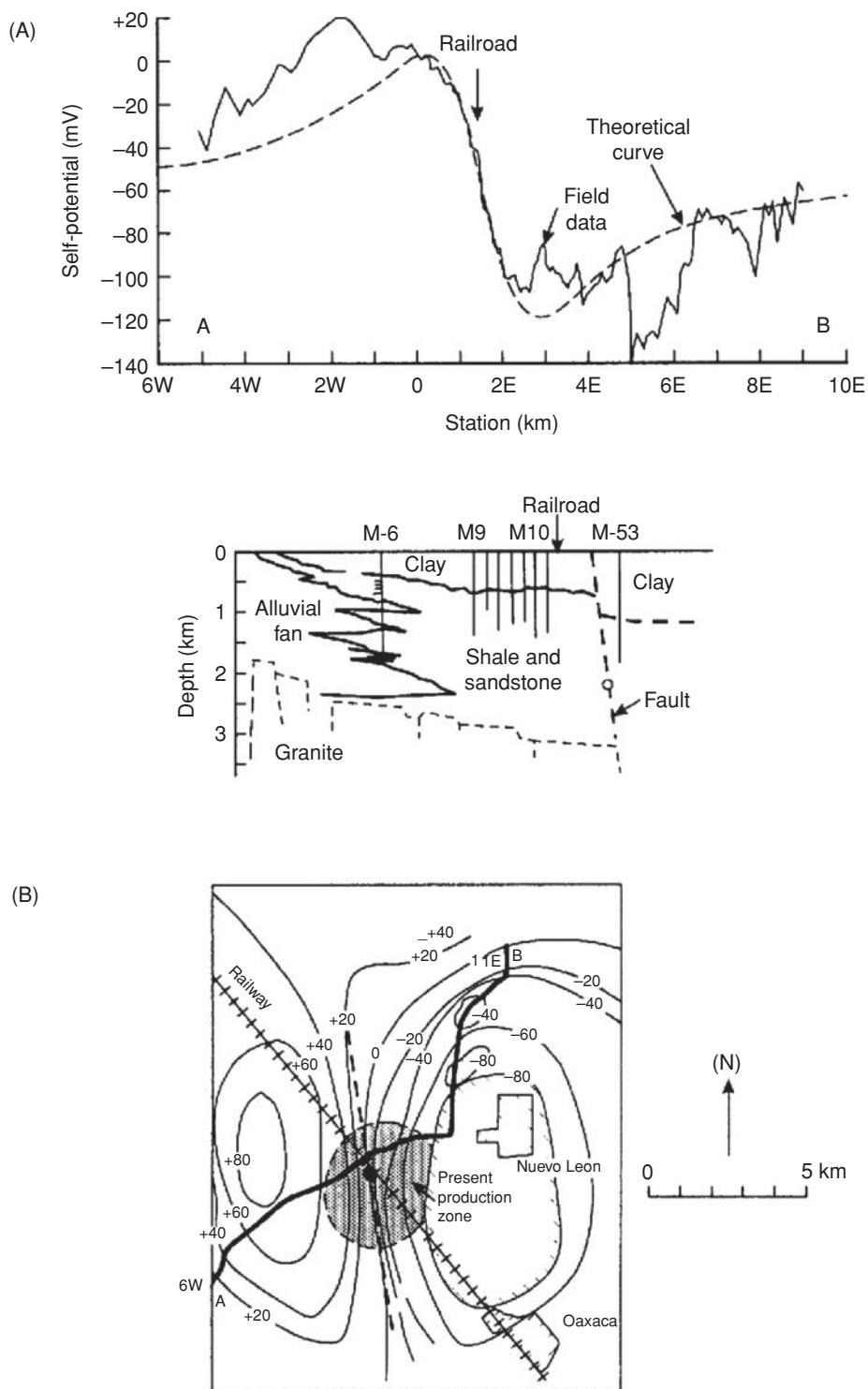


**Figure 8.12** (A) Self-potential anomaly along the profile A-B over the Cerro Prieto geothermal field, Mexico, with a simplified geological cross-section. After Corwin and Hoover (1979), by permission. (B) Self-potential map over the same field (profile line A-B marked) showing a distinct positive-negative couplet with the geothermal production area being midway between the two parts of the anomaly. After Fitterman and Corwin (1982), by permission.

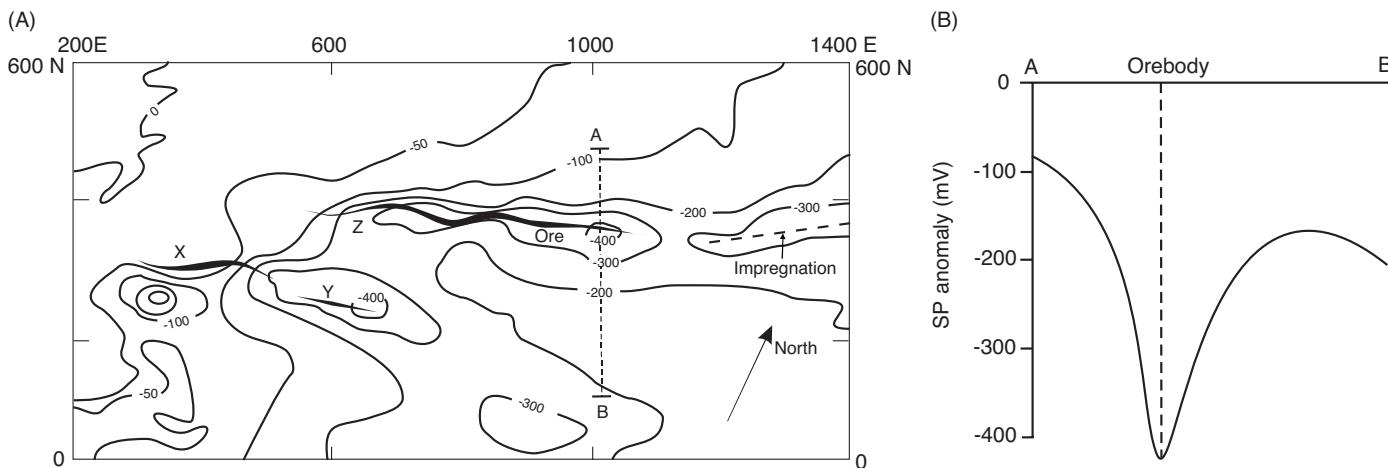


**Figure 8.13** (A) Self-potential map of the Kimheden pyrite orebody in northern Sweden. From Parasnis (1966), by permission. (B) The SP anomaly across profile A–B. Map contours are in mV.

which the one furthest downhill is pyritised and the three remaining zones have decreasing concentrations of copper from 14% on the downhill side to 1–2% on the upslope side. Each of these zones may be represented by a sphere whose SP anomaly contributes to the total anomaly observed (Figure 8.15B). The inflection points present on the observed profile can be modelled by changing the separation between the various model spheres.

This example demonstrates that subtle inflection points within an anomaly may be extremely important and should not be dismissed as being insignificant. In addition, the field data must be of very high quality in order to isolate such subdued features. For another example of the use of SP data in pyrite orebody investigations, see Logn and Bölviken (1974).

#### 8.7.2.4 High sulphidation gold deposits, Yanacocha, Peru

Large silica bodies associated with high-sulphidation oxide gold deposits in the Yanacocha district, Peru, have been characterised by significant self-potential anomalies up to  $-10.2\text{ V}$  in amplitude, the largest SP anomaly recorded to date (Goldie, 2002). One project site at Pabellon within the Yanacocha district reveals a highly resistive silica body ( $>10,000\text{ }\Omega\text{m}$ ) associated with an SP anomaly of  $-6.2\text{ V}$  over a volume of  $1000\text{ m} \times 1000\text{ m} \times 400\text{ m}$ . At another prospect, Puca Rumi, a large negative SP anomaly ( $-1.7\text{ V}$ ) was shown to correlate with a high-resistivity feature ( $>10,000\text{ }\Omega\text{m}$ ) over a high-silica body with a volume of  $400\text{ m} \times 600\text{ m} \times 100\text{ m}$  (Figure 8.16A). At Escalon, a resistive  $500\text{ m} \times 500\text{ m} \times 150\text{ m}$  granular silica unit that crops out gives rise to an SP anomaly of  $-4.946\text{ V}$  (Figure 8.16B). However, two subsurface, moderately resistive anomalies, proven by drilling to be associated with silica alunite, do not have a surface SP response, as the causative features are overlain by conductive clay. This clay appears to provide an impermeable barrier over the buried silica, and is thought to prevent the electrical potential from reaching the surface or perhaps to disperse the electropotentials so

that their magnitudes are too small to be identified unequivocally above noise levels. In contrast, a survey over the El Tapado deposit shows that a resistive ( $>1000\text{ }\Omega\text{m}$ ) silica body underlying resistive gravel can be detected using an SP survey. A moderate SP anomaly ( $\sim -1.5\text{ V}$ ) is clearly located over the bedrock massive silica unit under about 50 m of silica-rich alluvial cover (Figure 8.16C). Perhaps the most striking SP anomaly is that found at the Chaquecocha deposit, where an SP anomaly of  $-10.2\text{ V}$  was found associated with a highly resistive ( $>10,000\text{ }\Omega\text{m}$ ) silica body with dimensions  $1500\text{ m} \times 1500\text{ m} \times 300\text{ m}$  (Figure 8.16D). In each of the cases cited, there was no direct relationship between topography and SP responses.

### 8.7.3 Hydrogeology

Geothermal applications involving groundwater have already been discussed (Section 8.7.1), and the use of SP measurements in groundwater borehole testing were mentioned in Section 8.3.1. Other examples in hydrogeology are the use of SP measurements to detect the sites of leakages associated with manmade and natural dams (Ogilvy *et al.*, 1969; Bogoslovsky and Ogilvy, 1970a,b; Butler and Llopis, 1990; Jansen *et al.*, 1994), percolation of fresh groundwater through quartz gravels (Nayak, 1981), and in the study of groundwater movement (Schiavone and Quarto, 1984), for example.

Fournier (1989) used the SP method in conjunction with resistivity surveys to investigate the hydrogeology of volcanic aquifers in the Chaîne des Puys area of central France. He was able to delimit the catchment area of each spring, and found that an axial graben was the main aquifer and identified possible zones vulnerable to pollution. He also found that the water table provided the main source of SP anomalies and that their shape indicated the form of the water table. Fournier was able to characterise his SP anomalies in terms of hydrogeological significance (Table 8.3).

Lénat (2007) has provided an example of a regional-scale SP survey undertaken over Piton de la Fournaise on the island of La

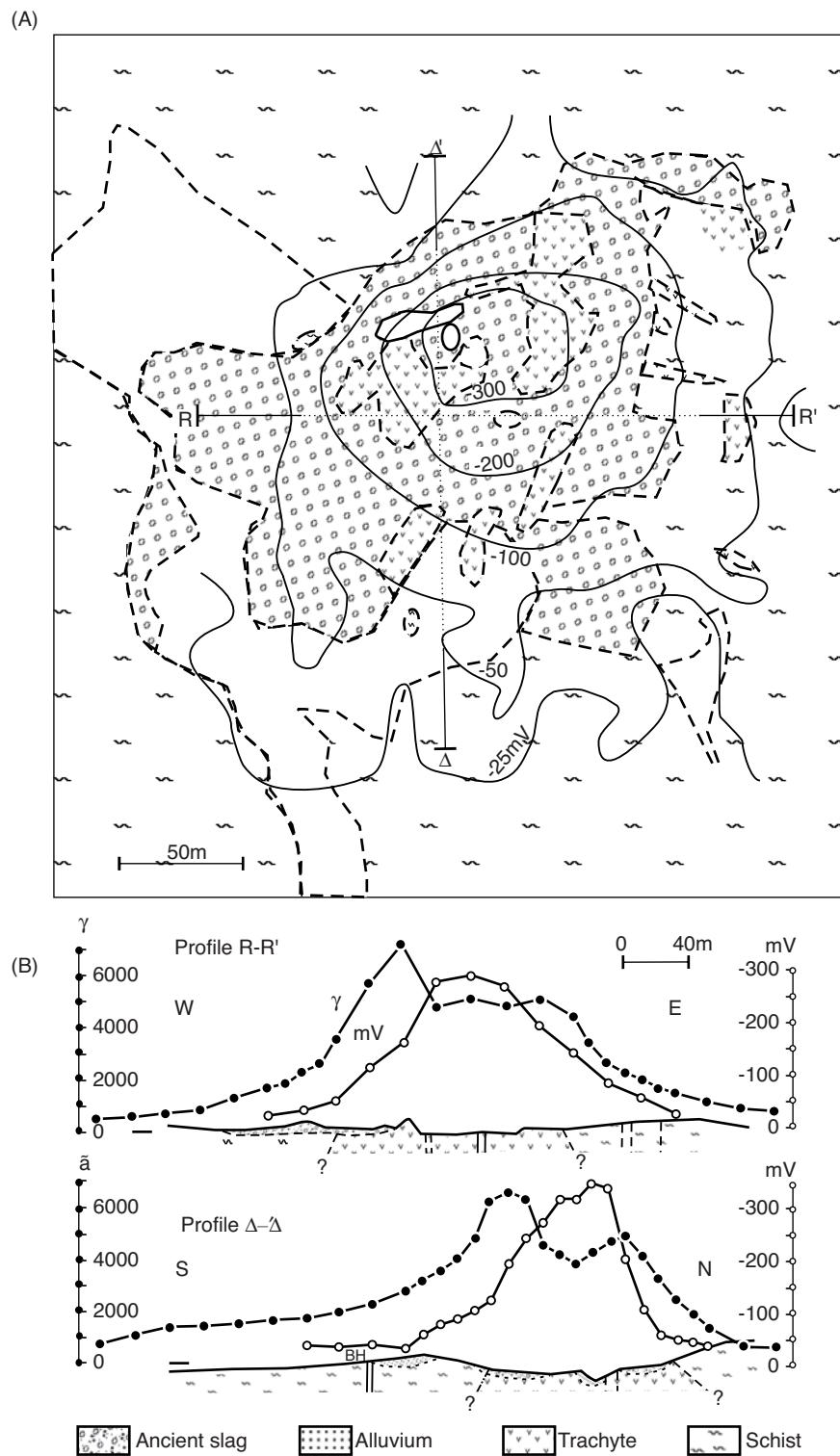


**Figure 8.14** (A) Map of the solid geology and self-potential values (in mV) in Chalkidiki, northern Greece. (B) SP and magnetic total field (in nT) profiles  $r-r'$  and  $\Delta-\Delta'$ . From Zachos (1963), by permission.

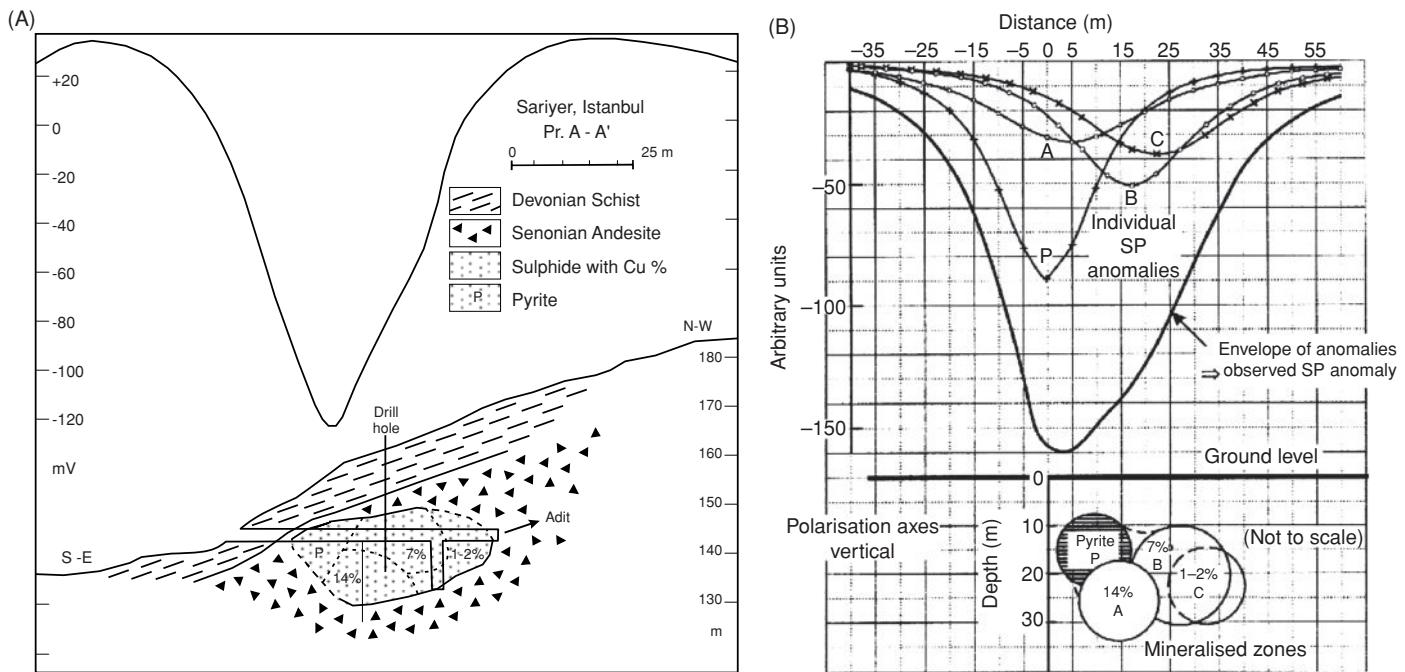


**Figure 8.15** (A) Self-potential anomaly across a pyrite ore body at Sariyer, Turkey. The borehole is located at the location of the topographically corrected SP minimum. (B) An equivalent model assuming each segment of the ore body conforms to a sphere with its axis of polarisation vertical, with the corresponding individual SP anomalies and their envelope. After Yüngül (1950), by permission.

Réunion to the east of Madagascar. The area is part of a highly active basaltic shield volcano that rises to an elevation of 2600 m. Linear trends in increasingly negative SP values with rising elevation are commonly found on the flanks of volcanoes. For example, at Kilauea, Hawaii, a linear trend of  $-1.7 \text{ mV/m}$  was found from sea-level to the main vent at an elevation of 550 m. A series of SP surveys has been undertaken over more than two decades at Piton de la Fournaise and combined over most of the active part of the volcano and a large part of its older, western flank. SP values range from over  $+200 \text{ mV}$  associated with the oldest more altered zones, to  $-3400 \text{ mV}$  (Figure 8.17A). On the stable outer flanks, SP values have remained stable over many years, fluctuating by no more than a few tens of mV. However, in the active central part, SP values are known to change in the areas where new eruptive fissures form. These anomalies have amplitudes ranging from a few tens to a few hundreds of mV, but subside to pre-eruptive values in the following months and years. Lénat (2007) has calculated the SP/elevation gradient for the SP grid data in order to highlight the different hydrogeological zones (Figure 8.18). The younger parts of the volcano are associated with more negative values of the SP/elevation gradient than the oldest, more altered zones. This technique shows promise in the differentiation of the various hydrogeological zones within an active volcano (perched water tables, hydrothermal zones, etc.). It has also been used successfully on two other volcanoes (Misti, Peru (Finizola *et al.*, 2004), and Stromboli, Italy (Finizola *et al.*, 2002)).

Associated with the hydrogeological applications of SP measurements is their possible use in earthquake prediction where the active fault planes are at very shallow depths and where deployment

of instrumentation is both feasible and viable. It has been noted previously (Rikitake, 1976) that natural electric fields within the ground may change prior to an earthquake, and therefore could act as sensible precursors to some types of seismic events. Renata (1977) attempted to argue that these electrical changes may be due to electrokinetic potentials associated with stress build-up/relaxation processes.

Further evidence of what is now called the ‘seismoelectric response’ has been presented by Butler *et al.* (1994). In an experiment using a sledgehammer source and electric field receivers, an electromagnetic signal was observed when the seismic wave impinged upon a boundary between organic-rich fill and impermeable glacial till. The depth to the interface (confirmed by drilling) was from 1 m to 3 m. It is believed that the electrical response was a transient streaming potential produced by a seismically induced flow of porewater at the interface. The critical combination in this experiment was the juxtaposition of a permeable material and an aquitard at shallow depth. It is postulated that this technique could be used to help map aquitards or the boundaries of permeable formations where they terminate against an impermeable material. This is discussed further in Section 8.8.

#### 8.7.4 Landfills and contaminant plumes

Steep-sided landfills containing significant volumes of highly conductive leachate that may leak through the margins are known to generate significant SP anomalies (Coleman, 1991). The reasons for this are primarily twofold. Firstly, there is an ionic imbalance

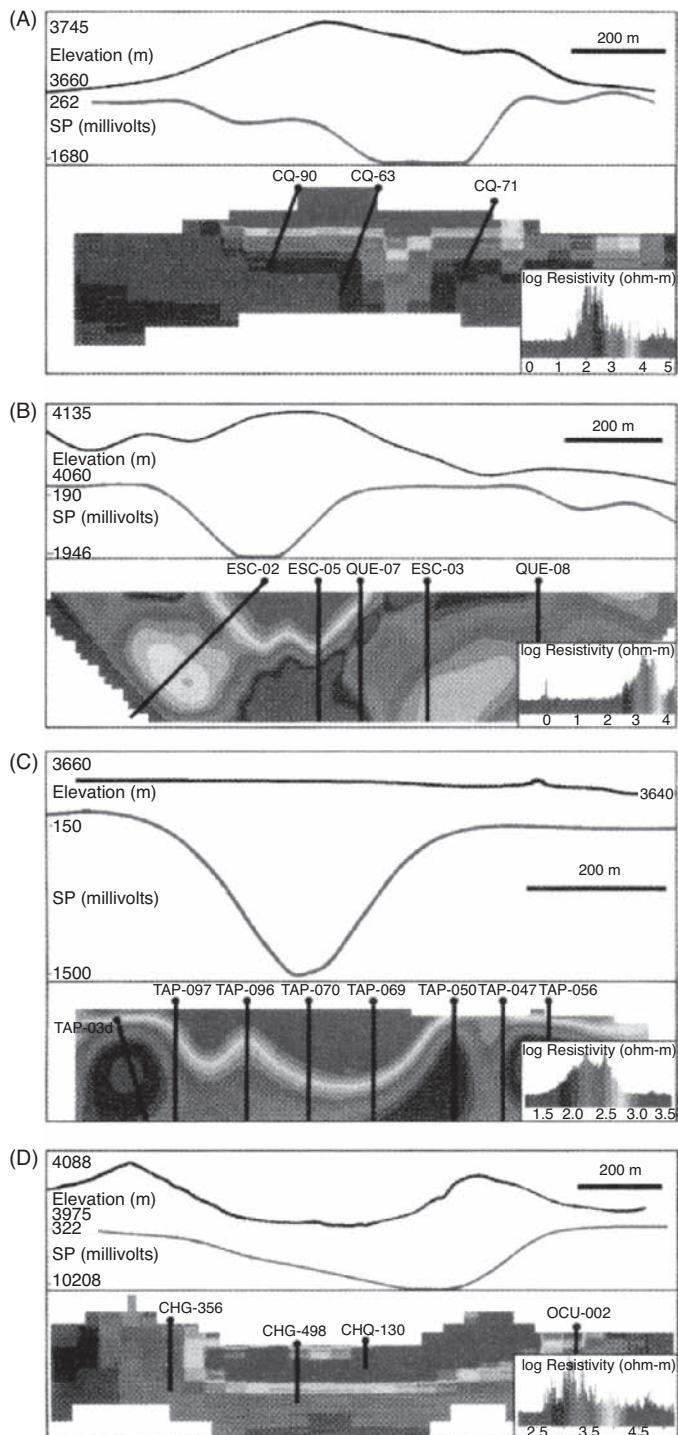


**Figure 8.16** Comparison of typical examples of the SP and resistivity responses at Yanacocha, Peru. Resistivity sections of pole-dipole IP/resistivity 2D inversion models with drill-hole locations compared with SP and topographic profiles at (A) the Puca Rumi, (B) Escalon and (D) Chaquicocha projects. (C) A CSAMT resistivity section of a 2D inversion model with drill-hole locations at the El Tapado deposit. From Goldie (2002), by permission. [C]

in concentrations each side of the landfill boundary, with high values within the landfill (due to the leachate) and low values outside (within the natural groundwater). In order to equilibrate the imbalance, diffusion occurs. As ions (which are charge carriers) move, their movement constitutes an electromotive force – an electrochemical potential. Secondly, if the leachate physically flows from the landfill outwards, a streaming potential may be generated. Consequently, if both electrochemical and streaming potentials are generated, it is highly probable that a measurable SP anomaly would be present at the landfill boundaries.

Coleman (1991) has produced an example of SP anomalies associated with the margins of a landfill (Figure 8.19). While there are small SP anomalies within the landfill, the largest SP events are associated with the boundaries, where the ionic imbalances are greatest and the rate of flow of leachate is most pronounced.

Nyquist and Corry (2002) have provided an example of the use of SP in monitoring and assessing bio-remediation of a site. They cite a proof-of-principle survey undertaken at a site near Oyster, Virginia, USA, which is located in Atlantic coastal sands. The site had been extensively investigated by both intrusive and non-intrusive testing and a substantial amount of information was already available about the site. However, it was discovered late on that there used to be a tomato-canning site nearby, and spoil was dumped in waste trenches up-groundwater gradient from the research site. Bacteria digesting the waste tomato liquor depleted the oxygen in the groundwater, resulting in an anaerobic groundwater plume that flowed across one corner of the site. Nyquist and colleagues undertook an SP survey over the site and compared the results with dissolved oxygen (DO) measurements that had been made in still-standing monitoring wells. A consistent correlation was found between SP values and dissolved oxygen levels. DO values decreased from about 8 ppm outside the anaerobic plume to <1 ppm inside, with a corresponding variation in SP values from -60 mV to -20 mV inside the plume to values in excess of +5 mV in unaffected groundwater outside the plume. It is also suggested that the SP technique can lend itself to surveys where the natural subsurface geochemistry is being altered to clean up contamination *in situ*. This can include monitoring thermal treatment, chemical injection, bio-remediation, reactive barriers, air sparging, and so on. It is perhaps important, therefore, for the careful consideration of what potential geochemical reactions might be taking place in an affected site and how best to detect and monitor them using a variety of time-lapse geophysical techniques including the self-potential method.

## 8.7.5 Leak detection

### 8.7.5.1 Artificial embankments

The SP method has been used to detect leaks in earth dam embankments for decades (e.g. Bogoslovsky and Ogilvy, 1970a,b). Although less well publicised, marine or boat-borne SP surveys have been made for at least 60 years. Where groundwater flows through such a structure by finding the path of least resistance (e.g. piping), electrokinetic streaming potentials may be generated with sufficient magnitude to be detectable. The concept of the generation of SP

**Table 8.3** Hydrogeological interpretation of SP anomalies (Fournier, 1989).

Aspect	Location	Hydrogeological significance
High horizontal SP gradient	On flat topography	Lateral limit of an unconfined aquifer
SP minimum	On a volcano flank	Ascent of water table in volcanic cone
SP maximum	On flat topography	Palaeo-valley axis
SP maximum	On a volcano flank or summit	Crest of the water table and underground watershed line
SP maximum	Above an unconfined aquifer	Depression of the water table due to better drainage
	Between two unconfined aquifers	Watershed line due to crest of the impervious basement

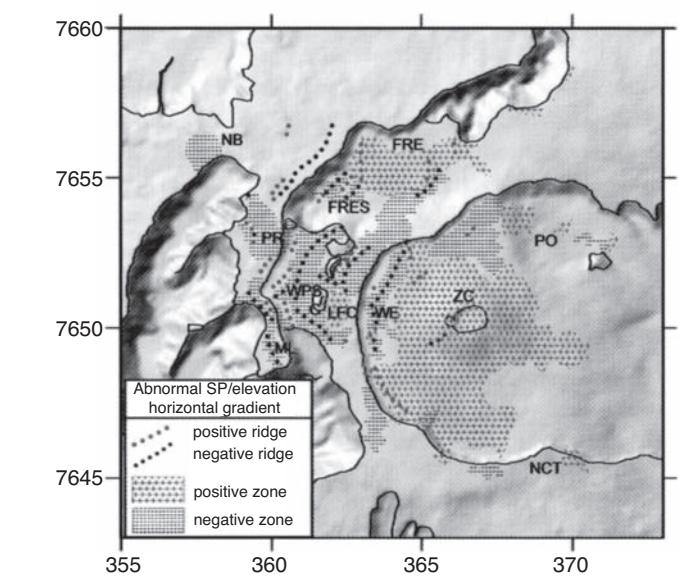
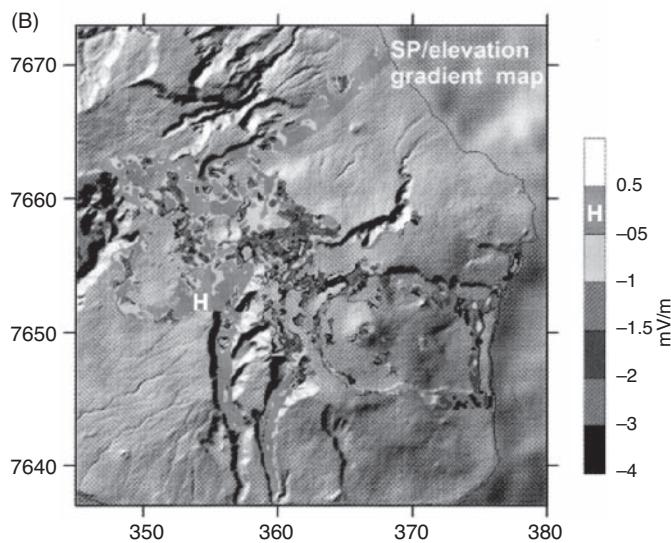
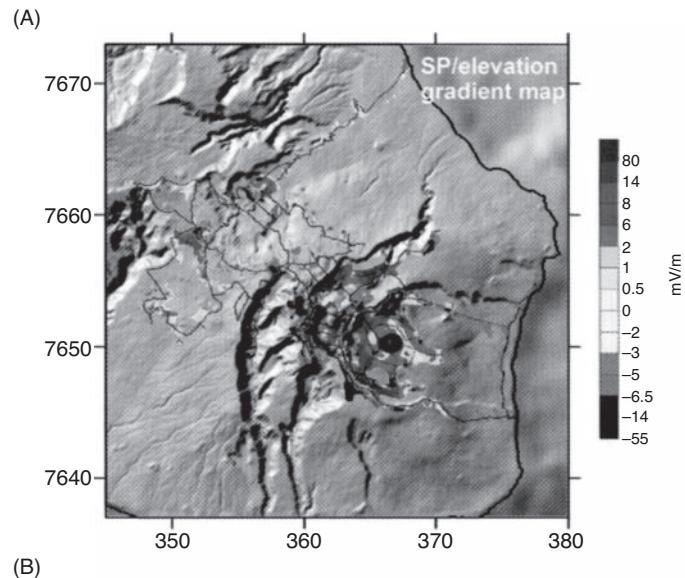
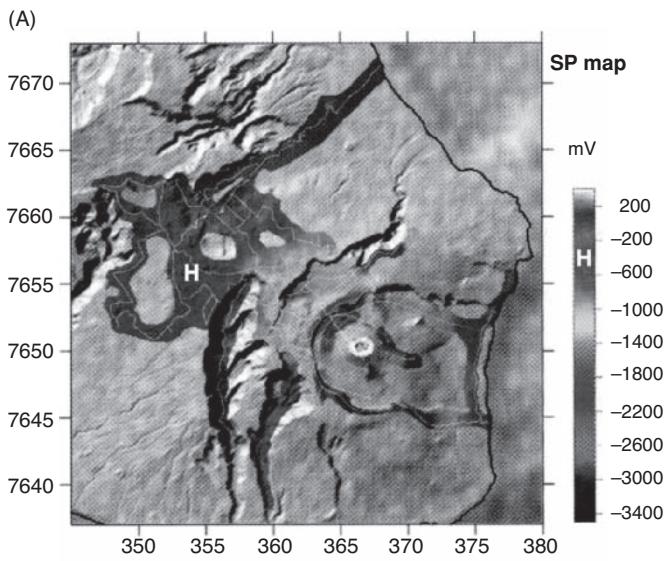


**Figure 8.17** Piton de la Fournaise, La Réunion, east of Madagascar: (A) SP (mV) map (white lines indicate profiles), and (B) SP/elevation gradient (mV/m) map. (UTM coordinates in km; north is upwards). From Lénat (2007), by permission. [C]

**Figure 8.18** (A) SP/elevation gradient (mV/m) map of Piton de la Fournaise and (B) map of the gradient anomalies. Lettering indicates place names in the original article. (UTM coordinates in km; north is upwards). From Lénat (2007), by permission. [C]

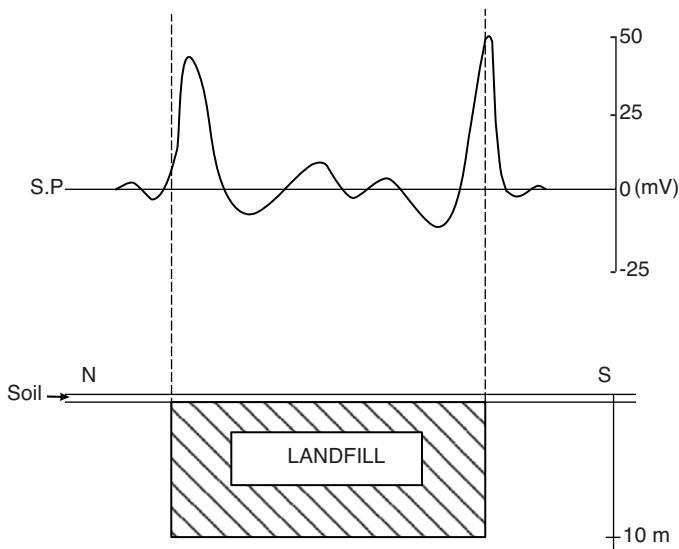


**Figure 8.19** SP anomaly over a closed landfill, showing the typically larger anomalies associated with the landfill boundaries compared with those observed in the interior. From Coleman (1991), by permission.

anomalies by leaks is shown schematically in Figure 8.20. Negative charges are associated with locations where leaks enter a dam, or above seepage paths where the flow is generally horizontal or descending. In contrast, positive anomalies may occur where the flow is generally ascending and where surface seepage takes place. Consequently, the presence of either or both a negative and/or positive anomaly may be physically significant.

Butler and Llopis (1990) have described an example of an SP survey to examine possible leaks at the Mill Creek Dam and Reservoir, Washington, USA (Figure 8.21). Since its first test filling in

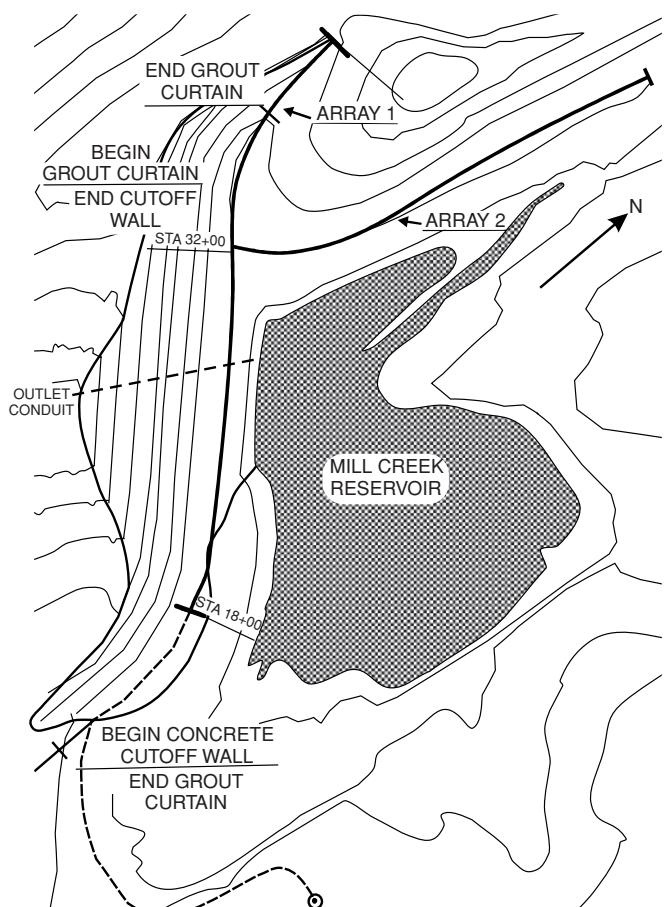


**Figure 8.21** Plan of Mill Creek Dam and Reservoir, Washington, USA, showing the locations of SP survey lines 'Array 1' and 'Array 2', grout curtains and the concrete cutoff wall. From Butler and Llopis (1990), by permission.

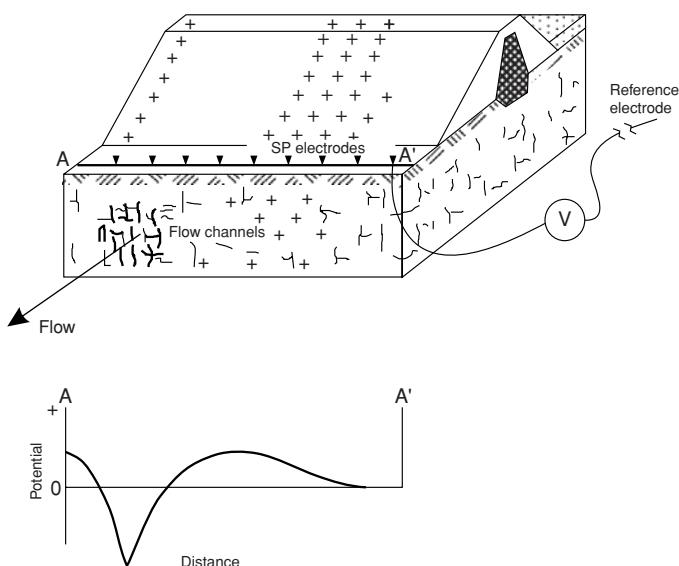


**Figure 8.20** Schematic of the concept of SP anomalies generated by features associated with seepages through earth dams. From Butler and Llopis (1990), by permission.

1941, considerable loss of stored water has been noticed. Attempts to change or stop the seepage have been unsuccessful. A concrete cut-off wall with flanking grout curtains was installed. The concrete wall was built on top of a massive basalt which underlies laterally variable conglomerate. Since the construction of these structures, the reservoir had not been filled but seepage was still evident.

In 1984, a geophysical investigation was instigated to detect anomalous seepage before, during and after test filling of the reservoir. Two SP electrode arrays comprising 85 metallic rods (copper-clad steel grounding rods) at 15 m spacings were installed two months before the first set of SP readings and four months before the first test filling. The reference electrode was located upstream. During the test, the reservoir level was raised by 10 m. The SP profile acquired along Array 1 (see Figure 8.21) before the filling of the reservoir is shown in Figure 8.22. Several notable features are evident:

- There is an anomaly of about  $-380$  mV associated with a 1.07 m diameter outlet conduit located about 20 m below the electrode array.

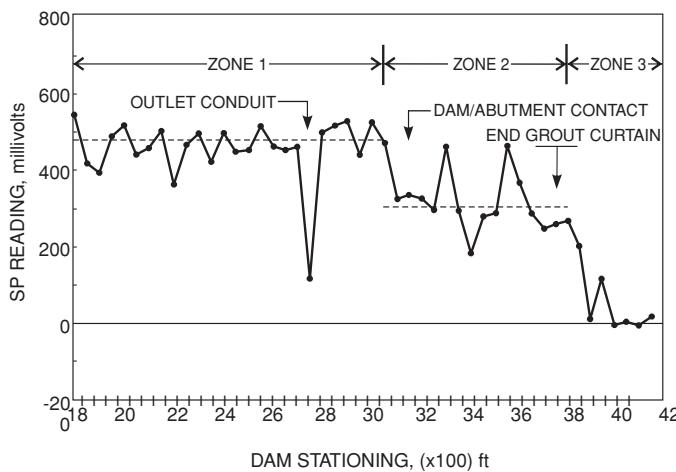


**Figure 8.22** Array 1 SP data acquired prior to the start of the filling of the Mill Creek Reservoir in Figure 8.21. From Butler and Llopis (1990), by permission.

- Three separate zones along Array 1 are distinguished by different base levels (indicated by dashed lines).
- The boundaries between zone 1/zone 2 and zone 2/zone 3 coincide approximately with the dam/right abutment contact and the end of the grout curtain, respectively. The anomaly associated with the boundary between zone 1 and zone 2 is thought to be due to a lateral change in material type. The zone 2/zone 3 boundary is caused by a lateral change in the groundwater flow regime as a result of the presence of the cutoff wall and the grout curtain.

As a test of the SP response to the raising of the level of the reservoir, values of the array averages responded immediately to the increase in water level, as indicated by the data in Figure 8.23. No

SP values were measured between 9 February and 5 March; the test fill began on 5 March. Note that the trend in SP anomaly with time is negative.

Further analysis of the SP data yielded an indication of several locations, most notably at station 18 (Figure 8.21) and at 30 + 50 (junction of zones 1 and 2). The cause at station 18 was thought to be seepage occurring under the cutoff wall in a very localised zone. The postulated seepage at 30 + 50 coincides with the end of the cutoff wall/grout curtain. The SP data, although not conclusive in themselves, provided valuable spatial and temporal data that aided a better understanding of the hydrogeological conditions of the site.

Marine surveys have typically been undertaken with a pair of silver-silver chloride electrodes (gradient array) behind a boat towed at the surface or at depth above the water bottom (Corwin, 1973). Alternatively, using an electrode fixed on the seabed, a mobile electrode is dragged along the bottom. Occasionally a borehole SP logging tool is used as the mobile tool. Other configurations include a pair of electrodes separated by only 1.25 m, suspended beneath a boat or lowered to the water bottom, and used with a third, fixed electrode planted by a diver remote from the profile line. An alternative to the surface-towed gradient array is the benthic gradient array where two electrodes are towed behind a weighted towfish and dragged along the water bottom in direct contact with the sediment. A development of this is the use of a fixed electrode, implanted by deploying the weighted electrode from the boat and letting it sink under gravity, and towing a weighted eel with a second electrode in its hind part, also in contact with the sediment.

Jansen *et al.* (1994) found that the benthic single roving electrode configuration produced much higher-quality data than using a benthic gradient array. Examples of data acquired using the two different methods over the same profile are shown in Figure 8.24. In the benthic gradient array dataset (Figure 8.24A), one main negative anomaly can be seen at location 410 ft north. The same feature is evident on the benthic single roving electrode data (Figure 8.24B). However, an additional feature is clearly seen at location 640 ft

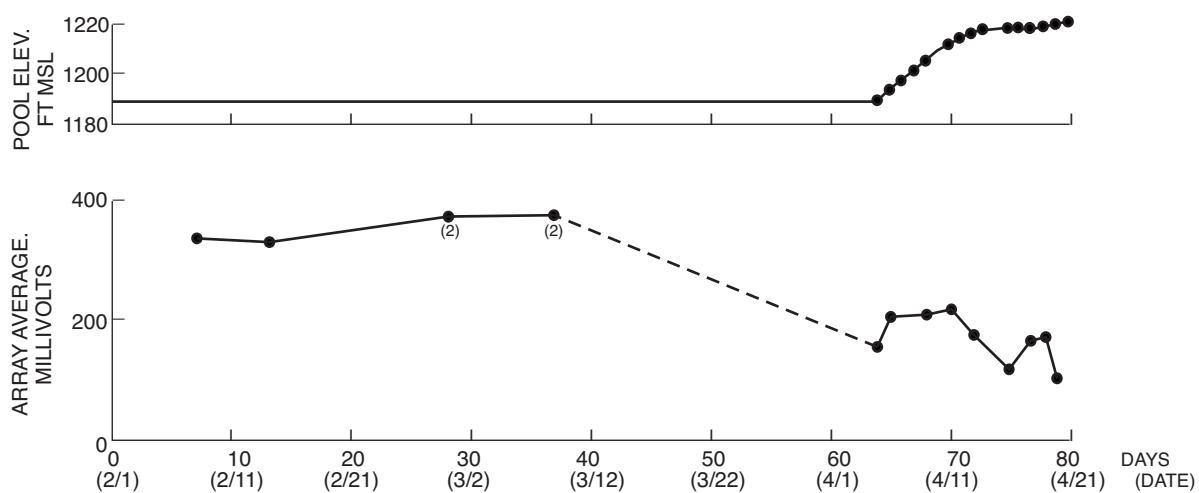


**Figure 8.23** Comparison of the reservoir water level with SP array average as a function of time (see Figure 8.21). Raising of the water level started on 5 April (4/5). From Butler and Llopis (1990), by permission.

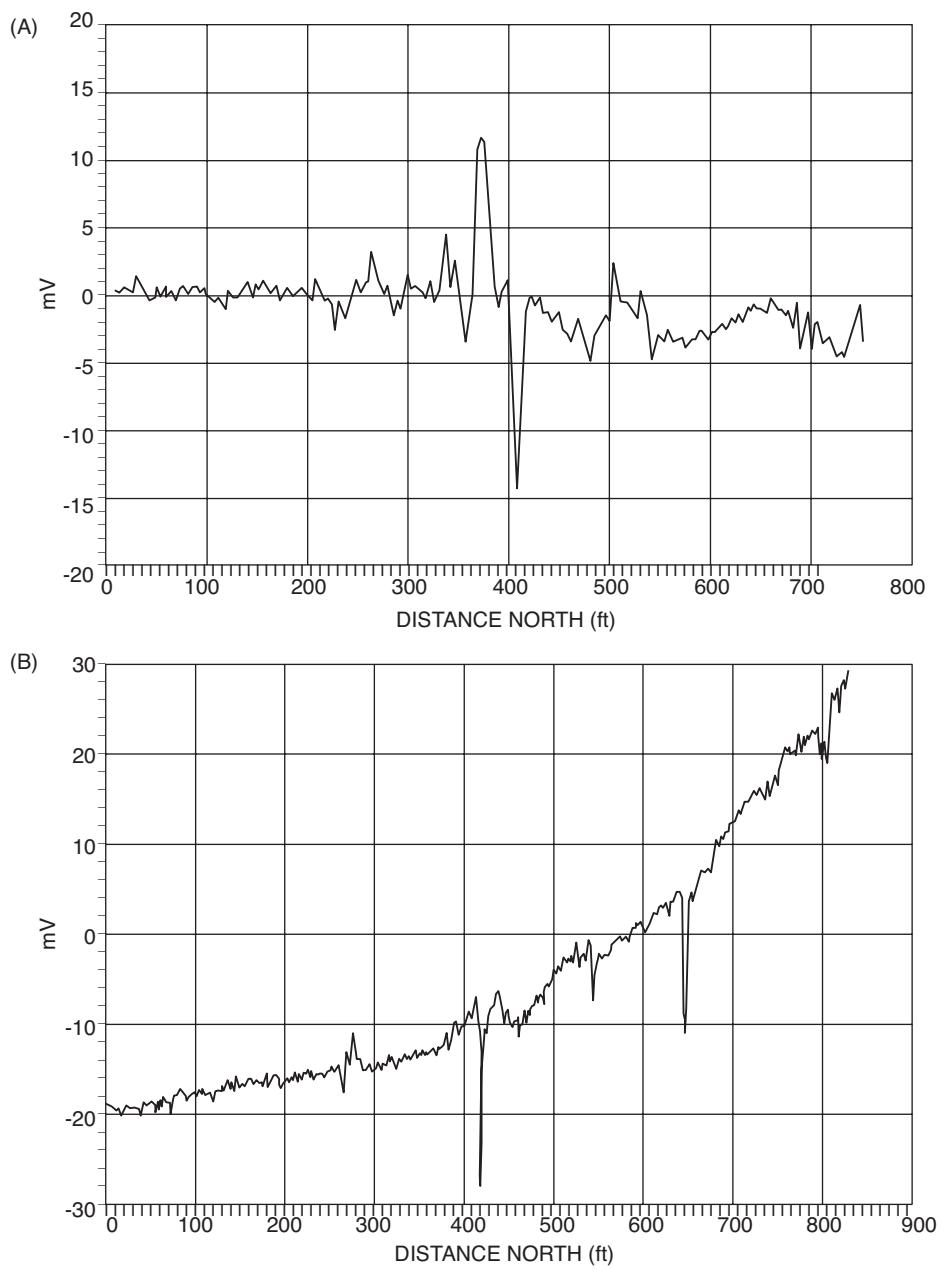


**Figure 8.24** Examples of boat-borne SP profiling along a test line in a fresh-water filled reservoir, using (A) a benthic gradient array with a 40 ft (12.2 m) electrode spacing, and (B) a benthic single roving electrode with remote reference electrode. From Jansen *et al.* (1994), by permission.

north. Other less significant features are evident on both datasets, which demonstrate the degree of repeatability, despite using a different electrode configuration in each case. The reason the potential increases with the roving electrode is related to the changing distance from the remote electrode. In the gradient array, it is the potential measured across the pair of electrodes at a separation of 40 ft (12.2 m). The units of measurement should be given as mV/unit length (e.g. per dipole length). In the roving electrode case, it is not a complicated task to remove the effects of distance on the data to residualise them in order to highlight anomalous zones.

### 8.7.5.2 Natural dams

The SP method has been deployed in many investigations of mine tailings dams, and the effectiveness of the method lends itself to the study of leakage through natural dams. One such situation is at Petrov Lake in the Tien Shan mountains of Kyrgyzstan. This lake has formed from the retreat of a large glacier and is currently contained by a moraine dam which is known to contain buried stagnant ice. The stability of this dam is of concern for two main reasons. Firstly, the lake is the primary source of fresh water for a mine camp associated with a local major gold mine. Secondly, the

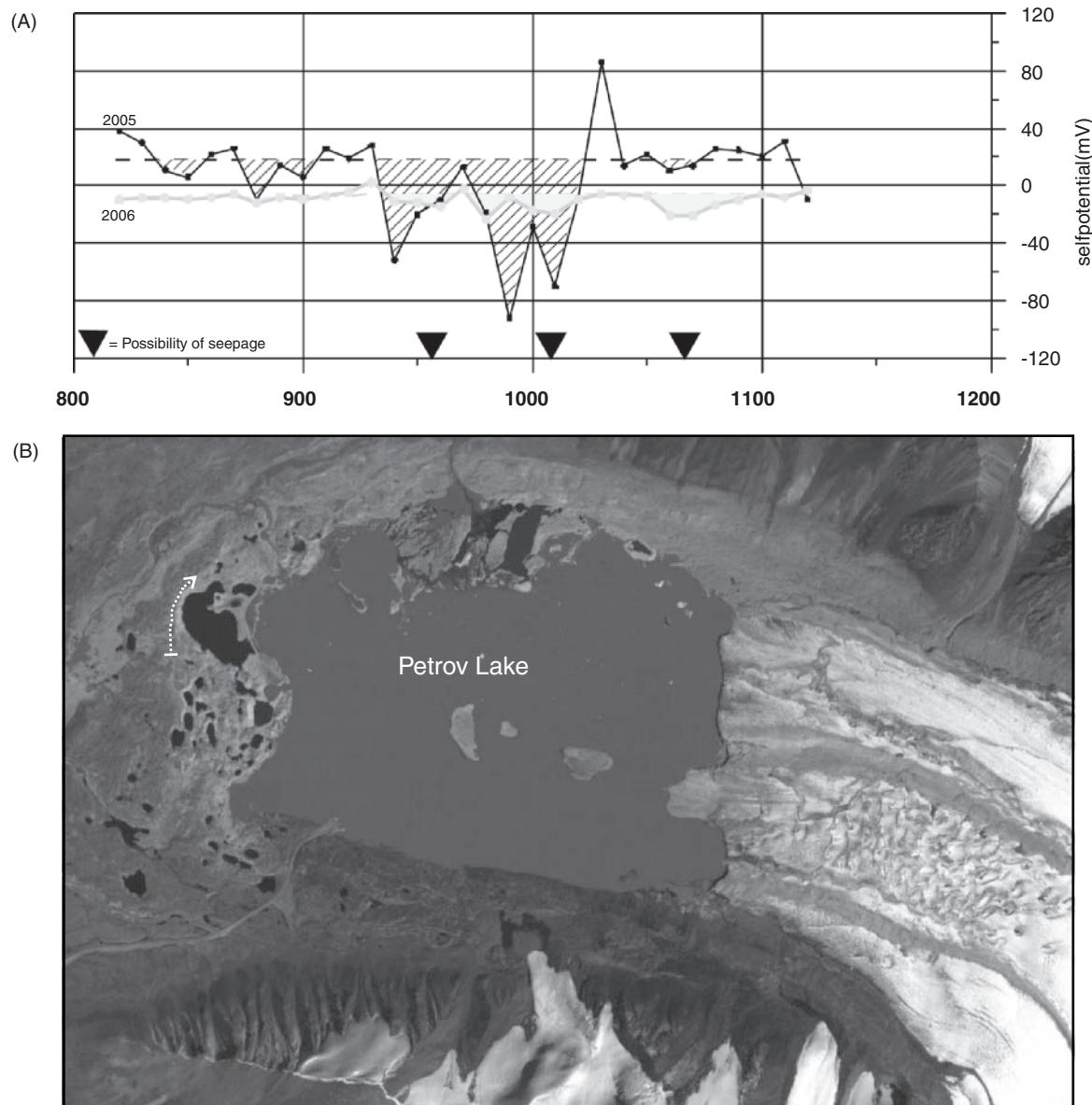


**Figure 8.25** (A) SP data acquired along the same transects in 2005 and independently in 2006 at Petrov Lake, Kyrgyzstan. Courtesy of Buhomír Janský, Charles University, Prague. The terminal moraine complex is shown in the satellite image (B) with the approximate line of the SP profile indicated.

moraine lies upstream of the tailings dam and there is concern that if the moraine should fail and a glacial lake outburst flood ensue, then the toe of the tailings dam might be affected leading to its potential failure, the consequences of which do not bear thinking about environmentally. This is part of an ongoing investigation, and further work is being considered.

Geophysical investigations have been undertaken at the terminal moraine complex over a number of seasons, including electrical resistivity tomography, microgravity and SP methods (Buhomír Janský, Charles University, Prague, pers. com. Janský). The ERT profiles have been very clear in helping to identify where ice is buried within the moraine complex. However, springs have been observed on the distal side of the moraine indicating that water is

flowing through the moraine, although it is not clear as to whether this is melt water from ice within the moraine itself, lake water, or a combination.

SP transects have been undertaken along a number of transects along and parallel to the moraine crest at slightly different times of the year in two successive seasons. The results (Figure 8.25) show two features. The first is the location of four possible subsurface water flows from the clear negative SP anomalies evident on the transects. The second is that the *location* of these anomalies is broadly consistent on profiles from two successive years, but that the *amplitude* of each anomaly is different. One survey was undertaken earlier in the summer before the main summer melt had started, while the second was conducted once the melt season had begun and flow rates

(i.e. streaming potentials) would be expected to be higher, hence the differences in anomaly amplitude. This time-lapse approach is further evidence that the SP method is useful not only in finding the location of leaks, but can give useful information about the relative flow rates of the water.

### 8.7.6 Mapping mine shafts

Patella's SPT method has been developed by Wilkinson *et al.* (2005), who have used it to detect mine shafts. Two mine shafts were known to occur at sites referred to as Site B and Site C. SP measurements were made using a standard porous-pot remote electrode 5 m outside each survey area, and a walking-stick roving electrode at 2 m intervals. Each survey area was approximately 50 m by 50 m in area. The SP results are shown in Figure 8.26. There are three reason-

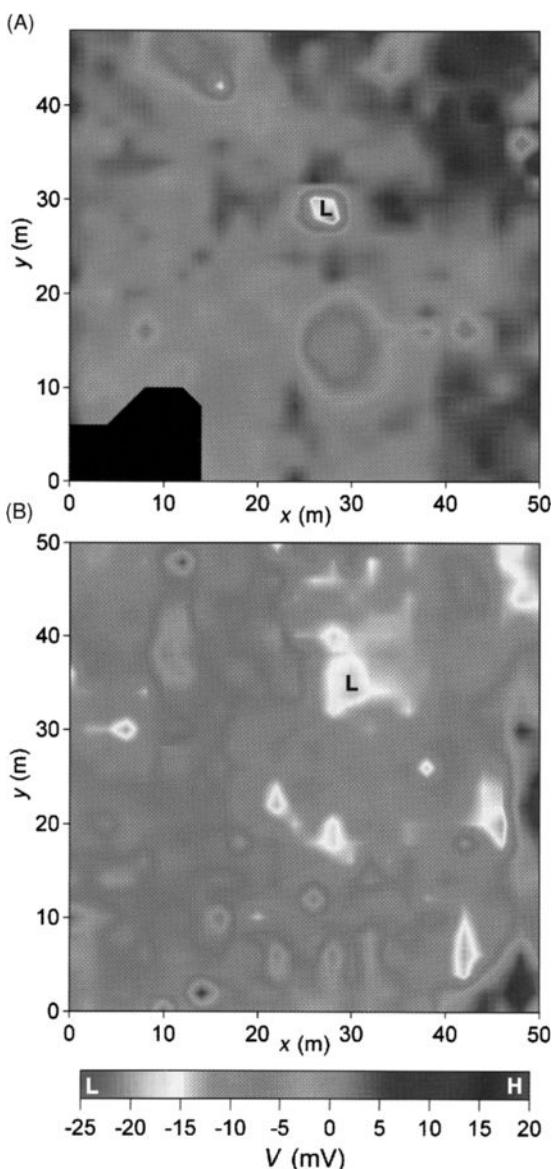


**Figure 8.26** Maps of self-potential ( $V$ ) measured at 2 m intervals as a function of ( $x, y$ ) for (A) Site B, and (B) Site C. From Wilkinson *et al.* (2005), by permission. [C]

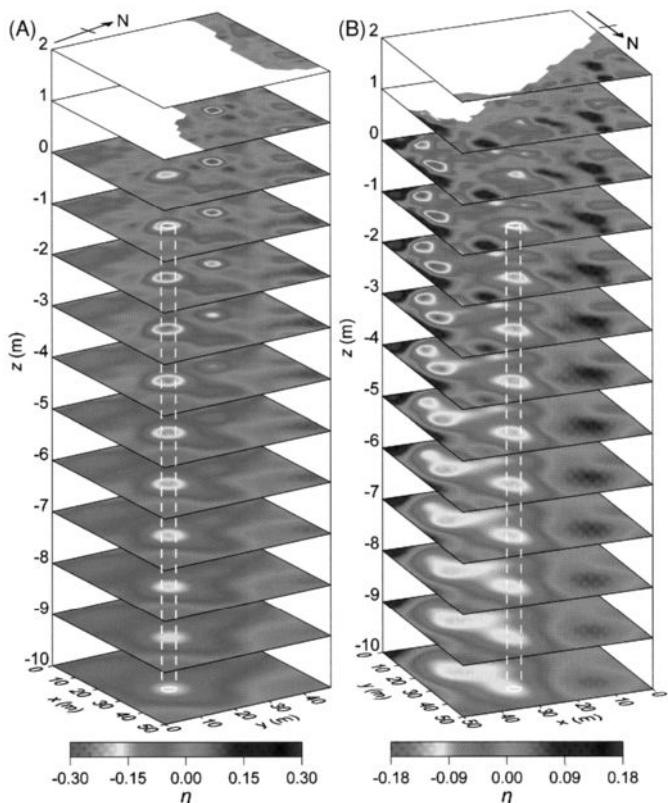


**Figure 8.27** Horizontal slices (tomopanes) showing charge occurrence probability ( $\eta$ ) values as a function of ( $x, y, z$ ) for (A) Site B and (B) Site C. The blank regions indicate points that are above ground level. For each site a dashed vertical cylinder with a 3-m diameter is shown to highlight anomalies associated with the mine shafts. From Wilkinson *et al.* (2005), by permission. [C]

ably well isolated negative SP anomalies at Site B (Figure 8.26A): a strong, roughly circular feature at  $x, y$  coordinates  $(27, 29)$ ; a slightly weaker, roughly circular feature at  $(29, 14)$ ; and a weaker, more irregular feature at  $(14, 44)$ . At Site C (Figure 8.26B) there are more anomalies than at Site B, but these are less well isolated and more irregular. It would be difficult on the basis of the SP map to interpret the location of a mine shaft.

Wilkinson *et al.* (2005) calculated the charge occurrence probability ( $\eta$ ) distribution at each site for planes at vertical depth increments of 1 m (Figure 8.27). For Site B (Figure 8.27A), the feature at  $(14, 44)$  decays quickly with depth and can be discounted. The strongly negative anomaly at  $(27, 29)$  has a strong signature at the surface but decays rapidly with depth and is indistinguishable by  $z = -4$  m. The SP anomaly at  $(29, 14)$  gives rise to a COP anomaly that can be clearly identified from  $z = 0$  m to  $-10$  m (annotated by a dashed cylinder in Figure 8.27A). This feature is associated with the mine shaft buried at a depth of 1 m below ground level. At Site C, where the SP results were more chaotic, several features are evident. Two strong negative COP anomalies occur at  $(45, 22)$  and  $(42, 7)$ . While the larger of these two anomalies persists with depth, its shape changes, broadening with depth. There is also a small positive COP anomaly at  $(48, 3)$  but this is only evident at shallow depths.

However, the COP anomaly at (30, 36) shows remarkably similar characteristics to the anomaly associated with the open mine shaft at Site B. The COP values are at their maximum between  $-2$  m and  $-3$  m and the roughly circular anomaly is persistent to a depth of  $-10$  m (indicated by the dashed cylinder in Figure 8.27B). This feature has been interpreted to be due to a mine shaft. However, the COP anomaly magnitude at Site C is about half that for the mine shaft at Site B. This can be explained by the mine shaft at Site B being open, allowing water to drain into it (hence higher streaming potentials), while the mine shaft at Site C is backfilled. Indeed, this was subsequently confirmed by the Coal Authority, who also indicated that the locations of both mine shafts determined from the SP/COP results were accurate to within 2 m, i.e. within one electrode increment. It is also notable that the ERT method was able to detect the mine shaft at Site B but was not able to locate the one at Site C, as the resistivity contrast between the backfill material and the host rock was insufficient.

## 8.8 Electrokinetic (EK) surveying

When a seismic wave travels through partially or fully saturated porous media, the seismic impulse effectively squeezes the rock, causing the pore fluid (electrolyte) to move. This generates a small electrical or electrokinetic signal that may be detected using electrodes implanted at the ground surface, an idea first mooted by Thompson in 1936. Around the same time, Russian workers were experimenting with similar systems (e.g. Ivanov, 1939). In 1959, Martner and Sparks reported a systematic study of seismo-electric coupling using explosives at various depths. They were the first to demonstrate that the conversion of seismic to electromagnetic energy at the water table could be detected using surface antennae. A review of the method was produced by Beamish (1999); see also Beamish and Peart (1998).

Theoretically there should be little or no seismo-electric response in partially or unsaturated media. A partially saturated vadose zone generates characteristic electrocapillary signals that are caused by the movement of air/water interfaces in pore throats, and electrophoretic signals that are caused by the displacement of bubbles within the pore fluid. However, fully saturated aquifers generate electrokinetic signals by the displacement of a single fluid (water or brine) when stimulated by a passing seismic wave. The difference between the two types of signal can be identified, leading to the determination of the depth to the water table in unconfined aquifers. The dry zone or basement or any non-aquifer rocks are characterised by the lack of any signal. The method is also referred to as seismo-electric or electroseismic surveying (Thompson and Gist, 1993). The signals to be measured are strongly dependent upon three main physical properties: porosity of rock, permeability and fluid chemistry. There are thought to be two types of signals (Butler *et al.*, 1996). The first is a non-radiating field that occurs in homogeneous media, and which is contained within and travels with the seismic P-wave. The second type is generated when the P-wave passes through a boundary across which there is a contrast in elastic and electrokinetic (fluid chemistry) properties. The electri-

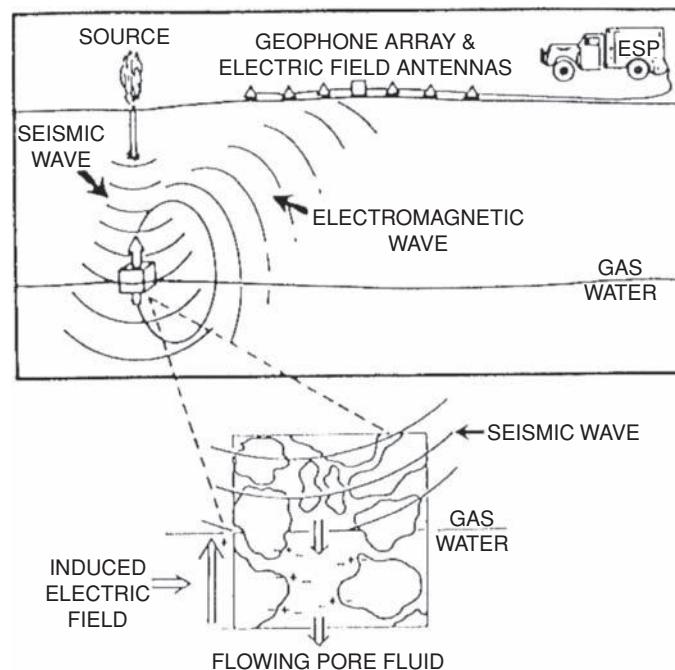


**Figure 8.28** Schematic of electroseismic prospecting as developed by Thompson and Gist (1993). Reproduced by permission.

cal signals generated diffuse towards the surface sensors faster than any P-wave. Consequently, such signals will arrive almost simultaneously across an array of dipole sensors at the ground surface (Rosid and Kepic, 2003).

The basic data acquisition system consists of a seismic source, usually a sledgehammer or shallow explosives (Figure 8.28). The seismic impulse propagates into the ground and any electrokinetic signals generated by the passage of the P-wave are detected using an electrode-pair dipole with an inter-electrode separation of between 0.5 m and 10 m.

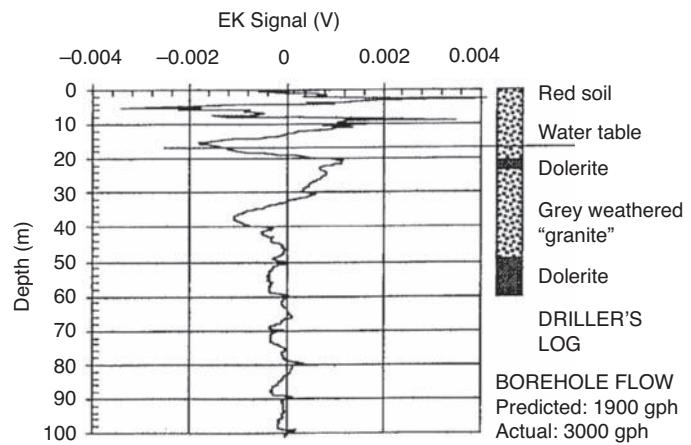


**Figure 8.29** Typical electrokinetic signal at a borehole site in Zimbabwe. Courtesy of GroundFlow Ltd.

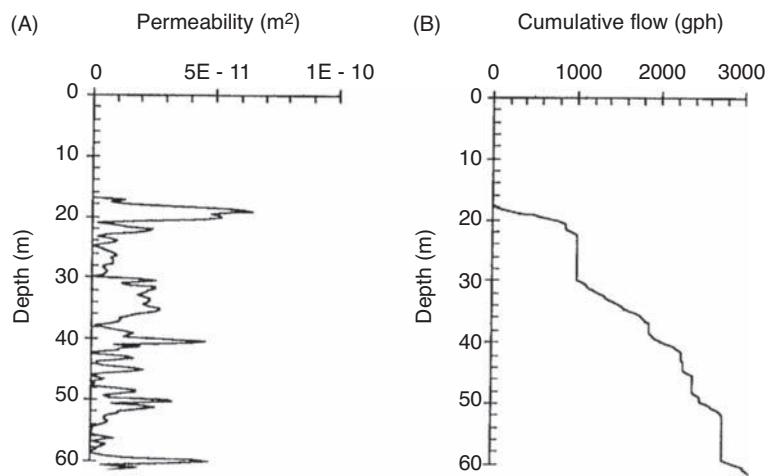


**Figure 8.30** (A) Permeability-depth profile, and (B) predicted flow derived from electrokinetic data at a borehole site in Zimbabwe.  
Courtesy of GroundFlow Ltd.

The technique was developed in the early 1990s in the USA under the name Electro-Seismic Prospecting (Thompson and Gist, 1993) for shallow (<1 km) hydrocarbon exploration, and in the UK by Clarke and Millar (GroundFlow Ltd; personal communication) for hydrogeological investigations, and by Butler *et al.* (1994) for mapping stratigraphic boundaries. Reference should be made to the papers indicated to see the fine differences between the methods proposed by various workers.

An example of the use of EK surveying is shown in Figure 8.29. The figure shows the EK response at a borehole site in Zimbabwe. The determination of depth has been undertaken using an assumed P-wave velocity of 1250 m/s. Note the strong EK responses at and around the position of the water table. Strong electrocapillary signals from the vadose zone are evident above the water table, with electrokinetic signals derived from the saturated zone from 17 m to 50 m. At greater depths, there is very little signal

response. The corresponding derived permeability-depth profile and cumulative flow responses are shown in Figures 8.30A and B, respectively.

Despite early promise this method has not been accepted generally, possibly due to the difficulties in measuring the very small electrical potentials generated (typically in the range of  $\mu\text{V}/\text{m}$  to  $\text{mV}/\text{m}$ ). Some workers have doubted the validity of the technique both to map the water table and to be able to determine cumulative flow profiles (quoted in units of gallons per hour) based on specific evaluation studies. However, it may be that the method is only applicable in remote areas where the background electrical noise is minimal and where, with appropriately sensitive recording systems, it might be possible to detect the small coherent electrical signals arising from the seismo-electric effects associated with the passage of a P-wave generated artificially. The method is generally not applicable in urban environments.

# 9

## Induced Polarisation

### 9.1 Introduction

The phenomenon of induced polarisation (IP) is reported to have been noted by Conrad Schlumberger as early as 1913. One aspect of IP, known as the *overvoltage effect*, has been known about since the nineteenth century. The induced polarisation method has been used since 1942, having been developed during the Second World War as part of a USA Navy project to detect mines at sea (Grow, 1982). In the 1950s there was a rapid increase in interest in the IP method in both the mining and petroleum exploration sectors. In the 1970s significant progress was made in instrumentation (Zonge and Wynn, 1975) which also led to the development of the *spectral IP* (SIP) method, especially leading into the early 1980s (Pelton *et al.*, 1978). In 1983, Canadian equipment was exported to China that led to a significant period of development of the IP method especially for mining. However, much of the output from this period was only produced in Chinese and was not available more widely until the monograph by Luo and Zhang was published in English by the SEG in 1998. More detailed histories of the IP method have been provided by Collett (1990) and Seigel *et al.* (2007).

The main current application of IP prospecting is in the search for disseminated metallic ores, especially porphyry coppers, bedded lead/zinc and sulphide-related gold deposits and, to a lesser extent, groundwater and geothermal exploration. Since the early 1990s, there has been an increased interest in the possible use of IP methods in environmental applications, based initially on laboratory measurements of IP effects associated with non-metallic minerals (e.g. Olhoeft, 1985; Börner *et al.*, 1996) and in archaeological investigations (Weller *et al.*, 2006). It is increasingly clear that the IP method shows significant promise in the detection of organic contaminants that are difficult to detect using other geophysical methods. As the analytical methods continue to improve, so the variety of applications will grow. However, it is important, especially within the environmental sector,

that the interpretations of field data are underpinned by more robust understanding of the polarisation processes at the particle scale and as a function of contaminant species and type.

Measurements of induced polarisation are made using conventional electrical resistivity electrode configurations (see Chapter 7) involving two current and two non-polarisable potential electrodes. When the current applied is switched off, the voltage between the potential electrodes takes a finite and measurable time (seconds to several minutes) to decay to zero (Figure 9.1) because the ground temporarily stores charge (i.e. becomes polarised) and acts somewhat like a capacitor. When the current is switched back on, the voltage does not peak instantaneously but builds up over the same time period (the *rise time*) to its maximum applied value. The voltage decay and rise time are dependent upon both instrumental and geological factors, and are thus diagnostic of the nature of the ground, as will be discussed later.

There are four systems of induced polarisation measurement. *Time domain* (or *pulse transient*) techniques measure the overvoltage as a function of time; and in *frequency domain* methods the apparent resistivity is measured at two or more different frequencies (usually lower than 10 Hz; Patella and Schiavone, 1977). In the *phase domain* technique, the phase lag between the applied current and the measured voltage is diagnostic of the subsurface mineralisation. In *spectral IP*, phase and magnitude are measured over a range of frequencies from  $10^{-3}$  to  $4 \times 10^3$  Hz.

The induced polarisation method is an active one because voltages, which can be as high as several thousand volts in time-domain surveys, are applied to the ground in order to generate measurable overvoltages. The equipment used is similar to, but much more elaborate than, that employed in electrical resistivity work. The induced polarisation method excites (induces) a response in the ground which is dependent upon the distribution and nature of mineral grains present, and is most effective when the mineral grains are disseminated rather than combined in a massive form, as explained in the next section.

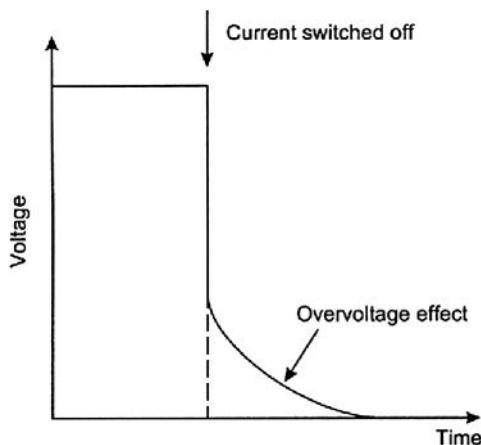


**Figure 9.1** The overvoltage effect produced by induced polarisation after an applied current is switched off.

## 9.2 Origin of induced polarisation effects

The exact causes of induced polarisation phenomena are still unclear, but the two main mechanisms that are reasonably understood are *grain (electrode) polarisation (overvoltage)* and *membrane (electrolytic) polarisation*, both of which occur through electrochemical processes.

### 9.2.1 Grain (electrode) polarisation

Grain or electrode polarisation occurs by the same process that results in self-potentials (see Chapter 8). If a metal electrode is placed in an ionic solution without a voltage being applied, charges with different polarities separate, resulting in the establishment of a potential difference between the electrode and the solution (Figure 9.2). The total magnitude of the potential is the Nernst potential, and the adsorbed layer gives rise to the zeta potential (see Section 8.3.2). When a voltage is applied, the ionic balance is disturbed; this causes a current to flow, which in turn changes the potential difference between the electrode and the solution. When the applied voltage is removed, the ionic balance is restored by the diffusion of ions.

In the geological situation current is conducted through the rock mass by the movement of ions within groundwater passing through interconnected pores or through the fracture and micro-crack structure within the rock. When an electronically conducting grain (e.g. a metal sulphide) blocks a flow channel, charge builds up (Figure 9.3) as in the electrochemical cell; this opposes the current flow and the grain becomes polarised, so creating a potential difference across the grain. Upon switching off the applied voltage, the ions diffuse back through the electrolytic medium and the potential difference across the grain reduces to zero in a finite time, giving the characteristic overvoltage decay measured in time-domain systems.

Grain polarisation is essentially a surface phenomenon, and this is why *disseminated* ores (with correspondingly large total surface areas) produce a significant IP response. (Sometimes an IP response

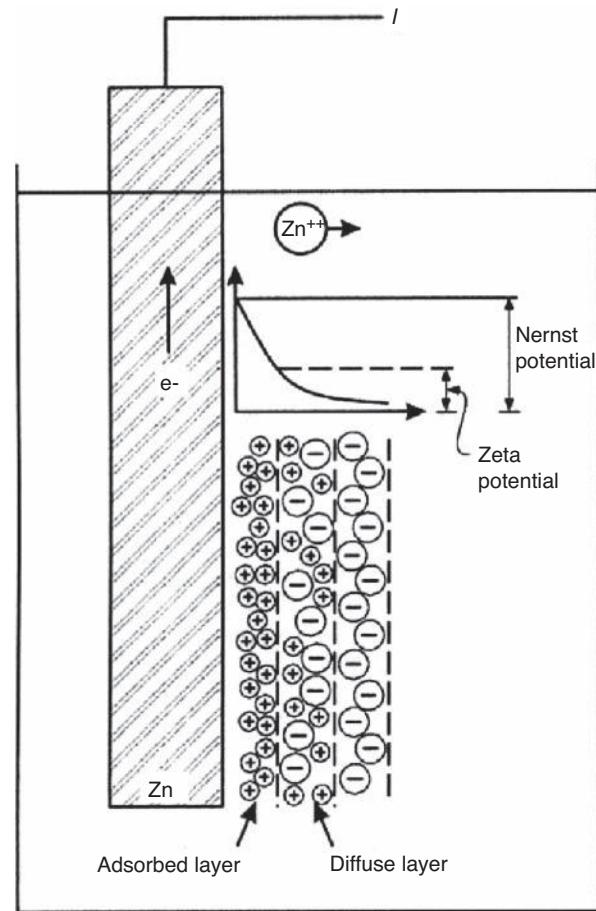


**Figure 9.2** The phenomenon of electrode polarisation with the physical processes by which the Nernst and zeta potentials are obtained. From Beck (1981), by permission.

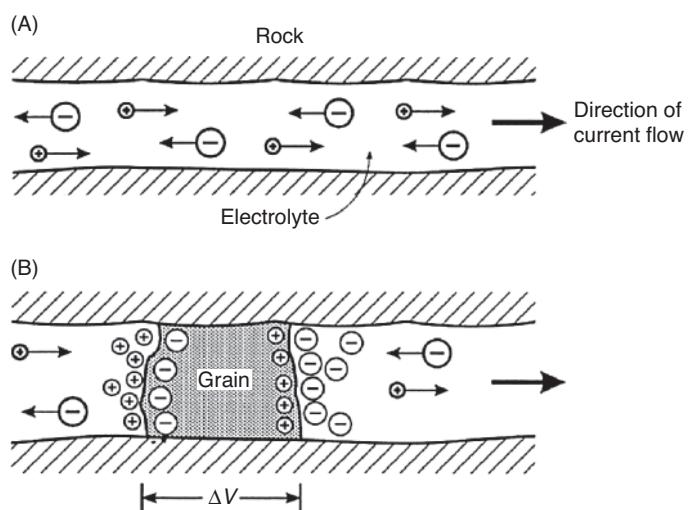


**Figure 9.3** Grain (electrode) polarisation. (A) Unrestricted electrolytic flow in an open channel. (B) Polarisation of an electronically conductive grain, blocking a channel.

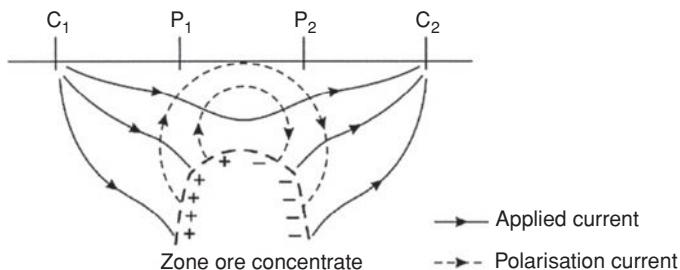


**Figure 9.4** Macroscopic effect of grain polarisation over a disseminated ore body.

is obtained over a halo of disseminated ore around a massive ore-body.) Although it is the individual electronically conducting mineral grains that become polarised, complete zones with significant concentrations of ore will also take on a net polarisation; this results in a macroscopic polarisation current flow in the ground which is measured as the IP response. For the Wenner electrode configuration (see Section 7.3.2) in Figure 9.4, current polarises the zone of ore concentration which, when the applied current is turned off, generates the transient polarisation current that is measured at the surface. The current field is more complicated for the more commonly used dipole–dipole electrode array (see Section 7.3.2). The factors affecting the rate at which the ionic balance is restored are extremely complex and may depend upon the pore shape and size, rock structure, permeability, electrolytic conductivity and ionic concentration, and upon the electronic conductivity of the mineral grain. Electrochemical processes in relation to the overvoltage effect have been discussed by Merriam (2007). Bornite, cassiterite, chalcopyrite, galena, graphite, ilmenite, agnetite, pyrite, pyrolusite and pyrrhotite all exhibit strong IP responses as they have high electronic conductivities. The sulphides sphalerite, cinnabar and stibnite have low electronic conductivities and do not produce significant IP responses. For the same reason, they tend to produce only minimal, if any, self-potentials.

## 9.2.2 Membrane (electrolytic) polarisation

An IP response measured over rocks that do not contain sulphide mineral grains can be indistinguishable from the IP overvoltage effect over rocks containing low concentrations of disseminated ores, especially if traditional methods of time- and frequency-domain measurement are used. However, the more modern spectral and phase-domain IP systems may provide sufficiently diagnostic results.

There are two causes of membrane or electrolytic polarisation (Ulrich and Slater, 2004; Scott, 2006). One is by the constriction within a pore channel, and the other is associated with the presence of clay within pore channels, such as in an impure sandstone. There is a net negative charge at the interface between most rock minerals and pore fluids. Positive charges within the pore fluid are attracted to the rock surface and build up a positively charged layer up to about 100 µm thick, while negative charges are repelled. Should the pore channel diameter reduce to less than this distance, the constriction will block the flow of ions when a voltage is applied. Negative

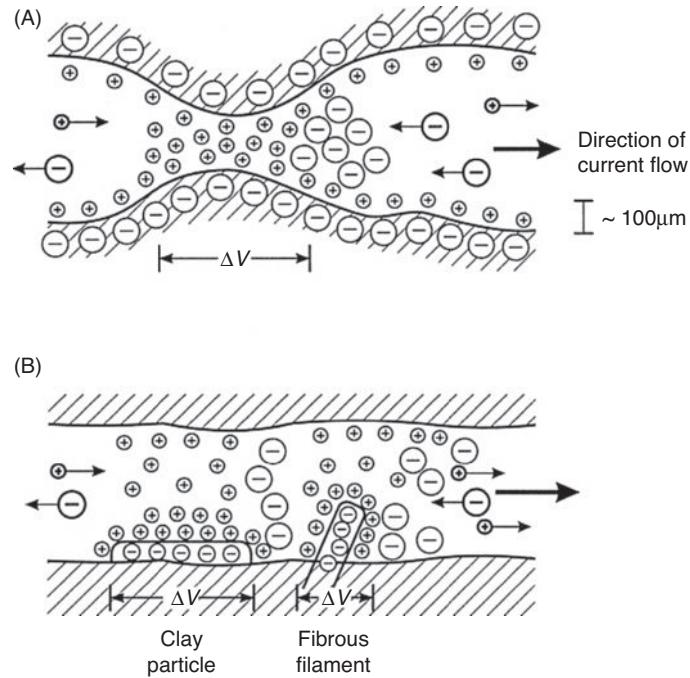


**Figure 9.5** Development of membrane polarisation associated with (A) a constriction within a channel between mineral grains, and (B) negatively charged clay particles (Fraser et al., 1964) and fibrous elements along the sides of a channel.

ions will leave the constricted zone and positive ions will increase their concentration, so producing a potential difference across the blockage (Figure 9.5A). When the applied voltage is switched off, the imbalance in ionic concentration is returned to normal by diffusion, which produces the measured IP response.

The second cause of membrane polarisation is the presence of clay particles or filaments of fibrous minerals, both of which tend to have a net negative charge. Positive ions are attracted to them, producing a positively charged cloud within the pore space. When a voltage is applied, positive charges can move between these similarly charged clouds, but the negatively charged ions are blocked, which produces a difference in ionic concentration (Figure 9.5B). When the applied voltage is switched off, the imbalances in ionic concentration decay to normal levels by diffusion, so causing a measurable IP response.

## 9.2.3 Macroscopic processes

Various attempts have been made to explain induced polarisation in a quantitative way (e.g. Bertin and Loeb, 1976) and to describe the phenomena qualitatively (e.g. Shuey and Johnson, 1973; Sumner, 1976). It is vital for interpretational purposes that any hypothesis should be able to explain the shape of the overvoltage decay curve with time and the variation of resistivity and phase with frequency. Indeed, the time-decay curve behaves in a complex manner proportionately to  $t^{-n}$ , where  $t$  is the time since the current was turned off, rather than being an exponential decay. Arguments involve the current density within and the dielectric constant (see Chapter 10) of the geological material, but the induced polarisation phenomenon

cannot be explained simply in terms of the dielectric constant of the rock. Models, which tend to be two-dimensional, fail to account adequately for three-dimensional reality, although Hohmann (1975) has attempted 3D modelling. Li and Oldenburg (2000) have developed a 3D inversion algorithm that also involves the inversion of DC resistivity data to help constrain the IP inversion. Not unsurprisingly, they also found that the joint inversion of surface and cross-hole data produced superior chargeability models to those obtained from discrete inversions of individual datasets. Some models have succeeded in identifying electric–circuit analogues in terms of resistor–capacitor systems (Bertin and Loeb, 1976), but these are not in themselves explanations of the physical processes within the ground that give rise to induced polarisation.

In the hydrocarbon setting, it is thought that the IP effects measured are caused by the presence of epigenetic pyrite microcrystals within the sedimentary rocks (Veeken *et al.*, 2009). These crystals occur in shallow halo-shaped mineralogical alteration zones that often overlie deeper-seated hydrocarbon accumulations. Local enrichment in pyrite occurs as a result of reducing geochemical conditions below an impermeable layer. An imperfect top seal of the accumulation allows small amounts of hydrocarbons to escape and migrate through the overlying rocks towards the surface. If, during this migration, hydrocarbons encounter an impermeable barrier, they may form an alteration zone that is detectable by its IP response.

It has also been found that organic matter (e.g. peat) can be highly chargeable (Slater and Reeve, 2002; Viezzoli *et al.*, 2006) and that clay also gives rise to characteristic IP responses, allowing the identification of clay units.

## 9.2.4 Ionic processes

Just as macroscopic theories have failed to provide an adequate solution, so too have those that consider processes on the microscopic level. Forces acting on the ions and their resultant motions have been considered under diffusion theory, which dates back to the end of the last century. The amplitude of the overvoltage in time-domain measurements should change as the square-root of the frequency, but, according to experiments, it does not. If electrical forces are considered in addition to general diffusion, which takes into account the electric field and the ionic mobility, then it is possible to obtain dielectric parameters which are much closer to those derived from actual measurements. The effect of thermal agitation has also been considered, and consequent mathematical modelling does reproduce the time-dependence of the overvoltage decay. Satisfactory physical explanations have yet to be found (Schufle, 1958; Wong, 1979).

Wenner, Schlumberger (gradient) and pole–dipole arrays are used. (For electrode array types, see Section 7.3.2.) Subsequent discussion of this method will be based on the use of the dipole–dipole array.

Electrode spacings are commonly tens to several hundred metres, but in broad reconnaissance surveys – for which the Schlumberger array tends to be used – the spacings can be even larger. The type of equipment used is bulkier and more elaborate than that used for resistivity surveys, and also depends on the type of IP survey being conducted. A transmitter is used to generate the applied current input into the ground, and the polarisation effects are detected by a receiver comprising non-polarisable porous-pots connected to the potential electrodes (see Chapter 8). Profiles are undertaken with fixed electrode spacings in much the same way as in the constant separation traversing of electrical resistivity surveys (Chapter 7). More details of the field arrangements are given by Telford *et al.* (1990) and Milsom (2003).

### 9.3.1 Time-domain measurements

When a current is applied to the ground and switched off a few moments later, an overvoltage decay results (Figure 9.6). The total magnitude of the observed voltage ( $V_o$ ) is equal to the actual voltage ( $V$ ) due to the applied current plus a polarisation voltage ( $V_p$ ) caused by the polarisation processes (Section 9.2). When the applied current is switched off, the voltage drops instantaneously by the amount  $V$ , leaving a residual voltage (the overvoltage) ( $V_p$ ) that decays with time. One measure of the IP effect is the ratio  $V_p/V_o$ , which is known as the *chargeability*, and is usually expressed in terms of millivolts per volt or per cent.

It is also possible to make IP measurements in a marine survey (Veeken *et al.*, 2009). A large current (up to 400–500 A (with power of 140 kW)) is injected into the water via a pair of subhorizontal current electrodes 1–2 m below the water surface and 200–500 m apart, with the nearest electrode to the towing vessel at least 50 m away. The current is applied for a 4 s period, then switched off. The receiver assembly consists of seven electrodes on a cable, with dipoles with dimensions from 196 m to 212 m, towed at or near the water surface 1–3 km behind the vessel. Several potential differences are measured in time during the subsequent switch-off stage. The decay of the potentials measured is recorded at 0.25 s time-sampling intervals and several attributes computed on the registered decay function. The current polarity is reversed for the following measurement cycle. The speed of the assembly through the water, typically being towed at 7–8 km/hr, helps to prevent the negative effects of gas release when the strong current is injected into the water column (ionisation of seawater). Productivity rates for this method are about 100 line-km per day at a cost comparable to that of standard seismic data acquisition. The typical station interval between measurement points along a profile varies between 0.2–1.0 km. The method has been used successfully in water depths up to 300 m.

Instrumentally, it is extremely difficult to measure  $V_p$  at the moment the current is switched off, so it is measured at a fixed time (typically 0.5 s) after cutoff. Measurements are then made of the decay of  $V_p$  over a very short time period (0.1 s) after discrete

## 9.3 Measurement of induced polarisation

Current is applied to the ground by means of two current electrodes, and the induced polarisation effect is measured between two potential electrodes, most commonly in a dipole–dipole array. Sometimes

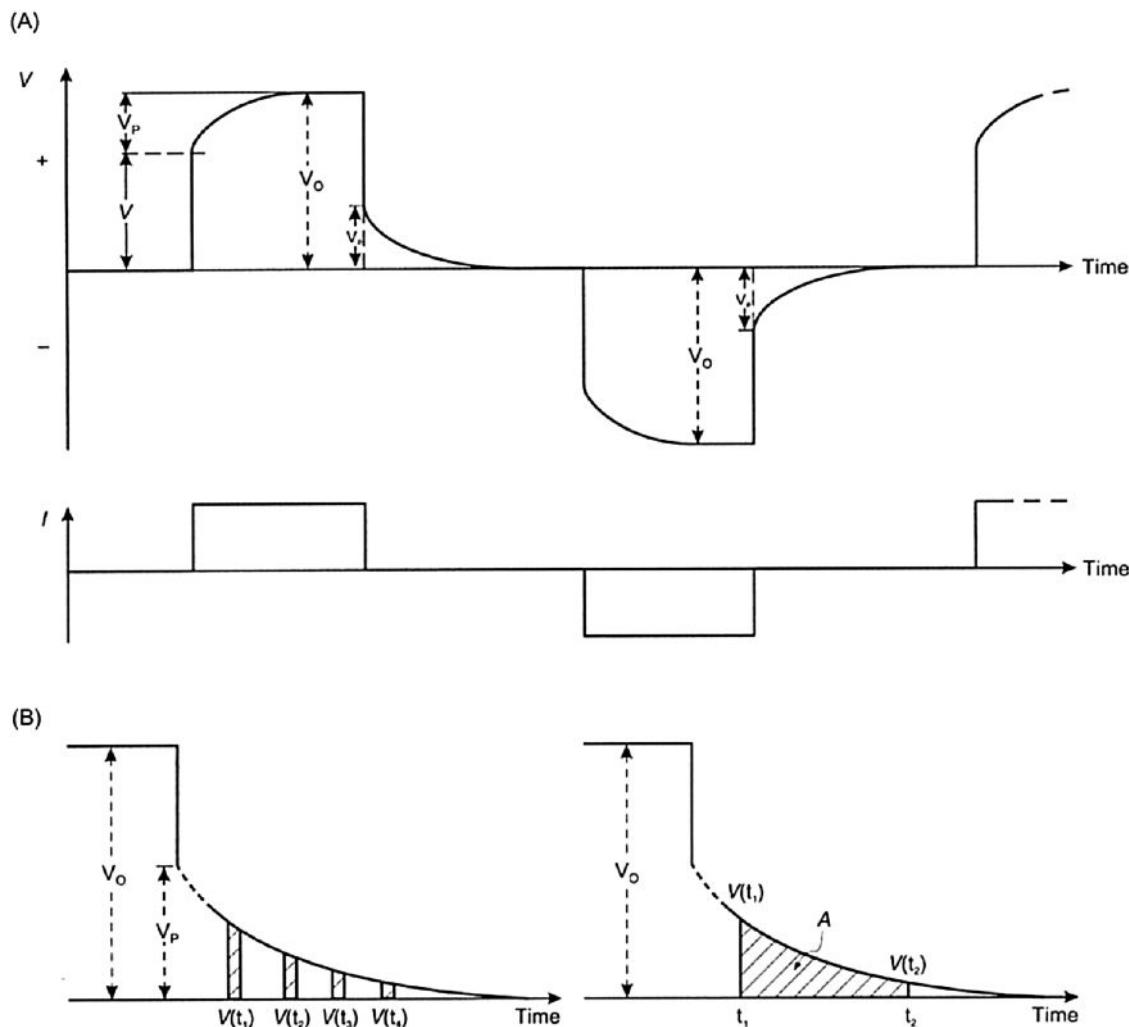


**Figure 9.6** (A) Application of a pulsed current with alternate polarity, and the consequent measured voltage showing the effect of the overvoltage ( $V_p$ ) and the rise-time on the leading edge of the voltage pulse. (B) Two forms of measurement of the overvoltage at discrete time intervals  $V(t_1)$ , etc., and by the area beneath the overvoltage curve ( $A$ ).

intervals of time (also around 0.5 s). The integration of these values with respect to time gives the area under the curve (Figure 9.6), which is an alternative way of defining the decay curve. When the integral is divided by  $V_o$ , the resultant value is called the *apparent chargeability* ( $M_a$ ) and has units of time (milliseconds) (see Box 9.1).

The *true* chargeability is virtually impossible to measure in the field situation as each layer within the ground will have its own absolute value of chargeability and of true resistivity. What is measured is a complex function of all true resistivities and absolute chargeabilities for all the media being sampled within the range of the equipment. A short charging period will produce a lower IP response than a longer charging period (Figure 9.7).

For given charging and integration periods (which differ between makes of IP equipment), the measured apparent chargeability is a diagnostic parameter that can be interpreted qualitatively in terms of the subsurface geology. For a charging time of 3 s, an integration period of 1 s and a 1% volume concentration, chalcocite has

a value of  $M_a$  of 13.2 ms, which is more than twice that of bornite (6.3 ms) and slightly higher than that of graphite (11.2 ms). In contrast, magnetite has a value of only 2.2 ms, and haematite has zero apparent chargeability.

The major advantage of integration and normalising by dividing by  $V$  is that noise from cross-coupling of cables and from background potentials is reduced. Care has to be exercised in selecting appropriate time intervals to maximise signal-to-noise ratios without reducing the method's diagnostic sensitivity.

### 9.3.2 Frequency-domain measurements

In frequency-domain (variable frequency) induced polarisation studies, the apparent resistivity is measured at two frequencies less than 10 Hz (e.g. 0.1 and 5 Hz, or 0.3 and 2.5 Hz) using the same electrode array as in time-domain and direct-current resistivity measurements. The apparent resistivity at low frequency ( $\rho_{a0}$ ) is greater than that at a higher frequency ( $\rho_{a1}$ ) for reasons that can be

**Box 9.1 Chargeability (see Figure 9.6)**

Chargeability:

$$M = V_p / V_o \text{ (mV/V or %)}$$

where  $V_p$  is the overvoltage, and  $V_o$  the observed voltage with an applied current.

**Apparent chargeability:**

$$M_a = \frac{1}{V_o} \int_{t_1}^{t_2} V_p(t) dt = \frac{A}{V_o}$$

where  $V_p(t)$  is the overvoltage at time  $t$ , and the other terms are as defined in Figure 9.6B.

appreciated by reference to Figure 9.7. For a short charging time the measured overvoltage is appreciably lower ( $V_{pa}$ ) than that obtained for longer charging times ( $V_{pb}$  and  $V_{pc}$ ).

The length of the decay is too short to be determined, so the total amplitude of voltage is measured with respect to the applied current, giving a value of the resistance ( $R$ ) which, when multiplied by the appropriate geometric factor (see Section 7.3.2), is the apparent resistivity. If the current is switched in polarity, and on and off, with a time delay comparable to the length of the charging time, then this is the same as applying an alternating current signal at a given frequency ( $f$ , Hertz). The shorter the charging and delay times, the higher the frequency, and so the apparent resistivity at low frequency is greater than that at a higher frequency. The two

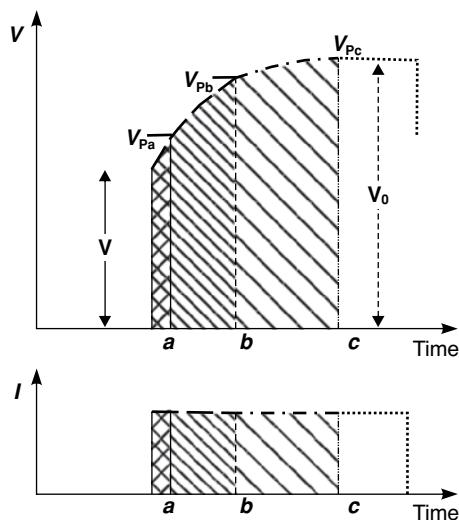


**Figure 9.7** Increasing the charging time (a to c), which decreases the frequency of measurement, has the effect of increasing the overvoltage ( $V_{pa}$  to  $V_{pc}$ ). Consequently, the apparent resistivity at lower frequency (e.g. at c) is greater than that at a higher frequency (e.g. at a).

**Box 9.2 Frequency effect (FE)**

**Frequency effect:**

$$FE = (\rho_{a0} - \rho_{a1}) / \rho_{a1} \text{ (unitless)}$$

where  $\rho_{a0}$  and  $\rho_{a1}$  are the apparent resistivities at low and higher frequencies respectively, and  $\rho_{a0} > \rho_{a1}$ .

**Percentage frequency effect:**

$$PFE = 100(\rho_{a0} - \rho_{a1}) / \rho_{a1} = 100 FE$$

and expressed in terms of conductivity ( $\sigma$ ),

$$PFE = 100[\sigma(\omega_1) - \sigma(\omega_0)] / \sigma(\omega_0)$$

where  $\sigma(\omega_0)$  and  $\sigma(\omega_1)$  are the formation conductivity magnitudes measured at low ( $\omega_0$ ) and high ( $\omega_1$ ) frequencies, and where  $\omega$  is the angular frequency ( $2\pi f$ ) and  $f$  the measurement frequency.

apparent resistivities are used to determine the *frequency effect* (FE) (unitless), which can be expressed alternatively as the *percentage frequency effect* (PFE) (%) (Box 9.2).

The frequency effect in the frequency-domain is equivalent to the chargeability in the time-domain for a weakly polarisable medium where FE is very much less than 1.

Marshall and Madden (1959) modified the expression involving the frequency effect to produce the *metal factor* (MF) (or the *metal conduction factor*) (Box 9.3). It is thought by some geophysicists that metal factor data delineate disseminated sulphide zones more effectively than frequency effect data.

Although disseminated orebodies can be located using IP data, chargeability, frequency effect and metal factor do not give a good

**Box 9.3 Metal factor (MF)**

**Metal factor:**

$$\begin{aligned} MF &= A(\rho_{a0} - \rho_{a1}) / (\rho_{a0}\rho_{a1}) \text{ (units : siemens/m)} \\ &= A(\sigma_{a1} - \sigma_{a0}) \end{aligned}$$

where  $\rho_{a0}$  and  $\rho_{a1}$  are the apparent resistivities, and  $\sigma_{a0}$  and  $\sigma_{a1}$  are the apparent conductivities ( $= 1/\rho_a$ ) at low and higher frequencies respectively;  $\rho_{a0} > \rho_{a1}$  and  $\sigma_{a0} < \sigma_{a1}$ ; and  $A = 2\pi \times 10^5$ .

Alternatively, the metal factor is given by:

$$MF = A \times FE / \rho_{a0} = A \times FE \times \sigma_{a0}$$

where FE is the frequency effect.

indication of the relative amount of the metallic mineralisation within the source of the IP response. It is necessary to go to more elaborate methods such as spectral IP, and even then the estimates obtained are not unambiguous.

One further frequency-domain method that has been used but which has been superseded by the spectral IP method is ‘phase IP’. Only one frequency is necessary. Induced polarisation is identified by the presence of a phase lag ( $\varphi$ ) between the applied current and the polarisation voltage measured.

### 9.3.3 Spectral IP and complex resistivity

Spectral IP is another name for complex resistivity, which in turn is related to the measurement of the dielectric properties of materials. (The term ‘complex’ refers to the mathematical definition of there being both real and imaginary components, not that the resistivity method is complicated.) An overview of the theoretical basis and interpretation of spectral IP (complex resistivity) data has been provided by Pelton *et al.* (1983) and Luo and Zhang (1998).

The same field arrangement is used as in time- and traditional variable-frequency surveys, but the equipment is considerably more sophisticated. It is important that the measurements be as precise as possible and that any noise be eradicated (see next section).

The magnitude of the complex resistivity ( $|Z(\omega)|$ ) and phase ( $\varphi$ ) of the polarisation voltage are measured over a wide range of frequencies (0.3 to 4 kHz) of applied current, which results in a diagnostic IP response spectrum (Figure 9.8). The frequency dependence is usually plotted as a binary function in the form of logarithms to base 2 rather than to base 10. The behaviour between the lower and upper frequency limits is known as the ‘relaxation’ of the electrical system (Shuey and Johnson, 1973) and the entire dispersion can be defined if four electrical parameters are known (Box 9.4), namely, the DC resistivity ( $\rho_0$ ), the IP chargeability ( $M$ ), the time constant of the IP response ( $\tau$ ; also known as the relax-

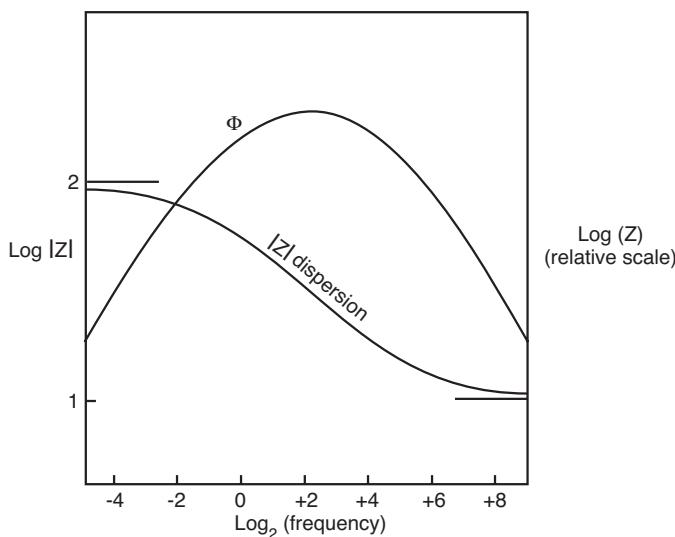


Figure 9.8 A typical IP spectral response (Pelton *et al.*, 1983).

#### Box 9.4 Spectral IP response

$$|Z(\omega)| = \rho_0 \left[ 1 - M \left( 1 - \frac{1}{1 + (i\omega\tau)^c} \right) \right]$$

where  $\rho_0$  is the DC resistivity,  $M$  is the IP chargeability,  $\omega$  is the angular frequency,  $\tau$  is the time constant,  $c$  is the frequency exponent or relaxation constant, and  $i = \sqrt{-1}$ .

ation time in dielectric studies), and the exponent of the angular frequency ( $\omega$ ).

The IP response reflects the degree to which the subsurface materials are able to store electrical charge, much like a capacitor. At high frequencies, the intrinsic capacity of a material is primarily determined by the high-frequency dielectric constant ( $\varepsilon_\infty$ ) (Box 9.5).

#### Box 9.5 Complex conductivity and normalised parameters (Slater and Lesmes, 2002)

Complex conductivity ( $\sigma^*$ ) has the form:

$$\sigma^* = \sigma' + i\sigma''$$

where  $\sigma'$  and  $\sigma''$  are the real and imaginary components and  $i = \sqrt{-1}$ .

High-frequency imaginary conductivity ( $\sigma''_\infty$ ) is given by:

$$\sigma''_\infty = \omega \varepsilon_0 \varepsilon_\infty$$

where  $\varepsilon_0$  is the permittivity of a vacuum,  $\varepsilon_\infty$  is the high-frequency dielectric constant, and  $\omega$  the angular frequency.

At low frequencies,

$$\omega \varepsilon_0 \varepsilon_\infty \ll \sigma''_{\text{surf}}(\omega),$$

where  $\sigma''_{\text{surf}}(\omega)$  is the imaginary component of the surface conductivity at angular frequency  $\omega$ .

Low-frequency complex conductivity is given by:

$$\sigma^* = (\sigma_{\text{bulk}} + \sigma'_{\text{surf}}(\omega)) + i\sigma''_{\text{surf}}(\omega),$$

where  $\sigma_{\text{bulk}}$  is the bulk conduction term.

Phase ( $\varphi$ ) is related to the real and imaginary components of conductivity by:

$$\varphi \cong \sigma''(\omega)/\sigma'(\omega).$$

Normalised parameters of IP parameters  $\varphi$ , PFE and  $M$  are obtained by weighting them by the measured conductivity ( $\sigma$ ) or dividing by the measured resistivity ( $\rho$ ), e.g.

Normalised chargeability  $M_N$  is given by:

$$M_N = M\sigma \text{ or } M/\rho$$

In the frequency range in which IP field measurements are made, the low-frequency *complex* conductivity of a material is made up of both bulk and real and imaginary components of surface conductivities (Box 9.5). Furthermore, the conductivities are also a function of bulk and surface conduction, and the relative proportion of each component is a function of the material type and frequency at which measurement is made.

One form of relaxation commonly used is the Cole–Cole relaxation spectrum (Figure 9.9), named after its originators Cole and Cole (1941). This can be characterised by the critical frequency ( $F_c$ ) which is the specific frequency at which the maximum phase shift is measured (Box 9.6). Note that this frequency is completely independent of resistivity. Phase angle and the critical frequency increase with increasing chargeability (Figure 9.10).

The fitting of two or more Cole–Cole dispersions to field spectra, a process known as *SIP inversion* (Song and Vozoff, 1985), is the means by which the various intrinsic dielectric parameters are obtained. The ‘texture’ of mineralisation, which is characterised by the grain size and grain-size distribution of the polarisable particles within each group of ore grains but which is less dependent on the type of metallic minerals present, dictates the behaviour of the time constant ( $\tau$ ) and the frequency exponent ( $c$ ). Where the polarisable mineralisation is coarse-grained, the relaxation time ( $\tau$ ) is large and the critical frequency ( $F_c$ ) is small (conversely for fine-grained mineralisation). Similarly, massive sulphide orebodies have a distinctly different chargeability-relaxation time behaviour compared with graphite (Hallop and Klein, 1982), and magnetite has a distinct chargeability-relaxation time behaviour compared with that of pyrrhotite (Pelton *et al.*, 1978) (Figure 9.11). The maximum value of  $c$  is 0.5, and for most massive sulphides  $c$  is in the range 0.25–0.35 (Hallop, 1983). Examples of the phase behaviour for several cases with various grain-size populations are illustrated in Figure 9.12. Where the two are distributed continuously, values of  $c$  fall to between 0.1 and 0.2 and the spectral curve is very flat. Computer analysis of such flat spectral curves is insensitive to variations in both  $c$  and  $\tau$ , and the estimations of grain-size distributions are likely to be ambiguous. Phase-angle spectra associated with dif-

#### Box 9.6 Critical frequency ( $F_c$ )

$$F_c = [2\pi\tau(1 - M)^{1/2c}]^{-1}$$

where  $\tau$  is the time constant, and  $M$  the IP chargeability.

ferent types of orebody are shown in Figure 9.13. If chargeability– $\tau$  data plot in an overlapping field (such as magnetite and massive sulphides in Figure 9.11), then the phase-angle spectrum can be used to differentiate between the two ore types (Pelton *et al.*, 1978).

Spectral IP parameters can be used to determine the mineralisation texture of an orebody, and so separate out zones of primary mineralisation that consist of veinlets of ore from those of disseminated ore. Where long zones of sulphide or oxide iron formations occur, spectral IP can indicate where base metal concentrations increase by variations in the spectral ‘texture’. In addition, changes in ‘texture’ along a pyrite zone may indicate the presence of gold, copper or zinc compared with barren areas (Hallop, 1983).

The interpretation of spectral IP remains limited by the continued lack of understanding of the dielectric and polarisation properties of rocks. The behaviour of the various dielectric parameters, such as the relaxation time, may vary with different physical conditions, such as with temperature (Saint-Amant and Strangway, 1970; Ogilvy and Kuzmina, 1972; Reynolds, 1985). Assuming that dielectric parameters behave isothermally may result in misleading interpretations. One example of where this temperature dependence may be of practical advantage has been given by Reynolds (1985, 1987b). The relaxation time for glacier ice is strongly temperature-dependent. Temperate glacier ice (i.e. ice at its pressure melting point throughout) has a diagnostically different temperature dependence of relaxation time compared with that for polar glacier ice (i.e. ice well below its pressure melting point) (Figure 9.14). Some glaciers have both temperate and polar ice zones with important implications for glacier ice flow and hazard evaluation, which can be differentiated by the dielectric measurement of relaxation time

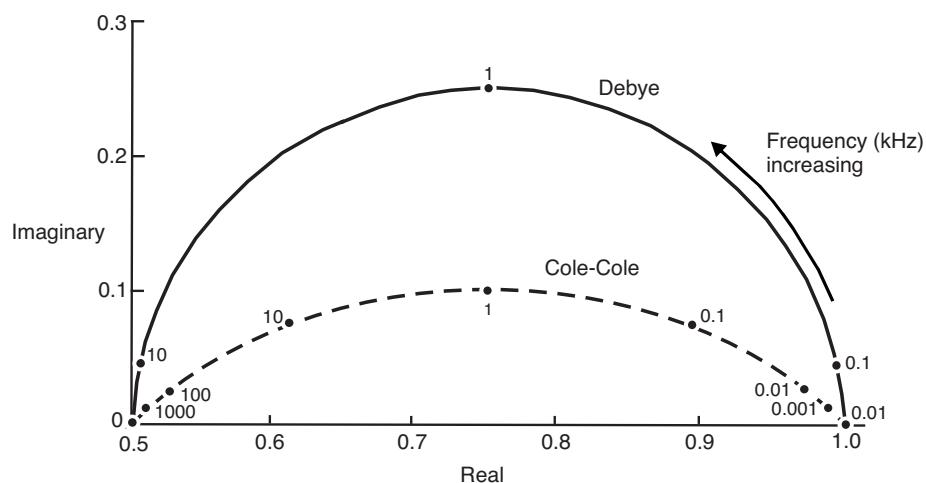


**Figure 9.9** Cole–Cole relaxation spectra for Debye and Cole–Cole dispersions for  $\tau = 1/2\pi$  and  $c = 0.5$  (Pelton *et al.*, 1983).

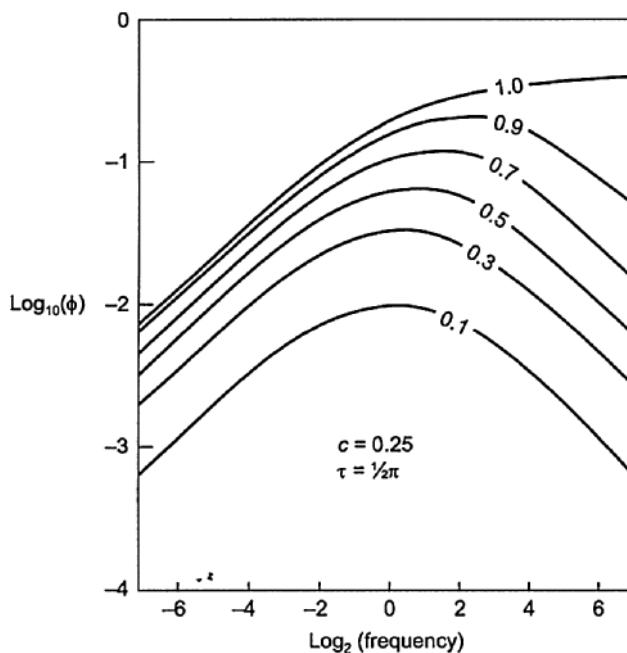


**Figure 9.10** Phase-angle curves for a typical Cole-Cole model with different chargeability ( $M = 0.1\text{--}1.0$ ) (Pelton *et al.*, 1983).

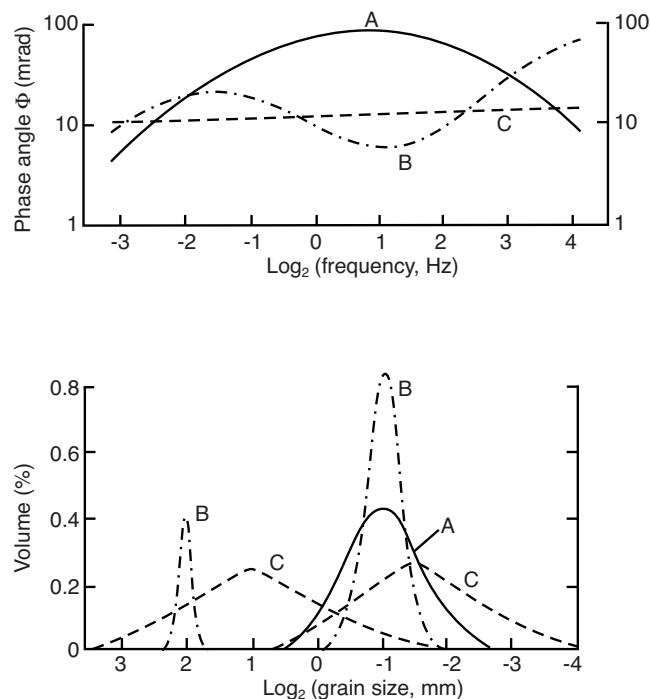


**Figure 9.12** Theoretical spectral plots of phase with three models (Halof (1983), by permission).

of ice samples (Reynolds, 1985). Spectral IP measurements have yet to be made over glaciers, but the information obtained should prove to be immensely useful glaciologically. Spectral IP could also have applications in mapping out and distinguishing between massive ice bodies and interstitial ice in permafrost, although this has yet to be tried.

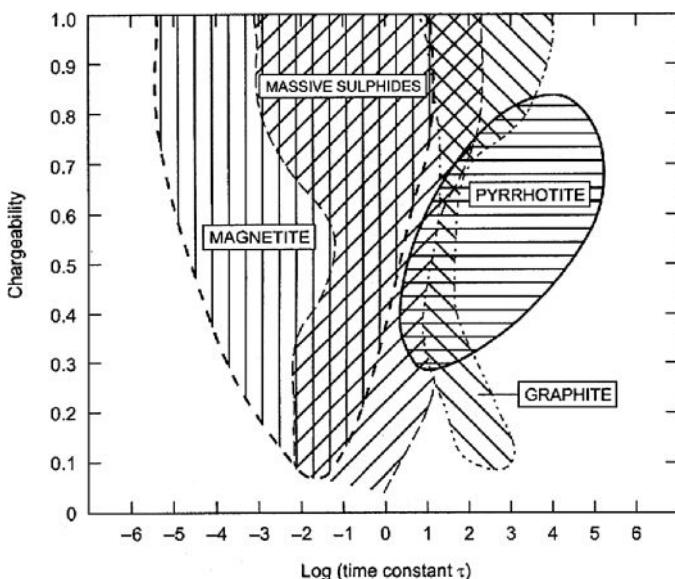


**Figure 9.11** Chargeability as a function of relaxation time constant  $\tau$ . After Halof and Klein (1992), and Pelton *et al.* (1978), by permission.

### 9.3.4 Noise reduction and electromagnetic coupling

To attain the high level of accuracy required for spectral IP, noise and electrical distortion of the IP response must be minimised before interpretation can proceed. There are four types of extraneous signal, of which three (current electrode variations, self-potentials and telluric currents) are regarded as ‘noise’ in IP work, and the remaining one (electromagnetic inductive coupling) is a distortion that occurs at higher frequencies and has to be estimated and removed from the data (Halof, 1974; Halof and Pelton, 1980).

The noise signals can be constrained within the instrument by the use of filters. Current electrode variations due to changing current flow and the frequency of the applied current cause distortions within the waveform of the applied current. To compensate for this, a multichannel approach is taken to measure voltage. Up to six pairs of potential electrodes are used to measure the IP voltage simultaneously, and the waveform of each pair is compared directly with that of the applied current so that the exact magnitude and phase of the signal waveform can be obtained for each of the six channels.

The most problematical effect is that due to electromagnetic coupling, which occurs particularly at large electrode separations and at higher frequencies. The highest frequencies used in IP work overlap with the lower frequencies used by electromagnetic prospecting methods where *induction* becomes important. If a wire carrying a current lies close to and parallel to another wire, a current will be induced into the second wire, such as happens close to power grid cables. If this induction occurs in wires connected to potential electrodes, spurious voltages will be measured. It is

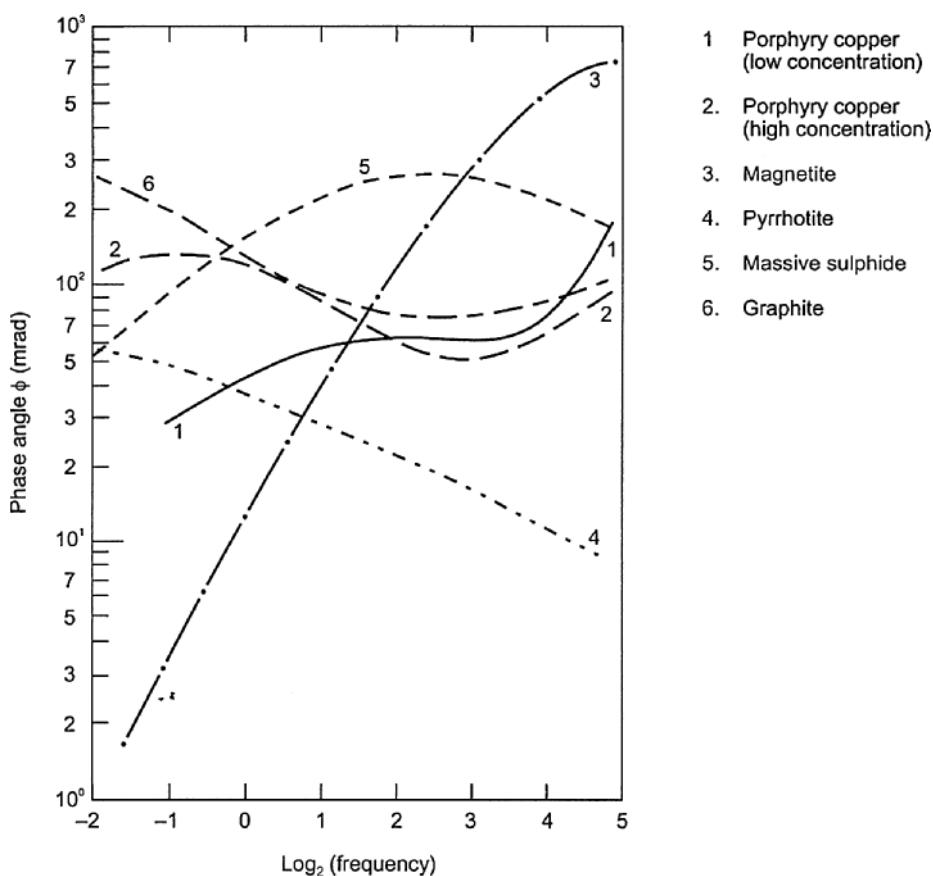


**Figure 9.13** Characteristic phase-angle plots for different types of mineralisation. Data from Pelton *et al.* (1978), by permission.

best to keep current-carrying cables well away from potential cables or to ensure that the two types of cable cross each other at right-angles. Furthermore, the current-carrying cables can induce a current into the ground which will distort the IP response. Fortunately, the frequency dependence of the electromagnetic coupling is recognisably different from that of the IP response and, if high enough frequencies are used, the coupling effects can be measured and then determined for the whole frequency range and removed from the data (Hohmann, 1973; Wynn and Zonge, 1975; Sumner, 1976; Rathor, 1977; Pelton *et al.*, 1978; Hallof, 1983). Pipelines have also been recognised as contributing to noise in IP surveys (Parra, 1984).

### 9.3.5 Forms of display of IP data

Induced polarisation data for a given electrode separation, particularly when measured in the time-domain, are commonly plotted as simple profiles and maps of chargeability (see Figure 8.6), metal factor or percentage frequency effect. In frequency-domain methods it is more usual to plot the data in the form of a pseudo-section (Figure 9.15).

Note that the spacing of the data points is dependent upon the integer value of  $n$  in dipole-dipole arrays and not on the actual dipole length. However, the increasing depth of penetration is implicit in the larger values of  $n$  and, as a guide, the depth of penetration is

approximately equal to  $a/2$  for  $n = 2$ ;  $\approx a$  for  $n = 3$ ; and  $\approx 2a$  for  $n = 4$  where  $a$  is the dipole length. Each data value is plotted at the intersection of two lines drawn at  $45^\circ$  to the midpoint of each dipole used in the measurement. Two positions are indicated, for example, in Figure 9.15. For  $n = 1$ , and dipoles 1–2 and 3–4, the measured data value is plotted at A; for  $n = 3$  and dipoles 4–5 and 8–9, the position is at B. It is usual for the apparent resistivity pseudo-section to be drawn inverted above those for other IP parameters. Apparent resistivity, which is often plotted in units of  $\Omega\text{m}/2\pi$ , can also be plotted the correct way up as convenient. The plotted values can then be contoured. The surface projection of zones with IP anomalies are indicated respectively by solid, dashed, or oblique dashed bars along the top of the pseudo-section to indicate the location of definite, probable and possible mineralisation (Figure 9.16).

The interpretation of such displays tends to be by qualitative comparison with those obtained for theoretical or experimental scale models. Examples of the apparent resistivity, apparent metal factor and apparent phase for two models are given in Figure 9.17. In both cases the patterns in all three IP parameters are symmetrical about the central position and form patterns in the form of an inverted V.

The apparent resistivity data over the horizontal rectangular block exhibit two ‘lows’ which correspond to end-effects of the block. Note also the lozenge shape anomaly ‘high’ in the apparent metal factor over the block model. From these two sets of data,

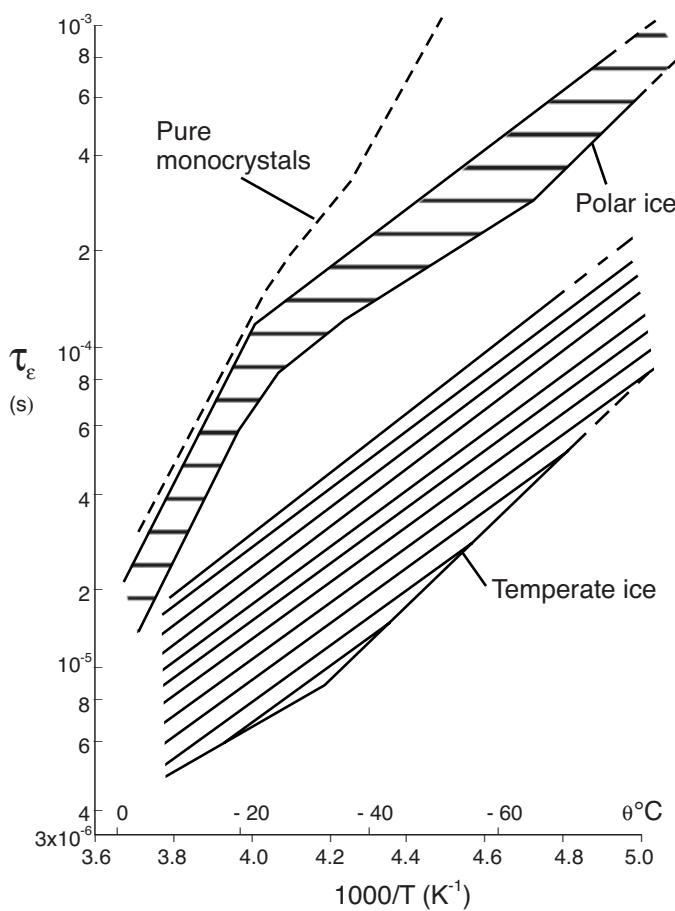


**Figure 9.14** Temperature dependence of relaxation time constant  $\tau$  for temperate and polar glacier ice, illustrating that  $\tau$  can be used to differentiate between thermal regimes of the two ice types. After Reynolds (1985), by permission.

the apparent frequency effect is less sensitive to the model and less diagnostic than the apparent metal factor.

Another form of display is the use of three-frequency spectra which are plotted on a modified form of a pseudo-section (Figure 9.18). Spectral IP parameters measured at up to five frequencies, for example 0.11, 0.33, 1.0, 3.0 and 9.0 Hz, are abstracted from the total frequency spectrum and normalised with respect to the value at mid-frequency (ratio = 1.0); i.e. for five frequencies the parameters are normalised to the value at 1.0 Hz; for three frequencies (0.11 to 1.0 Hz), they are normalised to the value at 0.33 Hz. The normalised values are then plotted against the frequency (Hallop and Pelton, 1981, Hallop, 1982) (Figure 9.18D). The shape of the graph at each plotting position can be categorised into ‘concave-up’ and ‘concave-down’ (Fraser *et al.*, 1964) or into specific and recognisable groupings based on the slope of the graph (Zonge and Wynn, 1975; Hallop and Pelton, 1981).

The most substantive development of both the display and interpretation of spectral IP is in the computer modelling of observed values of magnitude and phase according to Cole–Cole relaxation models (next section). These permit the recognition and subsequent removal of inductive coupling from the spectra; and in the course

of this, the four key IP parameters ( $\rho_0$ ,  $M$ ,  $\tau$ , and  $c$ ), which define the IP response, can be determined very accurately. An example of a spectra IP amplitude-phase diagram is given in Figure 9.19. It can be seen that at low frequencies the inductive coupling has little effect, whereas at high frequencies it becomes dominant.

### 9.3.6 Inversion and fitting dispersion spectra

Complex resistivity now allows the determination of many more parameters in addition to resistivity and chargeability. The problem is in both displaying the results and analysing them in a meaningful way. Luo and Zhang (1998) have provided a detailed account of the method and of the basics of the appropriate inversion theory. A key challenge is defining the four IP spectral parameters (resistivity,  $\rho$ ; the IP chargeability,  $M$ ; the time constant,  $\tau$ ; and  $c$ , the exponent of the angular frequency). Different authors have described various approaches. These have included the use of master curves (e.g. of  $M$  vs  $\tau$ ; Duckworth and Calvert, 1995). More recently, 1D and 2D inversions of IP parameters have been demonstrated theoretically and with practical applications (Hönig & Tezkan, 2007). The results of the inversion are displayed as separate pseudo-depth sections for each appropriate IP inversion parameter (resistivity, chargeability, relaxation time, or frequency constant). Parameter values are assigned to discrete pixels to give a parameter section. Each display shows the spatial distribution of the derived parameter with distance along the profile and with depth. In many cases the resistivity section may not be as detailed as would be achieved by undertaking an ERT profile on its own, whereby better spatial resolution might be achieved by using a different electrode array, finer electrode separation and more refined inversion of the resistivity model than would be achieved using the SIP method alone. It is suggested that a combination of methods would produce a better final resistivity result, especially in shallow environmental investigations.

In order to understand the inversion process better, laboratory studies have been undertaken from which developments of the inversion process have been made. For example, depending upon how the inversion process has been undertaken it can yield a time constant that can vary in magnitude over several decades, rendering evaluation of the results impossible (Nordsiek and Weller, 2008). For slag samples, they were able to determine that total chargeability indicates well the mass percentage of slag grains, and that the mean relaxation time is related to the grain size. Commonly programs use derivatives of the forward model using iterative Gauss–Newton algorithms to update Cole–Cole parameters from a set of initial values. The choice of such values can determine the outcome of the process, potentially making the results less robust. Chen *et al.* (2008) have provided an alternative stochastic computational approach, which also has limitations but which, when used with the Gauss–Newton method, can produce analytically more meaningful results.

The traditional approach to analysing geophysical data is to derive a 2D section, where the components are assumed to be semi-infinite perpendicular to the orientation of the profile so that edge effects can be ignored. However, in reality this is seldom true, and the edge effects of targets either across the line of the profile or indeed

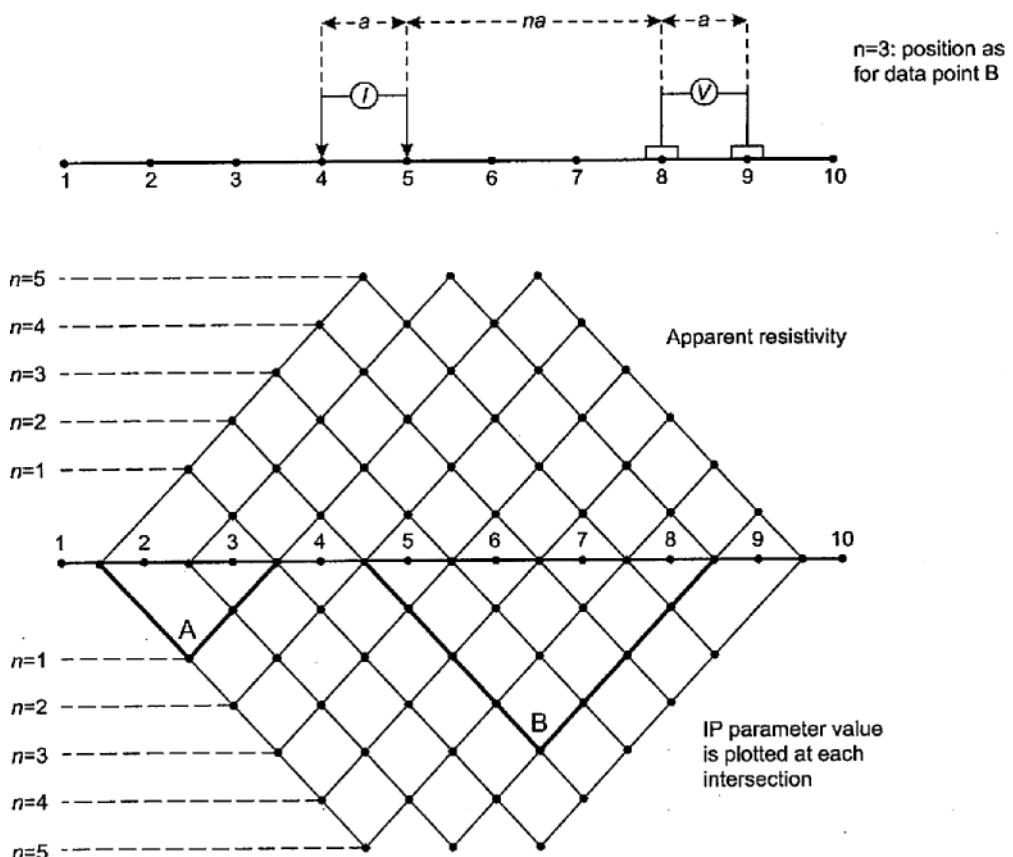


**Figure 9.15** How to plot a pseudo-section. For a dipole-dipole array with current and potential electrodes at 1-2 and 3-4 respectively ( $n = 1$ ), the measuring point is plotted at A; for dipoles at 4-5 and 8-9 ( $n = 3$ ), the data value is plotted at B.

those that lie offset from the section can have a strong influence on the 2D image that is produced. IP surveys are no different, and 3D targets will not be imaged as accurately when using only 2D surveys and inversion. To address this, Li and Oldenburg (2000) developed a 3D inversion process to take account of a topographically variable ground surface or including boreholes. They assumed that the chargeability would be small and developed a two-stage process. Firstly, the DC resistivity data were inverted to form a background conductivity that was used to generate a sensitivity matrix for the IP equations used. The 3D chargeability model was then generated by solving the system of equations, subject to the restriction that chargeability is everywhere positive and smaller than an upper limit. Their method requires a knowledge of the background conductivity as a precondition for the chargeability inversion, and this conductivity information in itself contains a degree of uncertainty. However, the ability to integrate both surface and borehole IP data into the 3D inversion process is an important step towards achieving more robust inversions that better reflect the three-dimensionality of geological features.

Sometimes, it is by the careful analysis of materials within the laboratory combined with developments in the analytical process that important new findings emerge. One such example is that described by Mansoor and Slater (2007) where they analysed 17 samples of clay and peat marsh soils. They found a linear relationship between

the normalised chargeability ( $M_N$ ) and the volumetric iron (Fe) concentration per unit volume of the bulk soil. This suggests that the spectral IP method may provide a new approach to probing soil geochemistry, iron cycling within soils and anaerobic microbial activity. This shows the interaction between developing understanding of the physical processes coupled with improvements in the analytical procedures.

The SIP method has significant potential in an increasing range of applications, and both field and laboratory experiments will help to generate future developments in conjunction with further progress in inversion programming.

## 9.4 Applications and case histories

### 9.4.1 Base metal exploration

A good example is the IP response over a disseminated copper-ore zone known as the Copper Mountain Orebody in Gaspe Area, Quebec, Canada (Figure 9.20). The orebody has been very well defined by many boreholes, and the mineralisation has been evaluated as an average 4% metallic mineralisation comprising both pyrite and chalcopyrite. The increasing thickness of weathering towards the

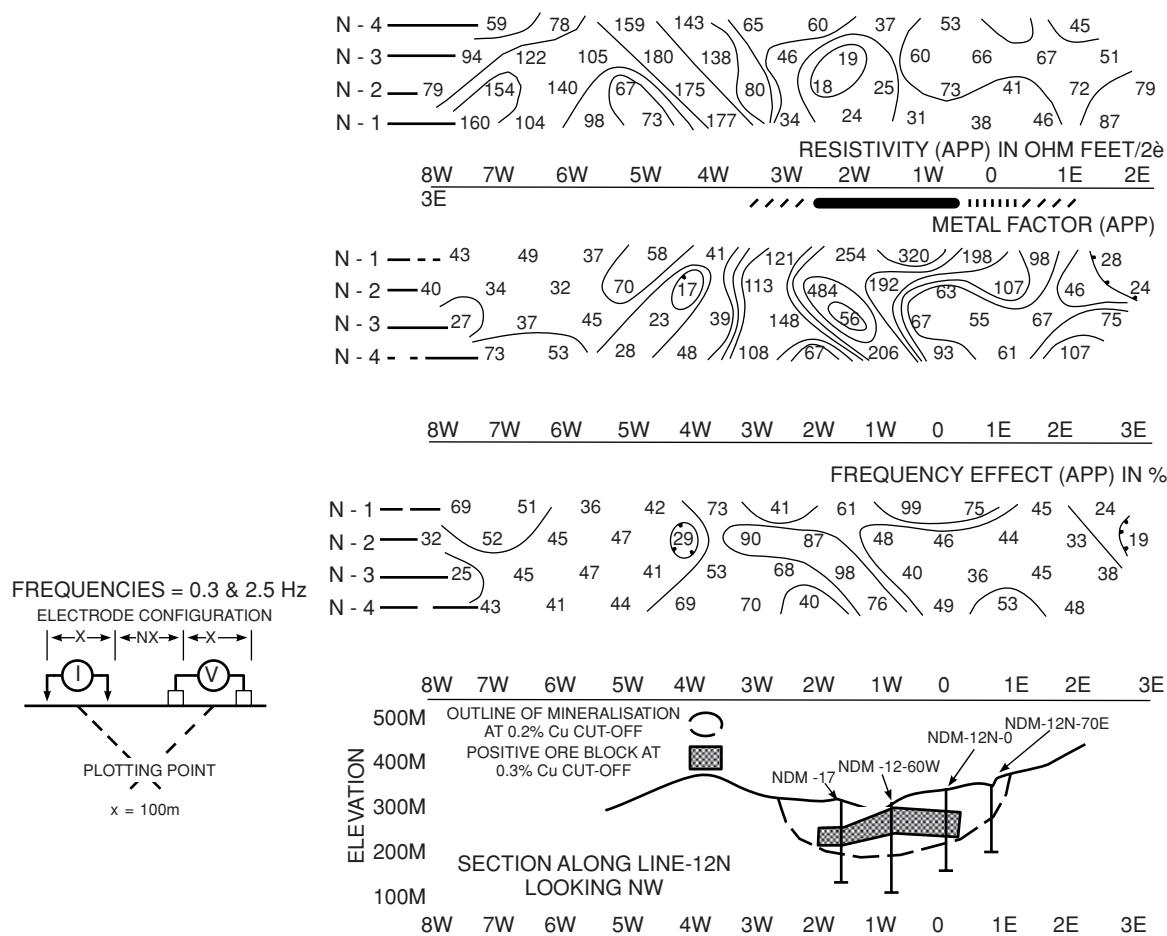


**Figure 9.16** Apparent resistivity, metal factor and frequency effect profiles over the Hinobaan deposit whose geological cross-section is shown schematically in the lower diagram. A dipole length of 100 m and frequencies of 0.3 and 2.5 Hz were used. From Pelton and Smith (1976), by permission.

south is picked out by the lower apparent resistivities. Low apparent resistivities, high apparent frequency effect and high apparent metal factor all coincide on  $n = 3$  and 4 at locations between 46 and 49N, which also correlates with known sulphide mineralisation.

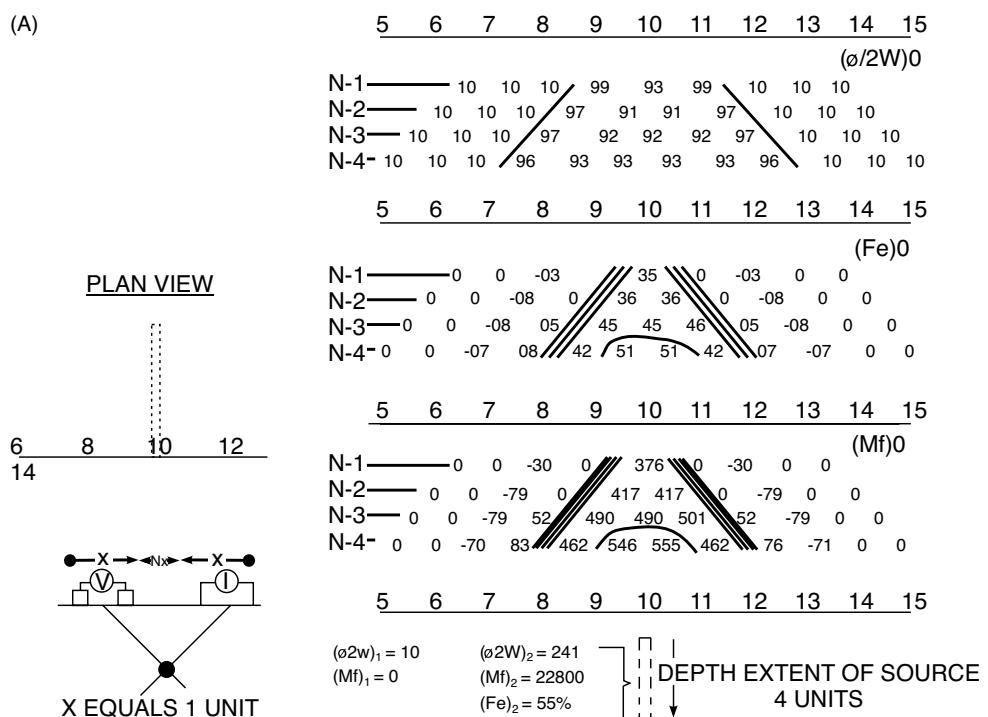
The IP method can produce valuable information about more massive types of mineralisation in cases where electromagnetic surveying fails. This is due to the mineralisation occurring in veinlets, which do not permit the formation of strong eddy currents in response to an induced electromagnetic field, rather than forming a totally massive orebody. One example of this is for Heath Steele Property, New Brunswick. IP data (apparent resistivity and apparent metal factor) and vertical loop EM data are shown in Figure 9.21, in which it is clear that the EM response is very weak in contrast to the IP effect. The characteristic inverted V-shape can be seen in the apparent metal factor data, indicating that the mineralisation is in near-vertical structures, as indicated by subsequent drilling.

Case histories of the application of spectral IP in the investigation of six Proterozoic sulphide, oxide and graphitic gneiss deposits in Finland have been described by Vanhala and Peltoniemi (1992). They found that deposits with large differences in texture, such as graphitic gneiss and coarse-grained disseminated sulphide, could

be separated on the basis of their diagnostic phase-spectra constants. They also found a good correlation between the observed grain size (from thin sections) and the grain size calculated from the apparent, field-survey phase spectra in the case of homogeneous disseminated textures.

The Sol sulphide system in Arizona, USA, consists of deep mineral deposits covered with thick, conductive overburden. The deposit was discovered in 1972 using a conventional time-domain IP survey over a gravity high. The original IP data have been reprocessed in the light of a recent magnetotelluric survey that has been used to extract natural field IP (NFIP) data (Gasperikova *et al.*, 2005). The specific details of the survey technique have been described by Gasperikova and Morrison (2001). A Laramide diorite porphyry intruded quartz monzonite, resulting in significant copper-molybdenum mineralisation with the highest concentrations of copper being found in the volcanic sediments adjacent to the porphyry. The generalised geology along the IP/MT profile is shown in Figure 9.22A. The derived IP resistivity and chargeability are shown in Figures 9.22B and C, respectively. The resistivity inversion (Figure 9.22B) shows an anomaly that correlates with the Cretaceous andesites between  $-2000\text{ m}$  and  $500\text{ m}$  along the profile, with the highest resistivities

(A)



(B)

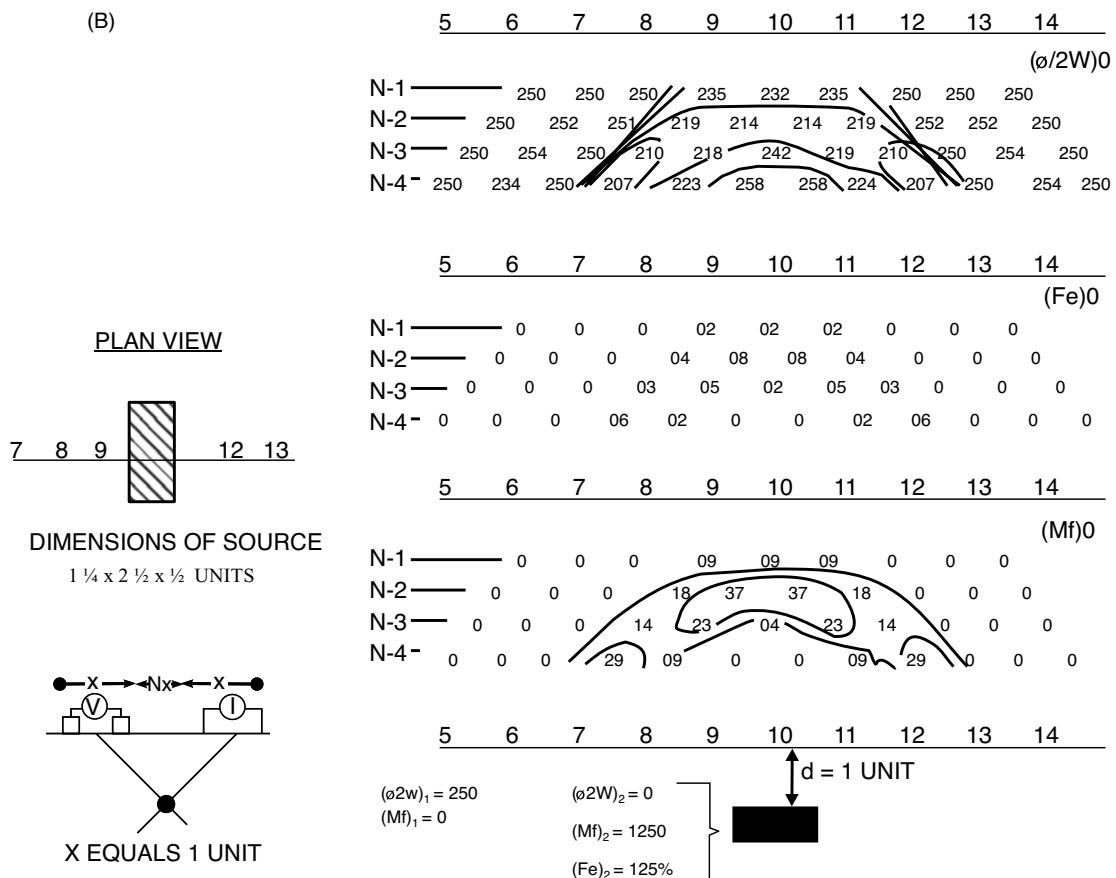
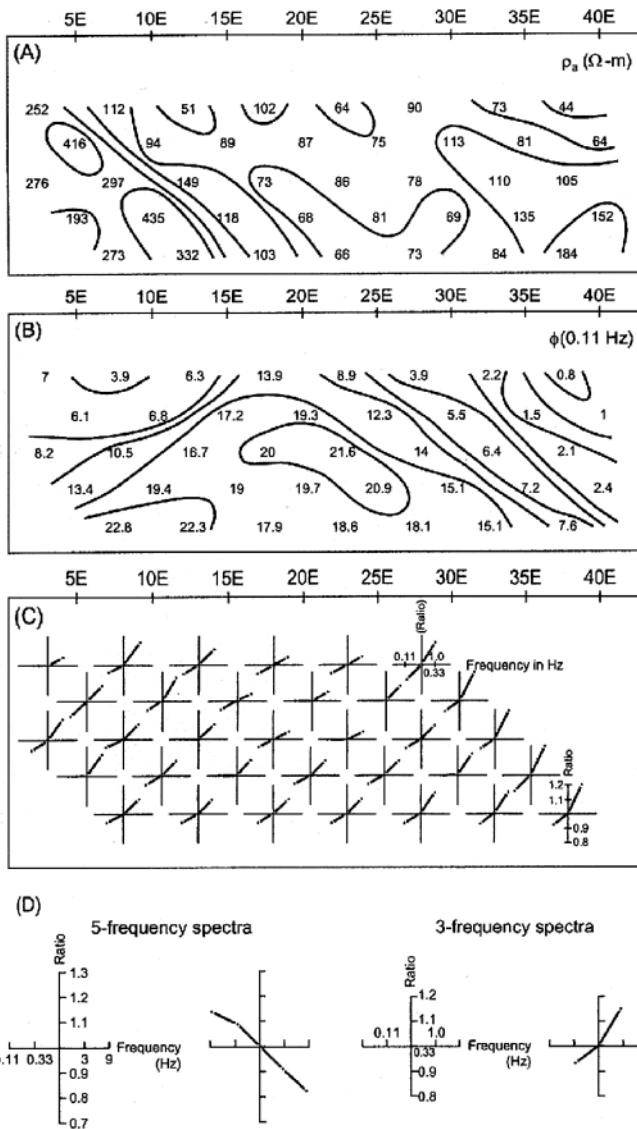


Figure 9.17 Two model experiments to illustrate the apparent resistivity, frequency effect and metal factor over (A) a thin vertical prism, and (B) a horizontal rectangular block. From Halløf (1967), by permission.



**Figure 9.18** Three forms of pseudo-section display of spectral IP data: (A) apparent resistivity at 1 Hz; (B) phase angle at 0.11 Hz, and (C) ratio of spectral parameters at three frequencies. From Hallof (1982), by permission. (D) Details of each plotting point, showing that the data are normalised to the mid-frequency value which always plots at 1.0 on the graphs (where the two axes cross).

being found between  $-1000$  m and 0 m interpreted to be at the edge of the porphyry shown in the geological cross-section. A wedge-shaped anomaly thickening from 0 m towards the west is associated with the conductive Tertiary sediments. The chargeability section (Figure 9.22C) shows a 30 ms anomaly between  $-2000$  m and 500 m, which correlates with the resistivity anomaly in the Cretaceous volcanic sediments. However, a large chargeability anomaly ( $>60$  ms) is found between  $-1000$  m and 0 m and in the depth range 500 m to 1000 m, which coincides with the location of the Laramide porphyry.

Porphyry copper deposits represent an important set of potential mineralisation prospects in the Philippines, where the use of

geophysics in mineral exploration is underdeveloped. Traditional IP surveys have been undertaken, although only recently have the data been inverted using methods to take into account topography. In one location, the original inversion was carried out assuming a flat surface (patently not correct) and borehole locations chosen. However, when the data were inverted allowing for topography, the original geophysical anomaly selected for drilling plotted over 80 m further along the profile. Had the original location been drilled, the association with the geophysics would have been incorrect. An example of an IP survey in the Philippines is shown in Figure 9.23. The survey was undertaken with a dipole-dipole survey and a dipole length of 100 m. It is clear that the resistivity section (Figure 9.23A) shows no significant resistive anomalies. However, the chargeability section (Figure 9.23B) reveals at least three if not four possible features (arrowed) that would be worth further investigation and correlation with other related geological information.

The Century zinc-lead-silver deposit in Queensland, Australia, occurs within sediments associated with the Proterozoic Mount Isa inlier, and is locally overlain unconformably by Cambrian dolomitic limestone, chert and chert breccia. The deposit is hosted within dolomitic siltstones and carbonaceous shales in which the 40-m thick mineralised sequence consists of four laterally continuous subdivisions (units 1–4). The bulk of the mineralisation occurs as strata-bound, banded sphalerite, galena and pyrite within black carbonaceous shales of units 2 and 4. A schematic north–south cross-section through the deposit is shown in Figure 9.24A (Mutton, 2000). There is a smaller, shallow southern block bounded by two faults and a deeper, larger, block completely concealed beneath the Cambrian limestone and recent alluvium. The deposit did not feature on early gravity or magnetic data prior to its discovery, which was based on zinc soil geochemistry. However, subsequently, significant amounts of geophysical investigations have been undertaken including ground and airborne surveys (gravity, magnetics, electromagnetics, IP/resistivity, reflection seismics), borehole logging and inter-borehole geophysical imaging. It was found early on in the exploration that the zinc-rich, low-sulphide mineralisation was not detected by EM methods. However, IP/resistivity traverses undertaken later were successful and are shown in Figure 9.24B and C. The major geological features shown in Figure 9.24A are superimposed in simplified form onto the IP inversion of chargeability in Figure 9.24C. The association of high chargeability values with especially the deeper deposit is clearly evident.

The range of geophysical techniques deployed at Rio Tinto's mine were used not only to establish the extent of the orebodies, but also to help with the geotechnical mine design and hydrogeological investigations. It is also worth reiterating Mutton's conclusion that 'the overall economic benefit of successful implementation of geophysical methods into all phases of resource definition and mining at Rio Tinto's operations is estimated at tens of millions of dollars annually'. Furthermore, mining operations that undertake, evaluate and successfully exploit geophysical developments, along with other forms of remote sensing (both airborne and satellite-based), in conjunction with better use of the access to be gained through boreholes (logging and inter-hole imaging), and geological and geochemical data, will become the most efficient and economically viable mines of the future. Mineral exploration and mining companies take note!

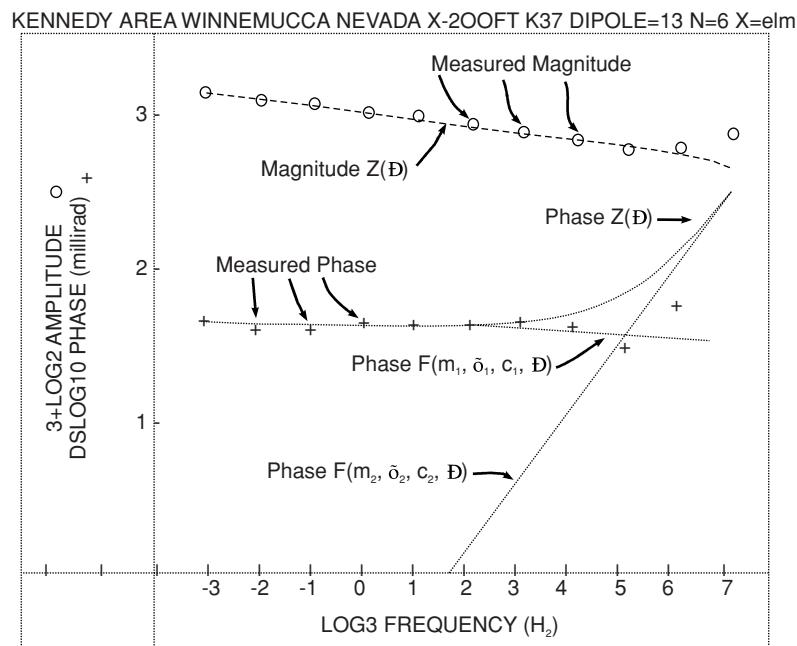


**Figure 9.19** Example of a spectral IP amplitude-phase diagram. The steep gradient at high frequencies is due to inductive coupling (dispersion 1), while the data at lower frequencies with almost flat graphs (dispersion 2) can be inverted to give the electrical parameters of the ground. From Hallof 1982), by permission.

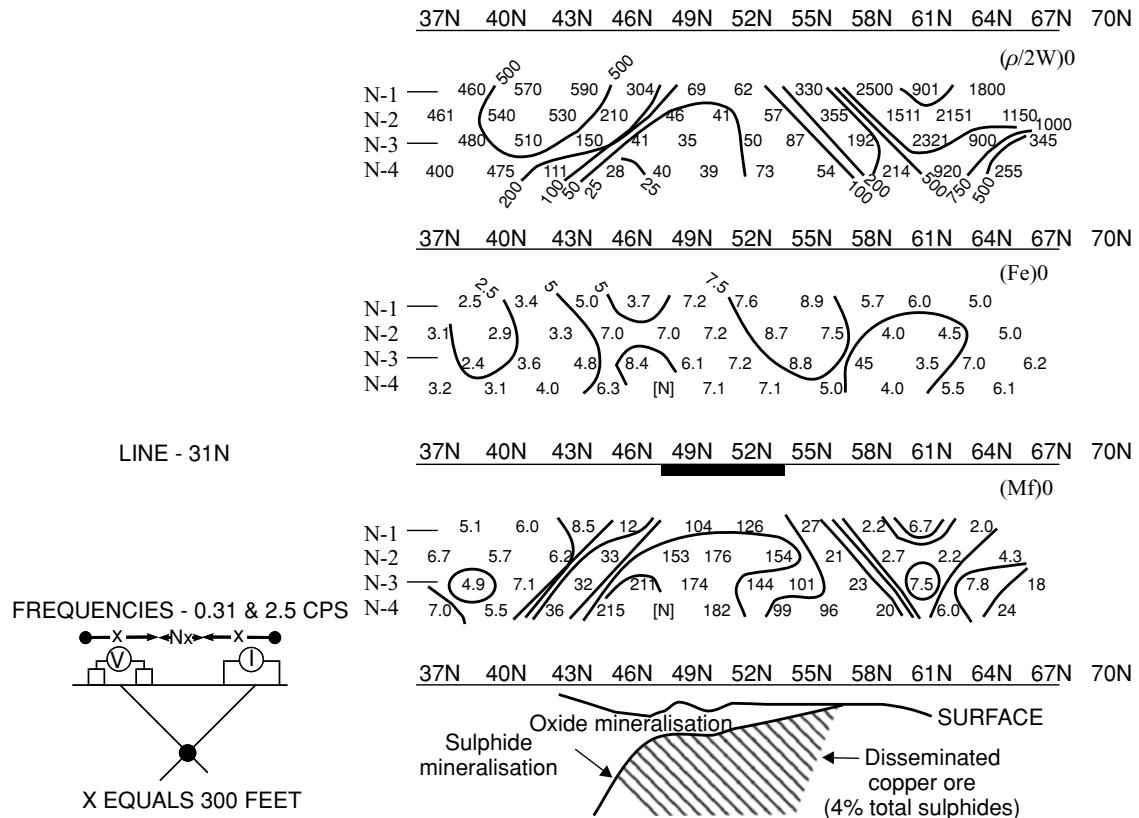


**Figure 9.20** Example of induced polarisation data for the Copper Mountain area, Gaspe, Quebec in Canada. From Hallof (1967), by permission.

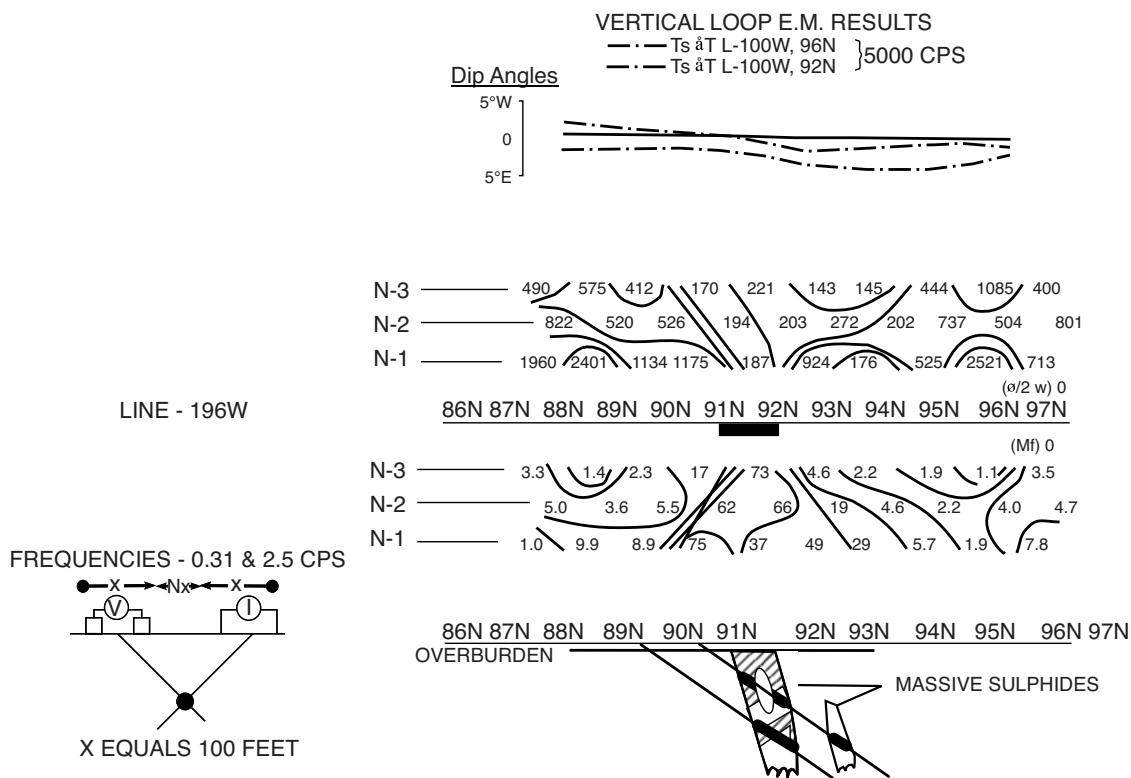


**Figure 9.21** Apparent resistivity and apparent metal factor data over a massive sulphide orebody at the Heath Steele Property, Newcastle, New Brunswick, compared with vertical loop EM data which show very poor resolution in contrast with the IP data. From Hallof (1967), by permission.

### 9.4.2 Hydrocarbon exploration

Electrical investigations (non-EM methods) for hydrocarbon exploration have been undertaken widely in the Arctic region, Siberia, Tatarstan, China, the Baltic Sea and the Caspian Sea (Veeken *et al.*, 2009) to complement seismic reflection surveys. EM methods for hydrocarbon exploration are discussed in Chapter 10. IP/resistivity investigations have been undertaken using marine configurations (see also section 9.3.1). Veeken *et al.* have been able to identify IP anomalies associated with shallow alteration haloes arising from hydrocarbon migration towards the seabed. They cite an example from a survey undertaken on the Severo-Guljaevskaya oil and gas field in the Barents Sea. IP data acquired were inverted in a 1D mode using the Cole–Cole model to produce resistivity, polarisation coefficient, relaxation time, and frequency exponent values.

They found a layered sequence with sedimentary rocks overlying a dolerite sill, which in turn overlies the hydrocarbon reservoir below. It is important, therefore, to be able to differentiate between these features. The overlying sediments were characterised by low resistivity values ( $<100 \Omega\text{m}$ ), the dolerite sill by high resistivity values (4000 to  $>20,000 \Omega\text{m}$ ), while the underlying reservoir rocks had resistivity values generally  $<400 \Omega\text{m}$ . There was no significant resistivity anomaly associated with the near-surface hydrocarbon diffusion zone. However, chargeability data ( $\eta$ ) clearly indicated that the diffusion zone had a prominent anomaly associated with

it, with values of  $\eta$  of 2–5%, whereas the unaffected sediments had values typically  $<1\%$ . The dolerite sill had  $\eta$  values  $>10\%$ . Similar anomalies also existed on relaxation time data.

Veeken *et al.* (2009) provided another example to illustrate the IP detection of a shallow diffusion zone over a much deeper hydrocarbon reservoir. The geoelectric section of polarisation coefficient  $\eta$  is shown in Figure 9.25A. The anomaly associated with the hydrocarbon diffusion zone is clearly evident (highlighted by an asterisk) and has  $\eta$  values between 11–13% compared with background values between 2 and 6%. The anomalous zone coincides with a geochemical permeability barrier at the top of a carbonate structure. A similar result is shown in Figure 9.25B, which is derived from IP data for the mid-Volga basin. Here the diffusion zone polarisation coefficient anomaly has a  $\eta$  value of 14–16% compared with background values of 12% or less. What is also evident is that in the area of the non-productive borehole there is no associated hydrocarbon diffusion zone, on the basis of there being no polarisation coefficient anomaly. This contrasts with a known hydrocarbon productive area (productive borehole) where there is the measured anomaly.

It is reported by Veeken *et al.* that in 124 out of 126 study cases in the former USSR, positive predictions of hydrocarbons were found and 40 successful wells have been drilled on IP anomalies identified by their methods. There is clearly a role for the marine IP method in hydrocarbon exploration to complement the rapidly developing controlled-source electromagnetic (CSEM) methods (see Chapter 10).

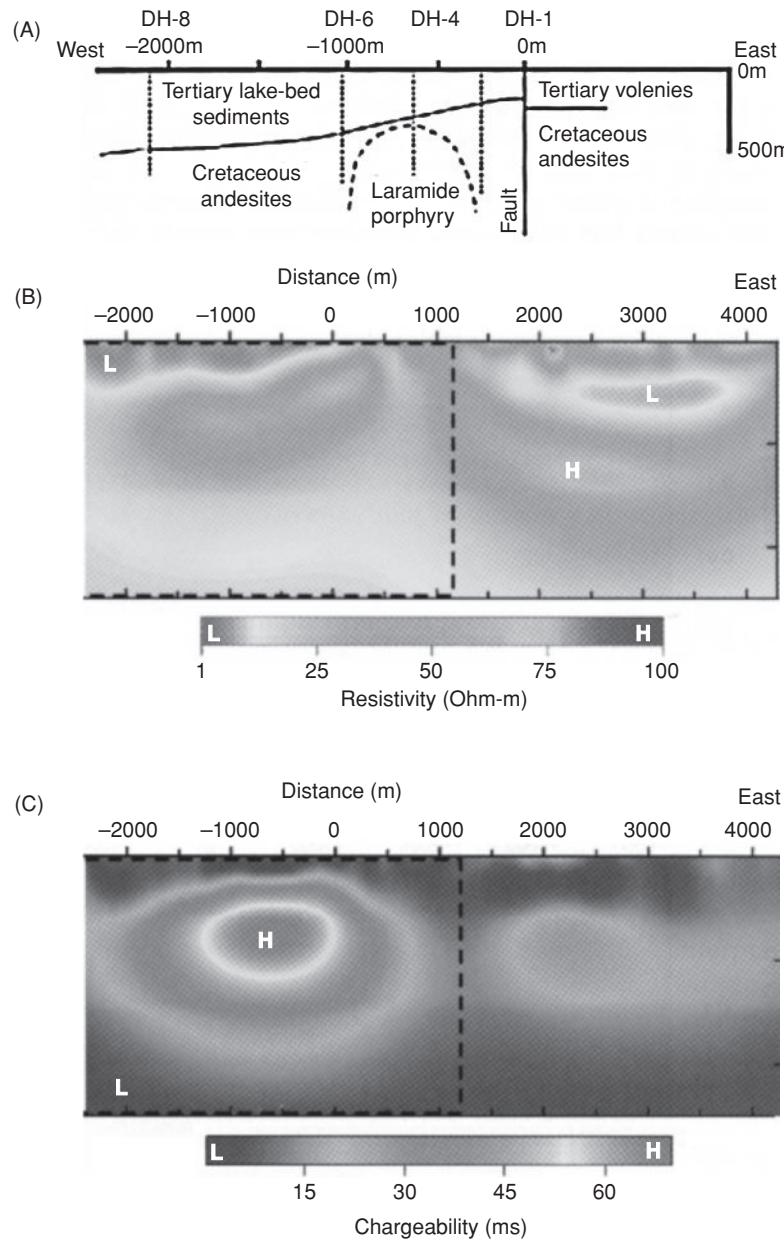


**Figure 9.22** (A) Schematic geological cross-section along an IP profile across the Sol sulphide system in Arizona, USA, and the corresponding (B) resistivity and (C) chargeability inversion sections of dipole-dipole data. From Gasperokova *et al.* (2005), by permission. [C]

### 9.4.3 Geothermal surveys

Geothermal sources often have high fluid mobility within circulating groundwater. This gives rise to low resistivities that can be detected using IP methods. The results on an IP survey over a possible geothermal field in Kenya are shown in Figure 9.26 (Hallot and Pelton, 1981), which illustrates low apparent resistivity values for  $n=5$  and 6 between locations 14 and 17. Computer analysis of these data produced a geologically plausible model of a poorly defined but major conductor at a depth of about 350–400 m and a width of about 250 m. Although the survey did not delineate the possible

geothermal centre absolutely, it did provide a constrained target for further, more detailed investigations.

Zohdy *et al.* (1973) have described a combined resistivity, self-potential and induced polarisation survey over a vapour-dominated geothermal field in the Yellowstone National Park, Wyoming, USA (Figure 9.27). The broad SP anomaly is caused by water upwelling (as indicated by the arrows in the bottom panel of the figure), and continues as far as it does to the southeast because the groundwater flows laterally until it enters more permeable material, at which point it can then descend. The resistivity profiles reflect the

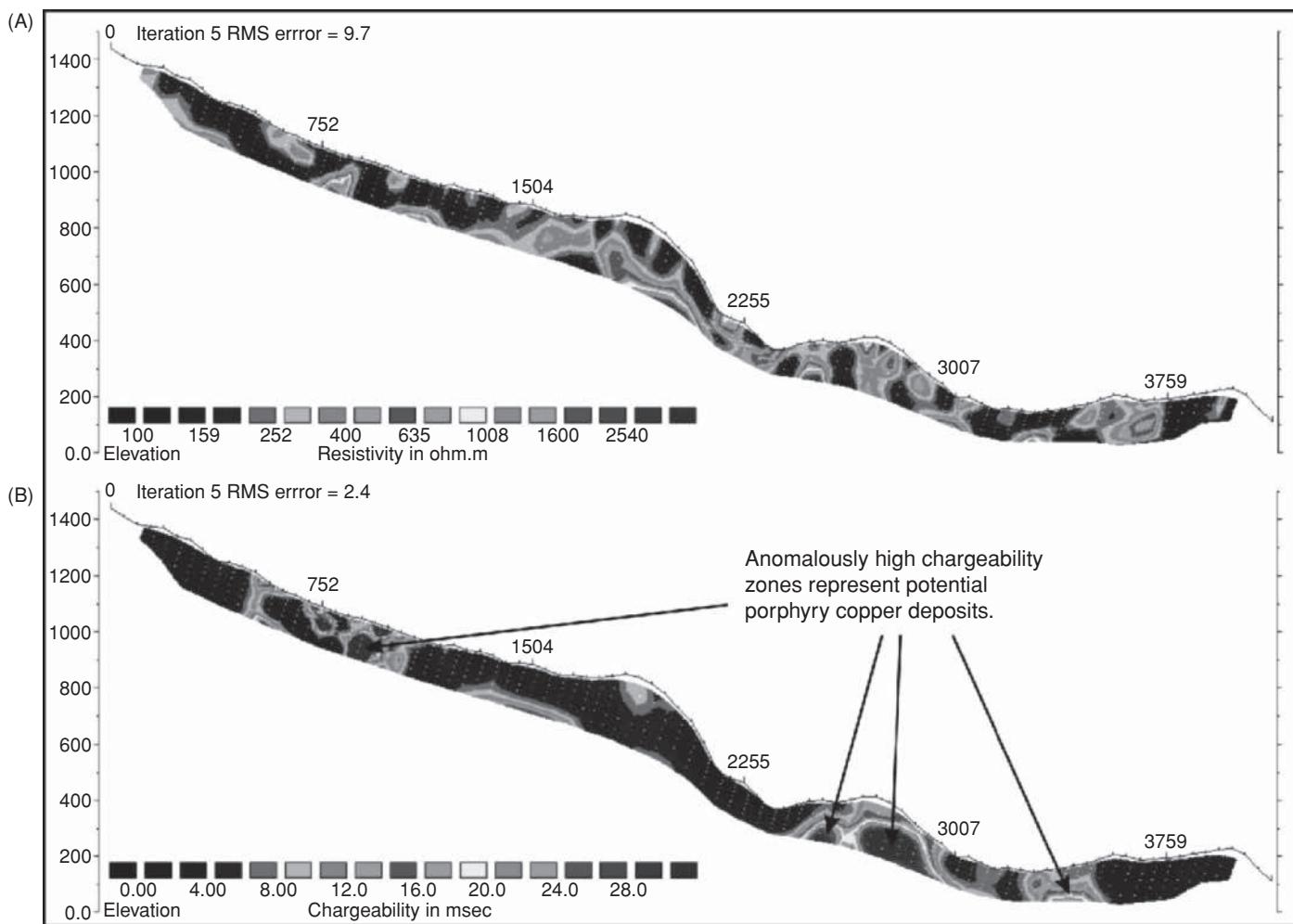


**Figure 9.23** (A) Dipole-dipole resistivity and (B) chargeability sections corrected for topography across a porphyry copper prospect in the Philippines. [C]

general distribution of formations, with those to the northwest having lower true resistivities ( $10\text{--}130 \Omega\text{m}$ ) than those to the southeast ( $>130 \Omega\text{m}$ ). The percentage-frequency effect profile has a significant background of around 5%, which has been attributed to the presence of clayey materials and pyrite in the near-surface materials. The IP anomaly which is particularly prominent with  $AO \approx 300 \text{ m}$  is due to an increase in disseminated pyrite deposited by circulating thermal waters, as indicated from borehole data in the area.

#### 9.4.4 Groundwater investigations

Vacquier *et al.* (1957), who were the first to use induced polarisation for hydrogeological investigations, described two useful case histories. The first is for a site near Carrizozo, New Mexico, in a valley bounded to the southeast by the Sierra Blanca which comprises volcanic rocks from which potable water is derived. To the north and west, Cretaceous sediments of the Tularosa Valley contaminate the groundwater with chlorides and gypsum, making it unusable.

Figure 9.28A shows a map of IP values 10 s after current shutoff; the contours are orientated approximately north–south and mirror

the existing drainage pattern, the boundaries of which correlate with contours of 2 mV/V in the east and 3 mV/V in the west. An irrigation well IR-1 produces about 4500 litres/minute of relatively poor quality water: hence the low IP overvoltage ( $\approx 3 \text{ mV/V}$ ). The closure with a value of 6 mV/V (L-1) was subsequently drilled and produced about 450 litres/minute of better quality water. The map shown in Figure 9.28B shows contours of the ratio of IP values 5 s after current shutoff to those after 10s. Vacquier and colleagues interpreted these contours as highlighting a buried channel, with the higher ratios being associated with finer-grained material.

Ogilvy and Kuzmina (1972) carried out a laboratory scale-model experiment to examine the effectiveness of time-domain IP measurements in locating groundwater accumulations in sandy-clayey overburden. While standard constant separation traversing over a hemispherical freshwater lens produced a broad apparent resistivity anomaly, the IP polarisability anomaly was both narrow and steep-sided (Figure 9.29A): a result which had also been obtained by Vacquier *et al.* (1957, p. 684). However, for a model with the same dimensions and geometry, but with a saline water lens, both the apparent resistivity and IP chargeability anomalies were broad

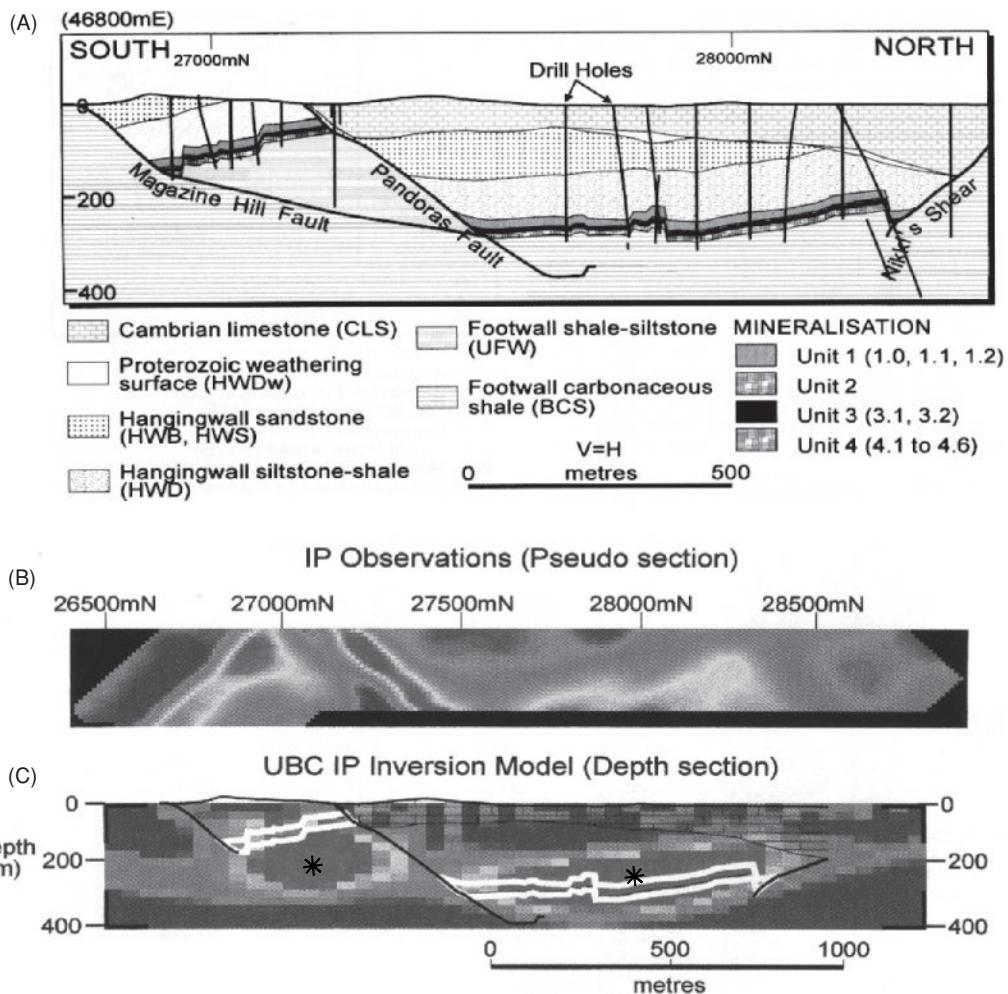


**Figure 9.24** (A) North-south geological section through the Century zinc deposit, Queensland, Australia, and (B) the corresponding IP pseudo-section and (C) IP inversion model with the orebody outline superimposed. Principal chargeability anomalies are denoted by an asterisk. From Mutton (2000), by permission. [C]

in contrast with the ratio of IP overvoltages 0.5 and 5 s after current shutoff (Figure 9.29B).

The examples from Vacquier and colleagues and from Ogilvy and Kuzmina demonstrate that for time-domain IP, maps of the ratio of the overvoltage for two different times can provide a sharper resolution of subsurface water bodies than maps of the overvoltage for single cutoff times. While the IP method can provide a useful interpretation of groundwater bodies, the field method is less practical than modern electromagnetic induction methods, and this may account for the paucity of recent examples of the use of IP in groundwater investigations.

## 9.4.5 Environmental applications

### 9.4.5.1 Slag deposits

Since the early 1980s, interest has been expressed in the possibility of using IP in the investigation of contaminated sites. Olhoeft (1985), for example, investigated the IP characteristics of rocks contami-

nated with organic pollutants. Organic chemicals can react with clay minerals so that the IP response of the clay mineral–electrolyte mixture changes. This work has been extended by Soininen and Vanhala (e.g. 1992), for example, who have investigated laboratory samples of glacial clays contaminated with ethylene glycol using spectral IP methods. They have found that both the phase and resistivity spectra (as functions of frequency) of contaminated samples differ significantly from those of uncontaminated samples. Whether this technique can be extended to achieve a fully commercial field survey technique has yet to be demonstrated.

Cahyna *et al.* (1990) have presented a case history where the field use of standard IP, in conjunction with appropriate laboratory measurements, was instrumental in mapping out an area seriously contaminated with cyanide complexes which originated from slag-type material from former plating works. They used both conventional resistivity sounding (using the Schlumberger array) and symmetrical resistivity profiling with IP (called SRP-IP by the authors). The resistivity survey failed to detect the contamination even though measured directly over a known slag deposit. In

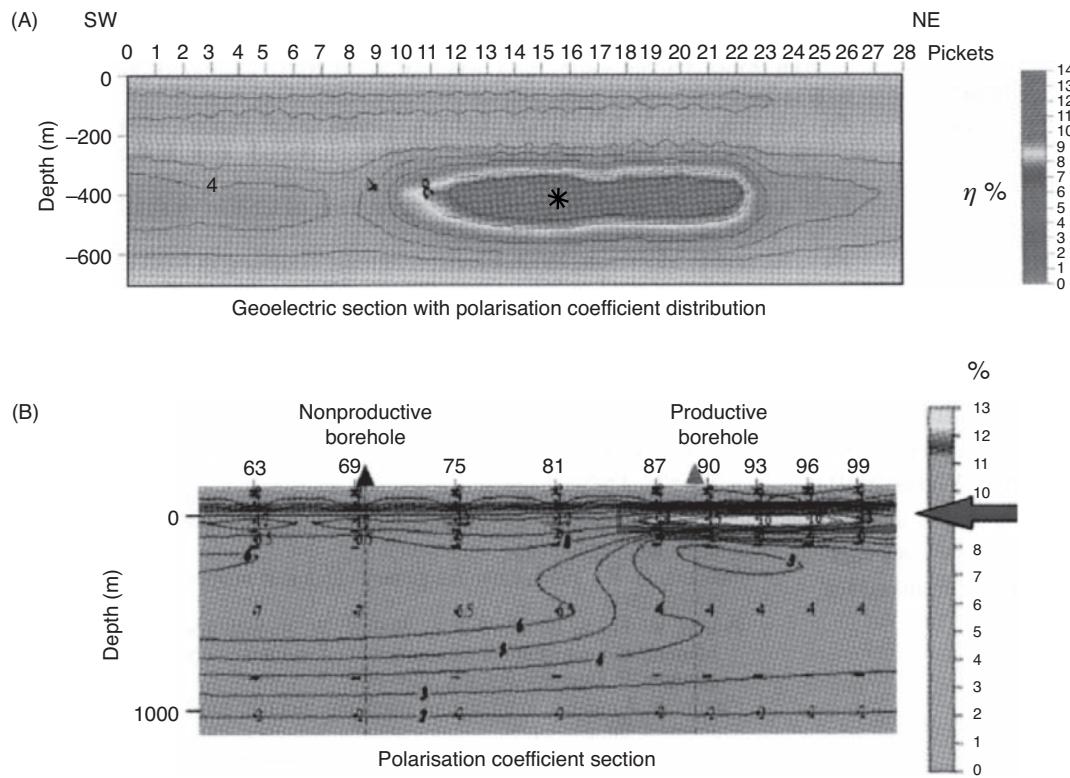


**Figure 9.25** (A) Geoelectric section of the polarisation coefficient  $\eta$  distribution (A) in the Severo-Guljaevskaya area, Barents Sea, and (B) mid-Volga basin. The IP anomalies are marked by an asterisk and horizontal arrow, respectively, and both overlie deeper accumulations of hydrocarbons. From Veenken et al. (2009), by permission. [C]

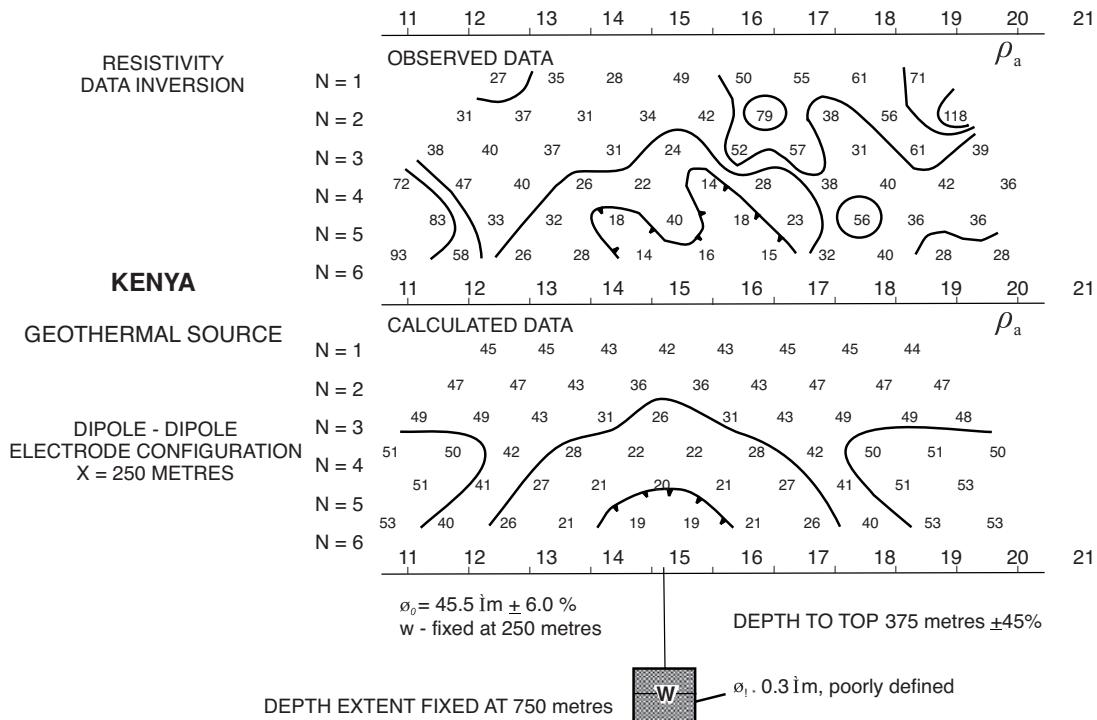


**Figure 9.26** Observed and calculated apparent resistivity data obtained during IP surveys of a low resistivity ( $0.3 \Omega m$ ) geothermal source in Kenya. From Hallof and Pelton (1981), by permission.

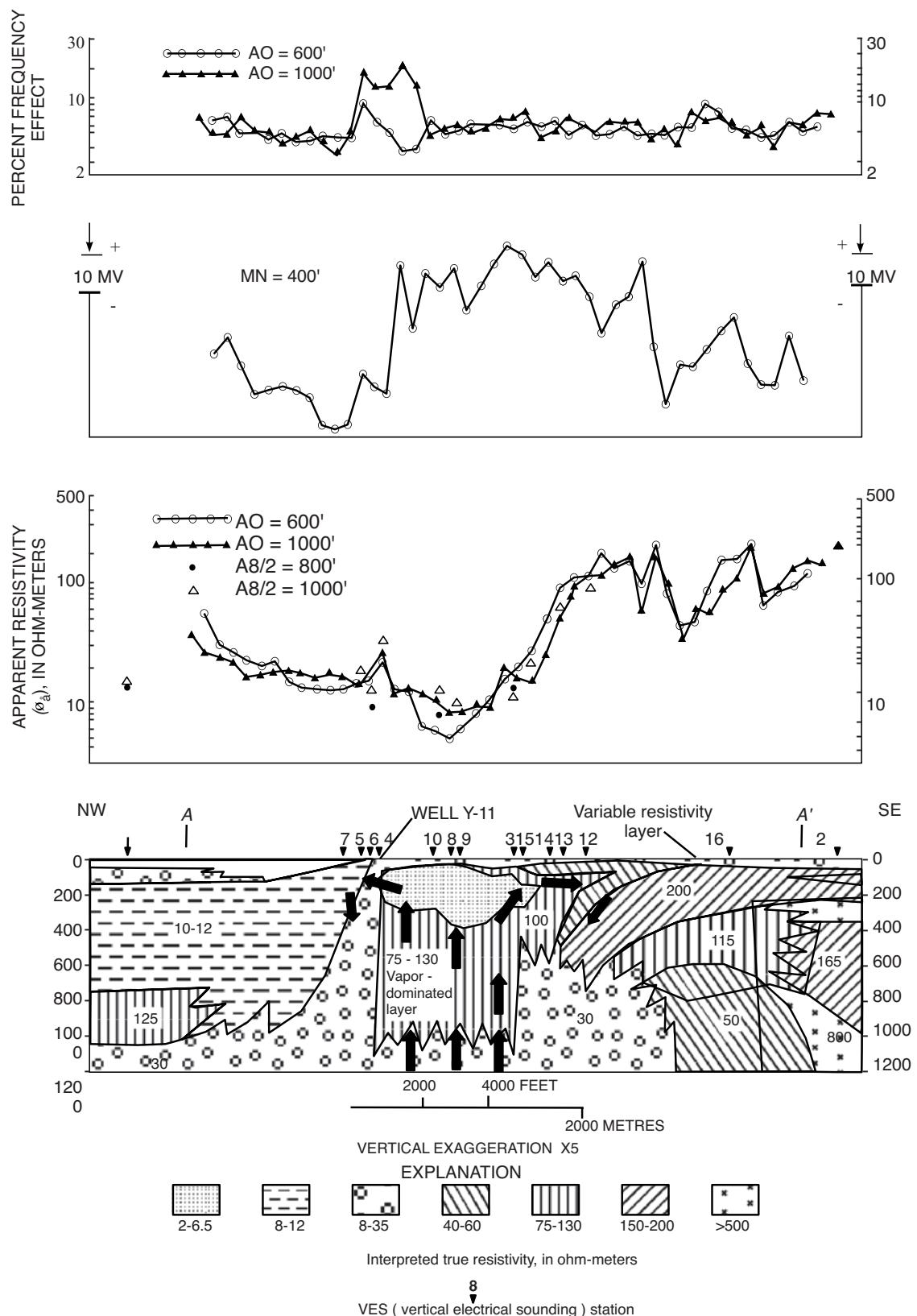


**Figure 9.27** Percentage frequency effect and apparent resistivity data across a vapour-dominated geothermal system in the Yellowstone National Park (interpreted geological cross-section shown in the lowest panel) compared with a self-potential profile across the same feature. From Zohdy *et al.* (1973), by permission.

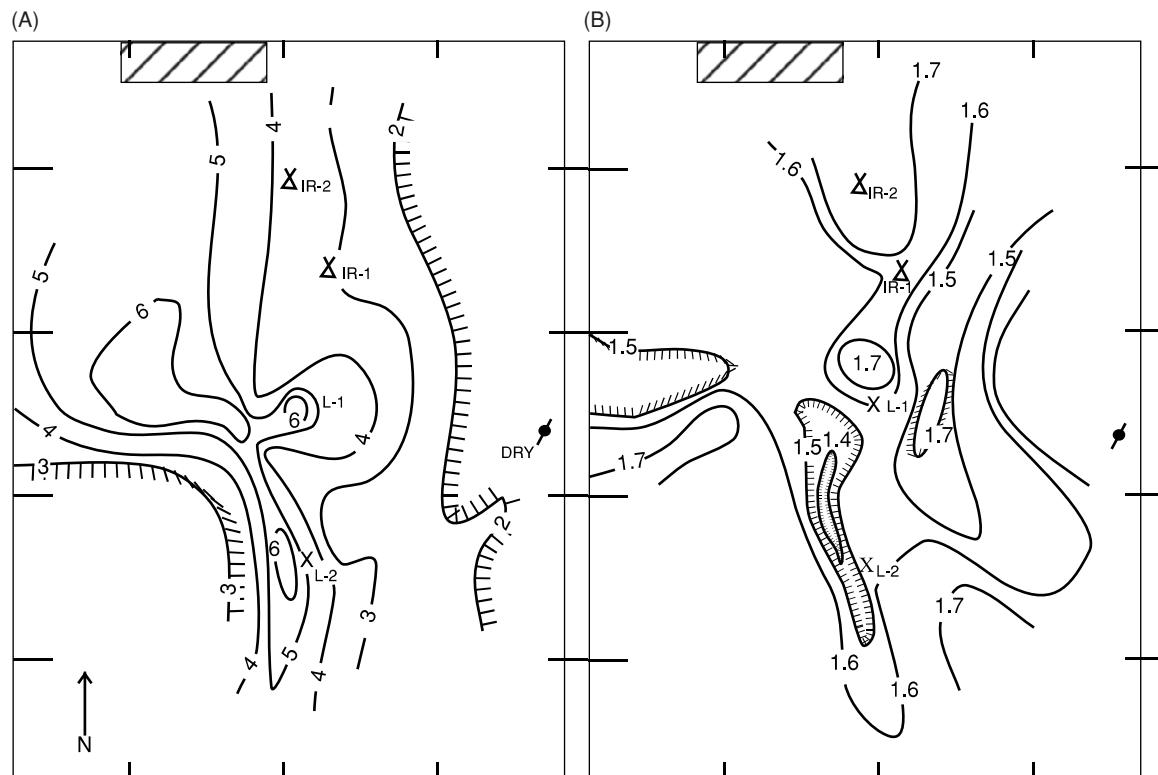


**Figure 9.28** Maps of: (A) induced polarisation overvoltage after 10 s (contours at 1 mV/V intervals); and (B) the ratio of IP data after 5 s and 10 s after current switchoff, over a buried valley aquifer near Carrizozo, New Mexico, USA. The well sunk at L-1 produced about 450 litres/minute of potable water. From Vacquier *et al.* (1957), by permission.

contrast, the SRP-IP survey, which was used to measure chargeability, was used successfully to identify not only the limit of the known slag, but also to detect a second and previously unknown area of contamination. A map of the SRP-IP chargeability was produced (Figure 9.30) on which the centres of contamination and the affected areas around them are clearly evident.

#### 9.4.5.2 Hydrocarbon contamination

A case history of the ability of the SIP method to detect hydrocarbon contamination has been provided by Kemna *et al.* (2004) for a kerosene-contaminated military site near Strasbourg-Entzheim airport in France. Contamination of the site occurred from 1957 until the 1970s when it operated as a jet fuel depot. In addition to occasional short-term but massive spillages of jet fuel during normal operations of the site, the subsurface has also been contaminated over a long time by slowly leaking underground storage tanks and pipelines. Jet fuel/kerosene, like other light non-aqueous phase liquids (LNAPLs), moves downwards by gravity until its progress is impeded either by a low permeability horizon or it meets the groundwater table. Soluble components may then develop dissolved contaminant plumes that flow with the hydraulic gradient. Hydrocarbon contamination was found over an area of 400,000 m<sup>2</sup> with

residual hydrocarbon concentrations of 1 g/kg. Principal components included aromatic hydrocarbons such as naphthalene and benzene/toluene/xylene (BTX) at concentrations of up to several hundred milligrams per litre.

The site consists of a sequence of fluvial sediments associated with the nearby Rhine and Bruche rivers, with a top layer of loess 1.5 m thick overlying sands and gravels. A clayey silt layer is found at a depth of around 9 m. At the time of the survey the groundwater table was at 8.6 m below ground level.

The survey consisted of deploying 16 equally spaced electrodes down each of several 13-m deep boreholes, with each borehole pair separated by about 8 m; the electrode separation was 0.75 m, with additional electrodes placed over the ground between the boreholes. Resistance and phase-angle data were acquired using a Zonge IP system. For each image plane a variety of dipole-dipole configurations were measured and both resistivity and IP images calculated. An example set of image sections is shown in Figure 9.31 along with a composite geological log.

The real conductivity ( $\sigma'$ ) component (Figure 9.31A) reflects the effects of the geological materials present. The top loess and deeper clayey silt layer are both evident as moderate to high conductivity zones, respectively, with a similar correspondence in the imaginary conductivity ( $\sigma''$ ) component (Figure 9.31B). In contrast the sand and gravel formations above (unsaturated) and below (saturated)

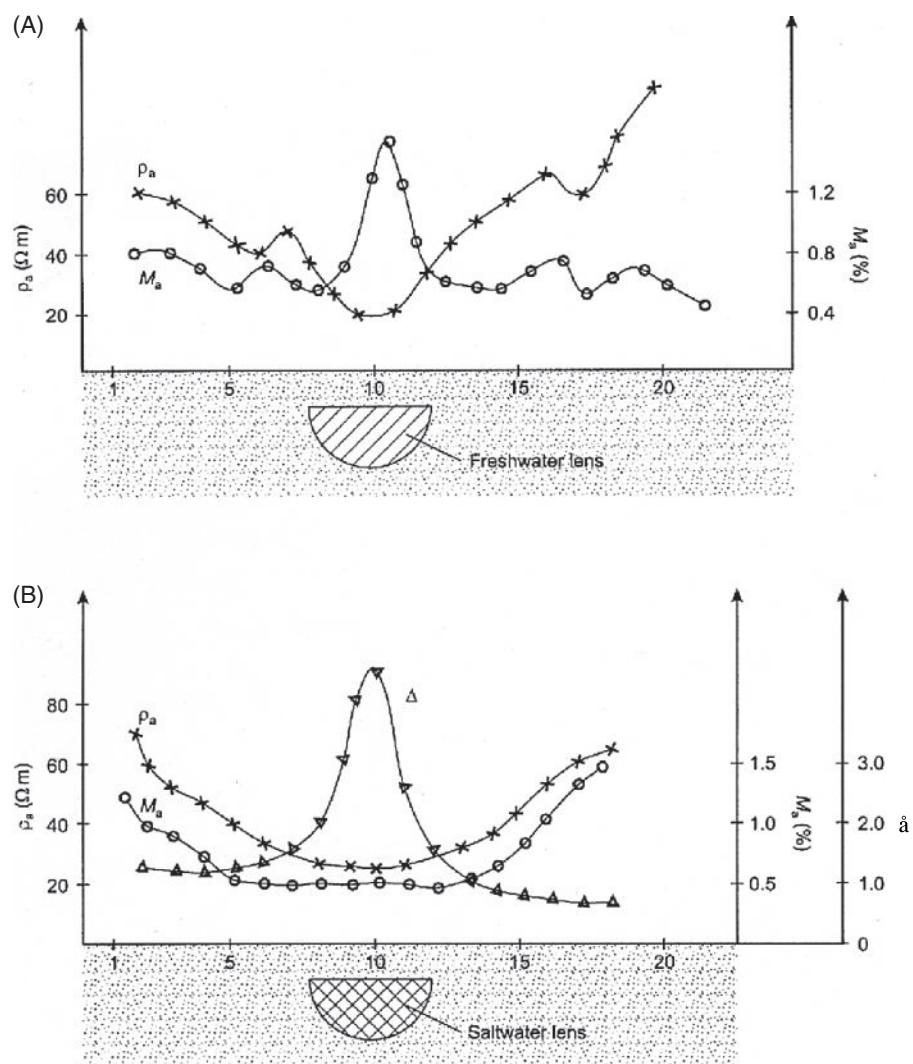


**Figure 9.29** Scale-model experimental results of apparent resistivity, chargeability, and ratio ( $\Delta$ ) of overvoltage measured 0.5 minutes and 5 minutes after current switchoff, obtained across a buried hemispherical lens of (A) fresh water and (B) salt water. After Ogilvy and Kuzmina (1972), by permission.

the clayey silt horizon exhibit low and intermediate conductivities, respectively. It is thought that the high  $\sigma'$  values in the loess and clayey silt are a function of the surface conduction from the higher clay mineral concentration. The increase in conductivity with saturation is thought to be a result of primarily electrolytic conduction. However, the conductivity phase ( $\varphi$ ; Figure 9.31C) shows a roughly 1-m-thick high-value zone above the top of the clayey silt horizon. This was found, following chemical core analysis, to coincide with residual hydrocarbon contamination at this depth. Similar surveys were undertaken upgradient of the polluted ground. While comparable conductivity anomalies were found (in the same geological materials), no phase response was found, indicating the absence of hydrocarbon contamination. In these cases, phase is clearly the parameter sensitive to the presence of the hydrocarbon contamination, not the conductivity.

#### 9.4.5.3 Fly-ash water pond leakage

Coal-fired power stations produce large amounts of fly ash as a product of burning coal to generate electricity. Hot ash is cooled using water that is then stored in open, clay-lined ponds where solids precipitate out and are later removed and disposed of. Fly-ash water tends to have high concentrations of total dissolved solids (TDS) and is highly conductive as a result (e.g. 1500 mS/m with TDS of  $10^4$  ppm). Viezzoli *et al.* (2006) describe the use of both TEM and IP surveys to help delineate a contaminant plume derived from a leaking fly-ash pond at Loy Yang coal-mine, Victoria, Australia. Information from shallow boreholes identified that conductive (200–400 mS/m) contaminated water had formed at least one if not two saline plumes from the fly-ash pond. However, the variability in the local geology and the spatial distribution of boreholes only allowed a relatively crude estimation of plume size

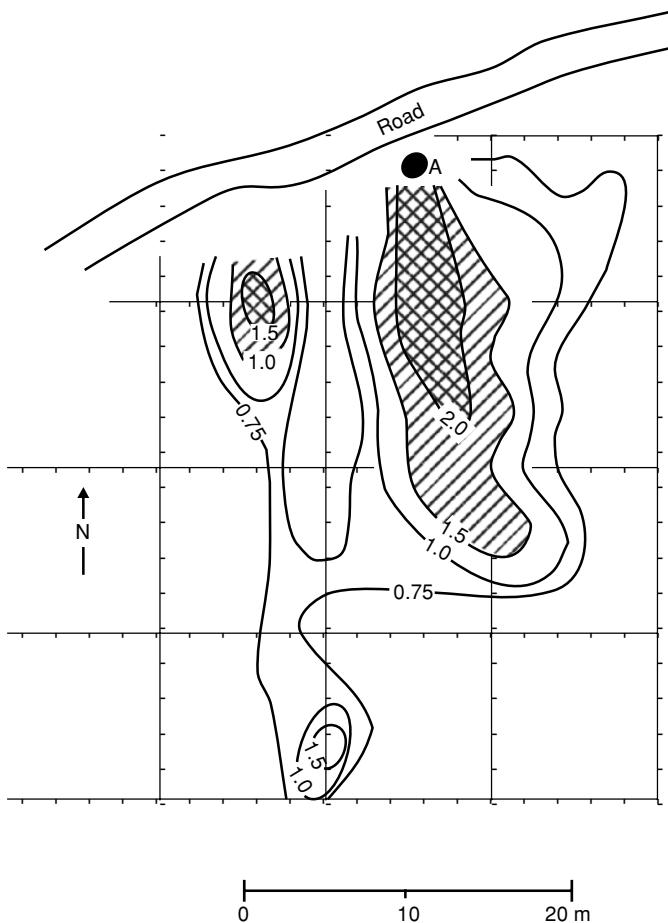


**Figure 9.30** Chargeability map over a site contaminated by cyanide complexes. The location of a known outcrop of slag is indicated at A. Contours are in percentage chargeability. Shaded areas indicate the interpreted extent of contaminated land. From Cahyna *et al.* (1990), by permission.

and direction. Consequently, geophysical methods were used over a number of transects orthogonal to the suspected plume flow directions. The general geography around the site is illustrated in Figure 9.32A, with plume flow directions derived from borehole data indicated by large open arrows (predominantly west-northwest); geophysical transects are shown by solid lines. The area to the northwest of the fly-ash pond is shown in greater detail in Figure 9.32B. It is apparent that the plume direction derived from TEM conductivity data is in a more northwesterly direction than had been indicated from the borehole data (as indicated by the 150 mS/m contour in Figure 9.32B).

An IP survey was conducted parallel to the TEM transects using a Wenner array with an electrode spacing of  $a = 5$  m and 10 m, combined with three soundings with  $a = 2$  m to  $a = 20$  m, in order to create a detailed electrical cross-section. IP data were inverted using a least-squares inversion (Loke and Barker, 1996a) with key IP Cole–Cole parameters ( $m$ ,  $c$  and  $\tau$ ) derived using the master-curve method of Duckworth and Calvert (1995). Integral chargeability ( $M$ ) and normalised integral chargeability ( $M_N$ ) were also derived.

The results of the IP survey along Line 3 are shown in Figure 9.33. The log from a borehole constructed adjacent to Line 3 is also shown with gamma-log results to 10 m depth. The geological sequence consisted of fill and ash to about 4 m (sampled also in a separate auger hole) over more fill made up of clay, sandy and clayey material down to 15 m.

The results shown in Figure 9.33 show different characteristics from southwest to northeast, with a transition at around 45 m along the profile. Northeast of 45 m, shallow conductive (300 mS/m) (Figure 9.33A) and highly chargeable ( $M_N \geq 50$  mS/m) (Figure 9.33B) anomalies are evident to a depth of around 5 m. This coincides with the dumped ash found in borehole 3766. Chargeability values decrease with greater depth, and coincide with increasing gamma values with depth attributable to an increase in the clay content. In the southwestern part of the profile, the conductivity and chargeability anomalies occur between 3 m and 10 m depth and are larger in magnitude than the more northern anomalies. The conductivity and chargeability anomalies are thought by Viezzioli *et al.* to relate to organic-, clay- and/or metal-rich soil, wet with saline porewater that has originated from surface precipitation percolating through dumped material and dissolving soluble minerals above the less permeable clay-rich strata.

Samples taken from the auger probe were tested in the laboratory for further IP parameters (percentage frequency effect,  $PFE$ ; and metal factor,  $MF$ ) of between 10 Hz and 100 Hz. Chargeability values were noticeable with phase lag,  $PFE$  and  $MF/a^*$  of the order of 100 mrad, 15%, and tens of mS/m, respectively. (\*The factor  $a$  is a dimensionless value equal to  $0.61\pi \times 10^5$  necessary to express  $MF$  in metric units). The chargeability of samples was noted to increase the higher the content of moisture, organic material, metals and TDS. The conclusion from the laboratory results is that the soil is organic-, metal- and clay-rich, which makes it very chargeable; the chargeability is further increased by the presence of saline porewater.

Lesmes and Frye (2001) showed that normalised chargeability ( $M_N$ ) relates directly to ground polarisation phenomena (both membrane and electrode polarisation), whereas integral chargeability ( $M$ ) is a measure of the ratio of ground polarisation to bulk conductivity. They also state that  $MF$  is the spectral equivalent of the integral normalised chargeability.

#### 9.4.5.4 Landfill

To demonstrate the efficacy of their 1D and 2D inversion processes, Höning and Tezkan (2007) described the results of a field IP survey undertaken over a former waste site near Düren, Germany. The former sand and gravel quarry was filled with household waste, building debris and industrial waste, and has an area of about 12,000 m<sup>2</sup>, a volume of about 55,000 m<sup>3</sup> and is between 3 m and 5 m deep. Since being backfilled the site has been covered with a layer of sand and gravel and recultivated.

Three IP profiles were surveyed (Figure 9.34A) using an IRIS transmitter with a 5-channel long-offset EM recording system allowing the simultaneous measurement of signals at five receiver

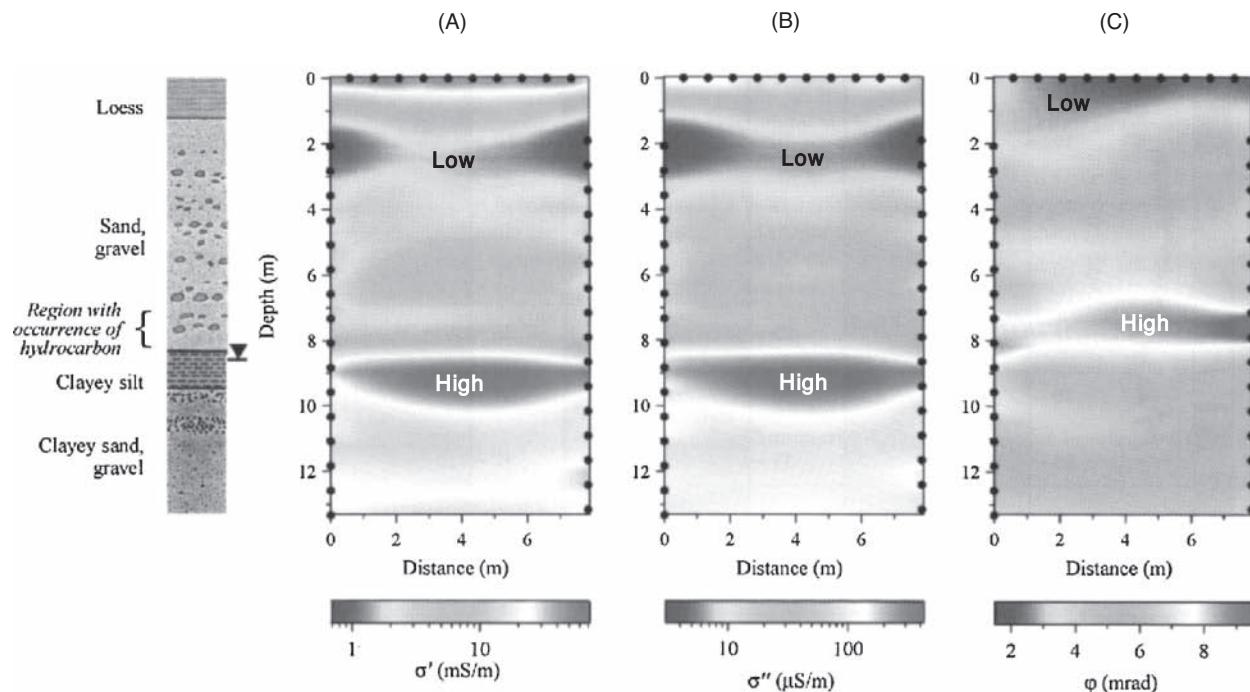


**Figure 9.31** Cross-hole IP imaging results from a site near Strasbourg-Entzheim airport, France, showing (A) the real component, (B) imaginary component, and (C) phase of complex conductivity. Solid circles indicate the position of electrodes. The geological log is derived from cores, and the occurrence of contamination was proved by chemical sample analysis. From Kemna *et al.* (2004), by permission. [C]

dipoles; electrode spacing was 6 m. Cole–Cole inversions were undertaken that yielded sections showing resistivity, chargeability, relaxation time and frequency exponent; those for Line 2 are shown in Figures 9.34B to E, respectively. The positions of the transmitter are shown as dots while the receiver dipole locations are shown as arrows. The orientation of each section shown in Figure 9.34 is northeast (left) to southwest (right). The waste is evident as a low-resistivity anomaly extending from –50 m to +50 m along the profile. The high resistivity between 50 m and 100 m is associated with unperturbed natural ground (sandy material). The resistivity section reveals the presence of a slightly deeper low-resistivity anomaly southwest of 100 m, with values of less than 100  $\Omega\text{m}$ . This has been interpreted to be associated with a well-known graben structure incorporating loess. Anomalies of chargeability, relaxation time and frequency component occur within the zone associated with the waste itself, with three prominent anomalies in each of the three parameters, perhaps indicating different types of waste material. However, what is particularly useful is that the general absence of a significant chargeability anomaly coincident with the southwestern low-resistivity anomaly helps to differentiate the area of waste from the loess. This example demonstrates the benefit of using SIP data to help to distinguish materials on the basis of their different spectral characteristics (chargeability, relaxation time and frequency component) compared with what could have been interpreted using resistivity alone.

#### 9.4.6 Geological investigations

Some applications require a more detailed breakdown of local geology and associated possible hydrogeological processes. One such application is site characterisation at nuclear waste disposal sites. Traditional geophysical methods may provide information about gross features, but more subtle aspects that might be physically important may go undetected. Kemna *et al.* (2004) have provided an example of the use of SIP to help address the issue of characterising heterogeneous glacial sediments through a 40-m deep section at the Drigg Low Level Radioactive Waste Disposal Site, Cumbria, UK.

Two 41-m deep boreholes were constructed about 15 m apart. Forty-five electrodes were installed in each borehole at 0.8-m intervals from 5.3 m to 40.5 m below ground level. Measurements were made of the DC resistivity and IP phase angle ( $\phi$ ), and cross-hole sections showing complex conductivity and phase-angle were produced (Figure 9.35). In addition, natural gamma-ray logs were acquired over part of the depth range in each borehole.

Comparison of the three IP parameters shown in Figure 9.35 reveal different aspects of the Quaternary sediments present. The real conductivity ( $\sigma'$ ) component shows high values associated with a silt/clay band between 6 m and 10 m, with a contrastingly low conductivity in the immediately underlying coarse-grained gravel to 12 m depth. The saturated fluvial outwash sands between 16 m

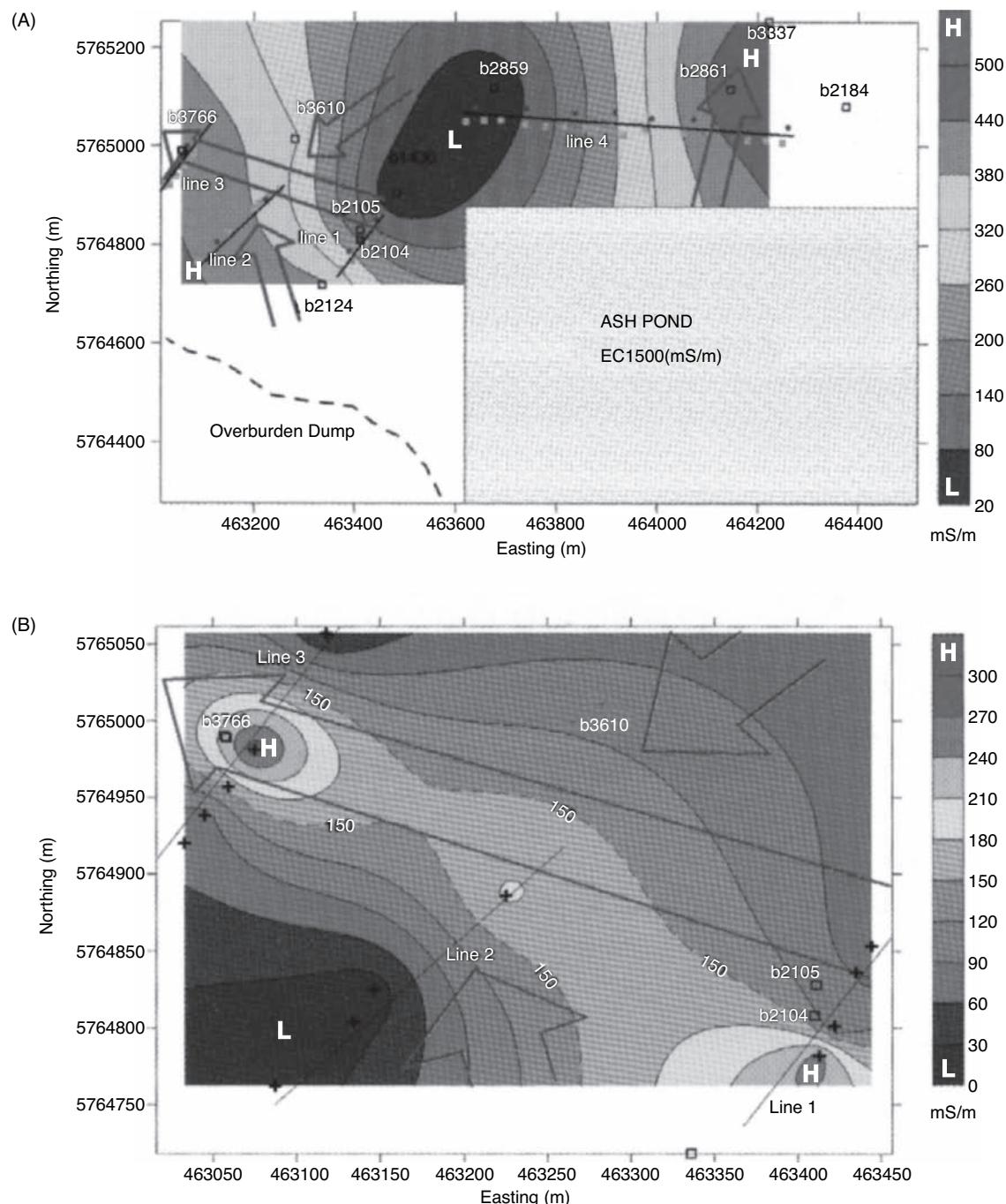


**Figure 9.32** (A) Groundwater electrical conductivity contours and fly-ash water-plume paths (large open arrows) as derived from boreholes (black squares). Individual survey lines are indicated. (B) TEM apparent conductivity slice (pseudo-depth  $\approx 25$  m) west of the fly-ash pond. The dashed line contour represents the interpreted centre of the plume. The large open arrow indicates the plume path as derived from the borehole data. From Vizzoli *et al.* (2006), by permission. [C]

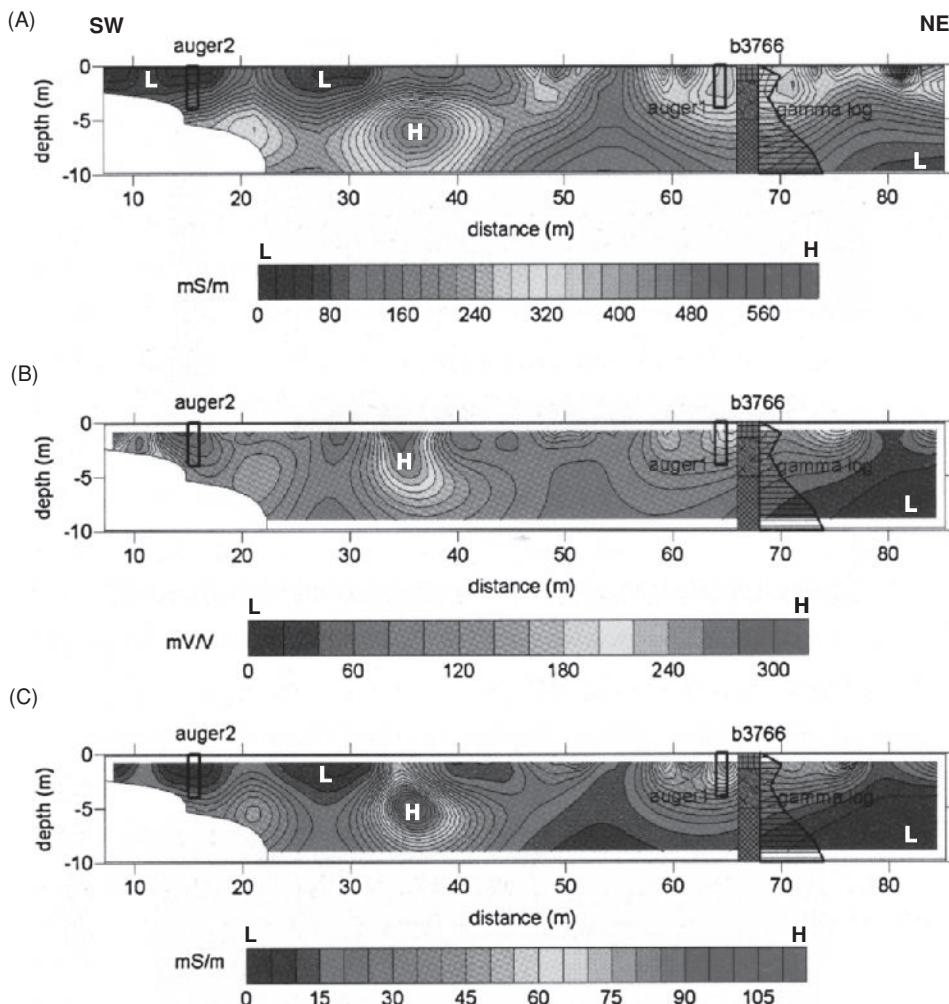


**Figure 9.33** Line 3 IP cross-sections: (A) conductivity ( $\text{mS}/\text{m}$ ), (B) integral chargeability ( $\text{mV}/\text{m}$ ), and (C) normalised integral chargeability ( $\text{mS}/\text{m}$ ). The borehole log for BH3766 reveals fill and ashes at the surface, ash, with fill beneath; a gamma-log is shown alongside. From Vizzoli *et al.* (2006), by permission. [C]

and 24 m show higher values of conductivity than the overlying unsaturated sediments. It is also clear from Figure 9.35A that the real conductivity component is unable to differentiate the fluvial sands, glacial sand and gravel, and lowermost sandstone units. There is, however, a weak, relatively resistive feature between 34 m and 36 m associated with the lower part of the deeper glacial till sequence, with a thin, moderately high conductivity band at around 32 m depth. In contrast, the imaginary conductivity ( $\sigma''$ ) component shows this thin band more prominently (Figure 9.35B), along with the lowermost sandstone unit (below 36 m depth). The saturated fluvial sands are clearly depicted (16 m to 24 m depth) as a high conductivity feature. These results suggest that the conduction in the fluvial sands is attributable to surface conduction associated with the greater surface area afforded by the finer grain size. The values of  $\sigma''$  in both the fluvial sands and lowermost sandstone unit are very similar, suggesting that perhaps the materials have similar

grain-size characteristics. Differentiation of the units shallower than 10 m depth is less clear on the imaginary conductivity component section (Figure 9.35B) than on the real conductivity component section (Figure 9.35A).

Examination of the phase-angle image (Figure 9.35C) shows different aspects of the inter-borehole section. The near-surface clays (6 m to 10 m) are clearly evident as having low phase-angle values (<5 mrad), probably due to the high ohmic conduction associated with the clays, while the uppermost sediments have slightly higher values (~5–7 mrad). A lower silt/clay band (around 24 m depth) is also identified by its low phase-angle (and high gamma count) as with the silt/clay band between 6 m and 10 m depth. The fluvial sands and the deeper sand/gravel units (below 26 m depth) have very similar phase-angle values and are not differentiated. Indeed, the fluvial sands are shown as having moderate phase-angle values, whereas the lowermost sandstone unit has

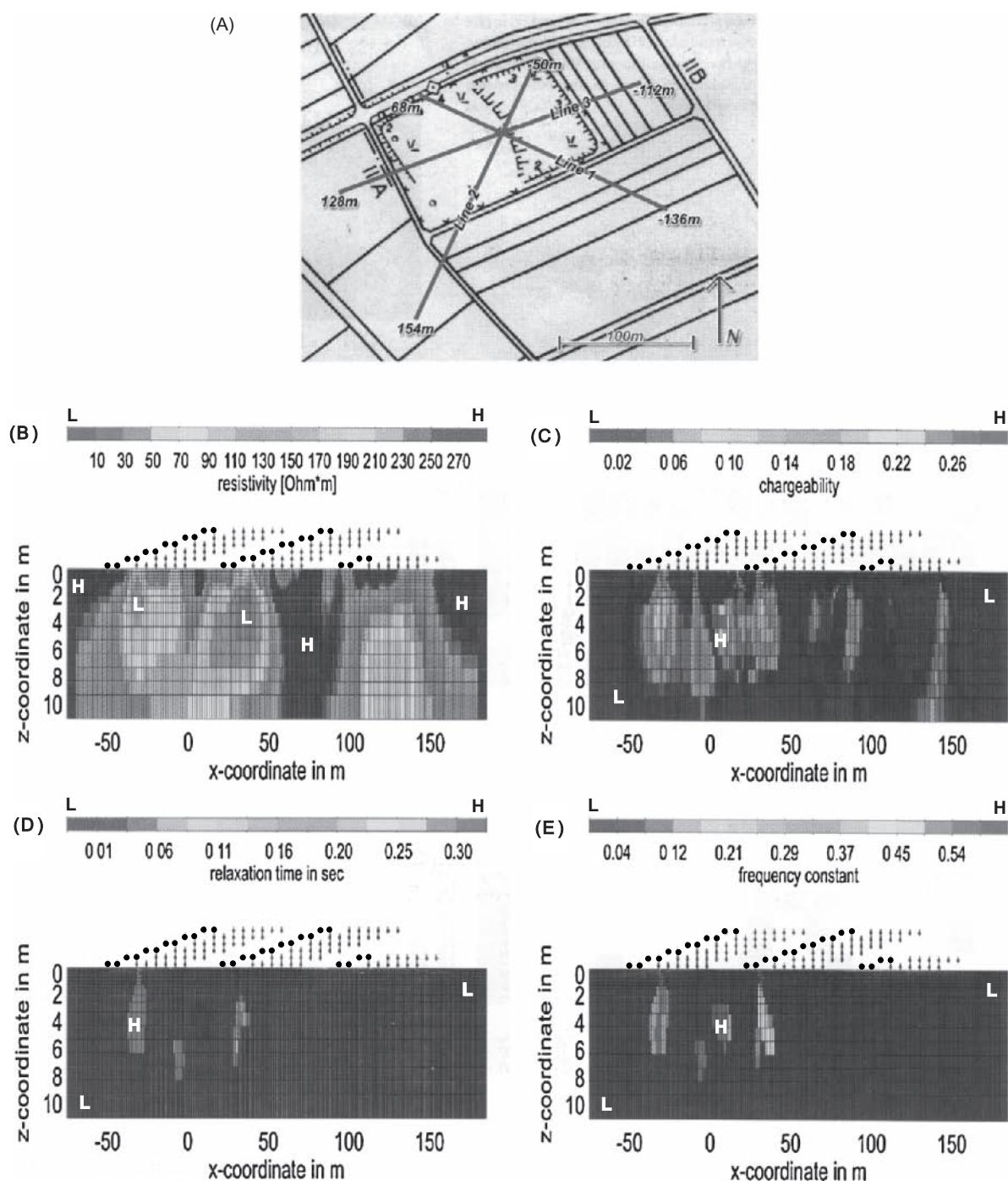


**Figure 9.34** (A) Layout of IP profiles across a former waste site near Düren, Germany; Cole-Cole inversion of the IP data from Line 2: (B) resistivity, (C) chargeability, (D) relaxation time, and (E) frequency exponent. Dots above the sections show the positions of the transmitter, the black arrows show the locations of the receiver dipoles. From Höning & Tezkan (2007), by permission. [C]

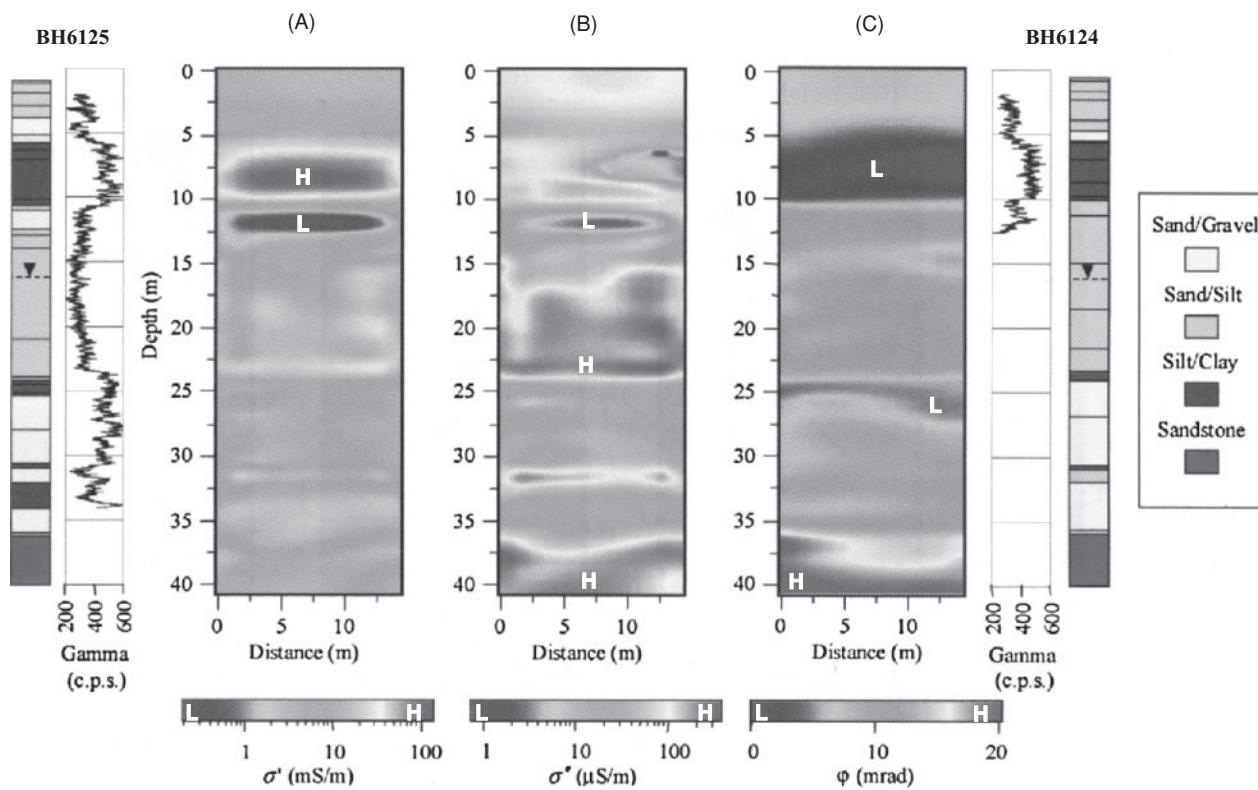


**Figure 9.35** Cross-hole IP imaging results from the Drigg Low Level Radioactive Waste Disposal Site, Cumbria, UK, showing (A) the real component, (B) imaginary component and (C) phase of complex conductivity. Geological logs and natural gamma-ray logs are shown for comparison. From Kemna *et al.* (2004), by permission. [C]

very high phase-angle values (e.g. up to  $\sim 20$  mrad). If the interpretation of the resistivity and phase-angle results alone had been used (i.e.  $\sigma_{dc}$  and  $\varphi$ ), the additional information about the nature of the fluvial sands and lowermost sandstone unit provided by the imaginary conductivity component would not have emerged.

This case history demonstrates that the IP method, when used with conventional resistivity, can help differentiate between various geological units and provide additional information about their physical, textural (e.g. particle-size distribution) and mineralogical variations resulting from differences in origin and nature of deposition.

# 10

## Electromagnetic Methods: Introduction and Principles

### 10.1 Introduction

#### 10.1.1 Background

Among all the geophysical methods, the electromagnetic techniques must have the broadest range of different instrumental systems of any, matched by the remarkable range of applications to which these methods are being applied. These methods also show the greatest geographical diversity, as some are used extensively and preferentially in the areas in which they were developed. For example, SIROTEM (see Section 11.3) is used predominantly in Australia where it was developed (named after the Australian Commonwealth Scientific Industrial Research Organisation, CSIRO), and Turam systems in Sweden. The range of EM instruments manufactured by Geonics Ltd, Canada, has been used predominantly in North America, particularly eastern Canada, and increasingly in Europe, although other manufacturers have now come onto the market. There have also been major changes in the commercial organisation of the market place, with acquisitions and mergers shaping the availability of different systems. There have been some major developments in the portability and ease of use of some instruments, and their ensuing popularity has resulted in the techniques being used more widely. Over the last decade there has been a significant growth in airborne systems especially for mineral exploration and regional surveys (Section 10.3). Similarly, a whole new area of marine Controlled Source EM (CSEM) systems (Section 10.4) have emerged for use predominantly for hydrocarbon exploration. The interpretation methods available are largely dependent upon the instrumentation used for each survey, and the information about the plethora of equipment available is widely scattered throughout the literature and on the Internet. However, the diversity of equipment provides a wide range of instruments to choose between in order to select

the most appropriate tool for the task in hand. This, rather than being a disadvantage, is a major strength. Modern EM systems provide a very powerful suite of sophisticated instruments. Coupled with major advances in computer interpretation techniques for the airborne and CSEM systems, EM methods are set to become much more heavily used.

Probably the first electromagnetic method to be used for mineral ore exploration was developed by Karl Sundberg in Sweden over two decades following the First World War (Sundberg, 1931). What is now known as the Sundberg method was developed in 1925 and was also used in structural mapping in hydrocarbon exploration (Sundberg and Hedstrom, 1934). Other pioneering work was done in the early 1930s by a Russian geophysicist V.R. Bursian, whose work is little known in the West. Other electromagnetic methods have been available commercially only since the Second World War and particularly since the mid-1960s. EM methods are especially important, not only in mineral and hydrocarbon exploration, but increasingly in environmental geophysics applications.

The different electromagnetic systems available are described briefly in Section 10.1.3 and in more detail in the next chapter. Chapter 12 is devoted to a discussion of ground-penetrating radar (GPR). A much more comprehensive and detailed discussion of the various electromagnetic methods, with the exception of ground-penetrating radar, has been produced by Misac Nabighian (1987, 1991) and by Nabighian and MacNae (1991). Further discussions and descriptions of the various methods have been given in the three-volume treatise *Geotechnical and Environmental Geophysics* edited by Stan Ward (1990). For marine CSEM in hydrocarbon exploration, see the special sections in *The Leading Edge* (August 2006) and *First Break* (May 2009). A review of airborne EM systems for metalliferous mineral exploration has been provided by Nabighian and Asten (2002).

## 10.1.2 Applications

The range of applications of EM methods is large. It is dependent upon the type of equipment being used but can be broadly categorised as listed in Table 10.1. Not all EM methods are equally appropriate to the applications listed. For example, ground-penetrating radar (GPR) has very limited use in the direct investigation of landfills by virtue of the high ambient conductivity and the corresponding high attenuation of radiowaves with depth. Conversely, ground conductivity mapping does not have the required resolution in comparison with GPR in some archaeological investigations. Furthermore, GPR can be used with care inside buildings, while ground conductivity methods cannot, by virtue of interference from ambient electrical noise from mains power lines, and so on.

One of the main advantages of the EM methods is that the process of induction does not require direct contact with the ground, as opposed to the case of electrical methods where electrodes have to be planted into the ground surface (see Chapter 7). Consequently, the speed with which EM surveys can be made is much greater than an equivalent survey using contacting electrical resistivity. Furthermore, the induction process also allows the method to be used from aircraft and ships, as well as down boreholes. Similar to electrical resistivity methods, scale-model experiments can be undertaken to illustrate particular structures (e.g. Frischknecht, 1987). However, numerical models and sophisticated inversion routines are now used preferentially. For small-scale surveys and shallow depths of investigation, one of the disadvantages of the EM methods available

is the lack of suitable inversion routines and restrictions in depth resolution. This remains an area for further development.

## 10.1.3 Types of EM systems

Electromagnetic methods can be classified as either time-domain (TEM) or frequency-domain (FEM) systems. Frequency-domain instruments use either one or more frequencies, whereas time-domain equipment makes measurements as a function of time. EM methods can be either passive, utilising natural ground signals (e.g. magnetotellurics), or active, where an artificial transmitter is used either in the near-field (as in ground conductivity meters) or in the far-field (using remote high-powered military transmitters as in the case of VLF mapping).

A basic classification of EM systems is given in Table 10.2, which is based on Swift (1988). Each system is described briefly in this section; VLF, ground-conductivity, time-domain EM, telluric and magnetotelluric systems are described in more detail in Chapter 11. Ground-penetrating radar is discussed comprehensively in Chapter 12.

Case histories are given where appropriate to illustrate the use of each of the main techniques. In most cases, the concept of each method is described rather than specific equipment systems, which may change through continuing development work.

The term ‘galvanic’ used in Table 10.2 describes the injection of electrical current directly into the ground via electrodes; these methods are discussed in detail in Chapters 7 and 9.

**Table 10.1** The range of applications for EM surveying.\*

Mineral exploration
Mineral resource evaluation
Hydrocarbon exploration
Monitoring hydrocarbon reservoirs
Groundwater surveys
Mapping contaminant plumes
Geothermal resource investigations
Contaminated land mapping
Landfill surveys
Detection of natural and artificial cavities
Location of geological faults
Geological mapping
Permafrost mapping
Brownfield site mapping
UneXploded Ordnance (UXO)
Sea-ice thickness mapping
Archaeological investigations

\*Independent of instrument type.

### 10.1.3.1 Magnetometric resistivity (MMR)

Commutated direct current is injected into the ground through two widely separated electrodes. The anomalous conductivity contribution is determined at the midpoint by measuring the secondary magnetic field arising from the flow of current using an extremely sensitive low-noise magnetometer aligned perpendicular to the line between the electrodes (Figure 10.1). For further details, see Chapter 7 and, in particular, the review by Edwards and Nabighian (1991).

### 10.1.3.2 Small-loop systems

A small-loop system is a frequency-domain EM system in which two small coils, one a transmitter and the other a receiver, separated by a constant distance of between 1 m and 100 m, are moved along a survey transect. The primary field is nulled so that the in-phase and quadrature components of the secondary field can be measured. The various combinations of coil orientation are shown in Figure 10.2. Slingram is synonymous with the *horizontal-loop method* (HLEM), Boliden, EM Gun, MaxMin and with Ronka EM methods. *Ground conductivity meters* (GCM) can be classified as being of this type of method. In this case, the quadrature component is normally taken to be a linear measure of the apparent conductivity of the ground. The coplanar coils are deployed both horizontally and vertically; Chapter 11 has more details. For a detailed discussion of small-loop systems, see the review by Frischknecht *et al.* (1991).

**Table 10.2** A classification of electrical and electromagnetic systems.

Transmitter type	Receiver type		
	Ground wire	Both wire and small coil	Small coil (ground)
<b>Grounded wire</b>			
Galvanic	Resistivity IP		Magnetometric resistivity (MMR)
Inductive		CSAMT	Magnetic IP (MIP) Some TEM systems Slingram Horizontal-loop EM Vertical-loop EM Tilt-angle method Ground conductivity meters (GCM) Some TEM systems Coincident loop Borehole systems Large-loop systems Sundberg method Turam Many TEM systems Borehole systems
<b>Small loop</b>			Airborne EM Time-domain towed-bird Helicopter rigid-boom
<b>Large loop</b> (long wire)			
<b>Plane wave</b>	VLF-resistivity		VLF
Vertical antenna	VLF		
Natural geomagnetic field	Telluric currents		

Grounded wires measure potential difference per length, thus electric field. Coils (or fluxgate magnetometers or SQUIDS) measure magnetic field, or its time derivative. A small loop is a 3D source (magnetic dipole). A long wire or the long edge of a large loop) is a 2D source. Natural EM sources are assumed to be 1D sources. Receivers can be frequency-domain, time-domain (TEM), or both. CSAMT = controlled-source audio magnetotelluric. This classification, which excludes the high-frequency techniques (radar, etc.), is based on Swift (1988, Table 1, p. 6).

### 10.1.3.3 Large-loop systems

There are two basic configurations in this classification, namely, the original method known as Sundberg's method, and the other, Turam.

Sundberg's method uses a long, grounded, insulated wire a few hundred metres to several kilometres long, or a rectangular loop with the long side laid in the direction of geological strike (Figure 10.3A and B). Typical loop dimensions are 1200 m by 400 m. Measurements are made along profiles at right-angles to the cable or long side of the loop. Phase reference is taken by using a feeding coil located close to the source loop/cable using the compensator system shown in Figure 10.3C. Normally, only the vertical magnetic field is observed using the receiver coil. If the coil is deployed in three mutually perpendicular planes, then the EM field can be determined completely.

The Turam technique overcomes a significant operational difficulty with the Sundberg method, that is, the necessity to have a feeding coil close to the source cable/loop. In the Turam method, two separate receiver coils are used which are maintained at a constant separation, typically 10–20 m (Figure 10.3D). After each measurement, the coils are moved so that the rear coil then takes the position formerly occupied by the forward one, and so on along the transect. The two coils provide a means whereby a measurement is made of the ratio of the resultant vertical-field amplitudes and phase difference of the vertical fields at two neighbouring points. In effect, by having a constant coil separation and measuring parameters at each of the two locations, the horizontal gradient of phase of the resultant vertical field is determined. A more complete discussion of these two methods has been given by Parasnis (1991).

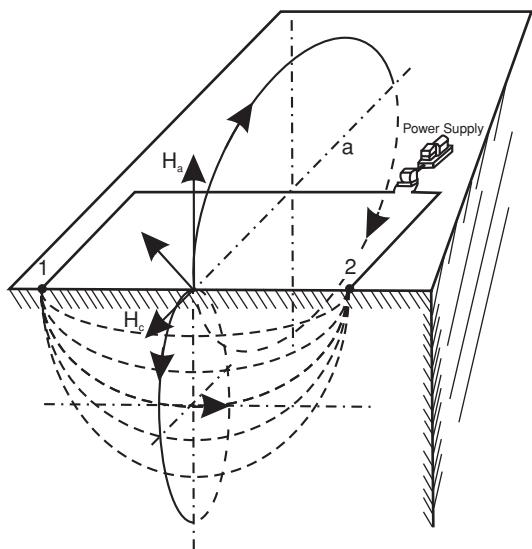


**Figure 10.1** Basic concept of a magnetometric resistivity (MMR) field survey layout. Electrodes (1 and 2) are used to inject direct current into the ground. The secondary magnetic field arising from the current flow in the ground is measured at the midpoint by an extremely sensitive magnetometer. From Edwards and Nabighian (1991), by permission.

#### 10.1.3.4 Time-domain systems

If a continuous EM field is produced by a transmitter, the secondary field is either determined by nulling the primary field so as to be able to detect the secondary field, or by measuring the resultant of both primary and secondary fields, and hence computing the secondary field parameters; those of the primary field are known by design. In time-domain or transient EM, the primary field is applied in pulses, typically 20–40 ms long, with the secondary field being measured once the primary field has been switched off over the following 100 ms, for example. One advantage of this is that the transmitter coil can also be used as the receiver. The basic field layouts are shown in Figure 10.4.

Typically a large ungrounded coil, through which a strong direct current is passed, is laid on the ground with the long axis parallel to any geological strike. A small receiver coil is moved along transects perpendicular to the long axis of the ungrounded loop to obtain profiles of the measured parameters as a function of distance along the transect. Alternatively, instead of profiling, TEM systems can be used very effectively for depth soundings. Increased depth penetration is achieved by measuring the decay of the secondary field as a function of time. As the secondary field decays, the field parameters are measured at discrete time intervals (typically logarithmically arranged). It is analogous to the induced polarisation (IP) method in resistivity surveying. A specific system (INPUT) was developed in 1958 for airborne work (Barringer, 1962). Following 1970, with improvements in technology and computing capabilities, a range of EM systems were developed by both academic institutions and commercial companies. By 1988, all instrument manufacturers had provided fully digital TEM systems.

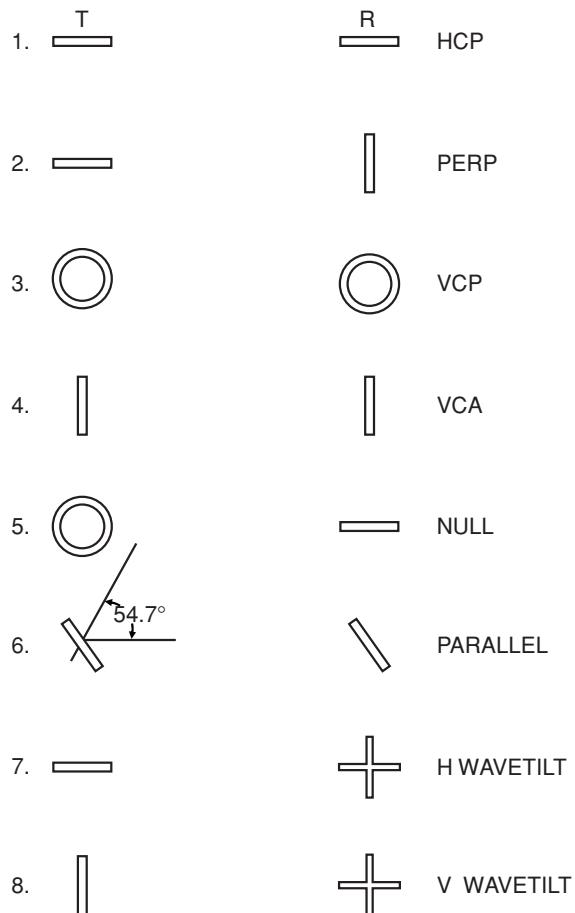


**Figure 10.2** Eight common dipolar loop configurations ( $T_x$  = transmitter;  $R_x$  = receiver). Each rectangle represents the edge-on view of a coil; e.g. to move from configuration 1 to 3, both coils are rotated about a horizontal axis; to move from 3 to 4, each coil is rotated about a vertical axis. HCP = horizontal coplanar; VCP = vertical coplanar; VCA = vertical coaxial; PEKP = perpendicular. From Frischknecht et al. (1991), by permission.

As a guide, but depending upon the actual configurations and equipment being used, 50 TEM soundings per day is not unreasonable. With increasing pressure to use TEM in environmental applications where depths of penetration of less than 50 m are required, ‘very-early TEM’ (VETEM) systems are being developed. VETEM could be used in surveys where depths of penetration of less than 25 m but high vertical resolution are required, such as over closed landfills. For more detailed descriptions of TEM systems and of depth sounding, see the reviews by Nabighian and Macnae (1991) and by Spies and Frischknecht (1991), respectively.

#### 10.1.3.5 Very low frequency (VLF)

High-powered military radio transmitters operating in the 15–24 kHz range (i.e. very low frequency in radio terms) are used to communicate with submarines even when submerged, and for long-range radio positioning. At very large distances from the transmitters, the EM field approximates to a plane wave which is used

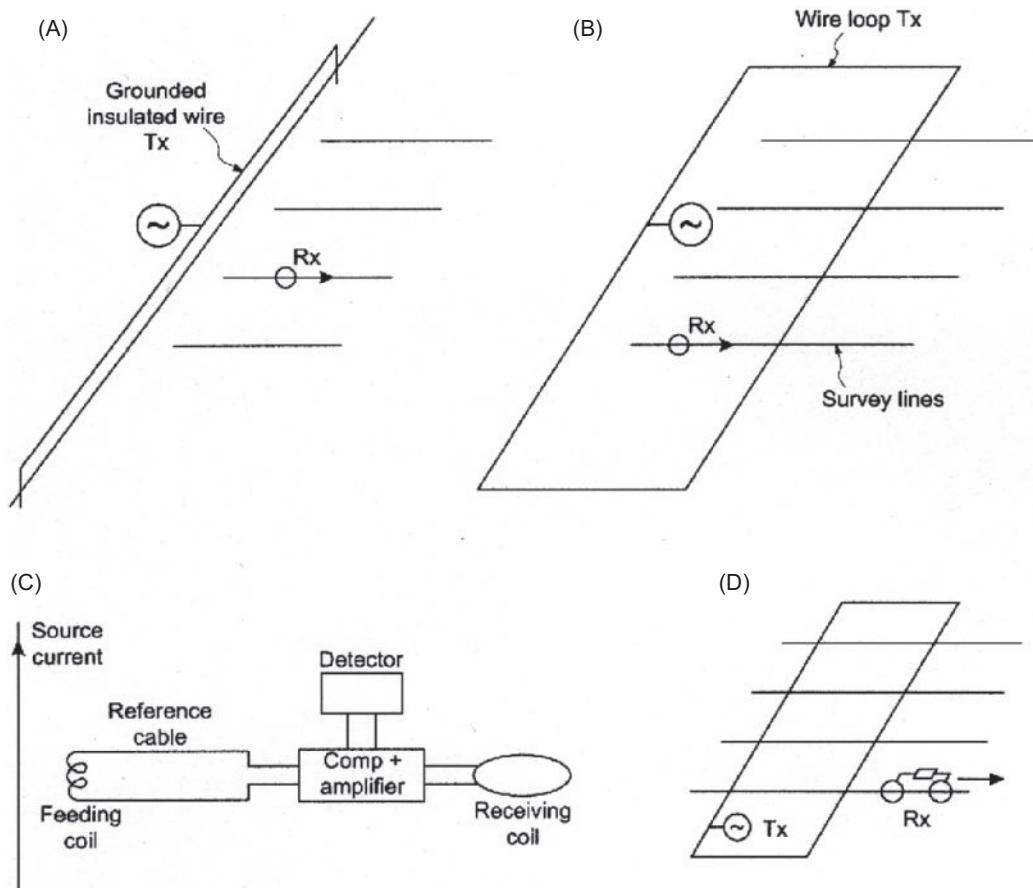


**Figure 10.3** (A) Survey layout for the Sundberg method with a long grounded wire, or (B) a grounded wire loop with survey profile lines indicated. Phase reference is determined using a compensator (C) close to the source wire. In the Turam method (D), two separate receiver coils are deployed with a constant separation.

in geophysical exploration (Figure 10.5). The method can be used either on the ground or from aircraft. The method is discussed in more detail in the next chapter and has been reviewed by McNeill and Labson (1991).

## 10.2 Principles of EM surveying

### 10.2.1 Electromagnetic waves

Electromagnetic methods use the response of the ground to the propagation of incident alternating electromagnetic waves which are made up of two orthogonal vector components, an electric intensity ( $E$ ) and a magnetising force ( $H$ ) (Figure 10.6), in a plane perpendicular to the direction of travel. An electromagnetic field can be generated by passing an alternating current through either a small coil comprising many turns of wire, or a large loop of wire. The frequency range of electromagnetic radiation is very wide (Figure 10.7), from atmospheric micropulsations at a frequency less than 10 Hz, through the radar bands ( $10^8$  to  $10^{11}$  Hz) up to X-rays and gamma-rays at frequencies in excess of  $10^{16}$  Hz. Of critical importance is the visible band ( $\approx 10^{15}$  Hz).

For geophysical applications, frequencies of the primary alternating field are usually less than a few thousand hertz. The wavelength of the primary wave is of the order of 10–100 km while the typical source–receiver separation is much smaller ( $\approx 4$ –100+ m). Consequently, the propagation of the primary wave and associated wave attenuation can be disregarded (Figure 10.8).

In general, a transmitter coil is used to generate the primary electromagnetic field, which propagates above and below ground. When the EM radiation travels through subsurface media it is modified slightly relative to that which travels through air. If a conductive medium is present within the ground, the magnetic component of the incident EM wave induces eddy currents (alternating currents) within the conductor. These eddy currents then generate their own secondary EM field which is detected by a receiver (Figure 10.9). The receiver also detects the primary field which travels through the air, so the overall response of the receiver is the combined (resultant) effect of both the primary and the secondary fields. Consequently, the measured response will differ in both phase and amplitude relative to the unmodulated primary field. The degree to which these components differ reveals important information about the geometry, size, and electrical properties of any subsurface conductor. Detailed discussions of electromagnetic theory, which are beyond the scope

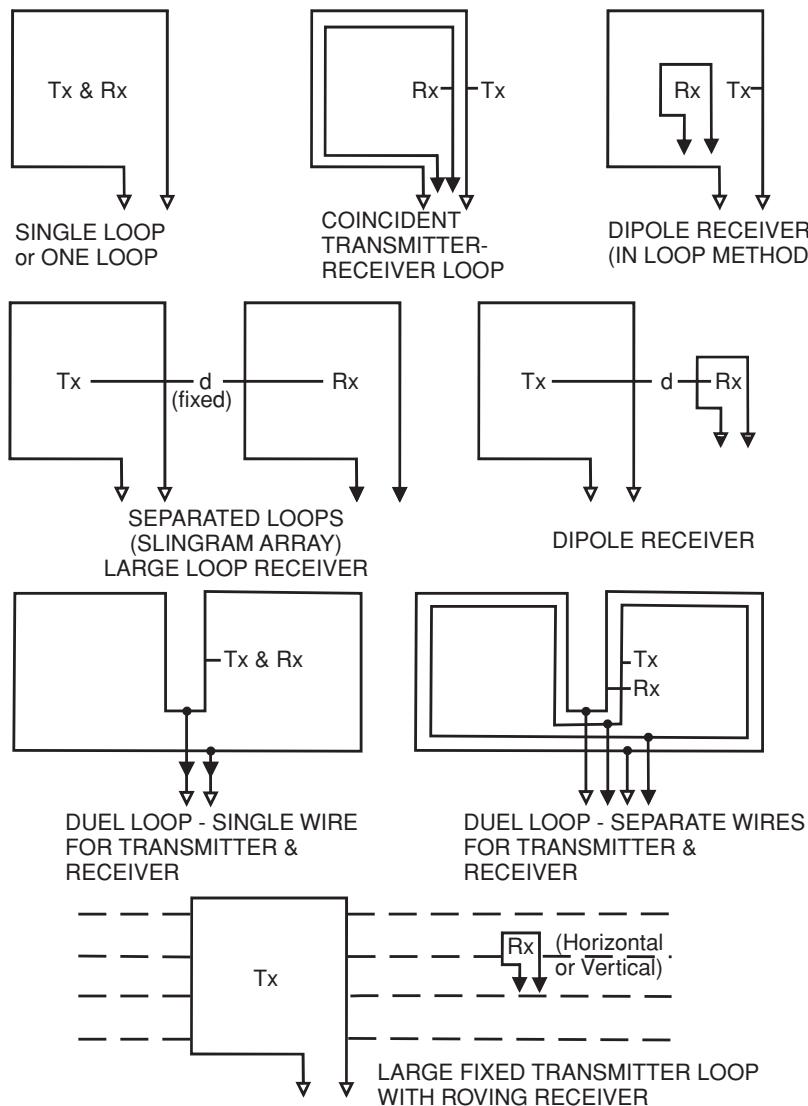


**Figure 10.4** Field configurations for time-domain EM surveys. From Nabighian and Macnae (1991), by permission.

of this book, have been given by Grant and West (1965), Telford *et al.* (1990), and Ward and Hohmann (1987), among others.

It is useful to regard the ground under investigation as comprising three components: inductive ( $L$ ), resistive ( $R$ ) and capacitive ( $C$ ); the electrical circuit equivalent is shown in Figure 10.10. The applied alternating voltage has the form of a sine wave with an angular frequency of  $\omega (= 2\pi f)$  and amplitude  $E_0$  which varies as a function of time, as described mathematically in Box 10.1. The current ( $I$ ) which flows lags behind the applied voltage by an amount  $\alpha$ , the phase lag. In EM exploration, a primary magnetic field is applied ( $P$ ) which, in accordance with the properties of an EM wave, is in phase with its orthogonal electric component ( $E$ ) (refer to Figure 10.6). Consequently, the form of the primary magnetic wave is  $P = H_0 \sin \omega t$ , where  $H_0$  is the peak amplitude of the magnetic wave (Figure 10.11A). The voltage induced into a secondary perfect conductor as a result of the incident primary magnetic field lags behind the primary field by  $\pi/2$ .

According to Faraday's Law of EM induction, the magnitude of the induced voltage is directly proportional to the rate of change of the magnetic field. The induced voltage is directly proportional to the rate of change of the magnetic field. The induced voltage will be zero when the magnetic field is either at its maximum or minimum (Figure 10.11B). Eddy currents within a conductor take a finite time to generate, arising from an induced voltage. This generation time is manifest as the phase lag  $\alpha$  (Figure 10.11C) which depends upon the electrical properties of the conductor. In good conductors this phase lag can be large, and conversely in poor conductors the phase lag is small. Once generated, the secondary magnetic field interacts with the primary to form a resultant magnetic field (Figure 10.11D) which has a total phase lag ( $\varphi$ ) behind the primary field.

The relationship between the primary, secondary and resultant fields can be represented in vector form (Figure 10.12A). The real (or in-phase) and imaginary (out-of-phase, or quadrature) components are shown on the vector diagram. The primary magnetic

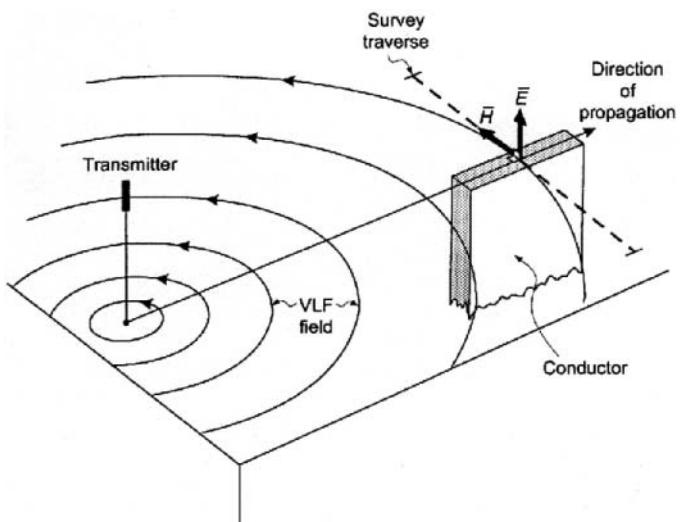


**Figure 10.5** An artificial VLF source (e.g. military transmitter) provides a primary EM field which, at a sufficiently large distance, equates to a plane EM wave. Preferred survey directions over a linear conductor are tangential to the VLF field.

field is designated  $P$  and relates to the time-varying wave shown in Figure 10.11A. The induced voltage (cf. Figure 10.11B) lags  $\pi/2$  ( $90^\circ$ ) behind the primary, and the secondary current or magnetic field lags behind by  $\alpha$  (cf. Figure 10.11C) and has a magnitude  $S$ . By normal conventions of vector diagrams, by completing the vector parallelogram, the resultant  $R$  of the primary and secondary fields (Figure 10.12A) is then defined with a total phase lag of  $\varphi$  (cf. Figure 10.11D). The secondary field  $S$  can be defined by the vectorial summation of its vertical and horizontal constituents (Figure 10.12B). Depending upon which equipment system is used, a number of these components can be measured from which an indication of the electrical properties of the subsurface materials can be obtained.

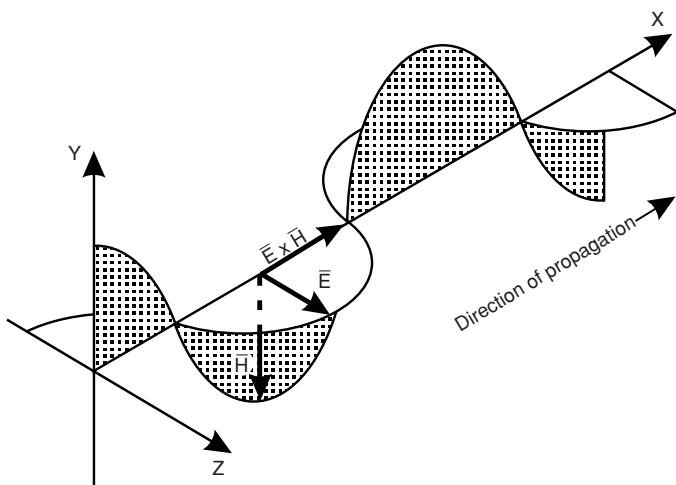


**Figure 10.6** Basic elements of an electromagnetic wave, showing the two principal electric ( $E$ ) and magnetic ( $H$ ) components. From Beck (1981), by permission.

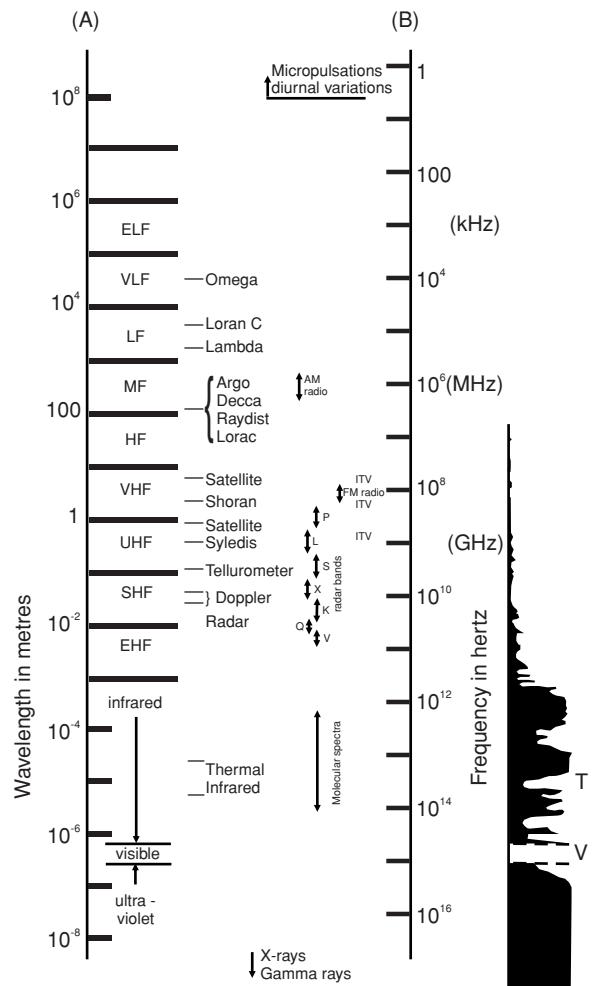


**Figure 10.7** The electromagnetic spectrum. (A) Designation of the various parts of the spectrum as a function of wavelength in metres. In (B), the dark portion of the graph shows zones of attenuation due to atmospheric absorption. Two windows are evident in the absorption spectrum at  $T$  (thermal infrared) and  $V$  (visible light). From Sheriff (2002), by permission.

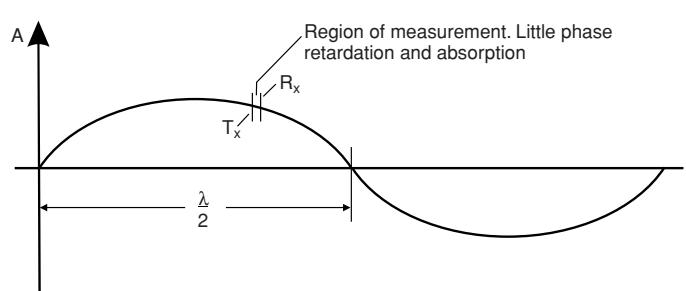


**Figure 10.8** The physical separation of a transmitter ( $T_x$ ) and receiver ( $R_x$ ) is very small in relation to the wavelength of EM waves with frequencies greater than 3 kHz. Consequently, attenuation due to wave propagation can be ignored. From Beck (1981), by permission.

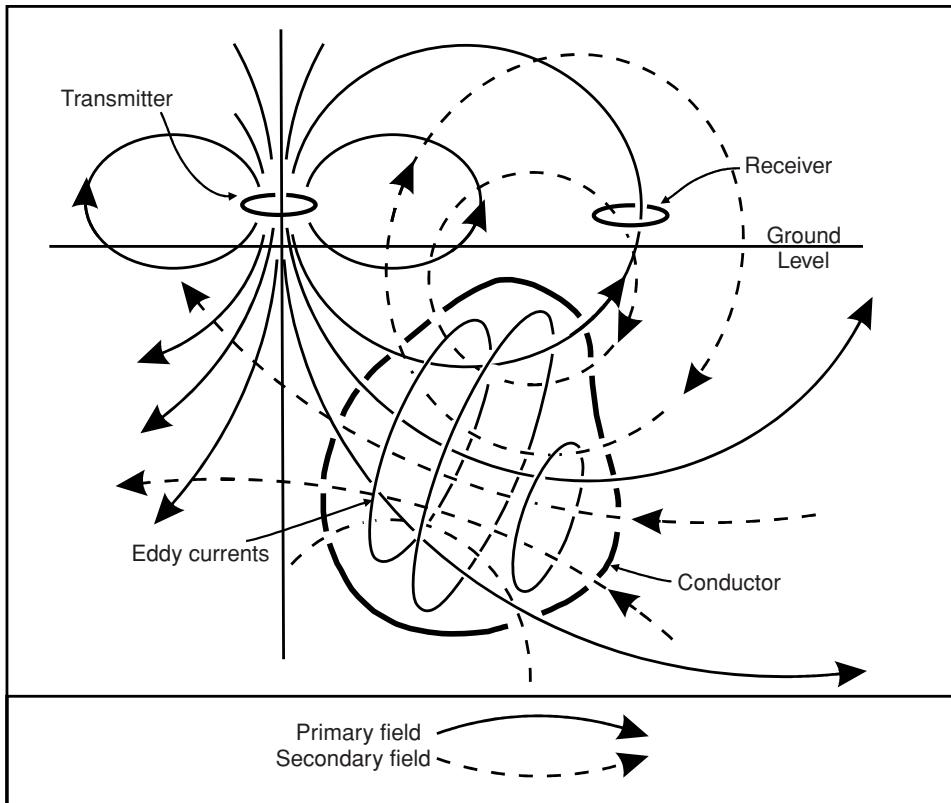
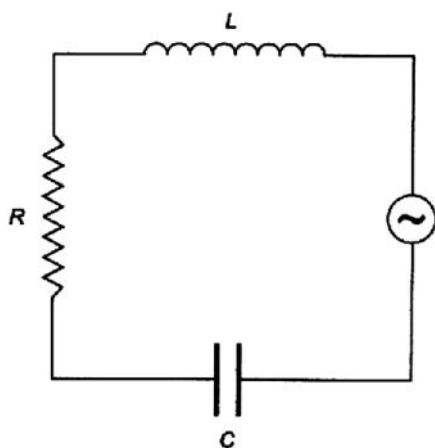


**Figure 10.9** Generalised schematic of the EM surveying method. From Grant and West (1965), by permission.

## 10.2.2 Polarisation

It is important to consider two vectors  $P$  and  $S$  which differ in space by a spatial angle  $\beta$  (Figure 10.13A) and in phase by a phase angle  $\varphi$ . In order to calculate the resultant of these two vectors, it is necessary to resolve each into its horizontal and vertical components, denoted by suffices  $x$  and  $y$ , respectively. The mathematical summation is given in Box 10.2. The consequence of this summation process is that

the resultant  $R$  always exists but varies continuously in magnitude and rotates in space. The tip of the resultant vector describes an ellipse in space, known as the ‘ellipse of polarisation’ (Figure 10.13C) which is inclined at an angle  $\theta$  to the horizontal. The angle  $\theta$  is known as the tilt or dip angle. Several EM methods (VLF and AFMAG) exploit this parameter and are known consequently as tilt-angle methods.



### Box 10.1 Time-varying electrical field

The amplitude ( $E$ ) of an alternating voltage is given by:

$$E = E_0 \sin \omega t.$$

The current ( $I$ ) within the equivalent circuit (see Figure 10.10) is described by:

$$I = E_0 \{[\omega L - (1/\omega C)]^2 + R^2\}^{-1/2} \sin(\omega t - \alpha)$$

where

$$\alpha = \tan^{-1} [\omega L - (1/\omega C)]/R$$

and  $L$  is the inductance,  $C$  the capacitance and  $R$  the resistance.

**Figure 10.10** Basic electrical circuit containing capacitance ( $C$ ), inductance ( $L$ ) and resistance ( $R$ ), the three electrical components that describe the equivalent behaviour of the ground.

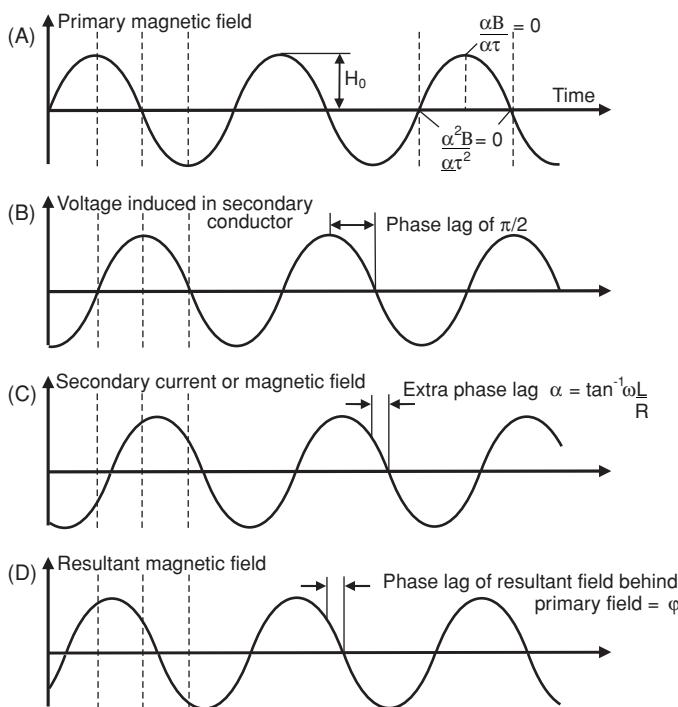


**Figure 10.11** Relationships between induced voltages and associated phase lags between primary, secondary and resultant magnetic fields. From Beck (1981), by permission.

There are several special cases which should be mentioned. When the angle  $\delta = 0$ , Equation (3) in Box 10.2 reverts to the equation of a straight line. This indicates that  $\mathbf{R}$  is then a simple alternating vector and that the radiation comprises plane-polarised waves. When  $\delta = \pi/2$ , the ellipse of polarisation is orientated such that axes are coincident with the  $x$ - and  $y$ -axes. The tilt angle  $\theta$  becomes either zero or  $n\pi/2$  when  $P$  and  $S$  are at right-angles and  $\varphi = \pi/2$ . A further special case is when  $\delta = \pi/2$  and  $X = Y$ , in which case Equation (3) simplifies to the equation of a circle and the radiation is then circularly polarised.

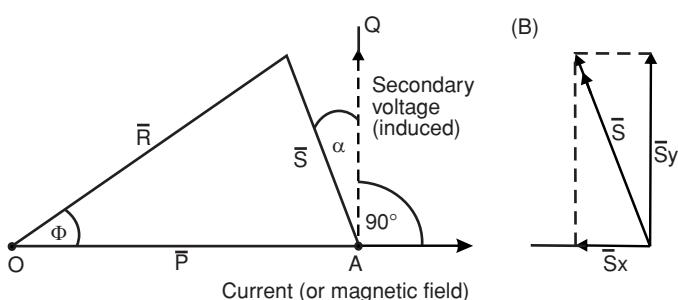


**Figure 10.12** (A) Vector diagram defining the magnitudes and phase relationships of the primary and secondary fields. (B) The vectorial components of the secondary field in terms of the secondary voltage ( $S_y$ ) and the current or primary magnetic field ( $S_x$ ).

### 10.2.3 Depth of penetration of EM radiation

Of prime importance in EM surveying are a consideration of the depth of penetration of the EM radiation and the resolution as a function of depth. In an isotropic resistive medium, EM waves would travel virtually indefinitely. However, in the real world, where surface conductivities are significant, the depth of penetration is often very limited. The depth of penetration is largely a function of frequency and the conductivity of the media present through which the EM radiation is to travel. At the usual frequencies (<5 kHz) used in EM exploration (excluding ground-penetrating radar), attenuation effects are virtually negligible, but signal losses occur by diffusion.

A common guide to the depth of penetration is known as the *skin depth*, which is defined (Sheriff, 2002) as the depth at which the amplitude of a plane wave has decreased to  $1/e$  or 37% relative to its initial amplitude  $A_0$ . The mathematical definition of skin depth is given in Box 10.3. Given a known frequency for a particular equipment system, the unknown is the vertical variation of conductivity with depth. Different instrument manufacturers commonly cite effective depths of penetration for their instruments. For example, Geonics Ltd give the depth of penetration of their FEM systems (EM38/EM31/EM34) as a function of the inter-coil separation (see Chapter 11 for details).

## 10.3 Airborne EM surveying

### 10.3.1 Background

The earliest known airborne EM (AEM) system was developed by Hans Lundberg in 1946 and first used in eastern Canada. It consisted of two coils mounted inside the cabin of a helicopter which had to fly at only 5 m above the ground if any conductors were to be detected! To denote the different aircraft platforms, AEM systems are herein denoted as *h*-AEM (helicopter) and *fw*-AEM (fixed-wing) systems. Also, AEM methods are divided into *frequency*- (FEM) and *time-domain* (TEM) systems (hence, *h*-TEM = helicopter-borne time-domain EM). Up until the 1960s all airborne systems operated in the frequency-domain; from the late 1970s, fixed-wing AEM systems were primarily time-domain. Since 1997, both *h*-AEM and *fw*-AEM systems have been almost equally split between frequency- and time-domain systems (Fountain, 2008). Airborne geophysical methods are commonly flown with multiple sensor types to acquire coincident datasets (e.g. radiometrics, magnetics (single sensor or gradiometry) and EM).

A detailed history of the development of airborne EM has been given by Pemberton (1962), Collett (1986), Becker *et al.* (1990), Palacky (1986), Palacky and West (1991), Nabighian and Asten (2002), Fountain *et al.* (2005), Fountain (1998, 2008) and Sattel (2006). Helicopter-borne EM methods for groundwater exploration have been reviewed by Siemon *et al.* (2009).

The first operational *fw*-AEM system was introduced in 1948, with the first operational *h*-EM system in 1955. Following on from the early enthusiasm for AEM in the search for strategic base metals

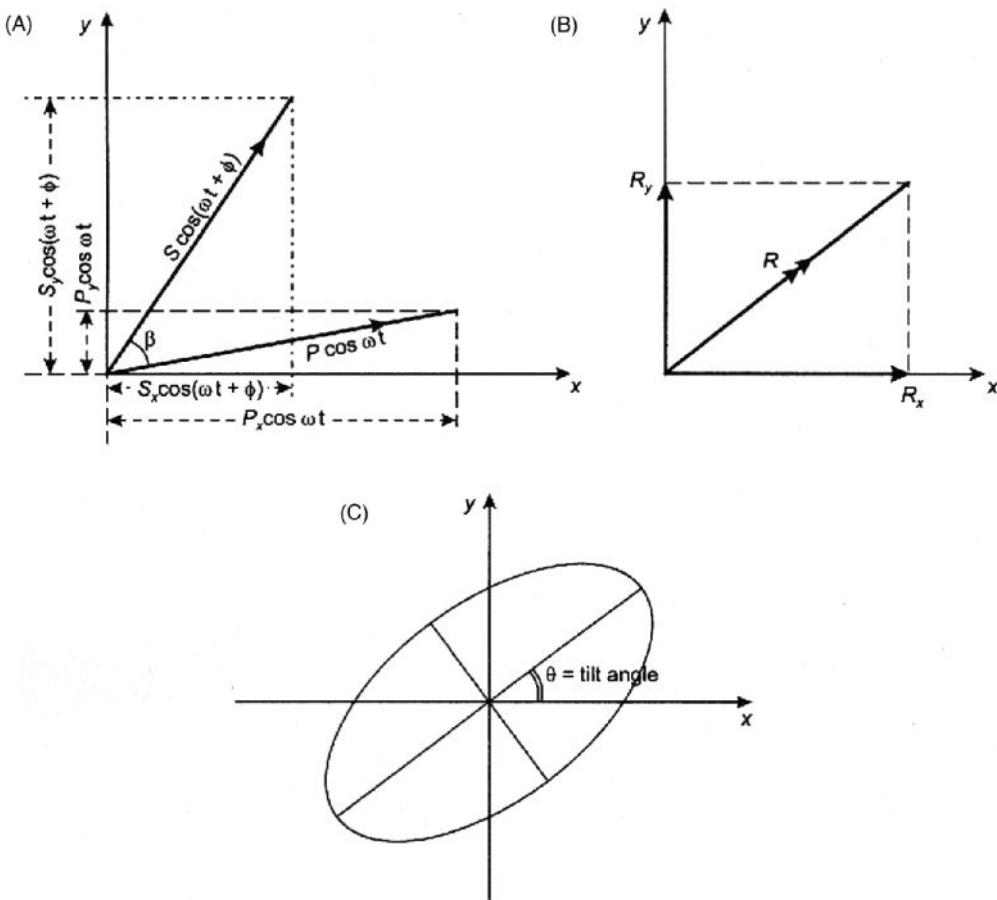


**Figure 10.13** (A) Secondary field orientated in space at an angle  $\beta$  to the primary field. (B) The horizontal and vertical components  $R_x$  and  $R_y$  of the resultant of the summation of primary and secondary fields. (C) The ellipse of polarisation inclined at the tilt-angle  $\theta$  to the horizontal.

(such as copper, lead, zinc and nickel), many other airborne systems were developed. The most successful system was that developed in the late 1950s (Barringer, 1962) and known as the INPUT system (INDuced PULSE Transient), the principle of operation of which is shown in Figure 10.14. INPUT was developed further in the late 1970s to obtain the greater depth penetration required in exploration for uranium, and is now operated under the names QUESTEM (operated by Questor Surveys) and GEOTEM (Geotrex Ltd now part of Fugro). Further improvements to these systems were made in the mid-1980s with more powerful transmitters and modern computer technology. At this time an additional system known as PROSPECT became available along with its South African equivalent SPECTRUM. Since 2000, there have been significant changes in the airborne geophysics market-place, with acquisitions and mergers of companies, as well as there having been a great deal of technological development within the airborne systems that are now available. Pre-1990s systems common in the USA since the 1980s have used 125 Hz transmitters, but since then lower-frequency (25 Hz) transmitters have been used, which can be useful for surveys where conductive cover screens basement conductors from being imaged using the older higher-frequency systems. A summary of

the various *h*- and *fw*-AEM systems developed since 1997 is shown in Figure 10.15 (Fountain, 2008; Fountain and Smith, 2003), and some of the systems are described below.

It has been recognised that airborne geophysics is potentially hazardous from an operational perspective, and as a consequence the International Airborne Geophysics Safety Association (IAGSA) was established to provide agreed minimum operational and safety standards for airborne geophysical surveys.

## 10.3.2 Frequency-domain EM (FEM)

### 10.3.2.1 Fixed-wing FEM (*fw*-FEM)

There are two types of sensor deployment from fixed-wing aircraft: (a) towed-bird receivers, such as in Russian multi-frequency systems (EM-4); and (b) wing-tip mounted rigid-coil systems, such as Geotech's HAWK system and the Joint Airborne geoscience Capability (JAC) system. The HAWK system has ten programmable frequencies in the range 200 Hz to 25 kHz. The Geological Survey of Finland (GTK) system was originally developed to use two

**Box 10.2 Polarisation ellipse**

The primary field  $\mathbf{P}(t)$  is given by:

$$\mathbf{P}(t) = \mathbf{P} \sin \omega t. \quad (1)$$

The secondary field  $\mathbf{S}(t)$  is given by:

$$\mathbf{S}(t) = \mathbf{S} \sin[\omega t - (\pi/2 + \varphi)] \quad (2)$$

The resultant ( $\mathbf{R}$ ) can be resolved into its horizontal and vertical components, suffices  $x$  and  $y$  respectively, where  $\mathbf{R} = i \mathbf{R}_x + j \mathbf{R}_y$  and  $R^2 = R_x^2 + R_y^2$ :

$$\mathbf{R}_x = \mathbf{P}_x \cos \omega t + \mathbf{S}_x \cos(\omega t + \varphi) = X \cos(\omega t + \varphi_1)$$

$$\mathbf{R}_y = \mathbf{P}_y \cos \omega t + \mathbf{S}_y \cos(\omega t + \varphi) = Y \cos(\omega t + \varphi_2)$$

By solving the above equations and eliminating  $\omega t$ , we obtain:

$$R_x^2 = R^2 - 2\mathbf{R}_x\mathbf{R}_y \cos \delta = \sin^2 \delta \quad (3)$$

where

$$\delta = \varphi_2 - \varphi_1.$$

Equation (3) is the equation of an ellipse with its major axis inclined at an angle  $\theta$  to the horizontal, where  $\theta$  is defined by:

$$\tan 2\theta = \frac{XY \cos \delta}{X^2 - Y^2}.$$

frequencies (3 kHz and 14 kHz) but since September 2004 it has been developed further as the JAC system as part of a joint programme with the British Geological Survey (BGS). BGS-JAC now operates a Twin Otter aircraft fitted with a wing-tip deployed system that uses four frequencies (912 Hz, 3005 Hz, 11,962 Hz and

**Box 10.3 Skin depth**

Amplitude of EM radiation as a function of depth ( $z$ ) relative to its original amplitude  $A_0$  is given by:

$$A_z = A_0 e^{-z/\delta}.$$

The skin depth  $\delta$  (in metres) is given by:

$$\delta = (2/\omega\sigma\mu)^{1/2} = 503(f\sigma)^{-1/2}$$

where  $\omega = 2\pi f$  (radians/s), and  $f$  is the frequency in Hz,  $\sigma$  is the conductivity in S/m, and  $\mu$  is the magnetic permeability =  $\mu_0 = 4\pi \times 10^{-7}$ . A realistic estimate of the depth to which a conductor would give rise to a detectable EM anomaly is  $\approx 8/5$ .

24,510 Hz). Flying heights for regional surveys are typically up to 150 m, with flight line spacings of 200 m. A magnetometer and radiometric system can also be deployed for simultaneous and coincident surveys. The early two-frequency GTK system was trialled for high-resolution surveys for environmental investigations in the UK in 1999. Flying heights ranged from 40–90 m, with flight line spacings of between 50 m and 200 m (Beamish, 2002). One application was to trace two buried water pipes (21-inch cast iron and 600/450 mm steel) linking water abstraction boreholes, and to map conductivity characteristics in the near surface associated with changes in total dissolved solids within the local groundwater. A second application was to compare the conductivity results obtained over a 3 km × 2 km area centred on the working Thoresby mine in the east Midlands, UK, with a flight line interval of 50 m. Strong conductivity gradients were found associated with the outline of the mine with highs linked to surface mineral concentrations. These trials demonstrated the role of *fw*-FEM low-level measurements for pathfinder reconnaissance surveys for mapping conductivity anomalies in environmental investigations.

**10.3.2.2 Helicopter FEM (*h*-FEM)**

A common mode of deploying EM systems is to mount all the electronics and transmitter and receiver coils inside a large cylinder, like a large cigar tube, which is suspended and towed below a helicopter. The Russian towed-bird system used in fixed-wing applications has been developed for use with helicopters (EM-4H) since 2006. Other towed-tube systems include Geotech's 1997 Hummingbird V, which uses five frequencies (880 Hz, 980 Hz, 6.6 kHz, 7 kHz and 35 kHz), and AeroQuest's IMPULSE and GEM2A systems (Figure 10.16A and B). These systems use a high-output transmitter driver to power individual horizontal coplanar and vertical coaxial transmitter coils, producing three fixed frequencies (IMPULSE: 870 Hz, 4.35 kHz, 21.75 kHz (co-axial); 903 Hz, 4.65 kHz, 23.25 kHz (coplanar)) or up to eight programmable frequencies (330 Hz to 96 kHz; GEM2A) in each coil configuration. Frequency-domain instruments are generally suitable for high-resolution surveys where the targets are located no deeper than 100 m. For deeper targets, time-domain systems are generally more suitable (helicopter or fixed wing).

The DIGHEM multi-frequency system was introduced in 1998 and is still used to locate mineral deposits and map surficial geology and bedrock geology to 150 m depth, and is operated in surveys for mining and environmental applications. This has been complemented since 2002 by the RESOLVE system, also operated by Fugro Airborne Surveys. This uses six frequencies, with five frequencies (400 Hz, 1.5 kHz, 6.4 kHz, 25 kHz and 100 kHz) with horizontal coplanar coils and one coaxial coil pair operating at 3.3 kHz. An example configuration of the use of this system for hydrogeophysical exploration is shown in Figure 10.16C.

Diamond exploration in the Canadian Arctic created a large demand for *h*-FEM surveys around the turn of the millennium, but demand has fallen significantly since then. However, these techniques are being increasingly used in groundwater, engineering and environmental investigations, a trend that is likely to continue.

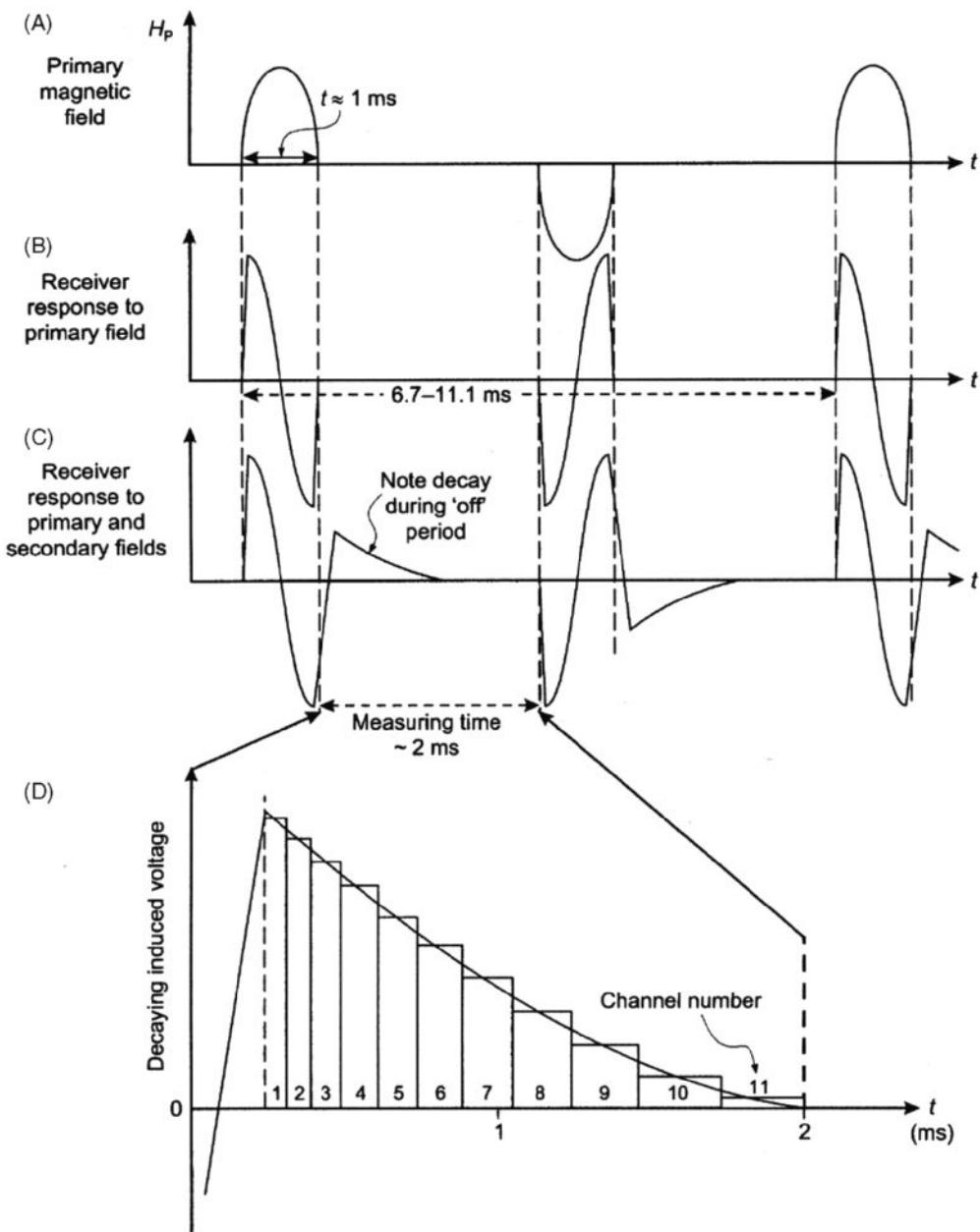


**Figure 10.14** Input TBM system for airborne EM. (A) A primary magnetic field is generated that excites a receiver response (B). The measured response of the receiver is modified by an element (C) that is a function of the ground properties. The decay curve (D) is sampled at designated intervals (channels).

### 10.3.3 Time-domain EM (TEM)

#### 10.3.3.1 Fixed-wing TEM (*fw-TEM*)

There has been considerable consolidation of the commercial *fw-TEM* operators around the millennium (Figure 10.15A) with few major new developments after 2002. One company has emerged as the principal player in fixed-wing TEM, namely Fugro Airborne Surveys with their MEGATEM, GEOTEM and TEMPEST systems (Figure 10.17). The MEGATEM II system provides the greatest transmitter power of the three systems and hence greatest potential

effective depth penetration as required in some geological terrains. The type of aircraft also dictate operational ranges and altitude limits, as the survey requirements for high-altitude mineral deposits in the Andes will be quite different than for the flat expanses of the Canadian Shield.

For the MEGATEM and GEOTEM systems, the transmitter loop is wound around the aircraft nose, wing tips and tail (Figure 10.17A and B), while in the TEMPEST system the transmitter is fixed in a boom. In each configuration it is also possible and common practice to measure the Earth's geomagnetic field. This is achieved using

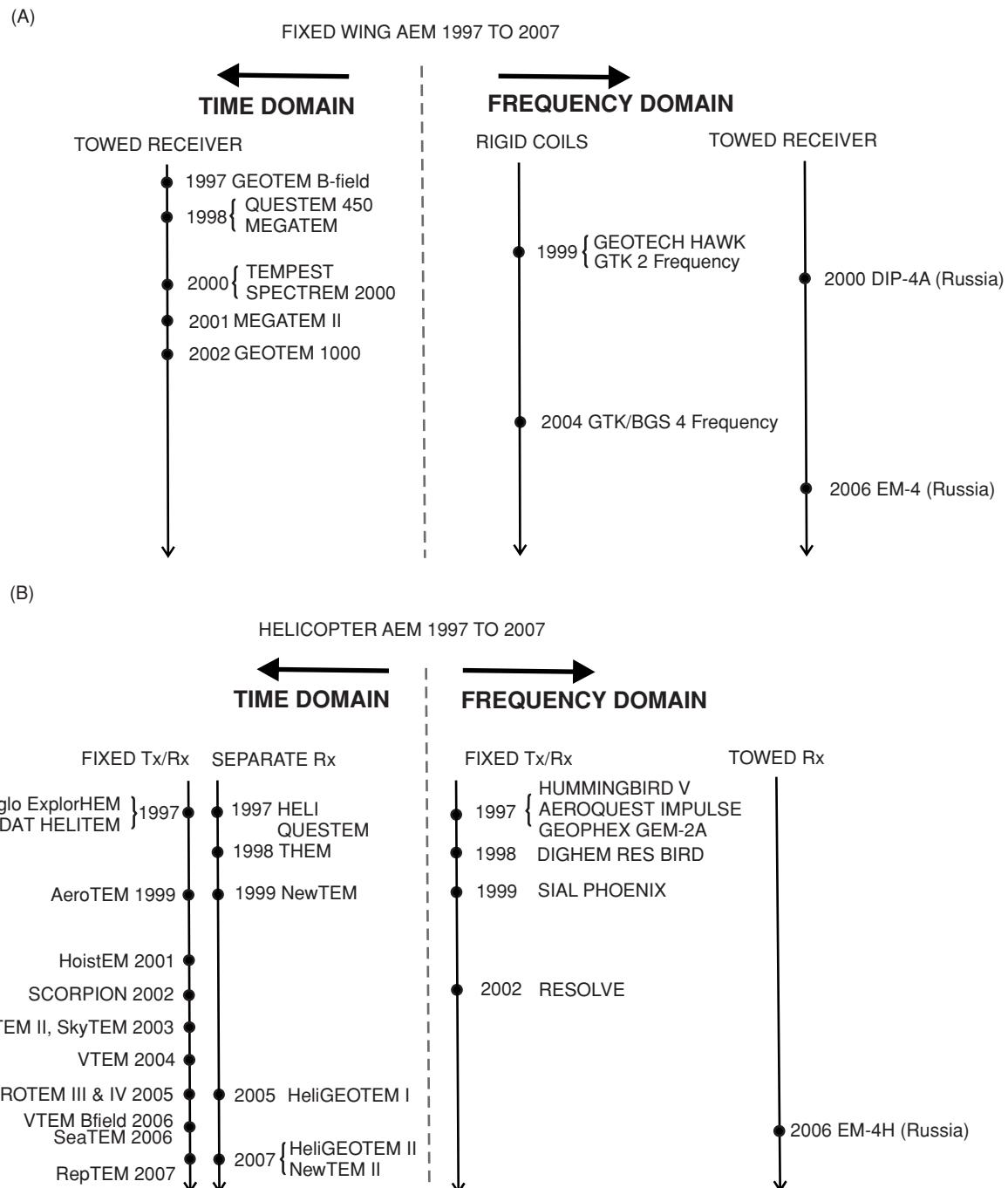
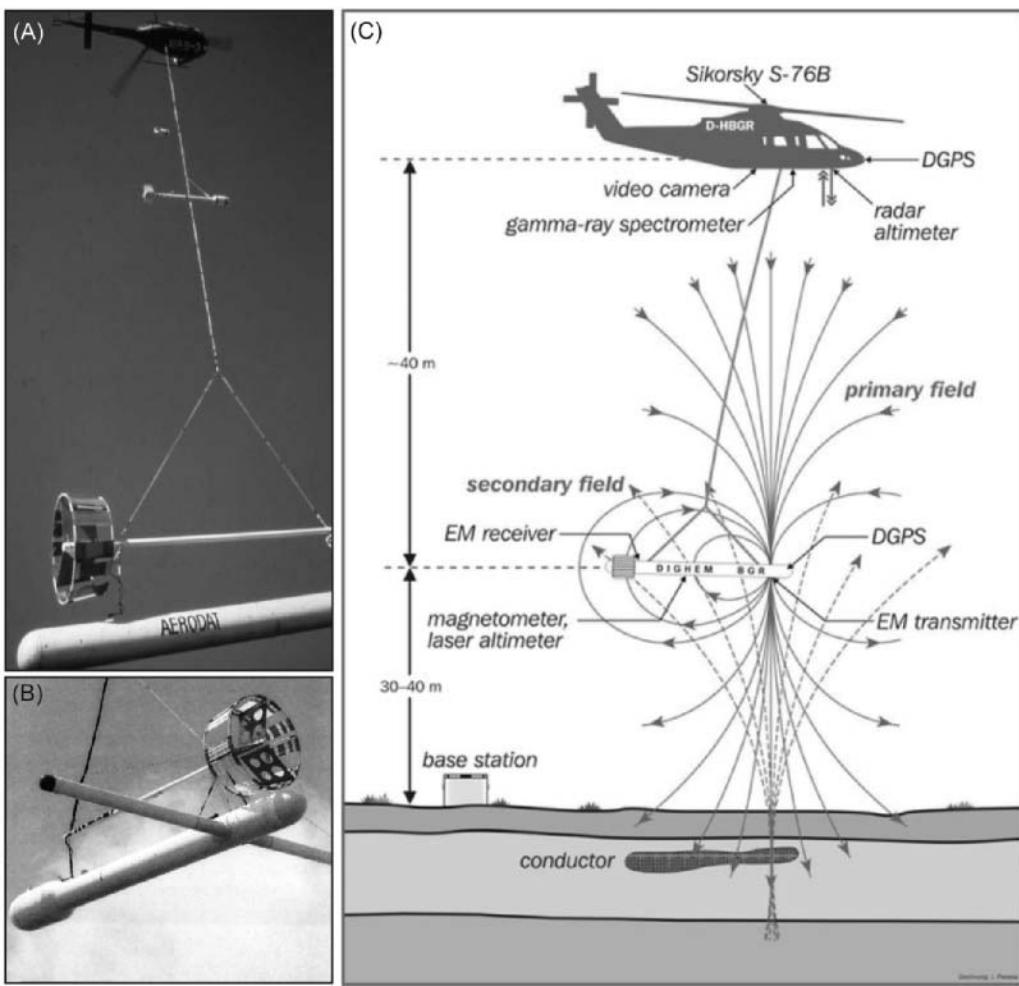


Figure 10.15 (A) Fixed-wing and (B) helicopter AEM system developments between 1997 and 2007. Modified from Fountain and Smith (2003) and Fountain (2008), by permission.

a caesium magnetometer mounted in a stinger in the TEMPEST configuration, and in separate towed birds around 45 m below and 80 m behind the aircraft in the case of MEGATEM and GEOTEM (Figure 10.19). A spectrometer is also commonly deployed at the same time in mineral exploration. Having magnetic data available helps to differentiate between potentially economic sulphides and other conductive features, such as graphites and clays, which are non-magnetic (Fountain *et al.*, 2005).

For both the GEOTEM and MEGATEM systems, the transmitter, which operates at low frequency (12.5–90 Hz), excites eddy currents in conductors within the ground with periodic pulses of the primary magnetic field (Figure 10.18). The decay of these currents is measured with a receiver located in a towed bird some 130 m behind and 50 m below the aircraft (Figure 10.19). The systems are flown with a terrain clearance of the towed bird of 120 m. The nearest equivalent helicopter system to the GEOTEM is the



**Figure 10.16** (A) Eurocopter AS350B towing three instrument pods. They are (from the top) 2-channel VLF-EM, total-field magnetometer, and 5-frequency electromagnetic induction system. (B) AeroQuest IMPULSE 6-frequency system. (A) and (B) courtesy of AeroQuest/Geophex, AeroDat Inc. (C) Schematic illustrating the deployment of the helicopter EM system operated by the Federal Institute of Geosciences and Natural Resources (BGR), Germany. From Siemon *et al.* (2009), by permission.

HeliGEOTEM system, although the sensor geometry is quite different (next section).

Where the systems permit, there is flexibility in choice of the base frequency of the transmitter both to suit ground conditions and the effective depth of penetration to be achieved. It is also possible to arrange the 30 receiving windows across the on-time and off-time, so that the system can be tuned to give the most diagnostic response characteristics of the targets being sought.

These systems measure three components ( $x$  – horizontal along the line of flight;  $y$  – horizontal transverse to the flight line; and  $z$  – vertical) of the secondary field. The transmitter ‘time-on’ and ‘time-off’ are also recorded. The receiver coils in all TEM systems are based upon induction from the secondary field induced in subsurface conductors by the transmitted primary field (Figure 10.19). An induction coil outputs a voltage proportional to the rate of change of the magnetic field ( $B$ ) in the EM bandwidth as a function of elapsed time, i.e.  $dB/dt$ . By integrating the digitised output from the induction coil, it is possible to obtain an indirect measurement

of the magnetic field in the same bandwidth. Modern AEM systems also measure  $dB/dt$  and increasingly  $B$  itself. The magnetic-field data are better for identifying, discriminating and interpreting good conductive features while suppressing the less conductive targets. Direct measurement of the  $B$ -field using a SQUID magnetometer as the sensor has demonstrated comparable amplitudes and features as derived from processing values of  $dB/dt$  (Smith and Annan, 2000). These systems have a number of time gates at set delay times at which the measurements are made. For example, a survey configuration might have a transmitter with a waveform with a period of 33 ms and pulse width of 4 ms. Fifteen time gates might be used (delay times of 0.19, 0.39, 0.63, 0.91, 1.2, 1.5, 1.9, 2.4, 2.9, 3.7, 4.7, 5.8, 7.3, 9.1 and 11.3 ms) in which to measure the decay parameters.

Given the transmitter power of the MEGATEM system and large survey footprint, it is possible to use a wider flight line separation (typically  $\geq 200$  m), although in areas of complex geological structure this may result in poorer spatial resolution than can be achieved using other systems, such as the VTEM helicopter system.

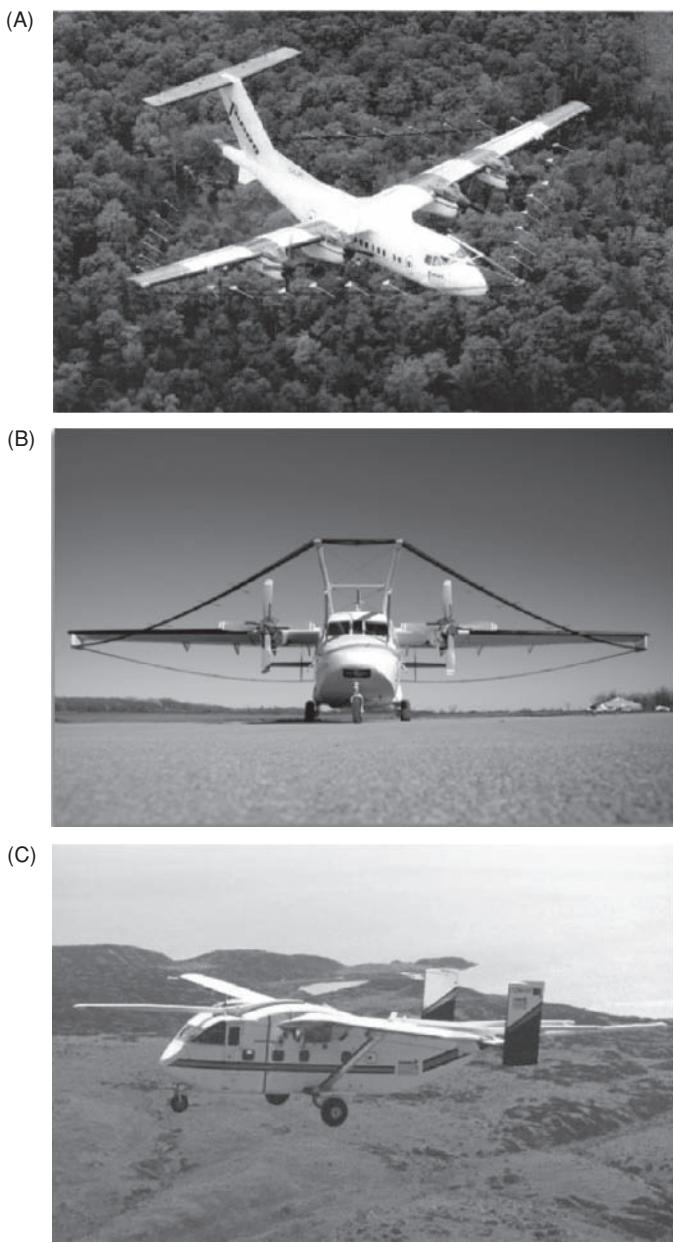


**Figure 10.17** Fixed-wing EM systems: (A) MEGATEM, (B) GEOTEM, and (C) TEMPEST. Courtesy of Fugro Airborne Systems, by permission. [C]

There are claims and counter-claims by the different survey operators as to the various merits (or otherwise) of these competing systems. It is important that when designing surveys, the total site and target conditions are considered along with practical logistical arrangements (distance from suitable refuelling locations, ground elevation and flying limits of the various aircraft, etc.) as well as the technical considerations regarding spatial resolution, effective depth of penetration, configuration of conductors and relative conductivity setting of the targets with respect to the host materials. Once these factors have been defined, then the most suitable systems can be selected.

### 10.3.3.2 Helicopter TEM (*h*-TEM)

There have been a significant number of new developments in *h*-TEM systems especially since 2005 (Figure 10.15B) with the emergence of the technique for mineral exploration. The rise in popularity of these techniques is attributable to the excellent horizontal accuracy (especially for coincident transmitter–receiver systems), ease of interpretation, cost-effective mobilisation/demobilisation, good depth of effective exploration and the ability to contour rough terrain. A brief overview of the various *h*-TEM systems has been provided by Sattel (2006) and Fountain (2008).

There are two different transmitter–receiver ( $T_x$ – $R_x$ ) arrangements: (a) fixed transmitter–receiver, and (b) where the receiver is separated from the transmitter. Fixed  $T_x$ – $R_x$  arrangements can include large diameter transmitter loops (e.g. AeroTEM systems, Figure 10.20A and B) from 5 m to 12 m across; or megaTEM 35 m diameter (Figure 10.20C) where the receiver is located either at the centre or near the edge of the  $T_x$  loop (AeroTEM IV system) – these are sometimes known as coincident systems. In other systems, such as the NewTEM system, the generator and  $T_x$  loop are suspended 30 m below a separate  $R_x$  bird which is itself towed 30 m below the helicopter; a separate magnetometer bird is also usually deployed (Figure 10.21). In hydrogeological surveys, the SkyTEM system has been specifically developed for groundwater investigations (Sørensen and Auken, 2004). Survey speeds of 45 km/h are usual but can be as low as 20 km/h, with a clearance altitude of the suspended transmitter loop of 15–20 m (Siemon *et al.*, 2009).

Given the range of different *h*-AEM systems available, it is important to recognise their different characteristics and range of parameters that they measure. All have vertical transmitter orientations, but the receiver configurations may measure one (typically  $z$ ), two (typically  $x$  and  $z$ ) or three ( $x$ ,  $y$  and  $z$ ). Only a minority have  $B$ -field processing capability within their systems. Although the size of the transmitter peak dipole moment (in  $\text{A.m}^2$ ) is an indicator of the possible effective depth of exploration, it does not necessarily mean that the more powerful systems will automatically give better results. There is a trade-off between the peak dipole moment, base frequency, transmitter waveform and receiver bandwidth as system parameters, even without considering target-related factors (such as depth of burial, conductivity contrast with host strata, dimensions, dip and strike, etc.). Peak dipole moment is sometimes given as *NIA*, which is the product of  $N$ , the number of turns in the transmitter loop,  $I$  the energising current applied (in amps), and the area of the transmitter loop (in  $\text{m}^2$ ), giving a value with units of  $\text{A.m}^2$ .

In contrast with the systems described above, an eight-channel time-domain system (TEM-8; Figure 10.22A) has been developed by Battelle/Oak Ridge Airborne Geophysical System Transient EM (ORAGS-TEM) for UXO surveys (Beard *et al.*, 2004; Doll *et al.*, 2006, 2008a, 2008b). This system has a dual-transmitter loop comprising two  $3 \times 4$  m multiple-turn loops mounted parallel to the long axis of each of the two transmitter loops. The typical flying height is only  $\sim 1$  m. Early results indicate that the TEM08 system can deliver comparable results to those from a multichannel vertical gradient helicopter magnetometer system (VG-22; Figure 10.22B). These systems have been developed for surveys over munitions testing ranges and military bombing grounds, for example, that cover

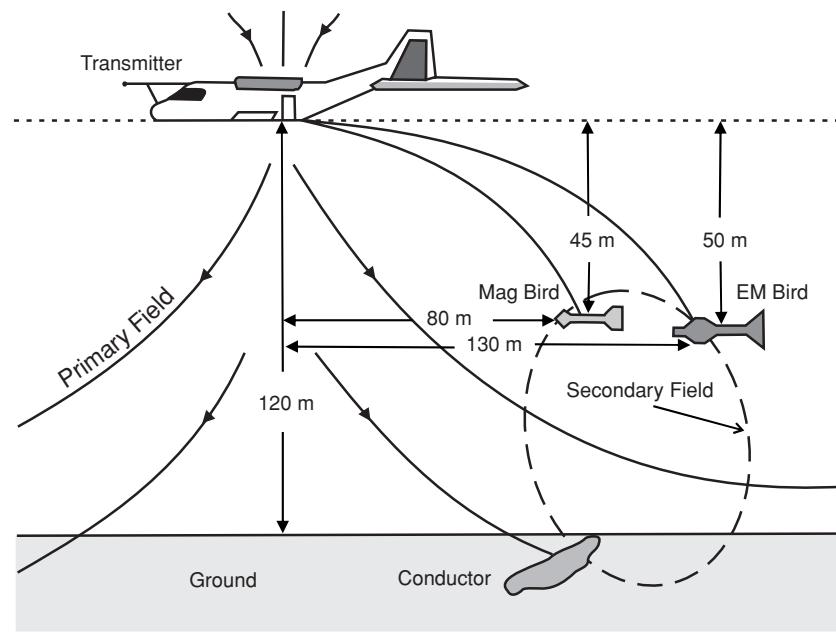


**Figure 10.18** Schematic diagram of the MEGATEM/GEOTEM system configuration. From Fountain *et al.* (2005), by permission.

large areas, where ground-based surveys would be logically and financially prohibitive, and potentially more dangerous from the risk of direct triggering of live ordnance. The scale of UXO contamination justifies the development of increasingly sophisticated detection systems, given that the USA Department of Defence has estimated that the cost of UXO clean-up efforts in the USA alone may be \$28–\$48 billion (Anon., 1996)! Further developments are likely to include the deployment of more channels and smaller flying platforms such as unmanned drones and remotely-controlled aircraft.

#### 10.3.4 Airborne VLF-EM

In addition to the active EM systems described above, airborne VLF-EM measurements can be made using small detectors which can be housed easily within a boomer or stinger that can be affixed to an aircraft or deployed in a separate towed bird suspended beneath a helicopter (e.g. Figure 10.16B).

### 10.4 Seaborne EM surveying

#### 10.4.1 Background

The principal difference between airborne and seaborne EM applications is largely one of scale. Whereas airborne surveys may involve flying heights of typically several tens to hundreds of metres, with transmitter–receiver distances of the order of 20–135 m, seaborne systems may have separations of tens of kilometres. Over-water EM surveying has been researched since the early 1980s. The main

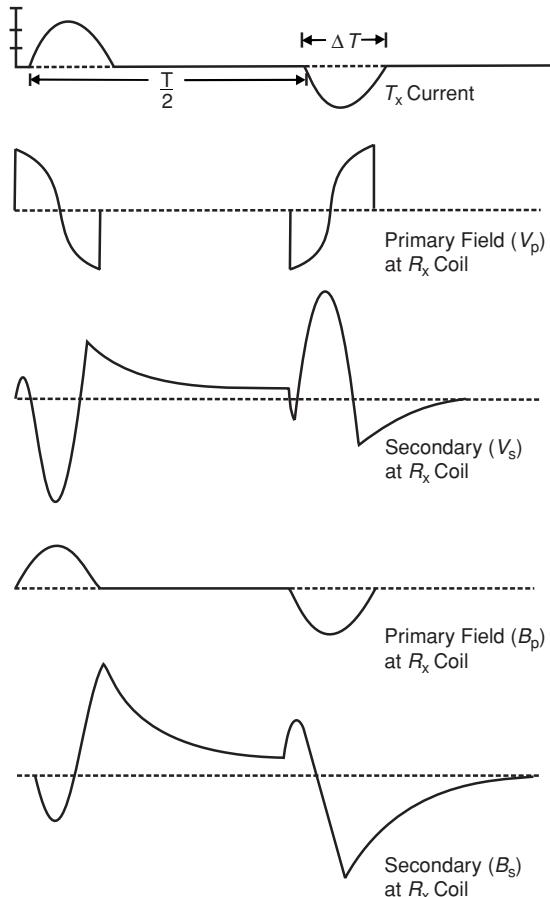


**Figure 10.19** The MEGATEM waveform. Courtesy of Fugro Airborne Surveys, by permission.



**Figure 10.20** (A) AeroTEM 2 system in flight with a magnetometer bird above, and (B) the coincident  $T_x$ - $R_x$  system on the ground (courtesy of AeroQuest); (C) VTEM system in flight (courtesy of Geotech Ltd). [C]

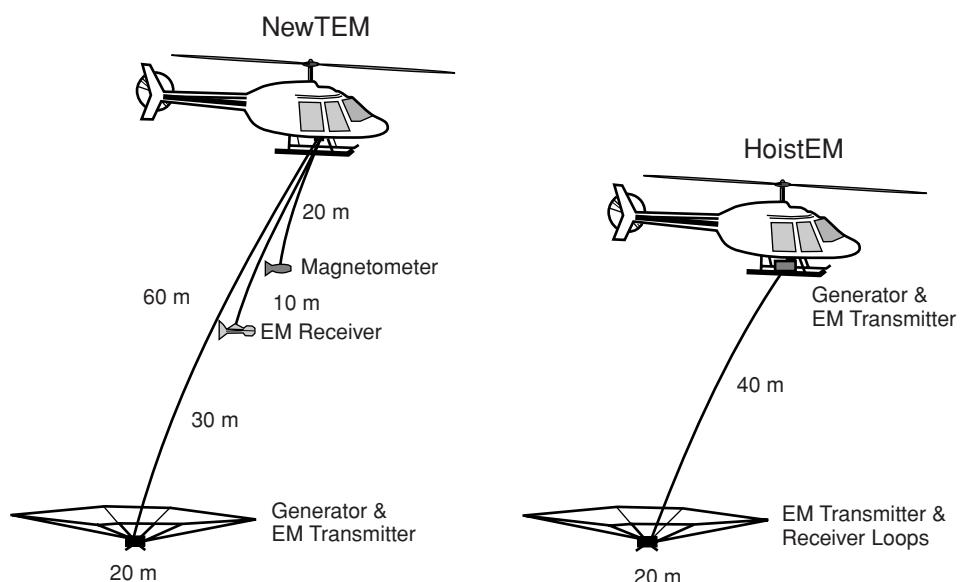


**Figure 10.21** NewTEM and HoistEM system layouts, courtesy of Newmont. From Fountain (2008), by permission.

methods that have been adapted for use in the marine environment are magnetotelluric, magnetometric resistivity, and frequency- and time-domain systems. The earlier work has been reviewed in detail by Filloux (1987) and Chave *et al.* (1991), and later work by, for example, Constable and Srnka (2007).

Marine deployment of EM systems using the concept of marine magnetotellurics (MMT) is usually for large-scale crustal investigations and requires specialised instrument packages (Chave *et al.* 1991). In the early 1990s an MMT consortium led by the Scripps Institute of Oceanography, University of California, adapted the MMT method initially for solving the problems associated with deep salt in the Gulf of Mexico. Independently, ExxonMobil developed the *Remote Reservoir Resistivity Mapping* (R3M) system for use in the hydrocarbon industry. In the late 1990s, the Norwegian company Statoil tested a marine controlled-source (CSEM) system for measuring the resistivity of structures previously identified on seismic reflection data. Since 2000, the oil exploration industry has increasingly used marine controlled-source electromagnetics (MCSEM) to determine the resistivity of deepwater (typically  $\sim 1000$  m) offshore geological structures already discovered using reflection seismology. These methods have proved to be successful in many areas, and the commercial exploitation of these techniques is expanding, although the costs are still quite high in what is a fiercely competitive market. In 2002, a spin-off company from Statoil, Electromagnetic Geoservices (EMGS), was formed to promote *seabed logging* (SBL; Ellingsrud *et al.*, 2002). Separately, other companies also began to provide similar services (e.g. Offshore Hydrocarbon Mapping (OHM); Western Geco; and in November 2004, MTM Ltd, since acquired in 2007 by PGS; and AGO, a Schlumberger company). In 2005, another Norwegian company, Petromarker, began to provide *Transient Electro-Magnetic Prospecting using Vertical Electric Lines* (TEMP-VEL) (Flekko *et al.*, 2009; Holten *et al.*, 2009). As the methods continue to be developed by existing companies, other operators will also enter the market, with enhancements of the older techniques or new approaches, such as *focused-source EM* (FSEM; Davydcheva and Rykhlnski, 2009). Fox and Ingerov (2007) have described a novel method of MMT that claims to provide similar information to that from MCSEM but at reduced cost. In contrast, other researchers (Anderson *et al.*, 2008) have developed what is called a *multi-transient EM* (MTEM) method that can be used both on land and over water as a direct indicator of the presence of hydrocarbons. There is also interest in developing systems for use in shallower water environments (Dell'Aversana, 2007; Mittet, 2008).

The marine EM methods have been the focus of several Special Topics in journals, for example, in 2006 (*The Leading Edge*, 25(8)), 2007 (*Geophysics*, 72(2), *The Leading Edge*, 26(3) and *First Break*, 25(Nov)) and 2009 (*First Break*, 27(May)). Undoubtedly more will follow given the growing importance of these techniques in hydrocarbon exploration and reservoir investigations.

The reason that EM methods are attractive tools for the potential reduction of risk in hydrocarbon exploration is that oil and gas have significantly lower electrical conductivity than salt water. Porous rock saturated with hydrocarbons will have a greater resistivity (lower conductivity) than one saturated with salt water. The contrast in resistivity can be as much as a factor of one hundred.

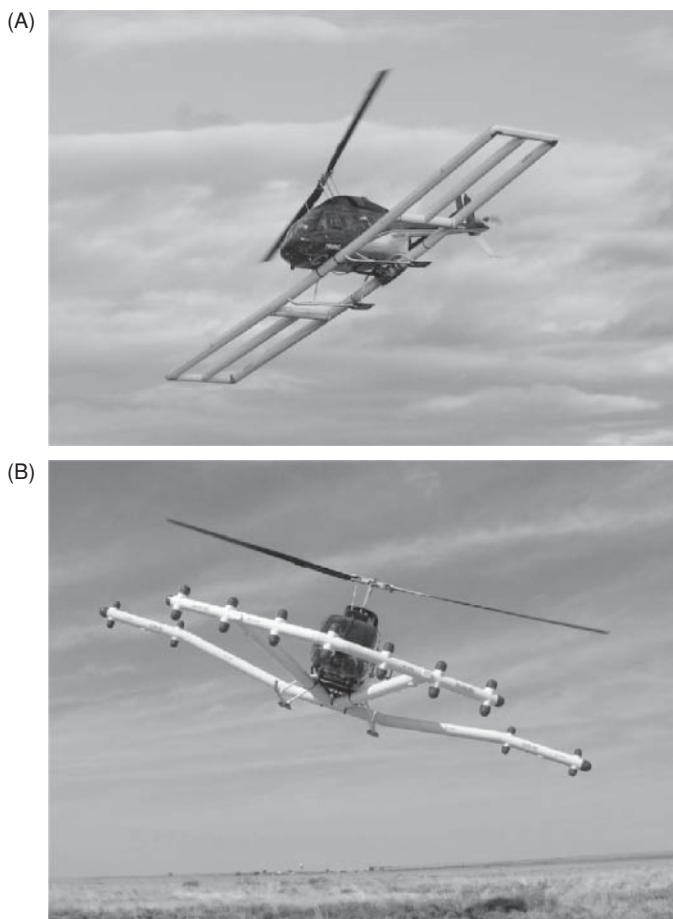


**Figure 10.22** Airborne UXO-detection systems: (A) Battelle TEM-8 and (B) the VG-22 multi-channel magnetic gradiometer. From Doll *et al.* (2008a, 2008b), by permission. [C]

While seismic methods provide images of the physical structure and acoustic impedance, EM techniques can yield information to differentiate between the types of pore fluids present, i.e. indicate the presence (or otherwise) of hydrocarbons, based on their resistivities.

The critical factor in all marine EM sounding is that the seawater is extremely conductive, and much more conductive than the geological materials at or below the sea floor. Seawater conductivity is strongly dependent upon salinity and temperature. The uppermost sediments under the ocean are usually water-saturated and have conductivities of the order of 0.1–1 S/m. This value decreases with increasing lithification and diagenesis, which reduce the *in situ* porosity. Basaltic crust and upper mantle peridotite have conductivities ranging from 0.1 S/m at the base of the overlying sediments to three orders of magnitude less at a depth of about 10 km.

In complete contrast, there are a few examples of where small-scale land-based dual-coil FEM systems, such as a Geonics EM34, have been deployed in rubber inflatable boats and towed over shallow freshwater lakes and rivers in engineering investigations.

## 10.4.2 Details of marine EM systems

### 10.4.2.1 Magnetotelluric (MT) methods

All oceanic MT work has been specifically to probe the deep lithosphere and asthenosphere to obtain a vertical EM structural model to depths of hundreds of kilometres. The MT method is currently the only geophysical method capable of obtaining information about the electrical properties at depths greater than 30 km.

The only commercially available instruments for the measurement of a magnetic field are fluxgate magnetic sensors, with sensitivities of the order of 0.5–1 nT. These sensors are deployed directly on the seabed.

There are two types of device for the measurement of the electric component: (a) long-wire units, and (b) short-arm salt bridges. The long-wire system comprises an insulated wire typically 500 m to 1000 m long with Ag–AgCl electrodes connected to the ends of the wire and to a recording unit (Webb *et al.*, 1985). The short-arm bridge apparatus utilises electrodes with spacings of only a few metres and salt bridges. Each salt bridge consists of a hollow tube attached to a Ag–AgCl electrode at one end and open to the sea at the other. The entire electrical unit has four arms (salt bridges and electrodes) that are spread out in the form of a horizontal cross which sits on top of a vertical cylinder housing the recording instruments. The base of this cylinder is located on a detachable tripod which, when lowered to the sea floor, is placed in contact with the seabed. Once measurements have been completed, the instrument module with salt bridges is released from the tripod and rises to the sea surface under slight positive buoyancy for subsequent recovery.

Marine MT surveys are often undertaken to complement MCSEM investigations by providing information about the background resistivity of sub-bottom sediments. Furthermore, MMT normally measures only the horizontal electric-field components (denoted as  $E_x$  and  $E_y$ ) and horizontal magnetic-field components (denoted  $H_x$  and  $H_y$ ). The method is passive, as it uses naturally occurring signals arising from variations in the Earth's magnetic field (Chave *et al.*, 1991; Vozoff, 1991). The MT source signal is a vertically-incident plane wave that is uniform over relatively large horizontal distances and generates nearly horizontal currents to flow in the sub-bottom sediments. A hydrocarbon target can be characterised as a thin, sub-horizontal resistive prism embedded within a much more conductive host material. Consequently the horizontal electric- and magnetic-field components measured by the MMT method are little affected by the presence of hydrocarbon targets.

In contrast to the horizontal fields, the vertical electric ( $E_z$ ) and magnetic ( $H_z$ ) fields of MMT are sensitive to lateral resistivity boundaries, such as occur at the edges of a sub-bottom (sub-)horizontal resistive hydrocarbon reservoir (Fox and Ingerov, 2007). Very sensitive three-axis magnetic sensors are deployed at specific locations across a possible reservoir and the vertical magnetic component ( $H_z$ ) recorded at each position as a function of frequency; see Section 11.6 for more details. The strongest horizontal gradients in  $H_z$  (i.e. how  $H_z$  varies as a function of horizontal distance along a profile) are found at the edges of the resistive reservoir. By using naturally occurring fields as the source signal, there is no air wave that is characteristic of marine controlled-source EM surveys, and

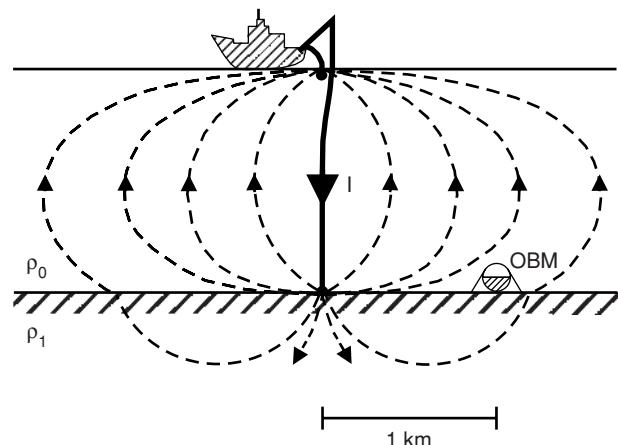


**Figure 10.23** Schematic to illustrate the principle of the MOSES method. Current is passed via two electrodes, one at the sea surface and the other on the sea floor. The relatively small amount of current that enters into the resistive crust is proportional to the ratio of the conductivity of the crust to that of seawater. Only this small current contributes to the azimuthal magnetic field measured at a point on the seabed. OBM = ocean bottom monitor. From Chave *et al.* (1991), by permission.

so this method can be used in shallow water as well as on land. It is also thought that this method could be used as a lower-cost alternative to MCSEM in exploration, but could also be deployed as permanent sea floor sensor arrays for reservoir monitoring.

### 10.4.2.2 Magnetometric resistivity (MMR)

The marine version of MMR developed by Edwards *et al.* (1985), known as MOSES (Magnetometric Off-Shore Electrical Sounding), has been used for deep crustal sounding, mapping sulphide deposits near mid-ocean ridges (Wolfgram *et al.*, 1986), and in the study of submarine permafrost below the Beaufort Sea. The general scheme of the MOSES method is shown in Figure 10.23.

The transmitter comprises a vertical long-wire bipolar which extends from the sea surface to the seabed. A commutated current is fed to two large electrodes at each end of the vertical wire. The return electrical current passes through the seawater and the near-surface materials of the seafloor. A remote receiver located on the seafloor consists of two orthogonal horizontal component fluxgate magnetometers. Two orthogonal components of the magnetic field are measured as a function of frequency and source–receiver distance. The remote receiver consists of a concrete anchor shaped like an inverted cone into which a spherical instrument housing is located. The magnetometers are located within the detachable pressure case, which can be released remotely from the concrete anchor for subsequent recovery.

A variation of the above system, called ICE-MOSES, was developed by Edwards *et al.* (1988) for use through sea-ice. The sensor design is quite different from the original MOSES version. The sensor is deployed folded (and subsequently recovered) through a 25 cm diameter hole cut in the sea-ice. Once through the hole, the unit unfolds to form a horizontal square which is lowered to the

seabed. Along two sides at right-angles to each other are located the sensors, which consist of coils wound on soft iron laminated cores and housed in stainless steel jackets.

ICE-MOSES is particularly important as it can be used to help to define the physical properties of seafloor sediments to a depth of several hundreds of metres. Of particular interest in the Beaufort Sea, where ICE-MOSES was first used, is a seismically important permafrost layer between 100 and 600 m thick under seawater 10–100 m deep. This permafrost horizon is of importance for two reasons. Firstly, a detailed knowledge of this layer is essential if reflection surveys undertaken in the same areas are to be interpreted accurately. Secondly, pockets of gas hydrate can be contained within the permafrost, and these can be a possible resource as well as a hazard to drilling to deeper targets.

#### 10.4.2.3 Controlled-source EM methods

Controlled-source EM systems use time-varying electrical and magnetic dipole sources of known geometry to induce electric currents in the various conducting media present. The electrical or magnetic character of the induced currents can be determined, from which estimates of the vertical electrical conductivity structure of the geological materials present can be made. There are four basic source–receiver types, but many combinations. The four are: *vertical and horizontal electric dipoles* (VED and HED) and *vertical and horizontal magnetic dipoles* (VMD and HMD).

In contrast to the land-based equivalent, marine controlled-source EM systems have both the source and receiver immersed in a conducting medium, and the electrical structure in both the seawater and the sub-sea floor materials affect the total induction achieved, and thus have to be taken into account in the interpretative modelling. In cases involving shallow water, for example over continental shelves, the position of the air/sea surface interface also has to be taken into consideration.

Three systems, two frequency-domain and one time-domain, will be described briefly to illustrate the diversity of systems currently being developed. The first is a submarine horizontal electric dipole (HED) frequency-domain system produced by Scripps Institution of Oceanography for deep sounding of the oceanic lithosphere. The source is a long (0.5–1 km) insulated cable terminating in stainless steel electrodes 15 m long. Receivers to detect the horizontal electric field are placed on the seabed between 1 and 200 km from the source. There are two types of electrical receivers (Figure 10.24):

- The electric field (ELF) free-fall recorder consists of a pair of rigid orthogonal antennae, each 9 m long, to the ends of which Ag-AgCl electrodes are fixed. ELF receivers are deployed between 5 km and 20 km from the transmitter.
- The long antenna EM recorder (LEM) consists of 200–300 m long insulated copper wire terminated by 0.5 m long Ag-AgCl electrodes. LEM recorders are placed up to 100 km or more away from the source.

The second basic system is also frequency-domain and is produced by Scripps for use over shallow continental shelves (Figure 10.25). The transmitter is made up of two 7 m long copper tubes 7 cm in diameter connected by 50 m of cable and powered directly by the survey vessel. The receiver array comprises a string of Ag-AgCl electrodes along a cable several hundred metres in length, all of which is in contact with the seabed. At the front end of the receiver array is a recording unit which is connected to a float and radio transmitter. The float is connected to the survey vessel by a floating rope, the length of which can be changed to alter the source–receiver separation. The point of having a surface radio transmitter is to allow the real-time relay of measured data from the submerged recorder unit (which also stores the data onto tape) directly to the survey vessel.

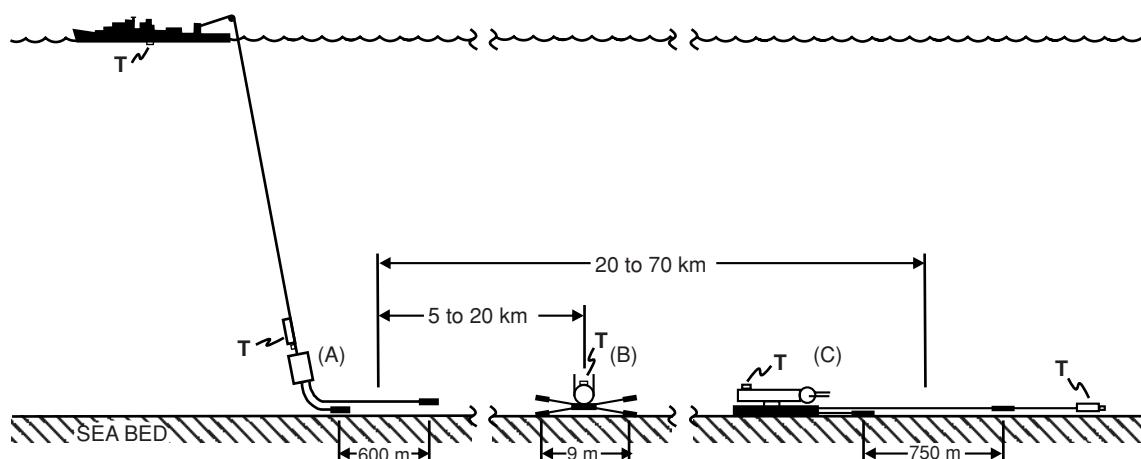


**Figure 10.24** Typical layout for a horizontal electric dipole (HED) deep-sounding experiment. Power is supplied from a surface source (e.g. ship) to the sea-floor transmitter (A) through a single conductor with a sea-water return. The transmitter comprises an insulated antenna (with bare ends) of about 600 m length. Receivers are placed at ranges from 5 km to over 70 km from the transmitter. Receivers may be either (B) an electric-field recorder (ELF) with a pair of rigid, orthogonal antennae of 9 m span, or (C) a long-antenna EM recorder (LEM), where the potential is measured between the ends of a 200–300 m insulated copper wire. Acoustics transponders (T) are used to locate all the seafloor components from a surface vessel. From Chave et al. (1991), by permission.

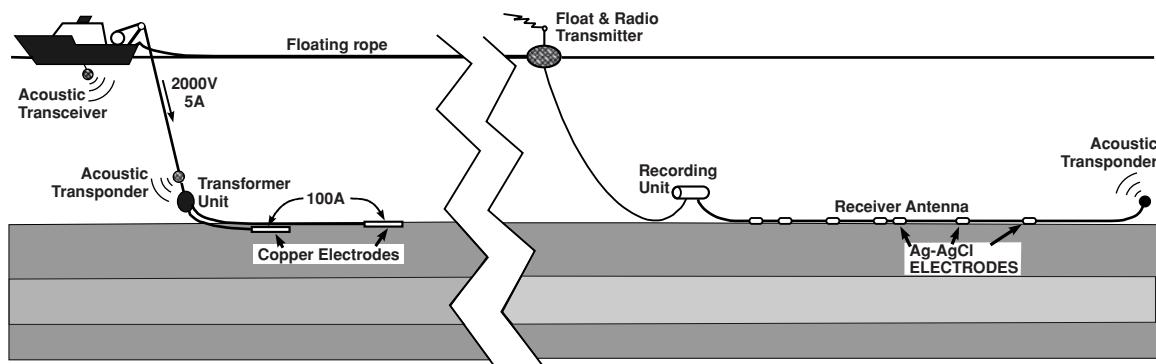


**Figure 10.25** Schematic to illustrate the components of a towed frequency-domain profiling system. The source antenna is towed immediately behind a research ship and is powered by the ship's generators. The receiving antenna is towed further behind from a radio-equipped buoy and consists of an array of Ag-AgCl electrodes. Acoustic transponders are used for location purposes. From Chave *et al.* (1991), by permission.

The third, time-domain, horizontal magnetic dipole (HMD) system (Figure 10.26) has been constructed by the University of Toronto, Canada. The transmitter comprises a 2 m long, 1 m diameter fibreglass cylinder in which 100 turns of wire are evenly embedded. Current is supplied to the transmitter from two car batteries located on the survey vessel. The polarity of the current is reversed every 5 ms to provide the transient EM signal. The receiver, which is made up of a modified iron core coil encased in a polycarbonate tube, is towed 50 m behind the transmitter. The entire source–receiver array is placed on to the seabed and is stationary during each measurement, which takes 90 s. The survey vessel is able to maintain headway by paying out additional cable during measurement periods and reeling in the extra cable between survey points. An advantage of this system is that the field source–receiver array is relatively small, with a consequential improvement in the ease of deployment over some of the larger, and more unwieldy, frequency-domain systems. For any of these systems to become op-

erational commercially, ease of operation is a major factor to be considered.

Constable and Srnka (2007) have described the basic method involved in CSEM surveying (Figure 10.27). A horizontal electric-field generator dipole is towed between 25 m and 50 m above the sea floor in order to maximise the energy that couples to the substrate and is the main source used in the hydrocarbon industry. Edwards (2005) provided details of other source configurations, such as vertical electric and horizontal dipoles. The source dipole is typically between 100 m and 300 m; longer than this and it becomes physically difficult to manage and control. A high-voltage AC current is passed down a cable to the transmitter dipole, which is towed over a series of tens of receivers along a survey profile that might be of the order of several tens of kilometres long, and the electrical and magnetic fields measured. The multicomponent electromagnetic receivers free-fall from the survey vessel to a seabed location with a positional accuracy of better than 25 m in 1500–2000 m of

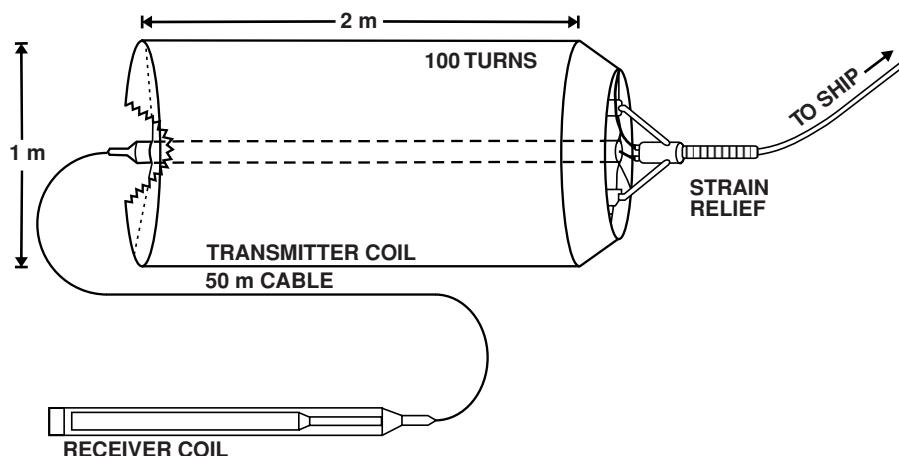


**Figure 10.26** Schematic of a horizontal magnetic dipole (HMD) transmitter that is connected to a surface vessel by an electric cable. The receiver is made up of a coil wound on an iron core and is encased in a protective plastic sleeve, all of which is streamed 50 m behind the transmitter. From Chave *et al.* (1991), by permission.

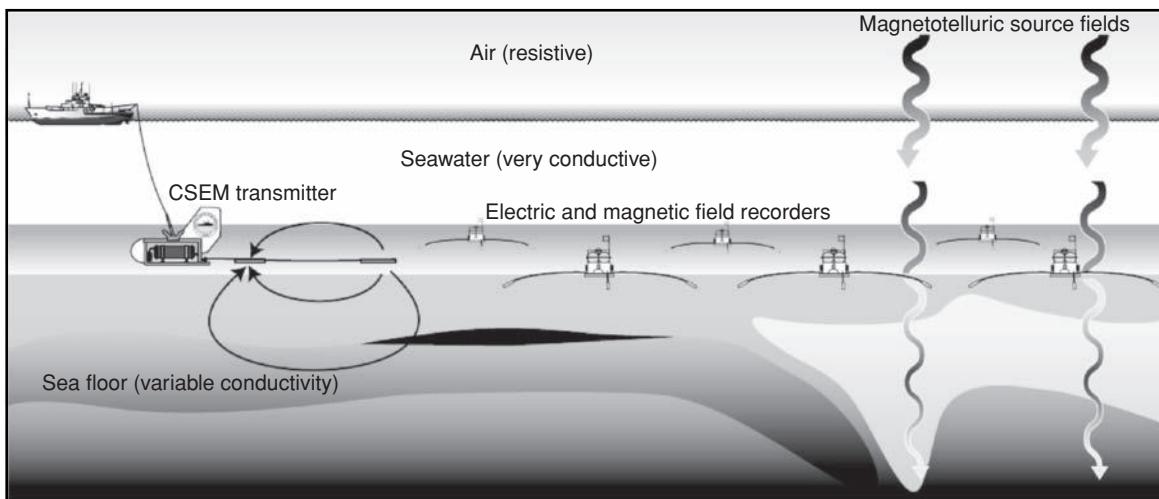


**Figure 10.27** Schematic representation of the horizontal electric dipole-dipole marine CSEM method. After Constable and Srnka (2007), by permission.

water. The receivers return to the surface after use for subsequent recovery and re-use. The source dipole provides a high-current, low-voltage oscillatory waveform at a low fundamental frequency, typically from 0.1 to 0.5 Hz. Such low frequencies allow effective depths of exploration to several kilometres below the sea floor. The receivers respond to the controlled-source signals but also respond to natural telluric EM sources, and also excitations due to seawater motion (Srnka *et al.*, 2006).

In addition to the source signal that couples with the substrate vertically below, energy propagates from the source dipole upwards as well. The multiple scattering within the water layer reverberations, including propagation to the sea-air interface, along this surface and back down to the receivers, is known as the 'air wave'. Management of the 'air wave' limited the use of the CSEM method in shallow water, but new developments in the processing of data (e.g. Um and Alumbaugh, 2007; Mittet, 2008) have been demonstrated to allow the application of the technique to sites with water depths as shallow as 40 m.

The layout used for the proof-of-concept CSEM survey offshore Angola in 2000 (Ellingsrud *et al.*, 2002; Constable and Srnka, 2007) is shown in Figure 10.28A, where the water depth was 1200 m. The locations of source receivers are shown by the large dots. The radial-mode horizontal electric field data recorded by receiver V (circled in Figure 10.28A) are shown in Figure 10.28B along with 1D and 2D modelled responses. The 2D modelled response shows a very reasonable agreement with the observed data, as the physical model shown in Figure 10.28B is a good approximation to the geology along the survey line.

Once the data have been collected, 1D inversions are undertaken to provide a vertical resistivity-depth profile at a given location. Adjacent 1D inversion results are collated along a profile and gridded to produce a *conductivity depth image* (CDI). The reason the first marine CSEM surveys were called seabed logging was because of the similarity of results to those produced by borehole resistivity logging. However, it is also recognised that an electric-field dataset for a given receiver location comprises two parts: data acquired

by the source being towed *towards* the receiver (the '*in-tow*') and those data acquired as the source is towed *away* from the receiver (the '*out-tow*'). Unless the geology and structure are symmetrical about the receiver position, the in- and out-tow electric field results will be different and thus should be inverted separately. Full 3D inversion of the data collected from a CSEM survey has yet to be undertaken routinely as a consequence of the computing power required. However, significant progress is being made in modelling and inversion processes. Further details of some of the 1D, 2D and 3D inversion of marine CSEM data have been described, for example, by Christensen and Dodds (2007); Li and Key (2007) and Li and Constable (2007); and Gribenko and Zhdanov (2007), respectively.

Marine CSEM techniques predominantly use a low-frequency alternating square-wave signal with measurements being made at discrete frequencies (i.e. in the frequency-domain). However, a time-domain system designed initially for use on land has now been developed by PGS for the marine environment (Anderson *et al.*, 2008). The *multi-transient EM system* (MTEM) uses a survey layout comparable to that for seismic reflection. A receiver cable based on ocean bottom cable (OBC) technology can be used in water depths from 10 m to over 500 m and is deployed in a linear configuration with a 200-m receiver bipolar interval on the seabed where it remains stationary. Having much shorter receiver intervals, and being contained in a cable, the receiver system can be deployed and retrieved far more quickly than discrete CSEM receivers. The transient EM source consists of two large electrodes connected to the source vessel by heavy cables and is deployed by a second vessel. As both the source and OBC are static at the time of measurement, it is possible to review the data quality during recording to ensure that the signal-to-noise ratio is sufficient before moving the source-receiver array to the next location. As with the MCSEM method, the MTEM method produces conductivity (or resistivity) depth images that can be superimposed over the corresponding seismic sections. High-resistivity anomalies are interpreted to be direct indicators of the presence of hydrocarbons.

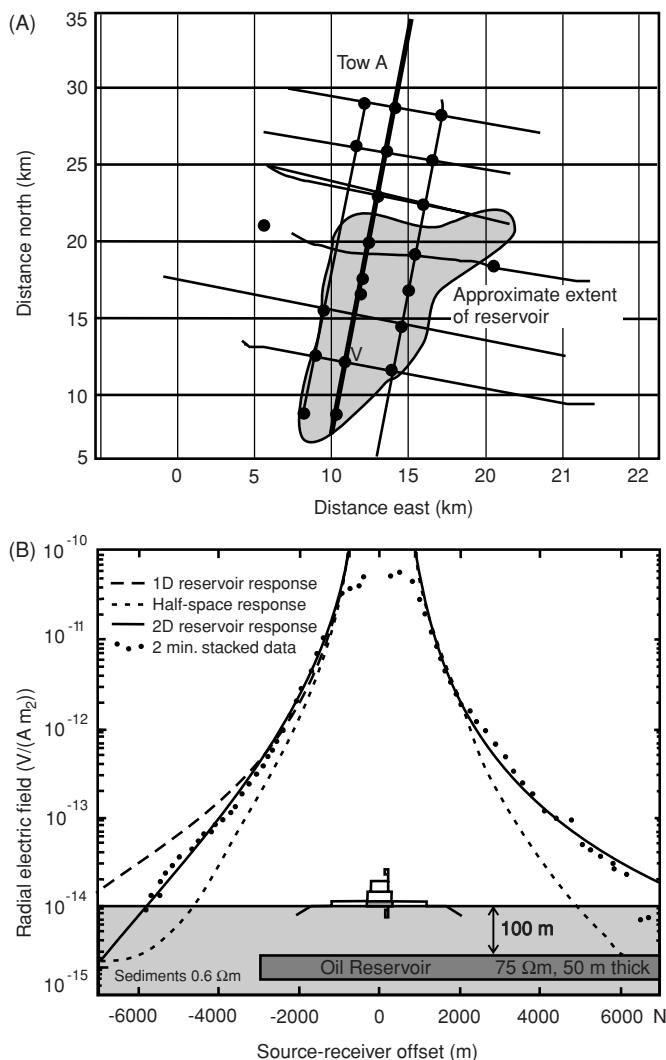


**Figure 10.28** (A) Survey layout and (B) radial-mode horizontal electric field data collected during Tow A on receiver V (circled) during the first proof-of-concept marine CSEM survey over the Girassol hydrocarbon reservoir, offshore Angola (Ellingsrud *et al.*, 2002). From Constable and Srnka (2007), by permission.

As has been mentioned before, a common limitation in CSEM methods, on land or in the marine environment, is the air wave effect that is also a function of water depth. However, another new technique that removes this effect is *focused-source EM* (FSEM; Davydycheva and Rykhlnski, 2009). Rather than use standard electric dipole receivers, multi-electrode receivers are required for the FSEM method; three or five electrodes can be used per receiver. Ratios of dipole and quadrupole measurements, or ratios of the first and second differences of the electric potential between the various electrodes are measured. The approach is also referred to as the *difference-normalisation method* (DNM; Davydycheva *et al.*, 2006) or *differentially normalised EM* (DNEM; Veeken *et al.*, 2009). It provides vertical focusing of the electric current, or elimination at the receiver of the influence of horizontally-directed axial current, which is typically strong on the axis of the exciting dipole

source. This helps to remove the effects of lateral near-surface effects, which often distort traditional dipole-dipole measurements on land. It also makes the method sensitive to a relatively narrow cylinder of material below the receiver. The modes of measurement also make it possible to separate the formation's EM and IP responses. When the electric current is on, geometric DC sounding is performed at a wide range of offsets to provide information on the formation's resistivity. The transient response of the formation is measured when the current is switched off. This reflects the spectral properties of the formation resistivity affected by the induced polarisation.

It is possible to model the FSEM field in 3D, but field data tend to have 1D inversions applied and then adjacent results stitched together and gridded to produce conductivity depth images (showing the lateral and vertical variation in conductivity) and the IP coefficient ( $\eta$ ) down to a depth of over 2 km (Davydycheva and Rykhlnski, 2009) (see also Section 9.4.2).

In contrast with the horizontal-source, horizontal-receiver of the older MCSEM systems, a vertical-source, vertical-receiver system called the *Transient Electro-Magnetic Prospecting using Vertical Electric Lines* (TEMP-VEL) (Flekkøy *et al.*, 2009; Holten *et al.*, 2009) has been developed by Petromarker. This system is shown schematically in Figure 10.29. It comprises a source system that is deployed from the survey vessel. Two generators work in parallel with a total capacity of 5000 A, with each transmitter dipole having a current

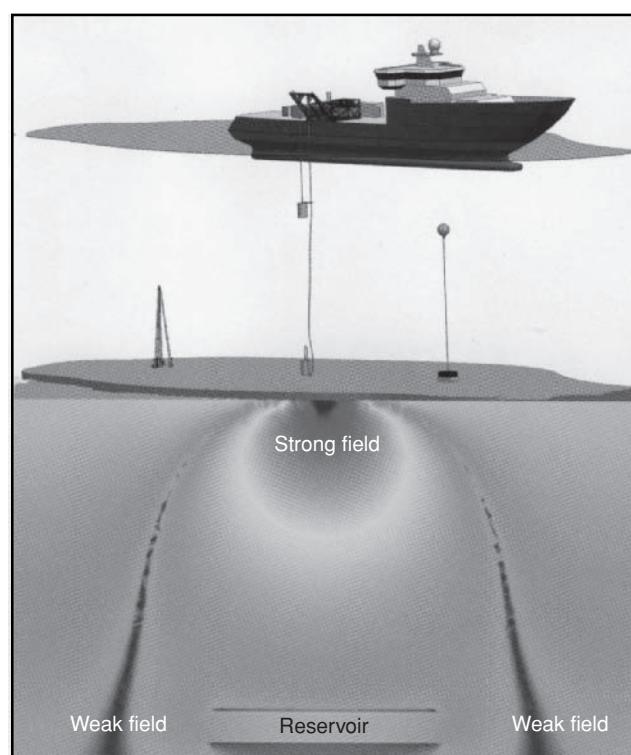


**Figure 10.29** An overview of the Petromarker TEMP-VEL system (not to scale) showing only one pulse system. To the left on the sea bottom is a tripod electrode. To the right is an alternative, older, flexible cable receiver. From Holten *et al.* (2009) and Petromarker, by permission. [C]

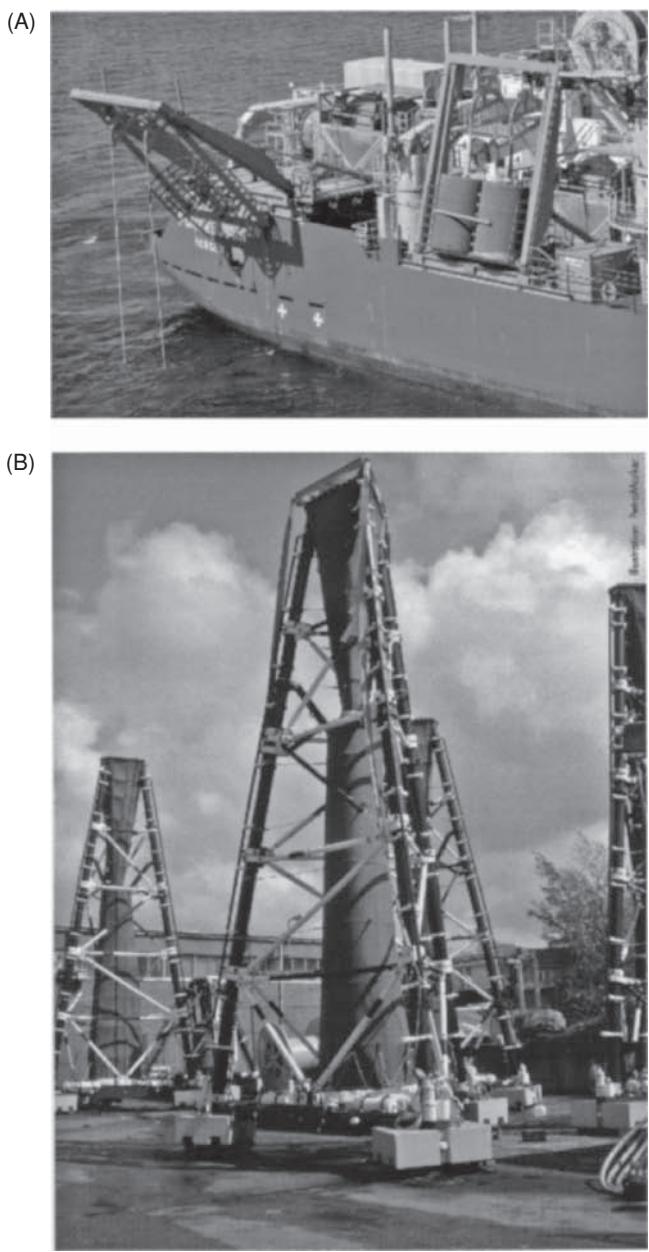


**Figure 10.30** TEMP-VEL equipment: (A) deployment of a transmitter electrode with another still in its gantry on board, and (B) 10-m tall vertical tripod antennae to be placed on the seabed. From Flekkøy *et al.*, (2009) and Petromarker, by permission. [C]

capacity of 2500 A. The transmitter dipole is made up of two electrodes that are connected to the vessel by cables (Figure 10.30A). The lower pulse electrode, connected to the pulse cable, is positioned accurately on the seabed. The upper electrode is lowered 50 m below the sea surface so that it lies vertically above the electrode on the seabed. A square pulse with alternating polarity followed by a pause is used. This alternating pulsing and recording eliminates the interference caused by the so-called air wave and the direct signal. The transmitter signal changes polarity in sequences of eight pulses (known as a *P-8 sequence*). Pulsing might last from four to

12 hours on a single station, with each pulse 8 s long with a 20 s listening pause between each pulse. Selected P-8-averaged response curves are averaged to produce a high-confidence, low-noise overall response curve which is later modelled.

Two types of receiver are used but both based on the same principle of a vertical dipole with an upper electrode and a base unit with the electronics, batteries, data storage and recording unit. The top electrodes are held vertically above the bottom unit by either a buoy with strong buoyancy as in the older version shown on the right in Figure 10.29, or by a rigid tripod system (Figure 10.30B). Each receiver has four pairs of Pb/PbCl electrodes. There is no physical connection between the survey vessel and the receivers, so recorded data are downloaded once the receivers have been recovered either by returning them to the survey vessel or by using a remotely operated vehicle. The survey vessel moves to a given location and the transmitters are pulsed while stationary. The optimal offset between source and receiver is in the range 500 m to 1500 m. The subsurface response is recorded while the transmitter is switched off so that any uncertainties in the location of the pulse electrodes do not lead to any time-dependent noise. The verticality of the system also eliminates the air wave components from the received signals. The magnitude of the vertical electric field ( $E_z$ ) is measured as a function of time.

The method is based on the diffusion principle that the vertical current will decay more quickly when a layer of lower electrical conductivity (i.e. a hydrocarbon reservoir) is present. The electric field distribution shown in Figure 10.29 is shown in the case of the presence of a cylindrical hydrocarbon-filled reservoir with a diameter of 400 m, height 100 m and a resistivity of 100  $\Omega\text{m}$ , with a 5000 Am source dipole shortly before the current is switched off. In the model, seawater has a resistivity of 0.3  $\Omega\text{m}$  and water-saturated sediments a resistivity of 1  $\Omega\text{m}$ . The greatest contrast in values of  $E_z$  occur between 2 s and 10 s. The decay of the electric field with time is recorded and modelled on the basis of a 1D horizontally layered earth, and assuming that induced polarisation effects and magnetisable materials are absent, neither of which might be absolutely valid. While 1D models assume semi-infinite layers, these clearly do not represent reality as the reservoir is restricted in all its dimensions and heterogeneous. Instead 3D models are used (e.g. Singer, 2008). Holten *et al.* (2009) have used these methods successfully across the Luva gas field in the Vøring Basin of the Norwegian Sea, even though the resistivity contrast of the reservoir (20–25  $\Omega\text{m}$ ) with surrounding shales (resistivity 1–7  $\Omega\text{m}$ ) is small. It is thought that this field would have been difficult to identify using the usual CSEM method because of this low resistivity contrast. However, the Luva gas field has been resolved using CSEM data constrained by use of vertical resistivity well-log data and seismic reflection data (Harris *et al.*, 2009).

## 10.5 Borehole EM surveying

Whereas surface and airborne EM systems have regular geometries of sources and receivers, the addition of the third dimension via a borehole leads to an increased number of possibilities with

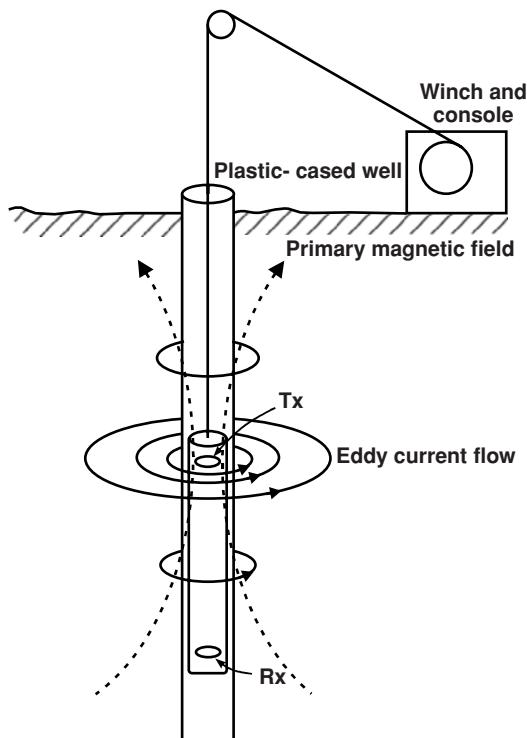


**Figure 10.31** The basic principle behind an electromagnetic induction logger for use in boreholes. From McNeill (1990), by permission.

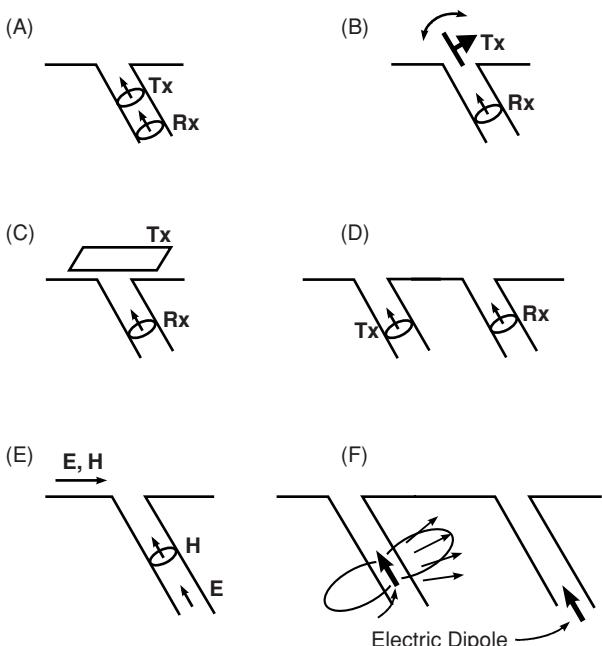


**Figure 10.32** Drill-hole EM systems. (A) Dipole-dipole EM. (B) Rotatable-transmitter EM (with transmitter  $T_x$  shown side-on). (C) Large-loop EM. (D) Hole-hole dipole EM (variation of (A)). (E) Remote transmitter (e.g. VLF radio source) for downhole measurement of electric and/or magnetic field. (F) Hole-hole wave propagation. From Dyck (1991), by permission.

associated complexities in interpretation. Borehole EM surveying differs from inductive well logging, which is used predominantly within the hydrocarbon industry, by virtue of the ability of being able to detect a conductive body at a significant distance away from the borehole. An induction logging device senses only those features through which the borehole has actually passed or within the near-field around the borehole (Figure 10.31).

The principle of operation of borehole EM surveying is the same as for ground conductivity meters. The system is able to measure the conductivity of the materials outside of a plastic-cased borehole or well with diameters in the range 5–20 cm. The measurements are insensitive to the usually much more conductive borehole fluid within the casing (McNeill *et al.*, 1988). Eddy currents are induced concentrically around the borehole using an intercoil separation of 0.5 m. This configuration provides a reasonable vertical resolution while at the same time maintains an adequate radial range of investigation (McNeill, 1990). Drill-hole EM methods have been reviewed by Dyck (1991), and more details can be found therein.

There are three types of system in borehole surveying: dipole–dipole EM, rotatable-transmitter EM, and large-loop EM (LLEM) methods, of which the last is the most commonly used in mineral prospecting. The basic transmitter–receiver geometries are shown in Figure 10.32.

The dipole–dipole system has two coaxial coils separated by fibreglass rods, with the transmitter preceding the receiver down the drill-hole. Measurement points are taken as being the midpoint

between transmitter and receiver. In-phase and quadrature components of the secondary magnetic field are measured as a percentage of the primary field. As the downhole system is deployed on a series of rods, the method can be used in near-horizontal and upwardly inclined holes, and is then limited only by the ability to move the probes within the hole.

The rotatable-transmitter system is a version of the dipole–dipole method, but the transmitter remains at the drill-hole collar throughout the survey, while the receiver is moved up and down the hole (Figure 10.33). The receiver probe is moved down the hole in discrete intervals of several metres at a time. At each measurement point, the surface transmitter coil is rotated until a null point in the sensor is reached and the corresponding angle of tilt is recorded. The method is analogous to the surface tilt-angle technique.

The general layout for borehole LLEM surveying is shown in Figure 10.34. A loop transmitter is deployed at the ground surface adjacent to the borehole down which a detector is run to obtain a profile. Typical ground loop dimensions range from 100 m to 1000 m and are comparable to the depth of the drill-hole being investigated. One ground loop, in conjunction with profiles down a number of drill-holes from the surface and from within a mine gallery, are sufficient to resolve a subsurface conducting target (Figure 10.35A). In contrast, if only one drill-hole is available, one loop on its own does not provide the azimuthal information necessary to locate the target. Consequently, a number of loop positions located around a collared borehole (Figure 10.35B) can be used to provide the additional information required.

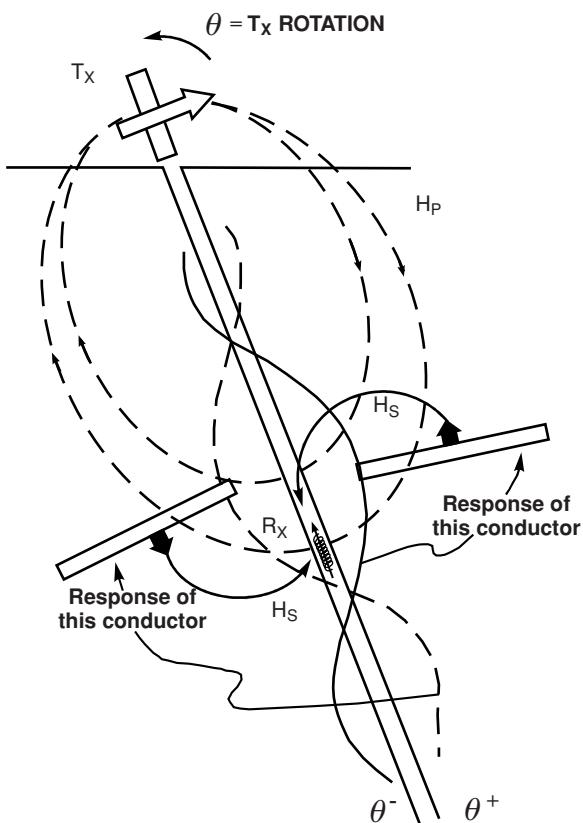


**Figure 10.33** Magnetic fields produced by a rotatable transmitter and target conductor. The transmitter coil is rotated about an axis perpendicular to the plane of the diagram. The conductor to the right of the drill-hole produces a negative (i.e. downward) component of secondary field  $H_s$  at the receiver position shown. A counter-clockwise ( $+θ$ ) rotation of the transmitter is required to achieve a null by offsetting  $H_s$  with a component of  $H_p$ , assuming negligible change in transmitter-conductor coupling as the transmitter is tilted. From Dyck (1991), by permission.

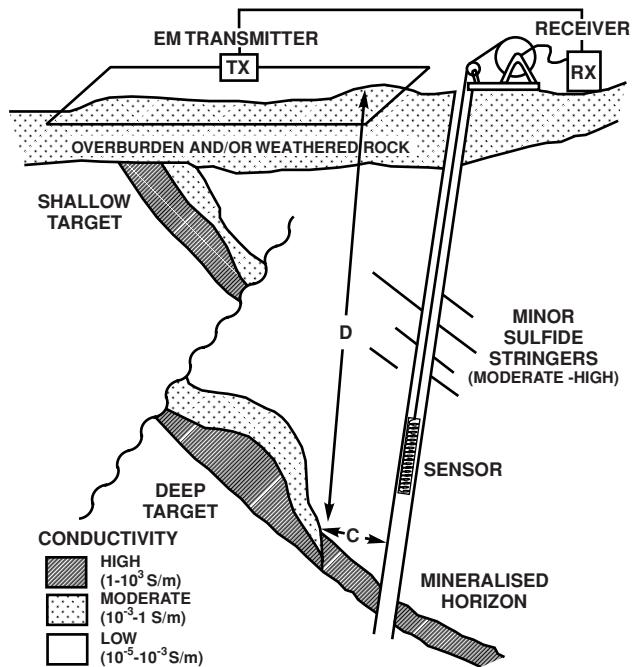


**Figure 10.34** Schematic to illustrate the use of the large-loop drill-hole EM method for massive sulphide exploration in highly resistive environments such as Precambrian rocks. The system comprises a transmitter ( $T_x$ ); a Clearance (C) is the critical distance in a drill-hole exploration problem involving a highly conductive target buried at depth D. There may be other bodies that are also conductive. From Dyck (1991), by permission.

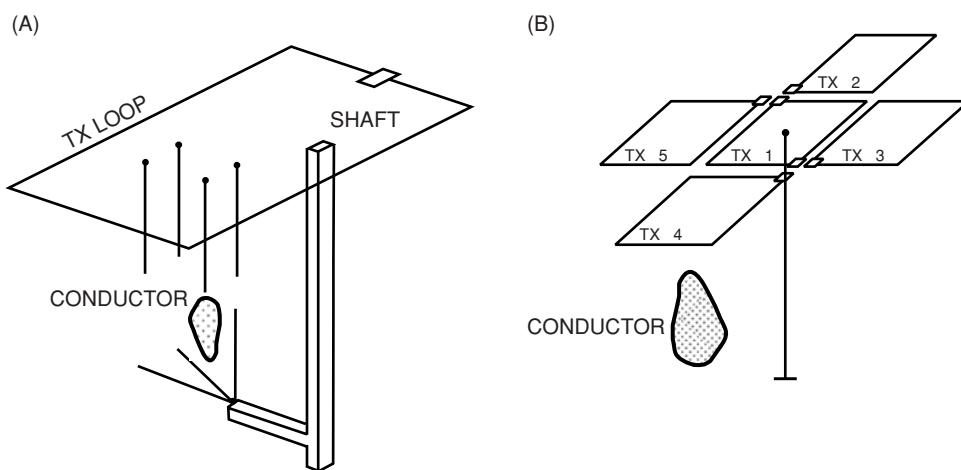


**Figure 10.35** Transmitter layouts for surveying (A) a group of drill holes collared underground; and (B) a single isolated drill-hole. Tx 1-5 are successive locations of the transmitter loop. From Crone (1986), by permission.

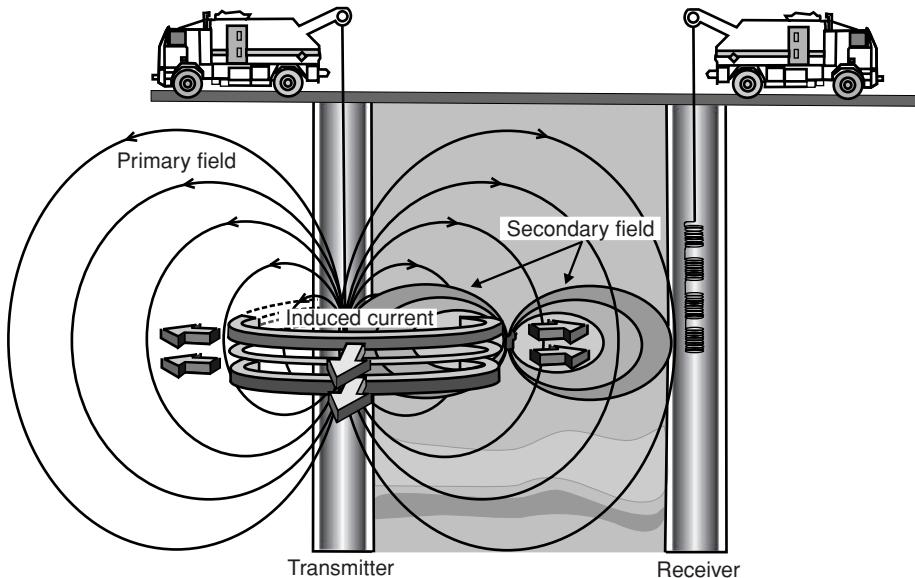


**Figure 10.36** DeepLook-EM system where both the primary magnetic field generated by the transmitter and the secondary magnetic fields resulting from the induced eddy currents are measured by four receiver sensors. Graphic provided courtesy of Schlumberger, by permission.

There are three types of LLEM system depending upon the received primary waveform of system function, namely impulse-type, step-function type (both of which are TEM systems), and multi-frequency (FEM) type. Further details of these systems are given by Dyck (1991). Other systems that are available include downhole VLF, and inter-hole wave propagation (e.g. Newman, 1994) which can include borehole tomographic techniques (see also 'borehole radar tomography' in Chapter 12). Three-component (magnetic field) systems have been developed and one such system successfully deployed by Boliden Mineral AB, in Sweden (Pantze *et al.*, 1986). A  $1 \times 1$  km ground loop was used in an FEM system which operated at two frequencies, 200 Hz and 2000 Hz. Three sensors were mounted in a 32 mm diameter probe with the  $y$ -axis always being horizontal,  $x$  parallel to the long axis of the probe, and  $z$  always at right-angles to  $x$  and  $y$ . In-phase residuals (computed after the removal of the primary field and the background response caused by the host rock) were plotted as a function of profile distance along the drill-hole. The shape and size of the excursion of each component away from a normal value provided information about the location (depth and azimuth) of a subsurface conductive target.

Borehole EM techniques have been used not only as part of primary exploration but also extended to mine production. The logging can help to identify ore-waste boundaries, reduce expensive core-drilling and provide information quickly about physical properties on ore intersections. It can also be applied to classify mineralisation, interpret lithology, and sometimes to transform physical responses to metal grades in ore (Hattula and Rekola, 2000). Borehole geophysics (including EM) coupled with lithogeochem-

ical data led to the discovery of a new volcanogenic massive sulphide (VMS) ore deposit at 500 m depth in the Pyhäsalmi area in Finland.

In marine hydrocarbon exploration, there has been a growth in interest in using both borehole EM as part of exploration surveys, but also to monitor reservoirs over time through the use of inter-borehole surveys. For example, Scholl & Edwards (2007) have described a technique to improve the detection resolution of horizontal hydrocarbon reservoirs by using an EM transmitter located beneath the reservoir in a borehole, but with receivers on the sea floor. Further modelling experiments have also been undertaken to take account of 3D media in borehole EM measurements (Hou *et al.*, 2006) and to undertake 2D inversion of large borehole EM datasets (Wang *et al.*, 2009).

A borehole EM system that has been developed since 2000 is the DeepLook-EM system, operated by Schlumberger, which is an enhanced crosswell reservoir monitoring system (Allegar, 2007). It can perform resistivity surveys on a reservoir scale between boreholes up to 1000 m apart, depending upon the type of casing present (Figure 10.36). The system comprises a 9.88 m transmitter antenna made up of a vertical-axis, magnetically permeable core wrapped with several hundred turns of wire that can generate a continuous sinusoidal signal at frequencies from 5 Hz to 1 kHz. Lower frequencies are used where the receiver is deployed in a well with steel casing, larger well separation or low formation resistivity.

The transmitter signal induces electrical currents to flow in the formation between the boreholes. These currents, in turn, induce a secondary magnetic field according to the electrical resistivity of the rock in which they are flowing. At the receiver borehole, the

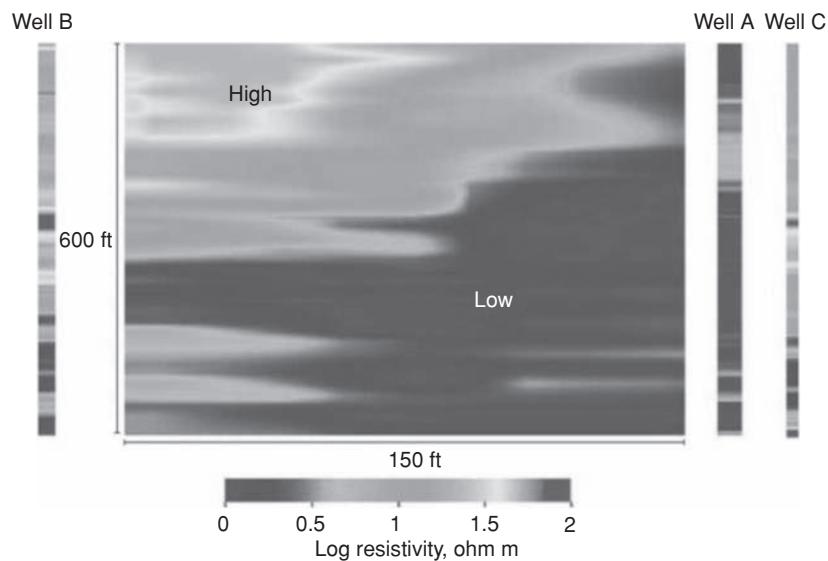


**Figure 10.37** The resistivity tomographic section derived from a DeepLook-EM survey shows an abrupt boundary midway between the area depleted of hydrocarbon by steam injection and unswept oil sands. Courtesy of Schlumberger, by permission. [C]

22.5-m long receiver comprises an array of four coils that record the signals simultaneously. For each receiver station, the transmitter in the other well is moved between the depths of interest while continuously transmitting signals. Once a complete transmitter traverse has been made per receiver location, the receiver tool is repositioned and the process repeated. After inversion of the recorded data for all receiver locations, a resistivity tomographic section is produced for each pair of wells. The technique is being used in time-lapse mode to monitor fluid movements to provide information about the efficiency of water- and steam-flood programmes, allowing inter-well saturation to be estimated, and to identify possible pay-zones that have been bypassed, and also in CO<sub>2</sub> sequestration.

Schlumberger have provided a case history where the DeepLook-EM system was used to identify the steam-front around cyclic injector wells in relation to the local geology. The hydrocarbon-field operator is using steam drive to produce from several reservoirs in a field in the San Joaquin Valley, California, USA. The field covers an area of 52 km<sup>2</sup> and has a complex steeply dipping geology and a variety of reservoirs. The DeepLook-EM transmitter and receiver tools were deployed in two wells (A and B) located 150 ft (~46 m)

apart to map the steam-affected zone between them. A baseline model for the inversion of the EM data was constructed from conventional wireline resistivity measurements made in the wells prior to injection and the DeepLook-EM survey. The derived resistivity tomographic section between wells A and B (Figure 10.37) shows the range of resistivity values measured. Lower resistivity values are characteristic of shale layers and steam-swept zones; the higher resistivity areas are characteristic of unswept oil sands. The contrast between the pre-injection resistivity logs from injector Well C and nearby observation Well A is extremely well defined. The abrupt boundary located 23 m from Well A on the tomographic section marks a resistivity change from 2 Ωm to more than 50 Ωm over a short distance. The lower resistivity identifies the depleted zone resulting from the replacement of oil by formation water and steam condensate, which matches the log in Well A.

It is interesting to conjecture whether the borehole EM systems either on their own when used tomographically, or as part of a borehole-surface survey, can be used effectively in near-surface applications to map and monitor shallow remediation of hydrocarbon contamination in environmental investigations.

# 11

## Electromagnetic Methods: Systems and Applications

### 11.1 Introduction

A basic introduction to the various types of electromagnetic systems and their respective operating principles has been given in Chapter 10. Here, two of the most commonly used types of method are discussed in more detail with case histories to illustrate their various applications, with a further four discussed in the next chapter. These systems can be classified into three groups:

- *near-field systems*, where the source is relatively close to the receiver;
- *far-field systems*, where the source is located at a very large distance from the receiver such that the EM wave can be treated as a plane wave (VLF surveying);
- *natural-source EM systems*, where no active generation of artificial electromagnetic radiation is necessary because naturally occurring ground currents provide the source.

The range of individual instruments is large, especially if airborne, seaborne and drill-hole systems are included along with those deployed solely from the ground surface. It is not possible, therefore, to provide an in-depth account of every system that is available. The selection presented here is of those techniques most likely to be used in engineering, environmental and archaeological applications, although in some cases some techniques are used almost exclusively in mineral and increasingly hydrocarbon exploration. More detailed descriptions of specific instrument types have been given, for example, by Nabighian and MacNae (1987, 1991), and within other papers cited in the appropriate sections; technical specifications of individual systems can be obtained from instrument manufacturers.

### 11.2 Continuous-wave (CW) systems

#### 11.2.1 Tilt-angle methods

Tilt-angle methods have been used extensively in both ground and airborne surveys, particularly for mineral exploration. The method obtains its name from the measurement of the angle (tilt) of the resultant of the applied primary field and the induced secondary fields arising from a buried conductive body (Figure 11.1), such as a buried massive sulphide orebody.

Given a horizontal primary field direction, induced eddy currents within a buried conductor generate a secondary magnetic field whose lines of force are concentric around the source of the currents, commonly taken as being the uppermost edge of the body. The secondary field is inclined upwards on the side nearest the transmitter and hence the resultant is also inclined upwards (positive tilt angle). Immediately above the conductive body, both primary and secondary fields are horizontal and in the same direction, hence the tilt-angle is zero. On the side furthest from the transmitter, the secondary field is inclined downwards and thus so too is the resultant (negative tilt angle). From a tilt-angle survey with a vertical coil axis (horizontal primary field), the conductive orebody is located at the point where the tilt angle passes from being positive to negative (the crossover point). When the primary field is orientated vertically downwards, the tilt angle passes through a minimum immediately over the conductive body (Figure 11.1).

When a conductive body is close to the ground surface, the steepness of tilt and the horizontal rate of change of tilt angle are greater than would be produced over a deep-seated conductive body. Furthermore, if the conductive body is vertical and the profile surveyed is at right-angles to the subsurface target, the tilt-angle profile should be symmetrical about the crossover point. If the profile is asymmetrical, then the amount of asymmetry is indicative of the degree of dip of the subsurface target. As the dip of the conductive target decreases (becomes less vertical relative to the ground), so the amount of asymmetry increases. Principal tilt-angle methods

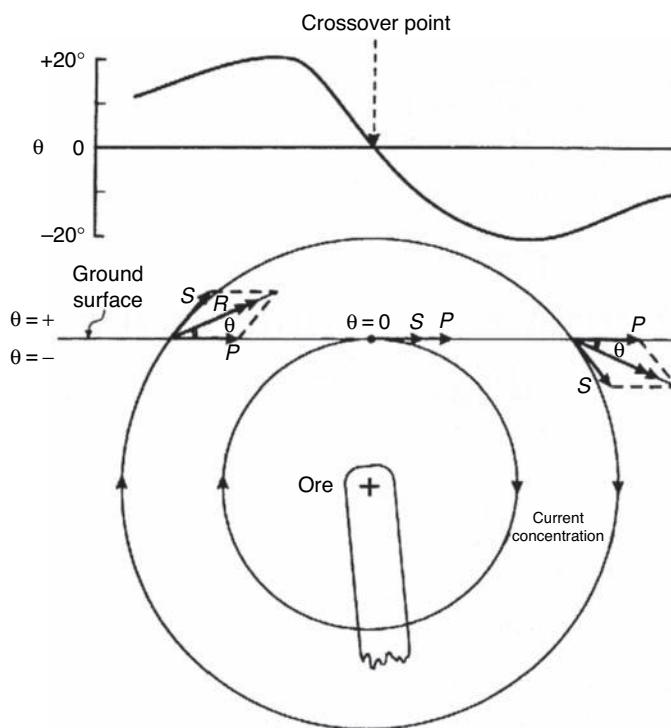


**Figure 11.1** Tilt-angle ( $\theta$ ) profile over a conductive orebody arising from a plane EM wave from a remote vertical transmitter.  $P$  indicates the direction of the primary field vector, and  $S$  and  $R$  are the secondary and resultant field vectors, respectively. After Parasnis (1973), by permission.

currently in use are the VLF and AFMAG techniques which are described in more detail in Sections 11.4 and 11.6 respectively.

### 11.2.2 Fixed-source systems (Sundberg, Turam)

Where a fixed source such as a large loop of wire or a long grounded cable is used, as in the Sundberg method, the primary magnetic field is inclined towards the ground (Figure 11.2). In the presence of a vertical, thin and laterally continuous conductor, eddy currents induced at the top edge of the subsurface body generate a secondary magnetic field which interferes with the primary field. The resultant or secondary vertical component of the magnetic field is measured by the receiver. In addition, the gradient of the secondary magnetic field can be measured and displayed as a profile.

In the case of a vertical thin conductor, the secondary magnetic field is inversely symmetrical about the crossover point immediately above the top of the subsurface target (Figure 11.2). At the same location, the gradient of the secondary field reaches a minimum value. If the conductive sheet is not vertical, the anomalies produced increase their degree of asymmetry with decreasing dip angle.

Care has to be exercised when using the Sundberg method because, as with many other EM techniques, topography affects the quality of data acquired. If the ground surface over which a survey

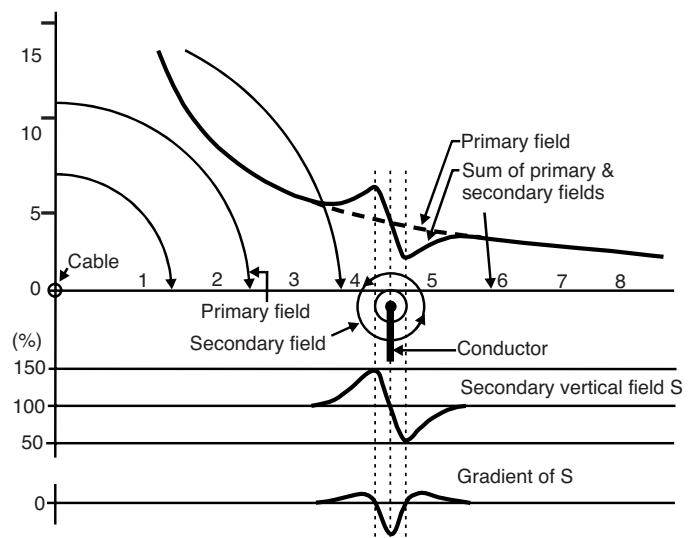


**Figure 11.2** In the Sundberg method, the source is a long wire which generates the primary field that produces a secondary field over a subsurface conductor. The anomaly due to the subsurface conductor is superimposed on the primary field but can be residualised by the removal of the primary field. The horizontal gradient of the residualised secondary field yields a minimum at a point directly over the top of the conductor. From Parasnis (1986), by permission.

is being undertaken is rough, such that the receiver is at an elevation significantly different from that of the source, appropriate topographic corrections have to be applied to the real component data of the vertical primary field in order to compensate.

In the case of the Turam method, two receiver coils (usually placed horizontally) are separated by a fixed distance ( $c$ ) and are moved along profiles at right-angles to the source wire. Given a number of stations (1, 2, 3, 4, ...) at which each coil is located in turn, the amplitude ( $V$ ) and phase ( $\alpha$ ) of the vertical electromagnetic field are measured at each location. The ratios of the amplitudes at each successive pair of stations (e.g.  $V_1/V_2, V_2/V_3, V_3/V_4, \dots$ ) and the horizontal gradient of the phases ( $(\alpha_2 - \alpha_1)/c, (\alpha_3 - \alpha_2)/c, (\alpha_4 - \alpha_3)/c, \dots$ ) are plotted at the location of the midpoint between the coils along the profile. In addition, as the primary field ( $P$ ) decreases in amplitude away from the source, the measured amplitude ratios are divided by the normalised amplitude ratios ( $P_1/P_2, P_3/P_2, P_4/P_3, \dots$ ) to give  $V_1P_2/V_2P_1, V_2P_3/V_3P_2, V_3P_2/V_4P_3, \dots$ , which are known as *reduced ratios* (RR). If either or both receiver coils are located at an elevation different from that of the source cable, then a topographic correction has to be applied to the reduced ratios.

It is usual to plot a Turam profile in terms of the reduced ratios and horizontal gradient of phase (e.g. Figure 11.3). As in the case of the Sundberg anomalies, symmetrical anomalies of both measured parameters should be obtained over a vertical conductor. If dip decreases from the vertical, the degree of asymmetry increases; higher values of the reduced ratio and smaller values of horizontal gradient of phase are measured over the downdip side of the conductive target.

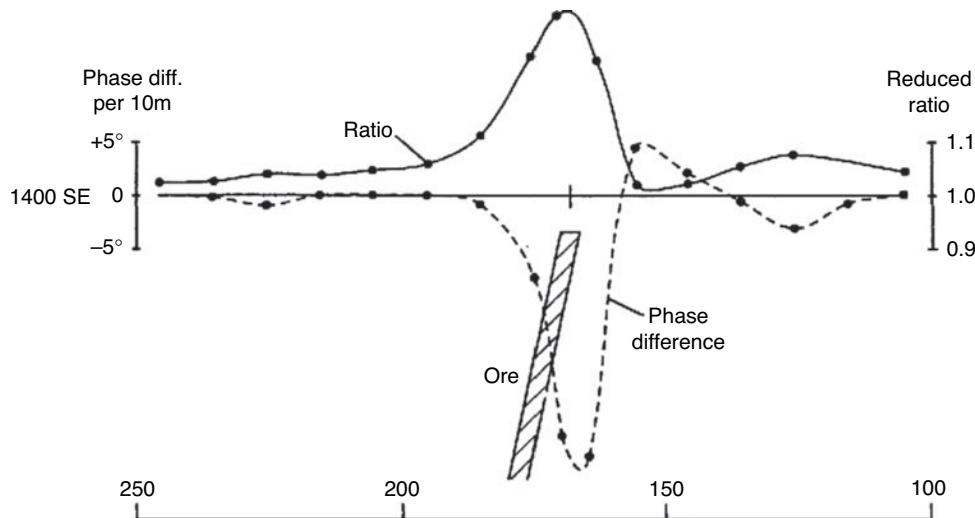


**Figure 11.3** Reduced-ratio and phase difference gradient profiles over an inclined conductor obtained using a Turam survey.

### 11.2.3 Moving-source systems

The most commonly used EM surveying method in environmental and engineering geophysics is the *moving-source dual-coil method* (McNeill, 1990). Two separate coils connected by a reference cable provide the basis of the system (Figure 11.4); one coil serves as a transmitter to generate the primary field and the other acts as a receiver. The inter-coil separation is maintained at a fixed distance and the dual-coil pair is moved along the survey transect in discrete intervals. The point of reference for the measurement is usually the mid-coil position. Typically, dual-coil systems measure the quadrature component only, or both the quadrature and in-phase components.

In the case of *ground conductivity meters* (GCMs), as manufactured by Geonics Ltd, for example (Figure 11.5), the instrument provides a direct reading of the quadrature component as the apparent conductivity ( $\sigma_a$ ) of the ground in units of milliohms per metre (SI equivalent units are milli-Siemens per metre (mS/m)). The in-phase component is measured in parts per thousand. These instruments can be used over land and in over-water investigations (Butler, 2009).

The ratio of the inter-coil spacing ( $s$ ) divided by the skin depth ( $\sigma$ ) is known as the *induction number* ( $B$ ) (see Box 11.1). Where the induction number is much less than one, then the ratio of the secondary to the primary magnetic fields at the receiver is directly proportional to apparent conductivity ( $\sigma_a$ ). If the ground is entirely homogeneous and isotropic, the instrument should give a measure of the true conductivity of the ground. However, real geological materials comprise a mixture of constituents, most notably a solid matrix with pore spaces that may be partially or fully saturated with pore fluids which, in some cases, can be highly conductive. Furthermore, the ground is made up of layers (soil over weathered material over bedrock, for example). Each material has its own diagnostic true conductivity and will contribute to the measured apparent conductivity value.

A ground conductivity meter responds to the conductivity composition of the ground, depending upon the orientation of the coils. Typically, there are two modes: horizontal coils with a vertical magnetic dipole (VMD), and vertical coils with a horizontal magnetic dipole (HMD). If a thin semi-infinite horizontal layer is located at a normalised depth  $z$  (where  $z$  is the actual depth divided by the inter-coil separation), then the relative contribution of that thin layer to the secondary magnetic field ( $H_s$ ) at the receiver is denoted by the impulse response function ( $\varphi$ ). The form of this response for both the vertical and horizontal magnetic dipoles (Figure 11.6) is very important. In the case of the vertical magnetic dipole, there is little relative contribution from the very near surface. Consequently, in this configuration, the technique is relatively insensitive to features very near to the surface. The maximum relative contribution arises from a normalised depth of  $z = 0.4$ . In contrast, the relative response for a horizontal magnetic dipole decreases with depth from a maximum at the surface. In this case, the dipole configuration makes the system very sensitive to near-surface features.

Rather than considering the relative contribution of a single thin layer at a depth  $z$ , the relative contributions of all materials within the depth  $z$  to the secondary magnetic field (or apparent conductivity) can be calculated. The sum of all the relative impulse responses

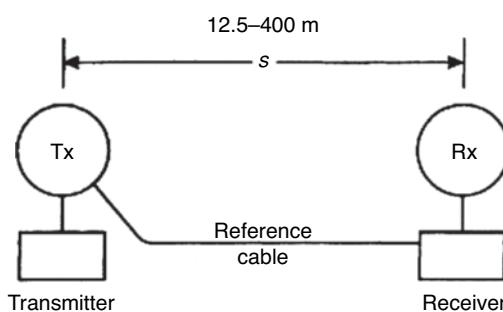


**Figure 11.4** Moving dual-coil EM system; circles indicate the transmitter (Tx) and receiver (Rx) coils.

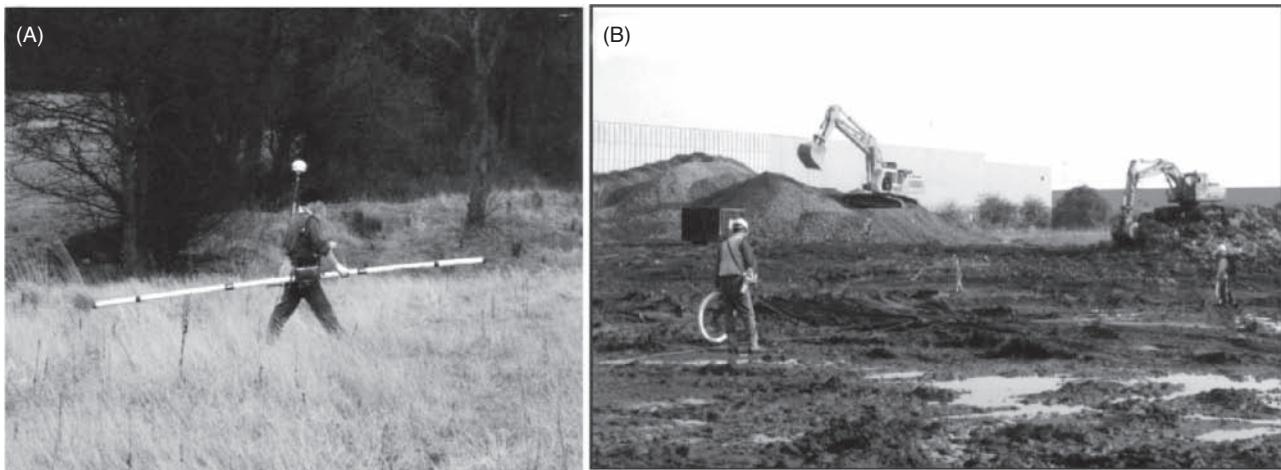


**Figure 11.5** Geonics (A) EM31 and (B) EM34 ground conductivity meters in use. [C]

**Box 11.1 Apparent conductivity at low induction numbers**  
(McNeill, 1980)

The skin depth ( $\delta$ ) is given by:

$$\delta = (2/\omega\mu_0\sigma)^{1/2} = (2i)^{1/2}/\Gamma$$

and

$$\Gamma s = (2i)^{1/2}s/\delta = (2i)^{1/2}B \quad [\text{as } B = s/\delta]$$

where:

$\omega = 2\pi f$  and  $f$  is the frequency (Hz)

$\mu_0$  = permeability of free space

$i = \sqrt{-1}$

$\Gamma = (i\omega\mu_0\sigma)^{1/2}$

$\sigma$  = conductivity

$s$  = inter-coil separation (m).

The ratio of the secondary ( $\mathbf{H}_s$ ) to primary ( $\mathbf{H}_p$ ) magnetic fields at the receiver at low induction numbers (i.e.  $B \ll 1$ ) is given by:

$$\mathbf{H}_s/\mathbf{H}_p \approx iB^2/2 = i\omega\mu_0\sigma s^2/4.$$

The measuring instrument is designed to ensure that with the selected frequency ( $f$ ), a given inter-coil separation ( $s$ ), and a designed response of  $\mathbf{H}_p$  for a given transmitter, the only unknowns are  $\mathbf{H}_s$ , which is measured by the instrument, and the ground conductivity ( $\sigma$ ).

Put another way:

$$\sigma_a = (4/\omega\mu_0 s^2)(\mathbf{H}_s/\mathbf{H}_p)_q$$

where the subscript  $q$  denotes the quadrature phase.

for all the depths to  $z$  is expressed mathematically as the integral of all the impulse response functions. The total contribution so calculated is called the *cumulative response function*,  $R(z)$ , and has different forms for the VMD and HMD configurations (Figure 11.7).

The graphs of cumulative response function for each dipole orientation can be used in the calculation of true conductivities for simple 2- or 3-layer models. An example of such a calculation is given in Box 11.2.

Consider the case of a model involving two semi-infinite horizontal layers where the inter-coil separation is much less than the

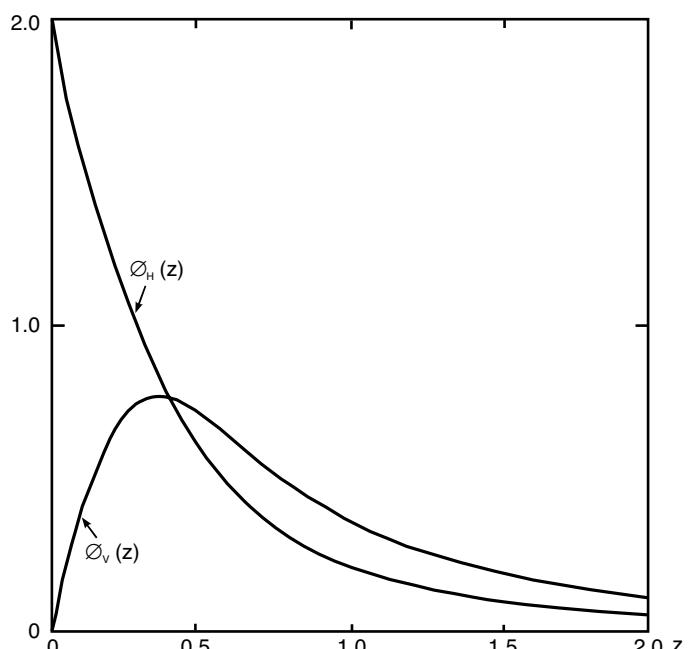


**Figure 11.6** Impulse response functions ( $\phi$ ) for horizontal and vertical magnetic dipoles as a function of normalised depth (McNeill, 1980).

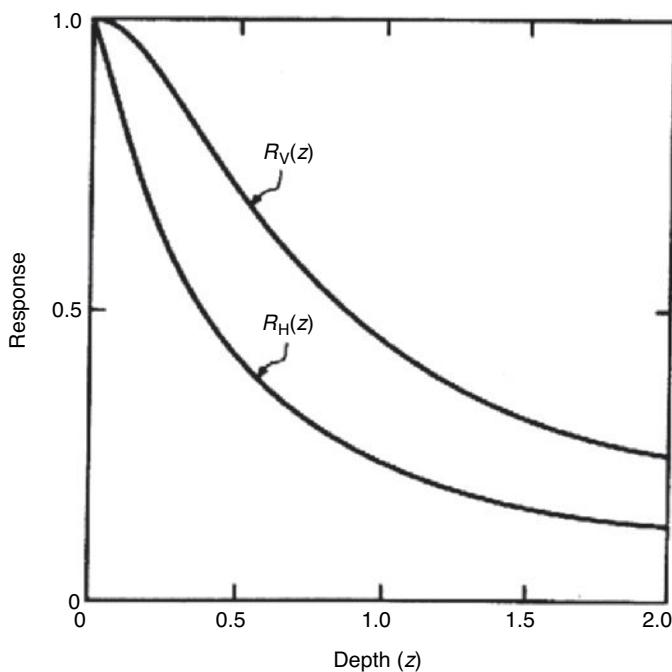


**Figure 11.7** Cumulative response functions ( $R$ ) for horizontal and vertical magnetic dipoles as a function of normalised depth (McNeill, 1980).

skin depth for all layers. The measured apparent conductivity is made up of the contribution of the first layer plus a contribution from the underlying material. The weighting of the conductivity contribution is provided by the cumulative response function. A similar logic follows for a 3-layer case.

This type of calculation is useful if the likely value of apparent conductivity is required over a model where layer conductivities have been estimated along with layer thicknesses. The values of apparent conductivity so obtained are estimates and will only be as accurate as the validity of the assumptions for a given situation. If the ground is not approximated by semi-infinite horizontal planar layers, and there is some lateral as well as vertical variation in conductivity and thickness, then the calculation will only be at best a rough guide. If there is a three-dimensional object within the sphere of influence of the EM measuring system, or if the interfaces between layers is sloping or non-planar, then the validity of this calculation will be substantially reduced.

In the 1980s Geophex developed a multi-frequency helicopter-towed EM system for bathymetry surveys over the shallow ocean. The first hand-held version (GEM-1) was completed in 1992. The latest system, the GEM-2 was completed in 1995 and is increasing in popularity especially in environmental investigations due in part to its light weight and portability. GSSI have the licence to manufacture commercial models of the GEM2, including the EMP-400, for use for very shallow investigations (comparable to those applications for which a Geonics EM38 would be a competing instrument). The GEM-2 (Figure 11.9) operates in a frequency range of 90 Hz to 24 kHz and measures the in-phase and quadrature component at a number of frequencies simultaneously (Won *et al.*, 1996). Like

**Box 11.2** Use of the cumulative response function to calculate a layered-earth model from a measured apparent conductivity

In a 2-layer model, the contribution from the upper layer to the measured apparent conductivity  $\sigma_a$  is given by:

$$\sigma_a = \sigma_1(1-R)$$

where  $\sigma_1$  is the true conductivity of the first layer and  $R$  is the cumulative response function for the appropriate dipole orientation (VMD or HMD).  $R$  is a function of normalised depth ( $z = d/s$ ), where  $d$  is the actual depth and  $s$  is the inter-coil separation.

The contribution arising from the underlying layer is given by:

$$\sigma_a = \sigma_2R$$

where  $\sigma_2$  is the true conductivity of the underlying material.

The total contribution to the apparent conductivity is the sum of these two contributions, such that:

$$\sigma_a = \sigma_1(1 - R) + \sigma_2R.$$

For a 3-layer case:

$$\sigma_a = \sigma_1(1 - R_1) + \sigma_2(R_1 - R_2) + \sigma_3R_2$$

where  $\sigma_{(1, 2, 3)}$  are the true conductivities and  $R_{(1, 2)}$  are the cumulative response function values of the first, second and third layers, respectively.

Examples of the calculation are given in the caption to Figure 11.8.

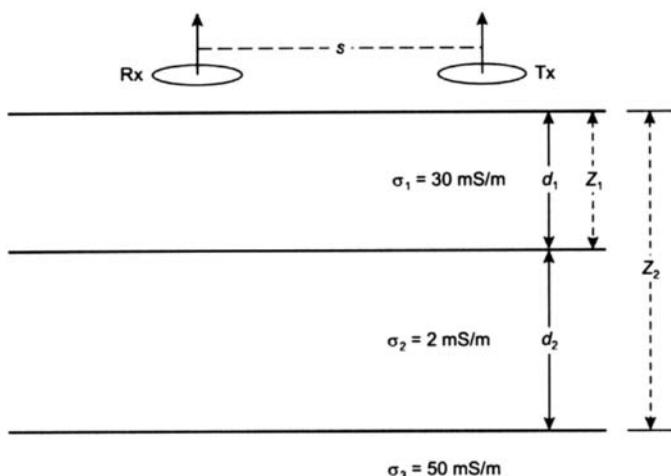


**Figure 11.8** Example of the use of cumulative impulse response functions ( $R$ ) and true conductivities ( $\sigma$ ) to calculate a theoretical value of apparent conductivity ( $\sigma_a$ ) for a given Earth model. Given  $R_1 = 0.71$  and  $R_2 = 0.31$ , and using Figure 11.7 for  $d_1 = 5$  m and  $d_2 = 10$  m, for  $s = 10$  m, then:  $\sigma_a = 30(1 - 0.71) + 2(0.71 - 0.31) + 50 \times 0.31 = 25.0$  mS/m, using the formula for a 3-layer case given in Box 11.2.



**Figure 11.9** GEM-2 multi-frequency ground conductivity instrument. [C]

the Geonics equipment, the dipole orientation of the GEM-2 can be changed between horizontal and vertical by simply rotating the instrument through 90° around the long axis so that the flat face of the instrument faces upwards (i.e. the coils are horizontal) or faces away from the operator (i.e. the coils are vertical). While the coils are horizontal, the dipole is vertical; similarly, when the coils are vertical, the dipole is horizontal, as the dipole is orthogonal to the plane of the coil. It is argued that varying depths of exploration are achieved by making measurements at different frequencies, with those at highest frequency giving information about the near surface, and increasing depth of exploration obtained by decreasing frequency, according to the skin depth (see Box 10.3). The instrument provides values of the *apparent* conductivity as a function of frequency.

There is, however, a long-running disagreement between manufacturers over the validity of an instrument with a fixed coil separation providing real depth discrimination purely by changing the frequency. Won *et al.* (1996) argued that a sweep through the frequency range is akin to undertaking a frequency sounding, i.e. measuring the conductivity as a function of ‘depth’ with greater depth of penetration being achieved with lower frequencies. This was strongly

#### Box 11.3 Horizontal Loop EM (HLEM) response parameter $\alpha$

The HLEM response parameter  $\alpha$  is given by:

$$\alpha = \mu\sigma\omega L^2$$

where  $\mu$  is the magnetic permeability of free space ( $4\pi \times 10^{-7}$  H/m),  $\sigma$  is the overburden conductivity,  $\omega$  is the angular frequency where  $\omega = 2\pi f$ ,  $f$  is the frequency of measurement, and  $L$  is the inter-coil separation (m).

disputed by McNeil (1996) who argued that to achieve information about the layering of the ground (i.e. depth discrimination) the highest frequency must be selected so that the skin depth in the ground is significantly shorter than the inter-coil spacing. To achieve such a condition for the GEM-2, which has an inter-coil separation of 1.67 m, would require a frequency of almost 4 MHz for ground with a conductivity of 25 mS/m, which is not achievable with the instruments available. McNeil argued that the GEM-2 is primarily a metal detector and should not be used for discriminating layered earth structure, whereas the EM31 is good at layer discrimination. Nonetheless, Won *et al.* (1996) gave an example of being able to locate and map an 18-inch diameter stainless steel pipe buried at a depth of around 9 m (30 ft) using a GEM-2 operating at a frequency of 7.29 kHz. Geonics have, however, developed a time-domain instrument for metal and UXO detection (the EM-61-3D).

In the case of an APEX MaxMin I-10 dual-coil system, up to ten different frequencies can be selected (110, 220, 440, 880, 1760, 3250, 7040, 14,080, 28,160 and 56,320 Hz), using one inter-coil separation which can be selected over the range 20 m to 500 m. The normal mode of operation is referred to as *horizontal loop EM* (HLEM), although measurements can also be made in the perpendicular dipole position and in the tilt-angle configuration (Frischknecht *et al.*, 1991). Commonly for mapping Quaternary sediments, an inter-coil separation of 100 m is used. Both the quadrature and in-phase components are measured at each frequency at a given station location and are displayed in a phasor diagram (Figure 11.10). The measured HLEM values depend on a response parameter  $\alpha$  (Box 11.3) that is directly proportional to the conductivity of the ground which it is trying to measure, and the frequency of measurement (one of the ten available frequencies) and the inter-coil separation, both of which are chosen by the system operators; other parameters are constants (Palacky, 1991). Master-curve phasor diagrams are used in the interpretation of the measured data (see next section).

Fixed-coil instruments should always be used keeping their dipole orientations the same way around when traversing a grid of data. For example, if the  $R_x-T_x$  are aligned so that the receiver is ahead of the transmitter (in-line profiling) along one line going from south to north, then for the next adjacent traverse which is surveyed in the opposite sense (north to south) the orientation of the dipole should be kept as for the previous line, in this case, the transmitter should be ahead of the receiver, and so on across the site. Similarly, the dipole orientation of the instrument should not be switched as the survey proceeds along a line, alternating between vertical and horizontal dipole orientations. To do this does not permit the decay of the EM field in the ground to occur before the field direction is switched, so the secondary fields are always transient. Data will be recorded but they will mean nothing sensible. To cover large areas of ground, a survey should be undertaken using one dipole orientation at a time, with two separate passes over the ground.

An operator who has a pronounced walking gait while carrying an EM31 can make the boom flex and bounce with each step. This causes the transmitter and receiver coils to vary their height above the ground and can affect the readings. The boom height should be kept as level and as constant as possible during each traverse of the

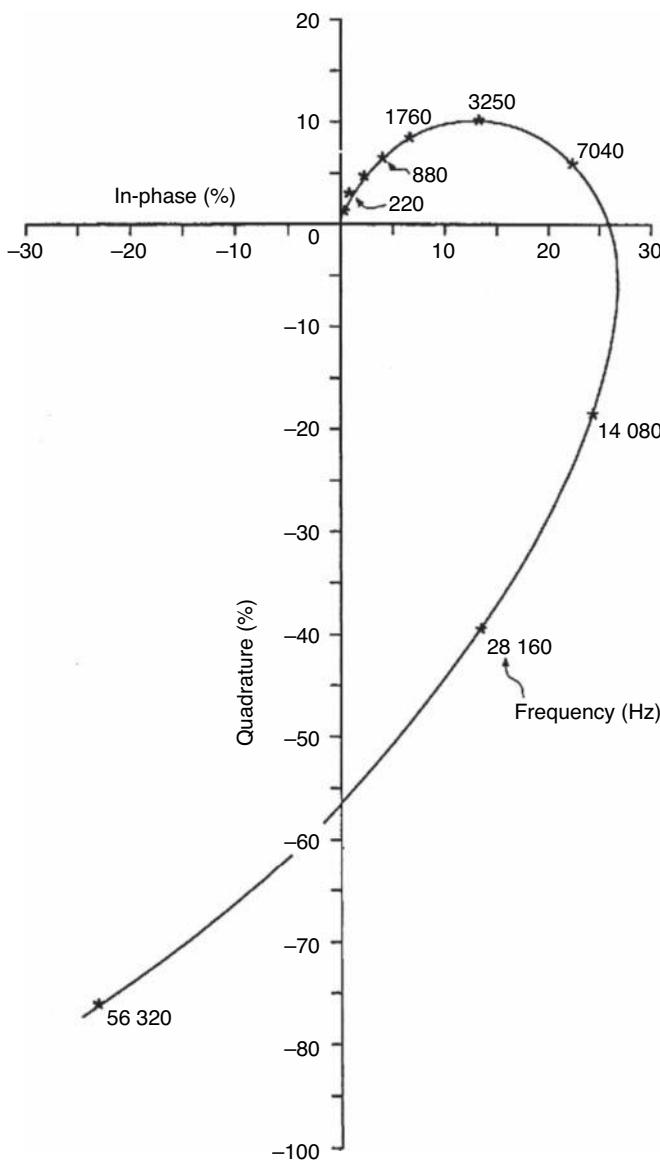


**Figure 11.10** Example of a phasor diagram where the in-phase and quadrature data for each frequency (shown by asterisks) are plotted and compared with a best-fit model (solid line) for a horizontal loop EM sounding (Palacky, 1991).

ground. When using an EM34 it is essential to keep the planes of the two separate coils parallel. Where coplanarity is not maintained, values recorded will be inaccurate.

## 11.2.4 Interpretation methods

### 11.2.4.1 Profiling and depth sounding

Electromagnetic data can be analysed in a number of different ways, according to the manner in which they have been acquired. Measured parameters may be plotted as profiles or as gridded and

contoured maps on which anomalous zones can be identified. These approaches tend to be qualitative and first-order interpretations.

For reconnaissance mapping or ‘anomaly spotting’, qualitative interpretation may suffice. However, there are certain pitfalls that can befall the unwary if the characteristic responses of certain features are not recognised. For example, it is a misconception when using a dual-coil system such as Geonics EM31 that a target produces only a single peak over a thin conductive target; spotting anomaly ‘highs’ is fraught with danger!

Consider a typical apparent conductivity profile produced over a 10 cm diameter metal gas pipe buried at around 1 m (Figure 11.11A). Two peaks are evident, with a strong low or even negative occurring immediately over the target. Note that the distance between the anomaly peaks is the same as the dipole length. Always check the inter-peak distance; if it is curiously similar to the inter-coil separation being used, then the target causing the anomaly is at the midpoint between coils. Depending upon the spatial sampling interval relative to the position of the target, the anomaly peaks and low may be slightly broader or narrower than one dipole length by the sampling being skewed relative to the target (see the subsampled profile in Figure 11.11B). The same effects may be more subdued with larger inter-coil separations.

Similarly, the shape of the anomaly will also vary depending upon which dipole orientation is used. An example of the difference of the output from both dipole orientations over a vertical conductor for the same inter-coil separation is shown in Figure 11.12.

The spatial smearing effect is also noticeable in gridded data. If the spatial sampling is too coarse, the anomalies arising from small (particularly 3D) targets may be effectively smoothed (aliased) and the targets may be missed. The resolution of ground conductivity mapping is discussed in Section 11.2.4.3.

### 11.2.4.2 Computer analysis

More quantitative analysis can be undertaken using specialist software. Two approaches are possible: (a) using EM data to form a depth-sounding at a single location; and (b) undertaking EM profiling along a line or over a grid to produce a two-dimensional geoelectric cross-section.

In the case of depth-sounding, a limited number of data are obtained as a function of inter-coil separation (which is in itself a function of frequency; greater depth penetration is achieved using the lowest frequencies and greatest inter-coil separations) and dipole orientation. For this discussion, the range of ground conductivity meters made by Geonics Ltd will be used as these instruments are employed commonly in environmental and engineering surveys. Data obtained with other makes of instruments can be interpreted in similar ways.

If a Geonics Ltd EM34-3 ground conductivity meter is used, three inter-coil separations and two dipole orientations are available, giving a maximum number of six data points obtainable using the one instrument at a given sampling point. The apparent conductivity values measured at each inter-coil separation and with each dipole orientation are entered into a program such as IX-1D v3 (Interpex Ltd, USA). The software can handle data from a

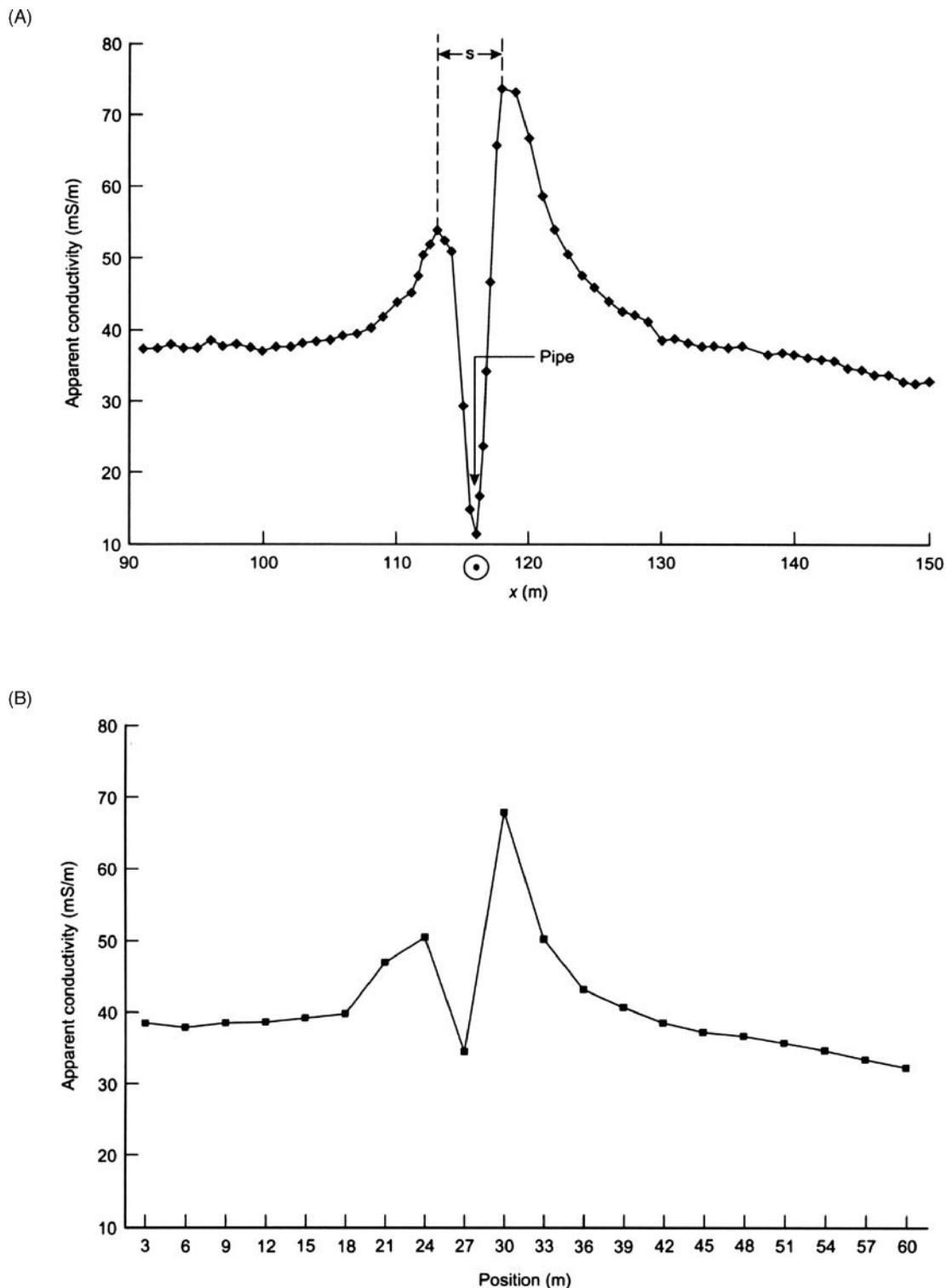


**Figure 11.11** Example of the effect of (A) a metal gas pipe on apparent conductivity data, and (B) the horizontal smearing of the anomaly caused by inadequate spatial sampling. Note that the peak-to-peak distance in (A) is equal to the inter-coil separation.

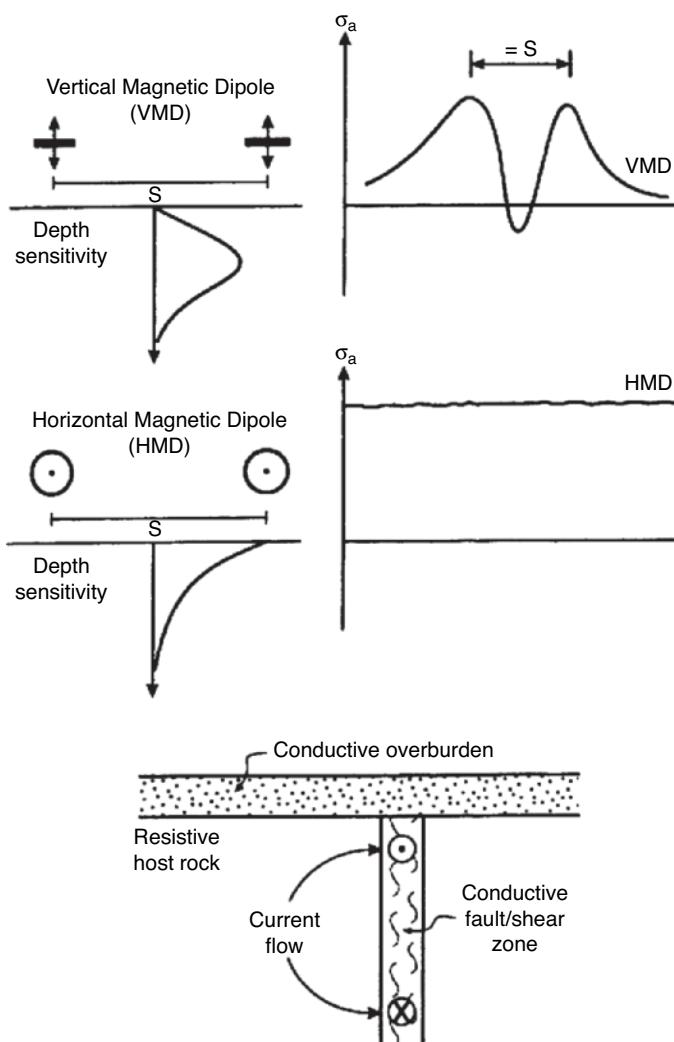


**Figure 11.12** Example of the difference in output from both vertical and horizontal magnetic dipoles over a vertical conductor for the same inter-coil separation.

variety of different instrument manufacturers. The program is used to invert the data to produce a layered-earth model in which the true conductivity of each layer and its associated thickness are estimated. Synthetic values of apparent conductivity are calculated for the selected model and compared with those actually observed. The computer model is automatically adjusted until the difference between the measured and observed apparent conductivities satisfies some statistical criterion, for example, a RMS error of less than 2%. The final output of the program is a vertical depth–true conductivity profile. Some versions of the software allow equivalence testing (see also Chapter 7). Correlation with borehole data can help to constrain the model layer thicknesses in order to obtain more realistic values for the layer true conductivities.

While the model so obtained may be statistically adequate, the question of geological reasonableness still has to be asked. For APEX MaxMin data, a series of master-curve phasor diagrams can be produced where the number of layers and their respective conductivity

values and thicknesses can be estimated from the fit with the observed phasor diagram. An example of an interpretation is shown in Figure 11.13.

An extension of the depth-sounding interpretation is the profile inversion. Instead of having one set of sounding data, a series of values of apparent conductivity for each inter-coil separation and dipole orientation are obtained along a survey line at discrete intervals. The ensuing apparent conductivity profile can also be inverted using the same program by taking each sounding and using the derived model as the starting model for the next adjacent sounding and moving along the profile, sounding by sounding. The final output is a pseudo-geological two-dimensional section displaying true conductivities and layer thicknesses along the profile line. It is important that sufficient data be collected to provide adequate sampling both spatially and as a function of depth. At least three different inter-coil separations are required for either depth-sounding or profile inversion to be achieved. As the Geonics family of EM ground conductivity meters measures relative values, and are separately nulled, the values measured cannot be compared directly between instruments. Consequently, data from the different types of instrument (EM38, EM31, and EM34) should not be modelled together. Care has to be taken in the calibration of each instrument when using more than one type on the same survey line, to ensure consistency. The variable-frequency instruments (e.g. GEM2) produce a family of data for all the frequencies measured. These can also be inverted using IX-1D v.3 to form a 1D layer model and subsequently a profile of true conductivity as a function of depth along a given traverse. However, there has yet to be an unequivocal demonstration of true depth discrimination being achieved using a fixed-dipole length, variable-frequency system. As with any modelled data, it is always sensible to test the results by using groundtruth information (e.g. from boreholes).

### 11.2.4.3 Resolution

As with any geophysical technique, consideration has to be given as to the resolution achievable. In the case of dual-coil systems, for example, a number of factors have to be taken into account in any survey if it is to be completed successfully.

Ground conductivity depth-sounding and profiling are best suited to horizontal or subhorizontal layered structures where the vertical conductivity contrast between horizons is significant. However, in environmental and engineering geophysics, EM techniques are increasingly being used at less than ideal sites. The criterion stated above is seldom applicable and, to complicate matters, the sites may often be cluttered with above-ground structures, old pipes and cables, buildings, tanks, metal fences, metal signposts, and so on, each of which may degrade the quality of data and reduce the reliability of, if not negate, any quantitative analysis. In some cases it may be possible to filter out the effects of a power line or pipe if the anomaly due solely to that feature can be identified clearly.

Edge effects associated with changes of slope, or margins of sites contained in old quarries, for example, also affect the data quality. Some of these effects can be reduced in the survey design stage if the presence of these features is known in advance.

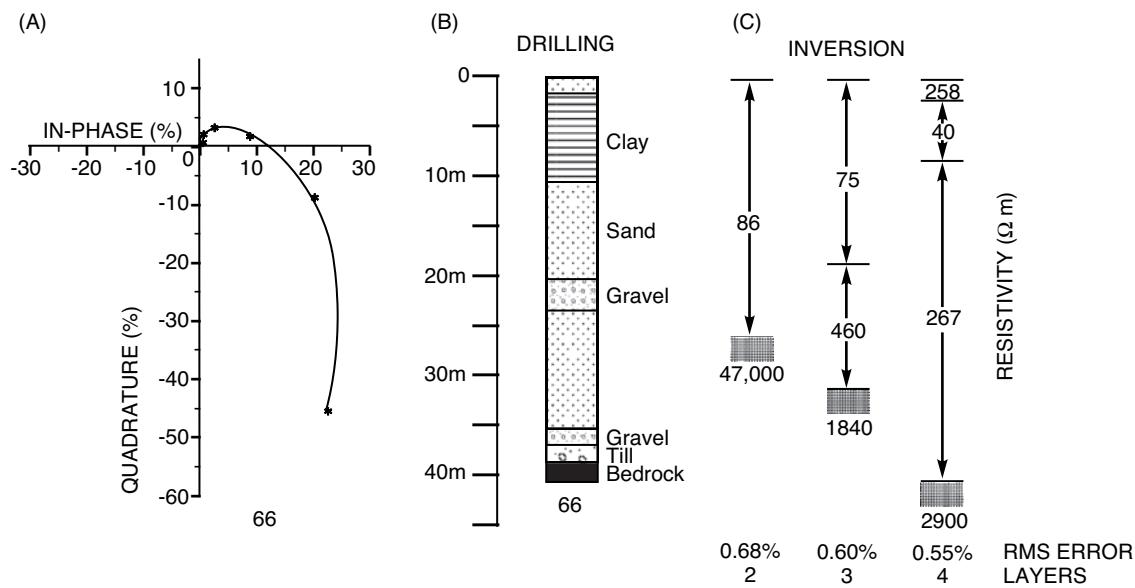


**Figure 11.13** Use of model phasor diagrams in the interpretation of HLEM data. (A) Eight frequency HLEM data acquired using an APEX MaxMin instrument; (B) the drilling log; and (C) the various inversions produced using 2-, 3- and 4-layer models. From Palacky (1991), by permission.

A further factor to be considered is the likely resolution of the method for a given type of subsurface target. The more a target deviates from being a semi-infinite homogeneous horizontal half-space (i.e. one that exists only in textbooks!), the more difficult it is to detect it. For example, consider the case of a steel drum buried at 2 m in an otherwise homogeneous ground. This target should be located readily using an EM31 given a fine enough survey grid. If, however, an EM34-3 is used with 40-m coil separations, the volume of ground being sampled is increased enormously compared with that being sampled by an EM31, and consequently the drum may be missed. Similarly, a conductive target of 1 m diameter buried at 10 m is unlikely to be resolvable with any EM method unless the utmost care is used and the site is virtually noise-free. Furthermore, a station interval of 1 m would have to be used to stand any chance of providing adequate spatial sampling. Most fixed-coil instruments now sample at rates of 5–10 times per second, so the spatial sampling along a particular profile can be very fine depending upon the speed at which the instrument travels across the ground.

A further consideration in the interpretation of EM data is the position of a subsurface target with respect to the dual-coil dipoles. If a survey is being conducted with both coils aligned along the survey transect (an ‘in-line’ configuration) with the transmitter preceding the receiver, and an apparent conductivity anomaly is observed, the source of that anomaly may not actually lie in the line of the transect but to one side (Figure 11.14). This makes the precise identification of the location of a subsurface target, such as a mineshaft, quite difficult. It is for this reason that one often finds that the location of an apparent conductivity anomaly does not necessarily coincide with that of a magnetic anomaly arising from the same metallic conductive target. This apparent lack of coincidence can lead to misinterpretation and the feature being

missed. To assist with determining lateral variability in ground conditions, it may be sensible on some sites to rotate the dual-coil system from being ‘in-line’ to being ‘broadside’ but keeping each dataset separate. Gridded and contoured maps of data from each dipole orientation can be viewed and compared. The datasets should not be merged.

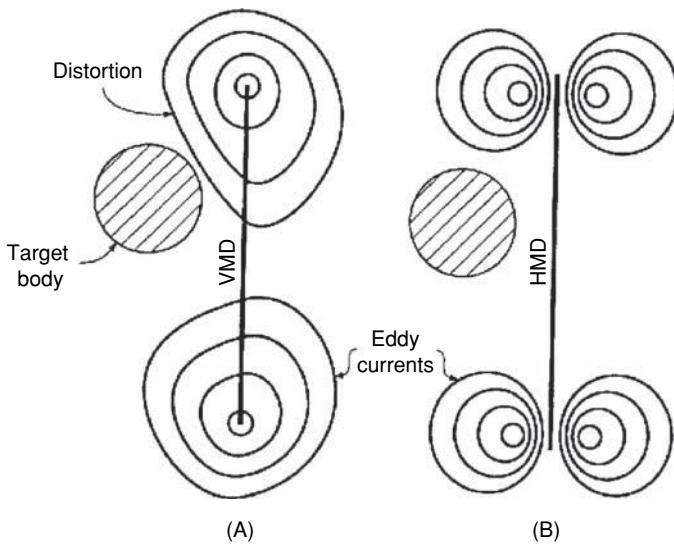


**Figure 11.14** Cartoon to illustrate the difference in eddy currents (plan view) produced by (A) the vertical and (B) the horizontal magnetic dipoles (Stoyer, 1989). A conductive (or resistive) target in a resistive (or conductive) medium will distort the eddy currents even when off the line of the survey section.

## 11.2.5 Applications and case histories

While there are a number of different types of EM instruments available, the majority of environmental case histories make reference to ground-based EM systems made by Geonics Ltd as they have been in use since the mid-1960s. Newer systems are becoming more widely available, and more case histories using these instruments will be forthcoming in due course. Additional information is available from various instrument manufacturers' websites (Appendix 1).

### 11.2.5.1 Mineral exploration

The most common use of EM techniques is undoubtedly exploration for mineral deposits, mostly as a means of locating possible targets. EM methods have been instrumental in the location of many significant economic orebodies (Frischknecht *et al.*, 1991): examples are the Temegami Mine, Ontario; the Poirier deposit, Quebec; the Faro Deposit, Yukon; the Caribou Deposit, New Brunswick; and the Kidd Creek Mine, Ontario, among many others.

EM results on their own are not usually diagnostic of whether a conductive body is economic or not. For example, it may be difficult to distinguish between a carbonaceous, a graphitic or a sulphide body purely on conductivity values alone. Consequently, other geophysical techniques, including other EM methods, are used in conjunction with each other to aid the interpretation.

There are many case histories describing the wide range of EM methods in mineral exploration, and a good number have been described by Frischknecht *et al.* (1991). It is important to note that the geophysical responses observed in one geological environment are not necessarily exactly the same in other areas. The specific geophysical responses are determined by the individual blend of mineral and structural associations present at a given site and, in some cases, may be unique to individual geographical locations.

One example is given here to illustrate the combined approach needed to differentiate between target types. Slingram and VLF EM methods were used by Barbour and Thurlow (1982) in exploration where long graphitic zones are common in Newfoundland. In addition, gravity data were used to help to differentiate between probable sulphide occurrences and massive sulphide deposits. At the Tulk East deposit, black graphitic shales and mudstones occur within 50 m of more conductive massive sulphides (Figure 11.15). Both quadrature and in-phase EM components (expressed as a percentage of the primary field) were measured using a MaxMin horizontal loop system. Two frequencies were used (222 Hz and 3555 Hz) but the greatest difference between target types was observed on the higher-frequency dataset (Figure 11.13). The massive sulphide deposit also gives rise to a peak in both the Bouguer gravity profile and the Fraser-filtered VLF transect.

A second example is presented which shows how important adequate signal processing may be to locating a mineral target accurately. A Turam profile across the Kimheden orebody in north Sweden (Parasnus, 1991) is shown in Figure 11.16A. Two components (reduced ratio and successive phase difference) are plotted as a function of distance and both show very distinctive positive (RR) and negative (phase difference) anomalies over a steeply dipping

pyrite orebody. The point of occurrence of an orebody is usually taken as corresponding with the reduced ratio maximum and phase difference minimum. The secondary fields calculated from the Turam profile in Figure 11.16A and normalised to the local primary field are shown in Figure 11.16B. The reduced ratio maximum is displaced by about 4 m relative to the true position of the current as revealed by the secondary fields. While a 4 m discrepancy in position may have little importance for shallow drilling, in cases where deeper drilling is required, this lateral shift could result in the subsurface target being missed or inadequately sampled.

An example of the use of HLEM has been presented by Palacky (1991) in an investigation over a conductor buried beneath Quaternary sediments in northeastern Ontario, Canada. An Apex Max-Min-I (eight-frequency) system with an inter-coil separation of 100 m was used along a 1 km profile south of Fraserdale. In-phase and quadrature components measured at each of eight frequencies are shown in separate families of graphs in Figure 11.17. It is clear that around station 600, the in-phase component goes negative and a corresponding trough-shaped anomaly is evident in the quadrature component data. The width of this anomaly at the zero level is equivalent to the inter-coil separation plus the width of the conductor. The character of this particular anomaly is typical of a narrow subvertical bedrock conductor of high conductance. In the case of a mineral exploration survey, such an anomaly would be indicative of a possible target zone. The reversal of the trough-shaped anomaly on the quadrature data at 14,080 Hz around station 600 (upside-down with respect to the other graphs) is a result of the presence of a moderately conductive overburden. The Quaternary sediments locally present comprise alternating clay-sand units 37 m thick, with 2 m of clay over 8 m of sand, 22 m of glacial till and 5 m of sand.

In contrast to the above example, Palacky (1991) also presented a HLEM profile over shear zones covered with thick clay (Figure 11.18) along a 12 km profile south of Kapuskasing, about 80 km southwest of Fraserdale, Ontario. Two shear zones are indicated around stations -375 and -635. A drill-hole located at station -500 passed through 35 m of massive clays. The measured amplitudes of both components are much larger than in the previous example and are due to the presence of the very conductive clay. The quadrature data are negative at the four highest frequencies, while the in-phase component is negative at 14,080 Hz.

Phasor diagrams obtained for HLEM data at three locations with different sediment types and at which borehole control was available are shown in Figure 11.19, with the simple borehole results. The phasor diagram for borehole 42 (which lies on the profile shown) shows that the fit between the measured data (as indicated by asterisks in Figure 11.19A) and the calculated response of the model (solid line) is imperfect. The overburden thickness was constrained at 35 m (the depth to bedrock as determined by drilling). However, an unconstrained inversion for a 2-layer model produced an interpreted thickness of 42 m and resistivity values of 51  $\Omega\text{m}$  for the upper layer and 8000  $\Omega\text{m}$  for the bedrock. The discrepancy of 7 m in depth estimates can be attributed to the effect on the HLEM response of the shear zones nearby.

The phasor diagram associated with the location of borehole 67 indicated a depth of overburden of 40 m with a resistivity of 210  $\Omega\text{m}$

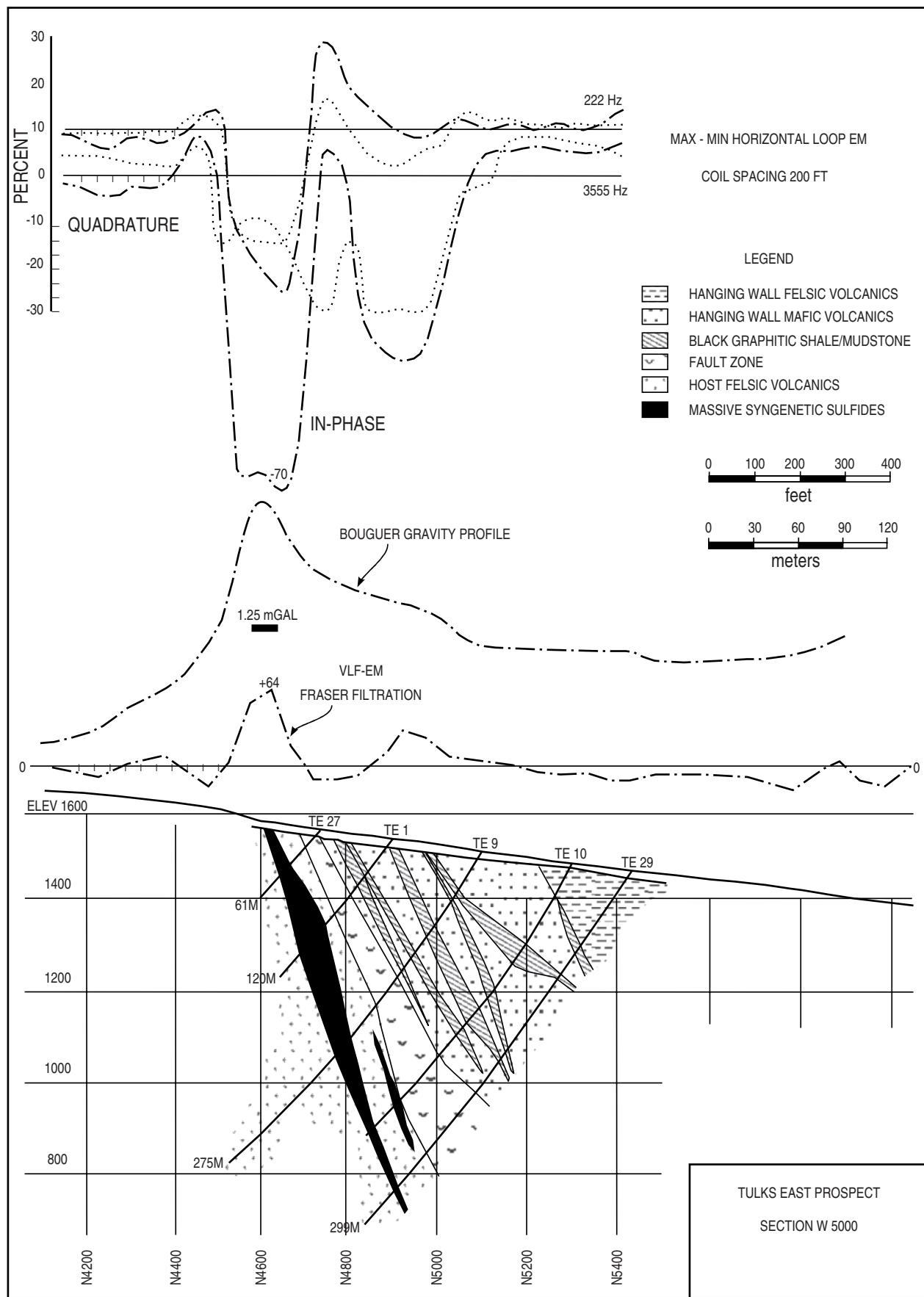
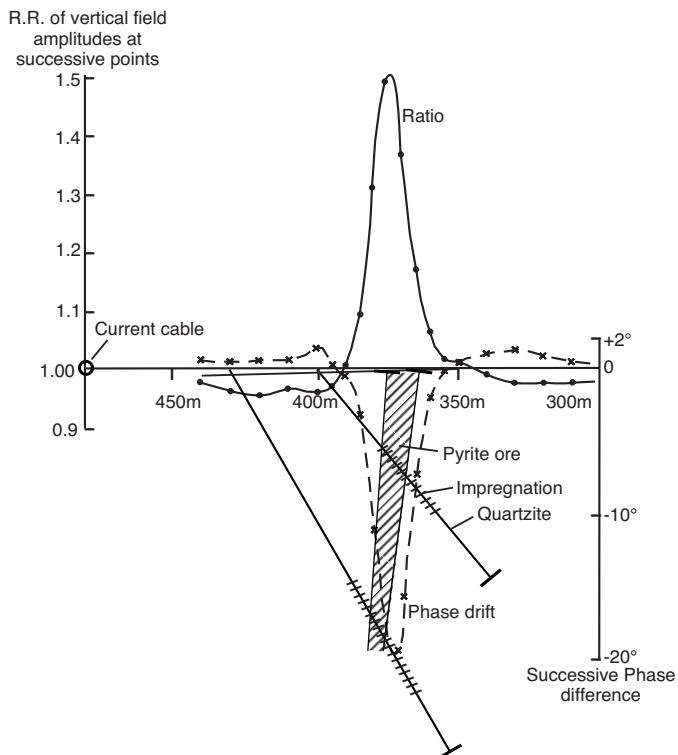


**Figure 11.15** HCP slingram, VLF, and Bouguer gravity profiles across the Tulk East Prospect, Newfoundland. The massive sulphide can be distinguished from graphitic shale at 222 Hz by the greater conductance of the sulphide. From Barbour and Thurlow (1982), by permission.

(A)



(B)

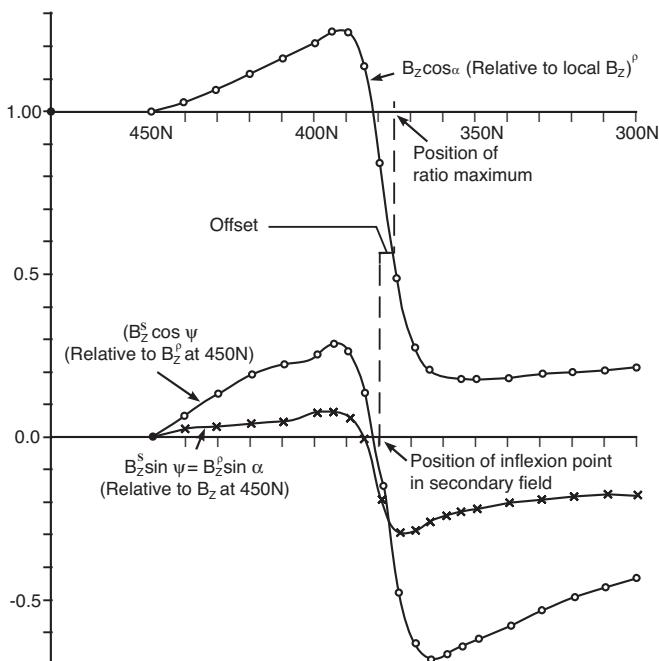


**Figure 11.16** (A) Turam profile across the Kimheden orebody in north Sweden, showing reduced ratio (RR) and successive phase differences. (B) The secondary field calculated from the Turam profiles in (A). Note the slight offset in location of the position of the RR maximum and that of the point of inflection in the field. From Parasnis (1991), by permission.

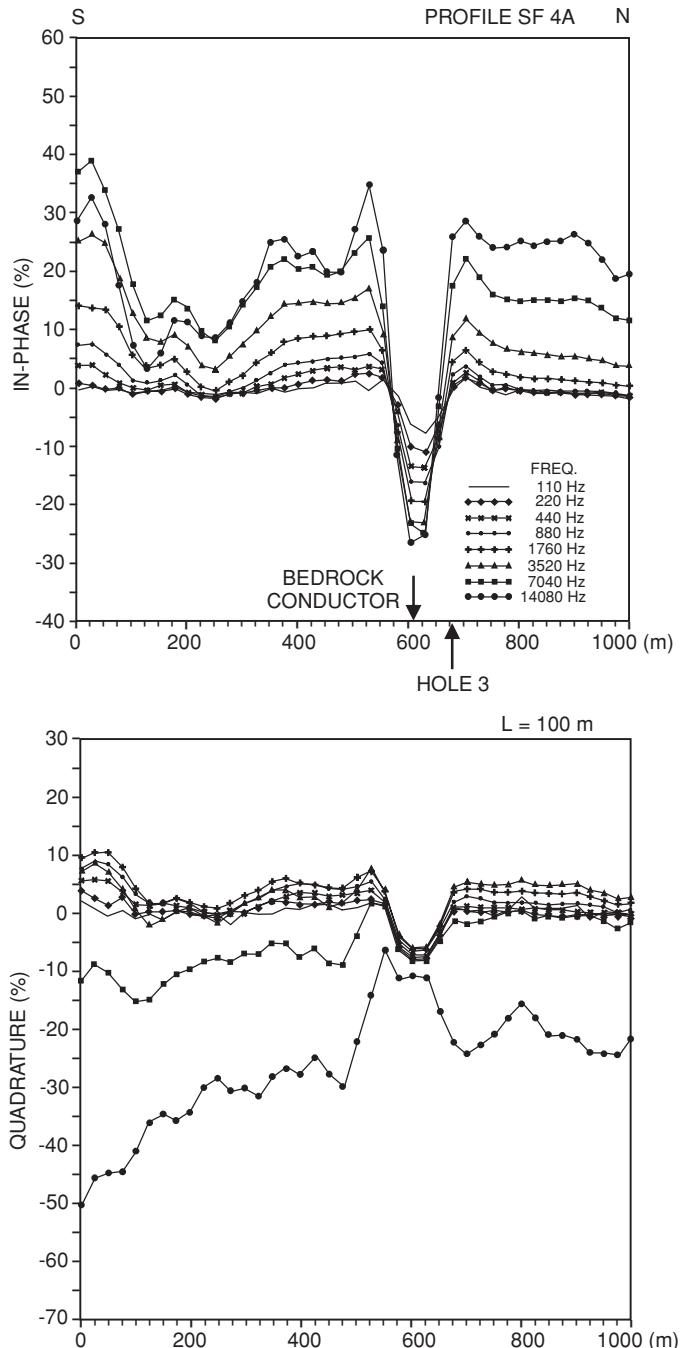


**Figure 11.17** HLEM profile over a 1000 m line, 20 km south of Frasdale, Ontario, over a bedrock conductor (at station 600) covered by Quaternary sediments. In-phase (top) and quadrature (bottom) data were acquired at the frequencies specified. Coil separation is 100 m. The location of borehole 3 is indicated. From Palacky (1991), by permission.

from an unconstrained model (Figure 11.19B). The drilled depth to bedrock was 39 m, which is in very close agreement. However, the bedrock resistivity was poorly resolved.

The third phasor diagram (Figure 11.19C) was obtained over thick sand. The best-fit model obtained produced an overburden

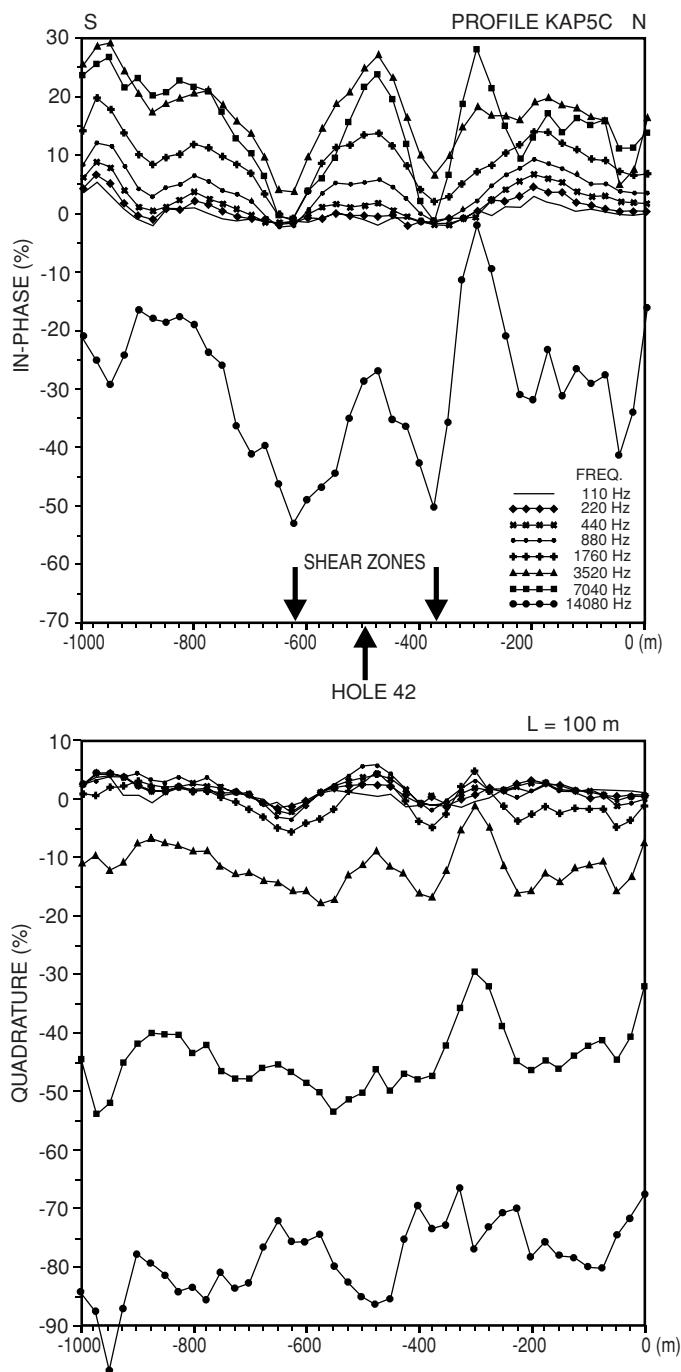


**Figure 11.18** HLEM profile over a 1000 m line, 12 km south of Kapuskasing, Ontario, with shear zones concealed by thick clay. From Palacky (1991), by permission.

41 m thick with a resistivity of 350  $\Omega\text{m}$  over bedrock with resistivity 500  $\Omega\text{m}$ . However, when the resistivity values are large and the contrast between layers is small, the determination of layer thicknesses becomes unreliable. Drilling in this case only went through 32 m of sand when the hole was terminated, as there was little point in going deeper through an esker where no basal till was expected.

These three examples provided by Palacky demonstrate the effectiveness of the use of HLEM profiling to locate shear zones

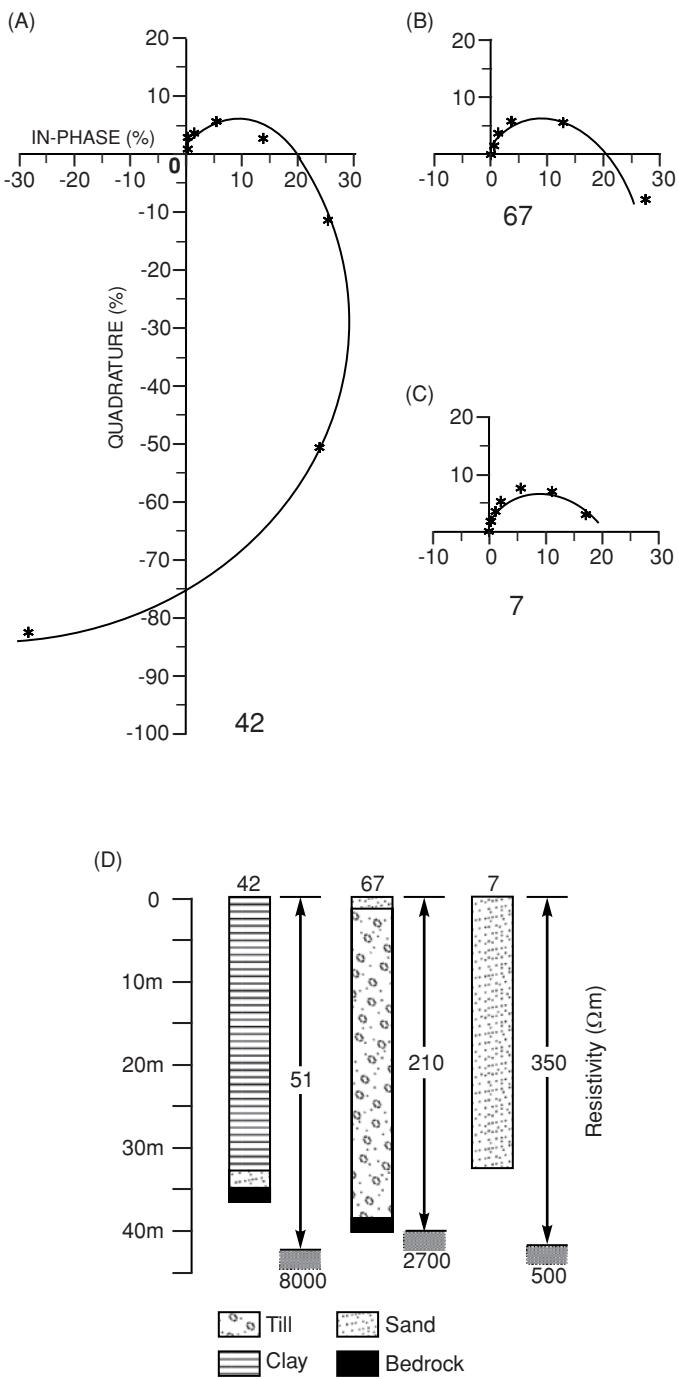


**Figure 11.19** (A)–(C) Phasor diagrams, and (D) corresponding borehole results, with HLEM-derived models over three sites with contrasting sediment types. (A) = thick clay adjacent to a shear zone (hence the discrepancy in depth estimates between the borehole and the HLEM model); (B) = glacial till; (C) = thick sand within an esker. From Palacky (1991), by permission.

and conductive targets beneath Quaternary sediments. The method produces phasor diagrams characteristic of the types of sediments present with different associated resistivities. The types of phasor diagrams can be used to help to discriminate between different material types and has obvious benefits in geological mapping.

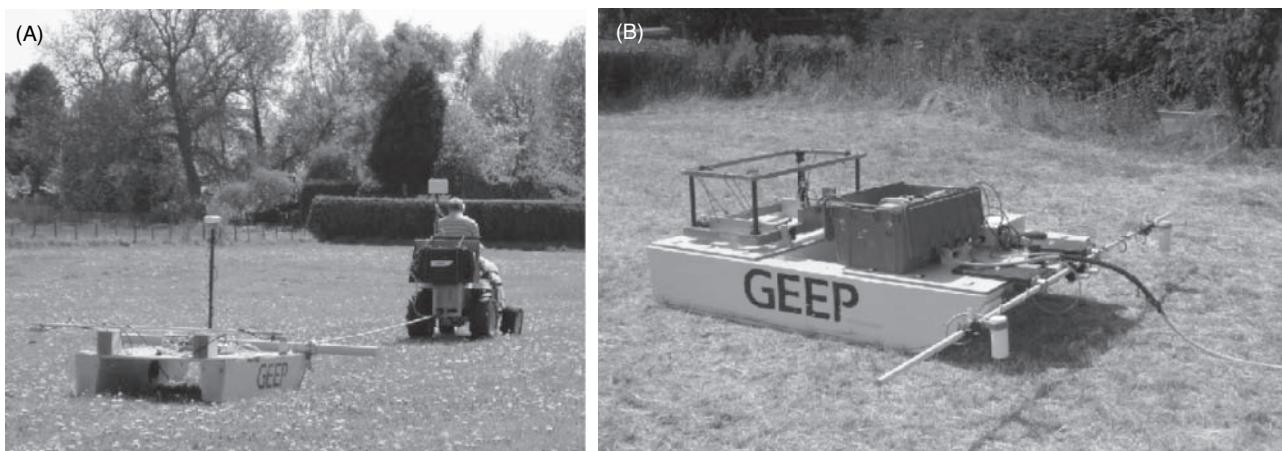


**Figure 11.20** Geophysical Multi-Sensor Platform or GEEP (A) equipped with two caesium magnetometers with a GPS antenna, and (B) with two magnetometer sensors (white pots on the front) and a Geonics EM61 dual coil system at the rear. Courtesy of Geomatrix Earth Science Ltd. [C]

In contrast to the examples above, several sensors have been deployed on a single platform, originally called a Multi-Sensor Platform (MSP; Figure 11.20A, Hill *et al.*, 2004), for an investigation of a site that forms part of the South Pennine ore field in Derbyshire. The local geology comprises a thick Carboniferous limestone succession with interbedded basic lavas. The lavas have been heavily altered and are clay-rich, making them electrically conductive and magnetic relative to the limestones. The location of the lavas is important with respect to mineralisation. The MSP had two caesium-vapour magnetometers with a horizontal separation of 2 m across the line of travel. In addition an EM31, EM38 and gamma-ray spectrometer were also deployed. The whole platform was towed behind a quad bike. The magnetometer data were used to provide information on the location of the basic lavas. The MSP has since been developed and commercialised into what is now known as the Geophysical Exploration Equipment Platform (GEEP; Figure 11.20B; Hill, 2008) which has exploited developments in dGPS and WiFi data communications.

Hill (2008) has described the use of the GEEP in a mineral exploration programme for the investigation of sand and gravel deposits at a site near Shelford, Nottingham, UK. For this the GEEP hosted EM31 and EM34-10 systems from which data are telemetered in real time to a static base station. The data from up to six systems can be logged simultaneously. The platform is towed by a quad bike; dGPS antennae are mounted on both the quad bike and on the GEEP itself. The survey area covered 63 hectares ( $0.63 \text{ km}^2$ ) and was made up of 80 line-km with 213,000 data values recorded just with the EM31. The entire investigation took only 12.6 hours over two days. Gridded apparent resistivity data acquired using the EM31 (Figure 11.21) show marked variation over the mineral deposit. Higher resistivity values correspond to coarser gravel. At the southeastern edge of the site there is a distinct step change in the resistivity values, which decrease to below  $20 \Omega\text{m}$  over mudstones. In the middle of the survey area, the resistivity data reveal a V-shaped anomaly which is thought to be a complex set of channels within the deposit.

### 11.2.5.2 Groundwater investigations

Electromagnetic methods have been demonstrated to provide a powerful suite of tools in hydrogeological investigations since the late 1970s. The methods lend themselves to environments where conductivity contrasts are high, but the ground surface precludes the simple deployment of DC resistivity methods owing to high surface resistances such as are found in very arid regions. There has been substantial development in the use of electrical and electromagnetic methods in hydrogeophysics.

Two approaches tend to be taken. One is for the general investigation of a groundwater regime, where the groundwater is prevalent within aquifers. The second approach is to search within the local bedrock for fractures that may contain small but usable reservoirs of potable water. The frequency-domain EM methods are generally used for near-surface mapping investigations within a hydrogeological investigation. For deeper investigations, TEM methods are used (see Section 11.3.3.1).

Mitsuhata *et al.* (2006) have described a comprehensive multi-system EM survey to investigate the distribution of saline groundwater in the Kujukuri coastal plain, southeast Japan, as illustrated schematically in Figure 11.22. This area comprises a coastal sandy ridge about 60 km long and 10 km wide. Quaternary formations forming the plain consist of marine sandstone and mudstone deposits over 3 km thick and have been formed by marine regression over the last 6000 years. Part of the sediment contains water-soluble natural gas and iodine that have been exploited commercially historically. Three different EM systems were used to investigate the saline groundwater: at the largest scale, AMT was used along a profile perpendicular to the coast and consisted of 22 stations. The resistivity section estimated by 2D inversion is shown in Figure 11.23. A very conductive zone ( $\sim 1 \Omega\text{m}$ ) is evident below about 100 m depth. This is the zone containing water-soluble gas and iodine dissolved in brine. The  $\text{Cl}^-$  concentration of this old brine is almost equal to that of seawater. Above this zone is a thin layer with a resistivity of  $\sim 3 \Omega\text{m}$ , less conductive due to dilution of the  $\text{Cl}^-$  by

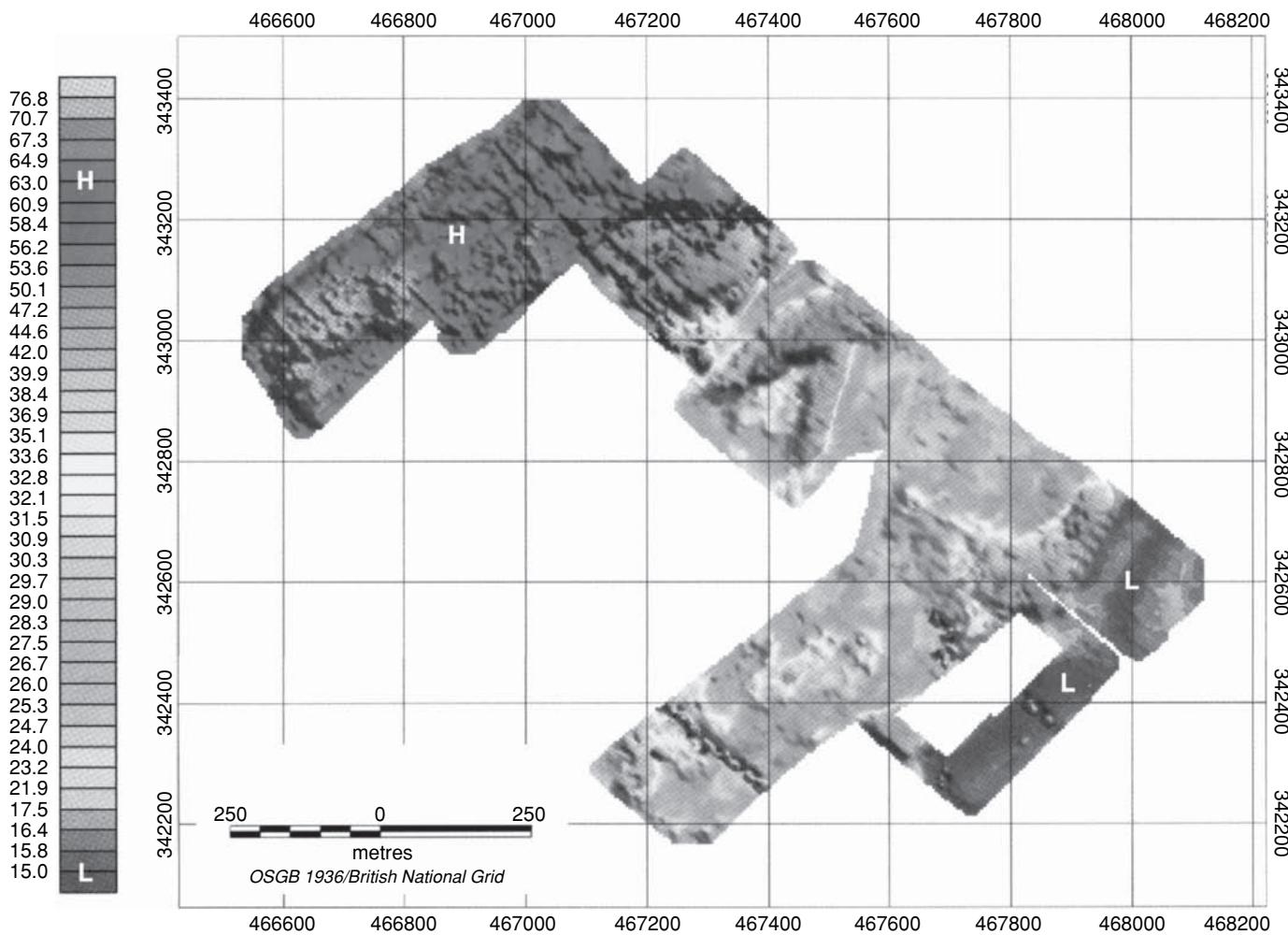


**Figure 11.21** EM31 apparent conductivity data collected over a sand and gravel deposit. From Hill (2008), by permission. [C]

rainwater. Between S18 and S22 (Figure 11.23) there is a relatively resistive zone shallower than about 150 m. This is associated with highly permeable sand or gravel layers and is part of the recharge area. The entire plain is covered by resistive, highly permeable sandy ridge and dune deposits.

A TEM survey was undertaken along a shorter profile (indicated by the dashed box in Figure 11.23) at stations S1–S10 using a Geonics PROTEM47 and a central-loop configuration with a 50-m sided square transmitter loop. By juxtaposing 1D inversions of the TEM data, a resistivity section was constructed which shows the variation

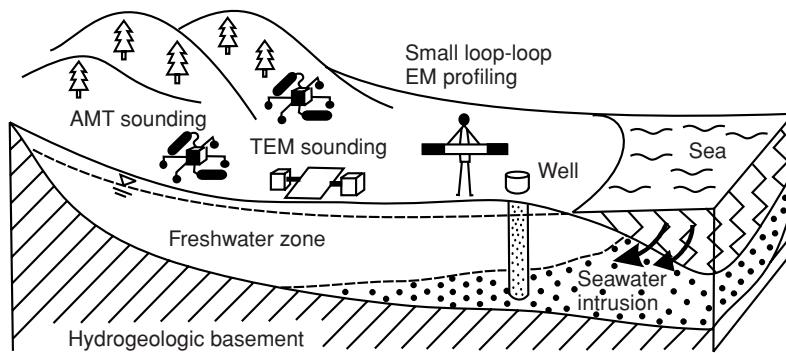


**Figure 11.22** Schematic diagram of three EM methods used in an investigation of seawater intrusion on the Kujukuri coastal plain, southeast Japan. From Mitsuhata *et al.* (2006), by permission.

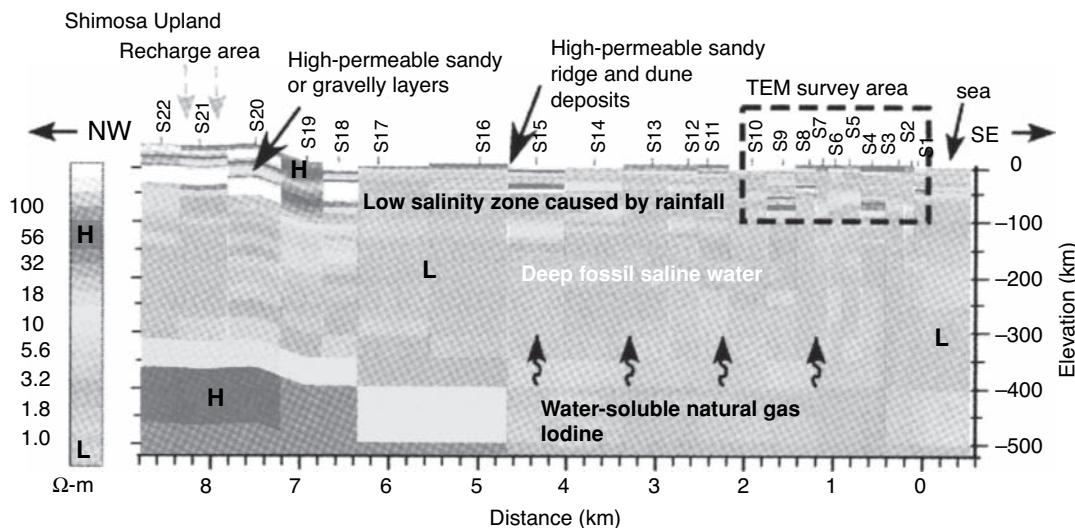


**Figure 11.23** Resistivity section estimated by 2D inversion of AMT data. The extent of a TEM survey (Figure 11.24) is indicated by the dashed rectangle. From Mitsuhashi *et al.* (2006), by permission. [C]

of resistivity along the profile to a depth of 100 m (Figure 11.24). At stations S1–S3, a very conductive zone is evident at a depth of about 30 m, and is thought to be caused by seawater intrusion as this area is closest to the shoreline. Another conductive zone is found between S5 and S7 at a depth of about 20 m. Being shallower, it is not thought that this zone is caused by saline intrusion. Instead, it is inferred that this conductor corresponds to salt-marsh deposits. Beach ridges may have formed on the seaward side of this zone during sporadic regressions such that a lagoon formed on the opposite side, which then turned into back marshes containing conductive high-salinity porewater. To investigate this further, the area indicated by a dashed rectangle in Figure 11.24 was surveyed using a small-loop EM system (GEM2) along profile line G1.

The GEM2 profile consisted of 168 stations located at 5-m intervals, and nine frequencies between 325 Hz and 47 kHz were transmitted at each station. Thirty-one data points were recorded at each frequency. The quadrature component, recorded at four

frequencies along the profile, was spatially averaged (Figure 11.25) and used in smoothness-constrained 1D inversions at each station. An example inversion from station  $x = 800$  m is shown in Figure 11.26. The resolvable depth range is considered to be down to 10 m. By amalgamating the 1D inversion results along the profile, a resistivity-depth section was produced (Figure 11.27). Two resistive sandy ridges are clearly defined and are presently being used as dry vegetable fields (see also in Figure 11.25). These form unconfined aquifers recharged by rainfall. At the lower right-hand corner of Figure 11.27 is a conductive zone, which is thought to be associated with the high-salinity salt-marsh deposits identified in the TEM survey.

Love *et al.* (2005) have presented a combined helicopter-borne and ground-based EM survey campaign in the Kettle Creek watershed, north-central Pennsylvania, USA, an area that has been heavily impacted by coal mining. Specifically, the survey was to locate mine discharges, map acidic pools in underground mines, and identify

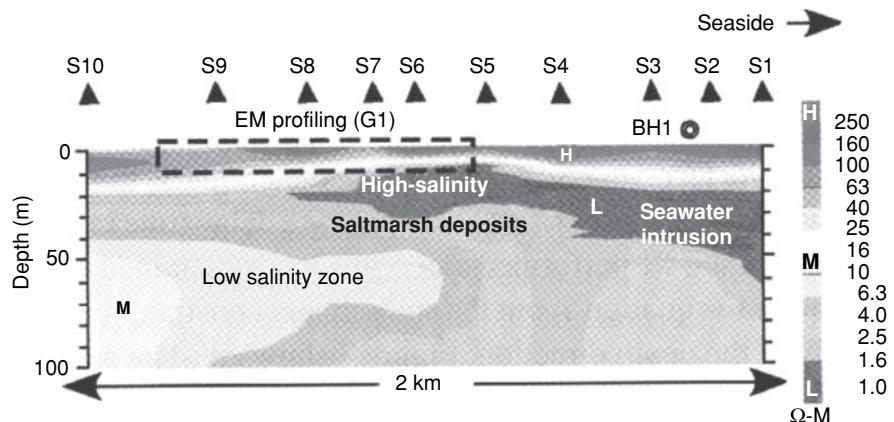


**Figure 11.24** Resistivity section constructed by juxtaposing 1D inversions of TEM data for the region shown by the dashed rectangle in Figure 11.23. The extent of EM profiling using a GEM2 is shown by a further dashed rectangle. From Mitsuhashi *et al.* (2006), by permission. [C]

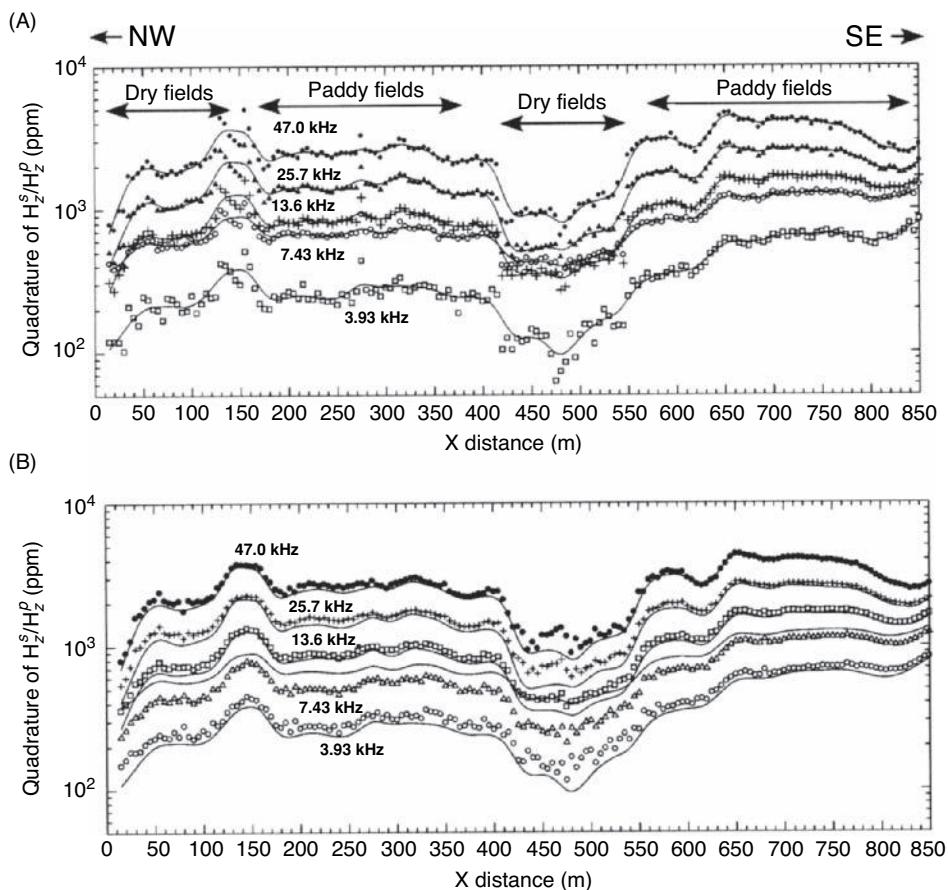


**Figure 11.25** (A) Quadrature component GEM2 data (symbols) and spatially-averaged values (solid lines) for the profile G1 shown in Figure 11.24. (B) Comparisons between the spatially averaged values (solid lines) and responses calculated using 1D inversions (symbols). From Mitsuhata *et al.* (2006), by permission.

spoil material generating acid drainage. The *h*-EM survey was undertaken in 2002 using the RESOLVE *h*-FEM system with a line spacing of 50 m and average sensor height above the terrain of 33.5 m. Data from this survey have been presented in two formats: (a) colour contour maps of apparent conductivity for each frequency

used, and (b) conductivity depth images (CDIs) that illustrate the conductivity (mS/m) distribution with depth along the flight lines. Apparent conductivity maps for four frequencies are shown in Figure 11.28A–D, with a map of the mine pools identified shown in Figure 11.28E. Two examples of CDIs, which were generated using

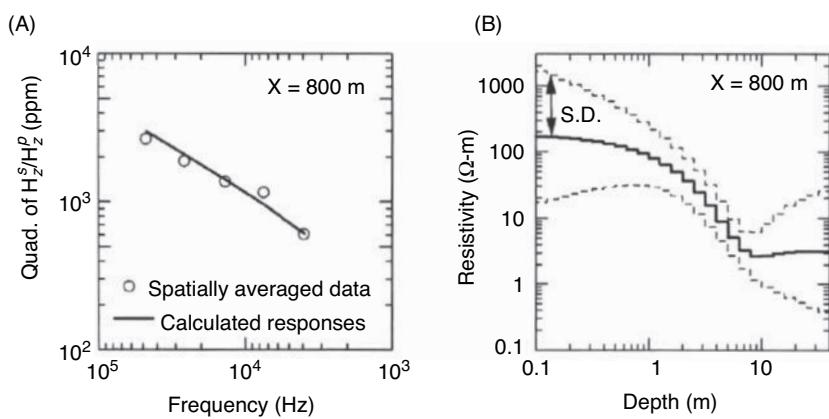


**Figure 11.26** (A) Smoothed GEM2 quadrature data obtained at  $x = 800$  m along profile line G1 and the 1D inversion results, with standard deviation (S.D.) indicated. (B) Resistivity profile obtained by 1D inversion of the smoothed quadrature data. From Mitsuhata *et al.* (2006), by permission.

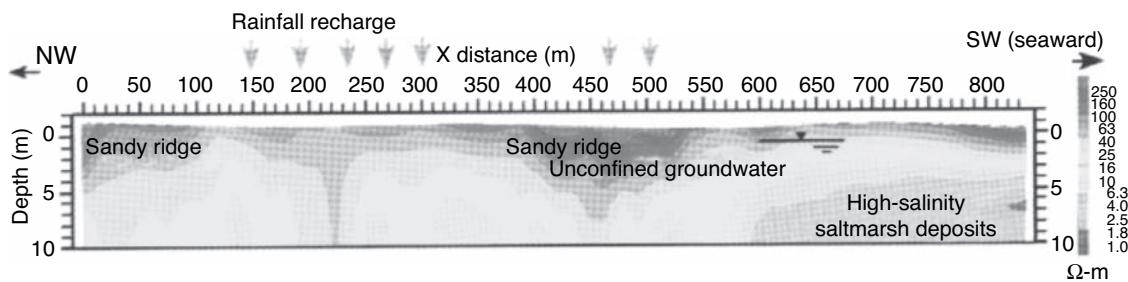


**Figure 11.27** Resistivity section along G1 compiled from 1D inversions of GEM2 quadrature data for the region shown by the dashed rectangle in Figure 11.24. From Mitsuhashi *et al.* (2006), by permission. [C]

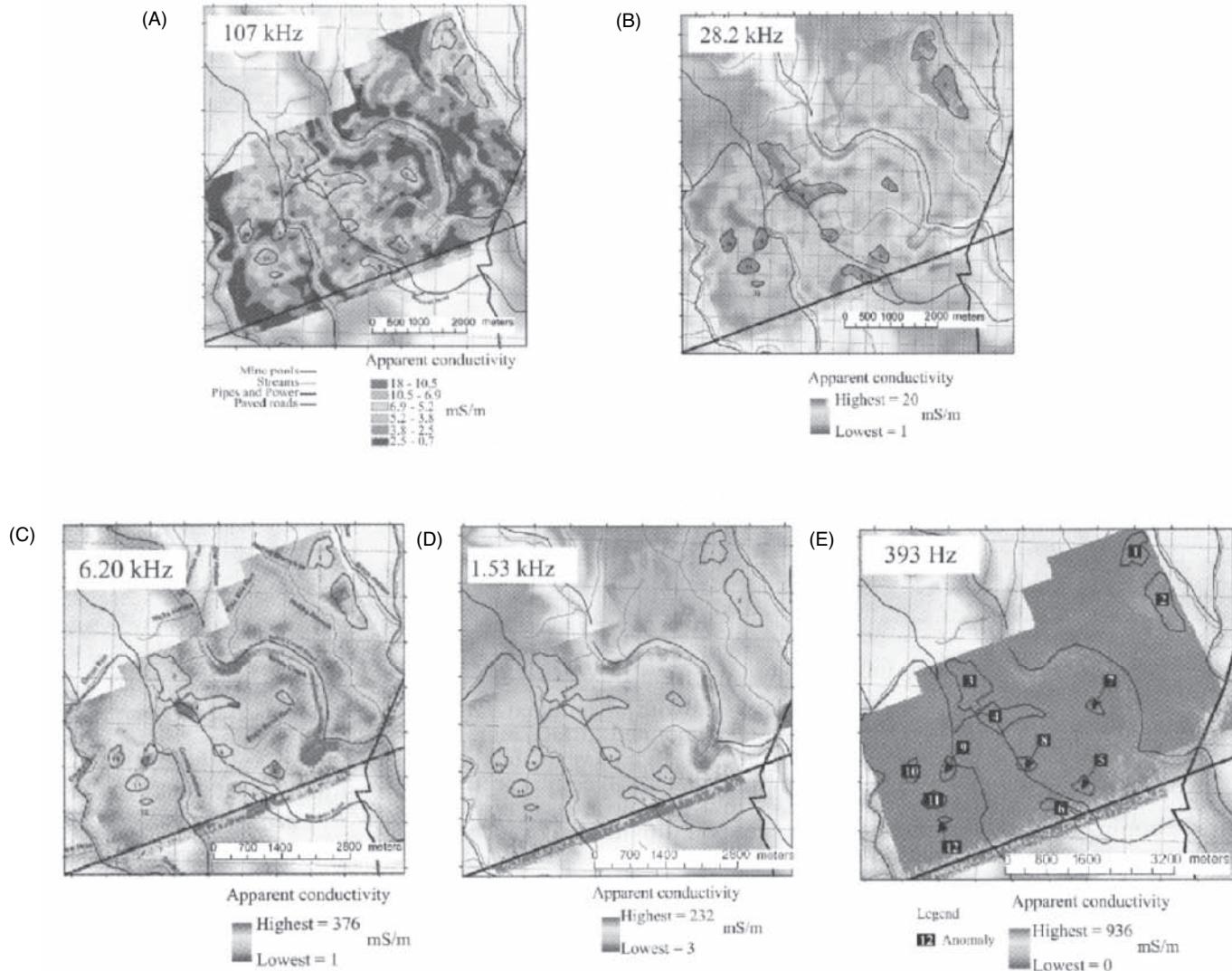


**Figure 11.28** HMEM survey across the Kettle Creek watershed, north-central Pennsylvania, USA. Apparent conductivity maps at (A) 107 kHz, (B) 28.2 kHz, (C) 6.2 kHz, (D) 1.53 kHz, and (E) 393 Hz; mine pools 1-12 defined from the HMEM survey are labelled. From Love *et al.* (2005), by permission. [C]

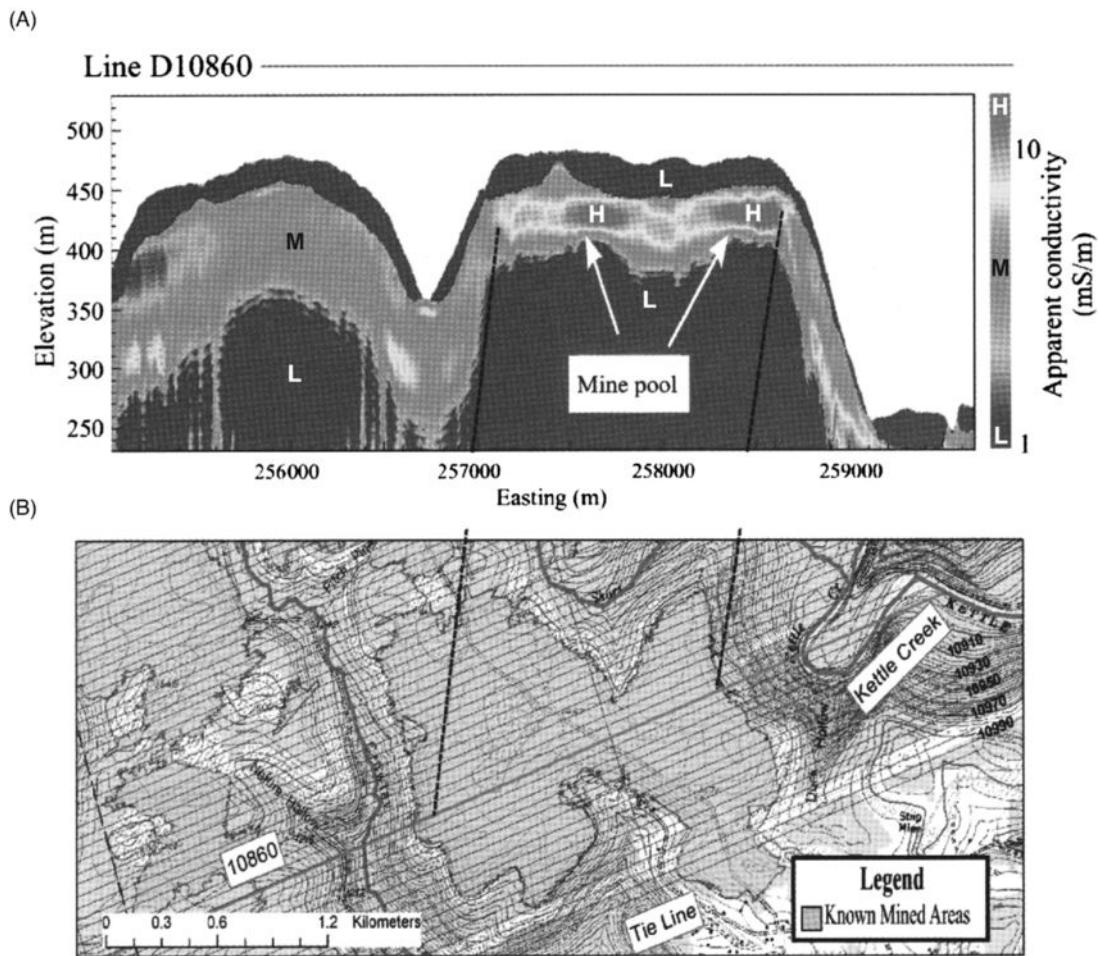


**Figure 11.29** (A) Conductivity depth image (CDI) indicating an apparent conductivity anomaly directly over a water-filled abandoned underground mine. (B) Georeferenced abandoned mine map indicating the location of the flight line and AMD-filled abandoned subsurface mine (mine pool). From Love et al. (2005), by permission. [C]

Encom Technology's EM Flow software, are shown in Figures 11.29 and 11.30. Figure 11.29 combines a mine map of an identified mine pool with an inset CDI for a flight line that crosses the pool, with the edges of the apparent conductivity anomaly identified in the CDI and interpolated onto the mine map, showing the high level of correlation between the two datasets. The second figure shows a CDI which is interpreted to show a mine pool and a breach of the barrier coal (outlined in black) by highly conductive acid mine drainage (AMD). Figure 11.30B is an enlargement from the main CDI in Figure 11.30A. Figure 11.30C shows an extract of the apparent conductivity map at 6.2 kHz across the abandoned mine pool anomaly 2. Its location is shown in Figure 11.28E.

Ground-based FEM profiles were conducted using a Geonics EM34-3XL ground conductivity meter along the ground paths coincident with two flight lines. The EM34 data for one line are shown in Figure 11.31, and *h*-FEM at two frequencies that most closely correlate in terms of skin depth and sensitivity. The *h*-FEM survey, being flown above the ground surface, has a larger footprint and thus lower spatial resolution than the ground-based EM34 survey. However, there is relatively good correlation between the ground-

based and *h*-FEM results. An extract from the corresponding CDI for this flight line is shown in Figure 11.31C. A surface barrier pillar was detected between the underground mine pool and conductive spoil back-filled against a high wall. This can be seen on the CDI (Figure 11.31C) represented by the break in the conductive anomaly for Flight Line 10300. This resistive surface barrier is also evident on the EM34 data (arrowed in Figure 11.31B). Overall, the comparison between the EM34 data and *h*-FEM results indicate that the EM34 responses in both dipole orientations were best matched against the 28-kHz data when the near surface was conductive, and with the 107-kHz data when the near surface was resistive.

The final groundwater case history has been provided by Lipinski et al. (2008), who have described using *h*-FEM surveys to evaluate disposal of water produced from coal bed natural gas (CBNG) production in the Powder River Basin, Wyoming, USA. CBNG is extracted by lowering a submersible pump into a well and extracting water from the underlying coal. This reduces the reservoir pressure and causes methane to desorb from the coal surface. The water is brought to the surface through tubing within the well, while the methane flows to the surface in the free space between the

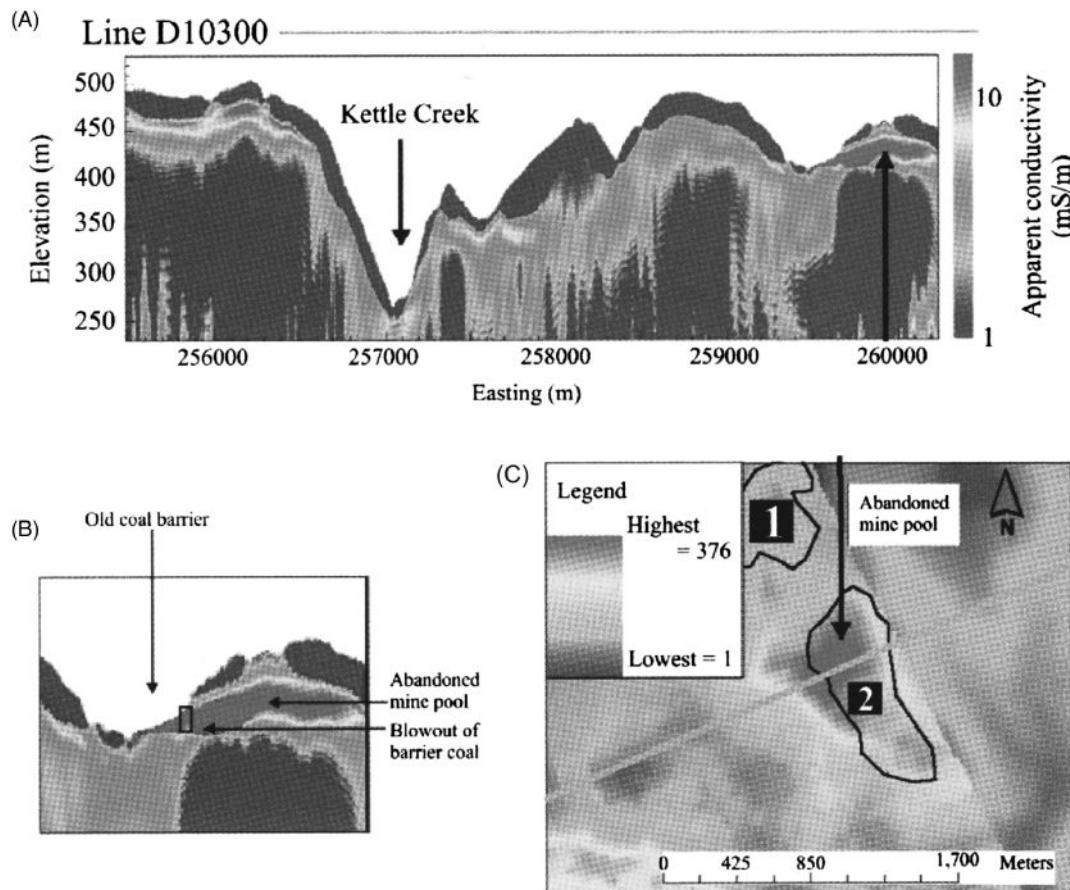


**Figure 11.30** Identification of an abandoned mine using a conductivity depth image (CDI) and apparent conductivity. (A) Along flight profile 10300; (B) identification of an abandoned mine pool and blowout of barrier coal in the unmapped eastern side of the study area using the CDI. (C) HEM 6.2 kHz conductivity map of abandoned mine pool anomaly 2 (whose location is indicated in Figure 11.28E). From Love *et al.* (2005), by permission. [C]

well casing and the pump tubing. Wells in the Powder River Basin generate 302 litres of water per 1000 cubic ft (MCF) of gas. A cross-section illustrating the generalised geology is shown in Figure 11.32. CBNG exploration and development are concentrated on the Palaeocene Fort Union Formation and the Eocene Wasatch Formation. These comprise sandstone interbedded with siltstone, mudstone, carbonaceous shale and coal. The production target is a coal zone within the Fort Union Formation that occurs at a depth of about 230 m.

Infiltration impoundments are the most widespread method of disposal of the CBNG water by-product. An infiltration impoundment is a man-made reservoir constructed without an impermeable liner so that water can infiltrate into the subsurface. In Wyoming there are more than 1100 permitted impoundments, but little research has been undertaken to evaluate their hydrogeological impact on the alluvial aquifer receiving CBNG water from the impoundments. The use of *h*-FEM methods provides a higher spatial resolution of hydrogeological features and water quality than can be achieved using traditional geochemical sampling methods.

A RESOLVE *h*-FEM system was used with 50 m flight-line spacing and instrument terrain clearance of 33–35 m. Data were inverted

using EM1DFM (UBC-GIF, 2000) to estimate layered earth parameters and produce conductivity depth images, one example of which is shown in Figure 11.33. The geophysical data were translated into geochemical terms (total dissolved solids, mg/l) using empirical relationships where the porewater electrical conductivity ( $\sigma_w$ ) was defined as a function of the formation conductivity ( $\sigma_f$ ). The concentration of TDS was defined as being equal to  $0.8\sigma_w$ . Plan maps were produced by interpolating geophysically-inferred TDS levels at each *h*-FEM sounding to a 10-m grid. These maps represent the inferred TDS concentrations within the unconfined aquifer, but not the surface water quality in the local river of CBNG impoundments themselves. An example TDS concentration map is shown in Figure 11.34, which demonstrates the consistency of the features identified between surveys undertaken in successive years.

The *h*-FEM data have produced inferred aquifer TDS levels in the range from 780 to 9900 mg/l in 2003, and with a slightly narrower range in the following year. TDS values were found to be relatively low (~1500 mg/l) near the Powder River, with significantly higher levels (up to 9900 mg/l) further away from the river. It is suggested that the Powder River water recharges the alluvial aquifer in which evapotranspiration raises TDS concentrations. Fluvial

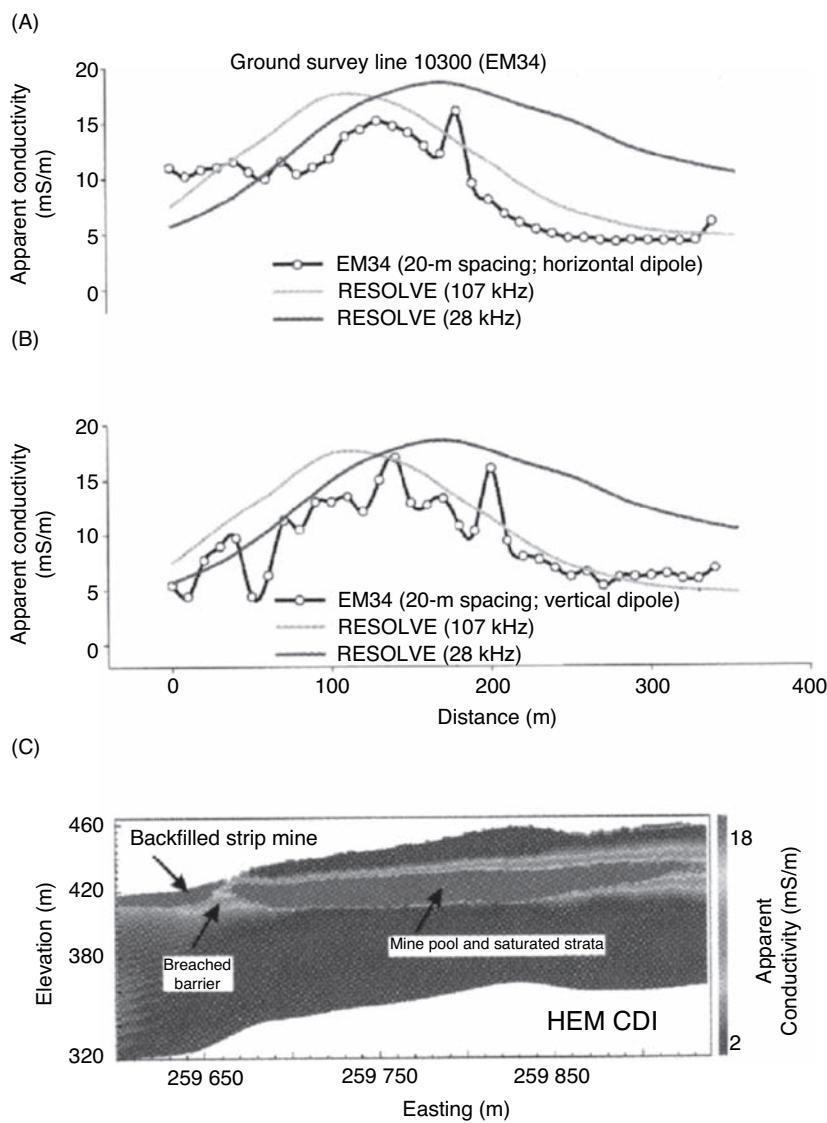


**Figure 11.31** Comparison of the airborne 107-kHz and 28-kHz responses to the EM34-3XL data collected with a 20-m coil separation with (A) horizontal and (B) vertical dipole orientations along profile 10300. (C) Conductivity depth image-derived apparent conductivity profile along the ground survey line 10300. From Love *et al.* (2005), by permission. [C]

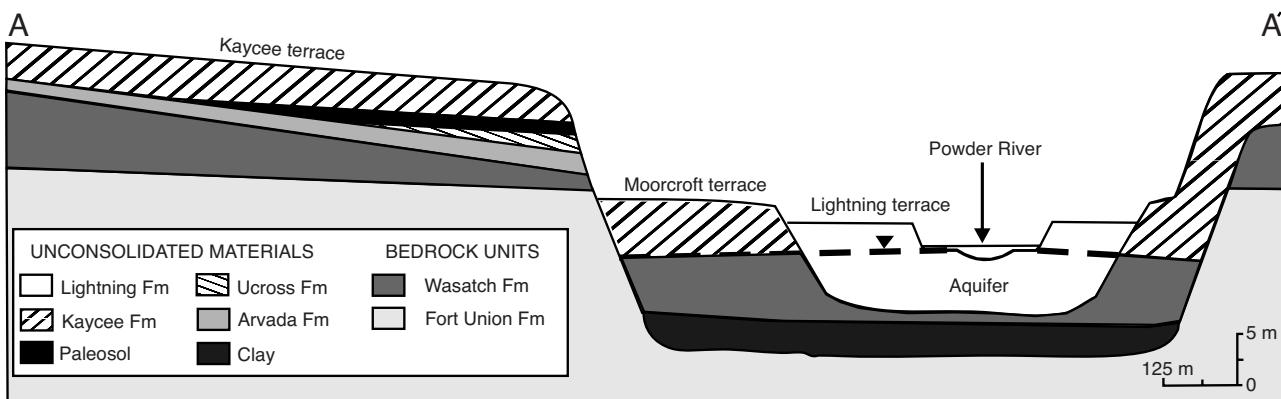


**Figure 11.32** Idealised east-west cross-section of Quaternary deposits across the Powder River Basin, Wyoming, USA. The water table surface is denoted by the solid triangle. From Lipinski *et al.* (2008). [C]

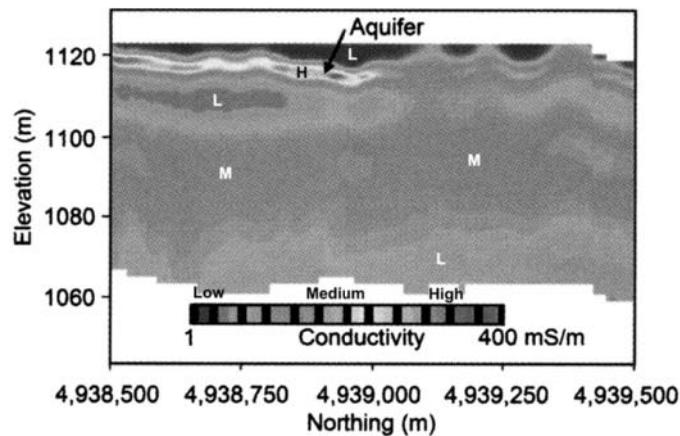


**Figure 11.33** Example conductivity depth image (CDI) depicting the interpreted aquifer location. From Lipinski et al. (2008). [C]

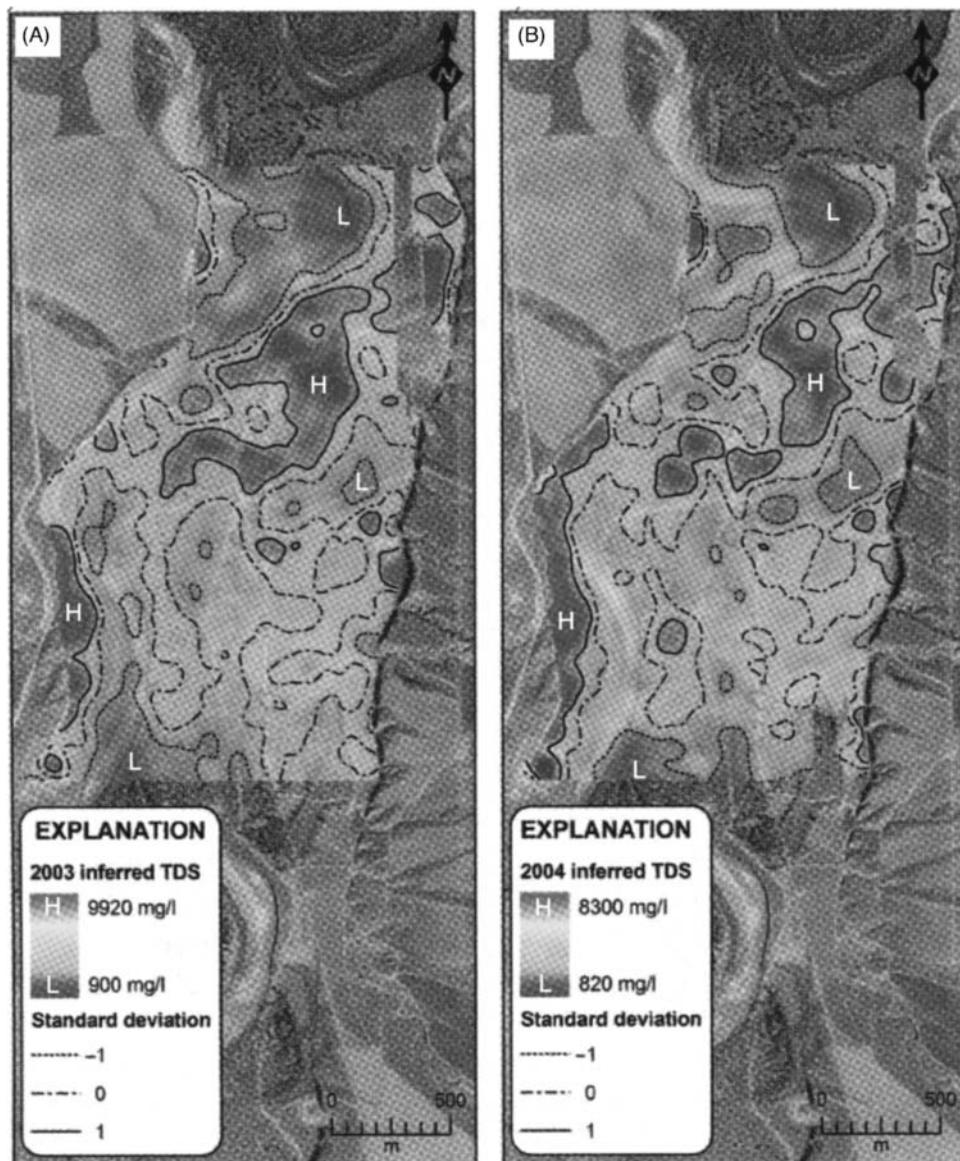


**Figure 11.34** Comparison of the (A) 2003 and (B) 2004 TDS distributions derived from HEM data. From Lipinski et al. (2008). [C]

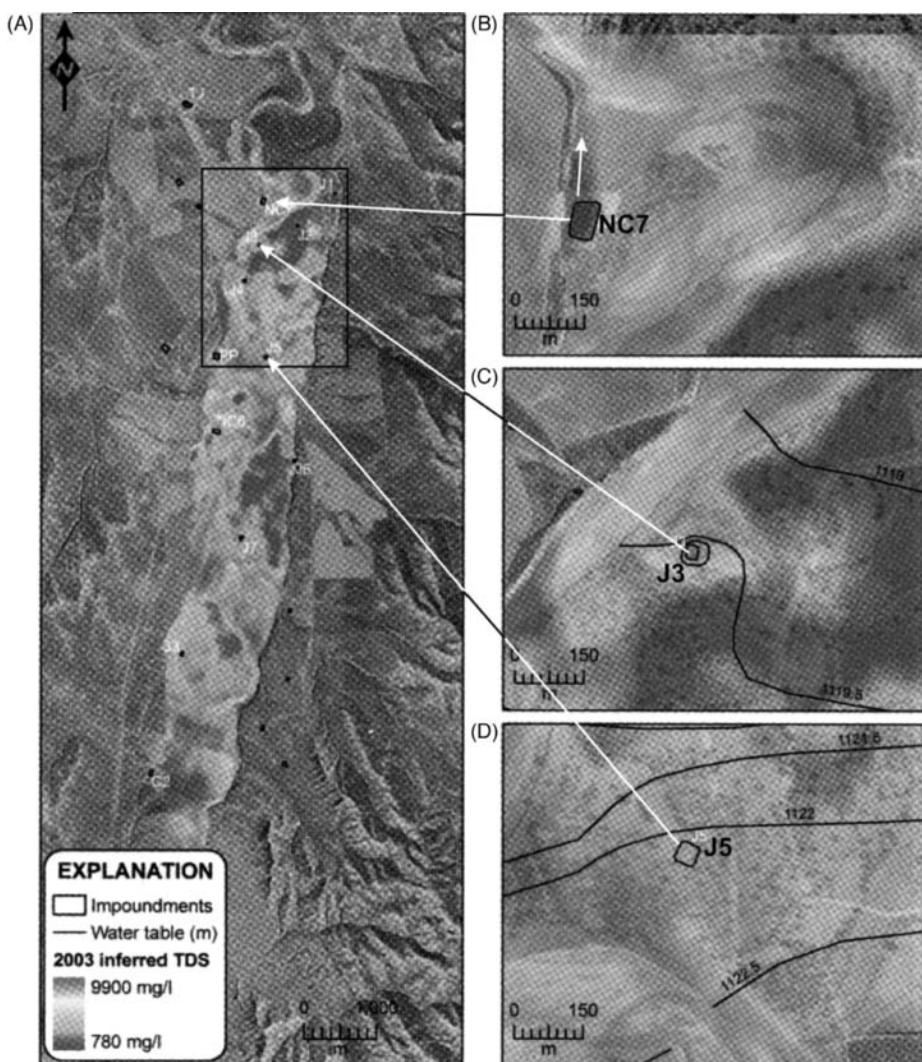


**Figure 11.35** Geophysically-inferred TDS levels in the alluvial aquifer on 25 July 2003 for (A) the entire site, impoundments (B) NC7, (C) J3, and (D) J5. Contours indicate water table levels in (C) and (D). From Lipinski *et al.* (2008). [C]

geomorphology is thought to control the inferred TDS distribution in some instances. Stream palaeochannels have higher TDS concentrations than the areas immediately adjacent to them (Figure 11.34). Conductive clay has accumulated in former oxbow lakes, which, by being low-lying, collect rainfall and runoff, thus influencing the type of vegetation present which could concentrate salts locally.

Based on the spatial distribution of inferred TDS concentrations, it was possible to determine the impact that several of the impoundments have on the alluvial aquifer. The geophysically-inferred TDS concentrations in the alluvial aquifer in 2003 are shown for the entire site in Figure 11.35A, on which the extent of the area shown in Figure 11.34 is indicated. Lipinski *et al.* (2008) interpreted three scenarios: (a) impoundments increase or (b) decrease TDS concentrations locally within the alluvial aquifer; or (c) they do not affect the aquifer TDS levels appreciably. This is demonstrated by reference to three impoundments (NC7, J3 and J5; Figure 11.35B–D, respectively).

Water TDS levels in the impoundment NC7, which is located on a point bar, were found to be around 2000 mg/l, whereas the river water was found to have a value of 1500 mg/l. However, the TDS values indicate a saline plume flowing northwards (arrowed in Figure 11.35B) towards the Powder River. White salt nodules (possibly gypsum) were observed in the vadose zone from hand-augering. It is thought that the salt accumulation has occurred as a result of the type of vegetation present.

Native alluvial groundwater around and upstream of impoundment J3 (Figure 11.35C) has TDS concentrations ranging from around 5000 to 7000 mg/l, whereas the water in the impoundment itself has a value of around 2000 mg/l. The infiltration of this water into the local aquifer effectively dilutes the TDS concentrations.

Impoundment J5 is located near a high-amplitude, low-wavelength stream meander that is thought to provide a preferential groundwater flow path from the Powder River. Native groundwater upstream of J5 has TDS concentrations around 2000 mg/l, comparable to that of the water in impoundment J5. TDS values downstream

of J5 were found to be slightly higher at 2500 mg/l (Figure 11.35D). This shows that there is insufficient contrast in TDS concentrations between the various water masses to determine the impact of the impoundment water infiltration on the local aquifer.

### 11.2.5.3 Detection of underground cavities and solution features

During a major investigation into the human biological history of the Near East, a Geonics EM31 ground conductivity meter was used as part of an archaeological study at Bab edh-Dhra in Jordan (Frohlich and Lancaster, 1986). The aim of the work was to locate and indicate the condition of shafts and tomb chambers. An example of an apparent conductivity profile over what was later found to be a shaft and two burial chambers is shown in Figure 11.36. Where a chamber was silted up, a slightly higher apparent conductivity was observed relative to a background value; where a chamber was intact (air-filled), a low apparent conductivity was observed. By mapping the excavation site with the EM31, various anomalous zones were identified. Of seven examined by direct excavation, all were found to be infilled tomb shafts about 1.5 m wide and about 2 m deep.

Where cavities are large relative to their depth, and there is good electrical contrast between the cavity and the host material, then such a feature should be readily detectable. However, small cavities with low contrasts in conductivity buried at depth are unlikely to be resolvable.

One of the many benefits of EM techniques is that they are environmentally benign and are thus suitable to use in environmentally sensitive areas. One such situation was described by Supper *et al.* (2009) who described the use of ground-based and helicopter-borne EM surveys in the investigation of karst aquifers in the Siam Ka'an

Biosphere Reserve in the Yucatán Peninsula, Mexico. They used ground-based geoelectric and EM methods to determine the electrical properties of the subsurface environment prior to committing to a helicopter-borne FEM survey. They were able to demonstrate clearly that seawater-filled caves could be detected using these techniques. One profile using a Geonics EM34 with a 10-m coil separation across a known cave branch is shown in Figure 11.37. The apparent conductivity high associated with the conductive seawater in the submerged cave is evident. The subsequent *h*-FEM survey was flown using a GEOTECH bird over a 40 km<sup>2</sup> survey area across the Ox Bel Ha cave system. The survey demonstrated that the signature of the cave system could be detected clearly. This example demonstrates the benefit of airborne EM techniques over an area where surface access is difficult and where widespread ground-based surveys would be severely restricted by the nature of the site.

In the southeast of England, large areas are underlain by carbonate rocks that are susceptible to dissolution. Using traditional intrusive methods alone to locate cavities and solution features tends to be a hit-and-miss process, and the consequences of failing to detect them can have serious technical and financial consequences. Furthermore, in parts of Hampshire, for example, elevated areas are covered by plateau gravels that in turn overlie clay-with-flints, which have historically been the source of flint for the manufacture of tools and arrowheads. Consequently, it can be important to map the conductive clay-with-flints as a means of targeting subsequent archaeological investigations and also identifying where solution features might lie for the design of engineered structures, such as foundation pads for columns in commercial retail developments. Knowing where the poor ground and deeper rockhead is at the design stage is much better than discovering that a solution feature exists at the same location at which it is intended to place a major load-bearing column. Whereas electrical resistivity tomography (ERT) provides a better way of discriminating properties with depth, such surveys are relatively slow if large areas are to be surveyed or if fine ground resolution is required. This is where the fixed-loop EM systems prove their worth. It is best to cover the ground rapidly using EM methods to provide the high resolution, and then follow up with selected ERT profiles with their better depth discrimination.

An example of the combined use of three EM survey systems (EM38, EM31 and EM34), using both horizontal and vertical magnetic dipole orientations with each system, and follow-up ERT profiling, has been provided for a site in Hampshire, England. EM31 vertical magnetic dipole apparent conductivity results are shown in Figure 11.38A, with a corresponding ERT profile in Figure 11.38B. The location of a solution feature with a corresponding overlying increased thickness of clay-with-flints is clear. The apparent conductivity data from the EM instruments were processed using EMIX34<sup>PLUS</sup> (Interpex Ltd) to provide elevations of interpreted interfaces. These data were gridded and maps of the elevations of each surface provided. The validity of this modelling was cross-checked by using the inversion of the ERT sections with RES2DINV, and both the layer thicknesses and values of layer true resistivity/conductivity compared for consistency.

Subsidence collapses commonly develop in parts of Texas, USA, as a result of the mining of lignite (brown coal) since the 1900s.

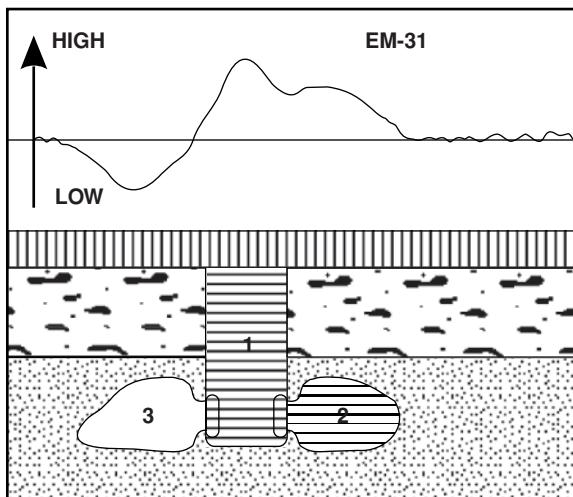


**Figure 11.36** An apparent conductivity profile over a shaft tomb at Bab edh-Dhra. The shaft (1) which leads down to the surrounding burial chambers (2 and 3) gives rise to an apparent conductivity high; the silted chamber (2) and the air-filled chamber (3) are associated with intermediate and low apparent conductivities, respectively. From Frohlich and Lancaster (1986), by permission.

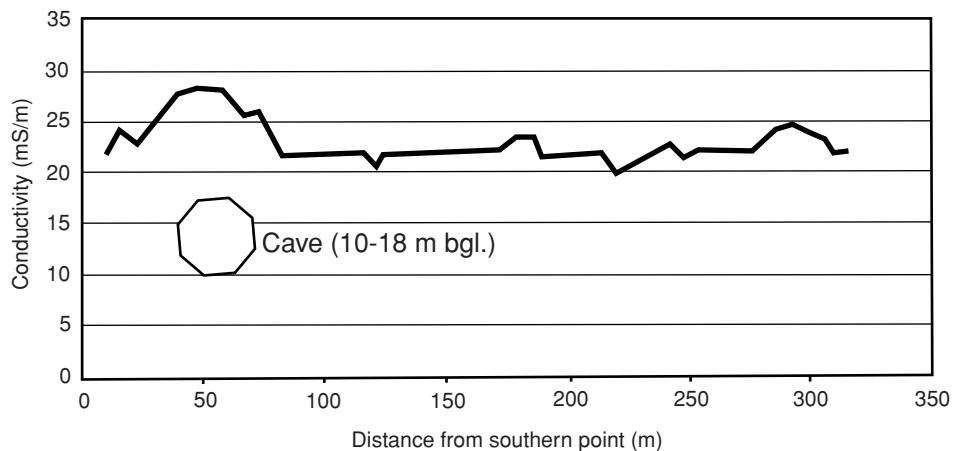


**Figure 11.37** EM34-20 apparent conductivity profile over a known cave branch in the Sian Ka'an Biosphere Reserve, Yucatán, Mexico.  
Modified from Supper et al. (2009), by permission.

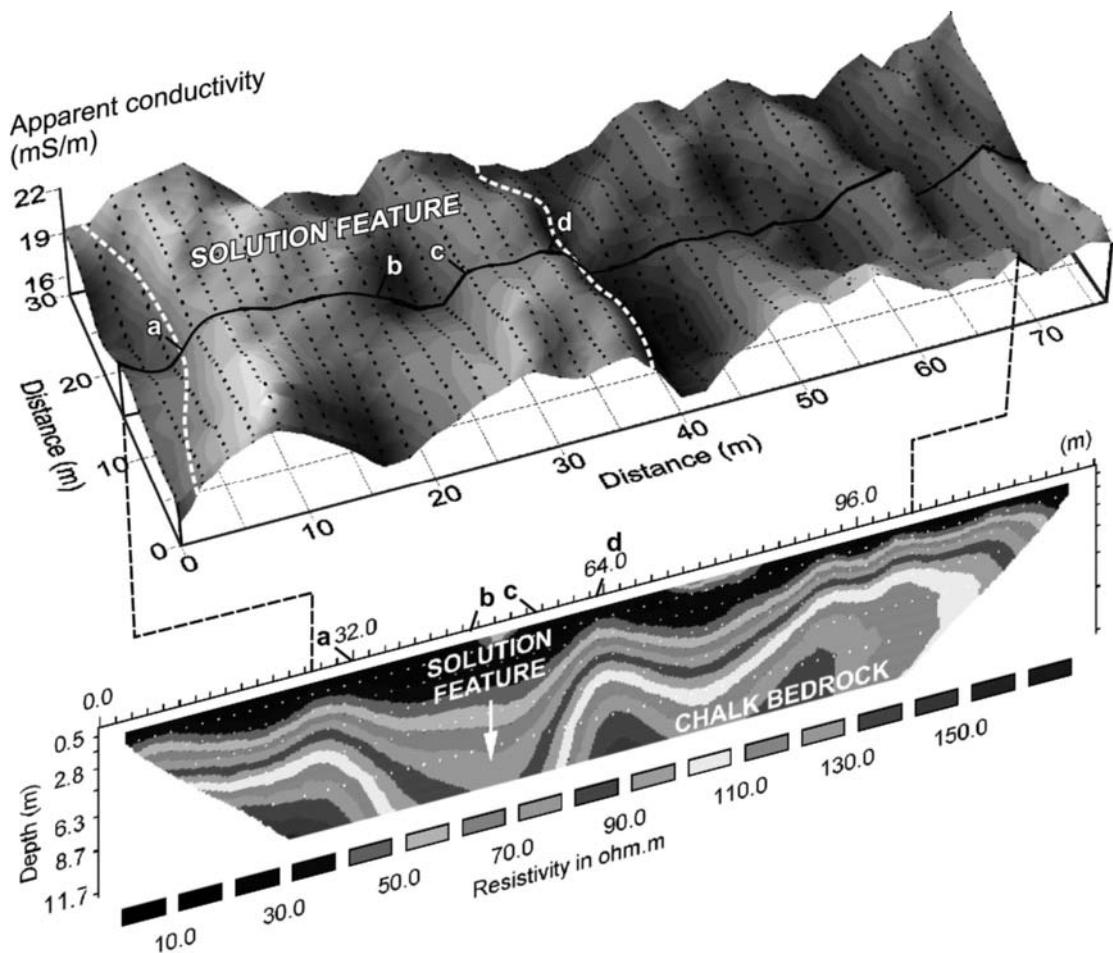


**Figure 11.38** (A) EM31 apparent conductivity surface across plateau gravels over chalk, Hampshire, England. (B) Corresponding electrical resistivity section across a solution feature in the chalk bedrock. [C]

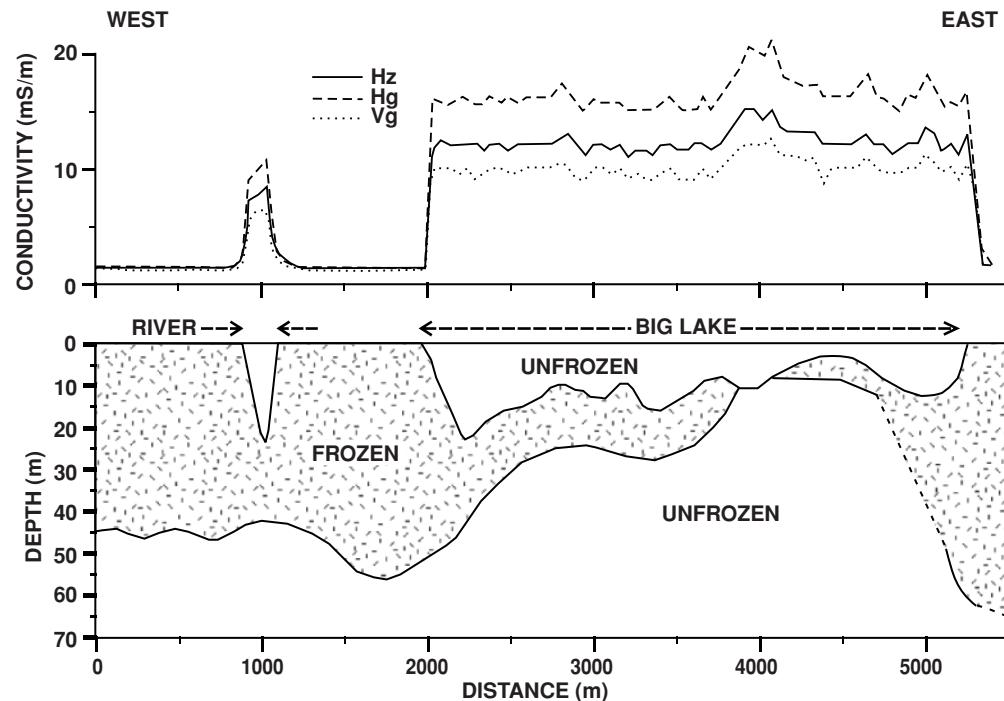


**Figure 11.39** Apparent conductivity profiles obtained with a Geonics EM31 ground conductivity meter over part of the Mackenzie Delta, Canada, showing areas affected by permafrost. From Todd *et al.* (1991), by permission.

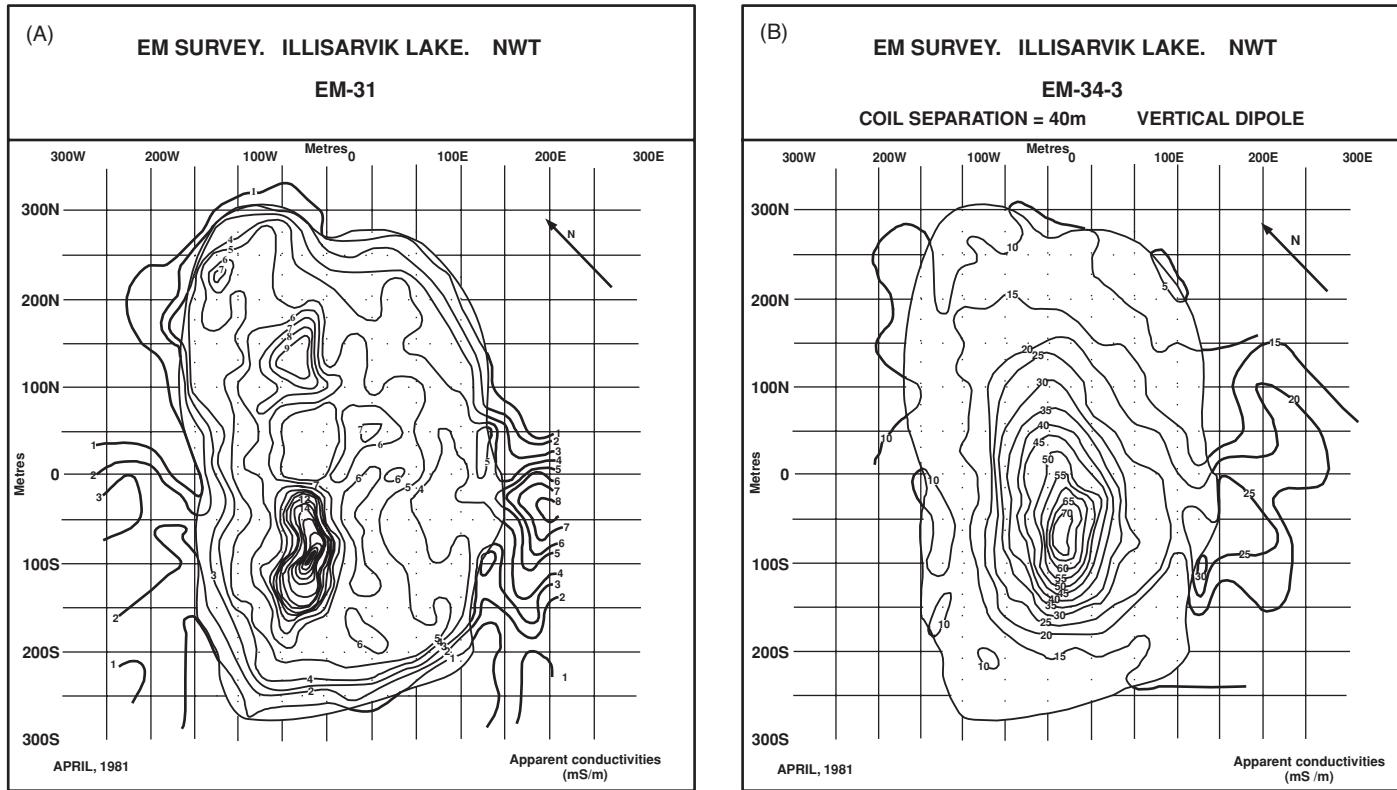
Many of the old mines, which exploited a 2.4 m thick lignite seam beneath about 7.6 m of cover, have not been properly sealed. The mines were developed using the ‘pillar and stall’ method and are prone to collapse. A heavily mined area at Malakoff in Henderson County was investigated by the Texas Railroad Commission, and between inspections a year apart, new cavities had become exposed. In January 2008 an EM survey was commissioned using a GEM fixed-loop instrument using five frequencies (Gochioco *et al.*, 2008). The EM system was reported to have been successful in detecting and imaging subsidence features and has encouraged the Texas Railroad Commission to undertake further surveys to map potential sinkholes.

#### 11.2.5.4 Location of frozen ground

In areas affected by extensive permafrost, it is of significant engineering importance to be able to differentiate between frozen and unfrozen ground. In the Arctic, the location of ice-bonded permafrost is vital when planning major projects such as pipelines. Ground frozen solid restricts the use of resistivity surveys because of the difficulty in implanting electrodes. Consequently, non-contacting inductive methods are very practical alternatives. This has been demonstrated in the first two case histories. While seismic reflection can be used in overwater surveys, EM dual-coil profiling can be much more rapid in covering the ground. An example of this is given in the third case history. A review of the use of geophysical methods in the investigation of permafrost has been given by Scott *et al.* (1990) and discussed more recently, for example, by Dobinski *et al.* (2008) and Hördt and Hauck (2008).

The first case demonstrates the use of a Geonics EM31 in providing a very rapid method of mapping the extent of frozen and unfrozen ground in the Mackenzie River Delta, Northwest Territories (Todd *et al.*, 1991). A 5 km traverse was undertaken across the ice of a small channel in the delta, over frozen tundra and across lake ice over Big Lake. The apparent conductivity profile obtained is shown in Figure 11.39. Apparent conductivity values were found to be around 1.5 mS/m over solidly frozen ground, but over 10 mS/m over unfrozen sediments and water. The lateral extents of the frozen/unfrozen portions at and near the surface correlate exactly with the marked changes in the values of the measured apparent conductivity. An example of the use of an EM31 to locate massive ice within frozen silt is shown in Figure 7.44 in Chapter 7 in a comparison with electrical resistivity profiling. Massive ice has a lower conductivity than frozen soil, and so gives rise to readily identifiable zones along a transect.

The second example, provided by Sinha and Stephens (1983), describes an EM ground conductivity survey over a drained lake at Illisarvik, Northwest Territories. Both an EM31 and an EM34 (with all three coil separations) were used over a  $300 \times 600$  m grid at 25 m centres. The apparent conductivity data from both vertical and horizontal magnetic dipoles for all three coil separations were contoured to give six apparent conductivity maps. Examples of the maps of EM31 and EM34(40) VMD data are shown in Figure 11.40. It is clear that there is an apparent conductivity anomaly centred around (25 mW, 100 mS). This relates in part to a residual pond of water at the surface. Note, however, that the centre of the conductivity anomaly on the 40 m dataset is at (25 mE, 75 mS). This is thought to be related to a zone of partially frozen sediments within



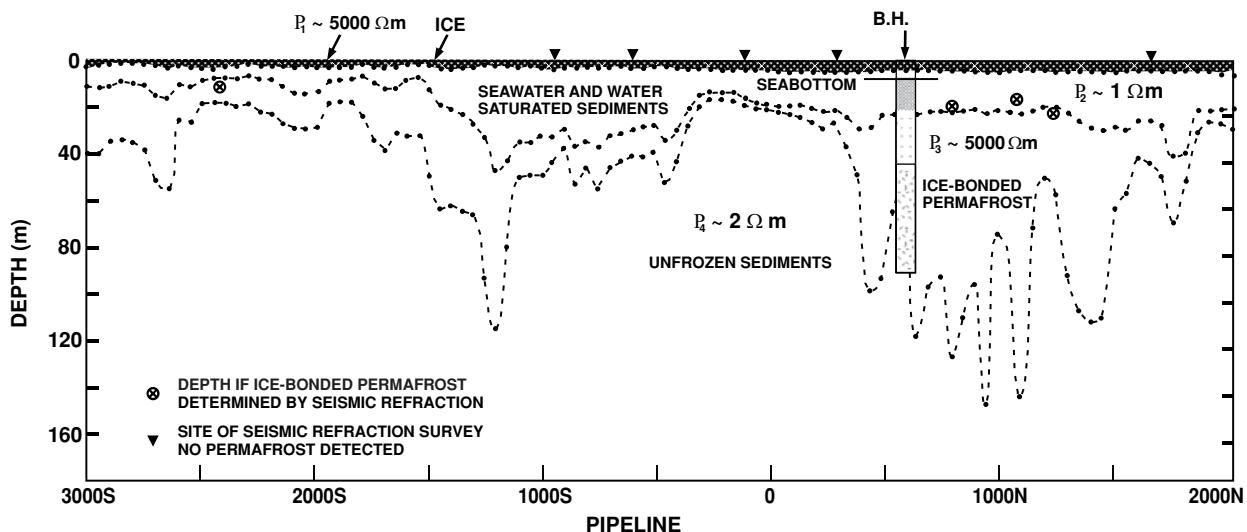


**Figure 11.41** Conductivity section of a 5 km profile over the Beaufort Shelf, Northwest Territories, Canada, obtained using an Apex MaxMin I horizontal loop EM (HLEM) system. Encircled crosses indicate depths interpreted from seismic refraction surveys to the top of the permafrost layer; triangles indicate seismic refraction surveys where no permafrost was found. From Palacky and Stephens (1992), by permission.

### 11.2.5.5 Brownfield site mapping

Dual-coil EM mapping provides a rapid means of surveying possibly heavily contaminated sites in a cost-effective and environmentally benign manner. As a trial survey, British Rail Research commissioned a combined EM and magnetometer survey over a trial

50 × 50 m area at a former railway welding yard at Dinsdale, Teesside, UK (Reynolds, 1994). It was known that part of the yard had previously been the site of an old iron foundry but the only plans of the works were unreliable. Geophysical methods were deployed to demonstrate what they could find and, in particular, to locate

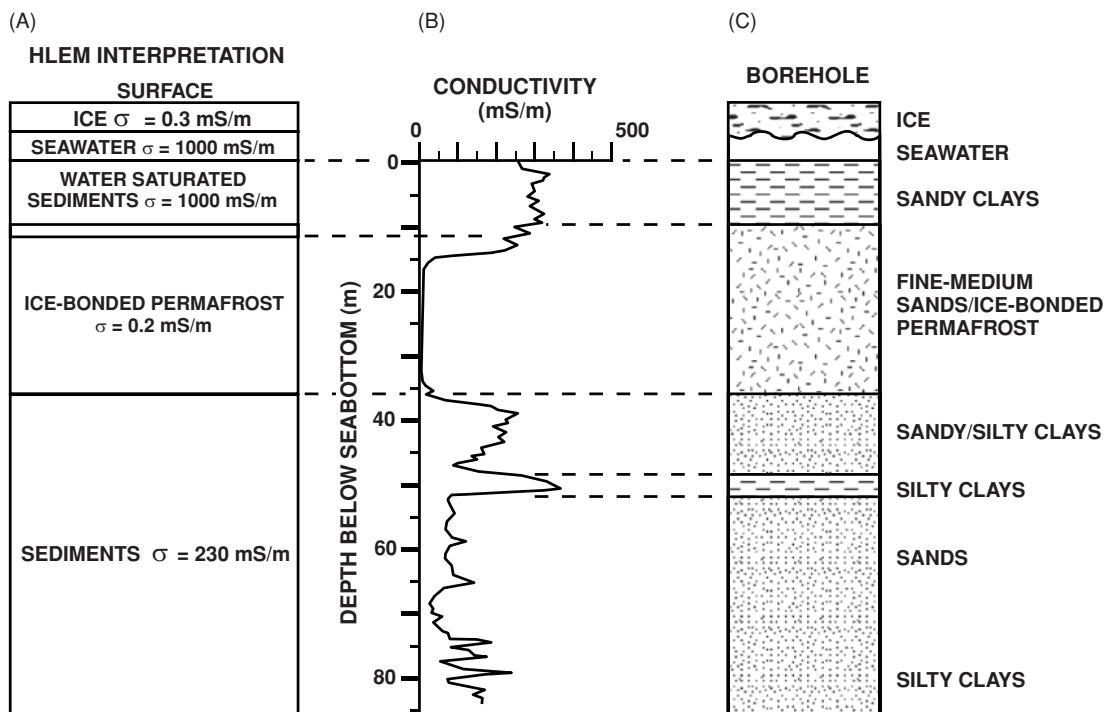


**Figure 11.42** (A) HLEM unconstrained conductivity model of the borehole shown in Figure 11.25. (B) Conductivity profile obtained by logging the borehole with Geonics EM 39 dual-coil probes. (C) Composite lithostratigraphical results of the drilling. After Palacky and Stephens (1992), by permission.

evidence of the iron foundry. The ground was featureless apart from the obvious lines where the railway tracks had once been, but was covered all over in railway ballast made of crushed limestone and dolerite. The two material types were laid in defined lines.

An EM31 was deployed on a  $1 \times 1$  m and  $2 \times 1$  m grid over the area, and both the quadrature and in-phase components were recorded. In addition, the Earth's magnetic field intensity was measured at two different heights above the ground and the difference between the two computed as a vertical gradient. Isometric projections of the apparent conductivity, in-phase component and magnetic gradient are shown in Figure 11.43A–C, respectively. On each, there is clearly an effect due to a major overhead metallic gantry used for moving welded railway track around. It is clear that, in addition to the effects of the gantry, different anomalies are present on each display. For example, in Figure 11.43A (conductivity), six conductive zones were found (lettered A to F). However, only anomaly A appears on the in-phase data, suggesting that the feature causing it is both conductive and metallic (as the in-phase component is particularly sensitive to metallic objects). The other anomalies (B–F) are not evident, suggesting that their cause is due to subsurface conductive material which is not metallic. This interpretation is consistent with the results of the magnetic gradiometer survey (Figure 11.43C) on which anomaly A is again clearly evident.

Direct excavation of each of these zones revealed anomaly A to be a series of I-shaped steel girders within reinforced concrete buried at a depth of 1 m. The anomaly width was 12 m and the concrete foundations (with subslab void!) were 11 m wide and contained within the extent of the anomaly. Furthermore, where anomaly A passes into anomaly D, it was found that the concrete foundations stopped and vitrified sulphurous slag was present. Sulphur had leached out from the slag to form yellow crystals on the surface of the slag, locally producing sulphuric acid which presumably gave rise to the elevated conductivities. Anomalies E and F were also found to be due to vitrified but broken-up pieces of sulphurous slag. Anomalies B and C were found to be buried tips of fine ash.

The linear anomalies evident on all three datasets relate to the surface ballast material. The orientation of the anomalies is exactly parallel to the lines of the former railway tracks. One linear feature (L1) was found to correlate with a cable duct that terminated in a metal box evident at the ground surface. On the conductivity data, the effect of this duct diminishes in amplitude towards the metal box. This effect is thought to be due to the increased depth of burial of the ducting below the ballast towards the box. No evidence of the ducting, either on the ground or within the three datasets, was found between the box and the location of anomaly A. In Figure 11.43A it can be seen that there is no conductivity anomaly over this zone either. Despite the site being so potentially noisy, and with railway ballast covering the area, the EM and magnetic surveys demonstrated that they could be used not only to locate anomalous material within the subsurface, but to differentiate between material types. By associating the nature of each target type with a characteristic geophysical anomaly, it was possible to highlight health and safety issues, especially regarding the physical handling of the acidic sulphurous slag.

Many major engineered structures are demolished to ground level once decommissioned, but the sites are then left derelict

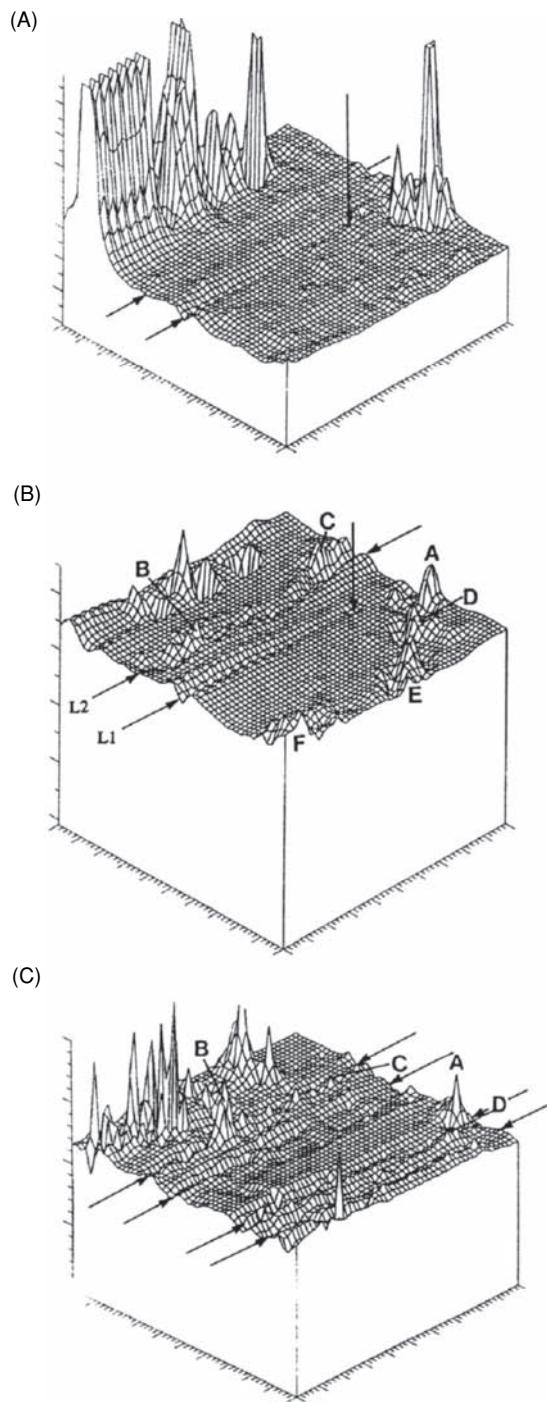


**Figure 11.43** Isometric projections of (A) apparent conductivity and (B) in-phase component, both measured using a Geonics EM31, and (C) vertical magnetic gradient, at a former railway welding yard at Dinsdale, Teeside, UK. Courtesy of British Rail Research (Reynolds, 1994).

until a new developer can be found, by which time the construction drawings of the original plant may have been lost. In order to determine what lies within the ground, trial pitting is traditionally used, but this is notorious for missing key features on such sites. A former steel rolling mill in northeast Wales, UK, had been demolished and

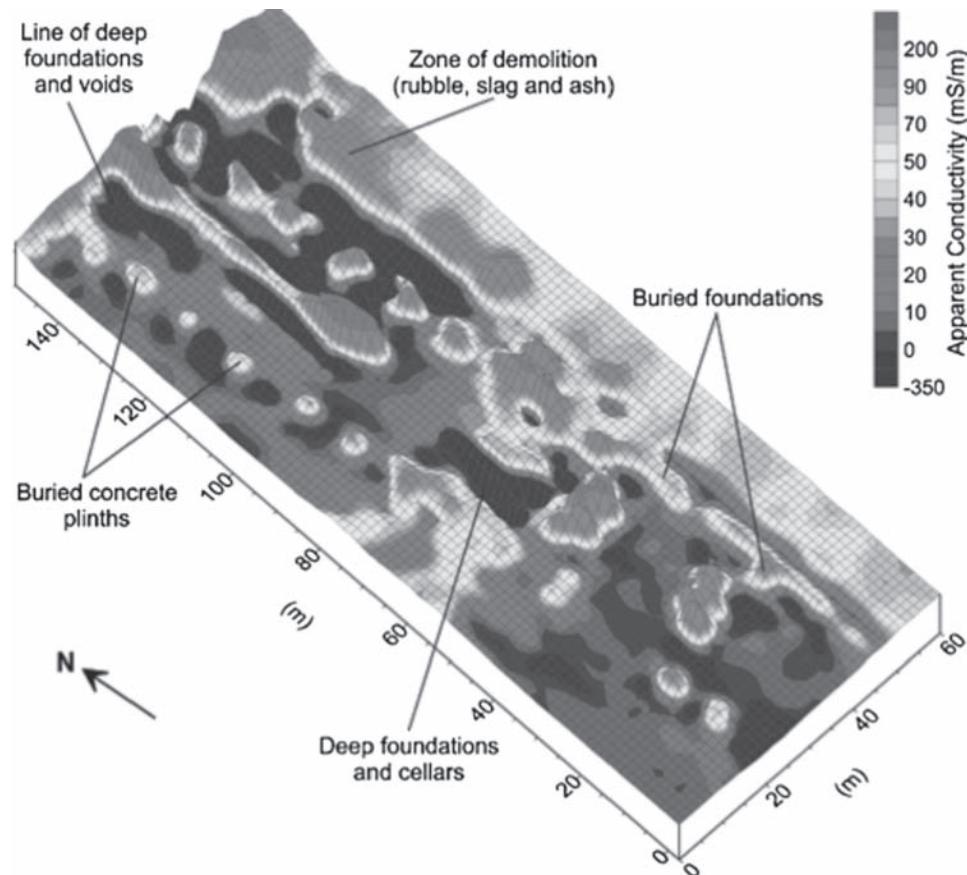


**Figure 11.44** EM31 apparent conductivity surface over part of the site of a former steel-rolling mill, NE Wales. [C]

the abandoned site had become used by local lads as a motorbike racing track, using some of the mounds of rubble as part of their racing circuit. However, the site was chosen for the construction of a combined heat and power station, and a geophysical survey using ground conductivity mapping with an EM31 was commissioned to investigate the site. Apparent conductivity data from part of the site are shown in Figure 11.44. Two parallel lines of conductive blobs can be seen across the site. These were associated with 2 × 2 m square by 6 m deep reinforced concrete pillars. They also merged into more continuous foundations, as can be seen along the eastern line of anomalies at the right hand side of the map. The demolition rubble from the building's superstructure had been buried along the eastern side of the site and is associated with elevated conductivities. Between the two lines of foundation anomalies, two areas were identified with negative apparent conductivity values. These were interpreted to be voids. Upon examination they were found to be cellars, with the one in the middle of the map having a concrete staircase descending into the pit. What was extremely worrying at the time, however, was the fact that these voids had been covered over only by thin plyboard and a veneer of soil scarcely a few centimetres deep. The lads' race track passed over this feature and, had the cover given way, someone could have been seriously injured. Furthermore, having mechanical excavators travelling across the site with their drivers unaware of the perilous state

of these features could have been potentially catastrophic. At another part of the site, which had been covered over by estuarine sands, a significant conductivity anomaly had been located which did not correspond to any known features on available historical plans. The depth of the source of the anomaly had been interpreted to be due to contamination. By using both horizontal and magnetic dipoles to acquire apparent conductivity data, it was possible to determine that the target lay below about 3 m depth. Upon careful excavation, the source of the anomaly was found to be a layer of tar, paint, oil and miscellaneous containers that had been dumped unofficially over many years into what had been a pond at the rear of the site. Upon decommissioning the site, it would appear that estuarine sand had been bulldozed across the pond area to fill it in and thus, being out of sight, was forgotten about. The EM survey was successful in locating the contamination, correctly identifying its relative depth of burial and defining its areal extent as well as mapping out the foundations and sub-floor structures of the old buildings.

A housing developer had purchased a former industrial site in northwest London. The site bordered onto a canal. However, following demolition of the buildings and stripping the ground cover off, the developer was served with notice to cease work by the Environment Agency. It had been noted that drain portals were clearly visible in the canal sides, and that pipes from the site must drain

into the canal. As the site was known to have been contaminated, it was essential that the possible sources of contamination and potential pathways to the canal were identified. It was a requirement of further work that non-intrusive methods were used so as to avoid risk of spreading contamination further. Magnetic and EM methods were chosen for reasons of speed of ground coverage, spatial resolution, and their suitability to detect the types of targets being sought. The apparent conductivity data acquired using an EM31 (vertical magnetic dipole) are shown in Figure 11.45A. The results were interpreted in the light of the total magnetic field data acquired across the site (Figure 11.45B). Linear low-conductivity anomalies

were identified that indicated the presence of cement pipes. Areas of negative apparent conductivity indicated buried reinforced concrete slabs. Two rectangular areas with negative apparent conductivities at the right-hand side of Figure 11.45A were subsequently found to be underground cellars, one of which was partially filled with oil-contaminated water. These had been covered over by wooden planks and represented a significant site hazard. This area had also been chosen by the developer as the location of his show homes. Had he proceeded with development without knowing what was there underground, he would have incurred even more expense and delay to his project. He indicated that just finding these two

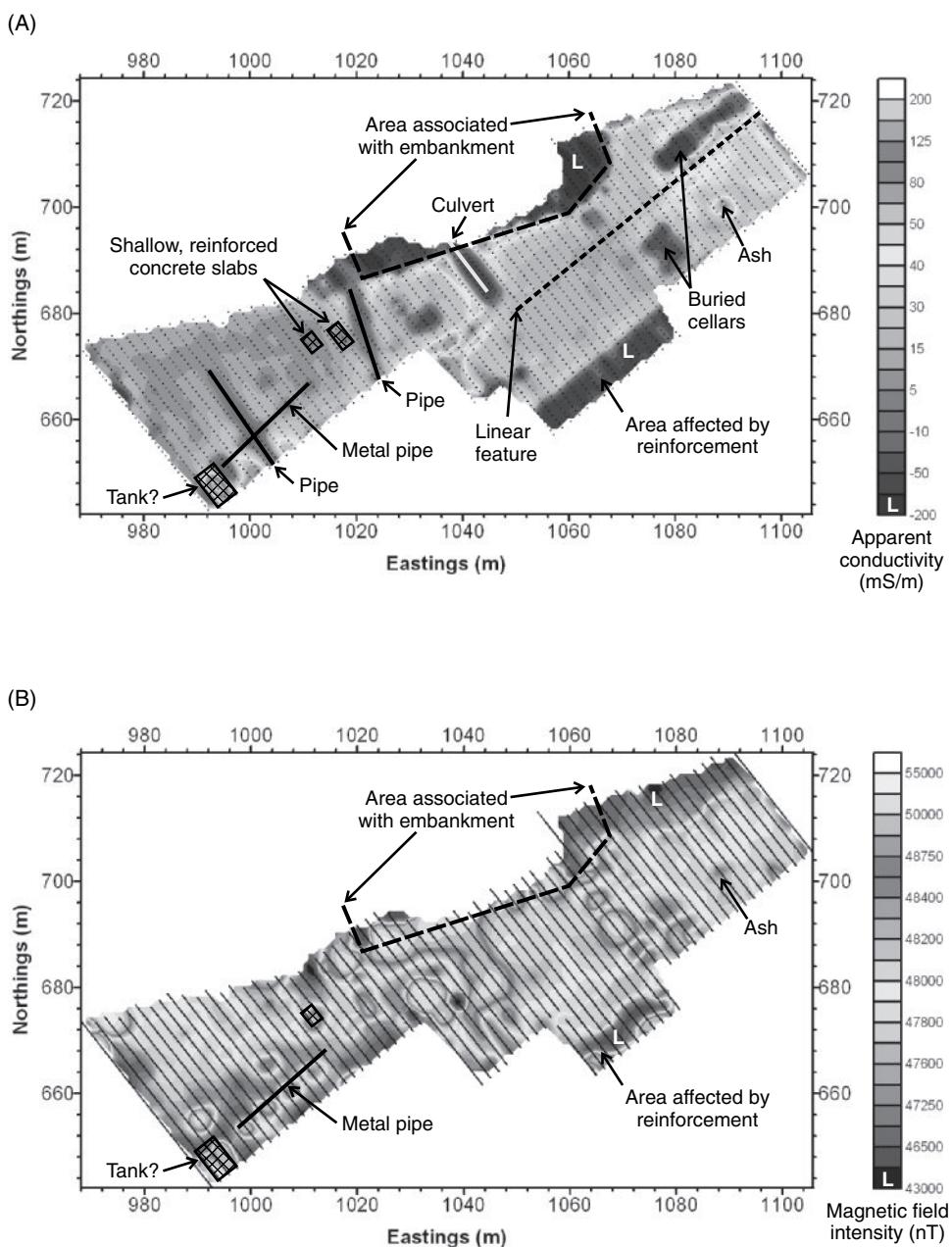


**Figure 11.45** Maps of (A) EM31 apparent conductivity and (B) magnetic total field strength across a redevelopment site in northwest London.

features alone justified the cost of the geophysical investigation. A further conductive, but non-magnetic, anomaly was found in this same area. This was found to be due to buried contaminated ash, which was excavated out and removed. A profile through the site from boreholes, trial pits, and ground stripping has been shown as Figure 1.2. It is also clear that had the investigation consisted solely of intrusive methods, virtually all of the key features of the site that would have materially affected the subsequent development and use of the site would have been missed. The use of these combined geophysical methods was successful in meeting the objectives of the investigation, satisfied the requirements of the environmental regulator and permitted the developer to target his remediation where it was needed. This reduced his clean-up costs, reduced the delays to his project and meant that he could proceed with his development.

### 11.2.5.6 Landfill investigations

Not only have FEM methods been used to detect contaminant plumes arising from landfills, they have also been used successfully at three stages in the life of a landfill. These stages are (a) site appraisal prior to the development of the waste facility, (b) investigation of the base of the site during excavation and construction, and, most commonly, (c) over closed landfills.

It is pertinent to consider the factors that need to be taken into account when contemplating undertaking a geophysical survey over any landfill site, at whatever stage of development. These factors are listed in Table 11.1 (from Reynolds and McCann, 1992). The types of waste material, the nature of the base and lining materials, the style of cover, and so on, all affect the deployment of geophysical methods. Of particular interest to waste regulatory authorities and those responsible for closed landfill sites, are the locations of the edges of the waste material, the depth of waste present, and any information concerning leachates. Three case histories are provided here, one to illustrate a simple method of determining the edge of a landfill, the second to show how EM methods have been used in leachate studies, and the third to demonstrate how ground conductivity meters can be used to provide a wide range of information about the type of fill material.

Of importance to those responsible for old closed landfills is a knowledge of the boundary of the waste. This is often required in relation to building new properties, which in the UK are not allowed to be within 250 m of the edge of a waste site for fear of gas and leachate migration. The other problem is that the responsible authority very often has many hundreds of sites within its jurisdiction, but insufficient money to investigate them all. What is required is a simple, cost-effective method that can be deployed without interfering with the site in any way.

To detect the edge of a landfill, a Geonics EM31 has been demonstrated to be a useful tool (Reynolds and McCann, 1992). A former North Wales landfill containing domestic waste up to 12 m thick and capped with about 1 m of inert soil was investigated using a variety of geophysical methods. The site was about 150 m long by 80 m wide. Trenches through the edges of the landfill had been constructed previously as part of a remediation programme, and these provided corroborative evidence against which to check the

**Table 11.1** Potential unknowns for any landfill (Reynolds and McCann, 1992).

<b>Type of void space:</b>
Hard-rock quarry
Sand/gravel quarry
Brick earth quarry
Shallow valley
Estuarine creek
Engineered site
Previous industrial site
<b>Type of lining:</b>
None
Mineral linear (compacted clay)
Artificial linear (e.g. HDPE geomembrane)
Combination linear (e.g. mineral + geomembrane, double membrane, etc.)
<b>Type of capping:</b>
None (natural venting)
Clay
Artificial (e.g. HDPE geomembrane)
<b>Site dimensions:</b>
Areal size
Depth
Shape, particularly of margins
<b>Tipping history:</b>
Types and mixtures of wastes
Duration of tipping (likely volumes)
Style and degree of compaction and cover during tipping operations
Age
<b>Geological factors:</b>
Type(s) of substrate
Local hydrogeology
Sub-site faulting
Previous resource activity at or beneath site (e.g. coal mining, quarrying)
Sub-site natural cavities
Site (slope) stability
<b>Factors related to infill material:</b>
Degree of saturation
Gas generation
Internal temperature and variability
Liquor/leachate generation
Mobility and conductivity of leachate
Compaction density and variability
Material composition (e.g. inert builder's rubble, putrescible material, industrial refuse, etc.)

geophysical interpretation. Short (<25 m) EM31 profiles were undertaken over the landfill site at right-angles to the perimeter hedge. Both vertical and horizontal dipoles were used, but only the quadrature (conductivity) component was measured.

One such profile is shown in Figure 11.46A, with the corresponding trench information (Figure 11.46C). It is clear that the apparent conductivity values increase sharply across the landfill boundary. It is also noticeable that the shallower penetrating EM31H has a less rapid change compared with the data obtained using the vertical

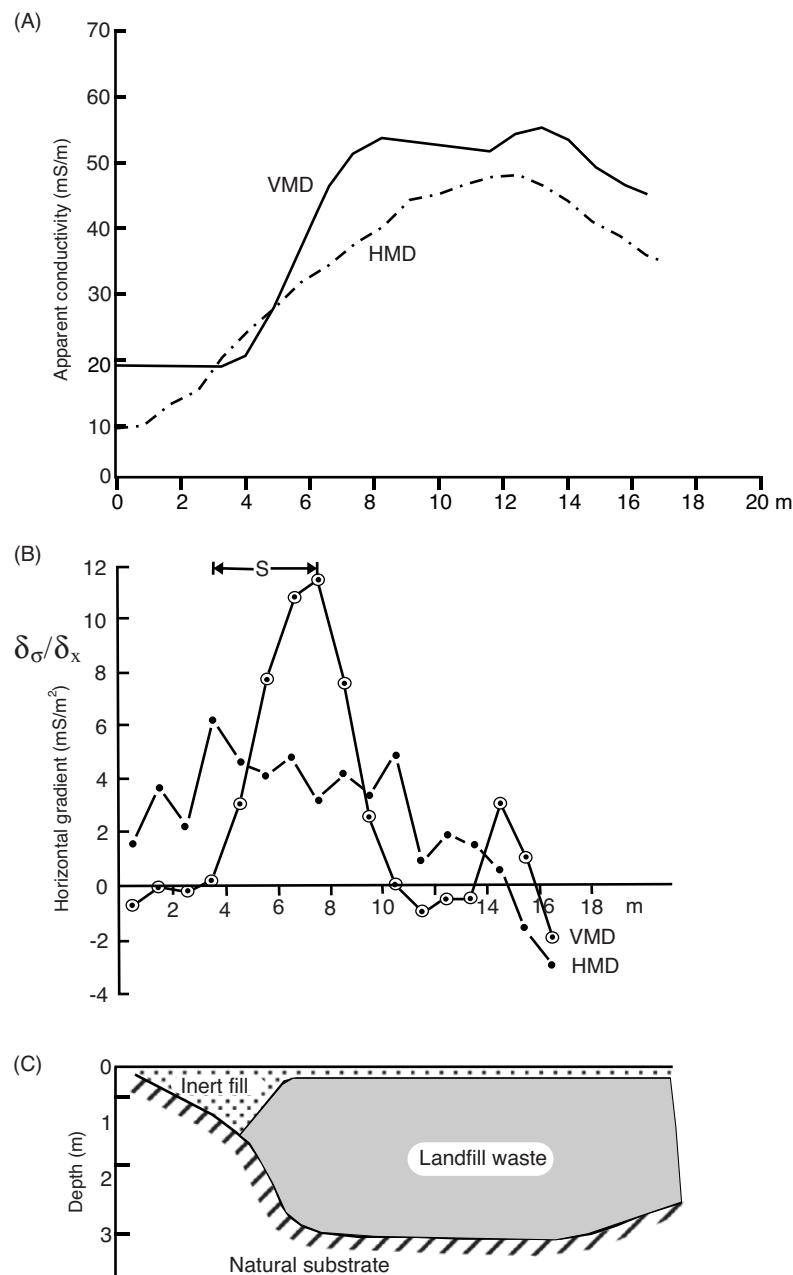


**Figure 11.46** (A) EM31 apparent conductivity profiles with both vertical and horizontal magnetic dipoles (VMD and HMD, respectively) over the edge of a shallow landfill in North Wales. (B) Schematic section of a trenched excavation. (C) Horizontal apparent conductivity gradients for the data in (A). After Reynolds and McCann (1992), by permission.

dipole. This reflects the slanted edge of the landfill. The EM31H responds to the gradually increasing thickness of the inert fill before finally responding to the refuse itself. The EM31V, however, responds more to the deeper material, which changes more abruptly from inert to refuse material. In order to highlight the effect, the horizontal gradient of each component has also been computed (Figure 11.46B). This demonstrates that the edge of the landfill as defined by the EM31H results lies outside that determined by the EM31V. This is clearly consistent with the observations within the trench.

By carrying out a series of short EM31 transects at right-angles to the site boundary, and using the criteria described above, the edge

of this landfill site was determined accurately (to within 1–2 m) using a survey which took one person about one day to execute. The results could be interpreted on-site and the landfill boundary marked with reasonable confidence. The approach taken here is very similar to that demonstrated by Zalasiewicz *et al.* (1985) for the interpretation of EM31 data in mapping geological boundaries at shallow depths.

A major problem with many landfills is the formation of leachate. As long as the liquor remains on-site and is treated it poses no significant problems. However, should leachate begin to migrate away from a site it may cause contamination of local potable water

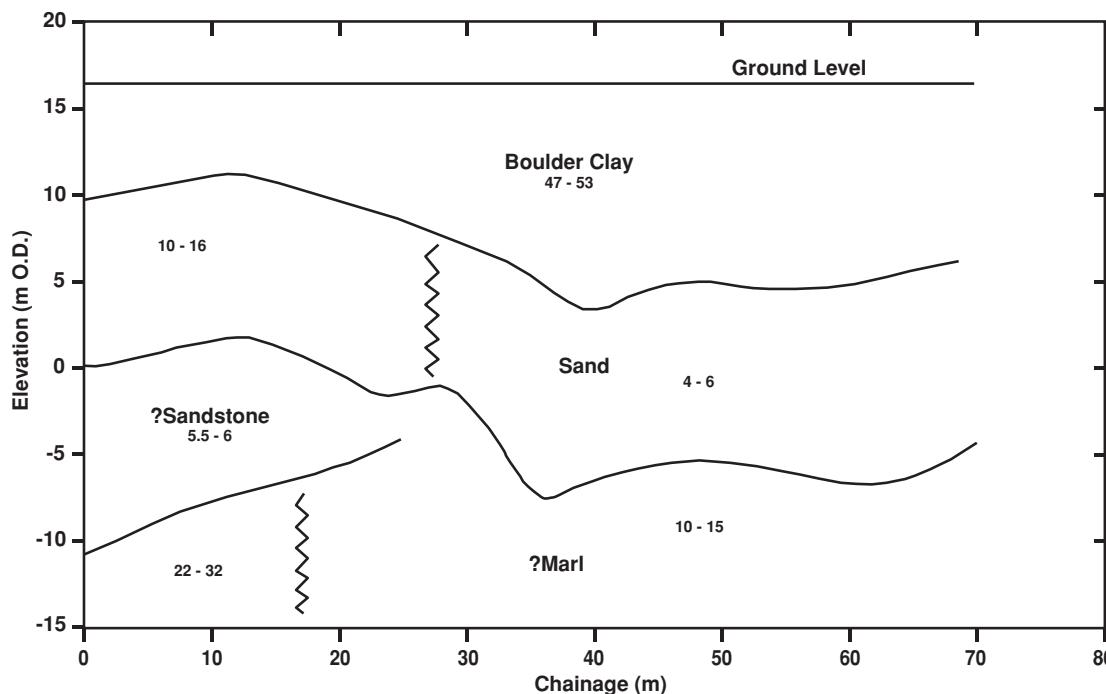


**Figure 11.47** Pseudo-geological cross-section derived from electromagnetic ground conductivity data derived from an EM31/34 survey over the base of a landfill being engineered with a natural clay liner. Values cited for geological materials are true conductivities in units of mS/m. From Reynolds and McCann (1992), by permission.

supplies. A further difficulty is in the treatment of wastes from some coal workings. Oxidation of pyrite associated with coal and coal-bearing strata causes increased acidity of minewater, which also typically contains high concentrations of iron, sulphates and trace metals, especially manganese and aluminium. Ladwig (1983) described several case histories associated with acid mine drainage (AMD). One of these examples relates to an abandoned strip mine in Butler County, Pennsylvania. The 8 ha site was thought to have been mined in the 1950s, but detailed records were no longer available.

In 1981 the mine was reclaimed, and a lake previously filling the mine was drained and the void space backfilled with mine spoil and regraded. Up to 7 m of soil was placed over the high-wall of the mine grading down to less than 2 m in the central and eastern parts of the site. A limestone-lined subsurface drain was built along the base of the high-wall to take away seepage. Following completion of the reclamation, discharge from the subsurface drain had been slightly acidic (acidity 20 mg/litre with iron 18 mg/l and sulphate 200 mg/l). Furthermore, an intermittent seep of acid water had occurred on the southeastern side of the site.

The second example is of a combined EM31 and EM34 survey over a site near Manchester at which a landfill facility was being constructed. The objective of the survey was to determine and map the thickness of the boulder-clay underlying the site, because a requirement for the site licence was a certain thickness of boulder-clay to act as an impermeable mineral liner. The survey was undertaken over a series of parallel traverses using both magnetic dipole orientations and 10 and 20 m coil separations with the EM34. The resulting six values of apparent conductivity per station were entered into EMIX34<sup>PLUS</sup> (Interpex Ltd) to produce two-dimensional in-

terpreted cross-sections through the site. The general stratigraphic sequence was boulder-clay over a saturated fine sand over bedrock. There was a reasonable conductivity contrast between the various layers, which were delimited on the interpreted models. One such profile is shown in Figure 11.47.

Borehole information available at the edge of the site was used to constrain the EM models. The interpreted thicknesses along each survey line were correlated between adjacent lines and an isopachyte map of clay thickness and a map of the elevation of the base of the clay layer were produced. As the landfill design required that a certain void volume be available to accommodate waste for the site to be commercially viable, a knowledge of the thickness of the clay and the elevation of its base were essential. As a consequence of the EM survey, various cell walls within the landfill were relocated. The geophysical survey provided the site operator with information of sufficient quality and reliability that he was able to modify his landfill design and construction appropriately, thereby avoiding potential problems later, had the clay liner been too thin.

One site contained a landfill in which municipal as well as inert waste had been dumped in a former sandstone quarry. Upon closure the landfill had been capped with about a metre of clay, top soil added and seeded with grass. The buried subsurface geometry of the quarry was not known. However, it was noted that some trees and vegetation on the downslope side of the site had begun to die. A geophysical investigation using both ground conductivity mapping and five ERT profiles was commissioned to map the extent of the landfill and to provide information about the structure and leachate distribution within the site. In open flat areas the EM31 instrument was mounted on a quad bike in vertical magnetic dipole

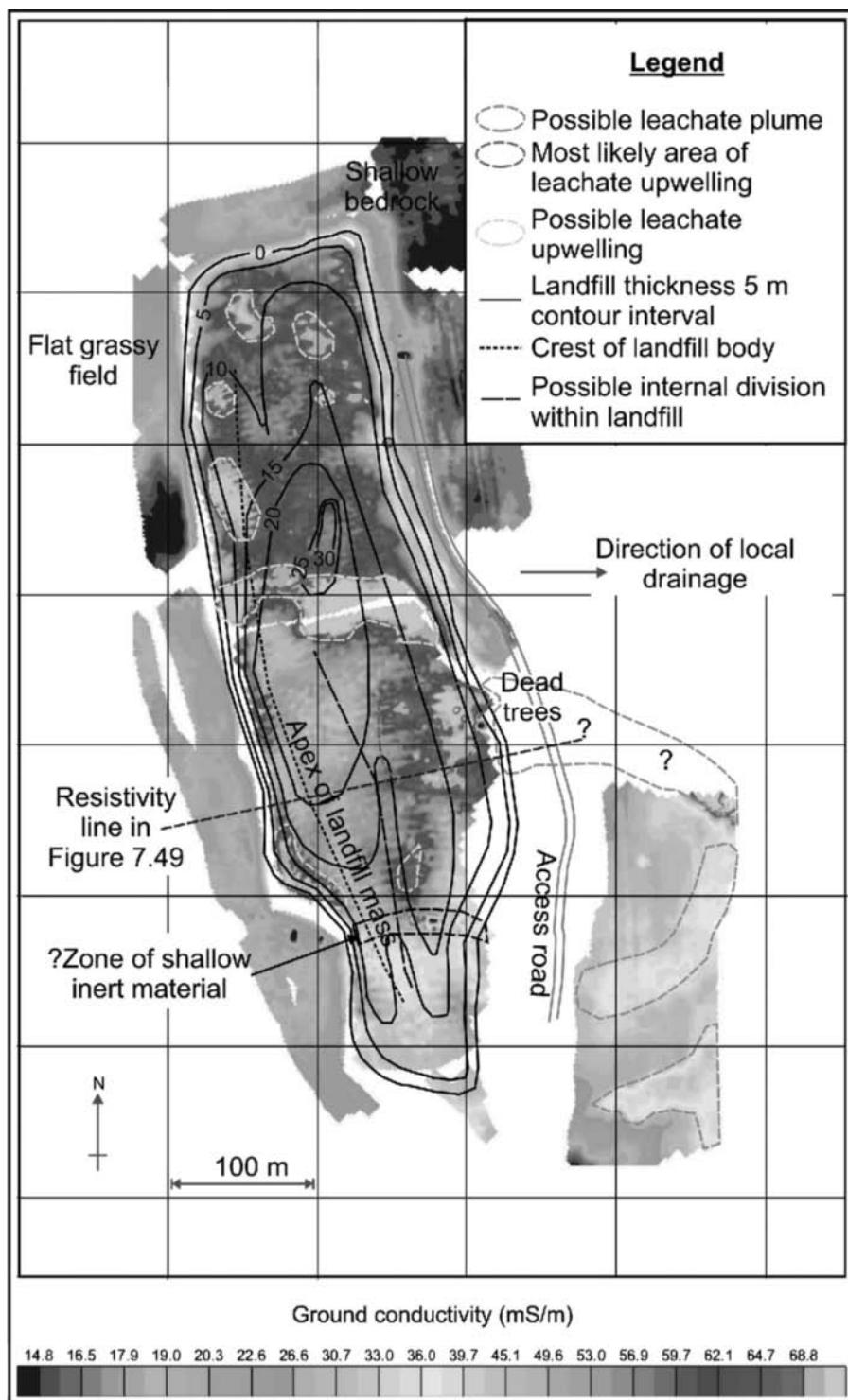


**Figure 11.48** An EM31 apparent conductivity map acquired across a capped closed landfill. The resistivity profile indicated along the dashed line is shown in Figure 7.49

mode to permit rapid areal coverage. In other areas data were acquired by an operator carrying the instrument. The EM31 survey was successful in defining the limits of the landfill by virtue of the elevated conductivities associated with the waste fill (Figure 11.48), as well as identifying a number of zones within the landfill bound-

ary with elevated conductivities thought to be associated with the disposal of different types of waste. The subsurface geometry of the former quarry was interpreted by interpolating inversions of the ERT profiles, one of which is shown in Figure 7.49. It became evident that upwelling of leachate through a defective capping layer

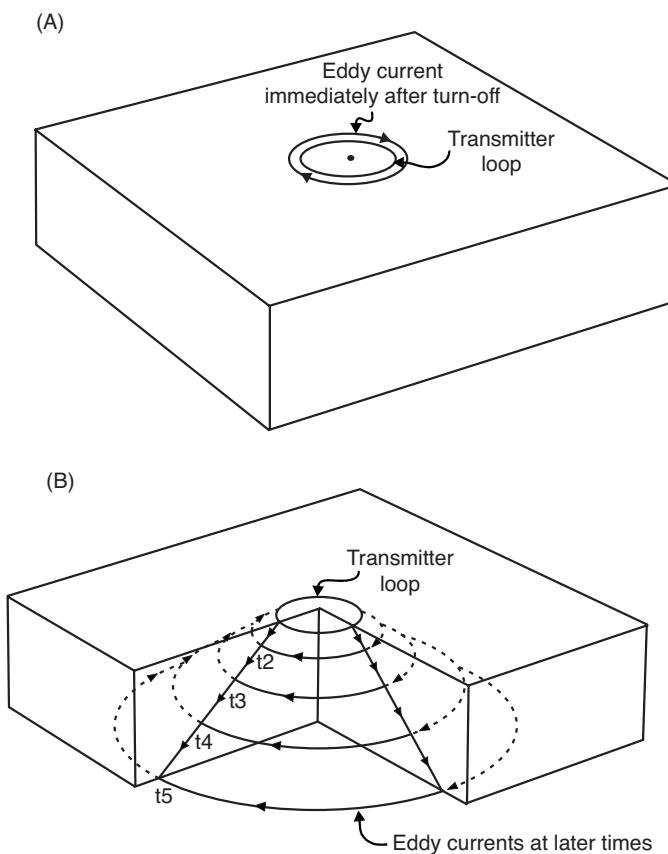


**Figure 11.49** (A) The form of an eddy current immediately after turn-off of the primary field. (B) Downward and outward propagation of the eddy current filament at successive intervals of time ( $t_2, \dots$ ) over homogeneous ground, rather like smoke rings.

and flow down-gradient was contributing to the demise of the vegetation.

These three case histories are but a small representation of what ground conductivity meters can be used for. It is worth reiterating, however, that in all cases, careful survey design is essential if the objectives of a survey are to be met. In addition, while iso-apparent-conductivity maps can provide excellent qualitative spatial information about a site, detailed quantitative analysis using specialist software can give highly reliable 2D models. When used as part of a grid of survey lines, the models along each line can be correlated between lines to produce a pseudo-3D model of the subsurface, under the right conditions. There are situations where no satisfactory model can be computed, which then suggests that there may be three-dimensional targets present within the ground. This in itself is useful information. For example, when modelling some EM data over an old colliery in the northeast of England, consistent layered models were successfully produced over much of the site. However, along one line, the data became erratic over a very short distance and no satisfactory models were producible. This effect was thought to be due to the presence of pillar and stall mine workings at shallow depths (<10 m). When the location of the anomalous zone was drilled, soft ground indicative of partially

collapsed mine workings was found, thus confirming the inference derived from the modelling.

## 11.3 Pulse-transient (TEM) or time-domain (TDEM) EM systems

### 11.3.1 TDEM/TEM surveys

In a typical TDEM survey, a direct current is passed through a large ungrounded loop transmitter to energise it. After a discrete period of time (a few tens of milliseconds), during which any effects due to switching the current on would have died away (known as ‘turn-on transients’), the applied current is interrupted abruptly. If a conductor is present within the vicinity, the sharp change in the primary field will induce eddy currents within the conductor, initially at its surface only. This is known as the ‘early-time’ stage of the transient process. These surface currents then start dissipating through ohmic losses. The zone immediately within the conductor then experiences a decreasing magnetic field with a consequential flow of eddy currents through it. Effectively, this is the start of the inward diffusion of the current pattern caused by the eddy currents towards the interior of the conductor. This is the ‘intermediate-time’ stage of the transient process. The final or ‘late-time’ stage of this process is reached when the induced current distribution is invariant with time. The only change observed is a decrease in the overall amplitude with time. If the conductor present is very large relative to the dipole source being used, the eddy currents may spread out laterally as well as diffuse into the interior of the conductor. The rate of change of these currents and of their respective magnetic field depends upon the size and shape of the conductor and on its conductivity. In contrast, the initial distribution of surface current is dependent only on the size and shape of the conductor, as this is a geometric phenomenon, not one due to the conductivity of the body. The whole process of the stepwise excitation of the current loop is repeated many times (Figure 11.49) and the data stacked for a given location. A detailed description of TEM prospecting methods has been given by Nabighian and Macnae (1991), which has been used as the basis for this section.

The transient electric field reaches a maximum at a distance known as the diffusion depth ( $d$ ), which is to TEM what the skin depth  $\delta$  is to frequency-domain EM (see Box 11.4). In the time domain the diffusion depth is directly proportional to  $\sqrt{t}$ , whereas in the frequency domain it is inversely proportional to  $\sqrt{\omega}$  (where  $\omega = 2\pi f$ ). This local maximum propagates downwards with a finite velocity ( $v$ ).

In the case of a semi-infinite half-space (i.e. uniform horizontally layered media), the ‘early-stage’ surface currents are located primarily in the vicinity of the transmitter loop. With the passage of time, diffusion occurs by the downward and outward spreading of the induced current loop, much like the downward movement of a system of smoke rings (Figure 11.50), with a consequential decay of the amplitude with time. The same principle applies in the

**Box 11.4 Diffusion depth ( $d$ ) and velocity ( $v$ )**

In a uniform conducting medium, the transient electric field achieves a maximum at the diffusion depth ( $d$ ) such that:

$$z = (2t/\sigma\mu)^{1/2} = d$$

where  $\sigma$  and  $\mu$  are the conductivity and the magnetic permeability of the medium. The maximum travels downwards with a velocity ( $v$ ) such that:

$$v = (2\sigma\mu t)^{-1/2}.$$

In a conducting half-space, the downward velocity is given by:

$$v = 2(\pi\sigma\mu t)^{-1/2}.$$

case of a horizontally layered earth. Normally, the ground materials are assumed to be non-polarisable and conductivity is taken to be independent of frequency or delay time. These induced polarisation effects have an impact on the reliability of interpretation.

Where materials within the ground have slight variations in magnetic permeability, typically of the order of 1% of the Earth's magnetic field intensity (e.g. 550 nT in a field of 55,000 nT), small TEM effects may be detectable. The TEM response is likely to be enhanced by about 1% in such cases. Where lateritic soils are present, super-paramagnetic effects may cause anomalous transient recordings with the SIROTEM system. It manifests as a  $1/t$  dependence, which results in erroneous determinations of apparent resistivity with time. Similar effects are also likely to occur where either the conductivity or the magnetic permeability of the ground varies as a

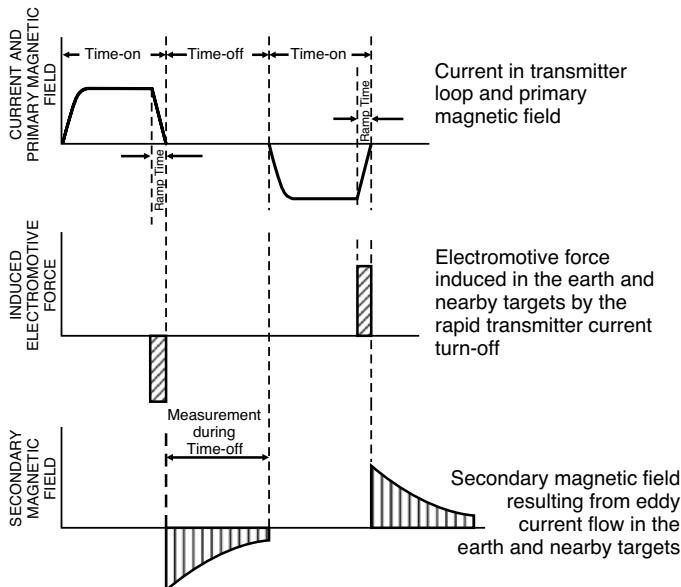


**Figure 11.50** Time-domain EM waveforms. From McNeill (1990), by permission.

function of frequency. Removal of super-paramagnetic effects can be achieved by displacing the receiving loop by 2–3 m relative to the transmitting loop where deployed in a coincident loop configuration.

There are three principal sources of error in TEM measurements: (a) geometric errors in transmitter–receiver positions and topographic effects; (b) static cultural noise; and (c) dynamic cultural noise.

Most TEM methods are largely insensitive to geometric errors, and in the case of a resistive ground are also relatively insensitive to topographic effects. However, where a conductive overburden is present, topography can produce severe coupling errors and deliberate procedures need to be followed to correct for such effects (Nabighian and Macnae, 1991).

Static cultural noise arises from the presence of pipes and cables, metal fences or other utilities present in the survey area. Some metallic utilities serve as current channellers which can cause distortions in the TEM data. Live electric cables have distinctive effects at particular frequencies and their harmonics, but these can be readily removed by notch filtering. The effect of channelling can be reduced by laying the transmitter loop symmetrically over the utility.

Dynamic cultural noise is caused by a number of sources. At frequencies less than 1 Hz, the source is geomagnetic signals from within and above the Earth's ionosphere. At frequencies above 1 Hz, typically in the 6–10 Hz range, signals generated by distant lightning discharges produce sferics which are natural EM transients. Higher-frequency sources of noise are AC power lines (50–60 Hz) and VLF transmitters (10–25 kHz). Of particular importance in airborne EM and in surveys undertaken in wide open spaces is wind noise, which causes motion of magnetic field sensors within the Earth's magnetic field. The fields used in TEM work are typically five orders of magnitude smaller than the Earth's magnetic field.

### 11.3.2 Data processing and interpretation of TEM surveys

There are many ways in which TEM data can be processed and these are largely dependent upon which instrument system is used to acquire the original data. Most TEM systems record the transient voltage at a number of discrete intervals during the voltage decay after the applied current is switched off. Each time the current is applied and then stopped, measurements are taken; when the current is applied again and switched off, a repeat set of measurements is taken. This process may be repeated many tens of times at a given location with all the data being logged automatically. Consequently, these many data can be processed to improve the signal-to-noise ratio. At the same time, the field data are checked for repeatability. Commonly, the data are normalised with respect to the transmitter current or other system parameter, and the effects of the time decay may be amplified in compensation by normalising the observed field at each point with the respective primary field value at the same point.

As the field measuring systems become more sophisticated and the amount of data increases, more careful thought needs to be given to the often quite involved data-processing sequences now available.

For example, Stephan *et al.* (1991) described a data-processing sequence for ‘long offset transient EM’ (LOTEM) sounding undertaken in Germany. Three data-processing stages were formulated: (a) pre-stack processing; (b) selective stacking; and (c) post-stack processing. Pre-stack processing was used to remove unwanted periodic noise using filtering such as a notch filter to remove noise associated with AC power lines and the German electric railway grid. A selective stacking algorithm was applied to average only a percentage of the data around the median of the individual time samples. The consequence of this was to reduce the noise content, thereby improving the signal-to-noise ratio. The final stage was to apply a slight time-variable smoothing filter. The culmination of this processing was the production of logarithmic plots of apparent resistivity as a function of decay time.

A variety of plots of processed data can be produced, such as transient decay (logarithmic) plots of voltage (in mV) versus decay time (in milliseconds); response profiles (graphs of measured voltage at a selected decay time at all stations in a survey area); response contours (the response profile data plotted in map form); apparent resistivity plots, either as profiles or maps; and vector plots, displaying components of the data in different orthogonal planes ( $xz$  or  $yz$  planes).

Interpretation methods are as varied as the different types of data plots and systems used to acquire the data. Typically, the interpretation is undertaken in two stages. The first is to locate a possible subsurface target on the basis of the shape, size and location of anomalies evident on profiles and maps of relevant parameters. The second, more quantitative, stage is to determine the ‘quality’ of the conductor using time constants determined from decay plots of the field intensity at one or more locations.

Various types of display parameter are useful for different applications. For example, apparent resistivity soundings can be extremely useful in hydrogeological investigations and in geological mapping, but provide very little information appropriate for mineral exploration. In the latter application, time-decay rates are more valuable as the curves produced can be characteristic of specific types of conductor. For example, the decay curve of an isolated conductor in a resistive medium shows a rapid decrease in amplitude in the ‘early-time’ stage, but this changes to a straight-line segment at late delay times. The gradient of this straight-line segment is used to derive a characteristic time constant ( $\tau$ ) when plotted logarithmically. These time constants are indicative of different types of causative bodies; examples of time constants for four target types are listed in Table 11.2. An analytical approach to the calculation of time constants is given in Box 11.5. For mineral exploration, time con-

**Table 11.2** Time constants for four common target types.

Conductor type	Time constant $\tau$
Sphere of radius $a$	$\sigma\mu a^2/\pi^2$
Cylinder of radius $a$	$1.71\sigma\mu a^2/\pi^2$
2D conducting plate of finite depth extent ( $l$ )	$2t\sigma\mu l/\pi^2$
Thin prism of thickness $t$ and average dimension $L$	$\sigma\mu L t/10$

### Box 11.5 Analytical approach to the calculation of time constants

The general expression for a time constant  $T$  of a conducting target is given by (Nabighian and Macnae, 1991):

$$\tau = K\sigma\mu A$$

where  $K$  is a numerical coefficient and  $A$  is proportional to the effective cross-sectional area of the conductor (see Table 11.2).

The time constant of a conducting target can be obtained from the straight-line segment of a TEM decay graph plotted on semi-log axes. The cotangent of the slope angle (in degrees) gives directly the value of the conductor’s time constant.

Analytically, given an initial amplitude  $A_0$ , then the decayed amplitude at a time  $t$  ( $A_t$ ) is given by:

$$A_t = A_0 \exp(-t/\tau).$$

Taking the logarithm of both sides, this can be rewritten as:

$$\ln(A_t) = \ln(A_0) - t/\tau$$

which is the equation of a straight line with negative gradient of  $1/\tau$ .

If the amplitudes at two times  $t_1$  and  $t_2$  are measured, the expression for the time constant becomes:

$$\tau = (t_2 - t_1)/\ln(A_1/A_2).$$

stants in the range 0.5–20 ms are of particular interest. Pyrrhotitic bodies often have very large time constants (several tens of milliseconds). With the exception of nickel associations, such targets are often of little economic interest. However, time constants alone should not be used to attach either geological or economic significance to any particular target.

The sense and degree of dip can be gauged from the asymmetry in measured components when plotted as functions of lateral distance along survey traverse lines.

While computer modelling is being used increasingly in the interpretation of TEM data, classical inversion is notoriously difficult to apply to 3D models. Software for such processing is largely still research-based and requires inordinately long computer execution times on mainframe computers. Consequently, such processing has yet to be applied routinely to commercial TEM projects when 3D modelling is required.

It is important also to consider the process of diffusion of the TEM fields into the ground; the subsurface conductivity structure dictates the diffusion depth and velocity. Inversion methods find the depth to an equivalent current filament as a function of time, from which the diffusion velocity and therefore the conductivity can be determined. The conductivity is then assigned to a depth

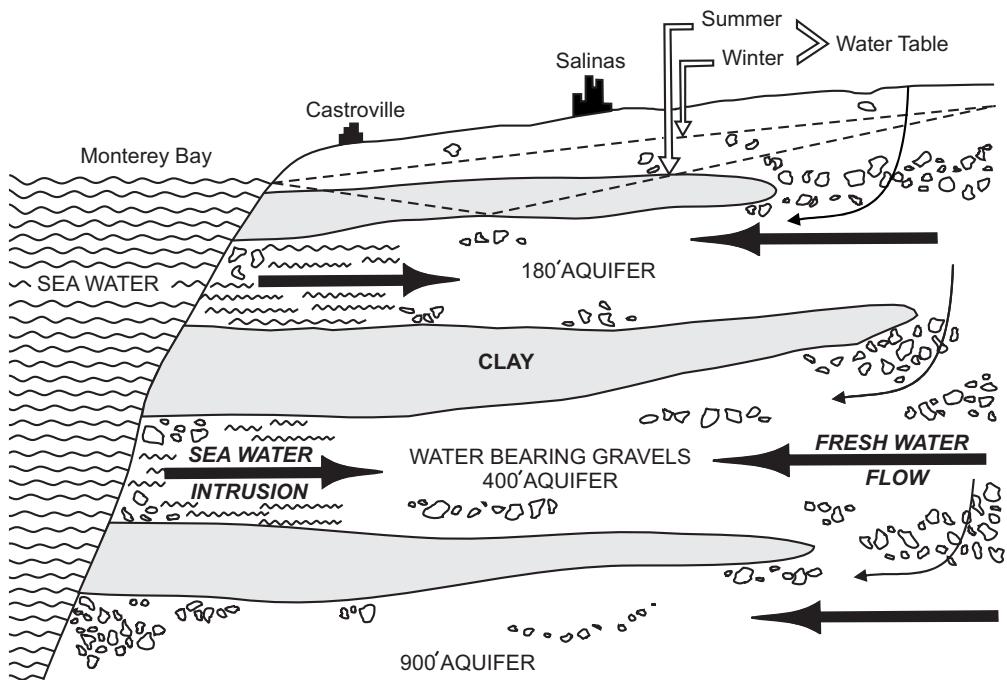


**Figure 11.51** Schematic hydrogeological section in the Salinas Valley, California. From Hoekstra and Blohm (1990), by permission.

equal to the image depth scaled with an *ad hoc* factor to produce the best results. Very detailed discussions of data processing and interpretational methods for a wide variety of EM systems have been given by Spies and Frischknecht (1991), Macnae *et al.* (1991), Nabighian and Macnae (1991) and Stoltz and Macnae (1997), among others.

One of the key aspects of successful *h*-EM surveys is efficient inversion of very large datasets. For example, data stacked for every 0.1 s at an acquisition speed of 25 m/s will yield 400 soundings per line-kilometre, corresponding to a million soundings for a survey of 2500 line-km. Such datasets are most commonly inverted using 1D schemes, but these assume that lateral changes in conductivity are gradual. Pseudo-2D images can be produced by juxtaposing successive 1D models along a profile to give a good approximation of the subsurface distribution of conductivity (e.g. Auken and Christensen, 2004). However, in areas where there are pronounced 3D structures, their effects may influence 1D inversions (Hördt and Scholl, 2004) and provide unreliable models and artefacts. Christensen (2002) has produced a fast approximate inversion method that has been updated in the subsequent paper by Christensen *et al.* (2009). Sattel (2005) has also demonstrated a fast inversion scheme using Zhody's method.

### 11.3.3 Applications and case histories

#### 11.3.3.1 Groundwater investigations

Electromagnetic methods have long been used in hydrogeological investigations. Most commonly, frequency-domain systems have been used for shallow investigations, and electrical resistivity depth-sounding for greater depth penetration. However, development

during the 1980s of TEM systems with faster shutoff rates and earlier time sampling resulted in an increased use of TEM in hydrogeology. A theoretical approach has been described by Fitterman and Stewart (1986), providing a range of hypothetical TEM responses for a range of commonly found hydrogeological problems. One advantage with TEM is that with the relatively small loop sizes available, measurements can be made on sites, such as public open spaces and sports fields, whose size may preclude the use of resistivity soundings, for example. Furthermore, in urban areas with high ambient dynamic electrical noise, the signal stacking capability of modern digital systems helps to improve the signal-to-noise ratio and recovery of the all-important signals from background noise.

TEM measurements have found increasing application in the mapping of saline-freshwater interfaces in coastal regions. A good case history describing such an application has been published by Mills *et al.* (1988) and Hoekstra and Blohm (1990). It describes the mapping of four overlapping aquifers shown schematically in Figure 11.51. These comprise a perched aquifer in which the groundwater has been heavily contaminated by fertilisers; a 60 m thick aquifer (known as the '180 ft') into which saltwater has intruded a significant distance inland; a 123 m thick aquifer (known as the '400 ft') into which saltwater has penetrated less far; and the deepest ('900 ft') aquifer which was untainted by saltwater at the time of the surveys. The layer-cake sequence of contaminated aquifers provided a difficulty in penetrating through the upper, more extensive saline intrusions to detect the lower ones. To this end, a TEM system employing 100 × 100 m transmitting loops was used to map the '180 ft' aquifer; for the deeper aquifers, a 200 × 200 m transmitter loop was used.

Four late-stage apparent resistivity sounding curves are shown in Figure 11.52, with the corresponding 1D inversions. These

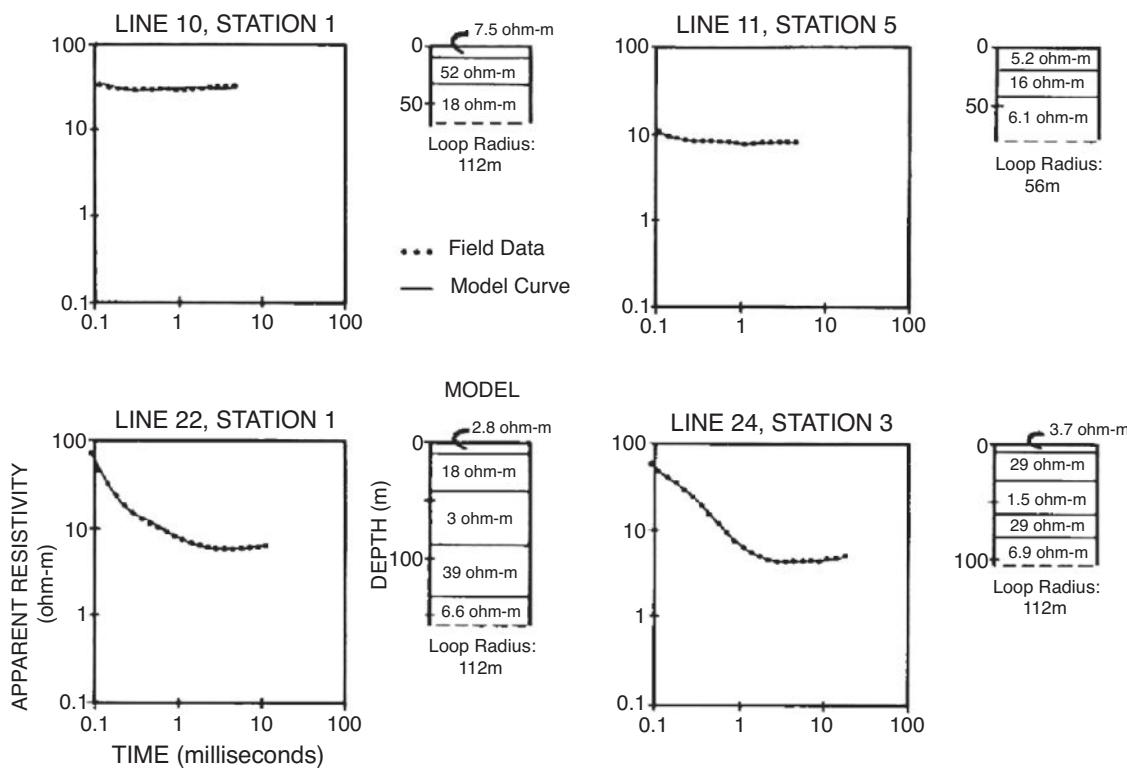


**Figure 11.52** Four late-stage apparent resistivity curves and their corresponding one-dimensional inversions along section B-B' (see Figure 11.53). From Hoekstra and Blohm (1990), by permission.

soundings relate to the positions on the interpreted geoelectric section B-B' shown in Figure 11.53. As an aid to interpretation, information from monitoring wells was used to constrain the number of layers used in the TDEM data inversion process. This information was also used to correlate derived true resistivities with equivalent chloride concentrations. It was found that a resistivity of approximately  $8 \Omega\text{m}$  correlated with a 500 ppm chloride concentration. Using this information, and the spatial information provided from the TDEM surveys, interpreted positions of the 500 ppm isochlor contours were plotted in map form for both the '180 ft' and '400 ft' aquifers and are shown in Figure 11.54. Also shown are the locations of the 500 ppm isochlor contours derived from monitoring wells. The greater detail on the TDEM-derived contours is a consequence of the greater spatial sampling provided by the TDEM survey compared with that of the monitoring wells.

A very similar application was described by Goldman *et al.* (1994) to map saline intrusion within the coastal strip immediately to the west of the Dead Sea in Israel. They carried out TDEM sounding using a Geonics PROTEM 37 with inversion and equivalence testing with TEMIXGL software (Interpex Ltd, USA). A feature

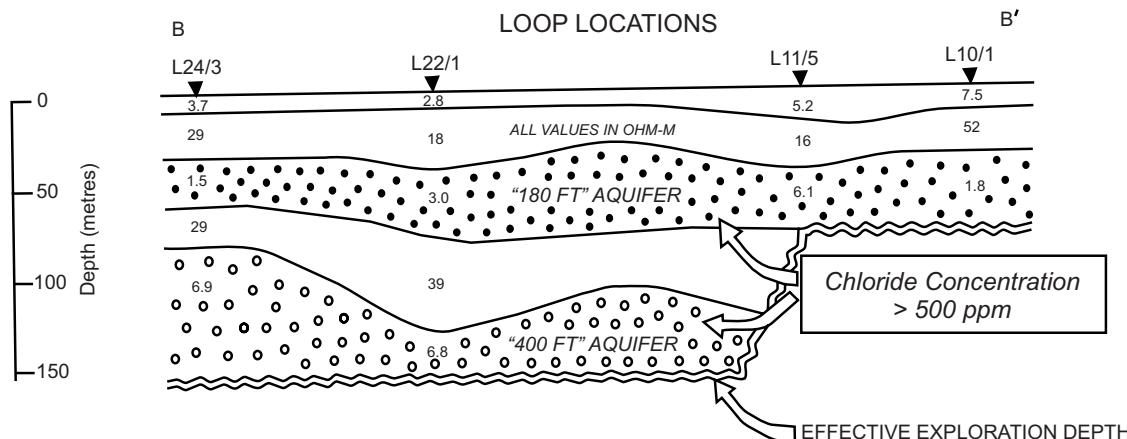


**Figure 11.53** Interpreted geoelectric section B-B' derived from TDEM soundings illustrated in Figure 11.52. From Hoekstra and Blohm (1990), by permission.

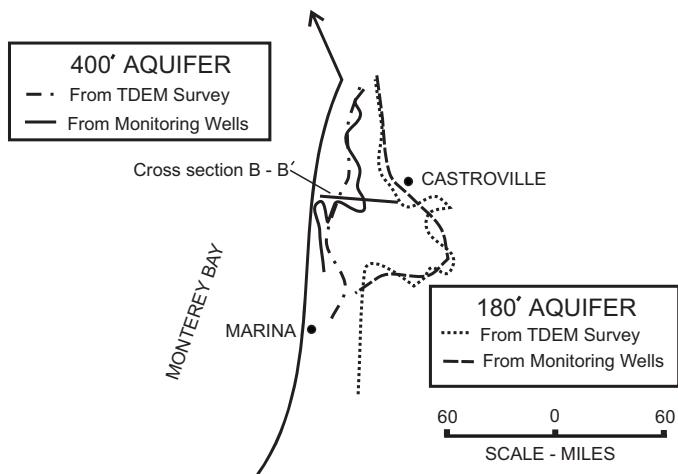


**Figure 11.54** Comparison of the position of the 500 ppm isochlor within the '180 ft' and '400 ft' aquifers derived from monitoring wells and TDEM soundings. From Hoekstra and Blohm (1990), by permission.

of this example was the use of TDEM to image the transition zone between the fully saline intrusion and the freshwater above.

Corriols *et al.* (2009) have described an investigation using TEM and continuous vertical electrical sounding (comparable to electrical resistivity tomography; see Chapter 7) to obtain information about the geology and hydrogeology of the León-Chinandega plains in the northwestern part of Nicaragua. This area represents the most important groundwater resource in the country. The aquifer consists of three hydrogeological units. The uppermost unit is an unconfined alluvial aquifer below which is a more consolidated volcanic aquifer. These rest on an ignimbrite unit that acts as the basement of the aquifer. Irrigation for agriculture comes from wells in the uppermost unconfined aquifer from depths normally less than 70 m. TEM profiles were achieved using TEMfast48 equipment made by the Russian company Applied Electromagnetic Research Company (AEMR Ltd). A total of 472 TEM soundings were acquired using a 25-m sided coincident loop configuration. The TEM soundings achieved a depth of exploration down to 100 m at most. The TEM surveys coupled with the electrical resistivity profiling produced generally three-layer models consistent with the known geology, with the CVES profiles providing more detail especially in areas of complex geology. The approach has demonstrated the value in undertaking combined EM/electrical surveys and is expected to become more widely used for the exploration, management and protection of groundwater resources in this area of Nicaragua.

Another aspect of hydrogeological investigations is understanding various aspects of fault–fluid interactions. Faults may act as either a conduit or barrier for flow, or some combination of barrier/conduit. An active fault may change over time, so its hydrological behaviour may also vary. Seismic activity has been linked to spatial and temporal distribution of the hydraulic properties of active faults. Furthermore, the role of faults in controlling fluid flow has important practical engineering and economic significance. For example, fluid flow is critical to the occurrence of mineral ore bodies, hydrocarbon migration and accumulation, and for the safe dis-

posal of nuclear waste. Hess *et al.* (2009) have provided an example where 3D seismic reflection and time-domain EM data have been used to develop a 3D model of hydraulic architecture in a predominantly dip-slip normal fault system as part of the fault-controlled Borax Lake Hydrothermal System (BLHS) in the Alvord Basin in southeastern Oregon, USA.

The Alvord Basin is a north-trending graben bounded on the east and west sides by north-trending normal faults. Basin fill, which in places is up to 1 km thick, comprises alluvial and lacustrine sediments on siltstones and claystones that overlie Miocene volcanic rocks. Within this basin about 175 geothermal springs occur along roughly north–south trending lineaments, with spring temperatures in the range of about 21–94°C emerging from a subsurface geothermal reservoir whose temperature is around 200–250°C. The faults within this area are thought to have been active within the last 2000 years, although the pronounced surface hydrothermal activity suggest active fault displacement.

Seismic and TEM data were acquired in an area centred on the left-lateral step-over in the trend of the Borax Lake springs. The seismic survey was made up of eight lines with 30 receiver stations in each line using a 240-channel receiver array. The source was a 7.62 mm semi-automatic rifle fired vertically into 0.3 m deep, 3 cm diameter holes. The TEM survey consisted of two orthogonal profiles within the 3D seismic survey area. Two horizontal coplanar loops were used with a 20-m sided square transmitter loop and a 5-m sided square receiver loop placed in the centre of the transmitter loop with a Zonge GDP-16 system. The results were inverted using TEMIX XL (Interpex Ltd). Example orthogonal seismic and TEM sections are shown in Figure 11.55A and B, and the layout of the seismic and TEM survey lines is illustrated in Figure 11.55C, in which the background is a seismic time-slice at 160 ms two-way travel time through the 3D seismic volume. This shows linear events that are subparallel to the trend of the hot springs. High spatial frequency linear features occur where the constant time slice intersects topographic irregularities in the reflection event R indicated in Figure 11.55. Two lines of hot springs occur (Figure 11.55C) and are referred to as the North Group (NG, line west of seismic profile C) and the South Group (SG, line east of seismic profile C), and these overlap in the middle, known as the overlap or step-over zone.

A strong reflection, labelled R at around 150 ms two-way travel time in the N–S profile in Figure 11.55A, is continuous across 75% of the survey area, and dips gently northwards. This event is truncated abruptly at what is interpreted by Hess *et al.* (2009) to be the eastward-dipping Borax Lake normal fault (BLF). The east–west seismic section shows an additional, westerly dipping normal fault (WF). The projections of the fault planes to the surface correspond respectively to the location of the North Group (WF) and South Group (BLF) of hot springs. A pair of orthogonal TEM profiles is shown in Figure 11.55B and whose locations are indicated in Figure 11.55C; the intersection of the two profiles is indicated by the finely dotted line. The dashed lines are the interpreted locations of the two faults from the seismic data. The profiles reveal a roughly 6-m thick high-resistivity layer underlain by a 1–2 m thick low resistivity layer, both of which lie roughly parallel with the surface topography.

On the east–west TEM profile, steeply dipping low-resistivity features are evident between 1200 m and 1225 m elevation and merge

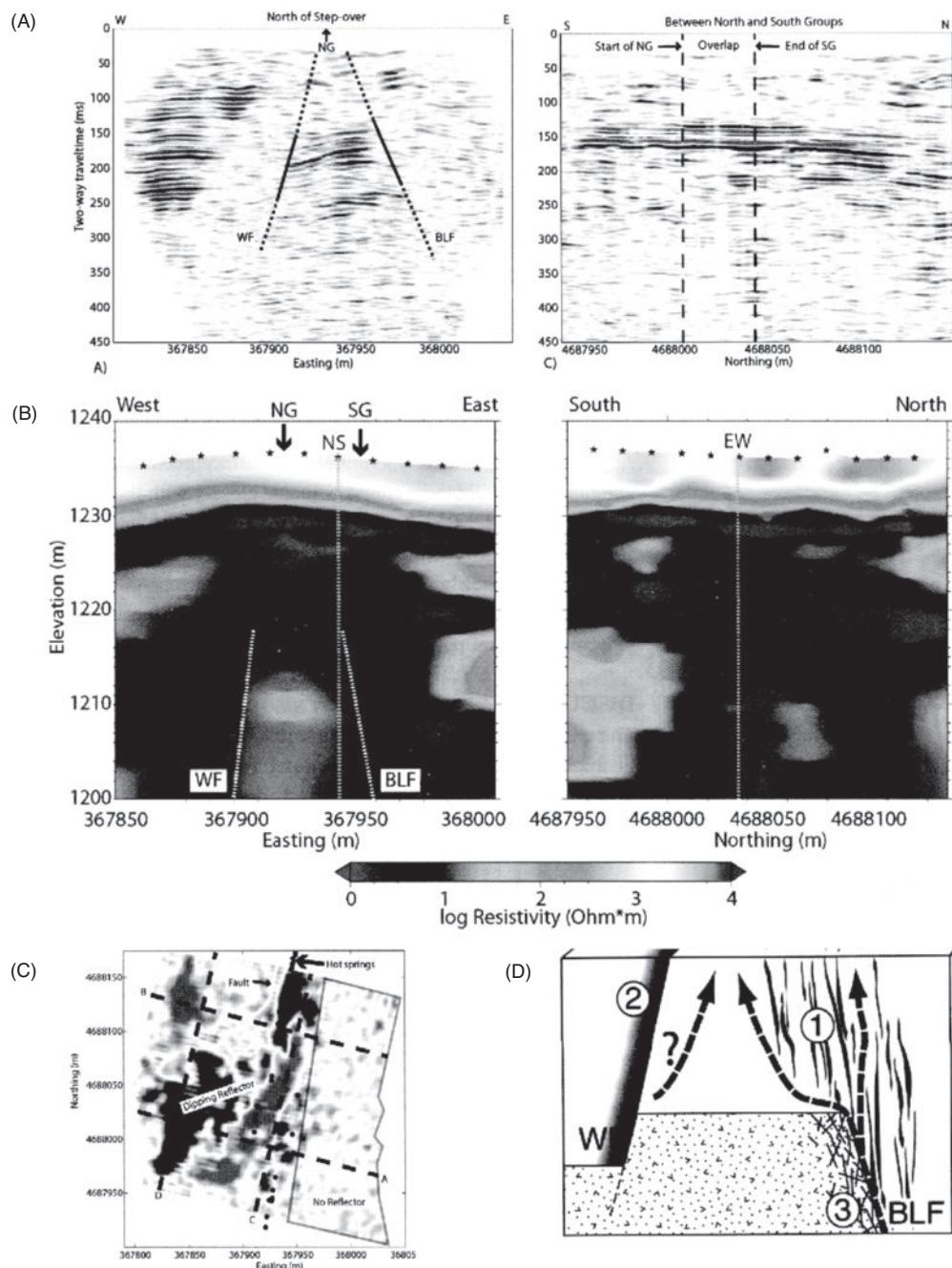


**Figure 11.55** (A) Orthogonal seismic sections east-west and north-south, with (B) the corresponding TEM profiles, (C) locations of TEM and seismic traverses, and of hot springs superimposed on a 160-ms two-way travel time slice, and (D) the schematic representation of hydraulic architecture in the step-over area of the Borax Lake Fault (BLF) zone. See text for details. Adapted from Hess *et al.* (2009), by permission. [C]

near the surface beneath the hot springs group. Their trend is consistent with those of the two faults identified from the seismic data and between which a relatively high-resistivity anomaly is evident centred at an elevation of around 1210 m. These features are likely to be associated with the geothermal fluid distribution along the fault zones.

A schematic representation of the hydraulic architecture of the BLHS is shown in Figure 11.55D. Arrows indicate flow paths for geothermal fluids rising up the Borax Lake Fault, and discharg-

ing through springs and as lateral flow through the near-surface sediments. Hess *et al.* (2009) postulate about three further elements of the model as indicated by the numbers in Figure 11.55D. These comprise: (1) zones of deformation banding and slip-slip surfaces, formed in sediments cemented by precipitates associated with geothermal discharge; (2) low-permeability mixed zone or deformation banding resulting from offset on the western fault (WF) and forming a barrier to westward fluid migration; (3) damage zone and/or deformation banding and slip-surface development at

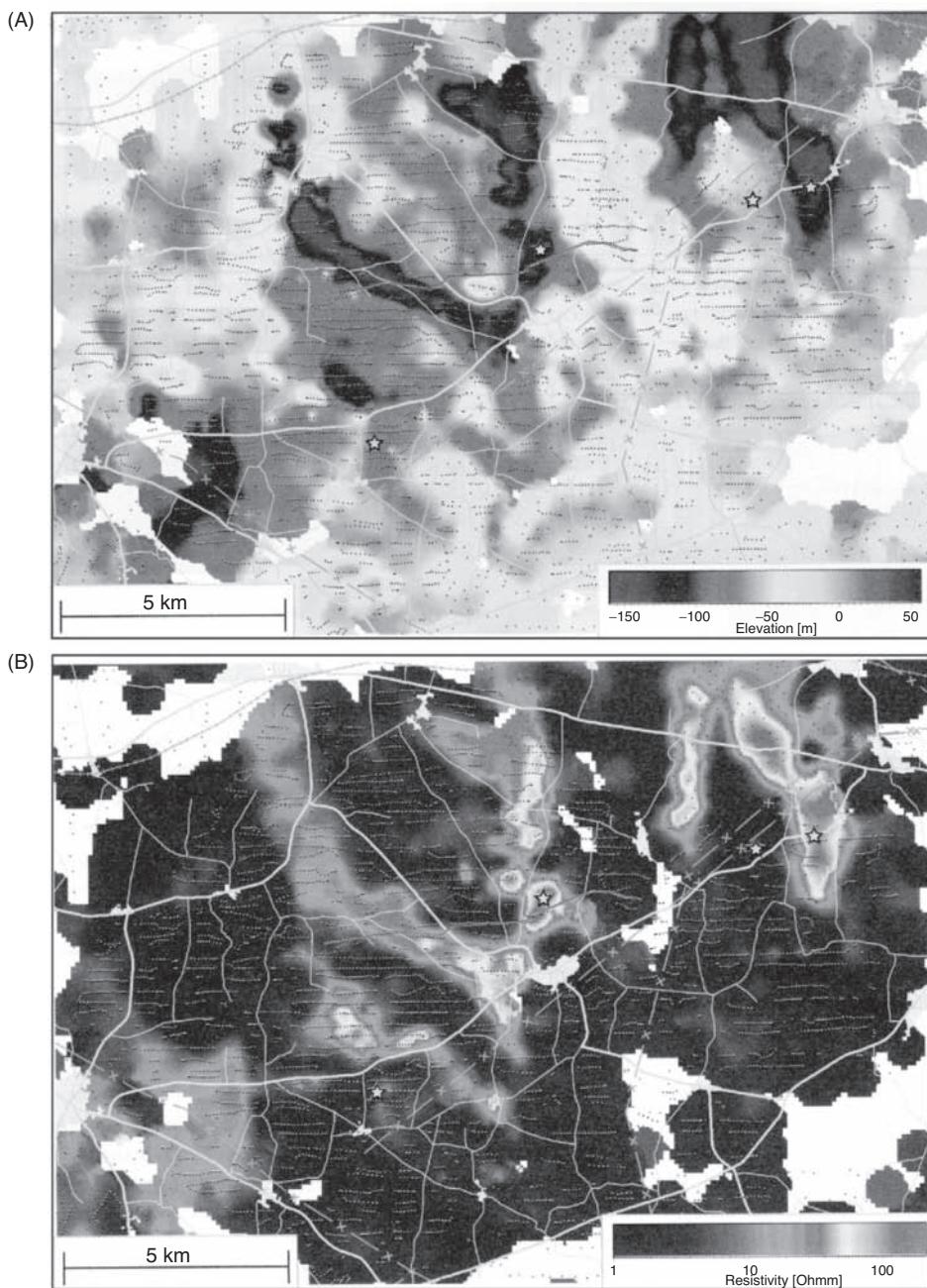


**Figure 11.56** (A) Elevation of conductor ( $<10 \Omega\text{m}$ ) and (B) average resistivity in the interval 80–90 m below sea level identified from a SkyTEM survey in northeast Jutland, Denmark. The profile line indicated is featured in Figure 11.57. Stars indicate positions of boreholes drilled after evaluation of the SkyTEM survey. From Siemon *et al.* (2009), by permission. [C]

the interface between bedrock (on the up-thrown block) and juxtaposed sediments (overlying the down-thrown block) across the Borax Lake Fault.

Since it was first introduced the SkyTEM system has been used to acquire many thousands of line-kilometres of data for hydrogeological investigations. Siemon *et al.* (2009) have described a large hydrogeological TEM survey in Vendsyssel, Northern Jutland, Denmark, undertaken to locate deep-lying aquifers as replacements for shallower aquifers as part of a water resources management programme. The SkyTEM system has been developed for groundwater investiga-

tions (Sørensen and Auken, 2004). For this survey, the transmitter loop comprised a four-turn  $300 \text{ m}^2$  loop divided into two segments, allowing transmittance of both a low and a high moment. The receiver coil was located on the rudder of the main loop. The entire system was suspended below the helicopter on its cargo hook. While normal flying speed with a SkyTEM system is about 45 km/h, this survey was flown at only 20 km/h. Spatial sampling was equivalent to 35–45 m along the flight path, with the carrier frame no lower than 15–20 m above the ground. The entire survey comprised 1250 line-km of data made up of over 9000 individual soundings.

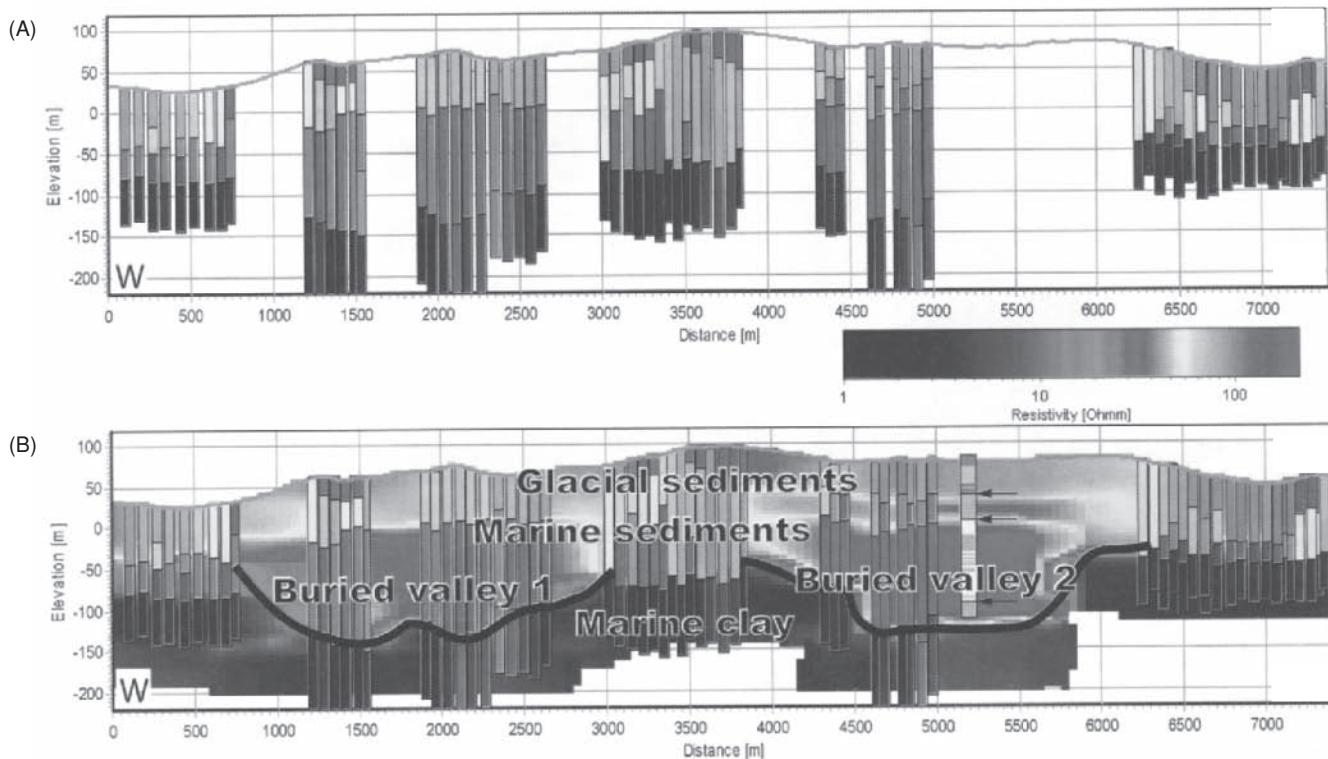


**Figure 11.57** (A) SkyTEM 1D inversions along a profile in northeast Jutland, Denmark, and (B) superimposed on a stack of average resistivity maps and a rough geological interpretation together with the nearest borehole. From Siemon *et al.* (2009), by permission. [C]

The TEM data were inverted using a 1D-inversion routine to derive the depths to a low-resistivity layer which was thought to be equivalent to a layer of marine clay that forms the base of any potential aquifer in the area. A map showing the elevation of this good conductor ( $<10 \Omega\text{m}$ ) is shown in Figure 11.56A. A map of the average resistivity in the interval 80–90 m below sea level is shown in Figure 11.56B. On both maps the line of an individual profile (shown in Figure 11.57) is indicated, along with locations of boreholes used for groundtruthing.

Figure 11.56A clearly shows the presence of previously unknown buried channels incised over 100 m into the clay. Such buried channels are very common in Denmark and often form an important groundwater resource, particularly if a coarse-grained valley fill is protected by a clayey cover. These newly-discovered buried channels have no surface expression morphologically; indeed, part of the landscape comprises a ridge up to 90 m high. By evaluating the average resistivity of the subsurface (Figure 11.56B) it is possible to differentiate the materials likely to be present within the buried channels. Areas with resistivities less than  $40 \Omega\text{m}$  are interpreted to be clay or clay-dominated sediments, while sand- and gravel-dominated sediments have resistivities over  $40 \Omega\text{m}$ . Consequently it is possible to identify those buried channels infilled with sands and gravels and which are therefore potential aquifers. For instance, one long buried channel in the west-central part of the area shows regions with resistivities in the range 20–30  $\Omega\text{m}$  for large parts of the northern end, indicating that this area is of little hydrological interest. To illustrate this further, the TEM pro-

file line indicated in Figure 11.56 is shown in Figure 11.57. The vertical bars show the 1D inversion results projected on to the profile line. In Figure 11.57A, only the 1D inversion results from the SkyTEM survey are shown for clarity. They are superimposed in Figure 11.57B onto a cut-through of a stack of average resistivity maps to give a schematic indication of the structures for the complete section. Also shown is an approximate geological interpretation together with the results of the nearest borehole (offset 300 m from the profile line). The ‘buried valley 1’ has an infill of sediments whose resistivities are in the range 20–30  $\Omega\text{m}$  and are likely to be dominated by clay-rich materials and thus of little interest hydrologically. The resistivity of the sediments in ‘buried valley 2’ is in excess of  $100 \Omega\text{m}$ , indicative of freshwater-saturated sands. Furthermore, there is indication of the presence of a capping layer of clay, providing protection of the aquifer to surface-derived pollutants.

In contrast with the *h*-TEM examples, Henderson (pers. comm.) has provided an example of the use of a ground-based survey using the terraTEM system as a comparison with the previously more widely used SIROTEM Mk-3 system. The comparative survey was undertaken in the state of Victoria, Australia, for the purpose of detecting groundwater in an aquifer thought to be fault-controlled on the flanks of Mt Major. The terraTEM survey consisted of a 50-m sided coincident loop configuration, with results obtained at 25 m and 50 m station intervals along lines perpendicular to the known strike of the fault. A comparable profile was acquired using a SIROTEM system and the results for one 875-m long profile are

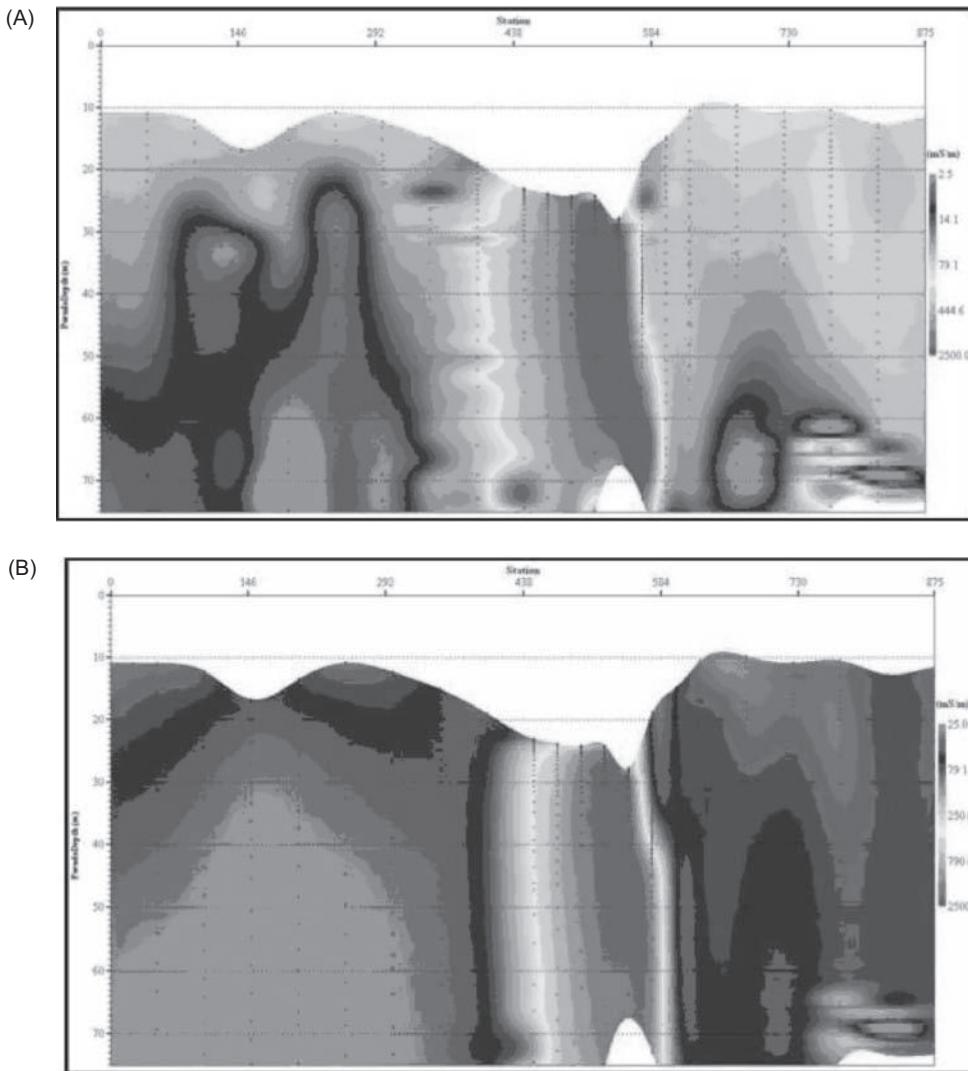


**Figure 11.58** Apparent conductivity depth images derived from (A) terraTEM data, and (B) SIROTEM data across a conductive fault-controlled aquifer on the flanks of Mt Major, Victoria, Australia. From Henderson (pers. com.), by permission

shown in Figure 11.58. A strong conductor is clearly shown between 400 m and 600 m along the profile for both systems, but there is more high-resolution information evident in the profile acquired using the terraTEM system.

These case histories demonstrate the usefulness of the TEM method in hydrogeological investigations. With the right combination of transmitter sizes and closely spaced soundings, profiles can be produced with a high degree of vertical and lateral resolution. Such spatial sampling, and the increasing reliability of inversion processes, enables detailed two-dimensional geoelectric sections to be produced much more cost-effectively than could have been achieved with boreholes alone.

### 11.3.3.2 Contaminant plume mapping

Hoekstra *et al.* (1992) have provided a case history which demonstrates the benefit of a combined deployment of both FEM and TEM soundings. The survey was conducted in the vicinity of a brine lagoon in southwest Texas, USA. A Geonics EM34–20H FEM

system was used to map variations in apparent conductivity around the brine pit. It is obvious from the resulting contour map (Figure 11.59) that elevated apparent conductivities are evident a considerable distance away from the brine pit. However, a single dipole configuration with a single inter-coil separation can provide only a qualitative impression of the distribution of this conductive contaminant plume. If both dipole orientations had been used with the 10 m and 40 m inter-coil separations, quantitative inversion would have been possible to determine the depth of the plume.

Instead of an increased number of measurements with the EM34, TEM soundings were undertaken using a Geonics EM37 with a transmitter loop side length of 100 ft (30 m). Examples of two TEM soundings are shown in Figure 11.60 with their respective 1D inversion results. It is clear that a layer about 10 m thick with a high conductivity is present on sounding 3 but is not seen on sounding 1, although the conductivities for deeper layers are the same for both. This high-conductivity zone is attributed to the saline contaminant plume. Using a series of soundings, a geoelectric section has been produced (Figure 11.61) on which the position of

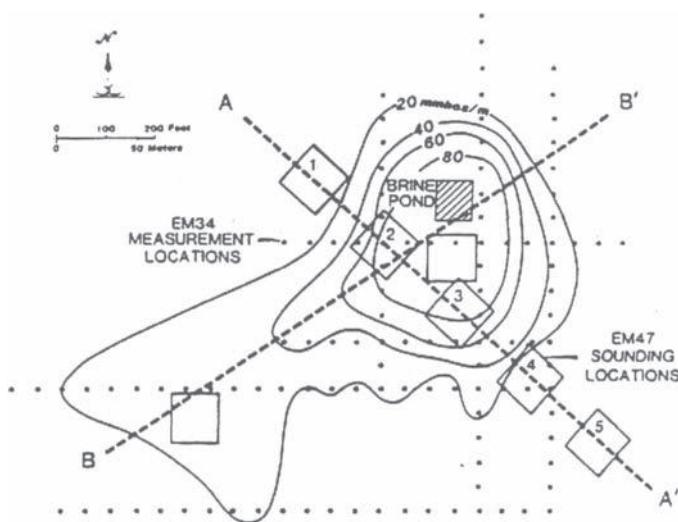


**Figure 11.59** Location map and apparent conductivity contour map derived from measurements made with a Geonics EM34 at 20 m coil separation, horizontal magnetic dipole, around a brine evaporation pit. Numbered squares indicate the locations of Geonics EM47 loop soundings. From Hoekstra *et al.* (1992), by permission.

the contaminant plume is obvious (shown as the shaded area). Not only can the EM data be used to map the contaminant plume spatially, but they have been demonstrated to provide an indication of the thickness too. The advantage of the TEM soundings in this case history is that a model of the probable migration pathways of the contamination can be developed using the TEM models (Figure 11.62). This knowledge is vital if any remediation is to be undertaken successfully.

Buselli *et al.* (1990) have provided examples of the use of TEM in mapping contaminant plumes near Perth in Western Australia. One of these has been selected for discussion here.

A waste disposal facility had been established at Morley, near Perth. Sand was quarried from the Pliocene–Holocene sequence of surficial sand formations and the resulting pit was then filled with domestic solid waste. The area underlain by the predominantly clay Osborne Formation was found to have a resistivity of 10  $\Omega\text{m}$ . The unsaturated zone within the sand was found to have a resistivity of 3600  $\Omega\text{m}$  and to be up to 50 m thick. The saturated zone of the surficial sand formation was between 20 and 30 m thick with a resistivity of 50  $\Omega\text{m}$ . The sand formations consist of unconsolidated, very fine to medium sand which coarsens progressively with depth to become gravelly at the contact with the Osborne Formation. The general direction of groundwater flow is towards the southwest.

TEM measurements were made using a SIROTEM system with a transmitter loop of either 25-m or 50-m side length with an in-loop geometry with a dipole receiver of  $10^4 \text{ m}^2$  effective area placed in the centre of the transmitter loop. The instrument had a capability of measuring the response in a delay time range of 49  $\mu\text{s}$  to 160 ms. The locations of all TEM loop centres are shown in Figure 11.63, and borehole locations in cross-section in Figure 11.64.

The results of the TEM survey are shown in Figure 11.65, in which values of resistivity of the sand formation derived from the TEM inversion are contoured. The contaminant plume arising from landfill has been interpreted to be where resistivity values less than or equal to 75  $\Omega\text{m}$  were determined (tinted area in Figure 11.65). The general orientation of this anomalous zone is the same as the direction of general groundwater flow. This is further confirmed by superimposing the isochlor concentrations as determined from chemical analyses of water samples from the various boreholes over the resistivity map.

The ease with which TEM measurements can be made makes it very simple to re-occupy the same survey locations after discrete intervals of time, such as every 3–6 months, in order to observe changes in the resistivity values. This provides a means of monitoring the flow of a contaminant plume not only with respect to space but also in time. The natural extension of this is the use of TEM to monitor any remediation undertaken.

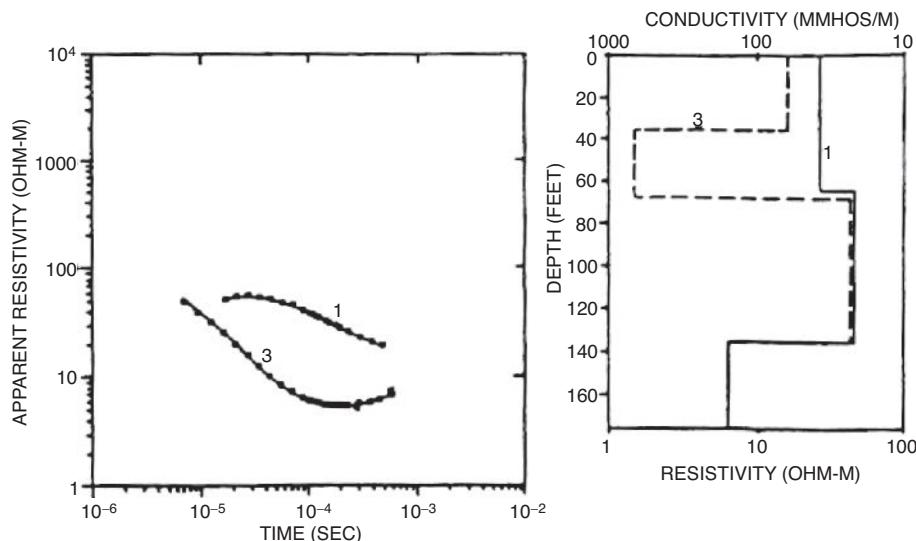


**Figure 11.60** TDEM apparent resistivity sounding curves and their corresponding one-dimensional inversions along cross-section A-A' (see Figure 11.59). From Hoekstra *et al.* (1992), by permission.

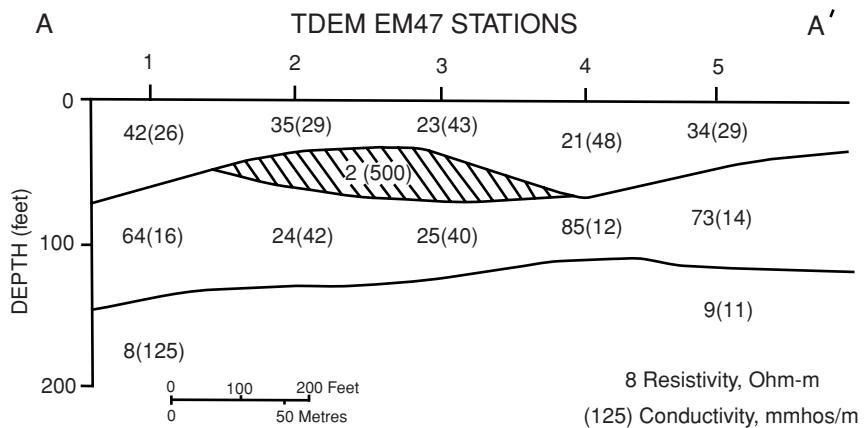


**Figure 11.61** Geoelectric section derived from one-dimensional inversions of TDEM soundings along A-A' (see Figure 11.59). From Hoekstra *et al.* (1992), by permission.

### 11.3.3.3 Mineral exploration

A surface DEEPEM survey was undertaken by Crone Geophysics Ltd for Cogema Canada Ltd in the Athabasca Basin, Saskatchewan, Canada. As a consequence of this survey, in conjunction with other techniques, a high-grade uranium deposit was discovered (Crone, 1991). The uranium deposit, which is a typical Athabasca type, comprises a long horizontal 'tube', of cross-sectional width less than 100 m, of high-grade uranium mineralisation which occurs at the base of flat-lying sandstone. The mineralised 'tube' is commonly associated with the upper interface of a large near-vertical graphitic structure that occurs in Archaean basement rocks. EM surveys may be employed to locate the graphitic conductors. Between the basement and the sandstone is an altered contact zone up to 100 m thick which is made up largely of clay and which is commonly found in areas of uranium mineralisation.

In this survey, a large-loop ( $400 \times 800$  m) pulse EM system was used, powered by a 2 kW waveform generator. Horizontal and vertical component measurements were made by the receiver coil at each survey location (Figure 11.66A). The data were filtered using a Fraser filter to emphasise selectively the response from currents at

up to a depth of five times the filter station interval. A 100 m station interval was used in the filter in order to pinpoint the location of the graphitic conductor. The filtered results of the survey are shown in Figure 11.66B. The data for the horizontal component are particularly revealing, with the location of the graphitic conductor being indicated by the node of the family of graphs as indicated in the figure.

Balch *et al.* (2003) have described an airborne TEM survey flown for FNX Mining Company to explore for Ni-Cu-PGE deposits in Sudbury, Ontario, Canada, during the summer of 2002. An AeroTEM helicopter system was used, with eight turns of wire, 5 m in diameter and a maximum current of 250 A that produces a peak moment of  $40,000 \text{ Am}^2$ . One receiver coil was orientated in a vertical plane ( $z$ -axis) and the other in an inline horizontal plane ( $x$ -axis). The rigidly mounted circular frame was towed beneath a helicopter at a nominal terrain clearance of 30 m and 40 m below the helicopter. A caesium-vapour magnetometer was deployed in a separate bird 10 m above the EM system. Previously known deposits were clearly detected (Figure 11.67), but so too was a previously unknown feature which subsequently became known as the Powerline Deposit, since it is located between two

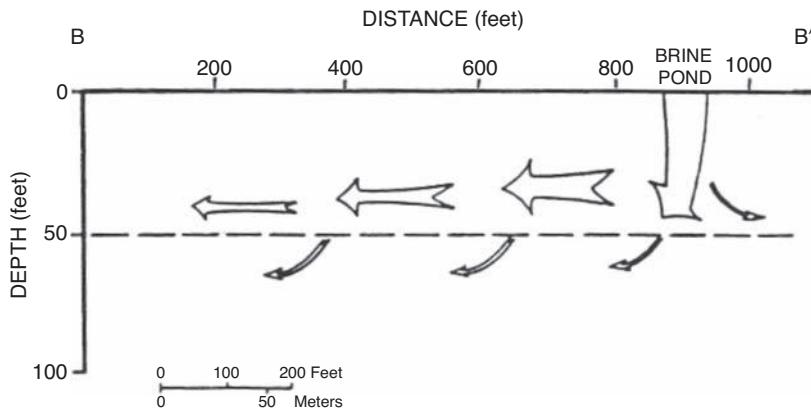


**Figure 11.62** Model of probable important pathways of brine migration, constructed from geophysical surveys. From Hoekstra *et al.* (1992), by permission.

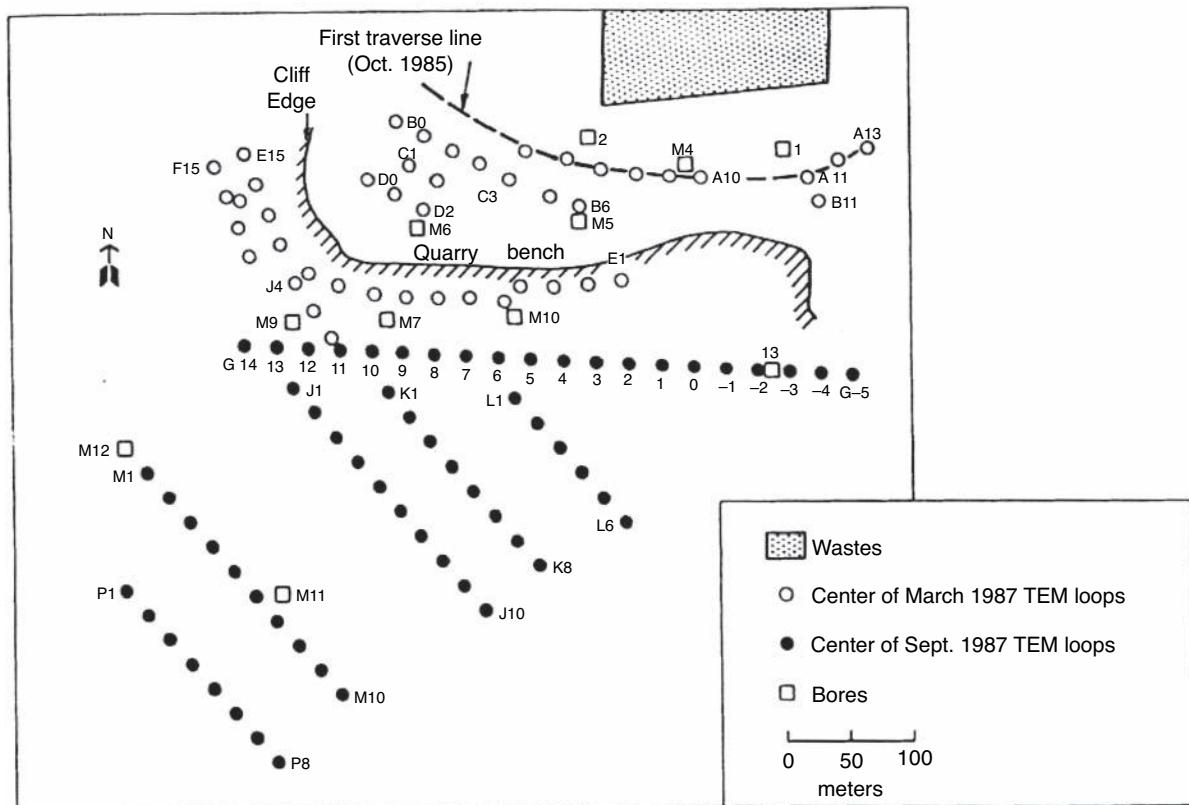


**Figure 11.63** Plan of the Morley landfill and survey area with centres of the 25 m TEM transmitter loops and borehole locations indicated. From Buselli *et al.* (1990), by permission.

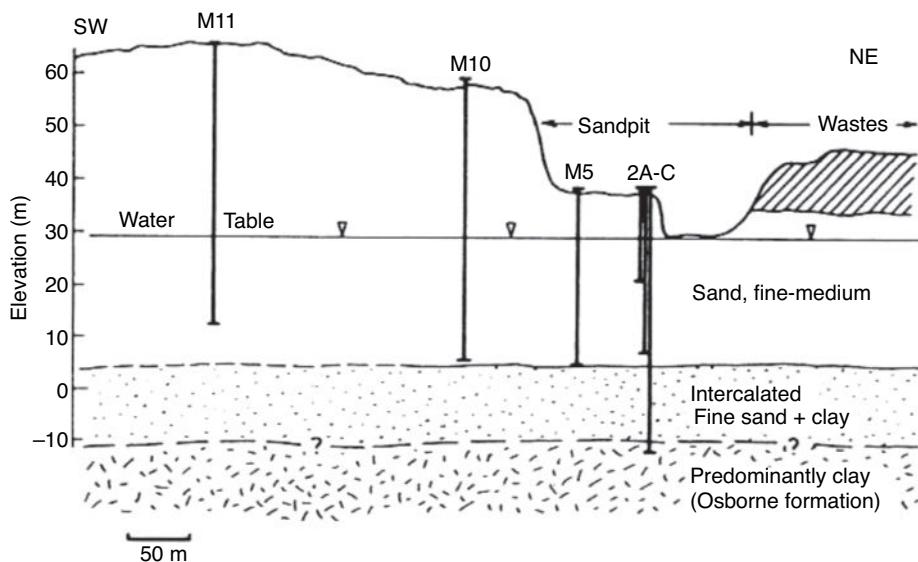


**Figure 11.64** Cross-section through the sequence of boreholes M11, M10, M5 and 2A-C and the landfill at Morley, Perth, Western Australia. From Buselli *et al.* (1990), by permission.

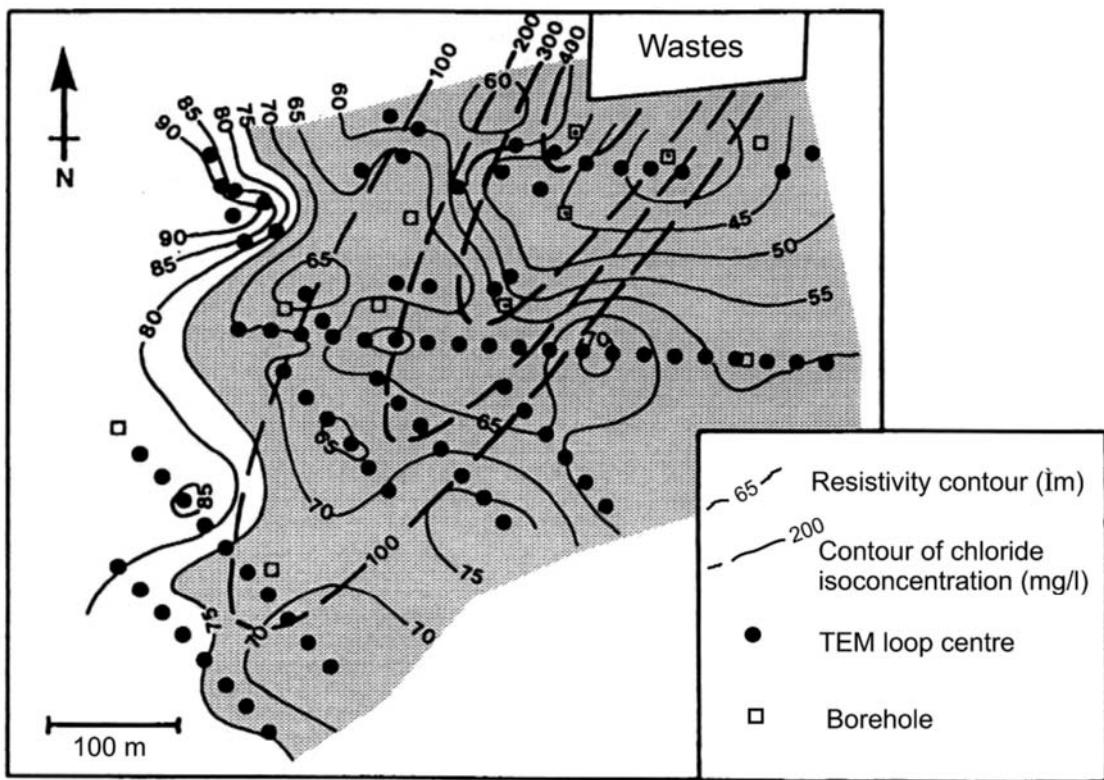


**Figure 11.65** Isoresistivity map derived from TEM sounding data with contours of isochlor concentrations determined from chemical analysis of water samples from the boreholes. The contaminant plume is indicated by a tint, as determined by resistivity values  $< 75 \Omega\text{m}$ . After Buselli *et al.* (1990), by permission.

powerlines. A  $z$ -axis profile across this deposit is shown in Figure 11.68. Despite the significant anomalies associated with the powerlines, it is still possible to detect the anomalies associated with both previously known and the newly-discovered Powerline Deposit. The Powerline Deposit anomaly was drilled directly without further ground-based geophysics, and was found to have 6.7% Cu, 1.3% Ni, and 13.3 g/t TPM over a 12.9 m segment in the discovery hole.

The same AeroTEM system was also flown over the Ni-Cu Montcalm Deposit owned by Falconbridge Ltd and originally discovered using  $h$ -EM in the 1970s. The very strong on-time response measured is characteristic of high-conductance targets such as nickel deposits. The concentric-coil configuration of the AeroTEM system produced EM responses that are diagnostic of conductor thickness for steeply dipping targets. A double-peak  $z$ -axis coil response and positive-to-negative  $x$ -axis coil crossover are diagnostic of a thin ( $< 8$  m thick) conductor. A thick tabular conductor ( $> 15$  m thick), such as a steeply dipping mineral deposit, is characterised by a single peak in the  $z$ -axis coil and a lower amplitude negative-to-positive  $x$ -axis coil crossover. For an 8–15 m thick conductor, the responses observed are transitional between the two cases described above. The responses for both thick and thin conductors recorded on the same flight line are shown in Figure 11.69.

Not all massive sulphide mineral deposits are necessarily good EM targets. For example, Cyprus-type massive sulphide deposits, which occur as mineralisation in altered conductive pillow lavas,

present very small physical parameter contrasts with the host rocks. Experiments using TEM over known mineral deposits in Cyprus failed to detect the orebodies (Cooper and Swift, 1994). Even when induced polarisation was used, only the true chargeability could discriminate between highly silicified structures and mineralised targets. Even chargeability was found to be an unreliable exploration parameter. The occurrence of extensive local disseminated pyrite masks electrical mineralisation anomalies at a survey scale typical of that used for mineral exploration. However, despite the lack of direct success with TEM in locating orebodies, it was used to help to delineate geological detail (faults, determination of lithology thicknesses, trends, etc.) which in turn can be used to build up a three-dimensional structure of a given area (Cooper and Swift, 1994).

#### 11.3.3.4 Mapping subsurface voids

A SIROTEM system was used in the investigation of a series of sinkholes along the route of the proposed Alice Springs to Darwin railway across the Wiso Basin, Northern Territories, Australia (Nelson and Haigh, 1990). The occurrence of sinkholes in this area was well known, but the sudden collapse of part of the Buchanan Highway into a sinkhole in 1982 highlighted the engineering hazard which then prompted a full-scale investigation.

Various geophysical methods were tested as to their effectiveness over terrain which was undulating and irregular, and which was

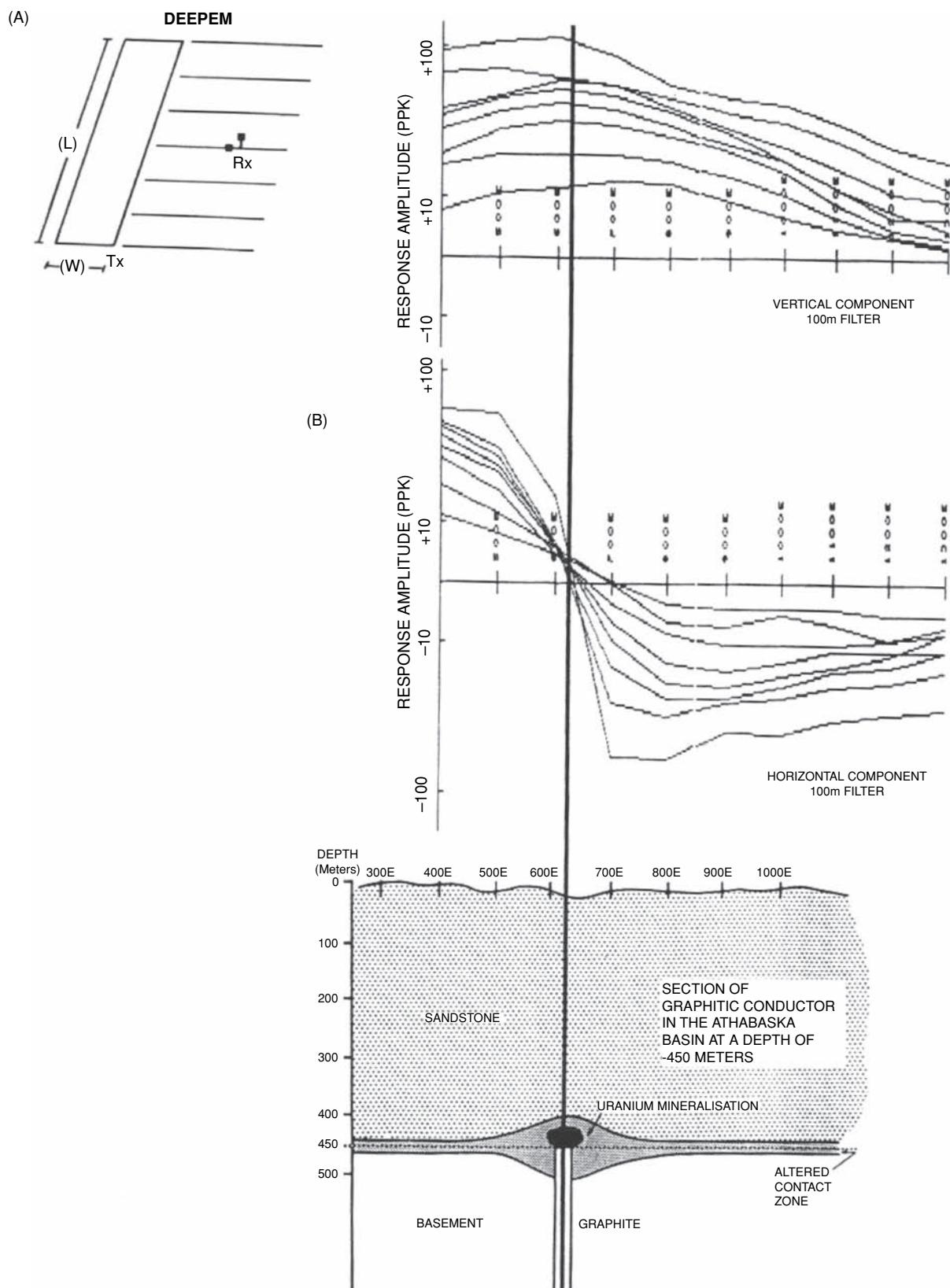


**Figure 11.66** (A) DEEPEM survey configuration. (B) Response amplitudes for both horizontal and vertical components (Fraser-filtered with a 100 m station interval filter gate). From Crone (1991), by permission.

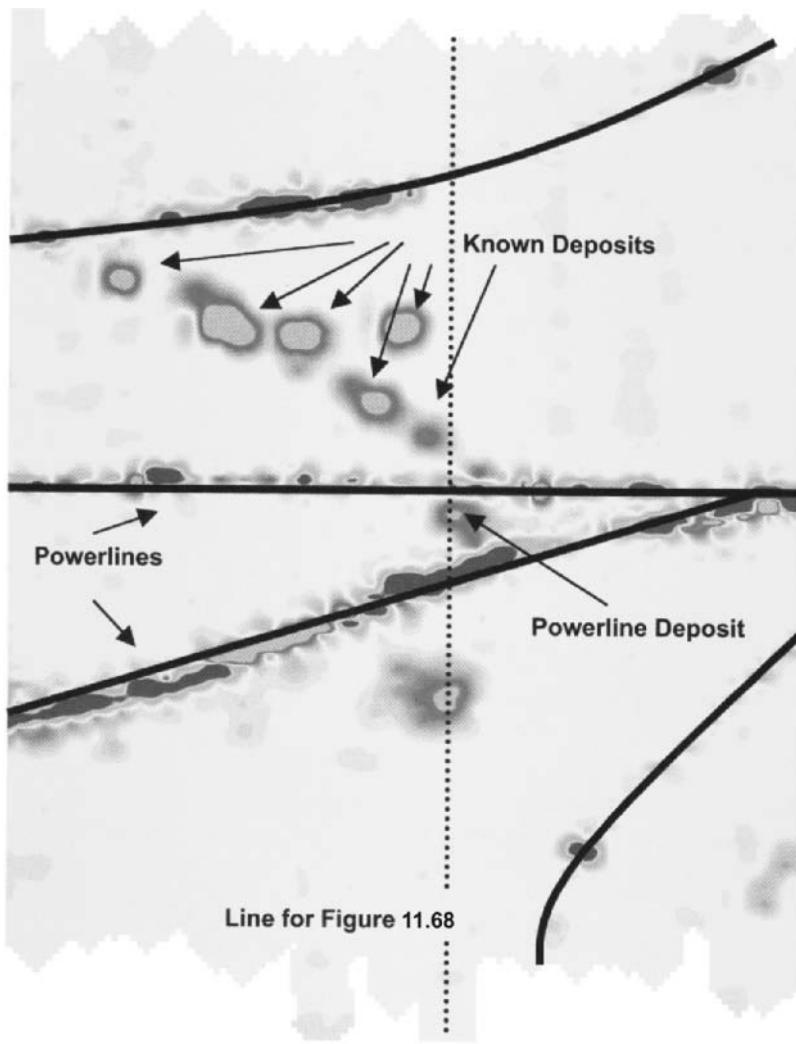


**Figure 11.67** Plan view of early-time z-axis response for the Victoria Property owned by FNX Mining Company. From Balch *et al.* (2003), by permission. [C]

covered with lateritic soils. Intuitively, air-filled cavities should give rise to resistive anomalies, but the contrasts found were sufficiently small that the method was not considered practicable for the required coverage of large tracts of land along the proposed railway route. It was found, however, that the walls and floors of known dolines tended to contain electrically conductive clay-rich material. Furthermore, the process of doline (sinkhole) formation was associated with leaching of silica, which produced pipes or structures with leached, weathered, transported or altered detritus that were also found to be characteristically conductive. Consequently, the target type for which the geophysics was selected was not the more intuitively obvious 'hole-in-the-ground' but the conductive secondary targets. Indeed, TEM would not have been suitable for air-filled voids owing to the diffusion velocity through the void being of the same order as the velocity of light. Similarly, these same silica-leached features also caused significant and detectable anomalies on time delays, relative amplitude attenuation and spectral content of seismic waves.

Following a considerable amount of trial work with a variety of methods, it was established that coincident-loop SIROTEM was the best method for rapid reconnaissance, with the seismic surveys being used over specific features. The seismic work, in addition to the SIROTEM investigation, has been described in considerable detail by Nelson and Haigh (1990).

Of several test areas, the Buchanan Highway Test Site, located 60 km west of the Stuart Highway, was known to be a major zone of doline formation. As part of this work, 25 m coincident-loop SIROTEM surveys were undertaken, with four turns of wire per loop to improve the signal strength. The rate of surveying with this system was up to 4 km per day. Two lines parallel to each other but 25 m apart were surveyed, with additional parallel lines with greater offset being investigated as required to help delimit the extent of features identified.

The general findings of the SIROTEM investigation were that the local geology was characterised by a generally uniform resistivity distribution, with apparent resistivities in the range 50–100  $\Omega\text{m}$ ,

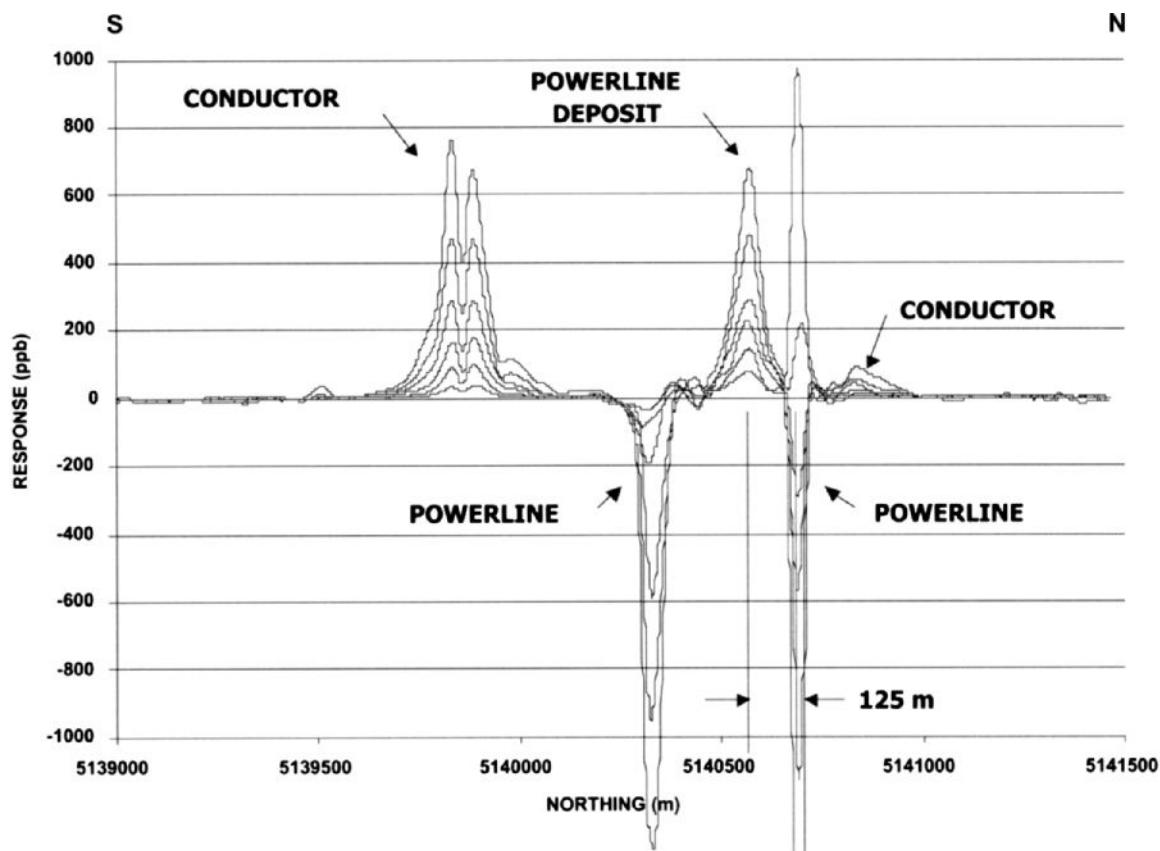


**Figure 11.68** Profiles of z-axis data for the Powerline Deposit. The responses from nearby powerlines are indicated. From Balch *et al.* (2003), by permission.

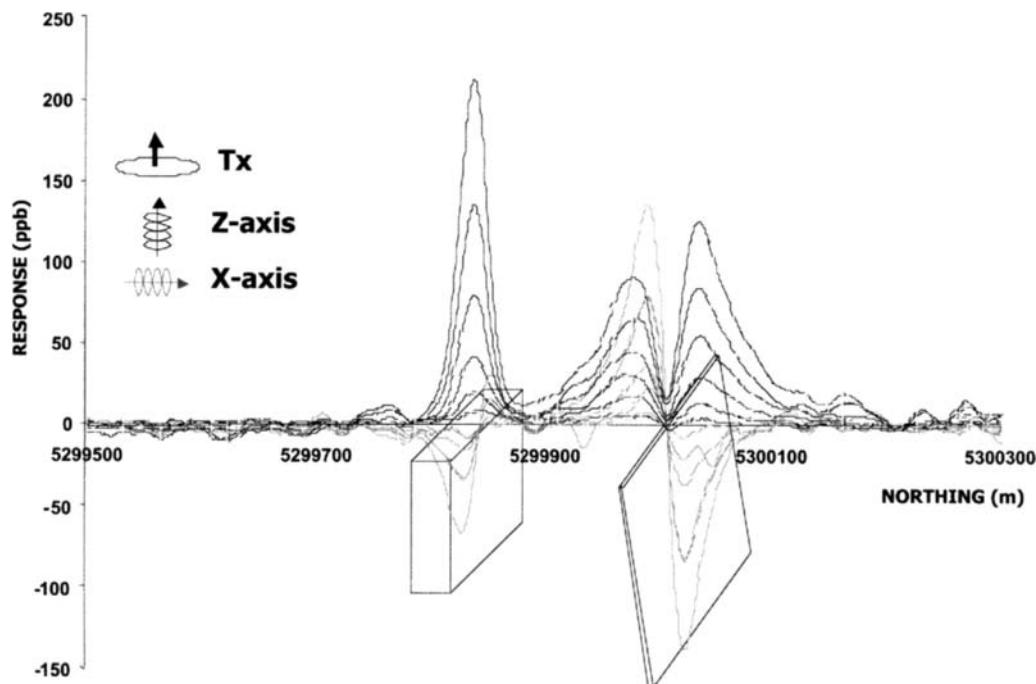


**Figure 11.69** Thick conductors have a characteristic single peak in the z-axis coil and a low-amplitude negative to positive cross-over in the x-axis coil. Steeply dipping conductors have a double peak in the z-axis and positive to negative peak cross-over in the x-axis of similar amplitude. From Balch *et al.* (2003), by permission. [C]

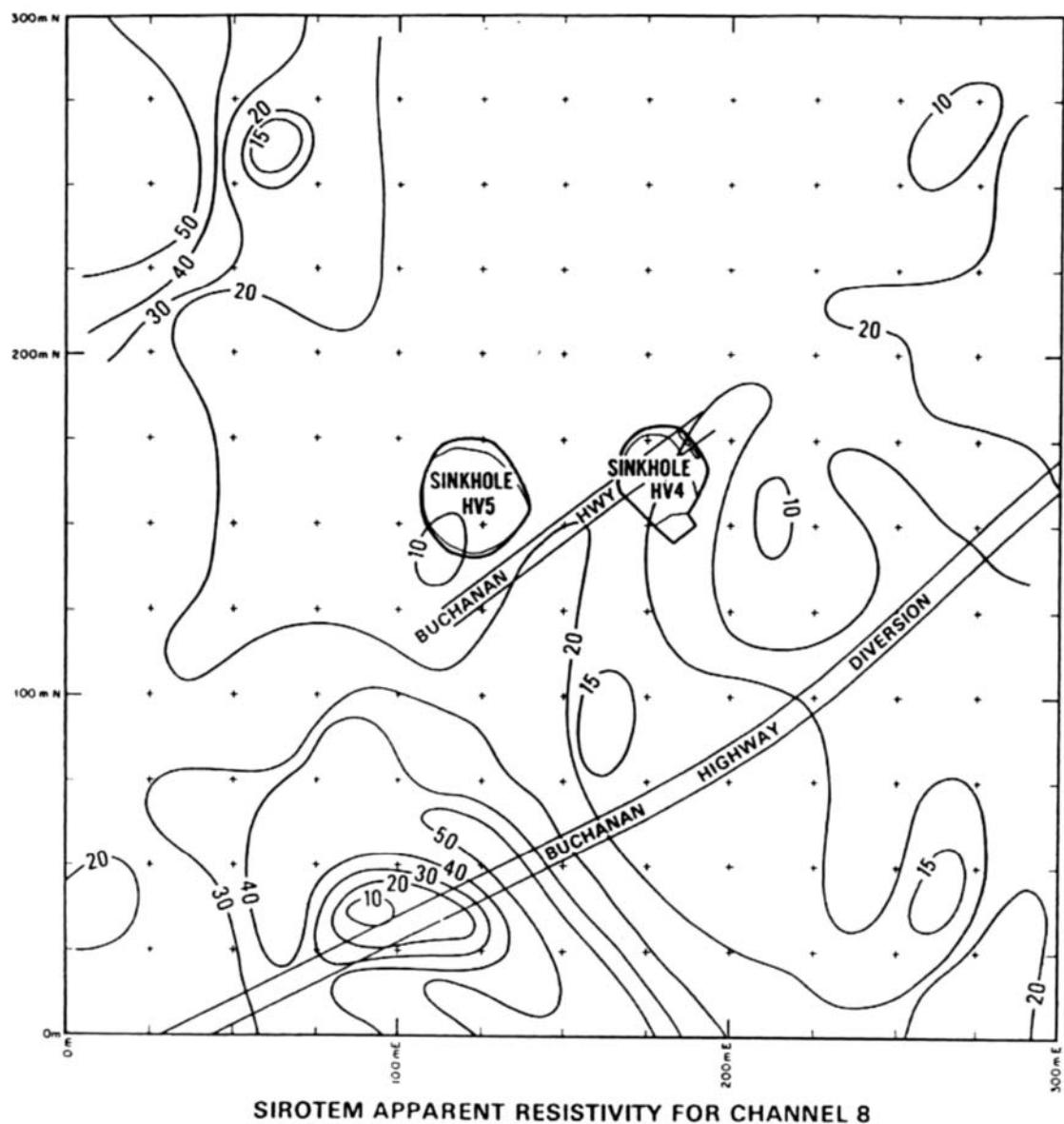


**Figure 11.70** SIROTEM apparent resistivity anomaly map over part of the Buchanan Highway test site, Northern Territory, Australia. From Nelson and Haigh (1990), by permission.

and with a gently dipping and consistently layered structure. In contrast, areas affected by dolines were found to have lateral resistivity fluctuations of up to  $20 \Omega\text{m}$  with a complex heterogeneous geometric appearance. A map of apparent resistivity values obtained using the SIROTEM system for part of the test site, where two dolines were known to occur, is shown in Figure 11.70. Sinkholes HV4 and HV5 were the two that occurred suddenly overnight in 1982. A car that drove into the newly formed hole was totally wrecked, but the driver escaped with only minor injuries! As a consequence of this incident, the highway was diverted along the route shown in Figure 11.70. However, a prominent apparent resistivity low (to  $10 \Omega\text{m}$ ) was found at coordinates (90 m E, 40 m N), almost on the diverted highway. This same feature correlated with seismic arrival

time anomalies and is interpreted to be an imminent doline collapse feature.

Figure 11.71 shows composite results of the two parallel SIROTEM traverses 25 m apart as contoured apparent resistivity values. A complex anomalous zone is evident between 89900 N and 90200 N on both traverses; in comparison with anomaly shapes over known dolines, this anomaly is characteristic of sinkhole-prone terrain. The SIROTEM anomaly is also consistent with the interpretation of seismic refraction results in terms of amplitude decay and travel-time delay over the anomalous feature. This combined correlation of the anomalous zone provides increased confidence in the overall interpretation. The full scope of the investigation carried out by Nelson and Haigh (1990) and coworkers deserves being read

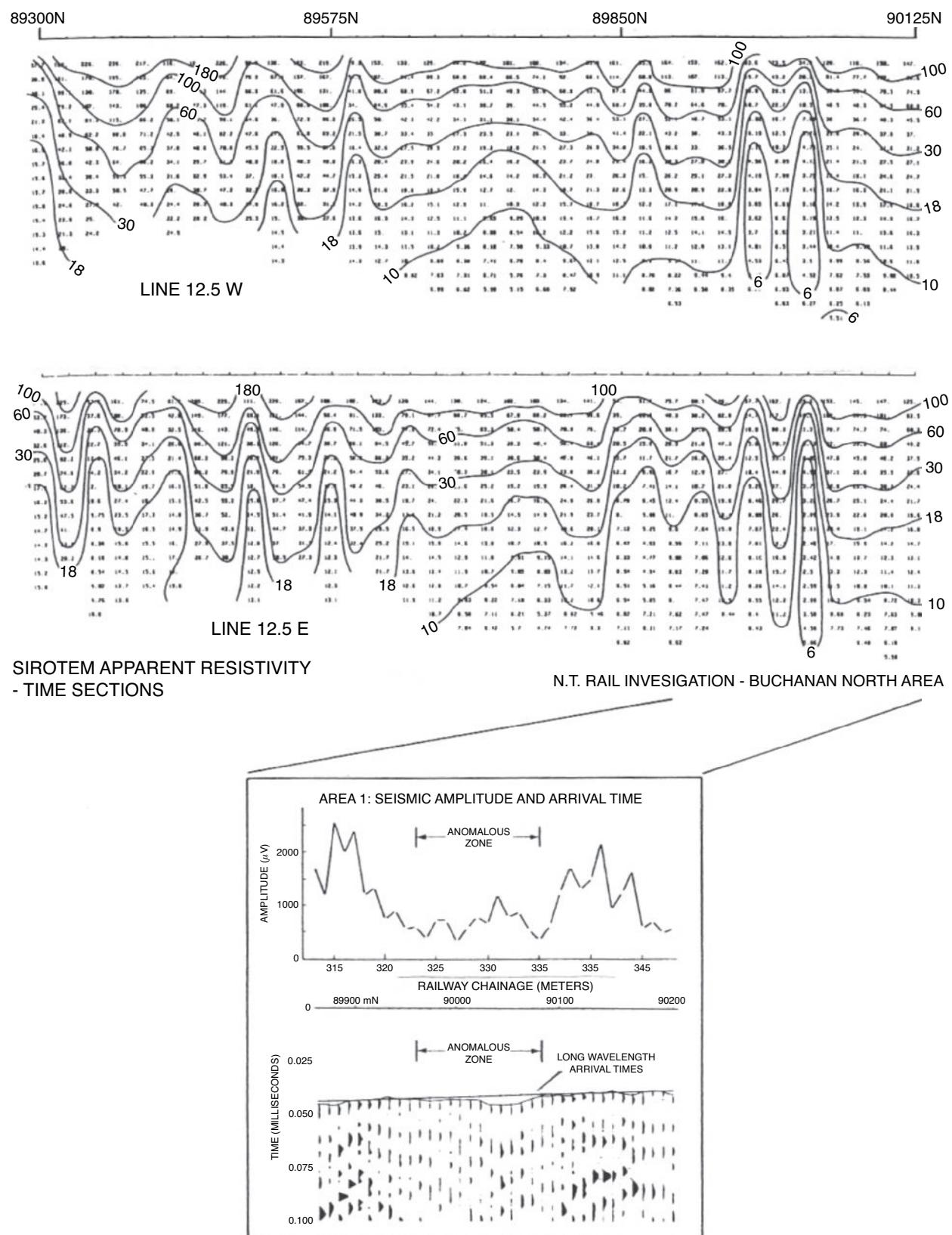


**Figure 11.71** SIROTEM 25 m coincident-loop apparent resistivity pseudo-sections along two lines 25 m apart, either side of the centre line of a proposed railway route at Buchanan Highway. Seismic amplitude and waveform sections over the SIROTEM anomalous zones confirm the probability of this region being sinkhole-prone terrain. From Nelson and Haigh (1990), by permission.

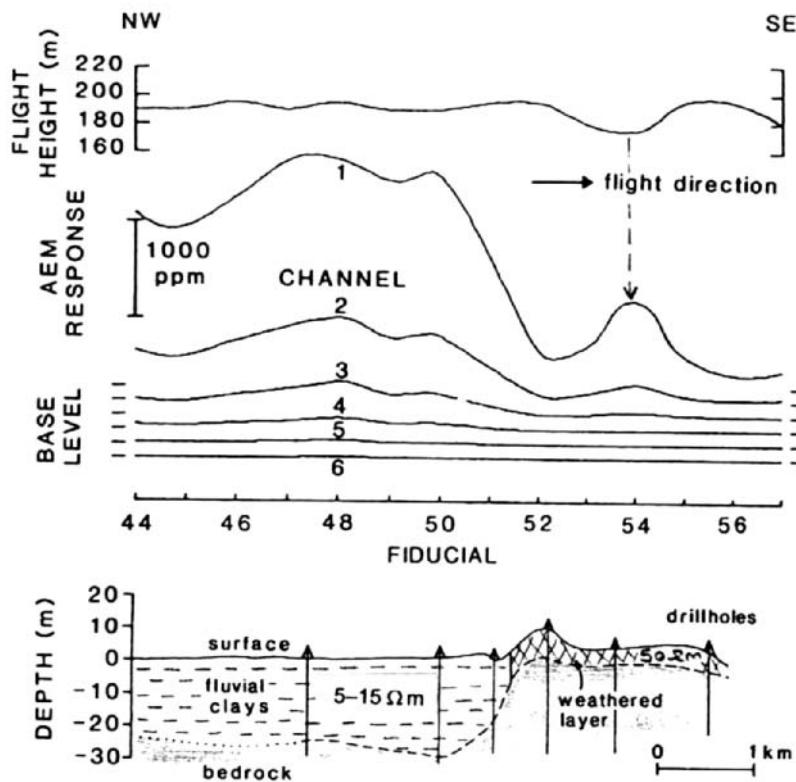


**Figure 11.72** (A) Altimeter trace for an airborne EM (AEM) survey at Dongling, Anhui Province, China. (B) AEM responses at six channels with respective base levels for each channel with fiducial fix numbers. (C) Interpreted geological section derived from AEM data and borehole information. The true resistivity ranges (in  $\Omega\text{m}$ ) of the superficial materials are indicated. From Huang and Palacky (1991), by permission.

in detail as it is an excellent example of a well-thought-out investigation that was well executed. As with so many projects like this, lack of finance at a critical stage denied the final conclusive direct investigative work. A series of appropriately sited boreholes could have helped to test the geomorphological model for the formation of these features over a very large tract of land in the Northern Territory of Australia, the incomplete funding of such work is a major oversight.

Guoqiang *et al.* (2004) have described the use of a Chinese TEM system for cavity detection for the Chinese Highway Department. They used a 100 m-sided square transmitter loop surrounding a 10-m sided receiver loop. The receiver station interval was 10 m with an inter-line separation of 15 m. Two high-value apparent resistivity anomalies were mapped and modelled and interpreted to be related to caverns formed by dissolution of limestone, which was subsequently verified by post-survey drilling.

### 11.3.3.5 Geological mapping using airborne EM

Huang and Palacky (1991) have described the use in 1983 of airborne EM surveying for geological mapping in Dongling, Anhui Province, China. The survey was undertaken using an INPUT-type system made in China (the M-1 instrument) which uses a transmitter made up of a seven-turn vertical axis loop mounted on a fixed-wing

aircraft. The receiver used was a towed bird, nominally 90 m behind and 63 m below the aircraft. Although designed for an optimum flying height of 120 m, the system was flown at significantly greater heights. The channels at which the signals were measured were 0.3, 0.5, 0.8, 1.2, 1.7 and 2.3 ms after the transmitter switch-off.

The survey area was known to contain lead-zinc mineralisation of the replacement type in Mesozoic limestones. The objective of the AEM survey was to locate previously unknown mineralised bodies and to determine the thickness of fluvial clays in the Yangtze River plain and the extent of the weathering in areas underlain by Mesozoic rocks. The line spacing was 500 m with a NW–SE flight line direction.

Figure 11.72 shows the AEM data and the corresponding geological section with the altimeter trace (top), and measured amplitudes at six channels with indicated base levels for each. The fiducial markers are at approximately 500 m intervals. The geological section was derived from the interpolation of drilling data. The peak observed on the AEM data at fiducial 54 for channels 1 and 2 (arrowed) is thought to be due to the change in flying height. Strong AEM anomalies evident on the early-time channels (1–3) are due to conductive fluvial clays. Resistivities of the local geological materials were obtained from ground-based electrical soundings, with the fluvial clays having a resistivity in the range 5–15  $\Omega\text{m}$  and the weathered material up to 50  $\Omega\text{m}$ , and the underlying Mesozoic strata having resistivities of hundreds to thousands of ohm-meters. The

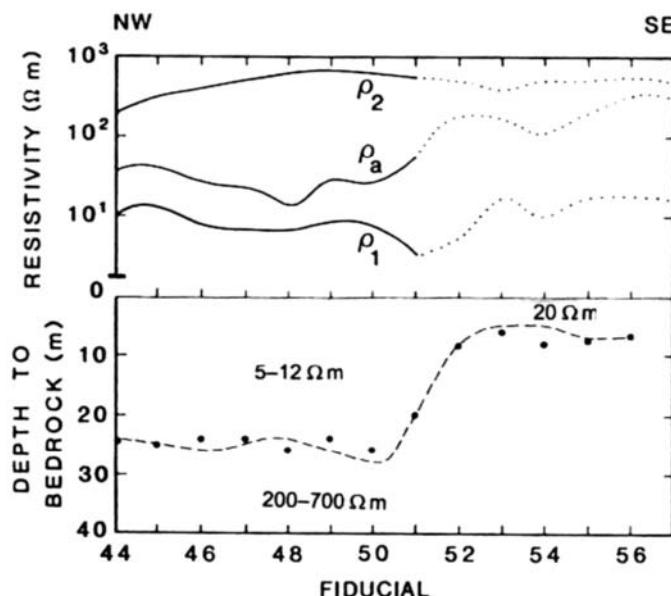


**Figure 11.73** Apparent resistivity ( $\rho_a$ ) and first- and second-layer resistivities ( $\rho_1$  and  $\rho_2$ ) obtained by inversion of the AEM data shown in Figure 11.72. The interpreted depth to bedrock at each fiducial position derived from the AEM inversion (dots) and from drilling (dashed lines) are shown for comparison. From Huang and Palacky (1991), by permission.

inversion results for the same data are shown in Figure 11.73. The apparent resistivity ( $\rho_a$ ) was derived from the inversion of the AEM data from all six channels, assuming a homogeneous half-space model. The marked increase in apparent resistivity near fiducial 51 is associated with the transition from the fluvial clays to Mesozoic sediments. The segments of the resistivity graphs shown dotted are indicative of less reliable results owing to the higher noise levels within the system.

The inversion was carried out using a two-layer model for which resistivities were found to be 200–700  $\Omega\text{m}$  for the Mesozoic strata, 5–12  $\Omega\text{m}$  for the Cenozoic fluvial clays and about 20  $\Omega\text{m}$  for the weathered Mesozoic sediments, all of which are in good accord with the results of the ground-based investigations. Furthermore, the depths derived from the inversion (dots) are in very good agreement with those found from drilling (dashed line) as shown in Figure 11.73. This example demonstrates the effectiveness of the AEM method coupled with appropriate inversion processing in mapping significant geological boundaries. The method shows that it is particularly the early-time responses that are sensitive to the conductivity contrasts in the near-surface.

An example of the development in inversion techniques has been described by Christensen *et al.* (2009) for a survey at Toolibin Lake, Western Australia, using the SkyTEM system. The problem being investigated is dry land salinity. Extensive previous geophysical investigations have been undertaken involving downhole induction logging, surface and airborne EM and airborne magnetic and radiometric surveys, plus shallow drilling. The geology of the area consists of Quaternary and Tertiary alluvial sediments overlying weathered Archaean granite and granite gneiss. The granitic bedrock contains

many Proterozoic mafic dykes. The cover overlying the bedrock is typically 25 m thick, but up to 60 m in places. Surface materials have been shown to have conductivities up to 700  $\text{mS/m}$  due to very high groundwater salinity ( $>50,000 \text{ mg/l}$ ). A deep and relatively transmissive palaeochannel system has been found that extends about 5 km northeast of the lake. Sands and clays up to 30 m thick comprise the sediments in the palaeochannels. Beneath the lake they are overlain by fine lacustrine clays up to 8 m thick.

The SkyTEM survey consisted of 340 line-km made up of 32 profiles and was conducted using both low and high transmitter moment (12,600 and 107,000  $\text{Am}^2$ , respectively) to ensure good near-surface resolution and depth of exploration. Nearly 8000 sets of combined high and low moment data were inverted jointly and it was concluded that a 1D inversion process gave sufficiently reliable results. Two profiles are illustrated in Figure 11.74 (lines 9 and 19). Line 9 shows a 5–10 m thick cover with an intermediate conductivity corresponding to alluvial sediments, underlain by a layer of high conductivity associated with saprolitic clays – intensely weathered bedrock with very saline groundwater. The base of this layer is found at 40–60 m depth over less conductive bedrock. Unweathered bedrock, characterised by low conductivities, occurs between positions 6.36 and 6.362.

Line 19 passes through the centre of the survey area and shows a conductive layer split into an upper and lower layer by a slightly less conductive layer at 20 m depth, which indicates fine-grained sediments beneath Lake Toolibin. From borehole results, these sediments have been found to have slightly lower conductivities than the sands and gravels in the underlying palaeochannel. It is interpreted by Christensen *et al.* that the groundwater in the clays is less saline than that in the saprolites and palaeochannel sequence.

From the inversion of the TEM data, contoured maps of the mean conductivity within specific 4-m depth intervals (8–12 m, 12–16 m, 16–20 m and 20–24 m) have been produced (Figure 11.75). A relatively low conductivity palaeochannel is evident (indicated by dots in Figure 11.75), trending northeast to southwest through the survey area; it is most clearly seen in the depth range 16–20 m. Relatively less conductive areas can be identified in the northwest and southeast of the survey area and show where more resistive bedrock lies closer to the surface.

A significant amount of Australia's coastal waters shallower than about 50 m are affected by turbidity. While laser scanning (LIDAR) is used for bathymetric mapping, it is affected detrimentally by the water turbidity. Furthermore, there are areas of palaeochannels infilled with sediments whose thicknesses are not known. A prototype *h*-TEM system has been developed (SeaTEM(0); Vrbancich, 2009) to provide a rapid method of bathymetric surveying coupled with determination of sediment cover thickness over bedrock.

SeaTEM(0) was based on the HoistEM system that has been used extensively for mineral exploration. The SeaTEM(0) framework comprises an 18-m centre pole with aerodynamically shaped 'wings' utilising carbon composite materials spanning ~23 m. A single-turn transmitter loop with an area of ~205  $\text{m}^2$  is fixed to the extremities of the frame. A three-turn receiver loop, concentric with the transmitter loop and with a combined area of ~96  $\text{m}^2$ , is mounted approximately midway between the extremities of the cross-frame and the intersection point of the centre pole and wings.

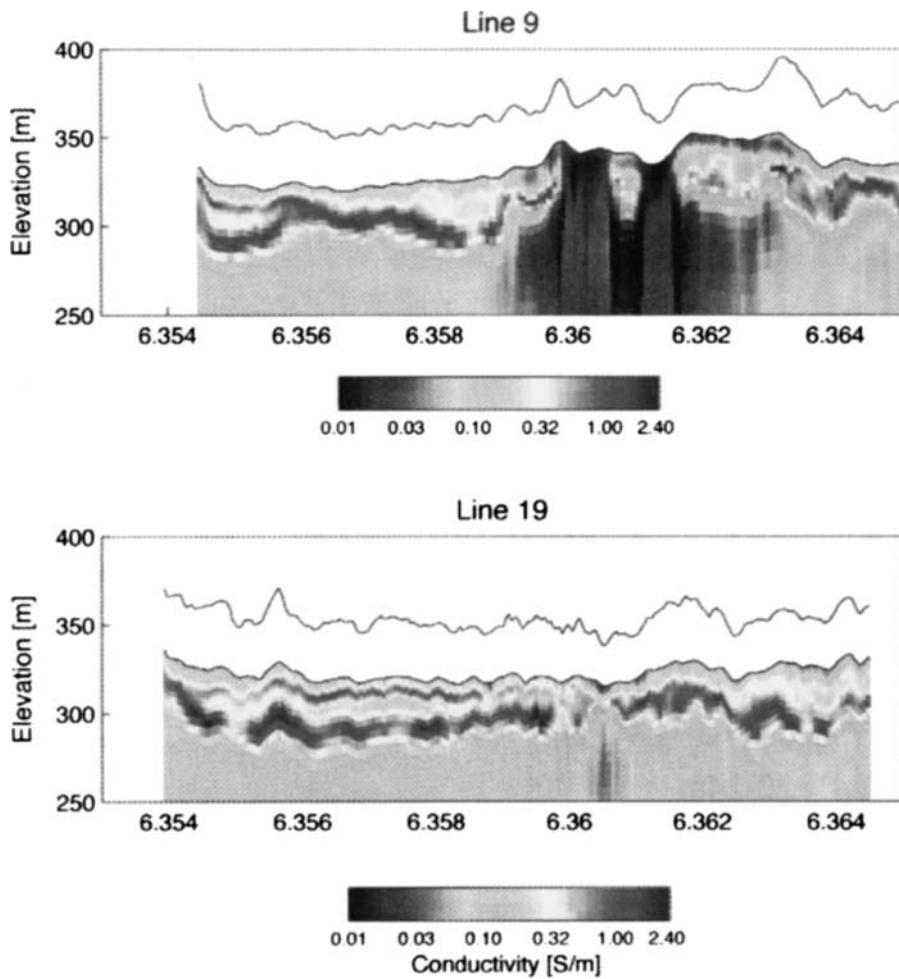


**Figure 11.74** Model sections of concatenated 1D models from lines 9 and 19 of a SkyTEM survey at Toolibin Lake, Western Australia. From Christensen et al. (2009), by permission. [C]

The SeaTEM(0) waveform is made up of 5 ms bipolar pulses transmitted at a fundamental frequency of 25 Hz (15 ms offtime). The current pulse is quasi-trapezoidal with an exponential rise time (750  $\mu$ s time constant), ~3.5 ms constant current, and a 27  $\mu$ s linear turn-off ramp. Decay voltages are measured over 112 channels binned into 21 windows.

Vrbancich (2009) described a trial survey using the SeaTEM(0) system in Broken Bay, New South Wales, Australia, where water depths are up to ~30 m. The survey area was selected as separate palaeo-drainage systems for the Hawkesbury River, Brisbane Water and Pittwater, which join in Broken Bay, give rise to palaeovalleys infilled with unconsolidated sediments to almost 200 m thickness, as well as exposed bedrock reefs. Measurements of seawater electrical conductivity were made and found to be typically around 4.72 S/m. Unconsolidated marine sand was assumed to have a conductivity of 1.25 S/m. These values were used in a 1D inversion of a three-layer model comprising seawater and sediment over bedrock with a conductivity of 0.1 mS/m. Water depths derived from the inversion were found to agree to within  $\pm 1$  m and  $\pm 0.5$  m for known water depths to 20 m and 6 m, respectively. Independent methods to determine bathymetry were obtained by chart sound-

ings and seismic reflection surveys. The trial survey revealed coarse topographic features of palaeovalleys to depth limits of ~60 m to 80 m below sea-level in 20–30 m water depth, as well as resolving bedrock ridges and exposed reefs in shallow waters. The *h*-TEM method also demonstrated that it could be used in areas of surf. An advantage of using *h*-TEM to measure bathymetry and sediment infill characteristics is the far greater speed with which the data can be acquired compared with surface-based over-water surveys using boats. However, the method depends on the conductivity of the layers modelled to be invariant within a given area, and errors, especially in the determination of sediment depths, may arise through local variations in electrical conductivity.

### 11.3.3.6 Geotechnical and environmental investigations

One of the previous limitations of using TEM in near-surface investigations has been the difficulty in measuring early time gates to yield information about the shallowest portion of the ground under investigation. Ambient cultural noise in urban environments

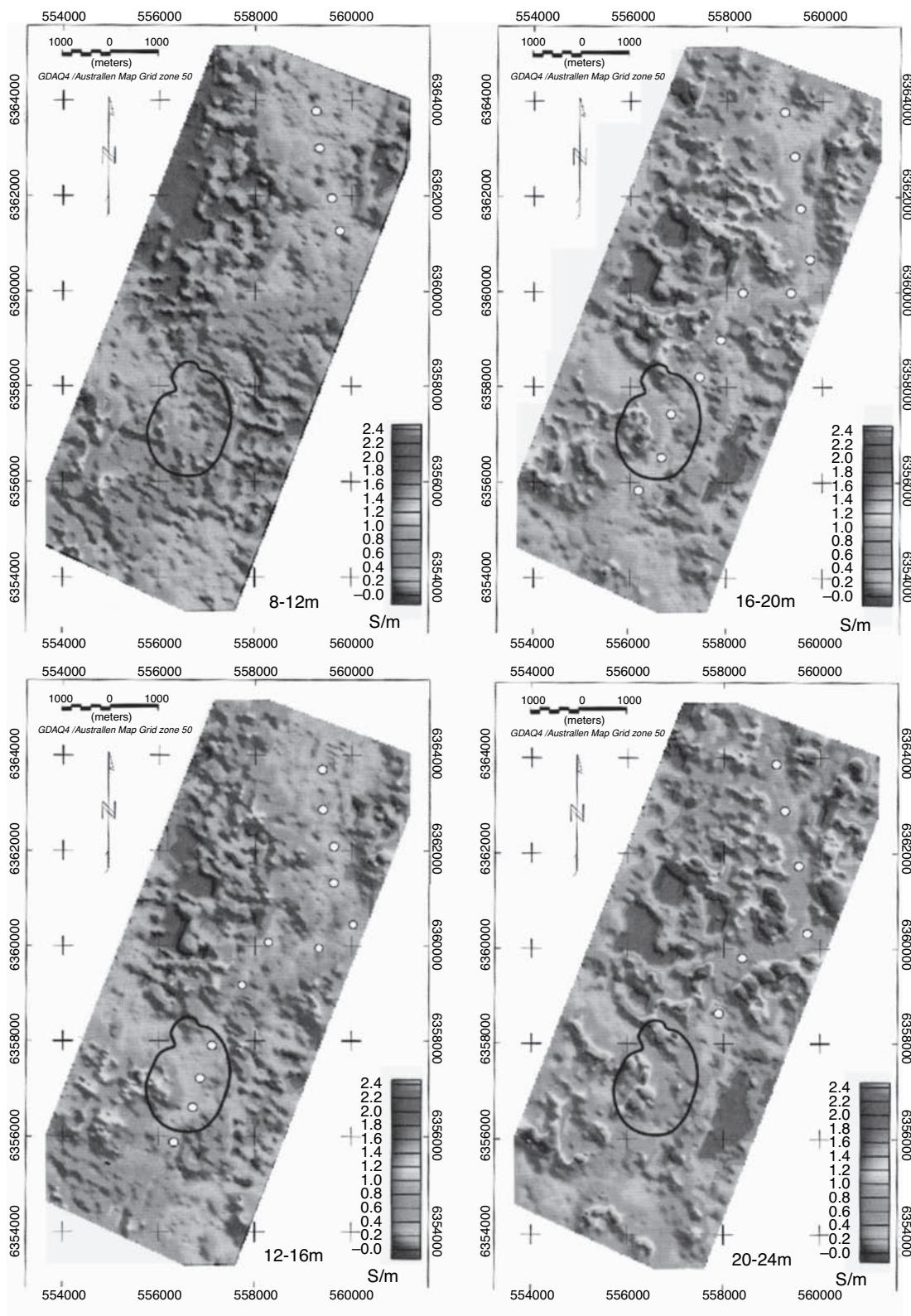


**Figure 11.75** Contoured maps of mean conductivity in the depth intervals 8–12 m, 12–16 m, 16–20 m and 20–24 m. The outline of Toolibin Lake is shown as a black contour in the southwest part of area; a palaeochannel is marked with white dots. From Christensen et al. (2009), by permission. [C]

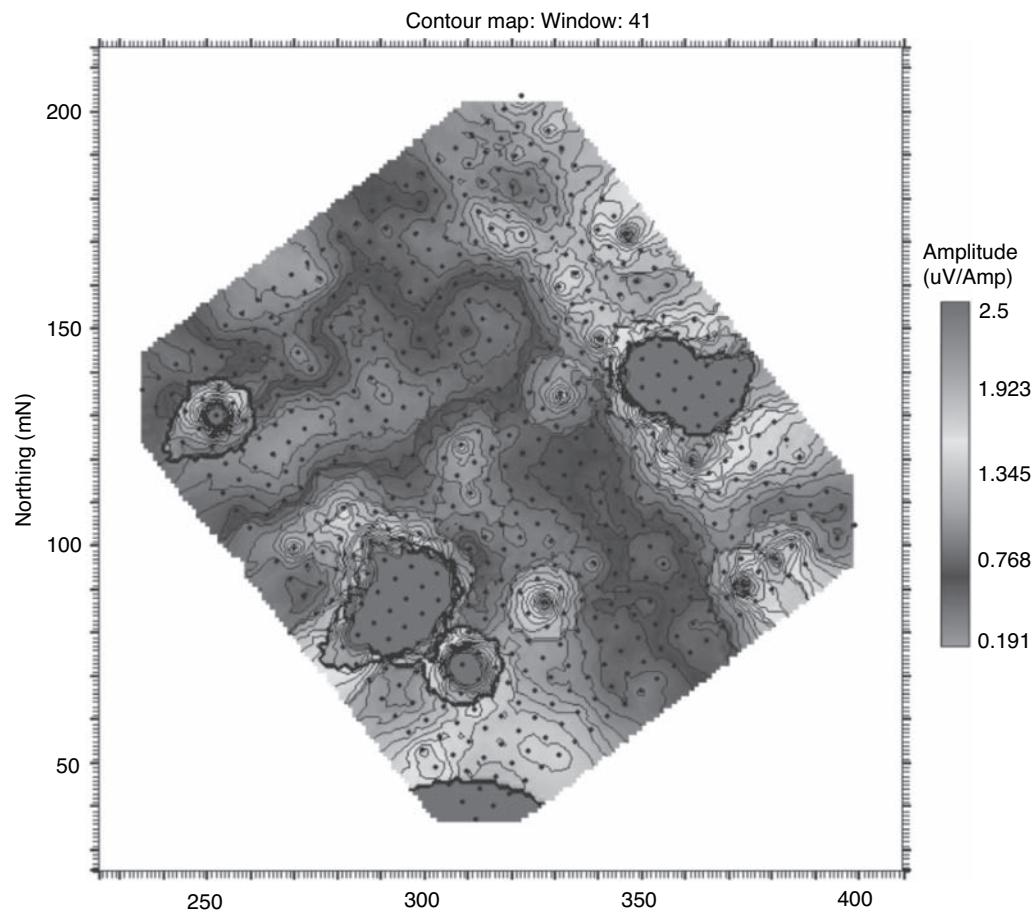


**Figure 11.76** TerraTEM amplitude time slice at 0.5285 ms delay. From Henderson (personal communication,) and Monex Geoscope Consulting, by permission. [C]

also restricted the use of such systems. Very Early (VETEM) TEM systems have now been developed where these limitations no longer apply, such as in the use of the TerraTEM system. Henderson (personal communication) has provided two examples of where the TerraTEM system has been used to good effect in both situations.

The first example is the use of the TerraTEM system to locate conductive foundations of former buildings. The foundation targets were thought to be of the order of 10–20 m across. A coincident loop geometry of 5 m by 5 m was used with a station interval of 5 m. A time slice of the amplitude values at a time delay of 0.5285 ms is shown in Figure 11.76. The most prominent features are the two large-amplitude anomalies measuring about 20 m across near the northeast and northwest sides of the survey area. These anomalies coincide with less distinct magnetic features and were interpreted to be the foundations that were the object of the survey.

The second example is a TEM survey to locate a possible landfill site originating from operations of a lead factory that had been removed previously and the site developed for housing (Figure 11.77A). Anecdotal information indicated that the material had been dumped into either a former quarry or trenches. Given the lack of detailed historical information, a geophysical survey was undertaken comprising both magnetic and transient EM techniques.

The site was complicated by the presence of reinforced concrete, above-ground ferrous objects and multiple subsurface utilities. The 2.1-ha site was covered with profiles at 2 m line intervals for the magnetic survey, during which 36,000 readings were recorded using a G856 magnetometer. The TerraTEM layout comprised a small-loop transmitter/receiver system using a  $10 \times 10$  m wire loop for both elements. The control console was offset from the transmitter/receiver loops and hard wire links used to connect with them. Data were acquired in a series of linear profiles that made up a grid over nominated areas. Loops were advanced at 10-m increments and 174 soundings completed. The magnetic total field intensity and TEM amplitude maps of the survey area are shown in Figure 11.77B and C, respectively. Discrete anomalies or clusters of magnetic anomalies have been delineated in Figure 11.77B; the position of a cyclone wire safety fence is indicated by a dashed line. Comparison of the two geophysical maps in Figure 11.77 shows that the largest area defined on the magnetic data coincides with a very prominent TEM high-amplitude anomaly. Three discrete magnetic anomalies in the middle of the survey area are also evident on the TEM data. The 10-m station interval on the TEM data provides a limit to the ground resolution of anomalies, and smaller features may not have been detected, although finer resolution of

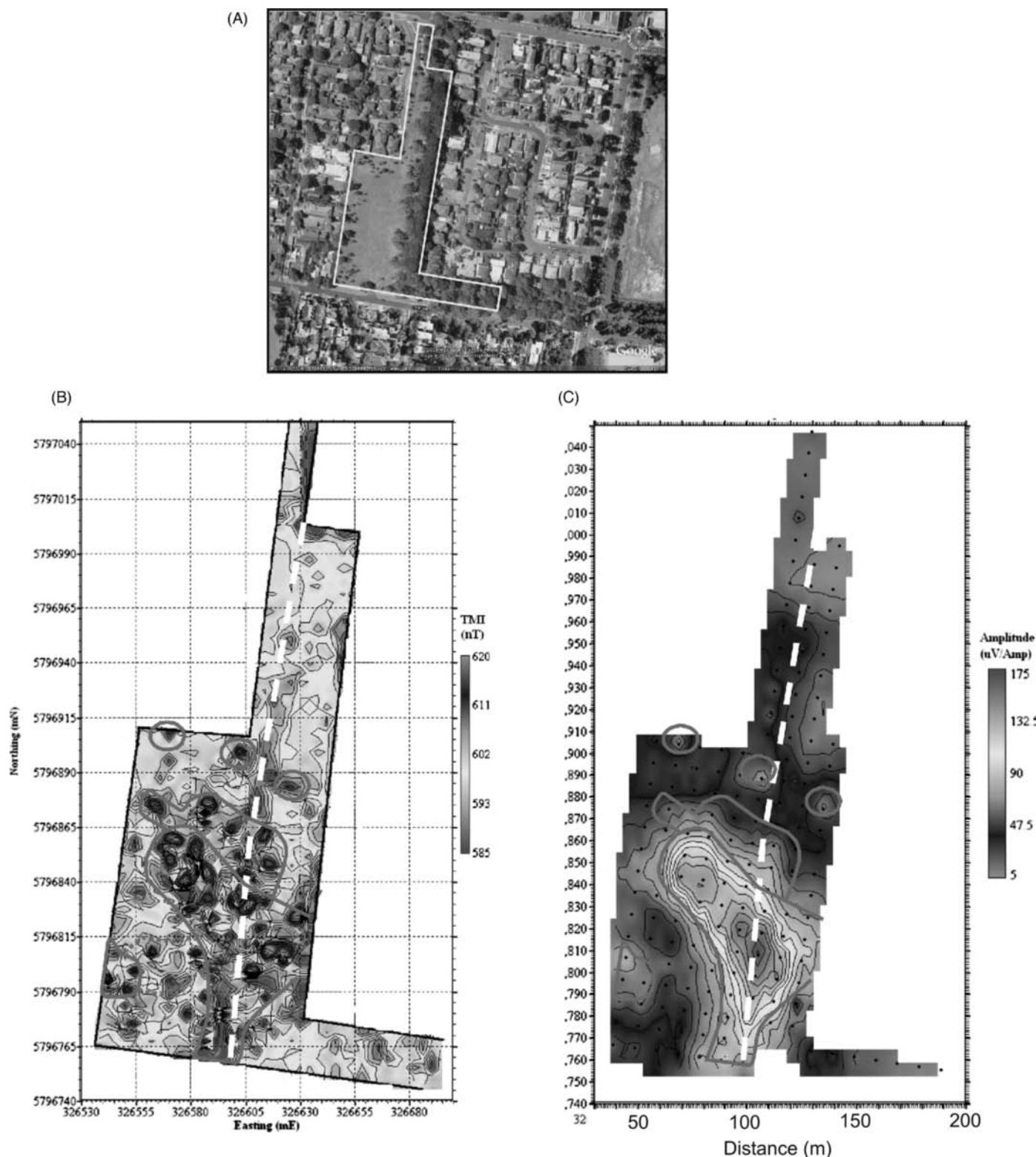


**Figure 11.77** (A) Location of a magnetic and TEM survey to locate an old landfill near Melbourne, Australia. (B) Total magnetic field intensity map and (C) TEM amplitude map of the survey area depicted in (A). Courtesy of Monex Geoscope Consulting and Henderson (personal communication), by permission. [C]

ferrous objects has been provided by the closer-spaced magnetic data.

### 11.3.3.7 Unexploded Ordnance (UXO) mapping

Sadly, one aspect of site investigation is having to detect unexploded ordnance (UXO), such as shells, mortars, rifle rounds, bombs, and so on, which might have been left after a military conflict or within designated military firing or bombing ranges. In the UK, for example, there still remains a considerable legacy of unexploded bombs from the Second World War, and with growing pressures to develop land, there is a need to be able to identify such features without them being detonated unintentionally. Between 2006 and 2008 about 15,000 items of ordnance, ranging from high explosive aerial-delivered German bombs to smaller items such as mortar shells and grenades (but excluding small-arms ammunition) have been removed from UK construction sites (Stone *et al.*, 2009). Clearly, similar problems exist to larger or smaller extents elsewhere, but there remains a need to be able to identify the presence of such hazards, preferably non-intrusively, and manage the ensuing risk. Geophysical techniques have been developed to service this need, and range from magnetic methods (for ferrous targets) through to EM systems (largely acting as metal detectors) that are ground-based or airborne. The use of ground-penetrating radar for UXO detection is discussed in Chapter 13. It is also important to note that many types of munitions, most notably landmines, are designed and manufactured to avoid methods of detection. A useful guide on unexploded ordnance for the construction industry in the UK has been produced (Stone *et al.*, *et al.*, 2009). Despite geophysical methods being widely used for UXO detection, this publication barely mentions them or in particular the limitations of such techniques. All too often, absence of evidence is used as evidence for absence, which, in the case of UXOs, may prove tragically incorrect! It is fundamental to any UXO risk assessment that the possibility of failure of detection is considered and the limits of detectability determined before declaring a site 'clear'. Nevertheless, these guidelines do provide a good introduction to the regulatory framework of UXO risk management.

Geonics Ltd have produced a range of TEM-based metal detectors for UXO detection, such as the EM61 family, and EM63 (Figure 11.78). The EM61 is available in a number of configurations ranging from the EM61-MK2 (Figure 11.78A), which comprises two vertically separated transmitter-receiver coils 0.5 m in diameter. The waveform is generated by a unipolar rectangular current and four time gates of secondary response are measured (in units of millivolts). Early time gates increase the maximum depth of detection of targets. The system can be pulled in a trailer, carried by an operator with a belt harness, or deployed as a single unit or with up to six sensors in an array. Data acquisition rates of 30 records per second can be achieved with travel speeds up to 10 km/h. The EM61 system is available in a variety of options including a hand-held (or wheeled) version (e.g. EM61-HH; Figure 11.78B), a submersible version (EM61S) for use in both fresh- and seawater, and as an airborne system (EM61-AB). A more advanced TEM system that operates with 26 time gates covering the range from 180  $\mu$ s to



**Figure 11.78** TEM metal detection systems: (A) EM61-MK2, (B) EM61-HH, and (B) EM63 instruments. Courtesy of Geonics Ltd, by permission. [C]

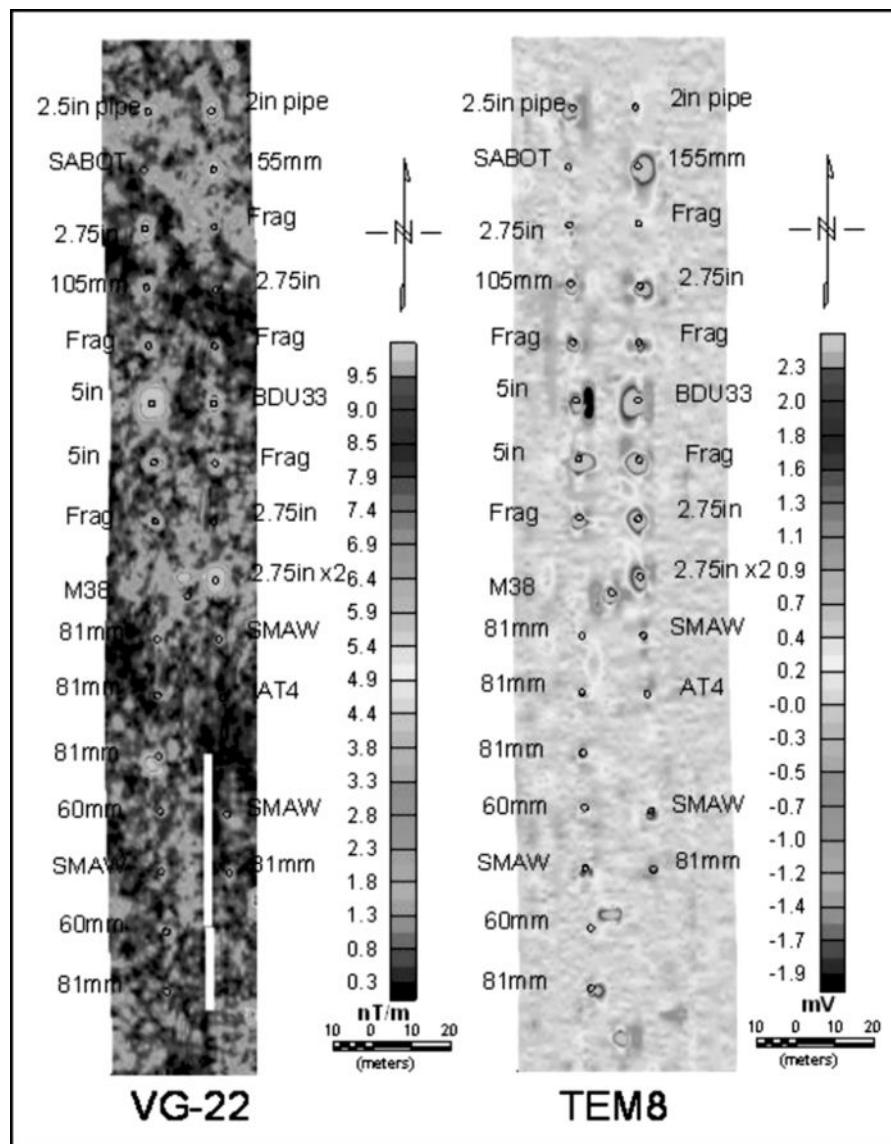


**Figure 11.79** Comparison of VG-22 magnetic gradiometer and TEM-8 results flown at 1-m ground clearance over two lines of ordnance test items laid on the ground surface. From Doll *et al.* (2008a), by permission. [C]

25 ms is available (EM63; Figure 11.78C) and offers greater resolution than the EM61 systems.

Military facilities such as bombing ranges typically cover very large tracts of land. If these are not to be sterilised for remnant UXO after each operation, then proactive clearance has to be undertaken. Given the large areas involved, ground-based search methods are likely to be inefficient and very time-consuming and costly. Consequently, much more rapid airborne mapping systems have been developed as described in Section 10.3.3.2 and shown in Figure 10.22. Helicopter-borne magnetic and TEM systems have been introduced that with very low terrain clearance can still differentiate small targets and provide a viable alternative to ground-based surveys. A further advantage of airborne systems is that the sensor system is not dependent upon contact with the ground, thereby

avoiding the potential of having survey operatives triggering any devices by stepping on them.

An example of airborne UXO mapping has been given by Doll *et al.* (2008a) with the Battelle VG-22 magnetometer and TEM-8 systems. They have demonstrated that airborne *h*-TEM UXO surveys flown at 1 m ground clearance can have comparable performance in target identification to that using helicopter magnetic gradiometer systems (Figure 11.79). In this case, two rows of ordnance of different types were laid at the ground surface at a site with moderate geological noise and overflown by both helicopter-borne sensor systems. The individual targets have been indicated. It is noted that the joint interpretation of both magnetic and EM datasets can reduce the number of false alarms.



# 12

## Electromagnetic Methods: Systems and Applications II

### 12.1 Very-low-frequency (VLF) methods

#### 12.1.1 Introduction

In 1963, Paal (1965) observed that radio waves at very low frequencies (VLF) could be used to look for conductive mineral deposits. The first commercially available ground VLF instrument was made in 1964 by Ronka (Paterson and Ronka, 1971) with others being manufactured within the following few years. The most widely accepted ground survey instrument has undoubtedly been the Geonics EM16. Its resistivity mapping mode is also very well used in the EM16R configuration. In recent years, new VLF instruments have been produced such as the WADI from ABEM, EDA's integrated magnetometer/VLF system called the OMNI IV, the 'VLF-3' and 'VLF-4' from Scintrex, and the 'VLF-2' from Phoenix, among others. Although VLF measurements can also be made from the air, only ground-based systems will be considered here. A comprehensive review of VLF methods has been given by McNeill and Labson (1991).

The VLF method has remained an excellent, cheap and rapid tool for reconnaissance mapping of conductive mineralised bodies and water-bearing fractures. Its use in engineering and environmental work has as yet remained small. However, with the advent of modern VLF systems with integrated data-loggers, auto-selection of appropriate transmitters and enhanced display and interpretation methods, the technique is gradually being tried for non-exploration purposes such as in cavity detection and in mapping landfills.

#### 12.1.2 Principles of operation

There are 11 major VLF transmitters distributed around the world used primarily for military communications. These provide very powerful EM waves which, when sensed from a distance greater than a few tens of kilometres, behave as plane waves propagating

outwards horizontally. Signal-level contours for two of the major VLF transmitters are shown in Figure 12.1. Areas enclosed within the 54 dB contours have good signal strengths, while those within the 48 dB contour have only marginal signal strength. Areas left unshaded have signal strengths too weak for the method to be used effectively or without special techniques being used.

If a vertical sheet conductor is orientated such that its long axis lies on a radial direction from an active transmitter, the magnetic vector acts tangentially (as depicted in Figure 10.5) across the conductor. Eddy currents are induced within the conductor to produce a secondary electromagnetic field. For a conductor not so aligned, the production of eddy currents is much less efficient and the strength of the induced secondary field is much reduced.

For a vertical sheet conductor in a resistive medium, for example, and a profile direction aligned along the magnetic vector, then the tilt-angle response obtained is derived from the vector summation of the primary and secondary components, as shown in Figure 12.2. The primary magnetic vector is horizontal. The induced electromagnetic field varies in amplitude and direction with position relative to the target. On one side of the target, the angle between the two vectors reaches a maximum and then passes to a minimum on the other side before returning to zero beyond the influence of the target. The point at which the tilt angle passes through zero from the positions of the maximum and the minimum, known as the 'crossover' point, lies immediately above the conductive target. If the target dips, then the anomaly shape is distorted with either the positive or negative element being emphasised at the expense of the other component. The largest amplitudes of the various electric and magnetic components lie at the ground surface and diminish with depth (Figure 12.3).

The VLF instrument contains one or more aerials whose characteristics are appropriate for specific transmitters. The VLF EM16 requires the correct crystal aerial for a given transmitter to be physically plugged into the device. To use the instrument, the operator holds the device out horizontally and then rotates it around a vertical axis until a null position is sensed using an audio signal. The

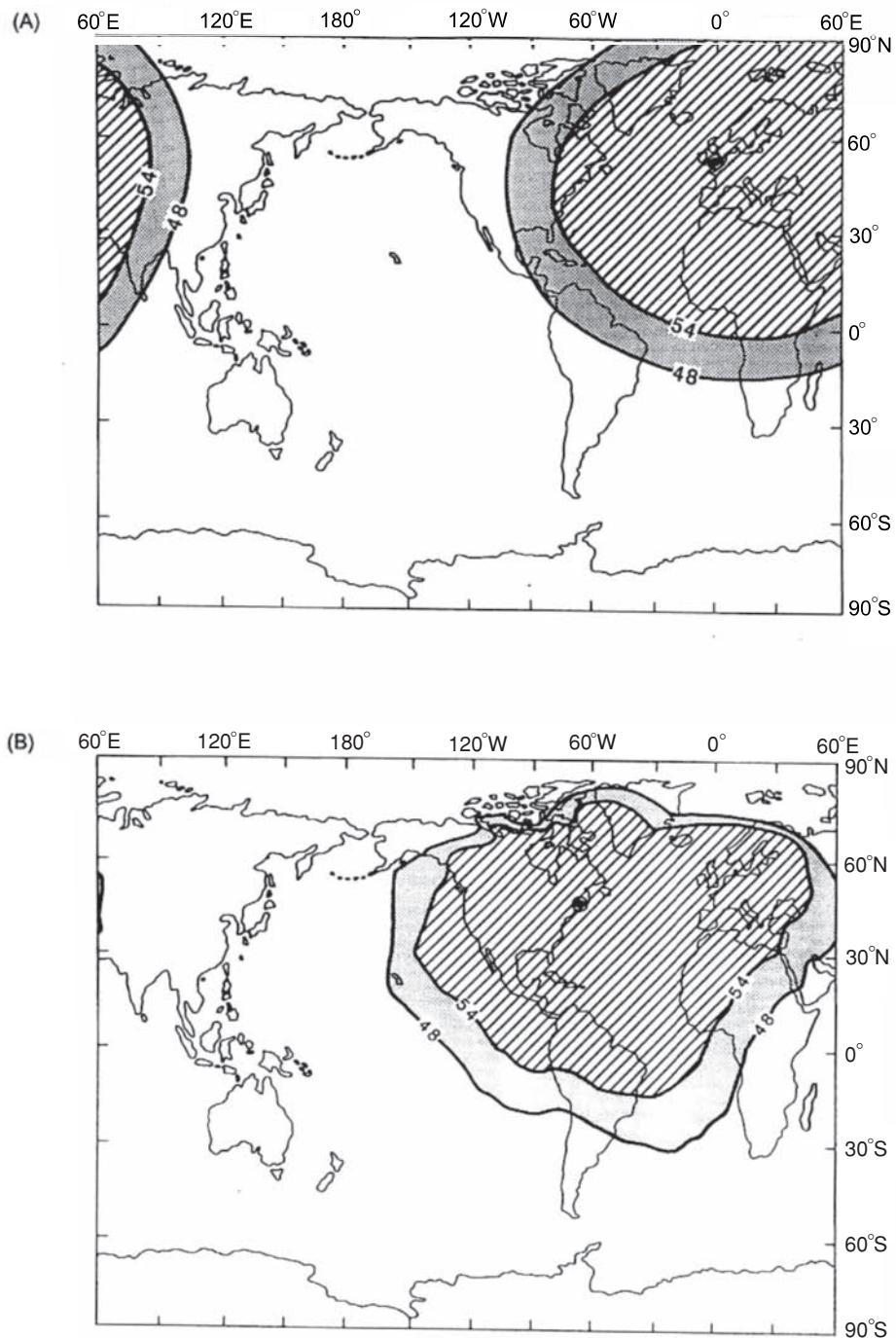


**Figure 12.1** Signal level contours for VLF transmitters at (A) GBR, Rugby, UK, and (B) NOAA, Cutler, USA. From McNeill and Labson (1991), by permission.

direction in which the device is then pointing is along the line of the horizontal component of the electric vector. Survey profiles are conducted at right-angles to this direction, i.e. along the line of the magnetic vector for the given transmitter. Once aligned along the profile direction, at each station, the device is rotated about a horizontal axis. The operator holds the device to his/her eye and views the tilt of the instrument through an eyepiece. The operator

rocks forwards and backwards to sense a null in the audio signal, at which point the tilt angle is then read from the instrument. VLF devices can also be used to measure the electric component by using a grounded dipole up to 5 m long made up of a piece of wire connected to the ground at each end. In this configuration (VLF-R) the apparent resistivity and phase of the horizontal electric field in the ground can also be determined.

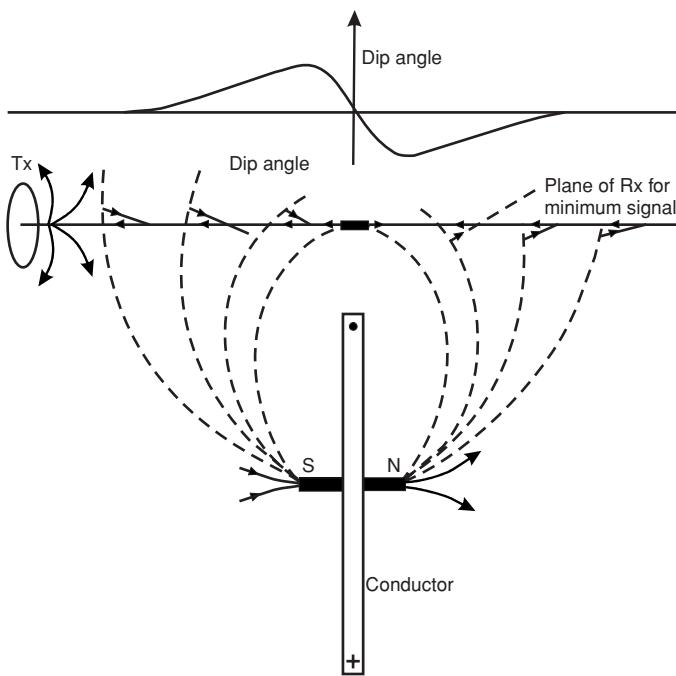


**Figure 12.2** Tilt-angle profile over a vertical sheet conductor.  
From Beck (1981), by permission.

In a modern instrument, such as the ABEM WADI, three different frequencies are used simultaneously and the device is able to sense from which transmitter the strongest signal is emanating. Without having to orientate the instrument, the operator walks along the chosen profile line and takes readings. While this has obvious benefits in reducing set-up time, there is one major disadvantage with auto-tuning devices. Repeatability of measurements is sometimes difficult along the same profile when surveyed on different occasions as the transmitter with the strongest signal may be different each time. Thus survey parameters are difficult to keep constant.

Another drawback with any VLF system is that the method is totally dependent on there being an appropriate transmitter oper-

#### Box 12.1 EM parameters

Measurement of the magnetic ( $H_y$ ) and electric ( $E_x$ ) components with the VLF-R method yields the surface Cagniard impedance ( $Z$ ), such that:

$$Z = E_x / H_y$$

The phase ( $\varphi_z$ ) between the electric and magnetic fields is related to real and imaginary parts of the impedance (denoted by suffices r and i, respectively) by:

$$\varphi_z = \arctan(Z_i / Z_r)$$

The frequency-normalised impedance (FNI,  $Y$ ) is given by:

$$Y = \frac{Z}{\sqrt{(i\omega\mu_0)}} = \frac{E_x}{\sqrt{(i\omega\mu_0)H_y}}$$

where  $\omega$  and  $\mu_0$  are the angular frequency and magnetic permeability of free space, respectively.

The Cagniard apparent resistivity ( $\rho_{aC}$ ) relates to the FNI by:

$$\rho_{aC} = \frac{1}{\omega\mu_0} |Z|^2 = Y_r^2 + Y_i^2$$

and phase by:

$$\varphi_z = \pi/4 + \arctan(Y_i / Y_r)$$

Linking the Cagniard apparent resistivity ( $\rho_{aC}$ ) and phase ( $\varphi_z$ ) (Basokur and Candansayar, 2003) gives:

$$\rho_{aF} = 2\rho_{aC} \cos^2(\varphi_z) \quad \text{for } \varphi_z \geq \pi/4$$

and

$$\rho_{aF} = \rho_{aC} / (2 \sin^2(\varphi_z)) \quad \text{for } \varphi_z \leq \pi/4.$$

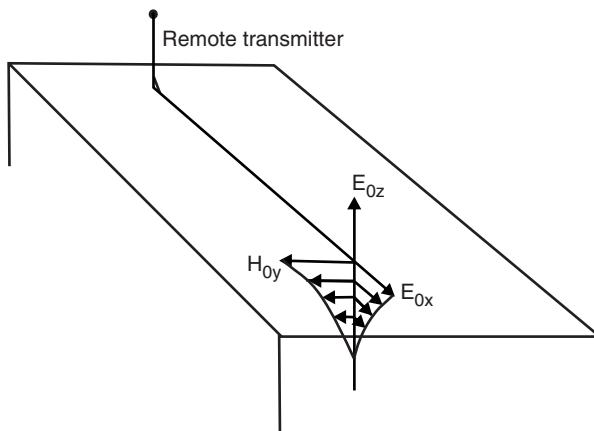


**Figure 12.3** Schematic of the diminution of the amplitude of field components with depth.  
From McNeill and Labson (1991), by permission.

ational. There are occasions when transmitters are off-air and no source signal from a transmitter with an appropriate azimuth to the target is available. Sometimes, a given transmitter can be switched off while an operator is in mid-survey. There is nothing within the control of that operator that can be done to rectify the situation unless another transmitter is available with a suitable azimuth and the instrument being used has the appropriate aerial.

With modern instruments it is now possible to measure the respective fields from two orthogonal transmitters with one instrument in the same pass along the survey line. The direction to one transmitter is parallel to the strike of the target with the other at right-angles. These two orientations are then referred to as the E- and H-polarisation modes. Thus with modern instruments in both VLF-EM and VLF-R modes using two orthogonal transmitters, eight parameters can be obtained at each station (in-phase and

quadrature components in VLF-EM mode; resistivity and phase in the VLF-R mode for each transmitter). In airborne VLF systems, the ratio of the horizontal and vertical electric fields (wave tilt) is used to determine the apparent resistivity, but only three components of the magnetic field are measured. The ratio between the vertical and horizontal magnetic fields ( $H_z/H_y$ ) measured in the  $y$ -axis direction is known as the *tipper* vector,  $B(y)$ . The horizontal derivative of the tipper is known as the *peaker* as it peaks directly over a conductor (Pedersen *et al.*, 1994).

### 12.1.3 Effect of topography on VLF observations

VLF measurements can be adversely affected by topography, and so some sort of topographic correction may have to be applied before a target anomaly becomes obvious. If a topographic high, such as a ridge, is parallel to the strike direction of the target body, and thus is at right-angles to the survey direction, the topographic effect is a subdued version of the actual topography. That is, on rising up the slope, the tilt angle is increased slightly, and on descending down the slope the other side, it decreases. If the survey is conducted parallel to the survey direction along the ridge, then no association with topography may be evident. The actual topographic response can be complex and depends upon the resistivity of the local materials. If the tilt-angle profile mirrors the actual topography, then this is strongly suggestive that topographic effects are present. Similarly, if positive polarity anomalies correlate with topographic highs and negative polarity anomalies are located at the bottoms of valleys, this also indicates the presence of topographic effects.

If the survey has been conducted over topography with a wavelength much longer than the width of the target along the survey line, topographic effects may be removed by the application of an appropriate filter.

### 12.1.4 Filtering and interpretation of VLF data

VLF tilt-angle data are commonly interpreted only qualitatively. The point where the tilt angle crosses over from being positive to negative polarity is usually interpreted as being immediately above the top of the conductor causing the anomaly. In profile, this crossover is usually quite clear. When plotted spatially in map form, however, the locus of all zero-points (a line joining the crossover points from each profile) is not as easy to identify.

One way by which this problem has been resolved is the use of a filter, such as those devised by Fraser (1969) and Karous and Hjelt (1983). Fraser's filter was designed to shift the tilt-angle data by  $90^\circ$  so that crossover and inflection points become peaks. The filter also attenuated long spatial wavelengths to help overcome some aspects of topographic effects and also to reduce the slow temporal variations in signal strength of the transmitter. Furthermore, his filter was designed not to increase the noise content of the data and, importantly, to be simple to apply.

The Fraser filter uses four consecutive data points, where the data have been acquired at a regular interval and can be ap-

#### Box 12.2 Fraser filtering VLF tilt-angle data

Given a sequence of tilt-angle data,  $M_1, M_2, M_3, \dots, M_n$  measured at a regular interval, then the Fraser filter  $F_i$  is applied as follows:

1. The first filtered value,  $F_1 = (M_3 + M_4) - (M_1 + M_2)$  is plotted halfway between stations 2 and 3.
2. The second filtered value,  $F_2 = (M_4 + M_5) - (M_2 + M_3)$  is plotted halfway between stations 3 and 4, and so on along the profile.

plied very simply using a hand calculator or spreadsheet. The sum of the first and second data points is subtracted from the sum of the third and fourth values and plotted at the midpoint between the second and third tilt-angle stations (see Box 12.2). It is important to remember to take account of the polarity of the tilt angle, whether positive or negative, in the calculation of the filtered values.

For interpretation, it is arguably better to use both the raw and filtered data. The effect of filtering the data can result in the anomaly peak being displaced laterally along the survey line. Thus for more accurate target location, the raw data should be used.

For more quantitative interpretation, two approaches can be taken. One is to use a set of *master curves* and associated interpretational aids as published by Madden and Vozoff (1971). However, these curves have not been widely used since most interpreters appear to favour their own empirical approach based on experience or on nomograms calculated for simple dipping sheet-like conductors (Sinha, 1990). For more detailed interpretation, especially in connection with two-dimensional and three-dimensional targets, numerical modelling can be used (e.g. Nissen, 1986; Ogilvy and Lee, 1989), although this tends to be undertaken more in research work rather than mainstream commercial surveys and has required substantial computing capacity for large datasets. A detailed discussion of earlier quantitative analysis of VLF data has been given by Telford *et al.* (1990) and by McNeill and Labson (1991). Transformation of VLF data into apparent resistivities and phases was described by Gharibi and Pedersen (1999), who discussed the use of the tipper vector in more detail, and Becken and Pedersen (2003). Further processing of VLF data can be undertaken using inversion techniques (e.g. Kaikkonen and Sharma, 2001). VLF measurements using magnetic measurements alone are commonly used to delineate lateral changes in electrical conductivity, such as caused by fracture zones in crystalline terrains or changes in lithology within sedimentary cover over basement rocks. While the main value in VLF surveying lies in its simplicity of use in the field for reconnaissance work for which qualitative interpretation is usually adequate, there is an increasing desire to extract depth information to the conductivity distribution. VLF data contain information about the host material through their decay away from conductors, and the position and depth of the dominating conductors through the relative contribution of in-phase and quadrature components of the VLF anomaly as well as to the rate of change of the anomaly close to the conductors. Further filter processing also using tipper vector data

can be used to derive the equivalent-current density distribution pseudo-section as a function of depth along a VLF profile. Depths to and dimensions of subsurface conductors can be determined from such displays (Pedersen and Becken, 2005). Sundararajan *et al.* (2006) have developed a simple, user-friendly Matlab code for processing and interpreting VLF-EM data which is available via the Internet (Appendix 1).

## 12.1.5 Applications and case histories

### 12.1.5.1 Detection of orebodies

A VLF profile acquired across mineralised metasediments at Sourton Tors adjacent to the Dartmoor granitic intrusion, Devon, is shown in Figure 12.4. The VLF profile shows a marked change in polarity at about 210 m along the survey line. This location

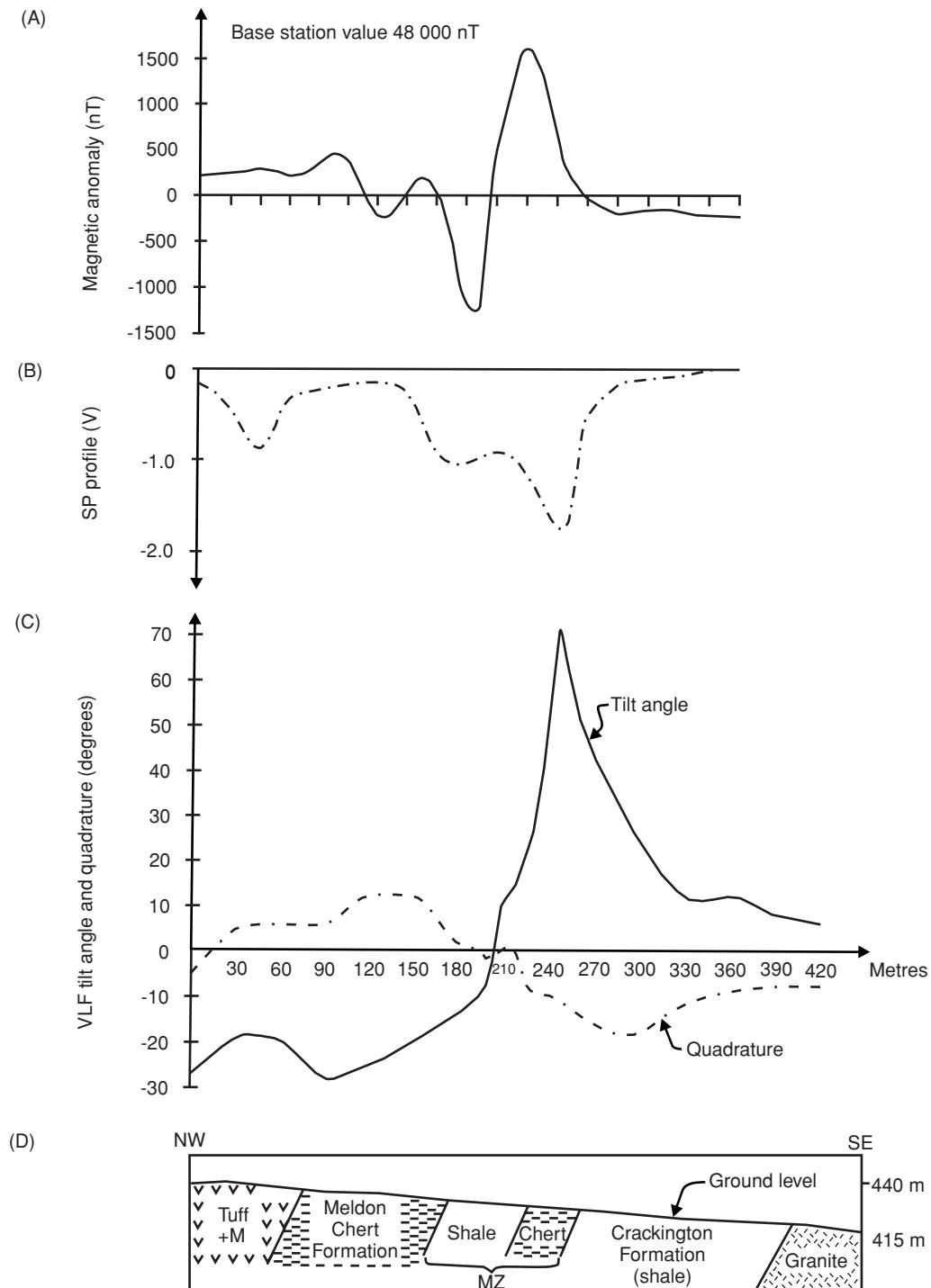


**Figure 12.4** A variety of geophysical profiles acquired using different geophysical methods over mineralised metasediments at Sourton Tors, Devon, UK: (A) magnetic total field; (B) SP; (C) VLF, and (D) the geological cross-section.

correlates with a known area of stratabound mineralisation within the chert/shale zone marked 'MZ'. For comparison, profiles obtained using SP and magnetometry are also shown. Both of these reveal anomalies around the same location and with the shapes of anomalies consistent with a conductive magnetic target dipping towards the northwest. Profiles showing microgravity and SP data across Sourton Tors are shown in Chapter 2 (Figure 2.48). The VLF data were acquired using a Geonics EM16 with GBR, Rugby, as the transmitter.

Measured total magnetic field data and observed in-phase and out-of-phase VLF-EM components were used in modelling and inversion as part of a survey in Raigarh district, Chhattisgarh, India, to investigate basement fractures associated with uranium mineralisation (Babu *et al.*, 2007). In this part of India, Sambalpur granitoids are exposed and basement fractures with uranium mineralisation occur along two distinct linear trends, N50E–S50W and N25E–S25W. The fracture zones contain breccia, cataclasite, or mylonite of acidic and basic composition representing origins from granite and basic rocks, respectively. The mineralised breccia/cataclasite is highly altered and generally associated with silicification.

Total magnetic field measurements were made along 17 traverses 40 m apart across the known strike of the structures, using a proton magnetometer at a 10-m station interval. VLF-EM data consisted of in-phase, out-of-phase, resistivity and phase-angle values acquired along 11 profiles coincident with the magnetic traverses. The VLF transmitter JJI Japan (frequency 22.2 kHz) was used as the source as it lies along the geological strike direction. Inversion of the VLF-EM data was undertaken using a modified code of Monteiro *et al.* (2006). Measurements were made in both magnetic and electric field mode and the observed and computed in-phase and out-of-phase results for one transect (N12) are shown in Figure 12.5A. The derived resistivity indicated a broad conductive anomaly ( $<100 \Omega\text{m}$ ) surrounded by resistive ( $800 \Omega\text{m}$ ) host rocks (Figure 12.5B). The VLF-EM data were processed using both Fraser and Karous-Hjelt filters and the 2D resistivity model and current density pseudo-sections derived (Figures 12.5B–D). These show two anomalous regions extending to over 50 m depth and provide greater clarity of the structures than the general resistivity section. The VLF-EM data are also shown in Figure 12.6 with a geological section derived with borehole data.

Detailed analysis of the magnetic data, including determining the amplitude of the analytical signal and Euler depth, was used to decipher the spatial locations of the fractures in the basement granitoids, and for planning the locations for inclined boreholes and their drilling directions. The modelling of the VLF-EM data delineated shallow vertical to subvertical conductors associated with the basement fractures. Crossovers of the in-phase and out-of-phase data demarcated the conductors. It is clear in Figures 12.5 and 12.6 that the in-phase data provide the greatest detail in response to the two steeply inclined conductors. Drilling confirmed the presence of the conductive zone associated with the fractures that were found to comprise pyrite, chalcopyrite, ilmenite, and brecciated matrix with haematite and magnetite.

Basokur and Candansayar (2003) have provided a brief case history of a VLF-R survey in an area known as the Killik orebody,

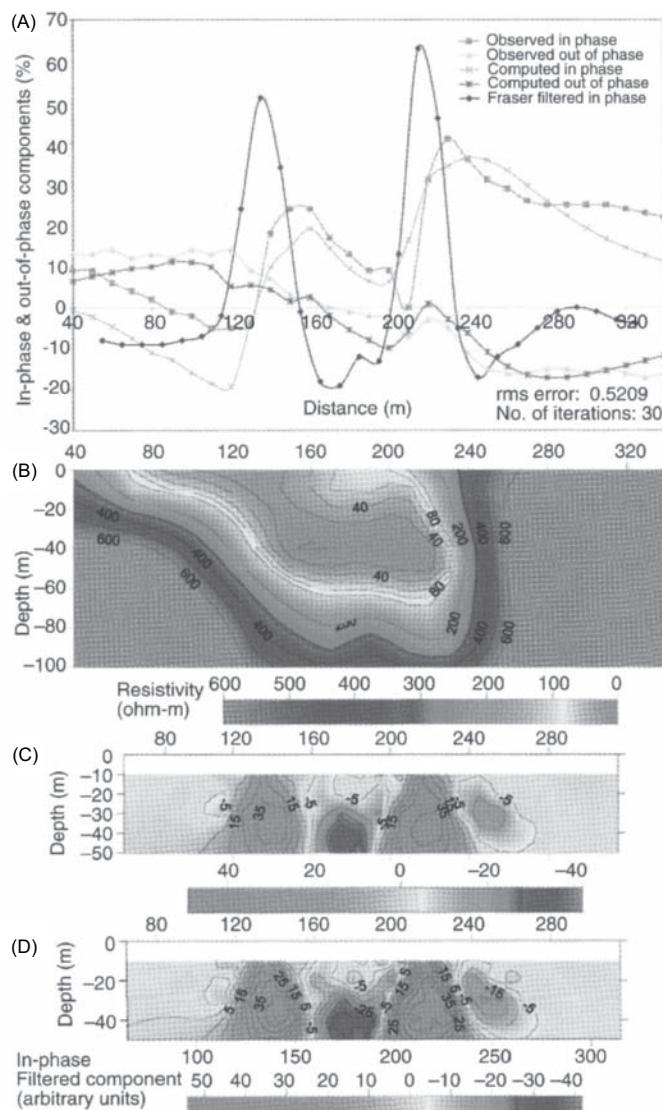


**Figure 12.5** VLF-EM response along profile N12. (A) Observed and computed in-phase and out-of-phase components with Fraser-filtered in-phase component; (B) 2D resistivity model derived from the inversion of the VLF-EM data; (C) Karous-Hjelt current density pseudo-section; and (D) Fraser-filtered current density pseudo-section. From Babu *et al.* (2007), by permission. [C]

close to the Lahanos deposit in the Black Sea region of Turkey. Here copper deposits occur within volcano-sedimentary units of Upper Cretaceous age formed in submarine environments. There are two units that have different depositional ages and physical properties. The massive chalcopyrite mineralisation always overlies the host dacitic tuff (resistivities 700–2500  $\Omega\text{m}$ ). The upper volcanogenic series, which was deposited after mineralisation, comprises dacite and andesitic tuff breccia (resistivities 100–300  $\Omega\text{m}$ ). The geometry of the ore is related to anticlinal and synclinal structures of the older series of dacitic tuff. A simplified geological section beneath the VLF profiles is shown in Figure 12.7A. The two-component target mineralisation lies at the base of the upper volcanogenic series above

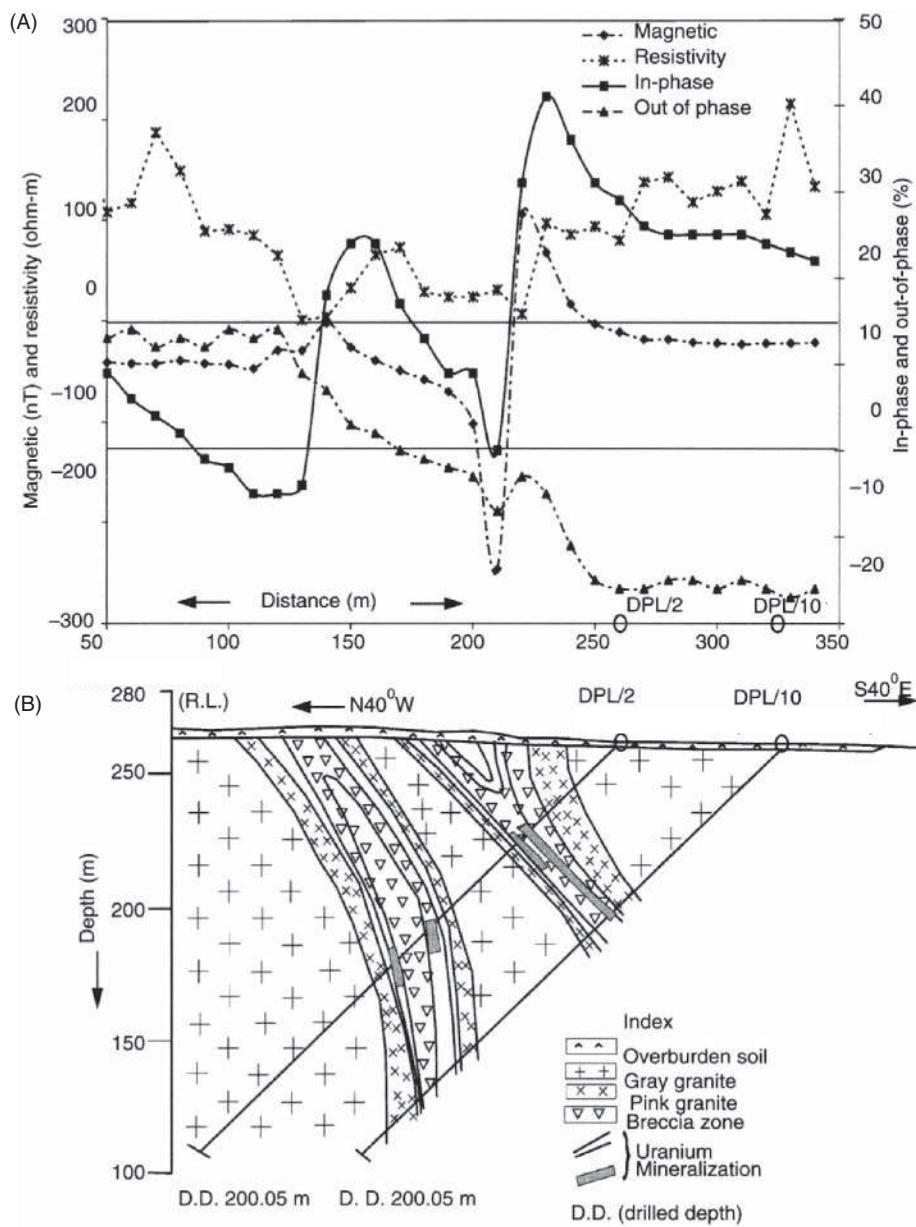


**Figure 12.6** (A) VLF-EM in-phase and out-of-phase components, resistivity and magnetic anomaly data along traverse N12, with (B) a schematic geological section derived from data from two inclined boreholes. From Babu *et al.* (2007), by permission.

the host rock. The VLF-R apparent resistivity and phase results are shown in Figures 12.7B and C, respectively.

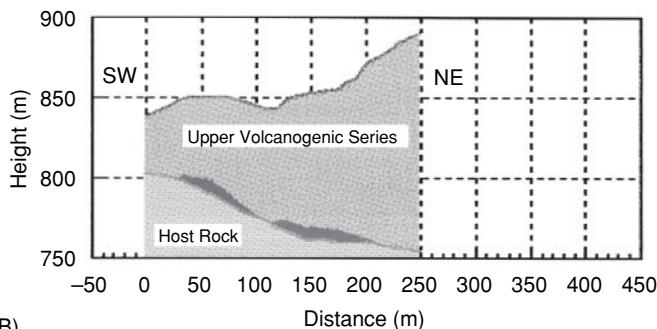
Three anomalies (A–C) are evident in the apparent resistivity and phase graphs in Figure 12.7. Anomalies A and B are characterised by low apparent resistivity values and large phase angles and are thought to be caused by the two discrete parts of the massive copper ore bodies. Anomaly C, however, is prominent on the phase graph but less distinct in comparison with anomalies A and B in terms of apparent resistivity. It is thought that the cause of anomaly C is associated with deep weathering due to the rainy climate, as no significant mineralisation was found at this location in drill-holes. In Figure 12.7B, two profiles are shown, one (with heavy dots) is the Cagniard apparent resistivity while the curve with stars has been

derived using the definitions of apparent resistivity ( $\rho_{aF}$ ) derived by Basokur and Candansayar (2003) (Box 12.1).

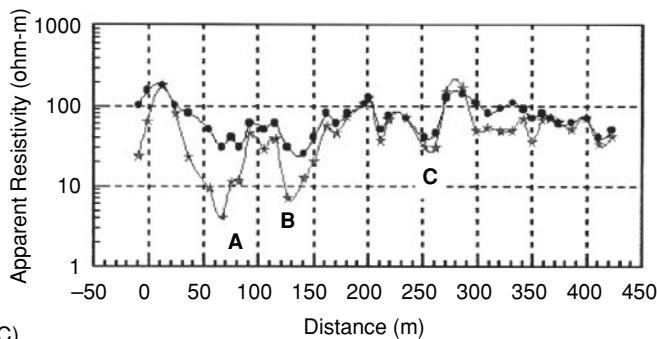
### 12.1.5.2 Location of subsurface cavities

Ogilvy *et al.* (1991) described a VLF survey undertaken near Alcalá de Henares, about 20 km east of Madrid, Spain. In medieval times, artificial galleries were constructed at a depth of 2–4 m to drain superficial Quaternary gravel terrace deposits which overlie an impermeable Tertiary clay formation in order to provide the town of Alcalá with fresh water. The location and the lateral extent of these galleries were uncertain. The shallowness of the galleries meant that they posed a potential for collapse. Indeed, one road

(A)



(B)



(C)

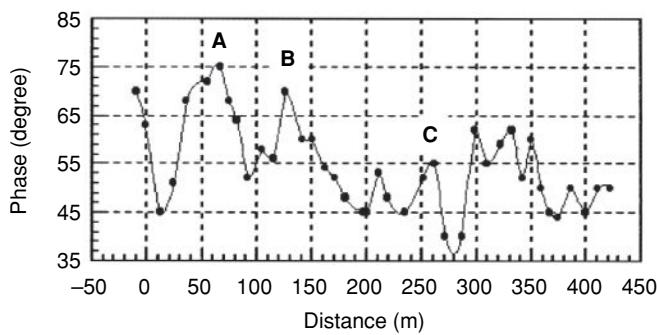


**Figure 12.7** (A) Interpreted geological cross-section; (B) Cagniard apparent resistivity (dots) and alternative definition of apparent conductivity (stars); (C) phase results. From Basakur and Candansayar (2003), by permission. [C]

subsided as a direct consequence of being constructed over one of these galleries.

An example of a geological cross-section through a typical gallery is shown in Figure 12.8A. The galleries are on average 1 m wide and 2 m high, and are largely free-standing and straddle the gravel-clay interface. At the time of the survey, the galleries were dry and thus constituted air-filled tunnels.

A  $100 \times 100$  m grid was established over one part of the known gallery system with lines orientated at right-angles to the direction of the galleries with an inter-line separation of 10 m or less. Station intervals along the lines varied between 5 m and 1 m, as required to sample the observed anomalies spatially. The position of the gallery system was also mapped underground by theodolite and compass so as to provide information with which to compare the VLF results.

The VLF instrument used was a Scintrex VLF-3 in both VLF-EM and VLF-R modes using two orthogonal VLF transmitters: NAA, USA (24 kHz) and Ste Assise, France (16.8 kHz) providing the *H*-polarisation and *E*-polarisation data, respectively. The type of current flow around an infinitely-resistive two-dimensional void, such as provided by the galleries, over a conductive substrate is shown in Figure 12.8B. There is obvious current channelling occurring as indicated by the closeness of the current flow lines around the gallery.

The VLF-EM survey produced absolutely no response from the gallery system. Given the true resistivities of the gravel beds ( $200 \Omega\text{m}$ ) and the underlying clays ( $10 \Omega\text{m}$ ), and the geometry of the gallery with respect to the *H*-polarisation, no vertical magnetic gradient is generated by such a structure.

In contrast, however, the VLF-R *H*-polarisation results produced anomalies which could be directly correlated with the gallery system and which could be modelled using 2D inversion routines. Pronounced apparent resistivity ( $52 \Omega\text{m}$ ) and phase ( $5^\circ$  peak-to-peak) anomalies were observed directly over a known gallery position (Figure 12.9). The decrease in phase above the gallery is indicative of a resistive structure below the uppermost layer. As it is known that the substrate is conductive clay, the only resistive target available is the gallery. This demonstrates the effectiveness of *H*-polarisation VLF-R measurements in the detection of air-filled voids over conductive media.

This example also demonstrates the importance of using orthogonal transmitters. The absence of any detectable VLF-EM magnetic field response for *H*-polarisation suggests that the observed anomaly must be caused by the electric field component  $E_x$  of the complex impedance ratio  $E_x/H_y$ . It is also a good example of the dominance of galvanic currents over vortex current flow arising from the deviation and concentration of current flow lines around the air-filled gallery. Such current flow results in larger-than-normal primary electric fields, with a consequent increase in apparent resistivities; hence the observed apparent resistivity high immediately over the target.

## 12.2 The telluric method

### 12.2.1 Principles of operation

As a consequence of the presence and fluctuation of the Earth's magnetosphere (see Chapter 3), natural low-frequency magnetotelluric fields occur which induce alternating currents within the ground. These currents flow parallel to the ground surface and cover huge areas. They are known as 'telluric' currents, named after Tellus, the Earth Goddess in Roman mythology. The electric current fields fluctuate continuously in direction and magnitude at any point in response to the temporal variations in the ionosphere and magnetosphere caused by extraneous influences (solar wind, and so on). Distant lightning gives rise to frequencies in the range 1–400 Hz, and changes in density of conductive plasma (solar wind) impinging on the Earth's magnetic field generate frequencies between

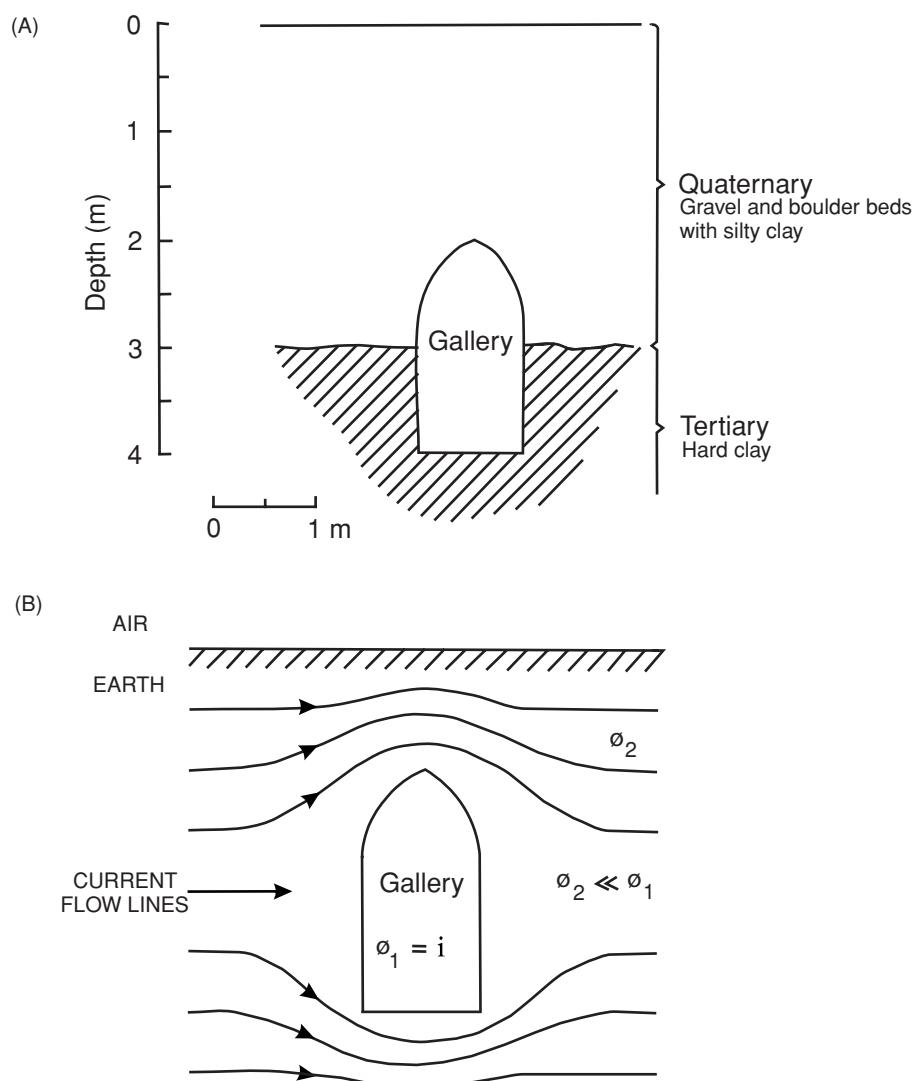


**Figure 12.8** (A) Typical cross-section, and (B) schematic representation of primary current flow lines around an air-filled (infinitely resistive) drainage gallery at Alcala, near Madrid, Spain. From Ogilvy et al. (1991), by permission.

0.0005 and 1 Hz. The magnitude of the electric field gradient is of the order of 10 mV/km. Electrical noise is also present, generated by electric storms, seawater currents, sferics, and manmade sources such as electrified railway and tram lines.

In a uniform conductive earth, the telluric currents flow parallel to the ground surface with decreasing amplitude with depth. If there is a large-scale resistive subsurface structure present, such as a salt dome or anticline, then the telluric current flow will be distorted and directed into the more conductive material above; similarly, if a large conductive target is present, such as a massive orebody, then the current will flow towards the more conductive material (Figure 12.10). The exploration method is designed to locate the distortions of the telluric fields. Historically, the telluric method has been used in the location of salt domes in exploration for hydrocarbons, particularly in Russia, Europe and North Africa. It has not been used widely in the USA as the salt domes there

are generally too small to give rise to significant telluric anomalies. The method has also been used in the search for massive sulphide deposits and in geothermal resource evaluation.

## 12.2.2 Field measurements

The potential gradient is measured across two pairs of orthogonal non-polarisable electrodes, at a base station located over ground that is thought to be electrically uniform or remote from the type of target being sought. A second pair of orthogonal non-polarisable electrodes are used as mobile search dipoles. The potential gradient across each dipole within each pair is measured at both the mobile and base stations simultaneously over a period of several minutes. If the ground is electrically uniform below the base station, the two horizontal components of the electric field measured at right-angles

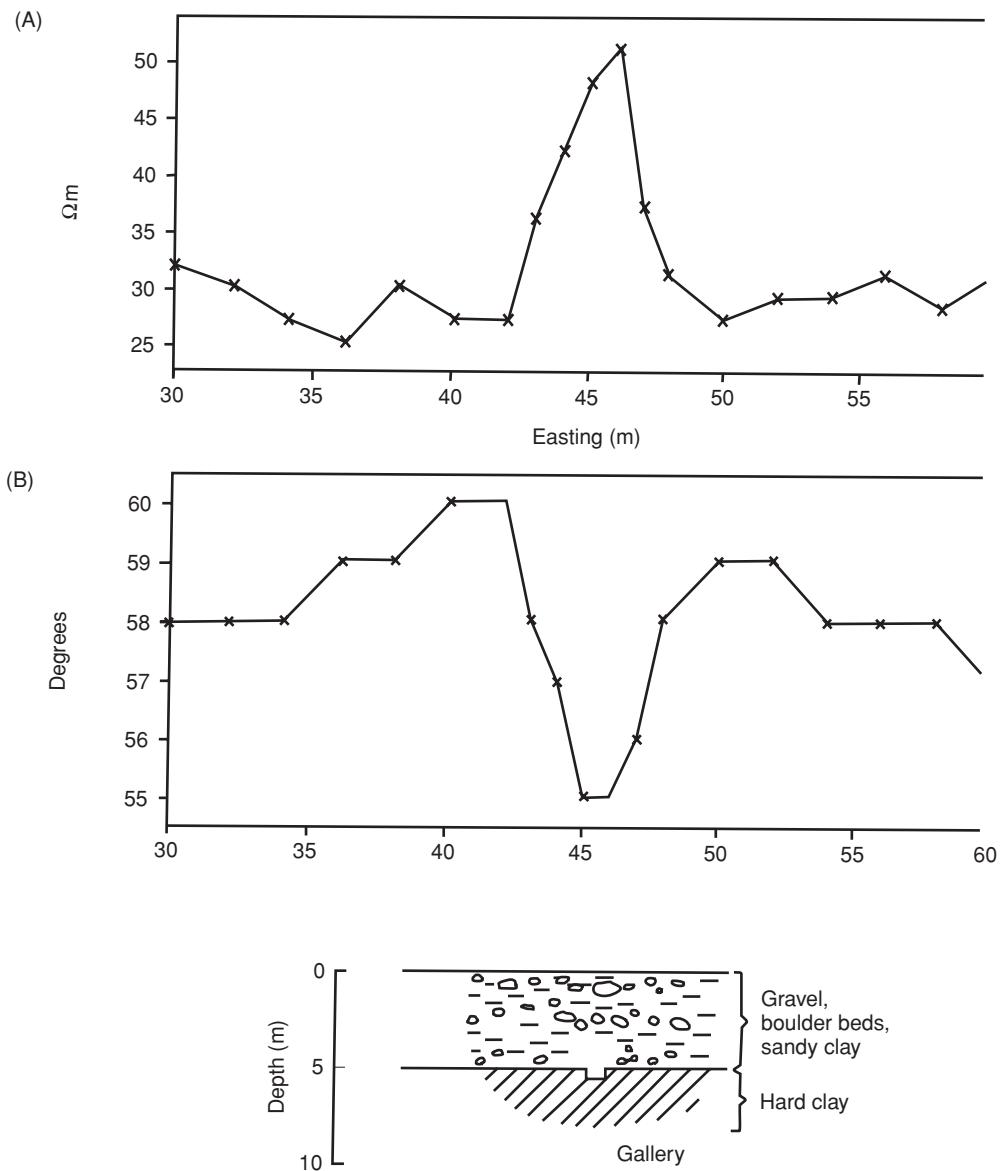


**Figure 12.9** (A) VLF-R apparent resistivity, and (B) phase profiles over a known drainage gallery: *H*-polarisation mode using the NAA, USA, transmitter (24 kHz). From Ogilvy *et al.* (1991), by permission.

should be the same, irrespective of azimuth. The locus of the electric vector at the base station should, therefore, describe a circle.

In actuality, with the presence of various components of electric noise in addition to the telluric currents, the base-station field vector does not describe a circle. However, a mathematical function can be applied to the data to constrain the results to conform to a circle with unit radius. This same mathematical function is applied to the dataset measured simultaneously at the mobile pair of dipoles in order to correct for the electric noise and time-variant field. By referring the measured signals at the mobile dipoles to those at the base station, the data from the mobile station are normalised. If there is no perturbation to the flow of telluric currents, the electric vector at the mobile station also describes a circle. If, however, there is some distortion due to the presence of a subsurface target, the field

vector at the mobile station describes an ellipse. The orientation of the major axis of the ellipse at the mobile station is aligned to the direction of maximum current flow at that point. The ratio of the area of the ellipse to that of the base-station circle gives a relative indication of the amplitude of the telluric anomaly.

Interpretation of telluric results can be qualitative, especially when the method is used for reconnaissance purposes. For more quantitative analysis, the effect of certain simple two-dimensional geological structures, such as an anticline, fault or horizontal cylinder, and three-dimensional shapes, such as a sphere or ellipsoid, can be calculated theoretically. Model curves can be produced against which measured anomalies can be matched. Detailed discussions of such procedures have been given by Keller and Frischknecht (1966) and by Telford *et al.* (1990).

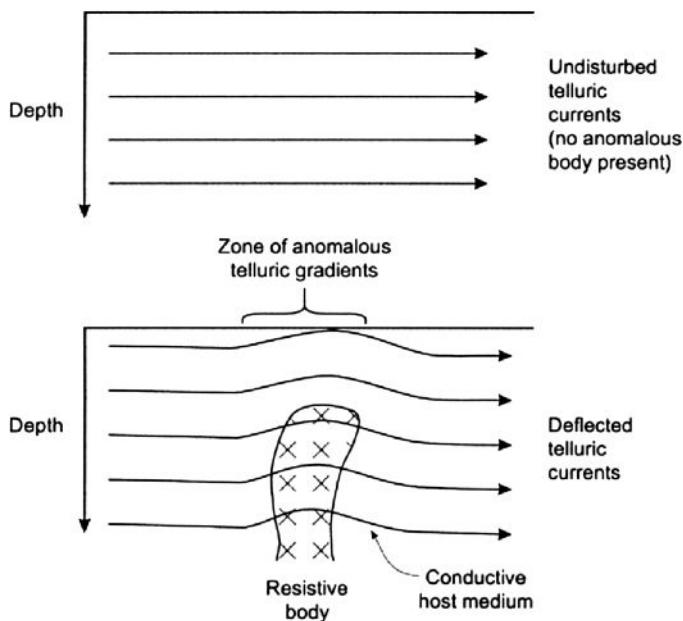


Figure 12.10 Telluric current flow around a subsurface structure.

## 12.3 The magnetotelluric (MT) method

### 12.3.1 Principles of operation

The magnetotelluric method uses measurements of both the electric and magnetic components of the natural time-variant fields generated as described in Section 11.5.1. The major advantage of this method is its unique capability for exploration to very great depths (hundreds of kilometres), as well as in shallow investigations, all without the use of an artificial power source (with the exception of ‘controlled-source’ versions of the method).

The *natural-source magnetotelluric* method uses the frequency range  $10^{-3}$  to 10 Hz, while the *audio-frequency MT* (AMT or AF-MAG) method operates within the higher range  $10\text{--}10^4$  Hz using sferics as the main energy source. Sferics are generated by lightning strikes that cause fluctuations of the Earth’s electromagnetic field in the frequency range from 1 to  $10^5$  Hz. The main disadvantage with the natural-source MT methods is the erratic signal strength. The variability in source strength and direction requires substantial amounts of stacking time (5–10 h) per site, thus making MT soundings expensive and production rates slow. AMT measurements can be made more rapidly owing to the slightly higher frequencies, but variability of local thunderstorm sources and signal attenuation around 1 Hz and 2 kHz can degrade data quality. For an example of the relative speed of measurements, three AMT soundings were made in six hours within the crater region of White Island, an active volcano 50 km to the north of North Island, New Zealand (Ingham, 1992).

A disadvantage with this method is that the sferics source – distant lightning activity – has a signal minimum between 1 and 5 kHz, the so-called AMT ‘dead’ band. The energy in this band

shows both diurnal and annual variations. Magnetic-field amplitudes measured during the day can be well below the noise levels of coil magnetometer sensors, thereby reducing the effectiveness of this method for high-resolution exploration of near-surface targets. To overcome this problem, García and Jones (2005) have described a hybrid acquisition and processing methodology that combines the telluric–telluric (T-T) and telluric–magnetotelluric (T-MT) methods in this frequency range. They suggested recording a large number of telluric channels at several sites and remote reference stations during the day. Two or three stations could be set to automatic data acquisition during the night and be used as base and remote stations at which the full magnetotelluric (MT) components would be recorded. By processing the data using transfer functions it is possible to obtain a reasonable approximation of the real AMT impedance tensors. They were able to demonstrate the effectiveness of the technique to acquire usable data in the dead band, but also found that the results can be affected severely by noise.

In the early 1970s, David Strangway and Myron Goldstein (Goldstein and Strangway, 1975), at the University of Toronto, introduced the principle of an artificial signal source which was dependable and strong enough to speed up data acquisition and improve the reliability of results. The controlled-source MT methods typically operate within the frequency band 0.1 Hz to 10 kHz. The first commercial systems were produced by Zonge Engineering and Research Organization Inc., from 1978. Excellent overviews of the range of methods included within the MT family have been given by Vozoff (1986, 1991), and for controlled-source audio-frequency MT (CSAMT) by Zonge and Hughes (1991).

AMT has been used in groundwater/geothermal resource investigations and in the exploration for major base-metal deposits over the depth range from 50–100 m to several kilometres. The main application of the MT method, however, has been in hydrocarbon exploration, particularly in extreme terrain and to penetrate below volcanic materials, both types of areas where reflection seismology is either extremely expensive or ineffective. It has also been used recently to investigate a meteoric impact structure in Brazil (Masero *et al.*, 1994).

Since the mid-1970s, CSAMT has been used in an increasing range of applications, and especially since the early 1980s within geotechnical and environmental investigations (Table 12.1). It is considered that CSAMT is an underutilised method with many potential applications in the future. For this reason, CSAMT is described in some detail here.

### 12.3.2 Field measurements

The general field layout for a magnetotelluric survey is shown in Figure 12.11. It comprises two orthogonal electric dipoles to measure the two horizontal electric components, and two magnetic sensors parallel to the electric dipoles to measure the corresponding magnetic components. The magnetic sensors are made up of coils with several tens of thousands of turns around highly permeable iron cores with a total sensor length typically of 2 m. A third sensor measures the vertical magnetic component. Thus at each location, five parameters are measured simultaneously as a function of frequency. By measuring the changes in the magnetic (*H*) and electric (*E*) fields

**Table 12.1** Applications of controlled-source audio magnetotelluric (CSMT) surveying

**Exploration for:**  
 Hydrocarbons  
 Massive sulphides  
 Base and precious metals  
 Geothermal resources

**Geological mapping:**  
 Structure  
 Lithology

**Environmental applications:**  
 Mapping brine leakage from wells  
 Mappings brine plumes from leaking tanks, etc.  
 Mapping spilled petroleum products  
 Monitoring leachate solution in *in situ* copper recovery projects

**Geotechnical applications:**  
 Structural analysis in mine planning  
 Void detection in underground mines  
 Mapping burn fronts in underground coal mine fires  
 Monitoring enhanced oil recovery

References to all published sources have been given by Zonge and Hughes (1991).

over a range of frequencies, an apparent resistivity sounding curve can be produced, analogous to that produced for electrical resistivity sounding but measured as a function of frequency rather than inter-electrode separation (Box 12.3). The lower the frequency, the greater is the depth penetration.

The data are displayed on log-log plots as apparent resistivity versus either frequency ( $f$ ) or period ( $1/2\pi f$ ). Over a uniform earth, the phases of the two orthogonal components differ by  $\pi/4$ , with the magnetic component lagging behind the electric component. If, however, the measured phase difference ( $\theta$ ) is not  $\pi/4$ , this is indicative of the ground being non-uniform. The basic definitions of apparent resistivity using magnetotelluric parameters were formulated by Cagniard (1953) whose name is given to the apparent resistivity and the impedance term, which is the ratio of the orthogonal electric and magnetic horizontal components. The definitions

**Box 12.3** Determination of apparent resistivity from magnetotelluric data

Apparent resistivity ( $\rho_a$ ) is approximated by:

$$\rho_a = \frac{0.2}{f} \frac{|E_x^2|}{|B_y|} \equiv \frac{0.2}{f} \frac{|E_{x^2}|}{|H_y|} = \frac{0.2}{f} |Z|^2$$

where  $E_x$  (nV/km) and  $B_y$  are the orthogonal electric and magnetic components, respectively.  $B_y$  is the magnetic flux density in nT, which is numerically equal in these units to the magnetising force  $H_y$  (A/m). The term  $Z$  is the *Cagniard impedance*.

apply to a layered earth; for more complex structures the full tensor impedance must be used (see later in this section).

For controlled-source MT surveys, either a loop or grounded dipole is used as a transmitter (the controlled source) with the same measurement configuration as described above. The grounded dipole is typically between 1 km and 3 km long; commonly two orthogonal grounded dipoles are used to provide two different source polarisations (Figure 12.12). The source may be several kilometres away from the receiver sensors. The location and orientation of the bipole source are important in determining the response of the ground at the receiver, and have implications for the style of interpretations appropriate. Particular aspects of source polarisation effects have been discussed by Kellett *et al.* (1994) with respect to two massive sulphide deposits in Australia.

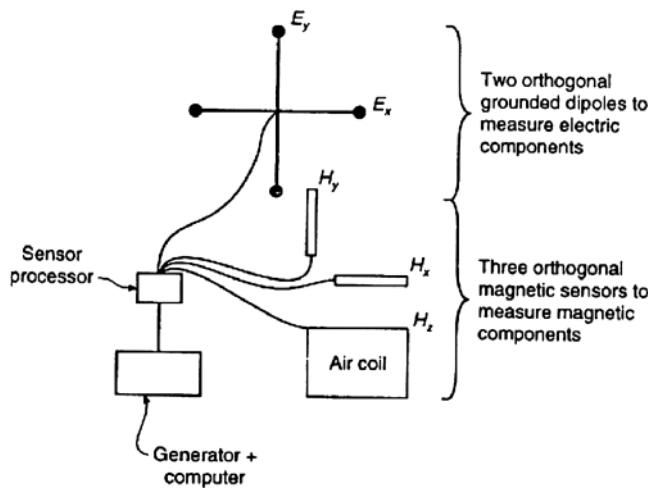


**Figure 12.11** Generalised field layout for a magnetotelluric survey.

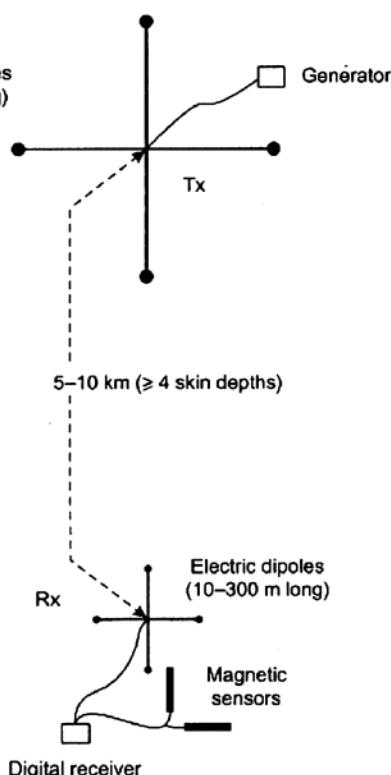


**Figure 12.12** Generalised field layout for a controlled-source magnetotelluric survey.

A variety of different field configurations are available, ranging from the simple scalar CSAMT, which provides a measure of the two orthogonal electric and magnetic components as shown in Figure 12.13A, to vector CSAMT with one source and two sets of orthogonal components (Figure 12.13B), and full tensor CSAMT with either coincident or separated sources (Figure 12.13C and D, respectively).

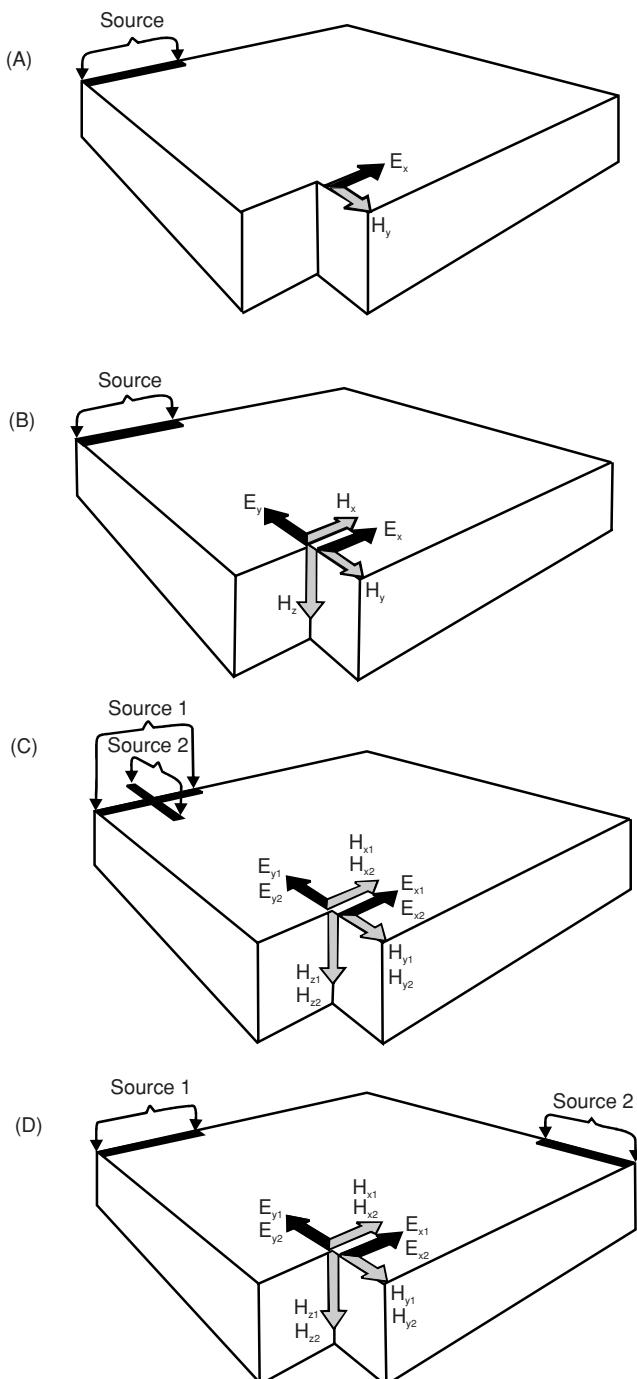


**Figure 12.13** Schematics of (A) scalar controlled-source audio-magnetotelluric sounding (CSAMT); (B) vector CSAMT; (C) tensor CSAMT with coincident sources; and (D) tensor CSAMT with separated sources. From Zonge and Hughes (1991), by permission.

### 12.3.3 Interpretation methods

Since the early 1980s there has been a tremendous advance in the interpretation of both magnetotelluric and controlled-source MT soundings, particularly in relation to the computer inversion of sounding curves. Detailed discussions of interpretational methods have been given by Telford *et al.* (1990), Vozoff (1991), and Zonge and Hughes (1991).

Two examples of magnetotelluric soundings are shown in Figure 12.14. It is evident that the combined interpretation of phase difference as well as apparent conductivity can yield important information. As frequency decreases, phase anticipates the resistivity behaviour. For example, Model A in Figure 12.14 is for a resistive basement. With decreasing frequency, the phase difference achieves a peak at mid frequencies while the apparent resistivity increases to reflect the basement value. Conversely, in the case of a conductive basement, the phase passes through a minimum while the apparent resistivity decreases with increasing depth penetration.

As long as the apparent resistivity is asymptotic to a constant value at low frequency, then phase difference should revert to  $45^\circ$  ( $= \pi/4$ ). The apparent resistivity profile, however, is sensitive to near-surface inhomogeneities which may reduce the reliability of a resistivity-only inversion. Furthermore, at middle and higher frequencies the phase difference is more sensitive to deeper structures than apparent resistivity. Very shallow features may not be evident on the phase difference sounding while they may be seen on the apparent resistivity data.

In CSAMT surveys, considerable amounts of data processing may be necessary prior to inversion (see Figure 12.15). The processing is

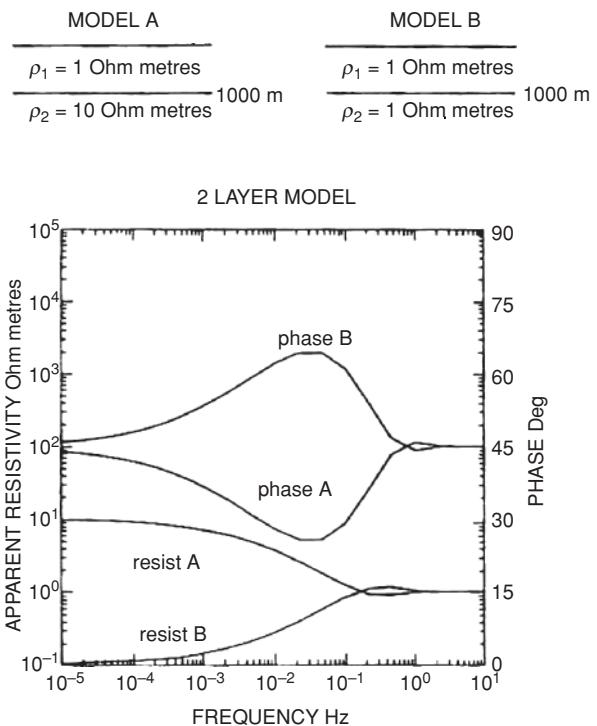
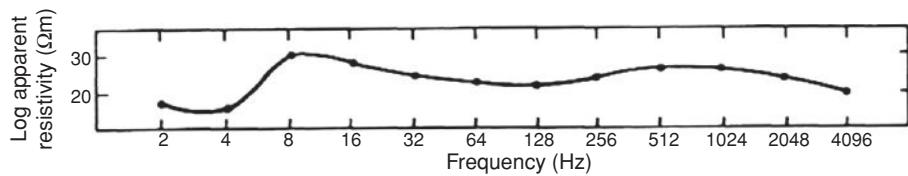


**Figure 12.14** Magnetotelluric apparent resistivity and phase responses of 2-layer models. Model A = resistive basement; Model B = conductive basement. From Vozoff (1991), by permission.

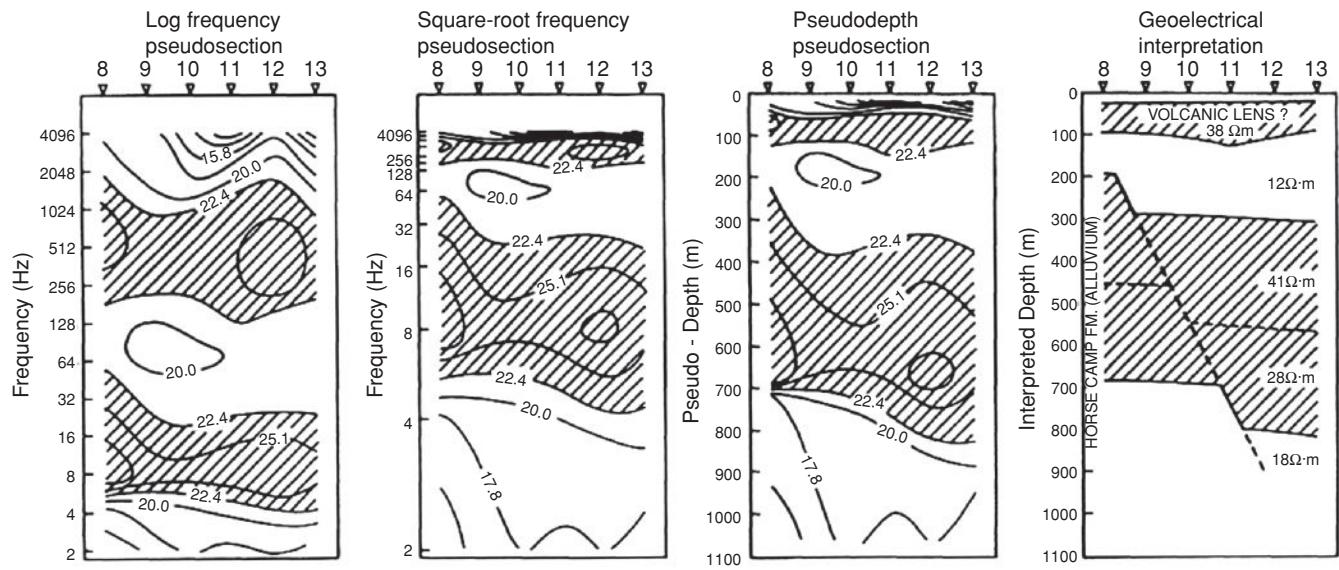
(A)

## INDIVIDUAL STATION PLOT



(B)

## PSEUDOSECTION PLOTS



## PLAN - VIEW PLOT

(C)



**Figure 12.15** Display types for CSAMT data. (A) Plot of log apparent resistivity versus frequency. (B) Pseudo-section displays with the corresponding geoelectric interpretation. (C) Plan-view plots. Other parameters, such as phase, may be plotted in similar ways. After Zonge and Hughes (1991), by permission.

usually undertaken in two stages: pre-processing and interpretative processing.

Pre-processing conditions the acquired data by the removal of errors and noise. Interpretative processing includes optimising plotting conventions for the particular measured or derived parameters. In addition, certain data enhancement processes may be applied such as normalising, static correction, filtering and derivative calculations. As explained by Zonge and Hughes (1991), normalisation removes the effects of layering by subtracting, dividing or other means of deconvolving equal-frequency or equal-depth average values from a set of data. Regional effects can be removed by deconvolution, which can also be used to enhance subtle lateral effects in survey areas with complex layering.

With multi-step processing it is important to compare the processed results with the original resistivity and phase information in order to maintain a sense of reality in the processing. If the basic trends evident in the original data cannot be observed in the processed results, then this suggests that something is wrong with the processing. The interpretative processing stages should emphasise particular trends in the original dataset, not create new ones.

One of the difficulties with the MT method is the amount of computer processing capacity required. This has previously limited the scope of the processing that can be undertaken, such as 1D (Avdeeva and Avdeev, 2006). The approach taken to try to resolve these difficulties is to use limited-memory quasi-Newton optimisation techniques. These have subsequently been developed further to permit a fully 3D MT inversion (Avdeev and Avdeeva, 2009). As the technology improves for the acquisition of greater quantities of data (more channels with more components), there is a need to be able to manage and invert the data appropriately and efficiently. Research is ongoing to improve the computational efficiency of 1D and 3D MT inversion techniques.

### 12.3.4 Applications and case histories

#### 12.3.4.1 Mineral exploration

A third of the Western world's uranium is produced from unconformity-type deposits found in the Athabasca Basin, northwest Saskatchewan and northeast Alberta, Canada. Many of the shallowest deposits have now been mined out, so deeper parts of the basin are now being explored. The uranium deposits are located where basement graphitic faults intersect the unconformity (Figures 12.16). Low electrical conductivity associated with the graphite provides a suitable target for EM exploration methods. Tuncer *et al.* (2006) have described the use of AMT methods at the McArthur River mine where the uranium orebody is 100 m long, 10 m wide, 60 m high, and is located between depths of 500 m and 600 m.

In the frequency range of 1000–1 Hz, the geoelectric strike direction is well defined at N45°E, parallel to a major fault. Apparent resistivities were computed from the along-strike electric currents (TE-mode) and also from the across-strike electric currents (TM-mode). For a 2D earth model, these two modes yield different apparent resistivity values and are sensitive to different aspects of

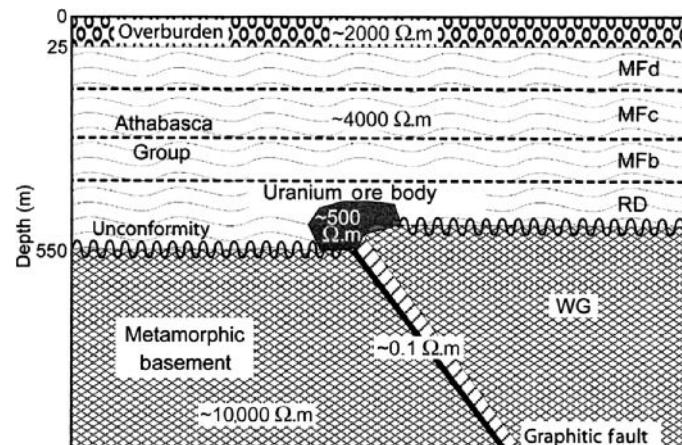


**Figure 12.16** Generic model of an unconformity-type uranium deposit in the Athabasca Basin. The Athabasca Group comprises four major units from bottom to top: the Read Formation (RD) - discontinuous basal conglomerate, intercalated coarse sandstone, conglomerate and red mudstone. The Manitou Falls Formation consists of: MFb: interbedded conglomerate and pebbly sandstone; MFc: granular sandstone; and MFd: medium-fine sandstone with mudstone intraclasts. WG is the Wollaston Formation. From Tuncer *et al.* (2006), by permission.

the subsurface geological structure. The TE-mode is the most sensitive to along-strike conductors, whereas the TM-mode is the most sensitive to resistors and shallow structures. AMT data for these two modes are shown as pseudo-sections in Figure 12.17A, and sample data curves of apparent resistivity and phase for the two modes are illustrated along three profiles in Figure 12.17B. The pseudo-sections in Figure 12.17A show limited site-to-site variation in apparent resistivity in TE-mode. This is because the electric field is parallel to the geoelectric strike. In contrast, the TM-mode pseudo-sections show greater variation because near-surface bodies affect the apparent resistivity strongly. In the TE-mode pseudo-section the location of the conductor is indicated by lower apparent resistivity values in the centre of the profile. The TM-mode data are less sensitive to the presence of the basement conductors than the TE-mode data. The TE-mode electric currents generate a vertical magnetic field ( $H_z$ ) which is related to the horizontal magnetic field by the relationship shown in Box 12.4. This real transfer function ( $T_{zy}$ ) changes polarity above a conductor, as can be seen in Figure 12.17A; positive values occur to the left of the conductor (at around 1.5 km distance) and negative values to the right. These tipper functions can also be

#### Box 12.4 Magnetic field transfer (tipper) function

A vertical magnetic field ( $H_z$ ) is related to the horizontal magnetic field by:

$$H_z = T_{zx}H_x + T_{zy}H_y$$

where  $T_{zx}$  and  $T_{zy}$  are components of the magnetic field transfer function (tipper).

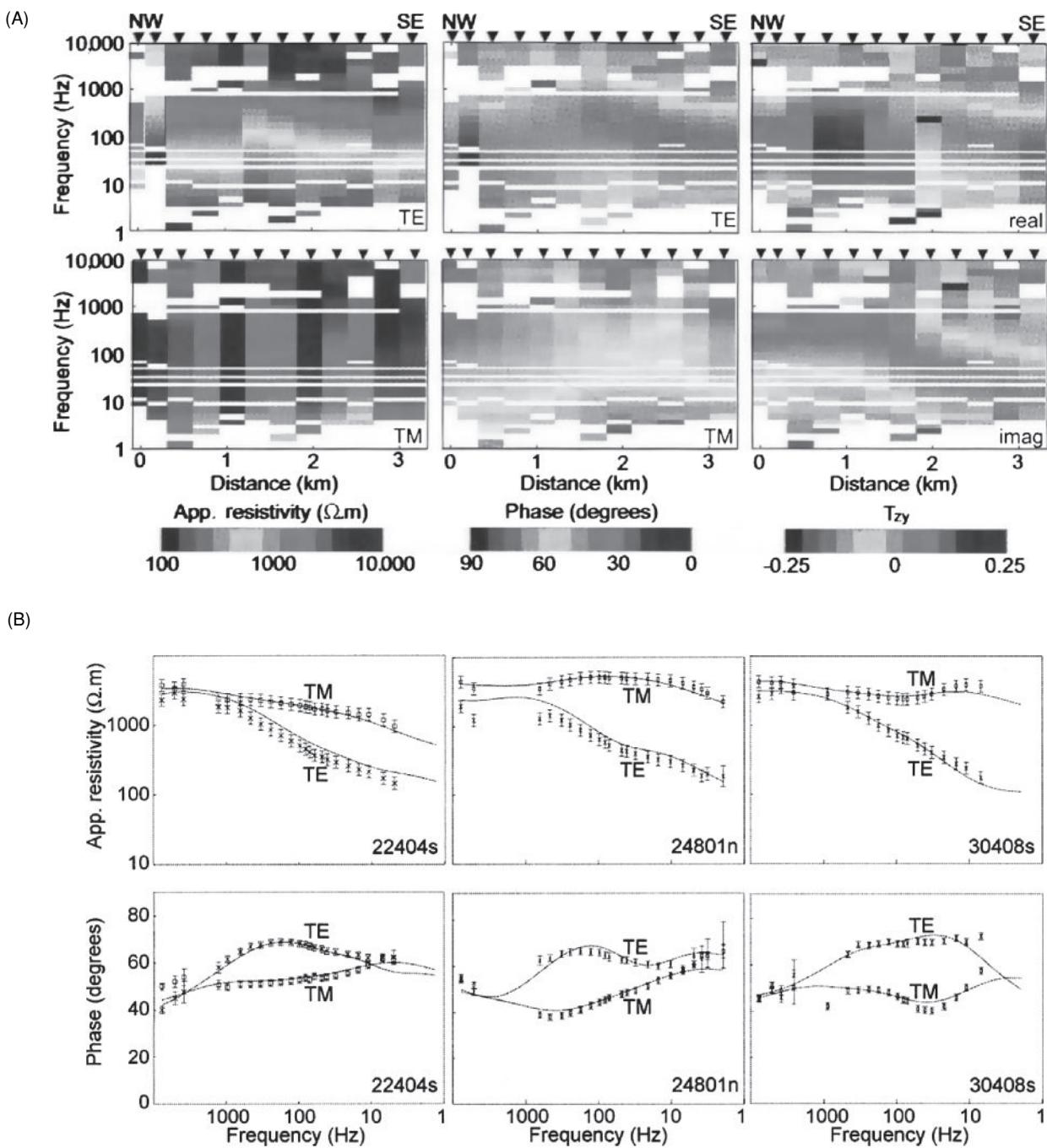


**Figure 12.17** (A) Pseudo sections for TE, TM, and magnetic field transfer function data from line 224. (B) Sample data curves of the TE and TM-mode for stations on lines 224, 248, and 304. Continuous lines show the response of inversion models. From Tuncer *et al.* (2006), by permission.

displayed as induction vectors at a given frequency, where the real part of the induction arrow points towards a conductor. Real induction vectors at a frequency of 100 Hz are shown in Figure 12.18. The direction of most vectors shows a reversal over the location of a basement conductor.

Tuncer *et al.* (2006) undertook detailed 2D inversion and 3D forward modelling of the AMT data. They produced resistivity-depths models for each profile surveyed. The interpretation of the resistiv-

ity model derived from a 2D inversion of the TE-TM- $T_{zy}$  data for profile 224 is shown in Figure 12.19. This indicates that a graphitic conductor terminates at the unconformity and dips to the east.

#### 12.3.4.2 Hydrocarbon investigations

At the Gemini Prospect in the Gulf of Mexico the dominant salt body has been investigated using seismic methods and comprises a

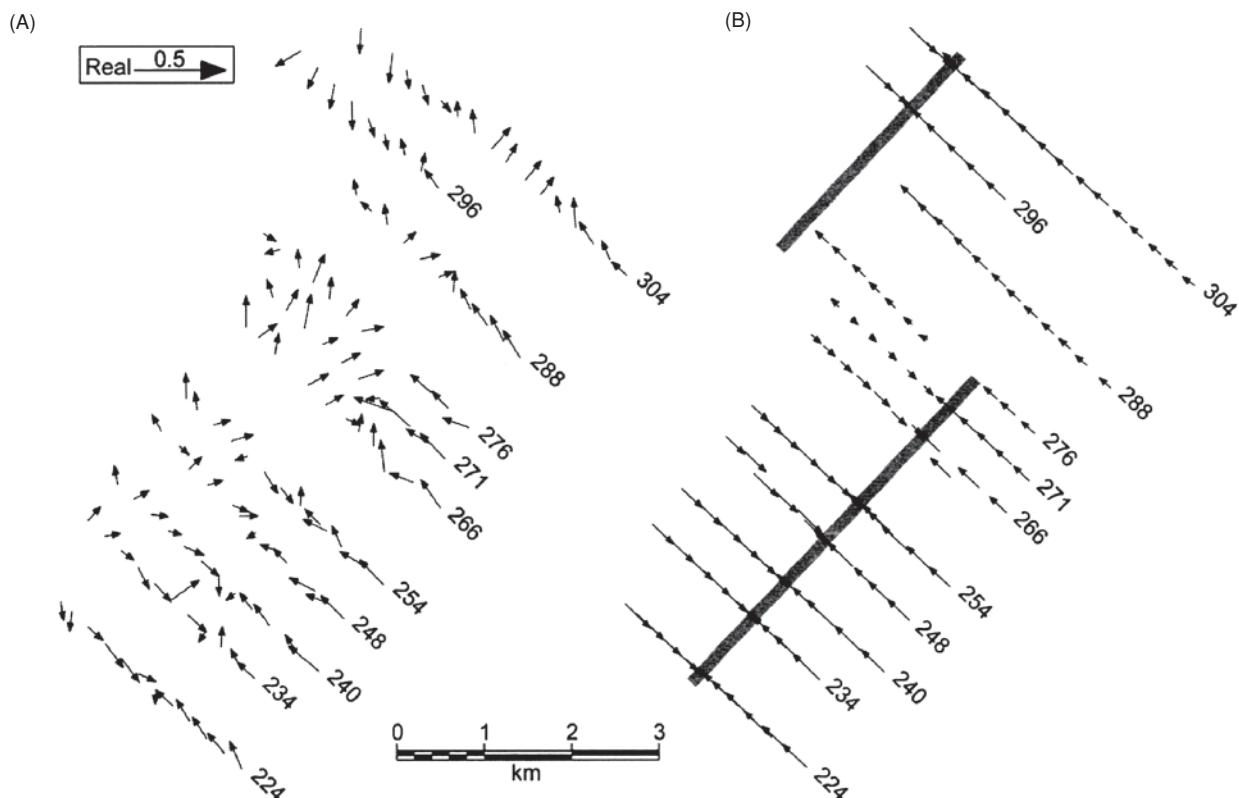


**Figure 12.18** (A) Induction vectors at 100 Hz frequency. The real induction vectors point at a conductor. (B) Synthetic induction vectors for a simple 3D model. Grey-shaded rectangular bars show the locations of the basement conductors. From Tuncer *et al.* (2006), by permission.

complex structure between 1 km and 5 km below the sea floor. The water depth is about 1 km. As seismic methods may not reveal sufficient detail of a complex salt body, and given the high contrast in electrical properties between the resistive salt and conductive host

rocks, marine MT methods have been developed progressively to provide additional resolution of the salt body structure and form (Key *et al.*, 2006). While controlled-source EM techniques are sensitive to thin resistive structures, the presence of massive, resistive salt roots surrounded by relatively conductive sediments provides a better target for MT surveys. Furthermore, the marine MT method also provides some logistical advantages over the CSEM technique by not requiring a separate ship (with all the associated costs) hosting a transmitter system. The Gemini Prospect has been used since the late 1990s as a test bed for developing marine MT techniques. A series of MT soundings has been acquired from which two profiles have been extracted: Line A was chosen as it crosses the NW–SE trending axis of the top-of-salt, while Line B lies predominantly along the shallow top-of-salt ridge. The locations of the 42 individual soundings and of the two profiles are shown in Figure 12.20. A broadband MT sensor was used to measure data in the period band of 1 to 3000 s at the sites indicated in Figure 12.20. An example of the data acquired is shown in Figure 12.21 for site s13, which is located over a thick, deep portion of the salt body. The slight increase in apparent resistivity observed at around a period of 10 s illustrates the sensitivity of the MT method to the presence of the salt body, which has a resistivity of  $> 10 \Omega\text{m}$ , compared with values of  $0.3 \Omega\text{m}$  and  $0.5 \Omega\text{m}$  for seawater and seawater saturated sediments, respectively. At periods longer than about 250 s the apparent resistivity and phase curves separate for each electric-field polarisation. At these long periods the MT skin depth becomes much greater than

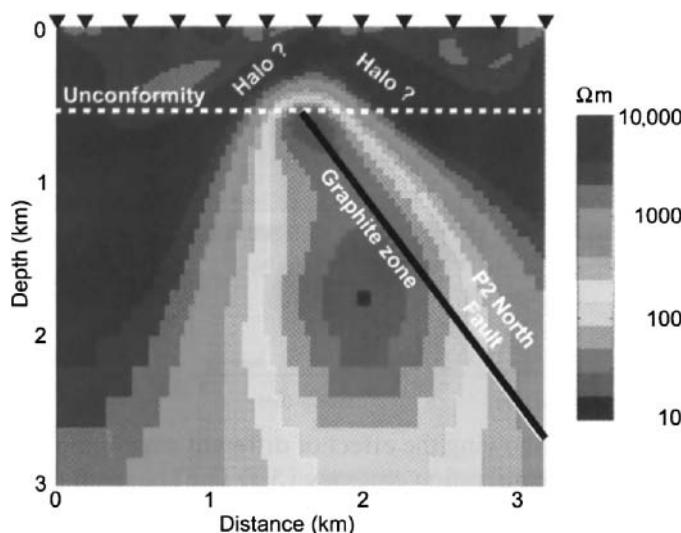


**Figure 12.19** Interpretation of the resistivity model derived from a 2D inversion of the TE-TM-T<sub>z</sub> data for profile 224. From Tuncer *et al.* (2006), by permission. [C]

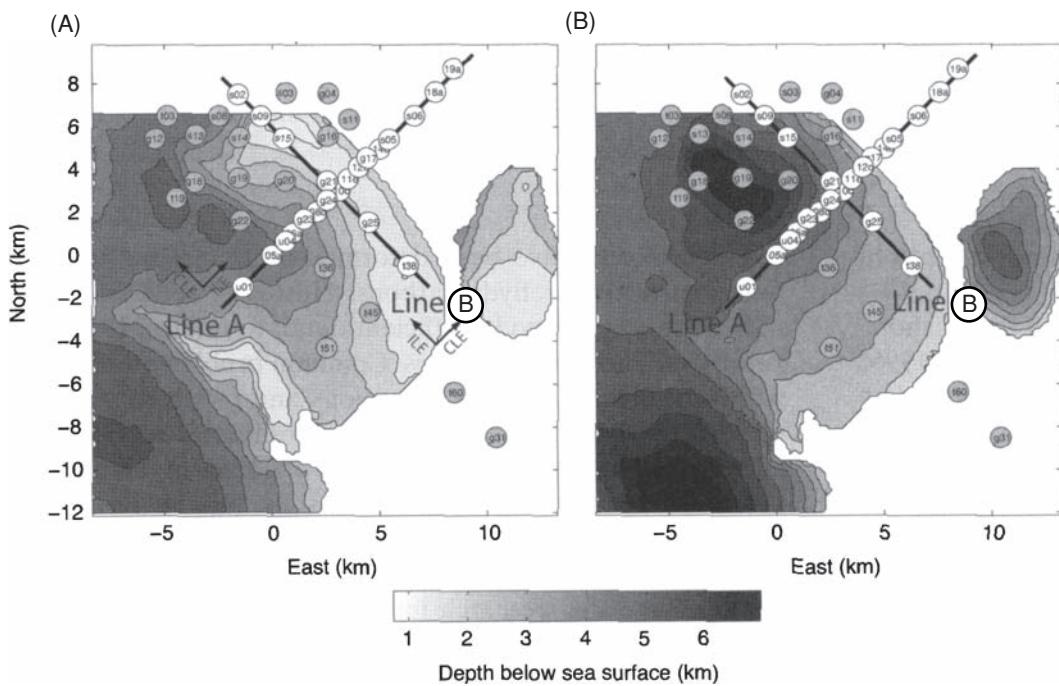


**Figure 12.20** Gemini Prospect, Gulf of Mexico – salt structure and MT sounding sites. Filled contours show the location of (A) top-of-salt and (B) base-of-salt surfaces determined from an industry 3D seismic survey. Black lines show the two MT transects shown in Figure 12.22. From Key *et al.* (2006), by permission.

the base-of-salt depth. This suggests that this split in MT responses is probably caused by a deep 2D or 3D structure and/or the conductivity contrast associated with the nearby continental shelf seafloor topography.

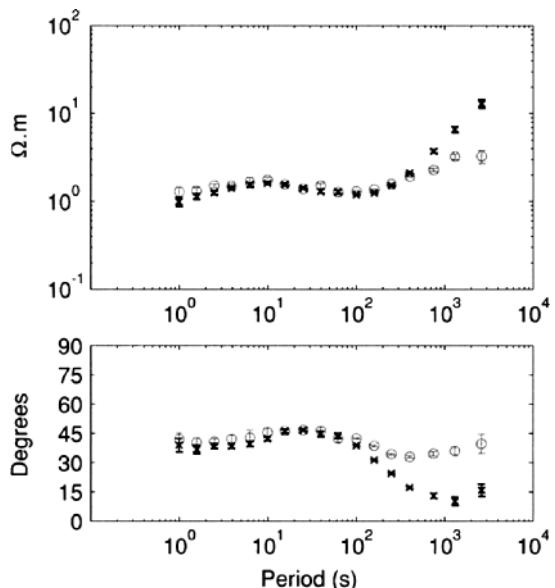


**Figure 12.21** High-quality marine MT apparent resistivity and phase data from site s13 (for location, see Figure 12.20), which is located over a thick portion of the salt. Symbols are for the off-diagonal impedance component with the electric field oriented to the southeast (black symbols) and to the northeast (grey symbols). From Key *et al.* (2006), by permission.

Key *et al.* (2006) undertook detailed 2D inversion of the MT results. They produced pseudo-sections for the period range 1–250 s for both Line A and B. They produced responses for the off-diagonal impedance components that correspond to the horizontal electric fields oriented either along the line (in-line electric, ILE) or across the line (cross-line electric, CLE), as referenced by the orientation of each line. This means that for Line A, the responses correspond to SW–NE (ILE) and SE–NW (CLE). Those for Line B are SE–NW (ILE) and SW–NE (CLE), respectively. The MT inversions with their ILE and CLE components were useful to delineate the structures along the corresponding profiles. However, to aid more detailed interpretation, the MT inversions were combined with depth-migrated seismic reflection profiles (Figure 12.22). The MT profiles extend beyond the end of the available seismic profiles. Line A ILE and Line B CLE were combined with the respective seismic sections showing the seismic and resistivity models derived. The outline of the salt body is clearly evident in Figure 12.22A by the top- and base-of-salt reflections at depths of less than 6 km (outlined in white dashed lines in the figure). What is clear in Figure 12.22A is that the seismic model corresponds extremely well with the higher resistivity anomaly between 2 km and 4 km depth. The wedge of salt depicted in Figure 12.22B (boundaries outlined by dashed white lines) also correlates well with higher resistivity values. The advantage of using a combined 2D/seismic approach is that areas where the resistivity–seismic model diverges indicates areas where the application of 3D MT inversion is required to help to resolve the deeper salt root structures.

Rubinat *et al.* (2010) have described the use of the MT method to investigate the characteristics of the Bicorb-Quesa salt diapir in southeast Spain. Thirty-four measuring sites were occupied using a

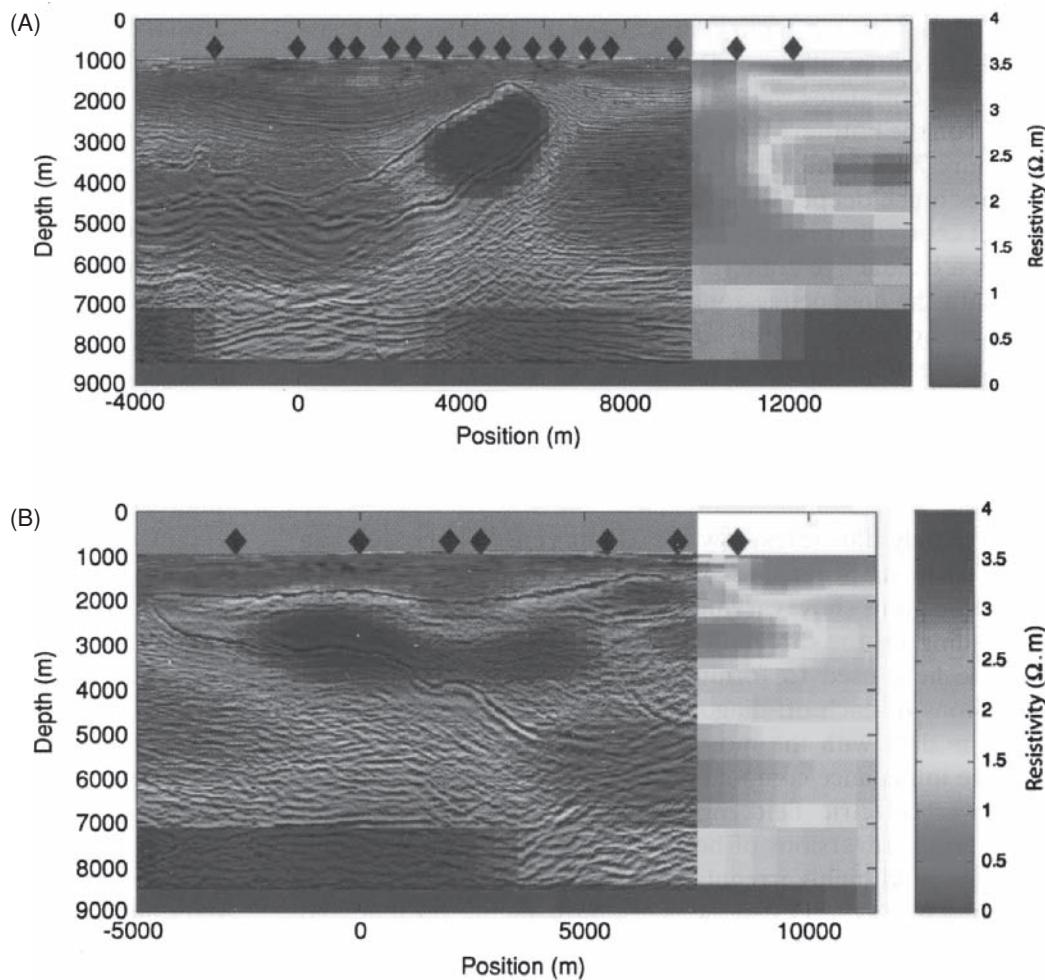


**Figure 12.22** (A) Line A and (B) Line B combined MT and reflection seismic models. Black lines show depth-migrated reflections from a 3D seismic survey. From Key *et al.* (2006), by permission.

broadband instrument measuring in the range  $10^{-3}$  s to  $10^{-2}$  s along a 13 km profile oriented perpendicular to the geological strike. Joint inversion of the TE- and TM-mode apparent resistivity and phase data was undertaken. The depth of investigation achieved was 2 km. The results indicated that the Keuper facies diapiric rocks are highly resistive only in the core of the diapir, whereas the rest of the diapir is conductive. The MT survey also provided information about the fluid nature and circulation in and around the diapirs. It showed that saline water is restricted to the top of the diapir and does not encroach into the surrounding overburden. It also indicated fluid circulation of slightly conductive water at the base of the limestone formation.

#### 12.3.4.3 Environmental applications

In the USA, there are thousands of abandoned, improperly plugged oil and gas wells. Where the producing horizon is over-pressurised following secondary hydrocarbon recovery techniques, these wells can allow injected oilfield brines to migrate up the borehole and into shallower potable-water aquifers. For example, at one oilfield

at Sac and Fox tribal lands of Lincoln County, Oklahoma, USA, oil has been recovered from the Prue Sand Unit since the 1930s. Brine injection has been used since the 1950s for enhanced oil recovery. At the same location, the Vamoosa Formation is the major source of drinking water and its base occurs at depths of between 45 m and 135 m. Test wells drilled in 1979 indicated significant brine concentrations.

CSAMT surveys in the area indicated the presence at depth of plumes of conductive material around abandoned injection wells. One such apparent resistivity section is shown in Figure 12.23 in which the conductive plume is self-evident. Some plumes were found to reach shallow depths. Following the CSAMT survey, two additional test wells were constructed, and bromide/chloride ratios established that the source of the contamination was undoubtedly the Prue Sand brines, as previously suggested by the CSAMT surveys.

In a similar vein, the migration of conductive fluids for *in situ* mining tests as well as injection tests have been mapped using CSAMT methods. In one example, an *in situ* leaching project was losing 90% of the injected fluid and it was important, therefore, to

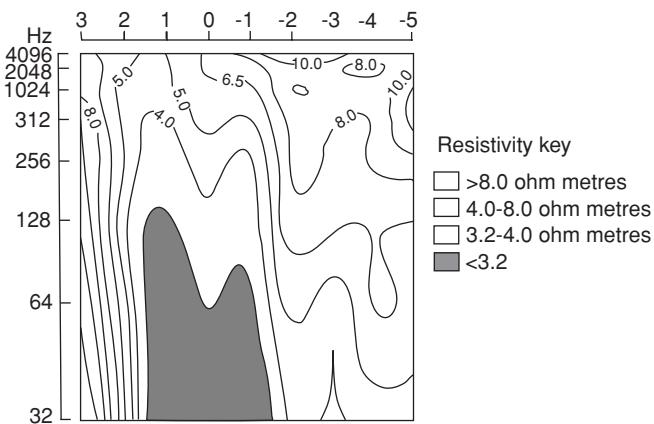


**Figure 12.23** Apparent resistivity pseudo-section near an abandoned injection well, showing the conductive plume (shaded) associated with upwardly migrating brine. From Zonge and Hughes (1991), by permission.

identify where the remainder of the injected material was going. A CSAMT survey was instigated and the resistivity results processed to provide depth-level resistivity slices (Figure 12.24). Conductive areas are shown shaded.

It is evident from Figure 12.24 that the main body of conductive material was centred at the 1600 level (as the areal extent is greatest at this level). It appeared that the fluid had migrated more slowly than

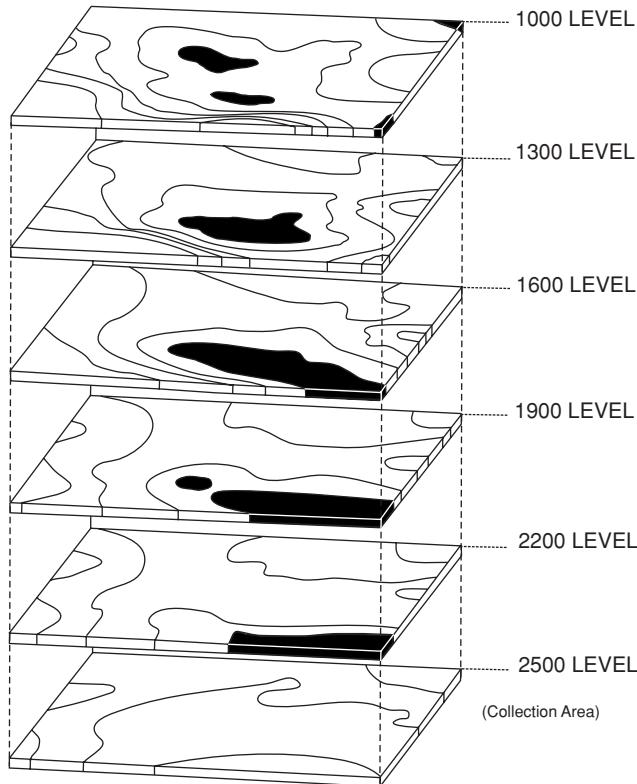


**Figure 12.24** CSAMT depth-level resistivity slices; conductive zones are shown shaded: The largest areal extent of contamination can be seen at the 1600 level. From Zonge and Hughes (1991), by permission.

hydrologists had suspected. Two CSAMT surveys were undertaken over exactly the same ground but one month apart to map the migration of the conductive plume. It was found that in some areas the apparent resistivity was changing by as much as 1% per day.

As with many geophysical methods, the use of the appropriate method(s) can yield valuable information about the three-dimensional spatial distribution of subsurface features. In environmental applications particularly, the spatial changes as a function of time are increasingly important. Where appropriate, CSAMT along with other EM and electrical methods can provide valuable information cost-effectively and without any environmentally detrimental effects.

Underground nuclear testing was undertaken at Amchitka Island in Alaska, USA, between 1965 and 1971. Since then there have been concerns about the possible release of radionuclides from the explosion sites into the overlying marine environment. The local hydrogeology comprises a rain-recharged freshwater layer overlying a deeper saltwater layer originating from intrusion of seawater, with salinity increasing with depth across a transition zone (TZ). Hydrogeological modelling of the groundwater regime had been undertaken on the timing and amount of nuclide release, but was inconclusive. To try to resolve this uncertainty, Unsworth *et al.* (2007) undertook a series of broadband MT soundings to investigate the subsurface porosity and salinity along profiles through three explosion test sites: Cannikin, Long Shot and Milrow.

Two-dimensional inversion of the MT soundings was undertaken using a starting model with the resistivity of seawater at  $0.3 \Omega\text{m}$  and seabed sediments at  $100 \Omega\text{m}$ . The results of the inversions are shown as resistivity-depth sections in Figure 12.25 for each of the three test sites; the location of each of the explosions is indicated by the radiation symbol. The transition zone was interpreted to be where the resistivity decreases with depth; the porosity also decreases linearly with depth. The top of the underlying saltwater layer is located where the resistivity begins to increase; the salinity within the saline layer is uniform, but as the porosity continues to decrease with depth, the overall resistivity (as determined by Archie's law) begins to increase.

In Figure 12.25A (Cannikin profile), relatively low resistivities ( $<30 \Omega\text{m}$ ) are observed within the top 500 m which are thought to be associated with fractures within the area of collapse above the explosion site. Unsworth *et al.* (2007) also speculated that in the high resistivity layer at 1000–2000 m depth in this profile, a lower-resistivity feature exists that is coincident with the cavity and collapse chimney caused by the explosion. The resolution achieved with the sounding spacings is insufficient to be sure of this. The location of each explosion cavity was found to lie within the transition zone. Porosities determined were found to be higher than those assumed in the hydrogeological modelling, and with longer transit times from the explosion site to the marine environment. It was calculated that for the Long Shot explosion site, radionuclides could reach the sea floor in 500–1000 years.

On a much smaller scale, radio-magnetotelluric surveys have been undertaken to map and monitor over time the hydrocarbon contamination associated with an oil refinery in Romania (Tezkan *et al.*, 2005). The Brazi Refinery is one of a number of oil refineries located close to Ploesti, about 60 km north of Bucharest. Oil products leaking from installations and sewerage in the area of the

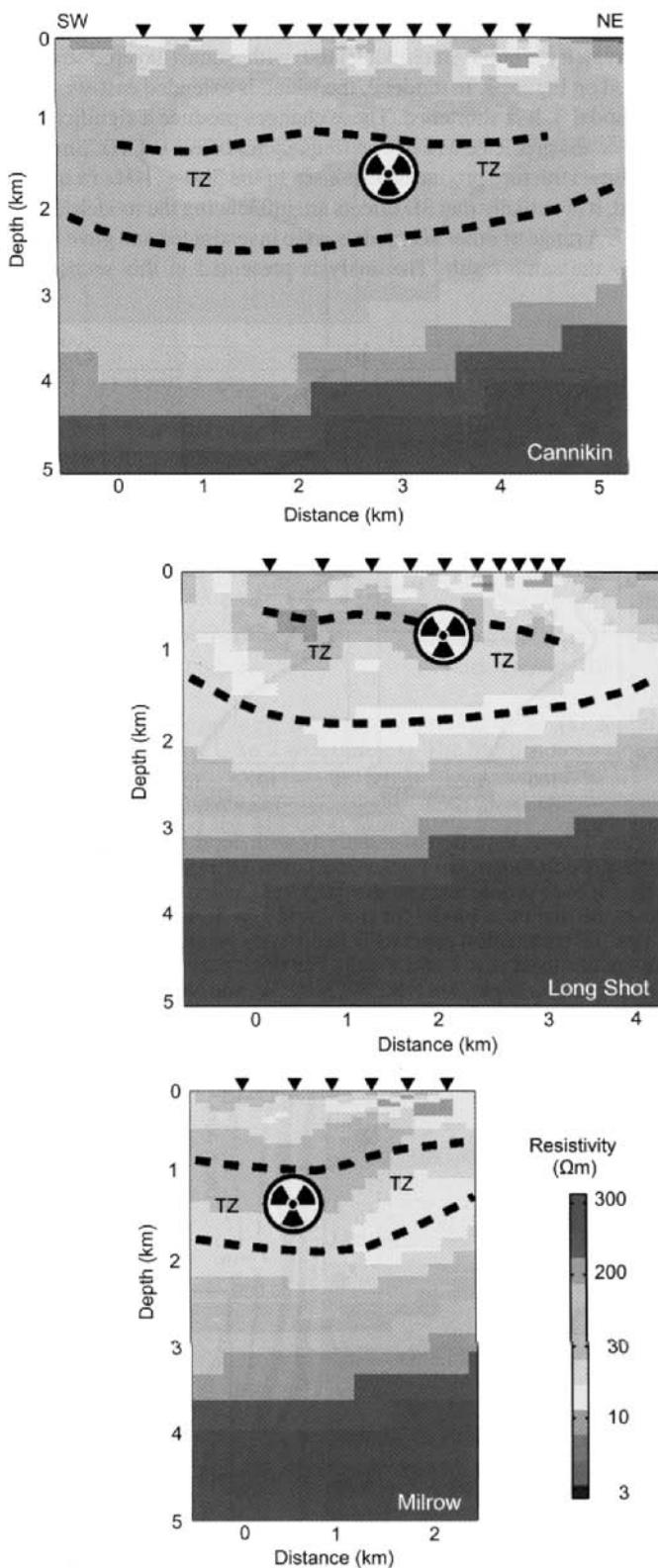


**Figure 12.25** Inversion models for Cannikin, Long Shot and Milrow profiles. Radiation symbols show the locations of the explosions; dashed lines denote the inferred boundaries of the transition zone (TZ). From Unsworth *et al.* (2007), by permission. [C]

refineries have led to the development of oil product films on the groundwater table, in some cases with a thickness of crude oil in excess of several metres. In fact, there has been so much oil contamination that local people have been able to extract residual oil from domestic wells using household tools! The most intense pollution (up to 4.8 m thick oil layer) was found beneath the Brazi Refinery, but this generally decreases towards the southeast along the direction of regional groundwater flow.

A test area of 150 m by 150 m was located southeast and downstream of the refinery in an area where the thickness of oil was thought to be around 1–1.5 m. Locally the geology comprises 0.2 m of top soil, 1 m of clay over 3.5 m of dry gravel with 1 m of oil-saturated gravel beneath, which in turn overlies 13 m of polluted water-saturated gravel. The aquifer base is located on a band of marl around 19 m below ground level. The water table varies seasonally from 1 m depth (wet season) to 5–8 m during dry periods. Locally the crude oil was found to have a resistivity of  $10^7 \Omega\text{m}$ , whereas that of the local groundwater was only  $3 \Omega\text{m}$ .

Apparent resistivity and phase measurements were made along 16 profiles at frequencies of 16, 60, 128.8, 198 and 243 kHz (TE-mode) and at 18.1, 49, 207 and 261 kHz (TM-mode). The response of the transmitters parallel to the strike (i.e. NW–SE direction) relate to the E-polarisation (TE-mode), while those perpendicular to it relate to the B-polarisation (TM-mode). The spatial distributions of the observed apparent resistivity and phase data for a frequency of 198 kHz are shown in Figure 12.26. There is a clear decrease in resistivity from west to east. The measured data were interpreted by 2D joint TE/TM inversion calculations and a resistivity–depth distribution for the survey area was obtained for every profile. Results for three selected profiles are shown in Figure 12.27. The sections reveal a conductive overburden over a resistive lens from 3 m to 13 m below ground level. Below this is a conductive zone attributable to the underlying marl. Within the resistive layer, a much more resistive lens was identified, and when correlated with boreholes was demonstrated to be most likely due to the presence of crude oil contamination.

Measurements were also taken across a similar-sized reference area located to the north and upstream of the Brazi refinery. A comparison of the spatial distribution of the TE-mode apparent resistivities for both the contaminated area and reference site is shown in Figure 12.28. The apparent resistivity values are fairly consistent for all frequencies measured, while at the contaminated site, high resistivity values are found for the higher-frequency datasets, attributable to shallow contamination. A further comparison was made for the contaminated site between measurements being made during a wet period in 1999 and a dry period in 2000. The results are shown in Figure 12.29. As might be expected, the general level of apparent resistivity values is lower ( $<100 \Omega\text{m}$ , western part;  $<50 \Omega\text{m}$  in the eastern part) during the wet period than during the dry time, when most resistivity values are  $>100 \Omega\text{m}$ . The biggest differences between the two sets of conditions occur in the zone interpreted to contain the crude oil contamination. This suggests that perhaps the greatest sensitivity to the resistivity contrast between crude oil contamination and host materials is obtained when the measurements are made during a dry period.

It should be noted, however, that the electrical resistivity of hydrocarbons does not necessarily stay constant with time. Dilution

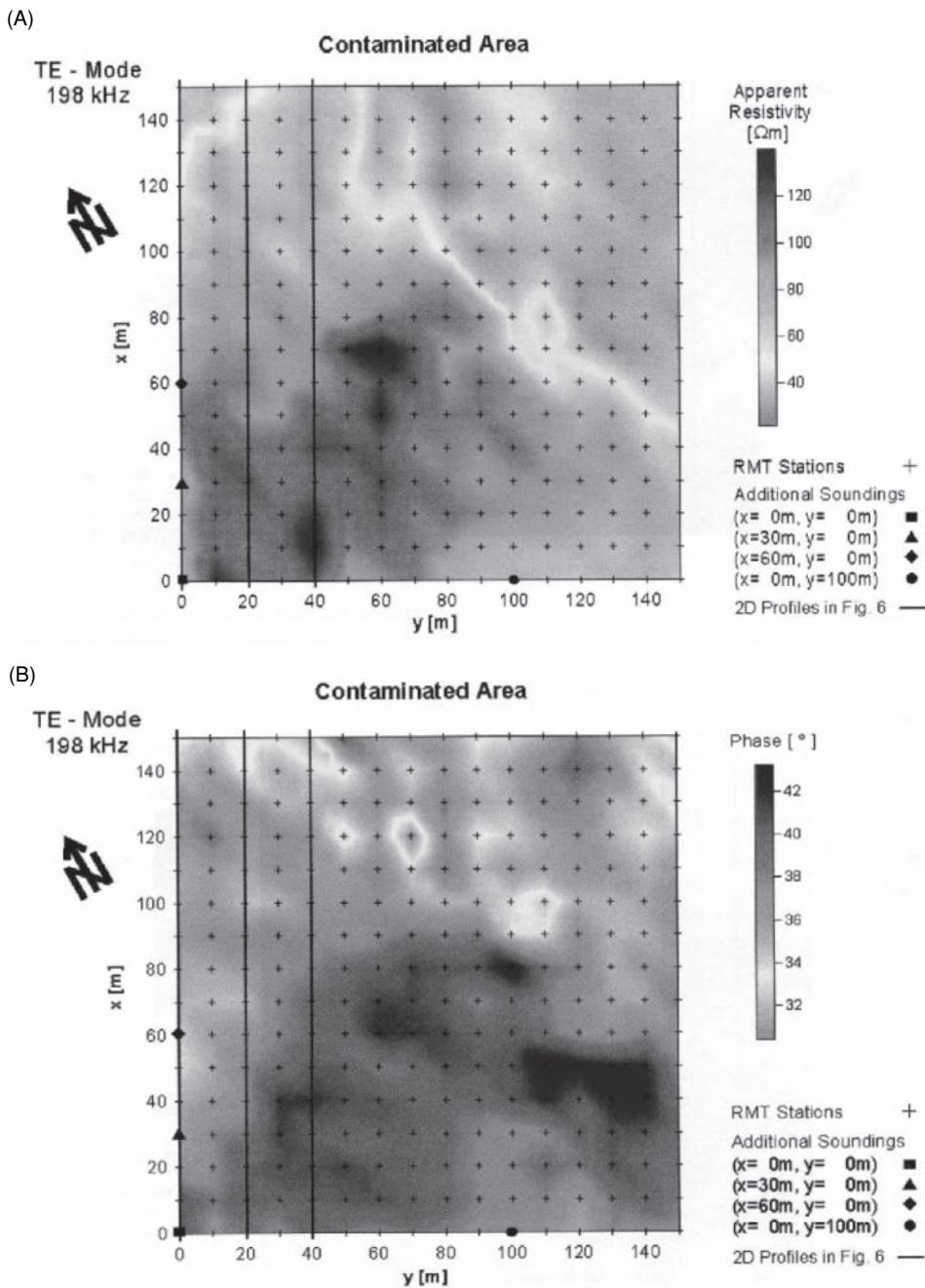


**Figure 12.26** Spatial distribution of (A) apparent resistivity and (B) phase for the frequency 198 kHz (TE-mode). Crosses indicate the location of radio-magnetotelluric stations. Additional soundings were undertaken at sites indicated by the symbols shown. Data were acquired during a wet period in 1999. From Tezkan *et al.* (2005), by permission. [C]

and dispersal effects might mute the resistivity contrast, but so can biochemical reactions. These may reduce the resistivity of the oil, even turning the affected oil conductive. It is thought that one of the diagnostic features associated with bioremediation of hydrocarbons using bacteria, for example, is elevated conductivities. Consequently, a geophysical model for crude oil floating on groundwater might be an upper resistive layer on top of a conductive layer. The behaviour of light non-aqueous-phase liquids (LNAPLs) in sandy sediments has been discussed, for example, by Sauck (2000).

#### 12.3.4.4 Groundwater investigations

Saltwater intrusion into coastal aquifers is a major environmental concern, especially as a significant proportion of the world's population is located in coastal areas. Electrical and electromagnetic methods are commonly used to investigate saltwater intrusion. However, it is often assumed that the seawater-freshwater transition is sharp and that flow is immiscible, neither of which may be appropriate near the coast where the mixing zone may be large and unstable.

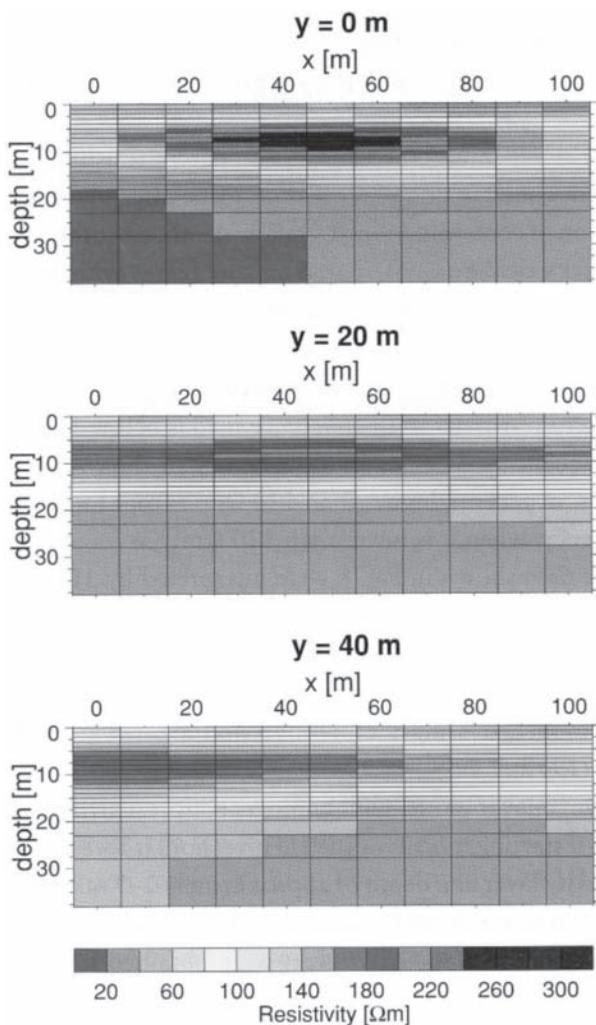


**Figure 12.27** Resistivity-depth sections for three profiles ( $y = 0$  m,  $y = 20$  m and  $y = 40$  m) indicated in Figure 12.26. From Tezkan *et al.* (2005), by permission. [C]

Falgàs *et al.* (2009) have undertaken an investigation of saltwater intrusion using AMT methods in the deltaic zone of the Tordera River, in the northeastern Iberian Peninsula. Every four months during the investigation period, AMT soundings were repeated over the same profile to provide time-lapse images comprising seven soundings along a 1700 m N–S trending profile. The freshwater–seawater transition zone was determined and monitored through one borehole and two multi-tube piezometers. The measured data were inverted to produce a sequence of time-lapse resistivity sections from April 2004 to May 2006 (Figure 12.30); the position of one of the piezometers (W-06) is also indicated. Throughout the experiment period the piezometric head level and rainfall were measured. The results indicate in models M-1 to M-3 that seawater retreats without lowering head levels during the summer due to significant amounts of precipitation. However, there was little precipitation during spring and summer 2005, so the head level lowered and the AMT results indicate seawater intrusion (models M-4 and M-5). This dry period was followed by a rainy autumn and head levels started to recover

with a corresponding retreat of seawater (models M-6 and M-7). In this last model, a time delay was observed between the head level changes and seawater content with an apparent regression of seawater. It was clear from the AMT and hydrometeorological results that the maximum seawater content (model M-5) occurred at the same time as the minimum piezometric head level (August 2005).

In MT surveys a galvanic distortion effect can shift apparent resistivity sounding curves by a scaling factor that is independent of the frequency while keeping phases unaffected. Such a static shift can be caused by charge accumulation at boundaries of shallow conductive features that disturb the regional electric field locally (Tournerie *et al.*, 2007). Presence of this vertical shift can lead to significant errors in the inverted model resistivity and depth values. It is important, therefore, to correct this static shift prior to inversion. Tournerie *et al.* provided an example of 3D AMT soundings undertaken in Las Cañadas Caldera, Tenerife, Canary Islands, and demonstrated their method of correcting the static shift. The objective of the survey was to reveal the shallow caldera structure of the island and to estimate the depths to the impermeable caldera floor (hydrothermalised lavas) to gain information on the geometry of local aquifers. Had several AMT soundings not been corrected for the static shift, modelled resistivity values and depths would have been incorrect and misleading information could have been produced about the aquifer geometries.

#### 12.3.4.5 Geotechnical investigations

Information about rock mass quality and the distribution of weak zones is essential for economical tunnel design and safety. Usually, such information is obtained by examining cores retrieved from drilling boreholes and laboratory testing of physical samples. High drilling costs and/or restricted access by rough terrain can result in too few boreholes being constructed and the design being made on the basis of too little information. To remedy this, it is possible to undertake surface geophysical methods such as electrical resistivity tomography (ERT) and controlled-source MT (CSMT) soundings along a proposed tunnel route. Kwon *et al.* (2006) have provided an example of the combined use of ERT and CSMT with the aid of borehole results to provide a rough estimate of the rock mass condition over a planned tunnel route in the Gangwon province in eastern Korea. The techniques are able to map weak zones (faults, fractures, and coal-bearing zones) that are locally characterised by lower resistivity values than the surrounding fresh rock mass.

The survey area is located in one of the most mountainous regions in Korea and in an area that contains coal mining. Ground subsidence from abandoned coal mines resulted in extensive rebuilding of existing railroads. To reduce costs and improve overall safety, a new railway route was proposed. Due to the mountainous terrain, which presented a significant elevation difference between the tunnel portals (400 m over a horizontal distance of 8 km), the new route comprised a loop tunnel to reduce the railway gradient; the new route extended to 18.15 km with 16.62 km being designed as a tunnel, whose depth below ground level ranged mostly between

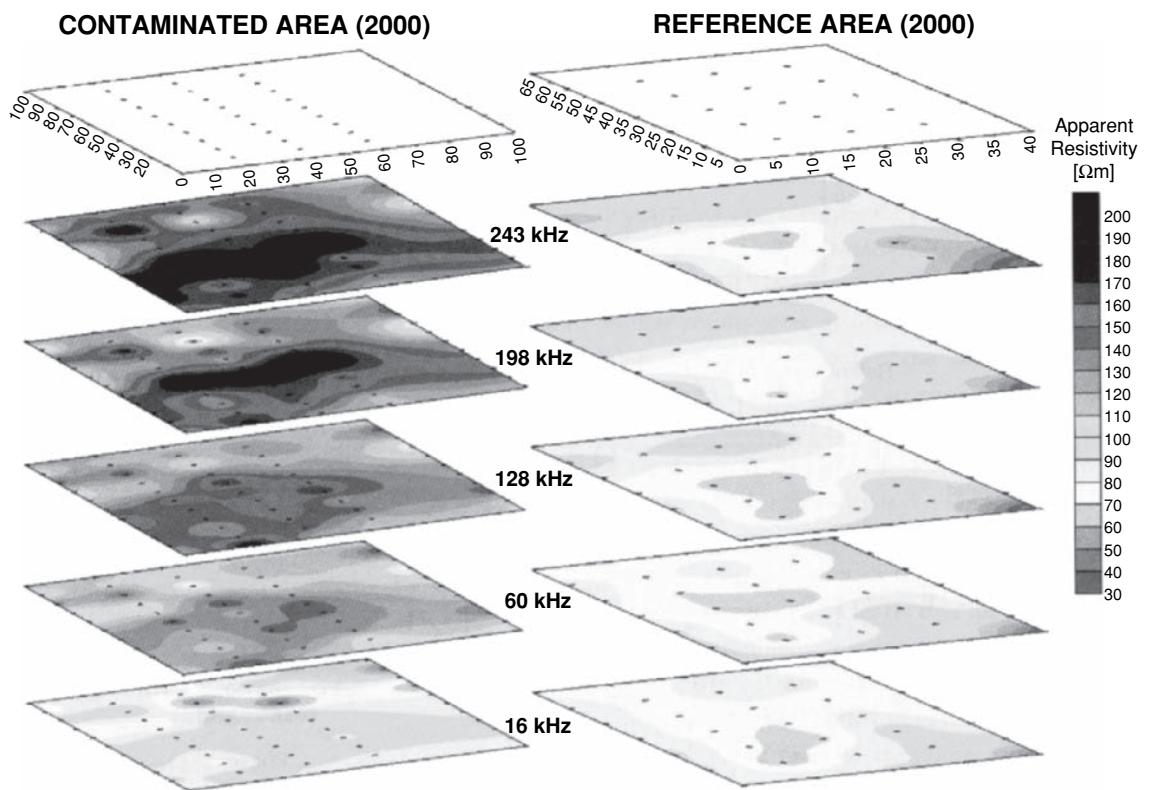


Figure 12.28 Apparent resistivity distributions of the contaminated area and reference field. From Tezkan et al. (2005), by permission. [C]

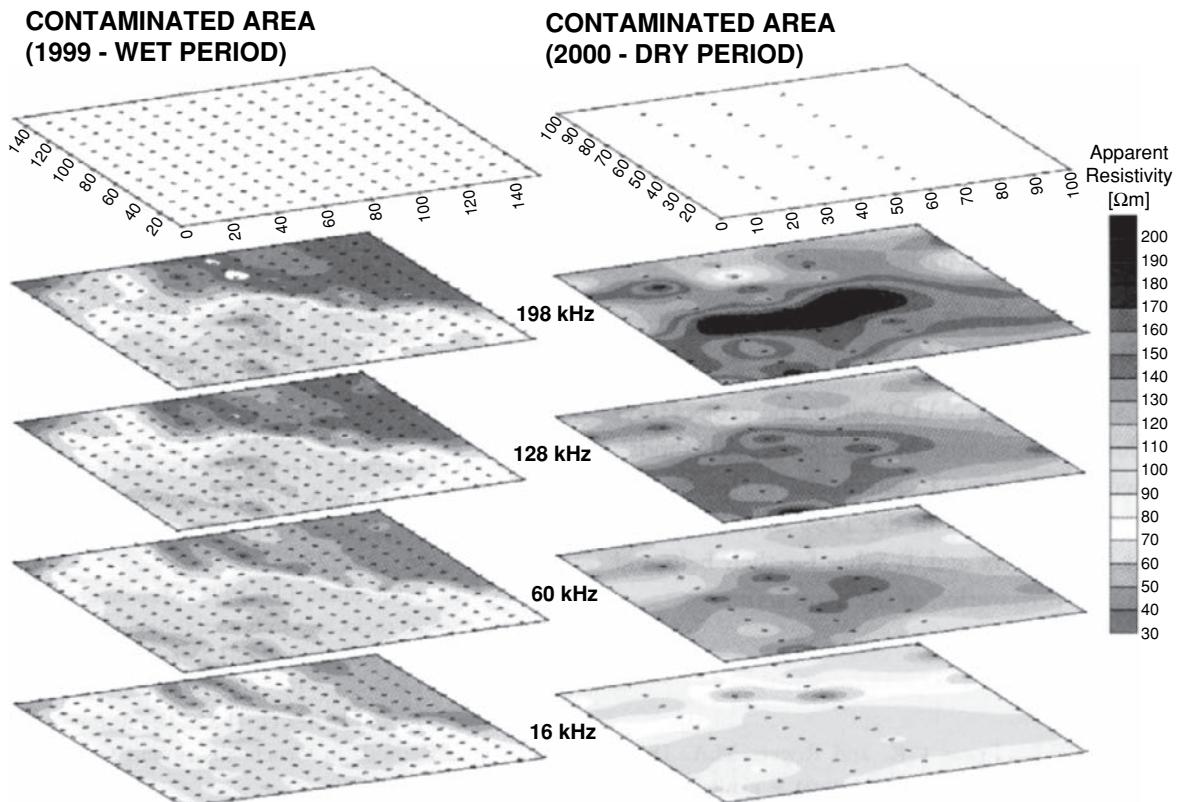
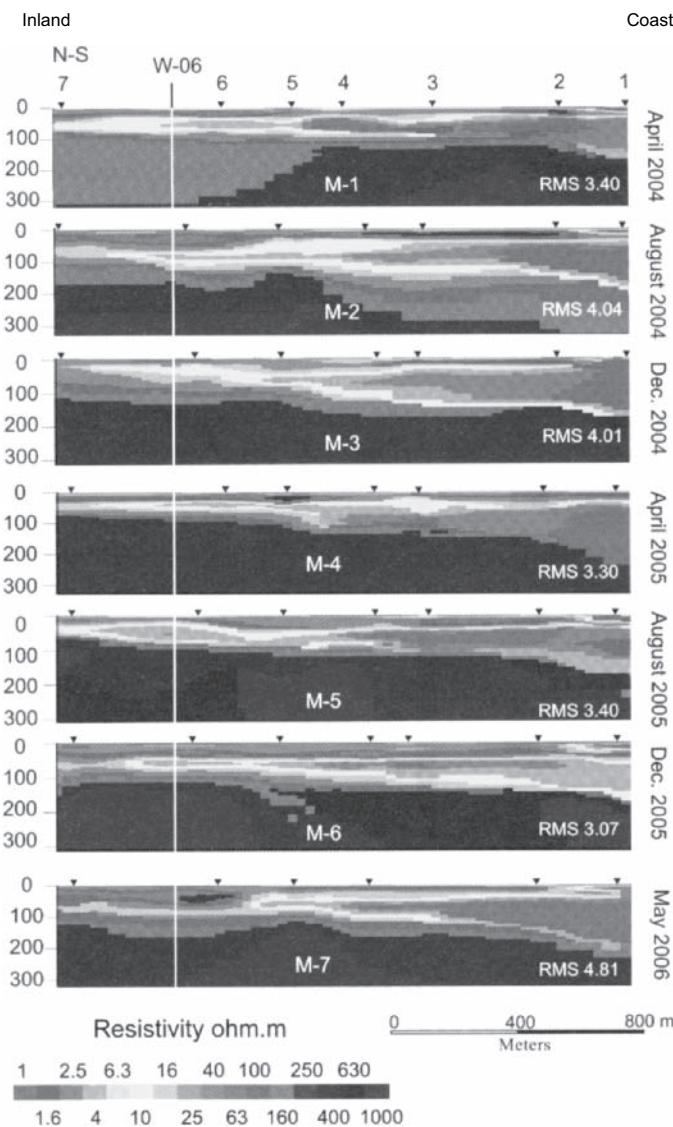


Figure 12.29 Apparent resistivity distributions (TE-mode) of the contaminated area obtained in the wet period (1999) and dry period (2000). From Tezkan et al. (2005), by permission. [C]



**Figure 12.30** Geoelectrical monitoring sequence from AMT models M-1 to M-7, obtained from April 2004 to May 2006. From Falgàs *et al.* (2009), by permission. [C]

200 m and 400 m, with a maximum beneath the mountain peak. The outline of the proposed route and local geology are shown in Figure 12.31. A CSMT survey was undertaken where the tunnel depth exceeded 200 m and in the coal seam area, where ERT surveys were also carried out to provide higher resolution. Kwon *et al.* used a StrataGEM system (Geometrics Inc.) to measure tensor electromagnetic impedance for the frequency range from 10 Hz to 75 kHz by measuring two mutually-orthogonal horizontal electric and magnetic fields. The ERT survey was carried out using an ABEM SAS 300 with a dipole-dipole array and a dipole length of 50 m.

The results of the CSMT and ERT surveys are shown in Figure 12.32 along with the locations of boreholes. The geological structures were estimated based on the results of a geological survey, comparison of the TE- and TM-mode CSMT data, and inverted

ERT images. Between 99 km and 106 km along the profile, the CSMT data reveal the presence of resistive base rock. The abrupt change in resistivity at around 103.5 km (anomaly A) is thought to be fractures due to faulting. Low-resistivity anomalies at B and C, seen on both the CSMT and ERT data, are attributed to the presence of coal seams and coaly shale. This example demonstrates the effectiveness of the combined use of these complementary techniques in detecting potentially problematic ground in relation to the proposed tunnel route.

## 12.4 Magnetic Resonance Sounding (MRS)

Magnetic Resonance Sounding (MRS), also known as the Proton Magnetic Resonance (PMR) and the Surface Nuclear Magnetic Resonance (SNMR) method, has been developed specifically for hydrogeological investigations and is the only geophysical technique to give a direct indication of the presence of water within the ground. The technique was first developed in Russia in the 1980s with the first soundings being undertaken between 1979 and 1981, with further developments in France, Germany and the Netherlands subsequently. In 1996 a new generation of MRS equipment became available commercially (NUMIS, Iris Instruments) and use of the method in groundwater surveys has been increasing since. The technique is designed to estimate the total quantity of water present at a given location, its depth, and the hydraulic permeability of the formation. The MRS method was the focus of a special edition of the *Journal of Applied Geophysics* in 2002 and of *Near Surface Geophysics* in 2005 (Yaramancı and Legchenko, 2005) and also in 2010. See also, for example, the overviews of the use of MRS in hydrogeology by Legchenko *et al.* (2002) and by Yaramancı and Hertrich (2009).

### 12.4.1 Principles of operation

The technique is based upon exciting hydrogen protons in water molecules with a magnetic field at a specific frequency (the Larmor frequency, depending upon the amplitude of the Earth's field) and measuring the field produced by these protons. It is a similar process to the way a proton magnetometer works – protons align themselves to an applied field and then precess when the field is switched off. A large loop of wire, with a side dimension of the order of the intended depth of investigation (e.g. 50–150 m), is used as both a transmitter and receiver (Figure 12.33). Pulses of alternating current generated by the transmitter excite protons in any underlying water that then align themselves with the direction of the net magnetic field. When the applied field is switched off, the protons precess, generating a magnetic field signal during the relaxation process (Figure 12.34). The analysis of the recorded data provides estimates of the water content and the mean pore size (permeability) of each layer at depth.

The Earth's ambient magnetic field ( $B_0$ , nT) determines the Larmor frequency of the hydrogen protons and varies between 0.8 and

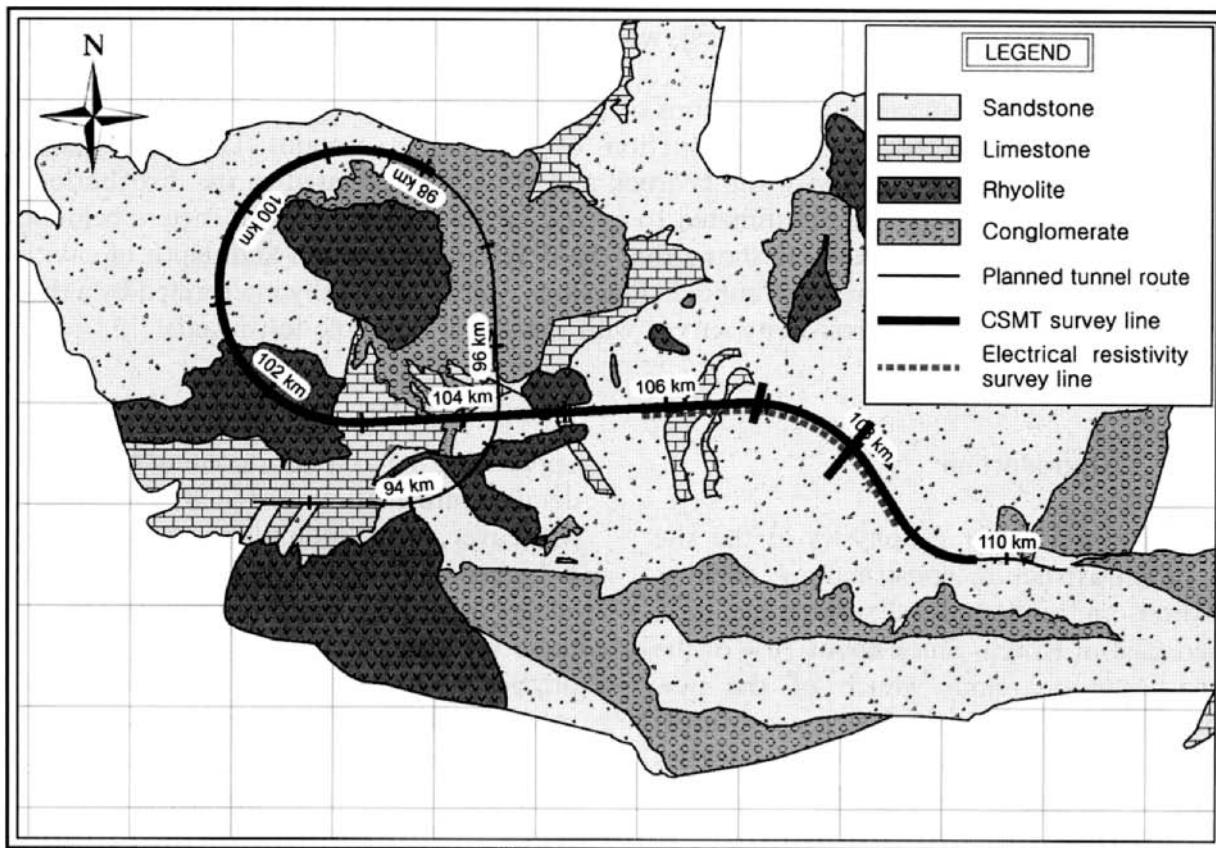


**Figure 12.31** Geological map of the survey route with the electrical resistivity and CSMT survey lines superimposed. From Kwon et al. (2006), by permission.

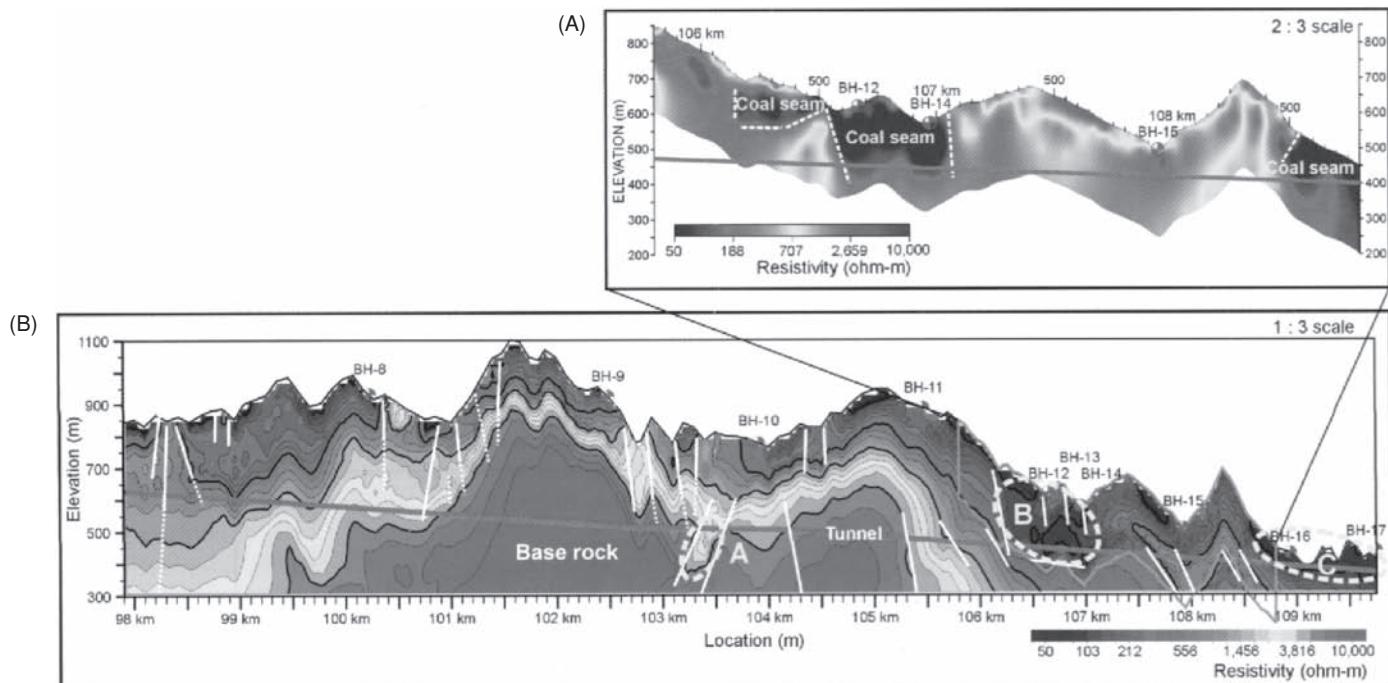


**Figure 12.32** Electrical resistivity images derived from (A) ERT and (B) CSMT surveys. The grey and white lines on the image denote the planned tunnel route and estimated geological structures, respectively. From Kwon et al. (2006), by permission. [C]

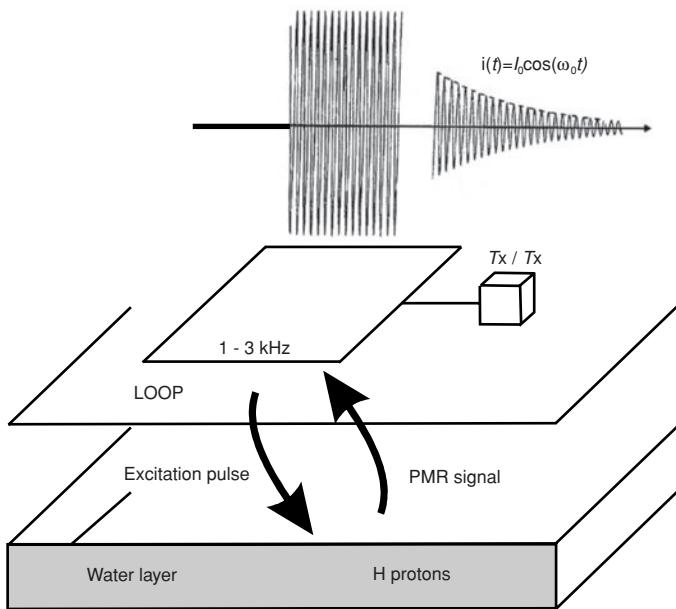


**Figure 12.33** Field layout and principle of the MRS method. After Bernard and Legchenko (2003), by permission.

3.0 kHz. Consequently it is necessary to measure the field intensity and inclination at the location of the intended MRS survey so as to be able to determine the locally correct Larmor frequency. The dynamic energising field ( $B_1$ ) (applied loop magnetic field) produces the nutation of the H protons' magnetic moment  $M_0$ : it tilts away from the static field at an angle  $\theta$ , while still precessing at the Larmor frequency (Figure 12.35). Once the energising field has been switched off, the protons return to equilibrium ( $M_0$  aligned with  $B_0$ ) after a relaxation decay characterised by an initial amplitude  $E_0$  and the *transverse* time constant  $T_2^*$ . This time constant relates to the component of the magnetic moment  $M_0$  perpendicular to the Earth's magnetic field (one-pulse technique measurement). The *longitudinal* time constant  $T_1$  relates to the component of the magnetic moment  $M_0$  parallel to the Earth's magnetic field (double-

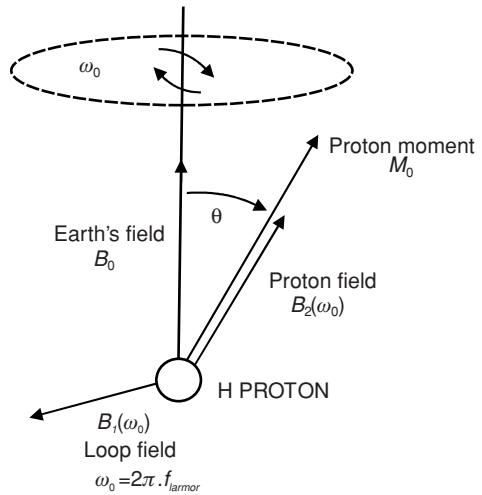


**Figure 12.35** Magnetic vectors in the proton precession process. After Bernard (2006b), by permission.

pulse technique measurement). The time constants relate to the permeability through the mean pore size. When pores are large, the protons lose their energy slowly (long time constant) by motion against adjacent rock grains compared with when pores are small, when energy loss is faster (short time constant). The water content (porosity) is proportional to the amplitude of the proton response and the time constant of the relaxation decay is determined by the pore size of the medium (which is linked to the permeability). The MRS method cannot distinguish between saline and fresh water, but just indicates the presence of water; electrical resistivity and/or EM methods should be used to determine water salinity. The moment of the energising pulse (intensity  $\times$  duration,  $\delta t$ ) determines the depth of investigation. A complete sounding is made up of a series of measurements made with different pulse moments. Current amplitudes of up to 400 A and voltages up to 4000 V are necessary over a period of a few tens of milliseconds (typically 40 ms) to achieve a depth of investigation of 150 m. Loop sizes are typically 50 m, 100 m or 150 m to achieve the same order of depth of investigation

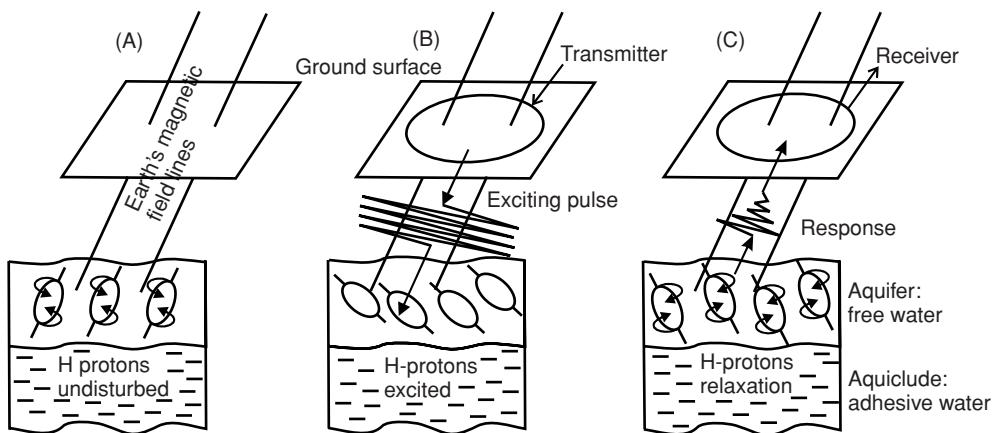


**Figure 12.34** Hydrogen protons (A) at equilibrium, and during (B) excitation and (C) relaxation in the MRS method relative to the Earth's magnetic field.

**Box 12.5 MRS relationships (Iris Instruments, 1998)**

*Proton precession frequency,  $f_0$ , subjected to the Earth's magnetic field  $H_0$  is given by:*

$$f_0 = H_0\gamma/2\pi$$

where  $\gamma$  is the gyromagnetic ratio of the protons [ $\gamma = 0.268 \text{ Hz/nT}$ ].

The *decay of the relaxation field* produced by the protons after turning off the excitation current is given by:

$$E = E_0 \exp(-t/T_2^*) \sin(2\pi f_0 t + \varphi_0)$$

where  $T_2^*$  is the transverse time constant and  $\varphi_0$  is the phase shift between the excitation current and the relaxation voltage measured in the transmitter-receiver loop.

The *relaxation voltage* measured at the ground surface just after the excitation current has been switched off is given by:

$$E_0 = \int_v 2\pi f_0 H_{\perp}(r) M_0 w(z) \sin[(\gamma/2)H_{\perp}(r)q] dv$$

where:

$M_0$  is the magnetic moment of the water molecules

$w(z)$  is the water content

$q$  is the pulse moment (intensity,  $I \times$  duration,  $\delta t$ )  
{units A.ms}

$H_{\perp}(r)$  is the component of the excitation field perpendicular to the Earth's field normalised for a unitary current ( $I = 1\text{A}$ ).

*Relationships for time constants  $T_1$  and  $T_2^*$*  (see Figure 12.36B; Bernard, 2006b):

$$E'_0 \approx E_0(1 - \exp(-\Delta t/T_1))$$

and

$$T_1 \approx -\Delta t/\log(1 - E'_0/E_0).$$

*Permeability* is derived from MRS readings using the expression:

$$\text{Permeability} = C \times \text{porosity} \times (T_1)^2$$

where  $C$  is a coefficient that may vary with geological context (Bernard and Legchenko, 2003).

(i.e. 50 m loop side for 50 m depth, etc.). Depending on the signal to noise ratio, a complete magnetic resonance sounding comprising 16 pulse moment values can take one to two hours to complete. The various relationships for the precession frequency, decay of the relaxation field and relaxation voltages measured at the ground surface are given in Box 12.5 (Iris Instruments, 1998). The form of the energising pulse and relaxation signal is shown in Figure 12.36A.

The time constants are important parameters and reveal different aspects of the subsurface hydrogeological conditions (Bernard and Legchenko, 2003).  $T_2^*$  for instance depends not only on the mean pore size of the local geological formations, but also on the inhomogeneities of the magnetic susceptibility of the rock grains, so  $T_2^*$  gives only an approximate indication of permeability. The longitudinal time constant  $T_1$ , which is usually two to four times larger than  $T_2^*$ , is determined by using a double-pulse technique (Figure 12.36B) (Bernard, 2006b). Two pulses of current are applied separated by a time interval ( $\Delta t$ ) greater than  $T_2^*$  but shorter than  $T_1$ . The initial amplitude after the second pulse ( $E'_0$ ) compared with the first ( $E_0$ ) is measured. The difference between the two amplitudes is due to the fact that the protons do not have sufficient time to relax back to their original starting position before the second current pulse is applied, which minimises the signal amplitude after the second energising pulse.  $T_1$  is related only to the mean pore size and thus is a more reliable parameter by which to estimate the permeability.

## 12.4.2 Field measurements

Commercial MRS systems are now available with a range of depths of exploration (e.g. NUMIS Plus for depths 100–150 m; NUMIS Lite for depths <50 m). The field configuration is illustrated in Figure 12.33. For the MRS method to be applicable, the Earth's magnetic field should not vary by more than  $\pm 20 \text{ nT}$  across the transmitter-receiver loop and its immediate vicinity. This corresponds to a variation of  $\pm 1 \text{ Hz}$  on the Larmor frequency. Also the magnetic susceptibility of the local rocks should be low enough not to perturb the relaxation of the hydrogen protons. Currently, magnetic resonance soundings are difficult to achieve successfully in areas with mafic volcanic rocks with their associated high levels of magnetic susceptibility (i.e.  $> 10^{-2} \text{ SI units}$ ); MRS may be successful with rocks with magnetic susceptibility values in the range  $10^{-3}$  to  $10^{-2} \text{ SI units}$ , but is best suited to areas with local susceptibility values smaller than  $10^{-3} \text{ SI units}$  (Bernard, 2006a).

As the measured voltages in the receiver coil are extremely small (of the order of nanovolts), the survey should be undertaken in a low EM-noise environment. The survey should be undertaken far enough away from power lines, pumps, metal fences, or anything else likely to generate EM-signals that could swamp the tiny signals arising from the proton relaxation process during magnetic resonance sounding.

To improve the signal:noise ratio, signal stacking can be achieved. In addition, it is possible to deploy a number of different loop configurations through which noise may be further reduced. For

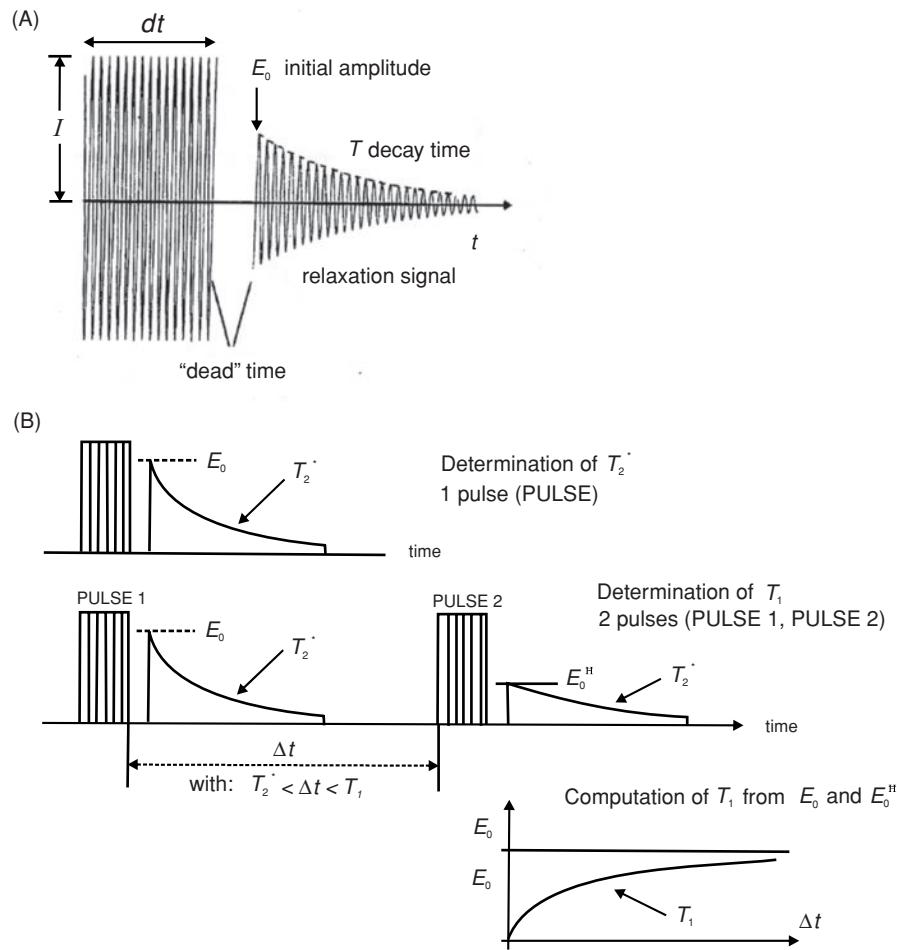


**Figure 12.36** (A) Excitation pulse and relaxation signal; (B) single and double pulse techniques to determine time constants  $T_1$  and  $T_2^*$ . After Bernard (2006b), by permission.

example, a figure-of-eight loop (Figure 12.37, middle) can improve the signal:noise ratio between two and ten times, depending upon site conditions compared with the response from the standard single loop (Figure 12.37, left). The figure-of-eight loop reduces the depth of exploration to half that of the same perimeter square loop producing the same current for a given output voltage (Bernard, 2006a). To achieve comparable depth of exploration, a compensation loop can be used (Figure 12.37, right). The noise from the compensation loop cancels a large proportion of noise from the main loop. Other loop configurations can also be used, including using separate transmitter and receiver loops (Hertrich *et al.*, 2005), subject to available space and local conditions.

There might be occasions when no discernable MRS signal is detected, even after signal stacking and optimising signal:noise with loop geometries. This might be due to one or more of the following:

- the excitation frequency selected is not close enough to the local Larmor frequency, perhaps due to a local magnetic field gradient;
- the EM noise is too high relative to the MRS signal;

- there is no water within the depth of exploration;
- the presence of magnetic rocks precludes acquisition of a sensible MRS signal.

Developments in equipment are likely to involve better noise suppression and multichannel instruments.

Once it has been determined that a sensible MRS signal is being detected, then a full sounding can be achieved. This is obtained by recording the relaxation amplitude at a given pulse moment amplitude (Figure 12.38B, left graph). This produces one data point on an amplitude–pulse moment graph. The pulse moment is then changed in sequence and another measurement of amplitude is obtained, and so on until amplitudes have been recorded for perhaps 16 different pulse moment amplitudes. The results are displayed on an amplitude–pulse moment graph (e.g. Figure 12.38A, left, and B, middle). Measurements of phase shift and noise are also made. From these parameters, profiles of water content (%) versus depth can be produced (Figure 12.38A and B, right).

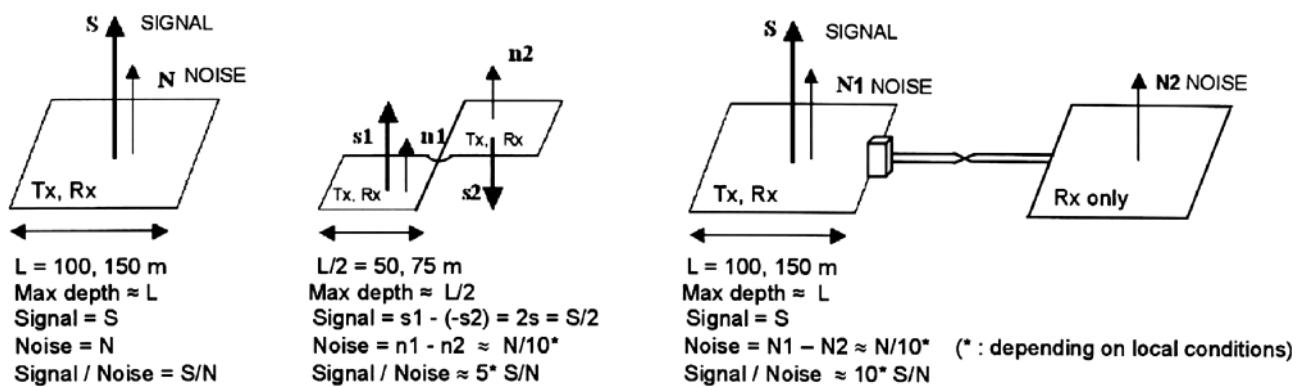


Figure 12.37 Square loop (left), eight-shape loop (middle), and compensation-square loop (right) configurations in magnetic resonance sounding. After Bernard (2006a), by permission.

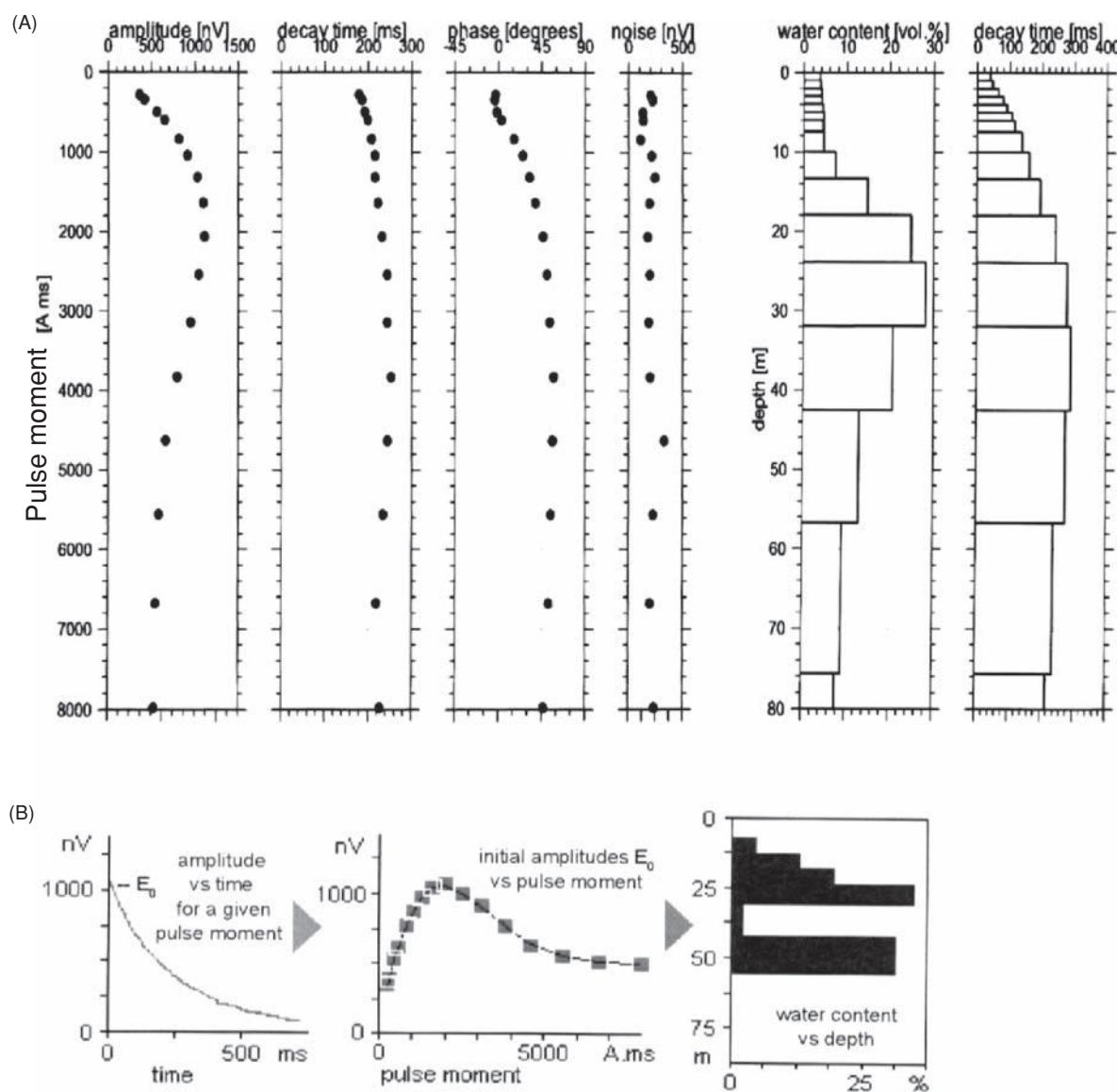


Figure 12.38 (A) Measured parameters as functions of pulse moment, and derived parameters as functions of depth (after Bernard, 2006a). (B) A sequence of displays showing the relaxation amplitude with time, amplitude-pulse moment, and estimation of water content (%) with depth (m) in magnetic resonance sounding. From Iris Instruments (1998), by permission. [C]

### 12.4.3 Interpretation methods

Basic interpretation can be undertaken by examining the MRS signal amplitude–pulse moment graphs to identify the basic shape of the curve. These can be related to the relative location and thickness of one or more aquifers within the depth of exploration of the system used (Figure 12.39). The forms of these graphs are diagnostic for a single shallow, medium or deep aquifer, and for two aquifers separated by a significant distance. These four situations can also be distinguished from the response of a thick aquifer or multilayered aquifer where the vertical distances between the layers is relatively small. However, it is difficult to distinguish between the thick aquifer and the multilayer aquifer. It is also possible to examine MRS amplitude–pulse moment graphs for models, such as shown in Figure 12.40. Two sets of graphs are shown, one for a very thick aquifer and the other for a relatively thin (10 m) aquifer with 20% water content as a function of pulse moment and water layer depths for a 100 m loop size. Bernard (2006b) has provided a simplified matrix linking values of  $T_2^*$ , mean pore size and permeability as a guide (Table 12.2).

Increasingly, modelling of the MRS responses is being undertaken to not only determine water content with depth but also to determine resistivity in a simultaneous inversion process (e.g. Braun *et al.*, 2009). Furthermore, the MRS method can field estimates of hydrodynamic parameters of detected aquifers (Lachassagne *et al.*, 2005), such as quantifying the specific yield (effective porosity) of aquifers and of the storage coefficient (the latter in unconfined aquifers only). It is also able to estimate the hydraulic conductivity (or transmissivity) of aquifers, and this is especially the case when borehole calibrations (pump tests, etc.) are available. If such direct calibration is not available, aquifers can be compared qualitatively.

### 12.4.4 Case histories

Geophysical techniques, especially electrical resistivity and EM methods, have long been used in hydrogeological investigations. The difficulty in the interpretations is being able to say with some confidence whether water is present and in what quantities. The MRS method has provided a new means of obtaining a direct indicator of the presence of water and quantifying some of the hydrogeological parameters.

In the sub-Saharan region, groundwater resources are scarce and exploration to find suitable locations for wells is logically and physically challenging. The MRS method can help to make such exploration more efficient and cost-effective. Vouillamoz *et al.* (2005) provided an example of the use of MRS to characterise the local aquifers within crystalline basement in Burkina Faso, West Africa. The conceptual model of the crystalline basement aquifers is shown in Figure 12.41. Alterites comprise weathered and decayed rocks of clayey-sandy composition and make up the regolith. The weathered fissured zone (saprock) is characterised by almost horizontal fractures that decrease in density with depth, coupled with vertical fissures and fractures that locally enhance the flow properties of the rock. The underlying bedrock is permeable only where it is fractured. Local aquifer characteristics were obtained from 13 boreholes in which pumping tests were also undertaken. Magnetic resonance soundings were carried out adjacent to the boreholes using NUMISPlus equipment and with a square loop with a side length of 125 m. MRS hydrogeological estimators were derived from MRS profiles and compared with the local borehole results. MRS results from one borehole (Sanon S1) are shown in Figure 12.42; the local Larmor frequency was 1412 Hz. The MRS results are also shown against the borehole data in Figure 12.43. It was found locally that for water in the alterite aquifers the average water content ( $w$ ) is

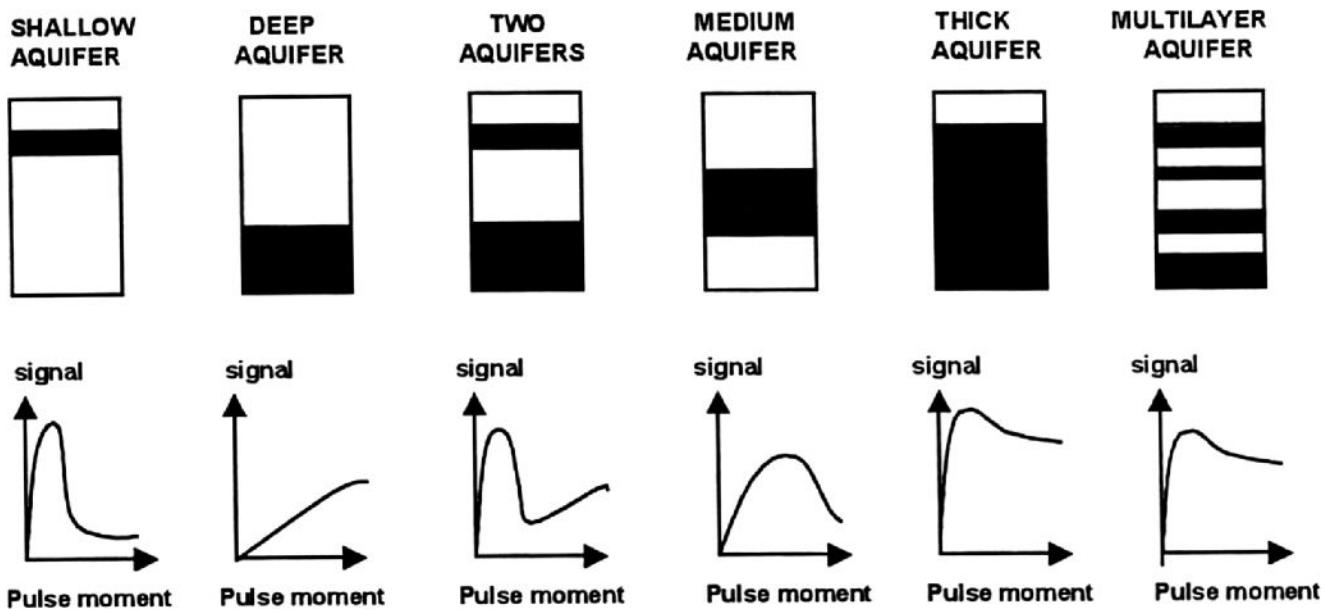
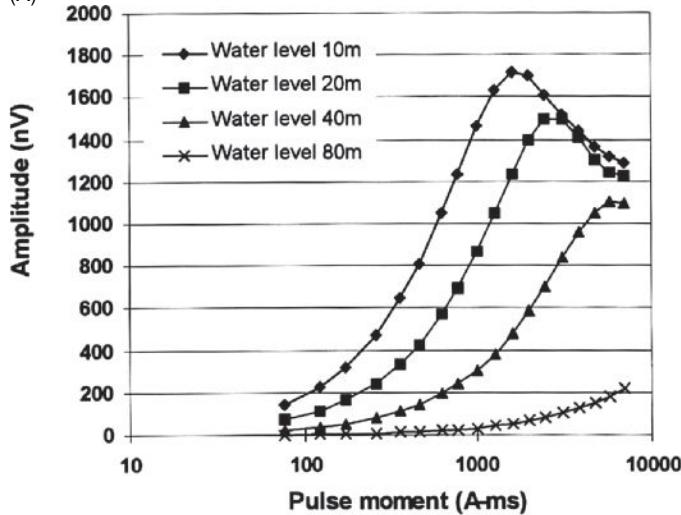


**Figure 12.39** Typical magnetic resonance sounding amplitude-pulse moment response curves for aquifer layers with different layer thicknesses and depths. After Bernard and Legchenko (2003), by permission.

(A)



(B)

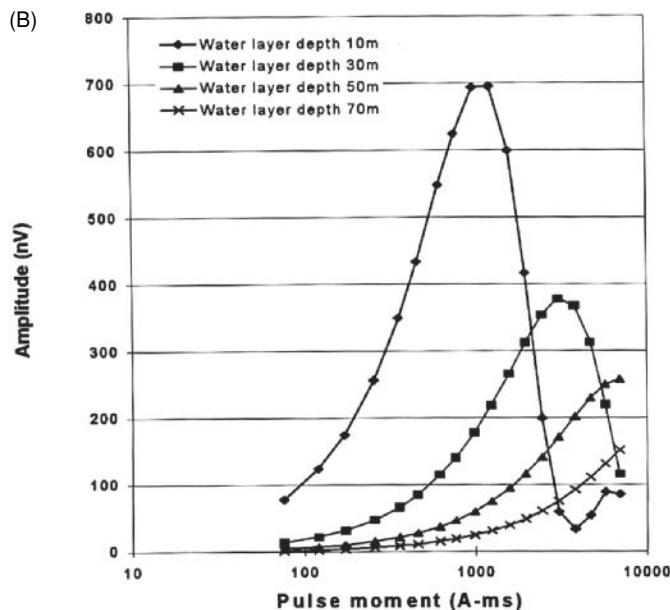


**Figure 12.40** Magnetic resonance sounding responses of (A) a very thick aquifer, and (B) a 10-m thick aquifer, both with 20% water content, as a function of pulse moment for various depths. Loop diameter is 100 m. After Iris Instruments (1998), by permission. [C]

higher and the average value of  $T_1$  is shorter than for water in the fissured-fractured reservoirs. There is a degree of ambiguity in the hydrogeological information using the MRS data alone as the range of MRS-derived transmissivity is the same for both the alterites and the fissured-fractured zones. However, when the interpreted resistivities, derived from Schlumberger soundings, are plotted as a function of the MRS-derived transmissivity values, the three geological components begin to separate out as can be seen in Figure 12.44.

**Table 12.2** MRS time constant ( $T_2^*$ ), mean pore size and permeability (Bernard, 2006b).

$T_2^*$ (ms) time constant	Mean pore size	Permeability
1000	(Free water)	
500	Lake, river	High
200	Gravel	
100	coarse	Medium
50	medium	
20	fine	
	Clay	Low
	(Bound water)	

In bedrock the MRS response can yield hydrogeological parameters that are unrepresentative when taken at face value. This is especially the case in fractured bedrock, which can be very conductive hydraulically if the fractures are open but they may not contain much water. Consequently the relaxation signal amplitude originating from the water in these fractures may be small and may remain undetected if the depth of this zone is greater than half the diameter of the transmitter-receiver loop. This is known as the principle of suppression. In addition, a screen effect may also be present. This manifests itself by reducing the interpreted MRS water content of a deep reservoir when topped by a shallower one such as occurs in bedrock aquifers that are known as multi-reservoir aquifers. This is evident in the results from the borehole and MRS results shown in Figure 12.45 for the Kombissiri borehole. The water content and  $T_1$

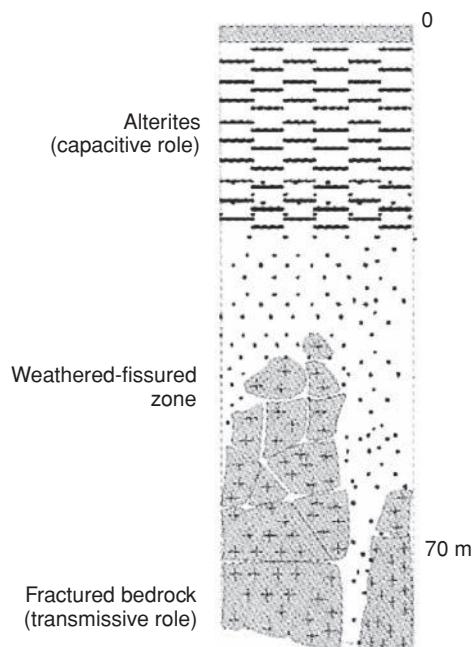


**Figure 12.41** Conceptual model of crystalline basement aquifers. From Vouillamoz et al. (2005), by permission.

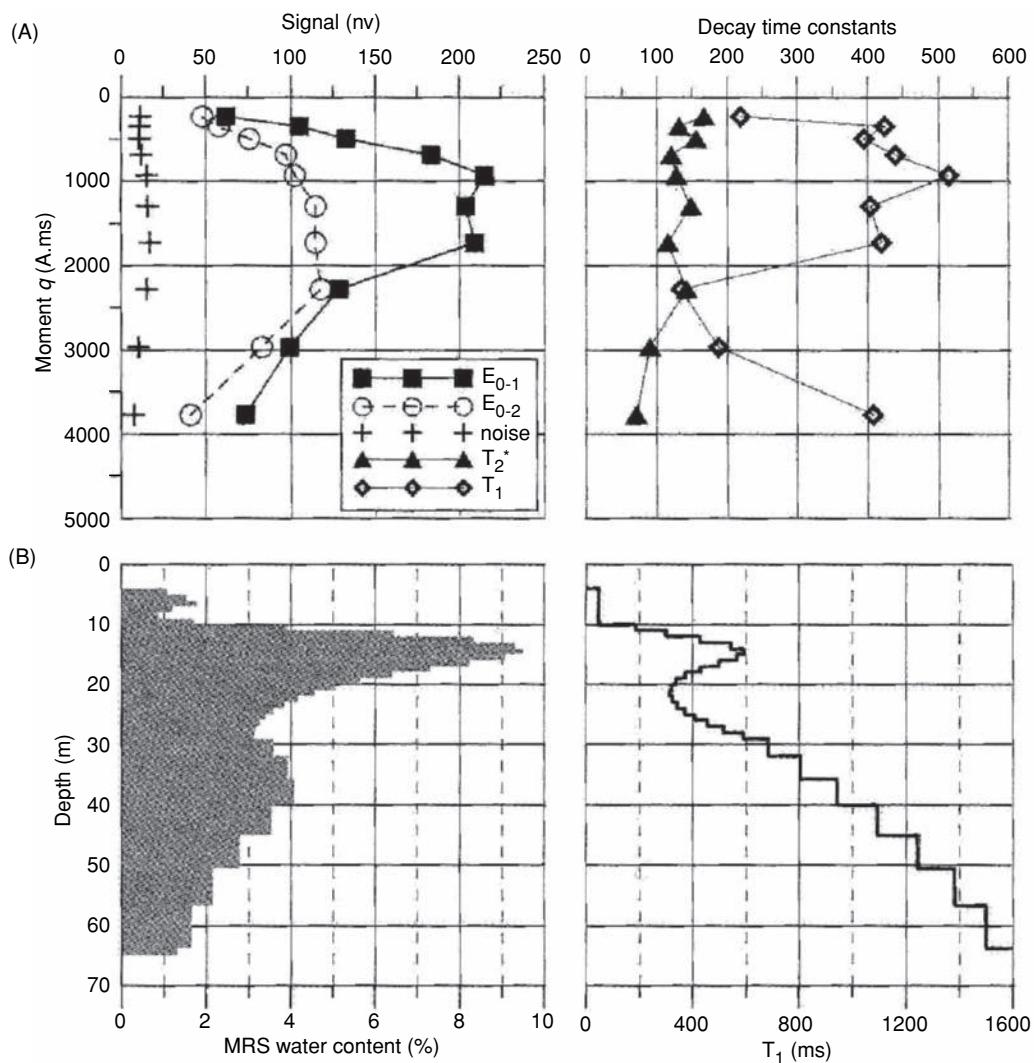


**Figure 12.42** Example of MRS data from the Sanon S1 borehole, Burkina Faso. (A) Recorded signal; (B) output parameters. From Vouillamoz *et al.* (2005), by permission.

decay-time constant are consistent for the alterites and weathered-fissured units, but almost no signal is detected below a depth of 40 m, whereas water-productive fractures were found to exist below this depth as detected by borehole electrical logging. The MRS transmissivity estimation clearly is insensitive to these and is three times lower than the pump test transmissivity. This case history demonstrates that the MRS results, coupled with surface electrical resistivity sounding and borehole logging and testing, can yield valuable information about the characteristics of complex aquifers in crystalline-basement zones.

Baltassat *et al.* (2005) provided a further example of the combined use of electrical resistivity tomography (ERT) with MRS in the exploration of small aquifers in heterogeneous superficial formations and in underlying weathered and fissured bedrock. They described an MRS investigation undertaken in the Ringelbach Catchment in the Vosges Massif in France. The local geology comprises granite or

partly overlain by Triassic sandstone, and forms a general structure made up of three blocks separated by faults. From 1999 to 2002, 26 MRS and seven ERT profiles were undertaken along transects crossing the principal geological formations of interest. The ERT transects were acquired using dipole-dipole arrays with 10 m and 20 m spacings with a maximum depth of investigation of about 40–50 m. The MRS measurements were acquired using NUMIS-Plus equipment with a figure-of-eight loop configuration with a loop side-length of 37.5 m, yielding a maximum depth of exploration of about 40 m. Despite the area being rural, there was a significant amount of ambient EM noise and not all MRS soundings were suitable for inversion. The MRS amplitude–pulse moment curves are shown in Figure 12.46A and the distribution of decay-time constant  $T_2^*$  and MRS maximum amplitudes in Figure 12.46B for a number of locations (indicated by RMP#). The MRS results fall within two discrete fields that correspond to the geology: granite or

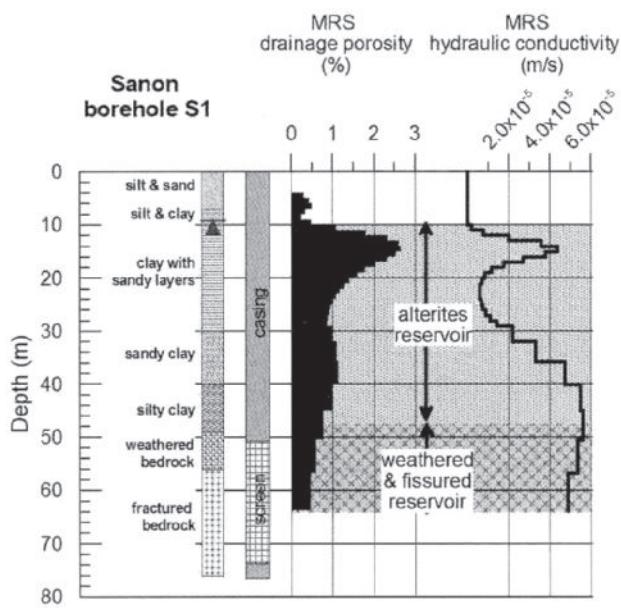


**Figure 12.43** Sanon S1 borehole results. Description of the reservoir units with corresponding MRS estimators. From Vouillamoz *et al.* (2005), by permission.

sandstone, differentiating one from the other. Electrical resistivity is unable to do this as both rock types are indicated by high resistivities (Table 12.3). Conversely, weathered (low resistivity) and fresh granite (high resistivity) cannot be differentiated by the MRS as these rock units have similar, low MRS water contents and short time constants. The distribution of background resistivity values

is shown in Figure 12.46 and range from  $50 \Omega\text{m}$  to over  $10,000 \Omega\text{m}$ . The locations of three ERT profiles are shown along with the positions of MRS survey points.

The MRS method can yield values of water content ( $w$ ) and aquifer thickness ( $e$ ). However, just as in resistivity sounding, the MRS results can produce equivalent models for a range of values of  $w$  and  $e$ , for a rock formation where the product  $w^*e$  is a constant. To reduce this ambiguity, the water volume per unit surface (known as the *water height*,  $V_w$ , in units of  $\text{m}^3/\text{m}^2$  or m) can be determined from the MRS data using the expression  $V_w = \sum w_i \cdot e_i$ . Values of  $V_w$  determined at the MRS locations are shown in Figure 12.47.

The results of the three ERT profiles and corresponding MR soundings are shown in Figure 12.48. The combination of these two geophysical techniques and their joint interpretation permits the definition of a rather complex geological structure in this area. Three main faults have been identified separating four blocks, each downthrown with respect to their neighbour from the lowest one in the southwest to the highest one (at Le Bunker in the SE) through to Heidenkopf (NW) and Le Hurlin (NE). Baltassat *et al.* concluded that the MRS confirmed that in the Ringelbach Catchment, sandstone (with MRS water content 2.7–2.9%) has better water storage than granite (MRS water content <1.5%). This value is particularly low for granite compared with values for granites in other areas (Table 12.4) where values of 2–7% are more prevalent. The low water content may be explained, however, by the fine-grained nature of the rock but also by the fact that the upper part of the weathered zone lies above the static water level.

In contrast with the previous two case histories that described the application of the MRS method over crystalline bedrock, Roy

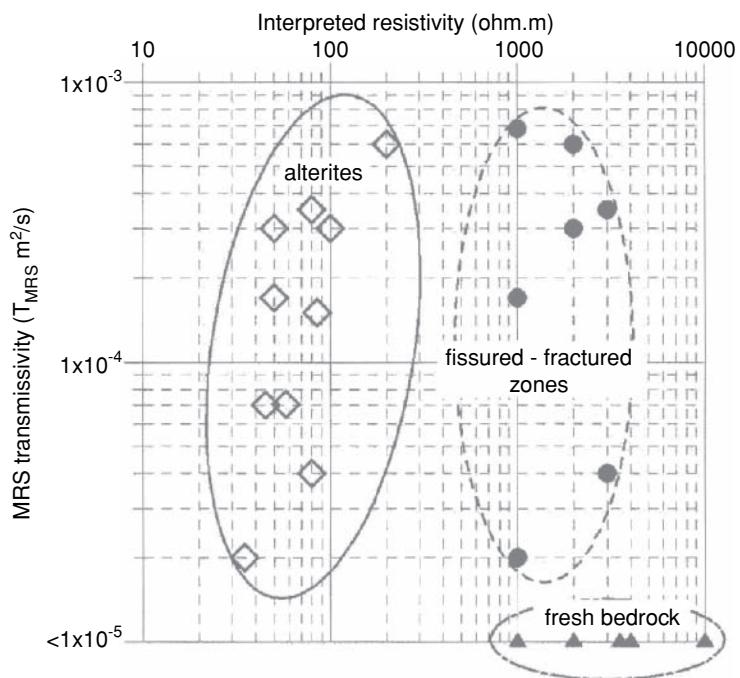


**Figure 12.44** Reservoir characterisation with MRS estimator and electrical resistivity obtained from Schlumberger soundings. From Vouillamoz *et al.* (2005), by permission.

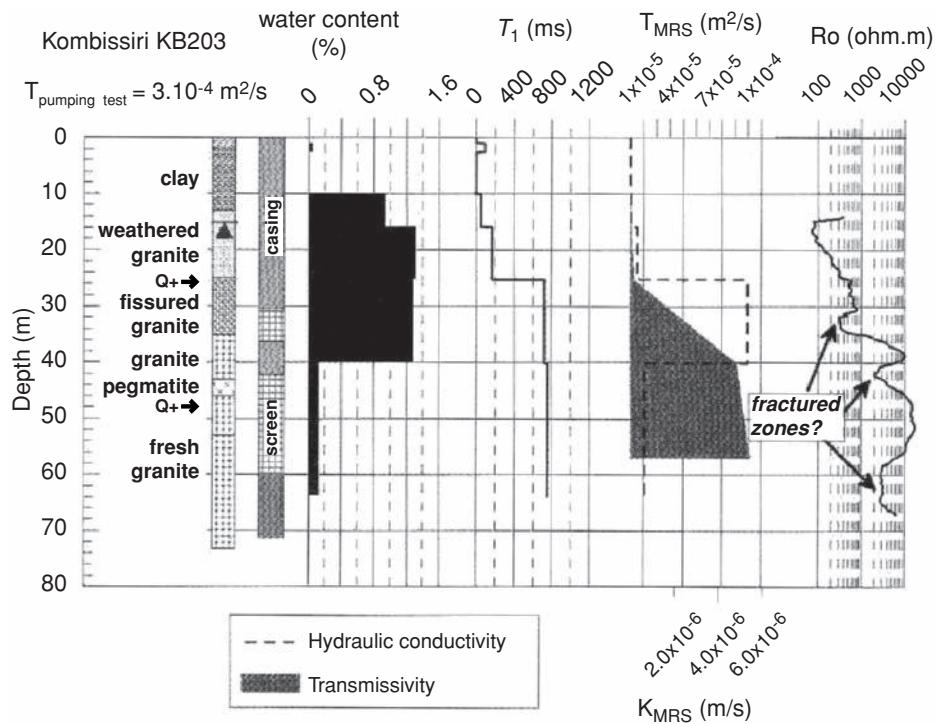


**Figure 12.45** Kombissiri borehole results. Principle of suppression and the screen effect in MRS. T: Transmissivity; K: hydraulic conductivity;  $R_o$ : apparent resistivity measured with borehole logging; Q+: water intake measured while drilling;  $T_1$ : MRS time constant. From Vouillamoz *et al.* (2005), by permission.

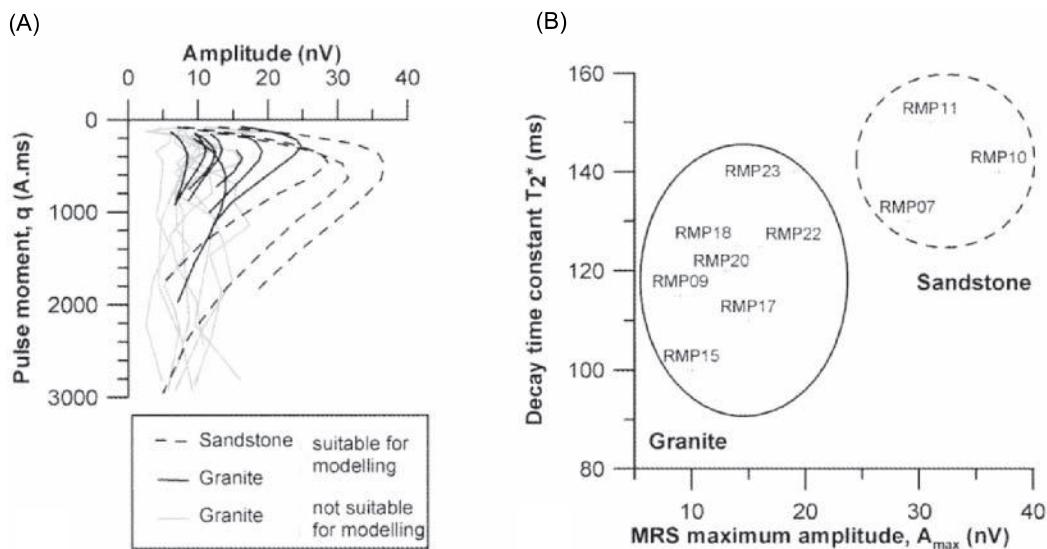


**Figure 12.46** (A) MRS curves, and (B) characteristics interpreted from various geological settings. From Baltassat *et al.* (2005), by permission.

**Table 12.3** Resistivity values and associated geology for the Ringelbach catchment (Baltassat et al., 2005).

<b>Geological formations</b>	<b>Interpreted resistivity (<math>\Omega\text{m}</math>)</b>
Fresh granite, sandstone	>1600
Moderately weathered granite	800-1600
Weathered granite	200-800
Highly weathered granite, valley surficial formation	30-200

(2009) has described an MRS example acquired in a park in the Netherlands at the margins of a sand dune. Data were acquired using a NUMISPlus system. The MRS results (signal amplitude versus pulse moment) and corresponding MRS inversion results are shown in Figure 12.49. In the left panel of this figure, one peak in, the  $E_0$  amplitude is evident without any inflections, which suggests the presence of only one aquifer. Where fine sediments occur or because of mixed grain sizes, the transition near the water table is gradual rather than abrupt. At the location shown in Figure 12.49 the water table occurs at  $\sim 8$  m depth as illustrated in the log on the right-hand side of the figure.

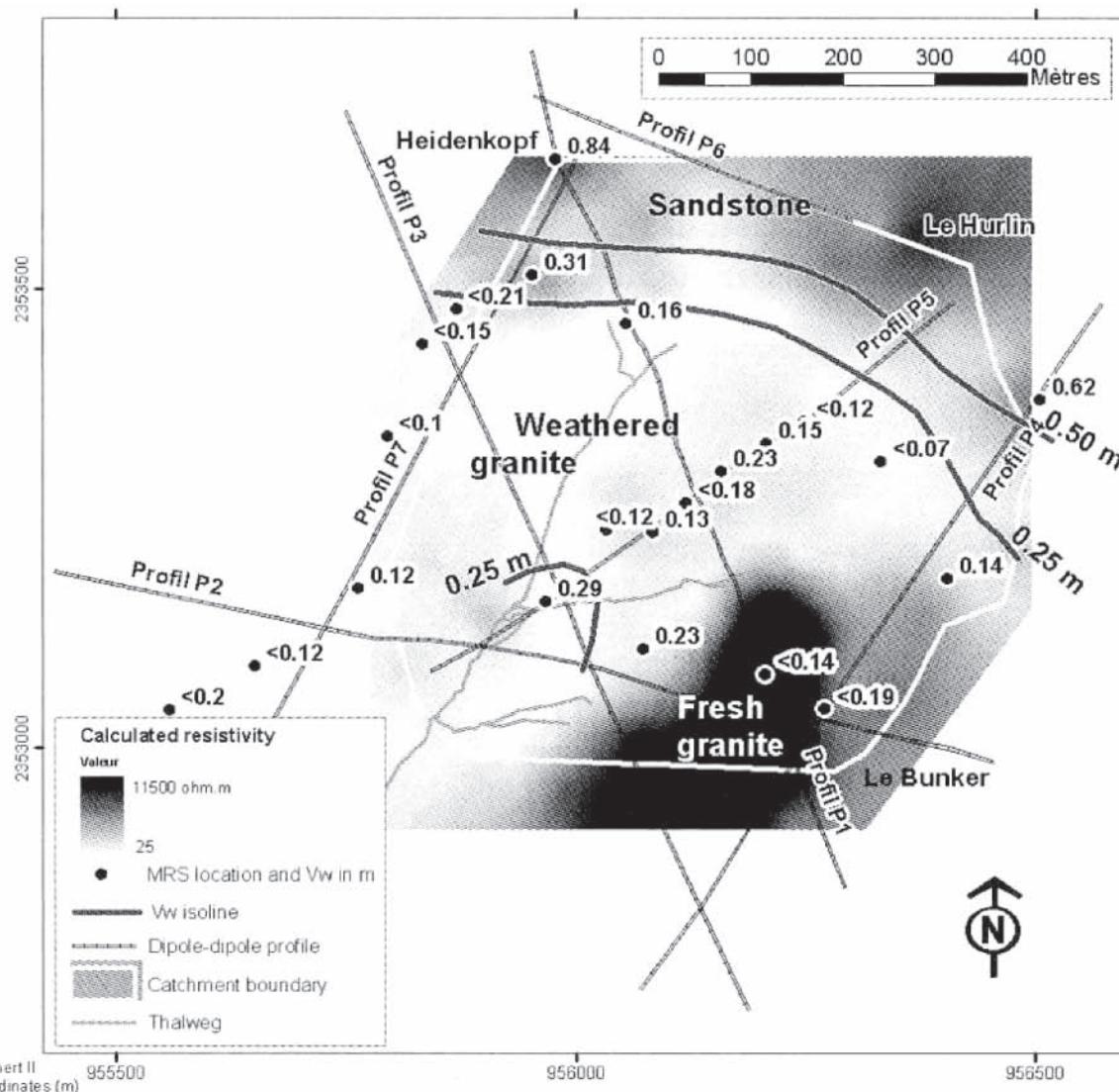


**Figure 12.47** Map of water volume per unit surface ( $V_w$ ) superimposed on the derived resistivity map for 13 m depth from electrical resistivity VES, with an indication of the solid geology. From Baltassat et al. (2005), by permission.

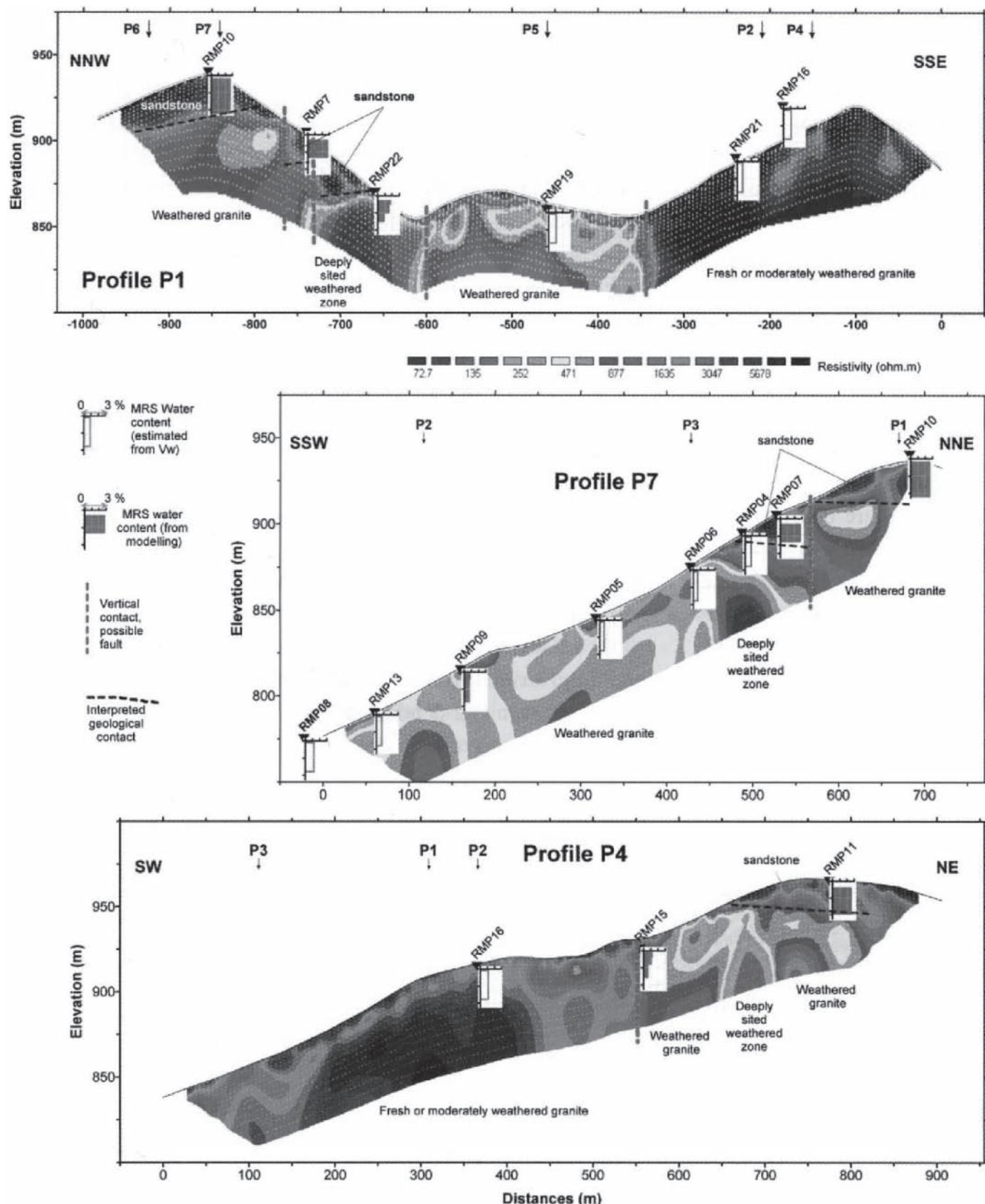


**Figure 12.48** MRS and electrical resistivity sections across the Ringelbach catchment with elements of the geological interpretation. From Baltassat et al. (2005), by permission. [C]

**Table 12.4** Geophysical characteristics of the Ringelbach granite compared with those from other granitic regions (Baltassat *et al.*, 2005).

Area	Weathered granite <sup>*1</sup>			Fresh or moderately weathered granite <sup>*2</sup>	
	Resistivity ( $\Omega\text{m}$ )	Water content w (%)	Relaxation time constant $T_2^*$ (ms)	Resistivity ( $\Omega\text{m}$ )	Water content w (%)
Ringelbach catchment	50-100	<1.4	110-140	>800	<1.3
Margeride (Massif Central)	30-500	3-7	150-350	>500	n.a.
Kerbennez catchment (Brittany)	80-600	2.7-5.5	150-350	>600	<2
Andalatanousy (Madagascar)	n.a.	2.2-5.5	50-180	n.a.	<1
Maheshwaram watershed (India)	10-200	2-6	50-150	>200	<1
Other sites in Brittany	n.a.	1.6	100-300	n.a.	<2

\*<sup>1</sup> Alterite - upper fissured zone; \*<sup>2</sup> lower fissured zone, fresh rock. n.a.: not available.

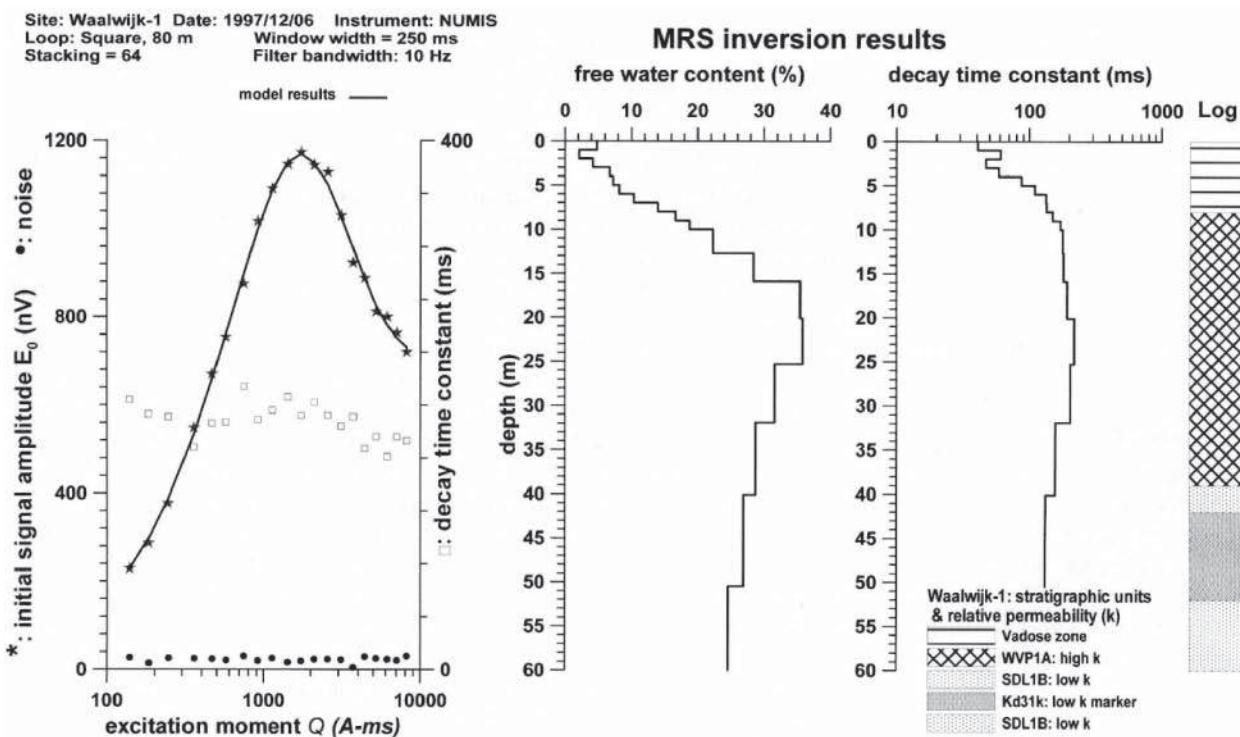


**Figure 12.49** MRS data for a site adjacent to a sand dune in the Netherlands. (A) MRS amplitude and decay-time constant-pulse moment curves; (B) MRS inversion results: water content and decay time constant as functions of depth. Also shown is a lithological log integrated from three adjacent boreholes - the WVP1A unit has a higher permeability than the SDL1B and Kd31k units - the formation references relate to the standard used in the Netherlands. From Roy (2009), by permission.

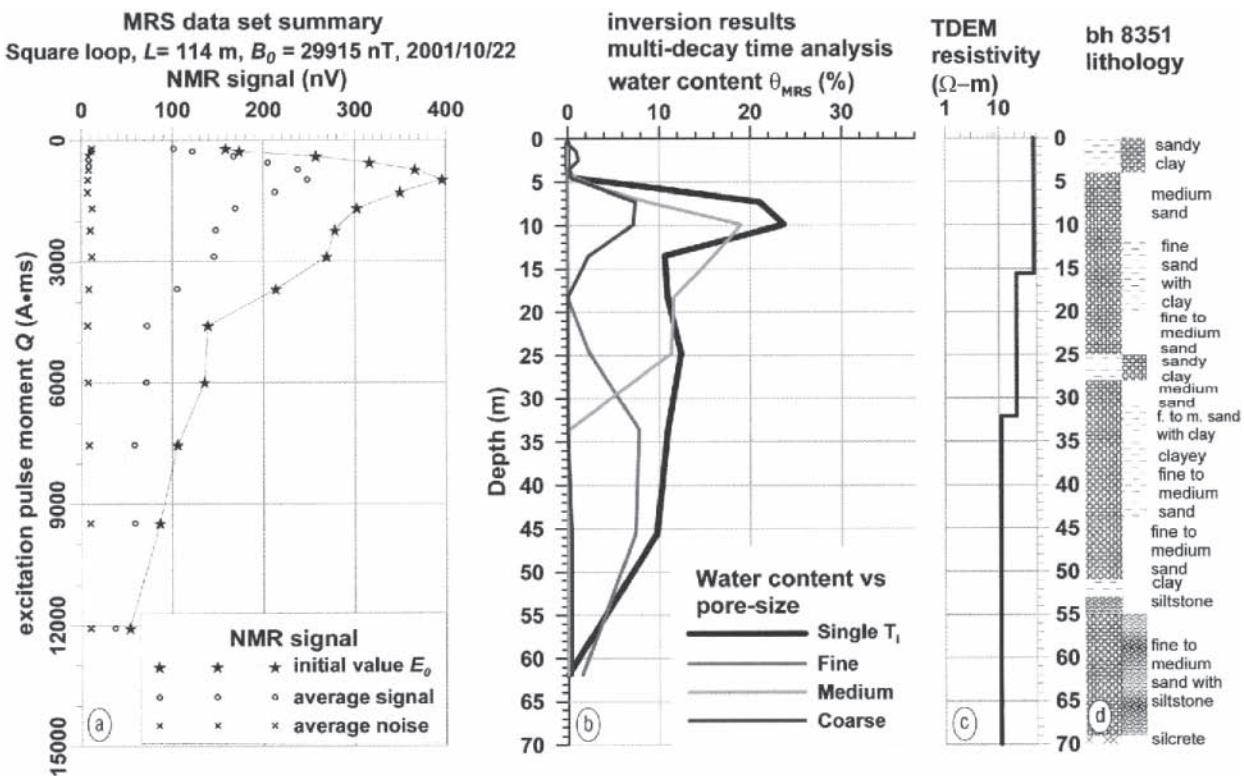


**Figure 12.50** MRS results from a site over a palaeochannel near Maun, Botswana. (a) MRS amplitude-pulse moment curves, and (b) inversion results with multi-decay time analysis; (c) TDEM-derived resistivity profile; (d) lithology derived from borehole BH 8351. From Roy (2009), by permission. [C]

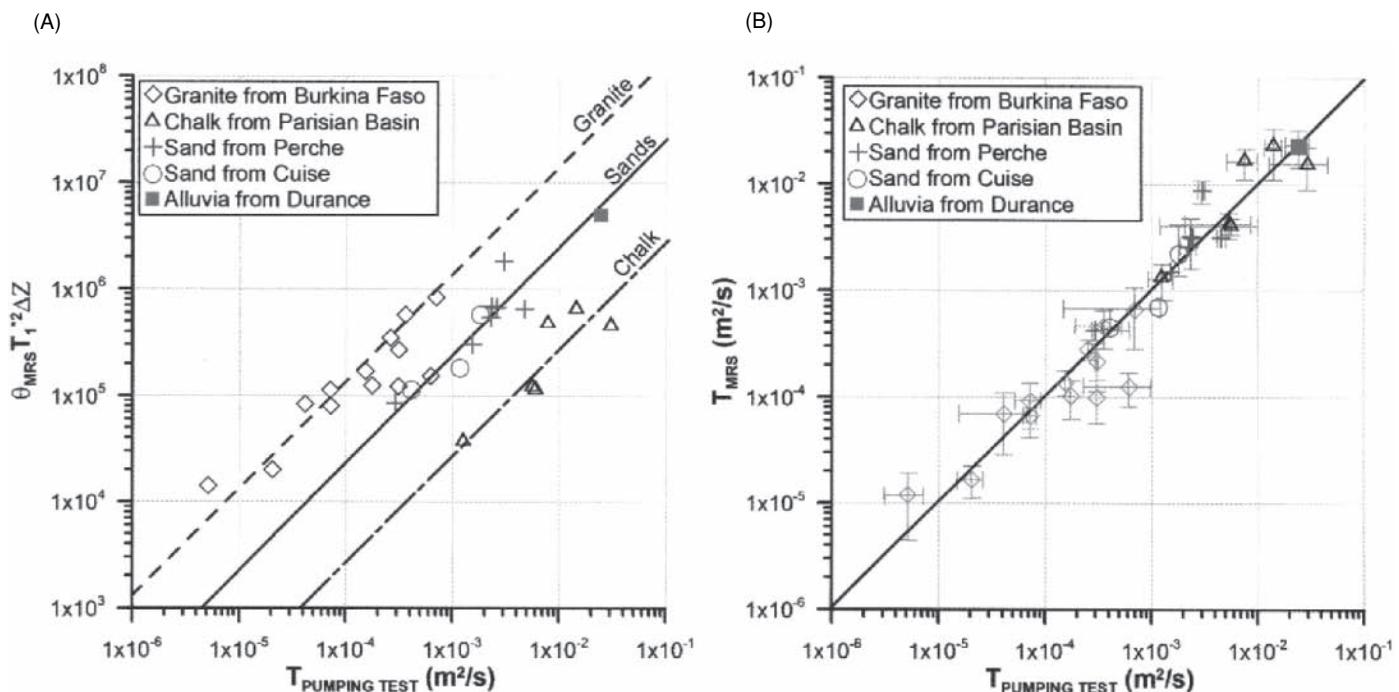


**Figure 12.51** Calibration of MRS-derived hydraulic parameters. (A) Pump test transmissivity versus MRS parameter  $P$  (see text for details) showing lithology dependence (broadly classified as granites, sands and chalk). (B) MRS-derived versus pump test transmissivities after integration of lithology-dependence factor. From Roy (2009), by permission. [C]

For MRS datasets where the signal:noise ratio is high, signal decay spectral analysis can be undertaken, which allows the water content to be resolved into categories of pore size (fine, medium and coarse) as illustrated in Figure 12.50. The data shown are from an MRS survey over a palaeochannel near Maun, Botswana. A square loop with side-length 114 m was used. It can be seen that the peak time constant occurs in association with a medium sand layer between 5 m and 12 m depth.

Roy (2009) also described a further development of correlations between MRS-derived hydraulic parameters and pump tests (e.g. Figure 12.51). This figure shows (left) the lithology dependence of the MRS-derived hydraulic parameter ( $P$ , which is a function of water content and time constant  $T_2^*$ ) with respect to pump test transmissivity  $T$  ( $\text{m}^2/\text{s}$ ). Vouillamoz (2003) developed a technique to remove the lithology sensitivity of the correlation between  $P$  and pump-test transmissivity, the benefits of which can be seen in Figure 12.51B.

# 13

## Introduction to Ground-Penetrating Radar

### 13.1 Introduction

Since the mid-1980s, *Ground-Penetrating Radar* (GPR) has become enormously popular, particularly within the engineering and archaeological communities. However, radar has been used for geological applications since the 1960s, especially in connection with the development of *radio echo-sounding* of polar ice sheets. Glaciological applications of radar are now very well developed. As technology has improved along with the power of computers, the GPR method has mushroomed in popularity and in the range of applications. This is matched by a growth in the available related literature. There continues to be enormous scope for the application of ground-penetrating radar and it is extremely exciting to anticipate what might be achieved in the near future. While the use of this technique is now probably more widespread than any other by virtue of the ease with which equipment and software can be obtained, the number of abuses of this method also is increasing. Too many people use it without understanding the basic physics or how to process and interpret the data. It is essential for good practice for intending GPR users/interpreters to obtain at least a grounding in the principles of the method and how to undertake basic data-processing and interpretation before using this method.

GPR applications can be divided into two virtually discrete classifications based on the main antenna frequencies. For geological applications, where depth penetration tends to be more important than very fine resolution, antennae with frequencies less than or equal to 500 MHz are used. For engineering or non-destructive testing (NDT) applications, antennae with frequencies of 500 MHz and higher are used, typically as high as 900 MHz or 1 GHz, and in some cases as high as 2.5 GHz. A list of the range of applications of GPR is given in Table 13.1

The first use of electromagnetic (EM) signals to locate remote buried objects is attributed to Hulsmeyer in a German patent in 1904, but the first published description of such investigations was by Leimbach and Löwy (1910), also in German patents.

The systems used in these investigations employed continuous wave (CW) transmission. Hülsenbeck & Co. (1926) developed the first use of pulsed radar to investigate the nature of buried features.

Pulsed techniques were developed substantially over the following five decades. Its early civilian development was in radio echo-sounding of polar ice sheets (Cook, 1960; Evans, 1965; Swithinbank, 1968). The first use of impulse radar for glaciological purposes was in the early 1970s (Watts *et al.*, 1975). There has been much pioneering research work carried out in the glaciological field: for example, see papers by Wright *et al.* (1990), Hammond and Sprenke (1991) and Narod and Clarke (1994), with a useful review of radio-glaciology published by Bogorodsky *et al.* (1985), and a special edition of the *Annals of Glaciology* in 2009. The earlier work was focused on investigations predominantly in polar regions, but since the mid-1990s there has been a huge growth in the use of commercial GPR systems in temperate glaciology and more recently for periglacial and permafrost investigations (e.g. Hauck and Kneisel, 2008). There has been wide acceptance of the radar method in certain areas of civil engineering, such as utility mapping, road pavement analysis, railway ballast testing and void detection behind tunnel linings. There has also been an expanding role for the method in geological applications, particularly in the rapid assessment of superficial deposits, location of swallow holes, and so on. GPR has been used in investigations of sedimentological sequences that might be suitable analogues useful for 3D hydrocarbon reservoir modelling, as well as for investigating aeolian and fluvial sediments (Bristow and Jol, 2003). In archaeological studies, too, GPR has been used extensively (Conyers, 2004; Daniels, 2007). A comprehensive overview of the GPR method, theory, data-processing and applications has been provided by Jol (2009).

Many uses of ground-penetrating radar have been described in the literature. These include the determination of permafrost thickness (Annan and Davis, 1976); the detection of fractures in rock salt (Thierbach, 1974; Unterberger, 1978; Nickel *et al.* 1983; Olsson *et al.*, 1983); and archaeological investigations (Bevan and Kenyon,

**Table 13.1** Range of applications of ground-penetrating radar.***Geological:***

- Detection of natural cavities and fissures
- Subsidence mapping
- Mapping sand body geometry
- Mapping of superficial deposits
- Soil stratigraphy mapping
- Glacial geological investigations
- Mineral exploration and resource evaluation
- Peat thickness mapping and resource evaluation
- Permafrost investigations
- Location of ice wedges
- Fracture mapping in rock salt
- Location of faults, (mineralised) dykes, coal seams, etc.
- Lake and riverbed sediment mapping

***Environmental:***

- Contaminant plume mapping and monitoring remediation
- Mapping and monitoring pollutants within groundwater
- Landfill investigations including capping effectiveness
- Location of buried fuel tanks and oil drums
- Mapping animal burrows and tree roots
- Groundwater investigations
- Detection of UXO

***Glaciological:***

- Ice thickness mapping
- Determination of internal glacier structures
- Ice movement studies
- Detection of concealed surface and basal glacier crevasses
- Mapping water conduits within glaciers
- Determination of thickness and type of sea and lake ice
- Subglacial mass balance determination
- Snow stratigraphy mapping
- Subglacial landform mapping
- Glacial hazard assessment

***Engineering and construction:***

- Road pavement analysis
- Railway trackbed testing
- Void detection
- Location of reinforcement (rebars) in concrete
- Location of public utilities (pipes, cables, etc.)
- Testing integrity of building materials
- Concrete testing
- Looking-ahead/sideways during horizontal directional drilling

***Archaeology:***

- Location of buried structures, graves, post-holes, etc.
- Detection and mapping of Roman roads, foundations, etc.
- Pre-excavation mapping
- Detection of voids (crypts, undercrofts, burial mounds, etc.)
- Investigation of ancient monuments, statues, building façades

***Forensic science:***

- Location of buried targets (e.g. bodies and bullion, etc.)

1975; Imai *et al.*, 1987; Bevan, 1991; Conyers and Goodman, 1997; Conyers, 2004). Examples of civil engineering and of other geological applications have been described by Darracott and Lake (1981), Leggo (1982), Ulriksen (1982), Leggo and Leech (1983), Davis and Annan (1989), Moorman *et al.* (1991), Doolittle (1993), Huggenberger *et al.* (1994), Neal (2004), Bristow (2009), Kim *et al.* (2007), Reynolds (2004, 2006), Saarenketo (2009), among others. Cross-hole radar systems for use in crystalline rock have been described by Nilsson (1983), Wright and Watts (1982) and Olsson *et al.* (1990) and for mining, by Kemp *et al.* (2009). GPR has also been used in police investigations to help to locate buried bodies, such as in a double murder inquiry on Jersey, Channel Islands, in the 1980s, and in a gruesome search for human remains at two houses in Gloucester in 1994. In the latter, radar was instrumental in detecting where the corpses of ten murdered women had been hidden within thick concrete inside the buildings, and in locating the remains of two other victims buried in a nearby field. Examples of a range of applications of the GPR method are described in more detail in Chapter 14.

For regional and large-scale investigations, radar measurements have been made increasingly from aircraft and satellites. Such remote sensing techniques are beyond the scope of this chapter. Nevertheless, for subsurface mapping in arid regions for hydrogeological purposes, for example, satellite radar (InSAR) imagery has been used to locate important features that would otherwise be extremely difficult to locate using ground-based surveys. An example of this is the identification of an ancient river drainage system now buried beneath desert sands in Africa, and which was later proven to be an important source of potable water.

Ground radar was developed further by the USA Army during the Vietnam War. Systems were constructed in order to locate labyrinths of tunnels excavated and used by the Viet Cong. At the end of the Vietnam War, the potential of GPR for civilian purposes was identified by Geophysical Survey Systems Inc. (GSSI). In recent years other manufacturers have developed GPR systems and examples of these have been listed in Table 13.2. Developing technologies also include one to look ahead and sideways from the drill tip of a horizontal directional drill, and another to significantly advance the penetration and accuracy of downward-looking radar. Manufacturers produce shielded and unshielded antennae. An unshielded antenna transmits radiation into the air as well as into the ground and will detect reflections from above-ground structures such as buildings, vehicles and overhead cables, especially high-voltage transmission lines, and other EM radiation from manmade sources such as TV broadcast and cell-phone aerials. Such signals represent noise and degrade the quality of the data acquired. To overcome this, antennae can be encased so that the coupling of the signals in air is reduced, effectively removing the excess noise. It is essential that shielded antennae are used where above-ground structures are present or where the GPR system is to be used inside buildings.

Antennae are identified by their frequency of operation, e.g. 100 MHz. This refers to the centre-frequency ( $f_c$ ), about which other frequencies are also transmitted within the designed bandwidth of the antenna. So both lower and higher frequency signals will also be present in the overall signal waveform.

**Table 13.2** Examples of commercial GPR systems (see Appendix A for website addresses).

Manufacturer	Models	Types
Cobham Technical Services (formerly ERA Technology)	SPRscan; Minehound™;	Cart-mounted system with interchangeable 250 and 500 MHz, 1 and 2 GHz antennae; Minehound™ is used for mine (UXO) detection.
GSSI	SIR, TerraVisionStructureScan UtilityScan, BridgeScan, RoadScan, BallastScan	Wide range of interchangeable antennae from 40 MHz to 2.2 GHz for cart-mounting, borehole and multichannel use. Multichannel (14) 400 MHz array (TerraVision).
IDS	RIS-ONE, RIS-PLUS RIS MF Hi-Mod	Single- and multi-(8) channel systems with a range of interchangeable antennae from 80 MHz to 2 GHz, and also integrated multifrequency units.
MALA Geoscience	ProEx (formerly Ramac)	Compact range of fully interchangeable antennae from 25 MHz to 1.6 GHz for cart mounting, borehole and multichannel use, and Rough Terrain Antennae (RTA).
Radar Systems Inc	Zond-12e	Dual-channel system with a range of ground-coupled antennae from 100 MHz to 2 GHz; two air-launched antennae either at a single frequency of 750 MHz or a 38/75/150 MHz combined unit.
Sensors & Software	PulseEkko PRO, Noggin, Conquest	Wide range of separable antennae from 12.5, 25, 50, 100, 200, 250, 500 MHz and 1 GHz options for cart-mounting, borehole and multichannel use. Noggin <sup>Plus</sup> uses 250, 500 MHz and 1 GHz antennae.
Utsi electronics	GroundVue 1 to 5	Wide frequency range of twin-array beam-focused antennae from 30-100, 125-500, 200-600 MHz, 1, 1.5 and 4 GHz for cart-mounting, borehole and multichannel use.
3d-radar	GeoScope	Digital stepped-frequency continuous wave system operating from 100 MHz to 2 GHz; multichannel integrated antennae (1 to 63 channels) available.

See the individual manufacturers' websites for product details (Appendix A).

The use of GPR is now governed under radio-frequency licensing legislation at national and international level, and intending users of GPR systems should check that they are legally permitted to use such equipment. For example, for operations in Europe, details of the licensing requirements are available through the Euro GPR Association. The licensing issue in the UK came to a head during the forensic use of GPR in the Gloucester murder investigation mentioned above. Unlicensed radio-transmitting devices (i.e. the GPR systems) were used to detect the remains of the murder victims, prompting the Radiocommunications Agency (RA) to step in to prevent the use of these systems. The RA threatened to seize and destroy the radar equipment and prosecute users, their managers and company directors, as appropriate. The Gloucestershire Police, however, took a different view and promptly offered to arrest any RA staff for impeding the course of a murder enquiry! To prevent further conflicts of interest, the issue of licensing GPR equipment was taken forward to cover equipment operating within the bandwidth 30 MHz to 12.4 GHz. Note that it is the user's organisation that needs to be registered, not the specific equipment itself. The issue of licensing GPR equipment in the USA began in 1993, and draft Federal Communication Commission (FCC) regulations were introduced in the USA in 2002 that restricted the bandwidth available to GPR to below 960 MHz and between 3.1 and 10.6 GHz. Further and up-to-date information of the licensing requirements in the USA is available from the FCC. Intending users outside of the USA and Europe need to check on the jurisdiction and details of

licensing requirements, if any, that apply to the geographical location of an intended GPR survey.

## 13.2 Principles of operation

A radar system comprises a signal generator, one or more transmitting and receiving antennae (depending upon the system and deployment method), and a control console for managing the signal generation and recording. Some systems record the raw signal, but filters and gains can be applied when viewing the results on the screen which do not affect the recorded data. Other systems may apply some filters prior to recording, which precludes post-processing removal of these filters if trying to view the raw data.

The basic constituents of a radar system are shown in Figure 13.1. The radar system causes the transmitter antenna ( $T_x$ ) to generate a wavetrain of radiowaves that propagates away in a broad beam. As radiowaves travel at high speeds (in air, 300,000 km/s or 0.3 m/ns), the travel time of a radiowave from instant of transmission through to its subsequent return to the receiving antenna ( $R_x$ ) is of the order of a few tens to several thousand nanoseconds (ns;  $10^{-9}$  seconds). This requires very accurate instrumentation to measure the transmission instant precisely enough for the final accuracy of the system to be reasonable with respect to the travel times in question. The antennae are used in either a monostatic or bistatic

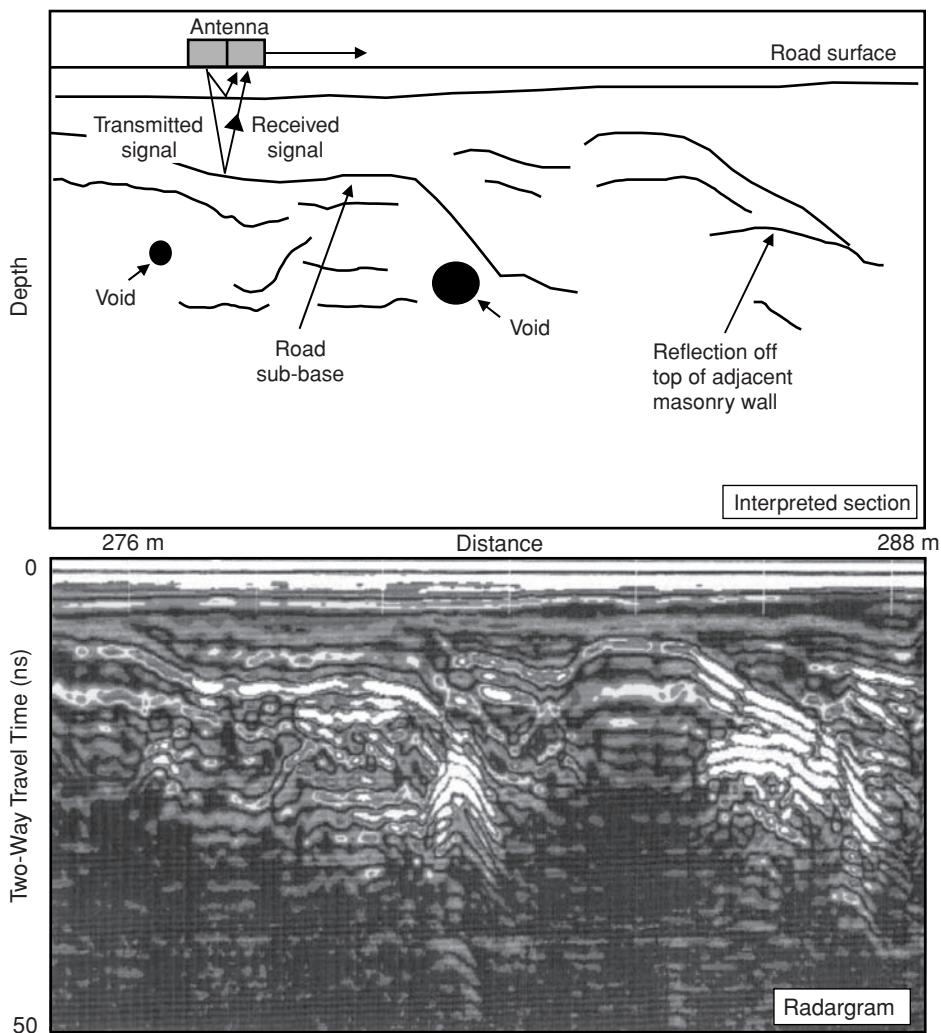


**Figure 13.1** (A) Interpretation of the radargram shown in (B) produced by moving an antenna along a profile and recording the returned signals. [C]

mode. *Monostatic mode* is when one antenna device is used as both transmitter and receiver, whereas *bistatic mode* is when two separate antennae are used with one serving as a transmitter and the other as a receiver. There are specific cases (such as in *wide-angle reflection and refraction* (WARR) measurements) when the bistatic mode is advantageous over the monostatic mode. For the majority of this chapter it can be assumed that any antennae are deployed in monostatic mode unless indicated otherwise.

The transmitter generates a pulse of radiowaves at a frequency determined by the characteristics of the antenna being used, at a repetition rate of typically 50,000 times per second. The receiver is set to scan at a fixed rate, normally up to 32 scans per second, depending upon the system being used. Each scan lasts as long as the total two-way travel time range, which can be set from a few tens to several thousand nanoseconds. Each scan is displayed on either a video screen or a graphic recorder or both. As the antenna is moved over the ground, the received signals are displayed as a function of their two-way travel time, i.e. the time taken from instant of transmission to time of detection by the receiver, in the

form of a *radargram*. This display is analogous to a seismic section (seismogram).

The pulse length of the transmitted radiowave should be short enough (typically <20 ns, depending upon antenna frequency and type) to provide resolvable reflections. It is important, therefore, that the shape and characteristics of the transmitted radiowave are both determinable and highly repeatable. The significance of this point will be discussed below (see Section 13.5). The manner in which the recorded signals are displayed is determined by the operator; a simplified output is illustrated in Figure 13.2. Signals with amplitudes greater than the set threshold are shown dark on the radar section as illustrated. In some cases, it may be most suitable to display signals as both positive and negative, or when just positive or just negative. Displays can also be output in terms of *variable area wiggle* or *wiggle trace* only (just as in seismic data displays). Commonly, the more sophisticated digital recording systems display the amplitudes of the signals according to a grey-scale or colour menu; for example, the strongest reflections can be picked out by the brightest colours.

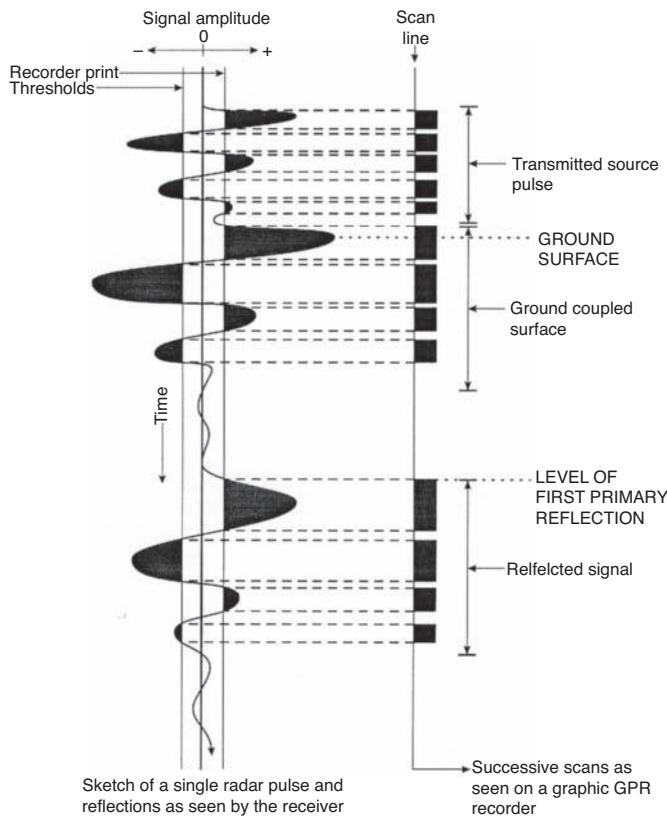


**Figure 13.2** Schematic example of the translation of the received waveform (one scan) on to a graphic recorder output.

Note that the source pulse consists of more than one wavelength and that it may have a complex wave shape. Ground coupling affects the shape and duration of the downgoing wavelet and thus the wave shape of any reflection is equally complex, but with a pulse-broadened duration due to attenuation of the higher frequency components of the signal. The reflection event consists of several wavelets, not just one, and it is imperative that this be borne in mind during the interpretation of radar data.

The measurement system should have sufficient dynamic range and sensitivity to be able to detect the low signal strengths associated with the returning radar pulses. It should also be able to produce printouts with adequate clarity for interpretation.

While the manufacturer's specifications may indicate the measurement accuracy of the timing within the instrument (e.g. to  $\pm 1$  ns), this should not be interpreted as being equivalent to the resolution capability of interpretation. Vertical and horizontal resolution are discussed in Section 13.5.

## 13.3 Propagation of radiowaves

### 13.3.1 Theory

The electromagnetic properties of materials are related to their composition and water content, both of which exert the main control

#### Box 13.1 Speed of radiowaves

The speed of radiowaves in a material ( $V_m$ ) is given by:

$$V_m = c / \{(\epsilon_r \mu_r / 2) [(1 + P^2) + 1]\}^{1/2}$$

where  $c$  is the speed of light in free space,  $\epsilon_r$  is the relative dielectric constant, and  $\mu_r$  is the relative magnetic permeability ( $= 1$  for non-magnetic materials).  $P$  is the *loss factor*, such that  $P = \sigma/\omega\epsilon$ , and  $\sigma$  is the conductivity,  $\omega = 2\pi f$  where  $f$  is the frequency,  $\epsilon$  is the permittivity  $= \epsilon_r \epsilon_0$ , and  $\epsilon_0$  is the permittivity of free space ( $8.854 \times 10^{-12}$  F/m).

In low-loss materials,  $P \approx 0$ , and the speed of radiowaves  $V_m = c/\sqrt{\epsilon_r} = 0.3/\sqrt{\epsilon_r}$ .

over the speed of radiowave propagation and the attenuation of electromagnetic waves in materials.

The speed of radiowaves in any medium is dependent upon the speed of light in free space ( $c = 0.3\text{m/ns}$ ), the relative dielectric constant ( $\epsilon_r$ ) and the relative magnetic permeability ( $\mu_r = 1$  for non-magnetic materials) (see Box 13.1). The success of the ground radar method relies on the variability of the ground to allow the transmission of radiowaves. Some materials, such as polar ice, are virtually transparent to radiowaves. Other materials, such as water-saturated clay and seawater, either absorb or reflect the radiowaves to such an extent that they are virtually opaque to radiowaves. It is the contrast in relative dielectric constant between adjacent layers that gives rise to reflection of incident electromagnetic radiation. The greater the contrast, the greater will be the amount of radiowave energy reflected. The proportion of energy reflected, given by the *reflection coefficient* ( $R$ ), is determined by the contrast in radiowave velocities, and, more fundamentally, by the contrast in the relative dielectric constants of adjacent media (see Box 13.2). In all cases the magnitude of  $R$  lies in the range  $\pm 1$ . The proportion of energy transmitted is equal to  $1 - R$ . The equations given in Box 13.2 apply

#### Box 13.2 Amplitude reflection coefficient

The amplitude reflection coefficient is:

$$R = \frac{(V_1 - V_2)}{(V_1 + V_2)}$$

where  $V_1$  and  $V_2$  are the radiowave velocities in layers 1 and 2 respectively, and  $V_1 > V_2$ . Also:

$$R = \frac{\sqrt{\epsilon_2} - \sqrt{\epsilon_1}}{\sqrt{\epsilon_2} + \sqrt{\epsilon_1}}$$

where  $\epsilon_1$  and  $\epsilon_2$  are the respective relative dielectric constants ( $\epsilon_r$ ) of layers 1 and 2, applicable for incidence at right-angles to a plane reflector. Typically,  $\epsilon$  increases with depth, so generally  $\epsilon_1 < \epsilon_2$ .

for normal incidence on a planar surface, assuming no other signal losses, and refer to the amplitude of a signal. The power reflection coefficient is equal to  $R^2$ .

It should always be remembered when dealing with ground radar that the radiation is electromagnetic and its propagation is described by Maxwell's equations with the electric ( $E$ ) component orthogonal to the magnetic ( $H$ ) component (Figure 13.3A and B). The specific shape and size of the directivity pattern lobes are functions of the

dielectric constant(s) of the host media. The main lobe may be as broad as  $\pm 45^\circ$  from the centre line of directional travel, indicating that the 'beam' has a finite and expanding width with depth (Figure 13.3C). There is a danger in making the comparison of radargrams to seismograms that the vector nature of radar may be overlooked, so that incorrect assumptions are made about the way the radiowaves behave in geological media. While seismic data processing can be used effectively in most cases, the electromagnetic polarisable characteristics of the radiowaves are more analogous to seismic S-waves than to P-waves.

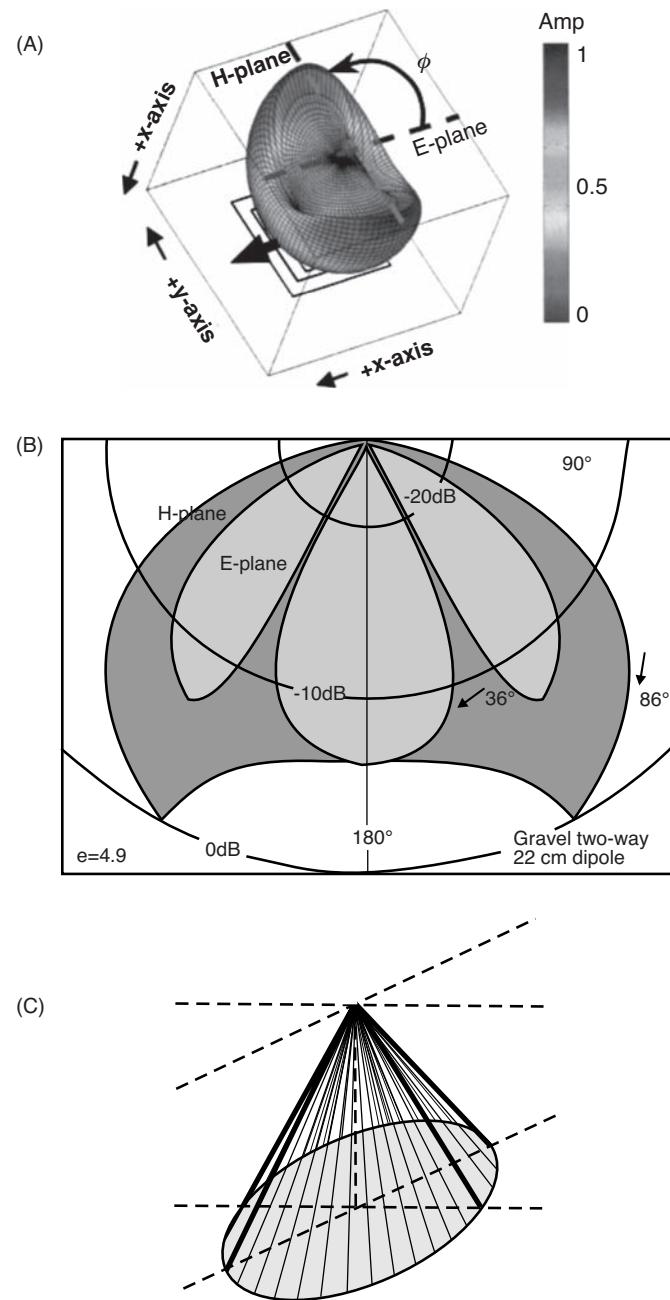


**Figure 13.3** (A) Upside-down 3D perspective on the far-field GPR radiation pattern in ice. (B) Theoretical  $E$ - and  $H$ -plane radar directivity patterns for a 22 cm resistively-loaded dipole situated over a medium with  $\epsilon = 4.9$ . (C) Simplified elliptical cone of incident radar beam. (A) From Moran *et al.* (2003) and (B) from Arcane *et al.* (1993), by permission. [C]

### 13.3.2 Energy loss and attenuation

Factors that result in a decrease in signal strength as it propagates through subsurface media are illustrated schematically in Figure 13.4. Energy loss occurs as a consequence of reflection/transmission losses about each interface and occur each time the radiowaves pass through a boundary. Furthermore, if there are objects with dimensions of the same order as the wavelength of the radar signal, these objects will cause scattering of energy in a random manner. This is known as *Mie scattering* with respect to scattering of light by dust particles, but as *Rayleigh scattering* for radar where the objects are smaller than the wavelength scattered, and causes 'clutter' noise on the radar section. It is analogous to the noise seen on marine radar screens caused by the backscatter from sea waves in rough weather. Where the objects are large enough relative to the radar wavelength, the objects may give rise to point diffractions. These serve to disperse the signal energy but also provide evidence to an interpreter that such objects are present. Coarse gravel in a channel lag deposit, for instance, can generate distinctive diffractions and broader, lower-frequency reflections than a finer-grained deposit and with a stronger reflection coefficient.

In addition to reflection/transmission losses at interfaces, energy is lost by *absorption* (turning the electromagnetic energy into heat). This is best pictured by analogy with a microwave oven which uses high-power radiowaves to cook food. A further loss of energy is caused by the geometric spreading of the energy. The radar signal is transmitted in a beam with a cone angle of  $90^\circ$ . As the radio signals travel away from the transmitter, they spread out causing a reduction in energy per unit area at a rate of  $1/r^2$ , where  $r$  is the distance travelled.

A fundamental cause of the loss of energy is *attenuation* which is a complex function of the dielectric and electrical properties of the media through which the radar signal is travelling. The attenuation factor ( $\alpha$ ) is dependent upon the electric ( $\sigma$ ), magnetic ( $\mu$ ) and dielectric ( $\epsilon$ ) properties of the media through which the signal is propagating, as well as the frequency of the signal itself ( $2\pi f$ ). The bulk behaviour of a material is determined by the corresponding physical properties of the various constituents present and their respective proportional abundances.

As with other electromagnetic waves, the depth by which the signal has decreased in amplitude to  $1/e$  (that is, to 37%) of the initial value is known as the skin depth ( $\delta$ ) and is inversely proportional to the attenuation factor (i.e.  $\delta = 1/\alpha$ ). Mathematical definitions of the attenuation factor and skin depth are given in Box 13.3.

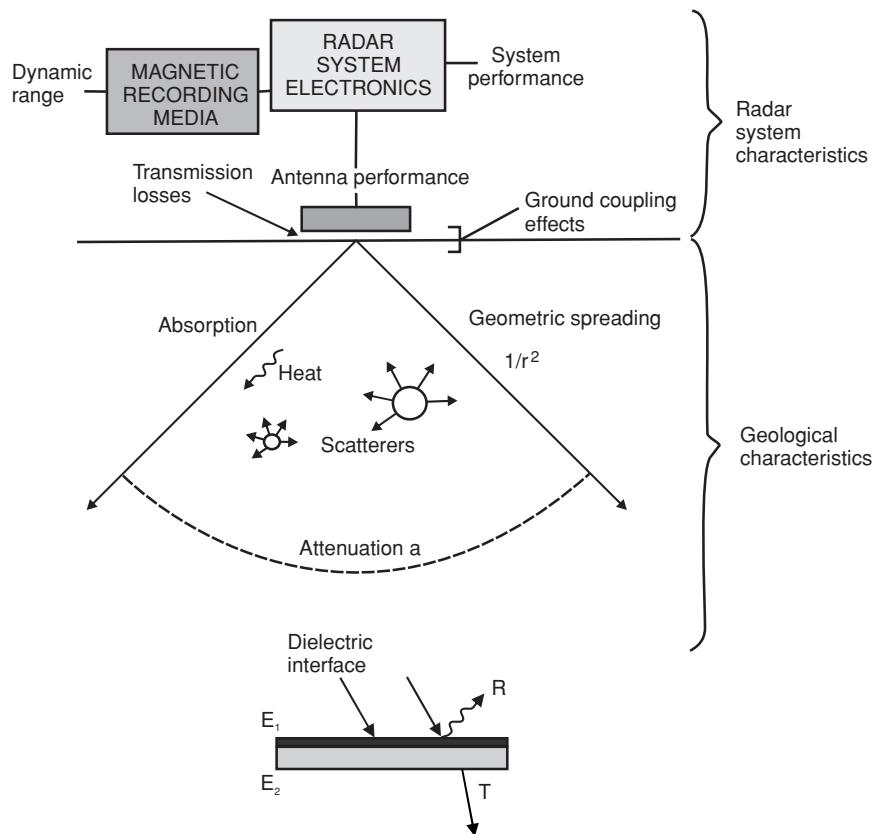


**Figure 13.4** Processes that lead to reduction in signal strength.

### Box 13.3 Energy loss and attenuation

If the peak electric field strength on transmission is  $E_0$  and at a distance  $x$  away it has reduced to  $E_x$ , the ratio of the two amplitudes is given by:

$$E_0/E_x = \exp(-\alpha x)$$

where  $\alpha$  is the attenuation coefficient;

$$\alpha = \omega \left\{ \left[ \frac{\mu \varepsilon}{2} \right] \left[ \left( 1 + \frac{\sigma^2}{\omega^2 \varepsilon^2} \right)^{1/2} - 1 \right] \right\}^{1/2}$$

where  $\omega = 2\pi f$  where  $f$  is the frequency (Hz),  $\mu$  is the magnetic permeability ( $4\pi \times 10^{-7}$  H/m),  $(\sigma$  is the bulk conductivity at the given frequency (S/m), and  $\varepsilon$  is the dielectric permittivity where  $\varepsilon = \varepsilon_r \times 8.85 \times 10^{-12}$  F/m and  $\varepsilon_r$  is the bulk relative dielectric constant. The formula is valid for non-magnetic materials only. The term  $(\sigma/\omega\varepsilon)$  above is equivalent to the loss factor ( $P$ ), such that:

$$P = \sigma/\omega\varepsilon = \tan D.$$

Also, skin depth( $\delta$ ) =  $1/\alpha$ . When  $\tan D \ll 1$ ,  $\delta = (2/\sigma)(\varepsilon/\rho)^{1/2}$ .

Numerically :  $\delta = (5.31\sqrt{\varepsilon_r})/\sigma$ , where  $\sigma$  is in mS/m.

Using the final term for the skin depth, and substituting typical values for seawater, it can be seen that the skin depth in seawater is only 1 cm, and for wet clay it is only 0.3 m. Where fresh dry rock is encountered, the conductivity term decreases substantially and hence the skin depth increases, and much greater depth penetration is likely. The variation in skin depth is shown in Figure 13.5 as a function of ground resistivity at the extremes of expected *in situ* relative dielectric constants (McCann *et al.*, 1988).

It is important to remember that the simplified version of skin depth is valid only when the loss factor is considerably less than one. In order to determine when such conditions are valid, the graph shown in Figure 13.6 should be used. The figure shows the theoretical conductivity values (in mS/m) when the loss factor is equal to one. Thus the observed conductivity for the condition of being much less than unity to apply should be of the order of 0.05 of the theoretical conductivity. For example, if the observed true conductivity is 15 mS/m, then the loss factor needs to be considered in its full form in all cases other than when a 900 MHz antenna is being used, as long as the relative dielectric constant is greater than or equal to six. If the full form of the attenuation factor is not used under these circumstances, the derived value of skin depth will be overestimated.

It should be noted that the skin depth does not equate to the depth of penetration of the ground radar. To determine radar range, instrumental factors also need to be taken into consideration in

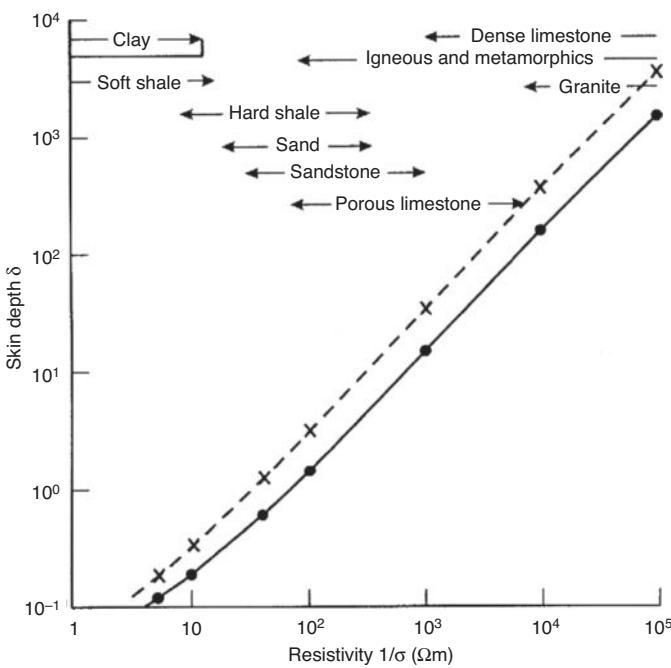


**Figure 13.5** Variation of skin depth ( $\delta$ ) as a function of resistivity for  $\epsilon_r = 8$  (solid line) and 40 (dashed line). After McCann *et al.* (1988), by permission.

addition to those related to the subsurface target and to the media through which the radiowaves travel. The total path loss for a given distance is made up of five terms: antenna losses; transmission losses between the air and the ground; losses caused by the geometric spreading of the radar beam; attenuation within the ground as a

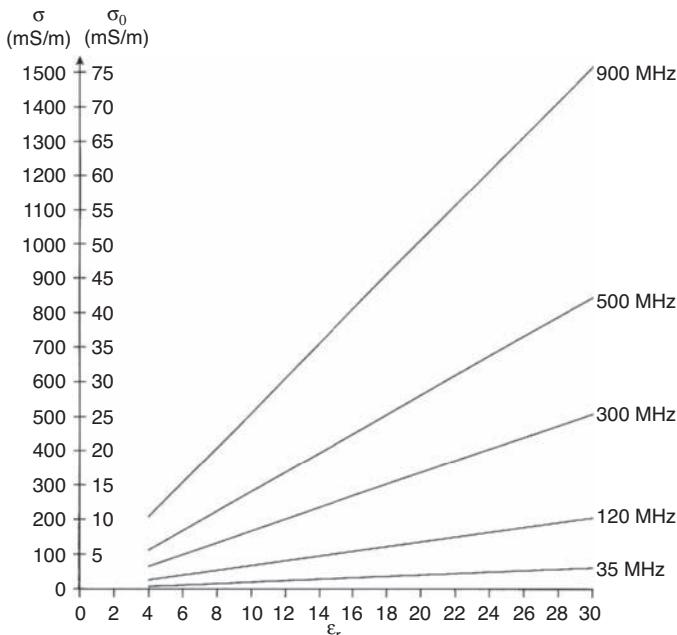


**Figure 13.6** Conditions under which the loss factor ( $\tan D$ )  $\ll 1$ .

**Box 13.4** Radar range equation and definition of  $Q$  (Annan and Davis, 1977) and Fresnel zone

**Radar range equation** (Ridenour, 1947)  $Q$  is the system performance (in decibels):

$$Q = 10 \log \left\{ \frac{E_{\text{Tx}} E_{\text{Rx}} G_{\text{Tx}} G_{\text{Rx}} V^2 (gF) \exp(-4\alpha z)}{64\pi^3 f^2 z^4} \right\}$$

The various terms are defined in Figure 13.7. Also:

$$Q = 10 \log(P_{\min}/P_s)$$

where  $P_{\min}$  is the minimum detectable signal power, and  $P_s$  is the source power.

In low-loss materials the range of  $z$  is approximately  $10D_2$ . In high-loss materials the range is approximately  $D_2/D_1$ , where:

$$D_1 = 2A/(40 - 10B_2)$$

$$D_2 = \left\{ \frac{-Q + 10 \log(S) + 10 \log V^2 + 10[B_1 + (B_3 - 2)\log f]}{40 - 10B_2} \right\}$$

$$S = E_{\text{Tx}} E_{\text{Rx}} G_{\text{Tx}} G_{\text{Rx}} / 64\pi^3$$

where  $B_1$ ,  $B_2$  and  $B_3$  are as listed in the table below.

Type of target	$gF$	$B_1$	$B_2$	$B_3$
Smooth, plane reflector	$\pi z^2 R$	$\log(\pi R)$	2	0
Rough, plane reflector	$\pi(V^2/16f^2 + Vz/2f)R$	$\log(\pi VR/2)$	1	-1
Rayleigh point target	$(64\pi^5 a^6 f^4 / V^4)R$	$\log(64\pi^5 a^6 f^4 / V^4)$	0	4

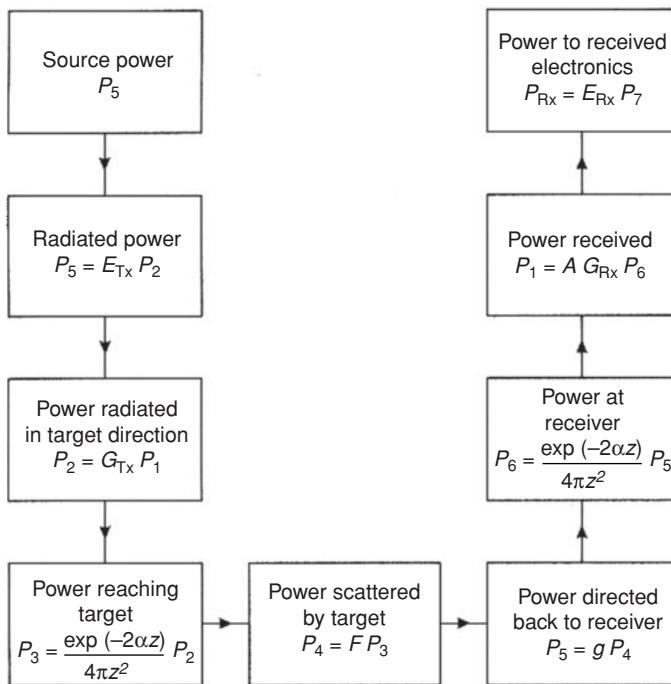
Radius  $r$  of the **Fresnel zone** (for a symmetrical wavefront) is given by:

$$r = ((\lambda c/4)^2 + \lambda_c z/2)^{1/2} \approx (z\lambda_c/2)^{1/2} \approx (\lambda_c/4) + z/(\epsilon - 1)^{1/2}$$

where  $\lambda_c$  is the centre-frequency wavelength and  $z$  is the depth to the reflecting surface.

function of the material properties; and losses due to scattering of the radar signal from the target itself. The radar range equation and definition of a radar system performance ( $Q$ ) are given in Box 13.4, and the components affecting radiated and return power are illustrated schematically in Figure 13.7.

Within Box 13.4 are listed three types of target: smooth and rough plane reflectors and a point target. Of particular importance is the  $gF$  term in the first equation in Box 13.4. This product defines the power scattered by the target and also directed back to the receiver. The term  $g$  is the backscatter gain of the target and  $F$  is the target scattering cross-sectional area.



$E_{Tx\cdot Rx}$	=	efficiency of transmitter/receiver antenna
$G_{Tx\cdot Rx}$	=	transmitter/receiver gain
$g$	=	backscatter gain of target
$F$	=	target scattering cross-sectional area
$z$	=	distance of target from antenna
$\alpha$	=	attenuation coefficient of medium
$V$	=	attradiowave velocity of medium
$A$	=	effective area of receiver antenna ( $= V^2 / 4\pi f^2$ )
$f$	=	Frequency of signal
$R$	=	power reflection coefficient

**Figure 13.7** Block diagram illustrating radiated and return power for a radar system. After Annan and Davis (1977), by permission.

For a smooth plane reflector, the incident signal returned appears to be an image of the source, albeit reduced in power by the power reflection coefficient  $R$  ( $= r^2$ , where  $r$  is the amplitude reflection coefficient) of the interface, radiating upwards from a distance twice as far away as the boundary. The theory behind this is the same as in simple optics for a plane reflector.

For a rough, specular reflector, there is difficulty in defining the cross-sectional area of the target. Cook (1975) suggested that it equates to the area of the first Fresnel zone (see Figure 13.8). Consequently, where the wavelength of the roughness of the surface is greater than the diameter of the first Fresnel zone, the cross-sectional area, and hence the  $gF$  product, can be estimated. Where the wavelength of the surface roughness is less than the diameter of the first Fresnel zone, and especially when the amplitude of the roughness is greater than one-quarter wavelength, the actual cross-sectional target area is difficult to calculate. The character of the reflection is also an indication of the nature of the reflector surface –

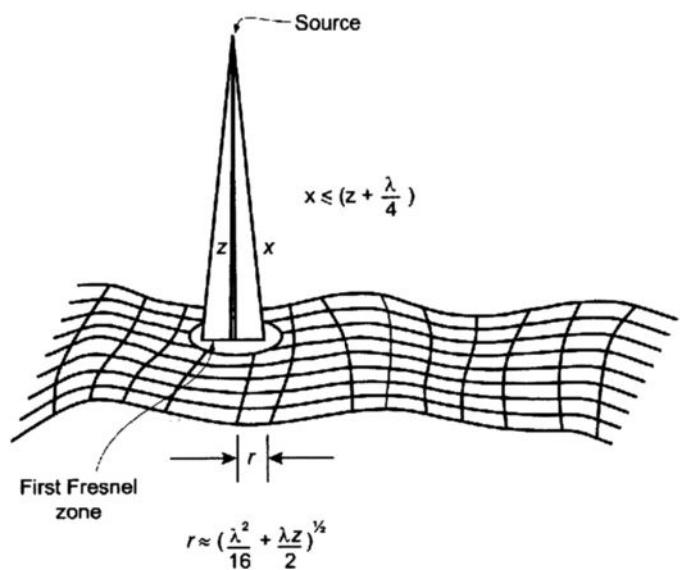
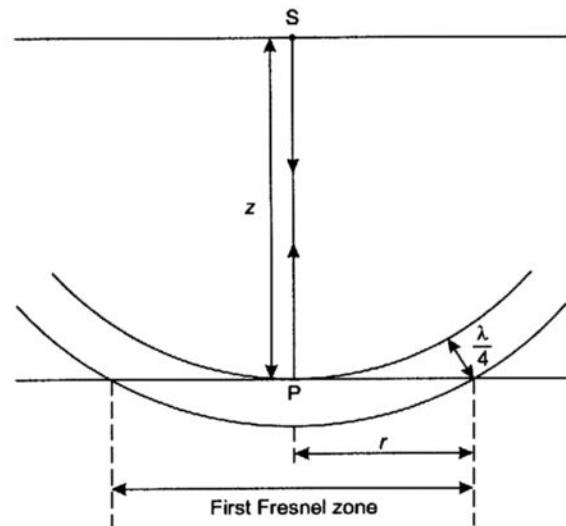


**Figure 13.8** Reflection from a rough, specular interface; the target cross-sectional area is equivalent to the area of the first Fresnel Zone. After Annan and Davis (1977), by permission.

a planar surface over a distance greater than the Fresnel footprint will give a stronger reflection signal than a specular reflector where the surface roughness has a wavelength much shorter than the Fresnel footprint (Figure 13.9). The power reflection coefficient would be reduced as a consequence of the greater scatter arising from such a surface roughness. The significance of the first Fresnel zone in terms of interpretation and resolution is discussed further in Section 13.3.3.

For a point target, the characteristics of the returned energy are described by the Rayleigh Law of scattering in which the  $gF$  product is very strongly dependent upon frequency (to the fourth power). It is assumed for the expression in Box 13.4 for a point source, that the radius of the target ( $a$ ) is much smaller than the wavelength of the incident radiation. In materials that consist of cobbles and gravel,

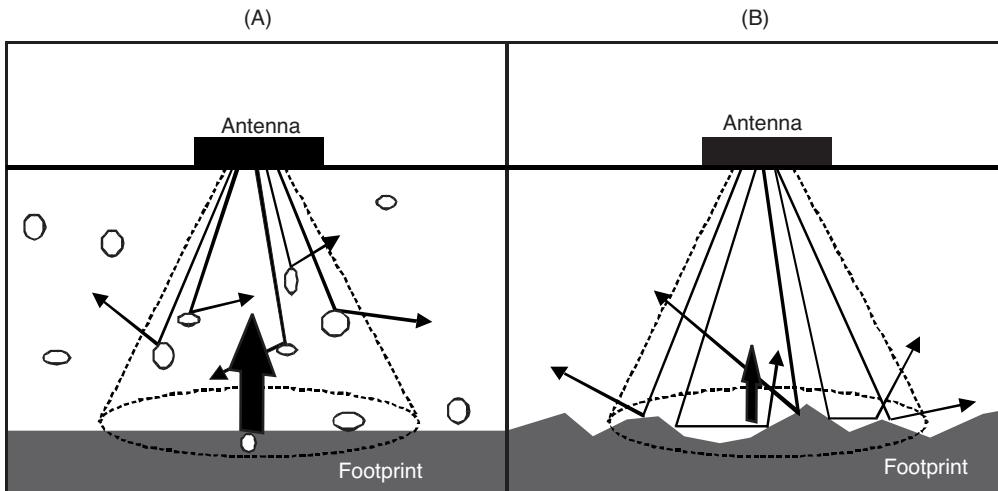


**Figure 13.9** Differences in reflection characteristics arising from (A) a planar reflector but with scatterers present, and (B) no scatterers but with a specular reflector. [C]

for example, or where the geological units are severely distorted over distances shorter than the wavelength of the incident energy, then the amount of energy scattered is likely to be large and the resulting radargram is likely to show very few, if any, coherent reflection events associated with such materials. This characteristic can in itself be used indirectly during interpretation as being diagnostic of such material.

It has been shown (see Box 13.3) that attenuation is directly proportional to frequency. The higher the frequency, the greater will be the amount of attenuation. It is also evident that the bulk relative dielectric constant ( $\epsilon_r$ ) and bulk conductivity at the given frequency ( $\sigma$ ) also affect attenuation significantly. Each of these properties is affected by the composition of the material and the electrical behaviour and relative abundance of each constituent. The loss factor ( $\tan D$  in Box 13.3) is directly proportional to conductivity and inversely proportional to the relative dielectric constant and frequency. For saturated granular media, the conductivity and the relative dielectric constant of the saturating fluid will dominate over the respective matrix values. The bulk relative dielectric constant ( $\epsilon_r$ ) is roughly equal to the product of porosity ( $\varphi$ ) and relative dielectric constant for the fluid ( $\epsilon_f$ ). The effect of this is that the more conductive the saturating fluid, and the greater the proportion of fluid present with a correspondingly high relative dielectric constant (remember:  $\epsilon_r$  for water = 81), the greater will be the attenuation. Similarly, the greater the clay content, the greater will be the loss factor and hence attenuation. The importance of clay is that it possesses bound water within its lattice structure. Clay minerals also exhibit particular electrical properties as a result of their physicochemical structure, the details of which are beyond the scope of this section.

For both geological and engineering materials, the electrical and dielectric properties, especially as functions of frequency, are still poorly understood. Furthermore, the petrophysical characteristics of such materials are largely unknown. The electrical and dielectric properties of materials are discussed in Section 13.4.

### 13.3.3 Horizontal and vertical resolution

*Vertical resolution* is a measure of the ability to differentiate between two signals adjacent to each other in time. Simplistically, vertical resolution is a function of frequency. Each radar antenna is designed to operate over a range of frequencies (bandwidth) where the peak power occurs at the centre frequency ( $f_c$ ) of the antenna. It is the centre frequency that labels an individual antenna; hence a 500 MHz antenna has a nominal centre frequency of 500 MHz, for instance. The centre frequency is also inversely proportional to the pulse period (in nanoseconds). The 500 MHz antenna, therefore, has a pulse period of  $1/500 \text{ MHz} = 2 \text{ ns}$ , and for 35 MHz the pulse period is  $1/35 \times 10^6$  or 28.6 ns. The equivalent length (in metres) of the pulse is the product of the pulse period and the radiowave velocity for the appropriate material. In a wet soil ( $V = 0.06 \text{ m/ns}$ ) and with a 100 MHz antenna (pulse period = 10 ns), the pulse (wave) length is  $0.06 \times 10 \text{ m}$  or 0.6 m. Resolution can be taken as one-quarter of the wavelength ( $\lambda$ ) of incident radiation;  $\lambda = V/f$ , where  $V$  is the radiowave velocity, and  $f$  is its frequency. In the last case, if the wavelength is 60 cm, the *theoretical* vertical resolution is 15 cm.

Examples of theoretical minimum resolutions for two different materials at three separate frequencies are listed in Table 13.3. The

**Table 13.3** Theoretical vertical resolution for two geological materials at three frequencies.

	Antenna frequency (MHz)		
	120	500	900
<i>Soil</i>			
Wavelength (cm)	62.5	15	8
Resolution (cm)	15.6	3.75	2
Bedrock Wavelength (cm)	92	22	12
Resolution (cm)	23	5.5	3

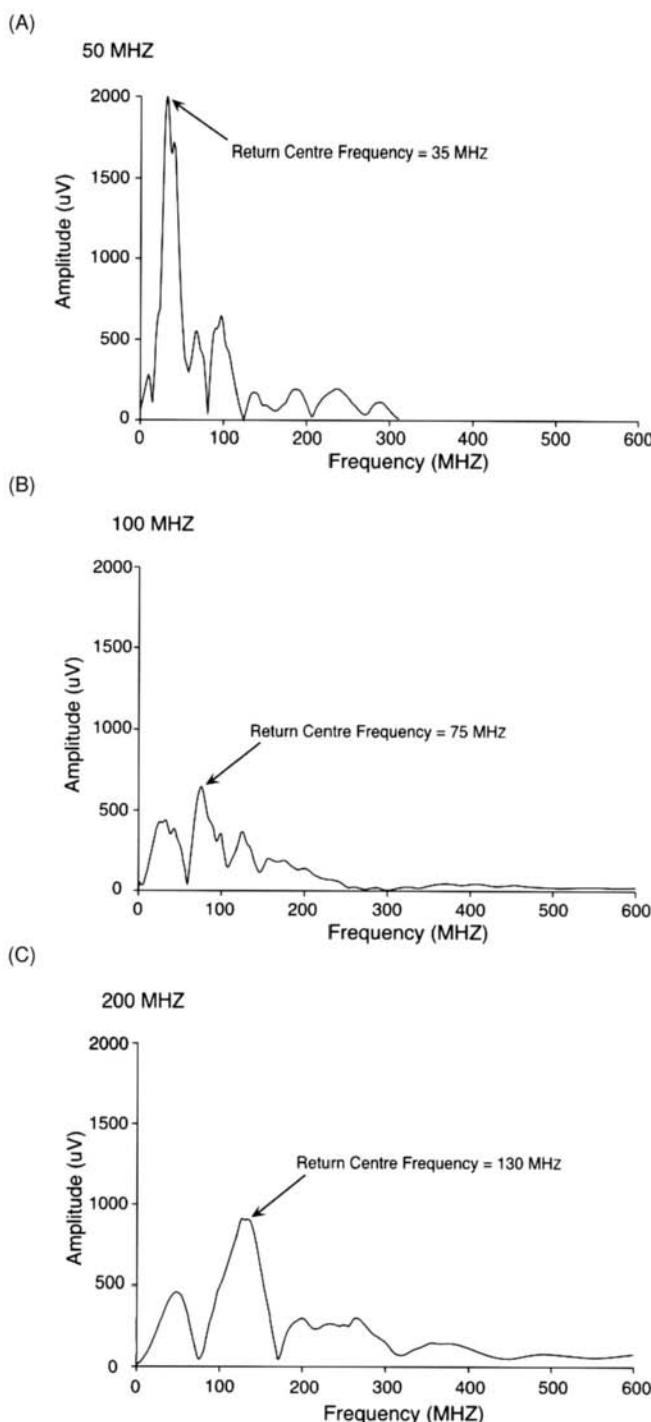


**Figure 13.10** Return centre-frequency spectra for three nominal centre-frequencies: (A) 50 MHz, (B) 100 MHz, and (C) 200 MHz. From Neal (2004), by permission.

first example in the table is for a typical soil with  $V = 0.075 \text{ m/ns}$ , and the second, a massive rock such as limestone with  $V = 0.110 \text{ m/ns}$ . The vertical resolutions given are the very best that could be achieved theoretically. In reality, the resolution is less than these figures owing to the complex nature of the source waveform and the ground responses.

An antenna placed directly on the ground will produce a ‘ground-coupled’ signal. That is, the transmitted waveform in air will not be reproduced when being transmitted into the ground. The material affects the shape, form and amplitude (power) of the downgoing source wave train and effectively filters it. The ground-coupled wave has a lower centre-frequency than that for the antenna when transmitting in air. This is illustrated by the amplitude–frequency spectra for three frequencies (50, 100, 200 MHz) shown in Figure 13.10. In each case the return centre-frequency is significantly lower than the nominated centre-frequency for that antenna, i.e. for the 50 MHz antenna, the peak return centre-frequency is 35 MHz. The source pulse length decreases with increasing frequency, but describes the main pulse lobe only. With ground coupling, and depending upon the transmitter efficiency, the downgoing wave train is usually several times longer than the pulse length described in the manufacturer’s literature for a given antenna. This complexity of source wave shape has serious consequences for interpretation.

If the downgoing radar wave has, for instance, three cycles with a total period of 25 ns, this means that a reflection from any interface will have equal if not greater complexity of shape and longer period. The lengthening is due to the loss of higher frequency components within the signal, as higher frequencies are attenuated preferentially with respect to lower frequencies.

If two interfaces are separated by only a few tens of centimetres, for example, and the radiowave velocity of the material in between is such that the time interval between a reflection from the first (uppermost) interface and one from the second is shorter than the period of the source wave train, the onset of the second reflection will be masked by the tail of the first, and thus may not be resolved. This principle is illustrated in Figure 13.11. Given two pulses, each with a half-width  $w_{1/2}$ , as long as the period ( $\delta t$ ) separating the two pulses is equal to or greater than  $w_{1/2}$ , then the two pulses will be distinguishable; if the time period is less than  $w_{1/2}$ , the two pulses effectively merge into one.

Another complexity is that the downgoing signal travels from the transmitter in a cone of radiation with a finite-sized footprint (see Figure 13.3C). The first Fresnel zone (Figure 13.8) describes the minimum area in which features with smaller dimensions will not be imaged. The finite size of this footprint affects both the vertical resolution (when interfaces are steeply dipping or have high-amplitude surface roughness relative to the wavelength of the incident radiowaves) and the *horizontal resolution*. The larger the first Fresnel zone, the lower will be the horizontal resolution in discriminating between adjacent targets. Note that when estimating the radius of the Fresnel zone, the centre-frequency within the ground will be significantly lower than that specified for the antenna (as discussed above), so the radius derived will in actuality be larger. Consequently, lateral or horizontal resolutions derived will also be overestimated – indicating better theoretical resolution than is actually achieved. The changes with depth in the Fresnel zone radar footprint for three nominal centre-frequencies (50, 100 and 200 MHz) are illustrated in Figure 13.12. These three profiles also relate to the amplitude–frequency spectra shown in Figure 13.10. It is important also to note that the depth scales are expanded below the water table due to the decrease in radar velocity in the saturated materials. Each profile was obtained along the same shore-parallel

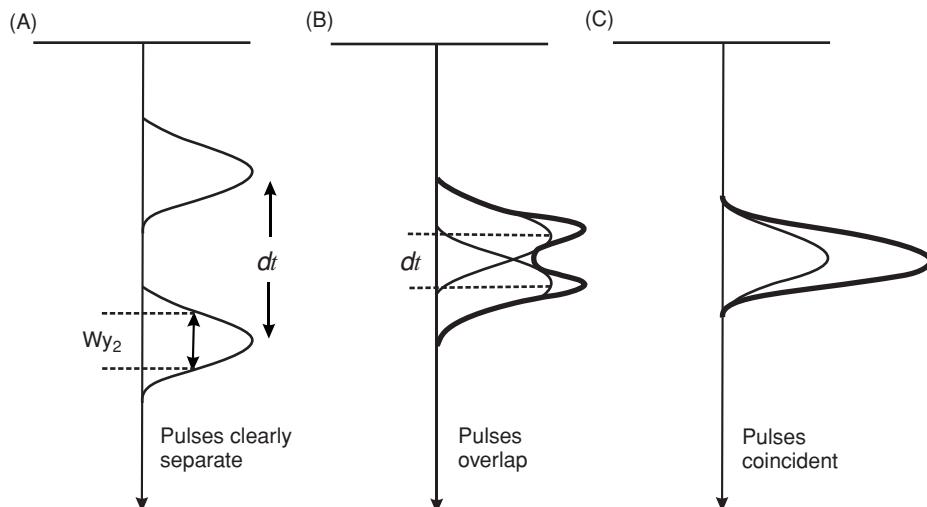


**Figure 13.11** Temporal resolution between two pulses. (A) Pulses with half-width  $w_{y_2}$  are clearly identifiable when  $\delta t \gg w_{y_2}$ . (B) The pulses remain distinguishable until  $\delta t \approx w_{y_2}$ . (C) the two pulses are indistinguishable when  $\delta t \ll w_{y_2}$ .

transect across sand-and-gravel-rich beach ridge-plain deposits at Beckfoot, outer Solway Firth, northwest England (Neal, 2004).

Whereas in seismology the Fresnel zone is circular (as sound travels omni-directionally), the EM footprint is elliptical depending upon the geometry of the *H*- and *E*-lobes (see Figure 13.3), although it becomes more symmetrical the larger the dielectric constant of the medium. The area of the Fresnel zone assuming a symmetrical zone (e.g. defined by the equation in Box 13.4) would be larger than the elliptical area as the minor axis of the ellipse would be shorter than the major axis, especially for small values of the dielectric constant. The eccentricity of the elliptical Fresnel zone also becomes important when considering the orientation of the antenna (and hence Fresnel zone major axis) with respect to the azimuth of particularly linear targets (e.g. metal pipes). The strength of the radar return from a pipe will be affected by the orientation of the *H*- or *E*-lobe so that when the pipe is aligned parallel to one vector (along the Fresnel ellipse major axis), the signal strength will be much stronger than when orientated at right angles (i.e. parallel to the other vector, along the minor axis of the Fresnel ellipse) (Roberts and Daniels, 1993). This can make the difference between detecting a linear target or not (Figure 13.13) and why undertaking a grid of orthogonal survey profiles can help to resolve linear targets whose orientation is unknown prior to the survey. However, for utility scanning, multi-array radar systems that image in 3D are becoming available that facilitate the detection of subsurface services.

Furthermore, spatial resolution is also affected by the conical beam width of the downgoing radiowaves (see Figure 13.14A); the narrower the beam width (such as might be achieved with a directional antenna), the greater will be the spatial resolution. Horizontal resolution is inversely proportional to  $\sqrt{\alpha}$ , where  $\alpha$  is the attenuation coefficient (Daniels *et al.*, 1988). Consequently, the horizontal resolution is actually better over a high-loss material than over a low-loss medium. Where radar systems permit horizontal stacking

of adjacent scans to improve the signal-to-noise ratio, horizontal resolution is reduced as the amount of horizontal stacking is increased. There is a practical compromise to be reached between optimising return signal strengths by horizontal stacking and reducing horizontal resolution. Also, illustrated in Figure 13.14B is the effect of a target within the Fresnel zone with equal area ( $A_1 = A_2$ ) but where the dielectric contrasts of the targets relative to that of the host medium differ (in this case  $R_2 >> R_1$ ) so that the reflection signal is larger than that for the target with the smaller contrast. Also, for a target with a smaller area ( $A_3$ ) than  $A_{1,2}$ , but with a much greater dielectric contrast, then the reflection strength may be similar in amplitude to that of the target  $A_2$ ,  $R_2$ . A target whose area is larger than that of the Fresnel zone is also more likely to be detected than one whose area is much smaller than the Fresnel zone, for an equivalent dielectric contrast.

When *synthetic aperture radar* (SAR) is used, measurements are made by a single antenna at a number of different positions and the results combined to simulate a narrower beam than would have been achieved by using just an isolated antenna at one location. Details of the SAR or holographic radar are beyond the scope of this chapter.

## 13.4 Dielectric properties of earth materials

The dielectric behaviour of a material is described in terms of its complex permittivity ( $\epsilon^*$ ) and complex conductivity ( $\sigma^*$ ), which are interrelated (see Box 13.5). The high-frequency permittivity ( $\epsilon_\infty$ ) is taken as the lowest real permittivity when the imaginary permittivity ( $\epsilon''$ ) is zero (see Figure 13.15). The real permittivity ( $\epsilon'$ ) increases as frequency decreases. When the material is a non-conductor, the frequency-permittivity behaviour is described by a

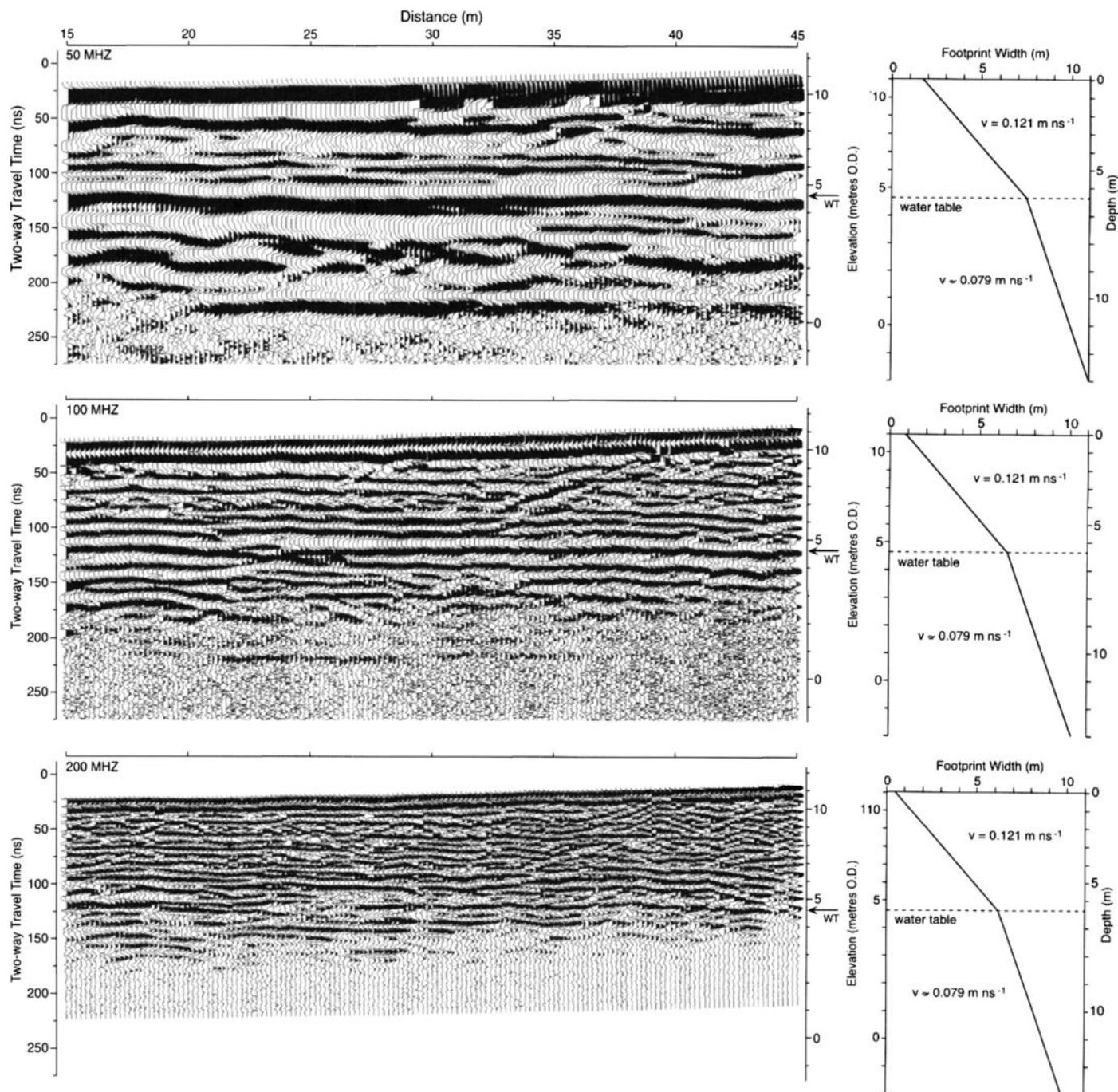


**Figure 13.12** Radargrams and Fresnel radar footprint size variations with depth for three profiles acquired with different nominal centre-frequencies along the same transect. From Neal (2004), by permission.

semicircle, the centre of which is located on the real permittivity axis halfway between the high-frequency and static permittivities ( $\epsilon_\infty$  and  $\epsilon_s$  respectively). The imaginary permittivity ( $\epsilon''$ ) indicates the absorption or energy loss within the dielectric material, and this in turn contributes to the absorption of radiowaves within the ground.

If the material is conductive, then an appropriate additional term has to be included within the definition of the complex permittivity

(Box 13.5). Conductivity also contributes to the loss within the material.

The relative dielectric constant ( $\epsilon_r$ ) varies from 1 in air through to 81 in water. For most geological materials,  $\epsilon_r$  lies in the range 3–30. Consequently, the range of radiowave velocities is large (see Box 13.1), from around 0.06 to 0.175 m/ns (Figure 13.16). The speed of radiowaves in air is 299.8 mm/ns. In trying to estimate depths to any given target it is *essential* to have a detailed knowledge of the

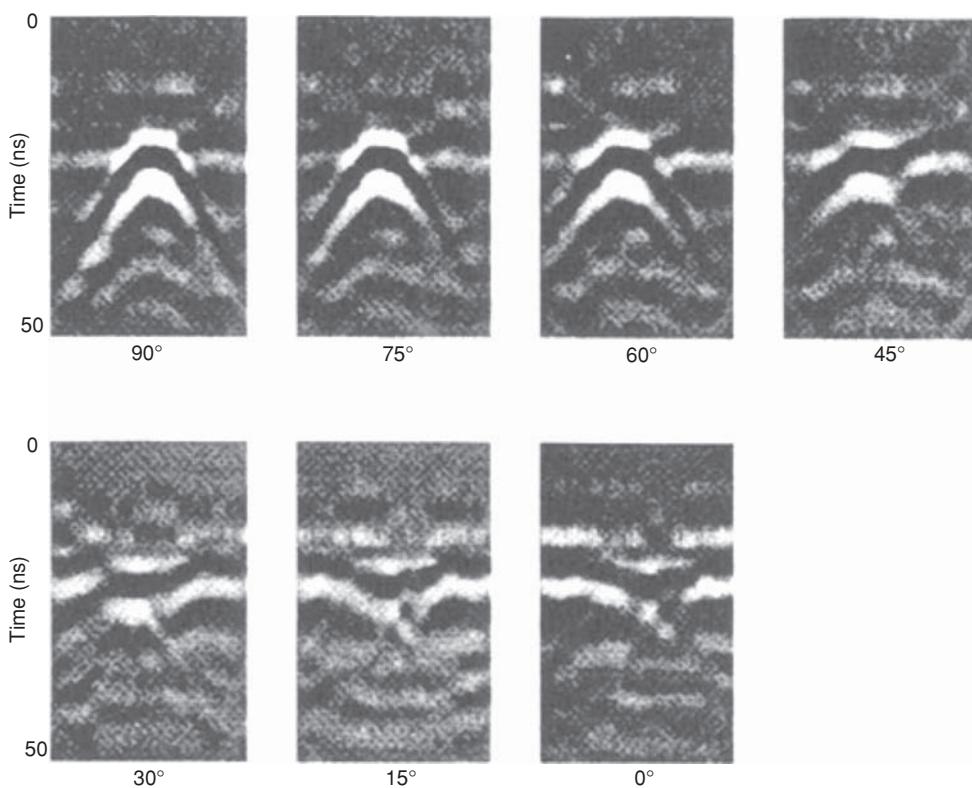


**Figure 13.13** Radargrams acquired over a 1.6 m pipe buried at 0.5 m depth at different azimuths, 0° indicates parallel profile and pipe; 90°, the profile crosses the pipe at right angles. From Roberts and Daniels (1993), by permission.

radiowave velocities through the subsurface materials present. This aspect of radar interpretation will be dealt with in Section 13.6.

A list of the relative dielectric constants and associated radiowave velocities for a variety of geological and manmade materials is given in Table 13.4. It should be emphasised that the values of both relative dielectric constants and radiowave velocities should be taken only as guide figures. The lack of ranges for some materials is due to the paucity of measurements made and is not meant to imply that there is no variation within these materials. The ranges given are also not meant to be extremes. As more results are published, the ranges listed may need to be extended as the true variability of both parameters becomes more widely realised. The frequencies at which these values have been determined range from 25 MHz to 100 MHz.

Cook (1975) produced a schematic illustration (Figure 13.17) to show the likely probing distances achievable for different geological materials over the frequency range from 1 to 500 MHz. Clay-rich materials have much shorter probing distances than more massive rocks such as granite and limestone.

Most materials, whether geological or manmade, are a complex mixture of components, each of which is likely to have different electrical and dielectric properties. Grain size and even grain shape can affect bulk electrical and dielectric behaviour. Most rocks contain a degree of moisture, either as 'free' liquid contained within pore spaces, or 'bound' within the mineral lattice as with many types of clay minerals. Since the relative dielectric constant of water is high (81) relative to that of dry rock, even a small amount of

water may increase the bulk permittivity of the rock. An example of the effect of soil moisture content of a variety of rocks on the relative dielectric constant is shown in Figure 13.18. Furthermore, the amount of water present within a rock will also affect the speed of propagation of radiowaves. The radar velocity through freshwater is 0.033 m/ns, whereas it is 0.12 m/ns through a low-porosity sandstone (McCann *et al.* 1988). From Figure 13.18 it can be seen that the dielectric permittivity ( $\epsilon_r$ ) increases with increasing soil moisture content as radiowave velocity decreases. Consequently, wetter materials have a better vertical resolution than dry materials, although the attenuation in wetter materials is greater than for dry, so depth penetration is likely to be smaller.

The relative dielectric constant of a layered material has been demonstrated to be related to porosity ( $\varphi$ ) by considering the proportion of constituents present and their respective relative dielectric constants. A number of relationships exist between saturation and dielectric constant. Topp *et al.* (1980) derived a series of equations that are widely used in soil hydrology using time-domain reflectometry (TDR) at gigahertz frequencies, but these tend to overestimate the volumetric moisture content. Another method in wide use is the complex refractive index method (CRIM) (Roth *et al.*, 1990). The relationships between constituent and bulk relative dielectric constants and porosity are given in Box 13.6; the variations of radiowave velocity with porosity for water-saturated and air-saturated porous media are illustrated in Figure 13.19. If the relative dielectric constant for each constituent of the material

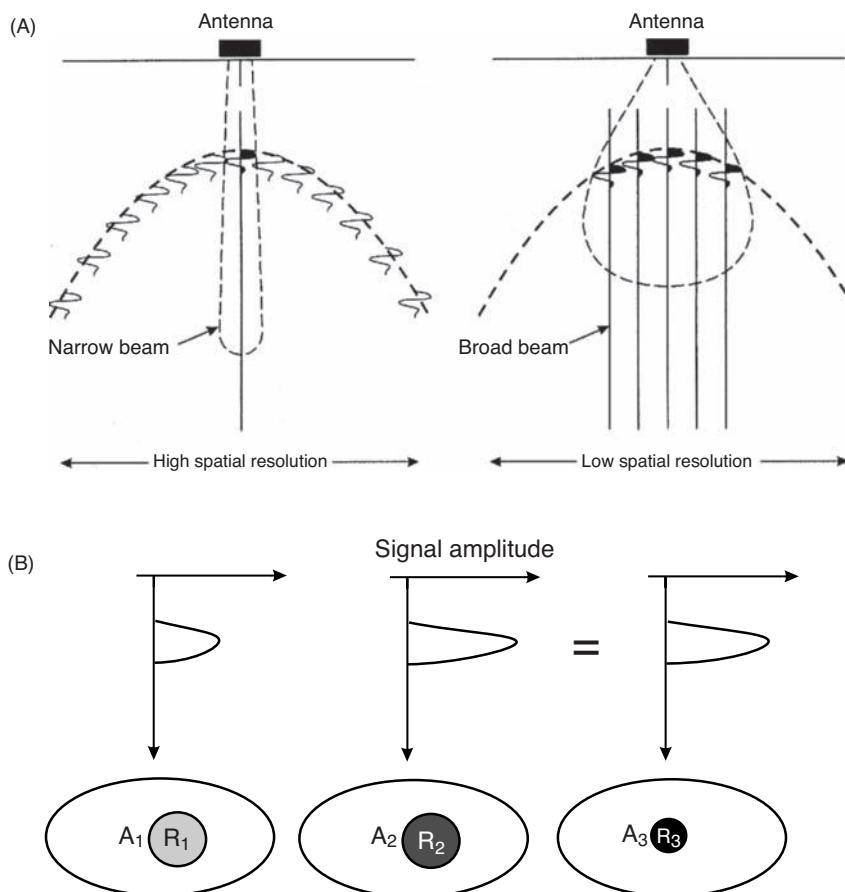


**Figure 13.14** (A) Horizontal resolution due to beam width. (B) Detectability of targets depending upon cross-sectional area relative to Fresnel zone and dielectric contrast. A small bright target may be more easily detected than a larger target with a smaller dielectric contrast with that of the host medium.

### Box 13.5 Complex permittivity and conductivity

Complex permittivity  $\epsilon^*$  of a non-conductive material is given by:

$$\epsilon^* = \epsilon' + i\epsilon''.$$

When  $\epsilon''$  is plotted as a function of  $\epsilon'$ , the resultant graph is a semicircle. The plot is known as a Cole–Cole plot after its originators, Cole and Cole (1941).

If the material has a conductivity  $\sigma$ , then:

$$\epsilon^* = \epsilon' + i(\epsilon + \sigma_s/\omega\epsilon_0)$$

where  $\sigma_s$  is the static or DC conductivity, and  $\epsilon_0$  is the permittivity of free space. At low frequencies, the DC term dominates and produces a characteristic low-frequency tail (see Figure 13.15). The  $\epsilon''$  term is the frequency-dependent loss related to the relaxation response phenomena associated with water molecules (King and Smith, 1981).

The complex conductivity ( $\sigma^*$ ) is given by:  $\sigma^* = \sigma' + i\sigma'' = j\omega\epsilon_0\epsilon^*$ .

is known, and that of the bulk material is measured or derived from the radiowave velocity, then the total porosity can be calculated.

The determination of porosity assumes only a two-component system made up of a matrix and pore spaces that are saturated with either air or another fluid of known relative dielectric constant. It also assumes that all the pore spaces are saturated with one fluid. This situation may not be achieved in many cases in nature.

*Total porosity* is the proportion of volume not filled by the solid constituents within a material and includes isolated pore/fracture space. The *effective porosity* is the porosity available to free fluids and excludes the isolated unconnected pores/fractures and space occupied by bound water in clays (Sheriff, 2002). The isolated pore/fracture space (*residual porosity*) is thus the difference between the total and effective porosities. The permeability of a material is a measure of the ease with which a fluid can flow through the pore spaces within a given medium and thus is a function of the connectivity of the pore space, i.e. the effective porosity. Permeability is also a function of the viscosity of the fluid, the rate of fluid flow and the hydraulic pressure gradient causing the flow.

When electrical resistivity is used to derive porosity of clean granular rocks, such as by using Archie's formula, it is the effective

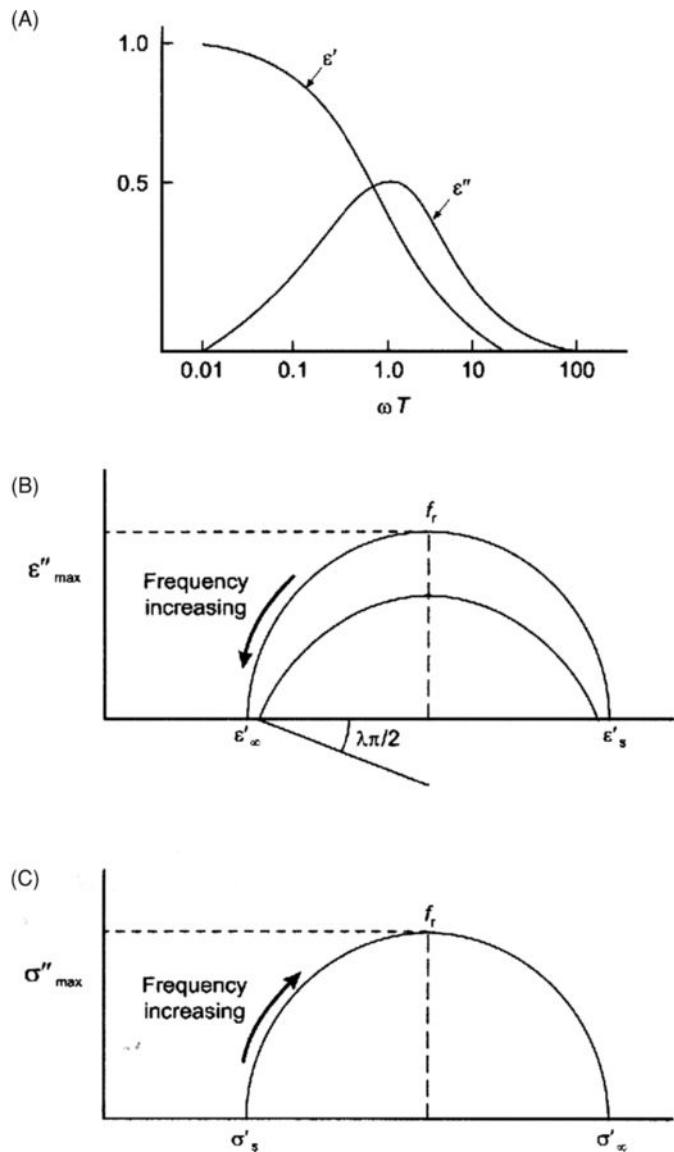


**Figure 13.15** (A) Frequency dependence of  $\epsilon'$  and  $\epsilon''$ ; (B) semi-circle and depressed arc forms of permittivity dispersions on a Cole-Cole diagram; (C) complex conductivity arc diagrams. The Debye relaxation frequency is  $f_r$ .

porosity which is being determined. Electrical continuity is provided by the electrolytes within the connected interstitial spaces. Dielectric measurements, however, are not dependent upon the connectivity and thus can be used to determine the total porosity. Conversely, values of porosity derived from the use of radiowave velocities are always likely to be overestimates of the effective porosity.

*Microporosity* (i.e. porosity at a scale of the order of microns but still large relative to the sensitivity of the electrical measuring system) becomes especially significant in dielectric analysis. Electrical conductivity is affected by pore geometry and pore surface area. Clay not only affects the physical communication between pores and pore throats (affecting permeability as well as porosity), but the type of clay provides differing surface areas for double-ionic

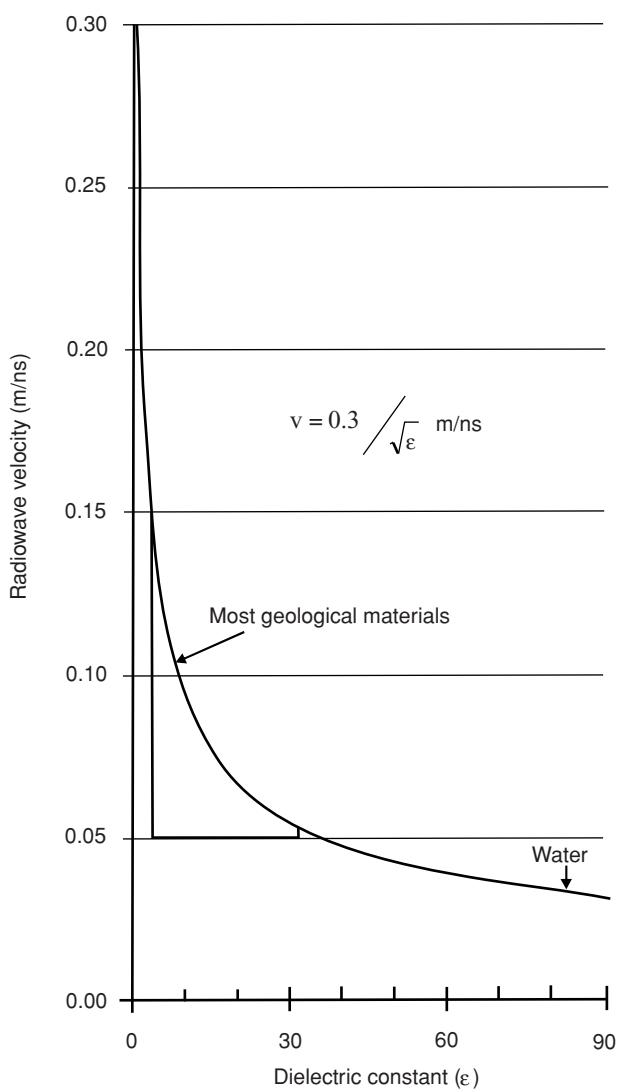


**Figure 13.16** Radiowave velocities as a function of relative dielectric constant.

polarisation (Reynolds and Taylor, 1992). For example, authigenic kaolinite occurs as disc-like 'booklets', whereas illite forms ribbons (Klimontos and McCann, 1990; Klimontos, 1991). The form of the clay, therefore, can affect the surface area within the pore space and it is probable that, at the scale of the order of microns, the microporosity has a measurable effect on the electrical properties. In contrast, ultrasonic acoustic methods appear to be less sensitive to this. This is not to say, however, that the microporosity does not influence the physical properties measured using acoustic methods, but that as yet the acoustic methods are not able to resolve the effects of microporosity. Indeed, electrical properties are being modelled by reference to the fractal nature of porosity (Ruffet *et al.*, 1991). As it is the *effective* porosity that is directly related to permeability, the latter will only be determinable once the former can be derived accurately.

**Table 13.4** Table of relative dielectric constants and radiowave velocities for a range of geological and manmade materials.

Material	$\epsilon_r$	V (mm/ns)	Conductivity (mS/m)
Air	1	300	0
Water (fresh)	81	33	0.5
Water (sea)	81-88	33	3000
Polar snow <sup>1</sup>	1.4-3	194-252	~0.05
Polar ice <sup>2</sup>	3-3.15	168-172	$\leq 0.06-0.08$
Temperate ice	3.2	167	$5 \times 10^{-8}$
Pure ice	3.2	167	$5 \times 10^{-8}$
Freshwater lake ice	4	150	$1-10^{-6}$
Sea ice	2.5-8	78-157	10-100
Permafrost	2-8	106-212	0.1-10
Active layer permafrost	25	60	
Gravel	5	134	10
Sand and gravel (unsaturated)	3.5-6.5	118-160	0.007-0.06
Sand and gravel (saturated)	15.5-17.5	72-76	0.7-9
Coastal sand (dry)	5-10	95-134	0.01-10
Sand (dry)	3-6	122-173	$10^{-4}-1$
Sand (coastal, dry)	5-10	95-134	0.01-1
Sand (wet)	10-32	53-95	0.1-10
Sand (golf course)	10-25	60-95	10
Silt (unsaturated)	2.5-5	134-190	1-100
Silt (saturated)	22-30	55-64	$\leq 100$
Clay (dry)	2-5	134-212	2-100
Clay (wet)	8-40	47-106	20-1000
Till (unsaturated)	7-21	65-113	2.5-10
Till (saturated)	24-34	51-61	2-5
Moraine	7-14	80-113	$10^{-5}-10^{-7}$
Marsh	12	86	
Peat (freshwater)	57-80	33-40	$\leq 40$
Agricultural land	15	77	
Pastoral land	13	83	
Soil (fine-grained)	41-49	43-47	40
Average 'soil'	16	75	5
Granite	5-8	106-120	$10^{-3}-10^{-5}$
Limestone (dry)	4-8	100-113	
Limestone (wet)	6-15	77-122	10-100
Dolomite	6.8-8	106-115	
Basalt (wet)	8	106	

(Continued)

**Table 13.4 (Continued)**

Material	$\epsilon_r$	V (mm/ns)	Conductivity (mS/m)
Norite	7.4	110	
Anorthosite	7.2-8.0	106-112	
Feldspathic pyroxenite	7.6-8.6	102-109	
Chromitite	11.7-12.2	86-90	
Pegmatoidal feldspathic pyroxenite	8.3	104	
Melanorite	8.2	105	
Shale (wet)	6-9	100-122	10-100
Sandstone (dry)	4-7	113-150	$10^{-3}$ - $10^{-7}$
Sandstone (wet)	6	122	$10^{-2}$ - $10^{-3}$
Coal	4-5	134-150	
Quartz	4.3	145	1-100
Concrete	4-30	55-150	1-100
Asphalt	3-5	134-173	
PVC, epoxy, polyesters	3	173	

Data from Allred *et al.* (2005), Berthling and Melvold (2009), Cassidy (2009), Johnson *et al.* (1979), McCann *et al.* (1988), Morey (1974), Neal (2004), Reynolds (1985, 1990b, 1991b), Rütschlin *et al.* (2007), and references therein.  
Note that the presence of water within materials significantly affects the dielectric properties and radiowave velocities.  
<sup>1</sup>Strongly dependent upon snow density ( $\epsilon_r = (1 + 000845\delta)^2$ , where  $\delta$  is the density of snow; Kovacs *et al.*, 1995).  
<sup>2</sup>Strongly temperature dependent below -5°C (Reynolds, 1985).

The significance of porosity, permeability and the dielectric properties of fluids is of particular importance in dielectric logging of hydrocarbon wells and in contamination mapping, for example.

Dielectric properties of concretes have also been demonstrated to exhibit a surprisingly large degree of variation (Reynolds, 1991b; Reynolds and Taylor, 1992). The relative dielectric constant can vary by more than 50% over a distance of less than 0.1 m within the same mix of concrete; the resulting change in radiowave velocity is of the order of 35%, with velocity decreasing with depth into the concrete. The effect is thought to be related to the amount of micro-cracking present within the concrete, with a greater amount of cracking present nearer the surface (hence more air present, thus the higher radiowave velocity). While this is but one isolated example, it does serve to demonstrate that even within a relatively controlled material like concrete, there is still a high degree of variability in the electrical properties.

tomography. The physical relationship between the transmitter and receiver antennae are different in each case. Where both transmitter and receiver are contained within the same unit, it is said to be a *monostatic* antenna. Where the transmitter and receiver dipoles are separate antenna and can be moved independently of each other, they are described as *bistatic* antennae. These may take the form of rigid flat antennae with handles to ease deployment, or can be wire dipoles attached to a towing cord that can be dragged across rough ground, and are known as *rough terrain antennae* (RTA).

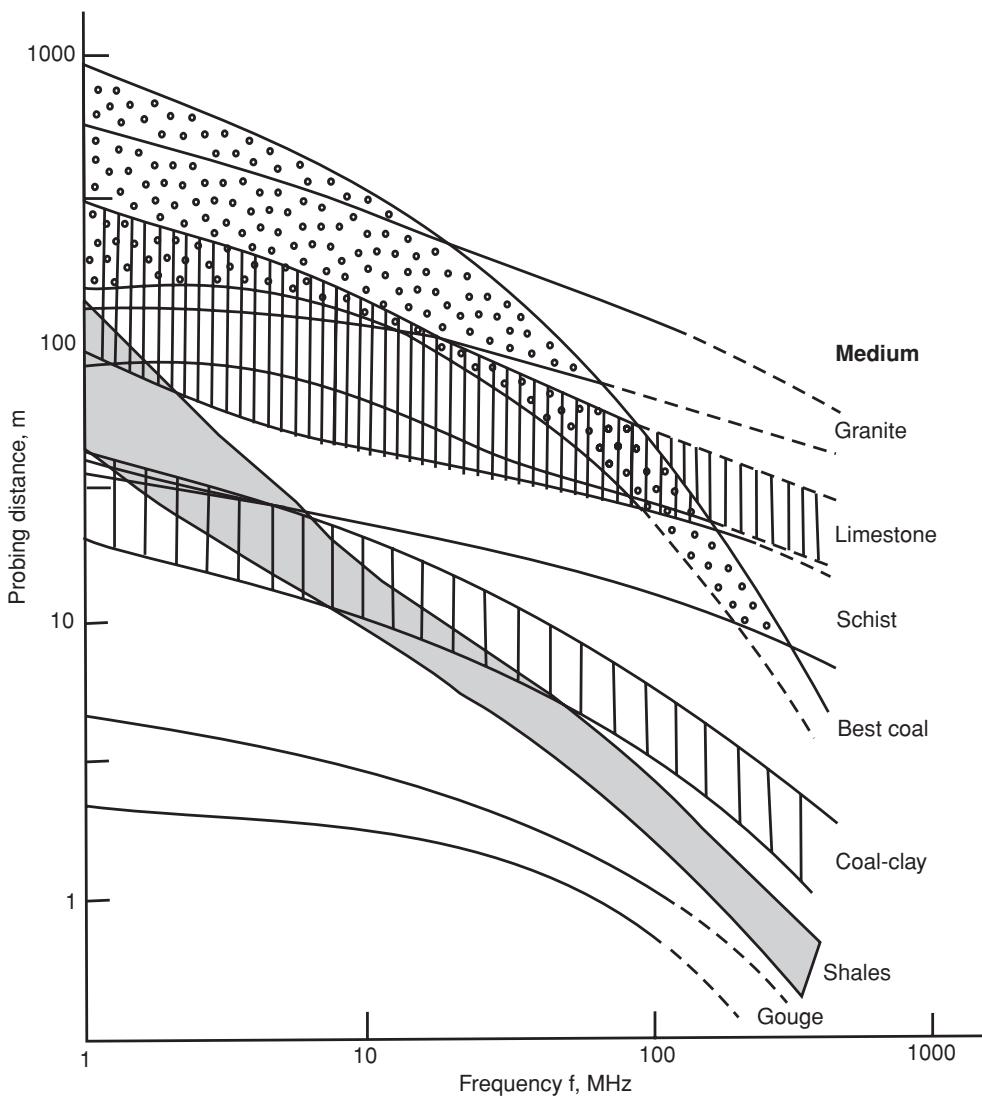
### 13.5.1 Radar reflection profiling

Figure 13.1 provides an example of radar being used to obtain a reflection profile. One or more radar antennae are moved over the ground surface simultaneously, with the measured travel times to radar reflectors being displayed on the vertical axis while the distance the antenna has travelled is shown on the horizontal axis. This mode of surveying is analogous to continuous seismic reflection profiling (see Chapter 6).

If the radiowave velocities have been measured independently (see next section) or reflections correlated with changes in ground characteristics observed from borehole data, then depths to the reflectors can be determined. See Section 13.7 for more details of interpretation techniques.

## 13.5 Modes of data acquisition

There are three modes of deployment of radar systems: reflection profiling; wide-angle reflection and refraction (WARR) or common midpoint (CMP) sounding; and trans-illumination or radar



**Figure 13.17** Probing distances as a function of frequency for different geological materials. From Cook (1975), by permission.

### 13.5.2 Wide-angle reflection and refraction (WARR) sounding

The WARR antenna configuration is shown in Figure 13.20A. The transmitter is kept at a fixed location and the receiver is towed away at increasing offsets. The location of a WARR sounding should be over an area where the principal reflectors are planar and either horizontal or dipping only at very shallow angles. It is also assumed that the material properties are uniform and that the reflector characteristics are the same over the subsurface area over which the WARR sounding is undertaken. This assumption may not be true in all cases.

To avoid having to make this last assumption, an alternative and preferable deployment for the same analysis is the common midpoint (CMP) sounding. In this case, both the transmitter and receiver are moved away from each other so that the midpoint between them stays at a fixed location (see Figure 13.20B). In the CMP case, the point of reflection on each subsurface reflector is used at

each offset, and thus areal consistency at depth is not a requirement. The equivalent positions between the WARR and CMP soundings are given as (i), (ii) and (iii) in Figure 13.20.

### 13.5.3 Trans-illumination or radar tomography

The trans-illumination mode of deployment is where the transmitter and receiver are on opposite sides of the medium under investigation (Figure 13.21). The method is used underground within mines, for example, where the transmitter is located in one gallery and the receiver is either in a gallery to one side of the transmitter, or in a gallery above or below. Alternatively, the radar antennae can be located down boreholes and the radar signals are then propagated from one, through the medium in between, to the other.

The trans-illumination mode is also common in non-destructive testing (NDT) investigations of manmade structures, particularly

**Box 13.6** Relative dielectric constants and porosity  
(Parkomenko, 1967)

The relationship between bulk relative dielectric constant ( $\epsilon_r$ ) and porosity ( $\varphi$ ) is:

$$\epsilon_r = (1 - \varphi)\epsilon_m + \epsilon_w \quad (1)$$

where  $\varphi$  is the porosity,  $\epsilon_m$  and  $\epsilon_w$  are the relative dielectric constants for the rock matrix and pore fluid water, respectively. This is valid when the external field is applied parallel to the bedding.

When the external field is applied perpendicular to the bedding, then:

$$\epsilon_r = \epsilon_m \epsilon_w / [(1 - \varphi)\epsilon_m + \epsilon_w].$$

Using the simplified relationship that  $V = c/\sqrt{\epsilon_r}$ , for low-loss materials, where  $c$  is the radiowave velocity in air, and substituting in Equation (1) for  $\epsilon_r$ , then:

$$V = c / [(1 - \varphi)\epsilon_m + \varphi\epsilon_w]^{1/2}.$$

*Complex Refractive Index Method* (CRIM) equation (Roth *et al.*, 1990):

$$\sqrt{\epsilon'} = (1 - \varphi)\sqrt{\epsilon_m} + \varphi S \sqrt{\epsilon_w} + \varphi(1 - S)\sqrt{\epsilon_a},$$

where  $\epsilon'$  is the bulk dielectric constant for an homogeneous mixture;  $\epsilon_a$  is the dielectric constant of air, and  $S$  is the saturation. The values of  $\epsilon_a$  and  $\epsilon_w$  are assumed to be equal to 1 and 81, respectively, in which case the CRIM equation simplifies to:

$$\sqrt{\epsilon'} = (1 - \varphi)\sqrt{\epsilon_s} + \varphi(1 + 8S).$$

using very high frequencies and hence small antennae (e.g. 900 MHz centre frequency). Examples include testing concrete columns and masonry pillars.

As the relative positions of the antennae are known at all times, and hence the distances between them, it is a simple matter to calculate the mean radiowave velocity of the appropriate raypath. If the signal amplitude is also measured, in addition to travel times, then attenuation can be determined. More details of this method have been given by Annan and Davis (1977). Sophisticated data-processing routines exist in order to produce tomograms that are analogous to seismic equivalents (see Chapter 6).

## 13.6 Data processing

Data processing of radar data can range from basic data display and application of gain while viewing radargrams during acquisition, through to complex and sophisticated post-acquisition processing

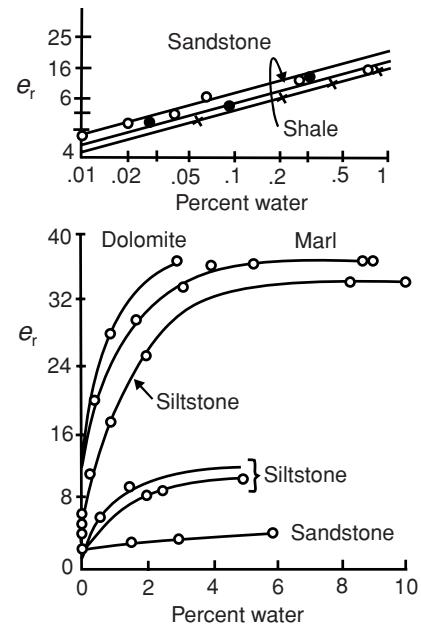


**Figure 13.18** Effect of soil moisture content of rock on  $\epsilon_r$ . From King and Smith (1981), by permission.

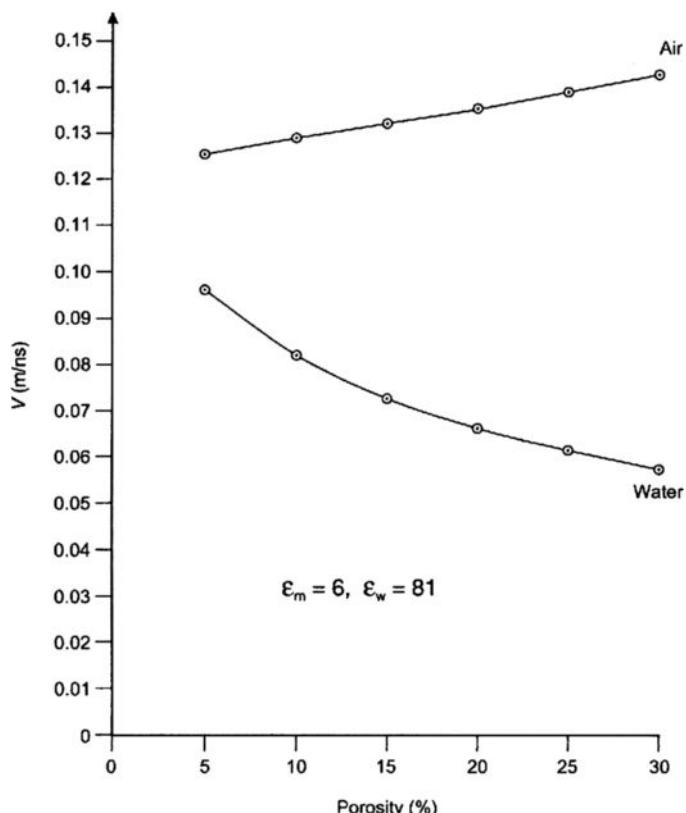


**Figure 13.19** Radar velocities as a function of porosity for air- and water-saturated granular materials.

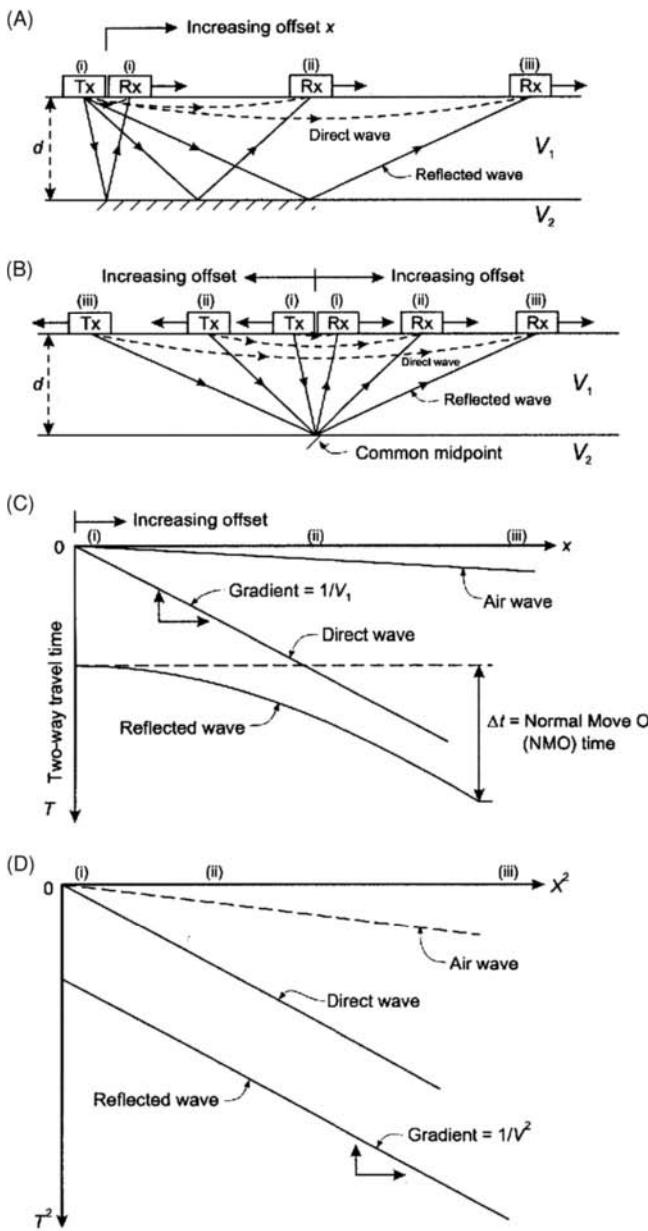


**Figure 13.20** (A) WARR sounding and (B) CMP sounding with (C) a time-distance ( $T$ - $X$ ) graph with normal moveout, and (D) the corresponding  $T^2$ - $X^2$  graph.

(Cassidy, 2009). An example of a data-processing work-flow is shown in Figure 13.22. It is important, the more so the more complex the processing work-flow, that the person involved in the data processing keeps a careful log of what processes have been applied to what data and in what order, otherwise confusion can quickly set in. It is preferable to design the anticipated work-flow before starting so that progress towards a desired outcome can be achieved and monitored. It is also important that the data processing achieves a specific benefit that aids the interpretation. It is possible to process data into oblivion! Like with any scientific experiment, applying a discrete data-processing step should be to test an idea and to measure an outcome. Data processing should never be used to try to

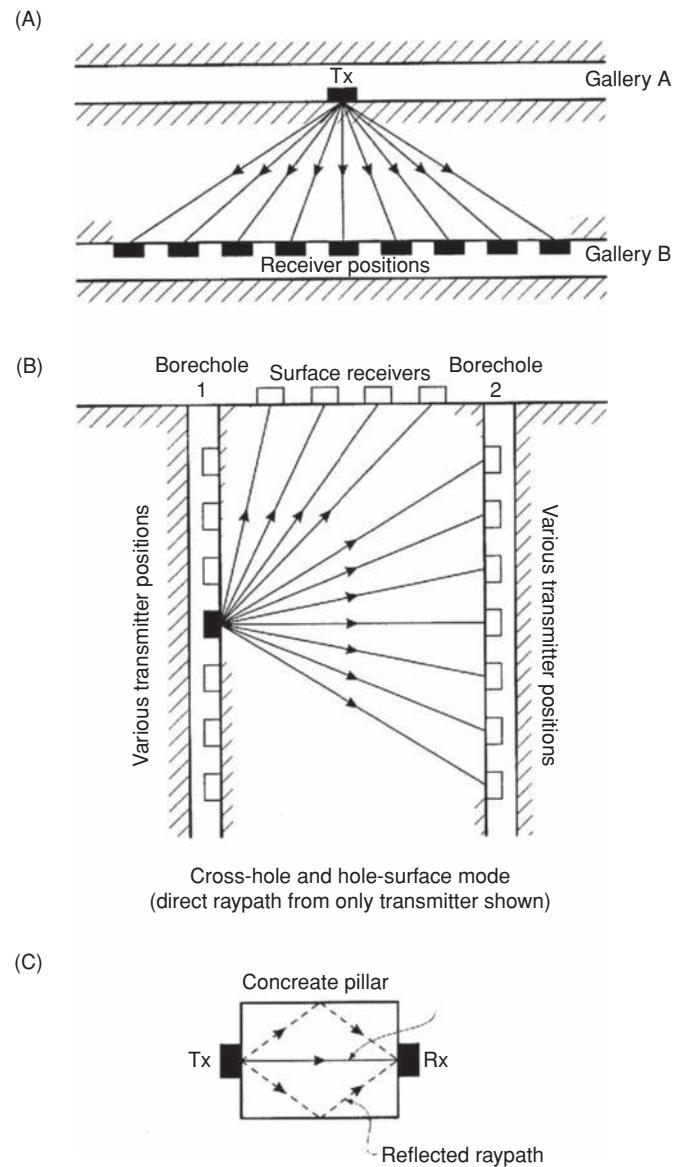


**Figure 13.21** Trans-illumination and cross-hole radar modes of data acquisition: (A) between galleries in a mine, (B) between boreholes or hole-surface, and (C) through a concrete pillar. In all cases the direct distance between transmitter (Tx) and receiver (Rx) antennae is known. Modes shown in (A) and (B) are also known as radar tomography.

extract sensible signals from poorly-acquired data; if they are not there, they will not appear as if by magic from all the noise! Field acquisition should always be optimised to achieve the best data quality and sufficient quantity (with areal coverage and appropriate spatial sampling). The level to which the data are processed should also be appropriate for the expected outcomes and available budgets.

Radar manufacturers have also been involved in developing software processing packages that are tailored to the type of surveys being undertaken; for example, utility scanning systems have viewing software with various degrees of sophistication to be able to map linear targets. It is then inappropriate to use such software for other

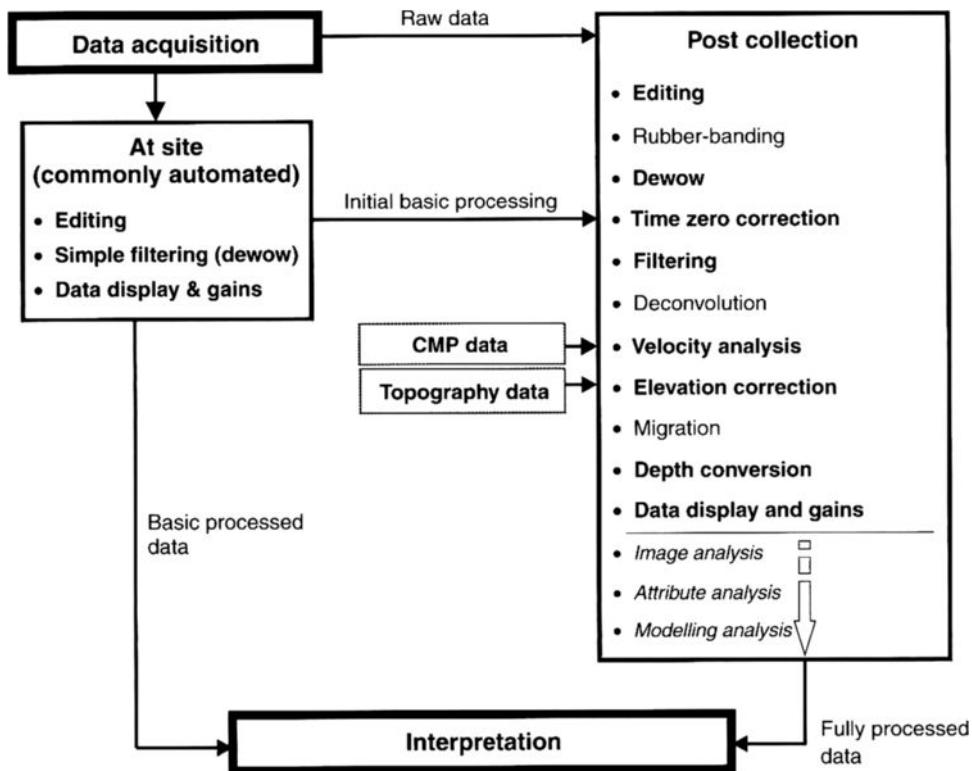


**Figure 13.22** An example of a data-processing work-flow for 2D bistatic, common-offset, reflection-mode GPR data. Processing steps in bold are usually essential for interpretation; the inclusion of any of the rest is dependent upon available time and budget, data quality and suitable software. After Cassidy (2009), by permission.

types of investigation, as the assumptions upon which the software is based may no longer be applicable and erroneous results may well be derived. Furthermore, blind processing without knowing what is being done to the data is also unhelpful.

It should also be remembered that radar data displayed on a radargram represent vectoral EM signals, not scalar signals such as in seismology. Some data-processing software treat both sets of waveforms as scalar commodities. In most instances this might be acceptable, but there might also be occasions when the EM responses arising from the electric and dielectric domains will result in characteristics that cannot be processed in scalar terms. Seismic software can be used for processing radar data and *vice versa* within limits. A good overview of radar data-processing has been provided by Cassidy (2009). Yilmaz (2001) has provided a comprehensive account of waveform data processing (focused on seismology) which can be applied in many cases to radar data, and many of the stages in data processing have been discussed briefly in Chapters 4 and 6. A list of the various data-processing stages is given in Table 13.5.

### 13.6.1 During data acquisition

All ground radar systems provide a means of filtering the data during acquisition. It is usually possible to set both highpass and lowpass filters to sharpen the signal waveform at the time of the survey. As with seismic filtering during acquisition, there is a significant element of qualitative feel to choosing appropriate filter settings.

More sophisticated digital systems allow vertical and horizontal filtering as well as more powerful gain-setting options with which to optimise the data quality. As a rule of thumb, it is advisable to keep the filter settings as broadband as possible so that potentially valuable data are not excluded during the acquisition phase. It is far cheaper to filter broadband data after the fieldwork has been completed than to realise that the data quality has been compromised by the use of filter settings that are too harsh, thereby necessitating a repeat of the fieldwork! Some radar systems allow the user to alter the gain and filters applied during acquisition but only affecting the displayed data; the raw data are recorded unfiltered and without signal amplification. This permits the interpreter to apply different filters and gain settings during post-acquisition processing.

Digital systems have the function of stacking a limited number of adjacent traces in order to improve the signal-to-noise ratio. This works well in areas where the structure is largely parallel or sub-parallel to the ground surface. When steeper structures are present, horizontal stacking over too many adjacent scans can produce lateral smearing and a defocusing of the radar image.

### 13.6.2 Wide-angle reflection and refraction (WARR) sounding

If two separate antennae are used, one as a transmitter and the other as a receiver, in bistatic mode, it is possible to determine the vertical variation in radiowave velocity (and hence relative dielectric

**Table 13.5** Data processing stages (modified from Cassidy, 2009).

Process	Description
<i>Editing</i>	Removal and correction of bad/poor data and sorting of data-files
<i>Rubber-banding</i>	Correction of data to ensure spatially uniform increments
<i>Dewow</i>	Correction for low-frequency and DC bias in data
<i>Time-zero correction</i>	Correction of start time to match with surface level
<i>Filtering</i>	1D and 2D filtering to improve signal-to-noise ratio and visual quality
<i>Deconvolution</i>	Contraction of signal wavelets to spikes to enhance reflection events
<i>Velocity analysis</i>	Determining radar wave velocities through media imaged
<i>Topographic correction</i>	Correcting for the effects of uneven topography
<i>Migration</i>	Removing diffractions and correcting the positions of dipping events
<i>Depth conversion</i>	Conversion of two-way travel time display to depth display
<i>Display gains</i>	Selection of appropriate amplification (gain) for data display to improve visualisation of data to aid interpretation
<i>Image analysis</i>	Using pattern or feature recognition tools on a radargram image
<i>Attribute analysis</i>	Transforming reflection data in terms of magnitude, frequency and phase (e.g. by using a Hilbert Transform)
<i>Modelling analysis</i>	Simulation of GPR responses to produce synthetic radargrams

constant). If only one antenna is available in monostatic mode, it is not possible to undertake WARR sounding and hence velocity determination can only be by either direct correlation with adjacent borehole logs, targets at known depths of burial, or by guesswork; the latter is the most commonly employed and may give depth estimates accurate to  $\pm 20\%$ .

In each of the WARR or CMP configurations, three types of wave may be identified:

- the airwave, travelling from the transmitter to the receiver through the air at the speed of radiowaves in air ( $0.3 \text{ m/ns}$ );
- the direct wave, travelling directly from the transmitter through the near-surface ground to the receiver at the speed of radiowaves in the near-surface medium ( $V_1$ );

- the reflected wave, travelling from the transmitter to the interface from which it is reflected to the receiver, also at the speed of radiowaves in the first layer ( $V_1$ ).

The travel times for both the airwave and the direct wave plot as straight-line segments on the  $T-X$  graph, but those for the reflected wave plot on a curved (hyperbolic) line. The difference in travel time between zero offset and at finite offset is the *normal moveout* (NMO) time (Figure 13.20C). However, when these travel-time data are plotted on a  $T^2-X^2$  graph, all the segments appear as straight lines (Figure 13.20D). The inverse gradients of each line are equal to the respective radiowave velocity squared. Further details of the velocity sounding techniques have been given by Arcone (1984).

The radiowave velocity determined for layer 1 is a time-averaged value over the interval from zero time to  $t_0$  and is hence a root-mean-squared velocity ( $V_{\text{RMS}}$ ). Where travel-time data are obtained for deeper reflections, the velocities determined from the above analysis for each layer are also RMS values. To determine a geologically more meaningful velocity for a particular layer, it is then necessary to use the Dix Formula to derive the ‘interval velocity’. This analysis is exactly the same as for seismic reflection data, and more complete details are given in Chapter 6.

### 13.6.3 Post-recording data processing

Only digital data can be processed post-recording. The degree of processing is often determined by (a) the budget available; (b) the time available; (c) data quality; (d) the available processing capability (software and hardware); (e) the requirement that the final interpretation justifies further analysis; and (f) the structural detail on the raw record meriting detailed quantitative data processing. Commercially available software for processing radar data includes RADAN (Geophysical Survey Systems Inc., USA) and REFLEXW (Sandmeier, Germany), among others.

The first step is to sort data-files, check trace headers, and edit the data to remove bad traces or traces with bad data. The edited data can be filtered in order to focus the image and to amplify the signals by applying a gain function. For many simple applications this is sufficient in order to locate subsurface features. For more detailed analysis, a wide range of processes is available, up to and including the same as for multifold seismic reflection data, including attribute analysis, details of which are given in Chapter 6.

It is essential that the trace geometry is checked and corrected as necessary to ensure that the traces are correctly located along a profile to adjust for variable speed of movement of the antennae when the transmit triggering is time-based. This means that the traces are triggered at a regular time increment (x traces per minute) and the spatial interval between traces is therefore dependent upon the speed of movement of the antennae along the profile. It is also important that fix marks are indicated along a radargram that tie to known positions. Correction for trace positions is known as *rubber banding*.

*Time-zero correction* is a useful technique as it allows the correction of jumps in the time of the reflection associated with ground level caused by electronic system effects, variations in the antenna-ground air gap, thermal drift, and so on, to a common time

datum, the so-called common *time-zero position* ( $t_0$ ). Correction of  $t_0$  improves lateral reflection continuity and helps with correlating reflections across sections.

Of particular significance is the ability to restore correct subsurface geometric relationships through the process of *migration*. Diffraction hyperbolae can be migrated back to the apex from which the diffraction originated. Dipping planar surfaces can be corrected to their correct position relative to ground locations. Otherwise, significant errors can be made by believing that the location of a particular subsurface feature on a raw radargram is exact, whereas it is only a virtual image and may be displaced from its actual position by significant horizontal and vertical distances. The principles of migration are discussed more fully in Chapter 6.

An example of successful migration of high-resolution radar data is given in Figure 13.23; a 1.5 GHz antenna was used to acquire data over the junction between two re-enforced concrete slabs 200 mm thick. Each slab contains re-enforcement dowels and a cage of re-enforcement bars ('rebars') at the slab boundary indicated in the dashed rectangle in the upper radargram, which shows the un-migrated data. The arrow points to the diffraction arising from the boundary between the two slabs. The edges of each slab sandwich a polystyrene sheet, which acts as a thermal expansion seal, about 2 cm wide, the top of which is sealed with bitumen. This leaves a small air gap about 1–2 cm deep below the top surface of the concrete slab. The air gap produces a strong signal evident as a bright event (at the head of the arrow). To provide rigidity to the slabs, each is fixed

to its neighbours by a series of single metal dowel rods, which can be seen as distinct diffractions except in the area of the cage, which shows a mess of diffractions (indicated by the dashed rectangle in Figure 13.23A). It would be difficult to separate out the individual rebars from this set of events. Furthermore, the diffraction tails from the dowels and rebar cage interfere with the coherency of the reflection from the base of the concrete slab and in turn from the roadway sub-base, making it difficult to be confident about the interpretation. However, by migrating the data, the diffraction tails are collapsed back to the points of origin and the individual rebars, especially in the rebar cage, can be picked out clearly. Although the migrated image shows the reconstituted signals from the rebars as circles, the metal re-enforcement was made of solid steel bars, not metal tubes. In the migrated radargram (lower part of Figure 13.23), the coherency of the reflections from the base of the concrete slab is significantly improved with that from the sub-base also showing greater lateral continuity compared with the un-migrated radargram.

*Depth conversion* is often a cause of significant interpretational errors as it usually requires the application of a single value of the dielectric constant across the entire time section, despite the fact that the dielectric constant may vary significantly both horizontally and especially vertically. If large variations in radiowave velocity are suspected, then great care must be taken when converting from the time domain to the depth domain if depths to targets are to be determined with any accuracy. More sophisticated software packages allow the application of time-variant values of dielectric constant, so results from such conversions are likely to be more meaningful. However, it is worth remembering that the radiowave velocity in materials such as concrete can vary by as much as 35% over vertical distances as short as 10 cm (Reynolds and Taylor, 1992). This variability is thought to be a function of the density of micro-cracking and the associated air content, both of which increase towards the surface of the concrete. An example of where a number of these data-processing steps have been applied to a coastal sedimentological investigation is shown in Figure 13.24.

*Attribute analysis* can also be undertaken on radar data. This is where, for example, a Hilbert Transform is applied to time-domain data to extract the magnitude, frequency and phase information contained therein. The magnitude is useful to display the raw energy reflected from an object or layer, helping to highlight *bright* or *dim spots*. Phase information may be more sensitive to dielectric changes (such as caused by contaminants, for instance) and can also help to identify thin layers and trace the continuity of reflections. Instantaneous frequency can help separate out reflections that arrive around the same time. Attribute analysis is only relevant in selected applications. With the right software it is easy to generate the attribute outputs; it is less easy to associate physical causality with the results. However, coupled with appropriate ground truth information, attribute analysis may be justified and beneficial in some cases.

Other methods of quantitative analysis are available through image analysis. Rather than operate on the waveforms of the data, the radargram is scanned for analysis of trends. For example, features such as reflections dipping in a particular direction can be picked out. Statistically significant trends can be identified from the entire

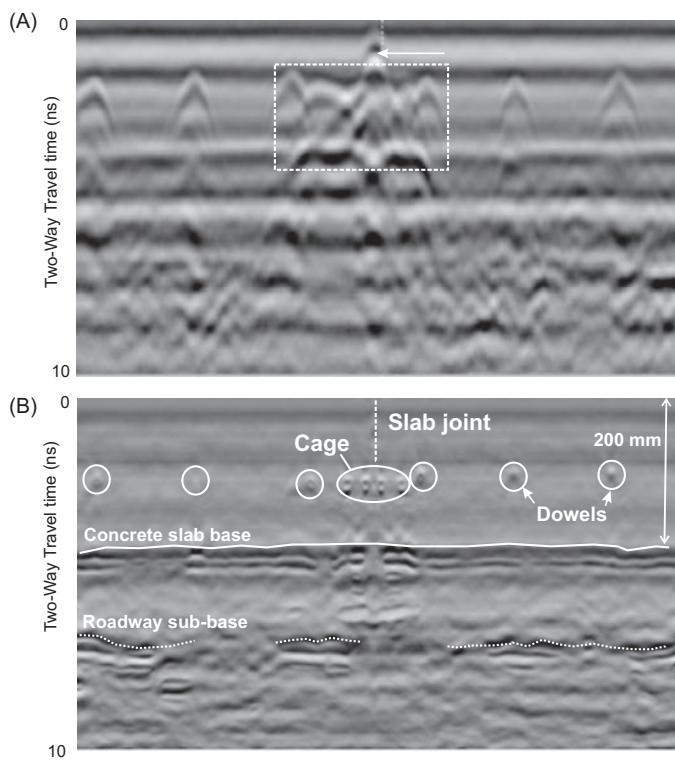


**Figure 13.23** (A) Unmigrated and (B) migrated high-resolution data (1.5 GHz) from a survey across the junction of two concrete road slabs. See text for details.

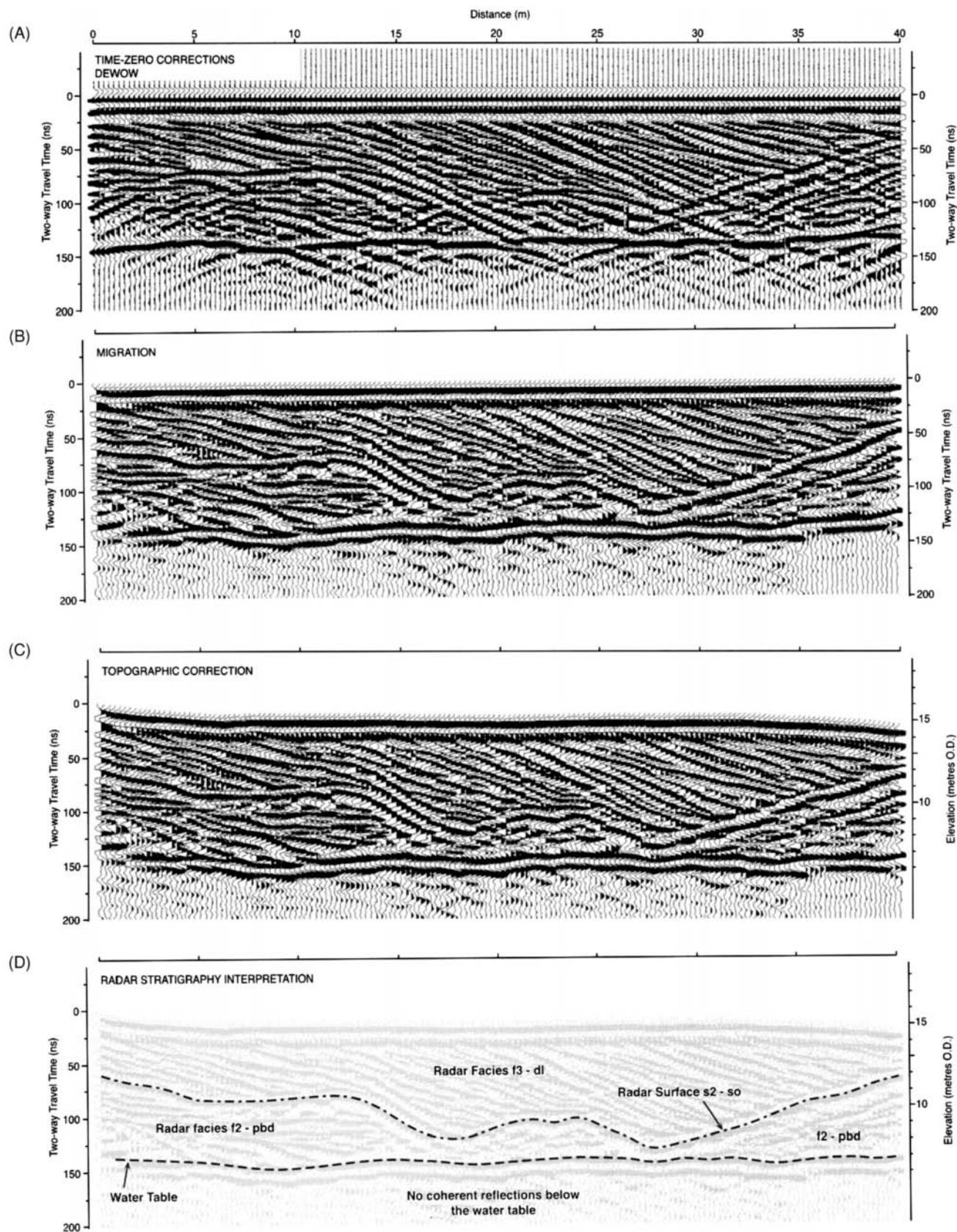


**Figure 13.24** Processing and interpretation sequence for a 100 MHz radar reflection profile acquired over a large coastal trough blowout at Raven Meols, Sefton, northwest England. From Neal (2004), by permission.

radargram and displayed automatically as line interpretations for subsequent manual analysis.

## 13.7 Interpretation techniques

### 13.7.1 Basic interpretation

Radargrams can be analysed in terms of identifying reflections and diffractions and measuring the two-way travel times to such identifiable events. By assuming, or having measured, a value for the appropriate relative dielectric constant – and hence obtained a realistic radiowave velocity – the two-way travel times to specific events can be translated into depths. Where radar data have been acquired over a regular grid, and reflections identified over significant areas, it is then possible to produce posted two-way travel time maps, or *isopachyte maps*, indicating the depth to, or thickness of, a particular layer, given a realistic measure of the radiowave velocity.

This approach is particularly prevalent in road pavement analysis, where the number of discrete layers is usually well constrained with up to four parallel to subparallel layers (bound layer of bitumen or concrete, granular layer, upper and lower subgrades). The travel times to interpreted interfaces can be extracted from radargrams and, using an appropriate radiowave velocity for each of the discrete layers, the depths to each interface can be determined. There would need to be careful consideration of the accuracy of picking the onset of the various reflections on the radargrams as well as the likely reliability of the radiowave velocities used to derive depths. Local variability in radiowave velocities can occur within concretes (see Section 13.4; different mixes, even though all within specification), or due to changes in moisture content (see Section 13.4). Individual horizons, such as the sub-base, may have been prepared in layers, and these may be detected. In some cases the boundary between layers may be fuzzy – so where does the radar reflection come from? Is it always from the same relative position? Sometimes, engineering as-built drawings show the major boundaries, but radar surveying may detect others, such as those formed by the process of construction. For example, in one major radar survey, engineering drawings indicated a thick ( $>7$  m thick) layer of uniform engineered fill. However, the radar data revealed consolidated horizons that had been formed by vehicles as they carried material across the site. The compacted material provided layers along which water flowed and changed the local dielectric permittivities so that these internal layers could be identified. These are often questions that need to be answered in engineering projects. In all cases, a statement as to the errors and limits of measurement should be made. There is no such thing as an absolute measure of depth using remote methods, particularly radar.

The interpreted data can be displayed in a wide range of ways using specialist 3D radar data-processing packages, computer-aided design (CAD) systems and 3D graphics software packages. While the final output may be extremely colourful and fancy, it should be remembered that the basic data analysis may be just that – basic! While the final drawings may indicate millimetre accuracy, is this justified? At present, the uncertainties and local variability in

the dielectric properties of materials and the subjective nature of defining the onset position of reflections tend to make claims of such accuracy unjustified. As the electrical and dielectric properties of materials used in road pavements become better known, accuracies and reliabilities will improve.

As the resultant radargrams are displays of waveforms as a function of two-way travel time with distance along a profile, the style of interpretation is very similar to that used in reflection seismology, as discussed in Chapter 6. Equivalent terms in seismic stratigraphy can be used in radar interpretation, such as radar *surfaces*, radar *packages* and radar *facies*, but not radar *sequence* or *sequence boundary* as confusion can arise from the specific meaning of the term ‘sequence’ in sequence stratigraphy. Reflection events can be defined according to the type of upper and lower boundary (Figure 13.25A), the 3D external form of the radar package (Figure 13.25B), and the configuration of the reflection (Figure 13.25C). The latter can be defined by their shape, dip and relationship between reflection events and by the degree of lateral reflection continuity (Neal, 2004). Neal recommended that radar reflection configurations should be described in terms of the shape and dip of reflections; the relationship between reflections; and reflection continuity. However, note must be taken that sedimentological facies are three-dimensional and often 2D radargrams are interpreted using radar facies analysis. Yet the radar characteristics can be as much a function of the relationship between the orientation of the sedimentological features and the azimuth of the radar profile and the orientation of the radar antennae. Consequently, radar facies characteristics are not unique and should be defined according to the style by which they are being analysed, i.e. 2D sections or 3D data volumes. Furthermore, different sedimentological regimes may give rise to different sets of definitions of radar facies and they are not readily transferable from one sedimentological regime to another. Consequently one set of investigators may define their radar facies differently to those of other people.

Facies analysis recognises that there can be zones within a radargram that display different styles of reflections, diffractions, noise, amplitudes, and so on, between discrete primary reflections, i.e. zones have a different *texture*. Their classification is by eye of an experienced interpreter. However, image analysis can take this process; quantitative measures of textures can be developed in conjunction with neural network classifiers. This has been discussed in detail by Moysey *et al.* (2006), for example.

In addition to facies mapping, it is possible to use the variations in amplitude displayed on the radargram as an indication of subsurface conditions relating to attenuation. For example, areas of high attenuation may reveal zones with elevated conductivities that may be associated with pollution, or clay pockets. Subsurface cavities may be evident by the resonance within the void space, indicated on the radargram as a series of large-amplitude pulses that are laterally very restricted. Zones of cobbles or severely distorted strata may be evident by the loss of coherency of primary reflection events, perhaps also associated with diffractions. Delamination of road pavements may also be indicated by diagnostic character changes on radargrams (delamination may also be evident when imaged using infrared thermography under appropriate conditions).

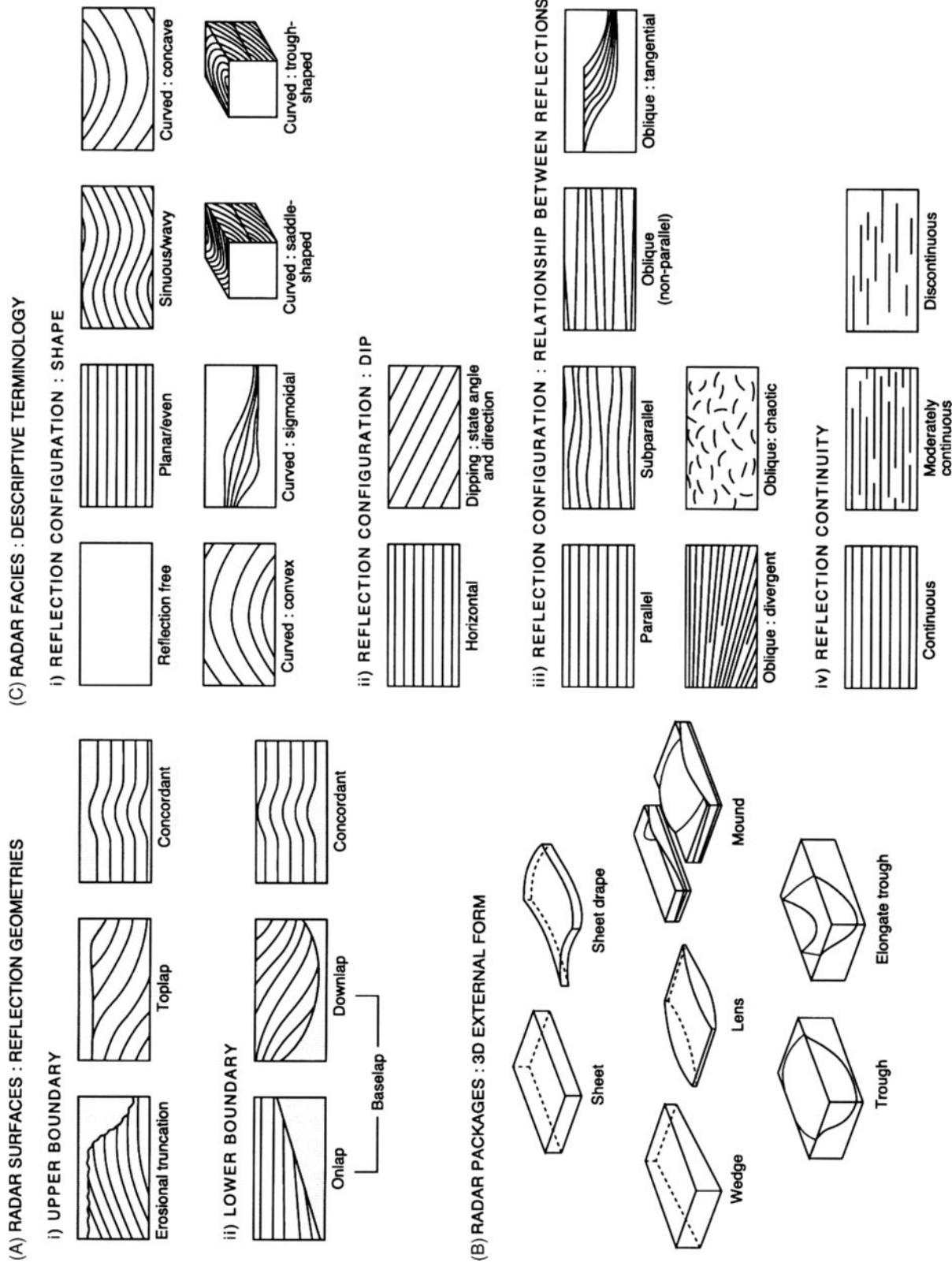


Figure 13.25 Terminology to define and describe radar facies, packages and surfaces. From Neal (2004), by permission.

### 13.7.2 Quantitative analysis

Basic depth determination depends upon an adequate knowledge of the radiowave velocity and its vertical and lateral variation within a given survey area. Where WARR/CMP data have been acquired, a detailed picture of the velocity field can be obtained. Consequently, geologically diagnostic values of the radiowave velocity, or more particularly of the relative dielectric constant, can be used to aid interpretation.

Where detailed quantitative attribute analysis has been undertaken of the recorded radiowave data, such as amplitude analysis, reflection coefficient determination, as well as variations in  $\epsilon_r$ , then a much more comprehensive understanding of a site can be gained. Indeed, given adequate data quality, careful processing may yield more valuable information about the petrophysics of a given geological or engineering regime than would otherwise have been possible. High-level processing and analysis are becoming much more important where detailed discrimination is required, such as in hydrocarbon exploration and reservoir engineering, and in contaminated land investigations. The use of ground radar in both cases is continuing to develop considerably.

### 13.7.3 Interpretational pitfalls

The two commonest pitfalls in the interpretation of radar data are (a) not being able to identify the ground surface, and (b) misidentifying each positive band on a radargram as being caused by a discrete horizon, even though the incident wave train comprises several positive pulses. The time zero ( $T_0$ ) is the transmit on time at the antenna, which lies at a finite distance above the ground even though the box in which the antenna is located is in contact with the ground, so the event associated with the ground surface will lie at some short time after  $T_0$ . The easiest way to identify ground level, especially with antennae with centre frequencies  $\geq 500\text{MHz}$  (some low-frequency antennae are too heavy to lift easily), is to raise and lower the antenna above the ground surface in what is called a *lift test*. A distinctive cusp appears on the radargram (Figure 13.26, between the white arrows) and clearly indicates where the ground level is represented as the travel time to the ground increases (indicated by the cursor arrow) as the antenna is lifted above it (Pringle *et al.*, 2009). This also serves an additional purpose as it helps to identify

where any system noise is present on the radargram. Some antennae generate characteristic system noise that occurs at a particular two-way travel time and which is independent of the position of the antenna or the ground conditions. The noise event remains at a constant travel time during the lift test. It is important to be able to identify noise on radargrams, both as a quality control check and also to be able to differentiate noise signals from primary events related to targets. In one radar survey, a contractor carefully extracted the travel times arising from an event that he had identified on radargrams across a survey area and produced a map showing apparent slight variations in this time. He interpreted this event to be due to a continuous buried surface at around 1 m depth. Upon excavation, nothing was found. He had misinterpreted the noise signal because he failed to do a lift test to identify such signals!

The over-identification of the number of layers highlights a real difficulty, especially with analogue radar data: how are the primary reflections to be identified from multiples, secondary events, and the tail of other primary reflections? Furthermore, when waveforms intersect each other, they cause interference which may give the appearance of a ‘termination’ of one dark band with respect to another. Geologically, this may be misinterpreted as one horizon abutting against another. If the geological conditions are such that the radargram is ambiguous in this regard, then there is justification for detailed quantitative analysis if the data have been recorded digitally. If the data have been produced as an analogue record, there is little that can be done to resolve the dilemma. The quantitative analysis can pick out likely multiple events (these are purely time repeats of earlier primary events), and by deconvolution, the shape of the downgoing wave train can be determined and hence primary reflection events identified. Subsequent migration can help to reduce diffraction hyperbolae and, by restoring some of the subsurface geometry of primary reflections, can help to resolve geologically significant detail that otherwise would have been obscured.

The difficulties in distinguishing between geologically significant reflections and extraneous reverberations, multiples, noise, diffractions, off-section ghosts, and so on, make the determination of soil and rock stratigraphy difficult in some cases. In others, the stratigraphy can be determined quite readily; one such example (from Best and Spies, 1990) is shown in Figure 13.27. An analogue record obtained in 1976 is compared with a digital radargram produced

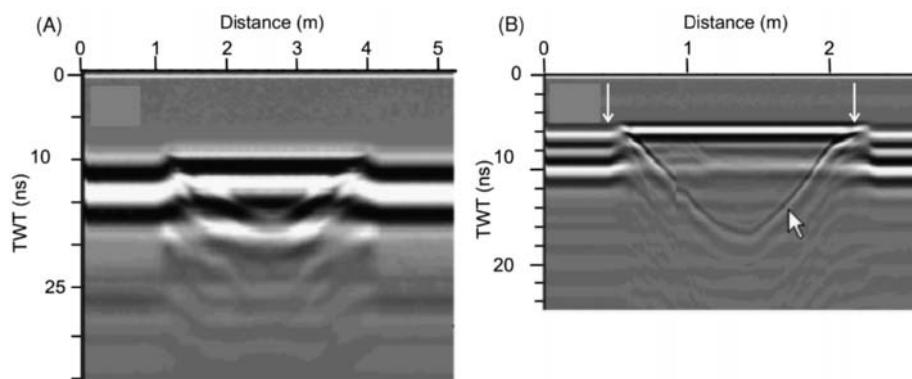


**Figure 13.26** Lift tests undertaken with (A) a 250 MHz and (B) a 500 MHz antenna inside a retail premises to help to identify the reflection associated with the ground surface and any static system noise. From Pringle *et al.* (2009), by permission.

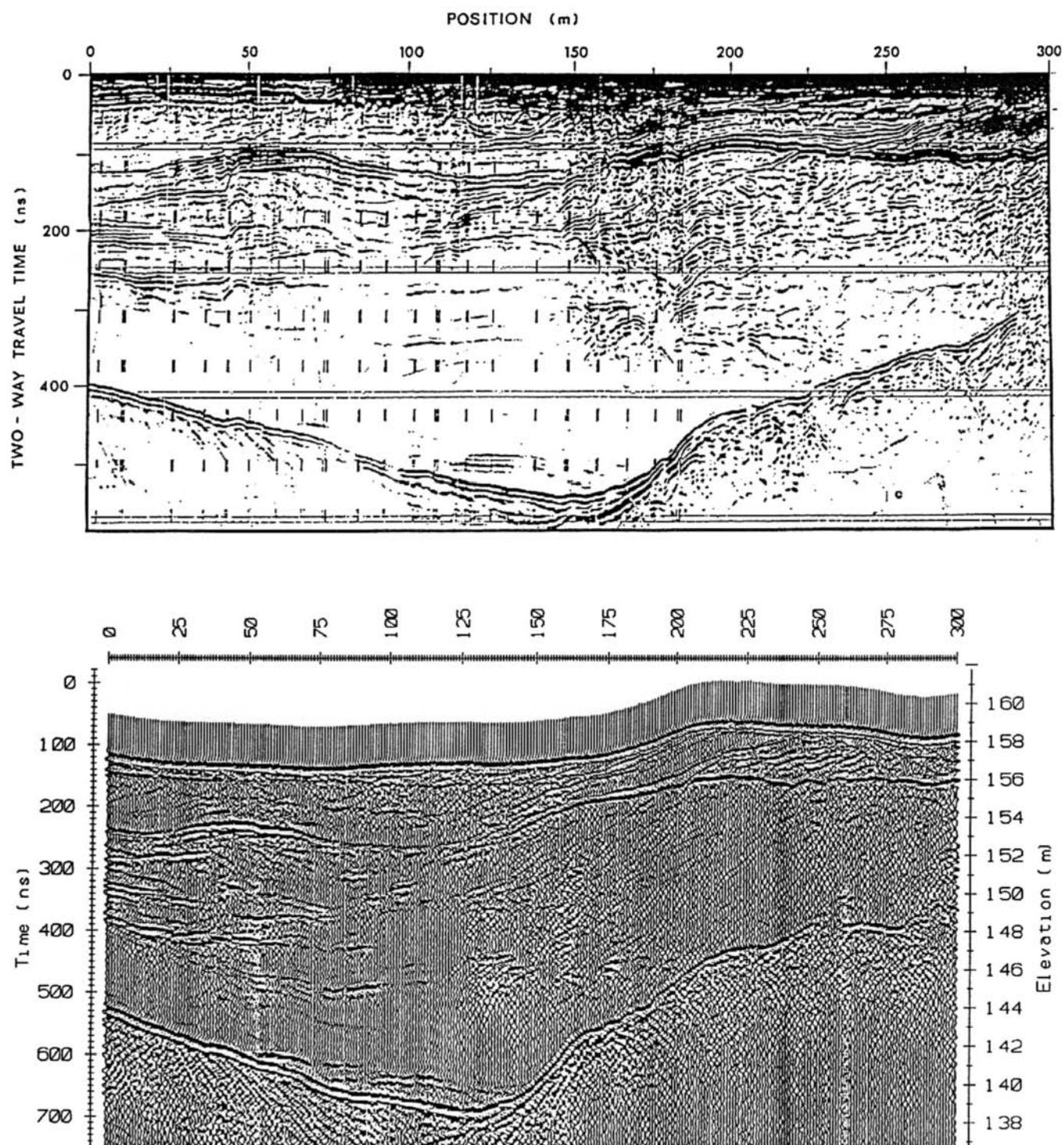
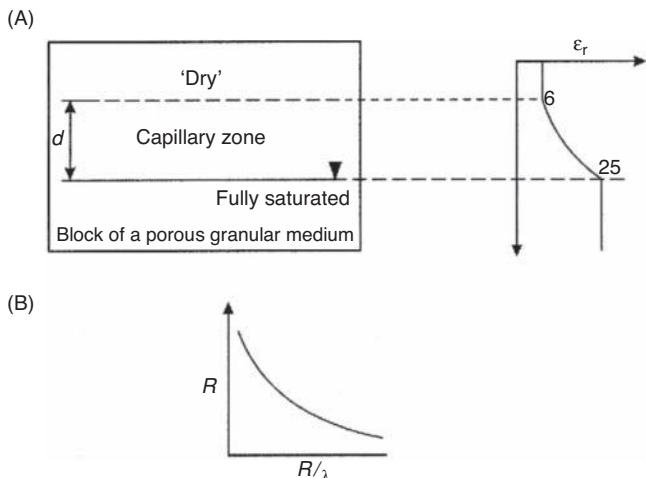


Figure 13.27 Radargram obtained in 1976 compared with one in 1990. From Best and Spies (1990), by permission.



**Figure 13.28** Effect of thickness of a capillary zone on the observed reflection strength arising from the water table. (A) A capillary zone of thickness  $d$  over the water table has a relative dielectric constant ( $\epsilon_r$ ) which increases to a maximum when fully saturated. (B) The amplitude reflection coefficient ( $R$ ) decreases as the ratio of the thickness of the capillary zone to wavelength of incident increases.

over the same area some 14 years later. While the gross structure is evident in the 1976 analogue record, the detail is much crisper in the later digital record.

There are situations when the water table is detectable on a radargram and others where it is not. The reason for this is that the ratio of the thickness of the capillary zone to the wavelength of the incident radiowaves needs to be small (i.e.  $d < \text{wavelength}$ ) in order to provide sufficient contrast in relative dielectric constant between the unsaturated and saturated material to reflect a significant proportion of the energy (Figure 13.28). If the capillary zone is thick with respect to the wavelength, then the rate of change of relative dielectric constant with depth through this zone is small. The effect of this is that, for each incremental increase in the relative dielectric constant, a proportion of the incident energy is reflected so that the total reflected energy is smeared from the capillary zone, and hence the resulting reflection amplitude is too low to be detected with any clarity. In contrast, if the transition from dry to saturated is virtually instantaneous (e.g. the change in relative dielectric constant is from 6 to 25), then the amplitude reflection coefficient  $|R|$  is 0.34 (using the expression in Box 13.2), which is a very strong return.

# 14

## Ground-Penetrating Radar: Applications and Case Histories

### 14.1 Geological mapping

Ground-penetrating radar has been demonstrated to be a valuable tool in mapping sediment sequences with a high degree of spatial resolution on both land and through freshwater. An example of the improvement in data quality in mapping soil stratigraphy was given in Figure 13.27. Other examples are given in Section 14.8. A common failing of the analysis of radargrams acquired in stratigraphic investigations is over-interpretation of the data. Too often, apparently coherent events are taken as indicating individual sedimentary interfaces without due regard for the physics of thin-bed interference, vertical and horizontal resolution limits, the finite size of the first Fresnel zone, migration effects, the complex form of the incident wave train, and so on. It is in these applications that data processing is likely to play an important role; for example, see the paper by Neal (2004).

#### 14.1.1 Sedimentary sequences

GPR has been applied extensively to sedimentological investigations and Neal (2004) has published a comprehensive review. Additional examples have been provided by Bristow and Jol (2003) and Bridge (2009), and, specifically for aeolian sand dunes, by Bristow (2009) and for coastal environments by Buynevich *et al.* (2009). Bristow and Pucillo (2006) have provided an example of using facies analysis to interpret a radargram acquired across a vegetated coastal fore-dune ridge at Guichen Bay in South Australia (Figure 14.1). The processed and topographically corrected profile is shown in the upper image. The middle picture shows an interpretation based upon radar facies analysis using reflection patterns to distinguish between foreslope accretion (seaward-dipping reflections) and rearslope accretion (landward-dipping reflections) within the foredune ridge. The water table beneath the dune sediments gives rise to a continuous high-amplitude subhorizontal reflection that cuts across the

inclined reflections associated with the sedimentary structures. The bottom image in Figure 14.1 shows the interpreted radar facies and dune facies. This radargram also shows a multiple reflection from the water table that produces a mirror image of the surface topography below the water table. Failure to identify these events as mirror multiples would lead to significant misinterpretation of the section.

The use of radar facies in the interpretation of coastal dune sequences has been discussed by Neal and Roberts (2000) for investigations at two locations near Formby Point on the Sefton coast, west Lancashire. This area comprises an extensive coastal dune barrier system comprising a series of unconsolidated Holocene sediments often over 30 m thick. A range of deposits associated with active and recently active coastal dunes is also present. In the southern part of this dune system, at Raven Meols, a large active trough blowout has developed covering an area 300 m long and 100 m wide, and which can easily be identified between Hightown and Formby Point on aerial photographs. A series of intersecting radar profiles were acquired using a 100 MHz antenna with a PulseEKKO system. Radar profiles through the long axis of the blowout and at right angles are shown in Figure 14.2. Radar surfaces (RM-A, B) and radar facies (RM-1, 2 and 3) are indicated. The water table is evident by a strong near-horizontal event (indicated by an arrowhead and WT). Note that due to the large difference in radiowave velocity above (0.135 m/ns) and below the water table (0.06 m/ns), the vertical depth axis scale shows different vertical distances above and below the water table. A description of the radar stratigraphy of the profiles and their geological interpretation is given in Table 14.1. It is important that the events on the radargram are described in terms of the waveforms present, whereas the interpretation describes the likely geological causes of those radar characteristics. The radar facies are separated by radar surfaces – the character of each can provide important information about the relative contrasts in physical properties and types of materials at that interface. The radar facies identified have reflection characteristics representative of primary sedimentary structures and their formation under differing depositional conditions.

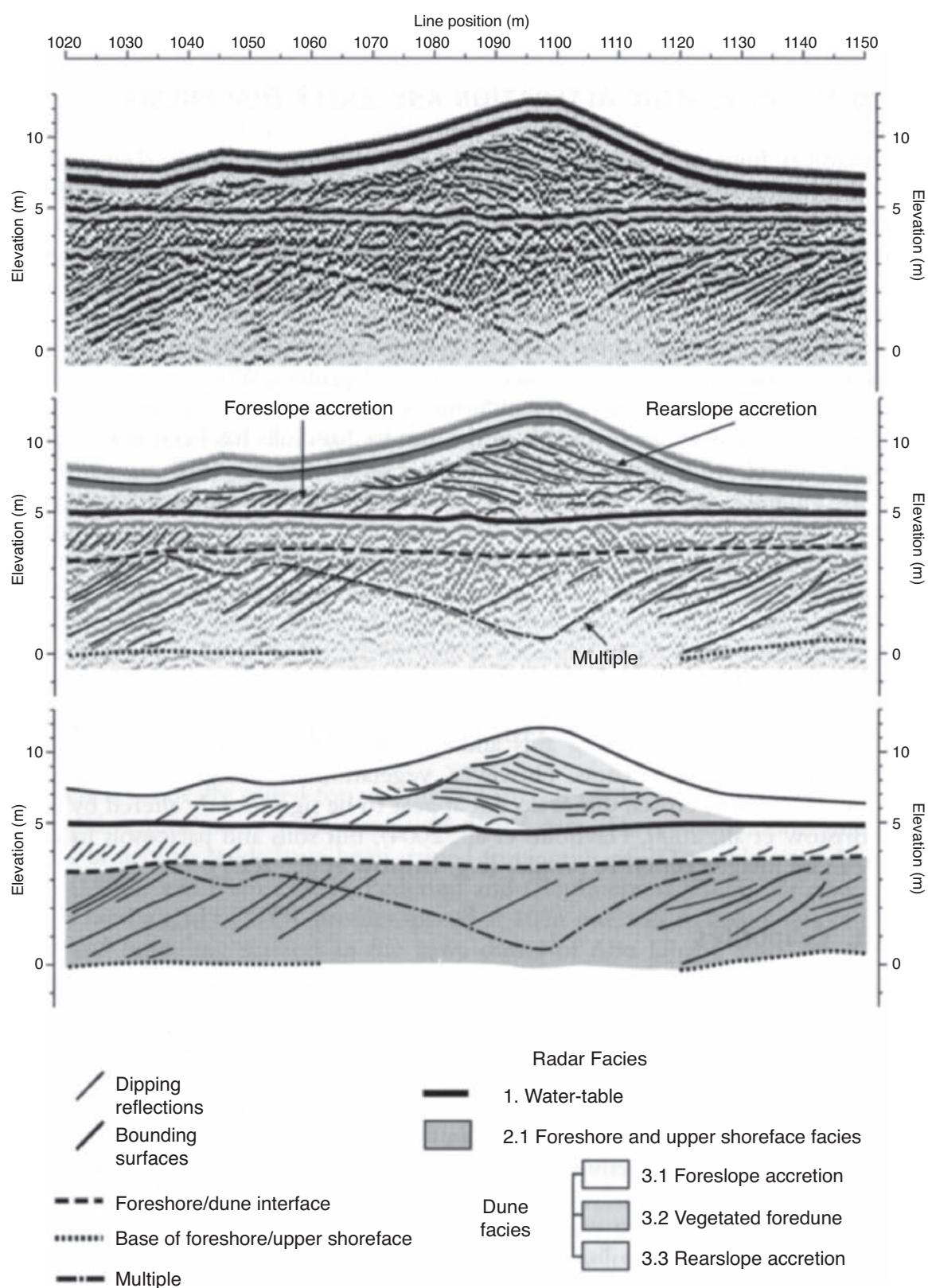


**Figure 14.1** (Top) Processed and topographically-corrected radargram across a vegetated coastal sand dune at Guichen Bay, South Australia; (middle) annotated radargram showing the radar facies interpretation; and (bottom) combined radar facies and dune facies interpretations. From Bristow and Pucillo (2006), by permission.

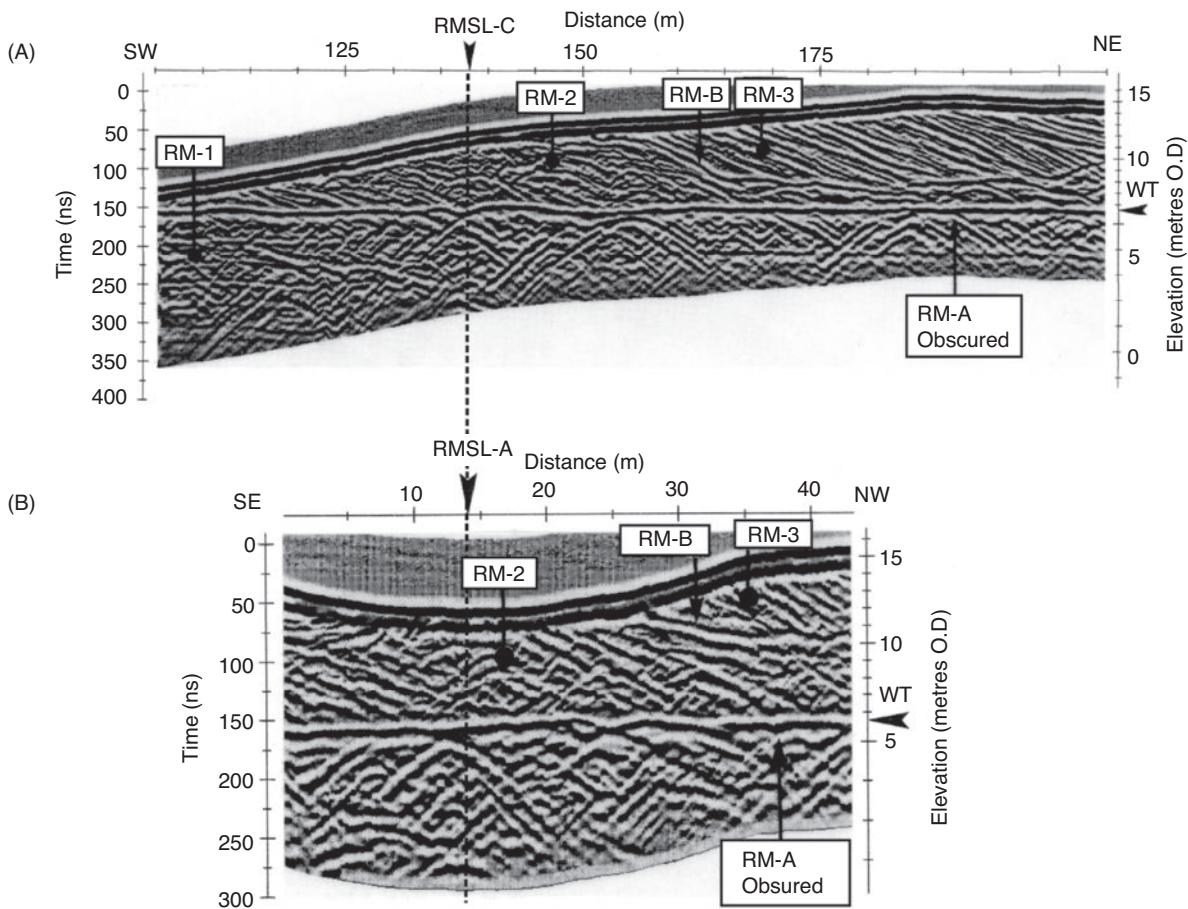


**Figure 14.2** 100 MHz radargrams for two orthogonal profiles across the Raven Meols dune blowout, Sefton, near Liverpool. (A) Profile A through the blowout long axis, and (B) Line C; the intersection of the two profiles is shown by the dashed line. Radar facies (RM) are discussed in the text. WT = water table. From Neal and Roberts (2000), by permission.

The second example in the Sefton coastal area is at Woodvale in the Ainsdale Hills. At this location the dune belt is about 3 km wide and consists of a series of aeolian dunes at least 12 m thick that extend well below the shallow water table (<1 m depth). Several boreholes have indicated that parts of the sequence comprise a series of peats and humic deposits that date back to around 5100  $^{14}\text{C}$  years BP. As the few boreholes available are widely spaced it is extremely difficult to correlate these peat horizons. However, radar profiles were undertaken approximately parallel to or at right angles to the presumed gross depositional strike. Two orthogonal profiles acquired at Woodvale are shown in Figure 14.3 on which the radar surfaces (WV-A, B) and radar facies (WV-1, 2) are indicated. The point of intersection between the two profiles is indicated by the dashed line. There appears to be little penetration beneath the base of the aeolian dunes (radar sequence boundary WV-A). This was thought to be due to the presence of an underlying peat horizon on top of thicker silt or muddy sands, as suggested by nearby boreholes. The aeolian deposits comprise two radar facies (WV-1 and 2) separated by radar surface WV-B. A series of broad, low, undulating dunes developed immediately on top of the peat. The second phase of dune formation, as represented by radar facies WV-2, was

probably due to extensive sand sheet development which rapidly buried the older dune topography.

### 14.1.2 Lacustrine environments

Ground radar can be deployed over frozen lakes and has been used to investigate sub-lake sediments through freshwater up to 27 m deep; an example of a through-ice survey is shown in Figure 14.4A. The lake ice provides a stable platform over which the radar was towed. The freshwater within the lake is virtually transparent to radiowaves and the lake sediments are clearly evident through 4.8 m of freshwater. The resolution of the system (100 MHz antenna) is such that individual horizons within the sediment can be picked out. Note that the reflection returns associated with the lake-bed comprise at least four bands owing to a ringy source. Furthermore, the period of the initial wave train (around 70 ns) might be misinterpreted by some as indicating the presence of up to 6 m of ice (radiowave velocity through ice is 0.167 m/ns). The actual thickness was only 0.15 m. The two-way travel time through the ice layer would only have been around 2 ns. This shows effectively that, using a low-frequency antenna (100 MHz), near-surface features cannot

**Table 14.1** Description and interpretation of the radar stratigraphy from Raven Meols blowout, as shown in Figure 14.2. After Neal and Roberts (2000) and Neal (2004).

	<i>Radiowave velocity</i>	<i>Description</i>	<i>Geological interpretation</i>
Radar facies RM-1	0.06 m/ns	Series of subhorizontal, laterally continuous, subparallel reflections. Partly obscured by a series of complex, interfering hyperbolae developed below the top of the water table	Upper foreshore sediments, deposited as part of a progradational beach-dune complex. Now lying below a fresh groundwater table
Radar surface RM-A		Obscured by complex series of interfering hyperbolae developed below the top of the water table	Contact between the underlying beach deposits of RM-1 and overlying dune deposits of RM-2
Radar facies RM-2	0.135 m/ns	Series of cross-cutting reflections with limited lateral continuity. Reflections have low to moderate apparent dips and downlap onto RM-A and toplap onto RM-B	Complex series of aeolian cross-strata separated by cross-cutting bounding surfaces. Indicative of dune development in the presence of at least a partial vegetation cover
Radar surface RM-B		Laterally continuous, undulating reflection with complex topography	Thin humic soil horizon representing a dune stabilisation surface that has been buried by the recently deposited aeolian sediments of RM-3
Radar facies RM-3	0.135 m/ns	Laterally continuous, subparallel, generally moderate to high-angle reflections. Occasionally display low-angle cross-cutting relationships. All reflections downlap onto RM-B	Packets of cross-strata deposited as the vegetation-free depositional lobe of the blowout has extended progressively northeastwards. Low-angle third order bounding surfaces occasionally seen representing minor reactivation surfaces

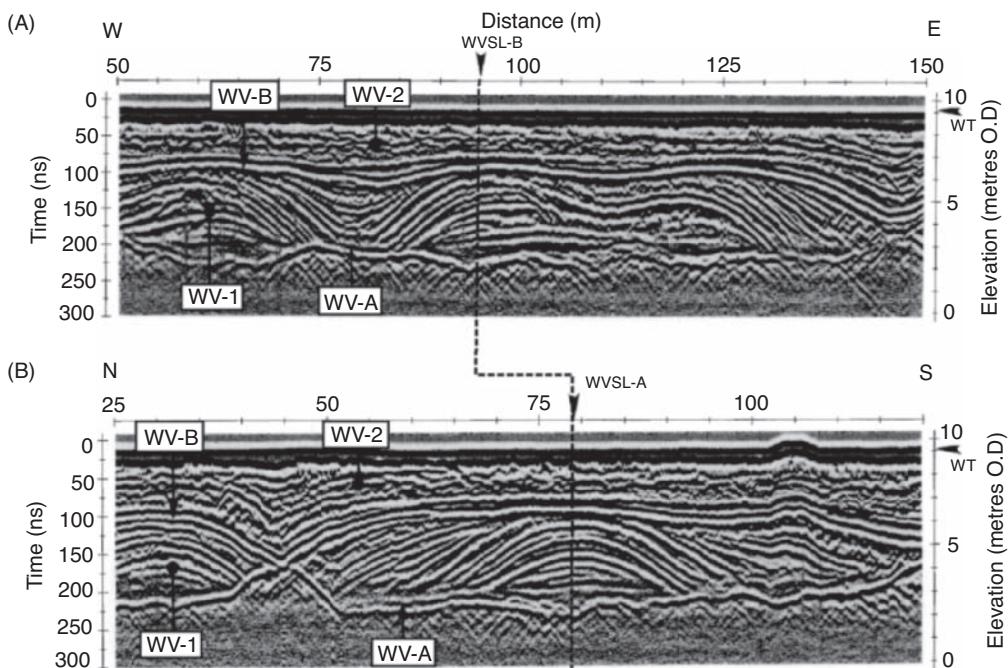


**Figure 14.3** 100 MHz radargrams for two orthogonal profiles at Woodvale, Sefton, Lancashire. (A) Profile A orientated perpendicular to the presumed gross depositional strike of the dune system, and (B) profile B, at right angles to Line A; the intersection of the two profiles is shown by the dashed line. Radar facies (WV) are discussed in the text. WT = water table. From Neal and Roberts (2000), by permission.

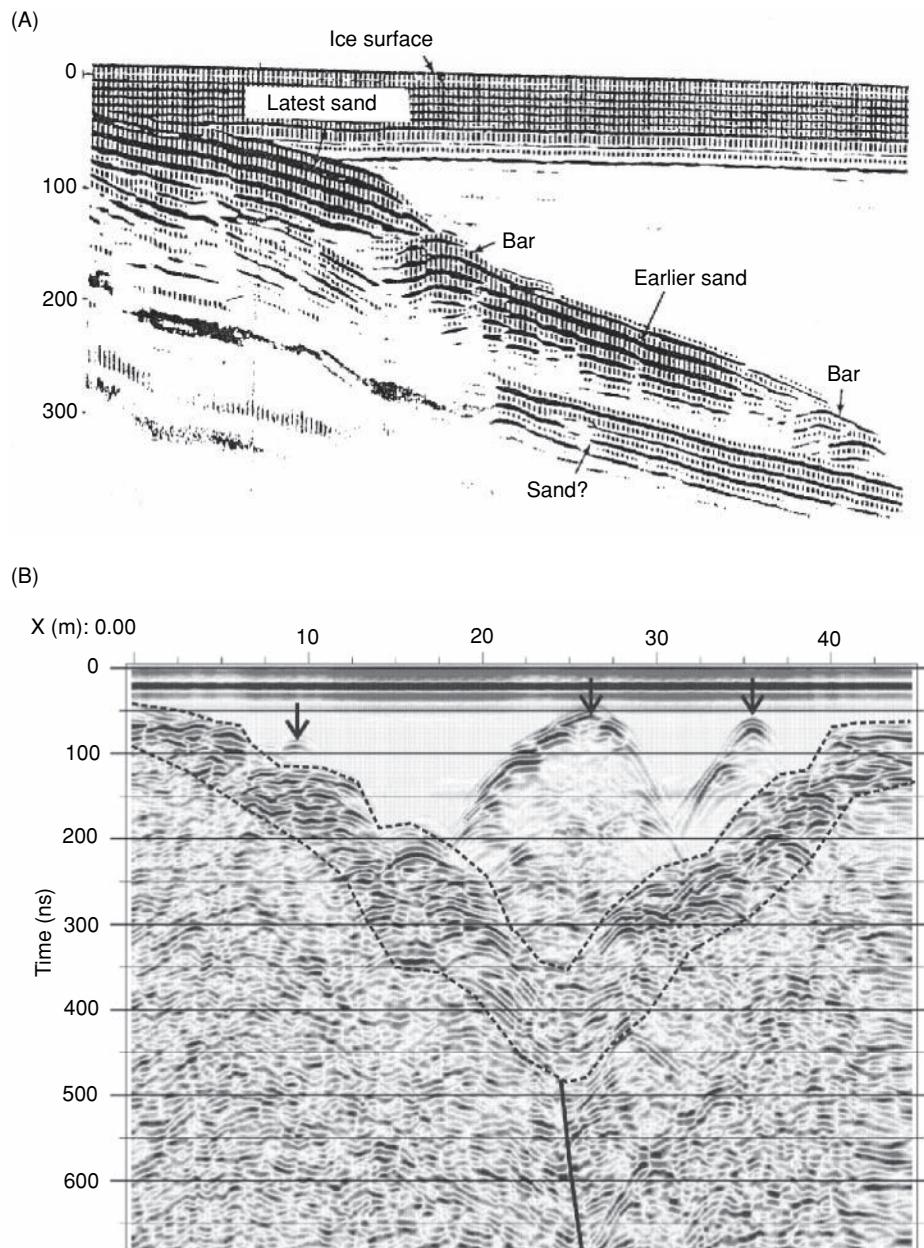


**Figure 14.4** (A) Radargram over an ice-covered lake obtained using a 100 MHz antenna. Maximum water depth is 4.8 m; width of profile is 25 m; 500 ns two-way travel time range. From Mellett (1993), by permission. (B) Mala RAMAC 100 MHz profile across part of Tsho Rolpa, a glacial lake in Nepal. See text for details. [C]

be resolved at all as they are totally masked within the initial ground-coupled wave train. The radiowave velocity through the freshwater can be calculated knowing the depth of water (about 4.8 m) and the total two-way travel time (around 300 ns). These values would give a radiowave velocity of 0.032 m/ns (from  $2 \times 4.8/300$ ), assuming low-loss media. As a double-check, the relative dielectric constant of water is 81, which thus gives a radiowave velocity of  $0.3/\sqrt{81}$ , or 0.033 m/ns (refer to Box 13.1 for the equation).

Another example of a radargram through water is shown in Figure 14.4B, which is for a 100 MHz profile across part of a glacial lake (Tsho Rolpa) in the Nepalese Himalayas. The radar system was

deployed in an inflatable boat with Mala RAMAC 100 MHz bistatic antennae situated on the wooden floor of the boat. Bright events can be seen in a surface zone highlighted between dashed lines. This zone was due to reflections and diffractions from coarse bouldery supra-glacial moraine overlying stagnant glacier ice. The travel time through the water (350 ns) indicates a depth of about 5.8 m. The ice (500 ns) with a radiowave velocity of 0.167 m/ns is at least 42 m thick at the start and end of the profile. The deepest part of the water overlies what was interpreted to be a former crevasse (indicated by the solid black line). Three sets of events are highlighted by arrows. These refer to reflections/diffractions off boulders that lie off the

line of the profile. The cause of these off-section reflections was well known as the boulders causing them had previously been above the lake level but had become submerged as the underlying ice had melted. This also nicely demonstrates the effect of off-section reflections. For more details of GPR in glacial hazards, see Section 14.3.4.

### 14.1.3 Geological faults

One of the advantages of the GPR method is the high resolution achievable compared with that possible using seismic reflection. This is exemplified by a detailed 3D GPR survey undertaken at Calf Paddock, in the north of South Island, New Zealand. The survey was designed to investigate a section of the Alpine Fault Zone that has ruptured various late Pleistocene and Holocene fluvial deposits of the Maruia River. The local geology comprises about 30 m of gravel overlying basement schist. A succession of offset terraces and stream channels provide direct evidence of recent vertical and horizontal displacements associated with the fault. One terrace is offset vertically by about 1.5 m, and an abandoned stream channel is dextrally displaced by about 10 m. The GPR survey, associated data processing and interpretation have been described by McClymont *et al.* (2008). This case history also demonstrates a very effective application of detailed data processing, including 3D migration and attribute analysis, and interpretation using the facies analysis approach promoted by Neal (2004). The survey was acquired using a PulseEKKO GPR unit linked to a self-tracking laser theodolite. A broadside acquisition geometry was used with 1.0-m offset 100 MHz bistatic antennae to record GPR traces (sampling rate 0.5 ns) at roughly 0.25 m intervals along 61, approximately 116-m long, lines separated by 0.5 m. The profile lines were oriented perpendicular to and centred about the principal fault trace. Various data-processing stages starting with the original unmigrated GPR data are shown in Figure 14.5. A thin, low-velocity ( $\sim 0.07$  m/ns) surface soil layer covers the site and contains boulders. These gave rise to dispersive diffractions (arrowed in Figure 14.5A) that could not be collapsed using standard migration techniques but were removed effectively using 3D  $f\text{-}k$  filtering (Figure 14.5B). The data were further processed using 3D topographic migration, depth conversion and  $3 \times 3$  trace  $f\text{-}xy$  deconvolution followed by muting the air- and ground-waves (Figure 14.5C). Depth conversion and migration were achieved using a CMP-derived velocity of 0.08 m/ns.

A so-called *chair diagram* (Figure 14.6) reveals a portion of the migrated and time-to-depth converted 3D GPR volume. The structural contrast associated with the fault is indicated by the change in reflection pattern at  $x = \sim 55$  m, which is coincident with the vertical offset of the terrace (annotated with a small arrow in Figure 14.6).

McClymont *et al.* (2008) undertook detailed coherence and texture-based attribute analysis of the 3D GPR data acquired at the Calf Paddock site and interpreted the results in terms of the radar stratigraphy (see Table 14.2 for details). The original migrated and time-to-depth converted GPR section (see also Figure 14.5C) and panels illustrating various attributes are displayed in Figure 14.7A–F. Relatively continuous reflections seen in the original data (bounding surface s1- and s2-bs) shown in Figure 14.7 are emphasised in the coherency section (Figure 14.7B). Differences either

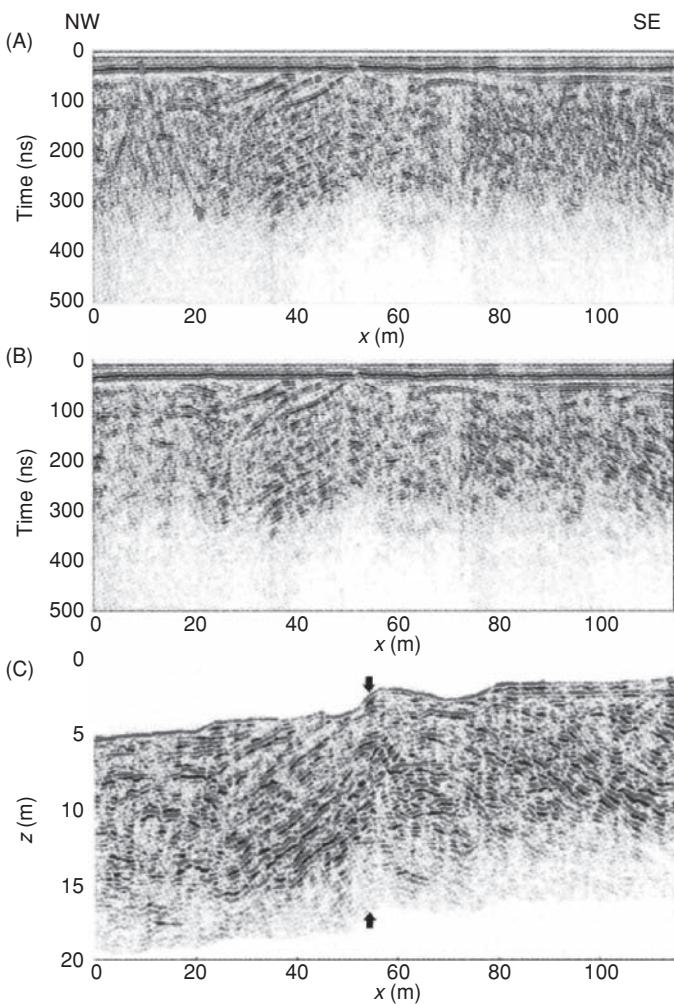


**Figure 14.5** (A) Unmigrated GPR section at Calf Paddock, New Zealand. (B) as for (A) but after 3D  $f\text{-}k$  filtering to remove the steeply dipping diffraction tails (arrowed in (A); (C) as for (B) after 3D topographic migration, depth conversion, and  $f\text{-}xy$  deconvolution. Black arrows identify the projected location of the Alpine Fault Zone. Vertical exaggeration is 3:1. From McClymont *et al.* (2008), by permission. [C]

side of the fault (indicated in the Figure by the pair of open arrows) are clear on the coherency section and help to identify four radar facies (f1-af, f2-tf, f3-fl and f4-fl) separated by the radar interfaces (s1- and s2-bs) and by a zone delineated by vertical dotted lines. This latter zone has been identified from a display of the contrast<sub>x</sub> and contrast<sub>y</sub> parameters (Figure 14.7D and F); as the analysis is undertaken for a 3D radar volume ( $x, y, z$ ) it is possible to extract texture attributes with specific orientations (*i.e.*  $x$  or  $z$ , as denoted by the respective suffix). The line of the fault is also clearly evident on the homogeneity section (Figure 14.7E). In some displays, high-amplitude attribute values occur as a result of low signal-to-noise below  $\sim 13$  m depth.

The results of the 3D GPR investigation at Calf Paddock, New Zealand, indicate that, within the top 15 m, the Alpine Fault Zone is characterised by a nearly 50-m wide zone of deformation that can be

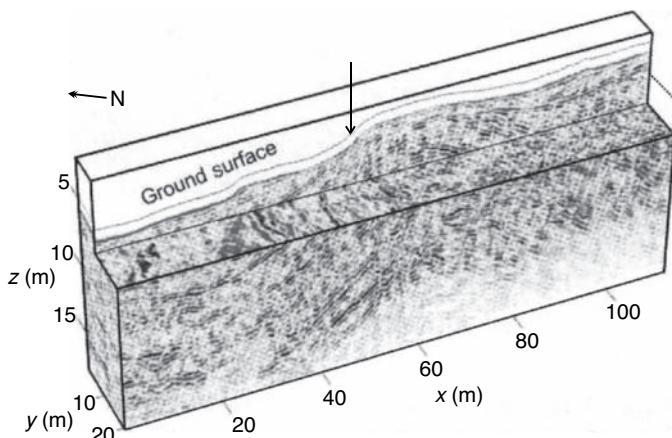


**Figure 14.6** A portion of the fully-processed 3D GPR volume from the Calf Paddock survey. Vertical exaggeration is 3:1. From McClymont *et al.* (2008), by permission. [C]

divided into three overlapping domains (McClymont *et al.*, 2008). A 30-m wide domain is characterised by a region in which older river gravel beds are tilted upwards towards the principal fault strand (Figures 14.7A and C). A 20-m wide domain is characterised by lateral fault drag of alluvial-fan deposits and an ancient river channel (identified on radar depth slices). These two domains, which represent the northwest footwall and the southeast hanging wall of the main fault, respectively, are themselves separated by a 15-m wide domain. This is associated with a steeply south-southeasterly dipping zone of shearing and stratal disruption of the main fault, which coincides with the zone of ground surface-fault displacements. The

overall interpretation is represented by the block model shown in Figure 14.8 on which the radar facies are indicated.

This particular GPR case history has demonstrated that, due to the strongly 3D characteristics of the geology and related structures, the most sensitive approach to resolving these features is by using 3D data processing and attribute analysis.

## 14.2 Hydrogeology and groundwater contamination

### 14.2.1 Groundwater contamination

As environmental protection measures become more stringent, and the pressure on preserving the quality of groundwater sources increases, so the need to identify groundwater pollution grows. Davis and Annan (1989) have demonstrated how ground radar was used to locate and map out a plume of contaminated water leaking out from a landfill site; a schematic plan of the site area is shown in Figure 14.9A. Along the line of the radar transect shown in this figure, the soil consists of fine sand and overlies bedrock which occurs at a depth of about 20 m. A radar survey was undertaken using a PulseEKKO III radar system and the resulting radargram is shown in Figure 14.9B.

Where penetration of the radiowaves into the superficial sediments occurs, reflections are seen and are thought to be due to horizons with different grain size and density, and hence different soil moisture contents. It is also very clear on this section that there are areas where either only very weak reflections occur, such as at 150 m along the profile at around 400 ns two-way travel time, or the

**Table 14.2** Description and interpretation of radar stratigraphy, Calf Paddock, New Zealand (after McClymont *et al.*, 2008).

	Description	Geological interpretation
Radar facies f1-af	Subparallel southwesterly dipping reflections with limited lateral continuity. Reflections have moderate ( $20^\circ$ - $35^\circ$ ) dips	Foreset beds of a prograding alluvial fan
Radar facies f2-tf	Subparallel northwesterly dipping reflections that are moderately continuous. Reflections have shallow to moderate ( $10^\circ$ - $25^\circ$ ) dips	Post-seismic alluvium beds deposited in the accommodation space provided by the repeatedly downthrown block northwest of the principal fault trace. The current alignment of the dipping strata with the fault plane suggests they were tilted upward by the fault
Radar surface s1-bs	Laterally continuous undulating reflection	Erosional surface formed by the Maruia River downcutting into the deposits characterised by radar facies f1-af on the southeast (hanging-wall) side of the fault zone
Radar facies f3-fl	Subhorizontal reflections that are moderately continuous	Fluvial deposits of the Maruia River
Radar surface s2-bs	Laterally continuous to discontinuous undulating reflection. Subhorizontal reflections of radar facies f4-dl onlap this surface	Contact at base of late Holocene river gravels resting unconformably over tilted alluvium beds on the northwest (footwall) side of the fault zone
Radar facies f4-fl	Subhorizontal reflections that are moderately continuous. They onlap radar surface s2-bs	Late Holocene fluvial deposits of the Maruia River

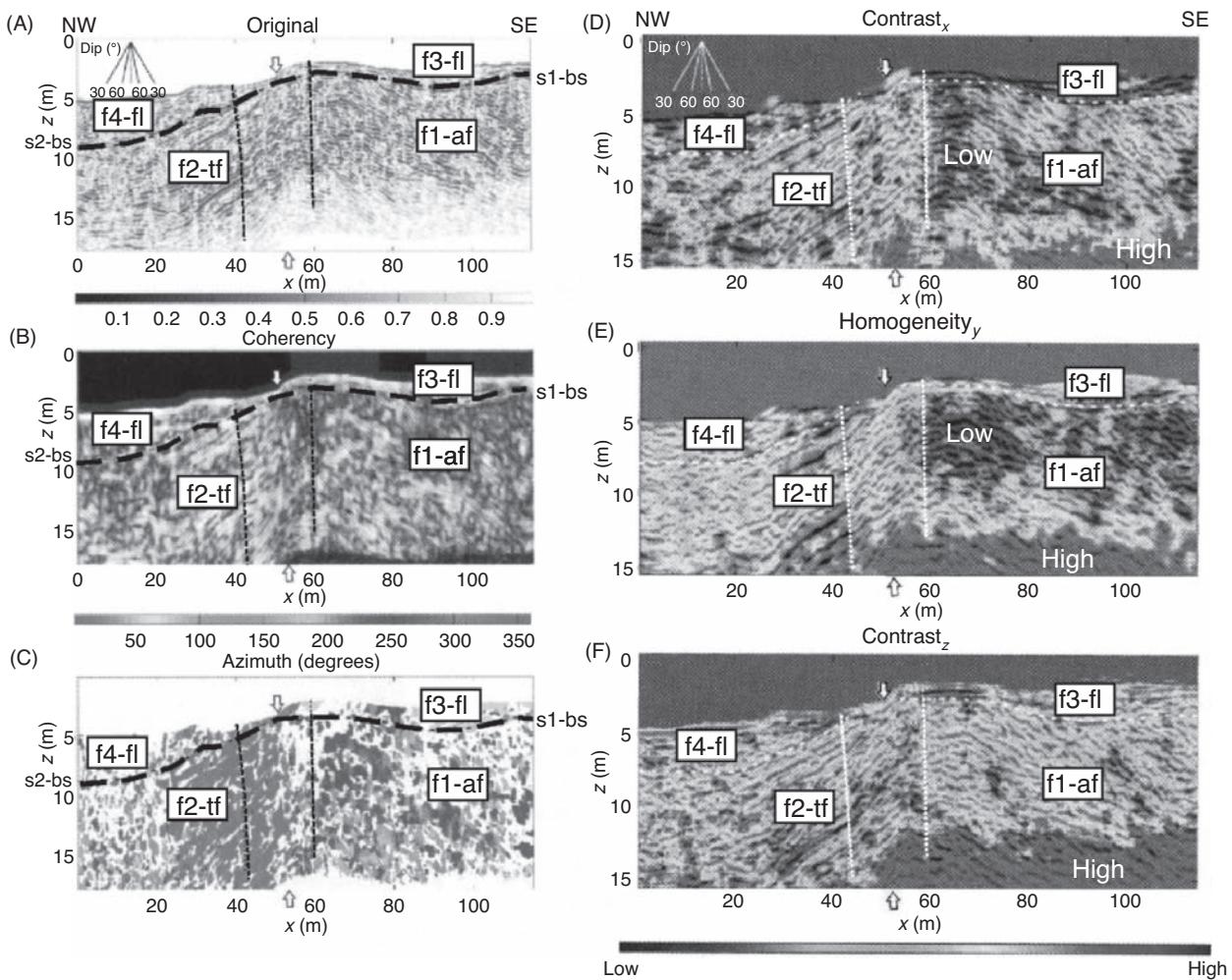


**Figure 14.7** (A) Original GPR section as shown in Figure 14.5C. (B) and (C) Coherence-based attribute sections (coherency and azimuth) with radar surfaces and facies indicated (see Table 14.2 for details). Texture attributes for the same section: (D) contrast<sub>x</sub>, (E) homogeneity and (F) contrast<sub>z</sub>. The open arrows indicate the projected location of the Alpine Fault Zone. Dotted lines outline a zone where reflections have reduced continuity and steeper dips (highlighted by the contrast<sub>x</sub> attribute in (D)). Vertical exaggeration is 3:1. From McClymont *et al.* (2008), by permission. [C]

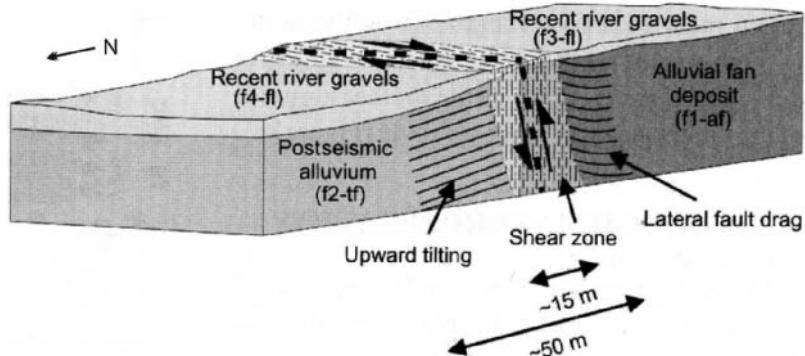


**Figure 14.8** Structural and depositional model based on the original 3D GPR data acquired across the Alpine Fault Zone at Calf Paddock and various attribute volumes. From McClymont *et al.* (2008), by permission.

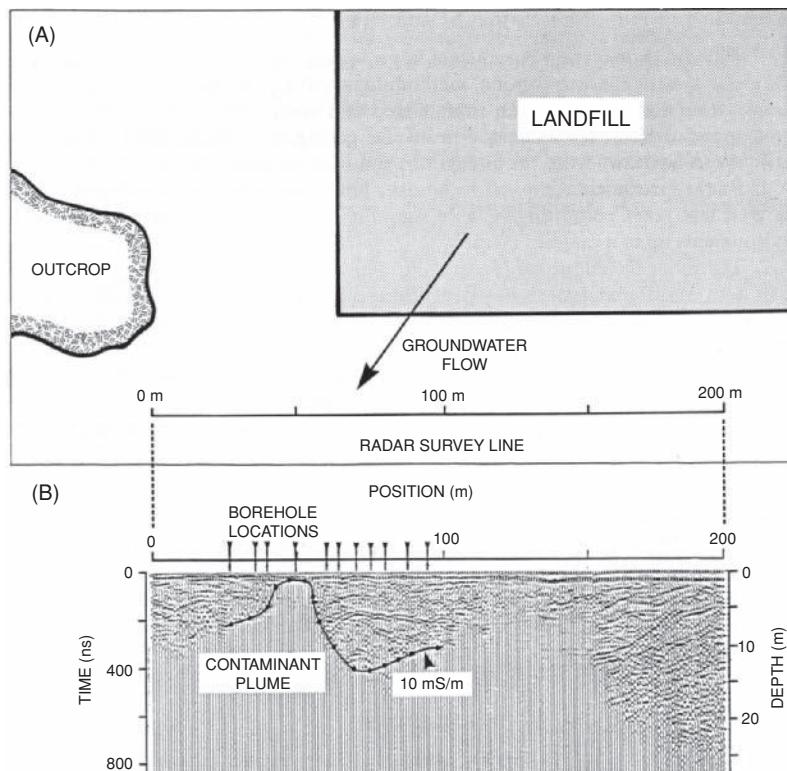


**Figure 14.9** (A) Schematic map showing the location of a GPR profile downstream of a landfill; (B) PulseEKKO III radargram along the profile in (A). The zone below the 10 mS/m contour is interpreted to be the conductive plume caused by leachate migrating from the nearby landfill. From Davis and Annan (1989) by permission.

signals are completely attenuated. The presence of contamination, which has an associated high electrical conductivity, attenuates the radar signals severely.

Several boreholes had been constructed along the survey line and the conductivity of the groundwater was measured. The solid line joining a series of black dots on Figure 14.9B indicates the position below which the pore water conductivity is greater than 10 mS/m. As it was known that the superficial deposits were reasonably consistent in their properties over the area of the site, it is evident, therefore, that the pollution plume approaches the surface between 40 and 60 m (as proven by the borehole data) and that it also extends between 110 and 150 m along the profile line at a depth of about 6 m below ground level. The second part of the plume had not been expected, and thus the results from the radar survey were extremely useful in providing this additional information. A ground conductivity survey to complement the radar work would have provided a non-invasive method of determining the spatial variation in subsurface conductivity without having to drill extra boreholes, which in themselves may make the spread of the pollution worse.

Where it can be demonstrated that radar surveys would be useful under the ambient geological and ground conditions, and that the pollution can be detected by radar, then changes in the pollution plume can be mapped. By undertaking repeat surveys along the same ground transects, it is possible to detect changes as a function of time. Furthermore, where remediation measures are undertaken,

the success of such treatment can be monitored using radar. For instance, where the conductivity of the formerly contaminated zone is reduced successfully by remediation, previously opaque areas on radargrams (due to high signal attenuation) gradually become transparent and signals associated with geological structures start to become visible. However, as radar is so sensitive to even moderate conductivity levels, it is often not the best technique to use; it is preferable to use measurements that respond directly to the conductivity such as rapid EM mapping and/or electrical resistivity tomography (ERT).

In addition to investigations into natural groundwater resources, there is a growing need to map groundwater contamination (Greenhouse *et al.*, 1993). Such pollution can arise from leachate migrating from a landfill, from saline water ingressing inland due to over-exploitation of freshwater sources, natural hydrocarbon contamination (from oil shales, etc.), through to chemical spillages (deliberate or otherwise) over timescales that can range from a few hours to many years. For example, could a chemical spill from an overturned railway tanker be monitored using geophysical methods? Or can petroleum products that have leaked from pipes at a refinery and which have ponded below ground at the water table be mapped?

Some chemicals can migrate from the source of contamination extremely quickly and would be difficult to detect by any means. However, an increasing amount of research is being undertaken to examine the protracted contamination of groundwater. The

reason is that there are enormous quantities of carcinogenic organic groundwater contaminants, such as DNAPLs (colloquially pronounced as 'dee-napples'). DNAPLs are dense, non-aqueous phase liquids. The main chemical concerned is perchloroethylene (PCE), which is one of the main constituents of the dry-cleaning and metal-cleaning industries. PCE is but one of a type of liquids known as 'chlorinated organic solvents'. Other well-known chemicals are trichloroethylene (TCE) and dichloromethane (DCM) which are paint-stripers and metal-degreasers. In 1986, it was reported that in the USA alone, 120 million litres of PCE and 200 million litres of TCE were manufactured. Once used, a small but significant proportion of these volumes were disposed of underground, around dry-cleaning establishments, car-service garages, in landfills and waste lagoons, and as residues on old industrial sites.

As their name suggests, DNAPLs are dense (with a density of  $1.623 \text{ Mg/m}^3$ ) and sink rapidly through the local groundwater leaving a residual trail of 5–20% of the pore volume, and eventually ponding for a time on a low-permeability layer such as a clay aquitard. DNAPLs also have low viscosity and low surface tension, which allows the chemicals to migrate rapidly through porous media. They can even pass through very fine fractures in clay given adequate time. It is estimated that in the USA, the cost of cleaning up the existing DNAPL contamination to acceptable standards is in excess of one thousand billion dollars.

An excellent overview of a controlled experiment to examine the detectability of DNAPLs has been presented by Greenhouse *et al.* (1993). A schematic of the experimental site is shown in Figure 14.10. A  $9 \times 9 \text{ m}$  cell was constructed by driving corrugated steel sheet piles, sealable at their joints, through the  $3.3 \text{ m}$  thick surficial aquifer into the underlying clay aquitard. Two concentric walls contained a  $0.5 \text{ m}$  wide moat which effectively isolated the inner section hydraulically from its surroundings, and allowed the interior water table to be maintained at a depth of  $0.15 \text{ m}$  below the ground surface. A tarpaulin covered the ground to restrict evaporation. The test cell was instrumented via nine vertical access tubes for radar tomography and borehole logging, and had four further vertical *in situ* probes to measure resistivity and relative dielectric constants (using time-domain reflectometry, TDR). Surface ground radar traverses were undertaken repeatedly over two sets of orthogonal profiles with a  $1 \text{ m}$  line interval using a PulseEKKO IV radar system with 200, 300, 500 and 900 MHz antennae. Over a period of 70 hours, 770 litres of liquid tetrachloroethylene (TCE, permittivity = 2.3) were injected under a constant head of  $2 \text{ m}$  of water at the centre of the test cell at a point  $0.6 \text{ m}$  below the ground surface. Geophysical imaging of the test cell began several days before the contaminant injection and continued over 912 hours after the injection had been completed. Measurements were made throughout the period of the experiment so as to obtain time-dependent datasets. Geophysical measurements continued for several weeks after the main experiment had been completed in order to monitor the removal of the TCE from the test cell, which was undertaken by flushing the cell with surfactants.

Of the substantial body of data obtained from this experiment, a time series of radargrams obtained along transect 5N (Figure 14.10) using a 200 MHz centre-frequency antennae is shown in Figure 14.11. Three radargrams are shown, ranging from one obtained

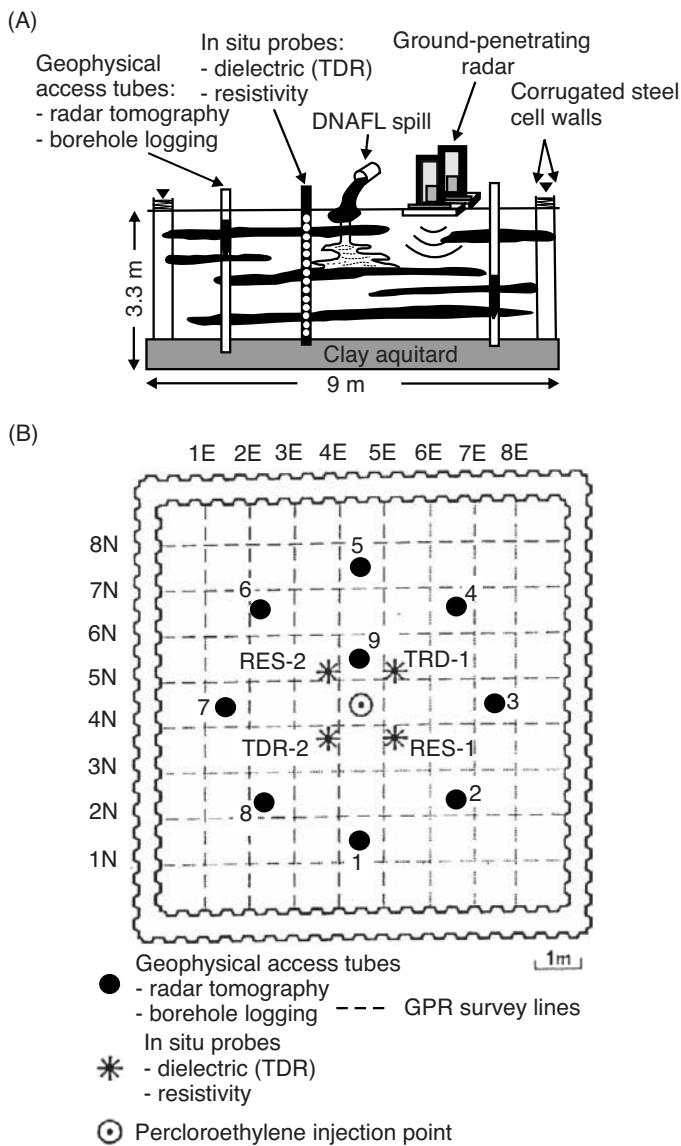


**Figure 14.10** (A) Schematic cross-section of the  $9 \times 9 \text{ m}$  Borden test cell. (B) Plan view of the Borden test cell showing access tubes AT-1 to AT-9, resistivity probe locations RES-1 and RES-2, TDR locations TDR-1 and TDR-2, the  $1 \text{ m}$  radar grid and the PCE injection point. From Greenhouse *et al.* (1993), by permission.

before any injection of TCE had occurred, and three acquired at 8.7, 16 and 178 hours after injection. What is clear from comparing the three radargrams after injection is that TCE appears to pond at a depth of  $1 \text{ m}$  and then drains laterally and downwards, leaving a residual at  $\sim 1 \text{ m}$  depth with ponding developing above the clay aquitard evident at  $\sim 2.8 \text{ m}$  depth. The small event indicated in Figure 14.11D was observed to grow laterally in extent and with stronger reflection amplitude by 920 hours after injection. The near-horizontal reflection at  $3.3 \text{ m}$  depth is from the clay aquitard, and the dipping events at the edges on all sections are diffractions from the sheet steel pile walling around the test cell. The travel time for the reflection from the aquitard shortens slightly with time due to the

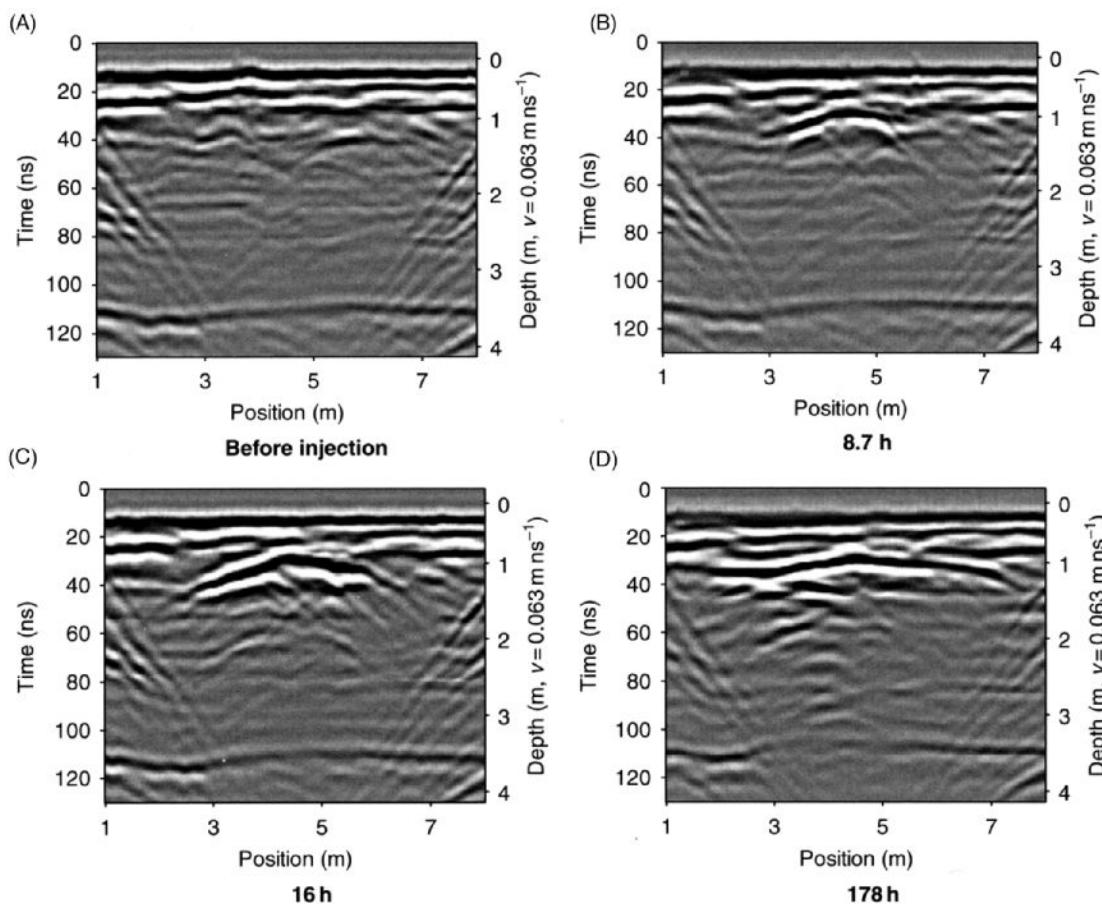


**Figure 14.11** Borden test cell GPR sections acquired using antennae with a centre-frequency of 200 MHz (A) before DNAPL injection; (B) at 8.7 h; (C) 16 h; and (D) 178 h after the start of the injection. From Redman (2009), by permission.

higher velocity associated with the injected TCE displacing water, causing velocity pull-up. In addition, the strength of the reflection from the aquitard decreases with time as energy is reflected back from the zones of high DNAPL saturation.

These experiments demonstrated that PCEs can be imaged successfully using a variety of geophysical methods, and that GPR can be used to monitor both the migration and the subsequent remediation of the contaminated ground. Further aspects of the radar surveys have been reported by Brewster *et al.* (1992a,b), for example. A GPR survey at a site where DNAPL contamination was known to have occurred has been described by Carpenter *et al.* (1994), although no DNAPLs were imaged directly using radar. Another experiment involving the injection of 50 litres of TCE into the Borden aquifer near the test cell and GPR monitoring has been described by Hwang *et al.* (2008). They monitored the dissolution of the pooled DNAPL over a 66-month period and demonstrated that GPR could be used to monitor the reduction in the areal extent of the pool and in the total DNAPL mass within this area during the monitoring period.

Redman (2009) has described the use of GPR to investigate LNAPL contamination from bi-weekly fire-training exercises at a former fire-training facility in Oscoda, Michigan, USA. The site geology comprises 20 m of uniform sands with a water table at

~5 m depth. A strong reflection from the water table is evident, but in a 40-m wide zone starting just below the water table reflection, the observed reflection strengths are diminished or absent, giving rise to a so-called 'shadow zone' of attenuated radar signals. This is thought to be associated with the elevated conductivity arising from the biodegradation of the LNAPL contamination as described by Sauck (2000). Marcak and Golebiowski (2006) have also used GPR to monitor the variability in hydrocarbon contamination with wet and dry seasons in former Soviet bases in Poland. Hagrey (2004) has undertaken controlled small-scale laboratory experiments using a 1.5 GHz antenna to map the infiltration of toluene (dielectric permittivity = 2.2) in a heterogeneous sand model. He found that the technique was able to identify areas of toluene within saturated and partially saturated zones but was not successful in dry areas. This is thought to be due to the poor dielectric contrast between the toluene and dry sand (dielectric permittivity 4.7), whereas in the saturated zones, the contrast is much stronger with the presence of water (dielectric permittivity in the experiment was 83). Generally speaking, hydrocarbons have lower values of dielectric permittivity and conductivity than groundwater. Their detectability is therefore a function of the dielectric contrast between the hydrocarbon and the groundwater and host medium.

## 14.2.2 Mapping the water table

Ground-penetrating radar is being used extensively in the Netherlands for hydrogeological assessment in groundwater management. Falling water tables and deteriorating water quality seriously affect agriculture, nature conservation and potable water supplies. Van Overmeeren (1994) has provided examples of types of hydrogeological applications current in the Netherlands where there are four main radar targets: (a) tectonic and sedimentary structures; (b) water tables within sandy deposits in push moraines, river terraces and sand dunes; (c) perched water tables as distinct from regional water tables; and (d) spatial extent and continuity of buried clay and peat layers within the superficial deposits.

A radargram acquired using a PulseEKKO IV with 25 MHz antennae and station interval of 1 m is shown in Figure 14.12. The profile was obtained over push moraine comprising mainly sand. The section has been corrected for topography and has identical horizontal and vertical scales. The water table is evident as a horizontal reflection with a large amplitude at around 30 m elevation. In the northern part of the section, the reflection is largely continuous whereas it is less so in the southern, most elevated part. This suggests that the depth of penetration of the radar is at its limits here and that the greater depth below ground level to the water table in the southern part results in the poorer data quality. Using a radiowave velocity of 0.145 m/ns (derived from CMP measurements), the water table is still evident at 42 m below ground level. The radargram also reveals reflections from interfaces above the water table. The oblique reflections are associated with interfaces between sandy layers of different grain sizes or between sandy and clayey sediments. In both cases, the interface marks a change in moisture content and hence a contrast in relative dielectric constant.

A conspicuous reflector with a large amplitude and dipping southwards is evident in the middle of the section. There is a small vertical offset (around 2 m) in the water-table reflection where it is intersected by the inclined event. The step in the water table is thought to be caused by an inclined clay layer that gives rise to the strong oblique reflection.

In an area of sandy ice-pushed ridges, where the water table is shallow, Van Overmeeren (1994) found significant, discrete steps in

the water table using 100 MHz antennae and a station interval of 0.5 m (Figure 14.13). The water table is clearly evident as a continuous, horizontal reflector with a large amplitude (around 15 m elevation at the eastern end of the section). What is also clear is the step in the groundwater table at a distance of ~285 m along the profile. It was thought that this step was an artefact of sharp changes in the radiowave velocity. However, radiowave velocity analyses (VA) undertaken using CMP tests (Figure 14.13) produced radiowave velocities of 130 mm/ns and 140 mm/ns either side of the step. The vertical offset of the water table is 2.5 m and could be traced on other parallel radar profiles for over 750 m southwards. It is thought that the step is a result of the sealing effect of a dipping clay layer, as also seen in Figure 14.12. The Dutch Geological Survey investigated the area using shallow boreholes but these could disturb the sealing layers of clay and peat. The radar survey, however, was able to map the water table continuously over large areas and identify features such as the near-vertical steps in the water table that would otherwise have not been identified using intrusive methods.

Van Overmeeren (1994) described another example of the hydrogeological usefulness of GPR, where a radargram (Figure 14.14A) was acquired using a PulseEKKO IV with 50 MHz antennae and a station interval of 0.5 m. The survey transect was over a valley with marine interglacial deposits passing into an uplifted ridge of ice-pushed sediments. A clay layer forms part of the marine formation. The objective of the radar survey was to map the lateral continuity of the clay layer and to locate its western limit (see Figure 14.14B, which is a schematic interpretation of part of Figure 14.14A). The clay layer, which occurs at a depth of 15 m below ground level, sustains an artesian aquifer which is recharged by infiltration in the higher ice-pushed ridge. The precise boundaries of the clay layer were required for groundwater flow modelling.

In the radargram (Figure 14.14A), the vertical exaggeration is 2.5 times the horizontal scale. The regional groundwater level is at a depth of about 7 m, as determined from a nearby observation well. A radar CMP test near the well produced a value of the radiowave velocity of 0.115 m/ns for the sediments above the water table. In the area of the survey, the average radiowave velocity was found to be 0.075 m/ns for sediments above the clay band, which is in close agreement with a known value of 0.06 m/ns for sand saturated with

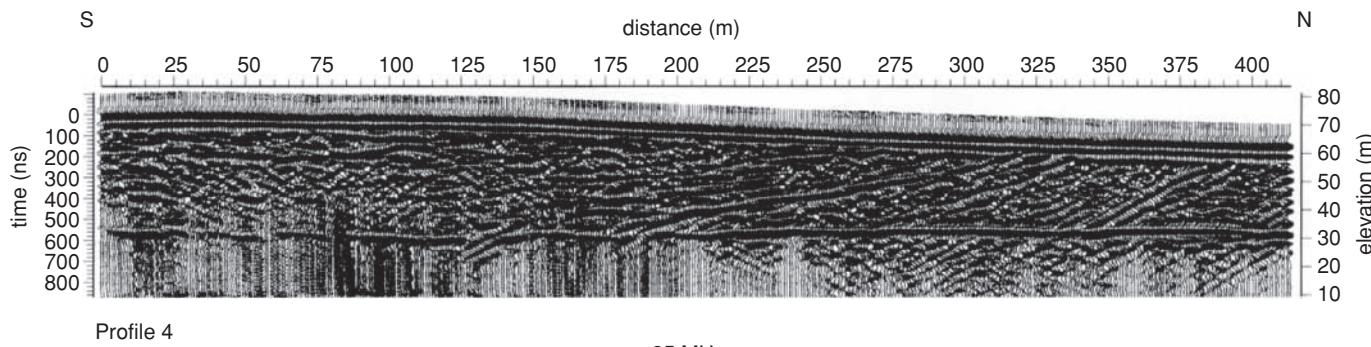


**Figure 14.12** Radargram acquired with 25 MHz antennae over a sandy ice-push moraine. The water-table reflection is evident at an elevation of 30 m. Note the slight vertical displacement in this reflection where an inclined reflection due to a clay layer intersects the water table at 185 m. From van Overmeeren (1994), by permission.

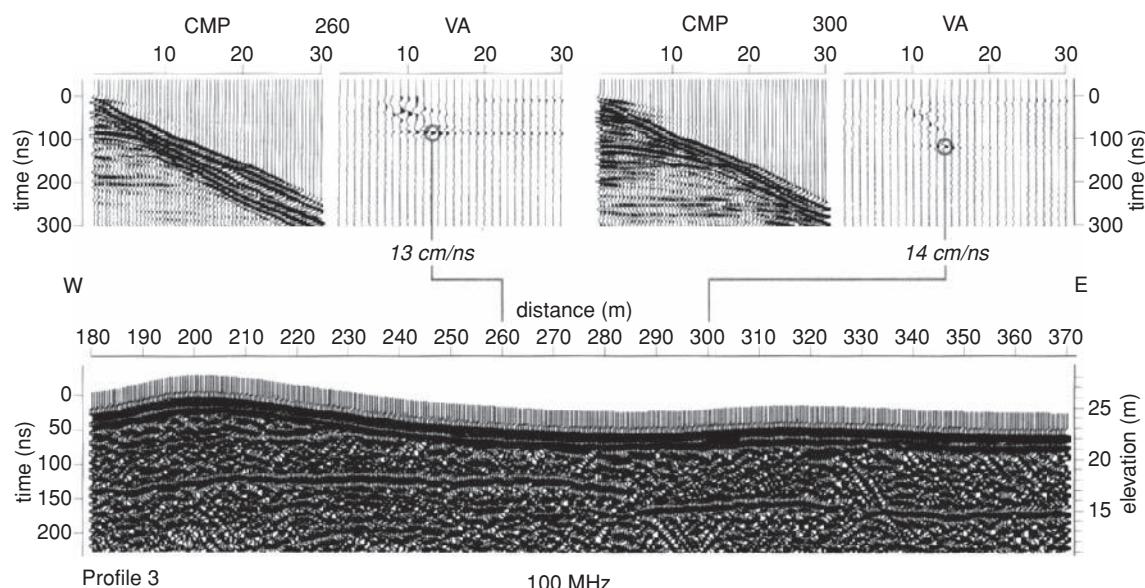


**Figure 14.13** Velocity analysis (VA) of CMP measurements made either side of a step in the water table observed in push moraine deposits imaged on a 100 MHz radargram. From van Overmeeren (1994), by permission.

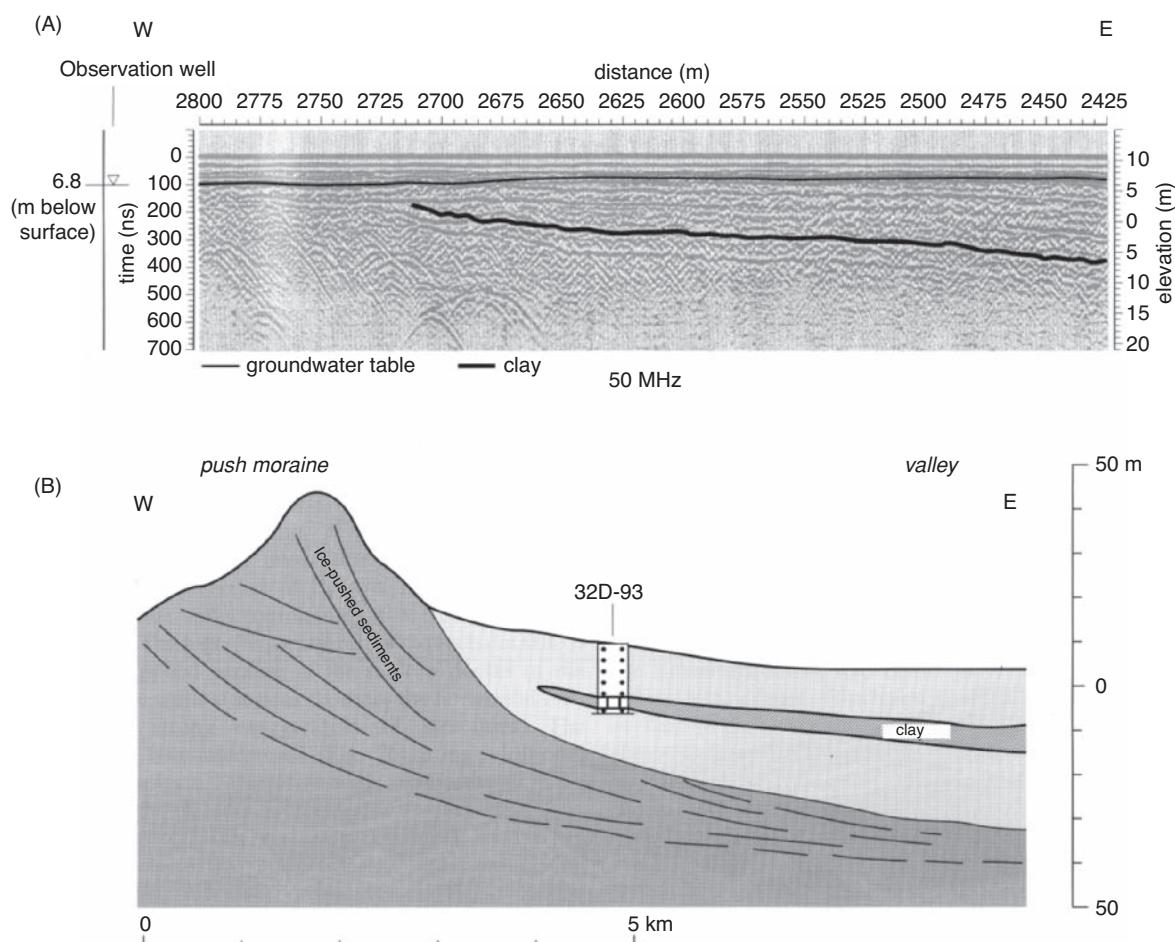


**Figure 14.14** (A) Radargram acquired with 50 MHz antennae over a sandy ice-push ridge on to which interglacial marine sediments, including a clay layer, onlap. The clay layer is indicated by a solid black line. The water table occurs at a depth of about 7 m. (B) General interpretation of the part of the radargram shown in (A). The clay layer has been verified by a borehole (32D-93). From van Overmeeren (1994), by permission.

freshwater. In contrast, dry sand has a radiowave velocity of 0.15 m/ns. The field-derived radiowave velocity is strongly indicative of freshwater-saturated sands above the clay layer, which can be identified on the radargram as a coherent reflection with large amplitude. The reflection from the clay layer persists clearly until station 2715 where it is cross-cut by an onlapping horizon.

The radargram shows that sensible reflection events arising from the subsurface geology can be identified to an interpreted depth of 12 m, with the exception of several diffraction-like events in the western part of the radargram which occur at interpreted depths of about 16 m. Note in Figure 14.14A that the reflections are largely coherent across the section, but become increasingly incoherent or disturbed west of station 2675 where the ice-pushed ridge is encountered. The more chaotic nature of reflection events here, due to diffraction hyperbolae, is typical of ice-pushed moraine in this area.

Although the water table occurs at shallow depth below ground level (around 3–5 m), reflection events at significant depth are still evident on the radargram. Elsewhere in the Netherlands, the detection of buried clay layers below the water table has proved impossible, yet at this location it is obvious that the radar survey has provided extremely valuable information about the clay layer. This is attributed to the high electrical resistivity of the surface layers, resulting in very little attenuation of the radar energy.

The transparency of freshwater-saturated sediments to radiowaves has also been demonstrated in North America using a PulseEKKO IV with 100 MHz antennae (Figure 14.15). The reflection arising from the water table is clearly seen as a coherent reflection with a large amplitude between stations 375 and 625 at an elevation of around 500 ft (about 152 m). Note that this radargram is displayed as a depth section using a constant radiowave velocity of 0.328 ft/ns and ignores the likely differences in radiowave velocity above and below the water table. Diffraction hyperbolae arising from two cables/pipes near the ground surface are also obvious (arrowed). Note that there are many reflections evident from the subsurface geology present to depths of around 33 ft (10 m). The data are published courtesy of the Michigan Department of Natural

Resources, Environmental Response Division, and of Sensors and Software Inc.

One of the key factors as to whether features below the water table can be imaged is where the water table is relative to the ground surface. If, as in the case above, the water table is at or just below the ground surface, sufficient radiowave energy is able to propagate through the water table to be reflected back by deeper interfaces. However, if the water table lies at significant depth, approaching the limits of penetration of the radar system being used, such as in the case shown in Figure 14.12, then little energy will be transmitted through the water table, due to its high reflection strength, which then effectively screens the underlying regions from being imaged.

## 14.3 Glaciological applications

### 14.3.1 Polar ice sheets

Radar mapping of the polar ice sheets has been one of the most widely used geophysical methods in both Greenland and Antarctica, initially to measure ice thickness but since expanded to explore other characteristics of polar ice sheets. Radio echo-sounding has been developed substantially since its early use in the 1960s. From the 1990s, use of commercial GPR systems in ground-based glaciological surveys has developed significantly, with uses extending to mapping crevasses, measuring sea-ice thickness, investigating polar, temperate and polythermal glaciers, especially within the near-surface, and within the snow pack itself. Determination of ice thicknesses is now accurate to around 1% and has provided excellent agreement with values derived from both seismic and gravity surveys, as well as with borehole control.

Ice is a remarkable material – it has a very narrow range of radiowave velocities ( $\sim 167$  m/ns) and dielectric constant ( $\epsilon = \sim 3.2$ ), and its electrical properties vary according to the type of ice. ‘Cold’ ice (ice well below its pressure melting point) has electrical resistivities three orders of magnitude lower than ‘warm’ temperate ice

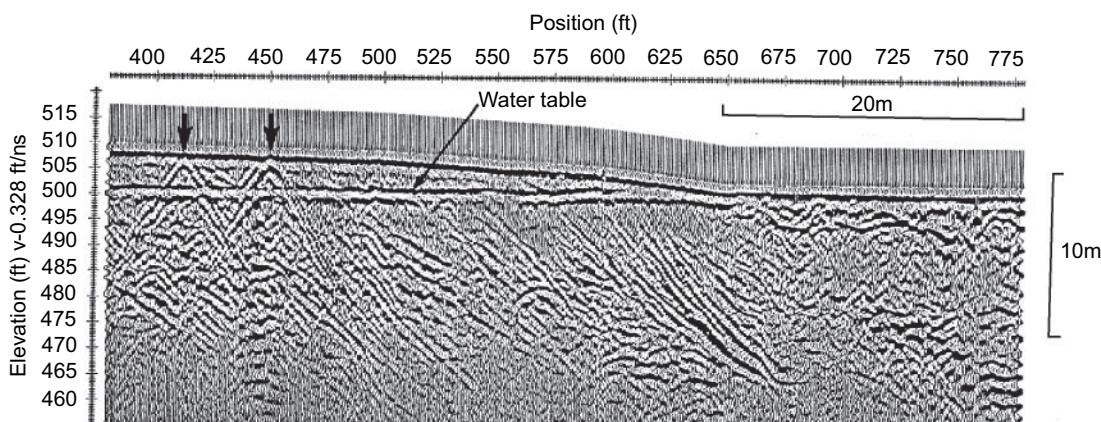


**Figure 14.15** Radargram acquired using 100 MHz antennae with a PulseEKKO IV system showing the water table (flat-lying reflection, arrowed) and two diffraction hyperbole from near-surface cables/pipes. Data courtesy of Michigan Department of Natural Resources, Environmental Response Division and Sensors and Software Inc.

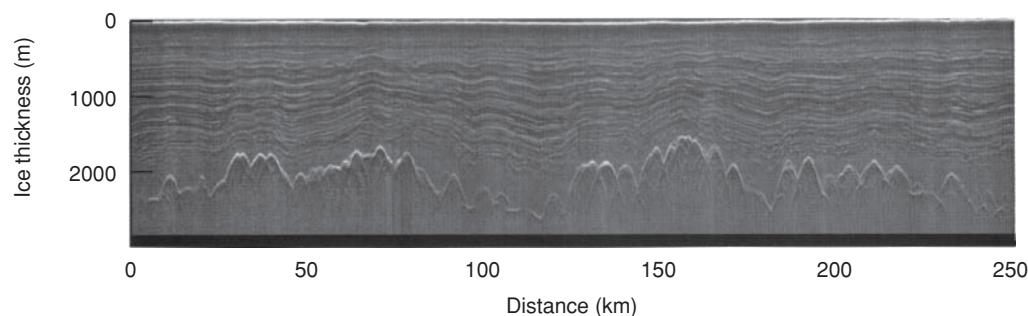


**Figure 14.16** Antarctic radio echo-sounding data collected in the 1970s showing distinctive internal layering over pronounced subglacial topography. From Bingham and Siegert (2007), by permission.

(ice at or around its pressure melting point) (Glen and Paren, 1975; Reynolds and Paren, 1980), and its resistivity values are strongly temperature-dependent (Reynolds, 1985). Glaciers can be classified as: *polar* – made up of cold ice and frozen at their base; *temperate* – made up of ice that is around the melting point apart from a surface layer that is subject to seasonal temperature cycles and wet-based; and *polythermal* – glaciers that consist typically of an upper cold ice zone over a temperate, wet, basal region. Polar ice is largely transparent to radiowaves, whereas temperate ice is variably transparent to radiowaves, depending upon the amount of internal water and the complexity of the glacier structure.

A radio echo-sounding (RES) profile acquired in the 1970s in Antarctica is shown in Figure 14.16 (Bingham and Siegert, 2007). Two principal features are evident on this profile. The first is that there are a series of subparallel reflections within the ice itself. Near the surface, the dielectric contrasts are likely to be between snow layers of different densities and ice layers. Some horizons may have undergone melting and annealing during the summer months (when the ice was at the surface) and subsequent refreezing. Ice has a thermal memory and the dielectric properties of the ice can be used to identify layers that have undergone melting and refreezing (Reynolds, 1985). Below about 1 km depth, the internal layers may represent snow layers that have been compressed to form ice and which may contain elevated concentrations of sulphate ( $H_2SO_4$ ). Particles from large volcanic eruptions from outside Antarctica are transported in atmospheric aerosols to become incorporated within the polar snow. Some of the most prominent internal reflections can be traced over thousands of square kilometres and appear to be interfaces formed at the same time, and thus can be used as *isochrons*. These can then be used in the analysis of the dynamics of the flow of the ice sheet. The second feature is that the bedrock surface can be seen very clearly and exhibits a range in elevation of about 1000 m. The bedrock topography comprises hidden ranges of mountains. At depths greater than 3 km, internal reflections may arise from variations in preferred orientations of crystal fabrics, although some of these causes are still a subject of debate. The mapping of internal reflections on RES profiles has provided information about accumulation and deformation rates within the ice sheets as well as other glacial geophysical problems.

Such RES profiles have also revealed huge freshwater subglacial lakes beneath the Antarctic ice sheet, such as those indicated in Figure 14.17. The contrast in relative dielectric constants between

the basal ice and the freshwater has given rise to this characteristic style of reflection.

In geophysical exploration it is not just the data themselves that are important, nor the compilation into striking 3D colour images, but that the information reveals information about subsurface processes – a dataset is *knowledge*, the interpretation leads to *understanding*, and this can be very exciting. There is considerable debate about the processes at the interface between ice sheets and

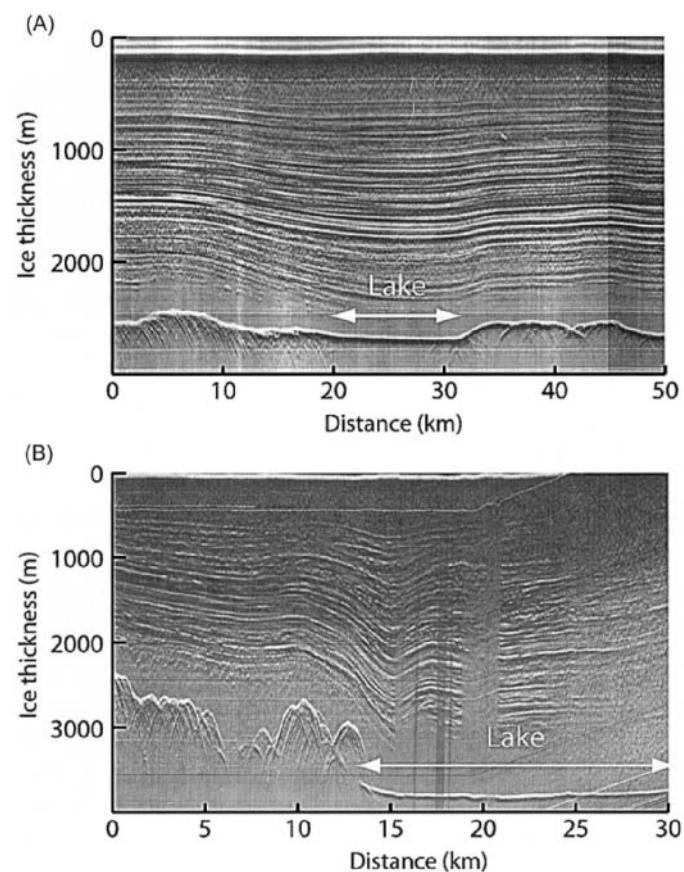


**Figure 14.17** Subglacial lakes identified on radio echo-sounding data collected during 1974–1979. (A) Subglacial Lake Aurora, close to Dome C, East Antarctica; (B) part of Lake Vostok, the largest known subglacial lake in Antarctica. From Bingham and Siegert (2007), by permission.

underlying sediments. Part of the problem has been the lack of data with a suitable resolution to be able to map the subglacial morphology in sufficient detail to be able to draw conclusions about this important interface. The reason this is so important is that large ice sheets, such as that in Antarctica, drain through fast-flowing ice streams. Their flow speed is strongly modulated by interactions between the ice and the underlying materials and this can affect the dynamics of the ice sheet. Seismic surveys and borehole investigations have revealed a spatial association between fast ice flow and saturated deformable sediments. It had previously been suggested that fast ice flow produces elongate bedforms known as *mega-scale glacial lineations* (MSGLs) (Clark, 1993).

To investigate this problem the British Antarctic Survey, Cambridge, UK, has developed a Deep Look Radio Echo Sounding system known as DELORES (King *et al.*, 2009). The highly portable system consists of a 3 MHz monopulse ground radar that can be mounted on a small sledge and towed overground across the snow surface. The system has a pulse repetition rate of 1 kHz and a digitisation period of 10 ns. The maximum depth of penetration so far recorded with this equipment is 3200 m.

King *et al.* (2009) described a radar survey undertaken across part of the Rutford Ice Stream in West Antarctica, where the surface ice flow speed is around 375 m/yr. Values of ice thickness were determined at 7.5 m intervals along profiles that were acquired perpendicular to ice flow and with an interline spacing of 500 m to form an overall grid of survey lines. The ice depth values were interpolated on to a 50-m grid and converted to bed elevations with a vertical resolution of  $\pm 3$  m. Ice thicknesses in the region were found to be over 2100 m. Example radar data and interpolated bed morphology are shown in Figures 14.18 and 14.19. The mean ice-surface elevation in the survey area was 300 m above geoid. It was found that the bed profile perpendicular to ice flow was 'W'-shaped, with a central ridge at 1800 m below geoid and flanking troughs 2100 m below geoid. Six seismic profiles had also been acquired in the area across the ice flow (C1 and C2) and four parallel to flow (F1–F4), at locations shown in Figure 14.20A; the radar-derived bedform elevations are also shown gridded across the survey area. Basal outcrops of stiff, unconsolidated till coincide with areas of subdued topography. Seismic profile C1 was repeated twice and indicated that one 500 m wide section of the bed was eroded by

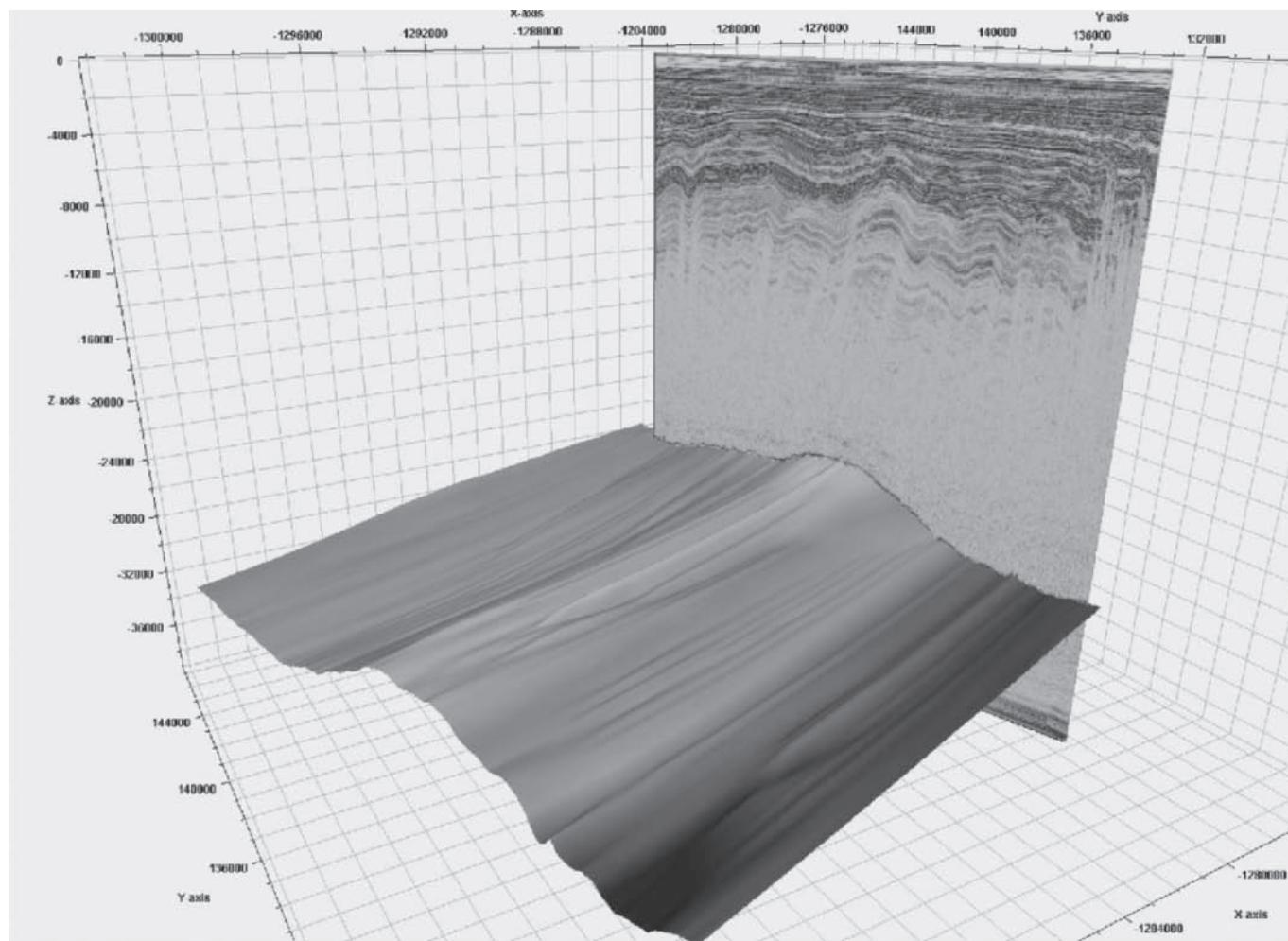


**Figure 14.18** Example radargram with part of the radar-derived subglacial landscape at Rutford Ice Stream, West Antarctica. Courtesy of E. King, British Antarctic Survey, by permission. [C]

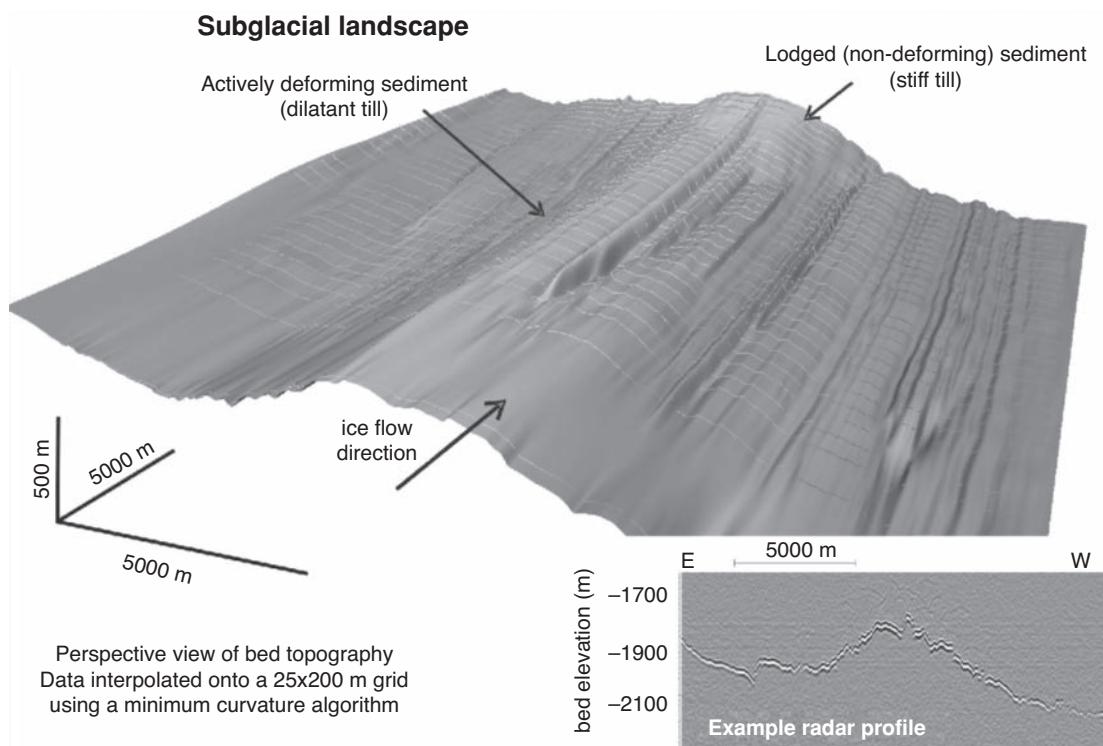


**Figure 14.19** Three-dimensional image of the bed of Rutford Ice Stream viewed downstream. The elongate mega-scale glacial lineations dominate the topography. Inset: example radargram. From King *et al.* (2009), by permission. [C]

6 m in six years. Subsequently, a 100 m wide, 10 m high bedform was deposited in a period of seven years. By removing the large-scale trend in bed elevation, the form of the residual topography can be seen (Figure 14.20B) along the profile A-AA indicated in Figure 14.20A. The radar data have revealed a series of linear features many kilometres long parallel to ice flow and with topographic amplitudes around 10 m and up to nearly 40 m. The radar bed reflection power was extracted from the radar returns and also gridded (Figure 14.20C). Warm colours associated with stronger reflections are thought to indicate free water at the ice–sediment interface; cool colours suggest that basal water is distributed within the sediment or exists in a thin layer (<0.04 m). The corresponding interpretation of a seismic profile along C1 is shown in Figure 14.20D (Smith and Murray, 2008). Dilatant till is relatively thin on the crest of the central ridge and thickens in the neighbouring troughs.

The parallel MSGL bedforms identified by the DELORES radar survey beneath the Rutford Ice Stream are indistinguishable from relict features reported from locations such as at the Dubawnt Lake palaeo-ice stream bed in northern Canada. The radar-derived bed elevation image is compared with a satellite image over the Dubawnt Lake site in Figure 14.21. The similarity is remarkable. However, the MSGL landforms beneath the Rutford Ice Stream have larger amplitudes. On the Dubawnt Lake ice stream, water-filled moats occur around some initiation points (white blotches in the image).

It is clear that the seismic and DELORES radar datasets acquired at the Rutford Ice Stream, West Antarctica, have produced a unique insight into the dynamic environment of subglacial sedimentary

beds. The surveys undertaken so far also provide a baseline against which future planned surveys across the same area can compare and so produce further important observations on the temporal evolution of bed processes beneath this ice stream, with implications for modelling of ice-stream dynamics.

### 14.3.2 Snow stratigraphy and crevasse detection

In contrast with the very low frequencies used in radio echo-sounding, higher-frequency commercial GPR systems are increasingly being used in glaciological applications. These can also be used to map snow stratigraphy within the near surface, but with significantly finer resolution than can be achieved with radio echo-sounding. An example of a radargram acquired along a 177-km profile, using a 400 MHz antenna with a GSSI SIR10B system, is shown in Figure 14.22 (Arcene *et al.*, 2005). In this figure, the small downward-pointing arrows indicate an internal reflection within the firn associated with a layer dated to 1875. The larger upward-pointing arrows indicate another isochron dated to 1734. The profile crosses the Bindschadler Ice Stream (BIS) obliquely. In several portions of the radargram, there is a general increase with depth in the dip of the limbs within any one fold. This is most evident between 70–130 km and 150–177 km, which are regions of higher ice-flow velocity. Also note that individual isochrons vary in elevation along the profile as highlighted by the two dated horizons.

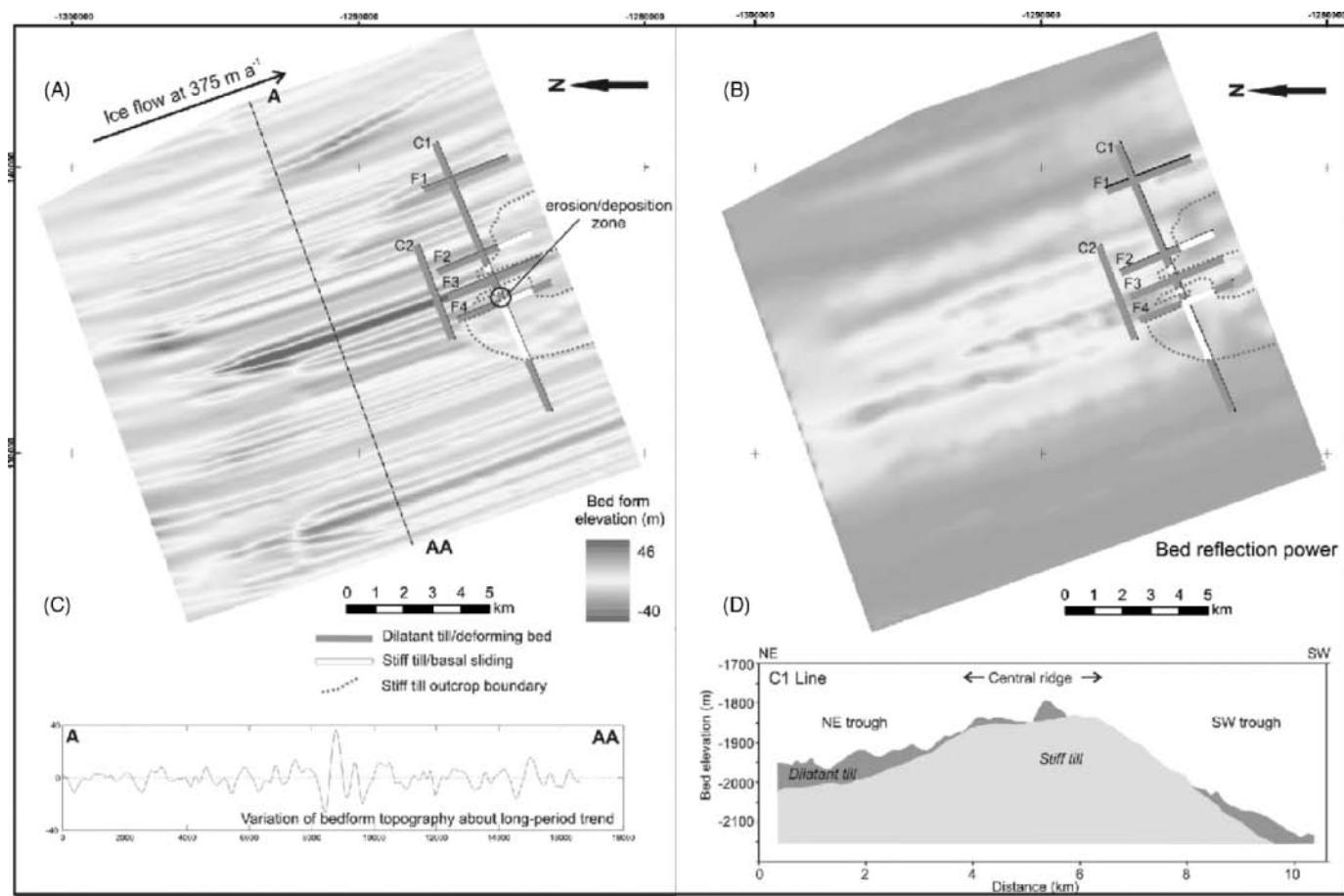


**Figure 14.20** Comparison between seismic and radar data at the Rutford Ice Stream, West Antarctica. (A) map view of the radar-derived bedform elevations with seismic traverses C1-2, F1-4, and line of cross-section A-AA indicated; (B) de-trended topographic profile showing the topographic expression of the lineations; (C) radar bed reflection power; (D) interpretation based on seismic section C1. See text for details. From King *et al.* (2009), by permission. [C]

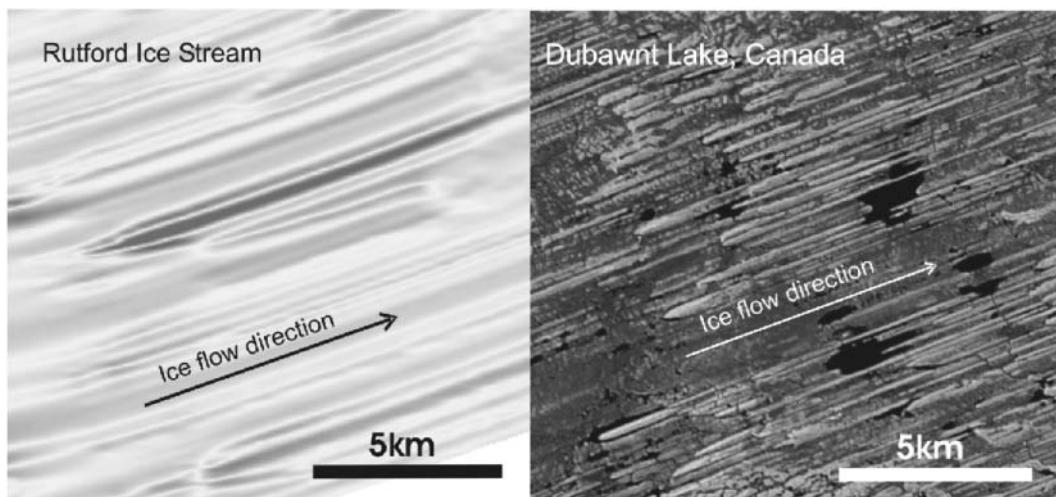


**Figure 14.21** Comparison of modern and relict landforms. (A) Rutford ice stream bedforms derived from radar data; (B) Landsat satellite imagery over relict bedforms on the present land surface at Dubawnt Lake palaeo-ice stream bed, northern Canada. The similarity between the two images is remarkable. From King *et al.* (2009), by permission. [C]

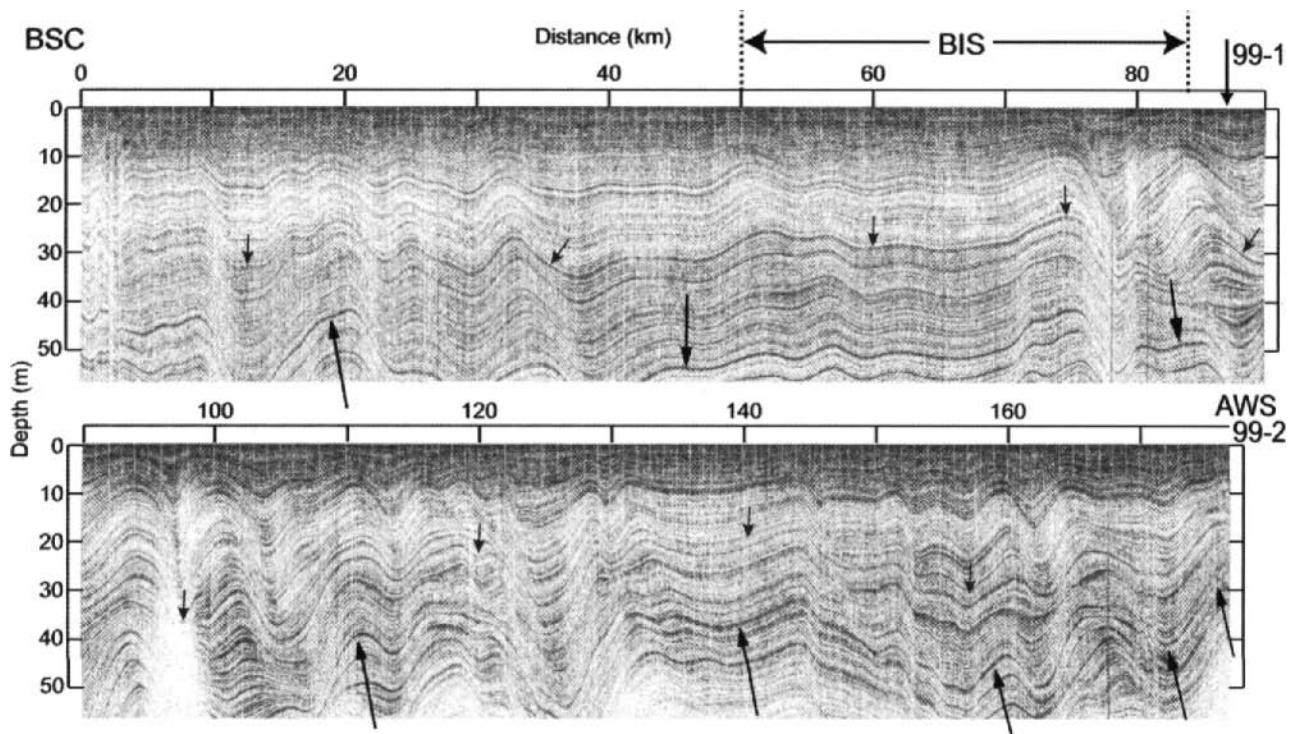


**Figure 14.22** A 400 MHz radar transect in West Antarctica showing internal reflections within the top 50 m of firn. The section has a vertical exaggeration of 350:1. The section obliquely crosses the Bindschadler Ice Stream (BIS). From Arcene et al. (2005), by permission. [C]

The same equipment was also used as a crevasse detection system. The radar antenna was located within an inflated rubber ring (vehicle inner tyre) attached to a 5 m rigid boom that was pushed ahead of a tracked snowcat. Radiation forward of the antenna, in the direction of travel of the vehicle, may be backscattered from the near-vertical side-walls of a hidden crevasse, revealing its presence. An example is shown in Figure 14.23 (Arcene, 2009). Diffractions are caused by the intersection of layers within the firn with the side-wall of the crevasse. The example shown indicates a complete snow bridge with no sagging above the crevasse, which appears as an inverted black cone. The reflections inside the firn either side of the crevasse are from snow layers. Crevasses as thin as only a few centimetres still generate strong responses. In some cases, crevasses may appear not to be open but are indicated by a zone of many diffractions arising from chaotic snow and ice within the crevasse.

### 14.3.3 Temperate glaciers

By their very nature, glaciers are logistically challenging and, especially in crevassed areas, can be extremely dangerous. It is therefore often beneficial to attempt airborne surveys rather than ground-based investigations. Airborne radar investigations of glaciers has predominantly been over dry polar ice sheets which are virtually transparent to radiowaves, and depths of investigation of up to 5 km are not unknown. However, temperate glaciers represent a different challenge due to the presence of surface and englacial water, and also complex structures within the ice. Freshwater can result in

significant signal attenuation, restricting the depth of penetration achievable. Commercial radar systems use frequencies higher than 50 MHz and are often affected by the numerous scatterers that lie on and within temperate glaciers. Better results at penetrating to the base of a temperate glacier and less sensitivity to scatterers can be achieved using a lower frequency radar system. Zamora et al. (2009) have described a new prototype 1 MHz impulse radar that is deployed from a Chilean Navy CASA 212 fixed-wing aircraft. The system, known as SIRAHT, a Spanish acronym for Airborne Radar System for Temperate Ice, comprises a bistatic system with a transmitter with 150 m long dipole that is deployed when the back-ramp of the aircraft is opened during flight. At its tail end is a drogue to help to stabilise the transmitter wire. An 80 m long monopole receiver is also trailed from the aircraft but is connected and grounded to the aircraft. The transmitter pod itself is located 250 m behind the aircraft in the centre of the transmitter dipole in an aerodynamic fibreglass casing 2 m long.

The SIRAHT system was tested over Glaciar Tyndall, Southern Patagonian Icefield, Chile. The system achieved a mean ground clearance of  $\sim 400$  m and was towed at speeds of  $\sim 100$  knots (185 km/h). An example profile is shown in Figure 14.24. The profile has been terrain-corrected and clearly shows reflections from the glacier bed, indicating an ice thickness of up to 600 m. Some events arise from within the glacier and, due to the long incident waveform, no information is produced for the near-surface of the glacier. The preliminary results are promising and indicate that the system has sufficient power to achieve significantly greater depths of penetration over thicker temperate glaciers in Patagonia.

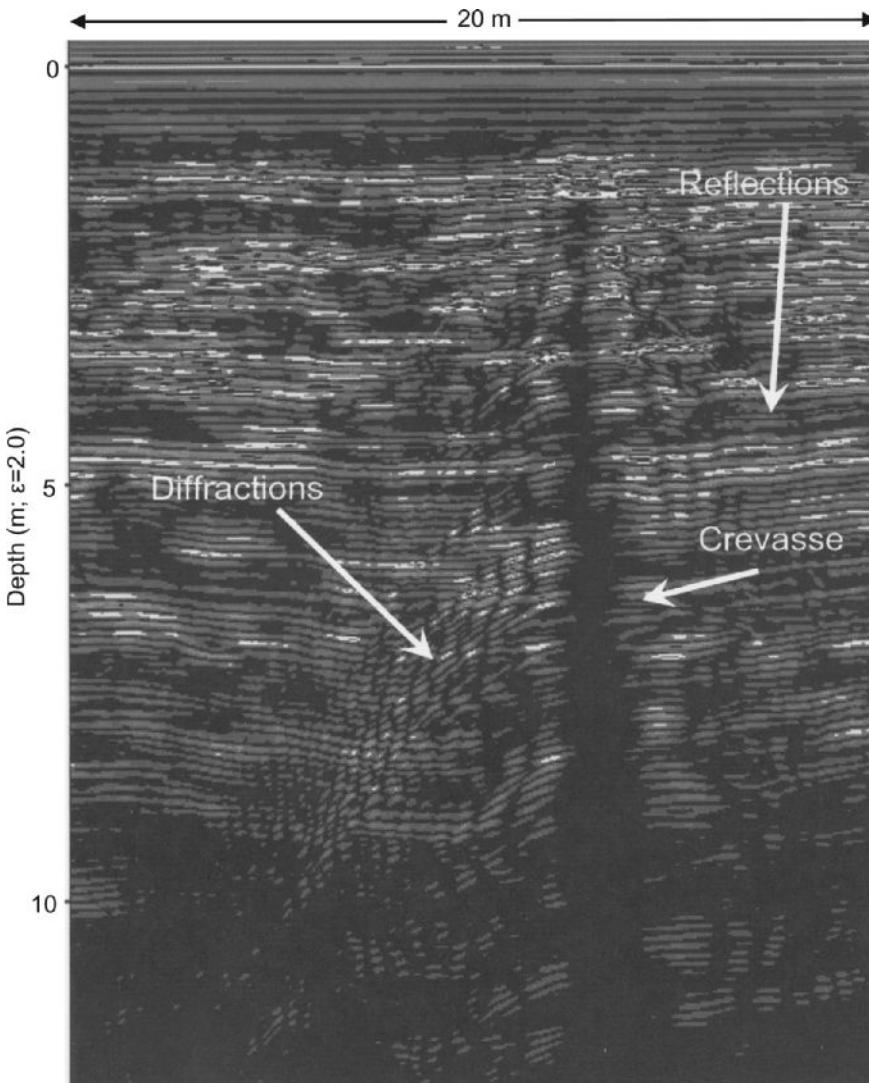


**Figure 14.23** A 400 MHz radargram across a concealed crevasse in Antarctica. From Arcone (2009), by permission. [C]

At the other end of the system size spectrum is a one-man portable 5 MHz radar system designed for ground-based surveys over glaciers (Matsuoka *et al.*, 2004). The entire system weighs no more than 13 kg; the antennae comprise half-wavelength dipoles that are laid on the ice surface. The system was trialled on the temperate Athabasca Glacier in Alberta, Canada. This glacier has significant amounts of surface water, and moulin through which the supra-glacial drainage enters at the glacier surface into englacial drainage systems. However, to ease the data acquisition, the survey profile was undertaken along a Snocoach bus route which runs over the glacier and is smooth and maintained daily. An example profile, which has been corrected for the topography, is shown in Figure 14.25. The glacier bed is clearly evident; so too are diffractions from scatterers within the glacier.

Another example of the seasonal effects of meltwater on radar profiles over a polythermal glacier was provided by Irvine-Fynn *et al.* (2006). They undertook repeat profiles across the same part of Stagnation Glacier, Bylot Island, Canada, in late June and late

July under different field conditions. Their surveys, using 50 MHz bistatic antennae with a PulseEKKO system, revealed significant differences on the resultant radargrams (Figure 14.26), which they attribute to changes in the amount of water present. For example, a prominent dipping reflection present in the late June survey (Figure 14.26A) is not present a month later (Figure 14.26B). They interpreted this as indicating that an englacial channel had drained between the two surveys. Reflection signals attributed to a temperate basal ice zone is present on both radargrams. The biggest differences occur in the shallow regions of the glacier. The late June survey shows significant amounts of noise attributed to slush in the base of supra-glacial streams. The slush had melted by the time of the second survey. The later survey indicated greater down-trace noise than was present on the earlier survey, and this was suggested as being associated with englacial water storage towards the base of the glacier. More details of this and other profiles over Stagnation Glacier have been described by Irvine-Fynn and Moorman (2009).

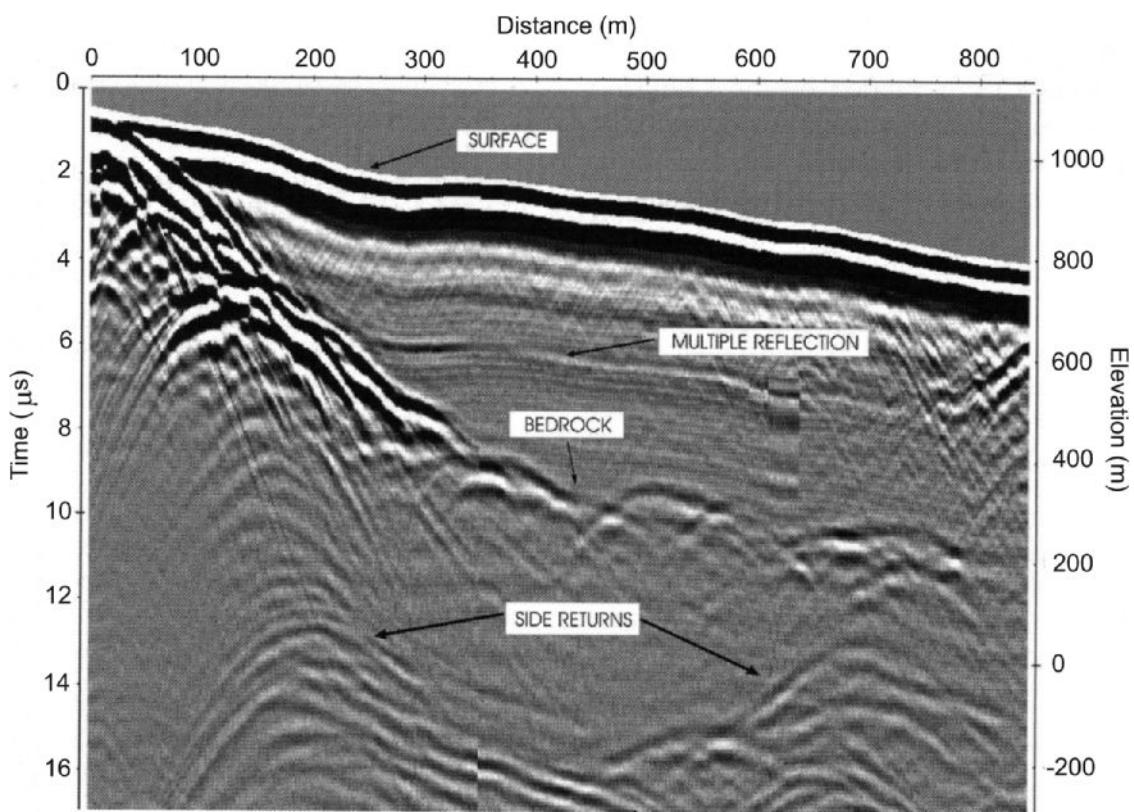


**Figure 14.24** Radargram acquired using the 1 MHz SIRAHT airborne radar system at Glaciar Tyndall, Southern Patagonian Icefield, Chile. From Zamora *et al.* (2009), by permission.

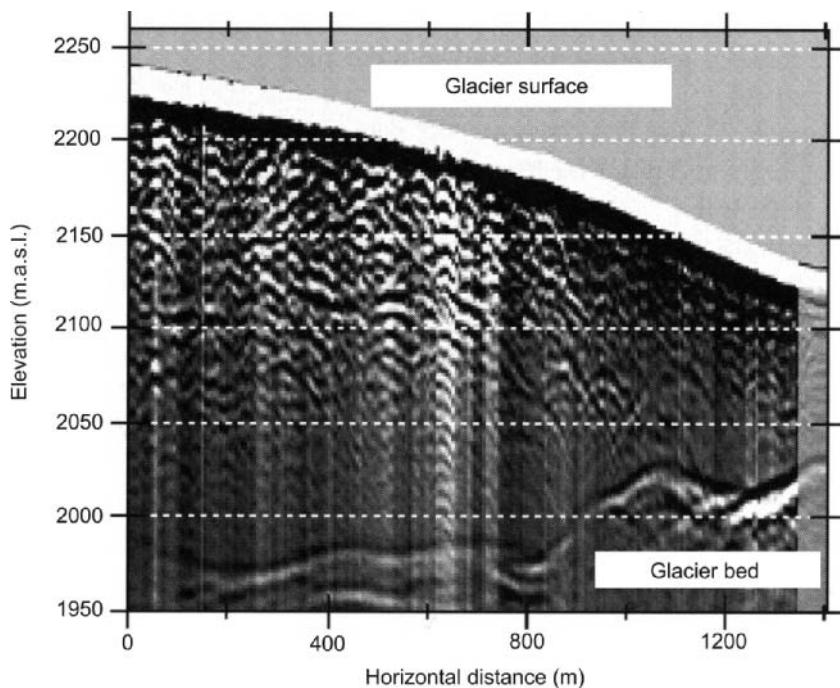


**Figure 14.25** Radargram acquired over the Athabasca Glacier using a 5 MHz portable radar system. From Matsuoka *et al.* (2004), by permission.

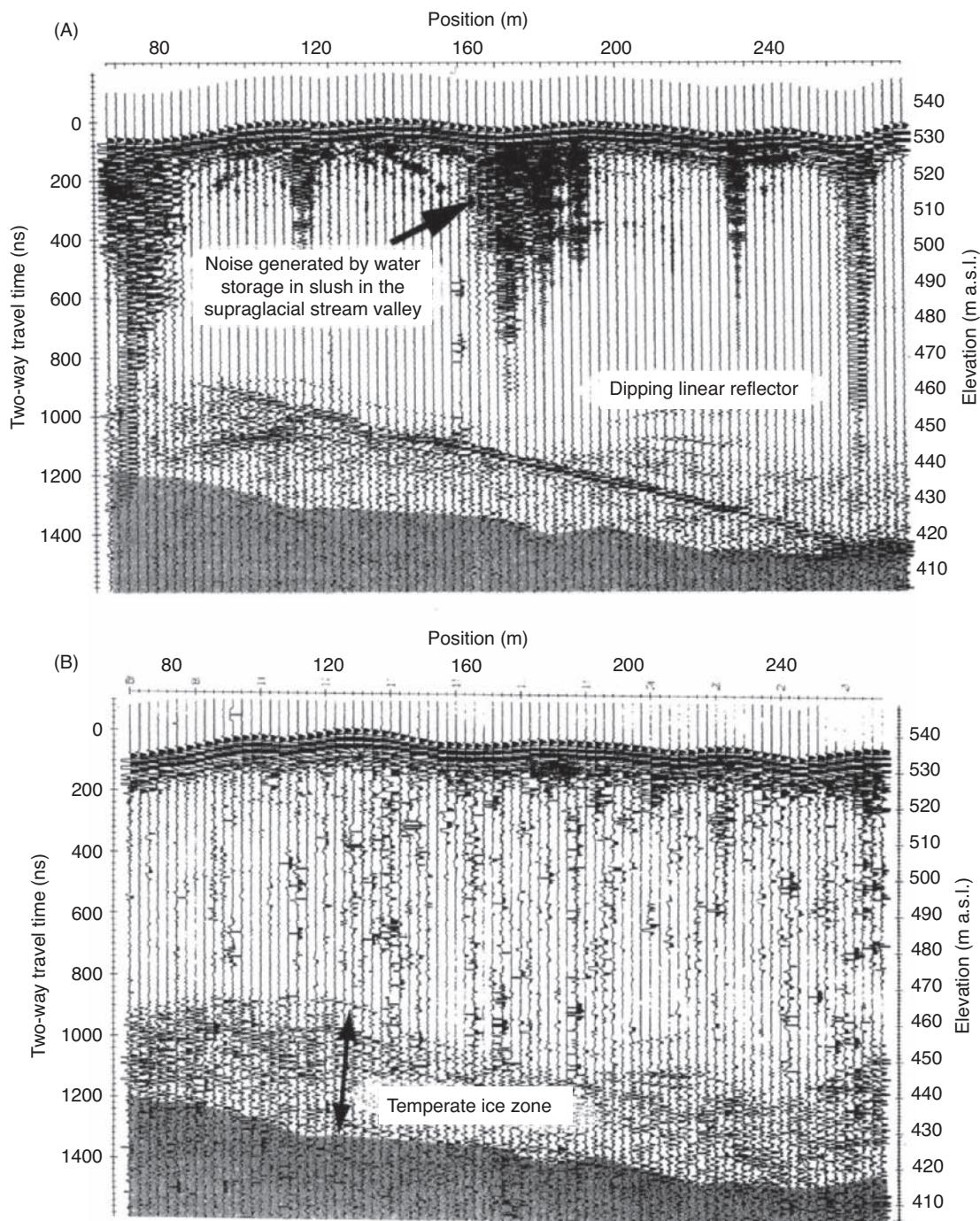


**Figure 14.26** Comparison of two radargrams acquired in (A) late June and (B) late July along the same profile on Stagnation Glacier, Bylot Island, Canada. From Irvine-Fynn *et al.* (2006), by permission.

#### 14.3.4 Glacial hazards

One of the adverse effects of climate change has been the catastrophic failure of moraine dams and ensuing outburst floods from glacial lakes in areas such as the Himalayas and the Andes. Many debris-covered glaciers develop large supra-glacial lakes that can have volumes of hundreds of millions of cubic metres of water. In themselves they represent a significant reservoir of fresh water.

However, when a glacial lake outburst flood (GLOF) occurs it can cause widespread damage for several hundred kilometres downstream, destroying whole communities, sweeping away bridges and houses, and damaging vital infrastructure. Many thousands of people have been killed by such floods. In Nepal, serious attention only started to be paid to such phenomena from around 1990. The focus of attention at that time was a glacial lake called Tsho Rolpa, in Rolwaling, a valley adjacent to the international border

with China. A small GLOF occurred from a neighbouring lake in 1991 and killed one elderly lady. The local villages raised the alarm about the much larger Tsho Rolpa lake. After a significant amount of field investigations from 1994, geophysical studies were carried out in 1999 and comprised electrical resistivity tomography and, for the first time in the Himalayas, ground-penetrating radar using a Malå 100 MHz system operated by staff from the Department of Hydrology and Meteorology, Kathmandu. The main concern was the possibility of buried ice within the terminal moraine itself. Melting of such ice would weaken the moraine and in time lead to its mechanical failure. Furthermore, to reduce the hazard posed by the 100 million m<sup>3</sup> of water stored in the lake, it had been proposed to lower the lake level by constructing an open spillway through the dam. Had ice been exposed by the excavation it could have triggered the failure of the dam. The GPR achieved depths of penetration in ice-free moraine of over 20 m and demonstrated that ice was not present. Subsequent excavation and construction of the spillway confirmed the absence of ice (Rana *et al.*, 2000); the lake level was lowered successfully by 3.5 m by July 2000. However, in another part of the terminal moraine, repeat observations since 1994 indicated that there was stagnant ice buried within part of the moraine complex. This was investigated using both ERT and GPR. Over the winter of 1996/97, some of the buried ice within the moraine melted very rapidly, leaving a roughly circular depression over 25 m deep and exposing an ice cliff beneath a thin veneer of debris (Figure 14.27A). This happened within 50 m of the moraine dam ridge and raised serious concerns that further melting could result in a possible catastrophic failure of the moraine. The recommendation was made that the lake level should be lowered by at least a further 11.5 m; this remains to be done. One of the radargrams acquired adjacent to this thermokarst feature is shown in Figure 14.27B. As the data have been topographically corrected, a constant radiowave velocity (0.167 m/ns) for the entire section has been applied (left-hand elevation scale). A short, flat reflection has been encircled in the radargram in Figure 14.27B. This was interpreted to be standing water located in a depression in the buried ice surface. The possible base of ice is indicated at the left-hand side and indicates that the base of ice dips towards the right (up-glacier). Several inclined reflections thought to be from within the temperate ice mass are also present. The ice cliff seen in the picture lies immediately at the right-hand edge of the radargram shown. The thin veneer of debris is clearly evident in the photograph overlying the dirty underlying glacier ice.

A radargram acquired from the base of the ice cliff depicted in Figure 14.27 and over the adjacent lake is shown in Figure 14.28; that shown in Figure 14.4 was also acquired across the water shown in Figure 14.27A. The reflections from two large boulders out of the line of the section occur at 53 m and 57 m along the profile. Note that a thin veneer of supra-glacial morainic debris is clearly evident as a layer of strong chaotic reflections and diffractions from boulders over the underlying glacier ice. The ice itself appears as a transparent zone best seen between the lake bed and lake bed multiple labels at the left of Figure 14.28. The bright reflection below 950 ns two-way travel time at 32 m along the profile is the lake bed multiple from the deepest part of the lake along this profile. The smudged appearance at the end of the profile is where the radar system

continued recording while the boat and antennae was stopped at the shoreline.

The interpretation of many of the radargrams acquired at Tsho Rolpa was aided by additional attribute analysis, which helped to distinguish areas of morainic debris, buried ice and structures within the ice and moraine. Tsho Rolpa continues to pose a serious hazard to villages and vital trails downstream, as well as an important hydropower installation at Khimte. Details of the interim remediation of Tsho Rolpa have been given by Rana *et al.* (2000).

Another similar example of the use of GPR and ERT to help to assess glacial hazards in the Nepalese Himalayas has been given in Section 7.6.4 and illustrated in Figures 7.57 and 7.58. These methods were applied at Imja Tsho and Solukhumbu, and the results discussed by Reynolds (2006) and Hambrey *et al.* (2008). At this location, depths of penetration through moraine exceeded 40 m, with greater depths achieved through underlying glacier ice.

These examples at Tsho Rolpa and Imja in Nepal clearly demonstrate the usefulness and success of GPR and especially in combination with electrical resistivity tomography in the assessment of glacial hazards associated with moraine dams. With the advent of wire dipole antennae to replace the rigid bistatic dipoles, fieldwork will not be quite as physically challenging as before, especially considering that these lakes lie at an altitude of around 4600 m.

## 14.4 Engineering applications on manmade structures

The radar technique has been developed into a range of specific applications in engineering: utility detection, bridge deck and railway ballast inspections, examination of engineered structures (e.g. concrete dams), road pavement investigations, non-destructive testing (NDT), and so on. In these cases, while the geometry and materials of each structure should be known, as-built records are often not kept. The method has also been used to investigate the internal composition of statues and of masonry facades of historic buildings. Also, what can be at odds is whether the structure has been constructed according to the required specifications. Indeed, the construction methods themselves may have left a legacy of subtle differences in physical properties within a particular structure. For example, an embankment made of fill material, which consisted largely of crushed dolerite, was thought to be uniform in its properties throughout. A radar survey using a 120 MHz antenna revealed subhorizontal layering within the fill which were interpreted to be associated with compacted horizons. These layers had been produced by the contractor's vehicles driving over the fill along roadways. Distinct reflections were evident from these horizons and occurred as a result of the reduction in soil moisture content (and hence altered dielectric constant) of the compacted horizons (Reynolds and Taylor, 1992).

(A)



(B)

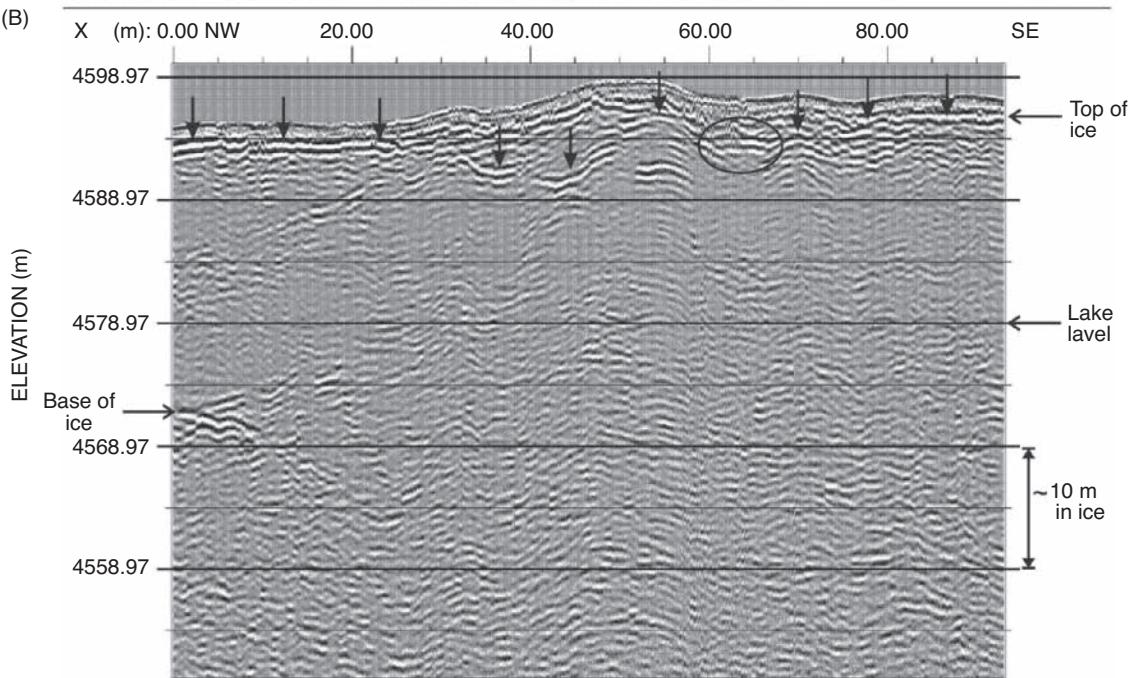


**Figure 14.27** (A) Picture of a newly formed ice cliff and lake at Tsho Rolpa, Rolwaling, Nepal, in May 1997.(B) Radargram acquired in 1999 with a 100 MHz Mala RAMAC system showing buried stagnant glacier ice beneath a veneer of morainic debris. Top of buried ice is indicated by downward-pointing arrows. [C]

#### 14.4.1 Underground storage tanks (USTs), pipes and cables

A very common application for radar surveying is to detect underground storage tanks (USTs), pipes and cables. However, it is also easy to misinterpret radargrams over USTs because of a number of

particular geometric aspects. Firstly, the synthetic response associated with a transect across the long axis of a single air-filled cylindrical tank at 200 MHz using zero-offset between transmitter and receiver antennae is shown in Figure 14.29 (Zeng and McMechan, 1997); free-surface and internal multiples were not simulated. The wall of the 3-m diameter PVC tank, the top of which is located at

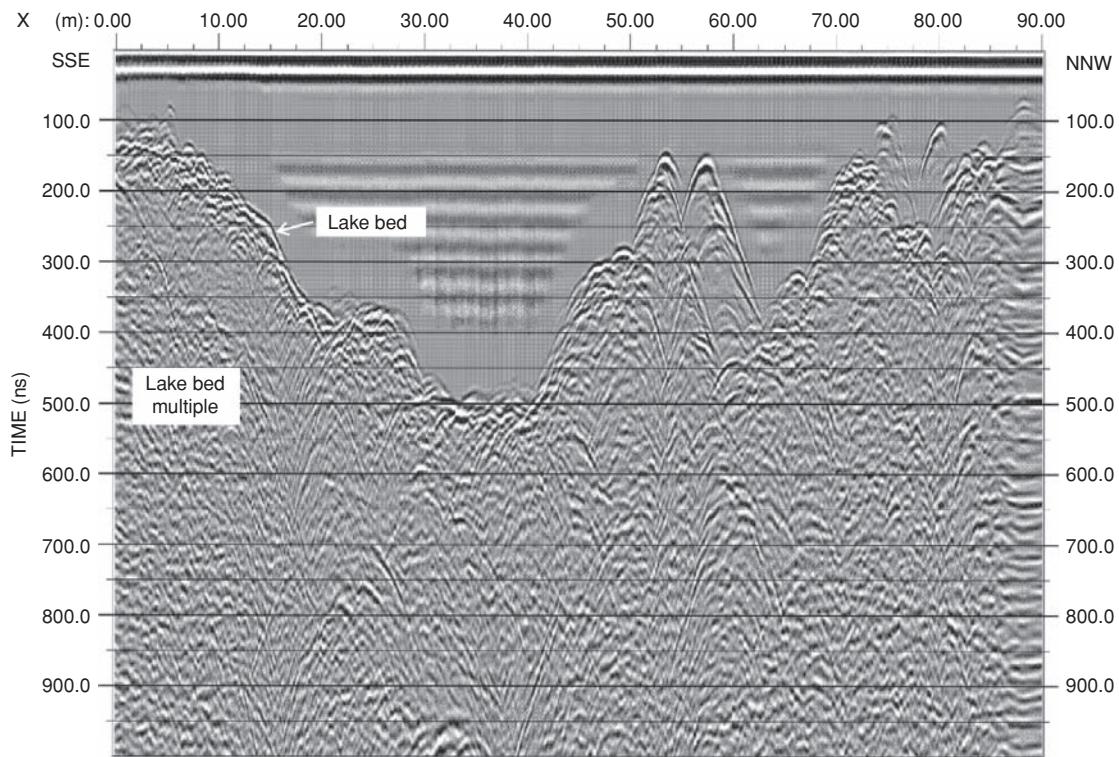


**Figure 14.28** A 100 MHz radargram acquired by boat across part of Tsho Rolpa, Rolwaling, Nepal.

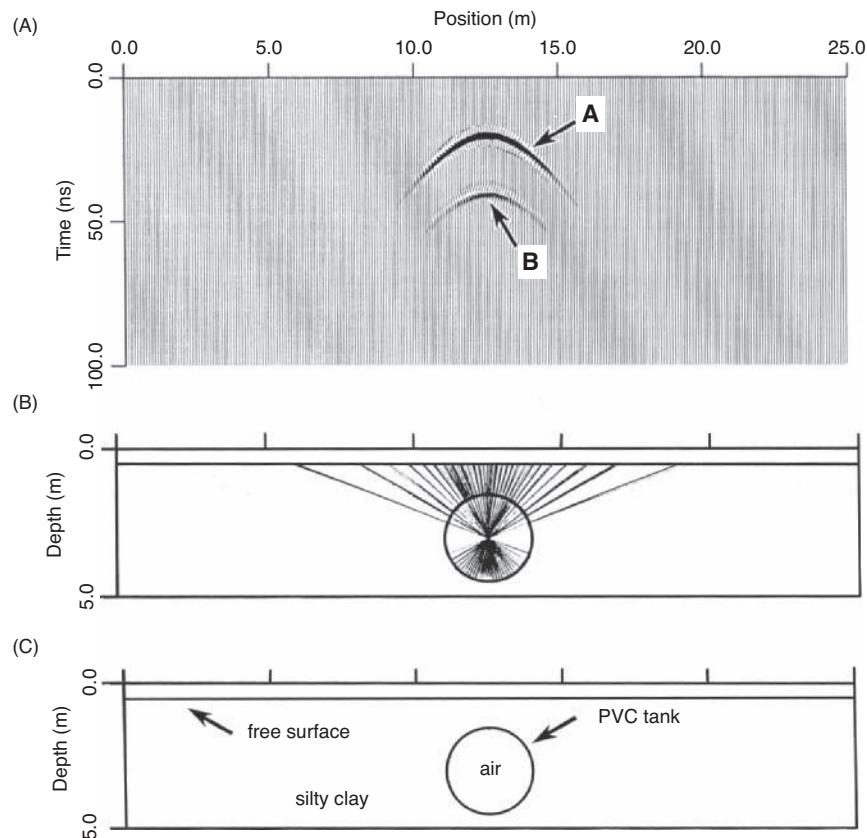


**Figure 14.29** Simulation of the zero-offset GPR response at 200 MHz across a cylindrical tank model. The synthetic radargram in (A) is produced by (B) ray tracing through the model (C) to obtain travel times. A and B are reflections from the top and bottom of the tank, respectively. From Zeng and McMechan (1997), by permission.

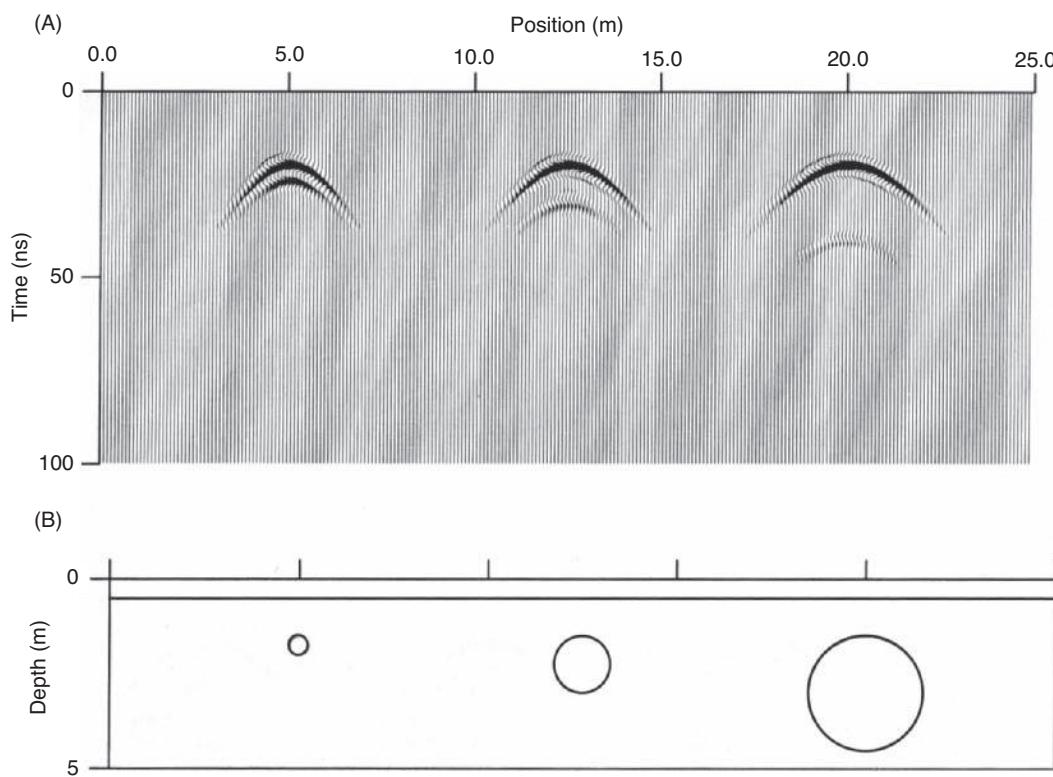


**Figure 14.30** (A) Synthetic radargrams at 200 MHz for three tank diameters shown in (B), 0.5 m (*left*), 1.5 m (*centre*) and 3.0 m (*right*). From Zeng and McMechan (1997), by permission.

1 m depth in silty clay, is 5 cm thick. Reflections from the top and bottom of the tank are clearly visible. However, the difference in curvature of the reflections from the top of the tank for different tank diameters is small (Figure 14.30), and this alone should not be used to determine the likely diameter of any UST. What is also clear from this figure is that the reflection from the bottom of the smallest tank occurs immediately on the tail of the reflection from the top of the tank and destructively interferes with it to reduce its overall amplitude. In real data with noise, this would be very hard to spot. For the other two, larger tanks, the time separation between the reflections from the top and bottom of the tank can be seen. If both the top and bottom reflections can be unequivocally identified, the time difference between them can be used to derive the diameter of the tank. In the case of the largest tank, the time difference should be twice the diameter (i.e. 6 m) divided by the radiowave velocity in air ( $\sim 0.3$  m/ns). This gives an expected time separation of 20 ns, which is what is observed in Figure 14.30. Zeng and McMechan (1997) also measured field profiles at a GPR test site at Borden, Manitoba, Canada, in which a number of pipes and cylinders have been buried. They have presented results for a 16-cm diameter plastic pipe buried at a depth of 1.25 m in sandy soil with dielectric permittivity of 8.5 from the surface to 0.5 m depth, and 6 from 0.5 to 1.0 m. The pipe was variously filled with air, tap water (conductivity, 29 mS/m), and salt water (conductivity, 4720 mS/m). The results for profiles across the pipe filled in turn as described are shown in Figure 14.31A (i)–(iii). Profile A(iv) is over a 15.5-cm diameter air-filled metal pipe. The synthetic 225 MHz

responses for the corresponding targets are shown in Figure 14.31B (i)–(iv) for comparison. As indicated by reference to Figure 14.31 for the smallest pipe, there is no obvious separate reflection from the bottom of the pipe, for the reasons previously explained. Figure 14.31A(ii) shows reflections from the top and bottom of the pipe, plus the first reflection multiple. That the reflections from the top and bottom of the tank are discernable is due to the longer time for the radiowaves to travel through the tap water compared with that through air. In contrast, for the case with the pipe being filled with saltwater, there is no bottom reflection. This was explained by the high conductivity of the saltwater attenuating the radiowaves.

It is also worth noting that the polarities of the first reflections in Figure 14.31A and B, (ii)–(iv), are all negative, while that for the air-filled pipe (Figure 14.31A and B, (i)) is positive. As the PVC pipe wall is thin, the pipe itself does not significantly influence the response (due to it being a small fraction of the skin depth). The polarity response is therefore in relation to the contrast between the dry soil and the material in the pipe, representing in each case a high to low velocity transition. The situation with an air-filled pipe is that the contrast is from low to high, with the air being a high radiowave velocity medium. In the case of the metal pipe, the skin depth is sufficiently small that the thickness of the pipe wall becomes dominant and the response of the metal pipe masks that of any material within it. Consequently, no reflection occurs from the bottom of the metal pipe. The detectability of the metal pipe in particular is due to the metal being conductive and also to a function of the orientation of the antennae dipoles with respect to

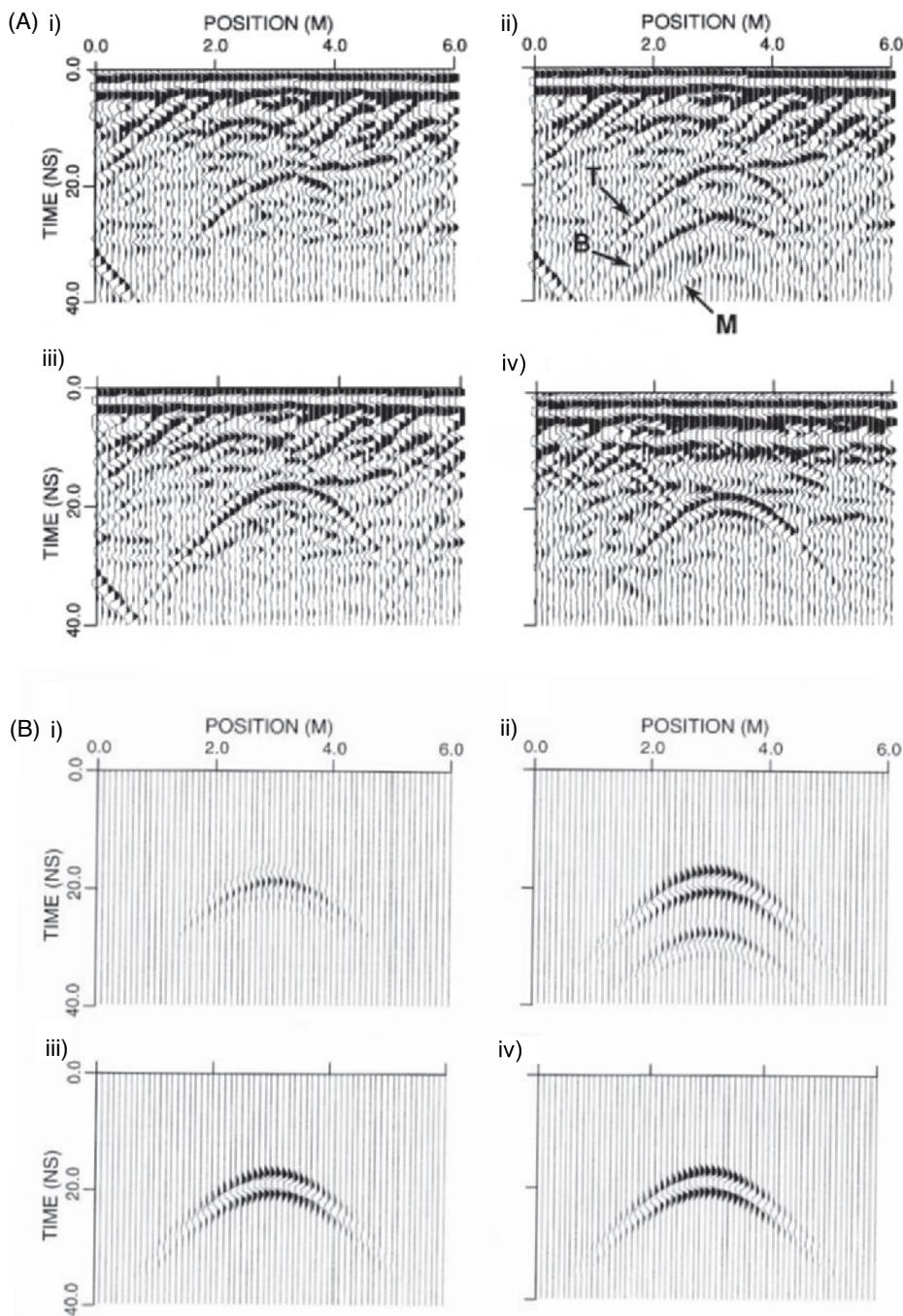


**Figure 14.31** (A) GPR records acquired at 225 MHz at 0.5 m offset across a plastic pipe filled with (i) air, (ii) tap water, and (iii) saltwater; (iv) is the response of a metal pipe buried at the same depth. Events T, B and M are from the top and bottom of the tank, and the first reflection multiple between the top and bottom of the pipe, respectively. (B) Synthetic 225 MHz responses for the same targets as in (A). From Zeng and McMechan (1997), by permission.

that of the pipe, as shown in Figure 13.13 and discussed in Section 13.3.3.

When more than one tank is present, the reflections observed include an artefact associated with their proximity as described by Porsani and Sauck (2007). They have described the raypaths from zero-offset transmitter-receiver antennae to a pair of buried steel tanks (Figure 14.32). Instead of just two reflections from the top

of each tank, a third event appears at the midpoint between the tanks but at a later two-way travel time. The raypath, simulated reflections and associated equations are shown in Figure 14.32. The occurrence of the artefact is clearly evident on field data as shown for a series of profiles across a pair of steel tanks buried in a test site acquired at 200 MHz and 400 MHz. In Figure 14.33A, it is possible to determine the edges of the excavated trench used to install the

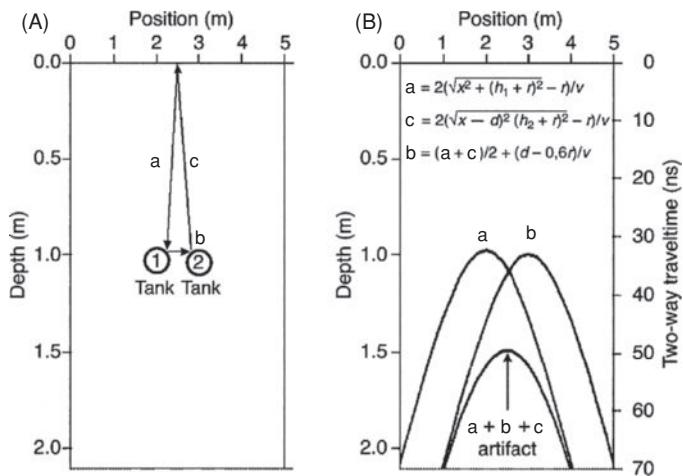


**Figure 14.32** (A) Schematic GPR raypath between two buried steel tanks. (B) Simulation of the wave propagation considering zero-offset between transmitter and receiver antennae, with the simplified equations for each raypath (a, b and c). From Porsani and Stauck (2007), by permission.

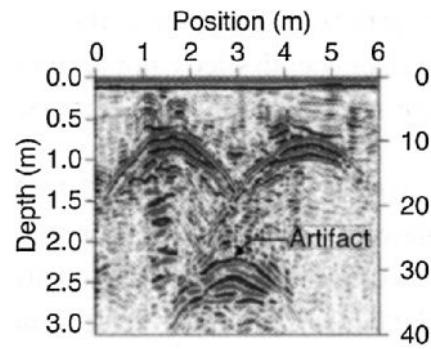


**Figure 14.34** A 500 MHz profile over two large steel tanks after standard processing without deconvolution. From Porsani and Stauck (2007), by permission. [C]

#### 14.4.2 Transportation infrastructure

The use of GPR for the inspection of bridge decks, railway running tracks and ballast, road pavements, airport runways and taxiways, and so on, is now extremely well developed, provides the basis for an entire radar industry sector, and has been reviewed by Saarenketo (2009). There has been substantial technical and software development specifically for these applications. GSSI, as an example of a GPR system and software manufacturer, has produced packages such as *BridgeScan* (1.6 GHz system), *RoadScan* and *BallastScan* (both use 2 GHz air-launch systems), and *Terravision™* (400 MHz, 14-channel 3D system) among others, which are illustrated in Figures 14.35 and 14.36. Software modules within the RADAN software family are also available for each application. Other radar manufacturers are developing their own suites of systems: see Appendix 1 for website details. Associated with this burgeoning market, there is also a substantial amount of literature relating to guidelines for the use of GPR such as provided by ASTM International, and in conjunction with Pavement Management Systems (e.g. the UKPMS), to

tanks, as well as identify the tops of the tanks. A third event is present, labelled 'artifact', as predicted. This feature also occurs on the 400 MHz profile. The benefits of higher-level processing of the 400 MHz data are shown in Figure 14.33B–D. A profile acquired at 500 MHz over another pair of steel tanks at another location is shown in Figure 14.34 with just standard data processing without deconvolution, and the artefact is clearly present.

When undertaking GPR profiles over metal tanks and pipes, it is important to be aware of reflections from the top and bottom, the time separation between such reflections if present, reflection polarity and the possible presence of reflection artefacts from additional lateral tank-to-tank raypaths.

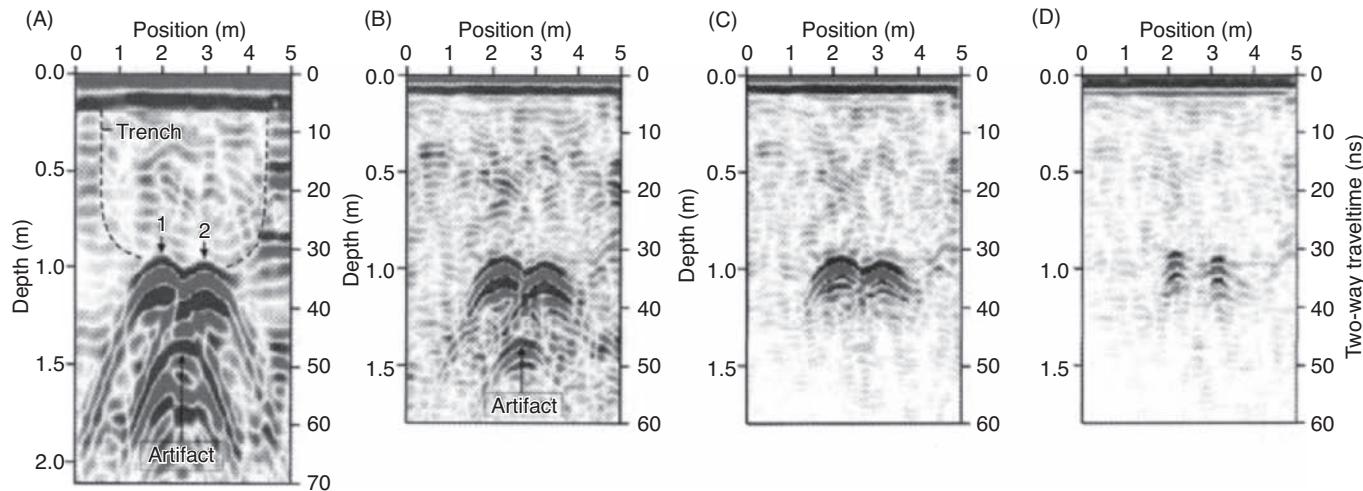


**Figure 14.33** Radargrams acquired over a pair of buried steel tanks at (A) 200 MHz, and (B) 400 MHz with standard processing without deconvolution; (C) as for (B) but with deconvolution and high-pass filtering; and (D) after Kirchhoff migration from (C). From Porsani and Stauck (2007), by permission. [C]

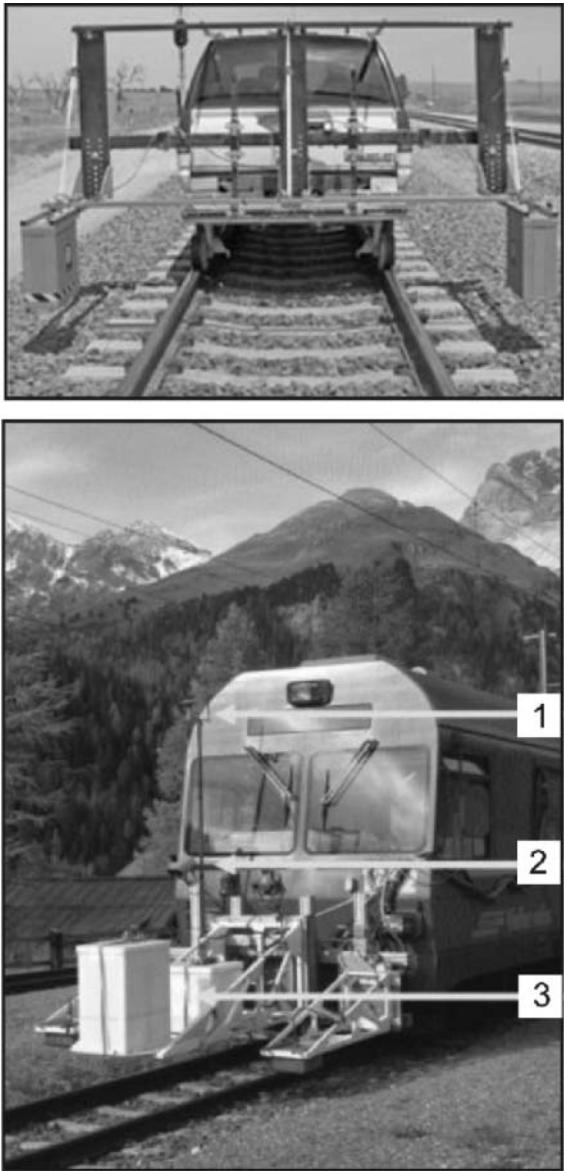


**Figure 14.35** Air-launch GPR antennae for railway ballast surveys (A) mounted on a dual-purpose road-rail vehicle, and (B) mounted on a train of the Rhätische Bahn, Switzerland: (1) dGPS antenna; (2) digital camera; (3) 400 MHz antennae. (A) Courtesy of GSSI, and (B) from Kathage et al. (2005), by permission. [C]

name but two. Details of the many sets of guidelines can be obtained from the respective websites (Appendix 1). While these systems are designed to manage vast quantities of data, users should always be sure to obtain groundtruth data to cross-check the results. Sometimes, the accuracies claimed by manufacturers and contractors are not fully justified, as the requirements for volume data management can result in generic application of default values and broad assumptions that may not be borne out in actuality. One of the key issues remains, as in all GPR interpretation, the lateral and vertical variation in radiowave velocity.

The ground radar method lends itself very well to the investigation of road pavements, bridge decks and railway ballast as they are

made up of discrete layers. For road pavements, radar can be used to measure layer thicknesses and to detect areas of delamination, where one horizon separates from another causing weakness in the road. This can lead to rapid deterioration of the road surface. As the depth of investigation is small (usually <1 m) and as fine vertical resolution is required, high-frequency antennae are used, typically 2GHz centre frequency as in the RoadScan system. One or more air-launch antennae are fixed to a frame on a vehicle so as to maintain a fixed and known geometry. The vehicle drives along the road being surveyed at speeds up to several tens of kilometres per hour. The lateral resolution is governed by the number of scans/second and the rate of travel of the antennae over the ground. If the scan rate is too slow or the travel rate too fast (or both), the number of traces produced may be too few to be able to resolve targets such as rebars. The graphical output is viewed for evidence of anomalous zones that might indicate potential problems within the road pavement and/or road base. Radar can also be used to check that the specified thickness of sub-base material has been put down during construction or if there are areas where the sub-base is defective. For railway ballast testing, the method is used to ensure that there has been no contamination of the ballast or upward reworking of the base beneath the ballast. For roads, bridge decks and railway ballast, another key target is the presence of voids.

In most of these applications, the radar method complements other non-destructive testing methods, such as acoustics (e.g. in bridge deck surveys), and falling weight deflectometers, nuclear density measurements and thermal imaging (e.g. road studies). As with all geophysical methods, some groundtruth data are invaluable for correlation purposes. In road pavement studies, cores are used to provide point-to-point correlation with radargrams. The major advantage of the radar method is that it is entirely non-destructive.

While the specialist systems are designed for acquiring very large quantities of data at anything up to traffic speed (e.g. up to 80 km/hr) and for covering as much ground as possible in the shortest reasonable time, there are occasions when the requirement is for higher resolution and finer detail. For this there is no substitute for hand-operated systems on the ground. One example of this is the detailed examination of concrete road slabs and the metal reinforcement at slab boundaries. A GSSI 1.5 GHz ground-based system was used to acquire data along each edge of every discrete concrete slab along 4.5 km of dual-carriageway. The concrete slabs were designed to be 200 mm thick, have metal rebars at mid-level around every 0.4 m along each edge, with a cage of smaller diameter reinforcement at the transverse edges of each slab, i.e. across the direction of traffic flow. The data underwent basic processing and where anomalies were identified from visual inspection, migration was carried out. This achieved a significant improvement in resolution as demonstrated by the data after basic processing and after migration shown in Figure 14.37. The border between each slab was filled by a thin polystyrene sheet and sealed at its top by bitumen. This formed a meniscus that left an air gap below the road surface and which generated bright diffractions on the radargrams at each slab edge (Figure 14.37A). The transverse metal cage also produced a profusion of diffractions that were hard to separate on the standard radargrams (Figure 14.37A). However, after migrating the data, the individual rebars could be differentiated. The



**Figure 14.36** (A) Air-launch GPR antennae for road pavement surveys mounted on the front of a pick-up truck. Additional radar antennae are towed behind the vehicle in contact with the ground. Positioning is achieved via a GPS antenna located behind the passenger cab. (B) Terravision™ 400 MHz multi-array 3D system. Courtesy of GSSI, by permission. [C]

migration process also collapsed the diffraction tails from the mid-level dowels that caused destructive interference with the normally horizontal reflection from the concrete slab base and road sub-base. The lateral continuity of these latter reflections was greatly improved by the migration process (Figure 14.37B).

In some cases, previous maintenance of the road had resulted in individual slabs being replaced. In such cases, mesh reinforcement was used instead of lateral dowels. However, in some cases, it appeared that the process of pouring the concrete had displaced segments of the mesh, resulting in an uneven level of reinforcement (Figure 14.38). In other cases, double-dowels were identified along with suspected open cracks through the slab (Figure 14.39A), and areas where the thickness of concrete was greater than expected, as well as no dowels having been installed (Figure 14.39B). These in-

dicate the usefulness of the GPR method in identifying areas where the road maintenance or construction is out of specification and where the method can be used for verification and quality control purposes.

#### 14.4.3 Dams and embankments

Water-retaining dykes along Dutch rivers have been provided at various locations with granular filters. The purpose of these filters is to reduce the groundwater potential inside and below the dyke in order to increase the stability and prevent bursting of a clay layer at the lee side of the dyke (Figure 14.40A). The gravel-filled filter must be in hydraulic contact with the underlying sandy layers.

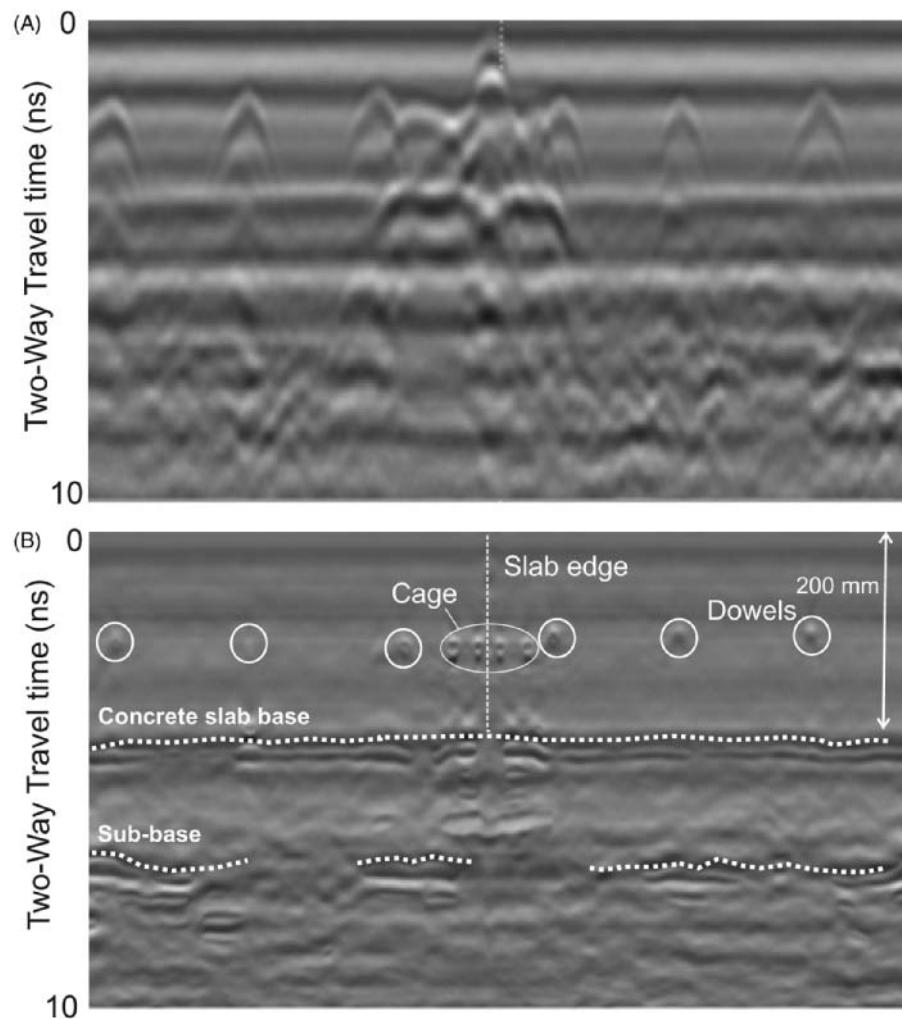


**Figure 14.37** (A) Standard and (B) migrated 1.5 GHz radargrams for a profile over a concrete roadway slab. The interpretation is indicated in (B); collapsed diffraction hyperbolae are circled and discrete events associated with metal reinforcement are highlighted within an ellipse.

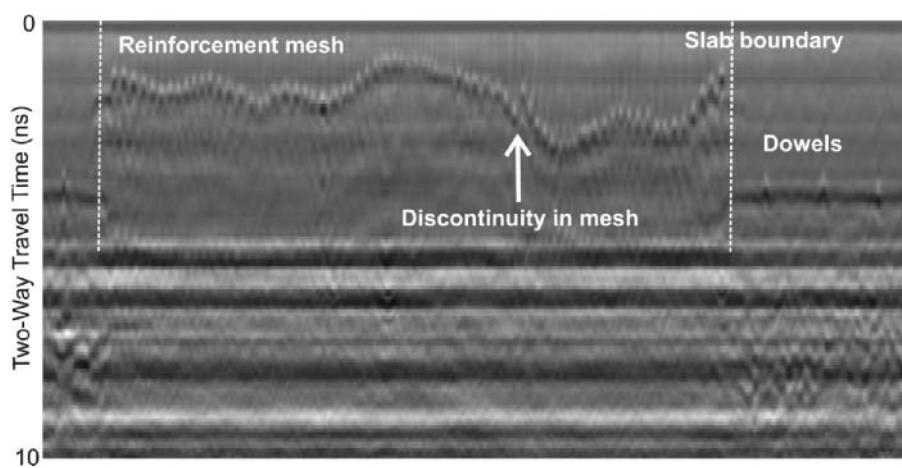


**Figure 14.38** A 1.5 GHz profile over a concrete roadway slab revealing an uneven reinforcement mesh.

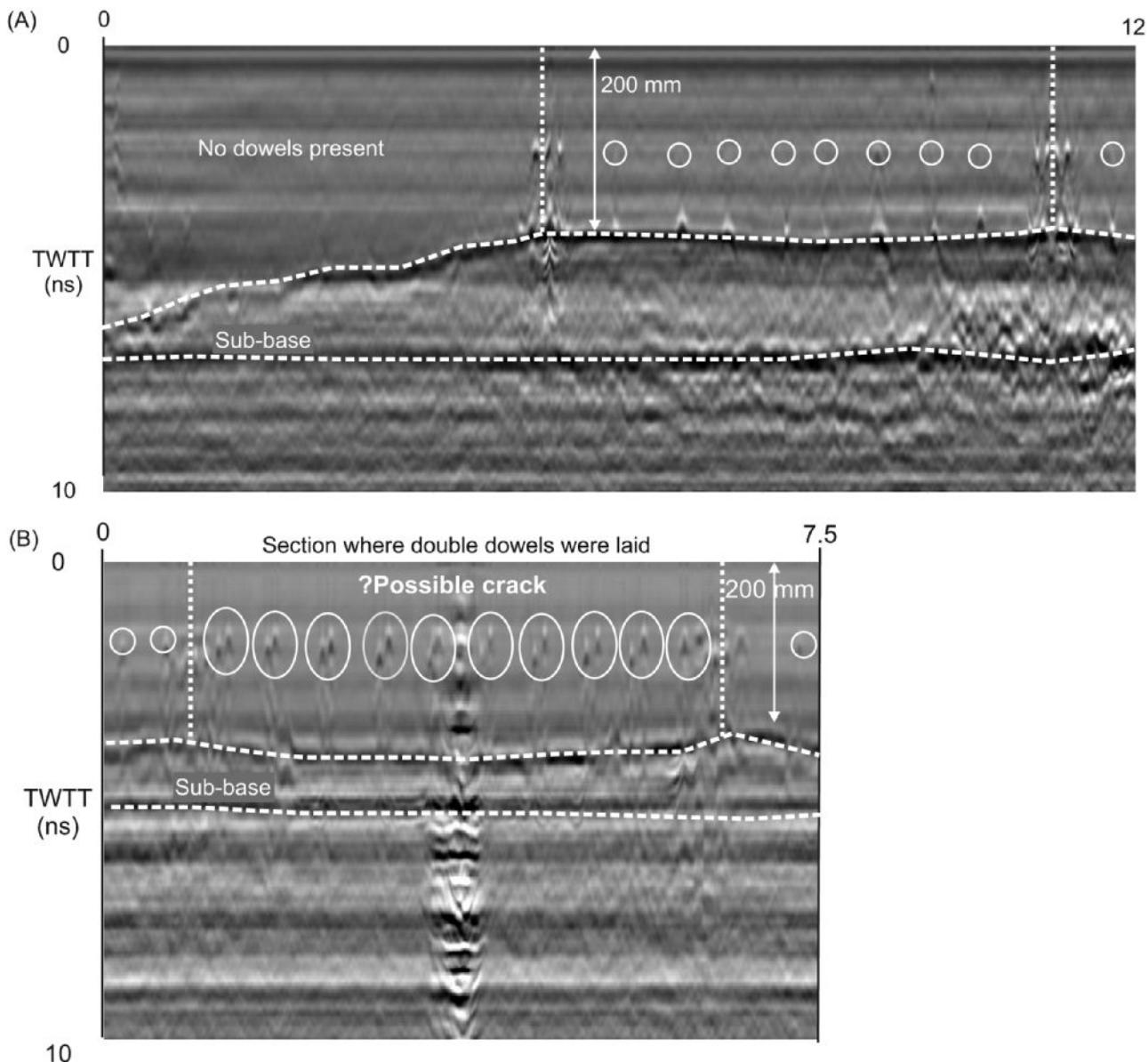


**Figure 14.39** Radargrams acquired using a 1.5 GHz antenna over a concrete roadway: (A) revealing an anomalously thick layer of concrete without reinforcement. Diffraction hyperbolae in the adjacent slab are shown circled. (B) A slab with double-dowels and evidence of a vertical crack through the concrete.

The filters have a working life of several decades but suffer with becoming clogged by finer particles. Consequently, it is necessary to monitor the filters periodically, preferably using non-destructive methods. Ground-penetrating radar has been used successfully in such investigations, as reported by de Feijter and van Deen (1990).

Radar surveys were carried out when the groundwater level was at its maximum and also at its minimum, over a time interval of several years. A sample radargram is shown in Figure 14.40B, which was obtained using a 300 MHz antenna with a GSSI radar system. The horizontal reflection (labelled 1) arises from the water table (with its multiple, 2). Reflection 3 is caused evidently by the filter–dyke interface. Note, however, that none of the horizontal layers within the dyke itself is imaged. Indeed, the zone to the right

of the filter–dyke interface shows significant attenuation of the radar energy, most probably because of the presence of water-saturated sandy clay and clay.

A common method of dam construction is to use an earth fill. However, degradation of the materials, ingress of water, voiding, and so on, can have an effect on a dam's integrity. Such a situation arose at an earth-filled dam in South Korea that had been constructed for water supply and retained about 100 million tons of water (Kim *et al.*, 2007). The dam, which is 55 m high and 407 m long, has a clay core that provides the main barrier to water flow. Following construction and upon filling with water, excessive water seepage was observed. While the maximum allowable seepage is 350 tons/day, the observed leakage ranged from 1200 to

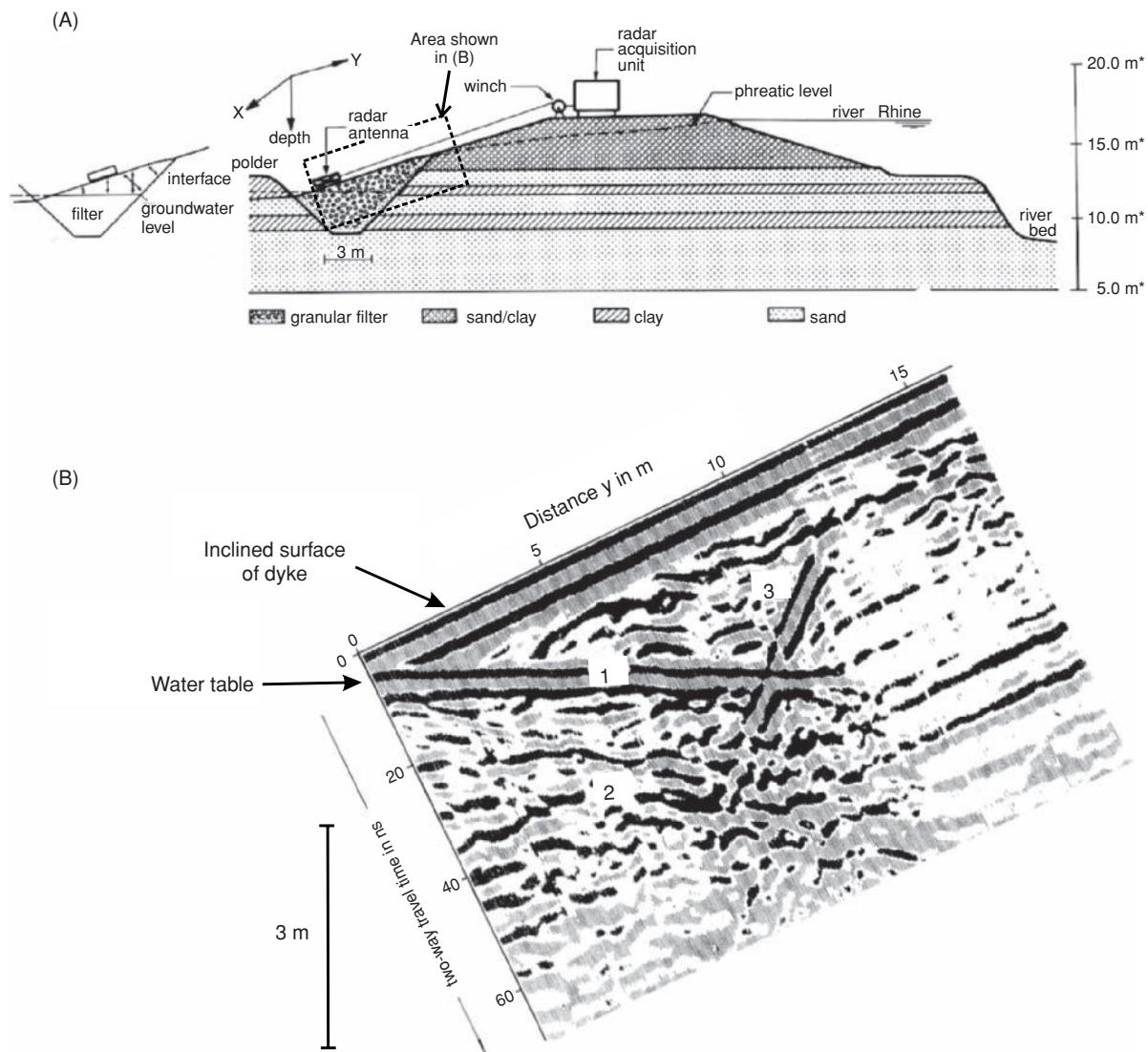


**Figure 14.40** (A) Cross-section of a dyke adjacent to the River Rhine, illustrating the engineered substructure, and the disposition of a radar transect shown in (B): 300 MHz radargram taken at highwater level. After de Feijter and van Deen (1990), by permission.

6000 tons/day. Furthermore, three sinkholes appeared on the dam crest and two areas of deformation or subsidence were identified at one end of the dam crest. A comprehensive geophysical investigation was launched and one of the methods used was GPR. A 50 MHz profile was obtained along the downstream edge of the dam crest (Figure 14.41A) in order to investigate the upper part of the clay core that was topped with gravel. There were known to be many buried services (cables, pipes, measuring instruments) and diffractions from these have been discounted. However, there still remain a significant number of diffractions unaccounted for (indicated by arrows in Figure 14.41A). These have been attributed to cavities in the near-surface. Although the radargram indicates a depth to 12 m, meaningful radar data are only evident to around 4 m due to the nature of the clay core.

Several six-fold 100 MHz radar profiles were acquired; one shown in Figure 14.41B was obtained along the upstream edge of the dam crest. The method of constructing the dam consisted of horizontal

dumping of material (clay, sand and gravels) followed repeatedly by hardening. This should produce largely horizontal layered structures and these should dominate the GPR sections. Reference to the radargram in Figure 14.41B shows that the layering is not continuously horizontal. Two discrete breaks in the reflection continuity are highlighted by vertical rectangles. Sections associated with subsidence are indicated by horizontal bars. A zone with reverse polarity is circled, although the cause of this is not known.

#### 14.4.4 Golf courses

An increasingly important sector is in the management and development of golf courses. In 1996 in the USA alone the annual cost of maintenance of golf courses was estimated as more than \$4.5 billion; by 2000, there were over 15,000 golf course facilities in the USA, with the number growing all the time. There is a significant case for the use of non-invasive geophysical techniques for

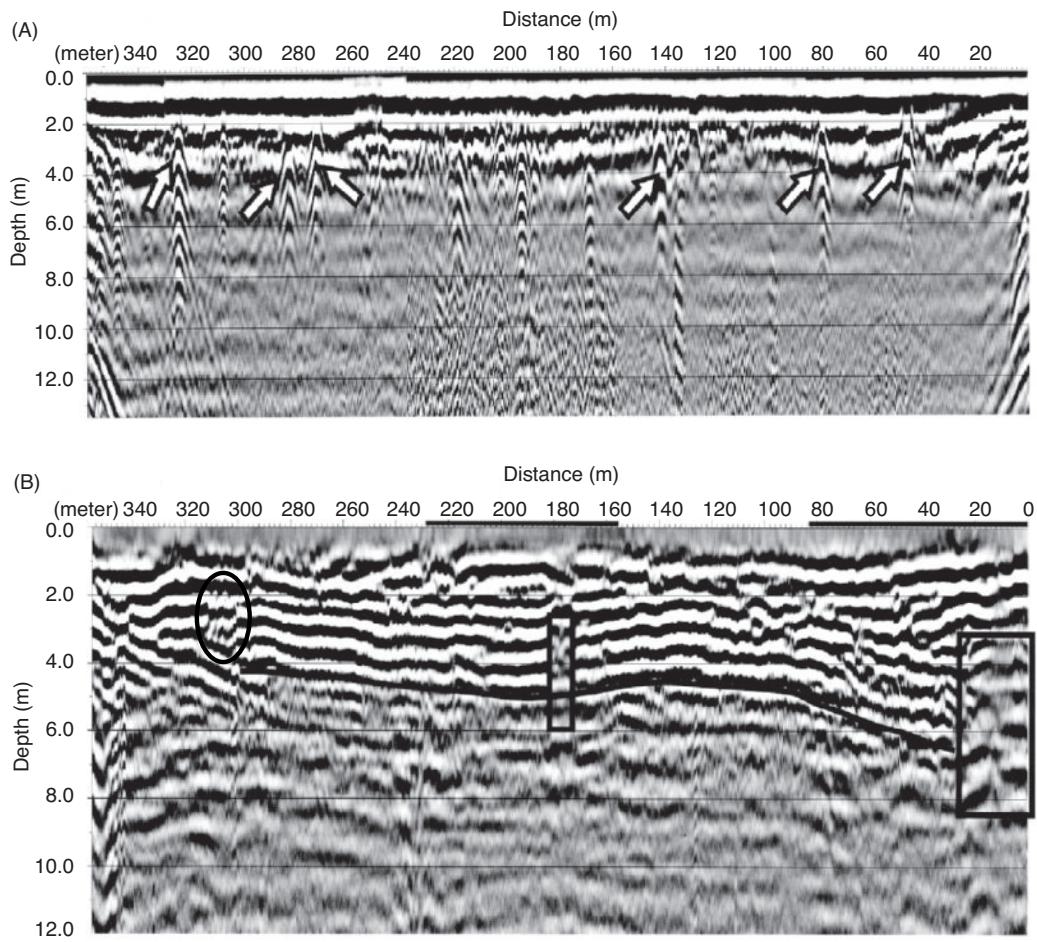


**Figure 14.41** (A) Unmigrated 50 MHz and (B) six-fold 100 MHz profiles acquired on the crest of an earth dam. See text for further details. From Kim *et al.* (2007), by permission.

the investigation of golf courses and, in particular, tees and greens. To achieve this, electromagnetic conductivity mapping and GPR are being used increasingly. Allred *et al.* (2005) have described tests undertaken on two golf courses using EM and GPR particularly to investigate the construction and drainage systems of greens. There are two main methods of green construction. The USA Golf Association method comprises a 0.3 m layer of sandy material below the surface that is underlain by a 0.1 m gravel layer resting on native soil, into which 0.25-m wide gravel-backfilled trenches with vertical sides 0.2 m high are cut to host 0.1-m diameter drainage pipes. The lateral edge of the sand and gravel layers is vertical. In contrast, the California Method comprises a 0.3 m layer of sandy material directly on top of native soil into which 0.15-m wide gravel-backfilled trenches with vertical sides 0.2 m high are cut to host 0.1-m diameter drainage pipes. The lateral edge of the sand and gravel layers is sloped typically at 45°. For either construction method, the drainage pipes are laid in either a rectangular or herringbone pattern. Representative radargrams at three different frequencies acquired using a Sensors & Software Noggin<sup>Plus</sup> system along the same line at the California Method practice green at the Golf Club of Dublin are shown in Figure 14.42. Time-slice amplitude maps for three time-depth ranges over the same green are shown in

Figure 14.43. The line of the profile in Figure 14.42 is indicated on Figure 14.43D. In each part of Figure 14.42, a diffraction arising from one drainage pipe is encircled. The depth values were calculated using a radiowave velocity of 0.082 m/ns derived from hyperbola curve-matching. The line interval used was 1 m and a trace interval of 0.05 m. Better horizontal resolution would have been achieved using a finer trace interval given that the pipe diameter is twice the trace interval used. Similarly, the radargrams in Figure 14.42 suggest a depth of penetration of less than 0.5 m and could have benefited from a shorter time window and finer trace sampling interval. Nevertheless, the bottom sand layer is well-defined, as are the sloping edges of the sand and gravel layers. In Figure 14.43, the broad herringbone pattern of the basal drainage system is clearly imaged, although the angular blotches (one example circled) along each arm of the drains appears to be a function of the spatial sampling of the survey lines coupled with the method of generating the time-amplitude slices, and is therefore an acquisition-processing artefact. The areal extent of the practice green is best indicated using the 250 MHz antenna (Figure 14.43A). A summary interpretation is presented in Figure 14.43D. This example demonstrates well the applicability of high-frequency radar mapping of golf course facilities.

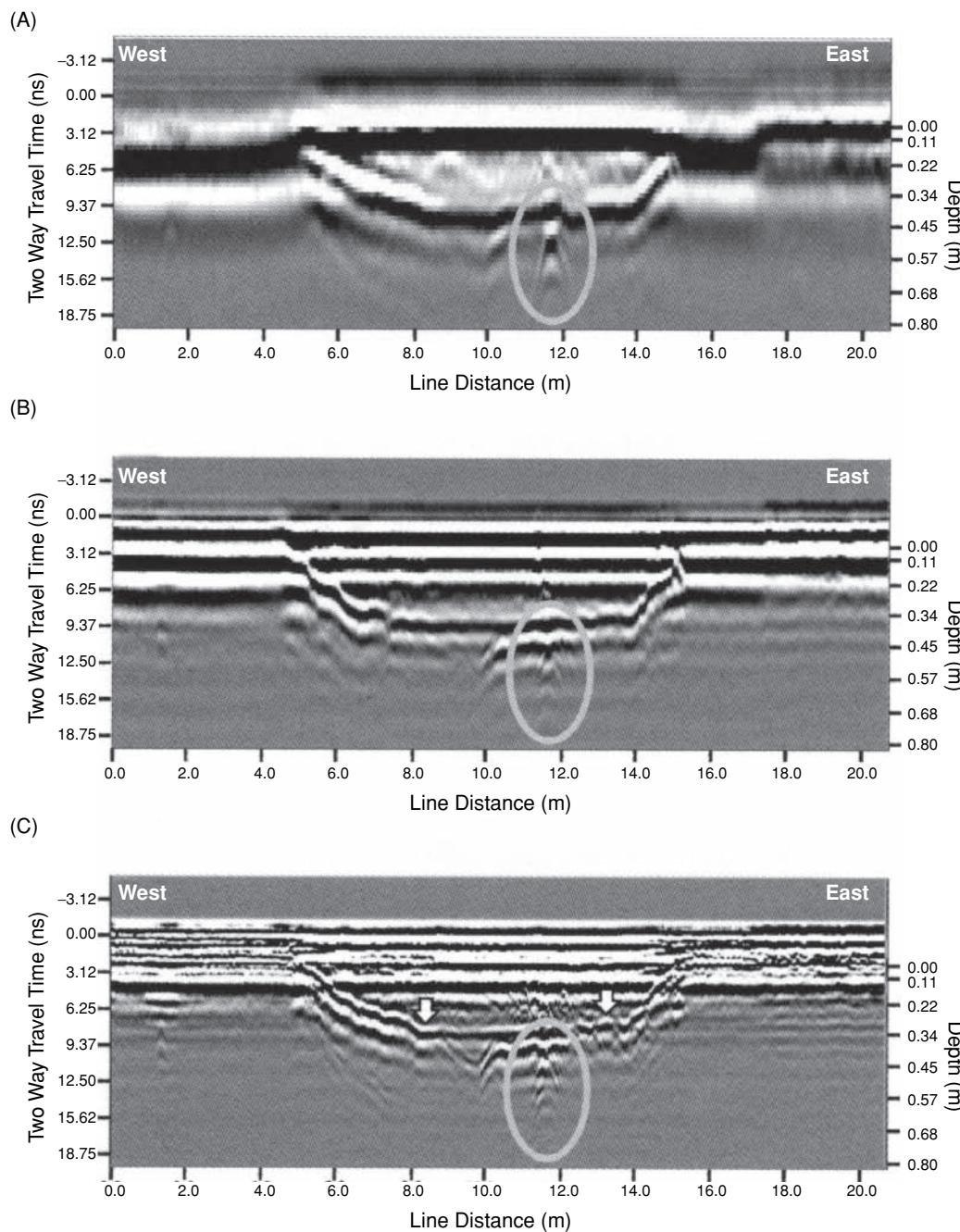


**Figure 14.42** GPR profiles acquired using (A) 250 MHz, (B) 500 MHz, and (C) 1 GHz antennae along the same line at the Golf Club of Dublin California Method practice green. The diffraction from a buried pipe is circled in each profile. The downward pointing arrows in (C) indicate the bottom of a sand layer. From Allred *et al.* (2005), by permission.

## 14.5 Voids within manmade structures

One of the commonest applications of ground-penetrating radar in the investigation of manmade structures is the detection and location of voids. Radar has been used extensively to inspect the condition of brick-lined tunnels and sewers. In the latter case, radar is often used in conjunction with closed-circuit TV (CCTV).

Two particular aspects of radar make the method particularly suited to such investigations. One is that the speed of radiowaves in air is around three times faster than in solid materials and thus produces a pronounced velocity 'pull-up' effect in association with a significant void. The second is the occurrence of resonance which happens when the wavelength of the incident radiowave energy is the same as, or shorter than, the dimensions of the void.

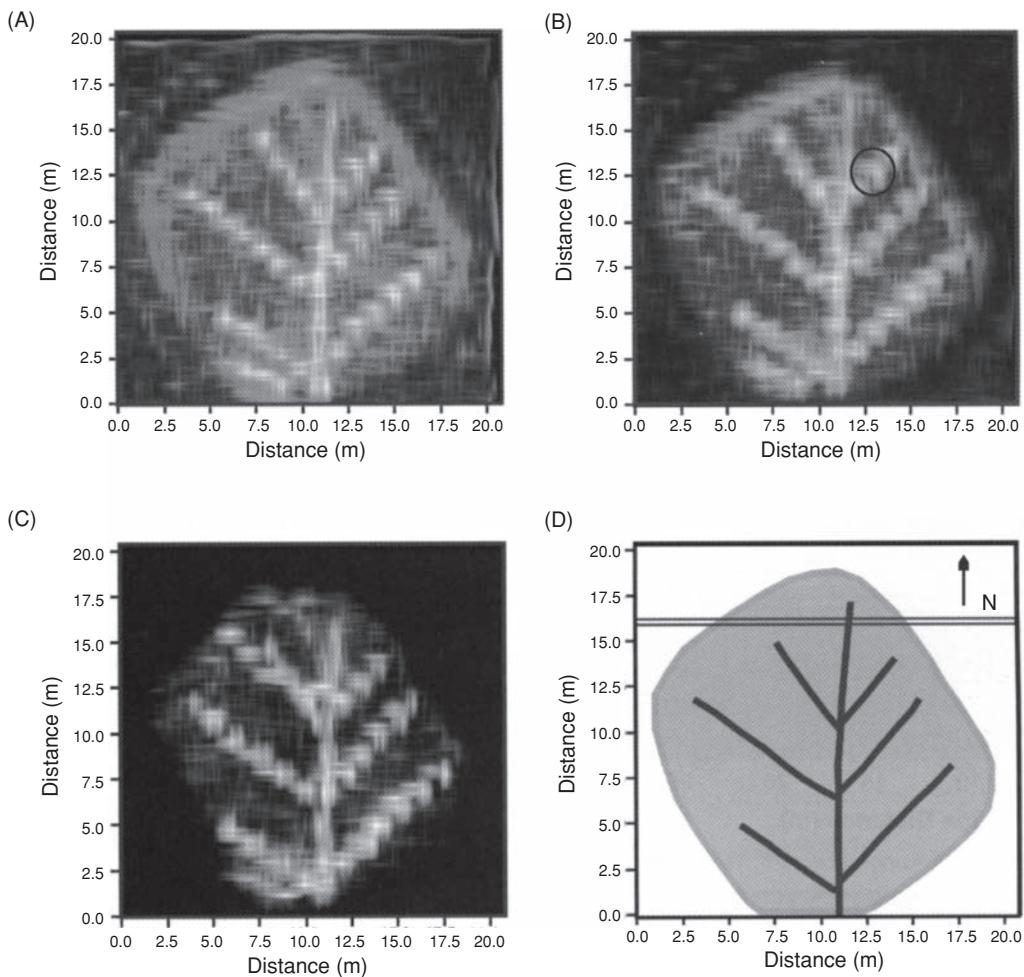


**Figure 14.43** Time slice amplitude maps from 8–15 ns (0.34–0.61 m) at (A) 250 MHz, (B) 500 MHz, (C) 1 GHz; (D) shows the interpreted schematic map with the areal extent of the green (grey shaded area) and drainage pipe locations (solid black lines). An acquisition-processing artefact is circled in (B). The double thin black lines in (D) indicate the position of the profile from which the radargrams in Figure 14.41 were acquired. From Allred *et al.* (2005), by permission.

### 14.5.1 Voids behind sewer linings

An example of a radargram acquired in a sewer survey is given in Figure 14.44A. This shows an extract of a radargram obtained where an air void was found above the crown of a sewer. Two features are evident on the radar section: one is the obvious difference in position of the crown of the sewer each side of the void (Figure 14.44B); the second is the obvious lozenge-shaped anomaly associated with the air void (picked out with white dashed lines in Figure 14.44A). The data were acquired using a vertical-looking 500 MHz antenna with a GSSI SIR-3 radar system.

### 14.5.2 Buried crypts and cellars

Not all air voids occur as failures in construction. There are examples where radar has been used to locate hidden crypts in churches and in other historic buildings, or old Second World War air-raid shelters whose locations have been lost.

An excellent example of a radargram showing the location of a crypt has been provided by Stratascan from a survey at Worcester Cathedral (Figure 14.45). This particular survey profile was carried out at right-angles to the long axis of the Charnel House, which has an arched roof. The stone–air interface of the roof of the Charnel House is obvious by the bright strong amplitude reflections, the apex of which is at 7.5 m along the profile (depicted by a dot-dashed line). Note that at about 6 ns above the top of the Charnel House roof reflection, there is a much weaker reflection which has the same shape as the reflection from the crypt (black dashed line). This is interpreted to be from the top surface of a line of stones used to construct the ceiling arch of the Charnel House.

The bright domed reflection at the bottom of the radargram is not due to a heap of rubble on the floor of the Charnel House, but is the reflection arising from the floor itself. That it is domed is purely due to the velocity pull-up effect from the air-filled crypt. Given an air-filled void 2 m deep, the reflection from the floor would occur at a two-way travel time some 26 ns ahead of a reflection from a

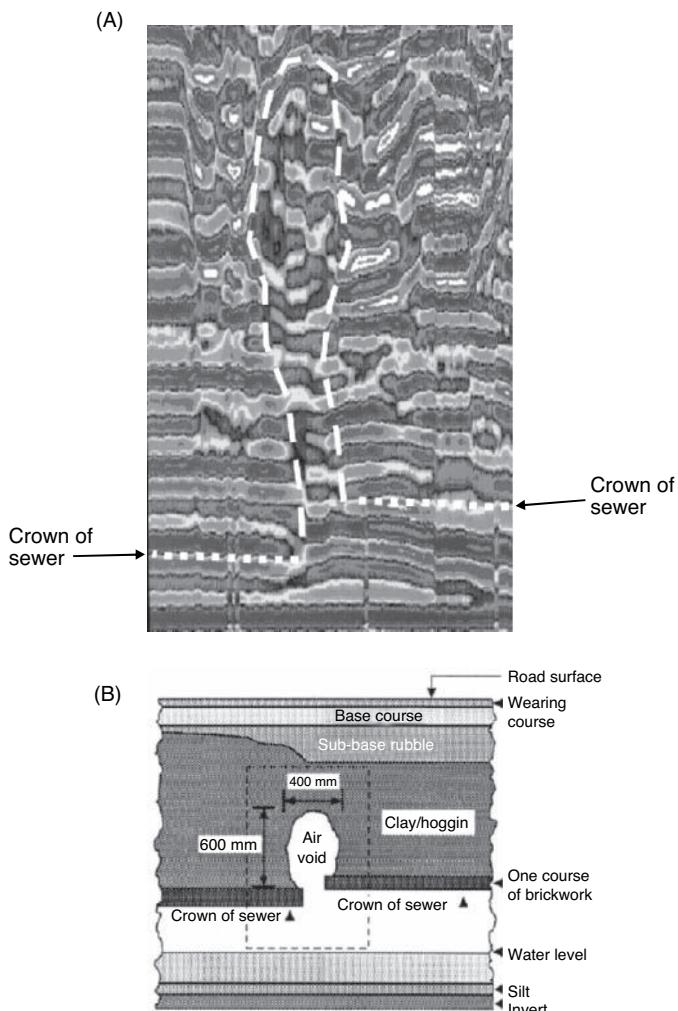


**Figure 14.44** (A) Radargram through clay hoggin material above a damaged sewer; a void is evident on the section and is delineated by dashed lines. The actual situation is shown in (B). Courtesy of Stratascan Ltd. [C]

comparable depth within the adjacent soil. Note also that the reflection from the stone-air interface at the ceiling of the Charnel House has the form of a leading white then positive, whereas the reflection from the floor (air-stone interface) has the form positive then negative white. The polarity change is attributable to the passage of radiowaves from (a) a slow to fast medium (stone to air) and then (b) from a fast to slow medium (air to stone). Consequently, the phase of the reflection changes, as does the sign of the reflection coefficient (see Section 13.3.1). Another bright event is highlighted by a black ellipse in Figure 14.45. It is possible that this is due to a void beneath the floor.

In some ancient buildings, additional complications can arise from the dimensions of the stone used in the construction of the building in relation to the wavelength of the incident radiowaves. Using a 500 MHz antenna over stone blocks ( $V \sim 0.1 \text{ m/ns}$ ), the wavelength is 0.2 m which is comparable to the dimensions of the blocks. Consequently, adverse phase interference can arise from internal reflections from the faces of individual blocks, making the

overall radargram much more chaotic than it would otherwise have been. Similarly, building materials used to fill-in behind stone walls can be of a wide variety of materials, ranging from stone rubble to soil that may compact to leave air-filled voids.

The city of Chester lies at the northern edge of the Cheshire Plain and has been the centre of human habitation for many centuries. A Roman fortress or *Principia* with an associated civilian settlement named 'Deva' was established by the Romans in the 8<sup>th</sup> decade AD. The site has been continually occupied through Anglo-Saxon, Norman and Medieval times, to the present day. Historically, construction within the city has re-used materials from former buildings, resulting in unique structures that are still present today. These include a series of interconnected frontages forming multi-level, raised walkways, known as 'The Rows', through commercial properties dating from different periods and with different architectural styles.

Near-surface site information was required for the potential redevelopment of an existing commercial shop premises in The Rows close to the known site of the *Principia*. There was also anecdotal evidence indicating the possible presence of relict Medieval cellars (undercrofts) and associated passageways beneath the premises. A high-resolution GPR investigation was undertaken within the shop to detect near-surface features, including a Medieval cellar, the location of which was unknown prior to the survey (Pringle *et al.*, 2009). One of the limitations placed on the survey was that there was to be little disruption to the layouts within the shop so that it could continue to operate during working hours as normal. Linear profiles were acquired on a 0.5-m square grid-pattern both within the premises and on an exterior raised walkway. Multifrequency (250, 500 and 800 MHz dominant-frequency antennae) repeat-surveys were acquired using a Malå RAMAC X3M system with shielded antennae over the same grid pattern to resolve progressively deeper structures. Within the limitations of the available space, orthogonal survey lines were established at 1 m intervals and a trace interval of 0.01 m.

A section across the undercroft produced using an 800 MHz antenna is shown in Figure 14.46. Fourteen regularly-spaced ( $\sim 0.6 \text{ m}$ ), shallow ( $\sim 5 \text{ ns}$  two-way travel time) hyperbolae were identified on the sections and were interpreted as representing walkway support beams. Absence of reflections from depths of around 0.2 m were interpreted to represent an open cellar, which turned out to be the air-filled undercroft. Three identified near-surface rectangular areas were found not to be associated with the undercroft. These were characterised by broad, hyperbolic reflections and interpreted to represent heterogeneous rubble backfill. Separate, isolated, raised areas were also identified  $\sim 1.5 \text{ m}$  below present floor level; these were interpreted to be relict brick column supports from a long-demolished Roman building. All of the targeted anomalies were intrusively investigated and provided positive confirmation of the geophysical interpretations. Floor-supporting wooden beams with steel supports, the Medieval undercroft, plus associated passageways and an unexpected trapdoor access position were all identified. This example demonstrated the ability to use GPR within a complex retail premises to locate and characterise the modern, Medieval and Roman features without extensive intrusive investigation and with minimal disruption to commercial operations.

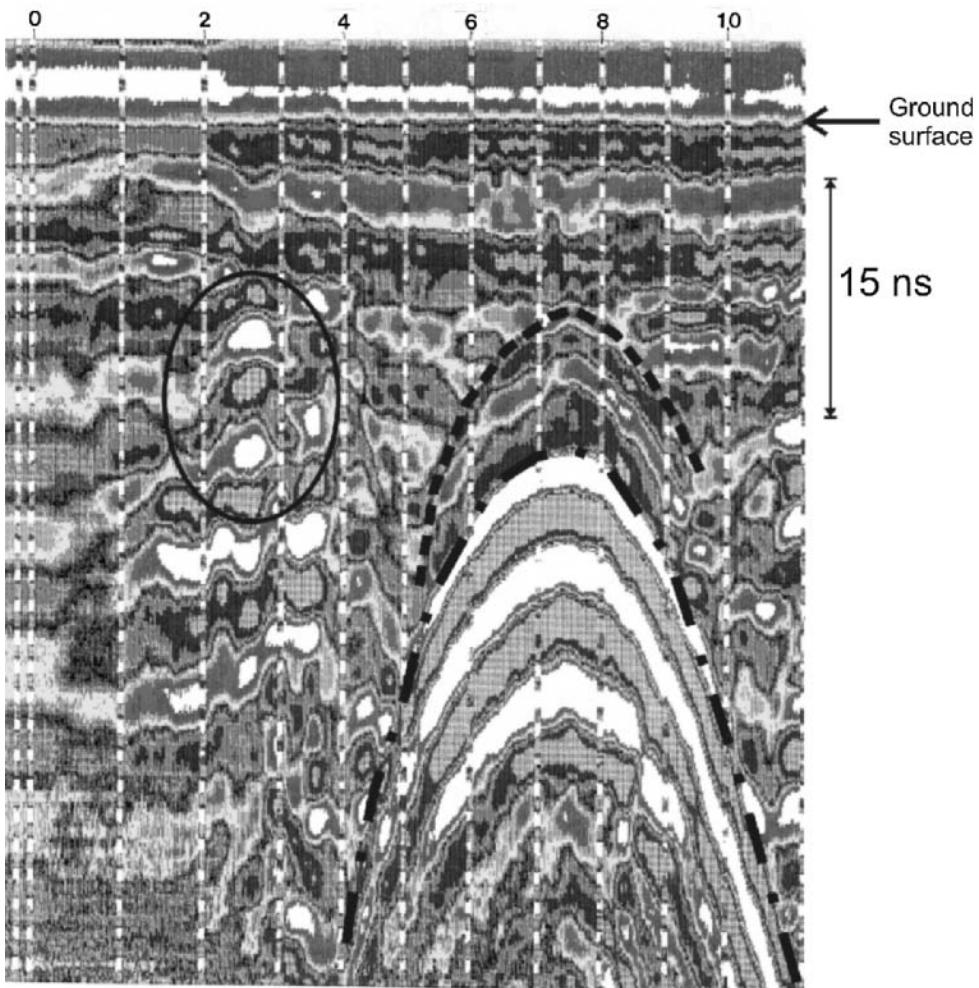


**Figure 14.45** Worcester Cathedral: radargram over a buried vault. See text for details. Radargram courtesy of Stratascan Ltd. [C]

### 14.5.3 Coastal defences

The case history in this section is to illustrate the detection of voids within a contemporary structure, namely the East Promenade in the coastal holiday resort of Rhyl, Denbighshire, on the north Wales coast, UK. The promenade acts as a sea defence to protect the shoreline and town from damage during stormy weather. It is subject to damage by marine scouring. The structure also provides a wide elegant dedicated pedestrian walkway along the sea front, and during the holiday season hosts many vendor kiosks that service a busy tourist destination. The original concrete sea wall at Rhyl was built between 1907 and 1913 over the edge of a prominent line of sand dunes up to 10 m high, but necessitated a seaward extension to form the present-day configuration. However, just before the start of the tourist season in April 1998, a segment of the promenade failed spectacularly during a maintenance programme and revealed the existence of a major cavity below the running surface of the promenade. The hole in the mass concrete un-reinforced slab measured 1.8 m by 2.2 m and the void ranged up to about 1.5 m deep (Figure 14.47A). In order to protect pedestrians using the promenade, sand was tipped into the hole to fill the void and the site barricaded. Sub-

sequent visual inspection of the remainder of the East Promenade revealed numerous shallow depressions and areas of water ponding as well as zones of longitudinal, radial and alligator cracking. Some cracks had displacements of up to 10 mm. There was serious concern about the state of the promenade and the possibility that substantial and costly remedial works might be needed if there was found to be more extensive voiding beneath the promenade. This would have disrupted the use of the promenade for a significant period of time and would have had serious economic effects on the tourist trade locally.

A GPR survey was undertaken using a GSSI SIR-2 system with a 900 MHz antenna along traverses separated by 1 m across the width of the promenade (Nichol and Reynolds, 2001). The profiles generated at the collapse site (e.g. Figure 14.47B) depict a uniform, featureless signal that corresponds with the air-filled void. A second smaller void is also evident between -61 m and -64 m. In addition, the pile of loose sand back-tipped into the hole forms a conspicuous anomaly. Using known targets within sand locally, the radiowave velocity was determined to be  $0.1 \pm 0.02$  m/ns. The radar survey indicated that the concrete slab at the collapse site varied up to 0.15 m thick compared with a typical thickness of 0.2 m elsewhere along the

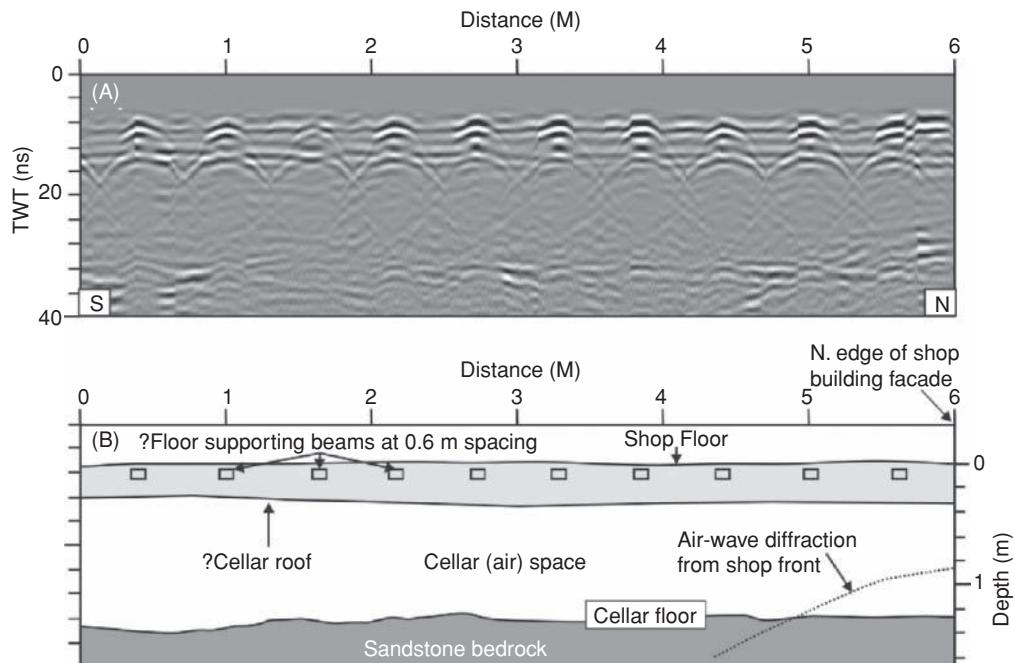


**Figure 14.46** An 800 MHz 2D radargram acquired over the exterior raised walkway at The Rows, Chester, UK, and (B) interpretation, showing reflections from the shop floor supporting beams, undercroft roof, open cellar space and the undercroft floor. The marked air-wave event is thought to be from the above-ground building. From Pringle *et al.* (2009), by permission. [C]

promenade. The concrete locally also appeared to be more friable and at a more advanced stage of deterioration than elsewhere along the promenade. The collapse was attributed to a combination of thinned, cracked and rotten concrete in conjunction with the presence of a sub-slab void formed most likely from marine scouring. Elsewhere along the promenade a range of shallow voids, generally less than 0.18 m deep, was identified and mapped from the radar results. These were attributed to the settlement of the underlying dune sand. The radar results were subsequently confirmed during later remedial work, the amount of which was substantially less than had been originally feared. Consequently there was minimal disruption to the activities along the promenade. The GPR survey provided the comprehensive understanding of the site needed to formulate a strategy to efficiently and economically repair the foundation support to the promenade and thereby ensure the safety of pedestrians using it.

over flat ground made up of alluvial silts, gravels and boulder clay at a site at Caersws, Powys, Wales, UK. The radargram shows very clearly the reflections arising from the surface of a Roman road with ditches on each side (emphasised by a dashed line). The swathe of the carriageway appears as a slightly depressed central zone.

## 14.6.2 Historical graves

The location of graves can be important for at least two reasons. As consecrated ground, there has to be considerable care exercised if the site is wanted for development. Also, there may be important archaeological information associated with the buried remains. It is doubly important, therefore, that the locations of graves can be determined non-destructively. One such survey of graves using GPR among other techniques has been described by Bevan (1991). Radargrams obtained in two orthogonal directions across a postulated grave are shown in Figure 14.49. To aid the interpretation of the radar results, an electromagnetic ground conductivity meter (an EM31) and a magnetometer were used for corroboration. As can be seen from Figure 14.49C and D, these other tools produced geophysical anomalies which are closed (form concentric contours) around the locations of the graves. It should be emphasised that it is the disturbed ground associated with the graves that tends to show up on radargrams, not the bodies themselves.

The location of old graves can have practical implications. A local council in Wales was responsible for a former cemetery that had been converted into a public amenity having removed the headstones. However, tarmac paths across the site had started to subside and holes develop, probably as a result of the collapse of individual grave

## 14.6 Archaeological investigations

### 14.6.1 Roman roads

Radar has many applications in archaeological investigations, especially as the depth of penetration required is usually small (commonly less than 3 m). Radar can be used as a first-look technique or as a fill-in method between areas of excavation. One example of the successful use of radar in imaging an archaeological feature is given in Figure 14.48. The radargram was obtained using a 300 MHz antenna (range setting = 40 ns) with a GSSI SIR-3 system

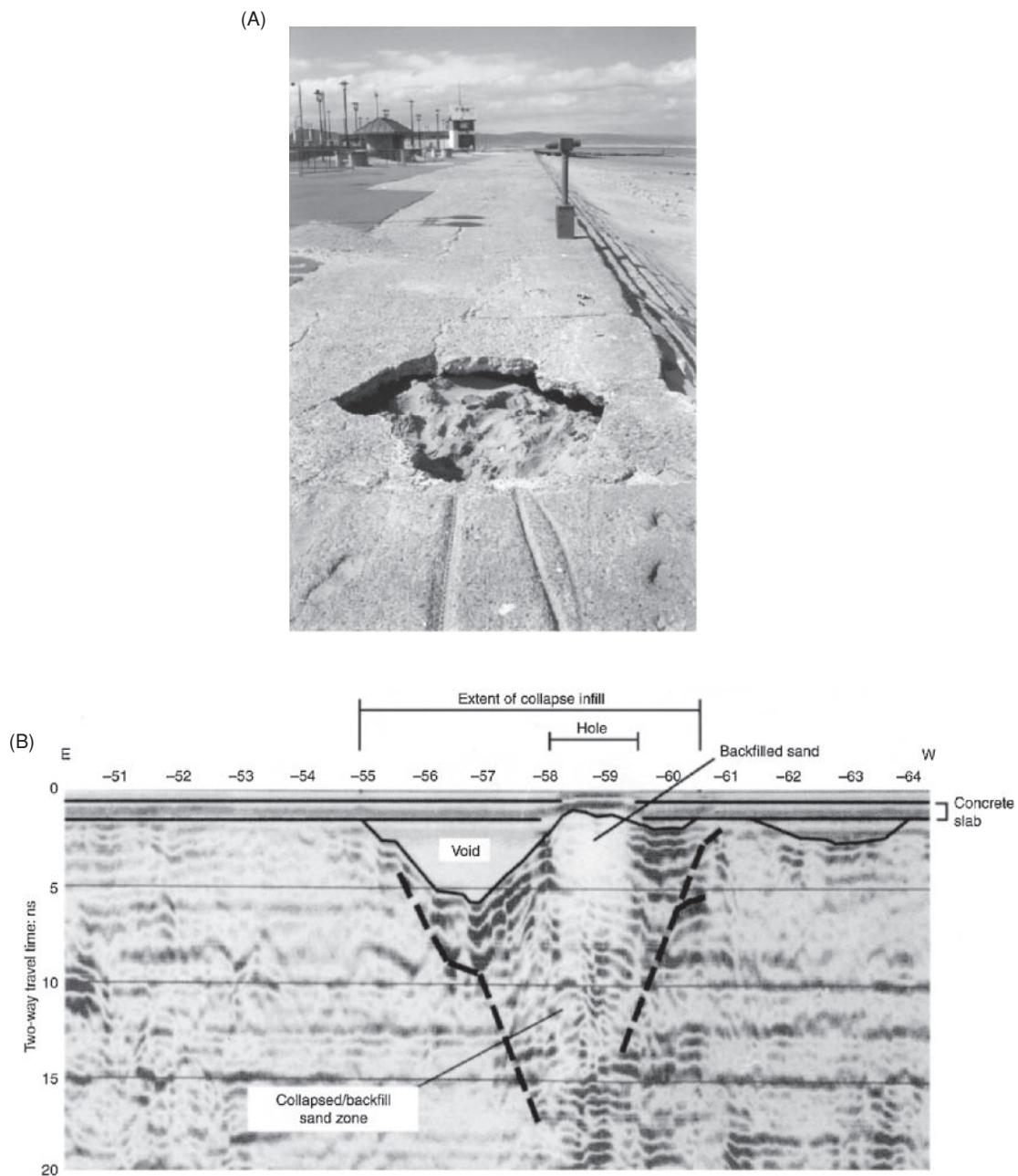


**Figure 14.47** (A) A partially backfilled void that formed catastrophically at Rhyl promenade, North Wales, in April 1998. (B) Radargram showing sub-slab voiding at the collapse site; from Nichol and Reynolds (2001), by permission. [C]

voids, putting those using the amenity at risk of injury. The council commissioned a detailed radar survey to locate the former graves so as to be able to protect them and to ensure that the pathways were properly reinstated to avoid further collapse.

Where human remains are thought to be located in specially protected sites – for example, those which may have been scheduled as ‘Ancient Monuments’ – radar can be particularly useful. The National Trust of Scotland has used radar in an attempt to locate the remains of the Duke of Northumberland’s redcoats who died at the Battle of Culloden in 1746 after the historic routing of Bonnie Prince Charlie and his army. The investigation of the site is impor-

tant as it is hoped that new information will be forthcoming about one of Scotland’s greatest defeats at the hands of the English. It is thought that the remains of some of the English soldiers are buried inside a turf dyke.

### 14.6.3 Buried Roman structures

Goodman *et al.* (2004) have described the use of GPR to map buried structures at a first century AD Roman amphitheatre and marketplace at the Forum Novum near Rome, Italy. The site had been investigated using magnetic techniques, but due to magnetic

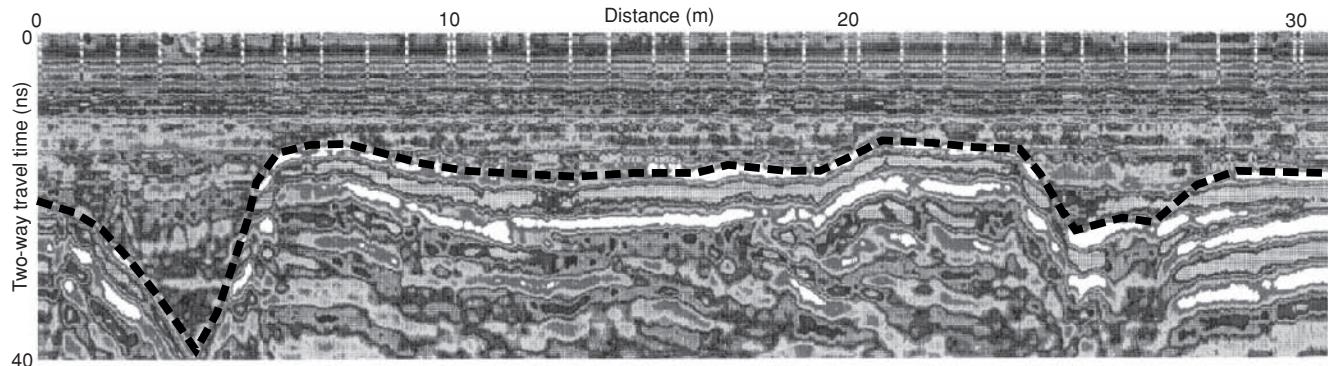


**Figure 14.48** Example of a 300 MHz radargram over a buried Roman road, Caersws, Powys, Wales. Courtesy of Stratascan Ltd. [C]

topsoils and metallic debris in some areas, the method was ineffective. These areas were targeted using GPR using a GSSI SIR-10 with 300 MHz and 500 MHz antennae with profiles surveyed on 0.5 m line separation. Due to the conductivity of the soil, depth penetra-

tion was restricted to the top 50 ns but was still sufficient to image the archaeological remains. In addition to revealing the outline of an amphitheatre, the GPR survey also identified the presence and layout of a marketplace on a series of time slices (Figure 14.50). These were computed using an 8-ns time window that proved to be better at indicating continuous features at variable depth. The shallowest time slice (Figure 14.50A) shows a Y-shaped anomaly attributed to surface effects associated with a dirt roadway. Rectangular anomalies are apparent on the later time slices (Figure 14.50B–D) and these are thought to be due to living quarters adjacent to the main marketplace, with doorways, corridors, and many rectangular rooms being imaged. The noisier data in the latest time slice (Figure 14.50D) is accounted for by the effects of rubble from fallen walls.

To improve the visualisation of the time slice data, an isosurface of the top 70% strongest events in the 3D reflection volume was produced (Figure 14.51). The render helps to indicate the possible orientation, shape and degree of preservation of buried wall foundations.

The use of GPR to map areas of archaeological interest can help to focus on areas of most interest that are likely to yield the most likely abundance of archaeological materials through direct excavation. Images of intact foundations in adjacent unexcavated areas help to place the retrieved material in a better spatial context. A useful overview of the use of GPR in archaeometry has been provided by Goodman *et al.* (2009).

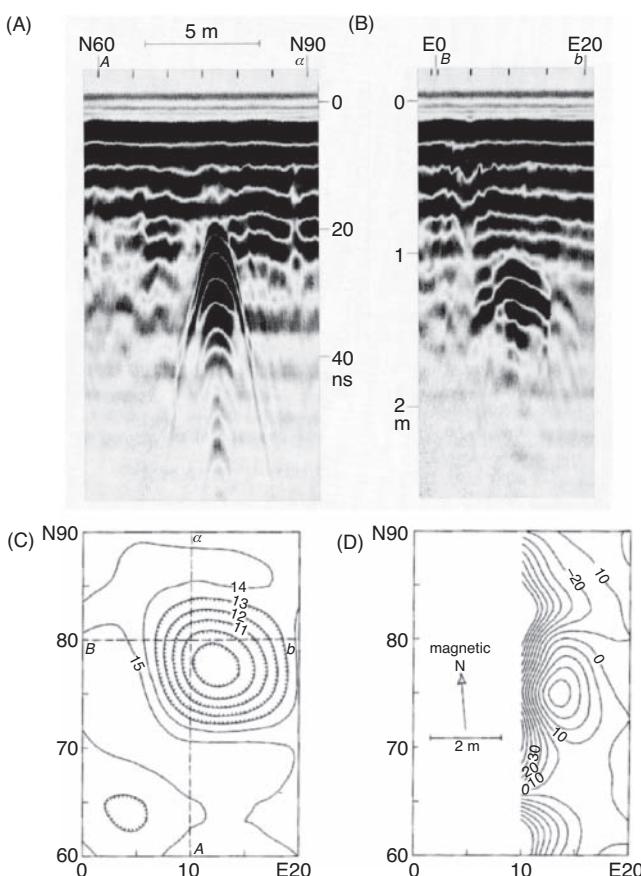


**Figure 14.49** (A) North-south radar profile over a possible grave. (B) An east-west profile shows that the object is wider in this direction. (C) Apparent conductivity map with a contour interval of 1 mS/m; dashed lines indicate the orientations of the two radar profiles. (D) There is also buried iron or fired brick; the contour interval of this magnetic anomaly map is 10 nT. From Bevan (1991), by permission.

#### 14.6.4 Burial mounds

While many radar surveys are undertaken over flat sites, those over pronounced topographic features, such as burial mounds, require adjustment for the effects of the changes in ground elevation. This is normally accounted for by a vertical displacement of adjacent traces using terrain correction. However, what is not accounted for by such a process is the variable tilt of the antenna and the degree of subsurface illumination that arises as a consequence. The concept is illustrated schematically in Figure 14.52: it assumed that the ray path from an antenna is perpendicular to the ground surface to produce the range of directions as indicated (Goodman *et al.*, 2007). In a medium with a slow radiowave velocity and hence limited ground penetration, each ray path covers a discrete and separate segment of

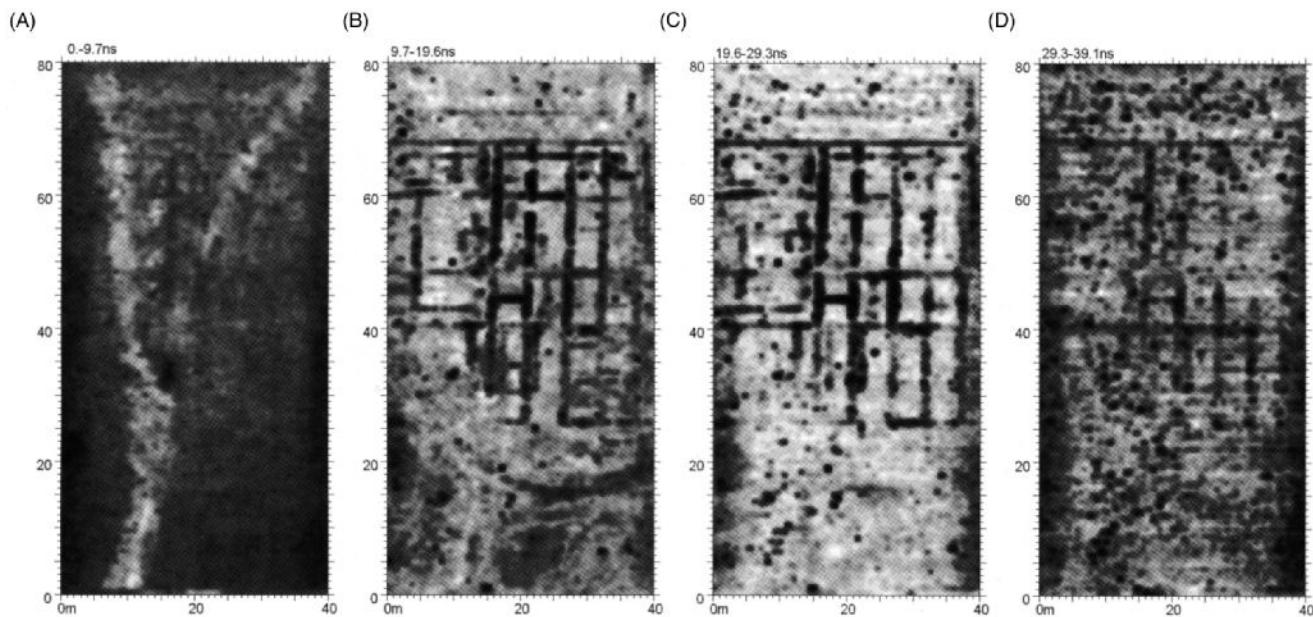


**Figure 14.50** GPR time-slices computed at the Forum Novum site, adjacent to the reconstructed market. (A) The shallowest time slice (0 to 9.7 ns) shows a Y-shaped feature that corresponds to a dirt road with vegetation removed along the roadway. Time slices (B) 9.7–19.6 ns, (C) 19.6–29.3 ns, and (D) 29.3–39.1 ns reveal anomalies below 10 ns associated with living quarters. From Goodman *et al.* (2004), by permission.

the subsurface. As the radiowave velocity and ground penetration increase, the ray paths may begin to cross over, such as when passing the antennae over a mound. Conversely, when passing through a hollow, the ray paths diverge and gaps may occur in the subsurface coverage. The areas of crossover and divergence are indicated by solid block arrows in Figure 14.52. These consequences of the tilt of the antenna can result in a degradation of the quality of the data and affect the continuity of subsurface reflections and misplace them spatially. The angle of each ray path can be calculated as the derivative of the topographic profile, and the degree of *tilt* ( $\varphi_t$ ) is calculated as the angle subtended between the vertical and the normal ray from the flat base of the antenna as indicated in Figure 14.52. Where gaps in the subsurface coverage occur, Goodman *et al.* (2007) have devised a method known as '*ray sweeping*' to sweep adjacent traces to interpolate across the gap. The amount of offset from the vertical is dependent upon the assumed *horizontal* radiowave velocity, with the greatest lateral offset occurring with fastest velocity. To reduce the need for such a process, the scan rate per metre should be increased so that the trace interval is small. The method also assumes that there are no side-looking reflections and does not take into account the Fresnel zone dimensions, so the real gaps in data may be artefacts of the way in which data are normally presented, not in the actual degree of subsurface radar illumination. The method also assumes a constant radiowave velocity throughout the subsurface. The question then arises: are the geospatial errors associated with the unknown degree of lateral and vertical variation in radiowave velocity greater or less than those from the effects of topography and antenna tilt? This highlights the need for careful consideration of field techniques in the placement and orientation of antennae. This is particularly true when dealing with bistatic

antennae, in which case the antennae should be held vertical, not perpendicular to the ground surface, so that the central line of subsurface illumination remains in the vertical.

Goodman *et al.* (2007) have demonstrated the improvement in data acquired over a Japanese burial mound arising from their tilt correction visualisation process, using 300 MHz data acquired with a scan rate of 32 scans/m and a time window of 300 ns. They presented a single profile with corrections at three different horizontal radiowave velocities: 0 m/ns, 0.06 m/ns and 0.12 m/ns (Figure 14.53A–C, respectively). It is assumed that there is no lateral offset in the first case and the traces remain in the vertical. As the horizontal velocity is increased, the lateral offset increases as shown in Figures 14.53B and C. The effect on the profile is to reduce the size of the bright anomaly within the mound that is associated with the burial chamber. It would be interesting to repeat the survey keeping the antenna vertical and comparing the resulting profile with those illustrated after tilt correction.

Another facet of acquisition artefacts is that associated with refraction of radar signals through local surface zones of high contrast in radiowave velocity, such as across a shallow stream, for instance (Nobes *et al.*, 2006). This focusing or lensing effect is brought about by the water, with its higher dielectric permittivity and consequent slower radiowave velocity than that of surrounding media, refracting the radiowaves more vertically into the subsurface. A small increase in the amplitude of higher frequencies is also observed. Combined, these have the effect of apparently increasing the depth of penetration and resolution beneath a shallow stream. The slowing of the signals also results in a larger time gap before the first multiple appears, so permitting the detection of events in this time window that might not otherwise have been visible.

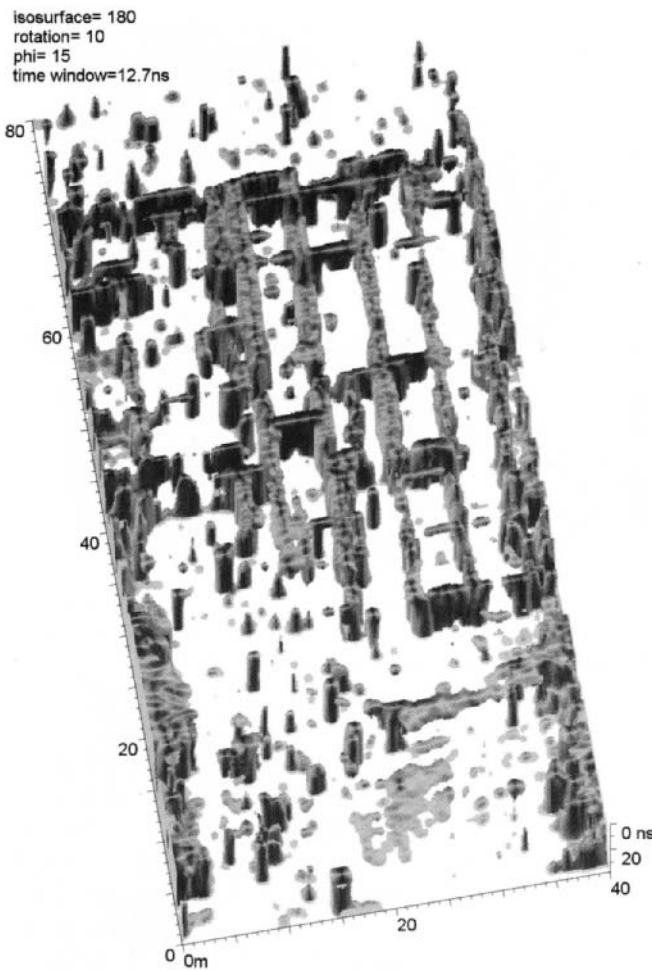


**Figure 14.51** Rendered isosurface of the top 70% strongest events in the 3D reflection volume computed for the car park at the Forum Novum. From Goodman *et al.* (2004), by permission.

## 14.7 Forensic uses of GPR

Radar has been used very successfully in the search not only for ancient graves but also for more recently buried bodies. It has been especially helpful where bodies have been concealed so as to avoid detection. Since the late 1980s, radar has been used increasingly by police in the search for disturbed ground which might indicate where a corpse has been hidden. For example, the States of Jersey, Channel Islands, employed radar to look for the bodies of a married couple which it was thought had been concealed in the back garden of their bungalow. Nothing was found. Radar also played an instrumental role in locating the remains of 12 corpses concealed at three locations in and around Gloucester, UK. A multiple murderer and his accomplice buried the bodies within the concrete foundations and inside newly plastered walls of their own house. The radar was able to identify anomalous targets within the concrete, thereby providing particular locations for excavation. Several more bodies buried in a nearby field were found with the help of radar.

In the USA, at Denton, Maryland, a high-school student Jamie Griffin was murdered, but neither his parents nor local police could locate his body for over seven years. Consequently, the person who had admitted perpetrating the crime could not be tried for murder. The body was thought to have been concealed somewhere within the 20 acres of Gunpowder Falls State Park, north of Baltimore. Previous searches using dogs, scuba divers and earth-moving equipment had been unsuccessful. It was only when a radar system was used that an anomaly was found which turned out to be due to Jamie Griffin's body. Not only was it then possible to convict the suspect of first-degree murder, but the victim's family was able to hold a proper funeral for their son.

In addition to aiding the location of concealed corpses, radar was used in the search for buried bullion following a major robbery in London in the late 1980s. With increasing publicity of such cases, so the forensic applications of radar increase. It is likely that, with the increasing reliability of radar, the applications for forensic investigations will become much more numerous.

Over the last ten years the use of GPR for forensic and police investigations has increased significantly, and particularly in the search for human remains. Research has focused on the best radar methods to detect bodies and to test whether there are ways in which the degree of decay can be determined from the radar data, commonly using dead pig as analogues for human bodies (e.g. Koppenjan *et al.*, 2003; Doolittle and Bellantoni, 2010).

Freeland *et al.* (2003) have described tests using multifrequency synthetic-aperture frequency-modulated continuous-wave (FM-CW) radar (200–700 MHz) and a commercial GSSI SIR-20 pulse system with 400 MHz and 900 MHz antennae over a test pit containing a human body (Figure 14.54). They used a burial plot 1.8 m by 2.4 m long containing a fleshed human cadaver. A folded plastic tarpaulin covered the lower body. The right half of the test pit comprised undisturbed soil, with the other half containing a grave 0.6 m deep and backfilled with the clay-rich excavated soil. A 10 cm thick concrete pad covered the pit.

Example radargrams from both the FM-CW and pulse radar at 400 MHz and 900 MHz are shown in Figure 14.55A–C, for two orthogonal profiles along and across the buried body as indicated in Figure 14.54. Depth of penetration of all systems was no more than 1 m due to the conductive and lossy clay soil. The FM-CW profiles reveal the body, particularly the torso, as high amplitude bright spots. The 400 MHz profiles show a horizontal bright reflection at the base of the concrete but with horizontal multiples beneath the position of the body. The 900 MHz system barely penetrated to 0.5 m beneath the concrete layer, but still resolved the base of the concrete layer and anomalies associated with the cadaver can just be determined.

## 14.8 Wide-aperture radar mapping and migration processing

Radar surveys are normally executed using one or two antennae in a profiling mode as a single-channel acquisition system. Fisher

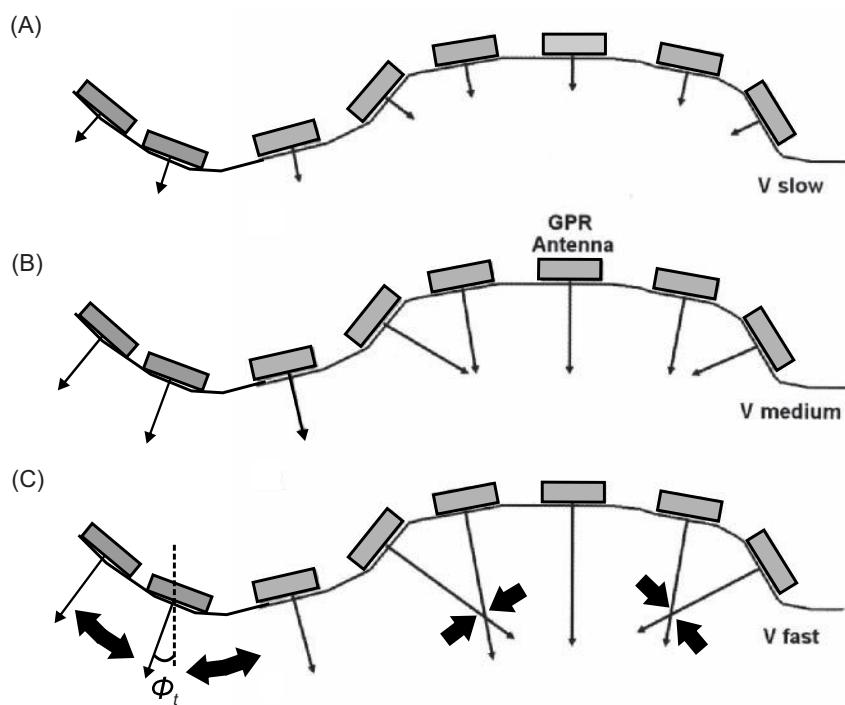


**Figure 14.52** Schematic showing the effect of abruptly changing topography on the tilt of normal radar scans in cases of (A) relatively slow, (B) intermediate, and (C) fast radiowave velocity media. Large solid arrows indicate ray crossover and ray path divergence. Modified from Goodman *et al.* (2007), by permission.

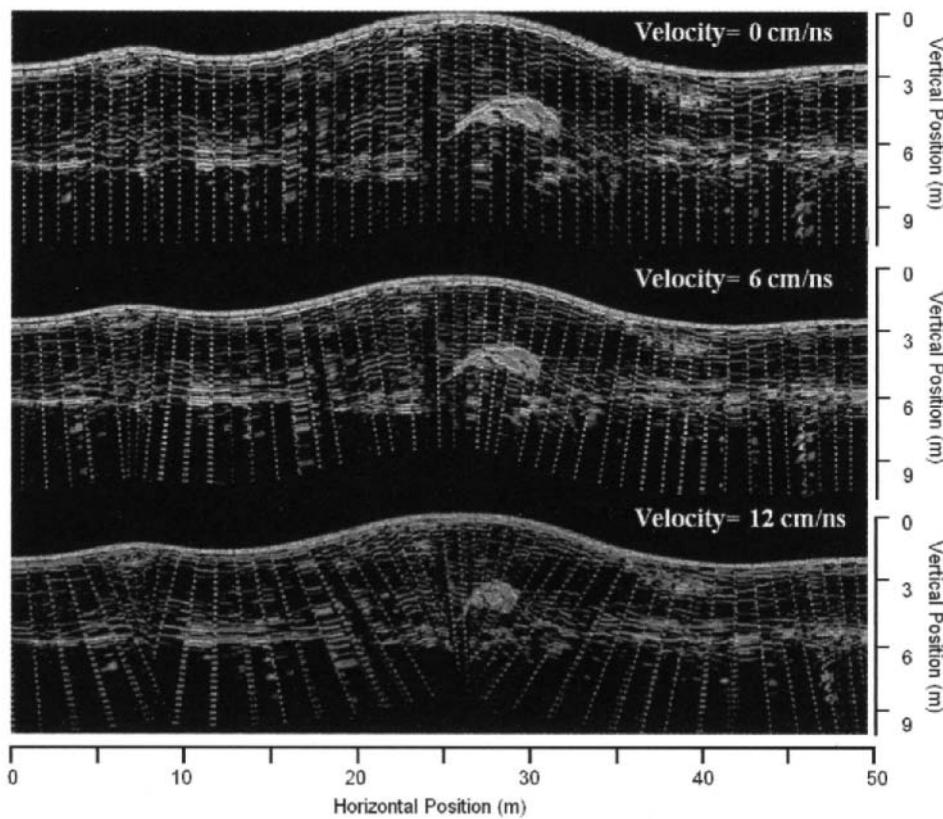


**Figure 14.53** Comparison of tilt corrections for radiowave velocities of (A) 0 m/ns, (B) 0.06 m/ns, and (C) 0.12 m/m.s. From Goodman *et al.* (2007), by permission. [C]

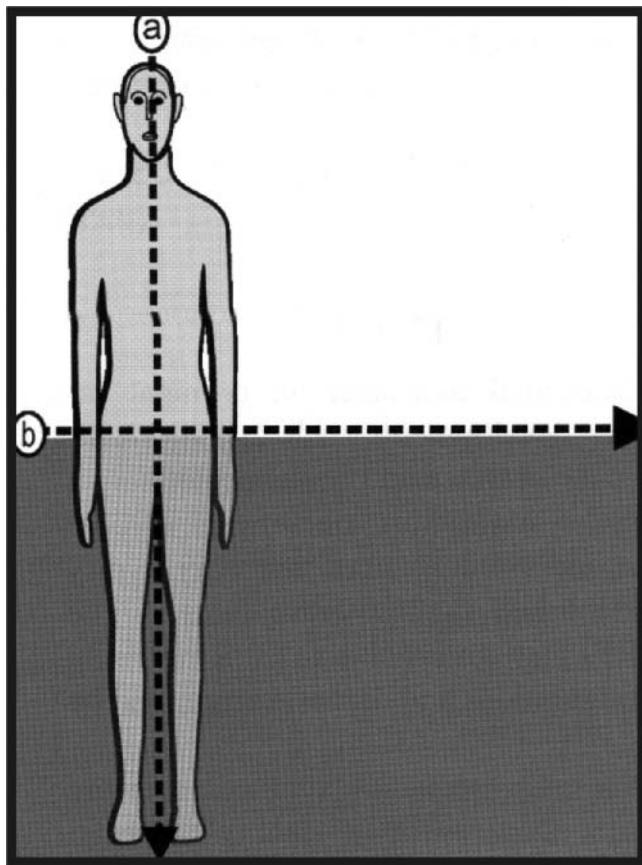


**Figure 14.54** Schematic showing the test pit layout with head-to-foot (a) and across hips (b) profile lines. The lower half of the pit was covered by a folded tarpaulin. From Freeland *et al.* (2003), by permission. [C]

*et al.* (1992a) carried out a 40-channel GPR survey in a complicated fluvial/aeolian environment in the Ottawa River valley approximately 300 km north-northeast of Toronto, Canada. The receiver antenna was placed at each of 441 survey points at 1 m intervals along the profile line. For each of these receiver locations, data were recorded with the transmitting antenna at each of 40 separate positions along the line, at 0.5 m intervals between 0.5 m and 20 m from the receiver (Figure 14.56). The antennae were orientated parallel to each other with the E-plane of the dipoles perpendicular to the survey line. Instead of the usual seismic analogue with a single source recording into a collection of receivers ('common-source gathers'), the common-receiver gathers were acquired. Traces could be sorted into common-source, common-receiver, common-offset or common-midpoint gathers irrespective of the method by which the data were acquired in the field. By obtaining the radar data in this way, traditional seismic processing could be undertaken on the common-midpoint (CMP) gathers.

A PulseEKKO radar system (Sensors & Software Inc.) with 100 MHz antennae was used, producing usable energy within the 50–150 MHz bandwidth. For each recording, 64 source excitations of the 400 V pulse were stacked to improve the signal-to-noise ratio. A total of 1280 samples were recorded with a time sample interval of 800 ps for a total time record of 1024 ns. Given a typical radiowave

velocity in soil of 0.065 m/ns, this time range provided a possible depth of penetration of up to 33 m.

The radar data were input into a standard seismic-processing sequence (filtering, statics corrections, common-midpoint gathering, velocity analysis, normal- and dip-moveout corrections, stacking and depth migration). More details of the data processing are given in Fisher *et al.* (1992a), and of the migration procedures in Fisher *et al.* (1992b). While the common-receiver and common-midpoint gathers for the radar data look very much like their seismic analogues, the derived RMS velocity estimates from three representative CMP gathers are shown in Figure 14.57. Whereas seismic velocities tend to increase with depth, these velocity panels show that the reverse is true for radar waves.

The results of the data processing are shown in Figures 14.58 and 14.59. Figure 14.58A shows a near-offset section; at each location the trace plotted is that recorded with the smallest (0.5 m) source-receiver separation. Figure 14.58B shows every fourth trace in the stacked time section; at each location, the trace plotted is the stack over the traces at the midpoint.

Note that the two panels in Figure 14.58 are shown as time sections. Compare those with the upper panel in Figure 14.59 which is a migrated depth image; the corresponding interpretation is provided in the lower panel. It is evident that significant detail has been obtained to a depth of over 25 m, as correlated with adjacent boreholes. The final migrated data are quite spectacular and show sub-metre vertical resolution even with a 100 MHz antenna to depths in excess of 20 m. Such success has to be tempered by the fact that, in the UK for example, sites where similar records could be obtained are rare, and comparable depths of penetration and similar resolution would be very difficult to achieve owing to the conductive nature of the soils. However, this example does demonstrate that, given the appropriate field conditions, equipment and processing facilities, exceptionally good results are possible with the method. Comparable results would not be possible using even high-resolution seismic reflection surveying.

## 14.9 Borehole radar

In parallel with developments in surface ground-penetrating radar, borehole systems have been in use since the early 1980s. They are used for environmental monitoring, hydrogeological and geotechnical investigations, and increasingly in mining – for mineral exploration, mine planning and safety. A system called RAMAC was developed as part of the International Stripa Project in Sweden and is manufactured by Malå Geoscience AB. The Stripa Project was undertaken in order to develop techniques suitable for use in underground nuclear fuel waste repositories. The short-pulse borehole radar was used primarily to obtain information about the structure and integrity of crystalline rock masses at a distance from tunnels and boreholes without affecting the rock in any way. In 1987, a RAMAC survey in Switzerland revealed fractures in granite 160 m away from the surveyed borehole.

Since then, RAMAC has been used to record reflections arising from structures at distances greater than 300 m within rock salt.

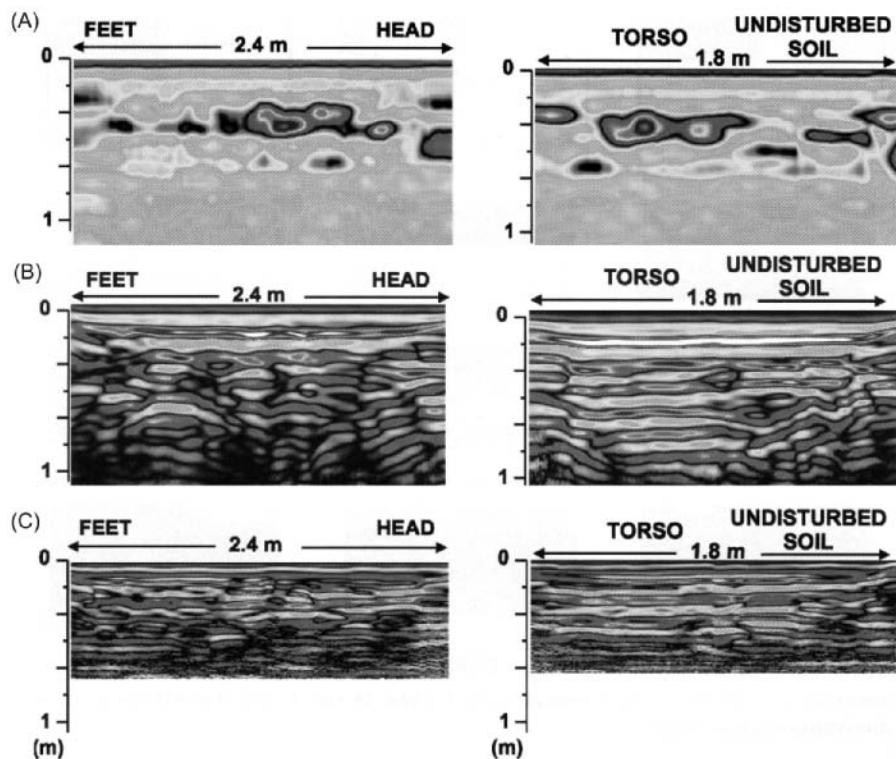


**Figure 14.55** Radar transects using (A) FM-CW radar (200–700 MHz), and GSSI SIR-20 with (B) 400 MHz, and (C) 900 MHz antennae along the head-to-toe and across hips profiles (*left* and *right* columns, respectively). Modified from Freeland *et al.* (2003), by permission. [C]

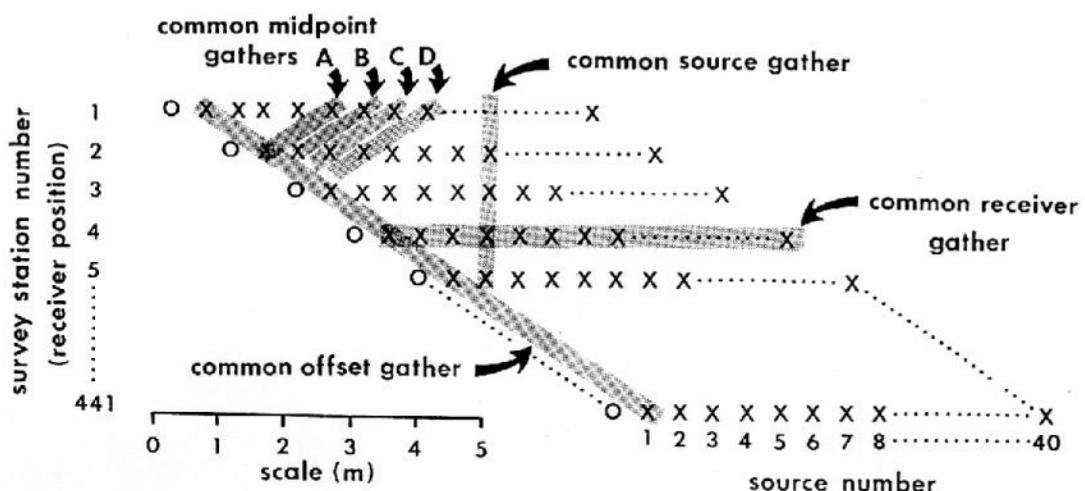


**Figure 14.56** Survey geometry and data-gather definitions. A common-receiver gather contains all the traces recorded at one receiver position. A common-source gather contains all the traces generated at one source position. A common-offset gather contains all the traces with a fixed source-receiver separation. A common-midpoint gather contains all the traces with the same centre point between source and receiver. For the geometry used, there are four common-midpoint positions (cf. A, B, C, D) per receiver position. There are 40 traces in each common-receiver and 40 in each common-source gather. Except at the end of the survey, there are 10 traces in each common-midpoint gather. From Fisher *et al.* (1992a), by permission.

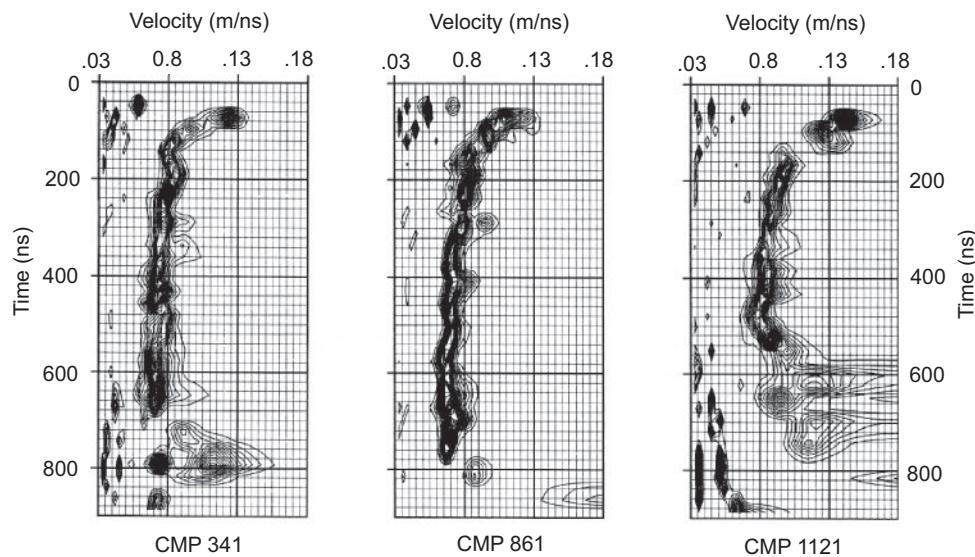


**Figure 14.57** RMS velocity estimates from three representative CMP gathers. Velocity generally decreases with increasing depth (i.e. with increasing travel time). Velocity estimates are not reliable at times greater than that at which the last coherent reflection occurs. From Fisher et al. (1992a), by permission.

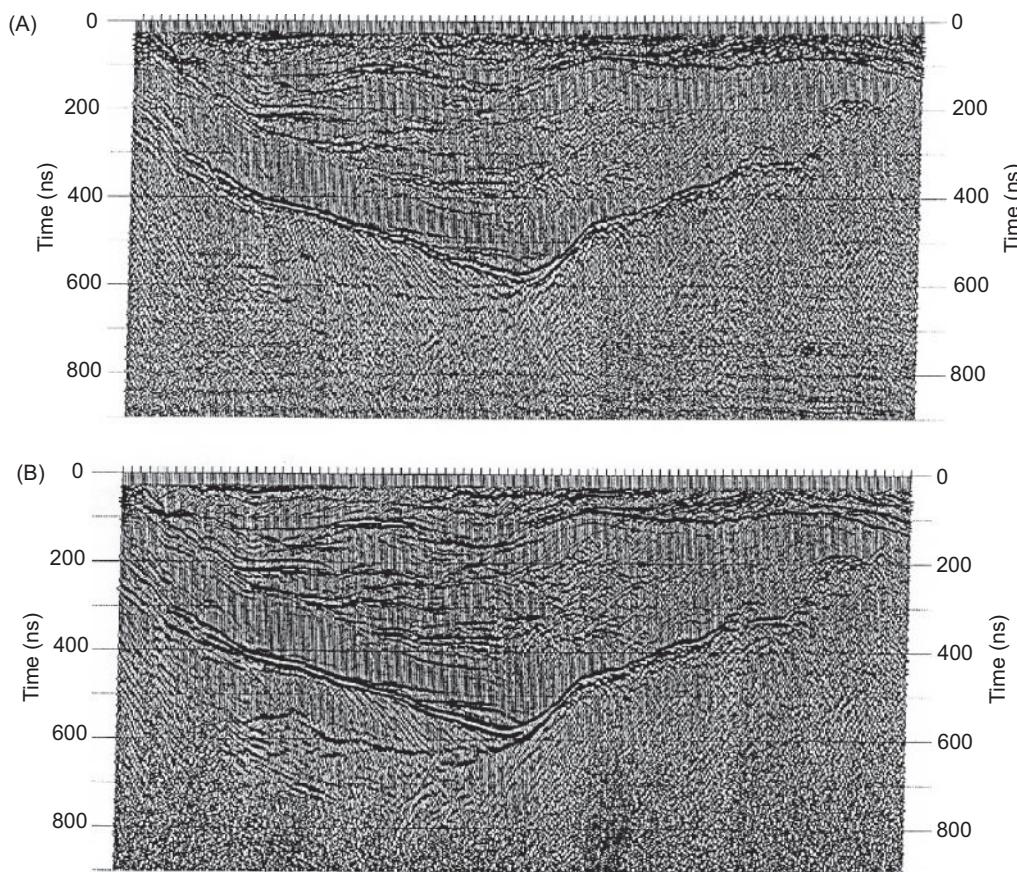


**Figure 14.58** Radar sections from a 40-channel radar survey in the Ottawa River valley, Canada. (A) A near-offset section, at each location the trace plotted is that recorded with the smallest (0.5 m) source-receiver separation. (B) Section displayed with every fourth trace of the stacked time section; at each location the trace plotted is the stack over the traces at that midpoint. Both (A) and (B) are plotted with AGC with a 200 ns window. From Fisher et al. (1992a), by permission.

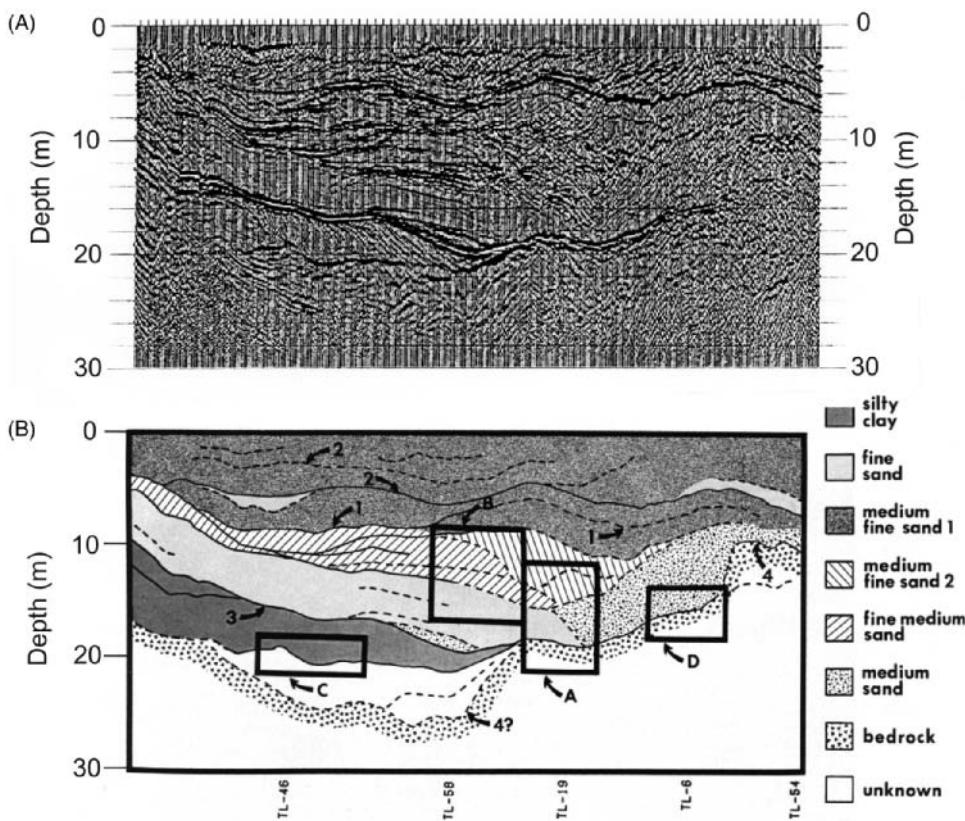


**Figure 14.59** (A) Migrated depth image and (B) its interpretation. The image is plotted with AGC and only every fourth trace is shown. Approximate locations of available drill cores are labelled at the bottom of (B). Reflector 1 is a garnet sand; 2 = silt layers; 3 = fine sand gravel; 4 = bedrock. From Fisher *et al.* (1992a), by permission.

The system is now well proven and has been used internationally in mining, hydrogeological and rock mechanical investigations. It is also being used to investigate sites for tunnels, dams and other construction type projects.

The basic system is illustrated schematically in Figure 14.60 with a simple radargram. A transmitter is used to generate the radiowaves with a pulse frequency of 43 kHz. A separate receiver is located a short distance further down the hole: typically 2–6 m when surveying in sedimentary rocks, and 5–15 m when in crystalline rocks. The receiver operates with a bandwidth of 10–200 MHz. Different frequency antennae can be used, either 20 MHz or 60 MHz using the standard RAMAC system, or 50, 100, 200 or 400 MHz with a newer version released in 1994. Measurements are made at fixed intervals of 0.5 m or 1 m. It takes at most about 30 seconds at each location to make the required measurements.

Two modes of operation are possible. One uses an omnidirectional dipole antenna, and the other uses directional antennae so that reflections from discretely identified quadrants surrounding the borehole can be identified. The RAMAC system can also be used in cross-hole tomographic configurations with the transmitter antenna in one borehole and the receiver down another. Additionally a receiver can be placed down a borehole while the transmitter is located either in a mine tunnel or on the ground surface, as illustrated in Figure 14.61. Processing of radargrams can be accomplished using on-screen interpretational software.

A simple example of the types of radargrams generated using the RAMAC system is shown in Figure 14.62. The radargram was obtained from one of three radar surveys made in three different boreholes to locate an abandoned drill string. Strong reflections from the drill string were observed on radargrams from all three boreholes. The radargrams also revealed the reason why the drill string became stuck – it had intersected an oblique major fault zone.

### 14.9.1 Hydrogeological investigations

In addition to radar being used increasingly in surface hydrogeological investigations, it is also being used down boreholes to investigate inhomogeneities within the saturated zone (Clement and Barrash, 2006), to detect water-filled fractures (Liu and Sato, 2006), to monitor vadose zone dynamics (e.g. Binley *et al.*, 2001, 2002), landfill capping effectiveness (Cassiani *et al.*, 2008) and temporal changes in subsurface fluid behaviour. This includes the investigation of water or oil-bearing layers within hydrocarbon reservoirs.

Clement and Barrash (2006) provided an example of cross-hole radar tomography between four pairs of boreholes in a line through the Boise Hydrogeophysical Research Site, Idaho, USA. The four boreholes provide three interlinking tomographic panels. A Malá RAMAC borehole system with 250 MHz antennae was used to acquire the data. The receiving antenna was held at a given depth while the transmitting antenna was lowered at 0.5 m intervals down the

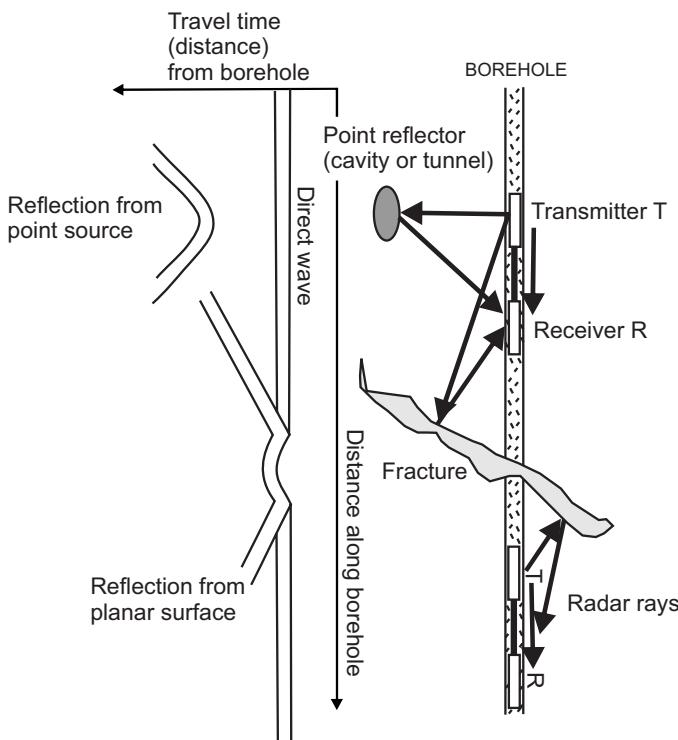


**Figure 14.60** Basic arrangement for a borehole radar system with typical radar section images of plane and point reflectors. The cylindrical symmetry of the dipole antennae creates V-shaped responses from planar reflectors. Hyperbolae arise from point sources. Courtesy of ABEM.

other paired borehole. Travel time data were acquired for each vertical increment of the transmitter to produce a receiver gather (Figure 14.63). The banding in the top 1.5 m and 3 m is associated with the dry and vadose zones at the top of the borehole. The receiver antenna was moved 0.2 m further down the hole and the transmitting antenna relocated to the top of its hole and then lowered in increments as before. The process was repeated until the receiving antenna had reached the bottom of its hole. Using all the gathers, a zero-offset profile can be produced (Figure 14.64). The effects of air and the vadose zone in the upper 2.5 m are self-apparent. The boreholes pass through a gravel bar adjacent to the Boise River where the local aquifer is shallow and unconfined. Boreholes were drilled through 18–21 m of unconsolidated fluvial deposits of cobbles and sand, and terminated in underlying red clay. In more detail, the sedimentary sequence comprised a sand-filled channel at the top of the saturated section (to ~4.5 m depth); strong porosity contrasts occur at the boundaries of local lenses at around 4.5 and 5.5 m depth. Water content affects the radiowave velocity: a high water content lowers the velocity, whereas a low water content increases the velocity. At this site, the mineralogy is fairly homogeneous so changes in radiowave velocity determined using the tomography indicates changes in porosity. The travel-time data were inverted to produce velocity tomograms for each borehole pair panel (Figure 14.65A). Using the relationship with radiowave velocity, the dielectric permittivities could be determined that in turn produce values of porosity, resulting in porosity panels (Figure 14.65B). The

radar-derived porosities were found to be similar to those derived from neutron log measurements. This example demonstrates the use of radar cross-hole tomography to provide information about the sedimentary architecture and an *in situ* estimate of subsurface porosity.

### 14.9.2 Mining

Borehole radar surveys are now commonplace in mapping an orebody ahead of mining, both as a strategic and tactical tool. Slimline borehole antennae can be deployed in a single radar ‘stick’ on the ends of drill rods through *cover holes* that ensure the competence of the hanging wall, and *geology holes* to determine the location and grade of ore within the prospect (Kemp *et al.*, 2009). It is preferable that the radar borehole approach angle relative to the target plane is less than 40°, whereas the norm is to drill at right-angles to the plane of the target. An example borehole radar layout for mining of a subhorizontal dyke is shown in Figure 14.66A. For instance, the borehole may pass through two parallel interfaces – the *hanging wall plane* and the *dyke plane*. When the radar tool passes through each plane, the intersection generates a diffraction hyperbola in the time section as shown in Figure 14.66B, along with apparently dipping reflections associated with both the hanging wall and dyke planes. Single-borehole radar systems are omnidirectional and reflections will be detected from 360° around the borehole. Time sections are often dominated by specular reflections from areas on the planes that straddle the so-called *nadir lines*, which are the loci of reflection points on a reflecting plane. The normals to the surface at these points collectively define the so-called *sagittal plane* (Figure 14.66A). It is important also to note that reflections from off the nadir line may generate side-swipe diffractions.

Kemp *et al.* (2009) described the use of borehole radar to image an orebody ahead of mining at the Snap Lake diamond mine, Northwest Territories, Canada. The orebody is a thin (average 2.8 m thick) shallowly dipping (~15°) diamondiferous kimberlite dyke intruded into a series of Archaean granite-gneiss and metavolcanic rocks. On an exploration scale the dyke is apparently a uniformly-dipping feature, but at a finer mining scale, the emplacement of the dyke is thought to have been controlled by a set of pre-existing low-angle fractures, giving rise to a series of ramps, steps, bifurcations and zig-zags (known as jogs) at a 1 m to 5 m scale. These have implications for efficient mining and are difficult to locate with traditional drilling methods alone, but they are mappable at the resolutions afforded by borehole radar.

The radar tool used comprises either a combined transmitter-receiver probe (stick) or two separate ~1.6-m long transmitting and receiving antennae on two separate probes with a 2-m fibre-optic spacer in-between. For practical reasons, the stick tool is more commonly used. The tool is broadband and covers the frequency range 20 MHz to 80 MHz and has a range in most hard-rock environments of at least 30 m from the borehole, and up to 80 m in some rock types. While directional single-probe borehole antennae exist by which it is possible to determine in which quarter reflections are generated, the tools are not yet slim enough to fit into underground mining holes that are typically ~48 mm diameter.

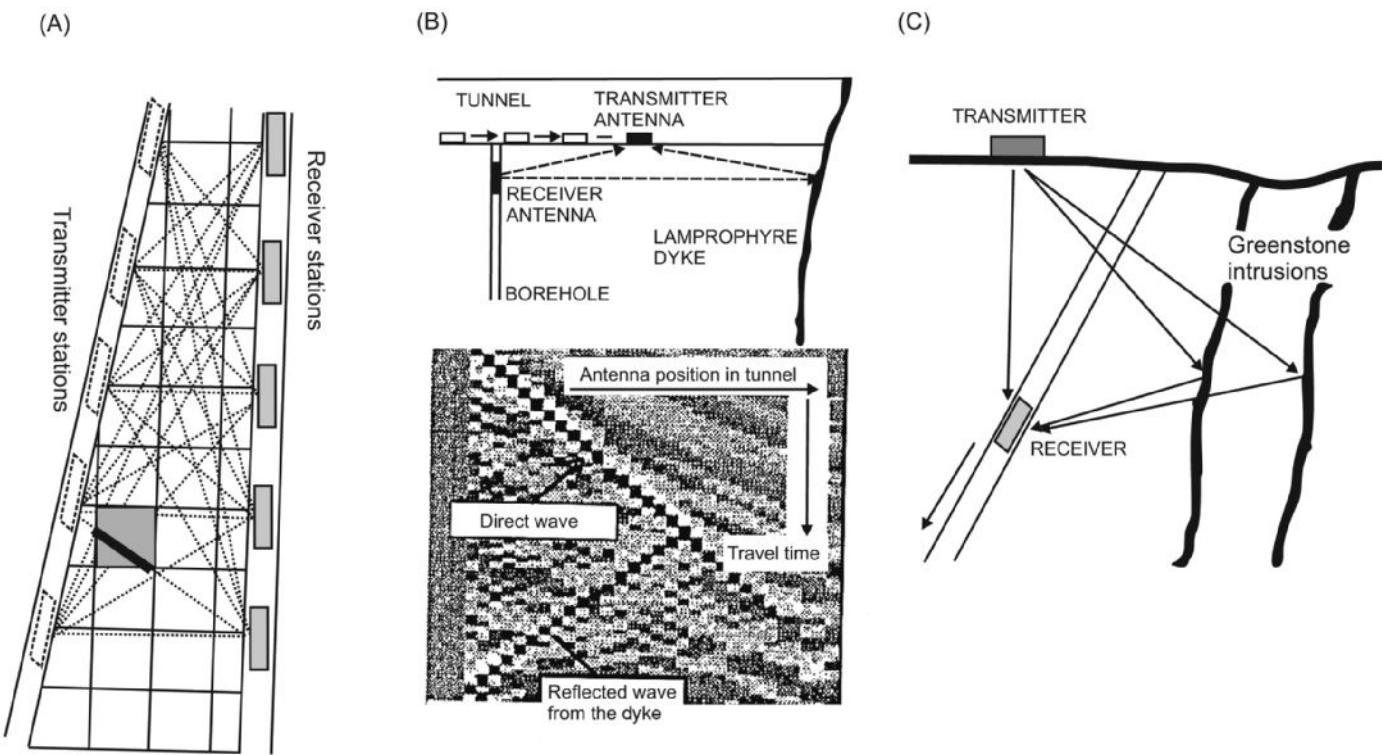


**Figure 14.61** Three configurations for borehole radar systems: (A) cross-hole tomography; (B) tunnel-to-borehole imaging, and (C) vertical radar profiling where the transmitter is on the ground surface and the receiver is down the borehole. Courtesy of ABEM.

In one case, surface drilling had indicated the possibility of a tear in the dyke. A probe hole was drilled and then surveyed using the borehole radar across the apparent tear zone in order to pick up the dyke with an intersection point on the other side of the 'discontinuity'. However, the drill hole encountered a second dyke about 300 m further downhole, so the tear was in fact a gap between two parallel dykes. The borehole radar successfully delineated the

extent of the two dykes. The corresponding radargram for this borehole is shown in Figure 14.67. The horizontal axis indicates the distance down the hole and the vertical axes show the radial range (m) and travel time ( $\mu$ s) from the borehole. There are two clear reflections arising from the two dykes (arrowed). The first reflection is seen moving away from the hole as the radar descends the hole, and this reflection originates from the dyke that was being mined at the time. The second reflection is seen moving towards the borehole as the radar descends further, and this arises from the second dyke. The reflections appear to intersect each other at around 170 m downhole. In fact the two dykes are parallel and the reflection from the first dyke should be rotated through  $180^\circ$  about the axis of the borehole, whereupon it lies parallel to the lower dyke. This visualisation is a consequence of the omnidirectionality of the single borehole radar system. Upon migration of the data, the correct geometric relationship between the two dykes becomes apparent.

Borehole radar has proved itself to be of significant financial benefit in mining. At one borehole, a radar survey costing  $\sim \$150,000$  was able to identify mineable areas that had not previously been exploited, and was able to add more than  $\$14.2$  million to the mine's resource base.

In South Africa, ruggedised borehole radar systems have been developed since 2004 and are now routinely deployed in cover holes in gold mines using 'on-the-rod' (OTR) techniques (Bray *et al.*, 2007). This is where a 1.6-m long broadband (10–125 MHz) radar probe is deployed through an air-driven diamond core drill on a double mining bar mount as a cover hole is being drilled. Each time

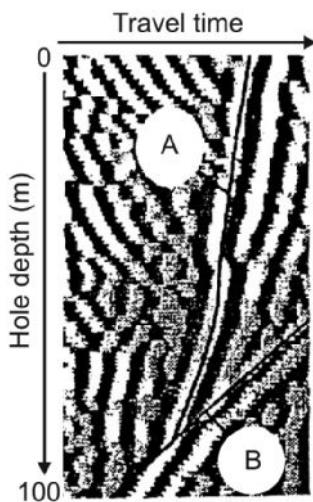


**Figure 14.62** Borehole radargram showing the location of an abandoned drill string (A) and a major fault zone (B) in which the drill bit was stuck. Courtesy of ABEM.

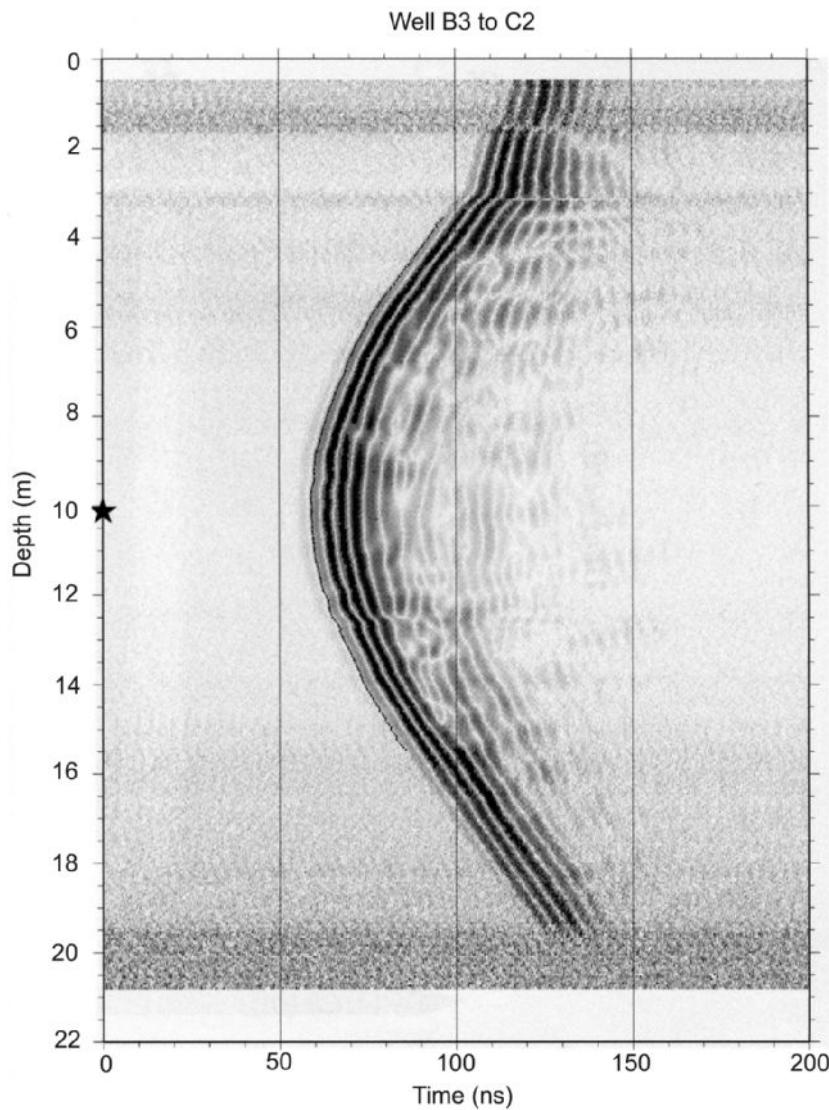


**Figure 14.63** Receiver gather from 10.12 m depth (asterisk) showing travel-time picks (black line) superimposed on the gather. From Clement and Barrash (2006), by permission.

the drill rod is changed, traces are recorded in an onboard flash memory that is downloaded via Bluetooth when the transceiver is returned to the surface. The radar is able to run deep downhole on lightweight cords, is self-supporting, self-adjusting and umbilical-free. A 133-m long cover hole can be surveyed using the OTR method in less than 50 minutes. Steeply dipping structures such as faults and dykes have also been identified using borehole radar in shaft pilot holes to depths greater than 3 km and with radial ranges in excess of 40 m from the borehole.

A further example of the use of borehole radar in a South African gold mine has been described by du Pisani and Vogt (2004). A significant proportion of South Africa's gold reserve is derived from the Venterdorp Contact Reef, which is a thin ( $<1.2$  m thick) tabular ore body concentrated in palaeochannels situated on river terraces. Five boreholes within a 200 m square block were surveyed using a borehole radar system, and the data combined into a single model to estimate the topography of the ore body within the block. Small

faults and other topographical changes were positioned accurately and gave warning of oncoming changes in mining conditions, facilitating planning of the optimal extraction of gold within the block.

The McConnell massive nickel-copper sulphide deposit near Sudbury, Ontario, Canada, has been used as a test site for a variety of geophysical survey methods. The ore deposit comprises a sheet-like structure that dips steeply to the south, subparallel to the stratigraphy. A number of deviated, north-dipping boreholes intersect the sulphide mineralisation. Borehole radar imaging surveys have been undertaken to evaluate the response of the massive sulphide deposit to radar illumination (Calvert and Livelybrooks, 1997). They used a Mala 60 MHz Ramac L1 borehole system in two boreholes, 78929 and 78930. First, single borehole imaging was undertaken in both boreholes with the source and receiver in the same hole. They then carried out cross-hole tomography with the transmitter placed in the upper hole (78929) and the receiver in the lower hole (78930), as illustrated in Figure 14.68.

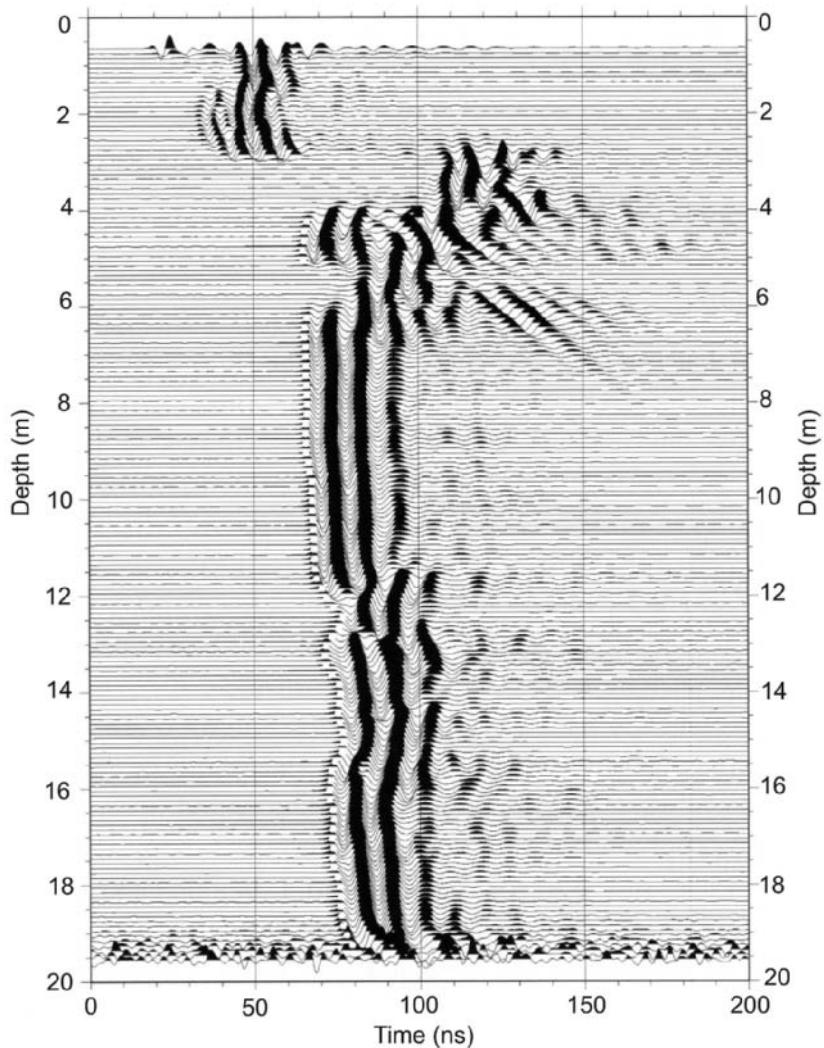


**Figure 14.64** Zero-offset profile showing travel-time picks corresponding to the zero-offset traces from each receiver gather. The early arrivals in the upper 2.5 m correspond to energy propagating through the air and vadose zone. From Clement and Barrash (2006), by permission.

The single-hole radar survey was undertaken with the receiver and transmitter separated by 4.7 m and radar signals measured every 0.25 m from 75 m to 130 m and 170 m measured depth in the upper and lower holes, respectively. The radar images obtained from the single-hole radar surveys, which recorded data from above, within and below the zone of massive sulphide mineralisation, are shown in Figure 14.69. The radar data are shown with no amplitude scaling (middle panel images) and with time-varying gain (AGC) applied (right-hand panels). The corresponding resistivity logs for the two boreholes are shown annotated as a function of lithology (left-hand panels in Figure 14.69). It is clear that the highly conductive massive sulphide orebody attenuates the radar signals, and no information from within the structure is visible. The host rock normally exhibits radiowave velocities in the range 100–140 mm/ns, but direct arrival travel times indicated that in the vicinity of the borehole, the host rock has been altered by fracturing as the local radiowave velocities were found to lie in the range 60–75 mm/ns. Weak downward-

dipping reflections can be seen in both sections arising from the interface between the top of the thick conglomerate above the orebody and the overlying metasediment layer. An upward-dipping reflection in Figure 14.69A (arrowed) can be seen arising from the top of the massive sulphide zone, although there is only a hint of something similar in Figure 14.69B arising from within the orebody and occurring at later range times. A downward-dipping reflection from the base of the orebody can be seen in Figure 14.69B.

The cross-hole radar survey was conducted using 18 locations in the upper borehole and at 25 receiver depths, with 3 m separation in the lower borehole. Inversion of the data provided a velocity tomogram (Figure 14.70) that revealed a number of distinct velocity anomalies above the orebody. Due to the sparsity of the ray coverage between the boreholes particularly at depth (i.e. immediately above the orebody), information about the orebody at mid-distance between the boreholes could not be resolved (Bellefleur and Chouteau, 2001). However, the results from these borehole radar surveys have

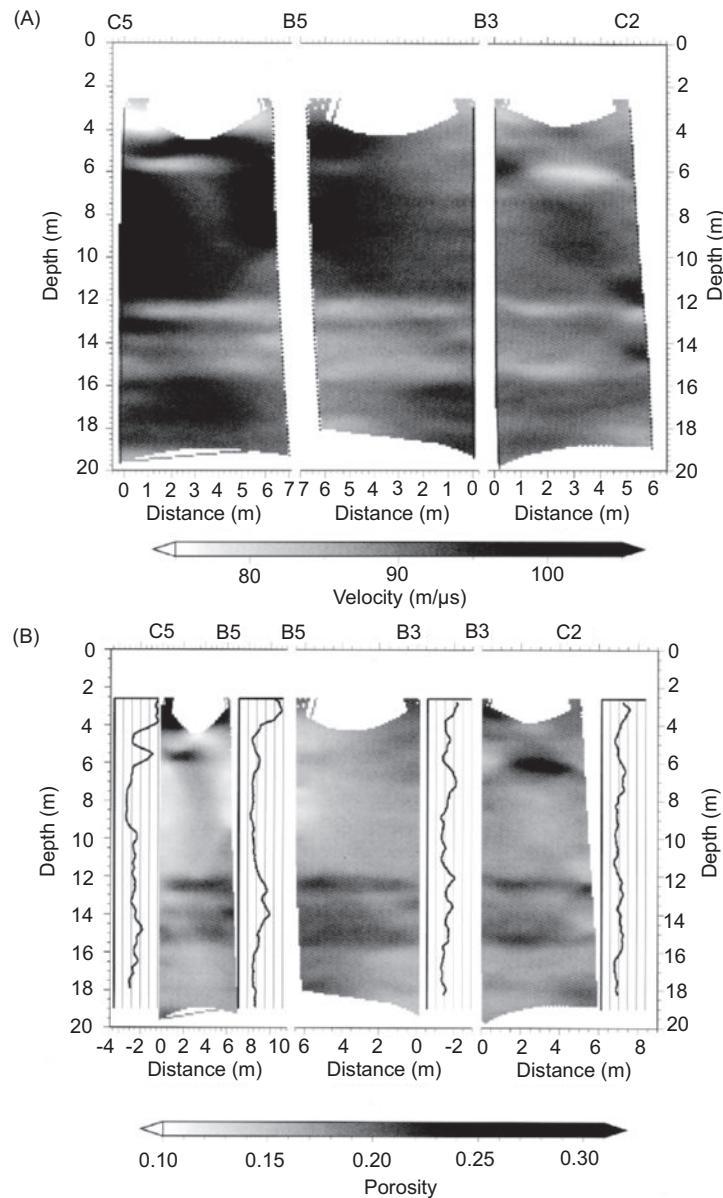


**Figure 14.65** (A) Radiowave velocity tomogram and (B) porosity profiles for three borehole panels between borehole pairs C5-B5, B5-B3 and B3-C2 at Boise, Idaho. From Clement and Barrash (2006), by permission.

provided important information on how to redesign the surveys to improve the resolution of the tomograms and thereby increase the usefulness of the borehole radar surveys to the mine geologists.

## 14.10 UXO and landmine detection

Ground-penetrating radar is sometimes used for the detection of UnExploded Ordnance (UXO) and landmines. UXOs by their nature tend to contain significant amounts of metal, whereas landmines have been designed to minimise the metal content specifically to confound mine detection systems. So-called minimum-metal mines contain less than 5 g of metal and are the most difficult to

detect. Explosives themselves have a dielectric permittivity of  $\sim 3$ , so when buried in dry sand have minimal dielectric contrast. Often it is not the explosive component that is detected but the housing or a void within the housing or the metal within a detonator. UXOs are easiest to locate using magnetic and EM methods. The difficulty with using GPR is not so much the detection of UXOs but reducing the false alarm rate (FAR) because the system might not discriminate between the responses identifiable that may come from miscellaneous metal fragments such as old nails or shrapnel, but also vegetation roots, stones, water pockets, or anything that presents a contrast in dielectric permittivity. Yarovoy (2009) has provided a brief overview of the use of GPR in detecting and classifying landmines and UXOs.

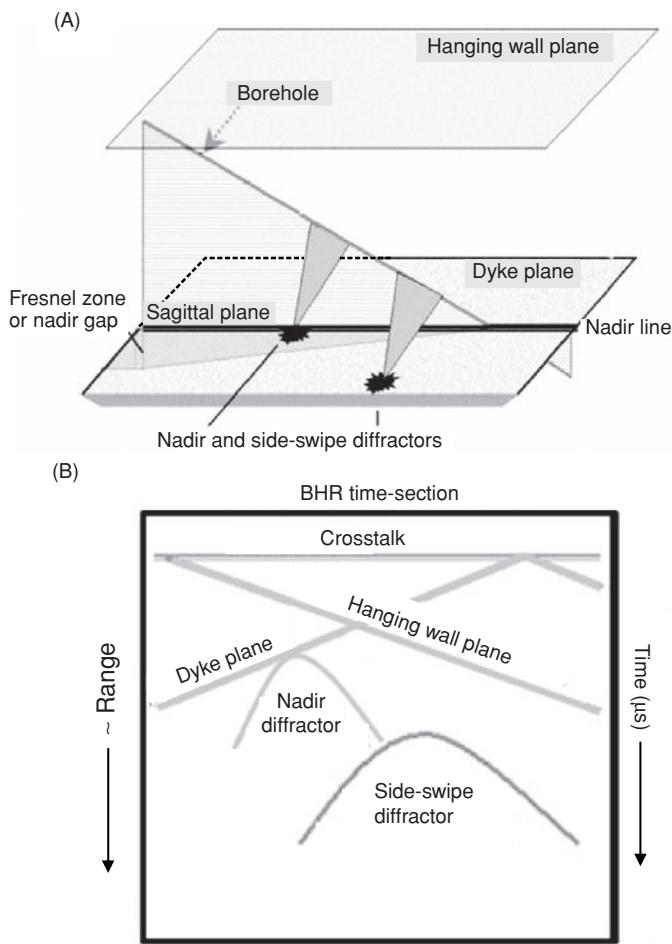


**Figure 14.66** (A) Schematic illustrating typical borehole radar (BHR) layout, and (B) resulting borehole radar time section. After Kemp *et al.* (2009), by permission.

It is important to bear in mind that UXOs are predominantly rotationally symmetric, strongly elongate and have metal casings, with a diameter in the range 0.2–0.4 m and 0.2–1.5 m long. They can have any orientation within the ground and lie at depths up to 15 m below ground level. Land and anti-personnel (AP) mines, however, need to be laid with minimal ground cover to be effective. Mines tend to be disc-shaped objects with a diameter of between 40 and 200 mm, with 50% of AP mines having a diameter greater than 100 mm. Anti-tank (AT) mines are several times larger. AP mines are between 30 and 80 mm thick. AP mines are usually buried shallower than 200 mm, while AT mines may be as deep as 1 m.

For UXOs it is possible to undertake radar surveys using ground contact with the antenna, but for AP mine detection it is advisable to have the radar antenna held above the ground so as not to detonate the device. Consequently GPR systems for landmine detection tend to be bespoke instruments often coupled with EM metal detection capability. Furthermore, given the small size of AP mines, traditional grid surveys would have to be undertaken on a very close spacing in order not to miss the targets. The UN defines an area as being safe only when 99.6% of all mines have been cleared. To ensure

that this is the case, handheld systems, such as the MineHound VMR2, are used by sweeping them in an arc in front of a forward-moving operator with one sweep per forward step. Detection of an anomaly is via an LED bargraph and by audio signal through a headset.

In situations where the radar data are recorded for post-processing and analysis, the success rate of the technique is dependent upon the software used to visualise the data and particularly to discriminate and classify target types to further reduce the false alarm rate.

It has been found that by combining a mine-detection GPR with metal detection increases the detection rate of mines significantly. On a Bosnian test site, for example, a GPR mine detector successfully located 94% of all the AP mines. It is thought that on its own, GPR is not sufficient to detect mines, but when used in conjunction with EM techniques, especially in combined sensors, it should be possible to detect almost all landmines and classify them as such.

## 14.11 Animals

Animal diggings pose a common problem wherever poorly consolidated sandy soils form the slopes of embankments and cuttings along transportation and waterway corridors. Engineered slopes with well-drained, firm and undisturbed ground frequently combine with landscaped areas of broad-leaved woodland adjacent to open pasture land to create ideal habitats for a wide variety of burrowing animals in general, and badgers in particular (Cresswell *et al.*, 1990). Animal excavations may have the potential to induce ground movements that may adversely affect roads, railways, buildings and flood defences, with potential consequences for neighbouring communities and the local economy. Furthermore, some burrowing animals, such as badgers and their dwellings, are protected in the UK under the protection of Badgers Act (1992) and the Wildlife and Countryside Act 1981 (for details, see the Joint Nature Conservation Committee website listed in Appendix A). Agencies responsible for flood defences such as canal embankments need to be able to investigate badger setts and tunnels in case they have the potential to provide water drainage routes that could lead to the catastrophic failure of the canal structures. In cases where individuals have been suspected of badger-baiting by using dogs to enter badger tunnels to kill the animals, the police are required to demonstrate that such habitations exist. Such activities are in breach of the Badgers Act (1992). The need to investigate such animal excavations can result in professional staff contravening the legislation if they use intrusive methods. However, ground-penetrating radar provides an environmentally benign method that enables such surveys to be undertaken without fear of breaking the law and without causing any disturbance to the actual underground structures themselves.

An example of the use of ground-penetrating radar to investigate a mature badger sett has been provided by Nichol *et al.* (2003). The site is located along the eastbound carriageway of the A55 St Asaph Bypass in north Wales, and comprises a 500-m long earthworks

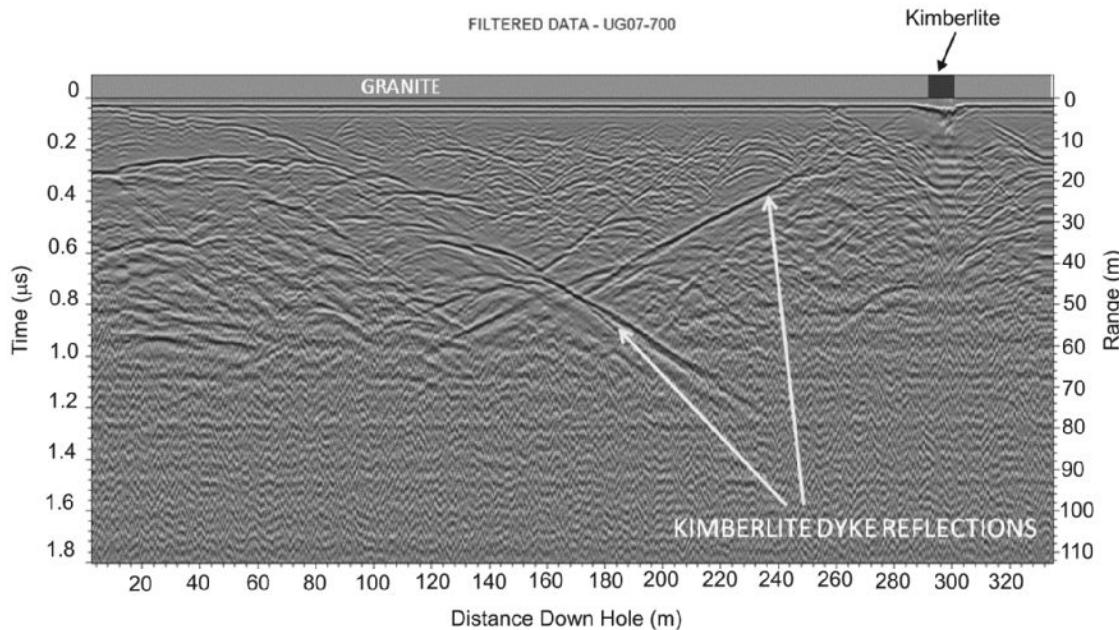


**Figure 14.67** Borehole radar time section. Distance downhole is shown on the horizontal axis; radial range is shown on the vertical axis. The geological log for the hole is overlain along the top of the section. From Kemp *et al.* (2009), by permission.

cutting. The slope profile contains numerous entrances and spoil heaps associated with badger setts. The presence of these structures in conjunction with the development of longitudinal cracks along the crest of the slope prompted concerns about slope stability and the potential threat posed to an extremely busy dual-carriageway. The cutting slope has an average gradient of 24° and a mean down-slope length of about 15 m. A flat platform 3–6 m wide is present at the top of the slope. The materials present include pale brown heterogeneous sandy and silty sands overlying brown clayey soils. On the slope badgers have created conical spoil mounds up to 3 m wide and up to 1.5 m high. Typically, each spoil mound surrounds a single entrance, but in places individual mounds have coalesced to form larger heaps with localised slope gradients of up to 38° (Figure 14.71).

A radar survey was undertaken using a GSSI SIR-2 system with 200 MHz and 400 MHz antennae across gridded transects at 0.5–2.0 m line interval between trees, with the closer line spacing being adopted in areas where features suggested that excavations were present. In order to obtain empirical estimates of the local radiowave velocities in the media present, calibration profiles were undertaken close to known entrances to the badger sett (Figure 14.72). From such measurements it was found that the local radiowave velocity was around 0.11 m/ns. Tunnels crossed by orthogonal sweeps were evident as parabolic reflections (Figure 14.73A). In contrast, tunnels crossed at oblique angles gave rise to broader and more complex anomalies (Figure 14.73B). The anomaly associated with an interpreted roof over a chamber can be seen in Figure 14.73C.

It was found that beneath the cutting slope the tunnels rarely extended beyond 1 m depth and below the top platform area they

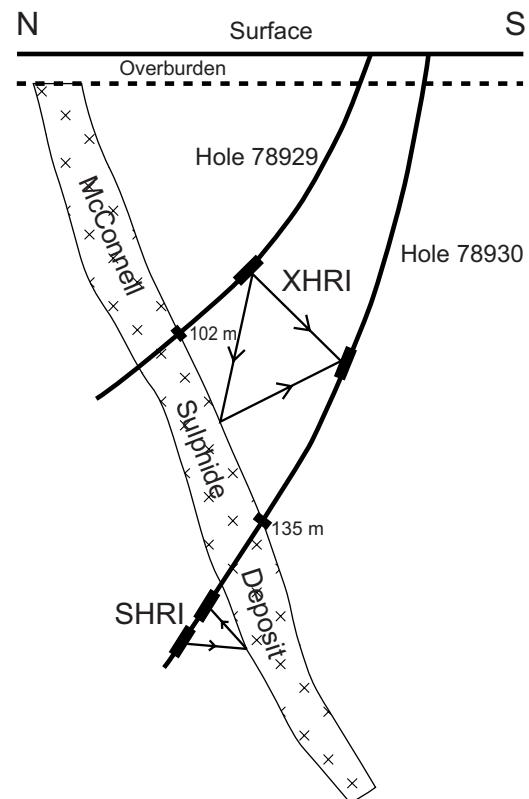


**Figure 14.68** Layout of the borehole radar survey at the McConnell nickel deposit, Sudbury, Ontario. From Calvert and Livelybrooks (1997), by permission.

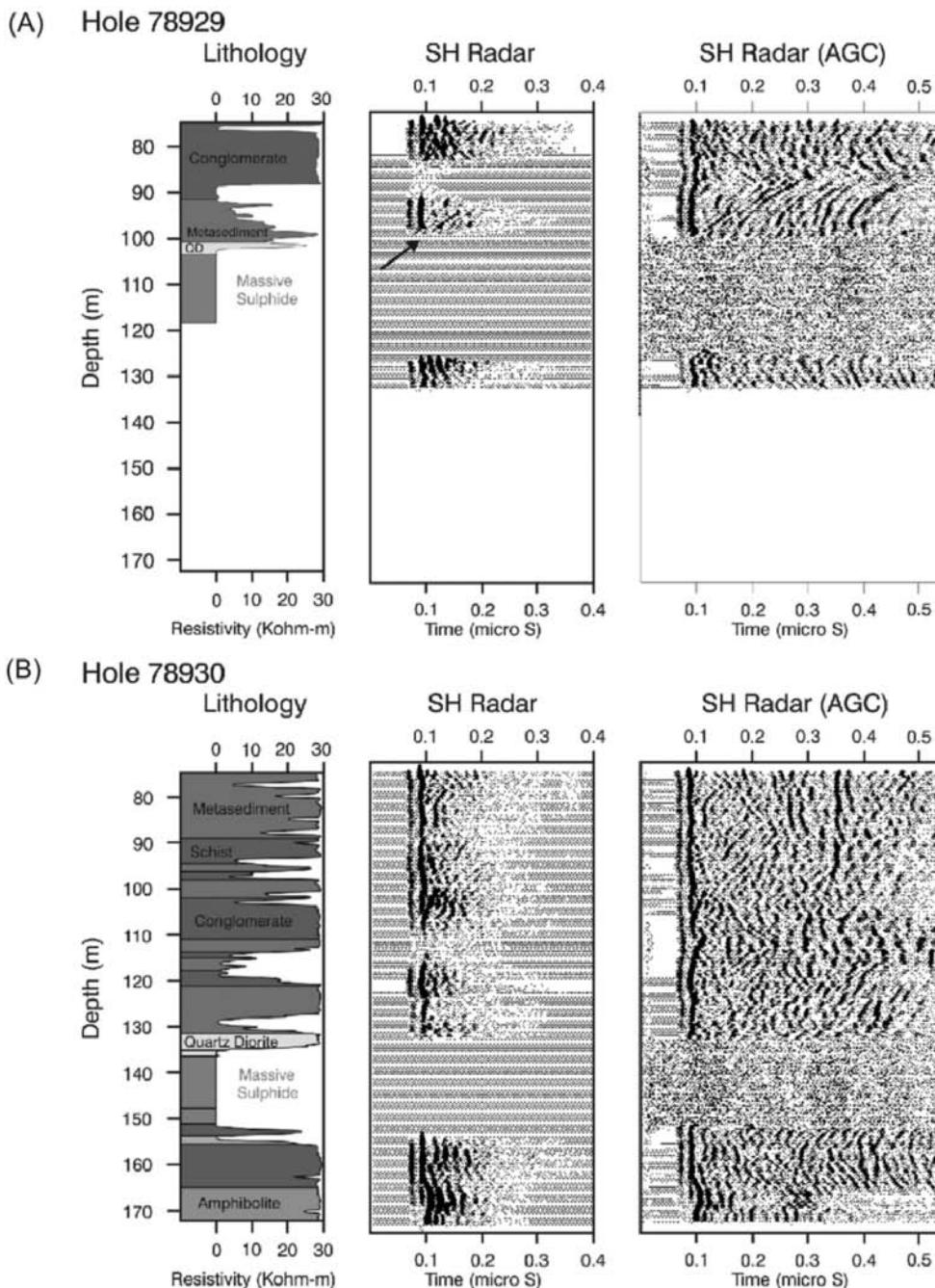


**Figure 14.69** Single-hole radar profiles recorded along boreholes (A) 78929 and (B) 78930 at the McConnell nickel deposit, Sudbury, Ontario. The radar data are shown with no amplitude scaling (*middle panels*) and with time-varying gain (AGC) applied (*right*). Resistivity logs coded as a function of borehole lithology are shown in the *left panels*. From Calvert and Livelybrooks (1997), by permission. [C]

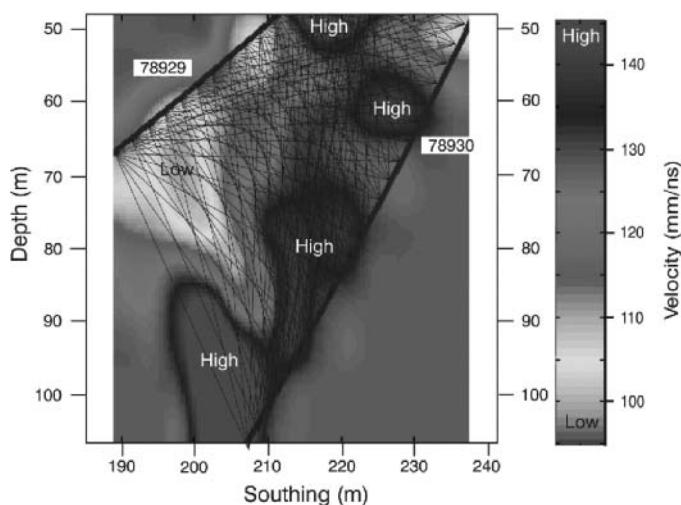


**Figure 14.70** Velocity tomogram derived from the cross-hole radar survey using the straight ray paths indicated. From Calvert and Livelybrooks (1997), by permission. [C]



**Figure 14.71** Excavation and deposition of soil in spoil mounds has produced over-steepening of the slope in a highway cutting at the A55 St Asaph Bypass, north Wales. [C]

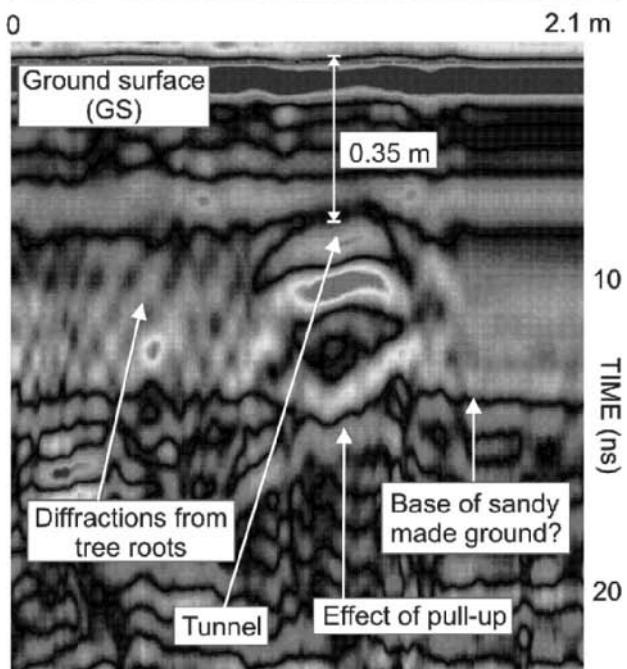


**Figure 14.72** (A) Calibration of 400 MHz radar profile above a tunnel of measured depth, and (B) interpreted radargram showing the calibrated section associated with a known badger sett entrance. [C]

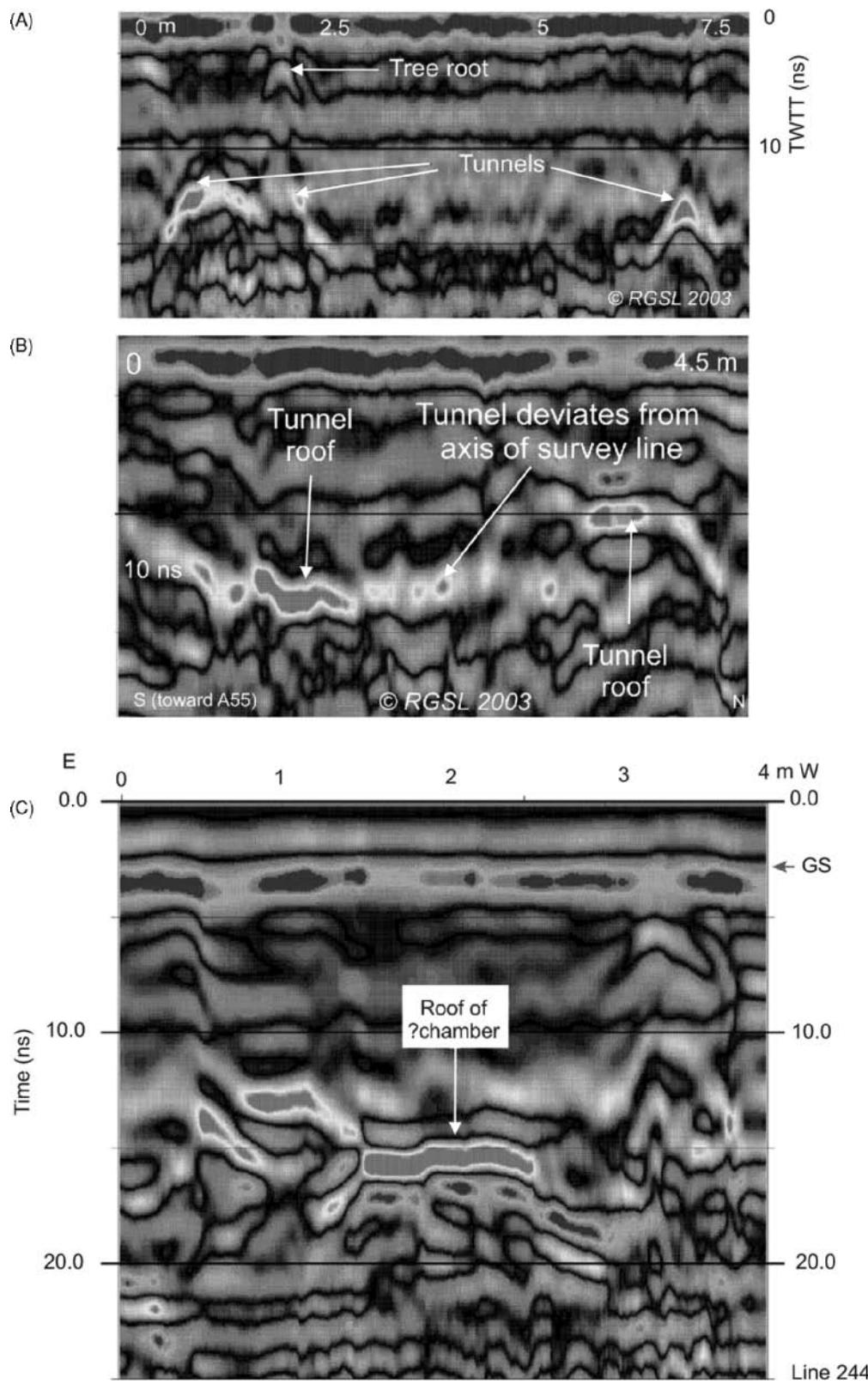


**Figure 14.73** Example of 400 MHz radargrams acquired (A) perpendicular and (B) subparallel to badger tunnels; (C) a strong elongate radar anomaly interpreted as representing a living chamber. [C]

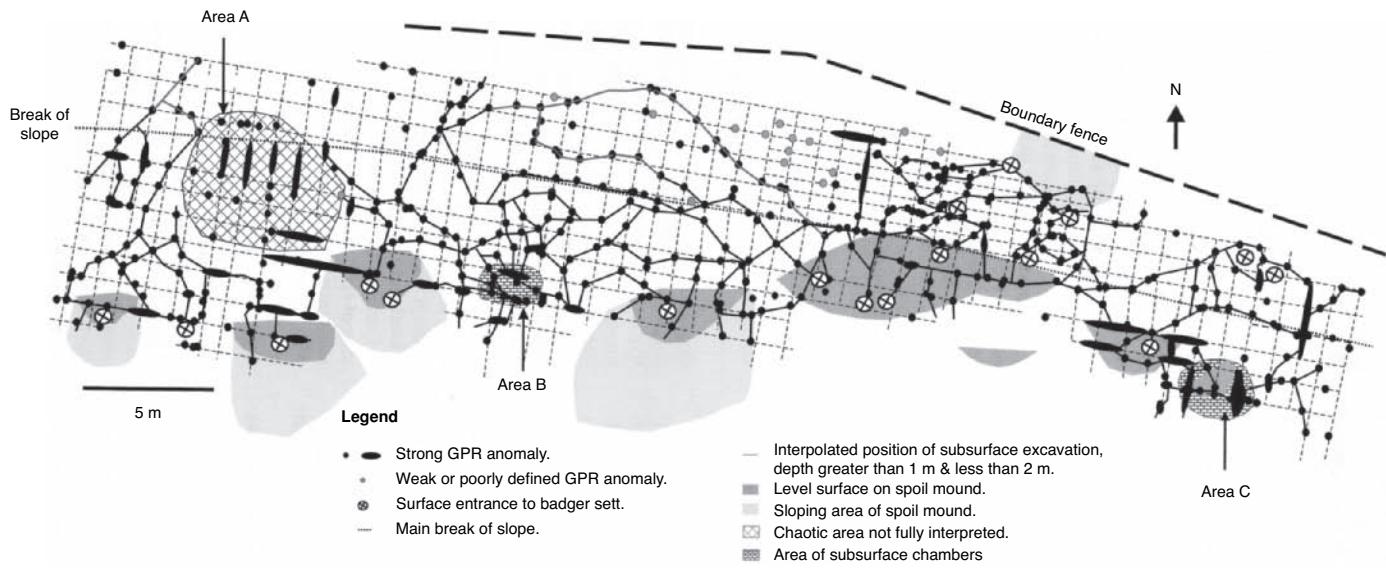


**Figure 14.74** Interpretation of the radar survey at the St Asaph Bypass, north Wales, showing the position of subsurface badger excavations. From Nichol *et al.* (2003), by permission.

typically ranged between 1 m and 2 m deep. No tunnels were found deeper than 2 m, and a change in the radargram characteristics around this level appear to correspond to the base of the sandy stratum. The survey identified a complex and extensive series of tunnels, living and nursery chambers and entrances (Figure 14.74), with a total identified tunnel length of 324 m. The volume of material excavated by the badgers was estimated to be  $46 \pm 9 \text{ m}^3$ , whereas the total tunnel volume was estimated from the radar survey to be  $31 \pm 6 \text{ m}^3$ . Although of the same order, a discrepancy in the volume remained. It is possible that the assumed dimensions of tunnels were underestimated during the volume calculation and/or that the

size of the badger sett was greater than that measured within the survey area and may have extended beneath the open pasture beyond the site boundary. Having mapped the probable reach of most of the badger setts and having found that the tunnels were limited to the sandy stratum in the uppermost 2 m of the cutting slope, no relationship was found with the surface cracking evident at the top of the cutting. Removal of spoil material from mounds in areas identified as being abandoned could be carried out safely without undue disruption to the local badger population. The radar survey also demonstrated that no expensive remedial engineering works were required.



# 15

## Radiometrics

### 15.1 Introduction

The phenomenon of radioactivity was discovered in 1896 by Antoine Becquerel, a year after Wilhelm Röntgen discovered X-rays. However, it was Pierre and Marie Curie who coined the term *radioactivity* in 1898 after their experiments on pitchblende, a uranium ore. The main motivator for exploration of uranium was to provide material for nuclear fuels and weaponry and began in the mid-1940s. The method has developed in phases depending upon the demand for uranium. Activity waned significantly in the 1950s, and only with a renewed interest in exploiting radioactive elements, such as uranium ( $^{238}\text{U}$ ), thorium ( $^{232}\text{Th}$ ) and potassium ( $^{40}\text{K}$ ), coupled with improvements in instrumentation, was the method re-awakened in the 1960s and 1970s. Natural gamma ( $\gamma$ )-ray logging down boreholes had been pioneered in 1939 for the hydrocarbon industry, and neutron logging followed around 1941. Gamma-gamma (density) logs were first used to determine density around 1957. Active and passive nuclear logging have become established components of the hydrocarbon industry ever since, and demand for these techniques has been largely unaffected by the vagaries of the mineral exploration market. The mineral exploration sector has been more variable, and it is only in the last couple of decades that radiometric surveying has become better established and used more routinely along with magnetic techniques, particularly in airborne exploration campaigns. Within the last few years, there has been significant development in the combination of radiometric survey data with remote sensing and digital elevation data, and *radiometric imaging* is now commonplace.

There are many hundreds of naturally occurring radioactive isotopes, but the majority are rare or are only weakly radioactive and thus are of little interest for mineral exploration. There are 45 minerals that exhibit strong radioactivity, and a further 225 that are very strong and to which exposure should be limited for health reasons; samples of these minerals have to be stored securely. Radiobarite is the most radioactive mineral known thus far and is potentially lethal. Radioactivity in minerals is caused by the inclusion of naturally-occurring radioactive elements and

is dependent upon the concentration and isotope present in the mineral.

While the earliest and most widespread applications of radiometric methods have been and continue to be for hydrocarbon and mineral exploration, the techniques are beginning to be applied to other areas, such as those listed in Table 15.1. These now include shallow archaeological and environmental investigations, non-destructive testing (NDT) of materials and in health monitoring such as for radon (and in medical procedures in hospitals).

### 15.2 Natural radiation

The fundamental part of all elements is the dense, positively charged nucleus, surrounded by negatively charged electrons, equal in number to the nuclear charge and never more than 92. The nucleus comprises positively charged protons, the number of which defines the element, and neutrons, which are neutral but have a slightly greater mass than a proton. Elements that have an equal number of protons and neutrons are stable; those that have a different number of neutrons than protons are termed *isotopes*. Conventional notation to describe an element A in terms of the number of protons (i.e. its atomic number)  $n$ , and atomic weight,  $w$  (which is the number of protons and neutrons) is  ${}_n\text{A}^w$ ;  $n$  ranges from 1 to 92 for naturally-occurring elements. Radioactive decay is the process by which a radioactive parent isotope loses elementary particles from its nucleus to become a progeny ('daughter') element. This occurs by the emission of alpha and beta particles, and gammarays, which are high-energy electromagnetic waves comparable to X-rays, which have lower energy. The rate of decay for this extremely precise process is constant for a given element.

#### 15.2.1 Isotopes

An isotope is an element whose atoms have a common number of protons and electrons (i.e. have the same atomic number,  $n$ ) but which vary in the number of neutrons in their nucleus. For

**Table 15.1** Applications for radiometric methods.

Mineral exploration, especially for uranium
Sediment distribution mapping
Archaeology
Soil mapping
Geological mapping
Mapping surface hydrocarbon seepages
Radiation hazard mapping, including from radon
Tracking artificial radioactive tracers
Monitoring radioactivity from low-level nuclear waste dumps
Monitoring seabed contamination by radioactive waste products
Borehole logging, predominantly in hydrocarbon exploration

example, hydrogen exists in three isotopic forms,  ${}_1\text{H}^1$  (one proton, no neutron),  ${}_1\text{H}^2$  (deuterium, one proton, one neutron), and  ${}_1\text{H}^3$  (tritium, one proton, two neutrons). In nature, there are 300 isotopes but only 92 elements. There are hundreds of artificial isotopes. Of greatest significance in radiometric surveying are isotopes of uranium, thorium and potassium.

## 15.2.2 $\alpha$ and $\beta$ particles, and $\gamma$ radiation

An *alpha* ( $\alpha$ ) particle comprises a helium nucleus  ${}_2\text{He}^4$ , with two protons and two neutrons, and a charge of +2. These are emitted during certain disintegrations from element A to form isotope B as denoted by the process:  ${}_n\text{A}^W \rightarrow {}_{n-2}\text{B}^{W-4} + {}_2\text{He}^4$ . Alpha particles are absorbed by a few centimetres of air.

A *beta* ( $\beta$ ) particle is an electron with a charge of -1, and a mass of 1/1840 of that of a proton, and may be emitted when a neutron splits into a proton and an electron, with the proton remaining in the nucleus. This results in a charge gain of +1 so that the atomic number increases by 1 but there is virtually no mass change. So for element A, the process is described by:  ${}_n\text{A}^W \rightarrow {}_{n+1}\text{B}^W + e^-$ . Beta particles can travel up to a metre in air and can be detected during ground surveys.

*Gamma* ( $\gamma$ ) rays are high-energy electromagnetic radiation with frequencies greater than  $10^{16}$  Hz with energy levels in the range of 0.1 MeV to 3 MeV (MeV = mega-electron volt). They can also be considered to behave like particles called *photons*. The energy of gamma radiation is diagnostic of the isotope from which it originated. In some natural radioactive elements, an additional disintegration process can occur known as *K capture*. This takes place when an electron from the innermost K-orbit enters the nucleus with the emission of  $\gamma$  radiation. As an electron is captured, the atomic number decreases by one and a different element is formed, as described by:  ${}_n\text{A}^W + e^- \rightarrow {}_{n-1}\text{B}^W$ . Gamma rays can travel for up to 300 m in air and so can be detected by airborne surveys, but are stopped by a few centimetres of soil, rock or water. It is important to recognise that the source of radiation measured is derived principally from the top 20–30 cm of soil or rock. If this is obscured then the results obtained will not be meaningful. Furthermore, where bedrock sources are being targeted in an exploration programme, diagnostic radiation may only be evident if the overlying soil contains sufficient minerals derived from the bedrock or if the bedrock is very close to or exposed at the ground surface.

The current convention to describe a radioactive isotope is to list it in terms of the atomic weight only, in the form  ${}^W\text{A}$ .

## 15.2.3 Radioactive decay series and radioactive equilibria

The radioactive decay process may result in the formation of a stable element or another radioactive substance that also undergoes decay. Radioactivity decays exponentially with time, and the time it takes for half the nuclei to disintegrate is termed the *half-life* ( $T_{1/2}$ ) (Box 15.1). The half-life values for different nuclei vary enormously – from  ${}^{212}\text{Po} \approx 10^{-7}$  s to  ${}^{204}\text{Pb} \approx 10^{19}$  years (i.e. this lead isotope is effectively stable). As the decay constants of isotopes are known very accurately, and are unaffected by environmental factors (temperature, pressure, chemical composition), they can be used as the basis of radiometric dating of rocks and of particular geological processes.

Radioactive activity of a mineral is measured in terms of the curie (Ci), the unit named after Marie Curie. One curie is defined as the activity that results in  $3.7 \times 10^{10}$  disintegrations per second, equivalent to the number of  $\alpha$ -particles emitted by 1 g of pure radium,  ${}^{226}\text{Ra}$ , in one second. One disintegration/second is defined as one *Becquerel* (Bq). One Ci =  $3.7 \times 10^{10}$  Bq. The intensity of gamma radiation is measured in *röntgen* (R), where one röntgen is the quantity of radiation that will produce one electrostatic unit of charge ( $2.08 \times 10^9$  ion pairs) per cubic centimetre in air at  $0^\circ\text{C}$  and normal pressure. Radiation anomalies are commonly quoted in units of  $\mu\text{R}/\text{hr}$ . The subunit milli-röntgen (mR) is used to define the maximum dosage permissible to humans exposed to radioactivity, equivalent to about 300mR/week.

### Box 15.1 Radioactive decay and half-life

The rate of radioactive decay is given by:

$$N = N_0 e^{-\lambda t}$$

where  $N$  is the number of atoms after time  $t$  from an initial number  $N_0$  at time = 0; the term  $\lambda$  is a decay constant that is characteristic of the specific element.

If half the nuclei disintegrate in a period of time, the half-life ( $T_{1/2}$ ), then:

$$N/N_0 = 1/2 = e^{-\lambda T_{1/2}}$$

and,

$$\lambda = 0.693/T_{1/2} \text{ and } T_{1/2} = \lambda/0.693$$

There are three radioactive decay series for uranium and thorium,  $_{90}\text{Th}^{232}$ ,  $_{92}\text{U}^{235}$  (called the actinium series) and  $_{92}\text{U}^{238}$ , as listed in Table 15.2. All radioactive decay eventually leads to stable isotopes of lead with a number of intermediate stages of radioactivity. The half-lives, decay type, and decay energy levels are listed for each intermediate stage. The decay energy levels remain constant for each isotope and can be used diagnostically to identify the isotopes present.

Radioactive decay can be said to be in *secular equilibrium* when the number of daughter atoms disintegrating per second is identical to the number being created by disintegrations of the parent isotope. The time taken for equilibrium to be reached is a function of the ratio of the decay constants for each isotope involved. Estimates of uranium ore grade based on radioactivity levels assume a state of near-secular equilibrium. It is also assumed that the radioactive decay is contained within the environment (i.e. a closed system) and that components of the decay have not been transported away (such as dissolved in groundwater). This assumption does not always hold, and errors can be introduced into estimates of uranium concentration as a result.

## 15.2.4 Natural gamma-ray spectra

As has been described above, the decay process for a particular isotope series generates diagnostic energy levels that can be measured remotely. Gamma rays from  $^{208}\text{Tl}$  have an energy of 2.62 MeV and are indicative of the presence of thorium; those from  $^{214}\text{Bi}$  have an

**Table 15.2A** Uranium decay series ([www.webmineral.com](http://www.webmineral.com)).

Isotope	Half-life	Half-life units	Half-life (seconds)	Decay	Decay energy (MeV)
$^{238}\text{U}$	$4.47 \times 10^9$	Years	$1.41 \times 10^{17}$	$\alpha$	4.270
$^{234}\text{Th}$	24.1	Days	$2.08 \times 10^6$	$\beta$	0.273
$^{234}\text{Pa}$	1.17	Min.	70.2	$\beta$	2.197
$^{234}\text{U}$	$2.48 \times 10^5$	Years	$7.82 \times 10^{12}$	$\alpha$	4.859
$^{230}\text{Th}$	$7.7 \times 10^4$	Years	$2.43 \times 10^{12}$	$\alpha$	4.770
$^{226}\text{Ra}$	1622	Years	$5.05 \times 10^{10}$	$\alpha$	4.871
$^{222}\text{Rn}$	3.82	Days	$3.3 \times 10^5$	$\alpha$	6.681
$^{218}\text{Po}$	3.05	Min.	183	$\alpha$	6.115
$^{214}\text{Pb}$	26.8	Min.	161	$\beta$	1.024
$^{214}\text{Bi}$	19.8	Min.	$1.19 \times 10^3$	$\beta$	3.272
$^{214}\text{Po}$	162	$\mu\text{sec.}$	$1.62 \times 10^{-4}$	$\alpha$	7.833
$^{210}\text{Pb}$	22.3	Years	$7.03 \times 10^8$	$\beta$	3.792
$^{210}\text{Bi}$	5.01	Days	$4.33 \times 10^5$	$\beta$	5.037
$^{210}\text{Po}$	138.4	Days	$1.2 \times 10^7$	$\alpha$	5.407
$^{206}\text{Pb}$	Stable				

(The specific activity associated with each decay stage is  $1.236 \times 10^7$  Bq/kg, equivalent to  $3.34 \times 10^{-4}$  Ci/kg).

**Table 15.2B** Actinium decay series ([www.webmineral.com](http://www.webmineral.com)).

Isotope	Half-life	Half-life units	Half-life (seconds)	Decay	Decay energy (MeV)
$^{235}\text{U}$	$7.04 \times 10^8$	Years	$2.22 \times 10^{16}$	$\alpha$	4.679
$^{231}\text{Th}$	25.5	Hours	$9.18 \times 10^4$	$\beta$	4.213
$^{231}\text{Pa}$	$3.25 \times 10^4$	Years	$1.02 \times 10^{12}$	$\alpha$	5.149
$^{227}\text{Ac}$	21.8	Years	$6.87 \times 10^8$	$\beta$	5.042
$^{227}\text{Th}$	18.5	Days	$1.6 \times 10^6$	$\alpha$	6.146
$^{223}\text{Ra}$	11.4	Days	$9.85 \times 10^5$	$\alpha$	5.979
$^{219}\text{Rn}$	4	Sec.	4	$\alpha$	8.130
$^{215}\text{Po}$	$1.78 \times 10^{-3}$	Sec.	$1.78 \times 10^{-3}$	$\alpha$	7.526
$^{211}\text{Pb}$	36.1	Min.	$2.17 \times 10^3$	$\beta$	1.373
$^{211}\text{Bi}$	2.13	Min.	$1.28 \times 10^2$	$\alpha$	6.751
$^{207}\text{Tl}$	4.77	Min.	$2.86 \times 10^2$	$\beta$	1.423
$^{207}\text{Pb}$	Stable				

(The specific activity associated with each decay stage is  $5.762 \times 10^5$  Bq/kg, equivalent to  $1.15 \times 10^{-5}$  Ci/kg).

**Table 15.2C** Thorium decay series ([www.webmineral.com](http://www.webmineral.com)).

Isotope	Half-life	Half-life units	Half-life (seconds)	Decay	Decay energy (MeV)
$^{232}\text{Th}$	$1.4 \times 10^{10}$	Years	$4.42 \times 10^{17}$	$\alpha$	4.083
$^{228}\text{Ra}$	5.8	Years	$6.93 \times 10^{11}$	$\beta$	5.520
$^{228}\text{Ac}$	6.1	Hours	$2.2 \times 10^4$	$\beta$	2.127
$^{228}\text{Th}$	1.9	Years	$5.99 \times 10^7$	$\alpha$	5.520
$^{224}\text{Ra}$	3.6	Days	$3.11 \times 10^5$	$\alpha$	5.789
$^{220}\text{Rn}$	55.0	Sec.	55.0	$\alpha$	0.800
$^{265}\text{Po}$	0.15	Sec.	0.15	$\alpha$	6.906
$^{212}\text{Pb}$	10.6	Hours	$3.82 \times 10^4$	$\beta$	0.574
$^{212}\text{Bi}$	61.0	Min.	$3.66 \times 10^3$	$\beta, \alpha$	2.254
$^{212}\text{Po}$	30.0	Sec.	30.0	$\alpha$	8.954
$^{208}\text{Tl}$	3.0	Min.	$1.8 \times 10^2$	$\beta$	5.001
$^{208}\text{Pb}$	Stable				

(The specific activity associated with each decay stage is  $4.075 \times 10^6$  Bq/kg, equivalent to  $1.101 \times 10^{-4}$  Ci/kg).

energy level of 1.76 MeV; while those from  $^{40}\text{K}$  have an energy level of 1.46 MeV. An example of a natural gamma-ray spectrum for a typical felsic intrusive rock measured during an airborne survey with a ground clearance of 120 m is shown in Figure 15.1. Peaks in counts per second, shown on a logarithmic scale, occur at each of these

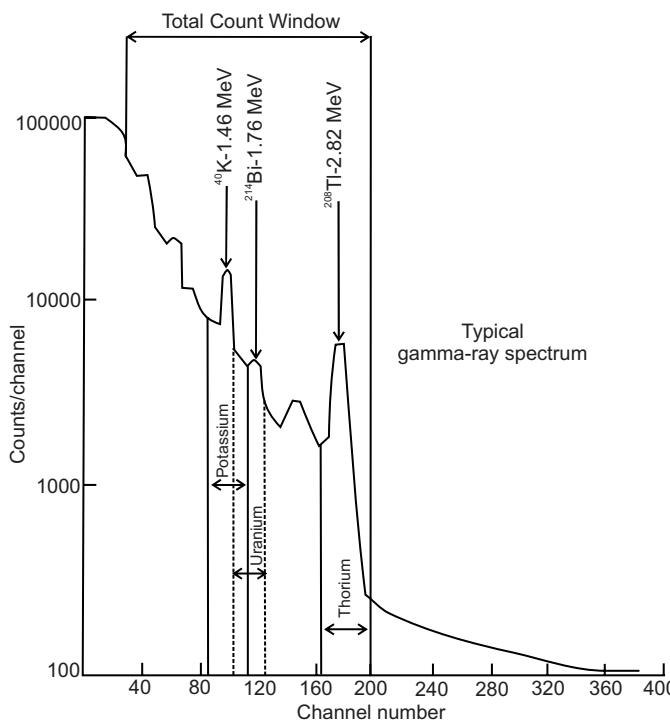


**Figure 15.1** A typical gamma-ray spectrum from felsic intrusive rock measured at 120 m terrain clearance. After Urquhart (2010), by permission.

energy levels in the spectrum shown in Figure 15.1. Note that the count rate falls off quickly beyond the thorium window as there are no naturally-occurring isotopes that emit gamma rays with higher energies than 2.62 MeV. Airborne radioactivity detection equipment measures counts per second in energy windows (channels), with the larger channel numbers relating to higher energy levels. The heights of the peaks are proportional to the amounts of the respective radioactive isotopes present in the rock at the ground surface. Consequently, by measuring spectra over different regions of exposed rock and comparing the results, it is possible to translate the relative heights in each energy window peak into corresponding variations in concentrations of potassium, uranium and thorium within the different rock types. However, the spectral shapes are related to the instrument detector response, the geometry of the source and the distance between the source and the detector, and are not only a function of the amounts of radioactive elements present, requiring corrections to be applied to the observed data prior to interpretation, as discussed in Section 15.5.

It can be seen from Figure 15.1 that there is a trend from high counts at lower energy levels, decreasing as the energy levels rise. This trend, called the *Compton continuum*, is due to a phenomenon known as *Compton scattering*. This occurs as a result of the loss in energy of the gamma ray from collisions with electrons. Furthermore, at each collision, the direction of travel of the gamma ray is deflected and will travel with a successively lower energy. Consequently, millions of gamma rays with well-defined initial energies will, as a result of having numerous collisions, form a continuum of energies with a steadily rising proportion trending towards lower

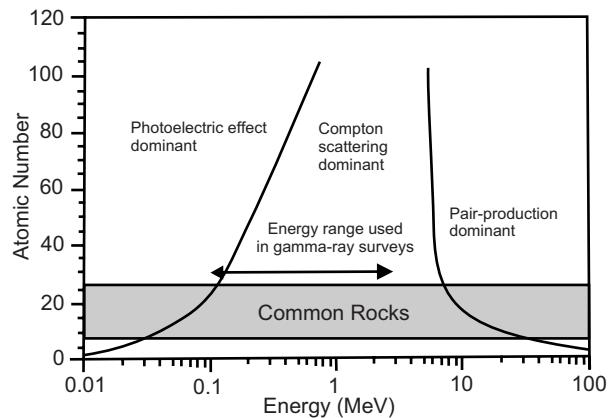


**Figure 15.2** The interaction of gamma rays with matter. Measurements in mineral exploration projects are normally made in the 0.1–3 MeV energy band. Adapted from IAEA (2003), by permission.

energy levels, hence the larger number of counts with decreasing energy levels. This scattering predominates at energies in the range 0.2–2.0 MeV (Figure 15.2). The eight most abundant elements in the Earth's crust (O, Si, Al, Fe, Ca, Na, K and Mg) have atomic numbers ranging from 8 to 26. Measurements in exploration surveys are normally made in the 0.1–3.0 MeV energy bands as indicated in Figure 15.2.

## 15.3 Radioactivity of rocks

Some of the naturally occurring radioactive isotopes are listed in Table 15.3, with the most significant isotopes for geological investigations highlighted. In addition, some of the common radioactive minerals of thorium and uranium are listed with their common occurrences in Table 15.4. More details of radioactive minerals have been provided by Durrance (1986) and are listed on [www.webminerals.com](http://www.webminerals.com). Potassium minerals are very widespread and their radioactivity often constitutes noise in the search for uranium and thorium minerals. Generally, activity is greater in sedimentary and meta-sedimentary rocks than it is in igneous and other metamorphic rock types, except for potassium-rich granites.

It is also important to recognise that trace concentrations of radioactive materials occur in all rocks. Cosmic radiation also contributes to background radiation, albeit in minute amounts, and radium is also found in water. Example values of background radioactivity for various rock types and water are shown in Table 15.5.

## 15.4 Radiation detectors

### 15.4.1 Geiger-Müller counter

A Geiger-Müller counter detects ionising radiation from beta particles. The detector comprises a sealed tube filled with an inert gas

**Table 15.3** Naturally occurring radioactive isotopes ([www.webmineral.com](http://www.webmineral.com)).

Element	Isotope symbol	Natural abundance	Half-life (years)	Primary decay mode
Tellurium	<b><math>^{130}\text{Te}</math></b>	33.97%	$2.4 \times 10^{21}$	
Vanadium	<b><math>^{50}\text{V}</math></b>	0.25%	$3.9 \times 10^{17}$	EC
Zirconium	<b><math>^{96}\text{Zr}</math></b>	2.80%	$3.6 \times 10^{17}$	
Samarium	<b><math>^{149}\text{Sm}</math></b>	13.80%	$1 \times 10^{16}$	$\alpha$
Samarium	<b><math>^{148}\text{Sm}</math></b>	11.30%	$7 \times 10^{15}$	$\alpha$
Osmium	<b><math>^{186}\text{Os}</math></b>	1.58%	$2 \times 10^{15}$	$\alpha$
Neodymium	<b><math>^{145}\text{Nd}</math></b>	8.30%	$1.1 \times 10^{15}$	$\alpha$
Platinum	<b><math>^{192}\text{Pt}</math></b>	0.79%	$1 \times 10^{15}$	$\alpha$
Indium	<b><math>^{115}\text{In}</math></b>	95.70%	$6 \times 10^{14}$	$\beta$
Gadolinium	<b><math>^{152}\text{Gd}</math></b>	0.20%	$1.1 \times 10^{14}$	$\alpha$
Tellurium	<b><math>^{123}\text{Te}</math></b>	0.89%	$1.3 \times 10^{13}$	EC
Platinum	<b><math>^{190}\text{Pt}</math></b>	0.01%	$6.9 \times 10^{11}$	$\alpha$
Samarium	<b><math>^{147}\text{Sm}</math></b>	15.00%	$1.08 \times 10^{11}$	$\alpha$
Rubidium	<b><math>^{87}\text{Rb}</math></b>	27.83%	$4.9 \times 10^{10}$	$\beta$
Rhenium	<b><math>^{187}\text{Re}</math></b>	62.60%	$4.5 \times 10^{10}$	$\beta$
Lutetium	<b><math>^{176}\text{Lu}</math></b>	2.59%	$2.2 \times 10^{10}$	$\beta$
Thorium	<b><math>^{232}\text{Th}</math></b>	100.00%	$1.4 \times 10^{10}$	$\alpha$
Uranium	<b><math>^{238}\text{U}</math></b>	99.28%	$4.46 \times 10^9$	$\alpha$
Potassium	<b><math>^{40}\text{K}</math></b>	0.01%	$1.25 \times 10^9$	$\beta$
Uranium	<b><math>^{235}\text{U}</math></b>	0.72%	$7.04 \times 10^8$	$\alpha$

Significant radioactive isotopes are highlighted in bold.

$\alpha$  (alpha),  $\beta$  (beta) and EC (= electron capture) decay modes.

**Table 15.5** Background radioactivity in selected rock types and waters (from Telford *et al.*, 1990).

Rock types	Activity (curies/g $\times 10^{-12}$ )
<i>Igneous</i>	
Granite	0.7-4.8
Basalts	0.5
<i>Metamorphic</i>	
Marble	1.9
Quartzite	5.0
Slates	3-8
<i>Sedimentary</i>	
Chalk	0.4
Dolomites	8
Sandstone	2-4

(usually helium, neon, or argon with halogens added) through the centre of which a thin axial anode wire is located. A voltage (typically 400 V) is maintained between a cylindrical cathode and the anode. Incoming beta particles ionise the gas and the resulting positive ions and electrons formed accelerate towards the electrodes, ionising more gas as they move. This process causes a current pulse that can be amplified and displayed by a needle on a meter and as an audible signal (click). Modern instruments can indicate radioactivity over several orders of magnitude. As Geiger counters measure beta particles, they are best suited to ground-based surveys where the distance between the source of the radioactivity and detector is less than a metre. Hand-held Geiger counters are also used to monitor low-level radioactivity contamination, and certain types of instrument can be used to measure gamma radiation also.

## 15.4.2 Scintillometers

A scintillation counter or scintillometer is used to detect and measure gamma radiation. When gamma radiation strikes a material

**Table 15.4** Radioactive minerals (from Telford *et al.*, 1990).

Element	Mineral	Occurrence
Potassium	Orthoclase and microcline feldspars [KAISi <sub>3</sub> O <sub>8</sub> ]	Main constituents in acid igneous rocks and pegmatites
	Muscovite [H <sub>2</sub> KAl(SiO <sub>4</sub> ) <sub>3</sub> ]	Main constituents in acid igneous rocks and pegmatites
	Alunite [K <sub>2</sub> Al <sub>6</sub> (OH) <sub>12</sub> SO <sub>4</sub> ]	Alteration in acid volcanics
	Sylvite, carnallite [KCl, MgCl <sub>2</sub> .6H <sub>2</sub> O]	Saline deposits in sediments
Thorium	Monazite [ThO <sub>2</sub> + rare earth phosphate]	Granites, pegmatites, gneiss
	Thorianite [(Th, U)O <sub>2</sub> ]	Granites, pegmatites, placers
	Thorite, uranothorite [ThSiO <sub>4</sub> + U]	Granites, pegmatites, placers
Uranium	Uraninite [oxide of U, Pb, Ra + Th, rare earths]	Granites, pegmatites, and with vein deposits of Ag, Pb, Cu
	Carnotite [K <sub>2</sub> O.2UO <sub>3</sub> .V <sub>2</sub> O <sub>5</sub> .2H <sub>2</sub> O]	Sandstones
	Gummite [uraninite alterations]	Associated with uraninite

such as thalium-activated sodium iodide it produces tiny flashes of light, i.e. it scintillates. These flashes are amplified by a photomultiplier tube (PMT), which results in a burst of electrons large enough to be detected at an anode where the signal is again amplified and the result displayed in counts per second by a needle on a meter, and as an audible click or digitally. It is used to provide a total count of radioactivity and can be deployed in hand-held devices, such as to monitor contamination in nuclear power stations, and also for mineral exploration in ground-based (man- or vehicle-mounted systems) or airborne configurations.

The sensitivity of a scintillometer depends upon the volume of the detector crystal, as larger crystals are able to detect more events. Detectors vary in their sensitivity also by virtue of how they have been shielded, using an aperture to detect radiation from a specific direction.

### 15.4.3 Gamma-ray spectrometers

While scintillometers measure total counts per second, they cannot indicate anything else about the type of radiation. To do this a gamma-ray spectrometer is used by which the energy of the radiation is measured as well as the activity level (associated with the radioactive element decay series). The number of light flashes within a specific time is proportional to the gamma ray energy. In large modern spectrometers, thalium-activated sodium iodide detectors are used with a high-speed (60 MHz) analogue-to-digital converter and processor assembly to convert the analogue signal from the NaI crystal detector to a digital spectrum with up to 1 million channel resolution. Using an energy calibration curve, the spectrum is linearised and compressed to a reduced number of channels (e.g. 256, 512 or 1024). More basic spectrometers have only four channels – one for the total count, and one specifically for potassium ( $^{40}\text{K}$ , 1.46 MeV), uranium ( $^{214}\text{Bi}$ , 1.765 MeV) and thorium ( $^{208}\text{Tl}$ , 2.614 MeV). Rather than measure the counts just at the peak energy level for these isotopes, there are recommended windows (IAEA, 1991) for energy bands for the three isotopes: potassium (1.37–1.57 MeV), uranium (1.66–1.86 MeV) and thorium (2.41–2.81 MeV) windows. In some cases these windows may overlap. The term ‘spectrometer’ should be reserved for instruments measuring the energy spectrum over at least 256 channels, while the four-channel instruments should strictly be termed ‘scintillometers’; however, they are commonly also referred to as spectrometers.

Gamma-ray spectrometers are produced with a range of crystal detector volumes: the larger the crystal volume, the greater the chance that gamma radiation will be detected, and so efficiency increases with crystal volume. Solid-state semiconducting detectors exist made from lithium-drifted germanium crystals, and they have superior resolving power (50–80 times better) compared with that of NaI crystal detectors. However, such germanium crystals are difficult to grow, and to operate effectively it is necessary to maintain them at liquid nitrogen temperatures and so are more difficult to deploy and are heavier than NaI detectors.

There are two types of gamma-ray measuring systems – integral and differential spectrometers. The crystal detectors are the same for both but the electronic analysers are different. Integral spectrome-

ters measure the total count of incoming gamma radiation above a specified energy threshold and do not differentiate between radiation from thorium, potassium or uranium sources, unless a number of sensors are deployed simultaneously with different energy-level thresholds. Integral spectrometers are used in hand-held systems for rapid prospecting work.

Differential spectrometers measure gamma radiation that falls within specified spectral windows of fixed energy bandwidth. These are centred on the  $^{214}\text{Bi}$ ,  $^{208}\text{Tl}$  and  $^{40}\text{K}$  energy peaks at 2.62 MeV, 1.76 MeV and 1.46 MeV, respectively. This form of spectrometer was the normal type of instrument used for airborne surveys in the 1970s and 1980s before multichannel spectrometers were introduced.

Multichannel spectrometers monitor the entire gamma-ray spectrum in discrete steps and can be used to record the spectra for potassium, thorium and uranium, and combined. The minimum crystal volume required depends upon the sensor altitude and aircraft speed. For slower helicopter operations at lower level, smaller crystal volume detectors can be used. For faster, higher altitude surveys, the largest volume crystals are needed, with volumes up to 32 litres, as the radiation flux decreases with altitude and therefore larger volumes are needed to compensate.

In order to convert the counting rates in the three or more spectral windows into gamma rays per unit time from  $^{214}\text{Bi}$ ,  $^{208}\text{Tl}$  and  $^{40}\text{K}$ , the instruments need to be calibrated. This is achieved by flying the sensors over an area of known radio-isotopic concentration and/or by placing the sensors above a ground-based slab that contains known proportions of radio-isotopes.

Examples of energy discrimination characteristics of integral and differential gamma ray spectrometers are shown in Figure 15.3. In each graph, the vertical axis shows the relative number of counts, and the horizontal axis, the energy gates. Figure 15.3A shows a single threshold system that records the number of counts within a single energy threshold window and does not differentiate the radio-isotopic source of the radiation. Figure 15.3B shows a multiple threshold system that uses the idea of single threshold sensors but where each is set to a different energy bandwidth. The contribution from each diagnostic energy peak can then be resolved. A spectrum from a window spectrometer is shown in Figure 15.3C where the energy peaks for potassium, uranium and thorium are centred on specific energy windows. The ultimate is the multichannel spectrometer (Figure 15.3D) which is able to sample the entire energy spectrum with many channels (256 to over 1000) and thus provide excellent energy resolution and discrimination.

A comprehensive overview of radioelement mapping using gamma-ray spectrometry has been provided by the IAEA (2003).

### 15.4.4 Radon detectors

Radon is the only radioactive element that exists in gaseous form. As it is a noble gas it does not react with other elements to form new compounds, and as a fluid it is highly mobile. Consequently it can migrate through pores, fractures, joints and faults both as a gas and dissolved in the groundwater. Radon gas is carcinogenic and represents a significant health hazard. Consequently, building regulations in areas known to contain radon require that suitable

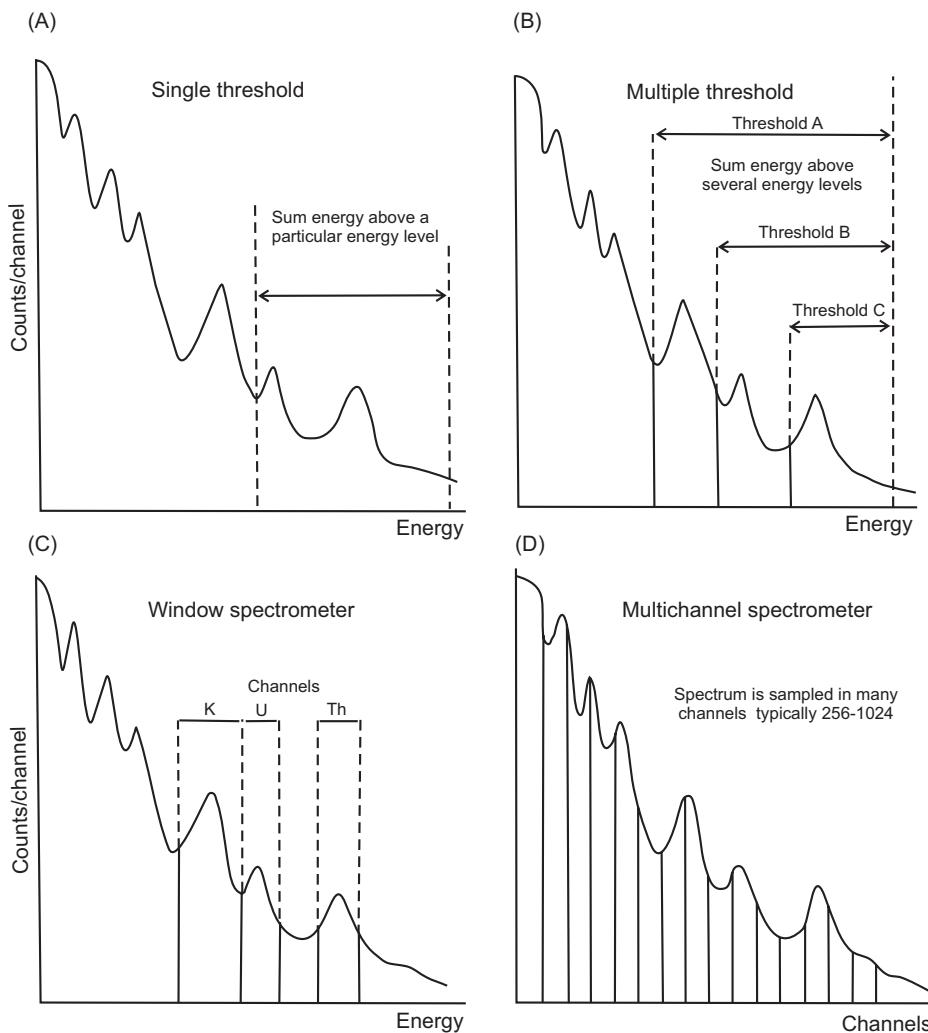


**Figure 15.3** Energy discrimination characteristics of integral and differential gamma-ray spectrometers. Modified from Hanson (1980), by permission.

ventilation or screening is installed to minimise the collection of and increased concentrations of radon gas within dwellings. In such areas, passive radon monitoring is achieved by placing small so-called Alpha Track devices in appropriate locations inside buildings. The devices contain a small strip of a special type of plastic that is mounted in a small, filtered container. When radon particles strike the strip, they leave an indication of their presence that can be measured once the strip has been removed for analysis. Other devices, such as a *radon emanometer* or *continuous radon monitor*, enable on-site measurements to be made but are slow to operate. Gas is extracted and drawn into the instrument where a detection chamber is located and in which the air quality is analyzed and the radiation level determined.

### 15.4.5 Seaborne systems

Seaborne systems comprise either towed scintillometer systems or static seabed measurements (Jones, 1999). In the latter mode of

deployment a total-count scintillometer is mounted in a pressure housing that is lowered to the sea floor on armoured conductor cable. A couple of measurements are made before the system is moved to a new location. An early towed system consisted of a 76 mm by 76 mm NaI(Tl) crystal detector and associated circuitry mounted inside a 1-m long stainless steel tube with a 60 keV  $^{241}\text{Am}$  source to act as a reference for gain stabilisation (Miller *et al.*, 1977). The probe was attached to 850 m of armoured conducting cable and was enclosed with the furthest 30 m of the cable in a flexible hose in which two 20-m lengths of steel chain were placed to give the so-called '*eel*' the same drag/weight ratio in water as the main conductor cable. The eel was designed to present minimal risk to becoming snagged on rocks or other seabed obstacles. Tow rates are typically around 5 knots (2.5 m/s).

The onboard system consisted of a four-channel pulse-height analyser to monitor the energy bandwidth at 0.1–3.0 MeV (total gamma activity), 1.31–1.61 MeV ( $^{40}\text{K}$ ), 1.62–1.94 MeV ( $\text{U}^{214}\text{Bi}$ ), and 2.475–2.97 MeV ( $\text{Th}^{208}\text{Tl}$ ). Other systems using multiple

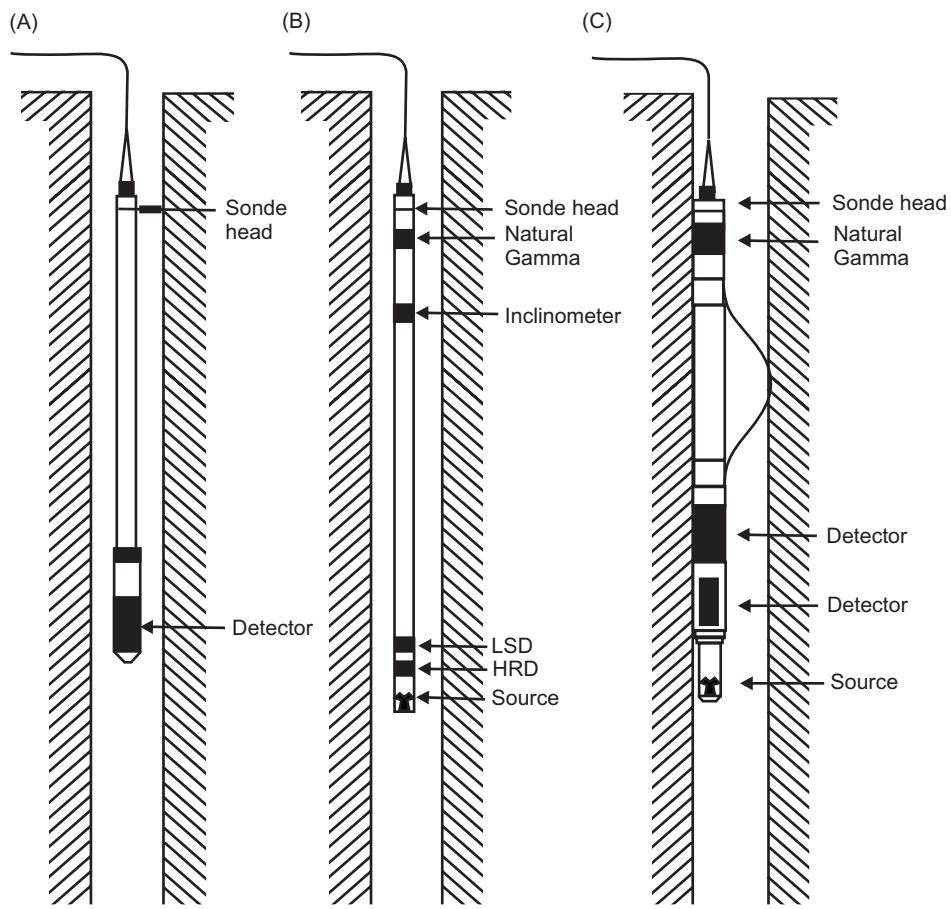


**Figure 15.4** Borehole logging tool systems for radiometric surveys: (A) natural gamma spectroscopy probe; (B) density gamma probe (trisonde); and (C) dual neutron probe. Courtesy of Robertson Geologging Ltd, by permission.

crystal detectors have also been developed (e.g. Jones DG, 1994; Jones EJW, 1989), including one developed by the British Geological Survey in the mid-1990s (Jones DG *et al.*, 2001).

Seabed radiation measurements have also been made from the USA submersible Alvin to investigate hydrothermal vents on the crest of the Juan de Fuca Ridge in the northwest Pacific. They found anomalously high count rates 2–4 m from baryte-rich deposits that contained high levels of radium ( $^{228}\text{Ra}$ ) (Stakes *et al.*, 1992).

Marine radioactive detectors can be towed across areas of sea floor where there are known concentrations of radioelements in order to calibrate them. Otherwise, calibration of detectors is carried out in air using the concrete slab method.

#### 15.4.6 Borehole logging tools

Borehole logging using active and passive nuclear systems have been long-established, especially in the oil industry, and a substantial volume of literature exists for these applications. There is a range of tools available, but broadly they comprise *gamma-ray logging*, *spectral logging*, and *neutron logging*. In each case a slimline tool is lowered into a borehole and parameters are measured as a function

of depth. A schematic showing the general layout of the down-hole tools for these three styles of logging is presented in Figure 15.4. Gamma-ray logging was first introduced in 1939 and neutron logging followed two years later.

Gamma-ray logging records radiation levels in terms of API units (API = American Petroleum Institute), as defined using the API calibration pit at the University of Houston, Texas, USA. This is a passive tool and measures the naturally occurring radioactivity in a qualitative sense; the results are affected by the diameter of the borehole and the borehole fluids present. The gamma-ray log records the total radiation present and cannot discriminate between isotopic sources. However, it is principally used to determine the shale content as the minerals that contain the radioisotopes (most commonly potassium) tend to be concentrated in clays and shales, which also tend to absorb uranium and thorium. Gamma-ray logging can be used through steel and cement walls of cased boreholes. The technique is used extensively for geological correlation purposes. Some other rock types can also exhibit elevated levels of gamma radiation, such as sandstone, which may contain uranium mineralisation; volcanic ash; potassium feldspar; clay fillings; and coal and dolomite may contain absorbed uranium. Evaporite deposits may also

contain potassium minerals such as carnallite (a hydrous chloride of potassium and magnesium). The technique is used for both qualitative and quantitative detection of economic materials (e.g. uranium and coal).

Gamma-ray logging is undertaken at 6–9 m/minute (20–30 ft/minute) but higher speeds may be used for logging deeper wells. Unstable nuclei of radioactive elements do not disintegrate in an entirely predictable manner. Consequently, a *time constant* circuit is used to average the counts over a defined period of time to provide a more representative and repeatable log. The interaction between the logging speed and the time constant results in a lag effect. Commonly, the logging speed and values of time constant are chosen to produce one foot (0.3 m) of lag, with the recorder being one foot (0.3 m) deeper than the measurement point in the hole.

Spectral logging is where the tool is able to measure the energy levels of the radiation and discriminate the isotopic sources at three energy levels: 1.46 MeV for potassium; 1.76 MeV for the uranium–radium series; and 2.62 MeV for the thorium series. To record a full spectrum (across the energy range 0.1–3 MeV; e.g. Figure 15.3D), using 256, 512 or 1024 channels, the tool is kept at a fixed depth in the borehole for several minutes. Downhole tools should be calibrated using special artificial blocks with known isotopic concentrations into which the tool can be inserted and by which the tools can be checked.

Neutron logging is an active technique that uses an artificial sealed source of neutrons, such as  $^{241}\text{Am}/\text{Be}$  (AmBe) to detect hydrogen in order to evaluate formation porosity. These sources emit fast neutrons that are slowed by collisions with hydrogen atoms until they are captured. The capture results in the emission of a secondary gamma ray. Some tools detect the captured gamma ray (*neutron–gamma log*, also the *pulsed neutron–gamma log*). Other tools detect intermediate (epithermal) neutrons or slow (thermal) neutrons (*neutron–neutron logs* in both cases). Thermal neutrons are counted in modern tools using a  $^3\text{He}$  type detector. Neutron logs are used to correlate between boreholes and can be used to detect gas in some circumstances, using the lower hydrogen density of gas compared with that in water or oil. Logging rates are comparable with those of gamma-ray logging and are also subject to the lag effect.

Further details of nuclear and other borehole logging techniques have been produced by Serra (1984), Keys (1990, 1996), Hearst *et al.* (2000), and the IAEA (2003).

## 15.5 Data correction methods

### 15.5.1 Detector calibration

As with any geophysical technique, the importance of checking equipment performance and stability also applies to radiometric techniques. Radiation detectors need to be calibrated. In the USA, Canada, Australia and handful of other countries, formal calibration sites have been set up. Instrument performance can be checked over concrete slabs that have been constructed to contain known concentrations of different radioactive isotopes, along with ‘null’ pads that

contain no known radioelements and by which background values can be determined. Similarly, areas with known natural radioactive material can be used for *in situ* cross-referencing. Both *in situ* sites and calibration slabs can be used to cross-check different instruments that are to be used in a single survey. Care also has to be taken to control the temperature of the detector, as instrument sensitivity varies with the temperature of the crystal and the photomultiplier tubes.

### 15.5.2 Thorium source test

One means of checking equipment is to undertake before and after instrument calibration, and before and after each day’s aerial survey, a thorium source test. Measurements are made using a thorium source placed at least 40 cm from the centre of each detector package to ensure that the crystals are adequately irradiated. Background measurements are made with the thorium source removed. The live time and background-corrected thorium window count rates must be within 3% of each other for the calibration checks and within 5% for the daily checks. If the results are greater than 5%, survey operations should be suspended until the source of the discrepancy is identified and rectified.

### 15.5.3 Dead time and live time

During the time that the radiometric instrument measures and analyses the scintillation from a single gamma ray or photon, all other incoming pulses are rejected and are uncounted. This time period during which the system is unable to process additional scintillations is known as the instrument *dead time* ( $T_d$ ), measured as a time period per pulse, typically of the order of 5–15  $\mu\text{s}/\text{pulse}$ ; the time during which the instrument is receptive to incoming radiation is known as the *live time*. In areas where the count rate is low or in airborne surveys, dead time may be insignificant. However, during borehole logging and in ground-based surveys where high count rates are experienced, dead time corrections (Box 15.2) may be required.

### 15.5.4 Geometric corrections

It is normally assumed that the extent of the radioactive source is extensive and at the ground surface so that the height of the radiometric sensor does not affect the count rate. To meet this so-called ‘ $2\pi$  geometry’, the lateral extent of the radioactive source should be greater than ten times the height of the sensor above

#### Box 15.2 Dead time correction (IAEA, 2003)

The true count rate ( $N_{\text{true}}$ ) can be estimated from the measured count rate ( $N_{\text{meas}}$ ) if the dead time ( $T_d$ ) is known using:

$$N_{\text{true}} = N_{\text{meas}} / (1 - T_d C) \text{ counts/s}$$

where  $C$  is the total count rate over all channels (counts/s).

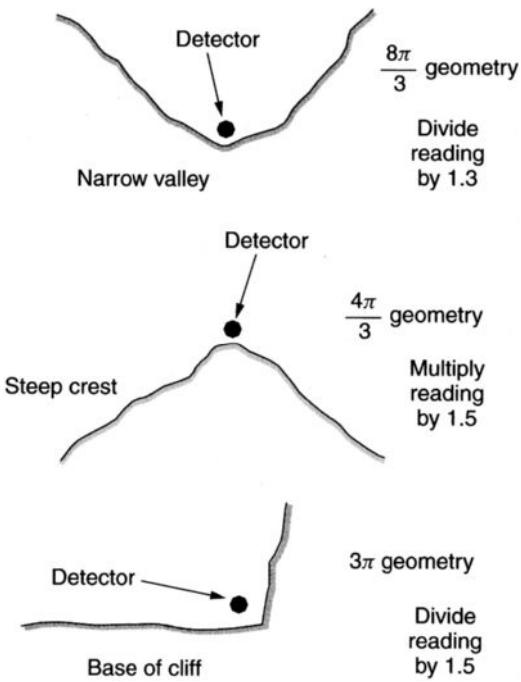


**Figure 15.5** Geometries and associated correction factors for ground-based radiometric surveys. From Milsom (2003), by permission.

it. This is seldom met in practice, particularly in ground-based surveys. Some examples of corrections to the count rates from different topographic effects are given in Figure 15.5. The reason that values have to be divided or multiplied by a geometric factor is due to the assumption that contributions to the counts detected arise additionally from adjacent hill slopes or a cliff face, hence the counts will be too high or not high enough as the ground slopes away from the detector.

### 15.5.5 Environmental factors

Radiometric surveys are affected by environmental factors arising from non-geological sources. These include atmospheric radon and humidity, cosmic rays, dirt on the detector housing and variations in soil moisture. Background cosmic radiation can be determined using an upward-looking photon detector. For ground-based surveys, measurements over a water body deeper than 1 m and with an area greater than 100 m<sup>2</sup> should be made, as this amount of water effectively attenuates all geologically derived radiation from beneath the water body. Alternatively, and less practically, measurements can be made above a large lead sheet – difficult to carry around on a field expedition! Airborne background levels can be checked by flying at a range of elevations (e.g. 1.0, 1.5, 2.0, 2.5, 3.0, 3.5 km) over water as most radiation from the ground surface is attenuated by this height and the water, and where atmospheric radon is minimal. More details as to how to undertake these corrections have been given by IAEA (2003). Atmospheric humidity can affect the background values as wet air absorbs radiation far more than dry air. Sometimes contamination of the detector housing by surface

dirt that itself contains some radioactivity can affect background values. It is important, therefore, to keep the detector surfaces as clean as possible. In the case of a ground-based survey, the mode of deployment may have an effect on background values. For example, if the detector crystal is located in a backpack, the operator's body will absorb some radiation. Also small sources of radioactivity may be inadvertently present, such as watches and compasses with luminous markings, although the former are now rare. If a micro-gravity survey is being undertaken simultaneously, be aware that there may be a small amount of radioactive material in the vacuum chamber of some micro-gravimeters with quartz springs. This is used to ionise the residual gas to prevent the build-up of static electricity on the spring devices.

In airborne surveys, a test flight of 8 km should be undertaken at the start and end of each day along the same profile. It enables the sensitivity of the equipment to be checked to ensure consistency and the radioactivity of the aircraft, and it is used to check the effects of changing soil moisture content in the survey area. The test line should be along a line that exhibits uniform radioactivity and should be typical of the survey area with respect to the soil cover. After live time, background, and height correction, the average thorium window count rate over the test line should be within 10% of the mean thorium window count rate for all previous test flight runs. If the change in soil moisture content has occurred because of precipitation, survey operations should be suspended or only undertaken in areas unaffected by the rain. Under these circumstances, a previous line flown in the area unaffected by the precipitation can be used as a local test line.

### 15.5.6 Compton scattering

It is necessary to take account of gamma rays not originating from their particular radioelement or decay series within the three radioisotope windows (K, U and Th). For instance, thorium-series gamma rays occur in both the uranium and potassium windows, and uranium-series gamma rays appear in the potassium window as a consequence of Compton scattering. If left uncorrected, the total counts in the uranium and potassium windows would be overestimated. This is particularly important if isotopic concentrations are to be estimated in a survey. Consequently, these over-counts need to be removed by a process known as Compton stripping. For each of the three channels, corrections can be applied as defined in Box 15.3. The stripping ratios ( $\alpha$ ,  $\beta$ ,  $\gamma$  and  $a$ ), defined in Box 15.3, are determined empirically over calibration pads, but correction for detector height above the ground must also be included for airborne surveys (Table 15.6). The stripping parameters used are illustrated in Figure 15.6 with respect to observed spectra and the three radio-element components

### 15.5.7 Terrain clearance corrections

In airborne surveys, the aircraft flies at a nominal elevation but this tends to vary along the line for operational reasons. The data recorded for each window needs to be adjusted to take account of these fluctuations in elevation. Window count rates vary

**Box 15.3** Compton stripping ratios (IAEA, 2003)

Compton stripping corrections for the three radioelemental series thorium (th), uranium (u) and potassium (k) are defined by:

$$\begin{aligned} n_{\text{th}(\text{corr})} &= (n_{\text{th}} - \alpha n_{\text{u}})/(1 - a\alpha) \\ n_{\text{u}(\text{corr})} &= (n_{\text{u}} - \alpha n_{\text{th}})/(1 - a\alpha) \\ n_{\text{k}(\text{corr})} &= n_{\text{k}} - \beta n_{\text{th}(\text{corr})} - \gamma n_{\text{u}(\text{corr})} \end{aligned}$$

where:

$\alpha$ ,  $\beta$ ,  $\gamma$  and  $a$  are the stripping ratios, whose values are:  $\alpha$ , the number of counts in the uranium window per unit count in the thorium window for a pure thorium source;  $\beta$ , the number of counts in the potassium window per unit count in the thorium window for a pure thorium source;  $\gamma$ , the number of counts in the potassium window per unit count in the uranium window for a pure uranium source; and,  $a$ , the number of counts in the thorium window per unit count in the uranium window for a pure uranium source (see Figure 15.6).

exponentially with height for the range of ground clearances (20–250 m) normally used in airborne surveying for subdued topography. Over rugged terrain, more accurate algorithms must be used such as described by Schwarz *et al.* (1992). The height correction is defined in Box 15.4 and must also be adjusted for ambient temperature and pressure. It is best if the temperature, pressure and altimeter data are lightly filtered before the altitude correction is applied.

### 15.5.8 Radio-element ground concentrations

Once the observed spectral data have been fully corrected, as described above, the resultant count rates in each channel can be converted to ground concentrations of the radio-elements using sensitivity coefficients. The coefficients for each window are determined from data obtained over the appropriate calibration ranges, test flights and concrete pads. The sensitivity coefficient ( $S$ ) is effectively the average background-corrected and stripped window count rate ( $n$ ) along the calibration test profile divided by the respective elemental concentration of the ground ( $C_g$ ), as measured by

**Table 15.6** Increase in Compton stripping ratios with altitude (IAEA, 2003).

Stripping ratio	Increase per metre
$\alpha$	0.00049
$\beta$	0.00065
$\gamma$	0.00069

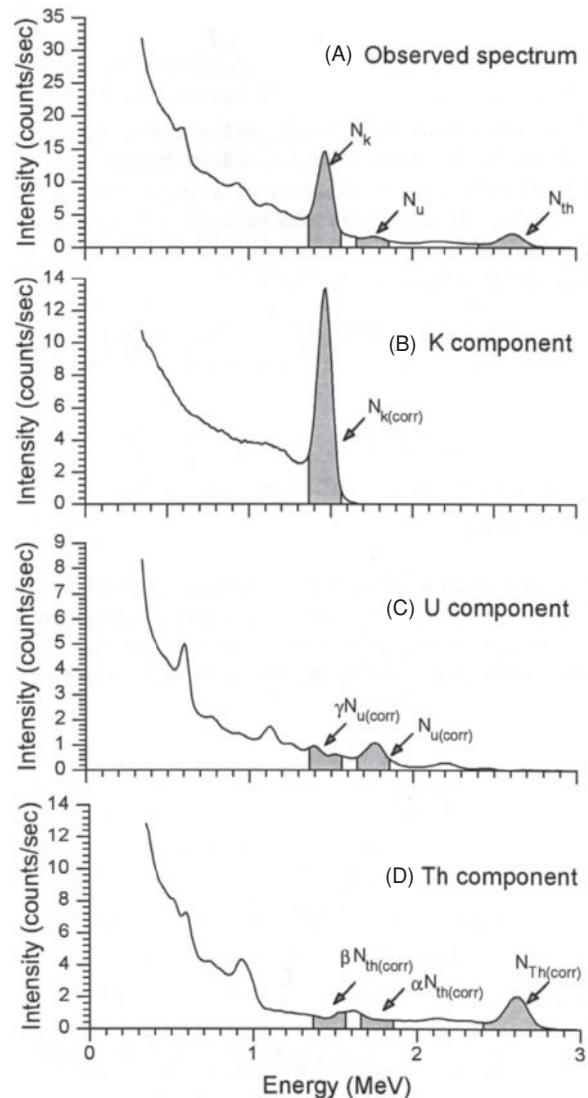


**Figure 15.6** Spectra showing the positions of the conventional potassium, uranium and thorium windows and the parameters used for spectral stripping. From IAEA (2003), by permission.

a calibrated portable spectrometer. If it is assumed that the daughter isotopes  $^{208}\text{Tl}$  and  $^{214}\text{Bi}$  are in secular equilibrium with their parent  $^{238}\text{U}$  and  $^{232}\text{Th}$  isotopes, the equivalent elemental concentrations can be estimated as defined in Box 15.5, combining with the first equation given in Box 15.4.

## 15.6 Radiometric data presentation

Radiometric data can be plotted as profiles of counts/s along a particular transect for each radio-element window or as a function of total counts. In airborne surveys, data are collected every 30–60 m along the flight path using a helicopter or at 50–80 m intervals using a faster fixed-wing aircraft. As the aircraft flies back and forth across the survey area the data form a grid based upon the flight line

**Box 15.4 Height corrections (IAEA, 2003)**

An estimate of the count rate ( $n$ ) at a nominal survey height ( $H$ ) is given by:

$$n = n_0 e^{-\mu(H-h)}$$

where:

- $\mu$  = the window attenuation coefficient (per metre)
- $n_0$  = the observed count rate at the STP height,  $h$ ; and,
- $n$  = the corrected count rate for the nominal terrain clearance,  $H$ .

The equivalent height ( $h_{STP}$ ) at standard temperature (273.15°K) and pressure (101.325 kPa) is defined by:

$$h_{STP} = 273.15 P h_{obs} / [101.325(T + 273.15)]$$

where  $h_{obs}$  is the observed height above ground level (metres),  $T$  is the air temperature (°C), and  $P$  is the barometric pressure (kPa).

coverage (Figure 15.7A). However, gaps may be evident between the flight lines but interpolation between flight lines allows these gaps to be filled in (Figure 15.7B). The number of counts at each position across the grid, including interpolated values, are assigned a colour according to the number of counts measured (Figure 15.7C) so that a colour map of the counts measured can be compiled.

The relative abundances of radioactive isotopes in different rock types can be plotted in a triangular diagram in relation to the three main radio-elements used in exploration (potassium, thorium and uranium) such as in Figure 15.8A. A similar way of illustrating the results of grid surveys is to combine the colours in a so-called ternary diagram (Figure 15.8B) where uranium is related to the

**Box 15.5 Equivalent concentrations of radio-elements (courtesy of GeoExplor Ltd)**

The equivalent concentrations of thorium and uranium ( $C_{th}$  and  $C_u$ , in parts per million) and potassium ( $C_k$ , %) are given by:

$$\begin{aligned} C_{th} &= S_{th} n_{th(\text{corr})} e^{-\mu_{th}(H-h)} \\ C_u &= S_u n_{u(\text{corr})} e^{-\mu_u(H-h)} \\ C_k &= S_k n_{k(\text{corr})} e^{-\mu_k(H-h)} \end{aligned}$$

where  $\mu_{th}$ ,  $\mu_u$  and  $\mu_k$  are the attenuation coefficients for the particular elements indicated, and the  $n_{e(\text{corr})}$  values are the corrected count rates for the element  $e$  (thorium, uranium or potassium); the sensitivity coefficient ( $S_e$ ) for each element is a function of calibrated ground concentrations for the appropriate element.

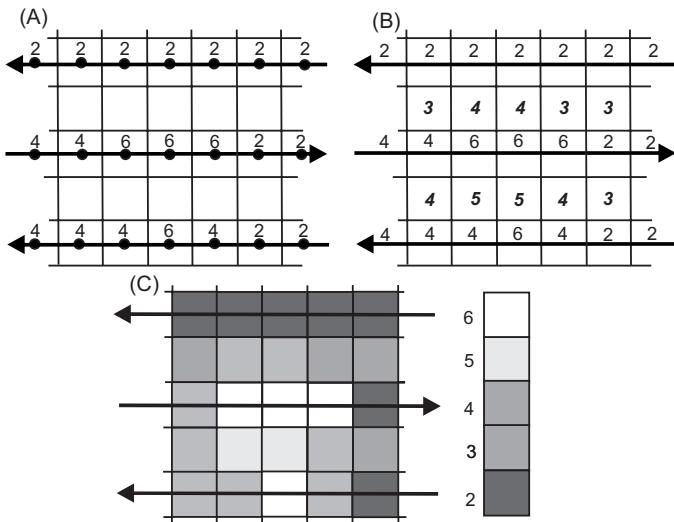


**Figure 15.7** Measurement and interpolation of radiometric data and map display. [C]

colour blue, potassium red, and thorium green. As modern spectrometers record data as total counts and in relation to the three radio-element windows, a variety of displays can be achieved. This includes radio-elemental ratios, by which different aspects of the surface radiation can be mapped in order to highlight particular features, as can be seen in the various case histories presented in the next section. As an example, a radiometric ternary map of Nova Scotia is shown in Figure 15.9 from which areas with high potassium counts are evident in the southwest and northern parts of the island, while the central part shows higher levels of uranium and thorium. As radiometric ternary displays are georeferenced datasets, the results can be draped over digital terrain models to produce a 3D surface display where the radioactivity results can be viewed in relation to the ground topography and morphology. Increasingly, radiometrics datasets are being combined with optical remote-sensing information through which sophisticated analysis of the ground surface characteristics can be undertaken. In addition, these same datasets can also be interpreted using airborne geophysical data, particularly aeromagnetic information, and integrated in geographic information systems, thereby providing even more opportunities for data analysis and visualisation.

## 15.7 Case histories

### 15.7.1 Mineral exploration

In February 2010, Sirius Resources NL announced the results of a radiometric survey from an airborne survey flown at its Lake Wells prospect, northeast of Perth in western Australia. They found three distinctive uranium anomalies associated with calcrete outcrops in a drainage system that drains a large area of granite and which is partly covered by sand dunes, which obscure the radioactivity from the underlying bedrock. The prospect tenements cover 2678 km<sup>2</sup> of

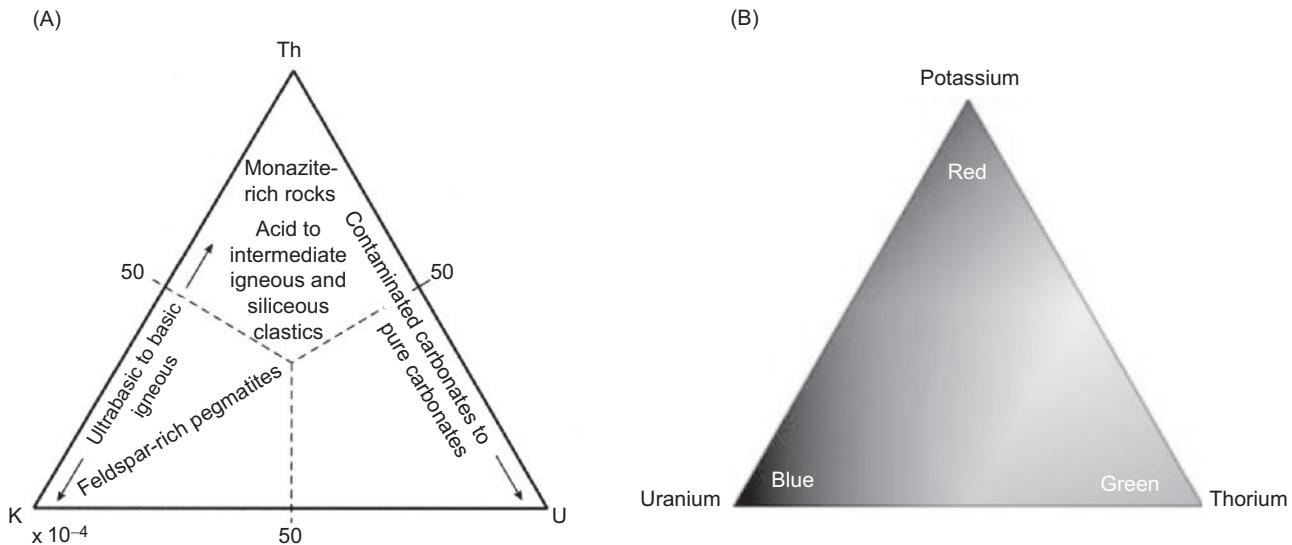


**Figure 15.8** (A) Relative abundances of radioactive elements in different rock types. Also shown are the relative radioactivities of the radio-elements. After Wollenberg (1977), by permission. (B) Red-green-blue ternary diagram. [C]

relatively unexplored greenstones and granites on the northeastern margin of the Yilgarn craton. The prospect contains major shear zones and banded iron formations. This area is prospective for the calcrete-hosted carnotite style of uranium deposits that can form extensive near-surface blankets of mineralisation.

The northern anomaly is 6 km long and 2 km wide, the central anomaly is 2 km in diameter and the southernmost anomaly

is 5 km long and 1 km wide. Each of these anomalies also contains a smaller zone of more intense radioactivity. The results were displayed in three forms: uranium, uranium squared divided by thorium, and as potassium–thorium–uranium ratios. The three displays for the northern and central anomalies have been extracted and are shown in Figure 15.10. In the uranium display (Figure 15.10A), the main anomalies are evident by high counts clustered

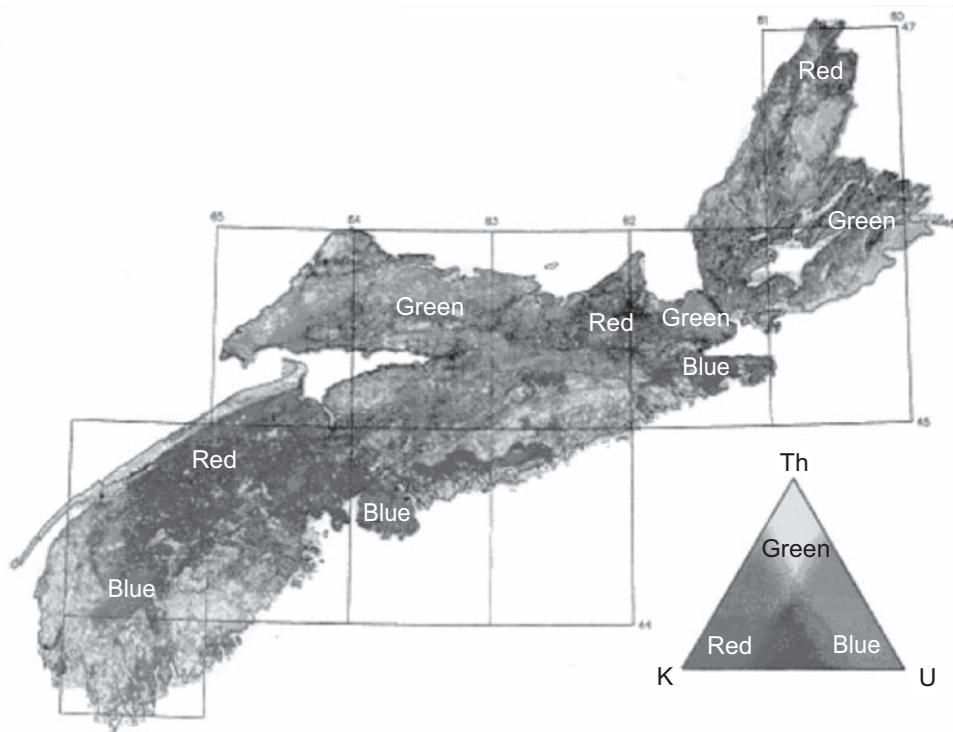


**Figure 15.9** Radiometric ternary display for the province of Nova Scotia, Canada. Courtesy of Natural Resources Canada. [C]

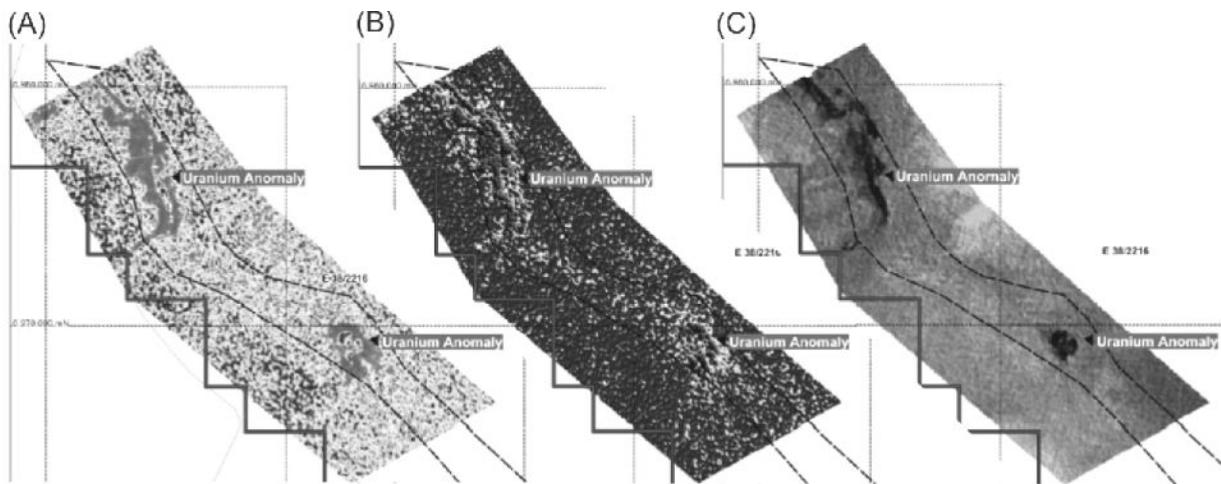


**Figure 15.10** Radiometric anomaly maps for the Lake Wells prospects, Western Australia: (A) uranium, (B) uranium<sup>2</sup>/thorium, and (C) ternary radiometric displays. Modified from Sirius (2010). [C]

around the centre of each anomaly with speckled values elsewhere. The uranium<sup>2</sup>/thorium display (Figure 15.10B) highlights the main anomalies with respect to the background, but also picks out details within the two uranium anomalies shown.

### 15.7.2 Engineering applications

In contrast to mineral exploration surveying, the use of surface radiometric measurements in geotechnical and archaeological applications has been extremely limited (see Ruffell and Wilson, 1998; Moussa, 2001; Ruffell *et al.*, 2006). However, it has been demonstrated (Ruffell *et al.*, 2006) that some structures buried within 10 cm of the ground surface can be identified using radio-elemental ratios of Th/K and Th/U to within 0.1 m horizontal resolution.

By way of example, Ruffell *et al.* (2006) presented two case histories using a Scintrex GIS-5 portable gamma-ray scintillometer that measured counts in four windows (total counts, K, U and Th). The instrument was calibrated using a thorium standard. Five measurements were made at each point on a 0.25-m sample grid; the lowest and highest values were discarded and the three remaining values were averaged. The first site, located on the shore of Belfast Lough, Northern Ireland, consisted of a known 45-year-old land drainage pipe that crosses sequentially a major road, a sandy-soil playing field (subject to the application of potassium-rich fertiliser), a beach (dominated by quartz and calcite sand) and emerges at the high-tide zone on the estuary shore. In profiles across the line of the 1.1-m diameter concrete pipe, total count values increased from 300 counts to around 500 counts over the drain, with comparable shaped profiles in potassium and uranium profiles. The thorium profile, however, revealed a prominent decrease in counts over the pipe, but without any clear anomaly that could be associated with the drain. When profiles using the thorium/potassium and thorium/uranium ratios were produced, a prominent, sharp-sided low

anomaly resulted that correlated well with the location of the drain. The thorium/potassium ratio profile was particularly clear.

The second example relates to a site in part of a static caravan park at the southern end of Ballywater Beach, County Down, Northern Ireland. The survey area covered the footprint of a partially-buried house foundation with complex geometry. The house was present at the site from 1890 to 1970 when it was demolished. Exposed 0.5-m wide foundations consisted of double-thickness red-brick and weathered rubble infill. The bricks were set in a loose aggregate of brick, greywacke and concrete rubble. The foundations extended beneath a sandy soil ranging in depth from a few centimetres to 0.3 m. A profile of the total counts across the site indicated two highs, one of which was associated with a neighbouring stream; the other was coincident with similar highs on the potassium and uranium profiles (Figure 15.11). As can be seen from the figure, the thorium profile appeared noisy with no discernable anomaly. However, a very prominent low anomaly is evident on the thorium/potassium ratio profile coincident with the buried foundation wall. The thorium/uranium anomaly was also indistinct. When presented in map form, the thorium/potassium ratio data clearly revealed a right-angled corner anomaly the width of which corresponded with the known thickness of the foundation, while the other forms of data presented a less clear result.

These two small surveys indicate that careful data acquisition with just a portable scintillometer can reveal interesting information about very near-surface structures. Clearly, it would be inappropriate to rely upon this technique alone to map such features, but the application of the technique to decimetre-scale surveys could be potentially useful.

In engineering investigations borehole logging is a commonly applied technique, although not used as much as perhaps it ought to be. One of the uses of natural gamma logging is that it provides a useful means of correlating marker horizons and delimiting possible fault structures. One such example has been provided by

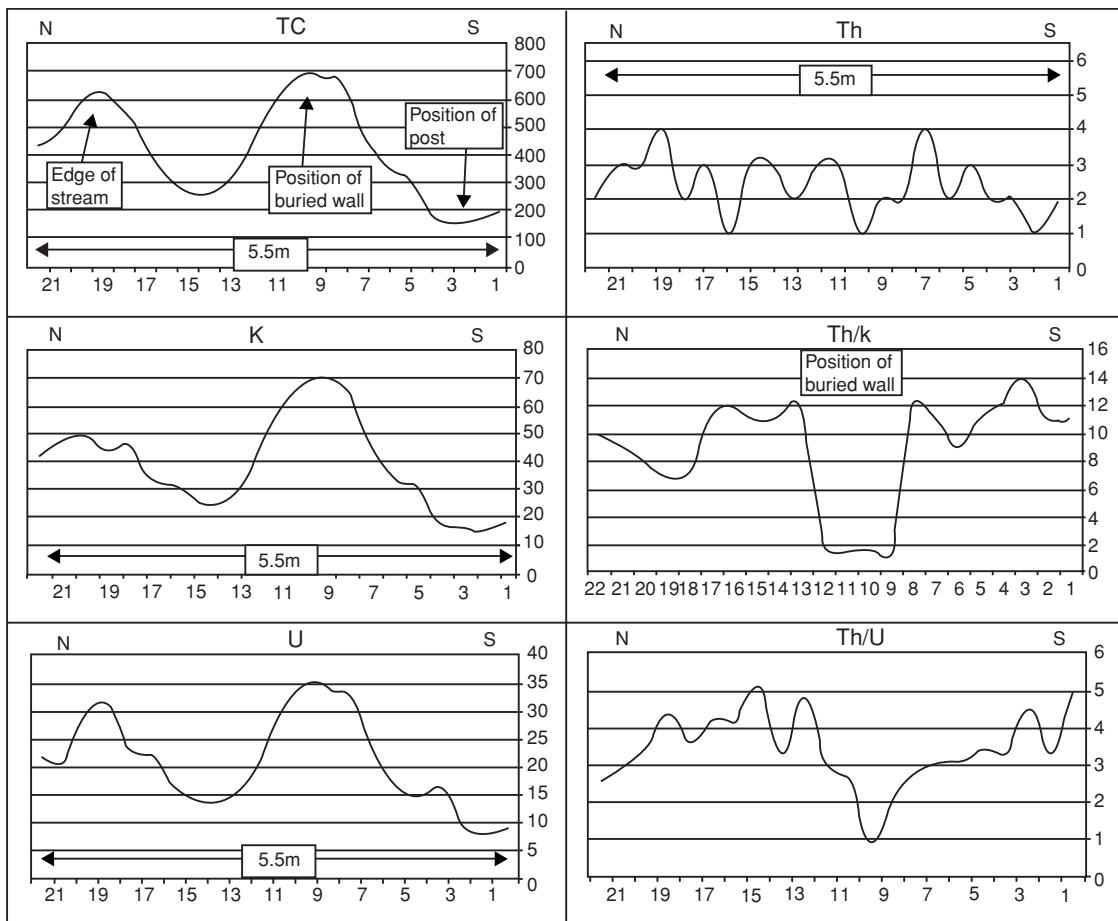


**Figure 15.11** Spectral gamma-ray cross-sections over buried foundations: TC = total count; Th, K and U = thorium, potassium and uranium counts; Th/K and Th/U = thorium:potassium and thorium:uranium ratios. From Ruffell et al. (2006), by permission.

Cripps and McCann (2000) where six boreholes were constructed during a standard site investigation. The marker horizon was a layer comprising fuller's earth (clay) that is clearly picked out by the high counts on the natural gamma logs (Figure 15.12); the single peak shallows between borehole 1 in the south towards borehole 4 to the north (see the plan view in Figure 15.12). However, the peak appears to split in boreholes 5 and 6, and appears displaced to a slightly greater depth, suggesting that this bifurcation of the clay horizon is downthrown about a metre by a fault.

### 15.7.3 Soil mapping

In Australia, environmental and natural resource management issues have become increasingly important in recent years. Land managers need information by which to assess soil, climate and water information over large catchment areas in order to provide more efficient land management. Traditional methods of mapping soils at a scale of less than 1:50,000 for such applications is too expensive. However, with the advent and availability of high-resolution airborne and ground radiometric data, soil maps at a scale of 1:25,000

and even 1:10,000 can be produced. Beckett (2008) has provided an example from the broad-acre sheep and wheat-farming community of Elashgin, 200 km northeast of Perth, Western Australia, of how using a tight grid of low terrain-clearance airborne radiometric survey can be used to discriminate key soil types.

Data were acquired with a terrain clearance of 20 m long flight lines 25 m apart, and with a sample interval of 25 m using a 256-channel radiometric spectrometer. The measured data were processed to remove the effects of Compton scattering and unwanted X-ray energies from the direct emissions, from which it was possible to resolve seven distinct photon peaks (Figure 15.13). New multi-spectral channels were generated subsequently by aggregating count rates over narrow windows centred on these seven peaks. This allowed the spatial distribution of a number of complementary photon emissions to be observed:  $^{208}\text{Tl}$  at 2.614 MeV and combined  $^{238}\text{Ac}$  emissions at 0.908 MeV, 0.960 MeV and 0.966 MeV from the thorium-232 decay series; and  $^{214}\text{Bi}$  emissions at 1.764 MeV and 1.12 MeV from the uranium-238 decay series.

Results using the thorium channels are illustrated in Figure 15.14 draped over a vertically-exaggerated digital elevation model. A standard ternary image (potassium: red; thorium: green; uranium: blue)

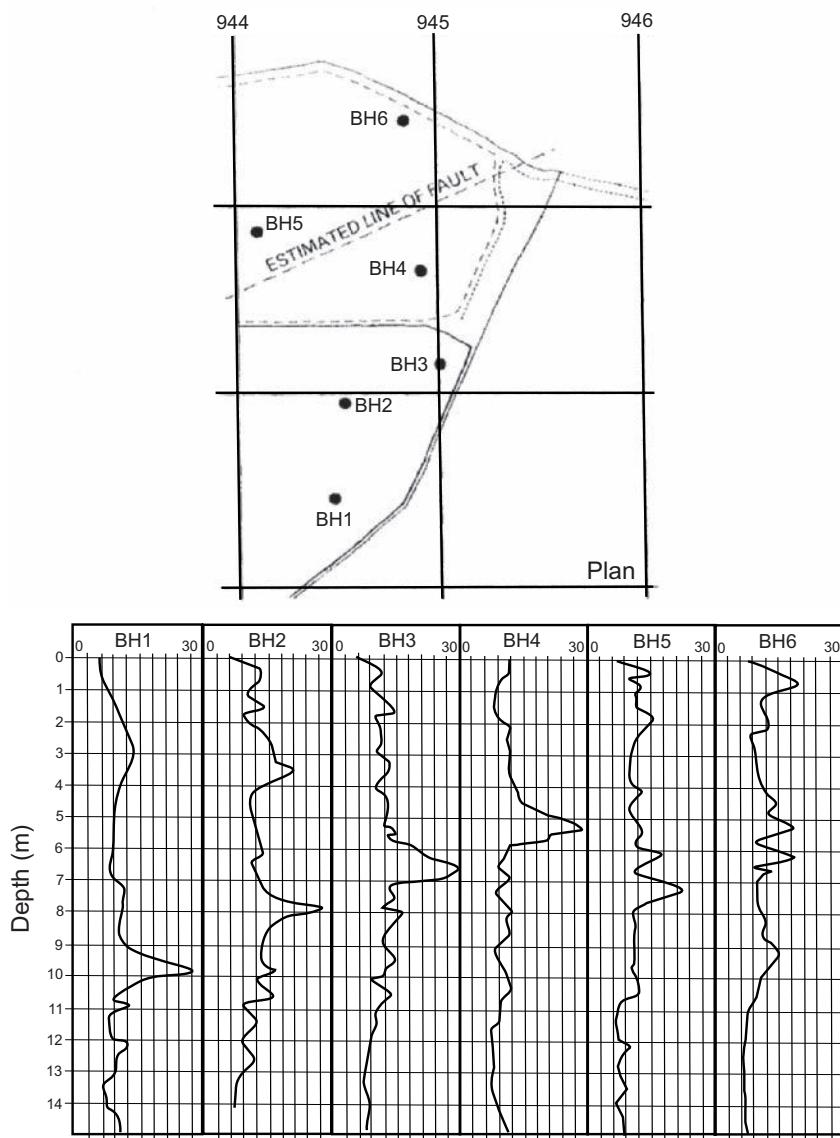


**Figure 15.12** Correlation of natural gamma logs between closely spaced boreholes in an engineering site investigation. Modified from Cripps and McCann (2000).

is shown in greyscale in Figure 15.14A. It is difficult to discriminate the ironstone gravel (laterite) soil unit from the clay-loam soil unit (both units are highlighted). The ironstone gravels are pisolithic iron accumulations formed under subtropical conditions and are often masked from field observations by a thin overburden layer. The gravel emits elevated  $^{238}\text{Ac}$  and  $^{208}\text{Tl}$  photons. In Western Australia, these gravel soil units are associated with high thorium response as highlighted by bright zones (labelled r) in Figure 15.14B. The local clay soils are formed by the weathering of the local granite-gneiss bedrock. Some thorium in the clay soil is locked within the clay particles from the original gneissic minerals, the clay also absorbs radionuclides from sources such as monzonite which increases the concentration of thorium in the clay. This results in elevated thorium values also as indicated in Figure 15.14B (labelled r). Figure

15.14C illustrates the complementary  $^{228}\text{Ac}$  channel. This results in a variation in the ternary diagram such that  $^{208}\text{Tl}$  is shown in red (r), the  $^{238}\text{Ac}$  1.29–1.64 MeV channel in blue (b), and the combined  $^{228}\text{Ac}$  0.908 MeV, 0.96 MeV and 0.966 MeV channels in green (g). There is now a distinct difference in colour and tone between the lateritic soil (white tone) and the clay soil (light green). The colouring associated with the lateritic soil indicates that  $^{228}\text{Ac}$  and  $^{208}\text{Tl}$  emit their energies in similar proportions, suggesting equilibrium conditions. In contrast, the colouring associated with the clay soil indicates that  $^{228}\text{Ac}$  is dominant over the  $^{208}\text{Tl}$ , which might indicate that equilibrium has yet to be reached. More detailed examination of the radiometric results yields additional information about the soil types such as soil texture, horizon changes and homogeneity in the top 0.4 m. The case history presented by Beckett demonstrates

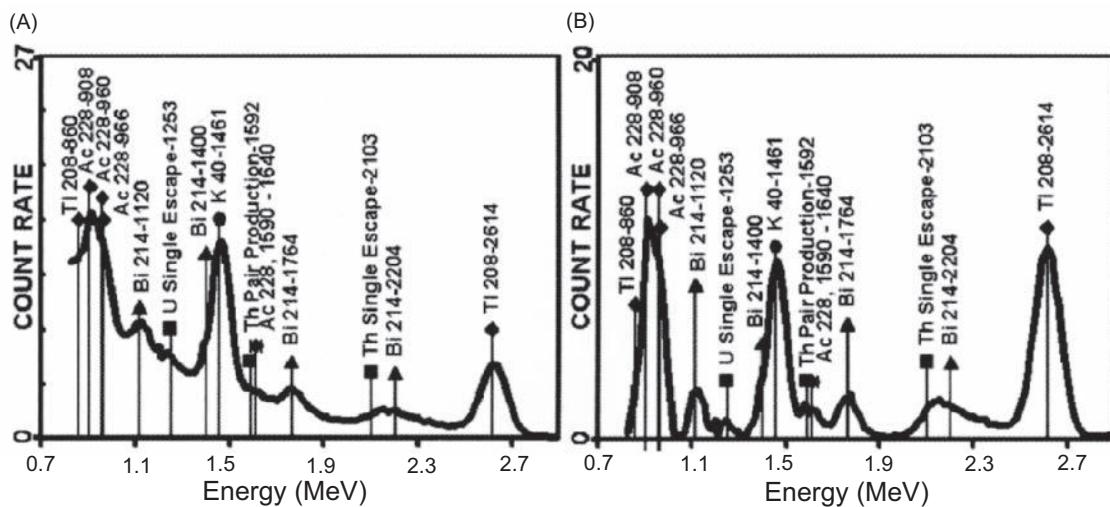


**Figure 15.13** (A) Original 256-channel radiometric spectrum for a typical soil sample, including Compton scattering energies; (B) data in (A) with the effects of Compton scattering removed. From Beckett (2008), by permission.

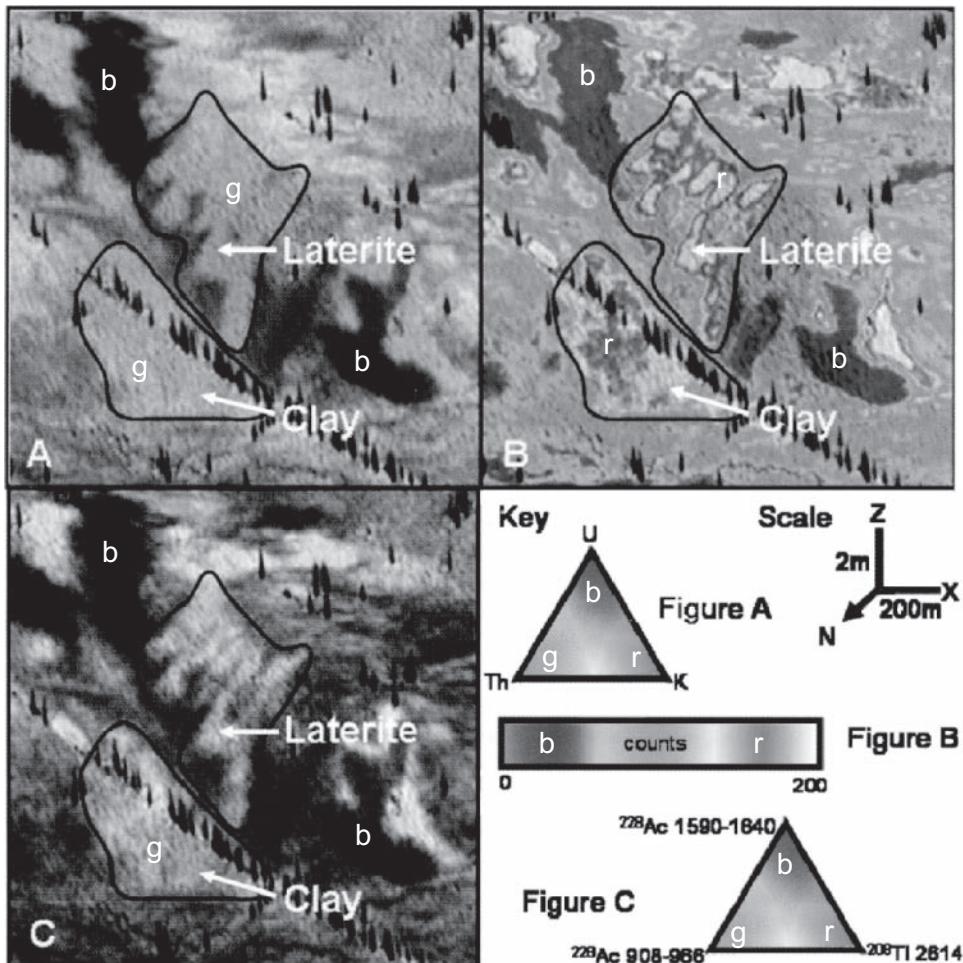


**Figure 15.14** Radiometric imagery used to differentiate an ironstone-gravel and clay-soil unit. (A) Standard ternary imagery produces tones (cy-gr) diagnostic of gravel and clay-soil units. (B) Grey-scale standard thorium channel imagery (white = high) shows a relatively high response for both clay- and gravel-soil units. (C) Thorium standard imagery within limits described in the text on which the gravel-soil unit is seen as white while the clay-soil unit produces diagnostic tones (g). All images are draped over a digital terrain model acquired while undertaking the airborne radiometric survey. From Beckett (2008), by permission. [C]

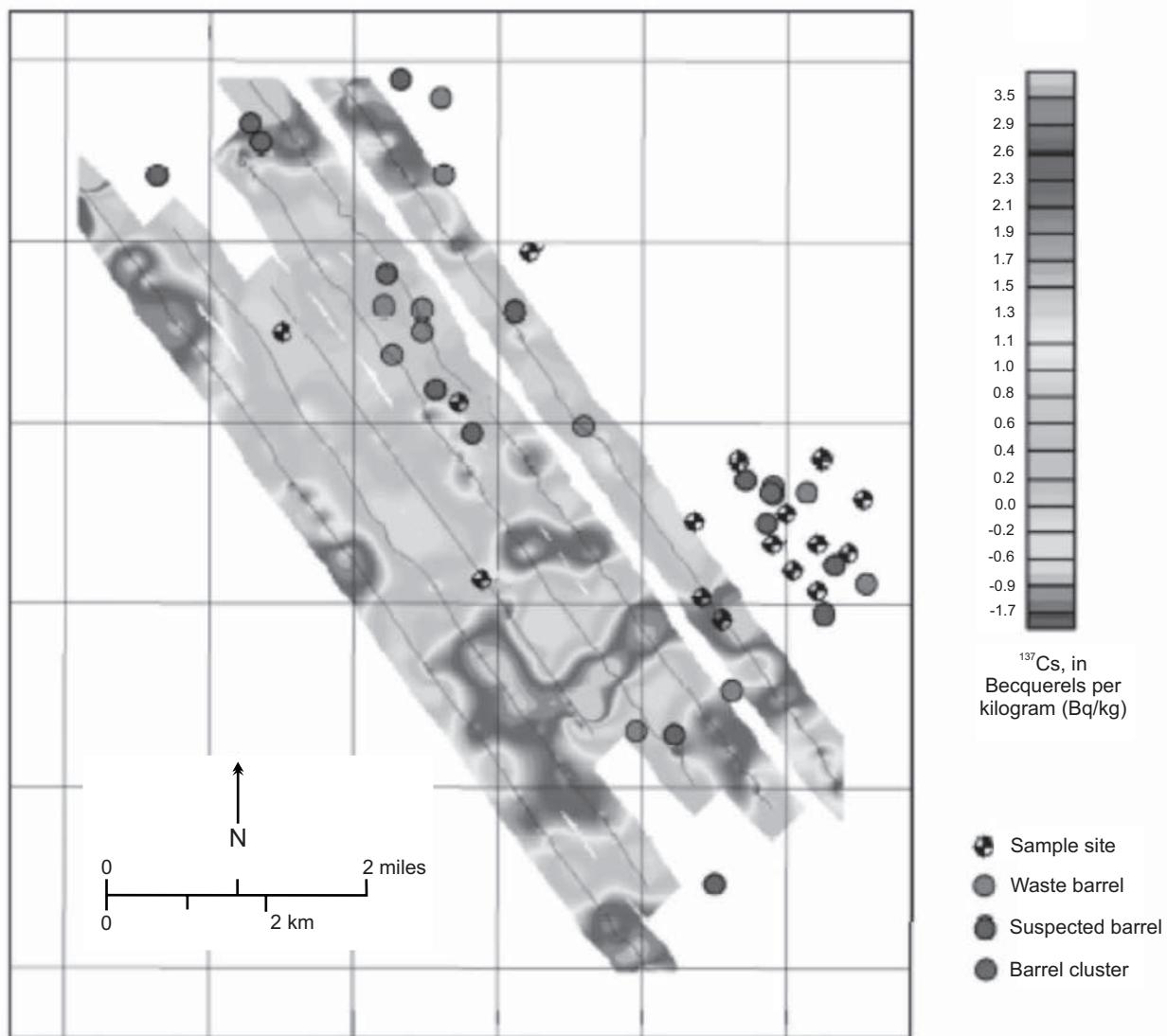


**Figure 15.15** Distribution of measured  $^{137}\text{Cs}$  radioactivity across the 900-m dump site south of the Farallon Islands west of San Francisco, USA. From Jones *et al.* (2001), by permission. [C]

the effectiveness of high-resolution radiometric spectrometry in soil mapping for land management planning.

#### 15.7.4 Nuclear waste disposal investigations

To the south and west of the Farallon Islands, offshore from San Francisco Bay, USA, is an area of about  $1400\text{ km}^2$  known as the Farallon Islands Radioactive Waste Dump (FIRWD). Some 47,800 large containers (55-gallon drums, concrete blocks and other containers) with low-level radioactive waste were dumped between 1946 and 1970. Although predominantly at three designated locations, con-

ainers litter the sea floor across the site in water depths ranging from 90 m to over 1800 m. Previous investigations of radioactive contamination had been undertaken using only sporadic surface sediment and habitat sampling with some side-scan sonar imaging. In 1998, the British Geological Survey (BGS) in conjunction with American agencies undertook a radiometric survey using the BGS EEL radiometric scintillometer system (Jones *et al.*, 2001). One of the concerns about the FIRWD is that the area, and especially the shallower water regions, forms part of commercial and sport fishing grounds and that the potential for radioactive contamination was considered to be the greatest in this portion.

Series of transects using the BGS EEL were surveyed at three locations with water depths nominally of 90 m, 900 m and into

deeper water at 1800 m. Sediment samples collected during the same survey were tested for radionuclide content, grain size and general geochemistry. Generally, the results indicated very low  $^{137}\text{Cs}$  contents across the survey areas and there were no suggestions of any significant regional-scale contamination of the sediments by  $^{137}\text{Cs}$ , nor any localised high concentrations of this radionuclide. Specific activity values (in Bq/kg) for the site at 900 m are shown in Figure 15.15 along with locations of waste barrels and drum clusters.

In some places higher activity levels were identified for which there were no obvious targets on the side-scan sonar. However, drums were observed to exist in a variety of physical states ranging from being still intact through to having disintegrated, in which case there might be no side-scan sonar target to be identified. This survey has demonstrated that the EEL scintillometer system is capable of being used to map sea-floor radioactivity from shallow-water environments through to significant water depths.



# Appendix 1

## Web addresses

### Learned societies

Description	Web address (www.-)
Society of Exploration Geophysicists (SEG)	seg.org
European Association of Geoscientists and Engineers (EAGE)	eage.org
The Environmental and Engineering Geophysical Society (EEGS)	eegs.org
Australian Society of Exploration Geophysicists (ASEG)	aseg.org.au
Canadian Society of Exploration Geophysicists (CSEG)	cseg.ca
South African Geophysical Association (SAGA)	sagaonline.co.za

### Other organisations

Organisation	Description	Web address (www.-)
ABEM Instruments AB	Geophysical equipment (electrical, VLF, seismic)	abem.se
Aeroquest Airborne*	Airborne EM contractor	aeroquestairborne.com
AGI Advanced Geosciences, Inc.	Resistivity survey systems	agiusa.com
ASTM International	Standards development organisation	astm.org
Austin Exploration, Inc.	Fluid damped dynamic marine gravity meter	austinex.com/newmeter.htm
Bartington Instruments	Magnetometer manufacturer	bartington.com
Battelle Ltd	Helicopter-based UXO detection systems	battelle.com
British Geological Survey	Geomagnetic pole information	geomag.bgs.ac.uk/poles.html
Caterpillar Tractor Company	Rippability charts	caterpillar.com
Cobham Technical Services (formerly ERA)	GPR instrument manufacturer	cobham.com/technicalservices
EuroGPR Association	Trade association; licensing information	eurogpr.org
Federal Communications Commission, USA	Radio-communications organisation	fcc.gov
Fugro Airborne Services	Airborne geophysics contractor	fugroairborne.com
GDD Instruments Inc.	IP equipment	gddinstruments.com
GDS Instruments	Geotechnical instruments including CSWS & SASW seismics	gdsinstruments.com
GEM Systems	Magnetometer manufacturer	gemsys.ca
GeoExpro	Magazine	geoexpro.com

Organisation	Description	Web address (www.-)
Geological Survey of Canada	National agency Geomagnetic pole information	gsc.nrcan.gc.ca html://gsc.nrcan.gc.ca/geomag/nmp/long_mvt_nmp.e.php
Geometrics	Geophysical instrument manufacturer	geometrics.com
Geomole Pty Ltd	Borehole radar contractor/manufacturer	geomole.com
Geonics Ltd	EM equipment manufacturer	geonics.com
Geophex*	EM and magnetic instrument manufacturer	aeroquestsensorstech.com
Geophysical Survey Systems, Inc.	GPR instrument manufacturer	geophysical.com
GeoProbing Technology	VibroPile S-wave source	geoprobeing.com
Geostuff	Land streamers	geostuff.com/landstreamers.htm
GeoTomo	Geophysical software	geotomo.com
Independent	Applets and calculators	martindalecenter.com
Ingegneria Dei Sistemi (IDS)	GPR instrument manufacturer	idscompany.it
Intelligent Resources Inc.	Seismic refraction software	rayfract.com
International Geomagnetic Reference Field (IGRF)-11	General information about the IGRF-11  Coefficients of IGRF-11	ngdc.noaa.gov/IAGA/vmod/igrf.html ngdc.noaa.gov/IAGA/vmod/igrf1coeffs.txt
International Society for Soil Mechanics and Geotechnical Engineering	Methods of site investigation using CPTs and SPTs, etc.	issmge.org/home
Interpex Ltd	Resistivity & EM software	interpex.com
IRIS Instruments	Resistivity, IP, VLF & MRS instruments	iris-instruments.com
Joint Nature Conservation Committee	Statutory adviser to UK Government	jncc.gov.uk
Kansas Geological Survey	MASW method and SurfSeis software	masw.com
LaCoste & Romberg	Gravity meters	lacosterromberg.com
Lankelma	CPT testing	cone penetration.com
Malå Geoscience	GPR instrument manufacturer	malags.com
Mitcham Industries Inc.	Streamer peripheral technologies	mitchamindustries.com/products
National Geodetic Survey, USA	National agency	nsg.gov
National Oceanic and Atmospheric Administration (NOAA), USA (absolute gravity measurements)	National agency	nsg.noaa.gov/GRD/GRAVITY/ABSG.html
Ordnance Survey of Great Britain	National agency	ordnancesurvey.co.uk
Park Seismic LLC	MASW method	parkseismic.com
Petroleum Geo-Services	Streamer technology	pgs.com/techlink
Polaris Explorer Ltd	Explorer 860 AWD	polarisgeo.com
Radiation Solutions Inc	Nuclear instrumentation/radiometrics	radiation-solutions-inc.com
Reynolds International Ltd	Geophysical consultants	reynolds-international.co.uk
Sander Geophysics Ltd	Airborne geophysics contractor	sgl.com
Schlumberger	DeepLook-EM borehole	slb.com
Scintrex Ltd	Gravity meters	scintrexltd.com
Sensors & Software Inc., Canada	GPR equipment manufacturers (PulseEKKO, etc.)	sensoft.ca
Sercel	Air guns and water guns	sercel.com
Sonardyne International Ltd	Sub-sea instrumentation	sonardyne.com
Sundararajan <i>et al.</i> (2006)	VLF-EM data processing Matlab code	iamp.org/CGEditor/index.htm
TC 16	Ground property characterisation by in-situ tests	webforum.com/tc16/home
Teledyne Benthos	Marine geophysical instruments & ROVs	benthos.com
UKPMS, now Pavement Condition Information System	UK Pavement Management System	pcis.org.uk
University of British Columbia (UBC)	Geophysical inversion software	eos.ubc.ca/research/ubcgif/home.htm
Utsi Electronics Ltd	GPR instrument manufacturer	utsielectronics.co.uk
Wessex Archaeology Ltd	Archaeological practice & educational charity	wessexarch.co.uk
Wireless Seismic Inc	Cable-less WiFi seismic systems	wirelessSeismic.com
ZLS Corporation	Burris gravity meter	zlscorp.com
Zonge Engineering & Research Organization, Inc.	Instrument manufacturer	zonge.com

\*Part of Aeroquest International group of companies.

**Disclaimer:** The website addresses listed were correct at the time of preparation of the list and have been provided in good faith for information only but some addresses may change or become deactivated.

This list is also available on the web-site ([www.wiley.com/go/reynolds/introduction2e](http://www.wiley.com/go/reynolds/introduction2e)) and will be updated in the event of changes becoming known.



# References

- Abbiss, C.P. (1981) Shear wave measurements of the elasticity of the ground. *Géotechnique*, **31**: 91–104.
- Abdelrahman, E.M., El-Araby, T.M. and Hassaneen, A.-R.G. (2003) New methods for shape and depth determinations from SP data. *Geophysics*, **68**: 1202–1210.
- Abdoh, A., Cowan, D. and Pilkington, M. (1990) 3D gravity inversion of the Cheshire basin. *Geophysical Prospecting*, **38**: 999–1011.
- Ackworth, R.I. and Griffiths, D.H. (1985) Simple data processing of tripotential apparent resistivity measurements as an aid to the interpretation of subsurface structure. *Geophysical Prospecting*, **33**: 861–887.
- Ahmad, M.U. (1961) A laboratory study of streaming potentials. *Geophysical Prospecting*, **12**: 49–64.
- Ahmed, H., Dillon, P.B., Johnstad, S.E. and Johnston, C.D. (1986) Northern Viking Graben multilevel three-component walkaway VSPs: a case history. *First Break*, **4** (10): 9–27.
- Airy, G.B. (1855) On the computation of the effect of the attraction of mountain masses, as disturbing the apparent astronomical latitude of stations in geodetic surveys. *Philosophical Transactions of the Royal Society, Series B*, **145**: 101–104.
- Ait-Messaoud, M., Boulegroun, M.-Z., Gribi, A., et al. (2005) New dimensions in land seismic technology. *Oilfield Review*, (Autumn issue 2005): 42–53.
- Aki, K. (1957) Space and time spectra of stationary stochastic waves with special reference to microtremors. *Bulletin of the Earthquake Research Institute*, **12**: 415–456.
- Al-Chalabi, M. (1972) Interpretation of gravity anomalies by non-linear optimisation. *Geophysical Prospecting*, **20**: 1–16.
- Aldridge, D.F. and Oldenburg, D.W. (1992) Refractor imaging using an automated wavefront reconstruction method. *Geophysics*, **57**: 378–385.
- Aleshkova, N.D., Golynsky, A.V., Kurinin, R.G. and Madrikov, V.S. (2000) Gravity mapping in the southern Weddell Sea region (explanatory note for free-air and Bouguer anomaly maps). *Polarforschung*, **67**: 163–177.
- Allegar, N. (2007) EM is becoming a major attraction. *First Break*, **25** (11): 97–102.
- Allis, R.G. and Hunt, T.M. (1986) Analysis of exploitation-induced gravity changes at Wairakei Geothermal Field. *Geophysics*, **51**: 1647–1660.
- Allred, B.J., Redman, J.D., Mccoy, E.L. and Taylor, R.S. (2005) Golf course applications of near-surface geophysical methods: a case study. *Journal of Environmental & Engineering Geophysics*, **10**: 1–19.
- Allred, B., Daniels, J.J. and Reza Ehsani, M. (2008) *Handbook of Agricultural Geophysics*, Taylor & Francis Group, Boca Raton, Florida, USA.
- Alnes, H., Eiken, O. and Stenvold, T. (2008) Monitoring gas production and CO<sub>2</sub> injection at the Sleipner field using time-lapse gravimetry. *Geophysics*, **73**: WA155–WA161.
- Am, K. (1972) The arbitrarily magnetized dyke; interpretation of characteristics. *Geoexploration*, **10**: 63–90.
- Amundsen, L. and Landrø, M. (2009) Seismic imaging technology: Part V: Shooting seismic in linked circles. *Geo ExPro*, **6**: 54–56.
- Amundsen, L. and Landrø, M. (2010a) Marine seismic sources. Part I: Air-guns for non experts. *Geo ExPro*, **7** (1): 32–35.
- Amundsen, L. and Landrø, M. (2010b) Marine seismic sources. Part II: Air-gun arrays for non-experts. *Geo ExPro*, **7** (2): 32–34.
- Ander, M., Summers, T. and Gruchalla, M.E. (1999) LaCoste & Romberg gravity meter: system analysis and instrumental errors. *Geophysics*, **64**: 1708–1719.
- Anderson, C., Long, A., Ziolkowski, A., et al. (2008) Multi-transient EM technology in practice. *First Break*, **26** (3): 93–102.
- Anderson, L.A. and Johnson, G.P. (1976) Application of the self potential method to geothermal exploration in Long Valley, California. *Journal of Geophysical Research*, **81**: 1527–1552.
- Annan, A.P. and Davis, J.L. (1976) Impulse radar sounding in permafrost. *Radio Science*, **11**: 383–394.
- Annan, A.P. and Davis, J.L. (1977) Radar range analysis for geological materials. Reports of Activities: Part B. *Geological Survey of Canada*, Paper 77–1B.
- Anon. (1996) *Unexploded Ordnance Advanced Technology Demonstration program at Jefferson Proving Ground (Phase II)* M. US Army Environmental Center, USA.

- Archie, G.E. (1942) The electrical resistivity log as an aid to determining some reservoir characteristics. *Transactions of the American Institute of Mining, Metallurgical, and Petroleum Engineers*, **146**: 389–409.
- Arcone, S.A. (1984) Field observations of electromagnetic pulse propagation in dielectric slabs. *Geophysics*, **49**: 1763–1773.
- Arcone, S.A. (2009) Glaciers and ice sheets, in *Ground Penetrating Radar: Theory and Applications* (ed. H.M. Jo1), Elsevier, Amsterdam, 361–392.
- Arcone, S.A., Lawson, D.E. and Delaney, A.J. (1993) Radar reflection and refraction profiles of seasonal thaw over permafrost in Fairbanks, Alaska. *Advanced Group Penetrating Radar: Technologies and Applications*, 26–28 Oct. 1993. Ohio State University, Columbus, Ohio, USA.
- Arcone, S.A., Spikes, V.B. and Hamilton, G.S. (2005) Stratigraphic variation within polar firn caused by differential accumulation and ice flow: interpretation of a 400 MHz short-pulse radar profile from West Antarctica. *Journal of Glaciology*, **51**: 407–422.
- Arkell, W.J. (1933) *The Jurassic System in Great Britain*, Oxford University Press, Oxford, UK.
- Arts, R., Chadwick, A., Eiken, O., et al. (2008) Ten years' experience of monitoring CO<sub>2</sub> injection in the Utsira Sand at Sleipner, offshore Norway. *First Break*, **26**: 65–72.
- Ates, A. and Kearey, P. (1995) A new method for determining magnetization direction from gravity and magnetic anomalies: application to the deep structure of the Worcester Graben. *Journal of the Geological Society*, **152**: 561–566.
- Auken, E. and Christensen, A.V. (2004) Layered and laterally constrained 2D inversion of resistivity data. *Geophysics*, **69**: 752–761.
- Avdeev, D. and Avdeeva, A. (2009) 3D magnetotelluric inversion using a limited-memory quasi-Newton optimization. *Geophysics*, **74** (3): F45–F57.
- Avdeeva, A.D. and Avdeev, D.B. (2006) A limited-memory quasi-Newton inversion for 1D magnetotellurics. *Geophysics*, **71** (5): G191–G196.
- Babu, V.R., Ram, S. and Sundararajan, N. (2007) Modeling and inversion of magnetic and VLF-EM data with an application to basement fractures: A case study from Raigarh, India. *Geophysics*, **7** (5): B133–B140.
- Baeten, G., Fokkema, J. and Ziolkowski, A. (1988) The marine vibrator source. *First Break*, **6**: 285–294.
- Baeten, G. and Ziolkowski, A. (1990) *The Vibroseis Source (Advances in Geophysics 3)*, Elsevier Science Publishers BV, Amsterdam, The Netherlands.
- Balch, S.J., Boyko, W.P. and Paterson, N.R. (2003) The AeroTEM airborne electromagnetic system. *The Leading Edge*, **22**: 562–566.
- Baltassat, J.M., Legchenko, A., Ambroise, B., et al. (2005) Magnetic resonance sounding (MRS) and resistivity characterisation of a mountain hard rock aquifer: the Ringelbach Catchment, Vosges Massif, France. *Near Surface Geophysics*, **3**: 267–274.
- Baoshan, Z. and Chopin, L. (1983) Shear wave velocity and geotechnical properties of tailings deposits. *Bulletin of the International Association of Engineering Geology* (26–27): 347–353.
- Baranov, V. (1957) A new method for interpretation of aeromagnetic maps pseudo-gravimetric anomalies. *Geophysics*, **22**: 359–383.
- Baranov, V. and Naudy, H. (1964) Numerical calculation of the formula of reduction to the magnetic pole. *Geophysics*, **29**: 67–79.
- Barbour, D.M. and Thurlow, J.G. (1982) Case histories of two massive sulphide discoveries in Central Newfoundland. In: Davenport, P.H. (ed.), *Prospecting in areas of glaciated terrane*. Canadian Institute of Mining and Metallurgy, Geology Division, Montreal: 300–321.
- Barker, R.D. (1979) Signal contribution sections and their use in resistivity studies. *Geophysical Journal of the Royal Astronomical Society*, **59**: 123–129.
- Barker, R.D. (1981) Offset system of electrical resistivity sounding and its use with a multicore cable. *Geophysical Prospecting*, **29**: 128–143.
- Barker, R.D. (1990) Improving the quality of resistivity sounding data in landfill studies, in *Geotechnical and Environmental Geophysics. Vol. 2: Environmental and Groundwater* (ed. S.H. Ward), Society of Exploration Geophysicists, Tulsa, USA, 245–251.
- Barker, R.D. (1992) A simple algorithm for electrical imaging of the subsurface. *First Break*, **10** (2): 53–62.
- Barringer, A.R. (1962) A new approach to exploration: the INPUT airborne electrical pulse prospecting system. *Mining Congress Journal*, **48**: 49–52.
- Barry, K.M. (1967) Delay time and its application to refraction profile interpretation, in *Seismic Refraction Prospecting* (ed. A.W. Musgrove), Society of Exploration Geophysicists, Tulsa, Oklahoma, USA, 348–362.
- Basokur, A.T. and Candansayar, M.E. (2003) Enhancing VLF data for qualitative interpretation: an example of massive chalcopyrite exploration. *The Leading Edge*, **22**: 568–570.
- Battaglia, M., Gottsmann, J., Carbone, D. and Fernández, J. (2008) 4D volcano gravimetry. *Geophysics*, **73** (6): WA3–WA18.
- Beamish, D. (1999) Characteristics of near-surface electrokinetic coupling. *Geophysical Journal International*, **137**: 231–242.
- Beamish, D. (2002) Airborne EM applied to environmental geoscience in the UK. *First Break*, **20**: 618–622.
- Beamish, D. and Peart, R.J. (1998) Electrokinetic geophysics – a review. *Terra Nova*, **10**: 48–55.
- Beard, L.P., Doll, W.E., Holladay, J.S., et al. (2004) Field tests of an experimental helicopter time-domain electromagnetic system for unexploded ordnance detection. *Geophysics*, **69**: 664–673.
- Beard, L.P., Doll, W.E., Gamey, T.J., et al. (2008) Comparison of performance of airborne magnetic and transient electromagnetic systems for ordnance detection and mapping. *Journal of Environmental and Engineering Geophysics*, **13**: 291–305.

- Beaudoin, B.C., Ten Brink, U.S. and Stern, T.A. (1992) Characteristics and processing of seismic data collected on thick, floating ice: results from the Ross Ice Shelf, Antarctica. *Geophysics*, **57**: 1359–1372.
- Becerra, C., Agudelo, W. and Guevara, S. (2009) Uncertainty analysis in static corrections obtained by tomographic inversion: application in a mountainous zone in Catatumbo (Colombia). *The Leading Edge*, **28**: 212–215.
- Beck, A.E. (1981) *Physical Principles of Exploration Methods*, Macmillan, London.
- Becken, M. and Pedersen, L.B. (2003) Transformation of VLF anomaly maps into apparent resistivity and phase. *Geophysics*, **68**: 497–505.
- Becker, A. and Telford, W.M. (1965) Spontaneous polarization studies. *Geophysical Prospecting*, **13**: 173–188.
- Becker, A., Barringer, A.R. and Annan, P. (1990) Airborne electromagnetics 1978–1988, in *Developments and Applications of Modern Airborne Electromagnetic Surveys* (ed. D.V. Fitterman), US Geological Survey Bulletin, **9**–20.
- Beckett, K. (2008) Multispectral processing of high-resolution radiometric data for soil mapping. *Near Surface Geophysics*, **6**: 281–287.
- Beer, K.E. and Fenning, P.J. (1976) *Geophysical Anomalies and Mineralisation at Sourton Tors, Okehampton, Devon*, Report Number 76/1, Institute of Geological Sciences.
- Bell, R.E. and Watts, A.B. (1986) Evaluation of the BGM-3 sea gravity meter system aboard R/V Conrad. *Geophysics*, **51**: 1480–1493.
- Bell, R.E. and Hansen, R.O. (1998) The rise and fall of early oil-field technology: the torsion balance gradiometer. *The Leading Edge*, **17**: 81–83.
- Bellefleur, G. and Chouetteau, M. (2001) Massive sulphide delineation using borehole radar: tests at the McConnell nickel deposit, Sudbury, Ontario. *Journal of Applied Geophysics*, **47**: 45–61.
- Bennett, B. (1990) A computer program to convert SEG-2 data to SEG-Y. *Geophysics*, **55**: 1272–1284.
- Berkhout, A.J. (1984) Seismic migration. *Developments in Solid Earth Geophysics*, **14B**.
- Bernard, J. (2006a) Instruments and field work to measure a Magnetic Resonance Sounding with NUMIS equipment, in *3rd Magnetic Resonance Sounding Workshop, Madrid, Spain, Oct. 2006*.
- Bernard, J. (2006b) Application use of the proton Magnetic Resonance Method (MRS) for groundwater investigations in various geological environments. AGU, San Francisco, California, USA.
- Bernard, J. and Legchenko, A. (2003) Groundwater exploration with the Magnetic Resonance Sounding method. *16th Geophysical Conference and Exhibition, Feb. 2003*, ASEG, Adelaide, Australia.
- Bertelli, L., Mascalin, B. and Salvador, L. (1993) Planning and field techniques for 3D land acquisition in highly tilled and populated areas: today's results and future trends. *First Break*, **11**: 23–32.
- Berthling, I. and Melvold, K. (2009) Ground-penetrating radar, in *Ground Penetrating Radar: Theory and Applications* (ed. H.M. Jol), Elsevier, Amsterdam, 81–97.
- Bertin, J. and Loeb, J. (1976) *Experimental and Theoretical Aspects of Induced Polarization* (Vols 1 and 2), Gerbrüder Borntraeger, Berlin.
- Bérubé, A.P. (2007) A graphical 3D finite element program for modelling Self-Potentials generated by flow through a porous medium. *Journal of Environmental and Engineering Geophysics*, **12**: 185–197.
- Best, M. and Spies, B. (1990) Recent developments in analysis and presentation of large data sets in mineral exploration. *Geophysics: The Leading Edge*, **9** (9): 37–43.
- Bevan, B.W. (1991) The search for graves. *Geophysics*, **56**: 1310–1319.
- Bevan, B.W. and Kenyon, J. (1975) Ground penetrating radar for historical archaeology. *MASCA Newsletter*, **11** (2): 2–7.
- Bhattacharya, B.B. (1986) Reply to comment by N.S. Rajan, N.L. Mohan and M. Narasumha Chary. *Geophysical Prospecting*, **34**: 1294–1295.
- Bhattacharya, B.B. and Roy, N. (1981) A note on the use of a nomogram for self-potential anomalies. *Geophysical Prospecting*, **29**: 102–107.
- Bhattacharya, P.K. and Patra, H.P. (1968) *Direct Current Electrical Sounding*, Elsevier, Amsterdam.
- Biegert, E., Ferguson, J. and Xiong, L. (2008) 4D gravity monitoring – introduction. *Geophysics*, **73** (6): WA1–WA2.
- Billings, S. and Wright, D. (2009) Optimal total-field magnetometer configuration for near-surface applications. *The Leading Edge*, **28**: 522–527.
- Bingham, R.G. and Siegert, M.J. (2007) Radio-echo sounding over polar ice masses. *Journal of Environmental & Engineering Geophysics*, **12**: 47–62.
- Binley, A., Cassiani, G., Middleton, R. and Winship, P. (2002) Vadose zone flow model parameterisation using cross-borehole radar and resistivity imaging. *Journal of Hydrology*, **267**: 147–159.
- Binley, A., Winship, P., Middleton, R., Pokar, M. and West, J. (2001) High-resolution characterization of vadose zone dynamics using cross-borehole radar. *Water Resources Research*, **37**: 2639–2652.
- Birch, F. (1960) The velocity of compressional waves in rocks to ten kilobars, Part 1. *Journal of Geophysical Research*, **65**: 1083–1102.
- Birch, F. (1961) The velocity of compressional waves in rocks to ten kilobars, Part 2. *Journal of Geophysical Research*, **66**: 2199–2224.
- Bishop, I., Styles, P., Emsley, S.J. and Ferguson, N.S. (1997) The detection of cavities using the microgravity technique: case histories from mining and karstic environments, in *Modern Geophysics in Engineering Geology* (eds D.M. McCann, M. Edleston, P.J. Fenning and G.M. Reeves), Geological Society Engineering Geology Special Publication, **12**: 153–166.

- Black, R.A., Steeples, D.W. and Miller, R.D. (1994) Migration of shallow seismic reflection data. *Geophysics*, **59**: 402–410.
- Blakely, R.J. (1995) *Potential Theory in Gravity and Magnetic Applications*. Cambridge University Press, Cambridge, UK.
- Blankenship, D.D., Morse, D.L., Finn, C.A., et al. (2001) Geologic controls on the initiation of rapid basal motion for the ice streams of the southern Ross Embayment: a geophysical perspective including new airborne radar sounding and laser altimetry results. *Antarctic Research Series*, **77**: 105–122.
- Blizkovsky, M. (1979) Processing and applications of microgravity surveys. *Geophysical Prospecting*, **27**: 848–861.
- Bloom, A.L. (1962) Physics of operation of the rubidium vapor magnetometer. *Applied Optics*, **1**: 61–68.
- Bloxham, J., Zatman, S. and Dumberry, M. (2002) The origin of geomagnetic jerks. *Nature*, **420** (7 Nov 2002): 65–68.
- Bogorodsky, V.V., Bentley, C.R. and Gudmansen, P.E. (1985) *Radio-glaciology*. D. Reidel Publishing Co., Dordrecht The Netherlands.
- Bogoslovsky, V.A. and Ogilvy, A.A. (1970a) Natural potential anomalies as a quantitative index of seepage from water reservoirs. *Geophysical Prospecting*, **18**: 261–268.
- Bogoslovsky, V.A. and Ogilvy, A.A. (1970b) Application of geophysical methods to studying the technical status of earth dams. *Geophysical Prospecting*, **18** (suppl.): 758–773.
- Bolt, B.A. (1982) *Inside the Earth*. W.H. Freeman, San Francisco, USA.
- Börner, F.D., Schopper, J.R. and Weller, A. (1996) Evaluation of transport and storage properties in the soil and groundwater zone from induced polarization measurements. *Geophysical Prospecting*, **44**: 583–601.
- Boslough, J. (1989) Searching for the secrets of gravity. *National Geographic*, **175**: 562–583.
- Bott, M.P.H. (1959) The use of electronic digital computers for the evaluation of gravimetric terrain corrections. *Geophysical Prospecting*, **5** (7): 45–54.
- Bott, M.P.H. (1960) The use of rapid digital computing methods for direct gravity interpretation of sedimentary basins. *Geophysical Journal*, **3**: 63–67.
- Bott, M.P.H. (1962) A simple criterion for interpreting negative gravity anomalies. *Geophysics*, **27**: 376–381.
- Bowles, L.G. (1990) The seismic fleet and the marine environment: a compatible relationship. *Geophysics: The Leading Edge*, **9** (9): 54–56.
- Branston, M.W. and Styles, P. (2003) The application of time lapse micro-gravity for the investigation and monitoring of subsidence at Northwich, Cheshire. *Quarterly Journal of Engineering Geology*, **36**: 231–244.
- Branston, M.W. and Styles, P. (2006) Site characterization and assessment using the microgravity technique: a case history. *Near Surface Geophysics*, **4**, 377–385.
- Braun, M., Kamm, J. and Yaramanci, U. (2009) Simultaneous inversion of magnetic resonance sounding in terms of water content, resistivity and decay times. *Near Surface Geophysics*, **7**: 589–598.
- Bray, A., Sindle, T., Mason, I., et al. (2007) Using slimline borehole radars from cover holes. *10th SAGA Biennial Technical Meeting and Exhibition*, 24–26 October 2007, Wild Coast, South Africa.
- Breiner, S. (1981) Magnetometers for geophysical applications, in *SQUID Applications to Geophysics* (eds H. Weinstock and W.C. Overton), Society of Exploration Geophysicists, Tulsa, 3–12.
- Brewster, M.L., Annan, A.P. and Redman, J.D. (1992a) GPR monitoring of DNAPL migration in a sandy aquifer. *Proceedings of the 4th International Conference of Ground Penetrating Radar*, Rovaniemi, Finland, June 1992.
- Brewster, M.L., Redman, J.D. and Annan, A.P. (1992b) Monitoring a controlled injection of perchloroethylene in a sandy aquifer with ground penetrating radar and time-domain reflectometry. *Symposium on the Application of Geophysics to Engineering and Environmental Problems*, Englefield, USA.
- Bruden, J.C., Clark, R.A. and Fairhead, J.D. (1982) Gravity and magnetic studies in the Channel Islands. *Journal of the Geological Society of London*, **139**: 35–48.
- Bridge, J. (2009) Advances in fluvial sedimentology using GPR, in *Ground Penetrating Radar: Theory and Applications* (ed. H.M. Jol), Elsevier, Amsterdam, 323–359.
- Bridle, R. (2007) Plus-minus method to solve large-amplitude near-surface static corrections. *Near Surface Geophysics*, **5**: 321–330.
- Bridle, R. (2009) Delay-time refraction methods applied to a 3D seismic block. *The Leading Edge*, **28**: 228–239.
- Bristow, C.S. (2009) Ground penetrating radar in aeolian sand dunes, in *Ground Penetrating Radar: Theory and Applications* (ed. H.M. Jol), Elsevier, Amsterdam, 273–297.
- Bristow, C.S. and Jol, H.M. (2003) *Ground Penetrating Radar in Sediments*. Geological Society, London, UK.
- Bristow, C.S. and Pucillo, K. (2006) Quantifying rates of coastal progradation from sediment volumes using GPR and OSL: The Holocene fill of Guichen Bay, southeast South Australia. *Sedimentology*, **53**, 769–788.
- British Standards Institution (1981) *BS 5930: Code of Practice for Site Investigations*. British Standards Institution, London, UK.
- Broadbent, M. and Habberjam, G.M. (1971) A solution to the dipping interface problem using the square array resistivity technique. *Geophysical Prospecting*, **19**: 321–338.
- Brock, J.S. (1973) Geophysical exploration leading to the discovery of the Faro deposit. *Canadian Institute of Mining and Metallurgy Bulletin*, **66**: 97–116.
- Brouwer, H. (2007) *In-situ Soil Testing*. Lankelma, UK.
- Brown, G.C. and Mussett, A.E. (1981) *The Inaccessible Earth*. George Allen & Unwin, London, UK.

- Bukovics, C. and Nooteboom, J.J. (1990) Combining techniques in integrated 3D land, shallow water and deep channel seismic acquisition. *First Break*, **8**, 375–382.
- Bullock, S.J. (1988) Future and present trends of navigation and positioning techniques in exploration geophysics. *Geophysical Journal*, **92**: 521.
- Buness, H. (2007) Improving the resolution of vibroseis data for very shallow high-resolution measurements. *Near Surface Geophysics*, **5**: 173–182.
- Busby, J.P. (1987) An interactive Fortran 77 program using GKS graphics for 2.5D modelling of gravity and magnetic data. *Computers and Geosciences*, **13**: 639–644.
- Buselli, G., Barber, C., Davis, G.B. and Salama, R.B. (1990) Detection of groundwater contamination near waste disposal sites with transient electromagnetic and electrical methods, in *Geotechnical and Environmental Geophysics, Vol. 2: Environmental and Groundwater*, (ed. S.H. Ward), Society of Exploration Geophysicists, Tulsa, USA, 27–39.
- Butcher, A.P. and Powell, J.J.M. (1996) Practical considerations for field geophysical techniques used to assess ground stiffness. *Proceedings of the International Conference held in London on 30–31 March 1995*: 701–714.
- Butler, D.K. (1984) Microgravimetric and gravity gradient techniques for detection of sub-surface cavities. *Geophysics*, **49**: 1084–1096.
- Butler, D.K. and Llopis, J.L. (1990) Assessment of anomalous seepage conditions, in *Geotechnical and Environmental Geophysics, Vol. 2: Environmental and Groundwater*, (ed. S.H. Ward), Society of Exploration Geophysicists, Tulsa, USA, 153–173.
- Butler, D.K., Llopis, J.L., Dobecki, T.L., et al. (1991) Comprehensive geophysics investigation of an existing dam foundation. *Geophysics: The Leading Edge*, **9** (9): 44–53.
- Butler, K.E. (2009) Trends in waterborne electrical and EM induction methods for high resolution sub-bottom imaging. *Near Surface Geophysics*, **7**: 241–246.
- Butler, K.E., Russell, R.D., Kepic, A.W. and Maxwell, M. (1994) Mapping of a stratigraphic boundary by its seismoelectric response. *Proceedings of the Symposium on the Application of Geophysics to Engineering and Environmental Problems, SAGEEP '94*, Vol. 2, Englefield, USA: 689–699.
- Butler, K.E., Russell, R.D., Kepic, A.W. and Maxwell, M. (1996) Measurement of the seismoelectric response from a shallow boundary. *Geophysics*, **61**: 1769–1778.
- Buynevich, I.V., Jol, H.M. and Fitzgerald, D.M. (2009) Coastal environments, in *Ground Penetrating Radar: Theory and Applications* (ed. H.M. Jol), Elsevier, Amsterdam, 299–322.
- Cagniard, L. (1953) Basic theory of the magneto-telluric method of geophysical prospecting. *Geophysics*, **18**: 605–635.
- Cahyna, F., Mazák, O. and Venhodová, D. (1990) Determination of the extent of cyanide contamination by surface geoelectrical methods, in *and Environmental Geophysics, Vol. 2: Environmental and Groundwater*, (ed. S.H. Ward), Society of Exploration Geophysicists, Tulsa, USA, 97–99.
- Calvert, A.J. and Livelybrooks, D. (1997) Borehole-radar reflection imaging at the McConnell nickel deposit, Sudbury. *Proceedings of Exploration 97: Fourth Decennial International Conference on Mineral Exploration*, 14–18 September 1997, Toronto, Canada, 701–704.
- Camacho, A.G., Nunes, J.C., Ortiz, E., et al. (2007) Gravimetric determination of an intrusive complex under the Island of Faial (Azores): some methodological improvements. *Geophysical Journal International*, **171**: 478–494.
- Cameron, G.W., Elliott, B.E. and Richardson, K.A. (1976) Effects of line spacing on contoured airborne gamma-ray spectrometry data. *Exploration for Uranium Ore Deposits, Proc. Series*, IAEA, Vienna, 81–92.
- Campbell, W.H. (1986) An interpretation of induced electric currents in long pipelines caused by natural geomagnetic sources in the upper atmosphere. *Surveys in Geophysics*, **8**: 239–259.
- Carbone, D., Zuccarello, L., Saccorotti, G. and Greco, F. (2006) Analysis of simultaneous gravity and tremor anomalies observed during the 2002–2003 Etna eruption. *Earth and Planetary Science Letters*, **245**: 616–629.
- Carey, H., Heinson, G. and Sexton, M. (2003) Lighting up the regolith: applied potential exploration methods, in *Advances in Regolith* (ed. I.C. Roach), CRC, Leme, 45–48.
- Carlson, D., Long, A., Söllner, W., et al. (2007) Increased resolution and penetration from a towed dual-sensor streamer. *First Break*, **25** (12): 71–77.
- Carmichael, R.S. and Henry, G. (1977) Gravity exploration for groundwater and bedrock topography in glaciated areas. *Geophysics*, **42**: 850–859.
- Carpenter, E.W. (1955) Some notes concerning the Wenner configuration. *Geophysical Prospecting*, **3**: 388–402.
- Carpenter, E.W. and Habberjam, G.M. (1956) A tripotential method of resistivity prospecting. *Geophysics*, **21**: 455–469.
- Carpenter, P.J., Calkin, S.F. and Kaufman, R.S. (1991) Assessing a fractured landfill cover using electrical resistivity and seismic refraction techniques. *Geophysics*, **56**: 1896–1904.
- Carpenter, P.J., Doll, W.E. and Phillips, B.E. (1994) Ground penetrating radar surveys over an alluvial DNAPL site, Paducah gaseous diffusion plant, Kentucky. *SAGEEP 1994*: 261–275.
- Cartwright, K. and McComas, M.R. (1968) Geophysical surveys in the vicinity of sanitary landfills in north-eastern Illinois. *Ground Water*, **16** (5): 23–30.
- Cassiani, G., Fusi, N., Susanni, D. and Deiana, R. (2008) Vertical radar profiling for the assessment of landfill capping effectiveness. *Near Surface Geophysics*, **6**: 133–142.
- Cassidy, N.J. (2009) Ground penetrating radar data processing, modelling and analysis, in *Ground Penetrating Radar: Theory and Applications* (ed. H.M. Jol), Elsevier, Amsterdam, 141–176.

- Casten, U. and Gram, C. (1989) Recent developments in underground gravity surveys. *Geophysical Prospecting*, **37**: 73–90.
- Caterpillar Tractor Company (2000) *Caterpillar Performance Handbook*, 31st edn, Caterpillar Tractor Company, Peoria, USA.
- Chapin, D.A. (1996) The theory of the Bouguer gravity anomaly: a tutorial. *The Leading Edge*, **15**: 361–363.
- Chapman, S. and Bartels, J. (1940) *Geomagnetism*, Clarendon Press, Oxford, UK.
- Chave, A.D., Constable, S.C. and Edwards, R.N. (1991) Electrical exploration methods for the seafloor, in *Electromagnetic Methods in Applied Geophysics*, Vol. 2B. (ed. M.N. Nabighian), Society of Exploration Geophysicists, Tulsa, USA, 931–966.
- Chen, J., Kemna, A. and Hubbard, S.S. (2008) A comparison between Gauss–Newton and Markov-chain Monte Carlo-based methods for inverting spectral induced-polarization data for Cole–Cole parameters. *Geophysics*, **73** (6): F247–F259.
- Christensen, E. (1992) Small vibrator development. *Abstracts of the EAGE Conference, 54th Meeting, Paris*, European Association of Exploration Geophysicists, Netherlands.
- Christensen, N.B. (2002) A generic 1-D imaging method for transient electromagnetic data. *Geophysics*, **67**: 438–447.
- Christensen, N.B. and Dodds, K. (2007) 1D inversion and resolution of marine CSEM data. *Geophysics*, **72** (2): WA27–WA38.
- Christensen, N.B., Reid, J.E. and Halkjær, M. (2009) Fast, laterally smooth inversion of airborne time-domain electromagnetic data. *Near Surface Geophysics*, **7**: 599–612.
- Christensen, N.I. and Fountain, D.M. (1975) Constitution of the lower continental crust based on experimental studies of seismic velocities in granulites. *Bulletin of the Geological Society of America*, **86**: 227–236.
- Cioni, R., Fanelli, G., Guidi, M., et al. (1992) Lake Bogoria hot springs (Kenya): geochemical features and geothermal implications. *Journal of Volcanology and Geothermal Research*, **50**: 231–246.
- Claerbout, J.F. (1976) *Fundamentals of Geophysical Data Processing*, McGraw-Hill, New York, USA.
- Claerbout, J.F. (1985) *Imaging the Earth's Interior*, Blackwell Scientific, Oxford, UK.
- Clark, C.D. (1993) Mega-scale glacial lineations and cross-cutting ice-flow landforms. *Earth Surface Processes and Landforms*, **18**: 1–29.
- Clement, W.P. and Barrash, W. (2006) Crosshole radar tomography in a fluvial aquifer near Boise, Idaho. *Journal of Environmental and Engineering Geophysics*, **11**: 171–184.
- Cole, K.S. and Cole, R.H. (1941) Dispersion and absorption in dielectrics. *Journal of Chemical Physics*, **9**: 341–351.
- Coleman, A.R. (1991) The use of the self-potential method in the delineation of a reclaimed landfill site. *Proceedings of the Conference on Planning and Engineering of Landfills*, 10–11 July 1991, University of Birmingham, The Midlands Geotechnical Society, UK.
- Collett, L.S. (1986) Development of the airborne electromagnetic technique, in *Airborne Resistivity Mapping* (ed. G.J. Palacky), Geological Survey of Canada, 9–18.
- Collett, L.S. (1990) History of the induced-polarization method. Induced polarization: applications and case histories, in *Invest. Geophys.* (eds J.B. Fink, E.O. McAlister, B.K. Sternberg, S.H. Ward and W.G. Wieduwilt), Society of Exploration Geophysicists, Tulsa, Oklahoma, USA, 5–22.
- Collette, B.J. (1958) Structural sketch of the North Sea. *Geologie Minjn*, **20**: 366–371.
- Colley, G.C. (1963) The detection of caves by gravity measurements. *Geophysical Prospecting*, **11**: 1–9.
- Constable, S. and Srnka, L.J. (2007) An introduction to marine controlled-source electromagnetic methods for hydrocarbon exploration. *Geophysics*, **72** (2): WA3–WA12.
- Conyers, L.B. (2004) *Ground Penetrating Radar for Archaeology*, AltaMira Press, Walnut Creek, California, USA.
- Conyers, L.B. and Goodman, D. (1997) *Ground Penetrating Radar: A Primer for the Archaeologist*, AltaMira Press, USA.
- Cook, J.C. (1960) Proposed monocycle-pulse very-high-frequency radar for air-borne ice and snow measurement. *AIEE Comm. Electron.*, **51**: 588–594.
- Cook, J.C. (1975) Radar transparencies of mine and tunnel rocks. *Geophysics*, **40**: 865–885.
- Cook, K.L. and Van Nostrand, R.G. (1954) Interpretation of resistivity data over filled sinks. *Geophysics*, **19**: 761–790.
- Cooper, G.R.J. (1997) SPINV: self-potential data modelling and inversion. *Computers and Geosciences*, **23**: 1121–1123.
- Cooper, G.R.J. (2009) Balancing images of potential-field data. *Geophysics*, **74** (3): L17–L20.
- Cooper, N.J. and Swift, R. (1994) The application of TEM to Cypress-type massive sulfide exploration in Cyprus. *Geophysics*, **59**: 202–214.
- Corriols, M., Nielson, M.R., Dahlin, T. and Christensen, N.B. (2009) Aquifer investigations in the León-Chinandega plains, Nicaragua, using electromagnetic and electrical methods. *Near Surface Geophysics*, **7**: 413–425.
- Corwin, R.F. (1973) *Offshore Application of Self-Potential Prospecting*, University of California, Berkeley, USA.
- Corwin, R.F. (1990) The self-potential method for environmental and engineering applications, in *Geotechnical and Environmental Geophysics*, Vol. 2: *Environmental and Groundwater*, (ed. S.H. Ward), Society of Exploration Geophysicists, Tulsa, Oklahoma, USA, 127–145.
- Corwin, R.F. and Morrison, H.F. (1977) Self-potential variations preceding earthquakes in central California. *Geophysical Research Letters*, **4**: 171–174.
- Corwin, R.F. and Hoover, D.B. (1979) The self-potential method in geothermal exploration. *Geophysics*, **44**: 226–245.

- Cosentino, M., Lombardo, G. and Privitera, E. (1989) A model for the internal dynamical processes on Mt Etna. *Geophysical Journal*, **97**: 367–379.
- Cox, M. (1999) *Static Corrections for Seismic Reflection Surveys*, Society of Exploration Geophysicists, Tulsa, Oklahoma, USA.
- Crampin, S. (1985) Evaluation of anisotropy by shear-wave splitting. *Geophysics*, **50**: 142–152.
- Crawford, W.G. (1995) *Construction Surveying and Layout*, 2nd edn, Creative Construction Publishing, West LaFayette, USA.
- Cresswell, P., Harris, S., and Jeffries, D.J. (1990). *The history, distribution, status and habitat requirements of the badger in Britain*. Nature Conservancy Council, Peterborough, UK.
- Cripps, A.C. and McCann, D.M. (2000) The use of the natural gamma log in engineering geological investigations. *Engineering Geology*, **55**: 313–324.
- Crone, J.D. (1986) Field examples of borehole pulse EM surveys used to detect and outline conductive ore deposits, in *Borehole Geophysics for Mining and Geotechnical Applications* (ed. P.G. Killeen), Geological Survey of Canada, 59–70.
- Crone, J.D. (1991) PEM case histories, Cigar and Winston Lakes, Canada, in *Electromagnetic Methods in Applied Geophysics, Vol. 2: Applications, Part A* (ed. M.N. Nabighian), Society of Exploration Geophysicists, Tulsa, Oklahoma, USA, 490–495.
- Cummings, D. (1988) Determination of depths to an irregular interface in shallow seismic refraction surveys using a pocket calculator. *Geophysics*, **44**: 1987–1998.
- Currenti, G., Del Negro, C. and Ganci, G. (2007) Modelling of ground deformation and gravity fields using finite element method: an application to Etna volcano. *Geophysical Journal International*, **169**: 775–786.
- Dagley, P., Mussett, A.E., Wilson, R.L. and Hall, J.M. (1978) The British Tertiary igneous province: palaeomagnetism of the Arran dykes. *Geophysical Journal of the Royal Astronomical Society*, **54**: 75–91.
- Dampney, C.N.G. (1977) Gravity interpretation for hydrocarbon exploration: a workshop manual. *Bulletin of the Australian Society of Exploration Geophysicists*, **8** (4): 161–178.
- Daniels, D. (2007) *Ground Penetrating Radar*, IEEE, London, UK.
- Daniels, D.J., Gunton, D.J. and Scott, H.F. (1988) Introduction to subsurface radar. *IEE Proceedings*, **135** (F4): 278–320.
- Danson, E. (2005) *Geotechnical and Geophysical Investigations for Offshore and Nearshore Developments*, International Society for Soil Mechanics and Geotechnical Engineering.
- Darracott, B.W. and Lake, M.I. (1981) An initial appraisal of ground probing radar for site investigation in Britain. *Ground Engineering*, **14**: 14–18.
- Darracott, B.W. and McCann, D.M. (1986) Planning engineering geophysical surveys, in *Site Investigation Practice: Assessing BS 5930* (ed. A.B. Hawkins), Geological Society Engineering Geology Special Publication No. 2, 85–90.
- David, A., Linford, N. and Linford, P. (2008) *Geophysical Survey in Archaeological Field Evaluation*, English Heritage, London, UK.
- Davis, J.L. and Annan, A.P. (1989) Ground-penetrating radar for high-resolution mapping of soil and rock stratigraphy. *Geophysical Prospecting*, **37**: 531–551.
- Davydycheva, S., Rykhlnski, N. and Legeido, P. (2006) Electrical-prospecting method for hydrocarbon search using the induced polarization effect. *Geophysics*, **71** (4): G179–G189.
- Davydycheva, S. and Rykhlnski, N. (2009) Focused-source EM survey versus time-domain and frequency-domain CSEM. *The Leading Edge*, **28**: 944–949.
- De Feijter, J.W. and Van Deen, J.K. (1990) Quality assessment of hydraulic engineering structures using ground radar, in *Geotechnical and Environmental Geophysics, Vol. III: Geotechnical* (ed. S. Ward), Society of Exploration Geophysicists, Tulsa, USA, 249–261.
- De Witte, L. (1948) A new method of interpretation of self-potential field data. *Geophysics*, **13**: 600–608.
- Deere, J. (2009) Introduction to this special section – Statics. *The Leading Edge*, **28**: 190.
- Dell'Aversana, P. (2007) Improving interpretation of CSEM in shallow water. *The Leading Edge*, **26**: 332–335.
- Dobinski, W., Zogala, B., Wzietek, K. and Litwin, L. (2008) Results of geophysical surveys on Kasprowy Wierch, the Tatra Mountains, Poland, in *Applied Geophysics in Periglacial Environments* (eds C. Hauck and C. Kneisel), Cambridge University Press, Cambridge, 126–136.
- Dobrin, M.B. (1976) *Introduction to Geophysical Prospecting*, McGraw-Hill, New York, USA.
- Dobrin, M.B. and Savit, C.H. (1988) *Introduction to Geophysical Prospecting*, McGraw-Hill, New York, USA.
- Docherty, P. (1992) Solving for the thickness and velocity of the weathering layer using 2-D refraction tomography. *Geophysics*, **57**: 1307–1318.
- Dodds, A.R. and Ivic, D. (1990) Integrated geophysical methods used for groundwater studies in the Murray Basin, South Australia, in *Geotechnical and Environmental Geophysics, Vol. 2: Environmental and Groundwater* (ed. S.H. Ward), Society of Exploration Geophysicists, Tulsa, Oklahoma, USA, 303–310.
- Dohr, G. (1981) *Applied Geophysics*, Halsted Press, New York, USA.
- Doll, W.E. (1994) How can environmental geophysics be advanced? *Geophysics: The Leading Edge*, **13**: 1035–1039.
- Doll, W.E., Gamey, T.J., Beard, L.P. and Bell, D.T. (2006) Airborne vertical magnetic gradient for near-surface applications. *The Leading Edge*, **25**: 50–53.
- Doll, W.E., Gamey, T.J., Beard, L.P., et al. (2008a) Advances in airborne geophysical systems for ordnance mapping and detection. *The Leading Edge*, **27**: 1463–1469.

- Doll, W.E., Sheehan, J.R., Gamey, T.J., *et al.* (2008b) Results of an airborne magnetic gradient demonstration, New Mexico. *Journal of Environmental and Engineering Geophysics*, **13**: 277–290.
- Dong, P., Fan, J., Chen, Z., *et al.* (2008) Applying Mise-a-la-masse method to determine the length of reinforcement in bored in situ concrete piles. *Journal of Environmental and Engineering Geophysics*, **13** (2): 51–56.
- Doolittle, J.A. (1993) Characteristics and monitoring the vadose zone with ground penetrating radar. *Advanced Ground Penetrating Radar: Technologies and Applications*, 26–28 Oct. 1993: 105–119.
- Doolittle, J.A. and Bellantoni, N.F. (2010) The search for graves with ground-penetrating radar in Connecticut. *Journal of Archaeological Science*, **37**: 941–949.
- Douma, J., Den Rooijen, H. and Schokking, F. (1990) Anisotropy detected in shallow clays using shear-wave splitting in a VSP survey. *Geophysical Prospecting*, **38**: 983–998.
- Drahor, M.G. (2004) Application of the self-potential method to archaeological prospection. *Archaeological Prospection*, **11**: 77–105.
- Du Pisani, P. and Vogt, D. (2004) Borehole radar delineation of the Veltersdorp Contact Reef in three dimensions. *Exploration Geophysics*, **35**: 319–323.
- Duckworth, K. and Calvert, H.T. (1995) An examination of the relationship between time-domain integral chargeability and the Cole–Cole impedance model. *Geophysics*, **60**: 1249–1252.
- Dunning, F.W. (1970) *Geophysical Exploration*, HMSO, London, UK.
- Durrance, E.M. (1986) *Radioactivity in Geology*, Ellis Horwood, Chichester, UK.
- Dyck, A.V. (1991) Drill-hole electromagnetic methods, in *Electromagnetic Methods in Applied Geophysics*, Vol. 2B (ed. M.N. Nabighian), Society of Exploration Geophysicists, Tulsa, Oklahoma, US, 881–930.
- Eaton, S. (2003) Gradiometers versus gravity meters. *New Technology Magazine*, April/May 2003: 3–4.
- Eaton, D.W.S., Stewart, R.R. and Harrison, M.P. (1991) The Fresnel zone for P-S waves. *Geophysics*, **56**: 360–364.
- Eddies, R.D. and Reynolds, J.M. (1988) Seismic character of infilled channels in Plymouth Sound and the River Tamar. *Proceedings of the Ussher Society*, **7**: 36–40.
- Edelmann, H.A.K. (1992) Circularly polarized shear waves used for VSP measurements. *Geophysics*, **57**: 643–646.
- Edwards, N. (2005) Marine controlled source electromagnetics: principles, methodologies, future commercial applications. *Surveys in Geophysics*, **26**: 675–700.
- Edwards, R.N., Law, L.K., Wolfgram, P.A., *et al.* (1985) First results of the MOSES experiment: sea sediment conductivity and thickness determination, Bute Inlet, British Columbia, by magnetometric offshore electrical sounding. *Geophysics*, **50**: 153–161.
- Edwards, R.N., Wolfgram, P.A. and Judge, A.S. (1988) The ICE-MOSES experiment: mapping permafrost zones electrically beneath the Beaufort Sea. *Marine Geophysical Researches*, **9**: 265–290.
- Edwards, R.N. and Nabighian, M.N. (1991) The magnetometric resistivity method, in *Electromagnetic Methods in Applied Geophysics*, Vol. 2A (ed. M.N. Nabighian), Society of Exploration Geophysicists, Tulsa, Oklahoma, USA, 47–104.
- Eggers, A.A. (1987) Residual gravity changes and eruption magnitudes. *Journal of Volcanology and Geothermal Research*, **33**: 201–216.
- Eiken, O., Degutsch, M., Riste, P. and Röd, K. (1989) Snowstreamer: an efficient tool in seismic acquisition. *First Break*, **7**: 374–378.
- Elkins, T.A. (1951) The second derivative method of gravity interpretation. *Geophysics*, **16**: 29–50.
- Ellingsrud, S., Eidesmo, T., Johansen, S., *et al.* (2002) Remote sensing of HC layers by seabed logging (SBL): results from a cruise offshore Angola. *The Leading Edge*, **21**: 972–982.
- Eloranta, E. (1984) A method for calculating mise-à-la-masse anomalies in the case of high conductivity contrast by the integral equation technique. *Geoexploration*, **22**: 77–88.
- Emanuel, D. (2002) *Field Road Chalk Mines Stabilisation Project – Phase 1 Volume 2: An Account of the Site and Subsidence Events*, Peter Brett Associates, Reading, UK.
- Emerson, D.W., Reid, J.E., Clark, D.A. and Hallett, M.S.C. (1992) The geophysical responses of buried drums – field tests in weathered Hawkesbury Sandstone, Sydney Basin, NSW. *Exploration Geophysics*, **23**: 589–617.
- European Association of Exploration Geophysicists (1991) *Standard Graphs for Resistivity Prospecting*, EAEG, The Hague.
- Evans, R.B. (1982) Currently available geophysical methods for use in hazardous waste site investigations, in *Risk Assessment at Hazardous Waste Sites* (eds F.A. Long and G.E. Schweitzer), American Chemical Society Symposium Series No. 204, 93–115.
- Evans, S. (1965) Dielectric properties of ice and snow: a review. *Journal of Glaciology*, **5**: 773–792.
- Ewing, M., Worzel, J. and Pekeris, C.L. (eds) (1948) Propagation of sound in the ocean. *Geol. Soc. America. Memoir* **27** pp. 205.
- Fajkiewicz, Z. (1986) Origin of the anomalies of gravity and its vertical gradient over cavities in brittle rock. *Geophysical Prospecting*, **34**: 1233–1254.
- Falgàs, E., Ledo, J., Marcuello, A. and Queralt, P. (2009) Monitoring freshwater–seawater interface dynamics with audiomagnetotelluric data. *Near Surface Geophysics*, **7**: 391–399.
- Fardis, M.N., Carvalho, E., Elnashai, A., *et al.* (2005) *Designers' guide to EN 1998-1 and EN 1998-5 EuroCode 8: Design of Structures for Earthquake Resistance. General Rules, Seismic Actions, Design Rules for Buildings, Foundations and Retaining Structures*, Thomas Telford Publishing, London, UK.

- Faust, L.Y. (1951) Seismic velocity as a function of depth and geologic time. *Geophysics*, **16**: 192–206.
- Ferguson, C.C. (1992) The statistical basis for spatial sampling of contaminated land. *Ground Engineering*, **25**: 34–38.
- Ferguson, J.F., Klopping, F.J., Chen, T., et al. (2008) The 4D microgravity method for waterflood surveillance: Part 3 – 4D absolute microgravity surveys at Prudhoe Bay, Alaska. *Geophysics*, **73** (6): WA163–WA171.
- Filloux, J.H. (1987) Instrumentation and experimental methods for oceanic studies, in *Geomagnetism*, Vol. 1, (ed. J.A. Jacobs), Academic Press, London, 143–246.
- Finizola, A., Sortino, F., Lénat, J.-F. and Valenza, M. (2002) Fluid circulation at Stromboli volcano (Aeolian Islands, Italy) from self-potential and CO<sub>2</sub> surveys. *Journal of Volcanology and Geothermal Research*, **116**: 1–18.
- Finizola, A., Lénat, J.-F., Macedo, O., et al. (2004) Fluid circulation and structural discontinuities at Misti volcano (Peru) inferred from self-potential and CO<sub>2</sub> measurements. *Journal of Volcanology and Geothermal Research*, **135**: 343–360.
- Fisher, E., McMechan, G.A. and Annan, A.P. (1992a) Acquisition and processing of wide-aperture ground penetrating radar data. *Geophysics*, **57**: 495–504.
- Fisher, E., McMechan, G.A., Annan, A.P. and Cosway, S.W. (1992b) Examples of reverse-time migration of single-channel, ground-penetrating radar profiles. *Geophysics*, **57**: 577–586.
- Fitterman, D.V. (1978) Electrokinetic and magnetic anomalies associated with dilatent regions in a layered earth. *Journal of Geophysical Research*, **83**: 5924–5934.
- Fitterman, D.V. (1979a) Calculations of self-potential anomalies near vertical contacts. *Geophysics*, **44**: 195–205.
- Fitterman, D.V. (1979b) Theory of electrokinetic-magnetic anomalies in a faulted half-space. *Journal of Geophysical Research*, **84** (B11): 6031–6040.
- Fitterman, D.V. and Corwin, R.F. (1982) Inversion of self-potential data from the Cerro Prieto geothermal field, Mexico. *Geophysics*, **47**: 938–945.
- Fitterman, D.V. and Stewart, M.T. (1986) Transient electromagnetic sounding for groundwater. *Geophysics*, **51**: 995–1005.
- Fitzpatrick, F. (1991) *Studies of sediments in a tidal environment*. Unpublished PhD thesis, University of Plymouth, UK.
- Flekkøy, E.G., Måløy, K.J. and Holten, T. (2009) EM: understanding the physics. *Geo ExPro*, **6** (4): 38–42.
- Flinn, D. (1977) A geological interpretation of the aeromagnetic map of east-central Shetland. *Journal of the Geological Society of London*, **133**: 111–121.
- Fofonoff, N.P. and Millard, R.C. (1983) Algorithms for computation of fundamental properties of seawater. *UNESCO Technical Papers in Marine Science*, **44**.
- Fountain, D. (1998) Airborne electromagnetic systems – 50 years of development. *Exploration Geophysics*, **29**: 1–11.
- Fountain, D. (2008) 60 years of airborne EM – focus on the last decade, *AEM2008, 5th International Conference on Airborne Electromagnetics, Haikko Manor, Finland*.
- Fountain, D. and Smith, R.S. (2003) 55 years of AEM: 50 years of KEGS. *KEGS 50th Anniversary symposium*, Toronto, Canada.
- Fountain, D., Smith, R., Payne, T. and Lemieux, J. (2005) A helicopter time-domain EM system applied to mineral exploration: system and data. *First Break*, **23**: 73–78.
- Fournier, C. (1989) Spontaneous potentials and resistivity surveys applied to hydrogeology in a volcanic area: case history of the Chaîne des Puys, (Puy-de-Dôme, France). *Geophysical Prospecting*, **37**: 647–668.
- Fox, L. and Ingerov, O. (2007) Natural source EM for offshore hydrocarbon detection offers potential cost savings. *First Break*, **25** (11): 87–94.
- Frangos, W. (1994) Electrical detection and monitoring of leaks in lined waste disposal ponds. *Proceedings of the Symposium on the Application of Geophysics to Engineering and Environmental Problems*, SAGEEP '94, Vol. 2, Englefield, USA, 1073–1082.
- Fraser, D.C. (1969) Contouring of VLF-EM data. *Geophysics*, **34**: 958–967.
- Fraser, D.C., Keevil, N.B. and Ward, S.H. (1964) Conductivity spectra of rocks from the Craigmont ore environment. *Geophysics*, **29**: 832–847.
- Freeland, R.S., Miller, M.C., Yoder, R.E. and Koppenjan, S.K. (2003) Forensic application of FM-CW and pulse radar. *Journal of Environmental and Engineering Geophysics*, **8**: 97–103.
- French, W. (1984) *Circular seismic acquisition system*. U.S. Patent 4486863, USA.
- Frischknecht, F.C. (1987) Electromagnetic physical scale modelling, in *Electromagnetic Methods in Applied Geophysics*, Vol. 1 (ed. M.N. Nabighian), Society of Exploration Geophysicists, Tulsa, Oklahoma, USA, 365–441.
- Frischknecht, F.C., Labson, V.F., Spies, B.R. and Anderson, W.L. (1991) Profiling methods using small sources, in *Electromagnetic Methods in Applied Geophysics*, Vol. 2: Applications, Part A (ed. M.N. Nabighian), Society of Exploration Geophysicists, Tulsa, Oklahoma, USA, 105–270.
- Frohlich, B. and Lancaster, W.J. (1986) Electromagnetic surveying in current Middle Eastern archaeology: application and evaluation. *Geophysics*, **51**: 1414–1425.
- Furness, P. (2002) The magnetic field of steel drums. *Journal of Applied Geophysics*, **51**: 63–74.
- Furness, P. (2007) Modelling magnetic fields due to steel drum accumulations. *Geophysical Prospecting*, **55**: 737–748.
- Gabell, A.H., Tuckett, H. and Olson, D. (2004) The GT-1A mobile gravimeter. *Australian SEG Airborne Gravity Workshop*.

- Gabriel, G. (2006) Gravity investigation of buried Pleistocene subglacial valleys. *Near Surface Geophysics*, **4**: 321–332.
- Gajewski, D. and Tessmer, E. (2005) Reverse modelling for seismic event characterization. *Geophysical Journal International*, **163**: 276–284.
- Gamey, T.J. (2008) Magnetic response of clustered UXO targets. *Journal of Environmental and Engineering Geophysics*, **13**: 211–221.
- García, X. and Jones, A.G. (2005) A new methodology for the acquisition and processing of audio-magnetotelluric (AMT) data in the AMT dead band. *Geophysics*, **70** (5): G119–G126.
- García-Abdeslam, J. and Ness, G.E. (1994) Inversion of the power spectrum from magnetic anomalies. *Geophysics*, **59**: 391–401.
- García-Abdeslam, J. and Martín-Atienza, B. (2001) A method to compute terrain corrections for gravimeter stations using a digital elevation model. *Geophysics*, **66**: 1110–1115.
- Gardener, R. (1992) Seismic refraction as a tool in the evaluation of rock quality for dredging and engineering purposes: case histories, in *Eurock '92, Chester* (ed. J.A. Hudson), British Geotechnical Society, London, 153–158.
- Gardner, L.W. (1939) An areal plan of mapping subsurface structure by refraction shooting. *Geophysics*, **4**: 247–259.
- Gardner, L.W. (1967) Refraction seismograph profile interpretation, in *Seismic Refraction Prospecting* (ed. A.W. Musgrove), Society of Exploration Geophysicists, Tulsa, Oklahoma, USA, 338–347.
- Garland, G.D. (1965) *The Earth's Shape and Gravity*, Pergamon, Oxford, UK.
- Gasperikova, E. and Morrison, H.F. (2001) Mapping of induced polarization using natural fields. *Geophysics*, **66**: 137–147.
- Gasperikova, E., Cuevas, N.H. and Morrison, H.F. (2005) Natural field induced polarization for mapping deep mineral deposits. *Geophysics*, **70** (6): B61–B66.
- Gay, S.P. (1963) Standard curves for the interpretation of magnetic anomalies over long tabular bodies. *Geophysics*, **28**: 161–200.
- Gay, S.P. (1967) A 1800 millivolt self-potential anomaly near Hualgayoc, Peru. *Geophysical Prospecting*, **15**: 236–245.
- Gay, S.P. (1986) The effects of cathodically protected pipelines on aero-magnetic surveys. *Geophysics*, **51**: 1671–1684.
- Geological Society Engineering Group Working Party (1988) Engineering geophysics. *Quarterly Journal of Engineering Geology*, **21**: 207–271.
- Geometrics Inc. and Oyo Inc. (2003) *SeisImager Manual*, Version 3, Geometrics Inc. and OYO Inc.
- GeoTomo (2007) *GeoCT-II*, GeoTomo, Houston, USA.
- GeoTomo Software (2009a) *RES2DINV ver. 3.58*, Geotomo Software, Penang, Malaysia.
- GeoTomo Software (2009b) *RES3DINV ver. 2.16*, Geotomo Software, Penang, Malaysia.
- Gharibi, M. and Pedersen, L.B. (1999) Transformation of VLF data into apparent resistivities and phases. *Geophysics*, **64**: 1393–1402.
- Ghosh, G.P. (1971) Inverse filter coefficients for the computation of apparent resistivity standard curves for a horizontally stratified earth. *Geophysical Prospecting*, **19**: 749–775.
- Gilbert, R.L.G. (1949) A dynamic gravimeter of novel design. *Proceedings of the Royal Society of London*, **62B**: 445–454.
- Glen, J.W. and Paren, J.G. (1975) The electrical properties of snow and ice. *Journal of Glaciology*, **15** (73): 15–38.
- Glusko, V.T., Cerednicenko, V.P. and Usatenko, B.S. (1981) *Reologija gornogo massiva*, Kiev. Naukowa Dumka, 22–49.
- Gochioco, L.M., Zhang, M. and Zhao, M. (2008) Environmental site assessment of an oil field and detection and imaging of sink-holes using a novel geophysical method. *The Leading Edge*, **27**: 1480–1486.
- Goldie, M. (2002) Self-potentials associated with the Yanacocha high-sulfidation gold deposit in Peru. *Geophysics*, **67**: 684–689.
- Goldman, M., Du Plooy, A. and Eckard, M. (1994) On reducing ambiguity in the interpretation of transient electromagnetic sounding data. *Geophysical Prospecting*, **42**: 3–25.
- Goldstein, M.A. and Strangway, D.W. (1975) Audio-frequency magnetotellurics with a grounded electric dipole source. *Geophysics*, **40**: 669–683.
- Goldstein, N.E., Benson, S.M. and Alumbough, D. (1990) Saline groundwater plume mapping with electromagnetics, in *Geotechnical and Environmental Geophysics, Vol. 2: Environmental and Groundwater* (ed. S.H. Ward), Society of Exploration Geophysicists, Tulsa, Oklahoma, USA, 17–25.
- Goodman, D., Piro, S., Nishimura, Y., et al. (2004) Discovery of a 1st century AD Roman amphitheater and other structures at the Forum Novum by GPR. *Journal of Environmental and Engineering Geophysics*, **9**: 35–51.
- Goodman, D., Hongo, H., Higashi, N., et al. (2007) GPR surveying over burial mounds: correcting for topography and the tilt of the GPR antenna. *Near Surface Geophysics*, **5**: 383–388.
- Goodman, D., Piro, S., Nishimura, Y., et al. (2009) GPR archaeometry, in *Ground Penetrating Radar: Theory and Applications* (ed. H.M. Jol), Elsevier, Amsterdam, 479–508.
- Goree, W.S. and Fuller, M. (1976) Magnetometers using RF-driven SQUIDs and their applications in rock magnetism and palaeomagnetism. *Review of Geophysics and Space Physics*, **14**: 591–608.
- Granser, H., Meurers, B. and Steinhauser, P. (1989) Apparent density mapping and 3D gravity inversion in the eastern Alps. *Geophysical Prospecting*, **37**: 279–292.
- Grant, F.S. and West, G.F. (1965) *Interpretation Theory in Applied Geophysics*, McGraw-Hill, New York, USA.
- Grant, F.S. and Dodds, J. (1972) *MAGMAP FFT Processing System Development Notes*, Paterson Grant and Watson Ltd, Canada.

- Green, R. (1960) Remanent magnetization and the interpretation of magnetic anomalies. *Geophysical Prospecting*, **8**: 98–110.
- Green, W.B. (1983) *Digital Image Processing*, Van Nostrand-Reinhold, New York.
- Greenhalgh, S.A. and Whiteley, R.J. (1977) Effective application of the seismic refraction method to highway engineering projects. *Australian Road Research*, **7**: 3–19.
- Greenhouse, J.P. (1991) Environmental geophysics: it's about time. *Geophysics: The Leading Edge*, **10**: 32–34.
- Greenhouse, J.P. and Slaine, D.D. (1983) The use of reconnaissance electromagnetic methods to map contaminant migration. *Ground Water Monitoring Review*, **3** (2): 47–59.
- Greenhouse, J., Brewster, M., Schneider, G., et al. (1993) Geophysics and solvents: the Borden experiment. *Geophysics: The Leading Edge*, **12**: 261–267.
- Greenway, J. (2009) A new generation of 3D seismic vessels. *Geo ExPro*, **6**: 44–45.
- Gribenko, A. and Zhdanov, M. (2007) Rigorous 3D inversion of marine CSEM data based on the integral equation method. *Geophysics*, **72** (2): WA73–WA84.
- Griffiths, D.H. and King, R.F. (1981) *Applied Geophysics for Geologists and Engineers*, Pergamon, Oxford, UK.
- Griffiths, D.H. and Turnbull, J. (1985) A multi-electrode array for resistivity surveying. *First Break*, **3** (7): 16–20.
- Griffiths, D.H., Turnbull, J. and Olayinka, A.I. (1990) Two-dimensional resistivity mapping with a computer-controlled array. *First Break*, **8** (4): 121–129.
- Grow, L.L. (1982) Induced polarization for geophysical exploration. *Geophysics: The Leading Edge of Exploration*, **1** (1): 55–56; 69–70.
- Gubbins, D. (1990) *Seismology and Plate Tectonics*, Cambridge University Press, Cambridge.
- Gubbins, D. and Herrero-Bervera, E. (2007) *Encyclopedia of Geomagnetism and Palaeomagnetism*, Springer Heidelberg, Germany.
- Guoqiang, X., Jianping, S. and Xian, Y. (2004). Detecting shallow caverns in China using TEM. *The Leading Edge*, **23** (7): 694–695.
- Gupta, V.K. and Fitzpatrick, M.M. (1971) Evaluation of terrain effects in ground magnetic surveys. *Geophysics*, **36**: 582–589.
- Guspí, F. and Novara, I. (2009) Reduction to the pole and transformations of scattered magnetic data using Newtonian equivalent sources. *Geophysics*, **74** (5): L67–L73.
- Habberjam, G.M. and Watkins, G.E. (1967) The reduction of lateral effects in resistivity probing. *Geophysical Prospecting*, **15**: 221–235.
- Hackney, R.I. and Featherstone, W.E. (2003) Geodetic versus geophysical perspectives of the 'gravity anomaly'. *Geophysical Journal International*, **154** (2): 35–43.
- Haeberli, W. and Fisch, W. (1984) Electrical resistivity soundings of glacier beds: a test study on Grubengletscher, Wallis, Swiss Alps. *Journal of Glaciology*, **30** (106): 373–376.
- Hagedoorn, J.G. (1959) The plus-minus method of interpreting seismic refraction sections. *Geophysical Prospecting*, **7**: 158–182.
- Hagrey, S.A.A. (2004) GPR application for mapping toluene infiltration in a heterogeneous sand model. *Journal of Environmental and Engineering Geophysics*, **9**: 79–85.
- Hahn, A., Kind, E.G. and Mishra, D.G. (1976) Depth estimation of magnetic sources by means of Fourier amplitude spectra. *Geophysical Prospecting*, **24**: 287–308.
- Hale, D.I., Hill, N.R. and Stefani, J.P. (1991) Imaging salt with turning seismic waves. *Expanded Abstracts of 61st Annual International Meeting of SEG*, 1171–1174.
- Hales, F.W. (1958) An accurate graphical method for interpreting seismic refraction lines. *Geophysical Prospecting*, **6**: 285–314.
- Hall, D.H. and Hajnal, J. (1962) The gravimeter in studies of buried valleys. *Geophysics*, **27**: 939–951.
- Hallof, P.G. (1967) *An Appraisal of the Variable Frequency IP Method after Twelve Years of Application*, Phoenix Geophysics Ltd, Markham, Ontario.
- Hallop, P.G. (1974) The IP phase measurement and inductive coupling. *Geophysics*, **39**: 650–665.
- Hallop, P.G. (1982) Reconnaissance and detailed geophysical results, Granite Mountain Area, Pershing County, Nevada. *Global Tectonics and Metallogeny*, **1**: 374–400.
- Hallop, P.G. (1983) *An Introduction to the Use of the Spectral Induced Polarization Method*, Phoenix Geophysics Ltd., Markham, Ontario, Canada.
- Hallop, P.G. and Klein, J.D. (1982) *Electrical Parameters of Volcanogenic Mineral Deposits in Ontario*, Phoenix Geophysics Ltd., Markham, Ontario, Canada.
- Hallop, P.G. and Pelton, W.H. (1980) The removal of inductive coupling effects from spectral IP data. *SEG 50th Annual International Meeting, Houston, Texas, 16–20 November 1980*.
- Hallop, P.G. and Pelton, W.H. (1981) *Recent and Future Advances in the Induced Polarization Method*, Phoenix Geophysics Ltd., Markham, Ontario, Canada.
- Halpenny, J.F. and Darbha, D.M. (1995) Airborne gravity tests over Lake Ontario. *Geophysics*, **60**: 61–65.
- Hambrey, M.J., Quincey, D.J., Glasser, N.F., et al. (2008) Sedimentological, geomorphological and dynamic context of debris-mantled glaciers, Mount Everest (Sagarmatha) region, Nepal. *Quaternary Science Reviews*, **27**: 2361–2389.
- Hamilton, S.M. and Hattori, K.H. (2008) Spontaneous potential and redox responses over a forest ring. *Geophysics*, **73** (3): B67–B75.

- Hammer, S. (1939) Terrain corrections for gravimeter stations. *Geophysics*, **4**: 184–194.
- Hammer, S. (1945) Estimating ore masses in gravity prospecting. *Geophysics*, **10**: 50–62.
- Hammer, S. (1963) Deep gravity interpretation by stripping. *Geophysics*, **28**: 369–378.
- Hammer, S. (1982) Airborne gravity is here! *Oil & Gas Journal*, 11 January.
- Hammer, S. (1984) Discussion on ‘Airborne gravity is here!’ *Geophysics*, **49**: 471–472.
- Hammond, S. and Murphy, C. (2003) Air-FTG™: Bell Geospace’s airborne gravity gradiometer – a description and case history. *Australian Society for Exploration Geophysics*, 24–26.
- Hammond, W.R. and Sprenke, K.F. (1991) Radar detection of subglacial sulfides. *Geophysics*, **56**: 870–873.
- Hanafy, S.M., Cao, W., Mccarter, K. and Schuster, G.T. (2009) Using super-stacking and super-resolution properties of time-reversal mirrors to locate trapped miners. *The Leading Edge*, **28**: 302–307.
- Hanisch, J., Delisle, G., Pokhrel, A.P., et al. (1998) The Thulagi glacier lake, Manaslu Himal, Nepal – Hazard assessment of a potential outburst. *Proceedings of the Eighth International IAEG Congress*, 21–25 September 1998, Vancouver, Canada, 2209–2215.
- Hansen, T., Kingston, J., Kjellesvik, S., et al. (1989) 3-D seismic surveys. *Oilfield Review*, **1** (3): 54–61.
- Hanson, D.A. (1980) Radiometrics, in *Practical Geophysics for the Exploration Geologist* (ed. R. van Blairicom), Northwest Mining Association, Spokane, Washington, USA.
- Hardage, B.A. (1985) *Vertical Seismic Profiling. Part A: Principles*, Geological Press, London, UK.
- Harris, P., Du, Z., Macgregor, L.M., et al. (2009) Joint interpretation of seismic and CSEM data using well log constraints: an example from the Luva Field. *First Break*, **27** (5): 73–81.
- Harrison, J.C., von Huene, R.E. and Corbato, C.E. (1966) Bouguer gravity anomalies and magnetic anomalies off the coast of southern California. *Journal of Geophysical Research*, **71**: 4921–4941.
- Hatherley, P.J., Urosevic, M., Lamborne, A. and Evans, B.J. (1994) A simple approach to calculating refraction statics corrections. *Geophysics*, **59**: 156–160.
- Hatton, L., Worthington, M.H. and Makin, J. (1986) *Seismic Data Processing: Theory and Practice*, Blackwell Scientific, Oxford, UK.
- Hattula, A. and Rekola, T. (2000) Exploration geophysics at the Pyhäsalmi mine and grade control work of the Outokumpu Group. *Geophysics*, **65**: 1961–1969.
- Hauck, C. and Kneisel, C. (2008) *Applied Geophysics in Periglacial Environments*, Cambridge University Press, Cambridge, UK.
- Hawkins, A.B. (1986) *Site Investigation Practice: Assessing BS 5930*, Geological Society Engineering Geology Special Publication No. 2, London, UK.
- Hayford, J.F. and Bowie, W. (1912) *US Coast and Geod. Survey*, Special Publication 10.
- Haynes, R., Davis, A.M., Reynolds, J.M. and Taylor, D.I. (1993) The extraction of geotechnical information from high-resolution seismic reflection data. Society for Underwater Technology. *Offshore Site Investigation and Foundation Behaviour*, **28**, 215–228.
- Hearst, J.R., Nelson, P.H. and Paillet, F.L. (2000) *Well Logging for Physical Properties*, John Wiley & Sons Inc., New York, USA.
- Heikes, R.R. and Ure, R.W. (1961) *Thermoelectricity. Science and Engineering*, Interscience, New York, USA.
- Heiskanen, W.A. (1938) Publ. Isostat. Inst., Int. Assoc. Geod., no. 1, Helsinki, Finland.
- Henriet, J.P., Verschuren, M. and Versteeg, W. (1992) Very-high-resolution 3D seismic reflection imaging of small-scale structural deformation. *First Break*, **10** (3): 81–88.
- Hermes, H.J. (1986) Calculation of pre-Zechstein Bouguer Anomaly in North-West Germany. *First Break*, **4** (11): 13–22.
- Herrod, L.D.B. and Garrett, S.W. (1986) Geophysical fieldwork on the Ronne Ice Shelf, Antarctica. *First Break*, **4** (1): 9–14.
- Hertrich, M., Braun, M. and Yaramanci, U. (2005) Magnetic resonance soundings with separate transmitter and receiver loops. *Near Surface Geophysics*, **3**: 141–154.
- Hess, S., Fairley, J.P., Bradford, J., et al. (2009) Evidence for composite hydraulic architecture in an active fault system based on 3D seismic reflection, time-domain electromagnetics and temperature data. *Near Surface Geophysics*, **7**: 341–352.
- Hildebrande, J.A., Stevenson, J.M., Hammer, P.T.C., et al. (1990) A seafloor and sea surface gravity survey of Axial Volcano. *Journal of Geophysical Research*, **95**: 12751–12763.
- Hill, I., Grossey, T. and Leech, C. (2004) High-resolution multisensory geophysical surveys for near-surface applications can be rapid and cost-effective. *The Leading Edge*, **23**(7): 684–688.
- Hill, I. (2008) Resolution and quality assurance in near-surface geophysical surveys: a multimethod field trial and results. *The Leading Edge*, **27**: 1516–1524.
- Hill, N.R. (1987) Downward continuation of refracted arrivals to determine shallow structure. *Geophysics*, **52**: 1188–1198.
- Hinze, W.J. (1985) *The Utility of Regional Gravity and Magnetic Anomaly Maps*, Society of Exploration Geophysicists, Tulsa, Oklahoma, USA.
- Hird, G.A., Karwatowski, J., Jenkinson, M.R. and Eyres, A. (1993) 3D concentric circle survey: the art of going in circles. *Extended Abstracts, 55th Meeting EAEG Stavanger Norway*, Paper A001.
- Hoekstra, P. and Blohm, M.W. (1990) Case histories of time domain electromagnetic sounding in environmental geophysics, in *Geotechnical*

- and Environmental Geophysics, Vol. 2: Environmental and Groundwater (ed. S.H. Ward), Society of Exploration Geophysicists, Tulsa, Oklahoma, USA, 1–15.
- Hoekstra, P., Lahti, R., Hild, J., et al. (1992) Case histories of shallow time domain electromagnetics in environmental site assessment. *Ground Water Monitoring Review*, Fall: 110–117.
- Hohmann, G.W. (1973) Electromagnetic coupling between grounded wires at the surface of a two-layered earth. *Geophysics*, **38**: 854–863.
- Hohmann, G.W. (1975) Three-dimensional induced-polarization and electromagnetic modelling. *Geophysics*, **40**: 309–324.
- Holten, T., Flekkøy, E.G., Singer, B., et al. (2009) Vertical source, vertical receiver, electromagnetic technique for offshore hydrocarbon exploration. *First Break*, **27** (5): 89–93.
- Holzschuh, J. (2002) Low-cost geophysical investigations of a palaeochannel aquifer in the Eastern Goldfields, Western Australia. *Geophysics*, **67**: 690–700.
- Hongisto, H. (1993) Self-potential interpretation using a surface polarization model. *Extended Abstracts of the 55th Meeting and Technical Exhibition, European Association of Exploration Geophysicists, Stavanger, Norway, 7–11 June 1993*, Paper D039.
- Hönig, M. and Tezkan, B. (2007) 1D and 2D Cole–Cole inversion of time-domain induced-polarization data. *Geophysical Prospecting*, **55**: 117–133.
- Hood, P.J. (1981) Aeromagnetic gradiometry – a superior geological mapping tool for mineral exploration programs, in *SQUID Applications to Geophysics* (eds H. Weinstock, H. and W.C. Overton), Society of Exploration Geophysicists, Tulsa, Oklahoma, USA, 72–76.
- Hood, P.J., Holroyd, M.T. and McGrath, P.H. (1979) Magnetic methods applied to base metal exploration, in *Geophysics and Geochemistry in the Search for Metallic Ores* (ed. P.J. Hood), Geological Survey of Canada Economic Geology Report No. **31**, 77–104.
- Hördt, A. and Scholl, C. (2004) The effect of local distortions on time-domain electromagnetic measurements. *Geophysics*, **68**: 87–96.
- Hördt, A. and Hauck, C. (2008) Electromagnetic methods, in *Applied Geophysics in Periglacial Environments* (eds C. Hauck and C. Kneisel), Cambridge University Press, Cambridge, 28–56.
- Hou, J., Mallan, R.K. and Torres-Verdin, C. (2006) Finite-difference simulation of borehole EM measurements in 3D anisotropic media using coupled scalar-vector potentials. *Geophysics*, **71**: G225–G233.
- Hovland, M. and Judd, A.G. (1988) *Seabed Pockmarks and Seepages*, Graham & Trotman, London, UK.
- Howell, B.F. (1990) *An Introduction to Seismological Research, History and Development*, Cambridge University Press, Cambridge, UK.
- Huang, H. and Palacky, G.J. (1991) Damped least-squares inversion of time domain airborne EM data based on singular value decomposition. *Geophysical Prospecting*, **39**: 827–844.
- Hubral, P., Schleicher, J., Tygel, M. and Hanitzsch, C. (1993) Determination of Fresnel zones from travel time information. *Geophysics*, **58**: 703–712.
- Huggenberger, P., Meier, E. and Pugin, A. (1994) Ground-probing radar as a tool for heterogeneity estimation in gravel deposits: advances in data processing and facies analysis. *Journal of Applied Geophysics*, **31**: 171–184.
- Hülsenbeck & Co. (1926) German patent no. 489434.
- Hülsmeye, C. (1904) German patent no. 165546.
- Hunt, S. (1992) The use of cone penetration testing and sampling techniques in the investigation of contaminated land, in *Second International Conference on Polluted and Marginal Land, 30 June–2 July, Brunel University, London* (ed. M.C. Forde), Engineering Technics Press.
- Hunt, T.M. (1977) Recharge of water in Wairakei Geothermal field determined from repeat gravity measurements. *New Zealand Journal of Geology and Geophysics*, **20**: 303–317.
- Hussein, A. (1983) Underground gravity surveys, in *Developments in Geophysical Exploration Methods*, Vol. 5 (ed. A.A. Fitch), Applied Science Publishers, 35–63.
- Hwang, Y.K., Endres, A.L., Piggott, S.D. and Parker, B.L. (2008). Long-term ground penetrating radar monitoring of a small volume DNAPL release in a natural groundwater flow field. *Journal of Contaminant Hydrology*, **97**: 1–12.
- IAEA (1991) Airborne gamma-ray spectrometer surveying. *Technical Report Series*, No. 323, International Atomic Energy Agency, Vienna, Austria.
- IAEA (2003) Guidelines for radioelement mapping using gamma ray spectrometry data. *IAEA-TECDOC-1363*, International Atomic Energy Agency, Vienna, Austria.
- Ikeda, A. (2008) Reassessment of DC resistivity in rock glaciers by comparing with P-wave velocity: a case study in the Swiss Alps, in *Applied Geophysics in Periglacial Environments* (eds C. Hauck and C. Kneisel), Cambridge University Press, Cambridge, UK, 137–152.
- Iliffe, J.C. (2008a) Flattening the Earth – or how to iron out geodetic problems on engineering and construction sites. *Geomatics World*, **16** (2): 22–24.
- Iliffe, J.C. (2008b) Engineering co-ordinate systems, Part II: datums and snakes. *Geomatics World*, **3** (16): 22–23.
- Iliffe, J.C., Arthur, J.V. and Preston (2007) The Snake Projection: a customised grid for rail projects. *Survey Review*, **39** (304): 90–97.
- Iliffe, J.C. and Lott, R. (2008) *Datums and Map Projections for Remote Sensing, GIS and Surveying*, Whittles Publishing, Dunbeath, Scotland, UK.
- Imai, T., Sakayama, T. and Kanemori, T. (1987) Use of ground probing radar and resistivity surveys for archeological investigations. *Geophysics*, **52**: 137–150.
- Ingham, M. (1992) Audiomagnetotelluric soundings in White Island volcano. *Journal of Volcanology and Geothermal Research*, **50**: 301–306.

- Interpex (2007) *IX1D v.3 Instruction Manual*, Interpex Ltd, Golden, Colorado, USA.
- Iris Instruments (1998) *The Proton Magnetic Resonance Method for Groundwater Investigations*. [www.iris-instruments.com](http://www.iris-instruments.com).
- Irvine-Fynn, T.D.L., Moorman, B.J., Williams, J.L.M. and Walter, F.S.A. (2006) Seasonal changes in ground-penetrating radar signature observed at a polythermal glacier, Bylot Island, Canada. *Earth Surface Processes and Landforms*, **31**: 892–909.
- Irvine-Fynn, T.D.L. and Moorman, B. (2009) Arctic glaciers and ground-penetrating radar. Case study: Stagnation Glacier, Bylot Island, Canada, in *Applied Geophysics in Periglacial Environments* (eds C. Hauck and C. Kneisel), Cambridge University Press, Cambridge, 178–190.
- Ivanov, A.G. (1939) Effect of electrization (sic) of earth layers by elastic waves passing through them. *Comptes Rendus (Doklady) de l'Academie des Sciences de l'URSS*, **24**: 42–45.
- Jackson, V.A. (1918) Panic in elephants during an earthquake. *Journal of Bombay Natural History Society*, **26**: 285.
- Jacobs, J.A. (1992) *Deep Interior of the Earth*, Chapman & Hall, London, UK.
- James, D.E. (1990) *The Encyclopedia of Solid Earth Geophysics*, Van Nostrand Reinhold, New York, USA.
- Jansen, J., Billington, E., Snider, F. and Jurcek, P. (1994) Marine SP surveys for dam seepage investigations: evaluation of array geometries through modelling and field trials. *Proceedings of the SAGEEP '94*, 27–31 March, Boston, USA, 1053–1071.
- Jenke, G. (1996) Geophysical exploration of palaeochannels in the Yilgarn of Western Australia. *Geophysics for Geologists and Engineers. Australian Inst. Geoscientists Bulletin*, **19**: 69–71.
- Johnson, R.W., Glaccum, R. and Wojtasinski, R. (1979) Application of ground penetrating radar to soil survey. *Soil and Crop Science Society of Florida Proceedings*, 68–72.
- Johnson, S. and Lohmann, K.J. (2008) Magnetoreception in animals. *Physics Today*, **61** (3): 29–35.
- Jol, H.M. (2009) *Ground Penetrating Radar: Theory and Applications*, Elsevier, Amsterdam.
- Jones, D.G. (1994) Towed sea-bed gamma ray spectrometer 'Eel' is radiometric instrument for wide range of offshore mineral exploration, environmental survey applications. *Sea Technology*, August 1994: 89–93.
- Jones, D.G., Roberts, P.D., Limburg, J., et al. (2001) *Measurements of seafloor radioactivity at the Farallon Islands Radioactive Waste Dump Site, California*. US Geological Survey Open-File Report 01-062.
- Jones, E.J.W. (1989) Radioactivity of the ocean floor and marine phosphorite deposits: observations with a new deep-tow scintillometer. *Geophysical Research Letters*, **16**: 123–126.
- Jones, E.J.W. (1999) *Marine Geophysics*, John Wiley & Sons Ltd, Chichester, UK.
- Jones, P.C., Johnson, A.C., Von Frese, R.R.B. and Corr, H. (2002) Detecting rift basins in the Evans Ice Stream region of west Antarctica using airborne gravity data. *Tectonophysics*, **347**: 25–41.
- Jones, R.B. (1958) In-situ measurements of the dynamic properties of soil by vibration methods. *Géotechnique*, **8**: 1–21.
- Jones, R. (1962) Surface wave technique for measuring the elastic wave properties and thickness of roads. *British Journal of Applied Physics*, **13**: 21–29.
- Jones, T.D. (1986) Pore fluids and frequency-dependent wave propagation in rocks. *Geophysics*, **51**: 1939–1953.
- Judd, A.G. and Hovland, M. (2007) *Seabed Fluid Flow: the Impact on Geology, Biology and the Marine Environment*, Cambridge University Press, Cambridge, UK.
- Kaikkonen, P. and Sharma, S.P. (2001) On of performances in linearized and global nonlinear 2-D inversions of VLF and VLF-R electromagnetic data. *Geophysics*, **66**: 462–475.
- Kane, M.F. (1962) A comprehensive system of terrain corrections using a digital computer. *Geophysics*, **27**: 455–462.
- Kanli, A.I., Tildy, P., Prónay, Z., Pinar, A. and Hermann, L. (2006)  $V_s^{30}$  mapping and soil classification for seismic effect evaluation in Dinar region, SW Turkey. *Geophysical Journal International*, **165** (1): 223–235.
- Kapoor, S., Moldoveanu, N., Egan, M., et al. (2007) Subsalt imaging. The RAZ-WAZ experience. *The Leading Edge*, **26**: 1414–1422.
- Karous, M. and Hjelt, S.E. (1983) Linear filtering of VLF dip angle measurements. *Geophysical Prospecting*, **31**: 782–794.
- Kathage, A., Niessen, J., White, G. and Bell, N. (2005) Fast inspection of railway ballast by means of impulse GPR equipped with horn antennas. *NDT.net*, **10** (9): 1–6.
- Kawasaki, K., Osterkamp, T.E., Jurick, R.W. and Kienle, J. (1983) Gravity measurements in permafrost terrain containing massive ground ice. *Annals of Glaciology*, **4**: 133–140.
- Kearey, P. and Vine, F.J. (1990) *Global tectonics*, Blackwell Scientific, Oxford, UK.
- Kearey, P., Brooks, M. and Hill, I. (2002) *An Introduction to Geophysical Exploration*, Blackwell Scientific, Oxford, UK.
- Keating, P. (2009) Improved use of the local wavenumber to potential-field interpretation. *Geophysics*, **74** (6): L75–L85.
- Keller, G.V. and Frischknecht, F.C. (1966) *Electrical Methods in Geophysical Prospecting*, Pergamon Press.
- Kellett, R., Bishop, J. and Van Reed, E. (1994) The effect of source polarization in CSAMT data over two massive sulfide deposits in Australia. *Geophysics*, **58**: 1764–1772.
- Kemna, A., Binley, A. and Slater, L. (2004) Crosshole IP imaging for engineering and environmental applications. *Geophysics*, **69**: 97–107.
- Kemp, C., Smith, K., Bray, A., et al. (2009) Imaging an orebody ahead of mining using borehole radar at the Snap Lake diamond mine,

- Northwest Territories, Canada. *Seventh International Mining Geology Conference, 17–19 August 2009*, Perth, Western Australia.
- Kennett, M., Laumann, T. and Lund, C. (1993) Helicopter-borne radio-echo sounding of Svartisen, Norway. *Annals of Glaciology*, **17**: 23–26.
- Kepic, A., Campbell, T. and Hinz, C. (2008) Mapping the extent and activity of tree root zones with self potential and misse (sic) a la masse. *SAGEEP*, 223–232.
- Keppner, G. (1991) Ludger Mintrop. *Geophysics: The Leading Edge*, **10** (9): 21–28.
- Ketelaar, A.C.R. (1976) A system for computer-calculation of the terrain correction in gravity surveying. *Geoexploration*, **14**: 57–65.
- Ketola, M. (1979) On the application of geophysics in the indirect exploration for copper sulphide ores in Finland, in *Geophysics and Geochemistry in the Search for Metallic Ores* (ed. P.J. Hood), Geological Survey of Canada, Economic Geology Report 31, 665–684.
- Key, K.W., Constable, S.C. and Weiss, C.J. (2006) Mapping 3D salt using the 2D marine magnetotelluric method: case study from Gemini Prospect, Gulf of Mexico. *Geophysics*, **71**: B17–B27.
- Keys, W.S. (1990) *Borehole Geophysics Applied to Ground-water Investigations*, Technical Water-Resources Investigations of the United States Geological Survey, Book 2, Chapter E2.
- Keys, W.S. (1996) *A Practical Guide to Borehole Geophysics in Environmental Investigations*, CRC Press, Taylor & Francis, London, UK.
- Kick, J.F. (1985) Depth to bedrock using gravimetry. *Geophysics: The Leading Edge of Exploration*, **4** (4): 38–42.
- Kilty, K.T. (1984) On the origin and interpretation of self potential anomalies. *Geophysical Prospecting*, **32**: 51–62.
- Kim, J.-H., Yi, M.-J., Song, Y., et al. (2007) Application of geophysical methods to the safety analysis of an earth dam. *Journal of Environmental and Engineering Geophysics*, **12**: 221–235.
- King, E.C. and Jarvis, E.P. (1992) Short-offset seismic refraction results near Rothera Station, Antarctic Peninsula. *Antarctic Science*, **4**: 479–480.
- King, E.C., Hindmarsh, R.C.A. and Stokes, C.R. (2009) Formation of mega-scale glacial lineations observed beneath the West Antarctic ice stream. *Nature Geoscience*, DOI: 10.1038/NGEO581.
- King, R.W.P. and Smith, G.S. (1981) *Antennas in Matter*, MIT Press, New York.
- King, W.C., Witten, A.J. and Reed, G.D. (1989) Detection and imaging of buried wastes using seismic wave propagation. *Journal of Environmental Engineering*, **115**: 527–540.
- Kirchner, J.F. and Bentley, C.R. (1979) Seismic short-refraction studies on the Ross Ice Shelf, Antarctica. *Journal of Glaciology*, **24**: 313–319.
- Klimentos, T. (1991) The effects of porosity-permeability-clay content on the velocity of compressional waves. *Geophysics*, **56**: 1930–1939.
- Klimentos, T. and McCann, C. (1990) Relationships among compressional wave attenuation, porosity, clay content, and permeability in sandstones. *Geophysics*, **55**: 998–1014.
- Knapp, R.W. (1991) Fresnel zones in the light of broadband data. *Geophysics*, **56**: 354–359.
- Kneisel, C. and Hauck, C. (2008) Electrical methods, in *Applied Geophysics in Periglacial Environments* (eds C. Hauck and C. Kneisel), Cambridge University Press, Cambridge, UK, 3–27.
- Knight, M.J., Leanard, J.B. and Whiteley, R.J. (1978) Lucas Heights solid waste landfill and downstream leachate transport: a case study in environmental geology. *Bulletin of the International Association of Engineering Geology*, **18**: 45–64.
- Koefoed, O. (1979) *Geosounding Principles*, Elsevier, Amsterdam, The Netherlands.
- Kohnen, H. (1974) The temperature dependance of seismic waves in ice. *Journal of Glaciology*, **13**: 144–147.
- Koppenjan, S.K., Schultz, J.J., Falsetti, A.B., et al. (2003) The application of GPR in Florida for detecting forensic burials. *SAGEEP 2003*: 635–649.
- Korvin, G. (1982) Axiomatic characterization of the general mixture rule. *Geoexploration*, **19**: 267–276.
- Kovacs, A., Gow, A.J. and Morey, R.M. (1995) The in-situ dielectric constant of polar firn revisited. *Cold Regions Science and Technology*, **23**: 245–256.
- Kovalevsky, V., Glinsky, B., Khairdinov, M. and Tatkov, G. (2009) Vibroseismic monitoring of the Baikal Lake Seismic active zone and Taman' mud volcano province. *European Geoscience Union General Assembly 2009, Vienna, Austria*, EGU-2009-4064.
- Kreitz, E. (1982) Evaluation of the Mors salt dome. Results of geological investigations for high-level waste disposal in the Mors Salt Dome, *Proceedings of a Symposium, 18–19 Sept. 1981, Copenhagen*, 74–98.
- Kruppenbach, J.A. and Bedenbender, J.W. (1975) Towed land cable: U.S. Patent 3 923 121.
- Kruppenbach, J.A. and Bedenbender, J.W. (1976) Towed land cable: U.S. Patent 3 954 154.
- Kulessa, B. and Woodward, J. (2007) Introduction to this Special Issue of JEG: The geophysics of glacial and frozen materials. *Journal of Environmental and Engineering Geophysics*, **12** (1): 1–2.
- Kuras, O., Meldrum, P.I., Beamish, D., et al. (2007) Capacitive Resistivity Imaging with towed arrays. *Journal of Environmental and Engineering Geophysics*, **12**: 267–279.
- Kwon, H.-S., Song, Y., Yi, M.-J., et al. (2006) Case histories of electrical resistivity and Controlled-Source Magnetotelluric surveys for the site investigation of tunnel construction. *Journal of Environmental and Engineering Geophysics*, **11**: 237–248.
- Laake, A. and Zaghloul, A. (2009) Estimation of static corrections from geologic and remote-sensing data. *The Leading Edge*, **28**: 192–196.
- Lachassagne, P., Baltassat, J.-M., Legchenko, A. and Machard De Gramont, H. (2005) The links between MRS parameters and the hydrogeological parameters. *Near Surface Geophysics*, **3**: 259–265.

- Lacombe, C., Butt, S., Mackenzie, G., *et al.* (2009) Correcting for water-column variations. *The Leading Edge*, **28**: 198–201.
- LaCoste, L.J.B. (1934) A new type of long period vertical seismograph. *Physics*, **5**: 178–180.
- LaCoste, L.J.B. (1967) Measurement of gravity at sea and in the air. *Rev. Geophys.*, **5**: 477–526.
- Ladwig, K.J. (1983) Electromagnetic induction methods for monitoring acid mine drainage. *Ground Water Monitoring Review*, (Winter): 46–51.
- Lafehr, T.R. (1982) Evaluation of surface and borehole gravity measurements at the Mors salt dome. Results of geological investigations for high-level waste disposal in the Mors Salt Dome, *Proceedings of a Symposium, 18–19 Sept. 1981, Copenhagen*, 196–232.
- Lakshmanan, J. (1991) The generalized gravity anomaly: endoscopic micro-gravity. *Geophysics*, **56**: 712–723.
- Langel R.A. (1987) The main field, in *Geomagnetism*, Vol. 1 (ed. J.A. Jacobs), Academic Press, London, 249–512.
- Langhammer, J. and Landrø, M. (1993) Temperature effects on airgun signatures. *Geophysical Prospecting*, **41**: 737–750.
- Lankston, R.W. (1990) High-resolution refraction data acquisition and interpretation, in *Geotechnical and Environmental Geophysics, Vol I: Review and Tutorial* (ed. S.H. Ward), Society of Exploration Geophysicists, Tulsa, Oklahoma, USA, 45–73.
- Lankston, R.W. and Lankston, M.M. (1986) Obtaining multilayer reciprocal times through phantoming. *Geophysics*, **51**: 45–49.
- Leaman, D.E. (1998) The gravity terrain correction – practical considerations. *Exploration Geophysics*, **29**: 467–471.
- Le Huy, M., Alexandrescu, M., Hulot, G. and Le Mouél, J.-L. (1998) On the characteristics of successive geomagnetic jerks. *Earth Planets Space*, **50**: 723–732.
- Lee and Schwartz. (1930) *Resistivity of Oil-Bearing Beds*, US Bureau of Mines Technical Paper 488.
- Leech, C. and Johnson, R.M. (1992) Locating buried drums using a proton precession magnetometer and magnetic gradiometer, in *Proceedings of the Second International Conference on Construction on Polluted and Marginal Land, 30 June–2 July 1992* (ed. M.C. Forde), Brunel University, 37–49.
- Legchenko, A., Baltassat, J.M., Beauce, A. and Bernard, J. (2002) Nuclear magnetic resonance as a geophysical tool for hydrogeologists. *Journal of Applied Geophysics*, **50**: 21–46.
- Leggo, P.J. (1982) Geological applications of ground impulse radar. *Transactions of the Institute of Mining and Metallurgy B: Applied Earth Sciences*, **91**: B1–5.
- Leggo, P.J. and Leech, C. (1983) Subsurface investigations for shallow mine workings and cavities by the ground impulse radar technique. *Ground Engineering*, **16**: 20–23.
- Leimbach, G. and Löwy, H. (1910) German patent no. 237944.
- Lénat, J.-F. (2007) Retrieving self-potential anomalies in a complex volcanic environment: an SP/elevation gradient approach. *Near Surface Geophysics*, **5**: 161–170.
- Lenham, J.W., Meyer, V.M., Edmonds, H., *et al.* (2006) What lies beneath: surveying the Thames at Woolwich. *Proceedings of ICE, Civil Engineering*, **159**: 32–41. Paper 14177.
- Lennox, D.H. and Carlson, V. (1967) Geophysical exploration for buried valleys in an area north of Two Hills, Alberta. *Geophysics*, **32**: 331–362.
- Lesmes, D.P. and Frye, K.M. (2001) Influence of pore fluid chemistry on the complex conductivity and induced polarization responses of Berea sandstone. *Journal of Geophysical Research*, **106** (B3): 4079–4090.
- Leung, T.M. (1997) Evaluation of seismic refraction using first arrival raytracing, in *Modern Geophysics in Engineering Geology* (eds D.M. McCann, D.M. Eddleston, P.J. Fenning and G.M. Reeves), Geological Society of London, London, 413–416.
- Leung, T.M., Win, A.W., Walker, C.S. and Whiteley, R.J. (1997) A flexible algorithm for seismic refraction interpretation using program REFRAC, in *Modern Geophysics in Engineering Geology* (eds D.M. McCann, D.M. Eddleston, P.J. Fenning and G.M. Reeves), Geological Society of London, London, 399–407.
- Li, Y. and Oldenburg, D.W. (2000) 3-D inversion of induced polarization data. *Geophysics*, **65**: 1931–1945.
- Li, Y. and Constable, S. (2007) 2D marine controlled-source electromagnetic modelling: Part 2 – the effect of bathymetry. *Geophysics*, **72** (2): WA63–WA71.
- Li, Y. and Key, K. (2007) 2D marine controlled-source electromagnetic modelling: Part 1 – an adaptive finite-element algorithm. *Geophysics*, **72** (2): WA51–WA62.
- Li, Y., Shearer, S.E., Haney, M.M. and Dannemiller, N. (2010) Comprehensive approaches to 3D inversion of magnetic data affected by remanent magnetization. *Geophysics*, **75**: L1–L11.
- Lines, L., *et al.* (1995) Integrated reservoir characterization: beyond tomography. *Geophysics*, **60**: 354–364.
- Lipinski, B.A., Sams, J.I., Smith, B.D. and Harbert, W. (2008) Using HEM surveys to evaluate disposal of by-product water from CBNG development in the Powder River Basin, Wyoming. *Geophysics*, **73** (3): B77–B84.
- Liu, S. and Sato, M. (2006) Subsurface water-filled fracture detection by borehole radar: a case history. *Journal of Environmental and Engineering Geophysics*, **11** (2): 95–101.
- Lliboutry, L. (1977) Glaciological problems set by the control of dangerous lakes in Cordillera Blanca, Peru. II. Movement of a covered glacier embedded within a rock glacier. *Journal of Glaciology*, **18**: 255–273.
- Logn, O. and Bölviken, B. (1974) Self potentials at the Joma pyrite deposit, Norway. *Geoexploration*, **12**: 11–28.
- Loke, M.H. (2010) [www.geoelectrical.com/downloads.php](http://www.geoelectrical.com/downloads.php). *Tutorial: 2-D and 3-D Electrical Imaging Surveys*.

- Loke, M.H. and Barker, R.D. (1996a) Rapid least-squares inversion of apparent resistivity pseudosections by a quasi-Newton method. *Geophysical Prospecting*, **44**: 131–152.
- Loke, M.H. and Barker, R.D. (1996b) Practical techniques for 3D resistivity surveys and data inversion. *Geophysical Prospecting*, **44**: 499–523.
- Love, E., Hammack, R., Harbert, W., et al. (2005) Using airborne thermal infrared imagery and helicopter EM conductivity to locate mine pools and discharges in the Kettle Creek watershed, north-central Pennsylvania. *Geophysics*, **70** (6): B73–B81.
- Lowes, F.J., Bondar, T., Golovkov, V.P., et al. (2000) Evaluation of the candidate Main Field model for IGRF 2000 derived from preliminary Ørsted data. *Earth Planets Space*, **52**: 1183–1186.
- Lowrie, W. (1990) Magnetic analysis of rock fabric, in *The Encyclopaedia of Solid Earth Geophysics* (ed. D.E. James), Van Nostrand Reinhold, New York, 698–706.
- Lück, E., Gebbers, R., Ruehlmann, J. and Spangenberg, U. (2009) Electrical conductivity mapping for precision farming. *Near Surface Geophysics*, **7**: 15–25.
- Lück, E. and Müller, M. (2009) Special section on the application of geophysics in agriculture Part II – forward. *Near Surface Geophysics*, **7**: 3.
- Lugg, R. (1979) Marine seismic sources, in *Developments in Geophysical Exploration Methods*, Vol. 1 (ed. A.A. Fitch), Applied Science Publishers, London, 143–203.
- Lumley, J.M., White, J.P., Barnes, G., et al. (2008) *A Superconducting Gravity Gradiometer Tool for Exploration*, Arkex Ltd, UK.
- Luo, Y. and Zhang, G. (1998) *Theory and Application of Spectral Induced Polarisation*, SEG, Tulsa, Oklahoma, USA.
- MacGregor, E., Fell, R., Mostyn, G.R., et al. (1994) The estimation of rock rippability. *Quarterly Journal of Engineering Geology*, **27**: 123–144.
- MacGregor, L.M., Barker, N., Overton, A., et al. (2007) Derisking exploration prospects using integrated seismic and electromagnetic data – a Falkland Islands case study. *The Leading Edge*, **26**: 356–359.
- Mackay, J.R. (1962) Pingos of the Pleistocene McKenzie delta area. *Geographical Bulletin*, **18**: 21–63.
- MacLeod, I.N., Jones, J. and Dai, T.F. (1993) 3-D analytic signals in the interpretation of total magnetic field data at low magnitude latitudes. *Exploration Geophysics*, **679**–688.
- Macmillan, S. and Maus, S. (2005) International Geomagnetic Reference Field – the tenth generation. *Earth Planets Space*, **57**: 1135–1140.
- Macnae, J., Smith, R., Polzer, B.D., et al. (1991) Conductivity-depth imaging of airborne electromagnetic step-response data. *Geophysics*, **56**: 102–114.
- Madden, T.R. and Vozoff, K. (1971) *VLF Model Suite*, 2nd edn, 17 Winthrop Road, Lexington, MA 02173, USA.
- Maillet, R. (1947) The fundamental equations of electrical prospecting. *Geophysics*, **12**: 529–556.
- Maio, X.-G., Moon, W.M. and Milkereit, B. (1995) A multioffset, three-component VSP study in the Sudbury Plain. *Geophysics*, **60**: 341–353.
- Mansoor, N. and Slater, L. (2007) On the relationship between iron concentration and induced polarization in marsh soils. *Geophysics*, **72**: A1–A5.
- Marcak, H. and Golebiowski, T. (2006) A stochastic interpretation of GPR data concerning the location of hydrocarbon plumes. *Near Surface Geophysics*, **4**(3): 163–176.
- Marsden, D. (1993a) Static corrections: a review. Part I. *Geophysics: The Leading Edge*, **12**: 43–49.
- Marsden, D. (1993b) Static corrections: a review. Part II. *Geophysics: The Leading Edge*, **12**: 115–120.
- Marsden, D. (1993c) Static corrections: a review. Part III. *Geophysics: The Leading Edge*, **12**: 210–216.
- Marsh, G.R. (1991) Geophysics and environmentalism. *Geophysics: The Leading Edge*, **10** (8): 32–33.
- Marshall, D.J. and Madden, T.R. (1959) Induced polarization: a study of its causes. *Geophysics*, **24**: 790–816.
- Martner, S.T. and Sparks, N.R. (1959) The electroseismic effect. *Geophysics*, **24**: 297–308.
- Masero, W., Schnegg, P.-A. and Fontes, S.L. (1994) A magneto-telluric investigation of the Araguainha impact structure in Mato Grosso-Goiás, central Brazil. *Geophysical Journal International*, **116**: 366–376.
- Masuda, H. (1981) *Seismic Refraction Analysis for Engineering Study*, OYO Technical Note 10, OYO Corporation, Japan.
- Matsuoka, K., Saito, R. and Naruse, R. (2004) A novel backpackable ice-penetrating radar system. *Journal of Glaciology*, **50**: 147–150.
- Matthews, M.C., Hope, V.S. and Clayton, C.R.I. (1996) The use of surface waves in the determination of ground stiffness profiles. *Proceedings of the Institution of Civil Engineers and Geotechnical Engineering*, **119** (April): 84–95.
- Mayne, P.W. (2007) *Cone Penetration Testing, A Synthesis of Highway Practice*, Transportation Research Board, Washington, DC, USA.
- Mazáč, O., Benes, L., Landa, I. and Skúthán, B. (1990) Geoelectrical detection of sealing foil quality in light-ash dumps, in *Geotechnical and Environmental Geophysics, Vol. 2: Environmental and Groundwater* (ed. S.H. Ward), Society of Exploration Geophysicists, Tulsa, Oklahoma, USA, 113–119.
- McCann, C. and Till, R. (1974) Demonstration of the use of an on-line terminal for teaching geophysical data processing techniques. *International Journal of Mathematics in Education Science and Technology*, **5**: 729–737.
- McCann, D.M., Jackson, P.D. and Fenning, P.J. (1988) Comparison of the seismic and ground-probing radar methods in geological surveying. *IEE Proceedings*, **135**: 380–390.
- McClymont, A.F., Green, A.G., Streich, R., et al. (2008) Visualization of active faults using geometric attributes of 3D GPR data: an example

- from the Alpine Fault Zone, New Zealand. *Geophysics*, **73** (2): B11–B23.
- McConnell, T. and Dragoset, W. (2006) Introduction to this special section: magnetic gradiometry. *The Leading Edge*, **25**: 45.
- McDowell, P.W., Barker, R.D., Butcher, A.P., et al. (2002) *Geophysics in Engineering Investigations*, Construction Industry Research and Information Association, Geological Society Engineering Geology Special Publication 19.
- McElhinny, M.W. (1973) *Palaeomagnetism and Plate Tectonics*, Cambridge University Press, Cambridge, UK.
- McGee, T.M. (1990) The use of marine seismic profiling for environmental assessment. *Geophysical Prospecting*, **38**: 861–880.
- McGinnis, L.D. and Jensen, T.E. (1971) Permafrost-hydrogeologic regimen in two ice-free valleys, Antarctica, from electrical depth sounding. *Quaternary Research*, **1**: 389–409.
- Mclean, M. and Reitmeyr, G. (2005) An airborne gravity survey south of the Prince Charles Mountains, east Antarctica. *Terra Antarctica*, **12** (2): 99–108.
- McNeill, J.D. (1980) *Electromagnetic Terrain Conductivity Measurement at Low Induction Numbers*, Technical Note TN-6, Geonics Ltd., Mississauga, Ontario, Canada.
- McNeill, J.D. (1985) *EM34-3 Measurements at Two Intercoil Spacings to Reduce Sensitivity to Near-Surface Material*, Technical Note TN-19, Geonics Ltd., Mississauga, Ontario, Canada.
- McNeill, J.D. (1990) Use of electromagnetic methods for groundwater studies, in *Geotechnical and Environmental Geophysics, Vol. 1: Review and Tutorial* (ed. S.H. Ward), Society of Exploration Geophysicists, Tulsa, Oklahoma, USA, 191–218.
- McNeill, J.D. (1996) *Why doesn't Geonics Limited build a multi-frequency EM31 or EM38?* Geonics Ltd., Mississauga, Canada.
- McNeill, J.D., Bosner, M. and Snelgrove, F.B. (1988) *A borehole induction logger for monitoring groundwater contamination*, Geonics Technical Note TN-25, Geonics Ltd, Mississauga, Canada.
- McNeill, J.D. and Labson, V.F. (1991) Geological mapping using VLF radiofields, in *Electromagnetic Methods in Applied Geophysics, Vol. 2: Applications, Part B* (ed. M.N. Nabighian), Society of Exploration Geophysicists, Tulsa, Oklahoma, USA, 521–640.
- McQuillin, R.M., Bacon, M. and Barclay, W. (1984) *An Introduction to Seismic Interpretation*, Graham & Trotman, London, UK.
- Meigh, A.C. (1987) *Cone Penetration Testing: Methods and Interpretation* (CIRIA ground engineering report: in situ testing), CIRIA, Butterworths, London, UK.
- Meinardus, H., Schleicher, K. and Sudhakar, V. (1993) A processing sequence for turning wave imaging. *Extended Abstracts of 62nd Annual International Meeting, Society of Exploration Geophysicists, New Orleans, Louisiana, USA, October 1992*.
- Meiser, P. (1962) A method for quantitative interpretation of self potential measurements. *Geophysical Prospecting*, **10**: 203–218.
- Mellett, J.S. (1993) Bathymetric studies of ponds and lakes using ground penetrating radar. *Advanced Ground Penetrating Radar: Technologies and Applications*, 26–28 Oct. 1993, 257–266.
- Menzies, B.K. (2001) *Near-surface site characterisation by ground stiffness profiling using surface wave geophysics*, in *Instrumentation in Geotechnical Engineering* (eds K.R. Saxena and V.M. Sharma), Oxford & IBH Publishing Co., New Delhi, India, 43–71.
- Merriam, J.B. (2007) Induced polarization and surface electrochemistry. *Geophysics*, **72** (4): F157–F166.
- Merrill, R.T. (1990) Rock magnetism, in *The Encyclopaedia of Solid Earth Geophysics* (ed. D.E. James), Van Nostrand Reinhold, New York, 946–950.
- Meyer De Stadelhofen, C. and Julliard, T. (1987) Truth is an instance of error temporarily appealing. *Geophysics: The Leading Edge of Exploration*, **6** (2): 38.
- Miller, C.R., Allen, A.L., Speece, M.A., et al. (2005) Land streamer aided geophysical studies at Saqqara, Egypt. *Journal of Environmental and Engineering Geophysics*, **10**: 371–380.
- Miller, J.M., Roberts, P.D., Symons, G.D., et al. (1977) A towed seabed gamma-ray spectrometer for continental shelf surveys. *Nuclear Techniques and Mineral Resources*, International Atomic Energy Agency, Vienna, 465–498.
- Miller, R.D., Pullan, S.E., Waldner, J.S. and Haeni, F.P. (1986) Field comparison of shallow seismic sources. *Geophysics*, **51**: 2067–2092.
- Miller, R.D., Pullan, S.E., Steeples, D.W. and Hunter, J.A. (1992) Field comparison of shallow seismic sources near Chino, California. *Geophysics*, **57**: 693–709.
- Miller, R.D., Pullan, S.E., Steeples, D.W. and Hunter, J.A. (1994) Field comparison of shallow P-wave seismic sources near Houston, Texas. *Geophysics*, **59**: 1713–1728.
- Miller, R.D., Anderson, N.L., Feldman, H.R. and Franseen, E.K. (1995) Vertical resolution of a seismic survey in stratigraphic sequences less than 100 m deep in southeastern Kansas. *Geophysics*, **60**: 423–430.
- Miller, H.G. and Singh, V. (1994) Potential field tilt – a new concept for location of potential field sources. *Journal of Applied Geophysics*, **32** (2–3): 213–217.
- Mills, T., Hoekstra, P., Blohm, M. and Evans, L. (1988) Time-domain electromagnetic soundings for mapping seawater intrusion in Monterey County, CA. *Ground Water*, **26**: 771–782.
- Milsom, J. (2003) *Field Geophysics*, 3rd edn, John Wiley & Sons Ltd, Chichester, UK.
- Mitsuhata, Y., Uchida, T., Matsuo, K., et al. (2006) Various-scale electromagnetic investigations of high-salinity zones in a coastal plain. *Geophysics*, **71** (6): B167–B173.
- Mittet, R. (2008) Normalized amplitude ratios for frequency-domain CSEM in very shallow water. *First Break*, **26** (11): 47–54.
- Monier-Williams, M.E., Greenhouse, J.P., Mendes, J.M. and Ellert, N. (1990) Terrain conductivity mapping with topographic corrections at

- three waste disposal sites in Brazil, in *Geotechnical and Environmental Geophysics, Vol. 2: Environmental and Groundwater* (ed. S.H. Ward), Society of Exploration Geophysicists, Tulsa, Oklahoma, USA, 41–55.
- Monk, D., Ross, J. and Mooney, W. (2004) A new look and an old source. *2004 CSEG National Convention*.
- Monteiro, S.F.A., Mateus, A., Figueiras, J. and Gonçalves, M.A. (2006) Mapping groundwater contamination around a landfill facility using the VLF-EM method – a case study. *Journal of Applied Geophysics*, **60**: 115–125.
- Montesinos, F.G., Camacho, A.G., Nunes, J.C., et al. (2003) A 3-D gravity model for a volcanic crater in Terceira Island (Azores) *Geophysical Journal International*, **154**: 393–406.
- Mooney, H.M. and Wetzel, W.W. (1956) *The Potentials about a Point Electrode*, University of Minnesota Press, Minnesota, USA.
- Moorman, B.J., Judge, A.S. and Smith, D.G. (1991) Examining fluvial sediments using ground penetrating radar in British Columbia. *Current Research: Part A*. Geological Survey of Canada, Paper 91-1A.
- Moran, M.L., Greenfield, R.J. and Arcone, S.A. (2003) Modeling GPR radiation and reflection characteristics for a complex temperate glacier bed. *Geophysics*, **68**: 559–565.
- Morelli, C. (1971) *The International Gravity Standard Net 1971 (IGSN 71)*, Special Publication No. 4, International Association of Geodesy, Bureau Central de l'Association Internationale de Géodésie, 19 Rue Auber, 75009, Paris, France.
- Morey, M. (1974) Continuous sub-surface profiling by impulse radar. *Subsurface Exploration for Underground Excavation and Heavy Construction*, ASCE Specialty Conference, Henneker, 213–232.
- Moritz, H. (1980) Geodetic Reference System 1980. *Journal of Geodesy*, **74**: 128–162.
- Morris, E. (1992) *Geophysical Lab Manual for Lotus 1-2-3 and Quattro Pro*, EcoTech Research Ltd, Regina, Canada.
- Moussa, M. (2001) Gamma-ray spectrometry: a new tool for exploring archaeological sites: a case study from East Sinai, Egypt. *Journal of Applied Geophysics*, **48**: 137–142.
- Moxhay, A.L., Tinsley, R.D. and Sutton, J.A. (2001) Monitoring of soil stiffness during ground improvement using seismic surface waves. *Ground Engineering* (January): 34–37.
- Moysey, S., Knight, R.J. and Jol, H.M. (2006) Texture-based classification of ground-penetrating radar images. *Geophysics*, **71** (6): K111–K118.
- Müller, M., Kurz, G. and Yaramancı, U. (2009) Influence of tillage methods on soil water content and geophysical properties. *Near Surface Geophysics*, **7**: 27–36.
- Mushayandebvu, M.F., Lesur, V., Reid, A.B. and Fairhead, J.D. (2004) Grid Euler deconvolution with constraints for 2D structures. *Geophysics*, **69**: 489–496.
- Mutton, A.J. (2000) The application of geophysics during evaluation of the Century zinc deposit. *Geophysics*, **65**: 1946–1960.
- Nabighian, M.N. (1972) The analytic signal of two-dimensional magnetic bodies with polygonal cross-section; its properties and use for automated anomaly interpretation. *Geophysics*, **37**(3): 507–517.
- Nabighian, M.N. (1984) Toward a three-dimensional automatic interpretation of potential field data via generalized Hilbert transforms: fundamental relations. *Geophysics*, **49**: 780–786.
- Nabighian, M.N. (1987) *Electromagnetic methods in applied geophysics, Volume 1 Theory*, Investigations in Geophysics No. 3, Society of Exploration Geophysicists, Tulsa, Oklahoma, USA, 513 pp.
- Nabighian, M.N. (ed.). 1991. *Electromagnetic methods in applied geophysics, Volume 2: Application*. Investigations in Geophysics No. 3, Society of Exploration Geophysicists, Tulsa, Oklahoma, USA, 2 volumes (A and B), 972 pp.
- Nabighian, M.N. and Asten, M.W. (2002) Metalliferous mining geophysics – state of the art in the last decade of the 20th century and then beginning of the new millennium. *Geophysics*, **67**: 964–978.
- Nabighian, M.N., Grauch, V.J.S., Hansen, R.O., et al. (2005a) The historical development of the magnetic method in exploration. *Geophysics*, **70** (6): 33ND–61ND.
- Nabighian, M.N., Ander, M.E., Grauch, V.J.S., et al. (2005b) Historical development of the gravity method in exploration. *Geophysics*, **70** (6): 63ND–89ND.
- Nabighian, M.N. and MacNae, J.C. (1991) Time domain electromagnetic prospecting methods, in *Electromagnetic Methods in Applied Geophysics, Vol 2A* (ed. M.N. Nabighian), Society of Exploration Geophysicists, Tulsa, Oklahoma, USA, 427–520.
- Nafe, J.E. and Drake, C.L. (1963) Physical properties of marine sediments, in *The Sea*, Vol. 3 (ed. M.N. Hill), Interscience Publishers, New York, 794–815.
- Nagata, T. (1961) *Rock Magnetism*, Maruzen, Tokyo.
- Narod, B.B. and Clarke, G.K.C. (1994) Miniature high-power impulse transmitter for radio-echo sounding. *Journal of Glaciology*, **40**: 190–194.
- Naudts, L., De Batist, M., Greinert, J. and Artemov, Y. (2009) Geo- and hydro-acoustic manifestations of shallow gas and gas seeps in the Dnepr paleodelta, northwestern Black Sea. *The Leading Edge*, **29**: 1030–1040.
- Nayak, P.N. (1981) Electromechanical potential in surveys for sulphides. *Geoexploration*, **18**: 311–320.
- Nazarian, S., Stokoe, K.H. and Hudson, W.R. (1983) Use of spectral analysis of surface waves method for determination of modulii and thickness of pavement systems. *Transport. Res. Record*, **930**: 38–45.
- Neal, A. (2004) Ground-penetrating radar and its use in sedimentology: principles, problems and progress. *Earth Science Reviews*, **66**: 261–330.
- Neal, A. and Roberts, C.L. (2000) Applications of ground-penetrating radar (GPR) to sedimentological, geomorphological and geoarchaeological studies in coastal environments, in *Coastal and Estuarine Environments: Sedimentology, Geomorphology and Geoarchaeology* (eds

- K. Pye and J.R.L. Allen), Geological Society Special Publications, London, 139–179.
- Nelson, R.G. and Haigh, J.H. (1990) Geophysical investigations of sink-holes in lateritic terrains, in *Geotechnical and Environmental Geophysics, Vol. 3: Geotechnical* (ed. S.H. Ward), Society of Exploration Geophysicists, Tulsa, Oklahoma, US, 133–153.
- Nestvold, E.O. (1992) 3-D seismics: is the promise fulfilled? *Geophysics: The Leading Edge*, **11** (6): 12–19.
- Nettleton, L.L. (1939) Determination of density for reduction of gravimeter observations. *Geophysics*, **4**: 176–183.
- Nettleton, L.L. (1940) *Geophysical Prospecting for Oil*, McGraw-Hill, New York, USA.
- Nettleton, L.L. (1942) Gravity and magnetic calculations. *Geophysics*, **7**: 293–310.
- Nettleton, L.L. (1954) Regionals, residuals and structures. *Geophysics*, **19**: 1–22.
- Nettleton, L.L. (1971) *Elementary Gravity and Magnetics for Geologists and Seismologists*, Society of Exploration Geophysicists, Monograph Series No. 1, Tulsa, Oklahoma, USA.
- Nettleton, L.L. (1976) *Gravity and Magnetics in Oil Exploration*, McGraw-Hill, New York, USA.
- New, B.M. (1985) An example of tomographic and Fourier microcomputer processing of seismic records. *Quarterly Journal of Engineering Geology*, **18**: 335–344.
- Newman, G.A. (1994) A study of downhole electromagnetic sources for mapping enhanced oil recovery processes. *Geophysics*, **59**: 534–545.
- Nichol, D. and Reynolds, J.M. (2001) Ground-penetrating radar survey to detect sub-slab voids beneath the East Promenade at Rhyl. *Proceedings of the Institution of Civil Engineers Water and Maritime Engineering*, **148**: 47–56.
- Nichol, D. and Reynolds, J.M. (2002) Application of reflection seismology to foundation investigations at A5 Pont Melin Rûg, North Wales. *Quarterly Journal of Engineering Geology and Hydrogeology*, **35**: 247–256.
- Nichol, D., Lenham, J.W. and Reynolds, J.M. (2003) Application of ground-penetrating radar to investigate the effects of badger setts on slope stability at St Asaph Bypass, North Wales. *Quarterly Journal of Engineering Geology and Hydrogeology*, **36**: 143–153.
- Nicholls, F. (1955) Effect of earthquake on elephants. *Journal of the Bombay Natural History Society*, **53**: 585.
- Nickel, H., Sender, F., Thierbach, R. and Weichert, H. (1983) Exploring the interior of salt domes from boreholes. *Geophysical Prospecting*, **31**: 131–148.
- Nilsson, B. (1983) *A New Borehole Radar System. Borehole Geophysics for Mining and Geotechnical Applications*, Geological Survey of Canada Paper 85-27, Ottawa, Canada.
- Nissen, J. (1986) A versatile electromagnetic modelling program for 2D structures. *Geophysical Prospecting*, **34**: 1099–1110.
- Nobes, D.C., Rother, H., Van De Kruik, J. and Jol, H.M. (2006) Radar ‘lensing’ by a small river: can a layer of surface water improve the signal? *Near Surface Geophysics*, **4**: 69–74.
- Noel, M. and Walker, R. (1990) Development of an electrical resistivity tomography system for imaging archaeological structures, in *Archaeometry ‘90* (eds E. Pernicka and G.A. Wagner), Birkhauser, Basel, 767–776.
- Nordsiek, S. and Weller, A. (2008) A new approach to fitting induced-polarization spectra. *Geophysics*, **73** (6): F235–F245.
- Nowell, D. (1999) Gravity terrain corrections: an overview. *Journal of Applied Geophysics*, **42**: 117–134.
- Nunn, K.R. (1978) Geophysical surveys at the landfill sites in the West Midlands. *Proceedings of a Symposium on the Engineering Behaviour of Industrial and Urban Fill, University of Birmingham, April 1978*, Midland Geotechnical Society, C45–C53.
- Nyquist, J.E. and Corry, C.E. (2002) Self-potential: the ugly duckling of environmental geophysics. *The Leading Edge*, **21**: 446–451.
- O’Connell-Rodwell, C.E. (2007) Keeping an “ear” to the ground: seismic communication in elephants. *Physiology*, **22**: 287–294.
- Odins, J. (1975) *The Application of Seismic Refraction to Groundwater Studies of Unconsolidated Sediments*. Unpublished MSc thesis. University of New South Wales, Australia.
- Ogilvy, A.A., Ayed, M.A. and Bogoslovsky, V.A. (1969) Geophysical studies of water leakages from reservoirs. *Geophysical Prospecting*, **17**: 36–62.
- Ogilvy, A.A. and Kuzmina, E.N. (1972) Hydrogeologic and engineering geologic possibilities for employing the method of induced potentials. *Geophysics*, **37**: 839–861.
- Ogilvy, R.D. and Lee, A.C. (1989) *KHFILTER: A Computer Program to Generate Current Density Pseudosections from VLF-EM In-Phase Data*, British Geological Survey, Technical Report WK/89/6R.
- Ogilvy, R.D., Cuadra, A., Jackson, P.D. and Monte, J.L. (1991) Detection of an air-filled drainage gallery by the VLF resistivity method. *Geophysical Prospecting*, **39**: 845–859.
- Ohta, Y. and Goto, N. (1978) Empirical shear wave velocity equations in terms of characteristic soil indexes. *Earthquake Engineering and Structural Dynamics*, **6**: 167–187.
- Olhoeft, G.R. (1985) Low-frequency electrical properties. *Geophysics*, **50**: 2492–2503.
- Olsen, N. and Mandea, M. (2007a) Investigation of a secular variation impulse using satellite data: the 2003 geomagnetic jerk. *Earth and Planetary Science Letters*, **255**: 94–105.
- Olsen, N. and Mandea, M. (2007b) Will the magnetic North pole move to Siberia? *Eos*, **88**: 293.

- Olsson, O., Sandberg, E. and Nilsson, B. (1983) *The Use of Borehole Radar for the Detection of Fractures in Crystalline Rock*, Stripa Project Report IR-83-06, SKB, Stockholm, Sweden.
- Olsson, O., Falk, L., Forslund, O., et al. (1990) *Crosshole Investigations: Results from Borehole Radar Investigations*, Stripa Project Technical Report 87-11, Stockholm, Sweden.
- O'Neill, D.J. and Merrick, N.P. (1984) A digital linear filter for resistivity sounding with a generalized electrode array. *Geophysical Prospecting*, **32**: 105–123.
- Oppiger, G.L. (1984) Three-dimensional terrain corrections for mise-à-la-masse and magnetic resistivity surveys. *Geophysics*, **49**: 1718–1729.
- Optim LLC (2002) *User's Manual SeisOpt® @2D™ Version 3.0*, Optim LLC, Reno, USA.
- Ordnance Survey (2008) *A Guide to Coordinate Systems in Great Britain v.1.9*. D00659, Ordnance Survey, UK.
- O'Reilly, W. (1984) *Rock and Mineral Magnetism*, Blackie, Glasgow, UK.
- Osterkamp, T.E. and Jurick, R.W. (1980) Detecting massive ground ice in permafrost by geophysical methods. *Northern Engineer*, **12** (4): 27–30.
- Ostrander, W.J. (1984) Plane-wave reflection coefficients for gas sands at non-normal angles of incidence. *Geophysics*, **49**: 1637–1648.
- Owen, T.E. (1983) Detection and mapping of tunnels and caves, in *Developments in Geophysical Exploration Methods, Vol. 5* (ed. A.A. Fitch), Applied Science Publishers, 161–258.
- Paal, G. (1965) Ore prospecting based on VLF-radio signals. *Geoexploration*, **3**: 139–147.
- Palacky, G.J. (1986) *Airborne Resistivity Mapping*. Geological Survey of Canada Paper.
- Palacky, G.J. (1991) Application of the multi-frequency horizontal loop EM method in overburden investigations. *Geophysical Prospecting*, **39**: 1061–1082.
- Palacky, G.J. and West, G.F. (1991) Airborne electromagnetic methods, in *Electromagnetic Methods in Applied Geophysics, Vol. 2B* (ed. M.N. Nabighian), Society of Exploration Geophysicists, Tulsa, Oklahoma, US, 811–879.
- Palacky, G.J. and Stephens, L.E. (1992) Detection of sub-bottom ice-bonded permafrost on the Canadian Beaufort Shelf by ground electromagnetic measurements. *Geophysics*, **57**: 1419–1427.
- Palmer, D. (1980) *The Generalised Reciprocal Method of Seismic Refraction Interpretation*, Society of Exploration Geophysicists, Tulsa, Oklahoma, USA.
- Palmer, D. (1991) The resolution of narrow low-velocity zones with the generalised reciprocal method. *Geophysical Prospecting*, **39**: 1031–1060.
- Palmer, D. (2009) Integrating long and short wavelength time and amplitude statics. *First Break*, **27** (6): 57–65.
- Pant, S.J. (2004) Tracing groundwater flow by mise-à-la-masse measurement of injected seawater. *Journal of Environmental and Engineering Geophysics*, **9** (3): 155–165.
- Pant, S.R. and Reynolds, J.M. (2000) Application of electrical imaging techniques for the investigation of natural dams: an example from the Thulagi Glacier Lake, Nepal. *Journal of the Nepal Geological Society*, **22**: 211–218.
- Pantze, R., Malmqvist, M. and Kristensson, G. (1986) Directional EM measurements in boreholes, in *Borehole Geophysics for Mining and Geotechnical Applications* (ed. P.G. Killeen), Geological Survey of Canada Paper, 79–88.
- Parasnis, D.S. (1966) *Mining Geophysics*, Elsevier, Amsterdam, The Netherlands.
- Parasnis, D.S. (1967) Three-dimensional electric mise-à-la-masse survey of an irregular lead-zinc-copper deposit in Central Sweden. *Geophysical Prospecting*, **15**: 407–437.
- Parasnis, D.S. (1973) *Mining Geophysics*, Elsevier, Amsterdam, The Netherlands.
- Parasnis, D.S. (1986) *Principles of Applied Geophysics*, Chapman & Hall, London.
- Parasnis, D.S. (1991) Large-layout harmonic field systems, in *Electromagnetic Methods in Applied Geophysics, Vol. 2A* (ed. M.N. Nabighian), Society of Exploration Geophysicists, Tulsa, Oklahoma, USA, 271–283.
- Park, C.B., Miller, R.D. and Xia, J. (1999) Multichannel analysis of surface waves. *Geophysics*, **64** (3): 800–808.
- Park, C.B., Miller, R.D., Xia, J. and Ivanov, J. (2007) Multichannel analysis of surface waves (MASW) – active and passive methods. *The Leading Edge*, **26**: 60–64.
- Park, C.B. and Miller, R.D. (2008) Roadside passive Multichannel Analysis of Seismic Waves (MASW). *Journal of Environmental & Engineering Geophysics*, **13**: 1–11.
- Parker, R.L. (1995) Improved Fourier terrain correction, Part I. *Geophysics*, **60**: 1007–1017.
- Parker, R.L. (1996) Improved Fourier terrain correction, Part II. *Geophysics*, **61**: 365–372.
- Parker, R.L. and Zumberge (1989) An analysis of geophysical experiments to test Newton's Law of Gravity. *Nature*, **342**: 29–32.
- Parkomenko, E.I. (1967). *Electrical Properties of Rocks*. Plenum Press, New York, USA.
- Parlowski, J., Lewis, R., Dobush, T. and Valleur, N. (1995) An integrated approach for measuring and processing geophysical data for the detection of unexploded ordnance. *Proceedings of SAGEEP-95, Orlando, USA*, 965–974.
- Parra, J.O. (1984) Effects of pipelines on spectral induced-polarization surveys. *Geophysics*, **49**: 1979–1992.
- Pasion, L.R., Billings, S.D., Kingdon, K.A., et al. (2008) Cooperative inversion of time domain electromagnetic and magnetometer data for

- the discrimination of unexploded ordnance. *Journal of Environmental and Engineering Geophysics*, **13**: 193–210.
- Patella, D. (1997a) Introduction to ground surface self-potential tomography. *Geophysical Prospecting*, **45**: 653–681.
- Patella, D. (1997b) Self-potential global tomography including topographic effects. *Geophysical Prospecting*, **45**: 843–863.
- Patella, D. (1998) Erratum. *Geophysical Prospecting*, **46**: 103.
- Patella, D. and Schiavone, D. (1977) Comparative analysis of time-domain and frequency-domain in the induced-polarization prospecting method. *Geophysical Prospecting*, **25**: 496–511.
- Paterson, N.R. and Ronka, V. (1971) Five years of surveying with the very low frequency electromagnetic method. *Geoexploration*, **9**: 7–26.
- Patterson, D.A., Davey, J.C., Cooper, A.H. and Ferris, J.K. (1995) The investigation of dissolution subsidence incorporating microgravity geophysics at Ripon, Yorkshire. *Quarterly Journal of Engineering Geology*, **28**: 83–94.
- Peddie, N.W. (1982) International geomagnetic reference field: the third generation. *Journal of Geomagnetism and Geoelectricity*, **34**: 309–326.
- Pedersen, L.B., Qian, W., Dynesius, L. and Zhang, P. (1994) An airborne tensor VLF system: from concept to realization. *Geophysical Prospecting*, **42**: 863–883.
- Pedersen, L.B. and Becken, M. (2005) Equivalent images derived from very-low-frequency (VLF) profile data. *Geophysics*, **70** (3): G43–G50.
- Pellerin, L., Holliger, K., Slater, L. and Yaramanci, U. (2009) Foreword – Special issue on hydrogeophysics – methods and processes. *Near Surface Geophysics*, **7**: 303–305.
- Pelton, W.H. and Smith, P.K. (1976) Mapping porphyry copper deposits in the Philippines with IP. *Geophysics*, **41**: 106–122.
- Pelton, W.H., Ward, S.H., Hallof, P.G., et al. (1978) Mineral discrimination and removal of inductive coupling with multi-frequency induced polarization. *Geophysics*, **43**: 588–609.
- Pelton, W.H., Sill, W.R. and Smith, B.D. (1983) Interpretation of complex resistivity and dielectric data, Part I. *Geophysical Transactions*, **29**: 297–330.
- Pemberton, R. (1962) Airborne electromagnetics in review. *Geophysics*, **27**: 691–713.
- Pendick, D. (1995) And here is the eruption forecast. *New Scientist*, **145** (1959): 26–29.
- Perrone, A., Iannuzzi, A., Lapenna, V., et al. (2004) High-resolution imaging of the Varco d'Izzo earthflow. *Journal of Applied Geophysics*, **56**: 17–29.
- Peters, L.J. (1949) The direct approach to magnetic interpretation and its practical application. *Geophysics*, **14**: 290–320.
- Petersen, N. (1990) Curie temperature, in *The Encyclopaedia of Solid Earth Geophysics* (ed. D.E. James), Van Nostrand Reinhold, New York, 166–173.
- Petrovski, A. (1928) The problem of a hidden polarized sphere. *Philosophical Magazine*, **5**: 334–358.
- Pfaffling, A., Haas, C. and Reid, J.E. (2007) Direct helicopter EM – sea-ice thickness inversion assessed with synthetic and field data. *Geophysics*, **72** (4): F127–F137.
- Phadke, S. and Kanasewich, E.R. (1990) The resolution possible in imaging with diffracted seismic waves. *Geophysical Prospecting*, **38**: 913–931.
- Poldini, E. (1939) Geophysical exploration by spontaneous polarization methods. *Mining Magazine*, **60**: 22–27; 90–94.
- Porsani, J.L. and Sauck, W.A. (2007) Ground-penetrating radar profiles over multiple steel tanks: artifact removal through effective data processing. *Geophysics*, **72** (6): J77–J83.
- Poster, C. and Cope, C. (1975) The location of backfilled quarries by high-resolution gravimetry. *The Arup Journal*, **10**: 7–9.
- Powell, J.J.M. and Butcher, A.P. (1991) Assessment of ground stiffness from field and laboratory tests. *Proceedings of the 10th European Conference on Soil Mechanics and Foundation Engineering*, Florence, May 1991, 153–156.
- Pratt, J.H. (1859) On the influence of the ocean on the plumb-line in India. *Philosophical Transactions of the Royal Society of London*, **149**: 779–796.
- Prentice, J.E. and McDowell, P. (1976) Geological and geophysical methods in the location and design of services. *Underground Services*, **4**: 15–18.
- Primdahl, F. (1979) The fluxgate magnetometer. *Journal of Physics E: Soc. Instrum.*, **12**: 241–253.
- Pringle, J.K., Lenham, J.W. and Reynolds, J.M. (2009) GPR investigations to characterize Medieval and Roman foundations under existing shop premises: a case study from Chester, Cheshire, UK. *Near Surface Geophysics*, **7**: 93–100.
- Pullan, S.E. and Hunter, J.A. (1990) Delineation of buried bedrock valleys using the optimum offset shallow seismic reflection technique, in *Geotechnical and Environmental Geophysics*, Vol. 3: *Geotechnical* (ed. S.H. Ward), Society of Exploration Geophysicists, Tulsa, Oklahoma, USA, 75–89.
- Pullan, S.E.C. and Subcommittee of the SEG Engineering and Ground-water Committee (1990) Recommended standard for seismic (/radar) files in the personal computer environment. *Geophysics*, **55**: 1260–1271.
- Pye, K. and Croft, D.J. (2003) *Forensic Geoscience: Principles, Techniques and Applications*. Geological Society of London Special Publication, **232**: 11–20.
- Quoqiang, X., Jianping, S. and Xian, Y. (2004) Detecting shallow caverns in China using TEM. *The Leading Edge*, **23**: 694–695.
- Rampton, V.N. and Walcott, R.I. (1974) Gravity profiles across ice-cored topography. *Canadian Journal of Earth Sciences*, **11**: 110–122.
- Rana, B., Shrestha, A.B., Reynolds, J.M., et al. (2000) Hazard assessment of the Tsho Rolpa Glacier Lake and ongoing remediation measures. *Journal of the Nepal Geological Society*, **22**: 563–570.

- Rao, C.V., Pramanik, A.G., Kumar, G.V.R.K. and Raju, M.L. (1994) Gravity interpretation of sedimentary basins with hyperbolic density contrast. *Geophysical Prospecting*, **42**: 825–839.
- Rao, D.B., Prakash, M.J. and Babu, N.R. (1993) Gravity interpretation using Fourier transforms and simple geometrical models with exponential density contrast. *Geophysics*, **58**: 1074–1083.
- Ratcliff, D.W., Gray, S.H. and Whitmore, N.D. (1991) Seismic imaging of salt structure in the Gulf of Mexico. *Expanded Abstracts of 61st Annual International Meeting of SEG*, 1164–1167.
- Rathor, B.S. (1977) Transient electromagnetic fields over a two-layer polarizable earth. *Geoexploration*, **15**: 137–149.
- Redman, J.D. (2009) Contaminant mapping, in *Ground Penetrating Radar: Theory and Application* (ed. H.M. Jol), Elsevier, Amsterdam, 247–269.
- Redmayne, D.W. and Turbitt, T. (1990) Ground motion effects of the Lockerbie air crash impact. *Geophysical Journal International*, **101**: 293.
- Redpath, B.B. (1973) *Seismic Refraction Exploration for Engineering Site Investigation*. National Technical Information Service.
- Reeves, C.V. and Macleod, I.N. (1986) A standard structure for geophysical data files on popular microcomputers. *First Break*, **4** (2): 9–17.
- Regueiro, J. (1990a) Seam waves: what they are used for (part 1). *Geophysics: The Leading Edge*, **9** (4): 19–23.
- Regueiro, J. (1990b) Seam waves: what they are used for (part 2). *Geophysics: The Leading Edge*, **9** (8): 32–34.
- Reid, A.B. (1980) Aeromagnetic survey design. *Geophysics*, **45**: 973–976.
- Reid, A.B., Allsop, J.M., Granser, H., et al. (1990) Magnetic interpretation in three dimensions using Euler deconvolution. *Geophysics*, **55**: 80–91.
- Reid, J.E., Kimber, B.A. and Worby, A.P. (2004) Calibration of a low induction number electromagnetic instrument for sea ice thickness measurements. *Journal of Environmental and Engineering Geophysics*, **9**: 43–50.
- Reilly, J.M. and Comeaux, L.B. (1993) 3D concentric circle survey: processing for steep dip imaging. *55th Meeting EAEG Stavanger Norway Extended Abstracts*, Paper A002.
- Renata, D. (1977) Electromechanical phenomena associated with earthquakes. *Geophysical Surveys*, **3**: 157–174.
- René, R.M., Kim, K.Y. and Park, C.H. (2008) Intra-inversion filtering for overlapping magnetic fields of unexploded ordnance (UXO), clutter and geology. *Journal of Environmental and Engineering Geophysics*, **13**: 147–164.
- Renner, R.G.B., Sturgeon, L.J.S. and Garrett, S.W. (1985) *Reconnaissance Gravity and Aeromagnetic Surveys of the Antarctic Peninsula*, British Antarctic Survey, Scientific Reports No. 110, Natural Environment Research Council, UK.
- Reynolds, J.M. (1982) Electrical resistivity of George VI Ice Shelf, Antarctica Peninsula. *Annals of Glaciology*, **3**: 279–283.
- Reynolds, J.M. (1985) Dielectric behaviour of firn and ice from the Antarctic Peninsula, Antarctica. *Journal of Glaciology*, **31** (109): 253–262.
- Reynolds, J.M. (1987a) The role of surface geophysics in the assessment of regional groundwater potential in northern Nigeria, in *Planning and Engineering Geology* (eds M.G. Culshaw, F.G. Bell, J.C. Cripps and M. O'Hara), Geological Society Engineering Group Special Publication No. 4, 185–190.
- Reynolds, J.M. (1987b) Dielectric analysis of rocks: a forward look. *Geophysical Journal of the Royal Astronomical Society*, **89**: 457.
- Reynolds, J.M. (1988) Surface geophysical anomalies associated with stratabound mineralisation at Sourton Tors, north-west Dartmoor. *Proceedings of the Usher Society*, **7**: 106.
- Reynolds, J.M. (1990a) High-resolution seismic reflection surveying of shallow marine and estuarine environments. *Marine Geophysical Researches*, **12**: 41–48.
- Reynolds, J.M. (1990b) Electrical properties of ice and the implications for ground penetrating radar. *Geophysical Journal International*, **101**: 268.
- Reynolds, J.M. (1991a) The need for recognized standards of applied geophysical software and the geophysical education of software users. *Computers and Geosciences*, **17**: 1099–1104.
- Reynolds, J.M. (1991b) The determination of the degree of 'Alkali Silica Reaction' (Concrete Cancer) using dielectric analysis: preliminary results. *Geophysical Journal International*, **104**: 674.
- Reynolds, J.M. (1994) Resolution and differentiation of sub-surface materials using multi-method geophysical surveys, in *Proceedings of 2nd International Conference on Construction on Polluted and Marginal Land*, 30 June–2 July 1992, Brunel University, London (ed. M.C. Forde), Engineering Technics Press, Edinburgh, 63–67.
- Reynolds, J.M. (1995) Environmental geophysics: towards the new millennium. *Geoscientist*, **5**: 21–23.
- Reynolds, J.M. (2002) The role of geophysics in the investigation of an acid tar lagoon, Llwyneinion, North Wales, UK. *First Break*, **20**: 630–636.
- Reynolds, J.M. (2004) Environmental geophysics investigations in urban areas. *First Break*, **22** (9): 63–69.
- Reynolds, J.M. (2006) Role of geophysics in glacial hazard assessment. *First Break*, **24**: 61–66.
- Reynolds, J.M. and Paren, J.G. (1980) Recrystallisation and electrical behaviour of glacier ice. *Nature*, **283** (5742): 63–64.
- Reynolds, J.M. and Paren, J.G. (1984) Electrical resistivity of ice from the Antarctic Peninsula. *Journal of Glaciology*, **30**: 289–295.
- Reynolds, J.M. and McCann, D.M. (1992) Geophysical methods for the assessment of landfill and waste disposal sites, in *Proceedings of 2nd International Conference on Construction on Polluted and Marginal Land*, 30 June–2 July 1992, Brunel University, London (ed. M.C. Forde), Engineering Technics Press, Edinburgh, 63–71.

- Reynolds, J.M. and Taylor, D.I. (1992) The use of sub-surface imaging techniques in the investigation of contaminated sites, in *Proceedings of 2nd International Conference on Construction on Polluted and Marginal Land, 30 June–2 July 1992, Brunel University, London* (ed. M.C. Forde), Engineering Technics Press, Edinburgh, 121–131.
- Reynolds, J.M. and Taylor, D.I. (1995) The use of geophysical surveys during the planning, construction and remediation of landfills, in *Engineering Geology of Waste Storage and Disposal* (ed. S. Bentley), Geological Society Special Publication No. 11, 93–98.
- Reynolds, J.M. and Edmonds, C.N. (2001) Micro-gravity investigation of Chalk mines at Field Road, Reading, in Proceedings of the 7<sup>th</sup> Meeting of the Environmental and Engineering Geophysics Society – European Section, Birmingham, England, 2–6<sup>th</sup> Sept., 130–131.
- Richter-Bernburg, G. (1982) Interior structures of salt domes. Results of Geological Investigations for High-Level Waste Disposal in the Mors Salt Dome. Proceedings of a Symposium, 18–19 Sept. 1981, Copenhagen, 50–73.
- Ridenour, L.N. (1947). *Radar system engineering*. McGraw-Hill Book Co., Inc., New York, USA.
- Rikitake, T. (1976) *Earthquake Prediction*, Elsevier, Amsterdam, The Netherlands.
- Rimbert, F., Erling, J.-C. and Lakshmanan, J. (1987) Variable density Bouguer processing of gravity data from Herault, France. *First Break*, 5: 9–13.
- Roberts, G.A. and Goultby, N.R. (1990) Directional deconvolution of marine seismic reflection data: North Sea example. *Geophysical Prospecting*, 38: 881–888.
- Roberts, R., Daniels, J.J. and Peters, L. Jr. (1993). Accounting for near field conditions when interpreting 3-D GPR data. *SAGEEP*, 6: 575–594.
- Roberts, R.L., Hinze, W.J. and Leap, D.I. (1990) Data enhancement procedures on magnetic data from landfill investigations, in *Geotechnical and Environmental Geophysics, Vol. II: Environmental and Groundwater* (ed. S.H. Ward), Society of Exploration Geophysicists, Tulsa, Oklahoma, USA, 261–266.
- Robin, G. De Q. and Swithinbank, C. (1987) Fifty years of progress in understanding ice sheets. *Journal of Glaciology* (Spec. Issue): 33–47.
- Robinson, E.S. and Coruh, C. (1988) *Basic Exploration Geophysics*, John Wiley & Sons, Ltd. New York, USA.
- Roest, W.R., Verhoef, J. and Pilkington, M. (1992) Magnetic interpretation using the 3-D analytic signal. *Geophysics*, 57: 116–125.
- Rohdewald, S. (2006) *RAYFRAC<sup>TM</sup> Manual*, Intelligent Resources Inc., Vancouver, Canada.
- Rollin, K.E. (1986) Geophysical surveys on the Lizard Complex, Cornwall. *Journal of the Geological Society of London*, 143: 437–446.
- Rosid, M.S. and Kepic, A.W. (2003) Electrokinetic sounding method to map hydrogeological boundaries, in *Advances in Regolith* (ed. I.C. Roach), CRC LEME, 364–368.
- Ross, R. (2008) Full azimuth imaging using Coil Shooting acquisition. *First Break*, 26 (12): 69–74.
- Roth, K.R., Schulin, R., Fluhler, H. and Attinger, W. (1990) Calibration of time domain reflectometry for water content measurement using a composite dielectric approach. *Water Resources Research*, 26: 2267–2273.
- Röthlisberger, H. (1967) Electrical resistivity measurements and soundings on glaciers: introductory remarks. *Journal of Glaciology*, 6 (47): 599–606.
- Roy, J. (2009) MRS: a new geophysical technique for groundwater work. *The Leading Edge*, 28: 1226–1233.
- Rubinat, M., Ledo, J., Roca, E., et al. (2010) Magnetotelluric characterization of a salt diapir: case study on Bicorb-Quesa Diapir (Prebetic Zone, SE Spain). *Journal of the Geological Society*, 167: 145–153.
- Ruffell, A. (2006) Forensic geoscience. *Geology Today*, 22 (2): 68–70.
- Ruffell, A. and Wilson, J. (1998) Shallow ground investigation using radiometrics and spectral gamma-ray data. *Archaeological Prospection*, 5: 203–215.
- Ruffell, A., McKinley, J.M., Lloyd, C.D. and Graham, C. (2006) Th/K and Th/U ratios from spectral gamma-ray surveys improve the mapped definition of subsurface structures. *Journal of Environmental and Engineering Geophysics*, 11: 53–61.
- Ruffell, A.R. and McKinley, J. (2008) *Geoforensics*, Wiley-Blackwell, Chichester, UK.
- Ruffet, C., Gueguen, Y. and Darot, M. (1991) Complex conductivity measurements and fractal nature of porosity. *Geophysics*, 56: 758–768.
- Russell, A. and Gee, R. (1990) The use of the dynamic probe on polluted and marginal sites, in *Proceedings of the International Conference on Construction on Polluted and Marginal Land, 28–29 June 1990, Brunel University, London*, Engineering Technics Press, 23–28.
- Rütschlin, M., Cloete, J.H., Mason, I. and Palmer, K.D. (2007) The radio frequency dielectric properties of the stratified UG1-UG2 geological unit in the Bushveld Complex. *Journal of Applied Geophysics*, 62: 354–360.
- Rymer, H. (1993) Predicting volcanic eruptions using microgravity, and the mitigation of volcanic hazard, in *Natural Disasters: Protecting Vulnerable Communities* (eds P.A. Merriman and C.W.A. Brownitt), Thomas Telford, London, 252–269.
- Rymer, H. and Brown, G.C. (1986) Gravity fields and the interpretation of volcanic structures: geological discrimination and temporal evolution. *Journal of Volcanology and Geothermal Research*, 27: 229–254.
- Rymer, H. and Brown, G.C. (1987) Causes of microgravity change at Poás volcano, Costa Rica: an active but non-erupting system. *Bulletin of Volcanology*, 49: 389–398.
- Rymer, H. and Brown, G.C. (1989) Gravity changes as a precursor to volcanic eruption at Poás volcano, Costa Rica. *Nature*, 342 (6252): 902–905.

- Rymer, H., Murray, J.B., Brown, G.C., *et al.* (1993) Magma eruption and emplacement mechanisms at Mt Etna 1989–1992. *Nature*, **361**: 439–441.
- Saarenketo, T. (2009) NDT transportation, in *Ground Penetrating Radar: theory and applications* (ed. H.M. Jol), Elsevier, Amsterdam, 395–444.
- Saint-Amant, M. and Strangway, D.W. (1970) Dielectric properties of dry, geologic materials. *Geophysics*, **35**: 624–645.
- Salem, A., Williams, S., Fairhead, J.D., *et al.* (2007) Tilt-depth method: a simple depth estimation method using first-order magnetic derivatives. *The Leading Edge*, **26**: 1502–1505.
- Salem, A., Williams, S., Fairhead, J.D., *et al.* (2008) Interpretation of magnetic data using tilt-angle derivatives. *Geophysics*, **73** (1): L1–L10.
- Sander, S.M., Argyle, M., Elieff, S., *et al.* (2004) *The AIRGrav Airborne Gravity System*. Australian SEG Airborne Gravity Workshop.
- Sanderson, T.J.O., Berrino, G., Corrado, G. and Grimaldi, M. (1983) Ground deformation and gravity changes accompanying the March 1981 eruption of Mount Etna. *Journal of Volcanology and Geothermal Research*, **16**: 299–315.
- Sandmeier, K.J. (2007) REFLEXW Version 4.2, Sandmeier Geo, Karlsruhe, Germany.
- Sargent, C. and Goult, N.R. (2009a) Seismic reflection survey for investigation of gypsum dissolution and subsidence at Hell Kettles, Darlington, UK. *Quarterly Journal of Hydrology and Hydrogeology*, **42**: 31–38.
- Sargent, C. and Goult, N.R. (2009b) Use of 3D seismic to image subsurface foundering due to gypsum dissolution. *First Break*, **27** (8): 61–67.
- Sasagawa, G.S., Crawford, W., Eiken, O., *et al.* (2003) A new sea-floor gravimeter. *Geophysics*, **68**: 544–553.
- Sasagawa, G., Zumberge, M. and Eiken, O. (2008) Long-term seafloor tidal gravity and pressure observations in the North Sea – Testing and validation of a theoretical tidal model. *Geophysics*, **73** (6): WA143–WA148.
- Sato, M. and Mooney, H.M. (1960) The electrochemical mechanism of sulphide self-potentials. *Geophysics*, **25**: 226–249.
- Sattel, D. (2005) Inverting airborne electromagnetic (AEM) data with Zodhy's method. *Geophysics*, **70**: G77–G85.
- Sattel, D. (2006) A brief discussion of helicopter time-domain EM systems. *AESC2006, Melbourne, Australia*.
- Saukk, W.A. (2000) A model for the resistivity structure of LNAPL plumes and their environs in sandy sediments. *Journal of Applied Geophysics*, **44**: 151–165.
- Saxov, S. (1956) Some gravity measurements in Thy, Mors and Vendsysel. *Geodet. Inst. Skrifter*, Ser. 3, no. 25.
- Schenck, F.L. (1967) Refraction solutions and wavefront targeting, in *Seismic Refraction Prospecting* (ed. A.W. Musgrave), Society of Exploration Geophysicists, Tulsa, Oklahoma, USA, 416–425.
- Schiavone, D. and Quarto, R. (1984) Self-potential prospecting in the study of water movements. *Geoexploration*, **22**: 47–58.
- Schnaid, F. (2009) *In Situ Testing in Geomechanics*, Taylor & Francis Group, New York.
- Scholl, C. and Edwards, N. (2007) Marine downhole to seafloor dipole–dipole electromagnetic methods and the resolution of resistive targets. *Geophysics*, **72** (2): WA39–WA49.
- Schufle, J.A. (1958) Cation exchange and induced electrical polarization. *Geophysics*, **24**: 164–166.
- Schuster, G.T. and Quintus-Bosz, A. (1993) Wavepath eikonal travel-time inversion. *Geophysics*, **58**: 1314–1323.
- Schwarz, G.F., Klingele, E.E. and Rybach, L. (1992) How to handle rugged topography in airborne gamma ray spectrometry surveys. *First Break*, **10**: 11–17.
- Scollar, I., Weidner, B. and Segeth, K. (1986) Display of archaeological magnetic data. *Geophysics*, **51**: 623–633.
- Scott, J.B.T. (2006) The origin of the observed low-frequency electrical polarization in sandstones. *Geophysics*, **71**: G235–G238.
- Scott, W.J., Sellman, P.V. and Hunter, J.A. (1990) Geophysics in the study of permafrost, in *Geotechnical and Environmental Geophysics, Vol. 1: Review and Tutorial* (ed. S.H. Ward), Society of Exploration Geophysicists, Tulsa, Oklahoma, USA, 355–384.
- Seigel, H.O., Hill, H.L. and Baird, J.G. (1968) Discovery case history of the Pyramid ore bodies, Pine Point, Northwest Territories, Canada. *Geophysics*, **33**: 645–656.
- Seigel, H., Nabighian, M.N., Parasnis, D.S. and Vozoff, K. (2007) The early history of the induced polarization method. *The Leading Edge*, **26**: 312–321.
- Semenov, A.S. (1980) *Elektrorazvedka metodom Estektvennogo Elektricheskogo Polya*, Nedra, Leningrad.
- Serra, O. (1984) *Fundamental of Well-log Interpretation, Vol. 1, The Acquisition of Logging Data*, Elsevier, Amsterdam, Dev. Pet. Sci. 15A.
- Shabtaie, S., Bentley, C.R., Blankenship, D.D., *et al.* (1980) Dome C geophysical survey. *Antarctic Journal of the United States*, **15** (5): 2–5.
- Shabtaie, S., Thyssen, F., and Bentley, C.R. (1982) Deep geoelectric and radar soundings at Dome C, East Antarctica. *Annals of Glaciology*, **3**: 342.
- Sharma, P.V. (1986) *Geophysical Methods in Geology*, Elsevier Science, New York, USA.
- Sheehan, J.R., Doll, W.E. and Mandell, W.A. (2005) An evaluation of methods and available software for seismic refraction tomography analysis. *Journal of Environmental and Engineering Geophysics*, **10**: 21–34.
- Sheffer, M.R. and Oldenburg, D.W. (2007) Three-dimensional modelling of streaming potential. *Geophysical Journal International*, **169**: 839–848.

- Sheriff, R.E. (2002) *Encylopedic Dictionary of Exploration Geophysics*, 4th edn, Society of Exploration Geophysicists, Tulsa, Oklahoma, USA.
- Sheriff, R.E. and Geldart, L.P. (1982) *Exploration Seismology*, Cambridge University Press, Cambridge, UK.
- Sherrell, F. (1987) 'I'll sue if I can...', aspects of professional liability. *British Geologist*, **13** (2): 66–71.
- Shuey, R.T. and Johnson, M. (1973) On the phenomenology of electrical relaxation in rocks. *Geophysics*, **38**: 37–48.
- Sieck, H.C. and Self, G.W. (1977) Analysis of high-resolution seismic data, in *Memoir 26: Seismic Stratigraphy: Applications to Hydrocarbon Exploration* (ed. C.E. Payton), American Association of Petroleum Geologists, Tulsa, Oklahoma, USA, 353–385.
- Siemon, B., Christiansen, A.V. and Auken, E. (2009) A review of helicopter-borne electromagnetic methods for groundwater exploration. *Near Surface Geophysics*, **7**: 629–646.
- Sill, W.R. (1983) Self-potential modeling from primary flows. *Geophysics*, **48**: 76–86.
- Singh, S.K. (1976) Fortran IV program to compute apparent resistivity of a perfectly conducting sphere buried in a half-space. *Computers & Geosciences*, **1**: 241–245.
- Sinha, A.K. (1990) Interpretation of ground VLF-EM data in terms of inclined sheet-like conductor models. *Pure & Applied Geophysics*, **132**: 733–756.
- Sinha, A.K. and Stephens, L.E. (1983) Permafrost mapping over a drained lake by electromagnetic induction methods. *Current Research, Part A, Geological Survey of Canada, Paper 83-1A*, 213–220.
- Sirius (2010) *Lake Wells radiometric survey confirms uranium anomalies*, Sirius Resources NL, Perth, Western Australia. Australian Securities Exchange announcement, 19 February 2010.
- Sjögren, B. (1984) *Shallow Refraction Seismics*, Chapman & Hall, London, UK.
- Sjögren, N.A., Öfthus, A. and Sandberg, J. (1979) Seismic classification of rock mass qualities. *Geophysical Prospecting*, **27**: 409–442.
- Slaine, D.D., Pehme, P.E., Hunter, J.A., et al. (1990) Mapping overburden stratigraphy at a proposed hazardous waste facility using shallow seismic reflection methods, in *Geotechnical and Environmental Geophysics, Vol. 2: Environmental and Groundwater* (ed. S.H. Ward), Society of Exploration Geophysicists, Tulsa, Oklahoma, USA, 273–280.
- Slater, L. and Lesmes, D. (2002) IP interpretation in environmental investigations. *Geophysics*, **67**: 77–88.
- Slater, L. and Reeve, A. (2002) Investigating peatland stratigraphy and hydrogeology using integrated electrical geophysics. *Geophysics*, **67**: 365–378.
- Slater, L. and Atekwana, E. (2009) Exploring the geophysical signatures of microbial processes. *Eos*, **90** (10): 83.
- Smith, A.M. and Murray, T. (2008) Bedform topography and basal conditions beneath a fast flowing West Antarctic ice stream. *Quaternary Science Reviews*, **28**: 584–596.
- Smith, R.A. (1959) Some depth formulae for local magnetic and gravity anomalies. *Geophysical Prospecting*, **7**: 55–63.
- Smith, R.A. (1960) Some formulae for interpreting local gravity anomalies. *Geophysical Prospecting*, **8**: 607–613.
- Smith, R.S. and Annan, A.P. (2000) Using an induction coil sensor to indirectly measure the B-field response in the bandwidth of the transient electromagnetic field. *Geophysics*, **65**: 1489–1494.
- Soames, C. (2000) Hole leaves 16 Reading families homeless. *New Civil Engineer* (20 January 2000), **6**.
- Soininen, H.T. and Vanhala, H. (2002) Spectral induced polarization method in mapping soils polluted by organic chemicals. *Extended Abstracts, 54th Meeting of EAEG, Paris, France*, 366–367.
- Song, L. and Vozoff, K. (1985) The complex resistivity spectra of models consisting of two polarizable media of different intrinsic properties. *Geophysical Prospecting*, **33**: 1029–1062.
- Sørensen, K. (1994) Pulled Array Continuous Electrical Profiling. *Symposium on the Application of Geophysics to Engineering and Environmental Problems SAGEEP '94*, **2**: 977–983.
- Sørensen, K.I. and Auken, E. (2004) SkyTEM – a new high-resolution helicopter transient electromagnetic system. *Exploration Geophysics*, **35**: 191–199.
- Sorgenfrei, T. (1971) On the granite problem and the similarity of salt and granite structures. *Geologiska Föreningens Förhandlingar*, **93**: 371–435.
- Sowerbutts, W.T.C. (1987) Magnetic mapping of the Butterton Dyke: an example of detailed geophysical surveying. *Journal of the Geological Society of London*, **144**: 29–33.
- Sowerbutts, W.T.C. (1988) The use of geophysical methods to locate joints in underground metal pipelines. *Quarterly Journal of Engineering Geology*, **21**: 273–281.
- Sowerbutts, W.T.C. and Mason, R.W.I. (1984) A microcomputer-based system for small-scale geophysical surveys. *Geophysics*, **49**: 189–193.
- Speake, C.C., Hammond, G.D. and Trenkel, C. (2001) The torsion balance as a tool for geophysical prospecting. *Geophysics*, **66**: 527–534.
- Spector, A. and Grant, F.S. (1970) Statistical models for interpreting aeromagnetic data. *Geophysics*, **35**: 293–302.
- Spector, A. and Parker, W. (1979) Computer compilation and interpretation of geophysical data, in *Geophysics and Geochemistry in the Search for Metallic Ores* (ed. P.J. Hood), Geological Survey of Canada, Economic Geology Report 31, 527–544.
- Spies, B.R. and Frischknecht, F.C. (1991) Electromagnetic sounding, in *Electromagnetic Methods in Applied Geophysics, Vol. 2A* (ed. M.N. Nabighian), Society of Exploration Geophysicists, Tulsa, Oklahoma, US, 285–425.
- Srnka, L.J., Carazzone, J.J., Ephron, M. and Eriksen, E.A. (2006) Remote reservoir resistivity mapping. *The Leading Edge*, **25**: 972–975.

- Stacey, F.D. and Banerjee, S.K. (1974) *The Physical Principles of Rock Magnetism*, Elsevier, Amsterdam.
- Stakes, D.S., Moore, W.S., Redding, S., et al. (1992) Cores drilled into active smokers on Juan de Fuca Ridge. *EOS, Transactions of the American Geophysical Union*, **73**: 273–283.
- Stanley, J.M. and Clark, P.J. (2003) *The Technology and Methodology for EOD Site Assessment*, Geophysical Technology Ltd, Armidale, NSW, Australia.
- Steeple, D. (1991) Uses and techniques of environmental geophysics. *Geophysics: The Leading Edge*, **10** (9): 30–31.
- Steeple, D.W. and Miller, R.D. (1994) Pitfalls in shallow seismic reflection. *Proceedings SAGEEP '94*, Englewood, US.
- Stenvold, T., Eiken, O. and Landrø, M. (2008) Gravimetric monitoring of gas reservoir water influx – a combined flow- and gravity-modeling approach. *Geophysics*, **73**: WA123–WA131.
- Stephan, A., Schniggenfittig, H. and Strack, K.-M. (1991) Long-offset transient EM sounding north of the Rhine-Ruhr coal district, Germany. *Geophysical Prospecting*, **39**: 505–525.
- Stephenson, S.N. (1984) Glacier flexure and the position of grounding lines: measurements by tiltmeter on Rutford Ice Stream, Antarctica. *Annals of Glaciology*, **5**: 65–169.
- Stephenson, S.N. and Doake, C.S.M. (1982) Dynamic behaviour of Rutford Ice Stream. *Annals of Glaciology*, **3**: 295–299.
- Stern, W. (1945) *Transactions AIME*, **164**: 189.
- Stevenson, J.M., Hildebrand, J.A., Zumberge, M.A. and Fox, C.G. (1994) An ocean bottom gravity study of the southern Juan de Fuca Ridge. *Journal of Geophysical Research*, **99**: 4875–4888.
- Stewart, R.R. (1991) *Exploration Seismic Tomography: Fundamentals*. Society of Exploration Geophysicists, Tulsa, Oklahoma, USA: SEG Continuing Education Short Course notes.
- Stolt, R.H. (1978) Migration by Fourier transform. *Geophysics*, **43**: 23–48.
- Stoltz, E. and MacNae, J.C. (1997) Fast approximate inversion of TEM data. *Exploration Geophysics*, **28**: 317–322.
- Stoltz, E. and MacNae, J.C. (1998) Evaluating EM waveforms by singular-value decomposition of exponential basis functions. *Geophysics*, **63**: 64–74. (Errata in *Geophysics*, **64**: 310).
- Stone, K., Murray, A., Cooke, S., Foran, J. and Gooderham, L. (2009). Unexploded ordnance (UXO) – a guide for the construction industry. CIRIA, London, 141 pp.
- Stone, P.M. and Simsky, A. (2001) Constructing high resolution DEMs from airborne laser scanner data. *Extended Abstracts, ASEG 15<sup>th</sup> Geophysical conference and exhibition, August 2001, Brisbane, Australia*.
- Stoyer, C. (1989) *EMIX34Plus<sup>TM</sup> User Manual*, Interpex Ltd, Golden, Colorado, USA.
- Studinger, M., Bell, R. and Frearson, N. (2008) Comparison of AIRGrav and GT-1A airborne gravimeters for research applications. *Geophysics*, **73** (6): I51–I61.
- Sumner, J.S. (1976) *Principle of Induced Polarization for Geophysical Exploration*, Elsevier, Amsterdam.
- Sundararajan, N., Ramesh Babu, V., Shiva Prasad, N. And Srinivas, Y. (2006). VLFPROS – A Matlab code for processing of VLF-EM data. *Computers & Geosciences*, **32** (10): 1806–1813.
- Sundberg, K. (1931) *Gerlands Beitr. Geoph. Ergänzungs-Hefte*, **1**: 298–361.
- Sundberg, K. and Hedström, F.H. (1934) Structural investigations by electromagnetic methods. Institute of Petroleum Technologists, *Proceedings of the World Petroleum Conference*, **V, B** (4): 102–110.
- Sunderland, J. (1972) Deep sedimentary basin in the Moray Firth. *Nature*, **236**: 24–25.
- Supper, R., Motschka, K., Ahl, A., et al. (2009) Spatial mapping of submerged cave systems by means of airborne electromagnetics: an emerging technology to support protection of endangered karst aquifers. *Near Surface Geophysics*, **7**: 613–627.
- Sutton, J.A. and Snelling, K. (1998) Assessment of ground improvement using the Continuous Surface Wave method. *4th Meeting of the Environmental and Engineering Geophysics Society, Barcelona, Spain*.
- Swift, C.M. (1988) Fundamentals of the electromagnetic method, in *Electromagnetic Methods in Applied Geophysics*, Vol. **1** (ed. M.N. Nabighian), Society of Exploration Geophysicists, Tulsa, Oklahoma, USA, 5–10.
- Swithinbank, C.S.M. (1968) Radio echosounding of Antarctic glaciers from light aircraft. *International Association of Hydrological Sciences, Publication*, **79**: 405–414.
- Syberg, F.J.R. (1972) A Fourier method for the regional-residual problem of potential fields. *Geophysical Prospecting*, **20**: 47–75.
- Szalai, S. and Szarka, L. (2008) On the classification of surface geoelectrical arrays. *Geophysical Prospecting*, **56**: 159–175.
- Takenaka, S., Yabuta, T. and Fukui, H. (2010) Distribution of dead ice inside moraine dam body of Imja Glacial Lake, Khumbu region, Nepal – internal structure of moraine dam of Imja Glacial Lake (in Japanese) *The Seppyo*, **72**: 3–12.
- Talwani, M. (1965) Computation with the help of a digital computer of magnetic anomalies caused by bodies of arbitrary shape. *Geophysics*, **30**: 797–817.
- Talwani, M. and Ewing, M. (1960) Rapid computation of gravitational attraction of three-dimensional bodies of arbitrary shape. *Geophysics*, **25**: 203–225.
- Talwani, M., Worzel, J.L. and Landisman, M. (1959) Rapid gravity computations for two-dimensional bodies with application to the Mendocino submarine fracture zone. *Journal of Geophysical Research*, **64**: 49–59.

- Talwani, M., Le Pichon, X. and Ewing, M. (1965) Crustal structures of the midocean ridges. 2: Computed models from gravity and seismic refraction data. *Journal of Geophysical Research*, **70**: 341–352.
- Tanner, J.G. and Gibb, R.A. (1979) Gravity method applied to base metal exploration, in *Geophysics and Geochemistry in the Search for Metallic Ores* (ed. P.J. Hood), Geological Survey of Canada, Economic Geology Report 31, 105–122.
- Tarling, D.H. (1983) *Palaeomagnetism*, Chapman & Hall, London, UK.
- Tauxe, L. (1990) Magnetostратigraphy, in *The Encyclopedia of Solid Earth Geophysics* (ed. D.E. James), Van Nostrand Reinhold, New York, 740–746.
- Taylor, D.I. (1992) Nearshore shallow gas around the UK coast. *Continental Shelf Research*, **12**: 1135–1144.
- Telford, W.M., Geldart, L.P., Sheriff, R.E. and Keys, D.A. (1990) *Applied Geophysics* (2nd edn), Cambridge University Press, Cambridge, UK.
- Tenghamn, R. and Dhelie, P.E. (2009) GeoStreamer – increasing the signal-to-noise ratio using a dual-sensor towed streamer. *First Break*, **27** (10): 45–51.
- Tezkan, B., Georgescu, P. and Fauzi, U. (2005) A radiomagnetotelluric survey on an oil-contaminated area near the Brazi Refinery, Romania. *Geophysical Prospecting*, **53**: 311–323.
- Thiel, E.C., Crary, A.P., Haubrich, R.A. and Behrendt, J.C. (1960) Gravitational determination of the ocean tide, Weddell and Ross seas, Antarctica. *Journal of Geophysical Research*, **65**: 629–636.
- Thierbach, R. (1974) Electromagnetic reflections in salt deposits. *Journal of Geophysics*, **40**: 633–637.
- Thimus, J.F. and Van Ruymbeke, M. (1988) Improvements in field technique for use of the LaCoste and Romberg gravimeter in microgravity surveys. *First Break*, **6** (4): 109–112.
- Thompson, A.H. and Gist, G.A. (1993) Geophysical applications of electrokinetic conversion. *The Leading Edge*, **12**: 1169–1173.
- Thompson, D.T. (1982) EULDPh: a new technique for making computer-assisted depth estimates from magnetic data. *Geophysics*, **47**: 31–37.
- Thompson, R.R. (1936) The seismic electric effect. *Geophysics*, **1**: 327–335.
- Thornburgh, H.R. (1930) Wavefront diagrams in seismic interpretation. *Bulletin of the American Association of Petroleum Geologists*, **14**: 185–200.
- Thurston, J.B. and Brown, R.J. (1994) Automated source-edge location with a new variable pass-band horizontal gradient operator. *Geophysics*, **59**: 546–554.
- Timco, G.W. (1979) An analysis of in situ resistivity of sea ice in terms of its microstructure. *Journal of Glaciology*, **22**: 461–471.
- Todd, B.J., Pullan, S.E. and Hunter, J.A. (1991) Electromagnetic studies across lakes and rivers in permafrost terrain, Mackenzie River Delta, Northwest Territories, Canada. *Expanded Abstracts of 61st Annual International Meeting*, 10–14 Nov., Society of Exploration Geophysicists, Tulsa, Oklahoma, US, 565–568.
- Tokimatsu, K., Shinzawa, K. and Kuwayama, S. (1992) Use of short-period microtremors for  $V_s$  profiling. *Journal of Geotechnical Engineering*, **118**: 1544–1558.
- Tonks, D.M., Hunt, S. and Bayne, J.M. (1993) Use of the conductivity probe to evaluate groundwater contamination. *Ground Engineering*, **26** (9): 24–29.
- Topp, G.C., Davis, J.L. and Annan, A.P. (1980) Electromagnetic determination of soil water moisture content: measurement in coaxial transmission lines. *Water Resources Research*, **16**: 574–582.
- Toteva, T. and Long, L.T. (2007) A seismic inversion experiment to identify scatterers in a granite outcrop. *Journal of Environmental and Engineering Geophysics*, **12**: 337–351.
- Tournerie, B., Chouteau, M. and Marcotte, D. (2007) Magnetotelluric static shift: estimation and removal using the cokriging method. *Geophysics*, **72**: F25–F34.
- Treloar, A.W. (1970) A simple theory for seismic diffractions. *Geophysics*, **35**: 762–784.
- Tucker, P.M. (1982) Pitfalls Revisited. *Geophysical Monograph* No. 3, Society of Exploration Geophysicists, Tulsa, Oklahoma, USA.
- Tucker, P.M. and Yorston, H.J. (1973) *Pitfalls in Seismic Interpretation*. Geophysical Monograph No. 2, Society of Exploration Geophysicists, Tulsa, Oklahoma, USA.
- Tuncer, V., Unsworth, M.J., Srirupunvaraporn, W. and Craven, J.A. (2006) Exploration for unconformity-type uranium deposits with audiomagnetotelluric data: a case study from the McArthur River mine, Saskatchewan, Canada. *Geophysics*, **71** (6): B201–B209.
- Tura, M.A.C., Greaves, R.J. and Beydoun, W.B. (1994) Crosswell seismic reflection/diffraction tomography: a reservoir characterization application. *Geophysics*, **59**: 351–361.
- UBC-GIF. (2000). *EM1DFM: a program library for forward modelling and inversion of frequency domain electromagnetic data over 1D structures*. University of British Columbia Geophysical Inversion Facility, Canada.
- Ulrich, C. and Slater, L. (2004) Induced polarization measurements on unsaturated unconsolidated sands. *Geophysics*, **69**: 762–771.
- Ulriksen, C.P.F. (1982) *Application of Impulse Radar to Civil Engineering*. Geophysical Survey Systems Inc., North Salem, NH, USA.
- Um, E.S. and Alumbaugh, D.L. (2007) On the physics of the controlled-source electromagnetic method. *Geophysics*, **72** (2): WA13–WA26.
- Unsworth, M., Soyer, W., Tuncer, V., et al. (2007) Hydrogeologic assessment of the Amchitka Island nuclear test site (Alaska) with magnetotellurics. *Geophysics*, **72** (3): B47–B57.
- Unterberger, R.R. (1978) Radar propagation in rock salt. *Geophysical Prospecting*, **26**: 312–328.

- Urquhart, W.E.S. (2010). *Airborne gamma-ray spectrometry surveys*. GeoExplor Ltda, Chile. ([www.geoexplo.com/airborne\\_survey\\_workshop\\_rad.html](http://www.geoexplo.com/airborne_survey_workshop_rad.html)).
- Vacquier, V., Steenland, N.C., Henderson, R. and Zietz, I. (1951) *Interpretation of Aeromagnetic Maps*. Geological Society of America Memoir 47, 151.
- Vacquier, V., Holmes, C.R., Kintzinger, P.P. and Lavergne, M. (1957) Prospecting for ground-water by induced electrical polarization. *Geophysics*, **22**: 660–687.
- Valliant, H.D., Halpenny, J. and Cooper, R.V. (1985) A microprocessor-based controller and data acquisition system for LaCoste and Romberg air-sea gravity meters. *Geophysics*, **50** (5): 840–845.
- Van Dam, J.C. and Meulenkamp, J.J. (1967) Some results of the geo-electrical resistivity method in ground water investigations in the Netherlands. *Geophysical Prospecting*, **15**: 92–115.
- Van Der Veen, M. and Green, A.G. (1998) Land streamer for shallow data acquisition: evaluation of gimbal-mounted geophones. *Geophysics*, **63**: 1408–1413.
- Van Der Veen, M., Spitzer, R., Green, A.G. and Wild, P. (2001) Design and application of a towed land-streamer for cost-effective 2D and pseudo-3D shallow seismic data acquisition. *Geophysics*, **66**: 482–500.
- Van Nostrand, R.G. and Cook, K.L. (1966) *Interpretation of resistivity data*. US Geological Survey Professional Paper No. 499.
- Van Overmeeren, R.A. (1980) Tracing by gravity of a narrow buried graben structure, detected by seismic refraction, for ground-water investigations in North Chile. *Geophysical Prospecting*, **28**: 392–407.
- Van Overmeeren, R.A. (1987) The plus-minus method for rapid field processing by portable computer of seismic refraction data in multilayer ground water studies. *First Break*, **5**: 83–94.
- Van Overmeeren, R.A. (1994) Georadar for hydrogeology. *First Break*, **12**: 401–408.
- Van Overmeeren, R.A. and Ritsema, I.L. (1988) Continuous vertical electrical sounding. *First Break*, **6**: 313–324.
- Vanhala, H. and Peltoniemi, M. (1992) Spectral IP studies of Finnish ore prospects. *Geophysics*, **57**: 1545–1555.
- Vaníček, P., Tenzer, R., Sjöberg, L.E., Martinec, Z. and Featherstone, W.E. (2004) New views of the spherical Bouguer gravity anomaly. *Geophysical Journal International*, **159**: 460–472.
- Varela, C.L., Rosa, A.L.R. and Ulryck, T.J. (1993) Modeling of attenuation and dispersion. *Geophysics*, **58**: 1167–1173.
- Varotsos, P. and Alexopoulos, K. (1984) Physical properties of the variations of the electric field of the earth preceding earthquakes. *Tectonophysics*, **110**: 73–98.
- Veeken, P.C.H., Legeydo, P.J., Davidenko, Y.A., et al. (2009) Benefits of the induced polarization geoelectric method to hydrocarbon exploration. *Geophysics*, **74** (2): B47–B59.
- Vermeer, G.J.O. (1991) Symmetric sampling. *Geophysics: The Leading Edge*, **10** (11): 17–27.
- Vidale, J. (1990) Finite-difference calculation of travel times in three dimensions. *Geophysics*, **55**: 521–526.
- Viezzoli, A., Cull, J.P. and Massie, D. (2006) Mapping fly-ash water pond leakage with TEM and IP data at Loy Yang coal-mine (Australia) *Near Surface Geophysics*, **4**: 305–311.
- Vouillamoz, J.M. (2003) *La caractérisation des aquifères par une méthode non-invasive: les sondages par résonance magnétique protonique*. University of Paris, Paris, France.
- Vouillamoz, J.M., Descloitres, M., Toe, G. and Legchenko, A. (2005) Characterization of crystalline basement aquifers with MRS: comparison with boreholes and pumping tests in Burkina Faso. *Near Surface Geophysics*, **3**: 205–213.
- Vozoff, K. (1986) *Magneto-telluric Methods*, Society of Exploration Geophysicists, Tulsa, Oklahoma, USA.
- Vozoff, K. (1991) The magneto-telluric method, in *Electromagnetic Methods in Applied Geophysics, Vol. 2: Applications, Part B* (ed. M.N. Nabighian), Society of Exploration Geophysicists, Tulsa, Oklahoma, USA, 641–711.
- Vrbancich, J. (2009) An investigation of seawater and sediment depth using a prototype airborne electromagnetic instrumentation system – a case study in Broken Bay, Australia. *Geophysical Prospecting*, **57**: 633–651.
- Wagner, C.A., Lerch, F., Brown, J.E. and Richardson, J.A. (1977) Improvement in the geopotential derived from satellite and surface data (GEM 7 and 8). *Journal of Geophysical Research*, **82**: 901–914.
- Wang, G.L., Torres-Verdin, C., Salazar, J.M. and Voss, B. (2009) Fast 2D inversion of large borehole EM induction data sets with an efficient Fréchet-derivative approximation. *Geophysics*, **74**: E75–E91.
- Ward, S.H. (1990) *Geotechnical and Environmental Geophysics*, Society of Exploration Geophysicists, Tulsa, Oklahoma, USA.
- Ward, S.H. and Hohmann, G.W. 1987. Electromagnetic theory for geophysical applications. In: Nabighian, M.N. (ed.). *Electromagnetic methods in applied geophysics, Volume 1 Theory*. Investigations in Geophysics No. 3, Society of Exploration Geophysicists, Tulsa, Oklahoma, USA, 131–311.
- Wartnaby, J. (1957) *Seismology*, HMSO, London, UK.
- Watanabe, T., Matsuoka, T. and Ashida, Y. (1999) Seismic travel time tomography using Fresnel volume approach, in *Expanded Abstracts, 69th Annual Meeting and Exposition*, Society of Exploration Geophysicists, Oklahoma, USA, 1402–1405.
- Waters, K.H. (1978) *Reflection Seismology: A Tool for Energy Resource Exploration*, 3rd edn, John Wiley and Sons, Ltd, New York, USA.
- Watts, R.D., England, A.W., Vickers, R.S. and Meier, M.F. (1975) Radio-echo sounding on South Cascade Glacier, Washington, using a long-wavelength, mono-pulse source. *Journal of Glaciology*, **15**: 459–461.

- Webb, S., Constable, S.C., Cox, C.S. and Deaton, T.K. (1985) A seafloor electric field instrument. *Journal of Geomagnetism and Geoelectricity*, **37**: 1115–1129.
- Weller, A., Nordsiek, S. and Bauerochse, A. (2006) Spectral induced polarization – a geophysical method for archaeological prospection in peatlands. *Journal of Wetland Archaeology*, **6**: 105–125.
- Wenner, F. (1912a) The four-terminal conductor and the Thompson Bridge. *US Bureau of Standards Bulletin*, **8**: 559–610.
- Wenner, F. (1912b) A method of measuring earth resistivity. *US Bureau of Standards Bulletin*, **12**: 469–478.
- Werban, U., Kuka, K. and Merbach, I. (2009) Correlation of electrical resistivity, electrical conductivity and soil parameters at a long-term fertilization experiment. *Near Surface Geophysics*, **7**: 5–14.
- Whitelaw, J.L., Mickus, K., Whitelaw, M.J. and Nave, J. (2008) High-resolution gravity study of the Gray Fossil Site. *Geophysics*, **73** (2): B25–B32.
- Whiteley, R.J. (1973) Electrode arrays in resistivity and IP prospecting: a review. *Bulletin of the Australian Society of Exploration Geophysicists*, **4**: 1–29.
- Whiteley, R.J. (2004) Shallow seismic refraction interpretation with visual interactive raytracing (VIRT). *Exploration Geophysics*, **35**: 116–123.
- Whiteley, R.J. and Eccleston, P.J. (2006) Comparison of shallow seismic refraction interpretation methods for regolith mapping. *Exploration Geophysics*, **37**: 210–214.
- Whitmore, N.D. and Garing, J.D. (1993) Interval velocity estimation using iterative prestack depth migration in the constant angle domain. *Geophysics: The Leading Edge*, **12**: 757–762.
- Wikramanayake, E., Fernando, P. and Leimgruber, P. (2006) Behavioral response of satellite-collared elephants to the tsunami in southern Sri Lanka. *Biotropica*, **38**: 775–777.
- Wilkinson, P.B., Chambers, J.E., Meldrum, P.I., et al. (2005) A comparison of Self-Potential Tomography with Electrical Resistivity Tomography for the detection of abandoned mineshafts. *Journal of Environmental & Engineering Geophysics*, **10**: 381–389.
- Williams, K.H., Ntarlagiannis, D., Slater, L., et al. (2005) Geophysical imaging of stimulated microbial biominerization. *Environmental Science & Technology*, **39**: 7592–7600.
- Witten, A.J., Gillette, D.D., Sypniewski, J. and King, W.C. (1992) Geophysical diffraction tomography at a dinosaur site. *Geophysics*, **57**: 187–195.
- Witten, A.J. and King, W.C. (1990a) Acoustic imaging of subsurface features. *Journal of Environmental Engineering*, **116**: 166–181.
- Witten, A.J. and King, W.C. (1990b) Sounding out buried waste. *Civil Engineering*, **60**: 62–64.
- Wolfgram, P.A., Edwards, R.N., Law, L.K. and Bone, M.N. (1986) Polymetallic sulfide exploration on the deep sea floor: the feasibility of the MINI-MOSES technique. *Geophysics*, **51**: 1808–1818.
- Wollenberg, H.A. (1977) Radiometric methods, in *Nuclear Methods in Mineral Exploration and Production* (ed. J.G. Morse), Elsevier, Amsterdam, 5–36.
- Won, I.J., Keiswetter, D.A., Fields, G.R.A. and Sutton, L.C. (1996) GEM-2: a new multifrequency electromagnetic sensor. *Journal of Environmental & Engineering Geophysics*, **1**: 129–137.
- Wong, J. (1979) An electrical model of the induced polarization phenomenon in disseminated sulphide ores. *Geophysics*, **44**: 1245–1265.
- Woodward, M.J. and Rocca, F. (1988) Wave-equation tomography, in *58<sup>th</sup> Annual International Meeting, SEG, Expanded Abstracts*, S21.3, Society of Exploration Geophysicists, Tulsa, Oklahoma, USA, 1232–1235.
- Woppard, G.P. (1950) The gravity meter as a geodetic instrument (surveys). *Geophysics*, **15**: 1–29.
- Woppard, G.P. (1959) Crustal structure from gravity and seismic measurements. *Journal of Geophysical Research*, **64**: 1521–1544.
- Woppard, G.P. (1975) Regional changes in gravity and their relation to crustal parameters. *Bulletin d'Information, Bureau Gravimetrique International*, **36**: 106–110.
- Woppard, G.P. and Rose, J.C. (1963) *International Gravity Measurement*, Society of Exploration Geophysicists, Tulsa, Oklahoma, USA.
- Wright, D.L., Hodge, S.M., Bradley, J.A., et al. (1990) A digital low-frequency, surface-profiling ice-radar system. *Journal of Glaciology*, **36**: 112–121.
- Wright, D.L. and Watts, R.D. (1982) A single-hole short pulse radar system. *Geophysical Investigations in Connection with Geological Disposal of Radioactive Waste*, OECD/NEA, Ottawa, Canada.
- Wright, D., Bennett, H.H. Jr., Ballard, J.H., et al. (2008) Portable magnetic/frequency domain electromagnetic induction sensor system development. *Journal of Engineering & Environmental Geophysics*, **13**: 237–245.
- Wu, C. (1990) Adequate sampling in magnetic surveys, the resolution of closely-spaced sources, and their importance to data processing, image-enhancement techniques and interpretation. (MSc thesis, ITC Delft.) *ITC Journal 1990–2*, 176–179.
- Wyllie, M.R., Gregory, A.R. and Gardner, G.H.F. (1958) An experimental investigation of factors affecting elastic wave velocities in porous media. *Geophysics*, **23**: 459–493.
- Wynn, J.C. and Zonge, K.L. (1975) EM coupling: its intrinsic value, its removal and the cultural coupling problem. *Geophysics*, **40**: 831–850.
- Wynn, J.C. and Zonge, K.L. (1977) Electromagnetic coupling. *Geophysical Prospecting*, **25**: 29–51.
- Wynn, J.C. and Sherwood, S.I. (1984) The self-potential (SP) method: an inexpensive reconnaissance and archaeological mapping tool. *Journal of Field Archaeology*, **11**: 195–204.
- Wyrobek, S.M. (1956) Application of delay and intercept times in the interpretation of multi-layer refraction time distance curves. *Geophysical Prospecting*, **4**: 112–130.

- Xia, J. and Sprowl, D.R. (1992) Inversion of potential-field data by iterative forward modelling in the wavenumber domain. *Geophysics*, **57**: 126–130.
- Yaghoobian, A., Boustead, G.A. and Dobush, T.M. (1992) Object delineation using Euler's inhomogeneity equation – location and depth determination of buried ferro-metallic bodies, in Proceedings of SAGEEP-92, San Diego, California, Environmental and Engineering Society, Englewood, USA.
- Yaramancı, U. and Legchenko, A. (2005) Special issue: Magnetic Resonance Sounding aquifer detection and characterization – Forward from guest editors. *Near Surface Geophysics*, **3** (3): 119–120.
- Yaramancı, U. and Hertrich, M. (2009) Magnetic resonance sounding, in *Groundwater Geophysics – a Tool for Hydrogeology* (ed. R. Kirsch), Springer, Berlin, 253–273.
- Yarovoy, A. (2009) Landmine and unexploded ordnance detection and classification with ground penetrating radar, in *Ground Penetrating Radar: Theory and Applications* (ed. H.M. Jol), Elsevier, Amsterdam, 445–478.
- Yilmaz, O. (2001) *Seismic Data Analysis, Processing, Inversion, and Interpretation of Seismic Data*, Society of Exploration Geophysicists, Tulsa, Oklahoma, USA.
- Yuanxuan, Z. (1993) Radon transform application to the improved gridding of airborne geophysical survey data. *Geophysical Prospecting*, **41**: 459–494.
- Yüngül, S.H. (1950) Interpretation of spontaneous-polarization anomalies caused by spheroidal orebodies. *Geophysics*, **15**: 237–246.
- Yüngül, S.H. (1954) Spontaneous-potential survey of a copper deposit at Sarıyer, Turkey. *Geophysics*, **19**: 455–458.
- Zablocki, C.J. (1976) Mapping thermal anomalies on an active volcano by the self-potential method, Kilauea, Hawaii. *Proceedings of the 2nd Symposium on the Development and Use of Geothermal Resources, San Francisco, US*, 1299–1309.
- Zachos, K. (1963) Discovery of a copper deposit in Chalkidiki Peninsula, northern Greece (in Greek with English summary) *Institute of Geology and Subsurface Research Publication*, **8**: 1–26.
- Zalasiewicz, J.A., Mather, S.J. and Cornwell, J.D. (1985) The application of ground conductivity measurements to geological mapping. *Quarterly Journal of Engineering Geology*, **18**: 139–148.
- Zamora, R., Ulloa, D., Garcia, G., et al. (2009) Airborne radar sounder for temperate ice: initial results from Patagonia. *Journal of Glaciology*, **55**: 507–512.
- Zanzi, L. (1990) Inversion of refracted arrivals: a few problems. *Geophysical Prospecting*, **38**: 339–364.
- Zanzi, L. and Carlini, A. (1991) Refraction statics in the wavenumber domain. *Geophysics*, **56**: 1661–1670.
- Zeng, X. and McMechan, G.A. (1997) GPR characterization of buried tanks and pipes. *Geophysics*, **62**: 797–806.
- Zeng, H. and Wan, T. (2004) Clarification of the geophysical definition of a gravity field. *Geophysics*, **69**: 1252–1254.
- Zhang, C., Mushayandebvu, M.F., Reid, A.B., et al. (2000) Euler deconvolution of gravity tensor gradient data. *Geophysics*, **65**: 512–520.
- Zhang, J. and Toksoz, M. (1998) Nonlinear refraction traveltime tomography. *Geophysics*, **63**: 1726–1737.
- Zhou, B. and Greenhalgh, S.A. (2001) Finite element three-dimensional direct current resistivity modelling: accuracy and efficiency considerations. *Geophysical Journal International*, **145**: 679–688.
- Zinni, E.V. (1995) Sub-surface fault detection using seismic data for hazardous-waste-injection well permitting: an example from St John the Baptist Parish, Louisiana. *Geophysics*, **60**: 468–475.
- Zohdy, A.A.R. (1974) Electrical methods, in *Applications of Surface Geophysics to Groundwater Investigations*, Book 2, Chapter D1, US Department of the Interior, 5–66.
- Zohdy, A.A.R. (1989) A new method for the interpretation of Schlumberger and Wenner sounding curves. *Geophysics*, **54**: 245–253.
- Zohdy, A.A.R., Anderson, L.A. and Muffler, L.J.P. (1973) Resistivity, self-potential and induced-polarization surveys of a vapor-dominated geothermal system. *Geophysics*, **38**: 1130–1144.
- Zonge, K.L. and Wynn, J.C. (1975) Recent advances and applications in complex resistivity measurements. *Geophysics*, **40**: 851–864.
- Zonge, K.L. and Hughes, L.H. (1991) Controlled-source audio-frequency magnetotellurics, in *Electromagnetic Methods in Applied Geophysics, Vol. 2: Applications, Part B* (ed. M.N. Nabighian), Society of Exploration Geophysicists, Tulsa, Oklahoma, USA, 713–809.
- Zumberge, M.A., Ridgway, J.R. and Hildebrand, J.A. (1997) A towed marine gravity meter for near-bottom surveys. *Geophysics*, **62**: 1386–1393.
- Zumberge, M., Alnes, H., Eiken, O., et al. (2008) Precision seafloor gravity and pressure measurements for reservoir monitoring. *Geophysics*, **73** (6): WA133–WA141.



# Index

Note: Page references in **bold** refers to Figures, page references in *italic* refer to Table and Boxes.

2D *see* two-dimensional

3D *see* three-dimensional

$\alpha$ -particles 626

absolute gravity 24–5, 25

absolute magnetic permeability 84

accelerated weight drop (AWD) 157, 157–8

accelerometers 170–3

acid mine drainage (AMD) 450, 465

acid tar lagoon surveys

geomagnetic methods 133–6, 136–7, 137

seismic refraction surveys 203–7, 205–7

acoustic blanking 458

acoustic impedance 246–7, 256–7, 257

acoustic turbidity 273

actinium decay series 627

active geophysical methods 3

adsorption potentials 351

AEM *see* airborne electromagnetic

aeromagnetic investigations

geomagnetic methods 105–7, 109, 114, 119, 121, 123–5, 124, 126

noise 13–14, 14–15

pattern analysis 105–7, 109, 114, 119, 121

station interval selection 12

agro-geophysics 1–2

AGS *see* Association of Geotechnical Specialists

airborne electromagnetic (AEM) methods 411–18, 414, 448, 450, 452, 455,

478, 486–8, 486–7

airborne investigations

geomagnetic methods 100, 100, 140

gravity systems 31–4, 32–3

radiometrics 634, 635–6, 641

airgun bubble pulse sources 160–1, 161–2

Airy's isotactic model 45

alkali vapour magnetometers 97–9, 99

AMD *see* acid mine drainage

amplitude–frequency spectra 545

amplitude–phase diagrams 388

amplitude–pulse moments 523–5, 524–5, 532

amplitude reflection coefficients 539, 564

AMT *see* audio magnetotelluric

analytical signal method 122–3, 123, 138

anhydrous remanent magnetization (ARM) 89

animals

ground-penetrating radar 618–23, 623

vibrator energy systems 166–70

anomalous mass 52–3

Antarctic ice sheets/shelves 81, 578–9

anti-ferromagnetism 86

anti-personnel (AP) mines 618

anti-tank (AT) mines 618

AP *see* anti-personnel

APEX MaxMin data 439–40, 440, 459

apparent chargeability 377–8

apparent conductivity

electromagnetic methods 434, 438, 446, 449–52, 455–8, 460–6, 476–7

ground-penetrating radar 605

apparent resistivity

electromagnetic methods 445–9, 470, 477, 484–7, 484–7

induced polarization 385–7, 389, 389, 394–6

magnetotelluric methods 505–7, 507–9, 511–12, 514–19

very-low-frequency methods 497, 501–2, 504

apparent susceptibility 88

applied geophysics 1–2, 2

applied seismology *see* seismology

aquifers

electromagnetic methods 525–6

seismic reflection surveys 263–7

*see also* hydrogeology

archaeo-geophysics 2

archaeological investigations

gravity methods 66–7, 75

ground-penetrating radar 536, 603–8

Archie's Law 292

ARM *see* anhysteretic remanent magnetization

array effect 231

artificial membranes 346–7

Askania gravimeters 27–8

Association of Geotechnical Specialists (AGS) 17

astatic/unstable gravimeters 27–31

asymmetric anomalies 116

AT *see* anti-tank

attenuation

ground-penetrating radar 540–4, 541, 575

seismology 153–4, 156

attribute analysis 558

audio-frequency magnetotelluric (AMT) method 505–8, , 517, 519

audio magnetotelluric (AMT) surveys 445–7

autocorrelation 236

automated array scanning 303–6

automatic sounding inversion techniques 318–21, 319, 323, 329

auxiliary curves 313–15, 314–15

AWD *see* accelerated weight drop

axial modulus 145–6

$\beta$ -particles 626

back-projection imaging 284–6, 286

back-propagation imaging 284–6, 286

backfilled voids

gravity methods 64, 69–70, 69, 71

ground-penetrating radar 602, 604

seismic refraction surveys 201–3

self-potentials 369–70

background potential 349

- badgers 618–23, **623**  
 Badlands Bombing Range (USA) **140–1**  
 balance magnetometers 95, **95**  
 Barkhausen jumps 87  
 base metal exploration 384–92  
 base-of-salt surfaces 511–12  
 bathymetry surveys 435  
 Bell marine gravimeter (BGM-3) 31–2  
 beta/gamma arrays 305–6, **305**  
 Betsy guns **158**  
*BGM-3* *see* Bell marine gravimeter  
*BGS* *see* British Geological Survey  
*BHR* *see* borehole radar  
*Bindschadler Ice Stream (BIS)* 581–3, **583**  
 bio-geophysics 2  
*BIS* *see* Bindschadler Ice Stream  
*BLHS* *see* Borax Lake Hydrothermal System  
 blind zones *see* hidden layers  
 block layout 222, **226**  
 blunderbuss approach 6  
 body waves 145–6  
 Boliden gravimeters 27–8  
 boomer  
   seismic reflection surveys 273, 276–83, **277–81**  
   seismology 162–3, 165, **165**  
*Borax Lake Hydrothermal System (BLHS)* 472–6, **473**  
*Borden test cells* 574–5, **574–5**  
 borehole radar (BHR) 609–20, **613–20**  
 boreholes 2–4  
   aquifers 263–7, **264–5**  
   correlations with seismic data 246–50, 277–8  
   cross-hole seismology 225–9  
   electrical resistivity 334, **338**, 340–3  
   electromagnetic methods 426–30, **427**, 459, 464–5, 474–5, 479–80, 525–9, **527**, **529**, **532**  
   ground-penetrating radar 573–4, 609–20, **613–20**  
   radiometrics 622, 632–3, 638–40  
   stratigraphic control 259  
   vertical seismic profiling 224–5, **227–8**, 249–50, 287  
*Bott criteria* 55, **59**, **60**  
 bottom-drag cables 182  
 Bouguer anomaly 44, **46**  
   Bott criteria 55, **59**, **60**  
   depth determinations 51–2, **51**  
   Euler deconvolution 54–5, **58**  
   geometric forms 47–53, **48–9**, **51**  
   interpretation 45–59, **64**, **70**  
   mass determination 52–3  
   principle of continuation 53–4, **57**  
   regionals and residual anomalies 46–7, **47**  
   second derivatives 53–5, **54–6**  
 Bouguer correction 35, **35**, 36–43, **36**, **42–3**  
 Bouguer gravity profiles **442**  
 bouldery rock glaciers 326, 329  
 British Geological Survey (BGS) 642–3  
 brownfield sites 3, 459–62  
 bubble pulse sources 159–62, **160–3**  
 Buffalo guns 203  
 building corrections 41, 43  
 bulk modulus 145–6  
 burial chambers *see* crypts  
 burial mounds **605–7**, **608–9**  
 buried channels 257–9, 475  
 buried container/object detection  
   geomagnetic methods 127–8, **131–3**, **136**  
   seismic reflection surveys 286, 288  
 buried dolines *see* sinkholes  
 buried foundations 326–8, 638–9  
 buried miner location 207–9, **208–9**  
 buried Roman structures 604–5, **605–7**, 607  
 buried valleys 67–8, **75**  
 Burris gravimeters 30  
 Butterton Dyke (England) 119–22  
 cables *see* underground pipe detection  
 CAD *see* computer aided design  
 Cagnard apparent resistivity 497, **502**  
 Cannikin profiles 514–15  
 capacitative coupling 307  
 capacitative resistivity imaging (CRI) 307–8, **308**  
 cavity detection  
   electromagnetic methods 455–7, 480–6, 501–2, **503–4**  
   gravity methods 63–6, 69–70  
   *see also* backfilled voids  
 CBA *see* cost-benefit analysis  
 CBNG *see* coal bed natural gas  
 CCS *see* concentric circle shooting  
 CCTV *see* closed-circuit television  
 CDI *see* conductivity depth images  
 cellars 600–1  
 Central Mineral Belt Uranium Project (Labrador) 59  
 centrifugal acceleration 20–1  
 Century zinc-lead-silver deposit (Australia) 387, 392  
 Cerro Prieto geothermal field (Mexico) 357–8, **360**  
 chair diagrams 570–1  
 Chalkidiki copper ore deposit (Greece) 359, **362**  
 charge occurrence probability (COP) 356–7, 369  
 chargeability 376–8, 378, **381**, 382, 384, 387, **390–1**, **397**, **400–1**  
 charged-body potential *see* mise-a-là-masse  
 chemical remanent magnetization (CRM) 89  
 chimney-collapse subsidence 265, 267–9  
 civil engineering pile testing 341–3, **343–4**  
 closed landfills 366  
 closed-circuit television (CCTV) 599  
 CMP *see* common midpoint  
 coal bed natural gas (CBNG) 450–5  
 coal mines 36–8  
 coastal defences 602–3  
 coercivity 87  
 coherence 239  
 coherent noise 14–15, **15**, 219–20  
 Cole–Cole relaxation spectra 379–81, **380–1**, 383, 389, 398, **401**  
 collapsed dolines *see* sinkholes  
 collapsed mines 207–9  
 Columbia Test Site (Canada) **122**  
 common midpoint (CMP)  
   ground-penetrating radar 553, 555, 557, 570, 576–8, 609–11, **610**  
   seismic reflection surveys 218–20, **219–20**, 227, 230, 236–41, **240–1**  
 common shot gathers 222, **230**  
 commutativity 228  
 complex conductivity 549  
 complex permittivity 549  
 complex refractive index method (CRIM) 548, 554  
 complex resistivity *see* spectral IP  
 Compton scattering 628, 634–5, 639, **641**  
 Compton stripping ratios 634–5, 635  
 computer aided design (CAD) 17  
 computer-based analytical methods 47, **50**, **54**  
 concentric circle shooting (CCS) 224  
 conductivity depth images (CDI) 424, 448–9, **450–1**, **453**  
 cone penetration testing (CPT) 140–1, 215, 247–51, **249–50**, 277–8  
 constant-velocity gathers (CVG) 238–9, **239**  
 constant-offset method 220–1  
 constant separation traversing (CST) 307–10, **307**, 336

- construction applications 536  
contact resistances 308–9  
contaminant plumes  
  electromagnetic methods 476–80  
  self-potentials 363–4  
continuation principle 53–4, 57, 102–3  
continuous surface wave systems (CSWS) 208, 209–11  
continuous velocity change 192–3  
continuous vertical electrical scanning (CVES) 304–6, 305  
continuous-wave (CW) systems 431–65  
  applications and case histories 441–68  
  brownfield site mapping 459–62  
  cavity detection 455–7  
  computer analysis 437–9  
  depth sounding 437–40  
  fixed-source systems 432–3  
  frozen ground 457–9  
  groundwater investigations 445–55  
  interpretation methods 437–40  
  landfill investigations 463–6, 463, 464–6  
  mineral exploration 441–5  
  moving-source systems 433–7  
  profiling methods 437–40  
  resolution 439–40  
  tilt-angle methods 431–2, 432  
controlled-source audio-frequency magnetotelluric (CSAMT) method, 505–8, 506, 507, 513–14, 514  
controlled-source electromagnetic (CSEM) methods 403  
  applications and case histories 511  
  induced polarization 389  
  seaborne EM surveys 420, 422–6, 425  
controlled-source magnetotelluric (CSMT) methods 517–20, 520  
convolution 233–6, 235  
COP *see* charge occurrence probability  
copper ore deposits  
  induced polarization 387, 391  
  self-potentials 359, 362  
correlation techniques 235–6, 246–50, 277–8  
cost-benefit analysis (CBA) 2–3, 7–8  
Covington aquifer (USA) 263–7, 267  
CPT *see* cone penetration testing  
crevasse detection 581–4  
CRI *see* capacitative resistivity imaging  
CRIM *see* complex refractive index method  
critical damping 170, 172  
critical distance 180–1  
critical frequency 380  
critical refraction 151–2, 152, 179–81  
CRM *see* chemical remanent magnetization  
cross-correlation 236  
cross-hole IP imaging 402  
cross-hole radar tomography 612–14, 614, 616–17, 621  
cross-hole seismology 225–9  
crossover distance 181, 183, 189  
cryogenic magnetometers 99  
crypts 75, 600–2, 603–4, 603  
CSAMT *see* controlled-source audio-frequency magnetotelluric  
CSEM *see* controlled-source electromagnetic  
CSMT *see* controlled-source magnetotelluric  
CST *see* constant separation traversing  
CSWS *see* continuous surface wave systems  
cumulative response functions 434–5, 435, 435  
Curie temperature 86, 94  
curve-matching by computer 314–17  
CVES *see* continuous vertical electrical scanning  
CVG *see* constant-velocity gathers  
CW *see* continuous-wave  
dams 366–9, 594–8  
Dar Zarrouk parameters 298  
data handling  
  geomagnetic methods 103  
  geophysical surveys 16–18  
  ground-penetrating radar 554–60  
  radiometrics 633–6, 635–6  
  seismic reflection surveys 217, 228–46, 229  
  smoothing statics 231  
dead time corrections 633  
decay of the relaxation field 522  
declination of magnetic fields 92, 94  
deconvolution  
  electrical resistivity 318–21, 319–21  
  ground-penetrating radar 592  
  seismic reflection surveys 228–9, 233–6, 236  
deep look radio echo sounding (DELORES) 580–1  
deep ocean surveys 269–70  
deep-well injection 263–5  
DEEPEM surveys 478, 481  
DeepLook-EM system 429–30, 429–30  
Definitive Geomagnetic Reference Field (DGRF) 93  
deghosting 234  
delay time method (DTM) 188–9, 188, 189, 193, 203, 207  
DELORES *see* deep look radio echo sounding  
Delta sparker system 165–6  
DEM *see* digital elevation models  
demagnetization factor 88  
demultiplexing data 229–30  
densities of geological materials 22–4, 22–4  
density logging tools 246–7, 248  
depth conversion 558  
depth determinations  
  electromagnetic methods 437–40  
  geomagnetic methods 112–15, 114–15, 115–16, 118–23  
  gravity methods 51–2, 51  
depth of penetration 411  
dereverberation 234, 242  
deringing 234  
detectable limits 252  
detrital remanent magnetization (DRM) 89  
DGRF *see* Definitive Geomagnetic Reference Field  
diamagnetism 85–7, 86  
diamond mining 613  
dielectric conduction 290  
dielectric permittivity 606  
dielectric properties of earth materials 546–52, 551–2, 554  
differential global positioning systems (dGPS) 3, 15–16  
differential spectrometers 630–1  
diffraction hyperbolae 244–5  
diffraction stack migration 243–5, 244  
diffraction waves 151–2, 152–4, 154  
diffusion depth 468  
diffusion potentials 350, 351  
DIGHEM system 413  
digital elevation models (DEM) 41, 205  
dip move-out (DMO) 236, 243, 245–6, 246, 252  
dip poles 90–1, 91  
dipolar field 90–2  
dipole-dipole arrays  
  electrical resistivity 294–8, 294, 296, 298, 301–4, 301–2, 304, 323  
  electromagnetic methods 424, 427  
  induced polarization 374, 375–6, 382, 384, 395  
dipping planes  
  raypath geometry 184–5  
  seismic reflection surveys 219, 243, 252–3  
  self-potentials 357

- discontinuous reflectors 253–4  
 dispersion curves 211–15, 383–4  
 dissolved oxygen (DO) 364  
 diurnal variations 95, 101–2, 102  
*Dix formula* 236  
*DMO* *see* dip move-out  
*DO* *see* dissolved oxygen  
 Doll-Maillet equivalence 318  
 domain theory 86–7  
 downward continuation 53–4, 57  
 dredging operations 247, 276–9  
 Drigg low level radioactive waste disposal site (England) 398, 400, 402  
 drinking water contamination 513–14  
*see also* aquifers; hydrogeological investigations  
 DRM *see* detrital remanent magnetization  
 drop-weight devices 156–7, 157–8  
 DTM *see* delay time method  
 dual neutron probes 632–3  
 dual-coil EM systems 420, 433, 433, 457, 459  
 dykes *see* embankments  
 dynamic corrections 236–41  
 dynamic probing 250
- earth dams 366, 596–8, 598  
 earthquake prediction  
*seismic reflection surveys* 265–6  
*seismic refraction surveys* 215–16  
*self-potentials* 363  
 Earth's magnetic field 89–95, 90  
*components* 89–94  
*dipolar field* 90–2, 92  
*non-dipolar field* 92–3  
*qualitative data* 104–5  
*time variable field* 94–5  
 echo sounding 266–8  
 eddy currents 407–8, 440, 467  
 editing data 230  
 EEL scintillometer 642–3  
 effective porosity 549–50  
 EGA *see* Engineering Geophysics Advisors  
 EGG *see* Exploration Gravity Gradiometer  
 EK *see* electrokinetic  
 elastic moduli 145–6, 145, 146  
 electric field (ELF) free-fall recorders 422  
 electrical reflection coefficient 299  
 electrical resistivity 289–347  
*2D and 3D modelling* 321–6, 322, 324–5  
*applications and case histories* 326–36  
*automated array scanning* 303–6  
*civil engineering pile testing* 341–3, 343–4  
*common materials and rocks* 291–2  
*constant separation traversing* 307–10, 307  
*current flow in a homogeneous earth* 292–3, 292, 293  
*curve-matching by computer* 314–17  
*electrode configurations* 294–8, 294–5, 295–7, 298  
*engineering investigations* 326–30, 341–3  
*equivalence and suppression tests* 317–18, 318  
*field problems* 308–11  
*generalized case* 293–4, 293  
*geomagnetic methods* 125–6, 128  
*geometric factors* 292, 293–301, 294–5  
*glaciological surveys* 333–7, 336–8  
*ground-penetrating radar* 335–6, 338–9, 344, 549–50  
*groundwater surveys* 330–1, 344–6, 346  
*historical development* 289  
*interpretation methods* 311–26  
*inversion and deconvolution* 318–21, 319–21, 323, 329  
*landfill surveys* 331–3, 332–5, 346–7  
*leak detection through artificial membranes* 346–7, 347  
*master curves* 313–15, 313–15  
*media with contrasting resistivities* 298–301, 299–300  
*mineral exploration* 59, 333, 338–41  
*mise-a-là-masse method* 336–46  
*modes of deployment* 301–11  
*noise* 13–14  
*principles* 289–93  
*qualitative methods* 311–13  
*saline intrusion* 9  
*seismic refraction surveys* 202–5, 205  
*tree root studies* 344, 344–5  
*true resistivity* 289–92, 290–1, 290, 299  
*vertical electrical sounding* 301–6, 303, 305, 309–11, 315, 317, 332, 334  
*electrical resistivity tomography (ERT)*  
*applications and case histories* 326–36, 344  
*electromagnetic methods* 455, 465  
*engineering investigations* 326–30, 329–30  
*geomagnetic methods* 133, 134  
*geotechnical investigations* 517–20, 520, 527–8, 531  
*glaciological surveys* 333–6, 336  
*gravity methods* 64, 68  
*ground-penetrating radar* 587  
*groundwater surveys* 330–1  
*interpretation methods* 321–6, 325  
*landfill surveys* 331–3, 332–5  
*mineral exploration* 333  
*modes of deployment* 306–7, 309–10  
*seismic refraction surveys* 203–5, 205  
*self-potentials* 369–70  
*electrochemical potentials* 351–2, 351–2  
*electrode configurations* 294–8, 294–5, 295–7, 298  
*electrode polarization* *see* overvoltage effect  
*electrokinetic (EK) surveying* 350–1, 350, 363, 370–2, 371  
*electrolytic conduction* 290  
*electrolytic polarization* 375, 375  
*electromagnetic conductivity* 9  
*electromagnetic coupling* 381–2  
*electromagnetic (EM) methods*  
*airborne* 411–18, 414, 448, 450, 452, 469, 478, 486–8, 486–7, 493  
*applications and case histories* 404, 404, 407, 441–68, 470–93, 499–502,  
 509–19, 525–33  
*boreholes* 426–30  
*brownfield site mapping* 459–62  
*cavity detection* 455–7, 480–6, 501–2, 504  
*classification* 405  
*computer analysis* 437–9, 468–70  
*contaminant plume mapping* 476–80  
*controlled-source methods* 403, 420, 422–6  
*depth of penetration* 411  
*depth sounding* 437–40  
*electromagnetic waves* 407–11  
*far-field systems* 431  
*field measurements* 503–7, 522–4  
*fixed-source systems* 432–3  
*focused-source methods* 420, 426  
*frozen ground* 457–9  
*generalized surveying schematic* 410  
*geological mapping* 486–8  
*geotechnical and environmental investigations* 488–93, 513–16, 517–19  
*glaciological surveys* 79  
*groundwater investigations* 445–55, 470–6, 516–17  
*hydrocarbon investigations* 510–13  
*hydrogeological surveys* 514, 525–33  
*interpretation methods* 437–40, 468–70, 498–9, 507–9, 525  
*inversions* 440, 487, 514–15

- landfill investigations 463–6, 463, **464–6, 479**  
large-loop systems 405, 407, 427–9  
magnetic resonance sounding 519–33  
magnetometric resistivity 404, **406**, 421–2  
magnetotelluric methods 505–19  
metallotelluric methods 420, 421  
mineral exploration 59, 441–5, 469, 478–80, 499–501, 509–10  
moving-source systems 433–7  
multi-transient methods 420  
natural-source 431  
near-field systems 431  
noise 468, 522–3  
polarization 410–12  
principles 403–30, 495–8, 502–3, 505, 519–22  
profiling methods 437–40  
pulse-transient methods 467–93  
resolution 439–40  
seaborne 418–26  
small-loop systems 404, 447  
surveying principles 407–11  
systems 404–7, 431–93, 495–533  
telluric method 502–5, **505**  
tilt-angle methods 431–2  
topographic effects 498  
unexploded ordnance mapping 492–3, **492–3**  
*see also* continuous-wave systems; frequency-domain electromagnetic methods; ground-penetrating radar; time-domain electromagnetic methods; very-low-frequency methods  
electromagnetic induction (EMI) 139  
electromagnetic spectrum **409**  
electronic conduction 290  
electroseismic response *see* electrokinetic surveying  
elephants 166, 169–70  
elevation corrections  
    gravity methods 36–8, 37  
    seismic reflection surveys 231, 233  
    self-potentials 363, **365**  
ELF *see* electric field  
Ellesmere Port (United Kingdom) 133  
ellipses of rotation **20**  
Elvis land vibrators **168**  
EM *see* electromagnetic  
embankments 364–8, 594–7, **597**  
EMI *see* electromagnetic induction  
energy loss 540–4, 541  
engineering applications  
    cavity detection 63–6, 69–70  
    electrical resistivity 326–30, **329–30**, 341–3  
    gravity methods 59–66, 69–70  
    ground-penetrating radar 536, 587–604  
    radiometrics 638–9  
    seismic refraction surveys 184  
engineering geophysics 1  
Engineering Geophysics Advisors (EGA) 6–7  
environmental geophysics 1–2  
environmental radiation sources 634  
EOC *see* Explosive Ordnance Clearance  
Eötvös correction 41–4, **44, 45**  
equipotential surfaces 20  
equivalence tests 317–18, **318**  
ERT *see* electrical resistivity tomography  
estuarine environments 281–3  
ETRS *see* European Terrestrial Reference System  
Euler deconvolution 120, **121, 127**  
    geomagnetic methods 118–23  
    gravity methods 54–5, 58  
European Terrestrial Reference System (ETRS) 16  
Exploration Gravity Gradiometer (EGG) 34  
exploration seismology *see* seismology  
explosive energy sources 159, **159**  
Explosive Ordnance Clearance (EOC) contractors 140–1  
facies analysis 560–1, 565–8, 571  
Faial Island 78, **80**  
FALCON airborne gradiometer 32–3  
false alarm rates (FAR) 136, 617  
fan shooting 143  
FAR *see* false alarm rates  
far-field electromagnetic (EM) systems 431  
Farallon Islands Radioactive Waste Dump (FRIWD) 642–3  
Faro lead-zinc deposit (Yukon) 59, **61**  
fault zones  
    geomagnetic methods 111–12, **119**  
    ground-penetrating radar 570–2, 614  
    seismic reflection surveys 278  
FE *see* frequency effect  
feathering 174, 233  
FEM *see* finite-element models; frequency-domain electromagnetic ferrimagnetism 85–7, **86**  
ferromagnetism 85–7, **86–7**  
field statics 230–3  
field strength 83–4, 84, 98, 105  
field surveys  
    electrical resistivity 308–11  
    electromagnetic methods 503–7  
    geomagnetic methods 100–1  
    seismic refraction surveys 181–2, 210  
figure of merit (FOM) ratings 98  
filtering techniques  
    electromagnetic methods 498–500  
    seismic reflection surveys 241–3, **242–3**  
finite-element forward modelling 319–20, **320**  
finite-element models (FEM) 72–3  
fixed-coil instruments 436  
fixed-source EM systems *see* Sundberg method; Turam method  
fixed-wing airborne electromagnetic (*fw*-AEM) methods 411–17  
Flexitor system 159  
flux density 83–4, **84**  
fluxgate gradiometers 99–100, 119  
fluxgate magnetometers 95–7, **95–7**  
fly ash water pond leakage 396–7, **399–400**  
FNI *see* frequency-normalized impedance  
focused-source electromagnetic (FSEM) methods 420, 425  
fold of coverage 218, **221**  
FOM *see* figure of merit  
forensic applications  
    ground-penetrating radar 536, 607, 609  
    seismic reflection surveys 286–8  
forensic geophysics 2, 5  
four-layer models 311–13  
Fourier analysis 242–3, 243  
Fraser filtering 498, **500**  
free-air correction 35–6, **35, 36**  
frequency effect (FE) 378, **385–6, 394**  
frequency-domain electromagnetic (FEM) methods  
    applications and case studies 445, 448, 450  
    principles 404, 411–13, **415, 420, 423, 429**  
frequency-domain IP measurements 373, 377–9  
frequency-normalized impedance (FNI) 497  
fresh-water surveys 271–2  
Fresnel zones  
    ground-penetrating radar 542–3, 545–7, **547, 606**  
    seismic refraction surveys 252  
seismology 150, **150, 150**

- FRIWD *see* Farallon Islands Radioactive Waste Dump  
 frozen ground 457–9  
*see also* permafrost  
 FSEM *see* focused-source electromagnetic  
 Full Tensor Gradient (FTG) gradiometers 33–4  
*fw-AEM* *see* fixed-wing airborne electromagnetic
- gamma-radiation 626, 627–8, **628**, 630–3, **631–2**, 638, **639–40**  
 gain recovery 230  
 Gallery correction 36  
 galvanic coupling 307  
 gas accumulations 272–6  
 gas gun bubble pulse sources 162  
 Gauss's theorem 52  
 GCM *see* ground conductivity meters  
 GDT *see* geophysical diffraction tomography  
 GEEP *see* geophysical exploration equipment platform  
 Geiger-Muller counters 628–9  
 GEM systems 413, 435–6, **436**, **447–8**, 460–3  
 Gemini Prospect 510–12, **512**  
 generalized reciprocal method (GRM) 190–1, **190**, **191**, **198–9**, 207  
 geo-battery model 352–3  
 GeoChirp 166, **170**  
 Geodetic Reference System 1967/1980 (GRS67/80) 21–2  
 geodetic surveys 20, 21  
 geoelectric basement 316  
 geoelectric sections 478  
 geoelectric surveys **393**  
 Geographical Information Systems (GIS) 16, 17  
 geoids 20–1, **21**  
 geological investigations  
     ground-penetrating radar 536, 548, 565–72, **566–72**, 568  
     induced polarization 398, 400, 402  
 Geological Long Range Inclined Asdic (GLORIA) 269–71  
 Geological Survey of Canada 25  
 geomagnetic methods 83–141  
     2D and 3D modelling 115–18, 126  
     acid tar lagoon surveys 133–6, **136–7**, 137  
     aeromagnetic investigations 105–7, **109**, **114**, **119**, **121**, 123–5, **124**, **126**  
     airborne magnetometer systems 100, **100**, 140  
     applications and case histories 83, 84, 123–41  
     buried container/object detection 127–8, **131–3**, **136**  
     concepts and units 83–7  
     cryogenic magnetometers 99  
     data reduction 103  
     depth determinations 112–15, **114–15**, **115–16**, 118–23  
     dia-, para-, ferri- and ferromagnetism 85–7, **86–7**  
     Earth's magnetic field 89–95, **90**, 104–5  
     Euler deconvolution 118–23  
     field strength 83–4, 84, 98, **105**  
     field surveys 100–1  
     flux density 83–4, 84  
     fluxgate magnetometers 95–7, **95–7**  
     geometric forms 110–12, **110–14**  
     gradiometers 99–100, 119, 122, **130**, 136, 139–40  
     historical development 83  
     induced and remanent magnetization 85, **85**, 88–9, 89, 112, 114, 123–4, **129**  
     instrumentation 95–100  
     intensity of magnetization 84–5, 85  
     Königsberger ratios 88–9, 89–90, 90, 125  
     landfill investigations 128, 133–4  
     magnetic properties of rocks 87–9  
     magnetic surveys 100–3  
     mineral exploration 125–6
- noise and corrections 101–3, 105, 127–9  
 pattern analysis 105–7, **109**, **114**, **119**, **121**  
 permeability 83–4  
 profile anomalies 105–8, **106–8**, **107**, 116–17, 126  
 qualitative data 103–7  
 quantitative data 107–23  
 reduction to the pole method 114–16  
 resonance magnetometers 97–9, **97–9**  
 susceptibility 84, 87–8, 87, **88**  
 time variable field 94–5  
 torsion/balance magnetometers 95, **95**  
 underground pipe detection 126–7, **130**  
 unexploded ordnance 135, 136–41, **138–41**
- geomagnetic poles 90–1  
 geomembranes 346–7, **347**  
 geometric corrections 633–4  
 geometric forms  
     electrical resistivity 292, 293–301, 294–5  
     geomagnetic methods 110–12, **110–14**  
     gravity methods 47–53, **48–9**, 51  
     self-potentials 355–7  
 geometrical spreading 152–3, **155**  
 Geometrics MagCat 133, **135**  
 geophones  
     seismic reflection surveys 218–21, 231–2, **234**, 249  
     seismic refraction surveys 181–2, **181**, 197–201, 203, 208–11  
     seismology 170–3, **171–2**  
 geophysical anomalies 9–13  
 geophysical diffraction tomography (GDT) 283–8, **287–8**  
 geophysical exploration equipment platform (GEEP) **445**  
 geophysical surveys 2–3  
     costs and budgeting 7–8, 8  
     data analysis 16–18  
     electromagnetic methods 407, 514, 517–20, 525–33  
     general philosophy/survey style 5  
     ground-penetrating radar 579–80, 597–8  
     induced polarization 387–8  
     intrusive investigations 2–5, 4  
     matching methods to applications 5–6, 6  
     noise 13–15, **14–15**  
     optimal line configuration and survey dimensions 9–11  
     planning strategies 5–7, 7  
     position fixing 3, 15–16, **17**  
     profiling and mapping 9  
     self-potentials 369  
     spatial aliasing 11–13, **11–13**  
     station interval selection 11–13, **11–13**  
     statistical sampling techniques 2–3, 3  
     survey constraints 7–8  
     survey design 9–18  
     target identification 9–10, **9–10**
- GeoStreamer 173  
 geotechnical surveys  
     electromagnetic methods 488–93, 517–19  
     seismic refraction surveys 199–201, **200–1**, 202, **205**  
     seismology 164–5
- GEOTEM system 412, 414–18, **417–18**
- geothermal surveys  
     induced polarization 390–1, 393–4  
     self-potentials 357–60
- GGI *see* gravity gradiometer instruments  
 GIS *see* Geographical Information Systems  
 glacial hazards 586–9  
 glacial lake outburst floods (GLOF) 334–5, 586–9  
 glacial stratigraphic control 259–63  
 glacier thickness determinations 79–81  
 glacio-geophysics 2

- glaciological surveys  
 electrical resistivity 333–7, **336–8**  
 gravity methods 78–81, **81**  
 ground-penetrating radar 536, 578–87
- global geophysics 1
- global positioning systems (GPS)  
 gravity methods 26  
 seismic refraction surveys 206
- GLOF *see* glacial lake outburst floods
- GLORIA *see* Geological Long Range Inclined Asdic
- gold deposits 361, 364, 614–15
- golf courses 597–600, **599–600**
- GPR *see* ground-penetrating radar
- GPS *see* global positioning systems
- gradient-amplitude ratio method 51–2
- gradient arrays 294, 295
- gradiometers 99–100, 119, 122, **130**, 136, 139–40
- grain polarization *see* overvoltage effect
- grain-size distribution 379–80, 548
- granite plutons 55, 59–60
- graphical methods 47–50
- graphite phyllites 355–6, 358
- graves *see* crypts
- gravity gradiometer instruments (GGI) 33–4
- gravity methods 19–81  
 absolute gravity 24–5, **25**  
 applications and case histories 20, 20, 59–81  
 archaeological investigations 66–7, **75**  
 Bott criteria 55, 59–60, 59, 60  
 Bouguer anomaly 44, 45–59, 46, 64, **70**  
 Bouguer correction 35, **35**, 36–43, 36, **42–3**  
 building corrections 41, 43  
 buried valleys 67–8, **75**  
 cavity detection 63–6, 69–70  
 corrections to gravity observations 34–45, 34–7, 40–1, **44**  
 densities of geological materials 22–4, 22–4  
 depth determinations 51–2, **51**  
 engineering applications 59–66  
 Eötvös correction 41–4, **44, 45**  
 Euler deconvolution 54–5, 58  
 free-air correction 35–6, **35**, 36  
 geometric forms 47–53, **48–9**, 51  
 glaciological surveys 78–81, **81**  
 Hammer charts 39–41, **39**, 40  
 hydrogeological applications 67–71  
 instrumental drift 34–5  
 instrumentation 24–34, **25–7**  
 interpretation of Bouguer anomaly 45–59, 64, 70  
 isotactic correction 44–5  
 latitude 20–2, 22, 35  
 marine and airborne gravity systems 31–4, **32–3**  
 mass determination 52–3, 52–3  
 matching methods to applications 5–6, 6  
 mineral exploration 59  
 oil industry applications 69–71  
 permafrost terrain 66, **74**  
 physical basis 19–24  
 principle of continuation 53–4, 57  
 regional and residual anomalies 46–7, **47**, **61–2**, 65–6, **74**, 79–81, **81**  
 relative gravity 25–6  
 second derivatives 53–5, **54–6**  
 stable gravimeters 27–8, **27–8**  
 technique and characteristics 19  
 terrain correction 38–41, **39**, 40–1  
 theoretical basis 19–20  
 tidal effects 34–5, 81
- units of gravity 20  
 unstable gravimeters 27–31, 29–30  
 variation of gravity with latitude 20–2  
 volcanic hazards 71–8
- GRAVMAG models 65, **72**
- Great Dyke (Zimbabwe) 125, 127, **127**
- GRM *see* generalized reciprocal method
- ground-based surveys 634
- ground conductivity 3, 16
- ground conductivity meters (GCM) 404, 433–4
- ground-penetrating radar (GPR) 335–6, **338–9**, 344, 535–623  
 animals 618–23  
 applications 404  
 applications and case histories 535–7, 536–7, 565–623  
 archaeological investigations 536, 603–8  
 boreholes 573–4, 609–20  
 commercial systems 537  
 data processing 554–60  
 dielectric properties of earth materials 546–52  
 energy loss and attenuation 540–4, 541  
 engineering and construction applications 536, 587–604  
 environmental investigations 536  
 forensic applications 536, 607, 609  
 geological investigations 536, 548, 565–72, **566–72**, 568  
 glaciological surveys 536, 578–87  
 groundwater investigations 571–5, **571–5**  
 historical development 535  
 horizontal and vertical resolution 544–6, 544, 549  
 hydrogeological investigations 562–4, **562–3**, 571–8, 612–13, 616  
 interpretation methods 538, 560–4, **561**  
 lacustrine environments 567–70  
 legislative issues 537  
 migration 558, **570**, 607–9, 612  
 mineral exploration 613–17  
 modes of operation 537–8, 552–7  
 post-recording data processing 557–60, 557, **559**  
 principles 403, 537–40  
 quantitative analysis 558–60, 562  
 radar range equation 542  
 radiowave propagation 539–46, 539, 550–2, **550**, 551–2, **577**, 578  
 sedimentary sequences 565–7  
 simultaneous data acquisition/processing 556  
 temporal resolution 545–6, **546**  
 theoretical principles 539–40  
 unexploded ordnance and landmine detection 617–18  
 voids within manmade structures 599–604  
 wide-aperture radar mapping 607–9
- ground radar 5
- ground roll 147
- ground stiffness 169, 208–12, **210**, **212**
- grounded wire electromagnetic (EM) methods 405
- groundwater investigations  
 electrical resistivity 330–2, 344–6, 346  
 electromagnetic methods 445–55, 470–6  
 ground-penetrating radar 571–5, **571–5**  
 induced polarization 391–2, 395, **399–400**
- GRS67/80 *see* Geodetic Reference System 1967/1980
- Gulf gravimeters 27–8, **28**
- h*-AEM *see* helicopter airborne electromagnetic
- Hagedoorn's Plus-Minus method 143–4, 187, 188–90, **188**, 189, 203–4
- half-life 626–7, 626
- Hammer charts 39–41, **39**, 40
- Hammerhead sensor array 140–1
- hazardous waste 258–9, 263–5  
*see also* radioactive waste
- HED *see* horizontal electric dipoles

- helicopter airborne electromagnetic (*h*-AEM) methods 411, 413, 415, 417–18, 419, 448, 450–1, 470, 488, 493  
 hidden layers 179, 191–2, 192  
 high-resolution seismic reflection surveys 217, 255, 257–65, 258–69, 266–83  
 high-resolution waterborne energy sources 162–6, 164  
 high sulphidation gold deposits 361, 364  
 historical graves 603–4, 603  
*HLEM* see horizontal loop electromagnetic  
*HMD* see horizontal magnetic dipoles  
 Hooke's Law 26–7, 27, 144  
 horizontal electric dipoles (HED) 422–4  
 horizontal gravity gradients 63  
 horizontal loop electromagnetic (HLEM) methods 404, 436, 443–4, 458–9, 459  
 horizontal magnetic dipoles (HMD) 422–3, 434–5, 464  
 horizontal resolution  
   ground-penetrating radar 544–6, 549  
   seismic reflection surveys 250–2  
 horizontal slab anomalies 111–12  
 horizontal velocity analysis (HVA) 239  
 Hoyt gravimeters 27–8, 28  
 Huygens' Principle 149, 149, 152  
 HVA see horizontal velocity analysis  
 hydro-geophysics 2  
 hydrocarbon contamination 395–6, 398, 398  
 hydrocarbon exploration  
   applied geophysics 2  
   electromagnetic methods 429–30, 510–13  
   geomagnetic methods 133–6  
   gravity methods 69–71  
   induced polarization 376, 393  
   seismic reflection surveys 220, 231, 251, 255  
   seismic refraction surveys 182, 203–7, 205–7  
   seismology 143–4, 164–5  
 hydrogeological investigations  
   electromagnetic methods 514, 525–33  
   gravity methods 67–71  
   ground-penetrating radar 562–4, 562–3, 571–8, 612–13, 616  
   self-potentials 361–3, 366  
   see also groundwater investigations  
 hydrographic surveys 266–72  
 hydrophones  
   seismic reflection surveys 220–1, 227, 272  
   seismic refraction surveys 182, 203–5  
   seismology 173–7, 174–7  
 hyperbolic move-out 228–9  
 hysteresis loops 87, 87
- ice-covered lakes 567–70  
 ICE-MOSES 421–2, 421  
 ice shelves 81  
 igneous rocks  
   geomagnetic methods 87–9  
   gravity methods 23–4  
 IGRF see International Geomagnetic Reference Field  
 IGSN71 see International Gravity Standardization Net 1971  
 image-processing methods 119  
 impact seismic devices 155–7  
 impulse energy sources 157–63  
 IMPULSE system 413, 416  
 impulsive energy sources 209  
 inclination of magnetic fields 92, 94  
 incoherent noise 14–15, 15, 237  
 induced magnetization 85, 85, 129  
 induced polarization (IP) 373–402  
   apparent resistivity 385–7, 389, 389, 394–6  
   applications and case histories 373, 384–402  
   base metal exploration 384–92  
   chargeability 376–8, 378, 381, 382, 384, 387, 390–1, 397, 400–1  
   Cole–Cole relaxation spectra 379–81, 383, 389, 398, 401  
   data display 382–3  
   dispersion spectra 383–4  
   electromagnetic methods 381–2, 406  
   environmental applications 392–8  
   fly ash water pond leakage 396–7, 399–400  
   frequency-domain measurements 373, 377–9  
   frequency effect 378, 385–6, 394  
   geological investigations 398, 400, 402  
   geothermal surveys 390–1, 393–4  
   groundwater investigations 391–2, 395, 399–400  
   historical development 373  
   hydrocarbon contamination 395–6, 398, 398  
   inversions 383–6, 390, 398  
   ionic processes 376  
   landfill investigations 397–8, 401  
   macroscopic processes 375–6  
   measurement 376–84  
   membrane/electrolytic polarization 375, 375  
   metal factor 378, 385–6, 389  
   mineral exploration 59  
   mineralization texture 379–80  
   noise 381–2  
   normalized parameters 380, 400  
   origins of IP effects 374–6, 374  
   overvoltage effect 373–5, 374, 377, 395–6  
   phase-angle spectra 379–80, 382, 395, 400, 402  
   phase-domain measurements 373  
   pseudo-sections 382–5, 387, 392  
   slag deposits 392–5, 397  
   spectral IP 373, 379–81, 379, 388, 395  
   time-domain measurements 373, 376–7, 391–2  
 induction numbers 433–4  
 induction vectors 511  
 INPUT system 412  
 instrumental drift 34–5  
 integral spectrometers 630–1  
 intensity of magnetization 84–5, 85  
 interglacial marine sediments 576–8  
 International Geomagnetic Reference Field (IGRF) 92–4, 93, 103  
 International Gravity Formula 21–2, 22  
 International Gravity Standardization Net 1971 (IGSN71) 25  
 International Terrestrial Reference System (ITRS) 16  
 intra-array effect 231  
 intrinsic attenuation 153–4, 156  
 intrusive investigations 2–5, 4  
 inversions  
   electrical resistivity 318–21, 319–21, 323, 329  
   electromagnetic methods 440, 487, 514–15  
   gravity methods 66  
   induced polarization 383–6, 390, 398  
   ionic processes, induced polarization 376  
   IP see induced polarization  
   IRM see isothermal remanent magnetization  
   iron ore deposits 126, 130  
   isolines 9  
   isoresistivity maps 480  
   isotactic correction 44–5  
   isothermal remanent magnetization (IRM) 89  
   isotopes 625–6  
 ITRS see International Terrestrial Reference System  
 Karous-Hjelt current density pseudo-sections 500  
 Kildonnan (Arran, Scotland) 105, 108

- Kimheden orebody (Sweden) 359, **361**  
Kirchhoff migration 243–5, **244**  
Königsberger ratios 88–9, 89–90, 90, 125
- LaCoste-Romberg gravimeters 29–30, **29–30**, 31–2, 34  
lacustrine environments 567–70  
Lake Windermere (England) 271–3  
land streamers 177  
land surveys  
  seismic reflection surveys 220, 257–65  
  seismic refraction surveys 181–2  
land vibrators 164–5, **167–9**, 168–9  
landfill investigations  
  electrical resistivity 331–3, **332–5**, 346–7  
  electromagnetic methods 463–6, 463, **464–6**, **479**, **491**  
  geomagnetic methods 128, 133–4  
  ground-penetrating radar 573  
  induced polarization 397–8, 401  
  seismic refraction surveys 201–3, **202–5**, 211–12  
  self-potentials 363–4, 366  
landmine detection 617–18  
landslides 328–31  
large-loop electromagnetic (LLEM) methods 405, 407, 427–9  
Larmor frequencies 519–21, 525  
Larmor precession frequency 97–9, 98  
latitude effects  
  geomagnetic methods 92, 111–13  
  gravity methods 20–2, 22, 35  
Laws of reflection 151  
layback diagrams 16–17  
layer equivalence 298  
layer resistivity 298, **312**, 317–18  
layer thickness 298, 317–18  
layered-earth model 435  
leachates 463, 573  
leak detection  
  electrical resistivity 346–7  
  induced polarization 396–7, 399–400  
  self-potentials 364–9  
Lee arrays 294, 295  
legislative issues 537  
LEM *see* long antenna EM recorders  
liability insurance 7–8  
LIDAR scanning 205  
lift tests **562**  
limit of visibility 252  
line shooting 222  
linear digital filters 314  
lithology dependence 533  
live time corrections 633  
Lizard Peninsula (Cornwall, England) 123–6, **124–6**  
LLEM *see* large-loop electromagnetic  
Lockerbie (Scotland) 286–8  
logistics constraints 8  
long antenna EM recorders (LEM) **422**  
long-offset transient EM (LOTEM) 469  
long-wavelength anomalies, gravity methods 20–1  
longitudinal conductance 298–9, 317–18  
longitudinal resistivity 298  
LOTEM *see* long-offset transient EM  
Love waves 146–7, **146**
- macroscopic processes 375–6  
MagCat system 203–6, **206**  
magnetic fabric analysis 88  
magnetic field transfer function 509
- magnetic gradiometry 3  
magnetic noise 101  
magnetic resonance sounding (MRS) 519–33, **521**  
  applications and case histories 525–33  
  field measurements 522–4, **523–4**  
  hydrogeological surveys 514, 525–33, **526–33**  
  interpretation methods 525  
  principles of operation 519–22  
  relationships and figures of merit 522
- magnetic storms 95
- magnetic surveys  
  data reduction 103  
  field survey procedures 100–1  
  geomagnetic methods 100–3  
  matching methods to applications 5–6, 6  
  noise and corrections 101–3  
  station interval selection 13  
  *see also* electromagnetic methods; geomagnetic methods
- magnetic tilt angle 114
- magnetizing field strength 84
- magnetometric resistivity (MMR) 404, **406**, 421–2
- magnetopause 89–90, **90**
- magnetosphere 89–90, **90**
- magnetostratigraphy 91
- magnetotellurics (MT) methods 505–19  
  applications and case histories 509–19  
  environmental investigations 513–16  
  field measurements 505–7, **506**  
  geotechnical investigations 517–19  
  groundwater investigations 516–17  
  hydrocarbon investigations 510–13  
  interpretation methods 507–9  
  mineral exploration 509–10  
  principles of operation 505, 506
- MALM *see* mise-a-là-masse
- manmade cavity detection 63–6, 69–70, **70–1**
- manmade structures *see* engineering applications
- marine gravity systems 31–4, **32–3**, 36
- marine hydrophones *see* streamers
- marine metallotellurics (MMT) 420, 421
- marine surveys  
  electromagnetic methods 418–26, 511–13, **512**  
  geoHazards 272–6  
  ground-penetrating radar 576–8  
  position fixing 16–17, **17**  
  radiometrics 631–2, 643  
  resource evaluation and dredging 247, 276–9  
  seismic reflection surveys 232–3, 256, 272–9  
  seismic refraction surveys 182  
  marine vibrators 165–6, 170  
  mass determination 52–3, 52–3  
  massive ice 66, **74**, **328**  
  massive sulphide ore deposits  
    electromagnetic methods **428**, **442**, 480  
    self-potentials 352–3  
  master curves 313–16, **313–15**, 498  
  MASW *see* multichannel analysis of shear waves  
  Maxipulse system **159**  
  MAZ *see* multi-azimuth  
  mega-scale glacial lineations (MSG) 580–1  
  MEGATEM system 414–18, **417–18**  
  membrane polarization 375, 375  
  metal factor (MF) 378, **385–6**, **389**  
  metal pipes *see* underground pipe detection  
  metallic minerals 24  
  metallotelluric (MT) methods 420, 421

- metamorphic rocks  
 geomagnetic methods 87–9  
 gravity methods 23–4  
 seismology 148
- MF *see* metal factor
- micro-gravity surveys 19, 26  
 applications 63–80, 65–8, 73, 75, 80  
 corrections to gravity observations 40–1
- microporosity 550
- microprocessor-controlled resistivity traversing system 304
- micro-tremor survey method (MSM) 215
- midpoint-offset coordinate systems 224–5, 224–5
- Mie scattering 154, 540
- migration  
 ground-penetrating radar 570, 607–9, 612  
 high-resolution radar data 558  
 seismic reflection surveys 228–9, 243–6, 243–6, 245
- Mill Creek Dam (USA) 366–7, 366–7
- mine collapses 207–9
- mine shafts  
 electrical resistivity 323–5  
 electromagnetic methods 450–1, 463  
 self-potentials 369–70
- mineral exploration  
 electrical resistivity 333, 338–41  
 electromagnetic methods 403, 441–5, 470, 478–80, 480–3, 499–501, 509–10  
 geomagnetic methods 87–9, 125–6  
 gravity methods 24, 59  
 ground-penetrating radar 613–17  
 radiometrics 636–8  
 seismology 164–5  
 self-potentials 352–3, 359–61
- mineral potentials 349, 352–3, 353
- mineralization texture 379–80
- mineralized graphite phyllites 355–6, 358
- Mini-Sosie land vibrators 168
- mise-a-là-masse (MALM) method 336–46  
 civil engineering pile testing 341–3, 343–4  
 groundwater surveys 344–6  
 mineral exploration 338–41, 339–44  
 tree root studies 344, 344–5
- MMR *see* magnetometric resistivity
- MMT *see* marine metallotellurics
- MOSES 421–2, 421
- moving-source EM systems 433–7
- MRS *see* magnetic resonance sounding
- MSGI *see* mega-scale glacial lineations
- MSM *see* micro-tremor survey method
- MSP *see* multi-sensor platforms
- MT *see* metallotelluric
- Mt Etna 71–4, 76–7
- MTEM *see* multi-transient electromagnetic
- multi-azimuth (MAZ) surveys 222–3
- multichannel analysis of shear waves (MASW) 208, 211–15, 213–15, 215
- multi-domain materials 86–7
- multilayer raypath geometry 183–4
- multiples 252–6, 253–4
- Multipulse 165–6
- multisensor magnetic gradiometers 139–40
- multi-sensor platforms (MSP) 445
- multi-step processing 509
- multi-transient electromagnetic (MTEM) methods 420, 424
- National Oceanic and Atmospheric Administration (NOAA) 25
- natural dams 368–9
- natural field IP (NFIP) 385
- natural radiation 625–8, 629
- natural remanent magnetization (NRM) 88–9
- natural-source electromagnetic (EM) systems 431
- natural-source magnetotelluric (MT) method 505, 506
- near-field electromagnetic (EM) systems 431
- Nernst potentials 350, 351, 374
- Nettleton method 37–8, 38
- neutron logging 632–3
- Newton, Isaac 19–20
- NFIP *see* natural field IP
- NMO *see* normal moveout
- NOAA *see* National Oceanic and Atmospheric Administration
- noise  
 electromagnetic methods 468, 522–3  
 geomagnetic methods 101–3, 105, 127–9  
 geophysical surveys 13–15, 14–15  
 ground-penetrating radar 556, 562, 570–1, 609  
 induced polarization 381–2  
 seismic reflection surveys 219–20, 237, 245  
*see also* signal-to-noise ratio
- non-dipolar field 92–3, 93
- non-explosive energy sources 159–62, 160–3
- non-metallic minerals 24
- normal moveout (NMO) 236–8, 237, 238
- normalized parameters 380, 400
- NRM *see* natural remanent magnetization
- nuclear power stations 222
- nuclear testing 514–15, 515
- nuclear waste *see* radioactive waste disposal
- ocean bottom cables (OBC) 424
- offset  
 electrical resistivity 323  
 seismic reflection surveys 218, 220–1, 222, 224–5, 224–5, 258–60, 258–60
- Wenner arrays 296–7, 297, 304, 311
- Ohm's Law 289–90
- oil industry *see* hydrocarbon exploration
- optical absorption magnetometers 98–9
- optimal line configuration 9–11
- optimum-offset method 220–1, 258–60, 258–60
- Ordnance Survey (OS) 16
- over-water surveys  
 electrical resistivity 307–8  
 hydrographic surveys 266–72  
 seismic reflection surveys 266–83  
 seismology 178
- overvoltage effect 373–5, 374, 377, 395–6
- P-waves  
 gravity methods 38, 68  
 seismic reflection surveys 224–5, 227–8, 249, 251  
 seismic refraction surveys 179, 202, 204–5  
 seismology 143, 145–8, 146, 147–8, 151  
 self-potentials 371–2
- PA-CEP *see* pulled array continuous electrical profiling
- palaeomagnetism 83, 91
- palaeontology 283–8
- parallel resistances 309
- paramagnetism 85–7
- passive geophysical methods 3
- patch arrays 219
- pattern analysis 105–7, 109, 114, 119, 121
- PDM *see* pre-stack depth migration
- PDRM *see* post-depositional remanent magnetization
- pebbly rock glaciers 326, 329
- PEG *see* propelled energy generator
- pegleg multiples 254–6, 256
- percentage frequency effect (PFE) 378

- permafrost  
electrical resistivity 326, **328**, 329  
electromagnetic methods 457–9  
gravity methods 66, **74**
- permeability  
electromagnetic methods 522, **532**  
geomagnetic methods 83–4  
ground-penetrating radar 574
- permeability-depth profiles 371–2, **371**
- Peters' half-slope method 113, **115**, 115
- Petrov Lake (Krygstan) 368–9, **369**
- PFE *see* percentage frequency effect
- phantomming 187–8, 193
- phase-angle spectra 379–80, **382**, 395, 400, 402
- phase-domain IP measurements 373
- phasor diagrams 440–4
- pile testing 341–3, **343–4**
- pingers 162–3, 251, 275–6
- pipes *see* underground pipe detection
- Piton de la Fournaise (La Réunion) 362–3, **365**
- plane boundaries 298–300
- Pleistocene subglacial valleys 67–8, **75**
- Plus-Minus method 143–4, 187, 188–90, **188**, 189, 203–4
- Plymouth Sound (Devon, England) 281–3
- PMR (proton magnetic resonance) *see* magnetic resonance sounding
- polar ice sheets 578–81
- polarization 410–13, 515  
*see also* induced polarization
- polarization ellipse **413**
- pole-dipole arrays 294, 295
- political constraints 8
- Pont Melin Rûg (Wales) 260–5
- porosity 548–9, **554**, 613, 617
- porous-pot electrodes 353–4, **354**
- porous rocks 148
- porphyry copper deposits 387, 391
- position fixing 3, 15–16, **17**
- post-depositional remanent magnetization (PDRM) 89
- potential amplitude method 353
- potential gradient method 353
- Pratt's isotactic model 45
- pre-stack depth migration (PDM) 239–41
- precession frequency 97–9, 98
- predictive deconvolution 235
- preprocessing data 229–30
- primary events 252–6
- principle of continuation 53–4, **57**, 102–3
- profile anomalies 105–8, **106–8**, 107, 116–17, 126
- propelled energy generator (PEG) 203
- PROSPECT 412
- proton free-precession magnetometers 97–9, **98**, 108
- proton magnetic resonance (PMR) *see* magnetic resonance sounding
- proton precession frequency 522
- pseudo-sections  
electromagnetic methods 500, 508–10, **508**, 510  
induced polarization 382–5, **387**, 392  
resistivity 319–21, 330, 335
- pull-ups 256, **258**
- pulled array continuous electrical profiling (PA-CEP) 307
- pulse-transient electromagnetic (TEM) methods 467–93  
applications and case histories 470–93  
cavity detection 480–6  
contaminant plume mapping 476–80  
data processing and interpretation 468–70  
geological mapping 486–8  
geotechnical and environmental investigations 488–93  
groundwater investigations 470–6, **471–6**
- mineral exploration 478–80
- principles 465–8  
unexploded ordnance mapping 492–3, **492–3**
- push-downs 256, **258**
- Pyramid lead-zinc deposit (NW Territories) 59, **62**
- Quad/Quad system 223–4, **227**
- qualitative methods  
electrical resistivity 311–13  
geomagnetic methods 103–7  
self-potentials 354–5
- quantitative methods  
electromagnetic methods 437–9  
geomagnetic methods 107–23  
ground-penetrating radar 558–60, 562  
self-potentials 355–7
- QUESTEM 412
- radar range equation **542**
- radar tomography 553–5
- radio echo-sounding (RES) 79, 578–9
- radioactive decay series 626–7, 626–7
- radioactive waste  
induced polarization 398, 400, **402**  
radiometrics 642–3  
seismic reflection surveys 222
- radioactivity of rocks 628, 629
- radio-element ground concentrations 635
- radiometrics 625–43  
applications and case histories 625, 626, 636–43  
boreholes 632–3, 638–40  
calibration 633  
data correction 633–5, 635–6  
data presentation 635–8  
detectors 628–33, 638  
engineering applications 638–9  
gamma-ray spectrometers 630–1, **631–2**  
Geiger-Muller counters 628–9  
historical development 625  
mineral exploration 636–8  
natural radiation 625–8, 629  
radioactive waste disposal 642–3  
radioactivity of rocks 628, 629  
radon detectors 630–1  
scintillometers 629–30, 638, 642–3  
seaborne systems 631–2, 643  
soil mapping 639–42
- radiowave propagation 539–46, 539, 550–2, **550**, 551–2, 577, 578
- radon detectors 630–1
- railway ballast surveys **593**
- RAMAC surveys 609–13
- Ramform Explorer 174–5, **176**
- random noise 219–20
- Rayleigh scattering  
ground-penetrating radar 540, 543–4  
seismic reflection surveys 251  
seismic refraction surveys 209–11, 211  
seismology 146–7, **146**, 154
- raypath diagrams **180**, **182–3**
- raypath geometry  
irregular interfaces 185–6, **186**, 189  
layered ground 149–53  
planar interfaces 182–5, 185
- raypath parameter 151
- RAZ *see* rich azimuth
- reciprocal method (RM) 144, 193
- reconnaissance surveys 7, 11

- redox potentials 351–2  
 reduced ratios (RR) 432–3, 441, **443**  
 reduction to the pole (RTP) method 114–16, **116, 116**  
 reflection coefficients 149–51, **150**, 218  
 reflection profiling 552, 559  
 refractor velocity analysis functions 191  
 regional anomalies 46–7, **47**, 66, 103  
 relative gravity 25–6  
 relaxation voltage 522  
 religious constraints 8  
 remanent magnetization (RM) 85, **85**, 88–9, 89, 112, 114, 123–4, **129**  
 Remotely Operated Vehicle-deployed Deep Ocean Gravimeter (ROVDOG) 31  
 RES *see* radio echo-sounding  
 reservoirs 366–9, **528**  
 residual anomalies  
     geomagnetic methods 103, **105**  
     gravity methods 46–7, **47, 61–2**, 65–6, **74**, 79–81, **81**  
 residual porosity 549  
 residual static analysis 231  
 resistivity–depth profiles 447–9, **447–9, 517**  
 RESOLVE system 413, 448, 451  
 resonance magnetometers 97–9, **97–9**  
 resource evaluation 276–9  
 rich azimuth (RAZ) surveys 222–3, **226**  
 rippability index 4, 201–2, **202**  
 riverbed geology 269, 271–2  
 RM *see* reciprocal method; remanent magnetization  
 road pavement studies 592–6, **594–6**  
 rock quality assessments 199–201, **200–1**  
 rockhead determinations 193–7  
 Roman roads 603, **605**  
 Roman structures 604–5, **605–7**, 607  
 Roosevelt Hot Springs (USA) 357, 359, **359**  
 rotatable-transmitter EM 427–8  
 rough specular reflectors 543–4  
 ROVDOG *see* Remotely Operated Vehicle-deployed Deep Ocean Gravimeter  
 RR *see* reduced ratios  
 RTP *see* reduction to the pole  
 rubber banding 557  
 Rutford ice Stream (Antarctica) 580–2, **581–2**
- S-waves  
     seismic reflection surveys 224–5, 227–8, 249, **251**  
     seismic refraction surveys 179, 210  
     seismology 143, 146–8, **146**  
 Saint Clair river (USA) 252–6, **253–6**  
 salinity  
     electrical resistivity 290, 330, 332  
     electromagnetic methods 446, 458, **470–1, 478**, , 516–17  
     geophysical surveys 9  
     ground-penetrating radar 573  
     seismology 148  
 sampling intervals 229  
 SAR *see* synthetic aperture radars  
 Saramäki ore body (Finland) 125–6, **128–9**  
 Sariyer sulphide ore deposit 359–61, **363**  
 SASW *see* spectral analysis of shear waves  
 satellite imaging 205  
 scanning functions 356  
 scattering of incident energy 154  
 Schlumberger arrays  
     electrical resistivity 294–8, **294, 296**, 298, **301**, 303–4, **304**, 310–13, **310–11**,  
     **315, 334, 337**  
     electromagnetic methods 526, 528  
     induced polarization 376, 392  
 Schmidt method 143  
 scintillometers 629–30, 638, 642–3
- seabed geology 272–9, **277–81**  
 seaborne electromagnetic (EM) methods 418–26  
 seaborne radiometrics 631–2, 643  
 SeaTEM system 487–8  
 seawater intrusion *see* salinity  
 Second Law of Motion 19  
 second vertical derivative (SVD) maps 53–4, **56**  
 secondary events 252–6  
 sedimentary basins 55, 59–60  
 sedimentary rocks  
     electrical resistivity 290  
     geomagnetic methods 87–9  
     gravity methods 22–3  
     ground-penetrating radar 565–7  
 SEG *see* Society of Exploration Geophysicists  
 seisloop layout 222, **226**  
 seismic reflection surveys 217–88  
     applications 217, 257–88  
     borehole logs and cones 246–50, 265  
     cone penetration testing 247–51  
     convolution and deconvolution 233–6, **235, 236**  
     correlation techniques 235–6, 246–50, 277–8  
     cross-hole seismology 225–9  
     data analysis 17–18  
     data processing 217, 228–46, **229**  
     dynamic corrections, velocity analysis and stacking 236–41, 236, **237–41**  
     earthquake prediction 265–6  
     estuarine environments 281–3  
     filtering 241–3, **242–3**  
     forensic seismology 286–8  
     fresh-water surveys 271–2  
     general considerations 217–18, **218**  
     geohazards 272–6  
     geophysical diffraction tomography 283–8  
     gravity methods 68  
     high-resolution 217, 255, 257–65, **258–69**, 266–83  
     historical development 143–4, 217  
     hydrographic surveys 266–72  
     interpretation methods 250–8  
     land surveys 220, 257–65  
     marine surveys 232–3, 256, 272–9  
     migration 243–6, **243–6, 245**  
     over-water surveys 266–83  
     palaeontology 283–8  
     position fixing 16–17  
     potential pitfalls 256–7  
     preprocessing data 229–30  
     primary and secondary events 252–6  
     principles 218–20  
     resource evaluation and dredging 247, 276–9  
     static corrections 230–3, **232, 233**  
     survey layouts 222–4, **226**, 231–2  
     three-dimensional surveys 221–4, **223**  
     tomographic imaging 225–8  
     tunnels 280–2  
     two-dimensional surveys 219–21  
     vertical and horizontal resolution 250–2, 260  
     vertical seismic profiling 224–5, **227–8**, 249–50, 287  
 seismic refraction surveys 179–216  
     acid tar lagoons 203–7  
     applications and case histories 184, 193–208  
     buried miner location 207–9, **208–9**  
     continuous velocity change 192–3  
     critical refraction 179–81  
     earthquake hazard studies 215–16  
     field surveys 181–2, 210  
     generalized reciprocal method 190–1, **190, 191, 198–9**, 207

- geomagnetic methods 136, 137  
ground stiffness profiling 208–12  
hidden layers 179, 191–2, 192  
historical development 143–4  
interpretation methods 186–93  
irregular interfaces 185–6, 186, 189  
landfill investigations 201–3, 202–5, 211–12  
multichannel analysis of shear waves 208, 211–15, 213–15, 215  
phantomming 187–8, 193  
planar interfaces 182–5, 185  
principles 179–82  
raypath geometry 182–6, 185, 189  
rock quality assessments 199–201, 200–1  
rockhead determinations 193–7  
shear wave methods 208–16, 211  
sinkhole location 197–9  
software applications 193, 211  
static corrections 205–7  
time-distance graphs 180–1, 181, 183–90, 183–5, 188–90, 194–8  
velocity analysis curves 193, 195–9  
waste disposal sites 193–7  
seismic waves 144–8  
attenuation/degradation 155  
body waves 145–6  
detection and recording 170–8  
stress and strain 144–8  
surface waves 146–7  
seismo-acoustic facies 278  
seismoelectric response *see* electrokinetic surveying  
seismography 177–8, 178, 211  
seismology  
accelerometers 170–3  
applications 144, 164–5  
critical refraction 151–2, 152  
detection and recording of seismic waves 170–8  
diffraction waves 151–2, 152–4, 154  
energy sources 154–70, 156  
explosive sources 159, 159  
geophones 170–3, 171–2  
high-resolution waterborne sources 162–3, 164  
historical development 143–4  
hydrophones 173–7, 174–7  
impact devices 155–7  
impulse sources 157–63  
intrinsic attenuation 153–4, 156  
loss of seismic energy 152–4  
non-explosive sources 159–62, 160–3  
raypath geometry in layered ground 149–53  
reflection and refraction of obliquely incident rays 150–1  
reflection and transmission of normally incident rays 149–50,  
150  
scattering of incident energy 154  
seismic waves 144–8  
seismography 177–8, 178  
spherical divergence/geometrical spreading 152–3, 155  
streamers 173–7, 174–7  
velocities 147–8, 147–8  
vibrator sources 163–70  
seismometers 171–3, 173  
self-oscillating split-beam caesium vapour gradiometers 100  
self-potential tomography (SPT) 355–6  
self-potentials (SP) 349–72  
applications and case histories 357–70  
contaminant plumes 363–4  
data corrections 354  
electrochemical potentials 351–2, 351–2  
electrokinetic surveying 350–1, 350, 363, 370–2, 371  
embankments 364–8  
geothermal exploration 357–60  
historical development 349  
hydrogeology 361–3, 366  
induced polarization 394  
interpretation of anomalies 354–7, 355–8  
landfill investigations 363–4, 366  
leak detection 364–9  
measurement 353–4  
mine shafts 369–70  
mineral exploration 352–3, 359–61  
mineral potentials 349, 352–3, 353  
occurrence 349  
origins 349–53  
qualitative interpretation 354–5, 355–7  
quantitative interpretation 355–7, 358–61  
semblance 239–40  
semicylindrical body anomalies 111–12  
separation/height ratio (SHR) 137–8  
sewer linings 600  
shadow zones 271  
shale potentials 351  
shallow gas accumulations 272–6, 273, 274–6  
shallow seismic reflection surveys 217, 223, 247  
shear modulus 145–6, 211–12  
shear wave methods 208–16, 211  
continuous surface wave systems 208, 209–11  
ground stiffness profiling 208–12, 210, 212  
multichannel analysis of shear waves 208, 211–15, 213–15, 215  
spectral analysis of shear waves 208, 209  
Shetland Islands (Scotland) 106–7, 109  
short-wavelength anomalies 20–1  
SHR *see* separation/height ratio  
side-scan sonar 268–72, 270–2  
signal-to-noise ratio (SNR)  
electromagnetic methods 522–3  
geophysical surveys 14–15, 15  
ground-penetrating radar 556, 570–1, 609  
seismic reflection surveys 220, 234, 237  
sinkholes  
electromagnetic methods 480–6  
gravity methods 66  
ground-penetrating radar 597  
seismic refraction surveys 197–9  
SIP *see* spectral IP  
SIROTEM system 468, 475, 476, 477, 482–5, 485  
skin depth 413, 542  
SkyTEM system 473–6, 474–5, 487–8, 488  
slag deposits 392–5, 397  
sledge hammer devices 155–6  
sleeve exploders 162  
sleeve guns  
bubble pulse sources 160–2, 162  
seismic refraction surveys 203, 206  
SLINGRAM electrical resistivity 125–6, 128  
Slingram methods 441–2, 442  
small-loop electromagnetic (EM) systems 404–5, 447  
small-scale land vibrators 164–5, 167–9, 168–9  
Smith rules 51–2, 52  
smooth plane reflectors 543–4  
Snell's laws of refraction 151, 179  
SNMR (surface nuclear magnetic resonance) *see* magnetic resonance sounding  
snow stratigraphy 581–3  
snow streamers 177  
SNR *see* signal-to-noise ratio  
social constraints 8  
Society of Exploration Geophysicists (SEG) 229–30

- soil surveys  
 electrical resistivity 305  
 radiometrics 639–42
- soil/sediment classification 250, 254, 263, 276–9
- Sol sulphide system 385, 390
- solid earth geophysics 1
- sonic logging tools 246–7, **248**, 256–7
- sonobuoys 182
- Soret Effect 351
- SOS call location 207–9
- source-receiver geometry 231–3
- source response 251–2
- Sourton Tors (Dartmoor, England) 59, **63**, 105, **108**, 126
- SP *see* self-potentials
- sparkers  
 seismic reflection surveys 251–2, **252**, 282  
 seismology 162–3, 165–6, **165–6**
- spatial aliasing 11–13, **11–13**, 101–2, 101
- spatial resolution 544–6, 544, 549
- spectral analysis of shear waves (SASW) 208, 209
- spectral IP (SIP) 373, 379–81, 379, **388**, 395
- SPECTRUM 412
- spherical divergence 152–3, **155**
- spiking deconvolution 235
- spontaneous polarization *see* self-potentials
- SPT *see* self-potential tomography; standard penetration testing
- square arrays 294, 295–8, 298, 303–4, **304**
- SQUID *see* superconducting quantum interference device
- Squid sparker system 165–6, **165–6**
- SRP-IP *see* symmetrical resistivity profiling with IP
- SSI (subsurface imaging) *see* electrical resistivity tomography
- stable/static gravimeters 27–8, **27–8**
- stacking 236–41
- Stagnation Glacier (Canada) **586**
- standard penetration tests (SPT) 215, 247, 250
- Starjet 162, **164**
- static corrections 205–7, 230–3, **232**, 233
- station interval selection 11–13, **11–13**
- statistical analysis 207
- statistical sampling 2–3
- steam gun bubble pulse sources 162, 164
- step discontinuities 185–6, **186**
- stratigraphic control 259–63
- streamers  
 electrical resistivity 307–8  
 seismic reflection surveys 220–1, **227**  
 seismic refraction surveys 182, 203–5  
 seismology 173–7, **174–7**
- strength-relaxation 63, 67
- Structural Index 120, 122
- subglacial landscapes 578–81, **579–82**
- subsidence  
 gravity methods 63–6  
 seismic reflection surveys 265, 267–9
- subsurface cavities *see* cavity detection
- subsurface collapse features 326
- subsurface coverage 188
- subsurface diagrams 222, 225
- subsurface imaging (SSI) *see* electrical resistivity tomography
- sulphide ore deposits  
 electromagnetic methods **428**, **442**, 480, **484**  
 induced polarization 385, **389–90**  
 self-potentials 359–61, 363
- Sundberg method 403, 405, **407**, 432–3, **432**
- superconducting quantum interference device (SQUID) magnetometers 99,
- 416
- suppression tests 317–18
- surface diagrams 222, 225
- surface nuclear magnetic resonance (SNMR) *see* magnetic resonance sounding
- surface roughness 150
- surface waves 146–7
- survey constraints 7–8
- susceptibility 84, 87–8, **87, 88**
- SVD *see* second vertical derivative
- swath bathymetry 268, **270**, **272**
- swathe shooting 222
- symmetric anomalies **116**
- symmetrical resistivity profiling with IP (SRP-IP) 392–5
- synthetic aperture radars (SAR) 546
- synthetic induction vectors 511
- synthetic seismograms 246–7, **248**, 271
- target identification 9–10, **9–10**
- TCRM *see* thermal-chemical remanent magnetization
- TDEM *see* time-domain electromagnetic
- TDR *see* time-domain reflectometry
- TDS *see* total dissolved solids
- telluric method 502–5, **505**  
 field measurements 503–5  
 principles of operation 502–3  
*see also* magnetotelluric methods
- TEM *see* pulse-transient electromagnetic
- TEMP-VEL *see* transient electro-magnetic prospecting using vertical electric lines
- temperate glaciers 583–6
- temperature effects 148
- TEMPEST system 414–17, **417**
- temporal resolution of spectra 545–6, **546**
- tensor gravity gradients 33, 33
- Terceira Island 74, **78–9**
- ternary radiometric displays 637–8, **637–8**, **641**
- terrain corrections  
 electrical resistivity **340**  
 geomagnetic methods 102  
 gravity methods 38–41, **39**, **40–1**  
 radiometrics 634–5
- TerraTEM system 475, **476**, 490–2, **490**
- Terrestrial Reference Frame (TRF) 16
- Thames River (London, England) 280–2, **280–2**
- thermal remanent magnetization (TRM) 89
- thermal-chemical remanent magnetization (TCRM) 89
- thermoelectric coupling 351
- thorium decay series 627, 639
- thorium source tests 633, 639–41
- three-dimensional analytical signal method 122–3, **123**, 138
- three-dimensional modelling  
 electrical resistivity 321–6, **322**, **324–5**  
 geomagnetic methods 115–18, 126
- three-dimensional seismic reflection surveys 221–4, **223**
- three-layer models 311–13, **312**, 317–18, 323
- three-layer raypath geometry 182–3, 184
- Thyssen gravimeters 29, **29**
- tidal effects 34–5, 81
- tilt-angle EM methods 431–2, **432**
- tilt-angle maps 114
- tilt-angle response 495, **497**, **498**
- time constants 469, 522
- time-depth functions 191, **199**
- time-distance graphs 180–1, **181**, 183–90, 183–5, **188–90**, **194–8**
- time-domain electromagnetic (TDEM) methods  
 applications and case histories 445–7, 470–93  
 cavity detection 480–6  
 contaminant plume mapping 476–80, **477–8**  
 geological mapping 486–8

- geomagnetic methods 139–41  
 geotechnical and environmental investigations 488–93  
 groundwater investigations 470–6, **471–4**  
 induced polarization 397  
 mineral exploration 478–80  
 principles 404, 406, **408**, 411, 414–18, **415**, 429, 465–8, **467**  
 unexploded ordnance mapping 492–3  
 time-domain IP measurements 373, 376–7, 391–2  
 time-domain reflectometry (TDR) 548  
 time-lapse micro-gravity surveys 64–5, 71, **76**  
 time migration 244–5  
 time-reverse mirrors (TRM) 208  
 time slice amplitude maps 600  
 time-variant deconvolution 235  
 time-varying electrical fields 410  
 time-zero correction 557–8  
 tipper function 509  
 TMI *see* total magnetic intensity  
 TOBI *see* Towed Ocean Bottom Instrument  
 tomographic imaging 225–8  
 tomoplanes 357  
 top-of-salt surfaces 511–12  
 topographic effects 498  
 topographic static corrections 231–2  
 torsion balances 26–7, **26**  
 torsion magnetometers 95, **95**  
 total dissolved solids (TDS) 396, 451–5  
 total magnetic intensity (TMI) 115, 117–18, 135  
 total porosity 549  
 Towed Ocean Bottom Instrument (TOBI) 269–71  
 trans-illumination 553–5  
 transient electro-magnetic prospecting using vertical electric lines  
     (TEMP-VEL) 425–6, **425–6**  
 transmission coefficients 149–51, 150  
 transportation infrastructure 592–6, **593–6**  
 transverse resistance 298–9  
 transverse resistivity 298  
 travel-time  
     ground-penetrating radar 613, 615  
     seismic refraction surveying 186–7, **186**, **187**  
     *see also* time-distance graphs  
 travel-time tomography 239  
 tree root studies 344, **344–5**  
 TRF *see* Terrestrial Reference Frame  
 trial pitting 2–4, 15–16  
 tripotential alpha arrays 305–6  
 TRM *see* thermal remanent magnetization; time-reverse mirrors  
 true resistivity 289–92, **290–1**, **290**, **299**  
 trunk sewer burial 326, 328  
 Tsho Rolpa (Nepal) 586–9, **588–9**  
 tunnels 280–2  
 TURAM electromagnetic surveys 59, **407**, 432–3, **433**, 441, **443**  
 turning wave migration 243–6  
 twin-parallel array system 231–2  
 two-dimensional modelling  
     electrical resistivity 321–6, **322**, **324–5**  
     geomagnetic methods 115–18  
 two-dimensional seismic reflection surveys 219–21  
 two-electrode arrays 295  
 two-layer master curves 322–3, **322**  
 two-layer master/auxiliary curves 313–14, **313–15**  
 two-layer raypath geometry 182–3  
 two-way travel time (TWTT) 217, 278, **282–4**  
 unconsolidated sediments 23  
 underdamping 170, 172  
 underground cavities *see* cavity detection  
 underground gravity methods 36–8  
 underground nuclear testing 514–15, **515**  
 underground pipe detection  
     electromagnetic methods **438**  
     geomagnetic methods 126–7, **130**  
     ground-penetrating radar 546, 548, 588–92, **591**, 600  
     magnetization 103, **104**, 126–7, **130**  
     radiometrics 638  
 underground sources of drinking water (USDW) 263–7  
 underground storage tanks (UST) 127–8, **130–3**, 588–92, **589–90**, **592**  
 unexploded ordnance (UXO) 3  
     electromagnetic methods 492–3, **492–3**  
     geomagnetic methods 135, 136–41, **138–41**  
     ground-penetrating radar 617–18  
 Universal Law of Gravitation 19  
 unstable/astatic gravimeters 27–31, 29–30  
 upward continuation 53–4, **57**, 102–3  
 uranium decay series 627  
 uranium deposits 509, 636–8  
 USDW *see* underground sources of drinking water  
 UST *see* underground storage tanks  
 UXO *see* unexploded ordnance  
 Van Allen radiation belts 89–90  
 Vaporchoc 162, **164**  
 VED *see* vertical electric dipoles  
 velocity analysis 193, **195–9**, 236–41, 236, **237**, **240**  
 velocity inversions 179  
 velocity semblance spectra 239–40  
 vertical dykes  
     electrical resistivity 299, 302, 325  
     geomagnetic methods 110–11, 113–14, **117–18**  
 vertical electric dipoles (VED) 422  
 vertical electrical sounding (VES) 301–6, **303**, **305**, 309–11, **315**, **317**, **332**, **334**  
 vertical gravity gradients 38, 63  
 vertical magnetic dipoles (VMD) 422–3, 434–5, **464**  
 vertical resolution  
     ground-penetrating radar 544–6, 544  
     seismic reflection surveys 250–2, 260  
 vertical seismic profiles (VSP) 164, 224–5, **227–8**, 249–50, **287**  
 very-early TEM (VETEM) systems 406, 490  
 very-low-frequency (VLF) methods 495–502  
     applications and case histories 441–3, 499–502  
     cavity detection 501–2, 504  
     distribution network 495–6  
     filtering techniques 498–500  
     interpretation methods 498–9  
     mineral exploration 499–501  
     modes of operation 497–8, 502  
     principles 406–7, **409**, 418, 495–8, **496–7**, 497–8  
     tilt-angle response 495, **496–7**, 498  
     topographic effects 498  
 VES *see* vertical electrical sounding  
 VETEM *see* very-early TEM  
 vibration energy sources 209–10  
 vibration strings 31, 31  
 vibrator energy sources 163–70  
 Vibroseis method 163–4, **167–8**  
 VIRT *see* Visual Interactive Ray Trace  
 viscous remanent magnetization (VRM) 89  
 Visual Interactive Ray Trace (VIRT) modelling 193  
 VLF *see* very-low-frequency  
 VMD *see* vertical magnetic dipoles  
 VMS *see* volcanic massive sulphide  
 voids within manmade structures 599–604  
     *see also* cavity detection  
 volcanic hazards 71–8

- volcanic massive sulphide (VMS) 341, 429  
VRM *see* viscous remanent magnetization  
VSP *see* vertical seismic profiles
- walking stick electrodes 353–4  
warping of the geoid 20–1, 21  
WARR *see* wide-angle reflection and refraction  
waste disposal  
  radiometrics 642–3  
  seismic reflection surveys 263–5  
  seismic refraction surveys 193–7  
  *see also* radioactive waste disposal  
waste treatment facilities 258–9  
water bathymetry surveys 17  
water gun bubble pulse sources 161–3, 163  
water-layer multiples (WLM) 253–4, 253–4, 256  
water table mapping 562–4, 576–8  
waterborne energy sources 162–6, 164  
waterborne surveys 182, 220  
wave dispersion 147, 211–15  
Wavepath Eikonal Travelttime (WET) modelling 193  
WAZ *see* wide azimuth  
weathered layer 231, 233–4  
weight-drop devices 156–7, 157–8
- Wenner arrays  
  electrical resistivity 294–302, 294, 296–7, 298, 301–2, 304–7, 304–5, 311, 323, 333, 335  
  induced polarization 376  
WET *see* Wavepath Eikonal Travelttime  
WGS84 *see* World Geodetic System 1984  
whitening 234–5  
wide-angle reflection and refraction (WARR) 538, 553, 555–7, 555  
wide-aperture radar mapping 607–9  
wide azimuth (WAZ) surveys 222–3  
wide-line layout 222, 226  
Wiener filters 235  
WLM *see* water-layer multiples  
Worcester cathedral (England) 600–2, 602  
Worden gravimeters 30–1, 30  
World Geodetic System 1984 (WGS84) 16, 22
- Yanacocha high sulphidation gold deposits (Peru) 361, 364  
Yellowstone National Park 390–1, 393–4  
Young's modulus 145–6
- zeta potentials 374  
zigzag layout 222, 226  
Zoeppritz's equations 149–51